CODEN: JASMAN 4966

THE JOURNAL of the Acoustical Society of America

Vol. 104, No. 4 October 1998

SOUNDINGS SECTION

(Continued)

CONTENTS—*Continued from preceding page*

(Continued)

CONTENTS—*Continued from preceding page*

(Continued)

CONTENTS—*Continued from preceding page*

NOTES CONCERNING ARTICLE ABSTRACTS

1. The number following the abstract copyright notice is a Publisher Item Identifier (PII) code that provides a unique and concise identification of each individual published document. This PII number should be included in all document delivery requests for copies of the article.
2. PACS numbers are for subject classification and indexing. See June and December issues for detailed listing of acoustical classes and subclasses.
3. The initials in brackets following the PACS numbers are the initials of the JASA Associate Editor who accepted the paper for publication.

ACOUSTICAL NEWS—USA

Elaine Moran
Acoustical Society of America, 500 Sunnyside Boulevard, Woodbury, New York 11797

Editor's Note: *Readers of this Journal are asked to submit news items on awards, appointments, and other activities about themselves or their colleagues. Deadline dates for news items and notices are 2 months prior to publication.*

Position Open

Assistant Professor—Audio Technology

Assistant Professor of Physics (Audio Technology), one-year temporary position, subject to budgetary approval, beginning fall semester 1998. The Department seeks a person with strong interests in the technology of sound for its Audio Technology Program. Responsibilities include: teaching (mostly undergraduate), research, student advising, departmental and University service. Candidates are preferred with research interests in acoustics and audio technology. The M.S. in Audio Technology or equivalent is required. Competitive salary. The search committee will begin reviewing applications immediately and continue until the position is filled. Send letter of application, resume, and the names of three references to:

Chair, Department of Physics
American University
Washington, DC 20016-8058

American University is an EEO/AA institution, committed to a diverse faculty, staff, and student body. Women and minority candidates are strongly encouraged to apply.

Reports of Technical Committees

(See November and December issues for reports of other Committees)

Musical Acoustics

The 1997–98 year for the Technical Committee on Musical Acoustics (TCMU) has been a banner year for musical acoustics. The ASA meeting in San Diego in December 1997 presented a diverse program of musical acoustics. Uwe Hansen organized a special session on the piano, which featured lectures covering the physical and subjective relationships between string, hammer, bridge and soundboard, and concluded with a demonstration of a computer-based piano performance reproduction system. A special session honoring Robert W. Young's contributions to acoustics was presented, which was co-sponsored by the Technical Committees on Noise, Underwater Acoustics, and Musical Acoustics. This session was followed by the plenary session, in which Bob Young was awarded the ASA Honorary Fellowship for his contributions encompassing many areas of acoustics, to international standards and acoustical terminology, and for sustained and devoted service to the Society. Jim Beauchamp organized a special session on computer jazz improvisation, which was followed by a concert featuring a number of the presenters.

The joint meeting of the 16th International Congress on Acoustics and the ASA was held in June 1998. Appropriate to the international character of musical acoustics, an exceptionally large number of musical acoustics sessions took place. Naotoshi Osaka and Julius Smith co-chaired a session on signal modeling in music synthesis and processing, which reviewed contrasting approaches to this rapidly evolving subject. A session organized by Ed Burns (and co-sponsored by Psychological and Physiological Acoustics) on the purposeful use of nonlinear distortion in musical performance celebrated the musical innovations of Eric Dolphy and Jimi Hendrix, and was combined with a musical performance by some of the presenters and friends. Shigeru Yoshikawa organized a pair of sessions on the physics and materials of musical instruments, which provided a comprehensive review of current research. Tom Rossing and Carleen Hutchins chaired a special session on bowed string instruments. This session was appropriately followed by the plenary session, in which Carleen Hutchins was awarded the ASA Honorary Fellowship for her unique role in combining the art of violin making with the science of acoustics. The theme next turned to the subject of musical timbre, which included a special session of invited papers organized by Jim Beauchamp and which attracted a robust number of contributed papers sufficient to generate a second contributed session on timbre. A final session comprised a broad range of contributed papers on musical acoustics. The ICA/ASA meeting was concluded with a flourish by the plenary lecture on musical acoustics presented by Neville Fletcher. This lecture exhibited the impact of nonlinear dynamics and complexity on current approaches in musical acoustics. Both the San Diego and Seattle meetings exhibited a strong representation from contributed research presentations.

The International Symposium on Musical Acoustics 1998 (ISMA98) immediately followed the ICA/ASA meeting. ISMA98 was organized by the ASA and the Catgut Acoustical Society, and was held in the Cascade mountains outside the town of Leavenworth, Washington at the Sleeping Lady Conference Center. Lectures and posters were presented by participants from 18 countries. The invited lecturers included Dean Ayers, Chris Chafe, Joseph Curtin, Brian Moore, Bernard Richardson, William Strong, and Shigeru Yoshikawa. As an experimental and successful innovation from past ISMA's, a series of workshops was organized on the general theme of bridging the gap between instrument makers and musical acousticians. The leaders of these well-attended workshops were Charles Besnainou, Uwe Hansen, William Hartmann, Carleen Hutchins, David Peterson, Oliver Rodgers, Martin Schleske, and Karen Strom. Music was heard throughout the Symposium in a set of invited concerts as well as from the participants themselves. A non-peer-reviewed Proceedings of ISMA98 has been published and an extremely limited number of copies are available from the ASA and the CAS offices. The preparations for ISMA98 included the largest TCMU technical initiatives over this year and last. ISMA98 committee members included: Carleen Hutchins (Honorary Chair), Maurits Hudig, Doug Keefe, and Charles Schmid (Organizing Committee), Tom Rossing [Chair], Joseph Curtin, Uwe Hansen, Bill Hartmann, and Oliver Rodgers (Technical Program Committee), Roger Hanson [Chair], Evan Davis, Ioana Park, Michael Park, and Karen Strom (Logistics Committee), Elizabeth McGilvray (Secretariat), Charles Schmid [Chair], Janet Jefferson, Ioana Park, and Michael Park (Proceedings Committee). ISMA98 was partially supported by a grant from The Experience Music Project Foundation.

Efforts to increase student involvement in musical acoustics have continued in 1997–98 through best student presentation contests and the inclusion of student socials at the San Diego and Seattle meetings. The winner of the San Diego contest for Best Student Presentation was John Hajda of UCLA, whose paper was entitled ''Relevant acoustical cues in the identification of Western orchestral instrument tones.'' The winner of the Seattle contest for Best Student Presentation was Leïla Rhaouti of France, whose paper was entitled ''Time-domain modeling and numerical simulation of timpani'' (co-authors Patrick Joly and Antoine Chaigne). It is a continuing goal of the TCMU to increase student participation in musical acoustics.

Outside of the society-sponsored meetings, a technical initiative during the past year supported educational workshops on acoustics for teachers conducted by Uwe Hansen.

Roger Hanson is the new TCMU representative on the ASA Medals and Awards Committee, and Ian Lindevald is our new representative on the ASACOS Committee. The representatives to the Technical Program Organizing Meetings were Dean Ayers for the San Diego meeting, and Ed Burns and Doug Keefe for the Seattle meeting. Carleen Hutchins and Max Mathews completed their terms of service this year on the TCMU, and Tom Rossing concluded service as representative on the Medals and Awards Committee. New members on the TCMU include R. Dean Ayers, Judith C. Brown, Courtney B. Burroughs, Robert D. Collier, Stephen F. Duncan, George F. Emerson, James H. Irwin, Bozena Kostek, Barry Larkin, Thomas D. Rossing, Julius O. Smith, and William J. Strong. The TCMU has increased in size to reflect increased international participation among musical acousticians in the ASA, and to better represent the broad diversity of approaches within musical acoustics.

The web site for the TCMU maintains current information on musical acoustics activities and is located at http://www.boystown.org/asamu/

DOUGLAS H. KEEFE
Chair

 0001-4966/98/104(4)/1879/9/$15.00

Noise

The TC Noise met two times since last September, in December 1997 in San Diego and in June 1998 in Seattle. Each two-hour meeting hosted about 70 visitors and members.

We discussed the amorphous committee structure and its purpose. With no officers, no formal committee structure, no clear procedure for nomination of successor Chair, we decided to address this issue at our Norfolk, VA meeting this October.

The committee has worked hard at organizing sessions for the ASA meetings. Seattle, Norfolk, and Berlin, with a combined total of about 45 special sessions have taken up a lot of the energy in the committee.

Many of our members put effort on the acoustics of classrooms and the effect of poor acoustics on learning. Working with the TC Architectural Acoustics, ASA members put on a very successful workshop, on the West Coast and expects a similar one on the East Coast in the near future.

We have had help from many people, from session organizers, program planners, to invited speakers, to people bringing refreshments, to workshop organizers, and to contributors to the lively discussions at the meeting. We continue to welcome new people to our open meetings and solicit their participation.

RICHARD J. PEPPIN
Chair

Structural Acoustics and Vibration

The primary business of the TC was conducted at its two regular meetings held at the Fall 1997 and Spring 1998 ASA meetings. A full picture of our activities are reflected by the Minutes of the Spring and Fall 1997 meetings, which have been approved by the Technical Committee. Certain activities occur on a regular basis. These include discussing the editorial activity for JASA as a way of monitoring the level of activity in the research area, discussing and approving topics for special sessions at future ASA meetings, supervising and approving the Best Student Paper Award for submissions at the ASA meetings, and responding to queries from the Technical Council regarding matters affecting the membership. Our committee is also responsible for organizing the technical sessions in structural acoustics and vibration, which is achieved by volunteer participation at the Technical Program Organizing Meetings.

We have begun an effort to expand interest in the structural acoustics and vibration area, both by expanding our student activities, and by attempting to expand the scope of our activities. Two items of note were a pizza luncheon for students held at the Seattle meeting in June 1998, and the technical session on ''New Challenges in Structural Acoustics,'' which was intended to highlight research areas that might benefit from expanded attention of the committee members. At the June 1998 meeting, we decided to expand the exchange of research ideas at the regular meetings. A number of concepts to achieve this objective are under consideration. Input from the membership is sought, and should be provided to the Chair.

Minutes of the SAV Technical Committee—Meeting of 19 June 1997

The TC Meeting was convened by the Chair at 8:00 p.m. in Room H of the Penn State Conference Center on 19 June 1997. The minutes of the previous TC meeting were read and approved.

Murray Strasberg requested the floor to make some remarks about the Acoustical Society Foundation that is being set up. The purpose of the foundation is to raise funds for new and on-going initiatives which support and enrich ASA programs.

The chair then reported on the issues brought up at the Technical Council Meeting. The first discussion was about the upcoming joint meeting with the European Acoustics Association (EAA) to be held in the Spring of 1999. Of the thirty members present nine indicated that they were planning to attend, and six said they would definitely not attend.

We then went on to discuss the electronic publishing items that are currently being pursued. These included the e-print, which is an electronic pre-print which will be open to comment, and not subject to review. The other item under discussion is that of short publications which will be subject to review but with a very quick turn-around time to appear in print. The aim is to have these publications in print in 8–10 weeks. One suggestion that was made by Phil Marston and seconded by others was to include abstracts of papers in the ''Off print'' publication which CD-ROM users receive.

The anticipated change in the dues structure was discussed a bit, but there were no serious objections. Allan Pierce talked about cooperation with the International Union of Theoretical and Applied Mechanics (IUTAM) in preparing a white-paper on ''Future Directions in Structural Mechanics.'' This was enthusiastically endorsed by the TC.

Jerry Ginsberg reported that two individuals with primary interest in SAV were endorsed by the Membership Committee to be Fellows of the Society.

The Associate Editors for SAV were both present and they presented the statistics for publication in the past year: 98 papers were received, 58 accepted, 7 rejected, and 44 have been sent back to the authors for revision. The SAV editors have the lowest rejection rates of all the JASA editors.

The Committee expressed its appreciation to the organizers of the Penn State Meeting a few of whom attended the TC meeting. Courtney Burroughs and Stuart Bolton were thanked for their participation in the TPOM.

We then went on to discuss Special Sessions for future meetings. Ken Cunefare will be organizing a ''Memorial Session for Manfred Heckl'' at the San Diego meeting. Greg McDaniel volunteered to organize a session on ''New Challenges in Structural Acoustics and Vibrations'' for the Seattle Meeting. Other suggested Special Sessions for the Seattle Meeting were: ''SEA and Fuzzy Structures'' by Dan Russell, and ''Non-linear vibrations and chaos'' by Sabih Hayek. Lou Herstein suggested a session for Norfolk that would review the work done at the Annapolis Detachment of CDNSWC. This detachment has been in existence for many years and will be closing down in 1998.

The winner of the Best Student Paper Award was Benjamin Bard for his paper ''Full-field visualization of ultrasonic waves in elastic solids,'' which was presented at the Hawaii meeting. Another Best Student Paper Award went to F. Honavar for his paper entitled ''Application of resonance acoustic spectroscopy to nondestructive evaluation of clad rods.'' The latter paper was presented at the Penn State Meeting. The Student Paper Award Committee for the Academic year 1996–97 consisted of Chair Joe Cuchieri, Scott Sommerfeldt, and Greg McDaniel. The Chair of next year's committee will be Scott Sommerfeldt. The Committee expressed its appreciation for a job well done to Joe Cuchieri who has organized the Student Paper Award presentations for the last two years.

The incoming SAVTC Chair Jerry Ginsberg was introduced and he made some remarks about trying to attract new non-Navy problem related researchers into our community. Some discussion ensued about the Seattle meeting and the possibility of inviting aerospace research managers to discuss the structural acoustics related problems that they are pursuing. After this discussion, the meeting was adjourned.

JERRY H. GINSBERG
Chair

USA Meetings Calendar

Listed below is a summary of meetings related to acoustics to be held in the U.S. in the near future. The month/year notation refers to the issue in which a complete meeting announcement appeared.

1998

12–16 Oct.	136th meeting of the Acoustical Society of America, Norfolk, VA [ASA, 500 Sunnyside Blvd., Woodbury, NY 11797, Tel.: 516-576-2360; FAX: 516-576-2377; E-mail: asa@aip.org, WWW: http://asa.aip.org].

1999

15–19 March	Joint meeting: 137th meeting of the Acoustical Society of America/2nd meeting of the European Acoustics Association [Acoustical Society of America, 500 Sunnyside Blvd., Woodbury, NY 11797, Tel.: 516-576-2360; FAX: 516-576-2377; E-mail: asa@aip.org; WWW: asa.aip.org].
27–30 June	ASME Mechanics and Materials Conference, Blacksburg, VA [Mrs. Norma Guynn, Dept. of Engineering Science and Mechanics, Virginia Tech, Blacksburg, VA 24061-0219, FAX: 540-231-4574; E-mail: nguynn@vt.edu; WWW: http://www.esm.vt.edu/mmconf/]. Deadline for receipt of abstracts: 15 January 1999.

Members of Technical and Administrative Committees and Technical Groups of the Acoustical Society of America

The Technical and Administrative Committees and Technical Groups listed below have been appointed by the Executive Council. These appointments, with such changes as may be made by the President from time to time, will be in effect until the Spring meeting of the Society in 1999.

Technical Committees 1998–1999

Acoustical Oceanography

	Term to
James F. Lynch, *Chair* to 2001	2001
Holly A. Burch	2001
Marshall Hall	2001
Darrell R. Jackson	2001
Jeffrey A. Nystuen	2001
Lev A. Ostrovsky	2001
Robert Pinkel	2001
Peter F. Worcester	2001
Manell E. Zakharia	2001
Robert W. Farwell	2000
Gary J. Heald	2000
Anatoliy N. Ivakin	2000
Subramanian D. Rajan	2000
Barbara J. Sotorin	2000
Ralph A. Stephen	2000
Alexander G. Voronovich	2000
Suk Wang Yoon	2000
Michael G. Brown	1999
Christian P. de Moustier	1999
James A. Mercer	1999
Marshall H. Orr	1999
Er-Chang Shang	1999
Robert D. Stoll	1999
Dajun Tang	1999
Alexandra I. Tolstoy	1999

Ex officio:
John C. Burgess, Associate Editor of JASA
David L. Bradley, Associate Editor of JASA
Stanley A. Chin-Bing, Associate Editor of JASA
Michael J. Buckingham, member of Medals and Awards Committee
Christopher Feuillade, member of Membership Committee
Er-Chang Shang, member of ASACOS

Animal Bioacoustics

	Term to
Whitlow W. L. Au, *Chair* to 2000	2000
Robert Hickling	2001
David A. Helweg	2001
Martin L. Lenhardt	2001
Peter M. Narins	2001
John R. Potter	2001
Daniel R. Raichel	2001
Robert H. Benson	2000
Ann E. Bowles	2000
William C. Cummings	2000
Charles R. Greene	2000
Mardi C. Hastings	2000
D. Vance Holliday	2000
David K. Mellinger	2000
Sam H. Ridgway	2000
Frank T. Awbrey	1999
William C. Burgess	1999
Daniel P. Costa	1999
Adam S. Frankel	1999
Darlene R. Ketten	1999
Larry L. Pater	1999
James A. Simmons	1999

Ex officio:
Whitlow W.L. Au, Associate Editor of JASA
David L. Bradley, Associate Editor of JASA
Stanley A. Chin-Bing, Associate Editor of JASA
Mardi C. Hastings, member of Medals and Awards Committee
Sam H. Ridgway, member of Membership Committee
Ann E. Bowles, member of ASACOS

Architectural Acoustics

	Term to
Ronald R. Freiheit, *Chair* to 2001	2001
Bennett M. Brooks	2001
Steven M. Brown	2001
Richard H. Campbell	2001
M. David Egan	2001
Richard M. Guernsey	2001
Mark A. Holden	2001
K. Anthony Hoover	2001
Dana S. Hougland	2001
David W. Kahn	2001
Gary S. Madaras	2001
Charles T. Moritz	2001
Paul B. Ostergaard	2001
Dennis A. Paoletti	2001
David J. Prince	2001
Neil A. Shaw	2001
Richard H. Talaske	2001
Ewart A. Wetherill	2001
George E. Winzer	2001
Michael R. Yantis	2001
Yoichi Ando	2000
David Braslau	2000
Dennis Fleisher	2000
John W. Kopec	2000
Robert F. Mahoney	2000
Daniel W. Martin	2000
Richard J. Peppin	2000
Scott Pfeiffer	2000
Roy L. Richards	2000
Ludwig W. Sepmeyer	2000
Gary W. Siebein	2000
David Still	2000
Robin M. Towne	2000
Lily Wang	2000
Christopher N. Blair	1999
John S. Bradley	1999
Christopher N. Brooks	1999
Angelo J. Campanella	1999
Antonio Pedro Carvalho	1999
Robert C. Coffeen	1999
Peter D'Antonio	1999
Timothy J. Foulkes	1999
J. Christopher Jaffe	1999
Mendel Kleiner	1999
David L. Klepper	1999
Edward L. Logsdon	1999
David Lubman	1999
Michael T. Nixon	1999
Jack E. Randorff	1999
H. Stanley Roller	1999
Carl J. Rosenberg	1999
Kenneth B. Scott	1999
Ben H. Sharp	1999
Noral D. Stewart	1999
Jason T. Weissenburger	1999

Ex officio:
Courtney B. Burroughs, Associate Editor of JASA
J. David Quirt, Associate Editor of JASA
Steven M. Brown, member of Medals and Awards Committee
Gregory C. Tocci, member of Membership Committee
George E. Winzer, member of ASACOS

Biomedical Ultrasound/Bioresponse to Vibration

	Term to
Ronald A. Roy, *Chair* to	1999
Paul E. Barbone	2001
Anthony J. Brammer	2001
Diane Dalecki	2001
J. Brian Fowlkes	2001
Leon Frizzell	2001
Alan K. Goble	2001
Mark Hollins	2001
Kullervo Hynynen	2001
T. Douglas Mast	2001
Doug Miller	2001
Pierre Mourad	2001
William D. O'Brien	2001
Gail R. ter Haar	2001
Stanley L. Bolanowski, Jr.	2000
Shira L. Broschat	2000
Robin O. Cleveland	2000
Inder R. S. Makin	2000
Janet M. Weisenberger	2000
Junru Wu	2000
Michalakis A. Averkiou	1999
Floyd Dunn	1999
John Erdreich	1999
E. Carr Everbach	1999
Christy K. Holland	1999
Wesley L. Nyborg	1999
William M. Rabinowitz	1999
K. Kirk Shung	1999

Ex officio:
Floyd Dunn, Associate Editor of JASA
Robert D. Frisina, Associate Editor of JASA
Joseph W. Hall, Associate Editor of JASA
Robert V. Shannon, Associate Editor of JASA
Wesley L. Nyborg, member of the Medals and Awards Committee
Anthony J. Brammer, member of the Membership Committee
Robin O. Cleveland, member of ASACOS

Engineering Acoustics

	Term to
Thomas R. Howarth, *Chair* to	2000
Mahlon D. Burkhard	2001
James Christoff	2001
Dennis F. Jones	2001
Jan F. Lindberg	2001
Yushieh Ma	2001
Elizabeth A. McLaughlin	2001
Alan Powell	2001
Roger T. Richards	2001
Harold C. Robinson	2001
Kenneth D. Rolt	2001
Neil A. Shaw	2001
James F. Tressler	2001
Kim C. Benjamin	2000
Allan C. Cummings	2000
Gary W. Elko	2000
Robert D. Finch	2000
Guillermo C. Gaunaurd	2000
Gordon Hayward	2000
Dehua Huang	2000
Sung Hwan Ko	2000
Victor Nedzelnitsky	2000
Ahmet Selamet	2000
James E. West	2000
Oscar B. Wilson	2000
George S. K. Wong	2000
Steven R. Baker	1999
David A. Brown	1999
Stephen C. Butler	1999
W. Jack Hughes	1999
K. Kirk Shung	1999
R. Lowell Smith	1999
Stephen C. Thompson	1999
Arnie L. Van Buren	1999
A. Mark Young	1999

Ex officio:
Henry E. Bass, Associate Editor of JASA
Stanley L. Ehrlich, Associate Editor of JASA
Robert D. Finch, member of Medals and Awards Committee
Sung H. Ko, member of Membership Committee
Mahlon D. Burkhard, member of ASACOS

Musical Acoustics

	Term to
Douglas H. Keefe, *Chair* to	1999
R. Dean Ayers	2001
Judith C. Brown	2001
Courtney B. Burroughs	2001
Robert D. Collier	2001
Stephen F. Duncan	2001
George F. Emerson	2001
James H. Irwin	2001
Bozena Kostek	2001
Barry Larkin	2001
Thomas D. Rossing	2001
Julius O. Smith	2001
William J. Strong	2001
James W. Beauchamp	2000
Rene E. Causse	2000
W. Jay Dowling	2000
William M. Hartmann	2000
Adrianus J. Houtsma	2000
Bruce A. Lawson	2000
James M. Pyne	2000
Shigeru Yoshikawa	2000
George A. Bissinger	1999
James P. Cottingham	1999
Uwe J. Hansen	1999
Peter L. Hoekje	1999
Ian M. Lindevald	1999
Daniel W. Martin	1999

Ex officio:
Stanley L. Ehrlich, Associate Editor of JASA
William J. Strong, Associate Editor of JASA
Roger J. Hanson, member of Medals and Awards Committee
Uwe J. Hansen, member of Membership Committee
Ian M. Lindevald, member of ASACOS

Noise

	Term to
Richard J. Peppin, *Chair* to	2000
Martin Alexander	2001
John P. Barry	2001
Leo L. Beranek	2001
Arno S. Bommer	2001
Anthony J. Brammer	2001
James O. Buntin	2001
Robert J. Cook	2001
Kenneth A. Cunefare	2001

Joseph P. Cuschieri	2001
Paul R. Donavan	2001
William D. Gallagher	2001
Gerald C. Lauchle	2001
Anna Maria Monslave	2001
Miomir Mijic	2001
Thomas Norris	2001
Larry H. Royster	2001
John P. Seiler	2001
Noral D. Stewart	2001
Michael R. Stinson	2001
Alice H. Suter	2001
Louis C. Sutherland	2001
Jiri Tichy	2001
Dennis Walton	2001
Keith Attenborough	2000
Sergio Beristain	2000
Robert D. Bruce	2000
John C. Burgess	2000
Angelo J. Campanella	2000
Robert J. Comparin	2000
T. James DuBois	2000
John J. Earshen	2000
Tony F. W. Embleton	2000
John Erdreich	2000
B. John Feng	2000
Robert D. Hellweg	2000
Robert M. Hoover	2000
Daniel L. Johnson	2000
Tor S. D. Kihlman	2000
Sonoko Kuwano	2000
Chantal Laroche	2000
Robert Lotz	2000
Alan H. Marsh	2000
Ralph T. Muehleisen	2000
Kenneth J. Plotkin	2000
Joseph Pope	2000
Julia D. Royster	2000
Brigitte Schulte-Fortkamp	2000
Jean Tourret	2000
Robert W. Young	2000
Elliott H. Berger	1999
Bennett M. Brooks	1999
Lawrence S. Finegold	1999
Jerry G. Lilly	1999
George A. Luz	1999
Luc Mongeau	1999
Mary M. Prince	1999
Jack E. Randorff	1999
Nancy S. Timmerman	1999
Laura A. Wilber	1999

Ex officio:
Michael R. Stinson, Associate Editor of JASA
Stanley L. Ehrlich, Associate Editor of JASA
Elliott H. Berger, member of Medals and Awards Committee
Daniel L. Johnson, member of Membership Committee
Arno S. Bommer, member of ASACOS

Physical Acoustics

	Term to
James M. Sabatier, *Chair* to	1999
David T. Blackstock	2001
David A. Brown	2001
Gilles A. Daigle	2001
Bruce Denardo	2001
Steven L. Garrett	2001
Logan E. Hargrove	2001
Craig J. Hickey	2001
Andres Larraza	2001
William Moss	2001
George Mozurkewich	2001
Vladimir Ostashev	2001
Victor W. Sparrow	2001
Keith Attenborough	2000
Yves H. Berthelot	2000
James P. Chambers	2000
Robin O. Cleveland	2000
Kerry W. Commander	2000
D. Felipe Gaitan	2000
Mark F. Hamilton	2000
Steven G. Kargl	2000
Philip L. Marston	2000
Thomas J. Matula	2000
Kenneth J. Plotkin	2000
Harry Simpson	2000
D. Keith Wilson	2000
Robert E. Apfel	1999
Anthony A. Atchley	1999
Lawrence A. Crum	1999
Floyd Dunn	1999
E. Carr Everbach	1999
David I. Havelock	1999
D. Kent Lewis	1999
Julian D. Maynard, Jr.	1999
Michael R. Moldover	1999
Ronald A. Roy	1999
Charles Thompson	1999
Wayne M. Wright	1999

Ex officio:
Henry E. Bass, Associate Editor of JASA
Mack A. Breazeale, Associate Editor of JASA
Mark F. Hamilton, Associate Editor of JASA
Courtney B. Burroughs, Associate Editor of JASA
Floyd Dunn, Associate Editor of JASA
Dale E. Chimenti, Associate Editor of JASA
Andrew N. Norris, Associate Editor of JASA
Paul J. Remington, Associate Editor of JASA
Louis C. Sutherland, Associate Editor of JASA
Anthony A. Atchley, member of Medals and Awards Committee
Steven L. Garrett, member of Membership Committee
Sameer I. Madanshetty, member of ASACOS

Psychological and Physiological Acoustics

	Term to
Donna L. Neff, *Chair* to	1999
Prudence Allen	2001
Robert P. Carlyon	2001
David F. Dolan	2001
Brent W. Edwards	2001
Nina Kraus	2001
John J. Rosowski	2001
David A. Eddins	2000
Mary Florentine	2000
John H. Grose	2000
Marjorie R. Leek	2000
Elizabeth A. Strickland	2000
Fan-Gang Zeng	2000
Leslie R. Bernstein	1999
Amy M. Donahue	1999
Gerald D. Kidd, Jr.	1999
Ruth Y. Litovsky	1999
Dennis McFadden	1999
Robert V. Shannon	1999

Ex officio:
D. Wesley Grantham, Associate Editor of JASA
Robert D. Frisina, Associate Editor of JASA

Joseph W. Hall, Associate Editor of JASA
Robert V. Shannon , Associate Editor of JASA
Brenda L. Lonsbury-Martin, Associate Editor of JASA
William A. Yost, member of Medals and Awards Committee
Richard R. Fay, member of Membership Committee
Christine M. Rankovic, member of ASACOS

Speech Communication

	Term to
Emily A. Tobey, *Chair* to 2001	2001
Fredericka Bell-Berti	2001
H. Timothy Bunnell	2001
Astrid Schmidt-Nielsen	2001
Winifred Strange	2001
Douglas H. Whalen	2001
Lynne E. Bernstein	2000
Sadaoki Furui	2000
Kenneth W. Grant	2000
Jody E. Kreiman	2000
Patricia K. Kuhl	2000
Richard S. McGowan	2000
Susan N. Nittrouer	2000
Douglas D. O'Shaughnessy	2000
Robert F. Port	2000
Mitchell S. Sommers	2000
Ann K. Syrdal	2000
Abeer Alwan	1999
Peter F. Assmann	1999
Thomas D. Carrell	1999
Carol Y. Espy-Wilson	1999
Robert A. Fox	1999
James M. Hillenbrand	1999
Diane Kewley-Port	1999
John C. Kingston	1999
Keith R. Kluender	1999
Mari L. Ostendorf	1999
Joseph S. Perkell	1999
Janet C. Rutledge	1999
Juergen Schroeter	1999
Christine H. Shadle	1999
Yoh-ichi Tohkura	1999
Gary G. Weismer	1999

Ex officio:
James L. Hieronymus, Associate Editor of JASA
Anders Lofqvist, Associate Editor of JASA
James M. Hillenbrand, Associate Editor of JASA
Winifred Strange, member of Medals and Awards Committee
Maureen L. Stone, member of Membership Committee
Diane Kewley-Port, member of ASACOS

Structural Acoustics and Vibration

	Term to
Jerry H. Ginsberg, *Chair* to 2000	2000
Paul E. Barbone	2001
Wen H. Lin	2001
Philip Marston	2001
James G. McDaniel	2001
Angie Sarkissian	2001
Benjamin Bard	2000
Alain C. Berry	2000
Hunter C. Cohen	2000
David Feit	2000
Guillermo C. Gaunaurd	2000
Karl Grosh	2000
Sabih I. Hayek	2000
Francis Kirschner	2000
Mauro Pierucci	2000
Andrew F. Seybert	2000
Scott D. Sommerfeldt	2000
Vasundara V. Varadan	2000
Richard D. Vogelsong	2000
Sean F. Wu	2000
John A. Burkhardt	1999
Courtney B. Burroughs	1999
Joseph M. Cuschieri	1999
Alison Flatau	1999
Richard F. Keltie	1999
Jean R. Nicolas	1999
Allan D. Pierce	1999
Victor W. Sparrow	1999

Ex officio:
Paul J. Remington, Associate Editor of JASA
Courtney B. Burroughs, Associate Editor of JASA and member of Membership Committee
Allan D. Pierce, member of Medals and Awards Committee
Louis A. Herstein, member of ASACOS

Underwater Acoustics

	Term to
George V. Frisk, *Chair* to 2000	2000
Michael G. Brown	2001
Dennis B. Creamer	2001
Christian P. de Moustier	2001
Stanley E. Dosso	2001
Stewart A. L. Glegg	2001
Zoi-Heleni Michalopoulou	2001
Marshall H. Orr	2001
Gregory J. Orris	2001
James C. Presig	2001
Daniel Rouseff	2001
William L. Siegmann	2001
David L. Bradley	2000
Curtis I. Caldwell	2000
William M. Carey	2000
Nicholas P. Chotiros	2000
Donald R. Del Balzo	2000
Frederick R. DiNapoli	2000
David R. Dowling	2000
Robert W. Farwell	2000
Roger C. Gauss	2000
Darrell R. Jackson	2000
Finn B. Jensen	2000
Roger W. Meredith	2000
John R. Preston	2000
Henrik Schmidt	2000
Ralph A. Stephen	2000
Robert D. Stoll	2000
Frederick D. Tappert	2000
Alexander G. Voronovich	2000
R. Jeffrey Wilkes	2000
Tsih C. Yang	2000
Robert A. Zingarelli	2000
Ralph N. Baer	1999
Shira L. Broschat	1999
Berlie A. Brunson	1999
Peter G. Cable	1999
Marshall V. Hall	1999
Samuel W. Marshall	1999
Dan J. Ramsdale	1999
Timothy H. Ruppel	1999
Natalia A. Sidorovskaia	1999
Kevin B. Smith	1999
Dajun Tang	1999
Christopher T. Tindle	1999
Alexandra I. Tolstoy	1999

Ex officio:
John C. Burgess, Associate Editor of JASA

Stanley A. Chin-Bing, Associate Editor of JASA
David L. Bradley, Associate Editor of JASA and member of Medals and Awards Committee
Peter H. Rogers, member of Membership Committee
Arnie L. Van Buren, member of ASACOS

Interdisciplinary Technical Group on Signal Processing in Acoustics

	Term to
James V. Candy, *Chair* to	2000
Martin Barlett	2001
David H. Chambers	2001
Elmer Hixson	2001
Ning Xiang	2001
John C. Burgess	2000
Christian P. deMoustier	2000
Gary W. Elko	2000
David I. Havelock	2000
Stergios Stergiopoulos	2000
Julius O. Smith, III	2000
Yoshio Yamasaki	2000
Edith L.R. Corliss	1999
John M. Noble	1999
James C. Rogers	1999
David C. Swanson	1999
Gary R. Wilson	1999

Ex officio:
John C. Burgess, Associate Editor of JASA

Administrative Committees 1998–1999

Archives and History

	Term to
Henry E. Bass, *Chair* to	2000
James C. Saunders	2001
Harry Schecter	2001
Rosalie M. Uchanski	2001
Richard K. Cook	2000
John W. Kopec	2000
Richard J. Peppin	2000
William J. Cavanaugh	1999
Logan E. Hargrove	1999
Carleen M. Hutchins	1999

Books[+]

	Term to
Mohsen Badiey, *Chair* to	1999
Stanley A. Chin-Bing	2001
Gordon E. Martin	2001
Victor W. Sparrow	2001
Robert D. Frisina	2000
Jerry H. Ginsberg	2000
Philip L. Marston	2000
Joseph Pope	2000
Robert A. Walkling	2000
Stephen N. Wolf	2000
Nancy S. McGarr	1999
Jeffrey A. Nystuen	1999
Neil A. Shaw	1999
Emily A. Tobey	1999

Ex officio:
James F. Bartram, Associate Editor of JASA for Book Reviews

Education in Acoustics

	Term to
Victor W. Sparrow, *Chair* to	2000
David A. Brown	2001
Robert D. Collier	2001
Corinne M. Darvennes	2001
Margaritis S. Fourakis	2001
Carole E. Gelfer	2001
Douglas R. Jones	2001
Sharon Y. Manuel	2001
Philip L. Marston	2001
Ana Maria Monsalve	2001
Ralph Muehleisen	2001
Andrew A. Piacsek	2001
Daniel R. Raichel	2001
Sally G. Revoile	2001
Thomas D. Rossing	2001
Ronald A. Roy	2001
Dawn R. Schuette	2001
Scott D. Sommerfeldt	2001
William Thompson, Jr.	2001
Robert A. Walkling	2001
George S.K. Wong	2001
Anthony A. Atchley	2000
Fredericka Bell-Berti	2000
E. Carr Everbach	2000
Uwe J. Hansen	2000
Elizabeth S. Ivey	2000
P. K. Raju	2000
Daniel A. Russell	2000
Emily A. Tobey	2000
D. Michael Daly	1999
Logan E. Hargrove	1999
Mardi C. Hastings	1999
Michel T.T. Jackson	1999
Murray F. Korman	1999
Diana F. McCammon	1999
James M. Sabatier	1999
James E. West	1999
Wayne M. Wright	1999
Michael K. Wynne	1999

Ethics and Grievances

	Term To
Robert E. Apfel, *Chair* to	2000
William J. Cavanaugh	2000
Carol Y. Espy-Wilson	2000
Mardi C. Hastings	1999
William A. Yost	1999

Investments

	Term to
John V. Bouyoucos and Leo L. Beranek, Cochairs to	2001
Kenneth M. Eldred	2001

William W. Lang, Treasurer, *ex officio*

Long Range Planning

	Term to
Anthony A. Atchley, *Chair* to	2000
Fredericka Bell-Berti	2001
Ervin R. Hafter	2001
Louis C. Sutherland	2001
Dana S. Hougland	2000
Scott D. Sommerfeldt	2000
Murray Strasberg	2000
Floyd Dunn	1999
Mardi C. Hastings	1999
Stephen C. Thompson	1999

Patricia K. Kuhl, President-Elect, *ex officio*

Medals and Awards

		Term to
Sabih I. Hayek, *Chair* to 1999		1999
Michael J. Buckingham	Acoustical Oceanography	2001
Robert D. Finch	Engineering Acoustics	2001
Roger J. Hansen	Musical Acoustics	2001
Winifred Strange	Speech Communication	2001
Mark F. Hamilton	Physical Acoustics	2000
Elliott H. Berger	Noise	2000
Wesley L. Nyborg	Biomedical Ultrasound/Bioresponse to Vibration	2000
William A. Yost	Psychological and Physiological Acoustics	2000
Steven M. Brown	Architectural Acoustics	1999
David L. Bradley	Underwater Acoustics	1999
Mardi C. Hastings	Animal Bioacoustics	1999
Allan D. Pierce	Structural Acoustics and Vibration	1999

Meetings—June 1998–October 1998

Gilles A. Daigle, *Chair* to 1999
William M. Hartmann, Vice President
Mardi C. Hastings, *Chair*, Fall 1999
Sabih I. Hayek, *Chair*, Spring 1997
Mauro Pierucci, *Chair*, Fall 1997 and Vice-President Elect
Lawrence A. Crum, *Chair*, Spring 1998
Kevin P. Shepherd, *Chair*, Fall 1998
Jiri Tichy, *Chair*, Spring 1999

Elaine Moran, ASA Office Manager, *ex officio*
Charles E. Schmid, Executive Director, *ex officio*

Subcommittee on Exhibits

Martin A. Alexander, *Chair*
Tony F. W. Embleton
Robert Finnegan
Sabih I. Hayek
Noland L. Lewis
Julia D. Royster

Membership

		Term to
Joseph W. Dickey, *Chair* to 2000		2000
Christopher Feuillade	Acoustical Oceanography	2001
Steven L. Garrett	Physical Acoustics	2001
Peter H. Rogers	Underwater Acoustics	2001
Gregory C. Tocci	Architectural Acoustics	2001
Richard R. Fay	Psychological and Physiological Acoustics	2000
Uwe J. Hansen	Musical Acoustics	2000
Sung H. Ko	Engineering Acoustics	2000
Maureen L. Stone	Speech Communication	2000
Sam H. Ridgway	Animal Bioacoustics	2000
Anthony J. Brammer	Biomedical Ultrasound/Bioresponse to Vibration	1999
Courtney B. Burroughs	Structural Acoustics and Vibration	1999
Burton G. Hurdle	Foreign Members	1999
Daniel L. Johnson	Noise	1999

Public Relations

	Term to
Paul A. Baxley, *Chair* to 2000	2000
E. Carr Everbach	2001
Charles Gaumond	2001
Christy K. Holland	2001
David Lubman	2001
Andrew A. Piacsek	2001
Anthony J. Brammer	2000
William J. Cavanaugh	2000
T. James DuBois	2000
Blas Espinoza-Varas	2000
Holly S. Haggerty	2000
Helen Ann McCaffrey	2000
Victor Nedzelnitsky	2000
Mauro Pierucci	2000
Thomas D. Rossing	2000
Bor-Tsuen Wang	2000
Ewart A. Wetherill	2000
John Erdreich	1999
Lawrence L. Feth	1999
Logan E. Hargrove	1999
Burton G. Hurdle	1999
Carlos R. Jimenez-Dianderas	1999
James F. Lynch	1999
Joanne L. Miller	1999
Joseph Pope	1999
Punita G. Singh	1999
Barbara J. Sotirin	1999

Daniel W. Martin, Editor-in-Chief, *ex officio*
Elaine Moran, ASA Office Manager, *ex officio*
Charles E. Schmid, Executive Director, *ex officio*
Thomas D. Rossing, Echoes Editor, *ex officio*

Publication Policy

	Term to
Floyd Dunn, *Chair* to 2000	2000
Sigfrid D. Soli	2001
Richard Stern	2001
Michael R. Stinson	2001
A. Simmons	2000
Robert C. Bilger	1999
James F. Lynch	1999
James H. Miller	1999
George S.K. Wong	1999
Allan J. Zuckerwar	1999

Patricia K. Kuhl, President-Elect, *ex officio*
Daniel W. Martin, Editor-in-Chief, *ex officio*

Regional Chapters

Roger T. Richards, *Chair* to 2000

Elmer L. Hixson	Austin
Angelo J. Campanella	Central Ohio
Courtney B. Burroughs	Central Pennsylvania
John W. Kopec	Chicago
Joseph V. Hendricks	Cincinnati
Edwin H. Toothman	Delaware Valley
Gary W. Siebein	Florida
Yves H. Berthelot	Georgia
Timothy J. Foulkes	Greater Boston
Robert M. Hoover	Houston
Michael J. Anderson	Inland Northwest
Neil A. Shaw	Los Angeles
Hari S. Paul	Madras, India
Marehalli G. Prasad	Metropolitan New York
Elizabeth A. McLaughlin	Narragansett
Larry H. Royster	North Carolina
Peter F. Assmann	North Texas
James R. Angerer	Northwest
R. Dean Ayers	Orange County
Mauro Pierucci	San Diego
David Braslau	Upper Midwest
Timothy S. Margulies	Washington, D.C.
Thomas M. Disch	Wisconsin

Victor W. Sparrow, *Chair*, Education in Acoustics, *ex officio*

Rules and Governance

	Term to
Tony F. W. Embleton, *Chair* to 1999	1999
William J. Cavanaugh	2001
Floyd Dunn	2001
Elaine Moran	2000
Charles E. Schmid	2000

Special Fellowships

	Term to
Wayne M. Wright, *Chair* to 1999	1999
John Erdreich	2001
Constantine Trahiotis	2001
James D. Miller	2000
Gary W. Elko	2000
Henrik Schmidt	1999

Standards

Executive Committee
Daniel L. Johnson, Chair (Standards Director)
Paul D. Schomer, Vice Chair
Avril Brenig, Standards Manager, *ex officio*

S1 Representation
John P. Seiler, Chair S1 and ASA representative on S1
George S. K. Wong, Vice Chair S1 and ASA alternate representative on S1

S2 Representation
David J. Evans, Chair S2 and ASA representative on S2
Richard F. Taddeo, Vice Chair S2 and ASA alternate representative on S2

S3 Representation
Lawrence S. Finegold, Chair S3 and ASA representative on S3
R. F. Burkard, Vice Chair S3 and ASA alternate representative on S3

S12 Representation
Paul D. Schomer, Chair S2 and ASA representative on S12
Bennett M. Brooks, Vice Chair S12
William J. Galloway, ASA alternate representative on S12

International TAGs (ex officio)
Paul D. Schomer, Chair, U.S. TAG for ISO/TC 43 and ISO/TC 43/SC1
Elliott H. Berger, U.S. TAG for ISO/TC 94/SC 12
David J. Evans, Chair, U.S. TAG for ISO/TC 108
Victor A. Nedzelnitsky, U.S. Technical Advisor for IEC/TC 29

ASA Technical Committee Representatives
William M. Hartmann, Chair of ASA Technical Council, *ex officio*
Er Chang Shang, Acoustical Oceanography
Ann E. Bowles, Animal Bioacoustics
George E. Winzer, Architectural Acoustics
Robin O. Cleveland, Biomedical Ultrasound/Bioresponse to Vibration
Mahlon D. Burkhard, Engineering Acoustics
Ian M. Lindevald, Musical Acoustics
Arno S. Bommer, Noise
Sameer I. Madanshetty, Physical Acoustics
Christine M. Rankovic, Psychological and Physiological Acoustics
Diane Kewley-Port, Speech Communication
Louis A. Herstein, Structural Acoustics and Vibration
Arnie L. Van Buren, Underwater Acoustics

ASA Officers
William W. Lang, Treasurer, *ex officio*
Charles E. Schmid, Executive Director, *ex officio*

Past Chair of ASACOS (*ex officio*)
Tony F. W. Embleton

Associate Editors for Standards News—JASA (*ex officio*)
Avril Brenig
George S. K. Wong

Tutorials

	Term to
Joseph Pope, *Chair* to 2000	2000
Ann E. Bowles	2001
Douglas D. O'Shaughnessy	2001
Gary W. Siebein	2001
Beverly A. Wright	2001
Kenneth E. Gilbert	2000
Kenneth J. Plotkin	2000
Yves H. Berthelot	1999
Uwe J. Hansen	1999
Alexandra I. Tolstoy	1999

Charles E. Schmid, Executive Director, *ex officio*

Women in Acoustics

	Term to
Barbara J. Sotirin, Chair to 1999	1999
Linda M. Carroll	2001
Lawrence A. Crum	2001
Corinne M. Darvennes	2001
Zoi-Heleni Michalpooulou	2001
Laura K. Smith	2001
Arlene E. Carney	2000
Chi-Fang Chen	2000
Peter H. Dahl	2000
Helen M. Hanson	2000
Elizabeth S. Ivey	2000
Bozena Kostek	2000
Dana S. Hougland	1999
Juliette Ioup	1999
Ellen S. Livingston	1999
Diana F. McCammon	1999
Sally G. Revoile	1999
Victor W. Sparrow	1999

ACOUSTICAL NEWS—INTERNATIONAL

Walter G. Mayer
Physics Department, Georgetown University, Washington, DC 20057

The International Commission on Acoustics—An update

The International Commission on Acoustics was instituted in 1951 as a subcommittee to the International Union for Pure and Applied Physics, IUPAP. Its mission has been to promote international development and collaboration in all fields of acoustics including the promotion of research and development, education, and standardization.

A few years ago the Commission initiated a change in its structure to link it more directly to the acoustical societies worldwide. This change was finally confirmed during the recent ICA/ASA Congress in Seattle where the reorganized Commission held its first General Assembly in which most acoustical societies in the world were presented.

The General Assembly elected new members and officers of the Commission who will serve from 1 October 1998 to 30 September 2001. The elected officers are:

Lawrence A. Crum, Acoustical Society of America, *President*
Gilles A. Daigle, Canadian Acoustical Association, *Secretary General*
Volker Mellert, German Acoustical Society, *Treasurer*
Tor Kihlman, Swedish Acoustical Society, *Past President*.

The other members of the Commission, representing their respective national or regional acoustical societies, are:

H. Tachibana (Japan), R. H. Zhang (China), C. Legros (France), G. Brambilla (Italy), A. S. Nikiforov (Russia), P. A. Nelson (United Kingdom), C. G. Don (Australia), S. N. Y. Gerges (Brasil), S. S. Agrawal (India), S. W. Yoon (Korea), and J. A. Gallego-Juarez (Spain).

Two associate members, J. Blauert (Germany) and S. H. Crandall (USA), were also elected.

The General Assembly approved new by-laws for the Commission. The close ties to IUPAP will be maintained but at the same time the Commission will be a more independent organization with increased economic resources which will be used for improved services to the member societies through strengthened secretarial functions. These will include:

(a) Providing an improved information service on societies, congresses, symposia, etc., as well as on research and education organizations in the field of acoustics.

(b) Taking an active role in coordinating the main international meetings within acoustics to avoid conflicts between the ever-increasing number of meetings.

(c) As in the past, convening the Triennial International Congresses on Acoustics.

In addition, ICA will sponsor or co-sponsor topical and special international conferences, including grants of some financial assistance. Further information on these initiatives and ICA in general is listed at http://gold.sao.nrc.ca/ims/ica

(Invited report by ICA Past President Tor Kihlman.)

The 7th Brekhovskikh conference on ocean acoustics—Moscow, May 1998

The 7th Brekhovskikh conference on ocean acoustics was held in the P. P. Shirshov Institute of Oceanology of the Russian Academy of Sciences in Moscow, 25–28 May 1998. This meeting continued the series of biennial conferences, which was initiated and supervised by Academician Leonid Brekhovskikh. The tradition was interrupted in 1990 due to dramatic changes in the scientific community related to political and economic crises in Russia. This year the tradition was renewed and the conference was held, jointly with the 7th meeting of the Russian Acoustical Society.

The conference attracted leading Russian researchers in the field of underwater acoustics. The official language was Russian, and 82 papers were presented by 79 participants. The presentations showed that the current research interests are concentrated on non-military applications of acoustical methods. The particular problems considered by keynote speakers included sound propagation in shallow water, inverse problems of acoustic tomography, sound scattering by volume and bottom inhomogeneities, generation of ocean noise, computer models, and acoustical instruments. Special attention was given to potential applications of acoustics to the study of region of the most active heat and salt exchange processes in the ocean and to problems of the Arctic. Proceedings containing extended abstracts of all reports were available at the meeting.

It is hoped that the series of conferences will continue on a regular basis and that, in the future, leading researchers from around the world will be invited to participate. The conference was supported by the Russian Foundation for Basic Research. Further information (in Russian) is available at the web-site: http://rav.sio.rssi.ru/shkola/mainl.html

YURI A. CHEPURIN
P. P. Shirov Institute of Oceanology
Russian Academy of Sciences
117851 Moscow, Russia

Papers published in JASJ(E)

A listing of Invited Papers and Regular Papers appearing in the latest issue of the English language version of the *Journal of the Acoustical Society of Japan*, JASJ(E), was published for the first time in the January 1995 issue of the Journal. This listing is continued below.

The May issue of JASJ(E), Vol. 19, No. 3 (1998) contains the following papers:

K. Soetanto, S. Takeuchi, and M. Okujima ''Numerical investigation on nonlinear response of free microbubble illuminated with ultrasonic pulse''
R. Makarewics and K. Masuda ''Highway noise under favorable conditions of generation and propagation''
T. Okubo and K. Fujiwara ''Efficiency of a noise barrier with an acoustically soft cylindrical edge''
H. Zheng, H. Yamaoka, N. Gohda, H. Noguchi, and A. Kaneko ''Design of the acoustic tomography system for velocity measurement with an application to the coastal sea''
A. Omoto, T. Matsui, and K. Fujiwara ''The behavior of an adaptive algorithm with a moving primary source''

International Meetings Calendar

Below are announcements of meetings to be held abroad. Entries preceded by an * are new or updated listings with contact addresses given in parentheses. Month/year listings following other entries refer to issues of the *Journal* which contain full calendar listings or meeting announcements.

October 1998

4–7	**euro-noise 98**, Munich. *4/98*
7–8	***1st Congress of the Slovenian Acoustical Society**, Portoroz, Slovenia. (E. Zelezic, Mechanical Engineering, University of Ljubljana, Askerceva 6, 1000 Ljubljana, Slovenia; Fax: +386 61 218 567; e-mail: erika.zelezic@fs.uni-lj.si)
12–16	**International Conference on Signal Processing (ICSP'98)**, Beijing. *6/98*
14–16	**16th Yugoslav Conference on Noise and Vibration**, Niš. *6/98*
15–16	**Autumn Meeting Swiss Acoustical Society**, Dübendorf. *8/98*
28–30	**Acoustics Week in Canada**, London, ON. *8/98*
31–2	**AES International Conference ''Audio, Acoustics, and Small Spaces,''** Copenhagen. *6/98*

 0001-4966/98/104(4)/1891/2/$15.00

November 1998

11–13 **1st Asia Pacific Conference on Acoustics and Vibration (APAV 98)**, Singapore. *6/98*

12–15 **Institute of Acoustics (UK) Autumn Conference: Speech and Hearing**, Windermere. *4/98*

16–18 **Inter-Noise 98**, Christchurch. *4/96*

20 **Recreational Noise**, Queenstown. *10/97*

23–27 **ICBEN 98: Biological Effects of Noise**, Sydney. *6/98*

30–4 **5th International Conference on Spoken Language Processing**, Sydney. *6/97*

December 1998

9–11 *__National Symposium on Acoustics-1998 (NSA-98)__, Calcutta, India. (Acoustical Society of India, c/o S. S. Agrawal, Central Electronics Engr. Res. Inst., CSIR Complex, Hillside Road, New Delhi-110 012, India; Fax: +91 33 471 4371)

15–16 **Sonar Signal Processing**, Loughborough. *4/98*

March 1999

15–19 **Joint Meeting of EAA Forum Acusticum, and 137th Meeting of the Acoustical Society of America**, Berlin. *6/97*

April 1999

27–29 **International Conference on Vibration, Noise, and Structural Dynamics**, Venice. *8/98*

May 1999

10–14 **4th International Conference on Theoretical and Computational Acoustics**, Trieste. *6/98*

24–26 **2nd International Conference on Emerging Technologies in NDT**, Athens. *8/98*

June 1999

28–30 **1st International Congress of the East European Acoustical Association**, St. Petersburg. *10/97*

28–1 **Joint Conference of Ultrasonics International '99 and World Congress on Acoustics '99 (UI99/WCU99)**, Lyngby. *6/98*

July 1999

4–9 **10th British Academic Conference in Otolaryngology**, London. *10/97*

5–8 **6th International Congress on Sound and Vibrations**, Copenhagen. *2/98*

September 1999

1–4 **15th International Symposium on Nonlinear Acoustics (ISNA-15)**, Göttingen. *10/97*

15–17 **British Society of Audiology Annual Conference**, Buxton. *8/98*

March 2000

20–24 *__Meeting of the German Acoustical Society (DAGA)__, Oldenburg, Germany. (DEGA, FB Physik, Universität Oldenburg, 26111 Oldenburg, Germany; Fax: +49 441 798 3698; e-mail: dega@aku.physik.uni-oldenburg.de)

October 2000

3–5 **WESTPRAC VII**, Kumamoto. *6/98*

16–20 *__6th International Conference on Spoken Language Processing__, Beijing, China. (ICSLP 2000 Secretariat, Institute of Acoustics, PO Box 2712, 17 Zhong Guan Cun Road, 100 080 Beijing, China; Fax: +86 10 6256 9079; e-mail: mchu@plum.ioa.ac.cn)

September 2001

2–7 *__17th International Congress on Acoustics (ICA)__, Rome, Italy. (A. Alippi, Dipartimento di Energetica, Università di Roma ''La Sapienza,'' Via A. Scarpa 14, 00161 Rome, Italy; Fax: +39 6 4424 0183; Web: www.uniroma1.it/energ/ica.html)

REVIEWS OF ACOUSTICAL PATENTS

Daniel W. Martin
7349 Clough Pike, Cincinnati, Ohio 45244

The purpose of these acoustical patent reviews is to provide enough information for a Journal reader to decide whether to seek more information from the patent itself. Any opinions expressed here are those of reviewers as individuals and are not legal opinions. Printed copies of United States Patents may be ordered at $3.00 each from the Commissioner of Patents and Trademarks, Washington, DC 20231.

Reviewers for this issue:

GEORGE L. AUGSPURGER, *Perception Incorporated, Box 39536, Los Angeles, California 90039*
SAMUEL F. LYBARGER, *101 Oakwood Road, McMurray, Pennsylvania 15317*
D. LLOYD RICE, *11222 Flatiron Drive, Lafayette, Colorado 80026*
CARL J. ROSENBERG, *Acentech Incorporated, 33 Moulton Street, Cambridge, Massachusetts 02138*
ERIC E. UNGAR, *Acentech Incorporated, 33 Moulton Street, Cambridge, Massachusetts 02138*
ROBERT C. WAAG, *University of Rochester Medical Center, 601 Elmwood Avenue, Rochester, New York 14642*

5,739,479

43.35.Pt GENTLE-BEVEL FLAT ACOUSTIC WAVE TOUCH SENSOR

Marcia M. Davis-Cannon *et al.*, assignors to ELO TouchSystems, Incorporated
14 April 1998 (Class 178/19); filed 4 March 1996

For an acoustic wave touch screen used as a computer input device, the screen substrate **10** is provided with a beveled edge **11**, with the beveled surface **12** extending to the extreme edge **13**. Ultrasonic transducer **21** directs an acoustic beam at the beveled edge, and an array **40** of acoustically partially reflective structures on touch surface **16**, when touched, modifies the transmission of the ultrasonic wave to the transducers located on the

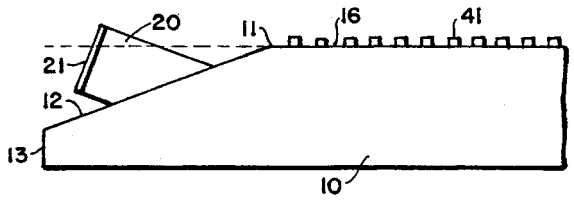

beveled edge of the substrate, in order to define the touch position on the screen. The principal feature of this patent is the beveled edge ''which is small as compared to the wavelength and a bevel angle such that the acoustic wave is attenuated by less than about 3 dB on transmission across the edge.''—DWM

5,750,941

43.35.Zc ULTRASONIC COORDINATES INPUT DEVICE

Hiroshi Ishikawa *et al.*, assignors to Fujitsu Limited
12 May 1998 (Class 178/19); filed in Japan 15 December 1994

In this patent the coordinates of a contact point on the plane surface of a rectangular plate are determined by contacting the point with input pen **1** to generate an ultrasonic wave in the surface, received by edge mounted transducers **3a**–**3e**. The input pen **1** contains a driver unit **1a** and a driver

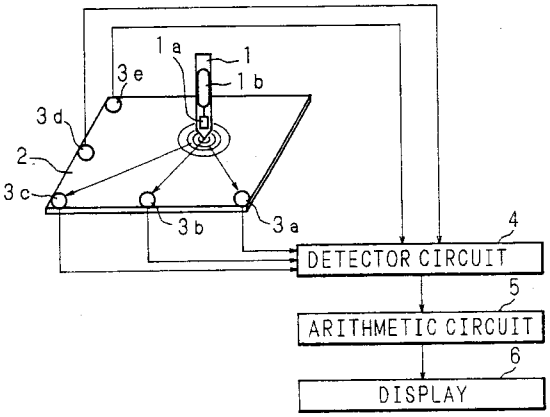

circuit **1b**. Output signals from the three transducers along each edge are received by detector circuit **4** and arithmetic circuit **5** which show the coordinate values (abscissa and ordinate) on a display screen **6**.—DWM

5,727,076

43.38.Fx AUDIO TRANSDUCER HAVING PIEZOELECTRIC DEVICE

Paul W. Paddock, assignor to Aura Systems, Incorporated
10 March 1998 (Class 381/190); filed 2 May 1994

Lightweight bridge **18** transfers the motion of piezoelectric disk **20** to curvilinear diaphragm **14**. The inventor holds several earlier patents in which his distinctive diaphragm is electromagnetically driven. This latest

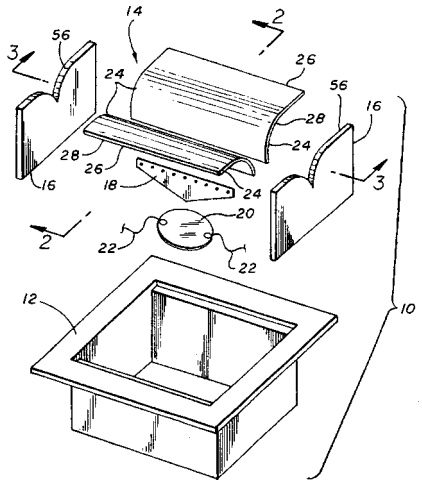

 0001-4966/98/104(4)/1893/10/$15.00

variation satisfies the ''...compelling need for a piezoelectric driven audio transducer for producing sound of higher fidelity than prior piezoelectric audio transducers.''—GLA

5,724,430

43.38.Hz AUDIO-VISUAL ARRANGEMENT AND SYSTEM IN WHICH SUCH AN ARRANGEMENT IS USED

Ronaldus M. Aarts and Willem F. Druyvesteyn, assignors to U.S. Philips Corporation
3 March 1998 (Class 381/59); filed in European Patent Office 24 March 1994

If a video screen is bordered by an array of small loudspeakers, then the resulting sound pattern is quite directional at high frequencies, making it presumably less annoying to other persons nearby. Side lobes can be suppressed by filtering or simple shading. Additional low-frequency isolation can be achieved with active sound cancellation. All of this is described in jargon that makes it sound highly important.—GLA

5,719,946

43.38.Ja LOUDSPEAKER FOR HIGHER AUDIO FREQUENCIES AND A MANUFACTURING METHOD THEREOF

Shouichiro Terauchi *et al.*, assignors to Pioneer Electronic Corporation
17 February 1998 (Class 381/195); filed in Japan 5 September 1994

A high-frequency loudspeaker is made with a relatively large center dome surrounded by a vestigial cone. Their relative geometries are designed such that response peaks from one are equalized by dips from the other. The patent includes numerous response curves and a lot of interesting information about the behavior of various diaphragm types.—GLA

5,721,786

43.38.Ja LOUDSPEAKERS

Simon Paul Carrington, Pipon, North Yorkshire, the United Kingdom
24 February 1998 (Class 381/202); filed in the United Kingdom 8 June 1990

Complicated device **16** is called an oscillator because it is ''...able to oscillate to create sound waves.'' The structure is hollow and contains a helical baffle which is flexible enough to allow both axial and rotary movement. Passage of air through the helical baffle, ''...operates as a pneumatic spring and air brake. ... The action of the unit as a pneumatic spring increases the efficiency of the drive unit and improves the attack of the speaker because there is more surface contact with the air and thus greater surface tension.''—GLA

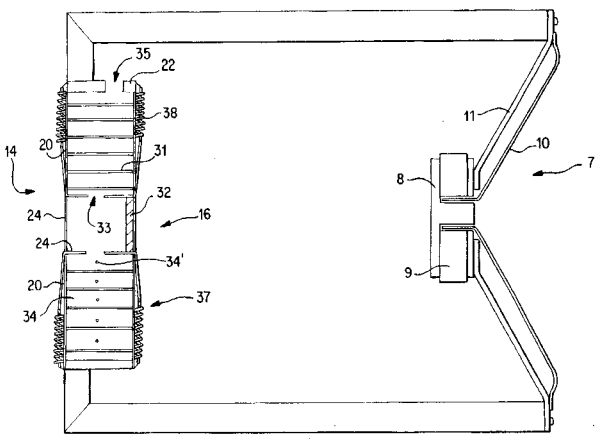

5,740,265

43.38.Ja LOUDSPEAKER UNIT AND LOUDSPEAKER SYSTEM EMPLOYING THE UNIT

Hidetoshi Shirakawa, assignor to Foster Electric Company
14 April 1998 (Class 381/199); filed in Japan 23 December 1996

Both a unit and a system are included in this patent. The unit is a dual-coil loudspeaker somewhat similar to JBL's design (US patent 5,748,760). In this case, however, coils **17a** and **17b** are deliberately offset from the centers of the two magnetic gaps; as one coil moves into its gap the other moves out. This is said to increase both driving efficiency and linear

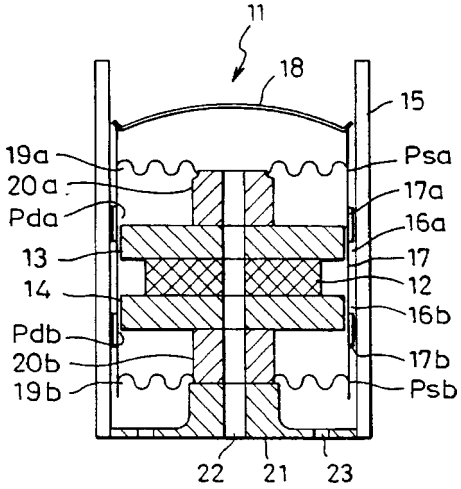

cone excursion. Centering spiders **19a** and **19b** are located above and below the coils. Sound is radiated by diaphragm **18**. Although an edge-driven diaphragm is shown, it could just as well be larger than the voice-coil bobbin. The patent also shows how two of these units could be mounted in dual, undamped tubes that might surround a TV screen.—GLA

5,729,614

43.38.Lc HOWLING REMOVER COMPOSED OF ADJUSTABLE EQUALIZERS FOR ATTENUATING COMPLICATED NOISE PEAKS

Yuichi Nagata *et al.*, assignors to Yamaha Corporation
17 March 1998 (Class 381/83); filed in Japan 9 September 1994

An automatic, computerized equalizer first identifies acoustical feedback frequencies, and then sets digital notch filters accordingly. An alternative mode allows the process to be controlled by a human operator. For a karaoke installation having a single microphone and fixed locations for the microphone and loudspeakers, the system may well be practical and effective.—GLA

5,734,731

43.38.Lc REAL TIME AUDIO MIXER

Elliot S. Marx, Winchester, MA
31 March 1998 (Class 381/119); filed 29 November 1994

A digital disco mixer includes both RAM and hard disk storage to facilitate the same effects that an operator normally achieves with dual, variable speed turntables. The patent is clearly written and includes interesting information about disco mixing techniques.—GLA

5,737,428

43.38.Lc CIRCUIT FOR PROVIDING VISUAL INDICATION OF FEEDBACK

John H. Roberts, assignor to Peavey Electronics Corporation
7 April 1998 (Class 381/58); filed 18 August 1995

Although intended for use with graphic equalizers, this simple circuit might well find other applications. A bank of light-emitting diodes (LEDs) represents a group of audio channels. At any time, only one LED is illuminated, identifying the sound channel with the highest level.—GLA

5,748,754

43.38.Lc SOUND SYSTEM GAIN AND EQUALIZATION CIRCUIT

Clifford Maag and Lance Parker, assignors to Night Technologies International
5 May 1998 (Class 381/104); filed 5 September 1995

The Langevin 252-A, manufactured in the 1960s, was a simple, passive graphic equalizer consisting of seven bandpass filters having outputs that were summed. Individual bandwidths were broad enough that summation always resulted in a smooth, ripple-free response curve with relatively little phase shift. The principle has been rediscovered in this patent, implemented with operational amplifiers.—GLA

5,751,825

43.38.Si COMBINATION ELECTRONIC METRONOME AND HEADPHONE UNIT

Robert A. Myers *et al.*, North Hollywood, CA
12 May 1998 (Class 381/118); filed 19 August 1994

This headset contains an electronic metronome circuit with its own transducer, in addition to the conventional earphones receiving audio signal input from an external source such as an electronic musical instrument or a sound system for a performing orchestra. The tempo of the metronome can be adjusted by a knob on the outside of the earphone shell. This system allows the wearer to play an electronic instrument heard only over his earphones while adjusting the playing tempo to match the metronome output; or allows an orchestra conductor to hear the metronome plus the output of the orchestra sound system, and to conduct the orchestra accordingly without having the metronome heard by the musicians or by the microphones picking up their musical sounds.—DWM

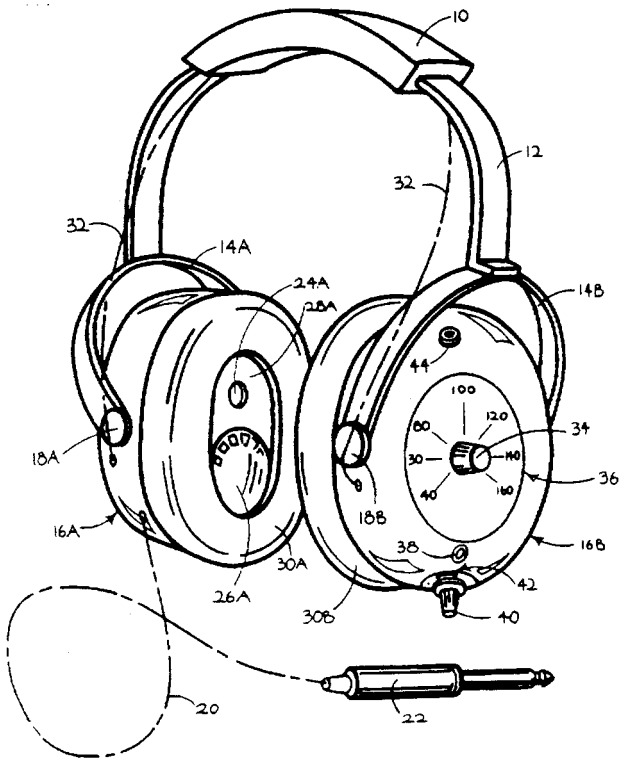

5,724,429

43.38.Vk SYSTEM AND METHOD FOR ENHANCING THE SPATIAL EFFECT OF SOUND PRODUCED BY A SOUND SYSTEM

Raja Banerjea, assignor to Lucent Technologies, Incorporated
3 March 1998 (Class 381/1); filed 15 November 1996

The operation of this asymmetric spatial enhancement circuit can be understood from the diagram. ''As a result, the loudspeakers produce sound

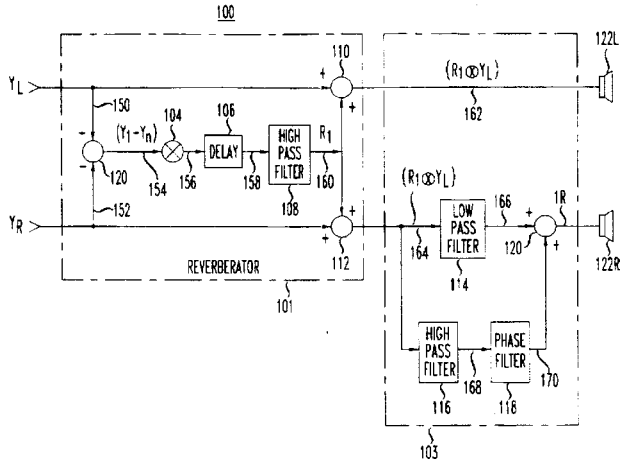

images located at several spatial positions, producing a perception that there is an array of loudspeakers surrounding a listener.''—GLA

5,727,066

43.38.Vk SOUND REPRODUCTION SYSTEM

Stephen John Elliott *et al.*, assignors to Adaptive Audio Limited
10 March 1998 (Class 381/1); filed in the United Kingdom 8 July 1988

Using digital filters and a fairly complicated least-squares algorithm the system attempts to, ''...compensate for crosstalk between the loudspeakers, the acoustic response of the listening space, and imperfections in the frequency response of the speaker channels.''—GLA

5,727,067

43.38.Vk SOUND FIELD CONTROL DEVICE

Masayuki Iwamatsu, assignor to Yamaha Corporation
10 March 1998 (Class 381/18); filed in Japan 28 August 1995

Dolby Prologic Surround encoding provides a single channel for surround sound information, to be reproduced (hopefully) as a diffuse, nonlocalized source. This is not easy to do in a small home theatre. The patented system adds synthetic room reflections and some additional processing to derive two decorrelated surround channels fed to left and right rear loudspeakers. The signals combine acoustically to generate a subjective sound field larger than the listening room itself.—GLA

5,705,769

43.40.Tm VIBRATIONALLY DAMPED STRUCTURE

Jeffrey S. Hanson, assignor to the United States of America
6 January 1998 (Class 114/20.1); filed 14 May 1996

This patent pertains to structures, such as the hulls of underwater vehicles, that are provided with constrained viscoelastic damping treatments. The damping treatment configuration described here employs a discontinuous, segmented constraining layer atop a continuous viscoelastic layer. The primary advantage of such an arrangement seems to be the relative ease with which the constraining layer can be installed inside tapered shell structures like the aft ends of torpedoes.—EEU

5,710,396

43.40.Tm ENERGY-DISSIPATING VIBRATION DAMPING STRUCTURE

Lynn C. Rogers, Jamestown, OH
20 January 1998 (Class 182/208); filed 2 January 1996

This patent describes a series of realizations of spaced viscoelastic damping. In spaced damping a ''spacer'' is introduced between the damping layer (consisting of a viscoelastic material) and either the structure (plate, beam, or shell skin) that is to be damped or a covering or ''constraining'' layer attached to the viscoelastic layer. The realizations of spacers set forth in this patent consist of V-shaped hinged flexures and of various stand-off lever arrangements.—EEU

5,711,350

43.40.Tm PIPING SYSTEM PROVIDING MINIMAL ACOUSTICALLY-INDUCED STRUCTURAL VIBRATION AND FATIGUE

Frantisek L. Eisinger, assignor to Foster Wheeler Energy International, Incorporated
27 January 1998 (Class 138/45); filed 31 July 1996

This patent describes an approach to designing piping near pressure-reducing valves so as to reduce the risk of structural fatigue of the piping due to acoustical pressures resulting from the pressure-reducing flow constriction. The patent document cites a relation that permits one to estimate the acoustic power level from fluid flow and pressure drop parameters and presents a relation between the allowable acoustic power level (that is, the power level at which no piping fatigue is expected) and the ratio of the piping diameter to the wall thickness downstream of the valve. The latter relation is derived from empirical data in limited diameter and thickness ranges.—EEU

5,698,788

43.40.Yq METHOD FOR ANALYZING REGULARLY RECURRING MECHANICAL VIBRATIONS

Hendrik Anne Mol and Cornelis Van Nijen, assignors to SKF Industrial Trading & Development Company B.V.
16 December 1997 (Class 73/659); filed in The Netherlands 22 November 1994

The method described in this patent is intended for the location of faults in rotating components, for example, cracks and pits in ball bearings, where at a given rotational speed specific fault locations are related to specific frequency components. In the presence of a fault the time signal derived from a sensor consists of a series of uniformly spaced impulses. This signal is divided into a series of short time intervals, each of which is subjected to frequency analysis. The resulting spectra then are used to observe how each frequency component varies with time and to obtain the dominant frequency with which each component varies.—EEU

5,710,715

43.40.Yq VIBRATION ANALYSIS METHOD

Motoshi Shitanda, assignor to Matsushita Electric Industrial Company
20 January 1998 (Class 364/508); filed in Japan 28 July 1994

This patent describes a method for detecting vibration abnormalities in production items, such as electric motors, by analyzing the time-varying vibrations produced by these items. The method involves sampling the vibration signature produced by an item at a number n of specified instants measured from a starting point, and assigning the sample values to an n-dimensional space. Abnormalities are determined by comparing the space for a given item with that for one that is designated as normal.—EEU

5,709,053

43.50.Gf PANEL FOR CONSTITUTING SOUND INSULATING WALL

Hideyuki Kuroda, assignor to Zeon Kasei Company
20 January 1998 (Class 52/145); filed in Japan 23 May 1994

This noise barrier (for use along a highway or railway or in an industrial high-noise environment) has a perforated face and a dense solid backing. The sound absorbing element, wrapped in plastic as a protection against the weather, is shredded magnetic tape from old floppy disks. The plastic does not wick or carry moisture.—CJR

5,714,713

43.50.Gf ACOUSTIC ABSORBING DEVICE

Jeffrey S. Hanson, assignor to the United States of America
3 February 1998 (Class 114/20.1); filed 14 May 1996

This device comprises a sound barrier layer that is spaced away from an enclosure (perhaps a torpedo), with absorbing material in the cavity.—CJR

5,723,831

43.55.Dt TACKABLE ACOUSTICAL BARRIER PANEL

David B. Martin *et al.*, assignors to Herman Miller, Incorporated
3 March 1998 (Class 181/287); filed 18 February 1997

This new office furniture panel has different construction systems below and above desk height. The system below desk height is designed to maximize durability, and the system above desk height is designed to maximize room absorption.—CJR

5,719,359

43.55.Ev LAMINAR DAMPER

Franz-Josef Wolf and Nenad Cvjeticanin, assignors to WOCO Franz-Josef Wolf & Co.
17 February 1998 (Class 181/286); filed in Germany 9 May 1994

This patent describes an acoustic absorber that does not use fibrous or porous materials and thus does not suffer the contamination problems associated with such materials. The absorber described here consists of an arrangement of strips that are supported at their ends and arranged so that their edges rub against each other as incident sound makes the strips vibrate. In a more complex design two layers of strips are used, arranged at an angle to each other and spaced so that friction between the two layers increases the damping of the assembly.—EEU

5,740,649

43.55.Ev FALSE CEILING

Helmut Fuchs and Dietmar Eckoldt, assignors to Fraunhofer-Gesellschaft zur Forderung der Angewandten Forschung E.V.
21 April 1998 (Class 52/506.06); filed in Germany 20 April 1993

This is a fiber-free acoustical false ceiling which absorbs wideband frequencies. The false ceiling uses staggered planes of microperforated metal panels as resonance dampers combining the properties of microperforated and membrane absorbers. The panels do not use any fibrous material.—CJR

5,744,763

43.55.Ti SOUNDPROOFING INSULATOR

Tadanobu Iwasa *et al.*, assignors to Toyoda Gosei Company
28 April 1998 (Class 181/286); filed in Japan 1 November 1994

This soundproofing insulator goes on the inside of an engine compartment. The panel has a sheet-like form, which engages and encapsulates grains of pulverized rubber of various sizes and kinds.—CJR

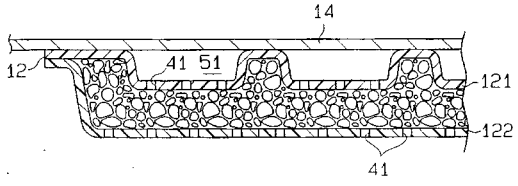

5,735,885

43.63.Qe METHODS FOR IMPLANTING NEURAL PROSTHETIC FOR TINNITUS

Matthew A. Howard III *et al.*, assignors to The University of Iowa Research Foundation
7 April 1998 (Class 607/55); filed 6 February 1996

The patent describes a method for implanting a neural prosthetic into a target zone of a patient's brain for reducing or eliminating the effects of tinnitus. The prosthetic includes a stimulation device for outputting processed electrical signals and an electrode which is arranged in the target zone having a plurality of electrical contacts. Each of the electrical contacts independently outputs electrical discharges in accordance with the electrical signals.—SFL

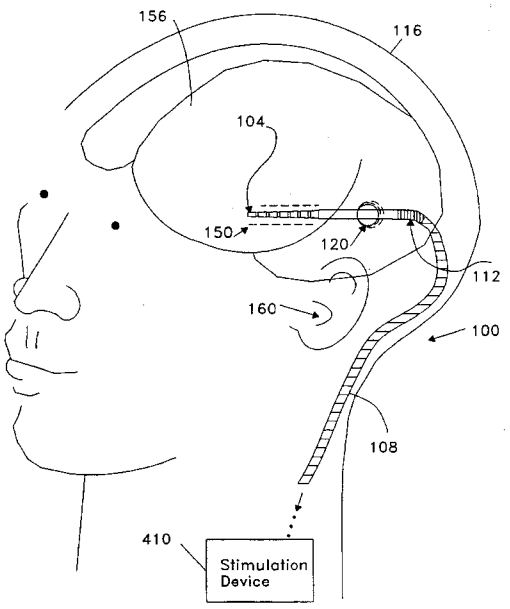

5,706,351

43.66.Ts PROGRAMMABLE HEARING AID WITH FUZZY LOGIC CONTROL OF TRANSMISSION CHARACTERISTICS

Oliver Weinfurtner, assignor to Siemens Audiologische Teknik GmbH
6 January 1998 (Class 381/68.2); filed in European Patent Office 23 March 1994

The hearing aid described has a fuzzy logic controller allocated to the amplifier and transmission circuit, which is connected between the microphone and the earphone for automatic switching and matching the transmission characteristics to the current ambient noise situation. The fuzzy controller makes a selection of parameters stored in a data carrier of the hearing aid for the modification of its transmission characteristics dependent on input quantities characteristic of the varying ambient noise.—SFL

5,706,352

43.66.Ts ADAPTIVE GAIN AND FILTERING CIRCUIT FOR A SOUND REPRODUCTION SYSTEM

A. Maynard Engebretson and Michael P. O'Connell, assignors to K/S HIMPP
6 January 1998 (Class 381/684); filed 7 April 1993

The patent describes a hearing aid that has a plurality of channels, each having adaptive compressive gain. Each channel includes a filter with a preset frequency response to receive the input signal and to produce a filtered signal, a channel amplifier to produce a channel output signal, a register to establish a channel threshold level, and a gain circuit to increase or decrease the gain of the channel amplifiers as needed. A transducer produces sound in response to the signal passed by the common circuit output. This is a very comprehensive patent, 110 pages long.—SFL

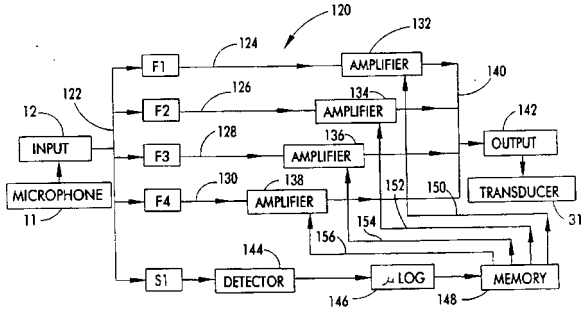

5,710,820

43.66.Ts PROGRAMMABLE HEARING AID

Raimond Martin *et al.*, assignors to Siemens Audiologische Teknik GmbH
20 January 1998 (Class 381/68.4); filed in European Patent Office 31 March 1994

A hearing aid has an analog part with a Class D final amplifier stage for audio signal processing, a digital part with an interface, a memory stage, as well as a supply stage for generating the voltage and control signals. The aid has an integrated circuit which includes a pre-amplifier stage with inputs for a microphone and a telephone coil. The aid is stated to be of small structural size and having especially low energy consumption.—SFL

5,730,699

43.66.Ts IMPLANTABLE HEARING SYSTEM HAVING MULTIPLE TRANSDUCERS

Theodore P. Adams and Kai Kroll, assignors to St. Croix Medical, Incorporated
24 March 1998 (Class 600/25); filed 7 August 1996

The patent shows multiple ceramic piezoelectric transducers implanted in the middle ear to drive various portions of the ossicular train. At least two transducers having nonidentical frequency response characteristics are specified. Details of the acoustical pickup and electronic amplification are not described except to show that separate output amplifiers for each piezoelectric transducer are employed.—SFL

5,735,790

43.66.Ts DEVICE IN HEARING AIDS

Bo Hakansson and Peder Carlsson, assignors to P & B Research AB
7 April 1998 (Class 600/25); filed in Sweden 2 December 1994

A device is shown for mechanically interconnecting an implant, anchored in the skull bone of a person having impaired hearing, with a bone conduction vibrator hearing aid unit. A female cup-shaped part attached to the threaded implant part receives a flexible part attached to the bone vibrator hearing aid for easy attachment or removal of the aid.—SFL

5,737,430

43.66.Ts DIRECTIONAL HEARING AID

Bernard Widrow, assignor to Cardinal Sound Labs, Incorporated
7 April 1998 (Class 381/68.1); filed 16 October 1996

A hearing aid has an array of five microphones across the chest, spaced 3.25 cm apart. In combination with the associated electronics with each microphone, the system acts as a beamformer that has high directivity, particularly at higher frequencies. The microphone output is further amplified and delivered to a neck loop that provides an audio frequency field

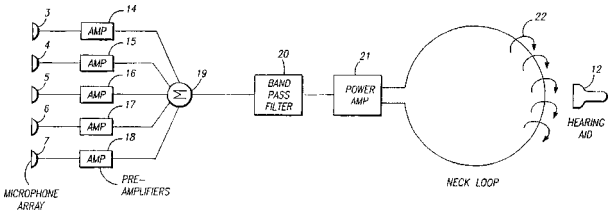

around the head that is picked up by the telecoil of a headworn hearing aid. The fact that telecoil response is usually lower at low frequencies, or that interference due to various stray magnetic fields could be a problem, are not mentioned.—SFL

5,742,692

43.66.Ts IN-THE-EAR HEARING AID WITH FLEXIBLE SEAL

Henri Garcia *et al.*, assignors to U.S. Philips Corpration
21 April 1998 (Class 381/68.6); filed in European Patent Office 8 April 1994

The patent shows an in-the-ear hearing aid with a collar **30** that forms

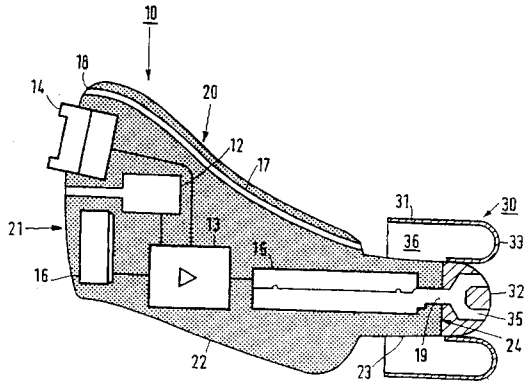

a flexible seal in the bony part of the ear canal so as to reduce the occlusion effect.—SFL

5,740,258

43.66.Vt ACTIVE NOISE SUPPRESSORS AND METHODS FOR USE IN THE EAR CANAL

Scott H. Goodwin-Johansson, assignor to MCNC
14 April 1998 (Class 381/72); filed 5 June 1995

A very small unit is shown that fits into only the central part of the ear canal diameter. A microphone at its outer end picks up incoming sound and delivers it to a lowpass filter. The output of the filter is inverted and delivered to an output transducer deeper in the ear canal, whose output will tend to cancel the low-frequency noise components. A final transducer, the farthest into the canal, receives its signal from the input microphone. The signal reaching the eardrum should have a reduced noise component. The device is formed largely on a common substrate on which microphones, amplifiers, receivers, and the filter are formed.—SFL

5,708,757

43.72.Ar METHOD OF DETERMINING PARAMETERS OF A PITCH SYNTHESIS FILTER IN A SPEECH CODER, AND SPEECH CODER IMPLEMENTING SUCH METHOD

Dominique Massaloux, assignor to France Telecom
13 January 1998 (Class 395/2.29); filed 22 April 1996

Several varieties of linear prediction speech coders use a pitch prediction (long-term) filter to reduce the output bitrate. Under certain conditions, the synthesis pitch filter can become unstable, resulting in a pop in the reconstructed speech, especially when transmission errors occur. This patent describes a method of estimating the range of unstable behavior for various error conditions and modifies the filter to avoid the most risky conditions.—DLR

5,708,759

43.72.Ar SPEECH RECOGNITION USING PHONEME WAVEFORM PARAMETERS

Emanuel S. Kemeny, Arlington, VA
13 January 1998 (Class 395/2.63); filed 19 November 1996

This patent describes a novel method of time-domain waveform analysis called the ''mainwave-ripple model'' to generate acoustic features for a speech recognizer system. Fine-structure parameters include amplitude and zero-crossing counts and their frame maxima and minima over 1 ms subframes. These provide a coarse classification into voiced, fricative, stop or

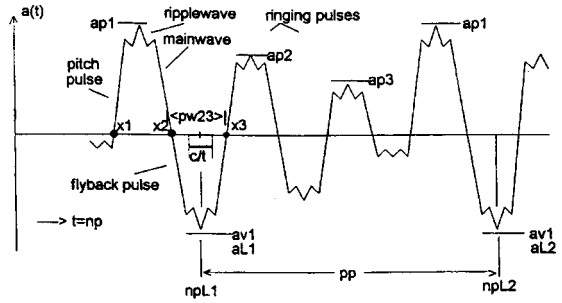

mixed. Main-structure separates the wave into mainwave (crosses zero) and ripple (noncrossing) and includes parameters pitch, flyback, damped ringing, ripple rate, and pitch period. These refine the phonetic classification of the frame.—DLR

5,712,956

43.72.Ar FEATURE EXTRACTION AND NORMALIZATION FOR SPEECH RECOGNITION

Eiko Yamada and Hiroaki Hattori, assignors to NEC Corporation
27 January 1998 (Class 395/2.43); filed in Japan 31 January 1994

This speech recognition analysis system uses a variation on cepstrum analysis to normalize the input signal to compensate for transmission line or other signal spectral characteristics. A parabola or higher order polynomial is fitted to a long-term average cepstral coefficient vector. The differences of individual cepstral vectors from the best-fit polynomial are then taken as the feature vectors.—DLR

5,715,363

43.72.Ar METHOD AND APPARATUS FOR PROCESSING SPEECH

Junichi Tamura *et al.*, assignors to Canon Kabushiki Kaisha
3 February 1998 (Class 395/2.14); filed in Japan 20 October 1989

This speech analysis system computes frame features in the form of smoothed mel-scale cepstral coefficients. The mel scale is approximated by an all-pass filter computation using a variable frequency warping factor. Ideally, if a phonetic transcription is available or obtained by recognition,

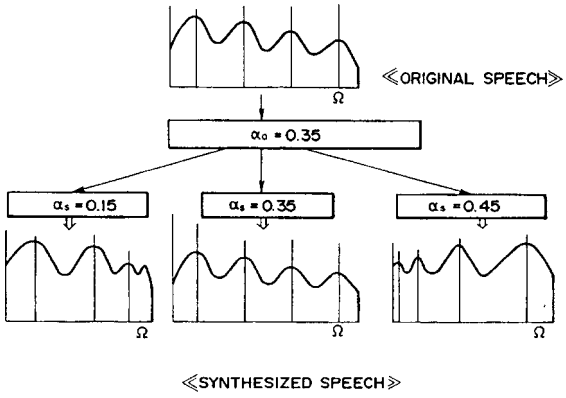

the mel warping factor is set from a table of phoneme-specific values. In addition, playback may be done using a different warping factor from that of the analysis, as shown in the figure.—DLR

5,717,818

43.72.Ew AUDIO SIGNAL STORING APPARATUS HAVING A FUNCTION FOR CONVERTING SPEECH SPEED

Yoshito Nejime *et al.*, assignors to Hitachi, Limited
10 February 1998 (Class 395/2.2); filed in Japan 10 September 1993

This patent describing a speech rate changer system is primarily concerned with issues of user control and varieties of application. The rate change system itself is a typical combination of duplicated or deleted pitch

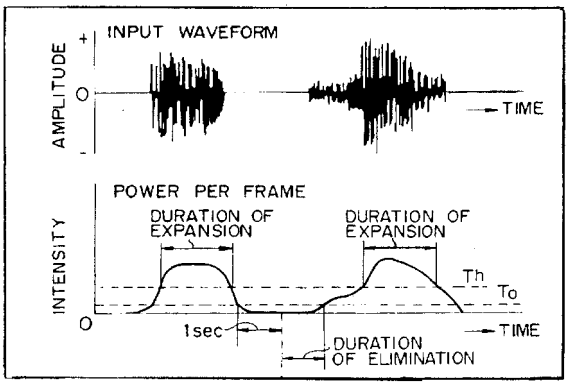

periods with fading mix of the joined segments and detection of specific portions of certain phonemes for possible deletion.—DLR

5,701,391

43.72.Gy METHOD AND SYSTEM FOR COMPRESSING A SPEECH SIGNAL USING ENVELOPE MODULATION

Shao Wei Pan and Shay-Ping Thomas Wang, assignors to Motorola, Incorporated
23 December 1997 (Class 395/2.21); filed 31 October 1995

This speech compression system represents the waveform of each 32 ms frame by a sum of sinusoids. Subframes of samples are normalized to a constant envelope shape and transformed via fast Fourier transform. For voiced frames, the three or four largest spectral components are fitted by a quadratic polynomial whose coefficients thus encode the spectral amplitudes. Phase values which best fit the normalized waveform are found for these components. For unvoiced frames, the largest spectral components are approximated as sum and difference components, as would result from a modulation process, and encoded as the carrier and modulating frequencies.—DLR

5,715,362

43.72.Gy METHOD OF TRANSMITTING AND RECEIVING CODED SPEECH

Marko Vaenskae, assignor to Nokia Telecommunications Oy
3 February 1998 (Class 395/2.1); filed in Finland 4 February 1993

This speech coder is a type of linear prediction coder in which reflection coefficients are vector quantized. If the best fitting codebook vector of coefficients is not close enough to the analyzed coefficients, then the actual coefficients are transmitted and the codebook is adapted. If the codebook vector is close, then the code and the differences from the code vector are transmitted.—DLR

5,717,819

43.72.Gy METHODS AND APPARATUS FOR ENCODING/DECODING SPEECH SIGNALS AT LOW BIT RATES

Stephen P. Emeott and Aaron M. Smith, assignors to Motorola, Incorporated
10 February 1998 (Class 395/2.3); filed 28 April 1995

This low bitrate coding method is said to produce high quality speech output in the 4–8 kbps range. Applicable to CELP, VSELP or other coders, the method uses the spectral envelope and pitch information to generate the set of harmonics up to a given fraction of half the sample frequency (Fs/2).

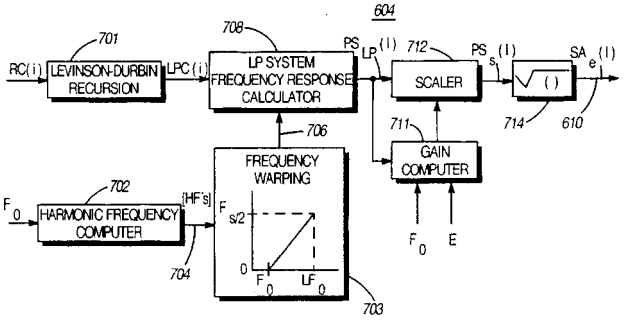

These are linearly warped, mapping F0 to 0 Hz and the highest harmonic to Fs/2. Log squared warped harmonics are fitted by cubic splines and interpolated to a given number, autocorrelated and converted to reflection coefficients, which are transmitted.—DLR

5,715,368

43.72.Ja SPEECH SYNTHESIS SYSTEM AND METHOD UTILIZING PHONEME INFORMATION AND RHYTHM INFORMATION

Takashi Saito and Masaaki Okochi, assignors to International Business Machines Corporation
3 February 1998 (Class 395/2.77); filed in Japan 19 October 1994

This speech synthesizer uses a strategy which makes a distinction between independent words and adjunct words such as adverbs and postpositional particles as used in the Japanese language. Phonetic clarity is a primary concern for independent words, while coarticulatory smoothness is of more concern for adjunct words. Prosodic factors, particularly rhythm, are treated differently according to the word type.—DLR

5,708,704

43.72.Ne SPEECH RECOGNITION METHOD AND SYSTEM WITH IMPROVED VOICE-ACTIVATED PROMPT INTERRUPT CAPABILITY

Thomas Drew Fisher, assignor to Texas Instruments, Incorporated
13 January 1998 (Class 379/410); filed 7 April 1995

This patent addresses a variety of problems concerned with the capabililty of a recognition system to allow a user to interrupt a voice prompt, often referred to as barge-in. The design of a barge-in system can be especially difficult when the system involves line echoes or transmission delays between the user and the system. Echo cancellation and controllable delay elements are combined to minimize transmission effects on barge-in operation.—DLR

5,710,866

43.72.Ne SYSTEM AND METHOD FOR SPEECH RECOGNITION USING DYNAMICALLY ADJUSTED CONFIDENCE MEASURE

Finelo A. Alleva *et al.*, assignors to Microsoft Corporation
20 January 1998 (Class 395/2.65); filed 26 May 1995

This speech recognition system performs vector quantization of spectra of the input speech frames. A hidden Markov model decoder is then used with and without linguistic constraints to classify the spectral code sequences. A confidence measure rates the linguistically constrained decoding against the unconstrained decoding and adjusts the decoding score accordingly. Linguistic constraints may represent phoneme, word, or other unit sequences according to a specified grammar.—DLR

5,712,957

43.72.Ne LOCATING AND CORRECTING ERRONEOUSLY RECOGNIZED PORTIONS OF UTTERANCES BY RESCORING BASED ON TWO *n*-BEST LISTS

Alex H. Waibel and Arthur E. McNair, assignors to Carnegie Mellon University
27 January 1998 (Class 395/2.49); filed 8 September 1995

Many current speech recognition systems provide a scored *n*-best list for each recognition attempt. This patent describes a strategy to use *n*-best lists to correct recognition errors. When a low best score occurs, the user is prompted to respeak the incorrect portion of the utterance. As one of several ways of locating the incorrect section, the system creates a grammar for the correction utterance consisting of all possible subsequences of the originally recognized utterance. *N*-best lists of the original and respoken inputs are then processed to locate and correct the original error.—DLR

5,715,367

43.72.Ne APPARATUSES AND METHODS FOR DEVELOPING AND USING MODELS FOR SPEECH RECOGNITION

Laurence S. Gillick and Francesco Scattone, assignors to Dragon Systems, Incorporated
3 February 1998 (Class 395/2.63); filed 23 January 1995

This speech recognition system uses a combination of dynamic time warping, decision tree classification, and phonetic context information to classify input feature vectors into phonetic units. In one version a preliminary decision tree classifies input feature vectors into phonetic groups using

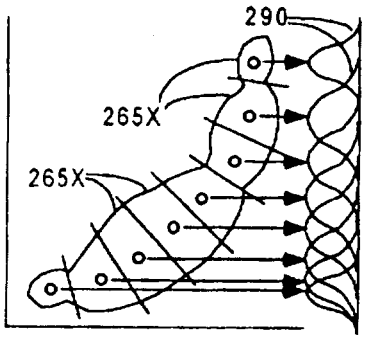

the context of neighboring vectors. The parameter sets are then reduced and then a new decision tree is built. Classifications of the second tree form the acoustic model of each phoneme.—DLR

5,717,826

43.72.Ne UTTERANCE VERIFICATION USING WORD BASED MINIMUM VERIFICATION ERROR TRAINING FOR RECOGNIZING A KEYBOARD STRING

Anand Rangaswamy Setlur *et al.*, assignors to Lucent Technologies, Incorporated
10 February 1998 (Class 395/2.61); filed 11 August 1995

This speech recognizer uses multiple special-purpose hidden Markov model (HMM) decoders to recheck keyword results from the primary HMM system. Detected keyword candidates are verified by the results from a keyword HMM, a misrecognition HMM, and a nonkeyword HMM, which, respectively, test the hypothesis, the null hypothesis, and the alternate hypothesis for each possible keyword.—DLR

5,717,828

43.72.Ne SPEECH RECOGNITION APPARATUS AND METHOD FOR LEARNING

Martin Rothenberg, assignor to Syracuse Language Systems
10 February 1998 (Class 395/2.79); filed 15 March 1995

This language teaching system presents the language learner with features of the language in such a way that specific sets of learner responses are most probable, some of which are correct and some incorrect. The recognizer grammar includes all such possible responses, allowing it to respond appropriately in most situations. When the learner is prompted to speak a foreign language item, the recognizer can spot deficient aspects of the pronunciation and offer specific help to improve that item.—DLR

5,719,996

43.72.Ne SPEECH RECOGNITION IN SELECTIVE CALL SYSTEMS

Lu Chang and Yan-Ming Cheng, assignors to Motorola, Incorporated
17 February 1998 (Class 395/2.65); filed 30 June 1995

This speech recognition system is designed for use as a call processor for accepting messages which are to be relayed to a subscriber's pager unit. In order to implement a hidden Markov model (HMM)-like recognizer with much reduced computational load, the system selects from precomputed sets of probability density functions for the best match to incoming speech.—DLR

5,736,660

43.75.Mn METHOD OF ADJUSTING LENGTH OF DUPLEX SCALE PORTION OF PIANO STRINGS

Daniel T. Frankel, New York, NY
7 April 1998 (Class 84/200); filed 19 June 1996

This patent describes a tool **22** designed to engage frets **16** resting on a piano plate **18** for moving the fret to a new position **16′**, in order to change the length of the duplex portion **10** of a piano string **11** between bridge pin **12** and the apex **14** of fret **16**. The purpose for moving the fret while the string is under tension is to adjust the modes of vibration of string segment **10** to frequencies that will enhance, through sympathetic vibration, the tone of the main tuned portion of the strings on the other side of the bridge.—DWM

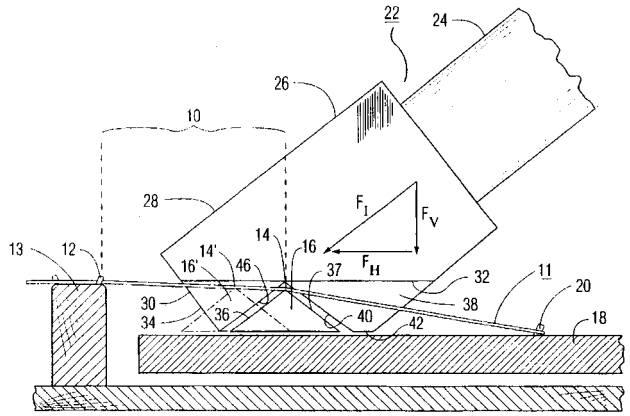

5,739,446

43.75.Pq HARMONICA AND METHOD OF PLAYING SAME

Henry T. Bahnson, Pittsburgh, PA
14 April 1998 (Class 84/377); filed 21 May 1992

The art of playing a 10-hole diatonic harmonica involves the combination of blowing and sucking modes in which either blow-reeds or draw-reeds are excited. A technique of overblowing or overdrawing enables players of great skill to produce additional members of the scale without having to resort to a chromatic harmonica having more reeds. The diatonic harmonica of this patent includes ''damping means for producing pure overblow and/or overdraw tones and making such tones less difficult to produce.'' One or more slides are used to damp reeds during an overblow or overdraw procedure. For additional details on the ''Acoustical and physical dynamics of the diatonic harmonica'' see Bahnson *et al.*, J. Acoust. Soc. Am. **103**, 2134–2144 (1998).—DWM

5,750,912

43.75.Rs FORMANT CONVERTING APPARATUS MODIFYING SINGING VOICE TO EMULATE MODEL VOICE

Shuichi Matsumoto, assignor to Yamaha Corporation
12 May 1998 (Class 84/609); filed in Japan 18 January 1996

This computer system analyzes the output signal from the microphone responding to a singer's voice, then compares the formant spectrum data to that of a model or reference voice, and automatically adjusts an electronic equalizer to modify the response-frequency characteristic of the sound system according to the detected spectral differences, ''so as to emulate the vocal quality of the model voice.'' Adjustments are made sequentially as the vowels change during singing.—DWM

5,701,897

43.80.Vj ULTRASONIC DIAGNOSIS APPARATUS AND IMAGE DISPLAYING SYSTEM

Akihiro Sano, assignor to Kabushiki Kaisha Toshiba
30 December 1997 (Class 128/661.09); filed in Japan 2 October 1992

This instrument, which is described by 95 figures and 46 columns of text, produces a gray scale *b*-scan image on which a color image of blood flow is superimposed.—RCW

5,704,105

43.80.Vj METHOD OF MANUFACTURING MULTILAYER ARRAY ULTRASONIC TRANSDUCERS

Venkat Subramaniam Venkataramani *et al.*, assignors to General Electric Company
6 January 1998 (Class 29/25.35); filed 4 September 1996

This method of fabricating a 1.5-dimensional or a two-dimensional multilayer transducer array **22** employs dicing saw kerfs **36**, **38**, **40**, **44** to provide acoustic isolation between rows. The kerfs are metalized **74**, **76** to

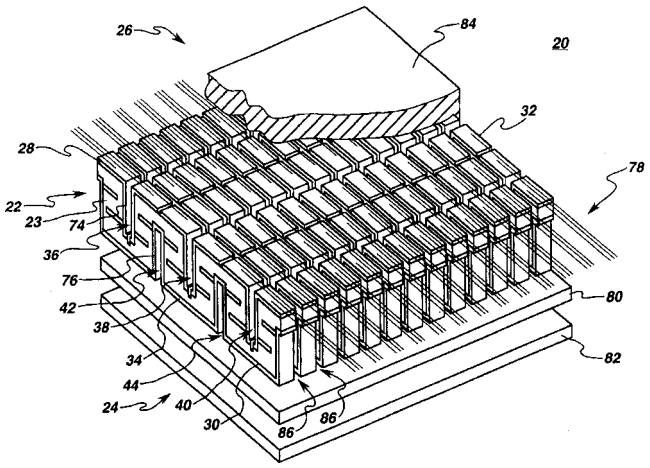

connect surface electrode layers and buried internal electrode layers. The method results in a higher element capacitance than in a corresponding single layer element.—RCW

5,706,816

43.80.Vj IMAGE PROCESSING APPARATUS AND IMAGE PROCESSING METHOD FOR USE IN THE IMAGE PROCESSING APPARATUS

Takashi Mochizuki and Mutsuhiro Akahane, assignors to Aloka Company
13 January 1998 (Class 128/660.07); filed in Japan 17 July 1995

In this method and apparatus, the transducer can be displaced to move the scan plane in a three-dimensional region. Included is a three-dimensional image data generator that determines the brightness of a voxel based on echo signal amplitude in that voxel and a memory to store the brightness data. The apparatus can produce a three-dimensional ultrasonic image in real time.—RCW

5,706,817

43.80.Vj FILTERING METHOD FOR ULTRASONIC COLOR DOPPLER IMAGING SYSTEM

Tai-kyong Song *et al.*, assignors to Medison Company
13 January 1998 (Class 128/661.09); filed in Korea 7 May 1996

This method employs a modified infinite impulse response filter to implement a moving target indicator that suppresses echoes from a stationary background. The filter also suppresses undesired transient signals that appear at the output of a conventional infinite impulse response filter and uses a small order to realize a steep transition between stop and pass bands. These characteristics permit higher frame rates.—RCW

5,715,823

43.80.Vj ULTRASONIC DIAGNOSTIC IMAGING SYSTEM WITH UNIVERSAL ACCESS TO DIAGNOSTIC INFORMATION AND IMAGES

Michael A. Wood *et al.*, assignors to Atlantis Diagnostics International, L.L.C. and Advanced Technology Laboratories, Incorporated
10 February 1998 (Class 128/660.01); filed 25 September 1996

This system can be connected through a communication network that makes ultrasonic images and other information accessible via a conventional personal computer and commercially available software.—RCW

5,724,974

43.80.Vj TWO-DIMENSIONAL ULTRASOUND DISPLAY SYSTEM

Leonard James Goodsell, Jr. *et al.*, assignors to Acuson Corporation
10 March 1998 (Class 128/661.09); filed 22 March 1996

A line of study is defined by two or more icons positioned on a two-dimensional motion image. At each point along the line of study, a velocity profile is displayed. Computations of velocity and spread are made from scan-converted information and user-specified direction angles.—RCW

Modeling nonlinearity in electrostrictive sonar transducers[a]

Craig L. Hom and Natarajan Shankar
Advanced Technology Center, Lockheed Martin Missiles & Space, Palo Alto, California 94304

(Received 23 December 1997; accepted for publication 29 April 1998)

Electrostrictive driver materials with large strain capability hold great promise for the advancement of sonar projector technology. However, the nonlinear induced strain of these materials can create acoustic distortion in transducers through higher-order harmonics. Electrostrictors also possess complicated prestress and temperature dependencies, and an elastic modulus that depends strongly on electric field. This investigation examined these issues with a nonlinear, frequency domain model for a flextensional transducer powered by an electrostrictive stacked actuator. A simple, linear lumped-parameter model of a flextensional shell and its surrounding acoustic medium were combined with a nonlinear model of the electrostrictive driver. This model accounted for the material's nonlinear dependencies and behavior. Predictions of the device's acoustic/electric response during operation compared favorably with experiments performed on a single element flextensional transducer. The model's results showed that proper adjustment of the power supply's parameters minimizes the level of distortion without completely sacrificing the transducer's improved source level. © *1998 Acoustical Society of America.* [S0001-4966(98)03808-9]

PACS numbers: 43.10.Ln, 43.38.Fx, 43.30.Yj [SLE]

INTRODUCTION

A continuing goal of underwater transducer design is to improve acoustic power output while maintaining or reducing size and weight. Since its driver ultimately limits a transducer's performance, devices with new, high strain electrostrictive and magnetostrictive materials have greater potential for meeting this goal than analogous transducers driven by traditional $Pb(Zr,Ti)O_3$ ceramics (PZT).[1–3] One family of electrostrictive relaxor ferroelectrics based on $Pb(Mg_{1/3},Nb_{2/3})O_3$–$PbTiO_3$–$BaTiO_3$ (PMN–PT–BT)[4,5] features high energy densities (6.4 kJ/m^3 at 1 MV/m) and large induced strains ($\sim 800\times 10^{-6}$ strain at 1 MV/m) with low hysteresis (<5% at 1 MV/m and 1 Hz) compared to PZT.

However, electrostrictive PMN–PT–BT materials possess a strong nonlinear induced strain and polarization response as shown in Fig. 1 (the exact composition was $0.97[0.9Pb(Mg_{1/3},Nb_{2/3})O_3$–$0.1PbTiO_3]$–0.03 $BaTiO_3$, and the test was performed at 5 °C and 1 Hz). Typical of both electrostrictive and magnetostrictive materials, this type of nonlinear behavior distorts a transducer's acoustic signal. In this context, distortion means a transducer excited by a single voltage harmonic input generates multiple acoustic harmonics, which are frequency multiples of the input. The higher-order harmonics divert power from the primary signal and complicate signal processing of the return signal, in turn limiting the operational use of the device. Nonlinear transduction modeling of electrostrictive and magnetostrictive devices can assess the distortion effects and offer guidance in tailoring the input signal to reduce distortion.

Sherman and Butler,[6] and Sherman *et al.*[7] studied the problem of harmonic acoustic distortion in nonlinear electrostrictive and magnetostrictive transducers using perturbation methods. They represented the constitutive behavior of the driver as a truncated polynomial expansion in both strain and electric field. For electrostrictors, difficult and extensive measurements of polarization and strain under compressive prestress were required to obtain the coefficients for their expansion. An attractive feature of Sherman and Butler's analysis was the solution of the problem in the frequency domain. This greatly simplified the analytical effort and provided a convenient way of interpreting the results. Their computations predicted the second and third harmonic amplitudes as a function of frequency. However, modeling of an electrostrictive transducer excited near saturation requires more higher-order terms. For this case, the perturbation method becomes tedious to formulate.

The work described in this paper examined the acoustic performance of a nonlinear PMN–PT–BT transducer for a broad range of electric fields up to saturation. A model of a class IV flextensional shell transducer with a PMN–PT–BT driver[2] was developed using the experimentally validated constitutive law of Hom and Shankar[8] for electrostriction. The material parameters for this constitutive law were measured from tests without compressive prestress, in contrast to Sherman and Butler's polynomial expansion. This significantly simplified the experimental requirements for material characterization. The Hom and Shankar constitutive law represents the nonlinear behavior over a full range of electric field up to saturation, and Brown *et al.*[9] have shown that it accurately predicts both the prestress dependency and the electric-field-dependent modulus. For example, they demonstrated that the elastic modulus changed nearly 30% as the electric field varied from 0.0 to 1.0 MV/m. The approach presented in this paper permitted solution of the sonar projector problem in the convenient frequency domain, like Sherman and Butler's perturbation method. However, the method maintained the full nonlinear saturation behavior of the ceramic shown in Fig. 1, and accurately modeled the prestress behavior and field-dependent modulus.

[a]Selected research articles'' are ones chosen occasionally by the Editor-in-Chief that are judged (a) to have a subject of wide acoustical interest, and (b) to be written for understanding by broad acoustical readership.

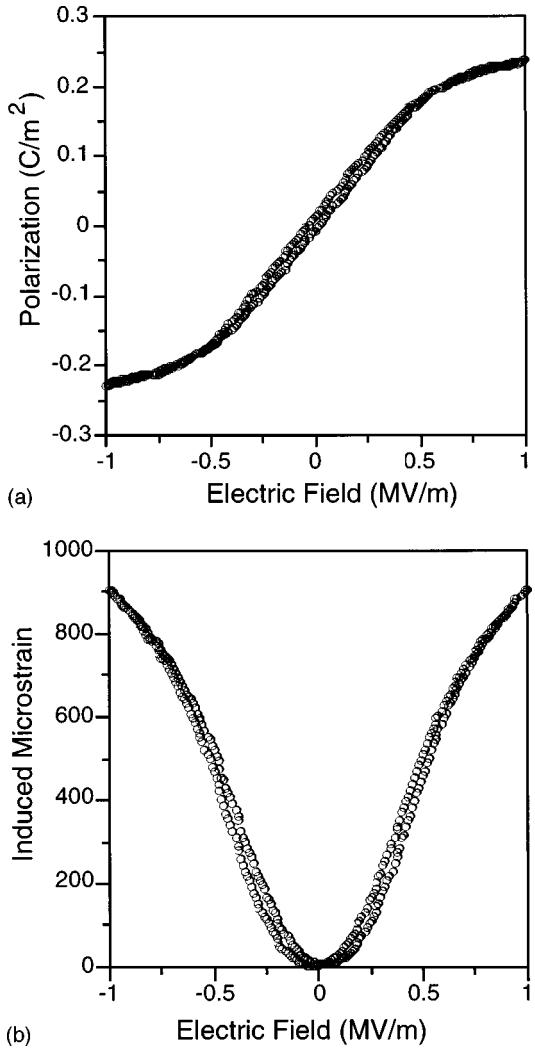

FIG. 1. (a) Induced polarization and (b) strain response of a PMN–PT–BT electrostrictor to a 1-MV/m electric field at 1 Hz and 5 °C (exact chemical formula provided in text). Data are displayed for one complete cycle.

I. NONLINEAR TRANSDUCER MODEL

Figure 2 shows the general layout of the class IV flextensional transducer modeled in this study. The transducer element consisted of two subelements, each containing an oval shell, a PMN–PT–BT ceramic driver, and two alumina/silica shims. End caps and tie rods fasten the two subelements in tandem, and rubber O-rings sealed the joints between the caps and the shells. The subelements were electrically staved together to operate simultaneously in phase. The electrostrictive ceramic driver was a stack of PMN–PT–BT plates sandwiched between alternating electrodes. Shims or end shanks placed between the shell and the stack provided a prestressed fit, which kept the stack in place during operation. In this design, the stack acted as an electric motor, while the shell's symmetric bending motion amplified its velocity output.

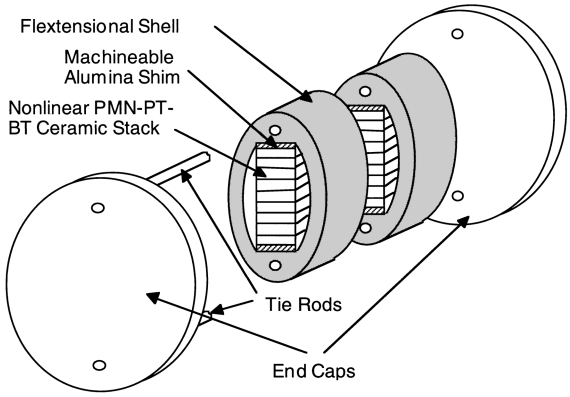

FIG. 2. Exploded view of a class-IV flextensional transducer with a nonlinear electrostrictive driver.

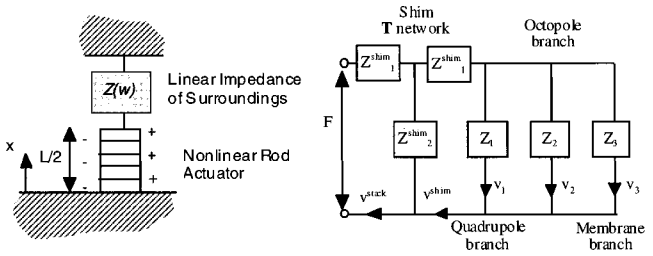

FIG. 3. Model of the flextensional transducer: (a) the ceramic driver as a nonlinear rod actuator constrained by a surrounding linear impedance, and (b) a lumped parameter model of the shim, shell, and acoustic medium.

The model broke the transducer into two parts: the nonlinear electrostrictive stack; and the surrounding linear shell, shims, and acoustic medium. The end caps, tie rods, and seals were not modeled. Nonlinear elastic behavior due to large deformation in the joints and other components was also ignored. Since the subelements operated in synchronization, the model examined a single shell/actuator assembly with twice the actual length.

A. The ceramic rod

The ceramic PMN–PT–BT stack consisted of N plates, each L/N thick with cross-sectional area A. The stack had a total length of L. Our analysis treated the driver as a nonlinear rod actuator constrained with the linear, frequency-dependent impedance of its surroundings. Figure 3(a) shows a schematic of the rod model and the external impedance. The axial coordinate x for the rod is also depicted in the figure. Due to symmetry of displacement relative to the middle of the stack, the rod was fixed at its base ($x=0$), and its length was $L/2$.

The goal of the rod model was to compute the velocity spectrum and static displacement for a given voltage. The force boundary condition at the end of the rod required

$$AT(L/2,t) = -K(C_0+\Delta) - \int_{-\infty}^{\infty} Z(\omega) V^{\text{stack}}(\omega) e^{i\omega t}\, d\omega. \tag{1}$$

Here, $T(x,t)$ is the axial stress in the rod, K and Z represent the surrounding structure's static stiffness and complex impedance, respectively, t is time, ω is frequency, V^{stack} is the complex Fourier transform of the velocity of the rod's end, $v^{\text{stack}}(t)$, and C_0 is the static displacement of the rod's end. Δ represents the mismatch between the stack and the shell created by alumina/silica shims. While this mismatch maintained a secure fit between the stack and the shell, it also prestressed the ceramic into compression. Δ diminished

slightly when submersed in water, since the external water pressure opened the shell with increasing depth. Appendix A describes how the mismatch was computed from finite-element analysis of the shell. Equation (1) shows that the nonlinear force generated by the actuator (the equation's left side) balanced the linear reaction of the surrounding medium (the equation's right side).

The constitutive response of the ceramic and the applied voltage determined the stress T. The ceramic's electromechanical behavior was modeled with the constitutive law of Hom and Shankar.[8] The one-dimensional version of this law consists of the coupled mechanical and electrical equations,

$$S(x,t)=s_{33}T(x,t)+Q_{33}P(x,t)^2 \tag{2}$$

and

$$E(x,t)=-2Q_{33}P(x,t)T(x,t)+\frac{1}{k}\operatorname{arctanh}\left(\frac{P(x,t)}{P_s}\right). \tag{3}$$

S, P, and E are the total strain, the polarization, and the electric field in the longitudinal direction, respectively. The material parameters Q_{33}, P_s, and k were measured experimentally from electrical tests without prestress. Q_{33} is the longitudinal electrostrictive coefficient, P_s is the saturation polarization, and k is a new material parameter introduced by Hom and Shankar. s_{33} represents the closed-circuit elastic compliance measured from a stress–strain test without applied field. As mentioned earlier, Brown *et al.*[9] showed that this model accurately predicts the drop in induced polarization and strain due to prestress effects and simulates the field-dependent elastic modulus.

The voltage applied to the positive electrodes controlled the electric field in the ceramic. The voltage was dc-biased, so the device oscillated on one wing of the strain–electric field curve shown in Fig. 1. This situation approximates linear behavior for a small ac voltage signal. In our case, the ac voltage was a single harmonic of arbitrary amplitude. The total voltage difference $\Delta\phi$ between alternating electrodes was

$$\Delta\phi(t)=V_0+\mathrm{Re}[Ve^{i\omega_0 t}], \tag{4}$$

where V_0 is the dc voltage, V is the complex ac voltage amplitude, and ω_0 is the frequency of the voltage source. The dielectric loss ($\tan\delta$) was modeled as a linear electric resistor in parallel with the actuator.

B. The surrounding medium

The impedance and stiffness of the shims, the flextensional shell, and the acoustic medium constrained the rod in Eq. (1). $Z(\omega)$ and K were computed using finite-element analysis and modal summation techniques. The analysis includes the response of the shell's quadrupole, octopole, and membrane modes. The result equaled the impedance of the lumped parameter system shown in Fig. 3(b), which was similar to the model developed by Brigham[10,11] to approximate his analytical shell solution to the class IV flextensional problem.[12] Appendix A describes the method used to obtain the total impedance of the surroundings and derives the impedance for each element in the lumped circuit shown in Fig. 3(b).

C. The acoustic response

After computing the rod's velocity spectrum, the transducer's underwater acoustic performance in terms of source level (SL) was predicted. The acoustical model treated the transducer as a radiating sphere of equivalent surface area. The shell's average velocity at the surface, $\langle v^{\mathrm{shell}}(\omega)\rangle$, was computed from the rod's velocity using the lumped parameter model in Fig. 3(b) and modal summation techniques. Appendix B describes the details of the computation. Both $\langle v^{\mathrm{shell}}(\omega)\rangle$ and the resulting pressure field consisted of several harmonics. Each pressure field harmonic was computed from its corresponding shell velocity harmonic by assuming spherical radiation in the water. Individual SLs for each harmonic were calculated from the predicted pressure harmonic at a distance of 1 m from source.

II. SOLUTION IN THE FREQUENCY DOMAIN

This section describes the solution of the electrostrictive transducer problem used to compute the rod's velocity spectrum. Once the rod's velocity was known, the transducer velocity spectrum and SL were calculated using the methods described in the previous section.

First, the polarization and stress in the stack were determined from the displacement and voltage. The standard definitions,

$$S=\frac{\partial u}{\partial x}\ \text{ and }\ E=-\frac{\partial\phi}{\partial x}, \tag{5}$$

related the displacement and voltage in the stack to its strain and electric field. Using Eq. (5), the electrical constitutive Eq. (3) became

$$-\frac{\partial\phi}{\partial x}=-2\frac{Q_{33}}{s_{33}}P\left(\frac{\partial u}{\partial x}-Q_{33}P^2\right)+\frac{1}{k}\operatorname{arctanh}\left(\frac{P}{P_s}\right). \tag{6}$$

For a multilayered stack, Eq. (6) was approximated by

$$\frac{N(V_0+\mathrm{Re}[Ve^{i\omega t}])}{L}=-2\frac{Q_{33}}{s_{33}}P\left(\frac{2u(L/2,t)}{L}-Q_{33}P^2\right)+\frac{1}{k}\left(\frac{P}{P_s}\right). \tag{7}$$

The left-hand side of this equation was the device's average electric field, and $2u(L/2,t)/L$ was the device's average strain. Given the end displacement at a specific time, the polarization for that time was computed from Eq. (7) by numerical iteration. The corresponding stress state was then calculated from Eq. (2).

The momentum balance in the rod required that

$$\frac{\partial T}{\partial x}=\rho\frac{\partial^2 u}{\partial t^2}, \tag{8}$$

where ρ represents the density of the electrostrictor. Since most electrostrictive ceramics have dielectric constants

above 10 000, Gauss's law for electrostatics was approximated by

$$\frac{\partial P}{\partial x} \approx \frac{\partial D}{\partial x} = 0, \tag{9}$$

inside each ceramic layer, where D is the electric displacement. From Eq. (9), P was effectively independent of x, except for the jump across the electrodes. Using Eqs. (2), (5), and (9), Eq. (8) became

$$\frac{\partial^2 u}{\partial x^2} = s_{33}\rho \frac{\partial^2 u}{\partial t^2}. \tag{10}$$

Assuming subharmonics did not exist, u had the same period, $2\pi/\omega_0$, as the voltage source. Then, the solution of Eq. (10) is the complex Fourier series,

$$u(x,t) = C_0 \frac{2x}{L} + \sum_{m=1}^{M} \frac{\sin(2m\bar{\omega}x/L)}{\sin(m\bar{\omega})} C_m e^{im\omega_0 t} + \sum_{m=-M}^{-1} \frac{\sin(2m\bar{\omega}x/L)}{\sin(m\bar{\omega})} C_m e^{im\omega_0 t}, \tag{11}$$

for a rod fixed at its base. $\bar{\omega}$ is a normalized frequency defined by

$$\bar{\omega}^2 = \frac{\rho s_{33} \omega_0^2 L^2}{4}. \tag{12}$$

C_m represents the complex Fourier coefficient of the mth displacement harmonic at the actuator's end. C_{-m} is the complex conjugate of C_m, so u in Eq. (11) was real. The two series in Eq. (11) were truncated after the $\pm M$th term. The corresponding strain at the rod's end was

$$S(L/2,t) = \frac{2C_0}{L} + \sum_{m=1}^{M} \frac{2m\bar{\omega}}{L} \cot(m\bar{\omega}) C_m e^{im\omega_0 t} + \sum_{m=-M}^{-1} \frac{2m\bar{\omega}}{L} \cot(m\bar{\omega}) C_m e^{im\omega_0 t}, \tag{13}$$

and the velocity of the stack's end was

$$v^{\text{stack}}(t) = \sum_{m=-M}^{M} im\omega_0 C_m e^{im\omega_0 t}. \tag{14}$$

Using Eq. (14), Eq. (1) was rewritten as

$$AT(L/2,t) - K(C_0 + \Delta) + \sum_{m=-M}^{M} Z(m\omega_0) im\omega_0 C_m e^{im\omega_0 t} = 0. \tag{15}$$

Fourier transforms of the right side of Eq. (15) are also zero, so

$$h_0 \equiv A \int_{-\pi/\omega_0}^{\pi/\omega_0} T(L/2,t)\,dt + \frac{2\pi}{\omega_0} K(C_0 + \Delta) = 0$$

and

$$h_m \equiv A \int_{-\pi/\omega_0}^{\pi/\omega_0} T(L/2,t) e^{-m\omega_0 t}\,dt + 2\pi Z(m\omega_0) m C_m i = 0, \quad \text{for } m > 0. \tag{16}$$

TABLE I. Material parameters for PMN–PT–BT at 5 °C.[a]

P_s (C/m)	k (m/MV)	Q_{33} (m^4/C^2)	$1/s_{33}$ (GPa)	$\tan\delta$	ρ (kg/m^3)
0.254	1.62	1.62×10^{-2}	104	0.035	7900

[a]Material composition given in the text.

Equation (16) represents a system of $2M+1$ nonlinear equations ($h_0 = 0$, Re$[h_m]=0$, and Im$[h_m]=0$) that was solved by Newton iteration for $2M+1$ variables (C_0, Re$[C_m]$ and Im$[C_m]$). h_m were the residuals for that procedure, and the derivatives of h_m with respect to C_m formed the Jacobian. The iteration procedure began by making an initial estimate for C_m. The polarization, strain, and stress were computed in succession from Eqs. (7), (13), and (2). Then, the stress and C_m were used to determine the residuals and Jacobian. Corrections to the displacement coefficients were calculated, and the initial estimate was updated. The iteration procedure continued until the correction to the device's average strain was less than 1.0×10^{-7} (giving 1/10th of a microstrain accuracy). Once C_m was determined, the rod's velocity was computed from Eq. (14). For the computations presented in this paper, $M=8$ was sufficient.

III. NUMERICAL RESULTS

A C++ computer program was written on a desktop computer to implement the electrostrictive flextensional sonar model described in the previous sections and the appendices. Using this program, calculations were performed to model a real transducer built by Lockheed Martin Laboratories, Baltimore, MD and tested by the Naval Undersea Warfare Center, Newport, RI. This flextentional device was designed to excite the shell's quadrupole mode at 4.5 kHz, underwater.

The ceramic stack contained ten PMN–PT–BT plates each 5.47 thick, 37.5 long, and 8.92 mm wide. The plates were stacked in the thickness direction. The alumina/silica shims had the same length and width as the electrostrictively active plates, but the thickness L^{shim} was 2.79 mm. Machining of the final stack assembly left an initial 0.152 mm mismatch, Δ_0, between the stack and the shell. The elliptical shell was constructed of aluminum with minor and major radii, a and b, of 17.1 and 39.4 mm, respectively. The shell had a length of 39.6 mm and a wall thickness of 4.3 mm. Since there were two elements, the effective length, W, of the shells was 79.2 mm.

The analysis consisted of a series of computations over a broad range of frequencies (3.0 to 8.0 kHz), where each calculation examined one specific ω_0. At that frequency, the SL for each harmonic ($m\omega_0$) and the electrical response were computed. The material properties used for PMN–PT–BT (exact composition was

TABLE II. Material parameters for flextensional components.

Material	Modulus $1/s$ (GPa)	Poisson's ratio	Density ρ (kg/m^3)
Aluminum	71.0	0.33	2700
Alumina/silica	64.1	⋯	2520

$0.97[0.9Pb(Mg_{1/3},Nb_{2/3})O_3-0.1PbTiO_3]-0.03\ BaTiO_3$) ceramic are shown in Table I, and correspond to data measured at 5 °C (the temperature of the experimental test data on this transducer). Table II shows the properties of the alumina/silica shim and aluminum shell materials. The speed of sound and density of the water medium for the calculations were 1500 m/s and 1026 kg/m^3, respectively. The depth of the transducer was 93 m for both the test and the simulation. The computations were first performed for specific ac voltages, V, and dc bias voltages, V_0, in order to compare with experimental measurements. Then, a parameter study was conducted to map distortion as a function of V, V_0, and ω_0.

A. Electrical response

The simulation predicted the transducer's electrical response using the electrostrictive model. Current I was directly computed from the polarization in the device and the electrostrictor's dielectric loss factor. I was the sum of a capacitive current, I_C, and resistive current due to dielectric losses, I_R. The loss tangent, tan δ, was defined as the ratio of resistive and capacitive current amplitudes. The capacitive current was

$$I_C(t)=\frac{\partial q}{\partial t}=\sum_{m=-M}^{M} ANm\omega_0 iP_m e^{im\omega_0 t}, \tag{17}$$

where q is the charge in the device, and P_m represents the complex Fourier coefficients of the computed polarization $P(t)$. I_C also included a resistance term due to the mechanical impedance of the acoustical medium. The resistive current due to dielectric loss was in phase with the applied voltage, so

$$I_R(t)=\sum_{m=-M}^{M} \frac{V}{|V|} ANm\omega_0|P_m|\tan\ \delta e^{im\omega_0 t}. \tag{18}$$

Combining the current of the two branches yielded

$$\begin{aligned} I(t)&=\sum_{m=1}^{M} \mathrm{Re}[i_m e^{im\omega_0 t}] \\ &=\sum_{m=1}^{M} 2\,\mathrm{Re}\Bigg[ANm\omega_0 iP_m \\ &\quad+\frac{V}{|V|} ANm\omega_0|P_m|\tan\ \delta e^{im\omega_0 t}\Bigg]. \end{aligned} \tag{19}$$

The magnitude and phase of the first current harmonic (I_1) versus frequency are plotted in Fig. 4 for $V=2.0\ \mathrm{kV_{RMS}}$ and $V_0=3.85$ kV. As expected, the result showed that the impedance to the electric load was almost purely reactive. The figure also plots the corresponding experimentally measured data for the first harmonic. The result demonstrates that reasonable agreement was obtained between the model and the experiment.

The electrical admittance characterizes a transducer's electrical response; however, by definition, admittance only applies to linear electrical systems. For the nonlinear electrostrictive problem, the electrical result was linearized by using the first harmonic of the current. Admittance was defined as

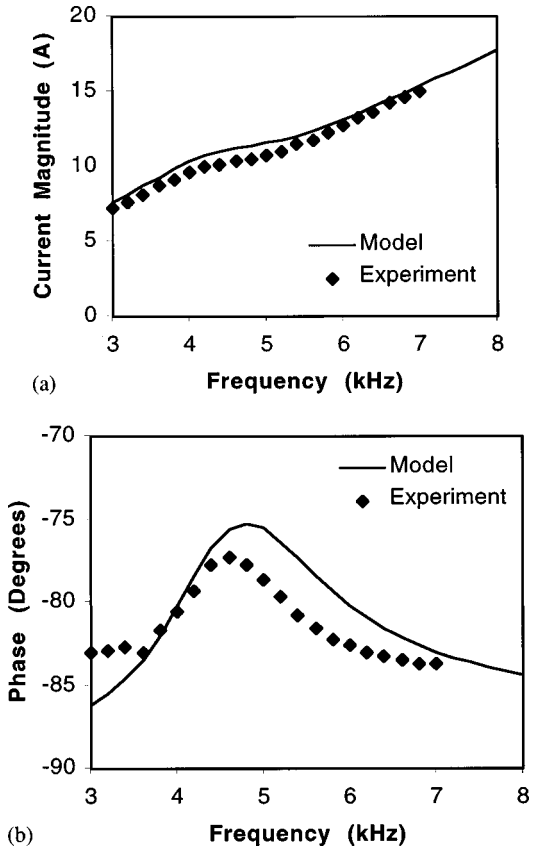

FIG. 4. (a) Magnitude and (b) phase angle of the transducer's first current harmonic ($m=1$) for $V=2.0\ \mathrm{kV_{RMS}}$ and $V_0=3.85$ kV. The solid line is the result predicted by the model, while the discrete points represent measured data.

$$\frac{I_1}{V}=G+iB, \tag{20}$$

where G is the conductance and B is the susceptance. Figure 5 shows the components of admittance as a function of frequency for $V=2.0\ \mathrm{kV_{RMS}}$ and $V_0=3.85$ kV. The corresponding experimental values, also plotted in the figure, agreed well with the model.

The simulation also computed the electrical power required by the device. The average electrical power input to the device was

$$\langle W\rangle=\frac{1}{T}\int_0^T \phi I\ dt, \tag{21}$$

for the period $T=2\pi/\omega_0$. Figure 6 plots the electric power as a function of frequency for $V=2.0\ \mathrm{kV_{RMS}}$ and $V_0=3.85$ kV. It is important to note that the power requirements for this device were nearly ten times that required for a similar PZT device run with the same ac drive voltage. The plot shows that the model overpredicted the peak power of the device at resonance. This result was consistent with the higher predicted conductance shown in Fig. 5, and the SL predictions presented in the next subsection. This inaccuracy was due to the crude equivalent sphere approximation used

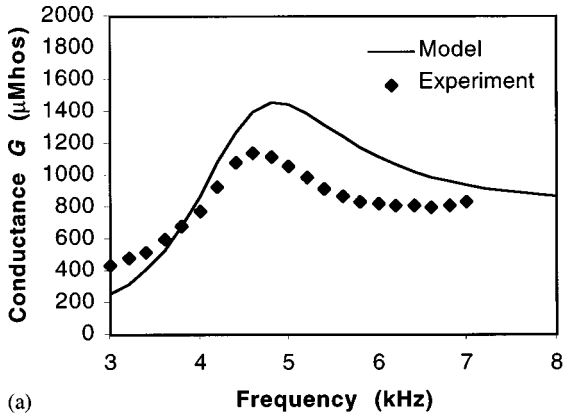

(a)

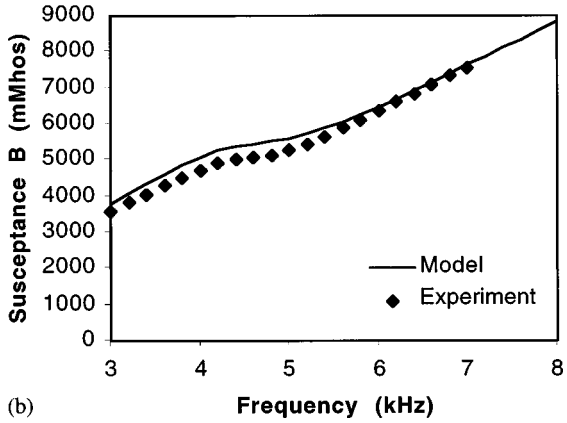

(b)

FIG. 5. The transducer's (a) conductance and (b) susceptance for $V=2.0\ \mathrm{kV_{RMS}}$ and $V_0=3.85$ kV. The solid line is the result predicted by the model, while the discrete points represent measured data.

to determine the acoustic impedance constraining the flextensional shell. This approximation overestimated the impedance resulting in the higher predicted conductance.

Finally, the model's electrical admittance computations were also used to calculate the device's in-air resonance. This prediction was performed to validate the linear lumped parameter model used for the shell. For $V_0=2.6$ kV dc with a weak field ac signal of $1.0\ \mathrm{V_{RMS}}$, the model predicts a 8.7 kHz out-of-water resonance of the flextensional's quadrupole

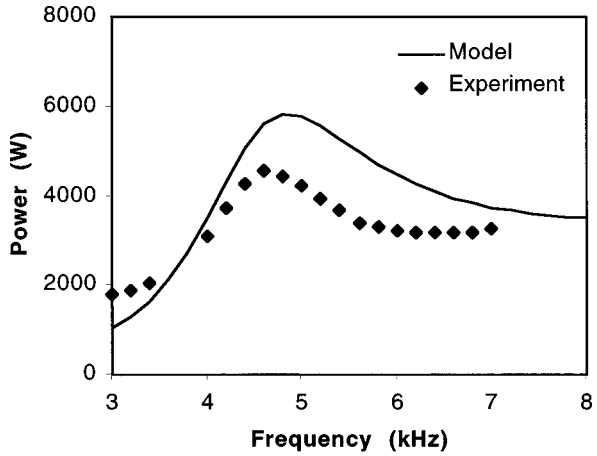

FIG. 6. A plot of the electric power for the transducer ($V=2.0\ \mathrm{kV_{RMS}}$ and $V_0=3.85$ kV). The solid line is the result predicted by the model, while the discrete points represent measured data.

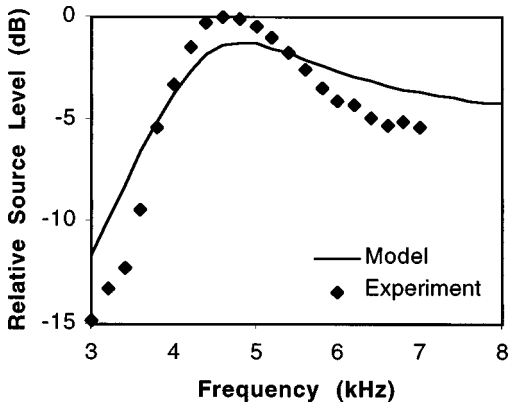

FIG. 7. SL plot of the first harmonic ($m=1$) for the transducer with $V=2.0\ \mathrm{kV_{RMS}}$ and $V_0=3.85$ kV. The solid line is the result predicted by the model, while the discrete points represent measured data.

mode compared to the 8.1 kHz resonance experimentally measured on the actual device.

B. Acoustic response

Figure 7 shows a plot of the SL for the first harmonic ($m=1$) of the transducer. This harmonic has the same frequency as the voltage source. A peak in primary harmonic's SL occurred at 4.8 kHz, when it excited the quadrupole mode of the shell. The figure also shows the performance measured by the Naval Undersea Warfare Center, New London, for the actual device under the same operating conditions. Comparison of the two results indicates reasonable agreement; the experiments and model were within 4 dB over the frequency range studied. A measured resonance occurred at 4.6 kHz, and the SL of the experiment at this frequency was 1.4 dB greater than the model. However, the predicted quality factor Q of the system was 1.3, which was significantly lower than the 2.7 measured in the experiment. The lower predicted peak and the shallow roll-off of SL at frequencies above resonance caused this disagreement.

The simulation also demonstrated that prestress has a weak effect on the primary harmonic's SL. From Eq. (1), the static prestress at the rod's end was

$$T_0=-\frac{K}{A}(C_0+\Delta). \tag{22}$$

For $\Delta_0=0.076$, 0.152, and 0.254 mm, the predicted prestresses for the case, $V=2.0\ \mathrm{kV_{RMS}}$ and $V_0=3.85$ kV, were 10.0, 22.7, and 39.6 MPa, respectively. However, the SLs of the primary harmonic for these three cases were within 0.5 dB of each other.

Acoustic distortion in the transducer occurred when the SL of the higher-order harmonics became significant relative to the primary harmonic. Figure 8 shows a waterfall plot of each harmonic's SL as a function of frequency for $2.0\ \mathrm{kV_{RMS}}$ and $V_0=3.85$ kV. The SLs provided in the figure are relative to the peak value of the primary harmonic. The results indicated that the distortion was at a minimum when the primary harmonic excited the shell's quadrupole mode into resonance. The next largest harmonic ($m=2$) was 24 dB below the primary harmonic at $\omega_0=4.6$ kHz. The distortion in-

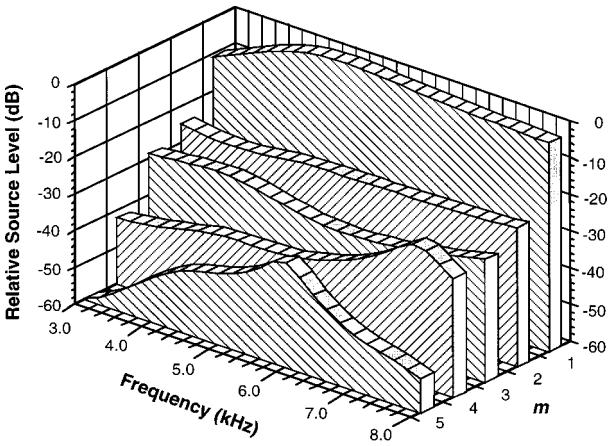

FIG. 8. Waterfall plot of each harmonic's relative SL as a function of frequency for the transducer with $V=2.0\ \mathrm{kV_{RMS}}$ and $V_0=3.85$ kV. The SLs are referenced to the peak SL of the primary harmonic.

creased above ($\omega_0 \sim 8.0$ kHz) and below ($\omega_0 \sim 3.0$ kHz) the primary harmonic's resonance frequency. Since the higher harmonics were frequency multiples of ω_0, they also excited the higher frequency stack resonance mode, and the shell's octopole and membrane modes. These resonances appeared as peaks in the 4th and 5th harmonics (Fig. 8), and they increased the level of distortion.

Figure 9 shows the model predictions and experimentally measured SL values of the first three higher-order harmonics ($m=2$, 3, and 4) versus frequency for $V_0=4.2$ kV with $V=1.5\ \mathrm{kV_{RMS}}$. The SLs were referenced to the SL of the primary harmonic ($m=1$). While the experiments showed the same general trend, the observed distortion differed from the model, particularly above resonance. Figure 10 displays the SL values for the higher harmonics with $2.0\ \mathrm{kV_{RMS}}$ and $V_0=4.2$ kV. As expected, the results showed that both the distortion predicted by the model and measured in the experiments were higher for the $2.0\ \mathrm{kV_{RMS}}$ ac signal. The figure also indicates that the model captured the general trend measured in the experiments.

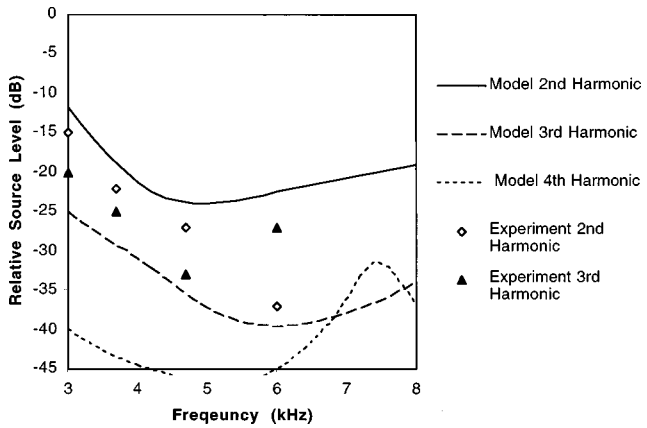

FIG. 9. Predicted SL of the higher harmonics relative to the primary harmonic compared to the experimentally measured values for $V=1.5\ \mathrm{kV_{RMS}}$ and $V_0=4.2$ kV.

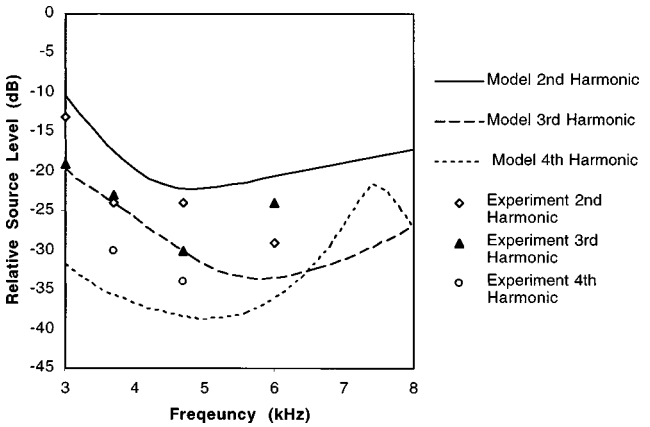

FIG. 10. Predicted SL of the higher harmonics relative to the primary harmonic compared to the experimentally measured values for $V=2.0\ \mathrm{kV_{RMS}}$ and $V_0=4.2$ kV.

C. Distortion maps

Parametric studies using the nonlinear model were also performed to determine the effect of dc bias voltage and ac voltage on the distortion. In this study, distortion was defined in terms of the acoustic pressure field as

$$\text{distortion}=\sqrt{\sum_{m=2}^{M} p_m^2}/p_1, \tag{23}$$

where p_m represents the Fourier components of the far-field water pressure. Physically, this distortion was the magnitude of the higher harmonic pressures relative to the primary pressure source.

Figure 11 is a contour plot of distortion in frequency-dc voltage space for a fixed ac voltage of $2.0\ \mathrm{kV_{RMS}}$. The plot's vertical dimension represents increasing or decreasing the bias voltage. The plot demonstrates that an optimum dc voltage of 3.4 kV existed that minimized distortion. This result quantified an intuitive assessment of the strain versus field curve (Fig. 1): if the bias was set too high, nonlinearity oc-

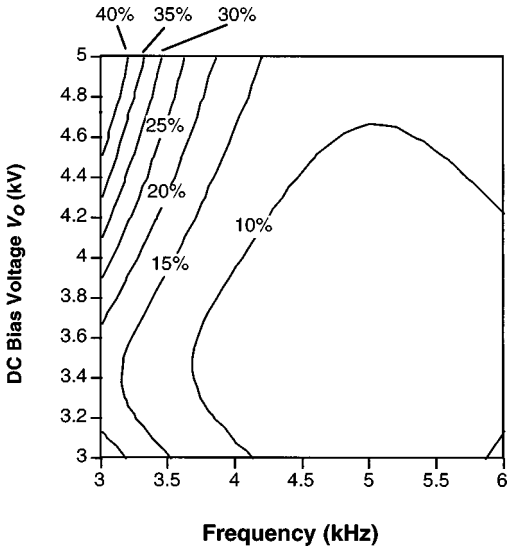

FIG. 11. Contour plot of the distortion level in frequency-dc voltage space for a fixed ac voltage of $2.0\ \mathrm{kV_{RMS}}$ and an initial mismatch Δ_0 of 0.152 mm. The plot gives a visual indication of the optimum dc bias voltage.

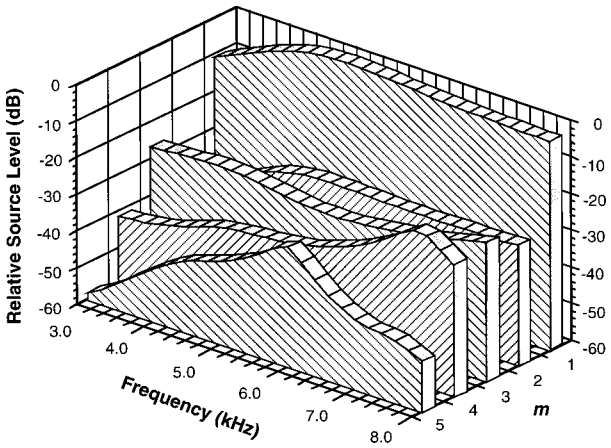

FIG. 12. Waterfall plot of each harmonic's relative SL as a function of frequency for the transducer at the optimum bias point ($V=2.0\ \mathrm{kV_{RMS}}$ and $V_0=3.4$ kV). The SLs are referenced to the peak SL of the primary harmonic. The result shows that distortion was minimized when the second harmonic ($m=2$) was lower than the third and fourth harmonics at $\omega_0=3$ kHz.

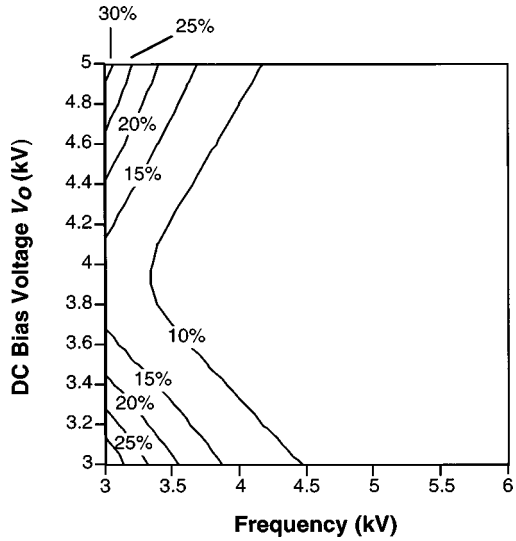

FIG. 13. Contour plot of the distortion level in frequency-dc voltage space for a fixed ac voltage of 2.0 $\mathrm{kV_{RMS}}$ and an initial mismatch Δ_0 of 0.254 mm. Compared with Fig. 12, this result shows the strong effect of prestress on the optimum bias point.

curred from saturation; if the bias was set too low, nonlinearity occurred from the quadratic strain response. The curve appears quasilinear somewhere in between these two extremes, and Fig. 11 quantifies that best bias point. Figure 12, a waterfall plot of the acoustic harmonic's SL with $V_0=3.4$ kV, reveals the nature of this optimization. The figure shows that the SL of the second harmonic drops below the third harmonic at frequencies below resonance ($\omega_0 \sim 3.0$ kHz). Indeed, the optimum bias point could be found experimentally by tuning the dc bias voltage and measuring the second harmonic. The results also showed that distortion limits the bandwidth of the transducer. For example, Fig. 11 shows that the device could not be operated below 3.7 kHz if a system-level requirement of a 10% distortion was imposed.

The optimum dc bias point also depended on the level of prestress. For the nominal case of $\Delta_0=0.152$ mm, the model predicted a 22.7-MPa compressive stress on the device and an optimum dc bias voltage of 3.4 kV. Figure 13 is a contour plot of distortion for a larger shim of 0.254 mm. The figure indicates that the optimum bias voltage for this shim size was 3.9 kV (a 15% increase in voltage). Compared to Fig. 11, the higher prestress has generally reduced the level of distortion. This sensitivity to shim size may explain why the model did not quantitatively agree with the distortion measurements shown in Figs. 9 and 10. The shell and stack were both machined to tolerances of 0.0254 mm. So the actual mismatch is within $\pm 33\%$ of the modeled value, which would make exact distortion predictions difficult for a specific transducer.

Finally, the model computed the distortion's dependence on the ac voltage. Figure 14 is a contour plot of distortion in frequency-ac voltage space for a fixed bias voltage of 3.85 kV. In this case, the plot's vertical dimension represents increasing or decreasing the ac voltage magnitude. The figure clearly shows that increasing the ac voltage increased the level of distortion, so an optimum ac voltage did not exist. The reader should view this plot as the operating envelope for the transducer for a given level of distortion. For example, if the distortion should not exceed 5% for a particular application, the 5% contour defines the maximum ac voltage that can be applied to the device. The maximum voltage in turn defines the maximum SL possible for the fixed distortion level.

IV. CONCLUSIONS

This paper introduces a new transducer model that simulates nonlinear material behavior in electrostrictive ceramics. The model predicts SL and acoustical distortion in the frequency domain as a function of the drive voltage parameters. The results offer guidance selecting the optimum dc bias voltage that minimizes distortion for a given material and transducer configuration. The model also defines the maximum ac voltage that could be applied to the device for a given level of distortion and predicted the resulting SL. This

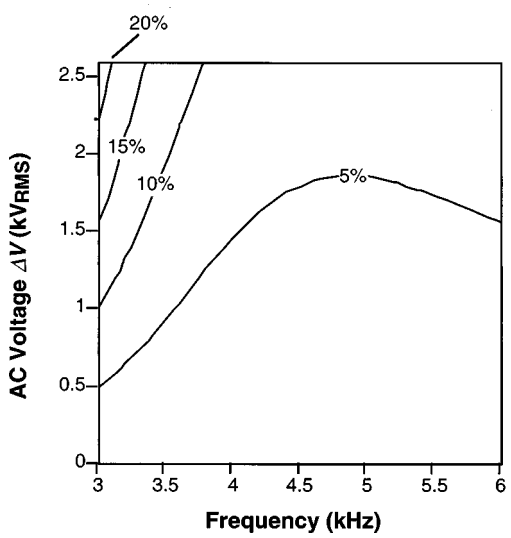

FIG. 14. Contour plot of the distortion level in frequency-ac voltage space for a fixed dc bias of 3.85 kV. This plot defines the operating envelope for a transducer with a fixed distortion requirement.

paper shows that electrostrictive transducers can be designed to minimize the effects of nonlinear material behavior without completely sacrificing the electrostrictor's acoustic power advantage. The results also show that the level of prestress on the electrostrictively active driver does not significantly affect the SL of the transducer's primary harmonic. However, the prestress strongly affects the level of distortion and the optimum dc bias point for the device.

The experimental measurements on the 4.5-kHz transducer generally agreed with the model results; measured and predicted resonances were within 300 Hz. However, the results of the comparison also indicated that the model was overconstrained by the acoustic impedance of the equivalent sphere approximation. The mechanical Q of the transducer was higher than predicted (2.7 vs 1.3), and the electrical conductance was lower than predicted (1150 vs 1400 μs at 4.6 kHz). In addition, the wavelengths of some of the higher harmonics were equivalent or even smaller than the major radius of the shell; the equivalent sphere approximation was invalid for the 4th harmonic and higher. Improved transducer predictions require the use of boundary element methods to model the near-field acoustic radiation. The acoustic impedance would be computed using the normalized velocities of the shell's eigenmodes. This approach is currently being investigated, and the results of an improved model will be reported in the future. The nonlinear electrostrictive model could also be validated using simpler transducer configurations (for example, a Tonpilz projector); however, to the authors' knowledge, no experimental data on electrostrictive nonlinearity in these configurations currently exist.

ACKNOWLEDGMENTS

The authors gratefully acknowledge helpful discussions with Dr. Roger Richards of the Naval Undersea Warfare Center; Mr. Phillip Kuhn, Mr. John Sewell, and Dr. Keith Bridger of Active Signal Technologies; Mr. David Erickson of Lockheed Martin Ocean & Radar Systems; and Dr. Steve Winzer of Lockheed Martin Missiles & Space. The experimental acoustical data presented in the paper were measured by the Naval Undersea Warfare Center, Newport, RI and provided by Dr. Richards. Mr. Steve Brown of Lockheed Martin Laboratories, Baltimore, MD made the experimental measurements depicted in Fig. 1. This work was sponsored under contract by the Office of Naval Research, and monitored by Mr. Richard Campbell of the Program Executive Office for Undersea Warfare.

APPENDIX A: FLEXTENSIONAL SHELL AND RADIATION IMPEDANCE

A lumped parameter approximation of the water-loaded flextensional shell's impedance was computed using the finite-element method and a simple approximation of the acoustic loading. The impedance $Z(\omega)$ computed characterizes the force response to a stack velocity of frequency ω, and was represented as the equivalent circuit shown in Fig. 3(b).

Using the ABAQUS general purpose finite-element program,[13] modal analysis was performed on the unconstrained shell without the stack or surrounding water to compute the impedances Z_1, Z_2, and Z_3. The analysis determined the free shell's natural frequencies (Ω_j) and mode displacements (ϕ_j). The mode displacements were a function of position ζ in the shell, and were normalized by the maximum displacement. Only the symmetric quadrupole mode ($j=1$), the octopole mode ($j=2$), and the membrane mode ($j=3$) were computed. The effective mass per length of shell for a mode was

TABLE AI. Modal finite-element results for the 4.5-kHz flextensional shell.

Mode	$\Omega/2\pi$ (kHz)	m_j (kg/m)	Γ_j	V_j (m)
Quadrupole ($j=1$)	4.66	0.7295	-0.2927	5.923×10^{-2}
Octopole ($j=2$)	23.76	0.8261	-0.2203	2.950×10^{-2}
Membrane ($j=3$)	29.8	1.2203	0.9919	8.466×10^{-2}

$$m_j=\int_{A^{\text{shell}}}\rho^{\text{shell}}\phi_j\cdot\phi_j\,dA, \tag{A1}$$

where A^{shell} represents the cross-sectional area of the shell. The modal participation factor, Γ_j, for the stack force is the displacement of the jth mode (ϕ_j) at the shell–shim point of contact.

Using the modal summation method,[14] the shell's kinematics with the acoustic load was constructed from the eigenmodes of the finite-element analysis. The shell's displacements, **a**, under load were defined in terms of the mode shapes as

$$\mathbf{a}=\sum_{j=1}^{3}\phi_j(\xi)q_j(t). \tag{A2}$$

q_j is the generalized coordinate for the jth mode, and by orthogonality it satisfied the linear vibration equation,

$$\frac{d^2q_j}{dt^2}+\Omega_j^2q_j=\frac{1}{m_j}\left(\frac{2F(t)\Gamma_j}{W}-\int_s p(t,s)\phi_j(s)\cdot\mathbf{n}(s)ds\right), \tag{A3}$$

where S is the arc length of the shell's surface, **n** is the outward normal of the shell surface, and s is the position on the shell surface. F is the force exerted by the stack, and p is the acoustic pressure on the shell. Ω_j is the eigenfrequency of the jth mode. We are interested in the shell's response to a single harmonic, so F, p, and q_j are single harmonic functions of frequency ω with complex amplitudes $\overline{F}$, $\overline{p}$, and $\overline{q_j}$, respectively. Using Eq. (A2), the velocity at the shell–shim interface was

$$v^{\text{shim}}(\omega)=\sum_{j=1}^{3}v_j(\omega)=i\omega\sum_{j=1}^{3}\Gamma_j\overline{q_j}(\omega), \tag{A4}$$

which is depicted in the lumped circuit of Fig. 3(b). v_j represents the velocities of the quadrupole, octopole, and membrane branches. The normal velocity at a point on the shell's surface was given by

$$v^{\text{shell}}(\omega,s)=i\omega\sum_{j=1}^{3}\phi_j(s)\cdot\mathbf{n}(s)\overline{q_j}(\omega). \tag{A5}$$

TABLE AII. K_{ij} for the 4.5-kHz flextensional shell from modal finite-element analysis.

K_{11} (m)	K_{22} (m)	K_{33} (m)	K_{12} (m)	K_{13} (m)	K_{23} (m)
5.668×10^{-2}	6.739×10^{-2}	4.592×10^{-2}	-5.033×10^{-3}	3.339×10^{-2}	1.758×10^{-2}

[a]Definition of K_{ij} given in the text.

The specific acoustic radiation impedance was approximated by an equivalent radiating sphere, so the pressure at the shell's surface was related to the shell velocity by

$$\overline{p}(s)=\frac{Z^{\text{water}}(\omega)}{SW}\,\nu^{\text{shell}}(\omega,s), \tag{A6}$$

where Z^{water} is the radiation impedance of a spherical source with the same surface area as the shell, SW. Replacing Eqs. (A5) and (A6) with Eq. (A3), yielded

$$-\omega^2\overline{q_j}(\omega)+\Omega_j^2\overline{q_j}(\omega)$$
$$=\frac{1}{m_j}\left(\frac{2\overline{F}(\omega)\Gamma_j}{W}-\frac{i\omega Z^{\text{water}}(\omega)}{SW}\sum_{\kappa=1}^{3}\overline{q_k}(\omega)K_{jk}\right), \tag{A7}$$

where

$$K_{jk}=\int_s \phi_k(s)\cdot\mathbf{n}(s)\,\phi_j(s)\cdot\mathbf{n}(s)\,ds. \tag{A8}$$

Equation (A7) represents a system of three linear algebraic equations, which determined the generalized coordinates in terms of the stack force $(\overline{q_j}/\overline{F})$. Solving this system and using Eq. (A4), the velocity at the point of contact with the shim was

$$v^{\text{shim}}(\omega)=\sum_{j=1}^{3} Y_j(\omega)\overline{F}(\omega)=\frac{\overline{F}(\omega)}{Z^{\text{shell}}(\omega)}, \tag{A9}$$

where the mechanical admittance Y_j for the jth mode was defined as

$$Y_j=i\omega\Gamma_j\frac{\overline{q_j}(\omega)}{\overline{F}(\omega)}. \tag{A10}$$

The inverses of these admittances were the impedances Z_1, Z_2, and Z_3 shown in Fig. 3. $Z^{\text{shell}}(\omega)$ was the total mechanical impedance of the water-loaded shell, which resisted the velocity of the shim. The results of the finite-element modal analysis are listed in Tables AI and AII for the 4.5-kHz shell described in Sec. III. The material properties for the shell's aluminum are given in Table II.

The impedance of the shim was modeled as the **T** circuit[15] depicted in Fig. 3(b), where the impedance of the elements was

$$Z^{\text{shim}}(\omega)=\frac{m^{\text{shim}}\omega i}{2}$$

and (A11)

$$Z_2^{\text{shim}}(\omega)=-\frac{K^{\text{shim}}\omega i}{2}.$$

The mass and stiffness of the shim were

$$m^{\text{shim}}=\rho^{\text{shim}}AL^{\text{shim}}$$

and (A12)

$$K^{\text{shim}}=\frac{A}{s^{\text{shim}}L^{\text{shim}}},$$

respectively. ρ^{shim}, s^{shim} are the shim's density and compliance, and are recorded in Table II. Solving the lumped circuit, total impedance seen by the stack was

$$Z(\omega)=Z_1^{\text{shim}}(\omega)+\frac{Z_2^{\text{shim}}(\omega)(Z_1^{\text{shim}}(\omega)+Z^{\text{shell}}(\omega))}{Z_1^{\text{shim}}(\omega)+Z_2^{\text{shim}}(\omega)+Z^{\text{shell}}(\omega)}, \tag{A13}$$

which was used in the force boundary condition of Eq. (1).

The real static stiffness K seen by the stack was obtained in a similar manner. The result was

$$K=\frac{K^{\text{shim}}K^{\text{shell}}}{K^{\text{shim}}+K^{\text{shell}}}, \tag{A14}$$

where

$$\frac{1}{K^{\text{shell}}}=\sum_{j=1}^{3}\frac{2\Gamma_j^2}{m_jW\Omega_j^2}. \tag{A15}$$

Equation (A14) was also used in the force boundary condition of Eq. (1).

The finite-element results also determined the mismatch between the shell/shims and the electroactive stack in Eq. (1). By design, an initial mismatch of Δ^o existed after transducer assembly. However, the actual mismatch decreased when the device was submerged in water, and the hydrostatic pressure, p^o, opened the shell. Using modal superposition for this static case, the shell opened by

$$u=-p^o\sum_{j=1}^{3}\frac{\Gamma_jV_j}{m_j\Omega_j^2} \tag{A16}$$

at the shell to shim interface. V_j was defined as

$$V_j=\int_s\phi(s)\cdot\mathbf{n}(s)\,ds. \tag{A17}$$

Ignoring the deformation of the shim, the actual mismatch was approximately

$$\Delta=\Delta^o+p^o\sum_{j=1}^{3}\frac{\Gamma_jV_j}{m_j\Omega_j^2} \tag{A18}$$

when the device was submerged. This value was used in Eqs. (1) and (20).

APPENDIX B: SHELL SURFACE VELOCITIES AND SOURCE LEVELS

After solving the loaded actuator problem, the stack velocity spectrum, $v^{\text{stack}}(\omega)$, was converted into a SL spectrum for the transducer. Two intermediate computations involved

computing the shim's end velocity from the stack's velocity, and the shell's average surface velocity from the shim's end velocity. Once the shell's average velocity was determined, the SL was computed assuming spherical radiation into the water.

The velocity of the shim's end in terms of the stack velocity was computed from the *T* circuit shown in Fig. 3(b) as

$$v^{\text{shim}}(\omega)=\frac{Z_2^{\text{shim}}(\omega)v^{\text{stack}}(\omega)}{Z_1^{\text{shim}}(\omega)+Z_2^{\text{shim}}(\omega)+Z^{\text{shell}}(\omega)}. \tag{B1}$$

Applying modal superposition, the average surface velocity of the shell was

$$\langle v^{\text{shell}}(\omega)\rangle = i\omega\sum_{j=1}^{3}\frac{V_j\overline{q_i}(\omega)}{S}, \tag{B2}$$

where V_j was defined by Eq. (A17). Using Eq. (A4), Eq. (B2) in terms of the shell's branch velocities, v_j, was

$$\langle v^{\text{shell}}(\omega)\rangle=\sum_{j=1}^{3}\frac{V_j v_i(\omega)}{S\Gamma_j}. \tag{B3}$$

From Eq. (A9), Eq. (B3) became

$$\begin{aligned}\langle v^{\text{shell}}(\omega)\rangle &= \frac{\overline{F}(\omega)}{S}\sum_{j=1}^{3}\frac{V_j Y_i(\omega)}{\Gamma_j}\\ &= \frac{Z(\omega)v^{\text{shim}}(\omega)}{S}\sum_{j=1}^{3}\frac{V_j Y_i(\omega)}{\Gamma_j},\end{aligned} \tag{B4}$$

which related the shell's velocity to the shim's end velocity. Given the shell's velocity, the pressure field and SL were computed, assuming spherical acoustic radiation described by Kinsler *et al.*[16] SL was computed for the pressure field at 1 m from the source's center relative to 1 μPa. For wavelengths greater than the shell's average dimension, this approximation gave a reasonable estimate of the far-field radiation.

[1] K. M. Rittenmeyer, ''Electrostrictive ceramics for underwater transducer applications,'' J. Acoust. Soc. Am. **95**, 849–856 (1994).
[2] S. M. Pilgrim, M. Massuda, J. D. Prodey, and A. P. Ritter, ''Electrostrictive sonar drivers for flextensional transducers,'' in *Transducers for Sonics and Ultrasonics*, edited by M. McCollum, B. F. Hamonic, and O. B. Wilson (Technomic, Lancaster, PA, 1993).
[3] M. B. Moffet, A. E. Clark, M. Wun-Fogle, J. Linberg, J. P. Teter, and E. A. McLaughlin, ''Characterization of Terfenol-D for magnetostrictive transducers,'' J. Acoust. Soc. Am. **89**, 1448–1455 (1991).
[4] L. E. Cross, ''Relaxor ferroelectrics,'' Ferroelectrics **76**, 241–267 (1987).
[5] S. M. Pilgrim, M. Massuda, J. D. Prodey, and A. P. Ritter, ''Electromechanical properties of some $Pb(Mg_{1/3}Nb_{2/3})O_3$–$PbTiO_3$–(Ba, Sr)TiO_3 ceramics: Part I,'' J. Am. Ceram. Soc. **75**, 1964–1969 (1992).
[6] C. H. Sherman and J. L. Butler, ''Analysis of harmonic distortion in electroacoustic transducers,'' J. Acoust. Soc. Am. **98**, 1596–1611 (1995).
[7] C. H. Sherman, J. L. Butler, and A. L. Butler, ''Analysis of harmonic distortion in electroacoustic transducers under indirect drive conditions,'' J. Acoust. Soc. Am. **101**, 297–314 (1997).
[8] C. L. Hom and N. Shankar, ''A fully coupled constitutive model for electrostrictive ceramic materials,'' J. Intell. Mater. Syst. Struct. **5**, 795–801 (1994).
[9] S. A. Brown, C. L. Hom, M. Massuda, J. D. Prodey, K. Bridger, N. Shankar, and S. R. Winzer, ''Electromechanical testing and modeling of a $Pb(Mg_{1/3}Nb_{2/3})O_3$–$PbTiO_3$–$BaTiO_3$ relaxor ferroelectric,'' J. Am. Ceram. Soc. **79**, 2271–2282 (1996).
[10] J. L. Butler, T. J. Peirce, and J. Lindberg, ''A desktop computer program for a flextensional transducer,'' Proceedings of the Institute of Acoustics **9**, 31–41 (1987).
[11] G. A. Brigham, ''Lumped-parameter analysis of the class IV (oval) flextensional transducer,'' Report TR4463 (NUSC, New London, CT, 1973.
[12] G. A. Brigham, ''Analysis of the class-IV flextensional transducer by use of wave mechanics,'' J. Acoust. Soc. Am. **56**, 31–39 (1974).
[13] ABAQUS Version 5.4, Hibbitt, Karlsson & Sorensen, Inc., Pawtucket, RI (1994).
[14] W. T. Thompson, *Theory of Vibration with Applications*, 4th ed. (Prentice Hall, Englewood Cliffs, NJ, 1993), pp. 345–358.
[15] G. E. Martin, ''On the theory of segmented electromechanical systems,'' J. Acoust. Soc. Am. **36**, 1366–1370 (1964).
[16] L. E. Kinsler, A. R. Frey, A. B. Coppens, and J. V. Sanders, *Fundamental of Acoustics* (Wiley, New York, 1980), 3rd ed., pp. 163–165.

Vortex sound in bass-reflex ports of loudspeakers. Part I. Observation of response to harmonic excitation and remedial measures[a)]

N. Bert Roozen
Philips Research Laboratories, Prof. Holstlaan 4, 5656 AA Eindhoven, The Netherlands

Marije Bockholts, Pascal van Eck, and A. Hirschberg
Eindhoven University of Technology, P.O. Box 513, 5600 MB Eindhoven, The Netherlands

(Received 24 December 1997; accepted for publication 13 May 1998)

At high sound pressure levels a bass-reflex port produces blowing sounds, especially in the case of small loudspeaker boxes with narrow bass-reflex ports. The blowing sounds are caused by vortex shedding of the acoustic flow at the end of the port at high flow velocities. It has been found that acoustic standing waves in the longitudinal direction of the port are excited in a pulsatile manner by the periodically generated vortices. This is demonstrated by time history measurements of the blowing sounds of a loudspeaker system with a bass-reflex port driven by a harmonic signal. Broadband turbulence sound appears to be weaker than these deterministic sounds. It has been found that, near the 1-kHz port resonance frequency, the power level of the blowing sounds can be reduced by 8 dB by using a port cross section that diverges gradually toward both port ends with a slope angle at the port ends of about 6°, and rounding the edges at both port ends. © *1998 Acoustical Society of America.* [S0001-4966(98)00909-6]

PACS numbers: 43.10.Ln, 43.38.Ja, 43.28.Ra [SLE]

INTRODUCTION

In the case of so-called bass-reflex boxes or vented loudspeaker boxes,[1,2] a port is applied. The port is an open pipe connecting the volume of air enclosed within the box with its surrounding environment. The port contributes to the sound reproduction in the lowest part of the frequency range around the Helmholtz frequency of the port-box system. Without a port, the box volume would have to be approximately a factor of 2 larger to achieve the same low-frequency acoustical performance. The typical improvement that can be obtained with a port is shown in Fig. 1.

The Helmholtz frequency can be calculated with the formula:[1]

$$f_{\text{Helmholtz}}=\frac{c}{2\pi}\sqrt{\frac{S_0}{L_{\text{eff}}V}}, \tag{1}$$

where c is the speed of sound, S_0 is a reference cross-sectional area of the port, V is the volume of the box, and L_{eff} is defined as

$$L_{\text{eff}}=\int_0^L \frac{S_0}{S(x)}\,dx. \tag{2}$$

In this equation L is the physical length of the port and x is the axial coordinate along the port axis. The port's effective length L_{eff} should additionally be corrected for end corrections. Appropriate end corrections can be found in the literature.[1,3]

In the case of boxes with a small box volume V, the port cross-sectional area S_0 has to be small on account of a limited physical port length L and a given Helmholtz frequency $f_{\text{Helmholtz}}$ [see Eq. (1)]. This means that in small boxes, with a small cross-sectional port area S_0, the acoustic flow velocity in the port has to be high in order to obtain a sound pressure level at low frequencies that is comparable with the sound pressure level that can be obtained with larger bass-reflex systems. The high air velocities which occur in such small ports cause vortex shedding, leading to blowing sounds and nonlinear acoustic losses. These blowing sounds are particularly annoying with respect to the reproduction of percussion or bass music.

In this article it will be shown that vortices are generated at both ends of the port during each cycle, and that these vortices excite acoustic standing waves in the longitudinal direction of the port in an impulsive manner. The spectrum of the blowing sounds appears to be dominated by these port resonances. Turbulent boundary layer noise was found to not be important because the critical Reynolds number for the onset of turbulence in oscillating viscous boundary layers is not achieved.[4]

Using time-history measurements of the acoustic pressure inside and outside the loudspeaker box, the deterministic behavior of the blowing sounds will be shown for both a standard and an improved bass-reflex port geometry.

In the final part of the article the dominant physical phenomena will be summarized and port geometry alterations for minimizing the blowing sound will be presented.

I. VISUALIZATION BY MEANS OF THE SCHLIEREN METHOD

The objective of the visualization was to obtain a better understanding of the physics of the air flow coming out of a bass-reflex port at high air speeds. Carbon-dioxide gas (CO_2) was used for the visualization of the flow by means of the Schlieren method.[5] The port used for this experiment was a

[a)]''Selected research articles'' are ones chosen occasionally by the Editor-in-Chief that are judged (a) to have a subject of wide acoustical interest, and (b) to be written for understanding by broad acoustical readership.

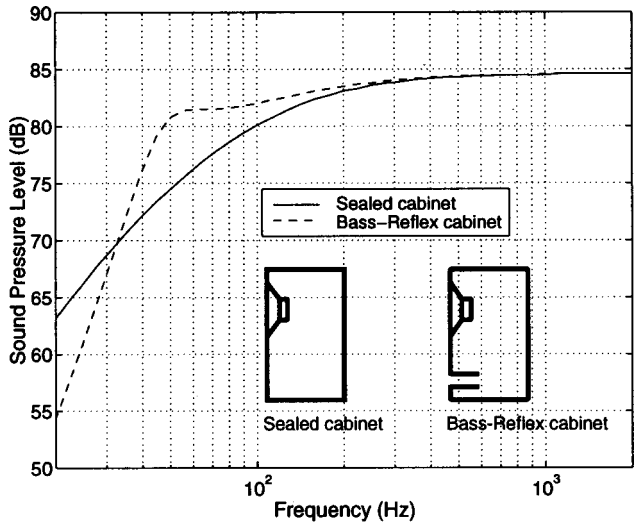

FIG. 1. A sealed cabinet versus a bass-reflex cabinet.

cylindrical port with rounded edges. The CO_2 was injected through porous walls made from sinter bronze around the port exit. With the aid of a stroboscope it was possible to take pictures at fixed moments of the oscillating period. A sketch of the test setup is shown in Fig. 2. The results are presented in Fig. 3.

As can be seen in Fig. 3, the vortex shedding takes place at the transitional area of the air flowing out of the port and the stagnant surrounding air. The mushroom-shaped vortices are produced each time the air flows out of the port. When the loudspeaker is driven at a frequency of for instance 45 Hz, a vortex will be generated 45 times per second at one end of the port and 45 times per second at the other end of the port. It can be seen in Fig. 3 that a vortex is generated during outflow and that this vortex moves away from the port. The vortex sounds produced by this mushroom-shaped vortex are the unwanted blowing sounds. Each time a vortex is generated, unwanted noises are produced. When a sharp-edged port termination is used, vortices are also observed during flow into the port in addition to vortices due to flow out of the port.

II. $\frac{1}{2}\lambda$ ACOUSTIC PORT RESONANCE

It was found that the periodic vortex shedding gives rise to a periodic excitation of acoustic resonances of the port. The first acoustic resonance corresponds to the $\frac{1}{2}\lambda$ acoustic wave in the longitudinal direction of the port. The resonance

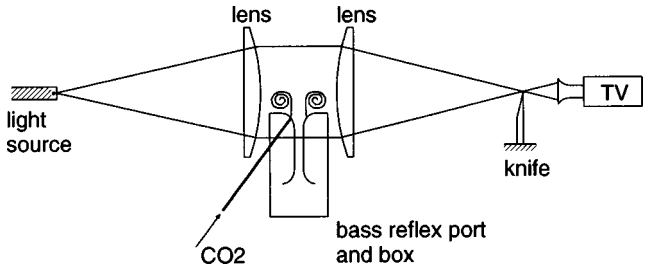

FIG. 2. Visualization test setup.

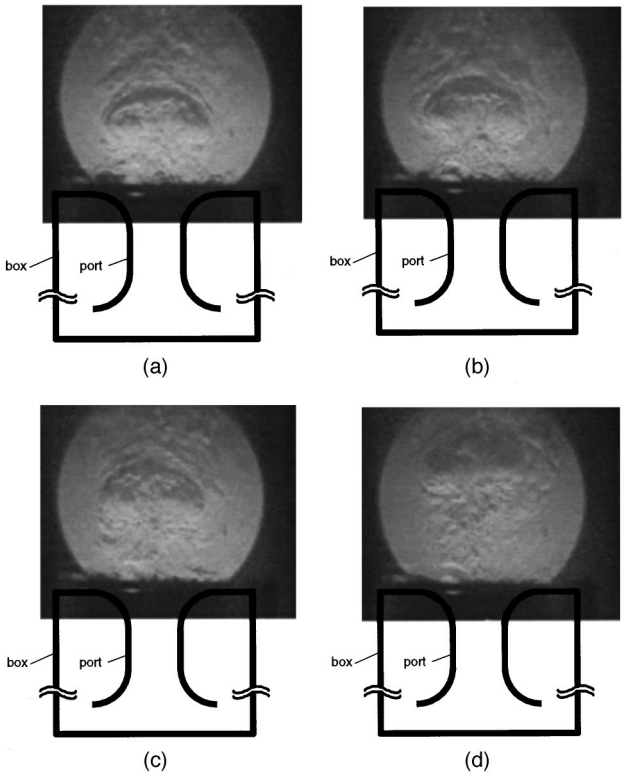

FIG. 3. Schlieren visualization of the vortex shedding for successive instants of the half-period of the harmonic cycle; (a)—the vortex develops; (b), (c), and (d)—the vortex moves away from the port.

frequency f_1 of this fundamental acoustic mode and its harmonics ($f_2, f_3, \ldots$) can easily be calculated with the formula

$$f_n \approx \frac{nc}{2L_{\text{eff}}}, \tag{3}$$

where n is an integer ($n=1,2,3,\ldots$). Measurements on a cylindrical bass-reflex port with a physical length $L=0.16$ m and a cross-sectional radius $a=0.01$ m yielded a fundamental resonance frequency of about 955 Hz, which agrees well with the above equation, with due allowance for the port's end effects.

The power spectral density of the sound pressure, measured at a distance of 1 m, is shown in Fig. 4. In this figure it can be clearly seen that the $\frac{1}{2}\lambda$ acoustic resonance at about 1 kHz is strongly excited. The harmonics of this resonance are also excited, but less strongly than the fundamental bass-reflex port mode at 1 kHz.

Although the loudspeaker was driven by an electrical signal with a frequency of 45 Hz only, harmonics of 45 Hz are also present. These harmonics, which are all 20 dB or more below the 45-Hz signal, are caused by harmonic distortion of the loudspeaker itself. This was confirmed by separate response measurements of the loudspeaker.

The width of the resonance peak at 1 kHz is rather large, which indicates that the resonance is strongly damped. Figure 4 shows the power spectral density of the sound pressure for various air velocities in the port. At low velocity amplitudes the damping of the 1-kHz resonance is due mainly to acoustic radiation into open space. At higher amplitudes the quality factor decreases due to dissipation of acoustic energy

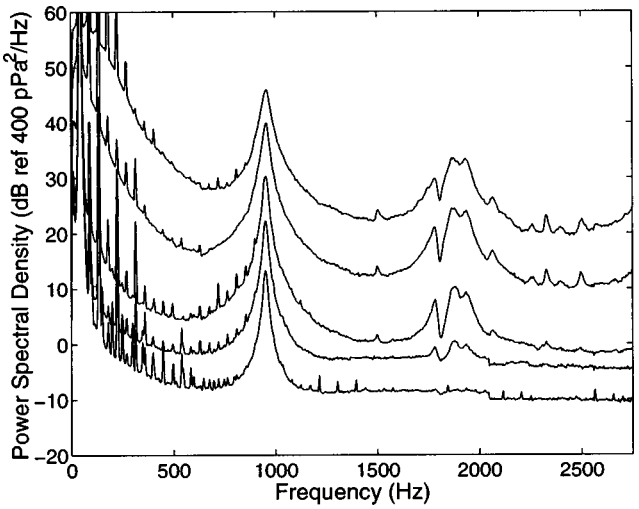

FIG. 4. Power spectral density of the sound pressure generated by a cylindrical bass-reflex port with sharp edges measured at a distance of 1 m for port velocity amplitudes ranging from 1 to 30 m/s, physical port length $L=0.16$ m, port cross-sectional radius $a=0.01$ m, loudspeaker driven at a single frequency of 45 Hz.

by convective effects. The quality factor Q, which is defined as the resonance frequency divided by the half-power bandwidth of the resonance (-3 dB bandwidth), can be estimated on the basis of Fig. 4 to be about 50 for air velocity amplitudes between 0 and 2 m/s, and about 20–30 for air velocity amplitudes between 10 and 20 m/s.

Theory indicates that the quality factor for a two-sided open pipe with flanged ends due to acoustical radiation at the $\frac{1}{2}\lambda$ acoustic port resonance frequency equals

$$Q=\frac{L^2}{2\pi a^2}, \tag{4}$$

where it is assumed that only plane waves propagate ($\lambda \gg a$). For a port with a physical length $L=0.16$ m and a cross-sectional radius $a=0.01$ m this yields a quality factor of 35. Assuming the port to be unflanged at both ends, the quality factor equals 70. In reality, the quality factor lies between these two values, which is in good agreement with the observed quality factor of the system at low air velocities.

The reduction of the quality factor Q at high air velocities is due to a transfer of energy from the acoustic oscillation of the port at 1 kHz to the free jet formed during the vortex shedding at the driving frequency. In this jet energy is dissipated by turbulence.[6]

III. HIGH-FREQUENCY SOUND PRESSURE COMPONENTS

To illustrate the periodic nature of the $\lambda/2$ port resonance excitation, the blowing sounds of a bass-reflex system driven at 40 Hz were measured in the time domain. The sound pressure signal was filtered using a high-pass filter. Below 500 Hz the filter reduces the level of the signal by more than 30 dB. The sound pressure was measured at a distance of 1 m from the port in a free-field condition (in an anechoic room) for both a port with sharp edges and a gradually converging–diverging port. No time averaging was employed. The results are shown in Fig. 5.

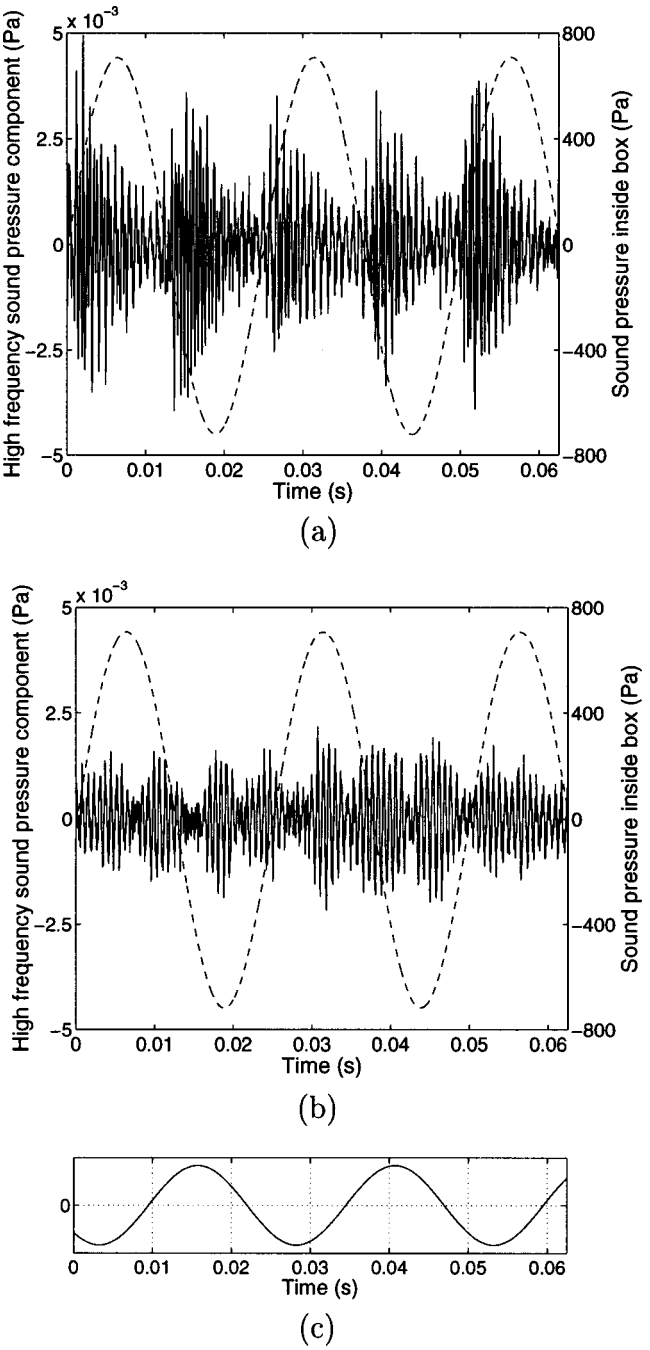

FIG. 5. High-pass filter results at the same sound pressure levels in the loudspeaker box at 40 Hz and at the same effective port lengths L_{eff}. Driving frequency 40 Hz. (a) Cylindrical port with sharp ends. Physical port length $L=0.13$ m, port cross-sectional radius $a=0.01$ m. Solid line: high-frequency sound pressure signal at 1-m distance outside box. Dashed line: sound pressure inside box. (b) Gradually converging–diverging port with rounded edges as shown in Fig. 6. Solid line: high-frequency sound pressure signal at 1-m distance outside box. Dashed line: sound pressure inside box. (c) Estimated port velocity (qualitatively), corrected for a time delay of 3 ms. Positive velocity indicates flow of air out of the loudspeaker box.

At this point it is interesting to consider the relationship between the sound pressure inside the box and the speed of the air particles in the port. Assuming nonlinear effects and friction not to be important for the flow in the port itself, the

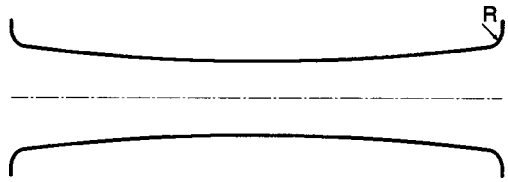

FIG. 6. A gradually converging–diverging port cross section, with rounded port edges. Physical port length $L=0.13$ m, radius of rounded edge $R=0.005$ m, port cross-sectional radius in the middle of the port $a=9.45\times10^{-3}$ m, widening angle at the port ends 6°. Effective port length L_{eff} corresponds to a cylindrical port with sharp edges ($L=0.13$ m, $a=0.01$ m).

moment in time at which flow reversal takes place is approximately the same as the moment in time at which the sound pressure in the loudspeaker box reaches its maximum or its minimum. In fact, during outflow, the sound pressure in the loudspeaker box will (in a first-order approximation) decrease because particles of air leave the box volume, and vice versa. On the basis of this reasoning the time dependency of the velocity in the port is deduced as shown in Fig. 5(c). A positive velocity indicates flow of air out of the box. Note that a small time delay of about 3 ms should be taken into account for the acoustic waves to travel from the loudspeaker port to the microphone at 1-m distance. The velocity in the port shown in Fig. 5(c) was corrected for this time delay.

The high-frequency components of the sound radiated from the port with sharp ends [Fig. 5(a)] clearly show a pulsatile behavior. The high-frequency blowing sounds have a deterministic character rather than a stochastic character. The frequency of these noises clearly corresponds to the $\lambda/2$ resonance of the port, as also illustrated by the frequency domain results in Fig. 4. Each time the acoustic resonance is excited, the high-frequency (1 kHz) component increases sharply. After this excitation an exponential decay is observed. Note that a pulsatile excitation takes place both during flow of air out of the box and during flow of air into the box.

As already mentioned above, a typical value of the quality factor Q of the port is about 50. The decay observed in Fig. 5(a) corresponds reasonably well to this value.

The high-frequency blowing sounds that are radiated from the gradually converging–diverging port with rounded port edges as shown in Fig. 6 appear to be more complex than those radiated from the port with sharp ends [see Fig. 5(b)]. The high-frequency pulses are produced at less distinct moments in time in comparison with the high-frequency blowing sounds that are radiated from the port with sharp ends.

It is important to realize that the blowing sound is not a broadband turbulence noise filtered by the port but a deterministic, pulsatile response of the port to vortex shedding. This phenomenon of pulsatile excitation of a pipe resonance by vortex shedding inspired Powell[7] to develop his theory of vortex sound. To quote Powell:[7] ''While watching a locomotive blow off steam soon after becoming interested in the subject of aerodynamically generated noise, the author was struck by the fact that each time that a particularly large eddy formed on the edge of the turbulent steam jet he heard a very definite impulsive sound. This focused attention upon the idea that the origin of aerodynamic sound might be attributed to the *process of formation* of eddies, or vortices.''

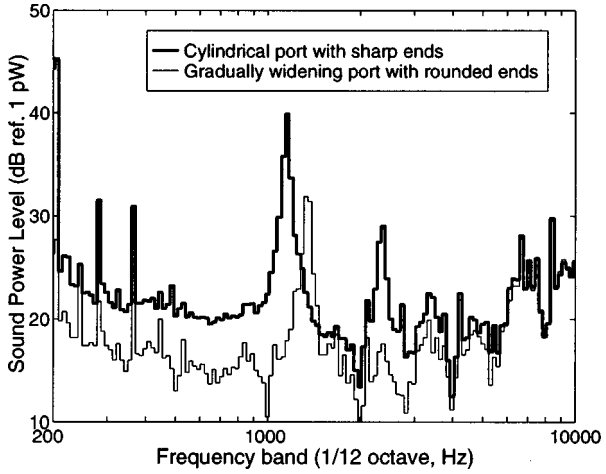

FIG. 7. Sound power level spectrum of blowing sounds for a cylindrical port with sharp edges (physical length $L=0.13$ m, port radius $a=0.01$ m) and a gradually widening port with rounded edges as shown in Fig. 6 at the same sound power levels at the driving frequency. Driving frequency is 40 Hz. Radiated sound power at 40 Hz is 90 dB.

Similar things happen in the present case of the bass-reflex port. In this case the vortices are periodically generated, resulting in a definite impulsive sound.

IV. MEASURES FOR REDUCING BLOWING SOUND

A significant reduction in the impulse due to vortex shedding can be achieved by gradually widening the port toward both port ends to obtain a converging–diverging port cross section as shown in Fig. 6. Reducing the port cross section in the middle of the port and widening the port toward both port ends effectively increases the cross-sectional area at both port ends, while maintaining a certain effective length L_{eff}. Because a larger port cross-sectional area at the port ends reduces the local air velocity, vortices are less likely to be generated, or will be less intense.

It is essential to widen the port toward both port ends as the flow is directed both inward and outward. The widening angle of the port should not be too large to avoid the risk of flow separation within the port. As a rule of thumb a slope angle of between 3° and 12° is proposed, but larger angles may be considered.

It is also important to round the port edges at both port ends. Rounding the edges at both ends eliminates the vortex shedding at the inlet side of the port and can considerably reduce the vortex shedding at the port's outlet side. Furthermore, rounding a port also has the advantage that any vortices produced will radiate noise less efficiently than vortices produced at a sharp port end. However, the rounding radius should not be too large because otherwise the blowing sounds may increase.[8]

A converging–diverging port with a slope angle of 6° at the port ends with rounded edges as shown in Fig. 6 will now be considered as well as a cylindrical port with sharp edges. The blowing sounds of these ports are shown in Fig. 7 at the same sound power levels at the driving frequency. From

these results it can be inferred that the sound power of the blowing sounds at the port resonance frequency of about 1.1 kHz are reduced by about 8 dB. The less dominant broadband noises in the frequency range from a few hundred Hertz to 3000 Hz are also reduced by about 8 dB. The vortices produced by the gradually widening port with rounded port ends are obviously less strong.

In a widening port geometry the exact location of the point of separation will vary depending on the air velocity. Because of the importance of the location of the point of separation with respect to the vortex shedding and the related production of blowing sounds and nonlinear acoustic losses, it is interesting to determine this point of separation. In part II of this paper a method will be presented for estimating the point of flow separation indirectly on the basis of a measurement of the sound pressure inside the loudspeaker box and a measurement of the sound pressure at a distance of 1 m from the port exit.

V. CONCLUSIONS

The high velocities in the port of a bass-reflex loudspeaker system driven at the Helmholtz frequency can cause serious vortex shedding, especially in the case of small boxes. The vortices created by the acoustic air flow have been visualized by means of a Schlieren method. It has been shown that the blowing sounds generated by the shedding of the vortices are dominated by deterministic noise rather than by broadband noise. This deterministic sound consists mainly of a single frequency which corresponds to the $\frac{1}{2}\lambda$ acoustic resonance of the port. The port resonance is excited in a pulsatile manner by the periodically generated vortices.

A reduction in the level of these blowing sounds can be obtained by modifying the port geometry to minimize the vortex shedding. The key in the design of a port with a minimum amount of blowing sounds due to vortex shedding is the point of flow separation from the wall at which vortices are formed. The larger the radius at which separation occurs, the less intense the vortex shedding will be.

A significant reduction in the vortex shedding can be obtained by gradually widening the port cross section toward both port ends to obtain a converging–diverging port cross section and rounding both port edges. With the adapted port geometry vortex shedding at the inlet side of the port is eliminated, and vortex shedding at the outlet side of the port is reduced significantly. A reduction of 8 dB in the sound power level of the blowing sounds relative to the sound power level of the blowing sounds radiated from a port with sharp ends has been demonstrated. This was a reduction not only in the level of the deterministic sounds but also in the (less dominant) broadband noise.

[1] J. Merhaut, *Theory of Electroacoustics* (McGraw-Hill, New York, 1981).
[2] L. L. Beranek, *Acoustics* (McGraw-Hill, New York, 1954).
[3] A. Cummings, ''Acoustics of a wine bottle,'' J. Sound Vib. **31**, 331–343 (1973).
[4] R. Verzicco, ''Direct simulation of transition in Stokes boundary layers,'' Phys. Fluids **8**, 1341–1343 (1996).
[5] W. Merzkirch, *Flow Visualization* (Academic, New York, 1974).
[6] M. C. A. M. Peters, A. Hirschberg, A. J. Reijnen, and A. P. J. Wijnands, ''Damping and reflection coefficient measurements for an open pipe at low Mach and low Helmholtz numbers,'' J. Fluid Mech. **256**, 499–534 (1993).
[7] A. Powell, ''Theory of vortex sound,'' J. Acoust. Soc. Am. **36**, 177–195 (1964).
[8] N. B. Roozen, J. E. M. Vael, and J. A. M. Nieuwendijk, ''Reduction of bass-reflex port non-linearities by optimizing the port geometry,'' AES 104th Convention, Amsterdam (1998), preprint No. 4661.

Vortex sound in bass-reflex ports of loudspeakers. Part II. A method to estimate the point of separation[a)]

N. Bert Roozen
Philips Research Laboratories, Prof. Holstlaan 4, 5656 AA Eindhoven, The Netherlands

Marije Bockholts, Pascal van Eck, and A. Hirschberg
Eindhoven University of Technology, P.O. Box 513, 5600 MB Eindhoven, The Netherlands

(Received 24 December 1997; accepted for publication 13 May 1998)

In part I of this paper, the vortex shedding that may occur in a bass-reflex port of a loudspeaker system was discussed. At the Helmholtz frequency of the bass-reflex port, air is pumped in and out at rather high velocities, vortex shedding occurs at the end of the port, and blowing sounds are generated. It was explained that the key in the design of a port with a minimum of blowing sounds is the point of flow separation from the wall at which vortices are formed. This paper presents a method for estimating the point of separation for an unsteady flow like the flow through a bass-reflex port. Assuming that the flow can be described by a potential flow up to the point where flow separation occurs, it was found that the point of separation can be estimated on the basis of measurement of the sound pressure inside the loudspeaker box and measurement of the sound pressure at a distance of 1 m from the port exit. Application of the proposed technique to a cylindrical port with rounded edges at both port ends revealed that the point of separation is determined by the particle displacement rather than by the particle velocity. It was also found that a good indicator of the onset of severe vortex shedding is the Strouhal number based on the radius of curvature of the port edges. © *1998 Acoustical Society of America.* [S0001-4966(98)01009-1]

PACS numbers: 43.10.Ln, 43.38.Ja, 43.28.Ra [SLE]

INTRODUCTION

In part I of this paper it was explained that a significant reduction in the blowing sounds of a port can be obtained by gradually widening the port cross section toward both port ends to obtain a converging–diverging port cross section and rounding both port edges. The key factor in judging a port with respect to the production of unwanted vortices and the related blowing sounds is the place in the port where the vortex is generated.

In a converging–diverging port or a cylindrical port with rounded port edges the separation does not occur at a fixed place on the wall surface, and is dependent on the air velocity amplitude. As the cross-sectional area of the port at which flow separation from the wall occurs determines the local air velocity at the point of separation (at a given fixed sound power), it also determines the intensity of the vortices formed. A smaller local air velocity amplitude results in a less intense vortex.

Because of the importance of the point of separation with respect to the vortex shedding and the related production of blowing sounds and nonlinear acoustic losses, it is interesting to determine the point of separation. This paper presents a method for estimating the point of flow separation on the basis of measurement of the sound pressure inside the loudspeaker box and measurement of the sound pressure radiated from the port into free space. The method employs an analytical model based on the unsteady Bernoulli equation.

All the measurements were carried out for a cylindrical port with rounded port ends. A sketch of the outlet of the port is shown in Fig. 1. The physical length of the port equals 0.13 m, the cross-sectional radius a_0 of the cylindrical part of the port equals 0.01 m and the radius of curvature R at both port ends equals 0.02 m.

I. THE UNSTEADY BERNOULLI EQUATION

Because flow with a high Reynolds number through relatively short pipes is considered, the effect of friction can be neglected except in the case of flow separation. At the Helmholtz resonance frequency the flow in the port is compact and can locally be assumed to be incompressible. Furthermore, it is assumed that the velocity vectors in the port are directed in the longitudinal direction of the port only, and that the velocity and pressure in the port depend on the axial coordinate x only.

Using these assumptions, the flow within the port can be described by a 1-D potential flow up to the point of flow separation. Furthermore, the abovementioned restrictions justify the use of a particular form of the unsteady Bernoulli equation, which reads[1]

$$\frac{\partial \phi(x,t)}{\partial t} + \frac{u^2(x,t)}{2} + \frac{p(x,t)}{\rho_0} = \text{constant}, \tag{1}$$

where $u(x,t)$ is the velocity in the x direction of the port, $p(x,t)$ is the sound pressure, ρ_0 is the mean fluid density and $\phi(x,t)$ is the flow potential defined by

$$\phi(x,t) = \int_0^x u(x',t)\,dx'. \tag{2}$$

Consider a cylindrical port whose edges are both rounded as indicated in Fig. 1. The cross section of the main cylindrical part of the port is denoted by S_0. The cross-sectional area of the port at an arbitrary point x is denoted by $S(x)$ (which equals S_0 in the main cylindrical part). The air velocity in the

[a)]''Selected research articles'' are ones chosen occasionally by the Editor-in-Chief that are judged (a) to have a subject of wide acoustical interest, and (b) to be written for understanding by broad acoustical readership.

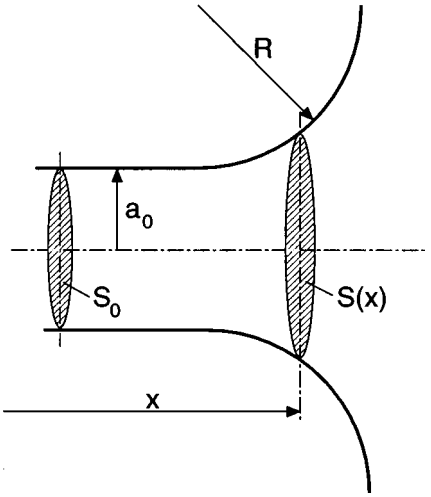

FIG. 1. Cylindrical port with rounded edges.

main cylindrical part of the port is denoted by $u_0(t)$. Making use of the incompressible flow approximation, the velocity $u(x,t)$ at an arbitrary point x in the port can be written as

$$u(x,t)=\frac{S_0 u_0(t)}{S(x)}. \tag{3}$$

The potential ϕ can be written as

$$\phi(x,t)=\int_0^x u(x',t)dx'=\int_0^x \frac{S_0 u_0(t)}{S(x')}\,dx' =l_{\text{eff}}(x)u_0(t), \tag{4}$$

where the effective length $l_{\text{eff}}(x)$ is defined similar to the definition of L_{eff} given in part I of this paper:

$$l_{\text{eff}}(x)=\int_0^x \frac{S_0}{S(x')}\,dx'. \tag{5}$$

Note that $u_0(t)$ does not depend on x and can therefore be separated from the integral over x' in Eq. (4).

With these definitions, the unsteady Bernoulli equation becomes

$$\frac{\partial}{\partial t}\left[l_{\text{eff}}(x)u_0(t)\right]+\frac{1}{2}u^2(x,t)+\frac{p(x,t)}{\rho_0}=\text{constant}. \tag{6}$$

Note that the first term in Eq. (6) is a term which takes the inertia of the air into account.

II. POINT OF SEPARATION

In this section the unsteady Bernoulli equation (6) will be used to determine the point of separation. It will be assumed that the port flow can be described by a frictionless incompressible potential flow up to the point where the flow separates from the port wall. As the point where the flow separates changes with the flow direction, the unsteady Bernoulli equation is applied along different trajectories during flow of air into the loudspeaker box and during flow of air out of the box. These two cases will be described below.

In the situation in which air flows out of the loudspeaker box the unsteady Bernoulli equation is applied along trajectory 1, from point 1A inside the loudspeaker box to point 1B

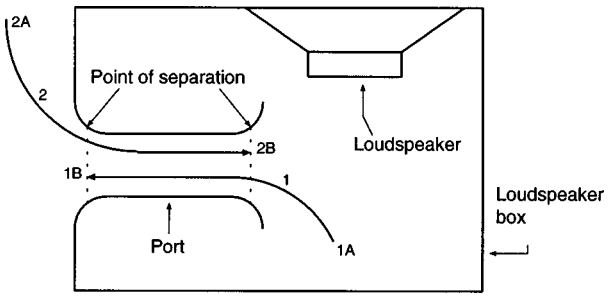

FIG. 2. Trajectories of air flowing out (1) and flowing into (2) the loudspeaker box.

where the flow separates (see Fig. 2). At point 1A the velocity u and the acceleration $\dot{u}$ both vanish. The origin of the axial coordinate x is chosen to coincide with point 1A in this case, so $l_{\text{eff}}(x_{1A})$ vanishes; the positive direction of x is directed out of the box and a positive velocity u denotes flow of air out of the box. At point 1B the velocity u is unknown. The sound pressure at point 1B is small and can be assumed to be negligible. We implicitly assume quasi-steady behavior of the free jet formed by the vortex shedding. Application of the unsteady Bernoulli equation along this trajectory yields

$$\frac{p_{\text{box}}}{\rho_0}=\frac{\partial}{\partial t}\left[l_{\text{eff}}(x_{1B})u_0\right]+\frac{1}{2}u_{1B}^2 \quad (u>0), \tag{7}$$

where p_{box} is the acoustic pressure inside the loudspeaker box (at point 1A) and u_{1B} is the velocity at the point of separation. Using the relationship given by Eq. (3) the velocity u_{1B} can also be expressed in terms of the velocity in the cylindrical part of the port u_0.

In the situation in which air flows into the loudspeaker box the unsteady Bernoulli equation is applied along trajectory 2, from point 2A far away from the box to point 2B where the flow separates (see Fig. 2). At point 2A the velocity u, acceleration $\dot{u}$, and sound pressure p all vanish. The origin of the axial coordinate x is chosen to coincide with point 2A in this case, so $l_{\text{eff}}(x_{2A})$ vanishes; the positive direction of x remains directed out of the box and a positive velocity u denotes flow of air out of the box. This choice implies that x_{2B} is a negative number, so $l_{\text{eff}}(x_{2B})$ is also negative. At point 2B the acoustic pressure is assumed to be equal to the acoustic pressure in the loudspeaker box p_{box}, which is measured by a microphone inside the box. Hence, application of the unsteady Bernoulli equation along this trajectory yields

$$0=\frac{\partial}{\partial t}\left[l_{\text{eff}}(x_{2B})u_0\right]+\frac{1}{2}u_{2B}^2+\frac{p_{\text{box}}}{\rho_0} \quad (u<0). \tag{8}$$

In this equation u_{2B} can be expressed in terms of u_0 using the relationship given by Eq. (3).

Merging of Eqs. (7) and (8) into one unifying equation yields

$$0=\frac{\partial}{\partial t}\left[l_{\text{eff}}(x_{1B,2B})u_0\right]+\frac{1}{2}\left(\frac{S_0}{S(x_{1B,2B})}\right)^2 u_0^2\pm\frac{p_{\text{box}}}{\rho_0}, \tag{9}$$

where use has been made of Eq. (3) and where the ''$-$'' sign applies for trajectory 1 and the ''$+$'' sign applies for trajectory 2.

By measuring the sound pressure in the box, p_{box}, and the velocity in the port, u_0, it should in principle be possible to calculate points $x_{1\mathrm{B}}$ and $x_{2\mathrm{B}}$ using Eq. (9). In this case the points of separation $x_{1\mathrm{B}}$ and $x_{2\mathrm{B}}$, which determine the effective length of the port l_{eff} and the cross-sectional area S at the points of separation 1B and 2B, are the only unknown variables in this set of equations. However, due to measuring errors the instantaneous time-varying point of separation cannot be determined accurately with the aid of these equations and the physical quantities measured. Therefore, the time-averaged point of separation will be determined instead. It will be assumed that the point of separation, by approximation, does not change in time. It will also be assumed that the points of separation during inflow and outflow are the same ($x_{1\mathrm{B}}=-x_{2\mathrm{B}}$). Using these assumptions, in an absolute sense, the effective lengths come to be equal to each other, as do the cross-sectional areas at the points of separation:

$$l_{\mathrm{eff}}(x_{1\mathrm{B}})=-l_{\mathrm{eff}}(x_{2\mathrm{B}}), \tag{10}$$

$$S(x_{1\mathrm{B}})=S(x_{2\mathrm{B}}). \tag{11}$$

III. DETERMINING THE PARTICLE VELOCITY IN THE PORT

Application of the unsteady Bernoulli equations involves the air velocity u_0 in the cylindrical part of the port. This velocity in the port can be determined in two ways, i.e., directly via laser Doppler anemometry, or indirectly via measurement of the sound pressure radiated by the port. Both methods will be explained below.

The viscous boundary layer is very thin in the present application, and the cross-sectional main velocity profile is flat. The dimensionless parameter that determines the velocity profile is the shear-wave number, which is defined as

$$\mathrm{Sh}=\sqrt{\frac{\nu}{\omega a^2}}. \tag{12}$$

The shear-wave number is the ratio of the thickness of the boundary layer δ, which equals $\delta=\sqrt{(2\nu/\omega)}$, and the port's cross-sectional radius a. It gives the ratio of viscous effects and inertia effects.[2] In the present case the boundary layer thickness will be approximately 0.3 mm for air oscillating with a frequency of 50 Hz. Compared with the cross-sectional radius a of 0.01 m, this is small. The velocity profile may hence be considered flat. The difference between the core velocity and the mean flow velocity (i.e., volume flux divided by cross-sectional area) is expected to be less than 3%.

A. Laser doppler anemometry

A direct method for determining the velocity of the air particles in the port involves using laser Doppler anemometry.[3] Laser Doppler anemometry using a Dantec FlowLite combined with a Dantec 57N10 burst spectrum analyzer was performed at two points, i.e., in the main flow at a point half-way along the centerline and at a point along the centerline, 1 cm in front of the port.

In order to be able to measure the velocity inside the port we used a port made of glass having a wall thickness of 1.4 mm. Because of the unknown influence of refraction of the laser beam passing the glass cylinder the measurements are to be interpreted qualitatively, not quantitatively. No special measures needed to be taken in the measurement of the velocity by means of laser Doppler anemometry in front of the port.

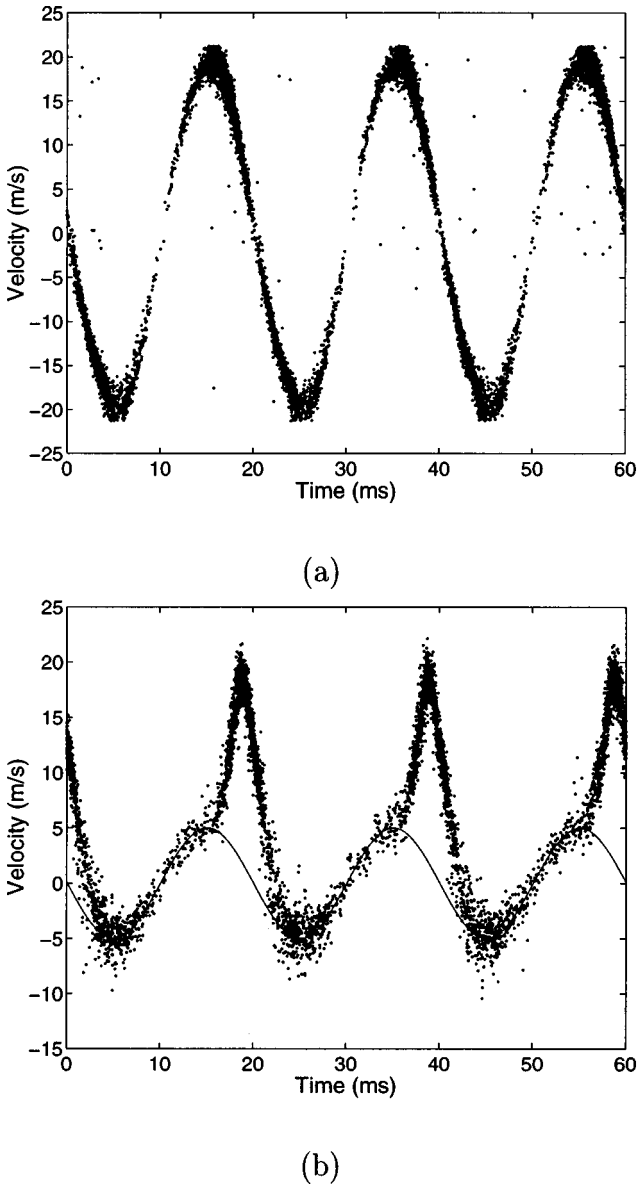

FIG. 3. Air velocity measurements obtained using laser Doppler anemometry; (a) laser Doppler anemometry measurement inside the port, half way along the centerline; (b) laser Doppler anemometry measurement along the centerline, 1 cm in front of the port; dotted: laser Doppler anemometry, Solid: Estimated velocity of a potential flow.

The air flow was seeded by means of smoke. Because of the very small smoke particles (submicron in size) the error due to the inertia of the smoke particles is small.

The measurement procedure was as follows. During a period of about 10 s the velocity of about 10 000 particles was measured with the aid of laser Doppler anemometry. The loudspeaker of the bass-reflex system was driven at a frequency of about 50 Hz. Hence, the velocity of only 20 particles are measured per cycle. In order to obtain more datapoints per period for purpose of presentation, some post-

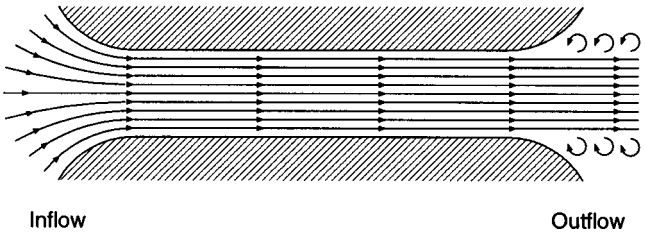

FIG. 4. Sinklike inflow (left) and jetlike outflow (right).

processing was performed. The time labels of the measurement points were modified so that they all lay within the first three cycles by shifting the time labels by an integer multiple of the period time T. The exact value of the period time T was determined by fitting the data with a sinusoidal function with a variable period time T, a variable amplitude, a variable phase and a variable dc offset in a least square sense.

The results obtained for a rather large velocity amplitude of 20 m/s in the main cylindrical part of the port can be seen in Fig. 3. The air velocity inside the port appears to have remained sinusoidal, also at large velocity amplitudes. More particles were measured around the maxima and minima of the velocity than around the abscissa. This difference is due to the greater effectiveness of laser Doppler anemometry at high particle velocities (because of the larger particle flux through the probe volume).

From the results obtained in front of the port it can be inferred that the velocity is much smaller during inflow than during outflow. This is rather obvious as during inflow the flow can be considered a potential flow. Air particles will move towards the inlet of the port from all directions, as illustrated in Fig. 4. However, during outflow, at air velocities high enough for flow separation to occur (i.e., at a Strouhal number $\mathrm{St}=\omega a/u$ of an order of 1 or smaller), the flow will be concentrated in a jet coming out of the port and vortices will be generated at the transition of moving air and stagnant air as observed in the flow visualization presented in part I of this paper. This causes the air speed in the jet to be much higher than the air speed during inflow in front of the port. The flow measured at the outlet of the port can be thought to consist of a small sinusoidal velocity due to the potential flow [indicated in Fig. 3(b) by a solid line] and a high velocity due to vortices and jet formed by flow separation.

B. Measurement of radiated sound pressure

An indirect way of determining the air velocity in the port is to measure the sound pressure radiated from the port. Using the relationships that exist between the radiated sound pressure and the volume velocity of the air movement in the port, the mean port velocity can be determined. Because the velocity profile is flat, the mean velocity can easily be translated into the core velocity.

The relationship used here follows from classical linear acoustics in which it is assumed that the radiation behavior of the bass-reflex port can be described by a compact acoustic source. This is justified if the acoustic wavelength is much larger than the dimensions of the bass-reflex port, which is certainly true in the present case. The relationship reads:[4]

$$p(r,t)=i\hat{u}\,\frac{\omega\rho_0\pi a^2}{4\pi r}\,e^{i(\omega t-kr)}, \tag{13}$$

where a is the inner radius of the bass-reflex port and r is the distance from the port where the sound pressure is measured. Note that this relationship holds for radiation into a free field (a 4-π field). Because at low frequencies the baffling effect of the loudspeaker box is negligible due to the long wavelengths, this is justified.

The sound pressure measurements were performed at a distance of 1 m from the exit of the port. In order to eliminate chaotic fluctuations induced by the pulsating air stream from the port, the microphone was placed at an angle of 45° relative to the axis of the port.

However, because the anechoic room in which the measurements were performed appeared to not be completely anechoic at frequencies below 100 Hz, the results have to be corrected to allow for the reflections of the anechoic room. This is done as follows. At very low port velocities (i.e., at Strouhal numbers $\mathrm{St}\gg 1$) the flow will not separate. As separation does not occur, the effective length becomes $L_{\mathrm{eff}}=l_{\mathrm{eff}}(L)$, where L is the physical length of the port. Applying the unsteady Bernoulli equation 9, the air velocity u_0 can be determined using the known effective length and the sound pressure p_{box} inside the box. The difference between the velocity u_0 obtained in this manner and that obtained indirectly in the measurement of the sound pressure at a distance of 1 m from the exit of the port yields a correction factor. This correction factor accounts not only for the reflections in the anechoic room, but also for the uncertainty of the exact distance between the microphone and the bass-reflex port. We assume this correction factor to be independent of amplitude. Note that the correction factor needs to be redetermined for different driving frequencies as the interference in the anechoic room is dependent on frequency.

C. A comparison of the two methods

In this section the velocity amplitude of the flow in the port measured by means of laser Doppler anemometry and that determined indirectly via measurement of the sound pressure at 1-m distance from the port in an anechoic room will be compared.

In Fig. 5 the velocity amplitudes obtained using these two methods are compared at different values of the loudspeaker voltage. The velocity amplitude obtained indirectly via measurement of the sound pressure radiated from the port is shown with and without correction for the reflections of the anechoic room. It can be seen in Fig. 5 that the velocity amplitudes obtained with laser Doppler anemometry are about 10% lower than that obtained indirectly via measurement of sound pressure. As already mentioned, the laser Doppler results are to be interpreted qualitatively, not quantitatively, as these results may show systematic errors due to laser beam distortion by the walls of the port.

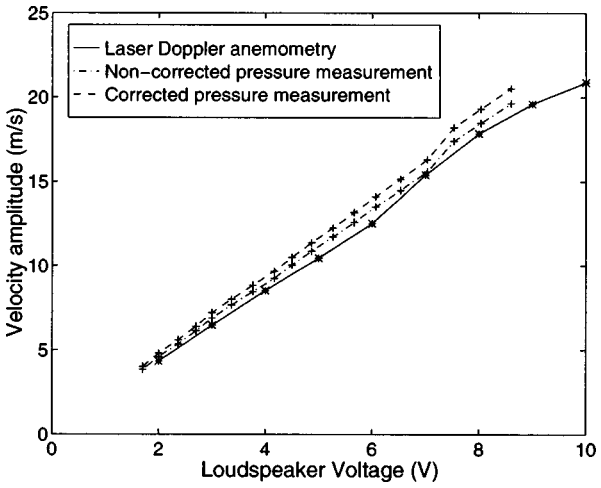

FIG. 5. Velocity amplitude measured by means of laser Doppler anemometry and that obtained indirectly via measurement of the sound pressure at a distance of 1 m from the port exit and at an angle of 45° relative to the axis of the port.

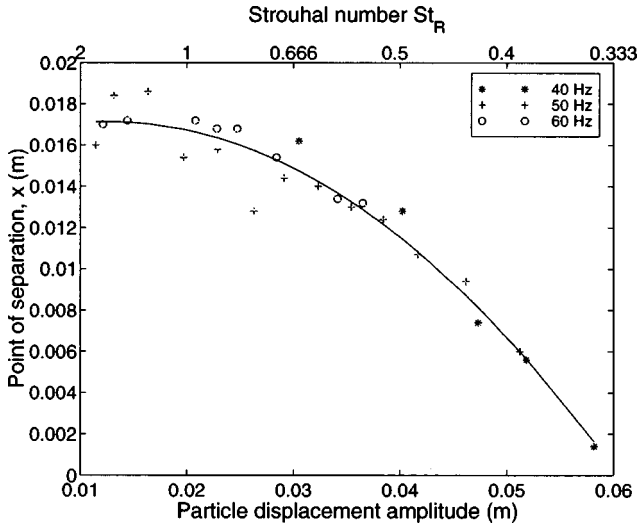

FIG. 6. Point of separation as a function of the particle displacement amplitude in the cylindrical part of the port and Strouhal number St_R.

IV. DETERMINATION OF THE POINT OF SEPARATION; A CYLINDRICAL PORT WITH ROUNDED EDGES

The time-averaged point of separation was determined for a port of physical length $L=0.13$ m, a cross-sectional radius of the cylindrical part $a_0=0.01$, and a radius of curvature $R=0.02$ m at both port ends, as shown in Fig. 1. The measurements were performed in an anechoic room. The sound pressure was measured both inside the loudspeaker box and outside the box at a distance of 1 m from the exit of the port and at an angle of 45° relative to the axis of the port. As explained above, the measurements of the sound pressure at 1-m distance were corrected to allow for reflections in the anechoic room at low frequencies.

The point of separation is expressed by the variable x, which is directed along the port axis and has its origin at the end of the cylindrical part of the port. Hence, $x=0$ corresponds to the point where the curvature just begins (immediate separation) and $x=0.02$ m corresponds to the point where the port passes into the baffle of the loudspeaker box (no separation at all). A valid range for the parameter x is between these two values.

A number of driving frequencies were considered: 40 Hz, 50 Hz, and 60 Hz. The results are shown as functions of the particle displacement amplitude and particle velocity amplitude in Figs. 6 and 7, respectively. The point of separation seems to be determined by the particle displacement and not by the particle velocity, as most of the curves in Fig. 6 coincide, especially at high values of the particle displacement, whereas they do not coincide in Fig. 7. A dimensionless quantity that determines flow separation in case of an unsteady flow is given by the Strouhal number based on the radius of curvature of the edges R as proposed by Peters *et al.*:[5]

$$\mathrm{St}_R=\frac{\omega R}{u}. \tag{14}$$

In the present case, separation begins at particle displacements of about 0.02 m (see Fig. 6), which corresponds to $\mathrm{St}_R=1$. From these data we may infer that rounded edges are a quite effective remedial measure as long as $\mathrm{St}_R>1$.

V. CONCLUSIONS

An objective indicator of a certain port geometry's ability to suppress blowing sounds is the point of separation. The larger the diameter at which separation occurs, the smaller the effect of vortex shedding due to the reduced local velocity.

The proposed method for estimating the time-averaged point of separation on the basis of measurement of the acoustic pressure inside the loudspeaker box and measurement of the sound pressure at a distance of 1 m from the port exit has been applied to a cylindrical port with rounded port edges at different driving frequencies and amplitudes. It is shown that the point of separation is determined by particle displacement and not by particle velocity. In particular, the Strouhal number $\mathrm{St}_R=\omega R/u$ based on the radius of curvature of the edges seems to be a good indicator of the onset of severe

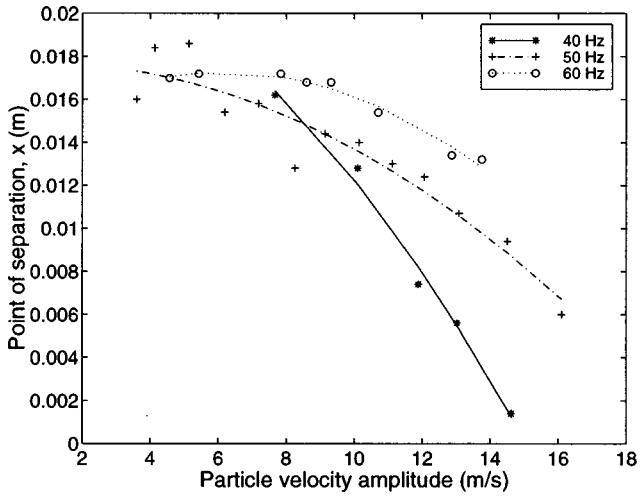

FIG. 7. Point of separation as a function of the particle velocity amplitude in the cylindrical part of the port.

vortex shedding. It was found that rounding the edges is a quite effective remedial measure as long as $\mathrm{St}_R > 1$.

[1] L. Prandtl and O. G. Tietjens, *Fundamentals of Hydro- and Aeromechanics* (Dover, New York, 1934).
[2] H. Tijdeman, ''On the propagation of sound waves in cylindrical tubes,'' J. Sound Vib. **39**, 1–33 (1975).
[3] F. Durst, A. Melling, and F. H. Whitelaw, *Principles and Practice of Laser-Doppler Anemometry* (Academic, New York, 1981).
[4] L. E. Kinsler, A. R. Frey, A. B. Coppens, and J. V. Sanders, *Fundamentals of Acoustics* (Wiley, New York, 1982).
[5] M. C. A. M. Peters, A. Hirschberg, A. J. Reijnen, and A. P. J. Wijnands, ''Damping and reflection coefficient measurements for an open pipe at low Mach and low Helmholtz numbers,'' J. Fluid Mech. **256**, 499–534 (1993).

The soft and the hard coated sphere within a point source wave field

Yani Arnaoudov
Technical University of Sofia, 1000 Sofia, Bulgaria

George Dassios and Vassilis Kostopoulos
University of Patras and ICEHT/FORTH, GR 265 00 Patras, Greece

(Received 14 October 1997; accepted for publication 9 July 1998)

An acoustically soft or hard sphere which is covered by a penetrable concentric spherical shell disturbs the propagation of an incident wave field emanating from a point source. The source is located in the exterior of the coated sphere. The medium, occupying the shell, is considered to be lossy while the dimensions of the coated sphere are much smaller than the wavelength of the incident field. For the case of a soft sphere covered with a penetrable lossy shell, the exact low frequency coefficients of the zeroth and the first order for the near field as well as the first and second order coefficients for the normalized scattering amplitude are obtained. In the case of the coated hard sphere, the zeroth and the first order coefficients of the near field, as well as the leading nonvanishing coefficient of the normalized scattering amplitude, which is of the second order, are obtained. For both cases of the soft and the hard sphere, the scattering and the absorption cross sections are calculated. The effect of the coating is expressed in terms of specific constants. A detailed discussion of the results and their physical meaning is included. For a sphere with a soft core and a point source located more than five radii away from the scatterer, or for a sphere with a hard core and a point source located more than two radii away from the scatterer, the results obtained are almost the same as if the scatterer was excited by a plane wave. © *1998 Acoustical Society of America.* [S0001-4966(98)06010-X]

PACS numbers: 43.20.Bi, 43.20.Fn [ANN]

INTRODUCTION

Scattering problems with an incident field generated at a point are not so customary in the literature of applied mathematics. Indeed, it comes as a surprise that the first reference that one can find is that of Jones in 1956,[1] while collected results for scattering of point source fields by simple shapes are included in the work of Bowman *et al.*[2] We refer also to the book[3] by Jones. Some results can also be found in the seismology literature, especially in the books by Aki and Richards[4] and that of Ben-Menahem and Singh.[5] Even more seldom in the literature are the corresponding low frequency results for scattering by small obstacles.[6–8]

On the other hand, there is great interest for such applied problems, which comes mainly from the theory of composite materials, the theory of acoustic emission, the theoretical analysis of biological studies at the cell level, from nondestructive testing and evaluation, from geophysics, from modeling in medicine and health sciences, from scattering problems connected to environmental data analysis, and from the fact that a point source field is much easier realizable in a laboratory. Nevertheless, the most important argument for scattering from point source illumination is due to the fact that the far field data, used in inversion algorithms, involve one more parameter than the case of plane wave illumination. This extra parameter concerns the distance between the point of excitation and the scatterer, and it is very useful in identifying the location of the scatterer via intersecting spheres.[6–8] In the above applications, the interest is concentrated on small scatterers which identifies the realm of low frequencies.

In a series of articles we have studied the problem of scattering of a modified point source field by a soft, or hard sphere,[6] by a sphere with an impedance boundary condition on its surface,[7] and by a penetrable sphere which could have either lossy, or lossless interior.[8] In these articles we provided analytic low frequency approximations for all possible boundaries, or transmission conditions of acoustic scattering. Of course, an analytic solution for such complicated problems is not possible if we abandon the simplicity of spherical geometry, but even the sphere is very useful in many applications, especially in the low frequency region. Furthermore, an analytic solution is always useful for testing computational algorithms and codes. Although the single sphere results are useful, the real interest, as far as the previously mentioned applications are concerned, is concentrated on the coated small scatterers. Biological cells involve a central nucleus coated by a cytoplasmic shell, granular material involve coated granules, nondestructive evaluation usually concerns the identification of core media within coated objects, human organs also form scattering obstacles buried within the body, and air or water pollutants are covered by all kind of substances.

The present work initiates a study of the effects that small coated scatterers have on the propagation of a point source field. It investigates the cases where the core is either an acoustically soft or hard scatterer which is covered with a lossy penetrable material. The case of a lossless coating is readily obtained if the compressional viscosity, which is re-

sponsible for the energy losses, is set equal to zero. The geometry of the scattering region is that of two concentric spheres and the point source is located in the exterior of both. Closed form near field solutions, accurate to $O(k^2)$ are obtained for the cases where the core behaves as a soft or as a hard sphere. The corresponding far field expressions are also provided in analytic form. A particular modification of the point source field allows recovery of all the corresponding results for plane wave excitation and comparison of the results in both cases.

Section I furnishes the mathematical formulation of the problem and explains the physical parameters involved. The low frequency theory of the two problems corresponding to the soft and to the hard coated sphere is developed in Sec. II. In Sec. III we provide the first two low frequency coefficients of the near field and the scattering amplitude, as well as the leading nonvanishing approximation of the scattering and the absorption cross section, for the case of the soft core scatterer. This is a very long task but only the final results are given. The same results, as in Sec. III, but for the hard core scatterer are provided, again in final form, in Sec. IV. In Sec. V we reduce all the results contained in Secs. III and IV to the case of plane wave excitation. Every known result,[2,6–11] that can be deduced from the content of the present work, has been reconfirmed, while particular attention has been given to the form of the results as to clearly indicate the effects that the core and the coating have upon the scattered field. The last section, Sec. VI, contains detailed numerical and physical discussion of the results obtained. This includes the dependence of the scattering and absorption cross sections on the mass density ratio, the thickness of the spherical shell, and the distance of the point source form the scatterer.

I. FORMULATION OF THE PROBLEM

We consider two concentric spheres in $\mathbb{R}^3$ with radii a_0 and a, where $a_0<a$. We denote by S_0 and S the sphere of radius a_0 and a, respectively. The exterior to S domain is denoted by V^+ and the spherical shell between S_0 and S is denoted by V^-. Within V^+ and at a distance $r_0>a$ from the center of the spheres, a point source is located emanating a time harmonic acoustic field at the frequency ω. We choose a coordinate system with its origin at the center of the spheres and its x_3-axis along the line connecting the origin with the point source, which is then located at the point $\mathbf{r}_0=(0,0,r_0)$.

Suppressing the harmonic time dependence $\exp\{-i\omega t\}$ and assuming the appropriate modification of the point source radiation, which is able to recover the corresponding plane wave results,[6] we specify the incident excess pressure field that illuminates the sphere as

$$u^i_{\mathbf{r}_0}(\mathbf{r})=\frac{r_0}{|\mathbf{r}-\mathbf{r}_0|}\,e^{ik(|\mathbf{r}-\mathbf{r}_0|-r_0)}, \tag{1}$$

where $\mathbf{r}\neq\mathbf{r}_0$ and k stands for the wave number in V^+.

Obviously, for fixed direction $\hat{\mathbf{r}}_0$,

$$\lim_{r_0\to\infty} u^i_{\mathbf{r}_0}(\mathbf{r})=e^{-ik\hat{\mathbf{r}}_0\cdot\mathbf{r}}, \tag{2}$$

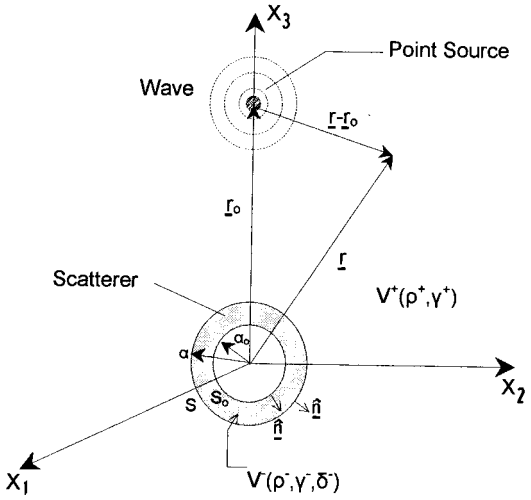

FIG. 1. Geometry of the scattering problem.

where the limit describes plane wave incidence in the direction $-\hat{\mathbf{r}}_0$. Here, and in what follows, the hat on the top of a vector indicates the corresponding unit directional vector.

We assume that V^+ is occupied by a linear, homogeneous, isotropic, and lossless acoustic medium characterized by the phase velocity c^+, the mass density ρ^+, the mean compressibility γ^+, and vanishing compressional viscosity $\delta^+=0$. A similar medium fills the spherical shell V^- which is characterized by the corresponding physical parameters c^-, ρ^-, γ^-, and δ^-. The medium in V^- could be either lossy where $\delta^->0$, or lossless, where $\delta^-=0$. This geometrical configuration is given in Fig. 1.

The scattering problem we consider here is the following. We want to find the total excess pressure field

$$u^+(\mathbf{r})=u^i_{\mathbf{r}_0}(\mathbf{r})+u^s(\mathbf{r}),\quad \mathbf{r}\in V^+-\{\mathbf{r}_0\}, \tag{3}$$

where the scattered field u^s is defined for $r>a$, and the interior excess pressure field u^- in V^-, which solve the equations

$$(\Delta+k^2)u^+(\mathbf{r})=0,\quad \mathbf{r}\in V^+-\{\mathbf{r}_0\} \tag{4}$$

and

$$(\Delta+(k^-)^2)u^-(\mathbf{r})=0,\quad \mathbf{r}\in V^-, \tag{5}$$

respectively, where k^- is the wave number in V^-.

The interior wave number k^- is complex for lossy media and it is related to k through the expression[3,8,12]

$$(k^-)^2=\eta_c^2k^2=\left(\frac{c^+}{c^-}\right)^2\frac{k^2}{1-i\omega\delta^-\gamma^-}=\eta^2\,\frac{k^2}{1-i\omega\delta^-\gamma^-}, \tag{6}$$

where η_c is the complex and η is the real index of refraction connecting the media V^+ and V^-. The branch of the square root is so chosen as to satisfy the dissipation condition $\mathrm{Im}\{k^-\}\geqslant 0$. For lossless media $\delta^-=0$, $\mathrm{Im}\{k^-\}=0$ and $\eta_c=\eta$.

Since the incident field is also generated in the finite domain it is the total field u^+ that has to satisfy the Sommerfeld radiation condition

$$\lim_{r\to\infty} r\left[\frac{\partial}{\partial r}-ik\right]u^+(\mathbf{r})=0 \tag{7}$$

uniformly over the unit sphere S^2 of the three dimensional Euclidean space.

On sphere S we demand the transmission conditions

$$u^+(\mathbf{r})=u^-(\mathbf{r}), \quad \mathbf{r}\in S \tag{8}$$

and

$$\frac{\partial}{\partial n}u^+(\mathbf{r})=B(1-ikc^+\delta^-\gamma^-)\frac{\partial}{\partial n}u^-(\mathbf{r}), \quad \mathbf{r}\in S, \tag{9}$$

where $\partial/\partial n$ denotes outward normal differentiation and

$$B=\frac{\rho^+}{\rho^-}. \tag{10}$$

Conditions (8) and (9) describe the continuity of the excess pressure field, as well as that of the normal component of the velocity field, as we cross the penetrable boundary S. On the surface S_0 of the core we assume, either the Dirichlet boundary condition

$$u^-(\mathbf{r})=0, \quad \mathbf{r}\in S_0, \tag{11}$$

which describes the fact that S_0 cannot sustain any pressure and identifies S_0 as an acoustically soft boundary, or the Neumann boundary condition

$$\frac{\partial}{\partial n}u^-(\mathbf{r})=0, \quad \mathbf{r}\in S_0, \tag{12}$$

which states that the normal velocity field vanishes, and identifies S_0 as an acoustically hard boundary. In either case, the excess pressure field u^- does not penetrate into the interior of S_0.

If we denote by

$$h(k|\mathbf{r}-\mathbf{r}'|)=\frac{e^{ik|\mathbf{r}-\mathbf{r}'|}}{ik|\mathbf{r}-\mathbf{r}'|} \tag{13}$$

the dimensionless fundamental solution for the Helmholtz operator with wave number k, then the exterior field u^+ assumes the well known integral representation

$$u^+(\mathbf{r})=u^i_{\mathbf{r}_0}(\mathbf{r})+\frac{ik}{4\pi}\int_S\Big[u^+(\mathbf{r}')\frac{\partial}{\partial n'}h(k|\mathbf{r}-\mathbf{r}'|) - h(k|\mathbf{r}-\mathbf{r}'|)\frac{\partial}{\partial n'}u^+(\mathbf{r}')\Big]ds(\mathbf{r}'), \tag{14}$$

where the integral term is defined in V^+ and the incident field in $V^+-\{\mathbf{r}_0\}$.

In the far field we have the asymptotic form

$$u^s(r)=g(\hat{r})h(kr)+O\left(\frac{1}{r^2}\right), \quad r\to\infty, \tag{15}$$

where the scattering amplitude g enjoys the representation

$$g(\hat{\mathbf{r}})=-\frac{ik}{4\pi}\int_{S^2}\Big[\frac{\partial}{\partial n'}u^+(\mathbf{r}')+ik(\hat{\mathbf{r}}\cdot\hat{\mathbf{n}}')u^+(\mathbf{r}')\Big] \times e^{-ik\hat{\mathbf{r}}\cdot\mathbf{r}'}\,ds(\mathbf{r}') \tag{16}$$

for $\hat{\mathbf{r}}\in S^2$. Representation (14) provides the scattered field everywhere outside the scatterer as a distribution of point sources of the monopole and of the dipole kind over S. On the other hand, representation (16) furnishes the angular dependence of the scattered field, far away from the scattering region, as the superposition of plane waves with amplitudes and directions of propagations distributed over S, while the radial dependence is that of a monopole at the origin.

Once the scattering amplitude is obtained, the scattering cross section is given by

$$\sigma_s=\frac{1}{k^2}\int_{S^2}|g(\hat{\mathbf{r}})|^2\,ds(\hat{\mathbf{r}}). \tag{17}$$

Similarly, for lossy coating, the absorption cross section, which does not vanish, is given by the formula

$$\sigma_a=\frac{1}{k}\,\mathrm{Im}\int_S u^+(\mathbf{r})\left(\frac{\partial}{\partial n}u^+(\mathbf{r})\right)^*ds(\mathbf{r}), \tag{18}$$

where a star indicates complex conjugation and the extinction cross section is given by the formula

$$\sigma_e=\sigma_s+\sigma_a. \tag{19}$$

Expression (18) furnishes the absorption cross section in terms of a surface integral over the exterior boundary S of the scatterer. A straightforward application of Green's second identity, as well as conditions (8), (9), Eq. (5), and formula (6), can be used to obtain the following expression

$$\sigma_a=\frac{B}{k}\,\mathrm{Im}\int_{S_0}u^-(\mathbf{r})\left(\frac{\partial}{\partial n}u^-(\mathbf{r})\right)^*ds(\mathbf{r}) + Bc^+\delta^-\gamma^-\,\mathrm{Re}\int_S u^-(\mathbf{r})\left(\frac{\partial}{\partial n}u^-(\mathbf{r})\right)^*ds(\mathbf{r}) + B\eta^2k^2\frac{c^+\delta^-\gamma^-}{1+(kc^+\delta^-\gamma^-)^2}\int_{V^-}|u^-(\mathbf{r})|^2\,d\nu(\mathbf{r}), \tag{20}$$

which provides σ_a in terms of a volume integral over the spherical shell V^- and two surface integrals over the interior and the exterior boundaries of the shell. In particular, for the soft or the hard core, the first integral on the right hand side of (20) vanishes and we arrive at

$$\sigma_a=Bc^+\delta^-\gamma^-\,\mathrm{Re}\int_S u^-(\mathbf{r})\left(\frac{\partial}{\partial n}u^-(\mathbf{r})\right)^*ds(\mathbf{r}) + B\eta^2k^2\frac{c^+\delta^-\gamma^-}{1+(kc^+\delta^-\gamma^-)^2}\int_{V^-}|u^-(\mathbf{r})|^2\,d\nu(\mathbf{r}). \tag{21}$$

If the spherical shell has zero compressional viscosity δ^-, then σ_a vanishes and the medium in V^- is lossless.

II. GOVERNING EQUATIONS AT LOW FREQUENCY

In the case where the wavelength of the incident field is much larger than the radius of the exterior sphere low fre-

quency techniques can be applied[13] and the scattering problem is reduced to a sequence of potential problems than can be solved iteratively.[11]

We consider the expansions

$$u^i_{\mathbf{r}_0}(\mathbf{r}) = \frac{r_0}{|\mathbf{r}-\mathbf{r}_0|} \sum_{n=0}^{\infty} \frac{(ik)^n}{n!} [|\mathbf{r}-\mathbf{r}_0| - r_0]^n \tag{22}$$

and

$$ikh(k|\mathbf{r}-\mathbf{r}'|) = \sum_{n=0}^{\infty} \frac{(ik)^n}{n!} |\mathbf{r}-\mathbf{r}'|^{n-1} \tag{23}$$

for the incident field and the fundamental solution, as well as the expansions

$$u^+(\mathbf{r}) = \sum_{n=0}^{\infty} \frac{(ik)^n}{n!} u_n^+(\mathbf{r}) \tag{24}$$

and

$$u^-(\mathbf{r}) = \sum_{n=0}^{\infty} \frac{(ik)^n}{n!} u_n^-(\mathbf{r}) \tag{25}$$

for the total and the interior field.

Note that every low frequency coefficient of the incident field has the same monopole singularity at the source point $\mathbf{r}_0$, while the corresponding monopole singularity at $\mathbf{r}'$ of the fundamental solution *ikh* appears in the leading term alone.

Substituting the above expansions into Eqs. (4), (5), the transmission conditions (8), (9), and boundary conditions (11), (12), we arrive, for each $n=0,1,2,...$, at equations

$$\Delta u_n^+(\mathbf{r}) = n(n-1)u_{n-2}^+(\mathbf{r}), \quad \mathbf{r} \in V^+ - \{\mathbf{r}_0\} \tag{26}$$

and

$$\Delta u_n^-(\mathbf{r}) = n(n-1)\eta^2 \sum_{\rho=0}^{n-2} \frac{(n-2)!}{\rho!} (c^+\delta^-\gamma^-)^{n-2-\rho} u_\rho^-(r), \quad \mathbf{r} \in V^-, \tag{27}$$

the transmission conditions

$$u_n^+(\mathbf{r}) = u_n^-(\mathbf{r}), \quad \mathbf{r} \in S \tag{28}$$

and

$$\frac{\partial}{\partial n} u_n^+(\mathbf{r}) = B\left[\frac{\partial}{\partial r} u_n^-(\mathbf{r}) - nc^+\delta^-\gamma^- \frac{\partial}{\partial r} u_{n-1}^-(\mathbf{r})\right], \quad \mathbf{r} \in S, \tag{29}$$

as well as the boundary condition

$$u_n^-(\mathbf{r}) = 0, \quad \mathbf{r} \in S_0 \tag{30}$$

for the soft core, or

$$\frac{\partial}{\partial n} u_n^-(\mathbf{r}) = 0, \quad \mathbf{r} \in S \tag{31}$$

for the hard core.

Note that dispersion relation (6) is recast in (27) as a geometric series in $(ikc^+\delta^-\gamma^-)$.

Similarly, from integral representation (14) we obtain the following asymptotic behavior of the total field as $r \to +\infty$

$$\begin{aligned} u_n^+(\mathbf{r}) = {} & \frac{r_0}{|\mathbf{r}-\mathbf{r}_0|} [|\mathbf{r}-\mathbf{r}_0| - r_0]^n \\ & - \frac{1}{4\pi} \sum_{\rho=1}^{n} \binom{n}{\rho} \int_S |\mathbf{r}-\mathbf{r}'|^{\rho-1} \frac{\partial}{\partial n'} u_{n-\rho}^+(\mathbf{r}') ds(\mathbf{r}') \\ & - \frac{1}{4\pi} \sum_{\rho=2}^{n} \binom{n}{\rho} (\rho-1) \int_S |\mathbf{r}-\mathbf{r}'|^{\rho-3} (\mathbf{r}-\mathbf{r}') \\ & \cdot \hat{\mathbf{n}}' u_{n-\rho}^+(\mathbf{r}') ds(\mathbf{r}') + O\left(\frac{1}{r}\right). \end{aligned} \tag{32}$$

The low frequency expansion of scattering amplitude (16) assumes the form

$$\begin{aligned} g(\hat{\mathbf{r}}) = {} & \frac{1}{4\pi} \sum_{n=0}^{+\infty} \frac{(ik)^{n+1}}{n!} \sum_{\rho=0}^{n} \binom{n}{\rho} (-1)^{\rho+1} \\ & \times \int_S (\hat{\mathbf{r}}\cdot\mathbf{r}')^\rho \frac{\partial}{\partial n'} u_{n-\rho}^+(\mathbf{r}') ds(\mathbf{r}') \\ & + \frac{1}{4\pi} \sum_{n=0}^{+\infty} \frac{(ik)^{n+2}}{n!} \sum_{\rho=0}^{n} \binom{n}{\rho} (-1)^{\rho+1} \\ & \times \int_S (\hat{\mathbf{r}}\cdot\mathbf{r}')^\rho (\hat{\mathbf{r}}\cdot\hat{\mathbf{n}}') u_{n-\rho}^+(\mathbf{r}') ds(\mathbf{r}') \end{aligned} \tag{33}$$

for $\hat{\mathbf{r}} \in S^2$.

Once the expansion for g is obtained, the corresponding expansion for the scattering cross section is readily drawn from (17). Using formula (21) and a straightforward application of Gauss's theorem, we can express the absorption cross section in the following form:

$$\begin{aligned} \sigma_a = {} & Bc^+\delta^-\gamma^-\eta^2 \sum_{n=0}^{\infty} k^{2n+2} \sum_{\sigma=0}^{n} \sum_{\rho=0}^{2n-2\sigma} (-1)^{n-\rho} \frac{(c^+\delta^-\gamma^-)^{2\sigma}}{(2n-2\sigma)!} \binom{2n-2\sigma}{\rho} \int_{V^-} u_\rho^-(r') u_{2n-2\sigma-\rho}^-(r') d\nu(r') \\ & + Bc^+\delta^-\gamma^- \sum_{n=0}^{\infty} \frac{k^{2n}}{(2n)!} \sum_{\rho=0}^{2n} (-1)^{n-\rho} \binom{2n}{\rho} \int_S u_\rho^-(\mathbf{r}') \frac{\partial}{\partial n'} u_{2n-\rho}^-(\mathbf{r}') ds(\mathbf{r}'). \end{aligned} \tag{34}$$

In the above expression of σ_a the contribution from the shell V^- and the one from the transmission surface S are explicit. Note that the contribution from the surface integral over S is by two orders of magnitude higher than the contribution from the volume integral over the shell V^-.

III. THE COATED SOFT SPHERE

The Rayleigh approximation for the near field is obtained by solving the following boundary value problems:

$$\Delta u_0^{+D}(\mathbf{r})=0, \quad \mathbf{r}\in V^{\pm}-\{\mathbf{r}_0\}, \tag{35}$$

$$\Delta u_0^{-D}(\mathbf{r})=0, \quad \mathbf{r}\in V^{-}, \tag{36}$$

$$u_0^{+D}(\mathbf{r})=u_0^{-D}(\mathbf{r}), \quad \mathbf{r}\in S, \tag{37}$$

$$\frac{\partial}{\partial n}u_0^{+D}(\mathbf{r})=B\frac{\partial}{\partial n}u_0^{-D}(\mathbf{r}), \quad \mathbf{r}\in S, \tag{38}$$

$$u_0^{-D}(\mathbf{r})=0, \quad \mathbf{r}\in S_0, \tag{39}$$

$$u_0^{+D}(\mathbf{r})=\frac{r_0}{|\mathbf{r}-\mathbf{r}_0|}+O\left(\frac{1}{r}\right), \quad \mathbf{r}\to\infty, \tag{40}$$

where the superscript D indicates Dirichlet boundary conditions on the core S_0. Long calculations, which are not included here, lead to the following exact solution for the leading low frequency approximation of the near field, for the soft sphere which is coated with a lossy medium:

$$\begin{aligned}u_0^{+D}(\mathbf{r})=&\sum_{n=0}^{\infty}\left(\frac{r}{r_0}\right)^n P_n(\cos\,\theta)\\&+\sum_{n=0}^{\infty}\left[K_n(1-l^{2n+1})-1\right]\\&\times\left(\frac{a}{r_0}\right)^n\left(\frac{a}{r}\right)^{n+1}P_n(\cos\,\theta)\end{aligned} \tag{41}$$

and

$$\begin{aligned}u_0^{-D}(\mathbf{r})=&\sum_{n=0}^{\infty}K_n\left(\frac{r}{r_0}\right)^n P_n(\cos\,\theta)\\&-\sum_{n=0}^{\infty}K_n\left(\frac{a_0}{r_0}\right)^n\left(\frac{a_0}{r}\right)^{n+1}P_n(\cos\,\theta),\end{aligned} \tag{42}$$

where P_n stand for the Legendre polynomials, the parameter

$$l=\frac{a_0}{a}\in(0,1) \tag{43}$$

indicates the thickness of the shell, and

$$K_n=\frac{2n+1}{(nB+n+1)+(n+1)(B-1)l^{2n+1}} \tag{44}$$

for every $n=0,1,2,\ldots$. References 12 and 14 contain all the basic expansions and functions needed.

Note that at the zeroth order of approximation the solution depends solely on the density ratio B. Hence, we can eliminate the shell by taking $B\to 1$. In that case, $K_n\to 1$ and solution (41) recover the corresponding solution [Ref. 6, Eq. (34)] for the single soft sphere. Consequently, the constants K_n provide the effect of the coating. Furthermore, since for $r<r_0$

$$\frac{r_0}{|\mathbf{r}-\mathbf{r}_0|}=\sum_{n=0}^{\infty}\left(\frac{r}{r_0}\right)^n P_n(\cos\,\theta) \tag{45}$$

the first series in expression (42) for u_0^{D-} shows that the shell modifies each interior harmonic component of the incident field through multiplication by K_n. We also indicate here that the Rayleigh approximation is not influenced by the lossy character of the shell.

Next, we look at the first order approximation which is determined as the solution of the equations

$$\Delta u_1^{+D}(\mathbf{r})=0, \quad \mathbf{r}\in V^{+}-\{\mathbf{r}_0\}, \tag{46}$$

$$\Delta u_1^{-D}(\mathbf{r})=0, \quad \mathbf{r}\in V^{-}, \tag{47}$$

which satisfy the transmission conditions

$$u_1^{+D}(\mathbf{r})=u_1^{-D}(\mathbf{r}), \quad \mathbf{r}\in S, \tag{48}$$

$$\frac{\partial}{\partial n}u_1^{+D}(\mathbf{r})=B\left[\frac{\partial}{\partial n}u_1^{-D}(\mathbf{r})-c^+\delta^-\gamma^-\frac{\partial}{\partial n}u_0^{-D}(\mathbf{r})\right], \quad \mathbf{r}\in S, \tag{49}$$

the boundary condition

$$u_1^{-D}(\mathbf{r})=0, \quad \mathbf{r}\in S_0, \tag{50}$$

and assumes the asymptotic form

$$\begin{aligned}u_1^{+D}(\mathbf{r})=&r_0\left(1-\frac{r_0}{|\mathbf{r}-\mathbf{r}_0|}\right)\\&-\frac{1}{4\pi}\int_S\frac{\partial}{\partial n}u_0^{+D}(\mathbf{r})ds(\mathbf{r})+O\left(\frac{1}{r}\right),\\&r\to\infty.\end{aligned} \tag{51}$$

In this case, the lossy character of the shell enters the scene through the transmission condition (49) where the constants δ^- and γ^- appear for the first time.

In solving this complicated interior–exterior boundary transmission value problem we first calculate the integral in (51), which by virtue of orthogonality and expression (41) gives

$$-\frac{1}{4\pi}\int_S\frac{\partial}{\partial n}u_0^{+D}(\mathbf{r})ds(\mathbf{r})=-a_0K_0B. \tag{52}$$

Then a long series of tedious calculations leads to the following form of the solution:

$$u_1^{+D}(\mathbf{r}) = a_0 K_0 B\left(\frac{a_0 K_0 B}{r} - 1\right) - r_0 \sum_{n=1}^{\infty} \left(\frac{r}{r_0}\right)^n P_n(\cos\,\theta)$$
$$- a \sum_{n=1}^{\infty} [K_n(1-l^{2n+1}) - 1]\left(\frac{a}{r_0}\right)^{n-1}\left(\frac{a}{r}\right)^{n+1}$$
$$\times P_n(\cos\,\theta) + Bc^+\delta^-\gamma^- \sum_{n=0}^{\infty} K_n^2 \frac{1-l^{2n+1}}{2n+1}$$
$$\times [n+(n+1)l^{2n+1}]\left(\frac{a}{r_0}\right)^n\left(\frac{a}{r}\right)^{n+1} P_n(\cos\,\theta) \quad (53)$$

in the exterior medium V^+, and

$$u_1^{-D}(\mathbf{r}) = K_0^2 Bl(a - c^+\delta^-\gamma^-)\left(\frac{a_0}{r} - 1\right) - r_0 \sum_{n=1}^{\infty} K_n \left(\frac{r}{r_0}\right)^n$$
$$\times P_n(\cos\,\theta) + a_0 \sum_{n=1}^{\infty} K_n \left(\frac{a_0}{r_0}\right)^{n-1}\left(\frac{a_0}{r}\right)^{n+1}$$
$$\times P_n(\cos\,\theta) + Bc^+\delta^-\gamma^- \sum_{n=1}^{\infty} K_n^2 \frac{n+(n+1)l^{2n+1}}{2n+1}$$
$$\times \left[\left(\frac{r}{r_0}\right)^n - \left(\frac{a_0}{r_0}\right)^n\left(\frac{a_0}{r}\right)^{n+1}\right] P_n(\cos\,\theta) \quad (54)$$

within the shell V^-.

If the medium in the shell is lossless, then $\delta^- = 0$ and the last series in both u_1^+ and in u_1^- vanish. Then, expressions (53) and (54) solve the corresponding problem for the soft sphere with lossless coating. On the other hand, $B \to 1$, $K_n \to 1$, $\delta^- = 0$ recovers the first order approximation of the single soft sphere case [Ref. 6, Eq. (38)]. Along the same line, we can take the limit $a_0 \to 0$, or $l \to 0$, of (41), (42) and of (53), (54) to arrive at the zeroth and the first order low frequency coefficients for the lossy sphere respectively, or for the lossless sphere, if we also set $\delta^- = 0$.[8]

The approximation of the far field, based on the knowledge of $u_0^{\pm}$ and $u_1^{\pm}$, is derived from (33) as

$$g^D(\hat{\mathbf{r}}) = -\frac{ik}{4\pi}\int_S \frac{\partial}{\partial n'} u_0^{+D}(\mathbf{r}')\,ds(\mathbf{r}')$$
$$+ \frac{k^2}{4\pi}\int_S \Big[\frac{\partial}{\partial r'} u_1^{+D}(\mathbf{r}') - (\hat{\mathbf{r}}\cdot\mathbf{r}')\frac{\partial}{\partial n'} u_0^{+D}(\mathbf{r}')$$
$$+ (\hat{\mathbf{r}}\cdot\hat{\mathbf{n}}')u_0^{+D}(\mathbf{r}')\Big] ds(\mathbf{r}'), + O(k^3), \quad k \to 0. \quad (55)$$

Using the values of integrals (A1)–(A4) in the Appendix, we arrive at the following expression for the scattering amplitude

$$g^D(\hat{\mathbf{r}}) = -i(ka)lK_0 B$$
$$+ (ka)^2\Big[-lK_0^2 B\Big(lB + \frac{1}{a}c^+\delta^-\gamma^-(1-l)\Big)$$
$$+ \frac{a}{r_0}(K_1(1-l^3)-1)P_1(\cos\,\theta)\Big] + O((ka)^3),$$
$$ka \to 0. \quad (56)$$

From (17) and (56) we easily obtain the following leading term approximation for the scattering cross section:

$$\sigma_s^D = 4\pi a^2 l^2 K_0^2 B^2 + O((ka)^2)$$
$$= 4\pi(a_0 K_0 B)^2 + O((ka)^2), \quad ka \to 0. \quad (57)$$

In the same fashion, from (34) we obtain

$$\sigma_a^D = Bc^+\delta^-\gamma^- \int_S u_0^{-D}(\mathbf{r})\,\frac{\partial}{\partial n} u_0^{-D}(\mathbf{r})\,ds(\mathbf{r}) + O((ka)^2),$$
$$ka \to 0, \quad (58)$$

and a lengthy evaluation of the integral yields

$$\sigma_a^D = 4\pi a B c^+\delta^-\gamma^- \sum_{n=0}^{\infty} \frac{K_n^2}{2n+1}\left(\frac{a}{r_0}\right)^{2n}(1-l^{2n+1})$$
$$\times (n+(n+1)l^{2n+1}) + O((ka)^2), \quad ka \to 0. \quad (59)$$

The far field expressions (56), (57), and (59) reduce to the corresponding formulae for the soft sphere when $B=1$ and $\delta^- = 0$,[6] to the lossy penetrable sphere when $l=0$, and to a lossless penetrable sphere when $l=0$ and $\delta^- = 0$.[8] Again, the constants K_n are to be interpreted as the influence of the coating, so that $K_n = 1$ for $B=1$.

IV. THE COATED HARD SPHERE

Indicating all the relative fields with a superscript N to denote the Neumann boundary condition on the surface S_0 of the core, the Rayleigh approximation $u_0^{\pm N}$ for the coated hard sphere has to satisfy the equations

$$\Delta u_0^{+N}(\mathbf{r}) = 0, \quad \mathbf{r} \in V^+ - \{\mathbf{r}_0\}, \quad (60)$$

$$\Delta u_0^{-N}(\mathbf{r}) = 0, \quad \mathbf{r} \in V^-, \quad (61)$$

the transmission conditions

$$u_0^{+N}(\mathbf{r}) = u_0^{-N}(\mathbf{r}), \quad \mathbf{r} \in S, \quad (62)$$

$$\frac{\partial}{\partial n} u_0^{+N}(\mathbf{r}) = B\,\frac{\partial}{\partial n} u_0^{-N}(\mathbf{r}), \quad \mathbf{r} \in S, \quad (63)$$

the Neumann boundary condition

$$\frac{\partial}{\partial n} u_0^{+N}(\mathbf{r}) = 0, \quad \mathbf{r} \in S, \quad (64)$$

and the asymptotic form

$$u_0^{+N}(\mathbf{r}) = \frac{r_0}{|\mathbf{r}-\mathbf{r}_0|} + O\left(\frac{1}{r}\right), \quad r \to \infty. \tag{65}$$

The particular constants that play the role that K_n played for the soft core case are now given by

$$L_n = \frac{2n+1}{(nB+n+1) - n(B-1)l^{2n+1}} \tag{66}$$

for every $n = 0,1,2,\ldots$. Here again $B \to 1$ implies that $L_n \to 1$, and the L_n's specify the effect that the coating has on the problem of scattering by a hard sphere.

The solution of (60)–(65) assumes the form

$$u_0^{+N}(\mathbf{r}) = \sum_{n=0}^{\infty} \left(\frac{r}{r_0}\right)^n P_n(\cos\,\theta) + \sum_{n=1}^{\infty} \left[L_n\left(1 + \frac{n}{n+1}\, l^{2n+1}\right) - 1 \right] \times \left(\frac{a}{r_0}\right)^n \left(\frac{a}{r}\right)^{n+1} P_n(\cos\,\theta) \tag{67}$$

and

$$u_0^{-N}(\mathbf{r}) = \sum_{n=0}^{\infty} L_n \left(\frac{r}{r_0}\right)^n P_n(\cos\,\theta) + \sum_{n=1}^{\infty} L_n \frac{n}{n+1} \left(\frac{a_0}{r_0}\right)^n \left(\frac{a_0}{r}\right)^{n+1} P_n(\cos\,\theta). \tag{68}$$

Similarly, since

$$\int_S \frac{\partial}{\partial n}\, u_0^{+N}(\mathbf{r})\, ds(\mathbf{r}) = 0, \tag{69}$$

the first order low frequency coefficient solves the following problem:

$$\Delta u_1^{+N}(\mathbf{r}) = 0, \quad \mathbf{r} \in V^+ - \{\mathbf{r}_0\}, \tag{70}$$

$$\Delta u_1^{-N}(\mathbf{r}) = 0, \quad \mathbf{r} \in V^-, \tag{71}$$

$$u_1^{+N}(\mathbf{r}) = u_1^{-N}(\mathbf{r}), \quad \mathbf{r} \in S, \tag{72}$$

$$\frac{\partial}{\partial n}\, u_1^{+N}(\mathbf{r}) = B\left[\frac{\partial}{\partial n}\, u_1^{-N}(\mathbf{r}) - c^+\delta^-\gamma^-\, \frac{\partial}{\partial n}\, u_0^{-N}(\mathbf{r})\right], \quad \mathbf{r} \in S, \tag{73}$$

$$\frac{\partial}{\partial n}\, u_1^{-N}(\mathbf{r}) = 0, \quad \mathbf{r} \in S_0, \tag{74}$$

and

$$u_1^{+N}(\mathbf{r}) = r_0\left(1 - \frac{r_0}{|\mathbf{r}-\mathbf{r}_0|}\right) + O\left(\frac{1}{r}\right), \quad r \to \infty. \tag{75}$$

Another sequence of long calculations concludes the solution of (70)–(75) that follows:

$$\begin{aligned} u_1^{+N}(\mathbf{r}) = & -r_0 \sum_{n=1}^{\infty} \left(\frac{r}{r_0}\right)^n P_n(\cos\,\theta) \\ & - a \sum_{n=1}^{\infty} \left[L_n\left(1 + \frac{n}{n+1}\, l^{2n+1}\right) - 1 \right] \left(\frac{a}{r_0}\right)^{n-1} \left(\frac{a}{r}\right)^{n+1} \\ & \times P_n(\cos\,\theta) + Bc^+\delta^-\gamma^- \sum_{n=1}^{\infty} L_n^2\, \frac{n}{2n+1} \\ & \times \left(1 + \frac{n}{n+1}\, l^{2n+1}\right)(1 - l^{2n+1}) \left(\frac{a}{r_0}\right)^n \left(\frac{a}{r}\right)^{n+1} \\ & \times P_n(\cos\,\theta) \end{aligned} \tag{76}$$

and

$$\begin{aligned} u_1^{-N}(\mathbf{r}) = & -r_0 \sum_{n=1}^{\infty} L_n \left(\frac{r}{r_0}\right)^n P_n(\cos\,\theta) \\ & - a_0 \sum_{n=1}^{\infty} L_n\, \frac{n}{n+1} \left(\frac{a_0}{r_0}\right)^{n-1} \left(\frac{a_0}{r}\right)^{n+1} P_n(\cos\,\theta) \\ & + Bc^+\delta^-\gamma^- \sum_{n=1}^{\infty} L_n^2\, \frac{n}{2n+1}\, (1 - l^{2n+1}) \left[\left(\frac{r}{r_0}\right)^n \right. \\ & \left. + \frac{n}{n+1} \left(\frac{a_0}{r_0}\right)^n \left(\frac{a_0}{r}\right)^{n+1} \right] P_n(\cos\,\theta). \end{aligned} \tag{77}$$

All special cases of the single hard sphere[6] and the lossy or lossless penetrable case[8] are recoverable from the above solutions.

Expressions (55) for the scattering amplitude hold for the case of the hard core too, and the integrals involved are given by (A5)–(A8) in the Appendix. The final form of g^N is

$$g^N(\hat{\mathbf{r}}) = (ka)^2\, \frac{a}{r_0}\, \frac{L_1}{3} \left[1 + \frac{1}{2}\, l^3 - B(1 - l^3) \right] P_1(\cos\,\theta) + O((ka)^3), \quad ka \to 0. \tag{78}$$

Similarly, the scattering cross-section formula (17) yields

$$\sigma_s^N = 4\pi a^2 (ka)^2 \left(\frac{a}{r_0}\right)^2 \frac{L_1^2}{27} \left[1 + \frac{1}{2}\, l^3 - B(1 - l^3) \right]^2 + O((ka)^4), \quad ka \to 0. \tag{79}$$

Formula (58) provides the leading approximation to the hard core sphere as well, and after the calculations are performed we conclude that

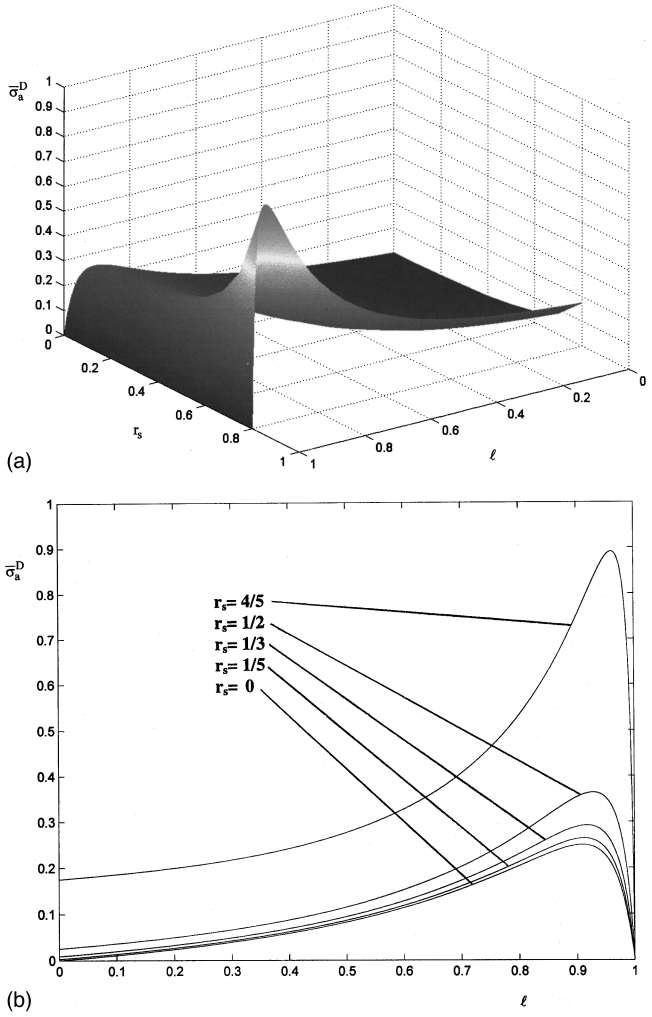

FIG. 2. The normalized absorption cross section, $\overline{\sigma}_a^D$, for $B=10^{-1}$ as a function of shell thickness (l) and distance from the source (r_s). (a) 3-D plot; (b) intersections (from top to bottom) at $r_s=4/5$, 1/2, 1/3, 1/5, 0.

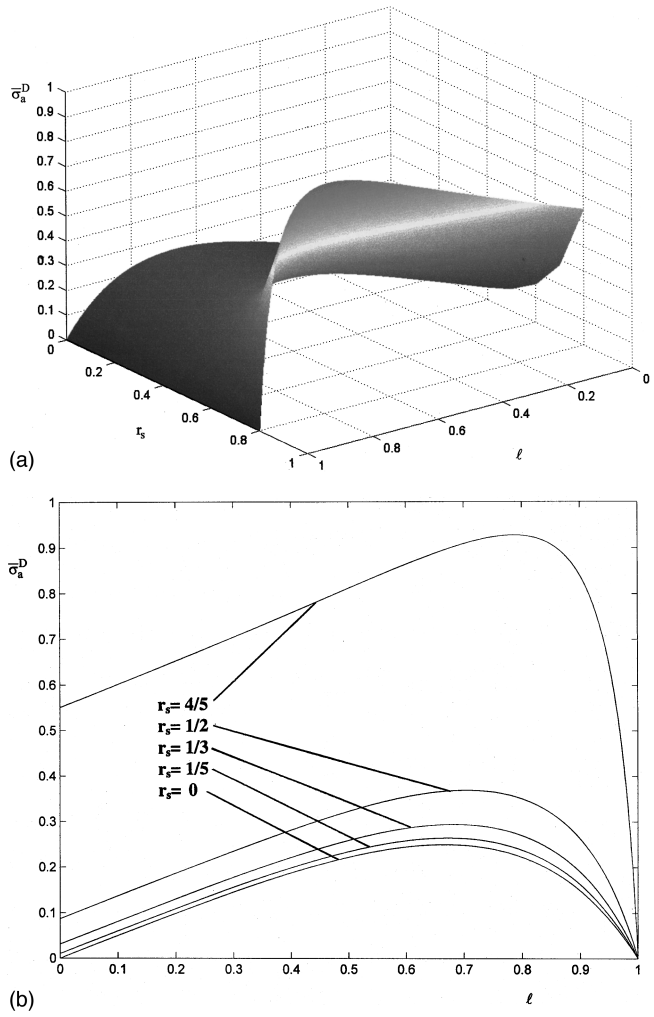

FIG. 3. The normalized absorption cross section, $\overline{\sigma}_a^D$, for $B=2^{-1}$ as a function of shell thickness (l) and distance from the source (r_s). (a) 3-D plot; (b) intersections (from top to bottom) at $r_s=4/5$, 1/2, 1/3, 1/5, 0.

$$\sigma_a^N = 4\pi a B c^+ \delta^- \gamma^- \sum_{n=1}^{\infty} \frac{n}{2n+1} L_n^2\left(\frac{a}{r_0}\right)^{2n} (1-l^{2n+1}) \times\left(1+\frac{n}{n+1} l^{2n+1}\right)+O((ka)^2), \quad ka\to 0. \tag{80}$$

Note that while for the coated soft sphere the low frequency order of the scattering and the absorption cross section are the same, for the coated hard sphere the absorption cross section is by two orders of magnitude more prominent than the scattering cross section.

V. REDUCTION TO PLANE WAVE INCIDENCE

As we explained in the beginning of Sec. I, our point source field is so modified by amplitude and phase as to be able to transform to a plane wave when the source approaches infinity. In fact, by (2) it is a plane wave propagating in the direction $-\hat{\mathbf{r}}_0$. By considering the same limiting case of $r_0\to\infty$ in our results, in Secs. III and IV, we confirm the following plane wave incidence counterparts. For the near fields corresponding to the soft core case, we obtain

$$u_0^{+D}(\mathbf{r}) = 1-\frac{B}{1+(B-1)l}\frac{a_0}{r}, \tag{81}$$

$$u_0^{-D}(\mathbf{r}) = \frac{1}{1+(B-1)l}\left(1-\frac{a_0}{r}\right), \tag{82}$$

and

$$u_1^{+D}(\mathbf{r}) = \frac{Ba_0}{1+(B-1)l}\left[\frac{Ba_0+c^+\delta^-\gamma^-(1-l)}{1+(B-1)l}\frac{1}{r}-1\right] - rP_1(\cos\theta) - \frac{(1-l)^3-B(1+2l^3)}{(B+2)+2(B-1)l^3}\frac{a^3}{r^2}P_1(\cos\theta), \tag{83}$$

$$u_1^{-D}(\mathbf{r}) = \frac{B(a_0-lc^+\delta^-\gamma^-)}{[1+(B-1)l]^2}\left(\frac{a_0}{r}-1\right) - \frac{3}{(B+2)+2(B-1)l^3}\left(r-\frac{a_0^3}{r^2}\right)P_1(\cos\theta), \tag{84}$$

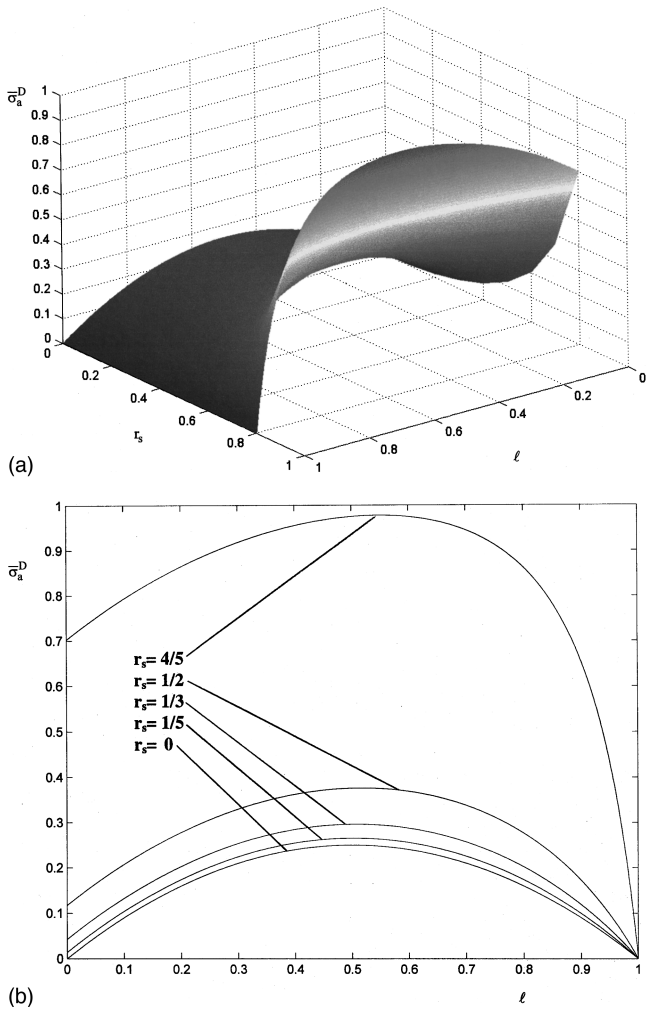

FIG. 4. The normalized absorption cross section, $\overline{\sigma_a^D}$, for $B=1$ as a function of shell thickness (l) and distance from the source (r_s). (a) 3-D plot; (b) intersections (from top to bottom) at $r_s=4/5$, 1/2, 1/3, 1/5, 0.

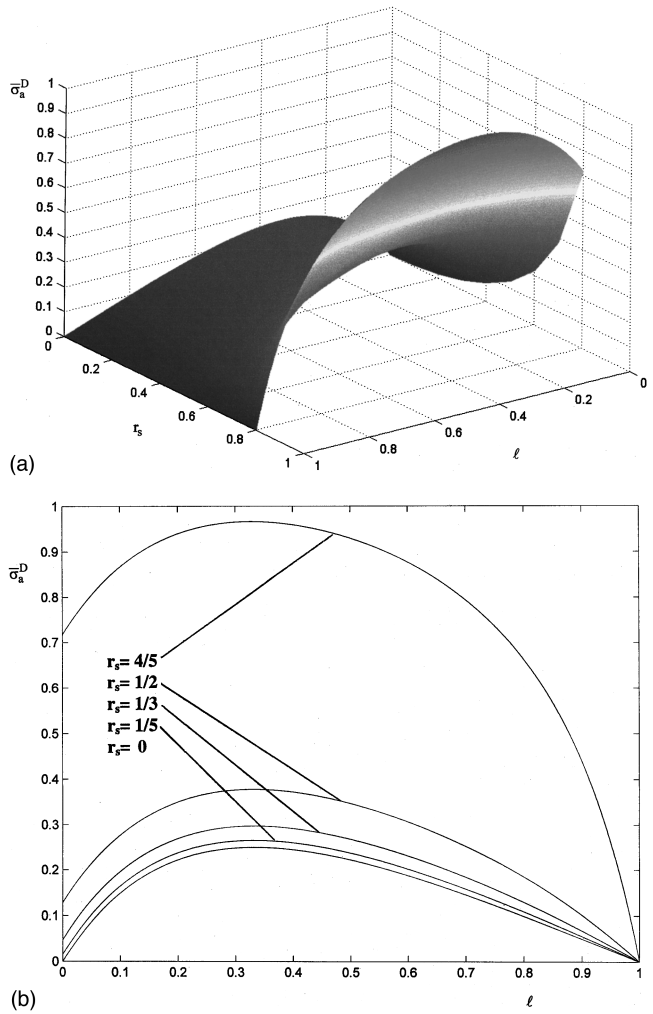

FIG. 5. The normalized absorption cross section, $\overline{\sigma_a^D}$, for $B=2$ as a function of shell thickness (l) and distance from the source (r_s). (a) 3-D plot; (b) intersections (from top to bottom) at $r_s=4/5$, 1/2, 1/3, 1/5, 0.

which, for $\delta^-=0$, coincide with Formulae (100), (101), (102), (103) in Ref. 10.

Similarly, in the far field we obtain

$$g^D(\hat{\mathbf{r}})=-i(ka)\,\frac{Bl}{1+(B-1)l}-(ka)^2\,\frac{Bl}{[1+(B-1)l]^2}\times\left[Bl+(1-l)\,\frac{c^+\delta^-\gamma^-}{a}\right]+O((ka)^3),\quad ka\to 0 \tag{85}$$

for the scattering amplitude,

$$\sigma_s^D=4\pi a^2\left[\frac{Bl}{1+(B-1)l}\right]^2+O((ka)^2),\quad ka\to 0 \tag{86}$$

for the scattering cross section, and

$$\sigma_a^D=4\pi a\,\frac{Bc^+\delta^-\gamma^-l(1-l)}{[1+(B-1)l]^2}+O((ka)^2),\quad ka\to 0 \tag{87}$$

for the adsorption cross section. Again, for lossless coating, (85) and (86) are included in (110) and (111) in Ref. 10, respectively.

Note that, as the source approaches infinity, the contribution from the highest multipole to every approximation of g vanishes.

In the case of the coated hard sphere the corresponding reductions to plane wave incidence are

$$u_0^{+N}(\mathbf{r})=1,\quad u_0^{-N}(\mathbf{r})=1, \tag{88}$$

$$u_1^{+N}(\mathbf{r})=-rP_1(\cos\,\theta)+\frac{(2B+1)(1-l^3)-3}{(B+2)-(B-1)l^3}\,\frac{a^3}{2r^2}\,P_1(\cos\,\theta), \tag{89}$$

$$u_1^{-N}(\mathbf{r})=-\frac{3a_0}{(B+2)-(B-1)l^3}\left(\frac{r}{a_0}+\frac{a_0^2}{2r^2}\right)P_1(\cos\,\theta) \tag{90}$$

for the near field, while in the far field the leading term approximations given by (78), (79), and (80) are all zero. Hence, the interaction of a coated hard sphere with an inci-

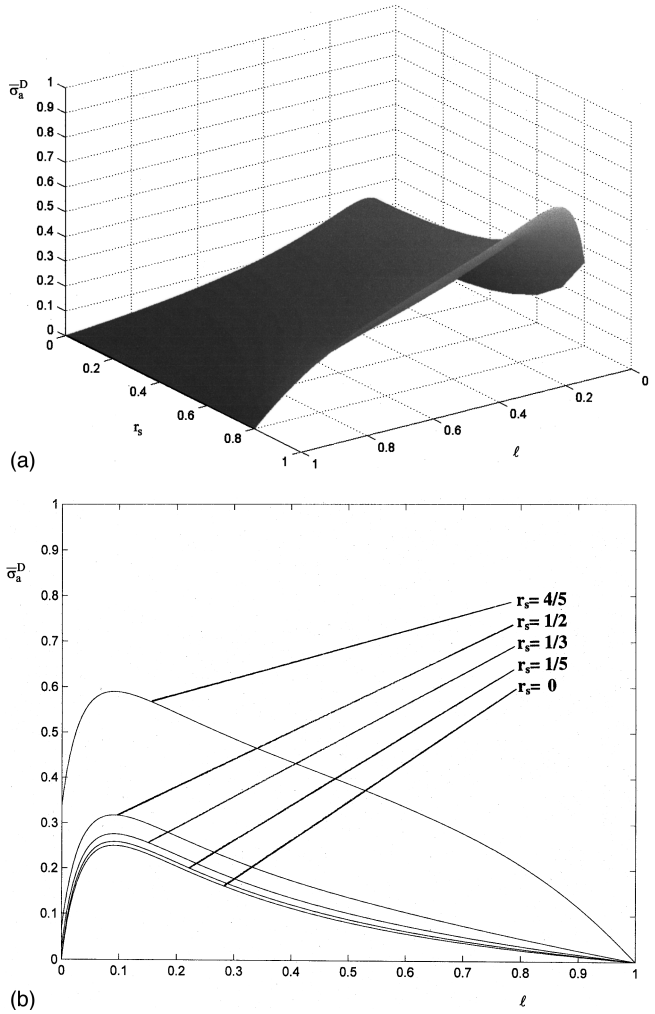

FIG. 6. The normalized absorption cross section, $\overline{\sigma_a^D}$, for $B=10$ as a function of shell thickness (l) and distance from the source (r_s). (a) 3-D plot; (b) intersections (from top to bottom) at $r_s=4/5$, 1/2, 1/3, 1/5, 0.

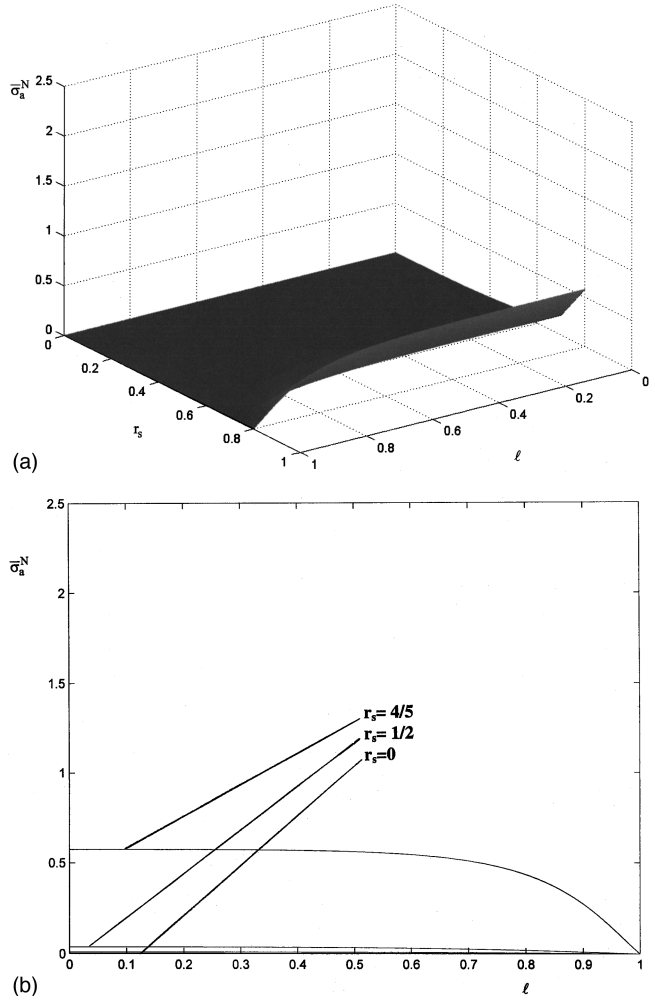

FIG. 7. The normalized absorption cross section, $\overline{\sigma_a^N}$, for $B=10^{-1}$ as a function of shell thickness (l) and distance from the source (r_s). (a) 3-D plot; (b) intersections (from top to bottom) at $r_s=4/5$, 1/2, 1/3, 1/5, 0.

dent low frequency field is weaker when the incident field is a plane wave than when it is a spherical wave.

VI. DISCUSSION AND CONCLUSIONS

In this section we discuss how the scattering cross section and the absorption cross section are dependent on the main physical and geometrical parameters of the problem. In particular, we observe that radius a of the exterior sphere, the phase velocity c^+ of the surrounding medium, and the mean compressibility γ^- as well as the compressional viscosity δ^- of the material that occupies the spherical shell, enter expressions (59) and (80) for the absorption cross section in a linear multiplicative way. Therefore, the interesting parameters of the problem are the ratio B of the mass densities, the parameter l that determines the thickness of the penetrable shell, and the parameter

$$r_s=\frac{a}{r_0} \tag{91}$$

that specifies the distance between the source and the scatterer.

The parameter B is a positive number which takes values less than one whenever the mass density in the shell is larger than the mass density of the exterior medium, and larger than one in the opposite case. If $B=1$, then the mass density of the spherical shell coincides with the mass density of the surrounding medium and the shell influences the scattering process only through the different mean compressibilities within V^- and V^+. The geometric parameter l varies between the value zero, which corresponds to a penetrable sphere[8] and the value one, which recovers either the soft or the hard sphere,[6] according to whether the surface of the core is assumed to be soft or hard. The parameter r_s also varies between zero and one. It actually varies between the zero value, which corresponds to plane wave excitation, and to some value strictly less than one, since at $r_s=1$ the point source lies on the surface and our formulation of scattering theory fails. In this case we deal with a radiation rather than a scattering problem. Note that all three basic parameters, B, l, and r_s, are dimensionless.

We start our discussion with the case where the core has a soft surface, i.e., S_0 is a pressure release boundary. From (44) and (57) we obtain

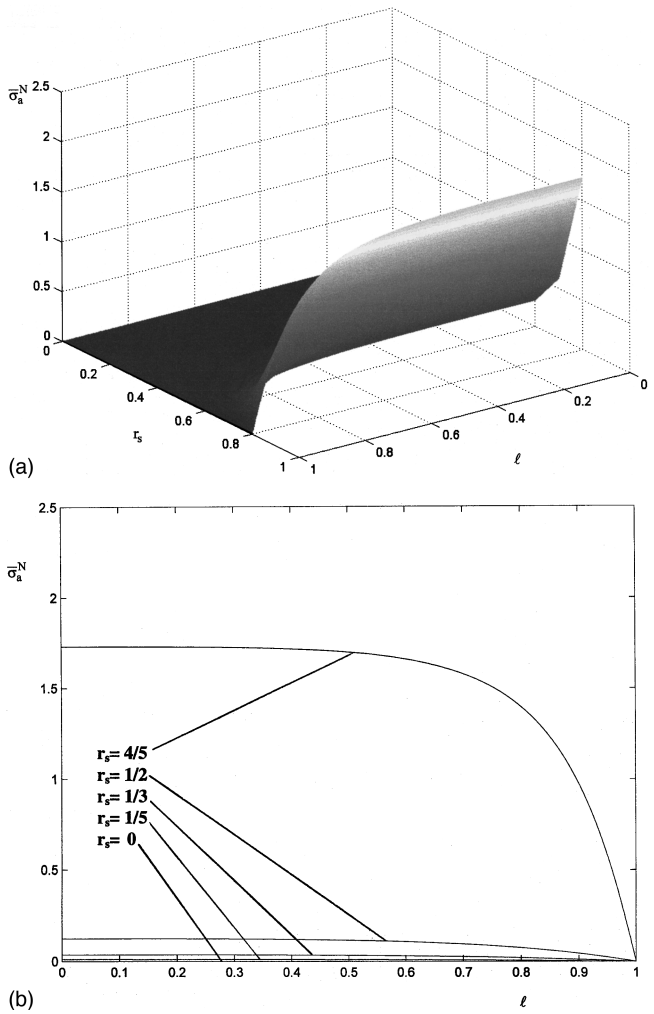

FIG. 8. The normalized absorption cross section, $\overline{\sigma_a^N}$, for $B=2^{-1}$ as a function of shell thickness (l) and distance from the source (r_s). (a) 3-D plot; (b) intersections (from top to bottom) at $r_s=4/5$, 1/2, 1/3, 1/5, 0.

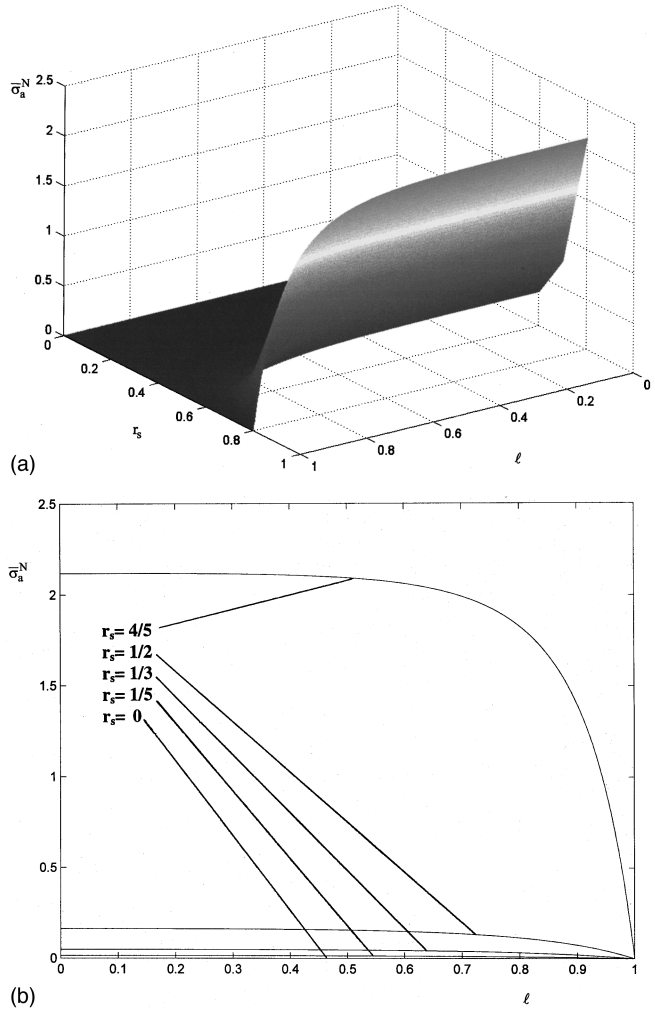

FIG. 9. The normalized absorption cross section, $\overline{\sigma_a^N}$, for $B=1$ as a function of shell thickness (l) and distance from the source (r_s). (a) 3-D plot; (b) intersections (from top to bottom) at $r_s=4/5$, 1/2, 1/3, 1/5, 0.

$$\overline{\sigma_s^D}=\frac{\sigma_s^D}{4\pi a^2}=\left[1+\frac{1}{lB}-\frac{1}{B}\right]^{-2}+O(k^2),\quad k\to 0 \tag{92}$$

from which it follows that the leading low frequency approximation, or Rayleigh approximation, of the scattering cross section is a monotonically increasing function of l. In other words, the thinner the shell the larger the scattering cross section. As $l\to 1$, the core disappears and (57) recovers the well known Rayleigh approximation for a soft sphere

$$\sigma_s^{\text{soft}}=4\pi a^2+O(k^2),\quad k\to 0, \tag{93}$$

which is the maximum value of σ_s^D as a function of l. At the other end, as $l\to 0$ the soft core disappears and we deal with a penetrable sphere for which the leading approximation of the scattering cross section is of order k^2.

Since

$$\frac{\partial\overline{\sigma_s^D}}{\partial B}=\frac{2Bl^2(1-l)}{(lB+1-l)^3}>0, \tag{94}$$

it follows that the scattering cross section is also an increasing function of B.

Hence for given shell thickness and mass density in V^+, as the mass density of the shell decreases the corresponding scattering cross section increases.

From our previous discussion on the variation of B and l, it follows that the quantity $(lB+1-l)$ is always positive so that no resonance occurs. We remark finally that the location of the point source has no influence on the leading term of σ_s^D, which coincides with the scattering cross section (86) for plane wave incidence.

A similar analysis of the scattering cross section (79) which provides the Rayleigh approximation for the case of a hard core leads to

$$\overline{\sigma_s^N}=\frac{3\sigma_s^N}{\pi a^4k^2}=r_s^2\left[\frac{2+l^3-2B(1-l^3)}{2+l^3+B(1-l^3)}\right]^2+O(k^2),\quad k\to 0, \tag{95}$$

where the denominator is always positive.

The dependence on r_s is obvious. The further away the point source, the less the scattering cross section, and for plane wave excitation the k^2-term vanishes leaving the Rayleigh approximation of σ_s^N to be of order k^4.

Rewriting (95) as

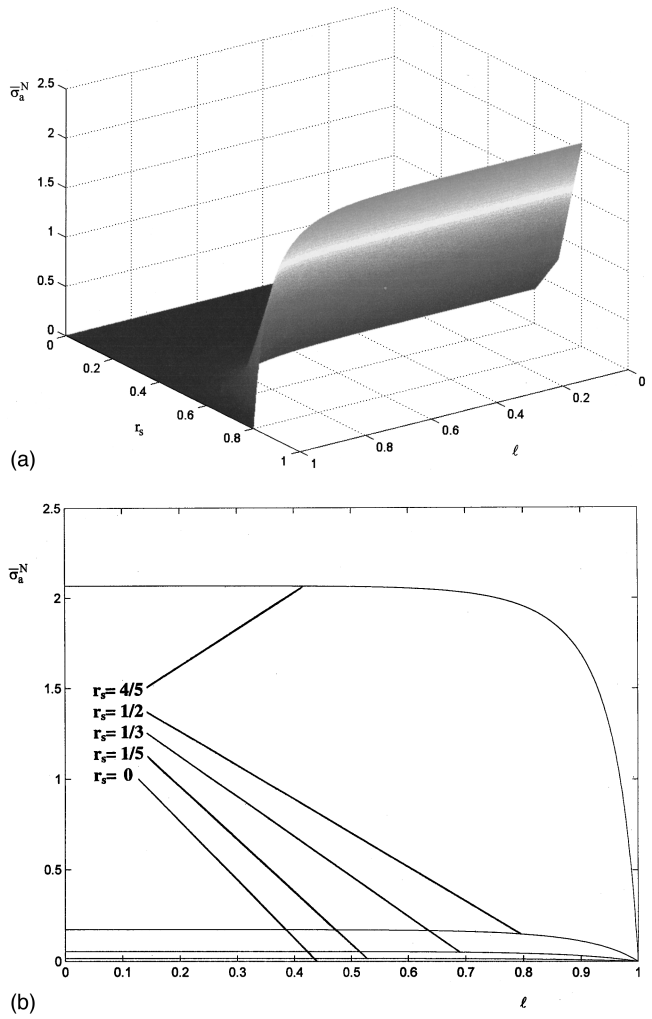

FIG. 10. The normalized absorption cross section, $\overline{\sigma}_a^N$, for $B=2$ as a function of shell thickness (l) and distance from the source (r_s). (a) 3-D plot; (b) intersections (from top to bottom) at $r_s=4/5$, 1/2, 1/3, 1/5, 0.

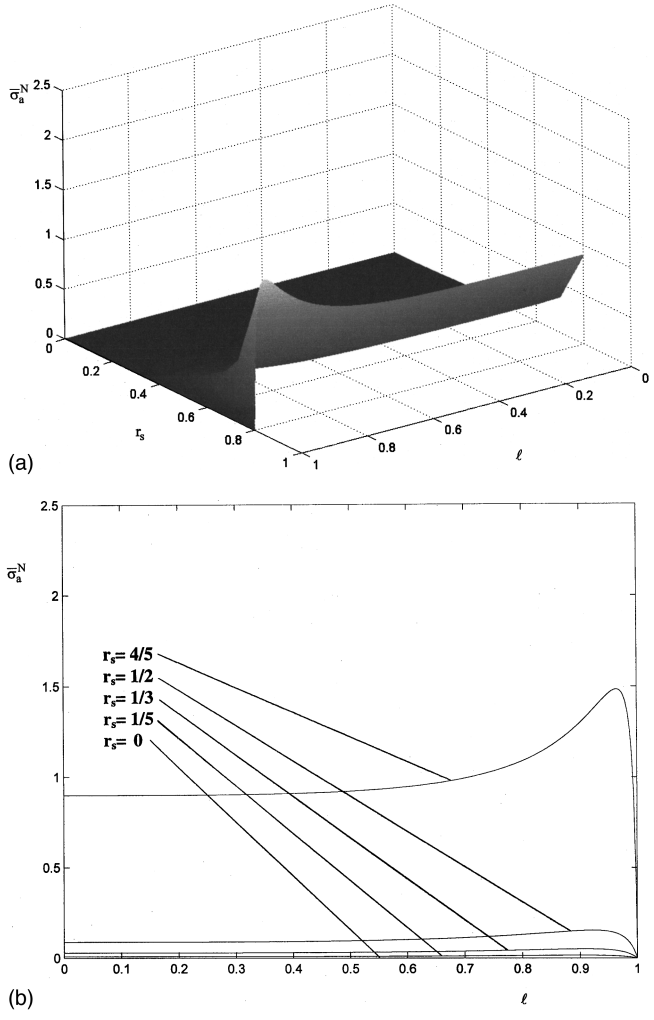

FIG. 11. The normalized absorption cross section, $\overline{\sigma}_a^N$, for $B=10$ as a function of shell thickness (l) and distance from the source (r_s). (a) 3-D plot; (b) intersections (from top to bottom) at $r_s=4/5$, 1/2, 1/3, 1/5, 0.

$$\overline{\sigma}_s^N = r_s^2\left[1-\frac{3B}{3/(1-l^3)-1+B}\right]^2+O(k^2), \quad k\to 0, \quad (96)$$

we observe that the scattering cross section is an increasing function of l. Hence, as the thickness of the shell diminishes, the scattering cross section increases and it assumes its maximum value

$$\sigma_s^{\text{hard}}=\frac{\pi a^6 k^2}{3r_0^2}+O(k^4), \quad k\to 0 \quad (97)$$

at $l=1$, which recovers the hard sphere.[6] On the other end, case $l=0$ which corresponds to a penetrable sphere recovers the scattering cross section of a penetrable scatterer[8] which is given by

$$\sigma_s^{\text{penet}}=\frac{4\pi a^6 k^2}{3r_0^2}\left(\frac{B-1}{B+2}\right)^2+O(k^4), \quad k\to 0. \quad (98)$$

In order to see the dependence on the physical parameter B, we rewrite (95) as

$$\overline{\sigma}_s^N = r_s^2\left[\frac{3(2+l^3)}{2+l^3+B(1-l^3)}-2\right]^2+O(k^2), \quad k\to 0, \quad (99)$$

which shows that the scattering cross section increases along with the mass density in the spherical shell. As $\rho^-\to\infty$, $B\to 0$, and (95) recovers the hard sphere result (97).

Next, we turn to the more interesting behavior of absorption cross sections (59) and (80) with respect to the parameters B, l and r_s.

A numerical investigation of the convergence of the series in (59) shows that 15 terms secure practically the exact value of the series at $r_s=0.8$ and the convergence is much better for smaller values of r_s. The value $r_s=0.8$ locates the point source one-fourth of the radius a away form the exterior sphere S. If the point source comes even closer to the scatterer, then the number of terms needed to calculate the value of the series increases drastically and as $r_s\to a$ the series diverges.

Figures 2, 3, 4, 5, and 6 show 3-D plots and corresponding 2-D intersections of the normalized absorption cross section

$$\overline{\sigma_a^D}=\frac{\sigma_a^D}{4\pi a c^+\delta^-\gamma^-}$$

$$\approx B\sum_{n=0}^{14}\frac{(2n+1)(1-l^{2n+1})(n+(n+1)l^{2n+1})}{[(n+1)(1-l^{2n+1})+B(n+(n+1)l^{2n+1})]^2}\times r_s^{2n}+O(k^2),\quad k\to 0. \tag{100}$$

for $B=10^{-1}$, 2^{-1}, 1, 2, and 10, respectively. Note that $\overline{\sigma_a^D}$ has a maximum which is translated from thinner shells to thicker shells as the mass density of the shell decreases. In fact, a relatively thin shell filled with a high mass density material absorbs more energy than a thicker shell with the same mass density. This seems to be a consequence of the low frequency character of the problem which allows the sphere to live in a succession of global compressions and global detonations setting the scatterer in small vibrations. On the other hand, if the shell is occupied by a low density material, it is a very thick shell that absorbs more energy. In this case, the incident pressure field is ''strong'' enough to impose vibrations to a thicker but ''lighter'' shell. When the mass densities within V^- and V^+ are equal, then maximum absorption occurs whenever the radius of the core is approximately 60% of the exterior radius.

It is obvious that many more results can be drawn from Figs. 2 to 6, but the most interesting geometrical conclusion is that when the source is located at a distance of more than five radii from the center of the scatterer, then the results are the same with the relative results corresponding to plane wave excitation. In other words, a modified point source five characteristic dimensions of the scatterer away from its center is ''seen'' by the scatterer almost as a plane wave. Furthermore, it seems that the point source should be less than two characteristic dimensions from the center of the obstacle in order to obtain significant discrepancy between the point source and plane wave excitation.

Figures 7, 8, 9, 10, and 11 provide the corresponding behavior of the normalized absorption cross section

$$\overline{\sigma_a^N}=\frac{\sigma_a^N}{4\pi a c^+\delta^-\gamma^-}$$

$$\approx B\sum_{n=1}^{25}\frac{n(2n+1)(1-l^{2n+1})(n+1+nl^{2n+1})}{(n+1)[nB(1-l^{2n+1})+n+1+nl^{2n+1}]^2}\times r_s^{2n}+O(k^2),\quad k\to 0 \tag{101}$$

for the hard core case. Note that in order to secure the same accuracy in the evaluation of the series, 25 terms have been used for the worst case where $r_s=0.8$. It is obvious from the plots that a scatterer with a hard core is less sensitive to the spherical characteristics of the point source fields, and in fact for a point source two radii away from its center no significant differences between point source and plane wave excitation is registered. In the cases of $B=10^{-1}$, 2^{-1}, 1, and 2, the absorption is stronger when the point source is close to the scatterer and decreases monotonically to zero as the thickness of the shell decreases. Nevertheless, for a shell with low mass density we observe, in Fig. 11, that if the source is close to the scatterer a local maximum of the absorption occurs in the thin shell neighborhood.

ACKNOWLEDGMENTS

This work is supported by the NATO International Scientific Exchange Programme between Greece and Bulgaria, under Linkage Grant No. 950960. The authors express their thanks to Dimitris Vlachos for his valuable help in the preparation of the plots.

APPENDIX

The values of the integrals appearing in (55), whenever the core has a soft surface, are

$$-\frac{1}{4\pi}\int_S \frac{\partial}{\partial n'}\,u_0^{+D}(\mathbf{r}')ds(\mathbf{r}')=-a_0K_0B, \tag{A1}$$

$$-\frac{1}{4\pi}\int_S(\hat{\mathbf{r}}\cdot\mathbf{r}')\,\frac{\partial}{\partial n'}\,u_0^{+D}(\mathbf{r}')ds(\mathbf{r}')=\frac{a^3}{3r_0}[2K_1(1-l^3)-3]P_1(\cos\,\theta), \tag{A2}$$

$$\frac{1}{4\pi}\int_S(\hat{\mathbf{r}}\cdot\hat{\mathbf{n}}')u_0^{+D}(\mathbf{r}')ds(\mathbf{r}')=\frac{a^3}{3r_0}K_1(1-l^3)P_1(\cos\,\theta), \tag{A3}$$

and

$$\frac{1}{4\pi}\int_S \frac{\partial}{\partial n'}\,u_1^{+D}(\mathbf{r}')ds(\mathbf{r}')=-a_0K_0^2B[a_0B+c^+\delta^-\gamma^-(1-l)]. \tag{A4}$$

When the surface S_0 of the core is hard, the four integrals in (55) assume the following values

$$\frac{1}{4\pi}\int_S \frac{\partial}{\partial n'}\,u_0^{+N}(\mathbf{r}')ds(\mathbf{r}')=0, \tag{A5}$$

$$\frac{1}{4\pi}\int_S(\hat{\mathbf{r}}\cdot\mathbf{r}')\,\frac{\partial}{\partial n'}\,u_0^{+N}(\mathbf{r}')ds(\mathbf{r}')=\frac{a^3}{3r_0}L_1B(1-l^3)P_1(\cos\,\theta), \tag{A6}$$

$$\frac{1}{4\pi}\int_S(\hat{\mathbf{r}}\cdot\hat{\mathbf{n}}')u_0^{+N}(\mathbf{r}')ds(\mathbf{r}')=\frac{a^3}{6r_0}L_1(2+l^3)P_1(\cos\,\theta), \tag{A7}$$

and

$$\frac{1}{4\pi}\int_S \frac{\partial}{\partial n'}\,u_1^{+N}(\mathbf{r}')ds(\mathbf{r}')=0. \tag{A8}$$

[1] D. S. Jones, ''A new method for calculating scattering with particular reference to the circular disc,'' Commun. Pure Appl. Math. **9**, 713–746 (1956).
[2] J. J. Bowman, T. B. A. Senior, and P. E. Uslenghi, *Electromagnetic and Acoustic Scattering by Simple Shapes* (North-Holland, New York, 1969).
[3] D. S. Jones, *Acoustic and Electromagnetic Waves* (Oxford U.P., Clarendon, 1986).
[4] K. Aki and P. G. Richards, *Quantitative Seismology. Theory and Methods. I, II* (Freeman, New York, 1980).
[5] A. Ben-Menahem and S. J. Singh, *Seismic Waves and Sources* (Springer-Verlag, New York, 1981).
[6] G. Dassios and G. Kamvyssas, ''Point source excitation in direct and inverse scattering: The soft and the hard sphere,'' IMA J. Appl. Math. **55**, 67–84 (1995).
[7] G. Dassios and G. Kamvyssas, ''The impedance scattering problem for a point source field. The small resistive sphere,'' Q. J. Mech. Appl. Math. **50**, 321–332 (1997).
[8] G. Dassios, M. Hadjinicolaou, and G. Kamvyssas, ''Direct and inverse scattering for point source fields. The penetrable small sphere,'' ZAMM, J. Appl. Math. Mech. (in press).
[9] G. Dassios, ''Convergent low-frequency expansions for penetrable scatterers,'' J. Math. Phys. **18**, 126–137 (1977).
[10] G. Dassios, ''Scattering of acoustic waves by a coated pressure-release ellipsoid,'' J. Acoust. Soc. Am. **70**, 176–185 (1981).
[11] G. Dassios, ''Low-frequency scattering theory for a penetrable body with an impenetrable core,'' SIAM (Soc. Ind. Appl. Math.) J. Appl. Math. **42**, 272–280 (1982).
[12] P. M. Morse and H. Feshbach, *Methods of Theoretical Physics. I, II* (McGraw-Hill, New York, 1953).
[13] R. E. Kleinman, ''The Rayleigh region,'' Proc. IEEE **53**, 848–856 (1965).
[14] E. D. Rainville, *Special Functions* (Chelsea, New York, 1960).

Generalized Bremmer series with rational approximation for the scattering of waves in inhomogeneous media

Mattheus J. N. van Stralen
Laboratory of Electromagnetic Research, Faculty of Electrical Engineering, Delft University of Technology, P.O. Box 5031, 2600 GA Delft, The Netherlands

Maarten V. de Hoop[a)]
Center for Wave Phenomena, Colorado School of Mines, Golden, Colorado 80401-1887

Hans Blok
Laboratory of Electromagnetic Research, Faculty of Electrical Engineering, Delft University of Technology, P.O. Box 5031, 2600 GA Delft, The Netherlands

(Received 8 June 1996; accepted for publication 15 June 1998)

The Bremmer series solution of the wave equation in generally inhomogeneous media, requires the introduction of pseudodifferential operators. In this paper, sparse matrix representations of these pseudodifferential operators are derived. The authors focus on designing sparse matrices, keeping the accuracy high at the cost of ignoring any critical scattering-angle phenomena. Such matrix representations follow from rational approximations of the vertical slowness and the transverse Laplace operator symbols, and of the vertical derivative, as they appear in the parabolic equation method. Sparse matrix representations lead to a fast algorithm. An optimization procedure is followed to minimize the errors, in the high-frequency limit, for a given discretization rate. The Bremmer series solver consists of three steps: directional decomposition into up- and downgoing waves, one-way propagation, and interaction of the counterpropagating constituents. Each of these steps is represented by a sparse matrix equation. The resulting algorithm provides an improvement of the parabolic equation method, in particular for transient wave phenomena, and extends the latter method, systematically, for backscattered waves.
[S0001-4966(98)06109-8]

PACS numbers: 43.20.Bi [ANN]

INTRODUCTION

Directional wave field decomposition is a tool for analyzing and computing the propagation of waves in configurations with a certain directionality, such as the waveguiding structure in Fig. 1. The method consists of three main steps: (i) decomposing the field into two constituents, propagating upward or downward along a preferred direction, (ii) computing the interaction of the counterpropagating constituents, and (iii) recomposing the constituents into observables at the positions of interest. The method is beneficial because it can be computationally efficient and it can be used to separate different propagation phenomena, which is of importance in the interpretation and inversion of measurements.

In the frequency-domain Bremmer series approach to modeling, we encounter pseudodifferential operators in the directional (de)composition, in the downward and up-ward propagation or continuation, and in the reflections and transmissions due to variations in medium properties in the preferred direction (De Hoop[1]). For the numerical implementation, we employ a total rational-approximation approach to find, upon discretization, sparse matrix representations of these pseudodifferential operators. The rational approximation has its roots in the parabolic equation (PE) method (Claerbout[2] and Tappert[3]), and has been extended and explored by Ma,[4] Greene,[5] Halpern and Trefethen,[6] and Collins.[7] The rational approximation should be carried out in a delicate way, to ensure conservation of acoustic power flow, see also Collins and Westwood.[8] The Bremmer series generates systematically the backscattered field, a topic investigated by Collins and Evans,[9] and Collins.[10] For fixed sampling rates, allowing the numerical grid to be coarse, we consider optimizations of the matrix representations for the three steps, (de)composition, propagation, and interaction, such that the numerical dispersion is minimized. The idea of optimization was exploited by Collins[11] and Cederberg *et al.*;[12] the numerical dispersion was carefully analyzed by Trefethen,[13] Beaumont *et al.*,[14] and Holberg.[15,16]

The improvement in accuracy and efficiency, and extensions of rational approximation techniques remain to get significant attention. Recent advances in the application to exploration seismics can be found in Graves and Clayton[17] and Rühl *et al.*[18] They controlled the errors at large scattering angles by initiating the propagation with a transversely homogeneous background phase shift. In the field of integrated optics, the PE method was introduced by Fleck *et al.*[19] Various extensions of the PE-style method have been developed since then. These are now known as beam propagation methods (BPMs). Examples of present BPMs are the method of lines,[20] the mode expansion method,[21] and wide-angle methods based upon higher-order rational approximations.[22–24] For a recent overview we refer to Hoekstra.[25] For the developments in ocean acoustics, we refer the reader to Collins.[7,26]

[a)]Electronic mail: mdehoop@dix.mines.edu

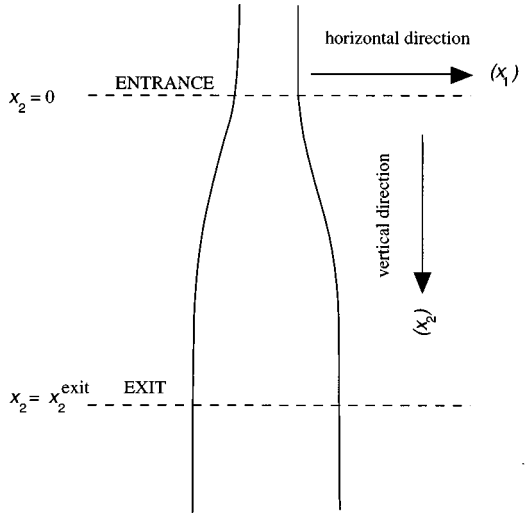

FIG. 1. A sample configuration. Between the entrance and the exit levels, the configuration's medium may vary in the vertical and horizontal directions. Outside that region the medium is constant.

A recent overview of PE methods in underwater acoustics is given by Lee and Pierce.[27]

The discretization of the ''one-way'' wave equation, the propagation step, is based on the third-order Thiele-type continued-fraction approximation of the left vertical wave-slowness symbol. We enforce the associated vertical slowness operator to be self-adjoint (''energy-conserving''), as the exact one is self-adjoint in the real L^2. This implies that we depart from the principal symbol analysis of De Hoop.[1] The one-way wave equation is thus approximated by a partial differential equation. By discretizing the transverse derivatives (the Laplace operator) according to a rational approximation of its spectrum, the partial differential equation is transformed into a system of ordinary differential equations. The solution of this system is formally written as a product integral. The exponent in the discretized version of the product integral is then replaced by its (n,n)-Padé approximation. Such a procedure guarantees numerical stability. We will pay most attention to the (1,1)-Padé approximation, which yields the Crank–Nicholson implicit finite-difference scheme in the preferred direction. The resulting algebraic equations, which now involve sparse matrices, can be solved rapidly with standard procedures available in various software libraries. In two dimensions, direct matrix inversions are carried out; in three dimensions, iterative techniques should be applied.

The vertical phase and group slownesses associated with the ultimate system of algebraic equations can be evaluated and are used to analyze the numerical artifacts introduced by the various rational approximations. The accuracy of the vertical group slowness as compared with the exact vertical slowness is indicative for the numerical anisotropy; the difference between the vertical phase and group slownesses is indicative for the numerical dissipation. To arrive at an optimal system of algebraic equations, fixing the bandwidth of the wave field and the sampling rate, a simultaneous optimization of the Thiele-type approximation, the transverse finite-difference, and the vertical finite-difference representations are carried out. Since the optimization will depend on the medium's wave speed, the optimal parameter set will vary with frequency and position as well. The optimization procedure is repeated for the composition, decomposition, reflection, and transmission operators. With the various matrix representations, the Bremmer coupling series solution of the wave equation can now be computed. For typical medium fluctuations, as a rule of thumb, one needs to consider three terms of this series to obtain an accurate representation. A general, *a priori*, rule for how many terms one should compute is hard to give, however. In this respect, note that in the Fourier domain the Bremmer series does not necessarily converge.

The outline of the paper is as follows. In the next section, a summary of the method of directional decomposition, leading to a coupled system of one-way wave equations is given. In Sec. II, the concept of generalized slowness surface is introduced, which is used in representations of the Green's functions of the one-way wave equations. In Sec. III, the Bremmer coupling series and its numerical implementation are discussed. The remainder of the paper is dedicated to the derivation and optimization of approximate, sparse, matrix representations. In Sec. IV, the one-way wave equations are discretized for the purpose of solving for the one-way Green's functions. In Sec. V, transverse, transparent boundaries are introduced. In Sec. VI, the optimization procedure for the one-way propagation is explained. Sections VII and VIII contain the discretizations and optimizations of the (de) composition and interaction operators. Finally, our algorithm is illustrated in Sec. IX by various numerical examples.

I. DIRECTIONAL WAVE FIELD DECOMPOSITION

For the details on the derivation of the Bremmer coupling series solution of the acoustics wave equation, we refer the reader to De Hoop.[1] Here we restrict ourselves to a summary of the method. Our configuration is two dimensional.

Let p=acoustic pressure [Pa], v_r=particle velocity [m/s], ρ=volume density of mass [kg/m^3], κ=compressibility [Pa^{-1}], q=volume source density of injection rate [s^{-1}], and f_k=volume source density of force [N/m^3]. We assume that the coefficient κ is smooth, and that ρ is constant, for the purpose of wave field decomposition. Furthermore, we assume that these functions are constant outside a compact domain. This provision enables us to formulate the acoustic wave propagation, when necessary, as a scattering problem in a homogeneous embedding. The smoothness entails that the singularities of the wave field (in particular the ones in the neighborhood of the wave arrival) arise from the ones in the signatures of the source distributions. The formation of caustics, associated with multipathing of characterictics, is captured in the numerical procedure developed in this paper.

We carry out our analysis in the time-Fourier domain. To show the notation, we give the expression for the acoustic pressure

$$\hat{p}(x_m,\omega)=\int_{t=0}^{\infty}\exp(-i\omega t)p(x_m,t)dt,\quad \mathrm{Im}\{\omega\}<0. \tag{1}$$

Under this transformation, assuming zero initial conditions, we have $\partial_t \rightarrow i\omega$. In the Fourier domain, the acoustic wave field satisfies the system of first-order equations

$$\partial_k \hat{p} + i\omega\rho\hat{v}_k = \hat{f}_k, \tag{2}$$

$$i\omega\kappa\hat{p} + \partial_r \hat{v}_r = \hat{q}. \tag{3}$$

The change of the wave field in space along a direction of preference can now be expressed in terms of the changes of the wave field in the direction transverse to it. The direction of preference is taken along the x_2 axis (or ''vertical'' axis) and the remaining (''transverse'' or ''horizontal'') coordinate is denoted by x_1.

Since we allow the medium to vary with all coordinates and hence also with the preferred direction, we are forced to carry out the wave field decomposition from the system of first-order equations rather than the second-order scalar Helmholtz equation.

A. The reduced system of equations

The procedure requires a separate handling of the horizontal component of the particle velocity. From Eqs. (2) and (3) we obtain

$$\hat{v}_1 = i\rho^{-1}\omega^{-1}(\partial_1 \hat{p} - \hat{f}_1), \tag{4}$$

leaving, upon substitution, the matrix differential equation

$$(\partial_2 \delta_{I,J} + i\omega\hat{A}_{I,J})\hat{F}_J = \hat{N}_I, \quad \hat{A}_{I,J} = \hat{A}_{I,J}(x_1, D_1; x_2), \quad D_1 \equiv \frac{i}{\omega}\partial_1, \tag{5}$$

in which the elements of the acoustic field matrix are given by

$$\hat{F}_1 = \hat{p}, \quad \hat{F}_2 = \hat{v}_2, \tag{6}$$

the elements of the acoustic system's operator matrix by

$$\hat{A}_{1,1} = \hat{A}_{2,2} = 0, \tag{7}$$

$$\hat{A}_{1,2} = \rho, \quad \hat{A}_{2,1} = -D_1(\rho^{-1}D_1) + \kappa, \tag{8}$$

and the elements of the notional source matrix by

$$\hat{N}_1 = \hat{f}_2, \quad \hat{N}_2 = D_1(\rho^{-1}\hat{f}_1) + \hat{q}. \tag{9}$$

It is observed that the right-hand side of Eq. (4) and $\hat{A}_{I,J}$ contain the spatial derivative D_1 with respect to the horizontal coordinate only. D_1 has the interpretation of *horizontal slowness* operator. Further, it is noted that $\hat{A}_{1,2}$ is simply a multiplicative operator.

To ensure that the medium is smooth, we employ equivalent medium averaging at any point over a box that is twice the spatial sample size. (This procedure is derived from the one by Coates and Schoenberg[28] for smoothing discontinuities making use of the equivalent medium averaging of Schoenberg and Sen.[29])

B. The coupled system of one-way wave equations

To distinguish up- and downgoing constituents in the wave field, we shall construct an appropriate linear operator $\hat{L}_{I,J}$ with

$$\hat{F}_I = \hat{L}_{I,J}\hat{W}_J, \tag{10}$$

that, with the aid of the commutation relation $(\partial_2 \hat{L}_{I,J}) = [\partial_2, \hat{L}_{I,J}]$, transforms Eq. (5) into

$$\hat{L}_{I,J}(\partial_2 \delta_{J,M} + i\omega\hat{\Lambda}_{J,M})\hat{W}_M = -(\partial_2 \hat{L}_{I,J})\hat{W}_J + \hat{N}_I, \tag{11}$$

as to make $\hat{\Lambda}_{J,M}$, satisfying

$$\hat{A}_{I,J}\hat{L}_{J,M} = \hat{L}_{I,J}\hat{\Lambda}_{J,M}, \tag{12}$$

a diagonal matrix of operators. We denote $\hat{L}_{I,J}$ as the composition operator and $\hat{W}_M$ as the wave matrix. The expression in parentheses on the left-hand side of Eq. (11) represents the two so-called *one-way* wave operators. The first term on the right-hand side of Eq. (11) is representative for the scattering due to variations of the medium properties in the vertical direction. The scattering due to variations of the medium properties in the horizontal direction is contained in $\hat{\Lambda}_{J,M}$ and, implicitly, in $\hat{L}_{I,J}$.

To investigate whether solutions of Eq. (12) exist, we introduce the column matrix operators $\hat{L}_I^{(\pm)}$ according to

$$\hat{L}_I^{(+)} = \hat{L}_{I,1}, \quad \hat{L}_I^{(-)} = \hat{L}_{I,2}. \tag{13}$$

Upon writing the diagonal entries of $\hat{\Lambda}_{J,M}$ as

$$\hat{\Lambda}_{1,1} = \hat{\Gamma}^{(+)}, \quad \hat{\Lambda}_{2,2} = \hat{\Gamma}^{(-)}, \tag{14}$$

Eq. (12) decomposes into the two systems of equations

$$\hat{A}_{I,J}\hat{L}_J^{(\pm)} = \hat{L}_I^{(\pm)}\hat{\Gamma}^{(\pm)}. \tag{15}$$

By analogy with the case where the medium is translationally invariant in the horizontal direction, we shall denote $\hat{\Gamma}^{(\pm)}$ as the *vertical slowness* operators. Notice that the operators $\hat{L}_1^{(\pm)}$ compose the acoustic pressure and that the operators $\hat{L}_2^{(\pm)}$ compose the vertical particle velocity, whereas the elements of $\hat{W}_M$ may be physically nonobservable.

In De Hoop[1] an Ansatz procedure has been followed to solve the generalized eigenvalue–eigenvector problem (15) in operator sense: in the *acoustic-pressure normalization* analog we have

$$[\hat{L}_2^{(\pm)}, \hat{A}_{2,1}\hat{A}_{1,2}] = 0. \tag{16}$$

In this normalization we find the vertical slowness operator to be

$$\hat{\Gamma}^{(+)} = -\hat{\Gamma}^{(-)} = \hat{\Gamma} = \hat{A}^{1/2}, \quad \hat{A} = \hat{A}_{2,1}\hat{A}_{1,2}, \tag{17}$$

while the generalized eigenvectors constitute the *composition* operator

$$\hat{L} = \begin{pmatrix} \hat{A}_{1,2} & \hat{A}_{1,2} \\ \hat{\Gamma} & -\hat{\Gamma} \end{pmatrix}. \tag{18}$$

Note that we have decomposed the pressure (up to a multiplication by density) viz., according to $\hat{F}_1 = \hat{F}_1^+ + \hat{F}_1^-$, $\hat{F}_1^+ = \hat{A}_{1,2}\hat{W}_1$, and $\hat{F}_1^- = \hat{A}_{1,2}\hat{W}_2$. In terms of the inverse vertical slowness operator, $\hat{\Gamma}^{-1} = \hat{A}^{-1/2}$, the *decomposition* operator then follows as

$$\hat{L}^{-1} = \frac{1}{2}\begin{pmatrix} \hat{A}_{1,2}^{-1} & \hat{\Gamma}^{-1} \\ \hat{A}_{1,2}^{-1} & -\hat{\Gamma}^{-1} \end{pmatrix}. \tag{19}$$

Using the decomposition operator, Eq. (11) transforms into

$$(\partial_2\delta_{I,M}+i\omega\hat{\Lambda}_{I,M})\hat{W}_M=-(\hat{L}^{-1})_{I,M}(\partial_2\hat{L}_{M,K})\hat{W}_K + (\hat{L}^{-1})_{I,M}\hat{N}_M, \tag{20}$$

which can be interpreted as a coupled system of one-way wave equations. The coupling between the counterpropagating components, $\hat{W}_M$, is apparent in the first sourcelike term on the right-hand side, which can be written as

$$-\hat{L}^{-1}(\partial_2\hat{L})=\begin{pmatrix}\hat{T} & \hat{R}\\ \hat{R} & \hat{T}\end{pmatrix}, \tag{21}$$

in which $\hat{T}$ and $\hat{R}$ represent the *transmission* and *reflection* operators, respectively. In the acoustic-pressure normalization analog, for constant density, we thus find

$$\hat{R}=-\hat{T}=\tfrac{1}{2}\hat{\Gamma}^{-1}(\partial_2\hat{\Gamma}). \tag{22}$$

II. THE ONE-WAY WAVE PROPAGATOR

To arrive at a coupled system of integral equations that is equivalent to Eq. (20) and that can be solved in terms of a Neumann expansion, we have to invert the operator occurring on the left-hand side. We set $\hat{G}^{(\pm)}=(\partial_2+i\omega\hat{\Gamma}^{(\pm)})^{-1}$. The one-sided elementary kernels $\hat{\mathscr{G}}^{(\pm)}(x_1,x_2;x_1',x_2')$ associated with these operators are the so-called one-way Green's functions. They satisfy the equations

$$\partial_2\hat{\mathscr{G}}^{(\pm)}+i\omega\hat{\Gamma}^{(\pm)}\hat{\mathscr{G}}^{(\pm)}=\delta(x_1-x_1')\,\delta(x_2-x_2'), \tag{23}$$

together with the condition of causality.

Now, consider $\hat{G}=\hat{G}^{(+)}$, $\hat{\mathscr{G}}=\hat{\mathscr{G}}^{(+)}$, and $\hat{\Gamma}=\hat{\Gamma}^{(+)}$. The operator $\hat{G}$ acts on a test field $\hat{u}$ as

$$(\hat{G}\hat{u})(x_1,x_2)=\int_{\zeta\in\mathbb{R}}\int_{x_1'\in\mathbb{R}}\hat{\mathscr{G}}(x_1,x_2;x_1',\zeta)\hat{u}(x_1',\zeta)dx_1'\,d\zeta. \tag{24}$$

Let us define the initial-value problem of determining a function $\hat{U}(x_1,x_2;\zeta)$ satisfying

$$(\partial_2+i\omega\hat{\Gamma})\hat{U}=0 \quad \text{for } x_2\geqslant\zeta, \quad \hat{U}(x_1,\zeta;\zeta)=\hat{u}(x_1,\zeta). \tag{25}$$

Then it is observed that

$$(\hat{G}\hat{u})(x_1,x_2)=\int_{\zeta=-\infty}^{x_2}\hat{U}(x_1,x_2;\zeta)d\zeta. \tag{26}$$

A. The product integral

We observe that the vertical slowness operators at different levels of x_2 do not necessarily commute with one another due to the heterogeneity of the medium. Thus we arrive at a ''time''-ordered product integral representation[30] of the one-sided propagators [cf. Eq. (25)] associated with the one-way wave equations, where ''time'' refers to the vertical coordinate x_2,

$$\hat{U}^{(\pm)}(.,x_2;x_2')=\pm H(\mp[x_2'-x_2])\times\left\{\prod_{\zeta=x_2'}^{x_2}\exp[-i\omega\hat{\Gamma}^{(\pm)}(.,\zeta)d\zeta]\right\}\hat{u}(.,x_2'). \tag{27}$$

In this expression, the operator ordering is initiated by $\exp[-i\omega\hat{\Gamma}(.,x_2')d\zeta]$ acting on $\hat{u}(.,x_2')$ followed by applying $\exp[-i\omega\hat{\Gamma}(.,\zeta)d\zeta]$ to the result, successively for increasing ζ.

If the medium in the interval $[x_2',x_2]$ were weakly varying in the vertical direction, the Trotter product formula can be applied to the product integral in Eq. (27). This results in the Hamiltonian path integral representations for the Green's functions,

$$\hat{\mathscr{G}}^{(\pm)}(x_1,x_2;x_1',x_2')=\pm H(\mp[x_2'-x_2])\times\int_P\mathscr{D}(x_1'',\alpha_1'')\times\exp\left[-i\omega\int_{\zeta=x_2'}^{x_2}d\zeta\{\alpha_1''(d_\zeta x_1'')+\hat{\gamma}^{(\pm)}(x_1'',\zeta,\alpha_1'')\}\right], \tag{28}$$

P being a set of paths $[x_1''(\zeta),\alpha_1''(\zeta)]$ in (horizontal) phase space satisfying $x_1''(\zeta=x_2')=x_1'$, $x_1''(\zeta=x_2)=x_1$. In Eq. (28), $\hat{\gamma}^{(\pm)}$ is the so-called left symbol of $\hat{\Gamma}^{(\pm)}$, i.e.,

$$\hat{\Gamma}^{(\pm)}(x_1,D_1;x_2)\exp(-i\omega\alpha_1x_1)=\hat{\gamma}^{(\pm)}(x_1,x_2,\alpha_1)\exp(-i\omega\alpha_1x_1). \tag{29}$$

The path integral in Eq. (28) is to be interpreted as the lattice multivariate integral

$$\hat{\mathscr{G}}^{(\pm)}(x_1,x_2;x_1',x_2')=\pm H(\mp[x_2'-x_2])\lim_{M\to\infty}\int\prod_{i=1}^{M}(\omega/2\pi)d\alpha_1^{(i)}\times\prod_{j=1}^{M-1}dx_1^{(j)}\exp\left[-i\omega\sum_{k=1}^{M}\{\alpha_1^{(k)}(x_1^{(k)}-x_1^{(k-1)})+\hat{\gamma}^{(\pm)}(x_1^{(k)},\zeta_k-\tfrac{1}{2}M^{-1}\Delta x_2,\alpha_1^{(k)})M^{-1}\Delta x_2\right\}, \tag{30}$$

with $x_1^{(0)}=x_1'$, $x_1^{(M)}=x_1$, and $\Delta x_2=x_2-x_2'$. All the integrations are taken over the interval $(-\infty,\infty)$, $M^{-1}\Delta x_2$ is the step size in ζ, and $(x_1^{(j)},\alpha_1^{(j)})$ are the coordinates of a path at the discrete values ζ_j of ζ as $j=1,...,M$. If Δx_2 is sufficiently small, the lattice integral reduces to the case $M=1$:

$$\hat{\mathscr{G}}^{(\pm)}(x_1,x_2;x_1',x_2')\simeq\pm H(\mp[x_2'-x_2])\int(\omega/2\pi)d\alpha_1''\times\exp[-i\omega\{\alpha_1''(x_1-x_1')+\hat{\gamma}^{(\pm)}(x_1,x_2-\tfrac{1}{2}\Delta x_2,\alpha_1'')\Delta x_2\}]. \tag{31}$$

B. The generalized slowness surface

In the acoustic pressure normalization analog, the characteristic differential operator [cf. Eq. (17)] is given by

$$\hat{A}=-D_1D_1-\rho^{-1}(D_1\rho)D_1+\rho^{-2}(D_1\rho)(D_1\rho) -\rho^{-1}(D_1D_1\rho)+\kappa\rho, \tag{32}$$

with left symbol $\hat{A}=\hat{A}_2+\hat{A}_1+\hat{A}_0$, in which

$$\hat{A}_2=-\alpha_1^2+\kappa\rho, \quad \hat{A}_1=-\rho^{-1}(D_1\rho)\alpha_1, \quad \hat{A}_0=-\rho^{-1}(D_1^2\rho)+\rho^{-2}(D_1\rho)^2. \tag{33}$$

In our configuration, we have $\hat{A}_1=\hat{A}_0=0$, since we assume the density to be constant. In $\hat{A}_2$ we can substitute $c=(\kappa\rho)^{-1/2}$, the wave speed in the medium.

Using the composition rule for symbols of pseudodifferential operators, the operator equation $\hat{\Gamma}^2=\hat{A}$ [cf. Eq. (17)] is transformed into a characteristic equation for the corresponding left symbols,

$$-(\omega/2\pi)\int_{x_1'\in\mathbb{R}}\int_{\alpha_1'\in\mathbb{R}}\hat{\gamma}(x_1,\alpha_1')\exp[i\omega(x_1-x_1')(\alpha_1-\alpha_1')] \times\hat{\gamma}(x_1',\alpha_1)d\alpha_1'dx_1'+\hat{A}(x_1,\alpha_1)=0. \tag{34}$$

This equation defines the generalized slowness surface and has solutions $\hat{\gamma}^{(\pm)}$, which appear in the thin-slab one-way Green's functions (31). The two branches are $\hat{\gamma}^{(\pm)}(x_1,\alpha_1)$ such that $\mathrm{Im}\{\hat{\gamma}^{(+)}(x_1,\alpha_1)\}\leqslant 0$ and $\mathrm{Im}\{\hat{\gamma}^{(-)}(x_1,\alpha_1)\}\geqslant 0$. These choices are consistent with the condition that $\hat{\mathscr{G}}^{(\pm)}$ are both causal. Due to the up/down symmetry of the medium we have $\hat{\gamma}^{(+)}=-\hat{\gamma}^{(-)}$. Note that as $\omega\to\infty$ the composition of symbols tends to an ordinary multiplication, and the solution of Eq. (34) reduces to the principal parts of the symbols. The principal part of the vertical slowness symbol corresponds to the vertical component of gradient of travel time, in accordance with the eikonal equation (which can be obtained from the high-frequency approximation of the path integral, see De Hoop[1]).

III. THE GENERALIZED BREMMER COUPLING SERIES

A. The coupled system of integral equations

Applying the operators with kernels given by Eq. (28) in Eq. (20) we obtain a coupled system of integral equations. In operator form, they are given by

$$(\delta_{I,J}-\hat{K}_{I,J})\hat{W}_J=\hat{W}_I^{(0)}, \tag{35}$$

in which $\hat{W}^{(0)}$ denotes the incident field. In our configuration the domain of heterogeneity will be restricted to the slab $(0, x_2^{\mathrm{exit}}]$, see Fig. 1, and the excitation of the waves will be specified through an initial condition at the level $x_2=0$, viz.,

$$\hat{W}_1^{(0)}(x_1,x_2)=\int_{x_1'\in\mathbb{R}}\hat{\mathscr{G}}^{(+)}(x_1,x_2;x_1',0)\hat{W}_1(x_1',0)dx_1', \quad \hat{W}_2^{(0)}(x_1,x_2)=0, \tag{36}$$

in the range of interest, $x_2\in[0, x_2^{\mathrm{exit}}]$; the second equation reflects the assumption that there is no excitation below the heterogeneous slab. The integral operators in Eq. (35) are given by

$$(\hat{K}_{1,1}\hat{W}_1)(x_1,x_2)=\int_{\zeta=0}^{x_2}\int_{x_1'\in\mathbb{R}}\hat{\mathscr{G}}^{(+)}(x_1,x_2;x_1',\zeta) \times(\hat{T}\hat{W}_1)(x_1',\zeta)dx_1'\,d\zeta, \tag{37}$$

$$(\hat{K}_{1,2}\hat{W}_2)(x_1,x_2)=\int_{\zeta=0}^{x_2}\int_{x_1'\in\mathbb{R}}\hat{\mathscr{G}}^{(+)}(x_1,x_2;x_1',\zeta) \times(\hat{R}\hat{W}_2)(x_1',\zeta)dx_1'\,d\zeta, \tag{38}$$

$$(\hat{K}_{2,1}\hat{W}_1)(x_1,x_2)=\int_{\zeta=x_2}^{x_2^{\mathrm{exit}}}\int_{x_1'\in\mathbb{R}}\hat{\mathscr{G}}^{(-)}(x_1,x_2;x_1',\zeta) \times(\hat{R}\hat{W}_1)(x_1',\zeta)dx_1'\,d\zeta, \tag{39}$$

$$(\hat{K}_{2,2}\hat{W}_2)(x_1,x_2)=\int_{\zeta=x_2}^{x_2^{\mathrm{exit}}}\int_{x_1'\in\mathbb{R}}\hat{\mathscr{G}}^{(-)}(x_1,x_2;x_1',\zeta) \times(\hat{T}\hat{W}_2)(x_1',\zeta)dx_1'\,d\zeta. \tag{40}$$

They describe the interaction between the counterpropagating constituent waves.

We can represent the action of the one-sided Green's kernels by product integrals, viz.,

$$\hat{W}_1^{(0)}(.,x_2)=\left\{\prod_{\zeta'=0}^{x_2}\exp[-i\omega\hat{\Gamma}^{(+)}(.,\zeta')d\zeta']\right\}\hat{W}_1(.,0), \tag{41}$$

while

$$(\hat{K}_{1,1}\hat{W}_1)(.,x_2)=\int_{\zeta=0}^{x_2}\left\{\prod_{\zeta'=\zeta}^{x_2}\exp[-i\omega\hat{\Gamma}^{(+)}(.,\zeta')d\zeta']\right\} \times(\hat{T}\hat{W}_1)(.,\zeta)d\zeta, \tag{42}$$

and so on.

B. Bremmer series

If $\omega=-is$ (and $\alpha_1=i\alpha_1^s\in i\mathbb{R}$) with s real and sufficiently large, the Neumann expansion can be employed to invert $(\delta_{I,J}-\hat{K}_{I,J})$ in Eq. (35). Such a procedure leads to the Bremmer coupling series,

$$\hat{W}_I=\sum_{j=0}^{\infty}\hat{W}_I^{(j)}, \quad \text{in which} \quad \hat{W}_I^{(j)}=\hat{K}_{I,J}\hat{W}_J^{(j-1)} \quad \text{for } j\geqslant 1, \tag{43}$$

can be interpreted as the j-times reflected or scattered wave. This equation indicates that the solution of Eq. (35) can be found with the aid of an iterative scheme. We will consider only a finite and small number of terms of the series in Eq. (43) and in fact take the frequencies ω close to real-valued.

C. An iterative scheme

To arrive at an iterative scheme for the solution of Eq. (35), consider the j-times reflected constituent wave. We split the interval $[0, x_2^{\text{exit}}]$ into M thin slabs with thickness Δx_2. Set

$$\hat{W}_I^{(j)}(.,k\Delta x_2)=\hat{I}_{I,1}^{(j)}(.,k)+\hat{I}_{I,2}^{(j)}(.,k), \tag{44}$$

$j=1,2,...$, and $k=0,1,...,M$, where [cf. Eq. (43)]

$$\hat{I}_{I,1}^{(j)}(.,k)=(\hat{K}_{I,1}\hat{W}_1^{(j-1)})(.,k\Delta x_2), \tag{45}$$

$$\hat{I}_{I,2}^{(j)}(.,k)=(\hat{K}_{I,2}\hat{W}_2^{(j-1)})(.,k\Delta x_2). \tag{46}$$

Upon comparison with Eq. (42) we find that

$$\hat{I}_{1,1}^{(j)}(.,k)=\int_{\zeta=0}^{k\Delta x_2}\left\{\prod_{\zeta'=\zeta}^{k\Delta x_2}\exp[-i\omega\hat{\Gamma}^{(+)}(.,\zeta')d\zeta']\right\}\times\hat{X}_{1,1}^{(j)}(.,\zeta)d\zeta, \tag{47}$$

with $\hat{X}_{1,1}^{(j)}(.,\zeta)=(\hat{T}\hat{W}_1^{(j-1)})(.,\zeta)$. Similarly,

$$\hat{I}_{1,2}^{(j)}(.,k)=\int_{\zeta=0}^{k\Delta x_2}\left\{\prod_{\zeta'=\zeta}^{k\Delta x_2}\exp[-i\omega\hat{\Gamma}^{(+)}(.,\zeta')d\zeta']\right\}\times\hat{X}_{1,2}^{(j)}(.,\zeta)d\zeta, \tag{48}$$

$$\hat{I}_{2,J}^{(j)}(.,k)=-\int_{\zeta=k\Delta x_2}^{x_2^{\text{exit}}}\left\{\prod_{\zeta'=\zeta}^{k\Delta x_2}\exp[-i\omega\hat{\Gamma}^{(-)}(.,\zeta')d\zeta']\right\}\times\hat{X}_{2,J}^{(j)}(.,\zeta)d\zeta, \tag{49}$$

with $\hat{X}_{1,2}^{(j)}(.,\zeta)=(\hat{R}\hat{W}_2^{(j-1)})(.,\zeta)$, $\hat{X}_{2,1}^{(j)}(.,\zeta)=(\hat{R}\hat{W}_1^{(j-1)})(.,\zeta)$, and $\hat{X}_{2,2}^{(j)}(.,\zeta)=(\hat{T}\hat{W}_2^{(j-1)})(.,\zeta)$. In a configuration with constant density, we have $\hat{R}=-\hat{T}$ and hence

$$\hat{X}_{2,1}^{(j)}=-\hat{X}_{1,1}^{(j)} \quad \text{and} \quad \hat{X}_{1,2}^{(j)}=-\hat{X}_{2,2}^{(j)}.$$

To construct the iteration scheme, we carry out the following steps. Let $\hat{P}$ denote the thin slab *propagator* [cf. Eq. (31)]

$$\hat{P}(.,k)=\left\{\prod_{\zeta'=(k-1)\Delta x_2}^{k\Delta x_2}\exp[-i\omega\hat{\Gamma}^{(+)}(.,\zeta')d\zeta']\right\}. \tag{50}$$

Then, using the semigroup property,

$$\begin{aligned}\hat{I}_{1,1}^{(j)}(.,k)=&\left\{\prod_{\zeta'=(k-1)\Delta x_2}^{k\Delta x_2}\exp[-i\omega\hat{\Gamma}^{(+)}(.,\zeta')d\zeta']\right\}\\&\times\int_{\zeta=0}^{(k-1)\Delta x_2}\left\{\prod_{\zeta'=\zeta}^{(k-1)\Delta x_2}\exp[-i\omega\hat{\Gamma}^{(+)}(.,\zeta')d\zeta']\right\}\\&\times\hat{X}_{1,1}^{(j)}(.,\zeta)d\zeta\\&+\int_{\zeta=(k-1)\Delta x_2}^{k\Delta x_2}\left\{\prod_{\zeta'=\zeta}^{k\Delta x_2}\exp[-i\omega\hat{\Gamma}^{(+)}(.,\zeta')d\zeta']\right\}\\&\times\hat{X}_{1,1}^{(j)}(.,\zeta)d\zeta,\end{aligned} \tag{51}$$

which can be written as

$$\hat{I}_{1,1}^{(j)}(.,k)=\hat{P}(.,k)\hat{I}_{1,1}^{(j)}(.,k-1)+\hat{Q}_{1,1}^{(j)}(.,k), \tag{52}$$

where

$$\hat{Q}_{1,1}^{(j)}(.,k)=\int_{\zeta=(k-1)\Delta x_2}^{k\Delta x_2}\left\{\prod_{\zeta'=\zeta}^{k\Delta x_2}\exp[-i\omega\hat{\Gamma}^{(+)}(.,\zeta')d\zeta']\right\}\times\hat{X}_{1,1}^{(j)}(.,\zeta)d\zeta. \tag{53}$$

Recursion relations similar to the one in Eq. (52) can be found for the other elements of $\hat{I}$, viz.,

$$\begin{aligned}&\hat{I}_{1,J}^{(j)}(.,k)=\hat{P}(.,k)\hat{I}_{1,J}^{(j)}(.,k-1)+\hat{Q}_{1,J}^{(j)}(.,k)\\&\qquad\text{for } k=1,2,...,M,\\&\hat{I}_{2,J}^{(j)}(.,k)=\hat{P}(.,k+1)\hat{I}_{2,J}^{(j)}(.,k+1)+\hat{Q}_{2,J}^{(j)}(.,k)\\&\qquad\text{for } k=M-1,\ M-2,...,0.\end{aligned} \tag{54}$$

Here

$$\hat{Q}_{1,J}^{(j)}(.,k)=\int_{\zeta=(k-1)\Delta x_2}^{k\Delta x_2}\left\{\prod_{\zeta'=\zeta}^{k\Delta x_2}\exp[-i\omega\hat{\Gamma}^{(+)}(.,\zeta')d\zeta']\right\}\times\hat{X}_{1,J}^{(j)}(.,\zeta)d\zeta, \tag{55}$$

$$\hat{Q}_{2,J}^{(j)}(.,k)=\int_{\zeta=(k+1)\Delta x_2}^{k\Delta x_2}\left\{\prod_{\zeta'=k\Delta x_2}^{\zeta}\exp[i\omega\hat{\Gamma}^{(-)}(.,\zeta')d\zeta']\right\}\times\hat{X}_{2,J}^{(j)}(.,\zeta)d\zeta. \tag{56}$$

The initial values for the recursive scheme (54) are given by

$$\hat{I}_{1,J}^{(j)}(x_1,0)=0, \tag{57}$$

$$\hat{I}_{2,J}^{(j)}(x_1,M)=0, \tag{58}$$

again, for $j=1,2,...$.

D. Numerical issues

The implementation of the iterative scheme is as follows. It is initiated by the calculation of the incident field, $\hat{W}_1^{(0)}$, according to

$$\hat{W}_1^{(0)}(.,k\Delta x_2)=\hat{P}(.,k)\hat{W}_1^{(0)}(.,(k-1)\Delta x_2)\qquad\text{for } k=1,2,...,M, \tag{59}$$

see Fig. 2, with the initial condition

$$\hat{W}_1^{(0)}(.,0)=\hat{W}_1(.,0), \tag{60}$$

according to Eq. (36). During the forward propagation, at each of the discrete levels, $\hat{X}_{J,1}^{(1)}$ are computed and stored; $\hat{X}_{J,2}^{(1)}$ are set to zero. The procedure is continued by the backward propagation defined by the second recursion in Eq. (54). At each of the discrete levels, $\hat{W}_2^{(1)}$ is computed [Eq. (44)] and used to calculate $\hat{X}_{J,2}^{(2)}$; the latter quantity is stored as before. The scheme continues to switch from backward to

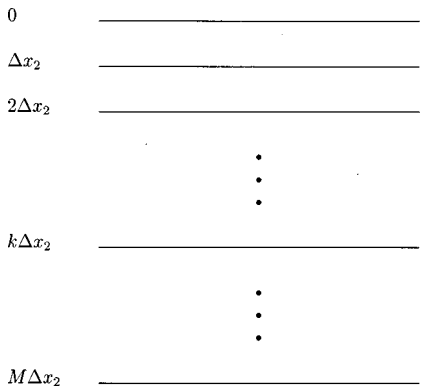

FIG. 2. The levels at which the field is calculated.

forward propagation based on the first recursion in Eq. (54), and so on.

To evaluate the elements of $\hat{Q}^{(j)}$, we apply the trapezoidal rule. Then

$$\hat{Q}^{(j)}_{1,J}(.,k) \simeq \tfrac{1}{2}\Delta x_2[\hat{X}^{(j)}_{1,J}(.,k\Delta x_2) + \hat{P}(.,k)\hat{X}^{(j)}_{1,J}(.,(k-1)\Delta x_2)], \tag{61}$$

$$\hat{Q}^{(j)}_{2,J}(.,k) \simeq -\tfrac{1}{2}\Delta x_2[\hat{X}^{(j)}_{2,J}(.,k\Delta x_2) + \hat{P}(.,k+1)\hat{X}^{(j)}_{2,J}(.,(k+1)\Delta x_2)], \tag{62}$$

which formulas are accurate $\mathcal{O}((\Delta x_2)^2)$.

The whole numerical scheme is elucidated in a flow chart, Fig. 3. In the remainder of this paper, we will derive approximate, sparse matrix representations for $\hat{\Gamma}$, $\hat{P}$, $\hat{\Gamma}^{-1}$, and $\hat{T}$.

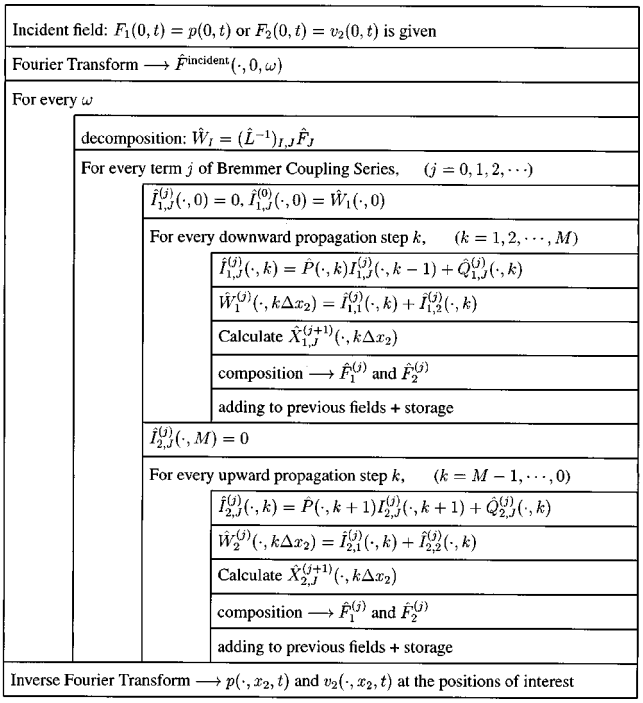

FIG. 3. Flow chart of the numerical implementation of the Bremmer coupling series.

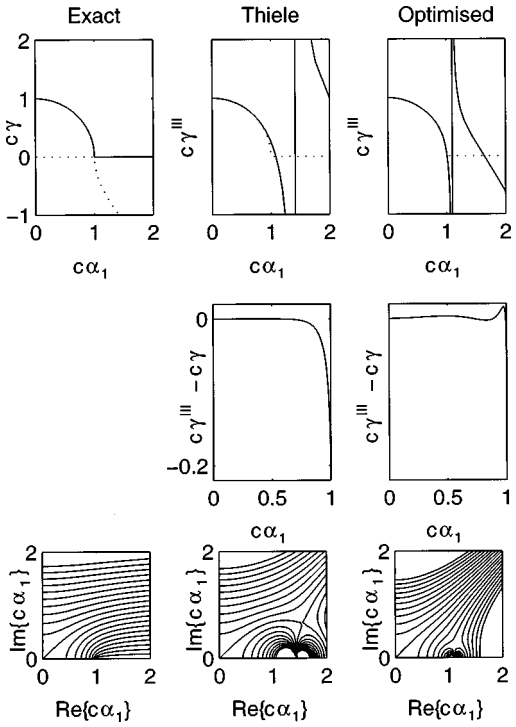

FIG. 4. The exact vertical slowness (left column) and its Thiele approximants with $\beta_1 = 1/2$, $\beta_2 = 1/8$, $\beta_3 = 1/2$ (middle) and with $\beta_1 = 0.531$, $\beta_2 = 0.364$, $\beta_3 = 0.825$ (right). In the upper left figure the dotted line corresponds to the imaginary part of the vertical slowness, while in the two other upper figures the dotted lines correspond to the real part of the exact vertical slowness. The figures in the second row show the differences between the approximants and the exact expression. In the bottom row, the real parts of the vertical slownesses as functions of complex α_1 are shown. The contour lines correspond to the values 0.1,0.2,...,2.0.

IV. SPARSE MATRIX REPRESENTATION OF THE PROPAGATOR

Consider the homogeneous one-way wave equation [cf. Eq. (20)]

$$\partial_2 \hat{W}^{(0)}_1 + i\omega\hat{\Gamma}\hat{W}^{(0)}_1 = 0, \quad x_2 \in (0, x_2^{\text{exit}}], \tag{63}$$

which is satisfied by the leading-order term of the Bremmer series. In this section we will derive a sparse matrix representation for its propagator, $\hat{P}(.,k)$. In the following approximations, we will maintain the hyperbolicity of the time-domain-equivalent equations, but we will deform the postcritical regime.

A. Approximating the vertical slowness leading to a partial differential equation

The principal part of the left vertical wave-slowness symbol is given by [cf. Eq. (34)]

$$\hat{\gamma}_{pp}(x_1,x_2,\alpha_1) = [c^{-2}(x_1,x_2) - \alpha_1^2]^{1/2}. \tag{64}$$

In the upper left corner of Fig. 4, $c\,\hat{\gamma}_{pp}$ is shown. The interval $c\alpha_1 \in [0,1]$ corresponds to wave propagation under an angle of 0°–90° and is called the precritical region. The interval $c\alpha_1 \in (1,\infty)$ corresponds to the evanescent wave constituents and is called the postcritical region.

For our numerical scheme, we consider Thiele's third-order continued fraction's approximation of the left symbol (see Serafini and De Hoop[31] and De Hoop and De Hoop[32])

$$\hat{\gamma}_{pp}^{III}=\frac{1}{c}+[1-\beta_3 c^2\alpha_1^2]^{-1}[-\beta_1 c\alpha_1^2+\beta_2 c^3\alpha_1^4]. \quad (65)$$

The wavefront associated with this approximation is free from artificial singularities in a cone of propagation angles about vertical, unlike the second-order approximation that is commonly used. The operator associated with this left symbol is not symmetric nor self-adjoint. To create a symmetric Thiele approximation, we extract the local wave speed c from the square root expression; the vertical slowness operator then becomes

$$\hat{\Gamma}\approx c^{-1/2}(1+\Xi)^{1/2}c^{-1/2}, \quad (66)$$

where

$$\Xi\equiv -cD_1^2(c\cdot). \quad (67)$$

This approximation is valid for small values of the commutator $[c,D_1]$, which will be the case for media varying smoothly on the scale of the dominant wavelength.

The third-order Thiele approximation is now applied to the symbol of the operator $(1+\Xi)^{1/2}$. This leads to a symmetric operator $\hat{\Gamma}^{III}$, the principal symbol of which still equals the expression in Eq. (65),

$$\hat{\Gamma}^{III}=c^{-1/2}\{1+[1+\beta_3\Xi]^{-1}[\beta_1\Xi+\beta_2\Xi^2]\}c^{-1/2}. \quad (68)$$

The internal structure of $\hat{\Gamma}^{III}$ is such that its symbol captures some of the contributions beyond the principal part. From now on we will freely omit the superscript III.

According to Thiele's formula, we have $\beta_1=1/2$, $\beta_2=1/8$, and $\beta_3=1/2$. The parameters, β_1, β_2, and β_3, however, can be adjusted by minimizing the difference between the exact spectral-domain vertical slowness and its continued-fraction approximation, defined by Eq. (65), with respect to the L_2 norm, over all the propagating modes (i.e., the real slowness surface). In this minimization, we must be aware of the fact that the pole [at $(\alpha_1^\gamma)^2=c^{-2}\beta_3^{-1}$] introduced by the Thiele-type approximation will lie outside the precritical region of the α_1 plane. The optimization procedure can be viewed as a replacement of Thiele's continued fraction by Newton interpolation. Using an optimization routine based on the simplex method,[33] the values $\beta_1=0.526$, $\beta_2=0.364$, and $\beta_3=0.825$ are obtained.

In case the propagation angles appearing in the wave field are restricted, the optimization should be carried out accordingly. This type of optimization was also considered by Lee and Suh[34] and followed by Bunks.[35]

Figure 4 shows the exact and approximated vertical slownesses with β_1, β_2, and β_3 set to Thiele's values and set to optimal values, respectively. In the second row of figures the differences with the exact slowness are drawn. In the bottom row the real part of the vertical slownesses as a function of complex-valued $c\alpha_1$ is shown. In these pictures we recognize the singularities in the vertical slownesses: a branch cut from $c\alpha_1=1$ to $+\infty$ in the exact vertical slowness and poles at $\sqrt{2}$ and 1.10 for the two approximated vertical slownesses, respectively. Since no singularities are present on the imaginary axis, the approximation is accurate for a large range of imaginary values of $c\alpha_1$.

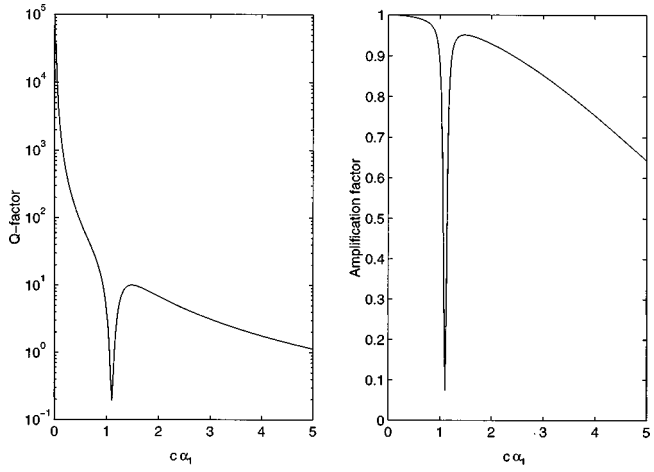

FIG. 5. The $\mathcal{Q}$ factor (left) and the corresponding amplification factor (right) associated with the dissipation trick in the third-order Thiele approximation; $\beta_1=0.526$, $\beta_2=0.364$, and $\beta_3=0.825$. The relative imaginary circular frequency $\Omega=0.02$. Note that the notch occurs beyond the critical angle.

Fundamental differences between the approximate and exact vertical slownesses occur near the singularities in the horizontal slowness plane. Since it is impossible to approximate a branch cut with a finite set of poles from a rational approximation, we have to restrict ourselves to approximating the precritical wave propagation as complete as possible. The influences of the artificial postcritical wave propagation must then be suppressed. A dissipation trick can be designed for that purpose.

B. The dissipation trick

To suppress artifacts, and aliasing (which may arise from the discretization to be carried out in the horizontal direction), from the large horizontal wave-number components, we may replace the real frequency ω by a complex one,

$$\omega'=\omega(1-i\Omega),$$

just in the expression for $i\omega\hat{\Gamma}$ [and later in $\hat{\mathsf{M}}$ and $\hat{\mathsf{M}}'$, see Eqs. (80)]. In a homogeneous medium, it implies per Fourier component or plane wave, $\mathcal{A}(x_2,\alpha_1,\omega)\exp(-i\omega\alpha_1 x_1)$, an amplification factor of the form

$$|\mathcal{A}(x_2+\Delta x_2,\alpha_1,\omega)/\mathcal{A}(x_2,\alpha_1,\omega)|$$
$$=\exp\left[-\frac{\omega\Delta x_2}{2c\mathcal{Q}(\alpha_1,\omega,i\Omega)}\right]. \quad (69)$$

The amplification factor is attenuative in nature. The $\mathcal{Q}$ factor is given by

$$\mathcal{Q}(\alpha_1,\omega,i\Omega)=\frac{1}{\mathrm{Im}\{2c\,\hat{\gamma}^{III}(\alpha_1;\omega(1-i\Omega))\}}, \quad (70)$$

and is plotted in Fig. 5. Here Ω is assumed to be very small ($\Omega\ll 1$). This particular complexification results in a local bandlimitation filter, suppressing the artifacts associated with the postcritically propagating modes.

C. The comoving frame of reference

To reduce discretization artifacts in the vertical derivative, the numerical computations are done in a comoving frame of reference, traveling in the direction of preference. The accuracy is improved, since this transformation enables us to take into account the leading phase shift exactly. The change of frame yields (see Claerbout[2])

$$\hat{h}(x_k,\omega)=\exp[i\omega\tau(x_k)]\hat{W}_1^{(0)}(x_k,\omega), \tag{71}$$

in which

$$\tau(x_k)=\int_{\zeta=0}^{x_2} c^{-1}(x_1,\zeta)d\zeta \tag{72}$$

is the local vertical travel time. Substituting Eq. (71) into Eq. (63) leads to

$$\partial_2\hat{h}+i\omega[\exp(i\omega\tau)\hat{\Gamma}\ \exp(-i\omega\tau)-c^{-1}]\hat{h}=0. \tag{73}$$

D. Discretization in the transverse direction

First, we introduce the discretization in the transverse direction, of the partial differentiation ∂_1^2. (In three-dimensional wave propagation this would be the two-dimensional Laplace operator.) Our starting point is a low-order, implicit, finite-difference approximation. The spectrum or symbol of the resulting operator is a rational function in horizontal slowness. The medium has to be smooth on the scale of the size of the operator. A uniform grid is employed in the horizontal direction. The horizontal sampling interval is denoted as Δx_1.

The discretization of the one-dimensional Laplace operator is formulated in terms of recursive filters based on the nearest-neighbors interaction (see Mitchell and Griffiths[36]). Our recursive filter acting on a function $\hat{h}$ is defined through

$$(1+a_2\delta_1^2)\langle\partial_1^2\hat{h}\rangle=(\Delta x_1)^{-2}a_1\delta_1^2\hat{h}, \tag{74}$$

where

$$\delta_1^2\hat{h}=\hat{h}(x_1+\Delta x_1)-2\hat{h}(x_1)+\hat{h}(x_1-\Delta x_1). \tag{75}$$

In Eq. (74), 1 denotes the identity and $\langle\partial_1^2\hat{h}\rangle=\langle\partial_1^2\rangle\hat{h}$ represents the approximate Laplace operator having acted on $\hat{h}$. Using a Taylor series expansion of $\hat{h}$ at $x_1\pm\Delta x_1$ about x_1, the values $a_1=1$ and $a_2=1/12$ are found (see Mitchell and Griffiths[36]). Then $\langle\partial_1^2\rangle=\partial_1^2+\mathcal{O}((\Delta x_1)^4)$. For a finite-bandwidth solution generated with a given sampling interval, however, we leave this order estimate, and use a_2 as a parameter to improve the overall accuracy. Requiring that in the limit $\Delta x_1\downarrow 0$ the spectrum of $\langle\partial_1^2\rangle$ tends to the spectrum of the Laplace operator up the lowest order, leads necessarily to $a_1=1$. The parameter a_2 is then determined by minimizing nonlinearly the difference between the approximate and the exact Laplace operator spectra with respect to the L_2 norm over the Nyquist interval. Thus a more accurate approximate spectrum is obtained over the spatial bandwidth as a whole. Using an optimization routine based on the simplex method,[37] the value $a_2=0.130$ is obtained. It is noted, however, that if it is known beforehand that the actual spatial bandwidth of the wave field to be extrapolated is limited by a horizontal wave number less the Nyquist wave number $k_{1,\mathrm{Nyq}}=\pi/\Delta x_1$, the optimization should be carried out over this sub-band only.

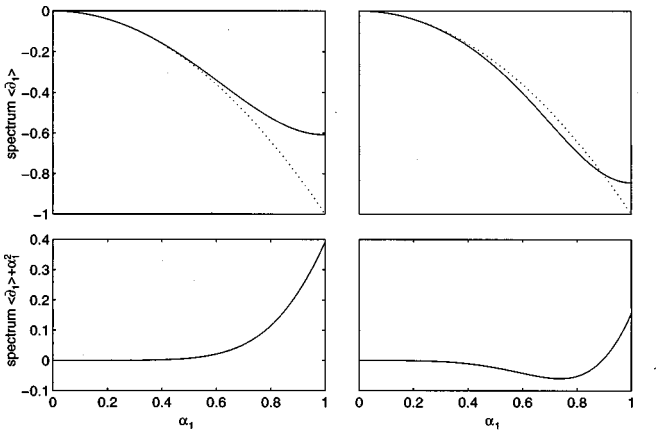

FIG. 6. The spectra or symbols of the approximate ∂_1^2 operators with $a_2=1/12$ (upper left) and $a_2=0.130$ (upper right). The bottom figures show the corresponding differences with the exact spectra, which are also dotted in the upper figures. We set $\omega=1\ \mathrm{s}^{-1}$ and $\Delta x_1=\pi m$.

Figure 6 illustrates the spectra of the exact and the approximate Laplace operators with optimal values and Taylor values for a_1 and a_2, respectively. The approximated Laplace operator has poles at

$$\alpha_1=\alpha_1^L=(\omega\Delta x_1)^{-1}\{\pm\arccos[1-\tfrac{1}{2}a_2^{-1}]+2m\pi\}, \tag{76}$$

$(m=0,\pm1,\pm2,...)$. In practice $a_2<1$, and these poles are situated in the complex α_1 plane at $\mathrm{Re}\{\alpha_1\}=\pi/(\omega\Delta x_1)$ (determined by the Nyquist theorem), far away from the real axis.

The poles of the approximate Laplace operator carry over in the approximation of the vertical slowness operator. The vertical slowness symbol becomes periodic in accordance with the Nyquist theorem, and the Laplace poles are slightly shifted:

$$\alpha_1^L\rightarrow(\omega\Delta x_1)^{-1}\{\pm\arccos[1-\tfrac{1}{2}(a_2^{-1}+\omega\Delta x_1\beta_3)]+2m\pi\}, \tag{77}$$

see Fig. 7. For example, taking $a_2=0.130$, $\beta_3=0.825$, and a sampling rate of 8 points per wavelength, the poles are located at

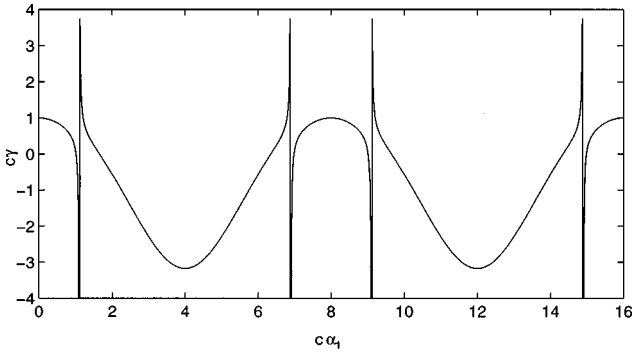

FIG. 7. The third-order Thiele approximation of the vertical slowness symbol including the spectrum of the discretized Laplace operator ($a_2=0.130$, $\beta_1=0.526$, $\beta_2=0.364$, $\beta_3=0.825$, and a sampling rate of eight points per wavelength). The poles are located at $\alpha_1\simeq 1.102$, 6.898, 9.102,... .

$$\alpha_1^{\gamma}=\pm 1.1023+8m \quad \text{and} \quad \alpha_1^{L}=\pm(4-2.4010i)+8m. \tag{78}$$

E. The system of ordinary differential equations

Substituting $\langle \partial_1^2 \rangle$, i.e., Eq. (74) into Eq. (67) and the result into the one-way wave equation (73) with vertical slowness (68), we obtain a system of ordinary differential equations of the form

$$\hat{\mathsf{M}}\partial_2 \hat{h} + i\omega \hat{\mathsf{M}}' \hat{\mathsf{C}}^{-1} \hat{h} = 0. \tag{79}$$

The operators involved are $\hat{\mathsf{M}}=\hat{\mathsf{M}}(x_2,\omega;x_1,\delta_1^2,\Delta x_1)$, $\hat{\mathsf{M}}'=\hat{\mathsf{M}}'(x_2,\omega;x_1,\delta_1^2,\Delta x_1)$, and $\hat{\mathsf{C}}=\hat{\mathsf{C}}(x_2,\omega;x_1,\delta_1^2,\Delta x_1)$; they are sparse, viz., 3, 5, and 3 bands, respectively, and are given by

$$\begin{aligned}
\hat{\mathsf{M}}\cdot &= (1+a_2\delta_1^2)(c^{-1/2}\exp(-i\omega\tau)\cdot) \\
&\quad + \beta_3\beta_8 c^{-2}\delta_1^2(c^{3/2}\exp(-i\omega\tau)\cdot), \\
\hat{\mathsf{M}}'\cdot &= \beta_1\beta_8 c^{-2}(1+a_2\delta_1^2)(\delta_1^2(\cdot)) \\
&\quad + \beta_2\beta_8^2 c^{-4}\delta_1^2(c^2\delta_1^2(\cdot)),
\end{aligned} \tag{80}$$

while

$$\hat{\mathsf{C}}\cdot = \exp(i\omega\tau)c^{-1/2}(1+a_2\delta_1^2)\cdot, \tag{81}$$

with horizontal sampling rate parameter

$$\beta_8=(\omega\Delta x_1/c)^{-2}. \tag{82}$$

The quantity $2\pi\beta_8$ equals the number of grid points per wavelength in the local medium.

F. Integration of the vertical derivative

The solution of Eq. (79) can formally be written as a product integral. This product integral will have to be evaluated, recursively, for every propagation step with size Δx_2. The product integral is given by [see also Eq. (27)]

$$\hat{h}(.,x_2+\Delta x_2) = \prod_{\zeta=x_2}^{x_2+\Delta x_2} \exp[-i\omega(\hat{\mathsf{M}}^{-1}\hat{\mathsf{M}}'\hat{\mathsf{C}}^{-1})(.,\zeta)d\zeta]\hat{h}(.,x_2). \tag{83}$$

It is approximated by

$$\hat{h}(.,x_2+\Delta x_2) \simeq \exp[-i\omega\Delta x_2(\hat{\mathsf{M}}^{-1}\hat{\mathsf{M}}'\hat{\mathsf{C}}^{-1})(.,x_2+\tfrac{1}{2}\Delta x_2)]\hat{h}(.,x_2). \tag{84}$$

To speed up the computations, the exponent is approximated by the solution of a unitary matrix equation. The (n,n)-Padé approximants can be used for this purpose. They are given by (see Numerical Recipes[38])

$$\exp(Z) \simeq \begin{cases} \dfrac{1+\beta_9 Z}{1-\beta_9 Z}, & \text{lowest order:}(1,1), \\ \left(\dfrac{1+\beta_{11}Z}{1-\beta_{11}Z}\right)\left(\dfrac{1+\beta_{10}Z}{1-\beta_{10}Z}\right), & \text{higher order:}(2,2), \end{cases} \tag{85}$$

where

$$Z \equiv \Delta x_2 \partial_2|_{x_2+1/2\Delta x_2}, \tag{86}$$

is the derivative that appears in Eq. (79). The higher the order of the approximation, the larger the stepsize Δx_2 can be. For stability considerations of the associated higher-order implicit finite-difference schemes, see Widlund.[39]

According to Padé's formula, we have $\beta_9=\frac{1}{2}$. Instead of taking this exact value, we let β_9 be a free parameter for an optimization procedure. Minimizing the difference for the precritical wave constituents, gives $\beta_9=0.766$ for two points per wavelength, $\beta_9=0.540$ for five points per wavelength, and $\beta_9=0.510$ for ten points per wavelength. The (1,1)-Padé approximation of the exponent yields the well-known Crank–Nicholson scheme (see Richtmeyer and Morton[40]), in our notation given by

$$\begin{aligned}
&(\hat{\mathsf{M}}\hat{\mathsf{C}})(x_2+\tfrac{1}{2}\Delta x_2)(\delta_{\|}\hat{h}'(x_2)) \\
&\quad = (-i\beta_9\omega\Delta x_2) \\
&\qquad \times \hat{\mathsf{M}}'(x_2+\tfrac{1}{2}\Delta x_2)(\hat{h}'(x_2)+\hat{h}'(x_2+\Delta x_2)),
\end{aligned} \tag{87}$$

with

$$(\delta_{\|}\hat{h}')(x_2)=\hat{h}'(x_2+\Delta x_2)-\hat{h}'(x_2), \tag{88}$$

where

$$\hat{h}'(\zeta)=\hat{\mathsf{C}}^{-1}(x_2+\tfrac{1}{2}\Delta x_2)\hat{h}(\zeta) \quad \text{for} \quad \zeta\in(x_2,x_2+\Delta x_2]. \tag{89}$$

The scheme Eq. (87) should be interpreted as a centered difference approximation of the vertical derivative, and hence is accurate up to $\mathcal{O}((\Delta x_2)^3)$.

G. Propagator matrix

To arrive at an explicit matrix representation for the one-way propagator, we introduce the array,

$$\hat{h}_i(x_2,\omega)=\hat{h}(x_{1i},x_2,\omega), \tag{90}$$

where $x_{1i}=i\Delta x_1$, and $i=1,...,N_{x_1}$ labels the samples in the tranverse direction. In this notation, with the aid of Eqs. (87) and (89), the approximate one-way wave propagation can finally be written in the matrix form

$$\hat{h}_i(x_2+\Delta x_2,\omega) = \hat{\mathsf{C}}_{ij}(\hat{\mathsf{A}}^{-1})_{jk}\hat{\mathsf{A}}'_{kl}(\hat{\mathsf{C}}^{-1})_{lm}|_{x_2+1/2\Delta x_2}\hat{h}_m(x_2,\omega), \tag{91}$$

where the matrices $\hat{\mathsf{A}}$, $\hat{\mathsf{A}}'$, and $\hat{\mathsf{C}}$ are functions of x_2 and ω, and are constructed from the operators $\hat{\mathsf{M}}$, $\hat{\mathsf{M}}'$, and $\hat{\mathsf{C}}$:

$$\hat{\mathsf{A}}=\hat{\mathsf{M}}\hat{\mathsf{C}}+i\beta_9\omega\Delta x_2\hat{\mathsf{M}}', \tag{92}$$

$$\hat{\mathsf{A}}'=\hat{\mathsf{M}}\hat{\mathsf{C}}-i\beta_9\omega\Delta x_2\hat{\mathsf{M}}'. \tag{93}$$

The matrices $\hat{\mathsf{A}}$ and $\hat{\mathsf{A}}'$ contain five nonvanishing bands, while $\hat{\mathsf{C}}$ has three nonvanishing bands only. Observe that

$$\hat{\mathsf{A}}'(\omega)=\hat{\mathsf{A}}(-\omega), \tag{94}$$

thus $\hat{\mathsf{A}}'(\omega)=\overline{\hat{\mathsf{A}}(\omega)}$ if ω is real-valued ($\Omega=0$).

The numerical scheme following Eq. (91) involves two matrix-vector multiplications and twice solving a matrix equation per propagation step:

$$\hat{\mathsf{C}}_{lm}\hat{h}'_m(x_2,\omega)=\hat{h}_l(x_2,\omega), \tag{95}$$

$$\hat{h}''_k(x_2,\omega)=\hat{\mathsf{A}}'_{kl}\hat{h}'_l(x_2,\omega), \tag{96}$$

$$\hat{\mathsf{A}}_{jk}\hat{h}'_k(x_2+\Delta x_2,\omega)=\hat{h}''_j(x_2,\omega), \tag{97}$$

$$\hat{h}_i(x_2+\Delta x_2,\omega)=\hat{\mathsf{C}}_{ij}\hat{h}'_j(x_2+\Delta x_2,\omega). \tag{98}$$

The last step adjusts for the change to the comoving frame of reference. Introduce the diagonal matrix T, representing the change of frame, with diagonal elements [cf. Eq. (71)]

$$\mathsf{T}_{mm}(x_2)=\exp[i\omega\tau(x_{1m},x_2)]. \tag{99}$$

Then the propagator matrix [cf. Eqs. (50) and (91)] is given by

$$\langle\hat{P}(k+1)\rangle_{im}=\mathsf{T}(x_2+\Delta x_2)_{ii'}\hat{\mathsf{C}}_{i'j}(\hat{\mathsf{A}}^{-1})_{jk}\times\hat{\mathsf{A}}'_{kl}(\hat{\mathsf{C}}^{-1})_{lm}|_{x_2+1/2\Delta x_2}. \tag{100}$$

The Appendix contains a discussion on absorbing boundary conditions to which the matrix $\hat{\mathsf{A}}$ is subjected. Several techniques exist for carrying out the matrix inversions.[41] The inversion of the tridiagonal matrix $\hat{\mathsf{C}}$ in Eq. (95) is carried out by forward/backward substitution (see Numerical Recipes[38]).

V. THE VERTICAL PHASE AND GROUP SLOWNESSES

Let $\hat{\gamma}^{\mathrm{ph}}$ and $\hat{\gamma}^{g}$ denote the vertical phase and vertical group *slowness* associated with a real-valued plane wave, respectively. We will analyze the accuracy of our numerical scheme with the aid of these quantities. The analysis of the accuracy of finite-difference propagation schemes with phase and group *velocities* can be found in Trefethen.[13] Beaumont *et al.*[14] and Holberg[15,16] assessed and improved the accuracy of such schemes.

A. General considerations

Substitute a plane-wave constituent into Eqs. (71) and (98):

$$\hat{W}_1^{(0)}(x_k,\omega)=\exp(-i\omega\hat{\gamma}^{\mathrm{ph}}\Delta x_2)\exp[-i\omega\alpha_1\Delta x_1], \tag{101}$$

or, in the moving frame of reference,

$$\hat{h}(x_k,\omega)=\exp(i\omega\tau)\exp(-i\omega\hat{\gamma}^{\mathrm{ph}}\Delta x_2)\times\exp[-i\omega\alpha_1\Delta x_1]. \tag{102}$$

We then obtain the *amplification* factor of the finite-difference scheme (see Richtmeyer and Morton[40]),

$$\mathsf{a}^{-1}\mathsf{a}'=\exp[-i\omega\hat{\gamma}^{\mathrm{ph}}\Delta x_2]\exp[i\omega c^{-1}\Delta x_2], \tag{103}$$

in which $\hat{\gamma}^{\mathrm{ph}}$, a, and a' are the left symbols of the numerical representation for $\hat{\Gamma}$, A, and A', respectively. For a homogeneous medium (constant c), we find

$$\mathsf{a}=\mathsf{A}_{ii}+2\mathsf{A}_{i\,i+1}\cos(\omega\alpha_1\Delta x_1)+2\mathsf{A}_{i\,i+2}\cos(2\omega\alpha_1\Delta x_1), \tag{104}$$

independent of i, together with a similar expression for a', replacing A by A'. For real-valued ω, we have $\mathsf{a}'(\omega)=\mathsf{a}(-\omega)$, thus $|\mathsf{a}^{-1}\mathsf{a}'|=1$ in a homogeneous medium. The symbol of the finite difference scheme is the vertical phase slowness $\hat{\gamma}^{\mathrm{ph}}$ given by

$$\hat{\gamma}^{\mathrm{ph}}(\alpha_1,\omega)=c^{-1}-\frac{\log(\mathsf{a}^{-1}\mathsf{a}')}{i\omega\Delta x_2}, \tag{105}$$

which reduces, if ω is real-valued, to

$$\hat{\gamma}^{\mathrm{ph}}(\alpha_1,\omega)=c^{-1}+\frac{2}{\omega\Delta x_2}\arg(\mathsf{a}). \tag{106}$$

From the vertical phase slowness the vertical group slowness $\hat{\gamma}^{g}$ can be derived, viz.,

$$\hat{\gamma}^{g}=\partial_\omega(\omega\hat{\gamma}^{\mathrm{ph}})=\hat{\gamma}^{\mathrm{ph}}+\omega(\partial_\omega\hat{\gamma}^{\mathrm{ph}}). \tag{107}$$

The term $c(\partial_\omega\hat{\gamma}^{\mathrm{ph}})$ can be identified with the delay of the envelope per wavelength. Together with Eq. (103) this leads to

$$\hat{\gamma}^{g}(\alpha_1,\omega)=c^{-1}-i(\Delta x_2)^{-1}\{\mathsf{a}^{-1}\partial_\omega\mathsf{a}-(\mathsf{a}')^{-1}\partial_\omega\mathsf{a}'\}, \tag{108}$$

and reduces, if ω is real-valued, to

$$\hat{\gamma}^{g}(\alpha_1,\omega)=c^{-1}-2(\Delta x_2)^{-1}\,\mathrm{Im}\{\mathsf{a}^{-1}\partial_\omega\mathsf{a}\}. \tag{109}$$

It is observed that $\hat{\gamma}^{\mathrm{ph}}$ and $\hat{\gamma}^{g}$ are functions of the horizontal and vertical sampling rates per wavelengths, $c/(\omega\Delta x_1)$ and $c/(\omega\Delta x_2)$. Note that $\hat{\gamma}^{g}-\hat{\gamma}$ is indicative for the numerical anisotropy, whereas $\hat{\gamma}^{\mathrm{ph}}-\hat{\gamma}^{g}$ is indicative for the numerical dissipation.

B. Optimization

The vertical phase and group slownesses are functions of our parameters $\{\beta_1,\beta_2,\beta_3,a_2,\beta_9,\Omega\}$ arising from the various approximations made to arrive at a sparse matrix representation for the propagator. So far, we have found two distinct parameter sets: one arising from consistent rational expansions, and one arising from stepwise optimization. For a sampling rate of 5 points per wavelength in both the horizontal and vertical directions ($\Delta x_1=\Delta x_2=0.2\lambda$) the phase and group slownesses for the first parameter set are shown in Fig. 8. The exact vertical slowness is shown in the same graph. Significant deviations are observed for large propagation angles. The parameter set corresponding to the stepwise optimization leads to a better result (Fig. 9). In the stepwise optimization, however, it is hard to control the movement of the poles in the complex horizontal slowness plane, introduced by the approximations. One can control this movement in an optimization scheme of the phase and group slownesses for all parameters together; then one expects a more accurate result as well.

The optimization of the phase and group slownesses results in a minimization of numerical anisotropy and numerical dissipation for the precritical wave constituents. In the optimization procedure special attention must be paid to the contraint that the poles of a stay outside the precritical region in the α_1 plane. The overall optimization is carried out for an objective function given by the sum of the squared differences between $\hat{\gamma}^{g}$ and $\hat{\gamma}$, and $\hat{\gamma}^{\mathrm{ph}}$ and $\hat{\gamma}^{g}$. The results are illustrated in Fig. 10, as before for five points per wavelength. From numerical tests, we find that the accuracy remains more or less the same when we vary the transverse

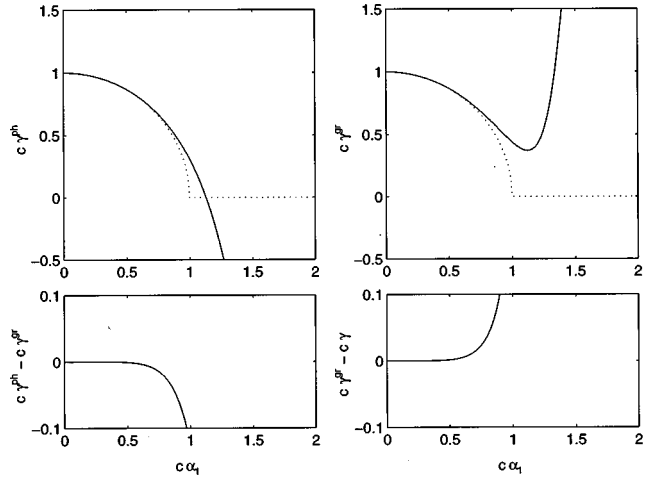

FIG. 8. The phase slowness (upper left) and the group slowness (upper right) associated with the discretized, approximate, one-way wave equation with $\beta_1=1/2$, $\beta_2=1/8$, $\beta_3=1/2$, $a_2=1/12$, $\beta_9=1/2$, and a sampling rate of five points per wavelength. The exact vertical wave-slowness symbol is dotted. In the bottom row the difference between the phase slowness and the group slowness, and the difference between the group slowness and the exact slowness are plotted.

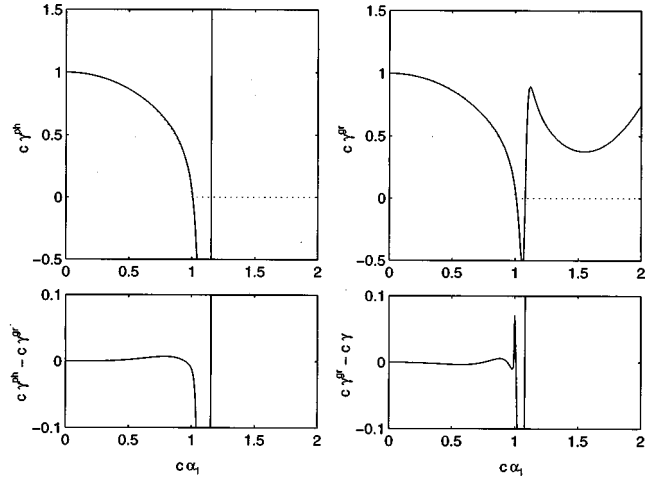

FIG. 10. The phase slowness (upper left) and the group slowness (upper right) associated with the discretized, approximate, one-way wave equation with $\beta_1=0.486$, $\beta_2=0.349$, $\beta_3=0.841$, $a_2=0.114$, $\beta_9=0.529$, and a sampling rate of five points per wavelength. The exact vertical wave-slowness symbol is dotted. In the bottom row the difference between the phase slowness and the group slowness, and the difference between the group slowness and the exact slowness are plotted.

sampling rate from 5 down to 2.5 points per wavelength, keeping the vertical sampling rate the same. The procedure is even less sensitive to the vertical sampling rate.

So far, the optimization procedure was focused on the real slowness surface. However, as we have seen in the preceeding sections, the approximations lead to artifacts in the postcritical regime. In fact, the postcritical constituents have been mapped on propagating constituents (slow waves). We have designed a dissipation trick to attenuate these constituents. Besides this trick, some of the artificial constituents are forced to leave the computational domain through the transparent boundary conditions. The dissipation trick induces a complexification of the parameters used in the optimization, and hence it seems to be natural to complexify the optimization procedure accordingly (see also Collins[42]). Pursuing this complexification, the optimization procedure is extended with the constraint that the postcritical power is attenuated strongly while the attenuation/amplification in the precritical region is kept minimal (less than 5%). The resulting parameter set is shown in the fourth column of Table I. The first column of this table represents the expansion values, and the second column represents the values obtained by stepwise optimization. The accuracy of the complex parameter set is illustrated in Fig. 11.

We note, however, that the complexification of parameters is not always desired. For example, in the application of our numerical scheme to long-range propagation in low-lossy waveguides, the accumulative power loss is of key importance. In such configurations, we set $\Omega=0$ and keep the parameters real. The optimization leads to the third column of Table I.

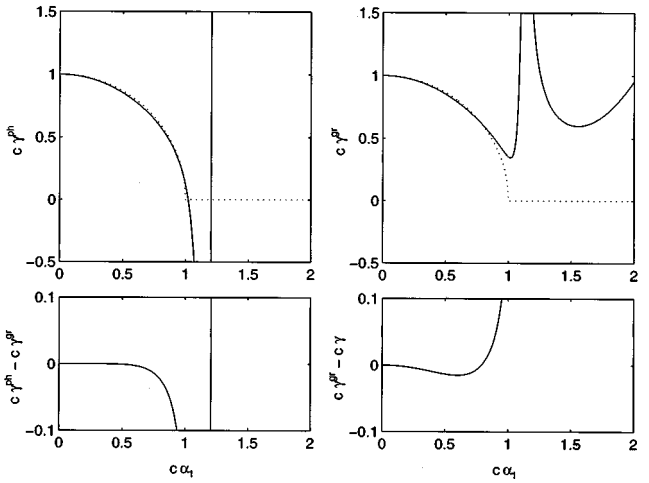

FIG. 9. The phase slowness (upper left) and the group slowness (upper right) associated with the discretized, approximate, one-way wave equation with $\beta_1=0.526$, $\beta_2=0.364$, $\beta_3=0.825$, $a_2=0.0888$, $\beta_9=0.529$, and a sampling rate of five points per wavelength. The exact vertical wave-slowness symbol is dotted. In the bottom row the difference between the phase slowness and the group slowness, and the difference between the group slowness and the exact slowness are plotted.

TABLE I. The parameter sets for propagation.

Parameter set	1	2	3	4
$\Delta x_1/\lambda$	0.2	0.2	0.2	0.2
$\Delta x_2/\lambda$	0.2	0.2	0.2	0.2
Re$\{\beta_1\}$	1/2	0.526	0.486	0.5104
Im$\{\beta_1\}$	0	0	0	−0.0340
Re$\{\beta_2\}$	1/8	0.364	0.349	0.2207
Im$\{\beta_2\}$	0	0	0	−0.0131
Re$\{\beta_3\}$	1/2	0.825	0.841	0.6685
Im$\{\beta_3\}$	0	0	0	−0.0310
Re$\{a_2\}$	1/12	0.089	0.114	0.1207
Im$\{a_2\}$	0	0	0	0.0063
Re$\{\beta_9\}$	1/2	0.540	0.529	0.4679
Im$\{\beta_9\}$	0	0	0	−0.0066
Ω	0	0	0	0.0406
Figures	8	9	10	11
			12	13
				18

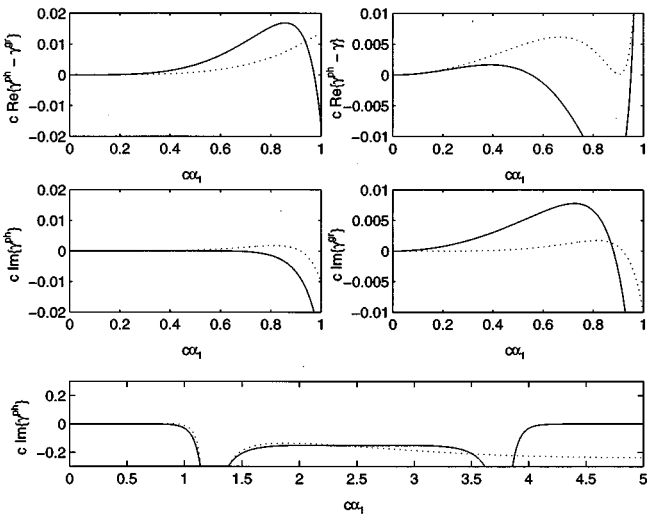

FIG. 11. The difference between the real parts of the phase slowness and the group slowness (upper left), and the difference between the real parts of the group slowness and the exact slowness (upper right). The middle row shows the imaginary parts of the phase slowness (left) and the group slowness (right). The parameter set is given in column 4 of Table I. Two sampling rates are shown: five points per wavelength (solid line) and ten points per wavelength (dotted line). The bottom figure shows the imaginary parts of the phase slowness (solid line) and the group slowness (dotted line on a larger scale).

The poles arising in vertical phase slowness, for the different parameter sets, are given in Table II.

C. A numerical example

We illustrate the final, optimized, one-way propagation by computing the wave field excited by a line source in a homogeneous medium. The wave speed of the medium is chosen to be $c=1900$ m/s. The numerical grid consists of 99 points along the x_1 direction and 60 points along the x_2 direction. The discretization step is 16 m in both directions. Given a source-signature with trapezoidal spectrum with corner frequencies 10, 20, 25, and 40 Hz, we encounter sampling rates of 2.97 to 11.9 points per wavelength. The line source is located at $x_1=800$ m, $x_2=0$ m, and we will show snapshots of the pressure field at 0.3 s. The source is a vertical force. For this configuration we have analytic expressions.

In Fig. 12 the snapshot is shown using the first parameter set, while in Fig. 13 the snapshot for the fourth parameter set is shown. The left parts of the figures ($0<x_1<800$ m) represent the numerical solutions, while the right parts ($800<x_1<1600$ m) represent the exact solution. The errors occurring in Fig. 13 are illustrated in Fig. 14, the absolute ones for $0<x_1<800$ m and the relative ones for 800

TABLE II. The poles of the numerical vertical phase slowness.

Parameter set	Pole 1	Pole 2
1	$1.4588+0.2807i$	$1.7135+1.3074i$
2	$1.1054-0.0040i$	$2.2899+1.7530i$
3	$1.0762-0.0271i$	$1.3686+1.1214i$
4	$1.5974-1.1406i$	$1.1816-0.1211i$

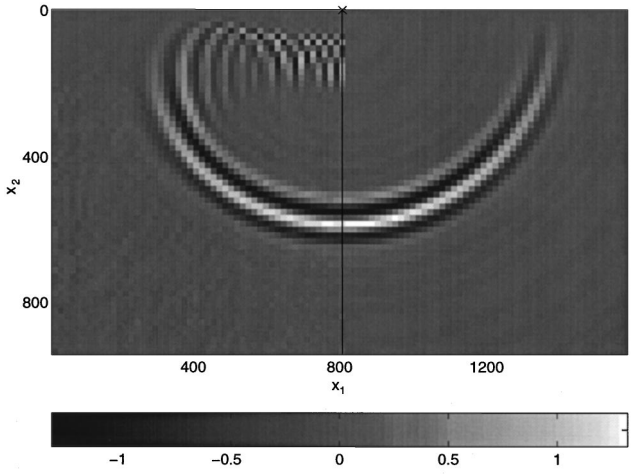

FIG. 12. Snapshot at 0.3 s of a vertical line force source response in a homogeneous medium ($c=1900$ m/s). The right-hand side is obtained analytically, while the left-hand side is obtained with our numerical scheme. Here we used parameter set 1 of Table I.

$<x_1<1600$ m. From this figure we find that the relative error at the numerical wave front is less than 2.5% up to angles of approximately 65°. Repeating this accuracy analysis for the other parameter sets, we conclude that the approximations are acceptable up to 20°, 40°, and 80° for the standard parabolic approximation, parameter set 1, and parameter set 3, respectively. The third parameter set is more accurate for higher angles than the fourth parameter set; however, postcritical artifacts remain apparent in the numerical results obtained with this real-valued parameter set.

VI. SPARSE MATRIX REPRESENTATIONS OF THE (DE)COMPOSITION OPERATORS

The computation of the generalized Bremmer coupling series starts with the decomposition of the initial field into up- and downgoing constituents in accordance with Eq. (19). Upon completing the calculation of a sufficiently large number of terms of the Bremmer coupling series, the constituents

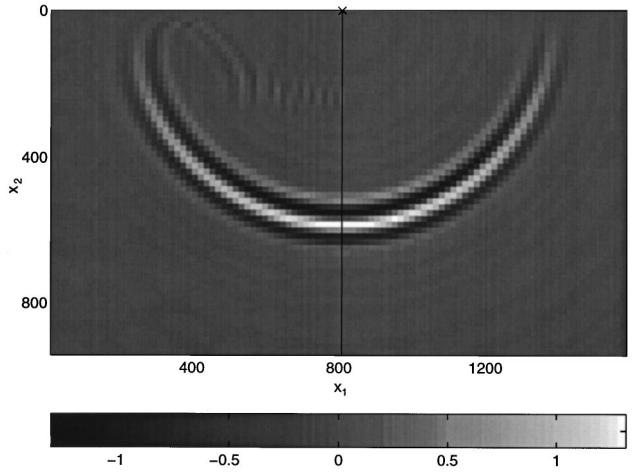

FIG. 13. Snapshot at 0.3 s of a vertical line force source response in a homogeneous medium ($c=1900$ m/s). The right-hand side is obtained analytically, while the left-hand side is obtained with our numerical scheme. Here we used parameter set 4 of Table I.

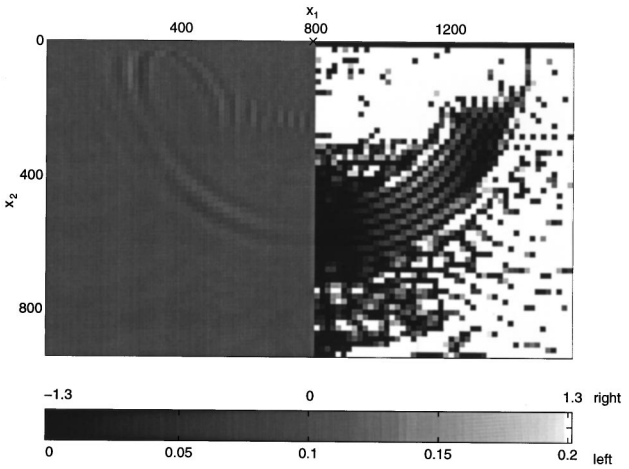

FIG. 14. The absolute error ($0<x_1<800$ m) and the relative error ($800<x_1<1600$ m) of the snapshot shown in the previous figure. The relative error is in percent.

are recomposed into observables with the aid of Eq. (18). In these procedures, the operator $\hat{\Gamma}$ and its inverse must be computed. Here using the results of Sec. IV, we will derive sparse matrix representations for these operators.

A. The composition operator

The composition operator contains the vertical slowness operator. To find a sparse matrix representation for this operator, we use the same approximation as in Eq. (68) for one-way wave propagation. We write, however, the fraction in a slightly different way,

$$\hat{\Gamma}^{III}=c^{-1/2}\{1+\beta_4\Xi+[1+\beta_3\Xi]^{-1}\beta_5\Xi\}c^{-1/2}, \tag{110}$$

with

$$\beta_4=\frac{\beta_2}{\beta_3}, \quad \beta_5=\beta_1-\frac{\beta_2}{\beta_3}. \tag{111}$$

We set

$$\hat{\Gamma}^{III}=\hat{\Gamma}_1^{III}+\hat{\Gamma}_2^{III}, \tag{112}$$

with

$$\begin{aligned}\hat{\Gamma}_1^{III}&=c^{-1/2}\{1+\beta_4\Xi\}c^{-1/2},\\ \hat{\Gamma}_2^{III}&=c^{-1/2}\{[1+\beta_3\Xi]^{-1}\beta_5\Xi\}c^{-1/2}.\end{aligned} \tag{113}$$

Substituting discretization Eq. (74) into Eq. (67) and the result into these operators, yields

$$\begin{aligned}&(1+a_2\delta_1^2)(c^{-1/2}\langle\hat{\Gamma}_1^{III}\hat{h}\rangle)\\ &\quad=[(1+a_2\delta_1^2)c^{-2}+\beta_4\beta_8c^{-2}\delta_1^2](c^{1/2}\hat{h}),\\ &[(1+a_2\delta_1^2)c^{-2}+\beta_3\beta_8c^{-2}\delta_1^2](c^{3/2}\langle\hat{\Gamma}_2^{III}\hat{h}\rangle)\\ &\quad=\beta_5\beta_8c^{-2}\delta_1^2(c^{1/2}\hat{h}).\end{aligned} \tag{114}$$

The two equations contain tridiagonal matrices only. Hence they can be solved rapidly with the forward/backward substitution procedure (see Numerical Recipes[38]).

B. The decomposition operator

The decomposition operator essentially contains the inverse of the vertical slowness operator. Using approximation (68) as before, we find that

$$c^{1/2}\hat{\Gamma}^{III}c^{1/2}=\beta_2[1+\beta_3\Xi]^{-1}[\beta_2^{-1}+\beta_2^{-1}(\beta_1+\beta_3)\Xi+\Xi^2]. \tag{115}$$

Factoring the operator between brackets, yields $\beta_2^{-1}+\beta_2^{-1}(\beta_1+\beta_3)\Xi+\Xi^2=[\beta_6-\Xi][\beta_7-\Xi]$. Then it is straightforward to invert the vertical slowness operator, viz.,

$$\begin{aligned}&(\hat{\Gamma}^{III})^{-1}\\ &\quad=c^{1/2}\{\beta_2^{-1}[\beta_7-\Xi]^{-1}[\beta_6-\Xi]^{-1}[1+\beta_3\Xi]\}c^{1/2}.\end{aligned} \tag{116}$$

Observe that the symbol of this operator has two poles on both sides of the origin (the zero crossings of $\hat{\gamma}^{III}$).

Using the factorization, we decompose the inverse vertical slowness into three operators,

$$(\hat{\Gamma}^{III})^{-1}=\hat{Y}_3^{-1}\hat{Y}_2^{-1}\hat{Y}_1, \tag{117}$$

with

$$\begin{aligned}&\hat{Y}_1=[1+\beta_3\Xi]c^{1/2}, \quad \hat{Y}_2=[\beta_6-\Xi],\\ &\hat{Y}_3=[\beta_7-\Xi]\beta_2c^{-1/2}.\end{aligned} \tag{118}$$

The inverse vertical slowness operator is then applied in two steps,

$$\hat{Y}_2(\hat{Y}_3((\hat{\Gamma}^{III})^{-1}\hat{h}))=\hat{Y}_1\hat{h},$$

which involves twice solving an equation. Substituting Eq. (67), with the aid of Eq. (74) the two equations are discretized

$$\begin{aligned}&[\beta_6(1+a_2\delta_1^2)-\beta_8c^{-2}\delta_1^2c^2](c^{-1}\langle\hat{Y}_3((\hat{\Gamma}^{III})^{-1}\hat{h})\rangle)\\ &\quad=[(1+a_2\delta_1^2)+\beta_3\beta_8c^{-2}\delta_1^2c^2](c^{-1/2}\hat{h}),\\ &\beta_2[\beta_7(1+a_2\delta_1^2)-\beta_8c^{-2}\delta_1^2c^2](c^{-3/2}\langle(\hat{\Gamma}^{III})^{-1}\hat{h}\rangle)\\ &\quad=(1+a_2\delta_1^2)(c^{-1}\langle\hat{Y}_3((\hat{\Gamma}^{III})^{-1}\hat{h})\rangle).\end{aligned} \tag{119}$$

The associated tridiagonal matrices are inverted using the forward/backward substitution procedure (see Numerical Recipes[38]).

C. A numerical example

At the computational boundaries we apply, as before, the Robin boundary conditions (Appendix). We also employ an optimization procedure for the (de)composition operators, considering the parameter subset $\{\beta_1,\beta_2,\beta_3,a_2,\Omega\}$. To avoid instabilities, we have to move the poles arising in the symbols of the approximate operators into the complex horizontal slowness plane. Table III contains the outcome of the optimization for a sampling rate of five points per wavelength. Figure 15 shows the symbols of the composition operator for different values of Ω.

To demonstrate the effect of wave field decomposition, we have computed the pressure excited by a line explosion source. The configuration was otherwise the same as in Figs. 12 and 13. Figure 16 shows a snapshot at 0.3 s. Note that the

TABLE III. The parameter set for (de)composition.

Parameter set	2′
$\Delta x_1/\lambda$	0.2
$\Delta x_2/\lambda$	0.2
Re$\{\beta_1\}$	0.526
Im$\{\beta_1\}$	0
Re$\{\beta_2\}$	0.364
Im$\{\beta_2\}$	0
Re$\{\beta_3\}$	0.825
Im$\{\beta_3\}$	0
Re$\{a_2\}$	0.13
Im$\{a_2\}$	0
Ω	0.01

artificial head wave enforces the approximate wave front to be vertical at the level of the source. The radiation pattern becomes close to isotropic as it should.

VII. SPARSE MATRIX REPRESENTATIONS OF THE REFLECTION/TRANSMISSION OPERATORS

Up to principal parts, we can simplify the reflection and transmission operators [cf. Eq. (22)] since then

$$\partial_2\hat{\Gamma}\simeq\tfrac{1}{2}\,\hat{\Gamma}^{-1}((\partial_2 c^{-2})\cdot). \tag{120}$$

Substituting this approximation into Eq. (22) yields

$$\hat{R}\simeq\tfrac{1}{4}\,\hat{A}^{-1}((\partial_2 c^{-2})\cdot); \tag{121}$$

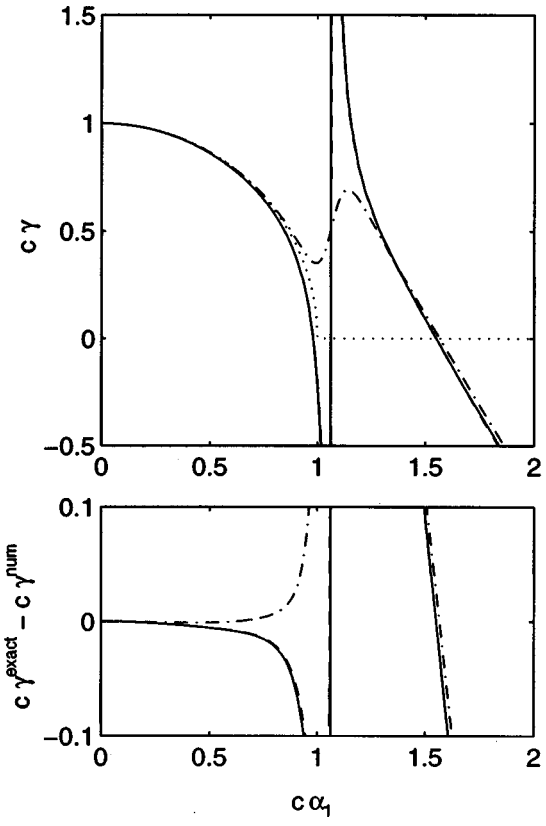

FIG. 15. The real part of the symbol of the vertical slowness (composition) operator (upper figure) and its difference with the exact symbol (lower figure). The dotted line corresponds to the real part of the exact slowness symbol; the other lines correspond to $\beta_1=0.526$, $\beta_2=0.364$, $\beta_3=0.825$, and $a_2=0.130$, while Ω equals 0 (solid line), 0.01 (dashed line), and 0.1 (dashdot line).

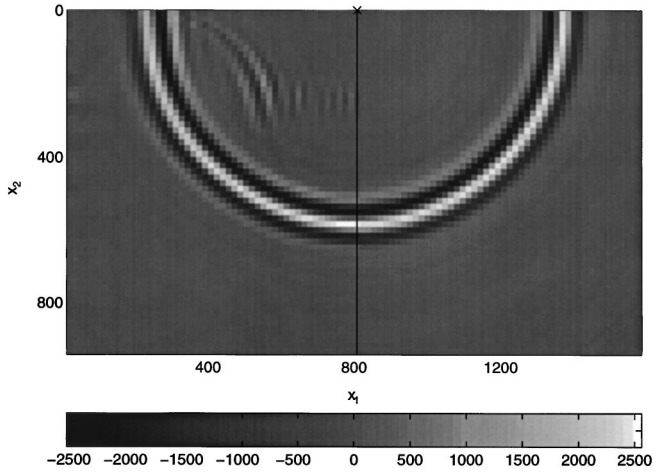

FIG. 16. Snapshot of an explosion line source in a homogeneous medium ($c=1900$ m/s). The right-hand side is obtained analytically, while the left-hand side is obtained with our numerical scheme.

no rational approximation is required to arrive at a sparse matrix representation, and its validity extends into the post-critical regime. To stay conceptually close to the original expression (22) we replace $\partial_2 c^{-2}$ by $2c^{-1}\partial_2 c^{-1}$. This replacement is justified only prior to applying the finite-difference (FD) approximation. In this approximation, we have

$$\frac{1}{2}\,c\,\partial_2 c^{-1}\overset{\text{FD}}{\rightarrow}\frac{1}{\Delta x_2}\,\frac{c^{-1}(x_2+1/2\Delta x_2)-c^{-1}(x_2-1/2\Delta x_2)}{c^{-1}(x_2+1/2\Delta x_2)+c^{-1}(x_2-1/2\Delta x_2)}, \tag{122}$$

which resembles the *exact* reflection coefficient at normal incidence.

On principal symbol level, the operator ordering can be further interchanged. Thus the reflection operator can be written in the symmetric form

$$\hat{R}\simeq\tfrac{1}{2}c^{-1/2}(\partial_2 c^{-1})^{1/2}\hat{A}^{-1}(c^{-1/2}(\partial_2 c^{-1})^{1/2}\cdot). \tag{123}$$

This form guarantees that the reflection/transmission operators vanish in any region where the medium is x_2 invariant. Upon discretizing this equation, using Eqs. (32) and (74), we get

$$\begin{aligned}&2[(1+a_2\delta_1^2)c^{-2}+\beta_8 c^{-2}\delta_1^2]((\partial_2 c^{-1})^{-1/2}c^{1/2}\langle\hat{R}\hat{h}\rangle)\\&\quad=(1+a_2\delta_1^2)(c^{-1/2}(\partial_2 c^{-1})^{1/2}\hat{h}).\end{aligned} \tag{124}$$

It is noted that the free change of order of operators in the frequency domain is accurate only near the diagonal of the integral kernel of their composition.

A. A numerical example

The discretized reflection operator contains only two free parameters: a_2 and Ω, through β_8. To optimize for these parameters, we would have to consider every possible change in wave speed. It turns out, however, that the optimization is rather insensitive to the medium changes, so that we can restrict ourselves to using a single parameter set, $a_2=1/12$, $\Omega=0.1$. The value of Ω is taken positive, to move the pole at 90° propagation angle into the complex horizontal slowness plane.

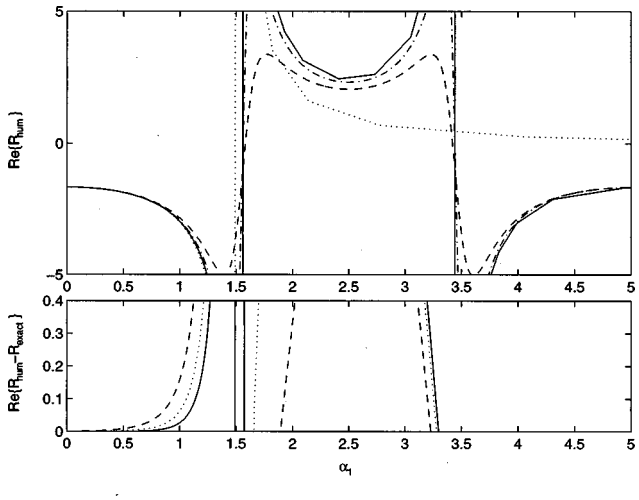

FIG. 17. The real part of the symbols of the discretized and the exact (dotted line) reflection operators (plane-wave reflection coefficients). The differences between the discretized and exact symbols are plotted in the lower figure. The wave speed equals 1 above and 2 below the interface. We used $a_2=1/12$ and $\Omega=0,0.1,0.05$ (solid, dashed, and dashdot lines, respectively).

Figure 17 shows the symbol of the discretized reflection operator for $a_2=1/12$ and $\Omega=0.0$ (the plane-wave reflection coefficient). In this figure are also shown the symbols for $\Omega=0.05$ and $\Omega=0.1$, as well as the exact reflection coefficient. In Fig. 18 we show a snapshot of the pressure field corresponding to the first two terms of the Bremmer series, excited by a vertical line force in a two-layer medium. The numerical grid, and the position of the source, are the same as in Figs. 12 and 13. The upper medium has a wave speed $c=1900$ m/s and the lower medium has a wave speed $c=3800$ m/s. The interface is located at $x_2=400$ m, and the snapshot time is 0.3 s, as before. The reflection and transmission are accurately modeled; the head wave, however, is only mimicked by our numerical scheme (for details, see De Hoop and De Hoop[43]).

VIII. NUMERICAL SIMULATIONS

In this section, we show examples of wave field modeling in various configurations, using our Bremmer coupling series algorithm. First, we consider two examples that originate from integrated optics. Here we have translated those configurations into their acoustic counterparts. Second, we consider an example from exploration seismics, viz., a salt structure embedded in a sparse system of sedimentary layers.

If N_ω denotes the number of frequencies relevant for the wave field computations, N_{x_1} denotes the number of discretization points of the configuration in the horizontal direction as before, M denotes the number of thin slabs of the configuration, i.e., the number of discretization points in the preferred direction as before, then the computational effort per term in the Bremmer series is of the order $2N_\omega 5N_{x_1}M$ (the factor 2 accounts for the propagator on the one hand and the reflection operator on the other hand; the factor 5 reflects the maximum number of nonvanishing bands in the matrices encountered in our numerical scheme). For waveguiding problems, N_ω is either one or small; for transient phenomena N_ω will be proportional to the number of time samples to be modeled. Our optimization approach allows us to employ a coarse computational grid; typically we sample the wave field by 2.5–5 points per wavelength.

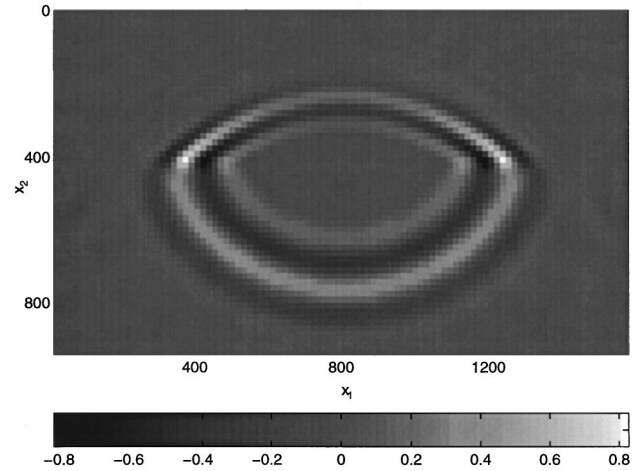

FIG. 18. Reflection and transmission at an interface.

A. Waveguide

Our first example is, in fact, a benchmark test (see Nolting and März[44]). It considers the propagation of a single mode through a waveguide (see, for example, Vassallo[45]), oriented under different angles with respect to the numerical grid. The details of this test configuration can be found in Nolting and März.[44] The wave speed is approximately 1825 m/s inside the waveguide and 1900 m/s outside. The waveguide has a thickness of approximately 180 m. The frequency is 190 Hz. We take a numerical grid with 779 points along the x_1 direction and 1360 points along the x_2 direction. The discretization step is approximately 1.5 m in both directions (about 6.7 points per wavelength). The total length of the waveguide is 2.04 km. In this simulation, we used the third (real-valued) parameter set. In this waveguide there exist only 11 discrete modes.

Two of the waveguiding modes (the fundamental and the tenth mode) are launched into the waveguide. In the first experiment the wall of the waveguide is parallel to the x_2 axis. In the second experiment, the waveguide is tilted with respect to the computational coordinate system by 20°. The field at the output level plane is compared with original field at the input level plane. Theoretically, these fields must be identical. Figure 19 shows the fundamental mode at the end of the vertical waveguide, while Fig. 20 shows the fundamental mode at the end of the tilted waveguide. Figures 21 and 22 are the same, but for the tenth-order mode. For the vertical waveguide, the symbols account for all the interactions; for the tilted waveguide, an interplay between the Bremmer coupling and the symbol interactions takes place. Up to the tenth-order mode the results are satisfactory. It is conjectured that some of the radiating modes can be properly modeled with our scheme as well.

B. Block

In the second example, we investigate the time-harmonic plane wave interaction in a homogeneous medium

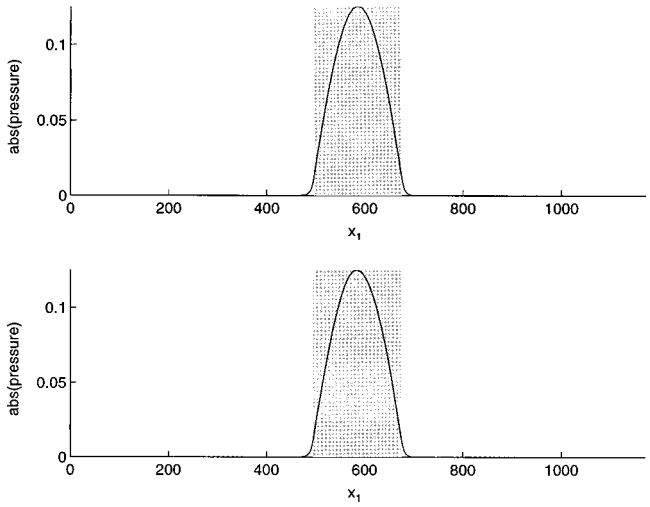

FIG. 19. The fundamental waveguiding mode at the entrance level (upper figure) and at the exit level (bottom figure). The waveguide is not tilted with respect to the coordinate system.

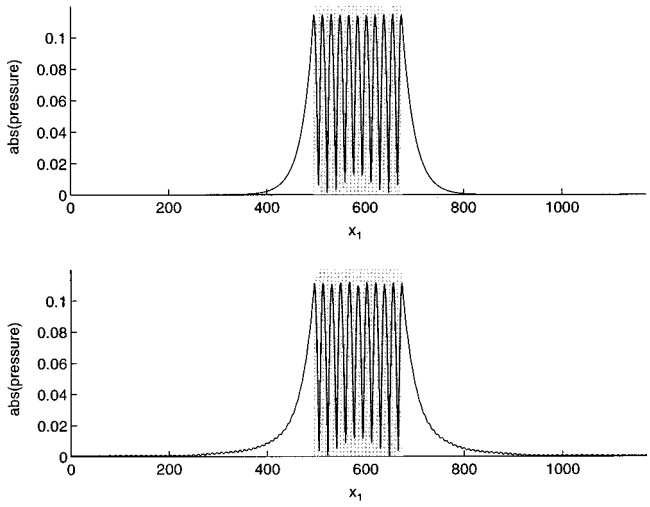

FIG. 21. The tenth-order waveguide mode at the entrance level (upper figure) and at the exit level (bottom figure). The waveguide is not tilted with respect to the coordinate system.

($c=1900$ m/s) with a square block (sized 100 by 100 m) with significantly smaller wave speed ($c=1344$ m/s). The frequency is 19 Hz. The numerical grid contains 99 points along the x_1 direction and 60 points along the x_2 direction. We plot only 59 points along the x_1 direction. The discretization step is 5 m in both directions (14 points per wavelength inside the heterogeneity). Full, accurate, numerical responses have been presented by Martin *et al.*[46] Our results, shown in Fig. 23, are very similar to theirs. (The right half of the figure is the Bremmer series solution, the left half is the full solution obtained by an iterative integral-equation technique based upon minimizing an integrated square error criterion.) Figure 24 corresponds to the second term of the Bremmer coupling series, while Fig. 25 shows the field corresponding to the leading term of the Bremmer coupling series. The higher-order terms in the Bremmer series become rapidly smaller. For the calculations we used parameter set 4; in the reflection operator, we set $\Omega=0.02$.

C. Geological dome

As a third example, we consider the salt model of Fig. 26. This model contains three sedimentary layers. The wave speed is constant in the upper and bottom layers, while the wave speed varies in the left part of the middle layer. An approximate, transient vertical line force is applied at $x_1=1600$ m, $x_2=0$ m. Figures 27–29 show snapshots at 0.75 s. For the calculations we used parameter set 4. The numerical grid contains 199 points in the x_1 direction and 156 points in the x_2 direction. The discretization step is 16 m in both directions. We used parameter set 4. In Fig. 27 we have calculated the first six terms of the Bremmer coupling series. Figures 28 and 29 show snapshots of the leading term and the second term of the series.

This example illustrates that our approximate scheme models the transmitted and reflected body waves accurately up to large scattering angles. Also the line diffraction at the major kink of the second deepest interface is captured by the

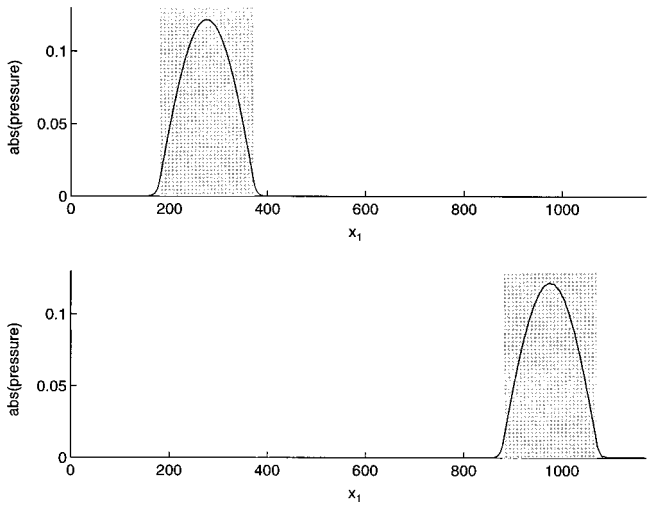

FIG. 20. The fundamental waveguiding mode at the entrance level (upper figure) and at the exit level (bottom figure). The waveguide is tilted with an angle of 20° with respect to the coordinate system. (Leading term of the Bremmer coupling series only.)

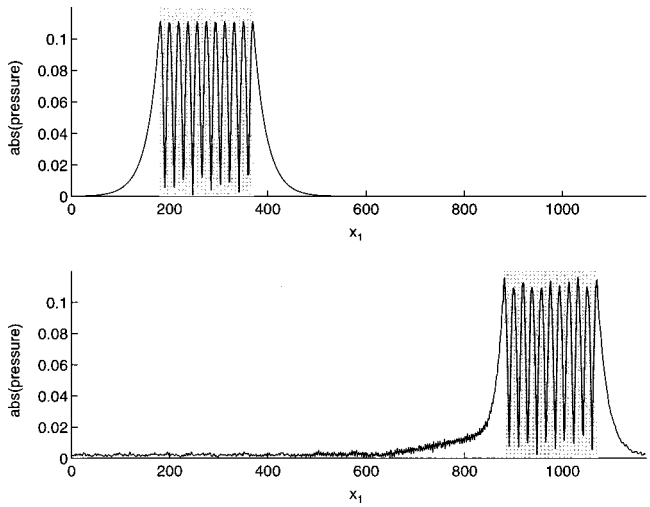

FIG. 22. The tenth-order waveguide mode at the entrance level (upper figure) and at the exit level (bottom figure). The waveguide is tilted with an angle of 20° with respect to the coordinate system. (Leading term of the Bremmer coupling series only.)

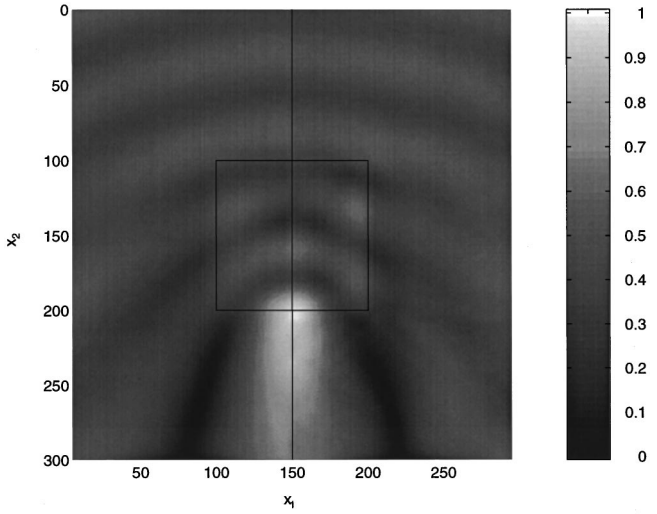

FIG. 23. Plane-wave (from the top) response in a configuration with a block in a homogeneous embedding.

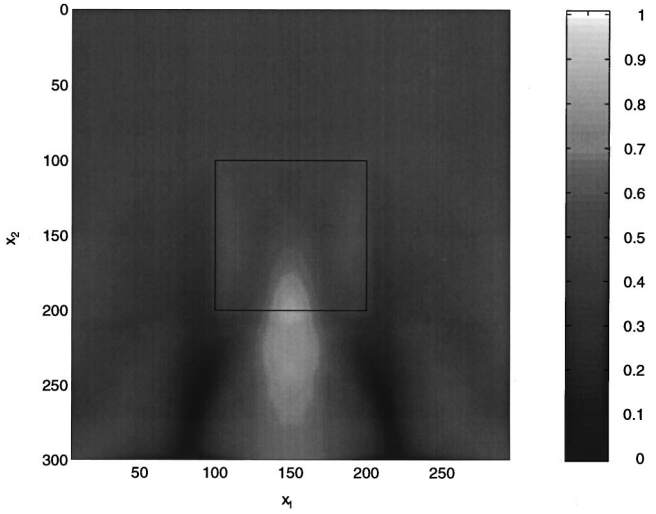

FIG. 25. Plane-wave (from the top) response in a configuration with a block in a homogeneous embedding. Leading term of the Bremmer coupling series.

method. Some head wave (postcritical) energy is mimicked by the artifacts of our approximations, but is inaccurate.

IX. DISCUSSION OF THE RESULTS

We have developed a fast numerical implementation of the Bremmer coupling series in two dimensions, for scattering angles up to critical. The key ingredient was a rational approximation of the vertical slowness in terms of the horizontal slowness. Our scheme has added to the various existing one-way wave propagation and BPM schemes in the following ways: we considered the third-order Thiele approximation rather than the first- or second-order one, to enhance the accuracy and to remove artificial body waves around the vertical direction; we enhanced the accuracy by optimizing the phase and group slowness surfaces for any desired sampling rates; we have improved the transformation to a moving frame of reference; we introduced (de)composition operators to incorporate any desired source- or receiver-type with the appropriate radiation characteristics; we have taken care of the backscattered field with the aid of the Bremmer coupling series. The backscattered field includes phenomena like turning ray waves. Though we have shown results in two dimensions only, the algorithm can be readily extended to three dimensions by employing a hexagonal grid in the horizontal directions (for reference, see Mersereau,[47] and Peterson and Middleton[48]).

We have illustrated the generalized Bremmer series with rational approximation with various examples. The examples have been taken from the different fields of application of the method. With a view to exploration geophysics, the waveguide is associated with coal beds. Figure 16 represents the wave-equation migration-operator response, the tangents to the front defining the dips. In migration, the Bremmer series approach is particularly useful if multiple arrivals play a role creating a proper image.

The efficiency of the method depends on the application. The method is designed in the frequency domain, and hence allows for a relatively coarse sampling of the field; the lower the frequency, the coarser the grid can be. If only a small

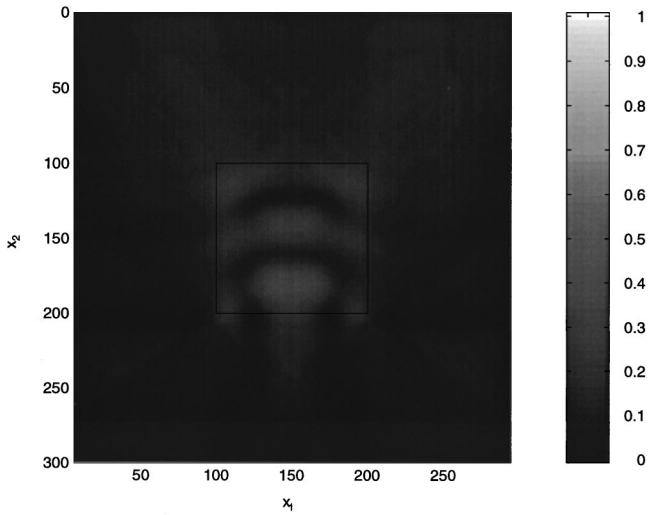

FIG. 24. Plane-wave (from the top) response in a configuration with a block in a homogeneous embedding. Second term of the Bremmer coupling series.

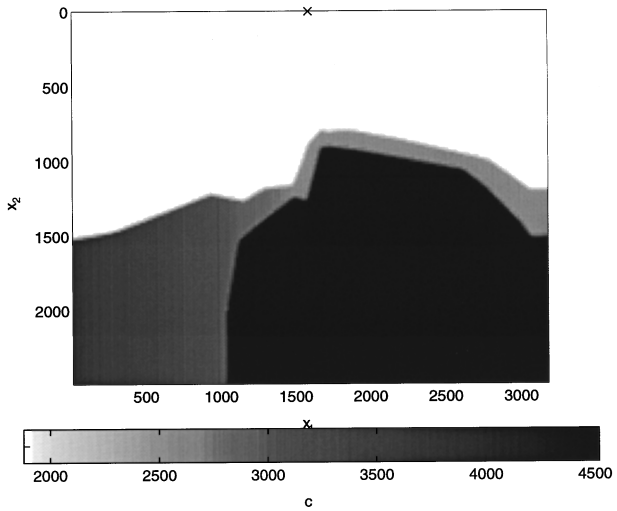

FIG. 26. Wave speeds of a two-dimensional salt model.

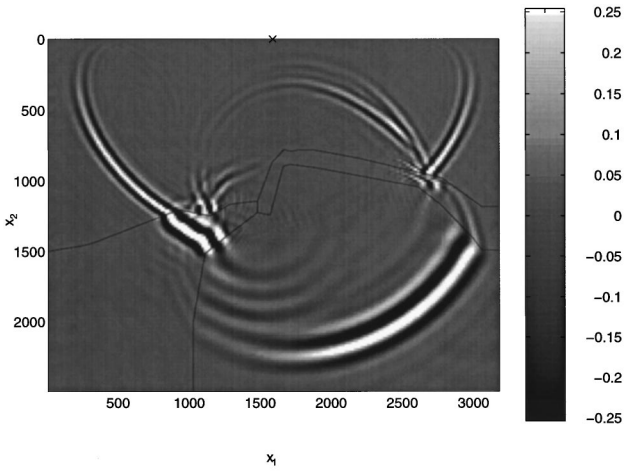

FIG. 27. Snapshot at $t=0.750$ s of the acoustic pressure due to a vertical line force in the model of Fig. 26. Six terms of the Bremmer coupling series.

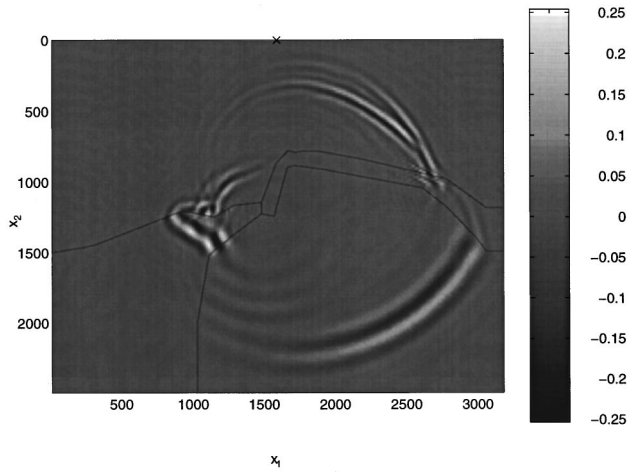

FIG. 29. Snapshot at $t=0.750$ s of the acoustic pressure due to a vertical line force in the model of Fig. 26. Second term of the Bremmer coupling series.

number of frequencies has to be evaluated, the Bremmer series approach has a particular advantage over full-wave modeling schemes. Though the range of scattering angles treated accurately is limited just below critical, the medium can be relatively strongly heterogeneous. If the medium is weakly heterogeneous, however, competing approaches exist to calculate the propagator. We mention the phase-shift (Gazdag and Sguazzero[49]), the split-step Fourier (Stoffa *et al.*[50]), the McClellan transform (Hale[51]), and the phase-screen (Wu[52]) representations. If the configuration consists of weakly and strongly heterogeneous regions, the different approaches can be combined into a hybrid scheme, matching them through the vertical phase slownesses.

In case critical angle phenomena are important, a more precise symbol for the vertical slowness operator has to be used. A candidate is the uniform expansion developed by Fishman and Gautesen.[53] Then the thin slab propagator is directly evaluated using Fourier transforms.

To incorporate variable density in the procedure developed in this paper, while keeping the numerical analysis the same, we refer to De Hoop.[1] The key is to port the wave field decomposition procedure from the acoustic-pressure normalization analog to the vertical-acoustic-power-flux normalization analog. The structure of the operator $\hat{A}$ remains the same (Laplacian plus medium slowness squared) but is subjected to a transformation of the wave speed function. The complication is hidden in the (de)composition operators, which now depend on a fractional power $\hat{A}^{-1/4}$. We can subject also this power to the sparsification procedure based on a continued-fraction expansion as discussed in the main body of this paper.

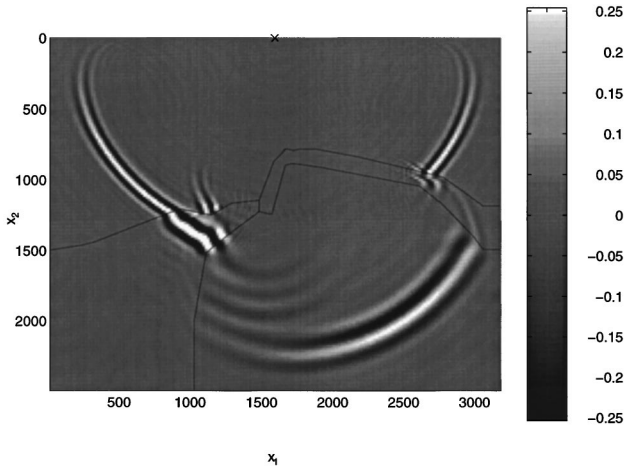

FIG. 28. Snapshot at $t=0.750$ s of the acoustic pressure due to a vertical line force in the model of Fig. 26. Leading term of the Bremmer coupling series.

ACKNOWLEDGMENTS

The research reported in this paper has been financially supported through a Special Research Fund of the Executive Board of the Delft University of Technology, Delft, the Netherlands and through research grants from the Stichting Fund for Science, Technology and Research (a companion organization to the Schlumberger Foundation in the USA). We also appreciate the financial support by the sponsors of the Consortium Project at the Center for Wave Phenomena.

APPENDIX: TRANSVERSE TRANSPARENT BOUNDARIES

Our discretization coexists with applying periodic boundary conditions in the transverse direction. It is standard practice to make the boundaries of the computational domain absorbing, to simulate an unbounded configuration instead. Several approaches have been developed for this adjustment; we mention the work of Clayton and Engquist[54] based on the parabolic equation in the transverse directions. Competing approaches are the transparent boundary condition by Hadley,[55] and the one by Bérenger[56] based on a perfectly matched layer for absorption at the boundary. We follow the methodology described by Arai *et al.*,[57] which is a generalization of Hadley's approach. Arai *et al.* arrived at a linear boundary condition and made it adaptive. We employ its simplest form, the so-called Robin conditions.

The Robin boundary condition employs the one-way wave equations [as in Eq. (63)] in both transverse directions at the edges of the computational domain,

$$\partial_1 \hat{h} + i\omega\eta^{(\pm)}\hat{h} = 0, \quad \text{at } x_1 = 0^{(-)} \text{ and at } x_1 = (N_{x_1}+1)\Delta x_1^{(+)}. \tag{A1}$$

By choosing $\eta^{(\pm)}$ adaptively, we will show that these boundary conditions can be made highly transparent.

The key matrices in our numerical scheme consist of five bands. Thus we require estimates of the field at two discretization points outside the computational domain, in accordance with transparent boundary conditions. The estimate of the field at the furthest sample points will be based on the additional constraint,

$$\partial_1^2 \hat{h} + i\omega\eta^{(\pm)}\partial_1 \hat{h} = \text{invariant}, \quad \text{at } x_1 = 0^{(-)} \text{ and at } x_1 = (N_{x_1}+1)\Delta x_1^{(+)}. \tag{A2}$$

We will illustrate the estimation procedure at the left boundary at $x_1 = \Delta x_1$. Then the field samples $\hat{h}_0$ and $\hat{h}_{-1}$ have to be determined. In terms of a lowest-order finite-difference representation, Eq. (A1) becomes,

$$\hat{h}_1 - \hat{h}_0 + i\omega\Delta x_1 \eta^{(-)}\hat{h}_0 = 0. \tag{A3}$$

This leads to

$$\hat{h}_0 = (1 - i\omega\Delta x_1 \eta^{(-)})^{-1}\hat{h}_1. \tag{A4}$$

The constraint (A2) is used to construct $\hat{h}_{-1}$, with the finite-difference representation

$$\frac{\hat{h}_1 - 2\hat{h}_0 + \hat{h}_{-1}}{(\Delta x_1)^2} + i\omega\eta^{(-)}\frac{\hat{h}_0 - \hat{h}_{-1}}{\Delta x_1} = \frac{\hat{h}_2 - 2\hat{h}_1 + \hat{h}_0}{(\Delta x_1)^2} + i\omega\eta^{(-)}\frac{\hat{h}_1 - \hat{h}_0}{\Delta x_1}, \tag{A5}$$

with the solution

$$\hat{h}_{-1} = \frac{\hat{h}_2 + \hat{h}_1[i\omega\Delta x_1\eta^{(-)} - 3 + (1 - i\omega\Delta x_1\eta^{(-)})^{-1}(3 - 2i\omega\Delta x_1\eta^{(-)})]}{1 - i\omega\Delta x_1\eta^{(-)}}. \tag{A6}$$

The numerical scheme associated with the Robin boundary condition is

(i) neutrally stable if $\mathrm{Im}\{\eta^{(-)}\}=0$,
(ii) stable if $\mathrm{Im}\{\eta^{(-)}\}<0$,
(iii) unstable if $\mathrm{Im}\{\eta^{(-)}\}>0$.

The boundary conditions reduce to the Neumann boundary condition for $\eta^{(-)}=0$, and to the Dirichlet boundary condition for $\eta^{(-)}\to\infty$.

We adapt the value of $\eta^{(\pm)}$ by assuming that the field behaves like a plane wave [$\sim\exp(-i\omega\eta^{(\pm)}x_1)$] near the computational boundaries. At the previous propagation step, the horizontal slowness associated with this plane wave can be estimated; at the current step, that value of $\eta^{(\pm)}$ can then be applied. At the left boundaries, with Eq. (A3), we get

$$\eta^{(-)} \simeq (i\omega\Delta x_1)^{-1}\left(1 - \frac{\hat{h}_2}{\hat{h}_1}\right). \tag{A7}$$

If the plane wave were to travel inward [$\mathrm{Re}\{\eta^{(-)}\}>0$ at the left boundary], $\eta^{(\pm)}$ is reset to its imaginary part $\mathrm{Im}\{\eta^{(\pm)}\}$. In this way, inward traveling waves are attenuated. The effectiveness of the transparent boundary conditions can be determined from the graph of reflection coefficient associated with a plane-wave hitting the boundary, see Clayton and Engquist.[54] Keys[58] extended the one-way absorbing boundary equation to the case where two distinguishable plane waves hit the computational boundary simultaneously.

In our numerical scheme the transparent boundary conditions are translated into an adjustment of the outer elements of the matrices A' and A. For example, the left boundary elements of A become [cf. Eqs. (A4)–(A6)]

$$\mathsf{A}_{11} \to \mathsf{A}_{11} + (1 - i\omega\Delta x_1\eta^{(-)})^{-1}[\mathsf{A}_{10} + (i\omega\Delta x_1\eta^{(-)} - 3 + (1 - i\omega\Delta x_1\eta^{(-)})^{-1}(3 - 2i\omega\Delta x_1\eta^{(-)}))\mathsf{A}_{1-1}], \tag{A8}$$

$$\mathsf{A}_{12} \to \mathsf{A}_{12} + (1 - i\omega\Delta x_1\eta^{(-)})^{-1}\mathsf{A}_{1-1}, \tag{A9}$$

$$\mathsf{A}_{21} \to \mathsf{A}_{21} + (1 - i\omega\Delta x_1\eta^{(-)})^{-1}\mathsf{A}_{20}. \tag{A10}$$

[1] M. V. de Hoop, ''Generalization of the Bremmer coupling series,'' J. Math. Phys. **37**, 3246–3282 (1996).
[2] J. F. Claerbout, ''Coarse grid calculations of waves in inhomogeneous media with application to delineation of complicated seismic structure,'' Geophysics **35**, 407–418 (1970).
[3] F. D. Tappert, ''The parabolic approximation method,'' in *Wave Propagation and Underwater Acoustics*, edited by J. B. Keller and J. S. Papadakis, Lecture Notes in Physics Vol. 70 (Springer-Verlag, New York, 1977), pp. 224–287.
[4] Z. Ma, ''Finite-difference migration with higher order approximation,'' Oil Geophys. Prosp. China **1**, 6–15 (1982).
[5] R. R. Greene, ''The rational approximation to the acoustic wave equation with bottom interaction,'' J. Acoust. Soc. Am. **76**, 1764–1773 (1984).
[6] L. Halpern and L. N. Trefethen, ''Wide-angle one-way wave equations,'' J. Acoust. Soc. Am. **84**, 1397–1404 (1988).
[7] M. D. Collins, ''Applications and time-domain solution of higher-order parabolic equations in underwater acoustics,'' J. Acoust. Soc. Am. **86**, 1097–1102 (1989).
[8] M. D. Collins and E. K. Westwood, ''A higher-order energy-conserving parabolic equation for range-dependent ocean depth, sound speed, and density,'' J. Acoust. Soc. Am. **89**, 1068–1075 (1991).
[9] M. D. Collins and R. B. Evans, ''A two-way parabolic equation for acoustic backscattering in the ocean,'' J. Acoust. Soc. Am. **91**, 1357–1368 (1992).

[10] M. D. Collins, ''A two-way parabolic equation for elastic media,'' J. Acoust. Soc. Am. **93**, 1815–1825 (1993).
[11] M. D. Collins, ''Minimax rational approximations for the parabolic equation method,'' J. Acoust. Soc. Am. **94**, 1884 (1993).
[12] R. J. Cederberg, M. D. Collins, and W. L. Siegmann, ''Applications of optimized rational approximations to parabolic equation modeling,'' J. Acoust. Soc. Am. **98**, 2971 (1995).
[13] L. N. Trefethen, ''Group velocity in finite difference schemes,'' SIAM (Soc. Ind. Appl. Math.) Rev. **24**, 113–136 (1982).
[14] C. M. Beaumont, J. F. Boyce, and R. Silva, ''Phase errors of finite difference migration,'' Geophys. Prospecting **35**, 267–280 (1987).
[15] O. Holberg, ''Computational aspects of the choice of operator and sampling interval for numerical differentiation in large-scale simulation of wave phenomena,'' Geophys. Prospecting **35**, 629–655 (1987).
[16] O. Holberg, ''Towards optimum one-way wave propagation,'' Geophys. Prospecting **36**, 99–114 (1988).
[17] R. W. Graves and R. W. Clayton, ''Modeling acoustic waves with paraxial extrapolators,'' Geophysics **55**, 306–319 (1990).
[18] T. Rühl, C. Kopp, and D. Ristow, ''Fourier finite-difference migration for steeply dipping reflectors with complex overburden,'' Geophys. Prospecting **43**, 919–938 (1995).
[19] J. A. F. Fleck, J. R. Morris, and M. D. Feit, ''Time-dependent propagation of high energy laser beams through the atmosphere,'' Appl. Phys. **10**, 129–160 (1976).
[20] J. Gerdes and R. Pregla, ''Beam-propagation algorithm based on the Methods of Lines,'' J. Opt. Soc. Am. B **8**, 389–394 (1991).
[21] R. Baets, J. Willems, and J. Haes, ''Diversity in beam propagation methods,'' ECIO , 13.1–13.3 (1993).
[22] G. R. Hadley, ''Wide-angle beam propagation using Padé approximant operator,'' Opt. Lett. **17**, 1426–1428 (1992).
[23] G. R. Hadley, ''Multistep method for wide-angle beam propagation,'' Opt. Lett. **17**, 1743–1745 (1992).
[24] H. J. W. M. Hoekstra, G. J. M. Krijnen, and P. V. Lambeck, ''New formulation of the beam propagation method based on the slowly varying envelope approximation,'' Opt. Commun. **97**, 301–303 (1993).
[25] H. J. W. M. Hoekstra, Opt. Quantum Electron. (to be published).
[26] M. D. Collins, ''Benchmark calculations for higher-order parabolic equations,'' J. Acoust. Soc. Am. **87**, 1535–1538 (1990).
[27] D. Lee and A. D. Pierce, ''Parabolic equation development in recent decade,'' J. Comput. Acoust. **2**, 95–173 (1995).
[28] R. T. Coates and M. Schoenberg, ''Finite-difference modeling of faults and fractures,'' Geophysics **60**, 1514–1526 (1995).
[29] M. Schoenberg and P. N. Sen, ''Properties of a periodically stratified acoustic half-space and its relation to a Biot fluid,'' J. Acoust. Soc. Am. **73**, 61–67 (1983).
[30] C. DeWitt-Morette, A. Maheshwari, and B. Nelson, ''Path integration in non-relativistic quantum mechanics,'' Phys. Rep. **50**, 255–372 (1979).
[31] H. C. Serafini and M. V. de Hoop, ''Even-versus-odd order Thiele approximations of the one-way operator in the space-time domain,'' 61st Ann. Mtg. Soc. Explor. Geophys., Expanded Abstracts, 1580–1583 (1991).
[32] M. V. de Hoop and A. T. de Hoop, ''Scalar space-time waves in their spectral-domain first- and second-order Thiele approximations,'' Wave Motion **15**, 229–265 (1992).
[33] We employed the routine E04CCF of the NAG FORTRAN Library Manual Mark 15 (1991).
[34] M. W. Lee and S. Y. Suh, ''Optimization of one-way wave equations,'' Geophysics **50**, 1634–1637 (1985).
[35] C. Bunks, ''Optimization of paraxial wave equation operator coefficients,'' 62nd Ann. Mtg. Soc. Explor. Geophys., Expanded Abstracts, 897–900 (1992).
[36] A. R. Mitchell and D. F. Griffiths, *The Finite Difference Method in Partial Differential Equations* (Wiley, Chichester, 1985).
[37] We employed the routine E04CCE of the NAG FORTRAN Library Manual Mark 15 (1991).
[38] W. H. Press, B. P. Flannery, S. A. Teukolsky, and W. T. Vetterling, *Numerical Recipes* (Cambridge U.P., Cambridge, England, 1986).
[39] O. B. Widlund, ''On the stability of parabolic difference schemes,'' Math. Comput. **19**, 1–13 (1965).
[40] R. D. Richtmeyer and K. W. Morton, *Difference Methods for Initial-Value Problems* (Wiley, New York, 1967).
[41] We employed the routines F07BRF and F07BSF of the NAG FORTRAN Library Manual Mark 15 (1991).
[42] M. D. Collins, ''Higher-order Padé approximations for accurate and stable elastic parabolic equations with application to interface wave propagation,'' J. Acoust. Soc. Am. **89**, 1050–1057 (1991).
[43] M. V. de Hoop and A. T. de Hoop, ''Interface reflections of spherical acoustic waves in the first- and second-order rational parabolic approximations and their artifacts,'' J. Acoust. Soc. Am. **93**, 22–35 (1993).
[44] H.-P. Nolting and R. März, ''Results of benchmark tests for different numerical BPM algorithms,'' IEEE J. Lightwave Technol. **13**, 216–224 (1995).
[45] C. Vassallo, *Optical Waveguide Concepts* (Elsevier, Amsterdam, 1991).
[46] O. J. F. Martin, A. Dereux, and C. Girard, ''Iterative scheme for computing exactly the total field propagating in dielectric structures of arbitrary shape,'' J. Opt. Soc. Am. A **11**, 1073–1080 (1994).
[47] R. M. Mersereau, ''The processing of hexagonally sampled two-dimensional signals,'' Proc. IEEE **67**, 930–949 (1979).
[48] D. P. Petersen and D. Middleton, ''Sampling and reconstruction of wave-number-limited functions in *N*-dimensional Euclidean spaces,'' Inf. Control. **5**, 279–323 (1962).
[49] J. Gazdag and P. Sguazzero, ''Migration of seismic data by phase shift plus interpolation,'' Geophysics **49**, 124–131 (1984).
[50] P. L. Stoffa, J. T. Fokkema, R. M. de Luna Freire, and W. P. Kessinger, ''Split-step Fourier migration,'' Geophysics **55**, 410–421 (1990).
[51] D. Hale, ''3-D depth migration via McClellan transformations,'' 60th Ann. Mtg. Soc. Explor. Geophys., Expanded Abstracts, 1325–1328 (1990).
[52] R.-S. Wu, ''Wide-angle elastic wave one-way propagation in heterogeneous media and an elastic wave complex-screen method,'' J. Geophys. Res. **99**, 751–766 (1994).
[53] L. Fishman and A. K. Gautesen, ''An exact, well-posed, one-way reformulation of the Helmholtz equation with application to direct and inverse wave propagation modeling,'' in *New Perspectives on Problems in Classical and Quantum Physics*, edited by A. W. Saenz and P. P. Delsanto (Gordon and Breach, Newark, 1996).
[54] R. W. Clayton and B. Engquist, ''Absorbing boundary conditions for wave-equation migration,'' Geophysics **45**, 895–904 (1980).
[55] G. R. Hadley, ''Transparant boundary condition for the beam propagation method,'' IEEE J. Quantum Electron. **28**, 363–370 (1992).
[56] J.-P. Bérenger, ''A perfectly matched layer for the absorption of electromagnetic waves,'' J. Comput. Phys. **114**, 185–200 (1994).
[57] Y. Arai, A. Maruta, and M. Matsuhara, ''Transparent boundary for the finite-element beam propagation method,'' Opt. Lett. **18**, 765–766 (1993).
[58] R. G. Keys, ''Absorbing boundary conditions for acoustic media,'' Geophysics **50**, 892–902 (1985).

Diffraction from simple shapes by a hybrid asymptotic-finite element method

Joshua M. Montgomery[a] and Paul E. Barbone
Department of Aerospace and Mechanical Engineering, Boston University, Boston, Massachusetts 02215

(Received 19 May 1997; revised 8 November 1997; accepted 8 June 1998)

The application of a hybrid asymptotic/finite element method to the problem of scattering from two-dimensional, submerged objects is considered. The hybrid method is based on patching a short-wavelength asymptotic expansion of the scattered field to a finite element interpolation of the near field. In patching, the diffracted field shape functions with unknown amplitude are forced to agree smoothly with the solution in the near field along a curve at a prescribed distance from the diffraction points. A new hybrid finite element on this artificial boundary represents the effect of the outer domain on the solution within this new boundary. This allows the replacement of the original boundary value problem with an asymptotically equivalent boundary value problem, the domain of which is small and efficiently discretized. The method is applied to diffraction by a blunted wedge, which in this context represents a degenerate prism. The hybrid scattering solution shall be compared to an analytic field representation found using an exact Dirichlet-to-Neumann map. [S0001-4966(98)04809-7]

PACS numbers: 43.20.Dk [ANN]

INTRODUCTION

We describe a hybrid method for scattering which combines short-wavelength asymptotics with the finite element method. In the hybrid approach, we attempt to draw on the benefits from both methods while eliminating their largest individual deficiencies. For example, an asymptotic approach can be computationally efficient for acoustically large scatterers; however, its applicability is limited since diffraction coefficients are unavailable for geometries with anything but simple discontinuities. Traditional numerical methods, on the other hand, can accommodate arbitrary geometries but are practically limited by their computational cost.

The hybrid method as presented here is related to the method of matched asymptotic expansions (MAE)[1] where, in the short wavelength limit, the scattered field contains two asymptotic regions. In the inner (local) region, the full Helmholtz equation must be solved. In the outer (global) region, the field can be found by means of a suitable short wavelength asymptotic technique, such as the geometrical theory of diffraction (GTD).[2] The representation of the outer field is written in terms of certain unspecified amplitude functions called ''diffraction coefficients.'' In the MAE method, the solutions in the two regions would be asymptotically matched, thus determining these coefficients.

In our hybrid method, on the other hand, the inner solution is found numerically by patching smoothly to the outer asymptotic approximation. The patching is imposed on an artificial boundary, Γ_R, which is introduced around diffraction points. This boundary is chosen to be located in an overlap domain where both the inner and outer solutions are valid. Patching the inner and outer fields on Γ_R is equivalent to using the GTD solution to specify a radiation boundary condition for the inner numerical problem. Thus, we replace the original boundary value problem (b.v.p.) with an asymptotically equivalent one.

The combination of the geometrical theory of diffraction (GTD) with traditional numerical methods in scattering applications dates back to 1975.[3] Burnside *et al.*[3] introduced the method and demonstrated its utility by computing the two-dimensional electromagnetic fields scattered by a perfectly conducting wedge and a perfectly conducting cylinder of square cross section. They substituted GTD-based shape functions for the fields diffracted by the vertices into a current-based integral formulation of the scattering problem. The GTD-based shape functions were used for distances greater than $\lambda/2$ from the vertices, while pulse shape functions were used for distances smaller than $\lambda/2$. A set of discrete equations was obtained by collocation. Agreement with exact and benchmark solutions was remarkable, especially considering that the near field ''numerical region'' extended only to a distance of $\lambda/2$.

Since 1975, Burnside's hybrid method has been applied to scattering from a tetrahedron,[4] has been augmented to address grazing incidence,[5] has been included within a Galerkin formulation, and applied to bodies of revolution.[6]

Wang[7] in 1991 was the first to introduce surface wave-based shape functions in a hybrid method. These he included for two-dimensional scattering and scattering from bodies of revolution. Wang noted that integration of the GTD-based shape functions in order to obtain the discretized equations was computationally expensive, and suggested that these integrals be evaluated asymptotically.

None of these authors address uniqueness issues associated with their boundary integral formulation for Helmholtz equation on exterior domains. Further, all rely on a surface integral equation formulation as a starting point of the analysis. Shape functions motivated by asymptotic expansions are

[a]Currently affiliated with Noise and Acoustics Division, The Boeing Company, Seattle, WA 98124.

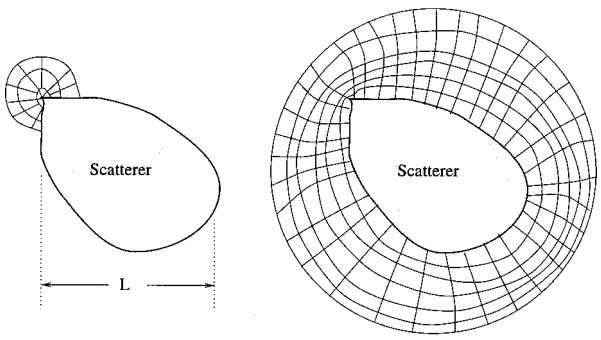

(a) Our hybrid approach (b) Far-field ABC approach

FIG. 1. Conceptual application of our hybrid method compared to a more typical ABC (artificial/absorbing boundary condition) approach. Our method is based on short-wavelength rather than far-field asymptotics. In our method, the condition on the artificial boundary comes from enforcing continuity of the function and its normal derivative with an outer asymptotic expansion. In the ABC approach, a boundary operator (usually a homogeneous differential operator) is applied on the artificial boundary.

then substituted into the equation in a straightforward manner.[8]

There are several distinctions between our approach and these previous approaches. First, we begin with a short wavelength asymptotic expansion of the overall solution, rather than with an integral equation formulation of the overall solution. Within the short-wavelength analysis we embed a well-posed boundary value problem that can be solved numerically. This is in contrast to simply using asymptotics-motivated shape functions in an otherwise traditional numerical formulation as in the works cited above,[3–7] or as in some applications of infinite elements.[9,10]

Second, we patch the inner numerical solution to the outer short-wavelength asymptotic solution. This concept might be compared to using a far-field asymptotic expansion to derive an approximate boundary condition to be applied on an artificial boundary.[11,12] Short wavelength expansions are valid when the wavelength λ is much shorter than all other dimensions in the problem. Far-field expansions, on the other hand, are valid when r, the distance from an origin ''near'' or in the scatterer, is much larger than all other distances in the problem. Only when λ and r are the only characteristic distances in a problem are the two expansions equivalent. (It so happens that the example we shall study in the following sections fits into this category.) One clear distinction between these two approaches is depicted in the cartoons in Fig. 1, which shows the numerical domains associated with each of the two approaches.

Even when the short wavelength expansion and the far-field expansion are equivalent, there is a considerable difference in the implementation of each approach. In the artificial/absorbing boundary condition (ABC) approach,[11,12] the far-field expansions are used to derive boundary operators that must be satisfied by the numerical solution. The high-order versions of such operators require the evaluation of high-order tangential derivatives of the finite element field. Since most finite element interpolations are only C^o, these implementations require special attention.[13] Further, this formulation yields only the solution inside the artificial boundary, and some extra postprocessing is therefore necessary to obtain the field outside the artificial boundary. In the general formulation of our hybrid method described in Sec. IV, on the other hand, we enforce continuity (of both the function and its normal derivative) between the short-wavelength asymptotic approximation and the numerical solution. We thus avoid the need to derive a boundary operator that must be satisfied by the finite-element field. Our boundary condition on the artificial boundary requires no derivatives of the finite-element interpolants for any order asymptotic approximation.

Alternatively, one might compare our hybrid method to an application of infinite elements. One distinction is that, in our formulation, the outer field is required to satisfy the Helmholtz equation (at least asymptotically) before we even formulate the numerical boundary value problem. In typical infinite element applications, on the other hand, the outer field is interpolated in some convenient,[14–17] or physically inspired,[9,10] manner. These interpolations are then substituted into a weak form that enforces the approximate satisfaction of the field equation (Helmholtz, in this case). Further, most infinite element formulations enforce continuity between the inner and outer fields strongly. Finally, our formulation is free of infinite or large domain integrals, while almost all infinite element formulations require infinite integrals of some kind. [The exceptions to these is the infinite element formulation devised by one of the authors (PEB) in collaboration with I. Harari, as described in Refs. 18 and 19.]

In addition, we remark that our hybrid approach is based on the formulation of an asymptotically equivalent boundary value problem defined on a small domain. We can choose any numerical method to solve this problem. (This is also in clear contrast to infinite elements, for example, in which the treatment of the outer domain is integral in the entire problem discretization.) Here we discuss solving this problem using finite elements, but in another contribution we discuss using the ''boundary strip method.'' [20]

The idea of patching a short-wavelength expansion to a collection of numerical solutions (as needed to supplement the validity of the outer expansion) can obviously be applied to a quite complicated scatterer. We have elected to first study and present our method in the context of the most basic of problems, diffraction from a truncated wedge. The formulation and asymptotic solution of this problem is presented in Sec. II. We follow this in Sec. III by discussing the issue of patching inner and outer fields together as opposed to matching them. Our hybrid method depends on patching, yet matching is known to yield the correct directivities. The comparison between patching and matching makes it clear that the patched directivity can provide a good approximation to the exact directivity. More importantly, it shows that the approximation can, in principle, be improved to arbitrarily high accuracy. This gives us reassurance that the proposed technique can be built into a reliable numerical method.

Patching of the numerical solution to the outer asymptotic solution gives rise to a boundary value problem defined on a finite (and relatively small) domain. This boundary value problem is outside the realm of application

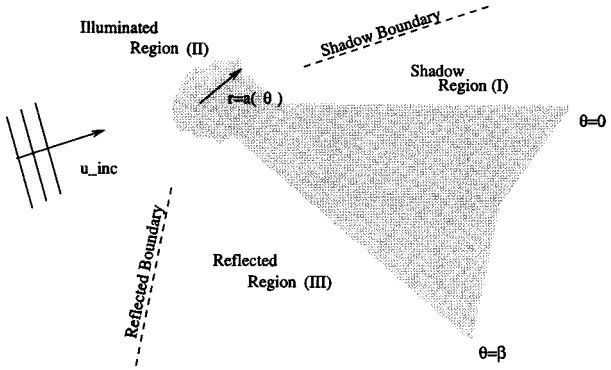

FIG. 2. Blunted wedge with incident plane wave.

of standard finite element methods because of the patching boundary conditions. In Sec. IV, we describe a weak formulation of the asymptotically equivalent b.v.p. as part of a finite element implementation. Here, we enforce the boundary condition by introducing a new ''hybrid'' finite element. The results from the hybrid method, utilizing this new element, are compared to a reference solution found by means of a Dirichlet-to-Neumann (DtN) map.[21]

I. FORMULATION

We imagine the wedge, of exterior angle β, positioned such that the tip coincides with the origin while one face lies on the positive x axis. The tip is blunted by a truncation described by $r=a(\theta)$ (see Fig. 2). We assume that the maximum of a is on the order of a wavelength (λ). Thus, $a(\theta)=O(k^{-1})$ or $ka=O(1)$. We let l be a predetermined distance from the tip with which we nondimensionalize all of our spatial coordinates. Then in the limit as $kl\to\infty$, the wedge appears to be acoustically infinite.

In all that follows we will work in terms of nondimensionalized coordinates as well as wave number, k. We shall also work in terms of a time-harmonic acoustic pressure:

$$p(x,y,t)=\Re\{u_{\text{tot}}(x,y)e^{-i\omega t}\}. \tag{1}$$

The time dependence will be suppressed from here on. The total field is then represented as the sum of an incident plane-wave and scattered field contributions:

$$u_{\text{tot}}=u_{\text{inc}}+u, \quad u_{\text{inc}}=e^{ik(x\cos\theta'+y\sin\theta')}. \tag{2}$$

In the absence of sources, u is governed by the reduced wave equation

$$(\Delta+k^2)u=0. \tag{3}$$

We consider a wedge with soft faces, such that $u_{\text{tot}}=0$ on the wedge. Equation (2) then yields

$$u=-u_{\text{inc}}\begin{cases} r=a(\theta), & \\ \theta=0, & r\geqslant a(0), \\ \theta=\beta, & r\geqslant a(\beta). \end{cases} \tag{4}$$

Further, the scattered field must satisfy a radiation condition as $r\to\infty$.

II. ASYMPTOTIC EXPANSION

We seek an asymptotic approximation of the solution to (1)–(4), valid in the limit as $k\to\infty$. In this section we discuss the process of obtaining the outer approximation to the field. We follow this by a description of the inner b.v.p. and characteristics of its solution. We then seek to compare the method used in patching these solutions to the method of matched asymptotics.

A. Outer solution

We assume a solution of the form

$$u(\mathbf{x})\sim w(\mathbf{x},k)e^{iks(\mathbf{x})}, \quad k\to\infty. \tag{5}$$

Here $w(\mathbf{x},k)$ is the amplitude, k is the wave number, and $s(\mathbf{x})$ is the phase. Substituting (5) into (3) yields

$$-k^2[(\nabla s)^2-1]w+2ik\nabla s\cdot\nabla w+ikw\Delta s+\Delta w=0. \tag{6}$$

To solve (6) for large values of k, we assume that w can be expanded in a series of inverse powers of ik:

$$w(\mathbf{x},k)\sim k^{-\alpha}\sum_{m=0}^{N} w_m(\mathbf{x})(ik)^{-m}+o(k^{-N-\alpha}). \tag{7}$$

Inserting (7) into (6) and equating powers of k yields the eiconal equation

$$(\nabla s)^2=1, \tag{8}$$

and the transport equations

$$2\nabla s\cdot\nabla w_m+w_m\Delta s=-\Delta w_{m-1}, \quad m=0,1,2,\ldots, \tag{9}$$

where $w_n=0$ for $n<0$. These equations can be solved by standard characteristic methods which provide the rays of GTD. The phase can be determined using Fermat's principle.[2] The scattered field can be expressed as the sum of a reflected plane wave, a shadow wave, a diffracted cylindrical wave, plus higher order terms

$$u\sim u_{\text{refl}}+u_{\text{shad}}+u_{\text{diff}}+O(k^{-3/2}). \tag{10}$$

The three different terms in the above equation represent the leading terms of three different expansions, each of the form (5) with (7). By defining an angle $\phi=\theta'-2\beta$, these contributions can be expressed as the following:

$$\begin{aligned} u_{\text{shadow}}&=-e^{ik(x\cos\theta'+y\sin\theta')} \quad \text{shadow region,} \\ u_{\text{refl}}&=-e^{ik(x\cos\phi+y\sin\phi)} \quad \text{reflected region,} \\ u_{\text{diff}}&=\frac{D(\theta,\theta')}{\sqrt{kr}}e^{ikr} \quad \text{everywhere.} \end{aligned} \tag{11}$$

Here, $D(\theta,\theta')$ is not yet determined. It represents the amplitude of the field diffracted into the θ direction due to an incident wave in the θ' direction. It is sometimes referred to as the ''diffraction coefficient'' associated with the wedge.

An immediate concern regarding this representation (11) is the discontinuity between the regions. In order to obtain a smooth transition across the boundaries, we introduce a boundary layer solution. Such solutions are readily available in many textbooks (e.g., Refs. 22–25).

As an example, we consider the boundary between the shadow region (I) and the illuminated region (II). We introduce a change of coordinates:

$$\xi = x\ \cos\ \theta' + y\ \sin\ \theta', \tag{12}$$

$$\eta = -x\ \sin\ \theta' + y\ \cos\ \theta'. \tag{13}$$

In terms of these new variables,

$$u_{\text{shad}} \sim \mathscr{H}(\eta) e^{ik\xi}. \tag{14}$$

Here $\mathscr{H}$ is the Heaviside step function. This solution is clearly not valid on $\eta = 0$, where there is a discontinuity predicted. Following the example in Ref. 22 yields the boundary layer solution:

$$u_{bl}(\xi, \eta) = \frac{1}{\sqrt{\pi}}\, e^{-i(\pi/4)} e^{ik\xi} \int_{-\eta\sqrt{k/2\xi}}^{\infty} e^{iz^2}\, dz. \tag{15}$$

Equation (15) shows that in the limit of $\|\eta\sqrt{k/\xi}\| \gg 1$ there exists a plane wave, $e^{ik\xi}$, for $\eta > 0$ and no first-order contribution for $\eta < 0$. On the boundary ($\eta = 0$) the amplitude of the field is the average of the amplitudes in (I) and (II). Replacing u_{shadow} in (11) with u_{bl} in (15) yields an asymptotic expansion for the field which is valid everywhere except at $r = 0$. We note that a representation that is uniformly valid in angle can be obtained without specific solution of a ''canonical'' or inner problem near the wedge tip. Until the solution of the inner problem is obtained, however, the directivity $D(\theta)$ that appears in (11) remains unknown.

B. Inner diffraction problem

It is the solution of the inner problem, or canonical problem, that provides the unknown diffraction coefficient. In the usual GTD or MAE approach, the inner solution is found analytically and then matched asymptotically to the outer solution. In our hybrid method, on the other hand, we shall find the inner solution numerically by patching it smoothly to the outer solution [Eqs. (11) and (15), or an equivalent solution]. In this section, we shall examine (analytically) the process of matching and patching to show that in some sense they are equivalent. This tells us that our hybrid method, based on patching, can provide a good approximation to the diffraction coefficient.

The inner problem is obtained by rescaling in ''inner'' variables:

$$R = kr; \quad \Theta = \theta; \quad U(R, \Theta) = u(r, \theta). \tag{16}$$

Rewriting the reduced wave equation (3) in polar coordinates gives the inner problem:

$$\left(\frac{\partial^2}{\partial R^2} + \frac{1}{R}\frac{\partial}{\partial R} + \frac{1}{R^2}\frac{\partial^2}{\partial \Theta^2} \right) U + U = 0, \tag{17}$$

$$U = -U_{\text{inc}} \begin{cases} R = ka(\theta), \\ \Theta = 0, \beta, \qquad R > ka, \end{cases} \tag{18}$$

$$U \text{ matches } u \text{ as } R \to \infty. \tag{19}$$

We note that in contrast to the outer equations, the limit $k \to \infty$ does not simplify the inner differential equation at all. We must solve the full Helmholtz equation.

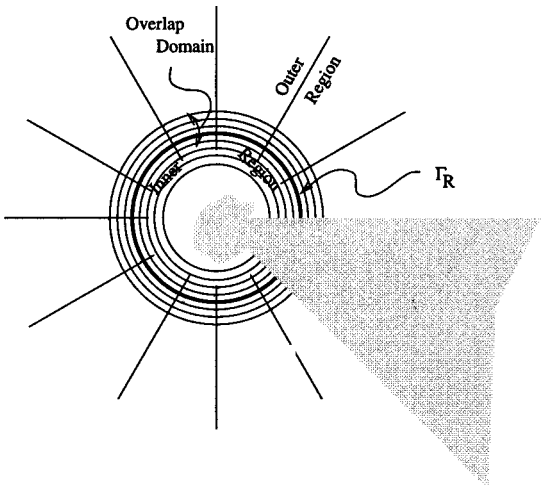

FIG. 3. Inner and outer regions.

In all that follows, we shall find it convenient to work in terms of $\hat{U} = U - U_{\text{sharp}}$. Here U_{sharp} represents the field (with minimum singularity) scattered by a sharp wedge due to an incident field U_{inc}.[23] Further, U_{sharp} can be shown to match the plane wave and boundary layer solutions in the outer field. Thus, the function $\hat{U}$ satisfies (17) and

$$\hat{U} = \begin{cases} -U_{\text{inc}} - U_{\text{sharp}} & \text{on } R = ka(\theta), \\ 0 & \text{on } \Theta = 0, \beta. \end{cases} \tag{20}$$

For a general $a(\theta)$, the solution for $\hat{U}$ cannot be obtained in closed form. Without the analytical form, we cannot match U to u as indicated in Eq. (19). Therefore, in Sec. IV, we shall describe a numerical method to find $\hat{U}$ subject to a patching condition replacing (19). For either outer boundary condition, $\hat{U}$ can be uniquely represented outside $R = ka_{\max}$ as

$$\hat{U}(R, \Theta) = \sum_{n=1}^{\infty} A_n H_{\nu_n}^{(1)}(R) \sin\ \nu_n \Theta + B_n H_{\nu_n}^{(2)}(R) \sin\ \nu_n \Theta. \tag{21}$$

Here, $H_{\nu_n}^{(1)}$ and $H_{\nu_n}^{(2)}$ are the Hankel function of the first and second kind of order ν_n,[26] where $\nu_n = n\pi/\beta$. A_n and B_n are unknown complex constants. For any given $a(\theta)$, there is a set of coefficients S_{nm} such that A_n and B_n can be related as follows:

$$A_n = A_n^o + \sum_{m=1}^{\infty} S_{nm} B_m. \tag{22}$$

A_n^o satisfies the inhomogeneous boundary condition (20). The sum $\Sigma_{m=1}^{\infty} S_{nm} B_m$ represents the amplitude of the nth scattered mode due to all incident modes with amplitude B_m.

We would now like to match (21) to the cylindrical wave in (11) to find $D(\theta)$ in terms of A_n and B_n. In the method of matched asymptotic expansions, this requires an overlap domain in which both (21) and (11) are valid (see Fig. 3). This domain occurs when

$$R = k^{\alpha}, \quad 0 < \alpha < 1. \tag{23}$$

The hybrid method, on the other hand, relies on patching. The inner solution will be found numerically and forced to agree smoothly with the outer asymptotic solution (11) along Γ_R. Here, Γ_R is chosen to be an arc of a circle lying in the aforementioned overlap domain.

C. Patching versus matching

The method of matched asymptotic expansions yields a solution which is asymptotic to the exact solution. Thus, we are guaranteed that the difference between the exact and asymptotic solutions vanishes in the limit as $k\to\infty$. Patching on the *fixed* curve $R=\text{const}$, on the other hand, has no such asymptotic validity. Here we shall compare the directivities obtained by patching $(\hat{D}_p(\theta))$ to those obtained by matching $(\hat{D}_m(\theta))$. In particular, we shall show that patching *in the overlap domain* leads to the result that

$$\hat{D}_p(\theta)\sim\hat{D}_m(\theta);\quad k\to\infty. \tag{24}$$

We denote the outer solutions to be used in the comparison as follows:

$$\hat{u}_p(r,\theta)=u_p-u_{\text{sharp}}=\frac{\hat{D}_p(\theta)}{\sqrt{kr}}\,e^{ikr}, \tag{25}$$

$$\hat{u}_m(r,\theta)=u_m-u_{\text{sharp}}=\frac{\hat{D}_m(\theta)}{\sqrt{kr}}\,e^{ikr}. \tag{26}$$

1. Patching

We shall patch along the curve $R=k^{\alpha}r_0$, or $r=k^{\alpha-1}r_0$:

$$\hat{u}_p(k^{\alpha-1}r_0,\theta)=\hat{U}(k^{\alpha}r_0,\theta), \tag{27}$$

$$\partial_r\hat{u}_p(k^{\alpha-1}r_0,\theta)=\partial_r\hat{U}(k^{\alpha}r_0,\theta). \tag{28}$$

Equations (21), (25), (27), and (28) then yield $\hat{D}_p(\theta)$ as

$$\hat{D}_p(\theta)=\sum_{n=1}^{\infty}\frac{-4i}{\pi}\frac{e^{-ik^{\alpha}r_0}}{\sqrt{k^{\alpha}r_0}}\times\frac{A_n\sin\nu_n\theta}{H_{\nu_n}^{(2)\prime}(k^{\alpha}r_0)-(i-1/2k^{\alpha}r_0)H_{\nu_n}^{(2)}(k^{\alpha}r_0)}. \tag{29}$$

In obtaining (29) we have used the identity[26]

$$H_{\nu_n}^{(1)}(z)H_{\nu_n}^{(2)\prime}(z)-H_{\nu_n}^{(2)}(z)H_{\nu_n}^{(1)\prime}(z)=-\frac{4i}{\pi z}. \tag{30}$$

Similarly, we can eliminate $\hat{D}_p(\theta)$ from (27) and (28) to obtain a relation between B_n and A_n:

$$B_n=\frac{(i-1/2k^{\alpha}r_0)H_{\nu_n}^{(1)}(k^{\alpha}r_0)-H_{\nu_n}^{(1)\prime}(k^{\alpha}r_0)}{(i-1/2k^{\alpha}r_0)H_{\nu_n}^{(2)}(k^{\alpha}r_0)-H_{\nu_n}^{(2)\prime}(k^{\alpha}r_0)}A_n=O(k^{\alpha}r_0)^{-2}. \tag{31}$$

Equations (22) and (31) show that patching yields

$$A_n=A_n^o+O(k^{\alpha}r_0)^{-2}. \tag{32}$$

2. Matching

We obtain $\hat{D}_m(\theta)$ by using Van Dyke's matching rule.[1] First we express the inner solution (21) in terms of outer variables:

Inner solution:

$$\hat{U}^{(0)}(R,\Theta)=\sum_{n=1}^{\infty}A_nH_{\nu_n}^{(1)}(R)\sin\nu_n\Theta+B_nH_{\nu_n}^{(2)}(R)\sin\nu_n\Theta. \tag{33}$$

In outer variables:

$$\hat{U}^{(0)}(kr,\theta)=\sum_{n=1}^{\infty}A_nH_{\nu_n}^{(1)}(kr)\sin\nu_n\theta+B_nH_{\nu_n}^{(2)}(kr)\sin\nu_n\theta. \tag{34}$$

We now expand (34) for large k to obtain the outer expansion of the inner solution:[26]

$$\hat{U}^{(0,-1/2)}(kr,\theta)=\sum_{n=1}^{\infty}\sqrt{\frac{2}{\pi kr}}\,[A_ne^{i(kr-(\pi/2)\nu_n-\pi/4)}+B_ne^{-i(kr-(\pi/2)\nu_n-\pi/4)}]\sin\nu_n\theta. \tag{35}$$

Outer solution:

$$\hat{u}^{(-1/2)}(r,\theta)=\frac{\hat{D}_m(\theta)}{\sqrt{kr}}\,e^{ikr}. \tag{36}$$

Inner of outer:

$$\hat{u}^{(-1/2,0)}\left(\frac{R}{k},\Theta\right)=\frac{\hat{D}_m(\Theta)}{\sqrt{R}}\,e^{iR}. \tag{37}$$

By Van Dyke's matching rule, (35) and (37) must be equivalent. Thus we conclude that

$$\hat{D}_m(\theta)=\sum_{n=1}^{\infty}\left[\sqrt{\frac{2}{\pi}}\,A_ne^{-i(\pi/2)(\nu_n+1/2)}\right]\sin\nu_n\theta, \tag{38}$$

$$B_n=0. \tag{39}$$

Equations (22) and (39) show that matching yields

$$A_n=A_n^o. \tag{40}$$

Therefore, we conclude from Eqs. (32) and (40) that matching and patching yield the same values for A_n to order $O(k^{\alpha}r_0)^{-2}$.

3. Error in directivity

We note that $\hat{D}_p(\theta)$ in (29) and $\hat{D}_m(\theta)$ in (38) appear to be different. Further, we note that $\hat{D}_p(\theta)$ depends explicitly on the location of our artificial boundary. This is a typical feature of patching. The matched directivity, $\hat{D}_m(\theta)$, is clearly independent of the purely artificial parameter r_0.

We measure the error in patching as the difference between $\hat{D}_m(\theta)$ in (38) and $\hat{D}_p(\theta)$ in (29). Thus, we define the following function:

$$\text{error}\ (\theta)=\sum_n E_n \sin \nu_n\theta \equiv \hat{D}_m(\theta)-\hat{D}_p(\theta). \tag{41}$$

Substituting Eqs. (29) and (38) into (41) leads to

$$E_n=A_n\Bigg[\sqrt{\frac{2}{\pi}}\,e^{-i(\pi/2)\nu_n-i(\pi/4)}-\frac{-4i}{\pi}\frac{e^{-ik^\alpha r_0}}{\sqrt{k^\alpha r_0}} \times\frac{1}{H_{\nu_n}^{(2)'}(k^\alpha r_0)-(i-1/2k^\alpha r_0)H_{\nu_n}^{(2)}(k^\alpha r_0)}\Bigg] + O(k^\alpha r_0)^{-2}. \tag{42}$$

Since $0<\alpha<1$, $k^\alpha r_0\to\infty$ as $k\to\infty$. Therefore, we can obtain an asymptotic approximation for E_n as $k\to\infty$ by expanding the Hankel functions for large argument. From Ref. 26 we have

$$H_{\nu_n}^{(2)}(k^\alpha r_0)=\sqrt{\frac{2}{\pi}}\left[1+i\frac{4\nu_n^2-1}{8k^\alpha r_0}\right]\frac{e^{-ik^\alpha r_0}}{\sqrt{k^\alpha r_0}}\,e^{i(\pi/2)+i(\pi/4)} + O((k^\alpha r_0)^{-5/2}). \tag{43}$$

Combining (42) with (43) yields an asymptotic approximation of the error as

$$E_n\sim -iA_n\sqrt{\frac{2}{\pi}}\frac{4\nu_n^2-1}{8k^\alpha r_0}\,e^{-i(\pi/2)\nu_n-i(\pi/4)}+O((k^\alpha r_0)^{-2}). \tag{44}$$

Clearly, as $k\to\infty$, $E_n\to 0$. We note, however, that E_n grows like n^2 for kr_0 fixed. For solutions with bounded energy, however, it can be shown[27] that $A_n=o(\nu_n^{-\nu_n})$ as $\nu_n\to\infty$. Therefore, (44) vanishes as $k\to\infty$ for all n.

III. THE HYBRID METHOD

Up to now we have considered the asymptotic aspects of the hybrid asymptotic-numerical method. Here we discuss a numerical formulation suitable for determining the inner solution. Patching the outer asymptotic solution to the numerical solution on the artificial boundary effectively enforces the radiation condition on the inner field. In this section, we describe a weak form developed by us[28] for this purpose. This is followed by a finite element discretization.

A. General formulation

We now describe a weak formulation of our boundary value problem that is suitably incorporated into our hybrid method. We denote the region outside of the scatterer by Ω. The ''internal'' boundary of Ω is denoted by Γ, which we assume to be piecewise smooth. We consider Γ as being partitioned into Γ_g and Γ_h, where $\Gamma=\overline{\Gamma_g\cup\Gamma_h}$. The classical or strong form of the problem is to find u in $\overline{\Omega}$ such that

$$(\Delta+k^2)u=-f \quad \text{in}\ \ \Omega, \tag{45}$$

$$u=g \quad \text{on}\ \ \Gamma_g, \tag{46}$$

$$\frac{\partial u}{\partial n}=ikh \quad \text{on}\ \ \Gamma_h, \tag{47}$$

$$\lim_{r\to\infty} r^{1/2}\left(\frac{\partial u}{\partial r}-iku\right)=0. \tag{48}$$

The unbounded domain Ω is decomposed by an artificial boundary Γ_R into a bounded inner domain Ω^i and its unbounded outer complement Ω^o. The solution to the original b.v.p. is decomposed into an inner and an outer field:

$$u=\begin{cases} u^i & \text{on}\ \ \Omega^i,\\ u^o & \text{on}\ \ \Omega^o.\end{cases} \tag{49}$$

In our hybrid method, we choose the outer field, u^o, to be given by the expansion in Eqs. (10) and (11), wherein the directivity $D(\theta)$ is unknown. [Or equivalently, when solving for $u-u_{\text{sharp}}$, by (25) with $\hat{D}_p(\theta)$ unknown.] Equations (45)–(47) are then supplemented by the patching boundary condition on Γ_R:

$$u^i=u^o \quad \text{on}\ \ \Gamma_R, \tag{50}$$

$$\partial_n u^i=\partial_n u^o \quad \text{on}\ \ \Gamma_R. \tag{51}$$

Standard finite element formulations are incompatible with the patching boundary conditions (50) and (51). Here we shall employ the weak formulation of Harari *et al.*:[28]

$$a(w^i,u^i)+\left(w^i,\frac{\partial u^o}{\partial n^o}\right)_{\Gamma_R}=L(w^i), \tag{52}$$

$$\left(\frac{\partial w^o}{\partial n^o},u^i\right)_{\Gamma_R}-\left(\frac{\partial w^o}{\partial n^o},u^o\right)_{\Gamma_R}=0. \tag{53}$$

It should be noted that $a(.,.)$ and $(.,.)_{\Gamma_R}$ are symmetric bilinear forms which are not inner products. Rather, they are defined as

$$a(w,u)=\int_{\Omega^i}(\nabla w\cdot\nabla u-wk^2u)\,d\Omega, \tag{54}$$

$$(w,u)_{\Gamma_R}=\int_{\Gamma_R} wu\,d\Gamma, \tag{55}$$

$$L(w)=\int_{\Omega^i} wf\,d\Omega+\int_{\Gamma_h} wikh\,d\Gamma. \tag{56}$$

We note that to evaluate the terms in (52) and (53), there is integration only over the inner region Ω^i and the artificial boundary, Γ_R. Thus, there is no integration over infinite or even large domains. For (52) and (53) to be valid, the outer solution u^o must satisfy the Helmholtz equation as well as the radiation condition. If the scatterer is not completely contained in Γ_R, then u^o must also satisfy all natural and essential boundary conditions in Ω^o. The functions w^i and w^o represent the arbitrary weighting functions of u^i and u^o, respectively. The Euler–Lagrange equations of (52) provide satisfaction of the governing differential equation in Ω^i and enforce continuity of normal derivatives across Γ_R. The relation in (53) enforces continuity of the unknown functions across Γ_R.

B. Finite element formulation

We now turn our attention to the problem of the imperfect wedge. In what follows, we shall be solving for $u_{\text{scat}} - u_{\text{sharp}}$. Thus, u^o will contain only a cylindrical wave contribution. Inside of Γ_R we use standard bilinear, quadrilateral elements with degrees of freedom representing the real and imaginary parts of the field. Let N and D denote shape functions with local support, defined on Ω^i and Γ_R, respectively. Then our inner field can be represented in the context of the finite element method.[29]

Inner solution:

$$u^i = \sum_A d_A^i N_A^i(r,\theta), \tag{57}$$

$$w^i = \sum_A c_A^i N_A^i(r,\theta). \tag{58}$$

Here each sum is over the total number of elements in our mesh. Similarly, we choose a finite element representation for $\hat{D}_p(\theta)$ on Γ_R, and so obtain the following representation of the outer field:

Outer solution:

$$u^o = \sum_M d_M^o D_M^o(\theta) \sqrt{\frac{r_0}{r}}\, e^{ik(r-r_0)}, \tag{59}$$

$$w^o = \sum_M c_M^o D_M^o(\theta) \sqrt{\frac{r_0}{r}}\, e^{ik(r-r_0)}. \tag{60}$$

Equations (59) and (60) reflect the GTD form of our outer solution (11), normalized by the radius of Γ_R.

To treat the boundary condition on Γ_R we introduce what will be referred to as a ''hybrid element.'' We shall assume that the shape functions N and D are both piecewise linear. Thus, for the special case treated here, the hybrid element has four nodes, two of which are shared with a Helmholtz element. The spatial coordinates of the two pairs match, forming what appears to be a one-dimensional element. We can then use (52) and (53) to find the following element stiffness matrix:

$$K^e = \begin{bmatrix} 0 & \mathscr{K} \\ \mathscr{K} & -\mathscr{K} \end{bmatrix}. \tag{61}$$

Here $\mathscr{K}$ is a 2×2 complex matrix with entries:

$$\mathscr{K}_{AB} = \int_{\Gamma_R^e} C_0 N_A^i N_B^i \, d\Gamma, \tag{62}$$

$$C_0 = \left(\frac{1}{2r_0} - ik\right). \tag{63}$$

We note that this matrix is symmetric. The lower half of the block weakly enforces continuity between the inner and outer fields. The upper right-hand block contributes to the continuity of normal derivatives.

C. Comparisons

We have implemented the hybrid element and performed calculations for a wedge of angle $\beta = 7\pi/4$. The interior domain Ω^i was meshed with a minimum resolution of ten elements per wavelength (Fig. 4). On the blunted tip, we define $a(\theta) = a_0 = \text{const}$, where $ka_0 = \pi$. We locate the artificial boundary, Γ_R, at $kr_0 = 4\pi$. The solution is forced by the inner boundary condition (20), where the infinite sum for U_{sharp} (Ref. 23) is truncated with negligible error.

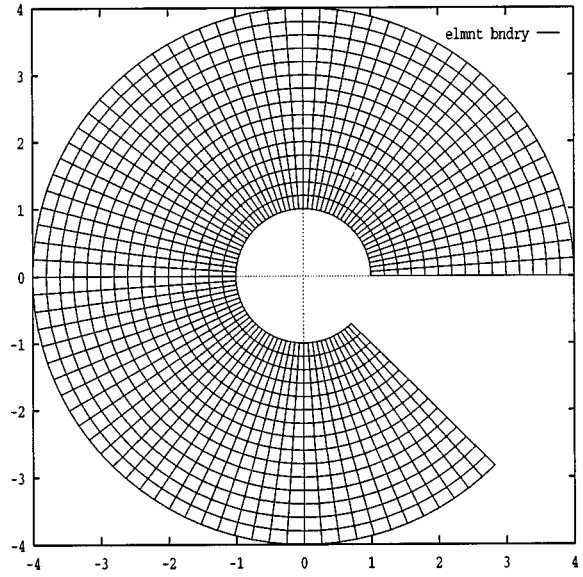

FIG. 4. Mesh used for radiation and scattering from a nonsharp soft wedge.

Our numerical interpolation is implemented twice: first we use the hybrid elements to represent the radiation boundary condition, and then we compare these results to those obtained using an ''exact'' DtN boundary condition.[30] The DtN map is derived in the Appendix. Although error will occur due to the finite element discretization of the interior problem, we expect this error to be identical in both the hybrid element and DtN methods. Thus, any difference in the results highlights inaccuracies in the hybrid formulation.

Here we consider a plane wave incident from $\theta = 7\pi/6$. At this incident angle, we expect both a shadow and a reflected region to exist. Figure 5 shows the magnitude of the pressure on Γ_R for both the hybrid element and DtN methods. The first thing we notice in comparing the two solutions is that they are hardly distinguishable from one another. The same is true when comparing the phase, although this is not shown. From these results we conclude that the hybrid and exact DtN representations compare favorably.

The shape of the curve (Fig. 5) is another point of interest. We note that the tip blunting does not significantly displace the shadow boundary from that formed by a sharp wedge. Such a displacement would be signaled by two infinities in $\hat{D}(\theta)$. One infinity would be associated with the new position of the shadow boundary. The other would be required to cancel the shadow boundary solution in u_{sharp}.

To better interpret the shape of the previous curve, the magnitude of the pressure on Γ_R is plotted for different incident angles (Fig. 6). In addition, we use our original numerical solution for $\hat{u}$, along with u_{sharp}, to construct a total field representation (Fig. 7). The repetition in the first plot reinforces our assumption that no shadow boundary correc-

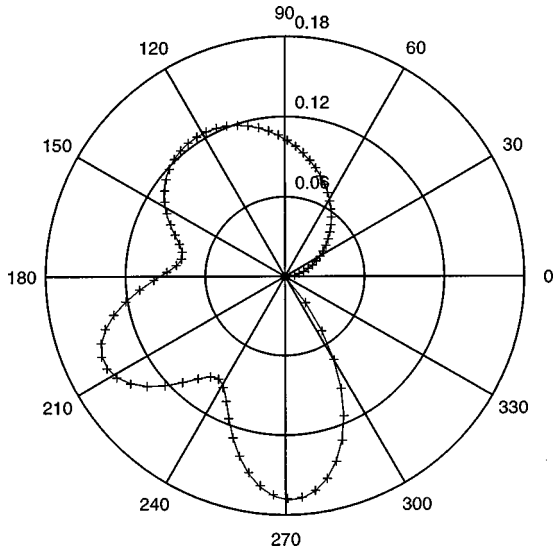

FIG. 5. Magnitude of the pressure on Γ_R as a function of θ. The solid curve represents the results obtained using the hybrid method. The ''+'' symbols mark the results obtained using an exact DtN boundary condition.

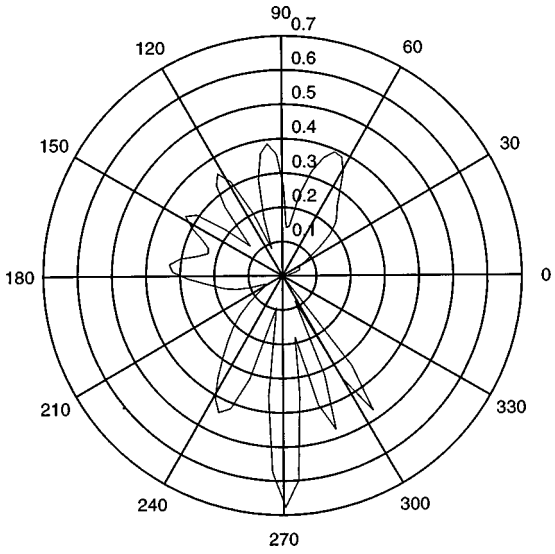

FIG. 7. Magnitude of the total field on Γ_R, due to an incident plane wave of angle $7\pi/6$ on a blunted wedge of angle $7\pi/4$.

tion is present. The three ''lobes'' represent backscattering and interference between the diffracted and reflected fields, which differ from the solution to the sharp wedge. This difference is small when compared to the magnitude of the total field (Fig. 7).

In examining the total field representation, given the original angle of incidence, we observe all of the expected phenomena. The first is our soft boundary condition, which requires the pressure to be zero on the wedge. We further observe sharp variations in the field in the reflected region due to interference between the diffracted and reflected fields. But most interesting are the smooth transitions across the shadow and reflected boundaries. In particular, we notice very small pressures in the shadow region compared to those on the other side of the shadow boundary.

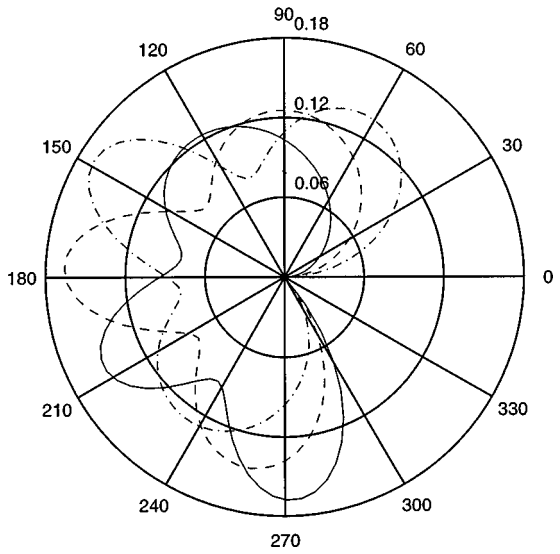

FIG. 6. Magnitude of $\hat{u}$ on Γ_R for incident angles: $5\pi/6$ –.–, π ––, $7\pi/6$ ———.

IV. CONCLUSIONS

We have described a hybrid GTD/FEM method to evaluate diffraction coefficients. The method depends on first performing an outer GTD analysis (less the diffraction coefficients) to obtain an outer asymptotic approximation of the field. An example of this procedure was presented in Sec. III. The outer approximation necessarily involves undetermined diffraction coefficients. To find those, an inner problem is formulated with a patching boundary condition on an artificial boundary. We found the relation between the patched directivity and the matched directivity in Sec. III C. In particular, we determined how their difference scaled with both kr_o and with ν_n.

In Sec. IV A, we described a weak formulation of the inner boundary value problem that allowed us to enforce the patching boundary condition within a FEM framework. In Sec. IV B, we specialized this to the problem at hand, diffraction from a wedge, and showed that the patching condition can be enforced by introducing a ''hybrid element.''

The results of our hybrid method in this simple geometry were compared to reference calculations performed using the DtN method. The DtN method provides an exact (modulo the truncation of an infinite series) representation of the artificial boundary condition. The two calculations were performed on the same inner mesh, and so any difference between the two highlights error in the patching boundary condition. We found the methods to be in excellent agreement with each other, and therefore conclude that our hybrid method might be successful in more complicated scattering geometries.

ACKNOWLEDGMENTS

The authors would like to thank Isaac Harari for many helpful discussions and ideas. This work was supported by the Office of Naval Research.

APPENDIX: DERIVATION OF DTN MAP

The DtN map, or Dirichlet-to-Neumann map, is simply the impedance map for the fluid outside the artificial boundary Γ_R. To find the DtN map, we must solve the following problem. Given $\overline{u}(\theta)$, find $\partial_r u|_{\Gamma_R}$ such that

$$(\Delta + k^2)u = 0 \quad \text{in} \quad \beta < \theta < 0; \quad r > r_0, \tag{A1}$$

$$u = \begin{cases} \overline{u} & \text{on} \quad \Gamma_R, \\ 0 & \text{on} \quad \theta = 0, \quad r > r_0, \\ 0 & \text{on} \quad \theta = \beta, \quad r > r_0. \end{cases} \tag{A2}$$

Further, u must satisfy a radiation condition as $r \to \infty$.

The solution of (A1) and (A2) can be written in the following form:

$$u(r,\theta) = \sum_{n=1}^{\infty} [A_n / H_{\nu_n}^{(1)}(kr_0)] H_{\nu_n}^{(1)}(kr) \sin \nu_n \theta. \tag{A3}$$

We recall that $\nu_n = n\pi/\beta$. The constants A_n are given by

$$A_n = \frac{1}{2\beta} \int_0^{\beta} \overline{u}(\theta) \sin \nu_n \theta \, d\theta. \tag{A4}$$

We now use (A3) to evaluate $\partial_r u$ on $r = r_0$:

$$\partial_r u(r_0,\theta) = k \sum_{n=1}^{\infty} [A_n / H_{\nu_n}^{(1)}(kr_0)] H_{\nu_n}^{(1)\prime}(kr_0) \sin \nu_n \theta. \tag{A5}$$

The DtN is obtained by combining (A4) with (A5), and substituting $u(r_0,\theta)$ for $\overline{u}(\theta)$. Thus we obtain

$$\partial_r u(r_0,\theta) = \frac{k}{2\beta} \sum_{n=1}^{\infty} \int_0^{\beta} u(r_0,\phi) \sin \nu_n \phi \, d\phi \times [H_{\nu_n}^{(1)\prime}(kr_0) / H_{\nu_n}^{(1)}(kr_0)] \sin \nu_n \theta. \tag{A6}$$

Equation (A6) is the exact DtN boundary condition for scattering from a soft truncated wedge. In practice, the infinite sum must be truncated, which causes the boundary condition to be inexact. In our calculations with $kr_0 = 2\pi$, we included ten terms in the sum.

[1] M. Van Dyke, *Perturbation Methods in Fluid Mechanics* (Parabolic, Stanford, 1975).

[2] J. B. Keller, ''A Geometrical Theory of Diffraction,'' in *Selected Papers on Geometrical Aspects of Scattering*, edited by P. L. Marston, SPIE Milestone Series, (MS 89):5-25 (SPIE Optical Engineering, Bellingham, WA, 1994); reprinted from *Calculus of Variations and its Applications*, Proc. of Symposia in Applied Mathematics, Vol. 8, pp. 27–51 (American Mathematical Society, New York, 1958).

[3] W. D. Burnside, C. L. Yu, and R. J. Marhefka, ''A technique to combine the geometrical theory of diffraction and the moment method,'' IEEE Trans. Antennas Propag. **AP-23**, 551–558 (1975).

[4] J. N. Sahalos and G. N. Thiele, ''On the application of the gtd-mm technique and its limitations,'' IEEE Trans. Antennas Propag. **AP-29**(5), 780–786 (1981).

[5] T. J. Kim and G. N. Thiele, ''A hybrid diffraction technique–general theory and applications,'' IEEE Trans. Antennas Propag. **AP-30**(5), 888–897 (1982).

[6] L. N. Medgyesi-Mitschang and D. S. Wang, ''Hybrid methods for analysis of complex scatterers,'' Proc. IEEE **77**(5), 770–779 (1989).

[7] D. S. Wang, ''Current-based hybrid analysis for surface-wave effects on large scatterers,'' IEEE Trans. Antennas Propag. **39**(6), 839–850 (1991).

[8] Z. El Hachemi, P. H. Gatignol, and M. Bentahar, ''On an hybrid technique for combining the uniform theory of diffraction with finite boundary elements,'' in *International Conference on Computational Acoustics and Its Environmental Applications*, edited by C. A. Brebbia, J. Kenny, and R. D. Ciskowski (Comp. Mechanics Publications, Ashurst, 1997), pp. 49–56.

[9] R. J. Astley, G. J. Macaulay, and J.-P. Coyette, ''Mapped wave envelope elements for acoustical radiation and scattering,'' J. Sound Vib. **170**, 97–118 (1994).

[10] D. S. Burnett, ''A three-dimensional acoustic infinite element based on a prolate spheroidal multipole expansion,'' J. Acoust. Soc. Am. **96**, 2798–2816 (1994).

[11] A. Bayliss and E. Turkel, ''Radiation boundary conditions for wave-like equations,'' Commun. Pure Appl. Math. **33**, 707–725 (1980).

[12] A. Khebir, A. Kouki, and R. Mittra, ''Higher order asymptotic boundary condition for the finite element modeling of two-dimensional transmission line structures,'' IEEE Trans. Microwave Theory Tech. **38**, 1433–1437 (1990).

[13] D. Givoli, I. Patlashenko, and J. B. Keller, ''High-order boundary conditions and finite elements for infinite domains,'' Comput. Methods Appl. Mech. Eng. **143**, 13–39 (1997).

[14] M. J. McDougall and J. P. Webb, ''Infinite elements for the analysis of open dielectric waveguides,'' IEEE Trans. Microwave Theory Tech. **37**, 1724–1731 (1989).

[15] P. Bettess, ''Infinite elements,'' Int. J. Numer. Methods Eng. **11**, 53–64 (1977).

[16] O. C. Zienkiewicz, K. Bando, P. Bettess, C. Emson, and T. C. Chiam, ''Mapped infinite elements for exterior wave problems,'' Int. J. Numer. Methods Eng. **21**, 1229–1251 (1985).

[17] O. C. Zienkiewicz, C. Emson, and P. Bettess, ''A novel boundary infinite element,'' Int. J. Numer. Methods Eng. **19**, 393–404 (1983).

[18] I. Harari, P. E. Barbone, M. Slavutin, and R. Shalom, ''Boundary infinite elements for the Helmholtz equation in exterior domains,'' Int. J. Numer. Methods Eng. **41**, 1105–1131 (1998).

[19] I. Harari, R. Shalom, and P. E. Barbone, ''Higher-order boundary infinite elements,'' Comput. Methods Appl. Mech. Eng. (in press, 1997).

[20] P. E. Barbone and O. Michael, ''Scattering from submerged objects by a hybrid asymptotic-boundary integral equation method,'' Wave Motion (in press, 1998).

[21] D. Givoli, *Numerical Methods for Problems in Infinite Domains* (Elsevier, Amsterdam, 1992).

[22] E. Zauderer, *Partial Differential Equations of Applied Mathematics* (Academic, New York, 1989), 2nd ed.

[23] D. S. Jones, *Acoustic and Electromagnetic Waves* (Clarendon, Oxford, 1986).

[24] A. D. Pierce, *Acoustics: An Introduction to its Physical Principles and Applications* (Acoustical Society of America, New York, 1989).

[25] L. B. Felsen and N. Marcuvitz, *Radiation and Scattering of Waves* (IEEE, New York, 1994).

[26] M. Abramowitz and I. A. Stegun, *Handbook of Mathematical Functions* (Dover, New York, 1972).

[27] J. M. Montgomery, ''Acoustic Scattering Calculations by a Hybrid Asymptotic-Numerical Method,'' M.Sc. Thesis, Dept. of Aerospace and Mechanical Engineering, Boston University, Boston, MA, 1997.

[28] I. Harari, P. E. Barbone, and J. M. Montgomery, ''Finite Element Formulations for Exterior Problems: Application to Hybrid Methods, Nonreflecting Boundary Conditions, and Infinite Elements,'' Int. J. Numer. Methods Eng. **40**, 2791–2805 (1997).

[29] Th. J. R. Hughes, *The Finite Element Method* (Prentice–Hall, Englewood Cliffs, NJ, 1987).

[30] D. Givoli, Revisions of the FEM code DLEARN found in Ref. 28 to accommodate Helmholtz elements.

Local sound field reproduction using two closely spaced loudspeakers

Ole Kirkeby[a] and Philip A. Nelson
Institute of Sound and Vibration Research, University of Southampton, Highfield, Southampton SO17 1BJ, United Kingdom

Hareo Hamada
Department of Information and Communication Engineering, Tokyo Denki University, Tokyo 101, Japan

(Received 2 December 1997; accepted for publication 5 June 1998)

When only two loudspeakers are used for the reproduction of sound for a single listener, time domain simulations show that it is advantageous that the two loudspeakers are very close together. The sound field reproduced by two loudspeakers that span 10 degrees as seen by the listener is simpler, and locally more similar to the sound field generated by a real sound source, than that reproduced by two loudspeakers that span 60 degrees. The basic physics of the problem is first explained by assuming that the sound propagates under free-field conditions. It is then demonstrated that when the influence of the listener on the incident sound waves is taken into account by modeling the listener's head as a rigid sphere, the results are qualitatively the same as in the free-field case. Consequently, two closely spaced loudspeakers are capable of accurately reproducing a desired sound field, not only at the ears of the listener but also in the vicinity of the listener's head. This result, although counter-intuitive, is very encouraging. In particular, it suggests that many low-fidelity audio systems, such as those currently supplied with most multi-media computers, can be greatly improved. © *1998 Acoustical Society of America.*
[S0001-4966(98)04309-4]

PACS numbers: 43.20.Fn, 43.20.Px, 43.60.Pt, 43.66.Pn [DEC]

INTRODUCTION

A virtual source imaging system attempts to give a listener the impression that there is a sound source at a position in space where no real sound source exists. The overwhelming part of current research into virtual source imaging relies heavily on binaural technology.[1–4] (A notable exception is when large arrays of loudspeakers are used for the reproduction. In that case it is possible to synthesize the entire sound field under certain conditions.[5]) Binaural technology is based on the sensible engineering principle that if a sound reproduction system can generate the same sound pressures at the listener's eardrums as would have been produced there by a real sound source, then the listener should not be able to tell the difference between the virtual image and the real sound source. In order to determine these binaural signals, or ''target'' signals, it is necessary to know how the listener's torso, head, and pinnae (outer ears) modify incoming sound waves as a function of the position of the sound source. This information can be obtained by making measurements on ''dummy-heads'' or human subjects.[6,7] The results of such measurements are usually called head-related transfer functions, or HRTFs.

When only two loudspeakers are used for the reproduction, it is necessary to consider how to deal with cross-talk.[8–12] Cross-talk in the context of sound reproduction is usually interpreted as the sound reproduced at a location where it was not intended to be heard.[8] For example, when a dummy-head recording[6] is played back over two loudspeakers, the sound emitted from the right loudspeakers, and heard at the left ear, is cross-talk. Similarly, the sound emitted from the left loudspeaker, and heard at the right ear, is also cross-talk. In 1966, the first method for cross-talk cancellation was developed by Atal *et al.*[13] Their method was based on a free-field model that did not account for the presence of a listener in the sound field. Since then, more sophisticated methods, some based on digital signal processing techniques, have been developed.[10–12,14–17]

With a few notable exceptions,[11,18] most researchers have concentrated on systems using loudspeaker arrangements spanning an angle of typically 60 degrees as seen by the listener. A fundamental problem that one faces when using relatively widely spaced loudspeakers is that convincing virtual images are experienced only within a very tight ''bubble'' surrounding the listener's head. In contrast, a system using two closely spaced loudspeakers is surprisingly robust with respect to head movement.[19] The size of the ''bubble'' around the listener's head is increased significantly without any noticeable reduction in performance. We use the term ''stereo dipole''[20,21] to describe such a virtual source imaging system since the inputs to the two closely spaced loudspeakers are close to being exactly out of phase over a wide frequency range.[22] Consequently, they reproduce a sound field very similar to that generated by a point dipole source. Strictly speaking, the field that they reproduce approximates that generated by a combination of a point dipole and a point monopole source.[23]

In this paper, time domain simulations are used to show the form of the sound fields that are reproduced by two loudspeakers placed symmetrically about the median plane in front of the listener. We concentrate on two loudspeaker ar-

[a]Now at the Department of Communication Technology, Institute for Electronic Systems, Aalborg University, Denmark.

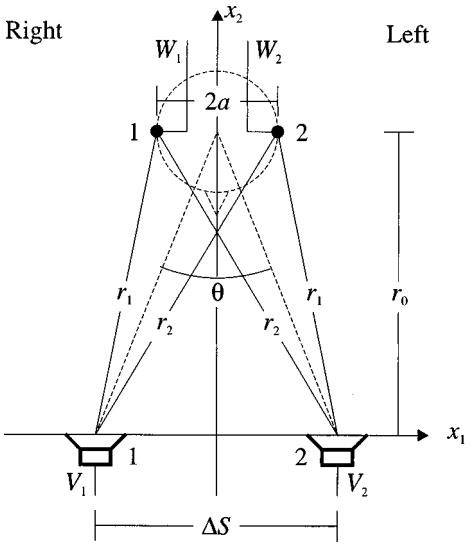

FIG. 1. The arrangement of the two loudspeakers and the two microphones. Note that ''left'' and ''right'' are defined to be relative to the listener.

rangements: a ''wide'' spacing where the loudspeakers span 60 degrees as seen by the listener, and a ''narrow'' spacing where the loudspeakers span 10 degrees as seen by the listener. The results calculated by using a free-field model are compared to the results calculated by using a rigid sphere model. The emphasis is on the basic physical principles, and so we do not attempt to include the detailed high-frequency information contained in HRTFs measured on human subjects, or dummy-heads, in this analysis.

I. GEOMETRY

The geometry of the problem is shown in Fig. 1. Two loudspeakers (sources), separated by the distance ΔS, are positioned on the x_1 axis symmetrically about the x_2 axis. We imagine that a listener is positioned r_0 meters away from the loudspeakers directly in front them. The ears of the listener are represented by two microphones, separated by the distance $2a$, that are also positioned symmetrically about the x_2 axis. Note that when we later refer to ''left'' and ''right,'' we consider this to be relative to the listener's point of view, as indicated in Fig. 1. The loudspeakers span an angle of θ as seen from the position of the listener. The shortest distance, in a straight line, from the loudspeakers to the microphones is the ''direct'' path r_1, and the furthest distance is the ''cross-talk'' path r_2.

When the system is operating at a single frequency, we can use complex notation. Thus, the inputs to the right and left loudspeaker are denoted by V_1 and V_2, respectively, and the outputs from the right and left microphone are denoted by W_1 and W_2, respectively. The variables V_1, V_2, W_1, and W_2 are all complex scalars.

II. ELECTROACOUSTIC TRANSFER FUNCTIONS

A. General notation

Since the loudspeaker–microphone arrangement is symmetric about the x_2 axis, only two of the four transfer functions relating the loudspeaker inputs to the microphone outputs are different. In complex notation, these are denoted C_1 and C_2. Similarly, the transfer functions relating the input D to a virtual source to the microphone outputs are denoted by A_1 and A_2. This is shown in Fig. 2.

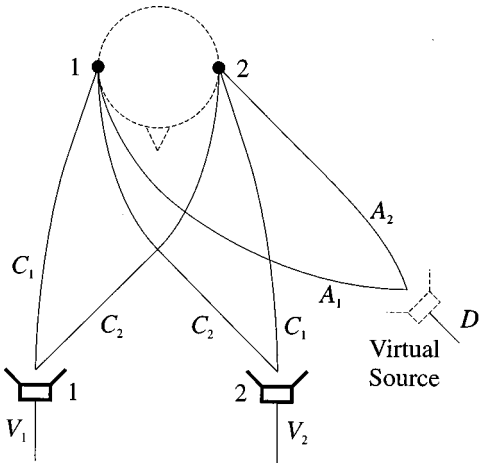

FIG. 2. Definitions of the electro-acoustic transfer functions C_1, C_2, A_1, and A_2.

Thus, for the two loudspeakers we have

$$C_1=\left.\frac{W_1}{V_1}\right|_{V_2=0}=\left.\frac{W_2}{V_2}\right|_{V_1=0} \tag{1a}$$

and

$$C_2=\left.\frac{W_2}{V_1}\right|_{V_2=0}=\left.\frac{W_1}{V_2}\right|_{V_1=0}. \tag{1b}$$

For the virtual source

$$A_1=\frac{W_1}{D} \tag{2a}$$

and

$$A_2=\frac{W_2}{D}. \tag{2b}$$

Using these two transfer functions, the output from the microphones as a function of the inputs to the loudspeakers is conveniently expressed as the matrix-vector multiplication

$$\mathbf{w}=\mathbf{C}\mathbf{v}, \tag{3}$$

where

$$\mathbf{w}=\begin{bmatrix}W_1\\W_2\end{bmatrix}, \tag{4}$$

$$\mathbf{C}=\begin{bmatrix}C_1 & C_2\\C_2 & C_1\end{bmatrix}, \tag{5}$$

and

$$\mathbf{v}=\begin{bmatrix}V_1\\V_2\end{bmatrix}. \tag{6}$$

The aim of the system shown in Fig. 1 is to reproduce a pair of desired signals D_1 and D_2 at the microphones. Consequently, we will generally want W_1 to be equal to D_1, and W_2 to be equal to D_2. The desired signals will sometimes be

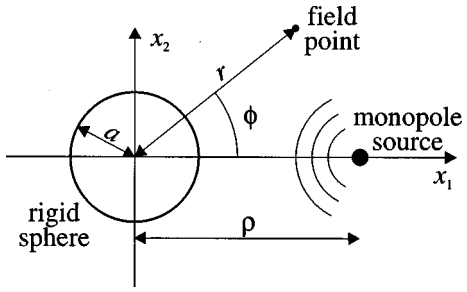

FIG. 3. The variables used when calculating the sound field scattered from a rigid sphere.

referred to individually as D_1 and D_2, and sometimes referred to as a vector $\mathbf{d}$ of the same type as $\mathbf{w}$,

$$\mathbf{d}=\begin{bmatrix} D_1 \\ D_2 \end{bmatrix}. \tag{7}$$

B. Free-field conditions

The sound field p_{ff} radiated from a monopole in a free-field is given by

$$p_{\mathrm{ff}}=j\omega\rho_0 q\,\frac{\exp(-jkr)}{4\pi r}, \tag{8}$$

where j is the square root of -1, ω is the angular frequency, ρ_0 is the density of the medium, q is the source strength, k is the wave number ω/c_0 where c_0 is the speed of sound, and r is the distance from the source to the field point.[24] If V is defined as

$$V=\frac{j\omega\rho_0 q}{4\pi}, \tag{9}$$

then the transfer function C_{ff} is given by

$$C_{\mathrm{ff}}=\frac{p_{\mathrm{ff}}}{V}=\frac{\exp(-jkr)}{r}. \tag{10}$$

This expression is easy to implement and quick to evaluate numerically, and it is therefore very suitable for computer simulations.

C. Rigid sphere model

An analytical expression for the total sound field produced by a plane wave impinging on a rigid sphere was first published by Rayleigh before the turn of the century.[25] Since then, Rayleigh's result has been used by many other authors (see, for example, Refs. 24 and 26). In the following, we will derive the expression for the total sound field produced by a *spherical* wave that impinges on a rigid sphere. This is straightforward to do once the spherical wave has been expanded into an appropriate infinite series. The results we need to do this are listed in the comprehensive work by Abramowitz and Stegun (Ref. 27).

The variables that are used in the derivation are shown in Fig. 3. A rigid sphere, whose radius is a, is positioned at the origin of the coordinate system. A monopole source is positioned on *the positive half* of the x_1 axis at a distance ρ from the origin. A straight line connecting the field point with the origin has the length r, and it forms the angle ϕ with the x_1 axis. The sound pressure p_t (subscript t is for total, and p, rather than P, is used in order to avoid confusion with the Legendre polynomial) at the field point can be written as the sum of two components: p_{ff}, the incident field, and p_s, the scattered field. Thus,

$$p_t=p_{\mathrm{ff}}+p_s. \tag{11}$$

The incident field p_{ff} is already known; it is given by Eq. (8). The scattered field p_s must be determined by imposing the relevant boundary conditions on the total field p_t. Since the sphere is assumed to be perfectly rigid, the particle velocity in the radial direction must be zero on the surface of the sphere. This is equivalent to requiring that the gradient of p_t in the radial direction must be zero on the surface of the sphere,

$$\left.\frac{\partial p_t}{\partial r}\right|_{r=a}=0. \tag{12}$$

In order to be able to impose this boundary condition on p_t, p_{ff} is expanded into an infinite series by using the results 10.1.45 and 10.1.46 listed on p. 440 in Ref. 27. These two results give series expansions for $\cos(kr)/kr$ and $\sin(kr)/kr$, and these series can be combined to give a series expansion for $\exp(-jkr)/kr$. By using the expression for V as defined in Eq. (9), we find

$$p_{\mathrm{ff}}=-jkV\sum_{m=0}^{+\infty}(2m+1)j_m(kr)\times[j_m(k\rho)-jn_m(k\rho)]P_m(\cos\phi). \tag{13}$$

In this expression, j_m and n_m are mth-order spherical Bessel functions of the first and second kind, respectively, and P_m is the mth-order Legendre polynomial. It can be shown that the scattered field p_s can be expanded into an infinite series of waves propagating *outwards*, away from the origin (Ref. 28, pp. 533–535),

$$p_s=kV\sum_{m=0}^{+\infty}b_m[j_m(kr)-jn_m(kr)]P_m(\cos\phi). \tag{14}$$

If the sign of $jn_m(kr)$, the second term in the square brackets, is reversed, then the series represents an infinite sum of waves converging on the origin rather than diverging from the origin. Although p_s could, in principle, contain such converging waves, we do not have to consider these components since they violate the so-called radiation condition at infinity (Ref. 28, p. 534). Consequently, the problem is now to choose the constants b_m such that the boundary condition given by Eq. (12) is satisfied. After some algebra we find

$$b_m=j(2m+1)\,\frac{j_m(k\rho)-jn_m(k\rho)}{1-j(n'_m(ka)/j'_m(ka))}, \tag{15}$$

where the prime denotes differentation with respect to the function's single argument. The scattered field is now readily calculated by substituting b_m back into Eq. (14). Note that the value of b_m for a given wave number k and order m does not depend on the position of the field point, and so it is possible to speed up the numerical evaluation of p_s dramatically by storing the constants b_m in a two-dimensional

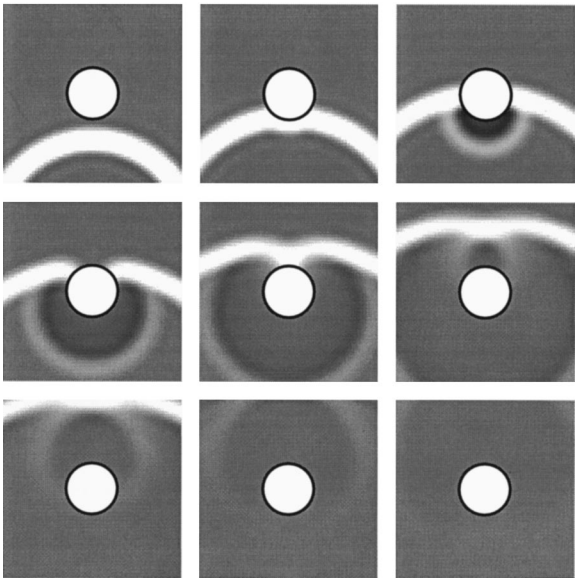

FIG. 4. The sound field produced by a sperical wave impinging on a rigid sphere. Note the secondary wave that starts radiating away form the ''bright spot'' at the back of the sphere.

lookup table rather than calculating them repeatedly for each field point. In addition, it is important to know that the series expansion of p_{ff} converges very slowly for large kr whereas the series expansion of p_s converges quite quickly for large kr. In fact, p_s converges most slowly when the field point is on the surface of the sphere ($r=a$). For values of ka smaller than about 10, it is more than enough to include only the first 20 terms of the series. Consequently, p_t should be calculated as the sum of the simple expression for p_{ff} given by Eq. (8), and the series expansion of p_s given by Eq. (14). It is not a good idea to calculate p_t from the single infinite series that can be obtained by adding together the series expansions of p_{ff} and p_s [Eqs. (13) and (14)]. Although this series looks quite compact when written out in full, it is not very efficient for calculating p_t numerically.

III. TIME DOMAIN SIMULATION OF SCATTERING FROM A RIGID SPHERE

In practice, we can calculate the field scattered by the sphere only at a finite number of discrete points and frequencies. Consequently, the time response at a given field point must be calculated by an inverse fast Fourier transform of the sampled frequency response at that point. In order to avoid the undesirable ''wrap-around'' effect,[29] p_t must be calculated at a relatively large number of frequencies even if we are interested in only a single ''snapshot'' of the total sound field. Thus, a time domain simulation typically requires several orders of magnitude more computational time than a frequency domain simulation. Nevertheless, it is still feasible to calculate the full time history of the scattered field on a fast PC. Figure 4 illustrates what happens when a short pulse emitted from a monopole source impinges on a rigid sphere.

Figure 4 shows nine ''snapshots,'' or frames, of the total sound field p_t. The frames are listed sequentially in a ''reading sequence'' from top left to bottom right; top left is the earliest time, bottom right is the latest time. The sound field is calculated at 65 frequencies between DC (0 Hz) and the Nyquist frequency f_{Nyq} (half the sampling frequency), both frequencies included. The sampling frequency f_s is 12.8 kHz, and the time increment between each frame is three sampling intervals, which is equivalent to the time it takes the sound to travel approximately 8 cm. In each frame, the value of p_t is calculated at 61×61 points over an area of $0.6\times0.6\ \mathrm{m}^2$. Values greater than 1 are plotted as white, values smaller than -1 are plotted as black, and values between -1 and 1 are shaded appropriately. The sphere, whose radius a is 9 cm, is positioned at the center of each frame. The source is positioned 0.5 m away from the sphere directly ''below'' it. Thus, the source is 20 cm below the bottom edge of each frame.

The pulse emitted by the source is a Hanning pulse (one period of a ''raised'' cosine) specified by

$$d_{\mathrm{pulse}}(t)=\begin{cases}(1-\cos\ \omega_0 t)/2, & 0\leqslant t\leqslant 2\pi/\omega_0,\\ 0, & \text{all other } t,\end{cases} \tag{16}$$

where ω_0 is chosen to be 2π times 3.2 kHz. The spectrum of this pulse has its first zero at 6.4 kHz, and the main part of its energy is concentrated below 3 kHz. This pulse, which is defined as a continuous function of time, is used for all free-field simulations. However, it is necessary to use a ''digital version'' of the Hanning pulse for the simulations based on the rigid sphere since in this case we do not have direct access to a time domain expression for the scattered field. Instead, the simulated time responses are calculated by an inverse Fourier transform of the sampled frequency response (inverse FFT). The digital Hanning pulse is given by the time sequence [0, 0.5, 1, 0.5, 0].

It is seen that when the incident wave hits the front of the sphere, it causes a ''reflected'' wave, which appears to be almost perfectly spherical, to radiate away from this point. This is not surprising since any hard obstacle reflects high-frequency components according to ray theory. However, it is interesting to observe that a similar wave starts to radiate away from the point directly at the back of the sphere a short while later. This phenomenon can be understood by realizing that the amplitude response at the point directly at the back of the sphere decays away quite slowly with frequency even though it is right in the middle of the shadow zone. All the paths the incident wave can follow around the sphere to this ''bright spot''[30] have the same length, and so all components of the incident field arriving at this point are bound to be in phase and interfere constructively. In the time domain, this is associated with a secondary wave that propagates away from the bright spot.

Note that the density plots in Fig. 4 are effectively ''clipped'' in order to make it easy to see the low-amplitude secondary wave. Had the sphere not been present, the amplitude of the incident field would have been two at the center of each frame, but since any value greater than one is plotted as white, the duration of the incident pulse looks greater than it really is.

IV. OPTIMAL SOURCE INPUTS

The pair of desired signals can be specified with two fundamentally different objectives in mind: cross-talk cancellation or virtual source imaging. Perfect cross-talk cancellation requires that a signal is reproduced perfectly at one ear of the listener while nothing is heard at the other ear, so if we want to produce a desired signal D_2 at the listener's left ear, then D_1 must be zero. Virtual source imaging, on the other hand, requires that the signals reproduced at the ears of the listener are identical (up to a common delay and a common scaling factor) to the signals that would have been produced there by a real source. For given values of D_1 and D_2, $\mathbf{v}$ must be calculated by solving $\mathbf{Cv}=\mathbf{d}$ for $\mathbf{v}$. In order to be able to determine the impulse responses corresponding to V_1 and V_2 for general choices of C_1, C_2, D_1, and D_2, it is necessary to use a modeling delay,[31] and it is usually also necessary to use regularization in order to avoid very large values of V_1 and V_2 caused by ill conditioning of $\mathbf{C}$.[12,17,32]

V. CROSS-TALK CANCELLATION SYSTEMS

A. Free-field conditions

It is advantageous to define D_2 to be the product of D_{pulse} and the phase factor $\exp(-jkr_1)$ since this ensures that the source inputs are both causal. The source inputs can be determined by solving the linear equation system $\mathbf{Cv}=[0,D_2]^T$ for $\mathbf{v}$. After an inverse Fourier transform of $\mathbf{v}$, we have the source inputs as a function of time. The solution for each source input[20,23] consists of an exponentially decaying train of delta functions convolved with d_{pulse} [which is a Hanning pulse defined as a continuous function of time, see Eq. (16)].

Figure 5 shows the two source inputs $v_1(t)$ and $v_2(t)$ for the two loudspeaker spans (a) 60 degrees and (b) 10 degrees. The x axis is normalized so that instead of showing time in seconds it indicates the distance in meters travelled by the sound as a function of time (assuming that c_0, the speed of sound, is 340 m/s). The distance to the listener is 0.5 m, and the microphone separation, which is an approximation to the head diameter, is 18 cm. In Fig. 5(a), it is seen that when the loudspeakers span 60 degrees, each of the pulses emitted by the sources are clearly separated. This is because the duration of the Hanning pulse is short compared to the interval between adjacent pulses. When the loudspeaker span is reduced to 10 degrees this is no longer the case. Figure 5(b) shows that the individual pulses then start to overlap because the interval between adjacent pulses is much shorter. This, in turn, increases the low-frequency energy content of the source inputs. As a rule of thumb, the interval between adjacent pulses is equivalent to a frequency f_0, which is reasonably well approximated by ''100 kHz divided by the loudspeaker span in degrees.''[20] We call f_0 the ringing frequency. For a loudspeaker span of 60 degrees f_0 is 1.9 kHz, for a loudspeaker span of 10 degrees f_0 is 11 kHz.

Figure 6 shows the sound field reproduced by the two loudspeaker spans (a) 60 degrees and (b) 10 degrees. Each of the two plots contains nine ''snapshots,'' or frames, of the sound field as in Fig. 4. The frames are listed sequentially in

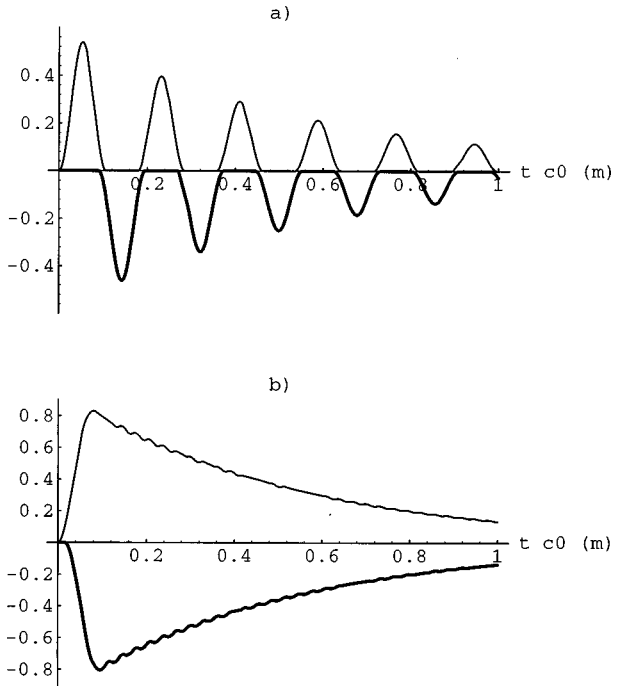

FIG. 5. The time response of the two source input signals $v_1(t)$ (thick line) and $v_2(t)$ (thin line) required to achieve perfect cross-talk cancellation at the listener's left ear under free-field conditions. The two loudspeaker spans are (a) 60 degrees and (b) 10 degrees.

a ''reading sequence'' from top left to bottom right; top left is the earliest time ($t=0.2/c_0$), bottom right is the latest time ($t=1.0/c_0$). The time increment between each frame is $0.1/c_0$ which is equivalent to the time it takes the sound to travel 10 cm. The normalization of D_2 ensures that the left loudspeaker starts emitting sound at exactly $t=0$; the right loudspeaker starts emitting sound a short while later. Each frame is calculated at 101×101 points over an area of $1\times1\ \text{m}^2$. The positions of the loudspeakers and the microphones are indicated by circles. As in Fig. 4, values greater than 1 are plotted as white, values smaller than -1 are plotted as black, and values between -1 and 1 are shaded appropriately.

Figure 6(a) illustrates the cross-talk cancellation principle when the loudspeakers span 60 degrees. It is easy to identify a sequence of positive pulses from the left loudspeaker, and a sequence of negative pulses from the right loudspeaker. Both pulse trains are emitted with a ringing frequency of 1.9 kHz. Only the first pulse emitted from the left loudspeaker is actually ''seen'' at the left microphone; consecutive pulses are cancelled out at both the left and right microphone. However, many ''copies'' of the original Hanning pulse are seen at other locations in the sound field, even very close to the two microphones. When the loudspeaker span is reduced to 10 degrees [Fig. 6(b)] the reproduced sound field becomes much simpler. The desired Hanning pulse is now ''beamed'' towards the left microphone, and a similar ''line of cross-talk cancellation'' extends through the position of the right microphone. The only disturbance seen at most locations in the sound field is a single attenuated and delayed copy of the original Hanning pulse. This suggests

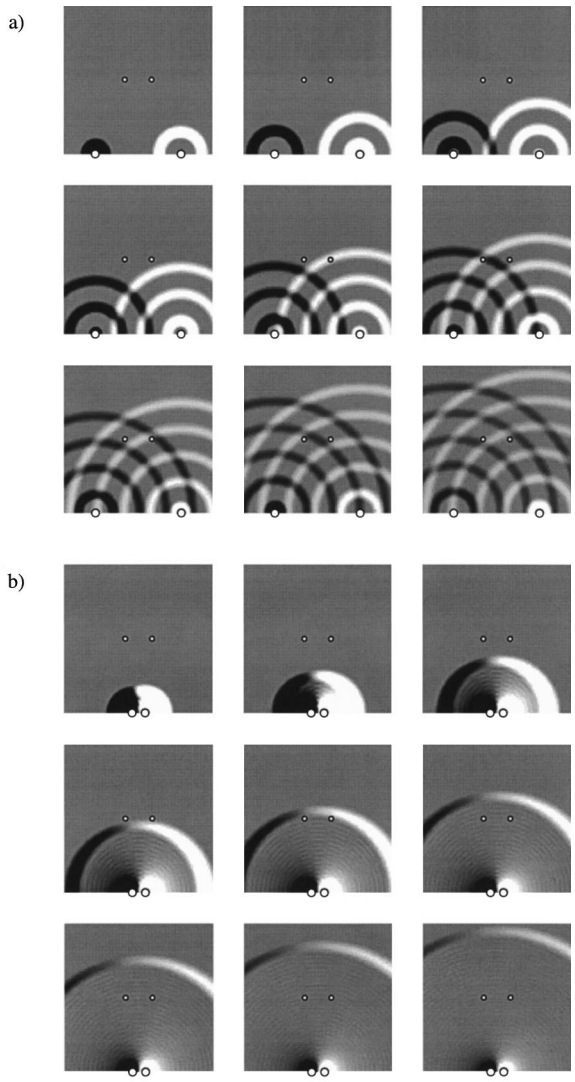

FIG. 6. The sound field reproduced by two monopole sources whose inputs are adjusted to achieve perfect cross-talk cancellation at the listener's left ear under free-field conditions. The two loudspeaker spans are (a) 60 degrees and (b) 10 degrees.

that reducing the loudspeaker span improves the system's robustness with respect to head movement.

B. Rigid sphere model

Figure 7 is equivalent to Fig. 5 but the source inputs are now calculated by using a rigid sphere model rather than a free-field model. For the purpose of visual presentation, the source inputs presented in Fig. 7, and also later in Fig. 11, have been calculated using a digital Hanning pulse given by the time sequence [0, 0.15, 0.5, 0.85, 1, 0.85, 0.5, 0.15, 0]. Since the duration of this sequence is twice as long as the sequence [0, 0.5, 1, 0.5, 0], the sampling frequency has also been increased by a factor of 2, from 12.8 to 25.6 kHz. Note that since these results are obtained by an inverse fast Fourier transform of sampled frequency data, there is no obvious way to calibrate the time axis, and so the time response has been manually shifted an integer number of sampling intervals in order to make Fig. 7 compatible with Fig. 5. It is seen that when the loudspeakers span 60 degrees [Fig. 7(a)], the

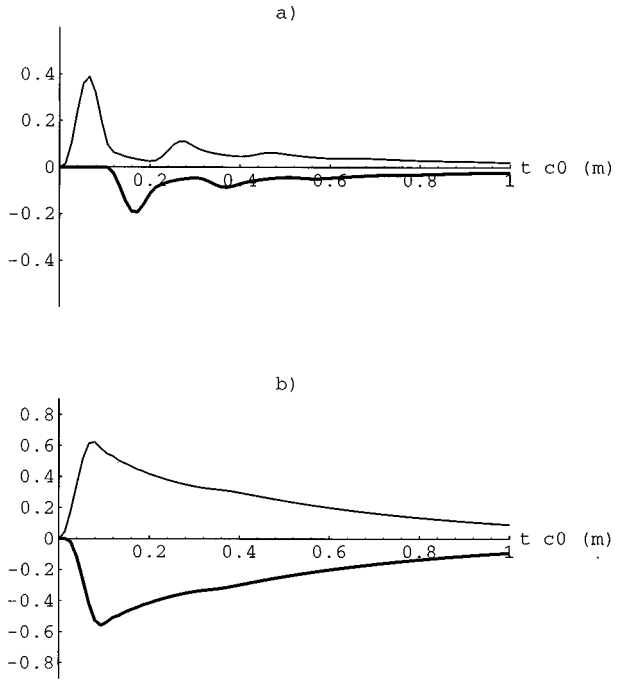

FIG. 7. As in Fig. 5 (cross-talk cancellation), but the listener's head is now modeled as a rigid sphere.

presence of the sphere causes the recursive source inputs to decay away much quicker with time than in the free-field case [Fig. 5(a)]. This is because the shadowing of the sphere reduces the amount of ''cross-talk'' that needs to be cancelled out. When the loudspeakers span only 10 degrees [Fig. 7(b)], the source inputs are very similar to the free-field case [Fig. 5(b)]. This is not surprising since in this case the two points on each side of the sphere are very close to being on the edge of the shadow zone, and so within the frequency range that we are considering the sphere does not modify the free-field transfer functions much.

Figure 8 is equivalent to Fig. 6 but the sound field is now calculated by using a rigid sphere model rather than a free-field model. As in Fig. 4, the sound field is plotted over an area of 0.6×0.6 m (note that this area is smaller than the 1×1 m^2 square used in the free-field case). The time is calibrated such that in frame four (first frame in second row) the center of the Hanning pulse is at the left ear. It is seen that the total sound field is qualitatively similar to the sound field generated by two monopoles in a free field. When the loudspeakers span 60 degrees [Fig. 8(a)], the zone of efficient cross-talk cancellation is still quite small even though the recursive nature of the source outputs is less pronounced than in the free-field case [Fig. 6(a)] whereas the 10 degrees loudspeaker span still produces a very ''clean'' sound field [Fig. 8(b)].

VI. VIRTUAL IMAGING SYSTEMS

It is, in principle, a trivial task to create a virtual source once it is known how to implement a cross-talk cancellation system. If the cross-talk cancellation problem can be solved for each ear separately, then any pair of desired signals can be reproduced by adding the two solutions together. In prac-

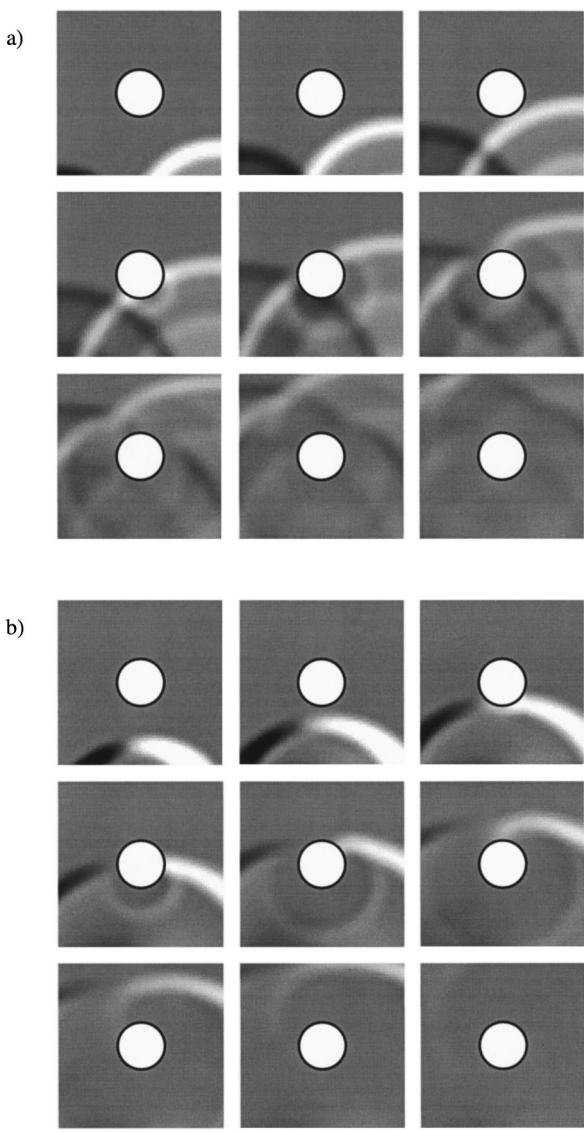

FIG. 8. As in Fig. 6 (cross-talk cancellation), but the listener's head is now modeled as a rigid sphere. Note that each frame represents a smaller area than each of the frames shown in Fig. 6.

tice it is far easier for the loudspeakers to create the signals due to a virtual source than to achieve perfect cross-talk cancellation at one point.

A. Free-field conditions

As in the cross-talk cancellation case, it is convenient to normalize the desired signals D_1 and D_2 in order to ensure causality of the source inputs. In addition, we want the loudest of the two desired signals to be equal to D_{pulse}, it must not be scaled no matter what the distance is from the virtual source to the center of the listener's head. The desired signals are therefore defined as

$$\mathbf{d}=e^{-jkr_1}\begin{bmatrix} A_1/A_2 \\ 1 \end{bmatrix}. \tag{17}$$

This definition assumes that the virtual source is to the left of the listener (at a coordinate for which $x_1>0$). The source inputs can be calculated by solving $\mathbf{Cv}=\mathbf{d}$ for $\mathbf{v}$, and the time domain responses can then be determined by taking the inverse Fourier transform. The result is that each source input is now the convolution of d_{pulse} with the sum of two decaying trains of delta functions, one positive and one negative.[20] The virtual source is positioned at (0.5 m, 0 m), which means that it is at an angle of 45 degrees to the left relative to straight front as seen by the listener.

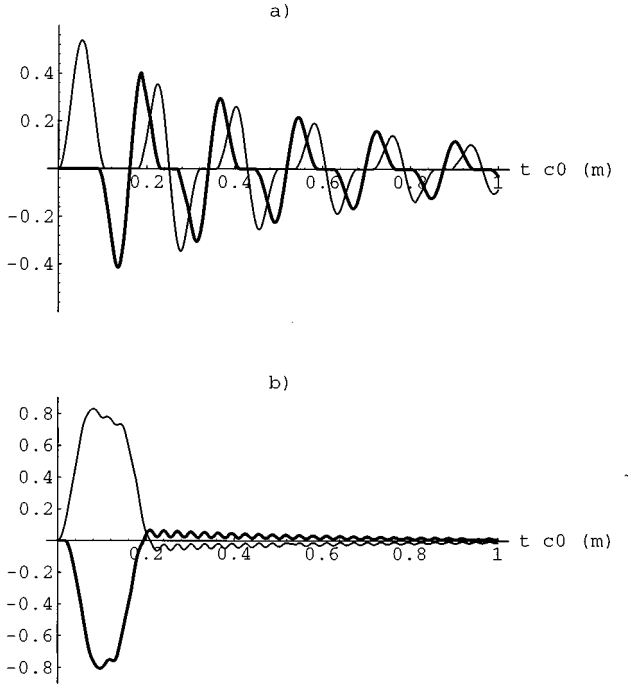

FIG. 9. The time response of the two source input signals $v_1(t)$ (thick line) and $v_2(t)$ (thin line) required to create a virtual source at the position (0.5 m, 0 m) under free-field conditions. The two loudspeaker spans are (a) 60 degrees and (b) 10 degrees. Note that the effective duration of both $v_1(t)$ and $v_2(t)$ decreases as the loudspeaker span is decreased.

Figure 9 shows the two source inputs $v_1(t)$ and $v_2(t)$ for the two loudspeaker spans (a) 60 degrees and (b) 10 degrees. When the loudspeakers span 60 degrees [Fig. 9(a)] both the positive and the negative pulse trains can be seen clearly in $v_1(t)$ and $v_2(t)$, just as in the cross-talk cancellation case [Fig. 5(a)]. However, as the loudspeaker span is reduced to 10 degrees [Fig. 9(b)], the positive and negative pulse trains start to cancel out. The two source inputs look roughly like square pulses of relatively short duration (this duration is given by the difference in arrival time at the microphones of a pulse emitted from the virtual source). The advantage of the cancelling of the positive and negative parts of the pulse trains is that it greatly reduces the low-frequency content of the source inputs, and this is why virtual source imaging systems in practice are much easier to implement than cross-talk cancellation systems.

Figure 10 shows another nine ''snapshots'' of the reproduced sound field. It is equivalent to Fig. 6, but for a virtual source at (0.5 m, 0 m) (indicated in the bottom right-hand corner of each frame) rather than for a cross-talk cancellation system. The plots show how the arrival times of the desired pulses are matched at the two ears, and they suggest, once again, that the reproduced sound field becomes simpler as the loudspeaker span is reduced from 60 degrees [Fig. 10(a)] to 10 degrees [Fig. 10(b)]. Note that the inputs to the two

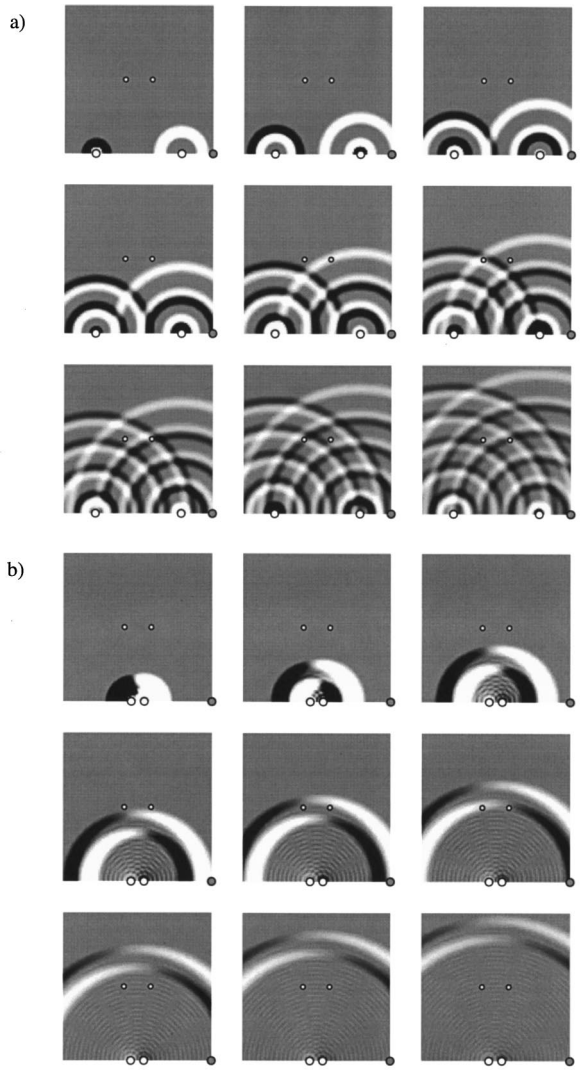

FIG. 10. The sound field reproduced by two sources whose outputs are adjusted to create a virtual source at (0.5 m, 0 m) under free-field conditions. The two loudspeaker spans are (a) 60 degrees and (b) 10 degrees.

loudspeakers contain roughly the same amount of energy. This means that the loudspeakers have to work almost equally hard even when the virtual source is quite close to the left loudspeaker, as is the case when the loudspeaker span is 60 degrees.

B. Rigid sphere model

Figure 11 is equivalent to Fig. 9, but the source inputs are now calculated by using a rigid sphere model rather than a free-field model. The source inputs will produce the same sound pressures at the listener's ears as would have been produced there by the virtual source [this means that the ''output'' from the virtual source is a delayed Hanning pulse in the free-field case, but $d_1(t)$ and $d_2(t)$ are no longer simple Hanning pulses]. It is seen, as in the cross-talk cancellation case, that the presence of the sphere makes the recursive nature of the source inputs less pronounced when the loudspeakers span 60 degrees [Fig. 11(a)], whereas it has little effect on the source inputs when the loudspeakers span only 10 degrees [Fig. 11(b)].

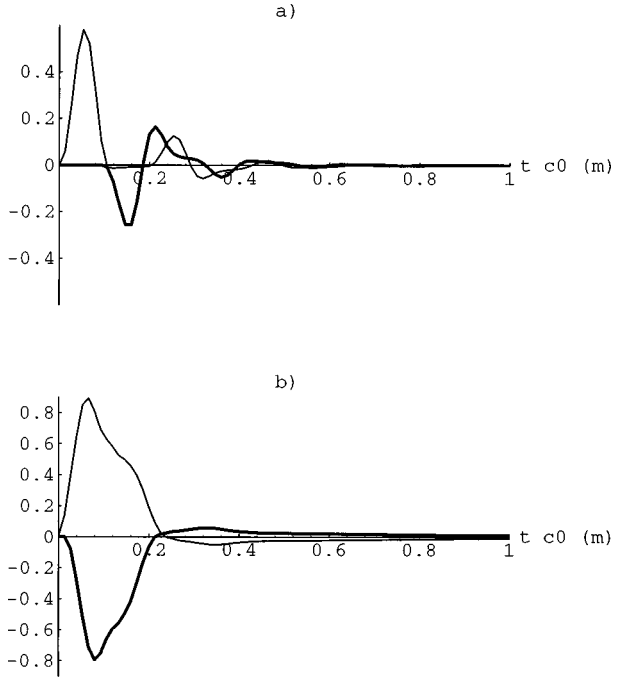

FIG. 11. As in Fig. 9 (virtual source imaging), but the listener's head is now modeled as a rigid sphere.

Figure 12 is equivalent to Fig. 8, but for a rigid sphere model rather than a free-field model. The first pulse from the virtual source is reproduced at the left ear at frame four, and a second pulse, which is significantly weaker than the first because of the shadowing of the sphere, is reproduced at the right ear at frame six. When the loudspeakers span 60 degrees [Fig. 12(a)], the reproduced sound field looks quite complicated. Since the amplitude of the desired pulse at the right ear is quite low, the total sound field is not too different from the sound field reproduced by the corresponding cross-talk cancellation system [Fig. 8(a)]. When the loudspeakers span 10 degrees [Fig. 12(b)], the properties of the reproduced sound field are qualitatively the same as in the free-field case [Fig. 10(b)], as expected.

VII. SUMMARY

When only two loudspeakers placed symmetrically in front of a single listener are used to control the sound field around the head of the listener, the area over which the sound field can be controlled is larger when the two loudspeakers are close together than when they are far apart. However, the smaller the loudspeaker span is as seen by the listener, the harder it is to achieve efficient cross-talk cancellation at low frequencies, and, in addition, the more low-frequency energy is required to create a virtual image at a position well outside the two loudspeakers. In practice, a loudspeaker span of 10 degrees is a good compromise.

The total sound field produced by a spherical wave impinging on a rigid sphere can be expressed as an infinite series. The scattered field, as opposed to the incident field, can be evaluated quite efficiently numerically from its series expansion. A time domain simulation shows that when the incident wave hits the front of the sphere, it causes a ''reflected'' wave to radiate away from this point, and that a

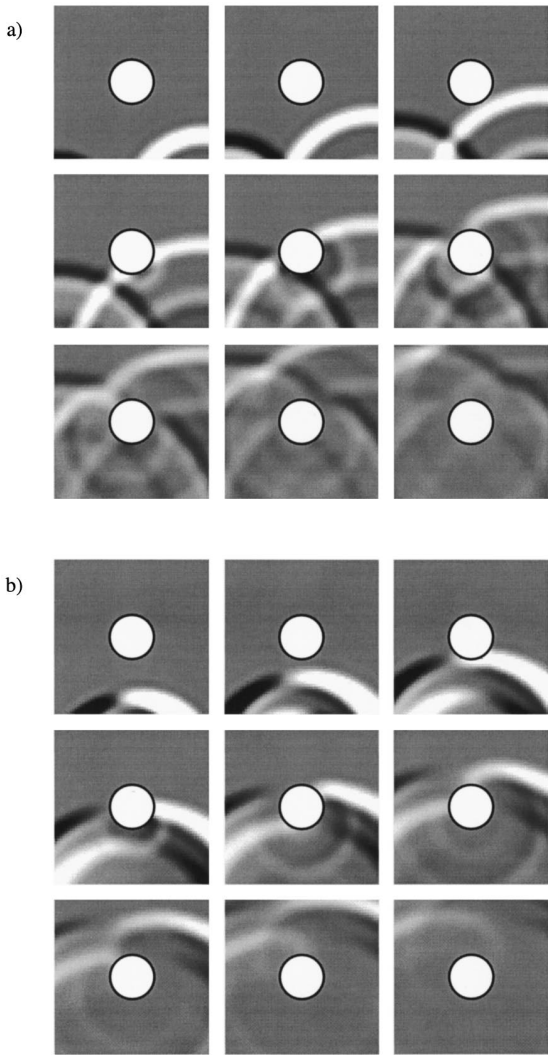

FIG. 12. As in Fig. 10 (virtual source imaging), but the listener's head is now modeled as a rigid sphere. Note that each frame represents a smaller area than each of the frames shown in Fig. 10.

short while later a similar, but weaker, wave starts to radiate away from the ''bright spot'' directly at the back of the sphere.

The properties of the sound field reproduced by a loudspeaker arrangement spanning 10 degrees as seen by the listener do not change markedly when a rigid sphere model is used instead of the simple free-field model. When the loudspeakers span 60 degrees, however, the shadowing of the sphere causes the series of impulses emitted from each of the two sources to decay away more rapidly than in the free-field case. Nevertheless, the ''zone of cross-talk cancellation'' still remains much smaller than when the loudspeakers span only 10 degrees.

[1] F. L. Wightman and D. J. Kistler, ''Headphone simulation of free-field listening Parts I and II,'' J. Acoust. Soc. Am. **85**, 858–867, 868–878 (1989).
[2] H. Møller, ''Fundamentals of binaural technology,'' Appl. Acoust. **36**, 171–218 (1992).
[3] D. R. Begault, *3-D Sound for Virtual Reality and Multimedia* (AP Professional, Cambridge, MA, 1994).
[4] J. Blauert, *Spatial Hearing, The Physchophysics of Human Sound Localization* (MIT, Cambridge, MA, 1997).
[5] A. J. Berkhout, D. de Vries, and P. Vogel, ''Acoustic control by wave field synthesis,'' J. Acoust. Soc. Am. **93**, 2764–2778 (1993).
[6] M. Kleiner, ''Problems in the design and use of 'dummy-heads,''' Acustica **41**, 183–193 (1978).
[7] H. Møller, C. B. Jensen, D. Hammershøi, and M. F. Sørensen, ''Evaluation of artificial heads in listening tests,'' presented at the 102nd Audio Engineering Society Convention, 22–25 March 1997, Munich, Germany. AES preprint 4404 (A1).
[8] P. Damaske, ''Head-related two-channel stereophony with loudspeaker reproduction,'' J. Acoust. Soc. Am. **50**, 1109–1115 (1971).
[9] D. Griesinger, ''Equalization and spatial equalization of dummy-head recordings for loudspeaker reproduction,'' J. Audio Eng. Soc. **37**(1/2), 20–29 (1989).
[10] D. H. Cooper and J. L. Bauck, ''Prospects for transaural recording,'' J. Audio Eng. Soc. **37**, 3–19 (1989).
[11] J. L. Bauck and D. H. Cooper, ''Generalized transaural stereo and applications,'' J. Audio Eng. Soc. **44**(9), 683–705 (1996).
[12] O. Kirkeby, P. A. Nelson, H. Hamada, and F. Orduna-Bustamante, ''Fast deconvolution of multi-channel systems using regularisation,'' IEEE Trans. Speech Audio Process. **6**(2), 189–194 (1998).
[13] B. S. Atal, M. Hill, and M. R. Schroeder, ''Apparent Sound Source Translator,'' United States Patent Office, No. 3,236,949 (22 February 1966).
[14] P. A. Nelson, H. Hamada, and S. J. Elliott, ''Adaptive inverse filters for stereophonic sound reproduction,'' IEEE Trans. Signal Process. **40**(7), 1621–1632 (1992).
[15] P. A. Nelson, F. Orduna-Bustamante, and H. Hamada, ''Inverse filter design and equalisation zones in multi-channel sound reproduction,'' IEEE Trans. Speech Audio Process. **3**(3), 185–192 (1995).
[16] P. A. Nelson and F. Orduna-Bustamante, ''Multi-channel signal processing techniques in the reproduction of sound,'' J. Audio Eng. Soc. **44**, 973–989 (1996).
[17] O. Kirkeby, P. A. Nelson, F. Orduna-Bustamante, and H. Hamada, ''Local sound field reproduction using digital signal processing,'' J. Acoust. Soc. Am. **100**, 1584–1593 (1996).
[18] F. Heegaard, ''The reproduction of sound in auditory perspective and a compatible system of stereophony,'' EBU Rev., Pt. A-Technical, No. 50, pp. 2–6 (1958 Dec.); reprinted in J. Audio Eng. Soc. **40**, 802–808 (1992).
[19] T. Takeuchi, P. A. Nelson, O. Kirkeby, and H. Hamada, ''Robustness of the performance of the 'Stereo Dipole' to misalignment of head position,'' presented at the 102nd Audio Engineering Society Convention, 22–25 March 1997, Munich, Germany, AES preprint 4464 (17).
[20] O. Kirkeby, P. A. Nelson, and H. Hamada, ''The ''stereo dipole''—binaural sound reproduction using two closely spaced loudspeakers,'' presented at the 102nd Audio Engineering Society Convention, 22–25 March 1997, Munich, Germany. AES preprint 4463 (I6). Also published in J. Audio Eng. Soc. **46** (5), 387–395 (1998).
[21] O. Kirkeby, P. A. Nelson, and H. Hamada, ''Stereo dipole,'' Patent Application, PCT/GB97/00415, 1997.
[22] O. Kirkeby and P. A. Nelson, ''Virtual source imaging using the 'stereo dipole''' presented at the 103rd Audio Engineering Society Convention, 26–29 September 1997, New York. AES preprint 4574 (J10).
[23] P. A. Nelson, O. Kirkeby, T. Takeuchi, and H. Hamada, ''Sound fields for the production of virtual acoustic images,'' J. Sound. Vib. **204**(2), 386–396 (1997).
[24] P. M. Morse and K. Uno Ingard, *Theoretical Acoustics* (McGraw–Hill, New York, 1968).
[25] J. W. S. Rayleigh, *The Theory of Sound* (Dover, New York, 1945), 2nd rev. ed., Vol. 2.
[26] I. Malechi, *Physical Foundations of Technical Acoustics* (Pergammon, New York, 1969).
[27] M. Abramowitz and I. A. Stegun, *Handbook of Mathematical Functions* (Dover, New York, 1965).
[28] D. G. Crighton, A. P. Dowling, J. E. Ffowcs Williams, M. Heckl, and F. G. Leppington, *Modern Methods in Analytical Acoustics* (Springer-Verlag, New York, 1992).
[29] A. V. Oppenheim and R. W. Schafer, *Digital Signal Processing* (Prentice–Hall, Englewood Cliffs, NJ, 1975).
[30] G. F. Kuhn, ''Physical acoustics and measurements pertaining to directional hearing,'' in *Directional Hearing*, edited by W. A. Yost and G. Gourevitch (Springer-Verlag, New York, 1987).
[31] B. Widrow and S. D. Stearns, *Adaptive Signal Processing* (Prentice–Hall, Englewood Cliffs, NJ, 1985).
[32] W. H. Press, S. A. Teukolsky, W. T. Vetterling, and B. P. Flannery, *Numerical Recipes in C*, 2nd ed. (Cambridge U.P., Cambridge, 1992).

Transducer misalignment effects in beam reflection from elastic structures

Han Zhang and D. E. Chimenti[a)]
Department of Aerospace Engineering and Engineering Mechanics and Center for NDE, Iowa State University, Ames, Iowa 50011

Smaine Zeroug
Schlumberger-Doll Research, Ridgefield, Connecticut 06877

(Received 5 November 1997; accepted for publication 17 June 1998)

In two-transducer, fluid-coupled ultrasonic reflection measurements phase matched to guided modes of elastic solid structures, the effects of misalignment (i.e., differences) between the receiver angle and the incident beam angle on the receiver voltage have been studied. The received voltage is typically due to contributions from the specular reflection and any of the several possible guided wave modes excited by the incident wave field. It is found that misalignment leads to changes in the relative amplitudes of the various contributions. Further, the more highly collimated the beam (or the contributor), the more pronounced are the effects. It is shown that the signal maximum is not a reliable indicator of receiver alignment. These conclusions are based on measurements and on calculations that have been performed at incident angles selected both close to, or far from, phase-matching angles to guided wave modes on plates, curved surfaces, and cylindrical shells. Receiver voltage coordinate scans have been performed with receiver angles misaligned from the incident beam axis by 1 to 4 degrees. The receiver voltage versus scan parameter in planar and curved structures is calculated by employing complex transducer points to synthesize two-dimensional, sheet-beam transducer fields with Gaussian apertures, spectral analysis to formulate the beam-structure interaction problem, and asymptotic methods to evaluate the resulting spectral integrals. The model predictions are generally in good agreement with the experiments. [S0001-4966(98)06709-5]

PACS numbers: 43.20.Fn, 43.35.Zc [ANN]

INTRODUCTION

Ultrasonic pitch–catch measurements performed with a pair of acoustic transducers, especially when critical angle phenomena play a role, represent a common characterization method in nondestructive evaluation.[1–9] One application of this technology is to near-field leaky wave (LW) measurements where material properties of immersed layered elastic structures can be determined. In LW measurements the acoustic transducer beams are aligned at phase-matching angles to excite efficiently one or more of the structure's propagating wave modes. The amplitude and phase of the scattered acoustic wave, detected and converted to a voltage by the receiving transducer, depend not only on the properties of the structure but also on those of the transducers. The aperture sizes and alignment angles are particularly significant parameters. Alignment issues are especially important for wide transducers that radiate or receive over a narrow angular range.

While transducer alignment in a pitch–catch geometry has been recognized as a potential problem among workers in ultrasonic materials characterization, difficulties remain in the quantitative assessment of its effect on measurements. The reason for these difficulties lies in the challenge of making high-resolution voltage measurements with the required transducer alignment precision in the incident and reflected angles. Yet, the importance of the misalignment effect is clear. In an experimental arrangement where the receiver voltage is a function both of extrinsic experimental parameters, such as the transducer aperture, beam shape, position, and alignment angle, and of intrinsic parameters such as the elastic properties of the structure, systematic errors in the extrinsic parameters could be misinterpreted as being the result of differing intrinsic parameters.

In near-field LW measurements, the option of relying on some attribute of the scattered signal (e.g., amplitude maximum of the specularly reflected component) to deduce the alignment accuracy is neither an unequivocal, nor independent measure of the effect. This is so because several acoustic components may impinge on the receiving transducer aperture at once, each with a ray bundle having a different average angle and with a different phase. To help assess quantitatively the effect of these questions, we have used a computationally efficient computer code built on an analytical model. The model is versatile enough to handle transducers with arbitrary apertures and alignments, as well as beam interactions with planar and cylindrical fluid-immersed elastic structures.

In our own previous research we have employed two transducers in a pitch–catch geometry to study nonspecular reflection of diverging acoustic beams from a planar interface and of collimated beams from a curved interface.[8,9] We measure the receiver voltage as a function of scan distance or

[a)]Author to whom correspondence should be addressed. Electronic mail: chimenti@iastate.edu

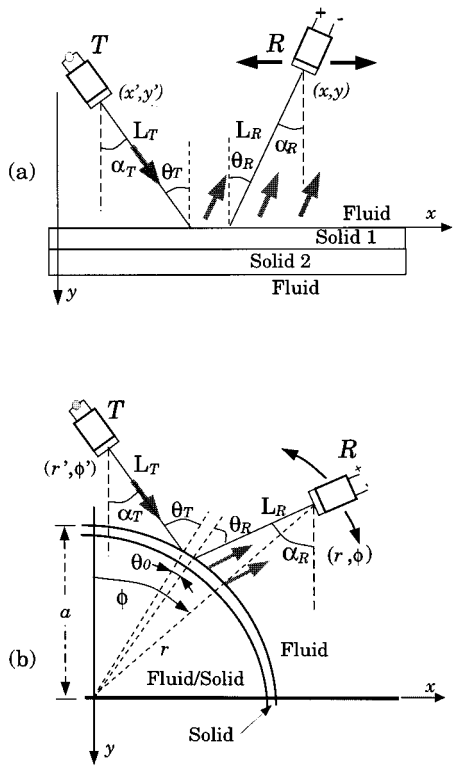

FIG. 1. Geometries for plane (a) and cylindrically (b) layered fluid-immersed elastic configurations excited by acoustic transducers. $\mathscr{T}$: transmitter, $\mathscr{R}$: receiver. Note that only a quadrant of the cylindrical structure is shown.

scan angle, and we have found that the experimental results are generally well predicted by an asymptotic complex-ray model.[10–12] In this article we investigate the influence of transducer misalignment in reflected acoustic beam measurements, where the transducer acoustic beams are incident at, or near, phase-matching angles to couple to one or to several of the structure's guided wave modes (Rayleigh or Lamb). In this circumstance the alignment of the transducers proves to be quite important. It is our purpose in this study to discover what effects small transducer misalignment will have on the receiver signal. We analyze the misalignment effects on the scattered beam both at and near the critical incidence for phase-matched coupling to structure-borne guided waves on plates, solid cylinders, and cylindrical shells.

In the next section we present a brief summary of the asymptotic complex-ray model, followed by the results of detailed experiments analyzed with the help of the model calculation.

I. THEORETICAL SUMMARY

The two-dimensional (2-D) configurations assumed and depicted in Fig. 1 consist of isotropic and homogeneous fluid-elastic layers excited by ultrasonic acoustic 2-D (sheet) transducers in a pitch–catch mode. A 2-D coordinate frame (x,y) is used with the layers and transducer fields extending uniformly out of the plane of the paper. The transmitting and receiving transducers, denoted by $\mathscr{T}$ and $\mathscr{R}$, respectively, are considered to be passive, linear, and electro-acoustically reciprocal. $\mathscr{T}$ is aligned at angle $\alpha_{\mathscr{T}}$ with respect to the y axis and insonifies the uppermost (outermost) fluid–solid interface at angle $\theta_{\mathscr{T}}$ with respect to the interface local normal. $\theta_{\mathscr{T}}$ is selected so as to excite one or more of the leaky waves that can be supported by the elastic structure. Similarly, $\mathscr{R}$ is aligned at angle $\alpha_{\mathscr{R}}$ and its beam axis defines the angle $\theta_{\mathscr{R}}$ with respect to the local normal of the interface. In a scan of the scattered pressure field, the receiver is displaced parallel to the interface maintaining a fixed angle $\theta_{\mathscr{R}}$.

TABLE I. Physical properties of experimental samples.

Format	Radius/thickness (mm)	v_l (km/s)	v_t (km/s)	ρ (kg m^{-3})
Plate	3.04	5.64	3.07	7900
Cylinder	76.2	5.66	3.12	7900
Shell	57.3/2.28	5.66	3.12	7900

The numerical code developed to simulate this measurement is based on an extension of a theoretical model that has been presented elsewhere.[8–15] The solution relies on spectral integral representations of the receiving transducer voltage and the acoustic beam-structure interaction. Within these two-dimensional representations, expressed in terms of plane waves for the planar geometry and angularly traveling waves for the cylindrical geometry, transducer beams are specified in terms of Gaussian beams generated through the complex-transducer-point (CTP) technique.[14] Asymptotic treatment of the spectral integrals involved leads to closed-form solutions for the dominant contributions to the scattered signal, namely, the specularly reflected (SR) field and the leaky waves excited. In the following, we restrict the presentation to the CTP procedure that is pertinent to our study. Detailed development of the approach is given in Refs. 8–15.

When piston transducers are employed experimentally in matched pairs, as they are here, their combined effect on the receiver signal voltage is nearly identical to the effect of a pair of transducers producing Gaussian beams. Demonstration of this correspondence and discussion of the reasons for its validity have recently been presented by Lobkis *et al.*[16] The point made in that article is that the averaging effect, in particular with respect to signal phase, of the receiving transducer works to suppress rapid variations present in the field of the transmitter. The result of that averaging is a voltage signal (versus angle or lateral coordinate) that is nearly indistinguishable from the voltage observed using a pair of reciprocal transducers that generate Gaussian fields, instead of piston fields. That is, the voltage signal received by an identical transducer tends to smooth angular variations present in the field of either device, leaving a Gaussian-like directivity function for the combined operations of generation and detection, despite the field profiles of the actual transducers. A collection of coaxial Gaussian beams can be employed for each transducer to achieve an accurate representation of the field of a piston radiator and also to obtain a highly accurate (better than 1%) modeling of the two-transducer voltage.[14]

In the CTP technique, each transducer ($\mathscr{T}$ or $\mathscr{R}$) aperture and alignment angle is specified through a set of complex coordinates that are conveniently given in terms of Car-

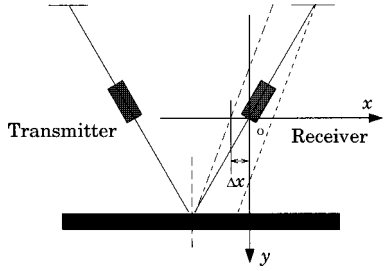

FIG. 2. Schematic illustrating the shift of maximum receiver voltage owing to its misalignment. Solid line denotes the aligned beam axis, the dashed lines denote the misaligned beam axis, and Δx is the shift distance of the maximum voltage when the receiver is misaligned.

tesian forms $(x_{\mathscr{T}},y_{\mathscr{T}})$ or $(x_{\mathscr{R}},y_{\mathscr{R}})$. These forms can be used directly in the planar geometry. For the cylindrical geometry, the coordinates must be adapted through the usual transformation from Cartesian to polar coordinates $(r_{\mathscr{T}},\phi_{\mathscr{T}})$ and $(r_{\mathscr{R}},\phi_{\mathscr{R}})$,[14]

$$r_{\mathscr{T},\mathscr{R}}=\sqrt{x^2_{\mathscr{T},\mathscr{R}}+y^2_{\mathscr{T},\mathscr{R}}},\quad \mathrm{Re}\{r_{\mathscr{T}},r_{\mathscr{R}}\}\geqslant 0,$$
$$\phi_{\mathscr{T},\mathscr{R}}=\tan^{-1}\{x_{\mathscr{T},\mathscr{R}}/y_{\mathscr{T},\mathscr{R}}\}, \tag{1}$$

where

$$x_{\mathscr{T}}=x'+ib_{\mathscr{T}}\sin\alpha_{\mathscr{T}},$$
$$x_{\mathscr{R}}=x-ib_{\mathscr{R}}\sin\alpha_{\mathscr{R}},\quad b_{\mathscr{T},\mathscr{R}}\geqslant 0,$$
$$y_{\mathscr{T}}=y'+ib_{\mathscr{T}}\cos\alpha_{\mathscr{T}}, \tag{2}$$
$$y_{\mathscr{R}}=y+ib_{\mathscr{R}}\cos\alpha_{\mathscr{R}},\quad \alpha_{\mathscr{T},\mathscr{R}}\geqslant 0.$$

The real positive parameters $b_{\mathscr{T}}$ and $b_{\mathscr{R}}$ specify the CTP beam Fresnel lengths, respectively. These lengths are related to the $1/e$ widths $W_{\mathscr{T}}$ and $W_{\mathscr{R}}$ of the distribution profiles of $\mathscr{T}$ and $\mathscr{R}$ through $W_{\mathscr{T}}=\sqrt{2b_{\mathscr{T}}/k_f}$ and $W_{\mathscr{R}}=\sqrt{2b_{\mathscr{R}}/k_f}$, respectively ($k_f=\omega/v_f$, v_f is the sound speed in the fluid). The beam waists of $\mathscr{T}$ and $\mathscr{R}$ are centered at (x',y') and (x,y), respectively. The CTP beams attain maximum amplitude along lines at angles $\alpha_{\mathscr{T}}$ and $\alpha_{\mathscr{R}}$, which are therefore defined as their alignment angles.

As mentioned previously, for an angle (ϕ) scan along a circular arc of radius r [as shown in Fig. 1(b)], the Cartesian coordinates of the receiving aperture center (x,y) are varied such that $x=r\sin\phi$ and $y=r\cos(\pi-\phi)$. The receiver angle $\alpha_{\mathscr{R}}$ is also updated, keeping the receiver incidence angle $\theta_{\mathscr{R}}$ on the cylindrical surface constant, where $\alpha_{\mathscr{R}}=\arcsin[a/r\sin\theta_{\mathscr{R}}]-\phi$, and a is the radius of the outermost interface. In the actual experiment and in Sec. III, the observation angle is measured more conveniently as the angular spread θ_0 between the intersection points of the transducer beam axes with the shell surface [see Fig. 1(b)]. We note that θ_0 is linearly proportional to ϕ.[13]

II. EXPERIMENTAL PROCEDURE

Stainless steel plates, solid cylinders, and cylindrical shells of various dimensions have been measured to test the limitations of the theoretical model. The geometrical and acoustical properties of the samples are listed in Table I. The surfaces of the specimens are carefully machined, but not

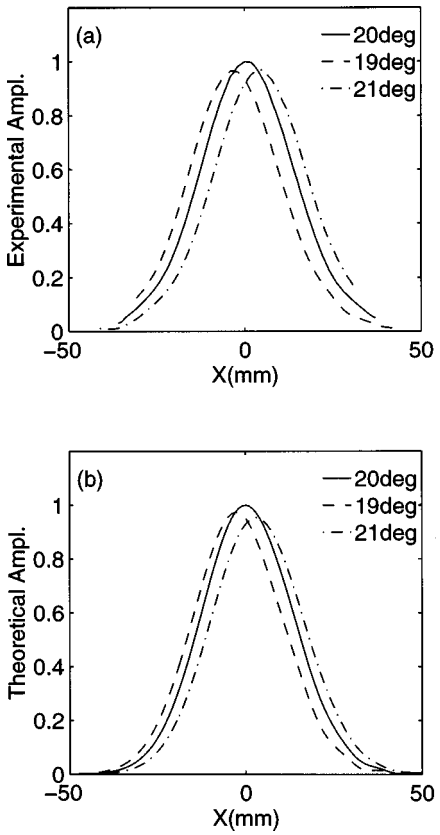

FIG. 3. Transducer voltage with pitch-catch geometry for sound beam interaction with a plate in water. Experimental data are in frame (a) and theoretical receiver voltage in (b) as a function of scan distance when $\mathscr{R}$ is aligned: $\theta_{\mathscr{R}}=\theta_{\mathscr{T}}=20°$, and when it is misaligned: $\theta_{\mathscr{R}}=19°$ and $\theta_{\mathscr{R}}=21°$. Note the position $x=0$ corresponds to the intersection of the scan line with the axis of the specularly reflected beam.

ground, and their flatness and parallelism are checked to assure these aspects do not contribute to significant systematic errors. All measurements are conducted using ULTRAN W575-1 19-mm-diam, 1-MHz, flat piston transducers.

Two scanning systems have been used in the experiments. A Parker–Daedel system with precision linear control is used for the experiments of planar structures. The scanning axes have a resolution of 0.01 mm and a position repeatability of of 0.03 mm. The transducer and receiver are mounted on precision rotary stages with a usable angular resolution of 0.01°. The mechanical system and the data acquisition electronics are described in detail elsewhere.[17] The transducer is excited with radio frequency (rf) tone bursts of 1-MHz center frequency. The entire received signal is amplified by a high-gain broadband receiver and averaged using a Lecroy 9340 digitizing oscilloscope.

The scanning system used for the cylindrical structures is a multi-axis positioning system manufactured by the Panametrics Company. The system provides five degrees of freedom for each transducer: translation along the x, y, and z axes, as well as rotation in the horizontal and vertical planes. Figure 1(b) shows a schematic of the experimental geometry. The transmitter and receiver are directed at the cylindrical sample at angles of $\theta_{\mathscr{T}}$ and $\theta_{\mathscr{R}}$ with respect to the surface normal. During an angular scan, the transmitter remains fixed while the receiver is scanned through an arc centered

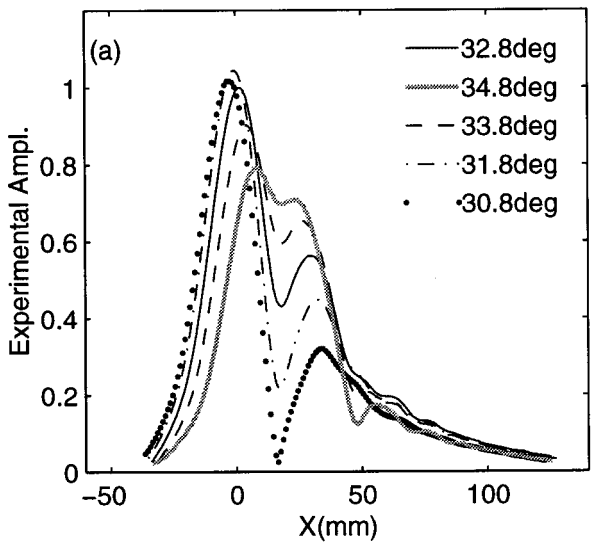

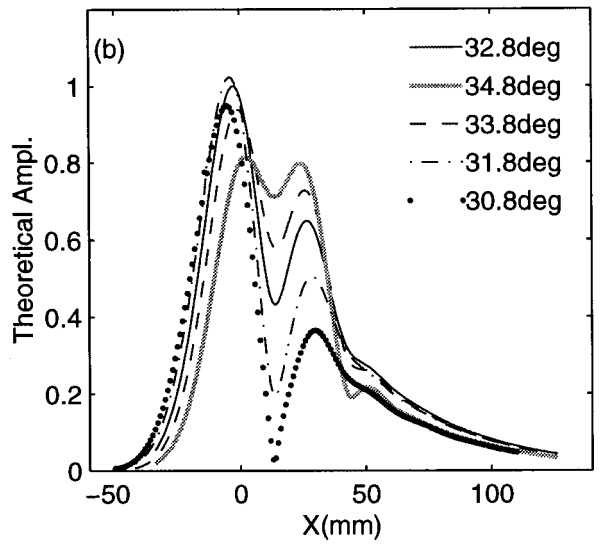

FIG. 4. Transducer voltage for a plate in water. Experimental data are in frame (a) and theoretical receiver voltage in (b) as a function of scan distance when $\mathscr{R}$ is aligned: $\theta_{\mathscr{R}}=\theta_{\mathscr{T}}=32.8°$, and when it is misaligned: $32.8°\pm1°$, and $32.8°\pm2°$. For all plots, $\theta_{\mathscr{T}}=32.8°$.

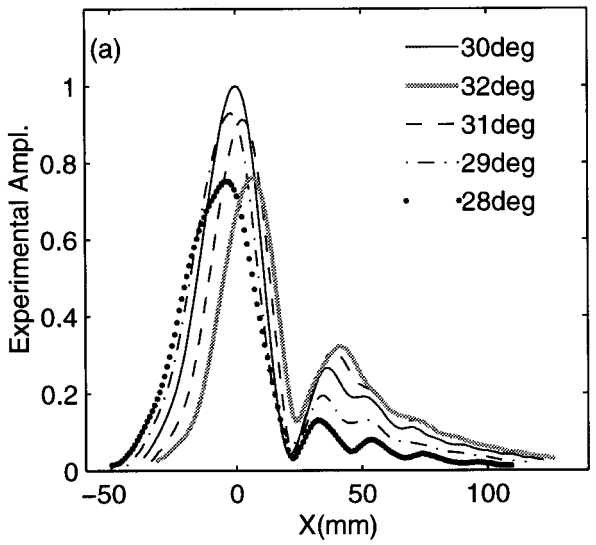

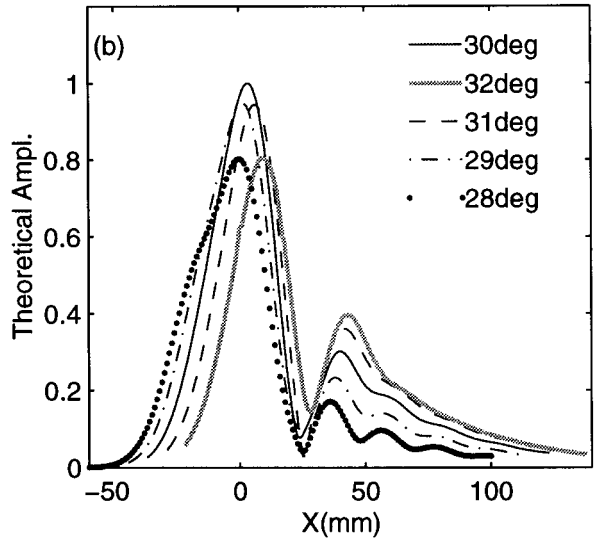

FIG. 5. Transducer voltage for sound beam interaction with a plate in water. Experimental data are in (a) and theoretical receiver voltage in (b) as a function of scan distance when $\mathscr{R}$ is aligned: $\theta_{\mathscr{R}}=\theta_{\mathscr{T}}=30°$, and when it is misaligned: $30°\pm1°$, and $30°\pm2°$. For all plots, $\theta_{\mathscr{T}}=30°$.

on the cylinder axis, maintaining the same incident angle. Both transducers remain at a constant distance from the interface throughout the scan. The observation angle (θ_0) is the angle on the cylinder surface between the intersection points of the central rays of the two transducers with the surface [see Fig. 1(b)]. The receiver beam axis denotes the axis of maximum far-field sensitivity or the center of the beam directivity function were the transducer to operate as a transmitter.

The entire waveform is digitized at 8 bits at each measurement point with a sampling rate of 20 MHz. We extract the 1-MHz component (the transducer center frequency) via a fast Fourier transform (FFT), and plot it as a function of observation angle θ_0. In the plots, the zero position is defined as the intersection of the two transducer central rays at the surface of the solid. Each plot contains the magnitude of the voltage for several receiver angular alignments. More complete descriptions of the apparatus and method can be found in Refs. 8, 16, and 18.

III. RESULTS AND DISCUSSION

Since the misalignment effects in planar and curved geometries display rather different characteristics, we discuss the results in these two cases separately. First, we address the planar structures, followed by the cylindrical ones.

A. Planar structures

For the 19-mm-diam transducer and at the 1-MHz transducer center frequency, four guided wave modes can be excited with varying efficiency in the 3.04-mm-thick steel plate used in this experiment, depending on the incident angle. These are the fundamental antisymmetric and symmetric modes, denoted A_0 and S_0, and the first two higher-order

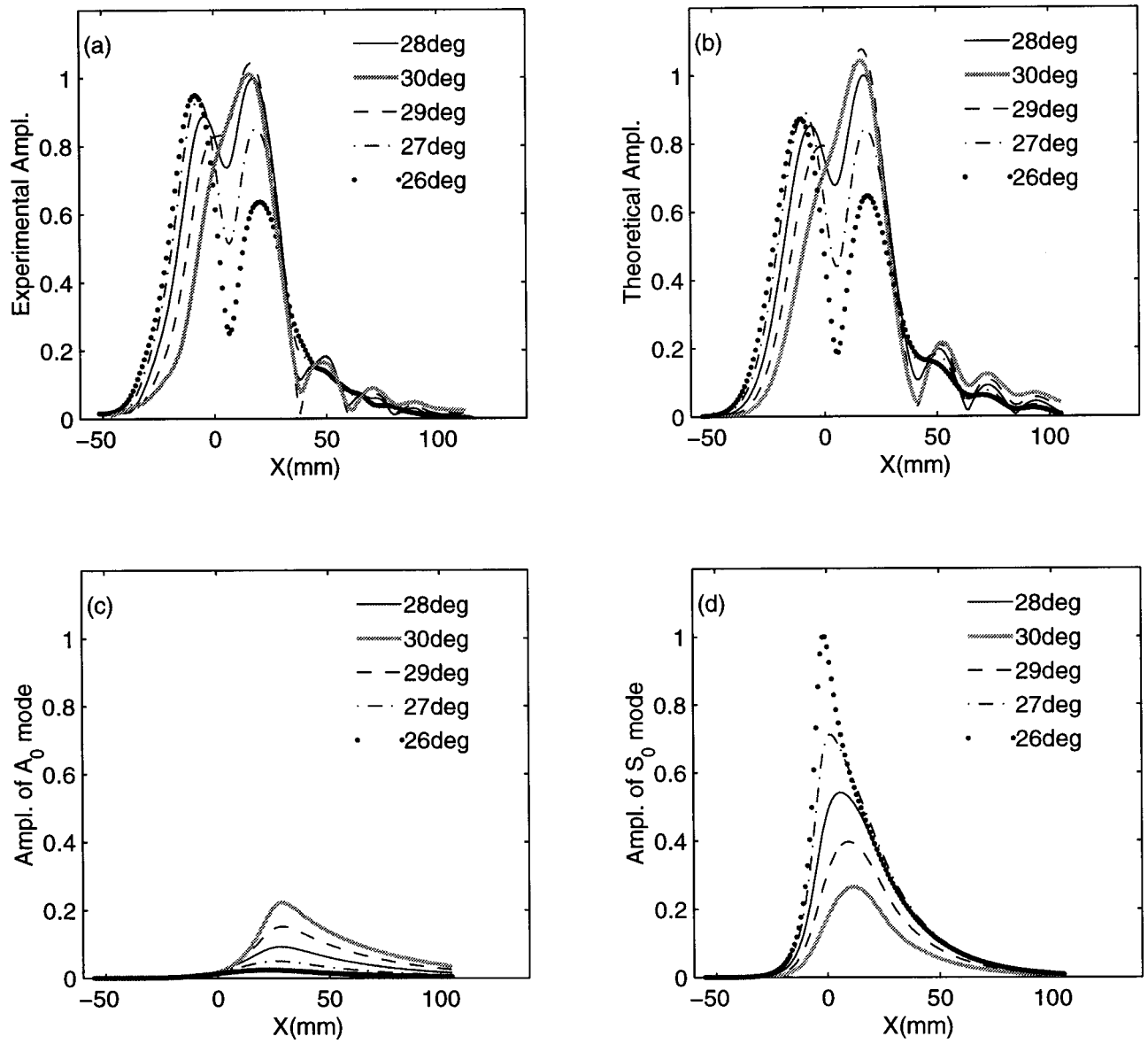

FIG. 6. Transducer voltage for sound beam interaction with a plate in water. Experimental data are in (a) and theoretical receiver voltage in (b) as a function of scan distance when $\mathscr{R}$ is aligned: $\theta_{\mathscr{R}}=\theta_{\mathscr{T}}=28°$, and when it is misaligned: $28°\pm1°$, and $28°\pm2°$. For all plots, $\theta_{\mathscr{T}}=28°$. The corresponding calculated profiles of the leaky A_0 mode (c) and S_0 mode (d) are shown for reference.

Lamb wave modes, denoted A_1 and S_1. These guided wave modes correspond to phase-match angles of 32.8°, 27.9°, 14.98°, and 14.15°, respectively.

Our experimental incident angle is chosen to be either at, or distant from, one of these Lamb mode angles, while the receiver angle is intentionally misaligned from the incident angle in a range from $-2°$ to 2°, usually at 1° increments. In a manner similar to the cylindrical geometry, the scan coordinate origin in the following plots is defined as the intersection of the transducer central rays at the sample surface. The receiver voltages at different receiver angles are recorded in a single plot in order to enhance direct comparison of the misalignment effects. When the receiver angle is misaligned from the incident angle, the amplitude of the received voltage decreases, since the position of the maximum shifts away from the transducer axis ($x=0$ mm). This situation is illustrated in Fig. 2. When the receiver angle decreases a small amount, the receiver voltage maximum will lie along the left-hand dashed line, with the receiver pointing at the center of the incident beam reflection. The voltage maximum occurs at the position for which the receiver aperture is in closest alignment with the scattered pressure wavefront.

We report first an experiment at an incident angle of $\theta_T=20°$. Since 20° is far from the phase-match angle for both the S_0 and A_1 modes, we can use this choice to isolate the effects of misalignment on the specular reflection. The experimental results and theoretical calculations at different receiver angles ($\theta_R=20°$, 19°, and 21°) are shown in Fig. 3(a) and (b). The voltage is dominated by the specularly reflected acoustic pressure, which has a nearly Gaussian profile.[16] The voltage maximum amplitude is smaller for the misalignment case because less acoustic energy impinges on the receiver aperture at the position where a maximum occurs. These results are similar to the theoretical pitch–catch

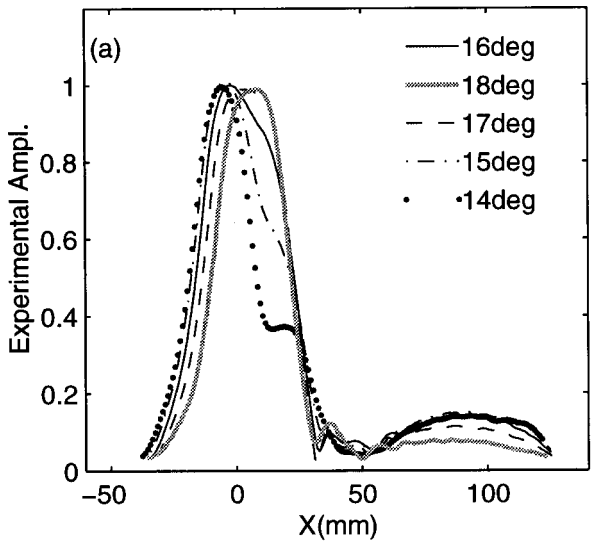

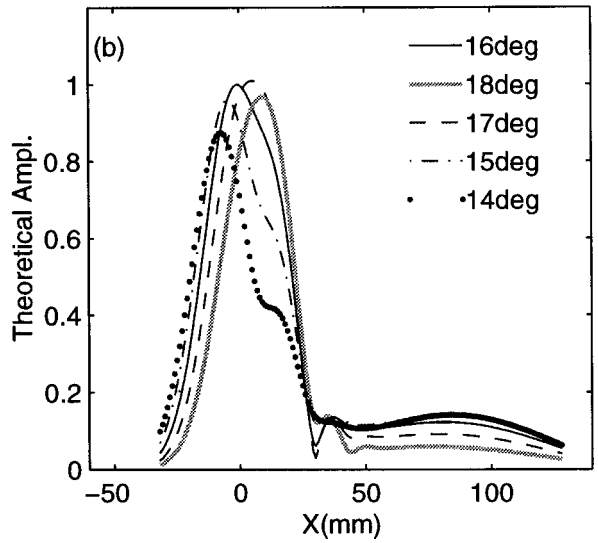

FIG. 7. Transducer voltage for sound beam interaction with a plate in water. Experimental data are in (a) and theoretical receiver voltage in (b) as a function of scan distance when $\mathscr{R}$ is aligned: $\theta_{\mathscr{R}}=\theta_{\mathscr{T}}=16°$, and when it is misaligned: $16°\pm1°$, and $16°\pm2°$. For all plots, $\theta_{\mathscr{T}}=16°$.

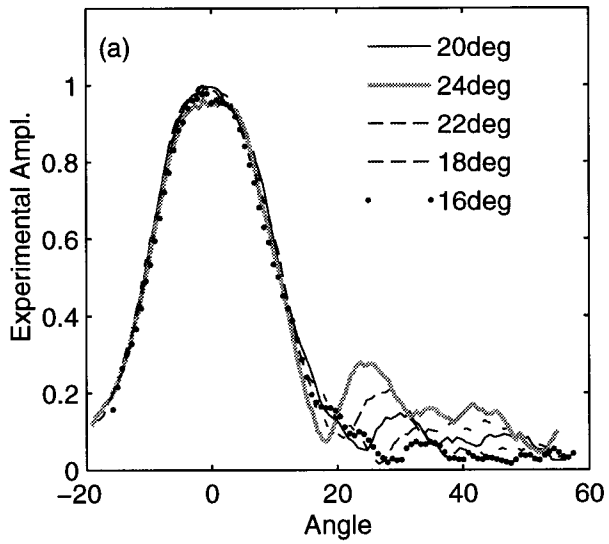

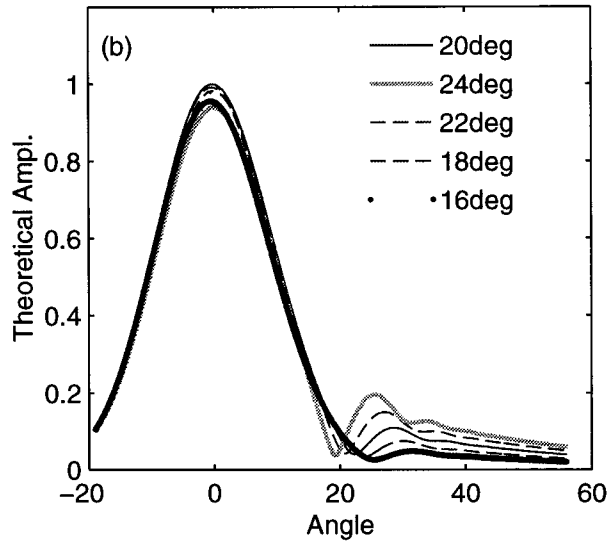

FIG. 8. Transducer voltage for a solid cylinder in water. Experimental data are in (a) and theoretical voltage in (b) as a function of scan angle for $\mathscr{R}$ aligned: $\theta_{\mathscr{R}}=\theta_{\mathscr{T}}=20°$, and when it is misaligned: $20°\pm2°$ and $20°\pm4°$. For all plots, $\theta_{\mathscr{T}}=20°$. The voltage is established primarily by the specularly reflected field except in the region above 20°, where the leaky Rayleigh wave dominates. Note that the dotted curve in (b) appears as a thick solid line because of a finer sampling rate.

calculations presented for the voltage amplitude in scanned lateral-coordinate measurements at a fixed range using Gaussian transducers.[14] The shift in the voltage maximum is not symmetric with respect to the receiver misalignment angle because of the asymmetry introduced by the reflection process, especially when there is an incident diverging beam. This asymmetry can be seen more clearly in the theoretical results of Fig. 3(b) than in the experimental results of Fig. 3(a).

The A_0 mode is excited at a phase-match angle of 32.8°. Voltage data corresponding to incidence at and near this angle are plotted as a function of scan coordinate in Fig. 4(a) for the measured and in Fig. 4(b) for the predicted receiver voltages. The voltage is a coherent sum of the specular reflection and the strongly excited leaky Lamb wave. At 32.8° incidence angle we expect that the A_0 mode will be the dominant contribution to the leaky wave signal. From Fig. 4 it can be seen that as the receiver angle is increased from 30.8° to 34.8°, the minimum at $x=20$ mm becomes less pronounced, indicating that the ratio of leaky wave to specular reflection decreases. At perfect alignment $\theta_{\mathscr{R}}=\theta_{\mathscr{T}}$, the specular reflection (SR) voltage contributes a larger amplitude than the A_0 wavefield, and, because they are out-of-phase (in this region), their interference leads to a mild dip as shown by the solid curve in Fig. 4(a) and (b). When the receiver angle decreases to 30.8° the leaky wave is strengthened at the expense of the specular reflection in the region $x>0$, and the two components become comparable in amplitude to each other, leading to a very pronounced minimum near $x=20$ mm. On the other hand, when the receiver angle increases to 34.8°, the leaky wave decreases faster than does the specular component, and the minimum can hardly be seen.

We also note that in the SR region ($x \approx 0$) the strength of the received voltage becomes larger as $\theta_{\mathscr{R}}$ decreases, as can be observed for the $\theta_{\mathscr{R}} = 31.8°$ curve. The increase, which is seemingly inconsistent with the conclusions obtained from Fig. 3, is ascribed to the effect of the S_0 mode which is excited in this region by the steep rays of the misaligned incident beam. A separate calculation of the S_0 leaky wave shows that it is in phase with the specular part in this region.

The misalignment effects at an incident angle of 30° are shown in Fig. 5 with experimental results in Fig. 5(a) and theoretical calculation in Fig. 5(b). With an incident angle of 30° between A_0 and S_0 mode angles, weaker coupling to the leaky waves is seen when compared with Fig. 4. The Gaussian-like shape of the SR (near $x = 0$ mm) is almost unperturbed, unlike the data of Fig. 4, except near $\theta_{\mathscr{R}} = 28°$. Here, the contribution of the S_0 mode is important enough to lead to an increase of the total voltage in the region $x < -10$ mm, whereas the decrease in the contribution of the A_0 mode leads to a decrease in the leaky wave amplitude beyond $x = 25$ mm.

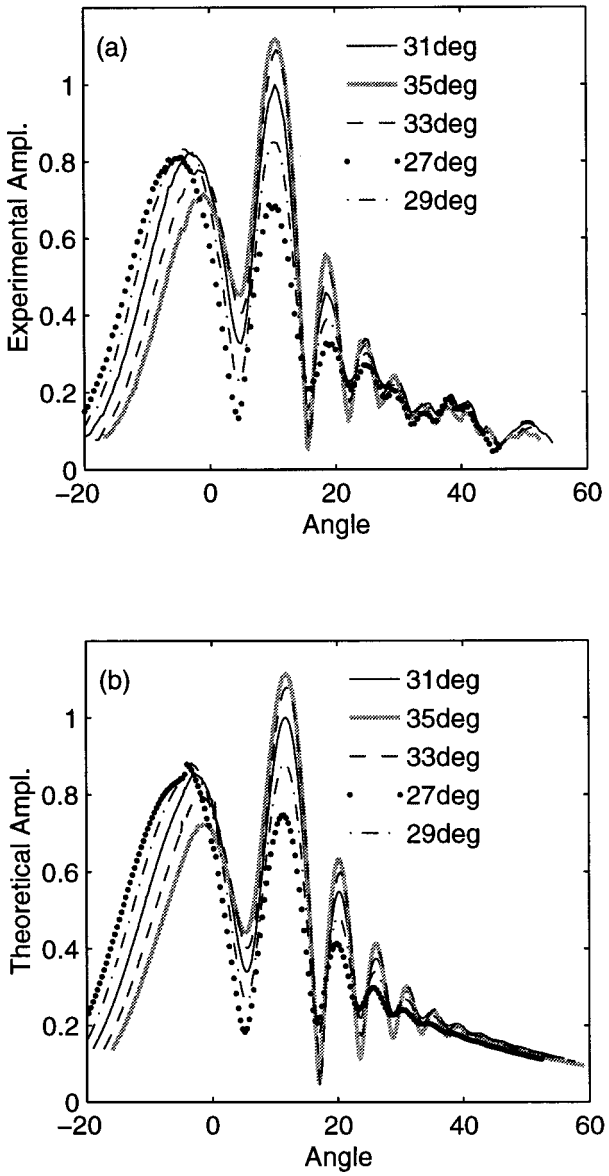

FIG. 9. Transducer voltage for a solid cylinder in water. Experimental data are in (a) and theoretical voltage in (b) as a function of scan angle when $\mathscr{R}$ is aligned: $\theta_{\mathscr{R}} = \theta_{\mathscr{T}} = 31°$, and when it is misaligned: $31° \pm 2°$, and $31° \pm 4°$. For all plots, $\theta_{\mathscr{T}} = 31°$.

Investigating misalignment for S_0-mode phase matching at an incidence angle of 28°, the experimental receiver voltages as a function of scan distance are plotted in Fig. 6(a). In Fig. 6(b) the theoretical amplitudes are recorded for the same conditions. For the aligned case, $\theta_{\mathscr{T}} = \theta_{\mathscr{R}} = 28°$, and for the misaligned cases, $\theta_{\mathscr{R}} = 26°$, 27°, 29°, and 30°. The curve for the aligned cases in either plot is shown in solid, and the others are indicated on the legend. For this incidence angle the S_0 mode dominates, but the A_0 mode is also excited. This hypothesis is confirmed by the plots in Fig. 6(c) and (d) for the calculated contributions of the A_0 and S_0 leaky modes, respectively. Similar to the case of 30° incidence shown in Fig. 5, the degree of excitation of these two modes depends on the receiver (mis)alignment. It can be seen that for $\theta_{\mathscr{R}} = 26°$, the excitation and detection of the S_0 mode is the strongest, while that for the A_0 is the weakest.

The situation reverses itself for $\theta_{\mathscr{R}} = 30°$. Quantifying the isolated contributions of these two modes helps explain some of the features seen in the receiver voltage. The amplitude of the voltage minimum near $x \approx 0$ in Fig. 6(a) and (b) follows the S_0 mode strength, that is, the S_0 mode interferes with the specularly reflected field to yield a minimum there, while the second peak after the dip correlates with the strength of the A_0 mode. Furthermore, the smooth decay of the voltage amplitude in the LW region ($x > 40$ mm) for $\theta_{\mathscr{R}} = 26°$ and 27° is a consequence of the fact that among the three components (S_0, A_0, and SR) only the S_0 is nonnegligible in that region. For $\theta_{\mathscr{R}} = 30°$, however, the voltage decay in this region is oscillatory owing to the interference between the S_0 mode and the A_0 mode, whose mode strength is clearly not negligible, as shown in Fig. 6(c).

Finally, we investigate misalignment effects at an incident angle of 16°, close to the A_1 mode and S_1 mode phase-matching angles. The experimental results and theoretical calculations at this incidence angle are shown in Fig. 7. Here, too, we see the effects of transducer misalignment on the receiver voltage. In this case, however, since the phase matching angles are close (14.98° and 14.15°) and both are smaller than the incident beam angle (16°), the decrease in the receiver angle favors both A_1 and S_1 modes, resulting in a strongly perturbed specular beam shape and a large, undifferentiated trailing field ($x > 50$ mm) amplitude in the receiver voltage. When the receiver angle is as low as 14°, the specular reflection is also highly distorted.

It should be noted that in all of the plots in Figs. 3–7, the agreement between theory and experiment is quite satisfactory, especially considering some of the intricate structure of the voltage owing to wave interference phenomena operating here. The agreement encourages confidence in the model predictions.

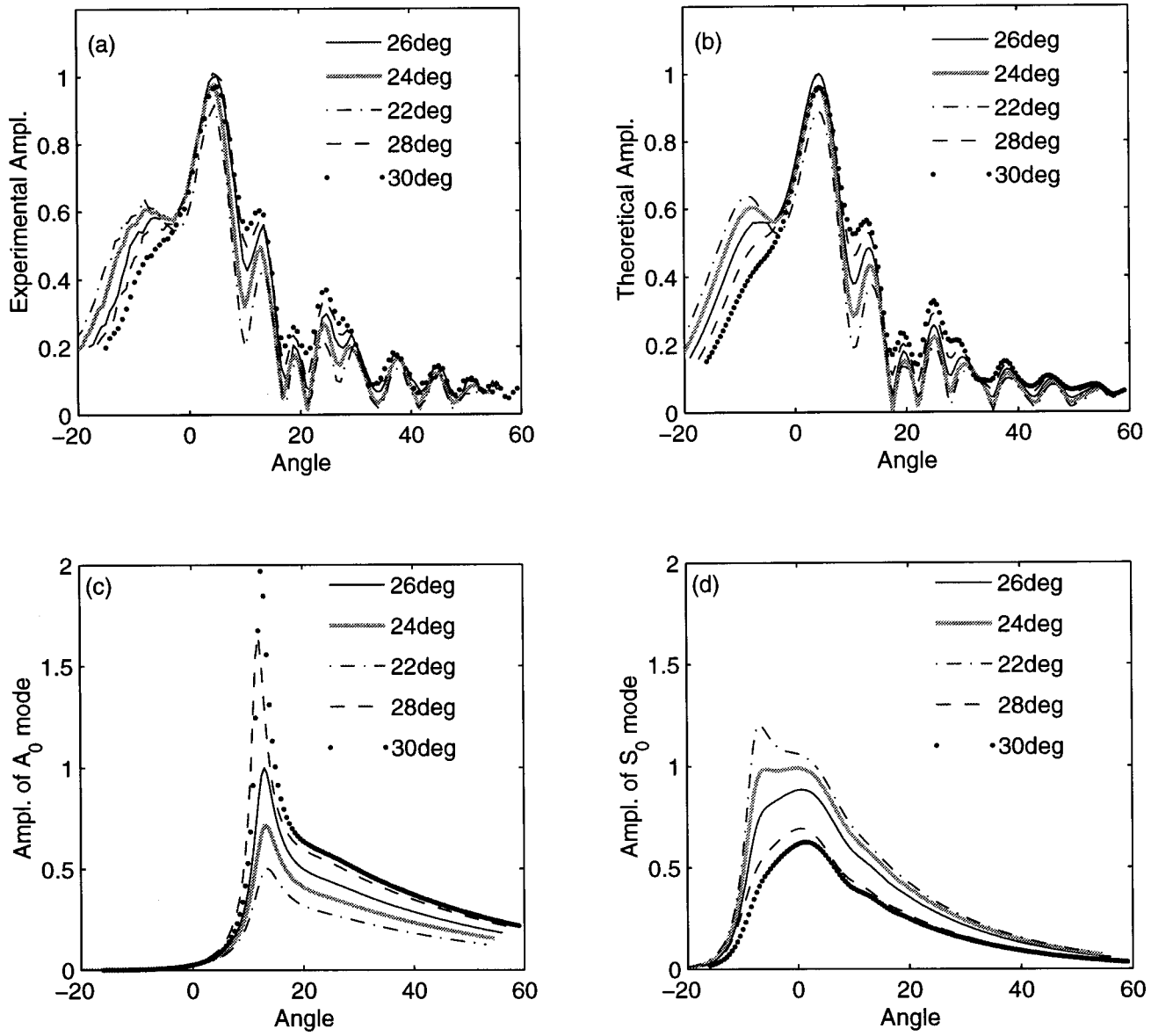

FIG. 10. Transducer voltage for a steel shell in water. Experimental data are in (a) and theoretical voltage in (b) as a function of scan angle when $\mathscr{R}$ is aligned: $\theta_{\mathscr{R}} = \theta_{\mathscr{T}} = 26°$, and when it is misaligned: $26° \pm 2°$ and $26° \pm 4°$. For all plots, $\theta_{\mathscr{T}} = 26°$. The corresponding calculated profiles of the leaky A_0 mode (c) and S_0 mode (d) are shown for reference.

B. Cylindrical interfaces

The misalignment effects on reflection from curved structures are investigated using steel solid cylinders and steel shells. Because only Rayleigh modes propagate on solid cylinders, the simpler case of the solid cylinder is presented first. To assess the misalignment effects on a specular beam reflected from a solid cylinder, we select an incidence angle that is far from the Rayleigh critical angle.

With a Rayleigh angle for the water-steel interface of 31°, a 20° incidence angle would mostly avoid Rayleigh wave excitation and permit us to examine the effect on the specular component. This assumption is confirmed by the experimental results and theoretical calculations shown in Fig. 8(a) and (b). For the SR region, we can see that when the receiver angle deviates from the incidence angle in either direction by 2°, the specularly reflected beam peak decreases very little, and its shape hardly changes. At a deviation angle of 4° the beam amplitude begins to weaken. Compared with planar structures, in which 1° of misalignment results in much larger amplitude decreases, the effect of misalignment on the specular reflection is really rather small here. This fact suggests that the curvature-induced divergence of the SR beam, as captured by the receiving aperture, is larger than a few degrees, such that there always are rays that are aligned with the receiving aperture axis, even when the receiver is misaligned with respect to the incident beam axis. This situation results in a weaker sensitivity of the receiving aperture to misalignments for the curved interface than for a planar interface. In the planar case, a collimated incident beam remains collimated upon reflection. We recall from our previous work[8,11] that the reflection of a collimated beam from a curved surface is equivalent to the reflection of a diverging beam from a planar surface. As the receiver angle exceeds 20° in Fig. 8, the leaky Rayleigh wave contribution becomes

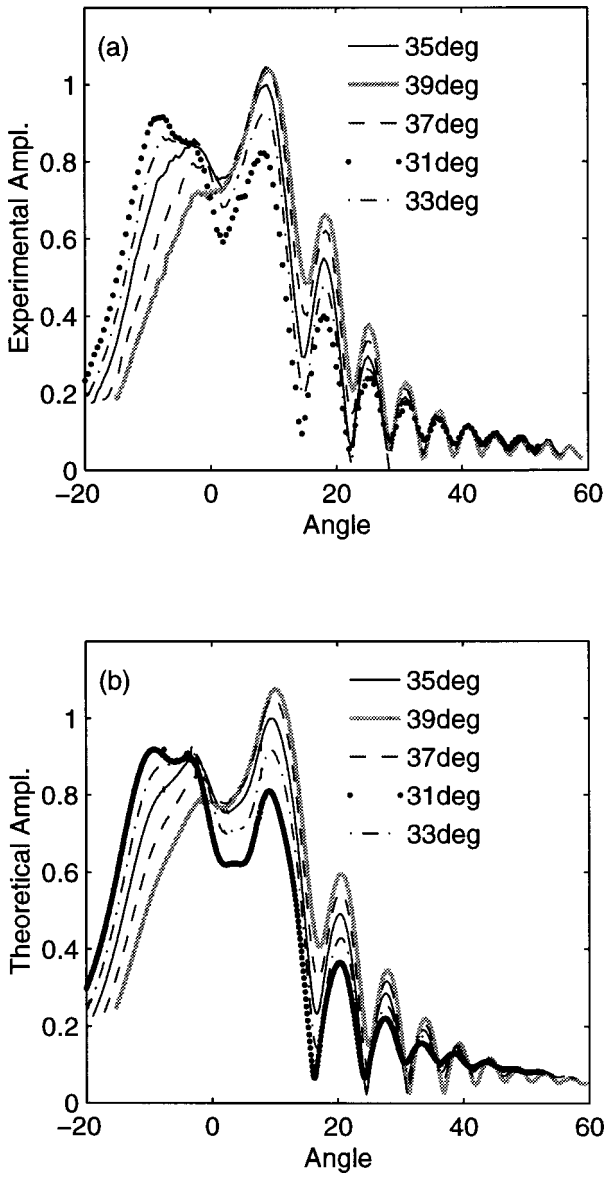

FIG. 11. Transducer voltage for a steel shell in water. Experimental data are in (a) and theoretical voltage in (b) as a function of scan angle when $\mathscr{R}$ is aligned: $\theta_{\mathscr{R}}=\theta_{\mathscr{T}}=35°$, and when it is misaligned: $35°\pm2°$ and $35°\pm4°$. For all plots, $\theta_{\mathscr{T}}=35°$.

more significant. At incident angles of 22° and 24° we see a distinct increase in receiver voltage in the scan angle range beyond 25°, where the Rayleigh wave, because of its constant-angle-leakage, radiates an angularly collimated beam (i.e., rays depart from the surface at a constant angle, regardless of scan angle coordinate[8,11]).

On the basis of the above analysis we examine the misalignment effects for incidence at the Rayleigh critical angle 31°. The experimental results and theoretical calculations for the receiver voltage are shown in Fig. 9 for various receiver misalignment angles. The curves for the aligned case are shown in dark solid. The Rayleigh wave is efficiently excited, and the minimum close to 0° scan angle follows the strength of the leaky Rayleigh wave, as verified in separate calculations. Separated by this minimum, the two main lobes show a decrease of one peak simultaneously with an increase in the other. This effect is mainly a result of the receiver aperture averaging process. For the specular peak (below 0° scan angle) the steep ray favors a receiver aperture with small receiver angle $\theta_{\mathscr{R}}$, while for the leaky wave (above 0° scan angle), the slant ray favors a receiver aperture with a larger receiver angle.

Moving to the case of cylindrical shells, we investigate misalignment effects on a 57.3-mm radius steel shell of thickness 2.28 mm. For the model calculations, we approximate the reflection coefficient of the curved shell by that of a planar structure having the same thickness. As shown in Ref. 19, this replacement is still acceptably accurate for our shell thickness and radius. At 1 MHz, the shell supports three principal Lamb modes, A_0, S_0 and A_1, with corresponding phase-match angles 33.3°, 20.5°, and 11.8°. In Fig. 10(a) and (b) we study misalignment from an incidence angle of 26°, lying between the A_0 and S_0 modes. The experimental results, together with the theoretical predictions, are shown in frames (a) and (b) of this figure and the calculated leaky wave mode analyses for the two candidate modes are shown in frames (c) and (d). At this incidence angle, we expect both modes to be efficiently excited. The changing receiver scan angle will favor one mode or the other. From $-20°$ to 0° scan angle, the misalignment effects on the S_0 mode are most prominent at any receiver misalignment angle from $-4°$ to $+4°$ with respect to 26°. The gradual increase in the predicted S_0 mode amplitude yields the receiver voltage increase shown in Fig. 10(a) and (b) at scan angles less than 0°.

Above scan angles of 10°, the misalignment has a more pronounced influence on the A_0 mode, but the situation is reversed here. The decrease of the receiver angle weakens the leaky wave and thus the total receiver voltage. It can also be seen that the largest peak in the receiver voltage, occurring near 5° scan angle in Fig. 10(a) and (b), for the case when the receiver angle is 26°, is almost identical to the case when the receiver angle is 28°. In this particular case, the leaky S_0 wave and the specular contribution are out of phase. The lower amplitude of the leaky S_0 wave at a receiver angle of 28° appears to compensate for the decrease in the specular component because of misalignment. This observation strongly reinforces the assertion made in the introduction that a simple amplitude test alone is an insufficient basis for a transducer alignment decision.

The experimental and theoretical results of transducer misalignment at an incident angle of 35° (5° above the Rayleigh angle) on the steel shell in water are shown in Fig. 11 frames (a) and (b). At this incident angle the A_0 mode leaky wave makes the dominant contribution to the signal. The misalignment effects observed earlier with the solid steel cylinder at Rayleigh angle incidence can be seen here also. As the receiver angle decreases, the excitation and reception strength of the A_0 mode increases, resulting in a larger total voltage for scan angles below about $-10°$ and in a more pronounced minimum near 0° in the total receiver voltage.

IV. CONCLUSIONS

In this article we have investigated the effects of receiver misalignment in leaky wave near-field measurements. We have, in particular, experimentally tested a computation-

ally efficient and approximate 2-D modeling code for piston transducers interacting with plates and cylinders in fluid. We have found that the effects of receiver misalignment are most pronounced (i.e., a drastic change in the voltage amplitude occurs) for cases where the signal is composed of more than one component. The effect is particularly strong when one, or more than one, of these components are collimated (linearly for the plane geometry and angularly for the cylindrical geometry) and impinge on the receiver at angles differing from each other. It is shown that misalignment effects lead to an enhancement of one or more components (specular reflection and/or leaky wave) at the expense of the other contributions. Having thus gained confidence in our model predictions, we propose to extend this study to the effects of transducer aperture size on the voltage amplitude and phase, and to the ramifications of these issues on material parameter characterization.

ACKNOWLEDGMENTS

This work has been supported in part by the Naval Surface Weapons Center under Contract No. N615339-K-0012. SZ acknowledges support from Schlumberger-Doll Research.

[1] H. L. Bertoni and T. Tamir, ''Unified theory of Rayleigh-angle phenomena for acoustic beams at liquid–solid interfaces,'' Appl. Phys. **2**, 157–172 (1973).
[2] L. E. Pitts, T. J. Plona, and W. G. Mayer, ''Theory of Nonspecular Reflection Effects for an Ultrasonic Beam Incident on a Solid Plate in a Liquid,'' IEEE Trans. Sonics Ultrason. **SU-24**, 101–109 (1977).
[3] T. J. Plona, L. E. Pitts, and W. G. Mayer, ''Ultrasonic bounded beam reflection and transmission effects at liquid/solid–plate/liquid interface,'' J. Acoust. Soc. Am. **59**, 1324–1328 (1976).
[4] J. Pott and J. G. Harris, ''Scattering of an acoustic Gaussian beam from a fluid-solid interface,'' J. Acoust. Soc. Am. **76**, 1829–1838 (1984).
[5] J. G. Harris and J. Pott, ''Further studies of the scattering of an acoustic Gaussian beam from a fluid–solid interface,'' J. Acoust. Soc. Am. **78**, 1072–1080 (1985).
[6] W. G. Neubauer, ''Observation of acoustic radiation from plane and curved surfaces,'' in *Physical Acoustics*, edited by W. P. Mason and R. N. Thurston (Academic, New York, 1973), Vol. 10, p. 85.
[7] F. L. Becker and R. L. Richardson, ''Ultrasonic Critical Angle Reflectivity,'' in *Research Techniques in Nondestructive Testing*, edited by R. S. Sharpe (Oxford U. P., London, 1970), Chap. 4.
[8] D. E. Chimenti, J.-G. Zhang, S. Zeroug, and L. B. Felsen, ''Interaction of acoustic beams with fluid-loaded elastic structures,'' J. Acoust. Soc. Am. **95**, 45–59 (1994).
[9] T. J. Cloutier, A. Safaeinili, D. E. Chimenti, S. Zeroug, and L. B. Felsen, ''An Experimental Study of Ultrasonic Beam Reflection From Fluids Loaded Cylindrical Shells,'' Rev. Prog. Quant. Nondestr. Eval. **14**, 131–138 (1995).
[10] S. Zeroug and L. B. Felsen, ''Nonspecular reflection of two- and three-dimensional acoustic beams from fluid-immersed plane-layered elastic structures,'' J. Acoust. Soc. Am. **95**, 3075–3098 (1994).
[11] S. Zeroug and L. B. Felsen, ''Nonspecular reflection of two- and three-dimensional acoustic beams from fluid-immersed cylindrically layered elastic structures,'' J. Acoust. Soc. Am. **98**, 584–598 (1995).
[12] S. Zeroug, ''Spectral integral formulae for the response of acoustic transducers in cylindrically curved configurations,'' IEEE Trans. Ultrason. Ferroelectr. Freq. Control **45**, 768–778 (1998).
[13] T. J. Cloutier, A. Safaeinili, D. E. Chimenti, S. Zeroug, and L. B. Felsen, ''Ultrasonic beam reflection from fluid-loaded cylindrical shells,'' J. Appl. Phys. **83**, 2408–2419 (1998).
[14] S. Zeroug, F. E. Stanke, and R. Burridge, ''A complex-transducer-point model for emitting and receiving ultrasonic transducers,'' Wave Motion **24**, 21–40 (1996).
[15] S. Zeroug, ''Efficient modeling of finite acoustic beam excitation and detection of interface and bulk waves on planar and cylindrical fluid–solid structures,'' Rev. Prog. Quant. Nondestr. Eval. **15**, 283–290 (1996).
[16] O. I. Lobkis, A. Safaeinili, and D. E. Chimenti, ''Precision ultrasonic reflection studies in fluid-coupled plates,'' J. Acoust. Soc. Am. **99**, 2727–2736 (1996).
[17] P. J. Shull, D. E. Chimenti, and S. K. Datta, ''Elastic guided waves and the Floquet concept in periodically layered plates,'' J. Acoust. Soc. Am. **95**, 99–108 (1994).
[18] T. J. Cloutier, ''Acoustic Beam Reflection from Curved, Layered Media,'' MS thesis, Iowa State University, 1995.
[19] I. A. Viktorov, *Rayleigh and Lamb Waves: Physical Theory and Applications* (Plenum, New York, 1967), pp. 113–116.

Stress effect on boundary conditions and elastic wave propagation through an interface between anisotropic media

A. D. Degtyar[a] and S. I. Rokhlin
The Ohio State University, Nondestructive Evaluation Program, 190 West 19th Avenue, Columbus, Ohio 43210

(Received 17 December 1997; accepted for publication 17 June 1998)

Elastic wave propagation through a plane interface between two generally anisotropic stressed solids is considered. The case when one solid is replaced with fluid is considered separately due to its importance for the development of immersion techniques for ultrasonic stress determination. The incident wave plane can coincide with or deviate from planes of material symmetry. Static stresses are assumed to be locally homogeneous and to satisfy static boundary conditions. The analysis is applicable for both applied and residual stresses. For numerical implementation a method and an analysis of the reflection-refraction problem on the boundary of separation between two anisotropic solids [Rokhlin *et al.*, J. Acoust. Soc. Am. **79**, 906 (1986)] is modified to take stresses into account. Simulations are performed to implement the theory described and to clarify the stress effect on elastic wave interaction with a solid interface. Changes in propagation directions, polarizations, and energy transmission and reflection coefficients due to the presence of stresses are discussed. The stress-induced birefringence is explored quantitatively. Conditions for destructive interference of shear waves are presented. [S0001-4966(98)05909-8]

PACS numbers: 43.20.Gp, 43.20.Fn [ANN]

INTRODUCTION

Ultrasonic wave propagation in prestressed materials has been studied extensively in the last 40 years. Most of this work has concentrated on the effect of stress on the velocities of different types of ultrasonic waves in homogeneous materials. Actually stresses affect not only the velocities of waves but also their amplitudes and propagation directions. Many practical applications of ultrasonic stress characterization involve wave propagation through an interface between fluid and solid or between two solids. For example, in immersion stress measurements an ultrasonic wave is incident from a fluid onto a stressed solid. The presence of stress leads to change in the propagation direction and energy redistribution. Also additional modes may be excited leading to stress-induced birefringence. These are all important phenomena which require rigorous quantitative description since the stress effect on ultrasonic wave propagation in general is very small. Another important problem is ultrasonic characterization of residual stresses in composite materials.[1] This involves wave propagation through an interface between layers with different properties and stress levels.

The cornerstone of the description of wave propagation through an interface between two media is the conditions at the boundary on wave displacements and stresses. Normally these conditions represent the continuity of particle movement and the balance of traction forces. Boundary conditions on a free surface for small perturbations in deformed isotropic materials were first formulated by Hayes and Rivlin,[2] when they considered Rayleigh wave propagation in a stressed medium. Generalized relations on a free boundary with an arbitrary orientation with respect to the principal stress directions were presented by Iwashimizu and Kobori.[3] The effect of prestress on the propagation of interface waves at the fluid/solid interface was recently treated by Norris and co-authors.[4,5]

Another important issue for any treatment of wave propagation in the prestressed medium is the nature of the stresses under consideration. Most papers use the conventional acoustoelastic theory which assumes that the medium is hyperelastic and the stresses result from elastic deformations. This makes the results inapplicable to the important case of residual stresses which usually arise from nonelastic processes. Man and Lu[6] developed a new theory which does not make a hyperelasticity assumption and thus is applicable to both applied and residual stresses. In this paper we follow their approach for the derivation of governing equations for wave propagation through interfaces in the prestressed medium. This makes all the results obtained applicable to the case of residual stress which is of greater practical interest.

The focus of this paper is the development of a unified approach for the solution of the reflection-transmission problem on the plane boundary of separation between two generally anisotropic stressed solids. The case when one of the solids is replaced by a fluid is described separately due to its importance. The approach is based on the theoretical treatment of wave propagation through a plane interface between two anisotropic media proposed by Rokhlin *et al.*[7] Stresses are assumed to be locally homogeneous and to satisfy static boundary conditions. It is shown that additional stress dependent terms, resulting from the interaction between dynamic and static fields, appear in the boundary conditions when static traction forces do not vanish at the interface. Calculation examples are presented for Ti/SiC as a model of a metal matrix composite, water/Plexiglas and water/aluminum inter-

[a]Present address: Thiokol Corporation, P.O. Box 707, M/S 245, Brigham City, UT 84302.

faces. Also computations are made for wave propagation through an interface between two crystallites with different orientations in a Ni polycrystal. Changes in propagation directions, polarizations, energy transmission and reflection coefficients are calculated using the proposed computational procedure. Stress-induced and texture-induced birefringence and the resulting shear wave interference is discussed in the examples of wave incidence from water onto isotropic Plexiglas and anisotropic aluminum. Some preliminary results of this work were described in Ref. 8.

In all computational examples, acoustoelastic constants are determined assuming hyperelasticity from second and third order elastic constants and stresses.[9] This is needed for simulation purposes only to calculate stress dependent elastic constants. In the theory itself no assumption is made on the nature of the stresses which can be both applied and residual resulting from elastic or plastic deformations.

I. WAVE PROPAGATION IN ANISOTROPIC STRESSED MEDIA

In this section we briefly review the derivation of equations which describe wave propagation in an anisotropic stressed medium. We follow the approach proposed by Man and Lu[6] who derived the generalized Christoffel equation for a stressed medium which is valid for both applied and residual stresses. Here we represent this equation in terms of the slowness vector, which plays an important role in the solution of the reflection-refraction problem. Next we derive equations for the energy flux density vector for a wave traveling in a stressed medium. This is needed to define energy reflection and transmission coefficients.

The prestressed configuration is the only reference configuration in this approach and the initial stress is included in the constitutive equation:

$$\sigma_{ij}=\sigma_{ij}^0+C_{ijkl}\epsilon_{kl}+u_{i,k}\sigma_{kj}^0, \tag{1}$$

where σ_{ij} is the first Piola–Kirchhoff stress tensor, σ_{ij}^0 is the initial static stress, ϵ_{ij} is the elastic strain due to wave propagation, $u_{i,k}$ is the displacement gradient and C_{ijkl} is the fourth rank tensor of stress-dependent elastic constants. Equation (1) gives the relation between stresses and displacements which arise due to wave propagation in the prestressed medium. It is an analog of Hooke's law for the unstressed case. The use of only one prestressed coordinate system makes the constitutive equation (1) applicable to the case of both applied and residual static stresses.

The equation for small elastic motion superimposed on the prestressed state is

$$\sigma_{ij,j}=\rho\ddot{u}_i, \tag{2}$$

where **u** is the displacement vector. Making use of Eq. (1), Eq. (2) can be written in component form:

$$(C_{ijkl}+\sigma_{jl}^0\delta_{ik})u_{k,jl}=\rho\ddot{u}_i. \tag{3}$$

The stress σ_{ij}^0 can be both applied and residual since there is no restriction that the resulting deformation be elastic. Now assuming that the material and local (over the size of the transducer) stresses are homogeneous and using a plane wave solution for **u**:

$$u_k=AP_ke^{iK(\mathbf{n}\cdot\mathbf{x}-V_pt)} \tag{4}$$

where A is the amplitude of the wave, P_k is the unit displacement vector, $\mathbf{K}=K\mathbf{n}=(\omega/V)\mathbf{n}$ is the wave number, V_p is the phase velocity, **n** is the wave normal, and **x** is the position vector, one has the Christoffel equation for an anisotropic material under stress:

$$[C_{ijkl}n_in_l+(\sigma_{il}^0n_in_l-\rho V_p^2)\delta_{jk}]P_k=0. \tag{5}$$

Equation (5) has nontrivial solutions when the determinant is equal to zero

$$|(C_{ijkl}+\sigma_{il}^0\delta_{jk})n_in_l-\rho V_p^2\delta_{jk}|=0. \tag{6}$$

In order to find the group velocity in a stressed medium Eq. (5) can be rewritten as

$$C_{ijkl}K_iK_lP_k+\sigma_{il}^0K_iK_lP_j=\rho\omega^2P_j. \tag{7}$$

Multiplying both sides of Eq. (7) by P_j and using the fact that $P_j'P_j=1$, we get

$$C_{ijkl}K_iK_lP_jP_k+\sigma_{il}^0K_iK_l=\rho\omega^2. \tag{8}$$

After differentiation of Eq. (8) with respect to the components of the wave vector **K** one has

$$2C_{ijkl}P_jP_kK_l+2\sigma_{il}^0K_l=2\rho\omega\frac{\partial\omega}{\partial K_i}. \tag{9}$$

The group velocity in the stressed medium is

$$V_{gi}\equiv\frac{\partial\omega}{\partial K_i}=\frac{1}{\rho\omega}(C_{ijkl}P_jP_k+\sigma_{il}^0)K_l$$

$$=\frac{1}{\rho V_p}(C_{ijkl}P_jP_k+\sigma_{il}^0)n_l. \tag{10}$$

In contrast to the group velocity for the unstressed medium,[10] here the elastic constants, phase velocity and polarization are all stress-dependent and there is an additional stress term $\sigma_{il}^0n_l$.

For further use it is more convenient to rewrite Eq. (6) in terms of the slowness vector $\mathbf{m}=\mathbf{n}/V=\mathbf{K}/\omega$:

$$\left|\frac{1}{\rho}(C_{ijkl}+\sigma_{il}^0\delta_{jk})m_im_l-\delta_{jk}\right|=0. \tag{11}$$

Also for the description of the energy reflection/refraction coefficients one needs to define the energy flux density vector. It is determined by

$$U_i=\overline{-\sigma_{ik}\dot{u}_k}, \tag{12}$$

where the bar indicates time averaging. For a stressed medium it can be calculated as

$$U_i=\tfrac{1}{2}A^2\omega^2(C_{ijlk}+\sigma_{il}^0\delta_{jk})m_lP_iP_k. \tag{13}$$

Comparing Eqs. (10) and (13) one can see that the vector **U** coincides with the direction of the group velocity $\mathbf{V}_g$ and thus **U** can be expressed in terms of $\mathbf{V}_g$:

$$U_i=\tfrac{1}{2}A^2\omega\rho V_{gi}. \tag{14}$$

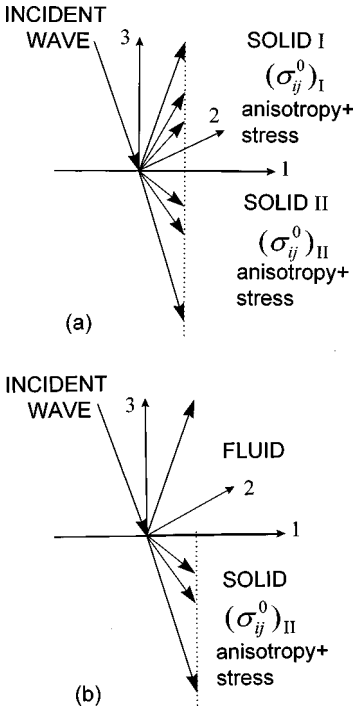

FIG. 1. Wave propagation through a plane boundary between (a) two anisotropic stressed solids and (b) fluid and anisotropic stressed solid.

The theory described in this section is applicable to the case of both applied and residual stresses σ_{ij}^0. Stress dependent elastic constants C_{ijkl} for orthotropic material are listed in the Appendix; they depend on second and third order elastic constants and stresses. The detailed derivation is given in Ref. 9. Only in the hyperelastic case can one provide simple explicit expressions for them. In the case of plastic deformations they also depend on the loading-unloading history.

An alternative approach to the treatment of wave propagation in anisotropic media is based on Stroh's formalism.[11] This approach combines constitutive and wave equations into one higher order equation which can be reduced to an eigenvalue problem. It has been applied to the solution of a wide range of reflection/refraction problems in piezoelectric and multilayered anisotropic structures.[12–14] The method can be extended to the case of stressed media.

II. BOUNDARY CONDITIONS FOR A PLANE STRESSED INTERFACE

In order to describe wave propagation through an interface between stressed media, we need to formulate boundary conditions. In this section boundary conditions on a stressed solid/solid interface are given and the necessary changes for a fluid/solid interface and a free solid surface are discussed.

Let us consider a plane interface between two generally anisotropic stressed media [Fig. 1(a)]. Index I refers to the upper medium and II to the lower medium. The initial static stresses are $(\sigma_{ij}^0)_I$ and $(\sigma_{ij}^0)_{II}$ for upper and lower media, respectively. For convenience we introduce the system of coordinates formed by incident and interface planes. 1-3 plane is the incident plane and the 2-3 plane is the plane of the interface [Fig. 1(a)]. Acoustical axes as well as principal stress directions do not necessarily coincide with coordinate axes. In the coordinate system selected the vector normal to the interface is $\boldsymbol{\nu}=(0,0,1)$ and traction force components are $T_i=\sigma_{ij}\nu_j=\sigma_{i3}$.

For the initial static stressed state the boundary conditions represent the continuity of the traction forces:

$$(\sigma_{i3}^0)_{\rm I}=(\sigma_{i3}^0)_{\rm II}, \quad i=1,...,3. \tag{15}$$

Consider a monochromatic plane wave (4) propagating from the upper to the lower medium. The boundary conditions at the interface represent continuity of displacements and traction forces. In the general case, for a wave incident from the upper medium there are three reflected (in the upper medium) and three transmitted (in the lower medium) waves. The boundary conditions are

$$\begin{aligned} &u_i^{\rm inc}+(u_i^{QL}+u_i^{QT_1}+u_i^{QT_2})_{\rm I}=(u_i^{QL}+u_i^{QT_1}+u_i^{QT_2})_{\rm II} \\ &\sigma_{i3}^{\rm inc}+(\sigma_{i3}^{QL}+\sigma_{i3}^{QT_1}+\sigma_{i3}^{QT_2})_{\rm I}=(\sigma_{i3}^{QL}+\sigma_{i3}^{QT_1}+\sigma_{i3}^{QT_2})_{\rm II}, \\ &\qquad i=1,...,3. \end{aligned} \tag{16}$$

Here QL, QT_1 and QT_2 refer to quasilongitudinal, fast and slow quasishear waves, respectively. Using Eq. (1) and taking into account static boundary conditions (15) each of the terms σ_{i3} in Eq. (16) can be written as

$$\sigma_{i3}=C_{i3kl}\epsilon_{kl}+u_{i,k}\sigma_{k3}^0. \tag{17}$$

Note that, in contrast to the boundary conditions for traction forces in the dynamic case of wave propagation through a plane boundary between two unstressed solids,[7] in Eq. (17) the elastic constants are replaced with stress dependent elastic constants C_{i3kl} and an additional term $u_{i,k}\sigma_{k3}^0$ appears. This represents the interaction between dynamic wave-induced deformation $\partial u_i/\partial x_k$ and static stress σ_{ik}^0. This happens when interfacial static traction forces are not equal to zero, that is when there is a load transfer between layers. The term $u_{i,k}\sigma_{k3}^0$ vanishes in Eq. (17) when there are no traction forces acting on the interfacial surface in the prestressed state $[(\sigma_{k3}^0)_I=(\sigma_{k3}^0)_{II}=0]$. In this case static stresses affect the boundary conditions (16) only through the stress dependent elastic constants C_{i3kl}. Boundary conditions for displacements have the same form as in the unstressed state[7] in all cases.

If one of the solids is replaced by a fluid with static pressure p_f^0 [upper medium (I) in Fig. 1(b)], static boundary conditions represent the lack of shear traction forces in the lower solid medium (II) and continuity of the normal traction force. Dynamic boundary conditions satisfy the continuity of normal traction forces σ_{33} and normal displacements u_3 and vanishing of shear traction forces σ_{13} and σ_{23}. If fluid pressure is small and can be neglected, the stresses in the solid affect the boundary conditions only through the stress dependent elastic constants because in the prestressed state the fluid/solid boundary is traction-free.

The boundary conditions on a free surface (medium I is vacuum and medium II is a stressed solid) require zero traction forces on the surface for the static and dynamic cases.

III. COMPUTATIONAL PROCEDURE

A simple unified algorithm for the solution of the reflection-refraction problem on a plane interface between two anisotropic unstressed solids has been described by Rokhlin *et al.*[7] In this section we will discuss the modifications needed in the computational procedure to take into account stresses. Because of its importance the computational procedure for critical angle determination is described separately.

A. Solid/solid interface

In the case of the solid/solid interface for stressed anisotropic solids the changes result from a different equation for wave propagation inside the stressed solid [Eq. (5)], use of stress dependent elastic constants and the modified boundary conditions [Eqs. (16) and (17)].

Since the slowness vectors for incident, reflected and transmitted waves all lie in the incident plane, they have only two nonzero components m_1 and m_3 in the selected coordinate system. From Snell's law, all projections of the slowness vectors on the interface m_1^α ($\alpha=\text{inc},1,...,6$, where inc refers to the incident wave, indices 1,...,3 to the three reflected waves and indices 4,...,6 to the three transmitted waves) are equal and thus they are known since m_1^{inc} is known. The unknown m_3^α components can be determined from Eq. (11).

Wave velocities and wave normal directions are determined from the slowness vectors for all existing waves. Then the wave polarizations are determined as the eigenvectors corresponding to the eigenvalues (velocities). This procedure should be carried out separately for upper and lower media. There will be six solutions for m_3 for each half space. To choose the three physical solutions for reflected and three for transmitted waves one must require that the energy flow be directed into the appropriate half space.

The unknown amplitudes A^α of the displacements for reflected ($\alpha=1,...,3$) and transmitted ($\alpha=4,...,6$) waves can be found from boundary conditions (16) using the determined slowness and polarization vectors. The boundary conditions can be written in the form of six linear algebraic equations:

$$\begin{aligned} &A^{\text{inc}}P_i^{\text{inc}}+\sum_{\alpha=1}^{6}A^\alpha P_i^\alpha=0,\\ &A^{\text{inc}}(C_{i3kl}P_k^{\text{inc}}m_l^{\text{inc}}+P_i^{\text{inc}}m_k^{\text{inc}}\sigma_{k3}^0)\\ &\quad+\sum_{\alpha=1}^{6}A^\alpha(C_{i3kl}P_k^\alpha m_l^\alpha+P_i^\alpha m_k^\alpha\sigma_{k3}^0)=0. \end{aligned} \tag{18}$$

Coefficients of reflection and refraction can be found as

$$R^\alpha=A^\alpha/A^0, \tag{19}$$

where A^α is the amplitude of the reflected or refracted wave and A^0 is the amplitude of the incident wave. It is more useful to discuss energy flow ratios than amplitude ratios. These transformation factors are defined in terms of the energy fluxes normal to the interfaces:

$$r^\alpha=U_3^\alpha/U_3^{\text{inc}}, \tag{20}$$

where the energy flux vector **U** is given by Eq. (14). r^α characterizes the redistribution of the incident energy between different reflected and transmitted modes. It can be calculated as

$$r^\alpha=\left(\frac{A^\alpha}{A^0}\right)^2\frac{\rho_\alpha}{\rho_0}\frac{V_{g3}^\alpha}{V_{g3}^0}. \tag{21}$$

B. Boundary conditions approximation

It is interesting to evaluate an approximation when the effect of static loading stresses is taken into account only through the stress-dependent elastic constants C_{ijkl}. In this case, in the boundary conditions (18) we neglect the stress terms $P_i^{\text{inc}}m_k^{\text{inc}}\sigma_{k3}^0$ and $P_i^\alpha m_k^\alpha\sigma_{k3}^0$, but the slowness vectors $\mathbf{m}^\alpha$ are calculated precisely using Eq. (11). This approximation is equivalent to using the unstressed case, with replacement of the second order elastic constants with the stress dependent elastic constants in the boundary conditions and using the wave velocities (slownesses) accounting for the stresses in the semispaces. Computational examples using the approximation and the exact solution will be given in the next section.

C. Fluid/solid interface

In the case of a wave incident from a fluid into the stressed solid there exist one wave reflected back into the fluid (with known velocity and polarization) and three waves transmitted into the solid. Thus Eq. (11) has to be solved for only the solid half space to find the slowness and polarization vectors of these transmitted waves. The system of linear equations (18) representing boundary conditions reduces from 6×6 to 4×4. The four unknowns are the amplitudes of the three waves transmitted into the solid and the one wave reflected into the fluid:

$$\begin{aligned} &A^{\text{inc}}P_3^{\text{inc}}+A^{\text{refl}}P_3^{\text{refl}}+\sum_{\alpha=4}^{6}A^\alpha P_3^\alpha=0,\\ &A^{\text{inc}}\rho_f V_f P_3^{\text{inc}}+A^{\text{refl}}\rho_f V_f P_3^{\text{refl}}+\sum_{\alpha=4}^{6}A^\alpha C_{33kl}P_k^\alpha m_l^\alpha=0,\\ &\sum_{\alpha=4}^{6}A^\alpha C_{i3kl}P_k^\alpha m_l^\alpha=0,\quad i=1,2. \end{aligned} \tag{22}$$

Here ρ_f is the fluid density and V_f is the wave velocity in fluid.

D. Critical angles

The critical angle is defined[7] as the incident angle at which the energy flow (group velocity) is parallel to the interface. For isotropic solids this definition coincides with the condition that the transmitted wave vector direction be parallel to the interface. Thus in this case the critical angle can be determined through Snell's law by letting the refraction angle equal 90°. For an anisotropic solid/solid interface (the

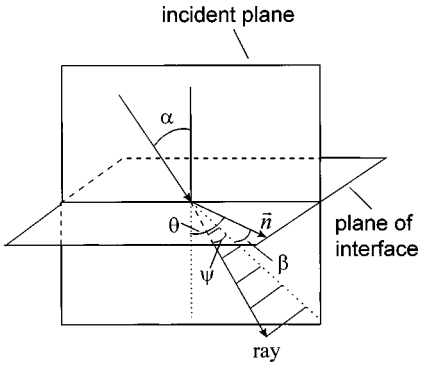

FIG. 2. Schematic illustration of the energy flow deviation (ray vector) from wave propagation direction (**n**). ψ is the out-of-incident-plane and β is the in-plane deviation angle of the ray vector.

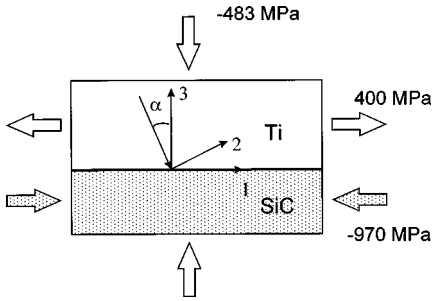

FIG. 3. Ti/SiC plane interface with stresses.

anisotropy can be stress induced) this definition is generally incorrect, since the group velocity (ray) and the wave normal vectors have different directions. The deviation between ray and propagation directions may be represented by out-of-incidence-plane ψ and in-incidence-plane β angles (Fig. 2). When the interface is the plane of symmetry for both semispaces[7] the definition of the critical angle through Snell's law is applicable since the energy flow vector and wave propagation vector at the critical angle are parallel to the interface simultaneously although they do not necessarily coincide[15] (at the critical angle, the in-plane deviation angle β is zero; however, the out-of-incidence-plane angle ψ may or may not be zero). The practical importance of the plane of symmetry interface case is that Snell's law can be used for the critical angle determination in the way done in the isotropic case.

The presence of stresses may or may not violate the correctness of the critical angle definition in terms of Snell's law depending on whether the stresses do or do not destroy the symmetry properties of the interfacial plane. This will be illustrated in the computational example in the next section. When the above definition is correct, the stresses can be determined from critical angle measurements using Snell's law.[16]

In the general case of wave propagation through an interface between two generally anisotropic stressed solids, the critical angle cannot be found from Snell's law. To find it, the following procedure is utilized. For every incident angle the phase velocity of the incident wave is calculated. The phase velocity and wave normal direction of the transmitted wave is determined by solving the Christoffel equation (11) for the appropriate semispace as described in Sec. III A. Next the group velocity vector (energy propagation direction) is found using Eq. (10). The incident angle is varied until the energy propagation direction of the transmitted wave becomes parallel to the interface. The incident angle found is the critical angle.

IV. CALCULATION RESULTS AND DISCUSSION

In this section we present computational examples based on the procedure described above to illustrate the effect of stress on wave propagation through solid/solid and fluid/solid boundaries. Also we discuss how stress influences shear wave interference.

A. Wave propagation through solid/solid interface

First as an example we consider wave propagation through a Ti/SiC plane interface, which models the fiber/matrix interface in Ti/SiC metal matrix composites. The stresses are chosen to be similar to the residual stresses in fiber (SiC) and matrix (Ti alloy). The composites are processed at high temperatures and during the subsequent cooling residual stresses develop due to the mismatch in coefficients of thermal expansion of fiber and matrix materials. These nonhomogeneous stresses were estimated by us using a concentric cylinders model.[17] In our calculations we take the average stress values for each phase. Thus we assume a compressional normal stress of 483 MPa perpendicular to the interface in both materials, tensional normal stress of 400 MPa along the interface direction in Ti and compressional normal stress of 970 MPa along the interface in SiC (Fig. 3). Shear stresses are assumed to be zero. Both substrates are considered to be isotropic and to determine the stress dependent elastic constants we assume the stresses result from elastic deformations.[9] Since the third order elastic constants for SiC are not available in the literature we replace them by those of Si. Second- and third-order elastic constants used for Ti and SiC are given in Table I. Figure 4(a) shows the energy conversion coefficient from the quasilongitudinal wave in Ti to the quasishear wave in SiC. The dashed line

TABLE I. Second- and third-order elastic constants for Ti and SiC (isotropic).

	Second-order elastic constants		Third-order elastic constants, GPa		
Material	Young's modulus, GPa	Poisson's ratio	C_{111}	C_{112}	C_{123}
Ti	97	0.33	−1358	−1105	−162
SiC	414	0.19	−821[a]	−448[a]	−104[a]

[a]Third-order elastic constants for Si.

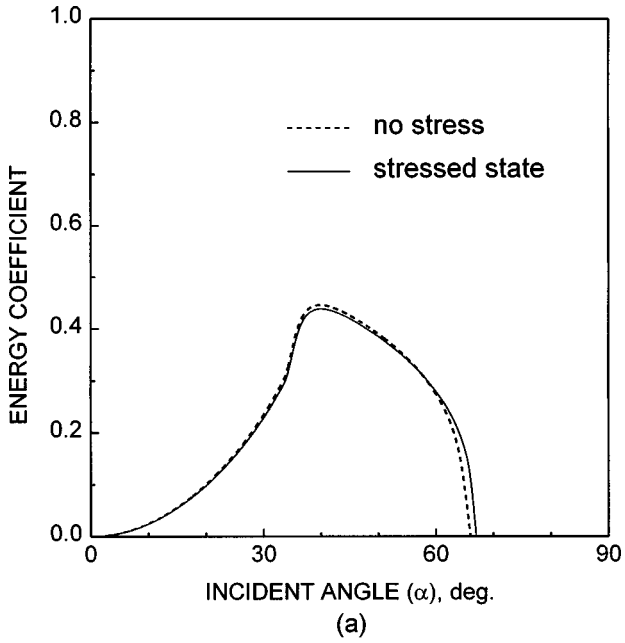

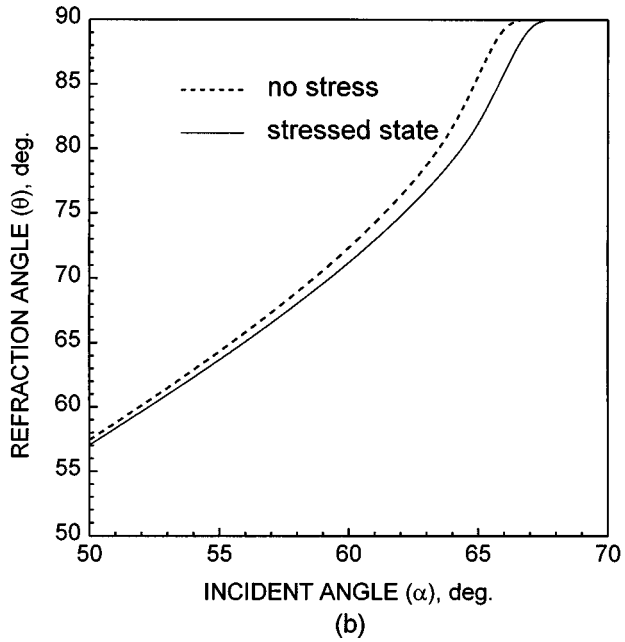

FIG. 4. Effect of stress on conversion of quasilongitudinal wave to quasishear wave on Ti/SiC interface: (a) Energy transmission coefficient and (b) refraction angle.

represents the results for the unstressed state and the solid line for the stressed state. Figure 4(b) displays refracted angle versus incident angle for the same case. One can see that the largest deviation is observed close to the second critical angle. However, despite the high stress level, the stress effect on energy redistribution is small.

Figure 5 illustrates the approximation described in Sec. III B when the additional stress term in the boundary conditions (18) is neglected and static stresses are accounted for only through the stress-dependent elastic constants C_{ijkl}. The results for the energy conversion coefficient for the example described above are presented in Fig. 5 with a dotted line. One can see that the approximation is close to the exact solution, so the direct effect of the stress terms in the boundary conditions (BC) is smaller than that of the stress-dependent elastic constants. Thus to account for the static stress effect in first approximation one need only replace the second-order elastic constants with the stress dependent elastic constants in the solution of the boundary conditions problem.

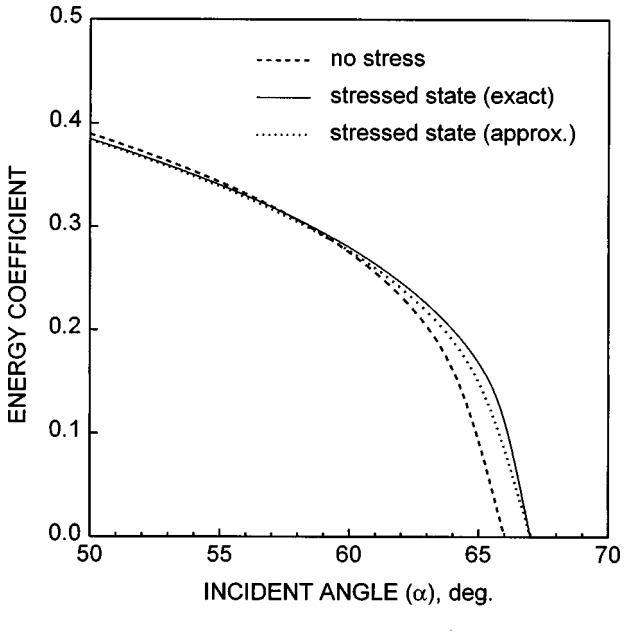

FIG. 5. Conversion of the quasilongitudinal wave to the quasishear wave at plane Ti/SiC interface. The dashed line is the energy transmission coefficient in an unstressed state. The solid line is the exact calculation for stressed state and the dotted line is approximation when the stress term is neglected in the boundary conditions.

As another example we consider wave propagation through the (001) plane interface of a Ni crystal of cubic symmetry. Second and third order elastic constants used for computations were taken from Ref. 18 and are given in Table II. For the upper medium the [100] and for the lower medium the [110] axes are perpendicular to the interface. The stressed state is shown in Fig. 6. There is a compressional stress of 200 MPa perpendicular to the interface and shear stresses of 100 MPa for both upper and lower media parallel to the interface. This example is motivated by analysis of the stress effect on reflection and transmission between differently oriented crystals of the same kind which is important for understanding of ultrasonic scattering in stressed polycrystals.

We consider a slow shear wave incident from the upper

TABLE II. Second- and third-order elastic constants for Ni crystal (cubic symmetry).

Second-order elastic constants, GPa			Third-order elastic constants, GPa					
C_{11}	C_{12}	C_{44}	C_{111}	C_{112}	C_{123}	C_{144}	C_{155}	C_{456}
270	170	123	−2030	−1040	−220	−138	−910	−70

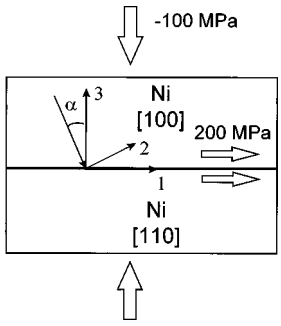

FIG. 6. Ni/Ni plane interface with stresses, [100] and [110] direction (in the Ni crystal of cubic symmetry) are perpendicular to the interface for upper and lower substrates, respectively.

medium and polarized in the 1-3 plane (Fig. 6). An interesting phenomenon occurs close to normal incidence for transmitted shear waves: in the unstressed state there is only one transmitted shear wave (solid line in Fig. 7), while in the stressed state there are two transmitted shear waves with orthogonal polarizations. In order to explain this effect one should take into account the polarization change of the incident slow shear wave. In the unstressed state this wave is polarized along the 1-direction (Fig. 6) but in the presence of stresses its polarization is slightly tilted in the 1-2 plane (plane of the interface). Therefore this wave propagating through the boundary generates two transmitted waves with polarizations in the 1 and 2 directions. Only shear waves with such polarizations are permitted to propagate in the lower medium. This phenomenon is called stress induced birefringence. It will be discussed in more detail below for the case of a wave incident from water into a stressed solid.

B. Determination of critical angles

To study the effect of stresses on critical angles we consider a quasilongitudinal wave incident from Ti to SiC (Fig. 8). As in the previous examples we select the 1-2 plane as the interface plane and the 1-3 plane as incident. We consider two stressed states: (a) pure shear stress in the 1-2 plane and (b) pure shear stress in the 1-3 plane. In both cases the same stress value of 300 MPa is assumed for both Ti and SiC semispaces. The in-plane and out-of-plane deviations between the ray and the wave propagation directions are calculated as a function of the refraction angle for the transmitted quasishear wave and are shown in Fig. 9 [(a): $\sigma_{12}=300$ MPa, (b): $\sigma_{13}=300$ MPa]. It can be seen in the case of the shear stress in the plane parallel to the interface that the in-plane deviation angle ψ equals zero at refraction angle 90°. This means that ray and wave propagation directions are parallel to the interface at the same time and Snell's law can be used to define the critical angle. This is possible because the stress does not destroy the symmetry of the interfacial plane. When the shear stress is in the plane perpendicular to the interface ($\sigma_{13}\neq 0$) there is in-incidence-plane deviation between ray and wave propagation direction when the refraction angle is 90° [Fig. 9(b)]. This happens because the interface plane loses its symmetry properties due to stress.

The critical angle as a function of shear stress in the 1-3 plane is shown in Fig. 10(a). It is determined from the condition that the ray direction (solid line) be parallel to the interface and from Snell's law (dashed line). Since the definition of the critical angle through Snell's law is incorrect in this case (the wave propagation direction is not parallel to the interface), the critical angle determined from Snell's law is erroneous. This leads to an error in velocity calculation from critical angle measurements using Snell's law. The error is shown in Fig. 10(b) as a function of shear stress σ_{13}. Thus in this case Snell's law cannot be used in stress determination from critical angle data and the general solution should be applied.

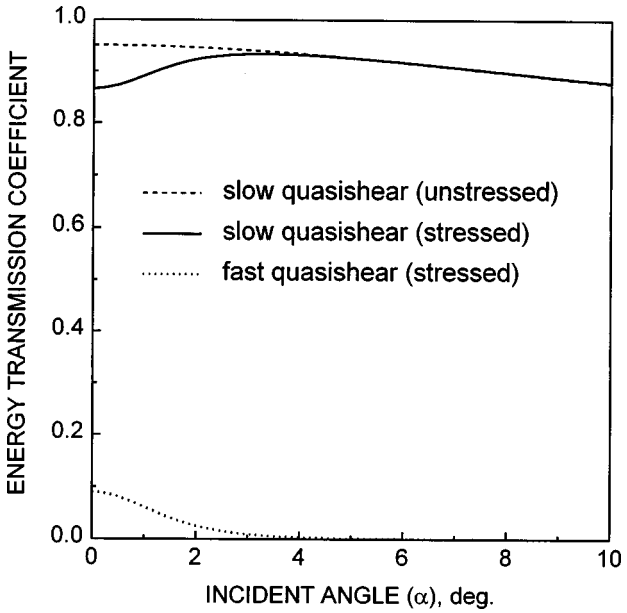

FIG. 7. Energy conversion coefficients of incident slow quasishear wave to transmitted slow quasishear for unstressed (dashed line) and stressed (solid line) states. The conversion to transmitted fast quasishear wave in stressed state is shown by a dotted line.

C. Wave propagation through water/solid interface. Stress-induced birefringence. Shear wave induced interference of the received field

A fluid is often used as a coupling medium in ultrasonic measurements. For stress measurements using immersion techniques it is important to understand different stress-induced phenomena for elastic wave propagation from a fluid into a stressed solid. Here we consider several examples of wave propagation through a fluid/stressed solid interface. In the first example it is demonstrated that the presence of stresses in isotropic material leads to birefringence. The

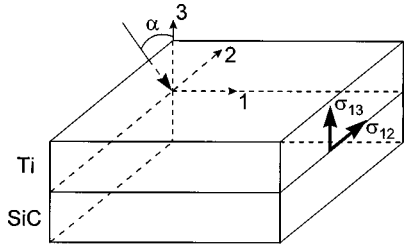

FIG. 8. Ti/SiC interface with nonzero shear stresses in the plane parallel and perpendicular to the interface .

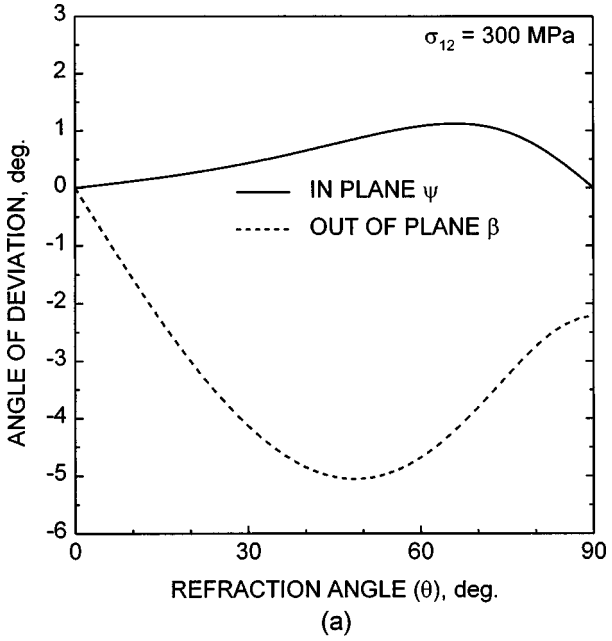

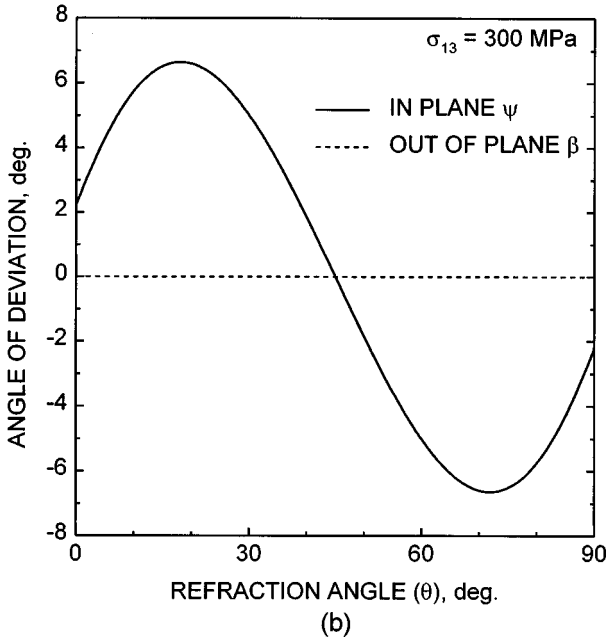

FIG. 9. Deviation angles between ray and wave normal (**n**) vectors for a transmitted quasishear wave through the stressed Ti/Sic interface; (a) σ_{12}(Ti)=σ_{12}(SiC)=300 MPa; (b) σ_{13}(Ti)=σ_{13}(SiC)=300 MPa.

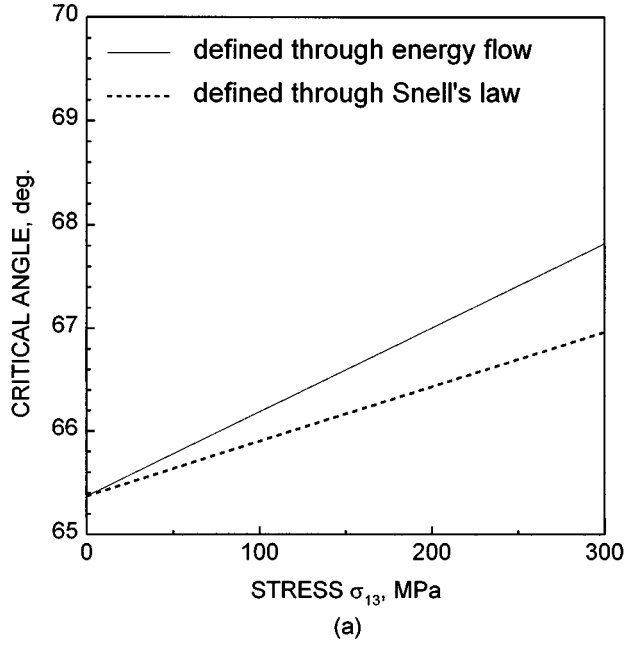

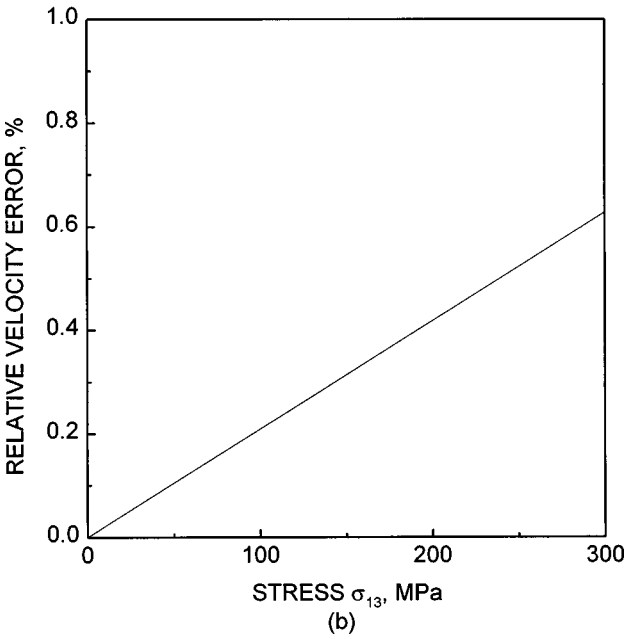

FIG. 10. Effect of stress induced anisotropy on critical angle. σ_{13}(Ti) $=\sigma_{13}$(SiC)=300 MPa. (a) Determination of critical angle from energy flow (solid line) and wave propagation (dashed line) directions for conversion of quasilongitudinal wave in Ti to quasishear wave in SiC. (b) Error in velocity calculation from critical angle using Snell's law.

wave incident from the fluid excites two waves in the solid. This happens because stresses make the solid effectively anisotropic, which puts conditions on the wave polarizations. Two shear waves must exist in the solid in order to satisfy BC on the fluid/solid interface. These two shear waves transform on the back surface of the plate into two longitudinal waves in the fluid. The interference of these waves in the fluid is described. The second example considers how the solid texture affects these phenomena.

First let us consider a wave incident from water on a plexiglass semispace. The plexiglass is considered to be isotropic and under uniaxial tensile stress 20 MPa. Its elastic constants are given in Table III. Calculations are made for an incident plane tilted by an angle $\varphi=45°$ with respect to the stress direction (11). Energy transmission coefficients for the shear wave in unstressed and stressed states are shown in Fig. 11(a). In the absence of stress there is only one shear wave excited in plexiglass (solid line), since the material is isotropic. The presence of stress causes birefringence and the appearance of two shear waves, slow (short dashed line) and fast (long dashed line). Upon transmitting back into the fluid these shear waves convert into two longitudinal waves separated in time and space which can be recorded by a receiver.

The two shear waves created on the interface [Fig. 11(b)] have very similar velocities and so must travel a significant distance to produce a measurable time delay differ-

TABLE III. Second- and third-order elastic constants for Plexiglas.

Lamé constants, GPa		Murnaghan constants, GPa		
λ	μ	l	m	n
1.16	4.00	−18.9	−13.3	−10.0

ence between them. To measure this time delay it is more feasible to consider the interference of the signals received by transducers from these waves. One should note that the two shear waves have mutually orthogonal polarizations and do not interfere in the solid, however, the electrical signals recorded by a transducer add with corresponding phases and an interference pattern is produced. Hsu[19] and Blinka and Sachse[20] demonstrated experimentally that stress-induced interference of shear waves produces minima in the spectrum of the received signal. They used a shear wave normal beam contact transducer to excite a shear wave in the direction perpendicular to the loading and demonstrated that the minimum position depends on the stress level. For historical background, one may refer to Pao *et al.*[21] Experimentally observed changes in acoustic microscopy contrast by Drescher-Krasicka[22] are attributed to stress-induced birefringence. Quantitative description of this phenomenon requires knowledge of energy distribution between interfering waves. The numerical procedure described above allows doing that and thus one can define exact conditions for destructive interference of the received signal[23] for both normal and oblique incidence.

In the previous example we assumed the material to be isotropic. Thus in the absence of stresses no birefringence is observed. In the next example we consider birefringence in anisotropic material. This phenomenon can be observed even in the unstressed case. Here we demonstrate that the presence of stresses significantly changes the birefringence pattern (spectrum of the interfered signal). We consider wave incidence from water into textured stressed aluminum alloy. Aluminum alloy is assumed to be orthotropic with degree of anisotropy of 1%. Most aluminum alloys have yield points exceeding 100 MPa.[24] That is why we consider the effect of the uniaxial stress of 100 MPa. The second and third order elastic constants of the material are given in Table IV. The angle (φ) between the incident plane and the axis of material symmetry is called the azimuthal angle [Fig. 12(b)]. The waves recorded by a transducer interfere even in the absence of stresses due to anisotropy. The amplitudes of the shear waves for this case are shown in Fig. 13(a) as a function of azimuthal angle φ for a fixed incident angle $\theta_i = 18°$. Strong

TABLE IV. Second- and third-order elastic constants for aluminum.

Second order elastic constants, GPa								
C_{11}	C_{22}	C_{33}	C_{12}	C_{13}	C_{23}	C_{44}	C_{55}	C_{66}
108.6	106.4	107.5	54.7	54.6	48.9	25.3	29.3	26.6
Third-order elastic constants, GPa								
l			m					n
−218[a]			−378[a]					−435[a]

[a]Third-order elastic constants are taken for isotropic Al.

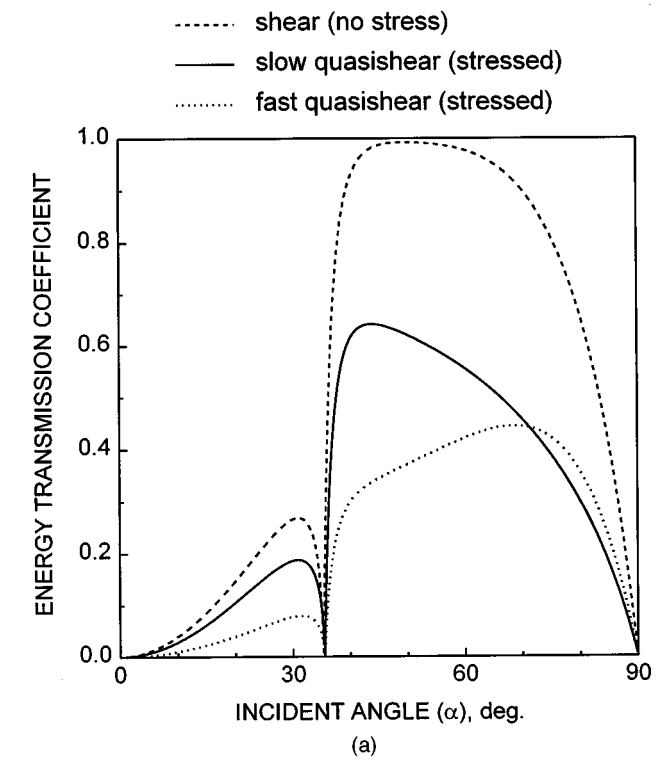

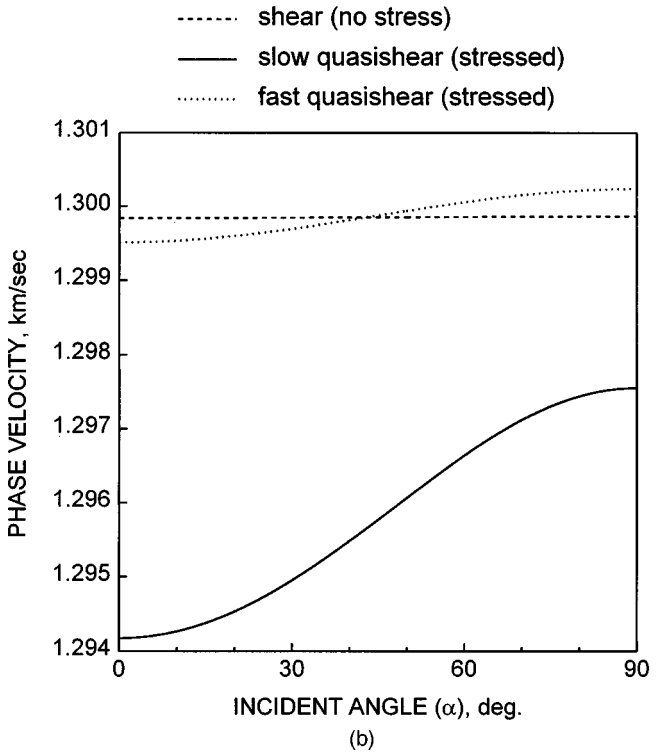

FIG. 11. (a) Energy transmission coefficient through water/Plexiglas interface for shear waves in unstressed and stressed states; (b) shear wave velocities in Plexiglas for the same cases.

destructive interference of the waves occurs in the receiver if two conditions are satisfied: (1) the amplitudes of the transmitted waves are similar, and (2) the waves have opposite phase. Fulfillment of the first condition depends on the elastic properties of the solid and on the angle of incidence. The second condition depends on velocity difference, plate thickness and signal frequency, or, more precisely, on the thick-

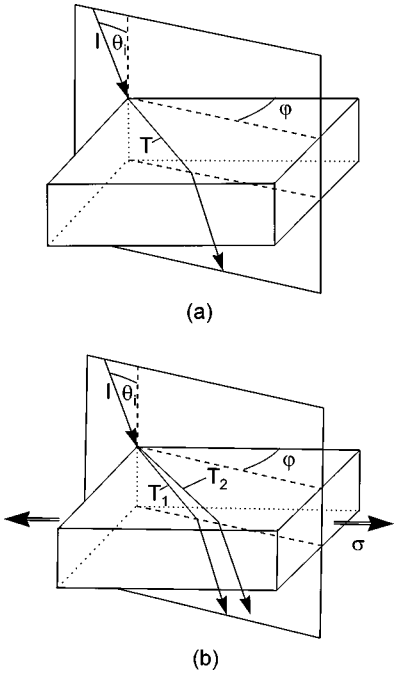

FIG. 12. Splitting of transmitted ray: (a) isotropic solid (no splitting) (b) stress or texture induced shear wave birefringence.

ness×frequency product. In our example the amplitudes of two shear waves are equal when the azimuthal angle φ is 32° and 46°. The frequency spectrum of the interference signal is shown with a dashed line in Fig. 14 for the incidence direction defined by $\theta_i = 18°$ and $\varphi = 32°$. The minimum occurs when the product of frequency and thickness is equal to 118 mm MHz. At this value the amplitude of the interference signal is almost 0. Figure 13(b) shows the amplitudes of shear waves in the presence of uniaxial stress of 100 MPa applied along the material axis. Changes are most pronounced in the angular range where the amplitude gradients are high. In this case there is no azimuthal angle φ at which the amplitudes of the waves are equal. Thus interference of these waves does not produce such a deep minimum, as in the unstressed case, as shown in Fig. 14 by a solid line. By

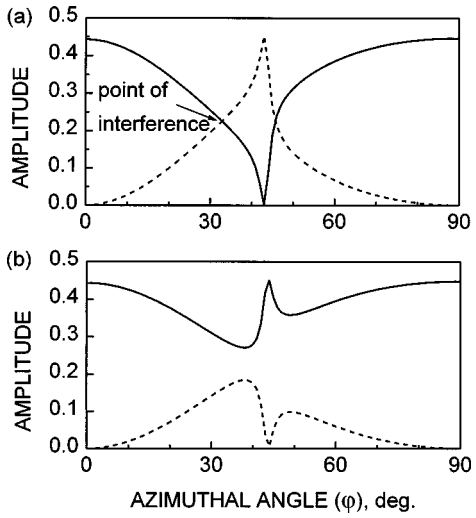

FIG. 13. Amplitudes of shear waves transmitted from water to textured aluminum (a) without and (b) with stress (note stress induced splitting).

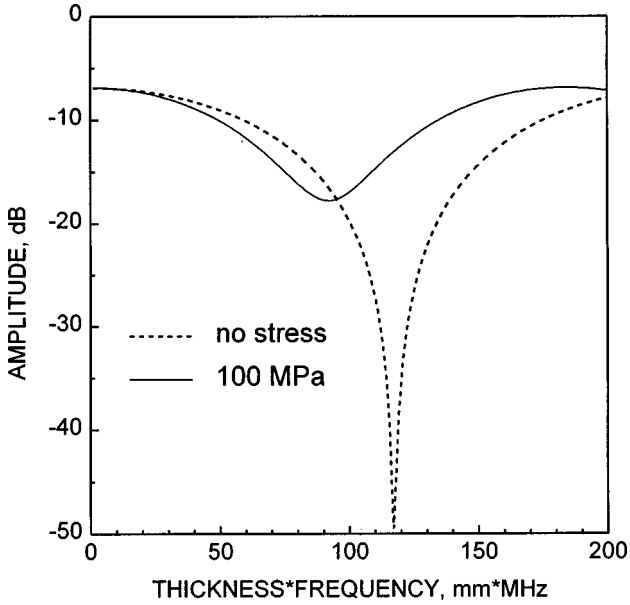

FIG. 14. Shear wave interference in unstressed and stressed textured aluminum.

comparing unstressed and stressed cases one can see that the presence of stresses and anisotropy both significantly affect the interference pattern recorded by a transducer, sometimes in opposite directions. One should take extreme care in the interpretation of interference patterns especially in such geometrically complicated cases as acoustic microscopy.

V. SUMMARY

We have presented a rigorous procedure to describe elastic wave propagation through a plane interface between two anisotropic stressed solids and between a fluid and a stressed anisotropic solid. The reflection/refraction problem is solved for arbitrary wave propagation direction and arbitrary incident wave type.

The presence of static stresses affects wave velocities in semispaces and boundary conditions at the interface. For a solid/solid interface stresses are accounted for in the boundary conditions by replacing the second order elastic constants with stress-dependent elastic constants and adding terms which provide interaction between static and dynamic stress fields. In the case of a fluid/solid interface boundary conditions are affected by stresses only through stress-dependent elastic constants of the solid. Thus, in general, to account for static stresses on elastic wave propagation through a plane interface, stress-induced changes in wave velocities and boundary conditions must be computed. The stress effect is accounted for through stress dependent elastic constants and direct stress terms in both velocities and boundary conditions. Computations show that the major part of the stress effect (approximately 90%) is accounted through the stress-dependent elastic constants.[9]

Calculation examples show that the stress effect on energy redistribution between reflected and transmitted waves is most pronounced near critical angles. This demonstrates

that the critical angle position is sensitive to the stresses. But the simple definition of the critical angle through Snell's law is only valid when the interface plane is a plane of symmetry. In other cases the general definition of a critical angle as the incident angle at which the energy flow is parallel to the interface must be used.

It was also shown that due to stress induced anisotropy an incident wave from a fluid transmits as two shear waves. Upon reflecting back into the fluid these shear waves convert into two longitudinal waves separated in time and space which can be recorded by a receiving transducer. Destructive interference in the transducer occurs only in directions where the shear wave amplitudes are equal or close to each other. This condition is satisfied only for a narrow angular range of the incident wave. The minimum position in the spectrum of the interference signal is sensitive to stresses.

APPENDIX: STRESS DEPENDENT ELASTIC CONSTANTS C_{ij} FOR GENERAL STRESS STATE IN ORTHOTROPIC MATERIAL

Assuming that deformations are hyperelastic and that the resulting strains are ϵ_{ij} and stresses σ_{ij} the stress-dependent elastic constants are

$$
\begin{aligned}
C_{11} &= C^o_{11} + C^o_{11}(3\epsilon_{11} - \epsilon_{22} - \epsilon_{33}) + C_{111}\epsilon_{11} + C_{112}\epsilon_{22} \\
&\quad + C_{113}\epsilon_{33}, \\
C_{12} &= C^o_{12} + C^o_{12}(\epsilon_{11} + \epsilon_{22} - \epsilon_{33}) + C_{112}\epsilon_{11} + C_{122}\epsilon_{22} \\
&\quad + C_{123}\epsilon_{33}, \\
C_{13} &= C^o_{13} + C^o_{13}(\epsilon_{11} - \epsilon_{22} + \epsilon_{33}) + C_{113}\epsilon_{11} + C_{123}\epsilon_{22} \\
&\quad + C_{133}\epsilon_{33}, \\
C_{14} &= (C^o_{12} + C^o_{13})\epsilon_{23} + C_{144}\epsilon_{23}, \\
C_{15} &= (C^o_{11} + C^o_{13} + 2C^o_{55})\epsilon_{13} + C_{155}\epsilon_{13}, \\
C_{16} &= (C^o_{11} + C^o_{12} + 2C^o_{66})\epsilon_{12} + C_{166}\epsilon_{12}, \\
C_{22} &= C^o_{22} + C^o_{22}(-\epsilon_{11} + 3\epsilon_{22} - \epsilon_{33}) + C_{122}\epsilon_{11} + C_{222}\epsilon_{22} \\
&\quad + C_{223}\epsilon_{33}, \\
C_{23} &= C^o_{23} + C^o_{23}(-\epsilon_{11} + \epsilon_{22} + \epsilon_{33}) + C_{123}\epsilon_{11} + C_{223}\epsilon_{22} \\
&\quad + C_{233}\epsilon_{33}, \\
C_{24} &= (C^o_{22} + C^o_{23} + 2C^o_{44})\epsilon_{23} + C_{244}\epsilon_{23}, \\
C_{25} &= (C^o_{12} + C^o_{23})\epsilon_{13} + C_{255}\epsilon_{13}, \\
C_{26} &= (C^o_{22} + C^o_{12} + 2C^o_{66})\epsilon_{12} + C_{266}\epsilon_{12}, \\
C_{33} &= C^o_{33} + C^o_{33}(-\epsilon_{11} - \epsilon_{22} + 3\epsilon_{33}) + C_{133}\epsilon_{11} + C_{233}\epsilon_{22} \\
&\quad + C_{333}\epsilon_{33}, \\
C_{34} &= (C^o_{33} + C^o_{23} + 2C^o_{44})\epsilon_{23} + C_{344}\epsilon_{23}, \\
C_{35} &= (C^o_{33} + C^o_{13} + 2C^o_{55})\epsilon_{13} + C_{355}\epsilon_{13}, \\
C_{36} &= (C^o_{13} + C^o_{23})\epsilon_{12} + C_{366}\epsilon_{12}, \\
C_{44} &= C^o_{44} + C^o_{44}(-\epsilon_{11} + \epsilon_{22} + \epsilon_{33}) + C_{144}\epsilon_{11} + C_{244}\epsilon_{22} \\
&\quad + C_{344}\epsilon_{33}, \\
C_{45} &= (C^o_{44} + C^o_{55})\epsilon_{12} + C_{456}\epsilon_{12}, \\
C_{46} &= (C^o_{44} + C^o_{66})\epsilon_{13} + C_{456}\epsilon_{13}, \\
C_{55} &= C^o_{55} + C^o_{55}(\epsilon_{11} - \epsilon_{22} + \epsilon_{33}) + C_{155}\epsilon_{11} + C_{255}\epsilon_{22} \\
&\quad + C_{355}\epsilon_{33}, \\
C_{56} &= (C^o_{55} + C^o_{66})\epsilon_{23} + C_{456}\epsilon_{23}, \\
C_{66} &= C^o_{66} + C^o_{66}(\epsilon_{11} + \epsilon_{22} - \epsilon_{33}) + C_{166}\epsilon_{11} + C_{266}\epsilon_{22} \\
&\quad + C_{366}\epsilon_{33}.
\end{aligned}
$$

Here we use the following symmetry properties:[18]

$$
\begin{aligned}
&C^o_{ijkl} = C^o_{klij} = C^o_{jikl} = C^o_{ijlk}, \\
&C_{ijklmn} = C_{jiklmn} = C_{ijlkmn} = C_{ijklnm} = C_{klijmn} \\
&\qquad = C_{mnklij} = C_{ijmnkl}.
\end{aligned}
\tag{A1}
$$

[1] A. D. Degtyar, W. Huang, and S. I. Rokhlin, ''Wave propagation in stressed composites,'' in *Review of Progress in Quantitative NDE*, Vol. 15B, edited by D. O. Thompson and D. E. Chimenti (Plenum, New York, 1996), pp. 1669–1676.

[2] M. Hayes and R. S. Rivlin, ''Surface waves in deformed elastic materials,'' Arch. Ration. Mech. Anal. **8**, 358–380 (1961).

[3] Y. Iwashimizu and O. Kobori, ''The Rayleigh wave in a finitely deformed isotropic elastic material,'' J. Acoust. Soc. Am. **64**, 910–916 (1978).

[4] A. N. Norris, B. S. Sinha, and S. Kostek, ''Acoustoelasticity of solid/fluid systems,'' Geophys. J. Int. **118**, 439–446 (1994).

[5] A. N. Norris and B. K. Sinha, ''The speed of a wave along a fluid/solid interface in the presence of anisotropy and prestress,'' J. Acoust. Soc. Am. **98**, 1147–1154 (1995).

[6] C.-S. Man and W. Y. Lu, ''Towards an acoustoelastic theory for measurement of residual stress,'' J. Elast. **17**, 159–182 (1987).

[7] S. I. Rokhlin, T. K. Bolland, and L. Adler, ''Reflection and refraction of elastic waves on a plane interface between two generally anisotropic media,'' J. Acoust. Soc. Am. **79**, 906–918 (1986).

[8] A. D. Degtyar and S. I. Rokhlin, ''Stress effect on ultrasonic wave propagation through the solid–solid and liquid–solid plane interface,'' in *Review of Progress in Quantitative NDE*, Vol. 16B, edited by D. O. Thompson and D. E. Chimenti (Plenum, New York, 1997), pp. 1699–1706.

[9] A. D. Degtyar and S. I. Rokhlin, ''Absolute stress determination in orthotropic materials from angular dependences of ultrasonic velocities,'' J. Appl. Phys. **78**, 1547–1556 (1995).

[10] F. I. Fedorov, *Theory of Elastic Waves in Crystals* (Plenum, New York, 1968).

[11] A. N. Stroh, ''Steady state problems in anisotropic elasticity,'' J. Math. Phys. **41**, 77–103 (1962).

[12] K. A. Ingebrigsten and A. Tonning, ''Elastic surface waves in crystals,'' Phys. Rev. **184**, 942–951 (1969).

[13] A. I. Shuvalov and J. Lothe, ''The Stroh formalism and the reciprocity properties of reflection-transmission problems in crystal piezo-acoustics,'' Wave Motion **25**, 331–345 (1997).

[14] S. I. Rokhlin and W. Huang, ''Ultrasonic wave interaction with a thin anisotropic layer between two anisotropic solids. II. Second-order asymptotic boundary conditions,'' J. Acoust. Soc. Am. **94**, 3405–3420 (1993).

[15] S. I. Rokhlin and W. Wang, ''Critical angle measurement of elastic constants in composite material,'' J. Acoust. Soc. Am. **86**, 1876–1882 (1989).

[16] J. Ditri, ''On the measurement of residual stress through changes in critical angle,'' J. Acoust. Soc. Am. **102**, 921–925 (1997).

[17] M.-J. Pindera, A. D. Freed, and S. M. Arnold, ''Effects of fiber and interfacial layer morphologies on the thermoplastic response of metal matrix composites,'' Int. J. Solids Struct. **30**, 1213–1238 (1993).

[18] Landolt-Börnstein, *Numerical Data and Functional Relationships in Science and Technology* (Springer, New York, 1979), Vol. III/11.

[19] N. N. Hsu, ''Acoustical birefringence and the use of ultrasonic waves for experimental stress analysis,'' Exp. Mech. **14**, 169–176 (1974).
[20] J. Blinka and W. Sachse, ''Application of ultrasonic-pulse-spectroscopy measurements to experimental stress analysis,'' J. Elast. **17**, 159–182 (1987).
[21] Y. H. Pao, W. Sachse, and H. Fukuoka, in *Physical Acoustics*, edited by W. P. Mayou and R. N. Thurston (Academic, New York, 1984), Vol. 17, Chap. 2.
[22] E. Drescher-Krasicka, ''Scanning acoustic imaging of stress in the interior of solid materials,'' J. Acoust. Soc. Am. **94**, 453–464 (1993).
[23] A. D. Degtyar, A. I. Lavrentyev, and S. I. Rokhlin, ''Effect of shear wave interference in anisotropic materials,'' in *Review of Progress in Quantitative NDE*, edited by D. O. Thompson and D. E. Chimenti (Plenum Press, New York, 1996), Vol. 15B, pp. 1645–1652.
[24] *Metals Handbook*, 9th ed., Vol. 2, *Properties and Selection: Nonferrous Alloys and Pure Metals* (American Society for Metals, Metals Park, OH, 1979).

Sound propagation in air-saturated random packings of beads

Jean F. Allard,[a] Michel Henry, and Julian Tizianel
Laboratoire d'Acoustique de l'Université du Maine, UMR CNRS 6613, Av. O. Messiaen, 72085 Le Mans Cedex 9, France

Luc Kelders and Walter Lauriks
Laboratorium voor Akoestiek en Thermische Fysica, Departement Natuurkunde, Katholieke Universiteit Leuven, Celestijnenlaan 200 D, B-3001 Heverlee, Belgium

(Received 4 February 1998; accepted for publication 10 July 1998)

In the pore space of packed grain material, transport properties are characterized by macroscopic parameters. Some of them, tortuosity, characteristic dimensions, viscous permeability, and trapping constant, are measured for a random packing of glass beads and compared to evaluations performed in previous studies. These parameters are used to predict the surface impedance at normal incidence of a layer of glass beads. The predictions are compared to measurements performed at normal incidence in a Kundt tube. © *1998 Acoustical Society of America.* [S0001-4966(98)04610-4]

PACS numbers: 43.20.Hq, 47.55.Mh, 44.30.+v [DEC]

INTRODUCTION

Disordered granular media, and among them bead packings, have been studied under different approaches.[1] A partial description of a granular medium at a macroscopic scale (over a volume large compared to the grain size) can be performed by evaluating different macroscopic parameters which depend only on the geometry of the granular structure. Some of them can be used to characterize sound propagation in air saturating the pore space, and conversely can be evaluated from acoustical measurements. Very commonly used by acousticians are the open porosity ϕ, i.e., the volume of free air per unit volume of porous medium, the viscous permeability k_0, related to the stationary flow resistivity σ and the viscosity of air η by

$$k_0 = \eta/\sigma, \tag{1}$$

and the tortuosity α_∞, which is the product of the formation factor F (the ratio of the resistivity r_p of the porous structure saturated by a conducting fluid to the resistivity r_f of the fluid) by the porosity ϕ (see Ref. 2):

$$\alpha_\infty = \phi r_p / r_f. \tag{2}$$

Other parameters that can be involved in the description of sound propagation are the characteristic viscous dimension Λ, the specific surface S, and the trapping constant Γ. The characteristic dimension Λ describes the fluid–solid structure viscous interaction at high frequencies.[3,4] The specific surface S is the total accessible area of the solid per unit mass of porous material and is usually measured with the BET method (after Brunauer, Emmet, and Teller[5]). This specific surface is related to a thermal dimension Λ', which characterizes the thermal exchanges between the saturating fluid and the solid structure at high frequencies,[6,7] by

$$\Lambda' = 2V/S, \tag{3}$$

where V is the volume of free fluid per unit mass of porous material. The trapping constant[8,9] is related to the mean survival time τ of a reactant produced and diffusing in the solid free region, and instantly absorbed on contact with the solid structure, by $\Gamma = 1/(\tau\phi D)$, D being the diffusion constant.

At sufficiently low frequencies, when the scattering by the beads is small,[10] the air inside the pore space can be replaced by a free equivalent fluid. This fluid is characterized by a complex density ρ_1, which takes into account the viscous and inertial interactions of air with the porous frame, and a normalized complex dynamic compressibility $\beta(\omega)$, defined as the actual compressibility divided by the adiabatic compressibility $(1/\gamma P)$, γ being the ratio of the specific heats and P the atmospheric pressure. It has been shown by Johnson *et al.*[4] that a good approximation for ρ_1 is given by

$$\rho_1/\rho = \alpha(\omega) = \alpha_\infty\left(1 + \frac{i\eta\phi}{\rho\alpha_\infty k_0\omega}\left(1 - \frac{4k_0^2\alpha_\infty^2 i\omega\rho}{\Lambda^2\phi^2\eta}\right)^{1/2}\right), \tag{4}$$

where ω is the radian frequency and ρ the air density [the time dependence is $\exp(-i\omega t)$]. With arguments similar to the ones developed in Ref. 4, Lafarge has shown[7,11] that β could be approximated by

$$\beta(\omega) = \gamma - (\gamma - 1)\left[1 + \frac{i\eta\phi}{\rho k_0' \mathrm{Pr}\,\omega}\left(1 - \frac{4k_0'^2\rho i\omega\,\mathrm{Pr}}{\Lambda'^2\phi^2\eta}\right)^{1/2}\right]^{-1}, \tag{5}$$

where Pr is the Prandtl number ($\mathrm{Pr} = \eta C_p/\kappa$, where C_p is the specific heat at constant pressure and κ is the thermal conductivity) and $k_0' = 1/\Gamma$ is the thermal permeability. Equations (4) and (5) provide a complete description of sound propagation in the pore space, the wave number k_1 and the characteristic impedance Z_1 being given by

$$k_1 = k(\alpha(\omega)\beta(\omega))^{1/2}, \tag{6}$$

$$Z_1 = Z(\alpha(\omega)/\beta(\omega))^{1/2}, \tag{7}$$

where k is the wave number and Z the characteristic impedance in free air.

The measurement of a set of macroscopic parameters for random packings of glass beads having a quasi-uniform di-

[a]Electronic mail: bal@laum.univ.lemans.fr

 0001-4966/98/104(4)/2004/4/$15.00

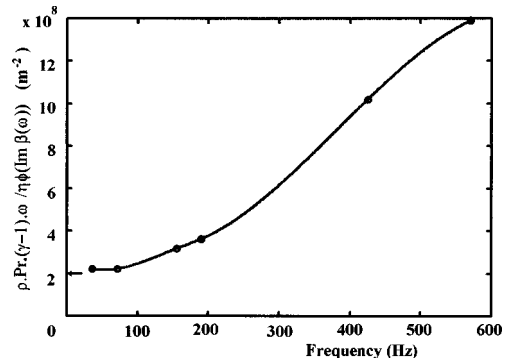

FIG. 1. Measured left-hand side of Eq. (8). The arrow indicates the predicted value of the trapping constant.

ameter is performed in Sec. I with nonacoustical methods for ϕ, k_0, α_∞, and Λ', and with acoustical methods for Λ and Γ. In Sec. II, the predicted and measured surface impedance at normal incidence of a layer of glass beads are compared in the audible frequency domain.

I. MACROSCOPIC DESCRIPTION OF THE RANDOM GLASS BEAD PACKING

Measurements were performed on glass beads manufactured by Negotec (Negotec, 49 rue du Paradis, 75010, Paris, France). The mean diameter is $d=1.46$ mm, with a standard deviation equal to 0.02 mm. The measured porosity for the natural disposal of beads is $\phi=0.4$. Previous measured porosity[12] for random close packings of monodispersive spheres with a weak dispersion is $\phi=0.37$, obtained by shaking containers of steel ball bearings and eliminating finite-size effects. For random loose packings obtained without shaking the containers, $\phi=0.4$. The measured viscous permeability k_0 for the glass beads is $k_0=1.51\times10^{-9}$ m^2. For beads of diameter close to 0.1 mm, previous measurements[13] give $k_0=10^{-11}$ m^2 for $\phi=0.4$. Multiplying this value by the squared ratio of the diameter (ϕ, F, and α_∞ are scale invariants, but the permeability is scale dependent in $[\mathrm{L}]^2$) gives $k_0=2.1\times10^{-9}$ m^2.

The tortuosity evaluated from conductivity measurements is $\alpha_\infty=1.37$. Previous measurements performed by Wong *et al.*[13] for $\phi=0.4$ give a formation factor $F=3.4$, leading to a tortuosity $\alpha_\infty=1.36$.

The trapping constant Γ can be evaluated from precise measurements of the imaginary part of the normalized compressibility β,[14] which can be obtained with a method developed by Tarnow.[15] From Eq. (5), a simple expression can be obtained for Γ:

$$\Gamma=\lim_{\omega\to0}\rho\frac{\mathrm{Pr}}{\eta\phi}(\gamma-1)\frac{\omega}{\mathrm{Im}\,\beta(\omega)}. \tag{8}$$

The right-hand side of Eq. (8), evaluated with the measured imaginary part of β, is represented in Fig. 1 as a function of frequency. The experimental set is described in Ref. 14. The limit of this expression when $\omega\to0$ is equal to $\Gamma=2.2\times10^8$ m^{-2}. The value predicted by Lee *et al.*[16] for a random packing of porosity $\phi=0.4$ is represented by an arrow at $\Gamma=2.0\times10^8$ m^{-2}.

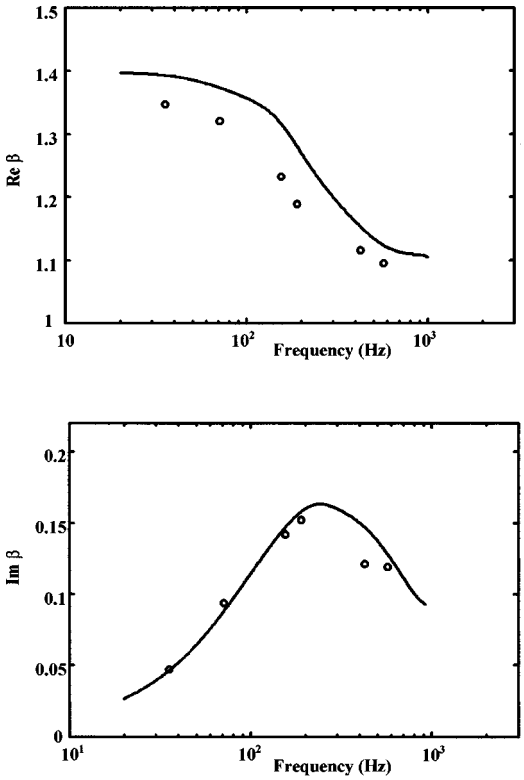

FIG. 2. Compressibility $\beta(\omega)$: measurement ○○○, prediction ———.

The parameter Λ' can be calculated with good precision by assuming identical beads of diameter $d=1.46$ mm for the actual beads, leading from Eq. (3) to $\Lambda'=\phi d/(3(1-\phi))=0.32$ mm. The normalized compressibility predicted from Eq. (5) with $\Gamma=2.2\times10^8$ m^{-2} and $\Lambda'=0.32$ mm measured at low frequencies with the Tarnow method is represented in Fig. 2. It may be noticed that there is a small systematic difference between the predicted and measured real parts of compressibility which has not been explained.

The viscous dimension Λ has been measured, for the case of reticulated foams, simultaneously with α_∞ and Λ' by measuring the velocity of ultrasonic pulses propagating inside the pore volume, the porous frame being successively saturated by different gases.[17] At high frequencies, from Eqs. (4)–(6), the squared ratio $(c_0/c)^2$ of the sound velocity in free air c_0 to the sound velocity c in the pore volume can be written in a simple form

$$\left(\frac{c_0}{c}\right)^2=\alpha_\infty\left\{1+\left(\frac{2\eta}{\omega\rho}\right)^{1/2}\left(\frac{1}{\Lambda}+\frac{\gamma-1}{(\mathrm{Pr}^{1/2}\Lambda')}\right)\right\}. \tag{9}$$

This equation shows that the squared ratio $(c_0/c)^2\to\alpha_\infty$ when $\omega\to\infty$, and $(c_0/c)^2-\alpha_\infty$ depends linearly on $(1/\omega)^{1/2}$. The validity of the modeling is limited toward the high frequencies by scattering[10] around 100 kHz for usual reticulated plastic foams and the asymptotic expression (9) is valid in a large range of frequencies for these materials.

The velocity for a sample of glass beads has been measured using a capacitive vibrating membrane to create an acoustic pulse in air. A B&K 4138 condenser microphone was used to detect the signal after transmission through a 26-mm-thick sample. The phase velocity was determined

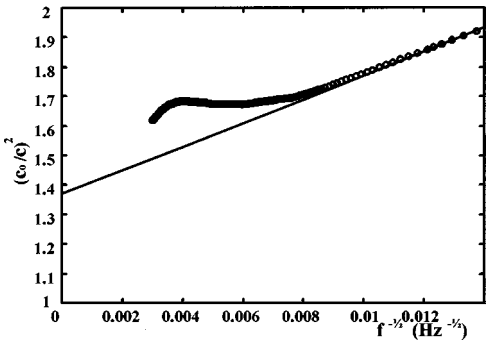

FIG. 3. $(c_0/c)^2$ as a function of $1/(f)^{1/2}$: measurement ○○○, prediction ———.

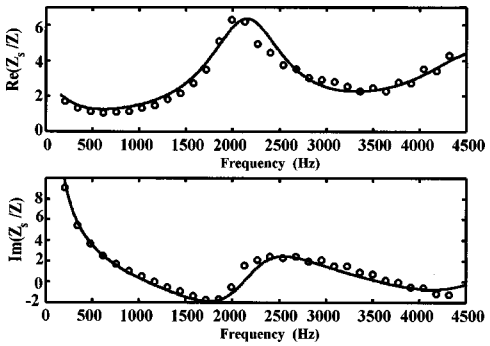

FIG. 4. Normalized surface impedance: measurement ○○○, prediction ———.

from the unwrapped phase of the Fourier transform of the received pulse. More details on the experimental procedure can be found in Ref. 17.

The measured squared ratio $(c_0/c)^2$ is represented in Fig. 3 and compared to predictions obtained without approximations from Eqs. (4)–(6) with the parameters ϕ, k_0, α_∞, k_0', and Λ' evaluated previously in this section, and $\Lambda = 0.9\times10^{-4}$ m. The agreement between prediction and measurement is good at frequencies lower than 15 kHz, but for higher frequencies the equivalent fluid model is not valid, due to scattering.[10] It may be noticed that the value of α_∞, determined from the phase velocity curve using the asymptotic expression (9) (as described in Ref. 17) is 1.37, very close to the value obtained from the conductivity measurements. Due to the scattering that occurs at 15 kHz, the asymptotic expression (9) is only accurate in a small interval and the precision on the ultrasonic measurement of α_∞ is less than reported in Ref. 17. Straley *et al.*[18] have shown that Λ and k_0 for random packings of beads are approximately related by $\Lambda = (4Fk_0)^{1/2}$. Using this relation with the measured values of α_∞, ϕ, and k_0 gives $\Lambda = 1.4\times10^{-4}$ m. The order of magnitude is the same as that of the measured value. In the following sections, the values for the set of parameters used in Eqs. (4) and (5) will be

$$\phi = 0.4, \quad k_0 = 1.5\times10^{-9}\ \text{m}^2, \quad \alpha_\infty = 1.37,$$

$$\Lambda = 0.9\times10^{-4}\ \text{m}, \quad k_0' = 5\times10^{-9}\ \text{m}^2,$$

$$\Lambda' = 0.32\times10^{-3}\ \text{m}.$$

A different model has been suggested previously by Attenborough.[19] The random bead packing is replaced by a system of parallel slits with a log-normal distribution for the semithickness. The macroscopic parameters related to a similar model have been calculated by Lafarge *et al.*[7] In the context of this last model, $\Lambda = \Lambda'$ and $k_0' = \alpha_\infty k_0$. For the glass beads of the present study, these relations are far from being satisfied by the measured parameters.

II. SURFACE IMPEDANCE AT NORMAL INCIDENCE OF A LAYER OF BEADS

The surface impedance at normal incidence of a porous layer is given by

$$Z_s = \frac{iZ_1}{\phi}\cot(k_1 l), \tag{10}$$

where l is the thickness of the layer. The surface impedance of a layer of the beads described in Sec. I, of thickness $l = 5.2$ cm, has been measured in an impedance tube. The surface impedance measured and predicted from Eqs. (4)–(7) and (10) with $\phi = 0.4$ are represented in Fig. 4. The agreement between prediction without any adjustable parameter and measurement is good. For the porous material studied, more sophisticated models, like the one by Pride *et al.*[20] for ρ_1, where a new parameter can be used to adjust $\mathrm{Re}\,\rho_1$ when $\omega\to0$, will not provide a noticeably better agreement with the measurement.

III. CONCLUSION

Acoustic properties of specific granular materials can be predicted accurately, without adjustable parameters, by using general transport parameters which have a precise physical meaning for other kinds of porous or fibrous structures. Conversely, acoustic measurements can provide a simple evaluation of these parameters, for instance, the trapping constant in the present work.

[1] D. Bideau and A. Hansen (Eds.), *Disorder and Granular Media* (North Holland, New York, 1993).

[2] R. J. S. Brown, ''Connection between Formation Factor of Electrical Resistivity and Fluid-Solid Coupling Factor in Biot's Equations for Acoustic Waves in Fluid-Filled Porous Media,'' Geophysics **45**, 1269–1275 (1980).

[3] D. L. Johnson, J. Koplik, and L. M. Schwartz, ''New Pore-Size Parameter Characterizing Transport in Porous Media,'' Phys. Rev. Lett. **57**, 2564–2567 (1986).

[4] D. L. Johnson, J. Koplik, and R. Dashen, ''Theory of Dynamic Permeability and Tortuosity in Fluid-Saturated Porous Media,'' J. Fluid Mech. **176**, 379–402 (1987).

[5] S. Brunauer, P. H. Emmett, and E. Teller, ''Adsorption of Gases in Multimolecular Layers,'' J. Am. Chem. Soc. **A11**, 309–319 (1938).

[6] Y. Champoux and J. F. Allard, ''Dynamic Tortuosity and Bulk Modulus in Air-Saturated Porous Media,'' J. Appl. Phys. **70**, 1975–1979 (1991).

[7] D. Lafarge, P. Lemarinier, J. F. Allard, and V. Tarnow, ''Dynamic Compressibility of Air in Porous Structures at Audible Frequencies,'' J. Acoust. Soc. Am. **102**, 1995–2006 (1997).

[8] S. Chandrasekhar, ''Stochastic Problems in Physics and Astronomy,'' Rev. Mod. Phys. **15**, 1–89 (1943).

[9] S. Torquato and M. Avellaneda, ''Diffusion and Reaction in Heterogeneous Media: Pore Size Distribution, Relaxation Times, and Mean Survival Time,'' J. Chem. Phys. **95**, 6477–6489 (1991).

[10] P. Leclaire, L. Kelders, W. Lauriks, J. F. Allard, and C. Glorieux, ''Ultrasonic Wave Propagation in Reticulated Foams Saturated by Different Gases—High Frequency Limit of Classical Models,'' Appl. Phys. Lett. **69**, 2641–2643 (1997).

[11] D. Lafarge, ''Propagation du Son dans les Matériaux Poreux à Structure

Rigide Saturés par un Fluide Viscothermique. Définition des Paramètres Géométriques, Analogie Electromagnétique, Temps de Relaxation,'' Ph.D., Le Mans, France, 1993.
[12] J. G. Berryman, ''Random Close Packing of Hard Spheres and Disks,'' Phys. Rev. A **27**, 1053–1061 (1983).
[13] Z. Wong, J. Koplik, and J. P. Tomanic, ''Conductivity and Permeability of Rocks,'' Phys. Rev. B **30**, 6606–6614 (1984).
[14] A. Debray, J. F. Allard, W. Lauriks, and L. Kelders, ''Acoustic Measurement of the Trapping Constant of Porous Materials,'' Rev. Sci. Instrum. **68**, 4462–4465 (1997).
[15] V. Tarnow, ''Measurement of Sound Propagation in Glass Wool,'' J. Acoust. Soc. Am. **97**, 2272–2281 (1995).
[16] S. B. Lee, I. C. Kim, and C. A. Miller, ''Random-Walk Simulation of Diffusion-Controlled Processes Among Static Traps,'' Phys. Rev. B **39**, 11833–11839 (1988).
[17] P. Leclaire, L. Kelders, W. Lauriks, M. Melon, N. Brown, and B. Castagnède, ''Determination of the Viscous and Thermal Characteristic Lengths of Plastic Foams by Ultrasonic Measurements in Helium and Air,'' J. Appl. Phys. **80**, 2009–2012 (1996).
[18] C. Straley, A. Matteson, S. Feng, M. Schwartz, W. E. Kenyon, and J. R. Banavar, ''Magnetic Resonance, Digital Image Analysis, and Permeability of Porous Media,'' Appl. Phys. Lett. **51**, 1146–1148 (1987).
[19] K. Attenborough, ''Models for the Acoustical Properties of Air-Saturated Granular Media,'' Acta Acustica **1**, 213–226 (1993).
[20] S. R. Pride, F. Dale Morgan, and A. F. Gangi, ''Drag Forces of Porous Medium Acoustics,'' Phys. Rev. B **47**, 4964–4978 (1993).

On the effect of spatial dispersion on the degeneracies of acoustic-wave branches in crystals

A. L. Shuvalov[a)]
Department of Mathematical Physics, University College Dublin, Belfield, Dublin 4, Ireland

(Received 9 September 1997; accepted for publication 30 April 1998)

The effect of spatial dispersion on the phase-speed degeneracies of acoustic waves in noncentrosymmetric crystals is explored in the framework of continuum elasticity. It is shown that the degeneracies, which in the nondispersive limit occur in directions neither lying in a symmetry plane nor parallel to a rotation inversion axis, are lifted on account of spatial dispersion. The degeneracies lying in symmetry planes change their in-plane orientation depending on the frequency, unless remaining fixed to a symmetry axis. Given that the degeneracy with regard for linear spatial dispersion occurs in some direction **m**, the value of degenerate phase speed coincides with the value of one of the speeds assigned to **m** in the nondispersive limit. Relations for the acoustic-wave parameters with dispersive corrections are derived and discussed for various particular cases. © *1998 Acoustical Society of America.* [S0001-4966(98)04008-9]

PACS numbers: 43.20.Jr [ANN]

INTRODUCTION

The degeneracy of acoustic branches is a significant concept both for elastic-wave propagation and for phonon phenomena in crystals. In the nondispersive limit, an essential attribute of wave propagation in the neighborhood of acoustic axes (directions, for which two modes have equal phase speeds) is the singularity of the polarization vector fields which underlies specific features of various effects, related to acoustic polarization, and stipulates the stability conditions of the phase-speed degeneracy with respect to external perturbations.[1,2] Linear spatial dispersion markedly disturbs acoustic properties of noncentrosymmetric crystals in the hypersonic frequency range, and its impact is especially salient when degeneracies are involved. It brings about the well-known phenomenon of the rotation of linear polarization upon the wave path along the high-symmetry axes (acoustic activity).[3,4] Also, it stipulates specific effects of acousto-optical diffraction, at which lifting of acoustic-wave degeneracy may allow for components of acousto-optical coupling forbidden in the nondispersive limit.[5] Dispersive properties of low-energy acoustic phonons, particularly in the neighborhood of degeneracies, manifest themselves vividly on the focusing patterns of phonon imaging, when spatial dispersion, affecting the degeneracies and, thereby, the corresponding singular points on the slowness surface, unfolds the phonon-focusing cusps.[6] Besides, degenerate and quasidegenerate acoustic phonons play important roles in such kinetic processes as thermal conductivity and dielectric losses.[7]

The frequency range, in which the lattice parameter a is much less than the wavelength λ, allows for the description of dispersive features of both elastic waves and acoustic phonons in the common setting of continuum elasticity generalized by taking account of the leading terms of the appropriate expansion in (a/λ).[3,8] Proceeding from the equations of elastodynamics with dispersive corrections, the effect of spatial dispersion on the acoustic axes coinciding with symmetry axes has been studied in Refs. 3, 6, 8, and 9. In terms of lattice dynamics, the properties of acoustic-phonon branches along the wave vector **k** parallel to symmetry axes were elicited with the aid of group-theoretic methods.[3,7,8,10] Both approaches established that in the directions of the rotation axes of symmetry, which are not lying in a symmetry plane, the degeneracy between sheets of the isofrequency surface is removed on account of linear spatial dispersion. At the same time, it was not clarified whether the degeneracy is lifted ''comprehensively'' from the neighboring domain under the effect of dispersive corrections, or the direction of degeneracy becomes nonstationary (frequency dependent) and shifts from the symmetry axis due to spatial dispersion. Neither the behavior of degeneracies in arbitrary (nonsymmetric) directions in response to spatial dispersion was analyzed generally, except for some particular comments [see, e.g., Refs. 5 and 6, in which the effect of spatial dispersion on nonsymmetrical acoustic axes in, respectively, quartz (symmetry class 32) and paratellurite (symmetry class 422) was considered].

The purpose of this paper is to study the impact of spatial dispersion on the problem of phase-speed degeneracies of acoustic waves in elastic media in the general context of unrestricted anisotropy. Both algebraic and perturbation-theory methods are applied to consider arbitrary nonsymmetric directions, and to evaluate the role of crystal symmetry. It is shown that, unless symmetry planes or rotation inversion axes intervene, an acoustic axis, which is established in a noncentrosymmetric crystal in the nondispersive limit, vanishes on account of spatial dispersion. This is in contrast to the effect of spatial dispersion in centrosymmetric crystals, in which such an acoustic axis acquires frequency-dependent orientation. In the former case, the polarization singularity, underlying the stability of the phase-speed degeneracy in the

[a)]Permanent address: Institute of Crystallography, Russian Academy of Sciences, Leninsky pr. 59, Moscow 117333, Russia.

nondispersive limit, is smoothed for the complex-valued amplitudes of dispersive acoustic waves.

I. BASIC EQUATIONS

Consider an anisotropic elastic medium, characterized by the density ρ and the elasticity tensor $\mathbf{c}$ with components $c_{ijkl}=c_{jikl}=c_{ijlk}=c_{klij}$. The propagation of elastic displacements $\mathbf{u}$ is governed by the equation of motion,

$$c_{ijkl}u_{k,jl}=\rho\ddot{u}_i \tag{1}$$

(comma in subscript and superposed dot implying the spatial and time derivatives, respectively). The solutions may be sought in the form of plane harmonic waves,

$$\mathbf{u}=U\mathbf{A}e^{i(\mathbf{kr}-\omega t)}, \tag{2}$$

where U is a scalar amplitude with the physical dimension of length, $\mathbf{A}$ is the unit polarization vector, $\mathbf{k}=\mathbf{m}\omega/v$ is the wave vector, $\mathbf{m}$ is the unit vector of wave normal, ω is the frequency, v is the phase speed. Insertion of (2) into (1) yields the Christoffel equation,

$$\Lambda\mathbf{A}=v^2\mathbf{A}, \tag{3}$$

where the Christoffel tensor Λ is represented in an arbitrary Cartesian base by the real symmetric positive-definite matrix,

$$\Lambda_{ik}=\frac{1}{\rho}\,m_j c_{ijkl}m_l\,. \tag{4}$$

Eigenvalue problem (3) entails the characteristic equation,

$$\det(\Lambda-v^2\mathbf{I})=0, \tag{5}$$

where $\mathbf{I}$ is the 3×3 identity matrix. The three bulk acoustic wave branches are characterized by real phase speeds $v_\alpha(\mathbf{m})$ [or slownesses $\mathbf{s}_\alpha(\mathbf{m})=v_\alpha^{-1}$, $\alpha=1,2,3$] and mutually orthogonal polarizations $\mathbf{A}_\alpha(\mathbf{m})$ delivered, respectively, by eigenvalues and eigenvectors of $\Lambda(\mathbf{m})$. In the direction of acoustic axes, phase speeds of two branches merge so that Λ has a repeated eigenvalue, and hence the corresponding polarization vector may take an arbitrary orientation in the plane orthogonal to the polarization of the nondegenerate wave. As a result of this multivalence, the polarization fields $\mathbf{A}_\alpha(\mathbf{m})$ of degenerate branches in the neighborhood of the acoustic axis are characterized by topologically invariant singularities underlying the stability properties of phase-speed degeneracy with respect to such perturbations which retain Λ in (3) as a real and symmetric tensor.[1,2]

The dispersive corrections may be incorporated into continuum elasticity by expanding the elastic coefficients in power series in the wave vector $\mathbf{k}$,

$$c_{ijkl}(\mathbf{k})=c_{ijkl}+id_{ijklp}k_p+\cdots\,, \tag{6}$$

so that linear spatial dispersion reveals itself in noncentrosymmetric crystals, in which the odd-rank tensor $\mathbf{d}$ is not vanishing (thereafter, noncentrosymmetric media are implied by default, unless otherwise explicitly specified). Under the assumption of time-reversal invariance,

$$d_{ijklp}=-d_{klijp}\,. \tag{7}$$

The expansion (6) and the symmetry (7) were given in Ref. 3 on phenomenological grounds. The link between the derivations of (6) by appealing to classical continuum mechanics and to microscopic lattice-dynamics description of vibrations was established in Ref. 8. It was shown that, although the coefficients of the expansion indeed acquire respectively different interpretations in the frameworks of continuum mechanics and lattice dynamics, their connection (including involved symmetry properties) is unique.

It is convenient to introduce the second-rank antisymmetric tensor,

$$g_{ik}^{\times}=\frac{1}{\rho}\,d_{ijklp}m_j m_l m_p\,, \tag{8}$$

which is dual to the axial vector $\mathbf{g}$ according to the definition $g_{ik}^{\times}\equiv\delta_{ikr}g_r=-g_{ki}^{\times}$, so that $\mathbf{g}^{\times}\mathbf{A}\equiv\mathbf{A}\times\mathbf{g}$ (δ_{ikr} is the Levi-Civita pseudotensor; $\times$ denotes the vector product).[9] It follows that the vector $\mathbf{g}$ and the tensor $\mathbf{d}$ are related as follows:

$$g_n=\frac{1}{2\rho}\,\delta_{nqs}d_{qjslp}m_j m_l m_p\,. \tag{9}$$

The order of magnitude of components g_n for a generic direction $\mathbf{m}$ may be evaluated by the condition $kg/v^2\sim ka\ll1$. The Christoffel equation, modified with regard for linear spatial dispersion, may be written with the aid of these notations in the form,[9]

$$(\Lambda+ik\mathbf{g}^{\times})\mathbf{A}=v^2\mathbf{A}, \tag{10}$$

in which the axial vector $\mathbf{g}$ encapsulates the contribution of linear spatial dispersion.

The piezoelectric effect may also be included in the consideration by standard augmenting Λ with coupled terms and, moreover, by incorporating the dispersive corrections to piezoelectric coefficients which modify the explicit form of $\mathbf{g}$.[8,11] However, for the sake of brevity, we are adhering to the framework of pure elasticity, because the contribution of electromechanical coupling preserves the intrinsic features of the wave Eq. (10) which make the subject of the foregoing study.

The characteristic equation associated with (10) may be written as

$$\det(\Lambda+ik\mathbf{g}^{\times}-v^2\mathbf{I})=\det(\Lambda-v^2\mathbf{I})-k^2\mathbf{g}\cdot(\Lambda-v^2\mathbf{I})\mathbf{g}=0. \tag{11}$$

Here we exploit the identity $\det(\boldsymbol{\alpha}+\boldsymbol{\beta})=\det\boldsymbol{\alpha}+\mathrm{tr}(\overline{\boldsymbol{\alpha}}\boldsymbol{\beta})+\mathrm{tr}(\boldsymbol{\alpha}\overline{\boldsymbol{\beta}})+\det\boldsymbol{\beta}$ for arbitrary 3×3 matrices $\boldsymbol{\alpha}$, $\boldsymbol{\beta}$ (tr denotes trace, and superposed bar implies adjugate of a matrix), the identities $\det\mathbf{g}^{\times}=0$, $\mathrm{tr}(\boldsymbol{\alpha}\mathbf{g}^{\times})=0$, $\overline{\mathbf{g}^{\times}}=\mathbf{g}\otimes\mathbf{g}$ ($\otimes$ denotes the dyadic product) for a symmetric matrix α and an axial vector $\mathbf{g}$, and the identity $\mathrm{tr}(\mathbf{a}\otimes\mathbf{b})=\mathbf{a}\cdot\mathbf{b}$ for arbitrary vectors $\mathbf{a}$, $\mathbf{b}$ (Ref. 12, §12). For a given direction $\mathbf{m}$, Eq. (11) defines three real roots $v_\alpha^2(k)$ ($\alpha=1,2,3$), provided that the wave number k is considered as a free parameter. This fits the interpretation in terms of acoustic-phonon branches characterized by the dispersion dependencies $\omega_\alpha=kv_\alpha(k)$ ($\alpha=1,2,3$) in the given direction $\mathbf{m}=\mathbf{k}/k$. Alternatively, the frequency ω may be regarded as a free parameter, thus matching the case of wave modes excited by a source at some ω and characterized by the dependencies $k_\alpha=\omega/v_\alpha(\omega)$ ($\alpha=1,2,3$). In the latter setting, recalling that $kg/v^2\ll1$, one may successively approximate k in Eq. (11)

by the values ω/v_α, where v_α ($\alpha=1,2,3$) are the phase speeds of the three modes traveling along $\mathbf{m}$ in the nondispersive limit. On such a substitution, the cubic equation in v^2, which follows from (11) for each of the three wave branches $\alpha=1,2,3$, yields a single appropriate solution satisfying the requirement that $v_\alpha(\omega)\to v_\alpha$ at $\mathbf{g}\to 0$.

We note that, in order to distinguish between values v_α, $\mathbf{A}_\alpha$ ($\alpha=1,2,3$) determined for the same direction $\mathbf{m}$, respectively, in the nondispersive limit and with regard for dispersive corrections, the values referred to in the latter case are hereafter supplied with an argument k or ω in parentheses, whereas the dependence on $\mathbf{m}$ is tacit.

II. CONDITIONS FOR DEGENERACY IN THE PRESENCE OF SPATIAL DISPERSION

A. General considerations

A double degenerate eigenvalue of the Hermitian matrix $\Lambda+ik\mathbf{g}^\times$, say $v_1^2(k)=v_2^2(k)\equiv v_d^2(k)$, must satisfy the condition

$$\overline{\Lambda+ik\mathbf{g}^\times-v_d^2(k)\mathbf{I}}=0 \tag{12}$$

(superposed line implies an adjugate matrix), which implicitly includes (11). The left-hand side may be cast into the form,

$$\overline{\Lambda+ik\mathbf{g}^\times-v_d^2(k)\mathbf{I}}=\overline{\Lambda-v_d^2(k)\mathbf{I}}-k^2\mathbf{g}\otimes\mathbf{g} -ik[(\Lambda-v_d^2(k)\mathbf{I})\mathbf{g}]^\times. \tag{13}$$

Here we use the identity $\overline{\boldsymbol{\alpha}+\boldsymbol{\beta}}=\overline{\boldsymbol{\alpha}}+\overline{\boldsymbol{\beta}}+\boldsymbol{\alpha}\boldsymbol{\beta}+\boldsymbol{\beta}\boldsymbol{\alpha}-(\mathrm{tr}\,\boldsymbol{\alpha})\boldsymbol{\beta}-(\mathrm{tr}\,\boldsymbol{\beta})\boldsymbol{\alpha}+(\mathrm{tr}\,\boldsymbol{\alpha})(\mathrm{tr}\,\boldsymbol{\beta})-\mathrm{tr}(\boldsymbol{\alpha}\boldsymbol{\beta})$ for arbitrary matrices $\boldsymbol{\alpha}$, $\boldsymbol{\beta}$ (Ref. 12, §12), which on substituting a symmetrical matrix $\boldsymbol{\alpha}$ and an antisymmetric matrix $\mathbf{g}^\times$ becomes $\overline{\boldsymbol{\alpha}+\mathbf{g}^\times}=\overline{\boldsymbol{\alpha}}+\mathbf{g}\otimes\mathbf{g}+\boldsymbol{\alpha}\mathbf{g}^\times+\mathbf{g}^\times\boldsymbol{\alpha}-(\mathrm{tr}\,\boldsymbol{\alpha})\mathbf{g}^\times$. It may be further shown that the antisymmetric matrix $\boldsymbol{\alpha}\mathbf{g}^\times+\mathbf{g}^\times\boldsymbol{\alpha}$ is dual to the vector, which is a scalar multiple of $(\mathbf{g}-\boldsymbol{\alpha}\mathbf{g})$, so that $\boldsymbol{\alpha}\mathbf{g}^\times+\mathbf{g}^\times\boldsymbol{\alpha}+(\boldsymbol{\alpha}\mathbf{g})^\times$ is proportional to $\mathbf{g}^\times$ with the factor equal to $\mathrm{tr}\,\boldsymbol{\alpha}$ (Ref. 13, §26). Inserting the standard spectral decomposition,

$$\Lambda=\sum_{\alpha=1}^{3} v_\alpha^2\mathbf{A}_\alpha\otimes\mathbf{A}_\alpha, \tag{14}$$

into (13) reveals that Eq. (12) may be decomposed into two real equations,

$$\overline{\Lambda-v_d^2(k)\mathbf{I}}-k^2\mathbf{g}\otimes\mathbf{g}=0, \tag{15}$$

$$\sum_{\alpha=1}^{3}[v_\alpha^2-v_d^2(k)]g_\alpha\mathbf{A}_\alpha=0, \tag{16}$$

where $g_\alpha\equiv\mathbf{g}\cdot\mathbf{A}_\alpha$.

Let $\mathbf{m}$ be the direction of phase-speed degeneracy established in the nondispersive limit, say $v_1=v_2\equiv v_d$. The corresponding necessary and sufficient condition is

$$\overline{\Lambda-v_d^2\mathbf{I}}=0. \tag{17}$$

By (15)–(17), it is seen that the degeneracy in the presence of linear spatial dispersion survives along a given $\mathbf{m}$ at varying k, if and only if $v_d(k)=v_d$ and the vector $\mathbf{g}$ defined by (9) identically vanishes for the given $\mathbf{m}$ [otherwise, incidental degeneracy with the third wave branch is possible at $g_1=g_2=0$ for the secluded value $k=|(\Lambda_{11}-\Lambda_{33})/g_3|$ where $\Lambda_{\alpha\beta}\equiv\mathbf{A}_\alpha\cdot\Lambda\mathbf{A}_\beta$].

Consider the conditions of degeneracy in a generic direction $\mathbf{m}$, which is not an acoustic axis in the nondispersive limit and for which $\mathbf{g}(\mathbf{m})\neq 0$. By (16), the degenerate value $v_d(k)$ must be equal to one of the speeds referred to in the nondispersive limit, say

$$v_d(k)=v_1, \tag{18}$$

and hence $g_2=g_3=0$. Inserting these equalities into (15), we infer the equation on g_1, so that the conditions for the degeneracy may be put together in the form of three restrictions,

$$g_1=\frac{1}{k}\{(v_2^2-v_1^2)(v_3^2-v_1^2)\}^{1/2},\quad g_2=0,\quad g_3=0, \tag{19}$$

imposed on the vector $\mathbf{g}$, which by definition (9) depends on $\mathbf{m}$ and k (or ω), i.e., on three real scalar parameters. The same results follow when the frequency ω is set as a free parameter, except that Eq. (19_1) modifies by the substitution of ω/v_1 instead of k. Hence, we may conclude that in noncentrosymmetric crystals the degeneracy of dispersive acoustic branches cannot persist at variation of $\mathbf{k}=k\mathbf{m}$ in both length and orientation in nonsymmetric directions, and may possibly come about only for some secluded values of k (or ω) and $\mathbf{m}$. This conclusion remains valid indeed with additional regard for the complementary effect of the next-order dispersive terms of the expansion (6). However, restrictions on the degeneracy subside for symmetry directions (see next subsection).

In centrosymmetric crystals, the principal (quadratic) dispersive corrections are represented by a real symmetric matrix added to the Christoffel tensor Λ. Acoustic axes of the general type, which are associated with the conical contact of the slowness sheets at the point of degeneracy, are stable with respect to such a perturbation,[1,2] hence in this case they merely shift their orientations $\mathbf{m}$ depending on k (or ω). On the other hand, the nonstability of degeneracies in nonsymmetric directions of noncentrosymmetric crystals with respect to spatial dispersion should not be put down just to the fact that the dispersive corrections to Λ in this case are complex valued. For instance, the effect of thermoelastic coupling in heat-conducting media, which also casts the wave problem into the complex-valued domain, modifies the acoustic-wave degeneracies but nevertheless retains their stability.[14]

B. Role of crystal symmetry

Regarding the nondispersive limit, consider an acoustic axis which lies in a symmetry plane m and normally implies the degeneracy between the out-of-plane polarized transverse mode and one of the in-plane polarized modes (e.g., Ref. 12, §25). For any direction $\mathbf{m}\in m$, the axial vector $\mathbf{g}$ (9) is orthogonal to m and therefore, according to (10), the wave branch with the out-of-plane transverse polarization is not affected by linear spatial dispersion. Condition (19) applied

to the acoustic axis in a symmetry plane m reduces to a single equation in two scalar parameters which are the angular coordinate of the acoustic axis in m, and k (or ω). Consequently, in noncentrosymmetric crystals there exist the curves of degeneracy of acoustic-phonon branches $\omega_\alpha(\mathbf{k})$ ($\alpha=1,2,3$), as $\mathbf{k}$ varies in its length and orientation in symmetry planes (whereas the similar curves in centrosymmetric crystals are not limited to symmetry planes). By virtue of (18), the values of degenerate phase speed $v_d(\mathbf{k})$ for $\mathbf{k}\in m$ are equal to the speed of the out-of-plane transverse mode taken for the same propagation direction $\mathbf{m}=\mathbf{k}/k$ in the nondispersive limit.

The symmetry axes, which represent the intersection of symmetry planes, and any of the rotation inversion axes, stipulate identical vanishing of $\mathbf{g}$, so the phase-speed degeneracy along such axes is not affected by linear spatial dispersion. Otherwise, the principal symmetry axes belonging to the groups 432, 23, 622, 6, 422, 4, and the threefold axes in the cubic groups 432, 23, provide a nonzero axial vector $\mathbf{g}$; hence the degeneracies, which are maintained along these symmetry axes in the nondispersive limit, are removed on account of linear spatial dispersion.[3,10] Furthermore, because these axes do not belong to symmetry planes, the effect of linear dispersion lifts the degeneracy from the neighborhood of the axes just as it is in the nonsymmetric case considered in Sec. III A.

We note that in the centrosymmetric crystals there is a single case when quadratic spatial dispersion disturbs the degeneracy referred to in the nondispersive limit to a symmetry axis, namely, the tangency of the slowness sheets in the directions of twofold axes in the group $m3$ splits into conicaltype degeneracies diverging from the axes.

III. PERTURBATION-THEORY APPROACH

A. Perturbation in the nondegenerate case

By virtue of (10), the polarization vectors $\mathbf{A}_\alpha(k)$ associated with nondegenerate speeds $v_\alpha(k)$ satisfy the relation,

$$\mathbf{A}_\alpha(k)\otimes\mathbf{A}^*_\alpha(k)\propto\overline{\Lambda+ik\mathbf{g}^\times-v^2_\alpha(k)\mathbf{I}}\quad(\alpha=1,2,3)\tag{20}$$

(asterisk denotes complex conjugation; $\propto$ implies that the two matrices in (20) are scalar multiples of each other). According to identities (13) and (14), the polarization related, say, to the wave branch $\alpha=1$, may be written as

$$\begin{aligned}A_1(k)\|&\{[v_2^2-v_1^2(k)][v_3^2-v_1^2(k)]-k^2g_1^2\}\mathbf{A}_1\\&+\{ik[v_3^2-v_1^2(k)]g_3-k^2g_1g_2\}\mathbf{A}_2\\&+\{-ik[v_2^2-v_1^2(k)]g_2-k^2g_1g_3\}\mathbf{A}_3,\end{aligned}\tag{21}$$

where $\|$ between two vectors indicates that they are parallel, and we recall the notation $g_\alpha\equiv\mathbf{g}\cdot\mathbf{A}_\alpha$. The exact relation (21) contains the roots $v_1^2(k)$ of Eq. (11). Provided that $|v_2-v_1|$, $|v_3-v_1|\gg|v_1(k)-v_1|$, i.e., that the given direction $\mathbf{m}$ is remote from acoustic axes determined in the nondispersive limit, the perturbation theory yields

$$v_1^2(k)=v_1^2+k^2\left(\frac{g_2^2}{v_2^2-v_1^2}+\frac{g_3^2}{v_3^2-v_1^2}\right).\tag{22}$$

Regarding the frequency ω as a free parameter, one needs to replace the parameter k by ω/v_1 in Eqs. (21) and (22). Similar relations for the branches $\alpha=2,3$ follow by obvious permutation of indices. It is seen that for directions, remote from degeneracies, linear spatial dispersion entails small ellipticity of polarizations proportional to (ka), and weak distortion of the phase speeds in the $(ka)^2$-order.[8,9] We note that, by (22), the effect of linear spatial dispersion increases the lowest of the three speeds and decreases the highest one; however, this conclusion may be violated on account of quadratic spatial dispersion which contributes to $v_\alpha^2(k)$ in the same $(ka)^2$-order.

As mentioned in Sec. III B, for any direction $\mathbf{m}$ lying in a symmetry plane m the vector $\mathbf{g}$ is orthogonal to m, therefore the out-of-plane transverse wave branch is not affected by linear spatial dispersion. According to (21) and (22), the displacement vectors associated with the other two modes circumscribe ellipses which lie in m and have principal axes along polarization vectors of these modes taken in the nondispersive limit.

B. Perturbation of the conicaltype degeneracy

Proceeding from the nondispersive limit, consider an arbitrary phase-speed degeneracy in some nonsymmetric direction denoted as $\mathbf{m}_{0d}$, and assume the general possibility for a contact of degenerate slowness sheets at $\mathbf{m}_{0d}$ which is the conicaltype contact. We denote the wave parameters, referred to as $\mathbf{m}_{0d}$ in the absence of spatial dispersion, as

$$\begin{aligned}&v_1(\mathbf{m}_{0d})=v_2(\mathbf{m}_{0d})\equiv v_{0d},\quad v_3(\mathbf{m}_{0d})\equiv v_{03},\\&\mathbf{A}_3(\mathbf{m}_{0d})\equiv\mathbf{A}_{03}.\end{aligned}\tag{23}$$

The distribution of the (real) polarization vectors $\mathbf{A}_\alpha(\mathbf{m})$ for each of the nondispersive wave branches $\alpha=1,2$ in the close proximity to $\mathbf{m}_{0d}$ represents a plane vector field with a singularity characterized by the Poincare index n. It measures in units of 2π the aggregate turn of the undirected vectors (segments) $\mathbf{A}_\alpha(\mathbf{m})$ accumulated on a closed circuit around $\mathbf{m}_{0d}$ (recall that the orientation $\mathbf{A}_\alpha$ at $\mathbf{m}=\mathbf{m}_{0d}$ is indefinite). In the case of the conicaltype acoustic axis, the Poincare index may take values $n=\pm1/2$ (see Fig. 1), which are specified by the criterion[2]

$$n=\tfrac{1}{2}\,\mathrm{sgn}\{[(\mathbf{A}_{01}\times\mathbf{A}_{02})\cdot\mathbf{m}_{0d}][(\mathbf{p}\times\mathbf{q})\cdot\mathbf{m}_{0d}]\},\tag{24}$$

where $\mathbf{A}_{01}$, $\mathbf{A}_{02}$ are arbitrary orthonormalized real vectors orthogonal to $\mathbf{A}_{03}$,

$$\begin{aligned}&\mathbf{p}=(\mathbf{A}_{01}\mathbf{c}\mathbf{A}_{01}-\mathbf{A}_{02}\mathbf{c}\mathbf{A}_{02})\mathbf{m}_{0d},\\&\mathbf{q}=(\mathbf{A}_{01}\mathbf{c}\mathbf{A}_{02}+\mathbf{A}_{02}\mathbf{c}\mathbf{A}_{01})\mathbf{m}_{0d}\end{aligned}\tag{25}$$

($\mathbf{A}_{0\alpha}\mathbf{c}\mathbf{A}_{0\beta}\mathbf{m}_{0d}\equiv A_{0\alpha_i}c_{ijkl}A_{0\beta_j}m_{0d_k}$), and $\mathbf{p}\times\mathbf{q}\neq0$, which embodies the assumption of the conical type of the degeneracy. The presence of such a topological singularity signals the stability of the degeneracy with respect to perturbations retaining the polarizations as real vectors. For instance, $n=-\frac{1}{2}$ in the case of conicaltype acoustic axis coinciding with a threefold symmetry axis.

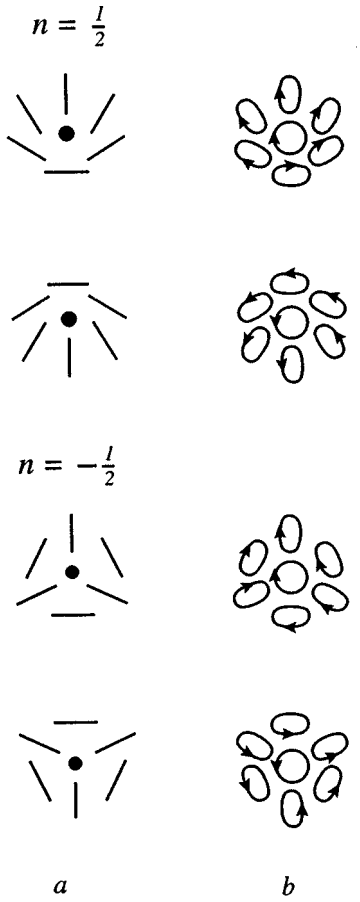

FIG. 1. The singular patterns of polarization fields $\mathbf{A}_\alpha(\mathbf{m})$ ($\alpha=1,2$) in the neighborhood of a conicaltype degeneracy in the nondispersive limit (a) and their transformation under the effect of linear spatial dispersion (b). [The filled circles in (a) imply arbitrary orientation of the polarization in the reference plane for the mode traveling strictly along the direction of degeneracy $\mathbf{m}_{0d}$; the arrows in (b) indicate the sense of traversal.]

Turning now to the effect of linear spatial dispersion, hereafter for definiteness we choose the frequency ω as a free parameter. Let us introduce the directions $\mathbf{m}$ in the neighborhood of $\mathbf{m}_{0d}$ as

$$\mathbf{m}(\theta,\varphi)\approx\mathbf{m}_{0d}+\theta\mathbf{e}_\varphi, \tag{26}$$

where θ ($\theta\ll 1$) is the small angle showing the deviation of the running vector $\mathbf{m}$ from the reference direction $\mathbf{m}_{0d}$; and $\mathbf{e}_\varphi$ is the unit vector, whose orientation in the plane orthogonal to $\mathbf{m}_{0d}$ may be described by the polar angle φ. We will also use the notation

$$g_{0\alpha}=\mathbf{g}_0\cdot\mathbf{A}_{0\alpha}, \quad \alpha=1,2,3, \tag{27}$$

where $\mathbf{g}_0\equiv\mathbf{g}(\mathbf{m}_{0d})$ is a constant vector (independent of θ, φ, ω) which is defined by (9) taken at $\mathbf{m}_{0d}$. By appeal to the perturbation-theory procedure for solving the perturbed Christoffel equation in the neighborhood of degeneracies,[2] the phase speeds $v_\alpha(\omega)$ and the polarization vectors $\mathbf{A}_\alpha(\omega)$ of the wave branches $\alpha=1,2$ in the leading approximation both in the dispersive corrections and in the deviation angle θ may be written in the form,

$$v_\alpha(\omega)=v_{0d}+\frac{1}{2v_{0d}}\left\{2v_{0d}\theta\mathbf{w}\cdot\mathbf{e}_\varphi \mp\left[(\theta\mathbf{p}\cdot\mathbf{e}_\varphi)^2+(\theta\mathbf{q}\cdot\mathbf{e}_\varphi)^2+\left(\frac{\omega}{v_{0d}}\right)^2 g_{03}^2\right]^{1/2}\right\}, \tag{28}$$

$$\mathbf{A}_\alpha(\omega)\|\left(\theta\mathbf{q}\cdot\mathbf{e}_\varphi+i\,\frac{\omega}{v_{0d}}\,g_{03}\right)\mathbf{A}_{01} +\left\{\theta\mathbf{p}\cdot\mathbf{e}_\varphi\mp\left[(\theta\mathbf{p}\cdot\mathbf{e}_\varphi)^2+(\theta\mathbf{q}\cdot\mathbf{e}_\varphi)^2+\left(\frac{\omega}{v_{0d}}\right)^2 g_{03}^2\right]^{1/2}\right\}\mathbf{A}_{02}, \tag{29}$$

where $\mathbf{w}=(1/2v_{0d})(\mathbf{A}_{01}\mathbf{c}\mathbf{A}_{01}+\mathbf{A}_{02}\mathbf{c}\mathbf{A}_{02})\mathbf{m}_{0d}$. Invoking (25), one may obtain, e.g., for the case of conicaltype degeneracy in the direction $\mathbf{m}_{0d}$ of the threefold axis in a trigonal crystal: $\mathbf{w}\cdot\mathbf{e}_\varphi=0$, $\mathbf{p}\cdot\mathbf{e}_\varphi=2(c_{14}\sin\varphi-c_{25}\cos\varphi)$, $\mathbf{q}\cdot\mathbf{e}_\varphi=2(c_{14}\cos\varphi+c_{25}\sin\varphi)$, where the angle φ is measured from the crystallographic axis X_1.

By (28), the effect of spatial dispersion lifts the degeneracy provided that $g_{03}\neq 0$. In accordance with the general considerations put forward in Sec. III A, the acoustic axis is not just removed from its ''original'' direction $\mathbf{m}_{0d}$, but the absence of degeneracy is ensured in the whole neighboring domain $\theta\leqslant\omega g/v^3\sim ka$. The complex polarization vectors $\mathbf{A}_1(\omega)$, $\mathbf{A}_2(\omega)$ approximated by (29) satisfy the Hermitian orthogonality condition $\mathbf{A}_1\cdot\mathbf{A}_2^*=0$ and lie in the common plane orthogonal to the real vector $\mathbf{A}_{03}$; hence (see Ref. 12, §45) the displacement vectors of the modes $\alpha=1,2$, propagating in the neighborhood of $\mathbf{m}_{0d}$, tend to circumscribe the coplanar orthogonal ellipses in mutually opposite directions. In particular, by (28) and (29), the speeds and polarizations of these modes, traveling strictly along the direction $\mathbf{m}_{0d}$ (i.e., at $\theta=0$), may be written in the leading approximation as

$$v_\alpha(\omega,\mathbf{m}_{0d})=v_{0d}\mp\frac{\omega|g_{03}|}{2v_{0d}^2}, \quad \mathbf{A}_\alpha(\mathbf{m}_{0d})\|\mathbf{A}_{01}\pm i\mathbf{A}_{02}, \tag{30}$$

where (30_1) reveals the (ka)-order impact of linear spatial dispersion, and (30_2) implies circular polarizations with opposite senses of traversal.[3,9] The latter property provides for the rotation of linear polarization (orthogonal to $\mathbf{A}_{03}$) of the coupled-modes disturbance traveling along $\mathbf{m}_{0d}$.

Thus, the acoustic-activity phenomenon of the polarization rotation pertains to the directions of acoustic axes in general, rather than just to those which coincide with the appropriate symmetry axes from the list[3,10] mentioned in Sec. III B. The difference is that in the case of symmetry axes, first, the rotation is concerned with pure transverse modes polarized in the plane orthogonal to $\mathbf{m}_{0d}$, and, second, Eqs. (30) prove to be exact to within the $(ka)^2$-order inclusively, which is because neither the vector $\mathbf{g}_0\|\mathbf{m}_{0d}\|\mathbf{A}_{03}$ in the second order of the perturbation theory, nor quadratic spatial dispersion, affects the wave solutions (see also Sec. IV C).

The patterns of the plane distribution of arbitrarily normalized polarization ellipses (29) in the close neighborhood of $\mathbf{m}_{0d}$ are schematically presented in Fig. 1(b). By sticking to principal axes of the ellipses, these distributions may be

understood as fields of the crosses assigned with orientation and length. On comparing with Fig. 1(a), which shows the singular patterns of fields of linear polarizations in the same plane in the nondispersive limit, we observe that it is the presence of the circular polarization (30) which smoothes the ''original'' topological singularity at $\mathbf{m}_{0d}$, and therefore allows for the vanishing of the degeneracy under the effect of spatial dispersion.

Let us envisage the remaining possibility, which is the orthogonality of the nonzero vector $\mathbf{g}_0 \equiv \mathbf{g}(\mathbf{m}_{0d})$ to $\mathbf{A}_{03}$, i.e., $\mathbf{g}_0 \cdot \mathbf{A}_{03} \equiv g_{03} = 0$, $\mathbf{g}_0^2 = g_{01}^2 + g_{02}^2 \neq 0$. Given that, perturbation theory yields the following relations for the wave branches $\alpha = 1,2$ in the neighborhood of $\mathbf{m}_{0d}$,

$$v_\alpha(\omega) = v_{0d} + \frac{1}{2v_{0d}} \left\{ 2v_{0d}\theta \mathbf{w}\cdot\mathbf{e}_\varphi + \frac{\omega^2 \mathbf{g}_0^2}{2v_{0d}^2(v_{0d}^2 - v_{03}^2)} \mp \left[\left(\theta \mathbf{p}\cdot\mathbf{e}_\varphi + \frac{\omega^2(g_{01}^2 - g_{02}^2)}{2v_{0d}^2(v_{0d}^2 - v_{03}^2)} \right)^2 + \left(\theta \mathbf{q}\cdot\mathbf{e}_\varphi - \frac{\omega^2 g_{01} g_{02}}{v_{0d}^2(v_{0d}^2 - v_{03}^2)} \right)^2 + \left(\frac{\omega g_3}{v_{0d}} \right)^2 \right]^{1/2} \right\}, \quad (31)$$

$$\mathbf{A}_\alpha(\omega) \| \left(\theta \mathbf{q}\cdot\mathbf{e}_\varphi - \frac{\omega^2 g_{01} g_{02}}{v_{0d}^2(v_{0d}^2 - v_{03}^2)} + i\,\frac{\omega g_3}{v_{0d}} \right) \mathbf{A}_{01} + \left\{ \theta \mathbf{p}\cdot\mathbf{e}_\varphi + \frac{\omega^2(g_{01}^2 - g_{02}^2)}{2v_{0d}^2(v_{0d}^2 - v_{03}^2)} \mp \left[\left(\theta \mathbf{p}\cdot\mathbf{e}_\varphi + \frac{\omega^2(g_{01}^2 - g_{02}^2)}{2v_{0d}^2(v_{0d}^2 - v_{03}^2)} \right)^2 + \left(\theta \mathbf{q}\cdot\mathbf{e}_\varphi - \frac{\omega g^2 g_{01} g_{02}}{v_{0d}^2(v_{0d}^2 - v_{03}^2)} \right)^2 + \left(\frac{\omega g_3}{v_{0d}} \right)^2 \right]^{1/2} \right\} \mathbf{A}_{02}, \quad (32)$$

where $g_3(\mathbf{m}) \equiv \mathbf{g}(\mathbf{m}) \cdot \mathbf{A}_{03}$.

The condition $\mathbf{g}_0 \cdot \mathbf{A}_{03} = 0$, stipulating (31) and (32), holds for $\mathbf{m}_{0d}$ lying in a symmetry plane m, so that $g_3(\mathbf{m}) = 0$. In this case the condition of zero radicand in (31) reduces to the system of equations,

$$\theta \mathbf{p}\cdot\mathbf{e}_\varphi + \frac{\omega^2(g_{01}^2 - g_{02}^2)}{2v_{0d}^2(v_{0d}^2 - v_{03}^2)} = 0, \qquad \theta \mathbf{q}\cdot\mathbf{e}_\varphi - \frac{\omega^2 g_{01} g_{02}}{v_{0d}^2(v_{0d}^2 - v_{03}^2)} = 0. \quad (33)$$

Bearing in mind that $\mathbf{p} \times \mathbf{q} \neq 0$, it may be shown that this system, regarded at any given frequency ω, always yields a unique solution for θ, φ. By (31), this solution defines the onset of the curve, which is traced in m by the orientation of the acoustic axis depending on frequency on account of spatial dispersion (see Sec. III B).

Also, the equality $\mathbf{g}_0 \cdot \mathbf{A}_{03} = 0$ may, in principle, come about as a result of incidental orthogonality of $\mathbf{g}_0 \equiv \mathbf{g}(\mathbf{m}_{0d})$ to $\mathbf{A}_{03}$ which is violated at deviating $\mathbf{m} \approx \mathbf{m}_{0d} + \theta \mathbf{e}_\varphi$ from $\mathbf{m}_{0d}$, so that $g_3(\mathbf{m}) \sim \theta a v^2$. In such a case, similarly to (28), Eq. (31) confirms the vanishing of the degeneracy in the domain surrounding $\mathbf{m}_{0d}$. At the same time, by (31), the $(ka)^2$-order effect of linear spatial dispersion is maintained throughout the neighborhood of $\mathbf{m}_{0d}$ which is different to (30_1); and by (32) the modes $\alpha = 1,2$ traveling strictly along $\mathbf{m}_{0d}$ are linearly polarized, which is in contrast to (30_2). However, by appeal to (32) it is plain to see that, once $g_3(\mathbf{m}) \neq 0$, the solution $\{\theta, \varphi, \omega\}$ of (33) delivers the frequency-dependent propagation direction $\mathbf{m}$ ($\mathbf{m} \to \mathbf{m}_{0d}$ at $\mathbf{g} \to 0$) of modes with the circular polarization, which smoothes the singularity of linear-polarization fields in accordance with the degeneracy lifting. It is worth mentioning that quadratic spatial dispersion provides the contribution of the same $(ka)^2$-order, but the third perfect-square term under the radical in (31) and (32), which underlies lifting of degeneracy, is stipulated particularly by linear spatial dispersion.

C. Perturbation of the tangentialtype degeneracy

In the nondispersive limit, typical occasions of the tangential degeneracies of slowness sheets are related to the directions $\mathbf{m}_{0d}$ of the axes of symmetry higher than threefold (plus the twofold axes in the 23 and $m3$ groups). These acoustic axes are characterized by the polarization singularities with the possible values of the Poincare index $n = \pm 1$.[1,2] Taking linear spatial dispersion into account and recalling that the nonzero vector $\mathbf{g}_0 \equiv \mathbf{g}(\mathbf{m}_{0d}) \| \mathbf{m}_{0d}$ exists for the principal symmetry axes $\mathbf{m}_{0d}$ in the groups 432, 23, 622, 6, 422, 4, we find in the leading approximation the phase speeds and polarizations of the (quasi) transverse waves $\alpha = 1,2$ propagating in the neighborhood of these axes,

$$v_\alpha(\omega) = \sqrt{\frac{c_{44}}{\rho}} + \frac{1}{4\sqrt{\rho c_{44}}} \left\{ \theta^2 \nu_3 \mp \left[\theta^4 (\nu_1^2 \cos^2 2\varphi + \nu_2^2 \sin^2 2\varphi) + 4\frac{\rho\omega^2}{c_{44}} g_{03}^2 \right]^{1/2} \right\}, \quad (34)$$

$$\mathbf{A}_\alpha(\omega) \| \left(\theta^2 \nu_2 \sin 2\varphi + 2i\omega \sqrt{\frac{\rho}{c_{44}}}\, g_{03} \right) \mathbf{A}_{01} + \left\{ \theta^2 \nu_1 \cos 2\varphi \mp \left[\theta^4 (\nu_1^2 \cos^2 2\varphi + \nu_2^2 \sin^2 2\varphi) + 4\frac{\rho\omega^2}{c_{44}} g_{03}^2 \right]^{1/2} \right\} \mathbf{A}_{02}, \quad (35)$$

where

$$\nu_1 = \Delta_{16} - \frac{d_{13}^2}{\Delta_{34}}, \quad \nu_2 = d_{12} - \frac{d_{13}^2}{\Delta_{34}}, \quad \nu_3 = \Delta_{14} - \Delta_{46} - \frac{d_{13}^2}{\Delta_{34}}, \quad \Delta_{ab} = c_{aa} - c_{bb}, \quad a,b = 1,...,6; \quad d_{ij} = c_{iijj} + c_{ijij}, \quad i \neq j = 1,2,3, \quad (36)$$

so that $\nu_1 = \nu_3$ and $\nu_1 = \nu_2$ for cubic and hexagonal symmetry groups, respectively (for brevity we assume that in the case of group 4 the choice of the axes X_1, X_2 ensures $c_{16} = 0$).

It is seen that the effect of linear spatial dispersion on the tangentialtype degeneracies has basically the same fea-

tures as in the case of the conicaltype degeneracies. In particular, the arrival of the circular polarizations smoothes the polarization singularity, which allows for the vanishing of degeneracy in the neighboring domain.

IV. SUMMARY

The effect of spatial dispersion on the acoustic properties of noncentrosymmetric crystals was studied in the neighborhood of directions established as acoustic axes in the nondispersive limit. It is shown that in the case of acoustic axes, which neither lie in a symmetry plane, nor prove to be parallel to a rotation inversion axis, the degeneracy is lifted in the whole local domain. An acoustic axis lying in a symmetry plane changes its in-plane orientation depending on the frequency, unless remaining fixed to a symmetry axis. Corresponding singularity of linear-polarization vectors, which is attached to the acoustic axis, is smoothed due to arrival of circular polarization stipulated by linear spatial dispersion. It is proved that, once the degeneracy with regard for linear spatial dispersion occurs in some direction, the value of degenerate phase speed coincides with the value of one of the speeds assigned to the same direction in the nondispersive limit. Relations for the acoustic-wave parameters with dispersive corrections are derived for various particular cases.

ACKNOWLEDGMENTS

This work has been supported by Forbairt under Grant No. SC/96/736, and by the Russian Foundation for Basic Research under Grant No. 97-02-16338.

[1] V. I. Alshits, A. V. Sarychev, and A. L. Shuvalov, Zh. Eksp. Teor. Fiz. **89**, 922–938 (1985) [English transl., Sov. Phys. JETP **62**, 531–539 (1985)].
[2] A. L. Shuvalov, ''Topological features of acoustic-wave polarization in anisotropic media,'' Proc. R. Soc. London, Ser. A **454**, 1–37 (1998).
[3] D. L. Portigal and E. Burstein, Phys. Rev. **170**, 673–678 (1968).
[4] A. S. Pine, Phys. Rev. B **2**, 2049–2054 (1970).
[5] S. V. Akimov, V. N. Belyi, V. M. Gorbenko, S. N. Kurilkina, V. V. Savchenko, and A. G. Khatkevich, Fiz. Tverd. Tela (Leningrad) **33**, 600–606 (1991) [English transl., Sov. Phys. Solid State **33**, 341–344 (1991)].
[6] A. G. Every, Phys. Rev. B **36**, 1448–1456 (1987).
[7] V. L. Gurevich, *Transport in Phonon System* (North-Holland, New York, 1986), Secs. 3.4; 5.2.
[8] D. P. DiVincenzo, Phys. Rev. B **34**, 5450–5465 (1986).
[9] Yu. I. Sirotin and M. P. Shaskol'skaya, *Fundamentals of Crystal Physics* (MIR, Moscow, 1982), Sec. 83.
[10] C. Herring, Phys. Rev. **95**, 954–965 (1954).
[11] R. D. Mindlin, Int. J. Solids Struct. **5**, 1197–1208 (1969).
[12] F. I. Fedorov, *Theory of Elastic Waves in Crystals* (Plenum, New York, 1968), Secs. 12, 25, 45.
[13] F. I. Fedorov, *Teoriya Girotropii* (*Theory of Gyrotropy*) (Nauka i Tekhnika, Minsk, 1976, in Russian), Sec. 26.
[14] A. L. Shuvalov and P. Chadwick, Philos. Trans. R. Soc. London, Ser. A **355**, 155–188 (1997).

Torsional wave scattering from a diameter step in a rod

Helge E. Engan
Department of Physical Electronics, Norwegian University of Science and Technology, N-7034 Trondheim, Norway

(Received 17 December 1997; accepted for publication 13 July 1998)

The propagation and scattering of torsional waves in circular rods of infinite length with a free surface that have an abrupt diameter change is discussed. A mode expansion technique involving propagating and cut-off modes is applied to obtain numerical results for a range of parameter values. The calculated results are compared with simplified models valid in the high- and low-frequency regions, respectively. The calculations show that higher radial modes have strong influence at higher frequencies. In particular, near the cut-off frequencies both amplitude and phase responses are strongly influenced. It is further found that the approximation accuracy results depend on the number of modes used in the modal expansion. It is demonstrated that in order to obtain an accuracy (as judged from convergence) that is sufficient for typical parameters chosen, all propagating modes plus a few cut-off modes should be included in the calculations. © *1998 Acoustical Society of America.* [S0001-4966(98)04410-5]

PACS numbers: 43.20.Ks, 43.20.Mv, 43.20.Fn, 43.35.Cg [ANN]

INTRODUCTION

Propagation of waves in cylindrical structures are of interest in many different applications such as medical ultrasound,[1] acoustic propagation along boreholes,[2] acoustic sensing,[3] and fiber acousto-optics,[4,5] etc. This problem has been studied for the special case when a semi-infinite rod is connected to an elastic half-space.[6] The problem of transient torsional waves in stepped rods has been investigated by a finite difference method.[7] In this study we address the scattering of the torsional mode group due to an abrupt rod diameter change. In comparison to the previous works, this is done for an extended range of various parameters such as radii, radius steps, and frequency. The theory includes scattering of modes by discontinuities both increasing and decreasing in the propagation direction.

In the next section we give a summary of torsional wave mode propagation in uniform rods. This is followed by a simplified theory giving the transmission of the fundamental mode in the low- and high-frequency limits, respectively. We then consider the scattered waves in more detail by expanding all fields in eigenmodes. Solving the resulting equations numerically, we first present detailed field patterns in the neighborhood of the discontinuity, followed by scattering parameters describing the reflection and transmission of a single mode. We consider mostly the scattering when a fundamental mode is incident on the discontinuity, but we also discuss the case of a higher-order mode as used in a trapped mode resonator configuration as reported in the literature.[8]

I. TORSIONAL MODES IN CIRCULAR RODS

We shall later need some detailed knowledge of the eigenmodes of the torsional mode group propagating along the z axis of a cylindrical rod of radius R with free boundaries (see Fig. 1). We first give a brief overview of some of the properties of these modes[9,10] pertinent to the present discussion. The displacement is circumferential and does not vary with φ, so it can be written

$$u(\vec{r},t)=u_{\varphi}(r)\exp j(\Omega t-Kz). \tag{1}$$

Suppressing the exponential part we have

$$u_{\varphi}=\begin{cases} C_0K_0^2r, & s=0,\\ C_sK_tJ_1(K_tr), & s>0, \end{cases} \tag{2}$$

where s denotes the fundamental mode, $K^2=K_0^2-K_t^2$, $K_0=\Omega/V_t$, $K_t=Z_s/R$, and Z_S is the sth zero of $J_2(Z)$. Some values for Z_s are 0, 5.136, 8.417, and 11.62 for $s=0$,1, 2, and 3, respectively. The angular frequency is Ω and V_t is the bulk shear wave velocity.

The Poynting vector is directed in the z direction and it has a complex magnitude $p=-\frac{1}{2}(v^*\cdot T)_z$. The asterisk denotes complex conjugate. Integrated over the cross section the total power in a given mode is

$$P=\int_0^{2\pi}\int_0^R pr\,dr\,d\varphi$$
$$=-\frac{1}{2}\int_0^{2\pi}\int_0^R (v^*\cdot T)_z r\,dr\,d\varphi=-\pi\int_0^R (v^*\cdot T)_z r\,dr, \tag{3}$$

where the relevant velocity and stress components are given by, respectively,

$$v=\frac{\partial u_{\varphi}}{\partial t}=jV_t\begin{cases} C_0K_0^3r, & s=0,\\ C_sK_0K_tJ_1(K_tr), & s>0, \end{cases} \tag{4}$$

$$T_4=T_{\varphi z}=-jc_{44}\begin{cases} C_0K_0^3r, & s=0,\\ C_sKK_tJ_1(K_tr), & s>0, \end{cases} \tag{5}$$

where the stiffness tensor element $c_{44}=\rho V_t^2$, is related to V_t and the density ρ. Substituting these expressions into Eq. (3), we find that for any given mode s we can write

$$P=\pi\Omega c_{44}K\int_0^R u_{\varphi,s}u_{\varphi,s}r\,dr, \tag{6}$$

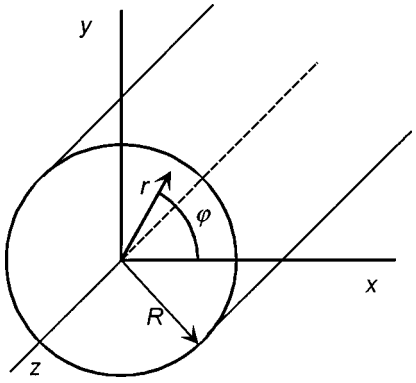

FIG. 1. Coordinate system for cylindrical rod.

taking into account that u is real (see below). The resulting expressions can be distinguished according to the value of s as follows.

(a) For $s=0$ we find

$$P=\frac{\pi}{4}c_{44}R^4V_tC_0^2K_0^6=\frac{\pi}{4}\rho R^4V_t^3C_0^2K_0^6. \tag{7}$$

Thus C_0 is

$$C_0=\frac{2}{K_0^3V_tR^2}\sqrt{\frac{P}{\pi\rho V_t}}=\frac{2V_t}{\Omega^3R^2}\sqrt{\frac{PV_t}{\pi\rho}}. \tag{8}$$

(b) For $s\geqslant 1$, we obtain when we apply the boundary conditions

$$\begin{aligned}P&=\pi c_{44}|C_s|^2KK_0V_t\int_0^{Z_s}J_1^2(K_tr)(K_tr)d(K_tr)\\&=\tfrac{1}{2}\pi c_{44}|C_s|^2KK_0V_tZ_s^2J_1^2(Z_s)\\&=\tfrac{1}{2}\pi\rho|C_s|^2KK_0V_t^3Z_s^2J_1^2(Z_s),\end{aligned} \tag{9}$$

so that

$$\begin{aligned}|C_s|^2&=\frac{1}{(V_tZ_sJ_1(Z_s))^2}\frac{2P}{\pi\rho KK_0V_t}\\&=\frac{1}{(V_tZ_sJ_1(Z_s))^2}\frac{2P}{\pi\rho\Omega K}.\end{aligned} \tag{10}$$

For propagating modes all quantities on the right side of this equation can be taken to be real and positive. For cut-off modes K is imaginary with a negative imaginary part. We choose this to be the case for P also. For normalization purposes we therefore define for all s values

$$P=\begin{cases}1, & \text{for propagating modes,}\\ -j, & \text{for cut-off modes.}\end{cases} \tag{11}$$

With this convention C_s is always real and positive. Therefore we can write the following relation valid for all values of s and for both propagating and cut-off modes:

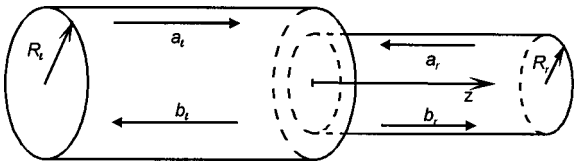

FIG. 2. Definition of geometry and incoming and scattered waves in problem of scattering from a single step.

$$C_s=\begin{cases}\dfrac{2V_t}{\Omega^3R^2}\sqrt{\dfrac{V_t}{\pi\rho}}, & s=0,\\ \dfrac{1}{V_tZ_s|J_1(Z_s)|}\sqrt{\dfrac{2}{\pi\rho\Omega|K|}}, & s>0.\end{cases} \tag{12}$$

Thus the normalized modes become

$$u_\varphi=\begin{cases}\dfrac{2V_t}{\Omega^3R^2}\sqrt{\dfrac{V_t}{\pi\rho}}K_0^2r=\dfrac{2}{\Omega R}\sqrt{\dfrac{1}{\pi\rho V_t}}\dfrac{r}{R}, & s=0,\\ \dfrac{1}{V_tZ_s|J_1(Z_s)|}\sqrt{\dfrac{2}{\pi\rho\Omega|K|}}K_tJ_1(K_tr) & \\ \quad=\dfrac{1}{V_tR}\sqrt{\dfrac{2}{\pi\rho\Omega|K|}}\dfrac{J_1(Z_s(r/R))}{|J_1(Z_s)|}, & s>0.\end{cases} \tag{13}$$

We want to eliminate K from these expressions. Substituting a previously stated relation and introducing the convenient normalized frequency parameter $X=R\Omega/V_t=K_0R$, we finally find that this can be written

$$u_\varphi=\frac{1}{X}\sqrt{\frac{2}{\pi\rho V_t^3|1-(Z_s/X)^2|^{1/2}}}\begin{cases}\sqrt{2}(r/R), & s=0,\\ \dfrac{J_1(Z_s(r/R))}{|J_1(Z_s)|}, & s>0,\end{cases} \tag{14}$$

which we note is always real.

II. STATEMENT OF THE SCATTERING PROBLEM

The scattering problem is defined as follows. Consider a solid rod with a circular cross section with a discontinuity in radius at $z=0$ changing from R_l in the left part to R_r in the right part, where we assume $R_l>R_r$ as shown in Fig. 2. The subscripts l and r will be used below in other variables to refer to the same two parts of the rod. Torsional waves are propagating in both directions on either side of the discontinuity. The amplitudes of incoming waves are denoted by a and outgoing waves by b, respectively. Relations between these amplitudes can be described by the scattering matrix S through

$$\begin{bmatrix}b_l\\ b_r\end{bmatrix}=\begin{bmatrix}S_{11} & S_{12}\\ S_{21} & S_{22}\end{bmatrix}\begin{bmatrix}a_l\\ a_r\end{bmatrix}. \tag{15}$$

We shall first develop formulas in special cases based on simplified theories in the high- and low-frequency limits, respectively. This is done to get a feeling for, in particular, the scattering of the fundamental mode. These results will also be used as a reference to compare results obtained by the more complete theory discussed subsequently. We point out that henceforth the subscript φ will be suppressed from the equations.

III. SIMPLIFIED THEORY

A. High-frequency limit

In the high frequency approximation the transmission of the wave can be found by modeling it as in classical beam propagation. In this limit the part of a fundamental mode that will propagate through a discontinuity is given by the fraction of the energy that is within radius R_r. Since the displacement of this mode varies linearly with radius, all of the transmitted energy will be excited in the right part with a radial distribution identical to a fundamental mode. Accordingly only this mode will propagate in the right part of the rod. If the impinging wave has unit power, we find that the power located between radius r and $r+dr$ is given by

$$dP = 4\frac{r^3 dr}{R_l^4}. \tag{16}$$

By integration of this expression from 0 to R_r we conclude that the amplitude scattering coefficient given by the power transmitted to the right part is

$$S_{21} = P_r = \left(\frac{R_r}{R_l}\right)^4. \tag{17}$$

The remaining part of the energy is reflected with partial mode conversion into various modes. We will not pursue this aspect any further here.

B. Low-frequency limit

In this case we assume that the problem involves only the fundamental mode. We consider the solution based on conservation of angular momentum and of energy. All four velocities being equal in this case, one can argue that the conservation of angular momentum can be expressed by integrating the product of the density and the local velocity over the cross sections, giving the following relation,

$$a_l \Omega \rho \int_0^{R_l} r u_l 2\pi r\, dr = b_l \Omega \rho \int_0^{R_l} r u_l 2\pi r\, dr + b_r \Omega \rho \int_0^{R_r} r u_r 2\pi r\, dr, \tag{18}$$

where the power normalized fields u_l and u_r according to Eq. (13) are proportional to r/R_l^2 and r/R_r^2, respectively. Substituting for these quantities and dividing out all common factors gives

$$a_l R_l^2 = b_l R_l^2 + b_r R_r^2. \tag{19}$$

Combining this condition with the condition of conservation of energy, i.e.,

$$a_l^2 = b_l^2 + b_r^2, \tag{20}$$

we find the relevant parameter to be

$$S_{21} = \frac{b_r}{a_l} = \frac{2R_{\mathrm{rel}}^2}{1+R_{\mathrm{rel}}^4}, \tag{21}$$

where $R_{\mathrm{rel}} = R_r/R_l$. We shall comment on these expressions later.

IV. MODAL ANALYSIS

We now consider the general torsional wave case, assuming an arbitrary field that can be expressed by a sum of eigenmodes. This is an approach that was developed for waveguide discontinuities in microwave engineering,[11] and it has also been used in various areas of acoustics.[9] If the number of modes is N, the scattering can be described by

$$\begin{bmatrix} b_{l1} \\ b_{l2} \\ \cdots \\ b_{lN} \\ b_{r1} \\ b_{r2} \\ \cdots \\ b_{rN} \end{bmatrix} = \begin{bmatrix} & \\ [S_{11}] & [S_{12}] \\ & \\ & \\ & \\ [S_{21}] & [S_{22}] \\ & \end{bmatrix} \begin{bmatrix} a_{l1} \\ a_{l2} \\ \cdots \\ a_{lN} \\ a_{r1} \\ a_{r2} \\ \cdots \\ a_{rN} \end{bmatrix}. \tag{22}$$

Here, the general expression for each wave consisting of N modes has been written in vector form so that, for example, the scattered wave in the left rod part is contained in the upper half of the column vector on the left side of this equation. The second index of a and b denotes the mode number. Also, each of the submatrices $[S_{ij}]$ is an $N \times N$ matrix.

In the general case an infinite number of modes are involved. Of these modes a finite number are propagating while the others are cut-off. For numerical calculations we have to limit the total number of modes N to be finite.

We consider the general case when there are incoming waves from both sides. To find the appropriate terms the following two boundary conditions must be satisfied for $z = 0$:

(a) for $r < R_r$, continuity of displacement and force across the interface, and
(b) For $r > R_r$, surface force is equal to zero.

The two variables we shall consider are u_φ and $T_{\varphi z}$, in which we will henceforth suppress the coordinate suffixes φ and z. We expand the u and T variables of the incoming wave on the left side (now called u_l^a and T_l^a to identify which wave and rod part) in eigenmodes, i.e.,

$$u_l^a = \sum_i a_{l,i} u_{l,i} \exp(-jK_{l,i} z), \qquad T_l^a = \sum_i T_{l,i} = -jc_{44} \sum_i K_{l,i} a_{l,i} u_{l,i} \exp(-jK_{l,i} z), \tag{23}$$

where $a_{l,i}$ denotes the amplitude of the incoming mode of radial mode number i in the left part of the structure. Similarly, the outgoing wave in the left guide is denoted by u_l^b and T_l^b and can be written

$$u_l^b=\sum_i\ b_{l,i}u_{l,i}\exp(jK_{l,i}z),$$

$$T_l^b=jc_{44}\sum_i\ K_{l,i}b_{l,i}u_{l,i}\exp(jK_{l,i}z). \tag{24}$$

In the right part incoming and outgoing waves can be written with a similar notation,

$$u_r^a=\sum_i\ a_{r,i}u_{r,i}\exp(jK_{r,i}z),$$

$$T_r^a=\sum_i\ T_{r,i}=jc_{44}\sum_i\ K_{r,i}a_{r,i}u_{r,i}\exp(jK_{r,i}z), \tag{25}$$

$$u_r^b=\sum_i\ b_{r,i}u_{r,i}\exp(-jK_{r,i}z),$$

$$T_r^b=-jc_{44}\sum_i\ K_{r,i}b_{r,i}u_{r,i}\exp(-jK_{r,i}z). \tag{26}$$

The discontinuity will generate scattered waves. From the cylindrical symmetry it is realized that no longitudinal or flexural mode is excited. All waves can therefore be expanded into torsional eigenmodes. For all modes in the left part we assume $\mathrm{Re}(K_{l,i})\geqslant 0$ for propagating modes and $\mathrm{Im}(K_{l,i})\leqslant 0$ for cut-off modes. The same relations hold for $K_{r,i}$.

We now apply the boundary conditions for velocity and stress at the step. They can be written

$$j\Omega u_l^a+j\Omega u_l^b=j\Omega u_r^a+j\Omega u_r^b,\quad r<R_r, \tag{27}$$

$$T_l^a+T_l^b=\begin{cases}T_r^a+T_r^b, & r<R_r,\\ 0, & r>R_r.\end{cases} \tag{28}$$

We expand all fields in eigenmodes to obtain

$$j\Omega\sum_i\ a_{l,i}u_{l,i}+j\Omega\sum_i\ b_{l,i}u_{l,i}=j\Omega\sum_i\ a_{r,i}u_{r,i}+j\Omega\sum_i\ b_{r,i}u_{r,i},\quad r<R_r, \tag{29}$$

$$-jc_{44}\sum_i\ K_{l,i}a_{l,i}u_{l,i}+jc_{44}\sum_i\ K_{l,i}b_{l,i}u_{l,i}=\begin{cases}jc_{44}\sum_i\ K_{r,i}a_{r,i}u_{r,i}-jc_{44}\sum_i\ K_{r,i}b_{r,i}u_{r,i}, & r<R_r,\\ 0, & r>R_r.\end{cases} \tag{30}$$

Equation (29) is complex conjugated and multiplied by $-\frac{1}{2}T_{r,m}=\frac{1}{2}jc_{44}K_{r,m}u_{r,m}$ where $T_{r,m}$ is the relevant stress component of mode m in the right part. After integration over the common cross section $0<r<R_r$ we obtain

$$\begin{aligned}&\sum_i\ \pi c_{44}\Omega K_{r,m}a_{l,i}^*\int_0^{R_r}u_{l,i}u_{r,m}r\,dr\\&+\sum_i\ \pi c_{44}\Omega K_{r,m}b_{l,i}^*\int_0^{R_r}u_{l,i}u_{r,m}r\,dr\\&=\sum_i\ \pi c_{44}\Omega K_{r,m}a_{r,i}^*\int_0^{R_r}u_{r,i}u_{r,m}r\,dr\\&\quad+\sum_i\ \pi c_{44}\Omega K_{r,m}b_{r,i}^*\int_0^{R_r}u_{r,i}u_{r,m}r\,dr.\end{aligned} \tag{31}$$

By complex conjugating this equation and introducing the normalized wave number $Q_{r,m}=K_{r,m}/K_0$, it can be written

$$\begin{aligned}&\sum_i\ \pi c_{44}\Omega Q_{r,m}^*a_{l,i}\int_0^{R_r}u_{l,i}u_{r,m}r\,dr\\&+\sum_i\ \pi c_{44}\Omega Q_{r,m}^*b_{l,i}\int_0^{R_r}u_{l,i}u_{r,m}r\,dr\\&=\sum_i\ \pi c_{44}\Omega Q_{r,m}^*a_{r,i}\int_0^{R_r}u_{r,i}u_{r,m}r\,dr\\&\quad+\sum_i\ \pi c_{44}\Omega Q_{r,m}^*b_{r,i}\int_0^{R_r}u_{r,i}u_{r,m}r\,dr,\end{aligned} \tag{32}$$

which can be changed to

$$Q_{r,m}^*\sum_i\ L_{im}a_{l,i}+Q_{r,m}^*\sum_i\ L_{im}b_{l,i}=P_{r,m}^*a_{r,m}+P_{r,m}^*b_{r,m}, \tag{33}$$

by introducing the real overlap integral

$$\begin{aligned}L_{im}&=\pi c_{44}\Omega K_0\int_0^{R_r}u_{l,i}u_{r,m}r\,dr\\&=\pi\rho V_t\Omega^2\int_0^{R_r}u_{l,i}u_{r,m}r\,dr=\pi\rho V_t^3\int_0^{X_r}u_{l,i}u_{r,m}x\,dx,\end{aligned} \tag{34}$$

where the normalized quantities $X_r=K_0R_r=R_r\Omega/V_t$ and $x=K_0r=r\Omega/V_t$ have been substituted. Further, $P_{r,m}$ equals 1 for a propagating mode, and $-j$ for cut-off modes.

Multiplication of Eq. (30) by $-\frac{1}{2}v_{l,m}^*=\frac{1}{2}j\Omega u_{l,m}$ and integration over the total cross section given by $0<r<R_l$ yields

$$\begin{aligned}&-\sum_i\ \pi c_{44}\Omega K_{l,i}a_{l,i}\int_0^{R_l}u_{l,i}u_{l,m}r\,dr\\&+\sum_i\ \pi c_{44}\Omega K_{l,i}b_{l,i}\int_0^{R_l}u_{l,i}u_{l,m}r\,dr\\&=\sum_i\ \pi c_{44}\Omega K_{r,i}a_{r,i}\int_0^{R_r}u_{r,i}u_{l,m}r\,dr\\&\quad-\sum_i\ \pi c_{44}\Omega K_{r,i}b_{r,i}\int_0^{R_r}u_{r,i}u_{l,m}r\,dr.\end{aligned} \tag{35}$$

Introducing the quantity P also for the left side, we write this relation,

$$-P_{l,m}a_{l,m}+P_{l,m}b_{l,m}$$

$$=\sum_i Q_{r,i}L_{mi}a_{r,i}-\sum_i Q_{r,i}L_{mi}b_{r,i}. \tag{36}$$

Provided all a's are known, the two equation systems in the most general case give an infinite set of linear equations to determine the infinite number of coefficients $b_{l,i}$ and $b_{r,i}$. For numerical calculations the summations are truncated to N terms which yield $2N$ equations to determine $2N$ coefficients.

To find the scattering parameters we write Eqs. (33) and (36) in the following form after dividing the first equation by $P^*_{r,m}$:

$$|Q_{r,m}|\sum_i L_{im}b_{l,i}-b_{r,m}=-|Q_{r,m}|\sum_i L_{im}a_{l,i}+a_{r,m}, \tag{37}$$

$$P_{l,m}b_{l,m}+\sum_i Q_{r,i}L_{mi}b_{r,i}=P_{l,m}a_{l,m}+\sum_i Q_{r,i}L_{mi}a_{r,i},$$

which is of the same form as Eq. (22). As an example, for $N=3$ these equations can be written for the left side

$$\begin{bmatrix} |Q_{r,1}|L_{11} & |Q_{r,1}|L_{21} & |Q_{r,1}|L_{31} & -1 & 0 & 0 \\ |Q_{r,2}|L_{12} & |Q_{r,2}|L_{22} & |Q_{r,2}|L_{32} & 0 & -1 & 0 \\ |Q_{r,3}|L_{13} & |Q_{r,3}|L_{23} & |Q_{r,3}|L_{33} & 0 & 0 & -1 \\ P_{l,1} & 0 & 0 & Q_{r,1}L_{11} & Q_{r,2}L_{12} & Q_{r,3}L_{13} \\ 0 & P_{l,2} & 0 & Q_{r,1}L_{21} & Q_{r,2}L_{22} & Q_{r,3}L_{23} \\ 0 & 0 & P_{l,3} & Q_{r,1}L_{31} & Q_{r,2}L_{32} & Q_{r,3}L_{33} \end{bmatrix} \begin{bmatrix} b_{l,1} \\ b_{l,2} \\ b_{l,3} \\ b_{r,1} \\ b_{r,2} \\ b_{r,3} \end{bmatrix}, \tag{38}$$

and for the right side

$$\begin{bmatrix} -|Q_{r,1}|L_{11} & -|Q_{r,1}|L_{21} & -|Q_{r,1}|L_{31} & 1 & 0 & 0 \\ -|Q_{r,2}|L_{12} & -|Q_{r,2}|L_{22} & -|Q_{r,2}|L_{32} & 0 & 1 & 0 \\ -|Q_{r,3}|L_{13} & -|Q_{r,3}|L_{23} & -|Q_{r,3}|L_{33} & 0 & 0 & 1 \\ P_{l,1} & 0 & 0 & Q_{r,1}L_{11} & Q_{r,2}L_{12} & Q_{r,3}L_{13} \\ 0 & P_{l,2} & 0 & Q_{r,1}L_{21} & Q_{r,2}L_{22} & Q_{r,3}L_{23} \\ 0 & 0 & P_{l,3} & Q_{r,1}L_{31} & Q_{r,2}L_{32} & Q_{r,3}L_{33} \end{bmatrix} \begin{bmatrix} a_{l,1} \\ a_{l,2} \\ a_{l,3} \\ a_{r,1} \\ a_{r,2} \\ a_{r,3} \end{bmatrix}. \tag{39}$$

With appropriate definitions of all Ms, these relations can be written in abbreviated form,

$$\begin{bmatrix} M_{11} & M_{12} \\ M_{21} & M_{22} \end{bmatrix} \begin{bmatrix} b_l \\ b_r \end{bmatrix} = \begin{bmatrix} -M_{11} & -M_{12} \\ M_{21} & M_{22} \end{bmatrix} \begin{bmatrix} a_l \\ a_r \end{bmatrix} \tag{40}$$

or

$$[M_b]\begin{bmatrix} b_l \\ b_r \end{bmatrix} = [M_a]\begin{bmatrix} a_l \\ a_r \end{bmatrix}, \tag{41}$$

with solution

$$\begin{bmatrix} b_l \\ b_r \end{bmatrix} = [M_b]^{-1}[M_a]\begin{bmatrix} a_l \\ a_r \end{bmatrix}. \tag{42}$$

The scattering matrix as defined in Eq. (22) is therefore given by

$$S=[M_b]^{-1}[M_a]. \tag{43}$$

We can also find the transmission matrix by reorganizing Eq. (37) to be

$$a_{r,m}+b_{r,m}=|Q_{r,m}|\sum_i L_{im}a_{l,i}+|Q_{r,m}|\sum_i L_{im}b_{l,i}, \tag{44}$$

$$\sum_i Q_{r,i}L_{mi}a_{r,i}-\sum_i Q_{r,i}L_{mi}b_{r,i}=P_{l,m}b_{l,m}-P_{l,m}a_{l,m}.$$

With the same notation as above, this equation system can be written

$$\begin{bmatrix} -M_{12} & -M_{12} \\ M_{22} & -M_{22} \end{bmatrix} \begin{bmatrix} a_r \\ b_r \end{bmatrix} = \begin{bmatrix} M_{11} & M_{11} \\ M_{21} & -M_{21} \end{bmatrix} \begin{bmatrix} b_l \\ a_l \end{bmatrix}, \tag{45}$$

which can also be written as

$$[M_r]\begin{bmatrix} a_r \\ b_r \end{bmatrix} = [M_l]\begin{bmatrix} b_l \\ a_l \end{bmatrix}. \tag{46}$$

With solution

$$\begin{bmatrix} a_r \\ b_r \end{bmatrix} = [M_r]^{-1}[M_l]\begin{bmatrix} b_l \\ a_l \end{bmatrix}, \tag{47}$$

the transmission matrix can be written

$$T=[M_r]^{-1}[M_l]. \tag{48}$$

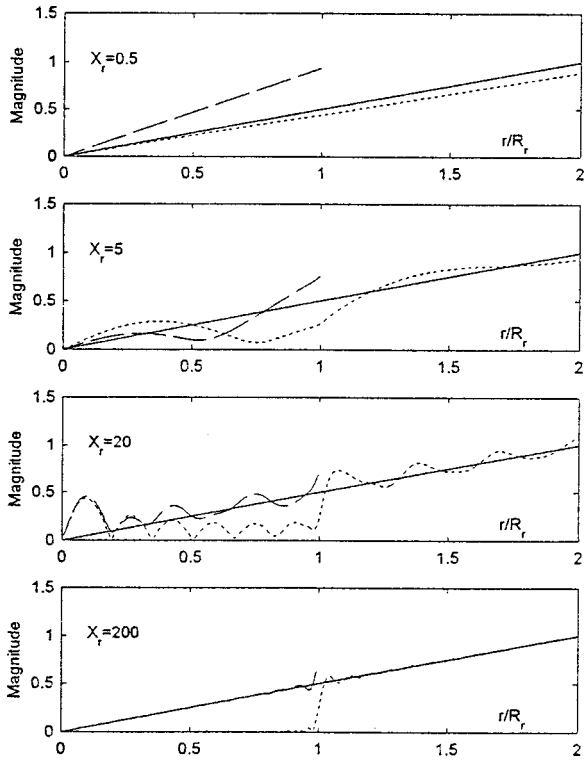

FIG. 3. Radial distribution of displacement with X_r as a parameter for $z=0$ with $R_r/R_l=0.5$. Full line is the incoming fundamental mode. Dotted curve is the reflected wave and dashed curve is the transmitted wave.

Although it is not necessary, we will consider the input port to be the left side. In this perspective we have until now assumed the ''downstep'' case where $R_l>R_r$. The opposite ''upstep'' case can be found easily from the solution already obtained by changing the notation so that the two sides of the rod are interchanged. By proceeding in this way we can refer to the ''input'' side as the left side independently of the direction of the step.

V. RESULTS

We shall present numerically calculated results below. We have investigated various cases describing the scattering process. This process will be considered from a field point of view. Power normalized transmission and reflection parameters are also discussed. In accordance with previous notation we have introduced the normalized frequencies $X_l=\Omega R_l/V_t$ and $X_r=\Omega R_r/V_t$ for the left and right parts of the rod, respectively. We have tested different numbers of modes in the mode expansion. The resulting curves are modes added up to a value where the result is not visibly dependent on additional modes when looking at it. Unless where specifically stated, the results shown are based on 50 modes in the field expansions.

The first example illustrates the displacement distribution across the step (i.e., $z=0$) when a fundamental mode is incident on the discontinuity. Its field amplitude is unity at the surface. We have chosen a geometry where the radius of the right part is half of the radius of the left part ($R_r/R_l=0.5$). In Fig. 3 we have shown the incoming distribution (magnitude of the complex phasor) of the fundamental mode as a straight line from the origin to the coordinates (2,1). In the four cases illustrated, X_r varies between 0.5, which is a very clear single mode case, up to 200, in which case the two parts can propagate 64 and 32 modes, respectively. The curves going from $r/R_r=0$ to 1 show the total transmitted field distribution for $z=0$ consisting of the sum of all mode contributions. In Fig. 4 we show the dependence on z and r of the displacement for the same parameters as in the previous figure.

These two figures show that for the lowest normalized frequency ($X_r=0.5$) the transmitted field pattern is dominated by the single propagating mode. For $X_r=5$ we can see the effect of, in particular, the next-higher-order mode ($s=1$) in the transmission, although this mode decays over a short transition region because it is slightly below its cutoff frequency of 5.14 and accordingly strongly attenuated. For $X_r=20$ five higher-order propagating modes contribute so that an irregular interference pattern occurs. In the high-frequency case ($X_r=200$) the incoming distribution is transmitted through the step as through a stop, at least when the immediate local field distribution is concerned. This is consistent with ray tracing methods well known from acoustics and optics. There seems to be a pronounced focusing effect of irregular character along the cylinder axis after a short distance.

We have also considered the upstep case. In Fig. 5 the axial variation of the fields are shown for the case $R_r/R_l=2$. We have again taken the incoming fundamental mode to be of unit amplitude at the surface, and we have used the same values for X_r as in the previous example. The same general features are demonstrated as before, although it appears that for the single-mode case the influence of the higher modes are somewhat more pronounced than before. We also note that in the high-frequency case the initially triangular excitation for $z=0$ spreads out quickly for increasing z, and that the focusing effect now seems to be stronger than in the downstep case.

Another illustration of the results can be obtained by calculating the scattering parameters for the power normalized modes as discussed earlier. We have calculated the scattering parameters for an incoming fundamental mode. The scattering into the two lowest modes in both transmission and reflection is shown for the downstep case in Fig. 6. The magnitude of the phasors are shown as functions of X_l with R_r/R_l as parameter. Only results for propagating scattered modes are shown. The frequency is normalized with respect to the left part of the rod. The figure shows that there are strong resonance effects associated with the left radius when the corresponding normalized frequency is equal to any of the zeros of the Bessel function of second order. For these values a mode is excited in the left part that is at the limit of cut-off. In this case the group velocity is near zero and accordingly the energy is stored in the neighborhood of the step for an extended time. We note that similar but weaker resonances can be observed in the responses for normalized frequencies corresponding to cut-off conditions for the right part. Transformation between normalized frequencies for the two parts can be done according to $X_r/X_l=R_r/R_l$.

In Fig. 7 we show similar curves for the upstep case. In

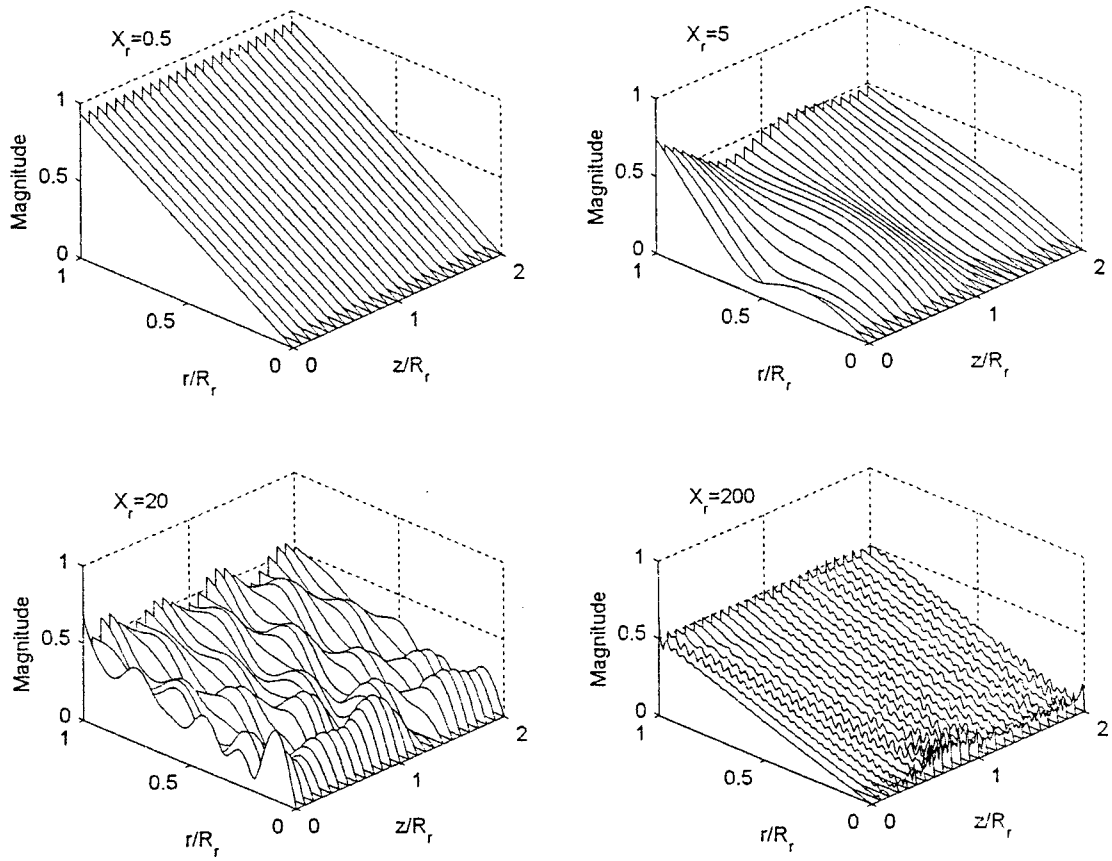

FIG. 4. Radial and axial distribution of displacement with X_r as a parameter for $z \geqslant 0$ with $R_r/R_l = 0.5$.

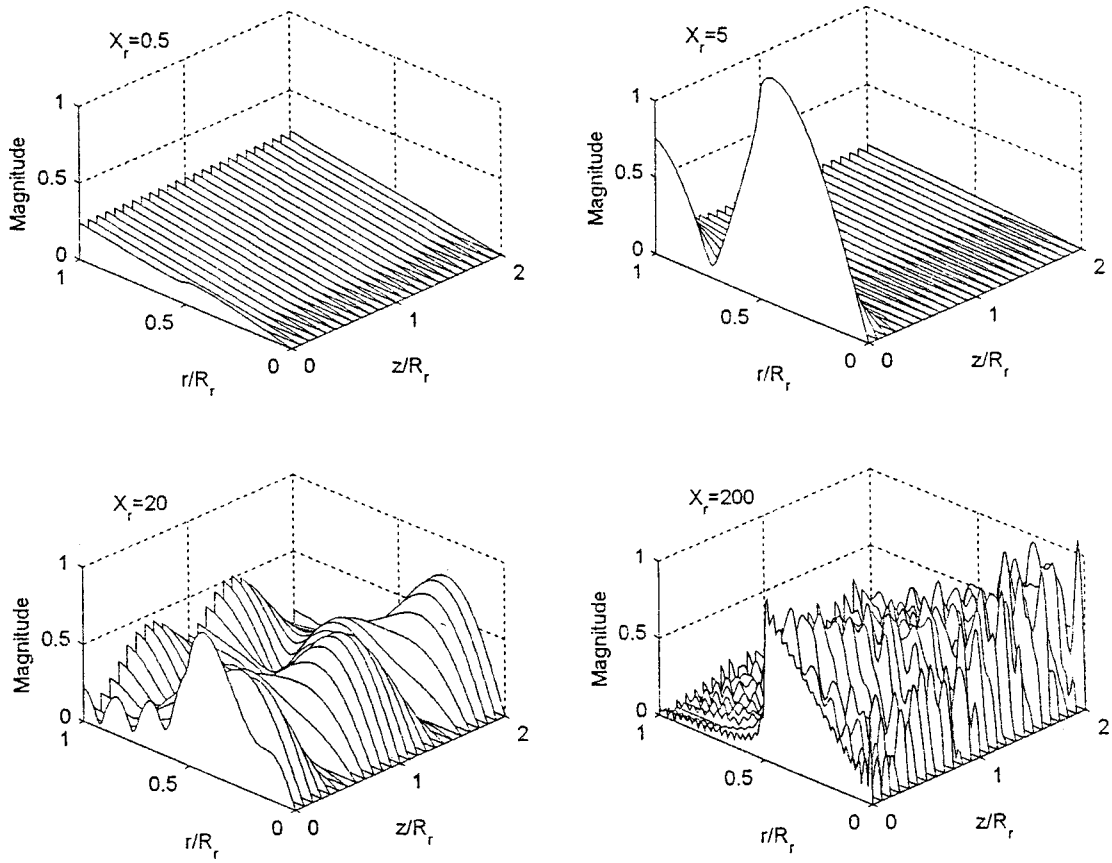

FIG. 5. Radial and axial distribution of displacement with X_r as a parameter for $z \geqslant 0$ with $R_r/R_l = 2$.

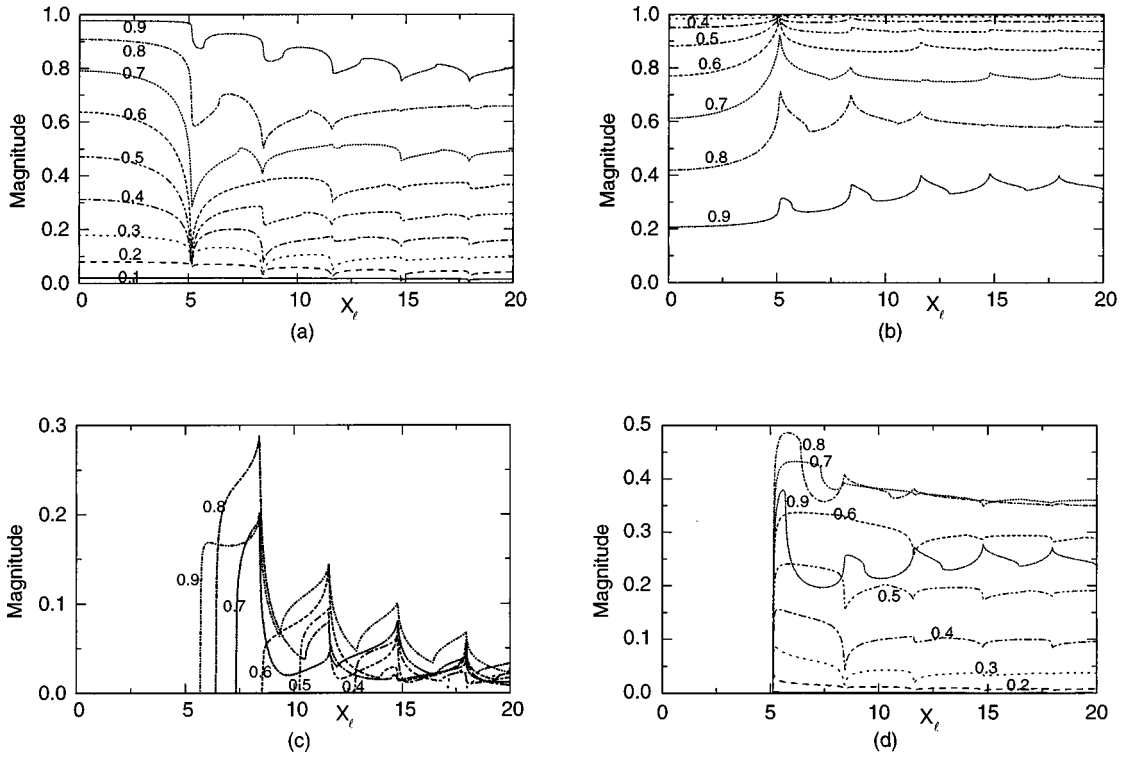

FIG. 6. Scattering from an incoming fundamental mode into the two lowest modes in transmission and reflection at a downstep. The parameter is R_r/R_l. The mode amplitudes are power normalized. (a) Transmitted mode $s=0$, (b) reflected mode $s=0$, (c) transmitted mode $s=1$, and (d) reflected mode $s=1$. Please observe the difference in vertical scale between the fundamental and the higher modes.

order to show similarities with the downstep case we have chosen to use X_r as variable and R_l/R_r as parameter here. In this format the curves for transmission into the fundamental mode is identical to the previous case when curves for corresponding parameters are compared. This is in accordance with symmetry properties of scattering matrices.[11] For low frequencies when no higher modes are propagating, energy conservation therefore implies that the reflected power is also

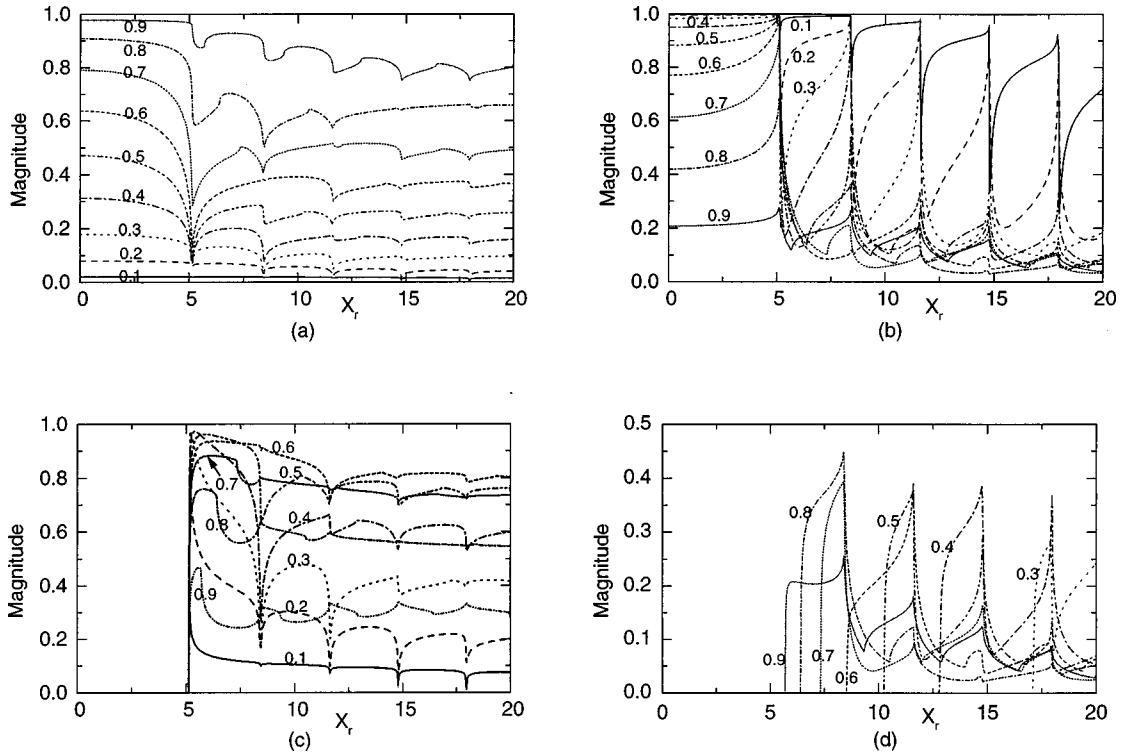

FIG. 7. As in Fig. 6, but for an upstep. The parameter is R_l/R_r. (a) Transmitted mode $s=0$, (b) reflected mode $s=0$, (c) transmitted mode $s=1$, and (d) reflected mode $s=1$.

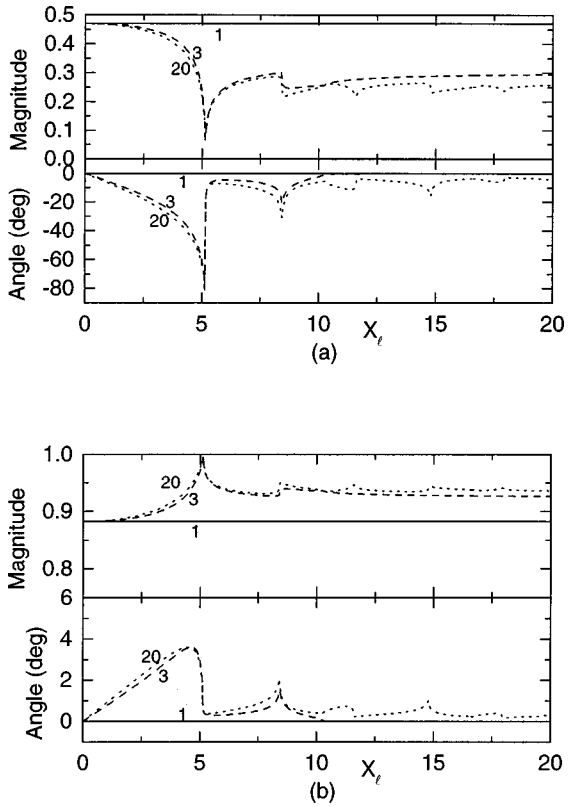

FIG. 8. Magnitude and phase angle of (a) transmitted and (b) reflected fundamental mode with number of modes used in the modal expansion as parameter. Incoming wave is the fundamental mode and $R_r/R_l=0.5$.

identical in the two cases. This is confirmed in the presented results. When higher modes are present, all curves except those for the transmitted fundamental will be different.

An illustrative example of how the results depend on the number of modes used in the expansion is shown in Fig. 8. Until now we have only presented the absolute values of the scattered amplitudes. Here we also show phase variation. We conclude from this figure that using a single mode in the expansion is accurate only when the frequency is considerably lower than the cut-off frequency of the next mode. In general, our calculations show that all propagating modes and a few of the cut-off modes are needed to get a reasonably accurate representation of the scattering process. Further, the calculations show that in a case when the amplitude may be represented with sufficient accuracy, it may be necessary to include even more modes to obtain a good accuracy of the phase.

We next compare our numerical results with the simplified theories for the high- and low-frequency approximations discussed earlier. We consider the case when the incoming and the transmitted wave are both the fundamental mode, and $R_r/R_l<1$. The comparison shown in Fig. 9 demonstrates good agreement between the low-frequency simplified theory and the modal expansion results for low frequencies for all values of $R_r/R_l<1$. In the high-frequency case the agreement appears to be adequate as long as the expansion takes into account all propagating modes. This agrees with results obtained above.

We finally discuss a case where the incoming wave is a

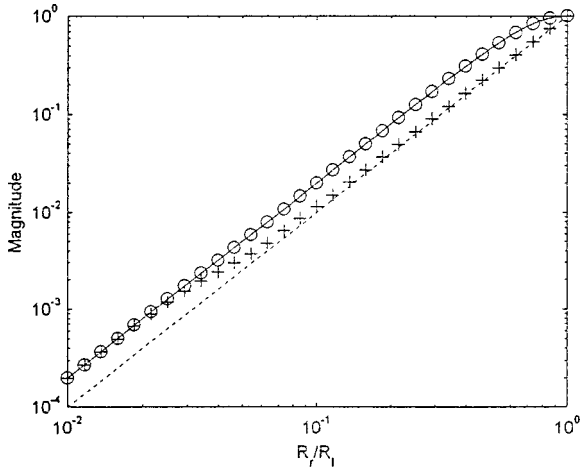

FIG. 9. Comparison between simplified theory and modal expansion calculations. Full and dotted lines describe the low- and high-frequency approximations of the simplified theory, respectively. ○: Modal expansion results for low frequencies ($X_l=0.1$). +: Modal expansion results for high frequencies ($X_l=400$). All modal expansion results apply 20 modes.

higher-order mode. We choose a value of $R_r/R_l=0.9896$. This corresponds to one of the samples discussed in a paper reported by Johnson *et al.*[8] where they considered trapping of higher torsional modes in solid rods obtained by reducing the rod diameter slightly in the two ends limiting the trapping region. In Fig. 10 we show the calculated scattering of the $s=2$ mode at and above its cut-off value of $X_l=8.417$. The magnitudes of the two modes $s=0$ and 1 are found to be

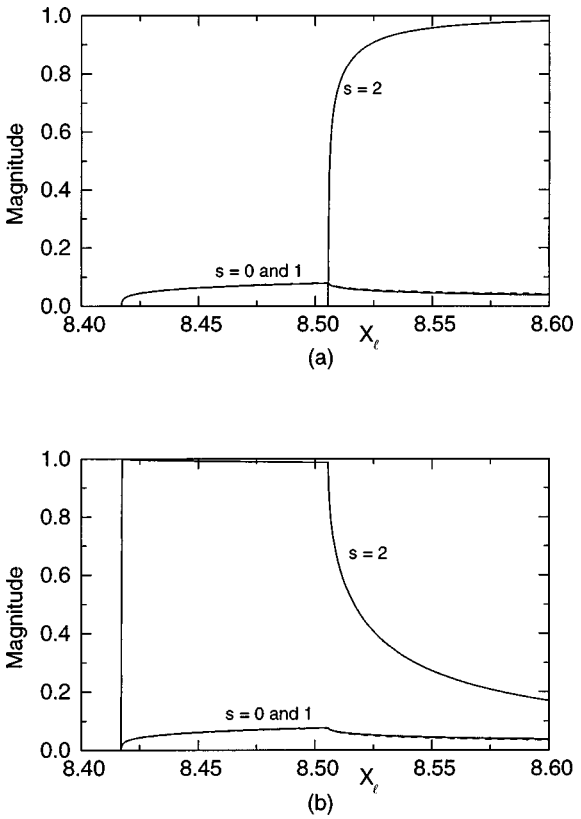

FIG. 10. Scattering characteristics for an incoming $s=2$ mode above its cut-off frequency $X_l=8.417$ when $R_r/R_l=0.9896$. (a) Transmitted modes and (b) reflected modes. Parameters refer to radial mode number. Please note that the curves for $s=0$ and $s=1$ are almost equal in the two cases.

almost equal but not identical in both transmission and reflection. From the figure we see that there is a small, but not negligible excitation of these modes. This cross coupling of the radial modes was not considered as a source for some extra resonances observed in Ref. 8. We suggest this interpretation as a possible explanation. This is supported by our calculations showing a monotonically increased excitation of the other modes and reduced reflection coefficient with frequency up to $X_l = 8.505$, at which point the mode is not trapped any more. Thus our calculations show that this effect may be small but not necessarily negligible. These features are also shown in the experiments in Ref. 8, although the axial distribution of the exciting transducers which can change this picture was not specified.

VI. CONCLUSION

We have presented numerical results of torsional wave scattering from abrupt diameter changes in a circular solid rod. The calculations are based on a theory applying modal expansion to the acoustic fields. We have included several modes in the expansion, and demonstrated that it may be necessary to include all propagating and some cut-off modes to obtain solutions of high accuracy. The results have shown that strong resonance effects are present in the scattering process when any of the scattered modes is at a cut-off frequency. We have also shown agreements to simplified theoretical expressions valid in the high- and low-frequency limits.

[1] E. Verdonk, ''Measurements of pulse mode behavior in weakly-clad waveguides,'' Proc. 1996 IEEE Ultrasonics Symposium, pp. 723–726.
[2] B. K. Sinha and S. Kostek, ''Borehole flexural waves in the presence of uniaxial stresses,'' Proc. 1994 IEEE Ultrasonics Symposium, pp. 665–670.
[3] C. K. Jen, ''Acoustic fibers,'' Proc. 1987 IEEE Ultrasonics Symposium, pp. 443–454.
[4] M. Berwick and D. A. Jackson, ''Coaxial optical-fiber frequency shifter,'' Opt. Lett. **17**, 270–272 (1992).
[5] H. E. Engan, ''Analysis of polarization mode coupling by acoustic torsional waves in optical fibers,'' J. Opt. Soc. Am. A **13**, 112–118 (1996).
[6] H. Wada, ''Reflection characteristics of torsional waves in a semi-infinite cylindrical rod connected to an elastic half-space,'' Int. J. Eng. Sci. **19**, 967–977 (1981).
[7] K. Liu and T. Yokoyama, ''Transient torsional waves in stepped circular bars,'' Japan Society of Mechanical Engineers International Journal A **39**, 86–92 (1996).
[8] W. Johnson, B. A. Auld, E. Segal, and F. Passarelli, ''Trapped torsional modes in solid cylinders,'' J. Acoust. Soc. Am. **100**, 285–293 (1996).
[9] B. A. Auld, *Acoustic Fields and Waves in Solids* (Wiley, New York, 1973).
[10] H. E. Engan, B. Y. Kim, J. N. Blake, and H. J. Shaw, ''Propagation and optical interaction of guided acoustic waves in two-mode optical fibers,'' J. Lightwave Technol. **LT-6**, 428–436 (1988).
[11] D. M. Pozar, *Microwave Engineering* (Addison-Wesley, New York, 1990).

Mandrel effects on the dipole flexural mode in a borehole

Chaur-Jian Hsu and Bikash K. Sinha
Schlumberger-Doll Research, Old Quarry Road, Ridgefield, Connecticut 06877-4108

(Received 30 March 1998; accepted for publication 21 July 1998)

The flexural mode is the lowest-order borehole mode with dipole excitation. The low-frequency asymptote of the flexural wave speed is used to estimate the formation shear speed in well logging. The borehole flexural mode measurement system consists of a mandrel that holds the transmitter and an array of receivers. This mandrel is, generally, designed to minimize the interference between any mandrel and the borehole flexural modes. A slotted sleeve housing that makes the sleeve arrival significantly slower than the formation arrival enables the processing of the recorded waveforms based on a model of fluid-filled boreholes without any mandrel. The objective of this work is to investigate the basic physics of mandrel effects on borehole flexural mode for the condition that the mandrel is in the form of a rod or pipe that is not necessarily slower than the formation arrivals. To this end, we describe an experimental and theoretical study of flexural modes in a borehole with a concentric mandrel and water annulus. The mandrels are of simple geometry such as a rod or a pipe, not intended to model any particular sonic tool in its entirety. However, the presence of a rod or a pipe can approximately represent the waveguide nature of the mandrel and its possible influence on borehole flexural modes. A fluid-filled (without any tool) borehole and a mandrel immersed in an infinite fluid (without any borehole) are two independent systems. Each supports a flexural mode that can be excited by a dipole source. These two uncoupled modes have distinct velocity dispersions. In a coupled mandrel-in-borehole system, two flexural modes are generated with a dipole source. These two coupled modes may resemble or significantly differ from the two uncoupled modes depending on the proximity of dispersions of these two uncoupled modes. [S0001-4966(98)05910-4]

PACS numbers: 43.20.Mv, 43.20.Hq, 43.40.Ph [ANN]

INTRODUCTION

Elastic wave propagation in cylindrical structures has been studied for different applications. Starting from fundamental studies of elastic wave propagation in plates and cylinders,[1,2] there has been a significant amount of work on wave propagation in composite cylindrical structures that have applications in the analysis of optical fiber acoustic waveguides.[3–10] Elastic waves propagating through the earth are routinely used to estimate physical properties of the formation.[11–13] A typical sonic measurement consists of a fluid-filled borehole where a source and an array of receivers are placed in the fluid. Two different types of sources are used: a monopole and a dipole. A monopole source excites axisymmetric waves propagating along the borehole. A dipole source directed perpendicular to the borehole axis excites flexural waves propagating along the borehole. Both axisymmetric and flexural waves in a borehole are dispersive. Sinha *et al.*[14] and Plona *et al.*[15] have presented a theoretical and experimental study of axisymmetric wave propagation in fluid-filled cylindrical shells. Recently, Hsu *et al.*[16] have reported on axisymmetric modes of an elastic or poroelastic mandrel in a liquid-filled borehole surrounded by a formation. The presence of a poroelastic mandrel causes a significant attenuation of tube modes that is useful in the design of sonic imaging tools. The lowest-order axisymmetric Stoneley mode dispersion may be utilized to estimate formation shear slowness under favorable conditions.[17] However, a preferable way of determining the formation shear slowness is to measure borehole flexural dispersion using a dipole source and an array of receivers in a liquid-filled borehole. The flexural dispersion asymptotically approaches the formation shear wave speed at low frequencies.

This paper describes a fundamental study of modal propagation of flexural waves in cylindrical structures and investigates the effect of interaction of rod or pipe flexural dispersion with that of the formation. It is helpful to study such interactions by analyzing the flexural dispersions of components of the coupled system separately. To this end, we analyze the flexural dispersion of a fluid-filled borehole in a formation; and a rod or a pipe immersed in an infinite fluid. Flexural dispersions of these two canonical cases provide a good indication of flexural dispersions of the coupled system consisting of a rod or a pipe in a fluid-filled borehole.

Numerical solutions have been obtained for these structures in terms of dispersion curves for the lowest-order flexural mode in the frequency range of interest. Since we are primarily interested in the propagating modes, dispersion curves extending into the imaginary and complex wave number domain are not included in this study. Nevertheless, attenuation of the leaky modes have been obtained directly from the imaginary part of the complex frequency for the cases when they exist.

I. MATHEMATICAL FORMULATION

In this section a brief review is given of the equations of motion for a cylindrical structure that are the building blocks of more complex cylindrically layered systems.

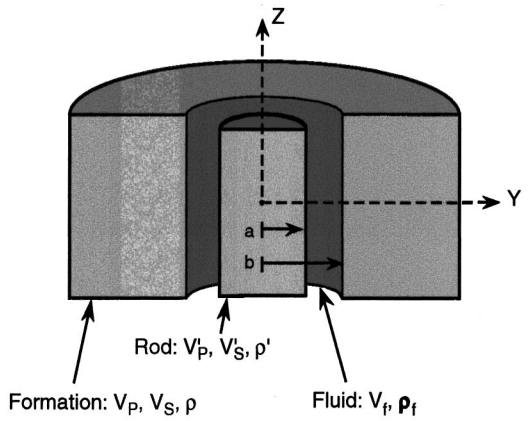

FIG. 1. Schematic diagram of a cylindrical rod in a fluid-filled borehole.

When referred to the coordinate system shown in Figs. 1 and 2, the equations of motion for harmonic waves in cylindrical structures may be given by[1]

$$\begin{aligned}
\rho\ddot{u}_r &= \frac{\partial \tau_{rr}}{\partial r} + \frac{1}{r}\frac{\partial \tau_{r\theta}}{\partial \theta} + \frac{\partial \tau_{rz}}{\partial z} + \frac{\tau_{rr}-\tau_{\theta\theta}}{r},\\
\rho\ddot{u}_\theta &= \frac{1}{r}\frac{\partial \tau_{\theta\theta}}{\partial \theta} + \frac{\partial \tau_{z\theta}}{\partial z} + \frac{\partial \tau_{r\theta}}{\partial r} + 2\frac{\tau_{r\theta}}{r},\\
\rho\ddot{u}_z &= \frac{\partial \tau_{rz}}{\partial r} + \frac{1}{r}\frac{\partial \tau_{z\theta}}{\partial \theta} + \frac{\partial \tau_{zz}}{\partial z} + \frac{\tau_{rz}}{r},
\end{aligned} \tag{1}$$

where τ_{rr}, $\tau_{\theta\theta}$, τ_{zz}, τ_{rz}, $\tau_{r\theta}$, and $\tau_{z\theta}$ are the stress components; u_r, u_θ, and u_z are the displacement components and ρ is the mass density of the material of the cylindrical structure at hand.

The constitutive relations for a homogeneous, elastic and isotropic material are

$$\begin{aligned}
&\tau_{rr}=\lambda\Delta+2\mu\epsilon_{rr}, \quad \tau_{\theta\theta}=\lambda\Delta+2\mu\epsilon_{\theta\theta},\\
&\tau_{zz}=\lambda\Delta+2\mu\epsilon_{zz}, \quad \tau_{r\theta}=2\mu\epsilon_{r\theta},\\
&\tau_{z\theta}=2\mu\epsilon_{z\theta}, \quad \tau_{rz}=2\mu\epsilon_{rz},
\end{aligned} \tag{2}$$

where $\Delta=\partial u_r/\partial r+u_r/r+(1/r)\partial u_\theta/\partial\theta+\partial u_z/\partial z$; ϵ_{rr}, $\epsilon_{\theta\theta}$, $\epsilon_{r\theta}$, $\epsilon_{z\theta}$, and ϵ_{rz} are the strain components and λ and μ are the Lamé constants for the material of the cylindrical structure at hand.

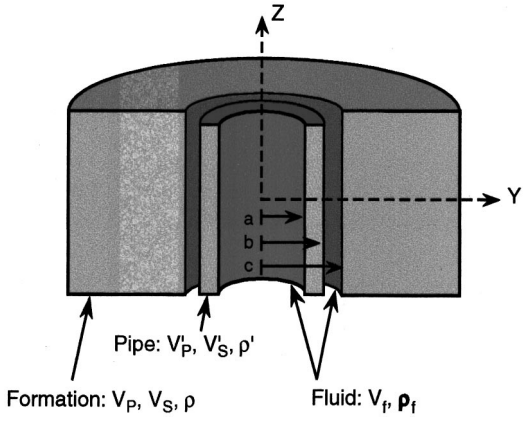

FIG. 2. Schematic diagram of a cylindrical pipe in a fluid-filled borehole.

The strain-displacement relations in cylindrical coordinates take the form

$$\begin{aligned}
&\epsilon_{rr}=\frac{\partial u_r}{\partial r}, \quad \epsilon_{\theta\theta}=\frac{1}{r}\frac{\partial u_\theta}{\partial\theta}+\frac{u_r}{r},\\
&\epsilon_{zz}=\frac{\partial u_z}{\partial z}, \quad \epsilon_{r\theta}=\frac{1}{2}\left[\frac{1}{r}\frac{\partial u_r}{\partial\theta}+\frac{\partial u_\theta}{\partial r}-\frac{u_\theta}{r}\right],\\
&\epsilon_{z\theta}=\frac{1}{2}\left[\frac{1}{r}\frac{\partial u_z}{\partial\theta}+\frac{\partial u_\theta}{\partial z}\right], \quad \epsilon_{rz}=\frac{1}{2}\left[\frac{\partial u_z}{\partial r}+\frac{\partial u_r}{\partial z}\right].
\end{aligned} \tag{3}$$

An eigensolution to any linear elastodynamic solution can be expressed in terms of a scalar potential ϕ and a vector potential H

$$\mathbf{u}=\nabla\phi+\nabla\times\mathbf{H}, \tag{4}$$

where $\nabla\cdot\mathbf{H}$ is arbitrary, and

$$V_1^2\nabla^2\phi=-\omega^2\phi, \quad V_2^2\nabla^2\mathbf{H}=-\omega^2\mathbf{H}. \tag{5}$$

We can express the displacement components in cylindrical coordinates in terms of these scalar and vector potentials

$$\begin{aligned}
u_r &= \frac{\partial\phi}{\partial r}+\frac{1}{r}\frac{\partial H_z}{\partial\theta}-\frac{\partial H_\theta}{\partial z},\\
u_\theta &= \frac{1}{r}\frac{\partial\phi}{\partial\theta}+\frac{\partial H_r}{\partial z}-\frac{\partial H_z}{\partial z},\\
u_z &= \frac{\partial\phi}{\partial z}+\frac{\partial H_\theta}{\partial r}+\frac{H_\theta}{r}-\frac{1}{r}\frac{\partial H_r}{\partial\theta}.
\end{aligned} \tag{6}$$

Substituting these displacement components into the constitutive relations and the stress equations of motion, we can write Eqs. (5) in the following form in terms of the scalar potential ϕ and the three components of vector potential $\mathbf{H}$

$$\begin{aligned}
-\frac{\omega^2}{V_1^2}\phi &= \frac{\partial^2\phi}{\partial r^2}+\frac{1}{r}\frac{\partial\phi}{\partial r}+\frac{1}{r^2}\frac{\partial^2\phi}{\partial\theta^2}+\frac{\partial^2\phi}{\partial z^2},\\
-\frac{\omega^2}{V_2^2}H_r &= \frac{\partial^2 H_r}{\partial r^2}+\frac{1}{r}\frac{\partial H_r}{\partial r}+\frac{1}{r^2}\left(\frac{\partial^2 H_r}{\partial\theta^2}-2\frac{\partial H_\theta}{\partial\theta}-H_r\right)\\
&\quad +\frac{\partial^2 H_r}{\partial z^2},\\
-\frac{\omega^2}{V_2^2}H_\theta &= \frac{\partial^2 H_\theta}{\partial r^2}+\frac{1}{r}\frac{\partial H_\theta}{r}+\frac{1}{r^2}\left(\frac{\partial^2 H_\theta}{\partial\theta^2}+2\frac{\partial H_r}{\partial\theta}-H_\theta\right)\\
&\quad +\frac{\partial^2 H_\theta}{\partial z^2},\\
-\frac{\omega^2}{V_2^2}H_z &= \frac{\partial^2 H_z}{\partial r^2}+\frac{1}{r}\frac{\partial H_z}{r}+\frac{1}{r^2}\frac{\partial^2 H_z}{\partial\theta^2}+\frac{\partial^2 H_z}{\partial z^2}.
\end{aligned} \tag{7}$$

A solution of Eqs. (7) may be written in the form

$$\begin{aligned}
\phi &= f(r)\cos n\theta e^{i\zeta z},\\
H_r &= h_r(r)\sin n\theta e^{i\zeta z},\\
H_\theta &= h_\theta(r)\cos n\theta e^{i\zeta z},\\
H_z &= h_z(r)\sin n\theta e^{i\zeta z},
\end{aligned} \tag{8}$$

which satisfies Eqs. (7) provided

$$\frac{\partial^2 f}{\partial r^2}+\frac{1}{r}\frac{\partial f}{\partial r}+\left(\frac{\alpha^2-n^2}{r^2}\right)f=0, \tag{9}$$

$$\frac{\partial^2 h_z}{\partial r^2}+\frac{1}{r}\frac{\partial h_z}{\partial r}+\left(\frac{\beta^2-n^2}{r^2}\right)h_z=0, \tag{10}$$

$$\frac{\partial^2 h_r}{\partial r^2}+\frac{1}{r}\frac{\partial h_r}{\partial r}+\frac{1}{r^2}(-n^2h_r+2nh_\theta-h_r)+\beta^2h_r=0, \tag{11}$$

$$\frac{\partial^2 h_\theta}{\partial r^2}+\frac{1}{r}\frac{\partial h_\theta}{\partial r}+\frac{1}{r^2}(-n^2h_\theta+2nh_r-h_\theta)+\beta^2h_\theta=0, \tag{12}$$

where

$$\alpha^2=\frac{\omega^2}{V_1^2}-\zeta^2, \quad \beta^2=\frac{\omega^2}{V_2^2}-\zeta^2, \tag{13}$$

where V_1 and V_2 are the compressional and shear wave velocities, respectively.

Subtracting and adding Eqs. (11) and (12), respectively, we obtain

$$\begin{aligned}\frac{\partial^2 h_1}{\partial r^2}+\frac{1}{r}\frac{\partial h_1}{\partial r}+\left(\beta^2-\frac{(n+1)^2}{r^2}\right)h_1=0,\\ \frac{\partial^2 h_2}{\partial r^2}+\frac{1}{r}\frac{\partial h_2}{\partial r}+\left(\beta^2-\frac{(n+1)^2}{r^2}\right)h_2=0,\end{aligned} \tag{14}$$

where

$$2h_1=h_r-h_\theta, \quad 2h_2=h_r+h_\theta. \tag{15}$$

Solutions of Eqs. (9), (10), (14), and (15), respectively, may be written in the form

$$f=AJ_n(\alpha r)+BY_n(\alpha r), \tag{16}$$

and

$$h_z=h_3=A_3J_n(\beta r)+B_3Y_n(\beta r), \tag{17}$$

$$2h_1=h_r-h_\theta=2A_1J_{n+1}(\beta r)+2B_1Y_{n+1}(\beta r), \tag{18}$$

$$2h_2=h_r+h_\theta=2A_2J_{n-1}(\beta r)+2B_2Y_{n-1}(\beta r), \tag{19}$$

where J_n and Y_n are Bessel functions of the first and second kind, respectively. Since $\nabla\cdot\mathbf{H}$ is arbitrary, we can eliminate one of the h_i. Following the work of Gazis,[1] we set $h_2=0$, and from Eqs. (18) and (19), we have

$$h_r=h_1, \quad h_\theta=-h_1. \tag{20}$$

The solution for the displacement components can now be written

$$\begin{aligned}u_r&=\left(\frac{\partial f}{\partial r}+\frac{n}{r}h_3+i\zeta h_1\right)\cos n\theta e^{i\zeta z},\\ u_\theta&=\left(\frac{-n}{r}f+i\zeta h_1-\frac{\partial h_3}{\partial r}\right)\sin n\theta e^{i\zeta z},\\ u_z&=\left(i\zeta f-\frac{\partial h_1}{\partial r}-(n+1)\frac{h_1}{r}\right)\cos n\theta e^{i\zeta z}.\end{aligned} \tag{21}$$

Substitution of Eqs. (16)–(20) into (21) yields the following expressions for the displacement components in the mth cylindrical layer that can be employed to satisfy the appropriate boundary conditions:

$$\begin{aligned}u_r=&\left[\left\{\frac{n}{r}J_n(\alpha_{(m)}r)-\alpha_{(m)}J_{n+1}(\alpha_{(m)}r)\right\}A^{(m)}\right.\\ &+\left\{\frac{n}{r}Y_n(\alpha_{(m)}r)-\alpha_{(m)}Y_{n+1}(\alpha_{(m)}r)\right\}B^{(m)}\\ &+i\zeta J_{n+1}(\beta_{(m)}r)A_1^{(m)}+i\zeta Y_{n+1}(\beta_{(m)}r)B_1^{(m)}\\ &+\frac{n}{r}J_n(\beta_{(m)}r)A_3^{(m)}\\ &\left.+\frac{n}{r}Y_n(\beta_{(m)}r)B_3^{(m)}\right]\cos n\theta e^{i(\omega t+\zeta z)},\end{aligned} \tag{22}$$

$$\begin{aligned}u_\theta=&\left[\left[-\frac{n}{r}J_n(\alpha_{(m)}r)\right]A^{(m)}+\left[-\frac{n}{r}Y_n(\alpha_{(m)}r)\right]B^{(m)}\right.\\ &+[i\zeta J_{n+1}(\beta_{(m)}r)]A_1^{(m)}+[i\zeta Y_{n+1}(\beta_{(m)}r)]B_1^{(m)}\\ &+\left\{-\frac{n}{r}J_n(\beta_{(m)}r)+\beta_{(m)}J_{n+1}(\beta_{(m)}r)\right\}A_3^{(m)}\\ &\left.+\left\{-\frac{n}{r}Y_n(\beta_{(m)}r)+\beta Y_{n+1}(\beta_{(m)}r)\right\}B_3^{(m)}\right]\\ &\times\cos n\theta e^{i(\omega t+\zeta z)},\end{aligned} \tag{23}$$

$$\begin{aligned}u_z=&[\{i\zeta J_n(\alpha_{(m)}r)\}A^{(m)}+\{i\zeta Y_n(\alpha_{(m)}r)\}B^{(m)}\\ &-[\beta_{(m)}J_n(\beta_{(m)}r)]A_1^{(m)}\\ &-\{\beta_{(m)}Y_n(\beta_{(m)}r)\}B_1^{(m)}]\cos n\theta e^{i(\omega t+\zeta z)},\end{aligned} \tag{24}$$

where the index m denotes the mth cylindrical layer parameter and

$$\alpha_{(m)}^2=\frac{\omega^2}{V_{1(m)}^2}-\zeta^2, \qquad \beta_{(m)}^2=\frac{\omega^2}{V_{2(m)}^2}-\zeta^2, \tag{25}$$

V_1 and V_2 are the compressional and shear wave velocities, respectively; $J_n(x)$ and $Y_n(x)$ are the Bessel functions of the first and second kinds, respectively, and of order n.

At this point, it should be noted that the solution given by Eqs. (22)–(24) is valid for a solid annulus. The corresponding solution for a solid rod is simply obtained by discarding the terms containing $Y_n(\alpha r)$ or $Y_n(\beta r)$ which diverge as $r\to 0$. On the other hand, the wave solution in a solid formation of infinite radial extent takes the form

$$\begin{aligned}u_r=&\left\{\frac{n}{r}H_n(\alpha r)-\alpha H_{n+1}(\alpha r)\right\}A^{(m)}\\ &+[i\zeta H_{n+1}(\beta r)]A_1^{(m)}\\ &+\left[\frac{n}{r}H_n(\beta r)\right]A_3^{(m)}\cos n\theta e^{i(\omega t+\zeta z)},\end{aligned} \tag{26}$$

$$u_\theta=\left[\left\{-\frac{n}{r}H_n(\alpha r)\right\}A^{(m)}+[i\zeta H_{n+1}(\beta r)]A_1^{(m)}+\left[-\frac{n}{r}H_n(\beta r)+\beta H_{n+1}(\beta r)\right]A_3^{(m)}\right]\times\sin n\theta e^{i(\omega t+\zeta z)}, \tag{27}$$

$$u_z=[\{i\zeta H_n(\alpha r)\}A^{(m)}-\{\beta H_n(\beta r)\}A_1^{(m)}]\cos n\theta e^{i(\omega t+\zeta z)}, \tag{28}$$

where $H_n(x)$ are the outgoing Hankel functions of the second kind consistent with the exp $i\omega t$ and are given by Eq. (29)

$$H_n^{(2)}(x)=J_n(x)-iY_n(x). \tag{29}$$

The corresponding displacement components in an inviscid fluid take the reduced form

$$u_r^f=\left\{\left[\frac{n}{r}J_n(\alpha^f r)-\alpha^f J_{n+1}(\alpha^f r)\right]C_1^{(m)}+\left[\frac{n}{r}Y_n(\alpha^f r)-\alpha^f Y_{n+1}(\alpha^f r)\right]C_2^{(m)}\right\}\times\cos n\theta e^{i(\omega t+\zeta z)}, \tag{30}$$

$$u_\theta^f=\left\{-\frac{n}{r}[J_n(\alpha^f r)C_1^{(m)}+Y_n(\alpha^f r)C_2^{(m)}]\right\}\sin n\theta e^{i(\omega t+\zeta z)}, \tag{31}$$

$$u_z^f=i\zeta[J_n(\alpha^f r)C_1^{(m)}+Y_n(\alpha^f r)C_2^{(m)}]\cos n\theta e^{i(\omega t+\zeta z)}, \tag{32}$$

where

$$\alpha^f=\frac{\omega^2}{V_f^2}-\zeta^2, \tag{33}$$

V_f is the compressional wave velocity in the fluid, and the superscript f refers the quantity to the fluid medium.

At this point, it should be noted that the solution given by Eqs. (30)–(32) is valid for a liquid annulus. The corresponding solution for a liquid column is simply obtained by discarding the terms containing $Y_{0,1}(\alpha^f r)$ which diverge as $r\to 0$. On the other hand, the wave solution in a fluid medium of infinite radial extent takes the form

$$u_r^f=-\alpha^f H_{n+1}(\alpha^f r)D_1^{(m)}\cos n\theta e^{i(\omega t+\zeta z)}, \tag{34}$$

$$u_\theta^f=\left\{-\alpha^f H_{n+1}(\alpha^f r)+\frac{n}{r}H_n(\alpha^f r)\right\}D_1^{(m)}\sin n\theta e^{i(\omega t+\zeta z)}, \tag{35}$$

$$u_z^f=i\zeta H_n(\alpha^f r)D_1^{(m)}\cos n\theta e^{i(\omega t+\zeta z)}, \tag{36}$$

where

$$H_n^{(2)}(x)=J_n(x)-iY_n(x), \tag{37}$$

are the appropriate outgoing Hankel functions of the second kind consistent with the exp $i\omega t$ time dependence.

The classical boundary conditions at a fluid–solid interface are given by

$$[\tau_{rr}^{(1)},\ \tau_{r\theta}^{(1)},\ \tau_{rz}^{(1)},\ u_r^{(1)}]_{r=a}=[\tau_{rr}^{(2)},\ \tau_{r\theta}^{(2)},\ \tau_{rz}^{(2)},\ u_r^{(2)}]_{r=a}, \tag{38}$$

where superscripts 1 and 2 refer to the media on either side of the surface of discontinuity $r=a$. However, it should be noted that the shear stress $\tau_{rz}^{(1)}$ and $\tau_{r\theta}^{(1)}$ in an inviscid fluid are identically equal to zero. At a solid–solid interface, the continuity conditions are

$$[\tau_{rr}^{(1)},\ \tau_{r\theta}^{(1)},\ \tau_{rz}^{(1)},\ u_r^{(1)},\ u_\theta^{(1)},\ u_z^{(1)}]_{r=a}=[\tau_{rr}^{(2)},\ \tau_{r\theta}^{(2)},\ \tau_{rz}^{(2)},\ u_r^{(2)},\ u_\theta^{(2)},\ u_z^{(2)}]_{r=a}, \tag{39}$$

whereas the normal stress components are set equal to zero at traction-free surfaces.

The unknown amplitudes associated with different cylindrical layers are determined by satisfying the boundary conditions at the relevant interfaces.

The solution to a cylindrically layered system can be obtained by satisfying appropriate boundary conditions at all the liquid–solid or solid–solid interfaces. These conditions can be expressed in terms of a matrix equation $\mathbf{Lc}=\mathbf{0}$, where the vector $\mathbf{c}$ denotes the unknown amplitude coefficients. For nontrivial solutions of this matrix equation, we require that the determinant of coefficient matrix $\mathbf{L}$ be zero. The appendix illustrates how these boundary conditions lead to the matrix equation for the case of a cylindrical pipe with its inner and outer radii of b and a, respectiveley, placed in a fluid-filled borehole of radius c surrounded by an infinite formation.

TABLE I. Material parameters for cylindrical components.

Material	V_1	V_2	ρ
Polyethylene	2380 m/s	932 m/s	960 kg/m^3
Limestone	3810	2230	2500
Lucite	2640	1270	1180
Steel	5790	3100	7900
Water	1480	0.0	1000

II. EXPERIMENTAL PROCEDURE

Experiments were conducted with the formation and mandrel immersed in water for all the cases discussed in this paper. Limestone and polyethylene blocks were used representing a fast and slow formations, respectively. The diameter of the borehole in each formation was 3.175 cm. The three mandrels used were a steel rod; a lucite rod; and a steel pipe. They all had an outside diameter of 1.905 cm. The mandrel to borehole diameter ratio was therefore 0.6 for all the cases. The steel pipe had an inner diameter of 1.575 cm. The wall thickness to radius ratio of the steel pipe was 0.17. Compared with a typical oil-field well of about 25 cm diameter, this experiment had a scale of 1/8. The mechanical properties of the relevant materials are listed in Table I.

In the experiment, acoustic waves were generated and received by two dipole ring transducers of the same design. Each dipole transducer was made of a PZT ring polarized along the radial direction. The electrode on the inner and outer surface of the PZT ring was electrically split into two halves and wired in such a way that the two halves vibrate

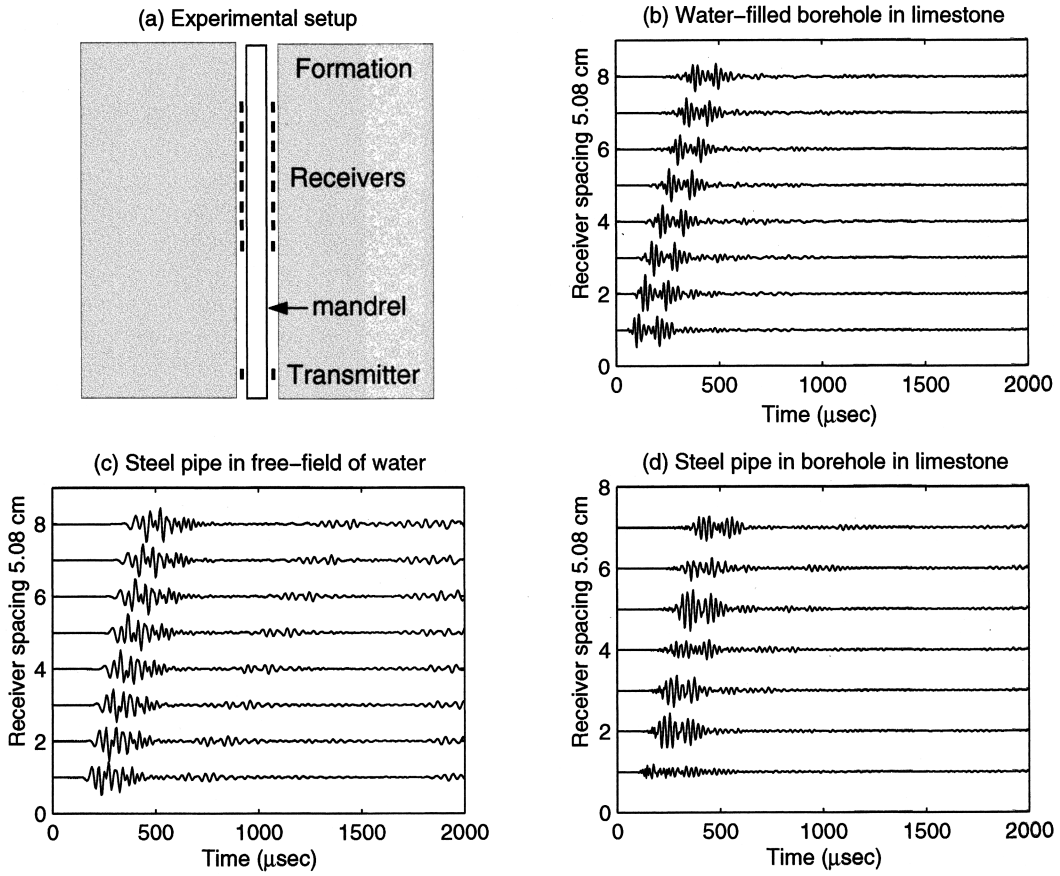

FIG. 3. (a) Schematic diagram of the experimental setup showing the ring source and receivers outside the cylindrical pipe in a fluid-filled borehole. (b) Recorded dipole waveforms at eight receiver positions in a fluid-filled borehole surrounded by a limestone formation. (c) Recorded waveforms on the outside of a steel pipe in infinite water. (d) Recorded waveforms on the outside of a steel pipe placed in a fluid-filled borehole surrounded by a limestone formation.

out of phase in response to an electric pulse drive. All cylindrical components of the experimental setup, including PZT rings, the rod or pipe, were placed concentrically in the borehole in order to minimize excitation of modes other than dipole flexural. Both the transmitter and receiver were aligned azimuthally to have the same dipole orientation which was perpendicular to the borehole axis. The transmitter was stationary, and the receiver stepped along the borehole axis in constant intervals to synthesize an array. The inter-receiver spacing was 1.27 cm. The transmitter was driven with repetitive electric pulses of a one-cycle sine wave. Waveforms were stacked and averaged to enhance the signal-to-noise ratio and then recorded as a function of time at each receiver position. These recorded waveforms were then processed with a modified matrix pencil algorithm developed by Ekstrom.[18] Other techniques may also be used for estimating slowness dispersions from arrays of sonic logging waveforms.[19,20]

The properties of these materials are listed in Table I.

III. EXPERIMENT AND THEORY COMPARISON

We describe experimental and theoretical analyses of three different configurations to study the mandrel effects on the borehole flexural mode. The three configurations are: (A) a steel pipe in a fast (limestone) formation, (B) a steel rod in a slow (polyethylene) formation, and (C) a Lucite rod in a slow (polyethylene) formation. A fast or slow formation refers to the formation shear wave speed being faster or slower than the compressional wave speed in the borehole fluid which is water in all the three cases.

The three cases are similar in geometry with a mandrel and a borehole in a formation. To aid the understanding of modal characteristics of each case, it is useful to understand characteristics of the three constituent parts of each case: (a) a water-filled borehole in a formation; (b) a mandrel in infinite water; and (c) a mandrel in a water-filled borehole in a formation. We will refer to the modes of cases (a) and (b) as uncoupled modes, since they are present in two completely independent systems and are measured separately. In case (c), there are two propagating modes coexisting in the combined mandrel and borehole system. They are referred to as coupled modes.

A. Flexural slowness dispersions

1. Case A: Steel pipe in a fast (limestone) formation

As mentioned earlier, we conducted experiments in three parts for each case. In Fig. 3(a), we show a schematic of experimental setup. The measurement system consists of a transmitter and an array of receivers placed in the annulus between the mandrel and formation. Figure 3(b), (c), and (d) displays, respectively, experimental waveforms recorded at an interval of 5.08 cm for the three configurations of this

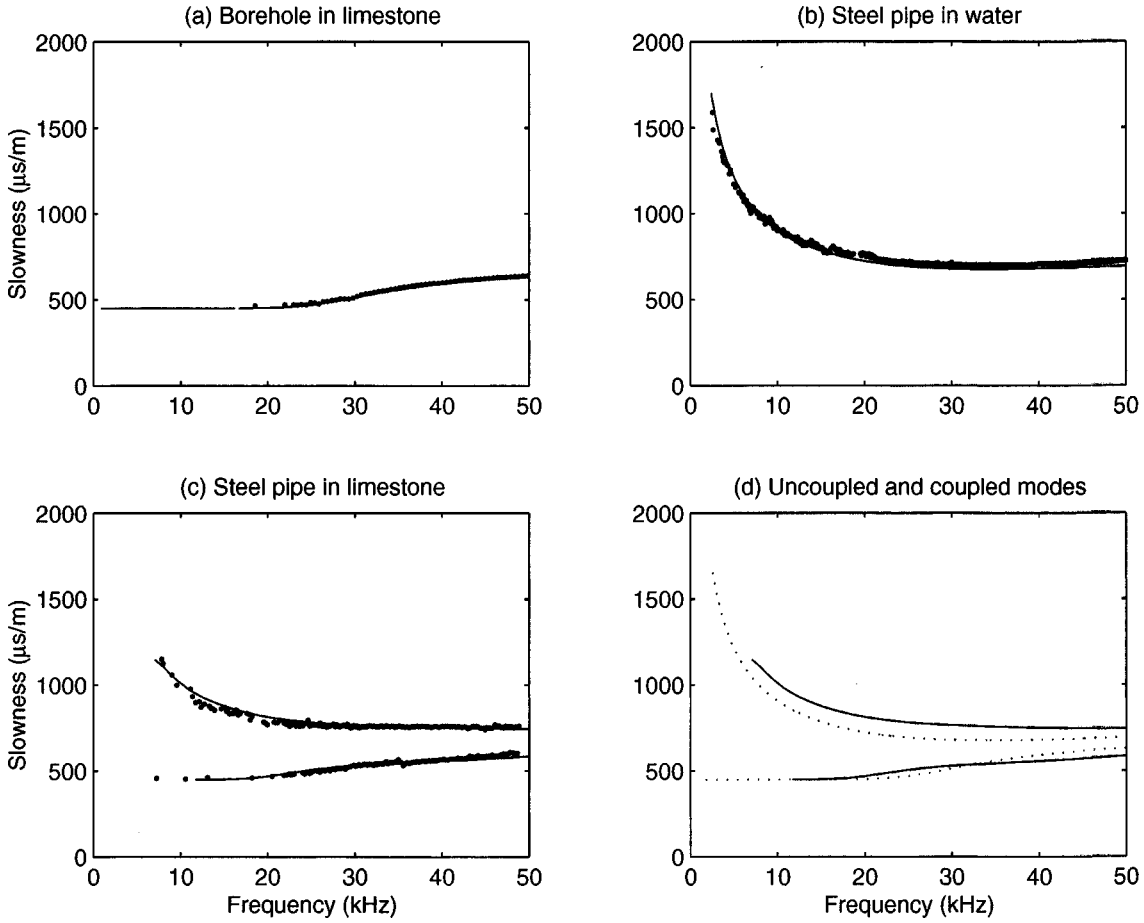

FIG. 4. (a) Borehole flexural dispersion for a limestone formation in the absence of any mandrel. The solid line denotes the theoretical dispersion obtained from a mode search program. The dots denote the measured dispersion obtained from a modified matrix pencil algorithm. (b) Steel pipe flexural dispersion in infinite water. The notation is the same as in (a). (c) Flexural dispersions of a steel pipe in a borehole surrounded by a limestone formation. The notation is the same as in (a). (d) The dotted lines denote uncoupled dispersions for the formation and steel pipe in infinite water from (a) and (b), respectively. The solid lines represent the two lowest-order modes of this composite system of a steel pipe in a borehole surrounded by a limestone formation from (c).

case: (a) a water-filled borehole in a limestone formation; (b) a steel pipe in infinite water; and (c) a steel pipe in a water-filled borehole in a limestone formation. These waves were generated by the same electric drive, which was a one-cycle sine wave of 10 kHz, applied to the same transmitter and acquired with the same receiver and electronic circuits. Even though about 30 waveforms were used in the processing, only eight of them sampled at intervals of 5.08 cm are displayed for brevity. The pipe flexural waves, shown in Fig. 3(c), contain more low-frequency energy as compared with the borehole flexural wave, shown in Fig. 3(b). Changes in the waveforms in Fig. 3(b) and (c) across the array suggest dispersive propagation of the acoustic disturbance. Figure 3(d) shows amplitude modulation as well as distortion in waveforms across the array. These changes are indicative of interference of waves propagating at different speeds across the array.

The dots in Fig. 4(a), (b), and (c) show slowness dispersions of flexural waves in the three configurations. These dispersions are obtained by processing time waveforms shown in Fig. 3(b), (c), and (d) by a modified matrix pencil algorithm. The solid lines denote slowness dispersions obtained by a numerical mode search routine for the three configurations. Excellent agreement is found between measured and theoretical dispersions in all of the three cases. Figure 4(a) and (b) shows that both the borehole and pipe flexural modes are dispersive, but with opposite dispersion trend. The borehole flexural mode, shown in Fig. 4(a), asymptotically approaches formation shear slowness at low frequencies and is slower at higher frequencies. The basic idea of dipole shear logging is to infer formation shear speed from the measured flexural dispersion. In contrast, the flexural mode of the steel pipe in infinite water propagates at vanishingly slow speed at low frequencies, as shown in Fig. 4(b).

In this case A, slowness dispersions of these two uncoupled modes are separated in the frequency range of this study with the borehole flexural mode being faster than the pipe mode. Figure 4(c) shows the dispersions of two flexural modes in the combined system of both the mandrel and borehole. Among these two coupled modes the slower one appears to resemble the steel pipe mode as shown in Fig. 4(b) and the faster one appears to resemble the borehole mode as shown in Fig. 4(a). To further compare these two coupled modes with the two uncoupled modes, we overlay the theoretical slowness dispersion curves of these four modes in Fig. 4(d) where the two uncoupled modes are shown in dotted lines which are duplicates of the solid lines in Fig. 4(a) and (b), and these two coupled modes are shown in solid

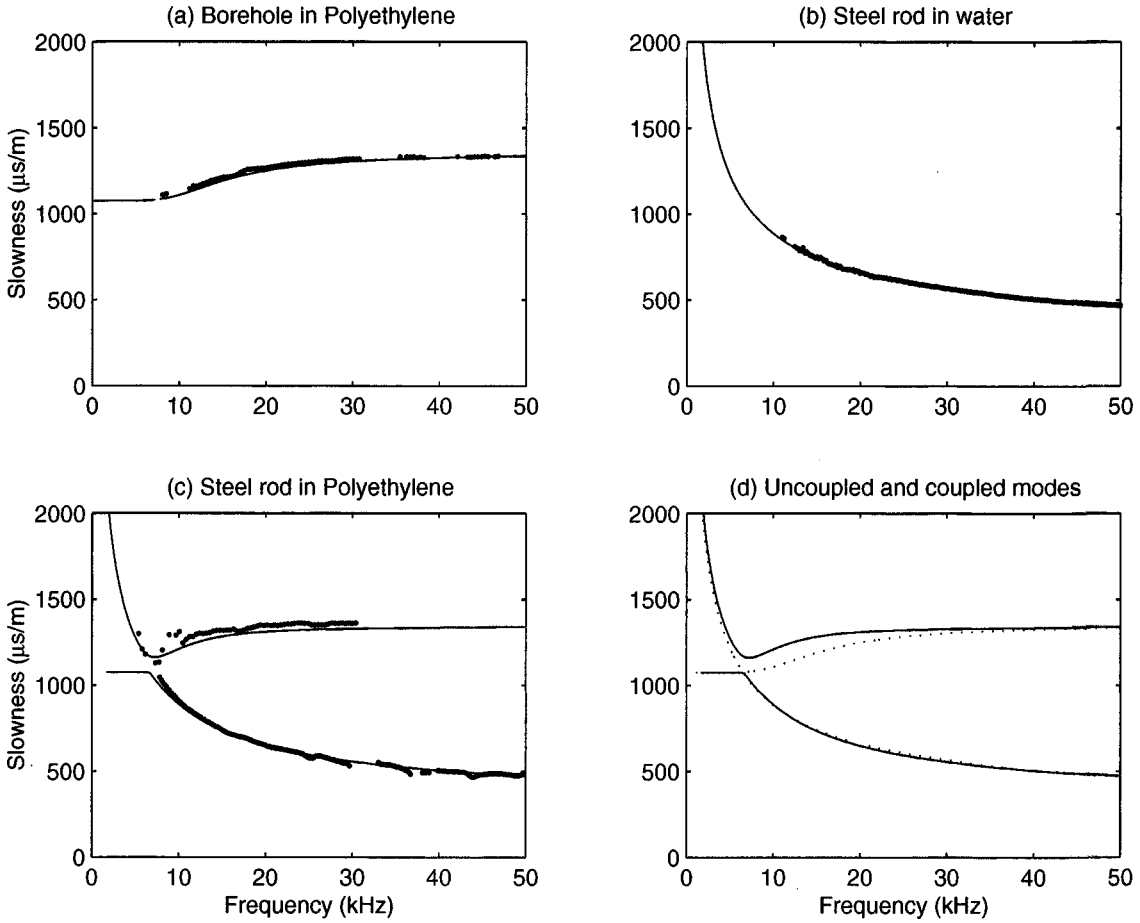

FIG. 5. (a) Borehole flexural dispersion for a polyethylene formation in the absence of any mandrel. The solid line denotes the theoretical dispersion obtained from a mode search program. The dots denote the measured dispersion obtained from a modified matrix pencil algorithm. (b) Steel rod flexural dispersion in infinite water. The notation is the same as in (a). (c) Flexural dispersions of a steel rod in a borehole surrounded by a polyethylene formation. The notation is the same as in (a). (d) The dotted lines denote uncoupled dispersions for the formation and steel rod from (a) and (b), respectively. The solid lines represent the two lowest-order modes of the composite system of a rod in a borehole surrounded by a polyethylene formation from (c).

lines which are duplicates of the solid lines in Fig. 4(c).

Figure 4(d) shows clearly that these two coupled modes are different from the two uncoupled modes. The separation in slowness between the two coupled modes is greater than the separation between the two uncoupled modes for all frequencies.

2. Case B: Steel rod in a slow (polyethylene) formation

Next we will discuss acoustic behavior of the two other cases in the frequency domain. Figure 5(a), (b), (c), and (d) shows similar results for a steel rod in a polyethylene formation. The notation is the same as in Fig. 4.

Figure 5(a) and (b) shows the two uncoupled modes for the first two configurations of case B. They are borehole flexural mode in polyethylene and steel rod flexural mode in infinite water, respectively. The dispersion characteristics of these two modes are similar to those shown in Fig. 4(a) and (b). However, in this case, the borehole flexural dispersion is slower than steel rod dispersion except below about 6.5 kHz where the two uncoupled modes cross each other. This is in agreement with theoretical predictions. Note that some portions of measured dispersions are missing because of rather small signal amplitude at those frequencies. Excellent agreement is again found between measured and theoretical dispersions as shown in Fig. 5(a) and (b).

Figure 5(c) shows two coupled modes of the combined system consisting of a steel rod in a water-filled borehole in a polyethylene formation. Theoretical dispersions from mode search routines agree very well with measured dispersions. Figure 5(d) shows overlays of theoretical results for these two uncoupled modes, shown in dotted lines, and the two coupled modes, shown in solid lines. Similar to the observations from Fig. 4(d), these two coupled modes are different from the two uncoupled modes, especially around the crossover frequency of about 6.5 kHz of the uncoupled modes. The separation in slowness between the two coupled modes is greater than the separation between the two uncoupled modes, especially around the crossover frequency.

3. Case C: Lucite rod in a slow (polyethylene) formation

Next we consider the case of a Lucite rod mandrel in a water-filled borehole in polyethylene formation. Figure 6(a), (b), (c), and (d) shows theoretical and experimental dispersions following the same notation as in Fig. 5.

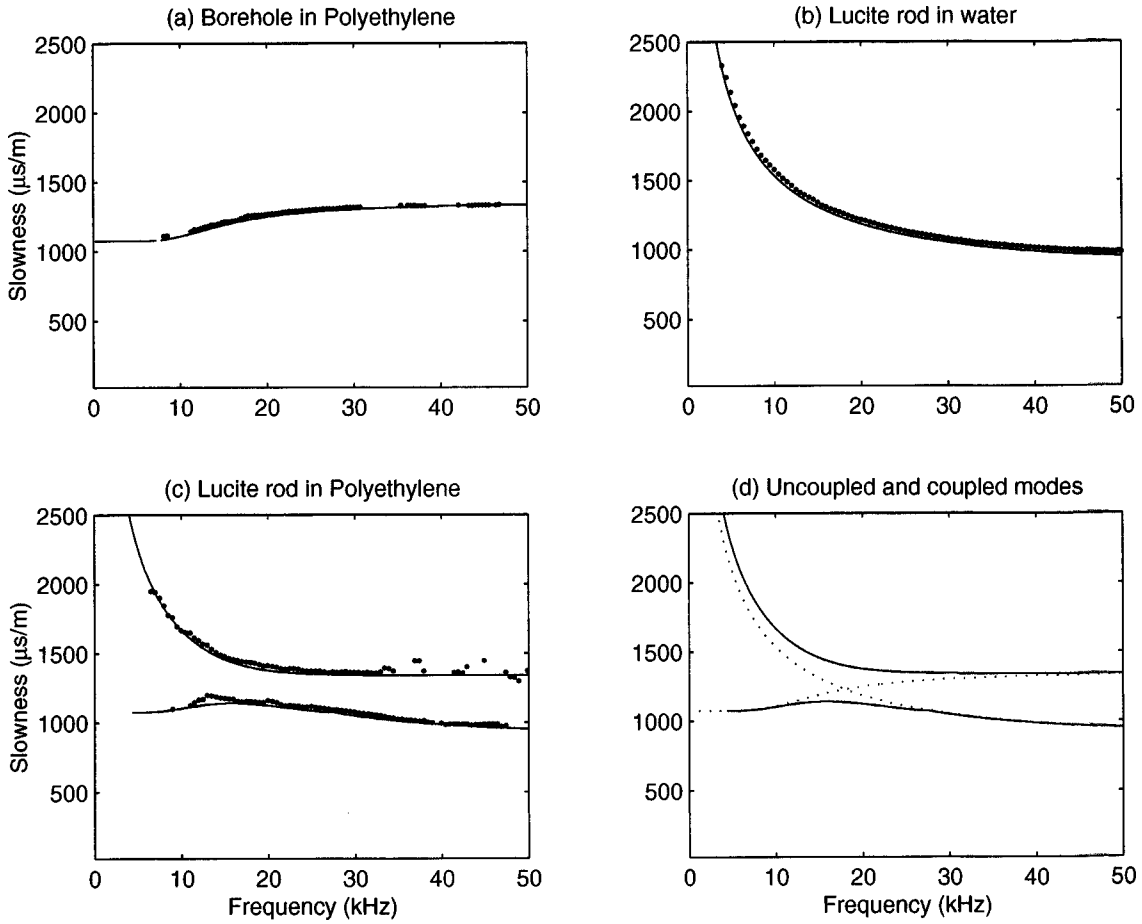

FIG. 6. (a) Borehole flexural dispersion for a polyethylene formation in the absence of any mandrel. The dots denote the measured dispersion obtained from a modified matrix pencil algorithm. (b) Lucite rod flexural dispersion in infinite water. The notation is the same as in (a). (c) Flexural dispersions of a lucite rod in a borehole surrounded by a polyethylene formation. The notation is the same as in (a). (d) The dotted lines denote uncoupled dispersions for the formation and lucite rod from (a) and (b), respectively. The solid lines represent the two lowest-order modes of the composite system of a lucite rod in a borehole surrounded by a polyethylene formation from (c).

Figure 6(a) and (b) shows theoretical and experimental slowness dispersions of the two uncoupled modes. The theoretical dispersion of these two modes are also shown in Fig. 6(d) as dotted lines. The two uncoupled modes cross each other at about 18 kHz where both modes are strongly excited.

The combined system of a Lucite mandrel in a borehole in polyethylene formation exhibits coupled mode dispersions is shown in Fig. 6(c). These dispersions are also duplicated in Fig. 6(d) as solid lines. In this case, the two coupled dispersions are strikingly different from the two uncoupled dispersions. However, changes are consistant with the general observation made from the previous two cases. The two coupled modes have greater slowness separation than the two uncoupled modes. Changes are mostly significant around the crossover frequency of these two uncoupled modes.

It is of interest to investigate the influence of strongly coupled mandrel (rod) and formation flexural modes on the recorded waveforms. Figure 7(a) shows the two slowness dispersions of the mandrel in a borehole system. The upper and lower curves in Fig. 7(a) denote the formation and mandrel dispersions, respectively. Figure 7(b) and (c), respectively, shows the waveforms synthesized from the slower and faster mode dispersions shown in Fig. 7(a). The green curves in Fig. 7(d) denote results from a superposition of the synthesized waveforms in Fig. 7(b) and (c). The black waveforms denote the measured (pressure) waveforms from the Lucite rod in a borehole surrounded by a polyethylene formation. The early arrivals in the measured waveforms denote the compressional headwaves that are not present in the synthesized waveforms as expected. Both the measured and synthesized waveforms in the presence of a strongly coupled mandrel and formation modes show a clear evidence of interference between the two modes manifested by incoherent amplitudes across the array. A strong coupling between the mandrel and formation modes occurs because of the close proximity of the two slowness dispersions even if the two independent modes do not intersect.

4. Summary of the slowness dispersion

It is known that a dipole source excites flexural mode in a fluid-filled borehole in a formation. However, a dipole source also excites flexural mode along a rod or a pipe in an infinite liquid. These two independent or uncoupled modes have slowness dispersions of opposite trend.

A study of flexural characteristics of systems consisting

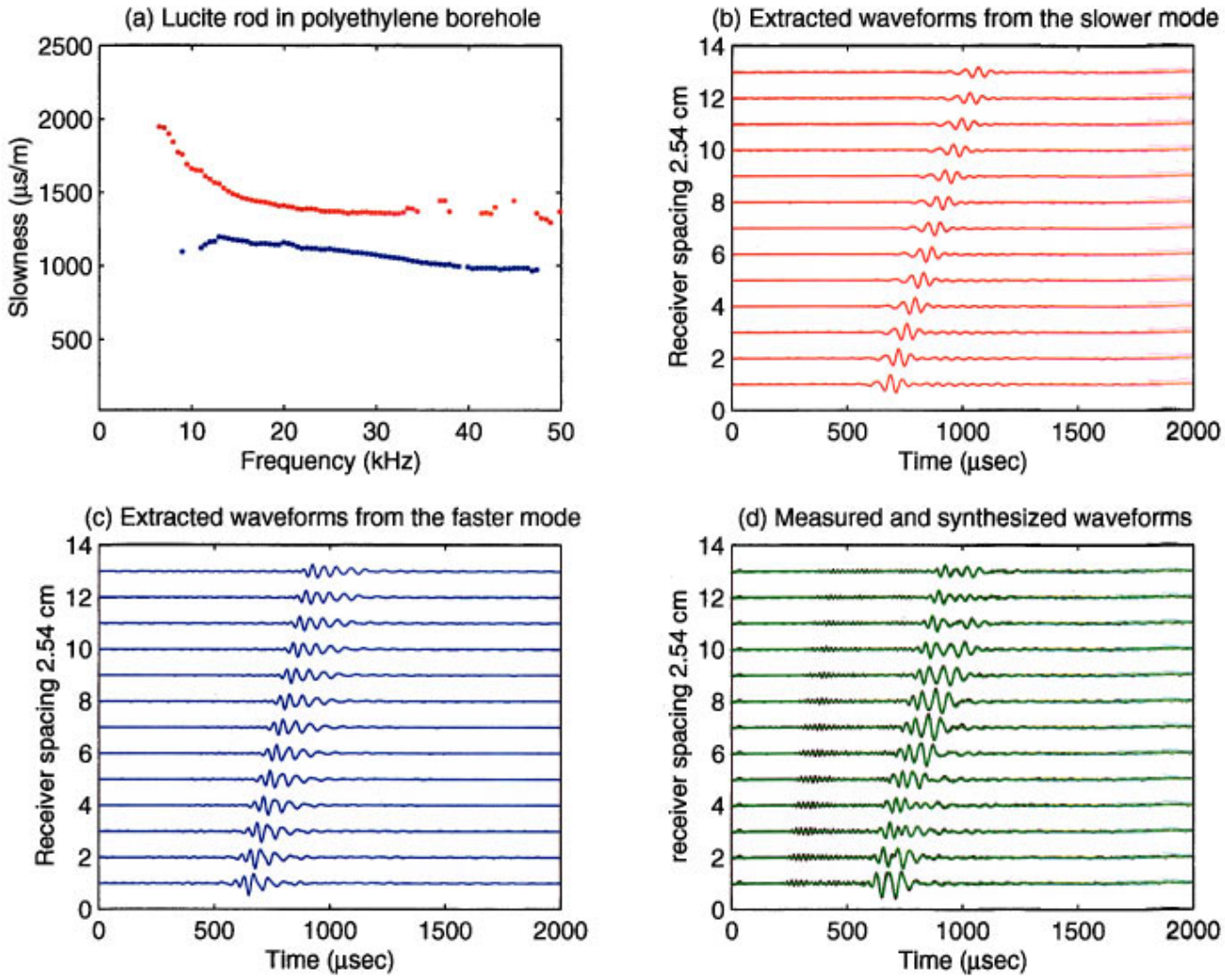

FIG. 7. (a) Measured flexural dispersions of a Lucite rod in a borehole surrounded by a polyethylene formation. (b) Synthetic waveforms from the slower mode dispersion shown in (a). (c) Synthetic waveforms from the faster mode dispersion shown in (a). (d) Comparison of the measured (pressure) waveforms (shown in black) with the superposition of synthetic waveforms (shown in green) from (b) and (c).

of a mandrel centered in a borehole in a formation reveals that a dipole source excites two coupled modes simultaneously. The slowness dispersions of these two coupled modes are *not* superposition of the two uncoupled modes. The difference between the two coupled modes and the two uncoupled modes is frequency dependent and may be small or significant. The degree of interaction depends strongly on the proximity of slowness dispersions of the two uncoupled modes. The slowness separation between the two coupled modes is greater than the separation between the two uncoupled modes in the frequency range of interest. This increase of slowness separation is more pronounced at frequencies where the two uncoupled modes are closer in slowness. Experiment and theory agree very well for all the cases studied.

The borehole flexural mode has been used in oil and gas exploration industry for measuring formation shear wave speed. In this application, the presence of a mandrel or tool in the borehole introduces changes in the water-filled borehole flexural mode. In addition, a second flexural mode is excited which is somewhat different from the flexural mode of the mandrel in infinite liquid. This study suggests that the significance of the mandrel or tool effect on borehole flexural mode depends on the proximity of the two uncoupled modes, i.e., the borehole mode and the mandrel mode. The closer these two uncoupled modes are, the stronger the mandrel effect is. This effect is insignificant only if the two uncoupled modes are widely separated in slowness for all frequencies of interest. This requires the mandrel to be flexible so that its flexural dispersion is significantly slower than the borehole flexural dispersion in formations of interest.

If the elastic waves propagating along the slotted sleeve receiver housing are sufficiently slow (flexible), the effect of sleeve on borehole flexural modes of most formations should be insignificant. However, it should be noted that a slotted tool will behave like an equivalent rod or pipe with a significantly *reduced* bending rigidity. Consequently, the slotted mandrel will affect the recorded waveforms when logging in a very slow formation whose shear velocity is close to the flexural velocity of the slotted mandrel. In contrast, for a smooth steel sleeve housing, the sleeve flexural mode is likely to be close to or intersect with the borehole flexural mode of most of the commonly encountered formations. In such cases, the mandrel effect on the borehole flexural dis-

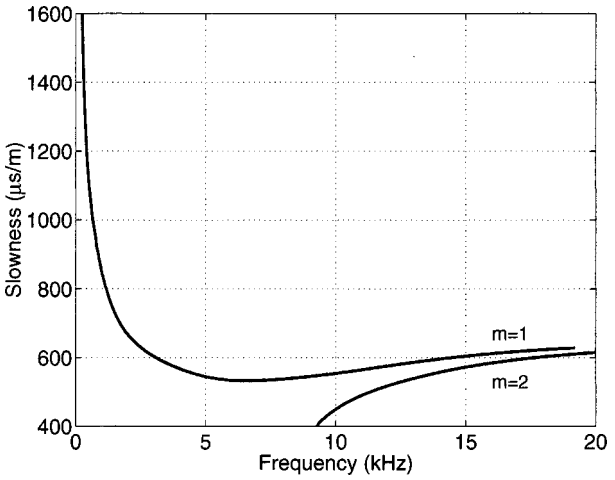

FIG. 8. Two lowest-order flexural modes ($m=1$ and 2) of a thick steel pipe in water: Inner and outer diameters are 12.7 and 20.32 cm, respectively.

persion must be considered in the waveform processing and inversion for the formation shear slowness. As an example, Fig. 8 shows calculated dispersions for the two lowest-order flexural modes of a steel pipe in water. The pipe has inner and outer diameters of 12.7 and 20.32 cm, respectively. This mandrel effect caused by a concomitant non-perforated steel sleeve makes dipole shear logging processing and interpretation more complicated. While the mandrel effect can be accurately modeled for a given tool design in a given formation, it becomes quite challenging to account for the formation dependent changes in the mandrel flexural dispersion.

B. Flexural attenuation

In this section, we investigate attenuation associated with dispersive modes in liquid-filled boreholes in the presence of a mandrel. Most waves we have discussed in this work are trapped modes which propagate along the borehole with phase velocities slower than the slowest formation shear wave speed. For these trapped modes, energy propagates only along the direction of the borehole axis, and therefore there is no attenuation caused by radiation. These trapped modes may still attenuate because of material viscous loss in the mandrel, fluid, or formation. However, if the phase velocity of a propagating mode exceeds the shear bulk wave speed in the surrounding medium, some wave energy radiates into the outer medium causing another form of attenuation.

For a real propagating wave number, a solution to such leaky eigenmodes is given by a complex frequency that is obtained from a complex search of the zeros of the boundary condition determinant shown in the Appendix. The imagi-

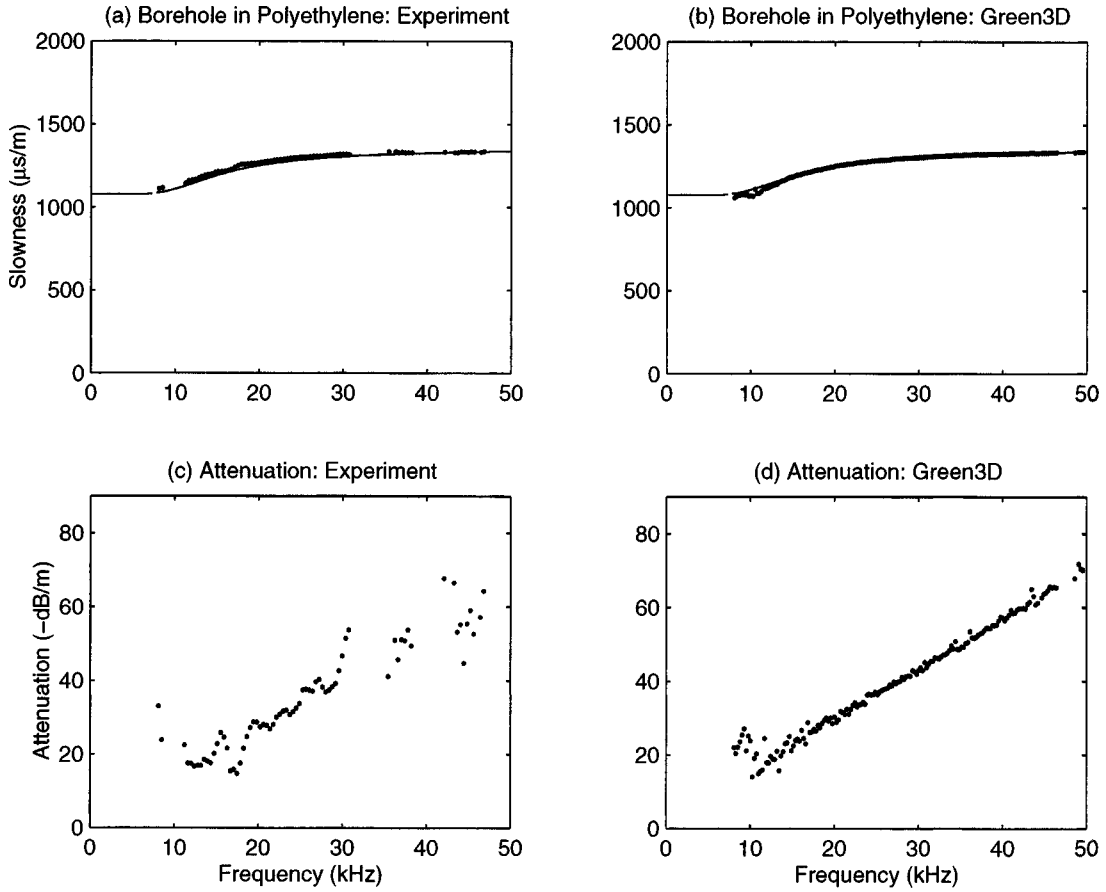

FIG. 9. (a) Borehole flexural dispersion for a polyethylene formation in the absence of any mandrel. The solid line denotes theoretical dispersion obtained from a mode search program. The dots denote measured dispersion obtained from a modified matrix pencil algorithm. (b) The dots denote theoretical dispersion obtained from synthetic waveforms (Green3D) by a modified matrix pencil algorithm. $Q=25$ for the formation in the Green3D calculations. (c) Attenuation of borehole flexural waves caused by finite Q of the formation. Results are obtained from experimental waveforms processed by a modified matrix pencil algorithm. (d) Attenuation results from synthetic waveforms processed by a modified matrix pencil algorithm.

nary part of the complex frequency can be converted into spatial attenuation at a given frequency with the aid of the relation

$$\delta = \omega_I / V \quad [\text{Np / m}], \tag{40}$$

where V is the phase velocity of the eigenmode at the selected frequency. The attenuation factor δ can also be expressed as

$$[\text{dB / m}] = 20(\log e)\delta \quad [\text{Np / m}]. \tag{41}$$

The radiation Q can be simply expressed as the ratio of the real to imaginary part of the complex frequency, multiplied by a factor of 0.5.

In cases A and C, we have flexural modes propagating at speeds slower than or close to the formation shear speed as shown in Figs. 4 and 6. In these cases, attenuation is dominated by material loss. In case B, the mandrel is a steel rod and the formation is polyethylene. The two flexural modes shown in Fig. 5(c) consists of both slow and fast modes. The attenuation of slow mode is largely caused by material loss. In contrast, the faster mode can have radiation loss in addition to material loss at frequencies above 6.5 kHz. We consider case B for the following discussions on attenuation. Similar to the discussion on slowness dispersion, we investigate attenuation associated with modes in case B in three parts: (a) a water-filled borehole in polyethylene formation; (b) a steel rod in infinite water; and (c) a steel rod in a water-filled borehole in polyethylene.

1. Water-filled borehole in polyethylene

The slowness dispersion of the flexural mode for a water-filled borehole in a polyethylene formation was shown in Fig. 5(a). Figure 9(a) shows comparison of measured (shown by dots) and theoretical (shown by a solid line) dispersions for a water-filled borehole in a polyethylene formation. The theoretical dispersion was obtained from a mode search code. Figure 9(b) compares dispersion (shown by dots) obtained from an array of synthetic waveforms processed by a modified matrix pencil algorithm and that from a mode search code (shown by a solid line) for a water-filled borehole in a polyethylene formation. The synthetic waveforms are generated from a three-dimensional dyadic Green's function for elastic waves in multilayer cylindrical structures and an assumed source function. Lu and Liu[21] have developed a Green3D code based on this algorithm which has been used in this study. Although the mode search did not include any material loss, the Green3D calculation was done with an assumed $Q=25$ for the polyethylene formation. Figure 9(c) displays measured attenuation as a function of frequency obtained by processing of recorded waveforms by a modified matrix pencil algorithm.[17] Figure 9(d) shows theoretical attenuation obtained by processing an array of Green3D waveforms for an assumed formation $Q=25$. Good agreement between the measured [as shown in Fig. 9(c)] and theoretical [as shown in Fig. 9(d)] attenuations suggest that it is a reasonable estimate of formation ($Q=25$) for shear wave propagation in polyethylene formation.

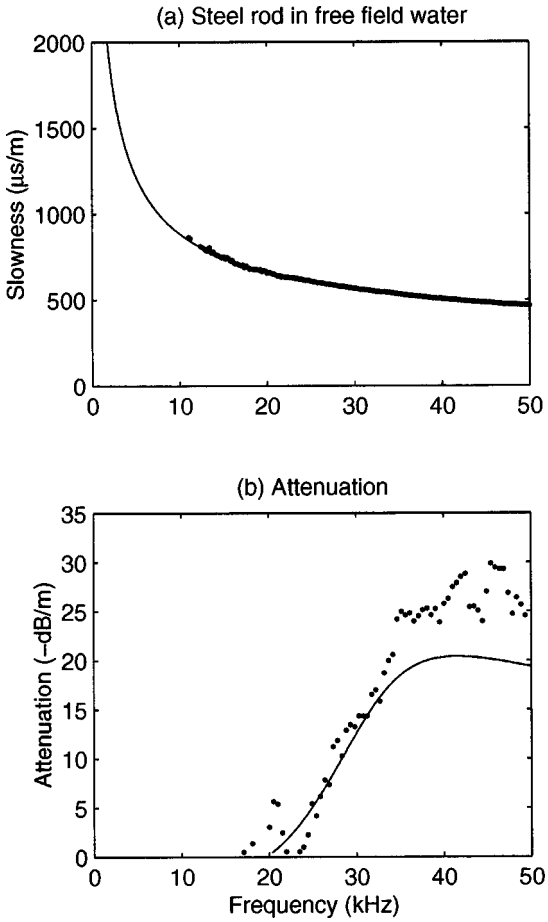

FIG. 10. (a) Slowness dispersion of flexural waves in a steel rod in infinite water. The solid line and dots denote results from a mode search and measured waveforms processed by a modified matrix pencil algorithm. (b) Attenuation of flexural waves in a steel rod in infinite water caused by radiation of acoustic energy from rod into water. The solid line denotes attenuation calculated by complex mode search program. The dots are obtained from measured waveforms processed by a modified matrix pencil algorithm.

2. Steel rod in water

Figure 10(a) shows the slowness dispersion of steel rod flexural mode in infinite water. The dots and solid line denote experimental and mode search results, respectively. Figure 10(b) shows the attenuation of this mode as a function of frequency. Again, the dots and solid line denote experimental and mode search results, respectively. Attenuation is observed for frequencies of about 20 kHz and above where the flexural mode propagates at a velocity faster than that of the compressional wave velocity in water. The compressional velocity in water is about 1480 m/s, or equivalently 675.7 μs/m in slowness. There was no material loss included in the mode search calculation. Clearly, radiation of acoustic energy from the steel flexural mode into the surrounding water is a dominant mechanism of the attenuation in this case.

3. Steel rod in a slow (polyethylene) formation

When a steel rod is concentrically placed in a borehole in polyethylene formation, two flexural modes are excited in the bandwidth of interest. Figure 11(a) compares measured and theoretical flexural dispersions for a steel rod in polyeth-

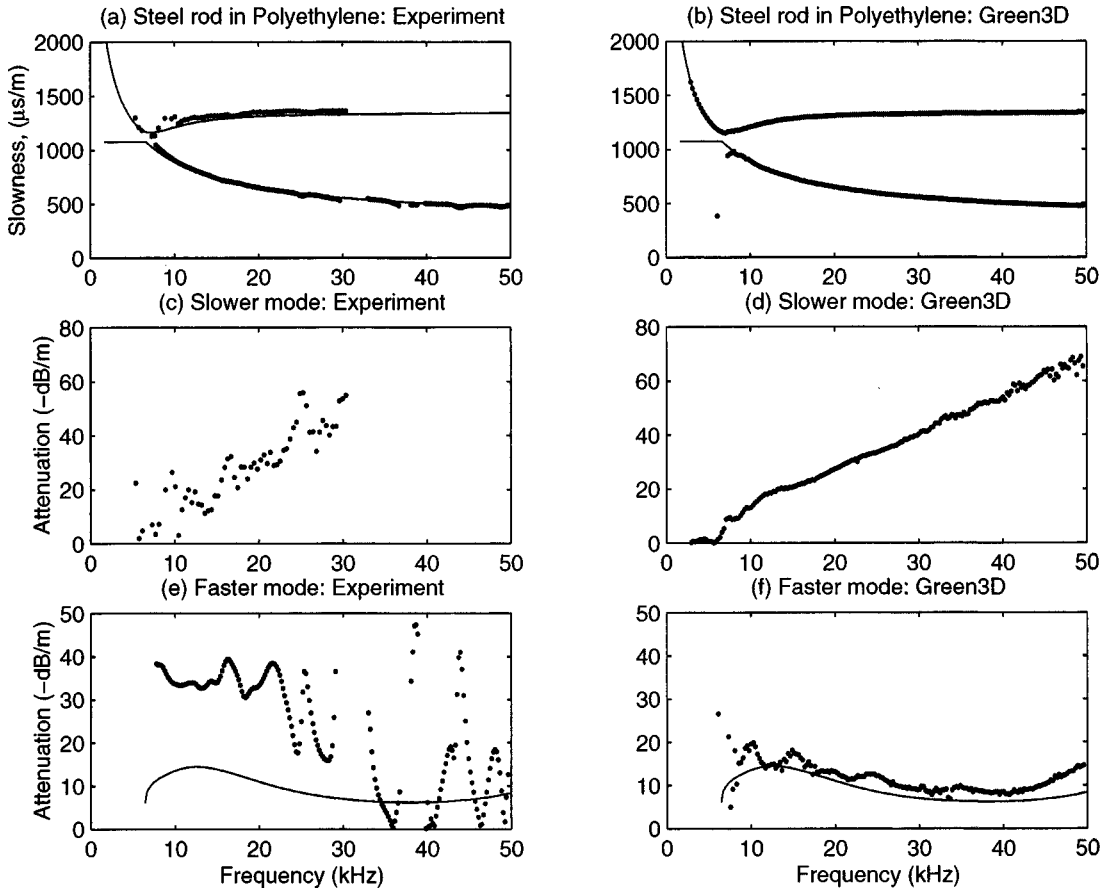

FIG. 11. (a) Flexural dispersions for a steel rod in polyethylene formation. The solid line denote theoretical dispersions obtained from a mode search program. The dots denote measured dispersion obtained from experimental waveforms processed by a modified matrix pencil algorithm. (b) The dots denote synthetic dispersion obtained from Green3D waveforms (with $Q=25$) processed by a modified matrix pencil algorithm. (c) Attenuation of slower (formation) mode in the composite geometry of steel rod in a borehole caused by a finite Q of polyethylene formation. Results are obtained from experimental waveforms processed by a modified matrix pencil algorithm. (d) Attenuation results are obtained from Green3D waveforms processed by a modified matrix pencil algorithm. (e) The dots denote attenuation results obtained from experimental waveforms processed by a modified matrix pencil algorithm. The solid line represents results from a complex mode search for the leaky steel (rod) flexural mode. (f) The dots denote attenuation results obtained from Green3D waveforms processed by a modified matrix pencil algorithm.

ylene formation. The measured slowness dispersion is obtained from experimental waveforms processed by a modified matrix pencil algorithm.[17] The theoretical dispersion is obtained from a mode search program descibed in the Appendix. The dots and solid line denote the measured and theoretical dispersions, respectively. As before, good agreement is obtained between the two results. Figure 11(b) compares calculated dispersion obtained from Green3D synthetic waveforms processed by a modified matrix pencil algorithm with that from a mode search code. The dots and solid line, respectively, represent the processed dispersion from synthetic waveforms and theoretical dispersion from a mode search code. Good agreement is obtained in the two cases.

Figure 11(c) and (d) shows the attenuation dispersion of the slower mode obtained from experimental and Green3D waveforms, respectively. $Q=25$ was assumed in the Green3D calculation for synthetic waveforms. The mode search predicts no attenuation without any material loss included. Therefore, the observed attenuation of this slower mode is largely attributed to the formation material loss.

Figure 11(e) and (f) shows the attenuation dispersion of the faster mode obtained from experimental and Green3D waveforms, respectively. The solid line denotes the radiation-induced attenuation as predicted by the complex mode search code without any material loss considered. Figure 11(f) suggests that acoustic radiation should be a dominant mechanism for the attenuation of this faster mode. It is interesting to note that the attenuation of the faster mode is quite different than that shown in Fig. 10(b), even though slowness dispersions are similar for these two modes. In Fig. 11(e), the measured attenuation is significantly larger than the predicted radiation loss. The cause of this discrepancy is not clear to us. It is possible that more accurate amplitude measurement may require greater precision in experimental setup than what we have, such as centering of the rod in the borehole and positioning of the source and receivers.

4. Summary of the attenuation dispersion

Two attenuation mechanisms caused by material loss and radiation are observed in both experimental and theoretical results. The estimated $Q=25$ for the polyethylene formation represents the material loss factor. Radiation loss occurs where the modal wave phase velocity along the borehole is faster than the bulk shear wave speed in the surrounding medium.

IV. CONCLUSIONS

The mandrel effect on a borehole flexural mode can be significant and complicated. It depends strongly on the proximity in phase slowness of the flexural modes of the two constituent components: a fluid-filled borehole and a mandrel in an infinite fluid. If the mandrel flexural mode dispersion is not well separated from the borehole flexural dispersion at all frequencies of interest, the mandrel effect will be significant. When the mandrel effect is deemed to be significant, the processing and interpretation of recorded waveforms must account for possible perturbations in borehole flexural dispersions caused by the presence of mandrel.

ACKNOWLEDGMENTS

We would like to thank Robert Bailey, Richard Lauer, and Richard Wells for helping in the experimental setup and data aquisition; John Ullo, David L. Johnson and Can-Yun Wang for helpful comments on the manuscript.

APPENDIX

Here we present the boundary equations for the case of a cylindrical pipe with its inner and outer radii of b and a, respectively, placed in a fluid-filled borehole of radius c surrounded by an infinite formation. These equations are obtained by substitution of appropriate solutions for flexural waves given by Eqs. (22)–(24), (26)–(28), and (30)–(32) into the relevant boundary conditions at the fluid-solid interfaces.

$$[L]\{c\}=\{0\}, \tag{A1}$$

where $[L]$ is a 12×12 matrix and $\{c\}$ is a 12×1 column vector of unknown amplitude coefficients. The elements of $[L]$ are given by

$$L(1,1)=-nJ_n(\alpha_{(1)}a)/a+\alpha_{(1)}J_{n+1}(\alpha_{(1)}a), \tag{A2}$$

$$L(1,2)=nJ_n(\alpha_{(2)}a)/a-\alpha_{(2)}J_{n+1}(\alpha_{(2)}a), \tag{A3}$$

$$L(1,3)=nY_n(\alpha_{(2)}a)/a-\alpha_{(2)}Y_{n+1}(\alpha_{(2)}a), \tag{A4}$$

$$L(1,4)=i\zeta J_{n+1}(\beta_{(2)}a), \tag{A5}$$

$$L(1,5)=i\zeta Y_{n+1}(\beta_{(2)}a), \tag{A6}$$

$$L(1,6)=nJ_n(\beta_{(2)}a)/a, \tag{A7}$$

$$L(1,7)=nY_n(\beta_{(2)}a)/a, \tag{A8}$$

$$L(2,1)=\lambda^{(1)}(\alpha_{(1)}^2+\zeta^2)J_n(\alpha_{(1)}a), \tag{A9}$$

$$L(2,2)=-[\lambda^{(2)}(\alpha_{(2)}^2+\zeta^2)+2\mu^{(2)}(\alpha_{(2)}^2-n(n-1)/a^2)]J_n(\alpha_{(2)}a)+2\mu^{(2)}\alpha_{(2)}J_{n+1}(\alpha_{(2)}a)/a, \tag{A10}$$

$$L(2,3)=-[\lambda^{(2)}(\alpha_{(2)}^2+\zeta^2)+2\mu^{(2)}(\alpha_{(2)}^2-n(n-1)/a^2)]Y_n(\alpha_{(2)}a)+2\mu^{(2)}\alpha_{(2)}Y_{n+1}(\alpha_{(2)}a)/a, \tag{A11}$$

$$L(2,4)=2i\mu^{(2)}\zeta\beta_{(2)}\{J_n(\beta_{(2)}a)-(n+1)J_{n+1}(\beta_{(2)}a)/\beta_{(2)}a\}, \tag{A12}$$

$$L(2,5)=2i\mu^{(2)}\zeta\beta_{(2)}\{Y_n(\beta_{(2)}a)-(n+1)Y_{n+1}(\beta_{(2)}a)/\beta_{(2)}a\}, \tag{A13}$$

$$L(2,6)=\mu_{(2)}\{2n(n-1)J_n(\beta_{(2)}a)/a^2-2n\beta_{(2)}J_{n+1}(\beta_{(2)}a)/a\}, \tag{A14}$$

$$L(2,7)=\mu_{(2)}\{2n(n-1)Y_n(\beta_{(2)}a)/a^2-2n\beta_{(2)}Y_{n+1}(\beta_{(2)}a)/a\}, \tag{A15}$$

$$L(3,2)=-2n(n-1)J_n(\alpha_{(2)}a)/a^2+2n\alpha_{(2)}J_{n+1}(\alpha_{(2)}a)/a, \tag{A16}$$

$$L(3,3)=-2n(n-1)Y_n(\alpha_{(2)}a)/a^2+2n\alpha_{(2)}Y_{n+1}(\alpha_{(2)}a)/a, \tag{A17}$$

$$L(3,4)=i\zeta\beta_{(2)}J_n(\beta_{(2)}a)-2i\zeta(n+1)J_{n+1}(\beta_{(2)}a)/a, \tag{A18}$$

$$L(3,5)=i\zeta\beta_{(2)}Y_n(\beta_{(2)}a)-2i\zeta(n+1)Y_{n+1}(\beta_{(2)}a)/a, \tag{A19}$$

$$L(3,6)=\{\beta_{(2)}^2-2n(n-1)/a^2\}J_n(\beta_{(2)}a)-2\beta_{(2)}J_{n+1}(\beta_{(2)}a)/a, \tag{A20}$$

$$L(3,7)=\{\beta_{(2)}^2-2n(n-1)/a^2\}Y_n(\beta_{(2)}a)-2\beta_{(2)}Y_{n+1}(\beta_{(2)}a)/a, \tag{A21}$$

$$L(4,2)=2i\zeta\alpha_{(2)}\{nJ_n(\alpha_{(2)}a)/\alpha_{(2)}a-J_{n+1}(\alpha_{(2)}a)\}, \tag{A22}$$

$$L(4,3)=2i\zeta\alpha_{(2)}\{nY_n(\alpha_{(2)}a)/\alpha_{(2)}a-Y_{n+1}(\alpha_{(2)}a)\}, \tag{A23}$$

$$L(4,4)=-n\beta_{(2)}J_n(\beta_{(2)}a)/a+(\beta_{(2)}^2-\zeta^2)J_{n+1}(\alpha_{(2)}a), \tag{A24}$$

$$L(4,5)=-n\beta_{(2)}Y_n(\beta_{(2)}a)/a+(\beta_{(2)}^2-\zeta^2)Y_{n+1}(\alpha_{(2)}a), \tag{A25}$$

$$L(4,6)=i\zeta nJ_n(\beta_{(2)}a)/a, \tag{A26}$$

$$L(4,7)=i\zeta nY_n(\beta_{(2)}a)/a, \tag{A27}$$

$$L(5,2)=nJ_n(\alpha_{(2)}b)/b-\alpha_{(2)}J_{n+1}(\alpha_{(2)}b), \tag{A28}$$

$$L(5,3)=nY_n(\alpha_{(2)}b)/b-\alpha_{(2)}Y_{n+1}(\alpha_{(2)}b), \tag{A29}$$

$$L(5,4)=i\zeta J_{n+1}(\beta_2 b), \tag{A30}$$

$$L(5,5)=i\zeta Y_{n+1}(\beta_2 b), \tag{A31}$$

$$L(5,6)=nJ_n(\beta_{(2)}b)/b, \tag{A32}$$

$$L(5,7)=nY_n(\beta_{(2)}b)/b, \tag{A33}$$

$$L(5,8)=-nJ_n(\alpha_{(3)}b)/b+\alpha_{(3)}J_{n+1}(\alpha_{(3)}b), \tag{A34}$$

$$L(5,9)=-nY_n(\alpha_{(3)}b)/b+\alpha_{(3)}Y_{n+1}(\alpha_{(3)}b), \tag{A35}$$

$$L(6,2)=-\lambda^{(2)}(\alpha_{(2)}^2+\zeta^2)+2\mu^{(2)}(\alpha_{(2)}^2-n(n-1)/b^2)\times J_n(\alpha_{(2)}b)+2\mu^{(2)}\alpha_{(2)}J_{n+1}(\alpha_{(2)}b)/b, \tag{A36}$$

$$L(6,3) = -\lambda^{(2)}(\alpha_{(2)}^2+\zeta^2)+2\mu^{(2)}(\alpha_{(2)}^2 - n(n-1)/b^2)Y_n(\alpha_{(2)}b) + 2\mu^{(2)}\alpha_{(2)}Y_{n+1}(\alpha_{(2)}b)/b, \quad \text{(A37)}$$

$$L(6,4) = 2\mu^{(2)}i\zeta\beta_{(2)}\{J_n(\beta_{(2)}b) - (n+1)J_{n+1}(\beta_{(2)}b)/\beta_{(2)}b\}, \quad \text{(A38)}$$

$$L(6,5) = 2\mu^{(2)}i\zeta\beta_{(2)}\{Y_n(\beta_{(2)}b) - (n+1)Y_{n+1}(\beta_{(2)}b)/\beta_{(2)}b\}, \quad \text{(A39)}$$

$$L(6,6) = 2\mu^{(2)}\{n(n-1)J_n(\beta_{(2)}b)/b^2 - n\beta_{(2)}J_{n+1}(\beta_{(2)}b)/b\}, \quad \text{(A40)}$$

$$L(6,7) = 2\mu^{(2)}\{n(n-1)Y_n(\beta_{(2)}b)/b^2 - n\beta_{(2)}Y_{n+1}(\beta_{(2)}b)/b\}, \quad \text{(A41)}$$

$$L(6,8) = \lambda^{(3)}(\alpha_{(3)}^2+\zeta^2)J_n(\alpha_{(3)}b), \quad \text{(A42)}$$

$$L(6,9) = \lambda^{(3)}(\alpha_{(3)}^2+\zeta^2)Y_n(\alpha_{(3)}b), \quad \text{(A43)}$$

$$L(7,2) = -2n(n-1)J_n(\alpha_{(2)}b)/b^2 + 2n\alpha_{(2)}J_{n+1}(\alpha_{(2)}b)/b, \quad \text{(A44)}$$

$$L(7,3) = -2n(n-1)Y_n(\alpha_{(2)}b)/b^2 + 2n\alpha_{(2)}Y_{n+1}(\alpha_{(2)}b)/b, \quad \text{(A45)}$$

$$L(7,4) = i\zeta\beta_{(2)}J_n(\beta_{(2)}b) - 2i\zeta(n+1)J_{n+1}(\beta_{(2)}b)/b, \quad \text{(A46)}$$

$$L(7,5) = i\zeta\beta_{(2)}Y_n(\beta_{(2)}b) - 2i\zeta(n+1)Y_{n+1}(\beta_{(2)}b)/b, \quad \text{(A47)}$$

$$L(7,6) = \{\beta_{(2)}^2 - 2n(n-1)/b^2\}J_n(\beta_{(2)}b) - 2\beta_{(2)}J_{n+1}(\beta_{(2)}b)/b, \quad \text{(A48)}$$

$$L(7,7) = \{\beta_{(2)}^2 - 2n(n-1)/b^2\}Y_n(\beta_{(2)}b) - 2\beta_{(2)}Y_{n+1}(\beta_{(2)}b)/b, \quad \text{(A49)}$$

$$L(8,2) = 2i\zeta nJ_n(\alpha_{(2)}b)/b - 2i\zeta\alpha_{(2)}J_{n+1}(\alpha_{(2)}b), \quad \text{(A50)}$$

$$L(8,3) = 2i\zeta nY_n(\alpha_{(2)}b)/b - 2i\zeta\alpha_{(2)}Y_{n+1}(\alpha_{(2)}b), \quad \text{(A51)}$$

$$L(8,4) = -n\beta_{(2)}J_n(\beta_{(2)}b)/b + (\beta_{(2)}^2 - \zeta^2)J_{n+1}(\beta_{(2)}b), \quad \text{(A52)}$$

$$L(8,5) = -n\beta_{(2)}Y_n(\beta_{(2)}b)/b + (\beta_{(2)}^2 - \zeta^2)Y_{n+1}(\beta_{(2)}b), \quad \text{(A53)}$$

$$L(8,6) = i\zeta nJ_n(\beta_{(2)}b)/b, \quad \text{(A54)}$$

$$L(8,7) = i\zeta nY_n(\beta_{(2)}b)/b, \quad \text{(A55)}$$

$$L(9,8) = -nJ_n(\alpha_{(3)}c)/c + \alpha_{(3)}J_{n+1}(\alpha_{(3)}c), \quad \text{(A56)}$$

$$L(9,9) = -nY_n(\alpha_{(3)}c)/c + \alpha_{(3)}Y_{n+1}(\alpha_{(3)}c), \quad \text{(A57)}$$

$$L(9,10) = nH_n(\alpha_{(4)}c)/c - \alpha_{(4)}H_{n+1}(\alpha_{(4)}c), \quad \text{(A58)}$$

$$L(9,11) = i\zeta H_{n+1}(\beta_{(4)}c), \quad \text{(A59)}$$

$$L(9,12) = nH_n(\beta_{(4)}c)/c, \quad \text{(A60)}$$

$$L(10,8) = \lambda^{(3)}(\alpha_{(3)}^2+\zeta^2)J_n(\alpha_{(3)}c), \quad \text{(A61)}$$

$$L(10,9) = \lambda^{(3)}(\alpha_{(3)}^2+\zeta^2)Y_n(\alpha_{(3)}c), \quad \text{(A62)}$$

$$L(10,10) = -\{\lambda^{(4)}(\alpha_{(4)}^2+\zeta^2)+2\mu^{(4)}(\alpha_{(4)}^2 - n(n-1)/c^2)\}H_n(\alpha_{(4)}c) + 2\mu^{(4)}\alpha_{(4)}H_{n+1}(\alpha_{(4)}c)/c, \quad \text{(A63)}$$

$$L(10,11) = 2i\mu^{(4)}\zeta\beta_{(4)}\{H_n(\beta_{(4)}c) - (n+1)H_{n+1}(\beta_{(4)}c)/\beta_{(4)}c\}, \quad \text{(A64)}$$

$$L(10,12) = 2\mu^{(4)}\{n(n-1)H_n(\beta_{(4)}c)/c^2 - n\beta_{(4)}H_{n+1}(\beta_{(4)}c)/c\}, \quad \text{(A65)}$$

$$L(11,10) = -2n(n-1)H_n(\alpha_{(4)}c)/c^2 + 2n\alpha_{(4)}H_{n+1}(\alpha_{(4)}c)/c, \quad \text{(A66)}$$

$$L(11,11) = i\zeta\beta_{(4)}H_n(\beta_{(4)}c) - 2i\zeta(n+1)H_{n+1}(\beta_{(4)}c)/c, \quad \text{(A67)}$$

$$L(11,12) = \{\beta_{(4)}^2 - 2n(n-1)/c^2\}H_n(\beta_{(4)}c) - 2\beta_{(4)}H_{n+1}(\beta_{(4)}c)/c, \quad \text{(A68)}$$

$$L(12,10) = 2i\zeta nH_n(\alpha_{(4)}c)/c - 2i\zeta\alpha_{(4)}H_{n+1}(\alpha_{(4)}c), \quad \text{(A69)}$$

$$L(12,11) = -n\beta_{(4)}H_n(\beta_{(4)}c)/c + (\beta_{(4)}^2 - \zeta^2)H_{n+1}(\beta_{(4)}c), \quad \text{(A70)}$$

$$L(12,12) = i\zeta nH_n(\beta_{(4)}c)/c, \quad \text{(A71)}$$

where the n refers to the cylindrical mode number. The elements of $L(12,12)$ not defined above are zero. The column vector $\{c\}$ is given by

$$\{c\} = (A^{(1)}, A^{(2)}, B^{(2)}, A_1^{(2)}, B_1^{(2)}, A_3^{(2)}, B_3^{(2)}, A^{(3)}, B^{(3)}, A^{(4)}, A_1^{(4)}, A_3^{(4)}). \quad \text{(A72)}$$

Equation (A1) constitutes a system of 12 linear homogeneous algebraic equations in the wave amplitudes $\{c\}$, which yields nontrivial solutions when the determinant of the coefficients of the wave amplitudes $\{c\}$ vanishes, i.e., when

$$|L| = 0. \quad \text{(A73)}$$

Equation (A73) is a complex algebraic equation, both the real and imaginary parts of which vanish simultaneously. A solution, i.e., values of ζ and ω satisfying the appropriate differential equations of motion and Eq. (A73) must be found numerically. Once the solution is obtained, the amplitude ratios can be solved for from Eq. (A1).

It should be noted that Eq. (A73) can be transformed into a *real* algebraic equation by redefining some of the amplitude coefficients in the following manner: $(A_1^{(2)}, B_1^{(2)}) \rightarrow (iA_1^{(2)}, iB_1^{(2)})$; and keeping the other coefficients the same as in Eq. (A72). However, in the case of leaky modes, Eq. (A73) becomes a complex algebraic equation in spite of the aforementioned transformation.

[1] D. C. Gazis, ''Three-dimensional investigation of the propagation of waves in hollow circular cylinders, I. Analytical foundation, and II. Numerical results,'' J. Acoust. Soc. Am. **31**, 568–577 (1959).
[2] T. R. Meeker and A. H. Meitzler, ''Guided wave propagation in elongated cylinders and plates,'' in *Physical Acoustics*, Vol. 1A, edited by W. P. Mason (Academic, New York, 1964).
[3] J. Lai, E. H. Dowell, and T. R. Tauchert, ''Propagation of harmonic waves in a composite elastic cylinder,'' J. Acoust. Soc. Am. **49**, 220–227 (1971).
[4] A. Safaai-Jazi, C. K. Jen, and G. W. Farnell, ''Analysis of weakly guiding fiber acoustic waveguide,'' IEEE Trans. Ultrason. Ferroelectr. Freq. Control **33**, 59–68 (1986).
[5] A. Safaai-Jazi, C. K. Jen, and G. W. Farnell, ''Cutoff conditions in an acoustic fiber with infinitely thick cladding,'' IEEE Trans. Ultrason. Ferroelectr. Freq. Control **33**, 69–73 (1986).
[6] A. Safaai-Jazi, C. K. Jen, G. W. Farnell, and J. D. N. Cheeke, ''Analysis of liquid-core cylindrical acoustic waveguides,'' J. Acoust. Soc. Am. **81**, 1273–1278 (1987).
[7] C. R. Fuller and F. J. Fahy, ''Characteristics of wave propagation and energy distributions in cylindrical elastic shells filled with fluid,'' J. Sound Vib. **81**, 501–518 (1982).
[8] C. R. Fuller, ''The input mobility of an infinite circular cylindrical elastic shell filled with fluid,'' J. Sound Vib. **87**, 409–427 (1983).
[9] C. R. Fuller, ''Monopole excitation of vibrations in an infinite cylindrical elastic shell filled with fluid,'' J. Sound Vib. **96**, 101–110 (1984).
[10] C. K. Jen, A. Safaai-Jazi, and G. W. Farnell, ''Leaky modes in weakly guiding fiber acoustic waveguides,'' IEEE Trans. Ultrason. Ferroelectr. Freq. Control **33**, 634–643 (1986).
[11] M. A. Biot, ''Propagation of elastic waves in a cylindrical bore containing a fluid,'' J. Appl. Phys. **23**, 997–1005 (1952).
[12] W. L. Roever, J. H. Rosenbaum, and T. F. Vining, ''Acoustic waves from an impulsive source in a fluid-filled borehole,'' J. Acoust. Soc. Am. **55**, 1144–1157 (1974).
[13] D. P. Schmitt, ''Shear wave logging elastic formations,'' J. Acoust. Soc. Am. **84**, 2215–2229 (1988).
[14] B. K. Sinha, T. J. Plona, S. Kostek, and S. K. Chang, ''Axi-symmetric wave propagation in fluid-loaded cylindrical shells. Part I: Theory,'' J. Acoust. Soc. Am. **92**, 1132–1143 (1992).
[15] T. J. Plona, B. K. Sinha, S. Kostek, and S. K. Chang, ''Axi-symmetric wave propagation in fluid-loaded cylindrical shells. Part II: Theory versus Experiment,'' J. Acoust. Soc. Am. **92**, 1144–1155 (1992).
[16] C-J. Hsu, S. Kostek, and D. L. Johnson, ''Tube waves and mandrel modes: Experiment and theory,'' J. Acoust. Soc. Am. **102**, 3277–3289 (1997).
[17] J. L. Stevens and S. M. Day, ''Shear velocity logging in slow formations using the Stoneley wave,'' Geophysics **51**, 137–147 (1986).
[18] M. P. Ekstrom, ''Dispersion estimation from borehole acoustic arrays using a modified matrix pencil algorithm,'' paper presented at the *29th Asilomar Conference on Signals, Systems, and Computers*, Pacific Grove, California, 31 October 1995.
[19] S. W. Lang, A. L. Kurkjian, J. H. McClellan, C. F. Morris, and T. W. Parks, ''Estimating slowness dispersions from arrays of sonic logging waveforms,'' Geophysics **52**, 530–544 (1987).
[20] L. L. Scharf, *Signal Processing: Detection, Estimation, and Time Series Analysis* (Addison-Wesley, New York, 1991), p. 407.
[21] C-C. Lu and Q-H. Liu, ''A three-dimensional dyadic Green's function for elastic waves in multilayer cylindrical structures,'' J. Acoust. Soc. Am. **98**, 2825–2835 (1995).

Acoustic performance of flexible bellows

M. L. Munjal and J. Vinay
Centre of Excellence for Technical Acoustics, Department of Mechanical Engineering, Indian Institute of Science, Bangalore—560012, India

(Received 31 March 1997; accepted for publication 6 June 1998)

Bellows are generally used for vibration isolation in ducts. However, conical expansions and contractions lead to acoustic transmission loss as well. In this paper plane wave propagation through a bellow has been investigated. The wave equation for a stationary medium has been solved exactly with the help of a practical assumption. But, for the case of mean flow, with its convective as well as dissipative effects, an equivalent simple expansion-contraction chamber model has been developed based on some parametric studies. Effects of different parameters like thickness of the bellow wall, radius, length, and Mach number of mean flow have been studied. A reasonable agreement has been found between the theoretical and experimental results. © *1998 Acoustical Society of America.* [S0001-4966(98)01710-X]

PACS numbers: 43.20.Mv, 43.20.Hq, 43.20.Bi [DEC]

LIST OF SYMBOLS

a slope of the conical portion of the bellow
c speed of sound
C compliance
E_{r0} storage modulus
I inertance
j $=\sqrt{-1}$
k_i wave number inside the bellow
l_e length of the simple expansion chamber
l_{eq} equivalent length
M mean flow Mach number
p acoustic pressure
r_i radius at the entrance of the expanding portion of the bellow
r_{eq} equivalent radius
$r_{i\text{av}}$ average inner radius
$r_{o\text{av}}$ average outer radius
S area of cross section
t_w thickness of the bellow wall material
u particle velocity
u_w particle velocity at the wall
v_v volume velocity
z distance along the axis of the bellow
ρ density of the fluid
ω circular frequency
ρ_w density of the bellow wall material
ν Poisson's ratio
η loss factor

Subscripts ''*i*'' and ''*o*'' denote the inside and outside medium, respectively.

INTRODUCTION

The effect of wall compliance has aroused interest in recent times due to its vibration isolation properties. Vibro-acoustics of hoses has been investigated by Munjal and Thawani,[1] among others. Practical hoses have been found to act like rigid pipes for acoustic waves. Similarly, wave propagation through rigid walled variable-area ducts has been studied by several researchers,[2–4] culminating in exact solutions for plane wave propagation in ducts of different shapes, with incompressible mean flow with the assumption that there is no separation of boundary layer.[5,6] However, the effect of wall compliance coupled with an area change, as would occur in flexible bellows, does not seem to have been investigated till now.

In this paper, an analytical model for prediction of the acoustic performance of flexible bellows is presented. The Helmholtz equation has been solved exactly for the case of stationary medium and an equivalent simple expansion–contraction chamber model is developed for incorporation of the convective as well as dissipative effects of mean flow. Results of some parametric studies have also been included.

I. AN ANALYTICAL MODEL FOR STATIONARY MEDIUM

The practical frequencies of interest in automotive applications being limited to about 2000 Hz, a plane wave model is found to suffice for typical bellows used in practice. Higher order modes will certainly be generated at the area discontiniuties. However, it is presumed here that their effect would be relatively negligible as compared to the plane wave. Considerable simplification in the governing equations occurs due to the assumption of a local reaction model, similar to the analysis of perforated elements.[7,8] Thus basic equations for a compliant wall, variable-area duct (see Fig. 1) for stationary medium are given as follows:

Continuity equation:

$$\frac{\partial \rho_i}{\partial t}+\rho_i\frac{\partial u}{\partial z}+\rho_i u\left(\frac{1}{S}\frac{dS}{dz}\right)+2\frac{\rho_i}{(r_i+az)}u_w=0; \tag{1}$$

Momentum equation:

$$\rho_i\frac{\partial u}{\partial t}+\frac{\partial p_i}{\partial z}=0. \tag{2}$$

 0001-4966/98/104(4)/2040/8/$15.00

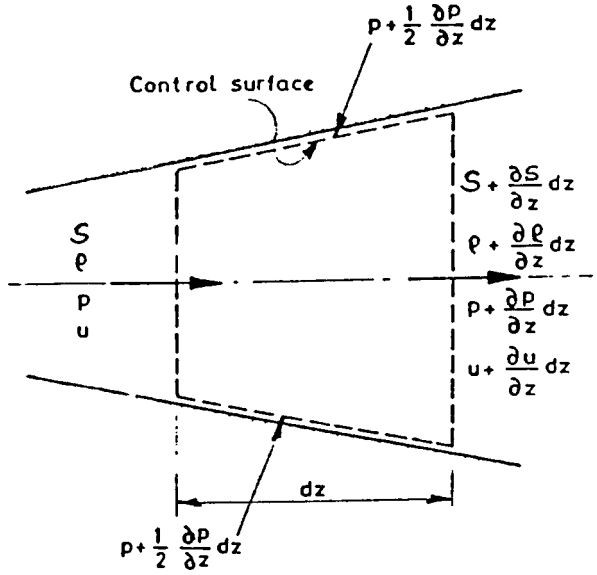

FIG. 1. Dynamics of the control surface.

Here, the radial particle velocity u_w is given by

$$u_w = \frac{p_i}{Z_w}, \tag{3}$$

assuming isentropicity,

$$\partial p_i = c_i^2 \, \partial \rho_i . \tag{4}$$

The area of cross section at any ''z'' is given by

$$S = \pi (r_i + az)^2. \tag{5}$$

Assuming the time dependence as $e^{j\omega t}$, Eqs. (1) to (5) yield the Helmholtz equation:

$$\frac{d^2 p_i}{dz^2} + \frac{2a}{(r_i + az)} \frac{dp_i}{dz} + p_i \left(k_i^2 - \frac{b}{(r_i + az)} \right) = 0, \tag{6}$$

where

$$b = 2jk_i X_i \tag{7}$$

and

$$X_i = \frac{\rho_i c_i}{Z_w}. \tag{8}$$

The dimensions of the bellow used in the expressions above are as shown in Fig. 2.

The radial wall impedance Z_w may be written as

$$Z_w = j\omega I + \frac{1}{j\omega C} + Z_o . \tag{9}$$

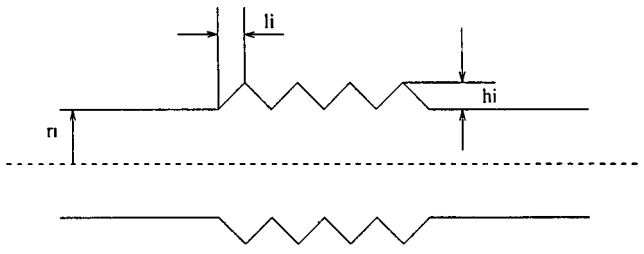

FIG. 2. A bellow.

Radiation impedance Z_o would generally be negligible. Inertance I is given by

$$I = \rho_w t_w \left(1 + \left(\frac{0.025}{ri} \right)^2 \right), \tag{10}$$

where a curvature factor has been incorporated from heuristic considerations.[1] Compliance is computed from the theory of shells:

$$C = \frac{r_{iav}}{E} \left(\frac{r_{oav}^2 + r_{iav}^2}{r_{oav}^2 - r_{iav}^2} + \nu \right). \tag{11}$$

The compliance is computed at the midpoint of the conical section in order to account for the variation of radius. A complex modulus is incorporated as

$$E = E_r (1 + j\eta), \tag{12}$$

where the frequency dependence of the storage modulus and loss factor is taken into account as follows:[1]

$$\eta = \eta_o \left(1 + \frac{f}{1000} \right), \tag{13}$$

$$E_r = E_{ro} \left(1 + \frac{f}{1000} \right), \tag{14}$$

''f'' being the frequency in Hz. When the outside medium is air, the radiation impedance Z_o is negligible in comparison with Z_w. Substituting in Eq. (6), the transformation

$$p_i = \frac{Q_i}{(r_i + az)}, \tag{15}$$

it yields

$$\frac{d^2 Q_i}{dz^2} + Q_i \left(ki^2 - \frac{b}{(r_i + az)} \right) = 0. \tag{16}$$

A solution to the above equation must satisfy the following self-consistency tests depending on the values of ''a'' and ''b'':

(i) If ''a''=0, it must reduce to the solution for a uniform hose pipe;
(ii) If ''b''=0, it must reduce to the solution for a rigid walled conical pipe;
(iii) If ''a''=''b''=0, then it must reduce to the solution for a rigid walled uniform pipe.

Although various solution methods were tried out, none were found to satisfy all the abovementioned self-consistency tests.[9] Practically, the ''az'' term is very small in comparison with ''r_i.'' Besides, k_i^2 is much larger than b/r_i. Therefore neglecting az with respect to r_i in Eq. (16), it yields

$$\frac{d^2 Q_i}{dz^2} + Q_i \left(ki^2 - \frac{b}{r_i} \right) = 0. \tag{17}$$

The solution of the above equation is easily obtained as

$$Q_i = Ae^{-jk_h z} + Be^{+jk_h z}, \tag{18}$$

where k_h, the hose pipe wave number, is related to the rigid pipe wave number k_i as follows:[1]

$$k_h^2 = k_i^2\left[1 - \frac{2jX_i}{k_i r_i}\right]. \tag{19}$$

Equations (15) and (18) give the solution for pressure p_i as

$$p_i = \frac{1}{(r_i + az)}\left[Ae^{-jk_h z} + Be^{+jk_h z}\right]. \tag{20}$$

This is seen to be a simple combination of the solutions of a uniform hose pipe and a rigid walled conical pipe. It satisfies all the aforementioned self-consistency tests. The particle velocity is obtained from the momentum equation (2) as

$$u = \frac{j}{\rho\omega(r_i + az)}\left[Ae^{-jk_h z}\left(\frac{-a}{(r_i + az)} - jk_h\right) + Be^{+jk_h z}\left(\frac{-a}{(r_i + az)} + jk_h\right)\right]. \tag{21}$$

The volume velocity is given by

$$v_v = \pi(r_i + az)^2 u. \tag{22}$$

The transfer matrix is then obtained by the elimination of constants ''A'' and ''B'' from the expressions for the pressure and volume velocity at ''$z=0$'' and ''$z=l$.'' The four-pole parameters thus obtained are:[9]

$$\mathrm{TM}(1,1) = \frac{j(r_i + al)}{2k_h r_i}\left[e^{+jk_h l}\left(\frac{a}{r_i + al} - jk_h\right) - e^{-jk_h l}\left(\frac{a}{r_i + al} + jk_h\right)\right], \tag{23}$$

$$\mathrm{TM}(1,2) = \frac{\rho_i\omega}{(r_i + al)2\pi k_h r_i}\left[e^{+jk_h l} - e^{-jk_h l}\right] = \frac{\rho_i\omega . j\ \sin(k_h l)}{\pi r_i(r_i + al).k_h}, \tag{24}$$

$$\mathrm{TM}(2,1) = \frac{1}{2\pi k_h}\left[\frac{\pi^2 r_i^2(r_i + al)}{\rho_i\omega} . e^{+jk_h l}\left(\frac{-a}{r_i} - jk_h\right) \times\left(\frac{-a}{r_i + al} + jk_h\right) - \frac{\pi^2 r_i(r_i + al)}{\rho_i\omega} \times e^{-jk_h l}\left(\frac{-a}{r_i} + jk_h\right)\left(\frac{-a}{r_i + al} - jk_h\right)\right], \tag{25}$$

$$\mathrm{TM}(2,2) = \frac{jr_i}{2(r_i + al)k_h}\left[e^{-jk_h l}\left(\frac{a}{r_i} - jk_h\right) - e^{+jk_h l}\left(\frac{a}{r_i} + jk_h\right)\right]. \tag{26}$$

The transfer matrix for a specified length of a bellow is obtained by successive multiplication of the constituent transfer matrices of the expanding and contracting portions, by choosing appropriate values of the slope parameter ''a.'' The axial transmission loss is determined as given in Ref. 8. A parametric study is carried out making use of the following data: Medium—Air; Density—1.18 kg/m^3; Material of the bellow—Rubber; Storage modulus—$2.0\times10^8(1+f/1000)$; Loss factor—$0.1(1+f/1000)$; Wall thickness—2.0 mm; Poisson's ratio—0.48; Density of the bellow material—1200 kg/m^3.

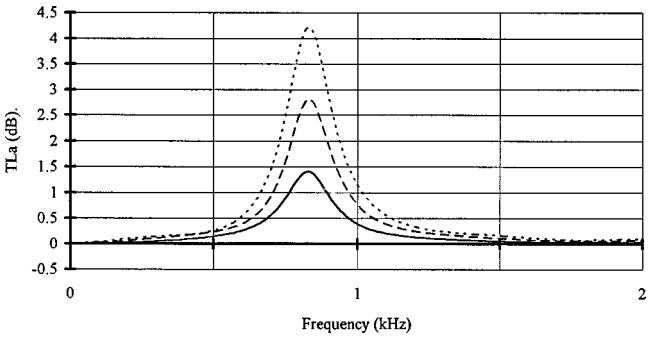

FIG. 3. Effect of number of steps (or serrations) on axial TL of a bellow ($r_i=10$ cm, ''a''$=1.0$). ——— nstep=5, ——— nstep=10, ----- nstep =15.

Effect of the variation of length of the bellow is seen in Fig. 3. It may be observed that the maximum TL_a increases with length. The frequency at which all the curves peak is that at which the imaginary part of wall impedance tends to zero [see Eq. (9)]. This frequency is known as ring frequency in the literature.

Variation of slope ''a'' of the conical portion of the bellow is seen in Fig. 4. As expected, the maximum TL_a increases with slope. In the limit, it tends toward a sudden area discontinuity, as the slope tends toward ∞. The frequency at which TL_a peaks remains practically unchanged with variation of ''a.''

Thickness ''th'' of the bellow wall material has an opposite effect to that of slope on the maximum TL_a, as it decreases with thickness, as can be seen in Fig. 5. The frequency at which TL_a peaks is seen to be unaltered by the variation in ''th,'' because inertance and compliance parts of the wall impedance Z_w increase linearly with thickness for thin hoses or bellows.

Variation of the radius ''ri,'' however, has a different effect on the TL_a. The frequency at which TL_a peaks is altered by the variation in radius, as seen in Fig. 6. TL_a peaks at a frequency at which the impedance Z_w tends to a mini-

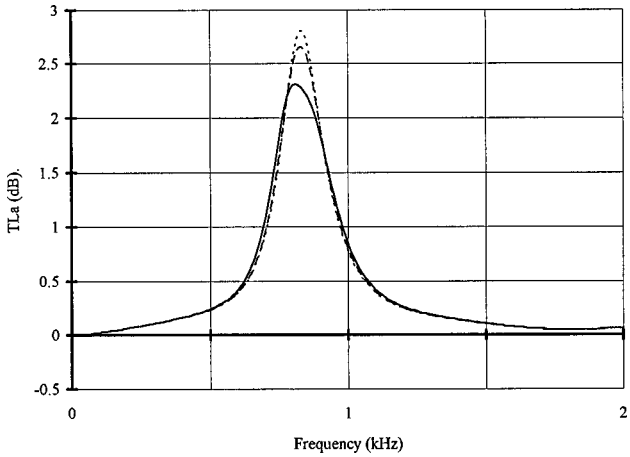

FIG. 4. Effect of the slope ''a'' on axial TL of a 200-mm bellow with 20-mm steps ($r_i=10$ cm). ——— $a=0$, ——— $a=0.5$, ----- $a=1.0$.

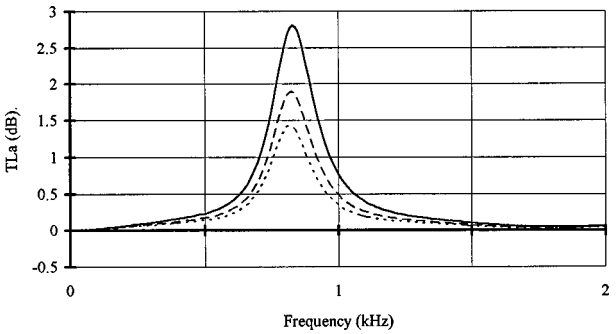

FIG. 5. Effect of thickness ''th'' of the wall material on axial TL of a bellow (r_i=10 cm, ''a''=1.0). ——— th=2 mm, ——— th=3 mm, ----- th=4 mm.

mum or at which the imaginary part of Z_w tends to zero, as can be seen in Fig. 7.

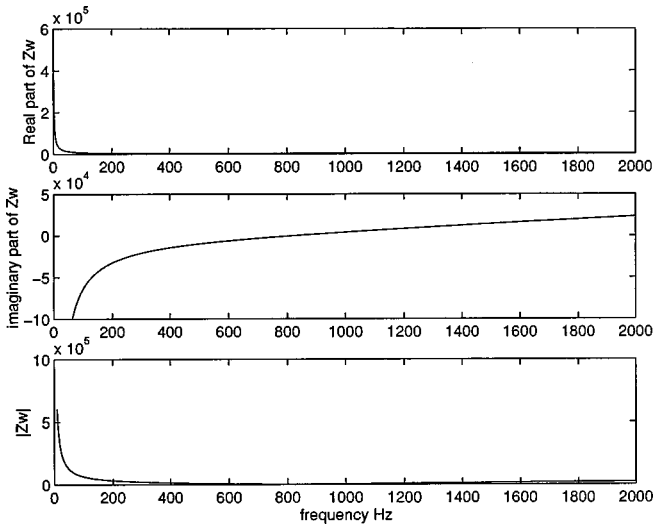

FIG. 7. Plot of real, imaginary, and absolute values of Z_w vs frequency.

II. A MODEL FOR MEAN FLOW

Formulation of basic equations of momentum and continuity for the case of mean flow without any dissipative effects yields

$$\rho_i \frac{Du}{Dt} + \frac{\partial p}{\partial z} = 0, \tag{27}$$

$$\frac{1}{a_o^2}\frac{Dp}{Dt} + \rho_i \frac{\partial u}{\partial z} + \rho_i u\left(\frac{2a}{r_i + az}\right) + \frac{2\rho_i}{r_i + az}\frac{p}{Z_w} = 0. \tag{28}$$

With the assumption of time dependence of the form $e^{j\omega t}$, elimination of the particle velocity yields the Helmholtz equation:

$$(1-M^2)\frac{d^2p}{dz^2} + \frac{dp}{dz}\left(\frac{2a}{r_i+az} - \frac{2\rho_i U}{Z_w(r_i+az)} - 2jk_iM\right) + p_i\left(k_i^2 - \frac{b}{r_i+az}\right) = 0. \tag{29}$$

As can be seen, a solution to the above equation conforming to all the limiting cases mentioned is very difficult to obtain. Besides, Eqs. (27) and (28), and thence Eq. (29), incorporate only the convectice effect of mean flow. They do not take into account the dissipative effect of mean flow arising out of boundary layer separation. Therefore, in what follows, an approximate simple expansion chamber model is developed for incorporation of the convective as well as dissipative effects of mean flow.

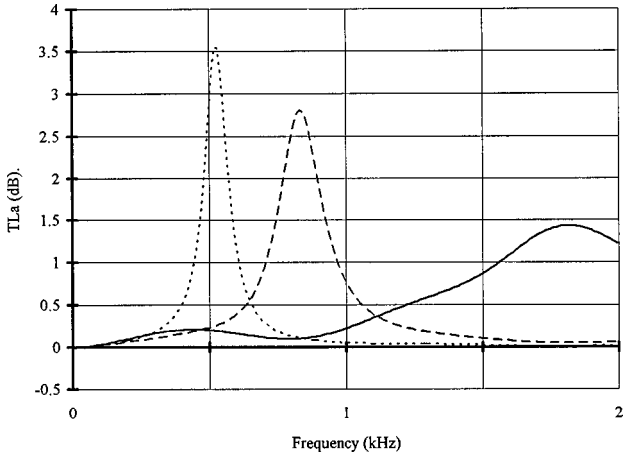

FIG. 6. Effect of internal radius ''r_i'' on axial TL of a bellow (length=200 mm, ''a''=1.0). ——— r_i=50 mm, ——— r_i=100 mm, ----- r_i =150 mm.

From the parametric studies carried out with stationary medium on bellows in the previous section, it can be intuitively deduced that a rigid walled conical expansion–contraction chamber can be approximated by an equivalent simple expansion chamber. Based on this heuristic principle, some parametric studies are carried out over a range of values of inner radius and radial height (i.e., the difference between the outer radius and the inner radius) and the length of area change.

The transmission loss of a simple expansion chamber is given by

$$\mathrm{TL}_a = 10\lg\left[1 + \frac{1}{4}\left(m - \frac{1}{m}\right)^2 \sin^2(kl_{\mathrm{eq}})\right], \tag{30}$$

where ''l_{eq}'' is the length of the expansion chamber and ''m'' is the area expansion ratio. The maximum transmission loss of a simple expansion chamber may be seen to be given by

$$\mathrm{TL}_{a_{\max}} = 10\lg\left[1 + \frac{1}{4}\left(m - \frac{1}{m}\right)^2\right], \tag{31}$$

when

$$\sin(kl_{\mathrm{eq}}) = 1$$

or

$$l_{\mathrm{eq}} = \frac{\pi}{2k}. \tag{32}$$

Thus the length of an equivalent simple expansion chamber can be deduced from the frequency corresponding to maximum TL_a. Also, by the solution of Eq. (31), rearranged as a quadratic in ''m,'' expansion ratio of the equiva-

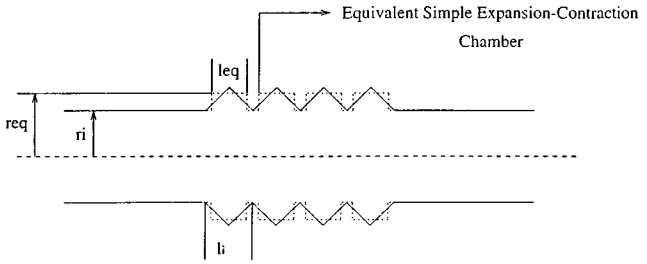

FIG. 8. Equivalent simple expansion chamber model.

lent chamber can be found out. This model is illustrated in Fig. 8.

This procedure is carried out for different values of the starting radius ''r_i'' and radial height ''h_i'' (the difference in the two radii) and length ''l_i.''

The values of ''r_i,'' ''h_i,'' and ''l_i'' used are

$r_i = 1.5,\ 2.0,\ \underline{2.5},\ 3.0,\ 3.5,\ 4.0$ cm,

$h_i = 0.5,\ \underline{1.0},\ 1.5,\ 2.0$ cm,

$l_i = \underline{3.0},\ 4.0,\ 5.0$ cm.

The underlined values are the default values used when the other one is being varied. Thus the following empirical relations have been deduced by means of the least squares technique:

$$r_{\text{eq}}(r_i,h_i,l_i) = 0.5526(1+1.414\,987.r_i) \times (1+0.282\,23.h_i), \tag{33}$$

$$l_{\text{eq}}(r_i,h_i,l_i) = 4.4428(1-0.007\,323.r_i)(1+0.030\,99.h_i - 0.006\,93.h_i^2)(1+158.9.l_i). \tag{34}$$

The comparison between the two models is seen in the Fig. 9.

Having obtained an equivalent simple expansion chamber model, a bellow can be modeled similarly by the inclusion of a factor ''b'' which is a function of the slope of the

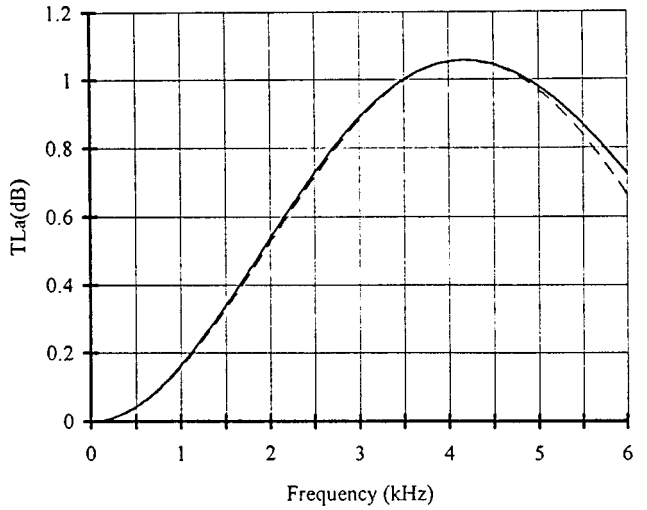

FIG. 9. Comparison between a conical chamber ($r_i = 2.5$ cm, $l_i = 3.0$ cm, $h_i = 1.0$ cm) and an equivalent simple expansion chamber ($r_{\text{eq}} = 3.215$ cm, $l_{\text{eq}} = 2.0697$ cm). ——— Rigid wall conical chamber, ——— equivalent simple expansion chamber.

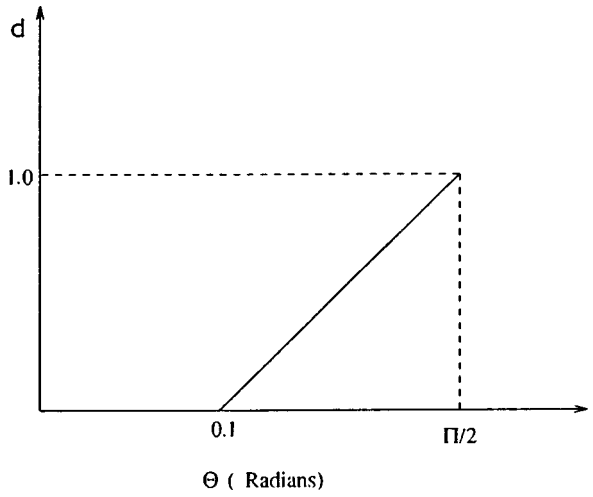

FIG. 10. Variation of the factor ''d'' with θ.

conical part in order to account for the separation of the mean flow boundary layer, as shown below. This is to be multiplied with the loss factor of a sudden area discontinuity.

The transfer matrix for a simple area discontinuity in terms of the convective state variables, as derived by Munjal,[10] is as follows:

$$\begin{bmatrix} p_{c2} \\ v_{c2} \end{bmatrix} = \begin{bmatrix} 1-\dfrac{KM_1^2}{1-M_1^2} & \dfrac{KM_1Y_1}{1-M_1^2} \\ \dfrac{(\gamma-1)KM_1^3}{(1-M_1^2)Y_1} & 1-\dfrac{(\gamma-1)KM_1^2}{1-M_1^2} \end{bmatrix} \begin{bmatrix} p_{c1} \\ v_{c1} \end{bmatrix}, \tag{35}$$

where ''K'' is the loss factor depending on whether it is a sudden expansion or sudden contraction. Thus

$$\text{for sudden expansion,} \quad K = \left(\frac{S_d}{S_u} - 1\right)^2, \tag{36}$$

$$\text{for sudden contraction,} \quad K = \frac{1}{2}\left(1 - \frac{S_d}{S_u}\right), \tag{37}$$

where S_d and S_u are the downstream and upstream areas of cross section at the discontinuity. The subscript ''c'' in the state variables denotes the convective state variables as defined by Munjal.[8] The relation between these convective

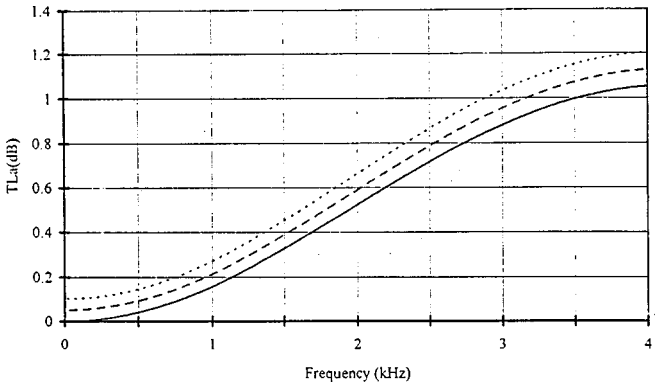

FIG. 11. Effect of mean flow Mach number (M, with dissipative effects taken into account) on TL_a of a bellow ($r_i = 0.025$ m, $r_o = 0.035$ m, $l_i = 0.03$ m). ——— $m = 0.0$, ——— $m = 0.1$, ----- $m = 0.2$.

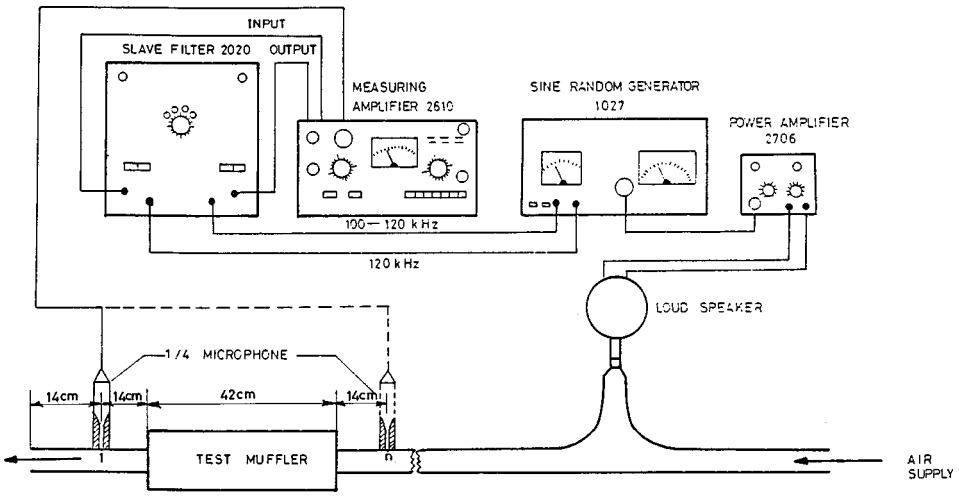

FIG. 12. A schematic arrangement of the excitation-cum-measurement system.

state variables and the classical acoustical variables, pressure, and mass velocity is given by

$$\begin{bmatrix} p_c \\ v_c \end{bmatrix} = \begin{bmatrix} 1 & MY_o \\ M/Y_o & 1 \end{bmatrix} \begin{bmatrix} p \\ v \end{bmatrix}, \tag{38}$$

where Y_o denotes the characteristic impedance, $\rho c_0/S$. If $M^2 \ll 1$, the transfer matrix in Eq. (35) would reduce to

$$\begin{bmatrix} p_{c2} \\ v_{c2} \end{bmatrix} = \begin{bmatrix} 1 & KM_1Y_1 \\ 0 & 1 \end{bmatrix} \begin{bmatrix} p_{c1} \\ v_{c1} \end{bmatrix}. \tag{39}$$

It has been observed that if the slope of a gradual expansion or a gradual contraction is less than 0.1, or if half the angle of convergence or divergence is less than 6 degrees, then flow separation losses are negligible, in the range of Mach numbers ($M^2 \ll 1$) encountered in practice. Based on this and the transfer matrices derived above, a new value of loss factor for a gradual area change with mean flow can be incorporated with a factor ''*d*,'' which varies as shown in the Fig. 10, which is to be multiplied with the loss factors for the sudden expansion or contraction as the case may be. Assuming a linear variation of this factor ''*d*,'' it would be given by

$$d = \frac{(\theta - 0.1)}{1.47}, \tag{40}$$

where ''θ'' is half the angle of convergence or divergence in radians.

Using this modified value of the loss factor, parametric studies were carried out to observe the effect of Mach number. Thus it can be seen from Fig. 11 that as the Mach number increases the axial transmission loss increases. This seems to justify the fact that the aeroacoustic losses due to vortex shedding at the area discontinuity increase with Mach number.

III. EXPERIMENTAL VALIDATION

The theoretical work is validated hereunder by means of experiments carried out on a bellow. Transfer matrices derived above may be used to evaluate insertion loss, IL, transmission loss, TL, and level difference (or noise reduction), LD. The last one being the easiest to measure, has been selected for the validation. Noise reduction was measured at two points, one on the exhaust and the other on the tail pipe side attached to the ends of the bellow. Noise reduction or level difference is given by (Ref. 8, pages 59–60):

$$\begin{aligned} \mathrm{LD} &= 20 \lg \left| \frac{p_n}{p_1} \right| \mathrm{dB}, \\ &= 20 \lg \left| \frac{\dfrac{p_n}{p_o}}{\dfrac{p_1}{p_o}} \right|, \\ &= 20 \lg \left| \frac{\mathrm{TM}(1,1) + \mathrm{TM}(1,2)/Z_0}{\cos kl_1' + (jY_n/Z_o) \sin kl_1'} \right| \mathrm{dB} \end{aligned} \tag{41}$$

and

$$Z_o = Y_n \left(\frac{(kr_o)^2}{4} - M_n + j(0.6kr_o) \right), \tag{42}$$

where r_o is the radius of the pipe element, TM is the transfer matrix, l_1' is the length of the tail pipe from the point at

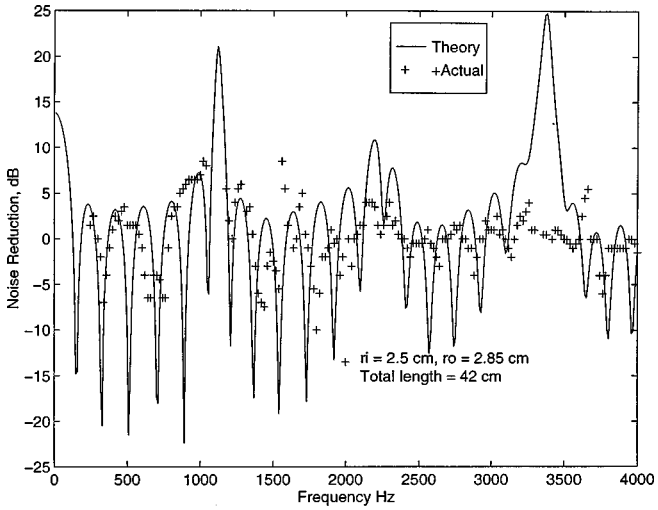

FIG. 13. Comparison between theoretical and experimental results for $M = 0.0$.

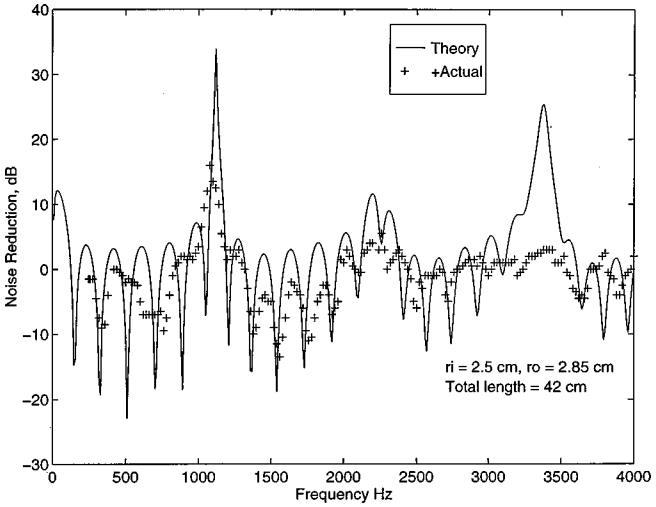

FIG. 14. Comparison between theoretical and experimental results for $M = 0.05$.

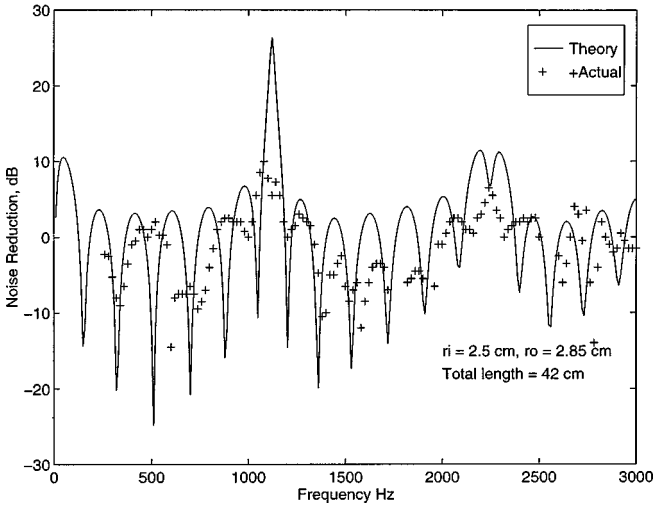

FIG. 15. Comparison between theoretical and experimental results for $M = 0.10$.

which the pressure is sensed to the radiation end, k_o is the wave number, Y_n is characteristic impedance of the tail pipe, Z_o is radiation impedance taking the mean flow effects into account, p_o is the acoustic pressure at the end of the tail pipe, and M_n is the mean flow Mach number at point n (see Fig. 12).

As would be observed from Eqs. (41) and (42), the effects of convection and radiation impedance have been duly incorporated. The effect of viscosity of the gaseous medium would be negligible for the typical diameters of bellows used in automotive applications (see Ref. 8, pages 24–25). Measurements were carried out upto a Mach number of 0.1 at frequency steps of 20 Hz. The experimental setup consisted of an air supply facility and the instrumentation for the measurement of noise reduction. The flow rate was measured using an orificemeter. Figure 12 shows the instrumentation used for the noise reduction measurements. The setup consisted of a loud speaker, a sine random generator, a heterodyne slave filter, and a power amplifier. In order to ensure that the sound source level would be sufficiently above the flow generated noise in the bellows, experiments were conducted for discrete frequency excitation. Measurements were restricted to frequencies above 250 Hz due to the loudspeaker diaphragm resonance at lower frequencies. As the model is valid for the plane mode only, measurements were carried out up to 4000 Hz only.

The total length of the bellow was 42 cm and the length of the tail pipe (from the end of the bellow to the exit) was 14 cm. The length of the pipe from the sensor to the bellow on the inlet side was also 14 cm.

Comparison between the theoretical and experimental results can be seen in Figs. 13, 14, and 15 for mean flow mach numbers 0.0, 0.05, and 0.1, respectively. As can be seen from these figures, peaks of noise reduction match quite reasonably upto frequencies of 4000 Hz, and there is reasonable general agreement between the predictions and experimental observations.

IV. CONCLUSIONS

An analytical model for prediction of the acoustic performance of flexible bellows has been developed, this being the first known attempt. For the case of stationary medium, the Helmholtz equation has been solved by using a practical assumption, and for the case of mean flow, based on some parametric studies, an equivalent simple expansion chamber model has been presented.

The axial transmission loss TL_a is seen to increase with the length of the bellow, and the slope of the expanding (or contracting portion) of the bellow, but decreases with the thickness of the bellow wall. With the inclusion of convective as well as dissipative effects of mean flow, TL_a is seen to increase with Mach number as expected. As also seen in the case of hose pipes, the wall compliance does not affect the acoustic performance parameters like TL_a significantly for a gaseous medium like air.[1]

There does not seem to be a significant difference between the rubber bellow and the equivalent rigid walled conical expansion-contraction chamber for the loss factors of the bellow material encountered in the present study. Bellows with higher loss factors are therefore preferable if they are to be used for acoustic applications.

ACKNOWLEDGMENTS

The investigation reported here would not have been possible without the facilities provided by the Department of Science and Technology of the Government of India for the Centre of Excellence for Technical Acoustics.

[1] M. L. Munjal and P. T. Thawani, ''Acoustic performance of hoses—A parametric study,'' Noise Control Eng. J. **44**, 274–280 (1996).
[2] J. H. Miles, ''Acoustic transmission matrix of a variable area duct or nozzle carrying a compressible subsonic flow,'' J. Acoust. Soc. Am. **69**, 1577–1586 (1981).
[3] R. J. Alfredson, ''The propagation of sound in a circular duct of continuously varying cross-sectional area,'' J. Sound Vib. **23**, 433–442 (1972).
[4] N. A. Eisenberg and T. W. Kao, ''Propagation of sound through a variable area duct with a steady compressible flow,'' J. Acoust. Soc. Am. **49**, 413–426 (1971).
[5] V. Easwaran and M. L. Munjal, ''Transfer matrix modeling of hyperbolic and parabolic ducts with incompressible mean flow,'' J. Acoust. Soc. Am. **90**, 2163–2172 (1991).

[6] V. Easwaran and M. L. Munjal, ''Plane wave analysis of conical and exponential pipes with incompressible mean flow,'' J. Sound Vib. **152**, 73–93 (1992).
[7] J. W. Sullivan and M. J. Crocker, ''Analysis of concentric tube resonators having unpartitioned cavities,'' J. Acoust. Soc. Am. **64**, 207–215 (1978).
[8] M. L. Munjal, *Acoustics of Ducts and Mufflers* (Wiley-Interscience, New York, 1987).
[9] J. Vinay, ''Flow acoustic performance of flexible bellows,'' M.E. thesis, Indian Institute of Science, Bangalore (1997).
[10] M. L. Munjal, ''Velocity ratio cum transfer matrix method for evaluation of a muffler with mean flow,'' J. Sound Vib. **39**, 105–119 (1975).

High modal density approximations for equipment in the time domain

Aravind Cherukuri[a] and Paul E. Barbone
Department of Aerospace and Mechanical Engineering, Boston University, Boston, Massachusetts 02215

(Received 19 May 1997; revised 12 January 1998; accepted 8 June 1998)

This article considers modeling the effect of complex subsystems on the dynamics of the main structure to which they are attached. It is proposed that the substructure (say a piece of equipment) be replaced by an equivalent set of forces which react back on the main structure. These forces are given as time convolutions of the displacements at the equipment attachment points. The convolution integral, which represents a time domain DtN (Dirichlet-to-Neumann) map, is approximated in the high modal density limit with determined error bounds. This approximation leads to a family of equipment representations. The simplest requires few measured equipment properties, though more information can lead to greater accuracy. Our approximate DtNs are demonstrated numerically in finite element simulations. © *1998 Acoustical Society of America.* [S0001-4966(98)04709-2]

PACS numbers: 43.20.Tb, 43.40.At [ANN]

INTRODUCTION

Analysis of problems involving simulations over large/infinite domains can often be simplified by replacing a portion of the domain by a Dirichlet to Neumann, or DtN map.[1] Here we utilize the concepts of Dirichlet to Neumann mapping to replace a dynamical subsystem by a set of forces $\mathbf{f}(t)$. We consider the subsystem to interact with the main structure through a finite number of degrees of freedom which we refer to as attachment points. The forces $\mathbf{f}(t)$ that the dynamical subsystem exerts on the main structure depend on the displacement histories of the attachment points. Thus a Dirichlet to Neumann map in this context is a map that takes displacement histories into current forces. Once the DtN map characterizing a dynamical subsystem is known, its effect on the main structure is completely determined.

Approximate representations of dynamical subsystems (equipment) have two important advantages over exact representations or models. First, the approximate DtNs often provide enough accuracy while reducing computational costs. Second, approximate DtNs require relatively little effort to formulate. Here we formulate an approximate DtN map based on a few gross parameters of the subsystem.

Many methods have been proposed to model the effects of complicated substructures on the dynamics of the main structure. Soize[2] has attempted to do so by treating the substructures as random structural elements, the parameters of which are imprecisely known. Because of the uncertainty in their structure, he has referred to them as ''fuzzy structures.'' Given a master (main) structure with random attachments, Soize sets out to find the ensemble average of the response of the main structure. Following Soize's example, many other authors have used different closure approximations in an attempt to achieve the same goal.[3–7] Statistical energy analysis is also concerned with finding the ensemble average response of a random system.

Pierce *et al.*,[8] on the other hand, found the ''typical response'' of a plate with a densely packed collection of oscillators. Crighton[9] has noted that in order to make predictions about an individual realization of a system, one must seek a ''typical response'' of a complicated system, rather than an average response. Any introductory statistics text makes the point that knowledge of the average response alone is insufficient to make judgments about the behavior of the individual. This has recently been emphasized in regard to fuzzy structures in Ref. 10.

Our approach is to examine a complicated *deterministic* system. We obtain a model for the system which can be exact if sufficient information about the system is given. We consider approximations for the response of the system which exploit the one thing that we have assumed from the outset: the subsystem is complicated. Therefore, the number of modes in the frequency range of interest in the system is large. Thus we obtain an approximation that is valid for any individual subsystem, and not only for an ensemble.

We conduct our analysis in the time domain (rather than the frequency domain) for two reasons. First, for dynamical simulations, this is the domain of interest. Second, the analysis of the causal limit of zero damping and high modal density in the frequency domain can be subtle. On the other hand, in the time domain we can more easily obtain results for zero damping than with damping, as we will show.

In the next section we formulate the problem for constructing the time domain DtN map for a general linear elastic subsystem. The exact equations are derived for the case of zero damping. We then solve the equations of motion to derive the exact DtN map for the subsystem. The effects of small damping are then incorporated approximately. We use a modal representation similar to that used by Pierce[6] and develop an approximate DtN map for the subsystem in the high modal density limit. We derive error bounds on the approximate DtN map based on the choice of parameters.

[a]Currently affiliated with Parametric Technologies Corporation, Waltham, MA.

Finally we compare the results of using an exact DtN map to those from an approximate DtN map in a dynamical simulation. The simulation is performed for the special case of a single attachment point subsystem whose components move unidirectionally.

I. FORMULATION

We consider a linear dynamical subsystem whose configuration is specified by $N+M$ generalized coordinates, ξ_i with $i=1,\ldots,N+M$. These generalized coordinates may be thought of as being the generalized displacements of the components of the subsystem from their equilibrium positions. This subsystem interacts with the outside world through the first N of the $N+M$ generalized coordinates ξ_β with $\beta=1,\ldots,N$. Henceforth we shall refer to these generalized degrees of freedom as the degrees of freedom of the attachment points. We denote the generalized forces that are applied to the system through the first N generalized coordinates by f_γ where $\gamma=1,2,\ldots,N$.

The equations of motion for the subsystem are:

$$\begin{pmatrix} \mathbf{M}_{11} & \mathbf{M}_{12} \\ \mathbf{M}_{21} & \mathbf{M}_{22} \end{pmatrix} \begin{pmatrix} \ddot{\boldsymbol{\xi}}_1 \\ \ddot{\boldsymbol{\xi}}_2 \end{pmatrix} + \begin{pmatrix} \mathbf{C}_{11} & \mathbf{C}_{12} \\ \mathbf{C}_{21} & \mathbf{C}_{22} \end{pmatrix} \begin{pmatrix} \dot{\boldsymbol{\xi}}_1 \\ \dot{\boldsymbol{\xi}}_2 \end{pmatrix} + \begin{pmatrix} \mathbf{K}_{11} & \boldsymbol{\kappa}_{12} \\ \boldsymbol{\kappa}_{21} & \mathbf{K}_{22} \end{pmatrix} \begin{pmatrix} \boldsymbol{\xi}_1 \\ \boldsymbol{\xi}_2 \end{pmatrix} = \begin{pmatrix} \mathbf{f}_1 \\ 0 \end{pmatrix}. \tag{1}$$

Here, $\boldsymbol{\xi}_1$ represents the generalized coordinates of the attachment points and $\boldsymbol{\xi}_2$ represents the generalized coordinates of the internal degrees of freedom. The **K**'s represent the stiffness parameters coupling the attachment degrees of freedom or the internal degrees of freedom to one another. The $\boldsymbol{\kappa}$'s represent the stiffness parameters coupling the attachment degrees of freedom to the internal degrees of freedom. The **M**'s represent mass elements, while the **C**'s are damping coefficients.

In the derivations that follow, we shall consider only the special case in which $\mathbf{C}_{11}=\mathbf{0}$ and $\mathbf{C}_{12}=\mathbf{C}_{21}^T=\mathbf{0}$. We shall also usually consider the case of zero damping, in which $\mathbf{C}_{22}=\mathbf{0}$. We shall, however, allow for the situations in which $\mathbf{M}_{11}=0$ and/or $\mathbf{M}_{12}=\mathbf{M}_{21}^T=\mathbf{0}$. The matrices $\mathbf{M}_{22}$, $\mathbf{K}_{11}$, $\mathbf{K}_{22}$ are all assumed to be positive definite.

In order to distinguish between the various blocks that appear in the matrices in (1), we shall adopt a summation convention where repeated subscripts are summed through their range. Since we require different ranges to distinguish between attachment points and internal degrees of freedom, we adopt the convention

$$\begin{aligned} &\alpha,\beta,\gamma,\ldots=1,2,\ldots,N, \\ &p,q,r,s,\ldots=N+1,\ldots,N+M. \end{aligned} \tag{2}$$

Thus $\mathbf{M}_{11}\rightarrow M_{\alpha\beta}$, $\mathbf{M}_{12}\rightarrow M_{\alpha p}$, $\mathbf{M}_{22}\rightarrow M_{pq}$, etc. Using this convention (2) allows us to rewrite (1) as

$$M_{\alpha\beta}\ddot{\xi}_\beta + M_{\alpha p}\ddot{\xi}_p + K_{\alpha\beta}\xi_\beta + \kappa_{\alpha p}\xi_p = f_\alpha \tag{3}$$

and

$$M_{pq}\ddot{\xi}_q + C_{pq}\dot{\xi}_q + K_{pq}\xi_q = -M_{p\alpha}\ddot{\xi}_\alpha - \kappa_{p\alpha}\xi_\alpha. \tag{4}$$

In Eq. (4) we see that the internal degrees of freedom are forced by the motions of the attachment points. Equations (3) and (4) are the equations of motion of the subsystem. We can now solve (4) for the unknown generalized coordinates, ξ_p, and use the result in (3) to formulate a Dirichlet to Neumann Map or DtN.[1] The DtN map can be written as

$$\mathbf{f}=\tilde{\mathbf{F}}(\xi_\alpha). \tag{5}$$

Here, $\tilde{\mathbf{F}}$ is the Dirichlet to Neumann map; the forces f_α represent the Neumann data and the displacements of the attachment points ξ_α represent the Dirichlet data. Thus the DtN describes the forces exerted by the subsystem on its environment in terms of the displacements of its attachment points. We note that in the case of linear systems, as are treated here, the Fourier transform of the time-domain DtN map (5) is directly proportional to the impedance of the subsystem.

II. EXACT SOLUTION FOR THE INTERNAL DEGREES OF FREEDOM

We now consider the special case of $\mathbf{C}_{22}=\mathbf{0}$. On that basis, we obtain an exact solution of (4) for the generalized displacements of the internal degrees of freedom ξ_p in terms of the displacements of the attachment points ξ_β. The solution may be obtained in terms of a normal mode expansion using the eigenvectors of the matrix $\mathbf{M}_{22}^{-1/2}\mathbf{K}_{22}\mathbf{M}_{22}^{-1/2}$. For details of this derivation we refer the reader to Ref. 11. Here we need not compute $\mathbf{M}_{22}^{-1/2}$ explicitly. We only need to note that $\mathbf{M}_{22}^{1/2}$ is the unique positive definite matrix that satisfies $\mathbf{M}_{22}^{1/2}\mathbf{M}_{22}^{1/2}=\mathbf{M}_{22}$.

The matrix $M_{sp}^{-1/2}K_{pq}M_{qr}^{-1/2}$ is symmetric because $\mathbf{K}_{22}$ is symmetric. We assume that $M_{sp}^{-1/2}K_{pq}M_{qr}^{-1/2}$ is positive definite; i.e.,

$$\mathbf{x}^T(\mathbf{M}^{-1/2}\mathbf{K}\mathbf{M}^{-1/2})\mathbf{x}>0, \quad \forall \mathbf{x}\neq 0 \in \mathbf{R}^M. \tag{6}$$

Since $M_{sp}^{-1/2}K_{pq}M_{qr}^{-1/2}$ is symmetric and positive definite, it has M positive eigenvalues, $(\omega^{(P)})^2$, $P=1,\ldots,M$, and M distinct orthonormal eigenvectors, $\boldsymbol{\gamma}^{(P)}$, $P=1,\ldots,M$.

In what follows summation is implied on repeated subscripts, but superscripts are not summed unless explicitly specified. We solve Eq. (4) subject to the conditions $\xi_\alpha(t)=0$, $\xi_p(t)=0$, $\forall t\leqslant 0$, and use the properties of $(M_{sp}^{-1/2}K_{pq}M_{qr}^{-1/2})$ to get

$$\xi_s(t) = -\int_0^t \sum_{Q=1}^{M} \frac{A_{sp}^{(Q)}}{\omega^{(Q)}} \sin(\omega^{(Q)}(t-\tau)) \times \{\kappa_{p\alpha}\xi_\alpha(\tau) + M_{p\alpha}\ddot{\xi}_\alpha(\tau)\}\, d\tau. \tag{7}$$

We note that the time integration starts at $t=0$ because the subsystem has no displacement history prior to this. In (7), we have denoted the outer product $\mathbf{M}^{-1/2}\boldsymbol{\gamma}\otimes\boldsymbol{\gamma}\mathbf{M}^{-1/2}$ by **A**:

$$A_{ps}^{(P)} = M_{pq}^{-1/2}\gamma_q^{(P)}\gamma_r^{(P)}M_{rs}^{-1/2}. \tag{8}$$

A. Exact Dirichlet to Neumann map

We now obtain an exact DtN map by substituting Eq. (7) into Eq. (3). This yields

$$f_\alpha = M_{\alpha\beta}\ddot{\xi}_\beta + K_{\alpha\beta}\xi_\beta - \left(\kappa_{\alpha p} + M_{\alpha p}\frac{d^2}{dt^2}\right)\int_0^t \sum_{P=1}^{M} \frac{A_{ps}^{(P)}}{\omega^{(P)}} \sin(\omega^{(P)}(t-\tau)) \times\{M_{s\beta}\ddot{\xi}_\beta(\tau) + \kappa_{s\beta}\xi_\beta(\tau)\}\, d\tau. \quad (9)$$

Various expressions for the exact DtN map may be constructed by rearranging the terms of Eq. (9).[11] It is, perhaps, most illustrative to conduct integration by parts on terms containing $\boldsymbol{\xi}$ and simplify the result to write

$$f_\alpha = [M_{\alpha\beta} - M_{\alpha i}M_{ij}^{-1}M_{j\beta}]\ddot{\xi}_\beta + [K_{\alpha\beta} - \kappa_{\alpha p}K_{ps}^{-1}\kappa_{s\beta}]\xi_\beta(t) + \int_0^t \sum_{P=1}^{M} \omega^{(P)} m_{\alpha\beta}^{(P)} \sin(\omega^{(P)}(t-\tau))\ddot{\xi}_\beta(\tau)\, d\tau. \quad (10)$$

Here we have used the relation[11]

$$K_{pq}^{-1} = \sum_{P=1}^{M} \frac{A_{pq}^{(P)}}{(\omega^{(P)})^2}. \quad (11)$$

In Eq. (10) we have introduced the modal mass tensor $m_{\alpha\beta}^{(P)}$. We define the modal mass tensor to be

$$m_{\alpha\beta}^{(P)} = \frac{1}{(\omega^{(P)})^4}(M_{\alpha p}(\omega^{(P)})^2 - \kappa_{\alpha q})\begin{pmatrix} A_{pr}^{(P)} & A_{ps}^{(P)} \\ A_{qr}^{(P)} & A_{qs}^{(P)} \end{pmatrix} \times \begin{pmatrix} M_{r\beta}(\omega^{(P)})^2 \\ -\kappa_{s\beta} \end{pmatrix}. \quad (12)$$

This modal mass tensor is a generalization of the modal mass definition of Pierce[6] and O'Hara and Cunniff.[12]

B. Properties of the modal mass tensor

The modal mass tensors have the property that their sum over all modes, $P=1,...,M$, yields the total mass of the subsystem.[11] This may be written as

$$\zeta_\alpha^i[M_{\alpha\beta} - M_{\alpha i}M_{ij}^{-1}M_{j\beta}]\zeta_\beta^j + \sum_{P=1}^{M} \zeta_\alpha^i m_{\alpha\beta}^{(P)}\zeta_\beta^j = M_{(T)}\delta^{ij}. \quad (13)$$

Here ζ_α^i represents a unit displacement of the attachment points in the ith Cartesian direction and δ^{ij} is the Kronecker delta function. Further, the modal mass tensors can also be shown to satisfy the relationship[11]

$$\sum_{P=1}^{M} (\omega^{(P)})^2 m_{\alpha\beta}^{(P)} = M_{\alpha p}M_{pq}^{-1}K_{qr}M_{rs}^{-1}M_{s\beta} - M_{\alpha p}M_{pq}^{-1}\kappa_{q\beta} - \kappa_{\alpha p}M_{pq}^{-1}M_{q\beta} + \kappa_{\alpha p}K_{pq}^{-1}\kappa_{q\beta}. \quad (14)$$

C. The role of damping

We now briefly reconsider Eq. (4) with $\mathbf{C}_{22} \neq 0$. We shall assume, however, that $\mathbf{C}_{22}$ can be diagonalized by the eigenvectors γ. Thus, we write

$$M_{rp}^{-1/2}C_{pq}M_{qs}^{-1/2}\gamma_s^{(Q)} = 2\eta^{(Q)}\omega^{(Q)}\gamma_s^{(Q)} \quad (\text{no sum on } Q). \quad (15)$$

Here, $\eta^{(Q)}$ is the fraction of critical damping of the Qth mode of the clamped subsystem. Assuming $\eta^{(Q)} \ll 1$ leads to the following solution of (4):

$$\xi_s = -\int_0^t \sum_{Q=1}^{M} \frac{A_{sp}^{(Q)}}{\omega^{(Q)}} \sin(\omega^{(Q)}(t-\tau)) \times \exp(-\eta^{(Q)}\omega^{(Q)}(t-\tau))\{\kappa_{p\alpha}\xi_\alpha(\tau) + M_{p\alpha}\ddot{\xi}_\alpha(\tau)\}d\tau. \quad (16)$$

Following the same steps as those leading to Eq. (10), gives an approximate DtN that includes the effects of small damping on the internal degrees of freedom:

$$f_\alpha = [M_{\alpha\beta} - M_{\alpha i}M_{ij}^{-1}M_{j\beta}]\ddot{\xi}_\beta + [K_{\alpha\beta} - \kappa_{\alpha p}K_{ps}^{-1}\kappa_{s\beta}]\xi_\beta(t) + \int_0^t \sum_{P=1}^{M} \omega^{(P)} m_{\alpha\beta}^{(P)} \times \sin(\omega^{(P)}(t-\tau))e^{-\eta^{(P)}\omega^{(P)}(t-\tau)}\ddot{\xi}_\beta(\tau)\, d\tau. \quad (17)$$

We emphasize here that (17) is exact for $\eta^{(P)} = 0$, but is only approximately valid for $\eta^{(P)} \neq 0$. We shall refer to results derived consistently from (17) as ''exact'' in the rest of the paper, with the understanding that they are exact for $\eta^{(P)} = 0$.

III. APPROXIMATE DTN MAP AND ERROR BOUNDS

We begin this section by introducing the modal mass function:

$$\mathbf{m}(\omega) = \sum_{P=1}^{M} \mathbf{m}^{(P)} H(\omega - \omega^{(P)}). \quad (18)$$

In (18), $H(\omega)$ is the Heaviside unit step function. This definition is similar although not identical to that of Pierce.[6] We note that the function $\mathbf{m}(\omega)$ is discontinuous. Therefore its derivatives are to be interpreted as delta functions. We also introduce a continuous damping function $\eta(\omega)$ such that $\eta(\omega^{(Q)}) = \eta^{(Q)}$, and that

$$\min_{\omega} \eta(\omega) = \min_{Q=1,\ldots,M} \eta^{(Q)}. \quad (19)$$

When the subsystem has many internal degrees of freedom and therefore many modes, we expect that the modal mass function $\mathbf{m}(\omega)$ is well approximated by a smooth function $\overline{\mathbf{m}}(\omega)$. We now show that the error in $\mathbf{f}(t)$ resulting from approximating the modal mass function is bounded for all time, subject to some conditions. We do this by rewriting our discrete DtN in (17) using (18) and (19):

$$f_\alpha = [M_{\alpha\beta} - M_{\alpha i}M_{ij}^{-1}M_{j\beta}]\ddot{\xi}_\beta + [K_{\alpha\beta} - \kappa_{\alpha p}K_{ps}^{-1}\kappa_{s\beta}]\xi_\beta(t) + \int_0^t \int_0^\infty \omega \frac{dm_{\alpha\beta}(\omega)}{d\omega} \times \sin\omega(t-\tau)e^{-\eta(t-\tau)}\ddot{\xi}_\beta(\tau)\, d\omega\, d\tau. \quad (20)$$

Here we emphasize that Eq. (20) is exact for the case of zero damping, and no ''fuzzy'' approximations have as yet been made. That (20) is indeed exact can be easily verified by substituting (18) into (20) and integrating the resulting sum of delta functions.

We now consider approximating $\mathbf{m}(\omega)$ by $\overline{\mathbf{m}}(\omega)$. Thus we introduce the difference function $\mathbf{m}^e(\nu)$ with $\nu=\omega/\epsilon$ such that

$$\mathbf{m}(\omega)=\overline{\mathbf{m}}(\omega)+\epsilon\mathbf{m}^e\left(\frac{\omega}{\epsilon}\right), \quad \epsilon\ll 1. \tag{21}$$

Here, $\epsilon\mathbf{m}^e(\omega/\epsilon)$ is a small but rapidly varying function which represents the error in approximating $\mathbf{m}(\omega)$ by $\overline{\mathbf{m}}(\omega)$. The fact that it is rapidly varying is accounted for explicitly through its dependence on the argument (ω/ϵ). The nondimensional parameter ϵ is a measure of the modal spacing. We now substitute Eq. (21) into (20) to get

$$\begin{aligned} f_\alpha=&[M_{\alpha\beta}-M_{\alpha i}M_{ij}^{-1}M_{j\beta}]\ddot{\xi}_\beta \\ &+[K_{\alpha\beta}-\kappa_{\alpha p}K_{ps}^{-1}\kappa_{s\beta}]\xi_\beta(t)+\int_0^t\int_0^\infty \omega\,\frac{d\overline{m}_{\alpha\beta}(\omega)}{d\omega} \\ &\times\sin\,\omega(t-\tau)e^{-\eta(t-\tau)}\ddot{\xi}_\beta(\tau)\,d\omega\,d\tau+\mathrm{error}_\alpha(t). \end{aligned} \tag{22}$$

The error term in Eq. (22) is given by

$$\begin{aligned} \mathbf{error}(t)=&\int_0^t\int_0^\infty \omega\,\frac{d\mathbf{m}^e}{d\nu}(\nu)\bigg|_{\nu=\omega/\epsilon}\sin\,\omega(t-\tau) \\ &\times e^{-\eta(t-\tau)}\ddot{\boldsymbol{\xi}}(\tau)\,d\omega\,d\tau. \end{aligned} \tag{23}$$

Here, $m^{e'}_{\alpha\beta}(\nu)$ is the derivative with respect to its argument. We now show that the error is bounded. We integrate (23) by parts once in time and twice in frequency to obtain:

$$\begin{aligned} \mathbf{error}(t)=&\epsilon^2\int_0^t\int_0^\infty \mathbf{m}^e_{-1}\left(\frac{\omega}{\epsilon}\right)(t-\tau)^2\cos\,\omega(t-\tau) \\ &\times e^{-\eta(t-\tau)}\boldsymbol{\xi}'''(\tau)\,d\omega\,d\tau. \end{aligned} \tag{24}$$

Here $\mathbf{m}^e_{-1}(\nu)$ is the integral of $\mathbf{m}^e(\nu)$ with respect to its argument. In deriving Eq. (24) the following assumptions were made regarding the choice of $\overline{\mathbf{m}}(\omega)$:

$$\begin{aligned} &\overline{\mathbf{m}}(0)=\mathbf{0}, \quad \overline{\mathbf{m}}(\infty)=\sum_{P=1}^{M}\mathbf{m}^{(P)}, \\ &\mathbf{m}^e_{-1}(0)=\mathbf{0}, \quad C\equiv\int_0^\infty||\mathbf{m}^e_{-1}(\nu)||\,d\nu<\infty. \end{aligned} \tag{25}$$

In Eq. (24) we observe

$$\begin{aligned} &\int_0^\infty\left\|\mathbf{m}^e_{-1}\left(\frac{\omega}{\epsilon}\right)\right\|d\omega=\epsilon C<\infty, \\ &|\cos\,\omega(t-\tau)|\leqslant 1, \\ &(t-\tau)^3e^{-\eta(t-\tau)}\leqslant\left(\frac{3}{\eta_{\min}}\right)^3e^{-3}. \end{aligned} \tag{26}$$

Substituting (26) into (24) yields

$$\begin{aligned} &||\mathbf{error}(t)|| \\ &\leqslant\begin{cases} \dfrac{\epsilon^3}{\eta^3}\,27e^{-3}C|\boldsymbol{\xi}'''(t)|_{\max}, & \eta\neq 0,\eta\ll 1,\forall t, \\ \epsilon^3t^3C|\boldsymbol{\xi}'''(t)|_{\max}, & \eta=0,\forall t. \end{cases} \end{aligned} \tag{27}$$

Equation (27) shows that the error incurred in replacing $\mathbf{m}(\omega)$ by a smooth $\overline{\mathbf{m}}(\omega)$ is bounded for all time in the presence of damping. When there is no damping, the error is small for simulation time less than $O(1/\epsilon)$.

IV. EXAMPLE APPLICATION OF DTNs

In this section we illustrate the application of our formulation and DtNs to a particular problem. We consider an elastic rod (main structure) that we model discretely using ten elastic finite elements. At one end of the rod we prescribe a unit step displacement at $t=0$. At the other end of the rod we attach a dynamical subsystem whose components are allowed unidirectional motion only. We represent the effect of the subsystem on the dynamics of the elastic rod through a DtN map. We use this special case to compare the results of the exact DtN map to an approximate (fuzzy) DtN map. The basis of our comparison is the force $\mathbf{f}(t)$ that the substructure exerts on the rod in each case.

The exact DtN for such a subsystem may be derived from Eq. (20) to be

$$\begin{aligned} f_0(t)=&K_0\xi_0(t)-\int_0^t\int_0^\infty\omega^3\frac{dm(\omega)}{d\omega}\sin\,\omega(t-\tau) \\ &\times e^{-\eta(\omega)(t-\tau)}\xi_0(\tau)\,d\omega\,d\tau. \end{aligned} \tag{28}$$

Here ξ_0 is the displacement of the attachment point between the rod and the subsystem (equipment), f_0 is the force exerted by the subsystem on the elastic rod, and K_0 is the high-frequency attachment point stiffness. For details of the formulation and derivation of Eq. (28) we refer the reader to Ref. 13. We consider exact and approximate modal mass functions of the form

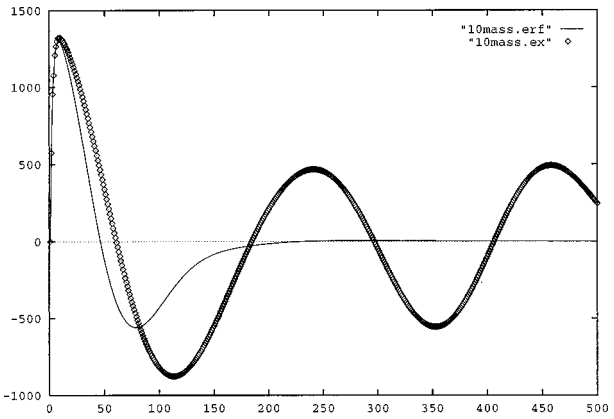

FIG. 1. Force at the attachment point plotted as a function of time. The full time scale is one unit. The parameters of the rod and subsystem are such that $\Omega\approx\omega_0\approx 10$. 10 internal d.o.f. subsystem.

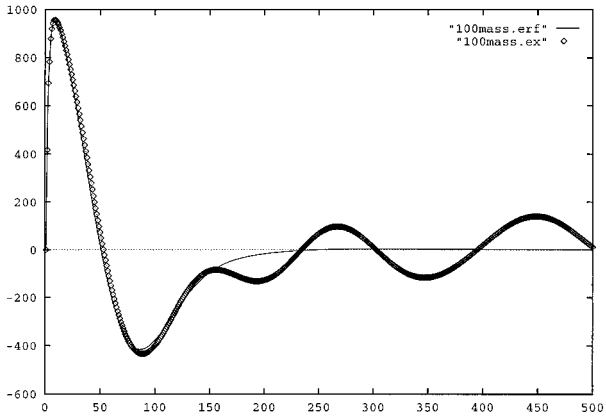

FIG. 2. The 100 internal d.o.f subsystem.

$$m(\omega)=\sum_{P=1}^{M} m^{(P)}H(\omega-\omega^{(P)}),$$

$$\overline{m}(\omega)=M_T \operatorname{erf}\left(\frac{\omega}{\sqrt{2}\Omega}\right). \tag{29}$$

Here erf (z) is the error function as defined in Ref. 14, M_T is the total mass of the subsystem, and Ω is a characteristic frequency scale of the subsystem. The frequencies $\omega^{(P)}$ are chosen randomly between 0 and $3\times\Omega$. The modal masses $m^{(P)}$ are chosen to approximate the continuous distribution $\overline{m}(\omega)$ in (29), thus satisfying the assumption (21).

We note further that the modal mass functions $m(\omega)$ and $\overline{m}(\omega)$ satisfy[13]

$$m(0)=0, \quad m(\infty)=M_T=\sum_{P=1}^{M} m^{(P)},$$

$$\frac{dm}{d\omega}\geqslant 0, \quad \int_0^{\infty}\omega^2\frac{dm(\omega)}{d\omega}\,d\omega=K_0. \tag{30}$$

From condition (30) we obtain $\Omega=\sqrt{K_0/M_T}$ in the approximate modal mass function. We use the modal mass functions from (29) in the DtN (28) to obtain our exact and approximate (fuzzy) DtN as[13]

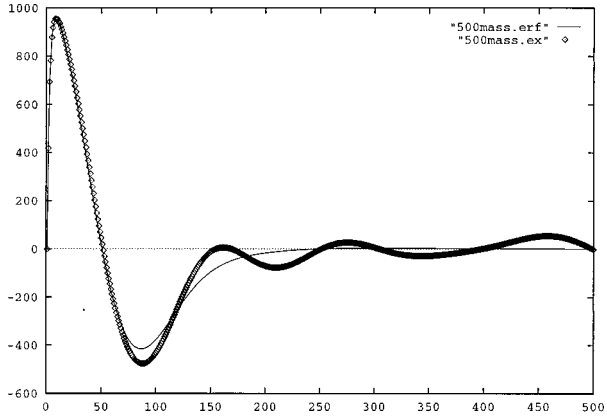

FIG. 3. The 500 internal d.o.f subsystem.

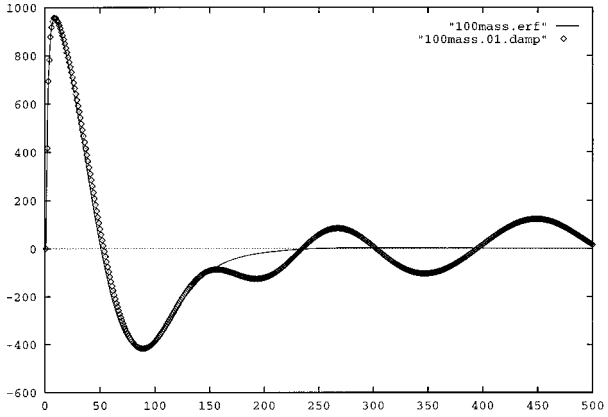

FIG. 4. The 100 internal d.o.f with 1% damping.

$$f_0(t)=K_0\xi_0(t)-\int_0^t\sum_{P=1}^{M}(\omega^{(P)})^3m^{(P)}\times\sin(\omega^{(P)}(t-\tau))e^{-\eta^{(P)}(t-\tau)}\xi_0(\tau)\,d\tau, \tag{31}$$

$$\overline{f}_0(t)=K_0\xi_0(t)-M_T\Omega^4\int_0^t[3-\Omega^2(t-\tau)^2]\times(t-\tau)e^{-(t-\tau)^2\Omega^2/2}\xi_0(\tau)\,d\tau. \tag{32}$$

We note that other choices of $\overline{m}(\omega)$ lead to different results.

A. Implementation and numerical results

We analyze the elastic rod described above using finite elements. The rod is discretized and represented by ten finite elements. The DtN boundary condition given by Eq. (31) or (32) is applied at the end of the rod at $x=L$. We apply a unit Heaviside step in displacement at the end $x=0$. We integrate the equations of motion explicitly to update the displacements in the rod and the force at the attachment point. The force at the attachment point at any time t depends on the value of ξ_0 at all *earlier* times. Therefore, we maintain a time history of the displacement of the node at $x=L$ and use this in (32) to evaluate the force f_0 at each time step. This allows us to compute the displacement of the rod at the next time step, and so on. Below we compare the forces between

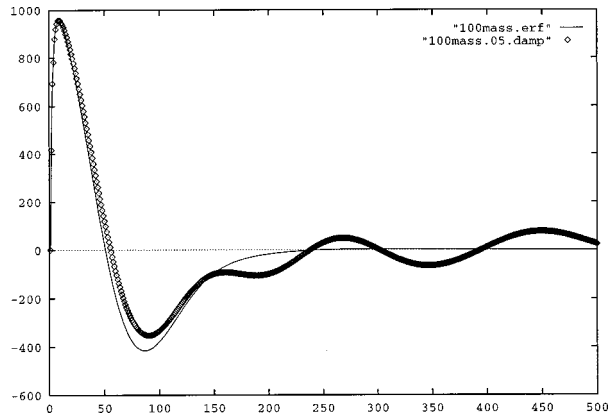

FIG. 5. The 100 internal d.o.f with 5% damping.

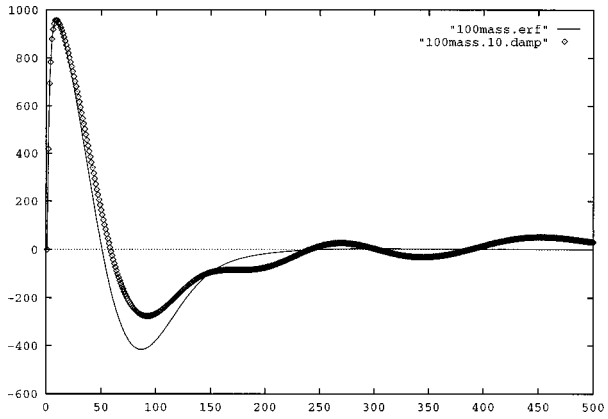

FIG. 6. The 100 internal d.o.f with 10% damping.

the rod and the equipment predicted by the exact DtN and the approximate DtN for various modal densities and modal damping.

The properties of the rod and the subsystem are chosen so that $\Omega \approx \omega_0 \approx 10$, where ω_0 is the lowest natural frequency of the rod. Further, the mass of the rod is approximately the same as the mass of the attachment. The rod has high ($\approx 10\%$) damping, which is the same throughout the simulations, and tends to make the travel time slightly faster than would be indicated by ω_0. The equipment has either zero dissipation or a value as stated in the figure captions. The full time range for the simulations is one time unit.

In Figs. 1–3 we see the effect of the number of internal degrees of freedom M (modes) on the exact and approximate DtNs (31) and (32), respectively. The number of modes is related inversely to the small parameter ϵ introduced in Eq. (21). Specifically, $\epsilon = O(1/M)$. Thus, as M increases, we expect the results from the approximate DtN (32) to better approximate the exact DtN results. From these figures we can see that the approximate DtN map in Eq. (32) indeed provides a more accurate representation of the subsystem as the number of internal degrees of freedom increase from 10 to 500.

In Figs. 4–6 we study the effect of subsystem damping on the validity of the DtN approximation. Based on the results from Sec. IV, we should expect that increasing damping (with M fixed) would control the long time error in the simulations. In Figs. 4–6, we see precisely this behavior as η increases from 1% to 10% of critical damping. We note that in all these figures the approximate DtN has zero added damping. We conjecture that better agreement in the ''over shoot'' region (near $t = 100$) would be realized by using an approximate DtN that included damping.

V. CONCLUSIONS

In Sec. III A we have shown that a general dynamical subsystem can be represented by an exact DtN map. The map can be used to replace the subsystem in a dynamical simulation. In Sec. IV we provided approximate representations for the dynamical subsystem. We showed that the error can be bounded. In the final section we studied an example problem and performed a dynamical simulation using both our exact and approximate DtNs. The simulation demonstrates the validity of our results when the number of modes is high. It also shows that the model improves with the presence of a small amount of damping.

The approximate structure model presented here requires knowledge of ''the limiting structure.'' That is, we need to know

$$\lim_{\epsilon \to 0} m(\omega) = \bar{m}(\omega). \tag{33}$$

Equation (33) is very restrictive in terms of developing approximations for real structures. In a future contribution,[15] we shall show that a given structure can be accurately modeled without full knowledge of the limit in (33). That is, we can construct an $\bar{m}(\omega)$ with knowledge of only a few relatively simple parameters that describe the system.

ACKNOWLEDGMENTS

The authors would like to thank Allan D. Pierce, Isaac Harari, Dan Givoli, Daniel Goldman, Raymond Nagem, Josh Montgomery and Brian Rush for many helpful discussions and ideas. They also thank the anonymous reviewers for their helpful comments. This work was supported by the Office of Naval Research.

[1] D. Givoli, *Numerical Methods for Problems on Infinite Domains* (Elsevier, Amsterdam, 1992), 1st ed.
[2] C. Soize, ''A model and numerical method in the medium frequency range for vibroacoustic predictions using the theory of structural fuzzy, J. Acoust. Soc. Am. **94**, 849–865 (1993).
[3] R. L. Weaver, ''The effect of an undamped finite degree of freedom fuzzy substructure: numerical solutions and theoretical discussion,'' J. Acoust. Soc. Am. **100**, 3159–3164 (1996).
[4] R. L. Weaver, ''Mean and mean-square responses of a prototypical master/fuzzy structure,'' J. Acoust. Soc. Am. **101**, 1441–1449 (1997).
[5] R. H. Lyon, ''Statistical energy analysis and structural fuzzy,'' J. Acoust. Soc. Am. **97**, 2878–2881 (1995).
[6] A. D. Pierce, ''Resonant-frequency-distribution of internal mass inferred from mechanical impedance matrices, with application to fuzzy structure theory,'' *Proceedings of ASME Symposium on Acoustics of Submerged Structures and Transduction Systems*, September 17–21, 1995 (ASME, New York, 1996).
[7] M. Strasberg, ''Continuous structures as fuzzy substructures,'' J. Acoust. Soc. Am. **100**, 3456–3459 (1996).
[8] A. D. Pierce, V. W. Sparrow, and D. A. Russel, ''Fundamental structural-acoustic idealizations for structures with fuzzy internals,'' ASME Transactions, Paper No. 93-WA/NCA-17, ASME Winter Annual Meeting, New Orleans, November 1993.
[9] D. G. Crighton, private communication.
[10] Y. K. Lin, ''On the standard deviation of change-in-impedance due to fuzzy subsystems,'' J. Acoust. Soc. Am. **101**, 616–618 (1997).
[11] A. Cherukuri and P. E. Barbone, ''Time Domain Dirichlet to Neumann Maps For Representing Complex Dynamical Subsystems,'' Boston University, Department of Aerospace & Mechanical Eng. Technical Report, No. AM-96-017, 1996.
[12] G. J. O'Hara and P. F. Cunniff, ''Elements of Normal Mode Theory,'' Naval Research Laboratory Report, 6002 (1963).
[13] P. E. Barbone, ''Equipment Representations for Shock Calculations: Time Domain Dirichlet to Neumann Maps,'' in *Acoustics, Vibrations, and Rotating Machines*, Proceedings of the 1995 Design Engineering Technical Conferences, Sept. 17–20, 1995 (ASME Press, New York, 1996), Vol. 3, Part B, pp. 223–228.
[14] M. Abramowitz and I. A. Stegun, *Handbook of Mathematical Functions* (Dover, New York, 1972).
[15] P. E. Barbone, A. Cherukuri, and D. Goldman, ''Canonical representations of complex vibratory subsystems, Part I: Single attachment point,'' Boston University Aerospace and Mechanical Engineering Technical Report No. AM-98-027, June 1998.

Reconstructing interior acoustic pressure fields via Helmholtz equation least-squares method

Sean F. Wu and Jingyou Yu
Department of Mechanical Engineering, Wayne State University, Detroit, Michigan 48202

(Received 17 March 1998; accepted for publication 28 June 1998)

This paper extends the Helmholtz equation least-squares (HELS) method previously developed by Wang and Wu [J. Acoust. Soc. Am. **102**, 2020–2032 (1997)] to reconstruction of acoustic pressure fields inside the cavity of a vibrating object. The acoustic pressures are reconstructed through an expansion of the acoustic modes generated by the Gram–Schmidt orthonormalization with respect to the particular solutions to the Helmholtz equation. Such an expansion is uniformly convergent because the selected acoustic modes consist of a uniformly convergent series of Legendre functions. The coefficients associated with these acoustic modes are determined by requiring the assumed-form solution to satisfy the pressure boundary condition at the measurement points. The errors incurred in this process are minimized by the least-squares method. Numerical examples of partially vibrating spheres and cylinders with various half-length to radius aspect ratios subject to different frequency excitations are demonstrated. The reconstructed acoustic pressures are compared with the analytic solutions and numerical ones obtained by using the standard boundary element method (BEM) codes. © *1998 Acoustical Society of America.* [S0001-4966(98)01110-2]

PACS numbers: 43.20.Tb, 43.20.Rz, 43.50.Yw [CBB]

INTRODUCTION

In engineering applications, it is often required to diagnose noise sources of vibrating structures, which includes identification of the locations and strengths of noise sources over the structural surfaces. With this information the design engineers can come up with more effective noise reduction measures. Traditionally, noise diagnosis is carried out by using an intensity probe that sweeps over the entire source surface at very close range. This approach is feasible when the source surface is smooth and flat. Even so, the diagnostic process can be costly and time-consuming.

One way of conducting a quick noise diagnosis is via the space transformation of sound field (STSF) method proposed by Bruel & Kjaer (1995). STSF combines the near field acoustic holography, originally developed by Williams *et al.* (1980), Maynard *et al.* (1985), and Veronesi and Maynard (1987), and the BEM-based Kirchhoff integral theory for acoustic radiation in the field. While STSF offers a quick result, it lacks a mathematical rigor in replacing a source by a finite planar surface on which acoustic pressure measurements are made. Such a replacement is inherently handicapped, and at best represents a crude approximation for an acoustic pressure distribution very close to the measurement plane. Even so, reconstruction of acoustic pressures is limited to a planar surface on one side of the source only.

To reconstruct the acoustic pressures over the entire surface of a vibrating object, one can utilize the Kirchhoff integral theory. This integral formulation correlates the radiated acoustic pressures to the surface acoustic quantities, which can be determined by solving an integral equation numerically using BEM (Gardner and Bernhard, 1988; Veronesi and Maynard, 1989; Kim and Lee, 1990; Ciskowski and Brebbia, 1991; Bai, 1992). The advantage of this BEM-based integral formulation is the reduction of dimensionality of the problem by one. However, precisely because of this transformation that gives its advantage, it also brings about several inherent drawbacks.

The first drawback is that the integral equation may fail to yield a unique solution when the excitation frequency is close to one of the characteristic frequencies of the related interior boundary value problem (Schenck, 1968). While this nonuniqueness difficulty can be overcome by the CHIEF method (Schenck, 1968), the efficiency and accuracy of numerical calculations may be affected. The second drawback is its inherent ill-conditioning difficulty (Wang and Wu, 1997) when the measured data are not error free. Singular value decomposition (SVD) can be used to truncate the order and regularize the matrix that correlates the measured data to surface acoustic pressures, thus reducing the reconstruction errors. Even with this regularization, the accuracy of reconstruction is still limited to the near field (Kim and Lee, 1990). Moreover, how to handle small singular values in SVD is still a problem open to investigation (Veronesi and Maynard, 1989). The last but not the least drawback is due to the fact that the number of measurements in the field must be comparable to that of the nodes discretized on the surface. Consequently, the effectiveness of this method can be severely hindered when hundreds of (or even more) discretized nodes are used to describe the surface acoustic pressure distribution, making diagnostics virtually impossible.

Recently, a Helmholtz equation least-squares (HELS) method (Wang *et al.*, 1995; Wang and Wu, 1997; Wu and Wang, 1998) was developed to reconstruct the radiated acoustic pressures from a vibrating object. This method employs an expansion of acoustic modes that satisfy the Helmholtz equation. Such an expansion is uniformly convergent because the selected acoustic modes consist of a uniformly convergent series of Legendre functions. The coefficients associated with these acoustic modes are determined by requiring the assumed-form solution to satisfy the pres-

sure boundary condition at the measurement points. The errors incurred in this process are minimized by the least-squares method. It is shown (Wang and Wu, 1997) that the solutions thus obtained are always unique. The number of measurements is no more than that of the acoustic modes needed to reconstruct the radiated acoustic pressure field, which is small when an appropriate coordinate system is selected for the particular source geometry under consideration. Consequently, numerical computation efficiency of the HELS method can be high. Notice that Hunt *et al.* (1974) have applied a similar expansion theory to the Kirchhoff integral formulation to solve acoustic radiation from an elastic structure. They express both the surface acoustic pressure and normal component of the surface velocity involved in the integral formulation as the spherical Hankel functions and Legendre functions. The coefficients associated with these functions are solved simultaneously, given the external excitation force acting on the structure.

In this paper, the previously derived HELS method (Wang and Wu, 1997) is extended to reconstruction of acoustic pressure fields inside the cavity of a vibrating structure. The results thus obtained are compared with analytical and numerical solutions using the standard BEM codes. Applications of such can be found in diagnoses of noise sources inside a vehicle passenger compartment and an aircraft cabin.

I. GENERAL FORMULATIONS

The acoustic pressure radiated from a finite vibrating object into an unbounded fluid medium satisfies the wave equation, whose Fourier transformation is known as the reduced wave equation or the Helmholtz equation,

$$\nabla^2 \hat{p} + k^2 \hat{p} = 0, \tag{1}$$

where $\hat{p}$ represents the complex amplitude of the acoustic pressure and $k = \omega/c$ is the acoustic wave number. Suppose that $\hat{p}$ satisfies the Dirichlet condition

$$\hat{p}(\mathbf{x}_B) = g(\mathbf{x}_B), \quad \mathbf{x}_B \in \partial B, \tag{2}$$

where ∂B represents a boundary surface. Solutions to Eq. (1) subject to boundary condition (2) can be expressed as an expansion of acoustic modes Ψ_{mj} (Wang and Wu, 1997; Note that there are some ambiguities in the indices of these acoustic modes Ψ_{mj} in the previous paper, which are corrected here);

$$\hat{p}(\mathbf{x}_m) = \rho c \sum_{j=0}^{\infty} C_{mj} \Psi_{mj}(\mathbf{x}_m), \tag{3}$$

where $\hat{p}$ represents the complex amplitude of the acoustic pressure at any point $\mathbf{x}_m$ in the field, ρ and c are the density and speed of sound of the fluid medium, respectively. The summation on the right side of Eq. (3) can also be written as

$$\sum_{j=0}^{\infty} C_{mj} \Psi_{mj}(\mathbf{x}_m) = \sum_{n=0}^{\infty} \sum_{l=-n}^{n} \tilde{C}_{nl} \tilde{\psi}_{nl}(\mathbf{x}_m). \tag{4}$$

The summations on both sides of Eq. (4) are equivalent. The right-hand side format may appear more frequently in the literature (Hunt *et al.*, 1974), but is cumbersome to use in the derivations because it contains a double summation. In this paper, the right-hand side format is utilized to facilitate the definition of the expansion functions $\tilde{\psi}_{nl}(\mathbf{x}_m)$. Once this is done, the expansion functions are rewritten in the left-hand side format to facilitate derivations of the formulations.

The expansion functions $\tilde{\psi}_{nl}(\mathbf{x}_m)$ on the right side of Eq. (4) can be generated by using Gram–Schmidt orthonormalization (Pinsky, 1991) with respect to the particular solutions to the Helmholtz equation ψ_{nl}

$$\langle \psi_{nl}(\mathbf{x}_B), \tilde{\psi}_{nl}(\mathbf{x}_B) \rangle = \int_{\partial B} \psi_{nl}(\mathbf{x}_B) \tilde{\psi}_{nl}(\mathbf{x}_B) dS. \tag{5}$$

Here a tilde is used to distinguish the expansion functions $\tilde{\psi}_{nl}$ from the particular solutions ψ_{nl}. The symbol $\langle\ \rangle$ on the left side of Eq. (5) indicates an inner product with respect to the boundary surface ∂B, and the particular solutions ψ_{nl} can be written in terms of the spherical coordinates as (Vekua, 1953)

$$\psi_{nl}(r, \theta, \phi) = h_n(kr) P_n^l(\cos\ \theta) \begin{Bmatrix} \cos\ l\theta \\ \sin\ l\theta \end{Bmatrix}, \tag{6}$$

where $h_n(kr)$ and $P_n^l(\cos\theta)$ denote the spherical Hankel functions and Legendre functions, respectively. The expansion functions $\tilde{\psi}_{nl}$ thus obtained are mutually orthonormal on ∂B and uniformly convergent, because ψ_{nl} consist of a uniformly convergent series of Legendre functions (Bergman, 1960).

Note that the orthonormalization defined by Eq. (6) is important for an arbitrary surface because it guarantees a mutual orthogonality of the basis functions. Without this process the reconstructed acoustic pressure fields may not converge to the true values. For a spherical surface, however, such a process is unnecessary because it produces the particular solutions ψ_{nl} themselves, namely, $\tilde{\psi}_{nl} \equiv \psi_{nl}$ for a spherical surface.

The coefficients associated with $\tilde{\psi}_{nl}(\mathbf{x}_m)$, or equivalently, those associated with $\Psi_{mj}(\mathbf{x}_m)$ in Eq. (4), can be determined by requiring the assumed-form solution, Eq. (3), to satisfy the boundary condition at the measurement point $\mathbf{x}_m$,

$$\rho c \sum_{j=0}^{J} C_{mj} \Psi_{mj}(\mathbf{x}_m) = \hat{p}_{Bm}(\mathbf{x}_m). \tag{7}$$

Suppose that an N-term expansion in Eq. (7) is used; then the total number of acoustic modes $\Psi_{mj}(\mathbf{x}_m)$ is equal to $J = (N+1)^2$. Accordingly, there are J unknown coefficients C_{mj}. To solve these unknowns, M measurements ($M \geqslant J$) must be taken, which leads to a set of J simultaneous algebraic equations. If the measured quantities $\hat{p}_B(\mathbf{x}_m)$, $m = 1$ to M, are exact, then the assumed-form solution converges to the true value as $N \to \infty$ (Davis and Rabinowitz, 1961). However, in reality $\hat{p}_B(\mathbf{x}_m)$ always contains errors due either to measurement uncertainties or to rapid decay of evanescent waves. Moreover, the number of measurements M is always finite, and so is the number of expansion terms N. Consequently, $\hat{p}(\mathbf{x}_m)$ will not converge to the true value. Neverthe-

less, the errors incurred in this process can be minimized by the least-squares method

$$I=\sum_{m=1}^{M}\left[\rho c\sum_{j=0}^{J}C_{mj}\Psi_{mj}(\mathbf{x}_m)-\hat{p}_B(\mathbf{x}_m)\right]^2. \tag{8}$$

Taking the derivative of I with respect to C_{mi} and setting the resultant equations to zero yield a set of simultaneous equations for the unknown coefficients C_{mi}, which can be written in a matrix form as

$$[T]_{J\times J}\{C\}_{J\times 1}=\{D\}_{J\times 1}, \tag{9}$$

where $[T]_{J\times J}$ represents the transformation matrix that correlates the measured data to the reconstructed acoustic pressures, and $\{D\}_{J\times 1}$ contains the measured information, whose elements are given, respectively, by

$$T_{ij}=\rho c\sum_{m=1}^{M}\Psi_{mi}(\mathbf{x}_m)\Psi_{mj}(\mathbf{x}_m), \tag{10a}$$

$$D_i=\sum_{m=1}^{M}\hat{p}_B(\mathbf{x}_m)\Psi_{mi}(\mathbf{x}_m). \tag{10b}$$

Note that the transformation matrix $[T]_{J\times J}$ is nonsingular. Therefore the coefficients $\{C\}$ can be solved by inverting the matrix $[T]_{J\times J}$

$$\{C\}_{J\times 1}=(\rho c)^{-1}[E]_{J\times M}\{\hat{p}_B\}_{M\times 1}, \tag{11}$$

where $[E]_{J\times M}$ is called the pseudoinverse matrix defined as

$$[E]_{J\times M}=([\Psi]^T_{M\times J}[\Psi]_{M\times J})^{-1}[\Psi]^T_{M\times J}, \tag{12}$$

where $[\Psi]_{M\times J}$ represents an $M\times J$ matrix that consists of the acoustic modes $\Psi_{ij}(\mathbf{x}_m)$ defined in Eq. (4). It can be shown that the condition number of the pseudoinverse matrix $[E]_{J\times M}$ is much smaller than that of a direct inverse (Stewart, 1973). Hence the matrix equation (11) is stable and the accuracy of numerical computations is high.

Note that in deriving Eq. (11) no restrictions are imposed on the measurement points, as long as they are noncoincident. The coefficients $\{C\}$ thus obtained will have errors to the second order. Once $\{C\}$ is determined, the surface acoustic pressures can be reconstructed by Eq. (3). In fact, one can use Eq. (3) to reconstruct acoustic pressures anywhere external to the vibrating object.

It is emphasized that Eq. (3) can be expressed in other coordinate systems. Table I summaries the coordinate systems that may be suited for reconstructing the acoustic pressures on various types of source geometry.

The advantages of the HELS method are that: (1) it is mathematically rigorous; (2) it allows for reconstruction of acoustic pressures over the entire surface; (3) solutions thus obtained are unique; and (4) the efficiency of numerical computations is high. This is because the number of measurements is determined by that of acoustic modes needed to reconstruct the radiated acoustic pressure field, which is small when an appropriate coordinate system is selected for the particular source geometry under consideration.

TABLE I. Summary of coordinate systems for various types of source geometry.

Representative aspect ratio x:y:z	Coordinate systems
1:1:1 (a chunky object)	Spherical Prolate spheroidal Oblate spheroidal Ellipsoidal
1:1:10 (a long object)	Prolate spheroidal Ellipsoidal
1:10:10 (a flat object)	Oblate spheroidal Ellipsoidal
1:10:100 (a long and flat object)	Ellipsoidal

II. INTERIOR PROBLEMS

The formulations derived above can be extended to reconstruction of the acoustic pressure fields in the interior region. Notice that the spherical Hankel function $h_n(kr)$ in Eq. (6) corresponds to outgoing waves, appropriate for reconstruction of acoustic pressure fields in the exterior region. Such a function is unbounded at $r=0$ and cannot be used to reconstruct the acoustic pressure fields in an interior region. This difficulty can be overcome by taking the real and imaginary parts of $h_n(kr)$ (Morse and Ingard, 1986)

$$h_n(kr)=\mathfrak{T}_n(kr)+\hat{\imath}\aleph_n(kr), \tag{13}$$

where $\hat{\imath}=\sqrt{-1}$, and $\mathfrak{T}_n$ and $\aleph_n$ are the spherical Bessel and spherical Neumann functions of order n, respectively. Since $\mathfrak{T}_n$ is finite at $r=0$ but $\aleph_n$ is not, and since the acoustic pressures are bounded, the spherical Neumann function $\aleph_n$ can be discarded on the physical reasoning basis, and only the spherical Bessel functions $\mathfrak{T}_n$ are retained in Eq. (6) to reconstruct the acoustic pressure fields in the interior region.

Note that the spherical Bessel functions $\mathfrak{T}_n$ are most suitable for reconstructing acoustic pressures radiated from a spherical source or sources with a characteristic aspect ratio x:y:z close to 1:1:1 (e.g., a chunky object). Under this condition, the number of acoustic modes needed to reconstruct the acoustic pressure fields is minimum, making it an extremely effective noise diagnostic tool. For an elongated or an arbitrarily shaped object, the Bessel functions can be expressed in terms of other coordinate systems as listed in Table I to reduce the number of acoustic modes necessary to approximate the acoustic pressure field. The major difficulty with these prolate, oblate, and elliptic coordinate systems, however, is that they are much harder to implement numerically than the spherical coordinate system, thus rendering them less attractive to use in practice.

III. NUMERICAL EXAMPLES

In this section numerical examples of reconstructing acoustic pressure fields inside the cavity of a vibrating object are demonstrated. To begin with, the cases for which analytical solutions are well known are considered in order to facilitate the validations of the HELS method. The first example is concerned with reconstruction of the radiated acoustic pressures from a partially vibrating sphere of radius

a. Assume that a portion of a spherical surface (with a vertex angle of $2\theta = 90°$) is vibrating at a constant frequency ω, and the rest of the surface is stationary,

$$\hat{V}_n(\theta) = \begin{cases} \hat{V}_0, & 0 \leqslant |\theta| < 45°, \\ 0, & \text{elsewhere}, \end{cases} \tag{14}$$

where $\hat{V}_0$ is constant.

The acoustic pressure field generated by this partially vibrating sphere can be determined analytically (Morse and Ingard, 1986). Without loss of generality, the interior field acoustic pressures at nine points along an arc of radius $r = 0.8a$ from $\theta = 0°$ to 180° with an equal interval, $\Delta\theta = 22.5°$, are calculated. Setting the number of measurements M to that of the acoustic modes yields $J = 9$ and $N = \sqrt{J} - 1 = 2$. Accordingly, the radiated acoustic pressure can be written as the following expansion:

$$\rho c \sum_{j=0}^{9} C_{mj} \Psi_{mj}(\mathbf{x}_m) = \rho c \sum_{n=0}^{2} \sum_{l=-n}^{n} \tilde{C}_{nl} \tilde{\psi}_{nl}(\mathbf{x}_m) = \hat{p}_B(\mathbf{x}_m). \tag{15}$$

The unknown coefficients C_{mj} can be determined by solving a set of nine simultaneous algebraic equations. Once this is done, the acoustic pressure field can be calculated anywhere, including the surface of the partially vibrating sphere. Note that in carrying out the numerical computations, the spherical Hankel functions involved in the expansion functions $\tilde{\psi}_{nl}(\mathbf{x}_m)$ must be replaced by the spherical Bessel functions, so that the reconstructed acoustic pressures are finite at $r = 0$.

It is emphasized that no axisymmetry property is taken into account in the numerical computations using the HELS method. The computer codes developed are suitable for a general three-dimensional finite object. The reconstructed acoustic pressures thus obtained are compared with the analytic solutions. Results show that excellent agreements in both field and surface acoustic pressures are obtained for all ka values tested. For brevity, only the comparison of the reconstructed surface acoustic pressures and the analytic ones at $ka = 10$ is demonstrated (see Fig. 1).

The second example deals with sound radiation in the interior region of a partially vibrating cylinder of radius a and half-length b with two spherical endcaps. As in the first example, the normal component of the surface velocity is assumed specified over a portion of one endcap (with a vertex angle of $2\theta = 90°$), and is zero elsewhere [see Eq. (14)]. Ideally, one would select the prolate spheroidal or ellipsoidal coordinates for this cylinder, especially when the aspect ratio b/a becomes large. Burnett (1994) shows examples of using prolate spheroidal multipole expansion functions for acoustic radiation from elongated three-dimensional (submarinelike) objects. Use of such coordinates for slender objects would enhance computation efficiency because the number of expansion functions is greatly reduced. In this paper, the spherical Bessel functions are used for cylindrical surfaces with various half-lengths to radii aspect ratios b/a and dimensionless frequencies ka. The main reason for doing that is for convenience sake, because the spherical Bessel functions are readily available. This also allows one to examine

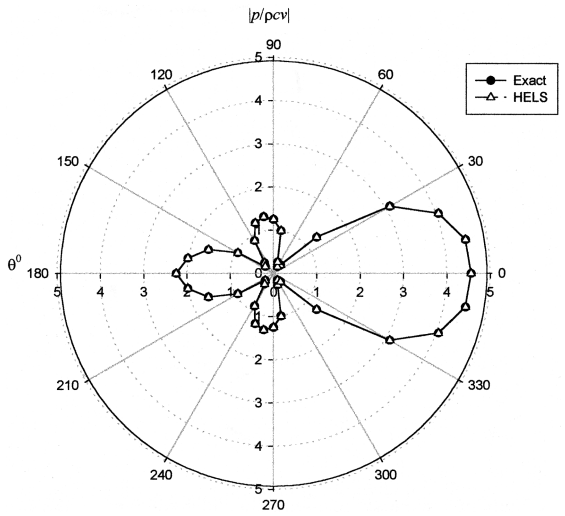

FIG. 1. Comparison of the reconstructed acoustic pressures on the interior surface of a partially vibrating sphere at $ka = 10$ and the analytic solutions.

the effectiveness of using the spherical Bessel functions to solve problems involving nonspherical surface, especially as the aspect ratio b/a and dimensionless frequency ka increase. Note that the partially vibrating sphere considered above is a special case of this cylinder with $b/a = 0$. Numerical results have shown that for a spherical surface, the reconstructed acoustic pressures are exact for all ka values. For a cylindrical surface, the accuracy of reconstruction is not only affected by the half-length to radius ratio b/a, but also by the dimensionless frequency ka. Since analytical solutions to the problems under consideration are not available, the results of Eq. (3) are validated against those of the standard BEM codes. It is emphasized here that both the BEM and HESL methods are programmed for general three-dimensional objects, thus no axisymmetry properties are taken into consideration.

The procedures of numerical validations are described as follows. First, the cylindrical surface is discretized into M_1 segments with a total of M_2 nodes. The acoustic pressures at these nodes are obtained by solving a set of M_2 simultaneous integral equations, based on the normal component of the surface velocity distribution given by Eq. (14). In carrying out the numerical integration, a nine-point Gaussian interpolation function is used for each element. Once the surface acoustic pressures are specified, the field acoustic pressures in the interior region are determined. As in the first example, the field pressures along an arc parallel to the generator of the cylindrical surface at a distance $0.1a$ are calculated, and the results are taken as the input to Eq. (3) to reconstruct the surface acoustic pressures. The reconstructed acoustic pressures are then compared with those of the BEM results.

To examine the effect of source elongation b/a and that of dimensionless frequency ka on the accuracy of reconstruction of the acoustic pressures, a relatively short cylinder, $b/a = 1$, at a lower frequency, $ka = 1$ is considered first. Note that in this case the input to Eq. (3) is not exact, hence the reconstructed acoustic pressures are approximate. In carrying out the numerical computations, the entire cylindrical surface is discretized into $M_1 = 464$ elements with a total of M_2

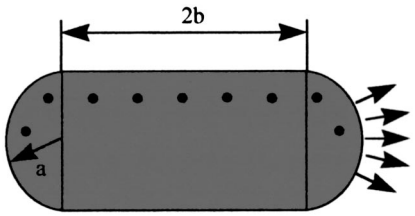

FIG. 2. Schematic of a partially vibrating cylinder of radius a and half-length b with two spherical endcaps. ●: measurement points.

$=1394$ nodes. Accordingly, the surface acoustic pressures are obtained by solving a set of 1394 simultaneous integral equations. Once the surface acoustic pressures are determined, the field pressures are calculated at 16 points along an arc parallel to the generator of the cylindrical surface at an equal interval (see Fig. 2). Setting the number of measurements to that of acoustic modes, $J=16$, leads to a three-term expansion $N=3$ in Eq. (15). Figure 3 demonstrates comparisons of the reconstructed magnitudes and phases of the dimensionless acoustic pressures and the BEM results along the generator of the cylindrical surface. Here S represents a dimensionless distance along the generator. In particular, $S=0$ corresponds to the center of the cylinder, $S=\pm 1$ to the joints where the cylinder and endcaps meet, and $S=\pm 2.5708$ to the centers of the endcaps (the vibrating surface is at the $S=2.5708$ end).

Figure 3 shows that by using the HELS method the acoustic pressures over the entire cylindrical surface can be accurately reconstructed with only 16 measurements inside the cavity. If the BEM-based Kirchhoff integral formulation is used, then one must take a comparable amount of acoustic pressure measurements as those of the discretized nodes on the surface. In this case, it would need more than 1000 measurements inside the cylinder, which would be impractical.

Note that the major effort in carrying out the above analysis is devoted to the generation of the surface acoustic

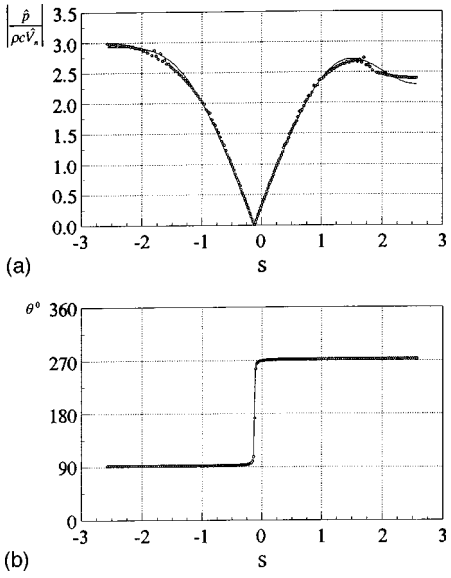

FIG. 3. Comparisons of the reconstructed acoustic pressures on the interior surface of a partially vibrating cylinder with two spherical endcaps at $b/a=1$ and $ka=1$. Solid line: HELS; ○: BEM. (a) Magnitudes; (b) phases.

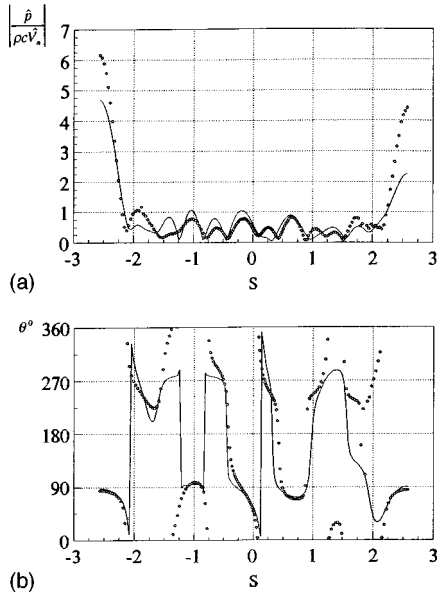

FIG. 4. Comparisons of the reconstructed acoustic pressures on the interior surface of a partially vibrating cylinder with two spherical endcaps at $b/a=1$ and $ka=10$. Solid line: HELS; ○: BEM. (a) Magnitudes; (b) phases.

pressures using the BEM codes. The time required for solving a set of 1000 or more simultaneous integral equation is in terms of hours on a Sun Spark Station 10. On the other hand, reconstruction of acoustic pressures using the HELS method with 16 acoustic modes takes less than 1 minute on the same workstation. Therefore the savings in computational time and effort can be very significant.

Now the effectiveness of the HELS method is examined for longer cylinders subject to higher frequency excitations. First, the dimensionless frequency ka is increased to 10, while the aspect ratio remains the same at $b/a=1$. To ensure a convergence of numerical solutions, the number of acoustic modes in Eq. (3) is increased to $J=36$, which is equivalent to taking 36 field acoustic pressure measurements inside the cylindrical cavity. Ideally, the numbers of the discretized segments and nodes on the cylindrical surface should also be increased, because the frequency is increased tenfold. To reduce the computational time, however, the same values of $M_1=464$ and $M_2=1394$ are used. The number of expansion terms in Eq. (15) becomes $N=5$.

Following the same procedures as described above, the surface acoustic pressures are reconstructed and compared with the BEM results along the generator of the cylindrical surface. Figure 4 shows that good agreement is obtained in general for both magnitudes and phases of the surface acoustic pressures. Some discrepancies in the magnitudes and phases around the centers of two endcaps are noted, however. They are caused by: (1) deterioration of the convergence of the spherical Bessel functions at high frequencies; and (2) numerical errors in the input to the HELS method and those in the benchmark surface acoustic pressures generated by the BEM codes. These discrepancies can be reduced by increasing the number of expansion terms in the HELS method, and the numbers of discretized segments and nodes on the cylindrical surface in generating the field and surface acoustic pressures using the BEM codes.

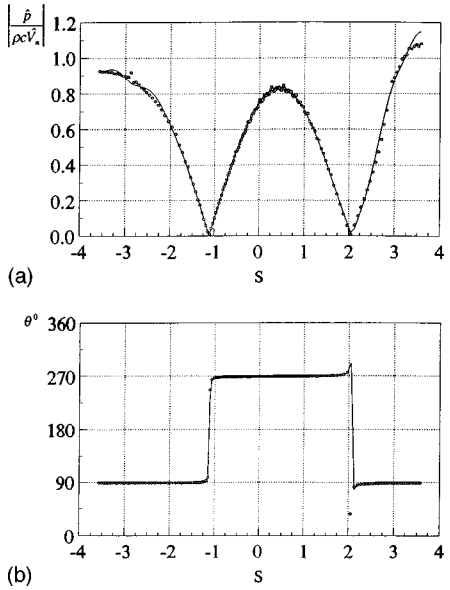

FIG. 5. Comparisons of the reconstructed acoustic pressures on the interior surface of a partially vibrating cylinder with two spherical endcaps at $b/a=2$ and $ka=1$. Solid line: HELS; ○: BEM. (a) Magnitudes; (b) phases.

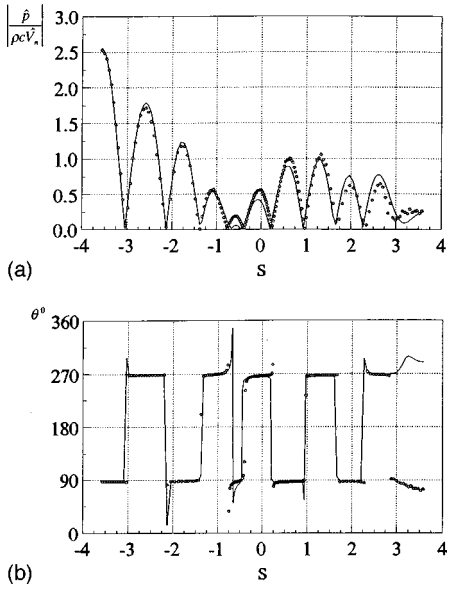

FIG. 6. Comparisons of the reconstructed acoustic pressures on the interior surface of a partially vibrating cylinder with two spherical endcaps at $b/a=2$ and $ka=5$. Solid line: HELS; ○: BEM. (a) Magnitudes; (b) phases.

Next, a longer cylinder of $b/a=2$ subject to a harmonic excitation at $ka=1$ is considered. Since the cylinder length is doubled, the discretized segments on the cylindrical surface are increased to $M_1=692$ with a total number of nodes $M_2=1898$. As before, 16 field measurements or 16 acoustic modes and 3 expansion terms are selected to reconstruct the acoustic pressure field. Comparisons of the reconstructed magnitudes and phases of the surface acoustic pressures and the BEM results are illustrated in Fig. 5. The agreement is almost perfect.

Now the dimensionless frequency is increased to $ka=5$ with the aspect ratio kept at $b/a=2$. Accordingly, the number of measurements or that of acoustic modes is increased to $J=25$, and the number of expansion terms in Eq. (15) becomes $N=4$. Once again, the numbers of discretized segments and nodes on the entire cylindrical surface remain unchanged to reduce the computational time. Figure 6 displays the comparisons of the reconstructed magnitudes and phases of the surface acoustic pressures with the BEM results. The agreements are quite satisfactory, except the phases over a portion of the vibrating endcap from $S=2.8$ to 3.57. The accuracy deteriorates, however, as the dimensionless frequency rises to $ka=10$ with $M_1=692$ and $M_2=1898$. The corresponding discrepancies in the magnitudes and phases between the reconstructed surface acoustic pressures and the BEM results are about the same as those shown in Fig. 4. Increasing the values of N, M_1, and M_2 can reduce these discrepancies. The corresponding plots are omitted here for brevity.

Finally, a relatively long cylinder is considered, which has a half-length to radius ratio $b/a=3$, a typical size cylinder in engineering practice. The cylindrical surface is discretized into $M_1=800$ segments with a total of $M_2=1898$ nodes. As before, the case of $ka=1$ is considered first, and 16 samples are taken along an arc parallel to the generator of the cylindrical surface. Accordingly, 16 acoustic modes or a three-term expansion are used in Eq. (15). Figure 7 exhibits the comparisons of the reconstructed magnitudes and phases of the surface acoustic pressures and the BEM results. These results demonstrate that the spherical Bessel functions can be used to acquire good results even for a relatively long cylinder. The accuracy of reconstruction becomes worse at high frequencies, as expected. Figure 8 displays the comparisons of the reconstructed surface acoustic pressures and the BEM results at $ka=10$ under $M_1=800$ and $M_2=1898$. The corresponding number of acoustic modes and that of expansion terms are $J=36$ and $N=5$, respectively. Results show that there are discrepancies in the magnitudes of the surface acoustic pressures. The agreements in phases, however, are much better.

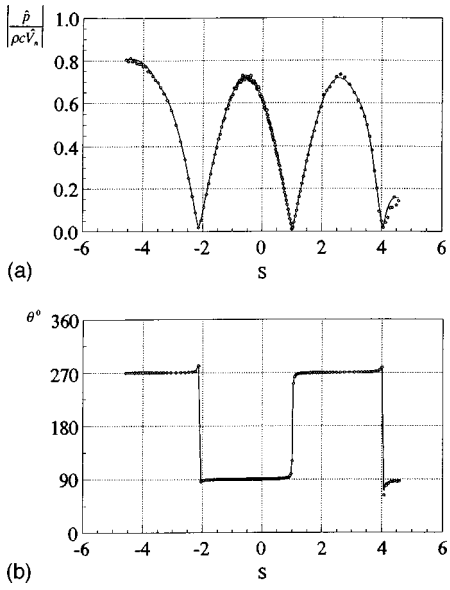

FIG. 7. Comparisons of the reconstructed acoustic pressures on the interior surface of a partially vibrating cylinder with two spherical endcaps at $b/a=3$ and $ka=1$. Solid line: HELS; ○: BEM. (a) Magnitudes; (b) phases.

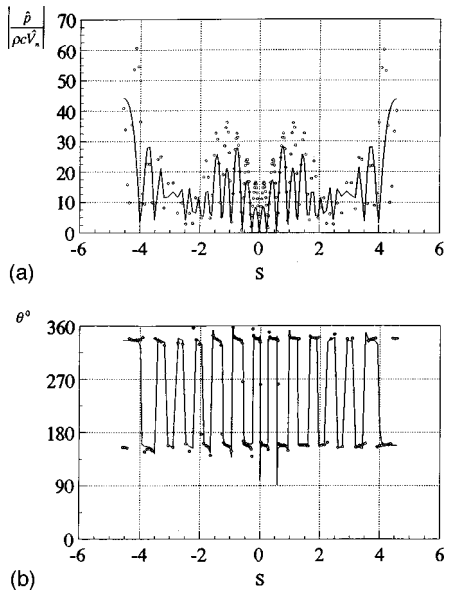

FIG. 8. Comparisons of the reconstructed acoustic pressures on the interior surface of a partially vibrating cylinder with two spherical endcaps at $b/a=3$ and $ka=10$. Solid line: HELS; ○: BEM. (a) Magnitudes; (b) phases.

These examples show that the spherical functions can be extended to reconstruction of the acoustic pressure fields generated by nonspherical sources. Needless to say, selection of the prolate and oblate spheroidal functions or ellipsoidal functions will require a lower number of acoustic modes to approximate the radiated acoustic pressure fields. Nonetheless, working with wave functions in nonspherical coordinate systems may not yet be practical from a computational efficiency standpoint. For the cases tested, the accuracy of reconstruction seems to be affected more by frequency than by elongation of an object. This is because the convergence of the expansion functions deteriorates at high frequencies, a difficulty inherent in all expansion theories, regardless of the types of coordinate systems employed. Under this condition, more expansion terms, or equivalently, more samples must be taken in the field. This high frequency difficulty also exists in BEM. To guarantee certain accuracy, one must increase accordingly the numbers of the discretized segments and nodes, which makes the BEM numerical computations even more time consuming.

IV. CONCLUDING REMARKS

The HELS method can be extended to reconstruction of acoustic pressure fields inside the cavity of a vibrating object. In particular, numerical examples demonstrate that the spherical Bessel functions can be used to reconstruct satisfactorily the interior acoustic pressure fields resulting from nonspherical or elongated vibrating objects. Unlike STSF, the HELS method enables one to reconstruct the acoustic pressures over the entire surface of a vibrating object. Also, the number of measurements taken in the field necessary to carry out reconstruction is much smaller than that of the BEM-based Kirchhoff integral formulation, which makes the HELS method very effective and attractive. Numerical results indicate that the accuracy of reconstruction of the acoustic pressures is affected more by the excitation frequency than by the elongation of a vibrating object. This is because the convergence of the expansion functions deteriorates at high frequencies. This high frequency difficulty is inherent in all expansion theories, regardless of the types of coordinate systems employed. The same difficulty also exists in the BEM-based integral formulation, for which more discretized segments and nodes must be used. This makes the numerical computations in BEM even more time consuming. Therefore other more effective approaches must be taken for handling high frequency problems.

Bai, M. R. (**1992**). ''Application of BEM (boundary element method)-based acoustic holography to radiation analysis of sound sources with arbitrarily shaped geometries,'' J. Acoust. Soc. Am. **92**, 533–549.

Bergman, S. (**1960**). *Integral Operators in the Theory of Linear Partial Differential Equations* (Springer-Verlag, Berlin), pp. 66–67.

Bruel & Kjaer Technical Review, No. 1 (**1995**).

Burnett, D. S. (**1994**). ''A three-dimensional acoustic infinite element based on a prolate spheroidal multipole expansion,'' J. Acoust. Soc. Am. **96**, 2798–2816.

Ciskowski, R. D., and Brebbia, C. A. (**1991**). *Boundary Element Methods in Acoustics* (Computational Mechanics Publications, Southampton, Boston; Elsevier Applied Science, London).

Davis, P. J., and Rabinowitz, P. (**1961**). ''Advances in orthonormalizing computation,'' *Advances in Computers*, edited by F. L. Alz *et al.* (Academic, New York), Vol. 2, pp. 55–133.

Gardner, B. K., and Bernhard, R. J. (**1988**). ''A noise source identification technique using an inverse Helmholtz integral equation method,'' Trans. ASME, J. Vib. Acoust. Stress and Reliability in Design **110**, 84–90.

Hunt, J. T., Knittel, M. R., and Barach, D. (**1974**). ''Finite element approach to acoustic radiation from elastic structures,'' J. Acoust. Soc. Am. **55**, 269–280.

Kim, G.-T., and Lee, B.-T. (**1990**). ''3-D sound source reconstruction and field reproduction using the Helmholtz integral equation,'' J. Sound Vib. **136**, 245–261.

Maynard, J. D., Williams, E. G., and Lee., Y. (**1985**). ''Nearfield acoustic holography: I. Theory of generalized holography and the development of NAH,'' J. Acoust. Soc. Am. **78**, 1395–1413.

Morse, P. M., and Ingard, K. U. (**1986**). *Theoretical Acoustics* (Princeton U.P., Princeton, NJ), pp. 337–338.

Pinsky, M. A. (**1991**). *Partial Differential Equations and Boundary-Value Problems with Applications* (McGraw-Hill, New York), pp. 18.

Schenck, H. A. (**1968**). ''Improved integral formulation for acoustic radiation problems,'' J. Acoust. Soc. Am. **44**, 41–58.

Stewart, G. W. (**1973**). *Introduction to Matrix Computations* (Academic, New York), pp. 184–230.

Vekua, I. N. (**1953**). ''On completeness of a system of metaharmonic functions,'' Dokl. Akad. Nauk SSSR **90**, 715–718.

Veronesi, W. A., and Maynard, J. D. (**1987**). ''Near field acoustic holography (NAH): II. Holographic reconstruction algorithms and computer implementation,'' J. Acoust. Soc. Am. **81**, 1307–1322.

Veronesi, W. A., and Maynard, J. D. (**1989**). ''Digital holographic reconstruction of sources with arbitrarily shaped surfaces,'' J. Acoust. Soc. Am. **85**, 588–598.

Wang, Z., and Wu, S. F. (**1997**). ''Helmholtz equation-least squares (HELS) method for reconstructing the acoustic pressure field,'' J. Acoust. Soc. Am. **102**, 2020–2032.

Wang, Z., Wu, S. F., and Su, S. (**1995**). ''An innovation in inverse acoustic radiation problems,'' in *Target Identification and Inverse Problems in Acoustics*, edited by R. J. Nagem, G. C. Gaunaurd, and M. C. Hastings, Proceedings of the ASME Noise Control and Acoustics Division, NCA-Vol. 21, pp. 127–136.

Williams, E. G., Maynard, J. D., and Skudrzyk, E. (**1980**). ''Sound source reconstruction using a microphone array,'' J. Acoust. Soc. Am. **68**, 340–344.

Wu, S. F., and Wang, Z. (**1998**). ''Noise diagnostic system,'' U.S. Patent No. 5,712,805 (27 January 1998).

Modeling of pulsed finite-amplitude focused sound beams in time domain

Jahangir Tavakkoli,[a] Dominique Cathignol, and Rémi Souchon
INSERM—Unité 281, 151 Cours Albert Thomas, 69424 Lyon Cedex 03, France

Oleg A. Sapozhnikov
Department of Acoustics, Physics Faculty, Moscow State University, Moscow 119899, Russia

(Received 10 June 1997; revised 11 June 1998; accepted 23 June 1998)

A time-domain numerical model is presented for simulating the finite-amplitude focused acoustic pulse propagation in a dissipative and nonlinear medium with a symmetrical source geometry. In this method, the main effects responsible in finite-amplitude wave propagation, i.e., diffraction, nonlinearity, and absorption, are taken into account. These effects are treated independently using the method of fractional steps with a second-order operator-splitting algorithm. In this method, the acoustic beam propagates, plane-by-plane, from the surface of a highly focused radiator up to its focus. The results of calculations in an ideal (linear and nondissipative) medium show the validity of the model for simulating the effect of diffraction in highly focused pulse propagation. For real media, very good agreement was obtained in the shape of the theoretical and experimental pressure-time waveforms. A discrepancy in the amplitudes was observed with a maximum of around 20%, which can be explained by existing sources of error in our measurements and on the assumptions inherent in our theoretical model. The model has certain advantages over other time-domain methods previously reported in that it: (1) allows for arbitrary absorption and dispersion, and (2) makes use of full diffraction formulation. The latter point is particularly important for studying intense sources with high focusing gains. [S0001-4966(98)02810-0]

PACS numbers: 43.25.Jh [MAB]

INTRODUCTION

Advances in the development of acoustic microscopes,[1] high intensity focused ultrasound surgery,[2] lithotripsy, and cavitation-induced tissue destruction[3] have generated renewed concern about finite-amplitude effects in focused sound beams. Each system is capable of transmitting focused sound that is strongly affected by the combined influence of nonlinearity, absorption, and diffraction. Existing analytical solutions fail to adequately describe these sound fields, and only recently have numerical solutions been developed that model the radiation of focused finite-amplitude sound from practical sources.

A series of theoretical models for studying the focusing of intensive acoustic waves has been developed during the last two decades. A model which seems to be best suited to the study of moderately focused acoustic beams and which accounts for diffraction, nonlinearity, and absorption is based on the Khokhlov–Zabolotskaya–Kuznetsov (KZK) parabolic equation.[4,5] In the original KZK equation, the effect of absorption is modeled by incorporating viscous and thermal conductivity losses, in which the absorption coefficient is assumed to be proportional to the square of frequency. However, such an assumption is not appropriate to most biological tissues which exhibit a nearly linear frequency dependence. Concerning the diffraction effect, the KZK model uses a so-called parabolic or quasi-optical approximation, which means that the angular spectrum is supposed to be narrow or, in other words, the wave is very close to a plane wave. This is not the case for strongly focused beams or for beams with strong irregularities in the transverse structure, e.g., near the edges or at the focal point of a focused source. This limits the validity of the model to the cases in which diffraction effects are relatively weak and focusing gains are relatively low. In general, the KZK equation is an accurate model of the sound field produced by directional sound sources ($ka \gg 1$, where k is the wave number and a the radius of the source) at distances beyond a few source radii and in the paraxial region. A complete discussion of the domain of validity of the KZK equation for plane and focused sources is provided in Refs. 6 and 7.

A number of computer algorithms has been proposed to solve the KZK equation numerically. One of the most popular algorithms for solving the KZK equation is a frequency-domain technique, called the spectral method, introduced by Aanonsen[8] and co-workers.[9] Most studies, based on the spectral method, focused initially on monochromatic waves or on tone bursts. However, in many biomedical applications the acoustic wave consists of a small number of cycles or even has the form of a single cycle. If, additionally, shock fronts are developed because of nonlinearity, the numerical analysis requires large amounts of computer time. The situation becomes even more complex if the absorption is frequency dependent and the beam is strongly focused.

To partially overcome these problems, Lee and Hamilton[10] developed a time-domain algorithm for solving the KZK equation. A marching scheme, based on the

[a]Current address: Institute of Biomedical Eng., University of Toronto, 4 Taddle Creek Road, Toronto, Ontario M5S 3G9, Canada.

operator-splitting method,[11,12] was used as the basis for the algorithm. In this technique, as the code marches along, at each step it takes separate account of nonlinear distortion, absorption, dispersion, diffraction, and any other effects. Cleveland *et al.*[13] used this algorithm to solve an augmented KZK equation that accounts for nonlinearity, thermoviscous absorption, relaxation, and diffraction in directive sound beams. Moreover, Averkiou and Hamilton[14] have recently presented new results of this time-domain model for the case of short pulses radiated by plane and focused circular pistons. Within the limits of the KZK model, they obtained very good agreement between their simulations and experiments.

In a related work, again based on the operator-splitting method, Cleveland *et al.*[15] presented a comparison of several time and frequency-domain codes for the propagation of sonic booms through idealized atmosphere. The main effects considered in these codes were nonlinearity, absorption, and dispersion.

A model of nonlinear diffractive field propagation, not based on the KZK equation, was developed by Christopher and Parker.[16] In this model, using an operator-splitting method, they solved the equations of diffraction and absorption in the frequency domain and the equation of nonlinearity in the time domain. This model has advantages over the KZK model in that it accounts for full diffraction and arbitrary absorption effects. Using a modified version of this model, Christopher[17] presented the modeling of an electrohydraulic, extracorporeal shock wave lithotripter as an example of an intense highly focused sound source.

On the other hand, the effect of acoustic nonlinearity on the focused beam can be predicted on the basis of simpler theoretical approaches. We have already proposed a simple model that makes it possible to study the focusing of an intense pulse on the basis of the spherical wave theory.[18] In this model, the focusing is associated with wave propagation along a rigid-wall tube. The dependence of the tube cross section on distance is chosen in such a way that the peak pulse pressure in the tube coincides with the peak pressure calculated by the Rayleigh diffraction integral in the linear regime. The nonlinear wave propagation along the tube is then described on the basis of a Burgers-type equation. Of course, such a simple model suffers from the same limitations as nonlinear spherical wave theory and is not accurate enough, especially in the focal region of a high-amplitude focused source. For this reason, we present another, more complete, model. As with the approach used by Christopher, our model accounts for full diffraction and arbitrary absorption effects. A second-order operator-splitting algorithm is used to solve a set of equations that account for the effects of diffraction, absorption, and nonlinearity. To avoid numerical errors associated with the transformations between the time and frequency domains, a pure time-domain approach has been adopted.[15] The basic theoretical approach and the results obtained are presented below. The model was used for simulating the pressure field of a highly focused source developed for tissue destruction studies.[19]

I. BASIC EQUATIONS

In general wave theory, differential equations of the evolution type are widely used to describe the propagation process:

$$\frac{\partial v(\tau,z)}{\partial z} \equiv \hat{L} \cdot v, \tag{1}$$

where v is the particle velocity, z is the coordinate in the direction of wave propagation, $\tau = t - z/c_0$ is retarded time, c_0 is the wave speed, and the operator $\hat{L}$ accounts for the effects changing the waveform. If $\hat{L} \cdot v = 0$, we have $v = F(\tau)$, i.e., the waveform does not change during propagation, which is the case of a plane wave traveling in an ideal linear medium. In reality, the waveform is distorted due to different effects. Consider, for instance, the equation for a linear plane acoustic wave propagating in a thermoviscous medium:[20]

$$\frac{\partial v}{\partial z} = \frac{b}{2\rho_0 c_0^3} \frac{\partial^2 v}{\partial \tau^2}, \tag{2}$$

where b is the dissipative coefficient of the medium and ρ_0 is the ambient density. In many practical situations, e.g., in biological tissues, the attenuation operator differs from that of Eq. (2). It can be written in the general form:[21]

$$\frac{\partial v}{\partial z} = \int_{-\infty}^{\tau} K(z, \tau - \tau') \cdot v(z, \tau') d\tau' \equiv \hat{L}_A \cdot v, \tag{3}$$

where the kernel K can be evaluated from the frequency dependence of the attenuation. The upper limit of the integral accounts for causality.

Another example is the evolution equation for a plane wave propagating in a lossless quadratically nonlinear medium:

$$\frac{\partial v}{\partial z} = \frac{\beta}{c_0^2} v \frac{\partial v}{\partial \tau} \equiv \hat{L}_N \cdot v, \tag{4}$$

where β is the coefficient of nonlinearity of the medium.

The third example is the so-called parabolic equation, describing diffraction of acoustical beams in linear lossless medium:

$$\frac{\partial v}{\partial z} = \frac{c_0}{2} \nabla_\perp^2 \int_{-\infty}^{\tau} v \, d\tau', \tag{5}$$

where z is the distance along the beam axis, $\nabla_\perp^2$ is a two-dimensional transverse Laplacian, and v is the axial component of particle velocity. Equation (5) describes the effect of diffraction properly only if the wave angular spectrum is narrow (quasi-plane wave). A more exact, wider-angle parabolic evolution equation was proposed by Hill.[22] On the other hand, the diffraction effect can be described by the Rayleigh integral over the initial source surface.[23] It is known that the Rayleigh integral presents an exact solution of the diffraction problem for the case of a plane surface. When the surface is curved, the integral gives an approximate, but fairly accurate solution.[24,25] Let us denote the corresponding diffraction operator as $\hat{L}_D$ and write a general form of the evolution equation for diffraction:

$$\frac{\partial v}{\partial z}=\hat{L}_D\cdot v. \tag{6}$$

In all of the above examples, each evolution equation is associated with only one effect. In the presence of multiple effects, if each is fairly weak, the evolution equation can be derived simply by summing the corresponding operators from the ''one-effect equations'':

$$\frac{\partial v}{\partial z}=\sum_{i=1}^{N}\hat{L}_i\cdot v. \tag{7}$$

For example, the combination of Eqs. (2) and (4) gives the Burgers equation and the combination of Eqs. (2), (4), and (5) results in the KZK equation. A more exact result than the KZK equation, accounting for the absorption and diffraction effects, is possible on the basis of combining Eqs. (3), (4), and (6). We write this combined equation in a general form:

$$\frac{\partial v}{\partial z}=\hat{L}\cdot v\equiv\hat{L}_A\cdot v+\hat{L}_N\cdot v+\hat{L}_D\cdot v, \tag{8}$$

which will be used for the development of our model for finite-amplitude acoustic pulse focusing. Note that $\hat{L}$ is a fairly complex integro-differential operator. One of the possible ways of solving it numerically is the use of the method of fractional steps with an operator-splitting procedure.[11,12] According to this method, the solution of the Eq. (8) at each step Δz is obtained on the basis of separate solutions of Eqs. (3), (4), and (6). This is why we will first consider each of these equations separately.

II. SOLVING THE ABSORPTION EQUATION

A. Minimum-phase digital filter model for absorption and dispersion

Here, a causal FIR (finite impulse response) digital filter for simulating the effects of frequency-dependent absorption and dispersion is presented. Let us consider Eq. (3) as accounting for dispersion and frequency-dependent absorption. After passing through the layer Δz, each spectral component $e^{i\omega\tau}$ changes its amplitude by a factor:

$$G_a(\Delta z,\omega)=\exp\{-\alpha(\omega)\cdot\Delta z+i\omega[c^{-1}(\omega)-c_0^{-1}]\cdot\Delta z\}, \tag{9}$$

where i is the imaginary unit, $c(\omega)$ is sound speed, $\alpha(\omega)$ is the absorption coefficient of the medium, and $\omega=2\pi f$ is angular frequency. The waveform v at distance $z+\Delta z$ can be evaluated from the waveform at distance z by a convolution integral:

$$v(z+\Delta z,\tau)=\int_{-\infty}^{+\infty}v(z,\tau')\cdot g(\Delta z,\tau-\tau')d\tau', \tag{10}$$

where the impulse response g is an inverse Fourier transform of the factor G_a:

$$g(\Delta z,\tau)=\frac{1}{2\pi}\int_{-\infty}^{+\infty}G_a(\Delta z,\omega)e^{i\omega\tau}\,d\omega. \tag{11}$$

The discrete analogy of the convolution integral (10) has the form of a convolution sum:

$$v_n(z+\Delta z)=\sum_{k=-\infty}^{+\infty}v_k(z)\cdot g_{n-k}(\Delta z), \tag{12}$$

where $v_n(z)=v(z,nT)$, $g_n(\Delta z)=T\cdot g(\Delta z,nT)$, and T is a uniform time-sampling period. In discrete regime, the Fourier integral (11) transforms to:

$$g_n(\Delta z)=\frac{1}{2\pi}\int_{-\pi}^{\pi}G(e^{i\Omega})e^{i\Omega n}\,d\Omega, \tag{13}$$

where

$$G(e^{i\Omega})=\frac{1}{T}\sum_{k=-\infty}^{+\infty}G_a\left(\Delta z,\frac{\Omega+2\pi k}{T}\right)$$

is a periodic function with a period of 2π, associated with the frequency response.[26] Supposing that $G_a=0$ for $\omega>2\pi/T$, we can therefore use within the interval $-\pi\leqslant\Omega\leqslant\pi$:

$$G(e^{i\Omega})=\frac{1}{T}G_a\left(\Delta z,\omega=\frac{\Omega}{T}\right). \tag{14}$$

The complex function $G(e^{i\Omega})$ can be considered to be a transfer function of a digital attenuater filter. Taking causality into account, the argument of $G(e^{i\Omega})$ is related to its magnitude by the minimum-phase condition. It is well known that for a minimum-phase filter, the log-magnitude and phase characteristics form a Hilbert transform pair.[26] Using the discrete-time Hilbert transform, the phase of the filter is equal to:

$$\arg[G(e^{i\Omega})]=\frac{1}{2\pi}P\int_{-\pi}^{\pi}\ln|G(e^{i\theta})|\cdot\cot\left(\frac{\theta-\Omega}{2}\right)d\theta, \tag{15}$$

where the symbol P denotes the Cauchy principal value of the integral. It is to be noted that as $T\to 0$, Eq. (15) transforms into the Kramers–Kronig relation between the attenuation coefficient and phase velocity.[27] Integral (15) can be rewritten in the following form:

$$\arg[G(e^{i\Omega})]=-\frac{1}{\pi}\int_0^{\pi}\frac{d[\ln|G(e^{i\theta})|]}{d\theta}\cdot\ln\left|\frac{\sin[(\theta+\Omega)/2]}{\sin[(\theta-\Omega)/2]}\right|d\theta. \tag{16}$$

The logarithmic singularity here does not need the Cauchy principal value integration. Using Eq. (16), it is possible to obtain the unit-sample response of the attenuater filter based only on the frequency dependence of the absorption coefficient $\alpha(\omega)$. Indeed, according to Eq. (14):

$$|G(e^{i\Omega})|=\frac{1}{T}\exp[-\alpha(\Omega/T)\cdot\Delta z]. \tag{17}$$

According to Eq. (16), the argument of G is also related to the function $\alpha(\omega)$:

$$\arg[G(e^{i\Omega})]=\frac{\Delta z}{\pi T}\int_0^{\pi}\dot{\alpha}(\theta/T)\cdot\ln\left|\frac{\sin[(\theta+\Omega)/2]}{\sin[(\theta-\Omega)/2]}\right|d\theta, \tag{18}$$

where $\dot{\alpha}(\omega)=d\alpha/d\omega$. Equations (17) and (18) give the complex function $G(e^{i\Omega})$. Based on this, the unit-sample response can be calculated from Eq. (13). The waveform after passing the layer Δz can be calculated from the convolution sum of Eq. (12). As the unit-sample response is a causal sequence, this sum is started from $k=0$.

To minimize the numerical errors induced by the FFT operations,[15] we chose to apply absorption by means of a convolution with an FIR filter in the time domain. For a waveform with M samples, the computation time for a convolution operation is proportional to M^2, whereas the time for an FFT operation is proportional to $M\cdot\log M$ (if M is not an integer power of 2, the computation time for an FFT operation is slightly higher). However, the absorption calculation takes up only a small portion of the total computation time in our algorithm (more than 80% of the total computation time is for the diffraction calculation). Using convolution for the absorption calculation does not, therefore, have a major influence on the total computation time.

B. Acoustic absorption in biological tissue

The acoustic absorption coefficient of soft tissue, when expressed in logarithmic units such as dB/cm, has been observed to increase approximately linearly with frequency. In order to simulate this absorption characteristic on a digital computer, a minimum-phase digital filter model was developed in Sec. II A. It has been argued that this filter model is appropriate for describing a physical medium exhibiting a linear-with-frequency absorption such as soft tissues.[28,29] Let the absorption coefficient of the medium, denoted by $\alpha(f)$, be a linear function of frequency (in MHz) with slope α_0:

$$\alpha(f)=\alpha_0\cdot f \quad \text{dB/cm}. \tag{19}$$

The log-magnitude transfer function of the attenuater filter for a Δz cm thick section of the medium, denoted by $L(f)$, is equal to

$$L(f)=-\alpha(f)\cdot\Delta z=-\alpha_0\cdot f\cdot\Delta z \quad \text{dB}. \tag{20}$$

The resulting magnitude function, denoted by $|G(f)|$, is then equal to

$$|G(f)|=10^{L(f)/20}=10^{-\alpha_0 f\Delta z/20}. \tag{21}$$

Now, using this magnitude function in Eq. (16) results in the phase function, and consequently, the complex transfer function of the minimum-phase filter:

$$G(f)=|G(f)|\cdot\exp\{i\cdot\arg[G(f)]\}. \tag{22}$$

The unit-sample response of the filter which is used for the convolution sum is equal to the real component of the inverse Fourier transform obtained from Eq. (13). Note that the imaginary component should be zero for a physical filter.

An example of implementation of this filter for simulating the absorption of acoustic pulses in liver tissue is shown in Fig. 1. In this example, the coefficient of absorption in the liver, α_0, was set equal to 0.5 dB $\text{cm}^{-1}\,\text{MHz}^{-1}$, and the distance Δz to 5 cm. Figure 1(a) and (b) shows the magnitude of the filter transfer function in linear and in logarithmic units respectively, and Fig. 1(c) shows its phase obtained from the Hilbert transform. The unit-sample response of the filter is shown in Fig. 1(d). Verification of the results obtained by applying this filter to a monochromatic sinusoidal wave demonstrated that it is possible to simulate exactly the frequency-dependent absorption of biological tissues.[28,30]

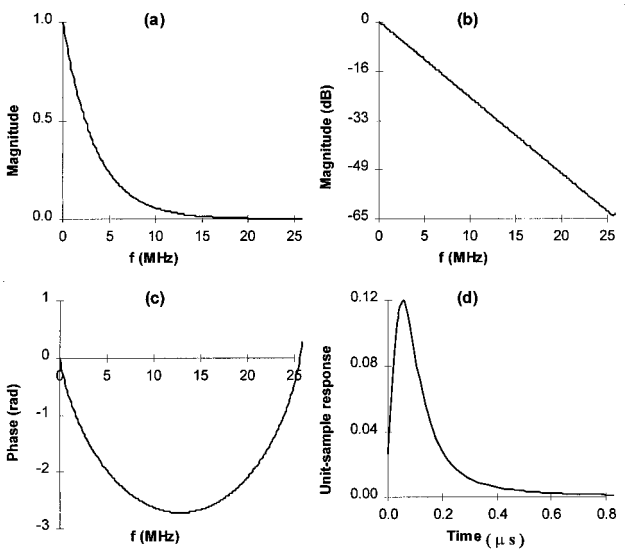

FIG. 1. Characteristics of the minimum-phase digital filter with $\alpha_0=0.5$ dB $\text{cm}^{-1}\,\text{MHz}^{-1}$ and $\Delta z=5$ cm. (a) Magnitude of the filter transfer function; (b) log magnitude of the filter; (c) phase of the filter obtained from Hilbert transform; (d) unit-sample response of the filter.

III. SOLVING THE NONLINEARITY EQUATION

The Eq. (4) for a nonlinear medium has an analytical solution, called the Poisson or the Earnshaw solution. This solution, with a second-order approximation, can be written as (see, e.g., Ref. 31, Chap. 4):

$$v(z,\tau)=\Psi(\tau+\beta v z/c_0^2), \tag{23}$$

where $\Psi(t)$ is the waveform at $z=0$. To describe the nonlinearly induced wave distortion during its propagation from z to $z+\Delta z$, this solution may be rewritten as:

$$v(z+\Delta z,\tau)=v\left\{z,\tau+\frac{\beta\Delta z}{c_0^2}\,v(z,\tau)\right\}. \tag{24}$$

Multivalued solutions are avoided if

$$\Delta z<\frac{c_0^2/\beta}{\max(\partial v/\partial\tau)}. \tag{25}$$

Solution (24) can also be easily obtained using the nonlinear theory of acoustic waves.[32] The nonlinearity equation (4) can be solved in discrete regime via a time-base transformation on the basis of Eq. (24):

$$\tau_m^{n+1}=\tau_m^n-\frac{\beta\Delta z_n}{c_0^2}\cdot v_m^n, \tag{26}$$

where m marks the mth sample of the temporal waveform and n denotes the nth step Δz_n in z. The discrete analogy of the inequality (25) has a form of:

$$\Delta z_n<T\cdot\frac{c_0^2/\beta}{\max(v_m^n-v_{m-1}^n)}, \tag{27}$$

where $T=\tau_m^n-\tau_{m-1}^n$. After calculating of τ_m^{n+1}, linear interpolation is used to resample the waveform and thus reestablish a uniform time sample spacing T.[33]

The necessary condition for avoiding multivalued solutions requires a trade-off between the maximum of particle velocity variation and the propagation length Δz. It means that as the degree of wave distortion increases during its propagation in the medium, smaller distances are needed. To fulfill this requirement a nonuniform plane spacing was adopted in our model. Detailed description of the grid generation is presented in Sec. V.

IV. SOLVING THE DIFFRACTION EQUATION

From the classical theory of sound for a linear and nondissipative medium, the instantaneous pressure $p(\mathbf{r},t)$ and particle velocity $v(\mathbf{r},t)$ at a point $P(\mathbf{r})$ and time t in the field of an ultrasound source can be expressed as:[23]

$$p(\mathbf{r},t)=\rho\,\frac{\partial\phi}{\partial t}\,(\mathbf{r},t), \tag{28}$$

$$v(\mathbf{r},t)=-\nabla\phi(\mathbf{r},t), \tag{29}$$

where ρ is the equilibrium density of the surrounding medium,

$$\nabla=\frac{\partial}{\partial x}\,\mathbf{i}+\frac{\partial}{\partial y}\,\mathbf{j}+\frac{\partial}{\partial z}\,\mathbf{k}$$

is the gradient operator, and $\phi(\mathbf{r},t)$ denotes the velocity potential.

For the case of a uniformly excited planar radiator of area S in an infinite rigid baffle, $\phi(\mathbf{r},t)$ is given by the Rayleigh integral:

$$\phi(\mathbf{r},t)=\frac{1}{2\pi}\int\int_S\frac{v_0(t-r'/c_0)}{r'}\,ds, \tag{30}$$

where $v_0(t)$ is the instantaneous normal particle velocity at the source and r' is the distance between the observation point P and the surface element ds at the source.

When the shape of the source is not plane, but convex or concave, the wave radiated by the source is diffracted by its own surface. This secondary radiation contributes theoretically to the pressure field but is not taken into account by Eq. (30). However, this equation can be used as an excellent approximation for most practical applications, where the diameter of the source is large compared to the ultrasound wavelength, and the source is only slightly curved.[24,25] Under these conditions, for a spherical focused source, the Rayleigh integral has to be evaluated over the spherical concave surface of the source. The geometry used for applying the Rayleigh integral is shown in Fig. 2 with the origin of coordinates at the focal point of the source. Let point P belongs to a planar intermediate surface that is normal to the z axis. Based on Eq. (30) for the Rayleigh integral, we can calculate the velocity potential at each point on this plane. Then, using Eqs. (28) and (29), the values of pressure and particle velocity can be calculated for each point.

Further, for implementing our fractional-step method, we need the value of normal particle velocity at each point of the intermediate plane. Based on Eqs. (29) and (30) we can derive the Rayleigh integral for normal particle velocity v_n at point P of the observing plane as follows:

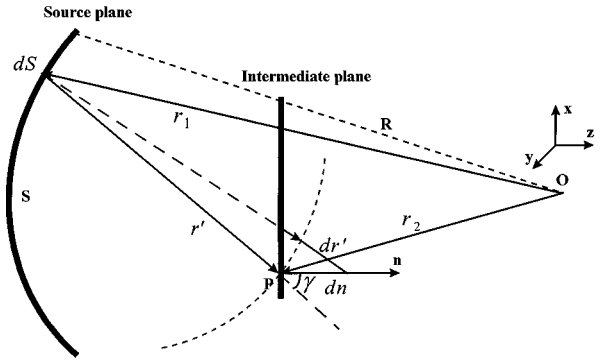

FIG. 2. Focused sound geometry used for calculation of the Rayleigh diffraction integral.

$$\begin{aligned}
v_n(\mathbf{r}_2,t)&=-\frac{\partial\phi}{\partial n}\\
&=-\frac{1}{2\pi}\int\int_S\frac{\partial}{\partial n}\left[\frac{1}{r'}\cdot v_n\left(\mathbf{r}_1,t-\frac{r'}{c_0}\right)\right]ds\\
&=-\frac{1}{2\pi}\int\int_S\left[\left(\frac{1}{r'}\right)\cdot\frac{\partial}{\partial t}\,v_n\left(\mathbf{r}_1,t-\frac{r'}{c_0}\right)\right.\\
&\quad\left.\cdot\frac{\partial}{\partial n}\left(-\frac{r'}{c_0}\right)+v_n\left(\mathbf{r}_1,t-\frac{r'}{c_0}\right)\cdot\frac{\partial}{\partial n}\left(\frac{1}{r'}\right)\right]ds\\
&=\frac{1}{2\pi}\int\int_S\left\{\left[\frac{1}{c_0r'}\cdot\frac{\partial}{\partial t}\,v_n\left(\mathbf{r}_1,t-\frac{r'}{c_0}\right)\right.\right.\\
&\quad\left.\left.+\frac{1}{r'^2}\cdot v_n\left(\mathbf{r}_1,t-\frac{r'}{c_0}\right)\right]\frac{\partial r'}{\partial n}\right\}ds,
\end{aligned} \tag{31}$$

where $r'=|\mathbf{r}'|=|\mathbf{r}_2-\mathbf{r}_1|$.

The surface element ds at the source surface in spherical coordinates is given as $ds=|\mathbf{r}_1|^2\sin\theta\,d\theta\,d\varphi$, where θ is the angle between $\mathbf{r}_1$ and z axis and φ is the angle between the projection of $\mathbf{r}_1$ on the xy plane and the x axis. As is shown in Fig. 2, $(\partial r'/\partial n)=\cos\gamma$, where γ is the angle between the $\mathbf{r}'$ and the z axis. Therefore, the normal particle velocity is given by:

$$\begin{aligned}
v_n(\mathbf{r}_2,t)=\frac{1}{2\pi}\int\int_S\left\{\left[\frac{1}{c_0r'}\cdot\frac{\partial}{\partial t}\,v_n\left(\mathbf{r}_1,t-\frac{r'}{c_0}\right)\right.\right.\\
\left.\left.+\frac{1}{r'^2}\cdot v_n\left(\mathbf{r}_1,t-\frac{r'}{c_0}\right)\right]\cdot\cos\gamma\right\}ds.
\end{aligned} \tag{32}$$

For this geometry, the Rayleigh integral for instantaneous pressure at point P of the intermediate plane can be rewritten as:

$$p(\mathbf{r}_2,t)=\frac{\rho}{2\pi}\int\int_S\left[\frac{1}{r'}\cdot\frac{\partial}{\partial t}\,v_n\left(\mathbf{r}_1,t-\frac{r'}{c_0}\right)\right]ds. \tag{33}$$

Equations (32) and (33) form the basic set of equations for simulating the effect of diffraction in our model. In discrete regime, the double integrals in Eqs. (32) and (33) were

solved numerically using a standard rectangular method.[34]

To obtain exact results, all calculations must be performed inside an extended volume which is a function of the geometrical characteristics of the source. This volume is defined as the envelope of a set of ellipsoids whose first foci are all placed on the source focal point and whose second foci are placed on different points of the source circular border. The eccentricity of these ellipsoids depends on the desired pulse length observed at the focal point (about 5 μs in our simulations).

The Rayleigh integral gives an exact solution to the diffraction problem for the case of a planar radiator in an infinite rigid baffle. Using this integral to simulate the effect of diffraction in our geometry therefore causes two kinds of errors: inherent and methodical. The inherent error relates to the geometry we used, i.e., a nonplanar source shape and a finite-baffle configuration. This source of error is not reducible. The methodical type of error is introduced by means of our fractional-step method. We studied the rate of this error for two different types of intermediate planes. In the first case, in our algorithm, we used the spherical-surface intermediate planes with the same center of curvature as the source, and in the second case, planar-surface intermediate planes were used. Comparison between these two different configurations revealed the superiority of the planar-surface intermediate planes. In fact, for this configuration, there exists a constant methodical error (about 3%) which is independent of the number of steps used, whereas for the spherical-surface plane configuration, this error is an increasing function of the number of steps (about 0.5% per step). The difference in the errors introduced by the two configurations of the intermediate planes is related to the fact that the solution of the Rayleigh integral over a curved surface introduces an error. When the planar-surface intermediate planes are used, this error is introduced only once, occurring only at the first step, i.e., from the source surface to the first intermediate plane. When the spherical-surface intermediate planes are used, however, a cumulative error is introduced at each step.

All simulations presented in the next sections were performed using the planar-surface intermediate planes.

V. FRACTIONAL-STEP METHOD WITH A SECOND-ORDER OPERATOR-SPLITTING ALGORITHM

The method of fractional steps with an operator-splitting algorithm has widely been used in numerical solutions to the problem of finite-amplitude sound beam propagation.[10–17] Besides, the technique was used in other physical problems, especially in optics.[35] A complete description of the technique can be found in Refs. 11 and 12. Using this method, we have developed a time-domain model for propagation of highly focused finite-amplitude ultrasonic beams by taking into account the effects of absorption, nonlinearity, and diffraction as independent phenomena. In this model, the acoustic beam propagates, plane-by-plane, from the surface of a highly focused spherical transducer up to its focus. The intermediate planes, all planar-surface type, are placed between the focused source and its focus. In each step, the abovementioned effects are applied sequentially: (1) by implementing the Rayleigh integral over the surface of the previous plane, the pressure and normal particle velocity are derived for each point of the current plane; (2) the effect of frequency-dependent absorption is applied to the pressure and normal particle velocity; (3) nonlinearly induced distortion is introduced to the resulted pressure and normal particle velocity to obtain the final values of these quantities for each point of the current plane; (4) code marches to the next step and the same procedure repeats.

The model was used to calculate the pressure field of an axisymmetric spherical highly focused piezocomposite shock-wave generator with an aperture diameter of 172 mm and with a 190-mm focal length (linear focusing gain $G \approx 30$, when driven by a sinusoidal pulse with a center frequency of 360 kHz). This source was developed in our laboratory for tissue destruction studies.[19,30] Because of the symmetry around the acoustical axis, in each observing plane, it is sufficient to calculate the acoustic field variables (instantaneous pressure and particle velocity) on a radial line, e.g., on x or y axes only.

In all simulations presented, the number of intermediate planes placed between the source front face and its focal point was set to be 23. This choice is a trade-off between the accuracy of calculations and the program run time. To have little changes of variable ν along each step Δz, as well as to avoid the problem of multivaluedness caused by nonlinear waveform steepening a nonuniform spacing was adopted: Axial step sizes were reduced by approaching the focus. Moreover, to satisfy inequality (27), especially in the region near the focus, after the first intermediate plane, each step was divided into 40 equally spaced substeps used only for nonlinearity calculation. Using this griding scheme, the minimum axial step sizes in the focal region were 2.02 mm for diffraction and absorption, and 50.5 μm for nonlinearity calculations. The number of surface elements, *ds*, for covering the surface of the source and each intermediate plane, was set to be 393 200, which is large enough to exactly calculate the Rayleigh integral: The minimum lateral step size in the focal region was about 2 μm.

The proper modeling of the shock fronts often requires a very dense temporal sampling. In our model, 5-μs pulses were sampled in 512-point vectors, i.e., with a sampling period less than 10 ns.

In the Appendix, we have proved a second-order accuracy operator-splitting algorithm used to solve numerically Eq. (8). In this algorithm there is a spatial shift between steps used for diffraction operation, $\hat{L}_D$, and those used for absorption, $\hat{L}_A$, and nonlinearity, $\hat{L}_N$, operations. Using this algorithm, it is possible to achieve a second order of accuracy with a running time not significantly higher than a first-order accuracy method. Figure 3(a) shows the basic geometry of nonuniform griding. Spatially shifted griding used for different operations in our second-order operator splitting method are shown schematically in Fig. 3(b).

At this time there is no analytical solution of the problem of beam propagation when multiple effects (diffraction, nonlinearity, absorption, etc.) are present. There is, therefore, no *a priori* reference to be used to assess the error from our

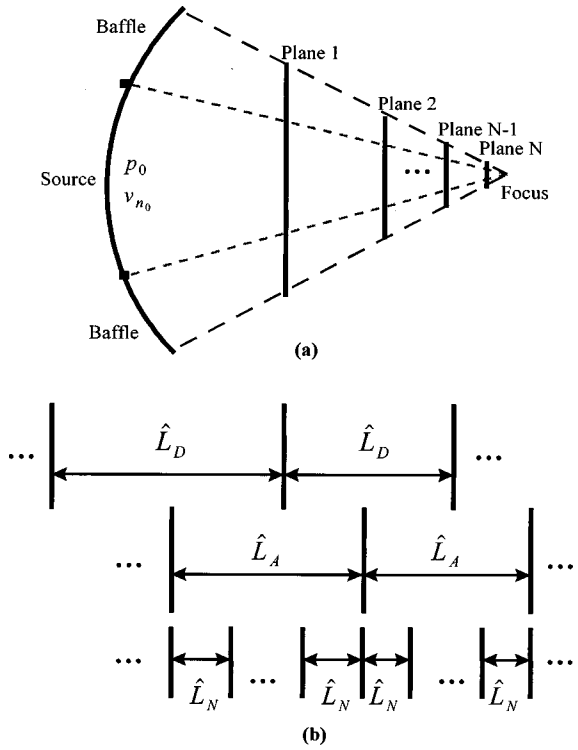

FIG. 3. (a) Axial griding scheme with nonuniform spacing; (b) spatially shifted griding for different operators in the second-order operator-splitting method.

numerical model. However, we investigated the stability of the code as a function of the number of steps. This study showed that the algorithm is convergent when the number of steps are increased (up to 79 intermediate planes). A similar study done by Lee and Hamilton to demonstrate the stability of their time-domain model for solving the KZK equation.[10]

An important characteristic of the operator-splitting method is that the final result is independent of the order of the effects when the steps Δz are small enough. To show this characteristic, we changed the order in which the effects (diffraction, absorption and nonlinearity) are applied in each plane. Specifically, we used two different orders:

Case 1: diffraction→absorption→nonlinearity

Case 2: absorption→nonlinearity→diffraction.

The discrepancy between the results of these two cases was reduced by increasing the number of planes. The maximum of the cross-correlation function was used as a criterion for comparing the waveforms obtained in each case. We studied the maximum of cross-correlation function applied to the pressure waveform as a function of number of the intermediate planes and for two different input pressures at source surface, i.e., $P_{\text{in}}=0.1$ MPa (linear regime) and $P_{\text{in}}=0.5$ MPa (nonlinear regime). This study showed that: even in nonlinear regime, by choosing a large enough number of planes, the maximum of the cross correlation would be close to 1 which shows that the algorithm is independent of the order of the effects. For example, for $P_{\text{in}}=0.5$ MPa and 17 intermediate planes, the maximum of cross correlation obtained was 0.991.[30]

TABLE I. Main acoustical parameters of water and 1,3-Butandiol.

	Water	1,3-Butandiol
Coefficient of attenuation (α_0)	0.0022 dB cm^{-1} MHz^{-2}	0.33 dB cm^{-1} MHz^{-1}
Frequency dependency of α	f^2	f^1
B/A	5.2	7.3
c_0	1500 m s^{-1}	1546 m s^{-1}
ρ	1000 kg m^{-3}	1000 kg m^{-3}

VI. NUMERICAL RESULTS AND COMPARISON WITH EXPERIMENTS

In this section, the results of implementing our numerical model and their comparisons with experimental results are presented. The initial version of the program was written in Matlab and then translated to C language and run on a Sun-UltraSparc workstation. For 23 intermediate planes and the griding scheme explained in the previous section, the program run time was about 3 h.

In Sec. VI A, the result of simulation for an ideal medium (linear and nondissipative) is presented. This simulation shows the validity of our model in linear regime. After verifying our algorithm in linear regime, we will present a series of simulation for real media by taking into account the effect of diffraction, absorption, and nonlinearity. The simulations, as well as experiments, were made for two different medium configurations. In the first configuration, an acoustic beam propagates from the source surface to its focus in degased and deionized water. In the second configuration, the propagation distance between the source front face and its focus is comprised of two parts. In the first part, the acoustic beam propagates from the source surface up to 5 cm from the focus in degased and deionized water, and in the second part, beam propagates the distance of 5 cm up to the focus in degased 1,3-Butandiol (ALDRICH, Steinheim, Germany) which is a tissue-mimicking liquid. These two medium configurations are called water and water-butandiol, respectively.[30] The relevant room temperature acoustical parameters of these media, as used in our simulations, are given in Table I.

A. Beam propagation in a linear and nondissipative medium

Here we present the simulation results for the propagation of a focused beam in an ideal medium, when only the effect of diffraction was accounted for. For this reason, the operator of nonlinearity, $\hat{L}_N$, was set to be zero, and only a small amount of absorption, $\hat{L}_A$, was introduced to provide stability of the numerical algorithm. In this simulation, input pressure at the surface of the transducer was considered as a Gaussian-modulated sinusoidal waveform with central frequency of 360 kHz and bandwidth of 120% [Fig. 4(a)]. The pressure calculations at the focus were made in two different cases. In the first case, using the linear wave theory, the pressure at the focus was calculated directly; i.e., without any intermediate plane; and in the second case, this pressure was calculated by means of our fractional-step method with 23 intermediate planes. These two pressure waveforms are presented in Fig. 4(b) and (c), respectively. The discrepancy

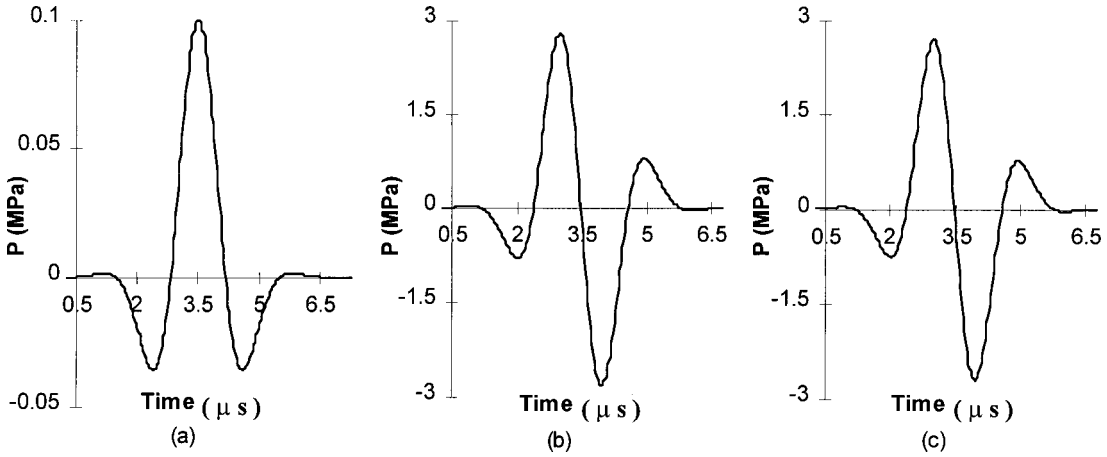

FIG. 4. Verifying the operator-splitting algorithm for the effect of diffraction. (a) Input pressure at the source surface; (b) calculated pressure waveform at the focus without any intermediate plane; and (c) with 23 intermediate planes.

between these two waveforms is about 3% for peak pressures which shows that it is possible to simulate the effect of diffraction quite accurately by means of our operator-splitting algorithm.

B. Pressure at the focal point in real media

Pressure-time waveforms at the focal point were calculated for different input pressure amplitudes at the source surface. For all of the simulations presented here and those that follow, the input pressure is the same as that measured at the surface of the generator using a PVDF bilaminar shielded membrane hydrophone.[19,30] Figures 5 and 6 show the calculated and measured pressure-time waveforms at the focus for the second configuration of the medium, i.e., water-butandiol, and for two different input pressure amplitudes (P_{in}=0.476 and 0.85 MPa). The presence of the nonlinearly induced shock fronts are notable in Fig. 6. For pressure measurements at the focus, a homemade PVDF shock-wave hydrophone was used.[36]

Comparison between the calculated and measured waveforms shows a very good agreement in the shape of waveforms. However, there exists some discrepancy between the pressure amplitudes. The maximum of this discrepancy was around 20% for positive pressure amplitudes. In the conclusion and discussion section, the sources of this discrepancy will be discussed.

Figure 7 shows the variations of the positive peak pressure at the focus as a function of input pressure amplitude at

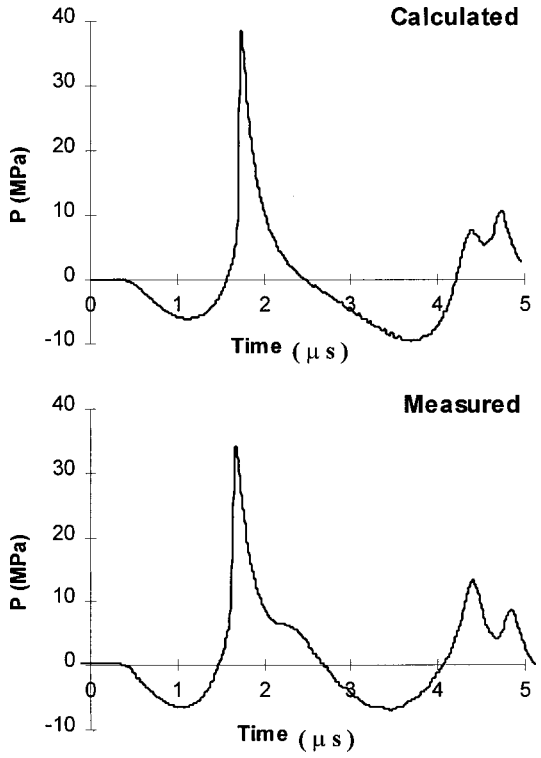

FIG. 5. Calculated and measured pressure-time waveforms at the focal point for P_{in}=0.476 MPa.

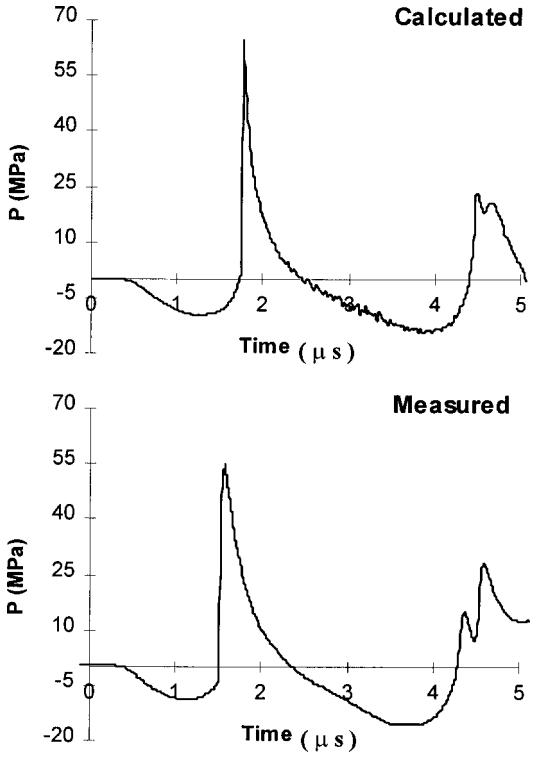

FIG. 6. Calculated and measured pressure-time waveforms at the focal point for P_{in}=0.85 MPa.

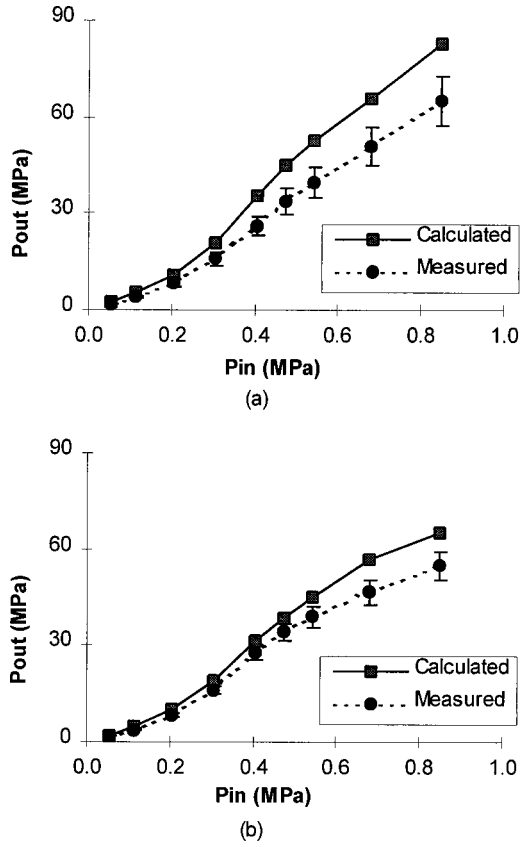

FIG. 7. Output pressure amplitude at the focus as a function of input pressure amplitude at the source surface for two medium configurations: (a) water; and (b) water-butandiol.

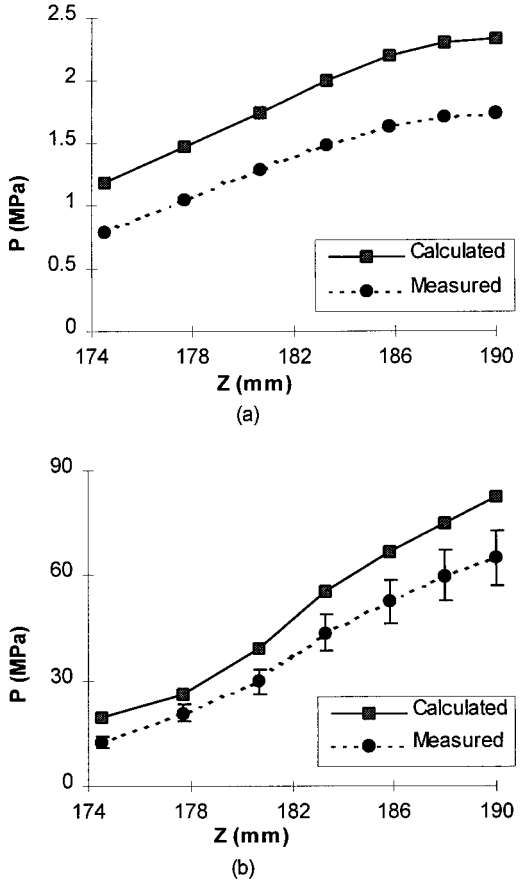

FIG. 8. On-axis pressure distributions in water. (a) $P_{in}=0.056$ MPa (linear regime); and (b) $P_{in}=0.85$ MPa (nonlinear regime).

the source surface for two medium configurations. For each medium, the results of theory and experiments have been shown. Both the theoretical and experimental results show three distinct regions of variations as: (1) acoustic pressure at the focus varies as a linear function of input pressure for very low input excitation levels ($P_{in}<0.1$ MPa); (2) for moderate levels of input pressures, there is an increase in slope of this variation (0.1 MPa$<P_{in}<0.4$ MPa); (3) and finally for high levels of input excitation, this slope decreases ($P_{in}>0.4$ MPa). The discrepancy between the theory and experiment increases by increasing the input pressure amplitude. This discrepancy may be explained by the pressure-averaging effect over the surface of the hydrophone active element that is larger than the real focus size. Increasing the input pressure amplitude leads to amplification of the nonlinearity effect with creation of the higher harmonics, and consequently to contraction of the focus size. The pressure-averaging effect over the surface of the hydrophone active element, therefore, becomes more important for higher input pressures.

C. On- and off-axis pressure distributions

Using our model, it is possible to simulate the plane-by-plane beam propagation in a medium. This simulation in linear regime shows that the waveform is mainly affected by diffraction which leads to a linear amplification of pressure during its propagation. In nonlinear regime, however, the situation is not so simple. Here, the nonlinearly induced wave distortion which leads to the creation of very steep shock fronts with higher harmonics in the signal spectrum, causes nonlinear amplification of the pressure. Also, the effect of frequency-dependent absorption becomes more important in this case.

Figures 8 and 9 show the theoretical and experimental on- and off-axis pressure distributions around the focus in water. These distributions are presented for both the linear ($P_{in}=0.056$ MPa) and nonlinear ($P_{in}=0.85$ MPa) regimes. Again, a good agreement between the theory and experiment is obvious. These distributions reveal the contraction of the focus dimensions in nonlinear regime.

VII. CONCLUSION AND DISCUSSION

In this work, we have presented a time-domain model for calculating the acoustic field of a finite-amplitude, highly focused source in pulsed regime. In this model, the main effects responsible in finite-amplitude beam propagation in a dissipative medium were taken into account. These effects, considered as independent phenomena, are: absorption, nonlinearity, and diffraction. Using general wave theory, we derived separate evolution-type differential equations for each of these effects and by combining these separate equations, the final evolution equation was derived in the form of Eq. (8). This equation was solved numerically, using the operator-splitting method.

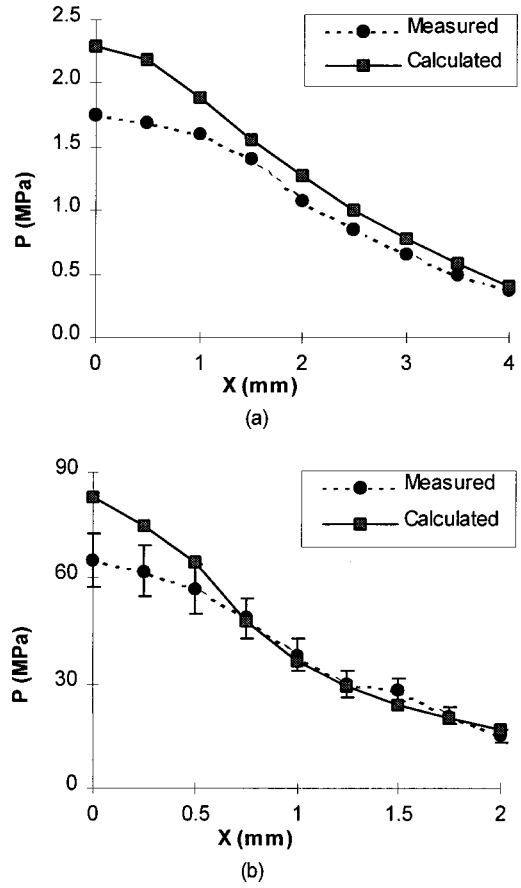

FIG. 9. Off-axis pressure distributions in water. (a) $P_{in}=0.056$ MPa (linear regime); and (b) $P_{in}=0.85$ MPa (nonlinear regime).

To solve the frequency-dependent attenuation equation, a minimum-phase digital filter model was developed. To be a causal filter, the log-magnitude and phase characteristics form a Hilbert transform pair. Using this filter model, the frequency-dependent attenuation and dispersion were exactly simulated without any waveform distortion even for a shock-wave pulse.

To simulate the effect of nonlinearity, we used the evolution equation for a plane wave propagating in an ideal quadratically nonlinear medium. Based on the analytical solution of this equation, the nonlinearly induced wave distortion was simulated via a simple time-base transformation.

To obtain an exact formulation of diffraction, we used the Rayleigh integral. The results of calculation in an ideal, linear, and nondissipative medium show the validity of our algorithm to simulate exactly the effect of diffraction. Full diffraction formulation enables our model to be used for simulating the finite-amplitude acoustic field of highly focused sources.

In a real medium, i.e., by taking into account the effects of diffraction, absorption, and nonlinearity, very good agreement was obtained in the shape of theoretical and experimental pressure waveforms. The discrepancy in the amplitudes may be explained by existing sources of error in our measurements from one hand and in the theoretical model on the other hand. The main sources of uncertainty in our measurements are: pressure-averaging effect over the surface of the hydrophone active element, error in the measured value of the shockwave hydrophone sensitivity,[36] and error in the measurement of the generator electro-acoustical conversion factor at its source surface.[30,37] Among these, we believe that the first one, i.e., the effect of pressure averaging over the surface of hydrophone active element, has had the most important influence on our measurements, especially in nonlinear regime when the focus dimensions become comparable with, or even smaller than, the hydrophone active element size ($\Phi=1$ mm in our measurements). To obtain an idea of the influence of this averaging effect on our results, we made a simple simulation in nonlinear regime and in water. In this simulation, based on calculated off-axis pressure distribution presented in Fig. 9, we derived the pressure amplitudes at 20 equally spaced points in the focal plane and on the *x*-axis, from the focus to a distance of 0.5 mm from the focus. We consider a circular-shape hydrophone active element with a radius of 0.5 mm. If the center of the hydrophone active element is placed at the focus, by dividing the active element area into 20 concentric and equal-width annuli, we can calculate the averaged value of the pressure by averaging the pressures at different annuli with the scaling factors proportional to the surface of each annulus. Using this method, the averaged pressure over the hydrophone active element in nonlinear regime ($P_{in}=0.85$ MPa) and in water was found to be about 11% smaller than the calculated pressure. As a result, we can conclude that a major part of the 20% discrepancy observed between the theory and experiments may be related to the averaging effect over the hydrophone active element.

The time-domain numerical model presented in this work can be used as a fairly simple theoretical tool for studying the intensive highly focused acoustic beam propagation in different medium configurations with a symmetrical source geometry. The technique has some advantages over other time-domain methods in the literature in that it allows (1) for arbitrary absorption and dispersion, and (2) does not make use of the parabolic approximation for diffraction. The latter point is particularly important because the trend in biomedical research is toward highly focused, intensive sources, and many current models cannot account for high focusing gains.

In the model presented, we have not considered the effects of reflection and refraction. These effects may have an important influence on wave propagation especially in multilayered media which cause an overestimation in the results of the simulation. The media used in this study (water and butandiol) have practically the same values of acoustic impedances and sound velocities: This source of error is therefore negligible in the results presented here.

Adding the effects of reflection and refraction, this model can be used to simulate the wave propagation in multi-layered media, such as a simplified model for the human body. Another field of application is to study electronic focusing along the acoustical axis of a high-amplitude two-dimensional focused source. Our method can easily be extended to asymmetrical sources, that makes it possible to simulate the focused finite-amplitude wave propagation in a medium with presence of arbitrary obstacles in the path of

propagation, as well as simulation of on- and off-axis electronic beam steering.

ACKNOWLEDGMENTS

The authors gratefully acknowledge the suggestions of Dr. Richard S. C. Cobbold, and wish to thank Dr. Valery P. Kandidov for discussions on the method of fractional steps. We also appreciate assistance of Brian Lim in reviewing the manuscript.

APPENDIX

Here, we describe and prove a second-order accuracy operator-splitting algorithm. For this reason, we calculate the solution of Eq. (8) at distance $z+\Delta z$ on the basis of the waveform ν at distance z within three steps:

Step 1. We consider the evolution equation (6) for diffraction:

$$\frac{\partial \nu_1}{\partial z}=\hat{L}_D \nu_1, \tag{A1}$$

with initial condition $\nu_1(z)=\nu_0$. As the first step, we calculate the waveform ν_1 at the distance $z+\Delta z/2$. Using a Taylor series expansion, it is possible to write:

$$\nu_1\left(z+\frac{\Delta z}{2}\right)=\nu_1(z)+\frac{\Delta z}{2}\cdot\frac{\partial \nu_1(z)}{\partial z}+\frac{\Delta z^2}{8}\cdot\frac{\partial^2 \nu_1(z)}{\partial z^2}+O(\Delta z^3). \tag{A2}$$

Note that within the Rayleigh integral approximation, the differential operator $\partial/\partial z$ commutes with the diffraction operator $\hat{L}_D$:

$$\frac{\partial}{\partial z}\hat{L}_D \nu_1(z)=\hat{L}_D\frac{\partial \nu_1(z)}{\partial z}. \tag{A3}$$

Indeed, the Rayleigh integral (32) represents an exact solution of the wave equation

$$\nabla^2 \nu-\frac{1}{c_0^2}\cdot\frac{\partial^2 \nu}{\partial t^2}=0$$

in case of the plane surface of integration, when the normal to the surface does not depend on coordinates. In our model, all intermediate observing planes are parallel with the *xy* plane, so $\partial/\partial z=\partial/\partial n$ over the surface of these planes (Fig. 2). In the case of $\vec{n}=\text{const}$, we obtain from the wave equation that the derivative $\partial v/\partial z$ is also a solution of the wave equation, so the integral (32) is valid for it. This proves that the diffraction operator $\hat{L}_D$ commutes with the differential operator $\partial/\partial z$. Using the result (A3), we obtain from Eqs. (A1) and (A2):

$$\nu_1\left(z+\frac{\Delta z}{2}\right)=\nu_0+\frac{\Delta z}{2}\hat{L}_D\nu_0+\frac{\Delta z^2}{8}\hat{L}_D^2\nu_0+O(\Delta z^3). \tag{A4}$$

Step 2. Consider the following evolution equation for the effects of absorption and nonlinearity:

$$\frac{\partial \nu_2}{\partial z}=\hat{L}_A\nu_2+\hat{L}_N\nu_2, \tag{A5}$$

with initial condition $\nu_2(z)=\nu_1(z+\Delta z/2)$. As the second step, we calculate the waveform ν_2 at distance $z+\Delta z$. The Taylor series expansion gives:

$$\nu_2(z+\Delta z)=\nu_2(z)+\Delta z\frac{\partial v_2(z)}{\partial z}+\frac{\Delta z^2}{2}\cdot\frac{\partial^2 \nu_2(z)}{\partial z^2}+O(\Delta z^3). \tag{A6}$$

Note, that according to Eq. (3) the differential operator $\partial/\partial z$ commutes with the operator $\hat{L}_A$, i.e.:

$$\frac{\partial}{\partial z}\hat{L}_A\nu_2(z)=\hat{L}_A\frac{\partial \nu_2(z)}{\partial z}. \tag{A7}$$

However, this is not the case for operators $\partial/\partial z$ and $\hat{L}_N$ in Eq. (4). Let us introduce a linear operator $\hat{\Lambda}_N=(\beta/2c_0^2)\times(\partial/\partial\tau)$, such that:

$$\hat{L}_N\nu_2=\hat{\Lambda}_N\nu_2^2. \tag{A8}$$

The operator $\hat{\Lambda}_N$ commutes with $\partial/\partial z$, therefore:

$$\frac{\partial}{\partial z}\hat{L}_N\nu_2(z)=2\hat{\Lambda}_N\left[\nu_2\frac{\partial \nu_2(z)}{\partial z}\right]. \tag{A9}$$

Equations (A4) to (A9) give the following expansion for the waveform ν_2 at distance $z+\Delta z$:

$$\begin{aligned}\nu_2(z+\Delta z)&=\nu_0+\Delta z\cdot\left[\tfrac{1}{2}\hat{L}_D\nu_0+\hat{L}_A\nu_0+\hat{\Lambda}_N\nu_0^2\right]\\&+\frac{\Delta z^2}{2}\cdot\left[\frac{1}{4}\hat{L}_D^2\nu_0+\hat{L}_A\hat{L}_D\nu_0+2\hat{\Lambda}_N(\nu_0\hat{L}_D\nu_0)+\hat{L}_A^2\nu_0\right]\\&+\frac{\Delta z^2}{2}\cdot\left[\hat{L}_A\hat{\Lambda}_N\nu_0^2+2\hat{\Lambda}_N(\nu_0\hat{L}_A\nu_0)+2\hat{\Lambda}_N(\nu_0\hat{\Lambda}_N\nu_0^2)\right]\\&+O(\Delta z^3).\end{aligned} \tag{A10}$$

Step 3. Consider Eq. (A1) again:

$$\frac{\partial \nu_3}{\partial z}=\hat{L}_D\nu_3, \tag{A11}$$

with initial condition $\nu_3(z+\Delta z/2)=\nu_2(z+\Delta z)$. As the third step, we calculate the waveform ν_3 at distance $z+\Delta z$. Using the Taylor series expansion, it is possible to write:

$$\nu_3(z+\Delta z)=\nu_3(z+\Delta z/2)+\frac{\Delta z}{2}\cdot\frac{\partial \nu_3(z+\Delta z/2)}{\partial z}+\frac{\Delta z^2}{8}\cdot\frac{\partial^2 \nu_3(z+\Delta z/2)}{\partial z^2}+O(\Delta z^3). \tag{A12}$$

Taking into account Eq. (A3), we obtain from Eqs. (A10) to (A12):

$$v_3(z+\Delta z)=v_0+\Delta z\cdot[\hat{L}_D v_0+\hat{L}_A v_0+\hat{\Lambda}_N v_0^2]$$
$$+\frac{\Delta z^2}{2}\cdot[\hat{L}_D^2 v_0+\hat{L}_D\hat{L}_A v_0+\hat{L}_A\hat{L}_D v_0$$
$$+\hat{L}_D\hat{\Lambda}_N v_0^2+\hat{L}_A^2 v_0+\hat{L}_A\hat{\Lambda}_N v_0^2]$$
$$+\frac{\Delta z^2}{2}\cdot[2\hat{\Lambda}_N(v_0\hat{L}_D v_0)+2\hat{\Lambda}_N(v_0\hat{L}_A v_0)$$
$$+2\hat{\Lambda}_N(v_0\hat{\Lambda}_N v_0^2)+O(\Delta z^3). \quad \text{(A13)}$$

Let $v(z)=v_0$, the following expression for the waveform at distance $z+\Delta z$ results from the evolution equation (8):

$$v(z+\Delta z)=v(z)+\Delta z\,\frac{\partial v(z)}{\partial z}+\frac{\Delta z^2}{2}\cdot\frac{\partial^2 v(z)}{\partial z^2}+O(\Delta z^3)$$
$$=v_0+\Delta z\cdot[\hat{L}_D v_0+\hat{L}_A v_0+\hat{\Lambda}_N v_0^2]$$
$$+\frac{\Delta z^2}{2}\cdot[\hat{L}_D^2 v_0+\hat{L}_D\hat{L}_A v_0+\hat{L}_A\hat{L}_D v_0+\hat{L}_D\hat{\Lambda}_N v_0^2$$
$$+\hat{L}_A^2 v_0+\hat{L}_A\hat{\Lambda}_N v_0^2]$$
$$+\frac{\Delta z^2}{2}\cdot[2\hat{\Lambda}_N(v_0\hat{L}_D v_0)+2\hat{\Lambda}_N(v_0\hat{L}_A v_0)$$
$$+2\hat{\Lambda}_N(v_0\hat{\Lambda}_N v_0^2)]+O(\Delta z^3). \quad \text{(A14)}$$

Comparing Eqs. (A13) and (A14), we conclude:

$$v(z+\Delta z)=v_3(z+\Delta z)+O(\Delta z^3), \quad \text{(A15)}$$

which proves the operator-splitting algorithm with the second-order of accuracy.

[1] L. Germain and J. D. N. Cheeke, ''Generation and detection of high-order harmonics in liquids using a scanning acoustic microscope,'' J. Acoust. Soc. Am. **83**, 942–949 (1988).

[2] J. Y. Chapelon and D. Cathignol, ''High energy ultrasound therapy: Part I—High intensity focused ultrasound (HIFU),'' in *Advances in Nonlinear-Acoustics*, edited by H. Hobaek, 13th International Symposium on Nonlinear Acoustics, Bergen, 28 June–2 July 1993 (World Scientific, Singapore, 1993), pp. 21–29.

[3] D. Cathignol and J. Y. Chapelon, ''High energy ultrasound therapy: Part II—Shock waves and cavitation,'' in *Advances in Nonlinear Acoustics*, edited by H. Hobaek, 13th International Symposium on Nonlinear Acoustics, Bergen, 28 June–2 July 1993 (World Scientific, Singapore, 1993), pp. 30–35.

[4] E. A. Zabolotskaya and R. V. Khokhlov, ''Quasi-plane waves in the nonlinear acoustics of confined beams,'' Sov. Phys. Acoust. **15**, 35–40 (1969).

[5] V. P. Kuznetsov, ''Equations of nonlinear acoustics,'' Sov. Phys. Acoust. **16**, 467–470 (1971).

[6] J. Naze Tjøtta, S. Tjøtta, and E. H. Vefring, ''Propagation and interaction of two collimated finite amplitude sound beams,'' J. Acoust. Soc. Am. **88**, 2859–2870 (1990).

[7] J. Naze Tjøtta, S. Tjøtta, and E. H. Vefring, ''Effects of focusing on the nonlinear interaction between two collinear finite amplitude sound beams,'' J. Acoust. Soc. Am. **89**, 1017–1027 (1991).

[8] S. I. Aanonsen, ''Numerical computation of the nearfield of a finite amplitude sound beam,'' Tech. Rep. No. 73, Department of Mathematics, University of Bergen, Bergen, Norway (1983).

[9] S. I. Aanonsen, T. Barkve, J. Naze Tjøtta, and S. Tjøtta, ''Distortion and harmonic generation in the nearfield of a finite amplitude sound beam,'' J. Acoust. Soc. Am. **75**, 749–768 (1984).

[10] Y. S. Lee and M. F. Hamilton, ''Time-domain modeling of pulsed finite-amplitude sound beams,'' J. Acoust. Soc. Am. **97**, 906–917 (1995).

[11] W. F. Ames, *Numerical Methods for Partial Differential Equations* (Academic, San Diego, 1992), 3rd ed.

[12] W. H. Press, S. A. Teukolsky, W. T. Vetterling, and B. P. Flannery, *Numerical Recipes in FORTRAN* (Cambridge U.P., New York, 1992), 2nd ed., pp. 847–848.

[13] R. O. Cleveland, M. F. Hamilton, and D. T. Blackstock, ''Time-domain modeling of finite-amplitude sound in relaxing fluids,'' J. Acoust. Soc. Am. **99**, 3312–3318 (1996).

[14] M. A. Averkiou and M. F. Hamilton, ''Nonlinear distortion of short pulses radiated by plane and focused circular pistons,'' J. Acoust. Soc. Am. **102**, 2539–2548 (1997).

[15] R. O. Cleveland, J. P. Chambers, H. E. Bass, R. Raspet, D. T. Blackstock, and M. F. Hamilton, ''Comparison of computer codes for the propagation of sonic boom waveforms through isothermal atmospheres,'' J. Acoust. Soc. Am. **100**, 3017–3027 (1996).

[16] P. T. Christopher and K. J. Parker, ''New approaches to nonlinear diffractive field propagation,'' J. Acoust. Soc. Am. **90**, 488–499 (1991).

[17] T. Christopher, ''Modeling the Dornier HM3 lithotripter,'' J. Acoust. Soc. Am. **96**, 3088–3095 (1994).

[18] D. Cathignol, O. A. Sapozhnikov, and J. Tavakkoli, ''One-dimensional theoretical model of high-intensity pulse focusing,'' in *Nonlinear Acoustics in Perspective*, edited by R. J. Wei, 14th International Symposium on Nonlinear Acoustics (Nanjing U.P., Nanjing, 1996), pp. 177–182.

[19] J. Tavakkoli, A. Birer, A. Arefiev, F. Prat, J. Y. Chapelon, and D. Cathignol, ''A piezocomposite shock wave generator with electronic focusing capability: Application for producing cavitation-induced lesions in rabbit liver,'' Ultrasound Med. Biol. **23**, 107–115 (1997).

[20] O. V. Rudenko and S. I. Soluyan, *Theoretical Foundations of Nonlinear Acoustics* (Plenum, New York, 1977).

[21] V. G. Andreev, V. A. Khokhlova, O. V. Rudenko, and O. A. Sapozhnikov, ''Suppression of nonlinear damping of a sound wave in a medium which contains a resonant absorber with a finite line width,'' Mosc. Univ. Phys. Bull. (USA), No. 3, 67–71 (1985).

[22] R. J. Hill, ''Wider-angle parabolic wave equation,'' J. Acoust. Soc. Am. **79**, 1406–1409 (1986).

[23] J. W. Strutt (Lord Rayleigh), *Theory of Sound* (Dover, New York, 1945), Vol. 2.

[24] H. T. O'Neil, ''Theory of focusing radiators,'' J. Acoust. Soc. Am. **21**, 516–526 (1949).

[25] A. Penttinen and P. M. Luukkala, ''The impulse response and pressure near field of a curved ultrasonic radiator,'' J. Phys. D **9**, 1547–1557 (1976).

[26] A. V. Oppenheim and R. W. Schafer, *Digital Signal Processing* (Prentice-Hall, London, 1975).

[27] M. O'Donnell, E. T. Jaynes, and J. G. Miller, ''Kramers-Kronig relationship between ultrasonic attenuation and phase velocity,'' J. Acoust. Soc. Am. **69**, 696–701 (1981).

[28] R. Kuc, ''Digital filter models for media having linear with frequency loss characteristics,'' J. Acoust. Soc. Am. **69**, 35–40 (1981).

[29] R. Kuc, ''Generating a minimum-phase digital filter model for the acoustic attenuation of soft tissue,'' 1983 Ultrasonics Symposium: Proceedings, 794–796 (1983).

[30] J. Tavakkoli, ''Study of intensive focused ultrasonic pulse propagation in biological media: application to shock wave-induced tissue destruction *in vitro* and *in vivo*,'' Ph.D. dissertation (English version), No. 65–97, University of Claude Bernard—Lyon 1 (1997).

[31] M. F. Hamilton and D. T. Blackstock, *Nonlinear Acoustics* (Academic, San Diego, 1998).

[32] R. T. Beyer, *Nonlinear Acoustics* (U.S. Naval Sea Systems Command, Washington, 1974).

[33] J. Lelong, ''Contribution à l'étude d'un dispositif piézo-électrique de puissance en vue de la creation d'ondes de choc,'' Ph. D. thesis, University of Pierre et Marie Curie—Paris VI, 1990.

[34] E. Kreyszig, *Advanced Engineering Mathematics* (Wiley, New York, 1979), Chap. 19.

[35] J. Martin, ''Simulation of wave propagation in random media: theory and application,'' in *Wave Propagation in Random Media (Scintillation)* (SPIE, Philadelphia, 1992), SPIE PM-09, pp. 463–486.

[36] J. Tavakkoli, A. Birer, and D. Cathignol, ''Development of a PVDF low-cost shock-wave hydrophone,'' Shock Waves **5**, 369–374 (1996).

[37] D. Cathignol, A. Birer, S. Nachef, and J. Y. Chapelon, ''Electronic beam steering of shock waves,'' Ultrasound Med. Biol. **3**, 365–377 (1995).

The influence of liquid temperature on the sonoluminescence hot spot

Vi Q. Vuong[a)]
University of California, Irvine, Department of Mechanical and Aerospace Engineering, Irvine, California 92697-3975

Marios M. Fyrillas[b)]
University of Cyprus, Department of Mathematics and Statistics, P.O. Box 537, 1678 Nicosia, Cyprus

Andrew J. Szeri
University of California, Berkeley, Department of Mechanical Engineering, Berkeley, California 94720-1740

(Received 27 August 1997; revised 7 July 1998; accepted 13 July 1998)

An explanation is provided for the influence of relatively small changes in liquid temperature on the hot spot within a sonoluminescence bubble. This influence derives from a change in the (stable) equilibrium mass of the bubble due to a variation of the gas solubility in the liquid with temperature. If the acoustic drive amplitude is held constant, a change in the liquid temperature has a large or small effect depending on the variability of the solubility with temperature. For a gas like xenon, which has rapidly decreasing solubility in water with increasing temperature, a decrease in water temperature shifts the stable mass exchange equilibrium to a smaller bubble size. This increases the ratio of maximum to minimum bubble radius over an acoustic cycle, resulting in a much higher hot spot temperature. In contrast helium has very little variation of solubility with temperature near room temperature; therefore the hot spot temperature is relatively insensitive to variations in the liquid temperature outside a helium bubble. © *1998 Acoustical Society of America.* [S0001-4966(98)04910-8]

PACS numbers: 43.25.Yw, 43.35.Ei [MAB]

INTRODUCTION

When a bubble is driven into sufficiently violent radial pulsations in sufficiently degassed water, the production of light is observed in the bubble interior. Careful management of gas transfer across the bubble wall was the key to the first successful observation of single bubble sonoluminescence (SL).[1] The tendency of the bubble to grow as a consequence of rectified diffusion driven by the nonlinear bubble oscillations must be counteracted by a reduction of the far-field gas concentration to low levels: in some cases a fraction of a percent of saturation.[2,3]

It has been observed repeatedly that in colder water SL appears brighter, when the bubble is driven at its maximum stable acoustic drive, which varies with liquid temperature, in general.[4–6] In the present work we present new physics that may play an important role in explaining this observation. The theory provides experimentalists with an additional way to exert control over the size of SL bubbles, beyond manipulation of the acoustic drive and the far-field gas concentration.

This work is relevant to bubbles of sparingly soluble gases where Henry's law applies.[7] Sonoluminescence experiments have been conducted on highly soluble gases as well, such as xenon in 1-butanol.[6] For such a system, one must instead make use of the much more complicated *ensemble Henry's law* in an analysis of mass exchange.[7]

I. MASS EXCHANGE EQUILIBRIUM

The condition for mass exchange equilibrium of an acoustically forced bubble is derived in Refs. 8 and 9. In the following equations C is the concentration (mass-fraction) field minus the far-field dissolved gas concentration C_∞. The dimensionless time is $\tau=\Omega_0 t$. The radius of the undisturbed bubble is a with natural frequency Ω_0. The dimensionless bubble radius is x. The Henry's law boundary condition involves the (dimensionless) saturation concentration outside a spherical bubble of radius $x(\tau)=1$: $C_{\mathrm{s,ref}}$. This parameter may be written as

$$C_{\mathrm{s,ref}}=\frac{m_G}{\frac{4}{3}\pi a^3}\,\frac{R_G T_\infty}{M}\,\frac{1}{k(T)}\equiv\frac{p_{\mathrm{ref}}}{k(T)},$$

where m_G is the mass of the gas in the bubble, $k(T,p)$ is the (temperature and pressure dependent) coefficient of Henry's law, M is the molecular weight of the gas, R_G is the universal gas constant, T_∞ and p_{ref} are the temperature and steady pressure of the fluid in the far field.

It is possible to repeat the analysis of Ref. 9 with the diffusivity and solubility of the gas in the liquid assumed to depend on temperature and pressure. One can exploit the fact that the mass transfer boundary layer is an order of magnitude thinner than the thermal boundary layer at sonoluminescence conditions. This allows one to evaluate the diffusivity in the boundary layer at the interface conditions of temperature and pressure. Proceeding in this way, one can derive a

[a)]Now at Kaijo America, Inc.
[b)]Now at University of Twente, The Netherlands.

TABLE I. Stable ambient radius a versus far-field temperature T_∞, and maximum internal gas temperature $T_{\max}$ and compression ratio at the end of the main collapse for bubbles of xenon in water driven at 1.3 atm and 26.5 kHz.

a (μm)	T_∞ (K)	$R_{\max}/R_{\min}$	$a/R_{\min}$	$T_{\max}$ (K)
4.000	289.6	80.44	7.794	242 000
4.500	300.0	70.72	6.691	173 000
5.000	311.5	62.79	5.801	137 000

threshold criterion including the effects of temperature- and pressure-dependent solubility and diffusivity.

However, the bubble spends only 10^{-2} to 10^{-3} of the period with elevated wall temperatures and pressures, and much less time at significantly elevated conditions. With reasonable models of temperature and pressure dependence of solubility and diffusivity, it is clear that transient departures from reference conditions have little effect. Therefore one need only use the usual threshold criterion of Eller and Flynn:[8]

$$\frac{C_\infty}{C_{\text{s,ref}}} = \langle p_G^*(\tau)\rangle \equiv \frac{\int_0^T x^4(\tau) p_G^*(\tau)\, d\tau}{\int_0^T x^4(\tau)\, d\tau}. \tag{1}$$

The right-hand side of (1) depends only on the response of the bubble to the forcing. If the reference temperature T_∞ is changed, and all other controllable experimental parameters are held constant, then $C_{\text{s,ref}}$ and $\langle p_G^*(\tau)\rangle$ must change to compensate, so as to maintain (1). If the transient departure from the reference Henry's law constant $k^*(T,p)$ and the transient departure from the reference diffusivity $D^*(T,p)$ are included, then the threshold criterion (1) is modified with D^*/k^* inserted into the integrand of the numerator on the right-hand side, and D^* inserted into the integrand in the denominator.

Confidence in application of (1) (without the previously mentioned modifications one can derive for the effects of transient departures from reference conditions) is obtained through the remarkable agreement of (1) with experiments.[3,10]

II. RESULTS

A clear demonstration of the consequences of changing the liquid temperature may be obtained as follows. We choose three different ambient bubble radii for three xenon bubbles: 4, 4.5, and 5 μm. These three bubbles are driven with the same ultrasound field. We assume they are all in (stable) mass exchange equilibrium in a sealed container, and hence have the same C_∞, but that the liquid temperatures are different.

By changing the liquid temperature, one changes $C_{\text{s,ref}} \equiv p_{\text{ref}}/k(T_\infty)$. The reference pressure is approximately constant for the results we report below. However, depending on the identity of the gas and liquid, $k(T_\infty)$ can vary quite dramatically with T_∞; this implies a similarly dramatic variation in bubble dynamics through an alteration in the value of $\langle p_G^*(\tau)\rangle_\tau$.

Then from (1), and the knowledge of $k(T_\infty)$,[11] we can determine what are the three temperatures consistent with mass exchange equilibrium. Finally, we can compare the internal gas dynamics within each bubble to see if there is a significant difference in the peak temperatures and pressures. The internal gas dynamics is computed with our previously published compressible Navier–Stokes solver[12] which includes temperature-dependent gas viscosity and thermal conductivity.

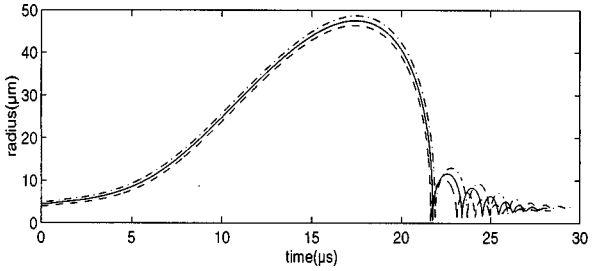

FIG. 1. Radius versus time for the three xenon bubbles in mass exchange equilibrium at three different far-field temperatures.

The results are shown in Table I. There one sees a quite remarkable trend. A 4.5-μm bubble is in mass exchange equilibrium at $T_\infty = 300$ K. If the far field temperature is decreased about 10°, the ambient radius shrinks to 4.0 μm and the peak gas temperature in the bubble interior *increases* by nearly 70 000°. Similarly, increasing the far-field temperature by about 10° increases the bubble size to 5.0 μm and *reduces* the maximum gas temperature by 36 000°. In Fig. 1 we show plots of the bubble radii as functions of time. In Fig. 2, we show the temperature profile with respect to mass at the instant when the origin is hottest at the end of the main bubble collapse.

Of course, the hot-spot temperatures can be expected to change somewhat from the values we report depending on

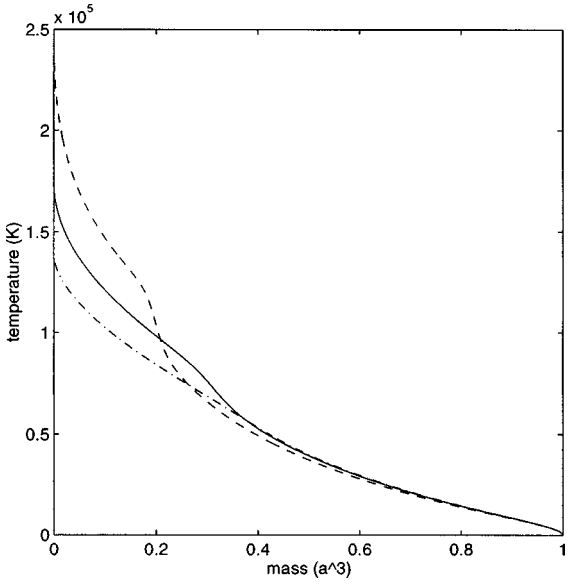

FIG. 2. Temperature profiles versus fraction of mass within the bubble at the hottest instant at the end of the main collapse of the three xenon bubbles in mass exchange equilibrium at three different far-field temperatures with the same far field concentration $C_\infty = 0.00\,173$. The dashed line is for the 4-μm bubble in equilibrium at 289.6 K. The solid curve is for a 4.5-μm bubble in equilibrium at 300 K. The dot–dashed curve is for a 5-μm bubble in mass exchange equilibrium at 311.5 K.

the details of the computational model one chooses. Unfortunately, it is not possible at present to measure, or even accurately to infer, the internal gas temperature in sonoluminescence experiments. However, dramatic changes in light output have been observed upon changing liquid temperature and driving the bubble as hard as possible. We return to the subject of experimental verification later.

The change in hot spot temperatures is easily understood from the changes in ''compression ratio'' which is $R_{\max}/R_{\min}$ over the cycle, also listed in the table. The compression from $R_{\max}$ to $R_{\min}$ is responsible for much of the heating of the bubble contents, with some heat loss to the surrounding liquid. A larger compression ratio therefore implies greater compression heating, as can be observed upon comparing profiles of the temperature versus mass in Fig. 2. This statement is independent of the details of the model.

The mass exchange equilibrium radii listed in Table I are all stable equilibria. Stability of these equilibria is established in the computations by checking that slightly larger bubbles would tend to shrink and slightly smaller bubbles would tend to grow over a cycle. The stability criterion of Ref. 13 were checked by finite differences, both with and without surface tension. We remark that if surface tension is included, another *unstable* mass exchange equilibrium appears at smaller radius.

It is most interesting to consider the fate of a still xenon bubble upon changing the liquid temperature. If two still bubbles are in mass exchange equilibrium in a liquid with temperature $T_{\infty,1}$ and $T_{\infty,2}$, with the same C_∞, then (1) implies

$$\frac{p_{\mathrm{ref},1}}{k(T_{\infty,1})}=\frac{p_{\mathrm{ref},2}}{k(T_{\infty,2})}.$$

Now we use the fact that the reference pressure is (rather weakly) related to the bubble ambient radius through the surface tension γ to obtain

$$\frac{p_a+2\gamma/a_1}{k(T_{\infty,1})}=\frac{p_a+2\gamma/a_2}{k(T_{\infty,2})}.$$

If we assume that the static pressure p_a is much larger than the contribution of surface tension, then we have approximately

$$1+\frac{2\gamma}{p_a}\left(\frac{1}{a_1}-\frac{1}{a_2}\right)=\frac{k(T_{\infty,1})}{k(T_{\infty,2})}.$$

Hence, if $T_{\infty,2}<T_{\infty,1}$ and solubility decreases with temperature as for xenon, then $a_2>a_1$. Static bubbles behave exactly opposite to the strongly driven bubbles when one changes the liquid temperature!

The strong influence of liquid temperature on the hot spot of a xenon sonoluminescence bubble is in stark contrast to the weak influence of liquid temperature on a helium bubble. This is shown in Table II. By adjusting the liquid temperature by about 10 K (plus and minus) relative to the reference temperature, the ambient radius of a helium bubble is shown to change by less than 1%. This is very little compared to the 11% change in the size of a xenon bubble over the same temperature range. The change in compression ratio and therefore also the hot spot temperature change is also very slight for a helium bubble. The main distinction between helium and xenon that is responsible for the differing response is the relative variability of the gas solubility with temperature, shown in Fig. 3 over a range about 300 K. The curves are the approximations we used, namely, for xenon solubility in water,

$$x_{\mathrm{Xe}}=\exp\left[-74.7398+\frac{105.210}{T/100}+27.4664\log\left(\frac{T}{100}\right)\right],$$

and for helium in water

$$x_{\mathrm{He}}=\exp\left[-41.4611+\frac{42.5962}{T/100}+14.0094\log\left(\frac{T}{100}\right)\right].$$

These are mole fractions with temperature in Kelvins.[11]

TABLE II. Stable ambient radius a versus far-field temperature T_∞, and maximum internal gas temperature $T_{\max}$ and compression ratio at the end of the main collapse for bubbles of helium in water driven at 1.3 atm and 26.5 kHz.

a (μm)	T_∞ (K)	$R_{\max}/R_{\min}$	$a/R_{\min}$	$T_{\max}$ (K)
4.470	289.2	94.00	8.885	45 100
4.500	300.0	93.40	8.815	44 700
4.495	311.8	93.50	8.827	44 700

III. CONCLUSIONS

We have argued that the hot spot in xenon SL bubbles in colder water is hotter as a consequence of a shift to smaller ambient radius that yields bubble dynamics characterized by larger compression ratios. The ambient radius decreases at colder liquid temperatures due to an increase in the solubility of xenon in water. In contrast helium bubbles show very little change in ambient radius over a similar temperature range, owing to the nearly constant helium solubility with varying temperature. Further study is needed to determine to what extent the vapor pressure of the liquid outside the bubble also contributes to this phenomenon.

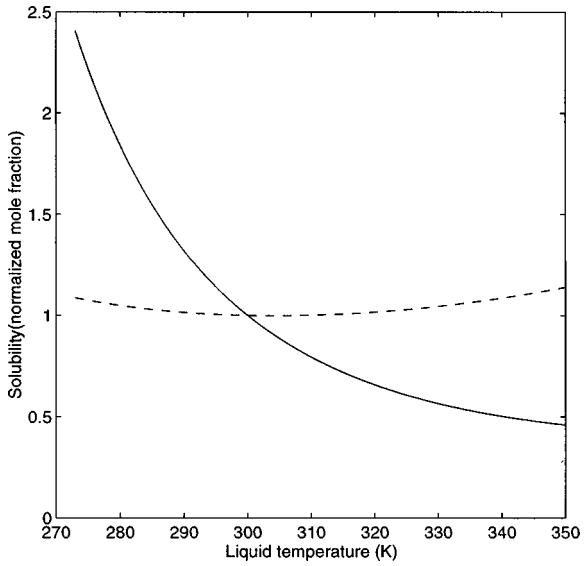

FIG. 3. Gas solubility in water, relative to the value at 300 K. The solid curve is for xenon, the dashed curve for helium.

A clearer version of the arguments presented can be obtained by formal differentiation of the threshold criterion (1) with respect to ambient radius a; in the case where p_{ref} is nearly constant, this yields

$$\frac{C_\infty}{p_{\mathrm{ref}}}\frac{dk}{dT_\infty}\frac{dT_\infty}{da}=\frac{d\langle p_G^*(\tau)\rangle_{\tilde{\tau}}}{da}.$$

For xenon, we argued that k increases with temperature. For a bubble in stable mass exchange equilibrium, the right-hand side is positive.[13] Hence, the equation allows one to conclude that $da/dT_\infty>0$, i.e., reducing the liquid temperature leads to a shrinking of a.

The theory presented in this work may be an important part of the explanation of why colder SL bubbles can be driven to shine more brightly. This observed effect may be partly due to the mechanism described in the present work, and must also be related to a change in the instability that limits the maximum acoustic drive amplitude that a bubble can sustain indefinitely.[14] Our work suggests that a fruitful experiment would be to observe changes in compression ratio and SL brightness of two different bubbles upon changing liquid temperature. This cannot be done at a constant amplitude and frequency of the transducers that drive the flask oscillations in a typical set up owing to a shift in the resonant oscillations of the flask with temperature. However, for both bubbles, either the transducer driving amplitudes or the frequencies could be adjusted similarly to follow the shifting resonance as the liquid temperature is changed. Bubbles of pure gases with rapidly varying solubility with temperature would be expected to change dramatically with temperature, while those with only slightly varying solubility with temperature would be expected to change little, if all other properties are similar for the two bubbles.

Because the ambient radius decreases for colder bubbles of xenon (or like gas), the bubble dynamics at a constant acoustic drive is more evident. The peak temperatures and pressures are increased, presumably increasing the light production by some as-yet unknown mechanism. These ideas have been the subject of previous speculation,[4] but the missing link that it is the shift in ambient radius with temperature that causes the effect has eluded explanation.

We note that these arguments do not address the question of the sometimes dramatic decrease in ambient radius with driving pressure amplitude that is observed in air bubbles or in bubbles of diatomic gases doped with a noble gas.[3,5] This effect is likely explained by the selective rectification of noble gases combined with the chemical destruction of other species.[15]

Finally, we note another possibly useful outcome of the present theory. In a carefully designed experiment, the extent of the change in ambient radius with liquid temperature may be a useful diagnostic of the *identity* of the gas within a SL bubble. This can be seen from the computational example in Sec. II, although in a physical experiment one must take into account the changes in resonance characteristics of the flask and contents with temperature.

ACKNOWLEDGMENTS

This research was funded by the Young Investigator Program of the Office of Naval Research, and by the National Science Foundation. The authors would like to thank the anonymous reviewers of an earlier version of this paper for their helpful comments.

[1] D. F. Gaitan, L. A. Crum, C. C. Church, and R. A. Roy, J. Acoust. Soc. Am. **91**, 3166 (1992); L. A. Crum and S. Cordry, in *Proc. IUTAM Symposium on Bubble Dynamics and Interface Phenomena*, edited by J. R. Blake and N. H. Thomas (Kluwer, Dordrecht, 1994).
[2] R. Löfstedt, K. Weninger, S. Putterman, and B. P. Barber, Phys. Rev. E **51**, 4400 (1995).
[3] R. G. Holt and D. F. Gaitan, Phys. Rev. Lett. **77**, 3791 (1996).
[4] R. Hiller, S. J. Putterman, and B. Barber, Phys. Rev. Lett. **69**, 1182 (1992).
[5] B. P. Barber, C. C. Wu, R. Löfstedt, P. H. Roberts, and S. J. Putterman, Phys. Rev. Lett. **72**, 1380 (1994).
[6] K. Weninger, R. Hiller, B. P. Barber, D. Lacoste, and S. J. Putterman, J. Phys. Chem. **99**, 14 195 (1995).
[7] J. J. Carroll, Chem. Eng. Prog. **87**(9), 48 (1991).
[8] A. Eller and H. G. Flynn, J. Acoust. Soc. Am. **37**, 493 (1965).
[9] M. M. Fyrillas and A. J. Szeri, J. Fluid Mech. **277**, 381 (1994).
[10] R. E. Apfel and J. A. Ketterling, J. Acoust. Soc. Am. **102**, 3076(A) (1998).
[11] H. L. Clever (ed.), *Helium and Neon—Gas Solubilities*, IUPAC Solubility Data Series, Vol. 1 (Pergamon, New York, 1979); *Krypton, Xenon and Radon—Gas Solubilities*, IUPAC Solubility Data Series (Pergamon, New York, 1979), Vol. 2.
[12] V. Q. Vuong and A. J. Szeri, Phys. Fluids **8**, 2354 (1996).
[13] M. P. Brenner, D. Lohse, D. Oxtoby, and T. F. Dupont, Phys. Rev. Lett. **76**, 1158 (1996); I. Akhatov, N. Grumerov, C. D. Ohl, U. Parlitz, and W. Lauterborn, *ibid.* **78**, 227 (1997).
[14] S. Hilgenfeldt, D. Lohse, and W. C. Moss, Phys. Rev. Lett. **80**, 1332 (1998).
[15] D. Lohse, M. P. Brenner, T. F. Dupont, S. Hilgenfeldt, and B. Johnston, Phys. Rev. Lett. **78**, 1359 (1997).

An improved ray-tracing algorithm for predicting sound propagation outdoors

Kai Ming Li,[a] Shahram Taherzadeh, and Keith Attenborough
Engineering Mechanics Discipline, Faculty of Technology, The Open University, Milton Keynes MK7 6AA, United Kingdom

(Received 14 May 1997; revised 18 May 1998; accepted 8 July 1998)

A new ray-tracing method for predicting the sound field near a flat impedance ground in a refracting atmosphere is developed that includes the effect of vector wind and turbulence explicitly. Improvements on previous ray-tracing schemes include the use of a generalized Snell's law, an integration by means of a Gaussian quadrature, and a bracketing method for finding the ray paths. For the turbulence calculations, the interray coherence is determined from turning point heights rather than from integrals along the ray paths. A more efficient algorithm is developed for computing the sound field above an impedance plane in a realistic atmosphere. Despite the inherent limitations of the ray-trace approach, particularly in respect of logarithmic wind profiles, the algorithm is valid over a wide range of practical situations. © *1998 Acoustical Society of America.* [S0001-4966(98)04010-7]

PACS numbers: 43.28.Fp, 43.20.Fn [LCS]

INTRODUCTION

The heuristic ray-tracing method[1] is a convenient and computationally undemanding way of predicting the sound propagation outdoors in the presence of wind and temperature gradients above an impedance plane. In a recent study,[2] Li has shown that the ground and surface wave terms can be included rigorously by using an asymptotic analysis. Raspet *et al.*[3] have demonstrated that the sound field predicted by the heuristic ray-tracing model,[4] using an effective sound speed gradient to represent the combined effects of wind and temperature, agrees remarkably well with that calculated by the fast field program (FFP) at long ranges. Furthermore, Salomons[5] has included atmospheric turbulence in his ray model for the computation of sound field in a temperature stratified medium. The purpose of this paper is to present an efficient numerical implementation of the theory developed in Ref. 2 in a way that includes the effect of vector wind and turbulence explicitly. It should be noted that the analytical solution for the sound field above an extended-reaction plane is derived in Ref. 2. However, most of the outdoor ground surfaces are locally reacting. Hence, although it is straightforward to derive a prediction for propagation over an extended reaction plane, we consider only the locally reacting plane.

The ray-tracing method used in the present paper differs from the traditional one.[6,7] First, when tracing the ray paths, we use a numerical integration algorithm instead of the Euler method. Alternatively, a fourth-order Runge–Kutta algorithm with adjustable step sizes may be used. Second, to search for the eigenrays, we use a bracketing method in place of the ''hit-and-miss'' approach. The traditional accuracy of computation of the phase angle is improved by using the modified Snell's law to calculate the ray angle along the ray path, and by using numerical integration to compute the acoustical path length. Turbulence is included in the formulation. However, the interray coherence coefficient is computed from the turning point heights rather than from detailed tracing of the ray paths. The inherent limitations of the ray-trace method for predicting the sound field above an impedance plane under logarithmic sound speed gradients are explored.

In Sec. I, the theoretical basis for the ray-trace implementation is outlined. Section II details the new computational features. Section III describes the method for including turbulence. Section IV presents results of computations and comparisons with FFP predictions. Finally, in Sec. V, we offer some concluding remarks.

I. MODIFIED WEYL–VAN DER POL FORMULA

In an earlier study, Li[2] has demonstrated that the sound field due to a monopole source above a porous ground in the presence of temperature and wind gradients can be written in form that is recognizably similar to the Weyl–Van der Pol formula. The theory may be summarized as follows. In a moving stratified medium, the index of refraction $m(z)$ is defined as

$$m(z)=\frac{n(z)}{1+M(z)\cos(\epsilon-\psi_w)\sin\mu}, \tag{1}$$

where $n(z)$ is the index of refraction in an otherwise homogeneous medium at height z above the impedance plane. The symbols, u and ψ_w, are the magnitude and direction of wind, $\mu(z)$ and ϵ are the polar and azimuthal angles of a wavefront normal, $c(z)$ is the speed of sound, and $M(z)=u/c$ is the Mach number. We note that the azimuthal angle ϵ is constant for a given wavefront normal, but the polar angle μ varies as a function of height in a moving stratified medium. Using the index of refraction in a moving medium, we can derive the modified Snell's Law for a wavefront normal as

[a]Corresponding author: present address: Department of Mechanical Engineering, Hong Kong Polytechnic University, Hung Hom, Kowloon, Hong Kong.

$$m \sin \mu = \sin \mu_0 = \text{constant}, \tag{2}$$

where μ_0 is a reference polar angle of a ray at $z=0$, for example. In other words, we can determine the wavefront normal of a particular ray by specifying a polar angle at a given height and its corresponding azimuthal angle. As pointed out by Ostashev,[8] the trajectory of the wavefront normal should be distinguished from the sound ray that travels from the source to receiver. In essence, the wavefront normal is not coincident with the sound ray in a moving medium. To aid theoretical and numerical analyses, we find it more convenient to define the acoustical path length, $R_L(\mu,\epsilon)$, the Doppler factor $D(z)$, the stratification factor $S(\mu,\epsilon)$, and the Jacobian factor $J(\mu,\epsilon)$ as follows:

$$R_L(\mu,\epsilon) = \int_{z_<}^{z_>} m \cos \mu \, dz + r \sin \mu_0 \cos \epsilon, \tag{3}$$

$$D(z) = [1 + M \cos(\epsilon - \psi_w)\sin \mu]^{-1}, \tag{4}$$

$$S(\mu,\epsilon) = \frac{D(z)}{D(z_s)} \sqrt{\frac{\rho(z)}{\rho(z_s)}} \sqrt{\frac{\cos \mu_0}{m \cos \mu}} \sqrt{\frac{\cos \mu_0}{m_s \cos \mu_s}}, \tag{5a}$$

and

$$J(\mu,\epsilon) = \left(\frac{1}{\sin \mu_0}\right)^2 \left| \frac{\partial^2 R_L}{\partial \mu_0^2} \frac{\partial^2 R_L}{\partial \epsilon^2} - \left[\frac{\partial^2 R_L}{\partial \mu_0 \, \partial \epsilon}\right]^2 \right|, \tag{5b}$$

where ρ is the density of air which is a function of height z and r is the horizontal separation between the source and receiver. The subscripts $<$ and $>$ denote the variables to be evaluated at $z_<$ and $z_>$, respectively, where $z_<$ and $z_>$ are the lesser and the larger of the source and receiver height.

In Ref. 2, an elaborate analysis has been used to derive an expression for the sound field above an extended reaction ground in a stratified medium. However, a heuristic model for the inclusion of the ground wave is found to be adequate for most practical situations in a homogeneous medium.[9] Since the interaction between the sound waves and ground should remain unaffected by the presence of wind and temperature gradients, it is proposed to use the same approach for the case of a stratified medium. Suppose that the polar and azimuthal angles of the wavefront normals of the direct and the reflected waves are θ, ψ, $\bar{\theta}$, and $\bar{\psi}$, respectively. Then, the sound field, above an extended reaction ground surface, can be approximated according to the heuristic model by[2,9]

$$p(r,0,z) = \frac{S_d e^{ik_0 R_1'}}{4\pi\sqrt{|J_d|}} + \{R(\bar{\theta}_0) + (1 - R(\bar{\theta}_0))F(w)\} \times \frac{S_i e^{ik_0 R_2'}}{4\pi\sqrt{|J_i|}}, \tag{6}$$

where k_0 is the reference wave number, $R(\bar{\theta}_0)$ is the plane wave reflection coefficient, $F(w)$ is the boundary loss factor, and w is known as the numerical distance. These parameters can be determined according to

$$R(\bar{\theta}_0) = \frac{\cos \bar{\theta}_0 - \beta_e}{\cos \bar{\theta}_0 + \beta_e}, \tag{7a}$$

$$F(w) = 1 + i\sqrt{\pi} w e^{-w^2} \operatorname{erfc}(-iw), \tag{7b}$$

$$w^2 = \tfrac{1}{2} i k_0 R_2' (\cos \bar{\theta}_0 + \beta_e)^2, \tag{7c}$$

where erfc( ) is the complementary error function, β_e is the effective admittance of the porous ground given by

$$\beta_e = e_\rho \sqrt{e_n^2 - \sin^2 \bar{\theta}_0}, \tag{8}$$

$e_\rho (\equiv \rho_0/\rho_2)$ and $e_n (\equiv k_2/k_0)$ are, respectively, the ratios of densities and wave numbers for the upper and lower media. The subscript 2 denotes the parameters of the lower medium, i.e., the porous ground, whilst the subscript 0 denotes those for the upper medium with the vertical height $z=0$.

As shown in Eq. (6), $k_0 R_1'$ and $k_0 R_2'$ are the total phase changes for the direct and reflected waves of the sound propagated from the source to the receiver. Hence, $R_1'[\equiv R_L(\theta,\psi)]$ and, $R_2'[\equiv R_L(\bar{\theta},\bar{\psi})]$ may be regarded as the corresponding acoustical path lengths. The quantities $S_d[\equiv S(\theta,\psi)]$, $J_d[\equiv J(\theta,\psi)]$, $S_i[\equiv S(\bar{\theta},\bar{\psi})]$, and $J_i[\equiv J(\bar{\theta},\bar{\psi})]$ are the corresponding stratification and Jacobian factors for the direct and reflected rays. Also, it is of interest to note that the receiver position is given in the cylindrical polar coordinate system with r as the range and z the height of the receiver. Without loss of generality, the azimuthal angle of the receiver is set at zero.

For a locally reacting surface, we have $|e_n| \gg 1$. Hence, it follows from Eq. (8) that the effective admittance becomes

$$\beta_e \approx e_\rho e_n = \frac{\rho_0 c_0}{\rho_2 c_2}, \tag{9}$$

which is the specific normalized admittance β of the ground. Furthermore, in the special case of a stationary medium where $M=0$, Eq. (6) can be reduced to the form given in Ref. 11 [see his Eq. (58)].

The above analysis is based on the method of Fourier transformation and the well-known WKB approximation in which the sound field can be expressed in terms of an integral representation. By evaluating the integral asymptotically, we can confirm the validity of the heuristic approximation used in the previous analyses[2] which include the ground wave term explicitly (the second term of the curly bracket) in Eq. (6). In addition, the previous analysis is valid for a relatively short separation between the source and receiver. This implies that, in an upward refracting medium, the analysis is invalid in the shadow zone and in close proximity to the shadow boundary. Also, in a downward refracting medium, the analysis is only satisfactory for a close range such that the reflected wave suffers only a single bounce. Also the receiver must not be close to a caustic where the Jacobian factor vanishes.

In another study,[10] Li has extended his previous work[11] to allow for multiple bounces in a temperature stratified but downward refracting medium. Although the analysis is based on a monotonically increasing function of $c(z)$, the principle should apply equally for other more intricate profiles that may include regions, where $dc(z)/dz$ is zero. This earlier work can be extended readily and straightforwardly to take account of the wind effects, but the details are not shown

here. The asymptotic solution for the total field above a locally reacting impedance plane can be derived to yield

$$p(r,0,z)=\frac{\exp[i(k_0R_1'-\chi_1)]}{4\pi R_d}+\sum_j Q_j\frac{\exp[i(k_0R_2'^{(j)}-\chi_2^{(j)})]}{4\pi R_r^{(j)}}, \tag{10}$$

where the subscript (j) represents the corresponding parameters of the reflected wave that hits the ground j-times before reaching the receiver. Since the sound field is expressed in an analogous form as the Weyl–Van der Pol formula, R_d $(\equiv\sqrt{J_d}/S_d)$ and $R_r^{(j)}(\equiv\sqrt{J_i^{(j)}}/S_i^{(j)})$, which have the dimension of length, may be treated as the effective path lengths for the direct and reflected waves. These terms are introduced for the ease of reference. The quantity Q_j is the spherical wave reflection coefficient for the reflected wave:

$$Q_j=\{\Gamma(\bar{\theta}_0^{(j)})+[1-\Gamma(\bar{\theta}_0^{(j)})]F(w(\bar{\theta}_0^{(j)}))\}^j \tag{11}$$

and, for an impedance plane, the plane wave reflection coefficient $\Gamma(\bar{\theta}_0^{(j)})$ is given by

$$\Gamma(\bar{\theta}_0^{(j)})=\frac{\cos\bar{\theta}_0^{(j)}-\beta}{\cos\bar{\theta}_0^{(j)}+\beta}, \tag{12}$$

where the specific normalized admittance β is used in favor of the effective admittance β_e. The boundary loss factor is determined by using Eq. (7b) with the numerical distance w_j given by

$$w(\bar{\theta}_0^{(j)})=\sqrt{\tfrac{1}{2}ik_0R_2'^{(j)}}(\cos\bar{\theta}_0^{(j)}+\beta). \tag{13}$$

It should be noted that one has to find all possible rays (or the so-called eigenrays) for a given j. Each eigenray, which hits the ground j-th time, has different values of $\bar{\theta}_0^{(j)}$, w_j, Γ_j, and Q_j.

Equation (10) describes the solution as the sum of contributions from all possible rays linking the source and receiver. We remark that there is at most one possible direct ray where the combined wind and temperature gradients give rise to monotonic profiles. When calculating R_1', R_d, $R_2'^{(j)}$, and $R_r^{(j)}$, it is crucial to include all possible branches of the ray traces. Furthermore, there are additional phase shifts, χ_1 and $\chi_2^{(j)}$ for the direct and reflected waves as a result of the ray grazing the caustic. There will be a phase reduction of $\pi/2$ each time the ray touches a caustic.[12]

II. AN IMPROVED SCHEME FOR RAY TRACING

In the past, Thompson's method[6,7] and its derivative[13] were commonly used as the basis for the ray-tracing algorithm in a moving stratified medium. These previous methods are based, in turn, on the theory derived by Blokhintzev.[14] Nevertheless, we have shown[2,15] earlier that the theoretical results of our present approach are identical to that of the previous methods. These earlier methods often involve a pair of first-order differential equations which can be solved either by numerical integration[13] or by the construction of a finite-step wavefront (i.e., by the Euler method).[6,7] More importantly, the search for an eigenray usually involves some form of hit-and-miss approach. A ray is launched in a given direction at the source and then it is determined whether the launched ray hits the ''target'' at the receiver location. To reduce computational time, the target is often restricted to a finite area. The numerical accuracy is controlled by setting the size of the target as well as the step size in tracing the ray path. The computational time increases as the step length and target are made smaller. In this paper, we propose a bracketing scheme that avoids the need for blind shooting.

Instead of using the eikonal equations as our starting point, we determine stationary points [(θ,ψ) for the direct wave and $(\bar{\theta},\bar{\psi})$ for the reflected wave] for $R_L(\mu,\epsilon)$ in Eq. (3). The eigenray can then be determined by solving a pair of nonlinear equations for μ and ϵ as follows:

$$r\sin\epsilon=\int_{z_<}^{z_>}\frac{M\sin(\epsilon-\psi_w)}{\cos\mu}\,dz \tag{14}$$

and

$$r\cos\epsilon=\int_{z_<}^{z_>}\frac{\sin\mu+M\cos(\epsilon-\psi_w)}{\cos\mu}\,dz. \tag{15}$$

To determine an eigenray, it is sufficient to specify the polar angle at a given height and the azimuthal angle of a wavefront normal because the polar angle at other heights can be found by using the modified Snell's law [i.e., Eq. (2)]. The small ratio between wind and sound speed ($M\approx0.03$) in the normal atmospheric environment means that the azimuthal angle of the wavefront normal is very close to the azimuthal angle of the receiver, and, therefore, $\epsilon=0$ may be used as the first approximation. We can determine $\mu(z)$ from Eqs. (2) and (15) for a given range r. A second approximation for ϵ can be found by using $\mu(z)$ and Eq. (14) to give

$$\epsilon=\tan^{-1}\left[\frac{\sin\psi_w\int_{z_<}^{z_>}(M/\cos\mu)dz}{\cos\psi_w\int_{z_<}^{z_>}(M/\cos\mu)dz-r}\right]. \tag{16}$$

The integration in Eq. (16) can be carried out numerically and hence ϵ evaluated. This iterative process in determining ϵ and $\mu(z)$ can be repeated until the required accuracy is achieved. In practice, ϵ is very small and one only needs two or three iterations for most situations.

Next, we describe an improved method of finding $\mu(z)$ for a given ϵ. We restrict our analysis to a monotonically increasing function of $m(z)$ and describe a ''sure-hit'' method in contrast to the conventional approach of trial-and-error. As mentioned earlier, it is sufficient just to specify $\mu_0[\equiv\mu(0)]$, for example, as the unknown variable in Eq. (15). The polar angle at other heights can be determined through the use of Eq. (2). Determination of μ_0 involves the evaluation of the integral given in Eq. (15). There is an integrable singularity at the turning point where the polar angle is $\pi/2$ (or the slope of the wavefront normal is zero). Substituting Eq. (14) into (15), we obtain

$$\int_{z_<}^{z_>}\tan\mu\,dz=\frac{r\sin\psi_w}{\sin(\psi_w-\epsilon)}. \tag{17}$$

Using partial integration, we can remove the integrable singularity of the left side of Eq. (17) and make the subsequent numerical analysis somewhat simpler. In this case, Eq. (17) can be rearranged in a more convenient form as

$$I(\mu_0)=\frac{r\ \sin\ \psi_w}{\sin(\psi_w-\epsilon)}-\left[\frac{m\ \sin\ \mu\ \cos\ \mu}{m'}\right]_{z_<}^{z_>}, \tag{18}$$

where

$$I(\mu_0)=\int_{z_<}^{z_>}\sin\ \mu\ \cos\ \mu[1+mm''/(m')^2]dz, \tag{19}$$

and the primes denote the derivatives with respect to z.

The above analysis is valid as long as the derivative of the index of refraction m does not vanish at any point along the ray path. Physically, this situation corresponds to the case of an infinitely narrow sound channel where a ray will be trapped. Numerical integration is required in general to calculate $I(\mu_0)$ in Eq. (19). On the other hand, the computation of definite integrals may be regarded as an initial value problem. By differentiating both sides of Eq. (19) with respect to z, we transform it into the following first-order differential equation:

$$\frac{dI}{dz}=\sin\ \mu\ \cos\ \mu\left[1+\frac{mm''}{(m')^2}\right], \tag{20}$$

with the initial condition of $I=0$ at $z=z_<$. We wish to compute the function I at $z=z_>$ with due consideration for tracing all branches for a complete ray path. It is adequate to just calculate the integral from $z_<$ to the turning point, from $z_>$ to the turning point, and from the ground surface to the turning point. The appropriate number of these portions are then added together to trace all eigenrays in all possible ways. A typical approach involves the use of a finite step size (Δz). The increment of I can be computed by multiplying the right side of Eq. (20) by Δz for each step. This method is sometimes called the Euler method. However, the Euler method is not recommended for practical use because other more sophisticated numerical methods provide a more accurate and stable solution.[16] Since a high degree of accuracy is required in computing $I(\mu_0)$, a fourth-order Runge–Kutta or the so-called adaptive Bulirch–Stoer technique may be used; see for example, Ref. 16. Nevertheless, we have also used a direct numerical integration method to compute $I(\mu_0)$. We find that a 10 point Gaussian quadrature[16] is sufficient for most practical purposes. It is also of interest to note that the height of the turning point $z_{\max}$ can be determined by using Eqs. (1) and (2), and by noting $\mu(z_{\max})=0$. The nonlinear equation for $z_{\max}$ can be solved readily by means of a standard Newton–Raphson method.[16]

To find all solutions for Eq. (18), we introduce the eigenray error function,

$$E(\mu_0)=\frac{r\ \sin\ \psi_w}{\sin(\psi_w-\epsilon)}-\left[\frac{m\ \sin\ \mu\ \cos\ \mu}{m'}\right]-I(\mu_0). \tag{21}$$

The eigenrays are then determined by minimizing $|E(\mu_0)|$ for a given source/receiver geometry and wind/temperature profiles. The error function $E(\mu_0)$ is sampled at a range of polar angles specified by the user. This allows the determination of zero crossings, which, in turn, provides information about a pair of bracketing polar angles. The spacing of the samples $\Delta\mu_0$ is also set by the user. A smaller $\Delta\mu_0$ and a large range of polar angles increase the probability that all eigenrays will be found at the expense of higher computational time. The Brent root finding algorithm[16] is used to find the eigenray solution when zero crossings are found. It is of interest to note that an initial examination of the wind velocity and sound speed profiles will provide some useful insight in the choice of upper and lower bounds of the polar angles. For example, suppose a ray launches upward at some polar angle μ_u that has its turning point at height $z_>$. In this case, it is clear that any ray launched upwards at a polar angle greater than μ_u cannot reach a receiver situated at a height greater than $z_>$. Figure 1 shows the schematic diagram for the typical rays launching at different polar angles. Hence, it is obvious μ_u provides a useful upper bound for the sampling range for the reflected rays. On the other hand, the choice of the sampling range may also be decided on a trial and error basis.

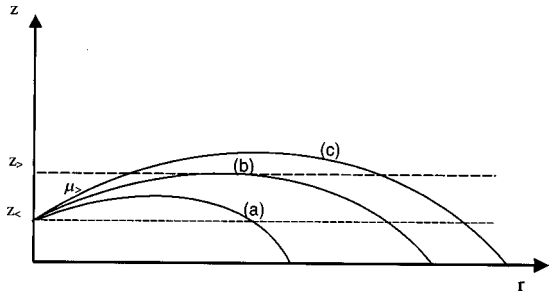

FIG. 1. Schematic diagram to show a ray is launched at an angle $\mu(z)$. (a) $\mu(z)>\mu_u$: Sound ray cannot reach the receiver at height greater than $z_>$. (b) $\mu(z)=\mu_u$: Critical ray, the ray reaches the receiver at height $z_>$ at the turning point. (c) $\mu(z)<\mu_u$: Sound ray can reach the receiver at height $z_>$ either at the ascending or descending branches.

We also note that, in a downward refracting medium, a ray launched at an angle $(\pi-\mu_u)$ has the same characteristic parameters as the ray launched upward with the polar angle μ_u. Therefore, the down-going rays can be searched at the same ''time.'' Once the polar angle $\mu(z)$ of the wavefront normal has been determined, its value is substituted into Eq. (16), and that allows ϵ to be found by a simple iteration procedure as described earlier. We wish to point out that the principle described above can be generalized to other more intricate profiles, but further developments are beyond the scope of the present paper.

On finding the polar and azimuthal angles of all eigenrays, it is straightforward to compute R_1', $R_2'^{(j)}$, J_d, and $J_i^{(j)}$ by direct numerical integration. Making use of Eq. (5a), the stratification factors, S_d and $S_i^{(j)}$ can be determined, and hence the effective path lengths R_d and $R_r^{(j)}$ can be computed. These parameters are used, in turn, to compute the total sound field using Eq. (10). The determination of J_d, $J_i^{(j)}$ and the reduction in phases [χ_1 and $\chi_2^{(j)}$] can be facilitated by noting

$$\frac{\partial^2 R_L}{\partial\mu^2}=-\cos^2\ \mu_0\int_{z_<}^{z_>}\frac{n^2}{m^3\ \cos^3\ \mu}\,dz, \tag{22a}$$

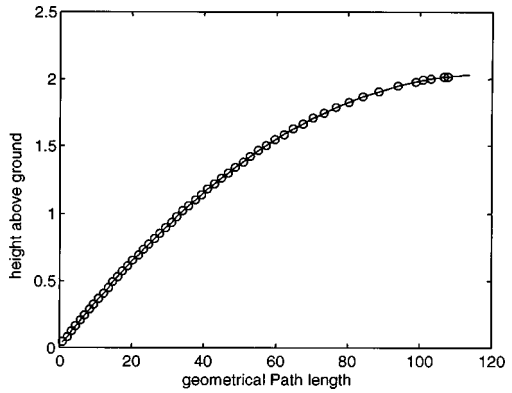

FIG. 2. Plots of the geometrical path length and the effective path length of the direct wave versus height from the ground up to the turning point. The solid line represents the geometrical path length calculated according to Eq. (24) and the circles represent the effective path length calculated by $\sqrt{J_d}/S_d$.

$$\frac{\partial^2 R_L}{\partial \epsilon^2} = -\sin^2\,\mu_0 \int_{z_<}^{z_>} \left[\frac{n}{m\,\cos\,\mu} + \frac{M^2\,\sin^2(\epsilon-\psi_w)\sin^2\,\mu_0}{m^3\,\cos^3\,\mu} \right] dz, \tag{22b}$$

and

$$\frac{\partial^2 R_L}{\partial \mu\,\partial \epsilon} = -\cos\,\mu_0\,\sin\,\mu_0 \times \int_{z_<}^{z_>} \frac{nM\,\sin(\epsilon-\psi_w)\sin\,\mu_0}{m^3\,\cos^3\,\mu}\,dz. \tag{22c}$$

The equation of the caustic can be found by setting the Jacobian factor J, given by

$$J = \left\{ \frac{\partial^2 R_L}{\partial \mu_0^2}\,\frac{\partial^2 R_L}{\partial \epsilon^2} - \left[\frac{\partial^2 R_L}{\partial \mu_0\,\partial \epsilon} \right]^2 \right\}^{1/2} \tag{23}$$

to zero,[1] and it is then possible to determine χ_1 and $\chi_{(j)}$ by examining whether the ray grazes the caustic.

In view of the fact that ray theory breaks down near caustics and it is computationally more expensive to compute the Jacobian factor, therefore, it is found more convenient to use the geometrical path lengths in favor of the effective path lengths of the direct and reflected waves, R_d and $R_r^{(j)}$.[4] The geometrical path length, $R_g(\mu,\epsilon)$ is defined as the length of the ray trajectory linking the source and receiver in a vertically stratified medium. From the geometrical consideration, it can be calculated by

$$R_g(\mu,\epsilon) = \int_{z_<}^{z_>} \frac{dz}{\cos\,\mu}. \tag{24}$$

Consequently, the geometrical path lengths of the direct and reflected waves can be determined according to R_1 $[\equiv R_g(\theta,\psi)]$ and $R_2[\equiv R_g(\theta,\psi)]$, respectively. Their numerical values can be computed efficiently by a standard numerical integration routine. Figure 2 compares R_1 with the effective path length $R_d(\equiv\sqrt{J_d}/S_d)$. It demonstrates that the corresponding geometrical path lengths are good approximations for replacing R_d and $R_r^{(j)}$ in Eq. (10) when the receiver is situated far from the caustics.

III. ALLOWANCE FOR TURBULENCE

A quantity that is of particular interest in studies of outdoor sound propagation near the ground is the excess ground attenuation in the presence of turbulence (A_e). Using a modified form of Eq. (10) and Ref. 4 [Eq. (35)], A_c may be defined by

$$A_e = 10\,\lg(\langle \overline{p^2}\rangle/\langle p_d^2\rangle), \tag{25}$$

where

$$\langle \overline{p^2}\rangle = \sum_{i=0}^{N} \frac{|q_i|^2}{R_i^2} + 2\sum_{i=1}^{N}\sum_{j=0}^{i-1} \frac{|q_i|\times|q_j|}{R_i R_j} \times \cos\left[k_0(R_j' - R_i') + \mathrm{Arg}\left(\frac{q_j}{q_i}\right) \right] \times \Lambda, \tag{26}$$

and p_d is the free field term. Note that Eqs. (25) and (26) are based on a study by Clifford and Lataitis[17] [but also see Eq. (35) of Ref. 4]. The mean pressure, $\langle \overline{p^2}\rangle$ is the total sum of interactions between any two rays of a total of $N+1$ rays (including the direct wave). The variables, R_i and R_i', represent the appropriate geometrical and acoustical path lengths. The term q_i is the appropriate spherical wave reflection coefficient, with $q_0=1$ which represents the direct wave term. Suppose that the i-th ray hits the ground l_i times, then the reflection coefficient is given by [see Eq. (11)]

$$q_i(\vartheta_i) = \{\Gamma(\vartheta_i) + [1-\Gamma(\vartheta_i)]F(w(\vartheta_i))\}^{l_i}, \tag{27}$$

where ϑ_i is the angle of incidence of the reflected wave, and $\Gamma(\vartheta_i)$ and $w(\vartheta_i)$ are, respectively, the plane wave reflection coefficient and the numerical distance [see Eqs. (12) and (13)]. The variable Λ is a turbulence parameter allowing for the destruction of coherence between the rays. The turbulence parameter is defined by

$$\Lambda = \exp[-\alpha\sigma^2(1-\zeta)], \tag{28}$$

where σ^2 and ζ are the variance of phase fluctuation along a path and the covariance between paired rays for equal source and receiver heights, respectively. They are defined as

$$\sigma^2 = \frac{\sqrt{\pi}}{2}\,\langle n^2\rangle k_0^2 R L_0 \tag{29a}$$

and

$$\zeta = \frac{\sqrt{\pi}L_0}{2h}\,\mathrm{erf}\left(\frac{h}{L_0}\right), \tag{29b}$$

where erf( ) is the error function with a real argument, $\langle n^2\rangle$ is the refractive index variance, L_0 is the outer scale of turbulence, h is the maximum separation between paired rays, $\alpha=1$ if $L_0 \gg \sqrt{d/k_0}$, $\alpha=0.5$ otherwise, and d is the distance between source and the receiver. The effect of atmospheric absorption is ignored in the present calculations, but it is straightforward to include it in our analysis. In previous ray-tracing methods,[4] h may be computed from predictions of the complete ray paths. Here we follow the method of Raspet and Wu[18] and define it as one-half of the vertical distance

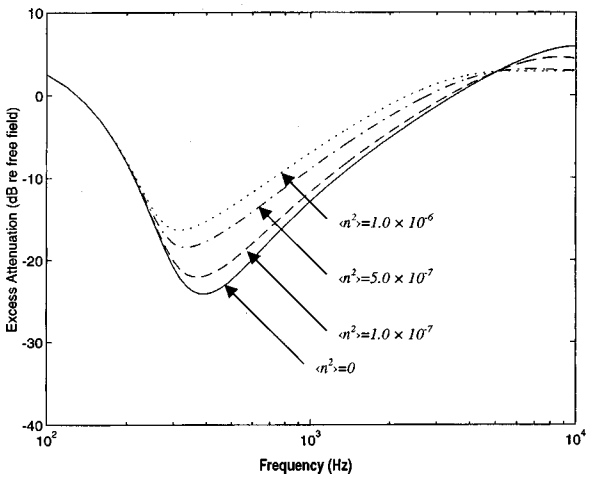

FIG. 3. Effect of turbulence on excess attenuation under downwind conditions with varying degrees of turbulence. Source and receiver heights are 1.5 and 1.8 m, respectively, and the horizontal separation is 1000 m. The assumed linear sound speed gradient is 10^{-4} s^{-1} and the ground impedance is calculated using the two-parameter model with $\sigma_e=300$ kPa s m^{-2} and $\alpha_e=20$ m^{-1}: solid line indicates $\langle n^2\rangle=0$, dashed line: $\langle n^2\rangle=1.0\times10^{-7}$; dash–dot line: $\langle n^2\rangle=5.0\times10^{-7}$; and dotted line: $\langle n^2\rangle=1.0\times10^{-6}$.

between the turning points of the two ray paths. Since the locations of the turning points are calculated in the routine anyway, no extra computation is necessary.

IV. NUMERICAL RESULTS AND DISCUSSIONS

In the following numerical calculations, the specific surface impedance of the boundary is represented by a two-parameter model which assumes a rigid porous ground in which the porosity decreases exponentially with depth. The specific normalized admittance β is given by a two-parameter model[19]

$$\beta=\frac{1}{0.436(1+i)(\sigma_e/f\,)^{0.5}+19.48i\alpha_e/f}, \tag{30}$$

where σ_e and α_e are, respectively, the effective flow resistivity and the effective rate of change of porosity with depth. The values chosen for these parameters here are 300 kPa s m^{-2} and 20 m^{-1}, respectively. They are typical of a grass-covered ground.

Figure 3 demonstrates the result of including turbulence in the manner described in Sec. III for a source and receiver at 1.5 and 1.8 m heights, respectively, horizontal separation 1000 m, a linear sound speed gradient of 10^{-1} s^{-1}, and $\langle n^2\rangle$ varying between zero and 10^{-6}. This figure essentially reproduces Fig. 8 in Ref. 4. Figure 4 compares predictions of transmission loss against range at a frequency of 1 kHz obtained from our ray-trace procedure with results of FFP calculations in the presence of a linear sound speed gradient of 0.1 s^{-1}. In this numerical example, 16 384 integration points and 1000 layers, each 0.5 m thick, were used to obtain the FFP results. However, the FFP calculations results have been plotted at 100 point intervals since finer interference structure than that shown will be destroyed by turbulence and has no practical significance. The ray-trace predictions are in good agreement with the ''smoothed'' structure predicted by the FFP out to the 4-km range.

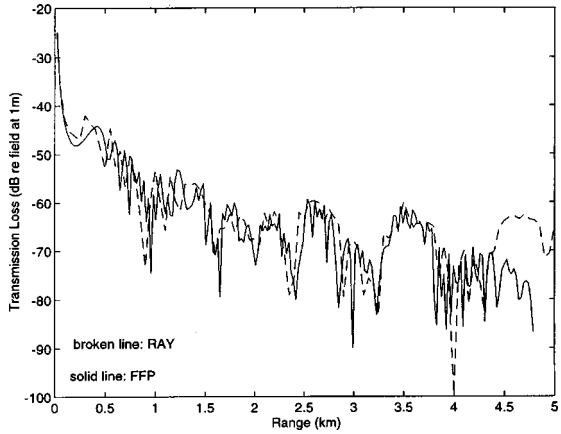

FIG. 4. Comparison between ray-trace and FFP calculations as a function of range at 1000 Hz under downward refraction conditions. The source and receiver heights and the ground impedance values are as for Fig. 2. The sound speed gradient is 0.1 s^{-1}.

A comparison of excess attenuation calculations, at shorter ranges and at 1 kHz, indicates significant discrepancies beyond 100 m (Figs. 4 and 5). This comparison is similar to that in Fig. 9 of Ref. 4 where the ray-trace predictions included turbulence whereas the FFP calculations did not. Here the ray-trace predictions are made both with and without turbulence thus showing that the discrepancy is the result of the ray-trace approximation.

Calculating the excess attenuation for sound downwind of a source in an atmosphere with a logarithmic wind speed profile $[u=1.73\ln(1+2.3z)]$ at a range of 250 m and with source and receiver heights 1.5 and 1.8 m, respectively shows clearly that the ray-trace method is deficient when compared with an accurate FFP calculation (Fig. 6). In this example, 1000 layers (with thickness increasing with height) were used in the FFP calculation.[20] The thickness of each layer near the ground plane was of order of a millimeter for accurate discretization of the logarithmic sound speed profile. The problem for the ray-trace method (as for the WKB–Airy formulation of the FFP[20]) arises from violation of the approximation that requires small change in sound/wind ve-

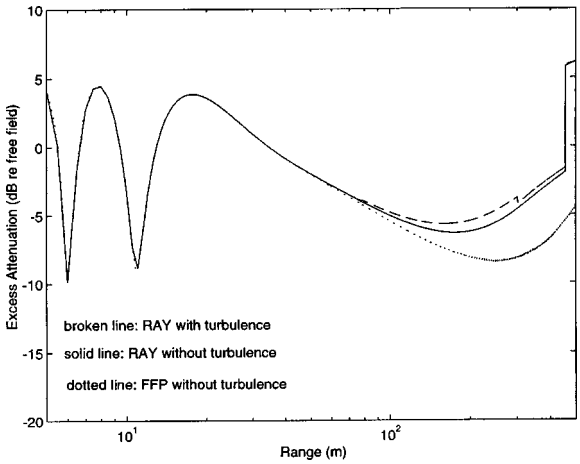

FIG. 5. Comparison of FFP and the ray-trace predictions at 1 kHz and short ranges including the effect of adding turbulence. The source and receiver heights are as for Fig. 2 and the positive sound speed gradient is 0.34×10^{-1} s^{-1}.

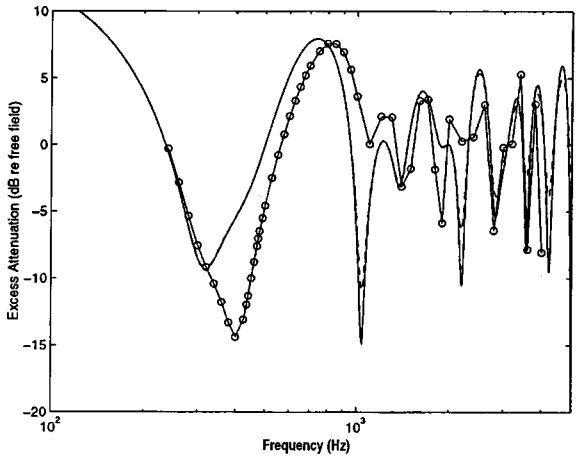

FIG. 6. Plot of excess attenuation for sound downwind of a source in an atmosphere with a logarithmic wind speed profile $[u=1.73\ln(1+2.3z)]$. The solid line is the prediction by the ray method, while the line with circles is that of the FFP program. A maximum of 1000 layers was used in the FFP calculations and the thickness of each layer increased with height. The layer thicknesses near the ground plane were of order of a millimeter for accurate discretization of a logarithmic sound speed profile. The range is 250.0 m and the source and receiver heights were 1.5 and 1.8 m, respectively.

locity per wavelength. However, for the logarithmic profile, the change is the steepest for regions close to the ground. This renders the use of ray-trace method to be inappropriate for the logarithmic profile.

V. CONCLUDING REMARKS

The heuristic ray-based method for calculating the sound field near an impedance plane beneath a refracting atmosphere has been extended to include the effect of vector wind and turbulence. Moreover the ray-based scheme has been improved computationally by using a generalized Snell's law, a ten-point Gaussian quadrature, and a bracketing method for finding the ray paths. For the turbulence calculations, the interray coherence has been determined from turning point heights rather than from integrals along the ray paths. The new ray-trace method should be accurate and efficient for predicting sound fields at short range in any monotonically and slowly increasing wind profile. However, despite the computational improvements, it has been demonstrated that the new ray-trace method is inaccurate when used to predict sound fields in logarithmic wind profiles.

ACKNOWLEDGMENT

This work was supported by the EPSRC, U.K. through Grant No. Ref. GR/J42052.

[1] J. S. Lamancusa and P. A. Daroux, ''Ray tracing in a moving medium with two-dimensional sound-speed variation and application to sound propagation over terrain discontinuities,'' J. Acoust. Soc. Am. **93**, 1716–1726 (1993).

[2] K. M. Li, ''A high frequency approximation of sound propagation in a stratified moving atmosphere above a porous ground surface,'' J. Acoust. Soc. Am. **95**, 1840–1852 (1994). [Two typographical errors are noted. The first equation of Eq. (55) should be $r=\int_{z_<}^{z_>}\cos(\xi-\psi)\tan\alpha\,dz$ and Eq. (58) should be $R_1'=R_L(\theta,\psi)=\int_{R_<}^{R_>} m\hat{\mathbf{a}}_n\cdot\hat{\mathbf{a}}_s\,dR_a$].

[3] R. Raspet, A. L'Esperance, and G. A. Daigle, ''The effect of realistic ground impedance on the accuracy of ray tracing,'' J. Acoust. Soc. Am. **97**, 154–158 (1995).

[4] A. L'Esperence, P. Herzog, G. A. Daigle, and J. R. Nicolas, ''Heuristic model for outdoor sound propagation based on an extension of the geometrical ray theory in the case of a linear sound speed profile,'' Appl. Acoust. **37**, 111–139 (1992).

[5] E. M. Salomons, ''Downwind propagation of sound in an atmosphere with a realistic sound-speed profile: A semianalytical ray model,'' J. Acoust. Soc. Am. **95**, 2425–2436 (1994).

[6] R. J. Thompson, ''Ray theory for an inhomogeneous moving medium,'' J. Acoust. Soc. Am. **51**, 1675–1682 (1972).

[7] M. M. Boone and E. A. Vermaas, ''A new ray-tracing algorithm for arbitrary inhomogeneous and moving media including caustics,'' J. Acoust. Soc. Am. **90**, 2109–2117 (1991).

[8] V. E. Ostashev, ''Ray acoustics of moving media,'' Izvestiya Atmos. Oceanic Phys. **25**, 661–673 (1989).

[9] K. M. Li, T. Waters-Fuller, and K. Attenborough, ''Sound propagation from a point source over extended-reaction ground,'' J. Acoust. Soc. Am. **104**, 679–685 (1998).

[10] K. M. Li, ''Propagation of sound above an impedance plane in a downward refracting atmosphere,'' J. Acoust. Soc. Am. **99**, 746–754 (1996).

[11] K. M. Li, ''On the validity of heuristic ray-trace based modification to the Weyl–Van der Pol formula,'' J. Acoust. Soc. Am. **93**, 1727–1735 (1993).

[12] L. M. Brekhovskikh, *Waves in Layered Media* (Academic, New York, 1980), 2nd ed., pp. 389–395.

[13] F. Walkden and M. West, ''Prediction of enhancement factor for small explosive sources in a stratified moving atmosphere,'' J. Acoust. Soc. Am. **84**, 321–326 (1988).

[14] D. I. Blokhintzev, ''Acoustics of a nonhomogeneous moving medium,'' NACA Tech. Memo 1399, Washington, DC (English translation) (1956).

[15] K. M. Li, S. Taherzadeh, and K. Attenborough, ''A new approach in predicting sound propagation outdoors,'' Proc. 6th International Symposium on Long-Range Sound Propagation (Ottawa, Canada, 1994), pp. 168–180.

[16] W. H. Press *et al.*, *Numerical Recipes in FORTRAN* (Cambridge U.P., London, 1992), 2nd ed., Chap. 4 for Gaussian quadrature, Chap. 9 for the Brent method, and Chap. 16 for the Bulirsch-Stoer method.

[17] S. F. Clifford and R. J. Lataitis, ''Turbulence effects on acoustic wave propagation over a smooth surface,'' J. Acoust. Soc. Am. **73**, 1545–1550 (1983).

[18] R. Raspet and W. Wu, ''Calculation of average turbulence effects on sound propagation based on the fast field program formulation,'' J. Acoust. Soc. Am. **97**, 147–153 (1995).

[19] K. Attenborough, ''Ground parameter information for propagation modeling,'' J. Acoust. Soc. Am. **92**, 418–427 (1992).

[20] S. Taherzadeh, K. M. Li, and K. Attenborough, ''Some practical considerations for predicting outdoor sound propagation in the presence of wind and temperature gradients,'' Appl. Acoust. **54**, 27–44 (1998).

Feedback mechanism of low-speed edgetones

Young-Pil Kwon
Department of Mechanical Engineering, Soongsil University, Dongjak, Seoul 156-743, Korea

(Received 25 June 1997; revised 8 June 1998; accepted 15 June 1998)

The feedback mechanism of low-speed edgetones is analyzed by using the jet–edge interaction model in which reaction of the edge is modeled by an array of dipoles. From the jet–edge interaction model the surface pressure of the edge and the upstream wave are estimated by assuming the downstream disturbance as a sinuously oscillating flow with a constant convection speed. The surface pressure distribution on the edge is found to increase from zero at the edge tip to a peak value around a quarter wavelength downstream, which may be regarded as the effective source point of the upstream-propagating sound wave. From the condition that the two wave trains should be phase-locked at the nozzle lip, $p=-\frac{1}{4}$ is obtained for low-speed edgetones in the phase criterion of the form, $h/\Lambda+h/\lambda=n+p$, where h is the stand-off distance, Λ and λ are the wavelengths of downstream and upstream, respectively, and n is the stage number. Based on the phase criterion, the ratio of the convection speed, U_c, to the jet speed, U_0, is estimated from the experimental data for low-speed edgetones and found to be about $U_c/U_0=0.6$ and to be almost independent of frequency. Finally, an approximate model for the frequency characteristics has been obtained in the form, $\mathrm{St}=(d/h)[(n-1/4)/(1/0.6+\mathrm{M}_0)]$, where d is the width of the two-dimensional nozzle, M_0 the Mach number of the jet velocity, St is the Strouhal number, $\mathrm{St}=fd/U_0$, and f is the frequency. The present model is confirmed substantially in comparison with available experimental data. © *1998 Acoustical Society of America.* [S0001-4966(98)05409-5]

PACS numbers: 43.28.Ra, 43.50.Nm [LCS]

INTRODUCTION

Self-sustained shear-layer oscillations, responsible for whistling flow noise and undesirable structural loading, have been observed for a wide variety of shear-layer impingement configurations as reviewed by Rockwell.[1] The edgetone, a typical phenomenon of these oscillations, is produced by an edge placed in the path of a plane jet issuing from a two-dimensional nozzle of high aspect ratio.

When the free shear layer near the nozzle lip is excited, a disturbance is initiated and convected downstream and amplified, if unstable, into organized vortices. When the vortices impinge on the edge, pressure waves are generated and propagate upstream to the nozzle lip to produce another disturbance as shown in Fig. 1. The upstream-propagating sound and the downstream-convected flow constitute a feedback loop and should be phase-locked at the nozzle lip in order to close the loop. Such a feedback theory was proposed first by Powell[2] in the following form, when the convection speed of the downstream disturbance is constant,

$$\frac{h}{\Lambda}+\frac{h}{\lambda}=n+p, \tag{1}$$

where h is the stand-off distance between the nozzle lip and the edge tip, Λ and λ are the wavelength of the downstream-propagating and the upstream-propagating disturbances, respectively, n is an integer representing sawtoothlike stages of frequency, and p is a nonintegral number for the factor associated with the possible phase delay in the process of jet–edge interaction. Powell[2,3] proposed $p=\frac{1}{4}$ based on a hypothesis about the relationship between the generation of the maximum pressure and the vortex motion. Later Powell[4] made some modification to the model by replacing h with the overall distance h' from the nozzle lip to the effective source point. Although it has never been justified rigorously, $p=\frac{1}{4}$ has been commonly used because it is in agreement with the experimental data obtained by Brown[5] through smoke-visualization experiment. Holger *et al.*[6] and Crighton[7] developed theoretical models for the phase criterion, but there was no established model in agreement with $p=\frac{1}{4}$. Recently, however, the author[8] proposed $p=-\frac{1}{4}$ based on a systematic analysis of the existing experimental data. He showed that Brown's data obtained by visualization experiment are not appropriate to compare with the phase criterion model of the form of Eq. (1). While the model is effective when the convection speed is almost constant along the jet, the experiment was performed at such low speeds that the wavelength decreased considerably with distance,[4] not consistent with the condition for Eq. (1).

Therefore, the objective of this study is to develop a theory to confirm $p=-\frac{1}{4}$ and clarify the feedback mechanism of low-speed edgetones. Generation of the upstream wave due to the edge is estimated by the simple model proposed by Kwon and Powell[9] for the jet–edge interaction, where the reaction of the edge is regarded as an array of dipoles and the downstream disturbance as a sinuously fluctuating flow with a constant convection speed. By imposing boundary conditions on the edge surface, the strength of each dipole is to be obtained. Using the dipoles, the pressure distribution on the edge surface and the upstream velocity are estimated. Then the phase criterion is obtained by the phase-locking condition on the nozzle lip and, based on this criterion, other features of the feedback mechanism such as the convection speed and frequency characteristics are obtained. The results are discussed in comparison with theoretical models or experimental data of previous investigators.

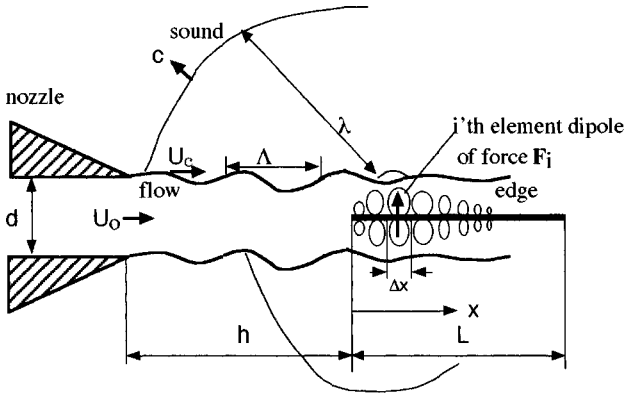

FIG. 1. Edgetone system modeled by an array of dipoles.

I. JET–EDGE INTERACTION

The basis of the present model for jet–edge interaction is replacement of the edge reacting to the impinging jet by an array of dipoles, in consideration of antisymmetry of the unstable jet about the central plane, as shown in Fig. 1. The edge with small wedge angle is regarded as a flat plate divided into small elements acting as dipole sources. Then, if the incident flow driven by impinging vortices is given, the strengths of the dipoles responding to this flow can be estimated by solving a simultaneous equation to be obtained by imposing boundary conditions on the surface of each element. The downstream-convected flow impinging on the edge can be regarded for simplicity as a sinuously fluctuating flow. Then the complex amplitude of the transverse velocity V_{im}, impinging on the edge surface, can be expressed by

$$V_{\mathrm{im}}(x)=V_0\ \exp[-(\alpha+2\pi\mathbf{i})x/\Lambda], \tag{2}$$

where V_0 is the amplitude at the tip, Λ is the wavelength of the sinuosity, $\mathbf{i}$ is the imaginary number $(-1)^{1/2}$, and x is the downstream distance from the edge tip. The constant α represents a parameter to take into account the amplitude attenuation due to the viscous damping or the generation of a secondary vortex with boundary separation in the process of interaction. In addition, the above expression is based on the assumption that the wavelength or the convection speed of downstream-propagating vortices is not affected by the interaction. The wavelength may be influenced by the configuration of vortex–edge interaction.[10] However, in the case of the edge aligned with the center line of plane jet, it has been observed that the wavelength is not altered.[11]

The edge, simplified as a thin plate of length L, is divided into dipole elements with force of complex amplitude F_i, as shown in Fig. 1. The complex amplitude of transverse velocity induced by the ith dipole element, $V_{r,i}$, can be obtained by the Hankel function $\mathrm{H}_1^{(2)}$ of the second kind of order 1 as

$$V_{r,i}(x)=\frac{F_i}{2\rho c|x-x_i|}\,\mathrm{H}_1^{(2)}(k|x-x_i|), \tag{3}$$

where ρ is the density, c is the sound velocity, and k is the wave number, $k=2\pi/\lambda$. When the length scale for the flow is much less than the acoustic wavelength as in the case of low-speed edgetones, compressibility may be neglected. Hence the flow around the edge by a dipole of Eq. (3) can be simplified by

$$V_{r,i}(x)=\frac{\mathbf{i}F_i}{\pi\rho\omega(x-x_i)^2}. \tag{4}$$

Then the amplitude of transverse velocity driven by the edge, V_r, is the sum of all the flows by the dipole elements, and is expressed by

$$V_r(x)=\sum_{i=1}^{N} V_{r,i}(x). \tag{5}$$

Now the resultant flow can be obtained by superimposing the reacting flow to the incident flow, that is, $V(x)=V_{\mathrm{im}}(x)+V_r(x)$. The boundary condition of the rigid wall requires $V(x)=0$ on the edge, the integral form of which yields

$$\sum_{i=1}^{N}\frac{\mathbf{i}F_i}{\pi\rho\omega}\int_{x_j-\Delta x/2}^{x_j+\Delta x/2}\frac{dx}{(x-x_i)^2}\,dx = -V_0\int_{x_i-\Delta x/2}^{x_j+\Delta x/2}\exp[-(\alpha+2\pi\mathbf{i})x/\Lambda]\,_{dx},$$
$$j=1,2,3,...,N. \tag{6}$$

Here the left side represents the upward volume flow rate through the jth element to compensate for the downward volume flow rate by the impinging jet, the right side. The integration near the singular point when $i=j$ can be performed along a semicircle circumventing the singular point or simply by considering the mass continuity of incompressible flow, that is,

$$\int_{-\Delta x/2}^{\Delta x/2}\frac{dx}{(x-x_i)^2}=-2\int_{\Delta x/2}^{\infty}\frac{dx}{(x-x_i)^2}.$$

Then Eq. (6) can be simplified in terms of a linear equation by

$$a_{ij}F_i=b_j,\quad i,j=1,...,N, \tag{7}$$

where

$$a_{ij}=\frac{1}{1-4(i-j)^2}, \tag{8}$$

$$b_j=-\frac{\mathbf{i}}{4}\,\pi\rho\omega\Delta x^2V_0e^{-(\alpha+2\pi\mathbf{i})x_j/\Lambda}. \tag{9}$$

The linear equation (7) for N unknown forces can be solved numerically.

Once the dipole force is obtained, the complex amplitude of surface pressure P_s on the upper side of the ith edge element is to be estimated by the relationship

$$P_{s,i}=\frac{F_i}{2\Delta x}, \tag{10}$$

where division by 2 is associated with the antisymmetry of pressure between the upper and the lower surfaces of the edge. The reliability of the numerical solution could be checked by the surface pressure. When the number of elements per wavelength $\Lambda/\Delta x$ of the downstream-propagating

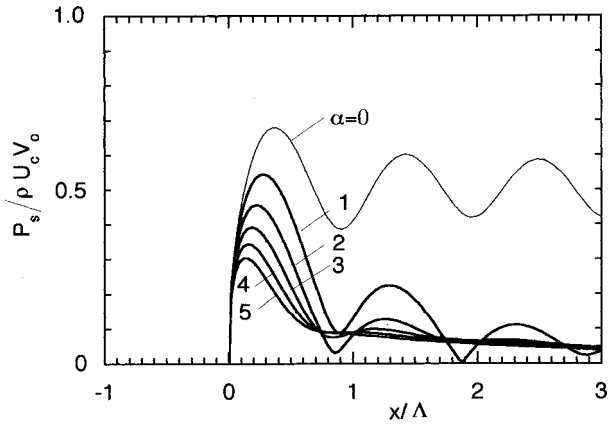

FIG. 2. Surface pressure distribution on the edge of length $L=5\Lambda$, for various attenuation constants α.

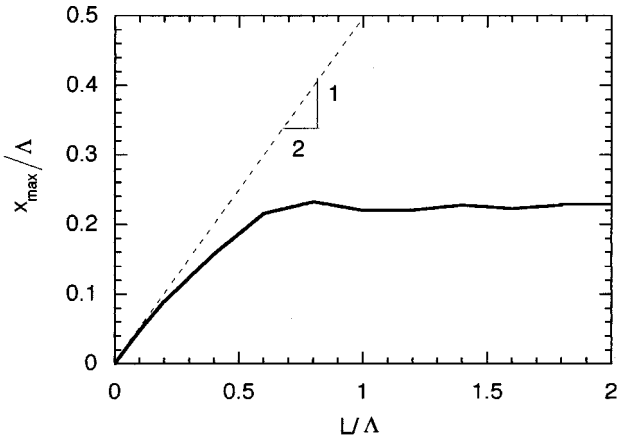

FIG. 3. Peak pressure point x_{max} on the edge surface as a function of the edge length, normalized by the convection wavelength Λ, for $\alpha=2$.

disturbance is more than 20, the surface pressure distribution on the edge became independent of further reductions in Δx.

Figure 2 shows the amplitude of the surface pressure on the edge for various attenuation constants α, for an edge of length $L=5\Lambda$. The surface pressure amplitude P_s has been normalized by $\rho V_0 U_c$, where U_c is the convection speed of the downstream disturbance, which is the surface pressure on an infinitely extended plate vibrating transversely with velocity amplitude V_0 and phase speed U_c far less than the sound speed c. It is shown that the pressure is zero at the edge tip and maximum at a little distance downstream as has been observed by Kakayoglu and Rockwell.[11] This feature is to be explained by the antisymmetry of the downstream disturbance about the central surface of jet, which is the physical basis of the present dipole model. It is shown from Fig. 2 that the point for the maximum pressure moves from half the wavelength to the edge tip with increase in α, and its mean value may be assumed to be about a quarter wavelength downstream. In addition, we can see in Fig. 2 that, although the normalized surface pressure decreases with the attenuation constant α, its maximum value is about $\frac{1}{2}$, that is,

$$P_{s,\max} \approx \tfrac{1}{2}\rho V_0 U_c . \tag{11}$$

The constant $\frac{1}{2}$ in Eq. (11) is associated with the antisymmetry of the surface pressure on both sides of the edge plate.

Figure 3 shows the point for the maximum surface pressure, $x_{\max}$, as a function of the edge length for $a=2$. When the edge is short enough, that is, $L \ll \Lambda/2$, the peak occurs at the center, $x_{\max}=L/2$, as to be expected by considering that the reaction of a short edge can be modeled by a single dipole instead of an array of dipoles.

Since the sound radiation by the edge is proportional to the surface pressure, the maximum pressure point can be regarded as the effective source point, although the exact point can be different somewhat depending on the radiating direction. In short, the effective source is located around a quarter wavelength downstream from the edge tip if the edge is not so short compared with the convection wavelength. Although it has been observed by many investigators, including Kaykayoglu and Rockwell,[11] that the source of sound radiation is not at the tip but a little distance downstream, there has been no analysis associated with this point.

II. UPSTREAM DISTURBANCE AND PHASE CRITERION

Transverse velocity of the upstream disturbance, $V_r(x)$, due to the jet–edge interaction in low-speed edgetones has been estimated by Eq. (5). Figure 4 shows how the amplitude of the upstream disturbance varies with x and α. The amplitude differs somewhat depending on the attenuation constant α and decreases steeply in the vicinity of the edge tip, then slowly with distance. Figure 5 shows the phase variation of the upstream disturbance, propagating at the sound speed, in comparison with that of the downstream disturbance propagating at the convection speed. The downstream phase decreases linearly in proportion to the propagating distance but the upstream phase is almost constant because the jet speed was assumed to be low enough to regard the upstream sound speed c as infinite. In the near vicinity of the edge tip, however, the upstream phase shows some variation due to the interference among the distributed dipole sources having different phases.

For both the upstream and the downstream disturbances to constitute a feedback loop between the nozzle lip and the effective source point of the edge, as described by Powell,[2] two conditions for phase and gain must be satisfied. First, the nozzle should be placed where the phase difference between

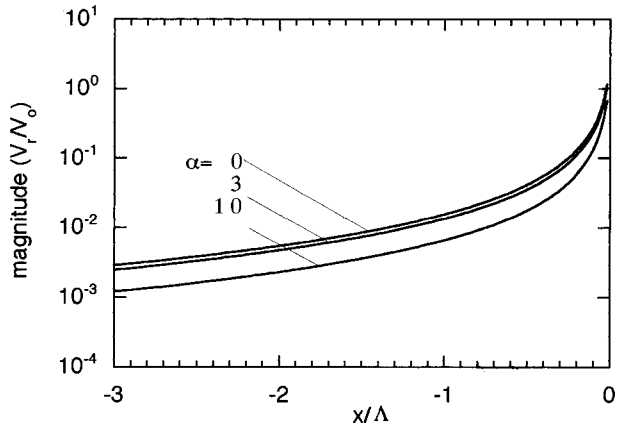

FIG. 4. Amplitude variation of the relative transverse velocity of the upstream disturbance with normalized distance, x/Λ, for three values of α.

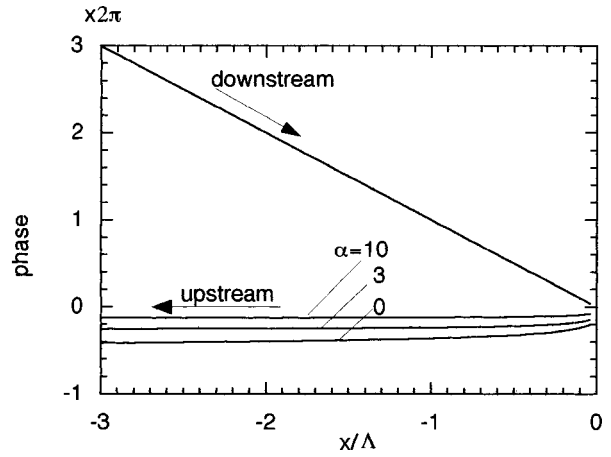

FIG. 5. Phase variation of the upstream and downstream disturbances with normalized distance, x/Λ, for three values of α.

the upstream and downstream disturbances is $2\pi n$ with positive integers n, under the assumption there is no phase delay associated with the interaction between the upstream sound and downstream disturbance at the nozzle exit. Second, the downstream disturbance must be amplified enough to compensate for the decay through the upstream propagation. However, the following sections are concerned primarily with the phase condition. Based on this condition, along with experimental results, the most important features of edgetones may be clarified. Since the estimation of the upstream decay is possible by the present model, the onset condition of the edgetone can be found if only the amplification of downstream-convected vortices is known. However, the amplification of the unstable shear layer is not known yet, from the quantitative point of view, so the second condition will not be dealt with here.

According to the phase-locking condition, the nozzle should be placed where the phase difference between the upstream and downstream disturbances is $2\pi n$. Then, when the Mach number of the convection speed is very low, that is, $M_c=\Lambda/\lambda \ll 1$, $n+p$ is the value of h/Λ for which the phase difference is just $2n\pi$ in Fig. 5. The phase factor obtained in this way is shown in Fig. 6. It is found here that p is not a universal constant, as noted by previous investigators,[4,7] but varies in the range $-\frac{1}{2}<p<0$, depending on the attenuation constant α, with less variation depending

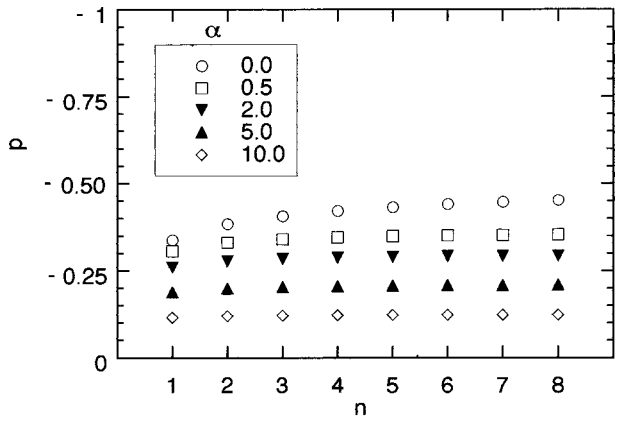

FIG. 6. Phase factor p estimated for various attenuation constants α.

on the stage n. However, its mean value can be approximated by

$$p=-\tfrac{1}{4}, \tag{12}$$

corresponding to the attenuation constant, in the range $2<\alpha<5$. This result shows a complete agreement with the previous model of the author[8] obtained by checking the experimental data of the previous authors.[5,12] Although $p=-\frac{1}{4}$ has been obtained by assuming the edge as a thin plate, it was found to be valid up to the edge of wedge angle 90°.

The effective source point may be regarded as the downstream extreme point of the feedback loop. The phase criterion requires an integer number of waves in the feedback loop over the distance h' between the two extreme points, if there is no phase shift at both extreme points. That is,

$$\frac{h'}{\Lambda}+\frac{h'}{\lambda}=n. \tag{13}$$

The above formulation indicates the phase factor in Eq. (1) is to be written by

$$p=-\left(\frac{\Delta h}{\Lambda}+\frac{\Delta h}{\lambda}\right), \tag{14}$$

where Δh is the distance from the edge tip to the effective source point. Then, in low-speed edgetones, $\Delta h=\Lambda/4$ leads to $p=-\frac{1}{4}$ in agreement with the approximation of Eq. (12). This agreement confirms the assumption that there is no phase shift at both extreme points. Then, the general formulation of the phase criterion, valid whether the convection speed (or wavelength) is constant or not, may be expressed by

$$\int_0^{h'}\left(\frac{1}{\Lambda}+\frac{1}{\lambda}\right)dh=n. \tag{15}$$

Hence the phase factor should be regarded as the factor associated with the phase delay for the disturbance to travel around the distance Δh, as noted by the author.[8] Since $\Delta h=0$ in the case of jet impinging on a normal surface, it is natural that $p=0$, as obtained by the author[8] based on the experimental data of Powell and Unfried.[12]

III. CONVECTION SPEED

Although it is a fundamental parameter in the feedback loop of edgetones, the convection speed U_c of downstream disturbance has not been established yet. Since the wavelength can be estimated from the phase criterion when the stand-off distance and the stage number are given, the convection speed can be estimated from experimental values of h, f, and n by the following equation,

$$\frac{h}{U_c}+\frac{h}{c}=\frac{n+p}{f}, \tag{16}$$

which is an alternative form of Eq. (1), based on the relationship $f\Lambda=U_c$ and $f\lambda=c$.

According to Eq. (16) with $p=-\frac{1}{4}$, the convection speed has been estimated and shown in Fig. 7 for the experimental data of Powell and Unfried[12] measured using a high-

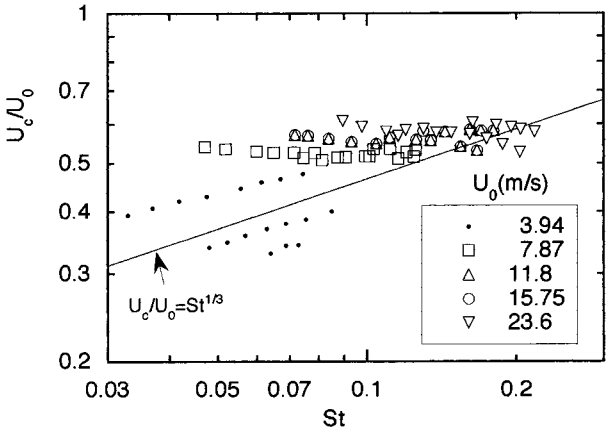

FIG. 7. Convection speed ratio U_c/U_0 versus Strouhal number St predicted from the data of Ref. 12 for a nozzle slit width of $d=0.92$ mm for various jet speeds.

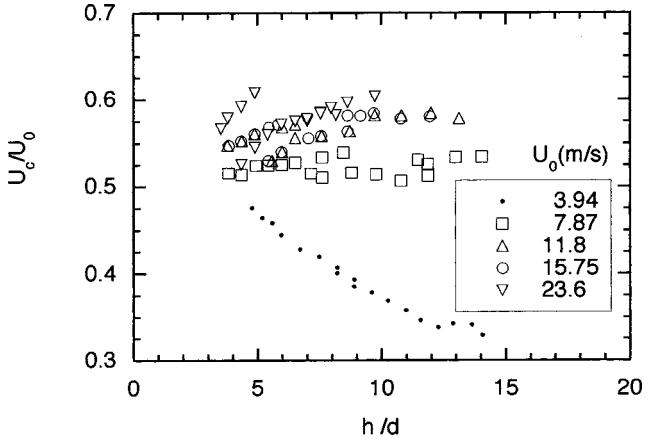

FIG. 8. Convection speed ratio U_c/U_0 versus normalized standoff distance h/d predicted from the data of Ref. 12 for a nozzle slit width of $d=0.92$ mm for various jet speeds.

aspect-ratio rectangular slit of width $d=0.92$ mm and breadth $b=38.1$ mm. The length of the parallel channel was 140 mm and the edge was made of a sharp-edged brass wedge having an included angle of 30 degrees, a breadth of 127 mm, and a length of 76 mm. In the figure, the ratio of the convection velocity U_c to the mean jet velocity U_0 is shown as a function of Strouhal number defined by $\mathrm{St}=fd/U_0$.

From Fig. 7 we can see that the convection speed ratio is about 0.6 and almost independent of frequency when the mean jet velocity is greater than 5 m/s. However, Sato[13] and Holger *et al.*[6] showed that the ratio increases with Strouhal number. The straight solid line in Fig. 7 shows the convection velocity ratio, $U_c/U_0=\mathrm{St}^{1/3}$, corresponding to the theoretical model developed by Holger *et al.*[6] Here it appears difficult to find any relationship between the normalized convection speed and the Strouhal number to support the theory. However, the convection speed ratio seems to be influenced by the jet speed rather than the frequency. The ratio increases as the jet speed increases. It is to be noted that the data for the speed of $U_0=3.94$ m/s seem to lie near the solid line, which had been regarded as the experimental evidence for the theoretical model. However, this is probably due to the deceleration of the convection speed along the jet as shown in Fig. 8.

Figure 8 shows the estimated convection velocity as a function of the edge distance for the same data of Fig. 7. In the figure the convection speed at $U_0=3.94$ m/s is shown clearly to decrease significantly with the edge distance, as noted by Powell.[4] However, the other data remain almost constant without deceleration. This feature suggests that the convection speed at a very low speed is not constant along the jet, so that the phase criterion in the form of Eq. (1) cannot be employed for the edgetone when the jet velocity is so low, as discussed previously by the author.[8] It may be deduced from Fig. 8 that, although free jets begin to spread around $5d$ downstream from the nozzle lip,[13] the impinging jet is not spreading up to $15d$ downstream when the jet speed is greater than 3.94 m/s. This is presumably due to the action of a vortex street. As long as the flow is controlled by the organized vortices, the velocity will remain unchanged with farther distance along the jet.

Figure 9 shows the convection velocity estimated for the experimental data of Powell and Unfried[12] as a function of Reynolds number defined by $\mathrm{Re}=U_0d/\nu$, where ν is the kinematic viscosity of the air. In this figure, the data for speeds lower than $U_0=5$ m/s were eliminated. It is shown in Fig. 9 that the convection velocity ratio is in the range between 0.5 and 0.7, with slight increase as the Reynolds number and/or the slit width d increases. These features suggest that the convection speed depends on the velocity distribution of the jet at the nozzle exit,[13] as it is controlled by the nozzle configuration and the Reynolds number of the jet. In spite of some variations of the convection velocity ratio, however, its average value may be taken to be roughly 0.6, in the range of the Reynolds number $\mathrm{Re}<3000$, associated with the low-speed edgetones by a slit, that is,

$$\frac{U_c}{U_0}\approx 0.6. \tag{17}$$

This result that the convection speed is almost independent of the Strouhal number is probably due to the low Reynolds number associated with the low-speed edgetones. The theory of Holger *et al.*[6] is based on potential flow with vortex street and that of Sato[13] on the linearized Orr–

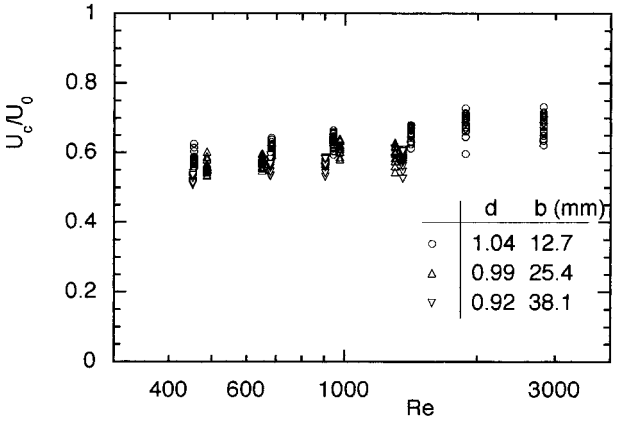

FIG. 9. Convection speed ratio U_c/U_0 as a function of the Reynolds number Re for various slits with different width d and breadth b.

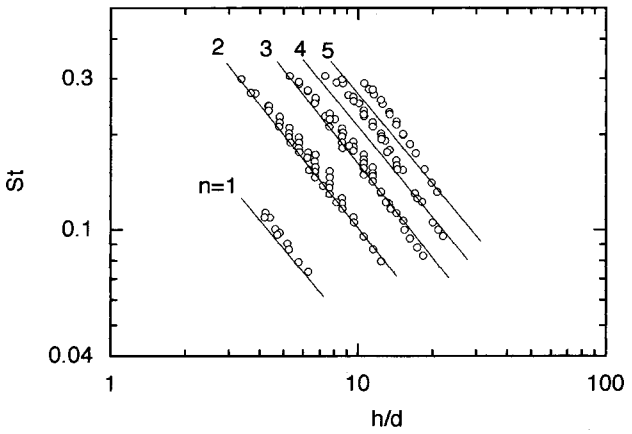

FIG. 10. Comparison of the present model with the data of Ref. 12 for the relationship between the normalized frequency and the stand-off distance.

Sommerfeld equation when the Reynolds number is very high. The Reynolds number for the low-speed edgetones might not be so high as to neglect viscosity relevant to the theory.

IV. FREQUENCIES OF OSCILLATION

According to the phase criterion in the form of Eq. (16) with $p=-\frac{1}{4}$ and the relationship $f=U_c/\Lambda=c/\lambda$, the frequency of oscillation can be obtained by the relationship,

$$f=\left(n-\frac{1}{4}\right)\frac{c/h}{(c/U_c)+1}. \tag{18}$$

The above equation shows that the frequency is dependent upon the stand-off distance, the convection speed, and the stage number. The stage number must be one of the integers corresponding to the frequencies associated with the unstable condition of the jet.[13]

If the relationship of Eq. (17) for the convection speed and the mean jet velocity at the nozzle exit is used, Eq. (18) can be rewritten in terms of Strouhal number by

$$\mathrm{St}=\frac{d}{h}\frac{n-1/4}{(1/0.6+\mathrm{M}_0)}, \tag{19}$$

where M_0 is the Mach number of the mean jet velocity U_0. Equation (19) shows that St is linearly proportional to d/h. According to formulations developed by both Holger *et al.*[6] and Crighton,[7] however, St was proportional to $(d/h)^{3/2}$ and U_c/U_0 was proportional to $\mathrm{St}^{1/3}$.

Figure 10 shows the prediction by Eq. (19) for the normalized frequency as a function of h/d in comparison with experimental data of Powell and Unfried[12] for the jet velocity $U_0>5$ m/s with the slit of width 1.04 mm. Among the three different slits in Fig. 9, the slit of $d=1.04$ mm was taken for comparison, since frequencies up to the stage $n=5$ occur at this slit, high compared with $n=3$ at the other slits, due to the difference of the aspect ratio of the rectangular slits. Some discrepancy between the prediction and the experimental data shown in Fig. 10 may be attributed to the approximation associated with $p=-\frac{1}{4}$ and $U_c/U_0=0.6$. However, the agreement is satisfactory enough to support the present simple analysis. A similar empirical relationship has been proposed by Rossister[14] in the case of cavity tones. Considering that the cavity tone is driven by the shear tone which has the same feedback mechanism as the edgetone, it is natural that the formulation for the frequencies is similar in the form.

V. CONCLUSION

The mechanism of the feedback system for low-speed edgetones has been studied by using the simple model of jet–edge interaction where the edge reaction is regarded as an array of dipoles. By assuming the downstream-convected disturbances as a sinuously fluctuating flow with a constant convection speed, the strength of the dipoles and then the pressure distribution on the edge surface have been estimated and the maximum pressure point, to be regarded as the effective source point, has been found to be around a quarter wavelength downstream from the edge tip. Based on the edge reaction, the upstream wave has been estimated in terms of its magnitude and phase. From the phase relationship the phase factor proved to be $p=-\frac{1}{4}$. The ratio of the convection speed to the mean velocity of the jet is approximately 0.6, almost independent of the Strouhal number, as far as the low-speed edgetones are concerned. Finally, a model for the frequency of oscillation has been obtained and confirmed by a close agreement with the experimental results.

ACKNOWLEDGMENTS

This work was supported by the Korea Science and Engineering Foundation. The author would like to thank Dr. Alan Powell at the University of Houston, Texas, for valuable references and discussions.

[1] D. Rockwell, ''Oscillations of impinging shear layers,'' AIAA J. **21**(5), 645–661 (1983).
[2] A. Powell, ''On edge tones and associated phenomena,'' Acustica **3**, 233–244 (1953).
[3] A. Powell, ''On the edgetone,'' J. Acoust. Soc. Am. **33**, 395–409 (1961).
[4] A. Powell, ''Aspects of edgetone experiment and theory,'' J. Acoust. Soc. Am. **37**, 535–536 (1965).
[5] G. B. Brown, ''The vortex motion causing edge tones,'' Proc. Phys. Soc. London **47**, 493–507 (1935).
[6] D. K. Holger, T. A. Wilson, and G. S. Beavers, ''Fluid mechanics of the edgetone,'' J. Acoust. Soc. Am. **62**, 1116–1128 (1977).
[7] D. G. Crighton, ''The jet-edge feedback cycle; linear theory for the operating stages,'' J. Fluid Mech. **234**, 361–391 (1992).
[8] Y. P. Kwon, ''Phase-locking condition in the feedback loop of low-speed edgetones,'' J. Acoust. Soc. Am. **100**, 3028–3032 (1996).
[9] Y. P. Kwon and A. Powell, ''A mechanism of jet-edge interaction and sound radiation,'' J. Acoust. Soc. Am. **92**, 2310(A) (1992).
[10] R. Kaykayoglu and D. Rockwell, ''Vortices incident upon a leading edge: instantaneous pressure fields,'' J. Fluid Mech. **156**, 439–461 (1986).
[11] R. Kaykayoglu and D. Rockwell, ''Unstable jet-edge interaction. Part 1. Instantaneous pressure fields at a single frequency,'' J. Fluid Mech. **169**, 125–149 (1986).
[12] A. Powell and H. Unfried, ''An experimental study of low speed edgetones,'' University of California, Los Angeles, Report No. 64-49 (1964).
[13] H. Sato, ''The stability and transition of a two-dimensional jet,'' J. Fluid Mech. **7**, 53–80 (1960).
[14] J. E. Rossiter, ''Wind tunnel experiments on the flow over rectangular cavities at subsonic and supersonic speeds,'' Aeronautical Research Council, R&M 3438, London, Oct. 1964.

Stochastic ray theory for long-range sound propagation in deep ocean environments

Michael G. Brown and John Viechnicki
Rosenstiel School of Marine and Atmospheric Science, University of Miami, 4600 Rickenbacker Causeway, Miami, Florida 33149

(Received 31 March 1998; accepted for publication 25 June 1998)

The motion of sound ray trajectories in deep ocean environments, including internal wave induced scattering, is considered. Using the empirical Garrett–Munk internal wave spectrum and results from the study of stochastic differential equations, a framework for studying and modeling stochastic ray motion is developed. It is argued that terms in the ray equations involving internal wave induced sound speed perturbations δc can be neglected, but those involving $\partial \delta c/\partial z$ cannot. It is then shown in that the (Markov) approximation that spatial variations of $\partial \delta c/\partial z$ are delta correlated is remarkably good. These results lead naturally to an extremely simple system of coupled stochastic ray equations (in ray depth z, ray slowness p and travel time T) in which stochasticity enters the system only through the equation for p. Solutions to the stochastic ray equations—or the corresponding Fokker–Planck equation—describe approximately the density of acoustic energy in range, depth, angle and time. Two dimensionless parameters are introduced: (1) an acoustic Péclet number which is a measure of the ratio of the strength of deterministic ray refraction to that of stochastic scattering induced ray diffusion; and (2) a measure of the ratio of the strength of scattering induced ray diffusion to that of wave diffraction. Numerical solutions to the stochastic ray equations are compared to full wave simulations. These results show that, even in the weak scattering regime (large acoustic Péclet number), the inclusion of internal wave induced scattering may lead to important qualitative corrections to predictions of distributions of acoustic energy. [S0001-4966(98)01810-4]

PACS numbers: 43.30.Cq, 43.30.Pc, 43.30.Re [JHM–DLB]

INTRODUCTION

In this paper we consider the motion of sound ray trajectories in deep ocean environments, including internal wave induced scattering. The empirical Garrett–Munk internal wave spectrum (Garrett and Munk, 1972, 1975; Munk, 1981) and results from the study of stochastic differential equations (see, e.g., Gardiner, 1985) are used to derive a simple set of equations which describe the stochastic motion of sound rays. Solutions to the stochastic ray equations describe the expected distribution of ray density, or, approximately, acoustic energy, as a function of range, depth, time and angle. Although the equations of motion that we derive are based on an approximate (ray) description of sound propagation, we argue that they are able to accurately account for a wide variety of ocean acoustic measurements made over the past two decades. Detailed model-data comparisons will be made in a forthcoming paper. The present paper is concerned with the theoretical basis for the new stochastic ray model.

This paper is organized as follows. Stochastic ray theory is developed in the following section (I). There is some overlap between this material and the work of Schneider (1991, 1994) and Sellschopp (1991). We focus our attention on ray scattering associated with internal wave induced sound speed fluctuations at midlatitudes in deep ocean environments. Details of the assumed form of the internal wave field are discussed in the Appendix; some of these details play an important role in the development of our stochastic ray model. Both ray-based (Langevin) and field-based (Fokker–Planck) equations are presented and discussed in Sec. I. In addition, in this section we introduce two dimensionless parameters which give insight into the importance of scattering effects and the domain of validity of the equations we derive. In Sec. II we present some numerical results based on stochastic ray theory and compare these to full wave (based on a parabolic equation) numerical simulations in the presence of internal wave induced sound speed fluctuations. Our results are discussed and summarized in the final section. Included in this section is a brief discussion of some of the connections between stochastic ray theory and the study of wave propagation in random media.

I. STOCHASTIC RAY THEORY

The acoustic ray equations on which our analysis is based are

$$\frac{dz}{dx} = \frac{\partial H}{\partial p}(p,z,x), \tag{1a}$$

$$\frac{dp}{dx} = -\frac{\partial H}{\partial z}(p,z,x), \tag{1b}$$

and

$$\frac{dT}{dx} = \mathscr{L}(p,z,x) = p\frac{dz}{dx} - H(p,z,x) \tag{1c}$$

where

$$H(p,z,x) = -\sqrt{C^{-2}(z,x) - p^2}. \tag{2}$$

 0001-4966/98/104(4)/2090/15/$15.00

In these equations z is ray depth, x is range, T is travel time, $C(z,x)$ is the sound speed, and p is the vertical ray slowness which may be thought of as a scaled angle variable. If ray angle θ is measured relative to the horizontal, the relationship between p and θ is

$$\tan\theta = \frac{dz}{dx} = \frac{\partial H}{\partial p}(p,z,x). \tag{3}$$

Using $H(p,z,x)$ defined in (2) this reduces to $Cp = \sin\theta$. Several points concerning these equations are noteworthy. First, these equations describe ray motion in the vertical plane (z,x). The extension to three space dimensions is straightforward but will not be considered here. Second, z and p evolve independent of T so that Eq. (1c) could be omitted, if desired. We have chosen to retain Eq. (1c) because travel time is an important observable. Third, these equations assume that following any ray path, z, p, and T are single-valued functions of x. In other words, these equation are based on a one-way propagation assumption. This assumption is almost always satisfied for the class of problems treated here—long-range sound propagation in deep ocean environments. Vertical plane problems for which backscattering is important can be treated by replacing Eqs. (1) by a system of $4+1$ ($+1$ if travel time T is of interest) equations. Fourth, we have written the ray equations in Hamiltonian form. This provides insight which is difficult to obtain otherwise. In addition, the Hamiltonian form of the ray equations facilitates the introduction of parabolic approximations, in which case the Hamiltonian function $H(p,z,x)$ is approximated but Eqs. (1) and (3) are unchanged. The Lagrangian function $\mathscr{L}$ can be treated as a function of z, dz/dx, and x; because we wish to treat Eqs. (1) as a system of three coupled ordinary differential equations, it is natural to treat $\mathscr{L}$ as a function of p, z, and x.

We assume that the sound speed C can be written as a sum of deterministic c and random δc components, $C = c + \delta c$. Both c and δc may be functions of z and x. In particular, we shall associate δc with internal wave induced sound speed fluctuations. The timescale associated with these fluctuations is sufficiently long that we may neglect this time dependence. The ratio $\delta c/c$ is $O(10^{-4})$ in the upper ocean and $O(10^{-6})$ in the deep ocean. [These estimates—due originally to Munk and Zachariasen (1976)—follow from arguments similar to those given in the Appendix.] Because $\delta c/c$ is everywhere small, it suffices to retain only first order correction terms in δc and $\partial\delta c/\partial z$ when $C = c + \delta c$ is substituted into the ray equations (1), (2). The resulting equations are

$$\frac{dz}{dx} = \frac{p}{(c^{-2}-p^2)^{1/2}}\left[1 + \frac{c^{-2}}{c^{-2}-p^2}\frac{\delta c}{c}\right], \tag{4a}$$

$$\frac{dp}{dx} = -\frac{c^{-3}}{(c^{-2}-p^2)^{1/2}}\left\{\left[1 + \left(\frac{c^{-2}}{c^{-2}-p^2} - 3\right)\frac{\delta c}{c}\right]\frac{\partial c}{\partial z} + \frac{\partial \delta c}{\partial z}\right\}, \tag{4b}$$

and

$$\frac{dT}{dx} = \frac{c^{-2}}{(c^{-2}-p^2)^{1/2}}\left[1 + \left(\frac{c^{-2}}{c^{-2}-p^2} - 2\right)\frac{\delta c}{c}\right]. \tag{4c}$$

The singularities in these equations when $cp = 1$ occur when the ray angle approaches 90°. These singularities are eliminated when a two-way ray formulation is used.

With this comment in mind, it is seen from Eqs. (4) that the terms involving $\delta c/c$ are everywhere small compared to unity. The only other term associated with internal wave fluctuations is that involving $(\partial\delta c/\partial z)$, which need not be small compared to $(\partial c/\partial z)$. Two points concerning the relative magnitudes of these terms are noteworthy. First, zeros of $\partial c/\partial z$ are not uncommon; these occur at the sound channel axis and at the base of a surface duct, for instance. At locations where the leading (deterministic) term in the expansion of dp/dx vanishes, one expects that it is important to retain the (stochastic) correction term. Second, even away from zero mean gradient conditions, $(\partial\delta c/\partial z)_{\rm rms}/(\partial c/\partial z)$ is much larger than $(\delta c)_{\rm rms}/c$. The depth dependence of $(\partial\delta c/\partial z)_{\rm rms}$ is described by Eq. (A18) in the Appendix. Using this estimate, it follows that typical values of $(\partial\delta c/\partial z)_{\rm rms}/(\partial c/\partial z)$ are $0.02\ {\rm s}^{-1}/0.05\ {\rm s}^{-1} \approx 0.4$ in the upper ocean and $2.\times 10^{-6}\ {\rm s}^{-1}/0.01\ {\rm s}^{-1} \approx 2.\times 10^{-4}$ in the deep ocean. These comments suggest that terms in Eqs. (4) involving $\delta c/c$ may be neglected, but the term involving $\partial\delta c/\partial z$ may not. This leaves only one stochastic term on the right side of Eqs. (4). It is shown below that the statistics of $\partial\delta c/\partial z$ are strongly inhomogeneous and anisotropic; the magnitude of this term may vary by several orders of magnitude. In contrast, the term $c^{-3}/(c^{-2}-p^2)^{1/2}$ that multiplies $\partial\delta c/\partial z$ varies by only a few percent under typical deep ocean, long-range propagation conditions. Thus, we may set $(c^{-3}/(c^{-2}-p^2)^{1/2})(\partial\delta c/\partial z) \approx c_0^{-2}(\partial\delta c/\partial z)$, where c_0 is a constant. With these approximations, Eqs. (4) reduce to

$$\frac{dz}{dx} = \frac{p}{(c^{-2}-p^2)^{1/2}}, \tag{5a}$$

$$\frac{dp}{dx} = -\frac{c^{-3}}{(c^{-2}-p^2)^{1/2}}\frac{\partial c}{\partial z} - c_o^{-2}\frac{\partial \delta c}{\partial z}, \tag{5b}$$

and

$$\frac{dT}{dx} = \frac{c^{-2}}{(c^{-2}-p^2)^{1/2}}. \tag{5c}$$

Equations (5a) and (5b) correspond to Eqs. (1a) and (1b) with

$$H(p,z,x) = -\sqrt{c^{-2}(z,x)-p^2} + \frac{\delta c}{c_o^2}. \tag{6}$$

That is, the approximations that we have made preserve the Hamiltonian structure of Eqs. (5a) and (5b). Equation (5c) does not, however, correspond to Eq. (1c) using $H(p,z,x)$ defined in (6)—a term $-\delta c/c_o^2$ is missing in (5c). The practical consequences of omitting this term are insignificant for two reasons. First, the evolution of z and p are unaffected by omitting this term. This is related to the fact that the travel time T plays the role of an auxiliary variable—Hamilton's

principal function—rather than a generalized coordinate or momentum variable. Indeed, T may be omitted entirely from our analysis. (We have chosen to retain T because we are interested in modeling transient wave fields.) Second, the omitted term produces nonnegligible corrections to the travel time spreads that are predicted using Eqs. (5) only at very short range. This can seen by noting that for small ray angles in an environment characterized by homogeneous fluctuations and a homogeneous background, the omitted term will give a contribution to travel time spreads that grows approximately like $\sqrt{x}$, whereas the retained term in (5ab) leads to travel time spreads that grow like x^2 [see Eq. (20), below]. We estimate that at ranges beyond a few tens of km, the contribution from the omitted term is negligible. In this context it is noteworthy that, on both physical and mathematical grounds, the stochastic framework developed below is not expected to be valid at very short ranges. We now proceed with the development of stochastic ray theory using Eqs. (5) as the basis of our analysis.

To further simplify Eqs. (5), the statistics of $\partial\delta c/\partial z$ must be described. The basic equation relating sound speed fluctuations and internal waves (see, e.g., Munk and Zachariasen, 1976, or Flatté *et al.*, 1979) is

$$\delta c(z,x) = c(z,x)\frac{\mu}{g}N^2(z,x)\zeta(z,x), \tag{7}$$

where $\mu = 24.5$ is a dimensionless constant, $g = 9.8\ \mathrm{ms}^{-2}$ is the gravitational acceleration, N is the buoyancy frequency in radian/s and ζ is the internal wave induced vertical displacement of a fluid parcel. We shall neglect the slow time dependence of δc and ζ—and that of c and N which vary on even longer timescales. Also, the range and depth scales which characterize variations in c and N are generally much longer than those which characterize variations in δc and ζ. In fact, variations in c are negligible relative to variations in N and ζ so that c may be replaced by the constant c_o. Statistics of $\zeta(z,x)$ are described by the empirical Garrett–Munk (hereafter GM) internal wave spectrum (Garrett and Munk, 1972, 1975; Munk, 1981); this topic is discussed in the Appendix. Equation (7) provides the link between the statistics of ζ and the statistics of δc.

With the aid of Eq. (7) we now seek to parameterize the stochastic term $\partial\delta c/\partial z$ in Eq. (5b) in an attempt to develop a simple stochastic ray theory. It is shown in the Appendix that rms fluctuations of $\partial\delta c/\partial z$ scale in depth like $N^{5/2}$. It is also shown in the Appendix that at each depth $\partial\zeta/\partial z$ is well approximated by a Gaussian white noise process. Specifically, it is shown that at each depth the horizontal wave number spectrum of $\partial\zeta/\partial z$ is very flat over the internal wave band and the horizontal correlation length of $\partial\zeta/\partial z$ is very short relative to all range scales which characterize the background sound speed structure. It follows from Eq. (7) that $\partial\delta c/\partial z$ is well approximated by a Gaussian white noise process. It follows that

$$\frac{\partial\delta c}{\partial z} = \alpha\left(\frac{N}{N_o}\right)^{5/2}\left(\frac{L_x}{2\pi}\right)^{1/2}\eta(x) \tag{8}$$

following horizontal rays. Here $\alpha \approx 0.030\ \mathrm{s}^{-1}$ is the same constant that appears in Eq. (A18), N_o is the surface extrapolated buoyancy frequency, and $\eta(x)$ is a Gaussian random variable which has a flat horizontal wave number spectrum out to $k_{\max}$—corresponding approximately to a horizontal correlation length L_x of $\pi/k_{\max}$. Setting $k_{\max} = 2\pi/1$ km gives $L_x \approx 0.5$ km. Our seemingly arbitrary choice of the constant α in (8) is justified because the variance of the random variable $\eta(x)$ has not yet been specified.

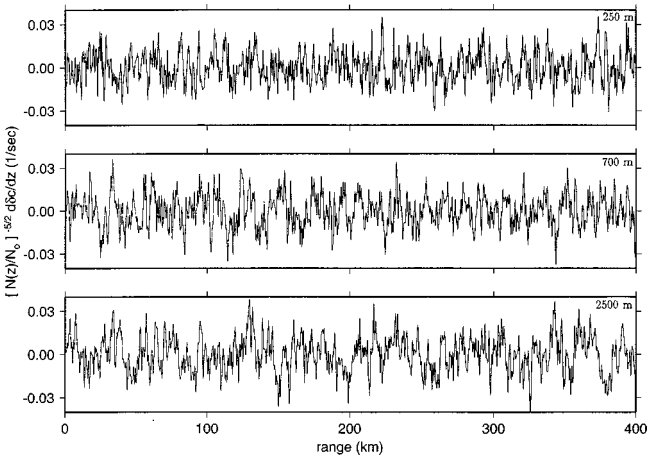

FIG. 1. Plots of $(N/N_o)^{-5/2}(\partial\delta c/\partial z)$ at three different depths as a function of range. These functions were generated using the internal wave eigenfunction expansion technique described in the Appendix. The plotted curves suggest that $\partial\delta c/\partial z$ scales like $N^{5/2}$ and that the horizontal correlation length of $\partial\delta c/\partial z$ is very short—less than 1 km—and does not depend on depth.

To determine the variance of η, we take the root-mean-square value of the left and right sides of Eq. (8),

$$\left(\frac{\partial\delta c}{\partial z}\right)_{\mathrm{rms}} = \alpha\left(\frac{N}{N_0}\right)^{5/2}\left(\frac{L_x}{2\pi}\right)^{1/2}\eta_{\mathrm{rms}}. \tag{9}$$

Comparison of Eq. (9) to Eq. (A18) dictates that $(L_x/2\pi)^{1/2}\eta_{\mathrm{rms}} = 1$. But η_{rms} is just σ where σ^2 is the variance of the (assumed Gaussian) probability density function which governs $\eta(x)$. It follows that $\sigma^2 = 2\pi/L_x$. Note that $\eta(x)$ has dimension $(\mathrm{length})^{-1/2}$. Figure 1 shows realizations of $(N/N_0)^{-5/2}(\partial\delta c/\partial z)$ as a function of x at three different depths, computed using the eigenfunction expansion technique described in the Appendix. These results are in good qualitative agreement with Eqs. (8) and (9) using the stated values of α and σ.

Missing from the preceeding discussion is consideration of the influence of the vertical correlation length L_z of $\partial\delta c/\partial z$ on nonhorizontal rays. It is shown in the Appendix that L_z scales like

$$L_z = L_{zo}\frac{N_o}{N(z)}, \tag{10}$$

where $L_{zo} \approx B/j_{\max}$ where $B \approx 1$ km is the thermocline depth scale and $j_{\max} \approx 50$ is the internal wave mode number cutoff. In Fig. 2 one realization of $\partial\delta c/\partial z$ as a function of z at a fixed x is shown. This curve shows that L_z increases from tens of meters in the upper ocean to approximately 1 km in the deep ocean, consistent with Eq. (10). In the upper ocean the short L_z will cause $\partial\delta c/\partial z$ to decorrelate more rapidly along steep rays than along flat rays. This effect is accounted

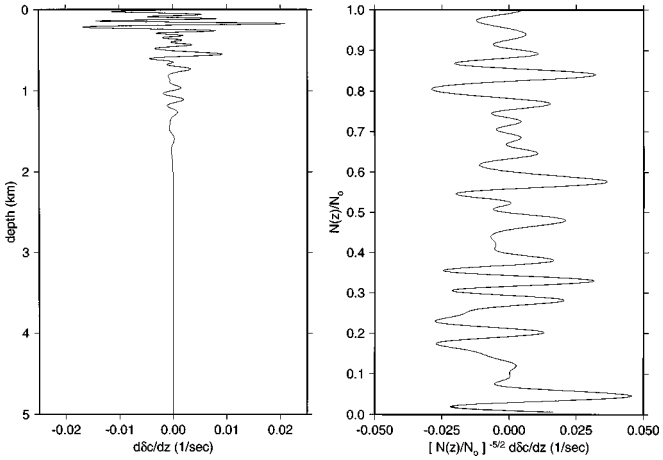

FIG. 2. Left panel: One realization of $\partial\delta c/\partial z$ vs z at a fixed range. Right panel: $(N(z)/N_0)^{-5/2}(\partial\delta c/\partial z)$ vs $N(z)/N_0$ for the curve plotted on the left. The function plotted was generated using the internal wave eigenfunction expansion technique described in the Appendix. The plot on the right suggests that $\partial\delta c/\partial z$ scales like $N^{5/2}$ and that the vertical correlation length of $\partial\delta c/\partial z$ is proportional to $N_o/N(z)$.

for by replacing the horizontal correlation length L_x in Eq. (8) by the appropriate ray angle- and depth-dependent correlation length $L(\theta,z)$. We have made the simple assumption that the correlation ''surface'' can be approximated by an ellipse, $L(\theta,z)=(\cos^2\theta/L_x^2+\sin^2\theta/L_z^2)^{-1/2}$ where $\theta=0$ and $\pi/2$ correspond to flat and vertical rays, respectively. This dependence of L on θ and z was tested numerically using the technique described in the Appendix to simulate realizations of internal-wave-induced sound speed perturbation fields and found to be an excellent approximation. Replacing θ by p gives

$$L(p,z)=\left[\frac{1-c^2p^2}{L_x^2}+\frac{c^2p^2}{L_z^2(z)}\right]^{-1/2}, \tag{11}$$

where $L_z(z)$ is defined by (10) and $L_x\approx 0.5$ km. Most ray paths of interest for long-range propagation have small ray angles—especially away from the sound channel axis—so $L(p,z)$ predicted by (11) generally stays close to L_x.

The fact that L_x and $L_z(z)$ depend on the horizontal wave number cutoff $k_{\max}$ and the mode number cutoff $j_{\max}$, respectively, deserves further comment. First, it should be noted that the values of these parameters that we have assumed are consistent with the observational foundation of the GM internal wave spectrum, on which our statistical description of the term $\partial\delta c/\partial z$ is based. Second, because this term is idealized as a white noise process below, such cutoffs are required on physical grounds so that the variance of $\partial\delta c/\partial z$ remains finite.

An alternative to using Eq. (8) with $L=L(p,z)$ as defined in (11) would be to employ a more general (two-way) ray formulation in which L_z and L_x appear independently. Such a formulation would involve more ray equations and would require that the statistics of both $\partial\delta c/\partial z$ and $\partial\delta c/\partial x$ be described. The approach we have adopted, using Eqs. (5), (8) and (11), is simpler, and, for this reason, preferable. The critical assumption on which our approach is based is that the spectrum of $\partial\delta c/\partial z$ fluctuations along all ray paths of interest should be nearly flat for $|k_{\text{ray}}|<\pi/L(p,z)$ where k_{ray} is the component of the internal wave wave number vector parallel to a ray.

Combining Eqs. (5) and (8) gives

$$\frac{dz}{dx}=\frac{p}{(c^{-2}-p^2)^{1/2}}, \tag{12a}$$

$$\frac{dp}{dx}=-\frac{c^{-3}}{(c^{-2}-p^2)^{1/2}}\frac{\partial c}{\partial z}-\alpha\left(\frac{N}{N_o}\right)^{5/2}\left(\frac{L}{2\pi}\right)^{1/2}\eta(x), \tag{12b}$$

and

$$\frac{dT}{dx}=\frac{c^{-2}}{(c^{-2}-p^2)^{1/2}}, \tag{12c}$$

where $L=L(p,z)$ is defined by Eq. (11) and α is as defined above. These equations provide the desired description of sound ray trajectories through an inhomogeneous ocean in the presence of internal wave induced sound speed fluctuations. Two alternative forms of these equations will now be presented. Both alternative forms are important and insightful. Our discussion of these alternative forms exploits well-known results from the study of stochastic differential equations (see, e.g., Gardiner, 1985). In addition, in the following discussion two dimensionless parameters are introduced which give insight into: (1) the relative importance of internal wave induced scattering effects; and (2) the domain of validity of Eqs. (12).

The alternative forms of the stochastic ray equations (12) require that the ratio of the correlation length L (for $\partial\delta c/\partial z$) to all length scales which characterize the background sound speed structure c be small. This ratio is $O(10^{-2})$, allowing us to proceed with some confidence. Because this ratio is small, the term $\eta(x)$ may be idealized as a true white noise process. With this interpretation, $\eta(x)$ is not a continuous function so Eqs. (12) must be interpreted cautiously. Multiplying Eqs. (12) by the differential dx gives

$$dz=\frac{p}{(c^{-2}-p^2)^{1/2}}dx, \tag{13a}$$

$$dp=-\frac{c^{-3}}{(c^{-2}-p^2)^{1/2}}\frac{\partial c}{\partial z}dx-\alpha\left(\frac{N}{N_o}\right)^{5/2}L^{1/2}\,dW(x), \tag{13b}$$

and

$$dT=\frac{c^{-2}}{(c^{-2}-p^2)^{1/2}}dx, \tag{13c}$$

where $dW(x)=(2\pi)^{-1/2}\eta(x)dx$. The function $W(x)$, whose dimension is $(\text{length})^{1/2}$, is known as a Wiener process; it is everywhere continuous but nowhere differentiable. The presence of the differential $dW(x)$ in Eqs. (13) precludes the interpretation, solution, etc. of these equations using the traditional calculus of smooth functions. These equations constitute a system of stochastic differential equations; the form of these equations shown in (13) involving the differentials dx, dW, etc. is referred to as the Langevin form. Two self-

consistent alternatives to traditional calculus have been developed to treat stochastic differential equations. These are known as the Itô calculus and the Stratonovich calculus. The Stratonovich interpretation of Eqs. (13) is most natural; in general, when continuous systems are described using stochastic differential equations, the Stratonovich interpretation is most natural. Stratonovich equations can be transformed to an equivalent Itô form, and vice versa (see, e.g., Gardiner, 1985).

The Langevin form of the stochastic differential equations (13) is equivalent to the second order partial differential (Fokker–Planck) equation

$$\frac{\partial \rho}{\partial x}+\frac{p}{(c^{-2}-p^2)^{1/2}}\frac{\partial \rho}{\partial z}-\frac{c^{-3}}{(c^{-2}-p^2)^{1/2}}\frac{\partial c}{\partial z}\frac{\partial \rho}{\partial p}+\frac{c^{-2}}{(c^{-2}-p^2)^{1/2}}\frac{\partial \rho}{\partial T}=\frac{\partial}{\partial p}\left(D(p,z)\frac{\partial \rho}{\partial p}\right), \tag{14}$$

where $\rho(p,z,T,x)$ is a ray density function and

$$D(p,z)=\frac{\alpha^2}{2}\left(\frac{N}{N_0}\right)^5 L(p,z) \tag{15}$$

is the diffusivity. Unlike the Langevin form of the stochastic ray equations (13), the Fokker–Planck form is amenable to interpretation/treatment using ordinary calculus. If, for a fixed initial condition, the Langevin form of the stochastic ray equations (13) is solved for a large ensemble of realizations of $\eta(x)$—or $dW(x)$—the resulting ray density function is just $\rho(p,z,T,x)$, the dependent variable in the Fokker–Planck equation. This fact is exploited in the following section. In the absence of internal wave induced sound speed fluctuations the Fokker–Planck equation reduces to a generalized (because of the inclusion of the auxiliary variable T) Liouville equation which can be solved by the method of characteristics. In this limit, ρ is constant following the deterministic ray equations (4 or 5 with $\delta c=0$). There is also a close connection between the Fokker–Planck equation and a more general (wave-based) radiation transport equation. This will be discussed in the final section. The form of the Fokker–Planck equation shown in (14) is appropriate if the Stratonovich interpretation of the stochastic ray equations (13) is adopted; if the Itô interpretation is adopted, the diffusion term in (14) has the form $\partial^2(D\rho)/\partial p^2$. If Eq. (13c) for T is omitted from the Langevin equations, the term involving $\partial\rho/\partial T$ is not present in the Fokker–Planck equation (14).

A general derivation of the Fokker–Planck equation from the corresponding system of Langevin equations can be found, for example, in Gardiner (1985) and will not be repeated here. It is, however, insightful to provide a heuristic derivation of a special case of Eq. (14) corresponding to a homogeneous background, $c=c_o$, and homogeneous internal wave fluctuations, $N=N_o$. Under these conditions the stochastic ray equation for p is decoupled from the equations for z and T, and can be considered in isolation; given $p(x)$, the functions $z(x)$ and $T(x)$ can be found. The argument that follows, due originally to Einstein, is adapted from Gardiner (1985). In discretized form, Eq. (12b) or (13b) is a statement that p is subjected to a sequence of random kicks. It follows that the ray density $\rho(p,x)$ must satisfy the condition

$$\rho(p,x+\Delta x)=\int \rho(p+\Delta p,x)\ \phi(\Delta p)\ d\Delta p,$$

where $\phi(\Delta p)\ d\Delta p$ is the probability that p changes by the amount Δp over the distance Δx. That is, ρ at $x+\Delta x$ is the sum of the ρ's at x with neighboring p-values, weighted by the probability that the appropriate jump in p is made over the distance Δx. It is assumed that $\phi(\Delta p)=\phi(-\Delta p)$ and $\int \phi(\Delta p)\ d\Delta p=1$. Because Δx is assumed to be small and only small values of Δp contribute appreciably on the right, the equation above reduces to

$$\rho+\Delta x\frac{\partial \rho}{\partial x}=\rho\int \phi(\Delta p)\ d\Delta p+\frac{\partial \rho}{\partial p}\int \Delta p\ \phi(\Delta p)\ d\Delta p+\frac{1}{2}\frac{\partial^2 \rho}{\partial p^2}\int (\Delta p)^2\ \phi(\Delta p)\ d\Delta p.$$

Because of the aforementioned properties of $\phi(\Delta p)$, the first terms on the left and right cancel and the second term on the right vanishes, leaving

$$\frac{\partial \rho}{\partial x}=D\frac{\partial^2 \rho}{\partial p^2}$$

with $D=\langle(\Delta p)^2\rangle/(2\Delta x)$ where angular brackets denote expected value. This diffusion equation is a special case of the Fokker–Planck equation (14). It follows from (5b) that $\langle(\Delta p)^2\rangle\approx c^{-2}\langle(\Delta c/c)^2\rangle(\Delta x/\Delta z)^2$, so

$$D\approx\frac{c^{-2}}{2}\left\langle\left(\frac{\delta c}{c}\right)^2\right\rangle\frac{\Delta x}{(\Delta z)^2}. \tag{16}$$

The fundamental solution to the diffusion equation is a Gaussian whose width grows like $\sqrt{2Dx}$, consistent with (18), below.

The general form of the Fokker–Planck equation (14) can be thought of as an advection-diffusion equation for ray density ρ. The fact that the diffusivity D (15) is proportional to the correlation length L is analogous to the fluid mechanical result that the molecular diffusivity is proportional to the mean *time* between successive molecular collisions. (Recall that in the one-way ray equations x plays the role of the timelike, or independent, variable.) In fluid mechanical mixing problems the Péclet number is a dimensionless measure of the ratio of the strength of advection [terms on the left side of Eq. (14)] to diffusion. The acoustic Péclet number corresponding to Eq. (14) is

$$Pe\approx\frac{cp/L_z}{D/p^2}.$$

It follows from this expression and (16) with Δx and Δz replaced by L_x and L_z, respectively, that

$$Pe\approx 2(cp)^3\frac{L_z}{L_x}\left\langle\left(\frac{\delta c}{c}\right)^2\right\rangle^{-1}. \tag{17}$$

Typical near-axial conditions are $cp=\sin(10°)\approx 0.17$, $L_z/L_x\approx 0.1$ and $(\delta c/c)_{\rm rms}\approx 1.\times 10^{-4}$, giving $Pe\approx 1.\times 10^5$.

One consequence of this large Pe—or, equivalently, the smallness of D—is that the Fokker–Planck equation (15) is difficult to accurately solve numerically using a finite difference scheme; such algorithms introduce numerical diffusion which overrides the true diffusion when Pe is large.

The relative smallness of the diffusive term in the Fokker–Planck equation (15) suggests that this term might be neglected. Unfortunately, solutions to Eqs. (15) for small D may be very different, especially for large x, than solutions to the $D=0$ limit of this equation. Mathematically, this can be understood from the observation that the small D limit of this equation constitutes a singular perturbation problem. Physically, a nonzero D—no matter how small—will cause ρ to become increasingly smooth as x increases; in contrast, in the $D=0$ limit, discontinuities in ρ at $x=0$ will persist for all x.

Before introducing a second dimensionless parameter it is necessary to briefly consider solutions to the stochastic ray equations (13a) under idealized conditions. Specifically, we assume that c, N and L in Eq. (12) are constant. In addition, we assume that ray angles are small so that $(c^{-2}-p^2)^{1/2} \approx c^{-1}$. For an initially flat ray, $p(0)=0$, the solution to (12b) is

$$p_{\mathrm{rms}}(x)=(2Dx)^{1/2}. \tag{18}$$

It then follows from (12a) and (12c), taking $z(0)=0$ and $T(0)=0$, that

$$z_{\mathrm{rms}}(x)=\tfrac{2}{3}c\sqrt{2D}x^{3/2} \tag{19}$$

and

$$T_{\mathrm{rms}}(x)=\frac{x}{c}+\frac{1}{2}cDx^2. \tag{20}$$

The result that $z_{\mathrm{rms}}(x)$ grows like $x^{3/2}$ for small ray angles under the assumed idealized conditions is well known (see, e.g., Tatarski, 1961).

Under the same idealized conditions, consider the ensemble of stochastic rays which connect a pair of fixed points separated by a distance x as shown in Fig. 3. Such an ensemble of stochastic trajectories is referred to as a ''Brownian bridge'' (see, e.g., Kloeden and Platen, 1992). The width R_B of such a Brownian bridge is approximately $z_{\mathrm{rms}}(x/2)$ where $z_{\mathrm{rms}}(x)$ is defined in (19):

$$R_B \approx \tfrac{1}{3}c\sqrt{D}x^{3/2}. \tag{21}$$

In the absence of fluctuations, deterministic ray paths also have a frequency-dependent characteristic width R_F, the Fresnel zone width (see Fig. 3). R_F is the maximum transverse ray perturbation consistent with the condition that the difference in path length between perturbed and unperturbed rays not exceed $\lambda/4$ where λ is the wavelength. In a homogeneous environment it is well known that

$$R_F \approx \tfrac{1}{2}(\lambda x)^{1/2}. \tag{22}$$

The ratio R_B/R_F is a dimensionless measure of the relative strengths of scattering and diffractive effects. The former are included in Eqs. (12), (13) and (14); the latter are not. Thus, our ray-based analysis can be a good approximation to a more difficult wave-based analysis only when R_B/R_F is larger than one. It follows from Eqs. (21), (22) and (16) that

$$\frac{R_B}{R_F}\approx\frac{2}{3}\sqrt{cD}f^{1/2}x\approx\left(\frac{\delta c}{c}\right)_{\mathrm{rms}}\frac{L_x}{L_z}(cL_x)^{-1/2}f^{1/2}x, \tag{23}$$

where $f=c/\lambda$ is the acoustic frequency. For near-axial conditions $(\delta c/c)_{\mathrm{rms}}(L_x/L_z)(cL_x)^{-1/2}\approx 1.\times 10^{-3}$ $\mathrm{s}^{1/2}$ km^{-1} corresponding to $R_B/R_F\approx(f/1\ \mathrm{Hz})^{1/2}(x/1000\ \mathrm{km})$. For most of the deep water tomography experiments conducted since 1979 (see Munk *et al.*, 1995) this ratio is approximately 10. This suggests that the solution to Eq. (14) should provide a useful, albeit approximate, description of the measured mean fields in these experiments.

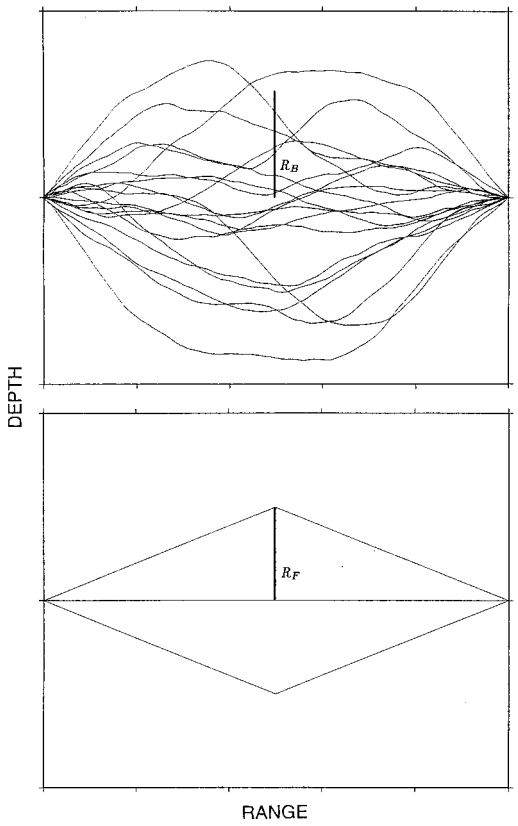

FIG. 3. A Brownian bridge (upper panel) is an ensemble of stochastic eigenrays. Its width R_B is a measure of the importance of ray scattering. A Fresnel zone (lower panel) is a measure of the frequency-dependent extent of a deterministic ray path. Its width R_F is a measure of the importance of diffractive effects.

II. NUMERICAL RESULTS

In this section numerical solutions to the stochastic ray equations are presented and compared to full wave solutions to the same set of problems. Prior to presenting these results, we discuss the issue of which ray- and wave-based quantities should be compared and the methods used to obtain our ray-based results.

The quantitative comparison of stochastic ray-based wavefield simulations to wave-based simulations is more difficult than might be anticipated. It must be understood that the ray density $\rho(z,p,T,x)$ describes only the mean distribution of acoustic energy. Higher order wave field statistics

must be computed using other techniques. For a point source in a 3-D model in which azimuthal coupling is negligible, energy flux conservation in *deterministic* ray tubes gives the expression

$$A^2 = A_o^2 \frac{l_o^2}{x} \frac{c}{c_s} \frac{\cos\theta_s}{\cos\theta} \left(\frac{\partial z}{\partial \theta_s} \right)^{-1} \tag{24}$$

for geometric intensities (squared amplitudes). Here z is ray depth, the subscript s denotes source, and A_o^2 is the acoustic intensity at a small distance l_o (usually taken to be 1 m) from the source. The range x is fixed when evaluating $\partial z/\partial \theta_s$. Unfortunately, Eq. (24) cannot be applied to stochastic rays; because each stochastic ray evolves independently of all others, $z(\theta_s)$ is not a continuous function and the derivative $\partial z/\partial \theta_s$ does not exist. A useful approximate stochastic equivalent of (24), written in terms of p rather than θ, is

$$\langle A^2 \rangle = A_o^2 \frac{l_o^2}{x} \langle (c^{-2} - p^2)^{-1/2} \rangle \frac{\Delta p_s}{\Delta z} n(z, \Delta z), \tag{25}$$

where the angular brackets denote average or expected value. Here it is assumed that a dense fan of rays is emitted at the source and traced out to a fixed range x; Δp_s is the increment (assumed constant) in p between neighboring rays at the source and $n(z,\Delta z)$ is the number of rays whose depths at range x fall between $z \pm \Delta z/2$. It is important that only rays with neighboring launch angles be included among the n rays counted; degeneracies associated with deterministic multipaths must be avoided. If the average of $(c^{-2} - p^2)^{-1/2}$ over the n constituent arrivals is taken to be its mean, then (25) reduces to

$$\langle A^2 \rangle = A_o^2 \frac{l_o^2}{x} \frac{\Delta p_s}{\Delta z} \sum_{j=1}^{n} (c^{-2} - p_j^2)^{-1/2}. \tag{26}$$

In this expression c is evaluated at the field point of interest.

Equations (25) and (26) have potentially serious shortcomings associated with improper treatment of both deterministic (macro) caustics and stochastic (micro) caustics. Furthermore, it is not clear what the full wave counterpart of $\langle A^2 \rangle$ is; the seemingly obvious choice $\langle u^2 \rangle$, where u is the pressure of the acoustic wave field, is difficult to justify because interference effects are not accounted for in $\langle A^2 \rangle$. Thus, while the ray density function $\rho(z,p,T,x)$ can be estimated without much difficulty, the question of how to quantitatively compare ρ to some measured wave field descriptor is difficult to answer. For some applications this shortcoming is not serious. In travel time tomography (Munk *et al.*, 1995), for example, having the ability to model internal wave induced spreads of acoustic energy in time, angle and depth is generally more important than having the ability to accurately predict absolute sound pressure levels. Our recommendation regarding Eq. (26) is that this expression be used only for temporally resolved arrival structures which correspond to isolated deterministic multipaths. For this type of arrival structure $\langle A^2 \rangle$ should provide a good approximation to $\langle u^2 \rangle$. To display stochastic ray tracing results we recommend plotting clouds of points—in (z,t) or (p,T) at fixed x, for example—where each point corresponds to a ray. Some examples are given below.

The most basic decision to be made concerning the numerical solution of the stochastic ray equations is which form of these equations is to be solved. We noted earlier that it is difficult to solve the Fokker–Planck equation (14) directly using finite differences because of the relative smallness of the diffusive term. The alternative is to numerically solve the Langevin equations (13) using techniques that make use of results from the study of stochastic differential equations. The latter approach has been taken. [For reasons to be discussed below, the numerical results presented in this paper are based on Eqs. (28), rather than (13). The same comments apply to both sets of equations.] The algorithm that we have used to integrate Eqs. (28) is due to Milshtein (1978); see Kloeden and Platen for a more complete discussion of numerical integration of stochastic differential equations. The Milshtein algorithm assumes an Itô interpretation of the stochastic differential equations being integrated, whereas the Stratonovich interpretation of the stochastic ray equations is more natural. Thus, prior to integrating Eqs. (28) using the Milshtein algorithm, they were transformed to an equivalent Itô form. Both the transformation and the numerical integration are straightforward. At each range step in the numerical integration, a zero mean, unit variance Gaussian random variable must be generated. This is efficiently done using the Box-Muller algorithm (see, e.g., Press *et al.*, 1986).

When comparing predicted transient wave fields to measurements it may be important to account for the temporal smearing of acoustic energy associated with finite duration (the reciprocal bandwidth) signals. A simple way to do this for stochastic rays is to randomly perturb the travel time T of each ray where the probability density function of the random perturbation is the normalized temporal envelope of the transmitted signal. Gaussian and boxcar (uniform within specified bounds) envelopes are particularly simple to treat in this fashion. This temporal smearing can be done either before or after the stochastic ray equations are numerically integrated. In the numerical results presented below this additional temporal smearing is not included.

The preceeding discussion outlines a method to calculate stochastic ray trajectories $[z(x),\ p(x),\ T(x)]$ and, in turn, ray density $\rho(z,p,T,x)$. The latter can be compared to measured wavefields. Comparisons of this type will be made in a forthcoming paper. In the present study simulations based on stochastic ray theory are compared to full wave simulations. This comparison is nontrivial because no efficient numerical technique is available to solve the full-wave counterpart of Eqs. (1) and (2), the time-dependent wave equation where $C(z,x)$ includes both an inhomogeneous background component and an internal wave induced stochastic component.

This problem can be circumvented by reformulating stochastic ray theory using a parabolic approximation (Tappert, 1977) and comparing numerical results based on the stochastic parabolic ray equations to numerical solutions to the corresponding parabolic wave equation; the latter can be computed using well known, efficient and robust techniques (see, e.g., Tappert *et al.*, 1995). There are many parabolic approximations from which to choose. For our purposes it is important only that our ray- and wave-based calculations are based

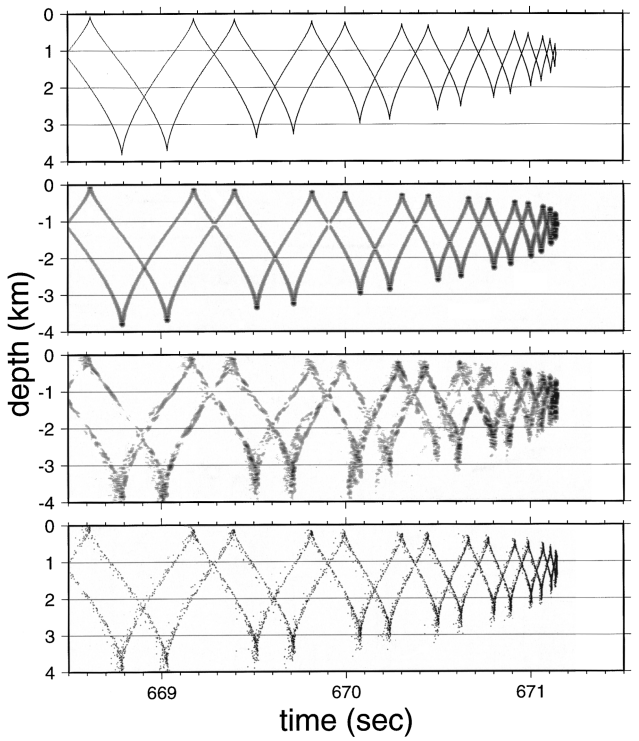

FIG. 4. Wave fields in the depth-time plane at a range of 1000 km in a canonical ocean model for a source on the sound channel axis at 1.1 km depth: (a) ray simulation without internal waves; (b) full-wave simulation without internal waves; (c) full-wave simulation with internal waves; (d) stochastic ray simulation which accounts for internal wave induced scattering. The dynamic range of the full-wave plots is 35 dB.

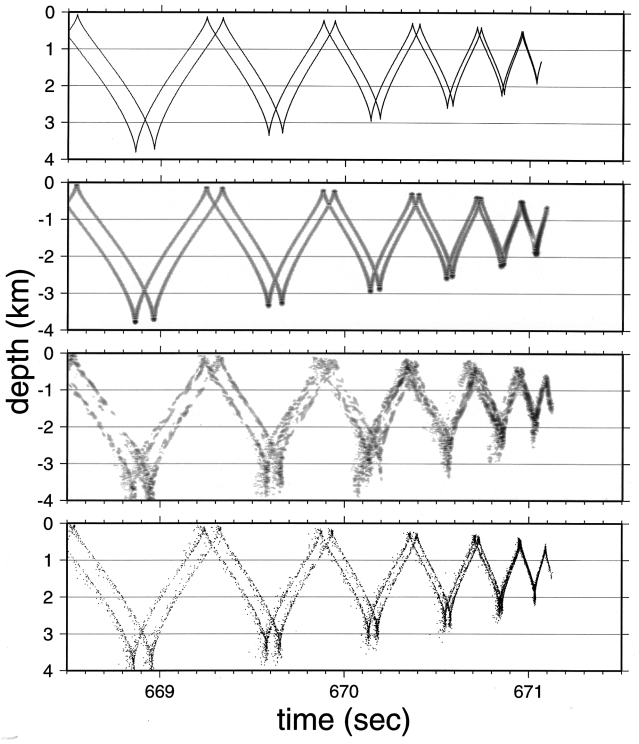

FIG. 5. Same as Fig. 4 for a source at 0.6 km depth.

on the same parabolic equation (PE). We have used the Thomson-Chapman PE (Thomson and Chapman, 1983), for which

$$H(p,z,x) = -\sqrt{c_o^{-2} - p^2} + c_o^{-1} - c^{-1}(z,x) + \frac{\delta c}{c_o^2}, \qquad (27)$$

where a stochastic correction term has been added to the deterministic Hamiltonian, as was the case in Eq. (6). Equations (1) and (3) still apply; the latter reduces to $\sin\theta = c_o p$. Our treatment of internal wave induced sound speed fluctuations is, of course, unaffected by use of a parabolic approximation. Using (27) in place of (6) gives, in place of Eqs. (13), the modified set

$$dz = \frac{p}{(c_o^{-2} - p^2)^{1/2}} dx, \qquad (28a)$$

$$dp = -\frac{1}{c^2}\frac{\partial c}{\partial z} dx - \alpha \left(\frac{N}{N_o}\right)^{5/2} L^{1/2}\, dW(x), \qquad (28b)$$

$$dT = \left[\frac{c_o^{-2}}{(c_o^{-2} - p^2)^{1/2}} + c^{-1} - c_o^{-1}\right] dx. \qquad (28c)$$

The assumed dependence of L on θ is unchanged; this leads to the replacement of c by c_o in Eq. (11). The comments concerning the numerical integration of Eqs. (13) also apply to Eqs. (28).

Full wave- and ray-based wave fields in the depth-time plane are shown in Figs. 4 and 5. These were computed at a range of 1000 km using a Munk (1974) sound speed profile with parameters $z_{\text{axis}} = 1.1$ km, $c_{\text{axis}} = 1.49$ km/s, $B = 1.0$ km and $\epsilon = 0.0057$, and an exponential buoyancy frequency profile, $N(z) = N_0 \exp(z/B)$, with $N_o = 2\pi/15$ min. The reference sound speed c_o was taken to be 1.5 km/s. Ray calculations were made with double precision arithmetic (64 bit floating point wordsize) using a fixed integration stepsize of 50 m. Approximately 12 000 rays with launch angles $|\theta_s| \leqslant 15^o$ were used in the ray simulations. The internal wave induced sound speed perturbation field $\delta c(z,x)$ that was used in our full-wave simulations is described in the Appendix. In the construction of $\delta c(z,x)$ it was assumed that $f_i = 2\pi/1$ day, $2\pi/100$ km $\leqslant k_x \leqslant 2\pi/1$ km with $\Delta k_x = 2\pi/1000$ km, and $j_{\max} = 50$. This choice of Δk_x produces a δc field which is periodic in range with a period of 1000 km. Internal wave modes with turning depths below 4.5 km were excluded from the modal sum; only a small number of modes with large j and small k_x (near $2\pi/100$ km) were affected. Other parameters which describe the internal wave field are specified in the Appendix. To compensate for missing energy outside of the k_x band considered, the dimensionless GM energy parameter E was increased by about 30% over its nominal value so as to make the numerical value of the vertically integrated internal wave potential energy density agree with the GM prediction [Eq. (A4)]. With this adjustment to E, rms vertical internal wave displacements at 250 m depth were 6.5 m. Full-wave calculations were made with single precision arithmetic using a range step of 50 m and a depth grid with 8 m spacing. A Gaussian starting field, whose width corresponds roughly to the initial ray angular aperture, was used. The source function used in the full-wave

calculations had a Hanning window spectral envelope whose total width was 100 Hz, centered at 250 Hz.

Consider first the wave fields shown in Fig. 4, computed for a source on the sound channel axis. Comparison of the ray- and wave-based calculations in the absence of internal waves [Fig. 4(a) and (b)] shows that the latter have cusps which are extended slightly in depth relative to the former, owing to diffraction. Some interference fringes can also be seen in the full-wave plot. The inclusion of internal waves in a full-wave calculation [Fig. 4(c)] is seen to lead to an overall blurring of the wave field, including an elongation (in depth) of the cusps. Finally, Fig. 4(d) shows that a stochastic ray calculation produces a distribution of energy which is quite similar to that produced in the corresponding full-wave calculation. Because scattering effects are included in the stochastic ray calculation but diffraction is not, this agreement suggests that, for the conditions treated, scattering effects dominate diffraction effects. This statement is consistent with Eq. (23) which gives the estimate (for near-axial rays only) $R_B/R_F \approx 16$. The ray depth and time spreads seen in Fig. 4(d) are comparable to those computed under similar conditions by Simmen *et al.* (1997) who traced rays through realizations of internal wave fields similar to those used in our full-wave simulations. The ray depth spreads seen in Fig. 4(d) are also in qualitative agreement with those predicted by Schneider (1994) using an approach which is similar to ours, but with a more idealized treatment of the small scale inhomogeneities.

Examination of the wave fields shown in Fig. 5—corresponding to an off-axial source at 0.6 km depth—shows behavior similar to that seen in Fig. 4, but an apparently new phenomenon can also be seen. In the absence of internal waves, diffraction is responsible for the elongation in time of the late arriving wave field branch [see Fig. 5(b)] relative to the ray theory prediction [see Fig. 5(a)]. In the full-wave calculation in which internal waves are present [Fig. 5(c)], the tail end of the arrival structure is seen to be further elongated in time, leading to the formation a new arrival branch, and broadened in depth. As was the case in Fig. 4, a stochastic ray calculation [Fig. 5(d)] gives a distribution of acoustic energy which is quite similar to the corresponding full-wave prediction. Reciprocity considerations dictate that the scattering of rays in depth that was discussed in the context of Fig. 4 must also produce new arrival branches, as seen in Fig. 5. Grabb and Birdsall (1995) have previously exploited reciprocity arguments to compute the travel times of diffracted (in the absence of internal wave induced scattering) near-axial arrivals.

The same set of stochastic rays that were used to produce Fig. 4(d) are plotted in z-p and p-T in Figs. 6 and 7, respectively. Figure 6 shows no discernible structure in phase space. Some structure can be seen in Figs. 4(d) and 7, however. Evidently, for the conditions considered, wave field structure in the ray limit can be resolved only when the wave field is viewed in the time domain. (Two caveats relating to structure in phase space should be mentioned. First, because z and p are conjugate variables, any wave-based structure in z-p must be constrained by an uncertainty relationship. Second, in the ray limit Liouville's theorem provides a strong constraint on the evolution of curves—corresponding to fans of rays—in phase space. Specifically, such curves may not break or intersect themselves. Our use of the Markov approximation—that all rays evolve independent of neighboring rays—precludes any consideration of curves in phase space, so that this constraint is overridden.)

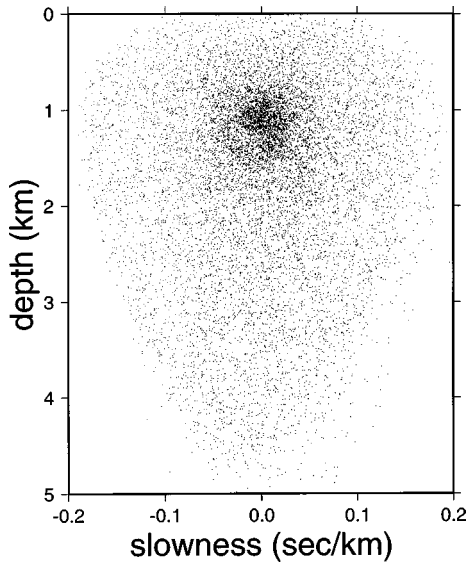

FIG. 6. Depth-slowness (phase space) plot of the same set of rays that are plotted in Figs. 4(d) and 7.

Our final remark concerning the comparisons shown in Figs. 4 and 5 is that we have made no attempt to adjust any parameters in the stochastic ray model to improve the fit between ray- and wave-based wavefield predictions. A significant source of uncertainty in the stochastic ray predictions is the choice of $j_{\max}$ and $k_{\max}$. An attempt to optimize the choice of these parameters—and possibly others—will be made when stochastic ray predictions are compared to measured wave fields.

III. SUMMARY AND DISCUSSION

In this paper we have investigated the behavior of sound rays in ocean models in which an inhomogeneous deterministic background sound speed structure is perturbed by inter-

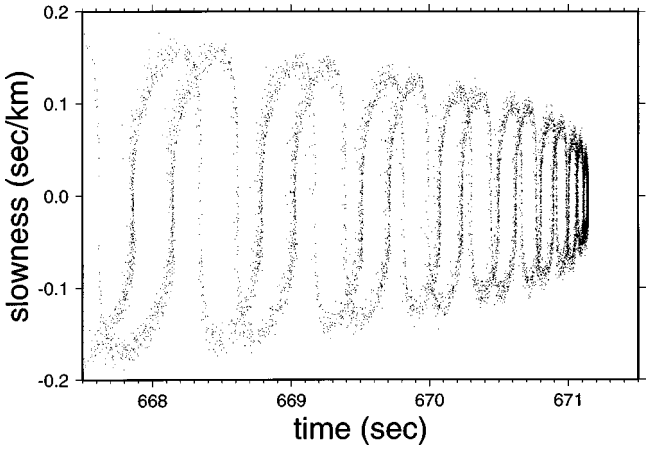

FIG. 7. Slowness-time plot of the same set of rays that are plotted in Figs. 4(d) and 6.

nal wave induced sound speed fluctuations. We have assumed that the internal wave field is describable using the empirical Garrett–Munk spectrum. It was argued that terms in the ray equations involving internal wave induced sound speed perturbations δc can be neglected but those involving $\partial \delta c/\partial z$ cannot. This led to a particularly simple set of stochastic ray equations. Application of well-known results from the study of stochastic differential equations led naturally to alternative (Langevin and Fokker–Planck) formulations of the stochastic ray equations. The results presented led naturally to a simple and robust algorithm to compute mean transient wave fields under conditions in which scattering effects dominate diffractive effects.

A dimensionless parameter R_B/R_F [Eq. (23)], which is a measure of the relative strengths of scattering and diffraction, was introduced. Our analysis should provide a useful, albeit approximate, description of wave fields when this ratio exceeds unity. For the problem treated, our $(R_B/R_F)^2$ is an $O(1)$ dimensionless constant times the quantity denoted $\Lambda\Phi^2$ in the work of Flatté *et al.* (1979). In that work the condition $\Lambda\Phi^2>1$ is one of two conditions which defines wave fields with ''saturated statistics'' or random phases. The approximate equivalence between the conditions $(R_B/R_F)^2>1$ and $\Lambda\Phi^2>1$ is reassuring inasmuch as our ray density function $\rho(z,p,T,x)$ can sensibly approximate the mean wave field only if the phase of each spectral component of the wave field is random.

There is also a close connection between stochastic ray theory and radiation transport theory (Wilson and Tappert, 1979; Chap. 13 of Flatté *et al.*, 1979). In the geometric limit, the radiation transport equation reduces to the Fokker–Planck equation which would result if the standard parabolic approximation (Tappert, 1977) to $H(p,z,x)$ were made and if the T-dependent term were omitted. Although stochastic ray theory is unable to describe frequency-dependent propagation effects which are included in radiation transport theory, it has some advantages over the latter: (1) simplicity; (2) there is no need to introduce a parabolic approximation; and (3) T-dependence is easily included, allowing time spreads to be computed directly. Because of the third point, stochastic ray theory as presented here is particularly well suited to the analysis/interpretation of transient wavefields. The importance of including T-dependence is vividly demonstrated by contrasting Figs. 4(d) and 7 to Fig. 6.

We anticipate that many other connections between the work presented here and work in wave propagation in random media can be made. In this regard, it is important to note that although we have confined our attention to the relatively simple problem of describing (approximately) the mean field, we have made no restrictive or unrealistic assumptions about the environment; the inhomogeneity of the background sound speed structure has been taken into account as has the inhomogeneity and anisotropy of the internal wave induced sound speed fluctuations.

A crucial element of our work is use of the (Markov) approximation that spatial variations of $\partial \delta c/\partial z$ are delta correlated. The Markov approximation is frequently used to describe spatial variations of δc in the ocean, in part because it leads to analytically tractable problems. We have demonstrated, using the GM spectrum, that there is strong justification for invoking the Markov approximation to describe internal wave induced spatial variations of $\partial \delta c/\partial z$.

We have focused our attention in this paper on sound propagation at midlatitudes in deep ocean environments. It is natural to inquire whether the results presented here might also hold in shallow water. (We exclude from consideration very high latitude and equatorial internal wave dynamics as these require special care.) One feature of our work that we expect to carry over to the shallow water problem is that $\partial \delta c/\partial z$ scales in depth like $N^{5/2}$. This relationship is a consequence of δc being proportional to $N^2\zeta$ and $\partial\zeta/\partial z$ scaling like $N^{1/2}$; the latter relationship is expected on the basis of the internal wave dispersion relationship and the fact that energy considerations suggest that ζ should scale like $N^{-1/2}$. Even if this relationship holds in shallow water, however, many unknowns and potential problems associated with the application of stochastic ray theory remain. Unfortunately, the deep water GM spectrum has no shallow water counterpart. Indeed, the notion of a quasi-universal shallow water internal wave spectrum is questionable. In shallow water the statistics of ζ generally vary as a function of location, direction (along vs cross shelf), and are generally not stationary in time. In order to sensibly apply the Markov approximation, the correlation lengths of $\partial \delta c/\partial z$ must be small compared to all length scales which characterize the background ray structure. This condition is often not satisfied in shallow water environments. In addition, in most shallow water environments, interactions with both the rough surface and bottom —and possibly also bottom penetration—must be accounted for. In short, the application of stochastic ray theory to shallow water propagation problems presents many problems that we have not considered.

Although the techniques described in this paper are limited to predicting the mean acoustic field, we feel that they should be very useful for the interpretation of measured wave fields, especially transient wave fields. Comparisons between measured deep water wave fields and stochastic ray-based predictions will be made in a forthcoming paper. In this regard, the comparisons with full wave simulations that we have presented are encouraging. In addition to the obvious need to compare predicted to measured wave fields, the connections between stochastic ray theory as presented here and various approaches to the study of wave propagation in random media should be further explored.

ACKNOWLEDGMENTS

We thank F. Tappert and M. Wolfson for the benefit of our discussions on stochastic ray theory, F. Tappert and X. Tang for assistance with the PE simulations, and S. Nikolic for providing computational assistance. This work was funded by the Office of Naval Research.

APPENDIX: INTERNAL WAVE INDUCED SOUND SPEED FLUCTUATIONS IN DEEP OCEAN ENVIRONMENTS

In this Appendix internal wave induced sound speed fluctuations in deep ocean environments are considered. It is

assumed that the field of internal waves is described by the empirical Garrett-Munk (GM) spectrum (Garrett and Munk, 1972, 1975; Munk, 1981; Flatté *et al.*, 1979). Two different but complementary descriptions of internal wave induced sound speed fluctuations are discussed. These are: (1) a local (in depth) power spectrum that has previously been used by Munk and Zachariasen (1976), Flatté *et al.* (1979) and others; and (2) an eigenfunction expansion technique that has previously been used by Dozier and Tappert (1978), Colosi *et al.* (1994) and others. The local power spectrum representation is used to derive some new results relating to spatial variations of $\partial\delta c/\partial z$. Previous work has considered only the statistics of δc. The eigenfunction expansion representation is used to test some of the predictions based on the local power spectrum representation and is required in the full-wave numerical simulations described in Sec. II.

Because internal wave induced sound speed perturbations are proportional to the vertical displacement of a fluid parcel,

$$\delta c = c\left(\frac{\mu}{g}\right) N^2 \zeta, \tag{A1}$$

we need only describe the statistics of ζ. [This equation also appears as Eq. (7) in Sec. I where all quantities are defined.] These statistics are described by the GM spectral density

$$F_\zeta(\omega, j) = \frac{2B^2E}{\pi M}\,\frac{N_o}{N}\,\frac{f_i}{\omega^3}(\omega^2 - f_i^2)^{1/2}(j^2 + j_*^2)^{-1}. \tag{A2}$$

Here ω is internal wave angular frequency, j is mode number, $j_* = 3$ and $E = 6.3\times10^{-5}$ are empirical dimensionless constants, f_i is the inertial frequency ($f_i = 2\pi/1$ day$\approx 7.3\times10^{-5}$ s^{-1} at 30° latitude), $B\approx 1$ km is the thermocline depth scale, N_0 is the surface extrapolated buoyancy frequency, and

$$M = \sum_{j=1}^{\infty} (j^2 + j_*^2)^{-1} \approx \frac{1}{2} j_*^{-2}(\pi j_* - 1)$$

is a constant. The spectrum is normalized so that

$$\langle \zeta^2 \rangle = \int_{f_i}^{N} d\omega \sum_{j=1}^{\infty} F_\zeta(\omega, j) = \frac{1}{2} B^2 E \frac{N_o}{N}, \tag{A3}$$

where the angular brackets denote average. Note that for internal waves $f_i \leqslant \omega \leqslant N$. The vertically integrated internal wave potential energy density is

$$\frac{\rho_w}{2}\int dz\; N^2 \langle \zeta^2 \rangle \approx \frac{\rho_w}{4} B^3 N_o^2 E \approx 810 \text{ J m}^{-2}. \tag{A4}$$

Here ρ_w is the density of sea water and we have used $B = \int (N/N_o) dz$. For some purposes it is convenient to replace the dependence of F_ζ on j by dependence on horizontal wave number $k = (k_x^2 + k_y^2)^{1/2}$. This transformation requires use of the dispersion relation,

$$m^2 = k^2 \frac{N^2 - \omega^2}{\omega^2 - f_i^2} \approx \left(\frac{\pi j}{B}\right)^2 \frac{N^2 - \omega^2}{N_o^2 - \omega^2}, \tag{A5}$$

where m is the vertical component of the wave number vector. The j-dependent form of the dispersion relation follows from a WKB modal analysis, as will be demonstrated below.

To describe the statistics of $\partial\delta c/\partial z$ the spectrum $F_{\zeta'}$ of $\partial\zeta/\partial z$ is required. Because $F_{\zeta'} = m^2 F_\zeta$ and $F_\zeta\, d\omega\, dj = F_\zeta\, d\omega\, dk(\partial j/\partial k)$,

$$F_{\zeta'}(\omega, k) = m^2(\omega, k) F_\zeta(\omega, j(\omega, k)) \frac{\partial j}{\partial k}(\omega, k). \tag{A6}$$

We shall adopt the convention that all spectra are normalized in such a way that the integral (or sum, as appropriate) of the spectrum of any physical quantity over the domain of its arguments yields the mean square value of the quantity. For this reason we have *multiplied* on the right by $\partial j/\partial k$. Making use of (A2) and (A5), Eq. (A6) reduces to

$$F_{\zeta'}(\omega, k) = \frac{2BE}{M}\,\frac{N_o}{N}\,\frac{f_i}{\omega^3}\,\frac{N^2 - \omega^2}{(N_o^2 - \omega^2)^{1/2}}\,\frac{k^2}{k^2 + k_*^2}, \tag{A7}$$

where

$$k_*^2 = \left(\frac{\pi j_*}{B}\right)^2 \frac{\omega^2 - f_i^2}{N_0^2 - \omega^2}. \tag{A8}$$

Noting that

$$2\pi \int_0^\infty dk\; kF(k) = \int_{-\infty}^{\infty} dk_x \int_{-\infty}^{\infty} dk_y\; F(\sqrt{k_x^2 + k_y^2}), \tag{A9}$$

we may replace $F_{\zeta'}(\omega, k)$ by

$$F_{\zeta'}(\omega, k_x, k_y) = \frac{BE}{\pi M}\,\frac{N_o}{N}\,\frac{f_i}{\omega^3}\,\frac{N^2 - \omega^2}{(N_o^2 - \omega^2)^{1/2}}\,\frac{\sqrt{k_x^2 + k_y^2}}{k_x^2 + k_y^2 + k_*^2}. \tag{A10}$$

Because of the horizontal isotropy of the internal wave field we may, without loss of generality, choose our coordinate system in such a way that the x-axis coincides with the vertical plane in range and depth in which sound propagates. To describe the fluctuations of $\partial\zeta/\partial z$ in this plane we must compute

$$F_{\zeta'}(\omega, k_x) = \int_{-\infty}^{\infty} dk_y\; F_{\zeta'}(\omega, k_x, k_y). \tag{A11}$$

This integral diverges so the limits must be replaced by $\pm k_{\max}$. To evaluate the integral it is helpful to first make the substitution (following Brill and Dozier, 1985)

$$q = \frac{k_*}{(k_x^2 + k_*^2)^{1/2}}\,\frac{k_y}{(k_x^2 + k_y^2)^{1/2}}. \tag{A12}$$

The resulting expression for $F_{\zeta'}(\omega, k_x)$ is

$$F_{\zeta'}(\omega, k_x) = \frac{BE}{\pi M}\,\frac{N_o}{N}\,\frac{f_i}{\omega^3}\,\frac{N^2 - \omega^2}{(N_o^2 - \omega^2)^{1/2}} I_{\zeta'}(k_x, k_*(\omega)), \tag{A13}$$

where

$$I_{\zeta'}(k_x,k_*(\omega)) = \ln\left[\frac{(k_x^2+k_{\max}^2)^{1/2}+k_{\max}}{(k_x^2+k_{\max}^2)^{1/2}-k_{\max}}\right] - \frac{k_*}{(k_x^2+k_*^2)^{1/2}} \times \ln\left[\frac{(k_x^2+k_*^2)^{1/2}(k_x^2+k_{\max}^2)^{1/2}+k_{\max}k_*}{(k_x^2+k_*^2)^{1/2}(k_x^2+k_{\max}^2)^{1/2}-k_{\max}k_*}\right]. \quad \text{(A14)}$$

Finally, we compute a pure longitudinal (in the propagation plane) horizontal wave number spectrum by integrating $F_{\zeta'}(\omega,k_x)$ over ω,

$$F_{\zeta'}(k_x) = \frac{BE}{\pi M}\frac{N_o}{N} J_{\zeta'}(k_x), \quad \text{(A15)}$$

where

$$J_{\zeta'}(k_x) = f_i \int_{f_i}^{N} d\omega \frac{1}{\omega^3}\frac{N^2-\omega^2}{(N_o^2-\omega^2)^{1/2}} I_{\zeta'}(k_x,k_*(\omega)) \quad \text{(A16)}$$

must be evaluated numerically. The result of such a numerical integration is shown in Fig. A1. Four curves are plotted corresponding to four different choices of $k_{\max}$. In all cases the parameters $f_i = 2\pi/1$ day, $N_o = 2\pi/15$ min, and $N = 2\pi/20$ min were used.

Important conclusions to be drawn from Fig. A1 are that the k_x spectrum of $\partial\zeta/\partial z$ is remarkably flat and not very sensitive to the choice of $k_{\max}$. Assuming $J_{\zeta'}(k_x)$ is zero for $|k_x| > k_{\max}$ allows

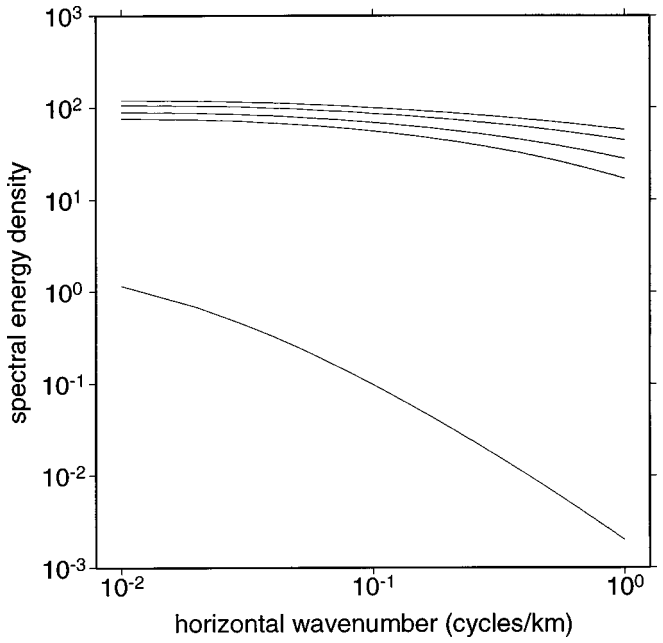

FIG. A1. Plots of $J_\zeta(k_x)$ (lower curve) and $J_{\zeta'}(k_x)$ (upper curves). After multiplication by $(BE/\pi M)(N_0/N)$—see Eqs. (A15) and (A19)—these correspond to the horizontal wave number spectra of ζ and $\partial\zeta/\partial z$, respectively. The four $J_{\zeta'}(k_x)$ plots correspond to $k_{\max}$ values of, from top to bottom, $2\pi/0.1$ km, $2\pi/0.2$ km, $2\pi/0.5$ km, and $2\pi/1.0$ km.

$$\left\langle \left(\frac{\partial\zeta}{\partial z}\right)^2 \right\rangle = \int_{-\infty}^{\infty} dk_x\, F_{\zeta'}(k_x) \quad \text{(A17)}$$

to be computed. The choice $k_{\max} = 2\pi/1.0$ km gives $(\partial\zeta/\partial z)_{\rm rms} \approx 0.15$ for the parameters chosen to construct Fig. A1. More generally, it follows from (A13) that $\langle(\partial\zeta/\partial z)^2\rangle$ scales in depth approximately like $N(z)$. Thus, at midlatitudes, $(\partial\zeta/\partial z)_{\rm rms} \approx 0.17(N/N_o)^{1/2}$. Using (A1) and assuming $N_0 = 2\pi/15$ min, this corresponds to

$$\left(\frac{\partial\delta c}{\partial z}\right)_{\rm rms} \approx \alpha\left(\frac{N}{N_o}\right)^{5/2} \quad \text{(A18)}$$

with $\alpha \approx 0.030$ s^{-1}. [More accurately, the term $N_o^{5/2}$ in Eq. (A18) should be replaced by $N_{\rm ref}^{5/2}$ with $N_{\rm ref} = 2\pi/15$ min; because typical values of N_o at midlatitudes are close to $2\pi/15$ min, we expect Eq. (A18) to be a good approximation.] Another quantity of interest in this study is the horizontal correlation length L_x of $\partial\delta c/\partial z$—or, using (A1), of $\partial\zeta/\partial z$. Because $F_{\zeta'}(k_x)$ is the Fourier transform of the autocorrelation function of $\partial\zeta/\partial z$, L_x can be defined as the x value of the first zero crossing of the inverse Fourier transform of $F_{\zeta'}(k_x)$. Assuming $F_{\zeta'}(k_x)$ is flat between $\pm k_{\max}$ gives $L_x = \pi/k_{\max} \approx 0.5$ km, independent of depth.

It is instructive to repeat the analysis above for the k_x spectrum of ζ. Details are very similar to those presented above for $\partial\zeta/\partial z$, but will not be given here. A closely related calculation was made by Brill and Dozier (1985). The counterparts of Eqs. (A15) and (A16) are, respectively,

$$F_\zeta(k_x) = \frac{BE}{\pi M}\frac{N_o}{N} J_\zeta(k_x) \quad \text{(A19)}$$

and

$$J_\zeta(k_x) = \frac{f_i B}{\pi j_*}\int_{f_i}^{N} d\omega \frac{(\omega^2-f_i^2)^{1/2}}{\omega^3} \times (k_x^2+k_*^2)^{-1/2} \ln\left[\frac{(k_x^2+k_*^2)^{1/2}+k_*}{(k_x^2+k_*^2)^{1/2}-k_*}\right]. \quad \text{(A20)}$$

It is not necessary to introduce a large k_y cutoff to compute $F_\zeta(k_x)$. $F_\zeta(k_x)$ is shown next to $F_{\zeta'}(k_x)$ in Fig. A1; the same parameters (f_i, N_o, N) were used to construct both functions. Note that the same factor multiplies both functions in Eqs. (A15) and (A19). An important observation is that the k_x spectrum of $\partial\zeta/\partial z$ is much more flat than the k_x spectrum of ζ. As a result, the horizontal correlation length for $\partial\zeta/\partial z$ is much shorter than that for ζ. This difference suggests that the justification for invoking the Markov approximation (discussed in Sec. I and III) to describe spatial variations of $\partial\delta c/\partial z$ is stronger than the justification for invoking this approximation to describe the spatial variations of δc.

The only remaining local power spectrum-based result that we require is the vertical correlation length of $\partial\zeta/\partial z$, L_z. To compute L_z it is most convenient to use the ω-j representation of $F_{\zeta'}$. It follows from (A2) and (A5) that

$$F_{\zeta'}(\omega,j) = \frac{2\pi E}{M}\frac{N_o}{N}\frac{f_i}{\omega^3}(\omega^2-f_i^2)^{1/2}\frac{N^2-\omega^2}{N_o^2-\omega^2}\frac{j^2}{j^2+j_*^2}. \quad \text{(A21)}$$

To compute L_z we need only find the first zero crossing of the inverse Fourier transform of $F_{\zeta'}$. Because the ω- and j-dependent pieces of $F_{\zeta'}$ separate, it suffices to examine

$$\sum_{j=1}^{\infty} \frac{j^2}{j^2+j_*^2}\cos\left(j\frac{N}{N_o}\frac{\pi z}{B}\right) \approx \int_0^{\infty}\left(1-\frac{j_*^2}{j^2+j_*^2}\right)\cos\left(j\frac{N}{N_o}\frac{\pi z}{B}\right)dj. \tag{A22}$$

We have used an approximate form of the dispersion relation (A5), $m\approx(\pi j/B)(N/N_o)$. Because the integral (and sum) in (A22) diverges, it is necessary to introduce a mode number cutoff, $j_{\max}$. The integral in (A22) is then approximated as

$$\int_0^{j_{\max}}\cos\left(j\frac{N}{N_o}\frac{\pi z}{B}\right)dj - j_*^2\int_0^{\infty}\frac{1}{j^2+j_*^2}\cos\left(j\frac{N}{N_0}\frac{\pi z}{B}\right)dj. \tag{A23}$$

For the purpose of estimating L_z, the second integral in (A23) gives a negligible correction to the first. The first zero crossing of the first integral gives the estimate

$$L_z=\frac{N_o}{N}\frac{B}{j_{\max}}. \tag{A24}$$

With $j_{\max}=50$, $B/j_{\max}\approx 20$ m so L_z is only a few tens of meters in the upper ocean.

We turn our attention now to an alternative to the local (in depth) spectral representation of the statistics of ζ. The alternative representation, introduced by Dozier and Tappert (1978), replaces the depth dependence implicit in $N(z)$ by an explicit eigenfunction expansion. The principal advantage of the eigenfunction expansion representation of ζ is that it provides a description of individual realizations of $\zeta(z,x)$— and hence also $\delta c(z,x)$. The ability to generate independent realizations of δc is important in our work to *test* the assumptions built into—and the predictions based on—stochastic ray theory. The material that follows should thus be considered as supplemental to the development of stochastic ray theory, and is included to explain the manner in which our numerical results which depend on individual realizations of $\delta c(z,x)$ were obtained.

In the eigenfunction expansion description of ζ, the GM dependence on j, k_x, and k_y is retained but the GM depth scaling is replaced by the z dependence of the internal wave normal modes. Let G_ζ take the place of F_ζ after introducing a new normalization constant and omitting the depth dependence of the latter. The new normalization constant is chosen so that the vertically integrated internal wave potential energy density is preserved. These considerations give

$$G_\zeta(\omega,j)=\frac{4B^3N_o^2E}{\pi M}\frac{f_i}{\omega^3}(\omega^2-f_i^2)^{1/2}(j^2+j_*^2)^{-1}.$$

The observation that $G_\zeta\, d\omega\, dj = G_\zeta\, dk\, dj(\partial\omega/\partial k)$ and use of the approximate form of the dispersion relation

$$\omega^2\approx\left(\frac{BN_o}{j\pi}\right)^2k^2+f_i^2$$

[see Eq. (A5)], gives

$$G_\zeta(j,k)=\frac{4B^3N_o^2E}{\pi M}(j^2+j_*^2)^{-1}\frac{k^2k_j}{(k^2+k_j^2)^2}, \tag{A25}$$

where $k_j=(f_i/N_o)(\pi j/B)$. Making use of (A9) gives

$$G_\zeta(j,k_x,k_y)=\frac{2B^3N_o^2E}{\pi^2M}(j^2+j_*^2)^{-1}\frac{\sqrt{k_x^2+k_y^2}k_j}{(k_x^2+k_y^2+k_j^2)^2}. \tag{A26}$$

The modal expansion for ζ is then

$$\zeta(x,y,z,t)=\mathrm{Re}\int\int dk_x\, dk_y\sum_j g(j,k_x,k_y) \times W_{jk}(z)e^{i(k_xx+k_yy-\omega_{jk}t)}. \tag{A27}$$

Each $g(j,k_x,k_y)$ is a complex Gaussian random variable with zero mean and variance

$$\langle g(j,k_x,k_y)g^*(j',k_x',k_y')\rangle = G_\zeta(j,k_x,k_y)\delta_{jj'}\delta(k_x-k_x') \times\delta(k_y-k_y'). \tag{A28}$$

The modes $W_{jk}(z)$, whose construction will be discussed below, satisfy the orthogonality condition

$$\int dz(N^2(z)-f_i^2)W_{jk}(z)W_{j'k}(z)=\delta_{jj'}. \tag{A29}$$

A useful approximate result that follows from the orthogonality condition is $\int dzN^2(z)W_{jk}^2(z)\approx 1$. The mean-square displacement is

$$\langle\zeta^2\rangle=\frac{1}{2}\int\int dk_x\, dk_y\sum_j G_\zeta(j,k_x,k_y)W_{jk}^2(z), \tag{A30}$$

and the vertically integrated internal wave potential energy density is

$$\frac{\rho_w}{2}\int dz\; N^2(z)\langle\zeta^2\rangle\approx\frac{\rho_w}{4}\int\int dk_x\, dk_y\sum_j G_\zeta(j,k_x,k_y) =\frac{\rho_w}{4}B^3N_o^2E, \tag{A31}$$

consistent with the local power spectrum-based result (A4) found earlier.

For numerical purposes it is advantageous to reduce the double integral over k_x and k_y in (A27) to a single integral. This is justified, in part, by invoking the horizontal isotropy argument used earlier; we can, without loss of generality, allow the propagation plane to coincide with the x-axis. The reduction of $G_\zeta(j,k_x,k_y)$ to $G_\zeta(j,k_x)$ can be done analytically. The result is

$$G_\zeta(j,k_x)=\frac{2B^3N_0^2E}{\pi^2M}(j^2+j_*^2)^{-1}\left[\frac{k_j}{k_x^2+k_j^2} +\frac{1}{2}\frac{k_x^2}{(k_x^2+k_j^2)^{3/2}}\ln\left(\frac{\sqrt{k_x^2+k_j^2}+k_j}{\sqrt{k_x^2+k_j^2}-k_j}\right)\right]. \tag{A32}$$

This result was derived originally by Brill and Dozier (1985) who made use of the substitution (A12). Previously, Dozier and Tappert (1978) had used an approximate form. In the modal expansion for ζ we may set $y=0$, as noted above, and $t=0$ because of the slow evolution of the internal wave field. In addition, elimination of the integral over k_y in (A27) requires that $W_{jk}(z)$ be approximated. Following Dozier and Tappert (1978) we replace $W_{jk}(z)$ by $W_{jk_x}(z)$, i.e., set $k_y=0$ when the modes are calculated. Equation (A27) is then replaced by

$$\zeta(x,z)=\mathrm{Re}\int dk_x \sum_j g(j,k_x) W_{jk_x}(z) e^{ik_x x}, \tag{A33}$$

where each $g(j,k_x)$ is a complex Gaussian random variable with zero mean and variance

$$\langle g(j,k_x) g^*(j',k_x')\rangle = G_\zeta(j,k_x)\,\delta_{jj'}\,\delta(k_x-k_x'). \tag{A34}$$

The mean-square displacement is now

$$\langle \zeta^2\rangle = \frac{1}{2}\int dk_x \sum_j G_\zeta(j,k_x) W_{jk_x}^2(z), \tag{A35}$$

and the vertically integrated internal wave potential energy density is

$$\frac{\rho_w}{2}\int dz\; N^2(z)\langle\zeta^2\rangle \approx \frac{\rho_w}{4}\int dk_x \sum_j G_\zeta(j,k_x) = \frac{\rho_w}{4} B^3 N_0^2 E, \tag{A36}$$

consistent with the results [Eqs. (A4) and (A31)] found previously.

We return now to the problem of constructing the internal wave modes, $W_{jk}(z)$, which satisfy

$$\frac{d^2W}{dz^2}+k^2\frac{N^2(z)-\omega^2}{\omega^2-f_i^2}W=0. \tag{A37}$$

For convenience we shall assume that the ocean is infinitely deep and impose the condition $W\to 0$ as $z\to-\infty$, together with $W(0)=0$. With these boundary conditions equation (A37) defines a Sturm–Liouville problem. Solutions, labeled $W_{jk}(z)$, satisfy the orthogonality condition (A29). Each W_{jk} corresponds to a discrete value of $k^2/(\omega^2-f_i^2)$; for our purposes it is most convenient to treat k as a continuous variable and set $\omega=\omega_{jk}$ where j is a positive integer.

For the purpose of constructing modes we have confined our attention to the class of $N(z)$ profiles which increase monotonically with increasing z (z increases upward). With this assumption each mode has a single turning depth $\bar{z}_{jk}$, where $N(\bar{z}_{jk})=\omega_{jk}$. For this class of problems, a uniform asymptotic nonnormalized solution to (A37) which vanishes as $z\to-\infty$ is

$$W_{jk}(z)=\left(\frac{dS_{jk}}{dz}\right)^{-1/2}\mathrm{Ai}\left(-\left(\frac{k^2}{\omega_{jk}^2-f_i^2}\right)^{1/3}S_{jk}(z)\right), \tag{A38}$$

where

$$S_{jk}(z)=\left[\frac{3}{2}\int_{\bar{z}_{jk}}^{z}(N^2(z')-\omega_{jk}^2)^{1/2}\,dz'\right]^{2/3} \tag{A39}$$

for $z\geq\bar{z}_{jk}$ and Ai denotes Airy function (Abromowitz and Stegun, 1972). [For $z<\bar{z}_{jk}$ the limits on the integral are reversed and $N^2(z')-\omega_{jk}^2$ in the integrand is replaced by $\omega_{jk}^2-N^2(z')$.] The surface boundary condition $W(0)=0$ gives

$$\mathrm{Ai}\left(-\left(\frac{k^2}{\omega_{jk}^2-f_i^2}\right)^{1/3}S_{jk}(0)\right)=0, \tag{A40}$$

which defines ω_{jk} and, in turn, $\bar{z}_{jk}$, $S_{jk}(z)$ and $W_{jk}(z)$. Equations (A1), (A33), (A38) (after normalization), (A39) and (A40) have been numerically evaluated/solved to produce the numerical results shown in Figs. 1, 2, 4 and 5.

Although the description of our internal wave eigenfunction expansion is now complete, it is insightful to further approximate (A40) to establish the approximate equivalence between this equation and (A5). Asymptotically, for large negative argument of the Airy function, (A40) reduces to

$$\frac{k}{(\omega_{jk}^2-f_i^2)^{1/2}}\int_{\bar{z}_{jk}}^{0}(N^2(z')-\omega_{jk}^2)^{1/2}\,dz'=\left(j-\frac{1}{4}\right)\pi, \tag{A41}$$

where $j=1,2,\ldots$ For the special case $N=N_o\exp(z/B)$ this integral can be evaluated analytically giving

$$\frac{kB}{(\omega_{jk}^2-f_i^2)^{1/2}}\left[(N_o^2-\omega_{jk}^2)^{1/2}+O\left(\frac{\omega_{jk}}{(N_0^2-\omega_{jk}^2)^{1/2}}\right)\right] = (j-\tfrac{1}{4})\pi. \tag{A42}$$

Neglect of the small correction term establishes the equivalence between the two forms of m^2 given in Eq. (A5). The factor j in (A5) applies to modes with no internal turning depths; $j-1/4$ in (A42) applies to modes with one internal turning depth. This difference is of no consequence in any of the results presented above.

Finally, we wish to point out that, although both the local power spectrum and eigenfunction expansion descriptions of inernal wave induced sound speed fluctuations involve approximations, predictions based on the former are consistent with numerical simulations based on the latter. This consistency is perhaps best illustrated in Fig. 2 where an individual realization of $\partial\delta c/\partial z$ vs z at fixed x is plotted. When $(N/N_o)^{-5/2}(\partial\delta c/\partial z)$ is plotted as a function of N_0/N, the magnitude of the oscillations are nearly constant, consistent with (A18) and (A1), and the spacing between zero crossings is nearly constant, consistent with (A24). Both the local power spectrum and eigenfunction expansion representations provide quantitatively useful descriptions of internal wave induced sound speed fluctuations in the ocean.

Abromowitz, M., and Stegun, I. A. (**1972**). *Handbook of Mathematical Functions* (Natl. Bureau of Standards, Washington, DC), Appl. Math. Series **55**.

Brill, M. H., and Dozier, L. B. (**1985**). ''Exact transition from two- to one-dimensional internal wave power spectra,'' J. Acoust. Soc. Am. **77**, 1248–1249.

Colosi, J. A., Flatté, S. M., and Bracher, C. (**1994**). ''Internal wave effects on 1000 km oceanic acoustic pulse propagation: Simulation and comparison with experiment,'' J. Acoust. Soc. Am. **96**, 452–468.

Dozier, L. B., and Tappert, F. D. (**1978**). ''Statistics of normal mode amplitudes in a random ocean. I. Theory,'' J. Acoust. Soc. Am. **63**, 353–365.
Flatté, S., Dashen, R., Munk, W., Watson, K., and Zachariasen, F. (**1979**). *Sound Transmission through a Fluctuating Ocean* (Cambridge U.P., Cambridge).
Gardiner, C. W. (**1985**). *Handbook of Stochastic Methods for Physics, Chemistry and the Natural Sciences* (Springer-Verlag, New York).
Garrett, C. J. R., and Munk, W. H. (**1972**). ''Space-time scales of internal waves,'' Geophys. Fluid Dyn. **2**, 225–264.
Garrett, C. J. R., and Munk, W. H. (**1975**). ''Space-time scales of internal waves: A progress report,'' J. Geophys. Res. **80**, 291–297.
Grabb, M., and Birdsall, T. (**1995**). ''Diffracted wavefronts,'' unpublished technical memorandum.
Kloeden, P., and Platen, E. (**1992**). *Numerical Solution of Stochastic Differential Equations* (Springer-Verlag, Berlin).
Milshtein, G. N. (**1978**). ''A method of second order accuracy integration of stochastic differential equations,'' Theor. Probab. Appl. **23**, 396–401.
Munk, W. H. (**1974**). ''Sound channel in an exponentially stratified ocean with application so SOFAR,'' J. Acoust. Soc. Am. **55**, 220–226.
Munk, W. (**1981**). ''Internal waves and small-scale processes,'' in *Evolution of Physical Oceanography*, edited by B. A. Warren and C. Wunsch (MIT, Cambridge), pp. 264–291.
Munk, W., Worcester, P., and Wunsch, C. (**1995**). *Ocean Acoustic Tomography* (Cambridge U.P., Cambridge).
Munk, W. H., and Zachariasen, F. (**1976**). ''Sound propagation through a fluctuating stratified ocean: Theory and observation,'' J. Acoust. Soc. Am. **59**, 818–838.
Press, W. H., Flannery, B. P., Teukolsky, S. A., and Vetterling, W. T. (**1986**). *Numerical Recipes* (Cambridge U.P., Cambridge).
Schneider, H. G. (**1991**). ''Average sound intensities in randomly varying sound speed structures,'' in *Ocean Variability and Acoustic Propagation*, edited by J. Potter and A. Warn-Varnas (Kluwer Academic, Dordrecht), pp. 283–292.
Schneider, H. G. (**1994**). ''Stochastic ray tracing,'' in *Theoretical and Computational Acoustics*, Volume 2, edited by D. Lee and M. H. Schultz (World Scientific, Singapore), pp. 957–969.
Sellschopp, J. (**1991**). ''Stochastic ray tracing in thermoclines,'' in *Ocean Variability and Acoustic Propagation*, edited by J. Potter and A. Warn-Varnas (Kluwer Academic, Dordrecht), pp. 283–292.
Simmen, J., Flatté, S. M., and Wang, G. (**1997**). ''Wavefront folding, chaos, and diffraction for sound propagation through ocean internal waves,'' J. Acoust. Soc. Am. **102**, 239–255.
Tappert, F. D. (**1977**). ''The parabolic approximation method,'' in *Wave Propagation and Underwater Acoustics*, Lecture Notes in Physics **70**, edited by J. B. Keller and J. S. Papadakis (Springer-Verlag, New York), pp. 224–284.
Tappert, F., Spiesberger, J. L., and Boden, L. (**1995**). ''New full-wave approximation for ocean acoustic travel time predictions,'' J. Acoust. Soc. Am. **97**, 2771–2782.
Tatarski, V. I. (**1961**). *Wave Propagation in a Turbulent Medium* (Dover, New York).
Thomson, D. J., and Chapman, N. R. (**1983**). ''A wide-angle split step algorithm for the parabolic equation,'' J. Acoust. Soc. Am. **74**, 1848–1854.
Wilson, H. L., and Tappert, F. D. (**1979**). ''Acoustic propagation in random oceans using the radiation tarnsport equation,'' J. Acoust. Soc. Am. **66**, 256–274.

A spectral approach to 3-D object scattering in layered media applied to scattering from submerged spheres

Nicholas C. Makris
Massachusetts Institute of Technology, Cambridge, Massachusetts 02139

(Received 25 November 1997; revised 5 June 1998; accepted 16 June 1998)

A spectral formulation for 3-D object scattering in a layered medium is described. The formulation is valid when the source and receiver are sufficiently far from the object that multiple scattering between the object and waveguide boundaries can be neglected and the scattered field can be expressed as a linear function of the object's plane wave scattering function. An analytic expression is then derived for the field scattered from a spherical object in a stratified medium. Since the expression is in terms of 1-D wave number integrals, it is computationally efficient to implement, allows detailed investigation of the scattered field in the vicinity of the object, and enables scattering of evanescent waves to be incorporated by analytic continuation. Computations for a noncompact sphere ($1<ka$) illustrate the essential characteristics of 3-D object scattering in a shallow but multi-modal waveguide. Relative to free-space scattering, a significant decrease in the level of the scattered field in the forward direction as well as a pronounced directional beaming effect in the vicinity of the sphere are discovered. Another primary finding is that multistatic observations of the scattered field, distributed over an azimuthal aperture greatly in excess of $\pi/(ka)$, will typically be necessary to classify an object submerged in a shallow-water waveguide at ranges exceeding the water column depth. © *1998 Acoustical Society of America.* [S0001-4966(98)01010-8]

PACS numbers: 43.30.Dr, 43.30.Gv, 43.30.Bp [SAC-B]

INTRODUCTION

The purpose of this paper is to elucidate some essential characteristics of 3-D scattering by potentially noncompact ($1<ka$) objects in a shallow-water waveguide. To simplify matters, it is assumed that the source and receiver are sufficiently far from the object that multiple scattering between the object and waveguide boundaries can be neglected and the scattered field can be expressed as a linear function of the object's plane wave scattering function. These assumptions are in keeping with both Ingenito's modal formulation[1] and the more recent spectral approach of Makris *et al.* for scattering from an object in a layered medium.[2] The latter is adopted in the present paper because accurate solutions can be obtained for source and receiver locations that are much closer to the object than in the former discrete modal formulation. This makes way for a detailed investigation into the 3-D structure of the scattered field from relatively close proximity to the submerged object out to horizontal ranges in great excess of the water column depth.

Primary attention is given to the important special case of scattering from a sphere in a layered medium. While the sphere shares many basic 3-D scattering characteristics with other objects, it also has a solution that is practical to implement. For example, separation of variables is fully exploited to analytically express the field scattered from a sphere in a layered medium in terms of 1-D wave number integrals. The resulting expression is evaluated numerically to delineate some fundamental characteristics of noncompact object scattering in a shallow-water waveguide.

The spatial structure of the scattered field is then computed as a function of range, depth, and azimuth so near to a noncompact sphere that a directional beaming effect, apparently peculiar to objects submerged in a shallow but multimodal waveguide, is discovered. A significant reduction in the relative level of the scattered field in the forward direction, over what would be expected in free space, is also discovered. The spatial structure of the scattered field at horizontal ranges greatly in excess of the water column depth is then analyzed. Implications for the remote classification of general noncompact objects in a shallow waveguide are discussed. Additionally, estimates of the scattered field intensity obtained by standard, but crude, target strength, and sonar-equation analysis are found to be in drastic error. The present formulation for a sphere, therefore, is expected to be especially useful in many canonical shallow-water active detection and estimation problems. For example, the solution has already been used in simulating the coherent localization of humpback whales[3] and other submerged objects whose scattered fields are buried in surface-generated noise.[4]

The problem of scattering from a 3-D object in a stratified medium has been treated by a number of authors.[1–11] Ingenito notes[1] that work prior to his 1987 paper focuses on adapting the T-matrix method to the waveguide problem. The most comprehensive work of this period is that of Hackman and Sammelmann,[6] who developed a modal solution that includes the effect of multiple scattering between object and waveguide boundaries, but which requires use of the *free-field* Green function and is restricted to media with constant sound speed layers. As Hackman and Sammelmann later note,[7] Ingenito's use of the *waveguide* Green function greatly simplifies the problem when *multiple scattering* between the *object* and waveguide boundaries can be neglected. Moreover, Ingenito's *single-scatter* model[1] fully accounts for waveguide propagation effects, such as multiple reflections of the scattered field between waveguide boundaries, because it is based upon the *waveguide* Green function.

As a result, multiple images of the object will appear at the receiver. However, there will be no rescattering between these multiple images in the single-scatter model because it employs the *free-space* scatter function for the object. The single-scatter approximation is typically valid when the object is not too close to the waveguide boundaries, relative to its scale and the wavelength,[1,2,6–11] and so is useful in many practical scenarios.

The spectral formulation adopted here generalizes Ingenito's single-scatter model. It was originally introduced to investigate the plausibility of detecting and localizing submerged objects by their perturbation of an ocean waveguide's ambient noise field.[2] It has not been previously applied to the standard 3-D object-scattering problem where the source is restricted to an isolated point in the waveguide. The primary advantage of the spectral approach is that it enables the scattered field to be computed much closer to the object than in previous modal formulations.[1,6,7,9–11] Moreover, it has an extremely compelling physical interpretation. Specifically, the source and receiver are assumed to be sufficiently far from the object that its free-space scattering function can be used to linearize the problem, as implied in Ingenito's original modal formulation.[1] The field emanating from the source is then decomposed into plane waves incident on the object. The object scatters each incident plane wave into all directions by its free-space scattering function. The scattered field from each incident plane wave then propagates through the waveguide to the receiver in accord with the waveguide Green function. The scattered fields from each incident plane wave are coherently superposed to form the total scattered field at the receiver. Just as the great practical advantage of Ingenito's modal approach is its ease of implementation by straightforward modification of existing normal-mode propagation software,[1] the spectral generalization is advantageous because it can be easily implemented by straightforward modification of existing wave number integration software. Like the modal approach, the spectral formulation can be used to compute the scattered field from an *arbitrarily shaped penetrable object* as long as its free-space scattering function is known either analytically, as is the case for many simple shapes,[12] or experimentally, as in submarine target scattering.[13] For example, Perkins, Kuperman, Tinker, Heaney, and Murphy have employed Ingenito's modal approach to treat the problem of scattering from a prolate spheroid in a deep ocean waveguide.[9,10] While the spectral approach described here is for a harmonic source, it is readily extended to the time domain by standard Fourier synthesis.

In related work, Collins and Werby[8] describe a parabolic equation (PE) method for 3-D object scattering in the ocean. The advantage of this approach is its ability to handle range-dependent waveguides. A primary disadvantage is that the 3-D PE must generally be used to properly handle diffraction about the object so that the entire 3-D field from the object must be marched to the range of the receiver even if the receiver is isolated at a single point in range, depth, and azimuth. Additionally, Perkins *et al.*[9,10] have used the adiabatic approximation to extend Ingenito's modal approach for 3-D object scattering to weakly range-dependent waveguides. As in the original modal formulation, this extension is only valid when the range from the source, and receiver, to the object is much greater than the waveguide depth.

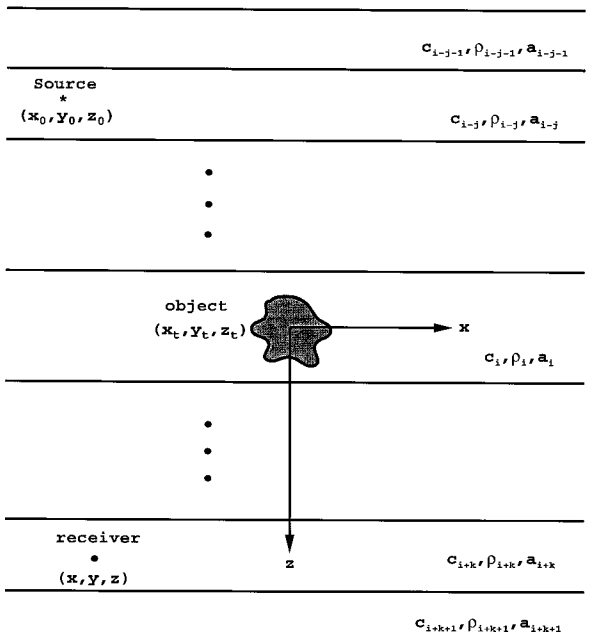

FIG. 1. Geometry of an object, source and receiver in a horizontally stratified medium. All coordinate systems are centered at the object centroid. Each layer i is characterized by sound speed c_i, density ρ_i, and attenuation a_i.

For economy, the notation of Ref. 2 is used here and in the remainder of this article. For example, the object centroid is at the center of all coordinate systems, as shown in Fig 1. Source coordinates are defined by (x_0, y_0, z_0), receiver coordinates by (x,y,z) and coordinates on the surface of the object by (x_t, y_t, z_t) where the positive z axis points downward and normal to the interfaces between horizontal strata. Spatial cylindrical (ρ, θ, z) and spherical systems (r, θ, ϕ) are defined by $x = r \sin\theta \cos\phi$, $y = r \sin\theta \sin\phi$, $z = r \cos\theta$, and $\rho^2 = x^2 + y^2$. Wave number coordinates for the incident $(\xi_{ix}, \xi_{iy}, \gamma_i)$ and scattered field (ξ_x, ξ_y, γ) are related to polar and azimuthal propagation angles (α, β) by $\xi_x = k \sin\alpha \cos\beta$, $\xi_y = k \sin\alpha \sin\beta$, $\gamma = k \cos\alpha$, where the horizontal wave number magnitude is defined by $\xi^2 = \xi_x^2 + \xi_y^2$ and the wave number magnitude k equals the angular frequency ω divided by the sound speed c. For example, the phase $\mathbf{k} \cdot \mathbf{r}$ is explicitly written as

$$\boldsymbol{\xi} \cdot \boldsymbol{\rho} + \gamma z = kr[\cos\alpha \cos\theta + \sin\alpha \sin\theta \cos(\beta - \phi)]. \tag{1}$$

I. AN APPROXIMATION FOR 3-D SCATTERING FROM AN OBJECT OF ARBITRARY SHAPE IN A LAYERED MEDIUM

The harmonic field $\Phi_s(\mathbf{r})$ scattered by an object can be expressed in terms of the medium Green function $G(\mathbf{r}|\mathbf{r}_t)$ and incident field $\Phi_i(\mathbf{r})$ by Kirchhoff's integral equation

$$\Phi_s(\mathbf{r}) = -\int\int_{A_t} [\Phi_i(\mathbf{r}_t)+\Phi_s(\mathbf{r}_t)]\,\frac{\partial G(\mathbf{r}|\mathbf{r}_t)}{\partial n_t} + G(\mathbf{r}|\mathbf{r}_t)\,\frac{\partial}{\partial n_t}[\Phi_i(\mathbf{r}_t)+\Phi_s(\mathbf{r}_t)]\,dA_t, \tag{2}$$

where $G(\mathbf{r}|\mathbf{r}_t)$ and $\Phi_i(\mathbf{r})$ each satisfy the Helmholtz equation, driven by a point source of unit strength at angular frequency ω.

In many practical applications, however, a number of simplifying assumptions can be made that lead to an approximate formulation that is both intuitively appealing and far less computationally expensive to solve than Kirchhoff's integral equation. This approximation is valid when: (1) the propagation medium is horizontally stratified and range independent; (2) the object is contained within a layer whose index of refraction can be well approximated as a constant; (3) multiple reflections between the *object* and waveguide boundaries make a negligible contribution to the scattered field at the location of a receiver; and (4) the range from the object to the source, and receiver, is large enough that the scattered field can be expressed as a linear function of the object's plane wave scatter function. This last assumption often requires that the range from the object is much greater than the object's spatial extent.

While the field scattered from an object in a horizontally stratified medium can always be expressed in terms of a 4-D horizontal wave number transform, this approach becomes particularly useful when the conditions listed above are satisfied. Then the kernel of the spectral transform can be approximated as a function that is independent of the horizontal positions of the source, potentially noncompact scatterer and receiver. In this case, Makris *et al.*[2] show that the scattered field becomes

$$\Phi_s(\mathbf{r}) = \frac{1}{\pi k}\int\int_{-\infty}^{\infty} F(z,z_0,\xi,\xi_i)e^{i(\boldsymbol{\xi}_i\cdot\boldsymbol{\rho}_0+\boldsymbol{\xi}\cdot\boldsymbol{\rho})}\,d^2\boldsymbol{\xi}_i\,d^2\boldsymbol{\xi}, \tag{3}$$

where the kernel,

$$\begin{aligned} F(z,z_0,\xi,\xi_i) \approx{}& \Psi^+(z_0)\Psi^+(z)S(\pi-\alpha,\beta;\pi-\alpha_i,\beta_i) \\ &+\Psi^+(z_0)\Psi^-(z)S(\alpha,\beta;\pi-\alpha_i,\beta_i) \\ &+\Psi^-(z_0)\Psi^+(z)S(\pi-\alpha,\beta;\alpha_i,\beta_i) \\ &+\Psi^-(z_0)\Psi^-(z)S(\alpha,\beta;\alpha_i,\beta_i), \end{aligned} \tag{4}$$

is a function of the object's plane wave scattering function in free space $S(\alpha,\beta;\alpha_i,\beta_i)$,[12] and down-going (positive superscript) and up-going (negative superscript) plane wave amplitudes $\Psi^+(z_0)$, $\Psi^-(z_0)$, $\Psi^+(z)$, and $\Psi^-(z)$. These plane wave amplitudes depend explicitly on the depth of the source or receiver, and implicitly on the depth of the object's centroid because the centroid is chosen to be at the origin of the coordinate system. By spectral transformation, these amplitudes can be used to express the incident field

$$\Phi_i(\mathbf{r}_t|\mathbf{r}_0) = \frac{1}{2\pi}\int_{-\infty}^{\infty}\left\{\Psi^+(z_0)e^{i\gamma_i z_t}+\Psi^-(z_0)e^{-i\gamma_i z_t}\right\} \times e^{-i\boldsymbol{\xi}_i\cdot(\boldsymbol{\rho}_t-\boldsymbol{\rho}_0)}\,d^2\boldsymbol{\xi}_i, \tag{5}$$

and waveguide Green function

$$G(\mathbf{r}|\mathbf{r}_t) = \frac{1}{2\pi}\int_{-\infty}^{\infty}\{\Psi^+(z)e^{i\gamma z_t}+\Psi^-(z)e^{-i\gamma z_t}\} \times e^{i\boldsymbol{\xi}\cdot(\boldsymbol{\rho}-\boldsymbol{\rho}_t)}\,d^2\boldsymbol{\xi}, \tag{6}$$

in terms of up and down going plane waves. In the former expression, the plane wave amplitudes relate transmission from the layer of the point source to a receiver in the layer of the object. In the latter they relate transmission from the layer of the object to that of the receiver. They also depend, therefore, on the magnitude of the horizontal wave number and the boundary conditions at the interfaces between the layers.

Equations (3)–(4) reveal a simple prescription for computing the field scattered from an object in a layered medium where preliminary propagation and scattering computations are made independently. For example, to set up the propagation component of the calculation, the up- and down-going plane wave amplitudes are computed just as they are for point–source to point–receiver propagation in a range-independent horizontally stratified media. Any of a number of standard techniques can be used for this purpose.[14,15] For the scattering component, the object's plane wave scattering function in free space may either be already known, as is the case for many simple shapes;[12] it may be experimentally measured, as for example in submarine target scattering;[13] or it may be computed by standard asymptotic methods.[12] The results of this preliminary analysis are then incorporated in Eqs. (3)–(4) and the scattered field is computed by wave number integration.

Equations (3)–(4) are also intuitively appealing. The incident field is decomposed into a continuum of up- and down-going plane waves in accord with propagation in a horizontally stratified waveguide, or specifically Eq. (5). Any one of these incident plane waves is scattered from the object into a continuum of directions. This continuum of scattered plane waves is then organized into an up-going and a down-going set, as required by the waveguide Green function in Eq. (6). When the approximation is valid, the total scattered field is then just the integral of all plane wave components scattered from every incident plane wave component.

II. SCATTERING FROM A SPHERICAL OBJECT IN A LAYERED MEDIUM

To derive an expression for the field scattered from a spherical object in a layered medium, Eq. (3) is first rewritten as

$$\Phi_s(\mathbf{r}) = \frac{1}{\pi k}\int_0^{\infty}\xi\,d\xi\int_0^{\infty}\xi_i\,d\xi_i\int_0^{2\pi}d\beta\int_0^{2\pi}d\beta_i \times F(z,z_0,\xi,\xi_i)e^{i(\boldsymbol{\rho}_i\cdot\boldsymbol{\xi}_0+\boldsymbol{\rho}\cdot\boldsymbol{\xi})}, \tag{7}$$

where each 2-D integral is expressed in terms of polar coordinates over the magnitude and direction of the respective horizontal wave number vector. As a consequence of the spherical symmetry of the object, a number of simplifications can be made. To this end, the plane wave scattering function for a spherical object is introduced.

As shown in Appendix A of Ref. 2, the addition theorem for spherical harmonics can be used to express the plane wave scattering function for a sphere in free space as

$$S(\alpha,\beta;\alpha_i,\beta_i)=\sum_{n=0}^{\infty} f(n)\left\{ P_n\left(\frac{\gamma}{k}\right)P_n\left(\frac{\gamma_i}{k}\right)+2\sum_{m=1}^{n}\frac{(n-m)!}{(n+m)!}\times P_n^m\left(\frac{\gamma}{k}\right)P_n^m\left(\frac{\gamma_i}{k}\right)\cos\, m(\beta-\beta_i)\right\}, \tag{8}$$

where

$$f(n)=i(-1)^n(2n+1)a_n, \tag{9}$$

and the coefficient

$$a_n=\frac{j_n'(ka)-(\rho c/\rho_t c_t)[j_n'(k_t a)/j_n(k_t a)]j_n(ka)}{h_n'(ka)-(\rho c/\rho_t c_t)[j_n'(k_t a)/j_n(k_t a)]\ h_n(ka)}, \tag{10}$$

is determined by boundary conditions at the sphere's surface given internal density ρ_t, sound speed c_t, and wave number $k_t=\omega/c_t$.[16] Equation (8) is convenient for two reasons. First, it factors the polar wave number components in such a way that they can be easily integrated out. Second, it expresses the vertical directionality of the incident and scattered waves in terms of the vertical wave number magnitudes. These attributes are essential for the scattered field to be expressed exclusively in terms of integrals over the horizontal wave number magnitudes. They also enable evanescent waves to be incorporated by analytic continuation to horizontal wave number magnitudes beyond k, which corresponds to imaginary incident and scattered angles.

After substituting this scattering function in Eqs. (4) and (7), integrals over the horizontal wave number's polar angle are carried out with the aid of the easily proven identities

$$\int_0^{2\pi} d\beta \int_0^{2\pi} d\beta_i\ e^{i\{\xi_i\rho_0\cos(\beta_i-\phi_0)+\xi\rho\cos(\beta-\phi)\}} = (2\pi)^2 J_0(\xi_i\rho_0)J_0(\xi\rho), \tag{11}$$

and

$$\int_0^{2\pi} d\beta \int_0^{2\pi} d\beta_i\ e^{i\{\xi_i\rho_0\cos(\beta_i-\phi_0)+\xi\rho\cos(\beta-\phi)\}}\cos\, m(\beta_i-\beta) = (2\pi)^2\cos\, m\pi\cos\, m(\phi_0-\phi)J_m(\xi_i\rho_0)J_m(\xi\rho). \tag{12}$$

After some straightforward algebraic manipulation, the field scattered from a sphere in a layered medium takes the form

$$\begin{aligned}\Phi_s(\mathbf{r},\mathbf{r}_0)=&\frac{(2\pi)^2}{\pi k}\sum_{n=0}^{\infty} f(n)\\ &\times\left\{\int_0^{\infty}\left[\Psi^+(z_0)P_n\left(-\frac{\gamma_i}{k}\right)+\Psi^-(z_0)P_n\left(\frac{\gamma_i}{k}\right)\right]J_0(\xi_i\rho_0)\xi_i\, d\xi_i\int_0^{\infty}\left[\Psi^+(z)P_n\left(-\frac{\gamma}{k}\right)+\Psi^-(z)P_n\left(\frac{\gamma}{k}\right)\right]J_0(\xi\rho)\xi\, d\xi\right.\\ &+2\sum_{m=1}^{n}\frac{(n-m)!}{(n+m)!}\cos\, m(\phi-\phi_0+\pi)\\ &\left.\times\left\{\int_0^{\infty}\left[\Psi^+(z_0)P_n^m\left(-\frac{\gamma_i}{k}\right)+\Psi^-(z_0)P_n^m\left(\frac{\gamma_i}{k}\right)\right]J_m(\xi_i\rho_0)\xi_i\, d\xi_i\int_0^{\infty}\left[\Psi^+(z)P_n^m\left(-\frac{\gamma}{k}\right)+\Psi^-(z)P_n^m\left(\frac{\gamma}{k}\right)\right]J_m(\xi\rho)\xi\, d\xi\right\}\right\}.\end{aligned} \tag{13}$$

This formula is particularly useful for computational purposes because it is expresses the 3-D field scattered from a sphere solely in terms of 1-D wave number integrals. The fourfold reduction in the dimensionality of the general spectral transform of Eq. (3) is a consequence of the spherical symmetry of the object. As a matter of practicality, the integrals typically converge in shallow-water acoustic applications when the horizontal wave number magnitude reaches an upper limit that exceeds, but is well within an order of magnitude of, k, while the summations generally converge after roughly $2ka$ terms are taken. It is noteworthy that the first term, $n=0$, of Eq. (13) is the general solution for an arbitrarily shaped *compact* object ($\lambda\gg a$) in a waveguide.

To examine the ranges within which Eq. (13) is valid, it is useful to consider the field scattered from a sphere in free space

$$\Phi_s(\mathbf{r})=-\sum_{n=0}^{\infty} i^n(2n+1)a_n h_n^{(1)}(kr)P_n(\cos\,\theta\cos\,\alpha_i+\sin\,\theta\sin\,\alpha_i\cos(\phi-\beta_i)), \tag{14}$$

by an incident plane wave propagating *in the direction* (α_i,β_i). Since

$$h_n^{(1)}(kr)\approx(-i)^{n+1}\frac{e^{ikr}}{kr}, \tag{15}$$

for $kr\gg 1$ and $kr>n$, the scattered field can be approximated by

$$\Phi_s(\mathbf{r})\approx\frac{e^{ikr}}{kr}S(\theta,\phi;\alpha_i,\beta_i), \tag{16}$$

for $kr\gg 1$ and $kr>2ka$, or $r>2a$, since satisfactory convergence typically occurs after $2ka$ terms are taken in Eq. (14). This approximation, therefore, can be a good one very close to the sphere's surface. For practical applications, it is usually valid well within the object's nearfield since $(2a)^2/\lambda$ thresholds onset of the far field. By similar reasoning, the Bessel functions in Eq. (13) can be approximated by their asymptotic forms for large arguments.

For objects in a shallow-water waveguide, however, neglect of multiple-scattering from the waveguide boundaries

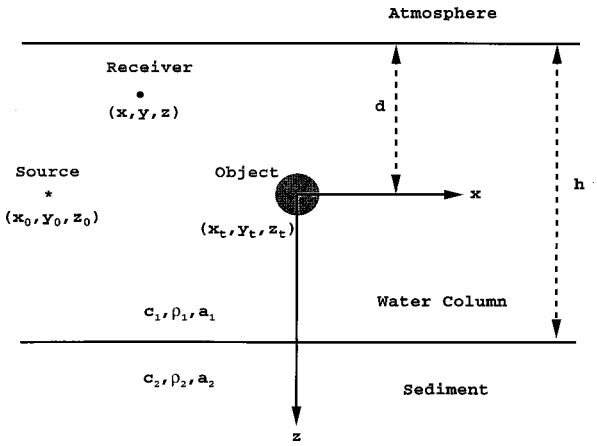

FIG. 2. Geometry of a spherical object in a Pekeris waveguide insonified by a point source. To be consistent with subsequent calculations, the point source and object centroid are shown at the center of the waveguide where $h=100$ m, $d=50$, and the sphere radius is $a=10$ m.

will sometimes lead to more stringent limitations on the range within which Eq. (13) remains a valid approximation. For most practical applications in shallow-water acoustics, however, the effects of multiple-scattering between the object and waveguide boundaries are only expected to be significant over horizontal ranges within roughly two diameters of the object centroid. They are expected to be most pronounced when the object's diameter is on the order of the strata thickness, and negligible when the diameter is much less than the strata thickness. Examples of multiple scattering and errors introduced by neglecting it have been given in Refs. 17 and 2.

III. SCATTERING FROM A SPHERICAL OBJECT IN A SHALLOW-WATER WAVEGUIDE

A. Pekeris waveguide

Equation (13) is used to numerically compute the field scattered from a spherical object in a shallow-water waveguide. For simplicity the waveguide is assumed to be Pekeris with water column sound speed $c_1=1500$ m/s, density $\rho_1=1000$ kg/m^3, and attenuation $a_1=3\times10^{-4}$ m^{-1} overlaying a sediment half-space of sound speed $c_2=1700$ m/s, density $\rho_2=1900$ kg/m^3, and attenuation $a_2=(0.1/\lambda)\mathrm{m}^{-1}$. The waveguide geometry is shown in Fig. 2. Analytic expressions for the up- and down-going plane wave amplitudes of the incident field and medium Green's function are provided in the Appendix.

Both the point source, of strength 0 dB re: 1 μPa at 1 m, and sphere centroid are located in the middle of the water column so that $d=h/2$ where $h=100$ m. The source, located at $(x_0=-4000\text{ m},\ y_0=0,\ z_0=0)$, is therefore separated from the sphere centroid by 4-km horizontal range. The homogenous sphere is assumed to have a radius of $a=10$ m and to satisfy pressure release boundary conditions at its surface. Computations are made at frequency $f=300$ Hz so that the number of wavelengths that fit across the sphere's circumference, ka, is roughly 12.6.

The results of the computations are shown in Figs. 3 and 4. To help understand their meaning, they are presented along with a standard but crude sonar-equation approximation for the field scattered from an object in a waveguide

$$\Phi_s(\mathbf{r})\approx\frac{4\pi}{k}\,G(\mathbf{r}|0)G(0|\mathbf{r}_0)S\left(\frac{\pi}{2},\varphi;\frac{\pi}{2},\phi_0-\pi\right), \quad (17)$$

where the scattering function, which determines target strength and is plotted for the given object in Fig. 5, factors from transmission coefficients to and from the object. This type of approximation has been discussed by Ingenito.[1] It becomes valid in Eqs. (3) and (4) when propagation is effectively horizontal, so that $\alpha_i\approx\alpha\approx\pi/2$, and the incident and received fields are effectively planar, so that $\beta_i\approx\phi_0+\pi$ and $\beta\approx\phi$. It also becomes valid for compact objects ($a\ll\lambda$) regardless of the waveguide's modal structure, as can be seen by taking *only* the first term, $n=0$, of Eq. (13) as the general compact-object solution, noting that z_t must vanish for a point target at the origin and that the plane wave scattering function reduces to $f(0)$ and so becomes independent of the incident and scattered angles. At 300 Hz, however, propagation in the waveguide of Figs. 2–4 is far from horizontal and the object is noncompact.

It is not surprising then that serious discrepancies arise between the sonar-equation approximation and the spectral formulation of Eq. (13). In particular, the sonar-equation approximation drastically overestimates the overall level of the scattered field, by tens of dB, as is evident in Fig. 3(a)–(b), where the scattered field is shown over a horizontal plane slicing through the center of the water column. This *absolute* error is *highly sensitive* to slight variations in the location of the source, target, and receiver, due to the complex interference structure within the waveguide. The sonar-equation approximation also significantly overestimates the level of the scattered field in the forward direction relative to other directions. But this error is *insensitive* to slight variations in source, target, or receiver locations because it is in *relative* level.

Besides the expected forward scatter beam of width $\pi/(ka)$, three other azimuthal beams of similar dimension are observed in Fig. 3(b). These fall within roughly two water column depths horizontal range of the object, between forward and backscatter directions. Since the beams are not observed in Fig. 5, they have no analogue in free-space scattering from an identical object. The beams apparently arise as interference from multiple images of the object. Since the beams are intimately related to the object's noncompactness, they are not present in the sonar-equation approximation. The 3-D nature of these beams can be explored by considering the range-depth plots of Fig. 4, where drastic azimuthal variations in the range–depth structure of the scattered field are observed in the vicinity of the object. While multiple images of the object are accounted for, as is consistent with waveguide propagation, multiple scattering between these images is neglected in the single-scatter formulation of Eqs. (3) and (4). The field structure within roughly two object diameters of the centroid, or roughly 40-m range, therefore may not be very accurate. But this has no affect on the noted beams which extend well beyond this range.

In the forward direction, Fig. 4(c), two vertical beams emerge from the object. The mean directions and relative

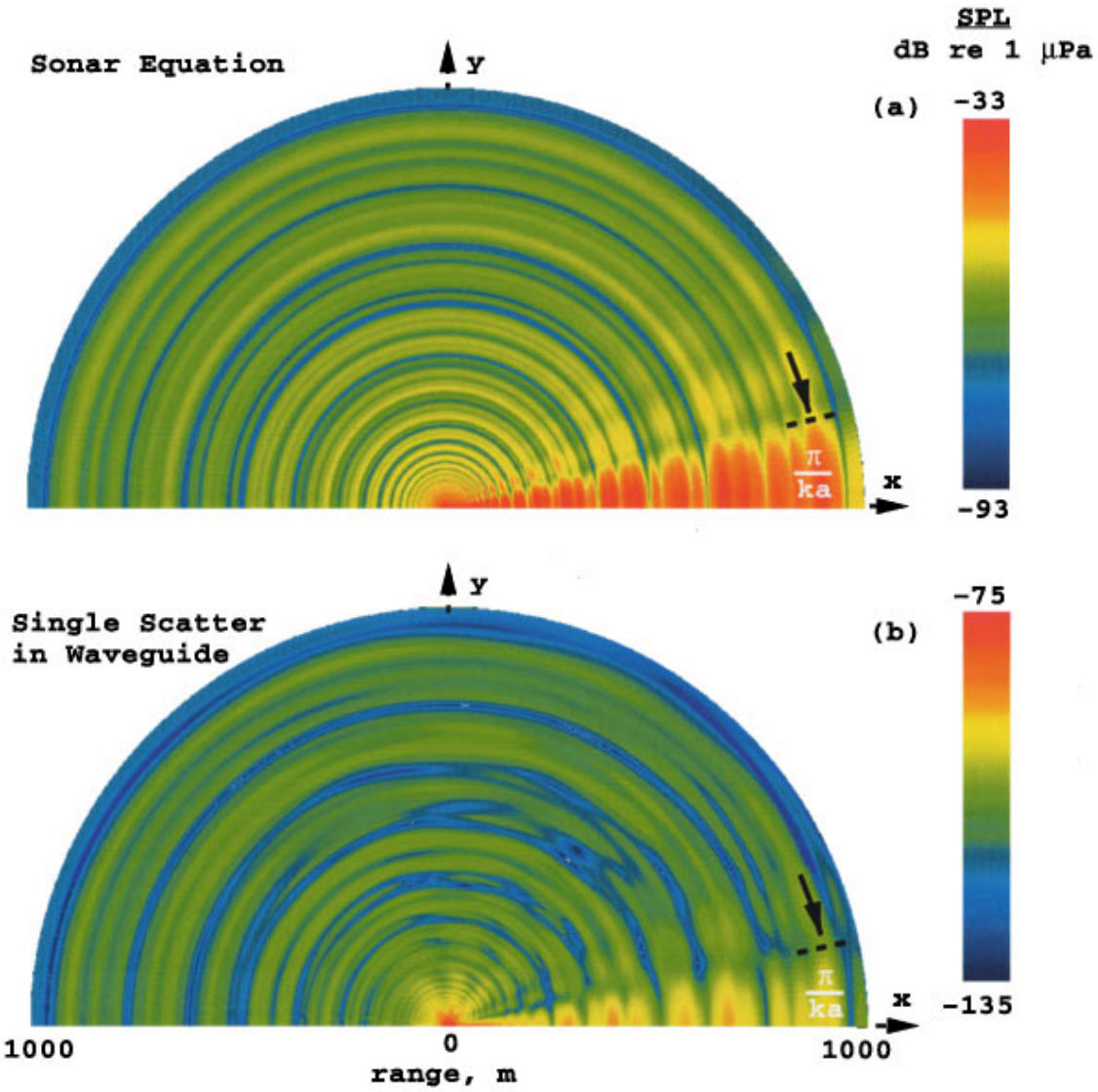

FIG. 3. Horizontal slice of the field scattered from a 10-m radius pressure release sphere, submerged in the middle of a 100-m-deep Pekeris waveguide, by a harmonic point source also in middle of the waveguide at ($x_0=-4000$ m, $y_0=0$, $z_0=0$) radiating at $f=300$ Hz. Image plane cuts through the object centroid placed in the middle of the waveguide. (a) For comparison, the sonar-equation approximation following Eq. (17) is shown for the noncompact object ($ka=12.6$). (b) Single-scatter calculation using Eq. (13).

intensities of these two beams roughly correspond to those of the equivalent up- and down-going plane waves for the most dominant discrete modes of the incident field. The forward scattered beamwidths can be interpreted as the convolution of this bimodal incident plane wave spectrum with the Poisson cone,[2,12] of angular width $\pi/(ka)$, for an individual plane wave.

B. Implications for remote classification of general objects submerged in shallow water

While the range-depth field structure predicted by the sonar-equation approximation is in serious error in the vicinity of the object, it becomes better with increasing range. Apparently, as horizontal range increases, the bandwidth of the vertical angular spectrum decreases, by bottom transmission and attenuation, to the point that it is on the order of or less than $\pi/(ka)$. Beaming and interference effects arising from the object's noncompactness are then *no longer resolvable by vertical apertures* within the waveguide, and the range-depth structure converges to that of a monopole source placed at the object centroid, as is evident upon comparison of Fig. 4(a) with Fig. 4(b)–(d). The *full complexity* of scattering from a noncompact object in a multi-modal waveguide, however, *is maintained by the azimuthal structure* of the scattered field regardless of range since no boundaries are present to provide a similar reduction in bandwidth over azimuthal angle.

At ranges in great excess of the water column depth, therefore, classification of the object by a *single vertical aperture* would require *a priori* knowledge of the aspect of the object relative to the source and receiver, since *only the absolute level* of the field can be used to characterize the object. With an *azimuthal aperture*, on the other hand, classification can be made at such distant ranges merely by examining the normalized *spatial structure* of the received field.

The implication here is that multistatic observations of

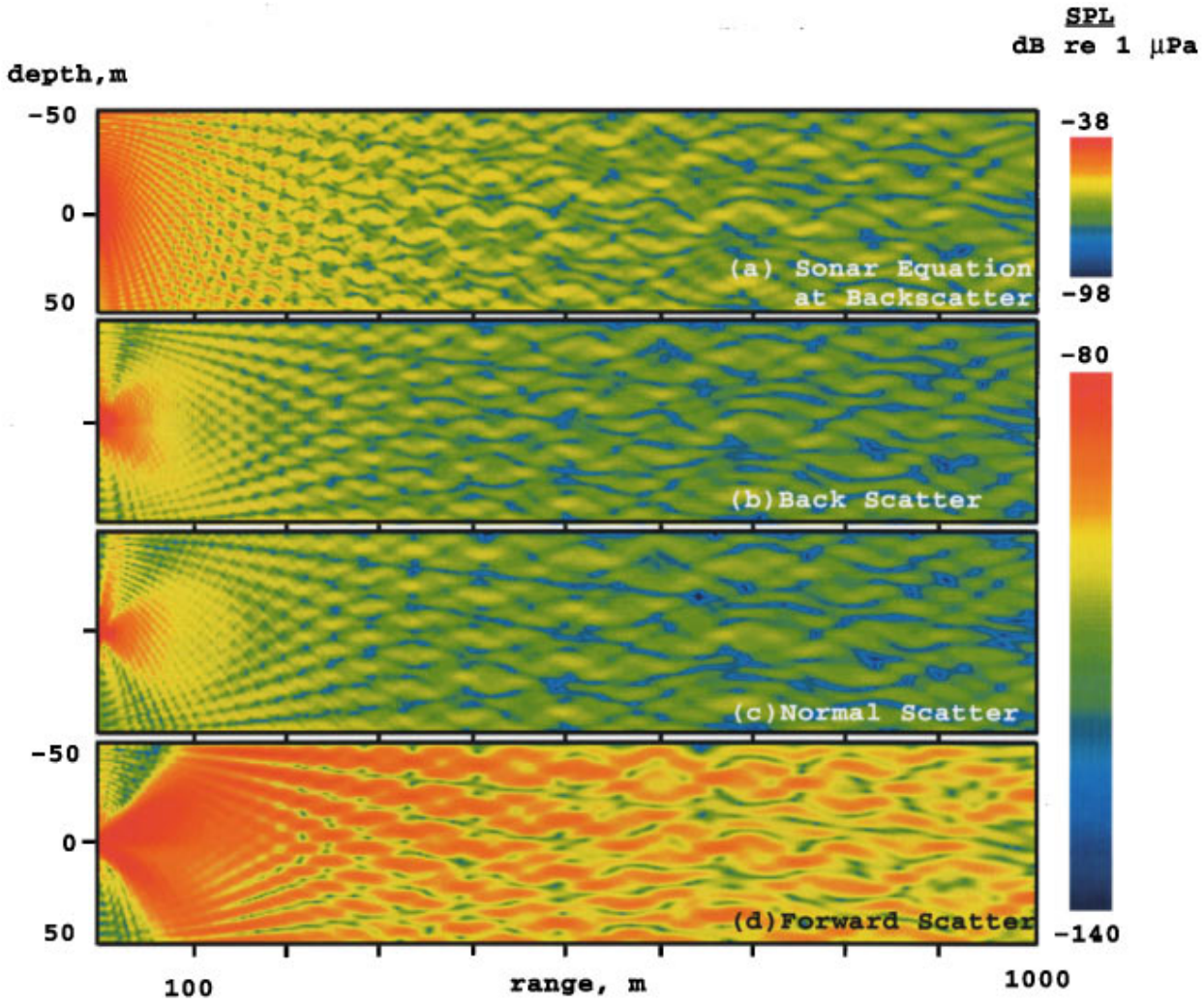

FIG. 4. Range-depth cross sections of the field scattered from a 10-m radius pressure release sphere, submerged in the middle of a 100-m-deep Pekeris waveguide, by a harmonic point source also in the middle of the waveguide at ($x_0 = -4000$ m, $y_0 = 0$, $z_0 = 0$) radiating at $f = 300$ Hz. (a) For comparison, the sonar-equation approximation of Eq. (17) is shown with levels corresponding to the backscatter azimuth. For the given noncompact object, Eq. (17) incorrectly yields range–depth *structure* that is invariant over azimuth and identical to point-source structure. To obtain the sonar-equation approximation at the forward scatter azimuth, uniformly augment the level by 24 dB over the entire Fig. 4(a). (b)–(d) Single-scatter calculation using Eq. (13) at azimuths corresponding to (b) backscatter, (c) normal scatter, and (d) forward scatter. Range increases along the negative x axis in (a) and (b), along the positive or negative y axis in (c), and along the positive x axis in (d). In single-scatter calculations, range-depth structure correctly shows drastic variation over azimuth in the vicinity of the noncompact object.

the scattered field, distributed over an azimuthal range greatly in excess of $\pi/(ka)$, will typically be necessary to classify an object submerged in a shallow-water waveguide at ranges exceeding the water column depth. By reciprocity, such multistatic observations may be made either by varying the relative azimuth of the source or receiver.

C. Implications for measurement of the scattered field

In reality, source signals have finite time duration. In active sonar systems, time separation between the incident and scattered waveform arrivals is generally built-in to the operational geometry to insure that the incident field will not significantly overlap the scattered field at the receiver, except in the forward direction where no time separation is possible. Time separation of this kind is often essential for the scattered field to be measured by a single *omni-directional* sensor because while the incident field only suffers spreading loss from the source, the scattered field suffers spreading loss from both the source to the object and from the object to the receiver. Given a *directional* sensor, with sufficient spatial aperture, however, the scattered field can be distinguished from the incident field even when there is no time separation by exploiting differences in propagation direction and field structure, as is done routinely in beamforming and matched field processing.

For the specific harmonic example described in Sec. III A, the total field, defined as the sum of the incident and scattered fields, has a sound pressure level that differs from the incident field by no more than a small fraction of a decibel over the regions shown in Figs. 3–4. In other words, relative to the incident field, the scattered field comprises an extremely small contribution to the total field amplitude. The reason for this can be understood better by analyzing the scattered field where it is strongest, namely in the two forward beams that appear in Fig. 4(d) within roughly one water

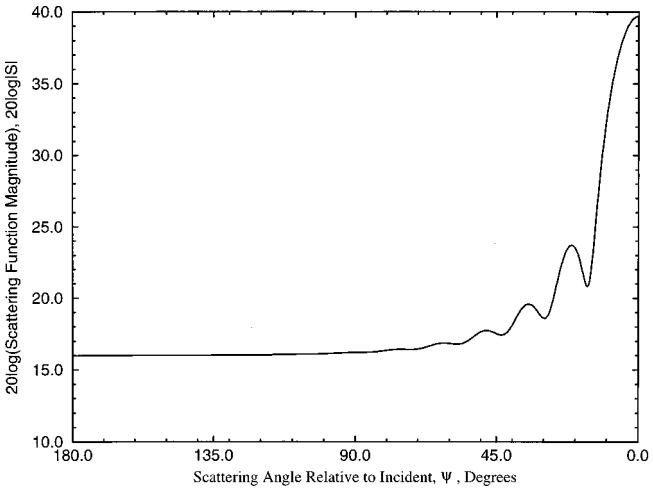

FIG. 5. The scattering function magnitude $|S(\psi)|$ for a pressure-release sphere of $ka=12.6$ is plotted as a function of the angle ψ between an incident plane wave *from the direction* (θ_0,ϕ_0) of a source and a plane wave scattered *in the direction* (θ,ϕ) of a receiver, where $\cos\psi=\cos(\pi-\theta_0)\cos\theta+\sin(\pi-\theta_0)\sin\theta\cos(\phi-\phi_0+\pi)$, and forward scatter occurs at $\psi=0$. For example, $\psi=\phi$ when $\theta_0=\pi/2$, $\phi_0=\pi$, and $\theta=\pi/2$, as is relevant in Fig. 3.

column depth in range from the object. At any point in these beams, the *incident* field is the *convergence* of a *broad directional spectrum* of incident plane waves, in keeping with waveguide propagation from a distant point source. At the same point within these beams, however, the scattered field emanating from the object is in the process of *diverging*. Moreover, as discussed in Sec. III A, each beam corresponds to the forward scatter of only a *fraction* of the incident spectrum, due to directional filtering by the object, whereas the incident field is comprised of the *entire* incident spectrum, by definition.

While the present harmonic analysis can be extended to finite-time duration and broadband source signals by Fourier synthesis, without loss of generality, it is already approximately valid for *narrow-band* waveforms. For example, distinct narrow-band conditions can be given for the free-space scattering and waveguide propagation problems, each of which must be satisfied for the narrow-band approximation to be made in the waveguide scattering problem. In the former, the waveform's bandwidth about the carrier frequency must be much smaller than the ratio of the mean sound speed to the object diameter, so that the spatial extent of the signal pulse is much greater than that of the object. In the latter, the Green function from the source to the object, and similarly from the object to the receiver, must effectively be constant within the signal band. This latter condition typically requires the bandwidth to decrease as the bistatic range from source to object and from object to receiver increases.

IV. CONCLUSIONS

A spectral formulation for 3-D object scattering in a layered medium is described. The formulation is valid when the source and receiver are sufficiently far from the object that multiple scattering between the object and waveguide boundaries can be neglected and the scattered field can be expressed as a linear function of the object's plane wave scattering function. Since these conditions are often satisfied in active sonar problems, especially those involving remote objects, and the formulation is relatively simple to implement, it is of practical value in a wide variety of ocean-acoustic applications.

An analytic expression is derived for the field scattered from a spherical object in a stratified medium. Since the expression is in terms of 1-D wave number integrals, it is computationally efficient to implement, allows detailed investigation of the scattered field in the vicinity of the object, and enables scattering of evanescent waves to be incorporated by analytic continuation.

Computations for a noncompact sphere illustrate the essential characteristics of 3-D object scattering in a shallow but multi-modal waveguide. For example, a significant decrease in the relative level of the scattered field in the forward direction, compared with free-space scattering, as well as a pronounced 3-D beaming effect in the vicinity of the sphere are discovered.

Another primary finding is that on vertical apertures, at sufficiently large ranges from the object, the structure of the scattered field converges to that of a monopole source placed at the object centroid. This convergence occurs when the bandwidth of the vertical angular spectrum decreases, by bottom transmission and attenuation, to the point that it is on the order of or less than $\pi/(ka)$. In this case only a constant scale factor is available to classify the object, given *a priori* knowledge of its aspect. As a result, multistatic observations of the scattered field, distributed over an azimuthal aperture greatly in excess of $\pi/(ka)$, will typically be necessary to classify an object submerged in a shallow-water waveguide at ranges exceeding the water column depth.

Finally, standard sonar equation analysis is found to be a highly unreliable method for estimating the level of the field scattered from noncompact objects submerged in shallow water.

APPENDIX

For a Pekeris waveguide of thickness h with object centroid at vertical distance d from the air–sea interface, as shown in Fig. 2, the plane wave coefficients for the incident field $\Phi_i(\mathbf{r})$ are

$$\Psi^+(z_0)=\frac{1}{4\pi i\gamma_i}\left(\frac{e^{i\gamma_i(z_0+2d)}-e^{-i\gamma_i z_0}}{1+R_i e^{i2\gamma_i h}}\right), \tag{A1}$$

$$\Psi^-(z_0)=\frac{R_i e^{i2\gamma_i h}}{4\pi i\gamma_i}\left(\frac{e^{i\gamma_i z_0}-e^{-i\gamma_i(z_0+2d)}}{1+R_i e^{i2\gamma_i h}}\right), \tag{A2}$$

when $h-d\geqslant z_t>z_0$, and

$$\Psi^+(z_0)=\frac{1}{4\pi i\gamma_i}\left(\frac{e^{i\gamma_i(z_0+2d)}+Re^{i2\gamma_i h}e^{-i\gamma_i z_0}}{1+Re^{i2\gamma_i h}}\right), \tag{A3}$$

$$\Psi^-(z_0)=-\frac{1}{4\pi i\gamma_i}\left(\frac{e^{i\gamma_i z_0}+Re^{i2\gamma_i h}e^{-i\gamma_i(z_0+2d)}}{1+Re^{i2\gamma_i h}}\right) \tag{A4}$$

when $z_0>z_t\geqslant -d$. These are in terms of the reflection coefficient between the water column and sediment

$$R_i = \frac{\rho_2 \gamma_i / \rho_1 \upsilon_i - 1}{\rho_2 \gamma_i / \rho_1 \upsilon_i + 1}, \tag{A5}$$

where the vertical wave number in the sediment υ_i is defined by $k^2(z) = \upsilon_i^2 + \xi_i^2$. Water column attenuation a_1 is included by setting $k(z) = \omega/c_1 + ia_1$, where c_1 is the sound speed in the water column. Sediment attenuation a_2 is included by setting $k(z) = \omega/c_2 + ia_2$, where c_2 is the sound speed in the sediment.

Conversely for the Green's function $G(\mathbf{r}|\mathbf{r}_i)$, the plane wave amplitudes are

$$\Psi^+(z) = \frac{1}{4\pi i \gamma} \left(\frac{e^{i\gamma_i(z+2d)} + Re^{i2\gamma h} e^{-i\gamma z}}{1 + Re^{i2\gamma h}} \right), \tag{A6}$$

$$\Psi^-(z) = -\frac{1}{4\pi i \gamma} \left(\frac{e^{i\gamma z} + Re^{i2\gamma h} e^{-i\gamma(z+2d)}}{1 + Re^{i2\gamma h}} \right), \tag{A7}$$

for $h - d \geqslant z > z_t$, and

$$\Psi^+(z) = \frac{1}{4\pi i \gamma} \left(\frac{e^{i\gamma(z+2d)} - e^{-i\gamma z}}{1 + Re^{i2\gamma h}} \right), \tag{A8}$$

$$\Psi^-(z) = \frac{Re^{i2\gamma h}}{4\pi i \gamma} \left(\frac{e^{i\gamma z} - e^{-i\gamma(z+2d)}}{1 + Re^{i2\gamma h}} \right), \tag{A9}$$

for $z_t > z \geqslant -d$.

[1] F. Ingenito, ''Scattering from an object in a stratified medium,'' J. Acoust. Soc. Am. **82**, 2051–2059 (1987).

[2] N. C. Makris, F. Ingenito, and W. A. Kuperman, ''Detection of a submerged object insonified by surface noise in an ocean waveguide,'' J. Acoust. Soc. Am. **96**, 1703–1724 (1994).

[3] N. C. Makris and D. H. Cato, ''Acoustic tracking of non-vocalizing whales using the scattered field of vocalizing whales,'' in Proceedings of the Australian Acoustical Society, Sydney, Australia (1994).

[4] N. C. Makris, ''Bistatic detection of underwater objects using directional surf noise as a source of opportunity,'' pp. A16-1–A16-7, in *ASW Surveillance Programs* (Office of Naval Research, Arlington, VA, 1996).

[5] While it may be the earliest reference on the general subject of scattering from an object in a waveguide, this paper is not directly relevant to ocean-acoustics since its treatment is restricted to cylindrical waveguides. A. Bostrom, ''The *T*-matrix method for scattering by an obstacle in a waveguide,'' in *Acoustic, Electromagnetic and Elastic Wave Scattering*, edited by V. V. Varadin and V. K. Varadin (Pergamon, New York, 1980), pp. 221–224.

[6] R. H. Hackman and G. S. Sammelmann, ''Acoustic scattering in an inhomogeneous waveguide: Theory,'' J. Acoust. Soc. Am. **80**, 1447–1458 (1986).

[7] R. H. Hackman and G. S. Sammelmann, ''Multiple scattering analysis for a target in an ocean waveguide,'' J. Acoust. Soc. Am. **84**, 1813–1825 (1988).

[8] M. D. Collins and M. F. Werby, ''A parabolic equation model for scattering in the ocean,'' J. Acoust. Soc. Am. **85**, 1895–1902 (1989).

[9] J. S. Perkins, W. A. Kuperman, K. D. Heaney, and G. T. Murphy, ''Scattering from an object in a three-dimensional ocean,'' Proceedings of the 20th Annual International Meeting of the Technical Cooperation Subgroup, Subgroup G, Technical Panel 9, October 1991.

[10] J. S. Perkins, W. A. Kuperman, L. E. Tinker, and G. T. Murphy, ''Active matched field processing,'' J. Acoust. Soc. Am. **91**, 2366 (1992).

[11] The following reference presents a single-scatter modal approach similar to Ingenito's except that it employs *T*-matrix techniques: G. V. Norton and M. F. Werby, ''A numerical technique to describe acoustical scattering and propagation from an object in a waveguide,'' J. Appl. Phys. **70**, 4104–4112 (1991).

[12] J. J. Bowman, T. B. A. Senior, and P. L. E. Uslenghi, Eds., *Electromagnetic and Acoustic Scattering by Simple Shapes* (North-Holland, Amsterdam, 1969). While the entire book is relevant, see Chap. 10 for application to spheres.

[13] R. J. Urick, *Principles of Sound in the Sea* (McGraw-Hill, New York, 1983), pp. 306–327.

[14] K. Aki and P. G. Richards, *Quantitative Seismology: Theory and Methods* (Freeman, New York, 1980), pp. 273–286.

[15] F. B. Jensen, W. A. Kuperman, M. B. Porter, and H. Schmidt, *Computational Ocean Acoustics* (AIP Press, New York, 1994), pp. 203–270.

[16] P. M. Morse and K. U. Ingard, *Theoretical Acoustics* (Princeton U. P., Princeton, NJ, 1986), pp. 418–436.

[17] J. A. Fawcett, ''Scattering from an elastic cylinder buried beneath a rough water/sediment interface,'' in *High Frequency Acoustics in Shallow Water* (NATO SACLANT Undersea Research Centre, La Spezia, Italy, 1997), pp. 147–154.

Measurement of viscous sound absorption at 50–150 kHz in a model turbid environment

Niven R. Brown and Timothy G. Leighton
Institute of Sound and Vibration Research, University of Southampton, Southampton SO17 1BJ, United Kingdom

Simon D. Richards
Defence Evaluation and Research Agency, DERA Winfrith, Winfrith Technology Centre, Dorset DT2 8XJ, United Kingdom

Anthony D. Heathershaw
Defence Evaluation and Research Agency, DERA Unit, Southampton Oceanography Centre, Southampton SO14 3ZH, United Kingdom

(Received 26 January 1998; accepted for publication 25 June 1998)

The visco-thermal absorption of sound by suspended particulate matter can be reliably measured using a reverberation technique. This absorption may have an adverse effect on the performance of sonars operating at 50–300 kHz in coastal waters where suspensions are often present in significant concentrations. A series of experiments has been performed to study the viscous absorption by suspensions in the frequency range of 50–150 kHz. In the test volumes employed, the effect is small. It is therefore measured by taking the difference in reverberation times of a volume of water with and without particles. This greatly reduces the effect on the measurement of the other sources of absorption. Even so, it is necessary to design the experiment to characterize and minimize acoustic losses which occur at the surfaces of the container, the hydrophones, and their cables, and losses associated with bubbles and turbulence. These effects are discussed and results for particulate absorption for suspensions of spherical glass beads are presented and compared to theoretical predictions. Measured absorption agrees well with that predicted by theory for concentrations above 0.5 kg/m^3 and up to 2.0 kg/m^3. [S0001-4966(98)01610-5]

PACS numbers: 43.30.Es, 43.35.Bf [DLB]

INTRODUCTION

The acoustic absorption properties of suspended particulate matter in natural bodies of water are not well characterized, although there are a number of applications (e.g., naval mine-hunting sonars, acoustic Doppler current profilers) where such knowledge would be important, particularly in shallow water in the frequency range 50–300 kHz. Typical suspensions contain particles in the size range 1–100 μm where a variety of shapes and concentrations from 0.1 kg/m^3 up to 4 kg/m^3 are possible. They are liable to produce significant absorption losses.[1] There may also be the potential for flocculation and turbulence. The acoustic absorption of such systems is not known and, if models or inversion procedures are to be successfully implemented, must be quantified.[2]

There are many potential contributory factors to signal loss in the water column. Most of the work concerning suspensions has focused on scattering. Absorption from certain phenomena other than particles is, by comparison with particulate absorption, well understood. Within the water column, temperature, salinity, pressure, and the concentrations of absorbed gas may vary, affecting the overall acoustic absorption.[3] If bubbles are present, they may contribute significantly to the loss of acoustic energy through thermal and viscous effects, and also through acoustic re-radiation.[4,5] It is possible to incorporate such factors individually into a description of the acoustic absorption. For deployments in the environment in question, however, it may not be sufficient simply to quantify the contribution from the suspended particulate matter: The possibility of synergy between these factors should be explored. There is, for example, an association between suspended particulate matter and the stabilisation of gas pockets.[6]

This paper presents results from an experimental study which aims to quantify the viscous absorption associated with suspended particulate matter. Recent theoretical descriptions of the phenomenon have been published by two of the authors,[1,7] and these are compared here with experimental measurements. The viscous absorption effects of the suspensions, once determined, can be incorporated into acoustic propagation models.

I. THEORY

The theory for visco-thermal attenuation by particles is well established and has been presented in some detail previously.[1,7] A brief synopsis is given here for clarity. Sound propagating in seawater is attenuated via a number of mechanisms such that the intensity, I, after propagation over range, r, is given by

$$I = I_0 e^{-2\alpha r}, \tag{1}$$

where α is the volume attenuation coefficient of the seawater. In this equation α is in units of Nepers/m but units of dB/m have been used in the remainder of the paper. The total

attenuation is the sum of the attenuation due to clear seawater, α_w, and that due to scattering and viscous absorption by the suspended sediment, α_s and α_ν, respectively, i.e.,

$$\alpha = \alpha_w + \alpha_s + \alpha_\nu . \tag{2}$$

Sound absorption in clear seawater is itself the sum of absorption due to pure water and ionic relaxation processes involving boric acid and magnesium sulphate. One expression for the seawater absorption term commonly employed is given by Fisher and Simmons,[8] which was derived from laboratory data using Lyman and Fleming artificial seawater.[9] A more recent and arguably more complete expression is given by Francois and Garrison.[3] The boric acid relaxation frequency is $O\{1\ \text{kHz}\}$, while that for magnesium sulphate is $O\{100\ \text{kHz}\}$. Both are temperature and pH dependent. For the frequency range of interest in this study only magnesium sulphate would make a significant contribution to the total attenuation and its behavior is well documented. Since the experimental protocol involved minimizing as far as practicable sources of absorption other than particles, the water used in the current study was filtered and degased.

Attenuation from scattering is due to sound energy being reflected and diffracted from the main propagation path by the suspended particles. A number of models for scattering exist. The scatterers can be modeled as homogeneous spheres, which may be rigid and movable, rigid and immovable, or elastic.[10,11] From the point of view of a closed reverberation volume, however, as is used experimentally here, scattering does not produce an attenuation *per se*. This is because, if the walls are perfectly reflecting, the acoustic energy would remain within the volume and continue to be attenuated by other loss mechanisms.

The method of attenuation of interest here is that due to viscous absorption which occurs in the viscous boundary layer surrounding the particles. The boundary layer is generated because the acoustic wave causes out-of-phase movement between the fluid and the particle which creates a velocity difference between the two. Unlike scattering, where the acoustic impedance mismatch at the particle surface is of importance, viscous absorption is an inertial effect governed by the density difference between the fluid and particle. Because of this, it is not possible to use neutrally bouyant particles as they would simply move in-phase with the fluid and, thus, create no viscous boundary layer. Using Urick's[12] expression for the viscous absorption coefficient, and taking the attenuation to be constant along the path length and assuming all particles are the same size, the attenuation coefficient due to viscous absorption may be expressed as

$$\alpha_\nu = (10 \log e^2)\left(\frac{\epsilon k(\sigma-1)^2}{2} \left[\frac{s}{s^2+(\sigma+\delta)^2} \right] \right) \text{dB/m}, \tag{3}$$

where

$$\delta = \frac{1}{2}\left[1 + \frac{9}{2\beta a} \right], \tag{4}$$

$$s = \frac{9}{4\beta a}\left[1 + \frac{1}{\beta a} \right], \tag{5}$$

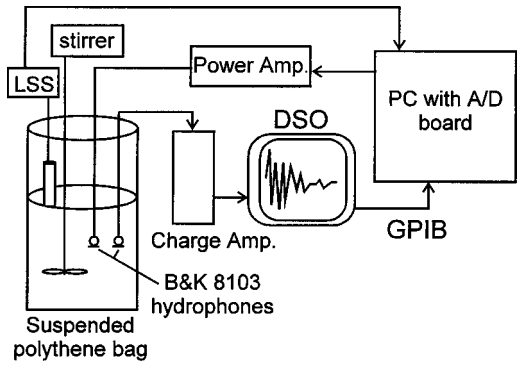

FIG. 1. Schematic diagram of the experimental apparatus.

$\sigma = \rho_s/\rho_0$, $\beta = \sqrt{\omega/2\nu}$ is the reciprocal of the viscous skin depth, ρ_s and ρ_0 are the densities of the particulate and fluid, respectively, ν is the kinematic viscosity of the ambient fluid, ϵ is the volume concentration of particulate, a is the particle radius, k is the acoustic wave number, and ω is the angular frequency of the incident pressure wave. The first term on the right-hand side of Eq. (3) is a constant which converts attenuation from Nepers/m to dB/m.

In this theory the assumption is made that the attenuation depends linearly on sediment concentration. Urick[12] showed that this linear dependence is valid up to volume concentrations of about 8%–9%. Below this concentration the suspension may be considered to be dilute, meaning that the effects of particle interaction, such as multiple scattering, may be ignored. The maximum mass concentration considered in this paper is 2 kg/m^3, which for quartz particles corresponds to a volume concentration of about 0.08%. The suspensions may therefore be considered to be dilute and the assumption of linear dependence on concentration is taken to be valid.

II. EXPERIMENTAL METHOD

The use of reverberation time to determine the attenuating characteristics of fluids has been credited by Kurtze and Tamm[13] to the work of Meyer and Skudrzyk. Differences in decay rates for a given volume of fluid may be equated to variations in the absorptive properties of the fluid and the boundaries of the volume. Preliminary tests[14] in the current study were performed in a large, thick-walled plastic tank containing approximately 0.6 m^3 of water. Decay traces from this apparatus were compared to traces taken from a smaller system comprising a suspended polythene bag containing only 16 ℓ of water. Although the ratio of surface area to volume was increased in the smaller system, the reverberation time increased, emphasizing the importance of reducing the losses at the boundaries in order to maximize the relative losses in the fluid. It should be noted here that the attenuation of pure water at 20 °C and 1 atm is only 0.002 dB/m at 100 kHz according to Fisher and Simmons.[8] Clearly any reduction in the boundary losses will greatly improve the estimation of the fluid losses.

The system used is shown in schematic form in Fig. 1. The signal generation, data acquisition, and signal processing are controlled by a personal computer running LABVIEW soft-

ware. The output signal is sent to a power amplifier and then to a Brüel & Kjær 8103 hydrophone. Signals are received by a second 8103 hydrophone and are monitored, after suitable amplification, by a LeCroy digital storage oscilloscope and are finally transferred to the computer via a GPIB interface for storage and analysis. The 16 ℓ of water is contained in a thin-walled polythene bag which is supported on a suspended ring. This provides an approximation to a pressure release surface around the whole volume, thus minimizing boundary losses. A mechanical stirrer is used to lift the particulate into suspension and is removed while data are being recorded. The dynamic concentration of the suspension can be monitored using a light scattering sensor (LSS). This monitors the settling out from suspension of the particulate. The acoustic and LSS measurements are performed separately as the presence of the LSS and the stirrer in the suspension represent additional absorbing surfaces which make measurement of the particulate contribution more difficult.

To measure the reverberation time of the volume it is necessary to record the decay of a sound field as a function of time. Ideally, the reverberation time is determined from the decay of a diffuse sound field. A diffuse sound field is one where the average energy density is the same throughout the volume considered and all directions of propagation are equally probable.[15] The onset of a diffuse sound field in an enclosure can be described by the Schroeder cutoff frequency. This gives an indication of the lowest frequency at which the modal density is sufficient to constitute a diffuse field. The Schroeder cutoff frequency, f_{Sch}, can be expressed as[16]

$$f_{\mathrm{Sch}}=\left(\frac{c^3}{4\ln 10}\right)^{1/2}\left(\frac{T}{V}\right)^{1/2}, \tag{6}$$

where T is the reverberation time of an impulsive noise source (i.e., the time for the sound pressure level to fall by 60 dB), c is the speed of sound in the fluid, and V is the volume of the enclosure. Values of f_{Sch} for the system used were between 50 and 75 kHz. This is near the lower limit of the frequency range under consideration in this project.

Two techniques have been used to generate a sound field: an impulse and a burst of uniform white noise. Both these techniques produce a broadband sound field. The advantages of a long burst are that the sound field is given time to build up to a constant level before being cut. This improves the signal-to-noise ratio. Also, because there is a more uniform sound field, the decaying sound field is less prone to large perturbations due to direct reflections and particular modes of the volume.

A typical test sequence consists of the suspension being stirred until the particulate is homogeneously spread throughout. The time for this to occur can be verified by the LSS and is of the order of a few seconds. Care must be taken to ensure that particulate does not collect in the eddies generated in the corners of the bag adjacent to the bottom seam during the stirring. Ten noise bursts are sent to the emitting hydrophone and their responses are recorded by the computer. The test sequence takes approximately 35 s. This is about the time limit before there is a significant change in the suspended particulate concentration as measured by the LSS.

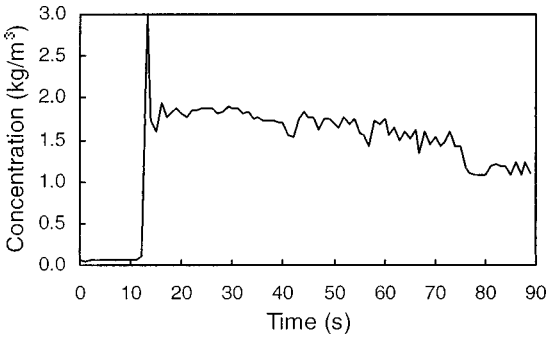

FIG. 2. Variation of suspended particulate concentration with time for a 2.0-kg/m^3 suspension.

Figure 2 shows a typical LSS output. In this instance the stirrer was turned on at 12 s and off at 32 s. The particle concentration is more accurately determined by weighing in the particulate to give the desired suspension concentrations. The LSS is simply used to verify the mixing and settling processes prior to acoustic tests being performed.

The particle size distribution was also determined independently of the acoustic tests by analyzing a sample of the particulate in a laser diffraction analyzer. This determines the volume distribution of particles over the size range, 0.4 μm–1000 μm. The dynamic variation of the particle size distribution cannot, however, readily be obtained by this method as a relatively substantial volume of water must be taken from the suspension. This would obviously affect the reverberation characteristics of the volume. Figure 3 shows the particle size distribution for the glass beads used in this study.

The decay rates were determined by applying the method of integrated impulse response[17] (IIR) to the sound field from the time that the driving signal was cutoff. This method was used, even for signals derived from nonimpulsional sources, as it gave a smooth estimate of the decay rate. The value of the integrated impulse response represents the ensemble average of the squared noise responses at time $t=t'$ after the onset of decay which is equal to the squared tone-burst response integrated from time $t=t'$ to $t=\infty$ or, in practice, to when the background noise level is greater than the signal of interest. The practical implementation of this method is as follows. The response of the volume to the burst of random noise (which contains the frequency range of interest) is squared, then backward integrated from an upper time limit (some time before the response is exceeded

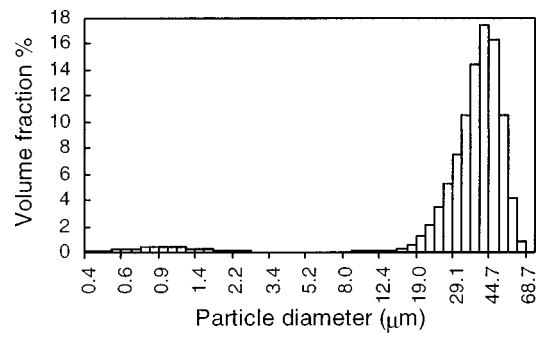

FIG. 3. Particle size distribution for glass beads.

by the background noise) to the lower time limit when the sound burst was cut off. This produces the IIR curves shown in the results section. The slope of this curve is determined from a linear regression over the initial, linear part of the curve. Typically, the lower time limit for the linear regression was 10 ms after the sound was cut off (the burst lasted 20 ms) and the upper limit was variable, the choice depending on the rapidity of the decay and the linearity of the response.

Post-processing of the results involved performing the IIR analysis at each of the desired frequency bands. The raw data were filtered after acquisition using a Butterworth bandpass filter in 10-kHz bands over the frequency range 50–150 kHz. Above this frequency, the response becomes increasingly nonlinear making it difficult to obtain an estimate for the linear decay of the sound field. The data were also reduced into time bins which represent the rms of the signal for a user-defined number of samples. This was typically 100 samples. The sampling frequency of the oscilloscope was 500 kHz and the sample duration was 0.2 s.

Measurements were made on particulate-free water and then on water containing varying concentrations of glass beads. Prior to experimentation, the water was passed through a reverse osmosis system, then filtered to remove any remaining particulate matter. The water was then degased under vacuum and the level of dissolved oxygen was monitored throughout the test to see what effect the addition of particles or the stirring process had. The dissolved oxygen content varied from 51% to 65% over the course of the measurements (approximately four hours). No bubbles could be detected. The glass beads have a high sphericity and are, thus, representative of the spherical particles used in the theoretical modeling. The difference in reverberation of the two systems determines the contribution of the particles to the total absorption according to the following analysis.

Determination of absorption from reverberation times

The decay of a diffuse sound field where absorption occurs at the boundary and within the propagating medium is characterized by the reverberation time, T, given by[18]

$$T = \frac{55.3V}{c(A + 8\alpha V)}, \tag{7}$$

where A is the total sound absorption at the boundaries of the volume, and α is the attenuation coefficient of the fluid in Nepers/m. The quantity $A = S\bar{a}$ is expressed in units of metric sabin, m^2, where S is the surface area of the volume (m^2) and $\bar{a}$ is the average Sabine absorptivity (dimensionless). The first term in the brackets, A, represents the sound absorption at the boundaries; the second term, $8\alpha V$, is the absorption in the medium. If T_w and T_s are the reverberation times of the particulate-free water and the water containing the particulate, respectively, then the difference in the attenuation coefficients of the fluids, $\Delta\alpha$, in dB/m is given by

$$\Delta\alpha = (10 \log e^2)\, \frac{55.3}{8c} \left(\frac{1}{T_s} - \frac{1}{T_w} \right). \tag{8}$$

This represents the attenuation due to the addition of the particulate. This equation makes three important assumptions:

(i) that the speed of sound of the suspension stays constant as particles are added;
(ii) that the volume remains constant; and
(iii) that the addition of the particles does not affect the absorptivity of the boundaries.

The sound speed in suspensions can be calculated by using the formulation developed by Ahuja.[19] Assuming a rigid particle (i.e., the particle ''viscosity'' is much greater than the fluid viscosity), then the change in sound speed for the suspensions considered in this work is less than 0.01%. The volume fraction of a 2-kg/m^3 suspension of glass beads having a density of 2400 kg/m^3 is only 0.08%, so that the assumption of constant volume is reasonable. Finally, if changes in acoustic impedance are principally responsible for changes in behavior at the boundary, then the product of the change in density and change in sound speed of the particulate suspension represents an error of less than 0.1%. Thus the properties of the bag can be assumed to have almost no contribution to the sound transmission at the boundary. This is reasonable to assume as the walls of the bag are thin (0.03 mm), certainly in terms of the wavelengths under consideration, and there is very little acoustic impedance mismatch with the water. Hence, the walls will move in phase with the water and be virtually acoustically transparent. The bag itself acts like an approximately pressure release surface and any change in behavior at the boundary will be due to changes in the properties of the fluid. There may be viscous boundary layer losses at the bag but these will be consistent between the clearwater and particulate suspension cases. These losses, along with losses due to the presence of the hydrophones, prevent a simple measurement of the absolute attenuation of the fluid as is the case for other measurement systems such as a spherical resonator, as noted by one of the early workers in that field.[13]

III. RESULTS

A series of tests was performed on water and glass bead suspensions with concentrations from 0.25 to 2.0 kg/m^3 in steps of 0.25 kg/m^3. Figure 4 shows typical binned time traces and their corresponding IIR curve at 100 kHz for pure water and a 1.0-kg/m^3 suspension of glass beads. The IIR curve clearly represents the decay rate of the sound energy in the volume. The y-axis scale is the sound pressure level (SPL) in dB re: 1 μPa. The two curves are offset because of the processing performed to obtain the IIR curve. At this frequency there is almost a 60-dB dynamic range. The output burst lasted 20 ms and the increase in the sound pressure over this time can be observed in the figures. The effect of the particulate is clearly seen. Note that for presentation purposes the time over which the IIR has been applied has been extended to cover the whole sample period, hence the tailing off of the IIR curve once the signal approaches the background noise level.

Figure 5 shows the reverberation time variation as the particulate concentration is increased. Each curve represents

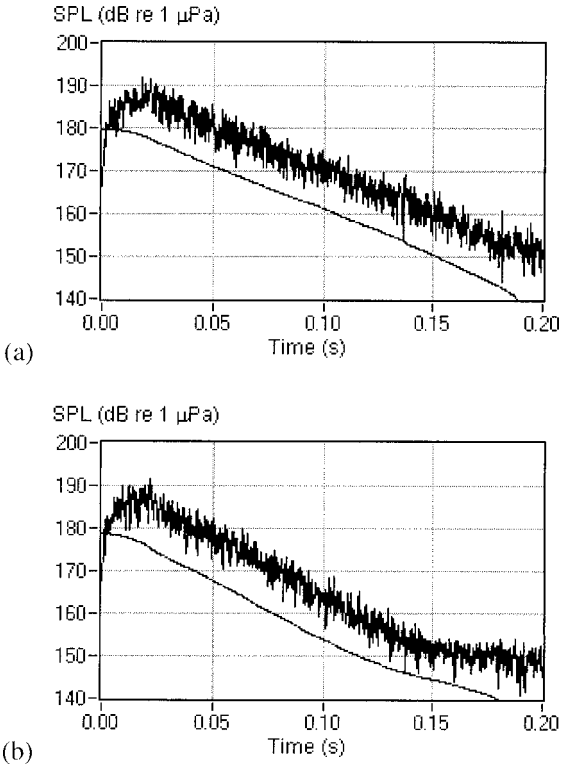

FIG. 4. Typical binned time traces at 100 kHz for reverberation time calculation (upper trace) with their corresponding integrated impulse response curve (lower trace) for (a) pure water, and (b) a 1.0-kg/m^3 suspension of glass beads.

the mean of three tests of ten pings each. Also shown are two curves for pure water: one for calm water and a second for stirred water. As the test suspensions containing particulate must be stirred, the stirred water response was taken as the reference signal for the subsequent calculation of the particulate attenuation. The error bars on the pure water curves represent the uncertainty in measuring the reverberation time at one point rather than throughout the volume. This is discussed fully in the following section. For clarity, only every other concentration is shown in Fig. 5. The decreasing trend

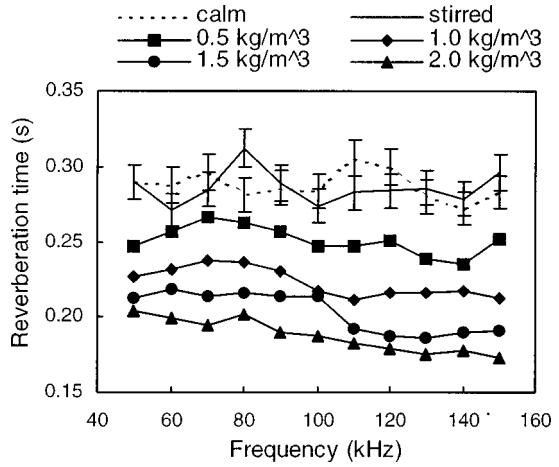

FIG. 5. Reverberation time for calm and stirred pure water and for various concentrations of glass beads. Error bars for water curves represent uncertainty due to measurement at a single location.

in reverberation time with increasing particulate concentration is quite apparent.

The reverberation times are converted to changes in attenuation according to Eq. (8) and are then normalized with respect to particle concentration. The units of dB m^2/kg can be converted to dB/m via multiplication by the given concentration. They can then be compared to a theoretical prediction [Eq. (3)] which has been calculated for a 1-kg/m^3 suspension having the same particle size distribution as shown in Fig. 3. The normalized attenuation due to the particles is shown in Fig. 6 at each of the measured concentrations. For all data, the theoretical prediction lies within two standard deviations of the data, and in most cases, within one. As expected, the magnitudes of both the uncertainty and the discrepancy between the data points and theory increase at the lowest concentrations. Appreciation of the errors is extremely important in interpreting these results, and these are discussed in the next section.

IV. DISCUSSION

The previous results show that this simple system is capable of producing reliable results for particulate suspensions once there is sufficient difference between the reference pure water signal and the particulate suspension signal. Taking a difference in this way in principle eliminates the effects of other loss mechanisms, such as the boundaries and the hydrophones. However, their effects should be minimized in order to enhance the behavior of the particulate attenuation. That is why the suspended thin-walled bag has been developed as opposed to using a solid containment vessel.

The principal difficulty of measuring the behavior of this type of suspension is maintaining the particulate in suspension. By stirring, the suspension becomes well mixed and the particulate remains suspended for a sufficiently long time to enable the measurements to be taken (see Fig. 2). However, the stirring process may affect the acoustics of the water volume, even when there is no particulate present. Acoustic energy may be absorbed by isotropic turbulence through perturbation of the turbulence field by the acoustic wave, leading to anisotropic Reynolds stress. Within the time taken for the Reynolds stress to return to isotropy, turbulent kinetic energy will have been redistributed among turbulence components as it cascades from the large scale to the dissipation scale, resulting in a net loss of energy from the acoustic wave. Noir and George[20] obtained an expression for the absorption coefficient resulting from this effect which may be used to estimate the absorption as a function of the rate at which turbulent kinetic energy in the system is dissipated. Consideration of the maximum rate of kinetic energy supplied by the mechanical stirrer leads to estimates of the turbulence absorption coefficient which are $O\{10^{-8}\,\mathrm{dB/m}\}$, which is several orders of magnitude smaller than the measured attenuation coefficient and the predicted viscous absorption coefficient. The effect of turbulence is also several orders of magnitude smaller than the error associated with the comparison between stirred and calm water in Fig. 5. It is therefore concluded that the effect of sound absorption by turbulence may be neglected in the present system.

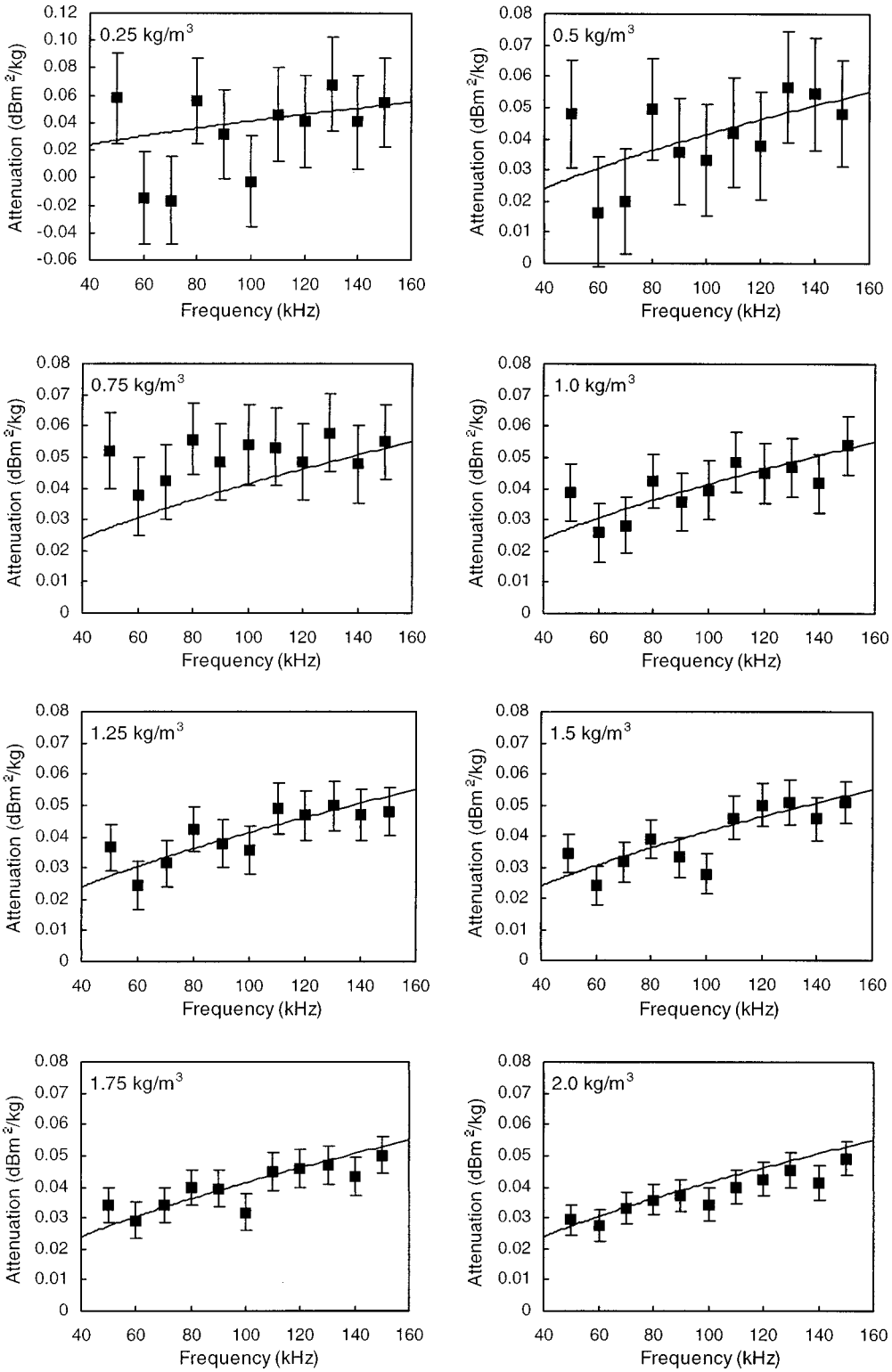

FIG. 6. Normalized particulate attenuation at the indicated concentrations compared to the prediction (solid line). Because of the normalization the prediction is always the same. An explanation of the error bars is given in Sec. IV.

Ideally the sound field would be measured at a number of places in order to obtain a spatial average throughout the bag. This would verify that the sound field was indeed diffuse and would give an indication as to how the settling process affects the attenuation. Measurements have been performed on pure water to assess the assumption of a diffuse sound field. However, the mere fact that more of the hydrophone was inserted into the water caused a very significant change in the level of absorption. For every 10 cm of cable inserted the increased absorption was of the same level as that due to 1 kg/m^3 of the particulate used in this study. It was, therefore, not possible to perform a volume average of the sound field. Instead the sound field was measured at a number of points at the same depth so that the same amount

of hydrophone was in the water. One standard deviation of these tests was equivalent to a 4% error in the estimation of the reverberation time if it were measured at one location rather than averaged in a plane. Error bars of 4% are shown for the calm and stirred water reverberation traces in Fig. 5. These show that the variation in reverberation due to stirring is within the range of error due to single location measuring. Other sources of error, such as the variation of the speed of sound with temperature, the estimation of the concentration based on the weight of added particulate, and the measurement of the water volume, were all significantly less than this and generally less than 1%. The error bars in Fig. 6 are, therefore, calculated using a 4% error in the measurement of the reverberation time and the cumulative error in the estimate of the suspension concentration, even though the ping-to-ping variation for reverberation measurements made at one location is less than 1%. It is clear from Fig. 6 that as the difference in the reverberation time between the reference pure water signal and the particulate suspension signal increases, the relative error in the attenuation, even after normalization, decreases.

The data in Fig. 6 support the trend predicted by theory (i.e., absolute values of attenuation and its gradient with respect to frequency). The contribution from random and systematic errors are such that it is not valid to suggest other trends which, at first sight, may appear to be present. For example, the necessarily inexact nature of the reference signal which is subtracted from each particulate measurement will impose artificial trends (such as a peak at 80 kHz) in the experimental results.

An alternative method of measuring the attenuation in fluids is the spherical resonator. The error in the measurement of absorption using this technique has been estimated[21] at 15%, which is of similar magnitude to the error for the normalized attenuation with this technique for suspensions with concentrations above 1.0 kg/m^3. Another technique for measuring attenuation in suspensions, the Kramers–Kronig technique,[22] is not applicable to the levels of attenuation observed in the suspensions under consideration here.

V. CONCLUSION

A series of reverberation tests performed on particulate-free water and water containing various concentrations of spherical glass beads has shown that the attenuation due to the particles is a readily measurable parameter using this technique. The measured attenuation agrees well with that predicted by theory for suspensions with a concentration greater than 0.5 kg/m^3 and improves as the difference in reverberation time increases.

ACKNOWLEDGMENT

This work is funded by DERA Winfrith (Contract No. SSDW3/0001) and their support is gratefully acknowledged.

[1] S. D. Richards, A. D. Heathershaw, and P. D. Thorne, ''The effect of suspended particulate matter on sound attenuation in seawater,'' J. Acoust. Soc. Am. **100**, 1447–50 (1996).

[2] A. D. Heathershaw and P. D. Thorne, ''Impact of suspended particulate matter on acoustic propagation in turbid coastal waters,'' in *Proceedings of the International Maritime Defence Exhibition and Conference* (Greenwich, London, 1995), Vol. 2, pp. 111–121.

[3] R. E. Francois and G. R. Garrison, ''Sound absorption based on ocean measurements: Part I: Pure water and magnesium sulfate contributions,'' J. Acoust. Soc. Am. **72**, 896–907 (1982).

[4] C. Devin, Jr., ''Survey of thermal, radiation, and viscous damping of pulsating air bubbles in water,'' J. Acoust. Soc. Am. **31**, 1654–1667 (1959).

[5] A. I. Eller, ''Damping constants of pulsating bubbles,'' J. Acoust. Soc. Am. **47**, 1469–1470 (1970).

[6] T. G. Leighton, *The Acoustic Bubble* (Academic, London, 1994), pp. 78–83.

[7] S. D. Richards, ''The effect of temperature, pressure and salinity on sound attenuation in turbid seawater,'' J. Acoust. Soc. Am. **103**, 205–211 (1998).

[8] F. H. Fisher and V. P. Simmons, ''Sound absorption in sea water,'' J. Acoust. Soc. Am. **62**, 558–564 (1977).

[9] J. Lyman and R. H. Fleming, ''Composition of sea water,'' J. Mar. Res. **3**, 134–146 (1940).

[10] A. E. Hay and D. G. Mercer, ''On the theory of sound scattering and viscous absorption in aqueous suspensions at medium and short wavelengths,'' J. Acoust. Soc. Am. **78**, 1761–1771 (1985).

[11] J. Sheng and A. E. Hay, ''An examination of the spherical scatterer approximation in aqueous suspensions of sand,'' J. Acoust. Soc. Am. **83**, 598–610 (1988).

[12] R. J. Urick, ''The absorption of sound in suspensions of irregular particles,'' J. Acoust. Soc. Am. **20**, 283–289 (1948).

[13] G. Kurtze and K. Tamm, ''Measurements of sound absorption in water and in aqueous solutions of electrolytes,'' Acustica **3**, 33–48 (1953).

[14] N. R. Brown, T. G. Leighton, S. D. Richards, and A. D. Heathershaw, ''Sound absorption by suspended particulate matter,'' in *High Frequency Acoustics in Shallow Water*, edited by N. G. Pace, E. Pouliquen, O. Bergem, and A. P. Lyons (NATO SACLANT Undersea Research Centre, La Spezia, 1997), pp. 75–82.

[15] L. E. Kinsler, A. R. Frey, A. B. Coppens, and J. V. Sanders, *Fundamentals of Acoustics* (Wiley, New York, 1982), 3rd ed., p. 313.

[16] A. D. Pierce, *Acoustics: An Introduction to its Physical Principles and Applications* (McGraw-Hill, New York, 1981), p. 294.

[17] M. R. Schroeder, ''New method of measuring reverberation time,'' J. Acoust. Soc. Am. **37**, 409–412 (1965).

[18] L. E. Kinsler, A. R. Frey, A. B. Coppens, and J. V. Sanders, Ref. 15, p. 319.

[19] A. S. Ahuja, ''Formulation of wave equation for calculating velocity of sound in suspensions,'' J. Acoust. Soc. Am. **51**, 916–919 (1972).

[20] D. T. Noir and A. R. George, ''Absorption of sound by homogeneous turbulence,'' J. Fluid Mech. **86**, 593–608 (1978).

[21] P. D. Edmonds and J. Lamb, ''A method for deriving the acoustic absorption coefficient of gases from measurement of the decay-time of a resonator,'' Proc. Phys. Soc. London **71**, 17–32 (1958).

[22] M. O'Donnell, E. T. Jaynes, and J. G. Miller, ''Kramers–Kronig relationship between ultrasonic attenuation and phase velocity,'' J. Acoust. Soc. Am. **69**, 696–701 (1981).

Effect of orientation on broadband acoustic scattering of Antarctic krill *Euphausia superba*: Implications for inverting zooplankton spectral acoustic signatures for angle of orientation

L. V. Martin Traykovski[a)]
Massachusetts Institute of Technology/Woods Hole Oceanographic Institution Joint Program in Oceanography and Applied Ocean Sciences and Engineering, Woods Hole Oceanographic Institution, MS 32, Woods Hole, Massachusetts 02543

R. L. O'Driscoll
Department of Marine Science, University of Otago, P.O. Box 56, Dunedin, New Zealand

D. E. McGehee[b)]
Department of Applied Ocean Physics and Engineering, Woods Hole Oceanographic Institution, Woods Hole, Massachusetts 02543

(Received 26 January 1998; accepted for publication 16 June 1998)

Acoustic scattering experiments involving simultaneous acquisition of broadband echoes and video footage from several Antarctic krill were carried out to determine the effect of animal orientation on echo spectral structure. A novel video analysis technique, applied to extract krill angle of orientation corresponding to each insonification, revealed that echo spectra from krill near broadside incidence relative to the incident acoustic wave exhibited widely spaced, deep nulls, whereas off-broadside echo spectra had a more erratic structure, with several closely spaced nulls of variable depth. The pattern of changes in echo spectra with orientation for the experimentally measured acoustic returns was very similar to theoretically predicted patterns based on a distorted wave Born approximation (DWBA) model. Information contained in the broadband echo spectra of the krill was exploited to invert the acoustic returns for angle of orientation by applying a newly developed Covariance Mean Variance Classification (CMVC) approach, using generic and animal-specific theoretical and empirical model spaces. The animal-specific empirical model space was best able to invert for angle of orientation. The CMVC inversion technique can be implemented using a generic empirical model space to determine angle of orientation based on broadband echoes from individual zooplankton in the field. [S0001-4966(98)05109-1]

PACS numbers: 43.30.Sf, 43.30.Pc [DLB]

INTRODUCTION

Antarctic krill provide a direct trophic link between the primary producers and the top predators (seabirds, whales, seals) of the Southern Ocean (Everson, 1977; El-Sayed, 1988; Nemoto *et al.*, 1988; Permitin, 1970). In addition, a commercially important krill fishery became established about 20 years ago, peaking in the early 1980s with landings of over 500 000 metric tons (Nicol and de la Mare, 1993). Because *Euphausia superba* plays such a central ecological role in the Antarctic marine food web, affecting the breeding success of the top predators that rely on it as a food source (Croxall *et al.*, 1988), it has become increasingly important to assess and manage the impact of the fishery on krill stocks. Consequently, accurate knowledge of krill distribution, abundance (biomass), and production is necessary in order to characterize the trophic interactions in the Southern Ocean food web, as well as to successfully manage krill stocks as a resource.

Conventional methods for estimating zooplankton biomass include measurement of displacement volume, wet weight, dry weight, or carbon (see Wiebe *et al.*, 1975) from net (e.g., MOCNESS-Wiebe *et al.*, 1985) or pump (Miller and Judkins, 1981) samples. As a result of the spatial patchiness of zooplankton populations in the ocean and extreme temporal variability in their abundance, it is estimated that there can be as much as seven orders of magnitude of variability in biomass on the spatial and temporal scales important for populations of macrozooplankton (Huntley and Lopez, 1992). For example, Antarctic krill are distributed over a vast area of ocean, aggregating in patches, shoals, schools, swarms, and superswarms, which can cover many square km and extend to 200-m depth, displaying complex, small-scale, horizontal, and vertical structure (Nicol and de la Mare, 1993). Conventional techniques for biomass estimation (nets, pumps, trawls) are not suited for simultaneous sampling of the entire water column over the relevant scales, nor to resolving ecologically important small-scale patterns of krill distribution. To make more accurate biomass estimates,

[a)]Address all correspondence and reprint requests to L. V. Martin Traykovski, Woods Hole Oceanographic Institution, MS 32, Woods Hole, MA 02543, Electronic mail: lmartin@whoi.edu, Tel.: (508) 289-2750, Fax: (508) 457-2134.
[b)]Present address: Tracor Applied Sciences, 4669 Murphy Canyon Road, Suite 102, San Diego, CA 92123.

high-resolution (~1 m) instruments capable of mapping variation in zooplankton biomass on large vertical (10–100 m), horizontal (100–1000 km), and temporal (days to months) scales are required. The use of high-frequency acoustics to make volume backscatter measurements of the water column has made it possible to do rapid, high-resolution, broad-scale synoptic surveys of krill abundance over the time and space scales of interest.

Traditional acoustic biomass estimation methods have employed single-frequency acoustic measures in conjunction with either theoretical models (e.g., Greenlaw, 1979) or empirical regression relationships between acoustic backscatter and biomass collected in simultaneous net samples (e.g., Flagg and Smith, 1989). Attempts to use volume backscatter measurements of the ocean as indicators of zooplankton type, size, and biomass rely on the accurate acoustic characterization of the zooplankton species of interest. Biomass estimates based on simple regression curves or on single-frequency echo energy measurements may be subject to large errors, particularly if important factors such as species-specific material properties, morphology, and animal orientation are overlooked. Much effort has been put toward characterizing the acoustic target strength of krill for the purposes of species identification, animal size classification, abundance estimation, and acoustic signal separation. Single-frequency target strength measurements have been made of krill and other elongated crustacean zooplankton (other euphausiids, shrimp), both experimentally constrained (by tethering or encagement, e.g., Greenlaw, 1977; Kristensen and Dalen, 1986; Everson *et al.*, 1990; Foote, 1990; Foote *et al.*, 1990; Wiebe *et al.*, 1990; Demer and Martin, 1995) and *in situ* (e.g., Hewitt and Demer, 1991, 1996). To obtain target strength information over a wide range of frequencies simultaneously, as well as to elucidate the frequency dependence of the scattering from elongated crustacean zooplankton, broadband insonifications have been made of tethered decapod shrimp (*Palaemonetes vulgaris*) as well as a species of euphausiid (*Meganyctiphanes norvegica*) found in the Northwest Atlantic (Chu *et al.*, 1992; Stanton *et al.*, 1994a, 1996) using a broadband chirp sonar. These single-frequency and broadband measurements have been used to develop and corroborate empirical and theoretical scattering models.

Empirical models (e.g., Greene *et al.*, 1991) have relied on relating a single parameter (e.g., zooplankton size or wet weight) to acoustic target strength through a simple regression relationship. Initial theoretical scattering models for zooplankton (including elongated crustacean zooplankton) were based on the Anderson (1950) fluid sphere model (e.g., Greenlaw, 1977, 1979; Johnson, 1977; Penrose and Kaye, 1979), which accounted for animal size and material properties. The first scattering model to consider the elongate and deformable morphology of some of the crustacean zooplankton was developed by Stanton (1988a,b, 1989a,b) to describe the scattering of sound by arbitrarily deformed cylinders of finite length. It became widely recognized that in addition to animal size and shape, animal orientation could have significant effects on the scattering from these elongated plankton (Greenlaw, 1977; Sameoto, 1980; Samovol'kin, 1980; Everson, 1982; Kristensen and Dalen, 1986; Chu *et al.*, 1993). The theoretical models were further developed and refined (Stanton *et al.*, 1993a,b, 1994a,b, 1996), and this orientational dependence was incorporated by describing scattering from these elongated zooplankton at normal incidence and at a distribution of orientations near broadside incidence using an approximate ray summation model (which takes advantage of the fact that many crustacean zooplankton behave acoustically as weakly scattering bent fluid cylinders). A more precise alternative to these ray models was developed for weakly scattering elongated zooplankton of arbitrary shape at all angles of orientation using a formulation based on the distorted wave Born approximation (DWBA) volume integral (Chu *et al.*, 1993; Stanton *et al.*, 1993b, 1998a,b). In fact, Chu *et al.* (1993) were able to predict observed echo levels for Antarctic krill at two discrete frequencies (38 and 120 kHz) using the DWBA model implemented with certain theoretical orientation distributions, but due to the absence of photographic measurements, were unable to verify actual krill orientation.

This paper summarizes an analysis of the effect of animal orientation on acoustic scattering by Antarctic krill. Both single-frequency and broadband acoustic scattering measurements were made of individual krill, and each animal was filmed during insonification with a high-magnification underwater video system. A separate paper (McGehee *et al.*, in press) is devoted to investigating the orientation-dependence of the single-frequency (120 kHz) target strength measurements. The work summarized herein is focused on interpretation of the broadband (500-kHz center frequency) scattering measurements in light of orientational information extracted using a novel video analysis technique. By coupling the collected broadband echo spectra with orientation data from the video footage, the effect of animal orientation on the frequency-dependent scattering characteristics of elongated, fluid-like zooplankton such as krill may be elucidated. The echo spectra collected from krill in different orientations are presented. These echoes are compared to the theoretical model results of the DWBA volume integral, which predicts echo spectra for all angles of orientation. Subsequently, a classification inversion using the model-based Covariance Mean Variance Classification (CMVC) technique (Martin Traykovski *et al.*, 1998) is carried out. Both theoretical and empirical models are employed to invert the echo spectra backscattered from the krill for angle of orientation; that is, the CMVC inversion technique uses these models to predict angle of orientation during each insonification based on the received echo spectrum.

I. METHODS

A. Scattering experiment

Acoustic and video data were collected during a week-long experiment (17 August–21 August 1995) at the Long Marine Laboratory of the University of California at Santa Cruz (UCSC). Antarctic krill (*Euphausia superba*) had been captured in the Southern Ocean near Palmer Station, Antarctica in February 1995, and placed in individual containers without food for long-term storage under refrigeration at the University of California at Santa Barbara, until transport to

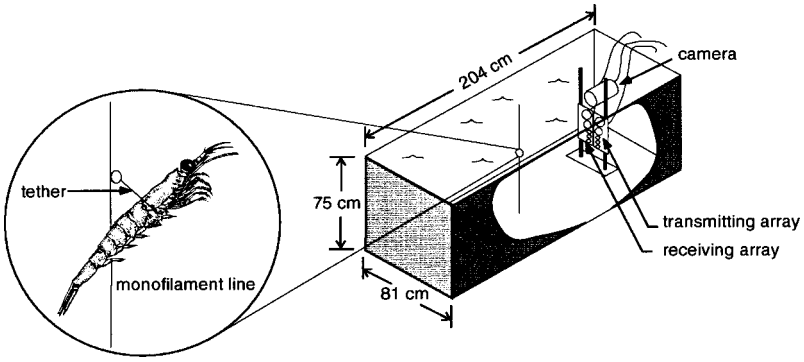

FIG. 1. Scattering experiments were carried out in a portion of a modified fiberglass dolphin transporter. To permit freedom of movement during insonification, the animals were tethered to a vertical section of monofilament line with an acoustically transparent fine strand around the abdomen. The tethered animal was lowered to the focal point of a side-looking transducer pair. A high-magnification underwater video camera was mounted above the transducer array, looking slightly downward at the animal. Each insonification was marked with an acoustic pulse on the audio track of the video tape, so that animal orientation at the time of insonification could be determined.

UCSC in August. Acoustic experiments included insonification of each live animal with a 200-μs duration broadband chirp of center frequency 500 kHz (~350–750 kHz).

Insonifications of the krill were made with a pulse–echo acoustic data acquisition system. The transmit/receive transducer pair was mounted in a side-looking transducer bank, and the animal was positioned at the focal point of the transducer pair at a range of 51 cm (Fig. 1). This bistatic experimental setup is similar to that described by Stanton (1990), and has been used extensively (e.g., Chu *et al.*, 1992; Stanton *et al.*, 1993b, 1994a,b, 1996) to make scattering measurements of zooplankton. During insonification, individual krill were suspended one at a time in a 2-m long by 0.8-m wide by 0.75-m deep tank (adapted from a fiberglass dolphin transporter) filled with filtered, chilled seawater (maintained between 2 and 5 °C). Each animal was tethered to a vertically suspended 0.12-mm monofilament line with a fine (55 μm), acoustically transparent synthetic strand tied around the first or second abdominal segment. This short tether allowed freedom of movement during insonification, while constraining the animal to remain within 1 cm of the focal point of the transducer pair. Target strength (TS) measurements made of these moving krill using the 500-kHz broadband transducer in this bistatic configuration are estimated to be within 0.5 dB (at 350 kHz) and 0.6 dB (at 750 kHz) of the actual values. Error estimates were based on both systematic and random sources of acoustic measurement error, including transducer misalignment and animal positional variability. To allow investigation of the relationship between the acoustic scattering of an organism and its orientation, each animal was filmed during insonification with a high-magnification underwater video system. The video camera was mounted directly above and slightly behind the transducer bank, looking across and slightly downward at the animal. Each insonification was marked with an acoustic pulse recorded on one audio track of the Hi-8 video tape, while a time code was continuously recorded on the other audio track. This allowed direct correlation between each acoustic return and the orientation of the animal at the time of insonification (to within 1/30 s). The freedom of movement permitted by the tether allowed the animal to assume a wide range of positions relative to the transducer, including lateral, dorsal, ventral, and end-on aspects.

After insonification, several measurements were made of each animal, including animal length, carapace height, carapace width, telson (central lobe of tail) length, and wet weight (Table I). If the telson was broken, total length (L2) for that animal was estimated by scaling the length (L1) to the end of the uropods (lateral lobes of tail) according to the ratio (L2/L1) observed in other individuals of similar size; telson length was also estimated by comparison to other animals of similar dimensions. Excess water was removed and

TABLE I. Summary of measurements made of Antarctic krill. Total length measured from center of eye to tip of telson; carapace height measured at maximum dorso-ventral width; carapace width measured at maximum lateral width. The asterisk indicates broken telson: for these animals, total length (L2) was estimated by scaling length to end of uropods (L1) according to the ratio (L2/L1) observed in other individuals of similar size; telson length also estimated by comparison to other animals of similar dimensions. Video analysis not possible for animals 12–14 due to blurring of the video images caused by condensation on the inside of the camera housing. Dimensions in mm, weights in g.

Animal No.	Total length	Carapace height	Carapace width	Telson length	Wet weight	Dry weight	No. of echoes collected	No. of video images analyzed
01	37.6	5.5	···	7.4	0.38	0.0872	1000	1000
02	42.2	5.9	···	8.6	0.51	0.1111	1000	400
03	41.4	5.4	4.4	8.4	0.55	0.1153	1000	400
04	38.9	4.8	4.35	7.7	0.38	0.0932	1000	400
05	41.4	5.3	4.4	7.1	0.56	0.1181	1000	1000
06	40.15	4.9	4.2	6.25	0.44	0.0916	1000	200
07*	33.3	4.4	3.65	6.2	0.24	0.0532	1000	1000
08	29.75	3.95	3.2	6.0	0.16	0.0363	1000	200
09	37.6	5.25	4.45	6.35	0.36	0.0702	1000	200
10	37.3	4.95	4.0	7.1	0.36	0.0689	1000	200
11	40.6	5.4	4.15	7.85	0.44	0.1016	1000	200
12	39.6	5.4	4.0	7.35	0.44	0.0884	1000	none
13*	42.9	6.0	4.9	8.1	0.55	0.1285	1000	none
14	42.45	6.15	4.6	7.7	0.58	0.1265	1000	none

each organism was frozen; dry weight was measured after oven-drying at a later date. During the experiment, 14 individuals were insonified and the return echoes from 1000 acoustic transmissions were collected from each animal.

B. Acoustic data processing

To obtain the echo spectrum representing the actual acoustic return from the animal, the raw signals received from the krill were combined with the results of calibration measurements, taken at the beginning (16 August 1995) and again at the end (24 August 1995) of the scattering experiments. During calibration, the transmit and receive transducers were aimed at each other with no target in the beam, and a calibration signal was transmitted. The transmitted and received voltage time series were collected for these calibration measurements [subscript C in Eq. (1)]. During the scattering experiments, the transducers were aimed forward, focused at a range of about half a meter, and the animal was placed in this focal region. The transmitted and received voltage time series were collected for the scattering measurements [subscript S in Eq. (1)], and for each received acoustic return the calibrated echo spectrum was computed as:

$$|f_{\mathrm{bs}}| = \left(\frac{V\mathrm{rec}_S}{V\mathrm{rec}_C}\right) \cdot \left(\frac{V\mathrm{xmit}_C}{V\mathrm{xmit}_S}\right) \cdot \left(\frac{r_S^2}{r_C}\right). \tag{1}$$

In Eq. (1), f_{bs} is the acoustic backscattering amplitude of the animal, and is a measure of the efficiency with which an object scatters sound back toward the sound source [f_{bs} is related to σ_{bs}, the differential backscattering cross section (Clay and Medwin, 1977), by $\sigma_{\mathrm{bs}} = |f_{\mathrm{bs}}|^2$]. $V\mathrm{rec}_C$ and $V\mathrm{xmit}_C$ were computed by taking the absolute value of the FFT of the received and transmitted voltage time series for calibration. $V\mathrm{xmit}_S$ was computed as the absolute value of the FFT of the transmitted voltage time series for scattering measured at the end of each run (every 200 pings). To compute $V\mathrm{rec}_S$, a fixed rectangular window was applied to the received voltage time series for each return (to capture only the echo from the animal) before applying the FFT. The scattering and calibration distances were $r_S = 50.9$ cm and $r_C = 57.8$ cm, respectively. The echo spectrum (TS $= 20 \log|f_{\mathrm{bs}}|$) for each return was then sampled at 203 points between 348.33 and 685 kHz (due to undesirable transducer frequency response characteristics in the upper end of its frequency range, the full bandwidth ($\sim$350–750 kHz) of the collected data was not used). It is this sampled echo spectrum that was used in analyzing the effects of orientation on the frequency-dependent scattering characteristics of Antarctic krill.

C. Video data processing

Video images for 11 of the 14 animals were analyzed to extract the angle of orientation of the krill corresponding to each echo spectrum (Table I). For some animals, orientation was extracted from only a subset of the 1000 images, since the video analysis procedure was extremely time-consuming. Condensation inside the video camera housing obscured the images for Animals 12–14, so that video analysis was not possible for these individuals.

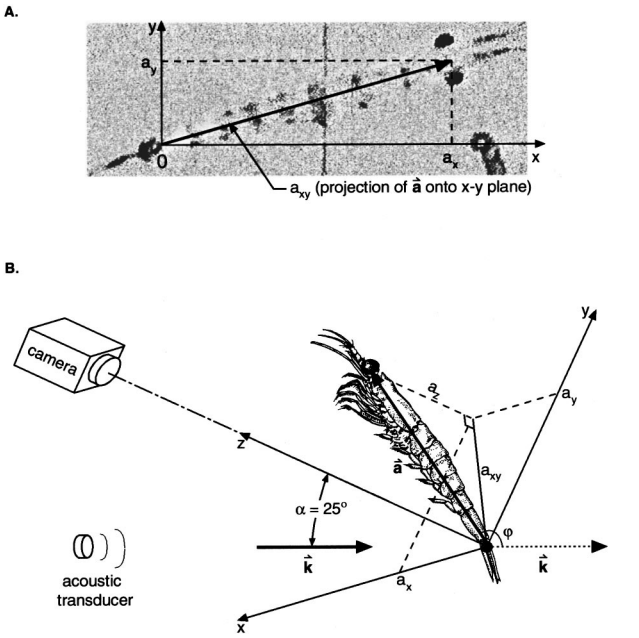

FIG. 2. Geometry for determination of angle of orientation φ from the video images. (A) Image gives the projection of the animal vector $\vec{\mathbf{a}}$ onto the x-y plane of a three-dimensional (3-D) coordinate system with origin situated at the base of the krill's telson. a_x and a_y computed directly from measurements made of the image; (B) 3-D sketch: a_z determined from geometry; φ computed using Eq. (2); incident acoustic wave vector $\vec{\mathbf{k}}$ is in the y-z plane, at an angle of $\alpha = 25°$ relative to the camera line of sight.

To determine the orientation of the animal corresponding to each received echo spectrum, it was necessary to extract from the video tape only the frames captured at the time of each insonification, as indicated by the acoustic pulses recorded on the audio track. To accomplish this, the audio and video channels of the original video tapes were duplicated, and a screen-burn of the time code was made on the duplicates to allow easier identification and location of frames of interest. The tapes were advanced frame-by-frame using a video editing deck which permitted frame-by-frame advancement with an audible audio track, and the time code of each frame in which an acoustic pulse occurred was noted. The video frames of interest were then identified upon playback by the screen-burned time code, captured, digitized, and stored in TIFF format using the public domain image processing and analysis program NIH *Image* for the Macintosh.

For each image, the origin of a three-dimensional rectilinear coordinate system was situated at the base of the animal's telson [Fig. 2(A)]. In this coordinate system, the video image represents the projection of the animal onto the x-y plane, as the camera looks in the negative z direction. The animal itself is then represented by a vector $\vec{\mathbf{a}}$ from the origin to the point midway between the center of the eyes. Measurements were made to determine the x and y coordinates of $\vec{\mathbf{a}}$ (a_x and a_y) for each image. Using a custom-built Matlab® measurement program, the location of the midpoint between the center of the eyes as well as the anterior edge of the conspicuous dark patch which marks the base of the telson were determined by clicking these points with a mouse; the colormap was adjusted to facilitate discrimination of these points on the images. The projected length of the animal a_{xy}

(in the x-y plane) was computed as $a_{xy}=\sqrt{a_x^2+a_y^2}$ directly from these measurements. The z coordinate a_z of $\vec{\mathbf{a}}$ was determined using the fact that $a_z=\sqrt{|\vec{\mathbf{a}}|^2-a_{xy}^2}$ [Fig. 2(B)], where $|\vec{\mathbf{a}}|$ is the length of $\vec{\mathbf{a}}$, as measured from an image in which the animal was estimated to be broadside to the camera (i.e., perpendicular to the camera line of sight, $a_z=0$). The sign of a_z was determined by noting whether the animal was head towards (a_z positive), broadside to (a_z 0), or head away from (a_z negative) the camera, as reflected by changes in the projected length of the animal a_{xy} for a succession of single images (a_{xy} attained its maximum $|\vec{\mathbf{a}}|$ when the animal was broadside to the camera). This was corroborated by watching the video in real time to estimate when broadside crossings occurred, and noting the head orientation before and after each crossing.

The angle of orientation of the animal was then determined for each image by computing the angle φ between the animal vector $\vec{\mathbf{a}}$ and the incident acoustic wave vector $\vec{\mathbf{k}}$ [Fig. 2(B)]:

$$\varphi=\arccos\left(\frac{\vec{\mathbf{k}}\cdot\vec{\mathbf{a}}}{|\vec{\mathbf{k}}||\vec{\mathbf{a}}|}\right), \tag{2}$$

where $\vec{\mathbf{k}}\cdot\vec{\mathbf{a}}$ is the inner product (dot product) of the two vectors; Eq. (2) follows directly from the definition of the inner product: $\vec{\mathbf{k}}\cdot\vec{\mathbf{a}}=|\vec{\mathbf{k}}||\vec{\mathbf{a}}|\cos\varphi$, with $0\leqslant\varphi\leqslant\pi$. For an animal located in the far field of the transducers, the incident acoustic wave is locally planar over the body of the krill, and $\vec{\mathbf{k}}$ is in the y-z plane (perpendicular to the x axis) of the coordinate system, so that $k_x=0$, and $\vec{\mathbf{k}}=|\vec{\mathbf{k}}|(k_x,k_y,k_z)=(2\pi/\lambda)(0,\sin\alpha,-\cos\alpha)$, where λ is the acoustic wavelength and α is the angle between the incident acoustic wave and the camera line of sight. With the animal positioned at the focal point of the transducer pair, this angle was measured as $\alpha=25°$ [Fig. 2(B)].

D. Theoretical modeling

Acoustic backscattering from a finite-length, arbitrarily shaped, weakly scattering (i.e., having density and sound speed similar to those of the surrounding medium) object in the far field can be described by the general volume integral formulation (Morse and Ingard, 1968) of the distorted wave Born approximation (DWBA):

$$f_{\mathrm{bs}}=\frac{k_1^2}{4\pi}\int\int\int(\gamma_\kappa-\gamma_\rho)e^{i2(\vec{k}_i)_2\cdot\vec{r}_0}d\nu_0. \tag{3}$$

Recently, Chu *et al.* (1993) and Stanton *et al.* (1993b) developed a DWBA model to describe the frequency-dependent scattering characteristics of elongated, fluid-like zooplankton at all angles of orientation. If the body has a circular cross section at every point along its lengthwise axis, the DWBA volume integral [Eq. (3)] may be reduced to a line integral along this axis (Stanton *et al.*, 1998b), yielding an accurate expression for the scattering from an elongated, weakly scattering fluid-like finite cylinder as a function of size, shape, material properties, and angle of orientation:

$$\mathrm{TS}=20\log\left|\frac{k_1}{4}\int_{\vec{r}_{\mathrm{pos}}}(\gamma_\kappa-\gamma_\rho)e^{i2(\vec{k}_i)_2\cdot\vec{r}_{\mathrm{pos}}}\times a\,\frac{J_1(2k_2a\cos\beta_{\mathrm{tilt}})}{\cos\beta_{\mathrm{tilt}}}\,|d\vec{r}_{\mathrm{pos}}|\right|. \tag{4}$$

In Eq. (4), $\mathrm{TS}=20\log|f_{\mathrm{bs}}|$, $k=2\pi/\lambda$ is the acoustic wave number ($\lambda=c/f$ where c is the sound speed in m/s and f is the acoustic frequency in Hz), $(\vec{k}_i)_2=\vec{k}_2=\vec{k}_1/h$, J_1 is a Bessel function of the first kind of order 1, $\gamma_p=(\rho_2-\rho_1)/\rho_2$, and $\gamma_\kappa=(\kappa_2-\kappa_1)/\kappa_1$ with compressibility κ defined as $\kappa_i=1/(\rho_i c_i^2)$; subscript 1 refers to the surrounding medium (seawater), subscript 2 refers to the fluid-like medium of the zooplankton body, so that $(\gamma_\kappa-\gamma_\rho)=(1/gh^2)+(1/g)-2$, where $g=\rho_2/\rho_1$ is the density contrast of the organism relative to water, and $h=c_2/c_1$ is its sound speed contrast. This model predicts the scattering from a deformed fluid-like cylindrical body of arbitrary shape (i.e., the cross-sectional radius of the cylinder a can vary along the lengthwise axis) for any angle of orientation relative to the incident acoustic wave by integrating the scattering contributions of each infinitesimally thin cross section (located at $\vec{r}_{\mathrm{pos}}$ along the lengthwise axis, at an angle β_{tilt} relative to the incident acoustic wave) over of the entire animal body.

The line-integral DWBA formulation in Eq. (4) can be implemented in a numerical integration scheme to model the orientational dependence of the scattering from an animal of known size, shape, and material properties. The animal body may be discretized into several cylindrical cross sections, each defined by a position $\vec{r}_{\mathrm{pos}}$ along the lengthwise axis of the animal body, a radius a, a density contrast g, and a sound-speed contrast h. This discretization was achieved by digitizing the outline of the animal from a video image (in lateral aspect if possible), capturing several points along the dorsal and ventral surfaces [refer to Figs. 4 and 5, parts (A) and (B)]. This outline was then scaled to size using the measurements made of the animal after insonification (Table I), and a and $\vec{r}_{\mathrm{pos}}$ were computed for each discrete segment from each dorso-ventral pair of points. The density contrast and sound-speed contrast were held constant over the animal body; values of $g=1.0357$ and $h=1.0279$ (as measured for *Euphausia superba* by Foote, 1990) were used. For a particular angle of orientation of the animal, the backscatter at each of 203 acoustic frequencies (between 348.33 and 685 kHz) was computed as the sum of the scattering contributions of each of the cylindrical cross sections due to an incident acoustic wave vector $\vec{k}_1=(|\vec{k}_1|\cos\beta_{\mathrm{tilt}},|\vec{k}_1|\sin\beta_{\mathrm{tilt}})$. Since the orientational dependence of the scattering predicted by the DWBA model is symmetrical about 180° for an arbitrary shape with circular cross section, the model was implemented by varying the angle of orientation in 1° increments between 0° and 180°. Appendix A of McGehee *et al.* (in press) contains Matlab® code to implement this numerical integration scheme.

E. Inversion for angle of orientation

If the acoustic backscattered energy from elongated, fluid-like zooplankton exhibits a strong orientational depen-

dence, biomass estimates for krill and other euphausiids based on the interpretation of acoustic survey data would be much improved by *in situ* determination of angle of orientation. Classification inversion schemes have been developed which can categorize individual zooplankton into distinct scatterer types (e.g., fluid-like, elastic-shelled, gas-bearing), as well as invert for specific parameters (e.g., animal size, animal orientation), based on the signature information contained in the return spectra of broadband insonifications of the animals (Martin *et al.*, 1996; Martin Traykovski *et al.*, 1998). Such a classification inversion approach was applied to the echo spectra collected from these krill to investigate the feasibility of inverting broadband acoustic returns for angle of orientation for these fluid-like zooplankton.

The Covariance Mean Variance Classifiers (CMVC) (Martin Traykovski *et al.*, 1998) are a set of advanced model-based techniques which classify observed echo spectra based on the correspondence between the observations and model predictions. Theoretical or empirical scattering models are used to construct a model space, which consists of model realizations representing predictions of the models for particular parameter values spanning the entire parameter space. For the *E. superba* data, the objective of this classification is to invert observed echo spectra for a specific parameter value: angle of orientation. The CMVC techniques can be implemented in several alternative configurations, one of which may be employed to search the entire physical model parameter space for the best-match model realizations for a set of observations, and report the parameter values of interest. Determination of the best match is based on the CMV metric (**C**), which quantifies the correspondence between an ensemble of observed echo spectra (**D**) and all the model realizations (**M**). The best-match model realization is determined by maximizing the CMV metric; to achieve a good match between an observation and a model realization, not only must the spectral structure (e.g., the location of peaks and nulls) be similar (as measured by the covariance **K**), but both the mean echo levels and the spectral variability (e.g., null depth) must also be comparable (quantified by the mean similarity **X** and the variance similarity **U**; Martin Traykovski *et al.*, 1998). The CMV metric (**C**) is computed as

$$\mathbf{C} = \mathrm{CMV}(\mathbf{M},\mathbf{D}) = \mathbf{K}\cdot\mathbf{X}\cdot\mathbf{U}. \tag{5}$$

Note that in Eq. (5), $\mathbf{C}_{ij} = (\Sigma_{k=1}^{n_p} \mathbf{D}_{ik}^T \mathbf{M}_{kj}) \cdot \mathbf{X}_{ij} \cdot \mathbf{U}_{ij}$, since $\mathbf{K} = \mathbf{D}^T\mathbf{M}$ is the covariance ($0 \leqslant \mathbf{K}_{ij} \leqslant 1$, see Papoulis, 1991) between the observed data matrix **D** and the model space matrix **M**. Each column of **D** contains a mean-subtracted, energy-normalized observed echo spectrum, whereas each column of **M** contains a mean-subtracted, energy-normalized model realization. **X** and **U** are the mean and variance similarity matrices ($0 \leqslant \mathbf{X}_{ij}, \mathbf{U}_{ij} \leqslant 1$, where $\mathbf{X}_{ij} = 1$ indicates that the *i*th observation and the *j*th model realization have the same mean echo levels, and $\mathbf{U}_{ij} = 1$ indicates that the *i*th observation and the *j*th model realization have identical variance), n_p is the number of points in each echo spectrum, and the centered dot ($\cdot$) indicates element-wise multiplication of matrices. The best-match model realization for the *i*th observed echo spectrum is found by determining the column *m* in which the maximum value in row *i* of **C** occurs, for example, for the first observation, $i = 1$ and the best-match *m* is the realization for which $\mathbf{C}_{1m} = \max(\mathbf{C}_{1j})$ over all *j*. The inversion result for observation *i* is then the angle of orientation associated with the model realization *m* that best predicts that observation.

The ability of the classifier to invert echo spectra for angle of orientation depends to a large extent upon the representativity of the model space, that is, whether it accurately predicts the scattering over the entire observed range of the parameter values with sufficient resolution. In this inversion of krill echo spectra for angle of orientation, two types of theoretical model spaces and two types of empirical model spaces were employed. The theoretical model spaces, consisting of model realizations generated from predictions of the DWBA model [Eq. (4)], include a single, size-constrained generic model space for all animals, and 11 animal-specific model spaces, one for each animal. The generic theoretical model space was based on several distinct discretizations of a euphausiid body, digitized from selected images to represent different animal shapes. Model predictions were made as described in the previous section, using each shape (scaled to approximately the size of the animal) as input into the DWBA. An animal-specific theoretical model space was generated for each of the 11 animals; the discretized shape used as input into the DWBA model was digitized from an image of the particular animal, so that it corresponded with the exact size and shape of that krill. The empirical model spaces included both a single generic empirical model space, constructed by interpolating the echo spectra received from Animal 01 over angle of orientation (with 1° resolution), and animal-specific empirical model spaces for Animals 01, 03, 05, and 09, generated by interpolating the empirical data in the same manner, but based on the observed echo spectra for that particular animal. Only these four animals exhibited a sufficiently wide range of orientations to generate a model with nearly complete angular coverage (see orientation distribution histograms in Fig. 3). For all 11 animals, inversions based on the generic theoretical model space, the appropriate animal-specific theoretical model space, and the generic empirical model space were carried out. Inversions based on the appropriate animal-specific empirical model space were performed for Animals 01, 03, 05, and 09 only.

II. RESULTS AND DISCUSSION

A. Variability in echo spectra with angle of orientation

Acoustic returns from the krill varied considerably with angle of orientation (Fig. 3). Echo spectra from animals near broadside incidence relative to the incident acoustic wave ($\varphi = 90°$) were characterized by widely spaced deep nulls (often 20 dB or greater), usually separated by 200 kHz, whereas the frequency response of off-broadside echoes exhibited a more erratic structure, with several closely spaced (<50 kHz) nulls of variable depth. The scattering from elongated, fluidlike zooplankton at broadside incidence is thought to be dominated by the constructive and destructive interference

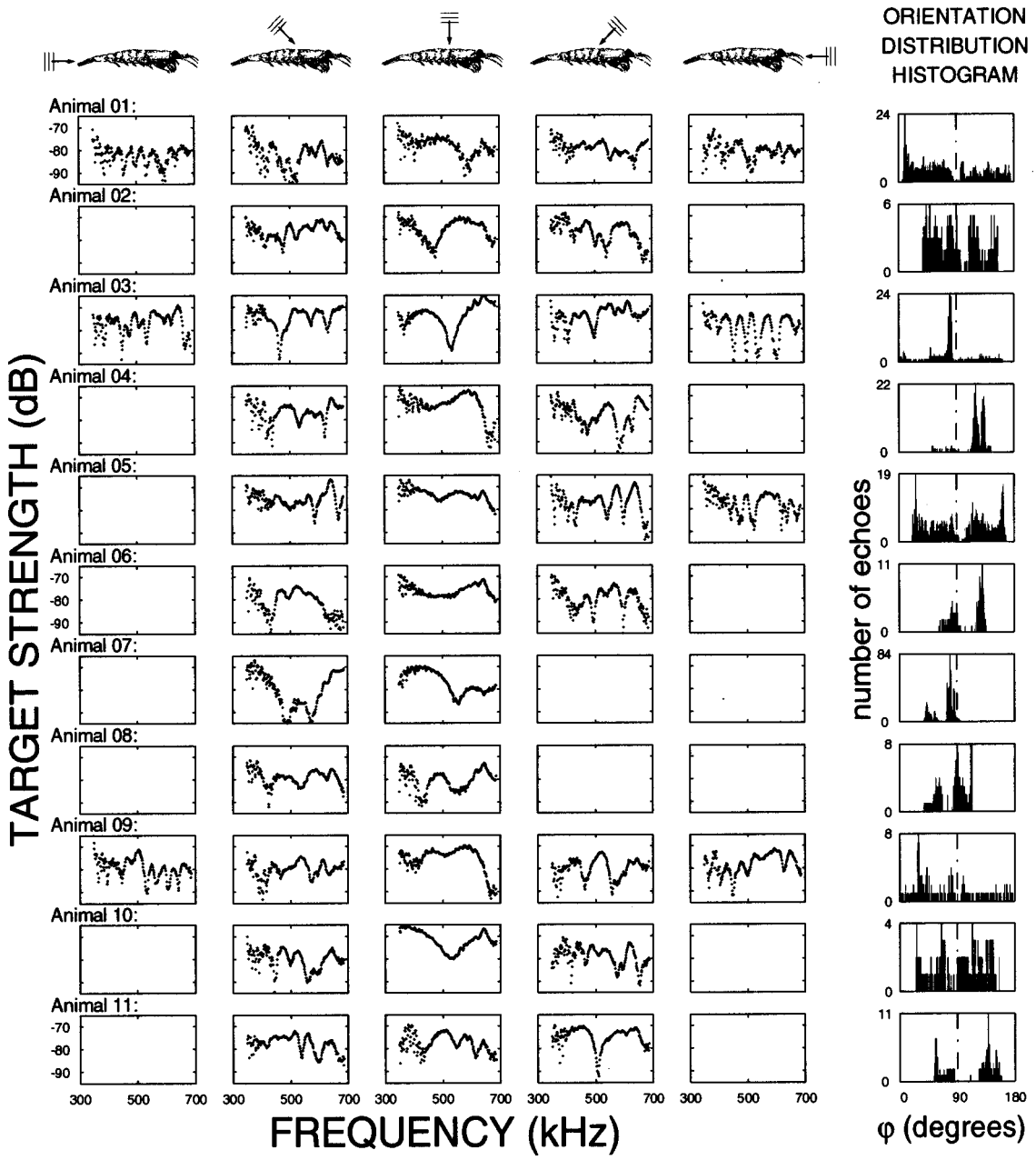

FIG. 3. Examples of echo spectra received from 11 krill (Animals 01–11, rows) at five angles of orientation, with acoustic wave incident at $\varphi \cong 0°$, 45°, 90°, 135°, 180° (±15°) (first five columns); empty plots indicate that the animal did not assume that orientation during the experiment. A histogram of the orientation distribution for each animal during insonification is shown at right.

between the echo from the front interface and the echo from the back interface of the animal (see Fig. 8, CASE 1). At off-broadside angles, contributions from other scattering features of the animal body are believed to become more significant, resulting in a more complicated/erratic interference pattern with many nulls (Stanton *et al.*, 1994b, 1998b).

The effect of orientation on average echo levels was investigated by computing the mean target strength over all frequencies ($\overline{\mathrm{TS}} = 10 \log|\overline{\sigma_{\mathrm{bs}}}|$) of the echo spectrum received at each angle of orientation φ. These spectrally averaged TSs (not shown) were found to be about 5 dB higher near broadside incidence versus off-broadside for most animals. For the larger animals (e.g., Animals 02, 03, 05, 06, 11), average target strengths over the frequency band were approximately −70 dB at orientations near broadside versus −75 dB off-broadside, whereas for the smaller animals (e.g., Animals 01, 08, 09, 10), the average TS near-broadside incidence was about −75 dB, versus off-broadside spectrally averaged target strengths of approximately −80 dB. These observations are consistent with what is expected based on the physics of scattering from elongated objects (Stanton, 1988a,b, 1989a, 1993a,b) since at broadside incidence, an elongated krill presents a much larger backscattering cross section to the incident acoustic wave than at any other angle of orientation.

There is a maximum of ±15° uncertainty in the calculation of φ using the video analysis method described to extract angle of orientation from two-dimensional images of the animal. Some of this uncertainty arises from possible

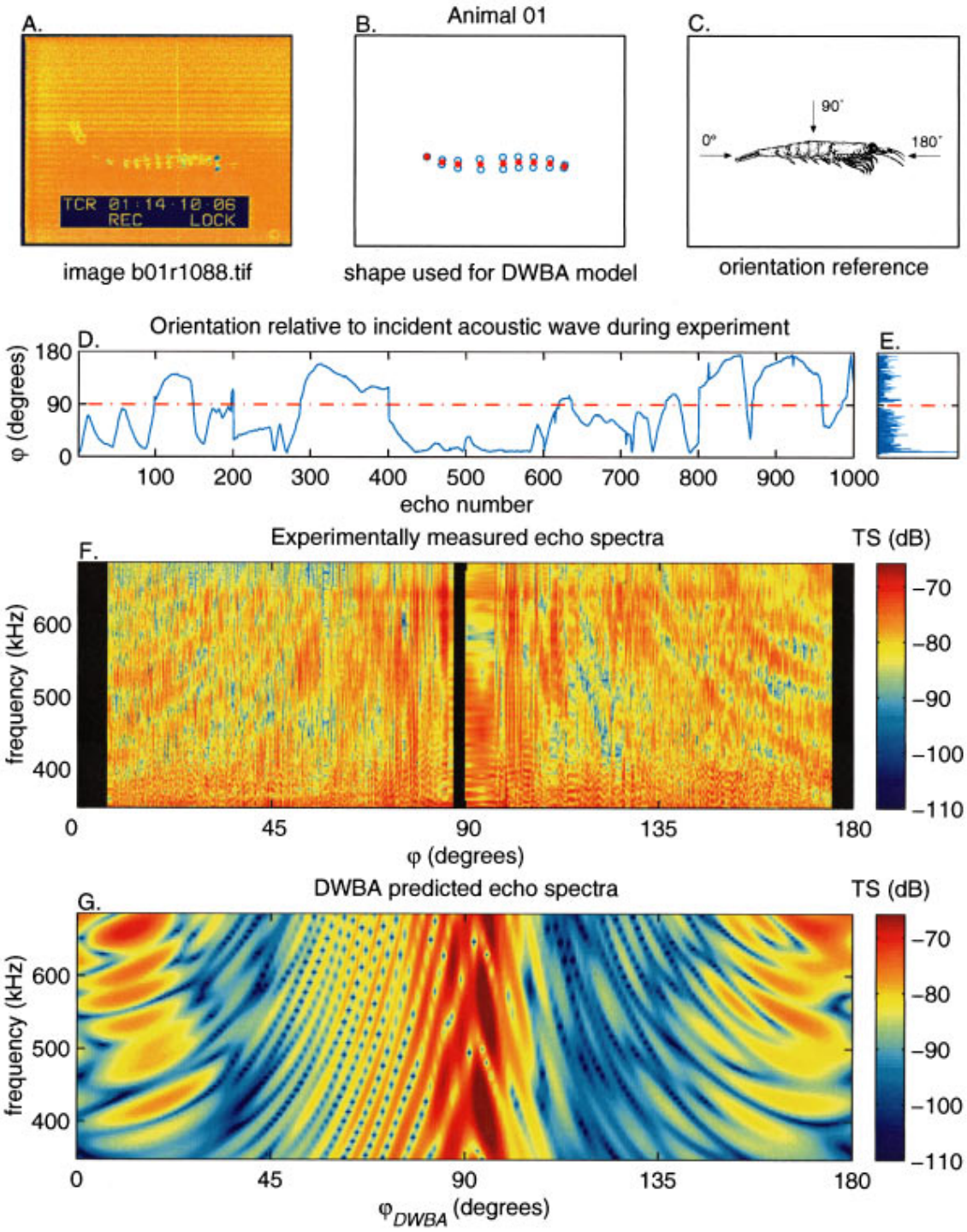

FIG. 4. Experimentally measured echo spectra versus DWBA model predictions for Animal 01: (A) video image used to digitize animal shape; (B) discretization of animal body; (C) orientation reference for DWBA modeling; (D) time series of φ during insonification; (E) orientation distribution histogram ($n=1000$); (F) measured echo spectra (y axis, TS in color) versus angle of orientation φ (x axis, interpolation over more than 1.5° is blacked out); (G) echo spectra predicted by DWBA model.

error during measurement of the video frames, as a result of the limited pixel resolution of the image and the curvature of the animal body, both of which can affect the measured projected length of the animal. Measurement error is greatest when the animal is broadside to the camera and decreases non-linearly at angles off-broadside, since very small changes (errors) in the measured length when the projected length is maximum result in greater changes in computed angle relative to measurement errors made when the animal is off-broadside relative to the camera. An additional source of error in the calculation of φ arises from small changes in the value of α [the angle between the camera line of sight and the transducer line of sight, see Fig. 2(B)] due to uncertainty in the exact fore–aft camera position relative to the

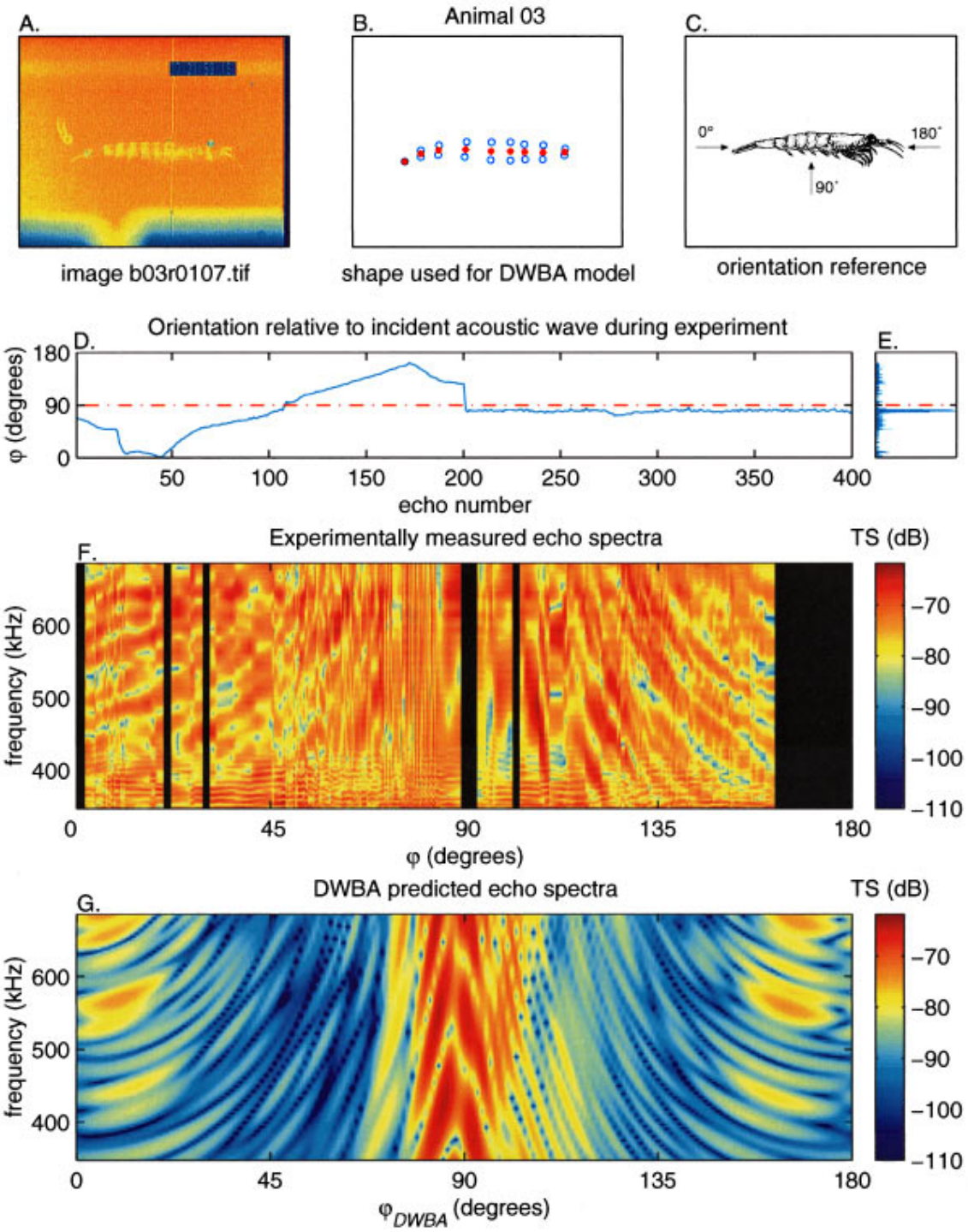

FIG. 5. Experimentally measured echo spectra versus DWBA model predictions for Animal 03: (A) video image used to digitize animal shape; (B) discretization of animal body; (C) orientation reference for DWBA modeling; (D) time series of φ during insonification; (E) orientation distribution histogram ($n=400$); (F) measured echo spectra (y axis, TS in color) versus angle of orientation φ (x axis, interpolation over more than 1.5° is blacked out); (G) echo spectra predicted by the DWBA model.

transducer bank. The maximum uncertainty of ±15° is a conservative estimate based on a sensitivity analysis of the effect of these sources of error on the calculated values of φ. The single-camera video system used to record animal orientation cannot provide the same accuracy as that obtainable by measuring animal orientation with a two-camera or a stereo-camera system. Future measurements would benefit from the implementation of a more sophisticated camera system. In the experiment, not all animals assumed all orientations during insonification, as is evident from the histograms of the orientation distribution measured for each animal (Fig. 3); Animals 01, 03, 05, and 09 were insonified at the widest range of angles φ. As a result of the extreme sensitivity of the measurement technique to very small changes in projected length near broadside, many of the histograms exhibit low echo counts at or near $\varphi=90°$.

B. Comparison to DWBA model theoretical predictions

Experimentally measured echo spectra versus angle of orientation φ were compared to theoretical model predictions based on a DWBA model for each animal. Two examples are presented: Animal 01 (Fig. 4) and Animal 03 (Fig. 5); results for these animals are shown because they assumed the widest range of orientations during insonification, providing the best angular coverage over which to visualize the comparison between observations and theory. The pattern of changes in echo spectra with φ is very similar for the experimentally measured data and the DWBA model predicted spectra for all 11 krill, with only one or two nulls apparent in the frequency responses near broadside incidence, whereas the spectra become much more oscillatory (more peaks and nulls) off-broadside. Although the patterns agree qualitatively, the DWBA model predicts a much greater drop in TS (about 20 dB) as orientation changes from broadside incidence to off-broadside (i.e., 20°–60° and 120°–160°) than was actually observed for these animals as they changed orientation [about a 5-dB drop going from broadside incidence to off-broadside; all values were well above the noise floor (−100 to −110 dB)]. Another feature of the theoretical model predictions not observed in the data is an increase in echo-levels closer to end-on (head-on and tail-on). In fact, the DWBA model consistently under-predicted off-broadside echo levels for all 11 animals, but model predictions of TS values near end-on were more consistent with the observations.

The DWBA theoretical model, which predicts scattering based on a highly simplified outline of the animal body by approximating it as a deformed cylinder, does not account for contributions of other scattering features of the complex animal body (e.g., rapidly moving legs). These unaccounted for scattering features appear to make significant contributions to the observed echo levels at off-broadside angles of incidence for these krill. Examination of the time series of angle of orientation throughout the experiment revealed that for some animals orientation was rapidly varying [e.g., Animal 01 (see Fig. 4(D)), 02, and 05], whereas other krill changed orientation slowly [e.g., Animal 03 (see Fig. 5(D)), 09, and 10], and still others (especially Animal 07) remained close to the same orientation throughout the experiment. Constraining the krill by tethering around the midsection likely affects their activity level by eliciting an escape response. The impact of animal activity on echo levels is unknown, although some correlation between rapid swimming and elevated echo levels has been observed by these authors and others.

C. Inversion for angle of orientation

The information contained in the broadband echo spectra collected from the krill was used to invert the acoustic returns for animal angle of orientation. To accomplish this, a classification inversion using the Covariance Mean Variance Classification approach was performed on the krill echo spectra. This model-based inversion was applied using both theoretical and empirical model spaces (Fig. 6 shows raw and bin-averaged Animal 03 inversion results for both theoretical and empirical model spaces). The raw inversion results tended to be quite variable, particularly for the theoretical model spaces, whereas the bin-averaged results (obtained by averaging over five nearest neighbors) were less sensitive to outliers, and more clearly delineated how each model space performed in inverting for angle of orientation. Surprisingly, inversions obtained using the animal-specific DWBA model space were no more accurate overall than could be achieved with the size-constrained generic DWBA model space (Table II). This indicates that the frequency response of the acoustic return, although sensitive to animal size, is relatively insensitive to animal shape; the animal-specific model space was generated using the digitized shape of each animal scaled to the exact measured size, whereas the generic DWBA model space, although constrained to be approximately the same size as the animal, was generated using several arbitrary shapes digitized from different euphausiid zooplankton. Although the generic DWBA theoretical model space was not able to accurately invert for angle of orientation for many of these animals, this generic theoretical model space has been shown to be quite powerful in discriminating between different types of scatterers; the generic DWBA model has been employed in conjunction with two other theoretical model spaces to classify several different species of zooplankton into three scattering classes (i.e., elastic-shelled, fluid-like, gas-bearing) based on broadband echo spectra (Martin Traykovski *et al.*, 1998). While the resolution of the generic DWBA theoretical model space is sufficient for identifying krill and other euphausiids as elongated, fluid-like scatterers, it is possible that modeling these animals as simple deformed cylinders is not adequate if the goal is to invert single broadband echoes for a particular parameter (e.g., angle of orientation).

Comparison of the inversion results achieved using the different model spaces reveals that a generic empirical model space based on acoustic returns collected from an arbitrarily chosen krill (in this case, Animal 01) may be better able to invert for angle of orientation than an animal-specific theoretical model space, which predicts the scattering with the DWBA model based on the actual size and shape of that particular animal (Table II). For 8 of the 11 krill, the animal-specific DWBA model space did not perform as well as the generic empirical model space [animal-specific DWBA: 36% correct inversions (s.d. 8.0); generic empirical: 68% correct (s.d. 8.2), based on an overall average ($n=8$); correct inversions are those within $\pm 15°$ of observed values]. Although the generic empirical model space was based on data collected from an animal of different size and shape, it did account for contributions of other scattering features of the complex animal body not included in the simplifying theoretical model. Orientations predicted using the animal-specific empirical model space were the most accurate overall for Animals 01, 03, 05, and 09, providing a more robust inversion than that achieved with the generic empirical model space (Table II, Fig. 7).

For these inversions (which are based on choosing the global maximum best-match echo spectra), symmetry about broadside incidence was assumed since both the observations

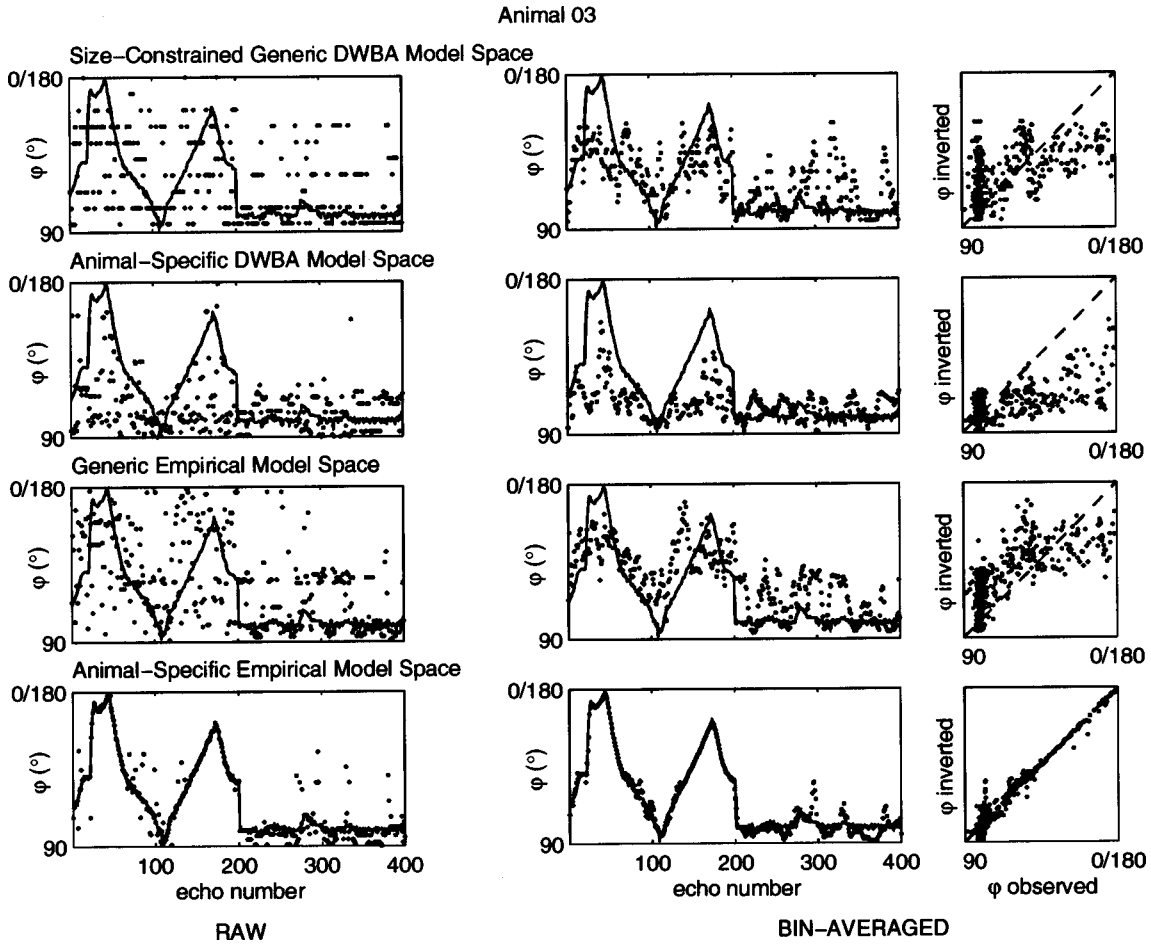

FIG. 6. Inversion of echo spectra from Animal 03 for angle of orientation using the CMVC inversion technique, assuming symmetry about broadside incidence (90°). Observed angle of orientation φ (solid line) shown together with inversion results (points) achieved using four different model spaces: generic DWBA model space constrained to approximate size of Animal 03 (top); animal-specific DWBA model space for Animal 03 (2nd row); generic empirical model space (based on data from Animal 01, 3rd row); animal-specific empirical model space (based on data from Animal 03, bottom). Raw results shown at left, bin-averaged (over five echoes) results shown at right, including scatter plot of inverted versus observed angle of orientation (dashed 45° line indicates perfect correspondence between inversion results and observations).

and the theoretical model predictions for all animals exhibited considerable symmetry around 90° [see Figs. 4 and 5, parts (F) and (G)], so that a good match to a 45° model realization will likely also be a good match to the similar 135° model realization. In applying the CMVC inversion algorithm, the mean similarity [as represented by **X** in Eq. (5)] was included only for inversions using the animal-specific empirical model space. This mean comparison was suppressed when classifying with the other three model spaces, since the theoretical models had been shown to under-predict mean echo levels at many angles of orientation, and an empirical model based on a different-sized animal will exhibit different mean echo levels. In these cases, the inversion was based only on correlation in spectral structure between the observed echo spectra and the model realizations in the model space, as well as the variance similarity of the observations and the model realizations.

For elongated, fluid-like zooplankton such as krill, the structure of the frequency response depends on both size and orientation, so that it is not possible to invert broadband echo spectra for angle of orientation without some *a priori* information regarding animal size. In fact, animal size and angle

TABLE II. Performance (percent correct, to within measurement uncertainty of ±15°) based on bin-averaged (over five echoes) inversion results (assuming symmetry about broadside incidence) for all 11 krill with the generic DWBA model space (constrained to approximate size of animal), the appropriate animal-specific DWBA model space, the generic empirical model space (based on data from Animal 01) and the appropriate animal-specific empirical model space (Animal 01, 03, 05, and 09 only).

	Animal number										
Model space	01	02	03	04	05	06	07	08	09	10	11
Generic DWBA	40%	61%	63%	78%	48%	62%	70%	60%	35%	60%	36%
Animal-specific DWBA	30%	52%	69%	33%	35%	48%	57%	54%	34%	43%	34%
Generic empirical	78%	65%	57%	74%	61%	70%	38%	47%	51%	66%	66%
Animal-specific empirical	78%	⋯	99%	⋯	90%	⋯	⋯	⋯	97%	⋯	⋯

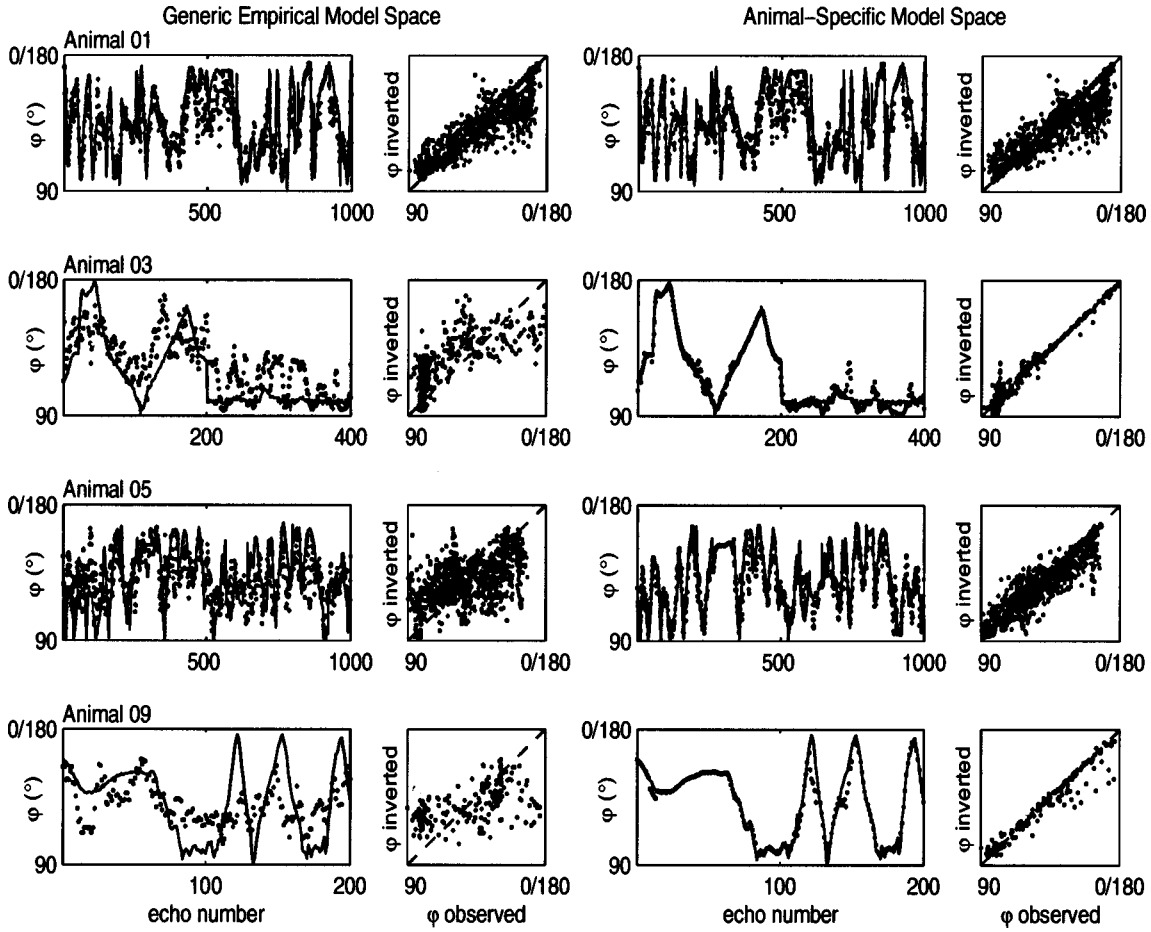

FIG. 7. Bin-averaged (over five echoes) inversion results for Animal 01, 03, 05, and 09 (top to bottom) using the CMVC inversion technique (assuming symmetry about 90°) with the generic empirical model space (based on data from Animal 01, left) and the animal-specific empirical model space (right). Observed orientation φ (solid line) shown together with inversion results (points); 45° dashed line in scatter plot indicates perfect agreement between inversion results and observations.

of orientation are confounded, so that the frequency response of an echo received from a large animal may have a structure similar to that received from a much smaller animal at a different orientation relative to the incident acoustic wave. To illustrate this, consider a simple scattering model which includes a summation of only two rays (Stanton *et al.*, 1993a,b), accounting for the constructive and destructive interference between the rays reflected from the front and back interfaces of a weakly scattering target such as a krill. The null spacing of the frequency response predicted by this two-ray model depends on the *apparent* size of the animal, that is, the distance the acoustic wave travels between the front and back interfaces of the animal. Apparent size is a function of both animal radius and angle of orientation, so that the echo spectrum of a large krill at broadside incidence can exhibit the same structure as that of a smaller animal oriented off-broadside relative to the direction of insonification (Fig. 8).

Knowledge of animal orientation during insonification could significantly improve acoustic biomass estimates of zooplankton, particularly for aggregations of similarly sized individuals of a single species, for example, swarms of Antarctic krill in the Southern Ocean. The *in situ* orientation distribution of *Euphausia superba* has not been measured quantitatively. Observations of freely swimming *E. superba* in an aquarium indicated that they assumed a wide range of orientations (corresponding to φ varying between 40° and 180°), but spent most of the time swimming upward at a steep angle, so that they would most often be oriented within 60° of end-on incidence relative to a downward-looking echosounder (Kils, 1981). It is probable that the animals in Kils' aquarium (as well as the tethered krill insonified in these scattering experiments) assumed a much wider range of orientations than would be observed in the field by a downward-looking sonar system. In fact, qualitative *in situ* observations of *E. superba* by Hamner *et al.* (1983) revealed that all individuals in a school assumed the same orientation, and that krill in an aggregation usually swam horizontally; descending at angles of less than approximately 10° relative to the horizontal.

Application of the CMVC inversion technique in the field could potentially allow prediction of the orientation of individual elongated, fluid-like zooplankton (e.g., krill) *in situ*. Information from broadband acoustic systems, combined with ground-truthing of animal size (e.g., from net samples), could be inverted for angle of orientation with the CMVC inversion technique using a generic empirical model space (e.g., the one constructed based on data collected from Animal 01, or alternatively, one based on data collected from krill at known orientations *in situ*). Certain technological

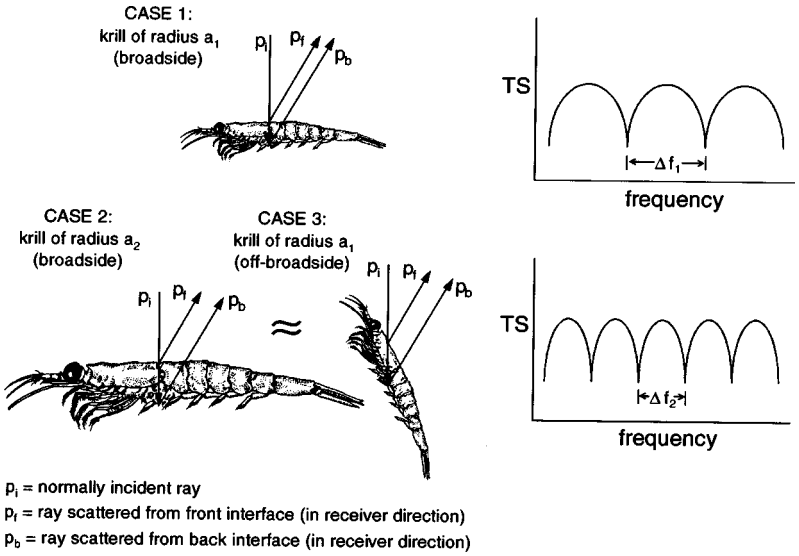

FIG. 8. Comparison of echo spectra predicted by a simplified two-ray theoretical scattering model [e.g., Stanton *et al.* (1993a,b)] received from krill insonified at high frequency ($\lambda \leqslant 4a$) for a small animal (radius a_1) at broadside incidence (CASE 1) and off-broadside (CASE 3), and a large animal (radius $a_2 > a_1$) at broadside incidence (CASE 2). Nulls in the echo spectra result from destructive interference between the echo from the front interface p_f and the echo from the back interface p_b of the animal, which occurs when the phase difference between them $\phi_{f/b}$ is $n\pi$ radians; for the three cases shown: $\phi_{f/b} = n\pi = (2\pi\Delta f_1/c)d_1 = (2\pi\Delta f_2/c)d_2 = (2\pi\Delta f_3/c)d_3$, where d is the distance the ray travels inside the body in each case, and c is the speed of sound in the body. When an animal is at broadside incidence (CASE 1 and CASE 2), $d_1 = 4a_1$ and $d_2 = 4a_2$, but off-broadside (CASE 3), the *apparent* size (to the acoustic wave) of the small krill is greater than a_1; i.e., $d_3 \neq d_1$. Here $d_3 \approx d_2$ so that the null spacing is the same for CASE 3 as for CASE 2 (i.e., $\Delta f_3 \approx \Delta f_2$).

challenges must be overcome to permit successful field implementation of a classification inversion for animal orientation based on broadband echo spectra. These include variable beam width and variable signal-to-noise ratio (SNR) over the bandwidth of current broadband sources suitable for field use. Development of constant beam width broadband transducers is underway by others. Orientational information obtained through inversion of the frequency response of broadband echoes may then be used in conjunction with single-frequency acoustic survey data to make more accurate biomass estimates of Antarctic krill stocks in the Southern Ocean.

III. SUMMARY

Biomass estimates of Antarctic krill (*Euphausia superba*) stocks in the Southern Ocean are often based on acoustic survey data. To make accurate estimates of zooplankton biomass from acoustic backscatter measurements, the acoustic characteristics of the species of interest must be well-understood. In particular, it has long been recognized that the acoustic target strength (TS) of elongated, fluid-like zooplankton such as *E. superba* varies with animal orientation. Acoustic scattering experiments were performed to elucidate the effect of animal orientation on the broadband scattering characteristics of Antarctic krill. During the experiments, individual, live krill were tethered and suspended in a tank filled with filtered, chilled seawater. One thousand echoes were collected from each of 14 animals during insonification with a broadband chirp of center frequency 500 kHz (~350–750 kHz), while their behavior was simultaneously captured on video tape. A novel video analysis technique was applied to images for 11 of the animals to extract the angle of orientation of the krill corresponding to each insonification. This analysis revealed that echo spectra from krill near broadside incidence relative to the incident acoustic wave were characterized by widely spaced (~200 kHz) deep (~20 dB) nulls, whereas off-broadside echo spectra exhibited a more erratic structure, with several closely spaced (<50 kHz) nulls of variable depth. Spectrally averaged echo levels were found to be about 5 dB higher near broadside incidence compared to off-broadside. The acoustic returns collected from the krill were compared to theoretical predictions for all angles of orientation based on a distorted wave Born approximation (DWBA) model for each animal. The pattern of changes in echo spectra with orientation is very similar for the experimentally measured data and the DWBA model predicted spectra for all 11 krill. However, the theoretical model predicts a much greater (by about 15 dB) drop in echo levels as orientation changes from broadside incidence to off-broadside than was actually observed for these animals as they changed orientation. Information contained in the broadband echo spectra of the krill was exploited to invert the acoustic returns for angle of orientation by applying a newly developed Covariance Mean Variance Classification (CMVC) approach, using generic and animal-specific theoretical and empirical model spaces. The animal-specific empirical model space (based on data collected from the appropriate animal) was best able to invert for angle of orientation. Employing a generic empirical model space (based on data collected from an arbitrarily chosen krill) resulted in more accurate inversions overall than could be achieved using the appropriate animal-specific theoretical model space (which predicts the scattering based on the actual size and shape of that particular animal). The CMVC inversion technique can be implemented using a generic empirical model space to determine angle of orientation based on broadband echoes from individual zooplankton in the field. Pending technological development of a broadband sonar for deployment in conjunction with single-frequency acoustic surveys of Antarctic krill, extraction of this orientational information has the potential to significantly improve biomass estimates of krill stocks in the Southern Ocean.

ACKNOWLEDGMENTS

The authors would like to thank Chuck Greene for coordinating the 1995 and 1996 Bioacoustical Oceanography Workshops, funded by the National Science Foundation and the Office of Naval Research, during which the scattering experiments and some of the data analysis were conducted. Many people contributed significantly to this work during

the workshops, especially Karen Fisher, Janice Jones, Andrew Remsen, and Kathy Vigness. Thanks also to Langdon Quetin and Robin Ross of UCSB for providing the krill, Dan Costa, Bernie LeBoeuf, and Betsy Steele for providing laboratory space at UCSC, Bill Lange at the Woods Hole Oceanographic Institution for providing the video equipment, and three anonymous reviewers for helpful suggestions for improvement of the manuscript. This work was completed in partial fulfillment of the requirements for a Ph.D., and L.V.MT. would like to thank her thesis committee: Tim Stanton (who also provided the pulse–echo acoustic data acquisition system and guidance regarding the theoretical models), Peter Wiebe and Jim Lynch at WHOI, and Penny Chisholm of the Massachusetts Institute of Technology, for their support, encouragement, and advice over the last five years. L.V.MT.'s research was supported by the Ocean Acoustics, Oceanic Biology and URIP programs of the Office of Naval Research Grant Nos. N00014-89-J-1729, N00014-95-1-0287, and N00014-92-J-1527, the Biological Oceanography program of the National Science Foundation Grant No. OCE-9201264, and the WHOI/MIT Joint Program Education Office. R.L.O. would like to thank Television New Zealand and the Claude McCarthy Fellowship Foundation for supporting his participation in the workshops. D.E.M. would like to thank Tracor and the WHOI Postdoctoral Fellowship program for support. This is Woods Hole Oceanographic Institution contribution number 9596.

Anderson, V. C. (**1950**). ''Sound scattering from a fluid sphere,'' J. Acoust. Soc. Am. **22**, 426–431.

Chu, D., Stanton, T. K., and Wiebe, P. H. (**1992**). ''Frequency dependence of sound backscattering from live individual zooplankton,'' ICES J. Mar. Sci. **49**, 97–106.

Chu, D., Foote, K. G., and Stanton, T. K. (**1993**). ''Further analysis of target strength measurements of Antarctic krill at 38 and 120 kHz: Comparison with deformed cylinder model and inference of orientation distribution,'' J. Acoust. Soc. Am. **93**, 2855–2988.

Clay, C. S., and Medwin, H. (**1977**). *Acoustical Oceanography: Principles and Applications* (Wiley, New York).

Croxall, J. P., McCann, T. S., Prince, P. A., and Rothery, P. (**1988**). ''Reproductive performance of seabirds and seals at South Georgia and Signy Island, South Orkney Islands, 1976–1987: Implications for Southern Ocean monitoring studies,'' in *Antarctic Ocean and Resources Variability*, edited by D. Sahrhage (Springer-Verlag, New York).

Demer, D. A., and Martin, L. V. (**1995**). ''Zooplankton target strength: Volumetric or areal dependence?,'' J. Acoust. Soc. Am. **98**, 1111–1118.

El-Sayed, S. Z. (**1988**). ''The BIOMASS program,'' Oceanus **31**, 75–79.

Everson, I. (**1977**). The living resources of the Southern Ocean. Food and Agriculture Organisation of the United Nations, GLO/SO/77/1, Rome, 156 pp.

Everson, I. (**1982**). ''Diurnal variations in mean volume backscattering strength of an Antarctic krill (*Euphausia superba*) patch,'' J. Plankton Res. **4**, 155–162.

Everson, I., Watkins, J. L., Bone, D. G., and Foote, K. G. (**1990**). ''Implications of a new acoustic target strength for abundance estimates of Antarctic krill,'' Nature (London) **345**, 338–340.

Flagg, C. N., and Smith, S. L. (**1989**). ''On the use of the acoustic Doppler current profiler to measure zooplankton abundance,'' Deep-Sea Res. Oceanogr. Abstr. **36**, 455–474.

Foote, K. G. (**1990**). ''Speed of sound in *Euphausia superba*,'' J. Acoust. Soc. Am. **87**, 1405–1408.

Foote, K. G., Everson, I., Watkins, J. L., and Bone, D. G. (**1990**). ''Target strengths of Antarctic krill (*Euphausia superba*) at 38 kHz and 120 kHz,'' J. Acoust. Soc. Am. **87**, 16–24.

Greene, C. H., Stanton, T. K., Wiebe, P. H., and McClatchie, S. (**1991**). ''Acoustic estimates of Antarctic krill,'' Nature (London) **349**, 110.

Greenlaw, C. F. (**1977**). ''Backscattering spectra of preserved zooplankton,'' J. Acoust. Soc. Am. **62**, 44–52.

Greenlaw, C. F. (**1979**). ''Acoustical estimation of zooplankton populations,'' Limnol. Oceanogr. **24**, 226–242.

Hamner, W. M., Hamner, P. P., Strand, S. W., and Gilmer, R. W. (**1983**). ''Behaviour of Antarctic krill, *Euphausia superba*: chemoreception, feeding, schooling and molting,'' Science **220**, 433–435.

Hewitt, R. P., and Demer, D. A. (**1991**). ''Krill abundance,'' Nature (London) **353**, 310.

Hewitt, R. P., and Demer, D. A. (**1996**). ''Lateral target strength of Antarctic krill,'' ICES J. Marine Sci. **53**, 297–302.

Huntley, M. E., and Lopez, M. D. G. (**1992**). ''Temperature dependent production of marine copepods: a global synthesis,'' Am. Nat. **140**, 201–242.

Johnson, R. K. (**1977**). ''Sound scattering from a fluid sphere revisited,'' J. Acoust. Soc. Am. **61**, 375–377.

Kils, U. (**1981**). ''The swimming behaviour, swimming performance and energy balance of Antarctic krill, *Euphausia superba*,'' BIOMASS Scientific Series **3**.

Kristensen, A., and Dalen, J. (**1986**). ''Acoustic estimation of size distribution and abundance of zooplankton,'' J. Acoust. Soc. Am. **80**, 601–611.

Martin, L. V., Stanton, T. K., Wiebe, P. H., and Lynch, J. F. (**1996**). ''Acoustic classification of zooplankton,'' ICES J. Marine Sci. **53**, 217–224.

Martin Traykovski, L. V., Lynch, J. F., Stanton, T. K., and Wiebe, P. H. (**1998**). ''Model-based Covariance Mean Variance Classification techniques: Algorithm development and application to the acoustic classification of zooplankton,'' IEEE J. Oceanic Eng. **23** (4).

McGehee, D. E., O'Driscoll, R. L., and Martin Traykovski, L. V. (in press). ''Effects of orientation on acoustic scattering from Antarctic Krill,'' Deep-Sea Res. Oceanogr. Abstr.

Miller, C. B., and Judkins, D. C. (**1981**). ''Design of pumping systems for sampling zooplankton, with descriptions of two high-capacity samplers for coastal studies,'' Biol. Ocean. **1**, 29–56.

Morse, P. M., and Ingard, K. U. (**1968**). *Theoretical Acoustics* (Princeton U.P., Princeton, NJ).

Nemoto, T., Okiyama, M., Iwasaki, N., and Kikuchi, T. (**1988**). ''Squid as predators on krill (*Euphausia superba*) and prey for sperm whales in the Southern Ocean,'' in *Antarctic Ocean and Resources Variability*, edited by D. Sahrhage (Springer-Verlag, New York), pp. 292–296.

Nicol, S., and de la Mare, W. (**1993**). ''Ecosystem management and the Antarctic Krill,'' Am. Sci. **81**, 36–47.

Papoulis, A. (**1991**). *Probability, Random Variables, and Stochastic Processes* (McGraw-Hill, New York), 3rd ed.

Penrose, J. D., and Kaye, G. T. (**1979**). ''Acoustic target strengths of marine organisms,'' J. Acoust. Soc. Am. **65**, 374–380.

Permitin, Y. E. (**1970**). ''The consumption of krill by Antarctic fishes,'' in *Antarctic Ecology Vol. I*, edited by M. W. Holdgate (Academic, New York), pp. 177–182.

Sameoto, D. D. (**1980**). ''Quantitative measurements of euphausiids using a 120 kHz sounder in their *in situ* orientation,'' Can. J. Fisheries Aquatic Sci. **37**, 693–702.

Samovol'kin, V. G. (**1980**). ''Backscattering of ultrasonic waves by shrimps,'' Oceanology **20**, 667–670.

Stanton, T. K. (**1988a**). ''Sound scattering by cylinders of finite length. I. Fluid cylinders,'' J. Acoust. Soc. Am. **83**, 55–63.

Stanton, T. K. (**1988b**). ''Sound scattering by cylinders of finite length. II. Elastic cylinders,'' J. Acoust. Soc. Am. **83**, 64–67.

Stanton, T. K. (**1989a**). ''Sound scattering by clinders of finite length. III. Deformed cylinders,'' J. Acoust. Soc. Am. **86**, 671–705.

Stanton, T. K. (**1989b**). ''Simple approximate formulas for backscattering of sound by spherical and elongated objects,'' J. Acoust. Soc. Am. **86**, 1499–1510.

Stanton, T. K. (**1990**). ''Sound scattering by spherical and elongated shelled bodies,'' J. Acoust. Soc. Am. **88**, 1619–1633.

Stanton, T. K., Clay, C. S., and Chu, D. (**1993a**). ''Ray representation of sound scattering by weakly scattering deformed fluid cylinders: Simple physics and application to zooplankton,'' J. Acoust. Soc. Am. **94**, 3454–3462.

Stanton, T. K., Chu, D., Wiebe, P. H., and Clay, C. S. (**1993b**). ''Average echoes from randomly oriented random-length finite cylinders: Zooplankton models,'' J. Acoust. Soc. Am. **94**, 3463–3472.

Stanton, T. K., Wiebe, P. H., Chu, D., Benfield, M. C., Scanlon, L., Martin,

L. V., and Eastwood, R. L. (**1994a**). ''On acoustic estimates of biomass,'' ICES J. Mar. Sci. **51**, 505–512.
Stanton, T. K., Wiebe, P. H., Chu, D., and Goodman, L. (**1994b**). ''Acoustic characterization and discrimination of marine zooplankton and turbulence,'' ICES J. Mar. Sci. **51**, 469–479.
Stanton, T. K., Chu, D., and Wiebe, P. H. (**1996**). ''Acoustic scattering characteristics of several zooplankton groups,'' ICES J. Mar. Sci. **53**, 289–295.
Stanton, T. K., Chu, D., Wiebe, P. H., Martin, L. V., and Eastwood, R. L. (**1998a**). ''Sound scattering by several zooplankton groups I: Experimental determination of dominant scattering mechanisms,'' J. Acoust. Soc. Am. **103**, 225–235.
Stanton, T. K., Chu, D., and Wiebe, P. H. (**1998b**). ''Sound scattering by several zooplankton groups II: Scattering models,'' J. Acoust. Soc. Am. **103**, 236–253.
Wiebe, P. H., Boyd, S., and Cox, J. L. (**1975**). ''Relationships between zooplankton displacement volume, wet weight, dry weight and carbon,'' Fishery Bull. **73**, 777–786.
Wiebe, P. H., Morton, A. W., Bradley, A. M., Backus, R. H., Craddock, J. E., Cowles, T. J., Barber, V. A., and Flierl, G. R. (**1985**). ''New developments in the MOCNESS, an apparatus for sampling zooplankton and micronekton,'' Mar. Biol. **87**, 313–323.
Wiebe, P. H., Greene, C. H., Stanton, T. K., and Burczynski, J. (**1990**). ''Sound scattering by live zooplankton and micronekton: Empirical studies with a dual-beam acoustical system,'' J. Acoust. Soc. Am. **88**, 2346–2360.

Theory of acoustic radiation near a hyperbolic ridge

Thomas K. Berger
Department of Physics, University of California, San Diego, 9500 Gilman Drive, La Jolla, California 92093-0238

(Received 17 December 1997; accepted for publication 20 June 1998)

A solution to the acoustic field due to a harmonic point source near a hyperbolic ridge with perfectly reflecting boundaries in an isovelocity ocean is derived and developed. An exact expression for the field is given as a modal sum of integrals. The integrals are in terms of eigenfunctions of the reduced wave equation in the three-dimensional elliptical coordinate system. The eigenfunctions are approximated away from the low-frequency limit by standard WKB techniques. The resulting integrals are estimated by first and second order stationary phase asymptotics, which are matched in the vicinity of the caustics, yielding a complete representation of the field. The field is given in terms of standard elliptic functions for which fast numerical routines are available. The solution includes the locations of the caustics and shadow zones, as well as predicting a complicated intramodal interference pattern resulting from the intersection of up to three rays in a given mode. The explicit representation of these features arising from horizontal refraction makes this theoretical model useful as a new fully three-dimensional benchmark solution. © *1998 Acoustical Society of America.* [S0001-4966(98)01510-0]

PACS numbers: 43.30.Bp [DLB]

INTRODUCTION

The modeling fof acoustic fields in the ocean environment, either analytically or numerically, has been extensively developed over the years, most often in two dimensions. However, in order to achieve a complete understanding of many situations, particularly those involving horizontal refraction, it is necessary to include explicitly the third spatial dimension in the models. Numerical modeling in fully three dimensions is computationally intensive; thus analytical models, though often highly idealized representations of the ocean, are useful in providing physical insight into the 3-D environment and serving as benchmarks for developing numerical codes. With this motivation in mind, an analytical solution to a canonical problem of ocean acoustics, namely sound propagation near a hyperbolic ridge, is developed and presented in this paper.

In the ocean ridge problem it is mostly horizontal refraction which causes difficulty for numerical modeling. The refraction mechanism is characterized by rays which are bent out of the plane of incidence by multiple reflections from a bottom of varying depth profile. The numerical difficulties brought about by the horizontal bending of rays are addressed in a recent extensive review by Buckingham[1] of numerical and analytical models. A standard numerical technique is to employ a 2-D PE (parabolic equation) routine and ''march'' out the field solution in particular azimuthal directions to achieve an effective 3-D solution. This method reduces computational time by employing both this ''$N\times 2$D'' approach and the parabolic approximation to the wave equation but does not take account of rays bent in and out of the plane by refraction. Other approaches include ray tracing techniques which are relatively fast but have difficulty with diffraction and caustics, which are manifest in problems involving horizontal refraction. More promising numerical alternatives include finite element/difference models which, at present, are restricted to lower frequencies because of computational intensity. As computational power increases, these methods should prove more practical but will still require analytic solutions as benchmarks for comparison.[2]

Analytic solutions to three-dimensional ocean acoustics problems, however, are still few in number. The most extensively explored problem is that of the wedge-shaped ocean.[3–6] The theoretical work on this problem serves as one of the few true benchmark analytic solutions to a 3-D environment. The solution to another problem involving a bottom of constant slope, that of a conical seamount, has also been addressed, most notably by Buckingham,[7,8] but not explored as extensively. Some work on a cylindrical island has also been recently performed.[9] This problem does not exhibit horizontal refraction but remains a useful benchmark because it is readily extended to arbitrary sound speed profiles, which is a difficulty for other analytic models including this study.

Some more general analytical work involving ray invariants is of particular interest here both because of its more universally applicable results and because the problem of this study, the hyperbolic ridge, has received most of its attention in this arena. Harrison[10,11] has developed general descriptions of ray paths in regions of varying depth profiles. The descriptions follow from ray invariants advanced by Weston[12] based on geometrical considerations involving reflections from locally inclined planes.

Harrison examined specific depth profiles including ridgelike structures and later collaborated to perform some numerical and experimental investigations that included the hyperbolic ridge.[13] These represent the bulk of the work that has been done regarding the hyperbolic ridge, although its potential usefulness as a benchmark problem is known.[1]

An analytic solution to this problem, the acoustic field due to a harmonic point source near a hyperbolic ridge in an

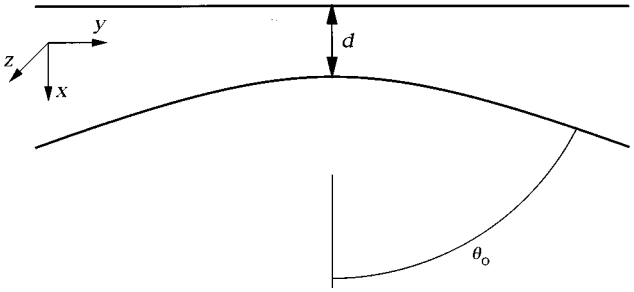

FIG. 1. Problem geometry.

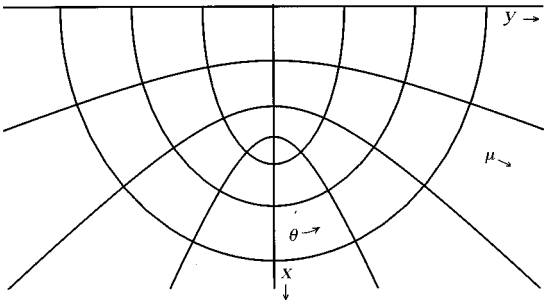

FIG. 2. Elliptical coordinate system: lines of constant μ and θ.

isovelocity ocean, is developed in this paper. Beginning by deriving the exact solution in terms of a sum over normal modes, the resulting expression, involving integrals whose solutions cannot be expressed explicitly, is approximated away from the low-frequency limit by standard asymptotic techniques. Specifically, WKB and stationary phase methods yield useful expressions for each mode, especially for the shallow slope and shallow depth conditions appropriate for the physical situation of ocean ridges and isovelocity sound speed profiles.

The resulting solution explicitly handles the aspects of horizontal refraction exhibited by this problem. The cutoff for modes propagating over the ridge and the locations of the shadow zones and caustics are provided by the theory. The solution further involves a complicated intramodal interference pattern that results from the intersection of up to three rays in a given mode; the field due to a given mode is just the sum of the contributions from each ray. This complicated intramodal interference makes this theory unique among analytic solutions to fully three-dimensional problems. The full field solution is obtained from the summation of the finite number of contributing modes. As such this paper hopes to provide a solution to a canonical problem of ocean acoustics and supply a new benchmark for useful comparison.

I. GEOMETRY AND FORMAL SOLUTION

The problem is to develop a solution to the acoustic field due to a point source near a hyperbolic ocean ridge, with perfectly reflecting boundaries on the ridge and ocean surface. The source is assumed to have a harmonic time dependence with angular frequency ω. The ocean surface is taken to be at $x=0$ with x increasing with depth. The z direction is parallel to the ridge apex and range is given by the y coordinate. Figure 1 illustrates that the ridge is characterized by two parameters, d, the depth at the apex, and θ_0, the angle from the x axis to which the ridge asymptotes.

The natural coordinate choice for this problem is the three-dimensional elliptical system; it has hyperbolas as surfaces of constant coordinate. The standard definitions are[14]

$$\begin{aligned} x&=(a/2)\cosh\,\mu\,\cos\,\theta,\\ y&=(a/2)\sinh\,\mu\,\sin\,\theta,\\ z&=z. \end{aligned} \tag{1}$$

Figure 2 shows the surfaces of constant μ and θ; z is perpendicular to the x-y plane. For this problem the boundaries are at $\theta=\pm\pi/2$, which defines the top surface, and $\theta=\pm\theta_0$, which defines the slope of the hyperbolic ridge. Notice that the depth at the apex of the ridge can be adjusted with the free parameter a, by $d=(a/2)\cos\,\theta_0$, and that for fixed depth a becomes large for the previously mentioned shallow slope condition, a fact that will prove useful in later approximation schemes.

Dirichlet boundary conditions representing an acoustically soft ridge are assumed. The extension to Neumann or mixed boundary conditions is trivial and comes into the definitions of the separated angular solutions; the modifications to the theory for an acoustically hard ridge will be noted at the relevant points. The problem then is the solution for the velocity potential ψ governed by the reduced wave equation including a point source of strength Q,

$$(\nabla^2+k^2)\psi=-4\pi Q\,\delta(\overline{r}-\overline{r'}), \tag{2}$$

with pressure release surfaces, $\psi=0$, at the boundaries. The Laplacian is denoted by ∇^2; $\delta(\ )$ is the Dirac delta function; $\overline{r}$ and $\overline{r'}$ are the receiver and source coordinates with the prime indicating the source. The wave number $k=\omega/c$, where c is the sound speed which is taken to be uniform throughout the medium. In the elliptic coordinate system the equation takes the following form:

$$\begin{aligned} &\left[\frac{4}{L^2}\left(\frac{\partial^2}{\partial\mu^2}+\frac{\partial^2}{\partial\theta^2}\right)+\frac{\partial^2}{\partial z^2}+k^2\right]\psi\\ &\quad=-4\pi Q\,\frac{4}{L^2}\,\delta(\mu-\mu')\,\delta(\theta-\theta')\,\delta(z-z'),\\ &L^2\equiv a^2(\sinh^2\,\mu\,\cos^2\,\theta+\cosh^2\,\mu\,\sin^2\,\theta). \end{aligned} \tag{3}$$

This form can be obtained by substitution of the coordinate definitions (1) into the Cartesian wave equation (2), but is more rigorously derived from a formal approach to coordinate transformations, involving the invariance of the length in different coordinate representations, found in most general texts on mathematical methods.[15,16]

Different techniques can be used to find a formal solution to ψ including integral transform methods or a standard Green function approach; the latter and its details are included in Appendix B. In any case, we rely on separation of variables which yields the separated equations:

$$\begin{aligned} &\frac{\partial^2}{\partial\theta^2}\,S(\theta)=-h^2(\tilde{\beta}_m+\sin^2\,\theta)S(\theta),\\ &\frac{\partial^2}{\partial\mu^2}\,J(\mu)=-h^2(-\tilde{\beta}_m+\sinh^2\,\mu)J(\mu), \end{aligned} \tag{4}$$

$$\left(\frac{\partial^2}{\partial z^2}+k_z^2\right)Z(z)=0,$$

where

$$h^2=\frac{a^2}{4}\,(k^2-k_z^2), \tag{5}$$

and k_z is the wave number in the z direction. As expected for the elliptical coordinate system, the first two expressions in Eq. (4) are the Mathieu's equation and the modified Mathieu's equation, respectively. The separation constants h and $\tilde{\beta}_m$ are free to vary subject to the Dirichlet constraint on the surfaces and the physical restrictions that the field be finite away from the source and no incoming waves are incident from infinity. The boundary conditions on S, that it vanish at the two pressure release surfaces, yield a discrete spectrum, indexed by m, for the eigenvalue $\tilde{\beta}_m$ for any given value of h. Because these boundary conditions are not the periodic ones, the angular and radial solutions are not the standard Mathieu functions; some care must be taken in trying to apply many of the useful relations for Mathieu functions found in the literature.[17] Further, it is important to note that there are two distinct regions of θ separated by the apex of the ridge, $\theta_0<\theta<\pi/2$ and $-\pi/2<\theta<-\theta_0$. For completeness it is necessary to define even and odd solutions:

$$\begin{aligned} S_{om}(-\theta)&=-S_{om}(\theta),\\ S_{em}(-\theta)&=-S_{em}(\theta), \end{aligned} \tag{6}$$

which are the same on the positive θ side and differ only by a minus sign on the negative θ side of the ridge. For continuity across the division between the two regions (the $\mu=0$ strip), we are restricted in our definition of the corresponding radial solutions to

$$\frac{\partial}{\partial\mu}\,J_{em}(0)=0,\quad J_{om}(0)=0, \tag{7}$$

which together with the eigenvalue $\tilde{\beta}_m$ fixes the behavior of the radial solutions; for normalization we take

$$J(\mu)\rightarrow\frac{\cos(h\,\cosh\,\mu+\varphi)}{\sqrt{h\,\cosh\,\mu}} \tag{8}$$

for large μ.

With these definitions and the details in Appendix B, the formal solution to the field due to a point source, in terms of a modal sum, is found to be:

$$\psi=\frac{16Qi}{a^2}\int_0^\infty dh\,\frac{h}{\sqrt{k^2-(4h^2/a^2)}}\sum_{m,i}\frac{S_{im}(h,\theta)S_{im}(h,\theta')}{M_m(h)}$$

$$\times J_{im}(h,\mu)J_{im}(h,\mu')e^{i\sqrt{k^2-(4h^2/a^2)}|z|}, \tag{9}$$

where

$$M_m(h)=2\int_{\theta_0}^{\pi/2}S_{im}^2(h,\theta)\,d\theta, \tag{10}$$

accommodating any normalization for S; the sum over i in the subscripts includes both even and odd solutions; and z', the z component of the source coordinates, is taken to be zero. A form approximate to Eq. (9) has recently been found by Harrison in a study involving more general depth variations including ridgelike structures,[18] but an explicit evaluation of Eq. (9) has not been performed.

II. WKB EIGENFUNCTION SOLUTIONS

To handle the integral in Eq. (9) we will use WKB techniques to approximate the Mathieu functions and stationary phase asymptotics to evaluate the resulting expression. Before proceeding it will be useful to examine the behavior of the angular and radial solutions. Writing them in a more convenient form, the differential equations are

$$\begin{aligned} \frac{\partial^2}{\partial\phi^2}\,S_{im}(\phi)&=-h^2(\beta_m-\sin^2\,\phi)S_{im}(\phi),\\ \frac{\partial^2}{\partial\mu^2}\,J_{im}(\mu)&=-h^2(-\beta_m+\cosh^2\,\mu)J_{im}(\mu), \end{aligned} \tag{11}$$

where $\phi=\pi/2-\theta$ ($\phi=-\pi/2-\theta$ for the negative y half-space) and $\beta_m=\tilde{\beta}_m+1$. In this form the Dirichlet surfaces are at $\phi=0,\pm\phi_0$—the angle ϕ_0 is between the top surface and the ridge far from the apex—and β_m is always positive. There are three regions of values for β that correspond to different behavior of S and J (subscripts dropped here and elsewhere for brevity; β, S, and J should always be understood to implicitly include the subscripts):

(1) $\beta<\sin^2\phi_0$: There is a turning point in the angular solutions; S is oscillatory for $|\phi|<\arcsin\sqrt{\beta}$ and exponentially decaying for larger ϕ. The radial solutions are pure oscillatory.
(2) $\sin^2\phi_0<\beta<1$: There are no turning points in either solution; both S and J are oscillatory.
(3) $\beta>1$: The angular solutions are oscillatory. The radial solutions are exponentially small for $\mu<\cosh^{-1}\sqrt{\beta}$ and then continue oscillatory.

It is the third domain that ensures the usefulness of the WKB approximation. For a given mode, m, and a given h there corresponds a unique eigenvalue β_m. Inverting this relationship we see that for a given β_m there is a corresponding h. Now, since the radial solutions are exponentially small for $\beta_m>\cosh^2\mu$, we can neglect larger β_m from the integral (9), which means that for a given mode there is a smallest $h=h^{\text{small}}$ which contributes to Eq. (9). A brief inspection of the angular equation (11) in the shallow slope limit, neglecting $\sin\phi$ (bearing in mind that small h implies large β_m since the number of oscillations is fixed by m), shows $h^{\text{small}}\approx m\pi/(\phi_0\,\cosh\,\mu_<)$, where $\mu_<$ is the smallest μ of the source and receiver. WKB, of course, becomes better as the large parameter h grows, making it particularly reliable at higher frequency and in the shallow slope limit. Note that we are not restricted to using WKB only in the shallow slope limit since the integrand in Eq. (9) is linear in h, negating contributions from small h, making inaccuracies in WKB for this small part of the integral negligible; only slightly greater care must be taken for larger values of ϕ_0. As will be seen later, a raylike picture corresponds to the field solution for each mode. The physical expectation that rays contribute to

the field allows contributions to the integral from small values of h to be neglected.

Before forging ahead into a WKB analysis of the angular solutions an inspection of the integral (9) will again be useful. The contribution to the integral for $h>ak/2 = kd/\sin\phi_0$ can be neglected because of the exponential term; if there is no z separation between source and receiver the highly oscillatory radial solutions will cancel this contribution, unless the receiver is at the source location in which case the integral will diverge. Now, since there is a largest h that contributes to the integral, there must be a smallest β_m for each mode. Focusing again on the shallow slope condition and Eq. (11), we can quickly make the estimate $\beta_m^{\text{small}} \approx (m\pi/h\phi_0)^2$. Note now that if $\beta_m^{\text{small}} \gg \sin^2\phi_0$ or, in terms of problem parameters, $m\pi/kd \gg \phi_0$, we can easily approximate the angular solutions as simple sine functions:

$$S_{em}(h,\theta)=S_{em}(h,\phi(\theta))\approx\sin\left(\frac{m\pi}{\phi_0}|\phi|\right),$$
$$S_{om}(h,\theta)=S_{om}(h,\phi(\theta))\approx\sin\left(\frac{m\pi}{\phi_0}\,\phi\right). \tag{12}$$

This gives the normalization $M_m(h)\approx\phi_0$. (For the ''hard'' ridge boundary conditions $m\to m-1/2$ in the argument of the sine.) Thus in the shallow slope, shallow depth limit, the modes expand and compress to adjust to slight variations in the depth of the waveguide, which yields the simple approximation. Again, we are not restricted to these limits but simplification can be achieved by assuming these physically appropriate conditions. Regardless of this approximation, the angular functions are determined essentially by m, depending only weakly on h, and are thus considered slowly varying in the subsequent stationary phase analysis of Eq. (9). For the case when Eq. (12) does not hold, the standard WKB approach detailed in Appendix C can be employed and the functions evaluated at the appropriate stationary phase point.

The radial solutions are also amenable to WKB. For $\beta_m<1$ the solutions are oscillatory everywhere and the boundary conditions at $\mu=0$ trivially determine the phase of the solution. For $\beta_m>1$ the solutions grow exponentially and then become oscillatory beyond $\mu=\mu_t\equiv\cosh^{-1}\sqrt{\beta_m}$. These solutions have the well known $-\pi/4$ phase.[19] The exponential growth is assumed to be strong enough, that is, h is taken to be large enough, that a sharp change in phase from $\beta_m<1$ to $\beta_m>1$ will occur. The WKB radial solutions then are

$$\beta_m<1 \qquad J_{em}(\mu)\approx\frac{\cos\left(h\int_0^\mu\sqrt{\cosh^2\mu-\beta_m}-\pi/2\right)}{h^{1/2}\sqrt[4]{\cosh^2\mu-\beta_m}},$$
$$J_{om}(\mu)\approx\frac{\cos\left(h\int_0^\mu\sqrt{\cosh^2\mu-\beta_m}\right)}{h^{1/2}\sqrt[4]{\cosh^2\mu-\beta_m}}, \tag{13}$$

$$\beta_m>1,\ \mu>\mu_t \qquad J_{e,om}(\mu)\approx\frac{\cos\left(h\int_{\mu_t}^\mu\sqrt{\cosh^2\mu-\beta_m}-\pi/4\right)}{h^{1/2}\sqrt[4]{\cosh^2\mu-\beta_m}}. \tag{14}$$

Again, we take $J=0$ for $\mu<\mu_t$ because of the rapid exponential behavior in this region. A more detailed development of Eqs. (13) and (14) is analogous to the angular case discussed in Appendix C and is not repeated here.

III. EVALUATION OF THE FIELD

A. Modal properties

The integral representation of the field equation (9) is well suited to a stationary phase analysis at higher frequency since the radial solutions and the exponential in z are highly oscillatory over the contributing range of h, giving significant contribution to the integral only at the stationary point. Writing Eq. (9) with a more convenient variable, it becomes:

$$\psi=4iQk\int_0^1 d\eta\sum_{m,i}\frac{S_{im}(\eta,\phi)S_{im}(\eta,\phi')}{M_m(\eta)} \times J_{im}(\eta,\mu)J_{im}(\eta,\mu')e^{i\eta k|z|}, \tag{15}$$

$$\eta=\sqrt{1-\left(\frac{2h}{ka}\right)^2}, \tag{16}$$

where the exponentially small contribution for $h>ak/2$ has been neglected. To take advantage of the WKB solutions (13) and (14) the field can again be rewritten for $\beta_m<1$ and $\beta_m>1$ as

$$\psi=\sum_m\psi_m^{\beta<1}+\psi_m^{\beta>1}, \tag{17}$$

$$\psi_m^{\beta<1}=4ikQ\int_0^{\eta_{\beta=1}}d\eta\,A_m(\eta,\phi,\phi') \times\frac{\cos[h(f(\mu,\beta)\pm f(\mu',\beta))]}{h\sqrt[4]{\cosh^2\mu-\beta}\sqrt[4]{\cosh^2\mu'-\beta}}e^{i\eta k|z|}, \tag{18}$$

$$\psi_m^{\beta>1}=8ikQ\int_{\eta_{\beta=1}}^{\eta_{\beta=\cosh^2\mu_<}}d\eta\,A_m(\eta,\phi,\phi') \times\frac{\cos[hf(\mu,\beta)-\pi/4]\cos[hf(\mu,\beta)-\pi/4]}{h\sqrt[4]{\cosh^2\mu-\beta}\sqrt[4]{\cosh^2\mu'-\beta}}e^{i\eta k|z|}, \tag{19}$$

$$A_m(\eta,\phi,\phi')=\frac{S_{em}(\eta,\phi)S_{em}(\eta,\phi')}{M_m(\eta)},$$
$$f(\mu,\beta)=\int_{0,\mu_t}^\mu\sqrt{\cosh^2\mu-\beta}\,d\mu, \tag{20}$$

where, as usual, β depends on h (or η) and m. Notice that the sum over even and odd solutions has already been found using elementary trigonometric relations. This produced the two following conditions:

(1) The $+(-)$ sign in Eq. (18) is taken for source and receiver on opposite (same) sides of the ridge.
(2) Expression (19) is only valid for source and receiver on the same side of the ridge. For source and receiver on opposite sides, $\psi_m^{\beta>1}=0$.

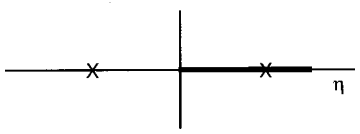

FIG. 3. Stationary phase points and path of integration.

To understand the integral limits in Eqs. (18) and (19), recall that for a given h and m there corresponds a unique β_m and that this relation can be inverted to find the h which corresponds to any β_m. Since η is a simple function of h, the limits of integration are just an expression of this eigenvalue condition. So, $\eta_{\beta=1}$ is the η which corresponds to $\beta_m=1$, and the $\eta_{\beta=\cosh^2\mu_<}$ limit explicitly halts the contribution to the integral when one of the radial solutions becomes exponentially small. It is these limits which contain some of the important physics of the problem. When the integration limit $\eta_{\beta=1}=0$ for a particular mode, there can be no propagation over the ridge. When $\eta_{\beta=\cosh^2\mu_<}=0$, the mode cannot be supported in the waveguide at this depth. Therefore, if $\mu_<$ is the source coordinate, all the energy must go into lower modes. The modal sum is, thus, in effect, always a finite sum; this, of course, is the motivation for the modal decomposition. With Eq. (16) and the eigenvalue condition derived in the Appendix, (C2), one can express the relation between η and β:

$$\eta_\beta=\sqrt{1-\left(\frac{2m\pi}{kaI}\right)^2},\quad I\equiv\int_0^{\phi_0}\sqrt{\beta-\sin^2\phi}\,d\phi, \tag{21}$$

where, for simplicity, the $\beta_m>\sin^2\phi_0$ case and Dirichlet conditions were assumed; the extension to Neumann conditions or other ranges of β_m are discussed in Appendix C. Substituting the appropriate values of β_m and using the cordinate definitions we find:

$$m\pi>kd\Rightarrow\text{no propagation over the ridge.}$$

For the shallow slope limit we also have:

$$m\pi>kd_\mu\Rightarrow\text{mode not supported,}$$

where d_μ is the depth at the source or receiver's μ coordinate.

B. Stationary phase

Focusing now on the evaluation of integrals (18) and (19), it is useful to write the cosine terms as exponentials. For Eq. (18) this gives two terms with phases:

$$(\pm)i\,\frac{ka}{2}\,\sqrt{1-\eta^2}[f(\mu_>,\beta)\pm f(\mu_<,\beta)]+ik\eta|z|.$$

Momentary consideration of these phases and their derivatives shows that only the phase with the plus (+) term yields a stationary phase point near the path of integration, as illustrated in Fig. 3. Thus Eq. (18) can be well approximated by:

$$\psi_m^{\beta<1}=\int_0^{\eta_{\beta=1}}d\eta\;D(\eta)e^{+ig_\pm(\eta,\mu,\mu')}e^{ik\eta|z|}, \tag{22}$$

$$g_\pm(\eta,\mu,\mu')\equiv\frac{ak}{2}\,\sqrt{1-\eta^2}[f(\mu_>,\beta)\pm f(\mu_<,\beta)], \tag{23}$$

$$D(\eta)\equiv\frac{2iQk}{(ak/2)\sqrt{1-\eta^2}\,\sqrt[4]{(\cosh^2\mu-\beta)(\cosh^2\mu'-\beta)}}\times\frac{S_{em}(\eta,\phi)S_{em}(\eta,\phi')}{M_m(\eta)}. \tag{24}$$

Again, the $+(-)$ sign in g is taken for source and receiver on the opposite (same) side of the ridge. Evaluating Eq. (22) at the stationary phase point and defining $g''_\pm$ as the second derivative of $g_\pm$ with respect to η, gives:

$$\psi_m^{\beta<1}=D(\eta_0)\;\sqrt{\frac{2\pi}{|g''_\pm(\eta_0)|}}\;e^{ig_\pm(\eta_0)+ik\eta_0|z|}e^{-i(\pi/4)}, \tag{25}$$

where η_0 is the solution, for $0<\eta_0<\eta_{\beta=1}$, to

$$\frac{\partial}{\partial\eta}\,g_\pm(\eta,\mu,\mu')=-k|z|. \tag{26}$$

Following the same procedure for Eq. (19), keeping only those terms with stationary phase points near the integration path, one arrives at:

$$\psi_m^{\beta>1}=\int_{\eta_{\beta=1}}^{\eta_{\beta=\cosh^2\mu_<}}d\eta\;D(\eta)[e^{+ig_-(\eta,\mu,\mu')}-ie^{+ig_+(\eta,\mu,\mu')}]e^{ik\eta|z|}, \tag{27}$$

which can be evaluated as:

$$\psi_m^{\beta>1}=D(\eta_0)\;\sqrt{\frac{2\pi}{|g''_-(\eta_0)|}}\;e^{ig_-(\eta_0)+ik\eta_0|z|}e^{-i(\pi/4)}-i\sum_{\eta_0}D(\eta_0)\;\sqrt{\frac{2\pi}{|g''_+(\eta_0)|}}\times e^{ig_+(\eta_0)+ik\eta_0|z|}e^{\mathrm{sgn}(g''_+)i(\pi/4)}, \tag{28}$$

where sgn( ) denotes the sign of the argument. The sum is over all (up to three) solutions to Eq. (26); both terms only include $\eta_{\beta=1}<\eta_0<\eta_{\beta=\cosh^2\mu_<}$.

Because the phase of the field represented by Eqs. (25) and (28) is very sensitive to g, or rather to $f(\mu,\beta)$ and η_β, approximations here are not as useful as elsewhere. Fortunately $f(\mu,\beta)$ and η_β (or I), Eqs. (20) and (21), are well behaved functions which can be exactly represented by standard elliptic functions:[20]

$$\beta<1:\quad f(\mu,\beta)=\frac{\sinh\,\mu\,\cosh\,\mu}{\sqrt{\cosh^2\,\mu-\beta}}+(1-\beta)F(\alpha,\beta^{1/2})-E(\alpha,\beta^{1/2}),\quad \alpha\equiv\arctan\left(\frac{\sinh\,\mu}{\sqrt{1-\beta}}\right)$$
$$I=E(\chi,\beta^{1/2})-(1-\beta)F(\chi,\beta^{1/2}),\quad \chi\equiv\arcsin\left(\frac{\sin\,\phi_0}{\sqrt{\beta}}\right)\underset{\sin^2\,\phi_0>\beta}{\equiv}\frac{\pi}{2}, \tag{29}$$

$$\beta>1:\quad f(\mu,\beta)=\coth\,\mu\sqrt{\cosh^2\,\mu-\beta}-\beta^{1/2}E(\gamma,\beta^{-1/2}),\quad \gamma\equiv\arccos\left(\frac{\sqrt{\beta-1}}{\sinh\,\mu}\right)$$
$$I=\beta^{1/2}E(\phi_0,\beta^{-1/2}). \tag{30}$$

Numerical routines for elliptic functions are widely available;[21,22] they can be considered ''known'' functions. Further, they have known derivatives,[23] again expressed in terms of elliptic functions, making Eqs. (25) and (28) a useful representation of the field. For the sake of brevity only the first derivatives of $f(\mu,\beta)$ and I are listed here:

$$\beta<1:\quad \frac{\partial}{\partial\beta}f(\mu,\beta)=-\frac{1}{2}F\left(\arcsin\left(\frac{\sinh\,\mu}{\sqrt{\cosh^2\,\mu-\beta}}\right),\beta^{1/2}\right)$$
$$\frac{\partial}{\partial\beta}I=\frac{1}{2}F(\chi,\beta^{1/2}), \tag{31}$$

$$\beta>1:\quad \frac{\partial}{\partial\beta}f(\mu,\beta)=-\frac{1}{2}\beta^{-1/2}F\left(\arcsin\left(\frac{\sqrt{\cosh^2\,\mu-\beta}}{\sinh\,\mu}\right),\beta^{-1/2}\right)$$
$$\frac{\partial}{\partial\beta}I=\frac{1}{2}\beta^{-1/2}F(\phi_0,\beta^{-1/2}). \tag{32}$$

Higher derivatives of g can also be expressed analytically but numerical derivatives prove more useful in ease of calculation and can be used since the field (particularly the phase) is not sensitive to small numerical errors in these higher derivatives.

It should be noted that although Eq. (26) is a transcendental equation, it is well behaved, allowing readily attainable numerical solutions. It can also be useful to parameterize the quantity of interest [e.g., field strength (25) and (28)] by η (or the β associated with it) and match it to the corresponding $kz(\eta_0)$ given explicitly by Eq. (26), so as to avoid a direct solution of the equation.

C. Eigenrays

The expression of the field given by Eqs. (25) and (28) is in terms of eigenrays corresponding to distinct values of η_0. By eigenray it is meant a horizontal ray path which is the projection of rays onto the horizontal plane, the explicit reflections on the two boundary surfaces are not indicated. These eigenrays represent upward and downward traveling wave fronts that interfere to satisfy the boundary conditions on the top and bottom of the waveguide. The easiest way to see that a particular value of η_0 defines an eigenray is to look at the z dependence of the phase of the field as expressed by Eqs. (25) and (28). For a ray we expect no change in z wave number k_z because of the translational similarity in z. The surfaces are all parallel to the z axis, which means $k_z=\eta_0 k$ is a constant.[10,12] Since η_0 is constant the corresponding β is also constant; it is a more useful defining parameter for the eigenrays. Typical plots of the eigenrays are shown in Fig. 4 for various values of β and two different mode numbers. Figure 4(a) involves a mode number low enough to allow propagation over the ridge. Note that for $\beta=1$ the eigenray propagates along the apex of the ridge and that for β slightly greater (less) than one, the eigenrays are slowly turned back (away) as they propagate along the apex. Since eigenrays corresponding to β close to unity are spread out in this way, there is no true shadow zone for lower modes. However, since the energy from this small region of β is distributed over a large space, the amplitudes are expected to be small and an effective shadow zone is recovered. Further, it is this slow turning back of eigenrays that leads to the possibility of three eigenrays intersecting at a point within a given mode. Compare this to another canonical problem that exhibits horizontal refraction, the wedge, in which intramodal interference can only result from the intersection of two eigenrays.[1] Figure 4(b) is for a mode number great enough to cut off propagation over the ridge. There is a true shadow zone beyond the caustics for this case and there is intramodal interference from only two eigenrays as in the wedge problem, which the ridge reduces to for high mode number.

D. Mode magnitude and intramodal interference

To clarify the character of the field, particularly this intramodal interference, it will be useful to examine each term in the field represented by Eqs. (25) and (28). The magnitudes of each term is shown in Figs. 5 and 6. These figures represent a typical case involving intramodal interference for receivers at a fixed μ (or y) location; the field has been normalized by $(4Q/a)A_m(\eta,\phi,\phi')$. As expected from Eq. (25), the case of source and receiver on opposite sides shows no intramodal interference. Notice, for the same side case, in the region of interference, two eigenrays have substantially higher magnitudes than the third, which corresponds to the

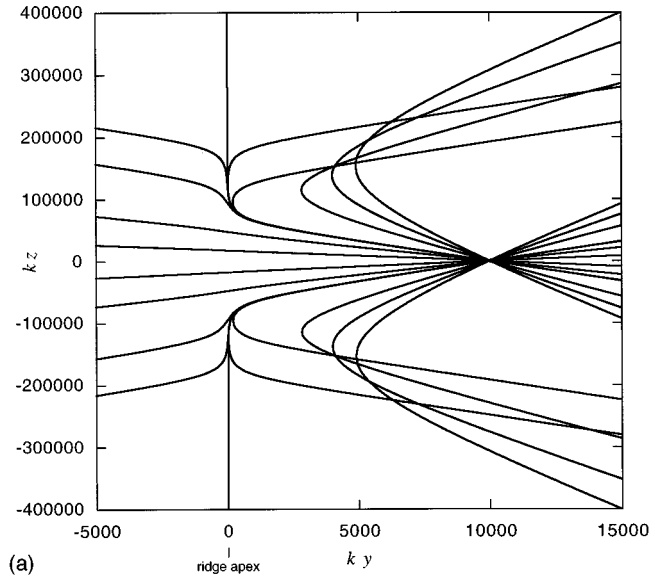

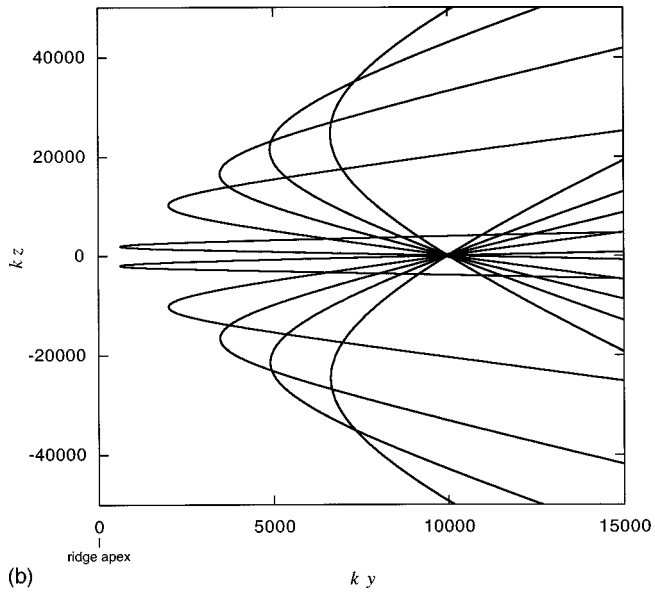

FIG. 4. (a) Eigenrays for $kd=100$, $\phi_0=0.05$, $m=5$, $ky'=10\,000$. β=0.1,0.5,0.99,0.9999,1,1.0001,1.01,3,5,7. (b) Eigenrays for $kd=100$, $\phi_0=0.05$, $m=33$, $ky'=10\,000$. β=1.1,2,4,7,12.

eigenray which has a β only slightly greater than one; this eigenray, however, as can be seen in the figure, is not in general negligible and should be considered in the approximation to the field. Also evident are two caustics, where the stationary phase evaluation of Eq. (27) fails because $g''(\eta)\approx 0$ there; this will be dealt with in the next section. Upon summation of the individual terms in Eq. (28) a complicated interference pattern due to the intersection of the three rays at any point is revealed, as shown in Figs. 7 and 8.

It is interesting to note that for this problem there are two caustics (and two more for the mirror image in the $-z$ half-space) for modes that exhibit propagation over the ridge. Between these caustics, as shown in Fig. 9, is the region of intramodal interference. Thus for $m\pi<kd$ there is no interference along the $z=0$ line and the field exhibits a nonoscillatory and predictable shape for the magnitude of the mode, as illustrated by Fig. 10.

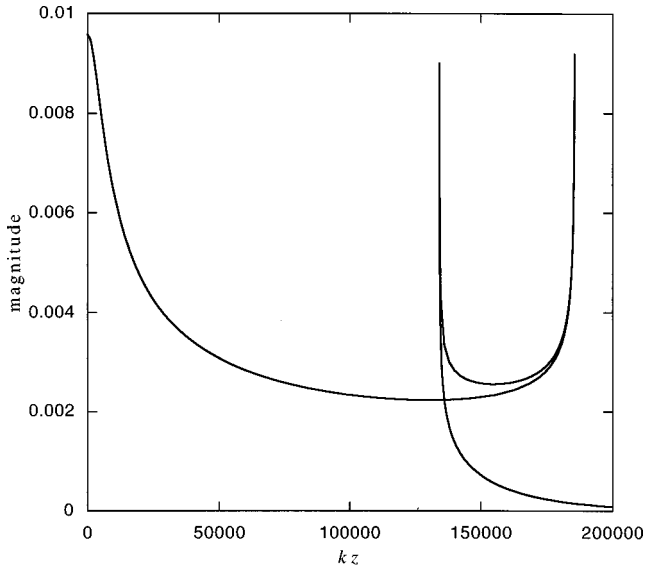

FIG. 5. Magnitude of the individual terms in the radial component of the field for $kd=100$, $\phi_0=0.05$, $m=5$, $ky=5000$, $ky'=10\,000$.

In the preceding, the only apparent failure of Eqs. (25) and (28) is at the caustics. In fact, we also expect a failure of the WKB approximation at the turning point, $\beta=\cosh^2\mu$, of the radial solutions. This is not exhibited in the figures because the expected region of failure is made so small by the very large values of h that the functions track smoothly through the offending point. This may not always be the case, particularly when a lower-frequency scale is considered. Fortunately, this problem is easily fixed by using matching formulas, which are similar to those used in Appendix C for the angular case, to approximate the radial function at the turning point and considering it slowly varying near that point for the subsequent stationary phase analysis.

E. Second order stationary phase

The failure of our approximate representation at the caustics deserves a more detailed discussion. This problem is

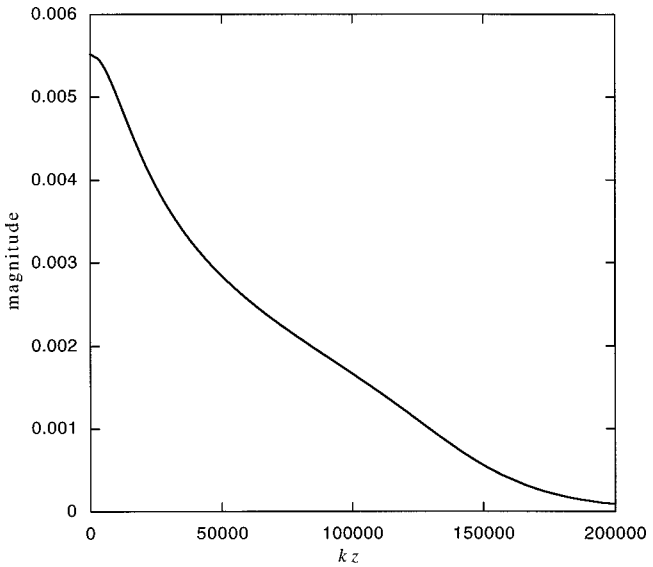

FIG. 6. Magnitude of the radial component of the field for $kd=100$, $\phi_0=0.05$, $m=5$, $ky=-5000$, $ky'=10\,000$.

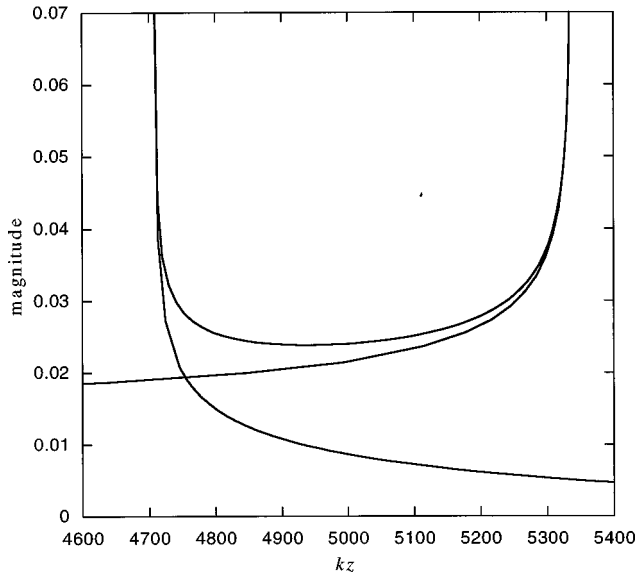

FIG. 7. Magnitude of the individual terms in the radial component of the field for $kd=20$, $\phi_0=0.05$, $m=4$, $ky=500$, $ky'=2000$.

a familiar one[3,24] and is readily treated by a second order stationary phase analysis first used by Sommerfeld. The difficulty arises from the second term in brackets in Eq. (27); two stationary points approach each other and $g''_+(\eta,\mu,\mu')\approx 0$. It is useful to separate out this part by rewriting Eq. (27):

$$\psi_m^{\beta>1}=\psi_m^c+\int_{\eta_{\beta=1}}^{\eta_{\beta=\cosh^2\mu_<}} d\eta\, D(\eta)e^{+ig_-(\eta,\mu,\mu')}e^{ik\eta|z|}, \tag{33}$$

$$\psi_m^c=-i\int_{\eta_{\beta=1}}^{\eta_{\beta=\cosh^2\mu_<}} d\eta\, D(\eta)e^{+ig_+(\eta,\mu,\mu')}e^{ik\eta|z|}. \tag{34}$$

Near the second order stationary point η_0^c, defined in Eq. (36), ψ_m^c can be evaluated by expanding $g_+(\eta,\mu,\mu')$ about

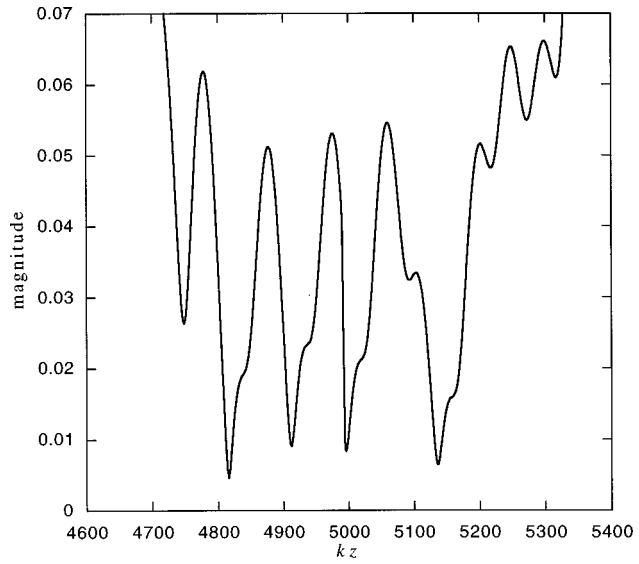

FIG. 8. Magnitude (individual terms summed) of the radial component of the field for $kd=20$, $\phi_0=0.05$, $m=4$, $ky=500$, $ky'=2000$.

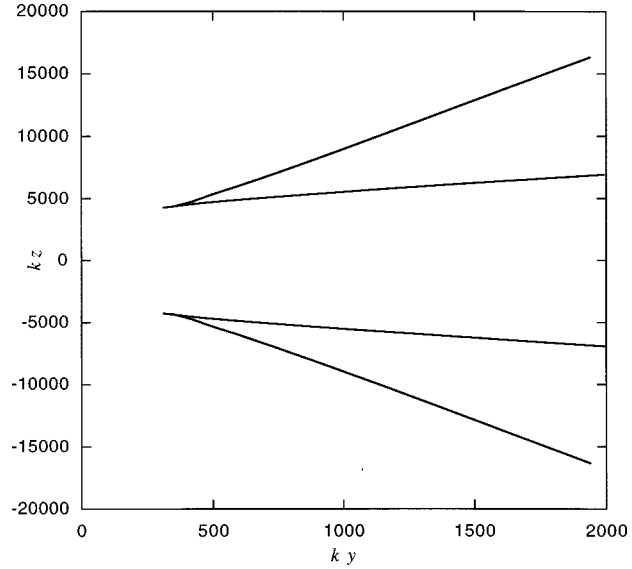

FIG. 9. Location of caustics for $kd=20$, $\phi_0=0.05$, $m=4$, $ky'=2000$.

η_0^c to third order, leaving Eq. (34) in the form of an Airy function. The details of this procedure are included in Appendix E and yield the following representation of Eq. (34) near the second order point [the integral (34) may still have another stationary point, associated with the third ray, whose contribution is obtained from Eq. (28)]:

$$\psi_m^{c,\eta_0^c}=-2i\pi D(\eta_0^c)e^{ig_+(\eta_0^c,\mu,\mu')+ik\eta_0^c|z|}\left(\frac{2}{|g'''(\eta_0^c)|}\right)^{1/3}$$
$$\times \mathrm{Ai}\left[\mathrm{sgn}(g'''(\eta_0^c))\left(\frac{2}{|g'''(\eta_0^c)|}\right)^{1/3}k(|z|-|z_0|)\right], \tag{35}$$

$$g''_+(\eta_0^c,\mu,\mu')=0, \tag{36}$$

where z_0 is the z location of the caustic. Using Eq. (35) in combination with Eq. (28) near the second order point, we have a complete representation of the given mode. Figure 11

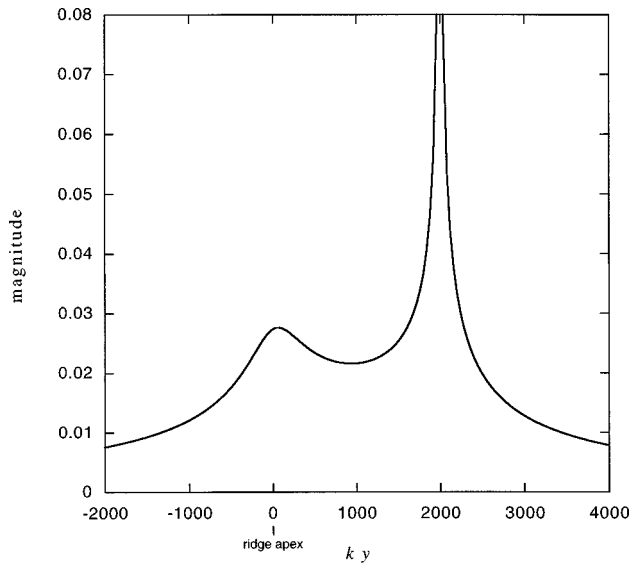

FIG. 10. Magnitude of the radial component of the field for $kd=20$, $\phi_0=0.05$, $m=4$, $ky'=2000$, $z=0$.

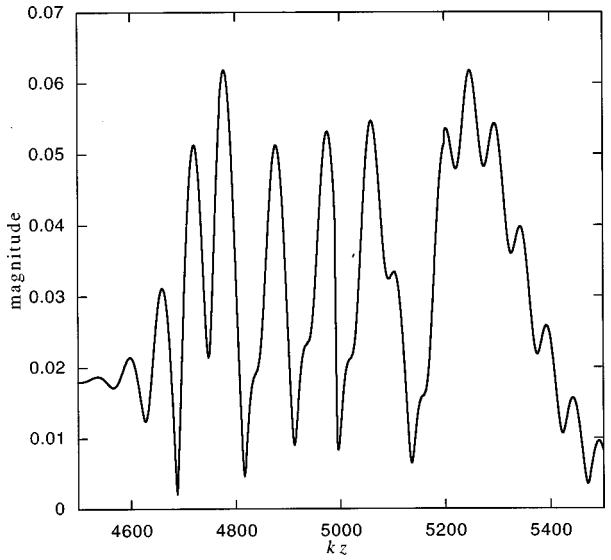

FIG. 11. Magnitude of the radial component of the field for $kd=20$, $\phi_0=0.05$, $m=4$, $ky=500$, $ky'=2000$ (failure at the caustics corrected).

is the same as the previous example in Fig. 8 except that it employs the corrected field representation near the caustics.

F. Field magnitude and intermodal interference

As previously mentioned, the full field representation is just a sum of the contributions from each of the modes. The sum is limited to those modes which can be supported in the waveguide at both the source and receiver locations. Figure 12 shows an example of the full field along the $z=0$ plane at $x=d/2$, a fixed receiver depth which is half the depth of the waveguide at the apex of the ridge. The field has been normalized by $4Q/(a\phi_0)$. Only four modes contribute here with two modes propagating over the ridge and contributions from the third and fourth modes adding as indicated. Of particular interest is the intermodal interference, the interference

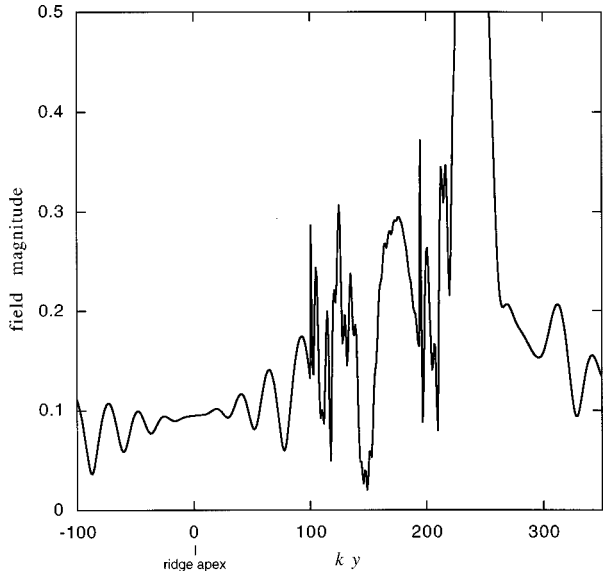

FIG. 12. Normalized field magnitude for $kd=8$, $\phi_0=0.05$, $ky'=240$, $x'=d/2$; $x=d/2$, $z=0$. Only four modes contribute significantly; modes 3 and 4 contribute only for ky greater than 100 and 194, respectively.

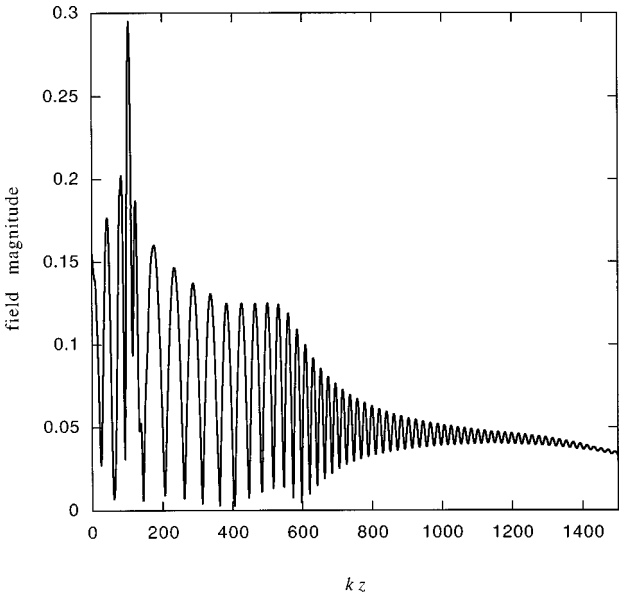

FIG. 13. Normalized field magnitude for $kd=8$, $\phi_0=0.05$, $ky'=240$, $x'=d/2$; $x=d/2$, $ky=120$. Mode 3 has a caustic at $kz=113$ beyond which only modes 1 and 2 contribute. Notice the drop off of mode 2 as its eigenvalue β_2 approaches unity. For $\beta_2=(1.1,1.01,1.001,1.0001)$, $kz=(624,857,1137,1426)$.

between different modes. Note that at the ridge apex this intermodal interference is suppressed because the second mode has a node there; the angular part of the second mode goes to zero and only the contribution from the first mode is seen. The intramodal inference can be seen as mode three and four contribute; note that it is not seen behind the source because the relative phase between the two eigenrays of a given mode is constant as both eigenrays propagate in the same direction. Figure 13 is for the same configuration but shows the variation parallel to the ridge halfway between the ridge apex and the source. Only the first three modes contribute for these receiver locations. The caustic associated with mode three is clearly visible. Beyond it, in the third mode's shadow zone, only the first two modes contribute, exhibiting the clear intermodal interference. Notice that the magnitude of mode two drops as its eigenvalue β_2 approaches unity; this is indicated in the width of the interference pattern. Although there is not a true shadow zone it can be seen that the contributions from a particular mode drop off rapidly as the only eigenrays that contribute are those that have essentially propagated along the apex of the ridge and are slowly turned back.

IV. CONCLUSION

The purpose of this study is to advance a solution to a canonical problem of three-dimensional ocean acoustics in which horizontal refraction plays an important role. A general expression, involving an integral over solutions to Mathieu's equation, is found for the acoustic field due to a harmonic point source in an isovelocity ocean over a hyperbolic ridge with perfectly reflecting boundaries. This expression is evaluated using simple WKB and asymptotic techniques, yielding a very accurate approximation to the field.

The representation is in terms of a finite modal sum involving elliptic functions and their derivatives. It can be further simplified by making assumptions appropriate to the physical situation of an ocean ridge in an isovelocity ocean, namely a gentle ridge slope and a shallow depth.

The results of the theory include a complete representation of the field providing for all the unique aspects of the horizontal refraction exhibited by this three-dimensional geometry. The mode cutoff for propagation over the ridge as well as the caustic and shadow zone locations are given by the theory. A unique aspect of this solution is that it involves a complicated intramodal interference pattern not seen in other analytic solutions to three-dimensional problems. This interference, resulting from the intersection of up to three rays in a given mode, may present an interesting challenge for numerical work in this hyperbolic geometry, making this analytical model especially useful as a comparison.

It is as a benchmark comparison, in fact, that this model is expected to be most useful. As with most analytical models, this model ignores much of the complicated components of physical environments (e.g., absorption at the boundaries, sound speed profiles, etc.) and is not easily extended to include them. Numerical models are typically more flexible, being easily generalized to cover more physical situations. They, however, can benefit greatly from benchmark verification. With this in mind, the present study is meant as the groundwork for further investigations into more realistic environments.

ACKNOWLEDGMENTS

I am indebted to Professor Michael J. Buckingham for suggesting this problem and have benefited greatly from his many constructive recommendations. This work was supported by the Office of Naval Research under Contract No. N00014-91-J-1127.

APPENDIX A: EIGENFUNCTION ORTHOGONALITY AND NORMALIZATION

Before proceeding with the derivation of Eq. (9), we need the normalization conditions for our eigenfunctions. As stated in the first section, because of the boundary conditions our eigenfunctions are not the standard Mathieu functions. Therefore a derivation of the proper orthogonality normalization is necessary.

For fixed h, Sturm–Liouville gives

$$\int d\vartheta\ S_m(h,\theta)S_n(h,\theta)=M_m(h)\,\delta_m^n. \tag{A1}$$

The integral is over all theta within the boundaries and the even/odd subscripts on S are considered implicit in m and n. This relationship, (A1), does not include $S_m(h,\theta)$ and $S_n(p,\theta)$ which are, in general, not orthogonal. Further, since the separation constant β depends on the other separation constant h, eigenfunctions S and J are not separately orthogonal. This is a standard problem of many coordinate systems including the elliptic one.[25] We continue, then, with the wave equation

$$\left[\frac{\partial^2}{\partial\mu^2}+\frac{\partial^2}{\partial\theta^2}+\frac{1}{2}\,h^2(\cosh 2\mu-\cos 2\theta)\right]\psi_{m,h}=0, \tag{A2}$$

$$\psi_{m,h}\equiv S_m(h,\theta)J_m(h,\mu), \tag{A3}$$

which, after multiplication by $\psi_{n,p}$ and subtraction of the same equation with the subscripts exchanged, yields

$$\begin{aligned}&\frac{\partial}{\partial\mu}\left[\psi_{n,p}\,\frac{\partial}{\partial\mu}\,\psi_{m,h}-\psi_{m,h}\,\frac{\partial}{\partial\mu}\,\psi_{n,p}\right]\\&\quad+\frac{\partial}{\partial\theta}\left[\psi_{n,p}\,\frac{\partial}{\partial\theta}\,\psi_{m,h}-\psi_{m,h}\,\frac{\partial}{\partial\theta}\,\psi_{n,p}\right]\\&\quad=-\tfrac{1}{2}(h^2-p^2)(\cosh 2\mu-\cos 2\theta)\psi_{m,h}\psi_{n,p}\,.\end{aligned} \tag{A4}$$

Upon integration and use of the boundary conditions, $S(\pi/2)=S(\theta_0)=0$ and $J'_{em}(0)=J_{om}(0)=0$, this becomes

$$\begin{aligned}&\frac{\int_{\theta_0}^{\pi/2}[\psi_{n,p}(\partial/\partial\mu)\psi_{m,h}-\psi_{m,h}(\partial/\partial\mu)\psi_{n,p}]_{\mu_0}d\theta}{-\frac{1}{2}(h^2-p^2)}\\&\quad=\int d\vartheta\int_0^{\mu_0}d\mu(\cosh 2\mu-\cos 2\theta)\psi_{m,h}\psi_{n,p}\,.\end{aligned} \tag{A5}$$

If we examine the LHS under an integral over p, we can arrive at the correct normalization for the double integral on the RHS. Specifically, we take the following limit

$$\begin{aligned}&\lim_{\epsilon\to 0}\lim_{\mu_0\to\infty}\int_{h_0-\epsilon}^{h_0+\epsilon}dp\\&\quad\times\frac{\int d\vartheta[\psi_{n,p}(\partial/\partial\mu)\psi_{m,h}-\psi_{m,h}(\partial/\partial\mu)\psi_{n,p}]_{\mu_0}}{-\frac{1}{2}(h^2-p^2)}.\end{aligned} \tag{A6}$$

A contribution to this integral arises only if the argument of the p integral diverges as $\epsilon\to 0$, that is, if $h=p$ to order ϵ. Thus the θ integral can be performed using Eq. (A1). Further, with definition (8) for large μ, Eq. (A6) becomes

$$\lim_{\epsilon\to 0}\lim_{\mu_0\to\infty}\int_{h_0-\epsilon}^{h_0+\epsilon}dp\ M_m(h)\,\delta_m^n\,\frac{h\,\sin(he^{\mu_0}+\varphi)\cos(pe^{\mu_0}+\varphi)-p\,\cos(he^{\mu_0}+\varphi)\sin(pe^{\mu_0}+\varphi)}{-\frac{1}{2}(h^2-p^2)\sqrt{hp}}. \tag{A7}$$

Employing simple trigonometric relations and keeping only the divergent piece of the argument, this turns into

$$\lim_{\epsilon\to 0}\lim_{\mu_0\to\infty}\int_{h_0-\epsilon}^{h_0+\epsilon} M_m(h)\,\delta_m^n\,\frac{\pi}{p}\,\frac{\sin((p-h)e^{\mu_0})}{\pi(p-h)}\,dp$$

$$=\begin{cases}(\pi/h)M_m(h)\,\delta_m^n, & |h-h_0|<\epsilon\\ 0, & |h-h_0|>\epsilon\end{cases}, \tag{A8}$$

where the equality is arrived at because this is a known integral and in fact a representation of the Dirac delta function under the integral.[26,27] This gives the desired normalization result for the RHS of Eq. (A5):

$$\int d\vartheta\int_0^\infty d\mu(\cosh 2\mu-\cos 2\theta)\psi_{m,h}\psi_{n,p}$$

$$=M_m(h)\,\delta_m^n\,\frac{\pi}{h}\,\delta(h-p). \tag{A9}$$

APPENDIX B: FORMAL SOLUTION

With the conclusion of the previous section, (A9), many standard methods can be employed to find the solution to the field. Ours begins by writing the most general form of the solution to

$$(\nabla^2+k^2)G=-4\pi\delta(\bar{r}-\bar{r}')$$

$$=-4\pi\,\frac{\delta(\mu-\mu')\,\delta(\theta-\theta')\,\delta(z-z')}{(a^2/8)(\cosh 2\mu-\cos 2\theta)}, \tag{B1}$$

the Green's function

$$G=\sum_{m,i}\int dk_z\,A_{i,m,k_z}J_{im}(h,\mu)S_{im}(h,\theta)e^{ik_z|z-z'|}, \tag{B2}$$

where h is given by Eq. (5) and the integral is over all k_z that give finite G at infinity and do not include incoming waves—all real and positive h. Next, integrate Eq. (B1) over z' from $z'-\epsilon$ to $z'+\epsilon$ and take the limit $\epsilon\to 0$, yielding

$$\sum_{m,i}\int dk_z\,A_{i,m,k_z}J_{im}(h,\mu)S_{im}(h,\theta)$$

$$=-4\pi\,\frac{\delta(\mu-\mu')\,\delta(\theta-\theta')}{(a^2/8)(\cosh 2\mu-\cos 2\theta)}. \tag{B3}$$

Multiplying both sides by $(\cosh 2\mu-\cos 2\theta)J_{im'}(h',\mu)S_{im'}(h',\theta)$, integrating over all space, and employing Eq. (A9) leaves a trivial integral involving the delta function which evaluates to the desired result

$$A_{i,m,k_z}=\frac{4iJ_{im}(h,\mu')S_{im}(h,\theta')}{M_m(h)}. \tag{B4}$$

A change of variables on Eq. (B2) completes our formal field representation

$$G=\frac{16i}{a^2}\int_0^\infty dh\,\frac{h}{\sqrt{k^2-\dfrac{4h^2}{a^2}}}\sum_{m,i}\,\frac{S_{im}(h,\theta)S_{im}(h,\theta')}{M_m(h)}$$

$$\times J_{im}(h,\mu)J_{im}(h,\mu')e^{i\sqrt{k^2-(4h^2/a^2)}|z-z'|}. \tag{B5}$$

APPENDIX C: WKB APPROXIMATION

As mentioned, we expect that for most physically interesting situations the angular solutions can be approximated by simple sine functions. For completeness, though, we can give the WKB approximation for situations where this simple approximation is not valid. For the case when there is no turning point, the oscillatory WKB approximation[28] holds everywhere:

$\beta_m>\sin^2\,\phi_0$:

$$S_{em}(h,\phi)=\frac{\cos(h\int_{|\phi|}^{\phi_0}\sqrt{\beta_m-\sin^2\,\phi}\;d\phi+\delta_\beta)}{h^{1/2}\sqrt[4]{\beta_m-\sin^2\,\phi}}. \tag{C1}$$

The boundary conditions determine the phase and the eigenvalue. Dirichlet, ''soft'' ridge, conditions dictate

$$S_{em}(h,\phi_0)=0\Rightarrow\delta_\beta=-\frac{\pi}{2},$$

$$S_{em}(h,0)=0\Rightarrow h\int_0^{\phi_0}\sqrt{\beta_m-\sin^2\,\phi}\;d\phi=m\pi. \tag{C2}$$

A ''hard'' ridge has

$$S'_{em}(h,\phi_0)=0\Rightarrow\delta_\beta=0,$$

$$S_{em}(h,0)=0\Rightarrow h\int_0^{\phi_0}\sqrt{\beta_m-\sin^2\,\phi}\;d\phi=(m-\tfrac{1}{2})\pi. \tag{C3}$$

For the case when even the above does not hold, we must approximate the function through the turning point and connect either side with the oscillatory and exponential solutions. This is a standard procedure done in many mathematical methods texts;[29–31] we repeat it here in brief for the Dirichlet case; the procedure for the ''hard'' ridge is analogous. On either side of the turning point we have:

$\beta_m<\sin^2\,\phi_0$:

$$\phi<\phi_t:\quad S_{em}(h,\phi)=\frac{\cos(h\int_{|\phi|}^{\phi_t}\sqrt{\beta_m-\sin^2\,\phi}\;d\phi+\delta_\beta)}{h^{1/2}\sqrt[4]{\beta_m-\sin^2\,\phi}},$$

$$\phi>\phi_t:\quad S_{em}(h,\phi)=C\,\frac{\exp(h\int_{|\phi|}^{\phi_0}\sqrt{\sin^2\,\phi-\beta_m}\;d\phi)-\exp(-h\int_{|\phi|}^{\phi_0}\sqrt{\sin^2\,\phi-\beta_m}\;d\phi)}{h^{1/2}\sqrt[4]{\sin^2\,\phi-\beta_m}}, \tag{C4}$$

where the form of the $\phi > \phi_t$ solution was determined by the boundary condition at ϕ_0. At the turning point our differential equation can be approximated by expanding about that point.

$$S'' = h^2 \sin(2\phi_t)(\phi - \phi_t)S, \tag{C5}$$

which has Airy functions as solutions:[32]

$$\begin{aligned}&\phi \approx \phi_t:\\ &S = A\ \mathrm{Ai}((h^2 \sin(2\phi_t))^{1/3}(\phi - \phi_t))\\ &\quad + B\ \mathrm{Bi}((h^2 \sin(2\phi_t))^{1/3}(\phi - \phi_t)).\end{aligned} \tag{C6}$$

The constants A, B, and C must be determined by boundary conditions and by matching the solutions through the turning point using the asymptotic expressions for the Airy functions;[33]

$$\mathrm{Ai}(z) \approx \frac{\exp(-\frac{2}{3}z^{3/2})}{2\pi^{1/2}z^{1/4}}, \quad \mathrm{Ai}(-z) \approx \frac{\sin(\frac{2}{3}z^{3/2} + \pi/4)}{\pi^{1/2}z^{1/4}}, \tag{C7}$$

$$\mathrm{Bi}(z) \approx \frac{\exp(\frac{2}{3}z^{3/2})}{\pi^{1/2}z^{1/4}}, \quad \mathrm{Bi}(-z) \approx \frac{\cos(\frac{2}{3}z^{3/2} + \pi/4)}{\pi^{1/2}z^{1/4}}. \tag{C8}$$

By inspection of the $z > 0$ expressions and the fact that the $S(\phi_0) = 0$, it is clear that $B \approx 0$. Connecting this onto the exponential $\phi > \phi_t$ solution, we arrive at C. Further, by matching onto the oscillatory $\phi < \phi_t$ solution, we find A and δ_β. The eigenvalue condition is again given by the $S(0) = 0$ boundary condition. The results are:

$$\begin{aligned}&A \approx \sqrt{\pi}(h^2 \sin 2\phi_t)^{1/3}, \quad B \approx 0,\\ &C \approx 2\sqrt{\pi}(h^2 \sin 2\phi_t)^{1/3}\\ &\quad \times \exp\left(-h\int_{\phi_t}^{\phi_0} \sqrt{\sin^2\phi - \beta_m}\, d\phi\right),\\ &h\int_0^{\phi_t} \sqrt{\beta_m - \sin^2\phi}\, d\phi = m\pi - \frac{\pi}{4}, \quad \delta_\beta = -\frac{\pi}{4}.\end{aligned} \tag{C9}$$

When the turning point gets very close to the boundary—$|(h^2 \sin(2\phi_t))^{1/3}(\phi_0 - \phi_t)| < 1$—the asymptotic expressions can not be used; one must employ Eq. (C6) up to ϕ_0. Boundary conditions and matching of solutions again determine the appropriate constants:

$$\begin{aligned}&A = \sqrt{\pi}(h^2 \sin 2\phi_t)^{1/3} \sin\left(\frac{\pi}{4} - \delta_\beta\right),\\ &B = \sqrt{\pi}(h^2 \sin 2\phi_t)^{1/3} \cos\left(\frac{\pi}{4} - \delta_\beta\right),\\ &\phi_t \approx \phi_0:\\ &h\int_0^{\phi_t} \sqrt{\beta_m - \sin^2\phi}\, d\phi + \delta_\beta = m\pi - \frac{\pi}{2},\\ &\delta_\beta = \arctan\left(\frac{\mathrm{Bi}((h^2 \sin(2\phi_t))^{1/3}(\phi_0 - \phi_t))}{\mathrm{Ai}((h^2 \sin(2\phi_t))^{1/3}(\phi_0 - \phi_t))}\right) - \frac{3\pi}{4}.\end{aligned} \tag{C10}$$

Note that these $\phi_t \approx \phi_0$ solutions should be used even when the turning point is just outside the boundary because Eq. (C1) fails near the turning point and is then not a valid means of determining the phase. Thus the above $\phi_t \approx \phi_0$ conditions together with Eqs. (C4) and (C6) should be used regardless of which side of the boundary the turning point is on.

It should be noted that turning points in the angular solutions arise for moderate slope and/or moderate depth conditions. For cases of extreme slope or depth the WKB solutions are still valid but the assumption that the angular solutions are slowly varying in h, which is required for the subsequent stationary phase analysis, is in jeopardy.

APPENDIX D: WKB NORMALIZATION

If the angular solutions are given by the WKB representations above, there is a nontrivial integral to perform to arrive at the normalization constant $M_m(h)$. Fortunately, one can employ a particular case of a general result of Sturm–Liouville theory to get a closed expression for the normalization. Consider the most general differential equation amenable to WKB,

$$u'' + q^2(x,\beta)u = 0, \tag{D1}$$

and two solutions whose parameters β are infinitesimally close: $u_1 \equiv u(x,\beta_1)$, $u_2 \equiv (x,\beta_2)$, $\beta_1 \approx \beta_2$. Now define a function W analogous to a Wronskian, differentiate it with respect to x, and employ Eq. (D1) to get:

$$W(x) \equiv u_1' u_2 - u_1 u_2', \tag{D2}$$

$$W' = [q^2(x,\beta_2) - q^2(x,\beta_1)]u_1 u_2. \tag{D3}$$

Expanding this to first order in $\delta\beta \equiv \beta_2 - \beta_1$, and integrating, we find an integral expression for W

$$W' = \delta\beta \frac{\partial q^2}{\partial \beta} u^2 \Rightarrow W = \delta\beta \int_{x_1}^{x} \frac{\partial q^2}{\partial \beta} u^2\, dx, \tag{D4}$$

where x_1 is a zero of u. We can also find an expression for $W(x)$ from our WKB approximation to the solutions, provided that x is in the oscillatory region of the eigenfunction. In general,

$$u = \frac{\cos(s(x,\beta))}{\sqrt{q}}, \quad u' \approx -q\frac{\sin(s(x,\beta))}{\sqrt{q}}, \tag{D5}$$

where $\partial s/\partial x = q$ defines s. In the derivative of u we have only kept terms due to the fast oscillation, an approximation that holds anytime the WKB approximation itself holds. With these expressions and a simple trigonometric relation, a simple expression for W for infinitesimal $\delta\beta$ is found.

$$W(x) \approx \left.\frac{\partial s}{\partial \beta}\right|_x \delta\beta. \tag{D6}$$

The two expressions for W, then, give

$$\left.\frac{\partial s}{\partial \beta}\right|_x = \int_{x_1}^{x} \frac{\partial q^2}{\partial \beta} u^2\, dx. \tag{D7}$$

By applying Eq. (D7) to our angular eigenfunctions and evaluating it at $\phi = 0$, which is always in the oscillatory region, we quickly get an expression for the desired normalization constant:

$$\left.\frac{\partial s}{\partial \beta}\right|_0 = h^2 \int_0^{\phi_0} S^2(h,\phi)\, d\phi = \frac{h^2}{2} M_m(h). \tag{D8}$$

Finally, notice the connection between $s(0)$ and the eigenvalue conditions of the previous section.

$$s(0)=h\int_0^{\phi_{0,t}}\sqrt{\beta-\sin^2\phi}\;d\phi+\delta_\beta=m\pi-\frac{\pi}{2}. \tag{D9}$$

As shown previously, this eigenvalue integral, defined in Eq. (21), and its derivative can be simply expressed in terms of elliptic functions. This gives the final expression for the normalization constant.

$$M_m(h)=\frac{2\pi}{h^2}\frac{\partial m}{\partial\beta}, \tag{D10}$$

where m is integral (D9).

APPENDIX E: SECOND ORDER STATIONARY PHASE

Integral (34) has a second order stationary point defined in Eq. (36) at η_0^c. Near η_0^c we can expand the argument of the exponential to third order giving the contribution to the integral near this point.

$$\psi_m^{c,\eta_0^c}=-iD(\eta_0^c)e^{ig_+(\eta_0^c,\mu,\mu')+ik\eta_0^c|z|}\times\int d\rho\; e^{i(g'_+(\eta_0^c,\mu,\mu')+k|z|)\rho+1/6g'''_+(\eta_0^c,\mu,\mu')\rho^3}. \tag{E1}$$

Because the argument of the integral becomes highly oscillatory, the limits of integration can be extended to $\pm\infty$; they were originally taken to define some region ''near'' η_0^c. The resulting integral is a representation of the Airy function,[34] giving the following approximation to Eq. (E1):

$$\psi_m^{c,\eta_0^c}=-2i\pi D(\eta_0^c)e^{ig_+(\eta,\mu,\mu')+ik\eta_0^c|z|}\left(\frac{2}{|g'''(\eta_0^c)|}\right)^{1/3}\times\mathrm{Ai}\left[\mathrm{sgn}(g'''(\eta_0^c))\left(\frac{2}{|g'''(\eta_0^c)|}\right)^{1/3}\times(g'_+(\eta_0^c,\mu,\mu')+k|z|)\right]. \tag{E2}$$

Recall that the z location of the caustic, z_0, is given by Eq. (26) and find the desired expression (35) for the contribution to the integral near the second order point.

[1] M. J. Buckingham, ''Ocean-acoustic propagation models,'' J. Acoust. **5**, 223–287 (1992).
[2] L. B. Felsen, ''Benchmarks: An option for quality assessment,'' J. Acoust. Soc. Am. **87**, 1497–1498 (1990).
[3] M. J. Buckingham, ''Theory of acoustic radiation in corners with homogeneous and mixed perfectly reflecting boundaries,'' J. Acoust. Soc. Am. **86**, 2273–2291 (1989).
[4] G. B. Deane and M. J. Buckingham, ''An analysis of the three dimensional sound field in a penetrable wedge with a stratified fluid or elastic basement,'' J. Acoust. Soc. Am. **93**, 1319–1328 (1993).
[5] S. A. Glegg and G. B. Deane, ''Experimental verification of the theory for sound propagation in a wedge with a shear supporting bottom,'' J. Acoust. Soc. Am. **92**, 2301–2302 (1992).
[6] L. S. Wang and N. G. Pace, ''Evaluations of the analytic solution for the acoustic field in an ideal wedge and the approximate solution in a penetrable wedge,'' J. Acoust. Soc. Am. **89**, 115–124 (1991).
[7] M. J. Buckingham, ''Theory of acoustic propagation around a conical seamount,'' J. Acoust. Soc. Am. **80**, 265–277 (1986).
[8] M. J. Buckingham, S. A. S. Jones, and Peter N. Harriman, ''Stationary phase evaluation of the integral for the acoustic field around a conical seamount,'' J. Acoust. Soc. Am. **80**, 278–281 (1986).
[9] G. A. Athanassoulis and A. M. Prospathopoulos, ''Three-dimensional acoustic scattering of a source-generated field from a cylindrical island,'' J. Acoust. Soc. Am. **100**, 206–218 (1996).
[10] C. H. Harrison, ''Three-dimensional ray paths in basins, troughs, and near seamouts,'' J. Acoust. Soc. Am. **62**, 1382–1388 (1977).
[11] C. H. Harrison, ''Acoustic shadow zones in the horizontal plane,'' J. Acoust. Soc. Am. **65**, 56–61 (1979).
[12] D. E. Weston, ''Horizontal refraction in a three-dimensional medium of variable stratification,'' Proc. Phys. Soc. London, Sect. A **78**, 46–52 (1959).
[13] M. A. Ainslie, L. S. Wang, C. H. Harrison, and N. G. Pace, ''Numerical and laboratory modeling of propagation over troughs and ridges,'' J. Acoust. Soc. Am. **94**, 2287–2295 (1993).
[14] P. M. Morse and H. Feshbach, *Methods of Theoretical Physics* (McGraw-Hill, New York, 1953), p. 657.
[15] G. Arfken, *Mathematical Methods for Physicists* (Academic, San Diego, 1985), pp. 86–92.
[16] P. M. Morse and H. Feshbach, *Methods of Theoretical Physics* (McGraw-Hill, New York, 1953), p. 1407.
[17] N. W. McLachlan, *Theory and Application of Mathieu Functions* (Oxford, Clarendon, 1951).
[18] C. H. Harrison, ''Wave solutions in three-dimensional ocean environments,'' J. Acoust. Soc. Am. **93**, 1826–1840 (1993).
[19] G. F. Carrier, M. Krook, and C. E. Pearson, *Functions of a Complex Variable* (Hod, Ithaca, 1983), pp. 296–297.
[20] I. S. Gradshteyn and I. M. Ryzhik, *Tables of Integrals, Series and Products* (Academic, New York, 1994), p. 326.
[21] M. Abromowitz and I. A. Stegun, *Handbook of Mathematical Functions* (Dover, New York, 1972), pp. 598–605.
[22] W. H. Press, S. A. Teukolsky, W. T. Vetterlin, and B. P. Flannery, *Numerical Recipes in C* (Cambridge U.P., Cambridge, 1992), pp. 261–269.
[23] I. S. Gradshteyn and I. M. Ryzhik, *Tables of Integrals, Series and Products* (Academic, New York, 1994), p. 301.
[24] C. L. Pekeris, ''Theory of propagation of explosive sound in shallow water,'' in *The Geological Society of America Memoir 27—Propagation of Sound in the Ocean* (Geological Society of America, New York, 1948), pp. 1–117.
[25] P. M. Morse and H. Feshbach, *Methods of Theoretical Physics* (McGraw-Hill, New York, 1953), p. 757.
[26] P. M. Morse and H. Feshbach, *Methods of Theoretical Physics* (McGraw-Hill, New York, 1953), p. 764.
[27] G. Arfken, *Mathematical Methods for Physicists* (Academic, San Diego, 1985), p. 481.
[28] G. F. Carrier, M. Krook, and C. E. Pearson, *Functions of a Complex Variable* (Hod, Ithaca, 1983), p. 293.
[29] M. Abromowitz and I. A. Stegun, *Handbook of Mathematical Functions* (Dover, New York, 1972), pp. 451–452.
[30] G. F. Carrier, M. Krook, and C. E. Pearson, *Functions of a Complex Variable* (Hod, Ithaca, 1983), pp. 295–297.
[31] P. M. Morse and H. Feshbach, *Methods of Theoretical Physics* (McGraw-Hill, New York, 1953), pp. 1096–1098.
[32] M. Abromowitz and I. A. Stegun, *Handbook of Mathematical Functions* (Dover, New York, 1972), p. 446.
[33] M. Abromowitz and I. A. Stegun, *Handbook of Mathematical Functions* (Dover, New York, 1972), pp. 448–449.
[34] M. Abromowitz and I. A. Stegun, *Handbook of Mathematical Functions* (Dover, New York, 1972), p. 447.

Very long-range source localization with a small vertical array

Kevin D. Heaney[a] and W. A. Kuperman
Marine Physical Laboratory, Scripps Institution of Oceanography, University of California, San Diego, La Jolla, California 92093

(Received 21 October 1997; revised 5 June 1998; accepted 16 June 1998)

Several processors are developed and used to perform source localization on the 3250-km San Diego–Hawaii path of the Acoustic Engineering Test (AET). Associated simulations are done to test the range-frequency limits of coherent matched-field processing using PE modeling through a simulated internal-wave environment. The AET experiment is presently well beyond the range of effective coherent matched-field processing. A mode filter was developed to extract 60 complex mode amplitudes from the data received on the 20-element vertical line array. A mode space depth estimator successfully localizes the source. A mode arrival time difference range estimator is developed and found to be biased by internal-wave induced mode coupling. The final processor developed utilizes the stability of early arriving wavefronts to determine the source range by matching wavefront arrival patterns. © *1998 Acoustical Society of America.*
[S0001-4966(98)05809-3]

PACS numbers: 43.30.Bp, 43.30.Pc, 43.30.Qd, 43.30.Re [SAC-B]

INTRODUCTION

In the past 10 years there has been a dramatic increase in interest in extremely long-range ocean acoustics.[1–5] The ability to receive transmitted sound and to determine travel times accurately to distances beyond 4000 km has been demonstrated.[6,7] Internal waves have been shown to cause significant degradation of long-range acoustic signals. The ability to passively locate an acoustic source using matched-field processing (MFP) is limited by mismatch between forward models and data. If localization is possible, limits are placed upon the extent that internal wave coupling has eliminated all source information from the signal.

Mode coupling from internal waves is expected to be larger at higher frequencies and larger propagation ranges. The range-frequency limits of coherent processing to localize a source are investigated in Sec. I. The simulation experiment by Book and Nolte,[8] at 20 Hz and a range of 1000 km, lies within the range-frequency limits expected. The AET experiment, at 75 Hz and 3250 km, is well beyond the expected limits of coherent processing. For this reason mode space and wavefront techniques are developed. Accessing the mode amplitudes with a 20-element vertical line array in deep water required a new mode filter. This filter is presented in Sec. II. A mode space method of determining the depth of the source is presented in Sec. III. In Sec. IV a range estimator is developed that uses the arrival time differences of the modes. A range estimator using the pattern of early arriving wavefronts is presented in Sec. V.

I. RANGE-FREQUENCY BOUNDS OF COHERENCE

In this section we look at the limitations internal-wave coupling places upon coherent matched-field processing.[9] In order to utilize beamforming and receive the associated array gain, the replica vectors and the signal must be partially coherent at the true source location. There have been few experiments to test the range limits of coherent matched-field processing in deep water. SLICE89, at a range of 1000 km and 250 Hz, was clearly outside of the envelope.

Two simulations were done for this calculation. The pressure field was computed every 20 km to a range of 3000 km with and without internal waves. The frequencies of 30 and 75 Hz were used. To determine the limits on coherence, the PE pressure field without internal waves will be used as the replica vector and will be compared with the data vector generated by the PE simulation with internal waves.

The coherence function is defined as

$$B(r,\omega)=\frac{|\Sigma_l p_l^*(r,\omega)d_l(r,\omega)|^2}{\sqrt{|\Sigma_l p_l(r,\omega)^2||\Sigma_l d_l(r,\omega)^2|}}, \tag{1}$$

where d_l and p_l are the PE fields with and without internal waves, respectively. It is the same as the normalized Bartlett processor. A correlation above 0.8 (or 2/10) indicates that coherent MFP is possible, depending upon the SNR.

Results for the correlation between range-independent and internal wave simulations for 30 and 75 Hz are shown in Fig. 1. The severe dependence upon frequency is clear. For each frequency five realizations of internal waves are shown. At 30 Hz, the correlation drops linearly with range. At 75 Hz, however, the correlation drops to below 0.8 within 500 km. The conclusion for this brief study is that without environmentally tolerant methods, coherent matched-field processing can be done at a range of 3000 km at 30 Hz and 500 km maximum range at 75 Hz.

II. ACOUSTIC ENGINEERING TEST (AET)

As a preliminary test of the Acoustic Thermometry of the Ocean Climate (ATOC) project source and receiver arrays the Acoustic Engineering Test was conducted in November 1994.[4] The 75-Hz source was suspended near the

[a]Present address: Science Applications International Corporation, 10260 Campus Point Dr. C-4A, San Diego, CA 92121. Electronic mail: heaney@trg.saic.com

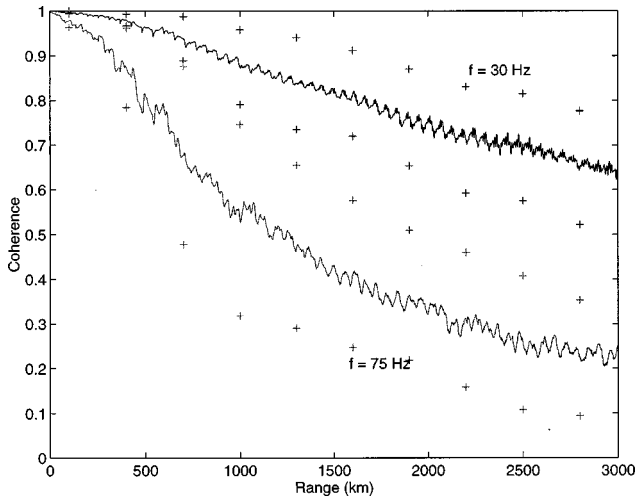

FIG. 1. Coherence of PE simulations through a range-independent profile and internal waves at 28 and 75 Hz. The standard deviations (+) are plotted around the means. The results of 20 simulations are plotted. This result indicates coherent MFP should be possible at a range of 3000 and 500 km for 28 and 75 Hz, respectively.

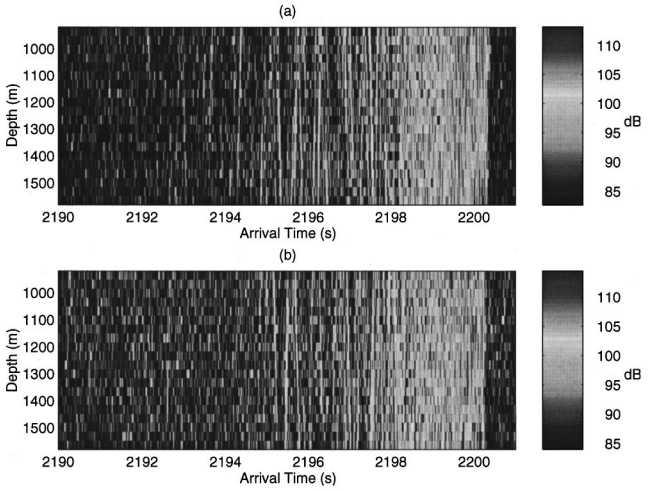

FIG. 2. Two consecutive AET receptions from the Hawaii vertical line array. The SOFAR crescendo is visible. Early arriving wavefronts are visible in both receptions.

sound channel axis off the coast of Southern California. Signals were transmitted for 7 days and received on a variety of receivers from the Aleutians to New Zealand. In this section we will outline the arrays which collected the data of interest for this paper, and present a few of the results.

The source was suspended at 650-m depth, near the sound channel axis. Receptions were recorded at two autonomous vertical line arrays (AVLA) receivers, one 75 km from the source, the other was east of Hawaii. All of the data used in this work are taken from the Hawaii AVLA. The range along a refracted geodesic was 3 252 382 m (WGS-84). Data was also successfully received at bottom mounted U.S. Navy Sound Surveilance System (SOSUS) hydrophones around the North Pacific and a single sonobouy deployed near the sound channel off the coast of New Zealand.

The vertical line arrays consist of 20 elements deployed from 935 to 1600 m. The element spacing was 35 m (1.75 wavelengths at the center frequency of 75 Hz). With the sound channel at 650 m this array aperture is poorly optimized for mode filtering. For this reason the tomography done in the paper by Worcester *et al.*[4] made use of only the axial cutoff time and the early arriving wavefronts.

Figure 2 is a plot of two consecutive AET receptions at the Hawaii AVLA. Plotted in a time/depth format the early arriving wavefronts ($t \sim 2190-2198$ s) are visible as well as the late arriving energy ($t \sim 1298-2201$ s) near the axis. There is significant breakup and spreading in the final 3 s of the arrival. The early arriving wavefronts are visible but there is significant fading across the wavefront and the doublet structure seen in simulations is barely visible. These two transmissions are 4 h apart in time. This is an indication that 4 h is beyond the coherence time of the ocean. In fact, Worcester *et al.*[4] found that the time coherence of the signal was on the order of 13 min.

In Fig. 3 two more receptions for the AET are shown. Figure 3(a) is another reception with the source at 650-m depth. This is the reception with the highest signal-to-noise ratio (33 dB). In Fig. 3(b), the reception with the shallow source (150 m) is shown. The change in arrival structure is visible. The depth estimator, developed in Sec. V, will use this change in relative energy between early and late arriving energy to localize the source.

In order to do tomography or source localization, identifiable information must be extracted from the received signal. The tomography inversion used the information from the arrival time and angle of the early arriving wavefronts. The final cutoff ($t \sim 2201$ s) was measured by stacking the received signals across phones. This was considered the mode 1 arrival in the tomographic inversion. The final 3 s of data were unusable in the analysis because of the lack of identifiable structure in a reception. With the SOFAR crescendo of a near axis source, this previously unusable portion of the reception contains a significant portion of the energy transmitted.

The late arriving energy, corresponding to the arrival of modes 1–30, contains information about the ocean structure from 300 to 1400 m. It also possibly contains enough infor-

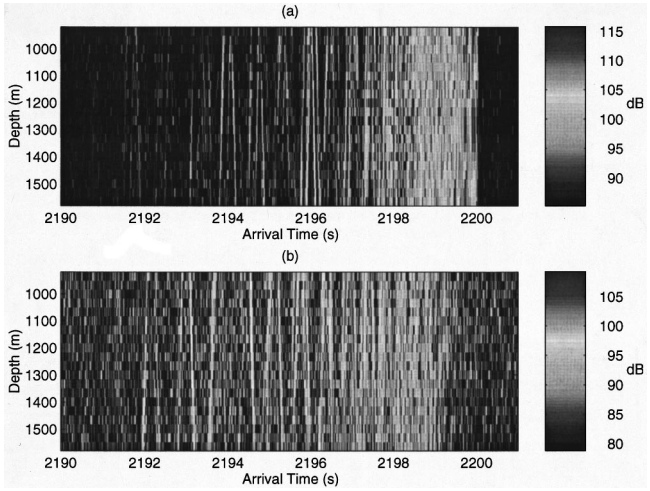

FIG. 3. AET receptions for the (a) deep source, $z = 650$ m, and (b) shallow source, $z = 150$ m. The excitation of higher modes from the shallow source is visible as a relative increase in the energy of early arriving wavefronts to the axial arrival.

mation to localize the source. With rays being unidentifiable in this region, the only choice for extracting useful information is to decompose to mode space.

The short array limits the abilities of the array to extract information from the modes. With 100 propagating modes in the water column arriving at each frequency, least-squares mode filtering is seriously underdetermined with only 20 elements in the array. This problem led to development of the Time-Windowed Mode Filter.

III. MODE FILTERING OF VERTICAL LINE ARRAY DATA

Several methods for extracting the complex mode amplitudes from the pressure field measured on a vertical array element will now be presented. The important characteristics of the array are the number of elements (N), the array spacing, and the array length. The number of propagating modes (M) is important in mode filtering and is a function of the frequency, water depth, and sound-speed structure. In many shallow-water experiments, like Swellex3[10,11] the number of receivers is much greater than the number of modes, i.e., $N \gg M$. In deep water, the opposite is generally the case. For the ATOC95 frequency band of 60–90 Hz, there are roughly 80–120 propagating modes in deep water.

A. Perfect mode filter

An array is considered perfect if its elements are densely spaced (relative to the acoustic wavelength) and extend from the surface to the bottom. The aperture of the array is such that the projection integral is well approximated by a sum over the elements:

$$b_n(\omega) = \int \frac{\varphi_n(z,\omega) p(z,\omega)}{\rho(z)}\, dz \cong \Delta z \sum_{i=1}^{N} \frac{\varphi_n(z_i,\omega) p(z_i,\omega)}{\rho(z_i)}, \tag{2}$$

where $\varphi_n(z,\omega)$ is the nth mode function at depth z and frequency ω, $p(z,\omega)$ is the pressure field recorded at the sensors, ρ is the density, and b_n is the correct amplitude of the nth mode.

B. Least-squares (LS) mode filter

A standard method of extracting modes from an array is the method of least-squares. Before deriving the solution, we will introduce the matrix notation used. The mode receiver matrix is defined as:

$$U = \begin{pmatrix} \varphi_1(z_1) & \cdots & \varphi_M(z_1) \\ \vdots & \ddots & \\ \varphi_1(z_N) & & \varphi_M(z_N) \end{pmatrix}, \tag{3}$$

where $U_{mn} = \varphi_m(z_n)$ is the mth mode function at the nth receiver. The pressure field at each depth can be written as the multiplication of the receiver matrix with the mode amplitude vector $\mathbf{b}(\omega)$:

$$p = Ub. \tag{4}$$

The least-squares solution in this notation is

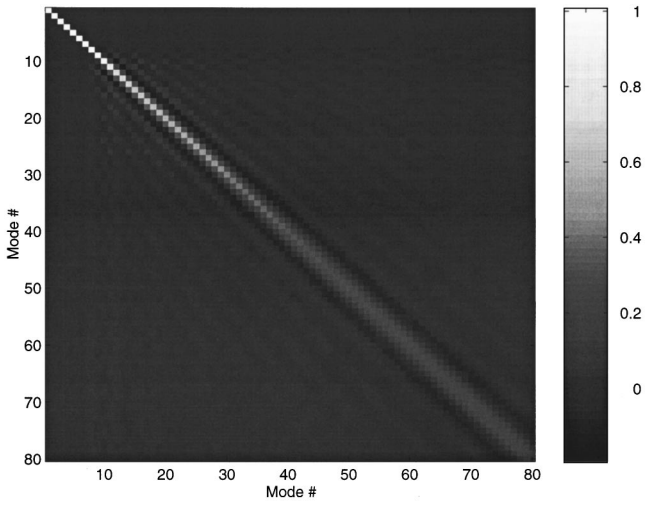

FIG. 4. Hawaii receiver array mode resolution matrix ($U'U$). The orthogonality of modes 1–10 is demonstrated by the unit diagonal matrix. The sidelobes for the higher modes are indications of the breakdown of the orthonormality of the modes, sampled across the array.

$$\hat{b} = (U'U)^{-1}U'p = (U'U)^{-1}U'Ub, \tag{5}$$

where the pseudoinverse must be used if the array is not fully spanning and the $U'U$ matrix is not full rank. The matrix $U'U$ is the projection of the modes with themselves. Each element corresponds to the summation of two modes across the array. In particular for the mnth element:

$$(U'U)_{mn} = \sum_i \varphi_m(z_i)\varphi_n(z_i). \tag{6}$$

This is the orthogonality condition expressed across the array. A plot of this matrix for the AET array is shown in Fig. 4. The array resolves the first eight modes well. If the array is perfect, the mode correlation matrix is the identity matrix. For this case the estimated mode amplitudes are equal to the true mode amplitudes.

C. Time-Windowed Mode Filter (TWMF)

For the AET experiment a processing algorithm was sought that could extract the mode information accurately for more than 15 modes. To overcome the problem of being underdetermined, either the number of phones must be increased or the number of modes must be reduced. The latter approach leads to the Time-Windowed Mode Filter (TWMF). Mode extraction for tomography purposes is possible with a single hydrophone in certain environments.[12] The relevant issue is the ratio of intermodal and intramodal dispersion of the profile. As discussed by Brown,[12] a single element would be able to determine the arrivals of modes 1–4 ($t \sim 2196$–2197 s) in this example.

The dispersion characteristics of the Central Pacific profile are shown in Fig. 5. The profile is for the range averaged climatology for the AET path and has a deep sound channel at 800 m. This dispersion curve presents the arrival times of each mode as a function of frequency at a range of 3250 km. The modes do overlap their arrivals, but at any particular time only 5–10 modes are arriving at the array. If the data is windowed in the time domain, then the filtered data will

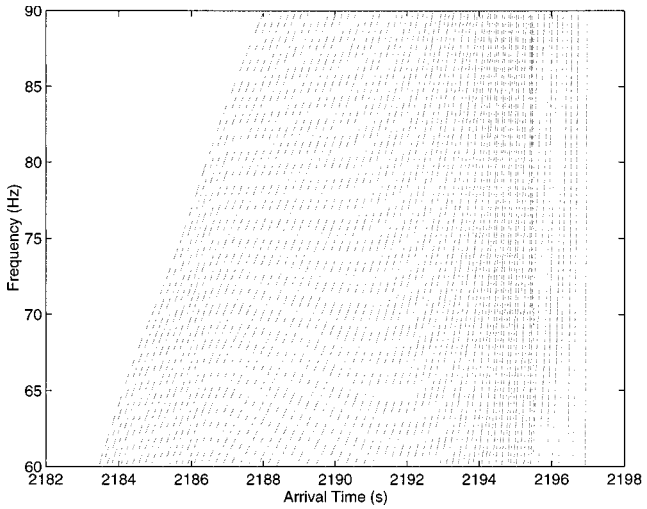

FIG. 5. Mode dispersion curves for the AET profile. Arrival times of modes 1–60 are plotted as a function of frequency. For the low modes there can be from 1 to 5 modes arriving at a particular time. For the higher modes, as many as 20 modes arrive at the same time.

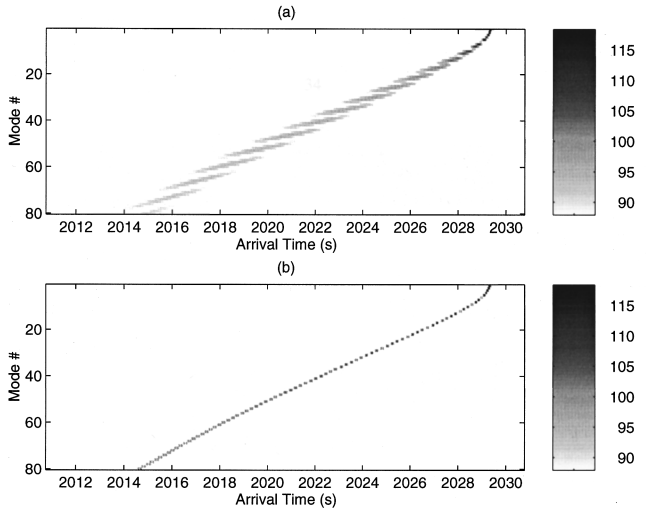

FIG. 6. Illustration of mode filtering technique. (a) Adiabatic 3000-km mode arrival on a perfect array. (b) Same array results with dispersion removed from each mode.

contain only a subset of modes. The dispersive properties of the ocean waveguide will be used to separate the modes and make the filtering problem well determined (i.e., make $M \sim N$).

Before processing the data, the modes at the receiver, as well as the range integrated adiabatic mode wave numbers must be calculated. The first step of processing involves removing the estimated dispersion from the pulse. This is done one mode at a time. If the propagation is adiabatic, this will collapse the received energy from the chosen mode (m) into a delta function. The dispersion removal process is

$$\hat{p}(t,z) = \mathfrak{I}[e^{-i\Delta k_m r}\mathfrak{I}^{-1}\{p(t,z)\}], \tag{7}$$

where $p(t,z)$ is the received pressure time series, and $\mathfrak{I}$ and $\mathfrak{I}^{-1}$ are the FFT and inverse-FFT, respectively. The dispersion for mode m is calculated by

$$\Delta k_m(\omega) = \overline{k}_m(\omega) - \overline{k}_m(\omega_0) - \frac{(\omega-\omega_0)}{\nu_{gm}}, \tag{8}$$

where $\overline{k}_m(\omega_0)$ is the unperturbed (by internal waves) wave number of the mth mode at the center frequency and ν_{gm} is the group velocity of the mth mode. Thus the dispersion is the second-order term in the Taylor expansion of the integrated wave number. The group velocities are calculated from the difference of the range integrated adiabatic mode wave numbers.

Once the dispersion is removed, the data is time-windowed around the predicted arrival time of the mth mode, t_m. The window chosen for filtering was a 4-s Tukey window[13] with a flat unit gain for 3 s. The width of the window was chosen to effectively reduce the number of arriving modes to 20. The windowed frequency domain pressure field is therefore

$$\hat{p}_m(z,\omega) = \int h(t-t_m)\hat{p}_m(z,t)e^{-i\omega t}\,dt. \tag{9}$$

The mode amplitude estimates of the replica are determined by using a 40×40 matrix $\hat{U}'\hat{U}$ centered on mode m. The filtered amplitude for the mth mode is the mth element of

$$\hat{b}_m = (\hat{U}'\hat{U})^{-1}\hat{U}'\hat{p}_m. \tag{10}$$

The filtering process is repeated for each mode and each frequency. Once the entire frequency band is processed Fourier synthesizing the complex mode amplitudes calculates the mode arrivals:

$$\hat{b}_m(t) = \int \hat{b}_m(\omega)e^{-i\omega t}\,dt. \tag{11}$$

This arrival of modal energy is used as the input data for many of the time-domain mode processors developed later in this thesis. Figure 6 is an illustration of the effects of the dispersion removal and the mode filter. The perfect array (1000 element) mode receptions are plotted in Fig. 6(a). In Fig. 6(b) the mode arrivals with the dispersion removed is plotted.

IV. MODE SPACE DEPTH ESTIMATOR

In this section the mode space method for determining the source depth of a passively received acoustic signal is derived. The *a priori* knowledge necessary for this processor is the sound-speed profile at the source and receiver, and the mode amplitudes of the received data at each frequency. If the profile at the source range is not known, it can be estimated and there will be an associated error due to environmental mismatch. The magnitude of the depth bias because of uncertainty in the ocean environment will depend upon the sensitivity of the mode excitation spectra to the ocean environmental uncertainty.

If the acoustic propagation is adiabatic, then the received mode amplitudes will be proportional to the modal excitation at the source. If the mode functions at the source location are known, the source depth can then be determined. The effectiveness of this processor is an important indication of the amount of energy transfer between modes. If internal-wave induced mode coupling has completely erased the source location (depth) information, and the received mode spectrum

is white[14–16] then the depth estimator will not work. If internal-wave scattering, which is certainly not adiabatic, is a diffusive process and does not have time (or range) to evolve to equipartition, then there will be source depth information in the signal, and a depth estimation should be possible.

This method was first introduced by Shang,[17,18] and later implemented and applied to experiments by Yang.[19,20] Based upon the properties of normal modes a single frequency (cw) beamformer will be derived. The corrections required because of imperfect array sampling of the normal modes will be applied.

A. Derivation of beamformer

Decomposing the received signal into normal modes is effective and natural because normal modes form a basis set of the depth separated part of the acoustic wave equation. From Sturm–Liuoville theory,[21] a basis set of functions will be orthonormal:

$$\int \frac{\varphi_n(z)\varphi_m(z)}{\rho(z)}\,dz=\delta_{m,n} \tag{12}$$

and complete:

$$\frac{\Sigma_n\varphi_n(z)\varphi_n(z_s)}{\rho(z_s)}\approx\delta(z-z_s), \tag{13}$$

where $\varphi_n(z)$ is the nth mode function at depth z. If the propagation is adiabatic, the received pressure field at a depth z will be:

$$P_{\text{adiabatic}}(\omega,z)=A\sum_n \frac{\varphi_n(z,\omega)\varphi_n(z_s,\omega)}{\sqrt{k_n(\omega)}}\,e^{ik_nr}, \tag{14}$$

where A is a complex constant which is a function of source excitation and inversely proportional to the square root of the range. The received experimental pressure field can be written as a complex modal sum:

$$P(\omega,z)=A\sum_n b_n(\omega)\varphi_n(z,\omega). \tag{15}$$

If the mode filtering is perfect (dense, fully spanning array) and the propagation is adiabatic, the identification of $b_n(\omega)$ can easily be made:

$$b_n(\omega)=\frac{\varphi_n(z_s,\omega)}{\sqrt{k_n(\omega)}}\,e^{ik_nr}. \tag{16}$$

Following the derivation of Yang,[19] we seek a beamformer of the form:

$$D\approx\frac{\Sigma_n\delta_n|b_n|}{\rho}. \tag{17}$$

Comparison of Eqs. (16) and (13) reveals that the correct normalization for the depth estimator will be

$$D(z,\omega)=\left(\frac{\Sigma_n|b_n||\varphi_n(z)|\sqrt{k_n}}{\rho(z)}\right)^2. \tag{18}$$

This function generates a beamformer output as a function of depth for each frequency.

The beamformer of Eq. (18) has been derived with the assumption that the array spans the water column and that there is no error in the mode filter. The orthogonality relation of Eq. (12) breaks down because of the reduced aperture of the array. In particular, integrating across the array:

$$B_n=\int \frac{|\varphi_n(z)|^2}{\rho(z)}\,dz=\Delta z\sum_i \frac{|\varphi_n(z_i)|^2}{\rho(z_i)}\neq 1. \tag{19}$$

In addition to the lack of normalization across the array, when the modal sum used in each of the beamformers is incomplete because of the lack of information of high mode numbers, the completeness relation of Eq. (13) breaks down as well. With this relation broken down, the beamformer replicas have different norms at different depths. The cw replica vector of Eq. (18) will be normalized so that it has unit norm. Thus with a perfect match, the beamformer output will be the power in the modal amplitudes. The normalization is

$$n(z)=\left(\sum_n k_n\varphi_n(z)^2\right)^2. \tag{20}$$

Applying the corrections to the lack of completeness and normalization as normalization constants the depth estimator beamformer is

$$D(z,\omega)=\frac{(\Sigma_n|b_n(\omega)/\sqrt{B_n}||\varphi_n(z,\omega)|\sqrt{k_n})^2}{(\Sigma_n k_n\varphi_n(z,\omega)^2)^2}. \tag{21}$$

For further benchmarking of the normalization calculations, see Heaney.[22]

B. Experimental results

Now we will apply the depth estimator to the AET experiment data set. Here there are several options of mode filters, and several receptions of interest. The mode filters of interest are the time-windowed (TW) mode filter with 60 modes, the least-squares mode filter with 40 modes and the least-squares mode filter with 80 modes. The three data sets of interest are the first one with a source depth of 650 m, one with a source depth of 150 m, and one when the source was off. For all the data there are 819 frequency samples that are summed in bins of 11 frequencies. This gives 74 frequency bins for averaging.

Before showing individual depth estimate results, the received modal energy for the two receptions of interest are presented. These are shown in Fig. 7. Figure 7 is the time-domain integral of the mode energy for the deep-water source. The lack of energy in mode 1 is due to the array being located below the sound channel. There is significantly more energy in the lower modes than in the higher modes. This is the information that the depth estimator keys in on to give a sound channel localization in depth. Figure 7(b) shows the received modal energy for the shallow source. The mode energy structure is significantly different than for the deep source. There is less energy and it is spread out more evenly amongst the modes.

The TWMF results will be presented because they consistently yielded answers with smaller standard deviations have those of the other estimators. Figure 8(a) is a plot of the

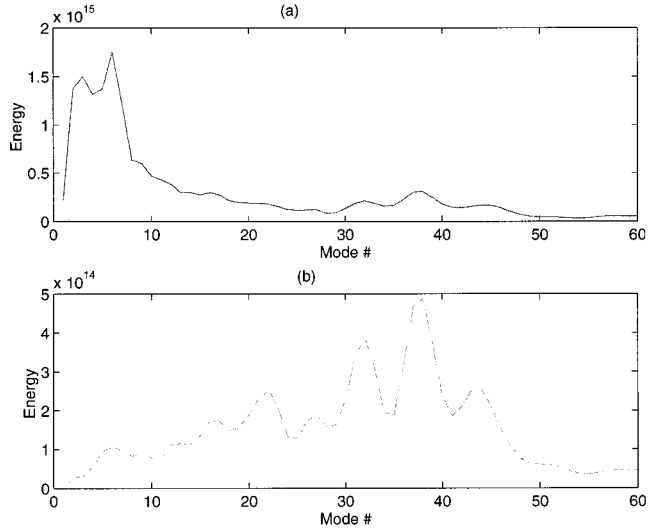

FIG. 7. Received mode spectra of the AET data for the source depth of 650 m (a) and 150 m (b).

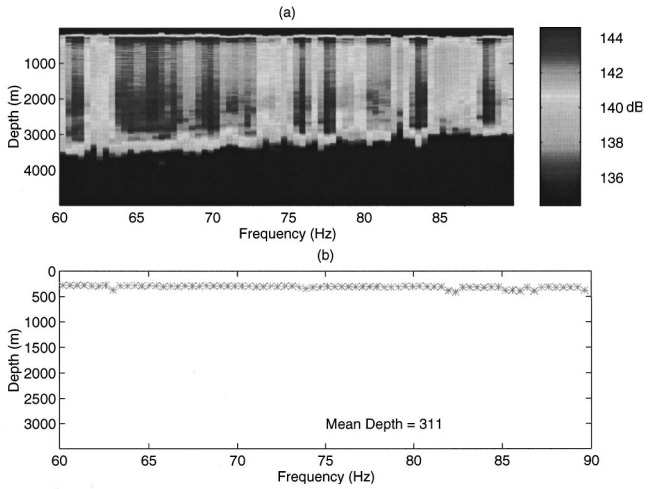

FIG. 9. Mode space depth estimator results for the shallow source. The depth estimator is stable across frequency. The mean estimate is 311 m with a 29-m standard deviation. The true source depth was 150 m.

beamformer power as a function of depth and frequency. It shows frequency patchiness indicative of the data, and reveals peaks for most frequencies around the sound channel. Figure 8(b) is a plot of the individual frequency depth estimates and they are scattered around a mean depth of 683 m. The standard deviation of the depth estimates is 115 m. This constitutes a correct depth localization, although with the large uncertainty it can only be said the source is near the sound channel axis.

The results for the shallow source are shown in the following figure. There is a significant peak near the surface. There is a strong sidelobe at 2800 m, which is the reciprocal depth. The individual frequency bin results shown in Fig. 9 show a stable localization with a mean of 311 m. The standard deviation of the depth estimate is 29 m. Although off of the true source depth (150 m), the beamformer clearly identifies the source as shallow as opposed to near the channel axis. The error is a result of an inadequate number of modes used for the localization. The peak of the ambiguity surface is at the shallowest point where there is any information in the mode replicas. If 80 to 100 modes could have been sampled by a longer array, the depth would have been correctly determined.

The final data set from the AET that the depth estimator was applied to was a reception when the source was not on. This reception serves as a measurement of ambient noise. The results of the cw depth estimator are shown in Fig. 10. The beamformer energy is scattered between 300 and 2800 m. As before, this is due to the reduced number of modes in the filter. The individual frequency peaks are scattered with a mean of 443 m and a standard deviation of 198 m. This large standard deviation, as well as the low power in the beamformer (128 dB), are indications that the depth estimator works well when the signal is present. The result that the ambient noise estimate for the source depth is not shallow is

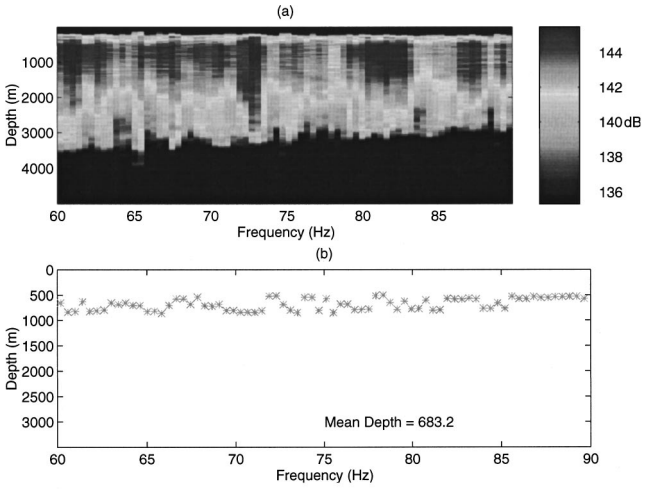

FIG. 8. Mode space depth estimator results for the AET deep-water source. The frequency/depth dependence of the beamformer output is plotted in (a). The localization to the sound channel is visible. In (b) the depth of maximum power is plotted for each frequency bin. The mean of the depth estimates is 683 m with a 115-m standard deviation. The true depth was 650 m.

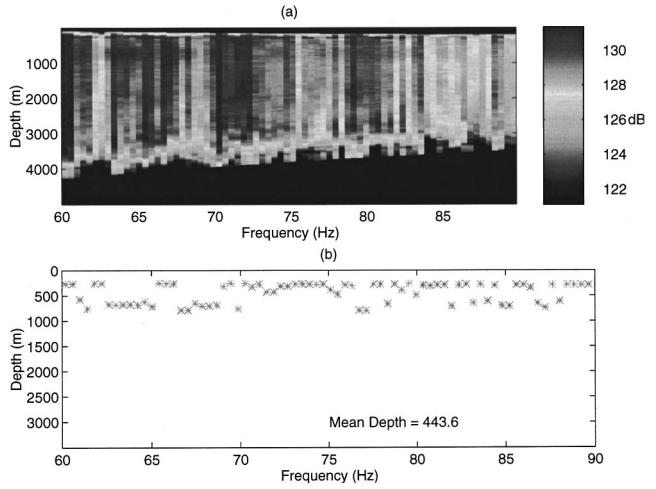

FIG. 10. Mode space depth estimates on an ambient noise measurement. The maximum power is 132 dB which is 12 dB lower than when the signal was present. The mean estimate is 444 m with a 198-m standard deviation.

an indication of the filling in of the noise notch in vertical directionality.

The ability to differentiate between near surface sources and deep-water sources indicates that the TWMF is separating mode energies effectively and that the internal-wave scattering has not whitened the mode spectra at 3250 km. The nonequipartition of mode energies implies either that we are not yet at equilibrium from random scattering, or that the equilibrium spectra are not white. We believe both to be true. Another method for mode-space source localization is to apply matched mode processing only to those modes, which are insensitive to internal wave fluctuations. A maximum-likelihood beamformer was developed by Tabrikian *et al.*[23] which only uses the statistically reliable mode information. With the lower-order modes more sensitive to internal wave coupling, this would involve only using the information from the higher modes. With a limited array size, this mode information is difficult to attain.

V. MODE DELAY RANGE ESTIMATION (MDRE)

The depth estimator results have demonstrated that there is source location information in the energy distribution of the modes. For an adiabatic environment, the depth information is in the received mode amplitudes, and the range information is in the relative phase of the individual modes. If the mode scattering is low, and coherent processing possible, the phase difference of the received modes can be used as an estimator of the range. The low correlation found in Sec. I indicates that the individual modal phases are perturbed by internal wave scattering, rendering coherent processing ineffective. In this section an incoherent method using the mode arrival times is implemented. The dispersive characteristics of the ocean profile are used to estimate the range of the source.

A. Inversion method

For a perfect mode filter the coherent modal range estimator proposed by Yang[19] is

$$R(r)=\left|\sum_n e^{ik_n r}\frac{b_n}{|b_n|}\right|^2\approx\left|\sum_n e^{ik_n(r-r_s)}\right|^2\approx\delta(r-r_s), \tag{22}$$

where b_n is the complex mode amplitude from Eq. (16).

It has been shown that internal-wave coupling is significant, and the coherent MFP was tried and found to be unsuccessful at 3500 km. The phase information of the mode is contained in the arrival times of the modal energy. For an adiabatic environment, mode group arrival times could be used. This is what is done in proposals of modal tomography.[24–26] In the presence of internal waves, this becomes more complicated. Individual peaks are not stable and there are many to choose from, so the definition of a mode arrival becomes ambiguous. To approach this problem, the first-order moment of the received mode energy (the centroid) is used as the statistic of mode arrival. The centroid is defined as

$$T_n=\frac{\int t|b_n|^2\,dt}{\int|b_n|^2\,dt}. \tag{23}$$

The uncertainty in this measurement will be a statistical quantity of great interest. It is the second moment of the received mode arrival and is the spread:

$$\sigma_n=\sqrt{\frac{\int(t-T_n)^2|b_n|^2\,dt}{\int|b_n|^2\,dt}}. \tag{24}$$

With the statistics of interest calculated from the data (T and σ) the range inversion algorithm is now presented. The relative arrival time inversion solves the following equation:

$$(T_0+\delta_n)=SR+\text{uncertainty}, \tag{25}$$

where δ_n is the relative mode arrival time, R is the source range,

$$S=\begin{bmatrix}1/\nu_{g1}\\ \vdots\\ 1/\nu_{gN}\end{bmatrix}\quad\text{and}\quad\Sigma=\begin{bmatrix}\sigma_1^{-2} & & 0\\ & \ddots & \\ 0 & & \sigma_N^{-2}\end{bmatrix} \tag{26}$$

is the group slowness vector and spread diagonal matrix, respectively. Since the reference time T_0 is not known, this is a linear equation with two unknowns (T_0 and R) and is easily solved using the method of least-squares. Each mode vector is normalized by the variance (uncertainty) in the arrival time estimate. The solution is

$$d=\begin{pmatrix}\hat{R}\\ \hat{T}_0\end{pmatrix}=(S'\Sigma S)^{-1}S\Sigma\,\delta. \tag{27}$$

B. Application to AET data

In order to place the time window in the mode filter, an initial range estimate must be made. This circular need for information (we need range to get modes and we need modes to get range) leads to the following iterative algorithm for determining the range of the AET data. The first step is to determine the mode arrival times using the straight LS mode filter. Then, using 30 modes (which are marginally trusted) the range is determined. With this range estimate as the *a priori* range for the TW mode filter, the arrival times of 60 modes are computed. These modes are then used to determine a less uncertain estimate of the range.

Summarizing the algorithm:

(i) Least-square mode filter data.
(ii) Use 30 modes in mode delay range estimator (MDRE) to get initial range.
(iii) TW mode filter data with estimated range
(iv) Use 60 modes in MDRE to get final range estimate and uncertainty.

Figure 11 shows a plot of the prediction, centroid, and spread of the data, and the results of the MDRE applied to the LS modes. The relative arrival time of the average of 50 receptions passed through the filter is plotted as stars. The mode uncertainties are indicated. The range estimator inversion is done using modes 2–30 since mode 1 is poorly sampled by the array. The range estimate is 3274 km with an uncertainty of 399 km. The large uncertainty is due to the small number of modes used and will be improved by continuing with the windowed mode data.

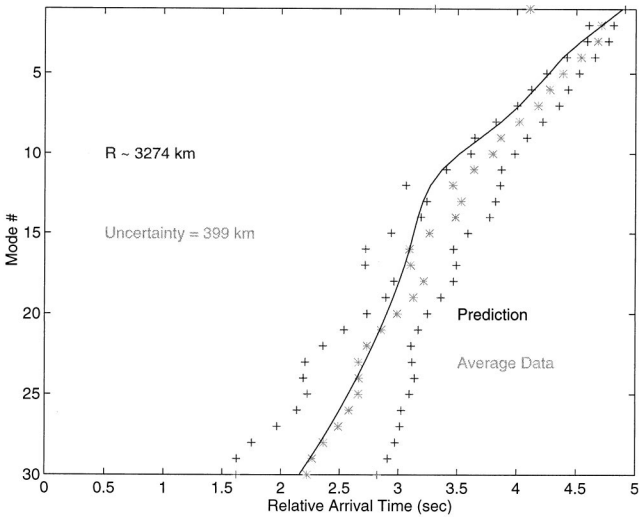

FIG. 11. AET data least-squares mode arrival times with the mode-delay range estimator results. The average mode arrivals (across 52 receptions) are shown (*) with spreads (+). The line is the predicted adiabatic mode arrival (offset to line up with mode 1). The range estimate using 30 modes is 3274 km with an uncertainty of 399 km.

This range (3274 km) was then used as an initial estimate for the range and the TWMF was run and these results are shown in Fig. 12. The MDRE gives a final range estimate of 2937 km with an uncertainty of 112 km. This estimate has a smaller uncertainty than the first pass, but is biased by 300 km.

The bias is a result of comparing mode arrival centroids (effective arrival times) of sound propagated through a real ocean environment (with internal waves) with adiabatic mode group velocities. The physics of the bias comes from the preferential direction (in the time domain) of mode scattering. The low modes receive energy from many higher modes, all of which travel faster. The extreme example is mode 1, which is the slowest traveling mode. It can only receive energy from faster traveling modes. In a random scattering environment the final arriving mode 1 energy will

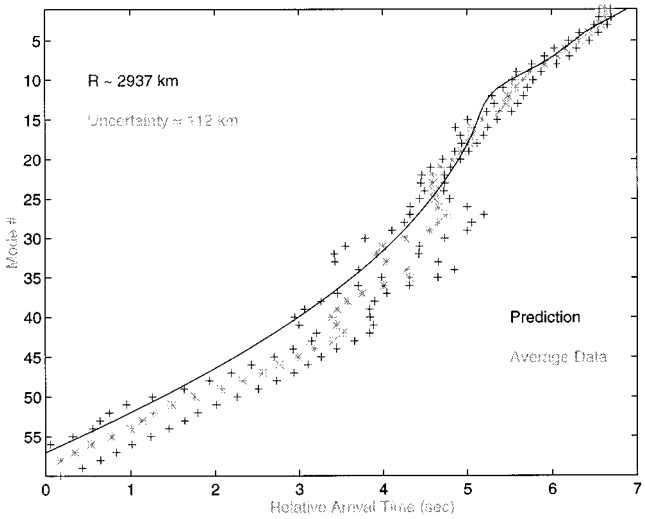

FIG. 12. AET data time-windowed mode filter arrival times with the mode-delay range estimator results. The range estimate using 60 modes was 2937 km with an uncertainty of 112 km.

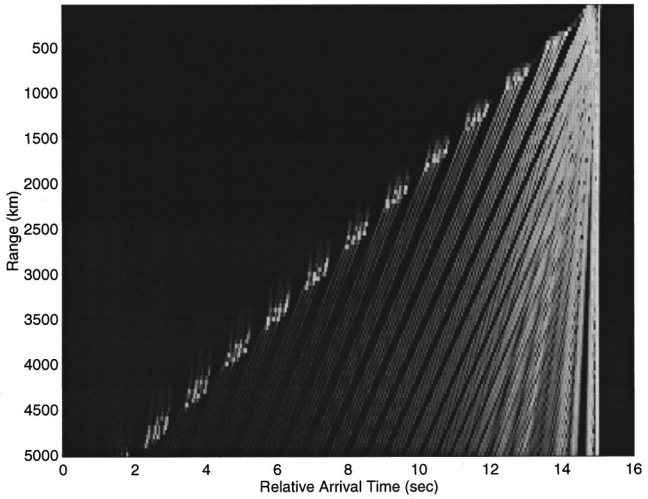

FIG. 13. Timefront receptions at 835 m depth as a function of range. The stretching of the accordian pattern is visible. The axial cutoff time of the arrival patterns have been aligned.

have a centroid that is biased faster than the adiabatic arrival time. For high modes there is scattering of energy from both faster and slower modes. Yet with the source located near the sound channel axis there is more initial energy in the lower modes. This causes the high modes to receive a preferential amount of energy from lower, slower modes. This gives their ''effective'' group arrival time a late bias. This bias tends to make the mode arrival time plot (mode no. versus time) more vertical. This translates through the range inversion to a bias short in range. For a perfectly vertical arrival pattern (all the modes arriving at the same time), the range estimate would be zero. This bias will be addressed in a subsequent paper on environmentally tolerant localization techniques.

VI. TIMEFRONT RANGE ESTIMATOR

A timefront is the arrival of acoustic energy across the array measured in a time-depth plot. As a wavefront of the acoustic field (measured in the depth/range/time) propagates, it crosses the array at a specific range. For a single hydrophone the arrival times of the timefronts correspond to the local peaks in the reception. Historically, timefronts have been thought of and analyzed as ray arrivals because of the correspondence between ray arrival times with those of timefronts. The identification and inversion of timefronts across an array is the basis of modern acoustic tomography.

In contrast to the late arriving axial energy, the early arriving energy exhibits surprising stability. It is this stability that has led to much of the success of tomography at long ranges.[4,5,27,28] We would like to make use of this stability in our localization of a broadband acoustic source. The dispersion of the water column produces a similar range effect in the timefronts as it does in the modes. Whereas the individual modal dispersion is linearly proportional to range, the timefront problem is not linear in range because of the combined effects of spreading and adding more timefronts. The timefront arrival pattern as a function of range for the Central Pacific is shown in Fig. 13 for a depth of 835 m. These

curves will be used as replicas in our correlation processor. As range increases from 0 to 5000 km the dispersion of the pulse is seen.

This section begins with a discussion of the stability of timefronts. The correlation processor is introduced and applied to several simulations. A few adjustments are mentioned to allow for better localization in the presence of internal waves.

A. Timefront stability

The work of Flatte and Colosi[14,29] has shown that the bias and wander of timefronts is two orders of magnitude smaller than that of the corresponding modes in the presence of internal-wave scattering. Mode biases have been measured as large as 1 s, whereas timefront biases are generally 10 ms. This continues to be a mystery for several reasons. Why are the early arriving timefronts more stable? Is coherent mode coupling occurring? How does this correspond to the equivalence of mode and ray solutions found by Traykovski?[30]

One comment should be made here concerning the comparison of timefront bias and mode bias. As was discussed earlier, it is the centroid of each individual mode that is measured and not the arrival time of a particular mode. The bias is the difference between the centroid and the adiabatic mode arrival time. The centroid, however, contains incoherent energy scattered from other modes. This leads to a bias in the centroid that is not a result of a change in the adiabatic group velocity.

B. Correlation processor

Arrival patterns from received data are correlated with predicted arrival patterns for various ranges. In order for the algorithm to work efficiently it is necessary to rapidly generate the received arrival pattern for each new range and depth. Raytrace algorithms are fast and can easily generate an arrival pattern but in order to move forward in range, the ray calculation must be done again from the source location. Adiabatic mode theory allows for the rapid recalculation of time domain arrival pattern replicas because only summations and FFT's need to be performed.

The correlation function, which yields the timefront range estimator, is now developed. For each receiver depth z_i the amplitude of the acoustic field with time forms the data vector $p^i_{\text{data}}(t)$. It must be noted here that it is the relative arrival time that is measured. Knowledge of the absolute arrival time assumes *a priori* knowledge of the source range. For each range estimate $\hat{r}$ an adiabatic mode replica vector $p^i_{\text{rep}}(\hat{r},\hat{t})$ is calculated. $\hat{t}$ is the relative time of arrival for the replica. Note that without knowledge of the source range, $\hat{t}$ and t are not aligned. If the pulses were exactly aligned a simple inner product (like the Bartlett) would work well for our processor. Without *a priori* alignment, we must define the correlation function:

$$C^i(\Delta t)=\frac{\Sigma_j p^i_{\text{data}}(t_j)p^i_{\text{rep}}(\hat{t}_j+\Delta t)}{\sqrt{\Sigma_l (p^i_{\text{data}}(t_l))^2 \Sigma_l (p^i_{\text{rep}}(\hat{t}_l))^2}}. \tag{28}$$

The correlation function is normalized such that for a perfect match the correlation is 1.0. The peak of $C^i(\Delta t)$ gives the best match and the relative offset between the two pulses. The final output of the timefront estimator is the sum across receivers of the correlation function peaks. Figure 14 demonstrates the beamformer for a particular replica. In Fig. 14(a) the replica and data vector for a PE calculation through internal waves at 1000 km is shown. The signals are not overlapping because of a mismatch in relative timing. Figure 14(b) shows the correlation function for these two vectors. The offset is correctly determined to be 0.3 s with a correlation of 0.8. This is significantly less than 1.0 expected for perfect correlation but we shall see that it is good enough for range estimation.

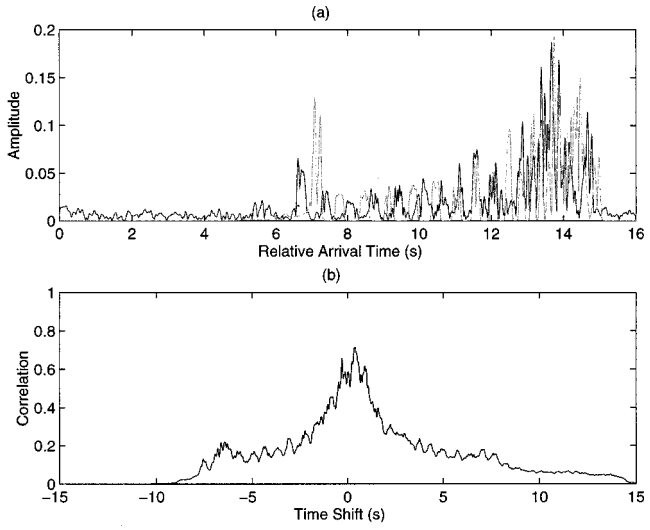

FIG. 14. Simulated data and replicas for a 1000-km reception across a single phone (a). The correlation, as a function of offset, is shown in (b). The FI-PE at 1000 km through internal waves is used as the data.

One final adjustment to the processor must be made in order to optimize it for localization of long-range sources in the presence of internal waves. Peaks (timefronts) in the final arrival cannot be identified for use in tomography. If this part of the reception is included in the timefront range estimator, it will swamp the range estimator with random noise because of its significant energy and lack of correlation with predictions. To remedy this problem a 2-s filter is applied to the data and replicas. This allows only the signals from the early arriving energy to be compared. This is equivalent to saying the source is more than 1000 km away. Such an assumption is not unmerited given the 8-s dispersion of the arriving data.

C. Localization of simulations

The timefront range estimator is applied to the series of frequency interpolation-parabolic equation (FI-PE)[31] simulations through internal waves. This is done first to test the normalization and then to examine the degradation caused by internal-wave coupling. Six simulated data sets were analyzed. The range-independent adiabatic-mode calculation and the FI-PE simulation with 1.0 GM internal waves were used at ranges of 1000, 2000, and 3000 km. The results are shown in Fig. 15. Each plot is the average across 20 individual depth receptions. The two lines are for the 2-s filtered data and the entire reception in the correlation processor. The lines with lower sidelobe energy are for the 2-s filtered pro-

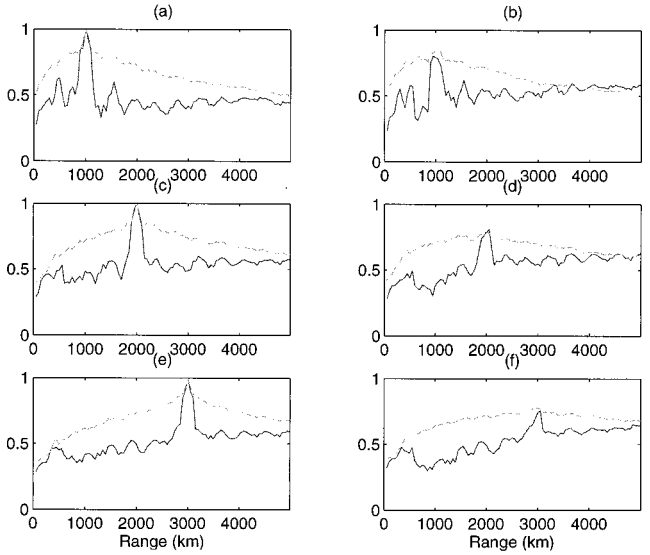

FIG. 15. Timefront range estimator results from simulations are presented. Adiabatic mode simulations were used as data at ranges of 1000 km (a), 2000 km (c), and 3000 km (e). The results for FI-PE simulations through 1.0 GM internal waves are shown at ranges of 1000 km (b), 2000 km (d), and 3000 km (f). The results with lower sidelobes and sharper peaks are for those with the final two seconds clipped from the data.

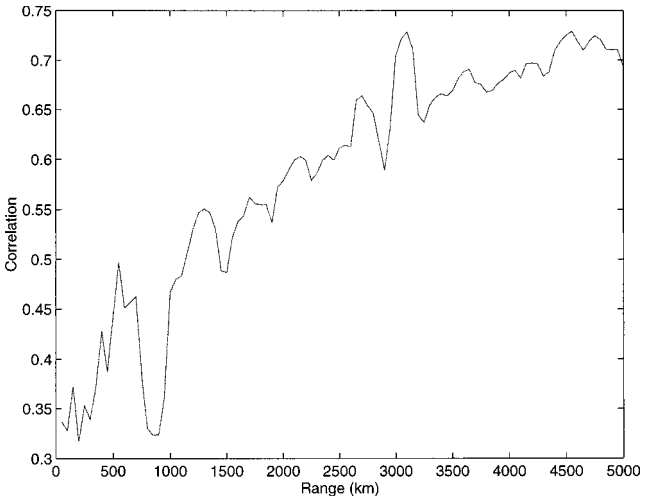

FIG. 16. Timefront range estimator results for the AET data. The average across 10 phones is plotted. The global maxima are at 3100 km, but there is growing noise with range. The true source was at 3250 km.

cessor. From the results of the adiabatic mode receptions we see the beamformer yields the correct range with a perfect correlation of 1.0. Internal waves reduce the correlation to 0.7 at the peak. The filtered correlation processor works even in the presence of internal waves, although the growing noise with range almost yields an incorrect localization at 3000 km.

D. Localization of AET data

The timefront range estimator was applied to the 20 element receptions of the AET data. 2 s were clipped from the data and replica fields. The average across phones for a single reception is shown in Fig. 16. There is a strong local maximum near the true source range of 3250 km. The peak is at 3100 km and is possibly off because of environmental mismatch. This peak is not, however, the global maximum. The noise floor appears to be growing with range, yielding a maximum at the largest range estimate of 5000 km. A possible explanation for this is the noise in the signal from internal waves or ambient noise. As the replica vector has more peaks, more of this incoherent energy is added to the output in the correlation processor.

VII. CONCLUSION

Data from the Acoustic Engineering Test has been analyzed from the perspective of the ability to do source localization. At a frequency of 75 Hz, and a range of 3250 km, this is well beyond the current expected range of successful localization, particularly using coherent processing. A short calculation of loss of coherence due to internal-wave scattering indicated that coherent MFP should work at a range of 300 km at this frequency. To determine what information remained in the signal, after internal-wave scattering, a mode filter algorithm was developed. By using time-domain processing, the complex amplitudes of 60 modes were extracted from a 20-element vertical line array. A processor was implemented to determine the depth of the source from the received modal amplitude spectra. The processor successfully differentiated between axial and near surface source depths.

Two methods were developed to determine the range of the source. The dispersion of the sound channel was used to determine the source range from relative mode arrival times. Identification of the mode arrival time with the centroid of arriving energy led to biases in range because of deterministic internal-wave scattering. The shift of energy from low modes to high modes by scattering causes the range estimator to be biased short. The stability of the wavefront arrival times relative to the mode centroids was used to develop a range estimator based upon the time-depth signature of the received signal. This estimator successfully determined the source range, although it was also biased short.

In this paper incoherent techniques were applied to extract residual information from the complex acoustic arrival. Hence the results in this paper should be interpreted as an indication that the ocean has not erased source localization information over multimegameter ranges in our particular frequency regime of 75 Hz. No heroic computational signal processing techniques involving data assimilation and/or combining environmental and acoustic modeling were attempted. Possibly such methods will yield better results in the future.

ACKNOWLEDGMENTS

The authors would like to thank Peter Worcester and the ATOC group for use of the AET data in this analysis. The results of this paper evolved from many discussions with Walter Munk, Peter Worcester, Matthew Dzieciuch, Bruce Cornuelle, and John Colosi. This work was supported by DARPA Grant No. MDA972-93-1-0003.

[1] B. E. McDonald, M. D. Collins, W. A. Kuperman, and K. D. Heaney, ''Comparison of data and model predictions for Heard Island acoustic transmissions,'' J. Acoust. Soc. Am. **96**, 2357–2370 (1994).
[2] W. H. Munk, W. C. O'Reilly, and J. L. Reid, ''Australia-Bermuda Sound Transmission Experiment (1960) revisited,'' J. Phys. Oceanogr. **18**, 1876–1897 (1988).
[3] W. Munk and A. M. G. Forbes, ''Global ocean warming: an acoustic measure?,'' J. Phys. Oceanogr. **19**, 1765–1778 (1989).
[4] P. F. Worcester, B. D. Cornuelle, M. Dzieciuch, W. H. Munk, J. A. Colosi, B. M. Howe, J. A. Mercer, R. C. Spindel, A. B. Baggeroer, K. Metzger, and T. G. Birdsall, ''A test of basin-scale acoustic thermometry using a large-aperture vertical array at 3250-km range in the eastern North Pacific Ocean,'' J. Acoust. Soc. Am. (submitted 1998).
[5] P. F. Worcester, B. D. Cornuelle, J. A. Hildebrand, Jr., W. S. Hodgekiss, T. F. Duda, J. Boyd, B. M. Howe, J. A. Mercer, and R. C. Spindel, ''A comparison of measured and predicted broadband acoustic arrival patterns in travel time-depth coordinates at 1000 km range,'' J. Acoust. Soc. Am. **95**, 3118–3128 (1991).
[6] A. B. Baggeroer, B. Sperry, K. Lashkari, C. S. Chiu, J. H. Miller, P. N. Mikhalevsky, and K. von der Heydt, ''Vertical array receptions of the Heard Island transmission,'' J. Acoust. Soc. Am. **96**, 2395–2413 (1994).
[7] W. H. Munk, R. C. Spindel, A. Baggeroer, and T. G. Birdsall, ''The Heard Island Feasibility Test,'' J. Acoust. Soc. Am. **96**, 2330–2342 (1994).
[8] P. J. Book and L. W. Nolte, ''Narrow-band source localization in the presence of internal waves for 1000-km range and 25-hz acoustic frequency,'' J. Acoust. Soc. Am. **101**, 1336–1346 (1997).
[9] A. B. Baggeroer, W. A. Kuperman, and P. N. Mikhalevsky, ''An overview of matched field methods in ocean acoustics,'' IEEE J. Ocean Eng. **18**, 401–424 (1993).
[10] N. O. Booth, P. A. Baxley, J. A. Rice, P. W. Schey, W. S. Hodgkiss, G. L. D'Spain, and J. J. Murray, ''Source localization with broad-band matched-field processing in shallow water,'' IEEE J. Ocean Eng. **21**, 402–412 (1996).
[11] W. S. Hodgkiss, D. E. Ensberg, J. J. Murray, G. L. D'Spain, N. O. Booth, and P. W. Schey, ''Direct measurement and matched-field inversion approaches to array shape estimation,'' IEEE J. Ocean Eng. **21**, 393–401 (1996).
[12] M. G. Brown, J. Viechnicki, and F. D. Tappert, ''On the measurement of modal group time delays in the deep ocean,'' J. Acoust. Soc. Am. **100**, 2093–2102 (1996).
[13] Fredric J. Harris, ''On the use of windows for harmonic analysis with the discrete Fourier transform,'' Proc. IEEE **66**, 51–83 (1978).
[14] J. A. Colosi and S. M. Flatte, ''Mode coupling by internal waves for multimegameter acoustic propagation in the ocean,'' J. Acoust. Soc. Am. **100**, 3607–3620 (1996).
[15] L. B. Dozier and F. D. Tappert, ''Statistics of normal mode amplitudes in a random ocean. I. Theory,'' J. Acoust. Soc. Am. **63**, 353–365 (1978).
[16] R. Dashen and W. Munk, ''Three models of global ocean noise,'' J. Acoust. Soc. Am. **76**, 540–554 (1984).
[17] E. C. Shang, ''Source depth estimation in waveguides,'' J. Acoust. Soc. Am. **77**, 1413–1418 (1985).
[18] E. C. Shang, C. S. Clay, and Y. Y. Wang, ''Passive harmonic source rangeing in waveguides by using mode filter,'' J. Acoust. Soc. Am. **78**, 172–175 (1985).
[19] T. C. Yang, ''A method of range and depth estimation by modal decomposition,'' J. Acoust. Soc. Am. **82**, 1736–1745 (1987).
[20] T. C. Yang, ''Broadband source localization and signature estimation,'' J. Acoust. Soc. Am. **93**, 1797–1806 (1993).
[21] G. Arfken, *Mathematical Methods for Physicists* (Academic San Diego, 1985), 2nd ed.
[22] K. D. Heaney, ''Simultaneous inversion for source location and internal wave strength using long range ocean acoustic signals,'' in *Scripps Institute of Oceanography* (University of California, San Diego, 1997), pp. 152–160.
[23] J. Tabrikian, J. L. Krolik, and H. Messer, ''Robust maximum-likelihood source localization in an uncertain shallow-water waveguide,'' J. Acoust. Soc. Am. **101**, 241–250 (1997).
[24] V. V. Goncharov and A. G. Voronovich, ''An experiment on matched-field acoustic tomography with continuous wave signals in the Norway Sea,'' J. Acoust. Soc. Am. **93**, 1873–1882 (1993).
[25] S. M. Jesus, ''Normal-mode matching localization in shallow water: Environmental and system effects,'' J. Acoust. Soc. Am. **90**, 2034–2041 (1991).
[26] E. C. Shang, ''Ocean acoustic tomography based on adiabatic mode theory,'' J. Acoust. Soc. Am. **85**, 1531–1537 (1989).
[27] J. L. Spiesberger and F. D. Tappert, ''Kaneohe acoustic thermometry further valicated with rays over 3700 km and the demise of the idea of axially trapped energy,'' J. Acoust. Soc. Am. **99**, 173–184 (1996).
[28] P. F. Worcester, ''Reciprical acoustic transmission in a midocean environment,'' J. Acoust. Soc. Am. **62**, 895–905 (1977).
[29] J. Colosi, S. Flatte, and C. Bracher, ''Internal-wave effects on 1000-km oceanic acoustic pulse propagation: Simulation and comparison with experiment,'' J. Acoust. Soc. Am. **96**, 452–468 (1994).
[30] P. Traykovski, ''Travel time perturbations due to internal waves: Equivalence of modal and ray solutions,'' J. Acoust. Soc. Am. **99**, 822–830 (1996).
[31] K. D. Heaney and W. A. Kuperman, ''Frequency Interpolation Technique for Broadband Parabolic Equation Calculations,'' J. Comp. Acoust. (to be published 1998).

An acoustic imaging system for the concurrent measurement of suspended sediment concentration and particle velocity

A. E. Adams,[a] O. R. Hinton, E. M. Valentine, and A. D. Tweedy
Department of Electrical and Electronic Engineering and Department of Civil Engineering, University of Newcastle upon Tyne, NE1 7RU, United Kingdom

(Received 20 October 1997; accepted for publication 16 June 1998)

This paper presents work on a system providing concurrent concentration and two-dimensional (2-D) particle velocity measurements on suspended sediments in water. The paper shows how one-dimensional methods for independent measurement of sediment concentration and particle velocity can be combined and extended to provide the concurrent 2-D information. An experimental system is described in which suspensions of 0.5-mm diameter sand are illuminated by acoustic burst signals of 1-MHz frequency from two transducers. The relevant theory for determining sediment concentration and particle velocity is presented. The system geometry provides for the illumination of a 5-cm^3 volume at ranges of up to 1.1 m, although longer ranges are possible. Results are presented for concurrent concentration and particle velocity measurements for a falling curtain of sediment, and these are shown to be consistent with predicted values. The measurements have sufficient resolution, and can be made sufficiently rapidly, to investigate short time-scale phenomena in hydraulics, such as the effect of wave dynamics on sediment transport. The method presented could form the basis of an instrument giving sequenced acoustic images of the transport phenomena occurring within an observed volume. [S0001-4966(98)06009-3]

PACS numbers: 43.30.Gv, 43.30.Ma, 43.30.Xm [DLB]

INTRODUCTION

Various sampling techniques have been used to measure sediment transport parameters. Several of these are intrusive and consequently alter the flow, affecting accuracy. The methods are usually applied separately to sediment concentration and fluid or particle velocity. Methods for the measurement of sediment concentration include optical systems (transmission and backscatter), and suction pumps, siphons, and grab samplers which require samples to be analyzed later.[1] Collection methods such as streamer traps[2] integrate longshore transport rates over periods of minutes at various levels above the bed and so cannot directly investigate the local transport physics. Velocity has been measured by a range of methods from Pitot tubes and current meters (propeller or electromagnetic) to laser-Doppler anemometers and video. All of these methods are either expensive, vulnerable, or imprecise.[3]

Acoustic techniques provide a much improved method for the nonintrusive measurement of underwater sediment transport parameters compared with traditional, intrusive, physical sampling techniques. In the past much effort has been put into empirical and theoretical model-based techniques of making acoustic sediment measurements.[4,5] Such work has concentrated on suspended sediment parameter measurements over long time periods, providing instrumentation for large scale events owing to tidal or large ocean current activity.

Although some work has considered high-resolution applications of these techniques,[6] disciplines with an interest in short time scale events have yet to benefit from the improved accuracy and resolution possible with the acoustic measurement of sediment transport. Typically, these events would be driven by (water) wave dynamics and current interactions with natural and artificial objects where both high spatial (of the order of a few millimetres) and time (subsecond) resolutions are required. The availability of instrumentation with higher resolution and accuracy is of special importance in civil engineering applications for sediment transport measurement and the subsequent verification of hydrodynamic models for natural and artificially influenced events. Numerical models of coastal sediment transport[7] require calibration, particularly with regard to vertical sediment concentration profiles through the wave period. These models presently depend on approximate estimates which this proposed acoustic technique could improve.

Until now, this has been very difficult owing to the relatively poor accuracy and resolution affordable with physical transport measurement techniques. This paper describes the development and evaluation of a sediment transport instrumentation system designed to provide measurements with high spatial and time resolution to support these areas.

Most current work in the acoustic sediment analysis field uses a single axis sonar [i.e., one dimension (1 D)] system to provide large-scale transport measurement. An extension of the measurement principles to provide a two-dimensional (2-D) transport imaging capability is here shown to provide an ideal solution for the high-resolution application.[8]

[a]Electronic mail: alan.adams@ncl.ac.uk

 0001-4966/98/104(4)/2160/7/$15.00

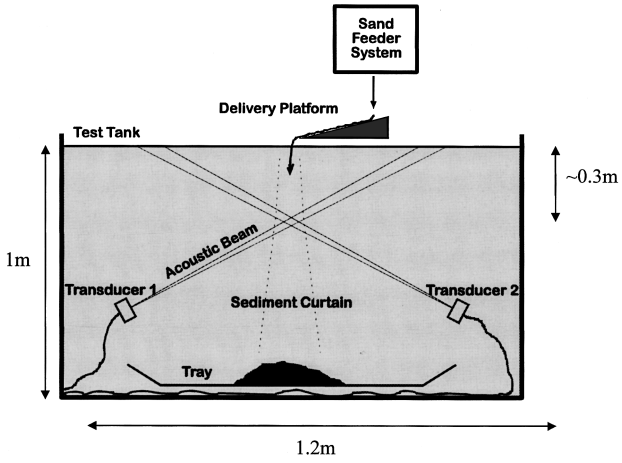

FIG. 1. Side view of experimental test tank.

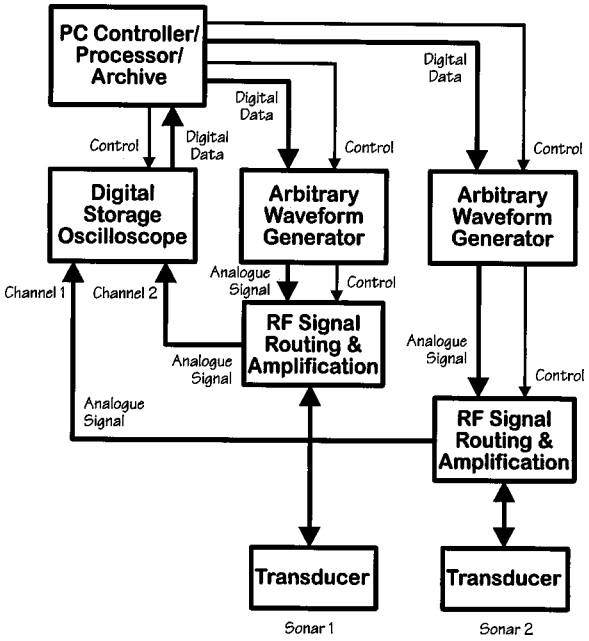

FIG. 2. Diagram of key system components.

I. SYSTEM CONFIGURATION

A. Tank and transducer design

The general configuration for the experimental system used in this work is shown in Fig. 1. The tank used was 1.2-m square, with a water depth of 1 m. Transducers were arranged to operate across one of the tank diagonals. The sediment target material used was well sorted beach sand with a mean diameter of 0.5 mm and a standard deviation in diameter of 0.33–0.71 mm. The sand was delivered from a screw feeder onto a sloping vibrating plate. The sand then dropped from the edge of the plate into the water, where it forms a falling curtain of terminal velocity. The sediment curtain concentration was estimated from the sand feed rate and system geometry, and also by physically sampling some of the measurement volume and filtering and weighing the solids within the sample. The sand was collected on a removable tray at the bottom of the tank, from which it could be retrieved for drying and reuse.

In these experiments 1-MHz transducers were used, since such a frequency provides a strong backscatter signal from the size of target particle employed (it is well known that scattering is related to $2a/\lambda$, where a is the particle radius and λ is the wavelength of the incident signal[9,11]). The transducers were disk types, with a Q factor of $\sim$10. In order to receive directly backscattered signals (i.e., receive acoustic returns at the point of transmission) a monostatic sonar geometry (one employing a single transducer to both transmit the insonification pulse and receive the acoustic backscatter) is the best system choice. In practice the range cell resolution of the sonar is proportional to beamwidth and the transducers were engineered to give narrow beams. For example, the 1-MHz transducers used had -3-dB beamwidths of 2°, providing a resolution of approximately 3.5 cm at 1-m range.

In the first set of experiments a single transducer was used for the concurrent measurement of sediment concentration and particle velocity, the component of velocity being that along the axis of the single transmit/receive transducer. These parameters were derived by measuring and analyzing the backscattered acoustic signal produced by the particles in the sediment curtain. Both signal strength and Doppler frequency shift were analyzed. The second set of experiments employed a pair of transducers whose beams intersect inside the falling sediment curtain. These transducers were pulsed alternately (at a rate of 650 Hz, which was high enough to ensure that no significant change in particle distribution and motion occurred between pulses). The resulting pair of Doppler measurements allowed the 2-D resolution of the motion of the sand particles. Results from these measurements and subsequent calculations were compared with measures obtained by direct physical means.

The configuration of the tank, the feeder system, and the signal processing system (described in Sec. II B) were deliberately designed so that they could be readily constructed from standard, commercially available units, resulting in a flexible development system.

B. The electronic system

Figure 2 gives an overview of the signal processing structure which was implemented. The full, twin sonar case is shown.

In experiments involving only one sonar, the waveform generation, signal routing, and transducer for the second channel are inactive. Overall system control and data transfer was achieved using a desktop PC, with system interconnection taking place via an IEEE-488 bus. The PC also provided a data processing and display platform, as well as hard disk, or digital audio tape (DAT) archiving. A programmable signal generator provided transmit signal generation and system synchronization. The excitation data for the generator is supplied (off-line) by the PC.

Amplification and routing of transmit and receive signals was achieved with the only part of the system to be custom built. This RF hardware, providing the necessary separation between receive and transmit signals, amplified the transmit signals from the waveform generator and ap-

plied them to the transducers, after which it switched roles and amplified signals from the transducers and routed them to an oscilloscope.

The digitization of the received backscattered signals was performed by a digital storage oscilloscope (DSO) with an extended memory facility, which provided an off-the-shelf, flexible acquisition system. Data acquired through the DSO could be visualized while a measurement was in progress. Real, carrier band received sampled data was temporarily stored in the DSO before being passed, via the IEEE-488 bus, to the PC for processing. A DSO with a sampling rate of 10 MHz was used for all of the experiments that are reported here.

II. SIGNAL PROCESSING

The received analog, transducer signals were preamplified prior to digitization using tuned preamplifiers. These amplifiers had gains of 60 dB at 1 MHz and -3 dB bandwidths of 400 kHz. After the digital data had been acquired by the DSO and transferred to the PC, it was quadrature down-converted from 1 MHz to yield complex baseband signals for each acquisition. The resulting baseband signals were low-pass filtered at 175 kHz. This data then provided the basis for two main concurrent signal processing activities; evaluation of sediment concentration from the real carrier band data and the evaluation of sediment suspension velocity from the complex baseband data.

A. Evaluation of sediment concentration

The principles of the acoustic instrumentation of ocean sediment suspensions have been developed over the last 30 years into a proven science.[4,5,10–12] A great proportion of the work has related to the laboratory calibration of acoustic backscatter systems with known sediment sizes and the extrapolation of the calibration results in order to develop concentration data from practical measurements.[13] More recently, Ref. 4 has shown that, by considering transducer geometries and acoustic properties, such as near- and far-field effects,[12] and the incident acoustic wave interaction with single and then multiple particles, using particle form functions which express particle backscattering properties,[11] it is possible to develop nonempirical expressions for sediment concentration at given ranges from a monostatic transducer system. The expressions depend only upon the acoustic calibration of the transducer used. The acoustic calibration of the transducers is a relatively trivial process in comparison to the empirical calibrations described above.

Beginning with an expression for the acoustic backscatter from a single particle:

$$P_z = \frac{d_s}{2} P_0 r_0 \frac{D^2}{2r_z^2} f_m \exp\{i[2r_z(k+ia_w)-\omega t]\}, \qquad (1)$$

where P_z is the transmitted pressure at range r_z, P_0 is the reference pressure at range r_0, d_s is the sediment particle diameter, D is a transducer directivity function, k is the wave number of the transmitted wave, ω is the transmit frequency (rad s^{-1}), a_w is the water attenuation factor, and f_m is a form function to represent particle scattering properties.

Developing the expression to allow for the insonified volume of the acoustic beam, particle size distribution functions, transducer near- and far-field range modifiers, sediment attenuation, and range to the target volume yields an expression for the mass concentration at a given range:

$$M(r) = K_1^2 e^{-4r\alpha}, \qquad (2)$$

where $M(r)$ is the mass concentration at range r from the transducer and α is the combined attenuation resulting from loss in the water and scattering from the sediment particles. K_1, which includes the effect of spreading, is given by

$$K_1 = \frac{\overline{P_{\text{rms}}}\psi r \sqrt{16\overline{a_s}\overline{\rho_s}/3\tau c}}{P_0 r_0 \sqrt{|\overline{f_m^2}|}(1/1.05ka_t)}, \qquad (3)$$

where P_{rms} is the rms backscatter signal pressure, Ψ represents a modifier function to allow for the transducer near field,[12] P_0 is a reference pressure at range r_0, f_m is a particle scattering form function,[11] τ is the transmit pulse duration, c is the speed of sound in the test water, a_s is the mean sediment particle diameter, ρ_s is the sediment material density, and a_t is the transducer diameter. These expressions show the interdependence of the mass concentration $M(r_n)$ on the previous concentration estimate through the overall attenuation α_{n-1}, where r is divided into p discrete range bins 0, 1,...,n,...,p. The calculation process is therefore iterative, starting at the transducer face (where it is a reasonable assumption in practical concentrations that the attenuation due to the sediment is negligible) and calculating concentration then attenuation in turn at each required range out to the maximum.

B. Doppler velocity processing

Measurement of the velocity of particles in the insonified region can be achieved by estimating the Doppler shifts evident in the sonar returns from the moving suspensions which have been illuminated by transmit pulses of known properties.

In Doppler signal processing two techniques can be used to provide particle velocity information from a frequency shifted acoustic return. The first is based upon Nyquist frequency or greater sampled returns from a single, arbitrary phased ping (pulse-to-pulse incoherent sonar). This technique suffers from the disadvantage that the Doppler shift must be evaluated within the coherent duration of the signal (or ping) duration. This would require pulses of several milliseconds width to allow effective Doppler measurement at resolutions suitable for this application (12 Hz in 1 MHz for 1 cm/s). However, the frequency resolution derivable from such a time window is too low to fully represent the necessary Doppler spectrum. There is, therefore, a need to measure the mean Doppler frequency inside range gates of several meters in length, which, considering the desired target range of around 1 m, eliminates the noncoherent method from consideration.

The second signal processing technique for the Doppler returns uses a series of coherent pings (pulse-to-pulse coherent sonar) and samples the sonar return once per range bin (representing the resolution with which the sonar range is to

be measured) at a frequency much lower than that of the incoherent sonar case. The phase change between successive pings in a given range bin can then be used to evaluate the velocity of the scatterers responsible for the return. The technique can be used over numbers of pings but commonly they are used in twos, that is, with successive Doppler estimates being made from pairs of pulses. The range bins used in this case can be very narrow because the minimum width of the sonar pulse depends only upon system bandwidth and noise considerations. This allows an adequate Doppler frequency resolution from the relatively long signal coherence period, as well as the centimeter range resolution required in the application.

Particle velocity information is extracted from the acoustic return signals by analysis of the first and second spectral moments,[14] given by the general expression:

$$\sigma_p = \int S_D(f)(f-\mu)^p \, df, \tag{4}$$

where σ_p is the pth spectral moment, $S_D(f)$ is the unity normalized Doppler spectrum, and μ is the first-order moment (mean) given by

$$\mu = \int S_D(f) f \, df. \tag{5}$$

It is efficient to use time-domain estimation of these spectral moments (which avoids the use of Fourier transforms) and one particular method, the autocovariance or ''pulse-pair'' estimator, is particularly useful here.[15] The estimator is described by the expressions:

$$f_m = \frac{\arg\{A(\tau)\}}{2\pi\tau}, \tag{6}$$

$$\tau = \frac{1}{\text{prf}}, \tag{7}$$

where f_m is the first spectral moment or mean signal frequency, prf is the pulse repetition frequency of the sonar, and $A(\tau)$ is the complex return signal autocovariance:

$$A(\tau) = S(t) \cdot S^*(t+\tau), \tag{8}$$

where $S(t)$ is the complex baseband sonar signal $I(t) + iQ(t)$ and the asterisk denotes the complex conjugate.

The pulse-to-pulse coherent acquisition and processing technique undersamples some of the sonar return signal resulting in calculated velocities which are aliased about the Nyquist frequency of this sampling rate. In addition to this limitation the prf has an effect on the maximum system range given that we must (in the absence of coded/frequency diverse pulses) allow only one pulse to be in the water at any given time. The combination of these two factors leads to the range-velocity ambiguity:

$$\nu_{\max} r_{\max} \leqslant \frac{\lambda c}{8}, \tag{9}$$

where $\nu_{\max}$ is the maximum unambiguous Doppler velocity, $r_{\max}$ is the maximum sonar range, λ is the transmit signal wavelength, and c is the speed of sound in the water.

TABLE I. Test system parameters.

Parameter	Value
Transmit pulse length	6 μs (6 cycles at 1 MHz)
Transmit power	1.0 W
prf	650 Hz
Maximum range	1.1 m
Receiver voltage gain	60 dB
Sampling frequency	10 MHz
Baseband frequency limit	175 kHz

This covariance estimator has been shown to be the maximum-likelihood estimator[8] and it has been used in all of the Doppler velocity processing discussed in this paper.

III. EXPERIMENTS

A. Test environment and methods

In the tests, up to two independent monostatic sonars were used in the tank at a given time. The transducer(s) were mounted near the bottom of the tank and angled to point their beams upward, through the path of the falling curtain of sediment, in such a way that the intersection volume of their beams coincided with the center of the sediment curtain. This arrangement allowed both the evaluation of single sonar beam axis (one dimensional) concentration and particle velocity measurement performance, as well as extending the measurements to the dual sonar, twin axis case, allowing the evaluation of resolved, 2-D, particle velocity parameters into axes perpendicular and parallel to the tank floor for the beam intersection volume.

B. Test parameters

Table I details the sonar system parameters used during the tests. These parameters imply a range bin length of ~0.9 cm and a Doppler aliasing velocity of $\sim \pm 0.25$ cm/s.

C. Test results

The initial tests involved characterizing the single-beam sonar performance with respect to concentration and velocity

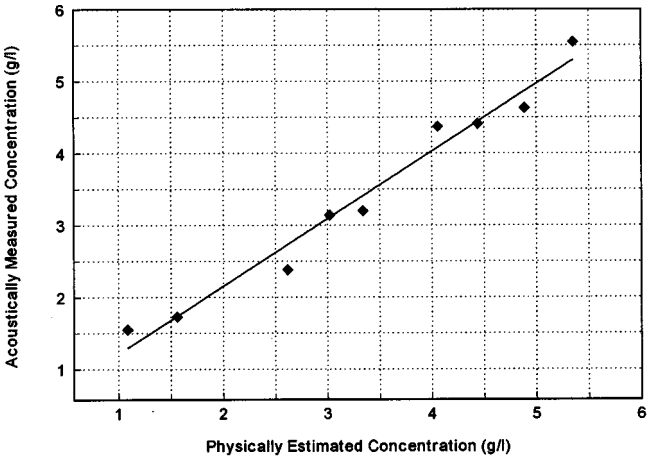

FIG. 3. Comparison between physically and acoustically measured concentrations.

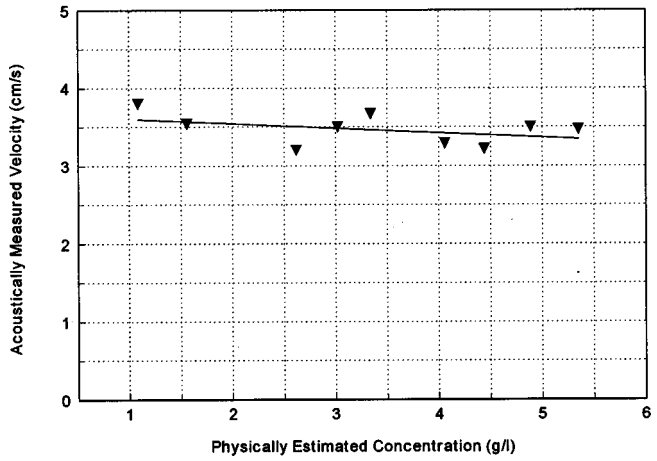

FIG. 4. Comparison of relative velocity estimates at different concentrations.

estimation. Experiments used concentrations in the range 1–6 g/l. It should be noted that, since the sand is of necessity dry to facilitate the feed mechanism, there is the possibility of entrained air bubbles entering the water with the sand particles. However, the measurement zone is approximately

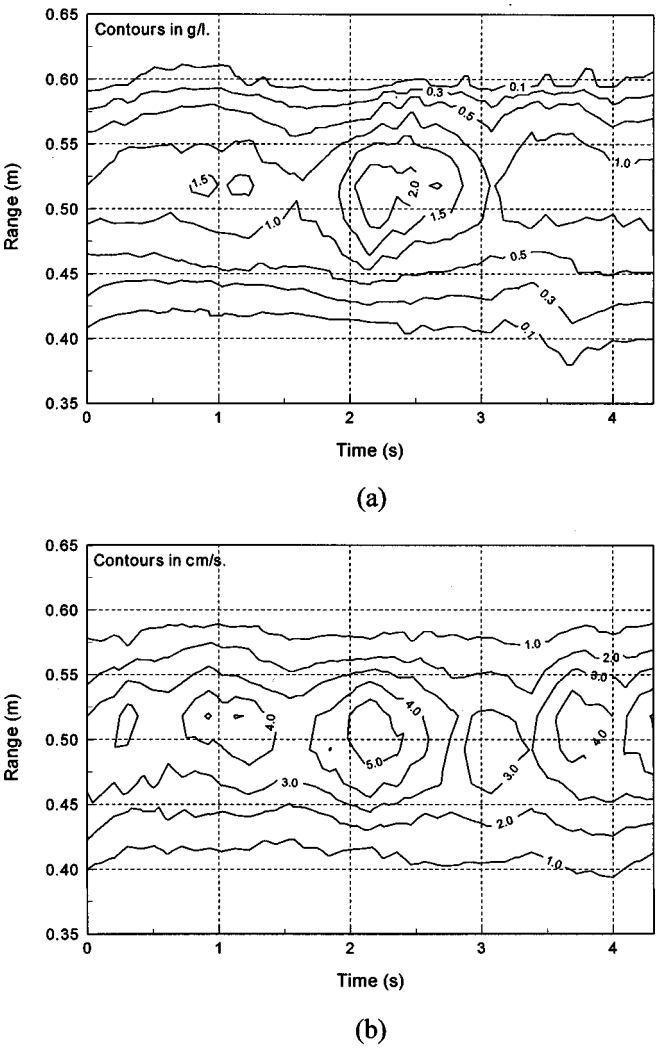

FIG. 5. Concentration (a) and velocity (b) results for a 1.2-g/l, 3.7-cm/s curtain at 0.5-m range over 4.62 s.

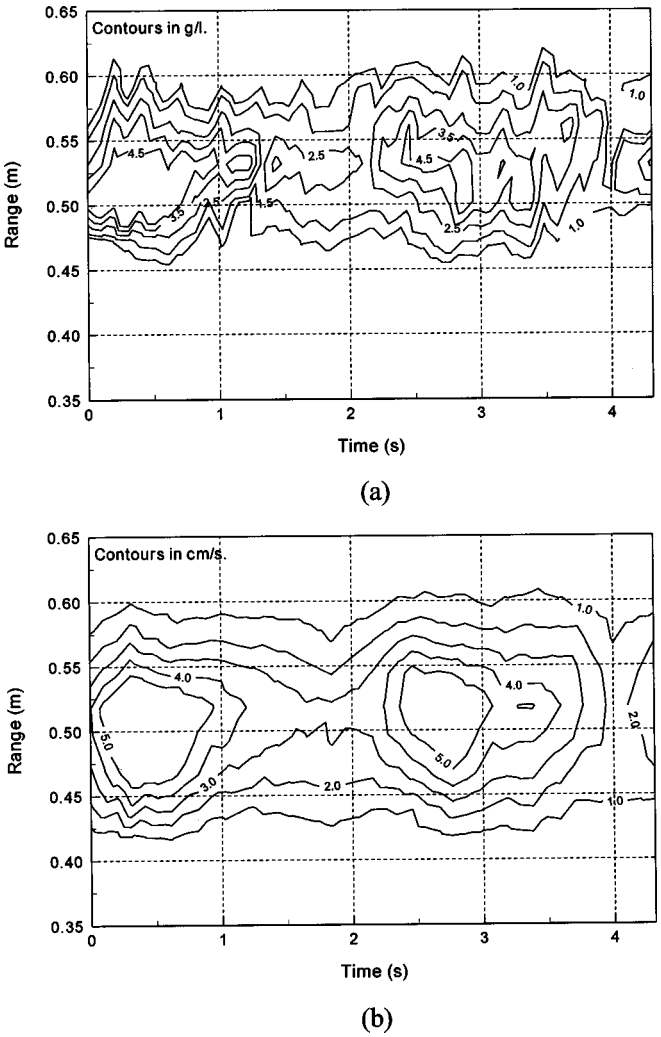

FIG. 6. Concentration (a) and velocity (b) results for a 3.4-g/l, 3.9-cm/s curtain at 0.5-m slant range over 4.62 s.

30 cm below the surface of the water and no free air bubbles were observed in this region. It is the case that any air still attached to the particles would provide a better than normal reflecting surface and hence would give a false increase in the concentration result. The results of acoustic measurement of concentration are compared with the physically estimated values in Fig. 3. This demonstrates the correlation between the acoustic estimate and one achieved through sampling volumes of the sediment curtain at the beam-curtain intersection point. The results represent the mean concentration at the midcurtain range over 30 successive pings, which was found to be a reasonable compromise between smoothing the apparent sediment concentration produced by the feeder and resolving the time variation in concentration inherent in the system. The acoustic measurements for the determination of concentration showed a standard deviation of 0.24 g/l. Overall, the correlation is encouraging, although the range of concentrations is small and the measurement does not represent the more difficult case, when there is significant sediment concentration along the entire sonar range. This situation may tend to increase errors in the estimate when allowing for the attenuation due to the suspension.

The range of known velocities available from the falling

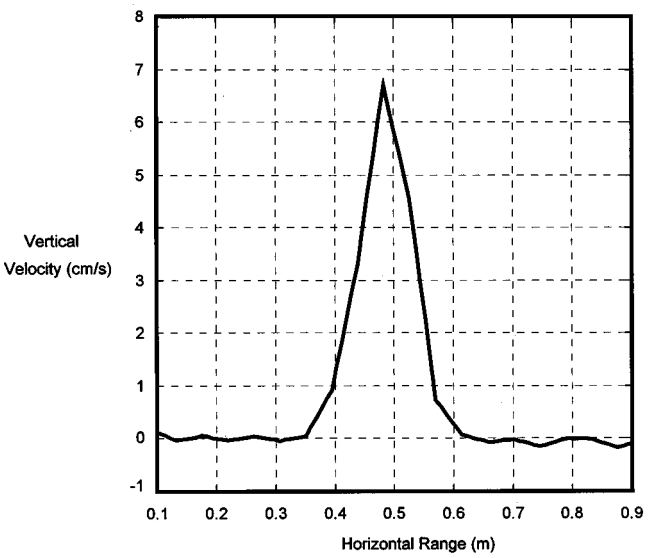

(a)

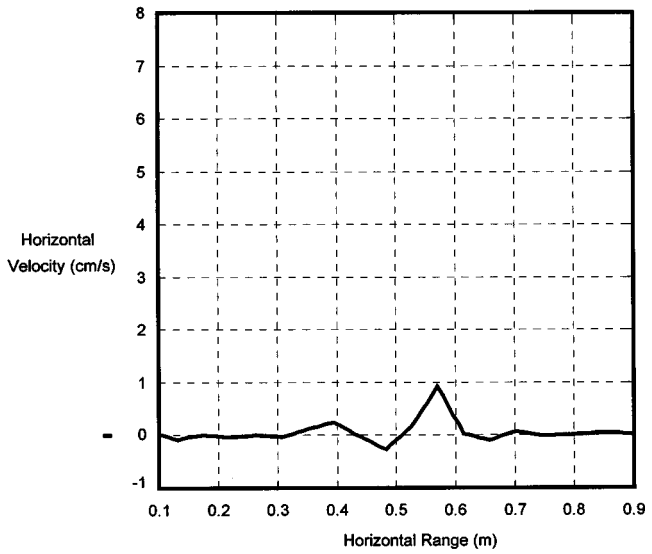

(b)

FIG. 7. Resolved 2-D components, 1.23-g/l curtain at ~0.5-m *y* axis range.

sediment curtain system is small and in the absence of any external effects, such as water, jets relates only to the terminal sediment velocity in the test tank (the particles reach their terminal velocity within a few centimeters of the surface, well before entering the insonified region). During the experiment there was no observed turbulence at this depth. It is accepted that once the Reynolds number is large (in the present case the particle Reynolds number is around 2.6), turbulence will be created in the wake of the particle. However, the turbulence in such a case is close to the surface of the particle.[16] The condition of fall in a calm fluid has been of limited interest to hydraulicians and little work has been done, but it is known that there is an increase in fall velocity due to the presence of turbulent fluctuations. This increase is greater in the case of fine sediments than medium sizes and it is therefore regarded as a minor effect here. It is possible that in natural flows the effects of turbulence may be significant. In these tests the terminal velocity was 7 cm/s. This is in accord with the predicted terminal velocity for natural sand particles of 0.5 mm calculated in accord with standard methods,[16] which include consideration of particle Reynolds numbers beyond the value of 1, the usual limit for Stokes' law. This figure was resolved to a 3.4 cm/s axial component in relation to the sensors. In this case velocity data represents an average over 15 successive pulse pairs. The results, as illustrated in Fig. 4, show the system to give a reasonable estimate of this prediction across a range of sediment concentrations. The maximum error compared to the calculated axial component of terminal velocity is of the order of 14% but, allowing for the instability of the sediment curtain, and the fact that the reference velocity is itself only estimated and may, in fact increase with concentration, the evidence is that the velocity measurement system and algorithms are realistic. The acoustic measurements for the determination of particle velocity showed a standard deviation of 0.18 cm/s.

The particle concentration and velocity measurements, used to produce Figs. 3 and 4, have been extended to examine the properties of the sediment curtain over a longer time interval, primarily with a view to assessing the variability present in the curtain, and secondarily to examine system performance over a more realistic time scale with respect to eventual applications. The results shown in Figs. 5 and 6 illustrate concurrent particle concentration-velocity results over a period of 4.62 s (3000 pings) looking at a curtain being dropped at a slant range of 0.5 m with measured concentrations 1.2 and 3.4 g/l, respectively. The offsets in the peaks of concentration show that the falling sediment was not exactly in the middle of the insonified region.

The concentration contours show a predictable overall distribution, the mean of which corresponds to the expected concentration level. However, the amount of variability in the curtain properties is evident, with the greatest concentration peak, between 2 and 3 s, showing a 60% deviation from the mean. Similarly, the velocity contour distribution is as would be expected and the mean velocity at the curtain slant range corresponds (within the velocity estimation limitations discussed) to that anticipated.

Experiments have been carried out which involve the use of both sonars, arranged so that their beams crossed in the center of the falling sediment curtain. The purpose of these experiments was to estimate the two-dimensional components of the sediment's velocity. The results of these tests are shown in Fig. 7.

When both sonars were in use their operation was time interleaved. Each sonar transmitted two pings and then paused for the other sonar to do the same. This results in a smoothing of the result data, but in this application, where the sediment moves relatively slowly, with the prf used, the effect is not significant.

These plots represent a composite result over 18 separate measurements with the beam intersection arranged in 5-cm increments along the horizontal axis (perpendicular to the sediment fall direction), at 0.32-m above the tank floor. Each measurement was formed from the mean velocity value given by 30 pulse pairs. The 2-D velocity results show the expected positive (towards the tank floor) vertical velocity

result of near 7 cm/s. The observed horizontal components are thought to be the result of gradual widening of the curtain as the falling sediment creates an outwardly moving (horizontal) component.

The resolution of the data in the plots is quite low at only 17 horizontal range bins over 0.8 m. This is because successive results were achieved by physically rearranging the transducers before each measurement and better than 5-cm accuracy in this process was not realistic. The result is, however, indicative of the possibilities of a multiple-beam system. The accuracy of the result is very encouraging considering the bins were not actually measured concurrently.

IV. CONCLUSIONS

The results presented indicate that the system geometry, processing techniques, and system parameters used have produced a technique which is suitable for the measurement of concurrent single axis sediment concentrations and particle velocities. Additionally, the twin axis results indicate that the technique may be developed to allow measurement of concurrent concentration and velocity in two dimensions. A limiting factor in determining the absolute accuracy of the technique is the difficulty in maintaining a consistent concentration level within the falling curtain. Although much more expensive, an active, pumped suspension system would generate a concentration level with less variability[12] though the mixing involved would introduce further problems in regard to a greater randomizing of particle direction and the disappearance of the sediment curtain ''edges'' which are useful markers.

The dual sonar tests showed that processing data from crossed sonar axes gives an estimate of 2-D sediment transport properties within 10%–15% of those predicted. This demonstrates the potential for development of the system into the transport measurement system proposed in Sec. I. The use of two beams can only give the 2-D information at one point in the measurement volume. However, the basic principle can be extended into a multiple-beam technique, where the number of intersections could be increased to provide a pixel image of a 2-D plane through the measurement volume.

There are two ways in which multiple beams might be formed:

(1) by mechanically moving a pair of sonar transducers through prescribed arcs to form the necessary intersections,

(2) using a pair of transducer arrays and actively forming the sonar beam using beamforming techniques.

In the first case the timing and speed of such a system is likely to prove problematic. In addition the mechanical stability and reliability of the electromechanical components would present problems. A better choice for a multiple-beam system would involve the electronic steering method. The resulting data would be processed in the same way as that discussed earlier. In using this technique, however, there would be considerable processing overhead involved in the beamforming and the imaging algorithms, and in dealing with the effects of the varying size of intersection volumes and varying sidelobe patterns.

In addition the use of coded pulses could be used to avoid the problem of Doppler aliasing velocity.

ACKNOWLEDGMENTS

This work was conducted as part of the UK Engineering and Physical Sciences Research Council (EPSRC) project No. GR/J42304.

[1] P. D. Osborne, C. E. Vincent, and B. Greenwood, ''Measurement of suspended sand concentrations in the nearshore field,'' Cont. Shelf Res. **14**, 159–174 (1994).
[2] P. Wang, ''Longshore sediment flux in water column and across surf zone,'' J. Waterway, Port, Coast., Ocean. Engrs, ASCE **124**, 108–117 (1998).
[3] H. A. Huntley and D. M. Hanes, ''Direct measurement of suspended sediment transport,'' in *Coastal Sediments*, edited by N. C. Kraus (ASCE, New Orleans, 1987), pp. 723–737.
[4] P. D. Thorne, P. J. Hardcastle, and R. L. Soulsby, ''Analysis of acoustic measurements of suspended sediments,'' J. Geophys. Res. **98**, 899–910 (1993).
[5] C. He and A. E. Hay, ''Broadband measurements of the acoustic backscatter cross section of sand particles in suspension,'' J. Acoust. Soc. Am. **94**, 2247–2254 (1993).
[6] L. Zedel, R. Cabrera, A. Lohrmann, and A. Hay, ''Single beam, high resolution pulse-to-pulse coherent Doppler profiler,'' IEEE Press, 0-7803-2437-4/95 (1995).
[7] R. Deigaard, J. Fredsoe, and I. B. Hedegaard, ''Mathematical model for littoral drift,'' J. Waterway, Port, Coast. Ocean. Engrs, ASCE **112**, 351–369 (1986).
[8] A. D. Tweedy, E. M. Valentine, O. R. Hinton, and A. E. Adams, ''The use of high frequency acoustic backscatter and Doppler measurements to determine sediment concentration and 2D velocity in water,'' Proc. OCEANS '96, Ft. Lauderdale, FL (1996), pp. 733–738.
[9] A. S. Schaafsma, ''In situ acoustic attenuation spectroscopy of sediment suspensions,'' Proc. European Conference on Underwater Acoustics, Luxembourg, 1992 (unpublished), pp. 177–180.
[10] G. H. Flammers, ''Ultrasonic measurement of suspended sediments,'' US Geol. Surv. Bull. **1141-A** (1962).
[11] J. Sheng and A. E. Hay, ''An examination of the spherical scatterer approximation in aqueous suspensions of sand,'' J. Acoust. Soc. Am. **83**, 598–610 (1988).
[12] P. D. Thorne, C. E. Vincent, P. J. Hardcastle, S. Rehmann, and N. Pearson, ''Measuring suspended sediment concentration using acoustic backscatter devices,'' Mar. Geol. **98**, 7–16 (1991).
[13] A. S. Shaafsma, ''Acoustic measurement of concentration and size of sediment particle suspensions,'' Ultrasonics International '89 Conference Proceeding, Madrid, 1989 (unpublished), pp. 388–393.
[14] K. S. Miller and M. M. Rochwarger, ''A covariance approach to spectral moment estimation,'' IEEE Trans. Inf. Theory **IT-18**, 588–596 (1972).
[15] R. Lhermitte, ''Pulse to pulse coherent Doppler sonar signal processing techniques,'' J. Atmos. Ocean Technol. **1**, 293–308 (1984).
[16] A. J. Raudkivi, *Loose Boundary Hydraulics* (Pergamon, New York, 1990), 3rd ed., p. 538.

The flattened surface parabolic equation

Richard B. Evans[a)]
Science Applications International Corporation, 21 Montauk Avenue, Suite 201, New London, Connecticut 06320

(Received 3 December 1997; accepted for publication 25 June 1998)

A simple surface flattening transformation is applied to the problem of underwater acoustic scattering from an irregular sea surface. The flattened surface elliptic wave equation is factored to obtain a parabolic equation that has the same high angle capability as recent parabolic equation models. The flattened surface parabolic equation contains an additional surface slope term, but includes forward scattering from the irregular sea surface. The transformation creates additional volume irregularities and irregularities in the water–sediment interface that the range and depth mesh need to resolve. The surface flattening transformation is easy to implement in a parabolic equation model. It compares very well with results obtained using boundary integral equations. An example is given of scattering at 400 Hz from a sea surface with wave heights of 3 m or nearly a wavelength. © *1998 Acoustical Society of America.* [S0001-4966(98)01410-6]

PACS numbers: 43.30.Hw, 43.20.Fn [DLB]

INTRODUCTION

The work described here was motivated by an attempt to understand how boundary perturbation theory is applied to problems in underwater sound scattering from an irregular sea surface. The main focus is, however, the application of the parabolic equation method to this irregular or rough surface scattering problem.

When boundary perturbation theory is applied to the rough surface scattering problem,[1] it is often implicitly assumed that the sound pressure field can be extended into the region above the irregular boundary, to a regular flat boundary. This may be possible, but it complicates the boundary perturbation theory. An alternative is to apply a simple translation of the independent depth variable[2] that flattens the irregular boundary. It converts the boundary perturbation problem to a volume perturbation problem, but places it in the context of a single Hilbert space,[3] i.e., a waveguide with a regular flat boundary. The latter setting is better understood. The simple surface flattening transformation, which measures depth from the sea surface rather than sea level, was applied to the elliptic wave equation by Konrady[4] (also see Abarbanel[5]). The transformation leads naturally to a small slope perturbation theory, but the perturbative aspects are not perused here.

The simple surface flattening transformation should also be useful in doing rough surface scattering calculations with the parabolic approximation,[6] in spite of the fact that it introduces an extra term proportional to the slope of the sea surface as well as other volume irregularities. Beilis and Tappert[7] augmented the simple surface flattening transformation with a transformation of the dependent field variable to eliminate the slope term. This composite surface flattening transformation has recently been applied by Barrios[8] to a parabolic approximation using the split-step Fourier method. An even more sophisticated transformation involving a conformal mapping, which preserves the form of elliptic wave equation, was developed and tested by Dozier[9] for the rough surface scattering problem. The conformal mapping procedure has been also been employed by Norton *et al.*[10] in a higher angle parabolic equation method. The simple surface flattening transformation, which retains the surface slope term, is still attractive because of its simplicity.

Procedures exist that do not rely on a transformation of independent variables. Tappert and Nghiem-Phu[11] explicitly extended the rough surface scattering problem into an image ocean replacing the free surface with an interface. The field is odd about the interface while the index of refraction is even and an extra term, proportional to the slope of the sea surface, appears in the image ocean. A transformation of the dependent field variable is again used to eliminate the slope term. This image ocean method is complementary to the composite surface flattening transformation derived by Beilis and Tappert.[7]

It is possible to place the rough free surface just inside the computational grid and explicitly enforce the free surface boundary condition. Rosenburg and Magruder[12] applied this procedure using extra zeros to fill out a regular grid in a finite element parabolic equation calculation. This numerical approach was used by Collins *et al.*[13] to allow the sea surface to intrude into the computational grid. The idea can be traced to Collins[14] where it was used in a rotated coordinate system.

Filling out the grid with zeroes is physically analogous to adjoining a fluid air layer above the sea surface. The free surface is replaced by the water–air interface. The air layer approach was developed and successfully used by Thomson *et al.*[15] in both finite difference and split-step Fourier parabolic equation calculations.

It is shown here that the original simple surface flattening transformation is useful in doing rough surface scattering calculations with the parabolic approximation and that it is easy to implement. It contains a readily identifiable contribution due to the irregular surface and maintains a potential connection to the small slope perturbation theory that is ab-

[a)]Research conducted while the author was a Guest Investigator at the Woods Hole Oceanographic Institution, MA.

sent in a purely numerical procedure. The simple surface flattening transformation places the rough surface scattering problem in the context of a waveguide with regular flat boundaries where the limitations of the parabolic approximation are ordinarily encountered and, hopefully, better understood.

I. THEORY

The partial differential equation used to describe the sound pressure in an underwater waveguide is first introduced. Assume that a harmonic source with circular frequency ω is operating in the waveguide. The time dependent complex pressure p can be factored into $p=\exp(i\omega t)P$ where the time invariant complex pressure P satisfies the elliptic or reduced wave equation

$$\frac{\partial^2 P(x,z)}{\partial x^2}+\rho(x,z)\frac{\partial}{\partial z}\left[\frac{1}{\rho(x,z)}\frac{\partial P(x,z)}{\partial z}\right]+k^2(x,z)P(x,z)=0 \tag{1}$$

in range x and depth z, where $\rho(x,z)$ is density, $k^2(x,z)=\omega^2/c^2(x,z)$ is the wave number squared, and $c(x,z)$ is the speed of sound. The density $\rho(x,z)$ is assumed to be piecewise constant in range x. Equation (1) is two dimensional and reflects a translational invariance in the cross range direction. It can also be used in the case of rotational invariance after the cylindrical spreading factor has been removed.

Boundary and interface conditions are also needed to define a solution of Eq. (1). It is assumed that there is an irregular or rough surface at the depth $z=s(x)$ where the complex pressure is required to satisfy the pressure release boundary condition $P(x,s(x))=0$.

The function $z=s(x)$ is the depth of the sea surface below mean sea level. It is also assumed that there is a copy of the sea surface buried, at a substantial depth D, in an absorbing bottom where the complex pressure satisfies the boundary condition $P(x,D+s(x))=0$.

The effect of this deep reflector, and its irregularity, is assumed to be minimized by the absorption in the bottom. The pressure and the normal component of the particle velocity are also required to be continuous at the water–sediment interface $z=d(x)$ where the density and sound speed may be discontinuous. A schematic of the problem is shown in Fig. 1.

The irregular free surface is flattened by choosing a new depth coordinate $\hat{z}$ according to

$$\hat{z}=z-s(x). \tag{2}$$

The complex pressure $\hat{P}$, considered as a function of the new depth variable $\hat{z}$, is

$$\hat{P}(x,\hat{z})=P(x,\hat{z}+s(x)),$$

and the density $\hat{\rho}$ and wave number squared $\hat{k}^2$ are defined in a similar fashion. The transformation has the obvious intent of flattening the two perfectly reflecting boundaries in Fig. 1. The water–sediment interface becomes more irregular, occurring at $\hat{z}=d(x)-s(x)$ as shown in Fig. 2. Other regions of rapid depth variability are likewise converted to regions of more rapid range variability by the transformation.

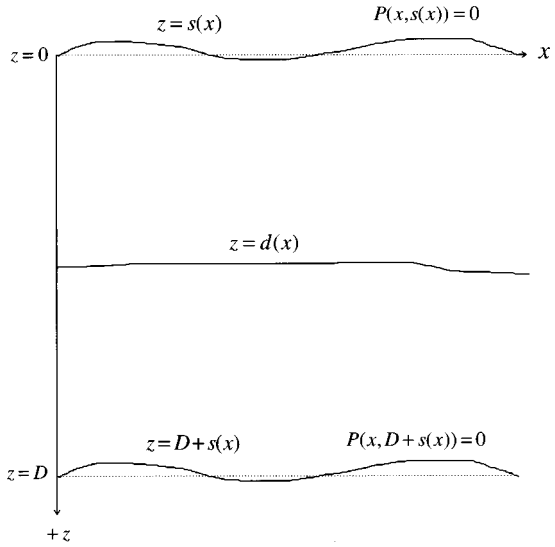

FIG. 1. Irregular or rough surface waveguide.

The effect of the transformation on Eq. (1) is best obtained by observing that

$$P(x,z)=\hat{P}(x,z-s(x))$$

and consequently

$$\frac{\partial P(x,z)}{\partial x}=\frac{\partial \hat{P}(x,z-s(x))}{\partial x}-s'(x)\frac{\partial \hat{P}(x,z-s(x))}{\partial \hat{z}}, \tag{3}$$

where $s'(x)$ is the slope of the sea surface. It is assumed that the irregular surface has a well defined tangent plane. Realizations of rough or irregular surfaces are usually many times differentiable[16] and are probably better called irregular since they are smooth, in a strict mathematical sense. Proceeding to apply Eq. (3) in Eq. (1) and substituting $z=\hat{z}+s(x)$ gives the flattened surface reduced wave equation

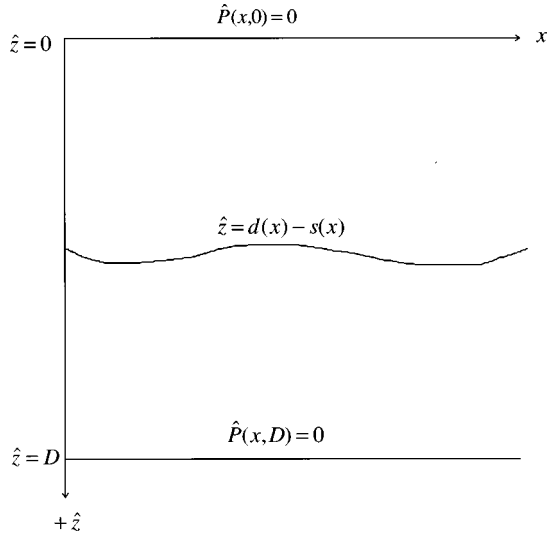

FIG. 2. Flattened surface waveguide.

$$\left[\frac{\partial}{\partial x}-s'(x)\frac{\partial}{\partial \hat{z}}\right]^2\hat{P}(x,\hat{z})+\hat{\rho}(x,\hat{z})\frac{\partial}{\partial \hat{z}}\left[\frac{1}{\hat{\rho}(x,\hat{z})}\frac{\partial \hat{P}(x,\hat{z})}{\partial \hat{z}}\right]$$
$$+\hat{k}^2(x,\hat{z})\hat{P}(x,\hat{z})=0, \tag{4}$$

with the boundary conditions $\hat{P}(x,0)=0$ and $\hat{P}(x,D)=0$.

A parabolic approximation to Eq. (4) is obtained, formally, by defining the linear partial differential operators

$$T=\frac{\partial}{\partial x}-s'(x)\frac{\partial}{\partial \hat{z}}$$

and

$$L=\hat{\rho}(x,\hat{z})\frac{\partial}{\partial \hat{z}}\left[\frac{1}{\hat{\rho}(x,\hat{z})}\frac{\partial}{\partial \hat{z}}\right]+\hat{k}^2(x,\hat{z}).$$

Then Eq. (4) becomes $[T^2+L]\hat{P}=0$ or

$$[(T+i\sqrt{L})(T-i\sqrt{L})+i(T\sqrt{L}-\sqrt{L}T)]\hat{P}=0. \tag{5}$$

The parabolic approximation is made by neglecting the effect of the commutator $(T\sqrt{L}-\sqrt{L}T)$ in Eq. (5) and selecting the outgoing wave to obtain $(T-i\sqrt{L})\hat{P}=0$. The flattened surface parabolic equation is then

$$\frac{\partial \hat{P}}{\partial x}=s'(x)\frac{\partial \hat{P}}{\partial \hat{z}}+i\sqrt{L}\hat{P}. \tag{6}$$

The first term on the right hand side of Eq. (6) is the result of the surface flattening transformation. The second term is a pseudodifferential operator that is often encountered when the parabolic approximation is applied to the reduced wave equation.

Note that the commutator in Eq. (5) is composed of two terms

$$T\sqrt{L}-\sqrt{L}T=\left(\frac{\partial}{\partial x}\sqrt{L}-\sqrt{L}\frac{\partial}{\partial x}\right)+s'(x)\left[\frac{\partial}{\partial \hat{z}}\sqrt{L}-\sqrt{L}\frac{\partial}{\partial \hat{z}}\right].$$

The neglect of the first term in the commutator is usually associated with the parabolic approximation, although its neglect is more significant here due to the added range dependence in L caused by the irregular surface. The neglect of the surface slope term in the commutator is a second additional approximation. The combination of these two approximations is the assumption that forward scattering is dominant. The second of these approximations will ultimately be used in solving Eq. (6) by operator splitting.[17] The two operators, on the right hand side of Eq. (6), will be applied in succession and it will be necessary that their order is unimportant or else nonunique results are obtained.

The pseudodifferential operator in Eq. (6) is handled by a linearlization procedure based on a rational linear Padé approximation.[18] The main range dependence of the complex pressure is removed by factoring $\hat{P}$ into $\hat{P}=\exp(ik_0x)U$, where U is a slowly varying envelope and k_0 is a reference wave number. Then Eq. (6) becomes

$$\frac{\partial U}{\partial x}=s'(x)\frac{\partial U}{\partial \hat{z}}+ik_0\left[\sqrt{1+\frac{L-k_0^2}{k_0^2}}-1\right]U. \tag{7}$$

At this stage the only approximation that has been made is the parabolic approximation. If it is assumed that the effect of the operator $(L-k_0^2)/k_0^2$ is small, then the pseudodifferential square root operator in Eq. (7) can be approximated by a finite sum of ratios of linear functions of L and Eq. (7) can be approximated by an equation of the form

$$\frac{\partial U}{\partial x}=s'(x)\frac{\partial U}{\partial \hat{z}}+ik_0\left[\sum_{\ell=1}^{M}\frac{\beta_\ell(L-k_0^2)}{k_0^2+\gamma_\ell^2(L-k_0^2)}\right]U, \tag{8}$$

where β_ℓ and γ_ℓ^2 are Padé coefficients and M is the order of the rational linear Padé approximation.[18] Properly formulated higher order approximations give more accurate solutions for higher angle propagation.

Equation (8) is solved by splitting,[17] which relies on the approximate commutativity of the operators on the right hand side of the equation. The field U is advanced by applying an implicit finite difference scheme in range, separately and successively, to each of the terms in the sum on the right hand side of Eq. (8). The equations involving the rational linear terms are linearlized by removing the denominators to the opposite sides of the equations. The splitting procedure used here was developed by Collins[19] who called it alternating direction. The splitting procedure is also described in the introductory section on the higher-order parabolic equation, in Ref. 20.

The separate application of the operator resulting from the surface flattening transformation

$$\frac{\partial U}{\partial x}=s'(x)\frac{\partial U}{\partial \hat{z}} \tag{9}$$

is one more step in the splitting. The exact explicit solution of Eq. (9) for a range step Δx and an infinite depth interval, including an image ocean, is

$$U(x+\Delta x,\hat{z})=U(x,\hat{z}+s(x+\Delta x)),$$

but it does not necessarily satisfy the boundary conditions. An implicit numerical approach is used that enforces the boundary conditions and retains the finite depth interval.

II. NUMERICAL IMPLEMENTATION

The numerical solution of the equation

$$\frac{\partial U}{\partial x}-s'(x)\frac{\partial U}{\partial \hat{z}}=0 \tag{10}$$

on the finite depth interval is described here. Equation (10) is just a restatement of Eq. (9) that better fits the discussion here. The numerical implementation uses the Galerkin method (alternatively called a finite element method) and is designed to be consistent with the finite element parabolic equation model, FEPE.[21]

The envelope function U is approximated using an expansion in terms of the basis set of piecewise linear hat functions[19,22]

$$U(x,\hat{z})\cong\sum_{j=1}^{N}U_j(x)\Psi_j(\hat{z}). \tag{11}$$

The $\Psi_j(\hat{z})$ are defined with the depth mesh $\hat{z}_j = j\Delta\hat{z}$ and $\Delta\hat{z} = D/(N+1)$. They are zero for $|\hat{z}-\hat{z}_j| \geqslant \Delta\hat{z}$, increase linearly from zero to one on the interval $[\hat{z}_{j-1}, \hat{z}_j]$, and decrease linearly from one to zero on $[\hat{z}_j, \hat{z}_{j+1}]$. The approximation of $U(x,\hat{z})$ is a piecewise linear function of $\hat{z}$ that need not be differentiable, with respect to $\hat{z}$, at the grid points $\hat{z}_j$. This is by design. The function $U(x,\hat{z})$ must fail to be differentiable at $\hat{z} = d(x) - s(x)$ to satisfy continuity of the vertical particle velocity when there is a discontinuity in the density. The discontinuity occurs at a grid point in the approximation. In the solution process, the operators T and L are only considered to operate under an integral over $\hat{z}$ and multiplied by a hat basis function. In this setting, the operator L is applied using integration by parts[23] and the continuity conditions.

The Galerkin method is as follows: The expansion in Eq. (11) is substituted into the left hand side of Eq. (10) and the result (the residual error) is required to be orthogonal to each member of the hat function basis set for $j = 1,N$. This yields the following system of ordinary differential equations for the expansion coefficients $U_j(x)$:

$$\frac{d}{dx}\left[\frac{U_{j-1}(x)+4U_j(x)+U_{j+1}(x)}{6}\right] = s'(x)\left[\frac{U_{j+1}(x)-U_{j-1}(x)}{2\Delta\hat{z}}\right], \tag{12}$$

where $U_0(x)$ and $U_{N+1}(x)$ are defined to be identically zero.

Equation (12) is solved, assuming $s'(x)$ is constant over a range step Δx, using a forward difference on the left hand side and an average of current and advanced values, of the quotient, on the right hand side. This implicit method is analogous to the implicit finite difference scheme (Crank–Nicolson) in Ref. 24. It results in a tridiagonal system of linear algebraic equations

$$(a+b)U_{j-1}(x+\Delta x)+cU_j(x+\Delta x)+(a-b)U_{j+1}(x+\Delta x) = (a-b)U_{j-1}(x)+cU_j(x)+(a+b)U_{j+1}(x),$$

where $a = 1/6\Delta x$, $b = s'(x)/4\Delta\hat{z}$, and $c = 2/3\Delta x$. The overhead of this additional tridiagonal solve is the same as adding one more higher angle term to the Padé sum and it incorporates forward scattering from the irregular sea surface.

III. EXAMPLES

The numerical implementation of the surface flattening procedure is checked against results for some bench mark problems.

A. Surface directed beam

The first example chosen is test case 1 from the Reverberation and Scattering Workshop held at Gulfport, MS on 2–6 May 1994. The problem is due to Thorsos[25] and consists of a 400 Hz Gaussian beam incident, from a half-space, on an irregular free surface at a grazing angle of $\theta = 10$ degrees.

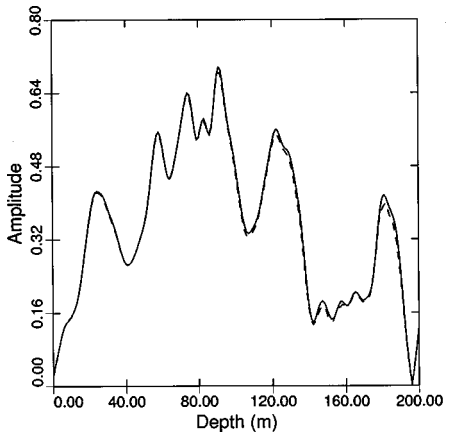

FIG. 3. Complex pressure amplitude versus depth for example A with the integral equation result as the solid curve and the flattened surface parabolic equation result as the dashed curve.

The beam's source is centered $z_s = 66.12$ m below the free surface and the beam has a half-width of $g = 27.55$ m. The starting field is

$$P(0,z) = \exp[-(z-z_s)^2/g^2]\exp[-i(k_0 \sin\theta)z],$$

where k_0 is the reference wave number corresponding to the half-space sound speed of 1500 m/s. The density is 1.0 g/cm^3. The surface is a single realization from a Pierson–Moskowitz spectrum for a wind speed of 15 m/s. A plot of the surface can be found in Ref. 26. The surface is sampled every tenth of a wavelength at 0.375 m increments over a range of 750 m and has excursions of 3 m, both above and below mean sea level. The geometry is such that the ray at the center of the beam, once reflected from a flat free surface, would return to the source depth at the range of 750 m.

The above formula for the starting field, defining the incident beam, and the realization of the irregular free surface were provided as part of test case 1. Solutions were obtained by Thorsos[25] using both first and second kind integral equations. The two integral equation solutions were essentially equivalent and one was provided as complex pressure versus depth at the range of 750 m.

The starting field and surface realization were input to a modified version of FEPE based on the flattened surface parabolic equation in Eq. (6). The half-space is represented by a water layer over an artificial sediment layer, or absorber, starting 132.24 m below the mean sea surface. The absorber will subsequently be replaced with a physical sediment layer in example B and the reason for starting at 132.24 m will become apparent. The absorber has the same sound speed and density as the water, but its attenuation is a function of depth. The attenuation in the absorber is held fixed at 0 dB per wavelength from 132.24 m to 300 m, increases linearly to 1 dB per wavelength at 400 m and again linearly to 10 dB per wavelength at 500 m, where the problem is terminated. A range step of 0.375 m and depth increment of 0.075 m are used with 4 terms in the rational linear Padé approximation. The results of the flattened surface parabolic equation calculation and the integral equation reference solution are both shown in Fig. 3. The amplitude of the complex pressure versus depth is plotted with the integral equation result as the

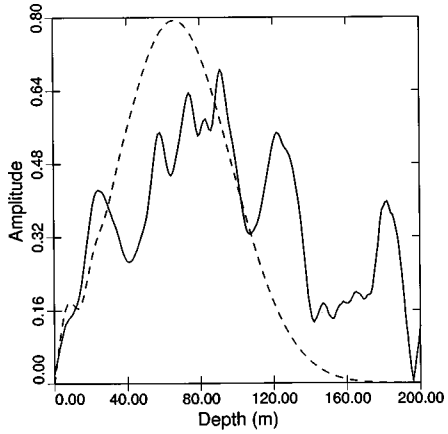

FIG. 4. Complex pressure amplitude versus depth for example A with the rough surface result as the solid curve and the flat surface result as the dashed curve. Both results were obtained from the flattened surface parabolic equation.

solid curve and the flattened surface parabolic equation result as the dashed curve. The small differences are probably due to the outgoing nature of the parabolic equation or the numerical differentiation of the sea surface heights. The integral equation incorporates backscattering and the analytic expression for the surface slope. There is very good agreement in the overall shape of the two curves.

The agreement of the two solutions, in Fig. 3, demonstrates the validity of the flattened surface parabolic equation for this case. This is especially impressive in view of the variations of the results from one realization to the next[25] and the complexity of the field in the beam reflected from a single realization of the irregular surface. The latter point starts to become apparent when the beam reflected from the irregular surface is contrasted with the beam reflected from the flat surface, as shown in Fig. 4. The dashed curve is the flat surface result. The scope of the scattering problem is brought home by the two gray scale contour plots of intensity level (including cylindrical spreading) versus range and depth in Figs. 5 and 6. There is no question of the effect of the irregular surface in Fig. 6.

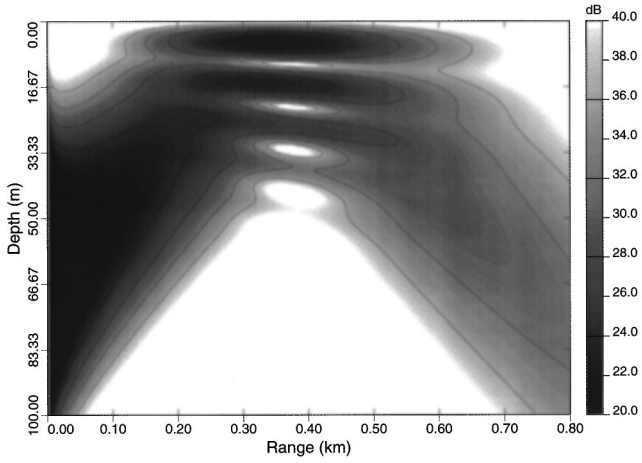

FIG. 5. Intensity level, with cylindrical spreading included, versus range and depth for the flat surface beam reflection problem of example A.

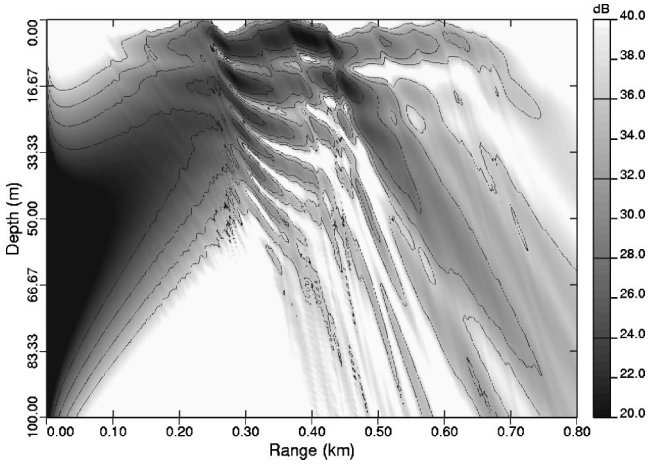

FIG. 6. Intensity level, with cylindrical spreading included, versus range and depth for the rough surface beam reflection problem of example A.

B. Bottom directed beam

Example A avoids the potential numerical complications caused by reflection from a bounding sediment layer and the associated waveguide propagation. The flattened surface parabolic equation is designed for such a situation. The example presented here includes a bounding sediment layer. A physical sediment layer is introduced in example A starting at a depth of 132.24 m and extending to a depth of 500 m. The sediment has a sound speed of 1700 m/s, a density of 1.5 g/cm^3 and an attenuation of 0.5 dB per wavelength. The physical attenuation replaces the 0 dB per wavelength used in the top of the absorber in example A. The beam used in example A is modified to be directed downward toward the water–sediment interface with a grazing angle of 10 degrees. The critical grazing angle of the bottom is approximately 28 degrees. The water depth is chosen so that the ray at the center of the bottom reflected beam returns to the source depth at the range of 750 m. The same irregular sea surface provided with test case 1 is used. The range and depth mesh used are the same as above.

In this example the flattened surface parabolic equation

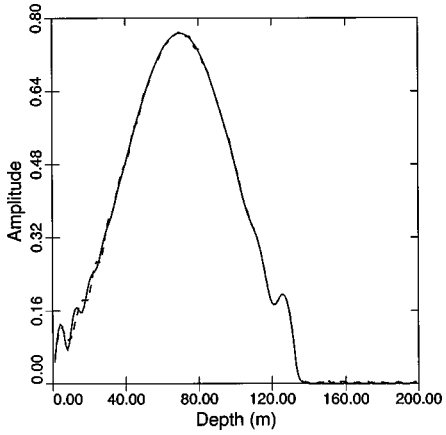

FIG. 7. Complex pressure amplitude versus depth for bottom reflected beam of example B in a waveguide with both an irregular and flat sea surface. The flat surface result is the solid curve and the irregular surface result is the dashed curve. The beam does not interact with the sea surface. Both results were obtained from the flattened surface parabolic equation.

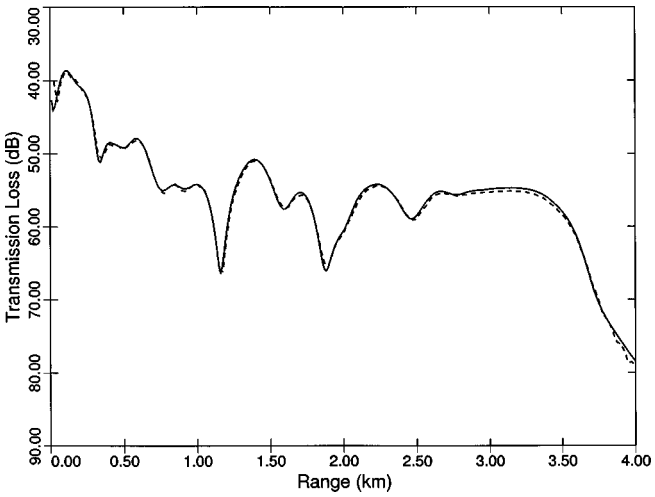

FIG. 8. Transmission loss versus range in the penetrable wedge of example C. The solid curve is the coupled mode result and the dashed curve was obtained with the flattened surface parabolic equation. The loss of energy, expected from the uncorrected parabolic equation calculation, does not occur.

is distinguished by what it should not do. The beam should not interact much with the irregular sea surface. In spite of the irregularities introduced at the water–sediment interface and the extra surface slope term in the partial differential equation, the results with the irregular sea surface should be essentially the same as the results with the flat sea surface. This is indeed the case as can be seen in Fig. 7 where the amplitude of the complex pressure versus depth at a range of 750 m is plotted. The result for the regular waveguide is the solid curve and the result for the irregular waveguide is the dashed curve.

C. Penetrable wedge

The last example is designed to further investigate the numerical consequences of the surface flattening transformation. It is known that some parabolic equation models fail to conserve energy in sloping environments;[27] they gain energy on the downslope and loose energy on the upslope. The loss, in excess of what would occur due to attenuation, is a consequence of not completely satisfying the interface conditions on the sloping bottom. It is possible to make a correction for this problem, but the version of FEPE used here did not have this correction. The correction is usually needed to obtain an accurate parabolic equation solution in the Acoustical Society of America benchmark penetrable wedge.[27] The material properties of the two fluid regions, forming the wedge, are the same as the two fluid regions in example B. The problem can be solved, with the flattened surface parabolic equation, by sloping the free surface[14] instead of the bottom. Since the surface is flat, the term surface flattening transformation is somewhat out of place, but the transformation may still be applied. The wedge is created by holding the depth of the water–sediment interface constant at 200 m and linearly increasing the depth of the free surface from 0 to 200 m over the range interval 0 to 4 km. A 25 Hz source is placed at a depth of 100 m at a range of 0 km. The transmission loss, including cylindrical spreading, to a receiver 30 m below the free surface is shown in Fig. 8 on the range interval 0 to 4 km. The solid curve is the coupled mode result[27] while the dashed curved was obtained with the flattened surface parabolic equation. The parabolic equation result does not suffer the loss of energy that would be expected from the uncorrected FEPE. The explanation for this is as follows: The simple surface flattening transformation is mathematical rather than physical and, if done correctly, it does not provide the opportunity for loss of physical energy. The energy conservation correction[27] can still be applied to the field as a function for the original independent depth variable z (not $\hat{z}$), but it would have no effect in this case since the interface is at a constant depth in z.

IV. CONCLUSIONS

The simple surface flattening transformation is useful in parabolic equation calculations with an irregular surface. In the flattened surface parabolic equation, the surface irregularities are transferred into volume irregularities and another term is introduced into the partial differential equation. The volume irregularities and the additional surface slope term are easily integrated in a high angle parabolic equation solution technique such as the one due to Collins.[19,21] Results obtained from the flattened surface parabolic equation compare well with results obtained from a boundary integral equation technique applied to a test case by Thorsos.[25]

The analysis reported here was motivated by an attempt to gain a better perspective on boundary perturbation theory. It subsequently became a diversion from perturbation theory. The simple surface flattening transformation is a reasonable alternative to perturbation theory that contains an identifiable contribution from the irregular surface. It is not the intent to imply that the simple surface flattening transformation is the best, or only, nonperturbative method for solving the forward scatter problem. In the course of study it was found that the numerical technique of Collins *et al.*[13] was just as useful when applied to example A. The conformal mapping procedure of Norton *et al.*[10] gives highly accurate results for example A. The agreement of these techniques on one or two test cases is not to be taken as indication that the problem is completely solved. It is an indications that an investigation of more comprehensive test cases should be undertaken to determined the strengths and weaknesses of the various methods.

ACKNOWLEDGMENTS

This work was conducted while the author was a Guest Investigator at the Woods Hole Oceanographic Institution (WHOI) and working for Science Applications International Corporation (SAIC). The author thanks WHOI for its gracious hospitality and SAIC for involving him in the project sponsored by the SSBN Security Program N87 under Contract No. N00014-94-C-0061. The author also thanks Mike Collins and Eric Thorsos for providing some essential ingredients. The efforts and comments of the reviewers are greatly appreciated.

[1] E. Y. Harper and F. M. Labianca, ''Perturbation theory for scattering of sound from a point source by a moving rough surface in the presence of refraction,'' J. Acoust. Soc. Am. **57**, 1044–1051 (1975).
[2] R. Courant and D. Hilbert, *Methods of Mathematical Physics* (Wiley–Interscience, New York, 1962), Vol. II, p. 474.
[3] T. Kato, *Perturbation Theory for Linear Operators* (Springer-Verlag, New York, 1976), 2nd ed., p. 424.
[4] J. A. Konrady, ''Scattering of sound from time-varying irregular free surface,'' J. Acoust. Soc. Am. **56**, 1687–1694 (1974).
[5] H. D. I. Abarbanel, ''Scattering from a random surface,'' J. Acoust. Soc. Am. **68**, 1459–1466 (1980).
[6] F. D. Tappert, ''The parabolic approximation method,'' in *Lecture Notes in Physics, Vol. 70, Wave Propagation and Underwater Acoustics*, edited by J. B. Keller and J. S. Papadakis (Springer-Verlag, New York, 1977).
[7] A. Beilis and F. D. Tappert, ''Coupled mode analysis of multiple rough surface scattering,'' J. Acoust. Soc. Am. **66**, 811–826 (1979).
[8] A. E. Barrios, ''A terrain parabolic equation model for propagation in the troposphere,'' IEEE Trans. Antennas Propag. **42**, 90–98 (1994).
[9] L. B. Dozier, ''PERUSE: A numerical treatment of rough surface scattering for the parabolic equation,'' J. Acoust. Soc. Am. **75**, 1415–1432 (1984).
[10] G. V. Norton, J. C. Novarini, and R. S. Keiffer, ''Coupling scattering from the sea surface to a one-way marching propagation model via conformal mapping: Validation,'' J. Acoust. Soc. Am. **97**, 2173–2180 (1995).
[11] F. D. Tappert and L. Nghiem-Phu, ''A new split step Fourier algorithm for solving the parabolic wave equation with rough surface scattering,'' J. Acoust. Soc. Am. Suppl. 1 **77**, S101 (1985).
[12] A. P. Rosenberg and S. F. Magruder, ''An accurate, efficient parabolic equation program that permits a rough ocean surface,'' STD-N-1004 (The Johns Hopkins University, Applied Physics Laboratory, Laurel, MD, September 1994).
[13] M. D. Collins, R. A. Coury, and W. L. Siegmann, ''Beach acoustics,'' J. Acoust. Soc. Am. **97**, 2767–2770 (1995).
[14] M. D. Collins, ''The rotated parabolic equation and sloping ocean bottoms,'' J. Acoust. Soc. Am. **87**, 1035–1037 (1990).
[15] D. J. Thomson, G. H. Brooke, and E. S. Holmes, ''PE approximations for scattering from a rough surface,'' Tech. Memo. 95-21 (Defense Research Establishment Pacific, Victoria, BC, Canada, March 1995).
[16] M. Shinozuka and C. M. Jan, ''Digital simulation of random processes and its applications,'' J. Sound Vib. **25**, 111–128 (1972).
[17] R. D. Richtmyer and K. W. Morton, *Difference Methods for Initial Value Problems*, 2nd ed. (Wiley–Interscience, New York, 1967), pp. 216–217.
[18] A. Bamberger, B. Engquist, L. Halpern, and P. Joly, ''Higher order paraxial wave equation approximations in heterogeneous media,'' SIAM (Soc. Ind. Appl. Math.) J. Appl. Math. **48**, 129–154 (1988).
[19] M. D. Collins, ''Applications and time-domain solutions of higher-order parabolic equations in underwater acoustics,'' J. Acoust. Soc. Am. **86**, 1097–1102 (1989).
[20] M. D. Collins, ''A split-step Padé solution for the parabolic equation method,'' J. Acoust. Soc. Am. **93**, 1736–1742 (1993).
[21] M. D. Collins, ''FEPE User's Guide,'' NORDA Tech. Note 365 (Naval Research Laboratory, Stennis Space Center, MS, October 1988).
[22] D. Huang, ''Finite element solution of the parabolic wave equation,'' J. Acoust. Soc. Am. **84**, 1405–1413 (1988).
[23] K. E. Gilbert and M. J. White, ''Application of the parabolic equation to sound propagation in a refracting atmosphere,'' J. Acoust. Soc. Am. **85**, 630–637 (1989).
[24] R. D. Richtmyer and K. W. Morton, *Difference Methods for Initial Value Problems*, 2nd ed. (Wiley–Interscience, New York, 1967), p. 17.
[25] E. I. Thorsos, ''Test Case 1: Sea Surface Forward Scattering,'' to appear in the proceedings of the Reverberation and Scattering Workshop, 2–6 May, 1994, Gulfport, MS (1998).
[26] F. D. Hastings, J. B. Schneider, and S. L. Broschat, ''A finite-difference time-domain solution to scattering from a rough pressure release surface,'' J. Acoust. Soc. Am. **102**, 3394–3400 (1997).
[27] F. B. Jensen, W. A. Kuperman, M. B. Porter, and H. Schmidt, *Computational Ocean Acoustics* (AIP Press, New York, 1994), pp. 396–399.

Matched-beam processing: Range tracking with vertical arrays in mismatched environments

T. C. Yang and Kwang Yoo
Naval Research Laboratory, Washington, DC 20375

T. Yates[a)]
Vector Research Corporation, 2101 Jefferson Street, Rockville, Maryland 20852

(Received 13 June 1997; accepted for publication 5 June 1998)

This paper addresses the problem of range tracking using one or more vertical arrays in certain mismatched shallow-water environments. The objective is to obtain continuous tracking of a target thereby allowing the target to be distinguished from false alarms. It is shown that bottom mismatch can cause large range errors at discrete source ranges as observed in previous experiments. Also, significant range errors (offsets) can result from unknown array tilt. Discrete range errors impede the ability to detect a target by integrating along the target track (track-before-detect) or by a probability based target detection and tracking algorithm. Large range errors impede the ability to localize and track the target from multiple vertical arrays. These problems are addressed using matched-beam processing whereby certain bottom mismatch is minimized by a beam filter and unknown array tilt is estimated by matching the measured beam pattern against the calculated one. Beam filtering and beam matching are simple and convenient methods to implement in practical systems. Comments are also given on other applications using beam domain processing. [S0001-4966(98)00310-5]

PACS numbers: 43.30.Wi, 43.30.Pc, 43.60.Gk [DLB]

INTRODUCTION

Matched-beam processing is matched-field processing[1] in the beam domain. It is based on conventional plane-wave beamforming, but extends the conventional processing to incorporate full-field processing. As such, it extends the advantage of matched-field techniques to existing systems where the conventional beam outputs are often the only data readily available. Matched-beam processing was applied to a horizontal line array in a previous paper.[2] It was shown to be a more efficient and robust approach for correcting bearing errors and signal gain degradation of a horizontal line array in shallow water.[2] Matched-beam processing has also been applied to a vertical array to improve the robustness of acoustic inversion of the bottom properties.[3,4]

In this paper, we apply matched-beam processing to range tracking using one or multiple vertical arrays. We address in particular how matched-beam processing handles certain environmental mismatch problems.

Source localization in range and depth can be achieved using matched-field[1] or matched-mode[5] processing. Source location is determined by the highest peak in the range–depth ambiguity where the correlation of the replica field and data field is the highest. This is the case, in principle, only when the replica field source is at the location of the true source (assuming signal propagation is accurately modeled). In the real world, the requirement of an accurate replica field that matches the data exactly is hard to achieve due to lack of information or inaccurate environmental data. Here lies the mismatch problem. Signal processing methods that deal with the mismatch problems are briefly reviewed in the next section.

Range tracking is an extension of the source localization problem involving a moving source. We shall assume that the source depth is known or it will be searched separately. The moving source problem is more complicated than the stationary source problem, since source localization is required not just at one range but at all ranges. Previous data have shown that range tracking can be discontinuous when large range errors occur at some ranges, such as when there is mismatch in bottom sound-speed profile.[6] The range estimate can be offset by a substantial amount due to mismatch in bottom depth.[7,8] Unknown array tilt can also interfere with range tracking resulting in either range errors or range offsets, prompting a direct or acoustic inversion approach for array shape estimation.[9]

Range tracking can encounter two problems. One problem is that the target is continuously tracked but range estimates have errors (e.g., constant offset). One expects that in this case the target is localized by the main lobe in the ambiguity surface. The other problem is frequent large range errors as when the sidelobe has a higher level than the main lobe at some source ranges. Both problems can occur at the same time; in that case, target tracking can be ambiguous. Range tracking is not possible when source localization yields inconsistent results as the source moves, as when the range versus time display becomes random.

Continuous target tracking is an important tool to distinguish the target from false alarms when the signal level is weak and when many peaks are present in the ambiguity surface due to clutter or noise. Continuous target tracking

[a)]Current address: Naval Surface Warfare Center Carderock Div., West Bethesda, MD 20817. Electronic mail: yates@wave14i.nrl.navy.mil

can be used to improve the detection of a weak signal by integrating the signal along the target track using the track-before-detect matched-field processing methods.[10–13] Track-before-detect matched-field processing involves intensive computations as various target tracks need to be searched. It requires that the environment (used for the replica field) supports consistent target localization as the target range changes, else the integration gain may be limited. This requirement must be satisfied even in the presence of environmental mismatch as real world environmental mismatch may be present but not *a priori* known.

A similar concept is used in the detection and tracking of a target using multiple vertical arrays. We note that while target tracking may be possible with a single vertical array,[14] in practice it is more likely that multiple ($\geqslant 3$) vertical arrays will be deployed to track the target. Let us first consider localization of a stationary source with multiple vertical arrays in a range-independent environment. The source can be localized in the x-y horizontal plane at the source depth by range estimates from the multiple vertical arrays.[15] A simple algorithm has been demonstrated in an Arctic environment using simulated data.[15] The algorithm works as follows: Since a vertical array has no bearing information, the range estimate applies to all bearing. Thus for each vertical array, a cylindrical range ambiguity surface centered at the array (x,y) position is created using the range ambiguity function. The range ambiguity surfaces, properly aligned with respect to the array positions, are next summed to create an ambiguity surface over the x-y plane. Target location is determined by the highest peak in this surface. We note that when a target is correctly localized in range with respect to all vertical arrays, the summation of the range ambiguity surfaces will produce a high peak at the target (x,y) location (main lobe). The summation of sidelobes, on the other hand, will produce a level weaker than the main lobe level since a strong sidelobe with respect to one array is unlikely to also be a strong sidelobe to another array.

This method can be used to track a target if the target shows up as a consistent and continuous peak in the x-y plane as the target moves. This requires consistent and continuous range tracking from each individual vertical array. One notes that using multiple vertical arrays, this method can often tolerate high sidelobes in individual range ambiguity functions as they conspire only occasionally to form a (local) peak in the x-y plane. One also notes that target depth can be determined by the x-y plane displaying the highest intensity target track.[15]

In shallow water, the problem is more complicated as each sensor produces a multiplicity of range possibilities which is difficult to resolve into a target track. A target detection and tracking algorithm for multiple vertical arrays has been formulated by converting the range ambiguity functions into a probability distribution (likelihood estimation) of a target as a function of the (x,y) coordinates.[16,17] The probability distribution of a target as a function of the (x,y) coordinates is continuously upgraded with each new contact using target motion (target state) analysis.[17] It was found that consistency in target tracking can be used to enhance the detection of a moving source by coherent fusion of the data along the target track (target state) with a nonlinear filter.[17] Discontinuous target tracking diminishes the probability of detection. (The nonlinear filter differentiates this algorithm from the track-before-detect method; the nonlinearity comes from the fact that the probability has to be normalized to one with each data fusion from multiple arrays.)

Based on the discussions above, our objective in this paper is to develop a method for consistent and continuous target tracking from a vertical array. We will consider certain mismatched environments. We note that in a research problem, there are plenty of opportunities to refine the acoustic environment until one localizes the source where it is supposed to be. Note that most of the matched-field processing work is done with a stationary source. In a practical problem, when target location is unknown, there is no ground truth to refine the acoustic environment (for the replica field) nor is there time to perform intensive searches for the correct acoustic parameters. A simple and robust method is desired. Our approach as illustrated below in this paper is to use matched-beam processing, whereby a beam filter is used to suppress the environmental mismatch.

I. ENVIRONMENTAL MISMATCH

As environmental mismatch is perhaps the primary issue for applications of matched field/mode processing to real world problems, we shall briefly review the various approaches to solve this problem and then discuss how matched-beam processing handles the environmental mismatch.

There are basically three different approaches. The first approach attempts to adjust the environmental parameters until there is a good match between the replica field and the data field. The search for the best match can be done using either the simulated annealing method,[18] the genetic algorithm method,[19] or the minimax method.[20] Alternatively, the environmental parameters and source location can be estimated using an *a posteriori* statistical model[21] assuming a certain probability distribution function for the environmental uncertainty. The acoustic model which agrees with the data has the highest probability, in theory, of yielding the highest matched-field correlation at the (true) target location. The model that best fits the data determines the parameters of the acoustic environment. A few cautionary notes are in order concerning the use of this method. First, it can happen that an environment that localizes the source at one range may not localize the source at another range. This can be avoided if the environment is close to being true or if there is ground truth to narrow down the search process for the true environment. Also, it may happen that the environment which localizes the source at one frequency may not localize the source at another frequency as indicated by some data.[22] Multiple tones or broadband signals can be used to suppress the sidelobes in the range–depth ambiguity[7] only if the main lobe is consistently located at the same place across the frequency band. Second, the ''optimal'' environment which localizes the source may depend on which and how many parameters are included in the search process. For example, should the vertical array tilt be included in the search? When the solutions (based on different assumptions) are not con-

sistent with each other, which one is the true solution? These issues are not a problem in a research project where the true source location is known. Different search parameters can be tried and the algorithm will eventually converge to a reasonable solution in agreement with the truth. Such options may not be available in a practical problem.

The second approach uses signal processing techniques such as the multiple constraints method,[23] the reduced maximum likelihood,[24] and the sector focusing method[25] to minimize the sensitivity of the processor outputs to the environmental mismatch. Robustness is obtained at the expense of resolution. Significant environmental mismatch may not be suppressed by signal processing alone.

The third approach uses the robust features of the signal field to localize the source. It assumes that certain properties of the signals will be insensitive to the variations or uncertainty in the environment. These properties may not be apparent from the raw data but can be extracted from the data using signal processing. In many cases, these robust features of the signals can be determined based on the physical analysis of sound propagation in a waveguide. For example, it is known that for low-frequency sound propagation in the Arctic, certain normal modes are insensitive to environmental mismatches.[5] In deep-water propagation, one can identify certain normal modes which are sensitive to sound-speed fluctuation in the upper water column due to surface warming[26] and/or internal waves.[27] In propagation through an oceanic front, certain normal modes are severely affected by mode coupling.[28] In shallow-water propagation, certain modes are less well sampled by the vertical array. Using mode filtering, one can suppress those modes which are either sensitive to environmental mismatch[26,29] or affected by the temporal and/or spatial variation in the sound channel.[27,28] The use of only the stable and predictable modes can improve source localization at the expense of lower signal gain and/or higher sidelobe levels.[26,29,30] Matched-mode processing has been applied to real data.[5,27,28]

Matched-beam processing handles the mismatch problem using a beam filter which follows a similar concept as the mode filter described above. We assume that the acoustic field can be conveniently characterized by discrete normal modes or by acoustic rays (as is the case for high frequencies). Conceptually, mode filtering or ray-selective processing could be used to discriminate against those modes or rays which are affected by the mismatch. In matched-beam processing, this discrimination process will be carried out using a beam filter, since each mode arrives on a vertical array with two specific arrival angles. Beam filtering can be more effective in shallow water than mode filtering when mode decomposition becomes ineffective due to the limited aperture of a vertical array (inability to sample acoustic energy which penetrates into the bottom); the beam filter is the equivalent of a mode cutoff which specifies which modes to discard. The fact that matched-beam processing relieves the requirement of exact mode decomposition could be an important consideration for shallow-water problems. For practical applications beam filtering is much easier to implement than mode filtering.

II. MATCHED-BEAM RANGE TRACKING

Matched-beam processing is matched-field processing in the beam domain. Matched-field processing was previously extended to the beam domain for a vertical array by Cox *et al.*[31] One notes that conventional beamforming has numerous applications to practical problems and its robustness is well recognized by the signal processing community. This prompts the following question: If one can apply coherent processing to a vertical array in the phone domain as in matched-field processing, what prevents one from applying coherent processing to the beam domain? Following this idea is the sub-array processing[31] approach. For a large aperture vertical array, it is generally agreed that the simple plane-wave assumption for the signal is invalid for the entire array due to the signal refraction and the presence of multipaths. However, the plane-wave assumption ought to be valid for a short vertical array. Hence the approach is to divide the array into several sub-arrays and use conventional beamforming for each short sub-array. The sub-array processor will then coherently combine the conventional beams for many sub-arrays according to the multipath arrival structure as a function of depth. The processor requires a proper choice for the sub-array aperture and a recipe for combining the beams on the sub-arrays.

Matched-beam processing uses a different approach than the sub-array approach; both start with conventional beam outputs. Matched-beam processing implements coherent processing by Fourier transforming both the data field and replica field into the beam domain. The data and replica beams are correlated to search for the source coordinates. As is well known, the correlation of signals in the time domain is the same as the correlation of the signals in the frequency domain (a Fourier transform). The equivalence of the two correlation results follows from the convolution theorem. By the same token, matched-beam processing, which is correlation in the beam domain, can be shown to be the same as its Fourier counterpart, i.e., matched-field processing. The Appendix shows the relation of matched-beam processing to conventional beamforming and matched-field processing. For practical applications, differences can occur for a short vertical array as discussed in the Appendix.

The matched-beam ambiguity surface for a vertical array is given by[3,4]

$$B(r,z)=\frac{\left|\int_{|\theta|<|\Theta_0|}A^{\mathrm{rplc}*}(\theta,r,z)A^{\mathrm{data}}(\theta-\theta_0)d\sin\theta\right|^2}{\left[\int_{|\theta|<|\Theta_0|}|A^{\mathrm{rplc}}(\theta,r,z)|^2 d\sin\theta\right]\left[\int_{|\theta|<|\Theta_0|}|A^{\mathrm{data}}(\theta-\theta_0)|^2 d\sin\theta\right]}, \tag{1}$$

where θ_0 is the angle shift corresponding to the array tilt, Θ_0 is the angle cutoff used for beam filter, and $A^{\text{data}}(\theta)$, $A^{\text{rplc}}(\theta)$ are the spatial Fourier transforms of the data and replica field, respectively, as defined by

$$A^{\text{data}}(\theta)=\sum_j e^{-ikz_j \sin\theta} p^{\text{data}}(z_j), \tag{2}$$

$$A^{\text{rplc}}(\theta,r,z)=\sum_j e^{-ikz_j \sin\theta} p^{\text{rplc}}(z_j,r,z), \tag{3}$$

where z_j is the receiver depth for the jth phone and r and z are the range and depth variable of the replica source. No assumption is made here that the acoustic field is a plane wave.

Next we turn our attention to source localization and range tracking. We note that in real data analysis, one often encounters incorrect source localizations and/or poor range tracking using the environmental data given. Often, one has no *a priori* clue as to why the incorrect answers. In research projects, as remarked above, successful source localizations can eventually be achieved after many adjustments of the environmental parameters or after employing an elaborate search method for these parameters. As such an option may not be feasible in practice, an alternative method will be needed. Our intention is to gain an understanding of the cause of the problem and devise a method to minimize the mismatch effect.

We note that for many data sets, one of the most common sources of mismatch is bottom mismatch as bottom properties are hard to measure and often least known. We shall hence examine how bottom mismatch affects range localization.[32] Let us discuss range estimation using normal modes.[5,33] We shall assume true source depth for the replica modes. We note that the range ambiguity function would have a (local) peak at range r if the modal phase of the replica field matches that of the data field

$$k_i' r - k_i r_s = 2n\pi, \tag{4}$$

where r_s is the true source range, and k_i and k_i' are the ith mode wave numbers of the data and replica fields, respectively. In Eq. (4), n is an integer; the solution with $n=0$ is the main lobe and the solutions with $n\neq 0$ are the sidelobes.

Equation (4) yields

$$k_i' \Delta r = -\Delta k_i r_s + 2n\pi, \tag{5}$$

where $\Delta r = r - r_s$ is the range bias, and $\Delta k_i \equiv k_i' - k_i$. Equation (5) can be used to address two kinds of range errors: the small and continuous range bias and the large and abrupt range errors; the latter causes range tracking to be intermittent and/or inconsistent.

Let us assume that the wave number mismatch in the low-order modes is small, i.e., $\Delta k_i / k_i' \ll 1$ for the low-order modes. An example is the constant or upward refractive sound-speed profile where the low-order modes are predominantly waterborne. The effect of the bottom is to cause a small mismatch in the low-order modes. From Eq. (5), one finds that range bias due to the mismatch in the low-order modes will be small, i.e.,

$$\Delta r = -\frac{\Delta k_i}{k_i'} r_s$$

and continuous with range.

[A comment is included here. Note that since the mode wave numbers calculated by a propagation code can never agree precisely with data (an uncertainty of 10^{-4}–10^{-3} in $\Delta k_i / k_i$ is not unusual), small range errors in the order of 0.01%–0.1% may be unavoidable.]

Assuming that the wave numbers of certain high-order modes disagree significantly between the data and replica fields, the effect on the range estimation including the mismatched modes will no longer be just a small range bias. Under certain circumstances the highest peak in the ambiguity surface will appear at a distance from the true range. This happens when the main lobes of the mismatched modes (denoted by j) coincide with the sidelobes of the low-order modes (denoted by i)

$$\Delta r = -\frac{\Delta k_i}{k_i'} r_s + \frac{2n_i\pi}{k_i'} \simeq -\frac{\Delta k_j}{k_j'} r_s, \tag{6}$$

where n_i is a different integer for a different mode. Neglecting $\Delta k_i / k_i'$ (for the low-order modes) as compared with $\Delta k_j / k_j'$, one finds

$$r_s \simeq -\frac{2n_i\pi}{k_i'} \left(\frac{k_j'}{\Delta k_j} \right).$$

We note that when Eq. (6) is satisfied for a majority of modes, the modes add coherently to produce a high peak at $r = r_s + \Delta r$ with Δr given by Eq. (6). If this peak has a higher intensity than the main lobe at $r = r_s$, the range estimation is in error.

Note that the above condition is only met at certain (discrete) ranges of the source r_s; the source is generally correctly tracked at other source ranges. At the ranges where Eq. (6) is satisfied, the range estimate would (abruptly) place the source outside the anticipated range-time track. As a result, source range tracking is discontinuous or intermittent along the expected range-time track. Large range errors at discrete ranges were found in previous experiments.[6]

Based on the mode analysis, the abrupt large range errors can be eliminated by suppressing the mismatch in the high-order modes. This can be done using mode filtering if mode amplitudes can be deduced from the phone data (mode decomposition[5]). Effective mode decomposition requires a vertical array which samples the depth functions of the dominant modes. In shallow water, there is a physical limitation to the vertical array size due to the water depth. If a significant portion of the acoustic field penetrates into the bottom and is not sampled by the vertical array in the water column, mode decomposition may not be effective.

An alternative method is to use beam filtering as embedded in matched-beam processing. We note that if the purpose is to suppress the high-order modes, a beam filter that discriminates the higher-order modes by the mode arrival angles will be just as good. No mode decomposition is required here.

Note that beam filtering has been used successfully for noise suppression in conventional beamforming. If the noise arrives at a different angle than the signal, it can be sup-

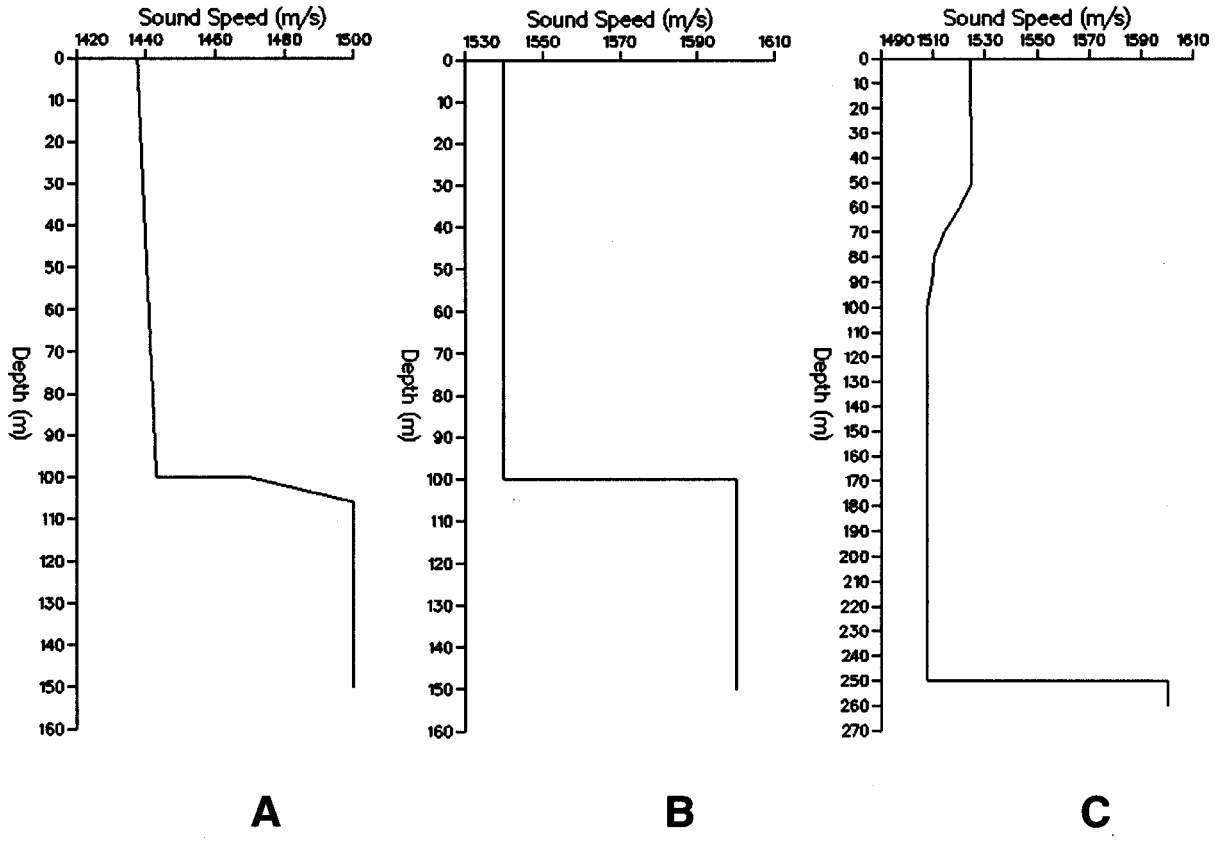

FIG. 1. Acoustic environments used in the simulation: (A) an upward refractive sound-speed profile, (B) a constant sound-speed profile, and (C) a downward refractive sound-speed profile.

pressed by (adaptively) steering the beam toward the source and away from the noise direction. The filtering of highly directional noise in the context of matched-beam processing is presented in a companion paper.[34] In the case of bottom mismatch we note that it affects different paths or different modes differently. Beam domain processing can be used to separate and filter the acoustic paths which have excessive mismatch.

The use of the beam filter in matched-beam processing will next be illustrated using three numerical examples. The effects of bottom mismatch are discussed in detail using simulated data. The hope is to develop a physical intuition which will be helpful in real data analysis. Note that the matched-beam analysis given below can be applied to real data to test if the underlying hypothesis of bottom mismatch is correct or not.

A. Upward refractive sound-speed profile

The first example involves a shallow-water environment with a winter sound-speed profile. The acoustic environment is illustrated in Fig. 1(A). The water depth is 100 m. The sound speed increases linearly with depth from 1437.5 m/s at the surface to 1443.0 m/s at the bottom. The bottom consists of a sediment layer of 6-m thickness with sound speed increasing with depth from 1470 m/s to 1500 m/s; the sediment has a density of 1.5 g/cm^3 and attenuation of 0.06 dB per wavelength. Under the sediment lies a (half space) basement with a sound speed of 1600 m/s, a density of 1.8 g/cm^3, and attenuation of 0.15 dB per wavelength. This sediment/bottom has been referred to as a soft bottom in previous literature.

A source is placed at the mid-depth of the water column (50 m), projecting a cw signal of 250 Hz. The acoustic field is received on a 31 element vertical array extending from 5 to 50 m, with a spacing of 3 m. The source moves from a range of 100 m to 10 km.

For the replica field, we assume a hard bottom with a sound speed of 1800 m/s, a density of 2 g/cm^3, and attenuation of 0.16 dB per wavelength.

Figure 2(A) plots the matched-field range ambiguity function which is the range–depth ambiguity function evaluated at the (true) source depth. (Throughout this paper, the replica field is focused at the source depth.) The vertical axis denotes the true source range which covers 100 m to 10 km. For a given source range, the range ambiguity function is displayed as a function of the search range. Note that the vertical axis in Fig. 2 can be displayed in time by dividing the source range by the speed of the source. The candidate track in Fig. 2 becomes then the range versus time track.

One notes that the (primary) range track in Fig. 2(A) is discontinuous (using the given replica environment). The reason is bottom mismatch which is discussed in more detail below. Note also that the bottom mismatch causes a significant signal gain degradation except at very close ranges (100 m).

Figure 2(B) shows a similar range ambiguity function plot using, in this case, matched-beam processing. Only

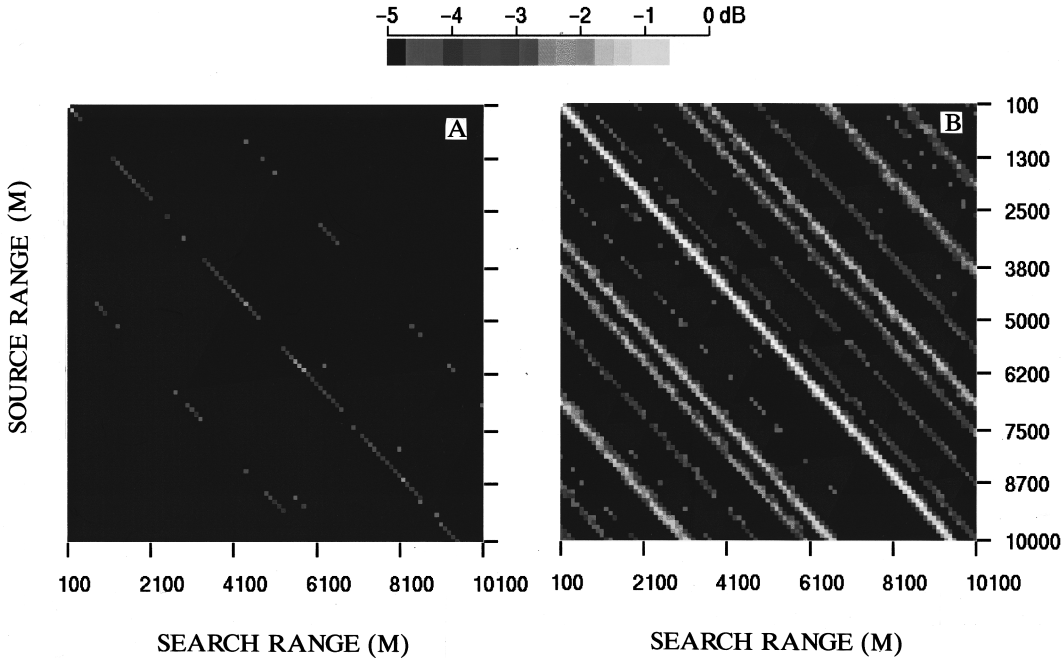

FIG. 2. Range ambiguity surface as a function of source range and search range in an upward refractive environment: (A) matched-field processing and (B) matched-beam processing with a beam filter.

beams with grazing angles $\leqslant 10°$ are included. Excluding the higher-order modes with arrival angles $>10°$ results in a relatively higher sidelobe level. One finds that the average peak-to-sidelobe level in Fig. 2(B) is slightly (1 to 2 dB) lower than in Fig. 2(A). The gain is that target tracking is consistent and continuous in Fig. 2(B). We find that the beam filter has some values from the point of view of improved target tracking.

Figure 3(A) and (B) shows the range error as a function of the source range for a search range from 100 m to 10 km. Range error is the difference between the estimated source range (associated with the highest peak of a range ambiguity function) and the true source range. Figure 3(A) shows the range error for matched-field processing, and Fig. 3(B) shows the range error for matched-beam processing with $\Theta_0 = 10°$. We see in both figures a small range bias that increases with range. For matched-field processing [Fig. 3(A)], there exists large range errors at many source ranges. If one excludes the points with large range errors ($\Delta r > 1$ km) in Fig. 3(A), one finds that range tracking is intermittent or discontinuous along the expected source track (similar to what was observed experimentally). With the beam filter, the large range errors are removed.

Naturally, the (next) question is how to select the beam filter. Before addressing that question, we first discuss how the beam filter is supposed to work. The physics of the beam filter is based on the bottom reflectivities for the two bottoms as shown in Fig. 4. Note in Fig. 4, the reflection loss for the hard bottom is negligible for grazing angles less than 35°. This coincides with the fact that the hard bottom has a criti-

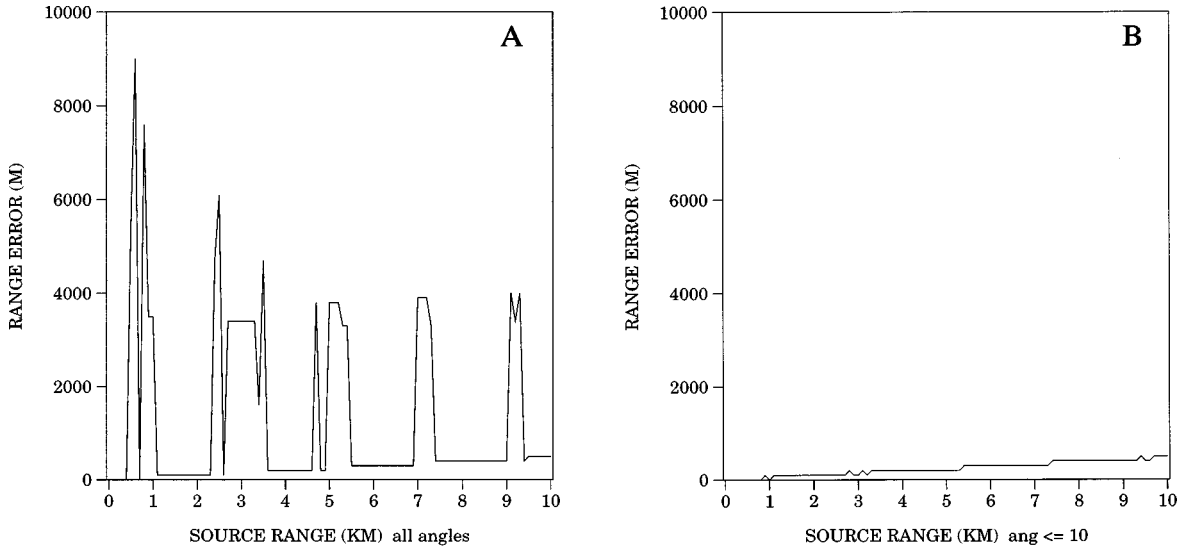

FIG. 3. Range error as a function of source range based on Fig. 2: (A) matched-field processing and (B) matched-beam processing with a beam filter.

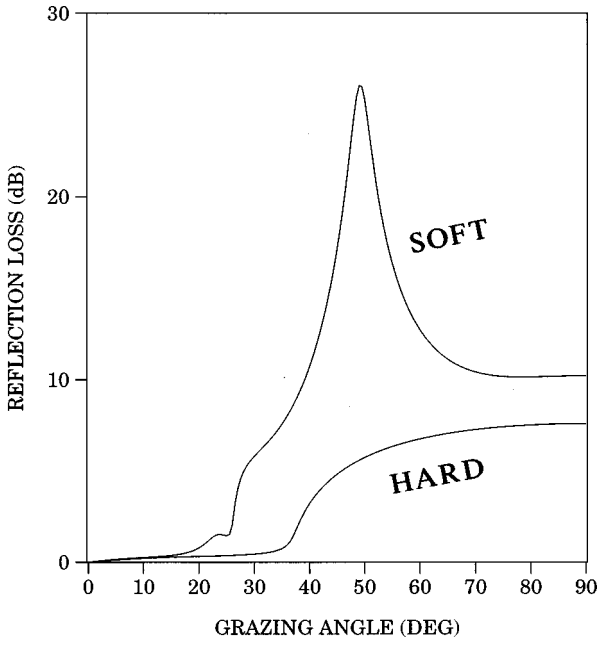

FIG. 4. Bottom reflection loss at 250 Hz as a function of incident grazing angle for the hard and soft bottom.

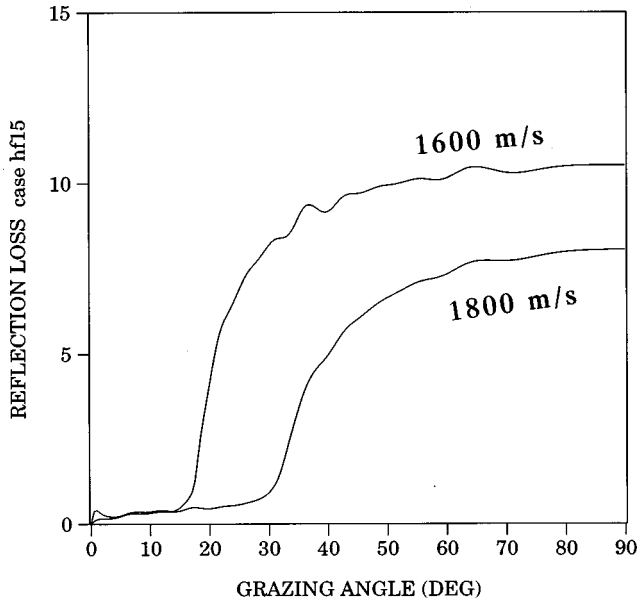

FIG. 5. Bottom reflection loss at 250 Hz as a function of incident grazing angle for two hard bottoms.

cal grazing angle of ~35° (small loss in Fig. 4 at angles <35° due to the evanescent waves). The soft bottom exhibits a substantial bottom reflection loss at grazing angles ≳25°. The mismatch of the reflection loss occurs at $\theta \gtrsim 15°$ between the soft and hard bottoms. Based on Fig. 4, we note that if we cut off beam correlations at angles ≳15° then bottom mismatch at angles ≳15° will be suppressed. This is the underlying principle for the beam filter.

In practice, since the bottom (and the bottom reflectivity) is not known, the beam filter has to be searched iteratively (see below). Note the angle estimate here is only approximate as the arrival angles changes with depth in a refractive sound-speed profile. In the above example we choose 10° to give us some safety margin.

B. Constant sound-speed profile

The next example involves a constant sound speed in the water column of 1540 m/s. See Fig. 1(B). The water depth is 100 m as above. The source and receiver configuration is the same as above. The cw frequency is also 250 Hz. The data are generated with a hard bottom which has a constant sound speed of 1600 m/s, density of 2 g/cm^3, and attenuation of 0.06 dB per wavelength. The replica fields are generated with a hard bottom with 1800 m/s with density and attenuation not changed. This is the same hard bottom used above.

Figure 5 plots the reflection loss for the two bottoms. We see that bottom mismatch starts at grazing angles ≳15°. We shall use a beam filter with $\Theta_0 = 10°$ as before.

Figure 6 shows the range ambiguity surfaces as a function of the source range and search range. Figure 6(A) and (B) uses matched-field processing and matched-beam processing ($\Theta_0 = 10°$), respectively. Figure 7(A) and (B) shows the range errors determined from Fig. 6(A) and (B), respectively. We see that the range error in Fig. 7(B) is much less than Fig. 7(A). We note that the average intensity along the target track in the matched-beam ambiguity surface [Fig. 6(B)] is about 2 dB higher than that in the matched-field ambiguity surface [Fig. 6(A)].

C. Downward refractive sound-speed profile

Last, we consider a summer environment with a downward refractive sound-speed profile. We use a linear sound-speed profile with a sound speed of 1524.4 m/s at the surface and 1507.7 m/s at the bottom as shown in Fig. 1(C). The water depth is 250 m. We use the same two bottoms as in the previous example. The source frequency is 100 Hz. The source depth is at 50 m. The receiver array consists of 31 phones spanning the water column from 5 m to 245 m, with a uniform spacing of 8 m.

Figure 8 plots the reflection loss for the two hard bottoms at 100 Hz. Compared with Fig. 5 (250 Hz), we note that the reflection loss is practically the same except for some minor details.

Figure 9(A) and (B) plots the range ambiguity surfaces as a function of the source range and the search range using matched-field processing and matched-beam processing (with $\Theta_0 = 13°$), respectively. One notes again that the intensity of the matched-field surface along the source track is (0.5–2 dB) weaker than the track in the matched-beam surface. Figure 10(A) and (B) plots the range errors for the two processors. One notes that for matched-field processing, source tracking has frequently been interrupted by erroneous peaks appearing ~4 km away. There are more occurrences of (>1 km) range errors in this case than the previous case because the sound is downwardly refracted and interacts more with the bottom than in the previous case.

D. Discussions

Some comments on the use of the beam filter are in order here. The approach used above assumes that the bot

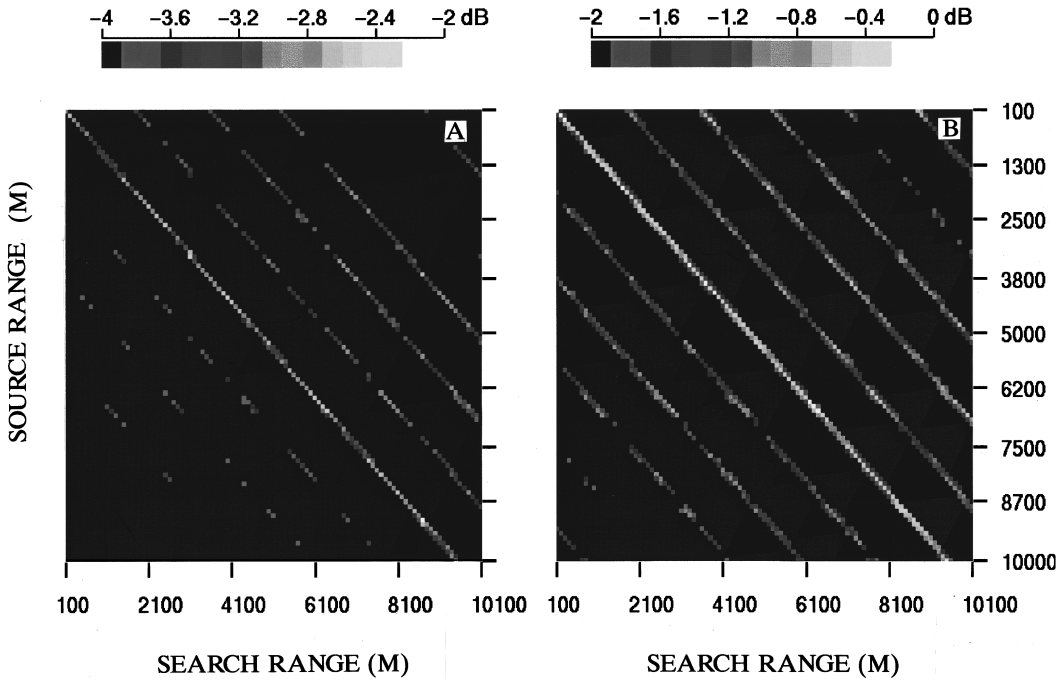

FIG. 6. Range ambiguity surface as a function of source range and search range in an environment with a constant sound-speed profile: (A) matched-field processing and (B) matched-beam processing with a beam filter.

tom mismatch is minimal or none for shallow angle arrivals (or low-order modes). For hard bottoms, these are the paths with grazing angles below the critical grazing angle. We note that although the bottom is interpreted as totally reflective at below the critical grazing angle, the bottom is not rigid for the low-order modes; the bottom affects the mode wave number since even the low-order mode penetrates into the bottom (the evanescent waves). For the case of soft bottom with a layer (or layers) of sediment, one needs to know the sound speed near the top of the sediment (e.g., from core samples). Note that the sediment (with sound speed equal or less than that in the water) modifies low grazing angle paths which penetrates into the sediment. In terms of the bottom reflection coefficient, the reflection loss (and phase) of the replica bottom and the real bottom should match at low grazing angles.

Note that in this method we use a minimum number of undistorted low-order modes (i.e., minimally affected by the bottom mismatch) to estimate the correct source range. Note further that if the bottom mismatch affects both the low-order modes and the high-order modes, correct source localization is impossible for the given replica field. In terms of practical applications, we note that if *a priori* information about the sediment is not available, one could calibrate the wave numbers of the low-order modes using acoustic data from a known source. This will be done using matched-beam

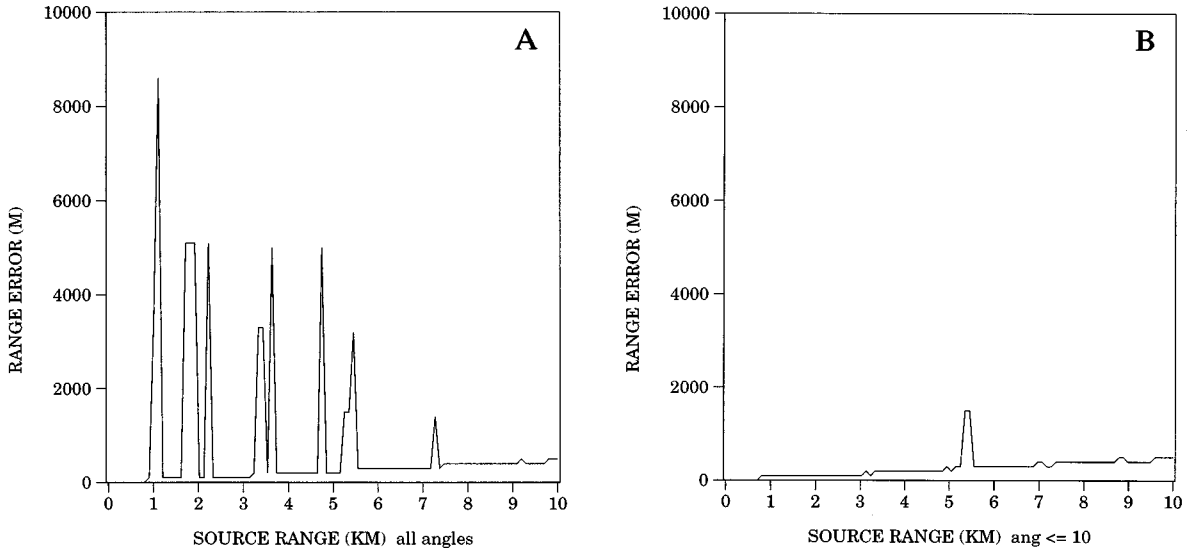

FIG. 7. Range error as a function of source range based on Fig. 6: (A) matched-field processing and (B) matched-beam processing with a beam filter.

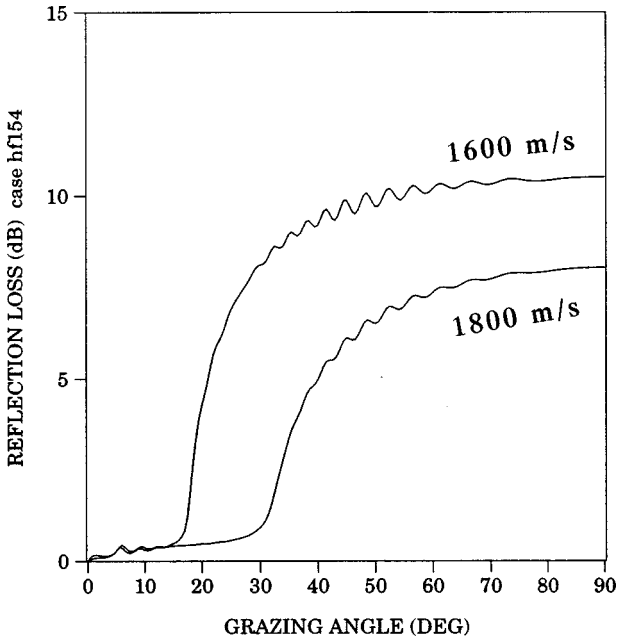

FIG. 8. Bottom reflection loss at 100 Hz as a function of incident grazing angle for two hard bottoms.

correlation including only the low angle beams. Otherwise one could empirically adjust the beam filter (as we did in example one) and check any improvement in tracking.

A comment on the beam filter itself. In the above analysis, the beam filter is implemented using a step function for the replica beams, i.e.,

$$\tilde{A}^{\mathrm{rplc}}(\theta,r,z)=A^{\mathrm{rplc}}(\theta,r,z)b(\theta), \tag{7}$$

where

$$b(\theta)=\begin{cases}0, & \text{for } |\theta|>\Theta_0,\\ 1, & \text{for } |\theta|\leqslant\Theta_0.\end{cases} \tag{8}$$

In practice, it may be preferred to use a smooth beam filter which decreases sharply above Θ_0 so that the edge effect at Θ_0 is minimized.

Next we comment on the use of the beam filter under various acoustic environments. Recall that the (large) range errors are caused by the range sidelobes overtaking (what should be) the main lobe when there is bottom mismatch. The distribution of range sidelobes and their magnitudes are determined by the sound-speed profile (SSP) in the water column and the water depth. As a result, the water column has a strong impact on the effectiveness of the beam filter in terms of removing the (large) range errors. We note that for a deep ocean, there are many waterborne normal modes available for source localization. One could then set Θ_0 to equal the angle of the steepest acoustic ray which grazes the bottom and thus excludes the bottom interacting arrivals. But for shallow water, the number of waterborne modes is often very limited and one needs bottom interacting modes for source localization. Typically one expects many sidelobes in the range ambiguity function which coupled with bottom mismatch can cause large range errors.

We note that there is more bottom interaction in a downward refractive SSP than an upward refractive SSP in shallow water. Hence the range error due to the bottom mismatch can be more severe for the downward refractive SSP than the upward refractive SSP. To illustrate this we consider these two environments with the same bottom, and bottom mismatch. The beam filter Θ_0 would be the same but the range error may be more severe in the downward refractive case than the upward refractive case. The reason is that the normal modes received by the vertical array are more con-

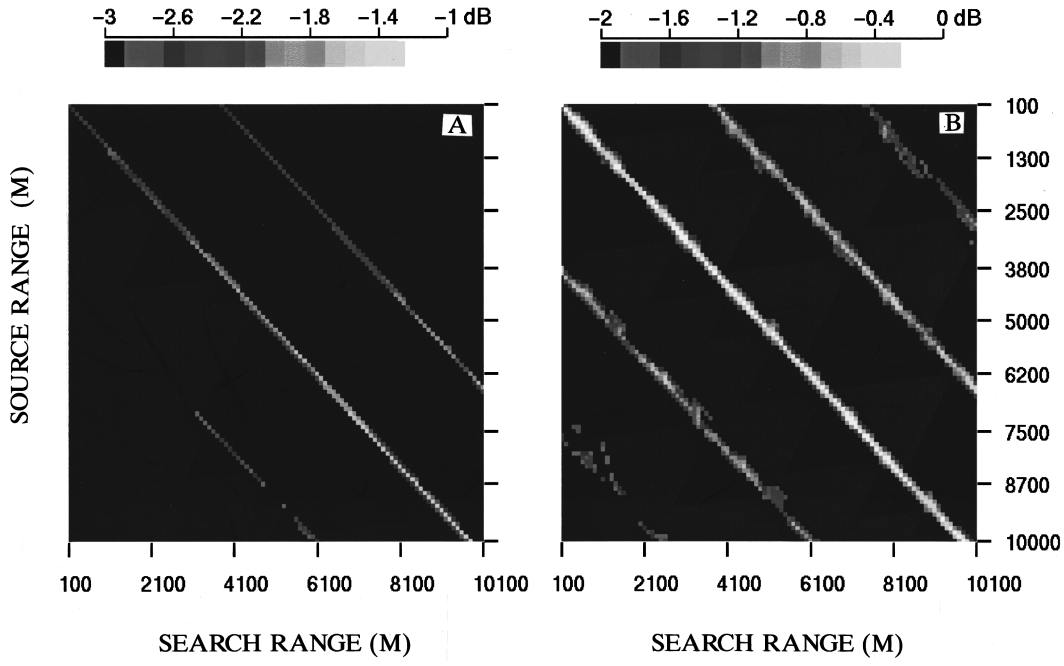

FIG. 9. Range ambiguity surface as a function of source range and search range in a downward refractive environment: (A) matched-field processing and (B) matched-beam processing with a beam filter.

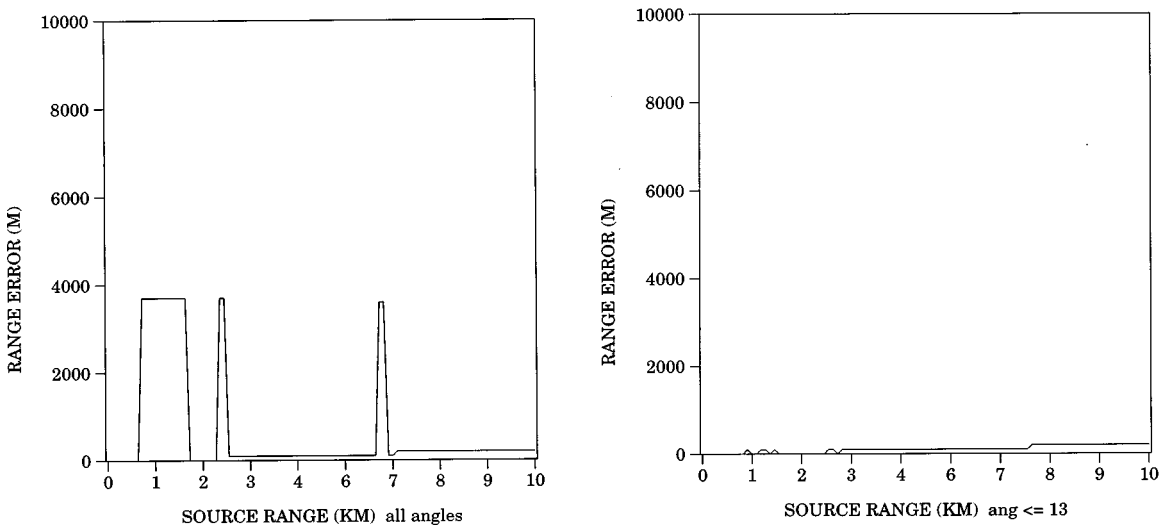

FIG. 10. Range error as a function of source range based on Fig. 9: (A) matched-field processing and (B) matched-beam processing with a beam filter.

centrated in the water column in the upward refractive case than the downward refractive case. As a result, the structure of the range sidelobes (and hence the range errors) are more favorable in the former than the latter case.

Note that the range error will also depend on the search range used in the ambiguity function calculation. As a wider search range is used, more erroneous peaks may show up. In practice, the search range may be limited to a certain range around where the target is expected. If one is only concerned with the sidelobes close to the target, the range spacings between the sidelobes and main lobe become the critical parameters in range errors.

We note that range tracking can be more ambiguous at high frequencies than at low frequencies due to the higher density of sidelobes (per range unit) at higher frequencies; the spacing between the range sidelobes and main lobe decreases with increasing frequency. This results in more sidelobes within a reasonable search range of the target at high frequencies. Range errors at high frequencies may be more sensitive to fluctuations in the water column than uncertainty in the bottom. At very low frequencies (e.g., wavelength of the same order as water depth), on the other hand, the bottom mismatch may be too severe to prevent source localization at all as the acoustic field is predominately bottom interacting. In the interpretation of data, whether the mismatch is due to bottom will depend on the signal frequency. This affects whether and how one will use the beam filter.

III. BEAM PATTERNS AND STATISTICS

We note that the input data to matched-beam processing [Eq. (2)] are none other than the beam outputs of conventional beamforming. For a large aperture vertical array, the signal arrivals are no longer plane waves due to the sound-speed variations with depth. As a result, the beam angle may deviate from the true signal arrival angle, and the beam width may be wider than the theoretical width (of a plane wave). Nevertheless, the conventional beams are well-defined quantities. They are physically measurable and can be simulated by numerical models. Vertical beam patterns of the signal have been widely used in the literature. They are often correlated with the multipath arrivals despite the distortion due to sound-speed variations with depth. We will study vertical beam patterns of the signal to discuss the estimation of array tilt and the formulation of a detection and estimation model for matched-beam processing.

A. Array tilt

Resolving the array tilt is critical for source localization when the array tilt is not known *a priori*. An incorrectly determined array tilt is another form of mismatch which can severely affect range tracking. In general one finds that matched-field source localization can be quite sensitive to the array tilt of, say, more than a few (e.g., 5) degrees.

Acoustic pingers have been widely used to measure the array element position, from which the array tilt is determined. Array element position is estimated by the pulse travel time to each element on a vertical array.[9] This adds to the hardware and uses more energy when the energy source may be limited. Array tilt can also be estimated using explosive or implosive sources deployed near the array. Distant broadband sources can also be used with less certainty due to fluctuations in sound propagation.

One can also use the phase differences of a narrow-band signal between the elements of a vertical array to determine the array tilt. In practice, it is extremely difficult to do so using a stationary source as the phase is sensitive to the source location for a nearby source and is subjective to the multipath interferences for a distant source. The situation is different for a moving source. We show that array tilt can be easily estimated from the vertical beam pattern as a function of range.

The estimation of the array tilt angle can be illustrated using data shown in Fig. 11. Figure 11(A) is the measured vertical beam patterns as a function of range and Fig. 11(B) is the simulated vertical beam pattern. The data were collected in shallow Arctic water with a typical Arctic sound-

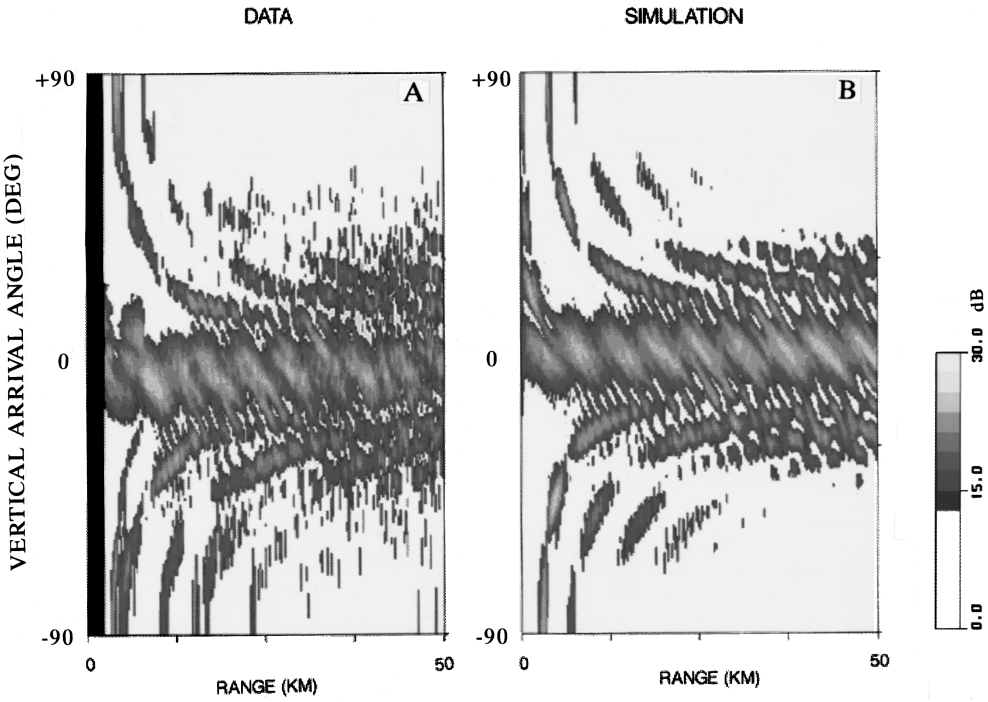

FIG. 11. A comparison of the vertical beam pattern between data (A) and replica (B).

speed profile. The environment was described in Ref. 35. For the simulation, the acoustic field was calculated using a nominal bottom profile estimated for the area.[36] The replica field (without array tilt) was beamformed the same way as the data was processed. One observes that Fig. 11(A) and (B) has nearly identical beam patterns for the waterborne paths ($\theta \lesssim 20°$) except for a shift in the arrival angle. By superposition of Fig. 11(A) with Fig. 11(B), one determines an angle offset of approximately 6°, which is the array tilt angle. We note that the detail of the acoustic model is not critical for the purpose of estimating the array tilt.

For high signal-to-noise data, the tilt angle can be estimated directly from the beam data as shown above. As is well known, the array tilt is manifested by a modified vertical arrival beam pattern. For a tilted line array as is often the case experimentally (when the tilt angle is small), the effect of the array tilt is a linear shift of the vertical beam pattern by an amount equal to the tilt angle θ_0. In matched-beam processing it is exactly represented by Eq. (1). If the array shape is not linear but (approximately) known, the array tilt can be estimated by incorporating the array shape in the replica beams.

For low signal-to-noise data, the tilt angle can be searched by correlating the data beams with the replica beams of a tilted array [which is matched-beam processing with an angle offset as given in Eq. (1)] and integrating over the target ranges. High noise and interfering signals in the nontarget directions can be removed using a beam filter. The estimation of array tilt has a high confidence when the source range is known (as is for a friendly source).

The concept as illustrated above is simple, but it has not been widely used in practice. In fact, using matched-field processing one would include the array tilt as another search parameter in the matched-field correlation calculation. The search process requires a new set of replica fields to be generated for all range–depth cells for each tilt angle. A separate range–depth ambiguity surface is generated for each tilt angle. The array tilt is determined by the ambiguity surface which yields the highest correlation coefficient; this ambiguity surface is used to determine the target range and depth. Note that the source can be incorrectly localized with the wrong tilt angle, hence one must search for range, depth, and tilt angle simultaneously. In contrast, using matched-beam processing the replica field is generated only once without array tilt and the correlation is done once for all range–depth cells. This reduces processing time by several folds, i.e., by the number of tilt angles used in the search process (e.g., $\pm 5°$ with a 1° step).

The effect of array tilt on source localization was examined using the same data described above (Fig. 11). Matched-field processing was used to estimate the source range. Since no array tilt information was available, the replica fields were generated assuming no array tilt. One found that the range estimation had many errors, and range tracking was intermittent. To improve the range tracking results, a great effort was devoted to modify the bottom sound speed, using simulated annealing, to improve the source localization and tracking results. It turned out that there was bottom mismatch (see below), but source localization was much more sensitive to the array tilt. If the array tilt angle was included as another search parameter in the simulated annealing algorithm, the range estimates with tilt and without tilt were different. The question is which answer is correct when the source range is not known in a practical problem. In theory, the range solution with a higher matched-field correlation coefficient should be the right answer. In practice, the difference in the coefficients may be small and the magnitudes of the coefficients may flip-flop with respect to range.

The source range was also estimated using matched-beam processing. When the vertical beam data were plotted and compared with calculation, array tilt was clearly demonstrated and was estimated from the data as shown above. After incorporating the array tilt, one found that the source range tracking was significantly improved even using the nominal bottom sound-speed profile estimated in nearby locations.[36]

The effect of the array tilt on source localization can be illustrated using Fig. 11. Incorrect source range estimation can result from array tilt since the replica beams [Fig. 11(B)] at a range not equal to the source range can match the data beams at the source range [Fig. 11(A)] better than the replica beam at the source range.

The purpose of the above discussions is to point out that array tilt can interfere with range tracking, but it can be estimated from the vertical beam pattern by beam matching. Matching beam pattern is simple and straightforward, and can be useful in practice. It can be applied to practical problems using, for example, signals from surface ships, or friendly sources with known ranges.

Figure 11 can also be used to illustrate the bottom mismatch between data and replica field. If we superimpose Fig. 11(A) with Fig. 11(B), after shifting the beam angle of the data by 6° due to the array tilt, we find that the beam intensity patterns of the data and replica fields agree very well with each other at grazing angles $\leqslant 30°$ but not at angles $\geqslant 40°$. Noting that the high angle arrivals are bottom bounced returns, the deviations in the vertical beam distributions between Fig. 11(A) and (B) suggest that there is bottom mismatch for this case.

Last, the comparison of the vertical beam patterns between the data and replica fields can be used for other purposes:

(1) It offers a simple means to estimate the degradation of the matched-field correlation due to the array tilt and to determine the maximum tolerable tilt angle for a system. Note that matched-beam processing with full beams is the same as matched-field processing. Array performance degradation is much easier to estimate in the beam domain than in the phone domain.

(2) It can be used to measure the array tilt (in the plane of propagation) as a function of time without using acoustic pingers, and study the array dynamics (as a function of current).

B. Detection and estimation

Source localization with matched-field processing has been successfully demonstrated in many experiments. When this method is applied to real world problems involving the detection and localization of a weak target, one faces two problems. One is the environmental mismatch problem as discussed above. The other is the difficulty of formulating a detection and estimation theory for matched-field processing. The problem is that the probability distributions of the signal and noise at the output of the matched-field correlation depend on the signal propagation model (the replica field). In other words, it is environment dependent. To this date, one does not know what the distribution should be like (to our knowledge no model has been proposed), nor has one measured it systematically from data. It is therefore no surprise to find that the probability of detection not only will vary from one range–depth cell to another (as the signal and noise level vary from one cell to another), but also will be environmentally dependent.

In contrast, the signal and noise at the output of the conventional beamformer follow certain well-established distributions which are almost independent of the environment. The beam statistics have been extensively measured from data and reasonably modeled. Detection has been formulated (such as the receiver operation curve) using the beam statistics.[37]

Using the beam domain formulation, it is possible to build a model of detection and estimation. This is based on the observation that the matched beam output can be expressed as a matrix multiplication of the conventional beam outputs. To illustrate this, we rewrite the numerator of Eq. (1) as

$$\tilde{B}(r_l) = \int A^{\mathrm{rplc}*}(\theta, r_l) A^{\mathrm{data}}(\theta)\, d\sin\theta$$

$$= \sum_i \alpha_i(r_l) A^{\mathrm{data}}(\theta_i)\cos\theta_i, \tag{9}$$

where $\tilde{B}(r_l)$ is the range ambiguity function, and

$$\alpha_i(r_l) = A^{\mathrm{rplc}*}(\theta_i, r_l) = \sum_j e^{-ikz_j \sin\theta_i} p_j^{\mathrm{rplc}}(r_l), \tag{10}$$

where r_l denotes the range variable. We have dropped the cutoff angle and the depth variable in Eq. (9). Equation (5) shows that the transformation from the input beams $A^{\mathrm{data}}(\theta_i)$ to the range ambiguity function $\tilde{B}(r_l)$ is a matrix multiplication.

Equipped with Eqs. (9) and (10), one could construct a statistical distribution for the range ambiguity function. We assume that the statistical distribution is known for the data beam $A^{\mathrm{data}}(\theta_i)$, e.g., a Rayleigh distribution for the signal and a Gaussian distribution for the noise. For the replica beams, we could assume the same distribution as the signal beams, e.g., a Rayleigh distribution with a mean determined by the replica field and a variance determined by the data. Otherwise, we could use a random propagation theory to calculate the variance for the replica beams. From Eq. (9), we find that the statistical distribution of the range ambiguity function is the product of two distributions. This complicated feature is not anticipated *a priori*. (It is no surprise then that the matched-field output did not seem to fit a simple distribution as commonly assumed.) Despite the complicated nature, the probability density function of the range ambiguity function can be calculated numerically using Eq. (9) given the input on the right-hand side of that equation. Detection statistics can be determined from this model. The study of the statistical distribution itself is beyond the scope of this paper.

IV. SUMMARY

In this paper, we apply matched-beam processing to range tracking for a moving source using a vertical array. We discuss how matched-beam processing suppresses the bottom mismatch (using a beam filter) to achieve consistent and continuous range tracking. We show how the vertical array tilt, which could easily mess up range tracking, can be estimated from the vertical beam pattern from a moving source. We present (for the first time) an approach to formulate a statistical distribution for the signal and noise at the output of the matched-field/beam processing using the beam representation.

We note that matched-beam processing is in essence matched-field processing in the beam domain. Matched-beam processing uses data beams and replica beams which are Fourier transformations of the acoustic fields into the wave-number domain. When all beams are used, matched-beam processing is identical to matched-field processing. When dealing with certain environmental mismatch and/or high noise, matched-beam processing can be more advantageous than matched-field processing by using only a subset of beams, i.e., a beam filter.

The work presented in this paper is aimed at practical applications, it has a different emphasis than most work published in the literature. We note that matched-field processing can achieve the same or better performance in range tracking (than presented above with a beam filter) but only after it has successfully searched for the correct environmental parameters. In this regard, matched-beam processing results would be inferior than the best results obtainable from matched-field processing. What matched-beam processing offers is a simple and robust method for consistent and continuous range tracking that can be applied to real world problems when bottom mismatch may be present. By using a beam filter to suppress the bottom mismatch rather than using a complicated search algorithm to search for the bottom parameters, matched-beam processing saves significant computation time over matched-field processing. Additional savings come from the fact that the number of signal beams is often smaller than the number of hydrophones which cuts the correlation calculation by several folds. These features, i.e., simplicity, robustness, and reduced processing time, may be important considerations when dealing with practical problems.

ACKNOWLEDGMENTS

This work was supported by the Office of Naval Research. We thank R. Heitmeyer and the reviewers for valuable comments.

APPENDIX: A SYNTHESIS OF CONVENTIONAL BEAMFORMING AND MATCHED-FIELD PROCESSING

This Appendix shows the relation of matched-beam processing with conventional beamforming for a plane wave on one hand and matched-field processing for a vertical array on the other hand.

We shall use matched-beam processing without a beam filter,

$$B=\frac{\left|\int A^{\mathrm{rplc}*}(\theta)A^{\mathrm{data}}(\theta)d\sin\theta\right|^2}{[\int|A^{\mathrm{rplc}}(\theta)|^2 d\sin\theta][\int|A^{\mathrm{data}}(\theta)|^2 d\sin\theta]}. \tag{A1}$$

For a plane-wave arrival on a horizontal array, the replica field can be assumed as a plane wave arriving in the look direction θ_l,

$$p_j^{\mathrm{rplc}}=e^{ikz_j\sin\theta_l}.$$

Substituting that into Eq. (3), one finds for a uniformly spaced array with spacing d,

$$A^{\mathrm{rplc}}(\theta)=\sum_{n=1}^{N} e^{-iknd(\sin\theta-\sin\theta_l)}, \tag{A2}$$

which becomes a delta function in $\sin\theta-\sin\theta_l$ as N increases, and matched-beam correlation becomes

$$\left|\int A^{\mathrm{rplc}*}(\theta)A^{\mathrm{data}}(\theta)d\sin\theta\right|^2 = |A^{\mathrm{data}}(\theta_l)|^2=\left|\sum_{n=1}^{N} e^{-iknd\sin\theta_l}p_n^{\mathrm{data}}\right|^2, \tag{A3}$$

which is the conventional plane-wave beamformer in the look direction θ_l. Thus matched-beam processing for a plane wave is equivalent to conventional beamforming for a horizontal array. There can be some numerical differences when the number of phones is small.

Next we show that for a vertical array, matched-beam processing reduces to matched-field processing when the correlation in Eq. (A1) is summed/integrated over the entire wave-number (angle) space. This is a consequence of the convolution theorem[38] which states that for discrete Fourier transforms

$$\begin{aligned} X(K)&=\sum_{n=0}^{N-1} x(n)e^{-i(2\pi/N)nK},\\ Y(K)&=\sum_{n=0}^{N-1} y(n)e^{-i(2\pi/N)nK}, \end{aligned} \tag{A4}$$

one has the equality

$$\sum_{n=0}^{N-1} x(n)y^*(n)=\frac{1}{N}\sum_{K=-K_0}^{N-1-K_0} X(K)Y^*(K), \tag{A5}$$

where $X(K)$ and $Y(K)$ are periodic functions with a period of N, and K_0 is an integer. We shall set $K_0=(N-1)/2$ for odd N. Equation (A4) says that for N phones uniformly spaced, we can form N beams. Comparing Eq. (A4) with Eqs. (2) and (3), one finds the beams are located at

$$\sin\theta_K=2K/N \quad \text{for } K=-(N-1)/2,\ldots,(N-1)/2$$

for a vertical array with half wavelength spacing. Note that Eq. (A5) also holds for a plane-wave signal (arriving on a horizontal line array).

While Eq. (A5) is exact, we note that we have a problem when the number of phones is small. The beams will be widely spaced and may not adequately sample the signal arrival angles which are concentrated at low grazing angles. In practice we may need to form beams at every degree at low grazing angles. For that purpose, we will modify the

right-hand side of Eq. (A5) by extrapolating to, say, 180 beams, but then the equality becomes approximate.

The equivalence of matched-beam processing and matched-field processing can also be illustrated for a continuous line array. The mathematical relationship comes through more clearly in this case. We can express Eqs. (2) and (3) as

$$A^{\text{data}}(\kappa)=\int e^{-iz\kappa}p^{\text{data}}(z)dz, \tag{A6}$$

$$A^{\text{rplc}}(\kappa)=\int e^{-i\tilde{z}\kappa}p^{\text{rplc}}(\tilde{z})d\tilde{z}, \tag{A7}$$

where $\kappa=k\ \sin\theta$. The source range and depth for the replica field are not explicitly shown. Matched-beam correlation becomes then

$$\left|\int A^{\text{rplc}*}(\kappa)A^{\text{data}}(\kappa)d\kappa\right|^2 = \left|\int\int\left[\int e^{-i(z-\tilde{z})\kappa}d\kappa\right]p^{\text{rplc}*}(\tilde{z})p^{\text{data}}(z)dz\ d\tilde{z}\right|^2. \tag{A8}$$

We note that the square bracket term in the above equation can be approximated by a delta function in $z-\tilde{z}$ if the wavenumber space is sufficiently large. In that case the above matched beam correlation becomes the matched-field correlation. In practice there may be some numerical differences which need to be checked. We have investigated the numerical difference for a vertical array with discrete elements in shallow water. In general the numerical differences are negligibly small as not worth reporting.

In summary, we find that matched-beam processing (with full beams) reduces to matched-field processing for signals received on a vertical array and reduces to conventional beamforming for a plane-wave signal received on a horizontal array. As such, matched-beam processing has put conventional beamforming and matched-field processing on equal footing; it is a synthesis of two processing methods.

[1] See reviews by A. B. Baggeroer and W. A. Kuperman, ''Matched field processing in ocean acoustics,'' in *Acoustic Signal Processing for Ocean Exploration*, edited by J. M. F. Moura and I. M. G. Lourtie (Kluwer, Dordrecht, The Netherlands, 1993), and A. Tolstoy, *Matched Field Processing for Underwater Acoustics* (World Scientific, Singapore, 1992).

[2] T. C. Yang and T. Yates, ''Matched beam processing: Applications to a horizontal line array in shallow water,'' J. Acoust. Soc. Am. **104**, 1316–1330 (1998).

[3] T. C. Yang and T. Yates, ''Improving the sensitivity of full-field geoacoustic inversion for estimating bottom sound speed profiles,'' *Full Field Inversion in Seismic and Ocean Acoustics* (Kluwer Academic, Dordrecht, 1995), pp. 323–328.

[4] T. C. Yang and T. Yates, ''Acoustic inversion of bottom reflectivity and bottom sound-speed profile,'' IEEE J. Oceanic Eng. **21**, 367–376 (1996).

[5] T. C. Yang, ''A method of range and depth estimation by modal decomposition,'' J. Acoust. Soc. Am. **82**, 1736–1745 (1987).

[6] D. F. Gingras and P. Gerstoft, ''Inversion for geometric and geoacoustic parameters in shallow water: Experimental results,'' J. Acoust. Soc. Am. **97**, 3589–3598 (1995).

[7] N. O. Booth, P. A. Baxley, J. A. Rice, P. W. Schey, W. S. Hodgkiss, G. L. D'Spain, and J. J. Murray, ''Source localization with broadband matched field processing in shallow water,'' IEEE J. Ocean Eng. **21**, 402–412 (1996).

[8] D. R. Del Balzo, C. Feuillade, and M. M. Rowe, ''Effects of water-depth mismatch on matched-field localization in shallow water,'' J. Acoust. Soc. Am. **83**, 2180–2185 (1988).

[9] See W. S. Hodgkiss, D. E. Ensberg, J. J. Murray, G. L. D'Spain, N. O. Booth, and P. W. Schey, ''Direct measurement and matched-field inversion approaches to array shape estimation,'' IEEE J. Ocean Eng. **21**, 393–401 (1996) and references therein.

[10] P. A. Baxley, R. B. Williams, and W. S. Hodgkiss, ''Track-before-detect matched-field processing,'' J. Acoust. Soc. Am. **94**, 1844 (1995).

[11] P. A. Baxley, ''Experimental evaluation of matched-field track-before-detect processing in shallow water,'' J. Acoust. Soc. Am. **98**, 2931 (1995).

[12] H. Bucker, ''Matched-field tracking in shallow water,'' J. Acoust. Soc. Am. **896**, 3809–3811 (1995).

[13] J. A. Fawcett and B. H. Maranda, ''A hybrid target motion analysis/matched-field processing localization method,'' J. Acoust. Soc. Am. **97**, 1363–1371 (1993).

[14] J. S. Perkins and W. A. Kuperman, ''Environmental signal processing: Three dimensional matched-field processing with a vertical array,'' J. Acoust. Soc. Am. **87**, 1553–1556 (1990).

[15] O. I. Diachok, T. C. Yang, and A. Livingston, ''Low frequency acoustic arrays in the Arctic,'' in *Proceedings of DOD Symposium on Arctic and Arctic-related Environmental Science* (Office of Naval Research, Washington, DC, 1987).

[16] T. C. Yang and S. D. Kuo, ''Active tracking in a shallow water environment,'' in *Proceedings of Undersea Defense Technology Symposium*, Cannes, France, 1993 (Read Exhibition Co., Turbridge Wells, UK).

[17] S. D. Kuo and L. D. Stone, ''Discrete non-linear data fusion for shallow water tracking and surveillance,'' Tech. Report, Metron Inc., Reston, VA, 1993.

[18] M. D. Collins and W. A. Kuperman, ''Facolization: Environmental focusing and source localization,'' J. Acoust. Soc. Am. **90**, 1410–1422 (1991).

[19] P. Gerstoft, ''Global inversion by genetic algorithms for both source position and environmental parameters,'' J. Comput. Acoust. **2**, 251–266 (1994).

[20] D. F. Gingras and N. L. Gerr, ''Minimax robust matched-field processing,'' J. Acoust. Soc. Am. **93**, 2798–2808 (1993).

[21] A. M. Richardson and L. W. Nolte, ''*A posteriori* probability source localization in an uncertain sound speed, deep ocean environment,'' J. Acoust. Soc. Am. **89**, 2280–2285 (1991).

[22] A. Tolstoy, ''Using matched-field processing to estimate shallow-water bottom properties from shot data taken in the Mediterranean sea,'' IEEE J. Oceanic Eng. **21**, 471–479 (1996).

[23] H. Schmidt, A. B. Baggeroer, W. A. Kuperman, and E. K. Scheer, ''Environmentally tolerant beamforming for high resolution matched-field processing: Deterministic mismatch,'' J. Acoust. Soc. Am. **88**, 1851–1862 (1990).

[24] J. M. Ozard, G. H. Brooke, and P. Brower, ''Improving performance for matched-field processing with a minimum variance beamformer,'' J. Acoust. Soc. Am. **91**, 141–150 (1992).

[25] G. M. Frichter, C. L. Byrne, and C. Feuillade, ''Sector-focused stability methods for robust source localization in matched-field processing,'' J. Acoust. Soc. Am. **88**, 2843–2851 (1990).

[26] T. C. Yang, ''Effectiveness of mode filtering: A comparison of matched-field and matched-mode processing,'' J. Acoust. Soc. Am. **87**, 2072–2084 (1990).

[27] K. Heaney, J. Colosi, and W. A. Kuperman, ''Estimation of internal wave strength from mode space source localization,'' J. Acoust. Soc. Am. **100**, 2582 (1996).

[28] D. D. Pierce, C.-S. Chiu, C. W. Therrien, and J. H. Miller, ''Matched-mode localization using conventional and cumulant-based MUSIC algorithms in a real, complex shallow water environment,'' J. Acoust. Soc. Am. **100**, 2636 (1996).

[29] J. Tabrikian, J. L. Krolik, and H. Messer, ''Robust maximum-likelihood source localization in an uncertain shallow-water waveguide,'' J. Acoust. Soc. Am. **101**, 241–249 (1997).

[30] C. L. Byrne, R. T. Brent, C. Feuillade, and D. R. Del Balzo, ''A stable data-adaptive method for matched-field array processing in acoustic waveguides,'' J. Acoust. Soc. Am. **87**, 2493–2505 (1990).

[31] H. Cox, R. M. Zeskind, and M. Myers, ''A subarray approach to matched-field processing,'' J. Acoust. Soc. Am. **87**, 168–178 (1990).

[32] See R. M. Hamson and R. M. Heitmeyer, ''Environmental and system effects on source localization in shallow water by the matched field processing of a vertical array,'' J. Acoust. Soc. Am. **86**, 1950–1959 (1989) and references therein.

[33] E. C. Shang, C. S. Clay, and Y. Y. Wang, ''Passive harmonic source, ranging in waveguides by using mode filter,'' J. Acoust. Soc. Am. **78**, 172–175 (1985).
[34] K. Yoo and T. C. Yang, ''Improved vertical array performance in shallow water with a directional noise field,'' J. Acoust. Soc. Am. (accepted for publication).
[35] B. Sotirin, ''Project spinnaker: Long term Arctic ambient noise measurement,'' J. Acoust. Soc. Am. **100**, 2732 (1996).
[36] See Ref. 3 for the bottom sound-speed profile.
[37] See, for example, W. S. Burdic, *Underwater Acoustic System Analysis* (Prentice-Hall, Englewood Cliffs, NJ, 1991).
[38] See, for example, A. V. Oppenheim and R. W. Schafer, *Digital Signal Processing* (Prentice-Hall, Englewood Cliffs, NJ, 1975), Chap. 3.

On the use of acoustic contrast to distinguish between agglomerates of finely dispersed polymeric particles

Sanjay Gupta[a] and Donald L. Feke[b]
Department of Chemical Engineering, Case Western Reserve University, Cleveland, Ohio 44106-7217

(Received 6 July 1997; accepted for publication 16 June 1998)

This paper demonstrates how differences in the morphology of agglomerates of fine particles can be detected based on the response of the agglomerates to a low-intensity resonant acoustic field. The technique is based upon observing whether the agglomerates are collected in nodal or antinodal positions when suspended in different fluids spanning an appropriate range of acoustic properties. Experiments performed with agglomerates of acrylonitrile–butadiene–styrene copolymeric particles suspended in 2-propanol–water mixtures illustrate the technique. © *1998 Acoustical Society of America.* [S0001-4966(98)00910-2]

PACS numbers: 43.35.Bf [HEB]

INTRODUCTION

Polymeric samples are routinely characterized for their physical or chemical properties using various analytical tools. Thermal characteristics such as heat capacity and stability to thermal decomposition can be examined using differential scanning calorimetry (DSC) or thermogravimetric analysis (TGA). The chemical makeup of polymers can be probed using various spectroscopies such as FTIR (Fourier-transform infrared), UV-VIS (ultraviolet-visible), or NMR (nuclear magnetic resonance). The mechanical and rheological behavior of polymers can be characterized using dynamic mechanical analysis (DMA).

Unlike thermal and chemical methods that can probe relatively small volumes of the polymer, conventional mechanical testing techniques for polymers require bulk samples. Often, there is a need to characterize finely dispersed polymer particles or agglomerates of particles in which the individual solids range from micron to millimeters in size. Quantitative information about the structure of agglomerates is generally very difficult to obtain experimentally. Techniques such as microscopy require the removal of the agglomerate from the suspending media or fixing the structure by infiltrating with a second liquid that eventually hardens and allows the agglomerate to be sectioned. Often, however, the very act of preparing the agglomerate for analysis severely alters its structure. Hence, a technique that senses agglomerate structure while it is in suspension may have significant technological applications.

In this article, we will describe a novel method of characterization of certain physical characteristics of fine polymer agglomerates using mild resonant ultrasonic fields. The method is based on comparing the sense of the acoustic response of such particles suspended in a variety of solvents that span a range of acoustic properties. To illustrate the sensitivity of the method, we have applied this approach to detect differences between two batches of agglomerates of polymeric powders. These agglomerates were comprised of individual particles that have identical chemical composition but were prepared in ways that lead to different agglomerate packing structures and morphology. As is typical of agglomeration processes, a wide range of morphologies was expected within each batch, and consequently each batch of agglomerates was expected to exhibit a range of acoustic responses. Although there may be overlap in the range of acoustic response of the two populations of agglomerates, we seek to detect differences in the mean response of each batch.

I. APPROACH

When a planar acoustic standing wave field is produced in a dilute suspension of particles (or droplets of an immiscible liquid), the dispersed phase experiences a time-averaged force known as the primary acoustic force. For a spherical particle (radius R) dispersed in an inviscid fluid, the acoustic force due to a one-dimensional standing wave field is given by[1]

$$F_{\mathrm{ac}} = 4\pi R^3 \kappa E_{\mathrm{ac}} F \sin(2\kappa x), \tag{1}$$

where x is the location of particle relative to the nearest pressure antinode of the wave field, κ is the wave number, E_{ac} is the acoustic energy density, and F is the acoustic contrast factor, evaluated from

$$F = \frac{1}{3}\left[\frac{5\Lambda - 2}{1 + 2\Lambda} - \frac{\gamma_p}{\gamma_f}\right]. \tag{2}$$

In Eq. (2), Λ is the ratio of particle to fluid density and γ_p and γ_f are the particle and fluid compressibilities. The acoustic force given by Eq. (1) is valid for any particle that is much smaller than the acoustic wavelength (λ). If this condition is met, then the acoustic contrast factor given by Eq. (2) is independent of particle size or shape. For nondilute suspensions, secondary acoustic forces, which are usually attractive, can act between suspended particles.

Analysis of Eq. (1) reveals that the primary acoustic force drives suspended particles to either the pressure nodes or antinodes of the acoustic field based on the algebraic sign of the acoustic contrast factor. If $F > 0$, collection at the pressure nodes occurs, whereas, if $F < 0$, the particles are driven to the pressure antinodes.

[a]Present address: Nestle R&D Center, Marysville, OH 43040-4002.
[b]To whom correspondence should be addressed.

 0001-4966/98/104(4)/2189/3/$15.00

Provided that the agglomerate size is smaller than the acoustic wavelength, expressions analogous to Eqs. (1) and (2), in which an effective density and compressibility of the agglomerate is used to compute the acoustic contrast factor, may be expected. However, we have not found any explicit analyses that describe how the acoustic contrast factor should be determined for agglomerates. Agglomerates comprised of identical particles but having different packing morphology may be expected to exhibit distinct values of F for two reasons. First, the effective density of the agglomerate will depend on the relative amounts of solid and fluid incorporated within the agglomerate structure. Second, different packing arrangements of the primary particles can lead to variations in the effective compressibility of the agglomerate.

Suppose that it is possible to identify two miscible liquids such that a given agglomerate exhibits a negative contrast when suspended in one of the liquids and a positive acoustic contrast when suspended in the other. Then, there should be some critical blend ratio of the two liquids at which the acoustic contrast of the agglomerate is zero. In this case, no acoustic response is expected, and the acoustic properties of this blend can be used as a lumped measure of the acoustic properties of the agglomerate. With proper theoretical analysis, this information can be linked to the agglomerate morphology.

For suspensions that contain two different types of agglomerates, it may be possible to select a fluid medium having acoustic properties intermediate between those of the two types. In this case, the two types of particles will have acoustic contrast factors of opposite sign. For a suspension containing a mixture of the two types of solids, one type of agglomerate should be collected at a pressure node while the other type is directed toward a pressure antinode provided that the suspension is dilute enough so that secondary acoustic forces are negligible. A continuous separation scheme for mixtures of unagglomerated polymer particles based on this principle has been previously reported.[2]

II. EXPERIMENTAL

A. Equipment

The characterization experiments were carried out in a rectangular acoustic chamber. The left and right walls of the acoustic chamber each consisted of a rectangular lead zirconate titanate (PZT) transducer (APC 880, $76.2\times38.1\times6.25$ mm^3, fundamental frequency 320 kHz, from American Piezo Ceramics, Inc., Mackeville, PA) mounted in an aluminum frame. These walls were aligned to be parallel to each other. The other four walls were constructed from Plexiglas plates outfitted with the necessary ports to allow feeding and removal of suspension from the chamber. In operation, only one transducer in the acoustic chamber was driven while the second served as a reflecting surface. The transducers were operated near 340 kHz by a continuous signal generated by a KROHN-HITE 2100 A signal generator and amplified by an ENI 240 L power amplifier. The spacing between the transducer and reflector was adjusted to maintain resonance in the chamber for the different suspension media used (which resulted in 6.5–8.5 mm gaps). The dimensions of the acoustically active portion of the chamber were thus $76.2\times38.1\times(6.5 \text{ or } 8.5)$ mm^3.

B. Materials

Two samples of polymeric powders [ABS (acrylonitrile-butadiene-styrene copolymers) supplied by GE Plastics, Washington, WV] were used for acoustic testing. According to the manufacturer's specification, the two samples were prepared from the same type of individual particle suspensions but different conditions were used to coagulate the particles. One sample was prepared under mild coagulation conditions, which generally leads to a dense, compact agglomerate structure. This type of agglomerate will be referred to as ''compact'' agglomerates. The second type of agglomerate was prepared under severe coagulation conditions, which usually results in loose, open agglomerate morphologies. This sample will be denoted as ''open'' agglomerates.

Quantitative information about the agglomerate structure was not available. Within each batch, a range of agglomerate structures (and correspondingly a range of acoustic response) was expected. In fact, it is possible that the batch of open agglomerates could contain substantial fractions of compact agglomerates, and vice versa. The dry powders received from the manufacturer were sieved and agglomerates having diameters in the range of 170–300 μm were selected for acoustic testing.

Based on a literature survey and some preliminary studies, aqueous solutions of 2-propanol was selected as the suspending medium. Both the open and compact agglomerates were expected to exhibit a positive acoustic contrast in pure 2-propanol but a negative acoustic contrast in pure water.

III. RESULTS AND DISCUSSION

Figures 1–3 show the acoustic response of the two types of agglomerates suspended in fluids having a range of blend ratio. In all of the photographs, the chamber was illuminated from behind, and the particles appear dark. The gap between the transducer and reflector was adjusted to two wavelengths for the particular fluid medium used. In the photographs, the reflecting wall is visible (the right side of each frame), but the transducer surface was obscured by the chamber supports on the left side of each photograph. The relative positions of the various surfaces are indicated in Fig. 1(a). In a resonant acoustic field, the first pressure node is one-quarter wavelength away from the reflecting wall, and the first pressure antinode is one-half wavelength from this wall.

Figure 1 shows the response of the two types of agglomerates in pure 2-propanol. Shown is the state of the chamber before the sound field is applied [Fig. 1(a)] as well as the response of the particles of the open agglomerates [Fig. 1(b)] and compact agglomerates [Fig. 1(c)]. Note that in both cases, the rightmost particle collection plane is significantly nearer to the reflector than the one-half wavelength spacing between the collection planes. This indicates that both types of agglomerates exhibited positive acoustic contrast in 2-propanol. Also, note that the collection planes for the com-

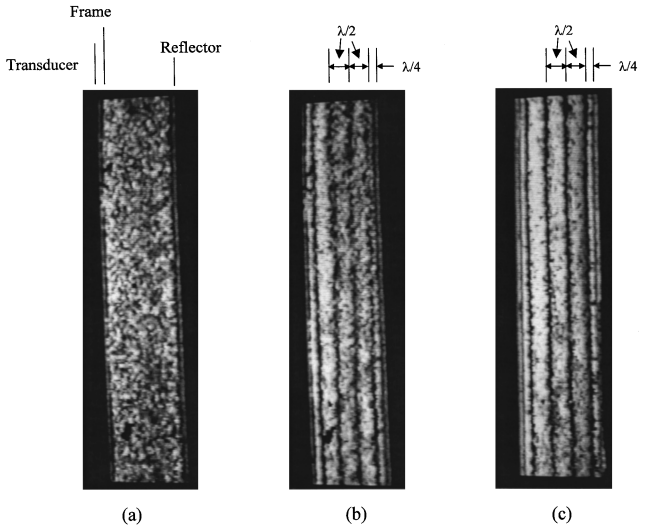

FIG. 1. Photographs showing the response of the agglomerates suspended in pure 2-propanol to the application of the resonant acoustic field. (a) No sound field applied. The markers at the top of the photograph indicate the relative position of the reflector and transducer surfaces. (b) Collection of open agglomerates into nodal planes. (c) Collection of compact agglomerates into nodal planes.

pact agglomerates [Fig. 1(c)] are crisper than those for the open agglomerates are. This suggests that the compact agglomerates have a larger magnitude of the acoustic contrast factor.

Figure 2 shows the acoustic response of the two types of agglomerates in a 20:80 2-propanol:water mixture (by volume). In both cases, the distance between the rightmost collection plane and the reflector wall is equal to the distance between the adjacent planes (i.e., one-half wavelength), indicating that both agglomerates show a negative acoustic contrast in this fluid. The crispness of the collection is slightly greater for the open agglomerates, suggesting that the open agglomerates have a larger (negative) value of the acoustic contrast factor.

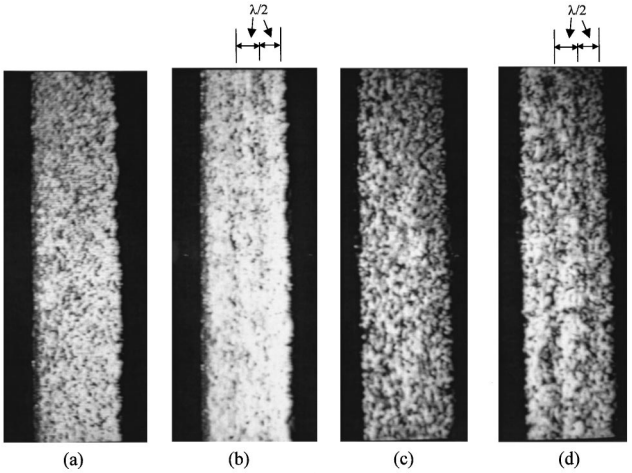

FIG. 2. Photographs showing the response of the agglomerates suspended in a 20-vol% mixture of 2-propanol in water. (a) Open agglomerates with no sound field applied; (b) collection of open agglomerates into antinodal planes; (c) compact agglomerates with no sound field applied; and (d) collection of compact agglomerates into antinodal planes.

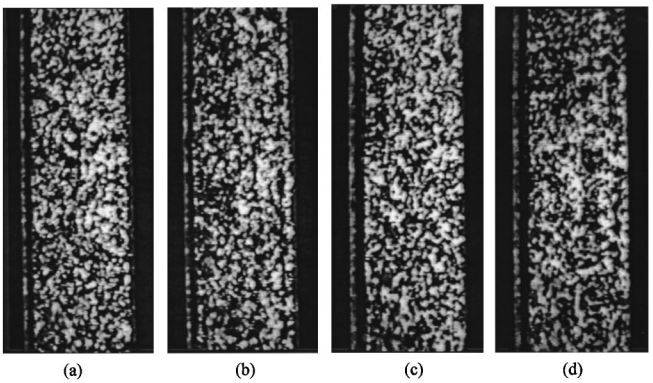

FIG. 3. Photographs showing the response of the agglomerates suspended in a 40-vol% mixture of 2-propanol in water. (a) Open agglomerates with no sound field applied; (b) weak collection of open agglomerates into nodal planes; (c) compact agglomerates with no sound field applied; and (d) weak collection of compact agglomerates into nodal planes.

Figure 3 shows the response in a 40:60 2-propanol:water mixture (by volume). Here, only a small amount of collection (into nodal planes) can be observed for both types of agglomerates. This result suggests that the acoustic properties of the agglomerates are nearly identical to those of this fluid mixture. However, the exact fluid composition for zero acoustic contrast could not be ascertained for these materials. Within each sample of the open and compact agglomerates used in this study there was expected to be a variation in the packing characteristics, and hence there would not be a unique fluid blend condition for zero acoustic contrast. Nevertheless, the experimental results suggest that F for the compact agglomerates is larger that F for the open agglomerates. This result is consistent with the expected differences in packing structure of the two types of agglomerates.

IV. CONCLUSIONS

The response of agglomerates suspended in an appropriately chosen fluid medium to a resonant ultrasonic field can be used to distinguish between samples. A variation in the magnitude of the mean acoustic contrast factor was observed for two samples of agglomerated polymer particles. This result was consistent with the expected differences in the packing structure of the two types of agglomerates. One motivation for reporting this method and these sample results is to stimulate theoreticians to analyze the acoustic response of agglomerated solids so that, eventually, a quantitative link between agglomerate morphology and the results of our technique can be established.

ACKNOWLEDGMENTS

The authors gratefully acknowledge the partial support of this work in the form of a Nestle Fellowship. The authors also thank GE Plastics for providing the agglomerate samples.

[1] R. Yosioka and G. Kawasima, ''Acoustic radiation pressure on a compressible sphere,'' Acustica **5**, 167 (1955).
[2] S. Gupta, D. L. Feke, and I. Manas-Zloczower, ''Fractionation of mixed particulate solids according to compressibility using ultrasonic standing wave fields,'' Chem. Eng. Sci. **50**(20), 3275 (1995).

Wave propagation in stressed composites

A. D. Degtyar,[a] W. Huang,[b] and S. I. Rokhlin
The Ohio State University, Nondestructive Evaluation Program, 190 West 19th Avenue, Columbus, Ohio 43210

(Received 10 December 1997; accepted for publication 13 June 1998)

The performance of high-temperature composites can be significantly affected by the presence of residual stresses. These stresses arise due to the mismatch of thermal expansion coefficients between matrix and fibers during cooling from fabrication temperature to room temperature. This effect is especially pronounced in metal matrix and intermetallic composites. It can lead to plastic deformation, matrix cracking and fiber/matrix interface debonding. Elastic wave propagation in homogeneously stressed media has been frequently addressed in the literature. However, the effect of nonhomogeneous stress distribution has not been investigated. This is especially important since the average residual stresses are zero in equilibrium and thus their distribution is inherently nonhomogeneous. In this paper, the feasibility of using ultrasonic techniques for residual stress assessment in composites is addressed. A theoretical method is presented for determining the velocities of ultrasonic waves propagating through a composite material with a nonhomogeneous distribution of residual stresses. It is based on the generalized self-consistent multiple scattering model. Calculated results for longitudinal and shear ultrasonic wave velocities propagating perpendicular to the fiber direction in SCS-6/Ti composite with and without residual stresses are presented. They show that velocity changes due to the presence of stresses are on the order of 1%.
 [S0001-4966(98)05609-4]

PACS numbers: 43.35.Cg [HEB]

INTRODUCTION

High-temperature composites have the potential to provide significant performance improvement and weight reduction in aircraft engines and other structures. For successful application of these materials in different environments their mechanical properties, life capability and reliability must be well known. The high cost of structures engineered from these materials makes experimental life determination very difficult. Thus nondestructive evaluation (NDE) of such composite structures becomes very important.

Metal matrix (MMC) and intermetallic (IMC) composites are manufactured at elevated temperatures. Due to thermal expansion mismatch between fibers and matrix, residual stresses occur as the material cools from processing temperature to room temperature. Residual stresses influence the strength properties of MMC and IMC composites. The levels of these stresses may vary significantly for different constraints, geometries and processing histories in composite structures. These stresses can be sufficiently large to cause the matrix material to yield. They can also lead to matrix cracking and fiber/matrix interface debonding, thus reducing the composite strength. Temperature changes during service (e.g., in aircraft engines) also influence the distribution of the residual stresses. All of this can significantly affect the performance of structural parts made from these composites.

Existing measurement techniques for residual stresses utilize x-ray or neutron diffraction. X-ray diffraction (the $\sin^2$-psi method) has been successfully applied to SCS-6 reinforced titanium matrix composites by several groups of researchers.[1,2] They have all obtained comparable results showing significant levels of matrix tension in both the fiber and transverse directions, with the fiber direction stresses being higher. X rays have small penetration depth, thus only near-surface stresses can be measured. More recently neutron diffraction was developed to measure residual stresses in bulk, and used for high-temperature composites.[3] Lattice strains are determined by measuring the shift in the diffraction peaks for the composite constituents between stressed and stress-free samples. Neutron irradiation has the advantage of deep penetration, thus allowing stress sensing for both fibers and matrix. However, neutron diffraction cannot be used *in situ* during processing. Also, it is extremely expensive and can be performed only at several national laboratories. This shows that there is still a great need for less expensive *in situ* techniques for nondestructive residual stress determination in composites. Ultrasonic methods are very attractive for this application. It has been demonstrated that ultrasonic wave velocity measurements can be successfully used for characterization of fiber-matrix interphase[4] and fatigue damage[5] in high-temperature composite materials.

The use of ultrasonic velocity temperature dependence has also been considered for determination of applied and residual stresses both theoretically and experimentally.[6,7] The approach is based on the fact that the ultrasonic velocity gradient with respect to temperature is a function of stress.

The purpose of this work is to describe quantitatively changes in ultrasonic wave velocities propagating through a composite material with residual stresses. This demonstrates the feasibility of the development of ultrasonic techniques

[a]Present address: Thiokol Corporation, P.O. Box 707, M/S 245, Brigham City, UT 84302.
[b]Present address: Digital Wave Corporation, 14 Inverness Drive East, B-120, Englewood, CO 80112.

for assessment of residual stresses in composite structures. Wave propagation through a nonhomogeneous medium with nonhomogeneous stress distribution is considered. The generalized self-consistent multiple scattering model[8,9] serves as a basis for the determination of velocity and attenuation of ultrasonic waves in unidirectional composites with multilayered fibers. This model is briefly reviewed in Sec. II A. It allows the consideration of an arbitrary number of fiber and matrix phases in the analysis of wave dispersion and scattering. In order to extend this model to the case of composites with residual stresses, we describe the governing equations for a wave propagating in a stressed medium with boundary conditions at the interface between two stressed media in Sec. II B. These equations provide a foundation for the description of wave propagation through a multilayered stressed structure. The detailed computational procedure for the solution of the reflection/refraction problem at the interface between two generally anisotropic stressed media is given in Ref. 10. Modifications in the model to take into account residual stresses in the composite are described in Sec. II C and in more detail in Ref. 11. Calculated results for ultrasonic wave velocities in SCS-6/Ti composite with and without residual stresses are presented in Sec. III. Preliminary results were given in Ref. 12.

I. CALCULATION OF RESIDUAL STRESSES IN HIGH-TEMPERATURE COMPOSITE MATERIALS

With the rapid development of new composite materials in the past three decades significant effort has been put into improving models and techniques for estimating residual stresses in composites.

Modeling of the thermal response in high-temperature composites can be performed using analytical concentric cylinder models (CCM)[13,14] or finite element models (FEM).[15,16] Today's models allow us to calculate residual thermal stresses in high-temperature composites and to explore the influence of material properties (fibers, matrices, interface coatings) and processing (cooldown history and fabrication temperature). Also, plastic and time-dependent deformations are included in most of these models. The advantage of CCM is computational speed and thus the possibility of performing parametric studies of the influence of fiber and matrix characteristics (fiber morphology, matrix yield strength) and fiber/matrix interface properties on the level of residual stress. The advantage of finite element analysis is the possibility of studying the effect of fiber packaging and different lamina orientation (i.e., cross-ply), but these calculations require powerful computational resources. Wright *et al.*[2] compared CCM, FEM, x-ray and neutron diffraction for different metal matrix composite materials. There is good agreement of model predictions with measurements by both x-ray and neutron diffraction techniques.

To predict the residual stresses in SCS-6/Ti composite which arise during the cooling from the processing temperature of 815 °C to room temperature (23 °C) we employ the local/global matrix formulation of the boundary value problem proposed by Pindera *et al.*[14] for an arbitrarily layered concentric cylinder. This formulation easily allows the incorporation of an arbitrary number of elastoplastic shells with

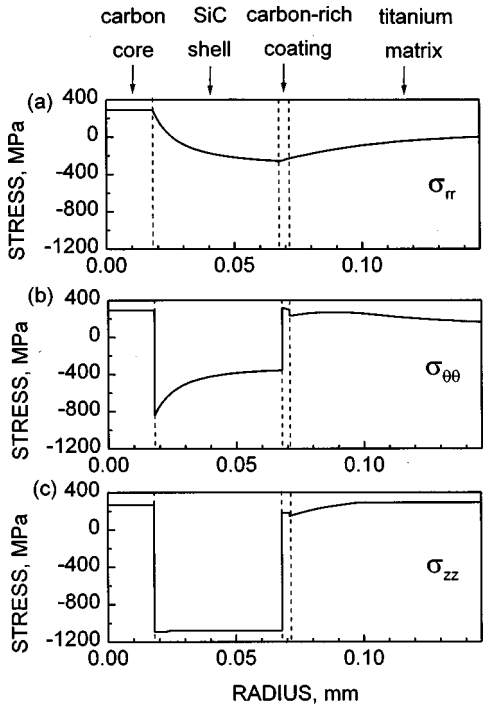

FIG. 1. Residual stresses resulted in SCS-6/Ti composite due to cooling from processing (815 °C) to room temperature. The stresses are calculated using the concentric cylinder model (CCM).

temperature-dependent properties into the concentric cylinder. The fiber is considered to have a multilayered structure consisting of a carbon core, SiC shell, and a carbon-rich coating [Fig. 1(a)]. The fiber volume fraction is 0.24. The temperature-dependent elastic properties of the Ti matrix are taken from Ref. 14. The CCM assumes zero shear stress, thus the only nonzero stress components are axial, radial and hoop [Fig. 1(b)]. To satisfy the boundary conditions at the interfaces, the radial stress is considered to be continuous. The continuity of radial displacements is incorporated automatically into the model. The results of the calculations are shown in Fig. 2. According to these calculations, the Ti matrix yields during cooling at 243 °C. One can see that the level of residual stress is high and that the stress distribution is nonhomogeneous. For example, the compressional axial stress in the SiC shell is around 1000 MPa, while the tensile axial stress in the Ti matrix is about 300 MPa. These stress levels lead to plastic deformations which may affect the performance of structural components made from this composite material.

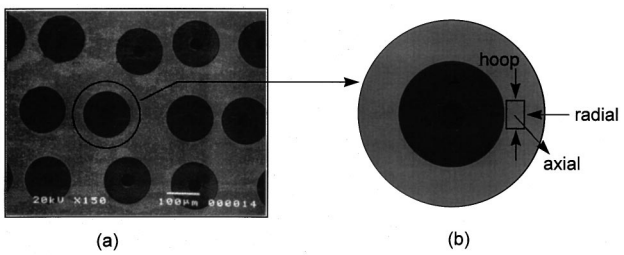

FIG. 2. (a) The SEM micrograph of a SCS-6/Ti unidirectional composite sample; (b) residual stress components.

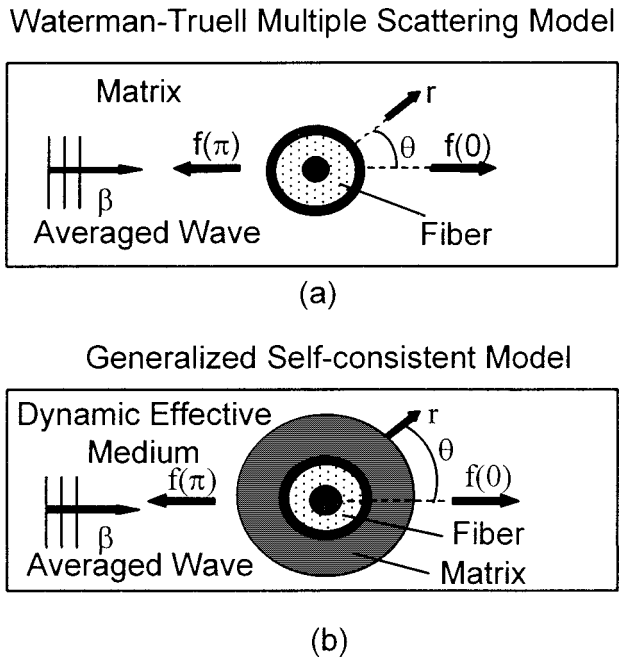

FIG. 3. (a) Waterman–Truell model: fiber with thin interphase is imbedded in the unbounded matrix. Multiple scattering is accounted by Eq. (1). (b) Generalized self-consistent multiple scattering models: fiber/matrix cell is imbedded in the composite effective medium.

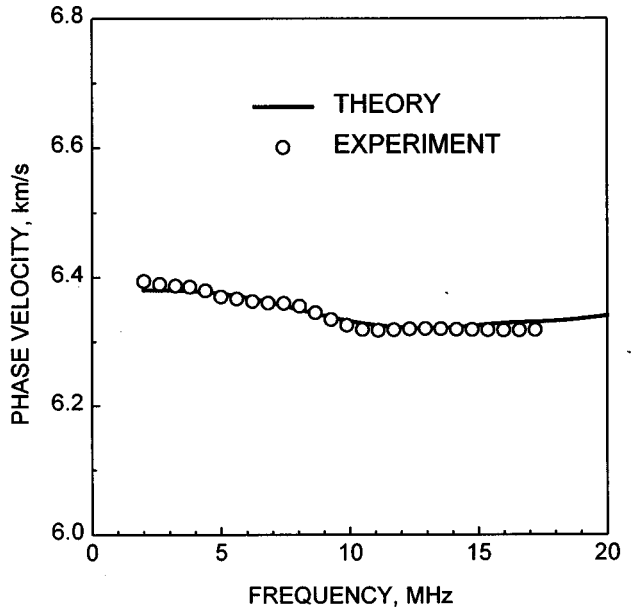

FIG. 4. Measured and predicted (by GSC model) frequency dependence of a longitudinal wave in SCS-6/Ti composite.

II. MODELING OF ELASTIC WAVE PROPAGATION IN COMPOSITES

As one can see, residual stresses of different sign resulted in the fiber and the matrix. An ultrasonic bulk wave propagating through a composite averages the properties of the constituents and the stress effect. In order to describe this averaging quantitatively and assess the effect of stresses in constituents on the wave propagation, we need to consider wave interaction with a multilayered structure of complex geometry.

A. Generalized self-consistent multiple scattering model

Interference of a wave scattered from different fibers in the composite results in scattering-induced wave attenuation and dispersion. If the fibers are sufficiently dense and closely spaced and the wavelength is comparable to the fiber size, the fibers cannot be considered as independent scatterers and a multiple scattering theory must be used. To calculate the velocities of ultrasonic waves propagating in the direction perpendicular to the fibers in a uniaxial composite, a modified Waterman–Truell multiple scattering model[8,9] is used.

In the Waterman–Truell model[17] the wave number is found by averaging a joint probability distribution over all scatterers. For a unidirectional composite with identical fibers, the multiple scattering field yields a complex wave propagation constant $\beta=\omega/V_c+i\alpha$ where

$$\left(\frac{\beta}{k}\right)^2=\left[1-\frac{2in_sf(0)}{k^2}\right]^2-\left[\frac{2in_sf(\pi)}{k^2}\right]^2, \tag{1}$$

where $n_s=c/\pi r_f^2$ is the number of fibers per unit area, r_f is the fiber radius and c is the fiber fraction; $k=k^m$ is the wave number of the matrix, and $f(0)$ and $f(\pi)$ are the forward and backward scattering amplitudes calculated from a single fiber embedded in a matrix with wave number k as shown in Fig. 3(a). One sees from Eq. (1) that both V_c and α are dependent on frequency.

For multilayered fibers scattering coefficients can be calculated using the transfer matrix method.[9,18] The solutions of Eq. (1) exhibit low-frequency velocity limits different from those predicted by the well-known static solutions [for example, the generalized self-consistent model (GSCM)[19]]. As static limit for a multilayered cylindrical medium the generalized self-consistent method is considered.[20] To satisfy the low-frequency limit, the Waterman–Truell model is modified as shown in Fig. 3(b), where the composite cylinder consisting of the multilayered fiber as the core and the matrix material as the annulus is considered embedded in the effective medium with properties the same as those of the composite which are assumed to be unknown and aimed to be determined as the problem solution. The forward and backward scattering amplitudes $f(0)$ and $f(\pi)$ are found for scattering from the multilayered cylinder by waves incident from the effective medium with wave number k^e and (1) is solved in a self-consistent manner which requires $\beta=k^e$. In this way, all the static solutions given in Ref. 20 match with the static limits of the longitudinal and transverse wave velocities. This dynamic model was developed by Mal and Yang[21] for study of SH shear wave propagation, and by Huang and Rokhlin[8] for longitudinal and SV shear wave propagation in composites. Figure 4 shows the comparison of experimental results (dots) and the theoretical prediction by the GSCM Waterman–Truell solution (solid line) for a longitudinal wave propagating perpendicular to the fibers in SCS-6/Ti composite. A description of the experiment and details of the computational procedure are given in Ref. 8. One can see that experiment and theory agree well.

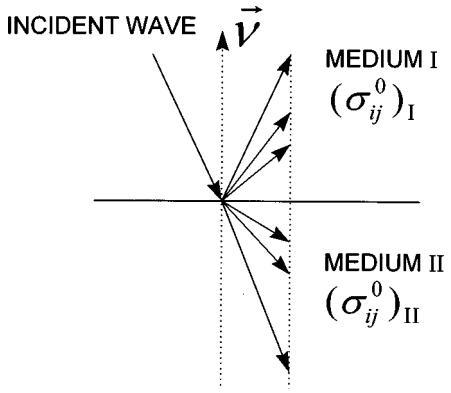

FIG. 5. Wave propagation through the plane boundary between anisotropic stressed media.

B. Wave propagation through a plane interface between two anisotropic stressed media

To introduce modifications in the above model for estimation of the wave velocities in a stressed composite, one must consider wave propagation in a stressed medium. In this section, we present the governing equations for a wave in a stressed homogeneous layer with boundary conditions at the interface between two stressed layers. We follow the approach proposed by Man and Lu[22] who derived the generalized Christoffel equation for a stressed medium. Next we formulate boundary conditions on the interface between two anisotropic stressed media. These equations serve as building blocks for modeling of ultrasonic wave propagation through, and scattering from, multiple interfaces between stressed fiber and matrix layers, which will be discussed in Sec. II C.

The prestressed configuration is the only reference configuration in this approach, and the initial stress is included in the constitutive equation:

$$\sigma_{ij}=\sigma_{ij}^0+C_{ijkl}\epsilon_{kl}+u_{i,k}\sigma_{kj}^0, \tag{2}$$

where σ_{ij} is the first Piola–Kirchhoff stress tensor, σ_{ij}^0 is the initial static stress, ϵ_{ij} is the elastic strain due to wave propagation, $u_{i,k}$ is the displacement gradient and C_{ijkl} is the fourth rank tensor of stress dependent elastic constants. Stress-dependent elastic constants are combinations of second and third order elastic constants and stresses.[23] In the case of plastic deformations they also depend on the loading–unloading history. Equation (2) gives the relation between stresses and displacements which arise from wave propagation in a prestressed medium. It is an analog of Hooke's law for the unstressed case. In general the stress σ_{ij} can be both applied and residual since there is no restriction that the resulting deformation be elastic.

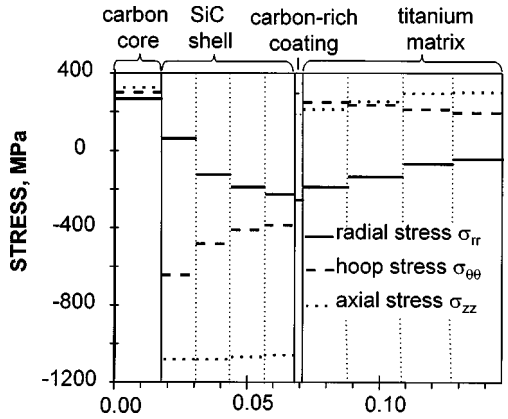

FIG. 6. Discretization of residual stresses in SCS-6/Ti composite.

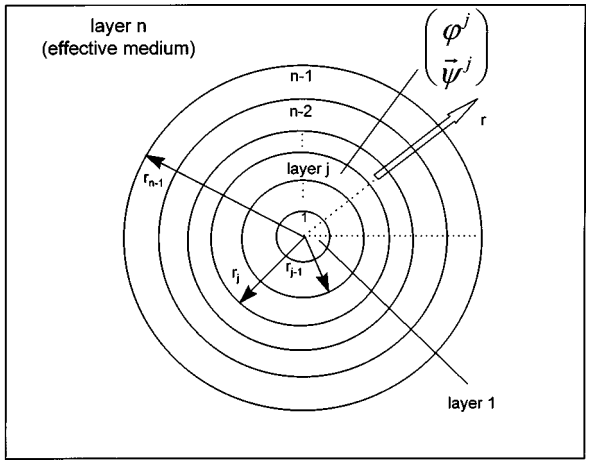

FIG. 7. Generalized self-consistent model for an N-layered cylindrical medium.

The equation of motion has the following form:

$$\sigma_{ij,j}=\rho\ddot{u}_i. \tag{3}$$

Using (2), (3) can be rewritten as

$$(C_{ijkl}+\sigma_{jl}^0\delta_{ik})u_{k,jl}=\rho\ddot{u}_i. \tag{4}$$

Now, assuming that the material and local (over the size of the transducer) stresses are homogeneous and using a plane wave solution for **u**,

$$u_k=AP_ke^{iK(\mathbf{n}\cdot\mathbf{x}-Vt)}, \tag{5}$$

where A is the amplitude of the wave, P_k is the unit displacement vector, $\mathbf{K}=K\mathbf{n}=(\omega/V)\mathbf{n}$ is the wave number, $\mathbf{V}=V\mathbf{n}$ is the wave velocity, **n** is the wave normal, and **x** is the position vector, one has the Christoffel equation for an anisotropic material under stress:

$$[C_{ijkl}n_in_l+(\sigma_{il}^0n_in_l-\rho V^2)\delta_{jk}]P_k=0. \tag{6}$$

Equation (6) has nontrivial solutions when the determinant is equal to zero,

$$|G_{jk}-\rho V^2\delta_{jk}|=0, \tag{7}$$

where G is the generalized Christoffel tensor with components

$$G_{jk}=(C_{ijkl}+\sigma_{il}^0\delta_{jk})n_in_l. \tag{8}$$

It can be shown that G is symmetric ($G_{ij}=G_{ji}$) and the eigenvalue problem has three real solutions as for an unstressed medium.

Let us consider a plane interface between two generally anisotropic stressed media. Here ν is the vector normal to the interface (Fig. 5). Index ''I'' refers to the upper medium and ''II'' to the lower medium. The initial stresses are $(\sigma_{ij}^0)_I$ and

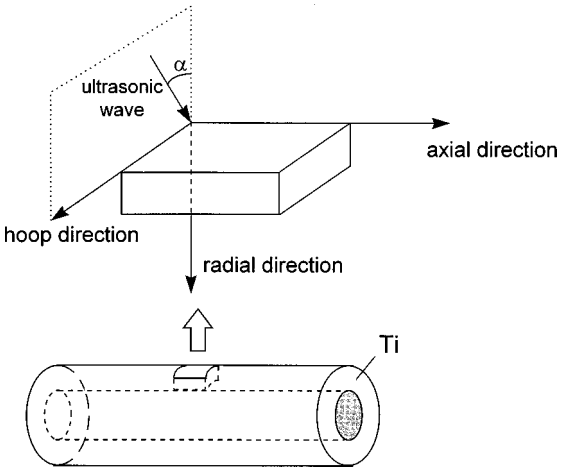

FIG. 8. Wave propagation in stressed Ti matrix with residual stresses.

$(\sigma_{ij}^0)_{II}$ for upper and lower media, respectively. For a static stressed state the boundary conditions represent the continuity of the traction forces:

$$(\sigma_{ij}^0)_I \nu_j = (\sigma_{ij}^0)_{II} \nu_j . \tag{9}$$

Consider a monochromatic plane wave (5) propagating from the upper to the lower medium. The boundary conditions at the interface represent continuity of displacements and traction forces. In the general case, for a wave incident from the upper medium there are three reflected (in upper medium, $\alpha = 1,...,3$) and three transmitted (in lower medium, $\alpha = 4,...,6$) waves. The boundary conditions are

$$\begin{aligned} &\mathbf{u}^{inc} + \sum_{\alpha=1}^{3} \mathbf{u}^{\alpha} = \sum_{\alpha=4}^{6} \mathbf{u}^{\alpha}, \\ &\sigma_{ik}^{inc} \nu_k + \sum_{\alpha=1}^{3} \sigma_{ik}^{\alpha} \nu_k = \sum_{\alpha=4}^{6} \sigma_{ik}^{\alpha} \nu_k . \end{aligned} \tag{10}$$

Using Eq. (2) and taking into account static boundary conditions (10), each of the terms $\sigma_{ij}\nu_j$ is equal to

$$\sigma_{ij}\nu_j = C_{ijkl}\epsilon_{kl}\nu_j + u_{i,k}\sigma_{kj}^0 \nu_j . \tag{11}$$

Note that, in comparison with the boundary conditions for traction forces in the unstressed case, the elastic constants are replaced with stress-dependent elastic constants and an additional term $u_{i,k}\sigma_{kj}^0\nu_j$ appears. Boundary conditions for displacements are the same as for the unstressed state.

C. Modeling of an ultrasonic wave propagation in a stressed composite

The model described in Sec. II A can be modified and used to estimate wave velocities in a stressed composite. As an example we will consider a four-phase SiC/Ti composite with the residual stress distribution shown in Fig. 2.

TABLE I. Transverse properties of each phase in a SCS-6/Ti composite.

Phase	C_{rr}^0 (GPa)	G_t^0 (GPa)	ρ (g/cc)	r (μm)
Core (carbon)	49	16	1.7	18
Shell (SiC)	446	177	3.2	68
Interphase (carbon-reach coating)	31	4.6	2.1	71
Matrix (titanium alloy)	193	45	5.4	146

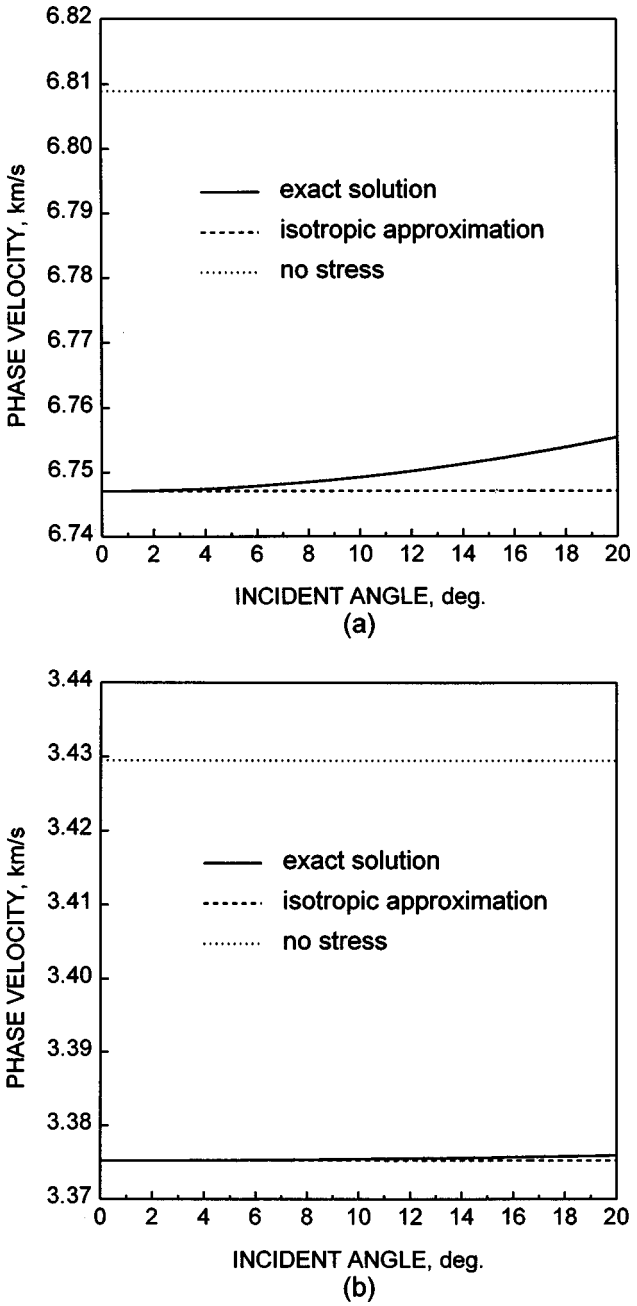

FIG. 9. (a) Longitudinal and (b) shear wave velocities in Ti matrix without and with residual stresses.

First the media with the nonhomogenous stress distribution is discretized. Each phase is divided into several layers and it is assumed that the stresses are constant within each layer. The stress level for each layer is assumed to be the average of the values on the inner and outer boundaries of that layer (Fig. 6). In doing so, a four-layered system is replaced by $n-1$ layers. Index 1 refers to the fiber core, index $n-1$ refers to the outer matrix layer and index n refers to the effective medium (Fig. 7). Each layer is characterized by the elastic properties of the corresponding phase and by three discretized stress components (radial, axial and hoop) which are assumed to be constant throughout the layer. Each layer is considered to be isotropic in the transverse (with respect to

TABLE II. Third-order elastic constants for Ti and Si.

Material	C_{111} (GPa)	C_{112} (GPa)	C_{123} (GPa)
Ti	−1358	−1105	−162
Si	−821	−448	−104

the fiber direction) plane. In the presence of residual stresses isotropy is violated since the radial and hoop stresses are different. However, radial symmetry still holds. Since the elastic field is decomposed into cylindrical waves propagating in the radial direction, the multiple scattering depends mainly on the material properties which define the velocities of longitudinal and shear waves in the radial direction. From the solution of the Christoffel equation (6) the velocities of the longitudinal and shear waves in the radial direction are

$$\rho V_l^2 = C_{rr} + \sigma_{rr}^0, \quad \rho V_s^2 = G_t, \tag{12}$$

where C_{rr} and G_t are the radial and transverse shear-stress-dependent elastic constants and σ_{rr}^0 is the radial component of the residual stress. Stress-dependent elastic constants can be determined from second and third order elastic constants and stresses assuming that the deformation is hyperelastic. Formulas for stress-dependent elastic constants are presented in Ref. 23.

The multiple scattering model described in the previous section assumes isotropy of each layer in the transverse plane. Since most of the scattering occurs within a small angular range in the radial direction, we assume that the isotropic moduli for each layer are equal to those which define the longitudinal and shear wave velocities (12) in the radial direction in the actual anisotropic layer. One can define the effective radial $C_{rr}^{\text{eff}} = C_{rr} + \sigma_{rr}^0$ and transverse shear $G_t^{\text{eff}} = G_t$ moduli. The effect of residual stresses is included in the stress-dependent elastic constants C_{rr} and G_t and as a direct stress term σ_{rr}^0 in C_{rr}^{eff}.

Thus, a four-phase composite with residual stress is approximated by a $(n-1)$-layered composite system, where the moduli of the jth layer are $(C_{rr}^{\text{eff}})_j$ and $(G_t^{\text{eff}})_j$. The generalized self-consistent multiple scattering model described in the previous section can be applied to this system to determine the dispersion of longitudinal and shear (polarized perpendicular to the fiber direction) waves propagating normal to the fibers.

To illustrate that the error in the velocities of scattered waves introduced by the isotropic approximation is small, we calculated longitudinal and shear wave velocities in the Ti matrix at different propagation angles α with respect to the normal to the fiber direction (Fig. 8). An axial stress of 300 MPa, a radial stress of 250 MPa and a hoop stress of 200 MPa were assumed in the matrix. These are averaged values of residual stresses predicted for the Ti matrix using CCM (Fig. 2). The results are presented in Fig. 9(a) and (b) for longitudinal and shear wave velocities, respectively. The dotted line shows velocities in unstressed material, the dashed line represents the isotropic approximation for the stressed case (which is described above) and the solid line gives the exact velocity value predicted by the acoustoelastic theory (Sec. II B). One can see that in the range of 10° from the fiber normal the difference between the exact solution and the isotropic approximation is only a few meters per second for a longitudinal wave. For a shear wave it is even smaller. Thus, the assumption of transverse isotropy of each layer is reasonable.

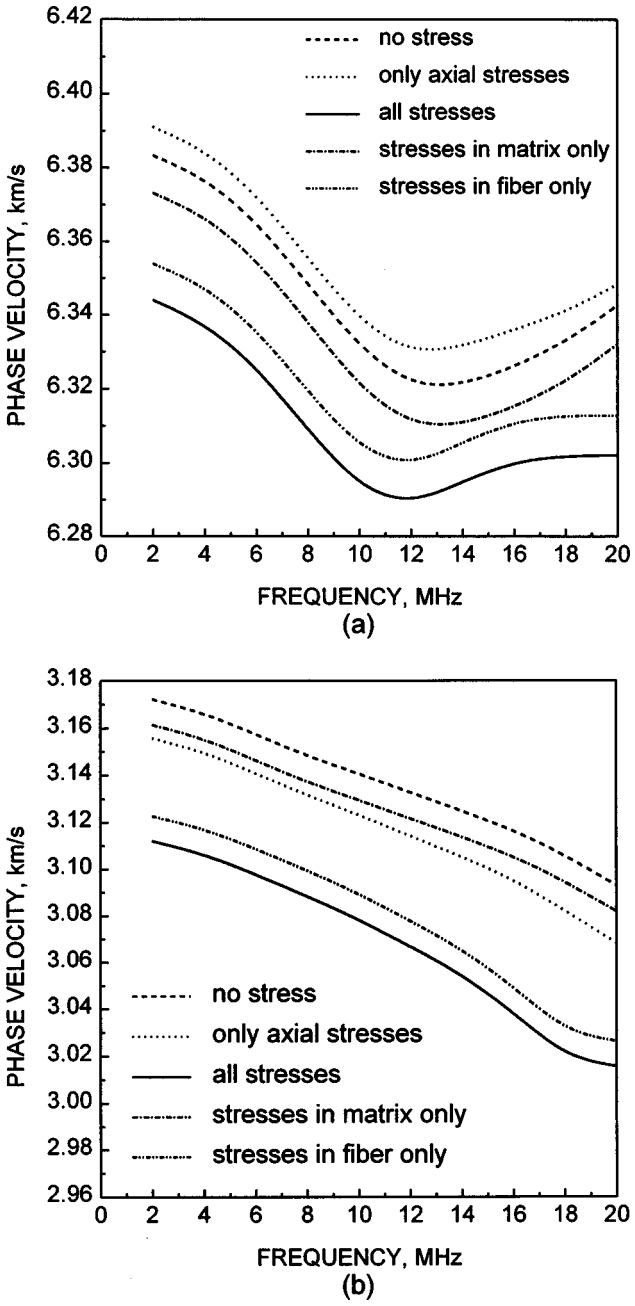

FIG. 10. Longitudinal (a) and shear (b) wave velocities in the perpendicular to fibers' direction in SCS-6/Ti composite with and without residual stresses.

III. APPLICATION OF THE MODEL FOR A COMPOSITE WITH RESIDUAL STRESSES

The approach described in Sec. II C was utilized to determine wave velocity changes due to the presence of thermally induced residual stresses in a four-phase SCS-6/Ti composite, consisting of carbon core, SiC shell, carbon-reach coating and titanium matrix. The residual stresses were estimated using CCM as described in Sec. I and are presented in

Fig. 2. The elastic properties of each phase in the transverse direction are presented in Table I. The third order elastic constants for all fiber phases (core, shell and coating) were taken from the handbook[24] to be those corresponding to Si and for the matrix, those for Ti. They are given in Table II. For stress discretization the SiC shell and Ti matrix were each split into five layers. The carbon core was left intact because it has constant stress. The carbon-rich coating is much thinner than the other phases, so it was not split either. Thus the total number of layers was 12.

Wave velocity calculations using the model described in the previous section were performed for different frequencies. The results are presented in Fig. 10(a) and (b) for longitudinal and shear waves propagating in the normal-to-fibers direction. The shear wave is polarized perpendicular to the fiber direction. Five cases are considered: unstressed composite (dashed line), the case when only the axial stresses (dotted line) in matrix and fiber are accounted for, the case when stresses are considered in the matrix and residual stress in the fiber are zero (dash-dotted line), and when stresses only in fibers are accounted for (dash-double-dotted line). Finally, the effect of all residual stresses is taken into consideration (solid line). One can see that the changes in velocities due to the presence of stresses are on the order of 1%.

This paper addresses the direct problem of determination of the effect of residual stress in composites on the ultrasonic velocity. Even though the average residual stress is zero, the average ultrasonic velocity over the acoustic path depends on stress distribution due to different sensitivity of the wave velocity to stress in the different material phases (fibers and matrix). While the overall velocity change is small, it is comparable to this in homogeneous materials.

The inverse problem, i.e., the determination of residual stress from experimentally measured velocity, is beyond the scope of this study. The practical solution is still far away even for homogeneous materials with homogeneous stress distributions. The main issue is the separation of the velocity variation due to material texture from that due to residual stress. For recent progress in this area, refer to Refs. 6, 25, and 26. In composites, the ultrasonic stress measurement is significantly more complicated due to possible local variations in fiber volume fraction, fiber matrix interphase properties, and matrix and fiber texture. Simultaneous reconstruction of elastic moduli and stress from the measured angle dependency of ultrasonic wave velocities[26] may help in overcoming these difficulties. Another possibility is to utilize the temperature dependence of ultrasonic velocity[6,7] on stress for stress measurement. Since the residual stress depends on temperature (Sec. I) it may be possible to exclude the effects of some microstructural characteristics on ultrasonic velocity.

IV. SUMMARY AND CONCLUSIONS

A numerical model has been developed to determine the velocities of ultrasonic waves propagating through a composite with residual stresses. The model is based on a modified generalized self-consistent method. The model accounts for multiple wave scattering and the multilayered structure of the composite. Simulation results performed for SCS-6/Ti metal matrix composite show that changes in the longitudinal and shear waves in the perpendicular-to-fibers direction are about 0.5% and 2.0%, respectively.

This work provides a foundation for the determination of changes in the ultrasonic wave velocities of composite materials induced by the presence of residual stresses. The main challenge in the development of a practical method for measurements of these changes for stress determination is the necessity of separating the stress effect from the influence of changes in the elastic properties of the constituents and the state of the fiber/matrix interphase.

[1] N. Jayaraman and P. Rangaswamy, ''Residual stresses in Ti3Al-SCS-6 fiber reinforced metal matrix composites'' Air Force Laboratory WL-TR-91-4020, February 1991, pp. 522–531.

[2] P. K. Wright, M. D. Sensmeier, D. Kupperman, and H. Wadley, ''Thermal stress effects in intermetallic matrix composites,'' HITEMP Review 1991, NASA Conference Publication 1991, pp. 45-1 to 45-14.

[3] S. Majumdar, J. P. Singh, D. Kupperman, and A. D. Krawitz, ''Application of neutron diffraction to measure residual strains in various engineering composite materials,'' Trans. ASME: J. Eng. Mater. Technol. **113**, 51–59 (1991).

[4] Y. C. Chu and S. I. Rokhlin, ''Effective elastic moduli of fiber-matrix interphases in high-temperature composites,'' Metall. Mater. Trans. A **27A**, 165–182 (1996).

[5] S. I. Rokhlin, Y. C. Chu, and W. Huang, ''Ultrasonic evaluation of fatigue damage in metal matrix composites,'' Mech. Mater. **21**, 251–263 (1995).

[6] J. H. Cantrell and K. Salama, ''Acoustoelastic characterization of materials,'' International Materials Reviews **36**, 125–145 (1991).

[7] K. Salama and C. K. Ling, ''The effect of stress on the temperature dependence of ultrasonic velocity,'' J. Appl. Phys. **51**, 1501 (1980).

[8] W. Huang and S. I. Rokhlin, ''Frequency dependencies on ultrasonic wave velocity and attenuation in fiber composites. Theory and experiments,'' Rev. Prog. Quant. Nondestr. Eval. **14**, 1233–1238 (1995).

[9] W. Huang, S. I. Rokhlin, and Y. J. Wang, ''Effect of fiber-matrix interphase on wave propagation along, and scattering from, multilayered fibers in composites. Transfer matrix approach,'' Ultrasonics **33**, 365–375 (1995).

[10] A. D. Degtyar and S. I. Rokhlin, ''Stress effect on ultrasonic wave propagation through the solid-solid and liquid-solid plane interface,'' Rev. Prog. Quant. Nondestr. Eval. **16**, 1699–1706 (1997).

[11] A. D. Degtyar and S. I. Rokhlin, ''Stress effect on boundary conditions and elastic wave propagation through an interface between anisotropic media,'' J. Acoust. Soc. Am. (submitted).

[12] A. D. Degtyar, W. Huang, and S. I. Rokhlin, ''Wave propagation in stressed composites,'' Rev. Prog. Quant. Nondestr. Eval. **15**, 1669–1676 (1996).

[13] Y. Mikata and M. Taya, ''Stress field in a coated continuous fiber composite subjected to thermal-mechanical loadings,'' J. Compos. Mater. **19**, 554–578 (1985).

[14] M-J. Pindera, A. D. Freed, and S. M. Arnold, ''Effects of fiber and interfacial layer architectures on the thermoplastic response of metal matrix composites,'' NASA Technical Memorandum 105802, August 1992.

[15] R. P. Nimmer, ''Fiber-matrix interface effects in the presence of thermally induced residual stresses,'' ASTM Journal of Composites Technology and Research **12**(2), 65–75 (1990).

[16] S. M. Arnold, V. K. Arya, and M. E. Melis, ''Elastic/plastic analyses of advanced composites investigating the use of the compliant layer concept in reducing residual stresses resulting from process,'' NASA TM 103204, September 1990.

[17] P. C. Waterman and R. Truell, ''Multiple scattering of elastic waves,'' J. Math. Phys. **2**, 512–537 (1961).

[18] W. Huang, Y. J. Wang, and S. I. Rokhlin, ''Oblique scattering of an elastic wave from multilayered cylinder in a solid. Transfer matrix approach,'' J. Acoust. Soc. Am. **99**, 2742–2754 (1996).

[19] R. M. Christensen, *Mechanics of Composite Materials* (Krieger, Malabar, FL 1991), 2nd ed.

[20] W. Huang and S. I. Rokhlin, ''Generalized self-consistent model for composites with functionally graded and multilayered interphases. Transfer matrix approach,'' Mech. Mater. **22**, 219–247 (1996).

[21] A. K. Mal and R. B. Yang, ''The influence of fiber-matrix interfacial properties on wave characteristics in metal matrix composites,'' Rev. Prog. Quant. Nondestr. Eval. **13**, 1453–1460 (1994).
[22] C.-S. Man and W. Y. Lu, ''Towards an acoustoelastic theory for measurement of residual stress,'' J. Elast. **17**, 159–182 (1987).
[23] A. D. Degtyar and S. I. Rokhlin, ''Absolute stress determination in orthotropic materials from angular dependences of ultrasonic velocities,'' J. Appl. Phys. **78**, 1547–1556 (1995).
[24] Landolt-Börnstein, *Numerical Data and Functional Relationships in Science and Technology* (Springer-Verlag, New York, 1979), Vol. III/11.
[25] R. B. Thompson, W. Y. Lu, and A. V. Clark, Jr., in *Handbook of Measurements of Residual Stresses*, edited by J. Lu (Fairmont, Lilburn, GA, 1996).
[26] A. D. Degtyar, A. L. Laurentyev, and S. I. Rokhlin, ''New Method for Determination of Applied and Residual Stresses in Anisotropic Materials from Ultrasonic Velocity Measurements,'' Mater. Eval. **55**, 1162–1168 (1997).

Elasticity of fused silica spheres under pressure using resonant ultrasound spectroscopy

Donald G. Isaak,[a] John D. Carnes, and Orson L. Anderson
Institute of Geophysics and Planetary Physics, University of California, Los Angeles, 405 Hilgard Avenue, Los Angeles, California 90095-1567

Hitoshi Oda
Faculty of Science, Okayama University, Okayama 700, Japan

(Received 24 October 1997; accepted for publication 26 May 1998)

Resonant ultrasound spectroscopy (RUS) is a powerful tool for determining the elastic properties of solids at high temperature. Before RUS can be used to measure the pressure derivatives of elasticity, however, effects of boundary conditions between the pressurizing gas and specimen must be understood. Data are presented that show effects of different pressurizing gases on the apparent or measured values of $(\partial G/\partial P)_T$ of fused silica spheres, where G is the shear modulus, P is pressure, and T is temperature. The value of $(\partial G/\partial P)_T$ is found to depend on the molecular mass, M, of the pressurizing gas via $-3.425(0.032)-5.9(1.6)\times 10^{-3}M$, when M is in grams. Extrapolating to zero gas mass gives $(\partial G/\partial P)_T=-3.42(0.03)$, a value bracketed by results from previous plane-wave, ultrasonic measurements. An alternative analysis in which effects of the pressurizing gas are removed by theoretical concerns is also presented and suggests that $(\partial G/\partial P)_T$ is $-3.32(0.03)$. Our results quantify the effect of pressurizing gas on measured pressure derivatives of G when using RUS and indicate that systematic problems in transducer-specimen bonding from previous acoustic plane-wave measurements on fused silica at elevated pressure are not yet measurable. © *1998 Acoustical Society of America.* [S0001-4966(98)05709-9]

PACS numbers: 43.35.Cg, 43.35.Yb [HEB]

INTRODUCTION

Information about the elastic properties of solids is important for a range of problems in material science, solid state physics, and geophysics. The temperature, T, and pressure, P, dependences of elasticity are often of particular importance. For example, information about the effects of pressure and temperature on elasticity are required when laboratory measurements are extrapolated to P, T conditions appropriate to the deep Earth. Elastic moduli are often called second order elastic constants because they are derived from the appropriate second strain derivatives of the free energy, and the dependences of the elastic moduli on stress can ultimately be related to third-order elastic constants (Birch, 1947; Bateman *et al.*, 1961; Thurston and Brugger, 1964). The special case of hydrostatic pressure dependence of elasticity has particular importance, and ultrasonic acoustic techniques have long been used to measure elastic properties and their dependences on pressure (see, for example, Lazarus, 1949; McSkimin, 1958; Daniels and Smith, 1958).

The ultrasonic methods used to perform elasticity measurements under pressure are primarily pulse-echo and continuous wave techniques, both of which rely on the propagation of plane waves through the specimen. In recent years resonant ultrasound spectroscopy (RUS) has emerged as a powerful tool to study single-crystal elastic properties (Ohno, 1976). RUS experiments at elevated temperature, albeit at ambient pressure (Goto and Anderson, 1989; Anderson and Isaak, 1995) have been especially fruitful. RUS single-crystal elasticity measurements to date have generally been done with specimens prepared as right-rectangular parallelepipeds (RPR) (Demarest, 1971; Ohno, 1976) or spheres (RST) (Oda *et al.*, 1992, 1993). Excellent overviews of the RUS technique are found in Maynard (1996), Leisure and Willis (1997), and Migliori and Sarrao (1997).

Although both plane wave and RUS methods of studying elasticity are useful, there are unique advantages to using RUS (Leisure and Willis, 1997). We consider the possibility of using RUS to determine third-order elastic properties. The prospect of measuring third-order elastic properties using RUS is attractive for a variety of reasons. RUS measurements are relatively simple to perform. The full set of elastic moduli are obtained from one frequency scan rather than from several measurements using different polarization and crystal directions. Using plane-wave techniques to measure the pressure dependences of the elastic moduli of a solid with orthorhombic crystal symmetry requires that nine separate pressure runs be done. Until somewhat recently, RUS techniques were amenable to much smaller specimens (Lei *et al.*, 1993; Spoor *et al.*, 1995) than were possible with routine interferometry measurements. Recent advances in acoustic interferometry techniques provide for elasticity measurements of very small specimens, in some cases using dimensions as small as 50 μm (Spetzler *et al.*, 1993, 1996; Li *et al.*, 1996). However, the experimental setups for interferometry (plane-wave) measurements of very small specimens are elaborate and are not used routinely. Furthermore, despite extensive studies of interferometry techniques (Spetzler *et al.*, 1993), outstanding questions about the effect of the transducer–specimen bonds on the pressure measure-

[a]Also at Department of Mathematics and Physics, Azusa Pacific University.

ments remain. Uncertainties pertaining to transducer–specimen bonding are eliminated in RUS since transducers are applied to the specimen without bonding agents.

The extension of RUS to measurements at elevated pressure has not received much attention, in part because of complications in data reduction. In RUS the conversion of the measured spectrum to elastic moduli requires the assumption that the surface of the resonating specimen is free of external stress (Demarest, 1971; Ohno, 1976; Migliori and Sarrao, 1997). With a specimen under hydrostatic pressure, this boundary condition is not met. This change in boundary condition has an unknown effect on the resonant modes. Only recently have attempts to quantify this effect been reported (Zhang *et al.*, 1997).

Ohno *et al.* (1991) did a preliminary study of the application of RST to isotropic steel spheres and reported results for the pressure dependence of the shear modulus, G. In that study, helium was used as the pressurizing gas so as to maximize the acoustic impedance contrast between the pressurizing gas and the specimen and container walls. By their choices of specimen and pressurizing gas, Ohno *et al.* (1991) attempted to minimize the energy exchange between the specimen and its surroundings. Ohno *et al.* (1991) analyzed the pressure dependence of one toroidal mode up to 0.0193 MPa (193 bar) and found that $(\partial G/\partial P)_T = 1.8$, in agreement with the range of 1.5–2.0 found from other acoustic techniques. Although the study by Ohno *et al.* (1991) clearly demonstrates the feasibility of using RUS to measure pressure dependences of elasticity, it provides no information about the effect of the pressurizing gas on the pressure derivatives.

We examine the pressure dependence of two pure toroidal resonant modes for two spherical specimens of fused silica. Three pressurizing gases (helium, nitrogen, argon) with a wide range of molecular mass were used. Our goal was to measure the effect of the molecular mass of the pressurizing gas on the apparent pressure dependence of elasticity. Only results for the shear modulus are reported here. Our results extrapolated to zero gas mass are compared with pressure data obtained from interferometry plane-wave experiments and provide information about the effects of bonding on the interferometry results. We also attempt to account for gas mass effects from theoretical concerns and compare this result with the extrapolation of the experiments.

I. BACKGROUND AND METHOD

The resonant modes of a vibrating sphere are readily calculated if the elastic moduli (C_{ij}), density, and radius of the sphere are known. Although the general case of an elastically anisotropic sphere has been solved (Oda *et al.*, 1993), since fused silica is isotropic we have a simplified situation in which the bulk and shear moduli fully represent the elastic properties of the material.

Vibrating spherical specimens produce two general resonant mode types, spheroidal and toroidal. The spheroidal frequencies of isotropic spheres depend on both the adiabatic bulk modulus, K_S, and G. The toroidal modes, however, depend only on G. The frequency can be expressed as a function $f(G,r,m)$, where G, r, and m are shear modulus, radius, and mass of the spherical specimen, respectively. The frequency change δf due to δG and δr, when the sample mass is kept constant, is given by

$$\delta f = \left(\frac{\partial f}{\partial G}\right)_{r,m} \delta G + \left(\frac{\partial f}{\partial r}\right)_{G,m} \delta r. \tag{1}$$

The derivative

$$\left(\frac{\partial f}{\partial r}\right)_{G,m} = \frac{f}{2r} \tag{2}$$

is obtained from the general energy equation of an elastic vibrating sphere (Oda *et al.*, 1993).

Substituting (2) into (1) gives

$$\delta f = \left(\frac{\partial f}{\partial G}\right)_{r,m} \delta G + \frac{f}{2r}\,\delta r. \tag{3}$$

Thus the measured pressure dependence of the resonant frequency is given by

$$\frac{df}{dP} = \left(\frac{\partial f}{\partial G}\right)_{r,m} \frac{dG}{dP} + \frac{f}{2r}\,\frac{dr}{dP}. \tag{4}$$

From the definition of the isothermal bulk modulus, K_T, given by

$$K_T = -V\left(\frac{\partial P}{\partial V}\right)_T \tag{5}$$

we can write dr/dP in (4) as

$$\frac{dr}{dP} = -\frac{r}{3K_T}. \tag{6}$$

Using (6) in (4) and solving for dG/dP results in

$$\frac{dG}{dP} = \frac{df/dP + f/6K_T}{(\partial f/\partial G)_{r,m}}. \tag{7}$$

In (7) the numerator of the right side is dominated by df/dP, a negative number. The $f/6K_T$ term represents less than 8% of the final magnitude of dG/dP. If measurements of df/dP are done at isothermal conditions, the resulting dG/dP in (7) becomes $(\partial G/\partial P)_T$.

We obtained two spherical specimens (hereafter referred to as spheres 1 and 2) of fused silica so as to make direct RUS measurements of $(\partial f/\partial P)_T$ and obtain $(\partial G/\partial P)_T$ for different pressure-loading gases. The respective radii of spheres 1 and 2 are 1.945 and 2.414 mm. In Table I we show calculated frequencies and their dependences on K_S, the adiabatic bulk modulus, and G for the first eight modes of the two fused silica specimens studied. For practical purposes, we need not distinguish between the numerical values of the adiabatic (K_S) and isothermal (K_T) bulk moduli when using (7) at ambient conditions. At room temperature the difference between K_S and K_T, about 1%, has no measurable effect on the calculated dG/dP results. The numbers in Table I assume respective values of 37 and 31.3 GPa for K_S and G and a density of 2.210 g cm^{-3}.

Pressure measurements for three pressurizing gases, helium, nitrogen, and argon, were done on both spheres. The maximum pressure attained was in the range of 0.011–0.015

TABLE I. Lowest calculated modal frequencies and their dependences on K_S and G for two fused silica spheres of constant mass.

	Frequency (MHz)	$(\partial f/\partial K_S)_{r,G}$ (10^{-2} MHz/GPa)	$(\partial f/\partial G)_{r,K_S}$ (10^{-2} MHz/GPa)
Sphere 1			
${}_0T_2$	0.770 22	0.0000	1.2304
${}_0S_2$	0.809 27	0.0353	1.2510
${}_1S_1$	0.998 52	0.5054	0.9976
${}_0S_0$	1.172 50	1.4171	0.1978
${}_0T_3$	1.190 12	0.0000	1.9012
${}_1S_2$	1.424 71	0.6515	1.5058
${}_0S_4$	1.522 05	0.1936	2.2025
Sphere 2			
${}_0T_2$	0.620 58	0.0000	0.9913
${}_0S_2$	0.652 04	0.0285	1.0080
${}_1S_1$	0.804 53	0.4072	0.8038
${}_0S_0$	0.944 70	1.1418	0.1594
${}_0T_3$	0.958 90	0.0000	1.5318
${}_0S_3$	0.961 98	0.0930	1.4268
${}_1S_2$	1.147 91	0.5249	1.2132
${}_0S_4$	1.226 34	0.1560	1.7746

MPa (110–150 bar), depending on the gas used. Pressure was measured with a Bourdon tube pressure gauge, accurate to 1%.

In general, the Q value of a resonant peak depends on both pressure and the type of gas used to pressurize the specimen. However, for the pure toroidal modes, i.e., modes having no dependency on K_S, we found Q to be insensitive to gas type and pressure. The toroidal modes ${}_0T_2$ and ${}_0T_3$ contained one or two degenerate frequencies, presumably due to small asphericity in the specimens. The ${}_0T_2$ degenerate modes of sphere 2 at three different pressures when pressurized with helium gas are illustrated in Fig. 1.

The temperature inside the pressure cell was monitored

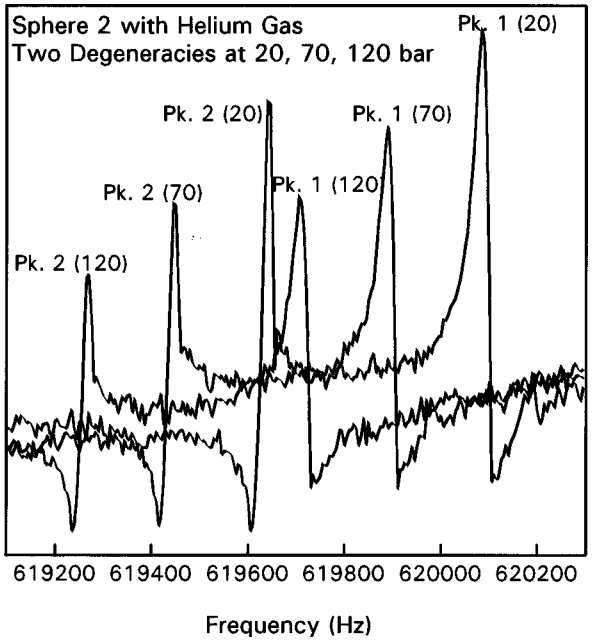

FIG. 1. Spectra of two degeneracies of the ${}_0T_2$ mode for sphere 2 shown at three different pressures. Numbers in parentheses with peak labels indicate pressure in bars.

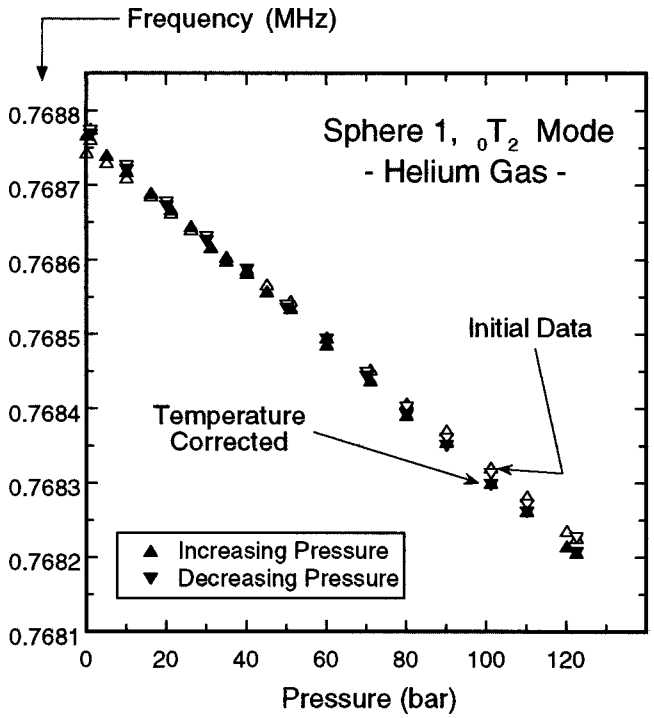

FIG. 2. Measured pressure dependency of the ${}_0T_2$ mode for sphere 1 using helium gas. The figure shows data before (open symbols) and after (closed symbols) temperature corrections were applied. These data were all obtained within a few tenths of a degree of each other.

with two type T Cu–CuNi thermocouples. Temperature was measured to 0.1°. The two thermocouples, placed on opposite sides of the specimen, never showed a difference of more than 0.1° from each other. After increasing or decreasing the pressure, we waited for the temperature inside the vessel to stabilize to within 0.1°, or so, of room temperature. Temperature corrections were applied to reference all frequency data to 25 °C. The frequency dependence on T is determined by

$$\left(\frac{\partial f}{\partial T}\right)_P = \left(\frac{\partial f}{\partial G}\right)_{r,K_S}\left(\frac{\partial G}{\partial T}\right)_P, \tag{8}$$

where $(\partial f/\partial G)_{r,K_S}$ is obtained from Table I and $(\partial G/\partial T)_P$ is from Bass (1995). Room temperature was usually near 25 °C throughout the pressure runs, requiring T corrections to the data of only a fraction of a degree. This situation is illustrated in Fig. 2, which shows the measured P dependence of the ${}_0T_2$ mode for sphere 1 using helium gas. Only small temperature corrections to the initial data (open symbols) were required throughout that pressure run. Figure 3 shows corrections required for the ${}_0T_3$ mode of sphere 1 using nitrogen gas. On that particular pressure run the starting room temperature was 20.8 °C, but there was a gradually warming to about 22.5 °C by the end of the run. The change in room temperature during the pressure run is reflected in the deviation of the open symbols in Fig. 3 at lower pressures. Nevertheless, in Fig. 3 we see excellent agreement in the up- and down-pressure data once they have all been referenced to isothermal conditions.

For sphere 1 we made one pressure run for each of the three loading gases and recorded frequency data while in-

creasing and decreasing pressure. We recorded data in intervals of 0.0005 MPa (5 bar) while increasing pressure up to 0.005 MPa (50 bar), after which intervals of 0.001 MPa (10 bar) were used. When decreasing pressure we used 0.001 MPa (10 bar) intervals throughout the pressure range. We analyzed two degenerate peaks of the ${}_0T_2$ mode and one peak of the ${}_0T_3$ mode for the helium and nitrogen runs. With argon only one degeneracy of the ${}_0T_2$ peak was clearly seen, thus we analyzed only one degenerate peak of each of the ${}_0T_2$ and ${}_0T_3$ modes. For sphere 2 we made three separate pressure runs for each of the three pressurizing gases and recorded data only when pressure increased. The one exception was the data recorded while decreasing pressure for the last argon pressure run with specimen 2. For each pressure run the measured value of $(\partial f/\partial P)_T$ for a particular mode, ${}_0T_2$ or ${}_0T_3$, was combined with the appropriate values of f, K_S, and $(\partial f/\partial G)_{r,m}$ (from Table I) in (9) so as to obtain an apparent value of $(\partial G/\partial P)_T$ for that particular gas.

II. EXPERIMENTAL RESULTS

The results for several pressure runs on the two spheres are summarized in Fig. 4. Fused silica is unusual in that the K_S and G moduli decrease, rather than increase, as pressure increases. Figure 4 shows the magnitude of $(\partial G/\partial P)_T$; the actual value of this derivative is negative. We refer to a value of $|(\partial G/\partial P)_T|$ determined from (7) as the apparent value of $|(\partial G/\partial P)_T|$ for a particular gas. The uncertainty in the apparent values for $|(\partial G/\partial P)_T|$ seen in Fig. 4 represents the standard deviation of all the results on the two spheres after the high and low values have been removed. The molecular mass, M, of the gas is the parameter by which these results are analyzed. Presumably, if the dependence of the apparent $|(\partial G/\partial P)_T|$ on pressurizing gas mass is known, then extrapolation to zero gas mass provides the correct value of $|(\partial G/\partial P)_T|$.

There is a monotonic increase in the apparent $|(\partial G/\partial P)_T|$ with increasing molecular mass. If a linear dependence on M is assumed, the apparent value of $(\partial G/\partial P)_T$ can be expressed by $-3.425(0.032)-5.9(1.6)\times 10^{-3}M$, when M is in grams. We have no prior reason to assign a linear dependence of $(\partial G/\partial P)_T$ on M. However, our results (Fig. 4) clearly show a monotonic increase in $|(\partial G/\partial P)_T|$ with increasing M, and a linear relationship is certainly admissible within the errors.

When our data are extrapolated to zero mass conditions, we find $(\partial G/\partial P)_T$ to be $-3.43(0.03)$, a result bracketed by values of -3.39 (Meister *et al.*, 1980) and -3.48 (Gerlich and Kennedy, 1978), both obtained from ultrasonic interferometry. We find no significant difference between the value of $(\partial G/\partial P)_T$ measured using helium gas and that of $(\partial G/\partial P)_T$ extrapolated to zero gas mass conditions; i.e., the magnitude of $(\partial G/\partial P)_T$ is 3.45 at 4 g (appropriate for helium), higher than the zero gas mass value by only about 0.7%. Thus the value of $(\partial G/\partial P)_T$ for fused silica, which has a relatively low acoustic impedance, can be quite accurately determined with RUS using only data from a helium gas pressure run. Our data show, however, that effects of different pressurizing gases on $|(\partial G/\partial P)_T|$ are noticeable.

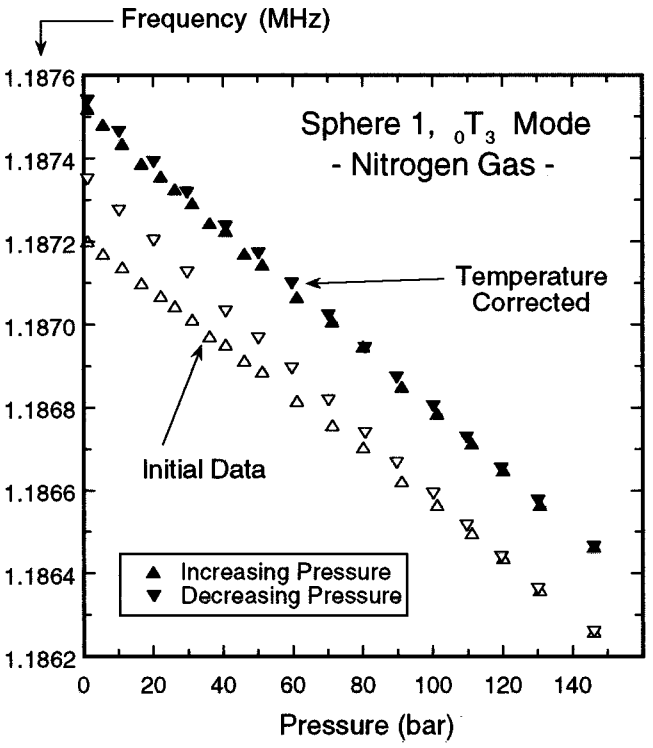

FIG. 3. Measured pressure dependency of the ${}_0T_3$ mode for sphere 1 using nitrogen gas. The figure shows data before (open symbols) and after (closed symbols) temperature corrections were applied. All data corrected to 25 °C. The ambient temperature was 20.8 °C at the start of the run, and gradually increased to 22.5 °C by the end of the run.

For instance, the $|(\partial G/\partial P)_T|$ from nitrogen gas is about 4% larger than at zero gas mass.

III. THEORETICAL CONSIDERATIONS

The preceding analysis provides an experimental account of effects of the pressurizing gas. We also attempted to account for gas effects from theory. We present here a simplified version of the full spherical harmonic acoustic radiation impedance development (Sorbello *et al.*, 1998). In the case of vibrating fused silica spheres we consider the finite viscosity of the pressurizing gas. Thus we account for the mass of the viscous gas layer surrounding the sphere in addition to the sphere mass.

A more general expression of (1) is when mass is not constrained to be constant. Thus (1) can be rewritten as (Oda *et al.*, 1993)

$$\delta f=\left(\frac{\partial f}{\partial G}\right)_{r,m}\delta G+\left(\frac{\partial f}{\partial r}\right)_{G,m}\delta r+\left(\frac{\partial f}{\partial m}\right)_{G,r}\delta m, \tag{9}$$

where

$$\left(\frac{\partial f}{\partial m}\right)_{G,r}=\frac{-f}{2m}. \tag{10}$$

Equation (4) then has an additional term and becomes

$$\frac{df}{dP}=\left(\frac{\partial f}{\partial G}\right)_{r,m}\frac{dG}{dP}+\frac{f}{2r}\frac{dr}{dP}-\frac{f}{2m}\frac{dm}{dP}. \tag{11}$$

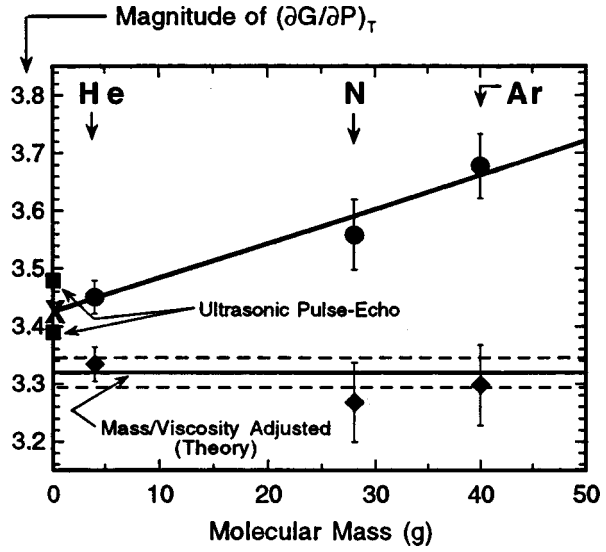

FIG. 4. Final results showing the dependences of the apparent values of $|(\partial G/\partial P)_T|$ on the molecular mass of pressurizing gas. Extrapolating (circle symbols) to zero gas mass shows RUS value (X) for $|(\partial G/\partial P)_T|$ bracketed by previous ultrasonic plane-wave (pulse-echo) results. Size of X reflects magnitude of uncertainty. Lower data set (diamond symbols) shows $|(\partial G/\partial P)_T|$ after gas layering is removed, as given by (12) and (20). Average value is shown by the solid line; dashed lines show standard deviation from the average.

In (11) m is the total mass, i.e., mass of the fused silica specimen plus the viscous gas layer. The additional term $(f/2m)(dm/dP)$ is nonzero because the mass of the gas layer changes with pressure. Thus we take dm/dP to be dm_g/dP, where m_g is the mass of the gas layer. The mass of the specimen is several orders of magnitude larger than the mass of the gas layer so that m in the denominator of (11) is essentially the sample mass, m_S. The general equation for dG/dP is then

$$\frac{dG}{dP}=\frac{df/dP+(f/2m_S)(dm_g/dP)+f/6K_T}{(\partial f/\partial G)_{r,m}}. \tag{12}$$

We note from (12) that dG/dP is negative for fused silica because df/dP is negative. The corrective term $(f/2m_S)\times(dm_g/dP)$ is positive, thus reducing the magnitude of dG/dP. As in (7), if isothermal conditions prevail as P increases, the dG/dP in (12) is $(\partial G/\partial P)_T$.

We now consider the evaluation of dm_g/dP via

$$\frac{dm_g}{dP}=\frac{d(\rho_g V_g)}{dP}=V_g\frac{d\rho_g}{dP}+\rho_g\frac{dV_g}{dP}, \tag{13}$$

where ρ_g and V_g are the respective densities and volumes of the viscous gas layer. The gas volume is given by

$$V_g=4\pi r^2\delta, \tag{14}$$

where r is the radius of the vibrating sphere and δ is the thickness of the viscous gas layer. The gas thickness, also called the penetration depth, is approximated in standard textbook derivations (see, for example, page 323 of Yih, 1969) as

$$\delta\sim\sqrt{\frac{\eta_g}{\pi\rho_g f}}, \tag{15}$$

TABLE II. Gas properties at 1 bar and 25 °C to be used in Eq. (20).[a]

Gas	Viscosity, η_g (poise)	Density, ρ_g (g/cm^3)
He	1.97×10^{-4}	0.165×10^{-3}
N	1.78×10^{-4}	1.131×10^{-3}
Ar	2.27×10^{-4}	1.635×10^{-3}

[a]Gas Encylopaedia reference.

where η_g is the absolute gas viscosity and f (in Hz) equals $\omega/2\pi$, ω being the angular frequency. From the perfect gas law we have

$$\frac{d\rho_g}{dP}=\frac{\rho_g}{P}. \tag{16}$$

Thus the first term on the right side of (13) is

$$V_g\frac{d\rho_g}{dP}=\frac{4r^2}{P}\sqrt{\frac{\pi}{f}}\sqrt{\eta_g\rho_g}. \tag{17}$$

The second term on the right side of (13) is evaluated by

$$\rho_g\frac{dV_g}{dP}=\rho_g 4\pi r^2\frac{d\delta}{dP}=\rho_g 4\pi r^2\frac{1}{\sqrt{\pi f}}\frac{d[(\eta_g/\rho_g)^{1/2}]}{dP}$$

$$=2r^2\sqrt{\frac{\pi}{f}}\sqrt{\frac{\rho_g}{\eta_g}}\left[\frac{d\eta_g}{dP}-\frac{\eta_g}{P}\right]. \tag{18}$$

We ignore $d\eta_g/dP$ in (18) because its magnitude at ambient pressure is 100–1000 times less than η_g/P (see the *Gas Encyclopaedia* reference). Finally we express (13) by the sum of (17) and (18)

$$\frac{dm_g}{dP}=V_g\frac{d\rho_g}{dP}+\rho_g\frac{dV_g}{dP}=\frac{2\sqrt{\pi}r^2}{P}\sqrt{\frac{\rho_g\eta_g}{f}} \tag{19}$$

and find the correction to df/dP in (11) and (12) to be

$$\frac{f}{2m_s}\frac{dm_g}{dP}=\frac{3}{4\sqrt{\pi}\rho_s}\frac{\sqrt{f\rho_g\eta_g}}{rP}, \tag{20}$$

where the m_S of the specimen is expressed in terms of the specimen radius (r) and density (ρ_S).

The adjustments to df/dP depend on the gas properties $(\eta_g,\ \rho_g)$ the specimen size (r), and the modal frequency (f). We wish to evaluate df/dP at $P=1$ bar. The relevant gas properties, from the *Gas Encyclopaedia* reference, are given in Table II. Table III shows the adjustments required for each modal frequency measured for each gas.

The dG/dP [or $|(\partial G/\partial P)_T|$] were determined using (12) and the results are shown in the lower part of Fig. 4. It is gratifying that the theory removes systematic effects of pressurizing gases. It is problematic, however, that the upper data points in Fig. 4, showing extrapolation to zero gas mass, converge to a slightly different value than when gas mass effects are accounted for as outlined in the above theory. The experimental extrapolation to $M=0$ of $|(\partial G/\partial P)_T|$ is 3.42(03), compared to an average value of 3.32(03) for the individual corrections from theory. There is a small but noticeable difference of 3%. Approximations we used, i.e., assuming the perfect gas law in (16) and ignoring pressure

TABLE III. Adjustments to measured df/dP required by (11), (12), and (20) to account for gas viscosity.

Gas	Specimen	Mode	Corrections to df/dP (Hz/bar)
He	1	${}_0T_2$	0.1557
		${}_0T_3$	0.1936
	2	${}_0T_2$	0.1127
		${}_0T_3$	0.1400
N	1	${}_0T_2$	0.3879
		${}_0T_3$	0.4822
	2	${}_0T_2$	0.2805
		${}_0T_3$	0.3487
Ar	1	${}_0T_2$	0.5262
		${}_0T_3$	0.6541
	2	${}_0T_2$	0.3806
		${}_0T_3$	0.4731

effects on η_g in (18), cannot account for this difference. Equations (12) and (20) indicate that fitting the apparent values of $|(\partial G/\partial P)_T|$ to $\sqrt{M}$ is more appropriate than fitting to M. This may be correct, but (12) and (20) also indicate that the apparent $|(\partial G/\partial P)_T|$ will vary systematically with $\sqrt{f}$. We do not observe such a variation, however. Indeed, when the average value of $|(\partial G/\partial P)_T|$ is found for a particular gas using (12) and (20), the standard deviation increases a little over that for the apparent $|(\partial G/\partial P)_T|$ found from (7) for that gas. Presumably, the corrections for f from (12) and (20) would result in smaller uncertainties for a particular gas, if these equations give an accurate description of the situation. It may be that (15) provides an inexact representation of the effective gas layer thickness. Another possibility is that the present data are not sufficiently precise to adequately resolve effects of frequency on the gas layer. More precise pressure measurements using a wider range of sphere radii, and thus modal frequencies, are required to further address these uncertainties.

IV. SUMMARY

In summary, we used RUS to determine $|(\partial G/\partial P)_T|$ for fused silica spheres. The effects of different pressurizing gases on $|(\partial G/\partial P)_T|$ are observed, and different methods of correcting for these effects are presented. Our results show that $|(\partial G/\partial P)_T|$ lies within the range of 3.32–3.42, depending on the method of analysis. These results overlap with the range of 3.39–3.48 found by interferometry techniques. Given the range of uncertainties, our results provide no clear evidence for systematic errors due to transducer bonds in interferometry (ultrasonic plane-wave) experiments (Gerlich and Kennedy, 1978; Meister *et al.*, 1980). We expect small differences to result from measurements of different specimens of fused silica since the thermal history of each specimen will have some effect on its physical properties. The overlap of our results with other ultrasonic data shows that specimen differences, systematic differences in measurement techniques, and uncertainties emanating from assumptions in analysis in combination affect the results by about 2% to 3%, at most.

ACKNOWLEDGMENTS

We thank I. Ohno (Ehime University, Japan), I. Suzuki (Okayama University, Japan), and M. Levy (University of Wisconsin-Milwaukee) for helpful comments and discussions. R. Sorbello (University of Wisconsin-Milwaukee) provided theoretical insights. The spheres used in this study were provided by I. Ohno. This work was supported by the Office of Naval Research. IGPP contribution no. 4950.

Anderson, O. L., and Isaak, D. G. (**1995**). ''Elastic constants of mantle minerals at high temperature,'' in *Mineral Physics & Crystallography: A Handbook of Physical Constants*, edited by T. J. Ahrens (American Geophysical Union, Washington, DC), pp. 64–97.

Bass, J. D. (**1995**). ''Elasticity of minerals, glasses, and melts,'' in *Mineral Physics & Crystallography: A Handbook of Physical Constants*, edited by T. J. Ahrens (American Geophysical Union, Washington, DC), pp. 45–63.

Bateman, T., Mason, W. P., and McSkimin, H. J. (**1961**). ''Third order elastic moduli of germanium,'' J. Appl. Phys. **32**, 928–936.

Birch, F. (**1947**). ''Finite strain of cubic crystals,'' Phys. Rev. **71**, 809–824.

Daniels, W. B., and Smith, C. S. (**1958**). ''Pressure derivatives of the elastic constants of copper, silver, and gold to 10,000 bars,'' Phys. Rev. **111**, 713–721.

Demarest, H. (**1971**). ''Cube resonance method to determine the elastic constants of solids,'' J. Acoust. Soc. Am. **49**, 768–775.

Gas Encyclopaedia (**1976**). Translated by N. Marshall, prepared under the auspices of L'Air Liquide (Elsevier, Amsterdam).

Gerlich, D., and Kennedy, G. C. (**1978**). ''Second pressure derivatives of the elastic moduli of fused quartz,'' J. Phys. Chem. Solids **39**, 1189–1191.

Goto, T., and Anderson, O. L. (**1989**). ''Apparatus for measuring elastic constants of single crystals by a resonance technique up to 1825 K,'' Rev. Sci. Instrum. **59**, 1405–1408.

Lazarus, D. (**1949**). ''The variation of the adiabatic elastic constants of KCl, NaCl, CuZn, Cu, and Al with pressure to 10,000 bars,'' Phys. Rev. **76**, 545–553.

Lei, M., Sarrao, J. L., Visscher, W. M., Bell, T. M., Thompson, J. D., Migliori, A., Welp, U. W., and Veal, B. M. (**1993**). ''Elastic constants of a monocrystal of superconducting $YBa_2Cu_3O_{7-\delta}$,'' Phys. Rev. B **47**, 6154–6156.

Leisure, R. G., and Willis, F. A. (**1997**). ''Resonant ultrasound spectroscopy,'' J. Phys.: Condens. Matter **9**, 6001–6029.

Li, B., Jackson, I., Gasparik, T., and Liebermann, R. C. (**1996**). ''Elastic wave velocity measurement in multi-anvil apparatus to 10 GPa using ultrasonic interferometry'' Phys. Earth Planet. Inter. **98**, 79–91.

Maynard, J. (**1996**). ''Resonant ultrasound spectroscopy,'' Phys. Today **49**(1), 26–29.

McSkimin, H. J. (**1958**). ''Elastic moduli of single crystal germanium as a function of hydrostatic pressure,'' J. Acoust. Soc. Am. **30**, 314–353.

Meister, R., Robertson, E. C., Werre, R. W., and Raspet, R. (**1980**). ''Elastic moduli of rock glasses under pressure to 8 kilobars and geophysical implications,'' J. Geophys. Res. **85**, 6461–6470.

Migliori, A., and Sarrao, J. L. (**1997**). *Resonant Ultrasound Spectroscopy* (Wiley, New York).

Oda, H., Anderson, O. L., Isaak, D. G., and Suzuki, I. (**1992**). ''Measurements of elastic properties of single crystal CaO up to 1200 K,'' Phys. Chem. Miner. **19**, 96–105.

Oda, H., Suzuki, I., and Ohno, I. (**1993**). ''Partial derivatives of eigenfrequencies of a rectangular parallelepiped and a sphere of elastically anisotropic solid,'' J. Phys. Earth **41**, 271–289.

Ohno, I. (**1976**). ''Free vibration of a rectangular parallelepiped crystal and its application to determination of elastic constants of orthorhombic crystals,'' J. Phys. Earth **24**, 355–379.

Ohno, I., Nishitake, T., Hanayama, Y., and Kimura, M. (**1991**). ''The resonance method to determine the pressure and temperature variations of elastic constants,'' Engineering Science Preprints-28, 28th Annual Meeting of the Society of Engineering Science (unpublished).

Sorbello, R. S., Feller, J., Levy, M., Isaak, D. G., Carnes, J. D., and Anderson, O. L. (**1998**). ''Gas mass and viscous loading effects on the RUS spectra of spheres'' (to be published).

Spetzler, H., Chen, G., Whitehead, S., and Getting, I. (**1993**). ''A new ultrasonic interferometer for the determination of equation of state parameters of sub-millimeter single crystals,'' PAGEOPH **141**, 341–377.

Spetzler, H., Shen, A., Chen, G., Herrmannsdoerfer, G., Schulze, H., and Weigel, R. (**1996**). ''Ultrasonic measurements in a diamond anvil cell,'' Phys. Earth Planet. Inter. **98**, 93–99.

Spoor, P. S., Maynard, J. D., and Kortan, A. R. (**1995**). ''Elastic isotropy and anisotropy in quasicrystalline and cubic AlCuLi,'' Phys. Rev. Lett. **75**, 3462–3465.

Thurston, R. N., and Brugger, K. (**1964**). ''Third-order elastic constants and the velocity of small amplitude elastic waves in homogeneously stressed media,'' Phys. Rev. **133**, A1604–A1610.

Yih, C.-S. (**1969**). *Fluid Mechanics: A Concise Introduction to the Theory* (McGraw-Hill, New York).

Zhang, H., Sorbello, R. S., Hucho, C., Herro, J., Feller, J. R., Beck, D. E., Levy, M., Isaak, D., Carnes, J. D., and Anderson, O. (**1998**). ''Radiation impedance of resonant ultrasound spectroscopy modes in fused silica,'' J. Acoust. Soc. Am. **103**, 2385–2394.

Experimental and numerical results for intensity modulated laser ultrasonics

Terry Sanderson, Charles Ume, and Jacek Jarzynski
Georgia Institute of Technology, School of Mechanical Engineering, Atlanta, Georgia 30332

(Received 14 October 1997; accepted for publication 17 June 1998)

This paper describes the experimental confirmation of a numerical model of laser-generated ultrasound, where a 100-μs-long laser pulse was intensity modulated using a Bragg cell. Temporal modulation was used to produce narrow-band ultrasound signals, which can substantially improve signal-to-noise ratios over ultrasound generated by *Q*-switched laser pulses. A curve fit function that represents Bragg cell modulation is given. Experimental results were obtained using a piezoelectric transducer (PZT) on an aluminum test block, and good agreement between theory and experiment was obtained while the modulated pulse train was on. Though the simple PZT model used here results in some discrepancies between theory and experiment late in the signals, it is concluded that the numerical model reliably predicts Bragg cell modulated laser-generated displacements. © *1998 Acoustical Society of America.* [S0001-4966(98)00610-9]

PACS numbers: 43.35.Cg, 43.35.Yb [HEB]

INTRODUCTION

The signal enhancement potential of modulated laser pulses has by now been well documented. Modulated laser pulses can narrow the bandwidth of ultrasonic signals, improving signal-to-noise ratios while providing a direct control over the center frequency of the ultrasound. Both spatial and temporal modulation of laser sources have been implemented experimentally using a variety of techniques for bulk[1] and surface wave[2] modes, and large improvements in signal-to-noise ratios have been reported. Spatial modulation has been achieved using cylindrical lenses in conjunction with diffraction gratings,[2] and by using lenticular arrays.[3] Temporal modulation has been achieved by mode locking the electronics inside the laser cavity,[4] by timing the firing of multiple laser cavities,[5] by using White cells,[6] and by using Bragg cells.[7] Spatial and temporal modulation have also been used simultaneously.[8] Weiner filtering techniques for digital signal processing of modulated laser pulses have been discussed in recent years.[9]

A problem with ultrasound generated by unmodulated lasers, such as *Q*-switched lasers, is that the signals are broadband in nature and do not display a clear center frequency. The selection and use of traditional narrow-band ultrasonic sensors such as PZTs (piezoelectric transducers) is therefore problematic, and the measurement of such broadband signals is susceptible to noise interference. The purpose of modulation, whether spatial or temporal, is to create a clear spike in the signal frequency spectrum, centered around some desired frequency, so that a narrow-band sensor such as a PZT can readily be used, and/or bandpass filters can be used in the receiving electronics for broadband sensors such as interferometers to improve noise rejection.

Results given here show that using Bragg cells to modulate laser pulses can produce the desired narrow-band spike in the frequency spectrum, and that a narrow-band sensor such as a PZT can be used to measure the resulting ultrasonic signals. Without modulation a suitable PZT center frequency is difficult to ascertain in advance, but with modulation the PZT center frequency is selected to match the modulation frequency.

To date, few comprehensive models of modulation for bulk wave modes have been presented. Huang *et al.*[2] gave results for surface waves using spatial modulation, and Spicer *et al.*[10] gave numerical results for temporal modulation, but neither was specifically for Bragg cells. Experiments using a Bragg cell to modulate long pulse lasers have been conducted by Pierce,[11] as later reported in Pierce *et al.*[7] Sanderson *et al.*[12] analyzed temporally modulated laser pulses, and recently[13] developed a comprehensive numerical model for Bragg cell modulation in particular.

The purpose of this work is to compare Pierce's experimental results[11] to the model developed by Sanderson *et al.*[13] to confirm the accuracy of the numerical model. Pierce generated ultrasound in aluminum and measured the ultrasound using PZTs. A model of the receiving electronics used by Pierce[11] is included here. Experiment and theory are compared and agreement is generally good at a 1-MHz modulation frequency.

I. EXPERIMENTAL SETUP

The experimental setup used by Pierce[7,11] is shown in Fig. 1. Ultrasound generation was in the thermoelastic regime. The laser was a General Photonics Series Two-45 Nd:YAG, with a nominal pulse duration of 100 μs, a 10-Hz

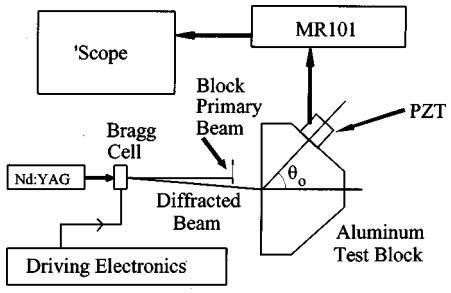

FIG. 1. Experimental setup.

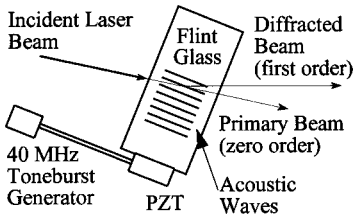

FIG. 2. Bragg cell construction and operation.

repetition rate, a nominal continuous output of 1 W, and a peak power of 1 kW. The Bragg cell was an InterAction Corporation model ADM-40N acousto-optic light deflector/modulator, used in intensity modulation mode. The Bragg cell, shown in Fig. 2, consists of a piece of flint glass epoxy bonded to a PZT, and the laser light passes through the flint glass. When a 30–50-MHz sinusoidal voltage is applied to the PZT, acoustic waves are generated in the flint glass. The interaction of the ultrasonic waves with the laser light deflects the primary (or zero order) transmitted laser beam, because the ultrasonic waves act as a moving diffraction grating. This diffracts the primary beam, and thus creates the diffracted (or first order) beam shown in Fig. 2. In Pierce's experiments a 40-MHz frequency-modulated signal was used to drive the Bragg cell and achieve various modulation frequencies in the first-order beam, as illustrated in Fig. 3 (Fig. 3 represents the theoretical Bragg cell output, as predicted by Jarzynski *et al.*[14]). The first-order beam was then directed at an aluminum block to generate ultrasound. Further details regarding Pierce's experimental setup, the operation of the Bragg cell, and the electronics required to drive it, are given by Jarzynski *et al.*[14] and Pierce.[7,11]

Pierce measured only longitudinal waves, at an observation angle θ_0 of 60° in Fig. 1, because the maximum longitudinal wave amplitude occurs at 60°. From Rose's point source theory[15] the maximum amplitude of the longitudinal waves should occur at 60° in aluminum, as can be seen in results given by Scruby *et al.*[16]

II. MATHEMATICAL MODEL

A block diagram of the experimental setup is shown in Fig. 4, and a numerical model[13] of Pierce's experiments was implemented using Laplace, Hankel, and Fourier transforms. Throughout this work lower case letters will be used to represent time domain functions, and upper case letters with overbars as in Fig. 4 will represent frequency domain functions. To model Pierce's experiments it was first necessary to represent the output of the Bragg cell, i.e., the time dependence of the first-order diffracted laser beam which was used to generate ultrasound. Next, the generation and propagation

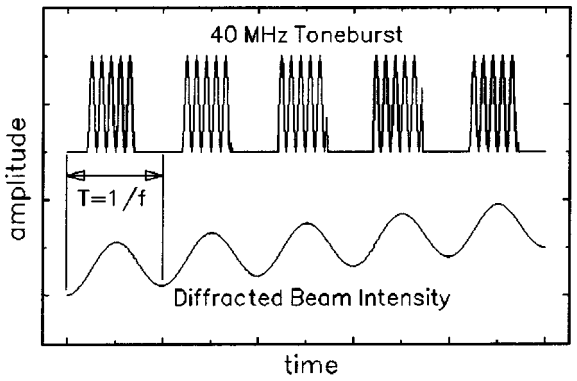

FIG. 3. Bragg cell input and output signals.

of the resulting ultrasonic waves was modeled. The transient response of the PZT was then assumed to obey Mason's model,[17] and finally the frequency response of the MR101 receiver was measured experimentally. These four steps will be discussed in turn.

A. Bragg cell output

Pierce modulated the first-order beam at frequencies ranging from 250 kHz to 2 MHz in his experiments, and he measured the temporal profiles using a photodiode. From this measured data the authors developed a function $h(t)$ to represent the temporal laser pulse profile,

$$h(t)=[1-u(t-\tau_s)]q_1(t)+u(t-\tau_s)Be^{-t/\tau_c},$$
$$q_1(t)=A(ft+1-\cos(\omega t)), \tag{1}$$
$$A=30, \quad B=2q_1(\tau_s),$$

where

$$\tau_s=\frac{n}{f}-\frac{0.03}{f}, \quad \tau_c=\frac{\tau_s}{\ln(2)},$$
$$f=\text{modulation frequency, Hz}, \quad \omega=2\pi f,$$
$$u(t)=\text{Heaviside step function}, \tag{2}$$
$$n=\text{number of pulses},$$

which gives a good approximation (within ±10%) to all of Pierce's measured temporal profiles.[7,11] Equation (1) can readily be Fourier or Laplace transformed. A time domain graph of the actual Bragg cell output (the intensity modulated first-order beam) as measured by Pierce[11] is shown in Fig. 5, as predicted by Eq. (1). Figure 5 is representative of the temporal profiles of the laser pulses used to generate ultrasound in Pierce's experiments.

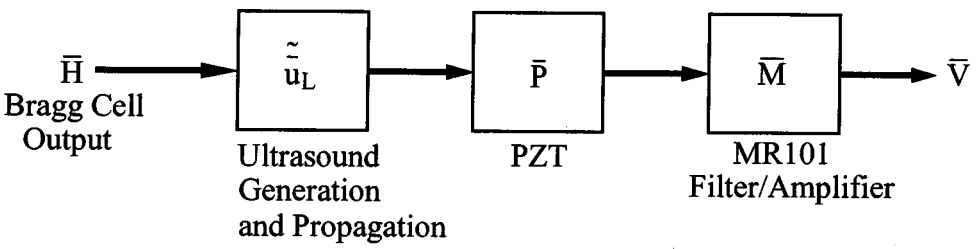

FIG. 4. Block diagram of experimental setup.

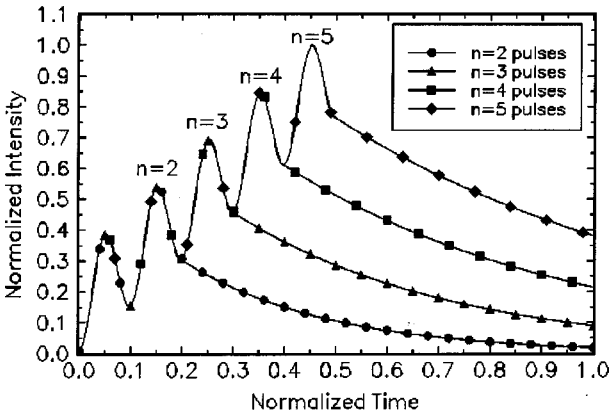

FIG. 5. Temporal profile of Bragg cell modulated laser pulse.

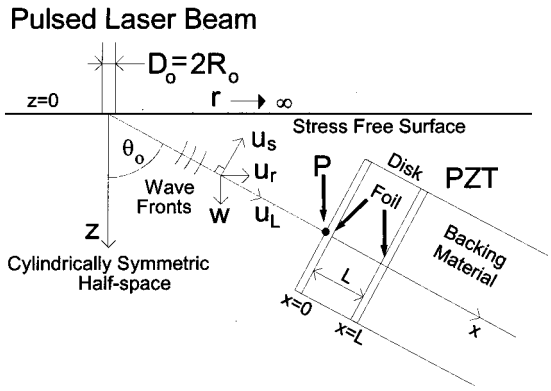

FIG. 6. Half-space and PZT coordinates.

B. Ultrasound model

A model to predict the ultrasound waves was presented by the authors in Ref. 13, and is summarized here. The governing equations for the displacement field, which were solved using simultaneous Hankel and Laplace transforms, are

$$
\begin{aligned}
&(\lambda+2\mu)\nabla e-2\mu\nabla\times\omega=\rho\,\frac{\partial^2 V}{\partial t^2}+\beta_0\nabla\theta,\\
&e=\nabla\cdot V,\quad \omega=\frac{1}{2}\,\nabla\times V,\\
&\nabla^2\theta=\frac{1}{\alpha}\,\frac{\partial\theta}{\partial t}+\frac{1}{c_H^2}\,\frac{\partial^2\theta}{\partial t^2},\\
&\nabla^2=\frac{\partial^2}{\partial r^2}+\frac{1}{r}\,\frac{\partial}{\partial r}+\frac{1}{r^2}\,\frac{\partial^2}{\partial\Theta^2}+\frac{\partial^2}{\partial z^2},
\end{aligned}
\tag{3}
$$

where

$T=$ temperature,	$V=u_r\hat{i}_r+w\hat{i}_z$ $=$ displacement
$T_i=$ initial temperature,	$\lambda,\mu=$ Lame constants,
$\theta=T-T_i$,	$\rho=$ density,
$k=$ thermal conductivity,	$c_S=\sqrt{\mu/\rho}$,
$\alpha=$ thermal diffusivity,	$c_L=\sqrt{(\lambda+2\mu)/\rho}$,
$\tau_R=$ thermal relaxation constant,	$\beta_0=\Gamma(3-4c_S^2/c_L^2)$,
$c_H=\sqrt{\alpha/\tau_R}=$ heat wave speed,	$e=$ dilation,
$\Gamma=$ coefficient of thermal expansion,	$\omega=$ rotation.

(4)

All initial conditions were taken as zero. Cylindrical coordinates were chosen because the incident laser beam is cylindrically symmetric. The half-space is shown in Fig. 6, where the z axis coincides with the axis of the laser beam, and the reference angle $\theta_0=60°$ is the same in Figs. 1 and 6. Half-space solutions to Eqs. (3) were obtained, and wave reflection at the PZT-specimen boundary was included later in the PZT model.

The laser light is assumed to be absorbed at the specimen surface, so the boundary conditions are continuity of heat flux at the surface, and the surface must remain stress free.

$$
\begin{aligned}
&\sigma_{zz}|_{z=0}=0,\quad \tau_{rz}|_{z=0}=0,\\
&-k\,\frac{\partial\theta}{\partial z}\bigg|_{z=0}=q''(r,t),\quad q''(r,t)=h(t)g(r),
\end{aligned}
\tag{5}
$$

where q'' is the heat flux, σ_{zz} is the axial normal stress, τ_{rz} is the shear stress, $h(t)$ is the Bragg cell output given by Eq. (1), and $g(r)$ is the spatial laser pulse profile, assumed Gaussian:

$$
g(r)=e^{-2(r/R_0)^2},
\tag{6}
$$

where $R_0=0.3$ mm is the Gaussian spot radius. Material properties of $c_S=3097$ m/s, $c_L=6108$ m/s, $k=177$ W/mK, $\alpha=73\times10^{-6}$ m^2/s, and $\Gamma=23.6\times10^{-6}$ were used.

C. Ultrasound transducer model

The analysis and modeling of PZTs is a well-established subject, and goes back at least as far as Mason.[17] Only the major assumptions are summarized here, and the interested reader is referred to the literature.[17–20] A cross section of a PZT is shown in Fig. 6. The foil, PZT casing, and couplant layer between the PZT and specimen are assumed to be sufficiently thin that their presence can be ignored.[17–20] Wave propagation within the disk is approximated as one dimensional.[17–20]

Letting the specific acoustic impedance $z=\rho c$, it can be shown[21] that the Laplace transformed PZT signal is

$$
\bar{P}=\frac{2c_1 zhs^2(a_1e^{-sL/c_p}+a_2e^{sL/c_p}+a_3e^{-2sL/c_p}+a_4e^{2sL/c_p}+a_5)}{(b_1e^{-sL/c_p}+b_2e^{sL/c_p})(b_3e^{-sL/c_p}+b_4e^{sL/c_p}+b_5)},
\tag{7}
$$

where c_1 is defined by a one-dimensional incident ultrasound wave, c is the wave speed, h is a piezoelectric material property, p subscripts denote the piezoelectric disk, b subscripts denote the backing, no subscripts are used for the specimen, and

$$a_1=2z_p(z-z_p), \quad a_2=-2z_p(z+z_p),$$
$$a_3=2z_p(z_p-z),$$
$$a_4=zz_b-zz_p-z_pz_b+z_p^2, \quad a_5=zz_b+zz_p+z_pz_b+z_p^2,$$
$$b_1=z-z_p, \quad b_2=z+z_p, \quad b_5=-\frac{4z_ph^2}{RA}, \tag{8}$$
$$b_3=\frac{1}{RA}\left\{\frac{a_4s}{C_0}+h^2(2z_p-z-z_b)\right\}+s^2a_4,$$
$$b_4=-\frac{1}{RA}\left\{\frac{a_5s}{C_0}-h^2(2z_p+z+z_b)\right\}-s^2a_5,$$

where A is the transducer cross-sectional area, R is the input impedance of the receiving electronics, and C_0 is the static capacitance of the transducer. Values of $z_b=0.9z_p$, $\rho_p=7500$ kg/m^3, $c_p=4474$ m/s, $C_0=3058$ pF, $R=1$ MΩ, and $h=1.19\times10^9$ C/N were used. Pierce used a Panametrics model V103 1-MHz longitudinal PZT with a 12.7-cm diameter. The frequency response $\bar{P}(j\omega)$ ($j=\sqrt{-1}$, $\omega=2\pi f$) of the PZT, as given by Eq. (7), is shown in Fig. 7.

To relate the one-dimensional PZT input signal $\bar{u}_i=c_1e^{-sx/c_L}$ (s is the Laplace transform variable) to the three-dimensional (3-D) solution of Eqs. (3), the 3-D longitudinal displacement $\tilde{\bar{u}}_L$ was evaluated at point P in Fig. 6, and used as the approximate incident wave on the PZT face. In this manner the 3-D ultrasound solution was tied to the 1-D PZT model.

$$u_i|_{x=0}\approx\tilde{\bar{u}}_L|_P. \tag{9}$$

This ignores the phase variation of the wavefront over the transducer face. However, the resulting error was assumed to be small because in Pierce's experiments there was a 0.08 wavelength difference between waves incident at the center and edges of the PZT.[11]

D. Transfer function of MR101 receiver

Pierce used a Metrotek MR101 amplifier/receiver to amplify the PZT output signal in his experiments. The MR101 is also capable of filtering the input signal, and Pierce used the MR101 as a 500-kHz high-pass filter with no attenuation. The present authors conducted a standard frequency response test on the MR101. A Bode plot of the measured amplitude response is shown in Fig. 8. A two stage op-amp circuit,

$$\bar{M}(s)=\frac{k(s+z_1)(s+z_2)}{(s+p_1)(s+p_2)} \tag{10}$$

with gain $k=109$, zeros $z_1=251{,}327$, $z_2=220\times10^6$, and poles $p_1=3\times10^6$, $p_2=1.75\times10^8$ was found to give a reasonable approximation of the measured response of the MR101. The frequency response $\bar{M}(s=j\omega)$ given by Eq. (10) is shown in Fig. 8. While Eq. (10) differs with the measured MR101 response above about 7 MHz, this was not expected to cause significant error in the final results. The bulk of the ultrasonic energy was below 7 MHz anyway, as will be seen in results given later.

Complete details on the mathematical model reported here can be found in Sanderson.[21]

III. COMPARISON OF PREDICTED AND MEASURED PZT SIGNALS

With the block diagram elements of the experimental setup defined, the next step is to multiply the block diagram functions together and invert the product to obtain predicted signals. The inversion process was carried out numerically. Crump's[22] method was used to numerically invert the Laplace transform, and Clenshaw–Curtis[23] quadrature, an efficient and progressive integration technique, was used to numerically invert the Hankel transform. To insure the numerical accuracy of the Hankel–Laplace inverter, the computer code was tested extensively against both functions that could be inverted analytically and against ultrasound waveforms found in the literature. Agreement was good in all cases.

The half-space solution for a longitudinal wave $\tilde{\bar{u}}_L$, corresponding to point P in Fig. 6, is shown in Fig. 9, for a train of five Bragg cell modulated pulses at 1 MHz, and the DFT (discrete Fourier transform) is shown in Fig. 10. The signal contains a substantial amount of low-frequency energy, but also has a clear peak centered around 1 MHz. This peak would not occur for a Q-switched laser pulse and is the de-

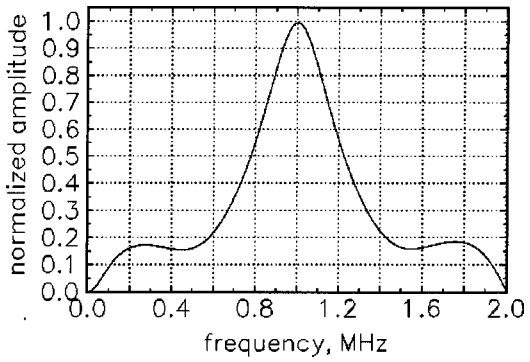

FIG. 7. Predicted frequency spectrum of PZT at 1-MHz center frequency.

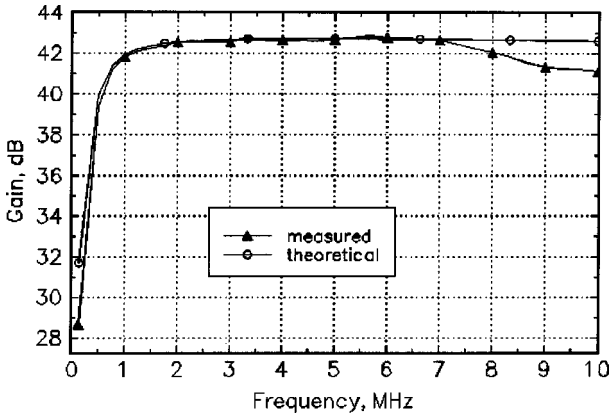

FIG. 8. Measured and predicted frequency response of the MR101 receiver.

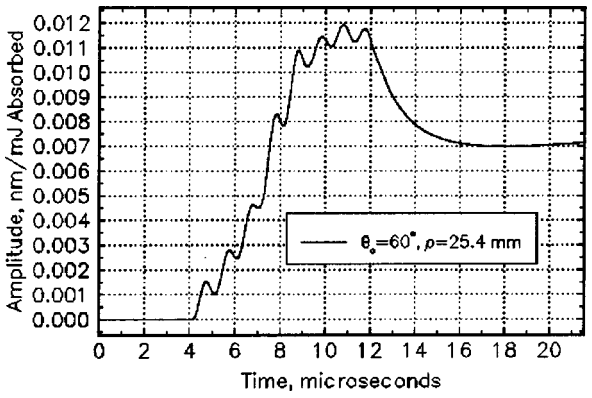

FIG. 9. Longitudinal wave, $n=5$ pulses at 1 MHz, $R_0=0.3$ mm.

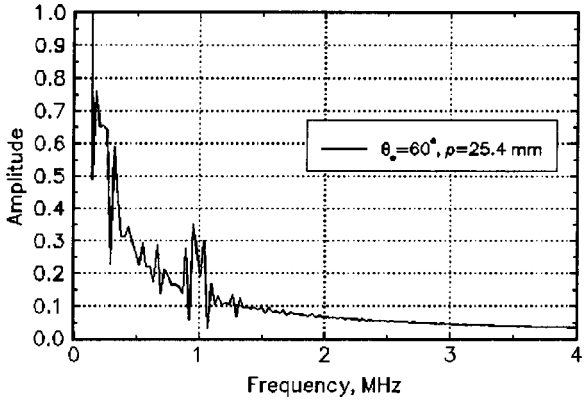

FIG. 10. DFT of the signal in Fig. 9.

sired effect of temporal modulation. The time domain waveform shown in Fig. 9 is the ultrasound wave just before it impinges on the PZT-specimen boundary in Fig. 6.

To carry out the convolutions indicated in the block diagram of the experimental setup, all signals and component responses in the block diagram (Fig. 2) were cast in the form of DFTs, multiplied together, and then the DFTs were inverted numerically using MATLAB.

Predicted voltage signals are shown in Fig. 11 for two, three, four, and five pulse modulated trains at a nominal 1-MHz modulation frequency, along with Pierce's experimentally measured signals.[11] Pierce manually set rotary dials to achieve the 1-MHz modulation frequency, and did not measure the actual modulation frequencies after setting the dials. Exactly 1-MHz modulation frequencies were not achieved experimentally. Modulation frequencies of 1.05 MHz for the two pulse train, 1.22 MHz for the three and four pulse trains, and 1.32 MHz for the five pulse train were used in the mathematical model to obtain the results shown in Fig. 11. The zero crossings in the predicted and measured signals show good agreement, which by the nature of PZTs seems unlikely to occur if the modulation frequencies of the ultrasonic signals were off by any significant amount.

For the two, three, and four pulse trains in Fig. 11 agreement is good, better than $\pm 20\%$, before the ends of the pulse trains. The pulse train is said to end when the modulated

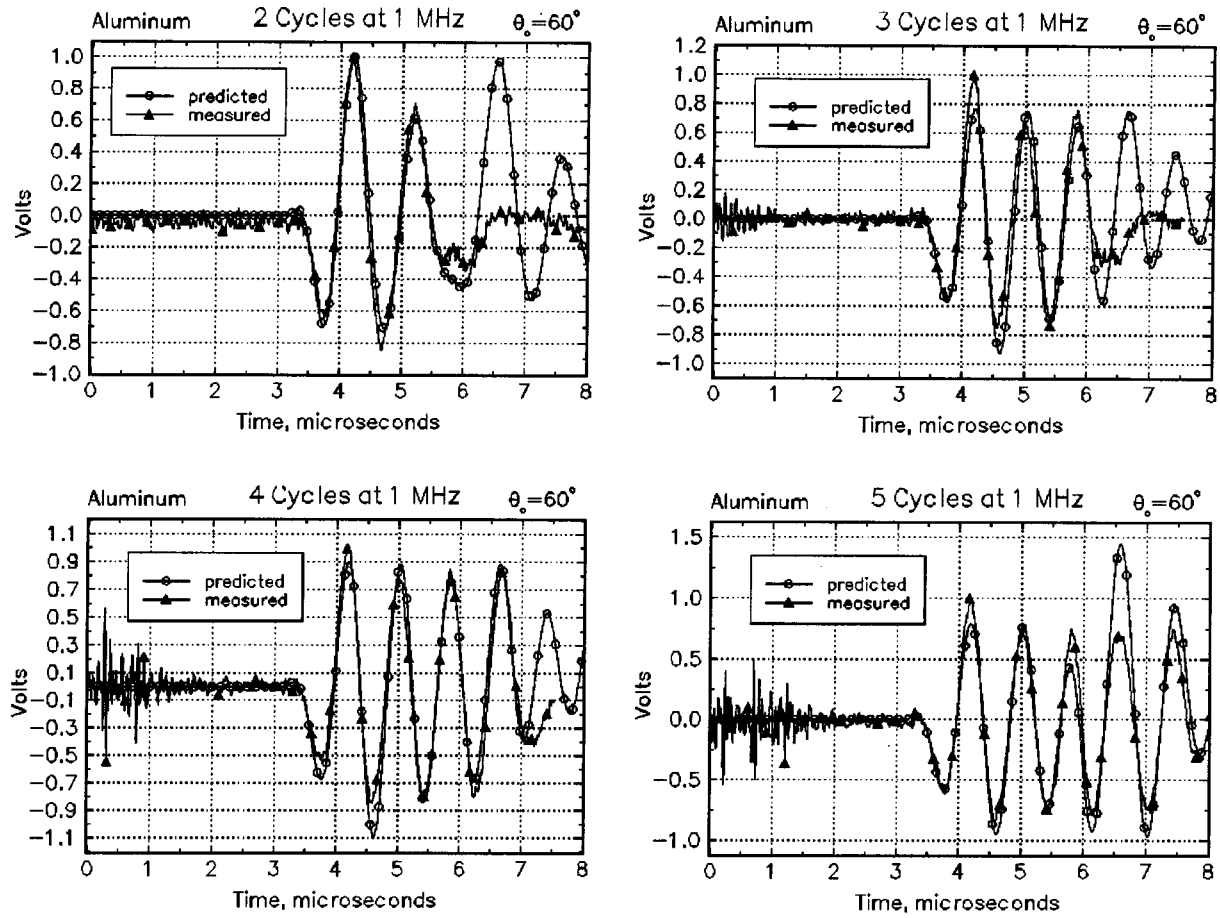

FIG. 11. Measured and predicted PZT voltages after filtering and amplification.

pulse begins its exponential decay at time τ_s [Eq. (1)], as can be seen in Fig. 5. After the pulse trains turn off, the predicted results show transducer ringing that did not occur in Pierce's experiments. The cause of this discrepancy is believed to be due to the simple model that was used for the PZT. Real PZTs typically contain built-in damping circuits to eliminate ringing, which was not included in the PZT model described earlier. A more accurate model of the PZT was not possible in this work because the design, construction, and material properties of the PZT are proprietary.

The results for the five pulse train in Fig. 11 show a large error at the fourth pulse in the train, with the predicted signal amplitude overshooting the measured amplitude by 71%. This is likely due to the above-mentioned limitations in the PZT model. The experimental center frequency of the five pulse train is also furthest from the PZT design center frequency of 1 MHz. Agreement between the predicted and measured signals was best while the modulated pulse train was on, and when the center frequency was closest to 1 MHz. The predicted and measured signals for the two pulse train gave the best agreement while the modulated pulse train was on, to within $\pm 12\%$, where the modulation frequency was 1.05 MHz. The three and four pulse trains, with 1.22-MHz frequencies, both yielded $\pm 20\%$ agreement while the pulse train was on, and the five pulse train at 1.32 MHz yielded the worst agreement at $\pm 71\%$.

As a final comment, Pierce *et al.*[7] reported signal enhancements on the order of 15–20 dB using Bragg cell modulation, compared to using the unmodulated laser pulse.

IV. CONCLUSIONS

A numerical model to predict laser-generated ultrasound due to intensity modulated laser pulses has been presented. The model was compared to experimental results obtained by Pierce.[11] The PZT and receiving electronics used by Pierce were modeled, and good overall agreement between theory and experiment during the modulation train was obtained at a 1-MHz modulation frequency. However, the PZT model predicted ringing after the modulated pulse train turned off that did not occur in the experimental results, probably because the damping circuit, couplant layer, transducer body, internal bond layers, the finite size of the PZT, and the finite dimensions of the backing material inside the PZT were neglected.

It is concluded that the numerical model of temporally modulated ultrasound is able to accurately predict longitudinal waves, because the discrepancies between theory and experiment can be attributed to limitations in the PZT model. This conclusion is substantiated by the good agreement between theory and experiment while the Bragg cell modulated pulse train was on. The model could therefore be used for signal enhancement optimization of temporally modulated laser pulses.

ACKNOWLEDGMENT

This work was supported by the Manufacturing Machines and Equipment program of the National Science Foundation under Contract No. DDM-9001733.

[1] J. B. Deaton, A. D. W. McKie, J. B. Spicer, and J. W. Wagner, ''Mode-locked laser generation of narrow-band ultrasound,'' Rev. Prog. Quant. Nondestr. Eval. **9A**, 493–497 (1991).

[2] J. Huang, S. Krishnaswamy, and J. D. Achenbach, ''Laser generation of narrow-band surface waves,'' J. Acoust. Soc. Am. **92**, 2527–2531 (1992).

[3] A. D. W. McKie, J. W. Wagner, J. B. Spicer, and J. B. Deaton, ''Narrowing the bandwidth of laser generated ultrasound by laser illumination of aluminum with an array of sources,'' Ultrasonics International 89 Conference Proceedings (unpublished), pp. 78–83.

[4] J. W. Wagner, J. B. Deaton, and J. B. Spicer, ''Generation of ultrasound by repetitively *Q*-switching a pulsed Nd:YAG laser,'' Appl. Opt. **27**, 4696–4700 (1988).

[5] T. W. Murray, J. B. Deaton, Jr., and J. W. Wagner, ''Experimental evaluation of enhanced generation of ultrasonic waves using an array of laser sources,'' Ultrasonics **34**, 69–77 (1996).

[6] J. S. Steckenrider, T. W. Murray, J. W. Wagner, and J. B. Deaton, ''Sensitivity enhancement in laser ultrasonics using a versatile laser array system,'' J. Acoust. Soc. Am. **97**, 273–279 (1995).

[7] R. Pierce, C. Ume, and J. Jarzynski, ''Temporal modulation of a laser source for the generation of ultrasonic waves,'' Ultrasonics **33**, 133–137 (1995).

[8] J. W. Wagner, A. D. W. McKie, J. B. Spicer, and J. B. Deaton, Jr., ''Modulated laser array sources for generation of narrowband and directed ultrasound,'' JNDE **9**, 263–270 (1990).

[9] J. B. Deaton, Jr. and J. W. Wagner, ''Weiner filtering of laser-generated multiple-pulse narrow-band ultrasound for enhanced detectability by a laser interferometer,'' Ultrasonics **32**, 187–193 (1995).

[10] J. B. Spicer, J. B. Deaton, Jr., and J. W. Wagner, ''Effects of laser source parameters on the generation of narrow band and directed laser ultrasound,'' Rev. Prog. Quant. Nondestr. Eval. **11**, 617–624.

[11] R. S. Pierce, ''Signal enhancement of laser generated ultrasound for nondestructive testing,'' MS thesis, Georgia Institute of Technology, 1992.

[12] T. Sanderson, C. Ume, and J. Jarzynski, ''Hyperbolic heat conduction effects caused by temporally modulated laser pulses,'' Ultrasonics **33**, 423–427 (1995).

[13] T. Sanderson, C. Ume, and J. Jarzynski, ''A numerical model of temporal intensity modulation for laser generated ultrasound,'' Rev. Prog. Quant. Nondestr. Eval. **16A**, 601–607 (1996).

[14] J. Jarzynski and Y. Berthelot, ''The use of optical fibers to enhance the laser generation of ultrasonic waves,'' J. Acoust. Soc. Am. **82**, 158–162 (1989).

[15] L. R. F. Rose, ''Point-source representation for laser-generated ultrasound,'' J. Acoust. Soc. Am. **75**, 723–732 (1984).

[16] C. B. Scruby and L. E. Drain, *Laser Ultrasonics* (Hilger, London, 1990).

[17] W. P. Mason, *Electromechanical Transducers and Wave Filters* (Van Nostrand, Princeton, 1948).

[18] V. M. Ristic, *Principles of Acoustic Devices* (Wiley, New York, 1983).

[19] M. Redwood, ''Transient performance of a piezoelectric transducer,'' J. Acoust. Soc. Am. **33**, 527–536 (1961).

[20] M. G. Silk, *Ultrasonic Transducers for Nondestructive Testing* (Hilger, London, 1984).

[21] T. M. Sanderson, ''Thermoelastic modeling of laser generated ultrasound for nondestructive materials testing,'' Ph.D. thesis, Georgia Institute of Technology, 1997.

[22] K. S. Crump, ''Numerical inversion of Laplace transforms using a Fourier series approximation,'' J. Assoc. Comput. Mach. **23**, 89–96 (1976).

[23] C. W. Clenshaw and A. R. Curtis, ''A method for numerical integration on an automatic computer,'' Numer. Math. **7**, 197–205 (1960).

Interaction between a Timoshenko–Mindlin plate and an attached rib

M. L. Rumerman
Naval Surface Warfare Center, Carderock Division, Signatures Directorate (Code 7200), 9500 MacArthur Boulevard, West Bethesda, Maryland 20817-5700

(Received 18 August 1997; revised 18 June 1998; accepted 29 June 1998)

In contrast to a thin plate having no shear component of deformation, a Timoshenko–Mindlin plate cannot support a concentrated line dipole moment exerted by a pair of equal and opposite line forces acting normal to its lateral surface. In this paper, it is argued that, in order to account for all the connectivity between a rib and the plate, it is necessary to assume a nonzero width footprint for the rib upon the plate. This footprint is idealized by a connection between the rib and plate along two lines parallel to the rib. The problem posed is one dimensional, with plate responses invariant in the direction of the rib; therefore, along each line of contact, the rib exerts upon the plate only a normal force and a tangential (shear) force perpendicular to the rib. These four initially independent forces combine to produce resultant opposing forces acting on the end of the rib which generate velocities of the rib that can be related to those of the plate. The response quantity of interest is the structural power reflected from the rib due to a wave propagating freely in a direction normal to the rib and incident upon it. It is shown that the rib footprint cannot be set equal to zero if the rib's rotational properties are to have a meaningful influence on the calculated reflected power.
[S0001-4966(98)02310-8]

PACS numbers: 43.40.At, 43.40.Dx [CBB]

INTRODUCTION

In describing the asymmetric transverse (flexural) displacement, w, of a planar elastic layer, Timoshenko–Mindlin (TM) thick plate theory accounts for shear deformation and rotatory inertia, as well as bending deformation and transverse inertia. As a result, TM theory distinguishes between the rotation of the cross section, ϕ, and the transverse slope of the deformed plate, w', which for thin plate theory are equal. A consequence of the inclusion of shear deformation is that a TM plate subjected to a line force acting normal to the plate's lateral surface has a transverse slope which is nonzero at and discontinuous across the line of force application, whereas the rotation of the cross section is zero and continuous at the line force. A more significant feature of TM plate theory, as noted by Smith and Dym[1] and Rumerman,[2] is that if the plate is subjected to a normal force dipole formed by equal and opposite parallel line forces of magnitude $|F|$ separated by a distance d, the transverse slope between the two line forces becomes unbounded as d approaches zero while the dipole moment $|F|d$ is kept constant. The cross section rotation again remains continuous and bounded.

It can be shown that only the nonpropagating part of the transverse slope diverges as d approaches zero, and that the propagating part is well-behaved. Therefore, if the line force dipole is independently specified, and only the plate response at some distance from the forces is of interest, a concentrated dipole can be a useful representation. On the other hand, if the interaction between a TM plate and a reinforcing rib is of interest, the problem is solved by enforcing equality of the interaction forces and displacements of the plate and rib at the rib location; therefore, the responses at the applied forces are important and a concentrated line dipole is an inappropriate model. Smith and Dym suggest that a proper resolution of this dilemma is to consider the line moment as being applied ''about the central plane'' (equivalently, to the cross section of the plate), rather than as a line dipole on the surface. Such would be the case for the built-up plate-rib structure shown in Fig. 1(a), in which the rib is attached to the cross section of the plate and can be viewed as exerting the tensile and compressive stresses on the plate's cross section which form the resultant moment. The difference between the bending moments in the two plate segments on either side of the rib is the driving moment on the rib, and the rotation of the plate's cross section, considered continuous across the rib, can be equated to the rotation of the rib at its ''root.'' (The rib's ''root'' is the end which is attached to the plate.) Similarly, the difference in the transverse shear forces on either side of the rib forms the driving force for transverse displacement. Therefore, if the rib is sufficiently thin with respect to wavelengths it supports, the Smith–Dym formalism will handle this configuration.

Most ribbed plates of interest, however, are not configured as shown in Fig. 1(a), but as the reinforced plate in Fig. 1(b), where the rib is joined to the plate's lateral surface and exerts a distribution of forces to this surface over its attachment width. The rib does not apply a moment directly to the plate's cross section, and the rotation of the rib at its root is kinematically related to the plate's transverse slope rather than to the cross section rotation. An attempt to represent the rib as an attachment along a single mathematical line leads to the conclusion that the rib cannot exert a concentrated normal force line dipole moment on the plate because the corresponding plate admittance is unbounded. As a consequence, in the limit of a concentrated line load, the rib's rotational impedance properties do not couple to the plate

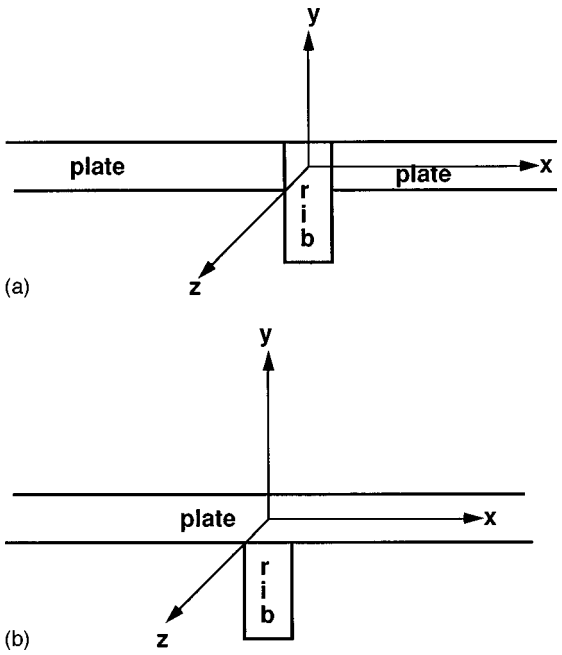

FIG. 1. (a) Built-up plate. (b) Rib-reinforced plate.

through a moment exerted between the plate and rib. The rib's rotational impedance properties do couple to the plate through the tangential force the rib applies to the plate because the reaction force is the shear force on the end of the rib, which also drives the rib's rotational response. It will be shown, however, that this drive may inadequately account for the effect of the rib's rotational impedance properties in estimating structural power reflected by the rib, and that a normal force dipole having nonzero ''footprint'' should be included in the analysis.

In order to examine how the rib's rotational properties might be coupled to a TM plate, this paper considers the interaction between such a plate and a rib attached to its lateral surface over a nonvanishing footprint. The driving excitation is a freely propagating flexural wave normally incident upon the rib (so that responses do not vary in the direction of the rib), and the response of interest is the reflected structural power. The focus is on the effect of the width of the rib's footprint over which forces are transmitted to the plate.

I. MATHEMATICAL DEVELOPMENT

A. Basic plate admittances

The principal interest is in the effect of the rib's footprint width, and analysis is considerably simplified by assuming that the rib is in actual contact with the plate only along two parallel mathematical lines, as indicated in Fig. 2, along each of which it exerts on the plate a normal force, F, in the y direction and a tangential force, T, in the x direction. These four forces are independently specified. The distance between the two lines of attachment is d, which is not necessarily equal to the thickness of the rib at its root. The system excitation and response are assumed to be independent of the z coordinate in the direction parallel to the rib.

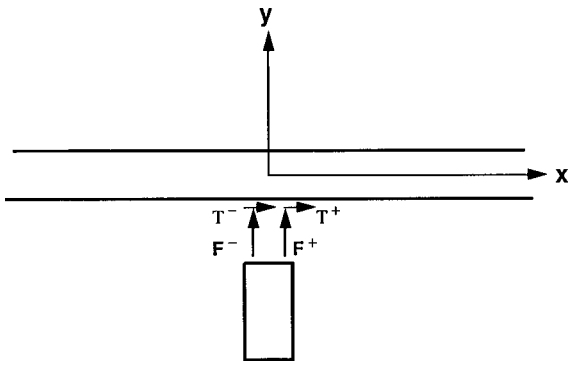

FIG. 2. Mutual plate-rib line forces.

In order to develop the formalism for handling the problem of Fig. 2, consider a TM plate driven by a single normal line force in the y direction and a single shear line force in the x direction, each at $x=0$. By extending the development by Junger and Feit[3] to include the shear force, the equations of motion are found to be given by Eqs. (1):

$$-\frac{Gh^3}{6(1-\nu)}\,\phi''-\kappa^2 Gh(w'-\phi)+\frac{\rho h^3}{12}\,\ddot{\phi}=-\frac{Th}{2}\,\delta(x), \tag{1a}$$

$$\kappa^2 Gh(w''-\phi')-\rho h\ddot{w}=-F\,\delta(x). \tag{1b}$$

In Eqs. (1), the dot signifies a time derivative ($\partial/\partial t$), and a prime signifies a spatial derivative ($\partial/\partial x$). Use has been made of the relationship among the shear modulus, Young's modulus, and Poisson's ratio. The shear adjustment factor κ^2 will be taken as $\pi^2/12$ after Mindlin,[4] rather than as the ratio of Rayleigh wave speed to shear wave speed after Junger and Feit. It is noted that the shear force, T, appears only in the product $Th/2$, and is equivalent to the moment of Smith and Dym in terms of its effect on the plate. The product $Th/2$ can, therefore, be considered as a moment ''about the central plane.'' With respect to the rib, T also acts as a shear force. The conventions for positive displacements and rotations are indicated in Fig. 3.

For time-harmonic motion, Eqs. (1) can be solved for $w(x)$ and $\phi(x)$ by Fourier transform techniques, and the solutions yield the set of plate transfer admittances, Y^p, given by Eqs. (2) for a force at $x=0$ and the observation point at $x\geqslant 0$, in which $u(x)=\phi(x)h/2$ represents the tangential displacement of the lower face of the plate (where the rib is attached) in the positive x direction, and the assumed

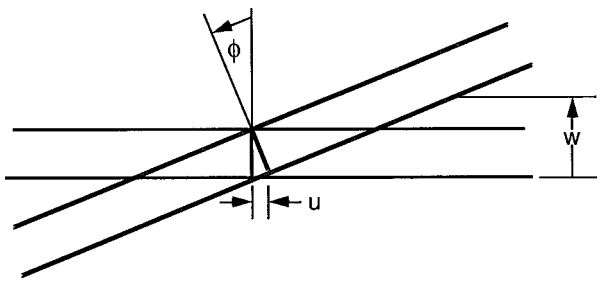

FIG. 3. Positive displacements and rotations for plate.

$\exp(-i\omega t)$ time factor is suppressed. For arbitrary force location x_f and observation point $x_0 > x_f$, x is replaced by $x_0 - x_f$:

$$\frac{\rho c h}{3(1-\nu)} \frac{A_1^2 - A_2^2}{K} Y^p_{\dot{w}F}(x) = \frac{(1-K^2/\pi^2) + 2A_1^2/(1-\nu)\pi^2}{A_1} \exp\left(\frac{iA_1 x}{h}\right) - \frac{(1-K^2/\pi^2) + 2A_2^2/(1-\nu)\pi^2}{A_2} \exp\left(\frac{iA_2 x}{h}\right), \tag{2a}$$

$$\frac{2\rho c h}{3(1-\nu)} \frac{A_1^2 - A_2^2}{iK} Y^p_{\dot{u}F}(x) = \exp\left(\frac{iA_1 x}{h}\right) - \exp\left(\frac{iA_2 x}{h}\right), \tag{2b}$$

$$\frac{4\rho c h}{3(1-\nu)} \frac{A_1^2 - A_2^2}{K} Y^p_{\dot{u}T}(x) = \frac{A_1^2 - 12K^2/\pi^2}{A_1} \exp\left(\frac{iA_1 x}{h}\right) - \frac{A_2^2 - 12K^2/\pi^2}{A_2} \exp\left(\frac{iA_2 x}{h}\right), \tag{2c}$$

$$Y^p_{\dot{w}T}(x) = -Y^p_{\dot{u}F}(x). \tag{2d}$$

The notation $Y^p_{\dot{w}F}(x)$ represents the velocity $\dot{w}$ at x due to force F at $x=0$, and other admittances are defined similarly.

These admittances are written for $x \geqslant 0$. $Y^p_{\dot{w}F}(x)$ and $Y^p_{\dot{u}T}(x)$ are symmetric about $x=0$; $Y^p_{\dot{w}T}(x)$ and $Y^p_{\dot{u}F}(x)$ are antisymmetric. In Eqs. (2), $K=\omega h/c$, where c is the shear wave speed of the plate material, ρ is its mass density, and ν is its Poisson's ratio. The quantities A_1/h and A_2/h represent the dimensional wave numbers for two antisymmetric modes in the plate, and the dimensionless forms are given by Eq. (3). For a lossless plate and $K<\pi$, A_1^2 is real and positive and A_2^2 is real and negative. For $\exp(-i\omega t)$ time dependence and $x \geqslant 0$, A_1 is positive and A_2 is positive imaginary. For frequencies such that $K>\pi$, the second mode becomes propagating. This higher-frequency range will not be considered:

$$A^2_{1,2} = \left(\frac{1-\nu}{4} + \frac{6}{\pi^2}\right) K^2 \pm \sqrt{\left(\frac{1-\nu}{4} + \frac{6}{\pi^2}\right)^2 K^4 + 6(1-\nu)\left(1 - \frac{K^2}{\pi^2}\right) K^2}. \tag{3}$$

B. Response of plate to assumed rib forces

Let the rib be attached to the plate along the two lines $x=\pm d/2$, along which the rib exerts the y directed normal forces F^+ and F^- and the x directed tangential forces T^+ and T^-, respectively. Additionally, the plate is subjected to an independently specified transverse velocity wave, $\dot{w}_0(x) = \dot{W}_0 \exp(iA_1 x/h)$, freely traveling in the positive x direction, along with the associated cross sectional rotation rate, $\dot{\phi}_0(x) = \dot{\Phi}_0 \exp(iA_1 x/h)$, where $\dot{\Phi}_0 = (\chi/h)\dot{W}_0$, and χ is given by Eqs. (4):

$$\chi = iA_1 \Gamma, \tag{4a}$$

$$\Gamma = \left[\left(1 - \frac{K^2}{\pi^2}\right) + \frac{2A_1^2}{(1-\nu)\pi^2}\right]^{-1}. \tag{4b}$$

The transfer admittances can be used to express the response of the plate at $x=\pm d/2$, as given in Eqs. (5) in which $\dot{U}_0 = \dot{\Phi}_0 h/2$:

$$\dot{w}(-d/2) = \dot{W}_0 \exp(-iA_1 d/2h) + F^- Y^p_{\dot{w}F}(0) + F^+ Y^p_{\dot{w}F}(d) - T^+ Y^p_{\dot{w}T}(d), \tag{5a}$$

$$\dot{w}(+d/2) = \dot{W}_0 \exp(+iA_1 d/2h) + F^+ Y^p_{\dot{w}F}(0) + F^- Y^p_{\dot{w}F}(d) + T^- Y^p_{\dot{w}T}(d), \tag{5b}$$

$$\dot{u}(-d/2) = \dot{U}_0 \exp(-iA_1 d/2h) - F^+ Y^p_{\dot{u}F}(d) + T^- Y^p_{\dot{u}T}(0) + T^+ Y^p_{\dot{u}T}(d), \tag{5c}$$

$$\dot{u}(+d/2) = \dot{U}_0 \exp(+iA_1 d/2h) + F^- Y^p_{\dot{u}F}(d) + T^+ Y^p_{\dot{u}T}(0) + T^- Y^p_{\dot{u}T}(d). \tag{5d}$$

These equations can be rewritten in a more convenient form by adding and subtracting Eqs. (5a) and (5b) to obtain Eqs. (6), and by adding and subtracting Eqs. (5c) and (5d) to obtain Eqs. (7):

$$\dot{w}_S = \dot{w}_{0S} + F_S \overline{Y}^S_{\dot{w}F} - T_D Y^p_{\dot{w}T}(d), \tag{6a}$$

$$\dot{w}_D = \dot{w}_{0D} + F_D \overline{Y}^D_{\dot{w}F} + T_S Y^p_{\dot{w}T}(d), \tag{6b}$$

$$\dot{u}_S = \dot{u}_{0S} - F_D Y^p_{\dot{u}F}(d) + T_S \overline{Y}^S_{\dot{u}T}, \tag{7a}$$

$$\dot{u}_D = \dot{u}_{0D} + F_S Y^p_{\dot{u}F}(d) + T_D \overline{Y}^D_{\dot{u}T}. \tag{7b}$$

The new symbols appearing in Eqs. (6) and (7) have the following definitions and interpretations:

$\dot{w}_S = \frac{1}{2}[\dot{w}(-d/2) + \dot{w}(+d/2)]$ is the average of the transverse velocities at $x=\pm d/2$.

$F_S = [F^- + F^+]$ is the total transverse force exerted on the plate by the rib.

$\dot{w}_D = [\dot{w}(+d/2) - \dot{w}(-d/2)]$, and $\dot{w}_D/d$ is the global transverse slope between the rib attachments at $x=+d/2$ and $x=-d/2$.

$F_D = \frac{1}{2}[F^+ - F^-]$, and $F_D d$ is the dipole moment exerted on the plate by the rib.

$\dot{u}_S = \frac{1}{2}[\dot{u}(-d/2) + \dot{u}(+d/2)]$ is the average of the tangential velocities at $x=\pm d/2$.

$T_S = [T^- + T^+]$ is the total tangential shear force exerted on the plate by the rib.

$\dot{u}_D = [\dot{u}(+d/2) - \dot{u}(-d/2)]$.

$\underline{T}_D = \frac{1}{2}[T^+ - T^-]$.

$\overline{Y}^S_{\dot{w}F} = \frac{1}{2}[Y^p_{\dot{w}F}(0) + Y^p_{\dot{w}F}(d)]$.

$\underline{Y}^D_{\dot{w}F} = 2[Y^p_{\dot{w}F}(0) - Y^p_{\dot{w}F}(d)]$.

$\overline{Y}^S_{\dot{u}T} = \frac{1}{2}[Y^p_{\dot{u}T}(0) + Y^p_{\dot{u}T}(d)]$.

$\underline{Y}^D_{\dot{u}T} = 2[Y^p_{\dot{u}T}(0) - Y^p_{\dot{u}T}(d)]$.

$\dot{w}_{0S}$, $\dot{w}_{0D}$, $\dot{u}_{0S}$, and $\dot{u}_{0D}$ are defined analogous to $\dot{w}_S$, $\dot{w}_D$, $\dot{u}_S$, and $\dot{u}_D$ except that $\dot{w}_0$ and $\dot{u}_0$ are used in the operations in place of $\dot{w}$ and $\dot{u}$.

Because the plate and rib are assumed to be connected along two lines, and these connections are symmetrical about

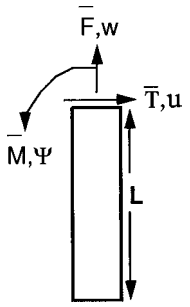

FIG. 4. Sign conventions for rib.

the ribs' mid-plane, $\dot{w}_S$ and $\dot{u}_S$ are the velocities of the root of the rib in the y and x directions, respectively, and $\dot{w}_D/d$ is the rotation of the rib's cross section at its root. $\dot{u}_D$ represents a Poisson contraction of the rib across its thickness (in the x direction) at the root. Similarly, F_S and T_S are the negative of the resultant forces exerted by the plate upon the end of the rib in the y and x directions, respectively, and $F_D d$ is the negative of the moment (in the x-y plane) exerted by the plate on the rib's root cross section. These are assumed to act on the root cross section as whole, and are not associated with any particular location on that cross section.

C. Coupling of rib to plate

Assume that the rib is attached below the plate and is symmetrical with respect to a plane through $x=0$ and normal to the x axis, and that the rib itself can be considered a plate lying in the y-z plane. Figure 4 shows the positive senses of the resultant shear force, $\bar{T}$, in the x direction, extensional force, $\bar{F}$, in the y direction, and bending moment, $\bar{M}$, in the x-y plane, all of which act on the rib's end cross section and the positive senses of the rib's extensional displacement, w_r, cross section rotation, ψ, and transverse displacement, u_r, at that location. The forces and moment are resultants and not identified with any particular point on the rib's root cross section.

The force and moment resultants acting on the rib are the negatives of the forces exerted by the rib on the plate; therefore, $\bar{F}=-F_S$, $\bar{T}=-T_S$, and $\bar{M}=-F_D d$. Because of the manner in which the rib is attached to the plate, $\dot{w}_r=\dot{w}_S$, $\dot{u}_r=\dot{u}_S$, and $\dot{\psi}=\dot{w}_D/d$. These responses are linked to the forces through the rib's input admittances, Y^r, at its root, as given by Eqs. (8) and (9);

$$\dot{u}_S=-T_S Y^r_{\dot{u}\bar{T}}-F_D d Y^r_{\dot{u}\bar{M}}, \tag{8a}$$

$$\dot{w}_D/d=-T_S Y^r_{\dot{\psi}\bar{T}}-F_D d Y^r_{\dot{\psi}\bar{M}}, \tag{8b}$$

$$\dot{w}_S=-F_S Y^r_{\dot{w}\bar{F}}. \tag{9a}$$

Equations (8) are related to the rib's velocity in the x direction and rotation in the x-y plane, and Eq. (9a) to its extensional velocity in the y direction. When Eqs. (8) are combined with Eqs. (6) for the plate, the forces T_S and F_D can be found. When Eq. (9a) is combined with Eqs. (7) for the plate, two quantities, $\dot{u}_D$ and T_D remain incompletely specified. The response $\dot{u}_D$ may be associated with the rib's Poisson strain in its thickness (x) direction due to its extensional motion and T_D can be considered a ''pinching'' force which allows full equality of resulting rib and plate displacements in the x direction. Because derivatives of extensional rib displacement are involved, the mathematical complexity required to complete the solution is probably not warranted by the ability to model the rib, nor for the purpose of showing the significance of a nonvanishing rib footprint; therefore, the last equation will be arbitrarily taken as (9b):

$$\dot{u}_D=0. \tag{9b}$$

(Alternatively, T_D could arbitrarily be set equal to zero.) Equations (7) and (9) can now be combined, and the forces F_S and T_D found. The system is now completely specified.

D. Reflected and transmitted structural power

As previously indicated, the response quantity of interest is the structural power reflected at the rib due to the incident structural wave. The reason for this choice is that plate-rib interaction is an important mechanism for backscattering of acoustic waves incident upon a ribbed plate or shell. When the frequency is greater than the critical bending frequency, so that the bending wave speed in the plate is greater than the sound speed in the ambient medium (approximately $K=0.5$, for steel or aluminum plates in water), the reflected structural power is carried by the supersonic structural wave and reradiated. Additionally, relevant input admittances for the plate in water above the coincidence frequency are well-approximated by their in vacuo values; therefore, the study in this paper can be used to provide guidance on modeling the rib-plate interaction for acoustic scattering problems above the coincidence frequency.

The structural power can be found from the propagating part of the transverse plate velocity, that is, that part varying as $\exp(iA_1 x/h)$, for $K<\pi$. Suppose that the plate without the rib is driven by a normal line force, F. The total time-averaged input power is $\frac{1}{2}|F^2|\text{Real}[Y^p_{wF}(0)]$, and the power propagating to the left (or the right) is $\frac{1}{4}|F^2|\text{Real}[Y^p_{wF}(0)]$. The square of the amplitude of the propagating part of the transverse velocity, $\dot{W}_{\text{prop}}$, on either side of the force is given by $|F\ \text{Real}[Y^p_{wF}(0)]|^2$. These two results can be combined to give the following expression for structural power, Π_s:

$$\Pi_s=\frac{1}{4}\frac{[\dot{W}_{\text{prop}}]^2}{\text{Real}[Y^p_{wF}(0)]}. \tag{10}$$

After the individual rib interaction forces are found, the power reflected by the rib can be found by finding the amplitude of the transverse plate velocity propagating to the left of $x=-d/2$, and substituting it into Eq. (10). The structural power transmitted through the rib can be found by finding that part of the transverse velocity propagating to the right of $x=+d/2$, which is generated by the action of the rib forces, adding it in phase to the incident transverse velocity (due to the source at $x=-\infty$), and substituting the amplitude of the result into Eq. (10). These are essentially independent calculations and, in the absence of structural dissipation, should sum to the incident power generated by the source at $x=-\infty$.

II. CALCULATIONS AND DISCUSSION

A. Rib model

Because the focus of this paper is the effect of the rib's footprint width on the response of the plate and not the detailed analysis of a particular rib, a simple rib model will be used in the calculations. Consider the rib in the form of a plate in the y-z plane having thickness b in the x direction and depth L in the y direction. The plate and the rib are of infinite length in the z direction, and all responses are independent of z. The following set of a mixed set of homogeneous boundary conditions on the far edge of the rib, at $y=-L$, is assumed: zero extensional stress resultant, zero shear stress resultant, zero cross section rotation in the x-y plane. The rib's extensional and rotational responses are uncoupled, and the rotational response is governed by the rib's bending properties in the x-y plane. Assuming the rib and plate to be of the same material, the rib's dimensionless bending wave numbers $A^r_{1,2}$ may be found from the right hand side of Eq. (3), with K replaced by $K^r=Kb/h$. The dimensional wave numbers are $(1/b)A^r_{1,2}$. If the rib has no dissipation and $K^r<\pi$, then $A^r_2=iB^r_2$, where B^r_2 is real and positive. If $(L/h)B^r_2$ is greater than about π, the input admittances for the rib's bending responses at the root may be approximated by Eqs. (11), with additional symbols defined by Eqs. (12):

$$\rho cb Y^r_{\dot{u}\dot{T}} \approx \frac{12i}{\pi^2} K^r \cos\left(\frac{A^r_1 L}{b}\right)[(B^r_2)^2\Omega_2+(A^r_1)^2\Omega_1]/\Delta, \tag{11a}$$

$$\rho cb^3 Y^r_{\dot{\psi}M} \approx 6i(1-\nu)K^r A^r_1 B^r_2 \sin(A^r_1 L/b) \times[\Omega_1(1+\Omega_2)-\Omega_2(1+\Omega_1)]/\Delta, \tag{11b}$$

$$\rho cb^2 Y^r_{\dot{\psi}\dot{T}} \approx -\frac{12i}{\pi^2} K^r A^r_1 B^r_2 \Omega_1\Omega_2[B^r_2 \sin(A^r_1 L/b) - A^r_1 \cos(A^r_1 L/b)]/\Delta, \tag{11c}$$

$$Y^r_{\dot{u}M} = Y^r_{\dot{\psi}\dot{T}}, \tag{11d}$$

$$\Delta = A^r_1 B^r_2[B^r_2\Omega_2(1+\Omega_1)\sin(A^r_1 L/b) - A^r_1\Omega_1(1+\Omega_2)\cos(A^r_1 L/b)], \tag{12a}$$

$$\Omega_1 = \frac{12(K^r)^2}{\pi^2(A^r_1)^2}-1, \tag{12b}$$

$$\Omega_2 = \frac{12(K^r)^2}{\pi^2(A^r_2)^2}-1. \tag{12c}$$

The admittance for extensional response is given by Eq. (13).

$$\rho cb Y^r_{\dot{w}\dot{F}} = i\sqrt{(1-\nu)/2}\cot(K^r\sqrt{(1-\nu)/2}L/b). \tag{13}$$

B. Sample results

1. Nonzero width footprint

Figure 5(a) and (b) each show the structural power reflection coefficients calculated for the rib described above with $b/h=0.5$, $d/b=0.5,0.67,1.0$ (equivalently, $d/h=0.25,0.33,0.5$), and with $L/h=5$ in Fig. 5(a) and $L/h=6$ in Fig. 5(b). The rib and the plate are both assumed to be free of structural dissipation. The major peaks in reflectivity are insensitive to the choice of d/h. Secondary levels (reflectivities greater than about 0.1) show some dependence on d/h and low levels are very sensitive to this parameter. A rule of thumb appears to be that reflectivities higher than 0.1 can be considered insensitive to d/h when the wave number width of the footprint, $A_1 d/h$, is less than $\pi/4$, but not so small that the admittance $Y^D_{\dot{w}F}$ begins to diverge. From a practical point of view, reflectivities smaller than 0.1 may be of no consequence, so that sensitivity to d/h is unimportant. The choice of $d/b=0.67$ appears to be a good compromise, which can be justified by considering the antisymmetric parts of the two normal line forces to represent the linear distribution of the normal component of stress on the cross section of a plate in bending (representing the rib bending in the x-y plane). Figure 6 shows the parameter $A_1 d/h$ as a function of K for the three values of d/b.

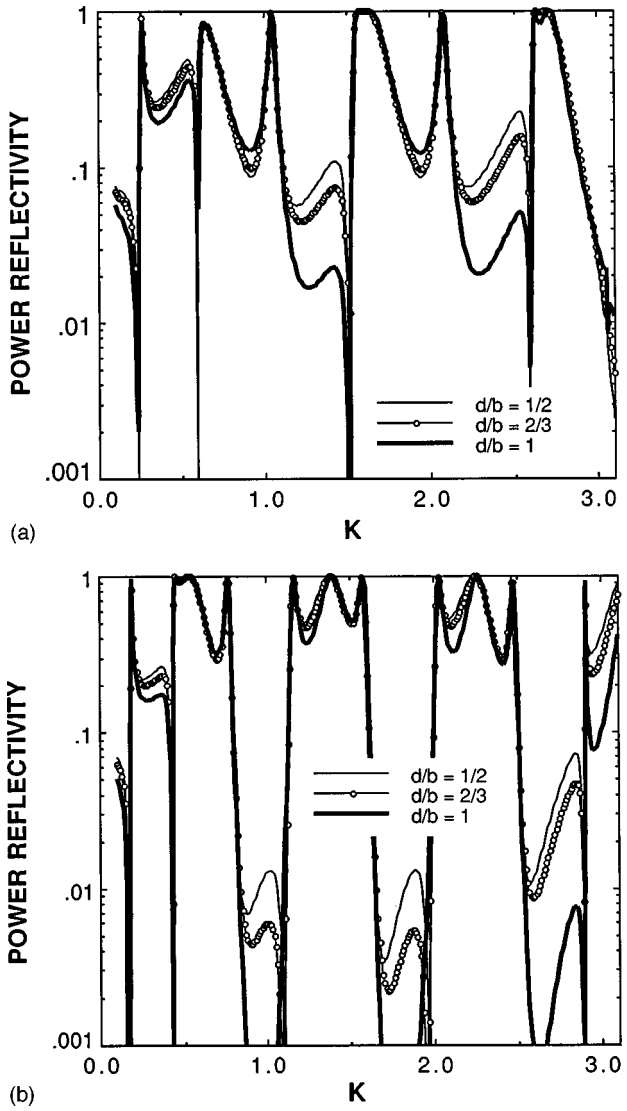

FIG. 5. (a) Power reflectivity with nonzero footprints: $L/h=5$; $b/h=0.5$, (b) Power reflectivity with nonzero footprints: $L/h=6$; $b/h=0.5$.

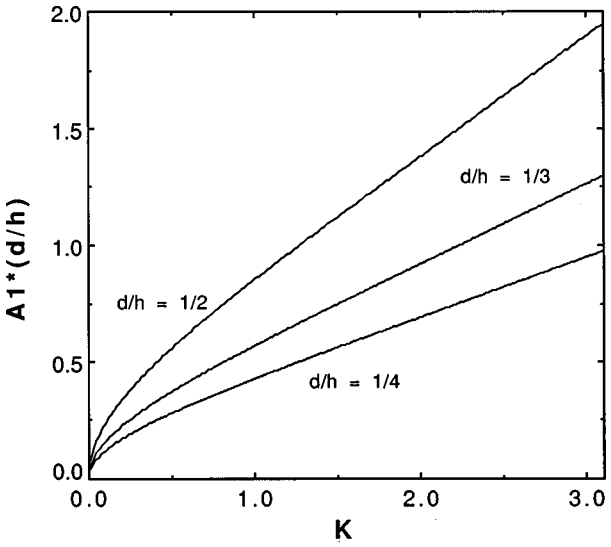

FIG. 6. Wave number width of footprint.

2. Limit of d/h→0

The consequence of assuming the rib to exert forces on the plate only along a single line can be determined by allowing d/h to approach zero in the admittances and incident wave terms appearing in Eqs. (6) and (7). Terms containing the lowest common order of d/h are kept, and Eqs. (14) and (15) are obtained:

$$\dot{W}_0 = -[Y^p_{\dot{w}F}(0) + Y^r_{\dot{w}F}]F_S, \tag{14a}$$

$$iA_1\dot{W}_0 = \frac{12i}{\rho ch\pi^2}KF_D - \left[\frac{3i(1-\nu)}{2\rho ch}\frac{K}{A_1+A_2} + hY^r_{\dot{\psi}T}\right]T_S, \tag{14b}$$

$$\frac{iA_1}{2}\Gamma\dot{W}_0 = -T_S[Y^p_{\dot{u}T}(0) + Y^r_{\dot{u}T}], \tag{15a}$$

$$-\frac{A_1^2}{2}\Gamma\dot{W}_0 = \frac{3i(1-\nu)}{2\rho ch}\frac{K}{A_1+A_2}F_S + \frac{3i(1-\nu)}{2\rho ch}KT_D. \tag{15b}$$

Equation (14a) shows that F_S is associated only with the transverse velocity of the plate and the extensional velocity of the rib. Equation (15a) indicates that, in the limit of vanishing d/h, T_S is associated only with the tangential plate velocity $\dot{u}$, and that the rib's rotational response couples to the plate only through the rib's shear admittance, $Y^r_{\dot{u}T}$, and not through the moment admittance, $Y^r_{\dot{\psi}M}$. Equations (14b) and (15b) are superfluous to subsequent calculations. Although F_D and T_D have nonzero finite values, they have no bearing on computing the response of the plate for $|x| \geqslant d/2$. This can be demonstrated by considering, for example, the admittance $Y(x)$, which relates any plate response to a transverse force, F. Writing $F^+ = \frac{1}{2}F_S + F_D$ and $F^- = \frac{1}{2}F_S - F_D$, that response for $|x| \geqslant d/2$ becomes $[\frac{1}{2}F_S + F_D]Y(x-d/2) + [\frac{1}{2}F_S - F_D]Y(x+d/2)$, which approaches $F_S Y(x)$ as d/h approaches zero.

Figure 7(a) and (b) show the power reflectivity, based on Eqs. (14a) and (15a), for $d/h \to 0$. Also shown in these figures is the power reflectivity obtained when $Y^r_{\dot{u}T} \to \infty$, so that the rib exerts only a normal force upon the plate.

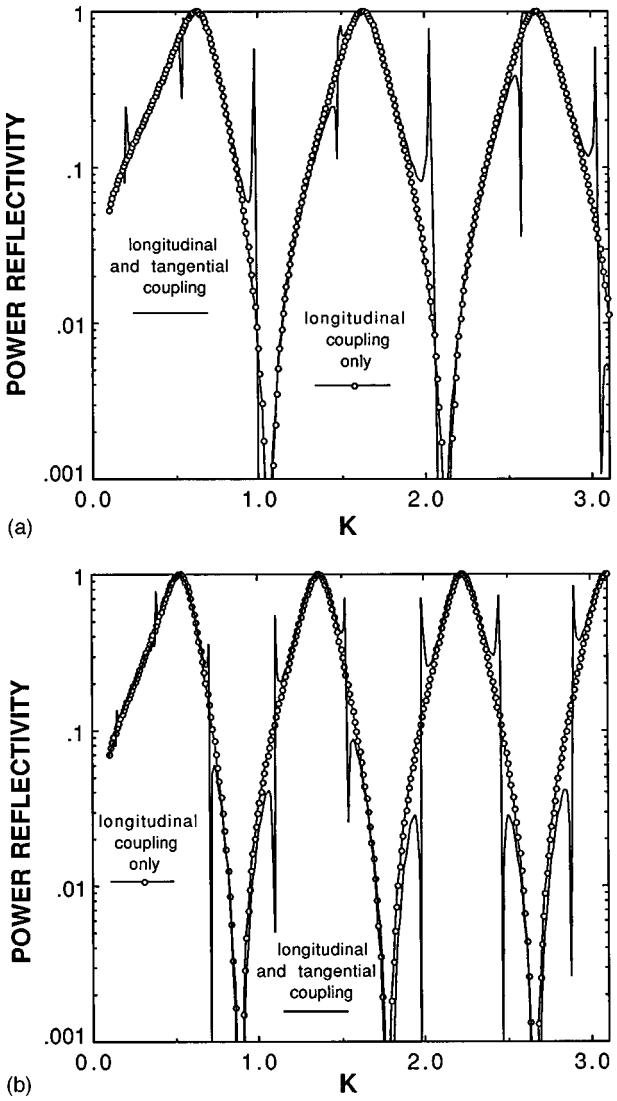

FIG. 7. (a) Power reflectivity with vanishing footprint: $L/h = 5$, single line drive. (b) Power reflectivity with vanishing footprint: $L/h = 6$, single line drive.

C. Discussion of results

There is a noticeable difference between the results in Fig. 5 and those in Fig. 7. In Fig. 7, the reflectivities are due principally to the rib's extensional admittance, and the broad peaks occur in the neighborhoods of the rib's extensional antiresonances or where $\mathrm{Imag}[Y^p_{\dot{w}F}(0) + Y^r_{\dot{w}F}] \to 0$; its rotational response plays almost no role. This conclusion is supported by the second curve in Fig. 7(a) and (b), which shows the power reflectivity for an attached rib which has the same extensional admittance but with $|Y^r_{\dot{u}T}| \to \infty$. In this case, no shear force on the end of the rib is developed and no rotational response, yet the power reflectivity closely matches the other, except for several narrow intervals. The reason for the similarity is that, for a Timoshenko–Mindlin plate, an impedance discontinuity for tangential motion, which produces a tangential force acting on the plate (equivalently a

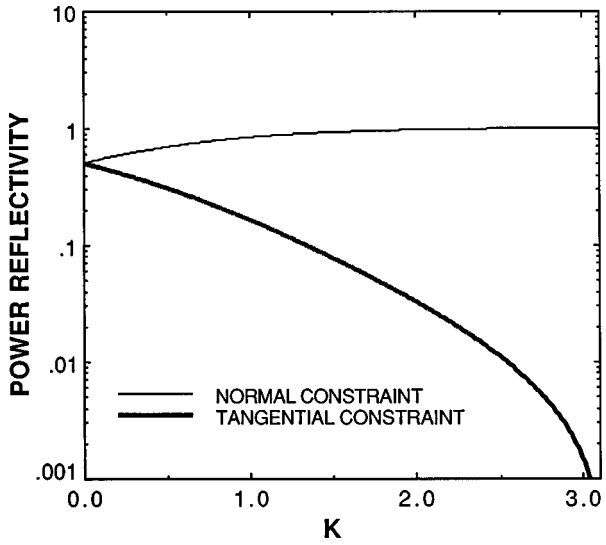

FIG. 8. Power reflectivity with vanishing footprint: perfect constraints.

''central moment''), develops little power in comparison with an impedance discontinuity for transverse motion which develops a normal force on the plate. This can be shown by considering a plate with a rib attached along a line. If the rib has zero extensional force admittance and infinite shear force admittance, then $T_S=0$, $F_S=-\dot{W}_0/Y^p_{wF}(0)$, and the time-averaged reflected power, P_F, is

$$\frac{1}{4}|\dot{W}_0|^2\,\frac{\mathrm{Real}[Y^p_{wF}(0)]}{|Y^p_{wF}(0)|^2}.$$

On the other hand, if the rib has zero shear force admittance and infinite extensional force admittance, then $F_S=0$, $T_S=-(\chi/2)\dot{W}_0/Y^p_{uT}(0)$, and the time-averaged reflected power, P_T, is

$$\frac{1}{4}\left|\frac{\chi}{2}\,\dot{W}_0\right|^2\,\frac{\mathrm{Real}[Y^p_{uT}(0)]}{|Y^p_{uT}(0)|^2}.$$

Each of these powers is shown in Fig. 8 as a function of K, and the results indicate that, for $K>1$, discontinuities associated with the plate's tangential motion (or bending rotation in the x-y plane) are much weaker reflectors of incident structural power than are discontinuities associated with the plate's transverse motion. This result is in marked contrast to that of thin plate theory, for which both an infinite impedance translational and rotational discontinuity acting alone reflect half the incident power. For the TM plate, the two reflectivities differ by more than 2 dB when K is greater than 0.3, corresponding to frequency thickness products which are larger than 14 kHz cm in steel. The narrow frequency bands in which the pairs of reflectivities in Fig. 7(a) and (b) diverge are due to antiresonance regions of $Y^r_{\dot{u}T}$, which are much narrower in frequency than are the rib's extensional antiresonances.

The reflectivities for the fully coupled case, shown in Fig. 5(a) and (b), have a richer structure in frequency because the rotational response of the rib is coupled to the plate through $Y^r_{\dot{\psi}M}$ and F_D. Because these involve the plate's transverse motion and normal forces acting on the plate, the effect on power is greater.

III. SUMMARY

The rotational component of response of a rib at its attachment to the lateral surface of a flat plate consists not only of a rotation of the rib's cross section at that attachment position, but also of a displacement of its cross section tangential to the plate. In order to account for this coupling, it is not sufficient to consider only the bending moment that the plate exerts on the rib and the equal but opposite normal force moment that the rib exerts on the plate's surface; the mutual shear forces that the rib and plate exert on one another must also be included. These shear forces have traditionally been neglected in problems of coupling between ribs and thin plates.

When the plate is modeled by Timoshenko–Mindlin (or similar) thick plate theory, which includes shear deformation, care must be taken because such a plate cannot sustain a concentrated normal force dipole on its lateral surface. Therefore, if it is desired to model the rib as a concentrated line attachment, coupling between the plate and the rotational response of the rib can only occur through the mutual shear forces between plate and rib. This interaction has small influence on the reflection of an incident structural wave by the rib when compared to the effects of the coupling between the plate's transverse response and the extensional response of the rib. With this choice of a model, the rib's rotational response may be of little consequence.

The situation changes when the rib's attachment to the plate is given a nonzero footprint width. If, for example, the rib is assumed to be attached to the plate along two parallel lines, the rib's end rotation is related to the difference in the plate's transverse displacement at those two positions, and the mutual moments are related to the difference in the two normal forces. The rotational response of the rib now has a greater influence on the reflection of an incident wave because it is coupled to the plate through normal forces.

It is noted that if the rib is modeled as a single concentrated line attachment, the relevant rotational admittance is not that of the rotational velocity due to a moment, $Y^r_{\dot{\psi}M}$, but the transverse velocity due to a shear force on its end, $Y^r_{\dot{u}T}$.

[1] P. W. Smith, Jr. and C. L. Dym, ''Input and transfer admittances of thick plates driven by a uniform line moment,'' J. Sound Vib. **60**, 441–447 (1978).
[2] M. L. Rumerman, ''Nonspecular acoustic backscattering from finite plates,'' J. Acoust. Soc. Am. **65**, 1121–1126 (1979).
[3] M. C. Junger and D. Feit, *Sound, Structures, and Their Interaction* (MIT, Cambridge, MA, 1972), pp. 152–156.
[4] R. D. Mindlin, ''Influence of rotatory inertia and shear on flexural motions of isotropic, elastic plates,'' J. Appl. Mech. **73**, 31–38 (1951).

A new bending wave solution for the classical plate equation

Christiaan Kauffmann
Delft University of Technology, Faculty of Technical Mathematics and Informatics, P.O. Box 5031, 2600 GA Delft, The Netherlands

(Received 22 January 1998; revised 30 June 1998; accepted 30 June 1998)

A new, flexural wave solution is derived for the Kirchhoff, thin plate equation on a semi-infinite domain with a free edge. This wave is a freely propagating wave that travels parallel to the edge, i.e., the curves of constant phase are straight lines perpendicular to the edge, while the wave amplitude falls off exponentially with distance from the edge, so the curves of constant amplitude are straight lines parallel to the edge. For a fixed frequency its speed is proportional to that of the standard bending wave speed. The constant of proportionality depends on the Poisson ratio only. Its value is slightly less than 1. © *1998 Acoustical Society of America.* [S0001-4966(98)02110-9]

PACS numbers: 43.40.Dx [CBB]

INTRODUCTION

The aim of this paper is to show that, according to Kirchhoff's theory, a semi-infinite, thin plate with a free edge supports nonuniform, flexural waves of a new type that travel along the edge without attenuation.

Analysis closely follows the same lines as in Refs. 1 and 2. The particular wave that is discussed here corresponds to the real-valued pole in the complex wave number space associated with the inverse Fourier transform integral for the response of an edge-excited, semi-infinite plate. A closed-form analytical expression for this pole was derived in Ref. 2. However, the associated wave mode has not been identified there since that paper merely evaluates structural power generated by localized forcing along the edge. For that purpose only input mobilities were needed. The total wave field—including the new wave mode investigated here—was not evaluated.

I. BASIC EQUATIONS

A thin, elastic plate occupies the semi-infinite region $x<0$, $-\infty<y<\infty$. The out-of-plane flexural motion is governed by Kirchhoff's plate equation

$$D\Delta\Delta w - m''\omega^2 w(x,y)=0, \quad x<0, \quad -\infty<y<\infty, \quad (1)$$

where $w(x,y)$ is the normal displacement, $D=Eh^3/12(1-\nu^2)$ is the bending stiffness, and $m''=\rho h$ is the density of mass per unit area, while E is Young's modulus, h is the plate thickness, ν is Poisson's ratio, and ρ is the volume density of mass of the plate. Only time-harmonic motion is considered (ω is the circular frequency) and the time factor $\exp(i\omega t)$ is omitted for brevity. The free edge conditions are

$$-D\,\frac{\partial}{\partial x}\left[\frac{\partial^2 w}{\partial x^2}(0,y)+(2-\nu)\,\frac{\partial^2 w}{\partial y^2}(0,y)\right]=0, \quad (2)$$

$$-D\left[\frac{\partial^2 w}{\partial x^2}(0,y)+\nu\,\frac{\partial^2 w}{\partial y^2}(0,y)\right]=0. \quad (3)$$

II. FREE EDGE PLATE WAVE

In Refs. 1 and 2 the edge-excited plate, i.e., Eq. (1) subject to the inhomogeneous counterparts of conditions (2) and (3), was analyzed using Fourier transforms

$$w(x,y)=\int_{-\infty}^{\infty}\tilde{w}(x,q)\exp(-iqy)\,dq, \quad (4)$$

$$\tilde{w}(x,q)=\frac{1}{2\pi}\int_{-\infty}^{\infty}w(x,y)\exp(iqy)\,dy. \quad (5)$$

The presence of a real-valued pole suggests that a particular wave mode might exist. So this paper deals with wave modes of the type

$$w(x,y)=\hat{w}(x,q)\exp(-iqy), \quad (6)$$

where q is real. Inserting into Eq. (1) yields

$$\frac{d^4\hat{w}}{dx^4}-2q^2\,\frac{d^2\hat{w}}{dx^2}+(q^4-k^4)\hat{w}(x,q)=0, \quad k^4=\frac{m''\omega^2}{D}, \quad (7)$$

where k is the flexural wave number. Solutions of the type

$$\hat{w}(x,q)=\exp(\lambda x) \quad (8)$$

satisfy

$$\lambda_1=(q^2+k^2)^{1/2}>0, \quad \text{for all } q, \quad (9)$$

$$\lambda_2=-\lambda_1, \quad (10)$$

$$\lambda_3=(q^2-k^2)^{1/2}=\begin{cases}|q^2-k^2|^{1/2}, & |q|>k,\\ i|k^2-q^2|^{1/2}, & -k<q<k,\end{cases} \quad (11)$$

$$\lambda_4=-\lambda_3. \quad (12)$$

Imposing the requirements for real physical modes, i.e.,

(1) $\mathrm{Im}[\lambda]=0\Rightarrow\mathrm{Re}[\lambda]>0$, which excludes the nonpropagating, exponentially increasing field components at infinity ($x\to-\infty$); and
(2) $\mathrm{Re}[\lambda]=0\Rightarrow\mathrm{Im}[\lambda]>0$, which excludes modes propagating from infinity towards the edge $x=0$; reveals that λ_2 and λ_4 are not admissible. Thus

$$\hat{w}(x,q)=A(q)\exp(\lambda_1 x)+B(q)\exp(\lambda_3 x), \quad (13)$$

where $A(q)$ and $B(q)$ are constants, but still functions of q. Unless $B(q)\equiv 0$ the condition $|q|>k$ should be satisfied for waves that travel parallel to the edge. Applying boundary conditions (2) and (3) leads to

$$\begin{pmatrix} \mu_+(p)M_-(p) & -\mu_-(p)M_+(p) \\ M_+(p) & -M_-(p) \end{pmatrix}\begin{pmatrix} A(q) \\ B(q) \end{pmatrix}=\begin{pmatrix} 0 \\ 0 \end{pmatrix}, \tag{14}$$

where $q=kp$ and

$$\mu_\pm(p)=(p^2\pm 1)^{1/2}, \quad M_\pm(p)=1\pm(1-\nu)p^2. \tag{15}$$

Note that $\lambda_1=k\mu_+(p)$ and $\lambda_3=k\mu_-(p)$. The condition $|q|>k$ is equivalent to $|p|>1$ and implies that the wave amplitude falls off exponentially with distance from the edge. System (14) has a nontrivial solution for $A(q)$ and $B(q)$ if

$$\det(p)=\mu_+(p)[M_-(p)]^2-\mu_-(p)[M_+(p)]^2=0. \tag{16}$$

Multiplying by

$$\text{adjdet}(p)=\mu_+(p)[M_-(p)]^2+\mu_-(p)[M_+(p)]^2 \tag{17}$$

yields

$$\begin{aligned}\triangle(p)&=-\det(p)\cdot\text{adjdet}(p),\\ &=2[-(3+\nu)(1-\nu)^3p^8+2(1-3\nu)(1-\nu)p^4+1]=0.\end{aligned} \tag{18}$$

The solutions read

$$p^4=\tau_+, \text{ or } p^4=\tau_-, \tag{19}$$

where $\tau_\pm$ are given by

$$\tau_\pm=\frac{1-3\nu\pm 2\sqrt{\nu^2+(1-\nu)^2}}{(1-\nu)^2(3+\nu)}. \tag{20}$$

One can show that $1<\tau_+<\frac{4}{7}(2\sqrt{2}-1)$ and $-\frac{4}{7}(1+2\sqrt{2})<\tau_-<-\frac{1}{3}$ for $0<\nu<\frac{1}{2}$. Consequently, the roots of $\triangle(p)=0$ are

$$p_1=\tau_+^{1/4}, \quad p_2=i\tau_+^{1/4}, \quad p_3=-p_1, \quad p_4=-p_2, \tag{21}$$

$$p_5=|\tau_-|^{1/4}e^{i\pi/4}, \quad p_6=|\tau_-|^{1/4}e^{3i\pi/4}, \quad p_7=-p_5, \quad p_8=-p_6. \tag{22}$$

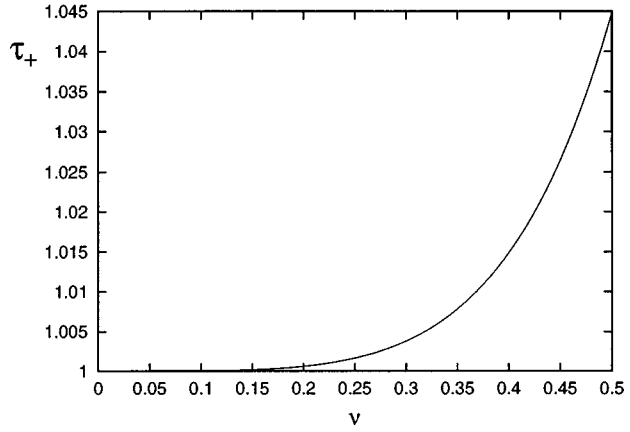

FIG. 1. Variation of τ_+ with ν.

Straightforward analysis reveals that:

$$\det(p_{1,2,3,4})=0 \quad \text{and} \quad \text{adjdet}(p_{5,6,7,8})=0. \tag{23}$$

Restricting the discussion to the real root $p_1>1$ (p_3 gives the same wave running in opposite direction) and inserting in (14) leads to

$$\frac{B(q_1)}{A(q_1)}=\frac{M_+(p_1)}{M_-(p_1)}=\frac{\mu_+(p_1)M_-(p_1)}{\mu_-(p_1)M_+(p_1)}. \tag{24}$$

The result is a nonuniform, plane wave of the form

$$\begin{aligned}w(x,y)=C\{&M_-(p_1)\exp[kx\mu_+(p_1)]\\ &+M_+(p_1)\exp[kx\mu_-(p_1)]\}\exp(-ikp_1y),\end{aligned} \tag{25}$$

where C is a constant. The wave speed or phase velocity is

$$c_{\text{ph}}=\frac{\omega}{kp_1}=\left[\frac{\omega^2D}{m''}\Big/\tau_+\right]^{1/4}. \tag{26}$$

The speed of this new wave is proportional to that of the classical bending wave. It differs from it only by the multiplicative factor $p_1^{-1}=\tau_+^{-1/4}$. This factor is slightly less than 1, indicating that the wave speed is slightly less than that of the classical bending wave. Figure 1 shows how τ_+ varies with ν. Since the correction factor p_1^{-1} depends on the Poisson ratio only, it is concluded that the persistence of this wave mode is due to a Poisson contraction effect at the free edge. The wave amplitude, i.e., $\hat{w}(q_1,y)$, falls off exponentially with distance from the edge at two different rates. However, since $\mu_+(p_1)\gg\mu_-(p_1)$, while $M_-(p_1)\approx\nu$ and $M_+(p_1)\approx 2-\nu$, the second term in (25), i.e., $M_+(p_1)\exp[kx\mu_-(p_1)]$, dominates over the first one. Actually, the decay rate is small. For steel plates ($\nu=0.3$) the $1/e$ value is attained for $k|x|\approx 22.93$ (about 3.65 wavelengths from the edge).

III. CLOSING REMARKS

Generally, at the plate edge one can impose two out of four uniform, homogeneous boundary conditions, i.e., those of Eqs. (2) and (3) and those expressing zero displacement and zero slope. Any of the six pairs of boundary conditions can be applied to the wave solutions of the type (6), (13). It is noted, however, that only those combinations representing clamped, simply supported, or free edges can be actually realized (the sliding condition makes sense for beams, not for plates). Nevertheless, any pair of conditions can be applied. However, this formal mathematical exercise, which will not be repeated here, leads nowhere, i.e. the free edge is the only case that supports a wave of the type (6), (13).

It should be noted that, whereas Kirchhoff's plate theory is an approximation derived from the three dimensional equations for a linear, isotropic, and homogeneous elastic solid, it is not clear as to what extent the wave mode (25) is an approximation of some wave solution for the three dimensional equations of elasticity, nor is it clear whether the wave mode (25) corresponds to a real physical phenomenon. How-

ever, this wave can be considered as a special case of a guided wave along the truncated tip of a wedge of zero internal angle, cf. Ref. 3.

[1] E. Eichler, ''Plate-edge admittances,'' J. Acoust. Soc. Am. **36**, 344–348 (1964).

[2] C. Kauffmann, ''Input mobilities and power flows for edge-excited, semi-infinite plates,'' J. Acoust. Soc. Am. **103**, 1874–1884 (1998).

[3] J. McKenna, G. D. Boyd, and R. N. Thurston, ''Plate theory solution for guided flexural acoustic waves along the tip of a wedge,'' IEEE Trans. Sonics Ultrason. **SU-21**, 178–186 (1974).

Range-dependent acoustic radiation from line-driven plates above the bending coincidence frequency

M. L. Rumerman
Naval Surface Warfare Center, Carderock Division, Signatures Directorate (Code 7200), 9500 MacArthur Boulevard, West Bethesda, Maryland 20817-5700

(Received 20 October 1997; accepted for publication 13 July 1998)

The leaky waves generated on plates driven in bending above the bending coincidence frequency radiate as extended sources; therefore, the standard saddle point evaluation of the radiated pressure, which yields a far-field result, may not be appropriate at the range of interest. The calculation can be modified by removing the contribution of the leaky waves from the original integrand, evaluating the remaining regular part by the saddle point method, and evaluating the effect of the leaky waves in terms of error functions and residue. Results showing range dependence are presented for radiation by a steel plate in water driven by normal and tangential line forces. The correctness of the results is made plausible by comparing independent calculations of acoustic power passing through a semicircle at finite range. [S0001-4966(98)05510-6]

PACS numbers: 43.40.Rj [CBB]

INTRODUCTION

For frequencies above bending coincidence, the vibration field of a plate driven in bending includes a leaky supersonic wave which radiates and decays exponentially in amplitude as it propagates away from the drive. Because this velocity component forms an extended source, rather than a compact source as formed by the other components of vibration, there may be ranges of interest at which the far-field estimate of radiated pressure is no longer adequate. Rigorous consideration of the acoustic beaming effects of supersonic surface waves and of the range dependence of the beam characteristics appear to have originated with Crighton.[1] Seren and Hayek[2] have considered the calculation of range-dependent radiation in a paper on scattering from rib-reinforced plates. Their approach is to decompose the original integral representation of the reradiated (i.e., scattered) field into ten integrals related to the zeros of the rationalized denominator of the original integrand, and to evaluate these integrals in terms of error functions. Their method uses zeros of the rationalized denominator which are not true poles of the system and zeros which are not associated with significant responses of the plate. Because only the leaky waves radiate as extended sources, only their contribution requires special treatment, and the calculation can be simplified by extracting the contribution of the leaky wave pole from the original integrand. The remainder is regular in the neighborhood of the saddle point and can be evaluated by the saddle point approximation; the extracted singular part is evaluated in terms of error functions. This has been pointed out by Stuart,[3] who quoted an algorithm similar to that used here, but presented no calculations illustrating the range dependence. The present paper shows sample range-dependence results, gives a rule of thumb for when the leaky wave should be given special treatment, and validates the algorithm by a power balance.

I. OUTLINE OF SOLUTION

The problem considered is the sound radiation due to a line normal force, F, or a line tangential force, T, acting on the vacuum side of an infinite steel plate bounded by a semi-infinite extent of water on the other side. As shown in Fig. 1, the plate, of thickness h, lies parallel to the x,y plane with the face $z=0$ in contact with the water and the face $z=-h$ driven by a y-independent line force applied along $x=0$.

The asymmetric flexural response of the plate will be modeled using the Timoshenko–Mindlin theory. By extending the development of Junger and Feit[4] to include the shear force, and including the pressure acting on the water side of the plate due to its normal velocity, the equations of time-harmonic motion, with radian frequency ω, are found to be given by Eqs. (1) in which $\exp(-i\omega t)$ time dependence is assumed and suppressed:

$$\frac{Gh^3}{6(1-\nu)}\,\Phi''+\frac{\pi^2}{12}\,Gh(W'-\Phi)+\frac{\rho_s h^3\omega^2}{12}\,\Phi=\frac{Th}{2}\,\delta(x), \tag{1a}$$

$$\frac{\pi^2}{12}\,Gh(W''-\Phi')+\rho_s h\omega^2 W-P=-F\,\delta(x). \tag{1b}$$

In Eqs. (1), $W(x)$ and $\Phi(x)$ are, respectively, the normal displacement and cross sectional rotation of the plate, $P(x,z=0)$ is the resulting acoustic pressure acting on the plate on the water side, and G, ν, and ρ_s are, respectively, the plate material shear modulus, Poisson's ratio, and mass density. The prime signifies a spatial derivative (d/dx). In arriving at these forms for the equations, use has been made of the relationship among the shear modulus, Young's modulus, and Poisson's ratio, and the shear adjustment factor was taken to be $\pi^2/12$.

Equations (1) can be solved by Fourier transform techniques to obtain W, Φ, and the acoustic field pressure $P(r,\theta)$, where r and θ are related to x and z by $x=r\sin\theta$

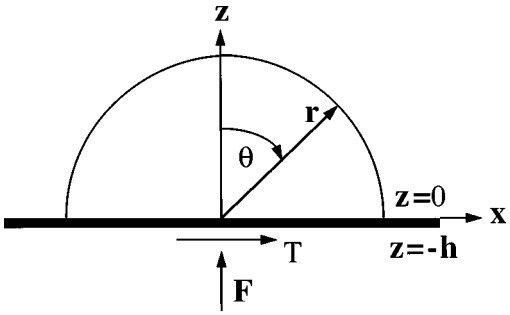

FIG. 1. Plate–fluid coordinate system.

and $z=r\cos\theta$. The pressures P_F due to F alone and P_T due to T alone are given by Eq. (2) with supplementary definitions in Eqs. (3).

$$P_\beta(r,\theta)=\frac{\mathsf{F}_\beta}{2\pi h}\frac{\rho}{\rho_s}\int_{-\infty}^{\infty}\frac{\Psi_\beta(A)}{\Delta(A)}\exp[(r/h)q(A)]dA \qquad \beta=F,T, \tag{2}$$

$$q(A)=iA\sin\theta-\sqrt{A^2-K^2}\cos\theta, \tag{3a}$$

$$\Delta(A)=N(A)\sqrt{A^2-K^2}+\frac{\rho}{\rho_s}D(A), \tag{3b}$$

$$N(A)=K_b^4\left(1-\frac{K_s^2}{\pi^2}\right)+A^2\left(\frac{K_b^4}{12}+\frac{12}{\pi^2}K_s^2\right)-A^4, \tag{3c}$$

$$D(A)=K_b^4\left(1-\frac{K_s^2}{\pi^2}\right)+\frac{12}{\pi^2}K_s^2A^2, \tag{3d}$$

$$\Psi_\beta(A)=D(A), \quad \mathsf{F}_\beta=F; \quad \beta=F, \tag{3e}$$

$$\Psi_\beta(A)=iK_b^4A/2, \quad \mathsf{F}_\beta=T; \quad \beta=T. \tag{3f}$$

In Eq. (2), ρ is the mass density of the acoustic medium and A is a dimensionless dummy wave number. In Eqs. (3), $K=kh$, $K_s=k_sh$ and $K_b=k_bh$, where k is the acoustic wave number of the ambient medium, k_s is the shear wave number of the plate material, and k_b is the classical thin plate bending wave number for the plate. It is noted that $K_b^4=6(1-\nu)K_s^2$.

The integral in Eq. (2) can be found for a far-field range ($r\to\infty$) by shifting the line of integration to the steepest descent path (SDP) through the saddle point $A=A_0=K\sin\theta$, and using the standard saddle point evaluation. For a non-far-field range, the SDP can still be used if the effects of poles of the integrand near the SDP are included in the integration along the SDP. Explicitly following the method as described by Felsen and Marcuvitz,[5] this is done by removing these poles from the integrand and leaving a regular function in the neighborhoods of these poles, using the standard saddle point evaluation for this regular part, and approximating the contribution of the singular part by error functions. Only the leaky wave poles are found to be important in this process, and the poles for the leaky waves traveling in both the $+x$ and $-x$ directions are included to preserve the proper symmetry of the pressure field about $\theta=0$. The frequency range considered is restricted to $K_s<\pi$ so that there is not more than one leaky wave type. The approximation for the pressure at the field point r,θ is given by Eqs. (4) in which $A_l=\alpha_lh$, where α_l is the wave number of the leaky wave and $\Delta'(A)=d\Delta/dA$:

$$\begin{aligned}\frac{2\pi h}{\mathsf{F}_\beta}\frac{\rho_s}{\rho}\exp(-ikr)P_\beta(r,\theta)=&\,2\pi i\frac{\Psi_\beta(A_l)}{\Delta'(A_l)}\exp\left(\frac{q(A_l)r}{h}\right)\exp(-ikr)\mathbf{H}(-\xi)\\&+2i\xi\sqrt{\pi}\frac{\Psi_\beta(A_l)}{\Delta'(A_l)}Q\left(-i\xi b(A_l)\sqrt{\frac{r}{h}}\right)\exp\left(-\frac{b^2(A_l)r}{h}\right)\\&+2i\sqrt{\pi}\frac{\Psi_\beta(-A_l)}{\Delta'(A_l)}Q\left(+ib(-A_l)\sqrt{\frac{r}{h}}\right)\exp\left(-\frac{b^2(-A_l)r}{h}\right)\\&+\sqrt{\frac{\pi h}{r}}\left[\sqrt{2K}\exp\left(-\frac{i\pi}{4}\right)\cos\theta\frac{\Psi_\beta(A_0)}{\Delta(A_0)}+\frac{\Psi_\beta(A_l)}{\Delta'(A_l)b(A_l)}-\frac{\Psi_\beta(-A_l)}{\Delta'(A_l)b(-A_l)}\right],\end{aligned} \tag{4a}$$

$$Q(y)=\int_y^\infty\exp(-\sigma^2)d\sigma, \tag{4b}$$

$$b(A)=\sqrt{q(K\sin\theta)-q(A)}, \tag{4c}$$

$$\xi=\frac{\mathrm{Im}[b(A_l)]}{|\mathrm{Im}[b(A_l)]|}, \tag{4d}$$

$\mathbf{H}(\phi)=1$ for ϕ positive, $\mathbf{H}(\phi)=0$ for ϕ negative.

Figure 2 shows a sketch of the poles in the complex A-plane appropriate to the indicated branch cuts, and the SDP through the saddle point $A=A_0=K\sin\theta$ which is found by setting $dq/dA=0$. (The angle θ is assumed to be nonnegative.) In addition to A_l, this choice of branch cuts results in the dimensionless poles A_d and A_s, which respectively correspond to the plate's bending attenuation field and subsonic surface wave. The function ξ defined in Eq. (4d) is a flag which marks the capture or noncapture of the leaky wave pole in the first quadrant as the path is shifted.

The first term on the RHS of Eq. (4a) is the residue contribution of the captured leaky wave pole and the second

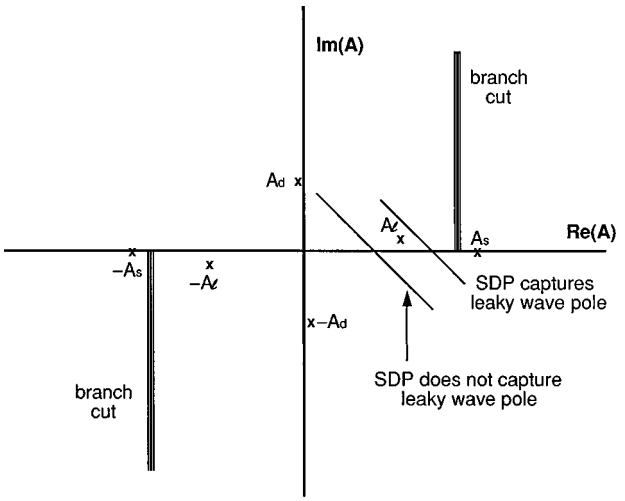

FIG. 2. Poles, branch cuts, and SDPs of complex A-plane.

term is the error function contribution of that pole. Their sum is continuous as the SDP crosses the pole. The third term on the RHS is the error function contribution of the leaky wave pole in the third quadrant, and is included to preserve symmetry of the pressure field about $\theta=0$. The fourth term is the contribution of the remaining regular part of the integrand, and represents radiation by a compact source.

II. SAMPLE CALCULATIONS

Calculations were performed for a lossless steel plate, with water on the side opposite the applied force, using the following dimensionless parameters: $\rho_s/\rho=7.8$; $\nu=0.3$; $k/k_s=2.07$. Figure 3(a), (b), (c) presents, for a normal force drive, $20\log|(P\sqrt{kr})/(kF)|$ as a function of θ, for three values of K_s (i.e., three dimensionless frequencies). For steel plates in water, the corresponding values of K are close approximations to the ratio of the frequency to the nominal thin plate bending coincidence frequency. For each frequency, results are given for the mathematical farfield and for two finite dimensionless ranges $kr=R$.

The finite ranges were chosen to test the condition under which the true far field would be approximated. For radiation problems, this condition is usually given as $r>L^2/\lambda$, where λ is the wavelength in the ambient acoustic medium and L is the effective length of the vibrating surface. In this case, and for radiation into the $+x$ quadrant, the important component of the surface vibration is that due to the leaky wave traveling in the $+x$ direction along the plate. This vibration component decays as it propagates, and its amplitude at any position x, relative to its value at $x=0$, is $\exp[-\mathrm{Im}(A_l)x/h]$. The question is, at what value of $x=L$ is the amplitude sufficiently reduced so that the leaky wave vibration for $x>L$ does not significantly contribute to the radiation? Let $\mathrm{Im}(A_l)L/h=\eta$. Then

$$L=\frac{\eta h}{\mathrm{Im}(A_l)},\quad r>\frac{1}{\lambda}\left[\frac{\eta h}{\mathrm{Im}(A_l)}\right]^2,$$
$$kr=R>\frac{1}{2\pi}\left[\frac{\eta K}{\mathrm{Im}(A_l)}\right]^2. \tag{5}$$

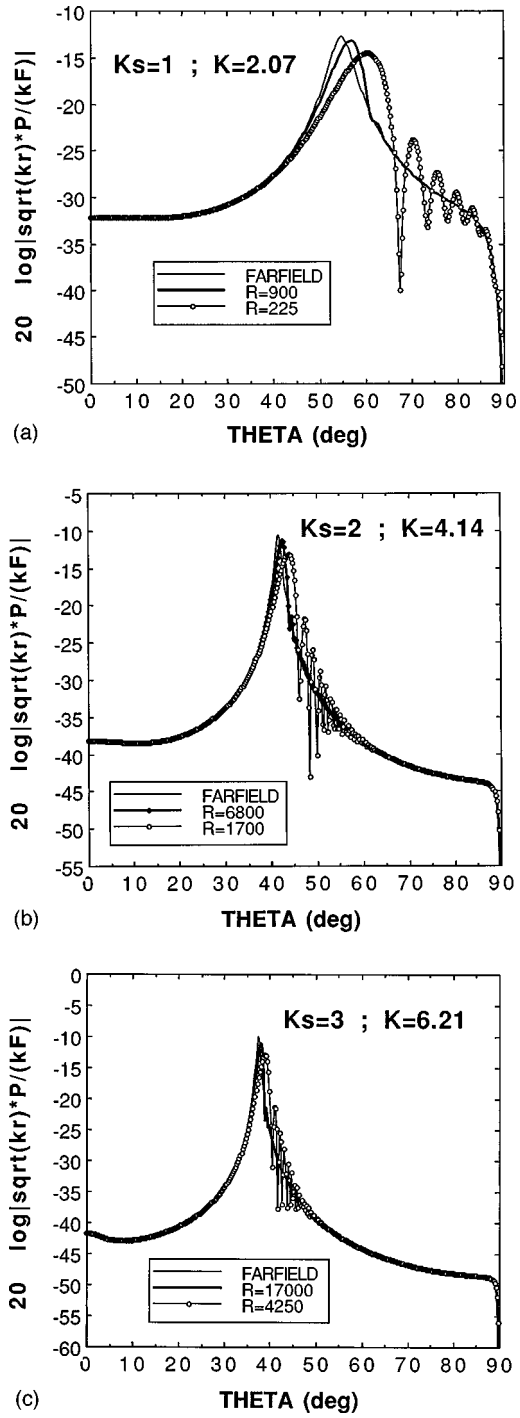

FIG. 3. (a) Normalized pressure vs θ; normal force drive, $K_S=1$. (b) Normalized pressure vs θ; normal force drive, $K_S=2$. (c) Normalized pressure vs θ; normal force drive, $K_S=3$.

The ranges chosen for calculation correspond approximately to $\eta=1$ and $\eta=2$, which represent vibration amplitude decays of e^{-1} and e^{-2}, respectively. Upon examining the results of the calculations, it is concluded that the choice of $\eta\approx 2$ appears to give a good approximation to the far field, but the pressure field at the range corresponding to $\eta\approx 1$ contains near-field effects.

Figure 4 presents analogous results for a tangential force drive with $K_s=1$, with pressure normalized to kT. Similar conclusions are reached.

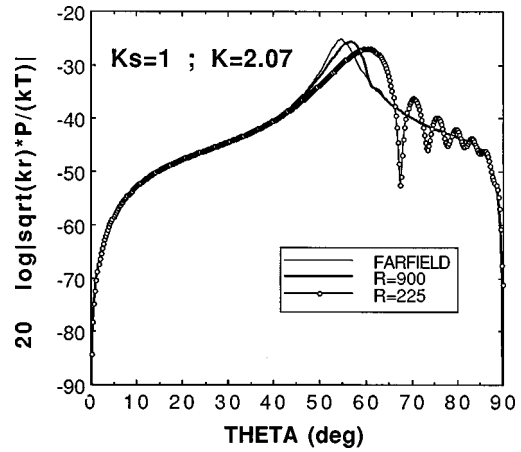

FIG. 4. Normalized pressure vs θ; tangential force drive, $K_S=1$.

III. VALIDATION BY POWER BALANCE

The total power radiated can be calculated by integrating the radial component of far-field acoustic intensity along a semicircular arc of radius r, as $r\to\infty$. For a plate without structural dissipation, this must equal the power input by the force less the power contained in the nonradiating subsonic wave. At short ranges, the acoustic power passing through the arc may be appreciably less than the total radiated power, and the difference should equal the power remaining in the leaky wave as it passes the locations $|x|=r$ on the plate. Because the calculations of the radial component of acoustic field intensity and of the various plate responses are independent, a power balance provides a reasonable check on the approach.

The radial component of the acoustic intensity is found by calculating the radial fluid velocity along the semicircle in a manner analogous to calculating the pressure, and appropriately combining it with the pressure. The power input to the plate is found by computing the real part of the plate velocity in the direction of the force at the drive point, and the total power in the subsonic and leaky waves are the contributions of their respective residues to the input power. The power in the leaky wave at distance $|x|$ from the line force is equal to $\exp[-2\,\mathrm{Im}(A_l)|x/h|]$ times the total leaky wave power. Equations (6) are integral relations for the transverse velocity, $-i\omega W_F$, of the plate due to a normal force F, and the tangential velocity, $-i\omega U_T$, of the plate surface at $z=-h$ to a tangential force T. These integrals were evaluated as the sum of residue and branch cut contributions:

$$-i\omega W_F(x)=\frac{iF}{2\pi\omega\rho_s h^2}\int_{-\infty}^{\infty}\frac{D(A)\sqrt{A^2-K^2}}{\Delta(A)}\exp\left(\frac{iAx}{h}\right)dA, \tag{6a}$$

$$-i\omega U_T(x)=\frac{iT/4}{2\pi\omega\rho_s h^2}\int_{-\infty}^{\infty}\frac{S(A)}{\Delta(A)}\exp\left(\frac{iAx}{h}\right)dA, \tag{6b}$$

$$S(A)=K_b^4\left[\left(A^2-\frac{12}{\pi^2}K_s^2\right)\sqrt{A^2-K^2}-\frac{12}{\pi^2}\frac{\rho}{\rho_s}K_s^2\right]. \tag{6c}$$

As an illustration, powers were calculated for $K_s=1$ and $kr=0.5K/\mathrm{Im}(A_l)=18.8$. The second condition means that the leaky wave amplitude at $|x|=r$ is 60% of its amplitude at its origin. Table I presents results obtained for normal force and tangential force drives. Powers are normalized with respect to $(k\mathsf{F}_\beta)^2/\rho\omega$, where β is F or T. For each case, the total (far-field) radiated power as calculated by integrating the acoustic intensity agrees with the total power available for radiation as calculated through the plate responses. The calculated acoustic power passing through the semicircle at $kr=18.8$ should agree with with the total radiated power less the structure borne power remaining in the leaky wave as it passes $|kx|=18.8$, and it agrees within 2.5 percent. The difference is attributable to the approximate integration of the singular part of the integrand.

TABLE I. Comparison of radiated power calculations.

Normalized power per unit width: $K_s=1$	F	T
Power input to plate by force	0.0157	0.000 85
Input power less subsonic wave power	0.0153	0.000 83
Acoustic power passing through far-field arc	0.0153	0.000 83
Input power less subsonic wave power less residual leaky wave power at $\|kx\|=18.8$	0.009 76	0.000 52
Acoustic power passing through arc at $kr=18.8$	0.009 99	0.000 53

IV. SUMMARY

The acoustic pressure radiated from a plate driven in bending by a concentrated force below the bending coincidence frequency may be considered as being due to a compact source in the neighborhood of the force and, for field points at least half an acoustic wavelength from the plate, may be evaluated by the standard saddle point or stationary phase approximation leading to the far-field result. Above the coincidence frequency, the leaky wave component of the plate response radiates as an extended source and, for ranges from the force less than $(2/\pi k)[K/\mathrm{Im}(A_l)]^2$, the field may exhibit range dependence other than cylindrical or spherical spreading. The calculation can be performed by removing the singular component of the integrand corresponding to the leaky wave, using the standard approximation for the remaining regular portion, and evaluating the singular part as an error function and possible residue contribution. An interpretation of the formulation is that the saddle point result for the regular portion of the integrand represents radiation by the compact portion of the plate response, and the residue and error function contributions represent radiation by the spatially extended leaky wave into the ''lit'' region and a ''transition'' function that preserves continuity and accounts for the leaky wave contribution away from its preferred angle of radiation.

[1] D. G. Crighton, ''Acoustic beaming and reflexion from wave-bearing surfaces,'' J. Fluid Mech. **47**, 625–638 (1971).
[2] C. Seren and S. I. Hayek, ''Acoustic radiation from an insonified elastic plate with a line discontinuity,'' J. Acoust. Soc. Am. **86**, 195–209 (1989).
[3] A. D. Stuart, ''Acoustic radiation from submerged plates I. Influence of leaky wave poles,'' J. Acoust. Soc. Am. **59**, 1160–1169 (1976).
[4] M. C. Junger and D. Feit, *Sound, Structures, and Their Interaction* (MIT, Cambridge, MA, 1972), pp. 152–156.
[5] L. B. Felsen and N. Marcuvitz, *Radiation and Scattering of Waves* (Prentice-Hall, Englewood Cliffs, NJ, 1973), Chap. 4, Sec. 4.4.

Numerical studies of acoustic boundary control for interior sound suppression

S. M. Hirsch and J. Q. Sun[a)]
Department of Mechanical Engineering, University of Delaware, Newark, Delaware 19716

(Received 2 May 1997; accepted for publication 13 May 1998)

There are two mainstream methods for the active control of noise in enclosures: active noise cancellation (ANC) and active structural acoustic control (ASAC). ASAC systems are most effective when the primary noise source is the radiation from a vibrating structure, but cannot efficiently control sound from other sources. ANC systems are effective when other noise sources are present, but will sometimes require a much higher dimensionality than ASAC systems to control structural radiation. This paper proposes a practically motivated implementation strategy for ANC actuator placement. Specifically, it proposes to implement an array of acoustic control sources in front of vibrating boundaries to form an acoustic boundary control layer. This provides low-power performance comparable to ASAC systems for controlling sound radiation from the boundary, but also an efficient system for controlling noise from other disturbances. Numerical simulations are presented to demonstrate the ability of the acoustic boundary control to suppress interior noise due to acoustic and structural sources. Because of the expense of implementing large active control systems, there is great interest in developing an actuator grouping strategy to reduce the control system dimensionality. A preliminary feasibility study, to establish under which conditions actuator grouping may be successful, is presented. A strategy in which actuators are grouped through an off-line analysis of the control problem is studied. [S0001-4966(98)00809-1]

PACS numbers: 43.40.Vn [PJR]

INTRODUCTION

Research on active structural control for suppressing aircraft interior noise has been very active. References 1–5 contain extensive reviews of the literature on this subject. It is sometimes found that a structural control system can achieve global interior noise reduction with a lower dimensionality than an active noise cancellation system. One of the main concerns with structural control is that it may cause fatigue damage to the structure. This issue is particularly sensitive to the aerospace industry. To avoid this problem of structural control, researchers have begun to consider placing actuators on noncritical structures such as interior trim panels of an aircraft.[6–9] The recent work by Silcox and his associates[7] represents significant progress in understanding some important issues regarding structural control applied to fuselage trim panels. In particular, they have found that with a small number of actuators, it is very hard to avoid structural control spillover which can cause the overall interior sound-pressure level to increase even though the sound pressure at error sensors is reduced. Others have proposed attaching a secondary structure to a heavy and stiff vibrating structure and placing actuators on the secondary structure for noise control.[10–12] Mason and his colleagues have proposed placing a loudspeaker directly on the radiating panel to achieve a zero net volume velocity.[13,14] Darlington has formulated interior noise control problems in terms of acoustic impedance and discussed the concept of active boundary control.[15]

One of the more difficult tasks facing an aircraft noise control engineer is to balance the ''best'' placement of control sources (both structural and acoustic) with the allowable placement, given restrictions on actuation on critical structures and the need to efficiently utilize cabin space. The authors propose a design and implementation strategy for active noise cancellation (ANC) which addresses this need, and provides efficient control of sound radiation from local ''hot spots'' of acoustic intensity. Using smart materials, the aircraft trim panels can be converted into lightweight, low-profile acoustic control sources which require no additional cabin space.[16,17] These sources can be clustered in front of radiating boundaries to control local structural radiation and distributed along the cabin walls to function as traditional ANC control sources. This strategy is termed acoustic boundary control (ABC). It is demonstrated in this work that the method by which ABC sources suppress radiation from a vibrating boundary is by actively canceling the ''near-field radiation'' before it enters the enclosure.

Acoustic boundary control shall be implemented by using a collection of piecewise smooth velocity sources, resulting in a potentially large number of control inputs. Because of the economic consideration, it is important to limit the number of control inputs. To do so, the authors propose grouping actuators through an off-line analysis of the control problem. By calculating actuator groups off-line, the dimension of the real-time controller can be reduced. The trade-off for this cost savings is a reduction in the degrees of freedom of the real-time control system, which can lead to a decrease in control performance. The goal of this work is to identify under what conditions actuator grouping may be successful,

a)Author to whom correspondence should be addressed.

by studying the performance of an active control system with estimated optimal control solutions.

In Sec. I, the proposed ABC method is described and some issues of the hardware for implementing the control are discussed. Preliminary issues relevant to the actuator grouping concept are presented in Sec. II. The results of numerical studies of steady-state frequency-domain optimal control with ABC and actuator grouping are presented in Sec. III. First, the ability of two ABC systems and an ANC system to control a simple acoustic field are compared, demonstrating the control behavior of ABC. As a preliminary feasibility analysis of the proposed actuator grouping strategy, the behavior of the optimal control solution for an ABC system is studied. The results of this study are used to develop a simple linear interpolation scheme for actuator grouping. The results of this paper are summarized in Sec. IV.

I. THE ABC METHOD

Motivated by the success of structural acoustic control systems for interior noise suppression and the low power consumption associated with acoustic control sources, the authors propose placing a distributed array of secondary acoustic sources at the structural–acoustic interface. This boundary control array may consist of a large number of acoustic point sources such as speakers, or a distributed acoustic actuation mechanism made of advanced smart materials. Specifically, actively controlled trim panels and low-profile piezoelectric speakers are being considered for this application.[16–18] In the present paper, a simple configuration is used to demonstrate the effectiveness of the method. The optimal control problem with ABC is now formulated.

Consider a reduced form of the Kirchhoff–Helmholtz integral for a harmonic sound field generated by M vibrating sources on the acoustic boundary:[19]

$$p(\mathbf{r})=\sum_{i=1}^{M}\int_{S_i} j\omega\rho\nu_n(\mathbf{r}_s)G(\mathbf{r},\mathbf{r}_s)dS(\mathbf{r}_s)+p_d(\mathbf{r}),\quad \mathbf{r}\in V, \tag{1}$$

where distance from the origin to a point within the domain V and to a point on the boundary $S=\cup_i S_i$ is indicated by $\mathbf{r}$ and $\mathbf{r}_s$, respectively. S_i forms an acoustic control element, G is the Green's function of the wave equation defined on V, ρ is the air density, p is the pressure distribution, ν_n is the normal velocity of the control source on the boundary, and p_d is the pressure distribution due to other disturbances. Note that the dependence on frequency ω is omitted in all functions for brevity. The Green's function for a system with orthogonal eigenfunctions $\phi_{\hat{n}}(\mathbf{r})$ can be expressed as

$$G(\mathbf{r}|\mathbf{r}_s)=\sum_{\hat{n}=0}^{\infty}\frac{\phi_{\hat{n}}(\mathbf{r}_s)}{k_{\hat{n}}^2-k^2}\phi_{\hat{n}}(\mathbf{r}), \tag{2}$$

where c is the speed of sound in air, $k=\omega/c$ is the acoustic wave number, and $k_{\hat{n}}$ is the wave number associated with $\phi_{\hat{n}}(\mathbf{r})$.

For simplicity in illustrating the method, we assume that each of the M acoustic control elements consists of a piston having a uniform normal velocity ν_n, which is a complex constant. Define a volume velocity as $q_n^i=\nu_n^i S_i$, where ν_n^i is the linear velocity and S_i is the area of the ith control piston. The pressure distribution can be expressed in a compact form in terms of the volume velocity and acoustic transfer impedance of the control sources as

$$p(\mathbf{r})=\mathbf{z}^T(\mathbf{r})\mathbf{q}+p_d(\mathbf{r}),\quad \mathbf{r}\in V, \tag{3}$$

where

$$\mathbf{q}=\{q_n^1,q_n^2,\ldots,q_n^M\}^T,$$
$$\mathbf{z}(\mathbf{r})=\left\{\frac{1}{S_i}\int_{S_i} j\omega\rho G(\mathbf{r},\mathbf{r}_s)dS(\mathbf{r}_s)\right\}_{M\times 1},\quad \mathbf{r}\in V. \tag{4}$$

The dynamics of a control element is determined in terms of its compliance as follows,

$$\mathbf{q}=\mathbf{H}(\mathbf{u}+\overline{\mathbf{p}}), \tag{5}$$

where $\mathbf{u}$ is the control force vector acting on the array of the pistons, $\mathbf{H}$ is a diagonal matrix consisting of the compliance of each control element, and $\overline{\mathbf{p}}$ is a force vector due to the pressure acting on the pistons defined by

$$\overline{\mathbf{p}}=\left\{\int_{S_i} p(\mathbf{r}_s)dS(\mathbf{r}_s)\right\}_{M\times 1}. \tag{6}$$

By using Eqs. (3) and (6), we can rewrite Eq. (5) as

$$\mathbf{q}=\mathbf{C}(\mathbf{u}+\overline{\mathbf{p}}_d), \tag{7}$$

where

$$\mathbf{C}_{M\times M}=(\mathbf{I}-\mathbf{HZ})^{-1}\mathbf{H},$$
$$\mathbf{Z}_{M\times M}=\left\{\int_{S_i} z_j(\mathbf{r}_s)dS(\mathbf{r}_s)\right\},$$
$$\overline{\mathbf{p}}_d=\left\{\int_{S_i} p_d(\mathbf{r}_s)dS(\mathbf{r}_s)\right\}_{M\times 1}, \tag{8}$$

and z_j is the jth element of $\mathbf{z}(\mathbf{r})$. $\mathbf{Z}$ involves an integration of the Green's function, which is singular at $\mathbf{r}=\mathbf{r}_s$. However, because of the Dirac delta-type nature of the singularity, the integral is well defined.

For interior noise control, one would like to minimize a global measure of the sound field. A common measure is the total potential energy of the sound field. The following performance index (cost function) is proportional to the total potential energy:

$$J=\int_V p(\mathbf{r})p^*(\mathbf{r})dV. \tag{9}$$

Inserting Eq. (3) into Eq. (9), and making use of the control element dynamics [Eq. (7)], J can be expressed in a standard quadratic form as

$$J=\mathbf{q}^H\mathbf{B}\mathbf{q}+\mathbf{q}^H\mathbf{b}+\mathbf{b}^H\mathbf{q}+J_0=\mathbf{u}^H\mathbf{A}\mathbf{u}+\mathbf{u}^H\mathbf{a}+\mathbf{a}^H\mathbf{u}+J_1, \tag{10}$$

where

$$\mathbf{B}=\int_V \mathbf{z}^*(\mathbf{r})\mathbf{z}^T(\mathbf{r})dV, \quad \mathbf{b}=\int_V \mathbf{z}(\mathbf{r})p_d(\mathbf{r})dV,$$

$$J_0=\int_V p_d(\mathbf{r})p_d^*(\mathbf{r})dV,$$

$$\mathbf{A}=\mathbf{C}^H\mathbf{B}\mathbf{C}, \quad \mathbf{a}=\mathbf{C}^H\mathbf{b}+\mathbf{A}\overline{\mathbf{p}}_d, \tag{11}$$

$$J_1=J_0+\overline{\mathbf{p}}_d^H\mathbf{A}\overline{\mathbf{p}}_d+\overline{\mathbf{p}}_d^H\mathbf{C}^H\mathbf{b}+\mathbf{b}^H\mathbf{C}\overline{\mathbf{p}}_d.$$

An optimal control vector which minimizes the performance index can be determined as

$$\mathbf{u}_{\text{opt}}=-\mathbf{A}^+\mathbf{a}, \quad \text{or} \quad \mathbf{q}_{\text{opt}}=-\mathbf{B}^+\mathbf{b}, \tag{12}$$

where $\mathbf{A}^+$ denotes the pseudo inverse of the matrix. In real-time applications, the optimal control vector can be obtained by using an adaptive algorithm such as least-mean-square.[20] Real-time issues are not discussed in this paper. Note that $\mathbf{B}=\mathbf{B}^H$ and $\mathbf{A}=\mathbf{A}^H$. When $\mathbf{C}$ is nonsingular, it can be shown that the inverse of $\mathbf{A}$ exists and that the optimal performance index is given by

$$J_{\text{opt}}=J_0-\mathbf{b}^H\mathbf{B}^{-1}\mathbf{b}. \tag{13}$$

The optimal performance index in this case is independent of $\mathbf{C}$, which includes the reverse acoustic loading on the control pistons.

In the above formulation, $\mathbf{B}$ is primarily determined by the transfer impedance $\mathbf{z}(\mathbf{r})$. $\mathbf{z}(\mathbf{r})$ is in turn determined by the Green's function of the enclosure and the placement and size of the control pistons. The matrix $\mathbf{HZ}$ describes the acoustic–actuator interaction. If $\mathbf{Z}$, the reverse acoustic loading on the control pistons, is neglected, the matrix ($\mathbf{I}$-$\mathbf{HZ}$) becomes a unit matrix $\mathbf{I}$. Then $\mathbf{q}=\mathbf{H}\mathbf{u}$ and $\mathbf{A}_s=\mathbf{H}^H\mathbf{B}\mathbf{H}$. On the other hand, when the acoustic medium and the control pistons are matched in impedance such that ($\mathbf{I}$-$\mathbf{HZ}$) is nearly singular, a small $\mathbf{u}$ will deliver a large volume velocity $\mathbf{q}$. Since the reverse acoustic loading becomes significant under this condition, actuator hardware design should take this factor into account. There is an optimization issue in the piston design for maximum acoustic power transfer, which will be studied in the future. It should be pointed out again that when $\mathbf{C}$ is nonsingular, the optimal control performance index is not affected by the reverse acoustic loading.

The cost function in Eq. (9) represents a physically unrealizable measure, but serves as an effective benchmark for numerical studies of active control applications. Instead of minimizing the squared pressure over the entire domain (global control), one can define a cost function as the squared pressure measured at L error sensors, located at $\mathbf{r}_l$ (sensor control):

$$J_s=\sum_{l=1}^{L} p(\mathbf{r}_l)p^*(\mathbf{r}_l)=\mathbf{q}^H\mathbf{B}_s\mathbf{q}+\mathbf{q}^H\mathbf{b}_s+\mathbf{b}_s^H\mathbf{q}+J_{0s}$$
$$=\mathbf{u}^H\mathbf{A}_s\mathbf{u}+\mathbf{u}^H\mathbf{a}_s+\mathbf{a}_s^H\mathbf{u}+J_{1s}, \tag{14}$$

where

$$\mathbf{B}_s=\sum_{l=1}^{L} \mathbf{z}^*(\mathbf{r}_l)\mathbf{z}^T(\mathbf{r}_l), \quad \mathbf{b}_s=\sum_{l=1}^{L} \mathbf{z}^*(\mathbf{r}_l)p_d(\mathbf{r}_l),$$

$$J_{0s}=\sum_{l=1}^{L} p_d(\mathbf{r}_l)p_d^*(\mathbf{r}_l),$$

$$\mathbf{A}_s=\mathbf{C}^H\mathbf{B}_s\mathbf{C}, \quad \mathbf{a}_s=\mathbf{C}^H\mathbf{b}_s+\mathbf{A}_s\overline{\mathbf{p}}_d, \tag{15}$$

$$J_{1s}=J_{0s}+\overline{\mathbf{p}}_d^H\mathbf{A}_s\overline{\mathbf{p}}_d+\overline{\mathbf{p}}_d^H\mathbf{C}^H\mathbf{b}_s+\mathbf{b}_s^H\mathbf{C}\overline{\mathbf{p}}_d.$$

A well-designed sensor system will render J_s proportional to J.[21]

II. ACTUATOR GROUPING

There is an interest in development of an actuator grouping strategy which will reduce the dimensionality of active noise control systems. The proposed approach is to take advantage of knowledge of the control system which can be obtained off-line to reduce the real-time computational requirements.

Consider the problem of active noise control in an enclosure. The optimal control inputs are related to the spatial wave-number distribution because the controls are determined such that they can create a sound field to match the primary noise both in time domain and in space.[22] Ideally, one should make use of wave-number information for actuator grouping. The spatial wave-number distribution in an enclosure may depend on many variables, such as the frequency of excitation, the relative phase of excitation sources, or the ambient temperature. As a simplification for this study, it is assumed that the driving frequency and relative phase of the disturbances vary while all other variables are fixed. A simplistic actuator grouping scheme in the frequency-phase domain is thus proposed. The steady-state control inputs are calculated and stored off-line (using the quadratic optimization outlined in Sec. I) as a function of the excitation frequency and relative phase of the disturbance sources. Active control is then implemented by recalling the appropriate stored set of control inputs for the given operating conditions. A two-dimensional linear interpolation is used to compute the actuator group (control inputs) for frequency-phase pairs at which the actuator group is not known.

Because any actuator grouping algorithm will introduce a deviation from the true optimal control vector, it is important to first consider the sensitivity of the control performance to these deviations. Consider a small deviation in the optimal control solution, as may be introduced through actuator grouping. Let the estimated control vector be

$$\hat{\mathbf{u}}_{\text{opt}}=\mathbf{u}_{\text{opt}}+\mathbf{v}, \quad \|\mathbf{v}\|\ll\|\mathbf{u}_{\text{opt}}\|, \tag{16}$$

where $\mathbf{v}$ is a complex vector of length M. Inserting the estimated control vector into the cost function for sensor control [Eq. (14)] yields a performance loss due to control vector estimation as

$$\hat{J}_{\text{opt}}-J_{\text{opt}}=\mathbf{v}^H\mathbf{A}_s\mathbf{v}. \tag{17}$$

For a system with more sensors than actuators, $\mathbf{A}_s$ will likely be nonsingular. In many physical systems, though, $\mathbf{A}_s$ may

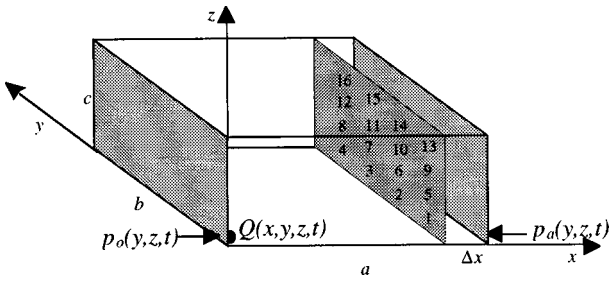

FIG. 1. Geometry of a three-dimensional enclosure.

be ill-conditioned. This is typical when the physical system contains a large number of modes in a wide range of frequencies. The condition number of $\mathbf{A}_s$, i.e., the ratio of the largest eigenvalue λ_1 to the smallest eigenvalue λ_M, can be very large, and $\mathbf{A}_s$ can have nearly zero eigenvalues. In this case, a small $\mathbf{v}$ can cause a large performance loss. Hence large condition numbers and near zero eigenvalues of $\mathbf{A}_s$ can make the system performance measure J very sensitive to errors in the optimal control vector. A more detailed analysis is presented elsewhere.

One way to reduce the condition number and increase the value of the near zero eigenvalues of $\mathbf{A}_s$ is to consider the following control performance index with actuator weighting:

$$J_u=\sum_{l=1}^{L} p(\mathbf{r}_l)p^*(\mathbf{r}_l)+\alpha\mathbf{u}^H\mathbf{u}$$

$$=\mathbf{u}^H(\mathbf{A}_s+\alpha\mathbf{I})\mathbf{u}+\mathbf{u}^H\mathbf{a}_s+\mathbf{a}_s^H\mathbf{u}+J_{0s}, \quad \alpha>0. \tag{18}$$

Note that the resulting time domain LMS algorithm associated with this performance index is the leaky LMS.[20] One can show that for this optimal control with actuator weighting,

$$\overline{\mathbf{A}}_s=\mathbf{A}_s+\alpha\mathbf{I}, \quad \overline{\mathbf{u}}_{\text{opt}}=-(\overline{\mathbf{A}}_s)^+\mathbf{a}_s. \tag{19}$$

By choosing α appropriately ($\lambda_1>\alpha\gg\lambda_M$), one can thus reduce the effects of errors in the optimal control vector on control performance.

III. NUMERICAL RESULTS

This section presents results of numerical simulations comparing the performance of the ABC method with a more traditional active noise control approach of scattering sources throughout an enclosure. The goals of this section are to demonstrate the effectiveness of ABC and to find out under what conditions an actuator grouping strategy may work.

The experimental geometry is a rigid-walled three-dimensional rectangular enclosure as shown in Fig. 1 with dimensions $(a,b,c)=(1.1,1.2,1.3)$ m along the x, y, and z directions, respectively. The end walls at $x=0$, a are simply supported 1-in.-thick aluminum panels, each excited by a 3000 N point force located at $(y,z)=0.01^*(a,b)$. These vibrating boundaries radiate sound into the enclosure. An acoustic source of 3000 m^3/s is placed in the corner at $(x,y,z)=0.01^*(a,b,c)$. The corner locations of the disturbance force and the acoustic source are chosen in order to excite as many system modes as possible. The source amplitudes are chosen such that each source generates similar pressure levels on average throughout the spatial domain. The computations utilize the Kirchhoff–Helmholtz integral for the harmonic sound field in a three-dimensional enclosure[19] and the quadratic forms of performance measures stated in Eqs. (10) and (18).

TABLE I. Coordinates of ANC control sources.

x/a (m)	y/b (m)	z/c (m)
0.2807	0.0219	0.4330
0.6551	0.4869	0.3310
0.1684	0.7708	0.2424
0.0505	0.0663	0.6665
0.2116	0.2978	0.8958
0.0958	0.9464	0.2083
0.7566	0.4240	0.6872
0.6307	0.6837	0.6300
0.9618	0.0712	0.6057
0.5642	0.8115	0.7920
0.6198	0.8592	0.3647
0.6136	0.0925	0.9101
0	0	1
0	1	1
1	0	1
1	1	1

The model is designed as a loose approximation of the noise control problem in business jets. The transmission of noise and vibration from the engines is often higher over some parts of the fuselage than others, leading to local ''hot spots'' of acoustic intensity radiated from the fuselage into the cabin. This behavior is represented in the model by the vibration of the walls at the ends of the enclosure. The noise field in a business jet cabin is due to many other sources, such as the air-conditioning system and aerodynamic loading of the fuselage. A single point source far from control sources is included in the model to mimic these remaining sources. The objective is to investigate the ability of the ABC configuration to cancel the sound due to the interior acoustic source and to the acoustic radiation from the structural sources.

Three configurations of control sources are considered. The first two follow the ABC strategy: a 4×4 array of acoustic pistons is placed over the vibrating boundary at either $x=0$ or $x=a$. The centers of the pistons are located at $y=0.2b$, $0.4b$, $0.6b$, $0.8b$ and $z=0.2c$, $0.4c$, $0.6c$, $0.8c$. The second typifies a traditional ANC implementation: four loudspeakers (modeled as acoustic point sources) are placed at corners of the enclosure; 12 more are scattered randomly throughout the enclosure. The coordinates for the 16 ANC sources are shown in Table I. Each piston is modeled as an 8-in.-square ideal velocity source, meaning that $\mathbf{H}$ is a constant gain matrix. Optimal steady-state control of a harmonic system, as outlined in the previous section, is employed.

The first part of this section compares the optimal control performance of the three control source configurations. The second part studies two issues relevant to the proposed actuator grouping strategy.

A. Control performance

Two numerical experiments are performed to demonstrate the ability of the ABC method to suppress ''near-field

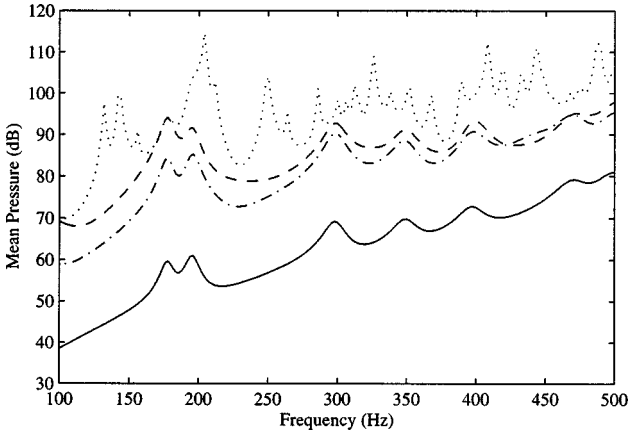

FIG. 2. The mean acoustic pressure in the three-dimensional enclosure with a primary sound field due to one vibrating boundary. Dotted line: before control. Solid line: after control, ABC-1. Dashed-dotted line: after control, ANC. Dashed line: after control, ABC-2.

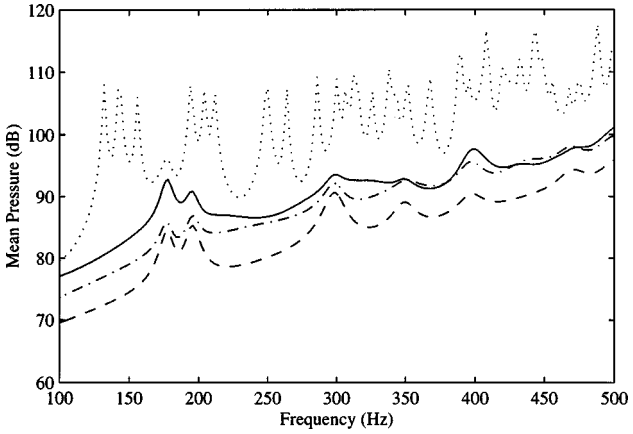

FIG. 3. The mean acoustic pressure in the three-dimensional enclosure with a primary sound field due to an internal acoustic source and two vibrating boundaries. Dotted line: before control. Solid line: after control, ABC-1. Dashed-dotted line: after control, ANC. Dashed line: after control, ABC-1 and ANC.

radiation'' from the vibrating structure, i.e., its nature of ''boundary control.'' In the first experiment, the only noise source included in the model is the vibrating boundary at $x=a$. In the second, the primary disturbance is generated by the vibration of the boundaries at $x=0$ and $x=a$ and the interior acoustic source. If the method by which acoustic boundary control cancels noise from a radiating boundary is in fact boundary control, one would expect ABC with the control source array located at the vibrating boundary (henceforth referred to as ABC-1) to outperform the other ABC array (distant from the disturbance source, ABC-2) and ANC in the first experiment, but not necessarily in the second experiment. In both experiments, the cost function is defined as the spatially averaged squared pressure [global control, based on Eq. (9)].

Figure 2 shows the mean pressure in the enclosure before and after optimal control is applied when the primary sound field in the enclosure is due only to radiation from the vibrating boundary at $x=a$. Throughout this section, ''mean pressure'' denotes the root-mean-squared pressure which has been spatially averaged over the entire volume. The best control performance is due to ABC-1, with the array located directly in front of the vibrating boundary. The very high attenuation levels are similar to that achievable by direct actuation on the vibrating structure. One of the advantages of noise cancellation with acoustic sources is that since the actuators act directly on the acoustic medium, the actuator impedance can be optimized so that less power of the controller will be needed to achieve a given level of noise reduction as compared to structural controls. This arises from the fact that the air does not contain much acoustic energy even when the noise level is high. The ANC system performs well, but not as effectively as the ABC configuration in front of the vibrating boundary. The ABC configuration far away from the vibrating boundary is seen to perform worse than the other two systems. This configuration is included to demonstrate that when an ABC array is placed in front of a vibrating boundary, the method by which it controls the radiated sound is control of the ''near-field radiation,'' while an ABC array away from a vibrating boundary functions as a traditional ANC system.

The results of the second experiment are presented in Fig. 3. In this experiment, the primary sound field is generated by the interior acoustic source and by vibrating boundaries at $x=0$ and at $x=a$. All sources are driven in phase. Only the ANC system and the ABC array at $x=a$ are considered. Significant reductions in mean pressure are observed with both methods. In general, the ANC system leads to greater attenuation than the ABC system due to its ability to couple more efficiently into the global acoustic space. The different abilities of these two control configurations suggest that significant benefits could be realized by combining the two strategies. The combined control system (using the 16 ANC actuators and the 16 ABC actuators) is observed to significantly improve on the performance of either system working independently over the frequency spectrum presented.

B. Actuator grouping study

In this section, the relationship between the optimal control inputs and the frequency and relative phase of the disturbance sources is studied. It is desired that this relationship be smooth, to allow for accurate reproduction of actuator groups with a small set of stored values. Next, the linear interpolation scheme for recalling actuator groups is implemented, and the performance results are compared with those achieved with the exact optimal control solution. It should be reiterated that this study intends only to find out when an actuator grouping scheme may work.

For the remainder of this work, the ABC array at the $x=a$ boundary is used to control the sound field generated by the acoustic point source and the two vibrating boundaries. The phase of the boundary excitation at $x=0$ is allowed to vary relative to the phase of the other two sources. The performance index is chosen as sensor control [Eq. (18)], with actuator weighting given as $\alpha=\lambda_1/100$. Microphone placement is based in part on the nodal placement theorem:[21,23,24] A linear evenly spaced array is placed in each principle

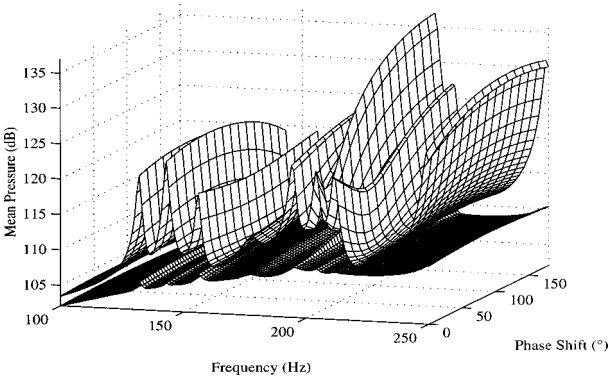

FIG. 4. Variation of the mean sensor pressure in the three-dimensional enclosure as a function of both frequency and the relative phase of the primary sources before and after control.

direction of the enclosure. Specifically, the coordinates of the microphones in these arrays are given as

$$(x,y,z)=([0.2\ \ 0.4\ \ 0.6\ \ 0.8]*a,\ \ 0,\ \ 0),$$

$$(x,y,z)=(0,[0.2\ \ 0.4\ \ 0.6\ \ 0.8]*b,\ \ 0),$$

$$(x,y,z)=(0,\ \ 0,\ [0.2\ \ 0.4\ \ 0.6\ \ 0.8]*c).$$

Additionally, a single microphone is placed in each corner of the enclosure, for a total of 20 microphones.

1. Spatial characteristics of the optimal control vectors

For an interpolation-based actuator grouping strategy to work, the variation of actuator groups with frequency and phase needs to be smooth so that the estimated actuator groups can be sufficiently accurate in real time. We first consider the cost function (sum of squared pressure from 20 error sensors) because its smoothness is often correlated with that of the optimal control solution. Figure 4 presents the variation in the mean pressure measured at the error sensors with frequency and relative phase of the disturbance sources. The upper curve is the mean sensor pressure before control is applied; the lower curve is the mean sensor pressure after steady-state quadratic optimal control is performed with the ABC array at $x=a$. It is observed that the mean sensor pressure before control varies significantly, but smoothly. Variations are most pronounced near resonance frequencies of both the structural sources and the acoustic enclosure. The active control system leads to a significant smoothing of the measured sound field, greatly reducing the pressure increases associated with the system resonances.

The optimal control solution is calculated as a volume velocity; the corresponding linear stroke for a given piston is computed as the ratio of the optimal volume velocity to the product of piston area and angular frequency (assuming harmonic behavior). The linear stroke and relative phase of a single actuator, as computed for the experiment presented in Fig. 4, are shown in Figs. 5 and 6. The control source phase has been unwrapped in the direction labeled ''Phase Shift.'' The stroke is observed to vary most significantly near resonance frequencies, such as the $(n_y,n_z)=(2,1)$ structural resonance at 178 Hz and the $(n_x,n_y,n_z)=(0,0,1)$ acoustic resonance at 132 Hz. n_i denotes a mode number in the i

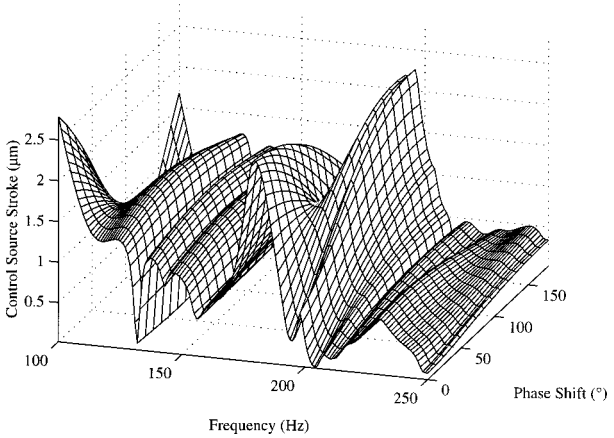

FIG. 5. Variation of the linear stroke of control source No. 10 for optimal control as a function of both frequency and the relative phase of the primary sources.

direction. The variation of the control source phase with frequency is generally smooth. The behavioral trends of this actuator typify that of all of the control sources.

It is interesting to note that one cannot judge the ''importance'' of an actuator simply based on the magnitude of its stroke required for optimal control. It is necessary to consider the coupling of the actuator with the enclosure to determine its contribution to the controlled sound field. For example, an actuator may have a very large stroke at a given frequency, but have little influence on the sound field because it is located near a pressure node. Conversely, an actuator with a small stroke located near a local pressure maximum could be extremely important. Due to the interaction of the pressure fields produced by each actuator, it is difficult to isolate the significance of a single actuator for control performance. The acoustic impedance on the surface of the pistons may be a better way to judge the importance of the actuators.[25–27]

2. Actuator grouping by linear interpolation

Having studied the variation of the optimal control vectors, we now explore this property for the actuator grouping study. As in the previous section, the phase of the boundary

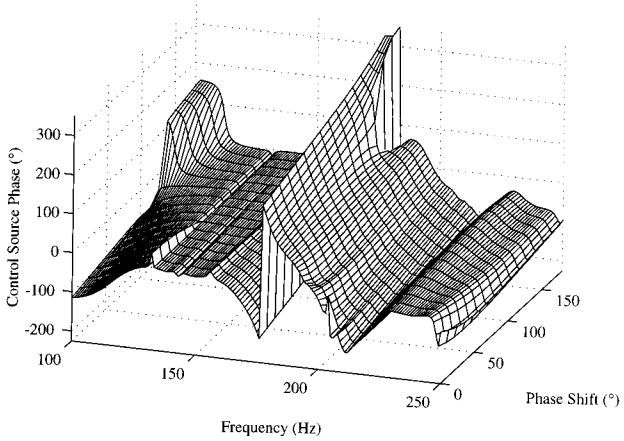

FIG. 6. Variation of the phase of control source No. 10 for optimal control as a function of both frequency and the relative phase of the primary sources.

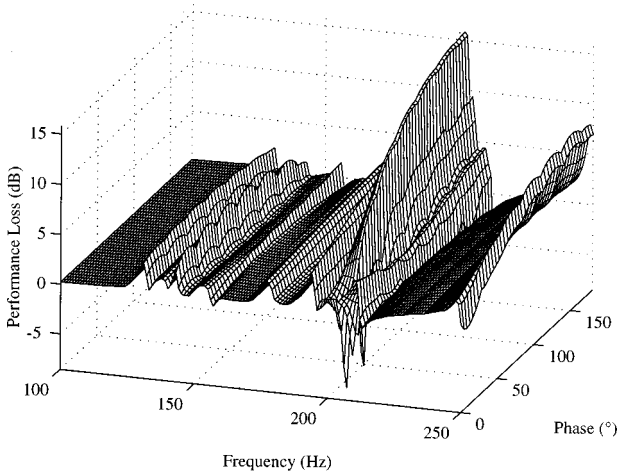

FIG. 7. The performance loss index of the interpolated optimal controls. The spacing is 8 Hz and 28°.

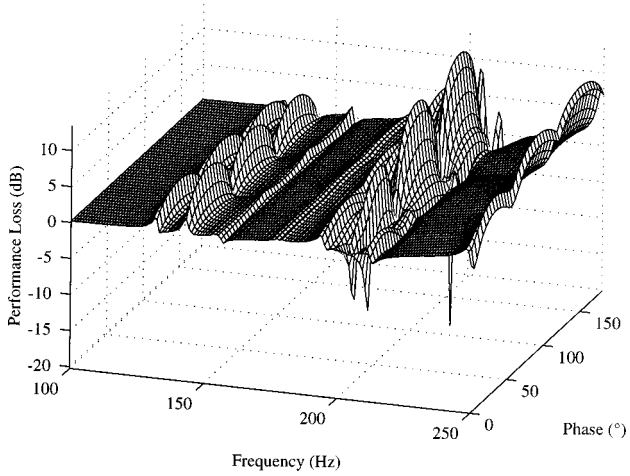

FIG. 8. The performance loss index of the interpolated optimal controls. The spacing is 2 Hz and 60°.

excitation at $x=0$ is varied relative to the phase of the other two sources. Again, the cost function is the mean-squared pressure measured at 20 microphones with actuator weighting $\alpha=\lambda_1/100$, and the control sources are the ABC array along the $x=a$ boundary.

The results of three numerical experiments are presented which study the ability of a two-dimensional linear interpolation to sufficiently approximate the actuator groups over a range of frequencies and relative phases of the primary sources. The first experiment does not use actuator grouping; this is the baseline to which the other two experiments will be compared. In this experiment, the control signal is the exact optimal control signal determined by steady-state quadratic optimization at the precise frequency and relative phase of the disturbance sources. The other two experiments determine the control signal by two-dimensional linear interpolation within a table of recorded actuator groups. In the first experiment, the actuator groups have been identified in increments of 8 Hz from 100 to 250 Hz and 28° as the phase of one disturbance source varies from 0° to 180° relative to the other sources. The second experiment is identical, except that the resolutions are 2 Hz and 60°. Note that the data at the edges of the frequency-phase domain are always included (specifically, 250 Hz and 180°).

To quantify the possible performance degradation due to control signal approximation, we define a performance loss index as the difference between attenuation of the mean pressure at the error sensors achieved with the exact control vectors and that achieved with the interpolated control vectors. Large values of the performance loss index indicate that the interpolation has not produced an adequate estimate of the exact control vector. The performance loss for the second and third experiments is shown in Figs. 7 and 8, respectively. Negative performance loss values are possible due to the use of actuator weighting in the cost function.

As predicted from the previous result that the optimal control signal varies most rapidly near system resonance frequencies, the performance loss is greatest near these frequencies. It is observed that away from resonance frequencies, a very small set of stored actuator groups is sufficient to preserve control performance. For example, the performance loss associated with storing the actuator groups in increments of 8 Hz and 28° is insignificant (<0.6 dB) over the range from 100 to 124 Hz, through which there are no system resonances. As the modal density increases, the optimal control signal varies more rapidly, leading to an increased performance loss. This is most evident in the neighborhood of 200 Hz. The acoustic resonances nearest the frequency are 194 Hz (0,1,1), 204 Hz (1,0,1), and 212 Hz (1,1,); the (1,2) structural resonance is at 195 Hz. This region is best characterized as being very sensitive to errors in the control solution, as the performance loss reaches appreciable negative values as well as large positive values.

Additional experiments have been performed over a range of resolutions of the stored data. Frequency resolutions of 2, 4, 8, and 12 Hz and phase resolutions of 4°, 8°, 16°, 28°, 60°, and 92° are considered. The maximum value of performance loss over the ranges 100–150 Hz and 151–250 Hz are calculated for each trial; these results are presented in Figs. 9 and 10, respectively. An increase in phase resolution up to 28° is observed to have little adverse effect on control

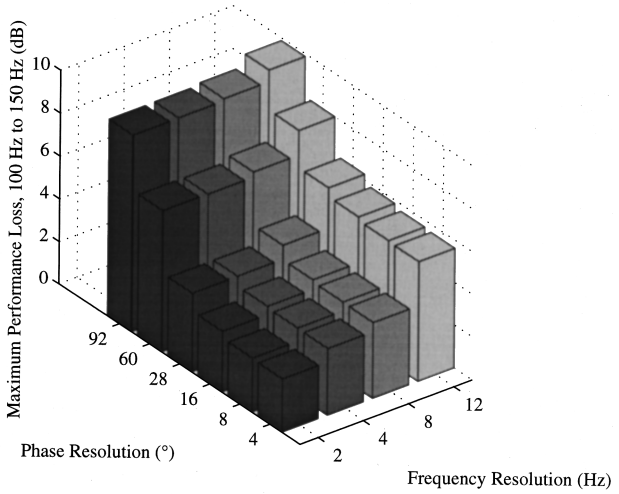

FIG. 9. Maximum value of performance loss from 100 through 150 Hz resulting from linear interpolation among actuator groups stored over a range of resolutions of disturbance source frequency and relative phase. The results cover a region of low modal density of the enclosure.

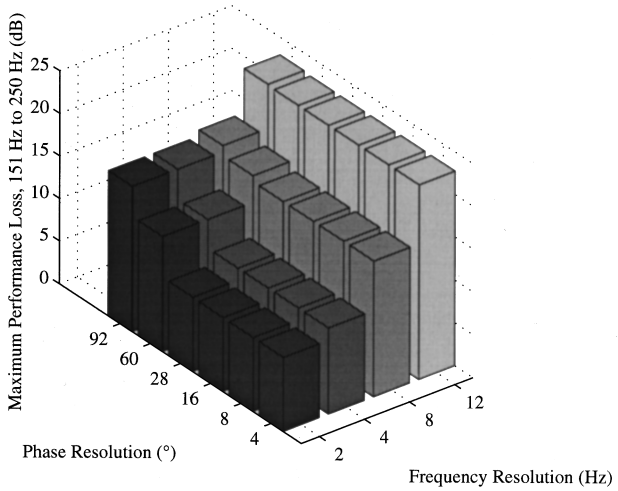

FIG. 10. Maximum value of performance loss from 151 through 250 Hz resulting from linear interpolation among actuator groups stored over a range of resolutions of disturbance source frequency and relative phase. The results cover a region of high modal density of the enclosure.

performance. Data storage with a phase resolution of 28° requires the computation of eight actuator groups for every frequency. The frequency resolution must be chosen with regard to the system behavior near the frequencies over which control is to be applied. Consider, for example, control of the primary engine tone in a business jet. If this tone does not sufficiently excite any system resonances, the results of this study suggest that a small set of actuator groups around this frequency will suffice for this actuator grouping strategy. If, on the other hand, the tone does excite system resonances, a much larger set of actuator groups may need to be computed.

In summary, we conclude that the linear interpolation scheme for grouping actuators based on the previously identified optimal control vectors is sufficient for the frequencies away from the system resonance frequencies. Near resonance frequencies, either a high resolution of the known optimal control vectors should be maintained or a more sophisticated interpolation scheme, such as a neural network, should be used. To develop a grouping scheme which can take into account other effects such as temperature, one needs to have a broader database of optimal control vectors and a robust interpolation scheme. This is a subject of on-going research. The goal is to develop a grouping strategy which takes the error sensor signals as input and selects the grouping of the actuators on-line.

IV. CONCLUSIONS

A new strategy for the placement of ANC actuators, termed acoustic boundary control (ABC), is presented. It is demonstrated through numerical simulations that the method by which ABC sources control radiation from a boundary is active cancellation of ''near-field radiation'' before it enters the enclosure, similar to the behavior of a structural control system. A combination of ABC arrays over local ''hot-spots'' of acoustic intensity and control actuators distributed throughout an enclosure is shown to be an effective actuator configuration for controlling interior sound field. The sensitivity of control performance to deviations in the optimal control vector is studied to find out when an actuator grouping scheme may work. An actuator grouping strategy which utilizes linear interpolation is studied. A preliminary study of this strategy suggests that linear interpolation among a small set of optimal stored actuator groups may provide adequate control performance for disturbances at most frequencies, but that a more complex strategy or much larger set of actuator groups may be required at frequencies near system resonances.

ACKNOWLEDGMENTS

This work was supported in part by a grant (CMS-9634672) from the National Science Foundation, and a grant from the State of Delaware Research Partnership program and Lord Corporation. We would also like to acknowledge the support for S. M. Hirsch by the Delaware Space Grant College Fellowship Program.

[1] K. K. Ahuja and J. C. Stevens, ''Recent advances in active noise control,'' AIAA J. **29**, 1058–1067 (1990).
[2] C. R. Fuller and A. H. von Flotow, ''Active control of sound and vibration,'' IEEE Control Syst. **15**, 9–19 (1995).
[3] G. Miccoli and A. Concilio, ''Recent advances in noise and vibration active control by means of piezoelectric transducers,'' in *Proceedings of the 3rd International Congress on Air- and Structure-borne Sound and Vibration*, edited by M. L. Crocker (International Scientific Publications, 1994), pp. 1377–1384.
[4] C. Ross, ''Current developments and future trends in active noise control,'' Noise Vib. Control Worldwide **20**, 171–173 (1989).
[5] J. Tichy, ''Current and future issues of active noise control,'' J. Acoust. Soc. Jpn. (E) **12**, 255–262 (1991).
[6] F. W. Grosveld, T. J. Coats, H. C. Lester, and R. J. Silcox, ''Numerical study of active structural acoustic control in a stiffened, double wall cylinder,'' in *Proceedings of the National Conference on Noise Control Engineering*, edited by J. M. Cuschieri, S. A. L. Glegs, and D. M. Yeager (Noise Control Foundation, Poughkeepsie, NY, 1994), pp. 403–408.
[7] R. J. Silcox, K. H. Lyle, V. L. Metcalf, and D. E. Brown, ''A study of active structural acoustic control applied to the trim panels of a large scale fuselage model,'' in *Proceedings of the First Joint CEAS/AIAA Aeroacoustics Conference* (Deutsche Gesellschaft fuer Luft-und Raumfahrt, 1995), pp. 1095–1104.
[8] R. L. St. Pierre, Jr., W. Chen, and G. H. Koopmann, ''Design of adaptive panels with high transmission loss characteristics,'' Proceedings of ASME Winter Annual Meeting (1995).
[9] D. R. Thomas, P. A. Nelson, S. J. Elliott, and R. J. Pinnington, ''Experimental investigation into the active control of sound transmission through stiff light composite panels,'' Noise Control Eng. J. **41**, 273–279 (1993).
[10] K. A. Burgemeister and C. H. Hansen, ''Use of a secondary perforated panel to actively control the sound radiated by a heavy structure,'' Proceedings of the ASME Winter Conference (1993).
[11] J. Pan, C. H. Hansen, and D. A. Bies, ''Use of a perforated panel for active control of sound radiated from vibrating structures, I. Low-frequency analysis,'' J. Sound Vib. **156**, 349–359 (1992).
[12] J. Pan and C. H. Hansen, ''Power transmission from a vibrating source through an intermediate flexible panel to a flexible cylinder,'' J. Vib. Acoust. **116**, 496–505 (1994).
[13] B. V. Mason, K. Naghshineh, and G. K. Toth, ''Broadband, wide-area active control of sound radiation from vibrating structures using local surface-mounted radiation suppression devices,'' in *Proceedings of Noise Con*, edited by J. M. Cuschieri, S. A. L. Glegs, and D. M. Yeager (Noise Control Foundation, Poughkeepsie, NY, 1994), pp. 467–472.
[14] B. V. Mason, G. K. Toth, K. Naghshineh, and J. W. Kamman, ''A feedforward controller for active reduction of radiated noise from a uniformly vibrating circular plate,'' Proceedings of ASME Winter Annual Meeting, 95-WA/NCA-8 (1995).
[15] P. Darlington, ''Active boundary control of enclosed sound fields,'' in *Proceedings of Inter-Noise 96* (Institute of Acoustics, London, 1996), pp. 1127–1132.

[16] V. Jayachandran, M. A. Westervelt, N. E. Meyer, and J. Q. Sun, ''Experimental studies of shallow spherical shell piezoceramic actuators as acoustic boundary control elements,'' Smart Mater. Struct. **7** (to be published).
[17] V. Jayachandran, N. E. Meyer, M. A. Westervelt, and J. Q. Sun, ''Piezoelectrically driven speakers for active aircraft interior noise suppression,'' Appl. Acoust. (to be published).
[18] V. Jayachandran and J. Q. Sun, ''Modeling shallow spherical shell piezoceramic actuators as acoustic boundary control elements,'' Smart Mater. Struct. **7**, 72–84 (1998).
[19] F. Fahy, *Sound and Structural Vibration—Radiation, Transmission and Response* (Academic, New York, 1985).
[20] P. A. Nelson and S. J. Elliot, *Active Control of Sound* (Academic, New York, 1992).
[21] J. Q. Sun, S. M. Hirsch, and V. Jayachandran, ''Sensor systems for global vibration and noise control,'' J. Acoust. Soc. Am. **103**, 1504–1509 (1998).
[22] C. R. Fuller and R. A. Burdisso, ''A wavenumber domain approach to the active control of structure-borne sound,'' J. Sound Vib. **148**, 355–360 (1991).
[23] L. Silverberg, ''Conjecture about orthogonal function,'' J. Guid. Control. Dyn. **20**, 198–202 (1996).
[24] L. Weaver, Jr. and L. Silverberg, ''Node control of uniform beams subject to various boundary conditions,'' J. Appl. Mech. **59**, 983–990 (1992).
[25] V. Jayachandran and J. Q. Sun, ''Impedance studies of active interior noise control systems,'' *Proceedings of the Eleventh VPI&SU Symposium on Structural Dynamics and Control*, edited by L. Meirovitch (1997).
[26] V. Jayachandran and J. Q. Sun, ''Impedance characteristics of structural acoustic control for interior noise suppression,'' Proceedings of ASME Sixteenth Biennial Conference on Mechanical Vibration and Noise (1997).
[27] V. Jayachandran and J. Q. Sun, ''Impedance characteristics of active interior noise control systems,'' J. Sound Vib. **211**, 716–727 (1998).

The influence of frequency-shaped cost functionals on the structural acoustic control performance of static, output feedback controllers

G. Clark Smith and Robert L. Clark
Department of Mechanical Engineering and Materials Science, Duke University, Durham, North Carolina 27708-0302

(Received 2 October 1997; accepted for publication 8 June 1998)

This paper investigates the level of modeling necessary to design static, output feedback controllers for structural acoustic control. The *acoustic performance* of three active control techniques is compared: active structural acoustic control (ASAC); active vibration control (AVC); and discrete active vibration control. The ASAC cost functional is created by the use of frequency-dependent models, which relate the structural response to radiated acoustic energy. A broadband measure of control signal power is developed and compensators are designed such that their power requirements are equal. These investigations are conducted on three different transducer arrangements. Results demonstrate that frequency-shaped cost functionals influence the design of frequency-independent controllers when the order of the control system is greater than one. With more than one sensor-actuator pair, the control energy bandwidth is shifted by the ASAC cost functional to provide increased low-frequency performance. © *1998 Acoustical Society of America.* [S0001-4966(98)00510-4]

PACS numbers: 43.40.Vn [PJR]

INTRODUCTION

In many application areas for adaptive structures, it is advantageous to apply feedback control. The primary motivation usually being the lack of a reference signal to implement broadband feedforward control. When applying feedback control, it is also desirable to utilize simple controllers. Control approaches, such as static, output feedback control, offer the potential for greater stability margins and are much easier to realize in hardware than more sophisticated adaptive or dynamic compensators. The primary disadvantage of static, output feedback control is that the compensator's action is fixed as a function of frequency.

If it is accepted that the ease of implementation and stability advantages associated with static, output feedback control outweigh the increased closed-loop performance achieved with dynamic compensation, it then becomes interesting to investigate the level of modeling necessary to implement structural acoustic control. For dynamic controllers it has been recognized that structural acoustic control requires a performance measure related to structural acoustic radiation. Baumann *et al.*[1] used frequency-shaping concepts[2] to develop radiation filters which augment the structural states of a plant model and, thus, proportionally weight each mode in terms of its radiation efficiency. This relates the structural response to the radiated acoustic energy. Their analytical study showed that, with a linear quadratic Gaussian (LQG) control law, radiation filters caused the compensator to focus energy into the frequencies of structural modes most responsible for sound radiation. Recently, Vipperman and Clark[3] have experimentally demonstrated the advantage of including a measure of sound power radiation into the cost functional of a dynamic multivariable feedback control system. Here, the H_2 control law was used for structural acoustic control with sensoriactuators.[4] Since the response of dynamic compensators can vary with frequency, it is understandable how shaping the performance measure as a function of frequency leads to superior results. However, it is unclear if developing frequency-shaped cost functionals for the design of static, output feedback compensators will greatly influence the final closed-loop structural acoustic control performance.

One of the major difficulties associated with comparing different cost functionals is that one compensator design can out-perform the other simply because more control effort is utilized by that compensator. Controllers designed using cost functionals based on different performance measures may employ varying amounts of control effort when all other design parameters have been held constant. In the reference by Baumann *et al.*[1] two performance measures were considered (modal velocity and radiation filter output) and it was noted that a relative weighting between the performance measure and control effort was adjusted such that the total energy used by each compensator was equal. This provided a level basis for the comparison of closed-loop results.

This work compares the structural acoustic control performance of three static, output feedback compensators with equal control signal power requirements. Each compensator is designed to minimize a weighted sum of control effort and one of the following measures: (1) radiated sound power; (2) plate modal velocity; and (3) plate velocity as measured at the center of 12 equal area rectangular sections. The three performance measures correspond to the three commonly referenced active control techniques, respectively: (1) active structural acoustic control (ASAC); (2) active vibration control (AVC); and (3) discrete active vibration control. The main goal of this comparison is to determine if it is necessary to use a measure of sound power radiation when designing

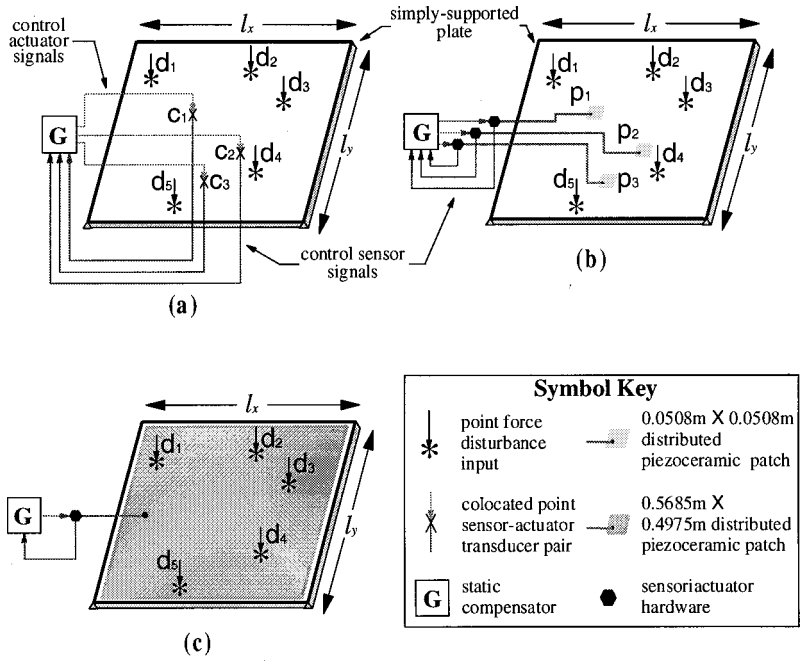

FIG. 1. Simply supported plate test-bed with five point force disturbances and (a) three colocated point sensor-actuator pairs; (b) three small sensoriactuator transducers; and (c) one large sensoriactuator transducer.

static, output feedback controllers for structural acoustic control. To calculate control signal power efficiently, a broadband measure proportional to control signal power usage per unit of input disturbance signal power is developed. As in Ref. 1, control signal power requirements are equalized by appropriately varying the weighting between control effort and the performance measure.

I. MODEL AND CONTROL FORMULATION

The comparison of the three active control techniques is considered on a variety of control system arrangements. As detailed in Fig. 1(a)–(c), the difference between the control systems investigated is the type, number, and size of the transducers applied to a simply supported plate. A description of the structure and three control system arrangements is given here; exact material parameters and dimensions are noted in Sec. II.

The ultimate goal of each control system arrangement is to reduce sound power radiated by the vibrating plate. It is assumed that the plate is located within an infinite baffle, the acoustic radiation of interest is into the half-space above the plate, and the medium above and below the panel is a homogeneous fluid (air) at rest. The plate in this investigation is vibrating due to five broadband, stochastic, point-force, disturbance sources, labeled d_1, d_2, d_3, d_4, and d_5 in Fig. 1(a)–(c). The positions of the disturbance sources are selected arbitrarily and held constant for all compensator design cases and control arrangements.

Figure 1(a) shows the first control system arrangement considered. Here the controller interfaces with the structure through three colocated point velocity sensor-point force actuator pairs, labeled c_1, c_2, and c_3. The positions of the control transducers are also selected arbitrarily and held constant for the three compensator design cases. Figure 1(b) shows the second control system, realized using three small, distributed piezoelectric sensoriactuators.[3,4] Each distributed transducer covers approximately 0.8% of the plate area and is comprised of two surface-bonded rectangular piezoelectric patches placed opposite one another on both sides of the structure and electrically wired out-of-phase. The centers of the three distributed transducers, labeled p_1, p_2, and p_3 in Fig. 1(b), are at the same positions as the point transducers in Fig. 1(a). In Fig. 1(b), each sensor signal is a measure of the rate of strain of the transducer due to the mechanical response of the plate and the actuator signal is voltage applied to the patch. The piezoelectric actuator couples to the plate through line moments at the edges of the patches. The third, and final, control system arrangement investigated is the large distributed piezoelectric sensoriactuator shown in Fig. 1(c). This single distributed transducer covers approximately 90% of the plate area and interfaces with the structure in the same method as the second control system arrangement discussed above.

Each compensator **G** in Fig. 1 is a fully populated, constant, real matrix. Thus in Fig. 1(a) and (b) **G** is a 3×3 matrix. The compensator realized for the single, large sensoriactuator in Fig. 1(c) is a single coefficient.

A. System model

The first step in the analysis of structural acoustic control performance is the derivation of the system model. This is presented here for the radiating plate shown in Fig. 1.

1. Plate model

Using the *assumed-modes method*,[5] the ordinary differential equation describing the plate generalized structural motion is expressed as follows:

$$\ddot{q}_n(t)+2\zeta_n\omega_n\dot{q}_n(t)+\omega_n^2 q_n(t)=Q_n^f(t), \tag{1}$$

where a proportional damping term is included in the model to bound the response on resonance and $Q_n^f(t)$ is the generalized force associated with a point force control or point force disturbance actuator. For this work, the localized mass, stiffness and damping of the point force disturbance sources,

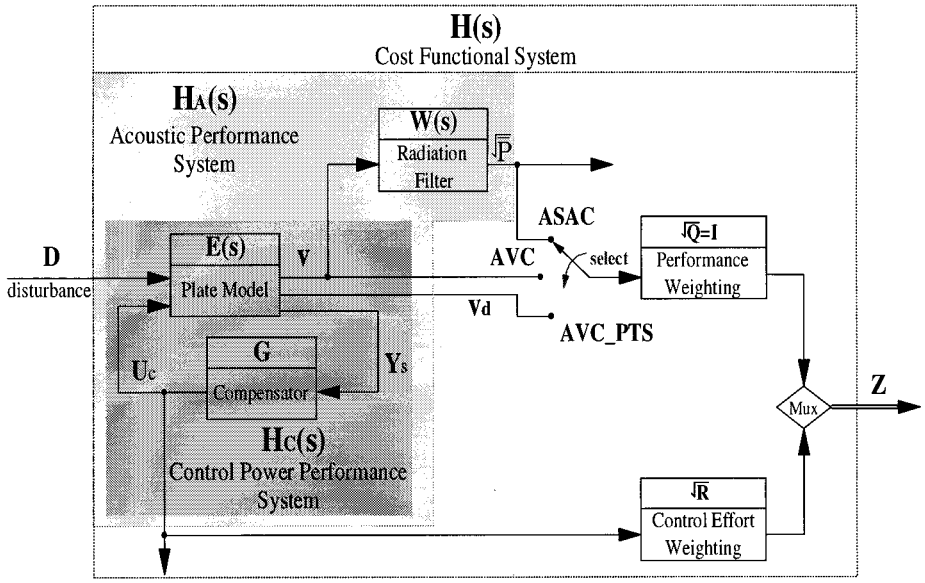

FIG. 2. Block diagram of cost functional and performance systems.

point velocity sensors and point force control actuators are assumed negligible.

The model of the control system arrangement utilizing piezoelectric sensoriactuator transducers is derived according to the techniques presented by Hagood *et al.*[6] The state-space model of a voltage-driven piezostructure is developed using a *Rayleigh–Ritz technique*[5] for coupled electromechanical systems. The localized mass and stiffness effects added by the piezoceramic patches are incorporated in the plate model, assuming simply supported plate eigenfunctions.[6,7] Throughout this investigation the portion of the current which represents the total strain-rate underneath the distributed piezoelectric transducer is assumed directly available to the control system. Implementation issues associated with the sensoriactuator are not considered, but are detailed by Vipperman and Clark in Ref. 3.

2. Structural acoustics

After the modal response of the plate has been characterized, the physics associated with the fluid-structure interaction needs to be developed to form a measure of radiated sound power. This is achieved by realizing frequency-dependent models of the structural acoustic coupling. These models are commonly called *radiation filters* and are used to develop the frequency-shaped cost functional for ASAC. Radiation filters were originally introduced by Baumann *et al.*,[1] and for the purpose of this study, the radiation filters designed by Clark and Cox[8] are utilized.

Assuming that the plate resides within an infinite baffle and radiating into an infinite half-space, an expression which relates the modal surface velocity to the radiated sound power can be written in vector form as

$$\overline{P}(j\omega)=\mathbf{v}(j\omega)\mathbf{M}(j\omega)\mathbf{v}^{H}(j\omega), \tag{2}$$

where $\mathbf{M}$ is the frequency-dependent matrix that defines the interaction of the structural modes in the acoustic field, $\mathbf{v}$ is a vector of modal velocities of the plate as a function of frequency and the superscript H is the Hermitian transpose. The diagonal entries of $\mathbf{M}$ are proportional to the self-radiation efficiencies and the off-diagonal entries are proportional to the mutual radiation efficiencies of the structural modes.[1,9] Expressing the Laplace domain equivalent of $\mathbf{M}(s)$ in terms of a filter and its para-Hermitian conjugate:

$$\tilde{\mathbf{M}}(s)=\mathbf{W}^{T}(-s)\mathbf{W}(s), \tag{3}$$

where $\mathbf{W}(s)$ is the radiation filter. The radiation filter is obtained through *spectral factorization* of $\mathbf{M}(s)$, as outlined by Francis.[10]

B. Performance metrics

In this section, the three cost functionals for compensator design and two quantitative measures used to identify the performance of the closed-loop control systems are discussed.

As detailed in Fig. 2, the *cost functional system*, $H(s)$, is used to form the appropriate weighted sum that is minimized during compensator synthesis. The transfer matrix $H(s)$ is composed of the *acoustic performance system* (shaded portion) and a bank of filters that weight the selected performance measure and control actuator signals. The desired performance measure is selected for each design case by moving the switch between one of the three signals. The frequency-shaped performance signal for the ASAC compensator design is the vector of radiation filter outputs. As presented in Sec. I A 2 and Ref. 8, this vector of signals leads to a measure of sound power, $\sqrt{\overline{P}}$, when averaged (rms). The performance measure for AVC compensator design is a vector of signals $\mathbf{v}$, the plate modal velocities. The discrete active vibration control performance measure is the plate velocity as measured at the center of 12 equal area rectangular sections, $\mathbf{v_d}$. This vector of signals is noted as AVC_PTS in Fig. 2. The discrete measurement locations are determined by

$$(x_i,y_j)=\left(\frac{l_x}{2N_x}(2i-1),\frac{l_y}{2N_y}(2j-1)\right), \tag{4}$$

where $i=1,2,\ldots,N_x$, $j=1,2,\ldots,N_y$, N_x is the number of sensor locations in the x direction and N_y is the number of sensor locations in the y direction.

The selected performance measurement is weighted by a parameter $\sqrt{\mathbf{Q}}$ where, for this work, $\sqrt{\mathbf{Q}}=\mathbf{I}$. For proper compensator design, each feedback control actuator signal, $\mathbf{U}_c$, is weighted by a parameter with a magnitude of $\sqrt{\mathbf{R}}$ where $\sqrt{\mathbf{R}}=R^{1/2}\mathbf{I}$. The parameter R is the specified scalar weighting variable and $\mathbf{I}$ is an appropriately sized identity matrix. Increasing or decreasing R decreases or increases, respectively, the amount of control effort the compensator uses. The two signals are joined into a single output vector, $\mathbf{Z}$, through the use of a multiplexer (Mux). Thus by appending the proper weighting filters to the selected performance measure and calculating the $\mathbf{H}_2$ norm of the cost functional system (discussed below), one obtains a single measure of both control system performance and required control effort. Optimum compensator synthesis involves minimizing this measure.

The equation for the $\mathbf{H}_2$ norm of the multiple-input, multiple-output (MIMO) *cost functional system* is written as

$$\|H\|_2=\left(\mathrm{Tr}\left[\frac{1}{2\pi}\int_{-\infty}^{\infty}H(j\omega)H^*(j\omega)d\omega\right]\right)^{1/2}, \tag{5}$$

where $\mathrm{Tr}[\bullet]$ is the trace operator and $H(j\omega)$ is the frequency response of the linear, time-invariant, stable system $H(s)$.[11] The physical interpretation being that the $\mathbf{H}_2$ norm is the rms value of the outputs when all the inputs are driven concurrently by independent, spectrally white input signals. By Parseval's theorem, the $\mathbf{H}_2$ norm can also be expressed as

$$\|H\|_2=\left(\mathrm{Tr}\left[\int_{-\infty}^{\infty}h(t)h(t)^T dt\right]\right)^{1/2} \tag{6}$$

$$=\left(\sum_{i=1}^{N_z}\sum_{k=1}^{N_w}\|H_{ik}\|_2^2\right)^{1/2}, \tag{7}$$

where $h(t)$ is the impulse matrix of $H(s)$, N_z is the number of performance signals, and N_w is the number of input disturbance signals. Equation (7) shows that the $\mathbf{H}_2$ norm of the MIMO transfer matrix H is the square root of the sum of squares of the $\mathbf{H}_2$ norm of its entries.

Using Eq. (7) and Fig. 2, the three cost functionals for compensator design in this work are written as

$$J_{\mathrm{ASAC}}=\left(\sum_{i=1}^{N_c}\left[\sum_{k=1}^{N_d=5}\int_0^{\infty}RU_{c_i}^k(t)^2\,dt+\int_0^{\infty}\overline{P}_i(t)dt\right]\right)^{1/2}, \tag{8}$$

$$J_{\mathrm{AVC}}=\left(\sum_{i=1}^{N_c}\left[\sum_{k=1}^{N_d=5}\int_0^{\infty}RU_{c_i}^k(t)^2\,dt+\sum_{j=1}^{N_p=N_m}\int_0^{\infty}v_i^j(t)^2dt\right]\right)^{1/2}, \tag{9}$$

$$J_{\mathrm{AVC\_PTS}}=\left(\sum_{i=1}^{N_c}\left[\sum_{k=1}^{N_d=5}\int_0^{\infty}RU_{c_i}^k(t)^2\,dt+\sum_{j=1}^{N_p=(N_x\times N_y)}\int_0^{\infty}(v_d)_i^j(t)^2\,dt\right]\right)^{1/2}, \tag{10}$$

where N_c is the number of control transducers in the respective control system arrangement, N_d is the number of input disturbance signals, N_p is the number of performance signals, $U_{c_i}^k$ is the portion of the ith control signal impulse response due to the kth disturbance, $\overline{P}_i$ is the portion of the radiated acoustic power impulse response due to the ith control signal, v_i^j is the jth modal velocity impulse response due to the ith control signal, and $(v_d)_i^j$ is the center velocity impulse response of the jth area due to the ith control signal. Since R is used to adjust the amount of control signal power, its value will vary for each control system arrangement and compensator design case. Due to the MIMO nature of the physical system, Eqs. (8)–(10) appear complicated, but all have the same basic form of a weighted control signal term added to the desired performance measure.

The two quantitative measures used to identify the performance of the output feedback controllers are also based upon evaluating the $\mathbf{H}_2$ norm of designated transfer matrices. A block diagram of the first transfer matrix is shown as the lightly shaded portion of Fig. 2. Called the *acoustic performance system*, H_A is composed of the plate, radiation filters and output feedback control system. The inputs to H_A are the five point force disturbance signals, D, and the output is the vector of signals proportional to the square root of plate radiated acoustic power. The performance measure based upon the $\mathbf{H}_2$ norm of H_A is the *active insertion loss* (AIL) of the controller.[12] Active insertion loss is defined as the reduction in noise transmission by the installation and use of the output feedback control system:

$$\mathrm{AIL}\equiv 20\,\log_{10}(S_{\mathrm{ol}}/S_{\mathrm{cl}}), \tag{11}$$

where S_{ol} is the $\mathbf{H}_2$ norm of the open-loop acoustic performance system (H_A where $\mathbf{G}=\mathbf{0}$) over the bandwidth of interest, and S_{cl} is the $\mathbf{H}_2$ norm of the closed-loop acoustic performance system over the same bandwidth. Thus positive values of AIL correspond to a reduction in radiated sound power. The second performance system is also designated in Fig. 2. The *control power performance system*, H_C, is the system from the disturbance input signals, D, to the control actuator signals, $\mathbf{U}_c$. The $\mathbf{H}_2$ norm of this transfer matrix forms a broadband measure of the amount of control signal power usage per unit of input disturbance signal power. The reader is encouraged here to understand that the terminology *control signal power* and *disturbance signal power* does not imply that the $\mathbf{H}_2$ norm of H_C has units of physical power for each control system arrangement considered. Historically, the $\mathbf{H}_2$ norm was used when discussing electrical signals of voltage or current and, as with the term *power spectral density*, the ''power'' terminology is a carryover.

C. Optimum output feedback gains

The dual Levine-Athans (DLA) algorithm is used to determine the static, output feedback gain matrix that minimizes the $\mathbf{H}_2$ norm of $H(s)$ in Fig. 2. The cost functional for the DLA algorithm was first described by Levine and Athans[13] and later developed for structural acoustic control by Clark and Cox.[8]

In summary, the procedure for calculating $\mathbf{G}_{\text{opt}}$, the optimal feedback gain matrix, involves first determining an initial gain matrix, $\mathbf{G}_o$, which stabilizes $H(s)$. Three nonlinear equations are then solved and $\mathbf{G}_o$ is updated. The process is repeated until $|\mathbf{G}_{i+1}-\mathbf{G}_i|<\epsilon$, where ϵ is a user specified convergence parameter. More specific details about the algorithm are given in Ref. 8. Since the DLA algorithm is a nonlinear optimization, the relationship between R and the amount of control signal power usage per unit of input disturbance signal power is also nonlinear. However, this globally convergent optimization algorithm is quite effective at determining a static matrix such that the weighted sum of the desired performance measure and control effort is minimized.[8] The focus herein is placed upon comparing levels of performance for structural acoustic control as opposed to advancing the algorithm for synthesizing the controller.

II. RESULTS

The following plate parameters are assumed in all the analytical runs: $l_x=0.6$ m, $l_y=0.525$ m, $l_z=2\times10^{-3}$ m, $\rho=7700$ kg/m^3, $\nu=0.2$, and $E_s=20.3\times10^{10}$ N/m^2. The material properties of this plate are consistent with that of steel. The state-space plate model is built assuming 5% proportional damping for all modes. The five fixed, point-force disturbance locations, in meters, are {(0.0552, 0.4002); (0.3161, 0.4779); (0.4207, 0.3865); (0.3923, 0.1378); (0.2496, 0.0249)}. Other constant run parameters are the number of structural modes in the plate model, $N_m=30$; the number of structural modes incorporated into the radiation filters, $N_f=10$; and the convergence parameter for the DLA algorithm, $\epsilon=1\times10^{-2}$. The number of plate modes was selected in order to ensure that the zeros of the colocated control transducer transfer functions had sufficiently converged.[14] However, the number of modes used in forming the radiation filters, N_f, need only be over the bandwidth of interest: 0–500 Hz. This frequency band represents the region in which plate acoustic energy is a maximum and passive noise control techniques are least effective. In forming the AVC_PTS performance measure, the number of sensor locations in each direction are $N_x=3$ and $N_y=4$.

A. Three colocated point velocity sensor-point force actuator pairs

The first control system arrangement to be tested was shown in Fig. 1(a). The exact locations of the point transducer pairs, in meters, are {(0.1680, 0.2992); (0.3000, 0.1680); (0.2700, 0.0788)}. The square of the $\mathbf{H}_2$ norm of the *control power performance system*, evaluated at each frequency, for each of the three active control techniques is given in Fig. 3. The total area under each curve (on a linear scale) is the sum of the mean square of the control actuator signals (i.e., mean square signal power) when all disturbance inputs are independent stochastic unit signals and its root is proportional to the $\mathbf{H}_2$ norm of the system H_C for each case. Notice that the control effort of the two vibration based techniques (AVC and AVC_PTS) differs very little over the bandwidth. Since the engineering units associated with the three different cost functionals vary, the value of R was adjusted such that the same amount of control signal power is expended in the implementation of each compensator.

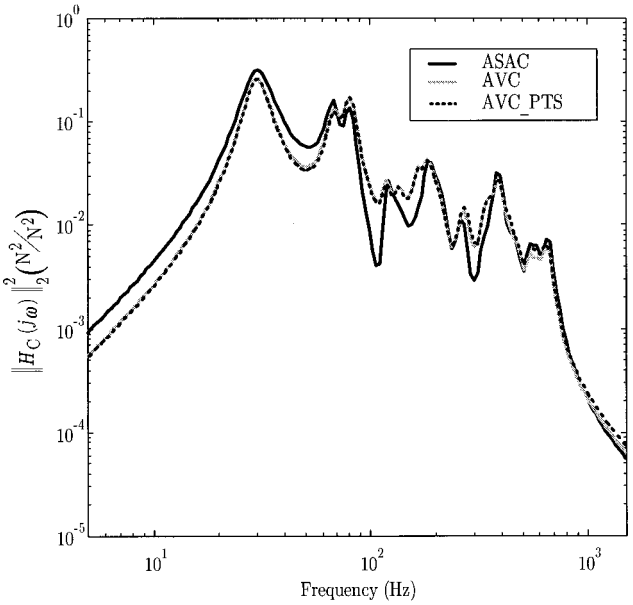

FIG. 3. Control signal power for arrangement with three colocated point sensor-actuator pairs.

Matching control power required some modeling iteration. First, a design guideline related to the ratio of mean square control signal power to input mean square disturbance signal power was assumed. For practical control system implementation, it is reasonable to expect that the amount of mean square control signal power input to the plate throughout the bandwidth of interest is approximately one order of magnitude below the amount of mean square disturbance signal power input to the plate. The ASAC performance signal was selected for the first compensator design case and, as shown in Table I and Fig. 3, with $R=3.0\times10^{-11}$ the mean square control signal power is approximately one order of magnitude less than the *unit* mean square disturbance signal power over the bandwidth, the primary exception being a peak at 30 Hz. This peak corresponds to the resonance of the fundamental plate mode where a significant amount of power is required for control. As reported in Table I, the control signal power over the entire bandwidth ($\mathbf{H}_2$ norm of H_C) for this ASAC design is 5.5344 N/N. The sequential quadratic programming (SQP) nonlinear optimization routine[15] was then used to converge the values of R for both the AVC and discrete AVC design cases. Values of R were optimized such that their control signal power over the entire bandwidth equaled 5.5344 ± 0.0001 N/N. Discussion of the SQP routine is omitted here for brevity; the work by Gill *et al.*[15] is an excellent reference. The values of R for the AVC and AVC_PTS designs are given in Table I. Please note that all

TABLE I. Control effort weighting and resulting control power for each controller arrangement and compensator design case.

	R	$\|\mathbf{H}_C\|_2$
Three point sensor-actuator pairs		
ASAC	3.0×10^{-11}	5.5344 N/N
AVC	2.1052×10^{-4}	5.5344 N/N
AVC_PTS	6.9910×10^{-4}	5.5345 N/N
Three small sensoriactuators		
ASAC	6.929×10^{-15}	349.1 V/N
AVC	4.15×10^{-8}	349.0 V/N
AVC_PTS	1.0865×10^{-7}	349.2 V/N
One large sensoriactuator		
ASAC	7.2549×10^{-12}	13.373 V/N
AVC	2.293×10^{-5}	13.374 V/N
AVC_PTS	7.497×10^{-5}	13.374 V/N
One large sensoriactuator with LQG compensation		
ASAC	$2.412\ 25\times10^{-6}$	13.373 V/N
AVC	4.507×10^{-3}	13.373 V/N
AVC_PTS	$8.212\ 65\times10^{-3}$	13.373 V/N

the values of R reported are exact; they have not been rounded up or down. As shown in Fig. 3, the mean square signal power guideline discussed above was also satisfied by these AVC and discrete AVC designs. The control signal power required by the two vibration criteria designs differ very little over the bandwidth. However, it is shown that the control system designed by the frequency-shaped cost function, ASAC, yields more control effort at low frequency and less control effort at high frequency.

Since the ultimate goal, no matter what the selected performance measure for compensator design, is structural acoustic control, Fig. 4 gives the square of the $\mathbf{H}_2$ norm of the *acoustic performance system*, evaluated at each frequency, for the open-loop system and the three closed-loop systems. The total area (on a linear scale) under each curve in Fig. 4 is proportional to the average sound power radiated by the plate when all inputs are independent white noise processes. The discrete AVC closed-loop system response rests on top of the AVC closed-loop system response for most frequencies. The AIL of the ASAC system, AVC system, and discrete AVC system in 1/3 octave bands is also shown in Fig. 4. The AIL ordinate is shown to the right of the figure. All three controller designs provide reduction in radiated acoustic power. A maximum reduction of 17.0 dB is seen in the 1/3 octave band centered at 31.5 Hz when using the compensator designed with the criteria of minimizing radiated acoustic power (ASAC). The AVC design provides 14.3 dB of reduction in the same frequency band. The discrete AVC design (AVC_PTS) provides 14.1 dB of reduction in that band. Since the fundamental mode of the plate is the most efficient acoustic radiator, the emphasis of the ASAC control system in frequencies that include both this structural mode and strongest acoustic response makes physical sense. Over all frequencies the AIL of the ASAC closed-loop system is 2.0 dB. The AIL of the AVC and discrete AVC closed-loop systems over the entire bandwidth is also 2.0 dB. The lack of significantly greater broadband performance between the ASAC system and structural vibration based designs is a result of the increased acoustic response of the (2,1) mode (the second peak at 135 Hz in Fig. 4) and lack of high frequency performance with the ASAC design. While the peak at 135 Hz is an order of magnitude down from the fundamental response, the 2.7 dB increase in radiated sound power seen in the 1/3 octave band centered at 63.0 Hz and the fact that the greater ASAC control performance is seen at lower frequencies causes the linear scale based broadband performance measures to be equal. The 1/3 octave band results are much more revealing and indicative of controller performance.

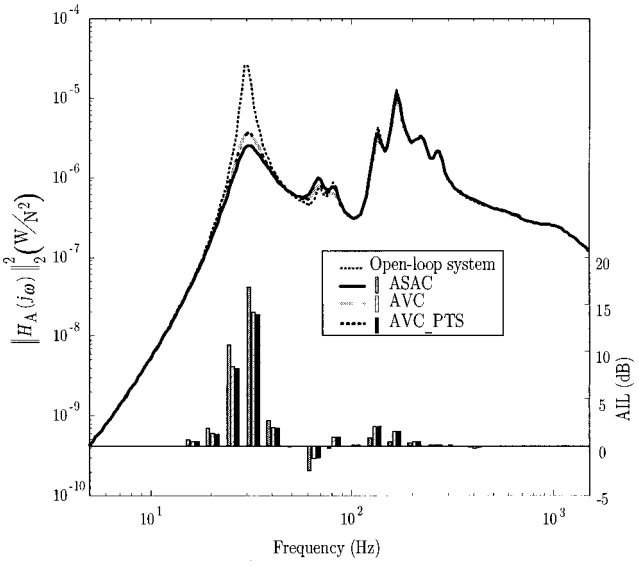

FIG. 4. Acoustic power spectrum and AIL over 1/3 octave bands for arrangement with three colocated point sensor-actuator pairs.

For this control system arrangement, the eigenvalues of the static output feedback gain matrix for all three controllers are positive and real. Thus each design results in positive dissipative controllers. However, **G** designed using the frequency-shaped (ASAC) cost functional provided greater structural acoustic control performance.

B. Three small piezoelectric sensoriactuator transducers

The second control system arrangement to be tested was shown in Fig. 1(b). Each piezoceramic patch is square in the xy plane with a dimension of 0.0508 m (2.0 in.) and a thickness of $l_z^p = 0.2\times10^{-3}$ m. The patches are assumed to be made of lead zirconate–titanate (PZT PSI-5A-S3).[16] The following parameters are specified for the PZT material: $\rho^p = 7650$ kg/m^3, $\nu^p = 0.3$, and $E_s^p = 4.9\times10^{10}$ N/m^2.[16,7]

The control signals to the piezoelectric sensoriactuator transducers have units of voltage. The actuator signals in Sec. II A had units of force. Therefore the guideline developed previously for specifying the amount of mean square control force per unit of input mean square disturbance force is inapplicable to this system. To provide some comparative association between this and the previous control system arrangement, the value of R for the three small piezoelectric sensoriactuator ASAC design was selected such that the broadband AIL of the system was 2.0 dB (the same amount of broadband control performance achieved by the three

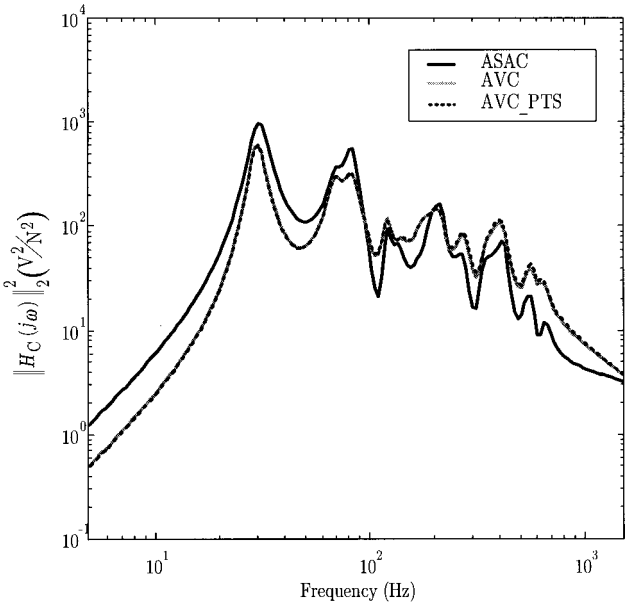

FIG. 5. Control signal power for arrangement with three small piezoelectric sensoriactuator transducers.

colocated point sensor-actuator pairs). As shown in Table I, the control power ($\mathbf{H}_2$ norm of H_C) for this ASAC system design is 349.1 V/N. Again using the SQP nonlinear optimization routine, values of R were selected for the two vibration based design cases such that their control power equaled 349.1 ± 0.1 V/N. The parameters' values and resulting control power are given in Table I. The sum of the squared singular values of H_C for the three small piezoelectric sensoriactuator control arrangement are shown in Fig. 5. As in the first control system arrangement, the AVC and AVC_PTS designs vary little over the bandwidth of interest and the ASAC compensator yields more control effort at lower frequency than the other two designs.

Figure 6 gives the square of the $\mathbf{H}_2$ norm of H_A, evaluated at each frequency, for the open-loop system and three

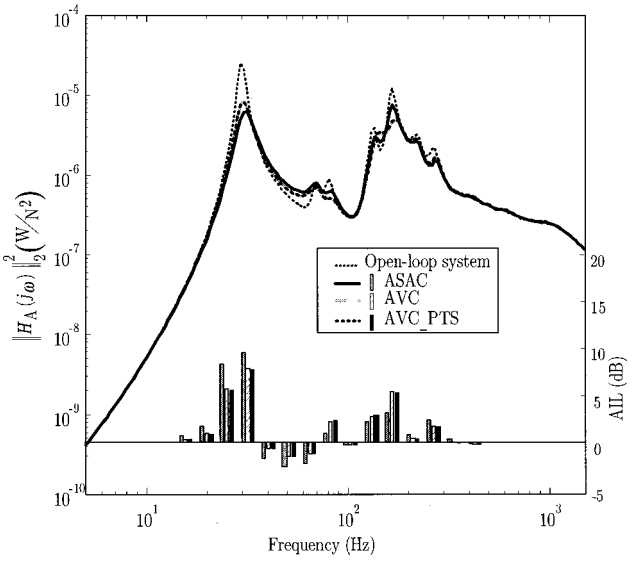

FIG. 6. Acoustic power spectrum and AIL over 1/3 octave bands for arrangement with three small piezoelectric sensoriactuator transducers.

closed-loop systems. All three controller designs provide reduction in radiated acoustic power. Over all frequencies, the AIL of the ASAC, AVC and discrete AVC closed-loop system is 2.0, 1.9, and 1.9 dB, respectively. In the 1/3 octave band centered at 31.5 Hz, the three active control techniques provide 9.2, 7.8, and 7.7 dB of reduction in sound transmission, respectively. Comparing Figs. 4 and 6 one sees that the three small piezoelectric sensoriactuators achieve reduction in the peaks of the higher-frequency acoustic response of the plate. Whereas the three colocated point sensor-actuator pairs arrangement provided very little control of the high-frequency response. This is due to the fact that the compliance of the piezostructure increases with frequency up to a limit set by the ratio of patch dimension to plate dimension.[7] Better coupling into the higher-frequency modes results from the spatial differentiation effect of the distributed strain transducer. This increase in coupling with frequency can lead to control stability issues associated with increasing phase and unmodeled high-frequency dynamics.[7]

The eigenvalues of each compensator designed for the three small piezoelectric sensoriactuators are positive and real. So, as in the first control system arrangement, all three controllers are dissipative. It is again noted that for this case the compensator designed using the ASAC cost functional provided greater structural acoustic control performance.

C. Single large piezoelectric sensoriactuator transducer

The third, and final, control system arrangement to be tested was shown in Fig. 1(c). The lower left corner of the large spatial transducer is located on the plate at (0.0150, 0.0131) m and the upper right corner is located at (0.5835, 0.5106) m. The piezoceramic material for this arrangement is assumed to be very thin, with a thickness of $l_z^p = 4.9 \times 10^{-7}$ m. This thin patch dimension is necessary to avoid greatly altering the plate response through localized mass and stiffness effects of the distributed transducer. Physical application of such transducers is the topic of future work and may be realized by sintering the piezoceramic material to the plate surface. The large spatial aperture of this transducer has been shown to provide greater closed-loop stability and less spillover than the smaller transducers used in Sec. II B.[17,7] The stability increase is due to the inherent roll-off of high-frequency plate dynamics associated with the large spatial aperture. Less spillover is due to the low structural wave number to aperture ratio and the fact that this transducer can only couple into odd structural modes. Excitation of even structural modes is not possible.

To again provide some association between the results for the three different control system arrangements, the value of R for the single, large piezoelectric sensoriactuator ASAC design was selected such that the broadband AIL of the system was 2.0 dB. The control power for this ASAC system design is 13.373 V/N. Values of R for AVC and AVC_PTS were optimized such that their control power equaled 13.373 ± 0.001 V/N and are given in Table I. The sum of the squared singular values of H_C for the large piezoelectric sensoriactuator control arrangement are given in Fig. 7. The control signal power required by the three designs does not

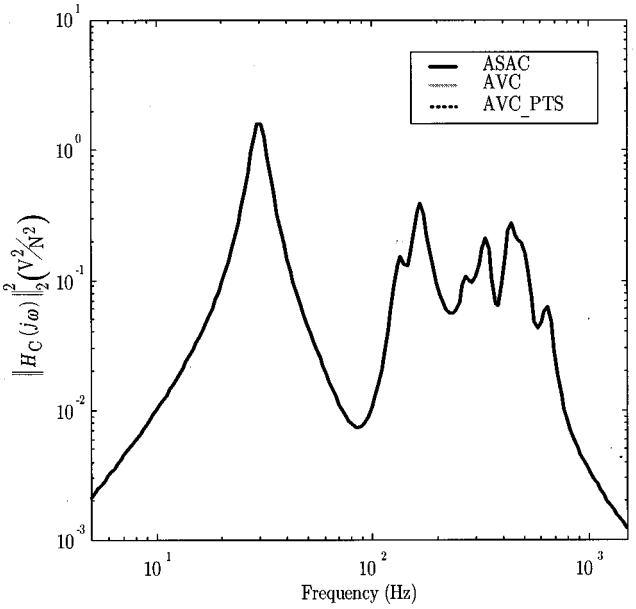

FIG. 7. Control signal power for arrangement with a single large piezoelectric sensoriactuator transducer.

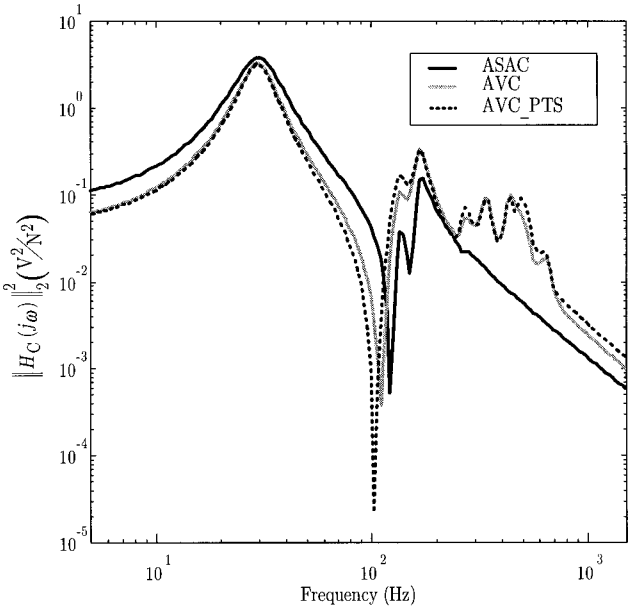

FIG. 9. Control signal power for arrangement with a single large piezoelectric sensoriactuator transducer and LQG compensation.

differ over the bandwidth: all three curves lie on top of each other. Due to the spatial aperture of the transducer, the response of the even structural modes is absent in Fig. 7 (compare with Fig. 5 or Fig. 3).

Figure 8 gives the square of the $\mathbf{H}_2$ norm of H_A, evaluated at each frequency, for the open-loop system and three closed-loop systems. As expected from Fig. 7, the closed-loop system response for all three controller designs rest on top of each other and all three controller designs provide the same reduction in radiated acoustic power. In the 1/3 octave band centered at 31.5 Hz, the three controllers provide 9.4 dB of reduction in sound transmission. Comparing Figs. 8 and 6, one sees that the single large piezoelectric sensoriactuator provides significantly less spillover in acoustic radiation, especially in the 50–100-Hz range.

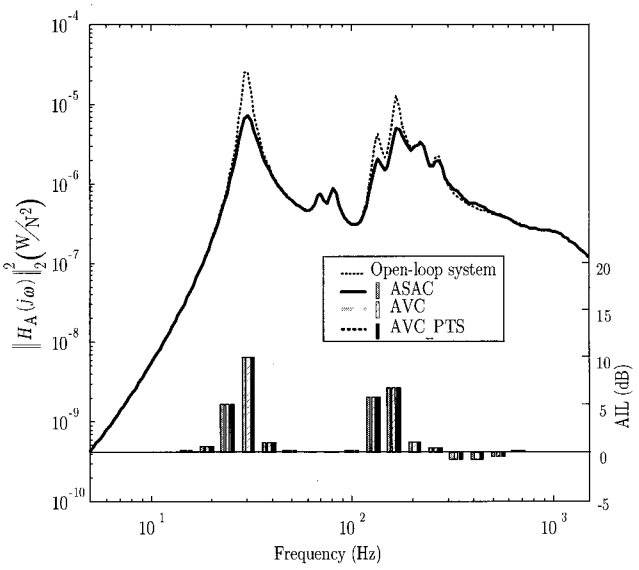

FIG. 8. Acoustic power spectrum and AIL over 1/3 octave bands for arrangement with a single large piezoelectric sensoriactuator transducer.

The compensator for all three designs was a positive, real number, which it must be for stability. As in the first two control system arrangements, the controller was dissipative. However, in this case the development and addition of frequency-shaped performance measures did not provide any additional closed-loop performance.

To verify that the results just presented for the single large piezoelectric sensoriactuator are not due simply to the spatial aperture of the transducer, dynamic compensation was also applied to this control system arrangement. Figure 9 shows the square of the $\mathbf{H}_2$ norm of H_C, evaluated at each frequency, when $\mathbf{G}$ is a linear quadratic Gaussian (LQG) compensator.[7] Due to space constraints, the presentation of the LQG controller design has been omitted. By evaluating the $\mathbf{H}_2$ norm of H_C when $\mathbf{G}$ is a full dynamic LQG compensator and using the design procedures discussed above, the values of R for the ASAC, AVC and AVC_PTS LQG control techniques were optimized such that their control power equaled 13.373 ± 0.001 V/N. For each control system arrangement, sensor noise was assumed to be approximately 1% of the rms sensor signal level and the system matrix of each controller has 204 states. The control effort weightings and resulting control power for this case are also noted in Table I. As shown in Fig. 9, the ASAC compensator design varies from the AVC and AVC_PTS LQG compensators. There is also a greater difference between the AVC and AVC_PTS designs then seen in the other transducer arrangements. Comparing Figs. 9 and 7, it can be concluded that the constant control signal power shown in Fig. 7 is due to the use of a single degree of freedom static, output feedback control system, not the shape or size of the transducer.

An interesting comparison can be made between the acoustic performance of static and dynamic compensators that have been designed with equal control power. Figure 10 shows the square of the $\mathbf{H}_2$ norm of H_A, evaluated at each frequency, and the AIL for the three LQG compensator de-

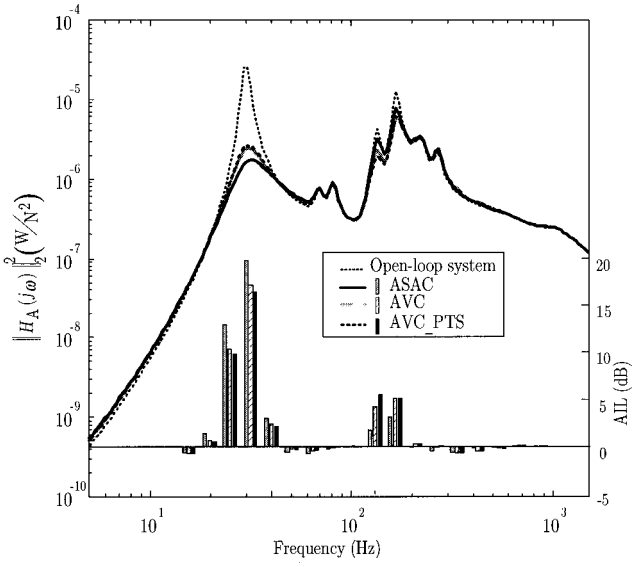

FIG. 10. Acoustic power spectrum and AIL over 1/3 octave bands for arrangement with a single large piezoelectric sensoriactuator transducer and LQG compensation.

signs. The ASAC, AVC, and AVC_PTS LQG compensator achieved 2.6, 2.4 and 2.4 dB of reduction in radiated acoustic power over all frequencies, respectively. In the 1/3 octave band centered at 31.5 Hz, the three compensators achieved 19.9, 17.1, and 16.5 dB of reduction, respectively. The performance of the LQG compensators is much greater than the three static, output feedback controllers (compare Figs. 9 and 7).

III. CONCLUSIONS

Frequency-shaped cost functionals were shown to affect the performance of multivariable, static, output feedback controllers. With more than one sensor-actuator pair, the bandwidth over which the control energy is expended was changed by the use of radiation filters. The ASAC control system demonstrated greater levels of sound power reduction in the proximity of the fundamental plate mode (strongest acoustic radiator) than that of the AVC and discrete AVC control system designs. However, for a single degree of freedom static, output feedback control system, control effort was not adjusted by the frequency-shaped cost functional for preferential treatment of a particular mode.

Dynamic (LQG) compensators were also built for the single degree of freedom control system. It was verified that the ASAC cost functional influenced the design of the frequency-dependent controllers and it was also shown that the dynamic compensators achieved greater control performance than the static compensators. The system matrix of each LQG controller required 204 states. Whereas, the static output feedback controller involved a single gain matrix and could be realized with simple analog circuitry. For practical application, the LQG compensator would have to be implemented in DSP hardware.

The balance of achievable performance with hardware complexity and stability issues will most certainly continue to be the topic of much work throughout the field of adaptive structures. However, the results presented here demonstrate that the frequency-shaped cost functional is important to control system design, even when static compensation is used.

ACKNOWLEDGMENTS

This work was supported by NSF Career Program CMS-9501470. The authors gratefully acknowledge the assistance of Duke University undergraduate J. D. Kemp in generating the analytical results for this work.

[1] W. T. Baumann, W. R. Saunders, and H. H. Robertshaw, ''Active suppression of acoustic radiation from impulsively excited structures,'' J. Acoust. Soc. Am. **90**, 3202–3208 (1991).
[2] N. K. Gupta, ''Frequency-shaped cost functionals: Extension of linear-quadratic-gaussian design methods,'' J. Guid. Control **3**, 529–535 (1980).
[3] J. S. Vipperman and R. L. Clark, ''Multivariable feedback active structural acoustic control using adaptive piezoelectric sensoriactuators,'' J. Acoust. Soc. Am. (to be published).
[4] R. L. Clark, J. S. Vipperman, and D. G. Cole, ''Adaptive piezoelectric sensoriactuator,'' U.S. Patent 5,578,761 (November 1996).
[5] L. Meirovitch, *Analytical Methods in Vibrations* (Macmilliam, New York, 1967).
[6] N. W. Hagood, W. H. Chung, and A. von Flotow, ''Modeling of piezoelectric actuator dynamics for active structural control,'' J. Intell. Mater. Syst. Struct. **1**, 327–354 (1990).
[7] R. L. Clark, G. P. Gibbs, and W. R. Saunders, *Adaptive Structures, Dynamics and Control* (Wiley, New York, 1998).
[8] R. L. Clark and D. E. Cox, ''Multi-variable structural acoustic control with static compensation,'' J. Acoust. Soc. Am. **102**, 2747–2756 (1997).
[9] K. A. Cunefare, ''The minimum multimodal radiation efficiency of baffled finite beams,'' J. Acoust. Soc. Am. **90**, 2521–2529 (1991).
[10] A. Francis, *A Course in $\mathscr{H}_\infty$ Control Theory* (Springer-Verlag, New York, 1986).
[11] S. Boyd and C. Baratt, *Linear Controller Design: Limits of Performance* (Prentice-Hall, Englewood Cliffs, NJ, 1991).
[12] G. C. Smith and R. L. Clark, ''Active insertion loss,'' Noise Control Eng. J. (submitted).
[13] W. S. Levine and M. Athans, ''On the determination of the optimal constant output feedback gains for linear multivariable systems,'' IEEE Trans. Autom. Control. **AC-15**, 44–48 (1970).
[14] F. M. Fleming and E. F. Crawley, ''The zeroes of controlled structures: Sensor/actuator attributes and structural modeling,'' AIAA Paper 91-0984, April 1991.
[15] P. E. Gill, W. Murray, and M. H. Wright, *Practical Optimization* (Academic, San Diego, CA, 1981).
[16] Piezo Systems, Inc., *Product Catalog*, 186 Massachusetts Ave., Cambridge, MA 02139.
[17] J. S. Vipperman and R. L. Clark, ''Implications of using colocated strain-based transducers for active structural acoustic control,'' J. Acoust. Soc. Am. (submitted).

Reactions to environmental noise in an ambient noise context in residential areas

James M. Fields
10407 Royal Road, Silver Spring, Maryland 20903

(Received 1 December 1997; revised 20 February 1998; accepted 13 June 1998)

Direct reanalyses of over 57 000 interview responses to 35 noise sources in 20 social surveys and reviews of publications for over 12 000 additional responses to 16 noise sources in 13 social surveys show that residents' reactions to an audible environmental noise (a target noise) are only slightly or not at all reduced by the presence of another noise source (ambient noise) in residential environments. The direct reanalyses account for type of noise source (aircraft, road traffic, railway, impulse noise), type of noise reaction question, type of activity disturbance, quality of noise data, type of regression analysis model (linear, logit, probit), two noise metrics (DNL, L_{Aeq}), and ten personal characteristics. Although there is considerable variation from survey to survey, the best direct estimate is that approximately a 20-dB increase in ambient noise exposure (95% confidence interval of 15–50 dB) has no more impact than approximately a 1-dB decrease in target noise exposure. Tabulations of 12 findings from laboratory studies in which subjects rated periods of multiple noise events also found that target noise annoyance is not consistently reduced by ambient noise. [S0001-4966(98)06809-X]

PACS numbers: 43.50.Qp, 43.50.Lj, 43.50.Ba [MRS]

INTRODUCTION

Studies in laboratory settings find that perceptions of the loudness of audible tones are reduced in the presence of a second, ambient noise. Figure 1 from a classic laboratory perceptual study shows that the loudness of a target tone presented at a fixed SPL of, for example, 60 SPL is no longer perceived to be the equivalent of a 60 SPL tone when an ambient noise is present. Instead the 60 SPL tone is perceived to decrease to the equivalent of about a 58 SPL tone in the presence of a 50 SPL ambient noise and then further to the equivalent of about a 30 SPL tone in the presence of a 80 SPL ambient noise.

As a corollary to these tone-perception studies, it has long been assumed that in residential settings annoyance with one audible noise (e.g., aircraft) will be reduced in the presence of another noise (e.g., road traffic). This article tests that assumption by analyzing all of the interview data that could be obtained from community social surveys of residents' reactions to one noise (the target noise) in neighborhoods with the presence of a second noise source (the ambient noise). In this article a ''target'' noise is the noise a respondent is asked to rate in a particular question. Aircraft noise is the target noise in this four-point verbal scale question:

> ''Taking all things into account, how much would you say the noise from aircraft around here bothers or annoys you: Very much, Moderately, A little, or Not at all?''

In this article, the term ''ambient'' noise can refer to a single other noise source, not necessarily the sum total of all other background noises. In one questionnaire the same noise (e.g., aircraft noise) can be the ''target'' noise in one question and the ''ambient'' noise in relation to a second question that asks about another target noise source (e.g., road traffic).

Reviews of previous discussions and research suggest two types of models for the relationship of target noise reactions to target and ambient noise exposure levels: the ***uniform ratio*** model and the ***varying ratio*** model. The central element of the uniform ratio model is the ambient effect ratio (''R'' in this article). A negative value of R is implicit in the common assumption that high ambient noise levels will reduce the impact of target noise. A value of $R=-1$ means that reactions depend on only the difference between target and ambient levels. The varying ratio model is represented by the relationships shown in Fig. 1 in which the ratio of the effect of target and ambient noise varies in some complex way that has not been expressed in a simple mathematical model.

The uniform ratio model is defined as a ratio of coefficients from the regression of annoyance on the target noise exposure level (regression coefficient B_T) and the ambient noise (B_A), $R=B_A/B_T$. The uniform ratio model can be represented by either of three regression models:

(1) the linear regression model in which the effects of the factors are assumed to be additive:

$$Y_i = a + B_T \cdot T_i + B_A \cdot A_i + U_i \tag{1}$$

(where Y_i = target annoyance score of individual i, a = intercept, B_T = linear regression coefficient for target noise level, T_i = target noise level for individual i, B_A = linear regression coefficient for ambient noise level, A_i = ambient noise level for individual i, and U_i = residual variation associated with individual i);

(2) the logistic regression model in which the effects are assumed to be multiplicative:

 0001-4966/98/104(4)/2245/16/$15.00

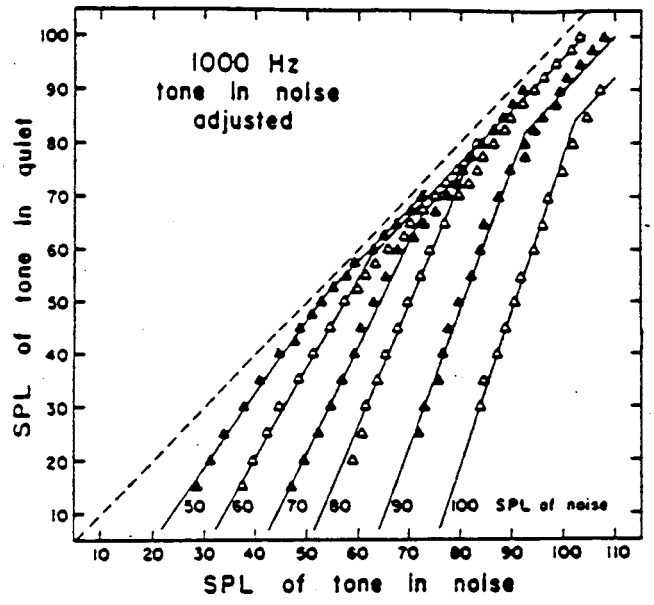

FIG. 1. Masked loudness functions obtained by adjusting the masked tone to equal the loudness of the tone in quiet (from Stevens and Guirao, 1967, p. 463).

$$Y_i = \frac{1}{1+e^{-(a+B_T \cdot T_i + B_A \cdot A_i + U_i)}} \tag{2}$$

(where e = base for the natural logarithm, a = locational parameter, B_T, B_A = indicators of the steepness of the slopes, and other parameters are as described in the previous equation), or

(3) the probit regression model (''normit'' model) based on a normal rather than logistic distribution:

$$Y_i = \frac{1}{\sqrt{2\pi}} \int_{-\infty}^{(a+B_T \cdot T_i + B_A \cdot A_i)} e^{-U_i^2/2}\, dU_i . \tag{3}$$

The logit and probit distributions are almost indistinguishable. The probit distribution's slightly ''thinner tail'' should be unimportant in this article (Hanushek and Jackson, 1977, p. 188).

The simple, dichotomous logistic regression model is used for estimating parameters for predicting truly dichotomous events (e.g., complaining or not complaining to authorities). For most annoyance measures, however, the underlying annoyance response is not a simple dichotomous response. Residents' reactions differ in degrees that are commonly captured with questions in which the respondent chooses from a number of numerical or verbally ordered ratings [e.g., ''On this scale from 0 (not at all disturbed) to 10 (unbearably disturbed) how do you rate aircraft noise?'']. The linear regression model captures this information by assuming that each of the adjacent answers to an annoyance question are separated by the same sized interval and thus, for example, the alternative answers of being ''not at all, a little, moderately, very much'' annoyed can be scored with the equally separated scores of 1, 2, 3, and 4. The cumulative logistic regression model used here does not make that assumption. This model captures some of the information contained in the order of the responses with a single slope parameter, but a separate locational parameter for the cumulative responses up to each point on the response scale (Agresti, 1989; DeMaris, 1992).

I. DATA FOR COMMUNITY RESPONSE ANALYSES

All of the 363 community noise surveys found in English language publications by the end of 1995 were examined for evidence on ambient noise impact [Fields (1991) catalogs 319 of these surveys]. A total of 32 social surveys were identified that meet the following six criteria for the present article: (1) The survey sought the respondent's direct reaction, feeling or rating. (2) The reaction question specified that ''noise'' or ''sound'' was to be rated. (3) The reaction question explicitly named the noise source. (4) The inquiry concerned reactions at the respondent's residence. (5) The noise exposure from the target noise source was determined. (6) Ambient noise was either measured or indirectly represented by a surrogate indicator (e.g., rural or urban area).

Each of the 32 surveys therefore had some indicator of the noise exposures from two noise sources. Since 19 of the 32 surveys asked respondents about both sources, a total of 51 data sets could be evaluated that contained over 70 000 evaluations of noises by over 45 000 respondents.

Steps were taken to attempt to obtain as complete and accurate information as possible about the 32 study designs, social surveys, and the accompanying 51 noise sources. The most complete, original-language reports were obtained and usually translated. The original researchers were sent detailed data-request forms to attempt to obtain more than 50 pieces of information about the social survey and noise measurement programs. Ambiguities were directly checked with these researchers. The original-language questionnaires were acquired for 31 of the 32 studies. The original respondent-level, social survey data file was obtained whenever possible.

Two different types of analyses could be performed with the 51 data sets. For 35 data sets (20 surveys) a standard, direct analysis of the original data was performed to directly estimate the ambient effect ratio (see Sec. II). For the remaining 16 data sets (12 additional surveys and one noise source from one of the previous 20 surveys) a weaker meta-analysis was performed to indirectly gauge the approximate importance of ambient noise using whatever type of information was presented in the publication (see Sec. III).

For the 35 data sets in the direct analysis, the annoyance data and acoustical indices were defined in the most comparable way possible before being merged into a single large data set in which each record was either a single interview-target noise evaluation (51 807 from 29 data sets) or a group of evaluations (often a study site) that was weighted to represent the number of interviews in the group (6 175 evaluations from six data sets). The annoyance data were prepared to produce at least one general target noise annoyance index for each data set, up to 17 other direct and indirect annoyance indicators, and as many as ten explanatory variables (see Table III). These 18 annoyance indicators were defined by the concepts measured (e.g., general annoyance, sleep dis-

turbance, etc.), but did not need to be scaled with the same numbers of scale points since the final objective is to calculate the ratio of regression coefficients (R), not the values of the individual regression coefficients. The general ''Multi-point question'' (defined in Table AI) that enters in many analyses is any single, multi-point question about annoyance with the noise source. This question is the dependent variable in cumulative logistic regression analyses. The general annoyance index (''Multi-item index'' in Table AI), the only reaction measure defined for every data set, is the average score of all the general questions about annoyance with the noise source after each was scored from 0 to 10. By combining several questions this index obtains a theoretically more reliable estimate of the respondent's position on the underlying annoyance dimension. This index is the dependent variable in linear regression analyses.

The available noise data for the two noise sources (target and ambient) for each of the 20 surveys were analyzed to provide estimates of both the 24-h, A-weighted, equivalent continuous sound level (L_{Aeq}) and the day–night average sound level (DNL). In an attempt to create comparable noise exposures, the various studies' noise exposure assessment procedures were examined to ensure comparability in time periods, noise events included and position (noisiest facade for the source with reflection effects removed). Each data set was then graded from Grade A to D depending upon the presumed accuracy of the derived estimates of DNL and L_{Aeq}. These two indices were used because they could be determined for large numbers of data sets and they are most likely to be relevant for regulatory purposes. Precise tests of many aspects of ambient noise theories would require more detailed data about the temporal and spectral characteristics of target noise events and the general background noise environment. Such data are not available for enough interviews to provide a sound basis for study. The survey publications do not mention that intermittent noise events were ever totally masked by the more pervasive types of noise sources (such as road traffic). In the absence of such indicators, it has been assumed that the investigators in these studies are reporting the noise levels from events that were audible outside dwellings. Additional information about the social survey data, noise data processing procedures and the noise quality grading procedure can be found in Table AI.

II. RESULTS FROM DIRECT ANALYSES OF 35 TARGET NOISE EVALUATIONS

This section provides the strongest tests for ambient noise effects in residential areas. Three techniques are used to examine the 35 target-noise data sets. First, the data are examined in figures. Second, the total-data-set regression analyses estimate the ambient effect ratios for the uniform ratio ambient response model. Third, subgroup regression analyses test the varying ratio model by examining responses within subgroups, including those defined by ranges of target/ambient differences.

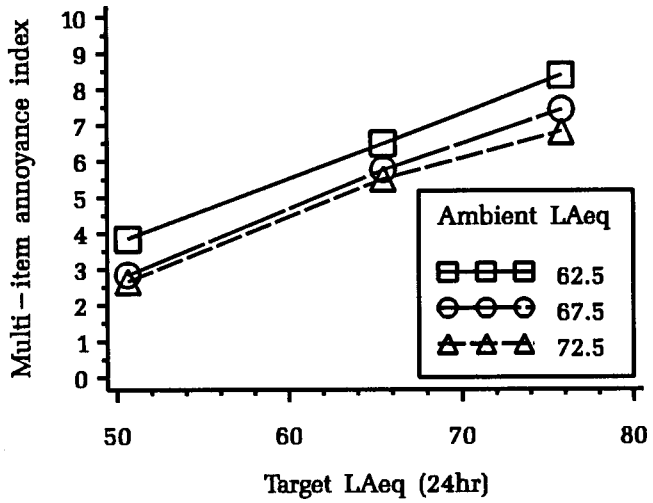

FIG. 2. Response to aircraft noise for three road traffic ambient noise exposures (1969 Heathrow aircraft survey, UKD-033).

A. Graphical displays

Relationships are first evaluated by examining a visual display of the degree of reaction in each target and ambient noise group in each of the 35 data sets. In Fig. 2, for example, each data point summarizes the reactions to aircraft noise on the multi-item index of at least 35 respondents by aircraft noise level at three road traffic ambient noise levels for a 1969 study around Heathrow airport. Thirty-five such figures were examined in the complete study report to determine whether the pattern of responses supported the uniform ratio model, the variable ratio model, or any other obvious pattern (Fields, 1996, Appendix E).

Only 2 figures (including Fig. 2) of the 35 figures in the complete report support the conventional expectation that target noise annoyance decreases as ambient noise levels increase. One figure supports the opposite pattern. The 32 remaining figures do not clearly support any model over all target noise levels or over any lesser 20-dB range of target noise levels. The type of noise source and quality of the noise data do not obviously differentiate the patterns found in the figures. Two of the data sets with the most consistent patterns (including Fig. 2) are in the lowest data-quality group.

The evidence from the 35 figures suggests that target noise annoyance consistently increases with increasing target noise levels, but that ambient noise has no clear effect. Given the variability present in these community survey data it is necessary to use more sensitive, multivariate statistical techniques to determine whether an ambient noise effect is present and statistically significant.

B. Multiple regression analyses to test the uniform-ratio model

Support for the standard, uniform-ratio model of ambient noise impact is tested in this section by directly estimating the value of the ambient effect ratio (R) from linear and nonlinear regression analyses. As was explained earlier, the ambient effect ratio (R) is defined by the ratio of the unstandardized regression coefficient for ambient noise di-

TABLE I. Estimates of the ambient effect ratio (R) from linear regression analyses of the multi-item annoyance index on target noise ($T_{LAeq24h}$) and ambient noise ($A_{LAeq24h}$) (35 data sets).

Target noise Study name (Catalog ID)[a]	Ambient noise source	No. of responses	Regression equation: Intercept	Target B_{TLAeq}	Ambient B_{ALAeq}	Ratio (B_{AlAeq}/B_{TlAeq}): Ratio (R)	95% confidence interval: $=R_{\pm}$	Lower limit	Upper limit
Aircraft target noise									
CEC/84 Glasgow (UKD-238)	Road	605	−13.02	0.23	−0.00	−0.01	±0.37	−0.37	0.36
CEC/84 French (FRA-239)	Road	570	−5.69	0.30	−0.10	−0.35	±0.92	−1.27	0.58
CEC/84 Schiphol (NET-240)	Road	581	−6.36	0.22	−0.04	−0.18	±0.54	−0.72	0.36
1978 Toronto (CAN-168)	Road	617	10.82	0.25	0.01	0.02	±0.31	−0.29	0.33
1982 Heathrow (UKD-242)	Road	413	17.05	0.37	−0.01	−0.03	±0.48	−0.51	0.45
Swiss 3-Airport (SWI-053)	Road	3940	−3.76	0.15	−0.04	−0.24	±0.44	−0.67	0.20
1977 Heathrow (UKD-148)	Road	5818	10.67	0.24	−0.00	−0.00	±0.08	−0.08	0.08
1989 Fornebu (NOR-311)	Road	3322	−8.10	0.19	0.02	0.09	±0.28	−0.19	0.37
USA 4-City 1967 (USA-022)	Road	3499	−3.34	0.16	−0.02	−0.14	±0.52	−0.66	0.38
USA 3-City 1969 (USA-032)	Road	2899	−6.38	0.19	0.03	0.16	±0.22	−0.07	0.38
USA 2-City 1970 (USA-044)	Road	1954	−1.63	0.14	−0.04	−0.29	±0.23	−0.52	−0.05
1967 Heathrow (UKD-024)	Road	4650	−2.14	0.14	−0.04	−0.26	±0.17	−0.43	−0.09
1969 Heathrow (UKD-033)	Road	315	2.39	0.18	−0.12	−0.70	±0.25	−0.95	−0.46
1976 Heathrow (UKD-130)	Road	2563	−4.81	0.16	−0.01	−0.04	±0.25	−0.29	0.20
1980 Brussels (BEL-288)	Road	677	14.20	0.28	−0.01	−0.05	±1.09	−1.14	1.04
Mean[b]		(Σ=32, 423)				−0.10	±0.10	−0.20	0.00
Railway target noise									
British Rail (UKD-116)	Road	1453	−1.30	0.08	0.01	0.15	±0.36	−0.21	0.51
1976 Gothenburg (SWE-165)	Road	464	−2.95	0.13	−0.07	−0.53	±1.40	−1.93	0.88
Mean[b]		(Σ=1917)				−0.01	±0.67	−0.68	0.65
Impulse target noise									
CEC/IMP French (FRA-252)	Road	451	−0.34	0.07	0.01	0.08	±0.70	−3.62	3.77
CEC/Imp German (GER-253)	Road	248	1.68	0.08	−0.04	−0.53	±0.51	−2.04	0.98
CEC/Imp Irish (IRE-254)	Road	454	−5.19	0.06	0.10	1.67	±0.18	−0.51	3.85
Mean[b]		(Σ=1153)				0.57	±1.34	−0.76	1.91
Road traffic target noise									
CEC/84 Glasgow (UKD-238)	Aircraft	605	3.22	0.16	−0.05	−0.28	±1.03	−1.31	0.75
CEC/84 French (FRA-239)	Aircraft	570	4.25	0.20	−0.09	−0.44	±0.78	−1.22	0.33
CEC/84 Schiphol (NET-240)	Aircraft	581	7.28	0.17	0.01	0.07	±1.17	−1.10	1.24
1978 Toronto (CAN-168)	Aircraft	597	1.58	0.25	−0.03	−0.10	±0.32	−0.43	0.22
1982 Heathrow (UKD-242)	Aircraft	410	6.16	0.18	−0.01	−0.05	±0.94	−0.98	0.89
British Rail (UKD-116)	Railway	1453	4.22	0.12	0.01	0.05	±0.20	−0.15	0.26
1977 Heathrow (UKD-148)	Aircraft	5882	6.04	0.20	−0.01	−0.07	±0.07	−0.14	0.00
1989 Fornebu (NOR-311)	Aircraft	3320	3.24	0.08	0.00	0.03	±0.52	−0.49	0.55
1967 Heathrow (UKD-024)	Aircraft	4638	2.50	0.13	−0.03	−0.22	±0.13	−0.35	−0.10
1969 Heathrow (UKD-033)	Aircraft	315	9.16	0.35	−0.00	−0.01	±0.11	−0.12	0.10
1976 Heathrow (UKD-130)	Aircraft	2502	3.36	0.13	−0.02	−0.18	±0.20	−0.38	0.03
1976 Gothenburg (SWE-165)	Tramway	464	2.20	0.05	−0.01	−0.18	±6.97	−47.15	46.79
CEC/Imp French (FRA-252)	Impulse	451	1.97	0.03	−0.00	−0.13	±1.26	−1.39	1.13
CEC/Imp German (GER-253)	Impulse	248	−0.65	0.01	0.05	6.26	±7.38	−71.12	83.63
CEC/Imp Irish (IRE-254)	Impulse	453	4.43	0.12	−0.01	−0.08	±0.30	−0.37	0.22
Mean[b]		(Σ=22 489)				−0.04	±0.17	−0.21	0.13
Mean for all sources[b]		(Σ=57 982)				−0.06	±0.09	−0.15	0.03

[a]Catalog identification number from Fields (1991).
[b]The ratios in these rows are the mean R weighted by the number of interviews in each survey.

vided by the unstandardized regression coefficient for target noise. This section summarizes the results from over 1200 regressions for 57 regression models that were performed and documented for the 35 data sets in the complete study report (Fields, 1996, Appendix D).

1. Overall estimates of the ambient effect ratio using target-noise reaction questions

The ambient effect ratio has been calculated for 39 regression models using target-noise reaction questions. Table I presents the results from each of the 35 data sets for 1 of

these 39 models, a linear regression model predicting the multi-item, direct annoyance index score (scored from 0 to 10 for every study) from the target and ambient noise levels. Each data set is represented by a row in the table. The 1969 Heathrow data set from Fig. 2, for example, appears under ''Aircraft target noise'' in the 13th row (UKD-033) and is shown in the first column with ''Road'' traffic as the ambient noise source. The entry for the road traffic annoyance data set from this study appears under ''Road traffic target noise'' in the last section of the table and represents the regression on road traffic noise annoyance. The next column (''No. of responses'') shows that the regressions for this study's analysis were based on 315 interview responses. Other columns in the table give the regression equation parameters for the ''Intercept'' and unadjusted regression coefficients for the target noise level (''Target B_{TLAeq}'') and ambient noise level (''Ambient $B_{\mathrm{AL_{Aeq}}}$''). The ''Ratio'' column shows that the ambient effect ratio for this data set of $R=-0.70$ is the strongest negative ratio found for any data set. The value of $R=-0.70$ indicates that the same increase in annoyance can be generated by either a 7/10 dB increase in target noise or a 1-dB decrease in ambient noise. The precision of the estimate of the ambient effect ratio is expressed as a 95% confidence interval. Thus the estimate of $R=-0.70$ for this study is surrounded by a 95% confidence interval that stretches from approximately $R=-0.46$ to $R=-0.95$. All confidence intervals in Tables I and II were calculated using the jackknife replication method that yields estimates of sampling errors that are appropriate for clustered study area data (Lee *et al.*, 1989) such as that found in community noise surveys (Fields, 1996, Appendix H.1).[1]

The linear regression model used in Table I may be criticized because the annoyance is measured by an arbitrary assignment of numerical values to the words used in annoyance scales. The logistic regression model, as explained earlier, avoids this assumption by analyzing proportions of respondents above a certain degree of severity. This is illustrated in Fig. 3 in which the 22 data points represent the percentage ''very much'' annoyed for a 1976 Heathrow survey. The five logistic regression curves with a single shape estimate the percentage ''very much'' annoyed by aircraft noise in five road traffic noise environments extending from 20 to 90 dB (LAeq) and illustrate how a regression analysis evaluates data from 22 differentially sized data points to identify patterns that are not apparent from visual inspection. The curves at 20 and 90 dB are extrapolated beyond the observed 40- to 70-dB range of ambient noise exposure and the observed target noise to clearly show the shape of the curves.

The values of the ambient effect ratios for each of the 35 data sets have been calculated for a logistic regression model just as they were for the linear model in Table I. This time, however, Fig. 4 graphically presents the values of these ratios (identified by a symbol) and their standard errors (represented by thin lines) grouped by target noise source. These ratios come from a cumulative, ordered logistic regression analysis of a single multi-point question from each survey on target and ambient noise. Each study is identified along the bottom scale by its catalog number.

A simple count of the 35 ratios indicates that 25 of the linear (Table I) and 22 of the logistic ambient effect ratios (Fig. 4) are negative (in conformity with the conventional assumption that ambient noise inhibits annoyance) but that only three of the linear and four of the logistic ratios are statistically significant. This is evident in Fig. 4 where all but four of the lines for the 95% confidence intervals cross the $R=0.0$ line.

A better summary of all of the studies is provided by weighting each study's estimate by its sample size and averaging the results to provide the ''Mean'' estimate represented in Fig. 4 by a dashed horizontal line at $R=-0.03$ (95% confidence interval of ± 0.09) and in Table I by the ''Mean'' rows for each type of noise and the 35 data sets as a whole ($R=-0.06\pm 0.09$ in last row). If both of these estimates are considered, their 95% confidence intervals span the range from $R=-0.15$ to $R=+0.06$. Two other types of weighted means appear in the main report (Fields, 1996, Appendix D) but were ultimately rejected. Weighting each study equally was rejected because it gives the same importance to a study with 315 respondents as to a study with 5818 respondents. Weighting each study by the inverse of the variance of ''*R*'' gave estimates that were similar to the number-of-interview weighting method, but was rejected because the estimates of the variance of ''*R*'' were very unstable for subgroups from studies with small numbers of study areas.

Table II summarizes the results from 39 target-noise regression models, including the model presented in Table I. Two rows in Table II contain the ambient effect ratio (''Mean *R*'' column) from Table I (first row of Table II) and Fig. 4 (thirteenth row). The most valid, direct estimates come from the 39 estimates in Parts I and II of the table, all of which are based on survey questions about target noise annoyance. A striking feature of these estimates is the rather narrow range of values from $R=-0.17$ to $+0.08$. Although they encompass both positive and negative estimates of the effect of ambient noise, none indicates that ambient noise has as much as 20% of the impact of target noise and none approaches the assumption that annoyance is a function of the difference between target and ambient noise (i.e., $R=-1.00$). Part I estimates are for overall annoyance with the target noise. Part II estimates are for annoyance with the target noise when there is speech interference, TV/radio interference, sleep interference, startle or vibration effects. The estimates in Part I vary in the type of regression model (linear or logistic), noise metric (DNL or L_{Aeq}), the method of scoring overall annoyance [multi-item index, single multi-point scale, dichotomous scale of any annoyance or dichotomous scale of high annoyance (as defined in Table AI)], and whether any of ten different control variables are introduced. Some uncertainty is introduced in comparing the analyses because, as the last column indicates, only 9 of the 35 data sets are included in the indirect rating analyses and from 7 to 29 are included in the analyses with control variables.

After considering the range of conditions in Table I it is proposed that the best conclusion from the data presented in this article is that the value of the ambient effect ratio lies between $R=-0.15$ and $R=+0.06$, the 95% confidence intervals for the simple linear regression of the multi-item in-

TABLE II. The 45 averages of ambient effect ratios (R) for 18 annoyance scales, two noise metrics and three regression models with controls for ten explanatory variables.

Type of annoyance scale	Regression model	Noise metric	Control[a] variables (−=None, TN=target noise)	Ratio (R) of B_{AL}/B_{TL}				No. of Responses	No. of Data sets
				Ratio (Mean R)[b]	95% Confidence interval				
					$=R\pm$	Lower limit	Upper limit		
Part I: Direct ratings of target noise									
Multi-item index	Linear	L_{Aeq}	–	−0.06	±0.09	−0.15	0.03	57 982	35
			Gender	−0.04	±0.10	−0.13	0.06	51 755	29
			Education	0.00	±0.15	−0.15	0.15	49 931	27
			Income	−0.03	±0.15	−0.18	0.11	13 155	7
			Social status	−0.10	±0.08	−0.19	−0.02	34 416	13
			Age	0.08	±0.30	−0.21	0.38	51 253	29
			Home owner	−0.01	±0.11	−0.13	0.10	50 843	27
			Dwelling type	0.06	±0.14	−0.08	0.20	28 072	20
			Employee of TN	−0.04	±0.13	−0.17	0.09	27 760	16
			User of TN	−0.05	±0.10	−0.15	0.04	31 537	11
			Fear of TN	0.02	±0.15	−0.12	0.17	32 800	20
		DNL	–	−0.07	±0.09	−0.16	0.02	57 982	35
Multi-point question	Logit	L_{Aeq}	–	−0.03	±0.09	−0.13	0.06	57 776	35
			Gender	−0.02	±0.10	−0.12	0.08	51 550	29
			Education	0.00	±0.12	−0.13	0.12	49 736	27
			Income	0.01	±0.17	−0.16	0.17	13 126	7
			Social status	−0.10	±0.08	−0.18	−0.01	34 365	13
			Age	0.00	±0.12	−0.12	0.11	51 051	29
			Home owner	−0.01	±0.11	−0.12	0.10	50 637	27
			Dwelling type	0.07	±0.14	−0.07	0.21	27 880	20
			Employee of TN	−0.01	±0.14	−0.15	0.13	27 719	16
			User of TN	−0.04	±0.11	−0.15	0.08	31 449	11
			Fear of TN	0.04	±0.15	−0.11	0.19	32 749	20
		DNL	–	−0.04	±0.10	−0.14	0.06	57 776	35
Any annoyance (0/1 dichotomy)	Logit	L_{Aeq}	–	−0.05	±0.09	−0.15	0.04	52 214	30
	Probit	L_{Aeq}	–	−0.05	±0.09	−0.15	0.04	52 214	30
High annoyance (0/1 dichotomy)	Logit	L_{Aeq}	–	−0.04	±0.09	−0.13	0.05	57 083	33
		DNL	–	−0.17	±0.23	−0.39	0.06	57 083	33
	Probit	L_{Aeq}	–	−0.05	±0.09	−0.14	0.05	57 083	33
Part II: Indirect ratings of target noise effects									
Talking (Multi-point)	Logit	L_{Aeq}	–	−0.07	±0.14	−0.21	0.07	22 376	9
Talking (''Any'' 0/1)			–	−0.09	±0.10	−0.19	0.02	22 376	9
TV/Radio (Multi-point)			–	−0.14	±0.13	−0.26	−0.01	22 370	9
TV/Radio (''Any'' 0/1)			–	−0.15	±0.08	−0.24	−0.07	22 370	9
Sleep (Multi-point)			–	−0.07	±0.27	−0.34	0.20	22 404	9
		DNL	–	−0.07	±0.27	−0.34	0.21	22 404	9
Sleep (''Any'' 0/1)	Logit	L_{Aeq}	–	−0.08	±0.16	−0.24	0.08	22 404	9
		DNL	–	−0.08	±0.17	−0.25	0.09	22 404	9
Startle (Multi-point)	Logit	L_{Aeq}	–	−0.03	±0.22	−0.24	0.19	22 378	9
Startle (''Any'' 0/1)			–	−0.13	±0.22	−0.34	0.09	22 378	9
Vibration (Multi-point)			–	−0.08	±0.20	−0.28	0.12	22 379	9
Vibration (''Any'' 0/1)			–	−0.14	±0.10	−0.23	−0.04	22 379	9
Part III: Analyses comparing the ratings of two target noise sources[c]									
Target #1 minus TN #2 score	Linear	L_{Aeq}	–	−2.11	±1.58	−3.69	−0.54	21 562	13
Target #1>Target #2 (0/1)	Logit	L_{Aeq}	–	−0.92	±0.23	−1.15	−0.69	21 562	13
Part IV: Questions with implied comparisons of two target noise sources									
Volunteer TN annoyance	Logit	L_{Aeq}	–	−0.03	±0.13	−0.16	0.10	40 495	27
Complain to authorities			–	0.30	±0.39	−0.09	0.68	22 954	12

[a]The control variables have been included in a multiple regression analysis with the target and ambient noise.
[b]The ratio (R) is the average of each survey's estimate of R weighted by the number of interviews.
[c]The Part III comparison ratings are for 13 regressions of annoyance differences (road traffic versus other annoyance) on road traffic noise and other noise (i.e., each study provides a single estimate). Including a second data set from the same study would be redundant since the same annoyance ratings would enter in both analyses (with opposite signs).

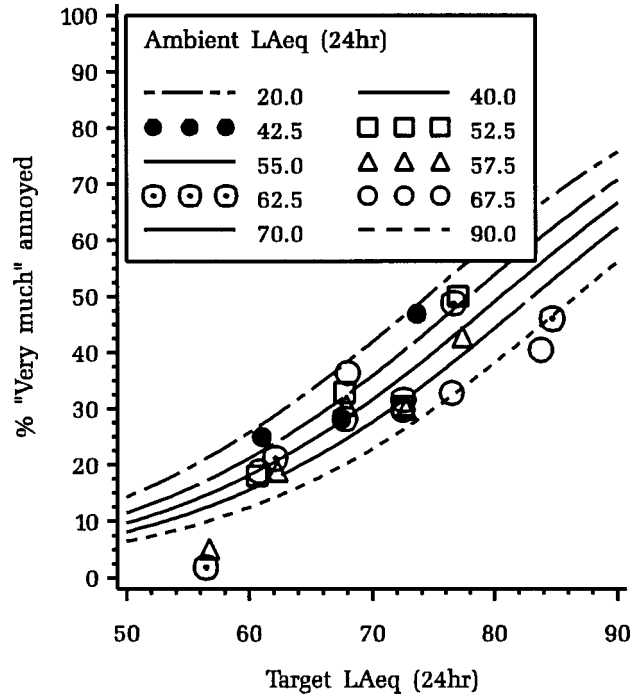

FIG. 3. Response to aircraft noise at five road traffic ambient noise levels (L_{Aeq24h}) (1976 Heathrow aircraft survey, UKD-130).

dex on L_{Aeq} of $R=-0.06$ and the logistic regression of the multi-point index on L_{Aeq} of $R=-0.03$. Both estimates weigh the individual data set estimates by their sample sizes, utilize the data from all 35 data sets and are based on annoyance measures that extract considerable information from the reaction questions. L_{Aeq} is less sensitive than DNL to errors in assumptions about nighttime exposures in some data sets. The preferred values of $R=-0.06$ and $R=-0.03$ are encompassed by the 95% confidence intervals of 39 of the 41 direct and indirect estimates of the ambient effect ratio in Table II.

a) *Conclusion.* This analysis of the best available data shows that the presence of a second, ambient noise does not reduce or only slightly reduces annoyance with an audible target noise. The small size of these effects and the implications of their confidence intervals are perhaps clearer when the ambient effect ratio is expressed as the number of decibels of ambient noise that have the same impact as a single decibel of target noise. The logistic model estimate of $R=-0.03$ implies that a 30-dB decrease ($1/-0.0331$) in ambient noise has no more impact than a single decibel increase in target noise. Even the most extreme proposed estimate of $R=-0.15$ implies that the 30-decibel decrease in ambient noise has less effect than a 5-dB ($4.5=30\bullet-0.15$) increase in target noise.

2. Testing for ambient effects in subgroups

This section considers the possibility that a strong effect of ambient noise has been obscured by ignoring differences between types of noise sources, adopting too simple an ambient effects model, or ignoring the quality of the noise data.

a) *Noise source differences.* It might be hypothesized that an ambient impact would only be expected for an intermittent target noise (such as aircraft) against a continuous background (such as road traffic). Although the average of

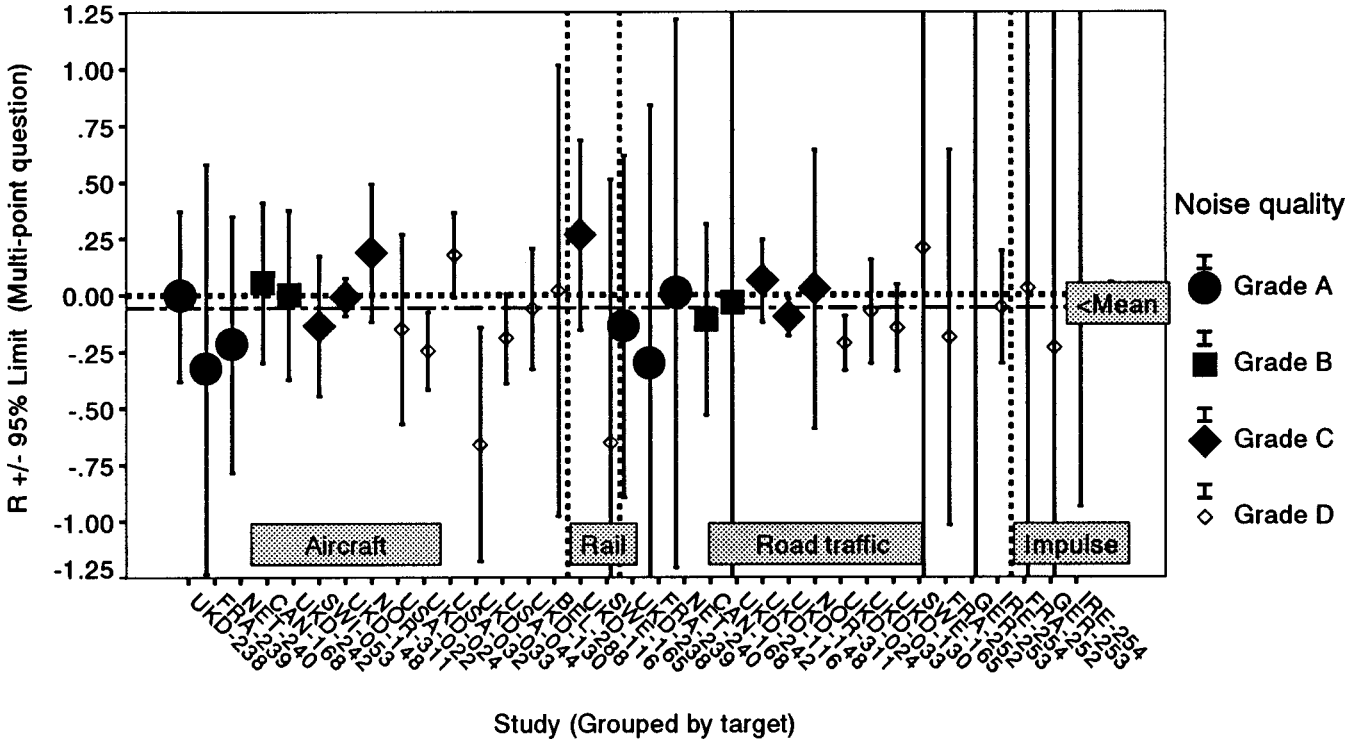

FIG. 4. Equivalent impact ratios (R) and 95% confidence intervals from cumulative logistic regression analyses for each of 35 data sets (identified by survey catalog number in Table AI) classified by noise source and noise data quality grade. (Two estimates are beyond the range in the figure. $R=1.43$ for impulse noise for IRE-254; $R=6.58$ for road traffic for GER-253.)

the ambient effect ratios for the aircraft target noises ($R = -0.10$) is slightly stronger than for the road traffic target noises ($R = -0.04$) in Table I, this difference is not statistically significant ($p > 0.05$) and better evidence does not support the hypothesis. The pair-wise comparison of the ten studies with both aircraft and road traffic evaluations in Table I shows that in seven of the ten comparisons road traffic target noise, rather than aircraft, is more strongly affected by the presence of a second noise source. In addition, the other two intermittent target noises in Table I (railway and impulse) are less affected by ambient noise than are the traffic noise sources. Similar results were found for the logistic regression analysis summarized in Fig. 4. The data for similar comparisons for all of the rating measures in Table II are available in the main report (Fields, 1996, Appendix D).

b) *Alternative ambient effect models.* The classic loudness perception experiments (e.g., Fig. 1) suggest the possibility that an ambient effect occurs over only a limited range of perhaps 30 dB when target and ambient noises are relatively equal. This pattern was tested with the social survey data in four sets of analyses by examining only those respondents for whom the difference between target and ambient values fell within four 30-dB ranges (L_{Aeq}). A second possibility is that an ambient effect might only exist at one end of the target noise range. This pattern was tested in four sets of analyses restricted to samples below 50 dB (L_{Aeq}), above 50 dB, below 60 dB and above 60 dB. None of these eight sets of linear or logistic regression analyses found a statistically significant-ambient effect ($p < 0.05$). The values of the ambient effect ratio ranged from $R = -0.07$ to $R = +0.31$ (Fields, 1996, Table 7, Tables D-2.9–D2.12). To reduce the possibility that inconsistencies in estimating the ranges of noise values could distort the estimates, these analyses excluded the 18 lowest quality data sets (labeled ''Grade D'' in Table AI).

c) *Quality of noise estimates.* The possibility that an ambient noise impact might be obscured by low-quality noise exposure data has been evaluated. In the absence of firm, statistically-based measures of the precision of the estimates of the long-term exposures (e.g., L_{Aeq} for 12 months), the noise data were graded into four quality groups (Grades A to D in Table AI) on the basis of ten quality factors and the range of measured noise levels (Fields, 1996, Appendix B). Grade A studies, for example, had direct estimates of L_{Aeq} for the nominal microphone location while Grade D studies lacked information about the noise metric or, for surface transportation, the location of the measurements relative to the noise source. No large or statistically significant differences were found in the estimates of the ambient effect ratio between the highest-graded and lowest-graded groups of data sets (Fields, 1996, pp. 29–31).

3. Comparisons of the simultaneous ratings of two target noises and the validity of the annoyance questions

Although the analyses in this section have shown that target noise evaluations are not affected by the presence of a second noise, other analyses do show that target noise evaluations are affected by target noise exposure and that a respondent's relative annoyance with two target noise sources is in general agreement with the relative noise exposures from the two target noises. The positive values for $B_{TL\,\mathrm{Aeq}}$ in Table I show that target noise evaluations are positively related to target noise exposure in all of the 35 data sets.

In part III of Table II, the difference between the annoyance rating for one target noise and a second target (ambient) has been regressed on the noise exposure from the two target noises. The strong negative values for the ambient effect ratios ($R = -1.21$ or $R = -0.64$) show that annoyance with one target noise relative to that of another target noise is just as expected: as the second target's noise levels become relatively high, the second target's annoyance levels become high, relative to those of the first target. This is true for both the simple classification of whether the first target is more highly scored ($R = -0.64$) and for the difference between the two scores ($R = -1.21$).

The estimates in part IV of Table II are for two low-validity measures of ambient effects that have occasionally been reported: volunteering target noise annoyance and complaining to authorities. As both of these questions tend to elicit only one noise source mention, they might also be expected to elicit measures of the relative rankings of two target noises rather than a measure of ambient noise impact. The weak, not statistically significant, relationships ($R = -0.03$, $R = +0.30$) in part IV of Table II do not support that conjecture.

III. RESULTS FROM A META-ANALYSIS OF 16 ADDITIONAL PUBLISHED TARGET NOISE EVALUATIONS

Other community studies have been reported in the noise literature for which the original data could not be obtained and the ambient effect ratio could not be directly estimated. In order to consider these studies, a meta-analysis was conducted by reading the publications, accepting the publications' diverse characterizations of the strength of the ambient noise effect and then tabulating their conclusions.

A. Data and methods

After a comprehensive review of the noise reaction literature some 16 additional ambient effect evaluations were located in 13 surveys.[2] In the absence of an exact estimate of R, the best of five alternative criteria is used to determine whether each of the 16 published findings indicates an ''important'' ambient noise effect. In descending order of validity the three standard (effect-size) criteria are

$\geqslant 3$ dB — a difference in annoyance scores that is the equivalent of at least a 3-dB difference in target noise exposure between respondents at different ambient noise levels,

TABLE III. Results and characteristics of 16 findings from 13 published surveys that appear in the meta-analysis.

Survey title (Catalog ID, see Fields, 1991)	Findings on ''important'' impact of ambient noise: Target noise control?	Criterion[a]	Standard quality?[b]	Target noise: Source	Target noise: Range	Ambient noise indicator[e]: Source	Ambient noise indicator[e]: Range	No. of interviews
Three findings that ambient noise reduces target noise annoyance								
1986 Sydney Aircraft/Road (AUL-307) (Putra, 1990, pp. 114, 353, 442; Lawrence and Putra, 1989, p. 894)	No	$\geqslant \Delta 5\%$	No	Aircraft	Unknown	Road	53–77 $=_{\Delta} 24\ L_{\mathrm{Aeq16h}}$	224
1989 Muroran Road/Rail (JPN-319)[c] (Izumi and Yano, 1990, pp. 281, 282)	√	$\geqslant$3 dB (sr)	√	Road	43–66 $=_{\Delta} 23\ L_{\mathrm{Aeq24h}}$	Rail	43–67 $=_{\Delta} 24\ L_{\mathrm{Aeq24h}}$	204
1990 Toronto Air conditioner (CAN-322)[c] (Bradley, 1993, p. 1981; Bradley, 1991, p. 31)	√	$\geqslant$3 dB	No	Air conditioner	Unknown	Community	53–69 $=_{\Delta} 16\ L_{\mathrm{Aeq24h}}$	550
Eleven findings that ambient noise has no important effect on target noise annoyance								
Swiss 3-Airport (SWI-053)[d] (Graf *et al.*, 1974, p. 144; Grandjean *et al.*, 1973, p. 648)	√	$\geqslant 0.01r^2$	√	Road	45–67 $=_{\Delta} 22\ L_{\mathrm{50(12h)}}$	Aircraft	5–37 $=_{\Delta} 32\ \mathrm{NNI}_{\mathrm{16h}}$	949
1979 Swiss General Aviation (SWI-180) (Institut für ..., 1980, pp. 56, 78, 79)	√	$\geqslant \Delta 5\%$ (ns)	√	Aircraft	30–69 $=_{\Delta} 39\ L_{\mathrm{Aeq12\,h}}$	Community	⟨41–47⟩ $=_{\Delta} 6$ dB (A)	1010
1964 Oklahoma City Sonic Boom (USA-012) (Borsky, 1965, Vol. I, pp. 25, 28, 30)	No	$\geqslant \Delta 5\%$ (ns)	No	Sonic boom	58–65 $=_{\Delta} 7\ L_{\mathrm{Cdn}}$	Area	Rural or urban	3000
1972 London Construction Site (UKD-074) (Large and Ludlow, 1976, p. 64)	√	$\geqslant 0.01r^2$ (ns)	√	Aircraft	32–32 $=_{\Delta} 0\ \mathrm{NNI}_{\mathrm{12h}}$	Road and construction	52–69 $=_{\Delta} 17\ L_{\mathrm{Aeq12h}}$ 30–70 $=_{\Delta} 40\ L_{\mathrm{Aeq12h}}$	535
1972 London Construction (UKD-074) (Large and Ludlow, 1976, pp. 62, 63; Ludlow, 1976, Table 23, Fig. 34)	√	$\geqslant$3 dB (ns)	√	Construction	30–70 $=_{\Delta} 40\ L_{\mathrm{Aeq12h}}$	Road	52–69 $=_{\Delta} 17\ L_{\mathrm{Aeq12h}}$	535
1972 Paris-Area Railway (FRA-063) [Aubree, 1973, p. 34 (p. 36 in English translation)]	√	$p<0.05$ (ns)	No	Rail	60–80 $=_{\Delta} 20\ L_{\mathrm{Aeq12h}}$	Community	47–67 $=_{\Delta} 20 L_{\mathrm{AeqDay}}$	350
1977 Dutch Railway (NET-153) (de Jong, 1983, p. 300; Peeters *et al.*, 1984, p. 47)	√	Vb	√	Rail	40–70 $=_{\Delta} 30\ L_{\mathrm{Aeq24h}}$	Community	37–44 $=_{\Delta} 7\ L_{\mathrm{95,24h}}$	670
1989 Muroran Road/Rail (JPN-319)[b] (Takahashi, 1991, p. 204, Fig. 8.11, Izumi, 1993)	√	$p<0.05$ (ns)	No	Rail	43–67 $=_{\Delta} 24\ L_{\mathrm{Aeq24h}}$	Road	43–66 $=_{\Delta} 23\ L_{\mathrm{Aeq24h}}$	204
1986 Sydney Aircraft/Road (AUL-307) (Putra, 1990, pp. 114, 353, 441, 443)	√	$\geqslant$3 dB	√	Road	53–77 $=_{\Delta} 24\ L_{\mathrm{Aeq16h}}$	Aircraft	⟨20–⟩25 $=_{\Delta} >5$ ANEF[f]	650
1978 Zurich Time-of-day (SWI-173) (Wehrli *et al.*, 1978, p. 145)	No	Vb	No	Road	20–75 $=_{\Delta} 55\ L_{\mathrm{Aeq16h}}$	Community	Rural or city[e]	1600
1977 Hampshire Village (UKD-160) (Hawkins, 1980, Fig. 6b, pp. 53, 54)	No	$\geqslant \Delta 5\%$ (ns)	No	Road	45–70 $=_{\Delta} 25\ L_{\mathrm{Aeq18h}}$	Area	Rural or national[e]	1595
Two findings that high ambient noise increases target noise annoyance								
1968 Coventry Railway (UKD-029) (Walters, 1970, p. 60)	No	Vb	No	Rail	40–450 m	Dwelling noise	Single unit or flats[e]	85
1987 Seoul Traffic (KOR-295) (Yu, 1987, pp. 986, 987)	No	$\geqslant$3 dB (sr)	No	Road	⟨61–⟩71 $\geqslant_{\Delta} 10 L_{\mathrm{Aeq}}$	Area	Resident or industry	351

[a]Definitions for $\geqslant$3 dB, $\geqslant \Delta 5\%$, $\geqslant 0.01r^2$, $p<0.05$, and ''Vb'' (Verbal) are given in the text. In addition, ns=not statistically significant ($p>0.05$) and sr=statistically significant (using unrealistically precise simple random sampling assumptions).

[b]The quality rating relates only to this ambient noise meta-analysis and not to other published analyses that achieved the surveys' planned, original goals.

[c]Two surveys (catalog Nos. JPN-319 and CAN-322) were not included in the survey catalog (Fields, 1991). Their descriptions can be obtained from the author.

[d]The aircraft noise evaluation for survey SWI-053 is a direct analysis data set.

[e]In four studies ambient levels were not measured but were assumed to be different because of the site location (rural or city; rural or nationally representative; resident in a single unit building or resident in a noisier, multiple-dwelling building consisting of many apartments).

[f]ANEF is the Australian Noise Exposure Forecast (dB) that contains a single weighting for both evening and nighttime hours that is less than the standard NEF nighttime weighting.

$\geqslant \Delta$ 5% a difference of at least 5% annoyed at different ambient levels,

$\geqslant 0.01r^2$ at least 1% of the variance in annoyance is explained by ambient noise.

In the absence of the above, the two nonstandard indicators are

$p < 0.05$ a statistically significant difference between respondents at different ambient noise levels ($p < 0.05$),

Verbal an unqualified, verbal assertion that ambient noise affects annoyance (i.e., no qualification such as ''small'' or ''slight'').

Each of the 16 study findings was classified by target noise source, ambient noise source, number of respondents, and overall quality (Table III). Standard quality findings used one of the three standard effect-size indicators given above and also controlled for the impact of target noise levels when drawing conclusions about reactions in different ambient noise exposure groups. A complete discussion of the rationale for these classifications is available elsewhere (Fields, 1996, Appendix F).

B. Results

Figure 5 shows that 11 of the findings, accounting for the vast majority of the respondents, indicate that the responses in the presence of ambient noise are about the same as those in the absence of ambient noise. Only 3 of the 16 findings, from studies with 978 (8%) of the 12 512 responses, suggested that there was an important tendency for annoyance with a target noise to be reduced in the presence of high ambient noise levels.

If the data in Fig. 5 are reanalyzed taking into account the noise source or the data quality rating, the same conclusions are reached. No important ambient noise effect is found for two of three aircraft findings or four of six road traffic findings. No important effect is found for five of the six standard quality findings. The results and bases for each finding are shown in Table III.

The evidence from the 12 512 responses in the 16 published findings in this section is consistent with the evidence from the 57 982 responses for the 35 analyzed reactions in the previous section. If ambient noise has any impact in a residential setting, it is not a strong impact.

IV. RESULTS FROM RATINGS OF NOISE DURING LABORATORY SESSIONS

In this section laboratory studies are examined to determine whether annoyance with complex environmental noises is affected by the presence of other, carefully measured noises in two laboratory rating situations: (1) when each target noise event is rated separately and (2) when the total session of exposures to a target noise is rated as a whole.

An attempt to locate all relevant studies published in English by the end of 1995 was made by reviewing eight journals, searching the PSYCHLIT electronic data base, scanning 162 article abstracts, and personally contacting every author of a relevant publication to ask about other publications. A total of 23 findings from 21 laboratory studies

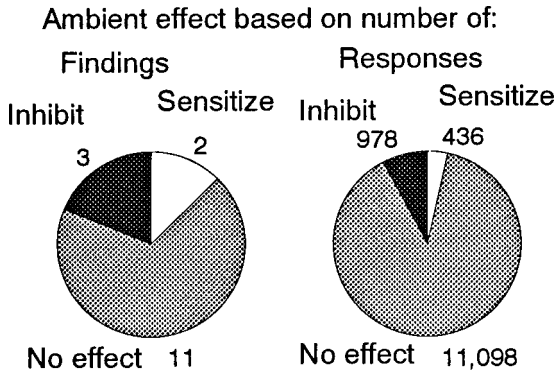

FIG. 5. Numbers of studies and responses in studies that indicate that annoyance with target noise stays the same or is reduced or increased to an important extent (source: 12 512 ratings of 16 noises from 13 surveys containing 11 549 respondents).

were located that contained all five of the following elements: (1) a target noise is itself rated (not the total noise environment), (2) the target noise is a complex environmental noise, (3) the rating is a subjective rating of the annoyance, loudness, or noisiness of the noise (not of its audibility), (4) an ambient noise is simultaneously presented, and (5) the impact of ambient noise is evaluated by contrasting reactions under conditions that differ in either target or ambient noise levels. The procedures followed and results of the search have been described in greater detail elsewhere (Fields, 1996, Appendix G).[3]

Single noise events were rated in 11 findings from ten studies. In these studies the subject rated a single presentation of a target noise before hearing the next target noise presentation. These studies generally support the pattern found in the tone perception studies. Nine findings (eight studies) indicated that reactions to a target noise were reduced by ambient noise (Berglund *et al.*, 1980; Fidell and Teffeteller, 1978, 1981; Fidell *et al.*, 1979; Pearsons, 1966; Pearsons *et al.*, 1979; Powell, 1979 (2 findings); Sternfeld *et al.*, 1974, pp. 14–17; Wells, 1971). Only 2 of the 11 findings did not find the expected pattern (Powell and Rice, 1975; Sternfeld *et al.*, 1974, pp. 3–11).

Total sessions of exposures to multiple target noise events (for example, a set of aircraft flyovers) were rated in 12 findings from ten studies (see Table AII). These findings differed from the single event ratings and resembled the findings from the field surveys. Nine either found no support for an ambient noise effect or found that ambient noise increased annoyance (Powell, 1978: 1st, 2nd (2 findings), and 3rd Session Experiments; Powell, 1978: 1st, 2nd, 3rd, and 4th Pilots; Powell and Rice, 1975). Only three studies found that ambient noise reduced target noise annoyance (Powell, 1978: 5th Pilot; Powell, 1978: 3rd Session Experiment; Vos and Smoorenburg, 1985). The only one of these later three that found a strong, statistically significant effect (Vos and Smoorenburg, 1985) was also the only 1 of the 12 findings for which the ambient noise was kept at an unvarying level during the entire rating session. In all of the other studies, the ambient noise fluctuated somewhat during the session so that, as in a residential environment, the subject could occasionally experience individual target noise events in the ab-

sence of high ambient noise levels. This suggests that ambient noise levels may not affect annoyance when, as in the normal living environment, people know what the noise level would be in the absence of ambient noise. In short, those laboratory studies that most closely match the residential environment do not support the traditional ambient noise hypothesis that residents in high ambient noise areas will be less annoyed by target noises.

V. CONCLUSIONS AND DISCUSSION

Laboratory studies show that the perceived loudness of tones and the annoyance with individually presented noise events are reduced in the presence of background noise. However, the present analysis has found that neither field nor laboratory studies show that annoyance with longer-term exposures to multiple noise events is reduced in the presence of a second noise. Because only a summary noise metric (LAeq) was available for the present analyses, it has not been possible to analyze variations in individual-event levels in rare situations in which target noises are always partially masked by ambient noises. None the less, by examining a wide range of combinations of target and ambient noise levels, the present analysis provides an adequate test for common variations in individual events from transportation noise sources.

It has often been assumed that residents' reactions to a target noise will be reduced if there are other environmental noises present. Why do the data from more than 70 000 evaluations of 51 noise sources by over 45 000 residents from 32 social surveys not show a strong effect of one noise source on the evaluations of another noise source? The wide range of surveys examined, the methods followed in preparing the surveys for this analysis, and the lack of variation in results for stronger and weaker surveys suggest that the answer is not weaknesses in the study methods. Furthermore, carefully controlled laboratory studies led to a similar conclusion.

Since the best available empirical data do not support the expectations about ambient noise impact, it is important to reexamine the theories that hypothesize an ambient noise effect. Except for theories about the perception and detection of partially masked noise events (e.g., Fidell and Teffeteller, 1981; Schultz, 1982, pp. 327–328; Stevens and Guirao, 1967), this author has been unable to find explicitly enunciated theories that give the basis for expecting an ambient noise effect. Some theories about reactions in low noise environments (Schultz, 1982, pp. 328–330) or reactions in apartments with a facade not exposed to a target noise (Fields, 1992a, pp. 117–120) turn out, on reflection, to be theories about reactions to low-level target noises, not about ambient noise effects. Previous survey publications have almost always implicitly, rather than explicitly, presented theories that ambient noise reduces target noise annoyance. Close examination of three such theories suggests that there are equally strong theoretical bases for hypothesizing that ambient noise should not affect target noise annoyance or should, instead, make residents more sensitive to a target noise.

A. Acoustical-perceptual theories

Acoustical-perceptual theories are based on the type of finding illustrated in Fig. 1; perceptions of the loudness of a target noise are inhibited when ambient noise levels approach or exceed those of a target noise level. There are at least three reasons for expecting that such perceptual inhibition is relatively unimportant in the residential environments.

First, because the ambient noise levels fluctuate greatly over time, residents may experience the target noise often enough without an ambient noise present that they form an accurate estimate of the target noise level regardless of the ambient noise conditions. The phenomenon of perceptual constancy may mean that as long as the target noise can be clearly identified, residents correctly estimate the target noise level rather than incorrectly assuming that the target noise is quieter when another noise is present.

Second, research on interior residential noise levels has shown that the total ambient noise environment in residences is dominated by the noises that the individual or other household members generate as they go about their normal daily routines of communicating, listening to audio equipment, performing household chores, moving about their environment or touching things that are close to their ears. If perceptions of a target noise in a residential environment are in fact inhibited by the ambient noise, a second, external transportation noise source would be expected to be a trivial contributor to that ambient noise.

Third, instead of inhibition there may be sensitization. Some residents who are exposed to multiple noise sources may react by becoming generally more aware of all noise sources (Schultz, 1978, p. 385).

One variant of an acoustical perception perspective is subject to the reductionist fallacy: the assumption that the physical laws that explain a phenomena at one level (e.g., the perceptions of individual noise events) can be simply extrapolated to the next level of abstraction (e.g., feelings about a total noise environment). An example is the assertion that people cannot be affected by individual noise events they do not hear. The reasonable part of this assertion is the assumption that people must perceive some instances of a noise source to form a judgment about the source. The fallacy is the assumption that the appropriate model for combining the effect of those events is a summation of only those events that were directly perceived. An alternative model assumes that people use their knowledge about physical phenomena to form their perception of the total noise environment (e.g., a noisy aircraft environment continues to be noisy even when I create a masking noise). The feelings about the noise environment produced by a single noise source do not need to be the sum of the sound pressure levels that are perceived at a resident's ear any more than the feelings about the visual environment produced by a neighborhood trash dump need to be the sum of the minutes that visual images of a trash dump are processed by a resident's retina. In short, the noise events that are partially or fully masked can affect residents' feelings if residents can estimate the unmasked noise levels of those events.

B. Environmental reference-point theories

Even if a second noise source does not directly affect perceptions, the environmental reference-point theory posits that judgments about the seriousness of one target noise will be reduced if there is another more serious target noise present. This is an understandable assumption for acoustical professionals who deal primarily with acoustical phenomena and limit their theories to acoustical variables. An equally logical alternative assumption is that residents judge the seriousness of target noises relative to the seriousness of other nonacoustical environmental nuisances in the neighborhood. Alternatively, residents may judge target noises relative to portable, omnipresent noise sources (people's voices, audio instruments) or may make judgments on an absolute, not a relative, basis. Another possibility is that residents judge target noises in their neighborhood relative to noises they have experienced in other neighborhoods. For all of these alternatives a target noise is not judged by reference to another transportation noise within the local neighborhood environment. Of course, the alternative sensitization theory is that the presence of one nuisance in the neighborhood (an ambient noise) makes residents environmentally more conscious of all environmental problems and thus sets a higher reference point for judging the target noise.

C. Quietness valuation theories

Quietness valuation theories assume that through self-selection or other processes the types of people who choose to live in a quiet area are the types of people who more highly value quiet. Residents who choose to live near a busy highway, for example, are assumed to have already judged that quietness is not highly valued and to thus be similarly insensitive to a second noise, for example, aircraft noise. The alternative assumption is that the value placed on quiet is uniformly distributed across residential areas. Direct evidence for this alternative assumption comes from a previous meta-analysis of the relationship between noise sensitivity and community noise levels for 17 noise ratings by over 31 000 respondents in 16 studies (Fields, 1992a, p. 25). Self-rated noise sensitivity was compared in high-noise communities and low-noise communities. In that meta-analysis no important differences in sensitivity were found in most studies (13 of the 17 noise ratings). Of course, the alternative sensitization theory is that some people begin to place a higher value on quietness from all noise sources when they live in an environment with a high ambient noise exposure.

Professional, community noise acousticians' beliefs in the standard quietness valuation theory can be easily explained by their contact with unrepresentative samples of the population at times when new noises are introduced. In this situation, an effective political argument is that residents who do not have other loud noises present should not be subject to a loud environmental noise. This is easily transformed into the untested empirical argument that people who do not have a second noise source present will be more bothered by the presence of a new noise source.

D. Summary

In summary, a careful consideration of the theoretical and experimental bases for forming hypotheses about ambient noise impact does not contradict the empirical findings in this report. If people are exposed to events for which they can develop a logical estimate of their long-term noise exposure (in the absence of ambient noise), then their annoyance may be related to the actual noise levels of the events, not the sum of the perceived levels of the directly experienced events. In this latter situation ambient noise does not reduce reactions to target noises in either short laboratory rating sessions or residential environments.

ACKNOWLEDGMENTS

This work was funded by the Office of Environment and Energy of the Federal Aviation Administration. The ESRC Data Archive at the University of Essex, United Kingdom, is a repository for many data sets. The analyses depended upon more than 40 community noise researchers who generously gave their time to provide data and patiently consulted their memories and archives to answer detailed questions about their studies. Special thanks are due to Marsha R. Annis, Dominique Aubree, Birgitta Berglund, Martin Björkman, Bernard F. Berry, Paul Borsky, John Bradley, Robert B. Bullen, Thomas L. Connor, William K. Connor, Ronald G. de Jong, Ian Diamond, Sanford Fidell, Eugene Galanter, Truls Gjestland, Fred L. Hall, Robert Hofman, Richard D. Horonjeff, Kiyoto Izumi, Soames Job, Deborah Jones, Robert E. Jonckheere, Anita Lawrence, John E. Ludlow, Michel Maurin, Aubree McKennell, H. M. E. Miedema, H. Myncke, Evy Öhrström, John Ollerhead, Karl S. Pearsons, C. A. Powell, Ardhana Putra, J. M. Rabrait, Chris Rice, David Rickert, Bernd Rohrmann, Alvin Rosenthal, Ragnar Rylander, Kevin Shepherd, Stephen A. Stansfeld, S. Martin Taylor, Henk Vos, Joos Vos, John Walker, and Takashi Yano.

APPENDIX: DESCRIPTION OF ANNOYANCE AND NOISE EXPOSURE DATA

TABLE AI. Data for the direct analyses of 35 target noise evaluations from 20 surveys (40 noise sources).

Identification					Major direct reaction meausures			Best published data to estimate L_{Aeq24h}		Adjustments to noisiest facade[e] (without reflections) (√=none, NA=unknown position)	Noise quality grade[f]		
Survey title (Catalog ID, see Fields, 1991)	No.	Noise source	No. of Interviews (G=grouped)[a]	No. of sites	Multi-point question (No. of points)[b]	High annoyance: verbal labels and fraction of scale points	Multi-item index-N[c]	Noise metric[d] (√=L_{Aeq})	No. of hours (√=24)		Grade for procedure	σ_{LAeq}[g]	Data set
CEC/84 Glasgow (UKD-238)	1.	Aircraft	605	6	Verb-4	1/4 ''Very much''	Index-2	√	√	√	A	5.6	A
(Diamond *et al.*, 1986)	2.	Road	605	6	Verb-4	1/4 ''Very much''	Index-2	√	√	−2.5	A	8.3	
CEC/84 French (FRA-239)	3.	Aircraft	570	9	Verb-4	1/4 ''Beaucoup''[i]	Index-2	√	√	√	A	9.6	A
(Vallet *et al.*, 1986)	4.	Road	570	9	Verb-4	1/4 ''Beaucoup''[i]	Index-2	√	√	−3	A	6.7	
CEC/84 Schiphol (NET-240)	5.	Aircraft	581	9	Verb-4	1/4 ''Heel erg''[i]	Index-3	√	√	√	A	5.6	A
(Diamond and Walker, 1986)	6.	Road	581	9	Verb-4	1/4 ''Heel erg''[i]	Index-2	√	√	√	A	6.5	
1978 Toronto (CAN-168)	7.	Aircraft	617	53	Verb-5 (Bipolar-9)	2/5 ''Considerably, Extremely''	Index-7	√	√	√	A	3.8	B
(Hall *et al.*, 1981)	8.	Road	597	53	Verb-5 (Bipolar-9)	2/5 ''Considerably, Extremely''	Index-7	√	√	√	A	5.6	
1982 Heathrow (UKD-242)	9.	Aircraft	413	10	Verb-4	1/4 ''Very much''	Index-3	√	√	√	A	4.1	B
(Brooker *et al.*, 1985)	10.	Road	410	10	Verb-4	1/4 ''Very much''	Verb-4	√	√	−2.5	A	7.9	
British-Rail (UKD-116)	11.	Rail	1453	300+	Verb-4	1/4 ''Very much''	Index-5	√	√	−2.4	A	12.3	C
(Fields and Walker, 1982)	12	Road	1453	300+	Numb-7	2/7	Index-2	√	Day[k]	−2.5	C	6.4	
1976 Gothenburg (SWE-165)	13.	Trams	464(G)	6	Verb-4	1/4 ''Very'' ''Mycket''	''Very''	√	√	−3	A	3.4	D
(Rylander *et al.*, 1977)	14.	Road	464(G)	6	Verb-4	1/4 ''Very'' ''Mycket''	''Very''	Traffic count	√	√	C	6.4	
Swiss 3-Airport (SWI-053)	15.	Aircraft	3940(G)	25[h]	Numb-11	3/11	3/11	NNI	16	Measured on balcony railings	C	10.9	C
(Graf *et al.*, 1974)		Road						L_{50}	12		C	6	
1982 Fornebu (NOR-311)	16.	Aircraft	3322	15	Verb-4	1/4 ''Very'' ''Svært''	Index-4	EFN	√	√	A	7.7	C
(Gjestland *et al.*, 1990)	17.	Road	3320	15	Verb-4	1/4 ''Very'' ''Svært''	Index-2	Traffic count	√	−3.0 (distance)	C	6.6	
1977 Heathrow (UKD-148)	18.	Aircraft	5818	200+	Numb-7	2/7	Numb-7	N, L	12	√	C	7.3	C
(Tarnopolsky and Morton-Williams, 1980)	19.	Road	5882	200+	Numb-7	2/7	Index-2	Traffic count	Off peak	−2.5	C	6.1	
1980 Brussels (BEL-288)	20.	Aircraft	677(G)	11	None	1/3	Indx-11[j]	NNI	√	√	B	6	D
(Jonckheere, 1989)		Other						√	√	NA	D	3	
1969 Heathrow (UKD-033)	21.	Aircraft	315(G)	9	Open-2	None	Index-6	N, L	12	√	C	10.4	D
(Bottom, 1971)	22.	Road	315	9	Open-2	None	Index-3	Traffic count	√	NA	C	4.1	
1967 Heathrow (UKD-024)	23.	Aircraft	4650	251	Verb-4	1/4 ''Very much''	Verb-4	N, L	√	√	B	8.4	D
(MIL Research, 1971)	24.	Road	4638	251	Verb-4	1/4 ''Very much''	Verb-4	Other	None	NA	D	5.4	
1976 Heathrow (UKD-130)	25.	Aircraft	2563	44	Verb-4	1/4 ''Very much''	Verb-4	N, L, Duration	12	√	B	6.7	D
(McKennell, 1977)	26.	Road	2502	44	Verb-4	1/4 ''Very much''	Verb-4	Other	None	NA	D	5.8	
USA-4-Airport (USA-022)	27.	Aircraft	3499	61	Numb-5	1/5 ''Extremely''	Numb-5	N, L	√	√	B	11	D
(Tracor, 1971)		Other						L_{50}	Daytime	NA	D	4.3	

TABLE AI. (*Continued.*)

Identification					Major direct reaction meausures			Best published data to estimate L_{Aeq24h}		Adjustments to noisiest facade[e] (without reflections) (√=none, NA=unknown position)	Noise quality grade[f]		
Survey title (Catalog ID, see Fields, 1991)	No.	Noise source	No. of Interviews (G=grouped)[a]	No. of sites	Multi-point question (No. of points)[b]	High annoyance: verbal labels and fraction of scale points	Multi-item index-N[c]	Noise metric[d] (√=L_{Aeq})	No. of hours (√=24)		Grade for procedure	σ_{LAeq}[g]	Data set
USA-3-Airport (USA-032)	28.	Aircraft	2899	187	Numb-5	1/5 ''Extremely''	Numb-5	N, L	√	√	B	8.4	D
(Tracor, 1971)		Other						L_{50}	Daytime	NA	D	4.4	
USA-2-Airport (USA-044)	29.	Aircraft	1954	24	Numb-5	1/5 ''Extremely''	Numb-5	N, L	√	√	B	9.1	D
(Connor and Patterson, 1972)		Other						L_{50}	Daytime	NA	D	5.1	
CEC/Imp French (FRA-252)	30.	Impulse	451	10	Verb-4	1/4 ''Very'' ''très''	Index-2	√	√	−3	A	20.7	D
(Groeneveld and de Jong, 1985)	31.	Road	451	10	Verb-4	1/4 ''Very'' ''très''	Index-2	√	√	NA	D	7.1	
CEC/Imp German (GER-253)	32.	Impulse	248	18	Verb-4	1/4 ''Very'' ''sehr''	Index-2	√	√	−3	A	7	D
(Groeneveld and de Jong, 1985)	33.	Road	248	18	Verb-4	1/4 ''Very'' ''sehr''	Index-2	√	√	NA	D	5.1	
CEC/Imp Ireland (IRE-254)	34.	Impulse	454	18	Verb-4	1/4 ''Very''	Index-2	√	√	−3	A	15.5	D
(Groeneveld and de Jong, 1985)	35.	Road	453	18	Verb-4	1/4 ''Very''	Index-2	√	√	NPA	D	5.4	

[a]Only group-level response data (averages) are available.
[b]The multi-point question is used in the cumulative logistic regression analysis in Fig. 4 and in Table II. For study UKD-033 the multi-point question is a volunteered mention of the noise source on an open question.
[c]The multi-item index is based on the average scores from ''N'' questions and used in the linear regression analysis in Tables I and II. Where the term ''Index'' is not used, only one question is used.
[d]Definition of metrics: N,L=number of noise events and the logarithmic average peak level of those events); EFN=Norwegian Equivalent Aircraft Sound Level index, dB. [This index contains a nighttime weighting, a graduated evening weighting and a Sunday weighting. Near Fornebu (Oslo) Airport, EFN is approximately equal to $L_{dn}+0.8$ dB.] ''Traffic count'' appears even if the noise metric value provided is derived from a traffic count.
[e]In the absence of study-specific estimates, exposures reported at 1 m before a dwelling facade are reduced by 2.5 dB for road traffic and 2.4 dB for railway noise.
[f]The quality rating relates only to this ambient noise meta-analysis and not to other published analyses achieving the surveys' planned, original goals.
[g]The noise quality grade is reduced to Grade D for standard deviations of less than $\sigma_{LAeq}=3.5$.
[h]Data for 25 noise ranges were aggregated from an unknown number of study sites (SWI-035).
[i]''Heel erg'' and ''Beaucoup'' are translated as ''very much.''
[j]Index-11 is based on 11 questions, but was collapsed into three scores when published (BEL-288).
[k]Road traffic is estimated with a single 10-minute measurement (UKD-116).

TABLE AII. Data from ratings of noise during laboratory session studies.

Study No.[a]	Target noise(s) rated	Length of period rated (min)	Ambient noise	No. of subjects	No. of ratings[b]	Results: Ratio (+/−) (S=statistically significant, $p<0.05$, NS=not significant)
			Findings that ambient noise reduces target noise annoyance (R is negative even if not significant)			
13	aircraft	10	road traffic	9	81	$R=-0.06$ (NS)
15a	aircraft	15	road traffic	64	576	$R=-?$ (Weak pattern)
17	gunfire, industrial road traffic	5	constant road traffic	32	512	$R=-0.3$ to -0.6 (less at higher target noise levels)
			Findings that ambient noise does not affect target noise annoyance (no estimates of R or inconsistent estimates)			
14a	aircraft	30	road traffic	27	126	(NS) (no estimate of R)
14b	road traffic	30	aircraft	27	126	(NS) (no estimate of R)
15b	road traffic	15	aircraft	64	512	$R=-$ and $R=+$ (varies) (NS)
16	aircraft	30	road traffic	27	162	(NS) (no estimate of R)
			Findings that ambient noise increases annoyance with a target noise ($R=+$)			
6b	aircraft	12	road traffic	12	24	$R=+$ (no estimate of R) (NS)
9	aircraft	10	road traffic	9	81	$R=+0.50$ (S)
10	aircraft	10	road traffic	9	81	$R=+0.17$ (S)
11	aircraft	10	road traffic	9	81	$R=+0.55$ (S)
12	aircraft	10	road traffic	9	81	$R=+0.18$ (NS)

Note: For detailed information about the study designs see Fields (1996), Table 15.

[a]Study numbers come from the main report (Fields, 1996). Location of information for each study number: 6b (Powell and Rice, 1975), 9 (Powell, 1978, pp. 60–62, ''1st Pilot Study''), 10 (Powell, 1978, pp. 62–64, ''2nd Pilot Study''), 11 (Powell, 1978, p. 64, ''3rd Pilot Study''), 12 (Powell, 1978, pp. 65–70, ''4th Pilot Study''), 13 (Powell, 1978, p. 70 ''5th Pilot Study''), 14a (Powell, 1978, pp. 79–95, ''2nd Session Exp.''), 14b (Powell, 1978, pp. 79–95, ''2nd Session Exp.''), 15a (Powell, 1978, pp. 95–110, ''3rd Session Exp.''), 15b (Powell, 1978, pp. 95–110, ''3rd Session Exp.''), 16 (Powell, 1978, pp. 70–78, ''1st Session Exp.''), and 17 (Vos and Smoorenburg, 1985).

[b]Activities during sessions: 13 of 14 studies allowed reading or other quiet activities (e.g., writing or silent handiwork). In study 6b, subjects were engaged in the rating of the individual noise events.

[1]Although the article's confidence intervals for the individual studies are unchanged from the main report (Fields, 1996), the intervals are slightly different for the summary measures that combine the results from several studies (for example, the ''Mean'' values in Table II) because this article always uses the jackknife-based variance estimates that have a stronger theoretical base than the weighted variance estimates that appeared in the main report. The differences, however, are slight. Of the 90 confidence intervals in text tables in the main report, 74 were within 1% point of the jackknife estimates in this article, 12 overestimated the precision and 4 underestimated the precision.

[2]The present article's meta-analysis includes fewer studies than in previous meta-analyses (Fields, 1992a, 1992b, 1993a, 1993b) because some of the studies could be analyzed in the more powerful direct analyses in the previous section of this article.

[3]Two of the 25 findings in the original report are not in this article's analysis because it was discovered that the subjects had rated the total noise environment rather than only the target noise.

Agresti, A. (**1989**). ''Tutorial on modeling ordered categorical response data,'' Psychol. Bull. **105**, 290–301.

Aubree, D. (**1973**). *Enquête Acoustique et Sociologique Permettant de Définir une Echelle des la Gêne Eprouvée par l'Homme dans son Logement du Fait des Bruits de Train* (Center Scientifique et Technique du Bâtiment, Paris) [English translation: *Acoustical and Sociological Survey to Define a Scale of Annoyance Felt by People in Their Homes Due to the Noise of Railroad Trains*, Technical Information Report No. 88 (Bolt Beranek and Newman, Cambridge, MA)].

Berglund, B., Berglund, U., and Lindvall, T. (**1980**). ''Loudness separation of community noises,'' in *Noise as a Public Health Problem, Proceedings of the Third International Congress*, ASHA Report 10 (American Speech-Language-Hearing Association, Rockville, Maryland), pp. 349–354.

Borsky, P. N. (**1965**). *Community Reactions to Sonic Booms in the Oklahoma City Area*, NORC Report No. 101, AMRL Report AMRL-TR 65-37 (AMRL, Wright Patterson Air Force Base, OH).

Bottom, C. G. (**1965**). ''A social survey into annoyance caused by the interaction of aircraft noise and traffic noise,'' J. Sound Vib. **19**, 473–476.

Bradley, J. S. (**1991**). *Survey of Outdoor Air Conditioner Noise*, Report No. CR-5954.2 (National Research Council Canada, Ottawa).

Bradley, J. S. (**1993**). ''Disturbance caused by residential air conditioner noise,'' J. Acoust. Soc. Am. **93**, 1978–1986.

Brooker, P., Critchley, J. B., Monkman, D. J., and Richmond, C. (**1985**). *United Kingdom Aircraft Noise Index Study: Main Report*, DR Report 8402 (Civil Aviation Authority, London).

Connor, W. K., and Patterson, H. P. (**1972**). *Community Reaction to Aircraft Noise Around Smaller City Airports*, NASA CR-2104 (National Aeronautics and Space Administration, Washington, DC).

de Jong, R. G. (**1983**). ''Some developments in community response research since the second international workshop on railway and tracked transit system noise in 1978,'' J. Sound Vib. **87**, 297–309.

DeMaris, A. (**1992**). *Logit Modeling: Practical Applications* (Sage, Newbury Park, CA).

Diamond, I. D., and Walker, J. G. (**1986**). *CEC Joint Research Project: Community Reactions to Aircraft Noise: Final Report* (ISVR, University of Southampton).

Diamond, I. D., Walker, J. G., Critchley, J. B., and Richmond, G. C. (**1986**). *CEC Joint Study of Community Response to Aircraft Noise 1984, Joint Report: The Influence of Residual Noise on Disturbance from Aircraft Noise*, DR Report 8601 (Civil Aviation Authority, London).

Fidell, S. A., and Teffeteller, S. (**1978**). *The Relationship Between Annoyance and Detectability of Low Level Sounds*, Report 3699 (Bolt Beranek and Newman, Canoga Park, CA).

Fidell, S. A., and Teffeteller, S. (**1981**). ''Scaling the annoyance of intrusive sounds,'' J. Sound Vib. **78**, 291–298.

Fidell, S. A., Teffeteller, S., Horonjeff, R., and Green, D. M. (**1979**). ''Predicting annoyance from detectability of low-level sounds,'' J. Acoust. Soc. Am. **66**, 1427–1434.

Fields, J. M. (**1991**). *An Updated Catalog of 318 Social Surveys of Residents' Reactions to Environmental Noise (1943–1989)*, NASA TM-187553 (National Aeronautics and Space Administration, Washington, DC).

Fields, J. M. (**1992a**). *Effect of Personal and Situational Variables on Noise Annoyance: with special reference to implications for en route noise*, NASA Report Number CR-189676, FAA Report Number FAA-EE-92-03 (Federal Aviation Administration, Washington, DC).

Fields, J. M. (**1992b**). *Impact of Ambient Noise on Noise Annoyance: An Assessment of the Evidence, Proceedings of Inter-Noise 92*, 1011–1016.

Fields, J. M. (**1993**). ''Effect of personal and situational variables on noise annoyance in residential areas,'' J. Acoust. Soc. Am. **93**, 2753–2763.

Fields, J. M. (**1993b**). ''Theories and evidence on the effect of ambient noise on reactions to major noise sources,'' in *Noise and Man '93: Noise*

as a Public Health Problem (Proceedings of the Sixth International Congress) (INRETS, Arcueil, France), Vol. 3, pp. 412–419.
Fields, J. M. (**1996**). *An Analysis of Residents' Reactions to Environmental Noise Sources within an Ambient Noise Context*, DOT/FAA/AEE-96/08 (U.S. Dept. of Transportation, Federal Aviation Administration, Washington, DC).
Fields, J. M., and Walker, J. G. (**1982**). ''The response to railway noise in residential areas in Great Britain,'' J. Sound Vib. **85**, 177–255.
Gjestland, T. T., Liasjø, K. H., Granøien, I., and Fields, J. M. (**1990**). *Response to Noise Around Oslo Airport Fornebu*, Report No. STF40 A90189 (ELAB-RUNIT, Trondheim, Norway).
Graf, P., Meier, H. P., and Müller, R. (**1974**). *Sozio-psychologische Fluglärmuntersuchung im Gebiet der drei Schweizer Flughäfen, Zürich, Genf, Basel* (Bern, 1974) [English translation: *Sociopsychological Airplane Noise Investigation in the Districts of Three Swiss Airports: Zurich, Geneva and Basel*, NASA TM-75787 (National Aeronautics and Space Administration, Washington, DC, 1980).]
Grandjean, E., Graf, P., Lauber, A., Meier, H. P., and Mueller, R. (**1973**). ''Survey of aircraft in Switzerland,'' in *Proceedings of the International Congress on Noise as a Public Health Problem, Dubrovnik, Yugoslavia, 13–18 May 1973*, USEPA 550-9-73-008 (U.S. Environmental Protection Agency, Washington, DC, 1973), pp. 745–659.
Groeneveld, Y., and de Jong, R. G. (**1985**). *CEC Joint Research Project Effects of Impulse Noise on Human Beings, the field survey*, NIPG-TNO publication 85008. (Netherlands Institute for Preventive Health Care—TNO, Delft).
Hall, F. L., Birnie, S. E., Taylor, S. M., and Palmer, J. E. (**1981**). ''Direct comparison of community response to road traffic noise and to aircraft noise,'' J. Acoust. Soc. Am. **70**, 1690–1698.
Hanushek, E. A., and Jackson, J. E. (**1977**). *Statistical Methods for Social Scientists* (Academic, New York).
Hawkins, M. M. (**1980**). *An Exploratory Study of Response To Sound (Including Noise) Occurring in Rural Hampshire and Wiltshire*, ISVR Contract Report 80/11 (Univ. of Southampton, England).
Institut für Praxisorientierte Sozialforschung (**1980**). *Störwirkungen durch den Lärm der Kleinaviatik. Bundesamt für Umweltschutz* (Berne) [English translation: *Annoyance Caused by Light Aircraft Noise*, NASA-TM-76533 (National Aeronautics and Space Administration, Washington, DC, 1981)].
Izumi, K., and Yano, T. (**1990**). ''A survey on the community response to road traffic noise in the mixed noise environment,'' *Proceedings of Inter-Noise 90*, pp. 279–282.
Izumi, K. (**1993**). Personal communication.
Jonckheere, R. E. (**1989**). ''Evaluation of noise exposure and annoyance around Brussels airport: energy descriptor versus exceedance-duration descriptor,'' Noise Control Eng. J. **32**, 93–98.
Large, J. B., and Ludlow, J. E. (**1976**). ''Community reaction to noise from a construction site,'' Noise Control Eng. **6**, 59–65.
Lawrence, A., and Putra, A. (**1989**). ''The combined effect of road traffic and aircraft noise on people,'' *Inter-Noise 89*, pp. 891–894.
Lee, E. S., Forthofer, R. N., and Lorimor, R. J. (**1989**). *Analyzing Complex Survey Data* (Sage, Newbury Park, CA).
Ludlow, J. E. (**1976**). *A Survey of the Effects of Noise Around a Construction Site*, ISVR Memo 553 (Univ. of Southampton, England).
McKennell, A. C. (**1977**). *Community Response to Concorde Flights Round London (Heathrow) Airport* (Social and Community Planning Research, London).
MIL Research (**1971**). *Second Survey of Aircraft Noise Annoyance Around London (Heathrow) Airport* (Her Majesty's Stationery Office, London).
Pearsons, K. S. (**1966**). *The Effects of Duration and Background Noise Level on Perceived Noisiness*, Technical Report No. FAA-ADS-78 (Federal Aviation Administration, Washington, DC).
Pearsons, K. S., Bennett, R. L., and Fidell, S. A. (**1979**). *Initial Study on the Effects of Transformer and Transmission Line Noise on People: Volume 1: Annoyance*, Report EA-1240, Vol. 1 (Bolt Beranek & Newman, Canoga Park, CA).
Peeters, A. L., de Jong, R. G., Kaper, J. P., and Tukker, J. C. (**1984**). *Hinder Door Spoorweggeluid in de Woonomgeving* (Railroad Noise Annoyance in Residential Areas), IMG-TNO Report D 60 (IMG-TNO, Delft).
Powell, C. A. (**1978**). *Annoyance Due to the Interaction of Community Noise Sources*, Ph.D. dissertation, School of Engineering and Applied Science, George Washington University, Washington, DC.
Powell, C. A. (**1979**). *Effects of Road-Traffic Background Noise on Judgments of Individual Airplane Noises*, NASA Technical Paper No. 1433 (National Aeronautics and Space Administration, Washington, DC).
Powell, C. A., and Rice, C. G. (**1975**). ''Judgments of aircraft noise in a traffic noise background,'' J. Sound Vib. **38**, 39–50.
Putra, A. (**1990**). *The Effect of Ambient Noise Levels From Road Traffic on Community Response to Aircraft Noise*, Ph.D. thesis, Graduate School of the Built Environment, University of New South Wales, Kensington, Australia.
Rylander, R., Björkman, M., Åhrlin, U., and Sörensen, S. (**1977**). ''Tramway noise in city traffic,'' J. Sound Vib. **51**, 353–358.
Schultz, T. J. (**1978**). ''Synthesis of social surveys on noise annoyance,'' J. Acoust. Soc. Am. **64**, 377–405.
Schultz, T. J. (**1982**). *Community Noise Ratings* (Applied Science Publishers, Barking, England).
Sternfeld, H., Hinterkeuser, E. G., Hackman, R. B., and Davis, J. (**1974**). *A Study of the Effect of Flight Density and Background Noise on V/STOL Acceptability*, NASA CR-2197 (National Aeronautics and Space Administration, Washington, DC).
Stevens, S. S., and Guirao, M. (**1967**). ''Loudness functions under inhibition,'' Percept. Psychophys. **2**, 459–465.
Takahashi, Y. (**1991**). *A Study on the Community Response to the Combined Noises of Railway and Road Traffic* (Japanese only), Master of Engineering Thesis, Muroran Institute of Technology.
Tarnopolsky, A., and Morton-Williams, J. (**1980**). *Aircraft Noise and Psychiatric Disorders* (Social and Community Planning Research, London 1980).
Tracor, Inc. (**1971**). *Community Reaction to Airport Noise*, NASA CR-1761, Vol. II, NASA CR-111316 (National Aeronautics and Space Administration, Washington, DC).
Vallet, M., Pachiaudi, G., Bruyere, J., Signolles, C., Tanguy, Y., Depitre, A., Fischl, M., Francois, J., and Abramowitch, J. (**1986**). *Réactions de La Communaute Au Bruit Des Avions* (Inrets-Laboratoire Energie Nuisances, Bron, France).
Vos, J., and Smoorenburg, G. F. (**1985**). ''Penalty for impulse noise, derived from annoyance ratings for impulse and road-traffic sounds,'' J. Acoust. Soc. Am. **77**, 193–201.
Walters, D. (**1970**). ''Annoyance due to railway noise in residential areas,'' in *Architectural Psychology*, edited by D. V. Center (R.J.B.A., England), pp. 56–61.
Wehrli, B., Nemecek, J., Turrian, V., Hofmann, R., and Wanner, H. U. (**1978**). ''Auswirkungen des straßenverkehrslárm in der nacht,'' Kampf dem Lärm **25**, 138–149.
Wells, R. J. (**1971**). ''Noise Complaint Potential: Ambient noise versus intrusive noise,'' in *Proceedings of the Seventh International Conference on Acoustics, Budapest*, pp. 321–324.
Yu, W. (**1987**). ''Accuracy of measurement for assessing human response to noise,'' *Inter-Noise 87*, pp. 985–988.

Differentiation of cochlear pathophysiology in ears damaged by salicylate or a pure tone using a nonlinear systems identification technique

Lin Bian and Mark E. Chertoff[a)]
Hearing and Speech Department, University of Kansas Medical Center, 39th Street and Rainbow Boulevard, Kansas City, Kansas 66160

(Received 12 December 1997; revised 6 July 1998; accepted 10 July 1998)

Mongolian gerbils were exposed to either α-ketoglutarate, salicylate, or an 8-kHz pure tone. Cochlear microphonic (CM) was recorded from the round window in response to 68 and 88 dB SPL Gaussian noise. A nonlinear systems identification technique provided the frequency-domain parameters of a third-order polynomial model characterizing cochlear mechano-electric transduction (MET). A series of physiologic indices were derived from further exploration of the model. Exposure to the 8-kHz pure tone and round window application of salicylate resulted in different changes in the polynomial parameters and physiologic indices even though the threshold shifts were similar. A general reduction of CM magnitude was found after the tone exposure, and an increase at low-mid frequencies was demonstrated in the salicylate group especially at the lower signal level. The slope of the MET curve was reduced by the acoustic overstimulation. The root or the operating point of the MET was shifted in opposite directions after the two treatments. Sound-pressure levels that saturate MET expanded in the tone exposure group and narrowed in the salicylate group. The signal level also had effects on these indices. © *1998 Acoustical Society of America.* [S0001-4966(98)05310-7]

PACS numbers: 43.64.Nf, 43.64.Kc, 43.64.Gz [RDF]

INTRODUCTION

Recently, a nonlinear systems identification (NLID) technique has been applied to the cochlear microphonic (CM) to quantify cochlear mechano-electric transduction (MET) in gerbils (Chertoff *et al.*, 1996, 1997). The NLID technique provided the frequency-domain parameters of a third-order polynomial equation which models MET. A series of physiologic indices characterizing the MET process were derived from further mathematical manipulations of the polynomial coefficients. These indices included slope, maxima, minima, and saturation sound-pressure levels at maxima (SPL_{max}) and minima (SPL_{min}). Exposure to an 8-kHz pure tone at 100 dB SPL for 20 min altered the polynomial coefficients, coherence functions, and physiologic indices. The slope, maxima, and minima of the transduction curve were reduced whereas the SPL_{max} and SPL_{min}, or the sound-pressure levels required to saturate the MET at the maximum and minimum output were increased. These results were interpreted as a decrease in outer hair cell (OHC) receptor currents, a change in the ion channels, and an alteration of the mechanics of the stereocilia.

Various cochlear pathologies may affect different aspects of the inner ear transduction. Noise exposure can damage the OHC stereocilia and lead to an uncoupling of the tectorial membrane (Patuzzi, 1995). Ototoxic drugs, such as salicylate, can alter MET by damaging the cell body (Stypulkowski, 1990; Shehata *et al.*, 1991). These changes in the inner ear may result in different changes in the polynomial model of MET and the corresponding physiologic parameters. If so, these indices may be helpful in describing the physiologic conditions of the inner ear and differentiating hearing losses due to different cochlear pathologies. The purpose of this study was to determine if the polynomial model and associated physiologic indices could characterize MET in damaged ears and distinguish among hearing disorders. In the present study, noise exposure and salicylate were selected as the damaging agents. In contrast with the alterations of the ultrastructure and micromechanics of the OHC stereocilia induced by noise exposure (Saunders *et al.*, 1991), salicylate toxicity targets the cell body, damaging the surface cisternal system (Dieler *et al.*, 1991) and reducing its turgor pressure (Shehata *et al.*, 1991). Therefore MET can be compared between ears with OHC stereocilia damage and those with cell body damage.

I. METHODS

A. Animal preparation

Twenty-four Mongolian gerbils weighing between 39 and 95 g, with normal hearing, served as subjects. Normal hearing was defined as round window compound action potential (CAP) thresholds at or below 25 dB SPL at 1, 2, 4, 8, and 16 kHz. Animals were sedated with an intraperitoneal injection of pentobarbital of 64 mg/kg as the initial dosage and 1/3 of that as a subsequent dosage administered every 60 min. Body temperature was monitored and maintained by a homeothermic blanket control unit (Harvard) with a rectal thermosensor insertion. The right pinna and its surrounding tissue were removed to expose the bulla. The bulla was opened with a dental drill (Volvere GX), and a ball-tip silver wire electrode was placed on the round window (RW). The

a)Electronic mail: mchertof@kumc.edu

electrode was insulated by #31 polymide tubing (Micro ML) and fixed on the bulla opening by super glue (cyanoacrylate ester). The RW niche was kept dry with a cotton wick. The bulla remained open throughout the experiment.

B. Signal delivery and processing

Acoustic signals were created in an array processor (Tucker-Davis Technology, TDT AP2), downloaded to a 16-bit digital-to-analog converter sampling at 65.536 kHz (TDT DA1), and passed through a headphone buffer (TDT HB6) to a headphone (Etymotic ER-2). The μ-metal encased headphone was connected to a tube that was sealed to the bony external ear canal. To monitor signal level, a calibrated probe microphone (Etymotic ER-7C) was sealed at the end of the tube, and positioned approximately 5 mm from the umbo of the tympanic membrane.

A sequence of 250-ms frozen Gaussian noise, windowed with a 5-ms $\cos^2$ ramp, was used to evoke CM responses. The noise was delivered at 68 and 88 dB SPL in random order. Because Chertoff *et al.* (1997) found differences in the polynomial parameters between 88 and 85 dB SPL, and previous studies showed that salicylate had greater effects at lower signal levels (Fitzgerald *et al.*, 1993; Kujawa *et al.*, 1992), the 68 dB SPL condition was used in the present study. The Gaussian noise was maintained at the desired level by measuring the input rms from the probe microphone and adjusting the attenuator through a feedback software routine. The noise spectrum was equalized between 0.1 and 10.24 kHz by an inverse filter procedure (Chertoff and Chen, 1996).

The CAP was elicited by 2-ms tone bursts windowed with a 1-ms $\cos^2$ ramp. Hearing threshold estimates were obtained by monitoring the CAP on a digital storage oscilloscope (Hitachi VC-6045A). Signal level was attenuated in 2-dB steps until the N_1 could only be detected approximately 50% of the time. This level was considered the CAP threshold.

C. Data acquisition and analysis

Cochlear responses between the RW electrode and a ground needle electrode in the neck musculature were band-pass filtered between 0.03 and 30 000 Hz (12 dB/oct) and amplified 500 times by a low-noise preamplifier (Stanford SR560). The electric signal was low-pass filtered at 16 kHz (54 dB/oct), amplified ten times by a dual variable filter (Steward VBF 10M), and digitized at 65.536 kHz (TDT AD2). The average of ten presentations of the same Gaussian noise sequence and the corresponding CM responses yielded one input/output record.

Each record (16 384 points) was divided into 64 sub-records of 256 points. Ten different sequences of Gaussian noise resulted in ten records, from which input/output spectral density functions were obtained. The time domain signal was Hanning windowed with 50% overlapping to correct the energy loss in the spectrum (Bendat and Piersol, 1986). The ratio of the cross-spectral density function and the input autospectral density function provided the gain and phase of the linear system frequency response function. The ratios of the uncorrelated cross- and input auto-spectral density functions yielded the gain and phase of the coefficients of the third-order polynomial model of MET (Chertoff *et al.*, 1996; Bendat and Palo, 1990; Bendat and Piersol, 1986):

$$y(f)=A_3(f)x^3-A_2(f)x^2-A_1(f)x+dc, \tag{1}$$

where x represents the input in pascals; y is the CM response in volts. Differentiation and algebraic manipulation of the polynomial equation resulted in a series of physiologic indices characterizing MET. Figure 1 demonstrates a mechano-electric transduction curve plotted from the polynomial equation of MET and its physiologic indices. Methods for deriving these indices were described previously (Chertoff *et al.*, 1997, Appendix).

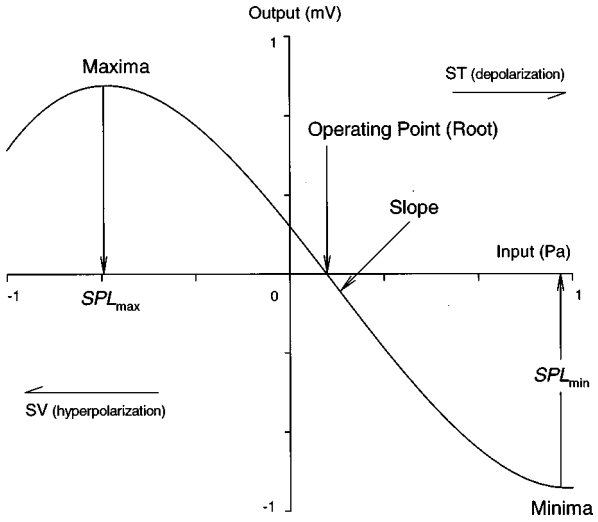

FIG. 1. Illustration of the MET transduction curve and the physiologic indices. SV and ST represent the directions of the input sound pressure towards scala vestibuli and scala tympani. Modified from Chertoff *et al.* (1997), with permission.

D. Experimental design

Animals were randomly assigned into a control group and two experimental groups. The number of subjects per group ($n=8$) was determined by performing a statistical power analysis on the previous data (Chertoff *et al.*, 1996, 1997). The control animals received 100 mM α-ketoglutarate (Sigma K-1875) which has a similar structure and formula weight (FW=168.1) to salicylate, but no ototoxic effect. The experimental animals received either 100 mM sodium salicylate (Sigma S-3007) solution or an 8-kHz pure tone (Mercer 9805) presented at 110 dB SPL for 10 min. The stimulus level of the damaging tone was monitored and maintained by tracking the peak amplitude of the spectrum with a signal analyzer (Hewlett–Packard 3561A Dynamic). The average sound-pressure level in the tone exposure group was 109.7 ± 0.28 (s.d.) dB SPL.

Preliminary studies of injecting salicylate into the femoral vein resulted in noticeable systemic alteration and minimal threshold shifts. However, dripping salicylate solution onto the RW produced acute high-frequency CAP threshold shifts. We also found that 100 mM salicylate could achieve a similar extent of threshold shift and audiometric configura-

tion to animals exposed to an 8-kHz tone for 10 min. All the solutions were freshly prepared and warmed to body temperature by placing a syringe in the animal's blanket. A micromanipulator was used to control the dripping of the solutions from a needle attached to a probe tube, which was connected to the syringe. Two drops of the solutions were kept in the RW niche for 10 min and then dried with cotton wicks. Both α-ketoglutarate and the salicylate were dissolved in phosphate buffered saline (pH$=7.3$). The pH of α-ketoglutarate was adjusted to 7.2 ± 0.21 (s.d.) by $5N$ NaOH. The average pH of sodium salicylate was 7.5 ± 0.13 (s.d.).

After the animal preparation and equipment setup, CAP thresholds were estimated and CM responses to Gaussian noise recorded. Next, the animals were allowed to rest for 10 min after which the CM recordings were repeated. This served as a within-subject control to determine the reliability of the experiment. Following this recording session, treatments of either an 8-kHz tone exposure or a perfusion of salicylate or α-ketoglutarate were initiated for a duration of 10 min. In both the control and the salicylate group, CAP threshold at 16 kHz was monitored during the exposures. Immediately after the treatments, the CM response to noise was recorded and CAP thresholds obtained. The recovery of the CAP threshold at 16 kHz was monitored in all groups for 60 min past the beginning of the treatments.

E. Statistics

The change of the dependent variables between the two consecutive recordings separated by a 10-min rest period was determined by subtracting the particular dependent variable of interest at time 2 from that variable at time 1. This is the effect of a 10-min rest. The treatment effect was determined by subtracting the variable at time 3 from that at time 2. The different scores for each group at each epoch were submitted to a between group (control, salicylate, and 8 kHz) two-factor (time and frequency) repeated measure analysis of variance (Statistica 4.5, StatSoft). If the general analysis of variance (ANOVA) was significant, a one-factor (frequency) three-way ANOVA was performed for rest and treatment conditions separately. If there was a significant group or group×frequency interaction, each experimental group was compared to the control group with a between group one-way ANOVA. The same statistical procedure was applied to the CAP threshold shift. If a group×frequency interaction was significant, a Newman–Keuls *post hoc* procedure was used to determine the frequencies where the threshold shifts differed between two groups. A probability of less than 0.05 was considered statistically significant.

Since the frequency effect was implied in the group by frequency interaction, the major focus of the statistical analysis for the present study was on the group or group×frequency effects. Violations of the homogeneity of variance and sphericity assumptions were controlled by adjusting the degrees of freedom with the Huyn–Feldt procedure (Marascuilo and Serlin, 1988). The estimates of effect sizes for the group and frequency×group effects were determined by calculating the η^2 (Young, 1993). Cohen's criteria (1988) were followed in the judgment of the effect size.

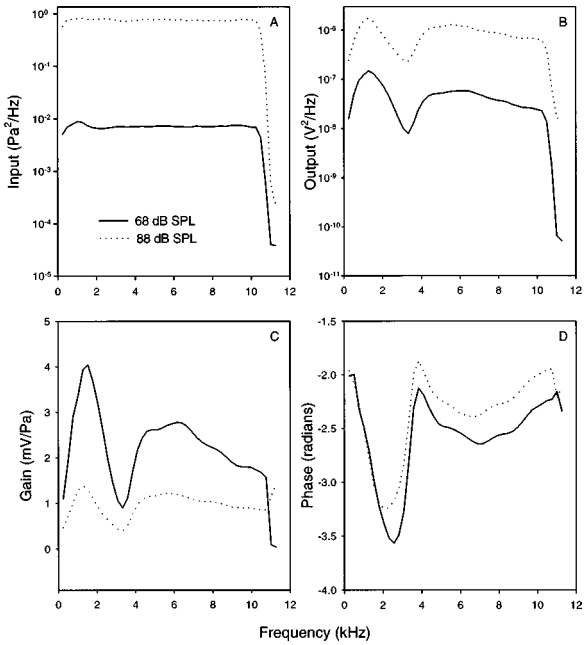

FIG. 2. Average input (panel A), output (panel B) spectral density functions for 68 and 88 dB SPL conditions. The magnitude and phase of the input/output transfer function are shown in panels (C) and (D), respectively.

II. RESULTS

A. Normative data

Statistical analysis showed no significant difference on the polynomial coefficients and physiologic indices between the first two recording sessions in all three groups, i.e., there was no change of these variables after the 10-min rest. However, data derived from the CM responses to 68 dB SPL Gaussian noise showed differences from that of 88 dB SPL.

1. Input/output

The average input/output spectral density functions computed across all animals for the first two recordings are shown in Fig. 2(A) and (B). The energy in the input spectra was evenly distributed, although a slight increase presented at about 1 kHz in the 68 dB SPL spectrum. The shapes of the output spectral density function for CM were similar at both levels, though the CM output for the 68 dB SPL Gaussian noise was about ten times smaller. The energy in the CM reached a maximum at approximately 1.3 kHz followed by a minimum at 3.3 kHz, and slowly rolled off above 6 kHz. The magnitude of the system transfer function was similar in shape to that of the output spectrum [Fig. 2(C)], however, the gain of the CM response for the 68 dB SPL signal was about 2.4 times larger than the 88 dB SPL condition. The average gain across frequency was 2.28 mV/Pa for 68 dB SPL and 0.96 mV/Pa for 88 dB SPL. The CM phases at both levels followed the same trend [panel (D)], but in general, the CM in response to the lower level signal was delayed more than the higher level. The largest phase delays, -3.25 rad for 88 dB SPL and -3.57 rad for 68 dB SPL, occurred at 2 and 2.6 kHz, respectively. The least phase delays (-1.87 rad for 88 dB SPL, -2.12 rad for 68 dB) were at 3.8 kHz.

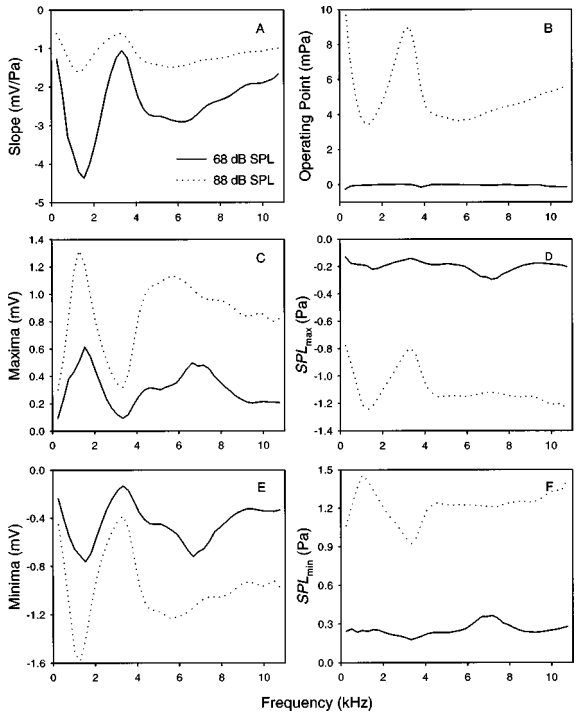

FIG. 3. Physiologic indices for 68 and 88 dB SPL. (A) slope of the MET curve; (B) operating point or the root of the polynomial model; (C) maxima or positive saturation CM; (D) SPL_{max} or sound-pressure level at maxima; (E) minima or negative saturation CM; (F) SPL_{min} or sound-pressure level at minima.

2. Physiologic indices

The physiologic indices derived from the third-order polynomial equation are illustrated in Fig. 3. The slope at the inflection point of the transduction curve represents the general sensitivity of the cochlear MET at a particular frequency. The absolute value of the slope at 68 dB SPL was always greater than at 88 dB SPL [panel (A)], indicating that the transduction curve for the lower signal level was steeper than that for the higher level. The slope at 68 dB SPL ranged across frequency from -4.5 to -1 mV/Pa, whereas the range for 88 dB SPL was from -1.6 to -0.6 mV/Pa. Panel (B) shows the effect of signal level on the root of the polynomial equation, which is the x intercept of the MET curve (Fig. 1), and represents the operating point (OP) of the cochlear partition. At 68 dB SPL, the root ranged from -0.25 to 0.02 mPa, and reached -0.15 mPa at 3.8 kHz. At 88 dB SPL, the lowest OP was 3.4 mPa at 1.3 kHz, and a peak of 9 mPa was present at 3.3 kHz.

The maximum output (maxima) and the sound-pressure levels required to reach this output (SPL_{max}) are shown in Fig. 3(C) and (D), respectively. The positive saturation voltages of the higher signal level was greater than that of the lower level. For 88 dB SPL, a peak as high as 1.3 mV occurred at 1.3 kHz, and a trough as low as 0.3 mV at 3.3 kHz. For 68 dB SPL, the highest maxima (0.6 mV) was at 1.5 kHz, the lowest (0.09 mV) was at 3.3 kHz. At 68 dB SPL, the SPL_{max} ranged from -0.14 to -0.3 Pa, and at 88 dB SPL it ranged from -0.8 to -1.25 Pa, and stayed around -1.15 Pa above 4600 Hz.

The minima is the saturation output for CM in the negative direction. The sound-pressure level needed for the saturation of the negative CM is the SPL at minima (SPL_{min}). As illustrated in Fig. 3(E), the absolute saturation output of the higher signal level was greater than that of the lower level. For 88 dB SPL, the largest output was -1.58 mV at 1.3 kHz, and the smallest output was -0.4 mV at 3.3 kHz. For 68 dB SPL, the minima ranged from -0.76 mV at 1.5 and 6.6 kHz to -0.1 mV at 3.3 kHz. Panel (F) shows that the SPL_{min} for 68 dB SPL was about 0.3 Pa, while that for 88 dB SPL ranged from 0.9 to 1.5 Pa.

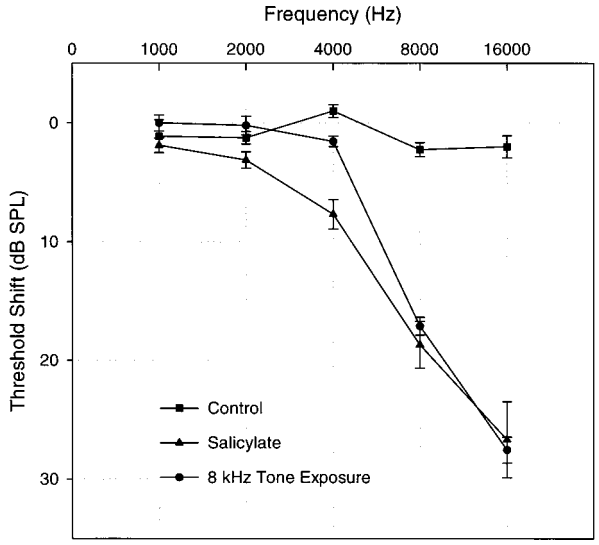

FIG. 4. The average CAP threshold shift±SEM for the three groups.

B. Effects of cochlear damage

1. Threshold shift

The CAP threshold change was determined by subtracting the thresholds before treatment from the thresholds after the treatment (Fig. 4). There were no considerable threshold shifts across frequency for the control group. The 8-kHz pure-tone exposure group and the salicylate group showed similar high-frequency threshold shifts. At 8 and 16 kHz, the average threshold shifts for the 8-kHz exposure and the salicylate groups were very similar and different from the control group. In contrast, at 4 kHz, the salicylate group had an average of 7.7 dB SPL threshold elevation, which was significantly different from the control group ($p<0.05$); whereas the 8 kHz tone exposure group had only a 1.6 dB SPL threshold change, which was not significantly different from the control group ($p=0.195$).

The threshold at 16 kHz was monitored from the onset of the treatment to 60-min post-exposure for the animals in the control and salicylate groups. In the 8-kHz pure-tone exposure group, the 16-kHz threshold could not be obtained during the 10-min exposure. Therefore it was measured immediately after the exposure and monitored for 50 min. One purpose of monitoring the threshold was to ensure the stability of the animals' hearing losses during the CM recordings. The time courses of the threshold shifts in the three groups are illustrated in Fig. 5. In the top panel, it is apparent that α-ketoglutarate did not result in a considerable threshold shift. In contrast, the salicylate and the 8-kHz pure-tone ex-

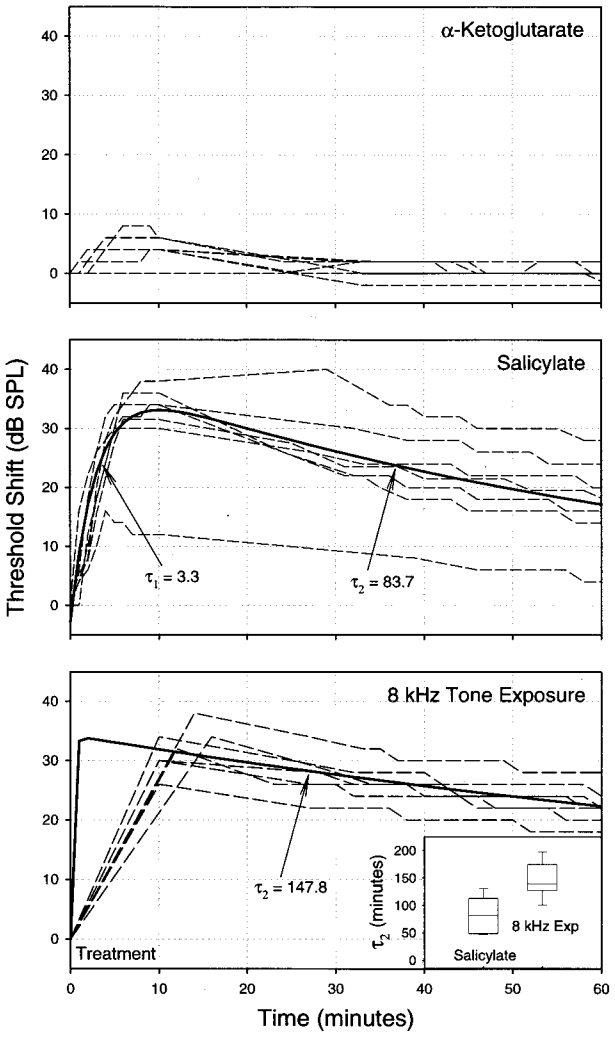

FIG. 5. Time courses of the CAP threshold shift at 16 kHz for each animal in the three groups (dashed lines). Treatments started at time zero and lasted 10 min. Solid lines indicate the best fitting double exponential decay curves and associated time constants τ_1 and τ_2. Inset in the bottom panel shows the medians and the 10th and 90th percentiles of the recovery time constants (τ_2) for the two experiment groups.

posure yielded a maximum threshold shift around 10 min, which was followed by a slow recovery (lower two panels). The time course of onset and recovery was fit by a double exponential decay function (SigmaPlot 3.03, Jandel):

$$\theta = ae^{t/\tau_2} - ce^{t/\tau_1}, \tag{2}$$

where τ_1 is the time constant of the onset of the threshold shift, and τ_2 is the time constant for the recovery from the maximum threshold shift; a and c are the curve fitting constants, so that the sum of them is the starting point of the curve at time zero.

The average τ_1 was about 3.3 min for the salicylate group; i.e., it took more than 3 min for the CAP threshold to reach 63% of the maximum shift (middle panel). For the 8-kHz exposure group, τ_1 was not available because the threshold was not recordable during the pure-tone exposure. As shown in the lower two panels, the recovery time constant (τ_2) of the salicylate group was significantly shorter than that of the 8-kHz exposure group (one tailed Mann–

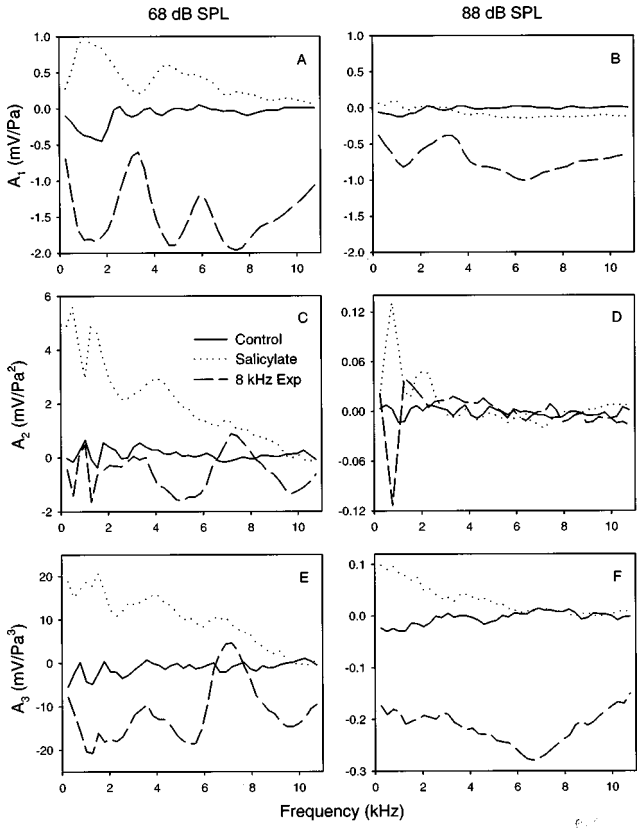

FIG. 6. Average changes in the polynomial coefficients for the three groups at 68 (left panels) and 88 dB SPL (right panels) conditions. Top panels, A_1; middle, A_2; bottom, A_3.

Whitney $T=8.0$, $p<0.05$). The τ_2 of the 8-kHz exposure group was 147.8 ± 35.7 (s.d.) min, while for the salicylate group τ_2 was 83.7 ± 35.1 (s.d.) min. The medians, 10th, and 90th percentiles of τ_2 for the two experimental groups are illustrated in the inset box-chart in the bottom panel of Fig. 5 for a direct comparison.

2. "A" polynomial coefficients

A set of three "A" polynomial coefficients [cf. Eq. (1)] were derived from the NLID procedure for each recording at different times. Figure 6 illustrates the changes in the magnitudes of the polynomial coefficients for the three groups at the two signal levels. At 68 dB SPL, salicylate increased A_1 primarily below 2 kHz and at 4.6 kHz (panel A). In contrast, A_1 was not affected by salicylate at the 88 dB SPL condition. Overstimulation with the 8-kHz tone dramatically reduced A_1 across the majority of the frequencies for both signal levels [panels (A) and (B)]. Moreover, A_1 was reduced more at 1.5, 4.6, and 7.4 kHz for the lower signal level and at 1 and 6 kHz for the higher level. For A_2, the salicylate group showed an increase at low frequencies for both signal levels, whereas the tone exposure group showed reductions at 5 and 9 kHz for 68 dB SPL [Fig. 6(C) and (D)]. Both panels (E) and (F) show that A_3 increased for some frequencies in the salicylate group, and decreased in the tone exposure group for both 68 and 88 dB SPL conditions. In the salicylate group, A_3 increased below approximately 8 kHz for the lower signal level, and at frequencies below 6 kHz for the

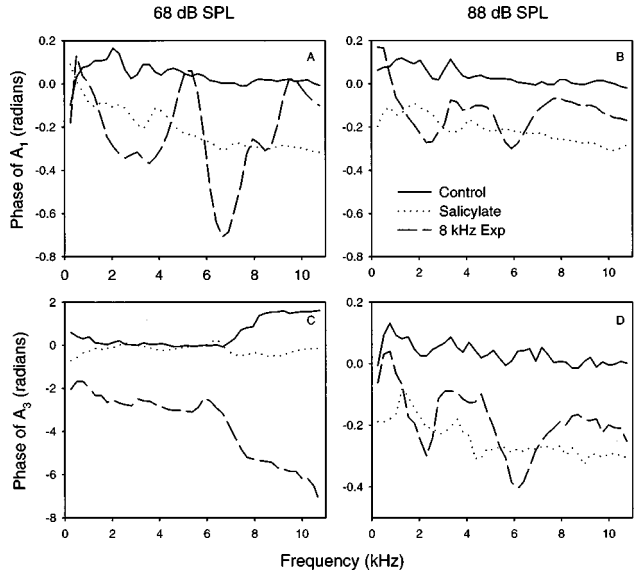

FIG. 7. Average change in phase of the polynomial coefficients. The left and right panels show the change scores for the phase of A_1 (upper panels) and A_3 (lower panels) under 68 and 88 dB SPL conditions, respectively.

higher level. However, in the tone exposure group, A_3 was reduced across the whole frequency range at 88 dB SPL, and in the frequency ranges below 6.1 and above 8.4 kHz at 68 dB SPL.

As illustrated in Fig. 7, salicylate and the tone exposure altered the phase of A_1 and A_3 but not A_2 (not shown). The phase delay of A_1 increased at both signal levels [panels (A) and (B)]. For 88 dB SPL, the phase of A_1 was delayed by about 0.1–0.3 rad in the salicylate group. A similar change occurred at 68 dB SPL. The phase delay caused by the 8-kHz tone exposure was not evenly distributed across frequency. As large as a 0.7-rad phase delay occurred at 6.7 kHz in the lower signal level condition; A_1 was delayed approximately 0.3 rad at around 2 and 6 kHz for the higher level. In the salicylate group, a change of A_3 phase occurred at 88 dB SPL but not at 68 dB SPL [Fig. 7(C) and (D)]. This amounted to approximately a 0.2- to 0.3-rad phase delay from low to high frequencies. Tone exposure increased the A_3 phase delay by about 6 rad at frequencies above 6 kHz in the lower stimulus level condition. Similar to A_1, at 88 dB SPL, A_3 phase was delayed more at 6.1 and 2.3 kHz.

3. Physiologic indices

The statistical results (F values and the adjusted degrees of freedom) for the changes in the physiologic indices compared to the control group are summarized in Table I. The group effects and the group by frequency interactions between each experimental group and control group are presented. Also included are the corresponding effect sizes (η^2) for the reader to determine the importance of one effect relative to the others.

Panels (A) and (B) of Fig. 8 illustrate the change in the slope or sensitivity of MET as a result of salicylate or 8-kHz pure-tone exposure. Positive change scores indicate that the slope became smaller or less sensitive; negative values represent steeper slopes. The tone exposure significantly decreased the slope of MET across almost all frequencies at both signal levels. The changes were more dramatic at 1.5, 4.8, and 6.9 kHz for 68 dB SPL, and at 1.3 and 6.4 kHz for 88 dB SPL. In contrast, for the salicylate group the slope became steeper with the greatest effects in the low frequencies and at the lower signal level. Limited changes occurred at the higher signal level.

The root of the polynomial equation or the OP of MET changed differently in the two treatments. For both signal level conditions, the value of the root was reduced, indicat-

TABLE I. Statistical results: effects and effect sizes on the physiologic indices. The F values, the adjusted degrees of freedom, and the η^2 were based on the ANOVA between each experimental group and the control group on the change scores of the indices.

		68 dB SPL						88 dB SPL					
		F[a]		df[b]		η^2[c]		F		df		η^2	
		Sal[d]	8 K[e]	Sal	8 K	Sal	8 K	Sal	8 K	Sal	8 K	Sal	8 K
Slope	$g\times f$[f]	7.35*	5.27*	3, 47	7, 98	0.18	0.05	5.39*	12.3*	4, 54	6, 80	0.17	0.05
	g[g]	65.4*	71.0*	1, 14	1, 15	0.34	0.62	1.78	116*	1, 14	1, 14	0.04	0.75
Root	$g\times f$	0.69	4.11*	39, 546	3, 45	0.01	0.07	2.24	5.58*	2, 31	2, 32	0.03	0.04
	g	0.01	16.0*	1, 14	1, 15	0.00	0.30	6.24*	9.70*	1, 14	1, 14	0.24	0.33
Maxima	$g\times f$	1.98	10.6*	7, 97	10, 155	0.08	0.18	1.64	9.72*	6, 81	7, 98	0.06	0.07
	g	0.88	51.0*	1, 14	1, 15	0.02	0.32	9.75*	113*	1, 14	1, 14	0.16	0.69
SPL_{max}	$g\times f$	3.72*	11.1*	11, 153	12, 191	0.11	0.30	3.24*	5.32*	13, 177	11, 147	0.08	0.15
	g	13.4*	0.06	1, 14	1, 15	0.20	0.00	30.1*	16.1*	1, 14	1, 14	0.35	0.17
Minima	$g\times f$	3.89*	2.01	8, 109	2, 28	0.18	0.10	3.46*	7.41*	6, 84	7, 98	0.10	0.07
	g	9.32*	21.3*	1, 14	1, 15	0.04	0.05	13.2*	57.3*	1, 14	1, 14	0.19	0.57
SPL_{min}	$g\times f$	2.52*	2.33	6, 81	2, 32	0.12	0.11	1.21	1.51	39, 546	4, 53	0.05	0.03
	g	22.1*	5.09*	1, 14	1, 15	0.08	0.01	20.2*	31.0*	1, 14	1, 14	0.20	0.43

*$p<0.05$.
[a]Each comparison involves each experimental group and the control group.
[b]Degrees of freedom were adjusted for any violation of assumptions.
[c]Effect size was judged as: large, if $\eta^2>0.14$; medium, if $0.14>\eta^2>0.01$; small, if $\eta^2<0.01$ (Cohen, 1988).
[d]Salicylate group.
[e]8-kHz pure-tone exposure group.
[f]Group×frequency interaction.
[g]Group effect.

ing that the OP shifted towards negative sound pressures as a result of the tone exposure [Fig. 8(C) and (D)]. In contrast, the salicylate group showed no effect on the OP at 68 dB SPL but an increase at 88 dB SPL. As shown in panel (D), salicylate moved the OP towards positive sound pressure.

The maxima of the CM were reduced in the two experimental groups, especially for the tone exposure group [Fig. 9(A) and (B)]. At 68 dB SPL, this reduction of output was dramatic at 1, 4.5, and 7 kHz for the tone exposure group. In the 88 dB SPL condition, the decrease of the maxima was significant throughout the whole frequency range, and more dramatic at 1.3 and 6.1 kHz. There was a reduction of maxima for frequencies above 4 kHz in the salicylate group for 88 dB SPL, and at 6.5 kHz for 68 dB SPL. Under both signal level conditions, less sound pressure (positive value) was needed to reach maxima (SPL_{max}) in the salicylate group [panels (C) and (D)]. For the 8-kHz exposure group, more sound pressure (negative value) was required to reach the maxima at 5.6 and 10 kHz for the low signal level; similarly, more sound-pressure level was required below 2.5 kHz and above 5 kHz for the higher level.

A reduction in the negative CM minima yielded a positive change score. From panels (E) and (F) of Fig. 9, it is obvious that the CM decreased for the tone exposure group at both signal levels. Greater reduction occurred at 6.9 kHz for 68 dB SPL, and in a wide frequency range for 88 dB SPL. In the salicylate group, the absolute value of minima increased at low frequencies ($<$ 1.5 kHz) for 68 dB SPL. Contrarily, it decreased in the 88 dB SPL condition above 5.5 kHz. The SPL_{min} was reduced around 7 kHz under the 68 dB SPL condition in both experimental groups [Fig. 9(G)]. In panel (H), for 88 dB SPL, the SPL_{min} was significantly increased by the tone exposure, indicating that more sound pressure was required to saturate MET. However, a decrease in the SPL_{min} occurred for the salicylate group, indicating that less sound pressure was needed to saturate the MET.

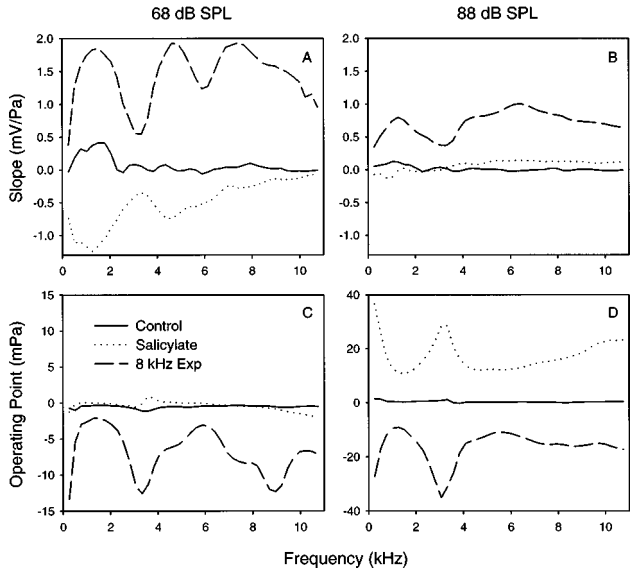

FIG. 8. Average change in physiologic indices. The change scores of the slope (upper panels) and the operating point (lower panels) for the 68 and 88 dB SPL signal levels are illustrated in the left and right panels, respectively. Positive change score indicates a decrease in the slope.

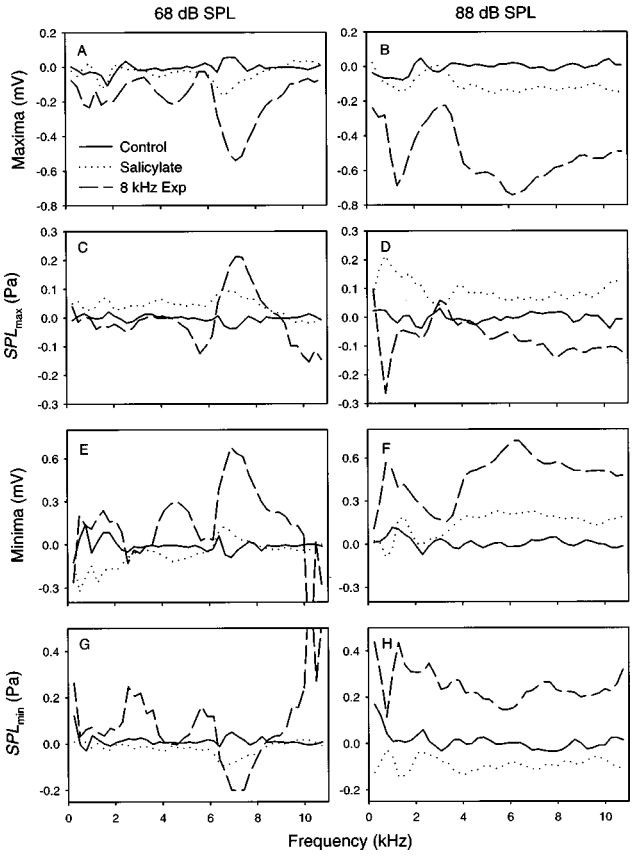

FIG. 9. Average change in physiologic indices. The change scores of the maxima, minima, SPL_{max}, and SPL_{min} under 68 and 88 dB SPL conditions are shown in the left and right panels, respectively. Panels (A) and (B) maxima; (C) and (D) SPL_{max}; (E) and (F) minima; (G) and (H) SPL_{min}.

III. DISCUSSION

A. Level effects

There were significant level effects on the overall amplitude, gain, and phase of the CM. The CM was larger at 88 dB SPL than at 68 dB SPL, but the gain was smaller, indicating that MET saturates at high stimulus levels. The phase delay was greater at 68 dB SPL than at 88 dB SPL. A change in phase may reflect a moving of the place in the cochlea where the CM is generated. That is, the greater delay of the CM for the 68 dB SPL condition suggests that the CM response moved towards the apex of the cochlea at the lower signal level. This is consistent with a previous investigation showing a level-related shift in CM response location (Honrubia and Ward, 1968) and other studies showing that maximal basilar membrane (BM) displacement shifts with stimulus level (Ruggero *et al.*, 1997; Zhang and Zwislocki, 1996).

The physiologic indices of MET changed with signal level. The steeper slope of the transduction curve at 68 dB SPL compared to 88 dB SPL indicates that MET is more sensitive at the lower signal level. This finding is in agreement with Patuzzi's (1995) demonstration of a decrease in a sensitivity parameter as a function of stimulus level. One explanation for the steeper slope (higher sensitivity) of MET at lower signal levels rests on the ''active process'' of the cochlear amplifier. The OHC is capable of fast or ac contractile movements in response to both electrical (Ashmore,

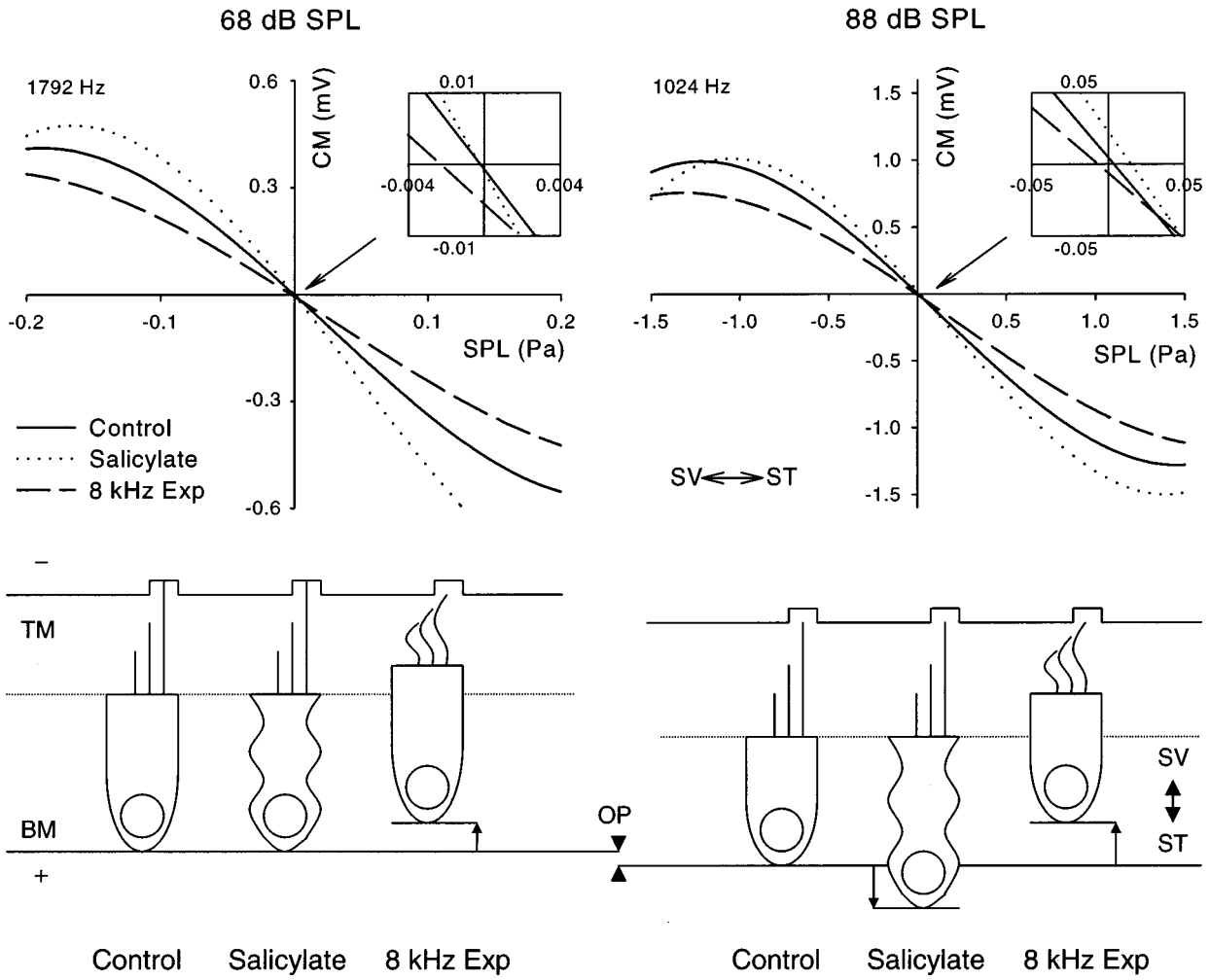

FIG. 10. Illustrations of MET curve and the hypothesized changes in the outer hair cell and the cochlear partition. Upper panels show the MET curves for the three groups at 1792 and 1024 Hz at 68 (left) and 88 dB SPL (right). Details of the operating point change are shown in the insets (*x* intercepts). Lower panels illustrate the anatomic and physiologic changes in the three groups at the two signal levels. The arrows represent the OP shifts. SV and ST are the directions towards scala vestibuli and scala tympani, respectively. BM: basilar membrane. TM: tectorial membrane.

1987) and mechanical stimulation (Brundin and Russell, 1994). These active processes, prevalent at low signal levels, may enhance the BM vibration, thereby increasing current flow through OHCs. At higher stimulus levels, the motile responses of the OHC and the number of ion channels being open for a given sound pressure may reach saturation, resulting in less steep MET slopes.

The reduced sensitivity of MET at the higher stimulus level could also result from the shift of the OP of the cochlear partition. As illustrated in the insets of the upper panels in Fig. 10 (the *x* intercepts of the solid lines), the root of the polynomial model of MET shifted towards positive sound pressures at 88 dB SPL. This root reflects the OP of the cochlear partition, or an equivalent sound-pressure level, at which 50% of the transduction channels are open (Patuzzi, 1995; Kirk and Patuzzi, 1997). This corresponds to a minimum stiffness of the stereocilia and maximum sensitivity of MET (Howard and Hudspeth, 1988). The shift of the OP towards positive sound pressure in the present study indicates that either the cochlear partition is displaced towards the scala tympani (ST), or the stereocilia on the OHCs are shifted to a hyperpolarized position (illustrated by the double arrow between the lower panels in Fig. 10). This is a less than optimal position for the opening and closing of the transduction channels, thereby decreasing the sensitivity.

The shift of the OP towards ST at the higher signal level in the present study is comparable to the finding of LePage (1987), that the RW summating potential showed a dc shift towards ST at the characteristic frequency where BM displacement was largest. The change in OP may be due to a dc contraction or a static change in stiffness of the OHC that alters the position of the cochlear partition at higher stimulus levels. The increase in the ion currents flowing through OHCs at the higher signal level could result in a cumulative elevation of extracellular K^+ concentration (Cody and Russell, 1988; Johnstone *et al.*, 1989), and cause a shortening of the OHCs via a voltage-dependent (Santos-Sacchi and Dilger, 1988) or an osmotic mechanism (Dulon *et al.*, 1988). This slow or dc contraction of OHC (shown by the comparison of the control OHCs in the lower panels of Fig. 10) could reduce the distance between the BM and the reticular lamina (Zimmermann and Fermin, 1996), consequently moving the OP towards ST. This static shift of the cochlear partition

towards the ST may be a protective mechanism for the vulnerable OHC stereocilia against high sound-pressure energy.

B. 8-kHz tone exposure

Even though the procedure of the pure-tone exposure in this study differed (level increased by 10 dB SPL, duration shortened by half) from our last study, the hearing loss, the CM response to 88 dB SPL noise, and the changes in the coefficients as well as the physiologic indices were consistent with our previous findings (Chertoff *et al.*, 1997). The threshold shift started at 8 kHz and was most prominent at an octave above, i.e., 16 kHz. The effects of the 8-kHz tone exposure included a reduction in the overall amplitude of the CM response and a decrease in the A_1 and A_3 coefficients. Furthermore, the absolute values of the slope, maxima, and minima decreased while those of SPL_{max} and SPL_{min} increased. In some cases, these changes were greater at 1 and 6 kHz for the 88 dB SPL condition (right panel of Fig. 9). This frequency effect was also found in our previous study (Chertoff *et al.*, 1997). The effects of the tone exposure are summarized in the upper panels of Fig. 10.

The reduced maxima, minima, and slope of the transduction curves could be due to the decrease in OHC receptor currents. Acoustic overstimulation damages the most vulnerable structure of the inner ear, i.e., stereocilia of the OHC (Saunders *et al.*, 1991). Many reversible anatomic alterations in stereocilia, such as bending, separation at the tips, disarray, and swelling of the cuticular plate were found in the acute stage of noise-induced temporary threshold shift (TTS) studies (Gao *et al.*, 1992; Clark and Pickles, 1996). All of these changes reduce the coupling between the hair cells and the tectorial membrane (Patuzzi, 1995), and could reduce the number of ion channels being opened at a given sound pressure. This would result in a reduction of hair-cell receptor currents and could account for the change in the physiologic indices of MET.

The observed increases in SPL_{max} and SPL_{min} after the tone exposure indicate that a larger cochlear partition displacement was required to drive the OHC receptor current into saturation. That is, more sound energy was needed to deflect the stereocilia so that the maximum number of channels are opened or closed. This could be due to a reduction of stereocilia stiffness such as that observed by Liberman and Dodds (1987) in their acute preparation of noise exposure *in vivo*, and by Saunders *et al.* (1986) in their water jet experiments on isolated cochlear turns *in vitro*. The loss of hair bundle stiffness could directly alter the displacement of the stereocilia and indirectly reduce the compliance of the cochlear partition. Both mechanisms would reduce the possibility of the opening and closing of the transduction channels at a given sound-pressure level. Therefore more sound pressure would be needed to saturate MET.

Another interesting finding is that the OP of the cochlear partition shifted towards negative sound pressure. This could be explained by an elevation of the cochlear partition towards scala vestibuli (SV) due to the structural changes in the stereocilia of the OHCs. As shown in the lower panels of Fig. 10, bending and disarray of stereocilia and decrease of hair bundle stiffness could reduce the distance between the BM and the tectorial membrane. The decrease in OHC length and volume after noise-induced TTS (Dew *et al.*, 1993) could also contribute to the OP shift. The direction of the OP shift in the present study is comparable to the shift in OP after a 200-Hz tone exposure for 3 min reported by Kirk *et al.* (1997).

There were various phase changes in the CM after tone exposure. The phases of A_1 and A_3 were delayed. One explanation for the change in phase is that the receptor currents normally flowing through hair cells are blocked, forming a longitudinal redistribution of the receptor currents. Because the CM was recorded from the RW, the vector summation of the receptor current included a greater contribution from a remote region. Responses from more remote regions would have more phase delay, since it takes longer for the traveling wave to reach the new contributing hair cells. Interestingly, the phase change was greatest at 2 and 6 kHz (Fig. 7). This may be attributed to different mechanisms involved in the change of MET. For example, uncoupling of stereocilia from the tectorial membrane may change MET at some frequencies, whereas blockage of transduction channels may be dominant at other frequencies.

C. Salicylate exposure

Dripping salicylate onto the RW caused a high-frequency hearing loss similar to that of an 8-kHz pure-tone exposure. However, the salicylate group demonstrated different changes in the polynomial parameters and the physiologic indices. The typical effects of salicylate on the CM were an increase in the magnitudes of the CM response and the ''*A*'' coefficients in the low-mid frequencies at low signal levels. Also the phase delay increased with frequency. These changes led to increases in slope, minima (low-mid frequencies), and reductions in maxima, SPL_{max} and SPL_{min} (upper panels in Fig. 10). Besides these changes, the OP shifted towards positive sound pressures in the 88 dB SPL condition.

The increase in the CM magnitude and the slope of MET were more dramatic at the lower signal level. These findings are consistent with the results of Stypulkowski (1990) and Fitzgerald *et al.* (1993). Furthermore, the increase in CM only occurred in certain frequency ranges, i.e., 1 to 2 kHz and 4–6 kHz. These effects due to signal levels and frequencies could explain the different results in some of the previous salicylate studies. For example, Puel *et al.* (1990) did not find alterations in CM evoked by a 10-kHz tone burst at 68 dB SPL, but they did find a ''slight'' reduction in CM magnitude at 98 dB SPL. In our Fig. 6, at 10 kHz, there is indeed no change of A_1 and A_3 for the 68 dB SPL condition, and a slight reduction of A_1 and A_3 for 88 dB SPL. The isopotential CM data reported by Didier *et al.* (1993) showed not only a decrease at 8 and 16 kHz, but also an increase at 2 kHz. These results are compatible with our findings. The frequency effects on the CM could be attributed to the local application of the salicylate in these studies.

The greater magnitude of the CM response, slope of MET curve, and maxima and minima after salicylate exposure may reflect an increase in the conductance of OHCs. Stypulkowski (1990) suggested that salicylate could increase

the permeability of the basolateral wall of the OHC, and thus increase the conductance of the cell membrane. Such an increase in conductance of OHCs would account for the increased receptor current from the OHCs and the consequent greater CM response for a given sound-pressure level. The increase in the slope occurred mainly in the 68 dB SPL condition. This could be due to the saturation of the OHC receptor current at the higher level.

Salicylate moved the OP in the positive sound-pressure direction at the higher signal level (lower right panel of Fig. 10). The shift of OP has also been suggested by Frank and Kössl (1996). They showed that injecting salicylate into the ST caused a decrease in cubic and an increase in quadratic distortion product otoacoustic emissions (DPOAE), an outcome of the change in asymmetry of the transduction curve. In the salicylate group, we also noted an increase in A_2, the quadratic component of the third-order polynomial model of MET, especially in the 68 dB SPL condition (Fig. 6). Furthermore, the peak voltage-dependent capacitance of the OHC, which corresponds to the most sensitive point of the reversible transduction curve (Iwasa, 1993), was reduced but shifted in the depolarizing direction with the application of salicylate to the isolated OHCs (Kakehata and Santos-Sacchi, 1996). This result is comparable to the OP shift towards ST in the present study.

Both *in vivo* and *in vitro* morphologic studies show that salicylate can induce swelling and vesiculation of the subsurface cisternae of OHCs (Douek *et al.*, 1983; Dieler *et al.*, 1991) and subsequently reduce the turgidity of the cell body (Shehata *et al.*, 1991). As hypothesized in the lower panels of Fig. 10, a reduction in OHC volume and surface area due to low cellular turgidity (Chertoff and Brownell, 1994), along with a decrease in the axial stiffness of the OHC (Russell and Schauz, 1995), may directly reduce the electromotility of the OHC (Shehata *et al.*, 1991). It is possible that the slow shortening of the OHC body at higher stimulus levels is blocked by the salicylate. This is in agreement with the finding that aspirin can potentiate the noise-induced TTS in humans (McFadden and Plattsmier, 1983), probably because the OP-shift protective mechanism is weakened. This inhibition of the slow movement of the OHC may lead to the shift of the OP towards ST at higher signal levels. Further studies on the OP shifts with respect to the stiffness of the cochlear partition and the radial morphometric changes of the organ of Corti are necessary to gain further insight into the mechanisms of the cochlear MET.

IV. SUMMARY AND CONCLUSION

The results of this study showed that the MET was altered in different manners by the two treatments. The amplitudes of the maxima and minima were decreased by the 8-kHz pure tone exposure, but increased in the mid- to low-frequency range by the salicylate. The pressures required to saturate the MET in both directions were reduced by salicylate and increased by the tone exposure. The slope of the MET transfer function (sigmoidal) at the inflection point was reduced by the tone exposure and increased by the salicylate. The cochlear partition OP shifted towards SV in the tone exposure group under both signal level conditions; however, the OP shifted towards ST in the salicylate group at the higher signal level. The results of the present study are encouraging for the development of clinical measures that are both sensitive and specific to alterations in cochlear physiology.

ACKNOWLEDGMENTS

We wish to thank Dr. John Belmont, Dr. Jeff Radel, Dr. Greg Ator, and Dr. John Ferraro for their valuable comments on the manuscript and help in the experiments. This study was supported in part by Research Grant No. 1 R29 DC02117-01A2 from the National Institute on Deafness and other Communication Disorders, National Institute of Health, and USPHS Grant No. HD02528 to the Smith Mental Retardation and Human Development Research Center.

Ashmore, J. F. (**1987**). ''A fast motile response in guinea-pig outer hair cells: the cellular basis of the cochlear amplifier,'' J. Physiol. (London) **338**, 323–347.

Bendat, J. S., and Palo, P. (**1990**). ''Practical techniques for nonlinear system analysis/identification,'' Sound Vib. **24**, 28–33.

Bendat, J. S., and Piersol, A. G. (**1986**). *Random Data: Analysis and Measurement Procedures* (Wiley, New York), 2nd ed.

Brundin, L., and Russell, I. (**1994**). ''Tuned phasic and tonic motile responses of isolated outer hair cells to direct mechanical stimulation of the cell body,'' Hearing Res. **73**, 35–45.

Chertoff, M. E., and Brownell, W. E. (**1994**). ''Characterization of cochlear outer hair cell turgor,'' Am. J. Physiol. **266**, C467–C479.

Chertoff, M. E., and Chen, J. (**1996**). ''An in-situ calibration procedure for click stimuli,'' J. Am. Acad. Audiol. **7**, 130–136.

Chertoff, M. E., Steele, T., Ator, G. A., and Bian, L. (**1996**). ''Characterizing cochlear mechano-electric transduction using a nonlinear system identification procedure,'' J. Acoust. Soc. Am. **100**, 3741–3753.

Chertoff, M. E., Steele, T. C., and Bian, L. (**1997**). ''Characterizing cochlear mechano-electric transduction in ears damaged with pure tones,'' J. Acoust. Soc. Am. **102**, 441–450.

Clark, J. A., and Pickles, J. O. (**1996**). ''The effects of moderate and low levels of acoustic overstimulation on stereocilia and their tip links in the guinea pig,'' Hearing Res. **99**, 119–128.

Cody, A. R., and Russell, I. J. (**1988**). ''Acoustically induced hearing loss: Intracellular studies in the guinea pig cochlea,'' Hearing Res. **35**, 59–70.

Cohen, J. (**1988**). ''The effect size index: *f*,'' in *Statistical Power Analysis for the Behavioral Sciences* (Erlbaum, Hillsdale, NJ), 2nd ed., pp. 274–288.

Dew, L. A., Owen, Jr., R. G., and Mulroy, M. J. (**1993**). ''Changes in size and shape of auditory hair cells in vivo during noise-induced temporary threshold shift,'' Hearing Res. **66**, 99–107.

Didier, A., Miller, J. M., and Nuttall, A. L. (**1993**). ''The vascular component of sodium salicylate ototoxicity in the guinea pig,'' Hearing Res. **69**, 199–206.

Dieler, R., Shehata-Dieler, W. E., and Brownell, W. E. (**1991**). ''Concomitant salicylate-induced alterations of outer hair cell subsurface cisternae and electromotility,'' J. Neurocytol. **20**, 637–653.

Douek, E. E., Dodson, H. C., and Bannister, L. H. (**1983**). ''The effects of sodium salicylate on the cochlea of guinea pigs,'' J. Laryngol. Otol. **93**, 793–799.

Dulon, D., Aran, J. M., and Schacht, J. (**1988**). ''Potassium-depolarization induces motility in isolated outer hair cells by an osmotic mechanism,'' Hearing Res. **32**, 123–130.

Fitzgerald, J. J., Robertson, D., and Johnstone, B. M. (**1993**). ''Effects of intra-cochlear perfusion of salicylates on cochlear microphonic and other auditory responses in the guinea pig,'' Hearing Res. **67**, 147–156.

Frank, G., and Kössl, M. (**1996**). ''The acoustic two-tone distortions $2f1-f2$ and $f2-f1$ and their possible relation to changes in the operating point of the cochlear amplifier,'' Hearing Res. **98**, 104–115.

Gao, W.-Y., Ding, D.-L., Zheng, X.-Y., Ruan, F.-M., and Liu, Y.-J. (**1992**). ''A comparison of changes in the stereocilia between temporary and permanent hearing loss in acoustic trauma,'' Hearing Res. **62**, 27–41.

Honrubia, V., and Ward, P. H. (**1968**). ''Longitudinal distribution of the cochlear microphonics inside the cochlear duct (guinea pig),'' J. Acoust. Soc. Am. **44**, 951–958.

Howard, J., and Hudspeth, A. J. (**1988**). ''Compliance of the hair bundle associated with gating of mechanoelectrical transduction channels in the bull-frog's saccular hair cell,'' Neuron **1**, 189–199.

Iwasa, K. H. (**1993**). ''Effect of stress on the membrane capacitance of the auditory outer hair cell,'' Biophys. J. **65**, 492–498.

Johnstone, B. M., Patuzzi, R., Syka, J., and Sykova, E. (**1989**). ''Stimulus-related potassium changes in the organ of Corti of guinea-pig,'' J. Physiol. (London) **408**, 77–92.

Kakehata, S., and Santos-Sacchi, J. (**1996**). ''Effects of salicylate and lanthanides on outer hair cell motility and associated gating charge,'' J. Neurosci. **16**, 4881–4889.

Kirk, D. L., Moleirinho, A., and Patuzzi, R. B. (**1997**). ''Microphonic and DPOAE measurements suggest a micromechanical mechanism for the 'bounce' phenomenon following low-frequency tones,'' Hearing Res. **112**, 69–86.

Kirk, D. L., and Patuzzi, R. B. (**1997**). ''Transient changes in cochlear potentials and DPOAEs after low-frequency tones: the 'two-minute bounce' revisited,'' Hearing Res. **112**, 49–68.

Kujawa, S. G., Fallon, M., and Bobbin, R. P. (**1992**). ''Intracochlear salicylate reduces low-intensity acoustic and cochlear microphonic distortion products,'' Hearing Res. **64**, 73–80.

LePage, E. L. (**1987**). ''Frequency-dependent self-induced bias of the basilar membrane and its potential for controlling sensitivity and tuning in the mammalian cochlea,'' J. Acoust. Soc. Am. **82**, 139–154.

Liberman, M. C., and Dodds, L. W. (**1987**). ''Acute ultrastructural changes in acoustic trauma: Serial-section reconstruction of stereocilia and cuticular plates,'' Hearing Res. **26**, 45–64.

Marascuilo, L. A., and Serlin, R. C. (**1988**). *Statistical Methods for the Social and Behavioral Sciences* (Freeman, New York).

McFadden, D., and Plattsmier, H. S. (**1983**). ''Aspirin can potentiate the temporary hearing loss induced by intense sounds,'' Hearing Res. **9**, 295–316.

Patuzzi, R. (**1995**). ''Monitoring cochlear homeostasis with automatic analysis of the low-frequency cochlear microphonic,'' in *Active Hearing*, edited by Å. Flock, D. Ottoson, and M. Ulfendahl (Elsevier, New York), pp. 141–153.

Puel, J-L., Bobbin, R. P., and Fallon, M. (**1990**). ''Salicylate, mefenamate, meclofenate, and quinine on cochlear potentials,'' Otolaryngol.-Head Neck Surg. **102**, 66–73.

Ruggero, M. A., Rich, N. C., Recio, A., Narayan, S. S., and Robles, L. (**1997**). ''Basilar-membrane responses to tones at the base of the chinchilla cochlea,'' J. Acoust. Soc. Am. **101**, 2151–2163.

Russell, I. J., and Schauz, C. (**1995**). ''Salicylate ototoxicity: effects on the stiffness and electromotility of outer hair cells isolated from the guinea pig cochlea,'' Aud. Neurosci. **1**, 309–319.

Santos-Sacchi, J., and Dilger, J. P. (**1988**). ''Whole-cell currents and mechanical responses of isolated outer hair cells,'' Hearing Res. **35**, 143–150.

Saunders, J. C., Canlon, B., and Flock, Å. (**1986**). ''Mechanical changes in stereocilia following overstimulation: observation and possible mechanisms,'' in *Basic and Applied Aspects of Noise-Induced Hearing Loss*, edited by R. J. Salvi, D. Henderson, R. P. Hamernik, and V. Colleti (Plenum, New York), pp. 11–30.

Saunders, J. C., Cohen, Y. E., and Szymko, Y. M. (**1991**). ''The structural and functional consequences of acoustic injury in the cochlea and peripheral auditory system: A five year update,'' J. Acoust. Soc. Am. **90**, 136–146.

Shehata, W. E., Brownell, W. E., and Dieler, R. (**1991**). ''Effects of salicylate on shape, electromotility and membrane characteristics of isolated outer hair cells from guinea pigs,'' Acta Oto-Laryngol. **111**, 707–718.

Stypulkowski, P. H. (**1990**). ''The mechanisms of salicylate ototoxicity,'' Hearing Res. **46**, 13–46.

Young, M. A. (**1993**). ''Supplementing tests of statistical significance: variation accounted for,'' J. Speech Hear. Res. **36**, 644–656.

Zhang, M., and Zwislocki, J. J. (**1996**). ''Intensity-dependent peak shift in cochlear transfer functions at the cellular level, its elimination by sound exposure, and its possible underlying mechanisms,'' Hearing Res. **96**, 46–58.

Zimmermann, U., and Fermin, C. (**1996**). ''Shape deformation of the organ of Corti associated with length changes of outer hair cell,'' Acta Oto-Laryngol. **116**, 395–400.

Temporal factors associated with cochlear nerve tuning to dual and single tones: A qualitative study

Kenneth R. Henry[a)]
Psychology Department, University of California, Davis, California 95616-8686

(Received 11 August 1997; revised 3 April 1998; accepted 12 June 1998)

The simultaneous presentation of a 10- and 10.86-kHz tone produces an 860-Hz cochlear nerve difference tone (DT) response in the gerbil which persists for the duration of the stimulus. Forward masking shows this response is generated by neurons sharply tuned to the stimulus frequencies. When compared with the DT response, the cochlear nerve compound action potential (CAP) to a single tone is smaller in amplitude, has a higher nonmasked threshold, and produces a less sensitive tuning curve (TC). Forward maskers can also produce amplitude enhancement of the CAP, but this was not observed for the onset portion of the DT response. The CAP TC is as sharply tuned as the TC of either the DT onset response or the entire DT response. A comparison was made of tuning of the DT response to the onset, the first half and second half of the 23-ms duration probe stimulus, using either a 5- or 15-ms masker-probe interval. An increase of the tip threshold of the TC to all three portions of the stimulus occurred as the interval was increased between the end of the masker and the midpoint of the portion of the stimulus under question. The 15-ms masker-probe interval produced sharper TCs. [S0001-4966(98)06209-2]

PACS numbers: 43.64.Qh, 43.64.Ri [RDF]

INTRODUCTION

Both temporal and filtering factors are important in the analysis of speech and other vocalizations (Evans, 1978; Langer, 1992). One commonly used method of assessing the spectral properties of the cochlea is the frequency threshold tuning curve, created by determining the minimal level of a single tonal stimulus, over a wide range of tonal frequencies, that can increase the firing rate of cochlear nerve fibers by a criterion amount (Tasaki, 1954). Alternatively, masker tuning curves for cochlear nerve axons can be obtained by using a method analogous to that used for obtaining the psychophysical tuning curve (Small, 1959). This involves stimulating the cochlea with an above-threshold tone at the characteristic frequency of the neuron, and determining the minimal intensity of a masker, over a wide range of masker frequencies, that can reduce this firing rate by a criterion amount (Bauer, 1978; Pickles, 1984).

Rather than measuring responses of individual neurons, masker tuning curves of cochlear nerve function are often (and more conveniently) generated by measuring changes of amplitude of the cochlear nerve compound action potential, or CAP (Dallos and Cheatham, 1976; Harris, 1979). The CAP is a response created by a rapid change (typically the onset edge) of stimulus intensity. But the sudden tonal onset required in order to obtain a robust CAP in response to a low level stimulus results in a considerable amount of acoustic splatter, thereby increasing the width of the masker TC. One purpose of the present experiments is to compare the CAP TC with a more recently developed (and equally convenient) method that does not have this disadvantage: The difference tone (DT) tuning curve.

When two phase-locked tones of equal amplitude are simultaneously presented, the acoustic waveform envelope is modulated at a frequency equal to the difference tone (DT $=F_2-F_1$, where F_2 has the higher frequency of the two tones). Even though this DT envelope frequency is not acoustically present in the stimulus, the nonlinear characteristics of the cochlear hair cells will result in a demodulation of the envelope frequency (Khanna and Teich, 1989). A DT response can be obtained from the firing rates of individual cochlear nerve axons, and is most robust if the axons have characteristic frequencies close to those of F_1 and F_2 (Kim *et al.*, 1980; Siegel *et al.*, 1982; Khanna and Teich, 1989). A DT response can also be recorded from the cochlear round window (RW) of the guinea pig (Nuttall and Dolan, 1993, 1994) and gerbil (Brown, 1994; Henry, 1996a). Tetrodotoxin reduces the magnitude of this response (Nuttall and Dolan, 1994; Henry, 1996a), suggesting the RW DT response is neural in origin. This interpretation is supported by forward masking of the RW DT response, which results in sharp tuning curves (TCs) having tip frequencies corresponding to the frequency of the two tones that comprise the probe stimulus (Henry, 1996b).

Another purpose of these experiments is to evaluate the influence of temporal factors on the tuning of the DT response. One conventional means of examining the effects of time on tuning curves is to vary the interval between the ending of the masker and the beginning of the probe stimulus. Studies using psychophysical tuning curves (PTCs) have shown that increasing this masker-probe interval elevates the TC tip threshold (Kidd and Feth, 1981; Nelson and Freyman, 1984; Lutfi, 1988) and broadens the TC (Kidd and Feth, 1981; Nelson and Freyman, 1984). Dallos and Cheatham (1976) also showed that increasing the masker-probe interval elevates the CAP TC threshold, but this only broadened the CAP TC if the masker was very brief (i.e., a 5-ms duration masker of a 15-ms duration probe stimulus). In addition to

a)Electronic mail: krhenry@ucdavis.edu

determining the influence of the masker-probe interval on the DT TC, the present experiments take advantage of a property that is not found in the CAP produced by the onset of a single tone: The DT response occurs throughout the duration of the stimulus. This allows the possibility of obtaining a measure of the tip threshold and sharpness of cochlear periodicity tuning to any portion of the stimulus, and not just to its onset.

I. METHODS

A. Subjects

Thirteen Mongolian gerbils (*Meriones unguiculatus*), aged 120 to 180 days, were used in these experiments. Six animals were used in the first, and seven in the second experiment. All animals were at least the sixth generation of gerbils raised in our colony under conditions of restricted ambient noise. Preliminary otoscopic screening and subsequent microscopic examination of the middle ear resulted in gerbils free of cholesteatomas (Chole *et al.*, 1981). Gerbils were only used if their CAP thresholds were within the range found to be normal in this laboratory ($\leqslant$25 dB SPL, with a 1-ms linear rise and fall time 8-kHz stimulus).

B. General stimulus considerations

The stimulus frequencies were chosen in order to provide a clear measurement and evaluation of both the acoustic stimulus and the DT response. Even though this response can easily be elicited by low intensity levels of stimuli having frequencies $\geqslant$38 kHz (Henry, 1997), frequencies were chosen to be within the range of the very sensitive probe microphone system (an Etymotic ER-10, custom made by the manufacturer to have a flat response up to 17 kHz).

Ten kHz and 10.86 kHz were chosen as the DT probe stimulus frequencies for the following reasons: The gerbil is most sensitive to frequencies ranging from approximately 2 to 15 kHz, and the upper end of this range has the sharper tuning curves; These probe frequencies allowed for a careful evaluation of maskers having frequencies of one-half octave above and one octave below the probe, thereby allowing a good tuning curve to be generated; And the 860-Hz separation of the two tones was chosen to result in a large amplitude DT response (see Sec. III).

Ten thousand four hundred and thirty Hz was chosen as the CAP probe stimulus because it is the midpoint of the 10.0-kHz and 10.86-kHz stimuli used to generate the DT TC, thereby allowing an appropriate comparison of the two functions.

C. Stimuli of the first experiment (Figs. 1–5)

The probe stimuli that were used to generate the CAP consisted of 30 dB SPL tones with a 1-ms linear rise and fall time and a 15-ms plateau duration. The polarities of the 100 stimuli used to generate an averaged CAP were alternated, in order to cancel out the cochlear microphonic (CM). The 30 dB SPL stimuli used to generate the DT response consisted of two simultaneously presented tone bursts (1-ms linear rise and fall time, 15-ms plateau), each beginning at the 0 degree position and alternating in polarity in order to cancel the CM. Forward maskers had a 4-ms linear rise and fall time and a 40-ms plateau. The duty cycle was 101 ms. The masker-probe interval (as measured from the termination of the masker to the initiation of the probe stimulus) was 5 ms.

D. Stimuli of the second experiment (Figs. 6 and 7)

The DT periodicity response was produced by simultaneously presenting two phase-locked, alternating polarity tones with an $\approx$4-ms Gaussian rise and fall time and a plateau duration of $\approx$15 ms. This more gradual, nonlinear onset and the lower intensity level (20 dB SPL) resulted in a stimulus that was relatively free of acoustic splatter and one which did not generate a CAP. Forward maskers had a 4-ms linear rise and fall time and a 40-ms plateau. The duty cycle was 101 ms. The masker-probe interval (as measured from the termination of the masker to the initiation of the probe stimulus) was either 5 or 15 ms.

E. Stimulus presentation

All probe stimuli and maskers were delivered to the right ear of the gerbil, and the output of the acoustic driver (which was tightly sealed to the external auditory meatus) was continuously monitored by a probe microphone at the level of the auditory meatus. The probe stimuli and forward maskers were transduced by an Etymotic ER2 acoustic driver, transmitted to the ear over a 0.5-m-long tube, and measured with an Etymotic ER10 low-noise probe microphone. The output of the probe microphone was analyzed over an 80-dB dynamic range by a Hewlett-Packard 3561A dynamic signal analyzer. The quality and intensity level of each stimulus and masker within the auditory meatus was evaluated individually for each subject by examination of the FFT of the probe microphone output.

When the probe stimuli were presented in the absence of the gerbil, no acoustic fundamental frequency was observed at -50 dB (*re:* probe stimulus level). Therefore, it is assumed that the cochlear response having a frequency equal to that of the stimulus periodicity must have arisen from within the animal itself, and was not a product of the acoustic delivery system.

F. Recording procedure

A ventral approach to the bulla of the animals was used to obtain cochlear nerve responses from the round window, in a manner described previously (Henry, 1995). The gerbils were pre-sedated with chlorprothixene and anesthetized with ketamine, after which the antrum of the RW was filled with artificial perilymph. Recordings were made from a silver wire electrode placed within this fluid. The amplified (10 000 $\times$) bioelectrical responses were actively filtered (48 dB/octave) with a bandpass of 300–5000 Hz to eliminate summating potentials, cochlear microphonics, and the $2F_1-F_2$ neural response. Averages were made with either 5- or 10-ms resolution over a 25-ms window in response to at least 100 stimulus presentations.

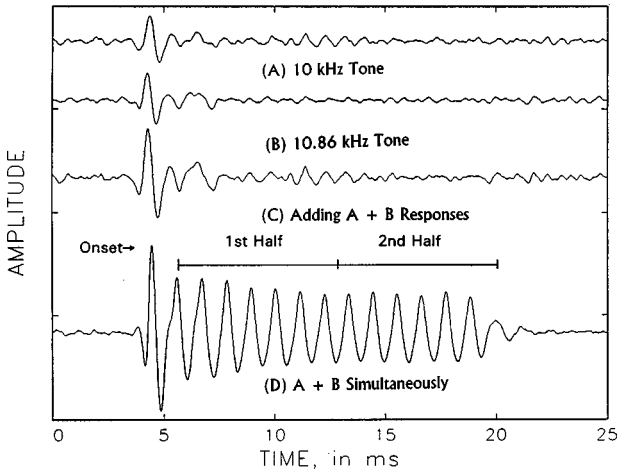

FIG. 1. Averaged cochlear round window responses to 10- and 10.86-kHz tone bursts, presented singly (A and B) or simultaneously (D). The intensity of the stimuli was 30 dB SPL, the linear rise and fall times were 1 ms, and the plateau durations were 15 ms. The 860-Hz difference tone (DT) response (fourth waveform) created by the simultaneous presentation of the 10- and 10.86-kHz tone bursts persists throughout the duration of the stimuli, and has a frequency which is equal to the modulation of the stimulus waveform (10.86 minus 10 kHz). The stimulus was created at the 0 point on the time axis, and an approximately 1.5-ms acoustic delay was introduced by the sound delivery tube. Each tic mark on the *X* axis represents 15 μV.

G. Evaluation of the cochlear response

Amplitudes of the CAP and the onset portion of the difference tone (DT) response were measured as peak-to-peak voltages. The DT response reflects the stimulus envelope; therefore, its duration equals that of the stimulus. This made it possible to measure the response to the entire stimulus, as well as to the first and second halves of the stimulus. This was achieved by a Fourier analysis conducted offline on the time-averaged response. When different portions of the DT response were used to obtain tuning curves, the interval after the probe was calculated as the masker-probe interval (either 5 or 15 ms) plus the time of the midpoint of either the first or the second half of the response (Fig. 7). In order to reduce the variability inherent in amplitude measurements of cochlear nerve activity, each masked response was immediately preceded by and followed by a nonmasked response. Tuning curves were created by determining the minimal level of forward masker (the masker threshold), over a wide range of masker frequencies, that was capable of reducing the amplitude of this response to 75% of the nonmasked amplitude.

II. RESULTS

A. Experiment 1

The difference tone (DT) response to two simultaneously presented 10- and 10.86-kHz tones is not equal to the summation of the CAP response to a 10-kHz tone and a 10.86-kHz tone (Fig. 1). The DT response is larger and persists for the entire stimulus duration, in contrast to the CAP which merely reflects the neural response to the stimulus onset. Unlike the stimulus, which has a 15-ms duration plateau, the DT response also shows adaptation, with the onset portion being largest, and a decline of amplitude from the first to the second half of the response.

Figure 2 illustrates other differences between the DT response and the CAP. A 10.43-kHz tone, at intensity levels of approximately 30 to 60 dB SPL, produces a well-defined compound action potential (CAP) in response to the onset edge of the stimulus. The simultaneously presented 10- and 10.86-kHz tones, over a wider range of stimulus intensities, generate an even larger DT response having a frequency of 860 Hz (10.86 kHz–10 kHz).

When probe stimulus levels of approximately 10–20 dB above detection threshold are used to generate RW responses, forward maskers can be used to generate tuning curves (TCs) that are similar for both one-tone and two-tone stimuli. Figure 3 shows three such TCs. The CAP TC is V-shaped, with its mean tip frequency (10 ± 0.1 kHz) and threshold (26.8 ± 2.1 dB SPL) corresponding closely with the values for its probe stimulus (10.43 kHz, 30 dB SPL). Two TCs were also obtained by forward masking of the dif-

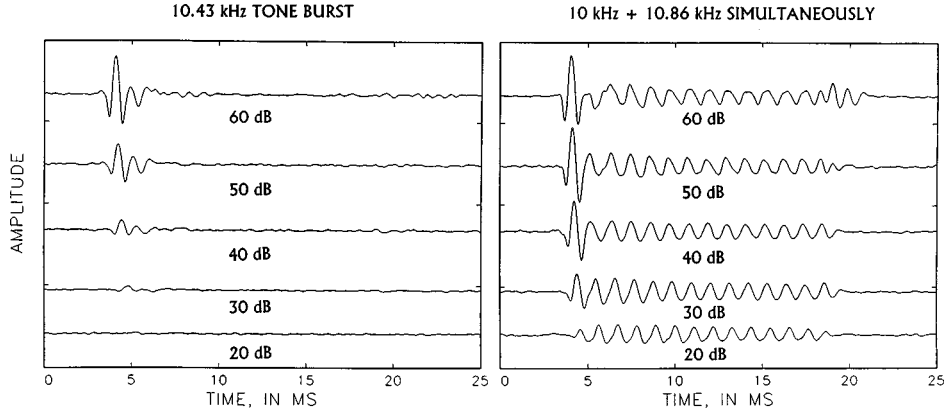

FIG. 2. (left) CAPs generated by a single 10.43-kHz tone burst (1-ms linear rise and fall time, 15-ms plateau) at intensity levels ranging from 60 (top) to 20 dB SPL (bottom). The CAP only occurs in response to the stimulus onset, and its amplitude drops rapidly as the stimulus intensity decreases (the visual detection threshold was 18 dB SPL in this gerbil). Each tic mark on the *X* axis represents 37.5 μV. (right) DT responses from the same animal generated by simultaneous presentation of 10- and 10.86-kHz tonal stimuli, each having a 1-ms linear rise and fall time and 15-ms plateau duration. The stimulus intensity levels ranged from 60 (top) to 20 dB SPL (bottom). At higher SPLs, these stimuli produce an onset response, an offset response, and a sustained response. As the intensity is lowered, only the sustained response remains. The amplitude of the sustained response does not drop as rapidly as the CAP amplitudes (the DT threshold was 7 dB SPL in this gerbil). Each tic mark on the *X* axis represents 37.5 μV.

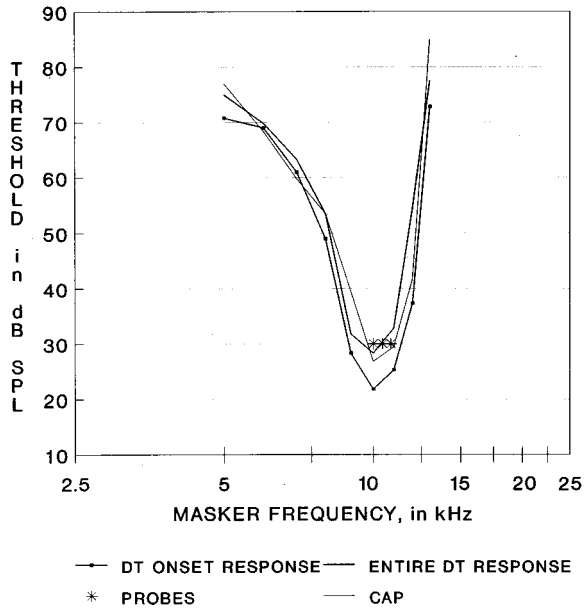

FIG. 3. Tuning curves (TCs) generated by forward masking of the CAP, the onset portion of the DT response, and the entire DT response. The probe stimuli for these TCs were the 30 dB SPL stimuli that created the responses that were illustrated as the fourth waveforms of Fig. 2, left and right. Each curve represents 25% amplitude reduction at each masker frequency (the masker threshold) from four gerbils. All three classes of TCs show comparable tuning, but the tip threshold is less for the onset DT response.

ference tone (DT) response to the two simultaneously presented stimuli. One of these TCs was created by evaluating the masker thresholds for reducing the peak-to-peak amplitude of the initial (onset) portion of the DT response. This DT onset response TC has a shape quite similar to that of the CAP TC, although its mean threshold is lower (21.8 $\pm$2.5 dB SPL). The second DT TC was determined by evaluating the influence of the forward masker on the amplitude of the DT response to the entire stimulus duration. The amplitude measurement for this method was obtained by a Fourier analysis of the entire 860-Hz DT response produced by the 10- and 10.86-kHz probe stimuli. This TC generated from the entire DT response was very similar to that generated by masking the CAP. The mean Q_{10} values for these 3 TCs were very similar (4.7 for both the CAP and the onset DT responses, and 4.9 for the entire DT response).

Although forward maskers are typically described in terms of their ability to decrease the response to the probe stimulus, an opposite effect is sometimes seen. In all but one of the gerbils involved in this experiment, preceding the 30-dB, 10.43-kHz CAP probe stimulus with a restricted frequency-intensity domain of forward maskers resulted in enhancement of the CAP amplitude. Figure 4 shows this effect for one gerbil, with a forward masker increasing the CAP amplitude by >50%. The regions (stippled area) of CAP enhancement and the CAP tuning curve for another gerbil are shown in Fig. 5. Note that enhancement only occurs within a limited range of masker frequencies and intensities outside the bounds of the TC. Enhancement of the DT response was never observed under conditions of forward masking.

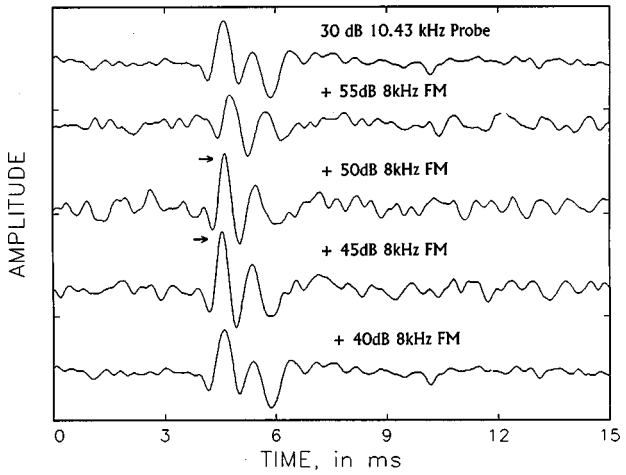

FIG. 4. Enhancement of the CAP, as a function of forward masking. The top waveform shows the response to the probe stimulus alone. The second through fifth waveforms show the CAP produced by the probe that was preceded by different intensity levels of an 8-kHz forward masker (FM). Note that the 50- and 45-dB levels of the forward masker result in an increase (enhancement) of the CAP amplitude, as indicated by an →. Each tic mark on the X axis represents 6.25 μV.

B. Experiment 2

This experiment examined the tuning of different portions of the DT response as a function of time (Fig. 6). It used two masker-probe intervals. A 4-ms Gaussian rise and fall time, 20 dB SPL probe stimulus was also used in order to minimize the effects of acoustic splatter on the initial portion of the DT response. These stimulus conditions resulted in a robust DT response, but were incapable of producing a CAP. When the magnitude of each DT response was evaluated by a Fourier analysis, the 15-ms interval resulted in a 25% response decrement, whereas the 5-ms interval resulted in a

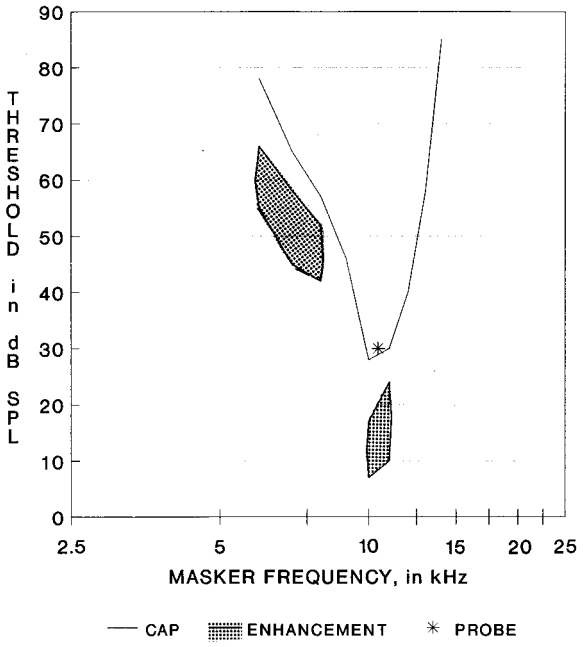

FIG. 5. Regions of CAP enhancement. The stimulus-intensity domains over which forward masking results in CAP amplitude enhancement (stippled region) lie outside the bounds of the forward masked TC for one gerbil.

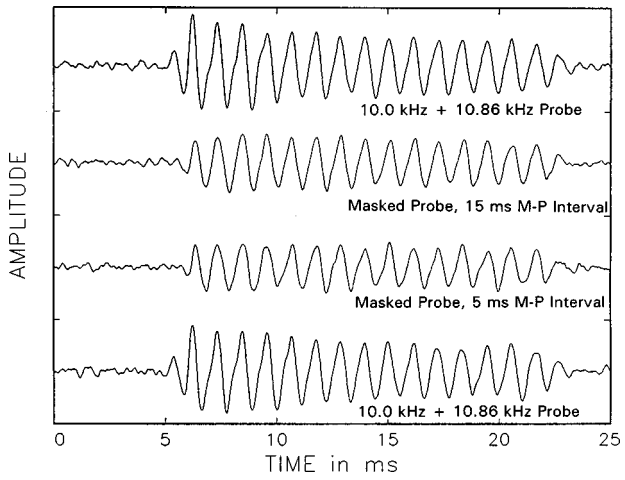

FIG. 6. Effects of different masker-probe intervals on the DT response. The masker-probe intervals were calculated as the time between the last portion of the masker and the initial portion of the probe stimulus. The probe stimuli were simultaneously presented 20-dB, 10-kHz and 10.86-kHz tone bursts, each having a 4-ms Gaussian rise and fall time and a 15-ms plateau. The top and bottom waveforms show the DT response to the probe stimulus alone. The second waveform is of the probe which is forward masked by a 30 dB SPL, 11-kHz tone, with a 15-ms masker-probe interval. The third waveform is as the second, but the masker-probe interval is 5 ms. These three regions of the DT response are illustrated in Fig. 1. Each tic mark on the *X* axis represents 12.5 μV.

35% decrement. The effects of masking were more evident in the initial portions of the DT response. Fourier analysis showed that, for the 15-ms masker-probe interval, the first half of the response had a decrement of 27%, whereas the second half of the response had an 18% decrement. For the 5-ms interval, these values were 47% and 27%, respectively.

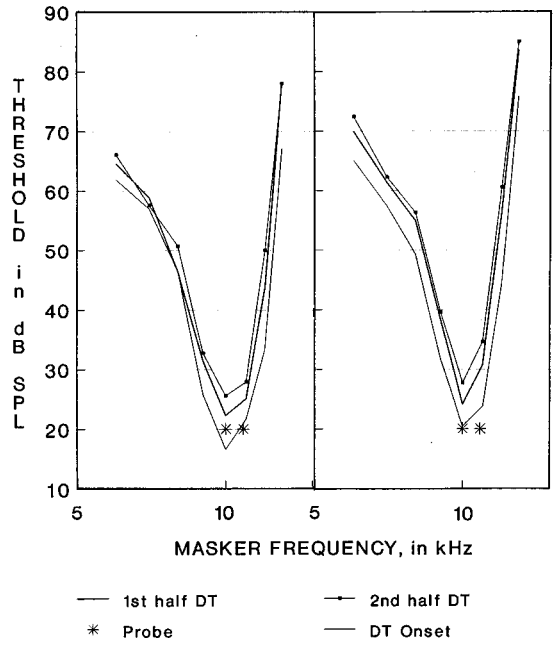

FIG. 7. TCs created by forward masking of the DT response created by the 20 dB SPL stimuli and the masker-probe intervals described in Fig. 6. These TCs were created for the initial (onset) portion, the first half, or the second half of the DT response. Each TC represents the average criterion amplitude reduction for each masker frequency from seven gerbils. The masker-probe interval was 5 ms (left) and 15 ms (right).

Figure 7 (left) shows the mean TCs from seven gerbils, produced when a 5-ms masker probe interval was used. The TC generated by masking the first large peak of the response (the DT onset response) was 4.9 dB more sensitive that those generated from the first half, and 7.7 dB more sensitive than those generated from the second half of the DT response. In addition, the TC generated from the first half of the DT response was marginally more sensitive than that generated from the second half of the response. The mean Q_{10} values of these three TCs were quite similar (4.06, 4.16, and 3.97 for the onset, first, and second halves, respectively).

Figure 7 (right) shows the mean TCs from these same seven gerbils, produced when a 15-ms masker-probe interval was used. The same trend was observed, with the DT onset response TC being more sensitive than the TC to either the first or the second half of the DT response, and the TC to the first half of the DT response being more sensitive than that to the second half. The Q_{10} values did not vary as a function of the portion of the response from which they were generated (the values were 5.93, 5.77, and 5.13 for the onset, first, and second halves, respectively).

There was a tendency of the tip thresholds of the TCs to vary as a function of time. But this was not merely a matter of the masker-probe interval. Rather, it varied as a function of the time between the end of the masker and the midpoint of the particular portion of the DT response that is being evaluated; i.e., the onset, first half, or second half.

The sharpness of tuning of these TCs also varied as a function of time, but in a different manner. The Q_{10} values were higher for every gerbil with the 15- than the 5-ms masker-probe interval. There was also a tendency for the Q_{10} values to become lower for TCs generated from later portions of the stimulus.

III. DISCUSSION

The DT responses described in this paper are quite distinct from F_2-F_1 difference tone responses which have been described in preneural cochlear measures such as the cochlear microphonic (CM; Gibian and Kim, 1982) and distortion products of otoacoustic emissions (DPOAE; Brown and Kemp, 1984). DPOAE TCs differ in several ways from the DT neural ensemble TCs described herein. For example, the DPOAE TCs can only be created by simultaneous maskers because forward maskers do not produce adaptation of these preneural responses (Brown and Kemp, 1984; Abdalla *et al.*, 1996). This appears to be one reason why DPOAE suppressor TCs are broader than psychophysical TCs, although they do appear to be quite similar in other respects (Abdalla *et al.*, 1996). In addition, the DPOAE is little influenced by TTX (Kujawa *et al.*, 1995), whereas the neural DT response described herein is clearly affected (Henry, 1996a). And, finally, the DPOAE reflecting $2F_1-F_2$ is larger than that which reflects F_2-F_1 (Brown, 1987; Abdalla *et al.*, 1996), whereas the gerbil's 10.86 kHz–10 kHz (i.e., F_2-F_1) neural response is much larger than its 2 (10 kHz)–10.86 kHz (i.e., $2F_1-F_2$) cochlear nerve ensemble response.

Several factors may contribute to the robust 860-Hz cochlear nerve DT response. For example, the simultaneous

presentation of these two tones produces an 860-Hz stimulus envelope modulation that is not reflected in the FFT of the stimulus. The ability of cochlear neurons to fire in a phase-locked fashion to the stimulus envelope (Gleich and Klump, 1995) is obviously restricted to those frequencies ($\approx \leqslant 4$ kHz) at which phase locking occurs. But this low-pass filter property of the cochlear nerve does not correspond to the bandpass range ($\approx$700–1100 Hz) over which the DT response is largest in the gerbil (Henry, 1996a). Dolan *et al.* (1990) described a spectral peak of approximately 800 Hz for spontaneous neural activity recorded from the round window of the guinea pig. Smith *et al.* (1993) described 800 Hz as the best modulation frequency for the gerbil. They hypothesized that this resulted from the biphasic time course of the contribution of spike activity from the ensemble of neurons that constituted this response, with the spikes acting as the impulse response of a second filter.

The DT response is much more robust than the CAP, especially in response to low intensity stimulus levels (Figs. 1–3). If one compares the CAP (which is an onset response) with that portion of the DT response that is elicited by the stimulus onset, the CAP amplitudes are smaller and its thresholds are higher (Fig. 2; Henry, 1996b). In addition, the forward masker tuning curves (TCs) generated by the onset portion of the DT response are more sensitive (have a lower tip threshold) than TCs produced from a CAP, even when the same level probe stimulus is used (Fig. 3).

The CAP produced by a low intensity, 1-ms linear rise time, high-frequency tone ($\geqslant$4 kHz) appears to be created by a restricted population of cochlear nerve axons having characteristic frequencies (CFs) at or near those of the stimulus (Özdamar and Dallos, 1978). This interpretation is supported in the present study, as evidenced by the agreement of the CAP TC tip frequencies (Fig. 3) with the frequency of the probe stimulus.

The DT response produced by a pair of low intensity tones also appears to be generated by a restricted number of cochlear neurons having CFs at or near those of the stimuli (Kim *et al.*, 1980), even though stimuli at higher levels (e.g., 60–80 dB) can generate DT responses from a wider range of cochlear preneural (Cheatham and Dallos, 1997) and neural (Henry, 1989) elements. The tip frequencies of the DT TCs created with 20- or 30-dB stimuli support the interpretation that they are generated by a restricted population of cochlear elements having CFs close to those of the tonal stimuli.

The CAP from the 1-ms rise time stimulus in this study has a detection threshold that is quite similar to the cochlear nerve axon detection threshold at CF, although both measures are higher than behavioral thresholds in the gerbils (Dallos *et al.*, 1978). By contrast, the sharply tuned tip of the DT TC and the detection threshold of the DT more closely approximate the behavioral threshold (Henry, 1996a, b). This may be related to the phase-locked activity that appears to underlie the DT response (Kim *et al.*, 1980; Siegel *et al.*, 1982): Phase locking has been observed to occur in response to stimuli at intensity levels that are 10 dB or more below the detection thresholds for these stimuli (Rose *et al.*, 1967; Palmer and Russell, 1986).

Enhancement of the CAP amplitude by a lower-frequency forward masker (Figs. 4 and 5) has been observed previously (Cacace and Smith, 1986; Henry, 1991a). The multiple enhancement regions bordering the CAP TC, such as those illustrated in Fig. 5, have also been described, occurring in approximately 70% of the gerbils. When it occurs, it is almost invariably found in response to tonal frequencies near and/or approximately 1 octave below the probe stimulus frequency; it is less likely observed in response to masker frequencies higher than that of the probe (Henry, 1991b). The forward masking conditions that result in enhancement of the RW-recorded CAP also produce amplitude enhancement of another response created by a rapid tonal onset—the scalp-recorded auditory brainstem response (Henry and Price, 1994). But these same forward masking conditions have not produced an observable amplitude enhancement at cochlear levels at or before the afferent synapse (Henry and Price, 1994). Although no definitive explanation has been presented to explain CAP amplitude enhancement, several mechanisms have been rejected (Cacace and Smith, 1986; Henry, 1991a, b). Enhancement of the onset portion of the DT response has not been observed in this laboratory as a function of forward masking, even though simultaneous masking can sometimes result in amplitude enhancement of the portion of the DT response that is produced by the plateau portion of the stimulus (Henry, 1996b).

In sum, the CAP and the onset portion of the DT response differ in several ways: The CAP amplitudes are smaller; CAP thresholds are higher; forward masker TCs have higher tip thresholds for the CAP than for the onset DT response; and forward masking can produce enhancement of the CAP, but this has not been observed for the initial portion of the DT response.

Nonetheless, forward masker TCs generated from the CAP and the DT response are quite similar in shape and sharpness of tuning. The same forward masking paradigm used in the present study has also been used to generate TCs as a function of decreased firing rate of single cochlear nerve fibers in the cat. These were quite similar in appearance to the frequency threshold curves (FTCs) of single cochlear units that were produced with singly presented tones (Bauer, 1978). Forward masking of a CAP has also been used to generate TCs that are quite similar to FTCs of individual cochlear nerve axons (Harris, 1979; Abbas and Gorga, 1981; Dolan *et al.*, 1985). Therefore, it appears that both the CAP TC and the DT TC can provide a convenient measure that reflects tuning of cochlear nerve fibers.

Acoustic splatter of the stimuli used to generate a CAP often results in some limitations in using this response as a measure of cochlear tuning. When the tone used to generate a CAP has a linear rise and fall time that is decreased from 4 to 1 ms, little difference is observed in the resultant TC (Mitchell, 1976). But further reductions do result in detuning (shifting of the TC tip toward a middle frequency of the audiogram; Mitchell, 1976; Dolan and Klein, 1987; Henry, 1989). Use of a nonlinear rise and fall time, even though it may not produce as robust a CAP, reduces this detuning, especially when higher stimulus levels are used (Dolan and Klein, 1987). These observations provided support for the use in the second experiment (Figs. 6 and 7) of low intensity

stimuli having long nonlinear rise and fall times.

The fact that the DT response persists for the duration of the stimulus allows an analysis of cochlear tuning as a function of adaptation to both the forward masker and to the probe stimulus, itself. This comparison separated the DT response into three portions: onset, first half, and second half. Increasing the interval between the termination of the masker and the midpoint of the portion of the DT response being analyzed resulted in an increase of the tip threshold. This is true for both forward masking paradigms shown in Figs. 6 and 7. Even though experiments utilizing psychophysical tuning curves (PTCs) obtained from human subjects did not compare tuning for different portions of the stimulus, the present data are compatible with the behavioral literature, in that increasing the masker-probe interval also elevates the PTC tip threshold (Kidd and Feth, 1981; Nelson and Freyman, 1984; Lutfi, 1988). Increasing the masker-probe interval allows for a longer recovery of the response from the adaptation effects of the masker (Harris and Dallos, 1979; Smith, 1979; Abbas and Gorga, 1981). This has been described as a two-compartment, nonlinear process (Kidd and Feth, 1981; Nelson and Freyman, 1984) which interacts with the masker level (Lutfi, 1988).

But a difference in the sharpness of tuning was found in the way in which the DT TC and PTC are influenced by the masker-probe interval. Increasing this interval broadens the PTC (Kidd and Feth, 1981; Nelson and Freyman, 1984). An opposite effect is seen for the DT TC: A 15-ms masker-probe interval results in a more sharply tuned TC than does a 5-ms interval. Therefore, the tuning of the gerbil's cochlear nerve to the stimulus envelope periodicity created by two simultaneously presented tones has some properties that differ from PTCs derived from a single tonal stimulus in humans. This difference could be due to the level (cochlear nerve versus behavioral) at which the response is made; the nature of the response (tuning of a single tone versus tuning to stimulus envelope periodicity); or to species-specific factors or other unidentified differences.

Abbas, P. J., and Gorga, M. P. (**1981**). ''AP responses in forward-masking paradigms and their relationship to responses of auditory-nerve fibers,'' J. Acoust. Soc. Am. **69**, 492–499.

Abdalla, C., Sinniger, Y. S., Ekelid, M., and Zeng, F. G. (**1996**). ''Distortion product otoacoustic emission suppression tuning curves in human adults and neonates,'' Hearing Res. **98**, 38–53.

Bauer, J. W. (**1978**). ''Tuning curves and masking functions of auditory-nerve fibers in cat,'' Sensory Processes **2**, 156–72.

Brown, A. M. (**1987**). ''Acoustic distortion from rodent ears: A comparison of responses from rats, guinea pigs and gerbils,'' Hearing Res. **31**, 25–38.

Brown, A. M. (**1994**). ''Modulation of the hair cell motor: A possible source of odd-order distortion,'' J. Acoust. Soc. Am. **96**, 2210–2215.

Brown, A. M., and Kemp, D. T. (**1984**). ''Suppressibility of the $2f_1-f_2$ stimulated acoustic emissions in gerbil and man,'' Hearing Res. **13**, 29–37.

Cacace, A. T., and Smith, R. L. (**1986**). ''Some poststimulatory effects on the whole nerve action potential,'' Hearing Res. **23**, 223–232.

Cheatham, M. A., and Dallos, P. (**1997**). ''Intermodulation components in inner hair cell and organ of Corti responses,'' J. Acoust. Soc. Am. **102**, 1038–1048.

Chole, R. A., Henry, K. R., and McGinn, M. D. (**1981**). ''Cholesteatoma: Spontaneous occurrence in the Mongolian gerbil, *Meriones unguiculatus*,'' Am. J. Otolaryngol. **2**, 204–210.

Dallos, P., and Cheatham, M. A. (**1976**). ''Compound action potential (AP) tuning curves,'' J. Acoust. Soc. Am. **59**, 591–597.

Dallos, P., Harris, D., Özdamar, Ö., and Ryan, A. (**1978**). ''Behavioral, compound action potential, and single unit thresholds: Relationship in normal and abnormal ears,'' J. Acoust. Soc. Am. **64**, 151–157.

Dolan, D. F., Nuttall, A. L., and Avinash, G. (**1990**). ''Asynchronous activity recorded from the round window,'' J. Acoust. Soc. Am. **87**, 2621–2627.

Dolan, T. G., and Klein, A. J. (**1987**). ''Effect of signal temporal shaping on the frequency specificity of the action potential in gerbils,'' Audiology **26**, 20–30.

Dolan, T. G., Mills, J. H., and Schmeidt, R. A. (**1985**). ''Brainstem, whole-nerve AP and single-fiber suppression in the gerbil: Normative data,'' Hearing Res. **18**, 203–210.

Evans, E. F. (**1978**). ''Place and time coding of frequency in the peripheral auditory system: Some physiological pros and cons,'' Audiology **17**, 369–420.

Gibian, G. L., and Kim, D. O. (**1982**). ''Cochlear microphonic evidence for mechanical propagation of distortion products (f_2-f_1 and $2f_1-f_2$),'' Hearing Res. **6**, 35–59.

Gleich, O., and Klump, G.-M. (**1995**). ''Temporal modulation transfer functions in the European Starling (*Sturnus vulgaris*): II. Responses of auditory-nerve fibers,'' Hearing Res. **82**, 81–92.

Harris, D. M. (**1979**). ''Action potential suppression, tuning curves and thresholds: Comparison with single fiber data,'' Hearing Res. **1**, 133–154.

Harris, D. M., and Dallos, P. (**1979**). ''Forward masking of auditory nerve fiber responses,'' J. Neurophysiol. **42**, 1083–1107.

Henry, K. R. (**1989**). ''Detuning of cochlear action potential tuning curves at high sound pressure levels: Influences of temporal, spectral and intensity variables,'' Audiology **28**, 19–36.

Henry, K. R. (**1991a**). ''Frequency-specific enhancement of the cochlear compound action potential: Influence of the forward masker,'' Hearing Res. **56**, 197–202.

Henry, K. R. (**1991b**). ''Enhancement of the cochlear nerve compound action potential: Sharply defined frequency-intensity domains bordering the tuning curve,'' Hearing Res. **56**, 239–245.

Henry, K. R. (**1995**). ''Auditory nerve neurophonic recorded from the round window of the Mongolian gerbil,'' Hearing Res. **90**, 176–184.

Henry, K. R. (**1996a**). ''Auditory nerve neurophonic produced by the frequency difference of two simultaneously presented tones,'' Hearing Res. **99**, 151–159.

Henry, K. R. (**1996b**). ''Tuning curves of the difference tone auditory nerve neurophonic,'' Hearing Res. **99**, 160–167.

Henry, K. R. (**1997**). ''Sharply tuned cochlear nerve ensemble periodicity responses to sonic and ultrasonic frequencies,'' J. Comp. Physiol. B **181**, 239–246.

Henry, K. R., and Price, J. M. (**1994**). ''Amplitude enhancement is seen in the cochlear nerve but not at, or before, the afferent synapse,'' Hearing Res. **79**, 190–196.

Khanna, S. M., and Teich, M. C. (**1989**). ''Spectral characteristics of the responses of primary auditory-nerve fibers to amplitude-modulated signals,'' Hearing Res. **39**, 143–158.

Kidd, Jr., G., and Feth, L. L. (**1981**). ''Patterns of residual masking,'' Hearing Res. **5**, 49–67.

Kim, D. O., Molnar, C. E., and Matthews, J. W. (**1980**). ''Cochlear mechanics: Nonlinear behavior in two-tone responses as reflected in cochlear nerve fiber responses and in ear canal sound pressure level,'' J. Acoust. Soc. Am. **67**, 1704–1721.

Kujawa, S. G., Fallon, M., and Bobbin, R. P. (**1995**). ''Time-varying alterations in the f_2-f_1 DPOAE response to continuous primary stimulation. I: Response characterization and contribution of the olivocochlear efferents,'' Hearing Res. **85**, 142–154.

Langner, G. (**1992**). ''Periodicity coding in the auditory system,'' Hearing Res. **60**, 115–142.

Lutfi, R. A. (**1988**). ''Interpreting measures of frequency selectivity: Is forward masking special?'' J. Acoust. Soc. Am. **83**, 163–177.

Mitchell, C. (**1976**). ''Frequency specificity of the N_1 potential from the cochlear nerve under various stimulus conditions,'' J. Aud. Res. **16**, 247–255.

Nelson, D. A., and Freyman, R. L. (**1984**). ''Broadened forward-masked tuning curves from intense masking tones: Delay-time and probe-level manipulation,'' J. Acoust. Soc. Am. **75**, 1570–1577.

Nuttall, A. L., and Dolan, D. F. (**1993**). ''Intermodulation distortion (F_2-F_1) in inner hair cell and basilar membrane responses,'' J. Acoust. Soc. Am. **93**, 2061–2068.

Nuttall, A. L., and Dolan, D. F. (**1994**). ''Comment on 'Modulation of the

hair cell motor: A possible source of odd-order distortion [J. Acoust. Soc. Am. **96**, 2210–2215)],'' '' J. Acoust. Soc. Am. **96**, 2583–2584.

Özdamar, Ö., and Dallos, P. (**1978**). ''Synchronous responses of the primary auditory fibers to the onset of tone burst and their relation to compound action potential,'' Brain Res. **155**, 169–175.

Palmer, A. R., and Russell, I. J. (**1986**). ''Phase-locking in the cochlear nerve of the guinea pig and its relation to the receptor potential of inner hair cells,'' Hearing Res. **24**, 1–15.

Pickles, J. O. (**1984**). ''Frequency threshold curves and simultaneous masking functions in single fibers of the guinea pig auditory nerve,'' Hearing Res. **14**, 245–256.

Rose, J. E., Brugge, J. F., Anderson, D. J., and Hind, J. E. (**1967**). ''Phase-locked response to low frequency tones in single auditory nerve fibers of the squirrel monkey,'' J. Neurophysiol. **30**, 769–793.

Siegel, J. H., Kim, D. O., and Molnar, C. E. (**1982**). ''Effects of altering organ of Corti on cochlear distortion products f_2-f_1 and $2f_1-f_2$,'' J. Neurophysiol. **47**, 303–328.

Small, Jr., A. M. (**1959**). ''Pure-tone masking,'' J. Acoust. Soc. Am. **31**, 1619–1625.

Smith, R. L. (**1979**). ''Adaptation, saturation and physiological masking in single auditory-nerve fibers,'' J. Acoust. Soc. Am. **65**, 166–178.

Smith, R. L., Passaglia, C., Relkin, E. M., Prieve, B., Nguyen, M., and Murnane, O. (**1993**). ''Modulation following responses from the auditory periphery: Some results from gerbils and humans,'' Association for Research in Otolaryngology Abstracts **19**, 93.

Tasaki, I. (**1954**). ''Nerve impulses in individual auditory nerve fibers of guinea pig,'' J. Neurophysiol. **17**, 97–122.

The effects of sensory hearing loss on cochlear filter times estimated from auditory brainstem response latencies

Manuel Don and Curtis W. Ponton
Electrophysiology Laboratory, House Ear Institute, 2100 West Third Street, Los Angeles, California 90057

Jos J. Eggermont
Departments of Physiology and Biophysics, and Psychology, University of Calgary, 2500 University Drive N.W., Calgary, Alberta T2N 1N4, Canada

Betty Kwong
Electrophysiology Laboratory, House Ear Institute, 2100 West Third Street, Los Angeles, California 90057

(Received 10 September 1997; revised 22 May 1998; accepted 16 June 1998)

Derived-band auditory brainstem responses (ABRs) were obtained in 43 normal-hearing and 80 cochlear hearing-impaired individuals using clicks and high-pass noise masking. The response times across the cochlea [the latency difference between wave V's of the 5.7- and 1.4-kHz center frequency (CF) derived bands] were calculated for five levels of click stimulation ranging from 53 to 93 dB p.-p.e. SPL (23 to 63 dB nHL) in 10-dB steps. Cochlear response times appeared to shorten significantly with hearing loss, especially when the average pure tone (1 to 8 kHz) hearing loss exceeded 30 dB. Examination of derived-band latencies indicates that this shortening is due to a dramatic decrease of wave V latency in the lower CF derived band. Estimates of cochlear filter times in terms of the number of periods to maximum response ($N_{\max}$) were calculated from derived-band latencies corrected for gender-dependent cochlear transport and neural conduction times. $N_{\max}$ decreased as a function of hearing loss, especially for the low CF derived bands. The functions were similar for both males and females. These results are consistent with broader cochlear tuning due to peripheral hearing loss. Estimating filter response times from ABR latencies enhances objective noninvasive diagnosis and allows delineation of the differential effects of pathology on the underlying cochlear mechanisms involved in cochlear transport and filter build-up times. © *1998 Acoustical Society of America.* [S0001-4966(98)06409-1]

PACS numbers: 43.64.Ri, 43.64.Wn [RDF]

INTRODUCTION

The latencies of waves in the auditory brainstem response (ABR) have been used extensively to help identify and quantify cochlear hearing loss (Jerger and Mauldin, 1978; Yamada *et al.*, 1979; Sohmer *et al.*, 1981; Rosenhamer *et al.*, 1981; Prosser *et al.*, 1983; Gorga *et al.*, 1985; van der Drift *et al.*, 1988; Collet *et al.*, 1992; Rupa and Dayal, 1993; Watson, 1996). However, when standard stimuli are used, the nonlinearity of cochlear processing makes standard latency measures problematic to interpret (Eggermont, 1982), especially in the presence of hearing loss. These standard stimuli, such as broadband clicks or mid- to low-frequency tonebursts presented at moderate to high levels, excite much of the cochlea within a few milliseconds (Eggermont, 1982). Inadequate place specificity of these stimuli has been shown in analyses of compound action potentials (CAPs). The CAP represents a convolution between the neural unit response and the compound poststimulus time histogram (PSTH) (Goldstein and Kiang, 1958). That is, the CAP represents a summation of responses from different eighth nerve units, each contributing responses with latencies according to its PSTH. These latencies, therefore, are dependent on factors involved in the response times of the units. The response times, in turn, depend on the characteristic frequencies of the units. The ABR is compounded activity similar to the CAP; it too represents convolved neural responses initiated in the brainstem by cochlear activation over time (Elberling, 1978). Thus, because of cochlear mechanics, standard latency and amplitude measures of ABRs obtained by simply averaging responses to broadband stimuli provide limited or even misleading information regarding place-specific cochlear function (Don and Eggermont, 1978; Don *et al.*, 1979; Eggermont and Don, 1980, 1982). These shortcomings become even more acute when evaluating impaired cochleae (Eggermont, 1982). Thus, while the status and health of both inner and outer hair cells in the cochlea are obvious critical factors in cochlear processing, they are also important to ABR latency measures. The core of this issue lies in understanding what an ABR latency measure represents and how cochlear hearing loss affects it.

ABRs—What do they reflect? The ABR is composed of several voltage deflections occurring within the first 15 ms after stimulus onset. These deflections (peaks and troughs) represent synchronous activity generated along the auditory brainstem pathway, beginning with the CAP of the eighth nerve. The peaks represent far-field activity produced by onset responses of neural elements and abrupt bends in the neural fiber tracts of the auditory brainstem pathway (Stegeman *et al.*, 1987; Deupree and Jewett, 1988). This activity has different latencies for different generating sites in the brainstem. In addition, contributions to this activity initiated from different parts of the cochlea result in different laten-

cies. Typically, latencies become gradually longer with progressive activation from base to apex of the cochlea. As a result, with broadband stimuli (e.g., clicks), phase cancellations of field activity from more apical regions of the cochlea occur so that the resulting peaks in the response largely reflect activity from the most basal regions.

The basic measures used in many ABR studies are the latencies of the peaks in the response. Peak latencies are determined by a number of mechanical and physiological processes in the cochlea, auditory nerve, and brainstem, including (1) the delay in the cochlea to the site of activation (cochlear transport time); (2) the filter impulse response time at the site of activation (cochlear filter build-up time); (3) the synaptic delay between inner hair cells (IHCs) and auditory nerve fibers, and finally, (4) the neural conduction time and any intervening synaptic delays to the point in the brainstem pathway responsible for the peak activity. Thus, nearly all cochlear and retrocochlear events affect the latency of the peak neural activity. If the peak response is dominated by activation of a specific region of the cochlea, then the cochlear response time related to that site in the cochlea is critically important in determining that peak's latency. The cochlear response time (Don *et al.*, 1993) consists of both transport and filter build-up times and has been referred to by Ruggero (1994) as the traveling-wave delay. If broadband clicks are used as stimuli, place-specific contributions to the overall response can be obtained from a high-pass noise masking procedure that results in derived-band responses (Don and Eggermont, 1978).

Effects of cochlear hearing loss. Whereas most of the afferent innervation of the cochlea is to the inner hair cells (IHCs) (Spoendlin, 1966; Davis, 1983), the outer hair cells (OHCs) have key roles in sensitivity and frequency tuning. Damage to OHCs results in loss of the ''cochlear amplifier,'' leading to threshold elevation and broadening of cochlear tuning (Davis, 1983). As demonstrated by Ruggero (1994), if tuning of the cochlear filter broadens, impulse response times decrease, resulting in shorter cochlear response times. Eggermont (1979a) showed that cochlear hearing losses in humans are similarly accompanied by shorter neural (CAP) response times. He explored these issues in sensory hearing loss patients with recruitment (most diagnosed with Meniere's disease) and in normal-hearing individuals. Estimates of the cochlear filter response times from the narrow-band CAPs demonstrated that many sensory loss patients had significantly shorter cochlear response times at several frequencies compared to the normal-hearing controls.

Contributions to ABR latencies. Peak latencies for the CAP or wave V of the ABR are dependent on the following factors: (a) place of generation along the cochlea (determined by its characteristic or center frequency, CF), (b) stimulus level, (c) degree of hearing loss, and (d) gender. The differential effects that these four factors have on the four major mechanical and physiological processes (cochlear transport time, filter build-up time, synaptic delay, and central conduction time) that contribute to the wave V latency of the derived band are described below.

''Cochlear response time'' (cochlear transport and filter build-up times). The cochlear response time up to a given CF location of the basilar membrane (BM) can be viewed as the sum of two parts, a cochlear transport time and a filter build-up time. We equate the cochlear response time with the group delay up to a given CF location (Goldstein *et al.*, 1971; Allen, 1983). Model studies have shown that the group delay consists of two parts (e.g., Fig. 9 in Neely, 1993) analogous to the two components of the cochlear response time. One part is a slowly changing delay for frequencies below CF (which we identify with the cochlear transport time up to CF); the other part shows a rapid change for frequencies in the vicinity of CF (which we identify with the filter build-up time at CF). Using this framework for the cochlea response times, we can now examine the effects of the passive BM properties and the cochlear active process on the two components of the cochlear response time. We can also postulate how OHC damage, which may alter both the passive BM properties and the cochlear active process, affects cochlear transport and filter build-up times.

The *cochlear transport time*, as defined, is determined solely by passive BM properties, specifically the stiffness gradient and, to a lesser extent, the mass loading. Thus, the cochlear transport time is the delay associated with the linear component of the BM filter, which in turn is affected by the structural integrity of the OHCs because the slow motile properties of OHCs influence the stiffness of the BM. This cochlear transport time is independent of stimulus level (Hall, 1974) because it mostly reflects the purely passive response time of a broadly tuned linear BM filter.

The *filter build-up time*, as defined, is equal to the increase in the cochlear response time above that due to passive BM properties alone. This increase is due to the cochlear amplifier which sharpens the tuning of the BM and shifts the place of resonance for a particular stimulus frequency to a more apical location, which means that the CF of a specific location on the BM increases. The filter build-up time is level dependent and is determined by the sharpness of tuning and by the CF of the BM location or auditory nerve fiber (Moller, 1983; Ruggero, 1992). For constant quality ($Q_{10\,\mathrm{dB}}$) filters across CF, the response time will be a constant number of periods of CF and thus inversely proportional to CF.

We have previously shown (Don *et al.*, 1993) that the cochlear response time (cochlear transport time + filter build-up time) is shorter in females than in males by an amount proportional to the shorter cochlear length found in females (Sato *et al.*, 1991). Assuming that the same frequency range is mapped on to the cochlea in females and males, this could be explained by the resulting greater stiffness gradient in females than in males (Don *et al.*, 1993). Thus, assuming that filter build-up time is not dependent on gender, this difference in cochlear response time reflects a gender difference in transport time. The assumption that filter build-up time is not gender dependent seems reasonable; otherwise, we would have to conclude that females are either more broadly tuned than males or have impaired cochleae. Neither of these conclusions seems reasonable.

Loss of OHCs that eliminates the action of the cochlear amplifier results in loss of the filter build-up time component of the cochlear response time. Thus, the cochlear response

time from a cochlea devoid of OHCs is a close estimate of the passive cochlear transport time (Eggermont, 1979a). With the loss of the cochlear amplifier, the resonant frequencies of the affected BM locations decrease (as much as half an octave) to values close to those for a purely passive BM filter, resulting in a basalward shift in the cochlear frequency-place map in the affected BM region (e.g., Neely, 1993). These changes are consistent with the apparent filter broadening for a given level of stimulation that is reflected by the tuning curve bandwidth increases ($Q_{10\,dB}$ decreases) in CF regions affected by cochlear hearing loss (Kiang *et al.*, 1970). Thus, changes in frequency tuning over a large region of the cochlea will result in a basalward shift in the cochlear frequency-place map and in shorter cochlear filter build-up times. These changes are intrinsically linked and occur simultaneously as a result of the elimination of active cochlear mechanisms due to OHC loss. The effect of these changes on ABR derived-band latencies are discussed below.

The ABR derived bands will cover the same frequency range in normal and cochlear hearing loss ears because the cutoff frequencies of the high-pass noise maskers are the same. However, if the cochlear map is shifted due to OHC loss, the derived response paradigm will not extract activity from the same regions of the BM in the two groups of ears. In normal ears, the latency difference between two adjacent derived-band regions is inversely proportional to the stiffness gradient across those regions (de Boer, 1979; Don *et al.*, 1993). A loss of OHCs can potentially decrease the stiffness of the affected region of the BM, thereby likely decreasing the stiffness gradient across that region and shifting the cochlear frequency-place map apicalward. Thus, the latency difference between two derived ABR bands *within* that region should increase if the shifting cochlear map is solely the result of passive changes (i.e., decrease in stiffness gradient) in BM properties. However, as discussed earlier, OHC loss also eliminates or greatly reduces the active component of cochlear frequency tuning. This results in the intrinsically linked downward shift of the resonant frequency (and for a given stimulus frequency, a basalward shift of its peak activation) and broadening of the filter described above. As a consequence, both the absolute latencies and the latency difference between the derived-band ABR responses decrease.

In summary, the changes in the cochlear frequency-place map as a result of diminished action of the cochlear amplifier due to OHC damage should be distinguished from those that are caused by changes in the passive membrane properties. It should be noted that because the effects of OHC loss on the passive and active aspects of cochlear transport time are expected to have opposite effects on derived-band latencies, they could potentially cancel each other. However, the effects of a loss of the cochlear amplifier (filter broadening) on the filter build-up time are larger and opposite to the effect of the passive changes (reduced stiffness) on the cochlear transport time. Thus, overall, it is likely that the effects on filter build-up time will dominate when the active process is heavily compromised by OHC damage and decreases in derived-band ABR latencies will result.

Synaptic delay. The synaptic delay between IHCs and auditory nerve fibers is dependent on the health of those synapses, but not on CF or stimulus level. Studies by Liberman and Kiang (1978) have shown that spontaneous activity of auditory nerve fibers after noise trauma is generally unaltered unless there is severe or complete loss for that nerve fiber's CF, suggesting that the synapses continue to function normally in moderate hearing losses. We assume that the synaptic delay for our group of subjects is independent of their amount of hearing loss (generally less than moderate) and also independent of gender.

Central conduction time. The central conduction time is the time between peak activity in the auditory nerve and the place in the brainstem responsible for the generation of wave V (the delay between waves I and V). The I–V delay from a place-specific region of the cochlea is gender dependent (Don *et al.*, 1993), but largely independent of CF (Don and Eggermont, 1978; Ponton *et al.*, 1992) and stimulus intensity (Eggermont and Don, 1980). In addition, it is reasonable to assume that conduction properties of the central neural pathway are typically unaffected by cochlear hearing loss. Our current data from derived-band ABRs indicate that I–V delays are not affected by hearing loss. These results from cochlear place-specific responses should not be confused with results from studies of *unmasked* ABRs. The I–V measures from unmasked ABRs to clicks do not necessarily estimate true neural central conduction times because the frequency region that dominates the latency of wave I is often different from that for wave V (Don and Eggermont, 1978; Eggermont and Don, 1986). Thus, the I–V delay in the unmasked response reflects not only neural conduction times but also differences in response times (transport and filter build-up times) of different parts of the cochlea that may dominate and determine the latency of waves I and V. In studies of the I–V delay in unmasked ABRs, the effects of stimulus level (Stockard *et al.*, 1979), amount and configuration of hearing loss (Coats and Martin, 1977; Coats, 1978; Sturzebecher *et al.*, 1985; Keith and Greville, 1987; Watson, 1996), as well as gender (Elberling and Parbo, 1987; Sabo *et al.*, 1992; Watson, 1996) have been examined. For the most part, the effects of these parameters on the I–V delay of the unmasked ABR are small and variable, and can be accounted for by the differential cochlear representation of waves I and V. However, these effects should not be interpreted as changes only in neural central conduction times. True neural conduction time can be estimated with waves I and V only when both waves represent activity initiated from the same place-specific region of the cochlea. Such is the case with derived-band ABRs.

Table I summarizes the proposed effects of the four factors on the four major processes reviewed above. These effects are based on empirical evidence, theoretical concepts (marked by superscript ''a''), or reasonable assumptions (marked by superscript ''b''). The cochlear transport time is dependent on CF and gender, but independent of stimulus level and hearing loss. The cochlear filter build-up time is dependent on CF, stimulus level, and amount of hearing loss, but considered independent of gender. The synaptic delay can be considered a constant, i.e., independent of CF, stimulus level, moderate hearing loss, and gender. Finally, the cochlear place-specific I–V delay is only affected by gender

TABLE I. The proposed dependency of the four major processes on various factors (DEP=dependent, IND=independent).

Processes	Factors			
	CF	Stimulus level	Hearing loss	Gender
Transport time	DEP	IND[a]	IND[b]	DEP
Filter build-up time	DEP	DEP	DEP	IND[b]
Synaptic delay	IND	IND[b]	IND	IND[b]
Central conduction time	IND	IND	IND	DEP

[a]Theoretical.
[b]Assumption.

and is independent of CF, stimulus level, and amount of hearing loss.

The purpose of this paper is to (1) demonstrate that cochlear filter build-up times can be estimated from derived-band wave V latencies, (2) specify the dependence of this filter build-up time on the amount of sensory hearing loss, and (3) demonstrate that changes of filter build-up times with hearing loss are not affected by gender.

I. METHODS

A. Subjects

1. Normal-hearing control group

This group consisted of 23 female and 20 male subjects ages 18–38 years. Subjects had normal hearing as defined by pure-tone thresholds of 10 dB HL (ANSI, 1989) or less for frequencies between 500–4000 Hz and 15 dB HL or less for 6000 and 8000 Hz. Anyone not meeting these criteria was classified as hearing impaired. Subjects were recruited from the staff at the House Ear Institute and House Ear Clinic and from the student bodies of local colleges and universities.

2. Cochlear hearing loss group

This test group was composed of 36 females and 49 males, ages 19–60 years, diagnosed with mild to moderate sensory hearing losses. The subjects were recruited from the House Ear Clinic and did not have a conductive impairment, Meniere's disease, or retrocochlear problems. All subjects were in good general health and reported normal neurological status. Otoscopic examinations were performed to identify existing conditions that would preclude audiometric and ABR testing. Pure-tone audiometric testing was performed with a Grason–Stadler GSI 16 audiometer and Telephonics TDH-50P earphones in P/N 10C017-1 cushions. Hearing thresholds were evaluated with use of the modified Hughson–Westlake procedure (Carhart and Jerger, 1959) in 2-dB steps. Each subject signed an informed consent form approved by an institutional review board before participating in the study. All subjects were paid for their participation.

B. Stimuli

Stimuli were rarefaction clicks produced by applying 100-μs rectangular voltage pulses to a TDH-50P earphone. Clicks were presented 22 ms apart at five levels: 53, 63, 73, 83, and 93 dB peak–peak equivalent sound pressure level (p.-p.e. SPL). The acoustic clicks were calibrated and measured with a B&K (Brüel & Kjaer) 4152 artificial ear with a 1-in. B&K microphone (4144), 6-cc coupler, and 2209 sound level meter. Perceptual detection thresholds were determined for 1-s bursts of clicks presented at the same interstimulus interval (ISI) used in recording the ABRs. This perceptual threshold was defined as the 79% point on the psychometric detection function obtained in a modified block up–down procedure (Weatherill and Levitt, 1965). For the group, 93 dB p-p.e. SPL was 63 dB above the average perceptual detection threshold.

Ipsilateral pink-noise masking was used to obtain derived-band ABRs (Don and Eggermont, 1978). The noise was produced by a General Radio Noise Generator (Type 1310) and presented at a level sufficient to mask the ABR to the clicks. For the 93 dB p.-p.e. SPL clicks, the required broadband pink-noise rms level was 92 dB SPL. For the remaining lower click levels, the noise was attenuated in 10-dB steps with the click to maintain a fixed click-to-noise masking ratio. There were six stimulus conditions for each stimulus level: clicks presented alone (unmasked condition), and clicks presented with ipsilateral noise high-pass filtered at 8, 4, 2, 1, and 0.5 kHz with a slope of 96 dB/oct. The high-pass filtering of the masking noise was achieved by cascading both channels of a Krohn-Hite (model 3343) dual filter, each with a 48 dB/oct slope. Previous work (Don *et al.*, 1993) has shown little effect of fatigue induced by noise exposure in a subset of 11 normal-hearing subjects. That is, ABR latencies and amplitudes showed little change for identical stimulus conditions before and after exposure to masking noise levels used in this study.

C. ABR recordings

Subjects were placed in a reclining chair in a double-walled sound-treated room (IAC). The ABRs were recorded differentially between electrodes applied to the vertex (*Cz*) and the ipsilateral mastoid ($M1$ or $M2$). The contralateral mastoid was used as ground. Scalp activity was amplified by 5×10^5 and filtered (cascading two Princeton Applied Research model 113 filters) with a passband of 0.1–3 kHz. The activity was sampled at a rate of 20 kHz for 15 ms after stimulus onset with use of an Ariel DSP-16 A/D-D/A board and a PC. After each block of 256 sweeps, the rms value of the averaged background noise was estimated according to procedures of Elberling and Don (1984). This noise estimate was used to form a weighted average by applying Bayesian estimation principles (Elberling and Wahlgreen, 1985; Don and Elberling, 1994). This technique minimizes the destructive effects of episodic high noise levels by weighting the average towards blocks of sweeps with low estimated background noise. Data collection for a run was terminated when the estimated averaged background noise reached 20 nV or less. Thus, all recordings had approximately the same low estimated residual background noise levels. The use of residual background noise level as the stopping criterion rather than a fixed number of sweeps reduces the substantial effect of physiological background noise variation on the interpretation of the ABR recordings (Don and Elberling, 1994, 1996).

D. Derived-band waveforms

Our analyses use derived-band ABRs (Don and Eggermont, 1978; Parker and Thornton, 1978a, b) based on the high-pass noise-masking technique (Teas *et al.*, 1962). The derived-band ABR technique consists of the simultaneous ipsilateral presentation of a broadband click and high-pass filtered noise. The cutoff frequency of the high-pass noise is successively lowered from one run to the next. Narrow-band contributions from the cochlea are then derived by successive subtraction of the responses to the successive high-pass noise masking conditions. The theoretical center frequency (CF) for each derived band is computed as the square root of the product of the two successive high-pass filter cutoff frequencies used to form the band (Parker and Thornton, 1978b). For the high-pass noise conditions used in this study, the CFs for the five resulting derived bands are 11.3, 5.7, 2.8, 1.4, and 0.7 kHz. The actual CF may differ slightly for each individual depending on the frequency response characteristics of the transducer (Donaldson and Ruth, 1993) and the peripheral auditory system.

As shown in many previous studies (e.g., Don and Eggermont, 1978; Parker and Thornton, 1978b, c), wave V latencies are longer for each successive (lower CF) derived-band ABR. These latencies reflect the cochlear response time composed of an apparent transport time and a frequency-dependent filter build-up time.

Don and Eggermont (1978) and Ponton *et al.* (1992) have demonstrated that wave I shows similar and parallel latency changes with CF of the derived band such that the I–V interval across frequency bands is constant. This relative constancy of the I–V delay across bands permits the use of wave V latency differences between derived bands as measures of cochlear response time. Don *et al.* (1993) present a more detailed justification for using this approach.

E. Cochlear response time measures

Figure 1 illustrates a series of derived-band ABR responses to clicks presented at 93 dB p.-p.e. SPL for one normal-hearing female subject. The delay between wave V for the 5.7- and 1.4-kHz derived bands ($\Delta V_{5.7-1.4}$) is the measure used because the latencies of these two bands can be reliably obtained.

II. RESULTS

Figure 2 plots the mean wave V latencies for the 5.7- and 1.4-kHz CF derived bands for normal-hearing males and females as a function of click level. The large change in latency with level for these two bands is, as argued by Eggermont and Don (1980), consistent with the impulse responses calculated for normal human cochleae based on their tuning properties (Eggermont, 1979b; de Boer, 1979). Although at high stimulus levels slightly shorter delays (consistent with shorter filter times) are observed, the latency-level curves for the two derived bands are essentially parallel. These data suggest that the delay between these two bands is, for the most part, not dependent on stimulus level.

This is confirmed in Fig. 3 which shows the individual (open circles) and mean (filled circles) $\Delta V_{5.7-1.4}$ as a func-

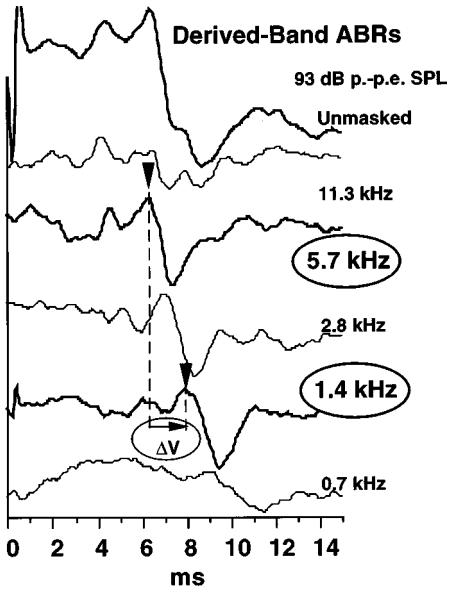

FIG. 1. An example of a series of derived-band ABRs from a normal-hearing female. The cochlear response time difference between the wave V latencies of the 5.7 and 1.4-kHz derived bands is the measure of interest in this study.

-

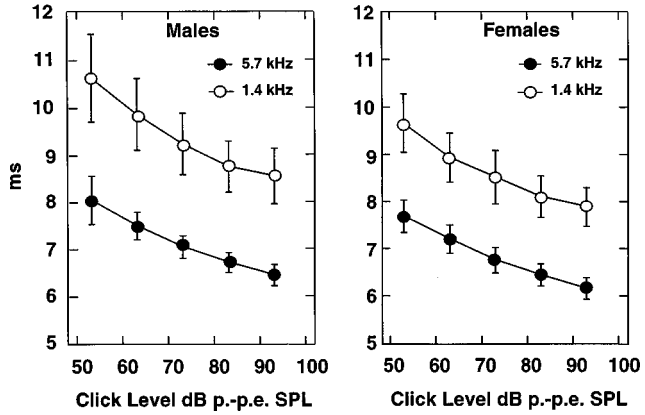

FIG. 2. Wave V latencies and standard deviations for 5.7 and 1.4-kHz CF derived bands as a function of click level for normal-hearing males and females. The range is shorter for females.

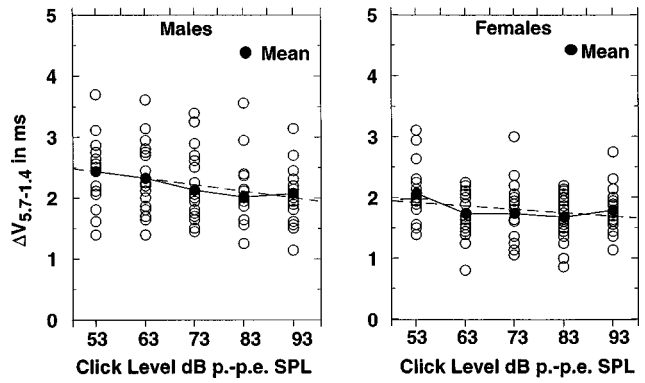

FIG. 3. Mean delay between 5.7- and 1.4-kHz CF derived bands as a function of click level for normal-hearing males and females.

tion of level for the normal-hearing subjects. The mean delay, at 93 dB p.-p.e. SPL, is 2.1 ms for males and 1.8 ms for females.

Figure 4(a)–(d) plots the latency of wave V to 93 dB p.-p.e. SPL clicks for the four major derived bands (CF $=5.7$, 2.8, 1.4, and 0.7 kHz) as a function of the weighted pure tone average (PTA_w) closest to the CF of the derived band. Frequency regions closest to the derived-band CF will normally contribute the most to the response. Therefore, hearing loss in that region should be weighted more heavily. In computing PTA_w, the threshold for the pure tone closest to the CF of the derived band was arbitrarily given twice the weight of the thresholds of the adjacent pure tones. For example, the PTA_w for the 5.7-kHz CF derived band was computed by multiplying the threshold for 6 kHz (the pure tone closest to 5.7 kHz CF) by 2, adding the thresholds for 4 and 8 kHz (the adjacent pure tones), then dividing by 4. For the highest CF derived band [5.7 kHz, Fig. 4(a)], wave V latency shows no change (or lengthens slightly) with increasing loss up to 60 dB in the CF region. For progressively lower CF

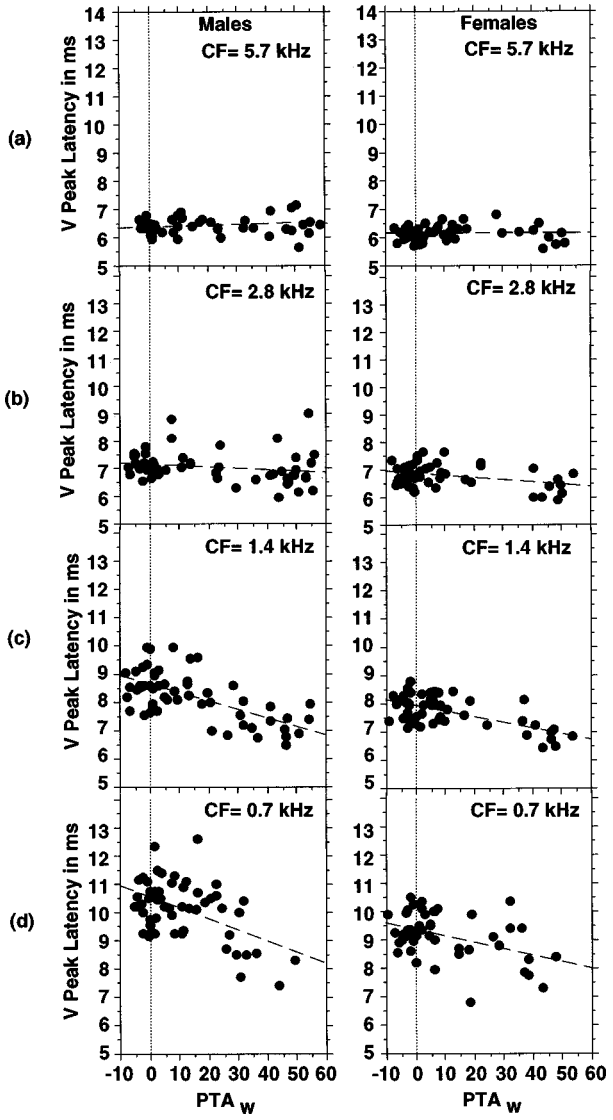

FIG. 4. Latency of wave V to 93 dB p.-p.e. SPL clicks for each CF derived-band ABR as a function of the related PTA_w threshold for males and females.

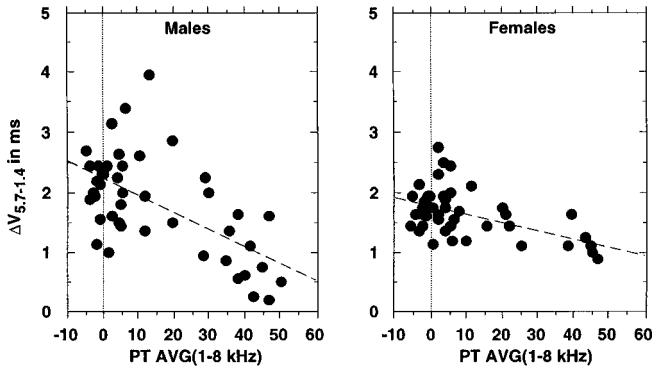

FIG. 5. Wave V latency delay between 5.7- and 1.4-kHz derived-band ABRs to 93 dB p.-p.e. SPL clicks as a function of pure tone average thresholds from 1 to 8 kHz.

derived bands, the latency tends to shorten as the loss becomes greater. The shortening is most evident for the lowest two bands [CF $=1.4$ and 0.7 kHz, Fig. 4(c) and (d)] and is clearly greater in males. In addition, the latencies become notably shorter when the PTA_w exceeds 20 or 30 dB. As discussed earlier, the effect of sensory hearing loss on cochlear transport time is opposite to that on cochlear filter build-up time. Thus, for the first 20–30 dB of hearing loss, the opposing effects may cancel, resulting in no net latency change. However, with greater losses, the effect on filter build-up time dominates and latencies become shorter.

Figure 5 demonstrates, as expected from the preceding figures, that $\Delta V_{5.7-1.4}$ in response to the same clicks shortens with increasing hearing loss (defined by averaging pure tone thresholds from 1–8 kHz). The basis for this shortening is revealed in the absolute latencies of the two derived bands. Figure 4(a) shows that for the 5.7-kHz CF derived band, virtually no change or only a slight increase in latency occurs with hearing loss at the CF region. However, as shown in Fig. 4(c), for the 1.4-kHz CF derived band, peak latency decreases with increases in hearing loss at that CF region.

Figure 6 illustrates a shorter $\Delta V_{5.7-1.4}$ of 1.1 ms for a hearing-impaired female subject (PTA 1–8 kHz $=45$ dB) compared to the 1.7 ms for a normal-hearing (PTA $=-2$ dB) female. The mean $\Delta V_{5.7-1.4}$ for normal-hearing females is about 1.8 ms (s.d. $=0.34$). Note also that the absolute latency

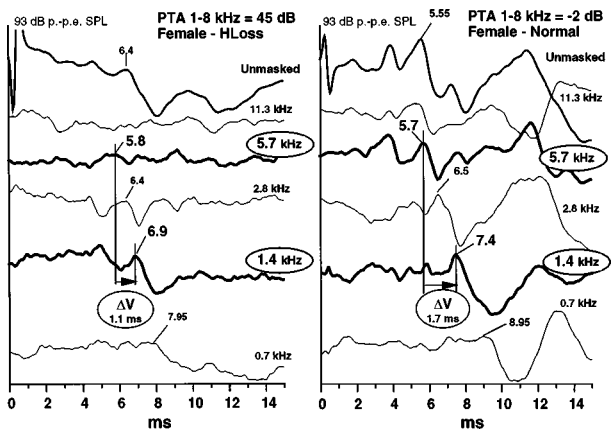

FIG. 6. Example of shorter delay between 5.7- and 1.4-kHz wave V derived-band latencies to 93 dB p.-p.e. SPL clicks for a hearing-impaired compared to a normal-hearing female.

of wave V for the 1.4-kHz derived band is shorter in the impaired ear than in the normal-hearing ear. The latency for the normal-hearing ear (7.4 ms) is about one standard deviation and the latency for the impaired ear (6.9 ms) is over two standard deviations below the mean (7.8 ± 0.42 ms) for normal-hearing females reported by Don *et al.* (1993).

A. Changes in width of the tuning filters

An obvious explanation for the decrease in derived-band latency with hearing loss is the known broadening of tuning in the part of the cochlea affected by hearing loss. That is, the $\Delta V_{5.7-1.4}$ mostly reflects differences in the response times of the cochlear filters. Assuming that response latency is related to synaptic delay and the width of the cochlear filter and that the transport time is minimal, the number of periods to maximum neural response ($N_{\max}$) as expressed by Eggermont (1979a) for the CAP is

$$N_{\max} = (\tau - 0.8)\mathrm{CF}, \tag{1}$$

where τ is the CAP peak latency in ms, 0.8 is the synaptic delay in ms, and CF is the center frequency of the derived band in kHz. (It should be noted that the neural response for all stimulus levels is likely to occur at the same fraction of the cycle and before the maximum of the impulse response.) However, as argued by Ruggero (1994), the transport time may be appreciable. Eggermont (1979a) estimated that for a significant amount of hearing loss (i.e., 60 dB or more) and, therefore, a very broad filter, the transport time in ms is the reciprocal of the square root of CF in kHz [$(\mathrm{CF})^{-0.5}$]. Thus, the transport time would be 1.0 ms for 1 kHz and about 0.32 ms for 10 kHz. Furthermore, as established by Don *et al.* (1993), shorter cochlear response times in females than males are more likely related to shorter cochlear length rather than broader tuning in females. Thus, to estimate the change in filter bandwidth as a function of hearing loss using $N_{\max}$ from latency measures, corrections for gender-dependent transport time in addition to the synaptic delay must be made. Finally, since wave V latency is being used instead of the CAP, the I–V delay must be subtracted from the wave V latency. Thus, the number of periods to maximum neural response using the wave V latency measure is

$$N_{\max} = [L_v - (\text{I–V delay}) - tt_g(\mathrm{CF}) - 0.8]\mathrm{CF}, \tag{2}$$

where L_v = the latency of wave V in ms, the (I–V delay) is the individual's time delay between the peak of wave I and wave V for the derived-band ABR, $tt_g(\mathrm{CF})$ is the gender-dependent transport time to that frequency region, 0.8 is the synaptic delay, and CF is the center frequency of the derived band in kHz. The gender-dependent $tt_g(\mathrm{CF})$ is estimated as follows: For female subjects,

$$tt_f(\mathrm{CF}) = \frac{1}{\sqrt{\mathrm{CF}}} \text{ in ms}, \tag{3}$$

and is simply the reciprocal of the square root of CF. For male subjects, the transport time is

$$tt_m(\mathrm{CF}) = tt_f(\mathrm{CF}) + [\overline{L}_{VM}(\mathrm{CF}) - \overline{L}_{VF}(\mathrm{CF})] - [\overline{(I-V)}_M - \overline{(I-V)}_F]. \tag{4}$$

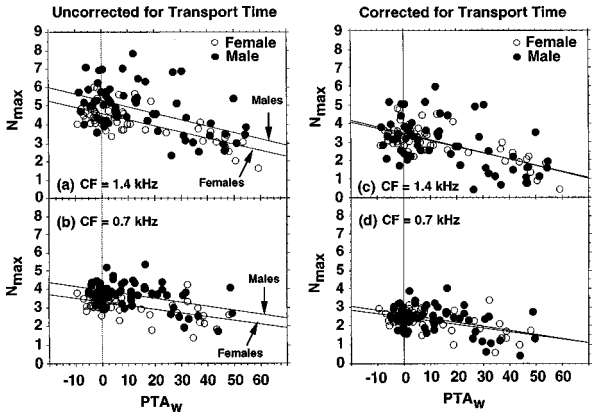

FIG. 7. Number of periods to maximum response ($N_{\max}$) as a function of PTA_w for CF = 1.4 and 0.7 kHz calculated from Eq. (2). Calculated values without correcting for transport time are shown in (a) and (b). Values after correcting for transport time are shown in (c) and (d). Little difference between males and females in estimated filter build-up time as a function of hearing loss is observed after correction for gender differences in central conduction (I–V) and cochlear transport times. Calculations were from responses to 93 dB p.-p.e. SPL clicks.

Equation (4) states that the transport time for male subjects is equivalent to the females' plus additional time to account for the longer cochlear length of males. Assuming no significant gender difference in synaptic delay and filter response, the gender difference in transport time is estimated by subtracting the mean gender difference of the I–V delay from the gender difference in the mean latency of wave V for a derived band. For the CF = 1.4 and 0.7 kHz derived-band responses, Fig. 7 plots $N_{\max}$ as a function of the PTA_w, without [Fig. 7(a) and (b)] and with [Fig. 7(c) and (d)] the transport time corrections. Here $N_{\max}$ is estimated for each individual according to Eq. (2) by subtracting both the individual's I–V delay and the mean estimated gender-dependent transport time to the derived-band CF from the wave V latency of the derived band. In some hearing-impaired individuals, a clear I–V delay could not be read due to the lack of an identifiable wave I. In those cases (about 20%), the mean I–V delay of the appropriate gender was used.

If gender differences in transport time are not included in the calculation of Eq. (2) [Fig. 7(a) and (b)], $N_{\max}$ is greater for males than females. However, if the latency is corrected for the gender difference in transport time before computing $N_{\max}$, the filter build-up time as a function of hearing loss is equivalent for males and females [Fig. 7(c) and (d)].

The estimated $N_{\max}$ as a function of CF for derived-band wave V latencies is shown for normal-hearing subjects in Fig. 8. For comparison, estimates by Bowman *et al.* (1997a) using a distortion product otoacoustic emissions (DPOAEs) f_2 sweep paradigm (Bowman *et al.*, 1997b) are also shown. There is close agreement between these two independent estimates. The data are plotted against a theoretical curve for delays produced by a gamma-tone filter with a dependence of bandwidth on CF, i.e., the order of the filter changed with CF as $6*\mathrm{CF}^{0.5}$. Note that both sets of data fit the curve fairly well.

The number of periods rises as CF increases, which is consistent with the observation that the cochlea is more nar

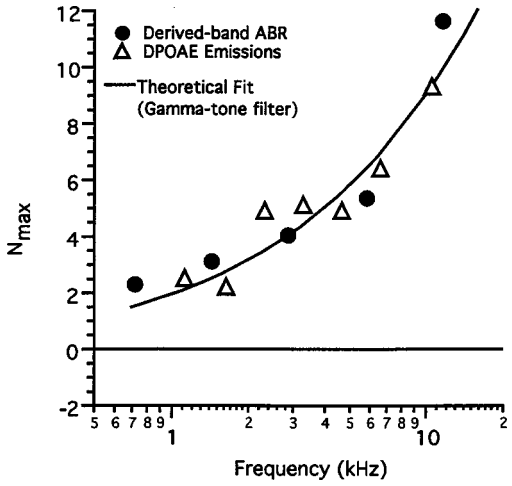

FIG. 8. Mean number of periods to maximum response (N_{max}) as a function of CF based on ABR derived-band corrected latencies (filled circles) and compared to estimates from DPOAE f_2 sweeps (open triangles) by Bowman *et al.* (1997a). Note the close correspondence. Both measures show the increase in the number of periods with CF. For comparison, the data are plotted against a theoretical curve based on a gamma-tone filter function.

rowly tuned in the higher than the lower frequency regions (Kiang *et al.*, 1965). However, as discussed later, the increase in N_{max} for the highest derived-band CF (11.3 kHz) may, in part, be a consequence of lower effective stimulus levels due to the use of clicks and earphones whose response decreases in the high frequencies.

III. DISCUSSION

The work presented here demonstrates that decreased cochlear filter times accompanying cochlear hearing loss can be estimated from the wave V peak latencies of ABRs derived from place-specific regions of the cochlea using high-pass noise-masking techniques. Latencies of these derived-band ABRs are determined by (1) cochlear transport time; (2) cochlear filter build-up time; (3) the synaptic delay between IHCs and auditory nerve fibers; and, finally, (4) the neural conduction time including any intervening synaptic delays to the point in the brainstem pathway responsible for the peak activity (i.e., the I–V delay). Gender differences reflected in these latencies result from differences in cochlear transport times (Don *et al.*, 1993, 1994) and well-documented differences in the I–V delays for both the unmasked responses (Elberling and Parbo, 1987; Sabo *et al.*, 1992; Watson, 1996) and the derived-band responses (Don *et al.*, 1993). There is no clear evidence for gender differences related to filter response times and synaptic delays. Cochlear hearing loss at the site of generation affects the cochlear filter build-up time, has little effect on synaptic delay if the hearing loss is not extreme (Liberman and Kiang, 1978), and does not affect cochlear transport time or neural conduction delays. Thus, if the latency measure is corrected for (1) gender differences in cochlear transport time for a response initiated from a given frequency region in the cochlea (i.e., the derived-band response), and (2) neural conduction time (i.e., the I–V delay), the effect of cochlear hearing loss on latency can be isolated. These corrected latencies can then be converted to number of periods to maximum response (N_{max}) in order to estimate the degree of filter broadening resulting from hearing loss. Assuming that initiation of unit spikes occurs at the same point on the envelope of the signal waveform responses for both normal-hearing and hearing-impaired subjects, our data indicate that N_{max} decreases with hearing loss. Over a 50–60-dB range of hearing loss, there is about a one to two period change (Fig. 7) that is more evident for the lower CF derived bands. This change was difficult to evaluate for the highest CF (11.3 kHz) derived-band responses because of the lower level of stimulation due to the use of relatively flat spectral clicks and the earphone's frequency response (Eggermont and Don, 1980). Often, little activity is seen in the CF=11.3 kHz derived bands when the related high-frequency hearing loss exceeds 30 dB. In addition, a one to two period change is a very small latency difference for this high CF and may be within the measurement variability for the lower level of stimulation. Therefore, the 11.3-kHz CF derived-band data were not analyzed for the hearing impaired. Rutten (1986) discusses this issue of stimulation level being a confound of the effects of hearing loss. Moreover, in contrast to our findings shown in Fig. 7 but similar to Eggermont's (1979a) results, Rutten (1986) concluded from derived CAP latencies that the number of periods did not change systematically with hearing loss. Although Brown and Abbas (1987) demonstrated similarities between AP and ABR tuning characteristics in animal studies, Klein and Mills (1981) demonstrated broader tuning of wave I relative to wave V in human ABRs. Therefore, the discrepancy may be due, in part, to differences in the tuning properties of ABRs and APs in humans. Another possibility for the lack of any systematic change in N_{max} with hearing loss may lie in the gender-dependent transport time differences. Neither Eggermont's (1979a) nor Rutten's (1986) studies attempted to analyze the data with respect to gender differences. If the subjects with the least amount of hearing loss were females and those with the most were males, then N_{max} calculated from the latencies may show little difference with hearing loss. Moreover, both studies included a large number of Meniere's disease patients. If transport times and/or frequency selectivity (Eggermont, 1979a) are differentially altered by Meniere's disease, this may also contribute to the insensitivity of N_{max} to sensory hearing loss. As shown in Fig. 8, the higher the CF, the greater the number of periods to reach response maximum. While this is consistent with differential tuning in the cochlea, a possible contributory factor for the ABR studies is lower physical stimulus levels in the higher frequencies due to the frequency response of the earphones (TDH-50P). However, the observed increase with CF is expected based on auditory nerve fiber data (Carney and Yin, 1988) and the theoretical curve fit derived from the assumption that the cochlear filter can be approximated by a gamma-tone filter. The good agreement of the derived-band ABR with the otoacoustic emission data also suggests that the effect of potentially lower stimulus levels at high CFs is small. Note, however, that this lower level effect may have contributed to the higher than expected N_{max} for the ABR 11.3-kHz derived-band data in Fig. 8.

One last factor that can affect ABRs is age (Elberling and Parbo, 1987). However, age appears to affect the neural aspects (e.g., I–V delay) rather than tuning *per se*. Data from comparisons between individuals with the same age but differing in hearing loss and between individuals differing in age but with the same hearing loss, revealed that the changes in filter-buildup time ($N_{\max}$) were related to hearing loss, not to age. Any correlation of $N_{\max}$ to age appears due to the correlation of age to hearing loss.

In summary, this study has explored three aspects of the relationship between sensory hearing loss and derived-band ABR latencies. First, cochlear filter build-up times can be estimated from derived-band wave V latencies that have been converted to $N_{\max}$. The use of latencies alone can be misleading because there is more absolute latency change for the lower CF bands that have longer periods. However, $N_{\max}$ essentially normalizes the latency data with respect to CF. Therefore, to determine the changes in the cochlear filter's response, latencies must be converted to $N_{\max}$.

Second, $N_{\max}$ is equivalent for males and females as a function of hearing loss after latencies are corrected for gender-related effects. This suggests that there is no gender-related effect of hearing loss on the filter selectivity and the filter response is gender independent.

Finally, cochlear transport time appears to be unaffected by cochlear hearing loss; but, as suggested by Thornton and Farrell (1991), Kim *et al.* (1994), and Donaldson and Ruth (1996), it may be affected by Meniere's disease. However, since their measures include both transport and filter build-up times, another explanation for their results is that Meniere's disease adversely affects the filter response to a greater degree than a cochlear hearing loss without hydrops (Eggermont, 1979a).

In conclusion, this work has shown that after removing gender-related effects, cochlear filter response times can be estimated from derived-band wave V latencies. In addition, this study has used derived-band latencies to demonstrate what tuning curve studies have observed: a broadening of the cochlear filter response with hearing loss that cannot be accounted for by stimulus level differences. Our method of estimating filter response times from derived-band ABR latencies enhances objective noninvasive diagnosis and allows delineation of effects of pathology on underlying cochlear mechanisms.

ACKNOWLEDGMENTS

Work supported in part by NIH Grant No. 1R01 DC00043. We thank the reviewers (Dr. Gail Donaldson and Dr. Robert Burkard) for their helpful criticisms and suggestions.

Allen, J. B. (**1983**). ''Magnitude and phase-frequency response to single tones in the auditory nerve,'' J. Acoust. Soc. Am. **73**, 2071–2092.

ANSI (**1989**). ANSI S3.6-1989, ''Specification for Audiometers'' (American National Standards Institute, New York).

Bowman, D. M., Brown, D. K., and Eggermont, J. J. (**1997a**). ''Estimating cochlear filter response properties from DPOAE phase delay measurements in normal hearing human adults,'' Poster presented at the 1997 ARO Midwinter Meeting, St. Petersburg, FL, 2–6 February 1997.

Bowman, D. M., Brown, D. K., Eggermont, J. J., and Kimberley, B. P. (**1997b**). ''The effect of sound intensity on f_1-sweep and f_2-sweep distortion product otoacoustic emissions phase delay estimates in human adults,'' J. Acoust. Soc. Am. **101**, 1550–1559.

Brown, C. J., and Abbas, P. J. (**1987**). ''A comparison of AP and ABR tuning curves in the guinea pig,'' Hearing Res. **25**, 193–204.

Carhart, R., and Jerger, J. (**1959**). ''Preferred method for clinical determination of pure-tone thresholds,'' J. Speech Hear. Disord. **24**, 330–345.

Carney, L. H., and Yin, T. C. T. (**1988**). ''Temporal coding of resonances by low-frequency auditory nerve fibers: single-fiber responses and a population model,'' J. Neurophysiol. **60**, 1653–1677.

Coats, A. C. (**1978**). ''Human auditory nerve action potentials and brain stem evoked responses: Latency-intensity functions in detection of cochlear and retrocochlear abnormality,'' Arch. Otolaryngol. **104**, 709–717.

Coats, A. C., and Martin, J. L. (**1977**). ''Human auditory nerve action potentials and brain stem evoked responses: Effects of audiogram shape and lesion location,'' Arch. Otolaryngol. **103**, 605–622.

Collet, L., Berger-Vachon, C., Desreux, V., and Morgon, A. (**1992**). ''Auditory brainstem response (ABR) latency: relative importance of age, gender, and sensory hearing-loss using a mathematical model of the audiogram,'' Int. J. Neurosci. (England) **67**, 187–197.

Davis, H. (**1983**). ''An active process in cochlear mechanisms,'' Hearing Res. **9**, 79–90.

de Boer, E. (**1979**). ''Travelling waves and cochlear resonance,'' Scand. Audiol. Suppl. **9**, 17–33.

Deupree, D. L., and Jewett, D. L. (**1988**). ''Far-field potentials due to action potentials traversing curved nerves, reaching cut nerve ends, and crossing boundaries between cylindrical volumes,'' Electroencephalogr. Clin. Neurophysiol. **70**, 355–362.

Don, M., and Eggermont, J. J. (**1978**). ''Analysis of the click-evoked brainstem potentials in man using high-pass noise masking,'' J. Acoust. Soc. Am. **63**, 1084–1092.

Don, M., and Elberling, C. (**1994**). ''Evaluating residual background noise in human auditory brainstem responses,'' J. Acoust. Soc. Am. **96**, 2746–2757.

Don, M., and Elberling, C. (**1996**). ''Use of quantitative measures of ABR peak amplitude and residual background noise in the decision to stop averaging,'' J. Acoust. Soc. Am. **99**, 491–499.

Don, M., Eggermont, J. J., and Brackmann, D. E. (**1979**). ''Reconstruction of the audiogram using brain stem responses,'' Ann. Otol. Rhinol. Laryngol. Suppl. **57**, 1–20.

Don, M., Ponton, C. W., Eggermont, J. J., and Masuda, A. (**1993**). ''Gender differences in cochlear response time: An explanation for gender amplitude differences in the unmasked auditory brain-stem response,'' J. Acoust. Soc. Am. **94**, 2135–2148.

Don, M., Ponton, C. W., Eggermont, J. J., and Masuda, A. (**1994**). ''Auditory brainstem response (ABR) peak amplitude variability reflects individual differences in cochlear response times,'' J. Acoust. Soc. Am. **96**, 3476–3491.

Donaldson, G. S., and Ruth, R. A. (**1993**). ''Derived band auditory brainstem response estimates of traveling wave velocity in humans. I. Normal-hearing subjects,'' J. Acoust. Soc. Am. **93**, 940–951.

Donaldson, G. S., and Ruth, R. A. (**1996**). ''Derived-band auditory brainstem response estimates of traveling wave velocity in humans. II: Subjects with noise-induced hearing loss and Meniere's disease,'' J. Speech Hear. Res. **39**, 534–545.

Eggermont, J. J. (**1979a**). ''Narrow-band AP latencies in normal and recruiting human ears,'' J. Acoust. Soc. Am. **65**, 463–470.

Eggermont, J. J. (**1979b**). ''Compound action potentials: tuning curves and delay times,'' Scand. Audiol. Suppl. **9**, 129–139.

Eggermont, J. J. (**1982**). ''The inadequacy of click-evoked auditory brainstem responses in audiological applications,'' Ann. (N.Y.) Acad. Sci. **388**, 707–709.

Eggermont, J. J., and Don, M. (**1980**). ''Analysis of the click-evoked brainstem potentials in humans using high-pass noise masking. II. Effect of click intensity,'' J. Acoust. Soc. Am. **68**, 1671–1675.

Eggermont, J. J., and Don, M. (**1982**). ''Analysis of click-evoked brainstem auditory electric potentials using high-pass noise masking and its clinical application,'' Ann. (N.Y.) Acad. Sci. **388**, 471–486.

Eggermont, J. J., and Don, M. (**1986**). ''Mechanisms of central conduction time prolongation in brain-stem auditory evoked potentials,'' Arch Neurol. **43**, 116–120.

Elberling, C. (**1978**). ''Compound impulse response for the brain stem de-

rived through combinations of cochlear and brain stem recordings,'' Scand. Audiol. **7**, 147–157.
Elberling, C., and Don, M. (**1984**). ''Quality estimation of averaged auditory brainstem responses,'' Scand. Audiol. **13**, 187–197.
Elberling, C., and Parbo, J. (**1987**). ''Reference data for ABRs in retrocochlear diagnosis,'' Scand. Audiol. **16**, 49–55.
Elberling, C., and Wahlgreen, O. (**1985**). ''Estimation of auditory brainstem responses, ABR, by means of Bayesian inference,'' Scand. Audiol. **14**, 89–96.
Goldstein, M. H., and Kiang, N. Y-S. (**1958**). ''Synchrony of neural activity in electric responses evoked by transient acoustic stimuli,'' J. Acoust. Soc. Am. **30**, 107.
Goldstein, J. L., Baer, T., and Kiang, N. Y. S. (**1971**). ''A theoretical treatment of latency, group delay, and tuning characteristics for auditory nerve responses to clicks and tones,'' in *Physiology of the Auditory System*, edited by M. B. Sachs (National Educational Consultants, Baltimore, MD), pp. 133–141.
Gorga, M. P., Worthington, D. W., Reiland, J. K., Beauchaine, K. A., Goldgar, D. E. (**1985**). ''Some comparisons between auditory brainstem response thresholds, latencies and pure-tone audiogram,'' Ear Hearing **6**, 105–112.
Hall, J. L. (**1974**). ''Two-tone distortion products in a nonlinear model of the basilar membrane,'' J. Acoust. Soc. Am. **56**, 1818–1828.
Jerger, J., and Mauldin, L. (**1978**). ''Prediction of sensorineural hearing level from the brain stem evoked response,'' Arch. Otolaryngol. **104**, 456–461.
Keith, W. J., and Greville, K. A. (**1987**). ''Effects of audiometric configuration on the auditory brain stem response,'' Ear Hearing **8**, 49–55.
Kiang, N. Y-S., Watanabe, T., Thomas, E. C., and Clark, L. F. (**1965**). *Discharge patterns of single fibers in the cat's auditory nerve* (Research Monograph No. 35) (Cambridge Univ. and Massachusetts Institute of Technology, Cambridge).
Kiang, N. Y.-S., Moxon, E. C., and Levine, R. A. (**1970**). ''Auditory-nerve activity in cats with normal and abnormal cochleas.'' in *Sensorineural Hearing Loss*, edited by G. E. W. Wolstenholme and J. Knight (Churchill, London), pp. 241–273.
Kim, Y., Aoyagi, M., and Koike, Y. (**1994**). ''Measurement of cochlear basilar membrane traveling wave velocity by derived ABR,'' Acta Otolaryngol Suppl. (Stockholm) **511**, 71–76.
Klein, A. J., and Mills, J. H. (**1981**). ''Physiological (waves *I* and *V*) and psychophysical tuning curves in human subjects,'' J. Acoust. Soc. Am. **69**, 760–768.
Liberman, M. C., and Kiang, N. Y.-S. (**1978**). ''Acoustic trauma in cats. Cochlear pathology and auditory-nerve activity,'' Acta Otolaryngol. Suppl. (Stockholm) **358**, 1–63.
Moller, A. R. (**1983**). ''Use of pseudorandom noise in studies of frequency selectivity: the periphery of the auditory system,'' Biol. Cybern. **47**, 95–102.
Neely, S. T. (**1993**). ''A model for cochlear mechanics with outer hair cell motility,'' J. Acoust. Soc. Am. **94**, 137–146.
Parker, D. J., and Thornton, A. R. D. (**1978a**). ''The validity of the derived cochlear nerve and brainstem evoked responses of the human auditory system,'' Scand. Audiol. **7**, 45–52.
Parker, D. J., and Thornton, A. R. D. (**1978b**). ''Frequency specific components of the cochlear nerve and brainstem evoked responses of the human auditory system,'' Scand. Audiol. **7**, 53–60.
Parker, D. J., and Thornton, A. R. D. (**1978c**). ''Cochlear traveling wave velocities calculated from the derived components of the cochlear nerve and brainstem evoked responses of the human auditory system,'' Scand. Audiol. **7**, 67–70.
Ponton, C. W., Eggermont, J. J., Coupland, S. G., and Winkelaar, R. (**1992**). ''Frequency specific maturation of the eighth nerve and brainstem auditory pathway: Evidence from derived auditory brain-stem responses (ABRs),'' J. Acoust. Soc. Am. **91**, 1576–1586.
Prosser, S., Arslan, E., Conti, G., and Michelini, S. (**1983**). ''Evaluation of the monaurally evoked brainstem response in the diagnosis of sensorineural hearing loss,'' Scand. Audiol. **12**, 103–106.
Rosenhamer, H. J., Lindstrom, B., and Lundborg, T. (**1981**). ''On the use of click-evoked brainstem responses in audiological diagnosis III: Latencies in cochlear hearing loss,'' Scand. Audiol. **10**, 3–11.
Ruggero, M. A. (**1992**). ''Response to sound of the basilar membrane of the mammalian cochlea,'' Curr. Opin. Neurobiol. **2**, 449–456.
Ruggero, M. A. (**1994**). ''Cochlear delays and traveling waves: Comments on 'Experimental look at cochlear mechanics' [A. Dancer, Audiology 1992; 31: 301–312],'' Audiology **33**, 131–142.
Rupa, V., and Dayal, A. K. (**1993**). ''Wave V latency shifts with age and sex in normals and patients with cochlear hearing loss: Development of a predictive model,'' Br. J. Audiol. **27**, 273–279.
Rutten, W. L. (**1986**). ''The influence of cochlear hearing loss and probe tone level on compound action potential tuning curves in humans,'' Hearing Res. **21**, 195–204.
Sabo, D. L., Durrant, J. D., Curtin, H., Boston, J. R., and Rood, S. (**1992**). ''Correlations of neuroanatomical measures to auditory brain stem response latencies,'' Ear Hearing **13**, 213–222.
Sato, H., Sando, I., and Takahashi, H. (**1991**). ''Sexual dimorphism and development of the human cochlea. Computer 3-D measurement,'' Acta Otolaryngol. (Stockholm) **111**, 1037–1040.
Sohmer, H., Kinarti, R., and Gafni, M. (**1981**). ''The latency of auditory nerve-brainstem responses in sensorineural hearing loss,'' Arch. Otorhinolarngol. **230**, 189–199.
Spoendlin, H. (**1966**). ''The Organization of the Cochlear Receptor,'' Adv. Otorhinolaryngol. **13**, 1–227.
Stegeman, D. F., Van Oosterom, A., and Colon, E. J. (**1987**). ''Far-field evoked potential components induced by a propagating generator: computational evidence,'' Electroencephalogr. Clin. Neurophysiol. **67**, 176–187.
Stockard, J. E., Stockard, J. J., Westmorland, B. F., and Corfits, J. L. (**1979**). ''Brainstem auditory evoked responses: Normal variation as a function of stimulus and subject characteristics,'' Arch. Neurol. **36**, 823–831.
Sturzebecher, E., Kevanishvili, Z., Werbs, M., Meyer, E., and Schmidt, D. (**1985**). ''Interpeak intervals of auditory brainstem response, interaural differences in normal-hearing subjects and patients with sensorineural hearing loss,'' Scand. Audiol. **14**, 83–87.
Teas, D. C., Eldredge, D. H., and Davis, H. (**1962**). ''Cochlear responses to acoustic transients. An interpretation of whole nerve action potentials,'' J. Acoust. Soc. Am. **34**, 1438–1489.
Thornton, A. R. D., and Farrell, G. (**1991**). ''Apparent travelling wave velocity changes in cases of endolymphatic hydrops,'' Scand. Audiol. **20**, 13–18.
van der Drift, J. F., Brocaar, M. P., and von Zanten, G. A. (**1988**). ''Brainstem response audiometry. I. Its use in distinguishing between conductive and cochlear hearing loss,'' Audiology (Switzerland) **27**, 260–270.
Watson, D. R. (**1996**). ''The effects of cochlear hearing loss, age and sex on the auditory brainstem response,'' Audiology **35**, 246–258.
Weatherill, G. B., and Levitt, H. (**1965**). ''Sequential estimation of points on a psychometric function,'' Br. J. Math. Stat. Psychol. **18**, 1–10.
Yamada, O., Kodera, K., and Yagi, T. (**1979**). ''Cochlear processes affecting wave *V* latency of the auditory evoked brain stem response,'' Scand. Audiol. **8**, 67–70.

Cubic distortion product otoacoustic emissions in young and aged chinchillas exposed to low-frequency noise

Sandra L. McFadden
Center for Hearing and Deafness, 215 Parker Hall, University of Buffalo, Buffalo, New York 14214-3001

Pierre Campo
INRS, BP 27, Vandoeuvre, 54501, France

(Received 6 March 1998; accepted for publication 13 July 1998)

The aim of this study was to examine susceptibility to noise-induced hearing loss in animals with and without age-related hearing loss (AHL), using cubic distortion product otoacoustic emissions (CDPs) to assess the functional status of the outer hair cell (OHC) system. Subjects were young (≤3-yr-old) and aged (10- to 15-yr-old) chinchillas. CDP thresholds and input/output (I/O) functions were measured before and after exposure to 95 dB or 106 dB SPL low-frequency noise. The results indicate that (a) aging in the chinchilla is associated with significant elevations of CDP thresholds and depression of CDP I/O functions, (b) noise exposures cause equivalent CDP threshold elevations and amplitude reductions in young animals with normal hearing and older animals with AHL, and (c) CDP threshold and amplitude measures provide information that complements evoked potentials measured from the auditory midbrain. © *1998 Acoustical Society of America.* [S0001-4966(98)05410-1]

PACS numbers: 43.64.Wn, 43.64.Jb, 43.80.Gx, 43.64.Ld [BLM]

INTRODUCTION

In a previous study (McFadden *et al.*, 1998a), we examined susceptibility to noise-induced hearing loss (NIHL) in chinchillas with and without age-related hearing loss (AHL), using inferior colliculus (IC) evoked potential (EVP) thresholds and amplitudes as physiological measures of damage. Subjects were 15 young (≤3-yr-old) and 15 aged (10- to 15-yr-old) chinchillas with recording electrodes implanted in the IC. Prior to noise exposure, there were clear differences between young and aged animals: aged animals had higher IC-EVP thresholds (by approximately 10 dB at 0.5–4 kHz, and 20 dB at 8 and 16 kHz) and depressed input/output (I/O) functions (i.e., functions relating response amplitude to stimulus level). The animals were subsequently exposed to a 0.5-kHz octave band (OB) noise. One group was exposed to the noise at a moderate level of 95 dB SPL for 6 h/day for 10 days. The other group was exposed to the noise at a higher level of 106 dB SPL continuously for 48 h. Analyses of the IC-EVP threshold and amplitude data revealed no differences between young and aged animals in their response to moderate-level noise. The 95-dB noise produced equivalent threshold shifts (TSs) and parallel recovery functions for the two age groups, with thresholds recovering to pre-exposure levels within 5 days after the exposure. High-level noise, on the other hand, produced greater physiological and histological deficits in aged animals. Physiologically, there were systematic differences in temporary TS (TTS), permanent TS (PTS), and IC-EVP amplitude functions following exposure to 106-dB noise. Histologically, aged noise-exposed ears showed greater outer hair cell (OHC) and inner hair cell (IHC) losses throughout the cochlea than young noise-exposed ears. In the 3–14 kHz region of the cochlea, OHC losses were greater than that predicted from the combined effects of noise exposure and aging, suggesting increased vulnerability of basal OHCs in older ears to damage from high-level noise. Overall, the results pointed to greater vulnerability of aged animals to cochlear and central auditory system damage following high-level, but not moderate-level, acoustic overstimulation.

The present study extends our earlier study of interactions between AHL and NIHL in the chinchilla, using a clinically relevant, noninvasive measure of OHC functioning, i.e., cubic distortion product ($2f_1-f_2$) otoacoustic emissions (CDPs). Previous studies have suggested that CDPs are sensitive and reliable indices of AHL and NIHL in both humans and chinchillas (Avan *et al.*, 1996; Lonsbury-Martin *et al.*, 1991; Eddins *et al.*, 1997; Hamernik *et al.*, 1996; Zurek *et al.*, 1982). Unlike evoked potentials recorded from the IC, which can show changes as a result of central compensatory mechanisms following acoustic trauma to the inner ear (Salvi *et al.*, 1990, 1992, 1996; Willott and Lu, 1982), CDPs are believed to reflect the functional status of the cochlear OHCs alone (Brownell, 1990; Trautwein *et al.*, 1996). Thus CDPs may provide a unique perspective on the functioning of OHCs in aged ears and on their vulnerability to damage from acoustic overstimulation. In addition, comparisons between CDPs and IC-EVPs may provide an important perspective on age-related and noise-induced dysfunction at different levels of the auditory system.

I. METHODS

A. Subjects

Subjects were 15 young (≤3 yr) and 15 aged chinchillas (*Chinchilla laniger*) that were among the animals described in a previous paper (McFadden *et al.*, 1997a). All animals were obtained from commercial breeders. Nine young and nine aged animals comprised the 95-dB exposure group. Six young and six aged chinchillas comprised the 106-dB expo-

 0001-4966/98/104(4)/2290/8/$15.00

sure group. Aged chinchillas in the 95-dB exposure group were 11 yr ($N=4$), 12 yr ($N=2$), 14 yr ($N=2$), and 15 yr ($N=1$), with a mean age of 12.3 yr (s.d.=1.6). Aged chinchillas in the 106-dB exposure group were 10 yr ($N=2$), 11 yr ($N=2$), and 12 yr ($N=2$), with a mean age of 11.0 yr (s.d.=0.9). The average life expectancy of the chinchilla has not been clearly established, as it has for short-lived laboratory rodents. Literature from the commercial breeder who supplied our aged chinchillas (Moulton Chinchilla Ranch) states that the average life span is 8–12 years, with some animals living to 22 years. Other sources (Clark, 1984; Bohne *et al.*, 1990; Sun *et al.*, 1994) indicate that the chinchilla's life span is between 12 and 20 years. All procedures regarding the use and care of the animals were reviewed and approved by the University of Buffalo Institutional Animal Care and Use Committee and conformed to state and federal guidelines for the humane treatment of animals.

B. Stimuli and procedures for recording CDPs

Testing was conducted in a sound attenuating booth (Industrial Acoustics Corp., Inc.) with an awake animal held in a custom-designed restraining device (Snyder and Salvi, 1994) that maintained its head at a constant orientation within a calibrated sound field. Tone stimuli were generated digitally (93-kHz sampling rate) by two D/A converters on digital signal processing (DSP) boards in a personal computer (PC). Stimuli were low-pass filtered (TDK HFL0030, roll-off 90 dB between 20 and 24 kHz) to prevent aliasing, attenuated by custom-built computer-controlled attenuators, amplified, and delivered by Etymotic ER2 transducers to the ear canal. Ear canal sound pressure was measured using a low-noise microphone (Etymotic ER10B). Output of the microphone was digitized by a 16 bit A/D converter on a third DSP board in the PC and sampled for 500 ms at a sampling rate of 31 kHz. Measurements made in a hard-walled cavity indicated that the distortion in the measurement system was less than 2 dB SPL for primary tone levels of 80 dB SPL.

The f_2/f_1 ratio was 1.2, and the level difference between f_1 and f_2 was 15 dB ($L_1>L_2$). These parameters were selected on the basis of a parametric study conducted in our lab using young, normal-hearing chinchillas (unpublished data). I/O functions for f_2 primaries of 1.2, 2.4, 3.6, 4.8, 7.2, 9.6, and 12.0 kHz were recorded in 5-dB steps from $L_1=0$ to 80 dB SPL ($L_2=-15$ to 65 dB SPL). The average noise floor level, represented by the low-level (0–15 dB input levels) portion of the I/O function, ranged from -8.4 to -14.2 dB SPL. Two or three sets of I/O functions were obtained from each ear of each animal before noise exposure, and 30 days after 106-dB noise exposure. Animals were tested once after 95-dB noise exposure. CDP threshold, defined as the first input level at which the emission amplitude clearly exceeded the noise floor (i.e., by at least 5 dB), was determined separately for each ear at each frequency, then averages for the group were computed.

C. Noise exposures

The noise used to produce TTS and PTS was an OB noise with a center frequency of 0.5 kHz. The noise was digitally generated with a D/A converter on a Spectrum DSP board (TMS320C25 system board) in a PC, routed through a manual attenuator (Hewlett-Packard 350D) to a low-distortion power amplifier (NAD 2200), and delivered by a compression driver (JBL 2445J) fitted to a bi-radial exponential horn (JBL 2360H) suspended from the ceiling in a sound-attenuating booth (Acoustic Systems). During exposures, animals were housed in separate cages beneath the loudspeaker and provided free access to food and water. Young and aged animals were exposed together in groups of four to six. Nine young and nine aged animals were exposed to 95-dB noise for 6 hr/day for 10 days; all other animals were exposed to 106-dB noise for 48 h continuously. These noise exposure parameters are frequently used in our lab, because they produce reliable TTSs, PTSs, and cochlear pathology in young, normal-hearing animals (e.g., Campo *et al.*, 1991; McFadden *et al.*, 1997b). Noise levels were measured with a Larson-Davis (model 800B) sound level meter and a 1/2-in. condenser microphone (LDL 2559). The microphone was placed in each cage at a height approximating the level of the external ear canal of a standing chinchilla. The SPL in each cage was estimated by averaging measurements made at each corner and the geometric center of the cage. SPL varied by less than 2 dB between cages. Animals were rotated to different cages each day of an exposure to minimize the effects of possible systematic differences in SPL between cages.

D. Data analyses

Data were typically obtained from both ears of a given animal, and treated independently for analysis. The assumption of independence between ears is justified by the nature of our noise exposure paradigm. Since animals were free to move around, eat, and sleep during the prolonged noise exposures, different amounts of damage could occur to the left and right ears of a given animal. Data are reported for all cases where CDPs could be reliably measured.

Linear regressions were used to obtain a rough estimate of the rate of change in CDP threshold as a function of age (3–15 yrs) at each f_2 frequency. Since the data are limited and data points are not available for all ages, the major value of the regression analysis is in providing slope estimates at each frequency for comparisons with previous IC-EVP slope data. Mean CDP thresholds of young and aged groups were compared using mixed factor analyses of variance (ANOVAs), with Age Group (young, aged) as a between-subjects factor, and Time (pre-exposure, post-exposure) and/or Frequency (1.2, 2.4, 3.6, 4.8, 7.2, 9.6, and 12 kHz) as within-subjects factors. Significant interactions were examined further using two-way ANOVAs, one-way ANOVAs, or Student *t*-tests. Mean threshold shifts at each frequency were compared using Student *t*-tests. For comparisons of CDP I/O functions between age groups or as a function of time (pre-exposure versus post-exposure), the 95% confidence interval for the difference between means was computed. Finally, within an age group, pre-exposure and post-exposure CDP thresholds were compared using paired *t*-tests, with a 0.01 criterion of significance.

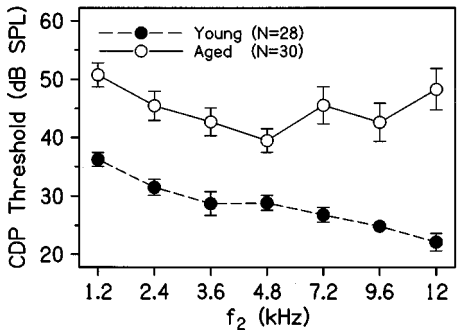

FIG. 1. DP-grams showing mean CDP thresholds as a function of primary tone (f_2) frequency for young ears ($N=28$; filled circles) and aged ears ($N=30$; open circles) prior to noise exposure. Threshold differences were significant at all frequencies. Bars are standard errors of the means (SEMs).

II. RESULTS

A. Pre-exposure CDP thresholds

Mean CDP thresholds of young and aged ears are shown in Fig. 1. Mean thresholds of young ears ($N=28$) ranged from 22.1 to 36.2 dB SPL (filled circles). Thresholds of aged ears ($N=30$) ranged from 39.5 to 50.8 (open circles). As shown by the error bars (SEM) in Fig. 1, variability was greater among the aged ears than among young ears. Standard deviations ranged from 11.1 to 19.4 dB for aged ears, compared to 5.0 to 10.6 dB for young ears.

Differences in mean thresholds between the two age groups ranged from 10.6 dB at $f_2=4.8$ kHz to 26.1 dB at $f_2=12$ kHz. A two-way mixed ANOVA (Age×Frequency) revealed a significant interaction between age and frequency [$F(6,324)=5.53$, $p<0.001$]. As shown in Fig. 1, the interaction reflects the greater threshold elevations at high frequencies ($f_2=7.2$, 9.6, and 12 kHz) compared to lower frequencies ($f_2=1.2$, 2.4, 3.6, and 4.8 kHz) in aged ears.

TABLE I. The relationship between age (3–15 yr) and CDP threshold at seven f_2 frequencies.

f_2 (kHz)	Slope	Intercept	R^2	$F(1,54)$	p
1.2	1.6	36.3	0.402	36.3	<0.0001
2.4	1.6	32.3	0.287	21.8	<0.0001
3.6	1.7	28.8	0.296	22.7	<0.0001
4.8	1.4	29.4	0.346	28.5	<0.0001
7.2	2.3	24.4	0.419	38.9	<0.0001
9.6	2.3	21.7	0.430	40.7	<0.0001
12.0	3.2	16.6	0.540	63.4	<0.0001

Linear regressions were performed to determine slopes (rate of change in threshold between 3 and 15 years) and intercepts at each frequency (Table I). The slope values obtained are consistent with a rate of change of threshold of 1.4–1.7 dB/yr at 1.2–4.8 kHz, 2.3 dB/yr at 7.2 and 9.6 kHz, and 3.2 dB/yr at 12 kHz.

B. Pre-exposure CDP amplitudes

Mean CDP I/O functions of young and aged ears are shown in Figs. 2 and 3 for animals in the 95-dB and 106-dB exposure groups, respectively. The thin lines show the mean CDP amplitudes for young animals, and the shaded regions surrounding them represent the 95% confidence interval for the difference between means. Means of aged animals are represented by the thick lines. Aged ears had consistently smaller suprathreshold response amplitudes at all frequencies tested. The CDP amplitude functions were very similar for the 95-dB and 106-dB exposure groups; however, it is interesting to note that the aged animals in the 95-dB group, who were slightly older than the aged animals in the 106-dB

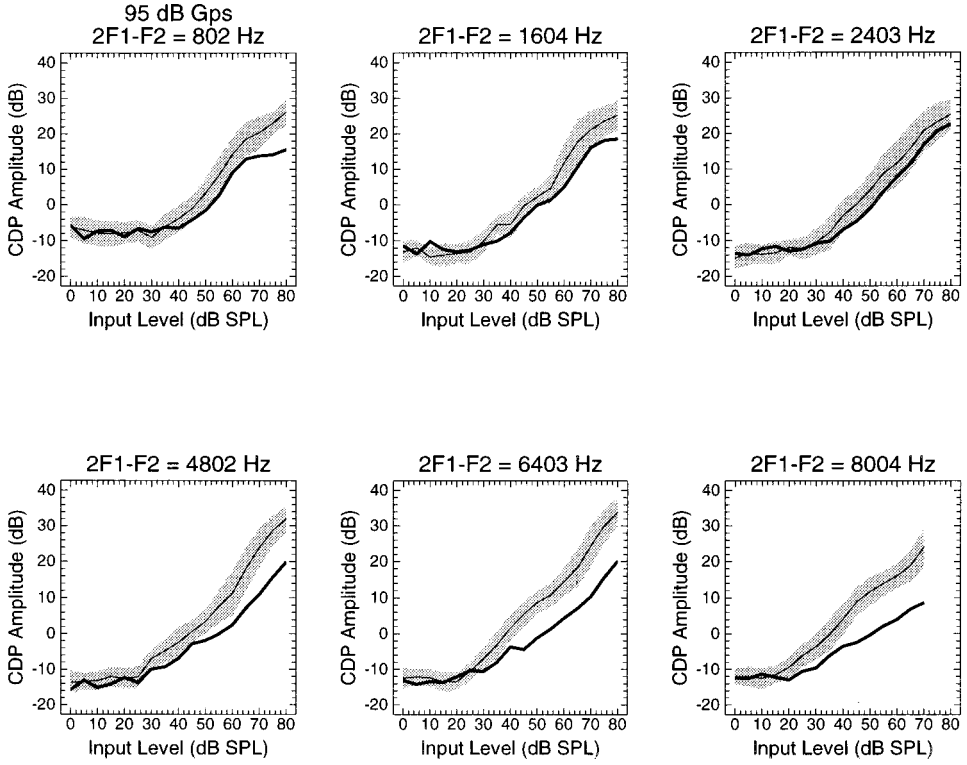

FIG. 2. Pre-exposure I/O functions for ears in the 95-dB exposure group, for primary tones (f_2) of 1.2, 2.4, 3.6, 7.2, 9.6, and 12 kHz. Thin lines represent means of young ears ($N=16$), and the hatched regions surrounding them represent the 95% confidence interval for the difference between means. Thick lines represent means of aged ears ($N=18$). I/O functions for $f_2=4.8$ kHz (data not shown) were very similar to those at $f_2=3.6$ kHz. For all CDP measurements, the level difference (L_1-L_2) was 15 dB, and the f_2/f_1 ratio was 1.2. Average noise floor levels were −8.4, −10.8, −14.2, −13.3, −13.8, and −12.0 dB SPL at 1.2, 2.4, 3.6, 7.2, 9.6, and 12 kHz, respectively.

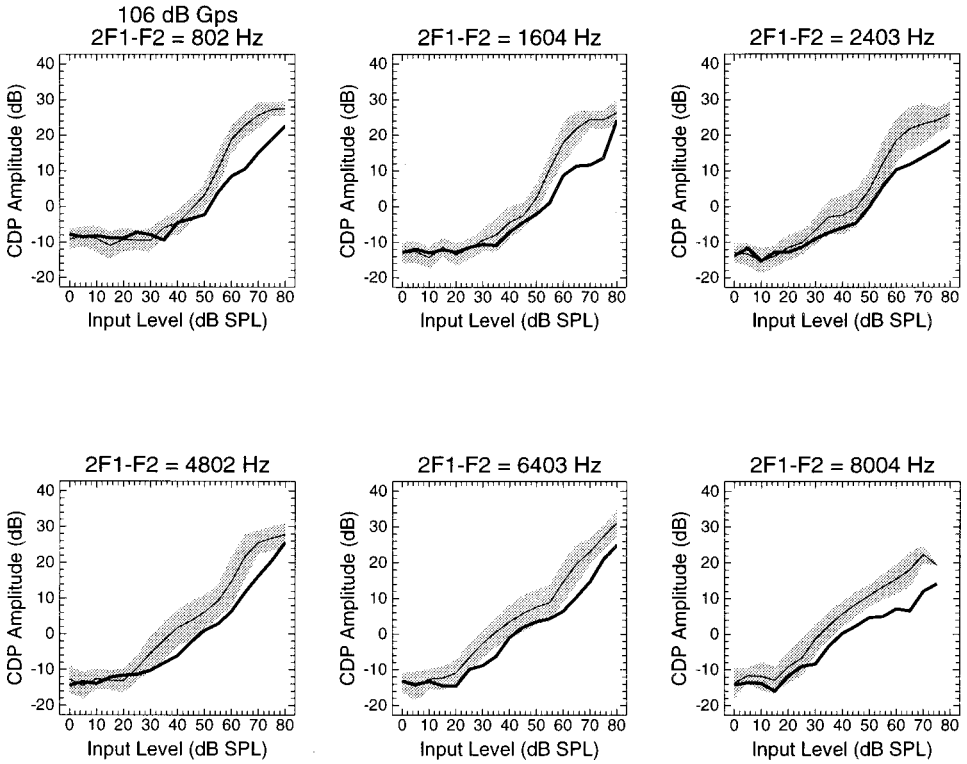

FIG. 3. Pre-exposure I/O functions for ears in the 106-dB exposure group, for primary tones (f_2) of 1.2, 2.4, 3.6, 7.2, 9.6, and 12 kHz. Thin lines represent means of young ears ($N=12$), and the hatched regions surrounding them represent the 95% confidence interval for the difference between means. Thick lines represent means of aged ears ($N=12$). I/O functions for $f_2=4.8$ kHz (data not shown) were very similar to those at $f_2=3.6$ kHz. Average noise floor levels were −8.8, −12.7, −14.0, −14.1, −13.4, −13.4, and −13.4 dB SPL at 1.2, 2.4, 3.6, 7.2, 9.6, and 12 kHz, respectively.

group ($M=12.3$ yrs versus 11.0 yrs, respectively), appeared to have slightly greater amplitude losses at the highest frequencies tested.

C. Effects of 95-dB noise exposure on CDP thresholds

Mean CDP thresholds measured 5 days after exposure to 95-dB noise are shown in Fig. 4A. Differences in mean thresholds between the young and aged groups ranged from 6 dB at 4.8 kHz to 26 dB at 12 kHz after exposure. A three-way mixed-factor ANOVA revealed a significant interaction between age group and frequency [$F(6,150)=5.44$, $p<0.001$], but no significant main or interaction effects involving time. The age×frequency interaction was examined further using Student *t*-tests. These analyses indicated that the interaction occurred because the low-frequency (1.2–4.8 kHz) threshold differences between young and aged ears prior to exposure were eliminated after exposure, whereas threshold differences at higher frequencies were maintained (Fig. 4A). That is, noise exposure made young and aged ears more similar at low frequencies. However, mean thresholds after noise exposure were not significantly different from thresholds prior to noise exposure for either age group, indicating that 95-dB exposure caused no permanent changes in CDP thresholds.

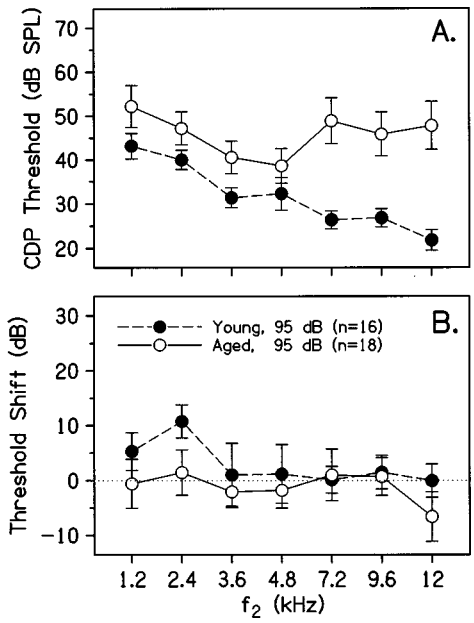

FIG. 4. Mean CDP thresholds (A) and threshold shifts (B) measured 5 days after 95-dB noise exposure. Bars show SEMs for each group.

Threshold shifts following 95-dB noise exposure are shown in Fig. 4B. Thresholds of young ears shifted by 0–10.8 dB, with the largest shifts occurring at 1.2 and 2.4 kHz. Thresholds of aged ears shifted by 1.5 dB or less at all frequencies. Although TSs tended to be slightly greater in young ears than in aged ears, there were no significant differences between age groups in TS magnitude at any frequency (Student *t*-tests, all p values >0.05).

D. Effects of 95-dB noise exposure on CDP amplitudes

Figure 5 compares CDP amplitudes of young and aged ears before [top three panels] and 5 days after [bottom three panels] 95-dB exposure, as a function of f_2 frequency and input level ($L_1=50$, 60, and 70 dB). Four main observations can be made from these suprathreshold DP-grams. First, CDP amplitudes were consistently lower for aged ears than for young ears at all input levels. Age differences were evident before as well as after exposure. Second, as input

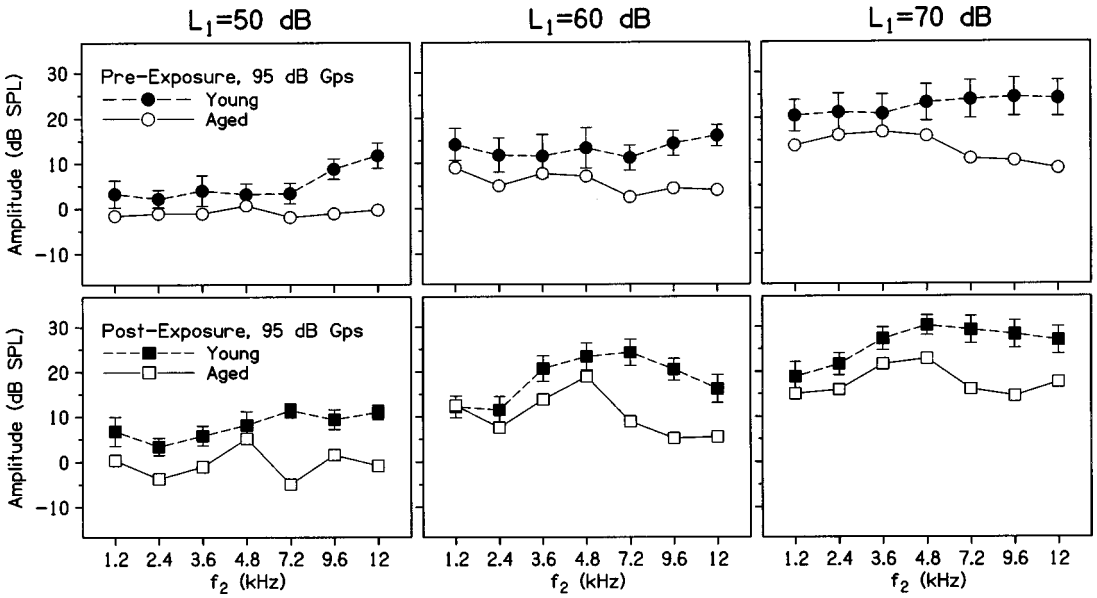

FIG. 5. CDP amplitudes as a function of frequency and input level ($L_1=50$, 60, and 70 dB SPL) for 95-dB exposure groups. Upper panels show amplitudes prior to exposure (see Fig. 2). Lower panels show amplitudes after exposure. The presentation facilitates comparison of differences due to age (filled symbols versus open symbols) and exposure (top panels versus bottom panels). Bars show 95% confidence intervals for the differences between means at each frequency.

level increased from 50 to 70 dB, differences between young and aged animals increased at high frequencies but not at low frequencies. Third, CDP amplitudes were not depressed after 95-dB noise exposure. In fact, amplitudes for both age groups actually increased at most frequencies, particularly at higher input levels (60 and 70 dB). After 95-dB exposure, amplitudes increased by as much as 13.1 dB for young ears (at 7.2 kHz, $L_1=60$ dB), and by as much as 11.8 dB for aged ears (at 4.8 kHz, $L_1=60$ dB). Fourth, the age-related differences seen prior to exposure were generally maintained after exposure, suggesting that suprathreshold responses of young and aged ears were affected similarly by 95-dB noise.

An examination of threshold shifts (Fig. 6B) shows why the interaction occurred. Whereas aged ears showed a relatively uniform TS across frequencies, young ears had greater TS at 12 kHz than at lower frequencies. Thus the pattern of TS across frequencies differed for young and aged ears.

Unlike 95-dB noise which caused no significant TS for either young or aged ears, the 106-dB exposure produced PTSs ranging from approximately 8 to 23 dB in young ears, and 10 to 14 dB for aged ears. Threshold shifts were significant at all frequencies for young ears. Because variability was greater among aged ears, only the mean TS at 9.6 kHz reached statistical significance [$t(11)=-3.5$, $p=0.005$].

E. Effects of 106-dB noise exposure on CDP thresholds

CDP thresholds and threshold shifts measured 30 days after exposure to 106-dB noise are shown in Fig. 6. An examination of these data suggests that high-level exposure made young ears more similar to aged ears by elevating high-frequency thresholds more than low (compare with Fig. 1), and that significant threshold elevations occurred for both age groups.

A three-way ANOVA for thresholds revealed significant main effects for age group, frequency, and time, and a significant interaction between time and frequency (all p values <0.005). Most importantly, there was a significant three-way interaction between age group, time and frequency [$F(6,156)=2.48$, $p=0.03$], indicating that high-level noise affected young and aged ears differently. Subsequent two-way ANOVAs (Time×Frequency) confirmed a significant interaction for the young group [$F(6,90)=7.6$, $p<0.001$], whereas there were significant main effects for time [$F(1,11)=8.4$, $p=0.01$] and frequency [$F(6,66)=2.9$, $p=0.01$] but no interaction for the aged group.

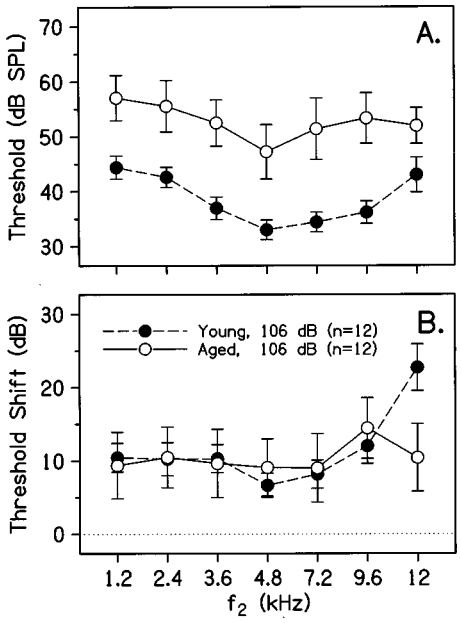

FIG. 6. Mean CDP thresholds (A) and threshold shifts (B) measured 30 days after 106-dB noise exposure. Bars show SEMs for each group.

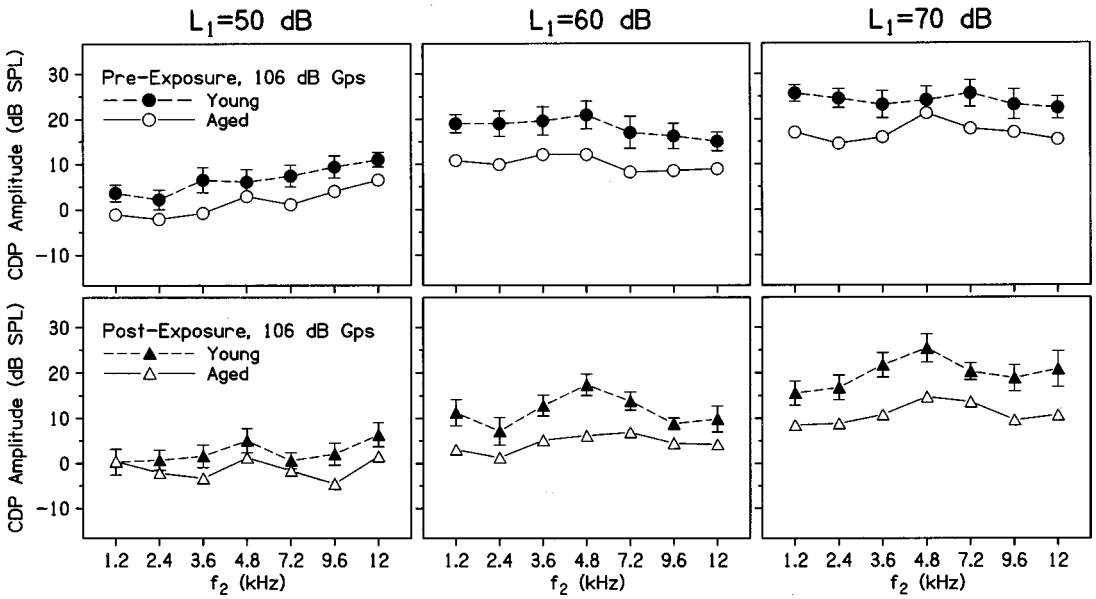

FIG. 7. CDP amplitudes as a function of frequency and input level ($L_1=50$, 60, and 70 dB SPL) for 106-dB exposure groups. Upper panels show amplitudes prior to exposure (see Fig. 3). Lower panels show amplitudes after exposure. The presentation facilitates comparison of differences due to both age (filled symbols versus open symbols) and exposure (top panels versus bottom panels). Bars show 95% confidence intervals for the differences between means at each frequency.

Threshold differences between young and aged ears persisted after exposure, with significant differences observed at all frequencies (p values <0.009) except 12 kHz ($p=0.6$).

F. Effects of 106-dB noise exposure on CDP amplitudes

Amplitudes of both young and aged ears tended to be depressed slightly after noise exposure, as illustrated in Fig. 7. However, there were no systematic differences between young and aged ears in either the pattern or the magnitude of amplitude decreases. Differences between young and aged ears seen prior to noise exposure (top panels) were well-preserved after noise exposure (bottom panels).

III. DISCUSSION

Prior to noise exposure, aged ears had significantly higher CDP thresholds and reduced CDP amplitudes compared to young ears. Thresholds were more elevated at high frequencies than at low frequencies. Regression analyses yielded slopes consistent with rates of threshold change between 1.4 and 3.2 dB/yr. After exposure, age-related threshold and amplitude differences were generally maintained, with one exception. After high-level noise exposure, young ears showed greater TS at $f_2=12$ kHz, the highest frequency tested, resulting in a threshold DP-gram that more closely resembled that of aged ears. Apart from this single difference, the CDP threshold and amplitude data suggest that young animals with normal hearing and aged animals with AHL do not differ in their susceptibility to either moderate-level or high-level noise. The results support a simple additive relationship between AHL and NIHL with respect to their effects on the functioning of surviving OHCs as assessed by CDPs.

In previous studies (McFadden *et al.*, 1997a, 1998a), we reported the results of EVP tests performed on young and aged chinchillas, including those used in the present study. Because the EVPs were measured from electrodes implanted in the auditory midbrain, a comparison between CDPs and IC-EVPs may provide an important perspective on peripheral versus central mechanisms contributing to AHL, NIHL, and the interaction between them.

A. Comparison of CDPs and IC-EVPs before noise exposure

Recent studies using chinchillas with selective IHC lesions produced by carboplatin (e.g., Burkard *et al.*, 1997; Jock *et al.*, 1996; McFadden *et al.*, 1998b) have shown that IC-EVP thresholds are sensitive to cochlear pathology involving significant OHC loss, but are surprisingly insensitive to IHC lesions. As long as OHCs are intact, even massive IHC lesions do not elevate IC-EVP thresholds (McFadden *et al.*, 1998b). Studies using the carboplatin-treated chinchilla model have also shown that IHCs make little or no contribution to CDPs, since even massive IHC lesions do not decrease CDP amplitude, as long as OHCs remain intact (Jock *et al.*, 1996; Hofstetter *et al.*, 1997; Trautwein *et al.*, 1996). Since both CDPs and IC-EVP thresholds are affected by OHC but not IHC loss, the two measures might be expected to provide similar information regarding the functional status of the OHC system. Data from the present study support this hypothesis, as CDP thresholds showed the same pattern of age-related elevation as the IC-EVP thresholds in our previous study (McFadden *et al.*, 1998a), i.e., greater elevations at high frequencies than at low, corresponding to greater basal OHC pathology. I/O functions of CDPs and IC-EVPs were also similar in pattern, with aged ears consistently showing smaller response amplitudes at all frequencies for both measures. However, CDP thresholds appear to increase some-

what more rapidly than IC-EVP thresholds with age. In our initial study of 21 young and 23 aged chinchillas (McFadden *et al.*, 1997a), IC-EVP thresholds increased by 0.8–1.1 dB/yr at 0.5–4 kHz, and by approximately 2.0 dB/yr at 8 and 16 kHz. In contrast, CDP thresholds for animals in the present study changed at rates corresponding to 1.4–1.7 dB/yr at $f_2 = 1.2–4.8$ kHz, 2.3 dB/yr at 7.2 and 9.6 kHz, and 3.2 dB/yr at 12 kHz. While these relatively small differences could be simply related to different sample sizes or to imperfect correspondence between test frequencies, they could also reflect a dissociation between peripheral and central pathology. The central nervous system is often able to compensate for peripheral losses, particularly when the peripheral changes occur slowly over time (Kaas, 1996; Robertson and Irvine, 1989; Willott *et al.*, 1993; Zheng *et al.*, 1998). The slightly slower decline in sensitivity seen in IC-EVPs compared to CDPs may therefore reflect central compensatory mechanisms similar to those described previously for C57 mice with AHL (Willott, 1996; Willott *et al.*, 1991, 1993). In the case of aging C57 mice, paradoxical differences in threshold shifts have been observed throughout the central auditory system. For example, mean age-related threshold shifts can be more than twice as large in the ventral cochlear nucleus as in the IC (Willott *et al.*, 1991). If differences in the rate of threshold decline observed between CDP and IC-EVP measures are due to central compensatory mechanisms, then the results demonstrate that aged animals are capable of exhibiting central auditory system plasticity in response to age-related peripheral damage. The clinical implication is that CDP threshold may be a more sensitive indicator of subtle damage to the OHCs than brain stem evoked potentials. However, it should be considered that EVPs may be more useful when large hearing losses are present.

B. Comparison of CDPs and IC-EVPs after noise exposure

The results of the present study suggest that young and aged OHCs do not differ in their physiological response to either moderate-level or high-level noise. For both exposure levels, the sensitivity and amplitude losses caused by noise exposure simply added to the losses already present from aging. The CDP results presented here are consistent with our previous findings from IC-EVP measurements (McFadden *et al.*, 1998a) in showing that 95-dB exposure produces no PTS for either young or aged ears, whereas 106-dB exposure produces significant PTS for both. However, the CDP and IC-EVP results differ in one important respect. Whereas the CDP data do not indicate a difference in the effects of moderate-level versus high-level noises, the IC-EVP data suggested that aged animals may be more susceptible to high-level noise than young animals, consistent with a recent study of the Mongolian gerbil (Mills *et al.*, 1997). One particularly notable difference that we observed in the previous study (McFadden *et al.*, 1998a) was that IC-EVP amplitude functions of young animals were *enhanced* after exposure, consistent with previous studies of young noise-exposed animals (Salvi *et al.*, 1990, 1992, 1996; Willott and Lu, 1982), whereas those of aged animals were not. The IC-EVP results suggested that high-level noise exposure altered the balance of excitation and inhibition differently in the central auditory system of young and aged animals.

Alterations in the balance of excitation and inhibition in central auditory nuclei could arise through a number of mechanisms. For instance, the strength of inhibition in the IC may already be diminished in aged animals (McFadden and Willott, 1994a, b), so that release from inhibition is less likely to be observed in their IC potentials. Alternatively, the strength of excitation in the IC may be diminished as a result of impaired OHC functioning and reduced neural input to the central auditory system. Results from the present study do not allow either of these hypotheses to be ruled out.

C. Clinical implications

Stover *et al.* (1996) assessed the clinical utility of CDP thresholds and amplitudes in the diagnosis of hearing status in 210 subjects ranging in age from 7 to 86 yrs. They found that CDP thresholds were slightly better than CDP amplitudes in correctly identifying ears with hearing loss. However, given the ambiguity inherent in CDP threshold estimation and the longer testing times required to obtain thresholds, Stover *et al.* (1996) recommended the use of suprathreshold DP-grams obtained with moderate level primaries in the clinical setting. Examination of the DP-grams from young and aged chinchillas (Figs. 5 and 7) shows that CDP amplitudes measured at input levels of 60–70 dB provide essentially the same information as the CDP threshold data from the same animals (Figs. 4A and 6A). Thus our data support the recommendation of Stover *et al.* (1996). At the same time, however, the differences we have observed between CDP and IC-EVP measures of auditory system pathology highlight the need to consider central as well as peripheral changes when assessing hearing loss in a clinical population. Aged subjects may have central deficits that are independent of peripheral pathology (see Willott, 1991), that would not be evident from CDPs. In addition, aged and/or noise-exposed individuals may have IHC lesions that would not be detected with either CDPs or IC-EVP thresholds (Burkard *et al.*, 1997; Hofstetter *et al.*, 1997; Jock *et al.*, 1996; McFadden *et al.*, 1998b; Trautwein *et al.*, 1996), emphasizing the need for suprathreshold measures of auditory function.

ACKNOWLEDGMENTS

Research supported by the Center for Hearing and Deafness at the University of Buffalo and by Grant No. DAMD17-96-1-6327 to SLM. The authors appreciate the assistance of Kimin Kim and Marty Howard in data collection.

Avan, P., Bonfils, P., and Loth, D. (**1996**). ''Effects of acoustic overstimulation on distortion-product and transient-evoked otoacoustic emissions,'' in *Scientific Basis of Noise-Induced Hearing Loss*, edited by A. Axelsson *et al.* (Thieme, New York), pp. 65–81.

Bohne, B. A., Gruner, M. M., and Harding, G. W. (**1990**). ''Morphological correlates of aging in the chincilla cochlea,'' Hearing Res. **48**, 79–92.

Brownell, W. E. (**1990**). ''Outer hair cell electromotility and otoacoustic emissions,'' Ear Hear. **11**, 82–92.

Burkard, R., Trautwein, P., and Salvi, R. (**1997**). ''The effects of click level, click rate, and level of background masking noise on the inferior colliculus potential (ICP) in the normal and carboplatin-treated chinchilla,'' J. Acoust. Soc. Am. **102**, 3620–3627.

Campo, P., Subramaniam, M., and Henderson, D. (**1991**). ''The effect of 'conditioning' exposures on hearing loss from traumatic exposure,'' Hearing Res. **55**, 195–200.

Clark, J. D. (**1984**). ''Biology and diseases of other rodents,'' in *Laboratory Animal Medicine*, edited by J. G. Fox, R. J. Cohen, and F. W. Loew (Academic, New York), pp. 183–206.

Eddins, A. C., Zuskov, M., and Salvi, R. J. (**1997**). ''Changes in distortion-product otoacoustic emissions in chinchillas with increasing levels of noise-induced asymptotic threshold shift,'' Assoc. Res. Otolaryngol. Abstr. **776**, 194.

Hamernik, R. P., Ahroon, W. A., and Lei, S. F. (**1996**). ''The cubic distortion product otoacoustic emissions from the normal and noise-damaged chinchilla cochlea,'' J. Acoust. Soc. Am. **100**, 1003–1012.

Hofstetter, P., Ding, D., Powers, N., and Salvi, R. J. (**1997**). ''Quantitative relationship of carboplatin dose to magnitude of inner and outer hair cell loss and the reduction in distortion product otoacoustic emission amplitude in chinchillas,'' Hearing Res. **112**, 199–215.

Jock, B. M., Hamernik, R. P., Aldrich, L. G., Ahroon, W. A., Petriello, K. L., and Johnson, A. R. (**1996**). ''Evoked-potential thresholds and cubic distortion product otoacoustic emissions in the chinchilla following carboplatin treatment and noise exposure,'' Hearing Res. **96**, 179–190.

Kaas, J. H. (**1996**). ''Plasticity of sensory representations in the auditory and other systems of adult mammals,'' in *Auditory System Plasticity and Regeneration*, edited by R. J. Salvi, D. Henderson, F. Fiorino, and V. Colletti (Thieme Medical, New York), pp. 213–223.

Lonsbury-Martin, B. L., Cutler, W. M., and Martin, G. K. (**1991**). ''Evidence for the influence of aging on distortion-product otoacoustic emissions in humans,'' J. Acoust. Soc. Am. **89**, 1749–1759.

McFadden, S. L., Campo, P., Ding, D., and Quaranta, N. (**1998a**). ''Effects of low-frequency noise on inferior colliculus evoked potentials and cochlear anatomy in young and aged chinchillas,'' Hearing Res. **117**, 1–16.

McFadden, S. L., Campo, P., Quaranta, N., and Henderson, D. (**1997a**). ''Age-related decline of auditory function in the chinchilla (*Chinchilla laniger*),'' Hearing Res. **111**, 114–126.

McFadden, S. L., Henderson, D., and Shen, Y.-H. (**1997b**). ''Low-frequency 'conditioning' provides long-term protection from noise-induced threshold shifts in chinchillas,'' Hearing Res. **103**, 142–150.

McFadden, S. L., Kasper, C., Ostrowski, J., Ding, D., and Salvi, R. J. (**1998b**). ''Effects of inner hair cell loss on inferior colliculus evoked potential thresholds, amplitudes and forward masking functions in chinchillas,'' Hearing Res. **120**, 121–132.

McFadden, S. L., and Willott, J. F. (**1994a**). ''Responses of inferior colliculus neurons in C57BL/6J mice with and without sensorineural hearing loss: Effects of changing the azimuthal location of an unmasked pure-tone stimulus,'' Hearing Res. **78**, 115–131.

McFadden, S. L., and Willott, J. F. (**1994b**). ''Responses of inferior colliculus neurons in C57BL/6J mice with and without sensorineural hearing loss: Effects of changing the azimuthal location of a continuous noise masker on responses to contralateral tones,'' Hearing Res. **78**, 132–148.

Mills, J. H., Boettcher, F. A., and Dubno, J. R. (**1997**). ''Interaction of noise-induced permanent threshold shift and age-related threshold shift,'' J. Acoust. Soc. Am. **101**, 1681–1686.

Robertson, D., and Irvine, D. R. F. (**1989**). ''Plasticity of frequency organization in auditory cortex of guinea pigs with partial unilateral deafness,'' J. Comp. Neurol. **282**, 456–471.

Salvi, R. J., Saunders, S. S., Gratton, M. A., Arehole, S., and Powers, N. (**1990**). ''Enhanced evoked response amplitudes in the inferior colliculus of the chinchilla following acoustic trauma,'' Hearing Res. **50**, 245–257.

Salvi, R. J., Powers, N. L., Saunders, S. S., Boettcher, F. A., and Clock, A. E. (**1992**). ''Enhancement of evoked response amplitude and single unit activity after noise exposure,'' in *Noise-Induced Hearing Loss*, edited by A. Dancer, D. Henderson, R. J. Salvi, and R. P. Hamernik (Mosby-Year Book, St. Louis, MO), pp. 156–171.

Salvi, R. J., Wang, J., and Powers, N. (**1996**). ''Rapid functional reorganization in the inferior colliculus and cochlear nucleus after acute cochlear damage,'' in *Auditory Plasticity and Regeneration*, edited by R. Salvi, D. Henderson, V. Coletti, and F. Fiorino (Thieme, New York), pp. 275–296.

Snyder, D. L., and Salvi, R. J. (**1994**). ''A novel chinchilla restraint device,'' Lab An. **23**, 42–44.

Stover, L., Gorga, M. P., Neely, S. T., and Montoya, D. (**1996**). ''Toward optimizing the clinical utility of distortion product otoacoustic emission measurements,'' J. Acoust. Soc. Am. **100**, 956–967.

Sun, J. C., Bohne, B. A., and Harding, G. W. (**1994**). ''Is the older ear more susceptible to noise damage?,'' Laryngoscope **104**, 1251–1258.

Trautwein, P., Hofstetter, P., Wang, J., Salvi, R. J., and Nostrant, A. (**1996**). ''Selective inner hair cell loss does not alter distortion product otoacoustic emissions,'' Hearing Res. **96**, 71–82.

Willott, J. F. (**1991**). *Aging and the Auditory System: Anatomy, Physiology, and Psychophysics* (Singular Publishing Group, San Diego, CA).

Willott, J. F. (**1996**). ''Auditory system plasticity in the adult C57BL/6J mouse,'' in *Auditory Plasticity and Regeneration*, edited by R. J. Salvi, D. Henderson, V. Coletti, and F. Fiorino (Thieme, New York), pp. 297–316.

Willott, J. F., and Lu, S. (**1982**). ''Noise-induced hearing loss can alter neural coding and increase excitability in the central nervous system,'' Science **216**, 1331–1332.

Willott, J. F., Aitkin, L. M., and McFadden, S. L. (**1993**). ''Plasticity of auditory cortex associated with sensorineural hearing loss in adult C57BL/6J mice,'' J. Comp. Neurol. **329**, 402–411.

Willott, J. F., Parham, K., and Hunter, K. P. (**1991**). ''Comparison of the auditory sensitivity of neurons in the cochlear nucleus and inferior colliculus neurons of young and aging C57BL/6J and CBA/J mice,'' Hearing Res. **53**, 78–94.

Zheng, X. Y., McFadden, S. L., and Henderson, D. (**1998**). ''Faster recovery in central than in peripheral auditory system following a reversible cochlear deafferentation,'' Neuroscience (NY) **85**, 579–586.

Zurek, P. M., Clark, W. W., and Kim, D. O. (**1982**). ''The behavior of acoustic distortion products in the ear canals of chinchillas with normal or damaged ears,'' J. Acoust. Soc. Am. **72**, 774–780.

Psychophysical evidence against the autocorrelation theory of auditory temporal processing

Christian Kaernbach[a)]
Institut für Allgemeine Psychologie, Universität Leipzig, Seeburgstraße 14/20, D-04 103 Leipzig, Germany

Laurent Demany[b)]
Laboratoire de Neurophysiologie, UMR CNRS 5543, Université Bordeaux 2, 146 rue Léo-Saignat, F-33 076 Bordeaux, France

(Received 6 July 1997; revised 30 January 1998; accepted 22 June 1998)

Nowadays, it is widely believed that the temporal structure of the auditory nerve fibers' response to sound stimuli plays an important role in auditory perception. An influential hypothesis is that information is extracted from this temporal structure by neural operations akin to an autocorrelation algorithm. The goal of the present work was to test this hypothesis. The stimuli consisted of sequences of unipolar clicks that were high-pass filtered and mixed with low-pass noise so as to exclude spectral cues. In experiment 1, ''interfering'' clicks were inserted in an otherwise periodic (isochronous) click sequence. Each click belonging to the periodic sequence was followed, after a random portion of the period, by one interfering click. This disrupted the detection of temporal regularity, even when the interfering clicks were 5 dB less intense than the periodic clicks. Experiments 2–4 used click sequences that showed a single peak in their autocorrelation functions. For some sequences, this peak originated from ''first-order'' temporal regularities, that is from the temporal relations between consecutive clicks. For other sequences, the peak originated instead from ''second-order'' regularities, relative to nonconsecutive clicks. The detection of second-order regularities appeared to be much more difficult than the detection of comparable first-order regularities. Overall, these results do not tally with the current autocorrelation models of temporal processing. They suggest that the extraction of temporal information from a group of closely spaced spectral components makes no use of time intervals between nonconsecutive peaks of the amplitude envelope. © *1998 Acoustical Society of America.* [S0001-4966(98)00810-8]

PACS numbers: 43.66.Ba, 43.66.Hg, 43.66.Mk [RHD]

INTRODUCTION

A complex tone with a rich spectrum, such as a vowel, is normally perceived as *one* sound with *one* pitch. The heard pitch is very close to that of a pure tone with the same period, even if the corresponding pure tone is actually absent in the spectrum of the complex tone (the ''missing fundamental phenomenon''). It is much more difficult to perceive a complex tone as a sum of pure tones with various pitches. This is very remarkable, for two reasons. First, the cochlea behaves as a spectral analyzer and resolves the lower harmonics of a vowellike sound. Second, these lower harmonics appear to play a more important role than the higher harmonics, unresolved by the cochlea, in the process of pitch extraction (Plomp, 1967; Ritsma, 1967; Moore *et al.*, 1985).

In the 1970s, ''pattern-recognition'' theories of pitch perception were proposed to account for the missing fundamental phenomenon and the importance of spectral resolution in pitch extraction (e.g., Terhardt, 1972; Goldstein, 1973). Basically, these theories assume that the pitch of a complex tone is extracted by a centrally located processor of the frequency relationships between resolved spectral components. The pattern-recognition theories can explain, in addition to the missing fundamental phenomenon, the pitch percepts induced by inharmonic complex tones, or the pitch ambiguity of complex tones consisting of only few harmonics. However, a fundamental problem for these theories is that pitch percepts can be elicited by the periodicity of sounds consisting of completely unresolved harmonics, or by other stimuli providing no spectral pitch cues (Burns and Viemeister, 1976, 1981; Moore and Rosen, 1979; Houtsma and Smurzynski, 1990).

To account for the latter fact, it is necessary to admit that pitch can be extracted by a mechanism working exclusively in the temporal domain. One may think that this temporal mechanism is used only for the processing of *amplitude envelopes*, and coexists with a completely different central processor of spectral cues (Terhardt, 1972; Carlyon and Shackleton, 1994). However, it is well established that the frequency of a resolved harmonic has in itself a temporal representation in the spike trains conveyed by the auditory nerve fibers responding to this harmonic (Sachs and Young, 1980; Horst *et al.*, 1986). Thus, temporal information might be used to identify the frequency of individual harmonics as a basis of a pattern recognition process (Srulovicz and Goldstein, 1983).

Moore (1977, 1997) argued that most of the psychophysical data concerning the pitch of complex sounds can be understood on the basis of a simpler model. According to Moore, the pitch of a complex sound would simply correspond to the most frequent interspike interval (ISI) occurring

a)Electronic mail: chris@psychologie.uni-leipzig.de
b)Electronic mail: Laurent.Demany@psyac.u-bordeaux2.fr

in the responses of all the auditory nerve fibers excited by this sound. In a nerve fiber excited by a resolved spectral component with frequency f (Hz), consecutive spikes will typically be separated by ISIs corresponding to $1/f, 2/f, 3/f, \ldots, n/f$ s (Sachs and Young, 1980). In other nerve fibers excited by another resolved component, the ISIs will be partly different, but common ISIs will occur if the two components are harmonically related (i.e., if the sound is periodic). The smallest of the common ISIs will correspond to the period of the sound. As the corresponding ISI should also occur in fibers excited by the sum of several harmonics rather than by a single harmonic (Evans, 1978), this ISI should be overall the most frequent one. Note that although Moore's model posits that the pitch extraction process is the same for spectrally resolvable sounds and unresolvable sounds, it is possible in this conceptual framework to make sense of the fact that resolved harmonics provide more salient pitch cues than unresolved harmonics (see Moore, 1997).

Moore's model identifies a possible correlate of the pitch of complex sounds at the auditory nerve level, but does not specify how pitch is neurally represented at higher levels of the auditory system. Because it seems that fine-grain temporal information cannot be represented directly in the auditory cortex (e.g., de Ribaupierre *et al.*, 1972; Steinschneider *et al.*, 1980), any temporal correlate of pitch in the auditory nerve is likely to be recoded beyond into place information (Pantev *et al.*, 1989; Langner, 1992; Langner *et al.*, 1997). How could this be done?

More than two decades earlier, Licklider (1951) hypothesized that the auditory system is able to calculate the autocorrelation (AC) function of a neural spike train, and to transform in this way temporal regularities into a place code for pitch. The neural scenario imagined by Licklider is depicted in Fig. 1. Nowadays, this specific neural scenario is often judged unrealistic, but Licklider's basic proposal is still very influential (Lyon, 1984; Slaney and Lyon, 1990; Lazzaro and Mead, 1989; Assmann and Summerfield, 1990; Meddis and Hewitt, 1991; de Cheveigné, 1993, 1998; Hartmann, 1993; Patterson *et al.*, 1996; Yost *et al.*, 1996; Cariani and Delgutte, 1996a, 1996b). Remark, however, that the temporal regularities liable to be picked up in a spike train by an AC process are not identical to those considered as relevant for pitch by certain pitch theorists (Goldstein and Srulovicz, 1977; Srulovicz and Goldstein, 1983; Ohgushi, 1978; van Noorden, 1982). These authors posited that the relevant information is limited to *first-order* ISIs, that is to intervals between *consecutive* spikes. By contrast, an autocorrelator will not distinguish first-order ISIs from higher-order ISIs, that is, consecutive spikes from nonconsecutive spikes (see Hartmann, 1997, p. 355).

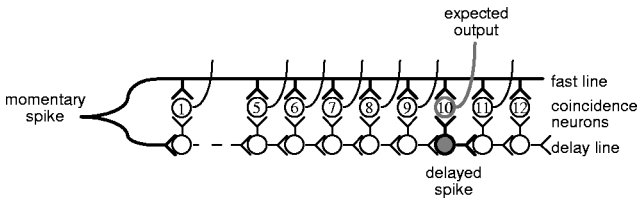

FIG. 1. A neural autocorrelator (after Licklider, 1951). A set of coincidence neurons is placed between a fast line and a delay line. The delay line is realized as a chain of neurons losing approximately 1 ms per synaptic transmission. The figure shows what happens when a spike enters into the system while another spike came in 10 ms earlier. The 10-ms coincidence neuron is about to fire. In Licklider's original model, each coincidence neuron is followed by another neuron doing some temporal integration.

The present study was intended to test the idea that the analysis of temporal regularity can be based on an AC process. To this end, we performed psychophysical experiments using sound stimuli that did not provide spectral cues and had the advantage of producing precisely predictable temporal patterns of neural activity. These stimuli were high-pass filtered nonperiodic click sequences, mixed with low-pass noise. They did not elicit truly *musical* pitch sensations, in so far as their pitches were weak and could not be used to build identifiable musical intervals. Nevertheless, it is reasonable to consider that they are able to provide information on a mechanism of pitch perception. Pitch can probably be derived from both spectral and temporal features of sound waves. In order to isolate the temporal mechanism of pitch perception, one has to eliminate spectral cues. By doing so one eventually reduces pitch strength up to a point where musical judgments can no longer be made. The remaining perceptual correlate of temporal regularity has been named ''rattle pitch'' by Plomp (1976, Chap. 7).

I. EXPERIMENT 1. THE POOR DETECTABILITY OF ''SECOND-ORDER PERIODICITY''

A. Preliminary observations

Consider a periodic click sequence in which consecutive clicks are separated by a constant interclick interval (ICI) of, e.g., 10 ms. Let us remove the resolvable spectral components of this stimulus by high-pass filtering it at, e.g., 6000 Hz. In addition, let us mix it with low-pass noise to ensure that its *internal* (i.e., auditory) power spectrum will not contain resolved components arising from cochlear nonlinearities (Plomp, 1976, Chap. 2). Under such conditions, one can hear a clear ''rattle pitch,'' which must be extracted from purely temporal information at the auditory nerve level. The AC function of the filtered click sequence shows a series of sharp peaks for delays of 10, 20, 30,... ms. It is reasonable to assume that, in the auditory nerve, each filtered click produces a short burst of activity, so that the ICIs are represented by ISIs of the same duration (Kiang *et al.*, 1965; Ruggero, 1992).

Suppose now that one ''interfering click'' is inserted at a random position within each 10-ms first-order ICI of the periodic click sequence. The top panel of Fig. 2 shows a segment of a stimulus obtained in doing so. There are no longer *first-order* temporal regularities in the click sequence: The ICIs of consecutive clicks have a flat statistical distribution. However, temporal regularities appear in the *second-order* ICI statistics, and the sequence can be said to have a ''second-order periodicity'' (SOP). Its AC function is displayed in the left part of Fig. 3. In spite of the interfering clicks, prominent peaks are still present for delays of 10, 20, 30,... ms. Yet, in informal listening tests, we found that the sequence does not sound regular. Instead, it is perceived as

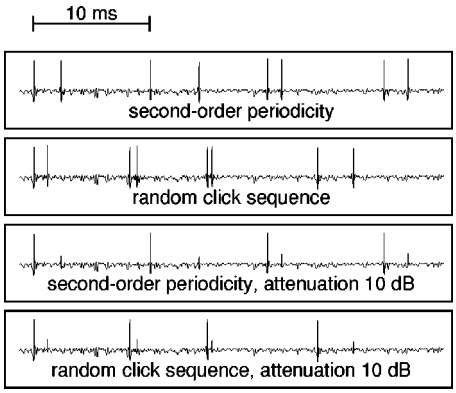

FIG. 2. High-pass filtered click sequences mixed with low-pass noise. The top panel shows a click train possessing a second-order periodicity (SOP) of 10 ms. It consists of an isochronous click train with one ''interfering'' click in each first-order ICI. It is not easy to realize visually that the first, third, fifth, and seventh clicks are equidistant. This click train looks basically similar to the random click train (without SOP) presented in the second panel. Here, each first-order ICI is randomly selected in the interval [0,10] ms. The SOP of the third train is much easier to see than the SOP of the first one. In this third train, the interfering clicks are three times smaller (10-dB attenuation) than the isochronous clicks. The bottom panel shows a comparable random click train with every even click attenuated by the same amount. While the SOP is easy to see with a 10-dB difference, it is difficult to hear.

similar to a sequence in which each first-order ICI is selected randomly, without any constraint, between 0 and 10 ms. We also noticed, however, that a perceptual discrimination between sequences with SOP and random sequences was possible on the basis of local (momentary) differences in click rate: In a random sequence, many short (or long) first-order ICIs sometimes occur in immediate succession; this cannot happen in a sequence with SOP. The corresponding discrimination cue disappears if, in the random sequences, the number of consecutive first-order ICIs falling above 5 ms, or below 5 ms, is prevented to exceed 2. Using this constraint, we observed that it was extremely hard to discriminate sequences with SOP from random sequences.

Experiment 1 was conducted to confirm this informal finding. In order to quantify the deleterious effect of the interfering clicks, we attenuated them by a variable amount, as illustrated in the third panel of Fig. 2. In the random sequence presented on the same trial as a given sequence with SOP, every even click was attenuated by the same amount (lowest panel of Fig. 2). For an attenuation of 20 dB, a sequence with SOP sounded perfectly regular. The goal of the experiment was to determine at which amplitude of the interfering clicks the detection of SOP would be disrupted.

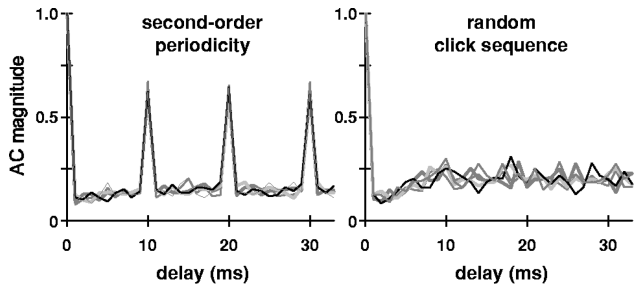

FIG. 3. Normalized AC functions of click trains used in experiment 1. Left part: AC functions of five click trains with a SOP of 10 ms. Right part: AC functions of five random click trains, excluding multiple repetitions of similar first-order ICIs (as explained in Sec. I A). The click trains analyzed here were composed of nonfiltered clicks with equal intensities. The AC functions were computed for delays of 0–33 ms, with a bin width of 1 ms.

B. Procedure

The click sequences were digitally generated at a sampling rate of 44 100 Hz. The unipolar clicks were high-pass filtered at 6000 Hz. The filter shape followed a logistic function with a 400-Hz transition region (from 10% to 90% of full amplitude). The low-pass noise mixed with the click sequences consisted of white noise filtered symmetrically, so that the entire stimulus had a flat spectral envelope (spectrum level: 35 dB) when the interfering clicks were unattenuated. The stimuli were presented diotically, via electrostatic earphones (Stax Lambda Pro), in a sound-proof booth.

On each trial, the subject was presented with two 1-s click sequences separated by a 333-ms pause. The low-pass filtered noise started 333 ms before the first sequence and ended 333 ms after the second one. The two sequences included a ''target'' sequence (with SOP) and a ''random'' sequence (excluding multiple repetitions of similar first-order ICIs, as explained in the previous section). The subject had to determine if the more regular sequence was the first or the second sequence. Feedback was provided following each trial. In a block of trials, the attenuation of the interfering clicks was initially set to 20 dB, and then varied according to the weighted up-down adaptive procedure (Kaernbach, 1991): Following a correct response, the attenuation decreased by 2 dB (before the first reversal) or 1 dB (after the first reversal); following each incorrect response, the attenuation increased by 3 dB. This continued until 60 trials were run. Three psychology students, without previous experience in psychoacoustic tasks, were tested each in two trial blocks.

C. Results

Since the results of the three subjects were very similar, they were pooled. (Author CK also produced similar results, which were not taken into account.) A psychometric function was fitted to the data using a maximum-likelihood procedure. Performance severely declined when the attenuation became smaller than about 10 dB. The 75% point of the psychometric function corresponded to an attenuation of 9.2 dB.

D. Discussion

This short experiment demonstrated that, for untrained subjects at least, the SOP of the target sequences was inaudible when the interfering clicks had the same intensity as the isochronous clicks, or when they were attenuated by as much as 5 dB. In the absence of any attenuation, the AC functions of the target sequences had prominent peaks at 10, 20, 30,... ms, as shown in the left part of Fig. 3. The prominence of the AC peaks was even larger when the interfering clicks were attenuated by 5 dB. Even then, the target sequences could not be discriminated from sequences with no

AC peak at all (right part of Fig. 3). This clearly casts doubts on the idea that the auditory system is able to compute AC functions.

The fact that the attenuation of the interfering clicks had to exceed as much as 5 dB before being effective is not so surprising if one considers data recently reported by Tsuzaki and Patterson (1998). These authors measured thresholds for the detection of amplitude jitter in high-pass filtered isochronous click trains. The obtained thresholds were remarkably high: For first-order ICIs of 10 ms (the shortest ICIs used by Tsuzaki *et al.*), they corresponded to interclick amplitude differences of no less than 7 dB.

It should be emphasized that the AC functions displayed in Fig. 3 are valid estimations of the AC functions of the activity produced by the click sequences in the auditory nerve. Consider, in this respect, a model of neural transduction assuming that the clicks are bandpass filtered in a number of frequency channels (with center frequencies exceeding 6 kHz), half-wave rectified, and finally low-pass filtered at about 1 kHz. In a given channel, the resulting signal will consist of smeared versions of the original clicks, spread over approximately 1 ms. Therefore, its AC function will be quite comparable to the AC function computed from the original click sequence with a bin width of 1 ms (the bin width we used). This will hold true as long as the clicks are all of the same amplitude and polarity. Meddis and Hewitt (1991) proposed that the neural AC functions should be averaged across channels. For high-pass filtered click sequences with a cutoff frequency as high as 6 kHz, the neural AC functions should be essentially identical across channels, so that averaging across the relevant channels will still produce results similar to those displayed in Fig. 3.

Our basic result is consistent with findings by Carlyon (1996) on the perception of mixtures of complex tones differing in fundamental frequency. In some of his experimental conditions, Carlyon mixed two spectrally unresolvable tones with identical spectral envelopes and amplitudes. He found that such a mixture is not heard as a sum of two tones differing in pitch but evokes instead a ''unitary noiselike or 'crackle' percept.'' This shows, like our own experiment, that the detection of a sound's periodicity can be dramatically disrupted by the simultaneous presentation of another sound which is not more intense. The disrupting sound was periodic in Carlyon's study, whereas it was not periodic in our experiment. In both cases, however, amplitude peaks of the disrupting sound occurred between consecutive amplitude peaks of the other (periodic) sound. Thus, both sets of data provide an indication that first-order time intervals are of paramount importance for the extraction of pitch in the temporal domain.

II. EXPERIMENTS 2 AND 3. THE PERCEPTUAL NONEQUIVALENCE OF FIRST-ORDER AND SECOND-ORDER TEMPORAL REGULARITIES

A. Purpose and general method

Experiment 1 demonstrated that second-order temporal regularities are difficult to hear in spectrally unresolvable click trains. It was the aim of experiments 2 and 3 to quantify the sensitivity of trained subjects to temporal regularities of different orders. The subject's task was again to discriminate ''target'' sequences with temporal regularities from irregular, ''random'' sequences. However, unlike the target sequences of experiment 1, those of experiments 2 and 3 had no ''periodicity'' of any kind. More precisely, there was only one peak in their AC functions. This peak originated from multiple occurrences of a fixed ICI, which was a first-order ICI for some targets (without second-order regularities), and a second-order ICI for other targets (without first-order regularities). In the targets with fixed first-order ICIs, the fixed ICI occurred more or less frequently, so that the AC peak was more or less prominent. The prominence of the AC peak was thus experimentally dissociated from the nature of the temporal regularities producing the peak.

In contrast to experiment 1, the component clicks of the sequences employed never differed from each other in intensity. They were always identical. Thus, discrimination performance was not assessed as a function of an intensity variable. In experiment 2 we manipulated instead of this the *length* of the sequences: For targets of various types, we measured how long a target sequence had to be, that is to say, how many fixed ICIs it had to contain, in order to be reliably discriminated from a random sequence of the same length.

B. Experiment 2: Procedure

In the target and random sequences presented on each trial of this experiment, the average click rate was the same and the first-order ICIs had an identical upper limit (of τ ms). Four types of targets were used. Their respective temporal characteristics are specified and illustrated in Fig. 4, as well as those of the comparison random sequences (constrained by a rule which was similar to that employed in experiment 1; see the caption of Fig. 4). Each target contained both fixed and random ICIs. The fixed ICIs were first-order ICIs for target types labeled **kxx**, **kxxx**, and **kxxxx**. In **abx** targets, by contrast, all the fixed ICIs were second-order ICIs; there was always one click at a random position between two clicks separated by the fixed ICI value. As shown in the bottom row of Fig. 4, the fixed ICIs of the various targets produced a single sharp peak in their otherwise noisy AC functions. (The singleness of this peak was due to the ''**x**'' ICIs.) The peak occurred at $\tau/2$ for the targets with first-order regularities, and at τ for the **abx** targets. Signal-to-noise ratios (S/N) were computed to quantify the prominence of each peak in the asymmetric noisy background surrounding it. In doing so, we selected the noise falling in a 6-ms region centered on the peak. Arranging the targets in order of decreasing S/N, one obtained: **kxx** (0.45), **abx** (0.34), **kxxx** (0.31), and **kxxxx** (0.24). There was no peak in the AC functions of the random sequences. Hence, under the assumption that the auditory system is able to perform operations akin to AC, one predicted that it would be easier to discriminate an **abx** target from a random sequence than to discriminate a **kxxx** or **kxxxx** target from a random sequence.

In the **kxx**, **kxxx**, and **kxxxx** targets, τ was always equal to 10 ms. In the **abx** targets, τ was set to 10 ms in some trial blocks, and to 5 ms in other trial blocks. This permitted a

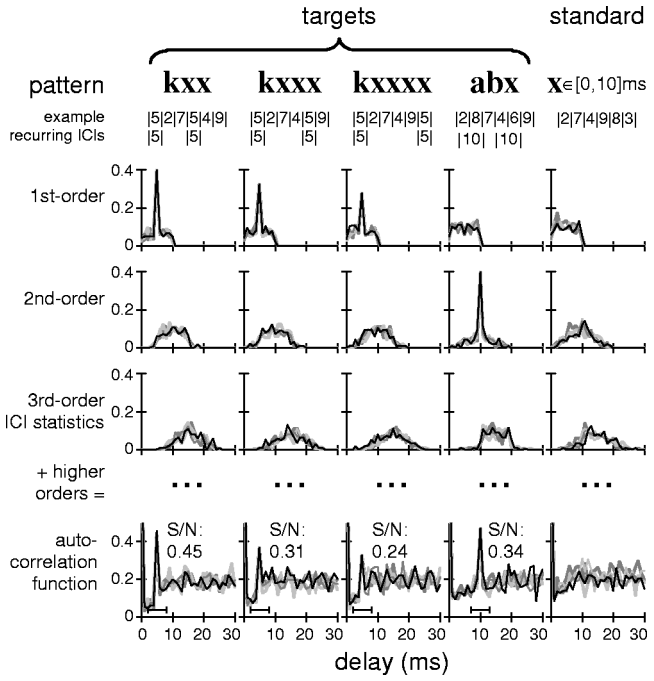

FIG. 4. Temporal characteristics of the sequences used in experiment 2. For each sequence type (patterns on the first row), we give on the second row a possible succession of first-order ICIs, in ms, τ being equal to 10 ms. The recurrence of a fixed ICI is emphasized on the third row. In a **kxx** sequence, a first-order ICI of $\tau/2$ (corresponding to **k**) is followed by two first-order ICIs (the **x**'s) which are randomly selected in the interval $[0,\tau]$; this pattern is then iterated. The **kxxx** and **kxxxx** sequences are constructed similarly, but with less frequent occurrences of the fixed ICI **k**. In an **abx** sequence, **a** is randomly selected in the interval $[0,\tau]$, **b** is such that $\mathbf{a}+\mathbf{b}=\tau$, and **x** is again taken randomly between 0 and τ. In a random (standard) sequence, all the first-order ICIs are taken randomly between 0 and τ, except that the number of consecutive first-order ICIs falling above $\tau/2$, or below $\tau/2$, cannot be larger than in the target sequence used on the same trial (e.g., larger than 3 for a **kxxx** target). Three rows of panels present normalized statistical distributions of the first-order, second-order, and third-order ICIs recorded in 1-s stimuli. The bin width is 1 ms. For the **kxx**, **kxxx**, and **kxxxx** sequences, the distribution of the first-order ICIs shows a peak and there is no peak in the higher-order distributions. In the **abx** case, by contrast, the peak occurs in the distribution of the second-order ICIs; the first-order ICIs are distributed exactly like the first-order ICIs of the random sequences. The sequences' AC functions, shown on the bottom row, are the sums of all their ICI statistics. The bar below each AC peak shows the region (−3 to +3 ms relative to the peak) that was integrated to compute S/N.

comparison between the detections of first-order and second-order temporal regularities for the same mean click rate (200 clicks per s) or for identical locations of the AC peak (a peak obtained for a 5-ms delay).

On each trial, the subject was presented with three successive click sequences, separated by 250-ms pauses. The clicks were high-pass filtered at 6000 Hz and mixed with low-pass noise as in experiment 1. The low-pass noise started 250 ms before the first sequence and ended 250 ms after the third one. The first sequence was a random sequence and served as a standard. The following two sequences included one target and one random sequence. The subject had to determine if the ''different'' sequence (the target) was the second or the third sequence. Feedback was provided immediately after the response. The stimuli were presented monaurally, via a Stax Lambda Pro earphone, at a 35-dB spectrum level.

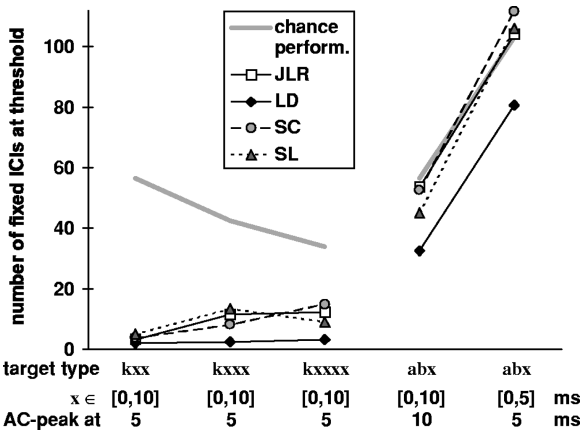

FIG. 5. Results of experiment 2. The ordinate shows the numbers of fixed ICIs needed by the four subjects to discriminate the various targets (abscissa) from random sequences. For the **abx** targets, the threshold estimates were strongly biased. A thick gray line indicates the results expected from a subject performing the task at chance level.

In each block of trials, the type of the targets and the value of τ were fixed. The duration of the sequences was initially set to 1 s and then varied following the same adaptive procedure as that used in experiment 1 (1 dB corresponding here to a duration change of approximately 26%). However, 1 s was the maximum possible duration. Due to the partial randomness of the ICIs, the number of fixed ICIs contained by a sequence of a certain duration could vary. Following each trial, we recorded the exact number of fixed ICIs which occurred on that trial. A block was finished after 100 trials. From the obtained data, we estimated the number of fixed ICIs for which the probability of a correct response was 0.75. This ''threshold'' was taken as the median of the numbers of fixed ICIs which had been presented on all the trials following the fourth reversal.

During a test session, one block of trials was run in each of the five experimental conditions. Each subject was tested for at least five training sessions before the formal experiment, run in five additional sessions. Four subjects were used: three students and author LD. Each subject had previously participated in other psychoacoustical experiments.

C. Experiment 2: Results

Figure 5 shows the mean threshold estimates obtained in the five final sessions. The thick gray line indicates the threshold estimates expected if the targets were actually not discriminated at all from random sequences. For a complete absence of discrimination, the adaptive procedure resulted in a random walk and simulations showed that the duration threshold would be estimated at 0.85 s (15% less than the maximum duration, 1 s). The number of fixed ICIs corresponding to this duration depended of course on the target type and on τ.

For the **abx** targets, the performance of three subjects did not differ significantly from the chance level indicated by the gray line; the measured thresholds were thus strongly biased by ceiling effects. By, contrast, unbiased thresholds could always be measured for the **kxx**, **kxxx**, and **kxxxx** targets. For each subject, the discrimination task was clearly

TABLE I. Percentages of correct responses obtained in the three conditions of experiment 3.

Target type		**kxxxx**	**abx**	**abx**
τ (ms)		10	10	5
Mean number of fixed ICIs		12	20	40
Subject	JLR	77.6	49.2	46.6
	LD	89.4	59.6	59.6
	SC	74.8	61.0	50.4
	SL	79.0	65.0	49.4
Mean		80.2	59.7	51.5

much more difficult for the **abx** targets than for all the targets with first-order regularities, even though S/N could be markedly smaller in the latter case.

D. Experiment 3

Experiment 3, a variant of experiment 2, was performed on the same subjects. In this new experiment, the duration of the three sequences presented on each trial was no longer varied adaptively but fixed at 300 ms. Thus, we did not measure discrimination thresholds but simply percentages of correct responses $[P(C)]$. This was done for three categories of targets: (1) **kxxxx** targets with $\tau=10$ ms; (2) **abx** targets with $\tau=10$ ms; and (3) **abx** targets with $\tau=5$ ms. In each of these three conditions, each subject was tested in five blocks of 100 trials. There was no need of preliminary training blocks as the subjects had been tested soon before in experiment 2.

Table I displays the $P(C)$ values obtained in the three experimental conditions. The third row of this table indicates the mean number of fixed ICIs contained by the various targets. Given that each subject performed 500 trials in each condition, a $P(C)$ larger than 55.3% exceeded the chance level with $p<0.01$. For the **abx** targets, $P(C)$ sometimes exceeded the chance level, but never markedly; two subjects (SC and SL) were more successful when τ was 10 ms than when τ was 5 ms, but this was not the case for the other two subjects (JLR and LD). For the **kxxxx** targets, $P(C)$ was always much higher, although the number of fixed ICIs contained by these targets was systematically smaller.

III. EXPERIMENT 4. SOME ADDITIONAL DATA ON THE DETECTABILITY OF FIRST-ORDER REGULARITIES

In experiment 4, we readopted the adaptive procedure used in experiment 2 to examine, in three trained listeners, the effect of τ on the discrimination of **kx** targets from random sequences. In a **kx** sequence, a fixed first-order ICI of $\tau/2$ ms alternates with a first-order ICI which is randomly chosen between 0 and τ ms. We employed such targets because these were the simplest sequences containing only first-order temporal regularities. The number of fixed ICIs necessary for their discrimination from random sequences (matched in average click rate, and with the same maximum first-order ICI) was measured using four values of τ: 5, 10, 20, and 40 ms. In ten blocks of 100 trials, ten threshold measurements were made for each subject and value of τ.

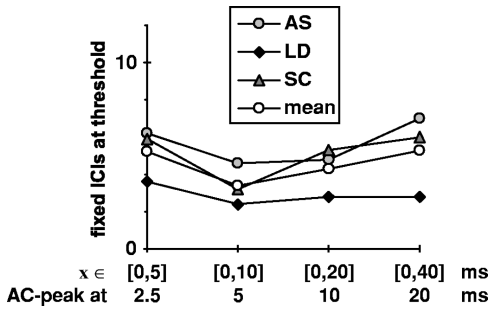

FIG. 6. Results of experiment 4. Numbers of fixed ICIs necessary to discriminate random sequences from **kx** targets with $\mathbf{k}=\tau/2$ and $\mathbf{x}\in[0,\tau]$, as a function of τ, for three subjects.

The average thresholds measured in the last five blocks of trials are displayed in Fig. 6. This figure shows that a reliable discrimination of the targets never required more than eight fixed ICIs. The best thresholds, corresponding to less than six fixed ICIs, were obtained for $\tau=10$ and 20 ms, that is, for the detection of pitches corresponding to 100 and 200 Hz. Remarkably, these are the typical pitches of male (100 Hz) and female (200 Hz) speech.

IV. GENERAL DISCUSSION

The present study was intended to test the idea that the auditory system acts as an autocorrelator in order to extract temporal information from a sound. A rudimentary version of that idea would be that the auditory system calculates the AC function of the sound waveform itself. To reject this model, it is sufficient to note that the AC function of a signal is independent of its phase spectrum but that the pitch of a complex tone consisting of unresolved harmonics does depend on the tone's phase spectrum (e.g., Moore, 1997; Houtsma and Smurzynski, 1990). More interesting is the idea that the AC is actually performed on sequences of neural spikes, after cochlear filtering. In recent years, this idea was supported by, e.g., Meddis and Hewitt (1991). They proposed a quantitative model of pitch perception according to which the auditory nerve response to a sound is processed by a bank of autocorrelators operating in different frequency-selective channels. The AC functions so obtained are supposed to be averaged across channels to generate a ''summary AC function,'' and the model assumes that the pitch of the sound corresponds to the highest point of this summary AC function. Other recent auditory models, especially the ''neural cancellation model'' of de Cheveigné (1993, 1998) and the ''auditory image model'' of Patterson (Patterson *et al.*, 1992, 1995), rest on very closely related assumptions.

Psychophysicists willing to test this family of models are clearly required to use stimuli that will have largely *predictable* temporal representations at the auditory nerve level. Such was the case of the high-pass filtered click sequences that we used. For a given auditory nerve fiber excited by these click sequences, one could reasonably consider that most of the ISIs would correspond to ICIs present in the stimuli (Kiang *et al.*, 1965; Ruggero, 1992). Moreover, it was reasonable to consider that the compound neural activity

of the fibers excited by the stimuli would be very similar to the stimuli themselves, each click being represented by many synchronous spikes (Cariani and Delgutte, 1996b). If this is admitted, then our results are not consistent with the models mentioned above. Especially, these models seem to be contradicted by our finding that it is much easier to detect temporal regularities in **kxxxx** sequences than in **abx** sequences (experiments 2 and 3). Our results apparently imply that very little or no information is conveyed by time intervals between nonconsecutive neural spikes.

From recent studies on the perception of ''iterated rippled noise'' (IRN), Yost (1996), Yost *et al.* (1996), and Patterson *et al.* (1996) concluded that the pitch of IRN is hard to explain in spectral terms but can be simply explained under the hypothesis that pitch extraction rests on the analysis of temporal regularities in the stimuli. More specifically, they suggested that the pitch salience of an IRN stimulus is determined only by the height of the first peak of its AC function. In support of this view, Yost *et al.* (1996) found that when two IRN stimuli have identical first AC peaks (for a delay d), they cannot be discriminated from each other, even when they differ with respect to the height of a second AC peak (at $2 \cdot d$). The representation of an IRN stimulus in a human auditory nerve is obviously more complex and less predictable than that of the click sequences used here. The first AC peak in the stimulus may be partly represented by first-order ISIs, but is probably also represented by higher-order ISIs. However, it is clear that a second AC peak will be represented by ISIs of an even higher order, on average. Thus, the finding that listeners are insensitive to the second AC peak is consistent with the idea that only first-order ISIs perceptually matter for pitch perception.[1]

We do not wish to conclude from our results that first-order ISIs at the auditory nerve level are a perfect predictor of pitch in any possible case. This conclusion would be at variance with some physiological data reported by Cariani and Delgutte (1996a). These authors conducted a large set of studies on the temporal correlates of pitch in the cat's auditory nerve. Their work shows that numerous pitch phenomena can be correctly predicted from the ISIs occurring in the auditory nerve. In one of their studies, the stimuli were periodic, vowellike complex tones. Such stimuli elicit a pitch corresponding to the period whatever the intensity. It was found that the highest point of the neural ''summary AC function'' (as defined by Meddis and Hewitt, 1991) did correspond to the period, and thus to the pitch heard, whatever the intensity. By contrast, when only the first-order ISIs were taken into account, the predicted pitch appeared to be somewhat dependent on intensity: It corresponded unambiguously to the period at 60 dB SPL, but not at 40 or 80 dB SPL.

It is plausible that the ''final'' temporal structure contributing to pitch sensations (either directly or after a conversion into a place code) does not occur in the auditory nerve but at a higher location in the auditory system. We believe that at this stage the ISIs that matter are first-order ISIs. However, the consecutive spikes bounding these ISIs may originate from nonconsecutive spikes at the auditory nerve level.[2]

It is important to keep in mind that our stimuli were spectrally unresolvable and that those having a detectable temporal regularity induced a percept of ''rattle'' pitch rather than ''musical'' pitch. We must acknowledge that the implications of our results may not be generalizable to spectrally resolvable sounds, which induce more salient and precise pitch sensations than those evoked by spectrally unresolvable sounds (Hoekstra, 1979; Houtsma and Smurzynski, 1990).[3] Carlyon and Shackleton (1994) provided experimental support for the idea that pitch extraction rests on different mechanisms for these two types of sounds. The task of their subjects was to detect differences in the periods of two simultaneous groups of harmonics, falling in separate frequency regions. Detection performance was good when listeners had to compare two resolvable groups, or two unresolvable groups, but poor when the comparison was between one resolvable group and one unresolvable group. It might be that the AC theory is in error for spectrally unresolvable sounds but is correct for resolvable sounds.[4]

Let us finally mention here some informal observations that we made using (high-pass filtered) click sequences which were not employed in the experiments described above. We constructed a sequence in which the first-order ICIs took two alternating values: 3, 5, 3, 5, 3, 5,... ms. This periodic sequence (''Period [3,5]'') sounds quite regular. It elicits a slightly ambiguous pitch, commonly identified as that of Period [5], but sometimes as that of Period [3] (very rarely as that of Period [8]). Period [3,5] sounds quite different from a sequence (''Random [3,5]'') in which the same two ICIs occur randomly, even when the randomness is limited by preventing an ICI to be repeated immediately more than once. This shows that the first-order ICI statistics are not sufficient to account for the perceptual effects of filtered click sequences. Period [3,5] and Random [3,5] are similar with respect to pitch, but Random [3,5] elicits a percept of temporal fluctuations that is not elicited by Period [3,5]. For more and more complex periodic sequences based on the same first-order ICIs, for instance, Period [3,3,5,5] or Period [3,3,5,3,5,5], there is an increasing perception of temporal fluctuations. However, these sequences still sound more regular than Random [3,5]. It does not seem reasonable to assume that the discrimination between Period [3,3,5,3,5,5] and Random [3,5] rests on the measurement of sixth-order ICIs (always equal to 24 ms in the periodic sequence, but variable in the random sequence). A neural model based on first-order ISI detection and fast synaptic plasticity (Kaernbach and Mohlberg, 1994) can account for such perceptual discriminations.

ACKNOWLEDGMENTS

We thank Peter A. Cariani, Robert P. Carlyon, Alain de Cheveigné, Bertrand Delgutte, Roy D. Patterson, and Lutz Wiegrebe for stimulating discussions. Special thanks are due to Christian Lorenzi for his useful computer simulations of the neural processing of our stimuli. We are also grateful to Ray Meddis, William A. Yost, and an anonymous reviewer for their helpful comments on a previous version of the manuscript. Part of the work was done while author CK was working at the Institut für Neuroinformatik, Ruhr-Universität Bochum, and supported by DFG Grant No. MA 697/4-2.

[1]Yost *et al.* (1996) submitted various IRN waveforms to a simple threshold device (including an absolute refractory period of 1 ms) and measured the first-order time intervals between successive threshold crossings. They found that the statistical distribution of these first-order intervals was a good predictor of the perceived pitch and pitch strength. This is consistent with our results. However, the waveforms used by Yost *et al.* were not high-pass filtered and, as acknowledged by these authors, their very simple processing of the waveforms did not provide a realistic picture of the neural spike trains induced by the corresponding sounds.

[2]Consider, for example, a small set of adjacent auditory nerve fibers responding to a vowellike complex tone (with a period of $p=1/f_0$ ms). If their characteristic frequency f_c is higher than about $4\cdot f_0$, they will not respond to a single harmonic. They will respond to a complex waveform resulting from the interaction of several, more or less attenuated, harmonics. The envelope of this complex waveform will have an amplitude peak every p ms. In a given fiber, many first-order ISIs may not be equal to p ms. They may often be close to $1/f_c$ and reflect time intervals between peaks of the waveform's fine structure. Across the set of fibers, however, peaks of the envelope will tend to elicit *synchronous* spikes, whereas peaks of the fine structure will fail to do so. One can imagine that at a higher stage of the auditory system, the synchronous spikes will produce excitation, thanks to some kind of summation effect, whereas many of the intervening nonsynchronous spikes will not survive. This could transform high-order ISIs at the auditory nerve level into first-order ISIs at the higher stage.

[3]The pitch of our target stimuli was weak because these stimuli were spectrally unresolvable but also because of their partial randomness.

[4]Moore (1997, Chap. 5) hypothesized that, in an auditory nerve fiber with characteristic frequency f_c, the temporal information on musical pitch is limited to ISIs smaller than about $15/f_c$. This would explain why a group of very high harmonics fails to evoke a sense of musical pitch corresponding to the fundamental.

Assmann, P. F., and Summerfield, Q. (**1990**). ''Modeling the perception of concurrent vowels: Vowels with different fundamental frequencies,'' J. Acoust. Soc. Am. **88**, 680–697.

Burns, E. M., and Viemeister, N. F. (**1976**). ''Nonspectral pitch,'' J. Acoust. Soc. Am. **60**, 863–869.

Burns, E. M., and Viemeister, N. F. (**1981**). ''Played-again SAM: Further observations on the pitch of amplitude-modulated noise,'' J. Acoust. Soc. Am. **70**, 1655–1660.

Cariani, P. A., and Delgutte, B. (**1996a**). ''Neural correlates of the pitch of complex tones. I. Pitch and pitch salience,'' J. Neurophysiol. **76**, 1698–1716.

Cariani, P. A., and Delgutte, B. (**1996b**). ''Neural correlates of the pitch of complex tones. II. Pitch shift, pitch ambiguity, phase-invariance, pitch circularity, rate-pitch, and the dominance region of pitch,'' J. Neurophysiol. **76**, 1717–1734.

Carlyon, R. P. (**1996**). ''Encoding the fundamental frequency of a complex tone in the presence of a spectrally overlapping masker,'' J. Acoust. Soc. Am. **99**, 517–524.

Carlyon, R. P., and Shackleton, T. M. (**1994**). ''Comparing the fundamental frequencies of resolved and unresolved harmonics: Evidence for two pitch mechanisms?'' J. Acoust. Soc. Am. **95**, 3541–3554.

de Cheveigné, A. (**1993**). ''Separation of concurrent harmonics sounds: Fundamental frequency estimation and a time-domain cancellation model of auditory processing,'' J. Acoust. Soc. Am. **93**, 3271–3290.

de Cheveigné, A. (**1998**). ''Cancellation model of pitch perception,'' J. Acoust. Soc. Am. **103**, 1261–1271.

de Ribaupierre, F., Goldstein, Jr., M. H., and Yeni-Komshian, G. (**1972**). ''Cortical coding of repetitive acoustic pulses,'' Brain Res. **48**, 205–225.

Evans, E. F. (**1978**). ''Place and time coding of frequency in the peripheral auditory system: some physiological pros and cons,'' Audiology **17**, 369–420.

Goldstein, J. L. (**1973**). ''An optimum processor theory for the central formation of the pitch of complex tones,'' J. Acoust. Soc. Am. **54**, 1496–1516.

Goldstein, J. L., and Srulovicz, P. (**1977**). ''Auditory-nerve spike intervals as an adequate basis for aural frequency measurement,'' in *Psychophysics and Physiology of Hearing*, edited by E. F. Evans and J. P. Wilson (Academic, London).

Hartmann, W. M. (**1993**). ''On the origin of the enlarged melodic octave,'' J. Acoust. Soc. Am. **93**, 3400–3409.

Hartmann, W. M. (**1997**). *Signals, Sound, and Sensation* (AIP Press, Woodbury, NY).

Hoekstra, A. (**1979**). ''Frequency discrimination and frequency analysis in hearing,'' Doctoral dissertation, University of Groningen, The Netherlands.

Horst, J. W., Javel, E., and Farley, G. R. (**1986**). ''Coding of spectral fine structure in the auditory nerve. I. Fourier analysis of period and interspike interval histograms,'' J. Acoust. Soc. Am. **79**, 398–416.

Houtsma, A. J. M., and Smurzynski, J. (**1990**). ''Pitch identification and discrimination for complex tones with many harmonics,'' J. Acoust. Soc. Am. **87**, 304–310.

Kaernbach, C. (**1991**). ''Simple adaptive testing with the weighted up-down method,'' Percept. Psychophys. **49**, 227–229.

Kaernbach, C., and Mohlberg, H. (**1994**). ''A neural sequence-learning model to explain auditory periodicity analysis,'' in *Proceedings of the 1994 International Congress on Artificial Neural Networks*, Sorrento, Italy, edited by M. Marinaro and P. G. Morasso (Springer-Verlag, New York).

Kiang, N. Y. S., Watanabe, T., Thomas, E. C., and Clark, L. F. (**1965**). ''Discharge Patterns of Single Fibers in the Cat's Auditory Nerve,'' Res. Monogr. 35 (MIT, Cambridge, MA).

Langner, G. (**1992**). ''Periodicity coding in the auditory system,'' Hearing Res. **60**, 115–142.

Langner, G., Sams, M., Heil, P., and Schulze, H. (**1997**). ''Frequency and periodicity are represented in orthogonal maps in the human auditory cortex: evidence from magnetoencephalography,'' J. Comp. Physiol. A **181**, 665–676.

Lazzaro, J., and Mead, C. (**1989**). ''Silicon modeling of pitch perception,'' Proc. Natl. Acad. Sci. USA **86**, 9597–9601.

Licklider, J. C. R. (**1951**). ''A duplex theory of pitch perception,'' Experientia **7**, 128–134.

Lyon, R. F. (**1984**). ''Computational models of neural auditory processing,'' in *Proceedings of the IEEE International Conference on Acoustics, Speech, and Signal Processing 36.1* (IEEE, New York), pp. 1–4.

Meddis, R., and Hewitt, M. J. (**1991**). ''Virtual pitch and phase sensitivity of a computer model of the auditory periphery. I: Pitch identification,'' J. Acoust. Soc. Am. **89**, 2866–2882.

Moore, B. C. J. (**1977**). ''Effects of relative phase of the components on the pitch of three-component complex tones,'' in *Psychophysics and Physiology of Hearing*, edited by E. F. Evans and J. P. Wilson (Academic, London).

Moore, B. C. J. (**1997**). *An Introduction to the Psychology of Hearing* (Academic, London), 4th ed.

Moore, B. C. J., and Rosen, S. M. (**1979**). ''Tune recognition with reduced pitch and interval information,'' Q. J. Exp. Physiol. **31**, 229–240.

Moore, B. C. J., Glasberg, B. R., and Peters, R. W. (**1985**). ''Relative dominance of individual partials in determining the pitch of complex tones,'' J. Acoust. Soc. Am. **77**, 1853–1860.

Ohgushi, K. (**1978**). ''On the role of spatial and temporal cues in the perception of the pitch of complex tones,'' J. Acoust. Soc. Am. **64**, 764–771.

Pantev, C., Hoke, M., Lütkenhöner, B., and Lehnertz, K. (**1989**). ''Tonotopic organization of the auditory cortex: Pitch versus frequency representation,'' Science **246**, 486–488.

Patterson, R. D., Allerhand, M. H., and Giguère, C. (**1995**). ''Time-domain modeling of auditory processing: A modular architecture and a software platform,'' J. Acoust. Soc. Am. **98**, 1890–1894.

Patterson, R. D., Handel, S., Yost, W. A., and Datta, A. J. (**1996**). ''The relative strength of the tone and noise components in iterated rippled noise,'' J. Acoust. Soc. Am. **100**, 3286–3294.

Patterson, R. D., Robinson, K., Holdsworth, J. W., McKeown, D., Zhang, C., and Allerhand, M. (**1992**). ''Complex sounds and auditory images,'' in *Auditory Physiology and Perception*, edited by Y. Cazals, L. Demany, and K. Horner (Pergamon, Oxford).

Plomp, R. (**1967**). ''Pitch of complex tones,'' J. Acoust. Soc. Am. **41**, 1526–1533.

Plomp, R. (**1976**). *Aspects of Tone Sensation* (Academic, London).

Ritsma, R. J. (**1967**). ''Frequencies dominant in the perception of the pitch of complex tones,'' J. Acoust. Soc. Am. **42**, 191–198.

Ruggero, M. A. (**1992**). ''Physiology and coding of sound in the auditory nerve,'' in *The Mammalian Auditory Pathway: Neurophysiology*, edited by A. N. Popper and R. R. Fay (Springer-Verlag, New York).

Sachs, M. B., and Young, E. D. (**1980**). ''Effects of nonlinearities on speech encoding in the auditory nerve,'' J. Acoust. Soc. Am. **68**, 858–875.

Slaney, M., and Lyon, R. F. (**1990**). ''A perceptual pitch detector,'' in

Proceedings of the IEEE International Conference on Acoustics, Speech, and Signal Processing, Albuquerque, New Mexico (IEEE, New York), pp. 357–360.

Srulovicz, P., and Goldstein, J. L. (**1983**). ''A central spectrum model: A synthesis of auditory-nerve timing and place cues in monaural communication of frequency spectrum,'' J. Acoust. Soc. Am. **73**, 1266–1276.

Steinschneider, M., Arezzo, J., and Vaughan, Jr., H. G. (**1980**). ''Phase-locked cortical responses to a human speech sound and low-frequency tones in the monkey,'' Brain Res. **198**, 75–84.

Terhardt, E. (**1972**). ''Zur Tonhöhenwahrnehmung von Klängen. II. Ein Funktionsschema,'' Acustica **26**, 187–199.

Tsuzaki, M., and Patterson, R. (**1998**). ''Jitter detection: a brief review and some new experiments,'' in *Psychophysical and Physiological Advances in Hearing*, edited by A. R. Palmer, A. Rees, A. Q. Summerfield, and R. Meddis (Whurr, London), pp. 546–552.

van Noorden, L. (**1982**). ''Two channel pitch perception,'' in *Music, Mind and Brain*, edited by M. Clynes (Plenum, New York).

Yost, W. A. (**1996**). ''Pitch of iterated rippled noise,'' J. Acoust. Soc. Am. **100**, 511–518.

Yost, W. A., Patterson, R. D., and Sheft, S. (**1996**). ''A time domain description for the pitch strength of iterated rippled noise,'' J. Acoust. Soc. Am. **99**, 1066–1078.

Temporal dynamics of pitch strength in regular interval noises

L. Wiegrebe[a] and R. D. Patterson[b]
Centre for the Neural Basis of Hearing, Physiology Department, Cambridge University, Downing Street, Cambridge CB2 3EG, United Kingdom

L. Demany[c]
Laboratoire de Neurophysiologie, UMR CNRS 5543, BP 63, Université Bordeaux 2, 146 rue Leo Saignat, F-33076 Bordeaux Cedex, France

R. P. Carlyon[d]
MRC Applied Psychology Unit, 15 Chaucer Road, Cambridge CB2 2EF, United Kingdom

(Received 14 January 1998; accepted for publication 10 July 1998)

The pitch strength of rippled noise and iterated rippled noise has recently been fitted by an exponential function of the height of the first peak in the normalized autocorrelation function [Yost, J. Acoust. Soc. Am. **100**, 3329–3335 (1996)]. The current study compares the pitch strengths and autocorrelation functions of rippled noise (RN) and another regular-interval noise, ''AABB.'' RN is generated by delaying a copy of a noise sample and adding it to the undelayed version. AABB with the same pitch is generated by taking a sample of noise (A) with the same duration as the RN delay and repeating it to produce AA, and then concatenating many of these once-repeated sequences to produce AABBCCDD$\cdots$. The height of the first peak ($h1$) in the normalized autocorrelation function of AABB is 0.5, identical to that of RN. The current experiments show the following: (1) AABB and RN can be discriminated when the pitch is less than about 250 Hz. (2) For these low pitches, the pitch strength of AABB is greater than that for RN whereas it is about the same for pitches above 250 Hz. (3) When RN is replaced by iterated rippled noise (IRN) adjusted to match the pitch strength of AABB, the two are no longer discriminable. The pitch-strength difference between AABB and RN below 250 Hz is explained in terms of a three-stage, running-autocorrelation model. It is suggested that temporal integration of pitch information is achieved in two stages separated by a nonlinearity. The first integration stage is implemented as running autocorrelation with a time constant of 1.5 ms. The second model stage is a nonlinear transformation. In the third model stage, the output of the nonlinear transformation is long-term averaged (second integration stage) to provide a measure of pitch strength. The model provides an excellent fit to the pitch-strength matching data over a wide range of pitches. [S0001-4966(98)05110-8]

PACS numbers: 43.66.Ba, 43.66.Hg, 43.66.Jh, 43.66.Mk [JWH]

INTRODUCTION

Random noise can be manipulated to elicit tonal sensations [for a review see Bilsen (1977)]. Yost (1998) has suggested the phrase ''regular interval noise'' (RIN) to characterize sounds that are derived from random noise but which have some form of temporal regularity in the waveform, and which thus produce a pitch percept as well as a ''hiss'' percept. The most common example of RIN is rippled noise (RN) which is produced by delaying a sample of Gaussian noise and adding it back to the undelayed version. The normalized autocorrelation function of RN has a single peak at the correlation lag corresponding to the delay d. The peak is referred to as $h1$ and its height is 0.5. Another form of RIN can be produced by concatenating many independent noise segments of the same duration d with the constraint that every noise segment is repeated once before the next independent segment is concatenated. If we denote independent noise segments with the letters A, B, C, etc., the general form for the sound will be AABBCC$\cdots$. For convenience, we will call this stimulus AABB. The normalized autocorrelation functions for AABB and RN with the same d are identical; an example for d equals 16 ms is shown in Fig. 1. Informal listening, however, indicated that, for a range of pitches, AABB produced a stronger pitch than RN. The current study was designed to investigate differences in the perception of RN and AABB systematically, and to provide some insight into how these perceptual differences might be explained.

I. EXPERIMENT I: RN-AABB DISCRIMINATION AS A FUNCTION OF PITCH ($1/d$)

We began by testing listeners' ability to discriminate an arbitrary sample of AABB with segment duration d from an arbitrary sample of RN with delay d.

A. Method

1. Stimuli

RN and AABB stimuli were produced exactly as described in the Introduction. The pitch which corresponds to

[a]Electronic mail: lutz.wiegrebe@mrc-cbu.cam.ac.uk
[b]Electronic mail: roy.patterson@mrc-cbu.cam.ac.uk
[c]Electronic mail: Laurent.Demany@psyac.u-bordeaux2.fr
[d]Electronic mail: bob.carlyon@mrc-cbu.cam.ac.uk

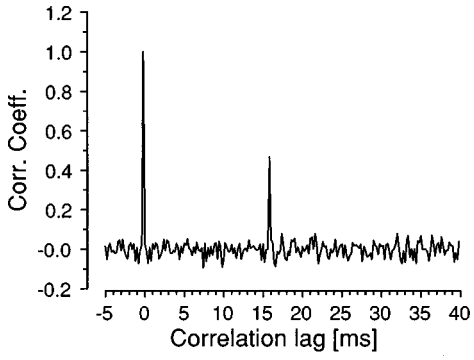

FIG. 1. Normalized long-term autocorrelation function for RN or AABB with $d = 16$ ms. A peak appears in the normalized autocorrelation function at a correlation lag of 16 ms ($h1$). The height of this peak is 0.5 for both AABB and RN.

$1/d$ ranged from 31.25 to 500 Hz in half-octave steps. Within each run, d was the same for RN and AABB, that is, their pitch was the same. The spectrum level was 20 dB sound-pressure level; the passband was 50–8000 Hz filtered with a TDT PF1 programmable filter (60 dB/oct). The stimulus duration was 409.6 ms including 20-ms cosine-square ramps. Stimuli were generated and played back digitally using the Tucker Davis System II and software delay lines. The sampling rate was 20 kHz. All sounds were presented binaurally via Sennheiser HD540 Reference Headphones. Listeners were tested individually in double-walled sound attenuating booths.

2. Procedure

Psychometric functions for the discrimination of AABB from RN were obtained using a two-alternative, three-interval, forced-choice task. The first interval was always an RN. Either the second or the third interval contained an AABB stimulus to be discriminated from RN whereas the remaining interval contained another RN. Each point on the psychometric function represents the mean of 100 trials obtained in four runs. Within a run, the value of d for each trial was chosen randomly from the full range. The listeners were instructed to chose the interval that differed from the other two. Listeners were provided with visual feedback.

3. Listeners

Three listeners aged between 23 and 32 took part in all experiments; L1 was the first author. All listeners had absolute thresholds at all audiometric frequencies within 10 dB of the 1969 ANSI standard.

B. Results

The psychometric functions for the AABB-RN discrimination are plotted in Fig. 2. The data for the three listeners are presented individually in panels L1–L3; the average psychometric functions are shown in the lower right-hand panel. For $1/d$ equals 500 Hz, an AABB stimulus is difficult to discriminate from an RN stimulus. With increasing d, however, discrimination performance becomes better rapidly. For low pitches, AABB is easily discriminable from RN for all listeners. Despite the fact that $h1$ is the same for RN and

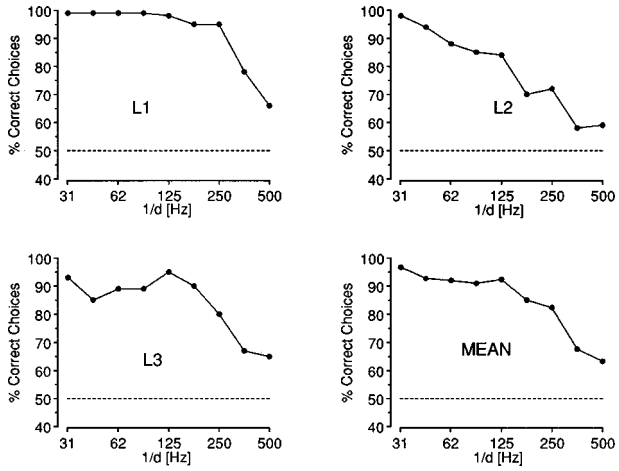

FIG. 2. Psychometric functions for the discrimination of AABB versus RN. The independent parameter is the inverse of the delay ($1/d$) of AABB and RN, respectively. Individual data are shown in the panels denoted L1–L3. The mean data, normalized for overall performance differences, are plotted in the lower right panel. For low pitches, discrimination was good. When the pitch of the stimuli was increased discrimination performance dropped steadily.

AABB, listeners reported hearing a stronger pitch in the AABB stimulus when it was discriminable from RN.

II. EXPERIMENT II: PITCH-STRENGTH MATCHING

Since experiment I employed a discrimination paradigm, it is not clear what the listeners used as the discrimination cue. To test the listeners' reports that they were using pitch strength, we performed a pitch-strength matching experiment. The pitch strength of RN can be increased by iterating the delay-and-add process and we used this iterated rippled noise (IRN) as a matching stimulus. Following Yost (1996a, b), we use the functional abbreviation IRN(d,g,n) to characterize an IRN stimulus in terms of the delay and gain in the delay-and-add loop (d,g) and the number of iterations (n). IRN is always produced in the ''same'' configuration (cf. Yost, 1996a, b): Gaussian noise is copied, delayed, and added back to itself. The output of the delay-and-add process serves as the input for the next delay-and-add process. By reducing the gain in the delay-and-add loop, the IRN-pitch strength can be continuously varied to match the pitch strength of AABB.

A. Method

1. Stimuli

Stimulus duration and presentation level were the same as in the previous experiment. AABB was generated as described above. IRN was generated with the same d and either 4 or 16 iterations. Pitch-strength matches were obtained for pitches between 31.25 and 500 Hz in half-octave steps.

2. Procedure

A two-alternative, forced-choice procedure was used to determine the pitch-strength matches. One randomly chosen interval contained a sample of AABB; the other interval contained an IRN. At the beginning of each run, the IRN gain was set to one so that the IRN pitch strength was initially

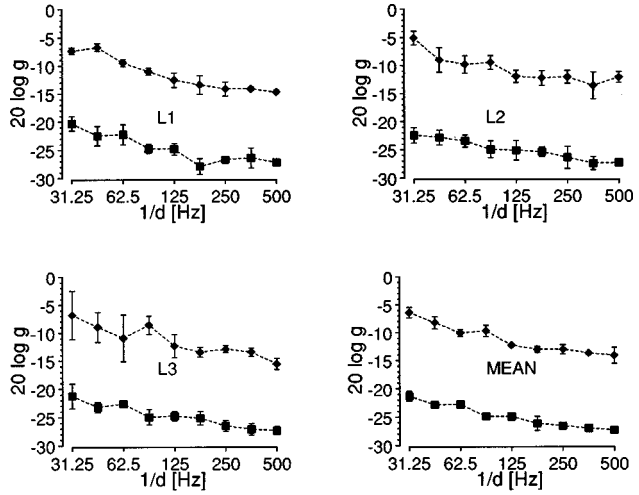

FIG. 3. Pitch-strength matches and standard deviations of an AABB test stimulus with IRN matching stimuli. The upper curves in each panel represent 20 times the logarithm of the matching IRN gain for an IRN with four iterations. The lower curves in each panel show the pitch-strength matches obtained with an IRN matching stimulus with 16 iterations. For the individual data (panels L1–L3) as well as for the mean data (lower right panel) a downward slope for the pitch-strength matches is observed. AABB test stimuli produced with longer d were matched with IRN with a greater pitch strength (a higher IRN gain) than AABB with shorter d.

greater than that of AABB. Listeners were instructed to choose the stimulus with the greater pitch strength. Feedback was not provided. When they chose the IRN stimulus, the IRN gain was reduced for the next trial, when they chose the AABB stimulus, the IRN gain was increased for the next trial. When listeners switched from choosing the IRN to the AABB or vice versa, a reversal was registered. The step size for the IRN gain initially was 3 dB which was reduced to 2 dB after the third and to 1 dB after the fifth reversal. The average gain from reversals 6 to 11 was taken as the matching gain for that run. For each condition, four runs were obtained and their matching points were averaged. The listeners were the same as in the previous experiment. They were trained until stable performance was reached which typically occurred after only a few runs for each value of d.

B. Results and discussion

The IRN gain required to match the IRN pitch strength to that of AABB is shown as a function of pitch $(1/d)$ in Fig. 3. The upper curve and the filled diamonds in each panel present the pitch-strength matches obtained with IRN$(d,g,4)$ as the matching stimulus; the lower curve and the filled squares present the matches with an IRN$(d,g,16)$. Individual data and standard deviations are shown in panels L1–L3; mean data and standard deviations across listeners are plotted in the lower right panel of Fig. 3. With 16 iterations, the IRN gain necessary to match the pitch strength of AABB increases by 7.5 dB, from -27.5 dB for $1/d=500$ Hz to -20 dB for $1/d=31.25$ Hz (lower curves). With four iterations (upper curves) the matching IRN gain increases 6 dB, from -12 dB for $1/d=500$ Hz to -6 dB for $1/d=31.25$ Hz.

$h1$ for the pitch-strength-matched IRNs in the average data of Fig. 3 is plotted in Fig. 4, with filled diamonds for 4 iterations and filled squares for 16 iterations. $h1$ is essentially the same for the two matching stimuli throughout the pitch range. $h1$ for the AABB stimuli is fixed at 0.5 for all values of d, and is indicated by the horizontal dashed line. The IRN data support Yost's (1996b) finding that the pitch strength of IRN is determined by $h1$, inasmuch as two different IRNs that match the same test stimulus have the same $h1$. However, contrary to Yost's hypothesis, the value of $h1$ for IRN deviates progressively from the value for the AABB test stimuli as pitch decreases. That is, $h1$ does not predict the pitch strength of AABB.

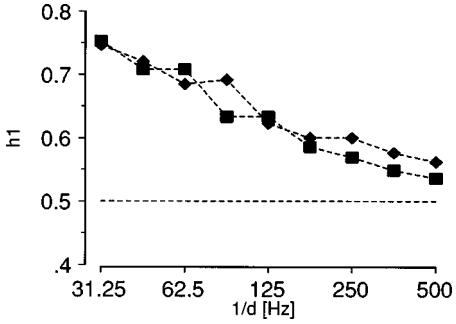

FIG. 4. Height of the first peak in the normalized long-term autocorrelation function ($h1$) for an IRN with either 4 iterations (diamonds) or 16 iterations (squares) pitch-strength matched to AABB as a function of $1/d$. Peak heights are based on mean data. The horizontal dashed line represents the d-independent $h1$ for AABB and RN (see the Introduction). The high similarity between the data obtained with 4 and 16 iterations confirms previous findings that pitch strength for IRN is a function of $h1$. The difference of both data plots from the value of 0.5 for AABB reveals that, for longer delays, $h1$ of pitch-strength matched IRN is considerably higher than that of AABB. Thus the pitch strength matches reveal that AABB violates the $h1$ dependence of pitch strength found for RN and IRN.

III. EXPERIMENT III: DISCRIMINATION OF AABB FROM IRN WITH MATCHING GAIN

Experiment I showed that AABB stimuli are discriminable from RN stimuli when the two have the same pitch $(1/d)$. Experiment II indicated that there are substantial pitch-strength differences between RN and AABB. In experiment III, listeners were asked to discriminate between an AABB and IRNs with gains in the region about the matching gain measured in experiment II. If pitch strength is the only discrimination cue then performance will drop to chance at the matching gain and rise in a V-shaped psychometric function as g deviates from the matching gain.

A. Method

1. Stimuli

The AABB and IRN stimuli had the same duration and level as in the previous experiments; the pitch, $1/d$, was either 357 or 44.2 Hz. IRNs were generated with 16 iterations and seven different gain values in 2.5-dB steps. For each listener, the fourth gain value corresponded to the value obtained for that individual in the pitch-strength matching experiment (experiment II).

2. Procedure

As in experiment I, psychometric functions for the discrimination of AABB and IRN were obtained using a three-

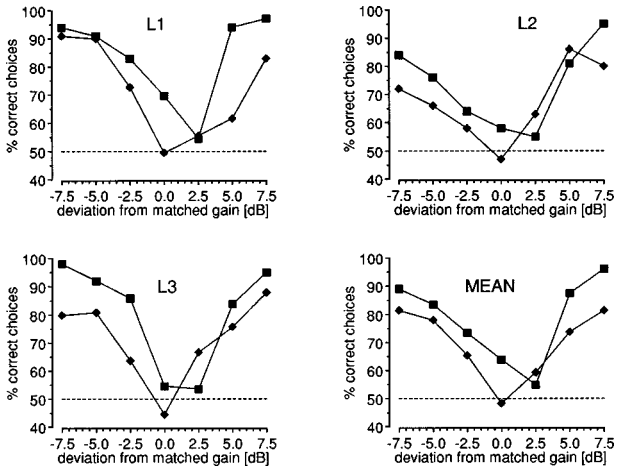

FIG. 5. Psychometric functions for the discrimination of AABB versus IRN with IRN gains ranging from 7.5 dB below the pitch-strength matched IRN gain to 7.5 dB above the matching gain. Individual data are shown in panels L1–L3; mean data are plotted in the lower right panel. Filled squares show the data for $1/d = 357$ Hz; filled diamonds represent the discrimination for IRN and AABB with $1/d = 44.2$ Hz. The mean psychometric functions as well as those for the individual listeners are V shaped. The dip of the functions is always at chance level indicating that when the IRN gain is pitch-strength matched to AABB the two are no longer discriminable.

interval, two-alternative, forced-choice paradigm. The first interval always contained an AABB stimulus, either the second or the third interval contained the IRN stimulus generated with one of the seven gain values; the remaining interval contained a sample of the given AABB stimulus. The listeners were the same as in the previous experiments.

B. Results and discussion

The psychometric functions for the discrimination of an AABB from its pitch-strength matched IRN are plotted in Fig. 5 for $1/d = 357$ Hz (filled squares) and 44.3 Hz (filled diamonds). The average psychometric functions are displayed in the lower right panel. For all subjects and both pitches, the psychometric functions are V-shaped with a minimum close to 50% correct. This means that when the pitch strength of an AABB and an IRN are matched, there is no longer any cue to discriminate between the two.

The psychometric functions for 357 Hz exhibit an asymmetry with the slope for gains less than the matching gain being shallower than the slope for gains greater than the matching gain. Moreover, the minima in the psychometric functions are shifted slightly towards IRN gains greater than the matching points measured in experiment II. This asymmetry may be explained as follows: Yost (1996b) showed that the pitch strength for IRN stimuli is a nonlinear function of $h1$. $h1$ itself grows nonlinearly with increasing IRN gain. So, when we used linear IRN gain step sizes of 2.5 dB, pitch-strength differences cannot be expected to change linearly. These nonlinear effects may be more pronounced for the high fundamental frequency in experiment III than for the low fundamental frequency because the overall pitch strength for the high pitch seems much stronger than for the low pitch. Thus nonlinear growth of pitch-strength differences may serve as a qualitative explanation for the asymmetry found in the psychometric functions in experiment III.

IV. MODELING THE PITCH STRENGTH OF REGULAR-INTERVAL NOISES

In Yost (1996b), pitch strength is based on the first peak of the long-term normalized autocorrelation function ($h1$). Pitch strength was found to be an exponential function of $h1$. $h1$ represents the average measure of temporal regularity of a stimulus over the whole stimulus duration. Yost (1996b) subjected this averaged value to the nonlinear transformation. Whereas, for RN and IRN this may be a reasonable approach, a measure of temporal regularity for AABB stimuli should fluctuate periodically. The following simulation suggests that these fluctuations are essential for the perceived pitch-strength difference between RN and AABB because averaging a fluctuating function before or after applying a nonlinear transformation leads to different results.

A. Calculation of the long-term autocorrelation and the running autocorrelation

The long-term autocorrelation of a signal $x(t)$ is given by

$$R(\tau) = \int_{-\infty}^{\infty} x(t)x(t-\tau)dt, \tag{1}$$

where τ is the correlation lag. This is the formulation used by Yost (1996a, b) and in this case, the integration period is only limited by the stimulus duration. Licklider (1951) suggested that the auditory system may use running autocorrelation; that is, the integration is limited by a time window. Licklider suggested an exponentially decaying window with a time constant λ. For a running autocorrelation, the integration period can be limited to three times λ because values beyond three times λ are small relative to the sum. The running autocorrelation of a signal, $x(t)$, is given by

$$RR(t,\tau) = \int_{t-3\lambda}^{t} x(s)x(s-\tau)e^{(s-t)/\lambda}\, ds, \tag{2}$$

where λ is the time constant, and s is the integration variable of the running autocorrelation. Note that the correlation lag τ and the time constant λ are independent time variables.

For each position of the sliding integration window, the running autocorrelation can be normalized according to

$$RRn(t,\tau) = \frac{RR(t,\tau)}{RR(t,0)}. \tag{3}$$

B. Running autocorrelations for RN and AABB stimuli

We applied normalized running autocorrelation to the stimuli used in the present study. As shown in Fig. 1, AABB and RN stimuli have only one peak in their long-term autocorrelation which occurs at the correlation lag corresponding to the RN delay or the AABB sample duration. For convenience, $RRn(t,\tau)$ was calculated only for this one correlation lag ($\tau = d$). In the following, $RRn(t,d)$ will be called

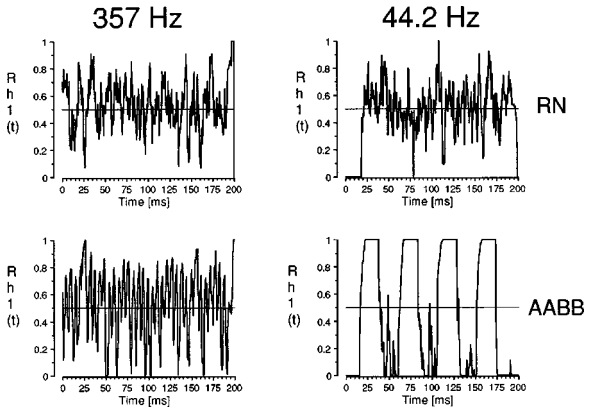

FIG. 6. $Rh1(t)$ as a function of time during the stimulus. A running autocorrelation was performed with an exponential time window with $\lambda = 1.5$ ms and a fixed correlation lag corresponding to d. $Rh1(t)$ is plotted for RN stimuli (upper panels) and AABB stimuli (lower panels) with $1/d = 357$ Hz (left panels) or 44.2 Hz (right panels). $Rh1(t)$ values averaged over the stimulus duration are shown as flat lines in the panels. Whereas for the RN stimuli (upper panels), $Rh1(t)$ fluctuates randomly around its average of 0.5, $Rh1(t)$ for AABB stimuli (lower panels) shows periodic fluctuations. The influence of the 1.5-ms time constant is reflected in the low-pass characteristic imposed on these periodic fluctuations.

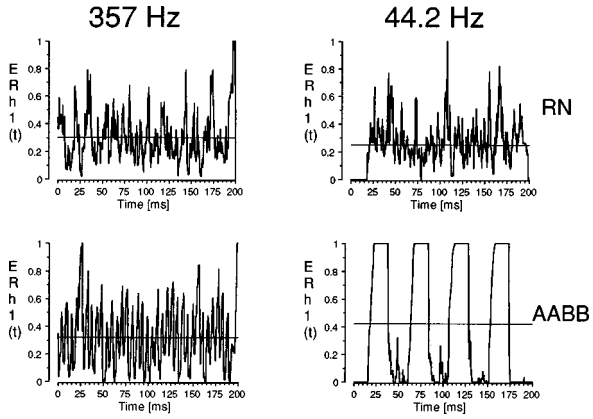

FIG. 7. $Rh1(t)$ as a function of time after being exponentiated with Eq. (4) $[ERh1(t)]$. $ERh1(t)$ averaged over the stimulus duration is shown by the horizontal line in each panel. As in Fig. 6, the functions are plotted for RN stimuli (upper panels) and AABB stimuli (lower panels) with $1/d = 357$ Hz (left panels) or 44.2 Hz (right panels). For RN and AABB with $1/d = 357$, the average value is about the same. For $1/d = 44.2$ Hz, the average value for AABB is considerably larger than the value for RN. If the average values are taken as a measure of the stimulus pitch strength, this pattern coincides with the experimental finding that, for low pitches, the pitch strength of AABB is higher than that of RN whereas pitch strengths are similar for high pitches.

$Rh1(t)$. $Rh1(t)$ is plotted in Fig. 6 for stimuli with pitches of 357 Hz (left panels) and 44.2 Hz (right panels). The upper panels show $Rh1(t)$ for RN, the lower panels show $Rh1(t)$ for AABB. Whereas for RN, there are only small, random fluctuations of $Rh1(t)$, for AABB, $Rh1(t)$ fluctuates periodically with a period equal to $2d$. The periodic fluctuations occur because, when the correlation lag equals the noise-segment duration, a given noise segment is correlated, in turn, with itself (giving a correlation of one) and with an independent noise segment (giving a correlation of zero). This is readily understandable by looking at the AABB waveforms symbolized by letters:

A	A	B	B	C	C	D	D	E	
	A	A	B	B	C	C	D	D	E

The exponential integration window smoothes this fluctuating correlation pattern to an extent given by the integration time constant. The smoothing has proportionately less effect on $Rh1(t)$ for stimuli with a pitch of 44.2 Hz than for stimuli with a pitch of 357 Hz. The horizontal lines show the value of $Rh1(t)$ averaged over the entire stimulus duration.

Yost (1996b) found that the pitch strength is proportional to 10 raised to the power of $h1$ in the long-term autocorrelation. We applied this exponentiation to $Rh1(t)$. For convenience, the resulting values were normalized and so the formula is

$$ERh1(t) = \frac{10^{k*Rh1(t)} - 1}{9}. \tag{4}$$

The parameter k is a constant whose value is determined in the modeling section (see below). $ERh1(t)$ derived from $Rh1(t)$ shown in Fig. 6 is presented in the same format in Fig. 7. As before, the horizontal lines show $ERh1(t)$ averaged over the entire stimulus duration. In the following, we define this average as the pitch strength of the stimulus.

For the higher pitch (left panels), the pitch strength is about the same for RN and AABB (about 0.3). For the lower pitch (right panels), the pitch strength for RN (upper panel) is about 0.25, but for AABB (lower right panel), the pitch strength is about 0.42, that is, considerably higher than the RN pitch strength. This distribution of pitch strength values mirrors that of the results from experiments I and II. For high pitches, the pitch strength of RN and AABB are about the same and the two stimuli are not discriminable. For low pitches, the stimuli are discriminable because AABB has a stronger pitch than RN.

The corresponding analysis for experiment III is presented in Fig. 8. $ERh1(t)$ and pitch strength (horizontal lines) for the AABB stimuli are presented in the lower panels and those for the pitch-strength-matched IRNs are presented in the upper panels in the same format as in Figs. 6 and 7. Now, the average values presented by the horizontal lines are essentially the same for the AABB and the corresponding IRN for the low and the high pitch. Experiment III showed that for the higher and, even more surprisingly, for the lower pitch, the discrimination of AABB and IRN fails when the two are pitch-strength matched despite the pronounced oscillation of $Rh1(t)$ and $ERh1(t)$ for the AABB stimuli.

C. A simulation of the pitch-strength matches

Unlike in previous autocorrelation models, where temporal integration was implemented in a single stage (Slaney and Lyon, 1990; Meddis and Hewitt, 1991a, b, 1992; de Cheveigné, 1998), the processing suggested here is based on two stages of temporal integration separated by a nonlinearity. The first integration stage is determined by the time constant of running autocorrelation, the second stage remains undetermined but can be approximated by averaging over the stimulus duration (see above and Fig. 8). While this kind of

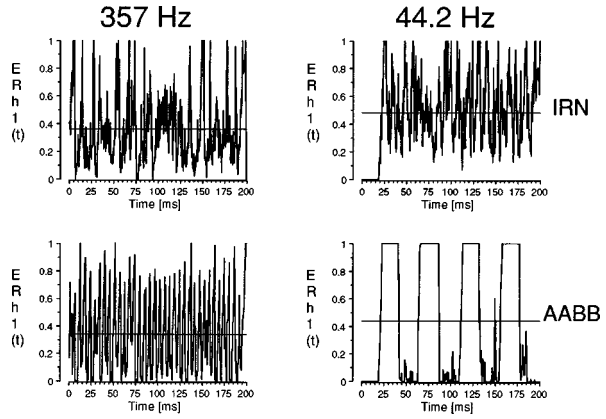

FIG. 8. Comparison of pitch-strength matched stimuli. In the left panels, stimuli have a pitch of 357 Hz, in the right panels, the pitch is 44.2 Hz. Upper panels show $ERh1(t)$ and averages for pitch-strength-matched IRN, lower panels show $ERh1(t)$ and averages for AABB. The average value for AABB and pitch-strength-matched IRN is about the same for both pitches. The short-term fluctuations of $ERh1(t)$, however, differ substantially between IRN and the corresponding AABB. From experiment III, it can be concluded that, nevertheless, the stimuli cannot be discriminated. The auditory system seems to be insensitive to the periodic fluctuations of $ERh1(t)$ for AABB stimuli.

processing may account for pitch-strength differences between AABB and RN or IRN, the results of pitch-strength matches between different IRN stimuli as in Yost (1996b) will not be changed when using this two-stage integration. The stimuli used by Yost (1996b) produce only relatively small, random fluctuations of $Rh1(t)$. These small fluctuations are not so sensitive to the nonlinear transformation, a fact which is also reflected in the current model's performance for stimuli with a relatively high pitch.

In this section, two-stage integration of pitch information is used to simulate the results of experiment II. For each interval of a simulated experimental trial, we calculated $Rh1(T)$, exponentiated according to Eq. (4), and averaged it over the stimulus duration to obtain a pitch-strength value. A block diagram for the simulation is shown in Fig. 9.

The simulation was run with the same stimuli and the same adaptive two-alternative, forced-choice (2AFC) procedure as in experiment II. On each trial, the simulated pitch strengths of the AABB and IRN were compared to determine the one with the greater pitch strength. Over trials, the IRN gain was adaptively changed with the same step sizes as in experiment II to determine the IRN gain that produced a pitch-strength match between the AABB and IRN. Model performance was also averaged over three runs. The free parameters in the simulation were the time constant of the running autocorrelation λ and the factor k [see Eq. (4)]. The pitch-strength-matching results of experiment II are represented by filled diamonds and filled squares for IRN$(d,g,4)$ and IRN$(d,g,16)$, respectively, in Fig. 10. The solid lines show the pitch-strength matches from the simulation with a time constant of 1.5 ms and k equals one.

The root-mean-squared deviation of the simulation from the average data is only 0.5 dB. Nevertheless, we attempted to determine if the goodness of fit could be improved further by varying k in the exponent of the nonlinear pitch-strength relation [Eq. (4)]. The influence of this parameter on the

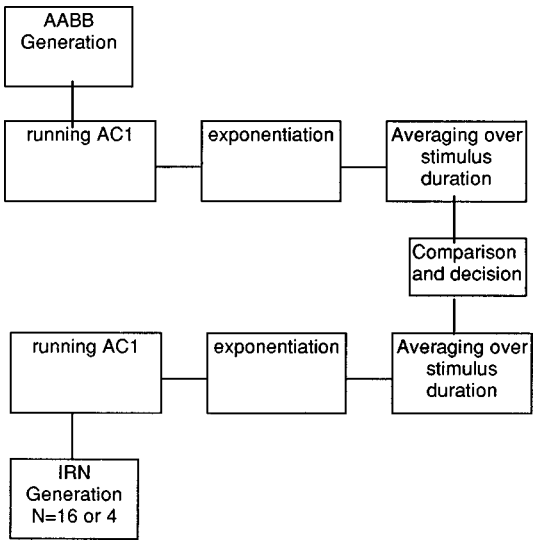

FIG. 9. Block diagram of the pitch-strength-match simulation of regular interval noises. The simulation was set up with the same adaptive 2AFC paradigm and was in each trial presented with an AABB stimulus and an IRN stimulus. For both stimuli, pitch strength was calculated by calculating the running autocorrelation, applying a nonlinear transformation, and averaging over the stimulus duration. When the calculated pitch strength for the IRN was higher than that of the AABB, the IRN gain was reduced for the following trial, when the AABB pitch strength was found to be higher than that of the IRN, the IRN gain was increased for the next trial.

goodness of fit is shown in Fig. 11 as a function of the time constant for values of k from 0.5 to 2. The figure shows that the best fit is obtained with k equal to one, at which point λ is 1.5 ms as reported above. When k is 1.2, the fit is essentially as good, and the optimal time constant shifts up to 2.5 ms. Values of k greater than 1.2 or less than 0.9 lead to significantly worse fits.

The results and simulations presented here do not prove unequivocally that pitch perception arises from the calculation of a running autocorrelation. Indeed, it has been argued that such models fail to account for certain aspects of temporal processing and pitch perception (Shackleton and Carlyon, 1994; Carlyon, 1998; Kaernbach and Demany, 1998). However, the success of the simulation presented in Fig. 10 shows that a temporally based model can account for the

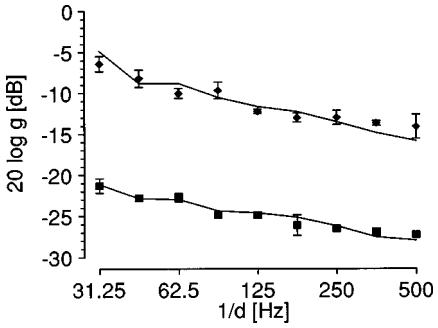

FIG. 10. Simulation results of the AABB-IRN pitch-strength matches. Mean data from experiment II are replotted from the lower right panel of Fig. 3. The filled diamonds represent the mean pitch matches with IRN with 4 iterations; the filled squares show the mean pitch-strength matches with IRN with 16 iterations. The solid lines represent the matches of the pitch-strength simulation obtained with the same matching stimuli, k equals one, and the time constant of running autocorrelation λ, is fixed at 1.5 ms.

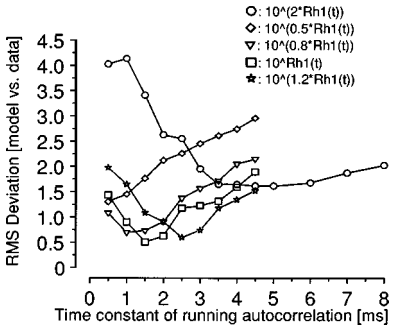

FIG. 11. Root-mean-squared deviations of the simulations from the experimental data of experiment II as a function of the time constant of running autocorrelation. Time constants tested ranged from 0.5 to 4.5 ms (8 ms for a factor of 2, circles) in 0.5-ms steps. The second free parameter in the model is the factor k applied to $Rh1(t)$. k was set to 0.5 (diamonds), 0.8 (triangles), 1 (squares), 1.2 (stars), or 2 (circles). The minimum root-mean-squared deviation from the data was reached with a factor of 1 and a time constant of 1.5 ms. A factor of 1.2 leads to a slightly worse fit and a best fitting time constant of 2.5 ms. For a factor of 0.8, the fit is also worse and the best fitting time constant is 1 ms.

pitch-strength differences occurring between RN and AABB. The results provide important limitations on the temporal dynamics of pitch perception, and suggest that the initial, instantaneous measures of temporal regularity are limited by a time constant of approximately 1.5 ms.

V. SUMMARY AND CONCLUSIONS

The present study compared the perceptions produced by two regular interval noises, rippled noise (RN) and AABB. Experiment I showed that for low pitches, listeners can discriminate between the two stimuli. Listeners reported that the AABB stimuli had a stronger pitch than the RN stimuli, despite the fact that $h1$ in the long-term autocorrelation is the same. Experiment II showed that listeners could match the pitch strengths of AABB and iterated rippled noise (IRN) and that, for low-pitched stimuli, $h1$ for the IRN that produces a match is invariably greater than that for the AABB. Experiment III showed that if the pitch strength of IRN is matched to that of AABB, the two cannot be discriminated which supports the interpretation that the discrimination observed in experiment I is based exclusively on differences in pitch strength. The data show that Yost's (1996b) suggestion that the pitch strength of regular interval noises is based on $h1$ is valid for the stimuli used in his study but does not hold for AABB stimuli. AABBs and IRNs with the same $h1$ have different pitch strengths, and AABBs and IRNs matched for pitch strength are not discriminable despite having different $h1$ values.

A three-stage model of pitch strength is introduced. It consists of (1) running autocorrelation with an integration window representing the first stage of temporal integration, (2) exponentiation according to Yost (1996b) and (3) averaging over the stimulus duration which approximates the second stage of temporal integration. The model provides an excellent quantitative fit to the pitch-strength-matching data with a time constant of running autocorrelation λ fixed at 1.5 ms. The value of 1.5 ms for the time constant of running autocorrelation is not readily comparable to the value of 2.5 ms suggested by Licklider (1951) and used by Meddis and Hewitt (1991a, b), or to the value of 10 ms used by Meddis and Hewitt (1992). These models consist of only one stage of temporal integration implemented as the time window for the running autocorrelation, whereas the current model uses two stages only the first of which is the autocorrelation time window. The nature of the second stage of temporal integration which is currently implemented by averaging over the stimulus duration remains to be determined.

ACKNOWLEDGMENTS

We would like to thank Guy Walker for his participation in the experiments and Alain de Cheveigné and Bill Yost for very helpful reviews of the manuscript. This study was supported by the Medical Research Council, Grant No. G9703469, UK, and by a research grant from the ''Deutsche Forschungsgemeinschaft'' to the first author.

Bilsen, F. (**1977**). ''Pitch of noise signals: Evidence for a 'central spectrum,' '' J. Acoust. Soc. Am. **61**, 150–161.

Carlyon, R. P. (**1998**). ''Comments on 'A unitary model of pitch perception,' '' J. Acoust. Soc. Am. **104**, 1118–1121.

de Cheveigné, A. (**1998**). ''Cancellation model of pitch perception,'' J. Acoust. Soc. Am. **103**, 1261–1271.

Kaernbach, C., and Demany, L. (**1998**). ''Psychophysical evidence against the autocorrelation theory of temporal processing,'' J. Acoust. Soc. Am. (submitted).

Licklider, J. C. R. (**1951**). ''A duplex theory of pitch perception,'' Experientia **7**, 128–133.

Meddis, R., and Hewitt, J. (**1991a**). ''Virtual pitch and phase sensitivity of a computer model of the auditory periphery. I: Pitch Identification,'' J. Acoust. Soc. Am. **89**, 2866–2882.

Meddis, R., and Hewitt, J. (**1991b**). ''Virtual pitch and phase sensitivity of a computer model of the auditory periphery. II: Phase sensitivity,'' J. Acoust. Soc. Am. **89**, 2883–2894.

Meddis, R., and Hewitt, J. (**1992**). ''Modeling the identification of concurrent vowels with different fundamental frequencies,'' J. Acoust. Soc. Am. **91**, 233–245.

Shackleton, T. M., and Carlyon, R. P. (**1994**). ''The role of resolved and unresolved harmonics in pitch perception and frequency modulation discrimination,'' J. Acoust. Soc. Am. **95**, 3529–3540.

Slaney, M., and Lyon, R. F. (**1990**). ''A perceptual pitch detector,'' in *Proceedings of the IEEE International Conference on Acoustics, Speech, and Signal Processing, Albuquerque, New Mexico* (IEEE, New York), pp. 357–360.

Yost, W. A. (**1996a**). ''Pitch of iterated rippled noise,'' J. Acoust. Soc. Am. **100**, 511–518.

Yost, W. A. (**1996b**). ''Pitch strength of iterated rippled noise,'' J. Acoust. Soc. Am. **100**, 3329–3335.

Yost, W. A. (**1998**). ''Auditory processing of sounds with temporal regularity: Auditory processing of regular interval stimuli,'' in *Psychophysical and Physiological Advances in Hearing, Proceedings of the 11th International Symposium on Hearing*, edited by A. R. Palmer, A. Rees, A. Q. Summerfield, and R. Meddis (Whurr, London).

Loudness perception and frequency discrimination in subjects with steeply sloping hearing loss: Possible correlates of neural plasticity

Hugh J. McDermott[a] and Margaret Lech
Co-operative Research Centre for Cochlear Implant, Speech, and Hearing Research, 384-388 Albert Street, East Melbourne, 3002, Australia

Michelle S. Kornblum
Department of Psychology, Monash University, Wellington Road, Clayton, 3168, Australia and Co-operative Research Centre for Cochlear Implant, Speech, and Hearing Research, 384-388 Albert Street, East Melbourne, 3002, Australia

Dexter R. F. Irvine
Department of Psychology, Monash University, Wellington Road, Clayton, 3168, Australia

(Received 4 May 1998; accepted for publication 30 June 1998)

Loudness functions and frequency difference limens (DLFs) were measured in five subjects with steeply sloping high-frequency sensorineural hearing loss. The stimuli were pulsed pure tones encompassing a range of frequencies. Loudness data were obtained using a 2AFC matching procedure with a 500-Hz reference presented at a number of levels. DLFs were measured using a 3AFC procedure with intensities randomized within 6 dB around an equal-loudness level. Results showed significantly shallower loudness functions near the cutoff frequency of the loss than at a lower frequency, where hearing thresholds were near normal. DLFs were elevated, on average, relative to DLFs measured using the same procedure in five normally hearing subjects, but showed a local reduction near the cutoff frequency in most subjects with high-frequency loss. The loudness data are generally consistent with recent models that describe loudness perception in terms of peripheral excitation patterns that are presumably restricted by a steeply sloping hearing loss. However, the DLF data are interpreted with reference to animal experiments that have shown reorganization in the auditory cortex following the introduction of restricted cochlear lesions. Such reorganization results in an increase in the spatial representation of lesion-edge frequencies, and is comparable with the functional reorganization observed in animals following frequency-discrimination training. It is suggested that similar effects may occur in humans with steeply sloping high-frequency hearing loss, and therefore, the local reduction in DLFs in our data may reflect neural plasticity. [S0001-4966(98)02910-5]

PACS numbers: 43.66.Ba, 43.66.Cb, 43.66.Fe, 43.66.Sr [RVS]

INTRODUCTION

Restricted cochlear lesions in adult animals have been shown to result in plasticity of the frequency tuning of auditory cortical neurons, and consequently in the functional tonotopic organization of auditory cortex. The general form of this reorganization is that neurons in the region of cortex deprived of its normal input by the lesion develop sharp tuning and low thresholds for a frequency close to the edge of the hearing loss, and the areal representation of that frequency is consequently greatly increased (see Irvine and Rajan, 1995 for review). This dynamic process of reorganization in auditory cortex is analogous to that seen in visual and somatosensory cortices after restricted retinal lesions and amputation of a digit or limb, respectively (see Kaas, 1991, 1995 for recent reviews). In each case, central reorganization results in an enlarged cortical representation of the peri-lesion area, or areas, of the receptor epithelium.

Cortical reorganization of this sort has been described in primary auditory cortex of adult mammals of a number of species, including simian primates, and after a variety of forms of cochlear lesion [guinea pig: Robertson and Irvine (1989); mouse: Willott *et al.* (1993); cat: Harrison *et al.* (1993), Rajan *et al.* (1993); macaque: Schwaber *et al.* (1993)]. It therefore seems likely that it would also occur in humans with partial deafness attributable to cochlear lesions of the types that have been studied in animal models. Since such reorganization would have the consequence that a stimulus activating peri-lesion areas of the receptor organ would produce a much larger than normal area of cortical activation by including neurons whose activation is normally associated with different stimuli and percepts, its occurrence would be expected to have perceptual consequences. The occurrence of such reorganization in the human somatosensory system is indicated by imaging studies in amputees (e.g., Elbert *et al.*, 1994; Flor *et al.*, 1995), and its perceptual consequences by some phantom limb phenomena (Ramachandran *et al.*, 1992). There have been no analogous studies in the auditory system. Our aim was to investigate pos-

[a]Electronic mail: h.mcdermott@medoto.unimelb.edu.au

sible perceptual correlates of putative cortical reorganization in humans with partial hearing loss.

Realization of this aim is complicated by at least two considerations. The first is that so far we have very little information on what characteristics of a particular cochlear lesion determine whether or not that lesion will result in cortical reorganization. Rajan and Irvine (1996) presented evidence from a cat with an idiopathic lesion which showed no evidence of cortical reorganization. The differences between this lesion and those produced experimentally suggested that a loss that slopes steeply from a region having relatively good thresholds to a region of severe deafness is a necessary condition for the occurrence of reorganization. We have therefore studied perceptual characteristics in a group of human subjects with steeply sloping loss. The second complication is that, in the absence of knowledge of the patterns of cortical activation associated with even the simplest auditory perceptual experience in either humans or animals, it is difficult to predict the nature of the perceptual changes that might result from such reorganization if it were to occur in humans. It would not be unreasonable to suppose, however, that the occurrence of cortical reorganization, such that a particular stimulus resulted in activation of a much larger than normal area of cortex, might result in a change in the perceived loudness and/or pitch of that stimulus.

Loudness perception has previously been studied in a group of subjects whose audiograms indicated near-normal hearing thresholds at low frequencies, followed by a steeply sloping loss at mid frequencies, with slopes greater than 50 dB/oct (Hellman, 1994). Loudness growth functions, measured by absolute magnitude estimation and production, were compared for tones at frequencies in the normal-threshold region, and for tones at the cutoff frequency (i.e., near the beginning of the slope). The slopes of the loudness functions were found to be significantly less steep, at mid-to-high levels, for the tones at the cutoff frequency than for the lower-frequency tones. A second group of subjects, who had hearing losses that were less steep (31–49 dB/oct), did not show this effect. To explain this result, it was assumed that the steep loss was indicative of a cochlear impairment that restricted the effective spread of the excitation from the tone at the cutoff frequency into higher-frequency regions of the cochlea. The reduction or absence of excitation above the cutoff frequency would cause a relatively slow growth of loudness with increasing level. Recently, models of loudness perception which can incorporate the effects of restricted cochlear hearing loss have been published (Florentine *et al.*, 1997; Moore and Glasberg, 1997). These models can account both qualitatively and quantitatively for the above observations, and thereby support the proposition that an appropriate explanation for these loudness effects can be found at the peripheral, rather than the cortical, level. However, it is still possible that some aspects of loudness perception in these subjects might relate to central plasticity, either instead of, or as well as, to peripheral activation patterns.

It is also possible that changes in pitch perception occur at frequencies near the lesion edge in subjects with steeply sloping high-frequency loss. This suggestion finds some indirect support in the reports that frequency-discrimination training in animals results in changes in the frequency selectivity of auditory cortical neurons, and in the frequency organization of primary auditory cortex, that are analogous to those produced by cochlear lesions (Recanzone *et al.*, 1993; Weinberger, 1995). Although the relationship between injury- and use-induced plasticity in auditory (and other) cortices, and the extent to which common mechanisms are involved, remains to be determined (Irvine and Rajan, 1996), these data nevertheless support investigation of frequency discrimination in subjects with putative auditory cortical reorganization.

TABLE I. Background information on the hearing-impaired subjects.

Subject	Sex	Age (years)	Tested ear	Etiology
S1	male	45	left	unknown (congenital)
S2	female	56	right	otitis media, ototoxic drug
S3	female	45	left	hereditary, progressive (congenital)
S4	male	37	left	unknown (congenital)
S5	female	55	right	progressive, suspected cochlear otosclerosis

In the following, we report on two experiments which investigated the perceptions of subjects with cochlear impairments resulting in a steeply sloping loss. In the first experiment, absolute thresholds and equal-loudness relations were obtained for pulsed pure tones over a wide range of frequencies. The second experiment measured frequency difference limens (DLFs) for pulsed pure tones presented at intensities corresponding to a fixed, comfortable loudness level.

I. EXPERIMENT 1: ABSOLUTE THRESHOLDS AND EQUAL-LOUDNESS CONTOURS

A. Method

1. Subjects

A group of five adults with steeply sloping sensorineural hearing loss (S1–S5) acted as subjects in all experiments described below. Some relevant background information about them is summarized in Table I. The subjects were selected on the basis of their audiograms (see filled circles in Fig. 1), which show three distinctive regions: (1) at low frequencies, normal hearing thresholds or slight to mild hearing loss, with absolute thresholds generally better than 33 dB HL; (2) a transition region where the loss increases abruptly from slight to severe; and (3) at higher frequencies, severe to profound hearing loss. Of the five subjects, only one (S2) usually wore a hearing aid. The ear tested was that with better hearing if the loss was not symmetrical. Audiological assessments indicated that the hearing loss in each case was likely to be of cochlear origin.

None of the subjects had experience in psychophysical tasks. They were not paid for participation in the two experiments, although costs such as travel expenses were reimbursed.

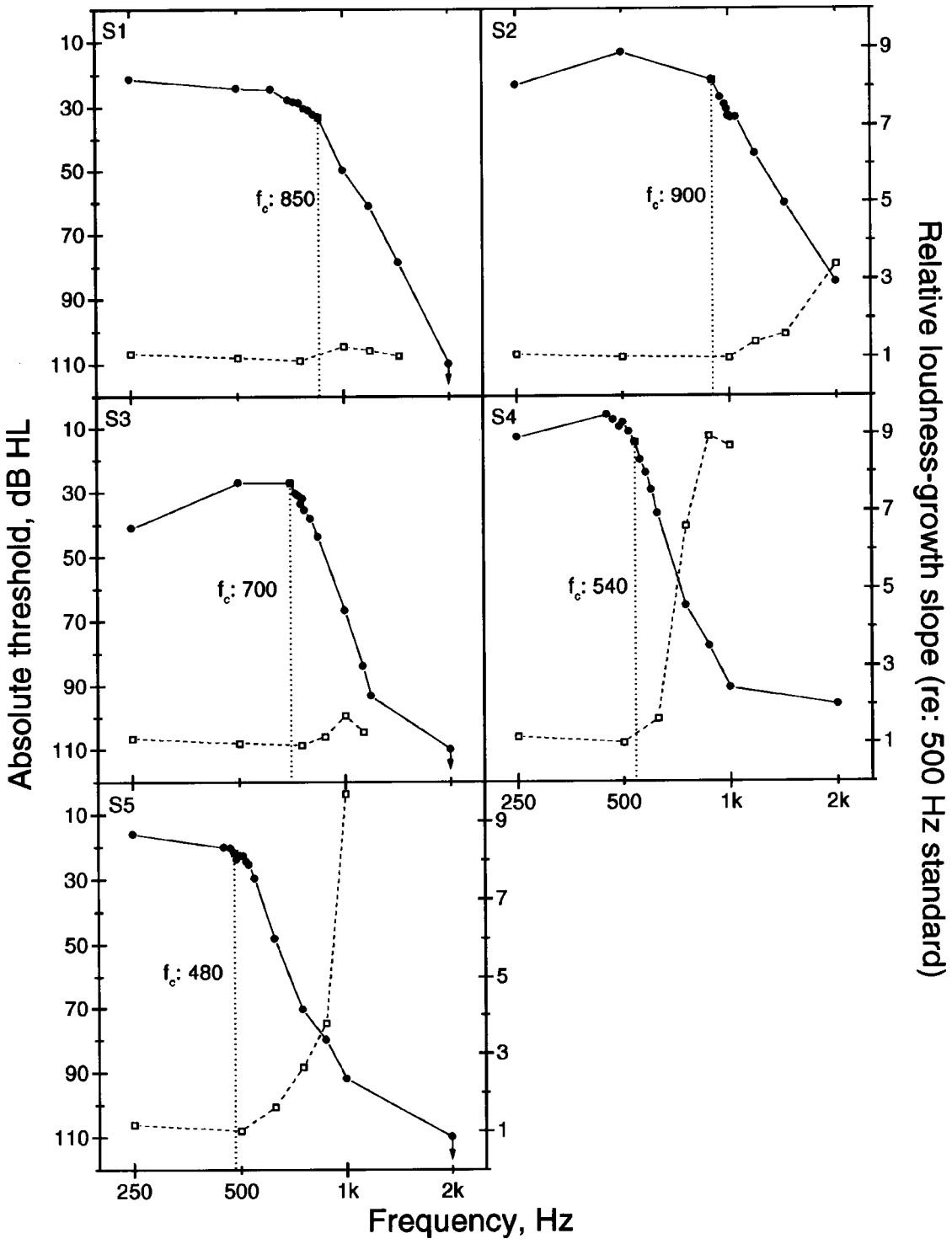

FIG. 1. Absolute thresholds and relative slopes of the loudness growth functions for each of the five subjects with steeply sloping hearing loss. Thresholds, in db HL (filled circles), are plotted against the left ordinate. The arrows indicate thresholds that could not be determined because they either exceeded the limit of the audiometer, or elicited uncomfortable sensations. The loudness-growth slopes (open squares, right ordinate) are scaled relative to the slope at 500 Hz, and were calculated from the data in Fig. 2 as illustrated in Fig. 3 (see text for details). The vertical dotted lines and adjacent numbers indicate the derived cutoff frequency (in Hertz) for each subject.

2. Stimuli

Subjects were tested individually in a double-walled sound-attenuating booth. Sounds were presented monaurally via a TDH-39 earphone with an Mx-41/AR cushion. All stimuli were pure tones generated using a programmable clinical audiometer (Madsen OB822), or a digital synthesizer (Korg 05R/W). They had 30-ms rise/decay ramps and a steady-state portion of 500-ms duration. The levels of the stimuli were computer-controlled via the audiometer. Specifically written software running on an IBM-compatible personal computer was used to control the stimuli and to collect each subject's responses. In the experiments, subjects used a custom-designed interface to initiate presentation of stimuli and to make their responses, as described further below. Be-

cause standard audiometric equipment was used, stimulus levels are reported below in units of dB HL.

3. Procedure

a. Absolute thresholds. Absolute thresholds were measured using an adaptive, four-interval forced-choice procedure, with a two-up, two-down decision rule. This rule converges on the 50% point on the psychometric function (Levitt, 1971). The frequencies of the stimuli were distributed between 250 Hz and at least 2 kHz. In the procedure, each trial was initiated by the subject and comprised a sequence of four observation intervals, each lasting 500 ms, and marked by lights. The intervals were separated by pauses of 300 ms. A stimulus was presented in only one interval, chosen at random. The subjects were asked to identify that interval. After two correct responses in three consecutive trials, the stimulus level was decreased, and after two incorrect responses in three trials, the level was increased. Six level reversals were obtained in each run. The levels were changed in 5-dB steps until the second reversal occurred, and in 2-dB steps thereafter. After each run, the arithmetic mean of the levels at the last four reversals was calculated. The results reported below are the averages for three such runs.

Thresholds were obtained at closely spaced frequencies near the beginning of the steep slope in the audiogram, so that the cutoff frequency (f_c) could be estimated precisely. The cutoff frequency was defined as the lowest frequency for which the threshold was greater (worse) than 15 dB HL, and the slope of the threshold curve at higher frequencies was greater than or equal to 50 dB/oct. As in Hellman (1994), we converted the dB HL data to equivalent free-field dB SPL units (ISO, 1996) before calculating the threshold slope. The order of the frequencies tested was randomized across sessions.

b. Equal-loudness contours. Equal-loudness contours were measured using an adaptive two-interval, two-alternative forced-choice procedure utilizing a two-up, two-down decision rule. Each trial consisted of two observation intervals, one containing a reference tone of 500 Hz presented at a fixed level, and the other containing a comparison tone at the frequency to be tested. The observation intervals were presented in random order, and the subject's task was to identify the interval which contained the louder tone.

The reference tone was presented at four or five levels, spaced at intervals of 15 dB, and chosen to encompass a wide range of loudness. The highest level was selected for each subject to avoid production of any uncomfortable sensations during the loudness matching procedure. This sometimes limited the number of matches that could be made at frequencies well above f_c. For example, with S3, loudness matches could be obtained only at two levels for a frequency of 1125 Hz.

For each subject, the comparison tone was presented at five frequencies, while the reference tone in each condition remained at 500 Hz. The lowest frequency was always 250 Hz, while the other four frequencies were above the 500-Hz reference. The highest comparison frequency was selected for each subject individually, because in some instances, high-frequency tones were found to produce anomalous sensations that made loudness matching impractical. The remaining comparison frequencies were distributed between the 500-Hz reference and the selected highest frequency. An attempt was made to sample the sloping region of the hearing loss fairly evenly. The order of testing was determined by random selection from among the entire set of frequency and level combinations for each subject.

In each run of the adaptive procedure, the level of the comparison tone was increased when it was judged less loud than the reference on two out of three consecutive trials, and reduced when it was judged louder on two out of three trials. The level was varied initially in 5-dB steps until the second level reversal occurred. Thereafter it was varied in 1-dB steps until four further reversals were obtained. The levels at these last four reversals were averaged for each run, and two such runs were obtained for each condition. The results shown are averages for these two runs.

B. Results

The graphs in Fig. 1 show the absolute thresholds across frequency for subjects S1–S5 (filled circles). The cutoff frequency calculated for each subject is indicated by a vertical, dotted line, and the adjacent number. Also shown is the estimated slope of the loudness function (open squares), the derivation of which is described below.

The equal-loudness contours for subjects S1–S5 are shown in Fig. 2. For completeness, the appropriate absolute thresholds, as plotted in Fig. 1, are also included in Fig. 2 (dashed lines). Below f_c, the curves in Fig. 2 are roughly parallel, indicating that the growth of loudness with intensity is similar across those frequencies. In contrast, above f_c the curves converge towards higher frequencies. This illustrates the phenomenon of loudness recruitment, which is commonly associated with severe sensorineural hearing loss. Essentially, the curves converge because the thresholds increase more steeply with frequency than the intensities corresponding to equal loudness at higher levels. This means that the growth of loudness with intensity becomes steeper at higher frequencies.

Because a loudness matching procedure was used, it is easy to compare the slopes of these loudness functions across frequency. To calculate the relative slopes, the data of Fig. 2 were replotted to show, for each comparison frequency, the levels of the reference (500 Hz) stimulus versus the levels of the comparison stimulus obtained in the experiment. These transformed data are shown in Fig. 3 for subjects S1–S5. Lines were fitted to these data using simple regression. Generally, straight lines fitted the data reasonably well in all cases except for frequencies above 1 kHz for subject S1 (see below). The slopes of these lines are plotted in Fig. 1 (open squares). Note that because estimates of loudness were not obtained in the experiment, the loudness-growth slopes at each frequency are plotted relative to that for the reference stimulus (i.e., at 500 Hz, the slope is 1.0 by definition).

At frequencies above f_c, there is a marked increase in loudness-growth slope, corresponding to recruitment, for each subject except S1, some of whose data were not well fitted by straight lines. However, an examination of S1's

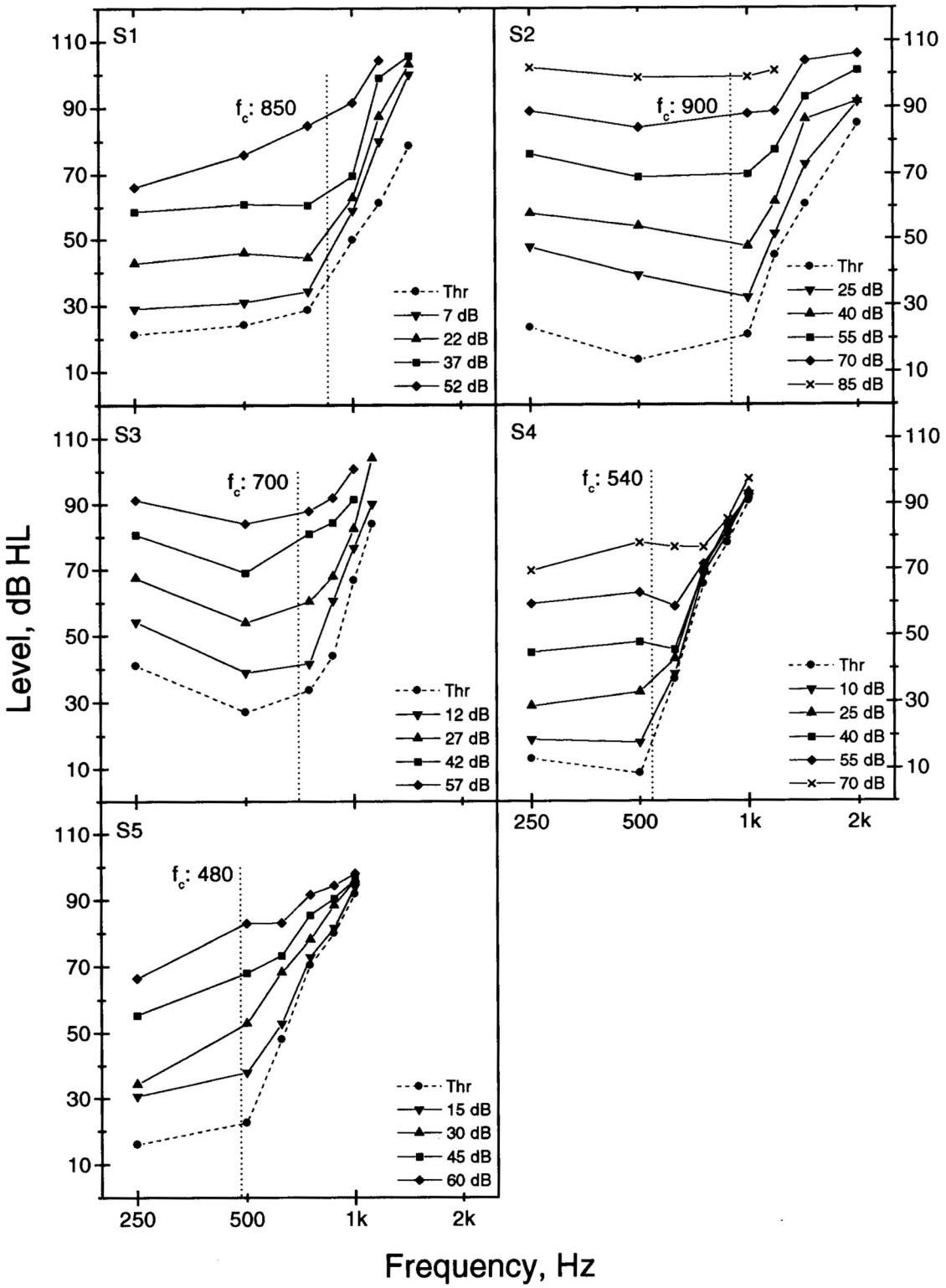

FIG. 2. Equal-loudness contours for the five subjects with steeply sloping hearing loss. The reference stimulus was a 500-Hz tone presented at four or five levels encompassing a range of loudness. The sensation levels of these 500-Hz reference tones for each subject are indicated in the legends. The contour containing levels at which stimuli were presented in the DLF experiment is marked by squares. Hearing thresholds are also shown (circles, dashed lines; Thr in the legends). The vertical dotted lines and adjacent numbers indicate the cutoff frequency (in Hertz) for each subject.

loudness-matching data in Figs. 2 and 3 indicates that the slope was in fact much steeper for supra-threshold levels at frequencies above f_c than below it. For all subjects, the slopes at frequencies below f_c are generally close to 1.0, as expected, but in each case reach a minimum value in the vicinity of f_c. This observation is consistent with previous reports on loudness perception with high-frequency hearing loss (Hellman, 1994; Florentine *et al.*, 1997; Moore and Glasberg, 1997) that were described briefly in the Introduction.

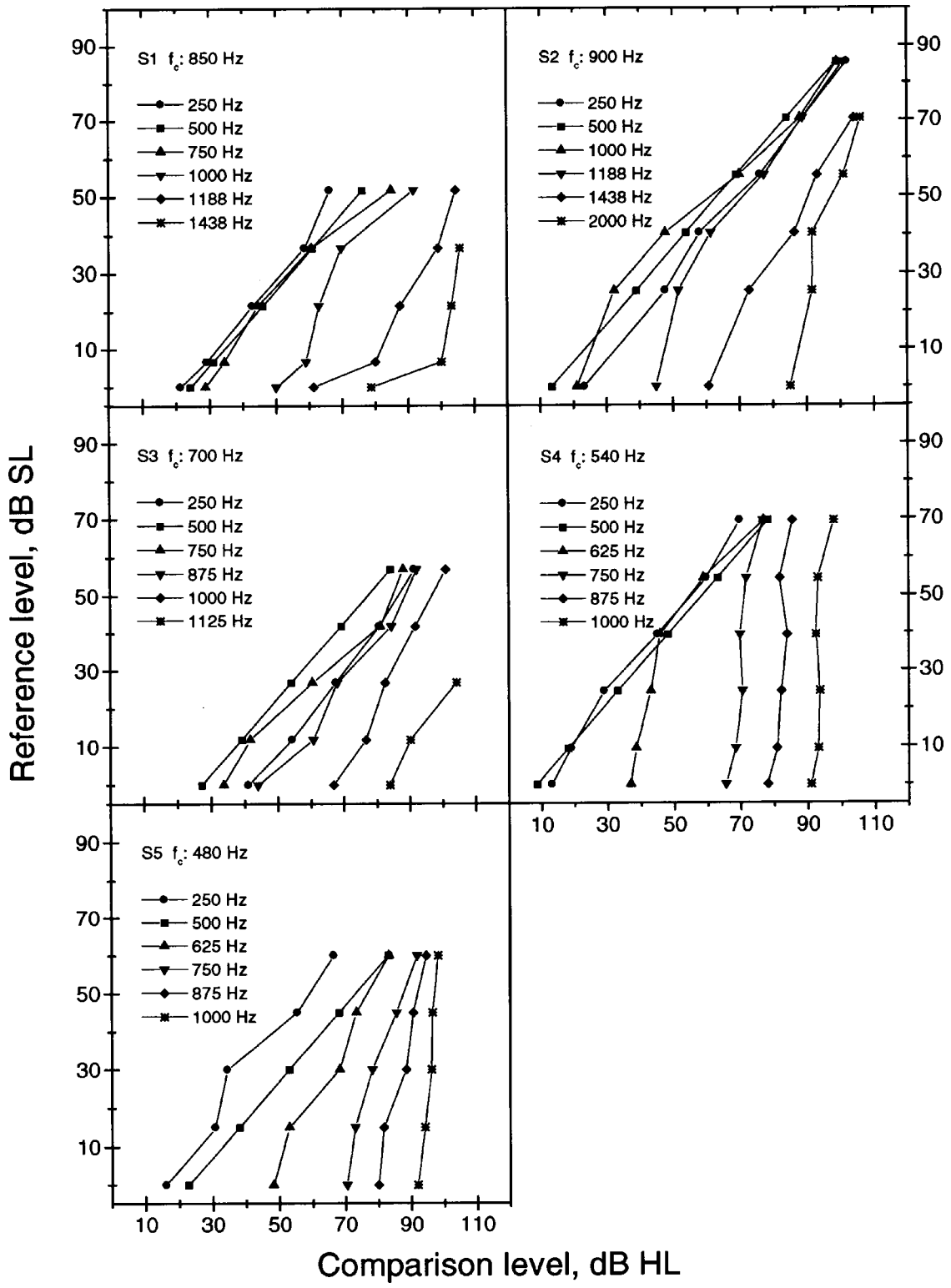

FIG. 3. The loudness-matching data shown in Fig. 2 transformed to facilitate estimation of the relative loudness-growth slopes plotted in Fig. 1. Each curve connects levels at which the loudness of the reference stimulus (ordinate) was judged equal to the loudness of the comparison stimulus (abscissa) at a given frequency. The frequency of the reference stimulus was 500 Hz (squares), while the comparison stimuli were presented at different frequencies, as indicated in the legends. Cutoff frequencies (f_c) for each subject are also shown.

To examine the reliability of this effect, the slope of the function at the frequency closest to f_c was compared with that at the next lower frequency in the region with near-normal hearing thresholds. Thus for subjects S1–S5 the near-f_c frequencies were: 750, 1000, 750, 500, and 500 Hz, and the adjacent lower frequencies were: 500, 500, 500, 250, and 250 Hz, respectively. Note that each of these frequency pairs includes the 500-Hz reference frequency. This facilitates comparison of the loudness-growth slopes, because in the experiment, subjects matched the loudness at these frequencies directly. When lines were fitted to the data at these frequencies (as explained above), the correlation coefficients

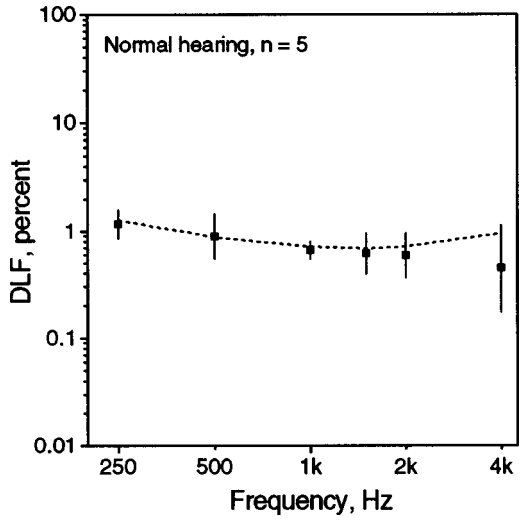

FIG. 4. Average DLFs for the five normal-hearing subjects, plotted on a log scale as a percentage of the frequency tested. Error bars indicate ± one standard deviation of the mean across subjects. The dashed line shows predictions from a general equation for DLFs (Nelson *et al.*, 1983).

(R^2) in each case were greater than 0.96. Thus these data are well described by linear functions, as would be expected. Averaging across subjects, the relative slope at the frequency near f_c was 0.97, while that at the lower frequency was 1.07. A *t*-test, paired for subjects, confirmed that this difference in slopes was statistically significant ($p<0.02$).

II. EXPERIMENT 2: FREQUENCY DIFFERENCE LIMENS FOR PURE TONES

A. Method

1. Subjects

In experiment 2, a control group of five subjects with normal hearing was tested in addition to the above five subjects with steeply sloping audiograms (S1–S5). The control subjects were three women and two men, ranging in age from 21 to 42 years. The absolute thresholds of their tested ears (chosen at random) were better than 15 dB HL at octave frequencies from 250 Hz to 4 kHz, and audiological assessments found no abnormalities. These subjects had no experience with the psychoacoustic procedures described below.

2. Procedure

Frequency difference limens (DLFs) for pure tones were measured using an adaptive, three-interval, forced-choice procedure. On each trial, two of the three observation intervals contained pure tones at a reference frequency, and one (selected at random) contained a pure tone of variable frequency, which was always higher than the reference frequency. The subject's task was to identify that interval. A three-down, one-up rule was used to estimate the frequency difference corresponding to the 79.4% point on the psychometric function (Levitt, 1971). The initial difference between the variable and the reference frequencies was 20% of the reference frequency for subjects with impaired hearing, and 10% of the reference frequency for subjects with normal hearing. After three consecutive correct responses, the difference in frequency was decreased by a factor of 0.75, while after each incorrect response the difference was increased by 1.25. For example, if the reference frequency was 1000 Hz and the variable frequency was 1100 Hz, a single step down would decrease the variable frequency to 1075 Hz, and a single step up would increase it to 1125 Hz. Each run proceeded until 12 frequency reversals had occurred, and the geometric mean was calculated for the last 8 reversals. Three such runs were performed for each reference frequency, and the DLF was calculated as the geometric mean over those three runs.

For each subject with impaired hearing, the reference frequencies were chosen to sample the frequency range from 250 Hz to the highest frequency at which a result could be obtained. The sampling was densest at frequencies close to and immediately above f_c, on the grounds that the results of the animal experiments outlined earlier suggest that reorganization would produce an expanded representation of frequencies in this region. The order of testing was randomized across sessions.

Because the results of experiment 1 showed that loudness would vary greatly for tones presented at a constant level across frequencies, it was considered inappropriate to attempt to measure DLFs at a constant SPL in these subjects. If a constant level had been used, subjects might have based their judgments in the DLF experiment on changes in loudness with frequency rather than on changes in pitch. Therefore, all stimuli were presented at an approximately constant loudness level, using each subject's equal-loudness contour obtained in experiment 1 when the 500-Hz reference tone was set to a medium (comfortable) loudness. These contours are plotted with squares in Fig. 2, and correspond to an average reference level of approximately 45 dB SL. Levels for frequencies between those tested in experiment 1 were calculated by linear interpolation. To prevent subjects from exploiting any residual loudness differences as the frequency changed in the adaptive procedure, the level of each stimulus was varied in each observation interval by a random value selected from a uniform distribution between −3 and +3 dB.

In order to familiarize subjects with the DLF task, a small number of training runs of the procedure were presented initially. In these runs the random level variation was not applied, and feedback was provided at the end of each trial. This was done by illuminating a light briefly to indicate whether the subject had correctly selected the interval containing the higher-frequency stimulus. Data were not collected during these training runs. Subsequently, in order to obtain additional data allowing any learning effects to be assessed, one practice run was performed before each experimental run. In the practice runs, neither level randomization nor correct-response feedback were provided. Data were collected for three such practice runs, but were analyzed separately from the data from the three experimental runs (i.e., those having randomized levels).

For the five subjects with normal hearing, DLFs were measured at reference frequencies of 250, 500, 1000, 1500, 2000, and 4000 Hz. The procedures were the same as those used with the hearing-impaired subjects, except that only one practice and one experimental run were performed for each frequency and each subject. This was considered adequate to

check the validity of a general equation predicting DLFs in normal-hearing subjects as a function of frequency and level, as discussed below. The levels of the stimuli were obtained from a published equal-loudness function for pure tones at the 70-phon loudness level (Robinson and Dadson, 1956). This was perceived as a comfortable level by the normal-hearing listeners.

B. Results

Before discussing the DLF results in detail, it is worthwhile considering the data obtained during the practice runs in which the stimulus levels were not randomly varied. For the normally hearing subjects, a two-way analysis of variance (ANOVA) was carried out on the log(DLF) data averaged across subjects, with factors of frequency and condition. The condition factor divided the DLFs into those obtained during practice runs (with fixed levels), and those obtained during experimental runs (with randomized levels). The analysis showed that neither the condition nor the frequency×condition factors were statistically significant ($p>0.05$). This was not unexpected, because the levels varied over a range of only 6 dB (see Moore and Glasberg, 1989). A similar ANOVA was carried out on the log(DLF) data for each of the hearing-impaired subjects S1–S5. Data could not be combined across these subjects because DLFs were not always obtained at the same frequency for each subject. For each subject, the effect of condition was significant ($p<0.01$), with the mean DLFs being higher in the randomized-level condition than in the practice condition. However, the shape of the DLF values across frequency for each subject was essentially identical for the two conditions. This is consistent with the results of the ANOVA, which showed that the frequency×condition factor was not significant ($p>0.05$) for each of S1–S5. This suggests that the generally lower DLFs for the fixed-level condition did not result from any residual loudness cues. If such cues had been present, and had assisted subjects to detect small frequency differences, then the effect of level randomization would probably not have been so consistent across frequencies. It is more probable that the distraction of random level changes in the post-training experimental condition adversely affected these subjects' judgments, resulting in a general elevation of DLFs. Averaged across subjects, the mean increase in DLFs for the randomized-level condition was by a factor of 1.35 (ranging from 1.23 for S1 and S2, to 1.74 for S5). Despite this effect, it can be concluded that the data obtained in the randomized-level condition for each subject are probably not confounded by loudness-related effects. Therefore, only the randomized-level data are considered in the following analyses.

The average DLFs for the five normal-hearing subjects are shown in Fig. 4, and the DLFs obtained for subjects S1–S5 are shown in Fig. 5. Note that the DLFs are expressed as the mean frequency difference (Δf) divided by the reference frequency, and are plotted as a percentage on a logarithmic scale.

The results for the normal-hearing subjects are consistent with those reported previously (e.g., Wier *et al.*, 1977; Nelson *et al.*, 1983; Emmerich *et al.*, 1989; Moore and Glasberg, 1989; Moore and Peters, 1992). They show a monotonic decrease from a mean of 1.2% at 250 Hz to about 0.6% at 4 kHz. There was considerable inter-subject variability, as indicated on the graph by the error bars. However, the mean DLFs are very close to those predicted by a general equation (Nelson *et al.*, 1983), shown as the dashed curve. This equation is

$$\log(\Delta f) = a\sqrt{f} + k + m/\mathrm{SL},$$

where f is the frequency, SL is the sensation level, and values for the constants appropriate for normal-hearing listeners are: $a=0.023$, $k=-0.25$, and $m=4.3$ (Moore and Peters, 1992). For our normal-hearing subjects, absolute thresholds at each frequency were, on average, close to 0 dB HL, so the SLs were taken to be equal to the published intensities (in dB HL) for the 70-phon equal-loudness level at which the DLFs were obtained (Robinson and Dadson, 1956). To enable direct comparison with our data, the predictions of the equation were scaled to account for the differences between our experimental procedure and that on which the equation was based. Our procedure, and that of Moore and Peters (1992), estimate DLFs corresponding to a d' value of 1.6, while that of Nelson *et al.* (1983) used a d' value of 0.78. Because DLF is a linear function of d' (Nelson and Freyman, 1986), the values calculated from the equation were increased by a factor of 2.05. As shown in Fig. 4, the mean DLFs we obtained are generally very close to the predictions of the equation. The mean squared error [in log(DLF) terms] is less than 0.02.

The DLFs for subjects S1–S5 are plotted individually in Fig. 5 (solid lines), and the hearing thresholds are included for convenience (dashed lines). In each case the DLFs are a nonmonotonic function of frequency. Overall, they did not exceed 20% for any subject over the range of frequencies for which data were obtained.

At frequencies well below f_c, the DLFs are higher than the mean DLFs for the normal-hearing subjects. This is true even for S4, who has thresholds well within the normal range below 500 Hz. However, his DLFs are within the range we obtained across the five normal-hearing subjects. The remaining four subjects have both poorer thresholds and higher DLFs than normal in this frequency region.

At frequencies well above f_c, the data generally show an increase in DLFs with frequency. Only in the case of S3 are the DLFs at the highest frequencies tested near those obtained at the lowest frequencies. For the remaining subjects, the increase in DLF coincides with the worsening of hearing thresholds.

The most interesting feature of the data in Fig. 5 is that, for most (if not all) subjects, the DLFs are reduced near the cutoff frequency relative to those at surrounding frequencies. To verify this observation objectively, we compared the DLFs near f_c with those at higher and lower frequencies. Because our definition of f_c is somewhat arbitrary, it seemed reasonable to include DLFs from a narrow range of frequencies around f_c in this comparison. Therefore, for each sub-

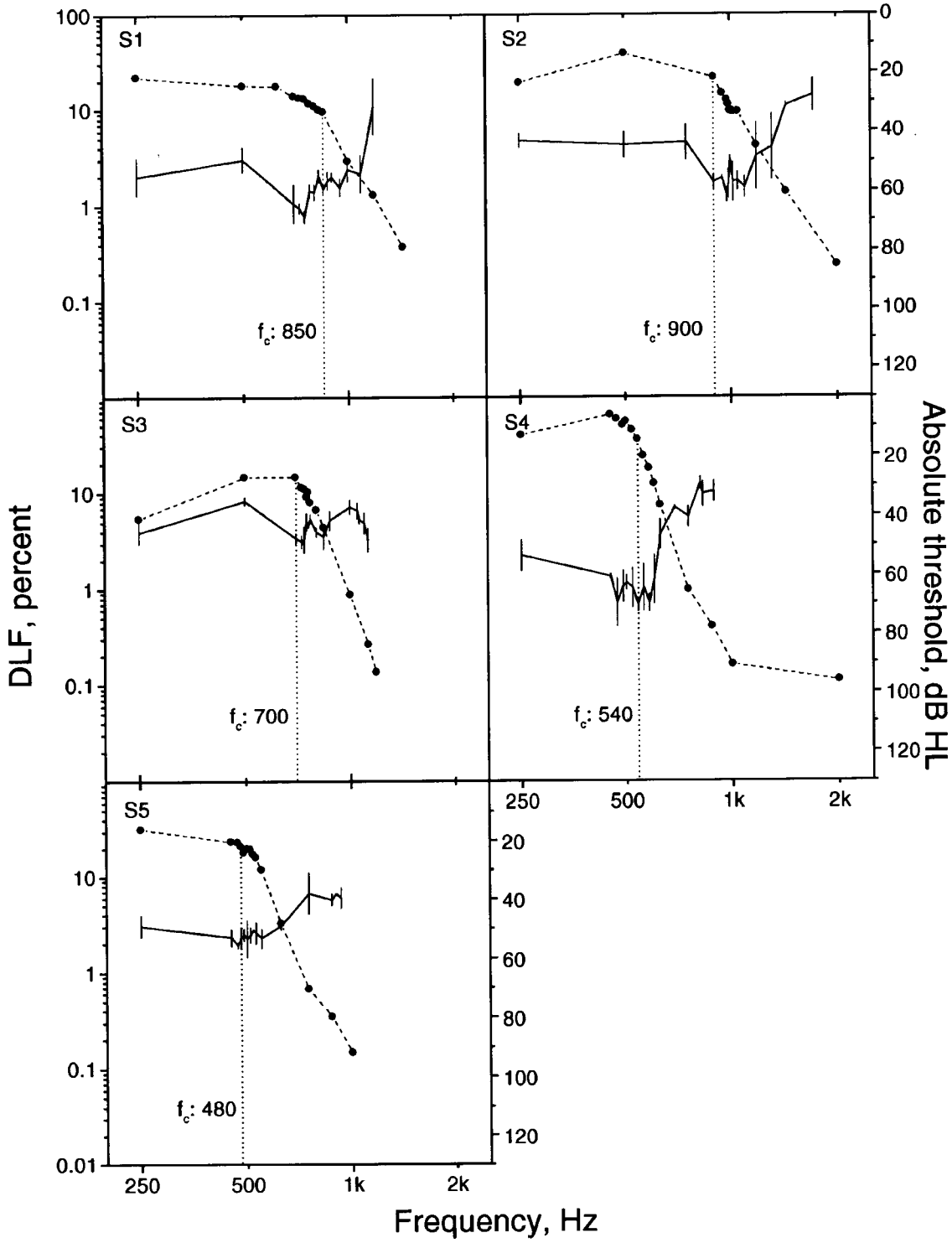

FIG. 5. Frequency difference limens (DLFs) for each of the five hearing-impaired subjects (S1–S5), plotted as in Fig. 4 (solid lines). Error bars indicate ± one standard deviation of the mean. The cutoff frequencies f_c (vertical dotted lines and adjacent numbers), and the absolute thresholds (dashed lines, right axes) are included for reference.

ject, the mean log(DLF) was calculated for frequencies in three bands: within one-third of an octave on each side of f_c; for all remaining lower frequencies; and for all remaining higher frequencies. A one-way ANOVA and Fisher's pairwise comparisons were used to determine, for each subject, whether the mean DLF was significantly lower in the band centered on f_c than in the other two bands. For S1–S4, this was the case ($p<0.05$). For S5, the mean DLF in the band centered on f_c was not significantly different from that in either the lower-frequency or the higher-frequency band. Although there are clear differences in the detailed data from each subject, the overall pattern of results is sufficiently consistent to suggest that there exist unusual perceptual characteristics affecting frequency discrimination near the cutoff frequency in the majority of these subjects. Possible explanations for these characteristics are discussed below.

III. GENERAL DISCUSSION

The results of experiments 1 and 2 reveal noteworthy features of both loudness perception and frequency discrimination that are associated with these subjects' steeply sloping high-frequency hearing loss. In particular, both the slopes of the loudness-growth functions and the DLFs exhibit local minima close to each subject's cutoff frequency. Although it is tempting to postulate that the same mechanism underlies both phenomena, further consideration suggests that, although cochlear excitation patterns may provide an adequate explanation for the loudness data, the DLF data are more likely to reflect partial functional reorganization in the auditory cortex (or subcortical auditory centers), at least in some subjects.

A. Loudness perception

The finding of significantly reduced loudness-growth slope near f_c is consistent with the results of Hellman (1994). Although the difference between the slope at the frequency near f_c and the slope at the lower frequency is smaller in our study (approximately 9%) than that reported by Hellman (approximately 17%), this disparity is not surprising, considering the differences in the procedures, in the ways in which the frequencies of the stimuli were selected, and between the subjects, particularly in their hearing thresholds. At least for frequencies up to f_c, our data are also consistent with recently published models of loudness perception with hearing impairment (Florentine *et al.*, 1997; Moore and Glasberg, 1997). As outlined in the Introduction, these models assume that subjects with steeply sloping high-frequency hearing loss, like our S1–S5, have cochlear impairment resulting in partial or total loss of sensitivity in a region having high characteristic frequencies. The lower boundary of this unresponsive region is presumed to be located close to the cutoff frequency. When stimuli are presented at frequencies below, but near, this boundary, the upward spread of excitation is effectively truncated. Therefore, the growth of loudness with intensity is less steep than at lower frequencies, where upward spread of excitation is presumed to be relatively normal. Thus it appears that the reduced slope of loudness functions near f_c is explicable in terms of peripheral mechanisms, and does not need an explanation based on central reorganization.

B. Frequency discrimination

The interpretation of the pattern of DLF results from experiment 2 is less straightforward. First, it is necessary to determine whether practice on the discrimination task could have led to an improvement in DLFs over time. This is important, because the subjects generally provided more DLF data for frequencies near f_c than for the remaining test frequencies. To investigate whether this additional experience could have caused the reduction in DLFs near f_c, we constructed scatter graphs for each subject containing the DLF estimate for each experimental run plotted against an integer representing the test sequence. Straight lines were fitted to these data. If reductions had occurred in DLFs as a consequence of practice, the lines would be expected to have negative slopes. However, in no cases were the slopes significantly different from zero ($p>0.05$). We repeated the analysis using exclusively data from the band of frequencies centered on f_c, with the same result for each subject. Together with the data showing an overall increase in DLFs across frequency in the randomized-level condition (compared with the fixed-level condition), these results strongly suggest that the DLF reductions near f_c are not a consequence of practice on the task for any subject.

To analyze the DLF data obtained with S1–S5 at the lowest frequencies, where hearing thresholds were near normal, the general equation predicting DLFs as a function of frequency and sensation level may be applicable, although it is important to note that it was based on DLFs obtained with normal-hearing listeners. To compare the data of S1–S5 with those obtained from our normal-hearing subjects, it is necessary to account for the different sensation levels used. For S1–S5, the sensation levels used at 250 and 500 Hz were, on average, about 17 dB lower than those used with the normal-hearing subjects. The equation predicts that this would result in an elevation of DLFs by a factor of approximately 1.07. Clearly this does not account fully for the DLFs we measured, which were, on average, about 3% for the hearing-impaired subjects, compared with about 1% for the normal-hearing subjects. However, for all hearing-impaired subjects except S4, hearing thresholds indicated a slight to mild hearing loss at the lowest frequencies, so it is likely that the elevation in the corresponding DLFs is related to a loss of hearing sensitivity. This is consistent with the observation that only S4 had both hearing thresholds and DLFs in the normal range at 250 and 500 Hz. Similar elevation of DLFs associated with various degrees of hearing loss have been reported previously (e.g., Turner and Nelson, 1982; Moore and Peters, 1992).

To interpret the DLF data at the higher frequencies, we need to consider current theories of frequency discrimination. One theory that has received much attention is based on auditory excitation patterns (e.g., Zwicker, 1970; Moore, 1989; Moore and Glasberg, 1989). The excitation pattern for a pure-tone stimulus is roughly triangular, with the peak located at a place corresponding to the frequency of the tone. A change in the stimulus frequency causes a shift in the excitation pattern, and consequently a change in excitation levels in the regions on each side of the peak. Because the slope of the excitation pattern is steeper on the low-frequency side of the peak, it has been suggested by some researchers that detection of changes in excitation level in that region might be sufficient to enable discrimination of changes in the stimulus frequency (see Moore, 1989; Moore and Glasberg, 1989). If this were an adequate explanation of frequency discrimination, however, it would be expected that random changes in the level of the stimuli (accompanying the frequency changes, as in our experiment 2) would result in elevation of the DLFs. This is inconsistent with most of the empirical data obtained with normal-hearing listeners and small level variations. For example, in one study where DLFs were measured in five subjects, both with fixed levels and with level randomization over a range of 6 dB, the effect of the randomization was to increase the average DLFs by a

factor of 1.15, but this increase was not statistically significant (Moore and Glasberg, 1989). In another study where a significant effect of level randomization was found (Emmerich *et al.*, 1989), the level was changed in steps ranging from 8 to 20 dB. Those steps were large enough to have directly affected the pitch perceived, and thereby to have affected the frequency discrimination. The insignificant effect of randomization over a narrower range of levels suggests that frequency discrimination may make use of information additional to, or other than, the level on the low-frequency edge of the excitation pattern. DLF data obtained when noise bands were applied to mask selected regions of the excitation pattern generally support this hypothesis. For example, DLFs were increased (relative to DLFs obtained in quiet) when tones were presented flanked by a low-pass or a high-pass noise, or in a notch created by combining a low-pass and a high-pass noise (Emmerich *et al.*, 1983, 1986). However, the increase was smaller than that expected if only information about excitation level is used in discriminating frequency changes, at least when only the upper side of the excitation pattern was masked by noise (Moore and Glasberg, 1989). This suggests that additional information is used to assist frequency discrimination. One possible source of such information is the phase locking of neural responses to temporal patterns in the stimulus. Presumably, temporal information, as well as excitation level information, would be available even in the responses of neurons that are tuned to frequencies somewhat distant from the stimulus frequency.

The steeply sloping hearing impairment of our subjects S1–S5 implies that, for stimulus frequencies below f_c, reduced information would be available from higher frequency regions. If, as suggested above, the cochleas of at least some of these subjects have an unresponsive high-frequency region, then for frequencies close to f_c, only information from the lower-frequency portion of the excitation pattern would be available. This condition is analogous to one where DLFs were obtained in normal-hearing listeners with a masking noise placed immediately above the stimulus frequency (Emmerich *et al.*, 1986; Moore and Glasberg, 1989). In those studies a statistically significant elevation in DLFs by a factor of about 1.5 was obtained relative to the unmasked condition. Furthermore, a study in which DLFs were measured in subjects who had normal hearing sensitivity up to 1500 Hz, and a loss of at least 20 dB averaged across higher frequencies, showed that DLFs at 1200 Hz were increased, on average, by a factor of 2 relative to normal (Turner and Nelson, 1982). This is in contrast to the results of our experiment. Although the DLFs obtained with our subjects S1–S5 were generally larger than normal, they tended to fall as the stimulus frequency was increased towards the cutoff frequency (Fig. 5). In fact, our data suggest that there is some additional mechanism contributing to frequency discrimination in these subjects which compensates partially for the effects of the reduced spread of excitation presumed to apply to stimuli near the cutoff.

Is it possible that this mechanism, and the local reduction in DLFs near f_c, can be understood in terms of neural plasticity? As outlined in the Introduction, there is experimental evidence of cortical plasticity in adult animals with restricted cochlear lesions. In these animal studies the region of cortex deprived of its normal input by a lesion was found to contain an expanded representation of lesion-edge frequencies. There is also evidence that training on frequency discrimination tasks in animals results in a similar expansion of the representation of the training frequencies (Recanzone *et al.*, 1993; Weinberger, 1995). If these results can be extended to humans, it is possible that the observed reduction in DLFs close to f_c reflects a related process. For example, if the high-frequency cochlear regions of subjects S1–S5 have been deprived of their normal acoustic input for a long time, as their etiologies seem to indicate, then it is plausible that frequencies near f_c would activate a larger than normal number of cortical neurons. Although the central (cortical or subcortical) mechanisms underlying frequency discrimination are not well understood, it is reasonable to assume that stimuli which can be discriminated must evoke different patterns of neural activity in the central nervous system. Because phase-locked frequency information is poorly preserved at levels above the brainstem, it is likely that the spatial distribution of activity would differ for stimuli that are discriminable in frequency. If circumstances result in a greatly expanded representation of a particular range of frequencies, it seems plausible that discrimination of frequencies in and around that range would be enhanced (relative to discrimination of other frequencies), because the expansion would increase the probability that different frequencies would generate different spatial patterns of activity. This supposition is supported by the animal studies suggesting an association between frequency discrimination ability and the spatial extent of the associated frequency representation (Recanzone *et al.*, 1993; Weinberger, 1995). Therefore, it is possible that the DLF reduction near f_c observed in our subjects might be a consequence of expanded cortical or subcortical (Irvine and Rajan, 1997) representation of those frequencies.

IV. CONCLUSIONS

The results of these two psychophysical studies on five subjects with steeply sloping high-frequency hearing impairment can be summarized as follows.

(1) Loudness perception

(a) Growth of loudness for tones presented near the cutoff frequency was less steep than that for tones presented at a lower frequency, although hearing thresholds were near normal at both frequencies. This was consistent with published models of loudness perception with sensorineural hearing loss, which assume that the upward spread of auditory excitation patterns is effectively truncated at a frequency near the cutoff.

(b) Growth of loudness at higher frequencies was steeper than at the cutoff frequency, consistent with the presence of recruitment where hearing thresholds were elevated.

(2) Frequency discrimination

(a) Across the range of frequencies tested, DLFs for pulsed

pure tones were generally elevated compared with DLFs for a control group of subjects with normal hearing.

(b) Below the cutoff frequency, the only subject having DLFs within the normal range was also the only subject with normal hearing thresholds at those frequencies.

(c) The DLF data from most subjects exhibited a local reduction near the cutoff frequency. It is speculated that this could be the result of functional reorganization of the auditory cortex (or subcortical auditory centers), similar to that observed in experimental animals with restricted cochlear lesions.

(d) For the normal-hearing subjects, the DLF data closely matched the predictions of a published general equation.

ACKNOWLEDGMENTS

The authors would like to thank all the subjects for their willing participation in this research. We also thank Michelle Dean, Dr. Harvey Dillon, Thomas Stainsby, Dr. Colette McKay, and Professor Graeme Clark for their help and advice, Professor Brian Moore of the University of Cambridge, England, for useful discussions, and Frank Devlin of Monash University for technical support. Constructive comments on an earlier version of this manuscript were provided by Dr. Bob Shannon and two anonymous reviewers. Financial support was provided by the Co-operative Research Centre for Cochlear Implant, Speech, and Hearing Research, and The Bionic Ear Institute.

Elbert, T., Flor, H., Birbaumer, N., Knecht, S., Hampson, S., Larbig, W., and Taub, E. (**1994**). ''Extensive reorganization of the somatosensory cortex in adult humans after nervous system injury,'' NeuroReport **5**, 2593–2597.

Emmerich, D. S., Brown, W. S., Fantini, D. A., and Navarro, N. C. (**1983**). ''Frequency discrimination and signal detection in band-reject noise,'' J. Acoust. Soc. Am. **74**, 1702–1708.

Emmerich, D. S., Fantini, D. A., and Brown, W. S. (**1986**). ''Frequency discrimination of tones presented in filtered noise,'' J. Acoust. Soc. Am. **80**, 1668–1672.

Emmerich, D. S., Ellermeier, W., and Butensky, B. (**1989**). ''A reexamination of the frequency discrimination of random-amplitude tones, and a test of Henning's modified energy-detector model,'' J. Acoust. Soc. Am. **85**, 1653–1659.

Flor, H., Elbert, T., Knecht, S., Wienbruch, C., Pantev, C., Birbaumer, N., Larbig, W., and Taub, E. (**1995**). ''Phantom-limb pain as a perceptual correlate of cortical reorganization following arm amputation,'' Nature (London) **375**, 482–484.

Florentine, M., Buus, S., and Hellman, R. P. (**1997**). ''A model of loudness summation applied to high-frequency hearing loss,'' in *Modeling Sensorineural Hearing Loss*, edited by W. Jesteadt (Erlbaum, Mahwah, NJ), pp. 187–198.

Harrison, R. V., Stanton, S. G., Ibrahim, D., Nagasawa, A., and Mount, R. J. (**1993**). ''Neonatal cochlear hearing loss results in developmental abnormalities of the central auditory pathways,'' Acta Oto-Laryngol. **113**, 296–302.

Hellman, R. P. (**1994**). ''Relation between the growth of loudness and high-frequency excitation,'' J. Acoust. Soc. Am. **96**, 2655–2663.

Irvine, D. R. F., and Rajan, R. (**1995**). ''Plasticity in the mature auditory system,'' in *Advances in Hearing Research*, edited by G. A. Manley, G. M. Klump, C. Koppl, C. Fastl, and H. Oeckinghaus (World Scientific, Singapore), pp. 3–23.

Irvine, D. R. F., and Rajan, R. (**1996**). ''Injury- and use-related plasticity in the primary sensory cortex of adult mammals: Possible relationship to perceptual learning,'' Clin. Exp. Pharmacol. Physiol. **23**, 939–947.

Irvine, D. R. F., and Rajan, R. (**1997**). ''Subcortical contributions to cortical reorganization consequent on restricted cochlear lesions in adult animals,'' Proc. Aust. Neurosci. Soc. **8**, 83.

ISO (**1996**). ISO 389-7, ''Acoustics—Reference zero for the calibration of audiometric equipment—Part 7: Reference threshold of hearing under free-field and diffuse-field listening conditions'' (International Organization for Standardization).

Kaas, J. H. (**1991**). ''Plasticity of sensory and motor maps in adult mammals,'' Annu. Rev. Neurosci. **14**, 137–167.

Kaas, J. H. (**1995**). ''The reorganization of sensory and motor maps in adult mammals,'' in *The Cognitive Neurosciences*, edited by M. S. Gazzaniga (MIT, Cambridge), pp. 51–72.

Levitt, H. (**1971**). ''Transformed up-down methods in psychoacoustics,'' J. Acoust. Soc. Am. **49**, 467–477.

Moore, B. C. J. (**1989**). *An Introduction to the Psychology of Hearing* (Academic, London), 3rd ed.

Moore, B. C. J., and Glasberg, B. R. (**1989**). ''Mechanisms underlying the frequency discrimination of pulsed tones and the detection of frequency modulation,'' J. Acoust. Soc. Am. **86**, 1722–1732.

Moore, B. C. J., and Glasberg, B. R. (**1997**). ''A model of loudness perception applied to cochlear hearing loss,'' Aud. Neurosci. **3**, 289–311.

Moore, B. C. J., and Peters, R. W. (**1992**). ''Pitch discrimination and phase sensitivity in young and elderly subjects and its relationship to frequency selectivity,'' J. Acoust. Soc. Am. **91**, 2881–2893.

Nelson, D. A., and Freyman, R. L. (**1986**). ''Psychometric functions for frequency discrimination from listeners with sensorineural hearing loss,'' J. Acoust. Soc. Am. **79**, 799–805.

Nelson, D. A., Stanton, M. E., and Freyman, R. L. (**1983**). ''A general equation describing frequency discrimination as a function of frequency and sensation level,'' J. Acoust. Soc. Am. **73**, 2117–2123.

Rajan, R., Irvine, D. R. F., Wise, L. Z., and Heil, P. (**1993**). ''Effect of unilateral partial cochlear lesions in adult cats on the representation of lesioned and unlesioned cochleas in primary auditory cortex,'' J. Comp. Neurol. **338**, 17–49.

Rajan, R., and Irvine, D. R. F. (**1996**). ''Features of and boundary conditions for lesion-induced reorganization of adult auditory cortical maps,'' in *Auditory System Plasticity and Regeneration*, edited by R. J. Salvi, D. Henderson, F. Fiorino, and V. Colletti (Thema, New York).

Ramachandran, V. S., Rogers-Ramachandran, D., and Stewart, M. (**1992**). ''Perceptual correlates of massive cortical reorganization,'' Science **258**, 1159–1160.

Recanzone, G. H., Schreiner, C. E., and Merzenich, M. M. (**1993**). ''Plasticity in the frequency representation of primary auditory cortex following discrimination training in adult owl monkeys,'' J. Neurosci. **13**, 87–103.

Robertson, D., and Irvine, D. R. F. (**1989**). ''Plasticity of frequency organization in auditory cortex of guinea pigs with partial unilateral deafness,'' J. Comp. Neurol. **282**, 456–471.

Robinson, D. W., and Dadson, R. S. (**1956**). ''A redetermination of the equal-loudness relations for pure tones,'' Br. J. Appl. Phys. **7**, 166–181.

Schwaber, M. K., Garraghty, P. E., and Kaas, J. H. (**1993**). ''Neuroplasticity of the adult primate auditory cortex following cochlear hearing loss,'' Am. J. Otolaryngol. **14**, 252–258.

Turner, C. W., and Nelson, D. A. (**1982**). ''Frequency discrimination in regions of normal and impaired sensitivity,'' J. Speech Hear. Res. **25**, 34–41.

Weinberger, N. M. (**1995**). ''Dynamic regulation of receptive fields and maps in the adult sensory cortex,'' Annu. Rev. Neurosci. **18**, 129–158.

Wier, C. C., Jesteadt, W., and Green, D. M. (**1977**). ''Frequency discrimination as a function of frequency and sensation level,'' J. Acoust. Soc. Am. **61**, 178–184.

Willott, J. F., Aitkin, L. M., and McFadden, S. L. (**1993**). ''Plasticity of auditory cortex associated with sensorineural hearing loss in adult C57BL/6J mice,'' J. Comp. Neurol. **329**, 402–411.

Zwicker, E. (**1970**). ''Masking and psychological excitation as consequences of the ear's frequency analysis,'' in *Frequency Analysis and Periodicity Detection in Hearing*, edited by R. Plomp and G. F. Smoorenburg (Sijthoff, Leiden).

Perceptual segregation and pitch shifts of mistuned components in harmonic complexes and in regular inharmonic complexes[a)]

Brian Roberts[b)] and Jeffrey M. Brunstrom
School of Psychology, University of Birmingham, Edgbaston, Birmingham B15 2TT, England

(Received 30 March 1998; accepted for publication 7 July 1998)

It is unclear whether the perceptual segregation of a mistuned harmonic from a periodic complex tone depends specifically on harmonic relations between the other components. A procedure used previously for harmonic complexes [W. M. Hartmann *et al.*, J. Acoust. Soc. Am. **88**, 1712–1724 (1990)] was adapted and extended to regular inharmonic complexes. On each trial, subjects heard a 12-component complex followed by a pure tone in a continuous loop. In experiment 1, a mistuning of ±4% was applied to one of the components 2–11. The complex was either harmonic, frequency shifted, or spectrally stretched. Subjects adjusted the pure tone to match the pitch of the mistuned component. Near matches were taken to indicate segregation, and were almost as frequent in the inharmonic conditions as in the harmonic case. Also, small but consistent mismatches, pitch shifts, were found in all conditions. These were similar in direction and size to earlier findings for harmonic complexes. Using a range of mistunings, experiment 2 showed that the segregation of components from regular inharmonic complexes could be sensitive to mistunings of 1.5% or less. These findings are consistent with the proposal that aspects of spectral regularity other than harmonic relations can also influence auditory grouping. © *1998 Acoustical Society of America.* [S0001-4966(98)03910-1]

PACS numbers: 43.66.Fe, 43.66.Hg, 43.66.Jh, 43.66.Ba [DWG]

INTRODUCTION

Many of the sounds to which the ear is exposed are periodic or nearly periodic in character. Hence, harmonic relations between the partials of a complex tone can provide a basis for the ascription of those partials to a common source. A number of studies have shown that the auditory system can discriminate a harmonic complex tone from a similar complex tone made inharmonic by the imposition of a small degree of mistuning on a single component (Moore *et al.*, 1985b; Carlyon, 1994; Lee and Green, 1994). However, Hartmann (1988) noted that a range of cues was potentially available to perform this task, including the perception of roughness or dissonance, in addition to the emergence of the mistuned component as a separate perceptual entity, with its own pure-tone-like pitch. The perceptual segregation of a mistuned component from an otherwise harmonic complex has been reported by Rasch (1978) and Martens (1984), and has been investigated systematically by Moore *et al.* (1986) and by Hartmann *et al.* (1990).

Moore *et al.* (1986) asked listeners explicitly to judge whether or not a mistuned component could be heard out from an otherwise harmonic complex at various degrees of mistuning for harmonic numbers 1–6. These authors found that segregation occurred for an approximately constant ratio of mistuning across these components, in the range 1.3%–2.1%. Hartmann *et al.* (1990) were concerned about the subjective nature of Moore *et al.*'s (1986) data. Therefore, they designed a discrimination experiment intended to provide an objective measure of the perceptual segregation of a mistuned partial, while minimizing the influence of other cues to inharmonicity (see Hartmann, 1988). These authors also extended the range of harmonic numbers tested up to the 16th, although their results for some partials above the 11th were subject to artifacts.[1] Listeners were presented with complex tones that were harmonic except for one mistuned component. Their task was to hear out the mistuned partial and to adjust the frequency of a pure tone until it matched that of the segregated partial. A match to within predefined criteria was accepted as a ''hit,'' and the proportion of hits obtained over a set of trials, the hit rate, was taken as a measure of the extent of segregation for that partial at that degree of mistuning. The results broadly confirmed and extended those of Moore *et al.* (1986).

As a by-product of their hits data, Hartmann *et al.* (1990) noted that there were small but systematic mismatches between the frequency of the mistuned partial and the preferred matching frequency of the adjustable pure tone. Following Terhardt (1971), they referred to these mismatches as pitch shifts, and found that they were generally exaggerations of the mistuning imposed on a partial. Pitch shifts were assumed to result from partial masking effects in the pitch model of Terhardt (1979) and his colleagues (Terhardt *et al.*, 1982). However, Hartmann *et al.* (1990) found that an implementation of Terhardt *et al.*'s (1982) model was unable to predict the pattern of pitch shifts that they observed. Instead, the model predicted positive pitch shifts for negative as well as for positive mistunings.

Hartmann and Doty (1996) have since confirmed Hartmann *et al.*'s observations in a study designed to obtain more accurate measures of these pitch shifts. In their study, the

[a)]A summary of this research was presented at the Joint 16th International Congress on Acoustics and 135th Meeting of the Acoustical Society of America, Seattle, WA, June 1998 [J. Acoust. Soc. Am. **103**, 2768(A) (1998)].

[b)]Electronic mail: b.roberts@bham.ac.uk

harmonic number tested was fixed for all trials in an experimental run, and a large degree of mistuning (8%) was used on the first trial to cue the subject to the appropriate frequency region for that run. Hartmann and Doty interpreted their findings in terms of a combined place-and-time model, based on partial masking interactions in the excitation pattern and predicted peak locations in the interspike-interval histogram of neural activity, but could not account for key aspects of the data. In particular, their hybrid model had difficulty in accounting for the apparent saturation, and sometimes supersaturation, of the pitch-shift effect for higher degrees of mistuning, and was unable to account for the pitch shifts evident for the fundamental component.

de Cheveigné (1997) has since pointed out that the pattern of displacement seen in the pitch-shift data of Hartmann *et al.* (1990) and Hartmann and Doty (1996) can instead be accounted for in terms of statistical decision theory. The operation of a template mechanism is assumed, perhaps like the ''harmonic sieve'' proposed by Duifhuis *et al.* (1982), and Scheffers (1983a, b). Consider a mistuned partial, lying on one side of a ''slot'' in a template that is optimally aligned with the partials of an otherwise harmonic complex tone. The extent of its perceptual segregation can be assumed to depend on its distance from the slot center, increasing with displacement from the center up to some asymptotic level. Furthermore, the internal representation of the frequency of any partial will be influenced from trial to trial by random processes. Since those trials in which the frequency of the mistuned partial is represented as more displaced from the slot center will lead to greater perceptual segregation, and hence give higher hit rates, it follows that the pitch estimates will be displaced from the center of the slot in either direction. This effect will saturate as the partial moves further away from the slot center. Although Lin and Hartmann (1998) have pointed out that de Cheveigné's (1997) model cannot account for both the pitch shifts and high hit rates observed by Hartmann and Doty (1996), it should be noted that this objection might be overcome if the model were modified to include noise in the neural representation of the target partial *within* a trial.

Consistent with de Cheveigné's (1997) proposal of a template mechanism, Lin and Hartmann (1998) have since shown that the pitch shifts found when a harmonic is mistuned are not primarily dependent on local interactions between partials. In particular, these pitch shifts can be found for partials isolated from the rest of the complex by gaps of one or more harmonic positions. Lin and Hartmann have interpreted their findings as evidence of an intimate connection between the ascription of pitch and the attribution of common source to a set of harmonics, namely that auditory organization is a consequence of the operation of a template-based pitch mechanism. However, de Cheveigné has pointed out that any arbitrary template, whatever its nature or origin, would produce similar pitch shifts for partials mistuned from their appropriate frequencies. Furthermore, while pitch perception is clearly of great importance in hearing [consider, e.g., Houtsma and Goldstein's (1972) demonstration that low pitch is ascribed even to dichotically presented two-component stimuli], the notion that it precedes auditory grouping is difficult to reconcile with the body of research showing that auditory attributes depend on the outcome of grouping processes (see Bregman, 1990).

Roberts and his colleagues (Roberts and Bregman, 1991; Roberts and Bailey, 1993a, b, 1996a, b; Roberts, 1998) have explored the role in auditory grouping of aspects of spectral patterning other than harmonicity. Roberts and Bregman (1991) showed that a single even harmonic in an otherwise odd-harmonic complex is typically more salient than its odd neighbors. Roberts and Bailey (1996b) have extended this finding to regular but inharmonic complexes, created by applying either frequency shift or spectral stretch manipulations to harmonic stimuli. These authors have suggested that their findings may indicate the operation of a principle of auditory grouping based on common spectral pattern.

Our informal listening to stimuli derived by applying moderate degrees of frequency shift or spectral stretch to multi-component periodic tones with consecutive harmonics suggests that these complexes sound far more coherent than randomly distributed partials. They also have some form of low pitch, although it may be weak and/or ambiguous. The experiments reported here have attempted to evaluate further the proposal that common spectral pattern can influence auditory grouping by applying the mistuned partial-matching paradigm of Hartmann *et al.* (1990) to regular inharmonic complexes of this kind. If common spectral pattern, in a broader sense than harmonicity, can influence spectral fusion, then regularly spaced but inharmonic components should also be sensitive to mistuning. Mistuning a partial should cause it to segregate just as in the harmonic case, allowing listeners to adjust a pure tone to a value near the frequency of the mistuned partial. One might also expect to find pitch shifts displaced from in-tune positions, as predicted by de Cheveigné (1997) for any template that mediates spectral fusion.

From a broader perspective, further evidence to support the notion that regularities other than harmonic relations can also act as a basis for spectral grouping would have considerable implications for our understanding of auditory perception. In particular, it would suggest a flexible system that can utilize a range of structures inherent in the spectra of a variety of sounds, rather than a mechanism equipped to deal solely with harmonic or near-harmonic stimuli.

I. EXPERIMENT 1

A. Method

1. Subjects

Three subjects participated, all of whom reported normal hearing. One subject was the second author and the others were research students from other laboratories in the School. All had some experience of taking part in auditory perception experiments, and one claimed to be musically experienced.

2. Task

Each trial consisted of a repeating cycle of a complex tone followed by a pure tone, with each sound separated from the next by a brief silent interval. One of the compo-

nents of the complex tone was mistuned from its appropriate frequency. The subjects' task was to adjust the frequency of the pure tone until its pitch matched that of the mistuned component. The ease with which this was possible depended on the perceptual salience of the mistuned component in relation to that of the other partials in the complex. There was no limit on the number of stimulus cycles that was permitted in a trial. The adjustment was made using a trackball mouse with two different sensitivity settings, which could be selected freely via a mouse button. The default was a coarse control that allowed rapid adjustment to the chosen frequency region. The fine control was ten times more sensitive, and subjects were encouraged to use this setting for final adjustments before selecting their best match using another mouse button. At the end of a trial, subjects were given feedback on their performance via a computer screen (see Sec. I A 4). Subjects chose when to start each trial, and were free to rest at any time between trials.

3. Stimuli and conditions

Within a trial, each stimulus cycle contained a 420-ms complex tone followed by a 310-ms pure tone, both including linear onset and offset ramps of 20 ms each. The durations of the within- and between-cycle silent intervals were 200 and 500 ms, respectively. These were chosen to create a rhythm that clearly identified the within-cycle order of the tones. The complex tone consisted of the first 12 partials of a nominal fundamental ($F0$) frequency, chosen randomly from a rectangular distribution with a width of $\pm 10\%$ around 200 Hz. All of the components were in sine phase and of equal amplitude, each set to a level of 60 dB SPL. The pure tone was set to the same level. The initial frequency of the pure tone was chosen randomly within the range of adjustment, 100–3200 Hz, quantized in steps of 2 Hz. This range was chosen to exceed that spanned by components 1 and 12 for the lowest and highest possible $F0$ frequencies, respectively, for all conditions. One of ten components of the complex tone, chosen from the set 2–11, was mistuned by $\pm 4\%$ from its appropriate frequency. Components 1 and 12, which constituted the spectral edges of the complex, were not tested.

There were three conditions, which differed in the type of complex tones used. For conditions 1–3, these were harmonic, frequency shifted, and spectrally stretched, respectively. The frequency shift used was 15% of the nominal $F0$ (e.g., 30 Hz added to the frequency of each component of a harmonic series with an $F0$ of 200 Hz). The spectral stretch used was 3% of the nominal $F0$ (e.g., a cumulative increment of 6 Hz added to the frequency spacing of the components with increasing component number for a harmonic series with an $F0$ of 200 Hz). This kind of spectral manipulation has previously been employed by Plomp (1964), Fine and Moore (1993), and Roberts and Bailey (1996b). The frequencies of the partials comprising the complex tones for a nominal $F0$ of 200 Hz are listed in Table I. The use of component numbers for the inharmonic conditions is analogous to their use in the harmonic condition.

All stimuli were generated using MITSYN software (see Henke, 1990) at a sampling rate of 16 kHz, and played with a precision of 16 bits via a D/A converter (Data Translation DT2823). They were low-pass filtered (corner frequency $=5.2$ kHz, roll-off$=100$ dB/oct.) and presented binaurally over Sennheiser HD 480-13II earphones. The levels of the stimuli were set using a programmable attenuator (0.25-dB steps), and were calibrated with a sound-level meter (Brüel & Kjaer type 2209, linear weighting) connected to the earphones by an artificial ear (type 4153). The stimuli were presented to the listeners in a sound-attenuating chamber (Industrial Acoustics).

TABLE I. For a nominal $F0$ frequency of 200 Hz, columns 2–4 show the in-tune frequencies (in Hz) of the components comprising the complex tones used in experiments 1 and 2.

Component No.	Condition 1 (harmonic)	Condition 2 (15% shifted)	Condition 3 (3% stretched)
1	200	230	200
2	400	430	406
3	600	630	618
4	800	830	836
5	1000	1030	1060
6	1200	1230	1290
7	1400	1430	1526
8	1600	1630	1768
9	1800	1830	2016
10	2000	2030	2270
11	2200	2230	2530
12	2400	2430	2796

4. Procedure

Each session consisted of three consecutive sets, each in a new randomized order, of all combinations of component number and direction of mistuning for one condition only, giving a total of 60 trials (3 sets$\times$10 components$\times$2 directions). Three sessions were run for each condition to give nine responses per stimulus. Each condition was completed, in the appropriate order, before the next was begun. The presentation order for the conditions across the three listeners was given by cyclic permutation. The total number of trials per subject was 540.

Feedback on performance was given to subjects at the end of each trial. If the chosen response was within $\pm 0.8 \times$nominal $F0$ of the correct value, the message ''within range'' was displayed. If the response was above or below this range, the message ''much too high'' or ''much too low'' was displayed, as appropriate.[2] Before the main experiment, subjects received two practice sessions to familiarize them with the full set of stimuli. Each session consisted of three consecutive sets, one for each condition, of all 20 combinations of component number and direction of mistuning, giving 60 trials in total. The order of the conditions was the same for each listener as in the main experiment.

5. Data analysis

The data analysis was based closely on that used by Hartmann *et al.* (1990), who used a simple classification of responses as ''hits'' or ''misses.'' Those authors noted that this approach obscured some aspects of the data, in particular the pattern of errors among the data points classified as

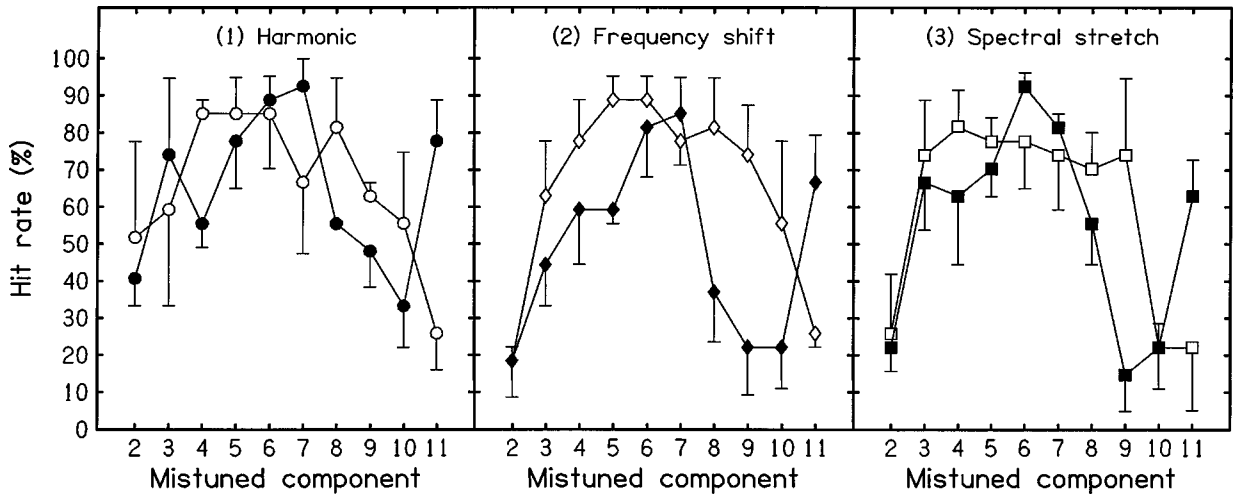

FIG. 1. Mean hit rates for three subjects (with intersubject standard errors) in conditions 1–3 of experiment 1. Parts 1–3 show these values for the corresponding conditions across component numbers 2–11. Hit rates for positive and negative mistunings are represented by filled and open symbols, respectively.

misses, but had the advantage of facilitating further quantitative analysis. However, they also noted that the classification of responses as hits or misses was complicated by pitch-shift effects—systematic mismatches between the pitch of a partial and an isolated pure tone of the same frequency (Terhardt, 1971). This problem was tackled by employing a two-stage procedure to classify the responses, as described below.

To be classified as a hit, a response was first required to fall within $\pm 1.0\times$nominal $F0$ of the frequency of the mistuned partial. This criterion was more lax than that used for feedback, owing to evidence of substantial pitch shifts for some stimuli. The second criterion was based on the clustering of the responses that passed the first criterion. A mean and standard deviation were calculated for these data. If the standard deviation exceeded 2.5% of the frequency of the mistuned component, then the data point most distant from the mean was rejected and a new mean and standard deviation were calculated. This procedure was repeated until the clustering criterion was met, or only two data points remained. In cases where these two data points failed the clustering criterion, the data point further from the frequency of the target component was rejected. In cases where only one data point passed the first criterion, that point was accepted as a hit. For each subject, the number of hits per stimulus (0–9) was converted to a percentage. A mean hit rate and intersubject standard error were then calculated for each stimulus.

Pitch shifts were calculated from those responses that were classified as hits. A pitch shift for a given stimulus was defined as the mean deviation of the hits, in units of component number, from the frequency of the mistuned partial. The use of a component number scale was to preserve as close an equivalence as possible across conditions for corresponding component numbers. To minimize the number of empty cells in a quantitative analysis of these pitch shifts, an estimate was calculated whenever a subject achieved at least one hit for a given stimulus. From these estimates, a mean pitch shift and intersubject standard error were then calculated for each stimulus.[3]

B. Results and discussion

1. Hit rates

The data are displayed in Figs. 1 and 2. Figure 1 shows the effects of direction of mistuning and component number in a separate panel for each condition. Figure 2 shows in one panel the effects of component number for all three conditions, when the data are collapsed across direction of mistuning. The data were assessed using a three-factor repeated-measures analysis of variance.

The most striking observation is the general similarity in the response profiles for the three conditions. The mean hit rates for conditions 1–3, collapsed across component number and direction of mistuning, were 65.2%, 57.4%, and 57.6%, respectively. Clearly, subjects were able to hear out mistuned components not only from harmonic complexes, but also from shifted and stretched complexes, because all of these values were well above chance.[4] The lower proportion of hits seen in the inharmonic conditions resulted chiefly from the lowest and highest component numbers tested, but the overall difference between conditions was not significant $[F(2,4)=2.02,\ p=0.247]$. A significant main effect was

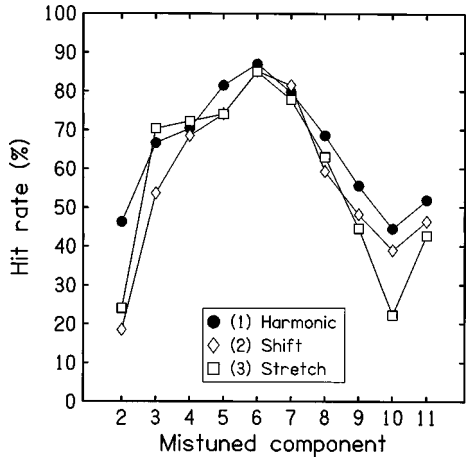

FIG. 2. Mean hit rates for three subjects (with intersubject standard errors) in conditions 1–3 of experiment 1. Hit rates in each condition are shown for components 2–11 when collapsed across direction of mistuning.

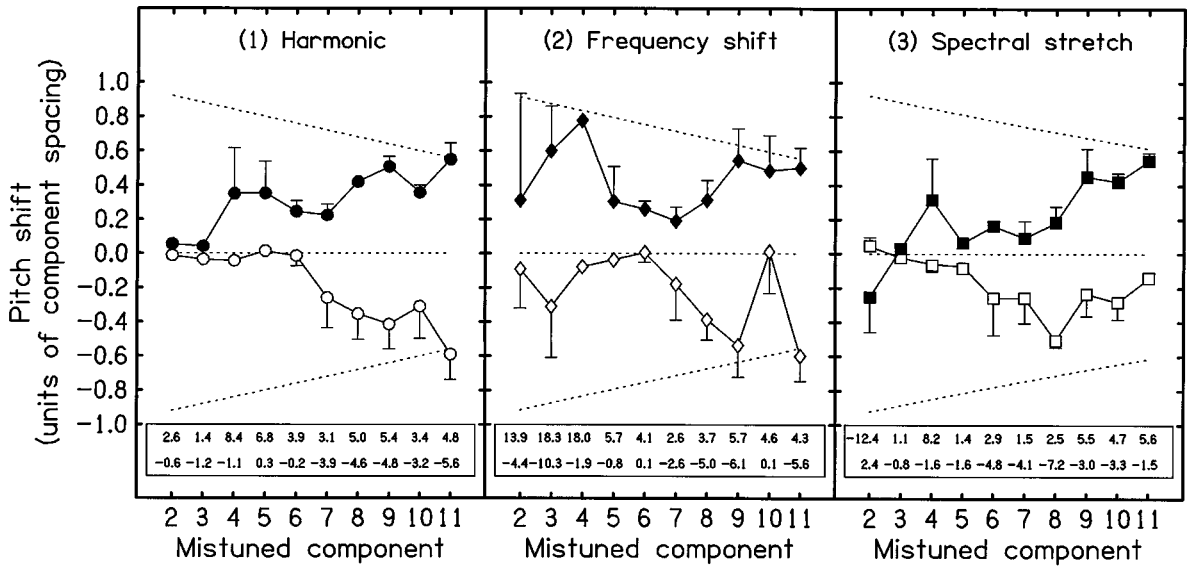

FIG. 3. Mean pitch shifts for three subjects (with intersubject standard errors) in conditions 1–3 of experiment 1. Parts 1–3 show these values for the corresponding conditions across component numbers 2–11. Pitch shifts for positive and negative mistunings are represented by filled and open symbols, respectively. The inset gives the mean pitch shifts expressed as percentage changes (for positive mistunings in the top row and for negative mistunings in the bottom row). The dotted lines indicate pitch shifts that would correspond to the frequencies of the components immediately adjacent to the mistuned component.

found for component number [$F(9,18)=6.69$, $p<0.001$]. Figure 2 shows that hit rates generally peaked in the region 5–7 and declined for higher and lower component numbers. The elevated hit rate for a positive mistuning on component 11 in all conditions was the only clear exception to this pattern (see Fig. 1). Although the main effect of direction of mistuning was not significant [$F(1,2)=3.67$, $p=0.196$], a significant two-way interaction was found for direction $\times$component [$F(9,18)=18.50$, $p<0.001$]. The origin of this interaction is evident in Fig. 1. In all conditions, the hit-rate profiles peak at components 6 and 7 for positive mistunings, but are broadly flat over the range 4–9 for negative mistunings. The reason for this difference in profiles is unclear. None of the other interaction terms was significant [condition$\times$component: $F(18,36)=0.66$, $p=0.822$; direction$\times$condition: $F(2,4)=0.97$, $p=0.455$; direction $\times$condition$\times$component: $F(18,36)=0.77$, $p=0.715$].

The peak region in the hit-rate profiles overlaps with, but does not correspond to, the dominant region of components (3–5) predicted for these $F0$ frequencies (Ritsma, 1967). A similar experiment using different nominal $F0$'s would be required to assess the effect on the profile of the absolute frequencies of the components tested. The hit-rate profile reported by Hartmann *et al.* (1990) for a mistuning of $\pm 4\%$ on a partial in a harmonic complex with a nominal $F0$ of 200 Hz was not an inverted U-shaped function. However, this is almost certainly because the performance of their highly trained subjects (the three authors) was nearly perfect for this condition. In conditions where the task was made more difficult by using smaller degrees of mistuning, the highest hit rates were found in the region 3–7.

2. Pitch shifts

The mean pitch shifts are displayed in Fig. 3, in units of component spacing (see Sec. I A 5). These data were assessed using a general linear model designed to provide an analysis similar to that of the balanced ANOVA used to assess the hit-rate data. This was necessary because of missing pitch-shift values in cases where none of a subject's responses to a stimulus was a hit (only seven cases in total).

The findings for the harmonic condition replicate the main observation of Hartmann *et al.* (1990) and of Hartmann and Doty (1996) that pitch shifts occur in the direction of the mistuning, representing an exaggeration of the displacement of the target component from its in-tune frequency. Hartmann *et al.*'s report of smaller pitch shifts for negative mistunings is also consistent with the pattern observed here, at least for components 2–6. In units of component number, the pitch shifts tended to grow progressively with an increase in component number, until coinciding almost exactly with the in-tune frequency of the nearest neighbor for component 11. Hartmann *et al.* (1990, Fig. 2) shows exactly this pattern for a mistuning of $+4\%$.

The pitch-shift profiles for the inharmonic conditions were like that for the harmonic condition in the most important aspect—that pitch shifts were an exaggeration of the direction of mistuning. Indeed, the main effect of direction of mistuning was found to be significant [$F(1,2)=153.97$, $p=0.006$]. However, the difference between the conditions was also sufficient to reach significance as a main effect [$F(2,4)=10.77$, $p=0.025$]. The profile for the shifted condition shows evidence of more extreme pitch shifts for positive mistuning of components 2–4, which resulted from a considerable number of matches close to the in-tune frequency of the next higher component. There was also an anomalous pitch shift for negative mistuning of component 10, but otherwise the profile for components 5–11 was similar to that seen in the harmonic condition. The profile for the stretched condition was more similar to that for the harmonic condition. The main difference was the finding of relatively

smaller pitch shifts for negative mistunings of the highest components. Overall, the dependence of pitch shift on component number is shown by the significant interaction term for direction×component [$F(9,18)=9.16$, $p<0.001$]. The main effect of component number was not significant [$F(9,18)=1.39$, $p=0.265$]. Also, none of the other interaction terms was significant [condition×component: $F(18,36)=1.05$, $p=0.431$; direction×condition: $F(2,4)=4.82$, $p=0.086$; direction×condition×component: $F(18,29)=1.51$, $p=0.156$].

The pitch shift evident in all conditions for a positive mistuning of component 11 suggests that the marked increase in hit rate seen for this manipulation was probably an artifact. This pitch shift corresponds closely in all cases to the in-tune frequency of component 12, which was the highest component in the complex. This component will have had a salient edge pitch associated with it (Kohlrausch and Houtsma, 1992; Moore and Ohgushi, 1993), and matches to it would be indistinguishable from those to the mistuned target.

The pitch-shift estimates obtained from this experiment were only supplementary to the computation of hit rates, for two reasons. First, subjects were not directed to listen to any particular frequency region within the complex, and so mistuned targets that were more difficult to hear out will have given rise to low hit rates and hence poor estimates of pitch shifts. Second, the feedback criterion needed to be lax to account for pitch shifts, and this would not have encouraged great accuracy in the matches made by the subjects. A procedure like that used by Hartmann and Doty (1996) would be required to study pitch shifts in greater detail. However, there were notable common features seen across the conditions in our pitch-shift estimates, despite these limitations. In particular, the finding of pitch shifts in the same direction as the mistuning for harmonic, shifted, and stretched complexes suggests the operation of a similar mechanism in the perceptual segregation of mistuned partials from the original complexes in all cases. We shall return to this point in the following section.

II. INTERIM DISCUSSION

The broad similarity in both hit-rate and pitch-shift profiles across conditions is consistent with the notion that the auditory system can be sensitive to the spectral regularity of inharmonic complex tones as well as harmonic ones. However, it is important to consider how well these findings can be accounted for by the quasiharmonic nature of shifted and stretched stimuli. The notion of a regular inharmonic template should only be invoked if an explanation in terms of a hypothetical device like the harmonic sieve proves inadequate.

Frequency-shifted stimuli have long been used to study the mechanisms of low pitch perception (de Boer, 1956, 1976; Schouten *et al.*, 1962; Patterson, 1973; Patterson and Wightman, 1976). The multi-component complexes used in Patterson and Wightman's (1976) study included examples very similar to those used in experiment 1 (nominal $F0=200$ Hz, component numbers 1–12 present, equal-amplitude components). The dominant components determining the low pitch of these frequency-shifted complexes were shown to be 4 and 5, and the slope of the near-linear function relating low pitch to the degree of frequency shift was estimated to be around 0.23. From this, we can estimate the low pitch of one of our stimuli, with a nominal $F0$ of 200 Hz and a fixed frequency shift of 15%, to be about 207 Hz. This is consistent with our informal observations of the low pitch of these complexes.

Taking this value as the $F0$ frequency for a harmonic sieve with a slot width of ±3%, components 3–12 would be passed when in tune.[5] This outcome supports the quasiharmonic account of the findings, which may also explain some details of the findings. In particular, partials above the fourth show a progressive displacement below the centers of their corresponding slots for a harmonic sieve with an $F0$ of 207 Hz, such that components 9 and 10 fit the sieve when they are mistuned by +4% about as well as when they are in tune. This might explain the marked depression in hit rates for positive mistunings of components 8–10 in the shifted condition. However, it should be noted that the same tendency is evident for those components in the other conditions, and such an account cannot explain the finding for the harmonic case. Furthermore, one would predict a marked dichotomy in hit rates between positive and negative mistuning on component 2 in the shifted condition, as −4% gives a value close to the center of slot 2, whereas +4% falls outside the slot. However, hit rates for both mistunings were equally depressed.

Less is known about the low pitches of stretched complexes, but best matches can be approximated by applying a harmonic sieve with an adjustable $F0$ to these stimuli. This was achieved using an implementation of Scheffers' (1983a, b) equations, with the slot width set to ±3%.[5] For a stretch factor of 3% and a nominal $F0$ frequency of 200 Hz, the best two matches were for sieve $F0's$ of 206 and 258 Hz. Both of these would pass 8 of the 12 components. The lower-$F0$ sieve would pass components 1–5 and 9–11 through slots 1–5 and 10–12, and the higher-$F0$ sieve would pass components 5–12 through slots 4–11. Both sieves pass components through slots 4 and 5, which are key components in the dominant region (Ritsma, 1967), although in each case the pass through one of these slots is very marginal. The lower-$F0$ sieve has the advantage of passing more of the components in the dominant region, but has the disadvantage of passing two nonconsecutive sets of partials. Informal listening suggested an ambiguous pitch with a primary value close to 206 Hz and a secondary value close to 258 Hz.

Whichever of these two pitches is assumed, the profile of hits in the stretched condition is hard to explain. If it depended on a quasiharmonic match to an $F0$ of 206 Hz, then components 6–8 should not integrate into the complex when in tune. These should present false targets for matching that would be expected to reduce markedly the overall level of hits, which did not happen. Moreover, mistunings of −4% on partials 6 and 7, and of +4% on partial 8, should cause them to pass through slots 6, 7, and 9, respectively. No corresponding decrements in hit rate were seen for these values. To the extent that the hit rate declined for +4% on partial 8, the decline was smaller than occurred for the same partial in

the harmonic case. Similarly, a quasiharmonic match to an $F0$ of 258 Hz would not predict the high hit rates to mistunings of partials 3 and 4, comparable to those found in the harmonic condition. Only by assuming some kind of blend of quasiharmonic matches to the two candidate low pitches can the hit-rate profile be understood. Even then, it is unclear how such a combination would operate in practice, as mistuning a partial so that it falls outside the slots of one sieve would often lead to it being passed by the other.

The slot width of $\pm 3\%$ chosen for our implementation of Scheffers' (1983a, b) harmonic-sieve model was based on the finding that a resolved harmonic ceases to make its full contribution to the low pitch of a periodic complex tone when it is mistuned by more than $\pm 3\%$ (Moore *et al.*, 1985a; Darwin *et al.*, 1994). This value was generous in relation to perceptual segregation. For example, Moore *et al.* (1986) found that only a small degree of mistuning, between 1.3% and 2.1%, was needed for listeners to report hearing a low partial in an otherwise harmonic complex as a separate tone. Indeed, Hartmann *et al.* (1990) have shown that it is sometimes possible to hear out a partial when it is mistuned from a harmonic value by as little as 0.5%. These findings make any attempt to explain the hit-rate profiles observed for the inharmonic conditions in terms of quasiharmonicity even more problematic.

It was noted earlier that the pitch shifts found for the shifted and stretched stimuli, although less regular across component number than for the harmonic stimuli, were typically in the same direction as the mistuning imposed on the target. According to de Cheveigné's (1997) template hypothesis, pitch shifts result from variability in the internal representation of a mistuned partial that falls on the sloping skirt of a slot in the template that is centered on or close to the in-tune frequency. From this, it follows that the slot centers for the hypothetical templates applied to our inharmonic stimuli must typically fall between the frequencies defined by $\pm 4\%$ mistuning for each of the set of target partials. A single harmonic template cannot meet this criterion. Rather, our findings imply once again either a blend of quasiharmonic matches to two or more candidate low pitches, or a single template with slots that are spaced inharmonically.

III. EXPERIMENT 2

A. Introduction

Mistunings of $\pm 4\%$ were used in experiment 1 to ensure reasonably high hit rates and relatively stable estimates of pitch shifts for the harmonic condition, against which the two inharmonic conditions could be compared. Experiment 1 showed few differences between the conditions, but more important differences might be revealed by testing other degrees of mistuning. In particular, the inclusion of smaller degrees of mistuning can provide more information on the spectral center and frequency tolerance of a slot in a hypothetical template aligned with the partials of a complex tone. Indeed, a demonstration for inharmonic stimuli of a sensitivity to displacement in either direction of a target partial from its in-tune frequency, across a set of component numbers, would strengthen the notion that a template can be constructed to mediate the fusion of regular but inharmonic complexes. As well as hits, evidence of pitch shifts of the same sign as the mistuning for smaller degrees of mistuning would also lend support to this concept. Therefore, an experiment was devised that would allow a cross-condition comparison of the function relating hit rate to degree of mistuning across a range of values.

B. Method

1. Stimuli and conditions

As before, there were three conditions in which harmonic, 15% frequency-shifted, and 3% spectrally stretched complex tones were used. However, the mistuning of a target partial varied in degree as well as in sign. To keep the number of trials within acceptable bounds, the set of component numbers tested was restricted to 3, 6, and 9. The range of mistunings available for testing that would not infringe on neighboring partials was more restricted in percentage terms for the higher component numbers, and so a different set of values was used for the three components tested. Mistunings of $\pm 0.75\%$, 1.5%, 3%, and 6% were used for all three components (eight values). For component 6, additional mistunings of $\pm 9\%$ were used (10 values), and for component 3, additional mistunings of $\pm 9\%$, 12%, and 18% were used (14 values).

2. Procedure and subjects

Each session consisted of all combinations of degree of mistuning, direction of mistuning, and condition for the three components tested, giving a total of 96 trials. The order of these trials was randomized anew for each session. Nine sessions were run per subject, giving a grand total of 864 trials. Feedback was changed to display the ''within range'' message to matches within $\pm 1.0\times$nominal $F0$ of the correct value. This was in response to the substantial pitch shifts found for some stimuli in experiment 1. The practice session given beforehand was the same as a single session in the main experiment.

C. Results and discussion

1. Hit rates

The hit rate data are displayed in Figs. 4–6, which show the results for components 3, 6, and 9, respectively. This depiction is used to facilitate cross-condition comparisons within corresponding component numbers. A separate repeated-measures ANOVA was used to assess the data for each component number.[6] These analyses are considered in turn.

For component 3, a significant main effect was found for degree of mistuning [$F(6,12)=9.62$, $p=0.001$], and for condition [$F(2,4)=11.06$, $p=0.023$], but not for direction of mistuning [$F(1,2)=0.17$, $p=0.724$]. None of the interaction terms was significant. Figure 4 shows that the mistuning profiles for component 3 were quite similar across conditions. All were trough shaped, centered around the in-tune position for the target, and of similar bandwidth (the functions asymptoted around $\pm 6\%$ mistuning). The conditions differed somewhat in their asymptotic hit rates, as reflected in the

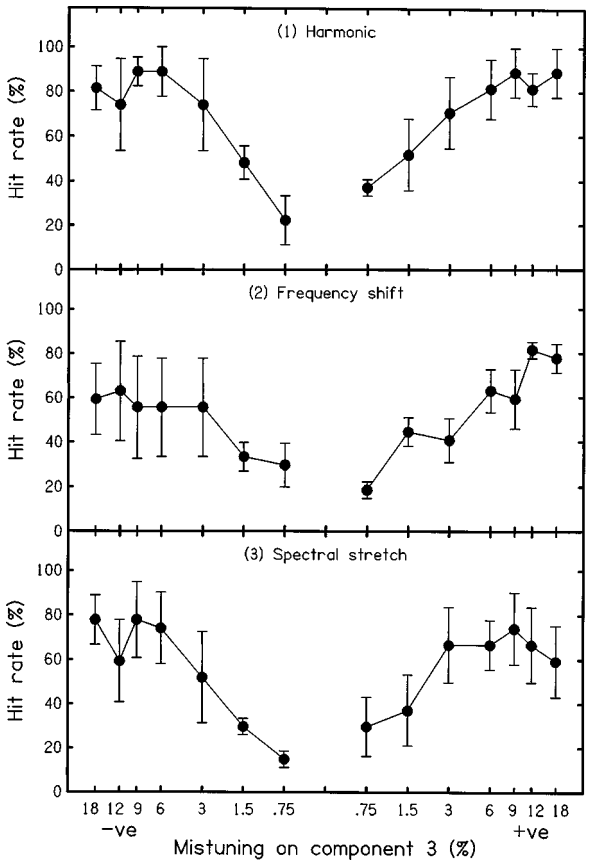

FIG. 4. Mean hit rates for three subjects (with intersubject standard errors) in conditions 1–3 of experiment 2. Each part shows these values for component 3 in the corresponding condition across the range of mistunings tested.

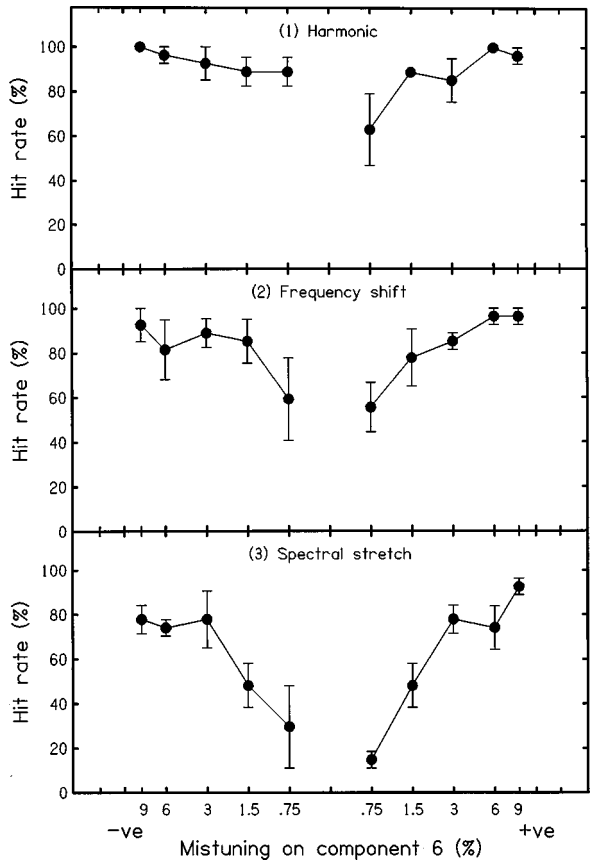

FIG. 5. Same as Fig. 4, except that component 6 was mistuned.

overall means of 69.8%, 52.6%, and 56.1% for harmonic, shifted, and stretched stimuli, respectively.[7] The lower performance in the inharmonic conditions probably reflected the increased likelihood of false targets resulting from a lower overall perceptual coherence for the inharmonic complex tones. The apparent compression of the profile for negative mistunings in the shifted condition resulted from poor performance for only one of the three subjects.

For component 6, a significant main effect was found for degree of mistuning [$F(4,8)=17.54$, $p=0.001$], and for condition [$F(2,4)=19.91$, $p=0.008$], but not for direction of mistuning [$F(1,2)=0.13$, $p=0.750$]. One interaction term, condition×degree, was significant [$F(8,16)=2.80$, $p=0.038$], but the others were not. The overall mean hit rates were 90.0%, 81.9%, and 61.5% for harmonic, shifted, and stretched stimuli, respectively.[7] Consistent with the results of experiment 1, the hit rates for the nearest equivalent mistunings (±3%) were higher than those of their counterparts for component 3. A comparison of Fig. 5 with Fig. 4 shows that the widths and depths of the mistuning profiles for component 6 differed across conditions more than did those for component 3. The profile was markedly narrower for condition 1, and to a lesser extent for condition 2, than it was for condition 3. However, the most parsimonious explanation for this effect is in terms of ceiling effects on asymptotic performance rather than underlying changes in bandwidth. Near-perfect matching behavior will occur when the perceptual salience of the target has risen above a certain level, relative to competing false targets. Beyond this level, further rises in salience with increased mistuning will not be reflected in the response profile, making the trough width appear narrower. By this analysis, the occurrence of more salient false targets in the stretched, and to a lesser extent shifted, stimuli than in the harmonic case removed these ceiling effects. The profile for the stretched stimuli suggests a trough width of approximately ±3%.

For component 9, a significant main effect was found for degree of mistuning [$F(3,6)=8.41$, $p=0.014$], and for condition [$F(2,4)=21.20$, $p=0.007$], but not for direction of mistuning [$F(1,2)=2.33$, $p=0.266$]. None of the interaction terms was significant. The overall mean hit rates were 50.9%, 40.3%, and 32.4% for harmonic, shifted, and stretched stimuli, respectively.[7] Consistent with the results of experiment 1, the hit rates for the nearest equivalent mistunings (±3%) were usually lower than those of their counterparts for components 3 and 6. More generally, Fig. 6 shows that the mistuning profiles for component 9 were broader and shallower than were their equivalents for components 3 and 6. Although the trough width is difficult to estimate, it must have been at least ±6%. For the stretched stimuli, performance was close to chance for all but the larger negative mistunings in the limited test set used for this component number.

The mistuning profiles for components 3 and 6 show a common trend for rising hit rates with increasing mistuning from ±0.75% to ±3% in all conditions. This finding con-

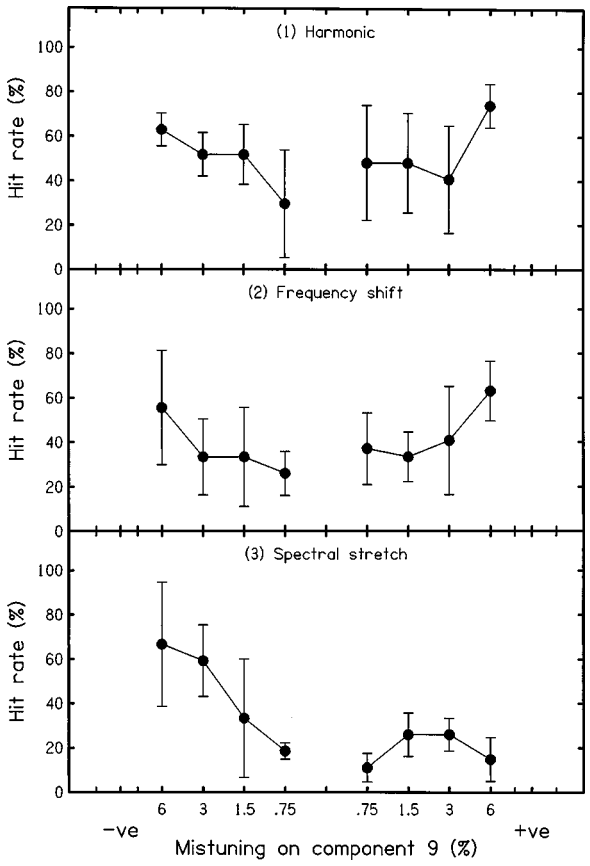

FIG. 6. Same as Fig. 4, except that component 9 was mistuned.

strains the slot centers of our hypothetical template to lie even closer to the in-tune frequencies of the target partials than did the results of experiment 1. Therefore, assuming that the results reflect the activation of only one template at a time, its slots must be distributed in a regular but inharmonic way when shifted and stretched stimuli are heard. The mistuning profiles for component 9 are less well defined for all conditions. However, it should be noted that the depressed hit rate for +6% mistuning in the stretched condition cannot be accounted for by harmonic sieves with $F0$'s of either 206 or 258 Hz (assuming a nominal $F0$ of 200 Hz for the stimuli) and a slot width of ±3% (see Sec. II).

2. Pitch shifts

We adopted a different approach from that used in experiment 1 to estimate the pitch shifts. Instead, the pitch shift for a given degree of mistuning in each condition was defined as the mean deviation from the mistuned frequency of all responses that were classified as hits when pooled across subjects and component number.[8] Only the pitch shifts for mistunings common to all three components tested were analyzed. These data are displayed in Fig. 7.

The pitch shifts were again clearly associated with the direction of mistuning in all three conditions. The only general exception was for the smallest degree of negative mistuning (−0.75%). The harmonic profile shows some evidence of saturation for the higher degrees of mistuning, which is consistent with the findings of Lin and Hartmann (1998). The shifted profile is quite similar to the harmonic

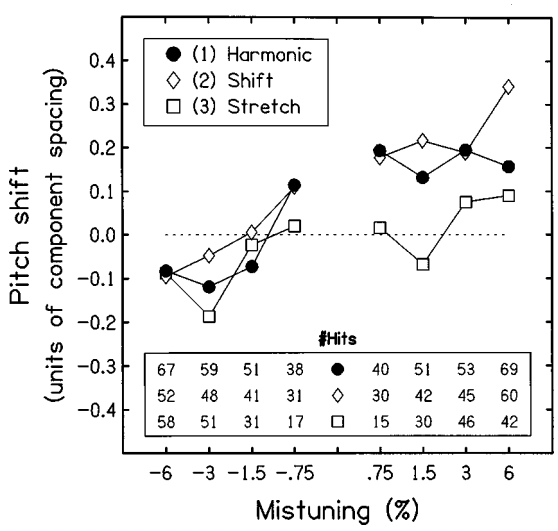

FIG. 7. Pitch shifts in conditions 1–3 of experiment 2 for mistunings in the range ±6%. These values were computed for each level of mistuning after pooling the hits of all three subjects across components 3, 6, and 9 (see text). The numbers of hits contributing to the computed pitch shifts are shown in the inset.

profile, except for +6% mistuning, which was influenced by a strong positive pitch shift for component 3. The same tendency was evident for +4% mistuning on component 3 for the shifted condition in experiment 1. The stretched profile is similar to the other two for negative mistunings, though much less so for positive ones. However, it should be noted that the difference between the stretched and harmonic conditions is not great for mistunings of +3% or more. Also, the pitch shifts for the lower degrees of positive mistuning in the stretched condition were computed from a rather small number of hits.

Two-sample *t*-tests were used to assess the overall effect of direction of mistuning in each condition, after further collapsing the data across degree of mistuning. All of these comparisons were highly significant and in the predicted direction [harmonic: $t(426)=10.27$, $p<0.0001$; shifted: $t(347)=9.55$, $p<0.0001$; stretched: $t(288)=5.36$, $p<0.0001$]. Together with the observed profile of pitch shifts, this analysis suggests that the slot centers in our hypothetical templates were not displaced substantially (i.e., <±3%) from the in-tune frequencies of the partials in our stimuli.

IV. FINAL DISCUSSION

A. How coherent are percepts of regular inharmonic complexes?

The sensitivity of our shifted and stretched complexes to small degrees of mistuning on their partials indicates that these stimuli have a significant degree of perceptual coherence. Indeed, the sounds produced by many kinds of environmental events consist of inharmonic partials, and yet may still be perceived as coherent. While our understanding of the perception of such sounds in general is limited (Gaver, 1993), there is a considerable body of knowledge concerning the sounds produced by musical instruments. These often exhibit nonlinear behavior, which may be severe for large-amplitude oscillations (McIntyre *et al.*, 1983). The extent to

which these nonlinearities are manifest as departures from harmonicity is generally small (e.g., piano strings, see Young, 1952), but can be marked for some kinds of instrument, notably carillon bells (e.g., Slaymaker and Meeker, 1954), tubular chimes (e.g., Hartmann, 1996), gongs, and drums. Pierce (1992) notes that the sounds produced by these instruments are typically heard as having distinct and identifiable timbres.

Pierce's (1966) consideration of the potential musical application of inharmonic sounds may be credited with initiating a study of their perceptual coherence (Slaymaker, 1970; Mathews and Pierce, 1980; Cohen, 1980a, b, 1984). All of these studies used a stretch transformation in which the logarithmic frequency ratios between the $F0$ component and its overtones in a harmonic complex were uniformly expanded to create sounds with systematic departures from harmonicity. Following Cohen (1980a), the frequency of the nth stretched partial can be calculated as shown:

$$f_n' = k x^{\log_2(n f_1)}, \quad \text{where } k = \frac{f_r}{x^{\log_2 f_r}},$$

and where f_1 is the fundamental frequency of the unstretched system, f_r is the reference frequency which acts as the center of the stretch transformation, and x is the base of the stretch factor, or octave ratio. If $x = 2.0$, the equation describes an untransformed harmonic series. Values above and below 2.0 result in logarithmic stretch and compression, respectively. When the reference frequency and the nominal $F0$ frequency are the same, the expression defining the transformation simplifies to

$$f_n' = f_1 x^{\log_2 n}.$$

Slaymaker (1970) used informal listening tests to establish how flat-spectrum tones with octave ratios in the range 1.7–2.4 were perceived, both individually and when formed into chords. The chords were made using intervals in a musical scale that was stretched from the conventional tempered scale by the same amount as the tones. Both stretched and compressed tones were reported to sound increasingly bell- or chime-like with greater departures from an octave ratio of 2.0. Chord sequences created from tones with an octave ratio up to about 2.1 were reported to sound increasingly out-of-tune as the intervals in the scale became more noticeably different from the familiar tempered scale, yet to retain an impression of conventional harmonic effect. However, chord sequences made with a larger octave ratio (around 2.4) lost all sense of this predictability, sounding ''smooth,'' but neither in-tune nor out-of-tune. Furthermore, Mathews and Pierce (1980) reported that stretched tones with an octave ratio of 2.4 did not sound fused. Pierce (1992) noted that the lower partials of these tones were usually distinguishable individually, with the upper partials heard as a group.

Cohen's (1980a) thesis represents the most extensive exploration of how the auditory system interprets regular inharmonic complex tones of the kind created by logarithmic stretching. In particular, she was interested to discover the point at which inharmonicity of the partials destroys tone fusion. Experienced musicians were asked to judge the degree of fusion/dispersion on a rating scale for tones generated with a range of octave ratios. No cues were provided to assist in hearing out particular partials. Each tone comprised eight partials, had a spectral envelope of -6 dB/oct, and was 200 ms in duration. The reference frequency for the stretch transformation was 256 Hz, and the $F0$ component in the harmonic case ($x = 2.0$) was either 196 or 440 Hz. Five different temporal envelopes were used, including trapezoidal and exponential. Tones with trapezoidal envelopes in the lower-$F0$ group were the most similar to our stimuli. Rated fusion was found to decline with increasing departure from harmonicity, asymptoting for the lower-$F0$ group beyond $x = 2.2$. However, a substantial degree of fusion remained for trapezoidal envelopes when $x = 2.05$, and an appreciable amount when $x = 2.1$. Tones with exponential envelopes were consistently rated as more fused than equivalent tones with trapezoidal envelopes, which has led Pierce (1992) to speculate that the sharp attack and slow decay of percussive sounds is important in holding together their partials. A multidimensional scaling experiment, in which listeners rated tone pairs for their degree of similarity with respect to tone fusion, confirmed the principal findings of the rating experiment. In another experiment, Cohen (1980a, 1984) asked listeners to ''tune'' two concurrent tones with the same octave ratio, one fixed and the other adjustable, to a designated musical interval. In the range $x = 1.9–2.1$, performance was determined primarily by the coincidence of partials (Plomp and Levelt, 1965), which is the aspect of interval size preserved by logarithmic stretching. However, beyond this range, listeners preferred to listen for salient partial pitches and to adjust them to a conventional ratio (e.g., 2:1 for the octave). A similar change in octave ratio changes the percept of a chord from a set of distinct notes to a blended timbre. Based on these experiments, Cohen (1980a) concluded that when the octave was stretched by more than about $\pm 5\%$ ($x = 1.9–2.1$), then the resulting inharmonic complex was no longer recognized as a whole.

We used a different kind of stretch transformation from that used by Cohen, such that ours resulted in less change to the frequencies of the lower partials, relative to the higher

TABLE II. Column 2 shows the component frequencies for our 3% stretched complex tones, for a nominal $F0$ frequency of 200 Hz. Columns 3 and 4 show the component frequencies for logarithmically stretched complex tones with octave ratios of 2.05 and 2.1, respectively. To facilitate comparison, both the reference and nominal $F0$ frequencies for these tones were set to 200 Hz.

Component No.	3% Stretched (Experiments 1 and 2)	log stretch (base=2.05)	log stretch (base=2.1)
1	200	200	200
2	406	410	420
3	618	624	648
4	836	841	882
5	1060	1059	1120
6	1290	1279	1361
7	1526	1500	1606
8	1768	1723	1852
9	2016	1947	2101
10	2270	2171	2352
11	2530	2396	2605
12	2796	2622	2859

ones, for a given degree of stretch. However, the similarity in the transformations is sufficient for a useful comparison to be made (see Table II). Both the nominal $F0$ frequency and the reference frequency were set to 200 Hz for the computation of the log-stretched stimuli, in order to facilitate the comparison with our stimuli. Note that our 3% spectral stretch results in a departure from harmonicity that is clearly less than that resulting from an octave ratio of 2.1 (5% stretch on the octave), and is of the same order as that resulting from an octave ratio of 2.05 (2.5% stretch on the octave). Hence, it seems reasonable to conclude that our stretched stimuli fell within the region of with appreciable fusion reported in Cohen's experiments.

B. How are perceptual fusion and low pitch related?

The degree of perceptual cohesion of complex tones with significant but systematic departures from harmonicity requires explanation. Hartmann (e.g., 1988, 1996) has argued strongly for the primacy of pitch in complex-tone perception. For example, the stretched partials of a chime tone give rise to a pitch (the ''strike tone'') that does not correspond to any of the modes of vibration, but rather to the best fit of a harmonic template. The perceptual fusion necessary for the distinctive timbre of the chime tone to be heard is then seen as a direct consequence of the acceptance of its partials by a pattern-recognition device that computes low pitch (e.g., Goldstein, 1973; Terhardt, 1974). The opinion that perceptual fusion is secondary to pitch perception is consistent with the results of Lin and Hartmann (1998, Expt. 5). These authors showed that increasing the $F0$ frequency of a harmonic complex tone from 200 to 800 Hz almost abolished the pitch shifts found for the $F0$ component when it was mistuned. The occurrence of these pitch shifts was taken to indicate the presence of an active slot in a harmonic template. Lin and Hartmann point out that 800 Hz is also the upper limit of the ''existence region'' for low pitch (Ritsma, 1962). However, an independent effect on both processes resulting from the progressive loss of phase-locking precision for partials above about 1 kHz (Anderson, 1973) could also account for this common upper limit. Indeed, the evidence in support of perceptual fusion as a process secondary to low pitch perception is at best equivocal. In particular, there is a clear mismatch in tolerance for component mistuning across the two processes in complex-tone perception. Moore *et al.* (1985a) found that a low partial made a full, linear, contribution to the estimation of low pitch when mistuned by up to $\pm 3\%$, but Moore *et al.* (1986) found that listeners often reported hearing out a separate pure tone when a low partial was mistuned by only half this amount. Unless some form of duplex perception is assumed (see Moore, 1987), this mismatch suggests that the two processes may be distinct. The problem with harmonic or near-harmonic stimuli is that it is hard to distinguish the effects of the pitch process from the grouping one.

C. Conjectures on inharmonic templates

As discussed earlier, the sensitivity to small degrees of mistuning imposed on the partials of shifted and stretched complexes reported here cannot easily be explained in terms of quasiharmonicity. In the context of template models, the patterns of hits and pitch shifts observed must reflect either a blend of harmonic-template fits to the in-tune frequencies of our shifted and stretched stimuli, or a single fit by an inharmonic template. In the latter case, what might plausibly be the basis for the construction or activation of such a template? Some speculation is necessary here. A reasonable starting position might be to assume that the auditory system is sensitive to equal spacing between consecutive partials, perhaps based on intermodulations evoked by partials not fully resolved by the auditory filterbank. This kind of sensitivity would encompass both harmonic and shifted complexes, as the rate of intermodulation between neighboring partials is unaffected by frequency shifting a harmonic complex. Moreover, an extension of this framework to encompass complex tones with moderate degrees of spectral stretch is also possible. We used stimuli with a spectral stretch of 3% and a nominal $F0$ frequency of 200 Hz. For these stimuli, each of the tested partials, 2–11, was displaced only slightly downwards (3 Hz) from equidistance with its immediate neighbors. In percentage terms, this ranges from -0.73% for component 2 to -0.12% for component 11. Most of the mistunings used in experiments 1 and 2 were substantial on this scale, and could, in principle, have been detected as deviations from equal spacing. The extension required here is that small local deviations from equal spacing are tolerated, and that the overall strength of perceptual fusion is built up by the ''chaining'' together of local consistencies among the partials across the spectrum. This kind of process would be ''blind'' to any marked changes over greater spectral distances resulting from the cumulation of small deviations, as in our stretched stimuli. This approach also avoids the need to hypothesize a set of preexisting templates able to to deal with varying degrees of spectral stretch, which there is no theoretical reason to expect. The idea of a template as a flexible device, built to utilize spectral regularities inherent in the stimulus, is not an implausible one. That sensitivity to spectral structure involves more than simply the *global* activation of the best-fitting template is clear even for harmonic stimuli. For example, Lin and Hartmann (1998, Expt. 3) showed a decline in the pitch-shift gradient for $\pm 8\%$ mistuning of a 200-Hz $F0$ component when harmonics 2–4 were progressively removed from the complex tone. This proximity effect suggests that the spread of activation to other harmonic positions from the partials defining the spectral pattern is not truly global, but rather attenuates with distance. The findings of Brunstrom and Roberts (1998), using hit-rate measures, led them to the same conclusion as Lin and Hartmann.

D. Can the ear recognize spectral structure in regular inharmonic complexes?

The findings of Roberts and his colleagues using variants of a stimulus configuration based on adding a single even harmonic to an otherwise odd-harmonic complex, including shift and stretch manipulations, have suggested that the auditory system may be sensitive to aspects of spectral pattern other than harmonicity (e.g., Roberts and Bailey, 1996b; Roberts, 1998). However, to move beyond conjec-

ture, a means must be found to evaluate directly whether or not a regular but inharmonic spectral structure can be recognized. As far as we are aware, only one attempt at this has previously been reported. Cohen (1980a, b) argued that if the ear is capable of recognizing the spectral structure of a logarithmically stretched complex as regular, then listeners should be able to reinsert a missing partial at the frequency predicted from the mathematical order of the other partials. Listeners (all experienced musicians) were presented with log-stretched complexes, created using various octave ratios, from which the second partial had been removed. The tones had flat spectral envelopes (partials 1–12, minus the second), a trapezoidal temporal envelope, and were one second in duration. The task was to ''tune'' an adjustable sinusoid to the position of the missing partial. The adjustment range was from the first to the third partial, and the stimulus could be repeated freely until the listener was satisfied with his or her choice. Within the range of octave ratios 1.9–2.1, but not outside it, there was a tendency for the chosen match to fall below twice the $F0$ component for compression and above it for stretch, although the slope of this function (estimated by eye) was not as predicted. However, there was considerable scatter in the data, with subjects having difficulty in adjusting the sinusoid even in the truly harmonic case (octave ratio $=2.0$). This difficulty probably reflected an attention-based segregation of the sinusoid from the complex induced by adjusting its frequency, as Cohen (1980a) acknowledged.

An approach that may prove more reliable than Cohen's design is one that avoids on-line adjustment of component frequency, and which uses complex tones with spectral gaps created by the removal of more than one consecutive partial. It should also prove informative to explore the effects of changing the degree of frequency shift or spectral stretch applied to harmonic stimuli. For example, it follows from our suggestion that the auditory system may be sensitive to equal component spacing that, unlike for stretch, increasing the degree of shift should have little effect on our ability to detect the mistuning of a partial.

E. Concluding remarks

At this point, it may be concluded that the auditory system can be sensitive to small mistunings imposed on the partials of complex tones with systematic departures from harmonicity. Indeed, for the 15% frequency-shifted and 3% spectrally stretched stimuli that we employed, both the hit-rate and pitch-shift profiles suggest that this sensitivity may approach that observed for truly harmonic stimuli. This finding cannot be explained in terms of a quasiharmonic fit to a harmonic template unless the responses of more than one concurrently active template are somehow blended together. Instead, the results may in each case reflect the best match of a single inharmonic template. Further study of the perceptual consequences of changing the spectral structure of regular inharmonic complexes is necessary to resolve these hypotheses. The results of experiments of this kind may also have implications for our understanding of how auditory grouping mechanisms process harmonic stimuli.

ACKNOWLEDGMENTS

This research was supported by Research Grant No. 6/S04782 from the Biotechnology and Biological Sciences Research Council (UK). Our thanks go to Peter Bailey for his comments on an earlier version of this manuscript. Thanks also go to Alison Statham and Nik Hargaden for agreeing to spend many hours in the acoustic chamber, and to the two anonymous reviewers.

[1]The behavior of listeners was markedly nonmonotonic for partials in this range. Typically, performance was poor for harmonics 12–14, but was good for harmonics 15 and 16. Hartmann *et al.* (1990) suggested that two modes of perception were involved in their task: A mistuned harmonic below the 12th was heard as a separate tone, whereas a higher-numbered mistuned harmonic evoked a beating sensation. For harmonics 15 and 16, this sensation took place in a region of tone height that was narrow enough for listeners' responses often to be classified as hits.

[2]Note that the frequency range around a perfect match was defined in terms of units of nominal $F0$ rather than of component number, making it constant in Hz across conditions and component numbers for a given nominal $F0$. Otherwise, the range would have increased (in linear terms) with component number for the stretched complexes used in condition 3.

[3]An alternative approach would have been to calculate mean pitch shifts that were weighted for the number of hits contributed by each subject. This could be justified on the grounds that the estimate obtained from a subject should be more stable when derived from a greater number of hits. This would minimize the impact of occasions on which an individual's pitch shift was based on a single, extreme, data point. However, this approach would also result in contributions from the three subjects that were unequal, sometimes heavily influenced by the scores of only one subject, and that varied in proportion from stimulus to stimulus. Since we were primarily interested in determining whether or not our stimulus manipulations expressed themselves across subjects, we preferred to accept the uncertainty introduced by pitch-shift estimates based on low hit rates rather than to lose the equal contribution of each subject.

[4]Chance performance is difficult to ascertain in a design of this kind. There are 12 consecutive components in each complex tone, giving a minimum spacing of 11 units of nominal $F0$ between the lowest and highest partials. Given this, and the first criterion of $\pm 1.0\times$nominal $F0$ around the target frequency for a response to be classified as a hit, an estimate of 2/11, or about 18%, would seem a reasonable estimate.

[5]The harmonic sieve as implemented by Duifhuis *et al.* (1982) and Scheffers (1983a,b) was designed to separate out the set of resolved partials in a complex-tone mixture that corresponded to one of two concurrent $F0$ frequencies. Since we are also interested in the ability of listeners to hear out mistuned partials above the sixth, which are less well resolved, and we are using this model only for illustrative purposes, we have extended it to include them. Our version was implemented using a template with 12 slots.

[6]This was done because the component numbers differed in the set of mistunings applied to them.

[7]Note that the means cannot be compared directly across component numbers, as different ranges of mistuning were used.

[8]This approach is an extension of the alternative that was considered and rejected (see footnote 1) for the calculation of pitch shifts in experiment 1. It was used here because of the especially low hit rates that sometimes resulted from the introduction of smaller degrees of mistuning, and that occurred more generally for component 9. Extensive pooling of the data was considered necessary to give stability to the estimates of pitch shifts. It was also felt that a confirmation, using a different method, of the finding in experiment 1 that pitch shifts are associated with the direction of mistuning would help to demonstrate that the finding was robust. A limited analysis, performed separately for each condition, replicated the previous finding that pitch shifts tend to be larger for higher components.

Anderson, D. J. (**1973**). ''Quantitative model for the effects of stimulus frequency upon synchronization of auditory discharges,'' J. Acoust. Soc. Am. **54**, 361–364.

Bregman, A. S. (**1990**). *Auditory Scene Analysis: The Perceptual Organization of Sound* (MIT, Cambridge, MA).

Brunstrom, J. M., and Roberts, B. (**1998**). ''Profiling the perceptual suppression of partials in periodic complex tones: Further evidence for a harmonic template,'' J. Acoust. Soc. Am. (submitted).
Carlyon, R. P. (**1994**). ''Detecting mistuning in the presence of synchronous and asynchronous interfering sounds,'' J. Acoust. Soc. Am. **95**, 2622–2630.
Cohen, E. A. (**1980a**). *The Influence of Nonharmonic Partials on Tone Perception*, doctoral thesis, Stanford University, CA.
Cohen, E. A. (**1980b**). ''Pitch processing of nonharmonic tones: A search for an auditory mechanism that recognizes spectral patterns,'' J. Acoust. Soc. Am. **68**, S110.
Cohen, E. A. (**1984**). ''Some effects of inharmonic partials on interval perception,'' Music Percept. **1**, 323–349.
Darwin, C. J., Ciocca, V., and Sandell, G. J. (**1994**). ''Effects of frequency and amplitude modulation on the pitch of a complex tone with a mistuned harmonic,'' J. Acoust. Soc. Am. **95**, 2631–2636.
de Boer, E. (**1956**). *On the 'Residue' in Hearing*, doctoral thesis, University of Amsterdam, The Netherlands.
de Boer, E. (**1976**). ''On the 'residue' and auditory pitch perception,'' in *Handbook of Sensory Physiology, Vol. 5*, edited by W. D. Keidel and W. D. Neff (Springer-Verlag, Berlin), pp. 479–583.
de Cheveigné, A. (**1997**). ''Harmonic fusion and pitch shifts of mistuned partials,'' J. Acoust. Soc. Am. **102**, 1083–1087.
Duifhuis, H., Willems, L. F., and Sluyter, R. J. (**1982**). ''Measurement of pitch in speech: An implementation of Goldstein's theory of pitch perception,'' J. Acoust. Soc. Am. **71**, 1568–1580.
Fine, P. A., and Moore, B. C. J. (**1993**). ''Frequency analysis and musical ability,'' Music Percept. **11**, 39–54.
Gaver, W. W. (**1993**). ''What in the world do we hear?: An ecological approach to auditory event perception,'' Ecol. Psychol. **5**, 1–29.
Goldstein, J. L. (**1973**). ''An optimum processor theory for the central formation of the pitch of complex tones,'' J. Acoust. Soc. Am. **54**, 1496–1516.
Hartmann, W. M. (**1988**). ''Pitch perception and the segregation and integration of auditory entities,'' in *Auditory Function*, edited by G. M. Edelman, W. E. Gall, and W. M. Cowan (Wiley, New York), pp. 623–645.
Hartmann, W. M. (**1996**). ''Pitch, periodicity, and auditory organization,'' J. Acoust. Soc. Am. **100**, 3491–3502.
Hartmann, W. M., and Doty, S. L. (**1996**). ''On the pitches of the components of a complex tone,'' J. Acoust. Soc. Am. **99**, 567–578.
Hartmann, W. M., McAdams, S., and Smith, B. K. (**1990**). ''Hearing a mistuned harmonic in an otherwise periodic complex tone,'' J. Acoust. Soc. Am. **88**, 1712–1724.
Henke, W. L. (**1990**). *MITSYN: A coherent family of high-level languages for time signal processing* (software package) (Belmont, MA).
Houtsma, A. J. M., and Goldstein, J. L. (**1972**). ''The central origin of the pitch of complex tones: Evidence from musical interval recognition,'' J. Acoust. Soc. Am. **51**, 520–529.
Kohlrausch, A., and Houtsma, A. J. M. (**1992**). ''Pitch related to spectral edges of broadband signals,'' in *Processing of Complex Sounds by the Auditory System*, edited by R. P. Carlyon, C. J. Darwin, and I. J. Russell (Oxford U.P., Oxford, UK), pp. 81–88.
Lee, J., and Green, D. M. (**1994**). ''Detection of a mistuned component in a harmonic complex,'' J. Acoust. Soc. Am. **96**, 716–725.
Lin, J.-Y., and Hartmann, W. M. (**1998**). ''The pitch of a mistuned harmonic: Evidence for a template model,'' J. Acoust. Soc. Am. **103**, 2608–2617.
Martens, J.-P. (**1984**). ''Comment on 'Algorithm for extraction of pitch and pitch salience from complex tonal signals','' J. Acoust. Soc. Am. **75**, 626–628.
Mathews, M. V., and Pierce, J. R. (**1980**). ''Harmony and nonharmonic partials,'' J. Acoust. Soc. Am. **68**, 1252–1257.
McIntyre, M. E., Schumacher, R. T., and Woodhouse, J. (**1983**). ''On the oscillations of musical instruments,'' J. Acoust. Soc. Am. **74**, 1325–1345.
Moore, B. C. J. (**1987**). ''The perception of inharmonic complex tones,'' in *Auditory Processing of Complex Sounds*, edited by W. A. Yost and C. S. Watson (Erlbaum, Hillsdale, NJ), pp. 180–189.
Moore, B. C. J., and Ohgushi, K. (**1993**). ''Audibility of partials in inharmonic complex tones,'' J. Acoust. Soc. Am. **93**, 452–461.
Moore, B. C. J., Glasberg, B. R., and Peters, R. W. (**1985a**). ''Relative dominance of individual partials in determining the pitch of complex tones,'' J. Acoust. Soc. Am. **77**, 1853–1860.
Moore, B. C. J., Glasberg, B. R., and Peters, R. W. (**1986**). ''Thresholds for hearing mistuned partials as separate tones in harmonic complexes,'' J. Acoust. Soc. Am. **80**, 479–483.
Moore, B. C. J., Peters, R. W., and Glasberg, B. R. (**1985b**). ''Thresholds for the detection of inharmonicity in complex tones,'' J. Acoust. Soc. Am. **77**, 1861–1867.
Patterson, R. D. (**1973**). ''The effects of relative phase and the number of components on residue pitch,'' J. Acoust. Soc. Am. **53**, 1565–1572.
Patterson, R. D., and Wightman, F. L. (**1976**). ''Residue pitch as a function of component spacing,'' J. Acoust. Soc. Am. **59**, 1450–1459.
Pierce, J. R. (**1966**). ''Attaining consonance in arbitrary scales,'' J. Acoust. Soc. Am. **40**, 249.
Pierce, J. R. (**1992**). *The Science of Musical Sound* (Freeman, New York).
Plomp, R. (**1964**). ''The ear as a frequency analyzer,'' J. Acoust. Soc. Am. **36**, 1628–1636.
Plomp, R., and Levelt, W. J. M. (**1965**). ''Tonal consonance and critical bandwidth,'' J. Acoust. Soc. Am. **38**, 548–560.
Rasch, R. A. (**1978**). ''The perception of simultaneous notes such as in polyphonic music,'' Acustica **40**, 21–33.
Ritsma, R. J. (**1962**). ''Existence region of the tonal residue. I,'' J. Acoust. Soc. Am. **34**, 1224–1229.
Ritsma, R. J. (**1967**). ''Frequencies dominant in the perception of the pitch of complex sounds,'' J. Acoust. Soc. Am. **42**, 191–198.
Roberts, B. (**1998**). ''Effects of spectral pattern on the perceptual salience of partials in harmonic and frequency-shifted complex tones: A performance measure,'' J. Acoust. Soc. Am. **103**, 3588–3596.
Roberts, B., and Bailey, P. J. (**1993a**). ''Spectral pattern and the perceptual fusion of harmonics. I. The role of temporal factors,'' J. Acoust. Soc. Am. **94**, 3153–3164.
Roberts, B., and Bailey, P. J. (**1993b**). ''Spectral pattern and the perceptual fusion of harmonics. II. A special status for added components?'' J. Acoust. Soc. Am. **94**, 3165–3177.
Roberts, B., and Bailey, P. J. (**1996a**). ''Regularity of spectral pattern and its effects on the perceptual fusion of harmonics,'' Percept. Psychophys. **58**, 289–299.
Roberts, B., and Bailey, P. J. (**1996b**). ''Spectral regularity as a factor distinct from harmonic relations in auditory grouping,'' J. Exp. Psychol. **22**, 604–614.
Roberts, B., and Bregman, A. S. (**1991**). ''Effects of the pattern of spectral spacing on the perceptual fusion of harmonics,'' J. Acoust. Soc. Am. **90**, 3050–3060.
Scheffers, M. T. M. (**1983a**). *Sifting Vowels: Auditory Pitch Analysis and Sound Segregation*, doctoral thesis, University of Groningen, The Netherlands.
Scheffers, M. T. M. (**1983b**). ''Simulation of auditory analysis of pitch: An elaboration on the DWS pitch meter,'' J. Acoust. Soc. Am. **74**, 1716–1725.
Schouten, J. F., Ritsma, R. J., and Cardozo, B. L. (**1962**). ''Pitch of the residue,'' J. Acoust. Soc. Am. **34**, 1418–1424.
Slaymaker, F. H. (**1970**). ''Chords from tones having stretched partials,'' J. Acoust. Soc. Am. **47**, 1569–1571.
Slaymaker, F. H., and Meeker, W. F. (**1954**). ''Measurements of the tonal characteristics of carillon bells,'' J. Acoust. Soc. Am. **26**, 515–522.
Terhardt, E. (**1971**). ''Pitch shifts of harmonics, an explanation of the octave enlargement phenomenon,'' in *Proc. 7th Int. Congr. Acoustics, Budapest, Vol. 3*, pp. 621–624.
Terhardt, E. (**1974**). ''Pitch, consonance, and harmony,'' J. Acoust. Soc. Am. **55**, 1061–1069.
Terhardt, E. (**1979**). ''Calculating virtual pitch,'' Hearing Res. **1**, 155–182.
Terhardt, E., Stoll, G., and Seewann, M. (**1982**). ''Algorithm for extraction of pitch and pitch salience from complex tonal signals,'' J. Acoust. Soc. Am. **71**, 679–688.
Young, R. W. (**1952**). ''Inharmonicity of plain wire piano strings,'' J. Acoust. Soc. Am. **24**, 267–273.

The pitch of short-duration fundamental frequency glissandos

Christophe d'Alessandro, Sophie Rosset, and Jean-Pierre Rossi
LIMSI–CNRS, BP 133 F-91403 Orsay, France

(Received 9 October 1997; accepted for publication 7 July 1998)

Pitch perception for short-duration fundamental frequency ($F0$) glissandos was studied. In the first part, new measurements using the method of adjustment are reported. Stimuli were $F0$ glissandos centered at 220 Hz. The parameters under study were: $F0$ glissando extents (0, 0.8, 1.5, 3, 6, and 12 semitones, i.e., 0, 10.17, 18.74, 38.17, 76.63, and 155.56 Hz), $F0$ glissando durations (50, 100, 200, and 300 ms), $F0$ glissando directions (rising or falling), and the extremity of $F0$ glissandos matched (beginning or end). In the second part, the main results are discussed: (1) perception seems to correspond to an average of the frequencies present in the vicinity of the extremity matched; (2) the higher extremities of the glissando seem more important; (3) adjustments at the end are closer to the extremities than adjustments at the beginning. In the third part, numerical models accounting for the experimental data are proposed: a time-average model and a weighted time-average model. Optimal parameters for these models are derived. The weighted time-average model achieves a 94% accurate prediction rate for the experimental data. The numerical model is successful in predicting the pitch of short-duration $F0$ glissandos.
[S0001-4966(98)03810-7]

PACS numbers: 43.66.Hg, 43.75.Bc [DWG]

INTRODUCTION

In natural audio signals like speech or music, fundamental frequency ($F0$) is almost never constant. The main psychological correlate of $F0$ is pitch. It is well known that the physical aspect ($F0$) and the psychological aspect (pitch) can differ significantly, particularly for sounds whose fundamental frequency changes. The aim of the present article is to report new measurements and to propose a numerical model for pitch perception of short-duration $F0$ glissandos. Short-duration $F0$ glissandos are thought of as prototypes or building blocks for the $F0$ contours that can be encountered in many natural signals, like notes in music or syllables in speech.

Several theories accounting for human *instantaneous* pitch detection are available, together with the corresponding pitch detection algorithms [see Hess (1983) or Hermes (1993) for reviews]. These theories and techniques focus on instantaneous, or at least short-term, attributes of the acoustic signal. Only a few periods of signals are considered in order to compute the time-varying instantaneous fundamental frequency. However, the link between instantaneous $F0$ contours and pitch perception for larger units, like $F0$ glissandos, is by no means straightforward. It is therefore important to distinguish between *instantaneous* $F0$, which is a relatively well-known problem, and pitch perception for *short-duration* $F0$ glissandos.

Perceptual thresholds for predicting under what conditions $F0$ changes are audible have long been studied. A first perceptual threshold is the glissando threshold, or absolute threshold of pitch change. It is expressed in frequency unit per unit of time. Below the threshold, a $F0$ glissando is perceived with constant pitch. Above the threshold, a pitch glissando is perceived. Data on the glissando threshold for speechlike sounds have been obtained by Klatt (1973), Rossi[1] (1971, 1978a), and Schouten (1985), following the pioneering work of Sergeant and Harris (1962) for pure tones. A unified view of this problem was presented by 't Hart (1976) and 't Hart *et al.* (1990), who conclude that the threshold can be approached by $G_t = 0.16/T^2$, where G_t is the glissando threshold (in semitones/s) and T the tone duration. When a glissando is above the glissando threshold, a separate perception of the high and low extremities of the $F0$ patterns appears. Nabelek *et al.* (1970) first studied this effect in a work on the pitch for tone bursts of changing frequency. They coined the term ''separation'' for when only the final part of the burst contributes to the pitch judgment, and the term ''fusion'' for when the overall $F0$ pattern contributes to the pitch judgment. Thresholds for separation and fusion are consistent with the glissando threshold.

Thresholds can predict whether a given $F0$ glissando (with a certain duration and a certain extent) will be perceived as a constant pitch tone or as a pitch glissando. However, the data on perceptual thresholds for pitch changes do not address the problem of what pitch is actually perceived, i.e., what the subjective pitch value is at the beginning and end of the $F0$ glissando. The first aim of this study is to give explicit measurements of the pitch perceived at the beginning and end of $F0$ glissandos. One of the few studies addressing this problem can be found in Rossi (1971, 1978a), where natural and synthetic vowels were used. Unfortunately, the experimental conditions used by Rossi were not likely to give accurate results, because of the choice of subjects (a group of students in phonetics whose individual capabilities in pitch discrimination were not tested) and because of the stimulus presentation method (loudspeakers in a classroom). Therefore, new and more accurate measurements were needed.

Another issue which needs to be reinvestigated is whether there are asymmetries in the perception of supraliminar rising and falling $F0$ glissandos. Several articles

have noted such asymmetries, but the results have not always been consistent. Hombert (1975) and Rump and Hermes (1996) found that the high register has more weight in intonation perception. Brady (1961) and Wieringen and Pols (1995) reported that for pure tone glides, the end of the tone has more perceptual weight than the beginning. For pure tones and complex tones, Demany and McAnally (1994) and Demany and Clément (1995, 1997), found an asymmetry between peaks and troughs for large frequency modulations. However, Rossi (1978a) reported that no differences occurred in the perception of rising and falling glissandos. In this article, we compare the perception of rises and falls over a wide range of conditions.

The final purpose of this work is to propose a numerical model of pitch perception for short-duration $F0$ glissandos. A first model addressing this problem was proposed by Rossi (1971, 1978a), using natural and synthetic vowels. Rossi postulated that for vowels with $F0$ glissandos (either rising or falling), the pitch perceived at the end of vowels corresponds to an averaging of $F0$ toward the end of the glissando. This is expressed in Rossi's so-called ''2/3 rule,'' which can be stated as follows:

> For dynamic tones in a vowel, the pitch perceived corresponds to a point between the second and the third third of the vowel.

For example, if a linear glissando between 100 and 200 Hz lasts 150 ms, this rule predicts that the pitch perceived is somewhere in the $F0$ values of the glissando in the time interval 100–150 ms, i.e., between 166.6 and 200 Hz. In Rossi's terminology, a dynamic tone is a tone with perceived pitch change. Of course, this rule applies only to the experimental situation envisaged in Rossi's experiments, namely pitch perception measured at the end of tones in vowels. This model was also applied to the pitch of glidelike $F0$ curves in folk songs. Ross (1987) reported good agreement between his experimental results and Rossi's rule. In mathematical terms, Rossi's rule is an example of a time-average (TA) model of pitch perception. Pitch is computed by averaging $F0$ on the time interval of the tone:

$$p=\frac{\int_{t1}^{t2} F0(\tau)\,d\tau}{\int_{t1}^{t2} d\tau}, \tag{1}$$

where p is the pitch perceived, $F0(\tau)$ is the time-varying fundamental frequency, $t1$ and $t2$ are the averaging time limits. In systems for automatic intonation analysis, several authors used ''pragmatic'' TA models. For instance, Mertens (1987) and House (1990) computed pitch as the average of $F0$ on 20–30 ms at the end of vowels in syllables.

In a study on pitch perception for short-duration vibrato tones in singing, d'Alessandro and Castellengo (1994) showed that TA models were not suitable in this situation. The main problem was that TA models were not able to give more perceptual weight to the end of tones. They proposed instead a weighted time-average (WTA) model of pitch perception. Pitch is computed as the time average of $F0$ viewed through a time window:

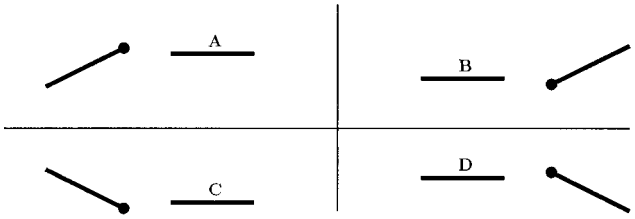

Part	first tone	second tone	adjustement at:
A	rise	flat	end
B	flat	rise	beginning
C	fall	flat	end
D	flat	fall	beginning

FIG. 1. The four parts ABCD of the experiments.

$$p=\frac{\int_{t1}^{t2}(e^{\alpha(\tau-t2)}+\beta)F0(\tau)\,d\tau}{\int_{t1}^{t2}(e^{\alpha(\tau-t2)}+\beta)\,d\tau}, \tag{2}$$

where the constants β and α define the raised exponential window. The constant α is the factor of the exponent in the window. It gives more or less weight to the final part of the tone. The constant β is the height of the raised exponential window, i.e., the height of a rectangular window, whose width is the tone duration. Contrary to α, the constant β gives equal weight to all parts of the tone. Thus β controls the weight given to the whole tone, while α controls the weight given to the end of the tone. The optimal parameters were $\alpha=22$ and $\beta=0.20$. This WTA model was also successfully applied to intonation stylization in speech in d'Alessandro and Mertens (1995).

In summary, the aim of the present study is to address the following matters: (1) to give new measurements of the pitch perceived at the beginning and end of short-duration $F0$ glissandos; (2) to study the asymmetries in perception of rises and falls; (3) to evaluate a WTA model of $F0$ integration for pitch perception. This model should be able to predict the pitch perceived at the beginning and end of an $F0$ glissando. In Sec. I, the experimental method is described. Then the results are presented and analyzed in Sec. II. A numerical model accounting for our data is proposed and discussed in Sec. III. Section IV concludes.

I. METHOD

A. Conditions

The aim of these experiments is to measure the pitch perceived for short-duration $F0$ glissandos. Linear $F0$ glissandos are of the form $F0(\tau)=a\times\tau+b$, where b is the frequency (in Hz) at the beginning of the tone, a is the slope of the tone (if d is the duration of the tone, $a\times d+b$ is the frequency at the end of the tone), and τ represents time. The stimulus are pairs of synthetic vowels, with a 300-ms silent interval between each member of a stimulus pair. One member of a pair is a glissando (either a rise or a fall). The other member of a pair is flat (constant $F0$) with the same duration. The test is divided into four parts ABCD, summarized in Fig. 1.

TABLE I. Experimental conditions. R: rise. F: fall. B: adjustment at the beginning. E: adjustment at the end. b: below the glissando threshold. g: glissando threshold. a: above the glissando threshold. ⋯ : condition not tested.

	50 ms				100 ms				200 ms				300 ms			
	B		E		B		E		B		E		B		E	
	R	F	R	F	R	F	R	F	R	F	R	F	R	F	R	R
0 ST	b	⋯	b	⋯	b	⋯	b	⋯	b	⋯	b	⋯	b	⋯	b	⋯
0.8 ST	b	b	b	b	b	b	b	b	g	g	g	g	a	a	a	a
1.5 ST	b	b	b	b	g	g	g	g	a	a	a	a	a	a	a	a
3 ST	g	g	g	g	a	a	a	a	a	a	a	a	a	a	a	a
6 ST	a	a	a	a	a	a	a	a	a	a	a	a	a	a	a	a
12 ST	a	a	a	a	a	a	a	a	a	a	a	a	a	a	a	a

In (A) the first member of a stimulus pair is a rise, and the second member is flat. The subjects are asked to adjust a flat tone to the end of a rise.

In (B) the first member of a stimulus pair is flat, and the second member is a rise. The subjects are asked to adjust a flat tone to the beginning of a rise.

In (C) the first member of a stimulus pair is a fall, and the second member is flat. The subjects are asked to adjust a flat tone to the end of a fall.

In (D) the first member of a stimulus pair is flat, and the second member is a fall. The subjects are asked to adjust a flat tone to the beginning of a fall.

All the stimuli are centered at 220 Hz, a typical $F0$ for a female voice. Four parameters are studied: the glissando direction (rise/fall), the extremity matched (beginning/end), duration (50, 100, 200, and 300 ms) and extent. The glissando extents are defined according to the glissando threshold, using data reported in 't Hart *et al.* (1990). For the 50 ms duration condition, $G_t = 0.16/(0.05)^2 = 64$ semitones/s. The extent of the glissando at threshold (G_{tr}) is $64 \times 0.05 = 3.2$ semitones. For this condition, the extents studied in the experiments are 0, 0.8, 1.5, 3, 6 and 12 semitones (or 0, 10.17, 18.74, 38.17, 76.63, and 155.56 Hz). This corresponds approximately to $0.25 \times G_{\mathrm{tr}}$, $0.5 \times G_{\mathrm{tr}}$, G_{tr}, $2 \times G_{\mathrm{tr}}$, $4 \times G_{\mathrm{tr}}$, in addition to the 0-Hz extent condition. The same values are used for the 100, 200, and 300 ms duration conditions. The extents are symmetric around the center value 220 Hz on a semitone (logarithmic) scale: $F0$ is within 220 Hz $\pm N/2$ semitones, where N is the extent of the stimuli in semitones. As the glissandos are linear functions of time in Hz, the value of 220 Hz is not reached at the center of the stimuli in time because of the wider interval in Hz for higher frequencies. In summary, there are 24 conditions for rises (including four ''0 semitone'' conditions, which are considered as rises) and 20 conditions for falls. The resulting 88 conditions are summarized in Table I, together with the glissando threshold. Glissandos above and below the glissando threshold are considered in the experiments.

B. Stimuli

The stimuli were synthetic posterior vowels /a/, computed by a digital parallel formant synthesizer. The center frequencies, bandwidth and relative amplitudes of the first four formants ($F1, F2, F3, F4$) were typical values for a female speaker: $F1 = (650\ \mathrm{Hz}, 80\ \mathrm{Hz}, 0\ \mathrm{dB})$, $F2 = (1100\ \mathrm{Hz}, 90\ \mathrm{Hz}, -8\ \mathrm{dB})$, $F3 = (2900\ \mathrm{Hz}, 140\ \mathrm{Hz}, -11\ \mathrm{dB})$, $F4 = (3300\ \mathrm{Hz}, 130\ \mathrm{Hz}, -20\ \mathrm{dB})$. Synthetic voice stimuli were chosen because they were fully controlled, and because they were closer to natural sounds (like speech and singing) than pure tones or square waves. The signals corresponding to all the experimental conditions were synthesized and stored on a computer disk. Signals were sampled at 16 kHz, using 16 bits per sample. Prestored examples were played at test time, following the procedure described below.

The signal peak amplitude was the same for all the stimuli. Sound intensity variation within all the stimuli was less than 2.4 dB. This was small enough to avoid consideration of the effect of intensity changes on pitch perception [see Rossi (1978b) for a discussion of interaction of amplitude and fundamental frequency glissandos in pitch perception].

C. Procedure

Previous data published on the pitch perceived for short-duration $F0$ glissandos were generally obtained using a forced-choice procedure (Rossi, 1971; 't Hart *et al.*, 1990). However, we preferred a method of adjustment similar to the method used in a study of pitch perception for short-duration vibrato tones in d'Alessandro and Castellengo (1994). The method of adjustment has a number of advantages: (1) each response of a subject gives an estimation of the pitch perceived; (2) the method helps concentration, as the subject is actively engaged in the adjustment process; (3) the data obtained are less variable than forced-choice data in frequency discrimination tasks, as shown by Wier *et al.* (1976).

Subjects were asked to adjust the frequency of the flat tone so that it was equal to the frequency at the beginning or at the end of the glissando. To make an adjustment, the subject pointed to a place on a one-octave scale on the computer screen, pressed a button, and heard a stimulus pair. If she/he was satisfied with this pair, the subject reported a match. If she/he was not satisfied with this pair, the subject moved the mouse pointer on the scale and listened to the corresponding stimulus pair. Low frequencies were on the left of the scale, and high frequencies on the right. For each match, the subject had no time limit for giving an answer, and could play any stimulus pair for the same condition. Subjects typically listened to about ten stimulus pairs while manipulating the frequency of the flat tone before reporting a match. The sub-

TABLE II. Experimental results. Means and standard deviations for the matches reported by the subjects, as a function of extent, duration, rise/fall, and begin/end (see parts ABCD in the text). Means and standard deviations are in Hz.

Extent ST (Hz)	50 ms	100 ms	200 ms	300 ms
		Part A		
0.0(220.9)	221.5±1.8	221.1±1.0	221.2±1.0	221.1±1.0
0.8(215.0–225.1)	224.0±7.1	225.5±6.9	226.2±8.7	227.0±9.5
1.5(210.6–229.4)	222.8±5.4	227.7±10.6	229.8±9.1	231.4±10.8
3.0(201.7–239.9)	234.7±15.5	238.6±12.4	241.1±11.6	242.0±12.7
6.0(185.0–261.6)	255.1±13.7	257.0±9.7	255.2±6.8	256.5±5.3
12.0(155.6–311.1)	281.9±12.4	283.7±12.8	291.0±13.7	292.0±12.7
		Part B		
0.0(220.9)	218.1±3.6	219.0±1.5	219.1±2.5	219.5±1.4
0.8(215.0–225.1)	219.0±2.0	218.3±3.4	218.1±2.9	218.1±4.0
1.5(210.6–229.4)	215.5±9.9	216.3±10.3	216.1±10.7	215.2±10.5
3.0(201.7–239.9)	213.9±12.4	216.0±13.1	213.3±11.6	212.4±11.3
6.0(185.0–261.6)	215.7±24.3	213.3±25.4	209.5±20.0	203.8±19.4
12.0(155.6–311.1)	215.9±39.7	213.8±41.1	208.2±35.7	201.8±29.1
		Part C		
0.8(215.0–225.1)	217.6±7.2	217.1±8.3	217.3±7.2	216.9±4.0
1.5(210.6–229.4)	217.9±2.0	217.5±2.6	215.3±4.9	214.6±5.4
3.0(201.7–239.9)	215.2±4.1	213.5±5.1	210.9±6.3	210.4±6.6
6.0(185.0–261.6)	208.1±15.9	205.7±13.8	201.0±12.2	198.0±10.0
12.0(155.6–311.1)	214.1±31.2	202.0±22.0	193.7±20.5	193.5±20.5
		Part D		
0.8(215.0–225.1)	220.2±2.0	221.1±2.8	223.1±4.4	222.5±3.0
1.5(210.6–229.4)	223.7±7.7	224.1±5.3	225.3±7.2	226.7±5.2
3.0(201.7–239.9)	228.3±7.8	231.1±9.5	234.0±11.4	235.0±6.7
6.0(185.0–261.6)	246.6±16.5	250.3±14.3	251.6±11.6	254.3±9.5
12.0(155.6–311.1)	267.4±18.8	272.1±18.9	275.9±22.0	282.0±16.6

jects were asked to always give an answer. For each test, a fixed scale spanning one octave was proposed to the subjects for adjustment of the flat tone. This scale was divided into steps of 2.25 Hz. This step size corresponded to about 1.4 times the difference limens reported by Moore (1973) for short-duration tones (about 1.6 Hz for 50 ms at 250 Hz). The signals were presented to both ears at a level of 80 dB SPL through Beyer DT48 headphones. The subjects participated in five test sessions divided into 20 min periods, with a comfortable pause between periods. A typical session lasted between 2 and 4 h. The first test session was considered as a training session, and was not used in the results.

D. Subjects

A group of eight musically trained subjects participated in the experiments. One of the subjects was one of the authors (CdA), and the others were music students who were paid for the experiments. Results are likely to be accurate with trained and selected subjects. However, interpretation of the results as representative of the general population may be questionable, because of the superior skills of our subjects in pitch discrimination. With 8 subjects and 4 sessions, 32 matches were made for each of the 88 experimental conditions.

II. RESULTS AND DISCUSSION

A. Results

Means and standard deviations averaged for all subjects are reported in Table II and plotted in Fig. 2. For each condition in Fig. 2, horizontal sides of the box represent duration and vertical sides of the box represent extent. The four empty circles near the corners of the boxes represent the means obtained for the four parts ABCD of the test. The coordinates of a circle represent the mean frequency (along the y axis) reported by the subjects, and the time (along the x axis) that corresponds to the instant when the glissando frequency was equal to the mean frequency. Thus the $F0$ rises can be represented in the boxes by a line between the bottom left corner and the top right corner. The falls can be represented in the boxes by a line between the top left corner and the bottom right corner. If the subjects were able to perfectly perceive the time-varying fundamental frequency, matches would place the four points in the four corners. Part A (rise/end) is generally in the right/top corner, part B (rise/beginning) is generally in the left/bottom corner, part C (fall/end) is generally in the right/bottom corner, and part D (fall/beginning) is generally in the left/top corner. Responses are always close to the extremity matched. This indicates that subjects did not take all the glissando into account, but rather made an average of the frequencies present near the extrem-

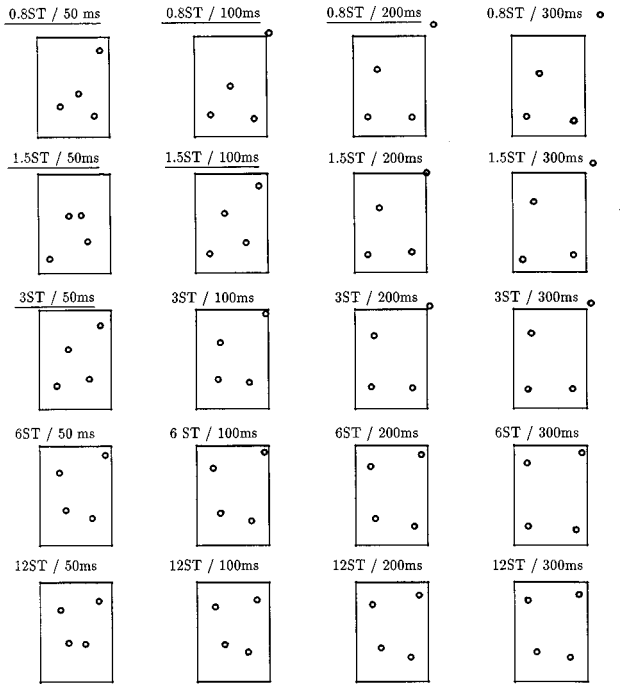

FIG. 2. Experimental results. Means reported in Table II. Each circle represents the mean obtained for each condition. Each box corresponds to the four parts ABCD of the experiments. For part A, rises adjusted at the end, results are generally in the right and top corner. For part B, rises adjusted at the beginning, results are generally in the left and bottom corner. For part C, falls adjusted at the end, results are generally in the right and bottom corner. For part D, falls adjusted at the beginning, results are generally in the left and top corner. The underlined conditions represent infraliminar glissandos, glissandos that are below the glissando threshold (they are marked ''b'' in Table I). The other conditions represents supraliminar glissandos.

ity. The underlined conditions in Fig. 2 represent infraliminar glissandos, glissandos that are below the glissando threshold (they are marked ''b'' in Table I). The other conditions represent supraliminar glissandos. For supraliminar glissandos, a ''butterfly'' pattern seems consistent across duration/extent conditions. Most butterflies share a similar form: part A is the nearest to the corner, and in several cases is matched even out of the box (average differences between means and extremities for part A are: 6.35 Hz); part B is the farthest from the corner (B: 20.12 Hz); point C is farther from the corner than point D (C: 16.43 Hz, D: 12.74 Hz). The parts can be classified in the order A<D<C<B as a function of their distances to the corresponding extremity.

The butterfly pattern shows a possible asymmetry between rises and falls. Pitch for rises (compared to falls) is closer to the end when matched at the end (compare parts A and C), and farther off the beginning when matched at the beginning (compare parts B and D). This might indicate different intervals for perceptual time averaging that may depend on the factor ''rise/fall.'' It seems that subjects are more influenced by the higher extremity than by the lower extremity. Typically, falls are adjusted closer to the beginning, i.e., the higher extremity (compare C and D), whereas rises are adjusted closer to the end, i.e., the higher extremity (compare A and B). Heuristic rules for drawing the butterfly patterns in Fig. 2 can be stated as follows:

(1) the high register has more weight in perception (because matches are closer to the higher extremity of the glissando).
(2) the integration interval is shorter at the end and longer at the beginning (because matches are closer to the extremity at the end than at the beginning).

Rule (1) states that A<B and C>D. Rule (2) states that A<D and B>C. Thus, one can deduce that A<D<C<B.

The same tendency can be seen for standard deviations. The standard deviations reported in Table II are an indication of the consistency of the adjustments. Generally, standard deviations are smaller for adjustments at the end (parts A and C), and higher for adjustments at the beginning (parts B and D). This could indicate that it was easier to make consistent adjustments at the end. Also, standard deviations are smaller for adjustment of the higher extremity (compare A and D, and B and C). For the large extent conditions (6 semitones and 12 semitones), the standard deviations can be ordered as: A<D<C<B. Thus it seems that when adjustments are farther from the extremity matched, they are also less consistent. For the smaller extent conditions, it is difficult to interpret the differences in standard deviation. For the 0 semitone condition, the standard deviations are small when adjusted at the end. In this case, they are close to the difference limens for short tones (Moore, 1973).

An analysis of variance was carried out with factors ''duration'' (four values), ''rise/fall'' (two values), ''beginning/end'' (two values), ''extent'' (five values), ''session'' (four values). The factor ''duration'' was not significant [$F(3,560)=20.055$; $p=0.9830$]. As a matter of fact, only a slight dependence on duration is noticeable in Fig. 2. Means followed a slightly rising or falling line as duration increased for a same extent, but this tendency was not significant. This showed that duration played only a minor role compared to other factors. No significant effect was found for the factor ''beginning/end'' [$F(1,560)=1.936$; $p=0.1646$]; subject responses averaged for parts A and C were not different from the subject responses averaged for parts B and D. The effect of the factor ''rise/fall'' was significant [$F(1,560)=26.94$; $p<0.0001$]. This indicates that the asymmetry observed in perception of rises and falls is significant. The factor ''extent'' was significant [$F(4,560)=72.67$; $p<0.0001$]. This was likely to occur, as for most conditions the extents were close to or above the glissando threshold. Interactions between ''rise/fall'' and ''beginning/end'' were very strong [$F(1,560)=1092.80$; $p<0.0001$] This indicates different behaviors for the different parts A, B, C and D. The interaction between ''rise/fall'' and ''extent'' was significant [$F(4,560)=3.07$; $p=0.0162$]. Again, this confirms an asymmetry in perception of rises and falls, which depends on extent. All other interactions were not significant.

B. Asymmetry between higher and lower extremities

Rule (1) states that the higher extremity is ''better'' perceived than the lower extremity. ''Better'' perceived means that adjustments are closer to the higher extremity, when it is the extremity matched, compared to the lower extremity,

again when it is the extremity matched. This experimental result suggests that the high register might be perceptually more important than the low register. Similar findings have already been reported in other works. A difference between rises and falls was noticed by Rump and Hermes (1996) in an experiment on prominence in intonation. The stimuli were /mamama/ utterances, with fundamental frequency around 100 Hz. They found that high pitch levels contributed to prominence more than low pitch levels. Demany and McAnally (1994) and Demany and Clément (1995, 1997) conducted a number of studies on perception of wide frequency modulations. In these experiments, pure tones or complex tones were used, between 250 and 4000 Hz. They consistently found that frequency peaks are better perceived than frequency troughs. This effect seems robust against factors like the carrier signal, modulation waveform, frequency register and intensity. In a study on perception of contour tones, Hombert (1975) asked subjects to adjust a static tone at the beginning of a rise or a fall. The results are very similar to ours: the beginning of a gliding tone is better perceived for falls than for rises. In other words, for a task rather similar to the present experiments, Hombert (1975) found the same type of effect: The higher extremity is better perceived than the lower extremity. This indicates that rule (1) might be a rather general effect for perception of supraliminar (or wide) frequency modulations.

C. Asymmetry between beginning and end

The second type of asymmetry found in our data, rule (2), is an asymmetry between adjustments at the beginning and at the end of tones. This type of asymmetry has been reported in several studies of wide frequency modulations, as in formant transitions between consonants and vowels in speech. Brady *et al.* (1961) suggest that a higher perceptual weight could be assigned to the most recent information. More recently, Porter *et al.* (1991), Wieringen and Pols (1995), Wieringen (1995), and Cullen *et al.* (1992) reported differences in sensitivity between initial and final transitions of short formant glides. All these studies conclude that the end is better perceived than the beginning. This indicates that rule (2) might be a rather general effect for perception of time-varying frequency modulation.

D. Asymmetries between rises and falls

The possible asymmetry in perception of rises and falls has been the subject of controversial discussion in many papers on tone or intonation perception. Dooley and Moore (1988) discussed asymmetry in difference limens for glide detection. In a two-alternative, forced-choice procedure, they measured frequency difference limens (DLF) for rises and falls. Rises and falls were presented randomly before and after a constant tone signal. Signals were merged, corresponding to parts A and B on the one hand and C and D on the other, and no effects between beginning and end were likely to occur. Pure tones were used, with center frequencies ranging from 500 to 8000 Hz, and durations ranging from 50 to 800 ms. Dooley and Moore (1988) found that UP–DL (DLF for rises) were consistently higher than DOWN–DL (DLF for falls). Thus it seems that rises are more difficult to perceive than falls. The opposite effect is reported by Gardner and Wilson (1979). Dooley and Moore conclude that these differences are difficult to interpret. The differences between rises and falls went unnoticed in many previous works on the glissando threshold, as 't Hart *et al.* (1990) pointed out. They also noted the large dispersion of the data on the glissando threshold found in the literature. All these studies were for difference limens. In this case, it is difficult to conclude about possible asymmetries between rises and falls. On the contrary, in the case of wide and supraliminar frequency modulations, it seems that the difference between rises and falls is consistent in many experiments (Hombert, 1975; Rump and Hermes, 1996; Demany and McAnally, 1994; Demany and Clément, 1995, 1997). In this case, the combination of rules (1) and (2) can shed some light on the possible asymmetry in perception of rises and falls, as it is discussed above.

E. Summary

In summary: (1) the mean frequency perceived for short-duration $F0$ glissandos is in the direction of the extremity matched; (2) distances of adjustments to the extremity differ for rises and falls; (3) adjustments are closer to the extremity for adjustments at the end, compared to adjustments at the beginning; (4) adjustments are closer to the higher extremity compared to the lower extremity; (5) ''duration'' plays a minor role; (6) ''extent'' is highly significant. As a consequence, the four parts ABCD for a given condition of extent and duration have distinct behaviors, which can be seen in the asymmetric butterfly patterns of Fig. 2.

Time averaging of $F0$ could explain pitch perception for $F0$ glissandos. It also seems that not all the glissando is taken into account for time averaging. These results are compatible with Rossi's 2/3 rule. One can easily check that most of our experimental data are comprised between the second and the third third of the glissandos.[2] However, this rule is not really a model, as it gives only an indication of where pitch is. It is of little use in the case of large extent. For example, if one considers the 12 semitone conditions, Rossi's rule predicts that the pitch perceived is between the second and the third third of the glissando, and one third of the glissando represents more than 50 Hz. Of course the result is correct, but not very accurate. In the next section, a more accurate model is discussed.

III. NUMERICAL MODEL

A. Equation of the model

A numerical model able to predict experimental data is searched for. The aim of this model is to predict the pitch perceived at the beginning and end of a given $F0$ glissando. The model should be able to give a response which is close to the subjects' mean response. Both TA and WTA models are studied. The TA model integrates $F0$ over a time interval of the glissando. The integration interval is near the extremity matched. Assuming a linear glissando $F0 = a\tau + b$, a TA model is

$$p=\frac{\int_{t1}^{t2}(a\tau+b)d\tau}{\int_{t1}^{t2}d\tau}=a\frac{t1+t2}{2}+b. \tag{3}$$

The model has only one parameter, δ, defined as follows. Let d be the glissando duration. Then δ is the length of the averaging interval for integration, expressed as a proportion of d. The time limits of integration are ($t1=0$, $t2=\delta\times d$) for an adjustment at the beginning, and ($t1=d-\delta\times d$, $t2=d$) for an adjustment at the end. The TA model is computed as

$$p(\delta)=\begin{cases}\dfrac{ad(2-\delta)}{2}+b & \text{adjustment at the end}\\ \dfrac{ad\delta}{2}+b & \text{adjustment at the beginning.}\end{cases} \tag{4}$$

Like the TA model, the WTA model integrates $F0$ on a time interval of the glissando, but $F0$ is modulated by a weighing function. The aim of this weighing function is to concentrate the integration of frequency on a part of the glissando. It is reasonable to assume that time plays a role in the averaging process, so more attention must be paid to the end in case of adjustment at the end, and to the beginning in case of adjustment at the beginning. This is the reason that the weighing function chosen is an exponential function. The model has two parameters. δ represents the duration of the averaging interval expressed as a proportion of the tone duration, and α is the exponential factor:

$$p(\alpha,\delta)=\frac{\int_{t1}^{t2}\exp(\alpha(\tau-t2))(a\tau+b)d\tau}{\int_{t1}^{t2}\exp(\alpha(\tau-t2))d\tau}$$

$$=\frac{at2-at1\exp(\alpha(t1-t2))}{1-\exp(\alpha(t1-t2))}+b-\frac{a}{\alpha}. \tag{5}$$

Let d be the glissando duration. Then the time limits of integration are ($t1=0$, $t2=\delta\times d$) for an adjustment at the beginning, and ($t1=d-\delta\times d$, $t2=d$) for an adjustment at the end. The WTA model is computed as:

$$p(\alpha,\delta)=\begin{cases}\dfrac{a-a(d-\delta d)\exp(-\alpha\delta d)}{1-\exp(-\alpha\delta d)}+b-\dfrac{a}{\alpha}\\ \quad\text{adjustment at the end,}\\ \dfrac{a\delta d}{1-\exp(-\alpha\delta d)}+b-\dfrac{a}{\alpha}\\ \quad\text{adjustment at the beginning.}\end{cases} \tag{6}$$

B. Estimation of optimal parameters

The TA model depends on one free parameter, and the WTA model depends on two free parameters. Optimal parameters of the models must be estimated. A classical means for estimation of optimal parameters is to minimize the root-mean-square (rms) distance between the model response and the experimental data.

Let $m(n)$ be the experimental mean (reported in Table II) for a particular condition n of factors ''duration,'' ''extent,'' ''rise/fall,'' and ''beginning/end.'' Let $p_{\delta,\alpha}(n)$ be the response of a model with parameters δ,α for condition n. The normalized rms distance is computed by

$$\mathrm{rms}(\delta,\alpha)=\frac{1}{N}\sqrt{\sum_{n=1}^{N}(p_{\delta,\alpha}(n)-m(n))^2}, \tag{7}$$

where n is between 1 and N, and where N is the number of conditions considered.

The minimum rms distance between the model and data, using an iterative minimization procedure, gives the optimal parameters. However, the raw distance between the model and the data is not very informative by itself. A good way to gain further insight into the model quality is to evaluate the fit to the data, by computing the number Q of conditions for which the model response is not statistically different from the subject's response: The larger the Q, the better the fit. Q is computed as follows. Let $e(n)$ be the experimental standard deviation (reported in Table II) for a particular condition n of factors ''duration,'' ''extent,'' ''rise/fall,'' and ''beginning/end.'' The statistical equivalence between this predicted value and the experimental data is computed by the Student t-test (recall that 32 responses are available for each test condition): $t(n)=[(m(n)-p_{\delta,\alpha}(n))\sqrt{31}]/e(n)$. Using a level of significance of 0.05, the critical value is 2.03 for a two-tailed test with df=31. The statistical equivalence between the predicted value and the experimental data for a condition n is computed using a function $q_{\delta,\alpha}(n)$ defined by

$$q_{\delta,\alpha}(n)=\begin{cases}1, & \text{if } -2.03<t(n)<2.03,\\ 0, & \text{otherwise.}\end{cases} \tag{8}$$

The quality $Q(\delta,\alpha)$ of the model with parameters δ,α is the number of conditions for which the model and the data are statistically equivalent:

$$Q(\delta,\alpha)=\sum_{n=1}^{N}q_{\delta,\alpha}(n), \tag{9}$$

n is between 1 and N, where N is the number of conditions considered. For instance, if the model is searched for all the conditions, then $N=80$; but if it is searched only for rises matched at the end, then $N=20$. The zero-semitone conditions are not considered, because every model will give the same answer in this case.

Discussion of the results reported above suggests that asymmetries between beginning versus end, higher versus lower extremities, and rises versus falls have to be considered. This indicates that each part ABCD should be considered separately for modeling. Thus four sets of parameters are considered for modeling, one for each part ABCD, with $N=20$ for each set. The optimization procedure described above is applied to each part. In addition, the optimization procedure is applied to the entire set of data (coined ''all data'' condition). Optimal parameters, and the corresponding number of conditions for which the predicted data are not significantly different from the experimental data, are reported in Table III. Results for each condition (using four sets of parameters) are displayed in Fig. 3. An empty circle indicates a condition for which the model response is statistically different from the data. A filled circle indicates a condition for which the model response is not statistically different from experimental data.

TABLE III. Optimal parameters for the TA and the WTAM models. ''*Q*'' represents the ''quality'' of the model: the number of conditions for which the predicted data are not significantly different from the experimental data (see text), and ''#'' represents the number of conditions for each part. ''%'' is the corresponding percentage ($100\times Q/\#$). ''All data'' means that a same parameter setting is used for all data. ''ABCD'' means that a different parameter setting is used for each part ABCD.

	TA δ	Q (#)	%	WTA δ	WTA α	Q (#)	%
All data	0.48	49 (80)	61	0.54	7.2	52 (80)	65
Part A	0.18	17 (20)	85	0.26	24.7	17 (20)	85
Part B	0.69	20 (20)	100	0.82	−7.5	20 (20)	100
Part C	0.59	16 (20)	80	0.75	13.5	20 (20)	100
Part D	0.45	15 (20)	75	0.56	−19.4	18 (20)	90
ABCD	···	68 (80)	85	···	···	75 (80)	94

C. Discussion

The TA and WTA models are able to predict 85% and 94% of the data, provided that the four parts ABCD are considered separately. The percentages are reduced to only 61% and 65% with the same parameter setting for all parts. This result is not surprising, given the asymmetries observed in the experimental data. Thus for modeling the four parts ABCD must be considered separately. In this case, good results are obtained for both models, though the WTA model performs better than the TA model.

The optimal α and δ parameters for the WTA model are different for the four parts of the test. The interpretation of δ is straightforward: It represents the proportion of the glissandos over which integration occurs. Interpretation of α is twofold. On the one hand, the sign of α indicates if more attention was paid to the beginning or end of the glissando. A positive α indicates that a higher perceptual weight is assigned to the most recent information (end). A negative α indicates that a higher perceptual weight is assigned to the most distant information (beginning). On the other hand, the magnitude of α represents the amount of damping introduced in averaging. A large magnitude means that a higher perceptual weight is assigned to the information close to the extremity matched. A small magnitude means that all the parts of the time interval used for averaging have almost the same weight. The averaging interval ($\delta=0.26$) is very short for part A: about 26% of the end of the glissando. The parameter $\alpha=24.7$ is positive, which means that the end of the glissando has more weight. The averaging window length in part B ($\delta=0.82$) is long: about 82% of the glide. The parameter $\alpha=-7.5$ is negative. This indicates that more attention was paid to the beginning of the glissando. The same remark holds for part D, where $\alpha=-19.4$ is negative, though for part D the averaging window ($\delta=0.56$) is shorter than for part B. For part C, the parameter $\alpha=13.5$ is positive, which indicates that more attention was paid to the end of the glissando. The averaging window ($\delta=0.75$) is long, about 75% of the tone duration. The same remarks hold for the TA model. The averaging window is shorter for part A (18%), longer for part B (69%). It is also long for parts C and D.

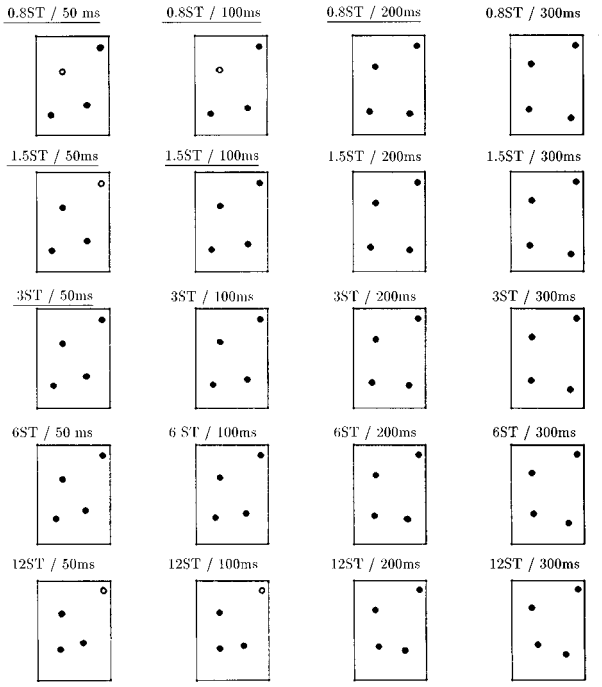

FIG. 3. Weighted time-average models. Each circle represents the value obtained by four weighted time-average models corresponding to the four parts of the test. A filled circle represents a conditions which is not statistically different from the experimental data. The underlined conditions represent infraliminar glissanndos, glissandos that are below the glissando threshold (they are marked ''b'' in Table I). The other conditions represent supraliminar glissandos.

The combination of the magnitude of α and δ can be used for computing the distance between the model responses and the extremity matched. Recall that in the results section, it was found that this distance is ordered as A<D<C<B for the experimental means. The constant α magnitude represents the damping factor. When it is high, damping is high and then the model response is close to the extremity. The distance of the model response and the extremity can be ordered as follows: A<D<C<B because the corresponding α are 24.7(A)>19.4(D)>13.5(C)>7.5(B). The parameter δ represents the proportion of the glissando used for integration. When δ is small, the model response is close to the extremity. We obtain the same order: A<D<C<B, because 0.26(A)<0.56(D)<0.75(C)<0.82(B). Therefore, the optimal parameters obtained for the WTA model are in good agreement with the heuristic rules derived

from the experimental results: The same order is found for the four parts ABCD of the test.

In summary, it seems that both the TA and the WTA models are able to predict a significant amount of the experimental data. However, the WTA model performs better than the TA model. This is not surprising, since the WTA model has two parameters compared to only one parameter for the TA model. The model's parameters give some insight into the experimental data, and are compatible with the butterfly patterns found in the experimental data. It must be pointed out that it is necessary to know the glissando direction and whether the match is at the beginning or end in order to select a set of parameters. This means that the WTA model in itself is not able to explain the asymmetries, but must be adapted to each situation. In this case it is able to predict the pitch perceived. The WTA model is a functional model, and not a model of the physiological or psychological processes that take place in pitch perception. It may help to compute the pitch perceived for an $F0$ glissando, but is not able to explain how this pitch is perceived. In particular, the explanation of experimental asymmetries in pitch perception is still unclear.

IV. CONCLUSION

In this study, we studied perception of short-duration linear $F0$ glissandos. Perception of rising and falling glissandos, matched at the beginning and at the end, was measured. Significant differences between the four main parts ABCD of the experiments (rises adjusted at the end, rises adjusted at the beginning, falls adjusted at the end, falls adjusted at the beginning) were found. This indicates that there is a difference between perception of rises and falls and perception of the beginning and the end of tones. This might be explained by a greater perceptual weight for the high register, compared to the low register. The experimental results showed that some sort of averaging of the $F0$ contours was performed by the subjects. Frequencies near the extremity matched (beginning or end) seemed more important. Simple numerical models for prediction of the experimental data were tried: a time-average model and a weighted time-average model of pitch perception. Optimal parameters for these models were estimated using a statistical distance criterion. The models performed well in predicting experimental data: 94% of the data computed with the best WTA models were not significantly different from experimental data. The optimal model's parameter settings varied significantly among parts ABCD (rises versus falls, adjustment at the end versus adjustment at the beginning). This was consistent with the finding of significant differences in the perception of the four parts. It can be concluded from our experiments that pitch perception for short-duration $F0$ glissandos corresponds to a weighted time average of $F0$. The WTA model proposed in the present study is close to the WTA model that was proposed for perception of short-duration vibrato tones in d'Alessandro and Castellengo (1994). However, the parameters obtained in both studies are different, as in this study they are also different among different parts.

ACKNOWLEDGMENTS

We are grateful to John P. Madden and Adrian Houtsma for their detailed constructive comments on an earlier version of this article, and to the editorial assistance and criticisms provided by D. Wesley Grantham. Thanks also to Olivier Piot, who helped in the experimental data collection.

[1]Mario Rossi, not to be confused with Jean-Pierre Rossi, one of the authors.
[2]Rossi's rule was stated for adjustment at the end of stimuli. The same type of rule can be formulated in the case of adjustment at the beginning, as follows: For dynamic tones in a vowel, the pitch perceived at the beginning corresponds to a point between the first and the second third of the vowel.

Brady, P. T., House, A. S., and Stevens, K. N. (**1961**). ''Perception of sounds characterized by a rapidly changing resonant frequency,'' J. Acoust. Soc. Am. **33**, 1357–1362.

Cullen, J. K., Houtsma, A. M. J., and Collier, R. (**1992**). ''Discrimination of brief tone-glides with high rate of frequency changes,'' Abstract of the Fifteenth Midwinter Meeting of the Association for Research in Otolaryngology, 67.

d'Alessandro, C., and Castellengo, M. (**1994**). ''The pitch of short duration vibrato tones,'' J. Acoust. Soc. Am. **95**, 1617–1630.

d'Alessandro, C., and Mertens, P. (**1995**). ''Automatic pitch contour stylization using a model of tonal perception,'' Comput. Speech Lang. **9**, 257–288.

Dooley, G. J., and Moore, B. C. J. (**1988**). ''Detection of linear frequency glides as a function of frequency and duration,'' J. Acoust. Soc. Am. **84**, 2045–2057.

Demany, L., and Clément, S. (**1995**). ''The perception of frequency peaks and troughs in wide frequency modulation. III. Complex carriers,'' J. Acoust. Soc. Am. **98**, 2515–2523.

Demany, L., and Clément, S. (**1997**). ''The perception of frequency peaks and troughs in wide frequency modulation. IV. Effects of modulation waveform,'' J. Acoust. Soc. Am. **102**, 2935–2944.

Demany, L., and McAnally, K. I. (**1994**). ''The perception of frequency peaks and troughs in wide frequency modulation,'' J. Acoust. Soc. Am. **96**, 706–715.

Gardner, R. B., and Wilson, J. P. (**1979**). ''Evidence for direction-specific channels in the processing of frequency modulations,'' J. Acoust. Soc. Am. **66**, 704–709.

Hermes, D. J. (**1993**). ''Pitch analysis,'' in *Visual Representation of Speech Signals*, edited by M. Cooke, S. Beet, and M. Crawford (Wiley, Chichester, UK).

Hess, W. (**1983**). *Pitch Determination of Speech Signals. Algorithms and Devices* (Springer-Verlag, Berlin).

Hombert, J. M. (**1975**). ''Perception of contour tones: an experimental study,'' Proc. 1st Annu. Meet. Berkeley Ling. Soc., pp. 221–232.

House, D. (**1990**). *Tonal Perception in Speech* (Lund U.P., Lund, Sweden).

Klatt, D. H. (**1973**). ''Discrimination of fundamental frequency contours in synthetic speech: Implications for models of pitch perception,'' J. Acoust. Soc. Am. **53**, 8–16.

Mertens, P. (**1987**). ''L'intonation du français. De la description linguistique á la reconnaissance automatique,'' Ph.D. thesis, Catholic University of Leuven, Belgium.

Moore, B. C. J. (**1973**). ''Frequency difference limens for short-duration tones,'' J. Acoust. Soc. Am. **54**, 610–619.

Nabelek, I. V., Nabelek, A. K., and Hirsh, I. J. (**1970**). ''Pitch of tone bursts of changing frequency,'' J. Acoust. Soc. Am. **48**, 536–553.

Porter, R. J., Cullen, J. K., Collins, M. J., and Jackson, D. F. (**1991**). ''Discrimination of formant transition onset frequency: Psychoacoustic cues at short, moderate, and long durations,'' J. Acoust. Soc. Am. **90**, 1298–1308.

Ross, J. (**1987**). ''The pitch of glide-like $F0$ curves in Votic folk songs,'' Proceedings of XIth International Congress of Phonetic Sciences, XIth ICPhS, Tallin, USSR, pp. 174–177.

Rossi, M. (**1971**). ''Le seuil de glissando ou seuil de perception des variations tonales pour les sons de la parole,'' Phonetica **23**, 1–33.

Rossi, M. (**1978**). ''La perception des glissando descendants dans les contours prosodiques,'' Phonetica **35**, 11–40.

Rossi, M. (**1978**). ''Interaction of intensity glides and frequency glissandos,'' Language and Speech **21**, 384–396.
Rump, H. H., and Hermes, D. J. (**1996**). ''Prominence lent by rising and falling pitch movements: Testing two models,'' J. Acoust. Soc. Am. **100**, 1122–1131.
Schouten, H. E. M. (**1985**). ''Identification and discrimination of sweep tones,'' Percept. Psychophys. **37**, 369–376.
Sergeant, R. L., and Harris, J. D. (**1962**). ''Sensitivity to unidirectional frequency modulation,'' J. Acoust. Soc. Am. **34**, 1625–1628.
't Hart, J. (**1976**). ''Psychoacoustic backgrounds of pitch contour stylization,'' IPO Ann. Prog. Rep. **11**, Eindhoven, The Netherlands, 11–19.
't Hart, J., Collier, R., and Cohen, A. (**1990**). *A Perceptual Study of Intonation* (Cambridge U.P., London).
van Wieringen, A. (**1995**). ''Perceiving dynamic speechlike sounds,'' Ph.D. thesis, Amsterdam University.
van Wieringen, A., and Pols, L. C. V. (**1995**). ''Discrimination of single and complex consonant-vowel- and vowel-consonant-like formant transitions,'' J. Acoust. Soc. Am. **98**, 1304–1312.
Wier, C. C., Jesteadt, W., and Green, D. M. (**1976**). ''A comparison of method-of-adjustment and forced-choice procedures in frequency discrimination,'' Percept. Psychophys. **19**, 75–79.

The role of the envelope in processing iterated rippled noise

William A. Yost
Parmly Hearing Institute, Loyola University Chicago, 6525 North Sheridan Road, Chicago, Illinois 60626

Roy Patterson
Centre for the Neural Basis of Hearing, Physiology Department, University of Cambridge, Cambridge CB2 3EG, England

Stanley Sheft
Parmly Hearing Institute, Loyola University Chicago, 6525 North Sheridan Road, Chicago, Illinois 60626

(Received 9 December 1997; revised 8 April 1998; accepted 10 July 1998)

Iterated rippled noise (IRN) is generated by a cascade of delay and add (the gain after the delay is 1.0) or delay and subtract (the gain is -1.0) operations. The delay and add/subtract operations impart a spectral ripple and a temporal regularity to the noise. The waveform fine structure is different in these two conditions, but the envelope can be extremely similar. Four experiments were used to determine conditions in which the processing of IRN stimuli might be mediated by the waveform fine structure or by the envelope. In experiments 1 and 3 listeners discriminated among three stimuli in a single-interval task: IRN stimuli generated with the delay and add operations ($g=1.0$), IRN stimuli generated using the delay and subtract operations ($g=-1.0$), and a flat-spectrum noise stimulus. In experiment 2 the listeners were presented two IRN stimuli that differed in delay (4 vs 6 ms) and a flat-spectrum noise stimulus that was not an IRN stimulus. In experiments 1 and 2 both the envelope and waveform fine structure contained the spectral ripple and temporal regularity. In experiment 3 only the envelope had this spectral and temporal structure. In all experiments discrimination was determined as a function of high-pass filtering the stimuli, and listeners could discriminate between the two IRN stimuli up to frequency regions as high as 4000–6000 Hz. Listeners could discriminate the IRN stimuli from the flat-spectrum noise stimulus at even higher frequencies (as high as 8000 Hz), but these discriminations did not appear to depend on the pitch of the IRN stimuli. A control experiment (fourth experiment) suggests that IRN discriminations in high-frequency regions are probably not due entirely to low-frequency nonlinear distortion products. The results of the paper imply that pitch processing of IRN stimuli is based on the waveform fine structure. [S0001-4966(98)04510-X]

PACS numbers: 43.66.Hg, 43.66.Jh, 43.66.Ki, 43.66.Mk [DWG]

INTRODUCTION

Iterated rippled noise (IRN) is produced by cascading a set of delay, attenuate, and add networks as illustrated in Fig. 1. The IRN stimuli have a pitch which varies with the reciprocal of the delay, d (Bilsen, 1966; Yost, 1996a), and the strength of the pitch increases with the number of iterations, n, and with the absolute value of the attenuation factor, g (Yost, 1996b, 1997). Recently, IRN stimuli have been used to study pitch perception, principally, in time-domain auditory models which suggest that pitch is mediated by regularity in the fine-structure of the IRN stimulus. The temporal information is extracted by autocorrelation either directly from the waveform (Yost, 1996a, b, 1997) or from the autocorrelogram (Meddis and Hewitt, 1991; Patterson *et al.*, 1996; Yost *et al.*, 1996). The transfer function of the IRN network has a spectral ripple, and, prior to the temporal hypothesis, the spectral peak spacing in the ripple was used to explain the perceived pitch (Bilsen, 1966; Bilsen and Ritsma, 1969/70). The spectral ripple can probably not be resolved in the spectral region above about the eighth harmonic of the reciprocal of the delay, and yet IRN stimuli restricted to this spectral region still produce strong pitch perceptions (Patterson *et al.*, 1996). So the spectral hypothesis has been rejected for high-pass-filtered IRN stimuli at least.

Recently, two experiments with bandpass-filtered IRN stimuli have been reported, one involving pitch-interval discrimination (Patterson and Akeroyd, 1995), the other involving the masking of a random noise signal by IRN stimulus, and the results of both have been interpreted to support the fine-structure hypothesis (Patterson and Datta, 1997). The passband for all of the stimuli was 800 Hz and the center frequency of the filter was varied from 800 to 8000 Hz. The IRN stimuli had 16 iterations and a delay of 16 ms (producing 62.5-Hz spectral peak spacing, which is unlikely to be resolved above 800 Hz). The paradigms were two-interval, forced-choice with a roving level. The data from the pitch-interval experiment showed that identification of the interval with the higher pitch remained extremely good as the center frequency increased from 800 to 4800 Hz, and, thereafter, as the pitch cue faded away, performance declined slowly to chance at 8000 Hz. The data from the masking experiment showed that at high frequencies detection of random noise presented in an IRN stimulus is about 14 dB easier than detection of random noise in random noise (Patterson and

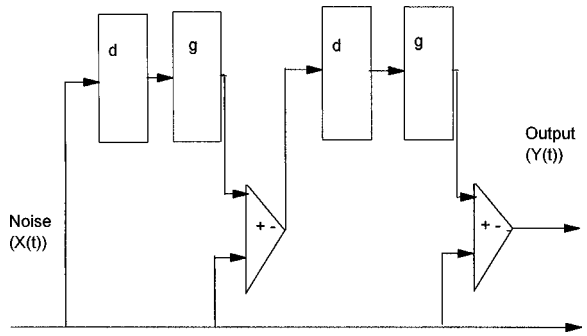

FIG. 1. A circuit diagram for an IRN stimulus with delay d in ms; gain; $-1 \leqslant g \leqslant 1$; and number of iterations, n ($n=2$ in this example).

Datta, 1997), and the result is independent of center frequency. When the masker is an IRN stimulus, the interval with the random-noise signal has a hiss component that is absent in the IRN stimulus, and this distinction persists at high center frequencies. The hiss is completely inaudible in random noise. The data were interpreted to suggest that some waveform fine-structure information is still available in some form up to 8000 Hz, even though a distinct pitch is no longer detected in bandpass-filtered IRN stimuli at high center frequencies.

There is, however, an alternative interpretation, which is that at high frequencies any pitch and timbre cues are, in some way, mediated by the envelopes of the stimuli. Both the spectral ripple and the temporal regularity of IRN stimuli are present in the envelope of the waveform as well as in its fine structure. The envelope has been used by Houtsma and Smyrzinski (1990) to explain the pitch of high-pass-filtered click trains, by Burns and Viemeister (1976) to explain the pitch of SAM noise, and by Viemeister (1979) and Dau (1996) to explain modulation detection. Other studies have argued that the pitch of complex stimuli may not be mediated by the envelope (de Boer, 1956; Plomp, 1976). The primary purpose of this paper is to determine the extent to which the perceptions associated with IRN stimuli should be attributed to the waveform fine structure and/or to the envelope of the stimulus.

I. HILBERT ENVELOPES AND LOW-PASS-FILTER ''ENVELOPES''

It is important to distinguish between the Hilbert envelope of a waveform, which is the true envelope in the mathematical sense, and the ''envelope'' produced by half-wave rectifying (HWR) a waveform (introducing a nonlinearity) and low-pass filtering (LPF). The HWR-LPF operation describes in a general sense the action of the haircell/auditory nerve complex in that the vibratory pattern of the basilar membrane produces neural impulses only when the vibration is in one direction (HWR) and the membrane properties limit the ability of the neurons to phase lock to high-frequency vibrations (LPF). Other forms of nonlinearity besides HWR can be used with a low-pass filter for envelope extraction, e.g., full-wave rectification (FWR) and squaring (energy). While the FWR-LPF and squaring-LPF operations have rarely been used to model auditory processing (see Jeffress, 1964), several models (e.g., Dau, 1996) assume that envelopes are extracted and used in the processing of several types of auditory stimuli and these two operations are ones that could be used in such models. In addition, these two operations help illustrate the general idea we wish to convey. That is, while the different operations that might be used to extract an envelope share many similarities, they also differ. The differences can be useful in deciding which operation may be appropriate for models of auditory processing. We want to distinguish among these forms of envelope extraction because one of these forms of envelope extraction (HWR-LPF) appears to be compatible with the auditory processing of IRN stimuli and the others do not.

A. Envelopes of frequency-shifted residue stimuli: Examples of envelope extraction

There is a noticeable difference in the pitch between stimuli produced by strictly harmonic components where the harmonics are all integer multiples of the fundamental, $f0$, and that produced when the harmonics are frequency shifted as a set by half the frequency of the fundamental. Such residue stimuli have been generated for tonal complexes (see, for example, Schouten *et al.*, 1962; Patterson and Wightman, 1976), alternating click trains (see, for example, Rosenberg, 1965), and iterated rippled noise (see discussion in the next section). These residue stimuli for tonal stimuli will be used to illustrate four types of envelopes, because the stimuli are deterministic and the lack of random fluctuations that occur for IRN stimuli makes it easier to observe the important distinctions among these envelopes. Waveforms that were produced by a set of harmonics in the region of 750–4625 Hz with a fundamental of 250 Hz are shown on the left side (Harmonics of $f0$) of Fig. 2; the frequency-shifted versions (Odd Harmonics of $\frac{1}{2}f0$) are shown on the right side. The important distinction is that peaks in the waveform at odd multiples of $\frac{1}{250}$ Hz (4 ms) are inverted in the frequency-shifted case. The remaining rows from the second row to the bottom row of the figure show envelopes after (1) half-wave rectification (HWR), (2) full-wave rectification (FWR), (3) squaring, and (4) the Hilbert envelopes (Hilbert). For the HWR, FWR, and squaring operations the same low-pass filter (LPF, two stages of a single-pole pair, 1200-Hz low-pass filter) was used to extract the envelope. The Hilbert envelope is the magnitude of the analytic signal derived from the stimulus. The mathematics of the Hilbert envelope are set out for use in psychoacoustics by Hartmann (1997). The figure shows that HWR-LPF operation can preserve the distinction (which is highly discriminable) between the two residue waveforms, inasmuch as the envelopes of the two waveforms are different. As such, time domain models of pitch processing could use the differences in the HWR-LPF envelope to describe discriminations among these stimuli.

B. IRN stimuli generated with $g=1.0$ (addition) and $g=-1.0$ (subtraction)

If $g=-1.0$ for IRN stimuli, then the delayed noise is subtracted rather than added ($g=1.0$) to the undelayed noise. In the case where $g=-1.0$ the spectrum has peaks at $1/2d$ and its odd integer multiplies instead of at $1/d$ and its integer multiplies when $g=1.0$. The pitch of wideband IRN stimuli

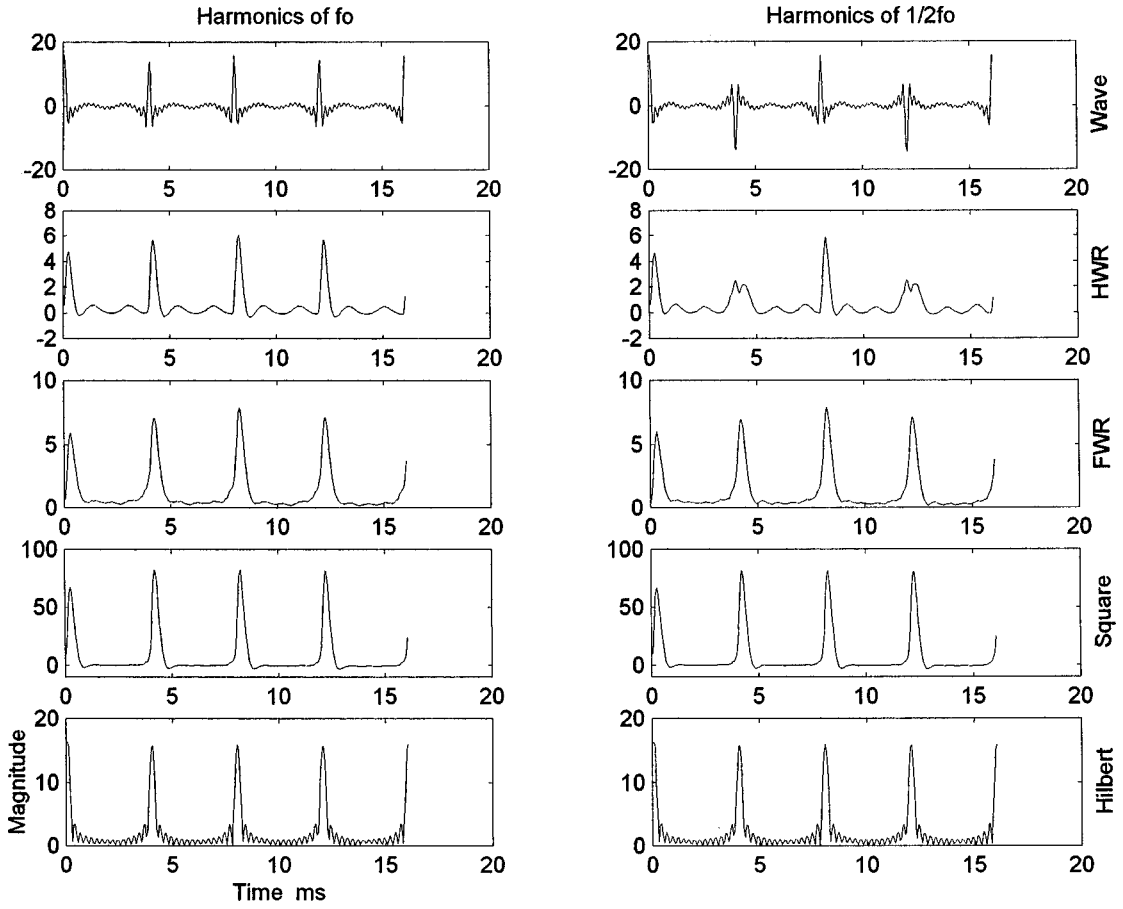

FIG. 2. The waveform and envelopes of two signals. The left-hand column is for stimuli based on the sum of the 16 harmonics of 250 Hz (Harmonics of $f0$) ranging from 750–4500 Hz. The right-hand column is for stimuli based on the sum of the 16 odd harmonics of 125 Hz (Odd Harmonics of $\frac{1}{2}f0$) from 875–4625 Hz. Envelopes based on half-wave rectification (HWR), full-wave rectification (FWR), squaring (Square), and the Hilbert envelope (Hilbert) are shown for each stimulus.

when $g=-1.0$ is different from that when $g=1.0$ (Yost, 1996a). For n less than 4, the pitch for wideband IRN stimuli when $g=-1.0$ is approximately $1/(1.1d)$ and $1/(0.9d)$. When n is greater than 4, the pitch for wideband IRN stimuli when $g=-1.0$ is at $1/2d$ (see also Bilsen and Wieman, 1980; Raatgever and Bilsen, 1995). In all cases the pitch for IRN stimuli when $g=1.0$ is $1/d$. In comparing the pitch of wideband IRN stimuli for cases of subtraction with those for cases of addition, the pitch difference for a low number of iterations is one of tone chroma, where as for a high number of iterations the pitch difference is one of tone height (an octave difference). Thus, there is a noticeable pitch difference between IRN stimuli generated with $g=1.0$ and those IRN stimuli generated with $g=-1.0$. Yost (1997) has also shown that there is a very small pitch strength difference between these two stimuli.

C. IRN waves and envelopes

The first row of Fig. 3 shows IRN waveforms produced by addition and subtraction; they have the same delay (4 ms) and the same number of iterations (8); the subtraction version is on the right. Differences between IRN stimuli produced by addition and subtraction are not obvious in the waveforms, but listeners can easily tell them apart (Yost, 1996a, 1997). The spectra (Spec) differ in the location of the spectral peaks and valleys (spectral peaks are shifted by 125 Hz for the subtraction case relative to that for addition). The differences are also revealed by autocorrelation (ACF) which emphasizes periodicity information and deemphasizes random fluctuations. The autocorrelation peaks for the case when $g=1.0$ are all positive, while those for $g=-1.0$ alternate between negative and positive values. The peaks in the autocorrelation function are used to explain the pitch of IRN stimuli in time-domain models (Meddis and Hewitt, 1991; Yost, 1996a).

The fourth row shows the Hilbert envelope (Env) for each IRN signal. As for the waveform, there is little apparent difference in the envelopes for IRN stimuli generated with $g=1.0$ and $g=-1.0$. The bottom two rows show the spectra (Spec Env) and autocorrelation functions (ACF Env) for the Hilbert envelopes. Despite the relatively flat envelopes, there is a spectral ripple and temporal regularity in the envelopes of IRN stimuli. However, the form of the envelope spectrum and regularity is the same for cases of subtraction and addition. These same envelope patterns also occur for cases of full-wave rectification and squaring, i.e., there is no difference in the envelope spectra and envelope autocorrelation functions between cases when $g=1.0$ (addition) and those when $g=-1.0$ (subtraction). In summary, if the pitch of IRN stimuli is based on the envelope, then it cannot be the

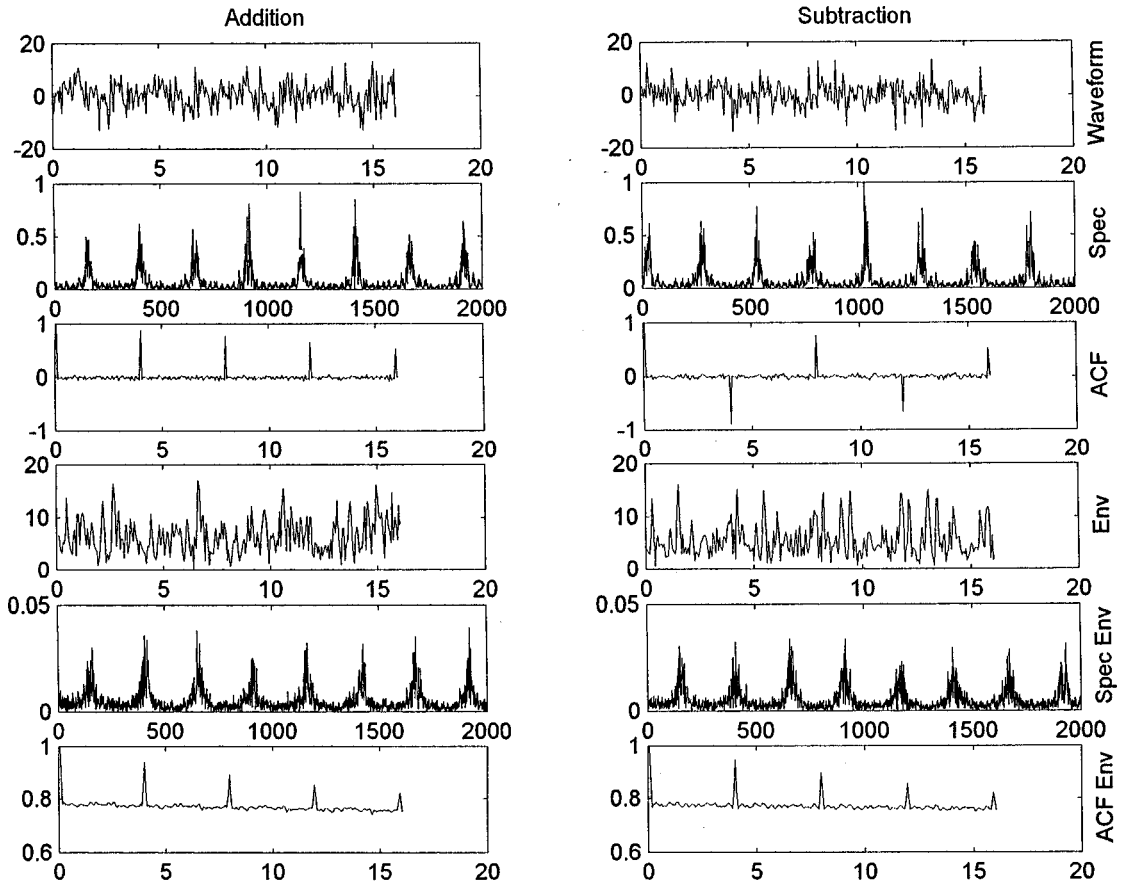

FIG. 3. The rows from the top to bottom display: waveforms (Waveform, units of amplitude and time in ms), waveform spectra (Spec, units of power and frequency in Hz), waveform autocorrelation functions (ACF, units of magnitude and lag in ms), Hilbert envelope (Env, units of amplitude and time in ms), spectra of the Hilbert envelope (Spec Env, units of power and frequency in Hz), and autocorrelation functions of the Hilbert envelope (ACF Env, units of magnitude and lag in ms) are shown for an IRN stimulus with $g=1.0$ (Addition) in the left column and with $g=-1.0$ (Subtraction) in the right column. The IRN stimuli were generated with $d=4$ ms and 8 iterations.

Hilbert envelope, the FWR-LPF ''envelope,'' or the squaring-LPF ''envelope'' because they do not distinguish wideband IRN stimuli produced by addition and subtraction and listeners do.

The autocorrelation pattern for half-wave rectification (HWR-LPF) IRN stimuli differs from the other forms of envelope extraction we have considered, in that the output of the HWR-LPF operation depends on the relationship between the spectral region of the IRN stimulus being evaluated relative to the cutoff of the low-pass filter used to extract the envelope. Figures 4 and 5 show autocorrelograms for IRN stimuli when $g=1.0$ (Fig. 4) and $g=-1.0$ (Fig. 5). Figure 6 shows the autocorrelogram for a noise that is not submitted to an IRN circuit (i.e., a flat-spectrum noise). The autocorrelograms were generated by first passing the stimuli (for IRN stimuli, $d=4$ ms and $n=8$ iterations) through a bank of 64 gammatone filters ranging in center frequency in equal ERB steps from 63 to 11 328 Hz. The output of each filter channel was half-wave rectified and low-pass filtered with a two-stage, one-pole pair, Butterworth filter with a 1200-Hz cutoff (see Patterson, 1994). Note that in Fig. 4 for the addition case, the alignment at lags of 4 and 8 ms is always at the peak of the autocorrelation function for every frequency channel. In Fig. 5 for the subtraction case, the alignment at 4 ms is at the valley for low-frequency channels but at the peak for the high-frequency channels. In Fig. 5, the alignment of the second autocorrelation peak at 8 ms is always at the peak as it was in Fig. 4. There is a similarity of the autocorrelation functions for the low-frequency channels to those shown for the waveform autocorrelation functions in Fig. 3. Thus, only in low-frequency channels of the autocorrelogram where waveform fine structure is still preserved is the difference between cases in which $g=1.0$ and those in which $g=-1.0$ also preserved. In Fig. 6 there is no apparent alignment in the autocorrelation peaks of the flat-spectrum noise for any channel at any particular delay. In particular notice the flat nature of the autocorrelation functions in the high-frequency channels. That is, the autocorrelation functions for IRN stimuli generated when $g=1.0$ and $g=-1.0$ differ in the low-frequency channels (where fine structure is preserved) but not in the high-frequency channels (where the envelope dominates). The exact frequency region in which fine-structure information is lost and the envelope is defined depends on the low-pass filter. Even frequency channels above the cutoff frequency of the filter will contain some fine-structure fluctuations since the filter only attenuates the waveform by an amount dependent on the order of the filter. The higher the frequency channel is relative to the filter cutoff, the less fine-structure information there is relative to envelope information. The autocorrelation functions for IRN

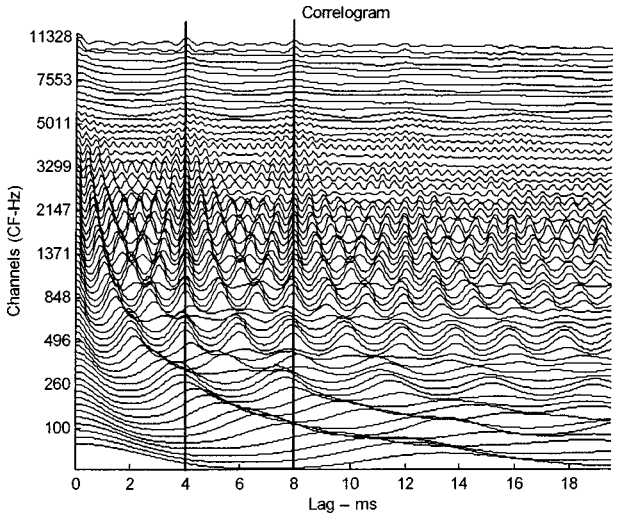

FIG. 4. Autocorrelograms for IRN stimulus with $g=1.0$, $d=4$ ms, and 8 iterations. The lines at lags of 4 and 8 ms mark the lags equaling the delay and its first higher integer multiple in the IRN circuit. In each case the lines mark the ACF peak. The correlograms plot the autocorrelation for each frequency channel (63 to 11 328). The correlograms are based on a 64-channel, gammatone filter-bank, rectification, lowpass filtering, and autocorrelation (see Patterson *et al.*, 1995).

stimuli differ from those for flat-spectrum noise in all channels. Since FWR-LPF, squaring-LPF, and the Hilbert envelope would produce no differences between cases of subtraction and addition in all frequency channels, only HWR-LPF appears to be a form of envelope extraction that is compatible with the observed discriminations.[1]

In this paper we will consider listeners' ability to discriminate between IRN stimuli generated with $g=1.0$ and those generated with $g=-1.0$, and their ability to discriminate IRN stimuli (independent of the sign of g) from flat-spectrum noise. These discriminations will be determined as a function of high-pass filtering. Recall that there is either a tone height or a tone chroma pitch difference for wideband IRN stimuli produced with $g=1.0$ and $g=-1.0$, and perhaps a small pitch strength difference. If the autocorrelograms of Figs. 4–6 represent auditory processing of these stimuli, then we predict that those IRN stimuli generated with $g=1.0$ can only be discriminated from those generated with $g=-1.0$ when the stimuli contain low frequencies where the fine structure is preserved. At high frequencies when discriminations between IRN stimuli are probably not possible, IRN stimuli might still be discriminated from flat-spectrum-noise stimuli on the basis of envelope cues.

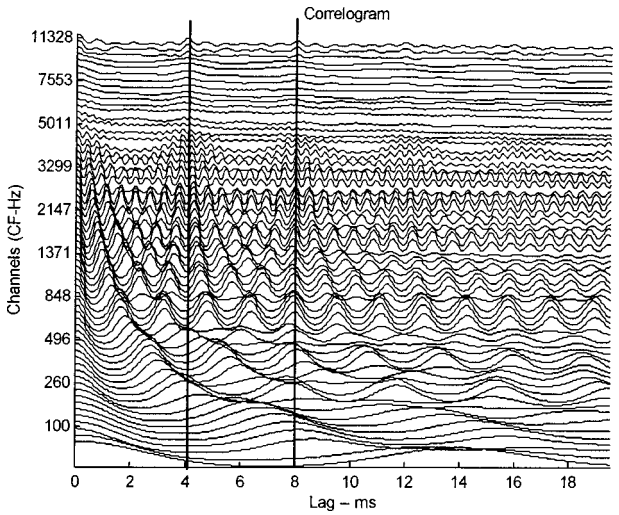

FIG. 5. Same as Fig. 4 except for the IRN stimulus when $g=-1.0$. Note that the line at a lag of 4 ms marks the valleys in the autocorrelation functions for low frequencies and the peaks at high frequencies. The line at a lag of 8 ms marks all peaks as it did in Fig. 4.

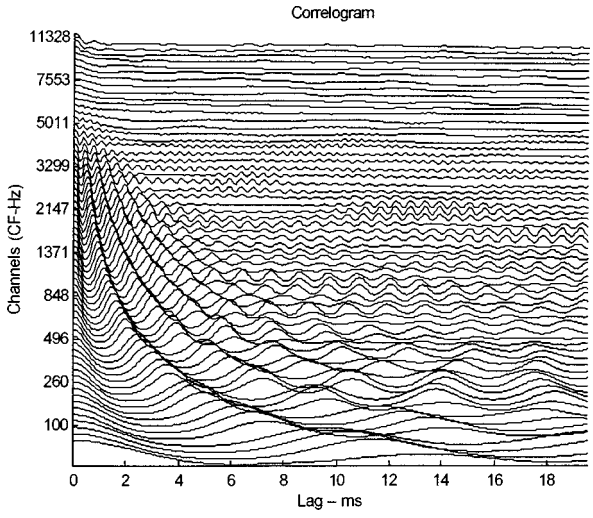

FIG. 6. Same as Figs. 4 and 5 except for the flat-spectrum noise. Note that there is little alignment of autocorrelation peaks at any particular lags, especially in the high-frequency channels.

II. EXPERIMENT 1

In experiment 1 listeners were presented IRN stimuli generated with $g=1.0$ or $g=-1.0$ or with a flat-spectrum noise that was not submitted to an IRN circuit. The goal was to determine how well listeners could discriminate the difference between IRN stimuli generated with $g=1.0$ and those generated with $g=-1.0$ as a function of high-pass filtering. In such an experiment, there are three possible outcomes. If listeners cannot discriminate between the two IRN stimuli generated with $g=1.0$ and $g=-1.0$, but they can tell these stimuli from a flat-spectrum noise, we will conclude that the envelope is most likely contributing to their discrimination. If listeners can discriminate between the two IRN stimuli, we will conclude that the IRN stimuli are most likely being discriminated based on the waveform fine structure. If they cannot discriminate between the two IRN stimuli and they cannot discriminate an IRN stimulus from a flat-spectrum noise, we will conclude that the IRN circuit no longer generates a perceptually relevant change in the noise.

A. Methods

Iterated rippled noises were generated on a Tucker Davis Technologies (TDT) system using software delay lines as described in Yost (1996b). The waveforms had a Gaussian distribution of instantaneous amplitudes and were played out of 16-bit D-to-A converters at 50 000 samples/s into a seventh-order Butterworth filter (programmable TDT, PF1 filters). The signals were 500 ms in duration, shaped with a

20-ms $\cos^2$ gate, and presented diotically. The overall level of the stimuli was 70 dB SPL and it was roved across each stimulus presentation over a ±6-dB range about 70 dB SPL (12-dB overall rove). The gain (g) was either 1.0 or −1.0, the delay was 4 or 16 ms, the number of iterations was 1 or 8, and the filter cutoffs were 100 to 2100 Hz, 4000 to 6000 Hz, 6000 to 8000 Hz, or 8000 to 10 000 Hz. New waveforms were generated for every observation interval. Five experienced listeners with normal hearing participated in the study.

On each trial of the single-interval experiment one of three stimuli was presented with equal probability: an IRN stimulus generated with $g=1.0$, an IRN stimulus generated with $g=-1.0$, or a noise not submitted to an IRN circuit (flat-spectrum noise). The listener indicated which of the three stimuli was presented and feedback was provided. A three-by-three stimulus-response table was generated for the last 50 trials of each 56-trial block. The first 6 trials for every 56-trial block were presented in the order: an IRN stimulus with $g=1.0$, an IRN stimulus with $g=-1.0$, and a flat-spectrum noise and then repeated another time in this order. Thus, these six initial trials served as practice for each block of trials to acquaint the listener with the differences among the three stimuli. The listeners were informed about these six practice trials. Five 50-trial blocks (250 total trials) were used for each stimulus–response table for each condition and listener.

Two measures of percent correct were obtained from the stimulus-response tables. Percent correct in discriminating between the two IRN stimuli, $P(C)_{+,-}$, was calculated based only on the trials in which either an IRN stimulus with $g=1.0$ or $g=-1.0$ was presented. $P(C)_{+,-}$ was the number of times the listener correctly identified the two IRN stimuli divided by the total number of times the two IRN stimuli were presented. That is, in calculating $P(C)_{+,-}$ the trials in which the flat-spectrum noise was presented were not used. Percent correct in discriminating between an IRN stimulus (independent of the gain, g) and flat-spectrum noise, $P(C)_{+/-,\text{noise}}$, was also determined. $P(C)_{+/-,\text{noise}}$ was determined by computing the number of times the listener correctly identified the flat-noise stimulus plus the number of times the listener correctly identified an IRN stimulus (independent of whether or not the IRN stimulus was generated with $g=1.0$ or $g=-1.0$) and dividing the sum by the total number of stimulus presentations.

B. Results and discussion

The results from the five listeners were similar [the largest $P(C)$ difference for any condition among the listeners was 8%], and therefore the data for each condition were collapsed into a single stimulus-response matrix across listeners before $P(C)_{+,-}$ and $P(C)_{+/-,\text{noise}}$ were calculated.[2] Figure 7 shows $P(C)_{+,-}$ versus the filter conditions and Fig. 8 shows the same relationships for $P(C)_{+/-,\text{noise}}$. As can be seen in Fig. 7, as long as the high-pass cutoff was 6000 Hz or lower, listeners were able to discriminate between the two IRN stimuli except perhaps for the 6000- to 8000-Hz condition when the delay was 16 ms with one iteration. The discriminations became more difficult as the delay increased

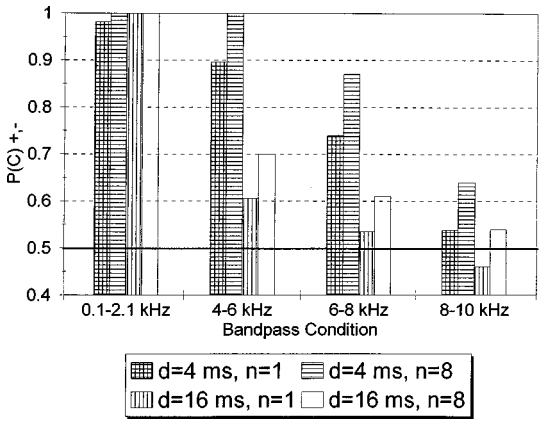

FIG. 7. Average percent correct discrimination $[P(C)_{+,-}]$ for four bandpass filter conditions and four IRN stimulus conditions: IRN stimulus with 4-ms delay and 1 and 8 iterations, and an IRN stimulus with 16-ms delay and 1 and 8 iterations.

from 4 to 16 ms, as the number of iterations decreased from 8 to 1, and as the high-pass filter cutoff was increased. The listeners were at or near chance in their ability to make these discriminations for the 8000- to 10 000-Hz conditions, except when the IRN stimulus was generated with 4-ms delay and 8 iterations, in which case average performance was near 63%. Figure 8 indicates that listeners were usually able to discriminate a flat-spectrum noise from an IRN stimulus for all filter conditions, except perhaps for the 8000- to 10 000-Hz condition with one iteration when the delay was 16 ms. Performance became worse as a function of increasing the highpass cutoff, and the task was more difficult for conditions with the longer delay and smaller number of iterations.

Since listeners could discriminate between IRN stimuli generated with $g=1.0$ and $g=-1.0$, these data suggest that for IRN stimuli with energy below approximately 6000 Hz the ability to process the IRN stimuli is based on the waveform fine structure. The difficulty in making these discriminations as the number of iterations decreased and the delay was increased is consistent with the literature on the pitch strength of IRN stimuli. Yost *et al.* (1996) and Yost (1996b, 1997) showed that the strength of the pitch increases with increasing number of iterations, and Bilsen (1966), Yost (1996b, 1997), and Yost *et al.* (1978) have shown that IRN

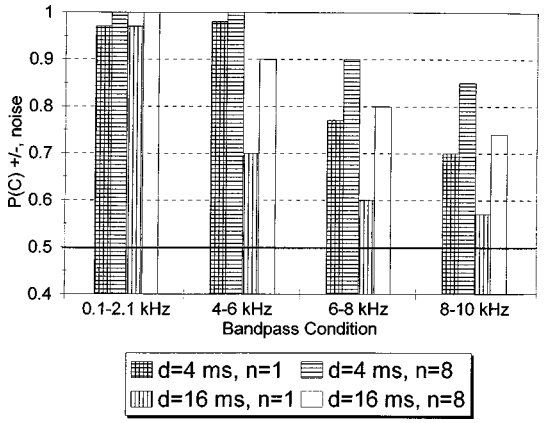

FIG. 8. Average percent correct discrimination $[P(C)_{+/-,\text{noise}}]$ for the four bandpass filter conditions and four IRN stimulus conditions shown in Fig. 7.

pitch strength decreases as the delay increases above about 5–8 ms. Suppin *et al.* (1994) also asked listeners to discriminate between IRN stimuli generated with $g=1.0$ and $g=-1.0$. They used bandpass IRN stimuli with $n=1$ iteration and center frequencies as high as 8000 Hz. Their data indicate that listeners can make this type of discrimination in the 8000-Hz spectral region when the delays used to generate the IRN stimuli were slightly less than 2 ms and the bandwidth of the IRN stimulus was about 2500 Hz. These results are consistent with those shown in Fig. 7 for the 6000- to 8000-Hz conditions.

The reason for the ability to tell IRN stimuli from noise even in the highest frequency regions is not entirely clear. In the 8000- to 10 000-Hz conditions, the listeners reported that all stimuli tended to sound like flat-spectrum noise. The only difference that they could use in making these discriminations was that the flat-spectrum noise sounded more ''hissy'' or ''noise-like'' than the IRN stimuli. The response bias of the individual listeners is consistent with these reports in that all listeners responded ''noise'' more than they did ''positive'' and ''negative.'' The overall stimulus-response table indicated a very slight bias for the ''positive'' response. All listeners agreed that these IRN stimuli did not have a pitch at these high frequencies.

While the pitch of complex stimuli is not due to nonlinear distortion products, it is possible that for the high-pass conditions of experiment 1, listeners were using such distortion products in low-frequency regions as the basis for their discriminations. The Appendix describes an experiment designed to address this problem.[3] These experiments used noise to mask both low-frequency regions (below 2000 Hz) for the 4000- to 6000-Hz IRN filtered conditions and the 4000- to 6000-Hz spectral region. The results of those experiments suggest that listeners are not using low-frequency distortion products as the only basis for making the discriminations described in this paper.

Although there is a small pitch strength difference between IRN stimuli presented with $g=1.0$ and $g=-1.0$, the major difference is a pitch difference. As pointed out earlier, the pitch difference is one of tone height or tone chroma depending on whether the pitch difference was a $\pm 10\%$ pitch difference (for cases in which the number of iterations was 1) or an octave difference (for cases in which the number of iterations was 8). In experiment 2 we investigate cases in which only a tone chroma pitch difference exists between the IRN stimuli to be discriminated.

III. EXPERIMENT 2

If the delay in an IRN circuit is changed by between 10% and 40% (especially if the delays are between 2 and 8 ms), the only perceptual change measured for these stimuli is a pitch chroma change (Yost, 1996a, 1997). Thus, by asking listeners to discriminate between two IRN stimuli generated with different delays, we assume that the only basis for discrimination is pitch. Thus, in experiment 2 listeners were presented with three stimuli as in experiment 1, except that the two IRN stimuli were generated with different delays and the same g (rather than the same delay and different g's as in experiment 1). As in experiment 1, the listeners had to decide whether a flat-spectrum noise was presented or which of the two IRN stimuli ($d=4$ ms for a high-pitched stimulus or $d=6$ ms for a low-pitched stimulus) was presented in the three-alternative, single-interval, forced-choice task.

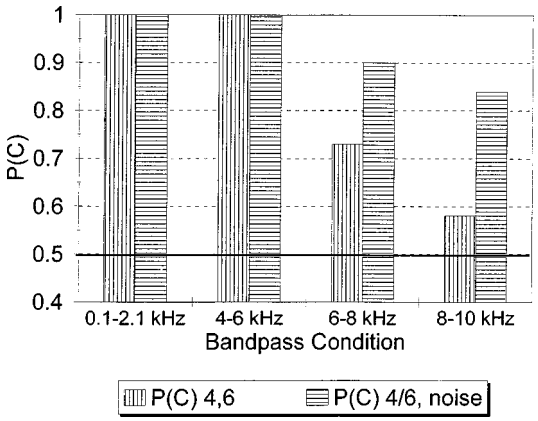

FIG. 9. Average percent correct discrimination for four bandpass filter conditions and for two $P(C)$ conditions: $P(C)_{4,6}$ for discriminating between an IRN stimulus with 4 ms and one with 6 ms delay ($g=1.0$ and $n=8$ for both IRN stimuli), and $P(C)_{4/6,\text{noise}}$ for discriminating between the IRN stimuli and flat-spectrum noise.

A. Methods

All stimuli, procedures, and listeners were the same in experiment 2 as in experiment 1, except that the two IRN stimuli were generated with $g=1.0$ and 8 iterations. A delay of 4 ms (250-Hz pitch) was chosen for one IRN stimulus and 6 ms (166.67-Hz pitch) for the other IRN stimulus. $P(C)_{4,6}$ and $P(C)_{4/6,\text{noise}}$ were computed in the same way that $P(C)_{+,-}$ and $P(C)_{+/-,\text{noise}}$ were computed in experiment 1. That is, $P(C)_{4,6}$ is the ability to discriminate between the two IRN stimulus generated with 4 and 6 ms of delay, and $P(C)_{4/6,\text{noise}}$ is the ability to discriminate between an IRN stimulus (independent of the delay) and flat-spectrum noise.

B. Results and discussion

Figure 9 shows the results for both $P(C)_{4,6}$ and $P(C)_{4/6,\text{noise}}$ as a function of cutoff frequency. Again the data among the five listeners were similar [the largest difference in $P(C)$ was 7%], so the data were collapsed into one stimulus-response table[2] across listeners as in experiment 1. Essentially the same results were obtained in experiment 2 as in experiment 1; listeners had difficulty telling the difference between the two IRN stimuli when the high-pass cutoff was in the region of 6000 Hz, but they could still tell the IRN stimuli from flat-spectrum noise. These results appear to reinforce the conclusions of experiment 1; the pitch of IRN stimuli is based on the waveform fine structure, but IRN stimuli can still be discriminated from flat-spectrum noise even at the highest frequencies. As in experiment 1, the listeners agreed that the basis of the ability to discriminate the IRN stimuli from flat-spectrum noise at high frequencies was not pitch but the perception of the flat-spectrum noise sounding more ''noisy'' or ''hissy'' than the IRN stimuli. Again, the response biases of the individual listeners are consistent with these reports in that all listeners responded ''noise''

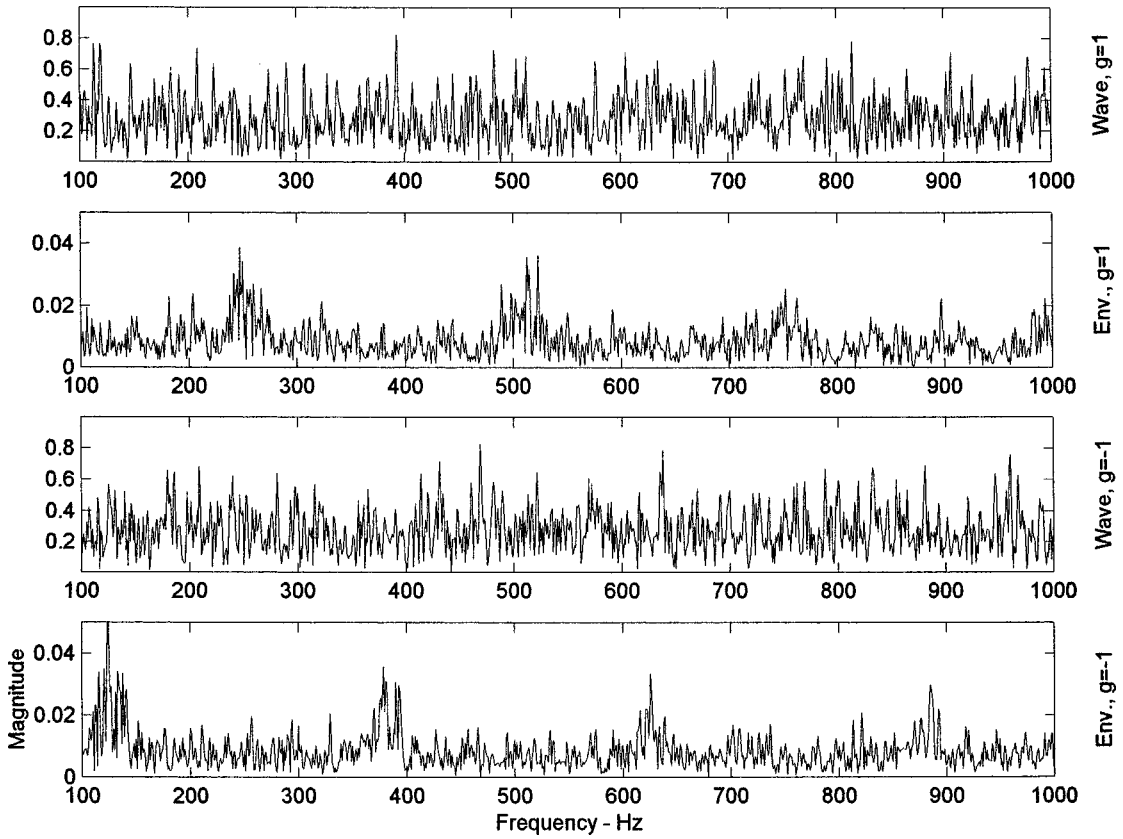

FIG. 10. The magnitude spectra for the waveform fine structure (top, Wave, $g=1.0$) and ''HWR-LPF envelope'' (second row, Env., $g=1.0$) for the condition in which wideband noise was modulated by a bandpass-filtered IRN stimulus generated with 4 ms delay, 8 iterations, and $g=1.0$. The same two plots are shown in the third row (Wave, $g=-1.0$) and fourth row (Env., $g=-1.0$) for the same IRN stimulus except when $g=-1.0$. Note that only the envelope contains the spectral ripple and that the ripple is different for $g=1.0$ than for $g=-1.0$.[4]

more than they did ''high-pitch'' and ''low-pitch.'' There was also a slight bias for the ''high-pitch'' response.

In experiments 1 and 2 the spectral and temporal structure associated with the IRN circuits are present in both the fine structure and in the envelope (although information may not always be used from both). It is possible to generate a stimulus such that *only* the envelope contains the spectral ripple and temporal regularity of an IRN stimulus. In experiment 3 we consider stimulus conditions in which the spectral ripple and temporal regularity are only in the envelope.

IV. EXPERIMENT 3

To produce a stimulus with an envelope, but not the fine structure, that contains the ripples and temporal regularity of an IRN stimulus, we bandpass filtered an IRN stimulus and multiplied it times a wideband noise carrier. The resulting stimulus has the random spectral fine-structure of the noise carrier, but an envelope that reflects the spectral ripples and temporal regularity of the IRN modulator. Thus, using a low-frequency, bandpass IRN stimulus as a modulator produces a stimulus with only the envelope containing the rippled spectrum and temporal regularity. Figure 10 shows the spectrum of the ''HWR-LPF envelope'' and waveform fine structure for a wideband noise multiplied by a 100- to 1100-Hz bandpass-filtered IRN stimulus with a 4-ms delay, 8 iterations, and $g=1.0$ or $g=-1.0$. The same two-pole, low-pass filter as was used in Fig. 2 was used for the envelopes shown in Fig. 10. If the IRN multiplier is generated with $g=1.0$, then the envelope has the spectral and temporal structure of an IRN stimulus generated with $g=1.0$ (note the spectral peaks at 250, 500, and 750 Hz).[4] The envelope of a noise multiplied with an IRN stimulus with $g=-1.0$ will have the spectral structure and temporal regularity of the IRN stimulus with $g=-1.0$ (note the spectral peaks at 125, 375, 625, and 875 Hz).[4] Thus, in this case the envelopes differ in their spectral ripples and temporal regularity as opposed to the conditions of experiment 1 where the envelopes were identical. While Fig. 10 shows the result of using the HWR-LPF operation, the same general outcome occurs if any of the other envelope extraction operations are applied. That is, no matter how the envelope is extracted, the spectrum of the extracted envelope for the stimulus based on multiplying a noise by an IRN stimulus differs when $g=1.0$ from when $g=-1.0$. Also, for this stimulus, there are no differences in the fine structure of the stimuli.

Sheft and Yost (1996) showed that listeners can discriminate a noise modulated with a low-pass IRN stimulus from an unmodulated noise, but the discrimination is difficult and the discriminations do not appear to be based on pitch.[5] In order to show that these stimuli with only a spectral ripple or temporal regularity in their envelope are probably not discriminated on the basis of pitch, we modified the three-alternative, forced-choice, single-interval experiment. The three basic stimuli used in experiment 1 were used in experi-

ment 3; that is, there was either no IRN multiplier (flat-spectrum noise), an IRN multiplier with $g=1.0$, or an IRN multiplier with $g=-1.0$. However, from trial to trial the delay used for the IRN multiplier was randomly varied over a small range. A wideband IRN stimuli generated with eight iterations generates a one-octave pitch shift between an IRN stimulus generated with $g=1.0$ and one generated with $g=-1.0$ (see Yost, 1996a). Thus, the small random change in delay, while producing a noticeable change in pitch, should not affect the ability to make a pitch discrimination between an IRN stimulus produced with $g=1.0$ and an IRN stimulus produced with $g=-1.0$ (see Yost *et al.*, 1978). Thus, we measured performance for IRN stimuli in the two conditions. We compared conditions (Condition 1-No Mod.) like those in experiment 1 in which both the waveform and envelope contain the spectral ripple and temporal regularity with conditions (Condition 2- Mod.) in which only the envelope contains these characteristics.

A. Methods

In the nonmodulated condition (No Mod.), the same general procedures as described for experiment 1 were used to generate IRN stimuli with a mean delay of 4 ms, with 8 iterations, and with $g=1.0$ and $g=-1.0$. On a trial by trial basis the delay for the IRN stimuli was randomly varied over a 12% range [Yost *et al.* (1978) showed that a 12% change in delay yielded about 100% correct discrimination between two IRN stimuli generated with different delays]. In the modulated condition (Mod.), these IRN stimuli were bandpass filtered between 100 and 1100 Hz. The 100- to 1100-Hz filter conditions were used to keep the same low-pass limit as used in experiments 1 and 2 and to use an upper cutoff similar to that employed by Sheft and Yost (1996). The peak amplitudes of the IRN stimuli were normalized to one, a dc shift added, and the result multiplied by a noise stimulus. If the IRN stimulus is I and the noise stimulus is n, then the resulting stimulus was $(1+I)n$ (see Fig. 10). The entire stimulus was then bandpass filtered between 100 and 2100 Hz as in the lowest filtered conditions of experiments 1 and 2. The psychophysical procedure for all experiments was the same as that used in experiment 1. Five new inexperienced listeners (all with normal hearing) were used in experiment 3.

B. Results and discussion

Figure 11 shows the results for both $P(C)_{+,-}$ and $P(C)_{+/-,\text{noise}}$ as a function of stimulus condition. Given the similarity among the listeners' data, the data from all listeners were collapsed into a single stimulus-response table.[2] The No Mod. condition involves IRN stimuli similar to those used in experiment 1 except that the delay was roved over a 12% range. As can be seen, discrimination for condition 1 is very similar to that measured in experiment 1. Thus, a 12% variation in pitch has little affect on the ability to make a pitch discrimination between IRN stimuli generated with $g=1.0$ and those generated with $g=-1.0$, when the waveform fine structure contains the ripple spectrum and temporal regularity.

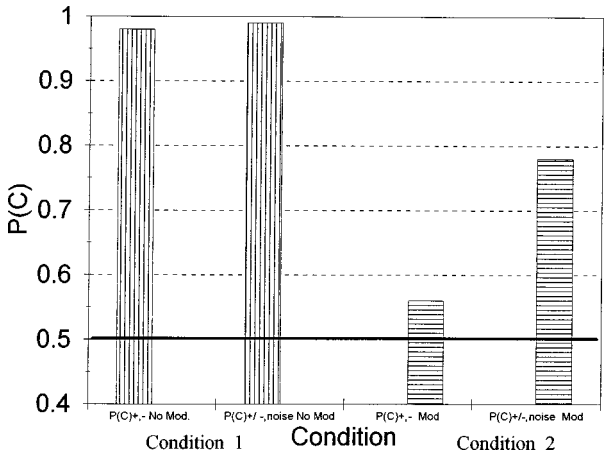

FIG. 11. Average percent correct discrimination for four conditions: $P(C)_{+,-}$ and $P(C)_{+/-,\text{noise}}$ for discriminating between a normal IRN stimulus generated with $g=1$ and one generated with $g=-1.0$ (No Mod, Condition 1), and $P(C)_{+,-}$ and $P(C)_{+/-,\text{noise}}$ for discrimination when the low-frequency, bandpass-filtered IRN stimulus was used to modulate a wideband noise (Mod, Condition 2).

The Mod. conditions are the cases in which low-frequency, bandpass IRN stimuli were used as multipliers for flat-spectrum noise. These are the conditions in which the spectral ripples and temporal regularity are *only* in the envelope. In condition 2 listeners had difficulty telling a stimulus generated with an IRN multiplier with $g=1.0$ from one with $g=-1.0$. That is, there is little evidence that they could use the pitch difference (or any other aspect of the stimuli) to discriminate between these two stimulus conditions. Listeners could tell a noise with a flat envelope (flat-spectrum noise) from one with the IRN envelope $[P(C)_{+/-,\text{noise}}]$ as was found by Sheft and Yost (1996), and this result is consistent with those from experiments 1 and 2, if one assumes that discriminations at very high frequencies are mediated by envelope cues. Thus, if the envelope is the only basis for discriminating IRN stimuli, then pitch discriminations cannot be made, but listeners do seem able to tell a stimulus with a ripple spectrum in its envelope from one in which there is no such spectral structure in the envelope.

In summary, information in the envelope of IRN stimuli is not sufficient to support the observed pitch discriminations; the information must be in the fine structure. Envelope information may, however, be sufficient to support discriminations of IRN stimuli from flat-spectrum noise.

V. OVERALL DISCUSSION

The discussion of IRN stimuli and their envelopes presented in the Introduction and summarized in Figs. 3–5 led to the prediction that if envelopes were based on HWR-LPF operations with a 1200-Hz low-pass filter, then discriminations between IRN stimuli generated with $g=1.0$ and those generated with $g=-1.0$ would only be possible for low-frequency IRN stimuli. And, it might be possible for listeners to use envelope cues for high-frequency stimuli to discriminate IRN stimuli (independent of the sign of g) from flat-spectrum stimuli. The results of experiments 1 and 2 appear to confirm these predictions. Thus, the HWR-LPF operation appears to be an appropriate way to model processing of IRN

stimuli. The results of the experiment described in the Appendix suggest that it is unlikely that the results of experiments 1 and 2 for high-frequency stimuli were based entirely on listeners' ability to use low-frequency distortion products as the basis for their discriminations. The data of experiment 3 further indicate that if a stimulus contains a spectral structure or temporal regularity only in its envelope, then pitch discriminations cannot be made, but stimuli with no spectral structure in the envelope can be discriminated from stimuli with a spectral structure. Thus, pitch discriminations of IRN stimuli are dependent on fine-structure information and the envelope of IRN stimuli may enable listeners to discriminate IRN stimuli from flat-spectrum stimuli.

These data as presented so far could be explained on the basis of the spectral (spectral ripple in the power spectrum) or on the basis of the temporal (temporal regularity as revealed by autocorrelation) aspects of the IRN stimuli, since autocorrelation is the Fourier transform of the power spectrum. However, it might be better to consider the effects of auditory processing of the stimuli used in many of these experiments rather than just the input waveforms. For instance, consider the 4000- to 6000-Hz conditions, in which two IRN stimuli with spectral ripples as dense as every 250 Hz can still be discriminated from each other. Four thousand Hertz is the 16th harmonic of 250 Hz (the peak spacing for an IRN stimulus with a 4-ms delay). Examination of the auditory spectra (generated as the integrated output of a gammatone filter bank; see Patterson, 1994; Patterson *et al.*, 1996; Yost *et al.*, 1996) for a 4000- to 6000-Hz bandpassed IRN stimulus generated with $d=4$ ms, 8 iterations, and for cases where $g=1.0$ and $g=-1.0$ indicated that there were no discernable spectral differences between the IRN stimuli generated with $g=1.0$ and $g=-1.0$ (see a similar analysis in Patterson *et al.*, 1996). Thus, it is highly unlikely that the spectral ripple (either in the waveform fine structure or in the envelope) can be spectrally resolved by the auditory system at these high frequencies, yet IRN stimuli with spectral ripples in these high-frequency regions can be discriminated from each other based on pitch. Thus, as we have argued before (see Patterson *et al.*, 1996), it is unlikely that these IRN stimuli are processed spectrally.

The data of this study show that, as the delay increased from 4 to 16 ms (spectral spacing in the rippled spectrum decreased from 250 to 62.5 Hz), performance became poorer. Performance also decreased as the number of iterations (n) decreased from 8 to 1. As n increases, the spectral peaks become narrower, and they are more likely to be resolved. Both the loss of performance with increasing delay and decreasing n are consistent with a spectral argument in that as the spectral peaks get closer together (i.e., the delay increases) and more broad (i.e., n decreases), the spectral differences would be more difficult to resolve, and thus performance would be predicted to become poorer, as it does. In the case of the high-pass-filtered conditions of this study we might argue that none of the spectral peaks are resolved for any IRN stimulus, so the auditory system could not discern these changes in these unresolvable spectral peaks. Also Yost (1979) and Meddis and Hewitt (1991) have both shown that the loss of pitch strength with increasing delay is compatible with an autocorrelation function explanation of the pitch of IRN stimuli. Likewise, Yost (1996b, 1997) and Patterson *et al.* (1996) have shown that the autocorrelation function can account for the loss of pitch strength with decreasing number of iterations.

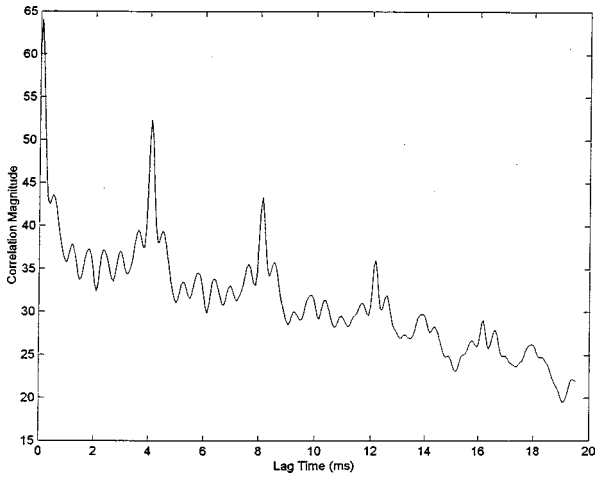

FIG. 12. Summary autocorrelogram based on the same autocorrelograms conditions that were used for Fig. 4. The summary autocorrelogram for an IRN stimulus with a delay of 4 ms, 8 iterations, and $g=1.0$. The IRN stimuli were bandpass filtered from 6000–8000 Hz. A summary autocorrelogram is generated by summing the correlograms across the high-frequency channels.

We argue that the pitch difference between IRN stimuli generated with $g=1.0$ and those generated with $g=-1.0$ is based on waveform fine structure in frequency regions that may be as high as 6000 Hz. Frequencies in the region of 6000 Hz are above the region where phase locking is usually assumed to operate. The auditory system would need to determine the temporal structure of the IRN stimuli based on the delay (d), which is on the order of 4–16 ms. That is, the auditory system does not need to follow short temporal events associated with the waveform fine structure of the high-frequency IRN stimuli, but rather much longer-duration regularities that are found in the IRN stimuli. Nevertheless, the ability to process even these longer temporal regularities in these very-high-frequency channels appears inconsistent with the use of a low-pass filter with a 1200-Hz cutoff as a model of the loss of phase locking at high frequencies. However, such a low-pass filter is only down 30 dB at 6000 Hz. Thus, it is possible that some fine-structure information will ''leak'' through at these high frequencies. Such fine-structure information might be made more clear if cross-spectral processing is used. Figures 12 and 13 show summary autocorrelograms for an IRN stimulus with $d=4$ ms, 8 iterations, $g=1.0$ (Fig. 12) and $=-1.0$ (Fig. 13), and a 6000- to 8000-Hz filter. These summary autocorrelograms were generated using the same modeling conditions used for Figs. 4–6, including the 1200-Hz low-pass filter to simulate the loss of phase locking. The summary correlogram is a cross-spectral processing scheme representing the sum of the autocorrelation functions of the individual channels across the 6000- to 8000-Hz region for each lag. As can be seen there are differences in the summary autocorrelogram between the $g=1.0$ and $g=-1.0$ conditions that might be the basis for discriminating these two stimuli. These differences in the

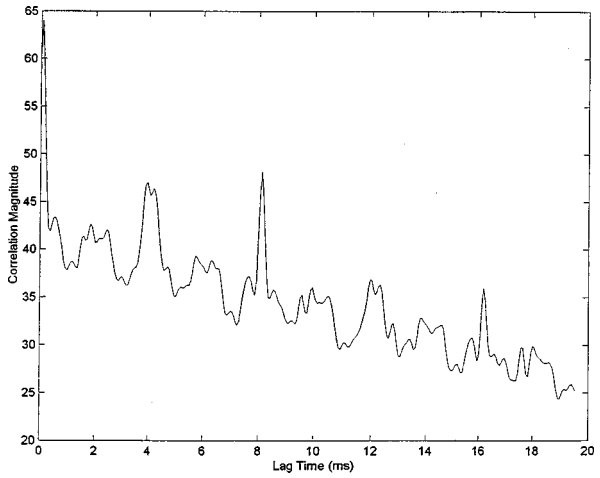

FIG. 13. The summary autocorrelogram for the same conditions used in Fig. 12, but for an IRN stimulus with a delay of 4 ms, 8 iterations, and $g = -1.0$. Note the double peak for the case where $g = -1.0$ at lag of 4 and 12 ms, indicating that some of the waveform fine structure of the IRN stimulus is still present in this summary correlogram for these high-pass conditions.

summary autocorrelograms are much smaller for the 8000- to 1000-Hz conditions. Thus, the long-duration temporal structure that differentiates conditions when $g = 1.0$ from those when $g = -1.0$ might still exist in the processed waveform fine structure even at high frequencies, if something like a summary autocorrelogram was used as a way to extract the information. Clearly a more quantitative model is necessary to test the ability of such summary-autocorrelogram differences to account for data like those shown in Figs. 7 and 9. In this paper, we simply want to indicate that such differences in the summary autocorrelograms do exist.

The work on IRN stimuli suggests that periodicities are not a necessary and sufficient condition for processing complex pitch, since there are no periodicities in the IRN waveform (see Yost *et al.*, 1996), yet they have a clear pitch (see Yost, 1996a). Our current work suggests that the information for processing the pitch of IRN stimuli is not in the envelope. That is, the envelope by itself cannot be used to explain the discriminations between IRN stimuli generated with $g = 1.0$ and $g = -1.0$. Thus, models based on either periodicity processing and/or pure envelope extraction would not be good ones for dealing with the pitch of IRN stimuli.[1] For instance, neural channels tuned to periodic envelope fluctuations would probably have a difficult time extracting the temporal regularity that appears to be responsible for the pitch of IRN stimuli. Any model of pitch based on envelope extraction would have to allow for fine-structure information to be available in the frequency regions below 6000 Hz.

Several physiological papers have shown that the information in the neural spike trains of auditory nerve fibers (Cariani and Delgutte, 1996a, b) and cochlear nucleus fibers (Shofner, 1991, 1998) can be analyzed with autocorrelation processes and these analyses reveal temporal regularities that are consistent with the psychophysically measured attributes of complex pitch. Of relevance to the arguments of this paper, Shofner (1991, 1998) has also argued that it is likely that the pitch of IRN stimuli is based on waveform fine structure since only neural units that phase lock to the waveform fine structure exhibit response properties consistent with processing the temporal structure of IRN stimuli. Fibers thought to be primarily sensitive to the envelope (e.g., chopper cells in the cochlear nucleus) are not very sensitive to the temporal structure of IRN stimuli as revealed by autocorrelationlike processing (Shofner, 1991, 1998). Thus, there are physiological data that support our contention that pitch discriminations for IRN stimuli are based on waveform fine structure.

We are unsure of the exact reason why listeners can discriminate IRN stimuli from flat-spectrum noise for the very-high-frequency conditions. It could be that the temporal regularities that are in the envelope of the IRN stimuli make it less ''noisy'' than the flat-spectrum noise stimulus whose envelope contains more random (irregular) intervals. If so, then it is the difference in the proportion of regular to irregular intervals in the envelope that accounts for the difference in perception of these two stimuli (i.e., noise with only irregular intervals is perceived as more ''hissy'' or ''noisy'' than IRN stimuli with more regular intervals in the envelope). It could also be that there is still a weak form of fine-structure temporal regularity that persists at high frequencies (see Figs. 12 and 13) that yields a discriminable difference between IRN and non-IRN stimuli, but this regularity is not strong enough to allow for a differentiation between IRN stimuli. However, even when the waveform's fine structure contains no spectral structure or temporal regularity and the envelope does (the stimulus conditions of experiment 3), listeners can discriminate a stimulus with an envelope spectral structure from without such a structure. This suggests that such discriminations are based on envelope cues only. We are not sure how these differences at high frequencies in the regularity of the intervals in the envelope and/or waveform fine structure are determined or how cues that are only in the envelope are determined.

Although autocorrelation or autocorrelograms appear to be good ways to process IRN stimuli to provide predictions for the pitch and pitch strength of IRN stimuli, autocorrelation is probably not the only mechanism that could be used. Yost *et al.* (1996) suggested that the interval histogram (first-order intervals) might be sufficient to reveal the temporal structure of IRN stimuli. Patterson *et al.* (1995) have proposed a mechanism, strobed temporal integration, that is like autocorrelation but is not true autocorrelation. In some informal testing it appears as if strobed temporal integration could also account for the pitch and pitch strength of IRN stimuli in a manner similar to that provided by autocorrelation. Obviously, experiments need to be designed to determine if one form or another of temporal analysis offers the best explanation of the pitch and pitch strength of IRN stimuli. However, no matter what the actual process is that might extract the temporal regularity in IRN stimuli, we believe this study along with several others (Yost *et al.*, 1996; Patterson *et al.*, 1996; Yost, 1996b, 1997) supports the contention that it is the temporal property of the waveform fine structure of IRN stimuli that provides the most parsimonious explanation for the pitch and pitch strength of IRN stimuli.

ACKNOWLEDGMENTS

This research was supported by grants from the NIDCD (Program Project Grant No. DC000293), from the Life Sciences Division of the Air Force Office of Scientific Research, and from DRA Farnborough. We would like to thank Dr. Shofner and Suzanne Sullivan, the 1996 Parmly Summer Intern, for sharing their ideas about our work with us.

APPENDIX: MASKING POSSIBLE DISTORTION PRODUCTS

An experiment with three listeners was undertaken to determine the extent to which performance in experiment 1 might be based on nonlinear distortions providing useable cues in low-frequency regions. The goal of this experiment was to determine the amount of noise that leads to a threshold difference in discriminating an IRN stimulus with $g=1.0$ from one with $g=-1.0$ and in discriminating an IRN from a flat-spectrum noise stimulus. The IRN and flat-spectrum noise stimuli were bandpass filtered between 4000 and 6000 Hz and two masking noises were used: a 2000-Hz low-pass noise and a noise occupying the same spectral region of the IRN stimuli (i.e., from 4000–6000 Hz). The IRN stimuli were generated with $d=4$ ms, and $n=8$ iterations. All filters were fourth-order Butterworth filters. The IRN and flat-spectrum noise stimuli were presented at an overall level of 70 dB SPL. The level of the masking noise was adaptively varied. All of the other stimulus conditions, with the exception that there was no overall level rove, were the same as in experiment 1. The 2000-Hz low-pass noise was used because it would mask the low-frequency region where distortion products might exist and it would reduce the effects of the upward spread of masking, since it is an octave away from the IRN stimuli to be discriminated. The masking noise with energy in the same spectral region as the stimuli to be discriminated was chosen to estimate the amount of noise that would disrupt IRN processing due to a direct interaction of the masker and the IRN stimuli within the frequency band of the IRN stimulus. Since thresholds were to be determined in an adaptive psychophysical task, we chose the 4000- to 6000-Hz condition with $d=4$ ms and $n=8$ iterations since the listeners in experiment 1 could make discriminations at a $P(C)_{+,-}$ of 100%. Performance for higher filter cutoffs was poorer, making it difficult to use these conditions in an adaptive task. In selecting five new, inexperienced listeners for these experiments only three could make these discriminations at a $P(C)$ of 100%, so only these three listeners were used. One of the listeners who had trouble with the discrimination performed between 70%–80% and the other between 80%–90%.

An adaptive, AA, AB, BB, BA same–different task (sometimes referred to as a roving-standard, same–different task) was used. In one set of conditions the A stimulus was IRN stimulus with $g=1.0$ and the masking noise and the B stimulus was the other IRN stimulus with $g=-1.0$ and the masking noise. In the other set of conditions the B stimulus was the 4000- to 6000-Hz, flat-spectrum stimulus plus the masking noise. The listener indicated whether the stimuli were the same or different in a 2-down, 1-up adaptive procedure with 2-dB step sizes. Thresholds were based on the average of three 50-trial blocks in which there were at least six reversals for each of the three threshold estimates.

The masker levels at threshold for discriminating between an IRN stimulus with $g=1.0$ and one with $g=-1.0$ when the masker was low-pass filtered at 2000 Hz were 58.7, 55.5, and 53.4 dB SPL; when the masker was filtered between 4000 and 6000 Hz the thresholds were 44.8, 41.7, and 40.7 dB SPL. The threshold masker levels for discriminating between an IRN stimulus and the flat-spectrum noise when the masker was low-pass filtered at 2000 Hz were 71.5, 74.2, and 72.6 dB SPL; and when the masker was filtered between 4000 and 6000 Hz the thresholds were 57.2, 55.6, and 50.9 dB SPL. Recalling that the level of the stimuli to be discriminated was 70 dB SPL, these results suggest that listeners are able to make the discriminations for high levels of masking noise. Thus, it is unlikely that for high-frequency IRN stimuli the ability to discriminate between two IRN stimuli or between an IRN stimulus and a flat-noise stimulus is due entirely to low-frequency distortion products. Further, given the magnitude of the thresholds when the masker and stimuli to be discriminated shared the same spectral region, it is possible that the difficulty in making the discriminations when the masker was low-pass filtered was due to upward spread of masking.

[1]As the discussion on envelopes makes clear, one has to be careful in using the term envelope. For the purposes of this paper, envelope will generally refer to the HWR-LPF operation and the envelope is extracted in frequency regions above the cutoff of the LPF. We believe this is consistent with the use of envelope in many auditory examples. However, we clearly recognize that other forms of envelope might exist or be proposed to exist in the auditory system. A point of this paper is that if such envelope mechanisms are like those of FWR, squaring, or the Hilbert transform, then they would have difficulty accounting for the IRN discrimination data obtained in this paper. We would further argue that such mechanisms would be poor candidates for explanations of pitch processing.

[2]Collapsing all data into a single stimulus-response table makes it difficult to calculate a measure of variability. As will be indicated for most experiments, the across-listener variability was very small as was the within-listener variability. The within-listener standard deviations ranged from 0.29% to 9% in experiment 1, 0.18% to 12.3% in experiment 2, and 0.64% to 14.8% in experiment 3. The maximum across-listener standard deviation was 3.6% in experiment 1, 3.8% in experiment 2, and 4.2% in experiment 3. Another way to indicate variability is to calculate the expected Bernoulli variance based on the 1250 trials (250 trials for each of 5 listeners) used in each of the three experiment stimulus-response tables. This Bernoulli variance ($\sqrt{\{[P(C)*(1-P(C))]/1250\}}$) ranges from 1.4% at $P(C)=50\%$ to 0.6% at $P(C)=95\%$.

[3]During the review of the paper, one reviewer suggested that we needed to rule out the possibility that listeners were using low-frequency distortion products for the high-pass conditions. Even though the pitch of complex stimuli does not depend on such distortion, the discriminations of this experiment could be based on low-frequency distortion. Thus, this was an excellent suggestion, and providing such evidence is crucial for our some of our arguments. We, therefore, performed the experiments described in the Appendix. While we did not redo all of the experiments with a low-pass noise, we feel that the results of the experiments described in the Appendix indicate that listeners are not using such distortion products as the only basis for making the discriminations described in experiment 1 and the rest of this paper.

[4]The envelope spectral differences shown in Fig. 10 result in autocorrelation functions like those shown in Fig. 3 for the IRN waveform. That is, the autocorrelation function for the envelope when the IRN multiplier was generated with $g=1.0$ has all positive peaks at a lag of 4 ms and its integer multiples (e.g., 8, 12, 16, 20, 24, 28, and 32 ms). The autocorrelation function for the envelope when the IRN multiplier was generated with $g=-1.0$ has negative peaks at a lag of 4 ms and its odd integer multiples

(e.g., 12, 20, and 28 ms) and positive peaks at a lag of 8 ms and its even integer multiples (e.g., 16, 24, and 32 ms).

[5]Sheft and Yost (1996) used IRN stimuli to modulate noise and determined the discriminability of such modulated stimuli from flat-spectrum noise stimuli. They showed that listeners could discriminate between the two with *d*'s of between 1.5 and 2 when the IRN multiplier was generated with a short delay (*d*) and multiple iterations, and was low-pass filtered with cutoffs of between 500 and 1000 Hz. Performance was much poorer for other IRN multipliers.

Bilsen, F. A. (**1966**). ''Repetition Pitch: Monaural Interaction of a Sound with the Repetition of the Same, but Phase Shifted Sound,'' Acustica **17**, 295–300.

Bilsen, F. A., and Ritsma, R. J. (**1969/70**). ''Repetition Pitch and its Implication for Hearing Theory,'' Acustica **22**, 63–68.

Bilsen, F. A., and Wieman, J. G. (**1980**). ''Atonal Periodicity Sensation for Comb Filtered Noise Signals,'' in *Psychophysical, Psychological and Behavioral Studies in Hearing*, edited by G. van Den Brink and F. A. Bilsen (Delft U.P., London).

Burns, E. M., and Viemeister, N. V. (**1976**). ''Nonspectral pitch,'' J. Acoust. Soc. Am. **60**, 863–869.

Cariani, P. M., and Delgutte, B. (**1996a**). ''Neural correlates of the pitch of complex tones. I. Pitch and pitch salience,'' J. Neurophysiol. **76**, 1698–1716.

Cariani, P. M., and Delgutte, B. (**1996b**). ''Neural correlates of the pitch of complex tones. II. Pitch shift, pitch ambiguity, phase invariance, pitch circularity, rate pitch, and the dominance region for pitch,'' J. Neurophysiol. **76**, 1717–1734.

Dau, T. (**1996**). *Modeling Auditory Processing of Amplitude Modulation* (BIS, Oldenburg Univ., Oldenburg, Germany).

de Boer, E. (**1956**). ''On the Residue in Hearing,'' Doctoral thesis, University of Amsterdam, The Netherlands.

Hartmann, W. M. (**1997**). *Signals, Sounds, and Sensation* (AIP, Woodbury, NY).

Houtsma, A. J. M., and Smyrzinski, J. (**1990**). ''Pitch identification for complex tones with many harmonics,'' J. Acoust. Soc. Am. **87**, 304–310.

Jeffress, L. A. (**1964**). ''Stimulus-oriented approach to detection,'' J. Acoust. Soc. Am. **36**, 766–774.

Meddis, R., and Hewitt, T. (**1991**). ''Virtual pitch and phase sensitivity of a computer model of the auditory periphery. I. Pitch identification,'' J. Acoust. Soc. Am. **89**, 1862–1882.

Patterson, R. D. (**1994**). ''The sound of sinusoid: Spectral models,'' J. Acoust. Soc. Am. **96**, 1409–1418.

Patterson, R. D., and Akeroyd, M. A. (**1995**). ''Time-interval patterns and sound quality,'' in *Advances in Hearing Research*, edited by G. A. Manley, G. M. Klumpp, C. Koppl, H. Fastl, and H. Deckinghaus (World Scientific, Hong Kong).

Patterson, R. D., Allerhand, M., and Giguere, C. (**1995**). ''Time-domain modeling of peripheral auditory processing: A modular architecture and a software platform,'' J. Acoust. Soc. Am. **98**, 1890–1895.

Patterson, R. P., and Datta, A. J. (**1997**). ''Detecting Iterated Rippled Noise (IRN) in IRN: The Spectral Position of the Listening Band,'' Brit. J. Aud. **31**, 131.

Patterson, R. P., and Wightman, F. L. (**1976**). ''Residue pitch as a function of component spacing,'' J. Acoust. Soc. Am. **59**, 1450–1459.

Patterson, R. P., Handel, S., Yost, W. A., and Datta, A. J. (**1996**). ''The relative strength of tone and noise components of iterated rippled noise,'' J. Acoust. Soc. Am. **100**, 3286–3294.

Plomp, R. (**1976**). *Aspects of Tone Sensation—A Psychophysical Study* (Academic, London).

Rosenberg, A. E. (**1965**). ''Effect of masking on the pitch of periodic pulse trains,'' J. Acoust. Soc. Am. **38**, 747–758.

Raatgever, J., and Bilsen, F. A. (**1992**). ''The Pitch of Anharmonic Comb Filtered Noise Reconsidered,'' in *Auditory Physiology and Perception*, edited by Y. Cazals, L. Demany, and K. Horner (Pergamon, Oxford).

Schouten, J. F., Ritsma, R. J., and Cardozo, B. L. (**1962**). ''Pitch of the residue,'' J. Acoust. Soc. Am. **34**, 1418–1424.

Sheft, S., and Yost, W. A. (**1996**). ''Discrimination of noise modulators,'' J. Acoust. Soc. Am. **100**, 2594(S).

Shofner, W. P. (**1991**). ''Temporal representation of rippled noise in the anteroventral cochlear nucleus of the chinchilla,'' J. Acoust. Soc. Am. **90**, 2450–2466.

Shofner, W. P. (**1998**). ''Evidence that primarylike units are the major CN subsystem which encodes pitch related information in their temporal discharge,'' Abst. Ass. Res. Oto., 1998.

Supin, A., Popov, V. V., Milekhina, O. N., and Tarakanov, M. B. (**1994**). ''Frequency resolving power measured with rippled noise,'' Hearing Res. **78**, 31–40.

Viemeister, N. F. (**1979**). ''Temporal modulation transfer functions based upon modulation thresholds,'' J. Acoust. Soc. Am. **66**, 1364–1380.

Yost, W. A. (**1979**). ''Models of the pitch and pitch strength of rippled noise,'' J. Acoust. Soc. Am. **66**, 400–411.

Yost, W. A. (**1996a**). ''Pitch of iterated rippled noise,'' J. Acoust. Soc. Am. **100**, 511–518.

Yost, W. A. (**1996b**). ''Pitch strength of iterated rippled noise,'' J. Acoust. Soc. Am. **100**, 3329–3335.

Yost, W. A. (**1997**). ''Pitch strength of iterated rippled noise when the pitch is ambiguous,'' J. Acoust. Soc. Am. **101**, 1644–1650.

Yost, W. A., Hill, R., and Perez-Falcon, T. (**1978**). ''Pitch and pitch discrimination of broadband signals with rippled power spectra,'' J. Acoust. Soc. Am. **63**, 1166–1173.

Yost, W. A., Patterson, R. D., and Sheft, S. (**1996**). ''A time domain description for the pitch strength of iterated rippled noise,'' J. Acoust. Soc. Am. **99**, 1066–1078.

The effects of varying signal intensity on the perceptual organization of rhythmic auditory patterns

Lynn D. Zimba and Donald A. Robin
Laboratory of Speech and Language Neuroscience, Department of Speech Pathology and Audiology, and The National Center for Voice and Speech, University of Iowa, 13 WJSHC, Iowa City, Iowa 52242-1407

(Received 8 April 1997; revised 13 March 1998; accepted 18 June 1998)

Cyclic repetitions of temporally structured sequences of sound bursts and gaps are perceived as rhythmic patterns. Some are perceptually unambiguous—the pattern organization is unique; others are perceptually ambiguous—the organization changes. Previous research suggests that the pattern of neuronal adaptation and recovery from adaptation associated with these stimuli determines how listeners perceptually organize the sequences. It follows that variations in the intensity of specific sound elements, which should produce specific changes in the underlying patterns of neuronal activation, should produce predictable changes in the perceptual organization of the sequences. The present study tested this hypothesis by observing the perceptual responses of listeners while varying the intensity of critical elements of unambiguous and ambiguous sequences. The results support the hypothesis in that an unambiguous sequence was made ambiguous and an ambiguous sequence was made less ambiguous. However, the unambiguous sequence did not completely reverse its perceptual organization, nor did the ambiguous sequence become completely unambiguous. The outcome is discussed focusing on the range of intensity increments tested, the type of stimuli used, and the possibility that neurosensory factors may interact with other organizing factors in determining the perceptual organization of rhythmic auditory sequences. © *1998 Acoustical Society of America.* [S0001-4966(98)01210-7]

PACS numbers: 43.66.Lj, 43.66.Mk [RHD]

INTRODUCTION

In the past decade there has been a concerted effort to understand complex sound perception in humans (e.g., Bregman, 1990; Handel, 1993). Included in this effort have been studies exploring the heuristic rules that lead to the organization of sounds into perceptual patterns. Within the broad area of auditory pattern perception, investigators have attempted to delineate organizational principles that are constrained by the temporal or rhythmic properties of stimuli (e.g., Essens, 1986, 1995; Essens and Povel, 1985; Handel, 1973, 1974; Handel and Oskinsky, 1981; Longuet-Higgins and Lee, 1982; Povel, 1981, 1984; Povel and Essens, 1985; Royer and Robin, 1986). A clear depiction of the temporal parameters that drive auditory pattern perception has an impact on the understanding of normal and impaired processing of both speech and music (e.g., Bregman, 1990; Deutsch, 1980, 1981; Efron, 1963; Gfeller *et al.*, 1997; Longuet-Higgins and Lee, 1984; Martin, 1972; Massaro, 1975; Pisoni and Swausch, 1975; Povel and Essens, 1985; Robin *et al.*, 1990b).

One set of auditory stimuli that has received close scrutiny involves the repetition of sequences of sounds over regular temporal intervals. When cyclic repetitions of sound sequences are presented to listeners with normal hearing abilities, they can identify rhythmic patterns in which a given sequence has a beginning point and an ending point, even though the sounds repeat continuously and there is no unique beginning or ending based on the physical structure of the stimuli (e.g., Garner and Gottwald, 1968; Handel, 1973, 1974; Royer and Garner, 1966, 1970; Royer and Robin, 1986). The perceived organization depends, among other things, on the temporal structure of the sequence, which includes the sounds and silent intervals (gaps) between the sounds that make up the sequence. The type of processing underlying the perception of rhythmic patterns depends on the rate of presentation of the sequence. With presentation rates of less than two sounds per second, pattern perception depends on an active learning process. The perceived beginning of the pattern is strongly influenced by the first sound element of the sequence that is presented. With faster presentation rates, pattern perception is holistic and automatic. The perceived beginning of the pattern is determined by the structure of the elements comprising the sequence, independent of the physical starting point (Garner and Gottwald, 1968). With very fast presentation rates, pattern perception breaks down and unitization occurs; the perception is of a repeating packet of sounds that includes the entire sequence. Although individual sounds can still be heard, the temporal structure of the sequence—the pattern—cannot be identified. With extremely fast presentation rates, only a continuous sound—an ''auditory texture''—is heard (Royer and Robin, 1986). The present study focused on the condition in which the presentation rates produced an automatic, integrated perception of a repetitive rhythmic pattern.

An extensive literature has been devoted to studying the perceptual organization of rhythmic auditory patterns (see Robin *et al.*, 1987, for a review). In brief, given an auditory sequence in which a sound element is represented by an ''X'' (a sound burst of some duration followed by a silent interval of the same duration) and a gap is represented by a

''–'' (a silent interval of the same duration as X), one can define perceptually unambiguous and perceptually ambiguous patterns that emerge based on the temporal structure of the stimuli. Two of the organizing principles that have been proposed to guide the perception of rhythmic auditory patterns are the *run* and *gap principles* (Garner, 1974; Garner and Gottwald, 1968; Preusser *et al.*, 1970). The run principle states that the longest run of sound elements will mark the perceived beginning of an auditory pattern, and the gap principle states that the longest gap will mark the perceived ending. Sequences in which runs and gaps predict the same organization are perceptually unambiguous; the rhythmic pattern has a unique perceptual organization. Sequences in which runs and gaps temporally conflict are perceptually ambiguous; the rhythmic pattern has multiple perceptual organizations. For example, the sequence X̲XX–X––– is unambiguous because the longest run and the longest gap are in accord and predict the same beginning (underlined) and ending of the pattern. When listeners are given the opportunity to describe their perceptions by tapping the pattern, or by written or vocal description, they almost always report hearing the pattern as beginning with the first sound element of the longest run, even though there are multiple possible starting points (e.g., Garner and Gottwald, 1968; Preusser *et al.*, 1970; Royer and Garner, 1966). In contrast, the sequence X̲X–X̲–X̲X– is ambiguous because there are two runs of equal length and three gaps of equal duration. Listeners describe the pattern as beginning with one of three sound elements (underlined), even though other organizations are possible. Ambiguous auditory patterns can change organization both during and between presentations, much like the visual Necker cube.

In an attempt to provide a neurophysiologic explanation of the run and gap principles, Robin *et al.* (1990a) reasoned that neuronal adaptation and recovery from adaptation might underlie the perceived rhythmic organization. They argued that because adaptation results in changes in the response of a neuron following repeated stimulation, the run and gap principles emerged as a result of the repetitive, cyclic nature of the auditory stimulus. They further argued that because the spacing among elements in the stimulus varied, the degree of adaptation would vary as well. Specifically, they hypothesized that the first element of a run receives psychological stress because it is associated with the greatest neuronal response (i.e., with the least adaptation). Moreover, the element after the longest gap also receives psychological stress because the greatest recovery from adaptation occurs during the longest pause in stimulation. Listeners appear to mark the beginning of patterns where psychological stress is greatest, that is, at the start of the longest run or following the longest gap. When there is a uniquely longest run preceded by a longest gap, one element in the sequence receives the greatest stress, and the emergent rhythmic organization is unambiguous. When there are multiple runs or gaps of equal length, or when the runs and gaps temporally conflict, there may be stress placed on more than one element of the sequence and the emergent rhythmic organization is ambiguous.

To provide support for this hypothesis, Robin *et al.* (1990a) examined adaptation in the eighth nerve, brain stem, and auditory cortex of cats. They used an unambiguous (XXX–X–––) and an ambiguous (XX–X–XX–) sequence. For the unambiguous sequence, it was predicted that the amplitude of the neuronal response would be greatest for the first sound element of the longest run (XXX), and that responses to each of the successive two elements would be progressively reduced in amplitude due to adaptation. There would then be a brief but incomplete recovery of the neuronal response amplitude following the first gap (–), and a greater degree of recovery following the longest gap (–––). The results supported this prediction as can be seen in the upper plot of Fig. 1, which depicts the pattern of neuronal responses reported by Robin *et al.* for the unambiguous sequence. The prediction for the ambiguous sequence was that the amplitude of the neuronal response would be equal for the first sound element of each of the two-element runs (XX), but higher than that for each of the immediately successive sound elements. The neuronal response amplitude associated with the single sound element (X) was predicted to be relatively high as well because there should be some recovery from adaptation after the pause (–). Overall, the pattern of neuronal response amplitude across the five sound elements of the ambiguous sequence was predicted to reflect the three possible perceptual organizations reported by human listeners. As before, the results supported this prediction as can be seen in the lower plot of Fig. 1, which depicts the pattern of neuronal responses reported by Robin *et al.* for the ambiguous sequence. It should also be noted that although there were differences in the absolute magnitude of the neuronal responses across the three recording sites (eighth nerve, brain stem, and auditory cortex), the patterns of neuronal

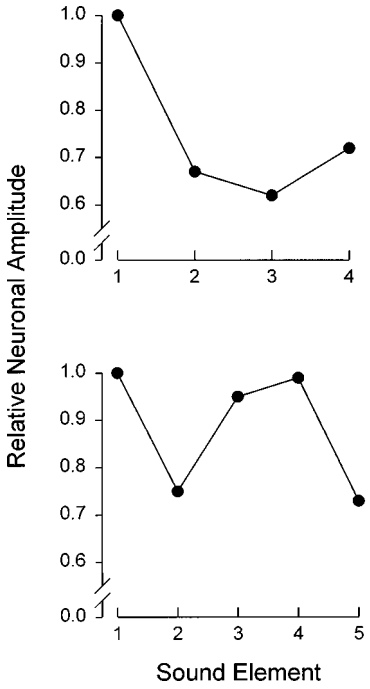

FIG. 1. Schematic representation of the normalized neuronal amplitude data reported by Robin *et al.* (1990a). The top graph represents data from the unambiguous sequence (XXX–X–––), and the bottom graph represents data from the ambiguous sequence (XX–X–XX–).

response amplitude were found to be the same regardless of the recording site.

If Robin *et al.*'s hypothesis is strictly true (i.e., it represents a strong form of the prediction), then a logical extension of it is that changes in the intensity of the sound elements within the cyclic patterns should result in predictable changes in listeners' perceptions. Changes in signal intensity will have a direct effect on the amplitude of the neuronal response. That is, increases in the intensity of specific sound elements will lead to a greater neuronal response amplitude for those elements. Thus if the strong form of Robin *et al.*'s hypothesis is true, changing the intensity of a given sound element in an unambiguous sequence should result in making the emergent pattern perceptually ambiguous. Moreover, if the intensity is sufficiently increased, it should be possible to systematically move from an unambiguous to an ambiguous pattern and, with further increases in intensity, to an unambiguous but new organization. Likewise, altering the intensity of a specific sound element of an ambiguous sequence should result in a perceptually unambiguous organization.

The purpose of the present study was to test these hypotheses. This was accomplished by varying the intensity of the fourth sound element of the unambiguous sequence (X̲XX–X–––) and the intensity of the first, third, and fourth sound elements of the ambiguous sequence (X̲X–X̲–X̲X–) and observing the perceptual responses of human listeners to cyclic repetitions of the altered stimuli. It was predicted that the unambiguous sequence, which is typically organized as XXX–X–––, would become perceptually ambiguous under certain intensity manipulations, and under the greatest increase in intensity it would reorganize as X–––XXX–, a new unambiguous pattern. It was also predicted that the ambiguous sequence, which is equally often organized as XX–X–XX–, X–XX–XX–, or XX–XX–X–, would become perceptually unambiguous under the greatest increase in intensity. It was expected that the particular perceptual reorganization of the ambiguous sequence would depend on the element being manipulated. When the intensity of the first sound element was increased, the pattern XX–X–XX– should predominate; when the intensity of the third sound element was increased, the pattern X–XX–XX– should predominate; when the intensity of the fourth sound element was increased, the pattern XX–XX–X– should predominate.

I. EXPERIMENT 1

A. Hypothesis

This experiment tested the hypothesis that variations in the intensity of the fourth sound element of the unambiguous sequence (XXX–X–––) would produce changes in the perceptual organization of the auditory pattern. The perceptual responses of human listeners were recorded in five intensity conditions. In the baseline condition, each sound element had the same intensity. This condition was similar to that of previous experiments (e.g., Garner and Gottwald, 1968; Preusser *et al.*, 1970; Royer and Garner, 1966; Royer and Robin, 1986), so it was expected that listeners would report hearing the conventional unambiguous pattern (XXX–X–––) on most of the trials. There were three conditions in which the intensity was greater than baseline. It was expected that as intensity increased, listeners would report hearing the conventional pattern on fewer trials and would report hearing the alternate organization (X–––XXX–) with increasing frequency. In the final condition, the fourth sound element was of a lower intensity than baseline. This condition was included to examine the possibility that changes in the frequency of hearing the alternate organization may be due simply to the presence of an altered sound element within the sequence, rather than to the direct effects of increased intensity on the magnitude of the neuronal response. If this possibility is correct, then the frequency of hearing the alternate pattern organization should increase under the condition of decreased intensity as well as under the condition(s) of increased intensity. On the other hand, if increased amplitude of neuronal response is the determining factor underlying changes in the perceived pattern organization, then the frequency of hearing the conventional pattern organization should not differ between the condition in which signal intensity of the fourth sound element was decreased and the baseline condition.

B. Method

1. Participants

Ten individuals from the University of Iowa community (seven females, three males) between the ages of 20 to 39 (mean age=25.6 years) volunteered to participate. All were naive regarding the aims of the study. Each participant was found to have hearing abilities within normal limits as determined by a pure-tone audiometric screening test. Participants were screened at each octave from 125 Hz to 8000 Hz at a constant intensity level of 20 dB. Each participant received monetary compensation. All of the participants in this study were treated in accordance with the guidelines established by the American Psychological Association (1992).

2. Stimuli and apparatus

The auditory stimulus consisted of 15 repetitions of an 8-element sequence. The sequence was composed of four computer-generated pulses of a 250-Hz tone and four gaps in which there was no tone. Each sound element had an on-duration and an off-duration of 44 ms; each gap was 88 ms. The temporal parameters of a single sequence are shown in Fig. 2. The digital output of the computer was converted to an analog voltage that was low-pass filtered, amplified, and used to drive an audio speaker. The intensity of the fourth sound element of the sequence was varied in five intensity conditions (see Fig. 2). In the baseline condition, each sound element had an intensity of 74 dB. Three of the conditions involved increases in the intensity of the fourth sound element of 3, 6, and 9 dB from the baseline intensity. The remaining condition involved a decrease in intensity of 9 dB from baseline. Thus while the intensity of the first, second, and third sound elements was always 74 dB, the intensity of the fourth sound element could be 65, 74, 77, 80, or 83 dB. Sound intensity was measured by placing a sound-level meter at the approximate position of the listener's head.

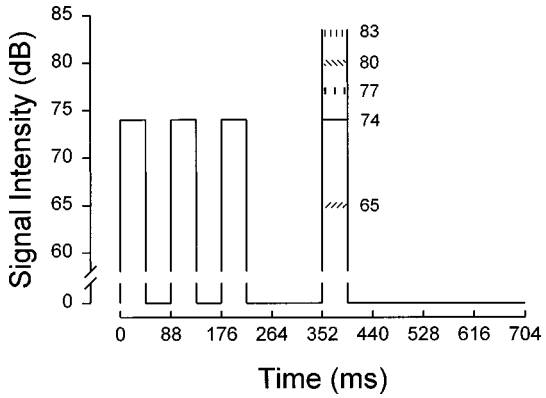

FIG. 2. Temporal structure of the unambiguous sequence (XXX–X–––) used in experiment 1. Each sound element consisted of a 250-Hz tone. The intensity of the first, second, and third sound elements was 74 dB. The intensity of the fourth sound element could be 65, 74, 77, 80, or 83 dB.

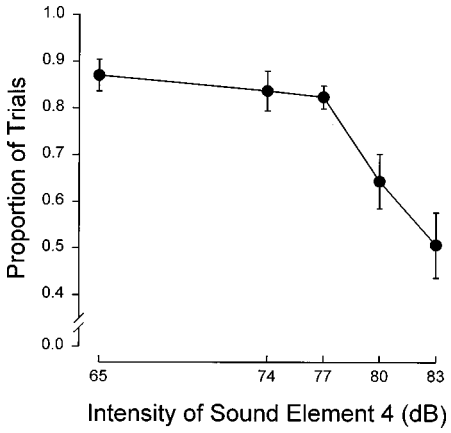

FIG. 3. Mean proportion of trials in which the standard unambiguous pattern (XXX–X–––) was reported as a function of the intensity of the fourth sound element. Data are from experiment 1. Bars=±1 SEM.

Testing was conducted in a dark, sound-treated booth. During testing, the participants were required to stay positioned in a chin rest to ensure that a consistent distance was maintained from the audio speaker located in the testing booth. A trial started with a visual ready message presented for 700 ms on a computer monitor visible through a plexiglass window in the testing booth. After a 300-ms delay, the auditory stimulus was presented, and then a visual response screen appeared on the monitor which displayed two patterns, XXX–X––– and X–––XXX–, one on the left and one on the right. The position of the patterns on the response screen (left, right) varied and was counterbalanced over each of the intensity conditions. The response screen remained visible until a response was made. A response box with three response keys was situated in front of the participant. Responses were made by pressing either the left or right key to indicate which pattern best characterized the perceptual pattern of the sequence during the trial. There was an inter-trial-interval of 2 s.

3. Procedures

Each participant was tested in one session that lasted about 1.25 h. The participant was first led through a demonstration block of three trials of the baseline intensity condition to become familiar with the experimental setup. This block could be repeated at the participant's request. It was followed by a 20-trial practice block consisting of 4 trials of each of the 5 intensity conditions. This block could be repeated once if the participant requested it. Finally, there was one 150-trial experimental block consisting of 30 trials of each intensity condition. There was a 2-min rest interval after trials 50, 90, and 120. This block was not repeated. For both practice and experimental blocks, the order of the intensity conditions was random, and for each trial, the starting element of the eight-element sequence was selected randomly.

C. Results and discussion

For each intensity condition, the proportion of trials in which the conventional unambiguous pattern (XXX–X–––) was reported was calculated for each participant. The means are presented in Fig. 3. A logarithmic transformation of the proportion scores was calculated (Kirk, 1982) after adding a constant of 1/60 (1 divided by twice the number of trials of each intensity condition). The constant was added to eliminate empty cells which could have occurred in cases in which the participant did not report perceiving the conventional unambiguous pattern. The log-transformed values were analyzed by a one-way repeated-measures analysis of variance (ANOVA). The main effect of intensity was significant [$F(4,36)=7.96$, $p<0.001$]. A Tukey pairwise comparison ($\alpha=0.05$) of the mean log scores indicated that performance in the 83-dB intensity condition was significantly different from performance in the 65-, 74-, and 77-dB levels. No other pairwise comparisons were significant.

The results generally support the predictions. In the baseline condition the conventional pattern was reported on the majority of trials—84% (see Fig. 3). This outcome was expected and replicates the results of previous studies (e.g., Garner and Gottwald, 1968; Preusser *et al.*, 1970; Royer and Garner, 1966; Royer and Robin, 1986). When the intensity of the fourth sound element was increased by 3 dB, the conventional pattern was reported on 82% of the trials—about the same as in the baseline condition. With further increases of 6 and 9 dB from baseline, the conventional pattern was reported less frequently—64% and 51%, respectively. The change in the perceived pattern organization from baseline was significant in the condition with the greatest (9 dB) intensity increment. This outcome supports the hypothesis that increasing the intensity of the fourth sound element of the unambiguous sequence would reduce the frequency of perceiving the conventional unambiguous pattern and, conversely, increase the frequency of perceiving the alternate pattern organization.

When the intensity of the fourth sound element was decreased by 9 dB, the conventional pattern was reported on 87% of the trials—about the same as in the baseline condition. This finding rules against the possibility that increases in the frequency of hearing the alternate pattern organization were due to an alteration in the intensity of the fourth sound element per se. Rather, the changes appear to be specific to increments in intensity.

II. EXPERIMENT 2

A. Hypothesis

The results of experiment 1 provide some support for Robin *et al.*'s (1990a) hypothesis. However, the hypothesis predicts that with a sufficient intensity increment of the fourth sound element, the emergent pattern should perceptually reorganize to a new unambiguous pattern beginning with the altered element (X−−−XXX−). This outcome was not obtained, but it may be that the intensity increment was not sufficient to produce the expected reorganization. The purpose of this experiment was to test the hypothesis that an intensity increment of greater than 9 dB would produce a perceptual reorganization of the unambiguous pattern into a new unambiguous pattern beginning with the altered sound element.

B. Method

1. Participants

Ten individuals from the University of Iowa community (nine females, one male) between the ages of 21 to 34 (mean age=23.9 years) volunteered. They were naive regarding the aims of the study. Each participant passed a pure tone audiometric screening test as in experiment 1. Each participant received monetary compensation.

2. Stimuli and apparatus

The stimuli and apparatus were identical to those used in experiment 1 with the exception of the intensity conditions. The intensity of the fourth sound element of the sequence (see Fig. 2) was varied in three, rather than five, conditions. In the baseline condition, each sound element was 65 dB rather than 74 dB. The other two conditions involved increments of 9 and 18 dB above baseline to 74 and 83 dB, respectively.

3. Procedures

For each participant, testing was conducted during one session that lasted about 50 min. The testing procedures were identical to those in experiment 1 with the following exceptions. Each practice block consisted of 24 trials, rather than 20, and there were 8 trials of each of the 3 intensity conditions. The experimental block consisted of 90 trials, rather than 150, with 30 trials of each intensity condition. There was only one 2-min rest interval which occurred after trial 50.

C. Results and discussion

For each intensity condition, the proportion of trials in which the conventional unambiguous pattern was reported was calculated for each individual. The means are presented in Fig. 4. A constant of 1/60 was added to the proportion scores, and the log-transformed values were analyzed by a one-way repeated-measures ANOVA. The main effect of intensity was significant [$F(2,18)=5.46$, $p<0.02$]. A Tukey pairwise comparison ($\alpha=0.05$) of the mean log scores indicated that performance in the 83-dB condition was significantly different from that in the baseline condition. No other pairwise comparisons were significant.

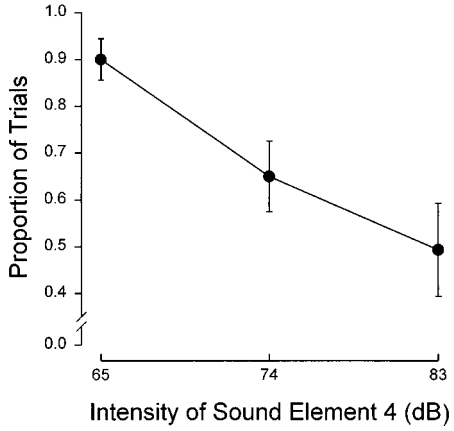

FIG. 4. Mean proportion of trials in which the standard unambiguous pattern (XXX−X−−−) was reported as a function of the intensity of the fourth sound element. Data are from experiment 2. Bars=±1 SEM.

These results replicate those of experiment 1. In the baseline condition the conventional pattern was reported on 90% of the trials (see Fig. 4). When the intensity of the fourth sound element was increased by 9 and 18 dB, the conventional unambiguous pattern was reported less frequently—65% and 50%, respectively. The change in performance from baseline was significant with the greatest (18 dB) intensity increment. However, the results do not support the hypothesis that an intensity increment greater than 9 dB would produce a perceptual reorganization of the auditory sequence to a new unambiguous pattern beginning with the altered sound element. Although the intensity increment was increased by 9 dB in this experiment compared to experiment 1, the same outcome was obtained.

III. EXPERIMENT 3

A. Hypothesis

This experiment tested the hypothesis that variations in the intensity of the first, third, or fourth sound element of the ambiguous sequence (XX−X−XX−) would produce changes in the perceptual organization of the auditory pattern. The perceptual responses of listeners were recorded in five intensity conditions for each of the three sound-element manipulations. In the baseline condition, each of the sound elements had the same intensity. This condition was similar to previous studies (e.g., Garner and Gottwald, 1968; Preusser *et al.*, 1970; Royer and Garner, 1966; Royer and Robin, 1986), so it was expected that listeners would report hearing each of the three different patterns (pattern 1: XX−X−XX−; pattern 2: X−XX−XX−; pattern 3: XX−XX−X−) with about equal frequency. There were three conditions in which the intensity of the manipulated sound element was greater than baseline. It was expected that as intensity increased, listeners would report hearing the pattern as beginning with the manipulated sound element more often than in the baseline condition, and they would report hearing the two

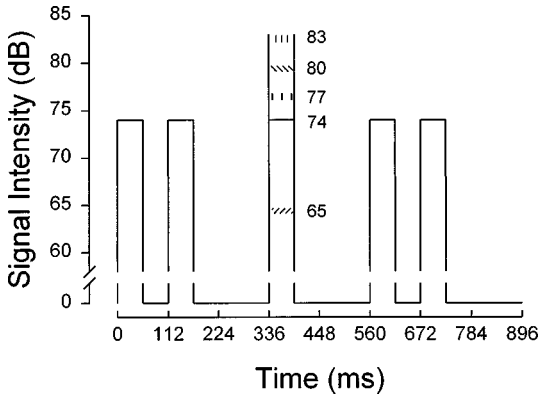

FIG. 5. Temporal structure of the ambiguous sequence (XX–X–XX–) used in experiment 3. Each sound element consisted of a 250-Hz tone. Depicted in the figure is the sound-element 3 manipulation. In this condition, the intensity of the third sound element could be 65, 74, 77, 80, or 83 dB. The other four sound elements had an intensity of 74 dB. For the sound-element 1 manipulation (not shown), the structure of the sequence was the same as depicted except the intensity of the first sound element varied. For the sound-element 4 manipulation (not shown), the intensity of the fourth sound element varied.

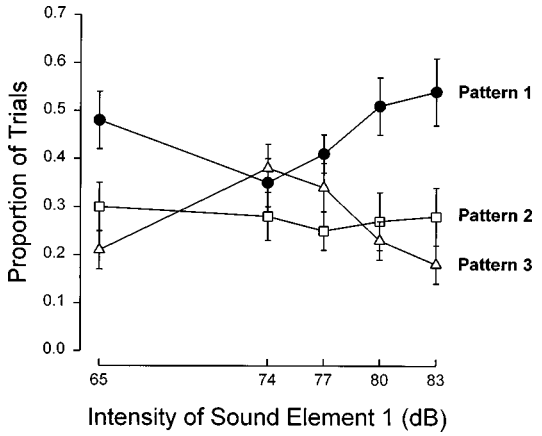

FIG. 6. Mean proportion of trials in which pattern 1 (XX–X–XX–; circles), pattern 2 (X–XX–XX–; squares), and pattern 3 (XX–XX–X–; triangles) were reported as a function of the intensity of the first sound element. Data are from experiment 3, sound-element 1 manipulation. Bars $=\pm 1$ SEM. Filled symbols indicate the pattern beginning with the manipulated sound element.

alternate organizations less often. There was also a condition in which the intensity of the manipulated sound element was less than baseline, as in experiment 1.

B. Method

1. Participants

Eighteen individuals from the University of Iowa community (nine females, nine males) between the ages of 16 to 33 (mean age=20.2 years) volunteered. They were all naive regarding the aims of the study. Each individual was screened for hearing impairments using a pure-tone audiometric screening test as in experiment 1. Each participant received monetary compensation.

2. Stimuli and apparatus

The auditory stimulus consisted of 15 repetitions of an 8-element sequence that was composed of 5 computer-generated pulses of a 250-Hz tone and 3 gaps. The on-duration and the off-duration of each sound element was 56 ms, and each gap was 112 ms. The temporal parameters of a single sequence are shown in Fig. 5. There were three sound-element manipulation conditions corresponding to manipulating the intensity of the first, the third, or the fourth sound element. For each of these conditions, the intensity of the manipulated element was varied in five conditions (see Fig. 5). These were the same as in experiment 1—65, 74, 77, 80, and 83 dB.

Testing was conducted in the same manner as before, and the structure of a trial was the same with the following exception. The response screen displayed the three patterns, XX–X–XX–, X–XX–XX–, and XX–XX–X–, one in the upper left, one in the center, and one in the lower right of the video monitor. Each of the three positions on the response screen corresponded to one of the three response keys on the response box. The participants responded by pressing the key that matched the position of the pattern that best characterized the perceptual pattern of the sequence during the trial.

3. Procedures

All of the participants were tested in each of the experimental conditions. Testing was conducted in three separate sessions that took place on three days within a 1- to 2-week period. Each testing session lasted about 1.25 h. The sound-element manipulation condition was blocked by session. At the start of the experiment, the participant was led through a demonstration block of three trials of the baseline intensity condition. This block could be repeated if the participant requested it. For each testing session, there was a 30-trial practice block composed of 6 trials of each of the 5 intensities. This block was not repeated. It was followed by one experimental block of 150 trials—30 trials of each intensity. There was a 2-min rest interval after trials 50, 90, and 120. The session order (i.e., the presentation order of the sound-element manipulation conditions) was counterbalanced across the 18 participants. Within each block, the presentation order of the five intensity conditions was randomized, and the starting element of the eight-element sequence was selected at random on each trial.

C. Results and discussion

The three sound-element manipulation conditions were analyzed separately. For the five levels of stimulus intensity, the proportion of trials in which pattern 1 (XX–X–XX–), pattern 2 (X–XX–XX–), and pattern 3 (XX–XX–X–) were reported was calculated for each participant. The means are presented in Figs. 6, 7, and 8 for the sound-element 1, 3, and 4 manipulations, respectively. A constant of 1/60 was added to each proportion score, and the logarithms of these values were calculated. To examine the effects of the intensity manipulation on the participants' responses across the different patterns, three planned contrasts were conducted for each sound-element manipulation condition. Separate contrasts were used because the frequency of responding to the three different patterns was not independent for a given intensity condition. Differences between the log-transformed proportions were calculated and used in the analyses. Using differ-

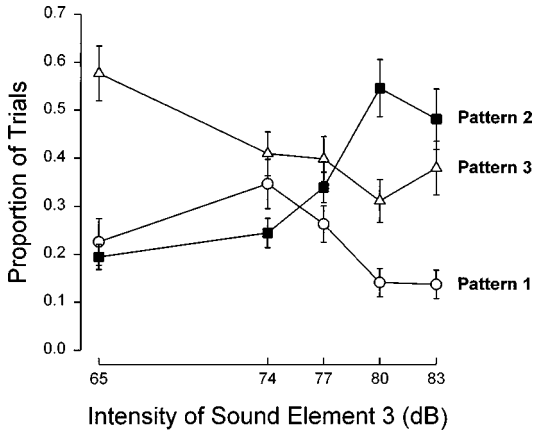

FIG. 7. Mean proportion of trials in which pattern 1 (XX–X–XX–; circles), pattern 2 (X–XX–XX–; squares), and pattern 3 (XX–XX–X–; triangles) were reported as a function of the intensity of the third sound element. Data are from experiment 3, sound-element 3 manipulation. Bars $=\pm 1$ SEM. Filled symbols indicate the pattern beginning with the manipulated sound element.

ence scores provided a way to directly examine changes in the relative frequency with which any two patterns were chosen as a function of the intensity of the manipulated element, while taking into account that there were absolute differences in the response frequency between the patterns in the baseline condition (see Figs. 6, 7, and 8, 74-dB intensity condition). The three planned contrasts examined the effects of the intensity manipulation on the response differences between patterns 1 and 2, 1 and 3, and 2 and 3. This amounted to three one-way repeated-measures ANOVAs on the difference in log scores. Because there were three analyses for each sound-element manipulation, significance levels were set at $\alpha=0.017$ (0.05/3) to minimize the possibility of a type I error (Keppel, 1991).

It was expected that the difference in log scores between the pattern beginning with the manipulated element and the other two patterns would increase with increasing intensity. No specific predictions were made regarding the differences between the two patterns that did not begin with the manipulated element, and there were no specific predictions made about the differences in the conditions in which the intensity of the manipulated element was less than the baseline intensity.

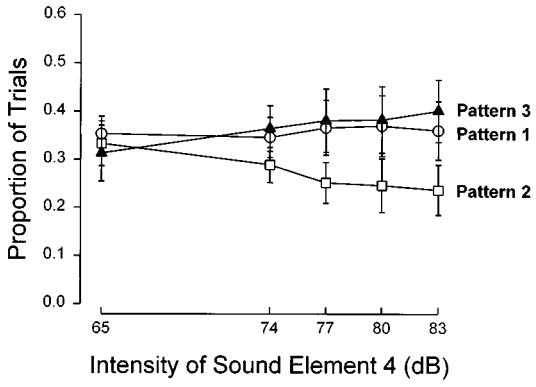

FIG. 8. Mean proportion of trials in which pattern 1 (XX–X–XX–; circles), pattern 2 (X–XX–XX–; squares), and pattern 3 (XX–XX–X–; triangles) were reported as a function of the intensity of the fourth sound element. Data are from experiment 3, sound-element 4 manipulation. Bars$=\pm 1$ SEM. Filled symbols indicate the pattern beginning with the manipulated sound element.

1. Sound-element 1 manipulation

The statistical analyses did not reveal a significant effect of intensity on the differences between patterns 1 and 2 [$F(4,68)=0.65$, $p>0.62$]. However, there was a significant effect on the differences between patterns 1 and 3 [$F(4,68)=6.03$, $p<0.001$], and 2 and 3 [$F(4,68)=4.17$, $p<0.005$]. Tukey follow-up comparisons ($\alpha=0.05$) were conducted on the mean differences involved in the significant contrasts. For the contrast of patterns 1 and 3, there were significant differences between the 74-dB condition and the 83-, 80-, and 65-dB conditions, and also between the 77- and 83-dB conditions. For the contrast of patterns 2 and 3 there were significant differences between the 74-dB condition and the 83- and 65-dB conditions. There were no other significant pairwise comparisons.

It was expected that as the intensity of sound-element 1 (underlined) was incremented, the difference in response frequency between pattern 1 (X̲X–X–XX–) responses and both pattern 2 (X–XX–X̲X–) and pattern 3 (XX–X̲X–X–) responses would increase compared to baseline levels. This outcome was obtained for the comparison of patterns 1 and 3 with the two largest intensity increments. As shown in Fig. 6, the increased difference was due to an increase in the frequency of pattern 1 responses and a concurrent decrease in the frequency of pattern 3 responses. In addition, decreasing the intensity resulted in a significantly greater difference between these patterns, which was also due to an increase in the frequency of pattern 1 responses and a decrease in the frequency of pattern 3 responses. For the comparison of patterns 1 and 2, the expected outcome was not obtained; the difference in the frequency of pattern 1 and pattern 2 responses did not change significantly as a function of intensity. This outcome most likely resulted from the fact that the frequency of pattern 2 responses remained relatively stable across all intensity conditions (see Fig. 6). For the comparison of patterns 2 and 3, the difference was significant at the two intensity extremes—65 and 83 dB. Although pattern 3 was reported more often than pattern 2 in the baseline condition, pattern 2 was reported more often than pattern 3 when the intensity of sound-element 1 was increased or decreased by 9 dB.

2. Sound-element 3 manipulation

Analyses revealed a significant effect of intensity on the response differences between patterns 1 and 2 [$F(4,68)=8.5$, $p<0.001$], and 2 and 3 [$F(4,68)=11.84$, $p<0.001$], and a marginally significant effect of intensity between patterns 1 and 3 [$F(4,68)=3.23$, $p<0.018$]. For the contrast of patterns 1 and 2, the Tukey follow-up tests revealed that the 74-, 77-, and 65-dB conditions were all significantly different from both the 80- and 83-dB conditions. For the contrast between patterns 2 and 3, the 80- and 83-dB conditions were significantly different from the 74- and 65-dB conditions,

and the 77-dB condition was significantly different from the 65-dB condition. For the marginally significant contrast of patterns 1 and 3, there was a significant difference between the 74- and 65-dB conditions. No other pairwise differences were significant.

It was expected that as the intensity of sound-element 3 (underlined) increased, the difference in response frequency between pattern 2 (X–XX–XX–) responses and both pattern 1 (XX–X–XX–) and pattern 3 (XX–XX–X–) responses would increase compared to baseline levels. This outcome was obtained. For the comparison of patterns 1 and 2, the difference in response frequency was significantly greater than baseline levels for the two largest intensity increments. This was due to an increase in the frequency of pattern 2 responses with a concurrent decrease in pattern 1 responses (see Fig. 7). For patterns 2 and 3, the differences were also significantly greater than baseline levels for the two largest intensity increments. As Fig. 7 indicates, the frequency of pattern 3 responses remained relatively stable across the 74-, 77-, 80-, and 83-dB intensity conditions, but the frequency of pattern 2 responses increased with increasing intensity. As a result, although pattern 3 was reported significantly more often than pattern 2 in the baseline condition, pattern 2 was reported more often than pattern 3 in the 80- and 83-dB conditions. Also, decreasing the intensity of the third sound element resulted in a significantly greater difference in the frequency of both pattern 2 responses and pattern 1 responses compared to pattern 3 responses. The frequency of pattern 3 responses increased with decreasing intensity of the manipulated sound element, whereas the frequency of both pattern 1 and pattern 2 responses remained about the same as baseline (see Fig. 7).

3. Sound-element 4 manipulation

The analyses did not reveal a significant effect of intensity on the response differences between patterns 1 and 2 [$F(4,68)=0.35$, $p>0.84$], 1 and 3 [$F(4,68)=1.02$, $p>0.4$], or 2 and 3 [$F(4,68)=2.46$, $p>0.05$]. It was expected that as the intensity of sound-element 4 (underlined) increased, the difference in response frequency between pattern 3 (XX–XX–X–) responses and both pattern 1 (XX–X–XX–) and pattern 2 (X–XX–XX–) responses would increase compared to baseline levels. This outcome was not obtained. As Fig. 8 indicates, the pattern of responding was relatively stable across the five intensity conditions, although the frequency of pattern 2 responses tended to decrease slightly with increasing intensity of the fourth sound element, while the frequency of pattern 1 and pattern 3 responses tended to increase slightly.

4. Baseline conditions

A final analysis was conducted to test for overall differences in the frequency of responses to patterns 1, 2, and 3 in the baseline condition. For each participant, the proportion of trials on which pattern 1, pattern 2, and pattern 3 were reported was averaged over the three sound-element manipulation conditions. A constant of 1/60 was added to the average proportions, and the logarithms were calculated. The log-transformed values were analyzed by a one-way repeated-measures ANOVA, which did not reveal a significant effect of pattern [$F(2,34)=1.09$, $p>0.34$]. This outcome supports the expectation that listeners would report the three patterns about equally often in the baseline condition. The averages across sound-element manipulation conditions were 35% (SE=±4%) for pattern 1, 27% (SE=±3%) for pattern 2, and 38% (SE=±4%) for pattern 3.

IV. DISCUSSION

The results of this study generally support Robin *et al.*'s (1990a) hypothesis that the amplitude of the neuronal response influences the perceptual organization of rhythmic auditory patterns. In experiments 1 and 2, increasing the intensity of the fourth sound element of the perceptually unambiguous sequence (XXX–X–––) resulted in a perceptually ambiguous pattern organization; overall, listeners reported perceiving both of the alternative pattern organizations about equally often with the greatest intensity increments. Likewise, in experiment 3 it was found that increasing the intensity of either the first or third sound element of the perceptually ambiguous sequence (XX–X–XX–) biased the perceptual organization in favor of the pattern beginning with the altered sound element. Thus by manipulating the signal intensity of specific sound elements in the auditory sequences, which should have a direct effect on the underlying pattern of neuronal response amplitude, it was possible to produce predictable changes in the perceived pattern organizations.

Additional support for the hypothesis emerges in considering the results of experiment 3 when the intensity of either the first or third sound element of the ambiguous sequence was decreased. Under these conditions, the altered sound element appears to have taken on some of the qualities of a gap which then biased the perceptual organization of the sequence in specific ways. For example, when the intensity of sound element 3 was decreased (e.g., XX–x–XX–), the perceptual organization of the sequence was biased in favor of pattern 3 responses (e.g., XX–XX–x–). The reduced amplitude of the sound element effectively increased the size of the gap and, by increasing the degree of neuronal recovery from adaptation, produced an increase in the neuronal response amplitude associated with the fourth sound element. Thus listeners most often perceived the pattern as beginning with the sound element associated with the greatest neuronal response amplitude (i.e., pattern 3), as Robin *et al.*'s hypothesis predicts. When the intensity of sound-element 1 was decreased (e.g., xX–X–XX–), the perceptual organization of the sequence was biased in favor of pattern 1 responses (e.g., xX–X–XX–). In this case, the amplitude of the neuronal response associated with the second sound element would have been effectively increased, biasing perception of the pattern in favor of one beginning with the second sound element (e.g., X–X–XX–x). However, this pattern was not one of the response alternatives available to the listeners. Of the three available response alternatives, pattern 1 (XX–X–XX–) most closely resembles what listeners may have perceived, that is, a pattern containing a single sound

element in the middle position and ending with two consecutive sound elements.

The same logic can be applied to experiment 1 when the intensity of sound-element 4 was decreased (e.g., XXX–x–––). In this case, the reduced intensity effectively increased the degree of recovery from neuronal adaptation during the gap, thereby increasing the amplitude of the neuronal response associated with the first sound element. However, because the frequency of responses to the standard unambiguous pattern was already high in the baseline condition (see Fig. 3), it would have been difficult to detect a significant increase in the frequency of responses in this condition. It is unlikely that when the intensity of the fourth sound element was increased, the listeners perceived a pattern organization other than the two available response alternatives.

There are some aspects of this study that are equivocal regarding Robin *et al.*'s hypothesis. For example, the hypothesis predicts that by increasing the intensity of the fourth sound element of the unambiguous sequence it should be possible to completely reverse the perceptual organization so that a new, unambiguous pattern beginning with the fourth sound element would emerge. This outcome was not obtained in experiment 1, nor was it obtained in experiment 2 even though the intensity increment from baseline was 9 dB greater than that in experiment 1. However, the averaged results do not accurately reflect the responses of all of the listeners. In experiment 1, the expected reversal in pattern perception was evident in the response patterns of two of the ten listeners (from 93% to 10% and from 80% to 20% in the baseline and 83-dB intensity conditions, respectively). On the other hand, performance remained relatively stable across all of the intensity conditions for three of the ten listeners, while the remaining five individuals demonstrated performance patterns similar to the averaged data. About the same degree of between-subjects variability was evident in the data from experiment 2. Three of the ten listeners demonstrated the expected reversal in pattern perception (from 97% to 7%, from 100% to 37%, and from 97% to 3% in the baseline and 83-dB conditions, respectively), and performance remained relatively stable across all intensity conditions for two of the ten listeners. The remaining five individuals showed performance patterns represented in the averaged data.

Furthermore, in experiment 3, increments in the intensity of the first and third sound elements of the ambiguous sequence biased the perceptual organization in favor of the pattern beginning with the altered sound element, but in neither condition did the pattern change from a perceptually ambiguous organization to a perceptually unambiguous organization. In addition, increments in signal strength of the fourth sound element did not have a significant effect on the perceived pattern organization. In general, the changes in pattern organization with increases in signal intensity observed in this study were significant but incomplete.

There are several possibilities that might explain why some of the expected results were not obtained. First, it may be that the magnitude of the intensity increments used in this study was insufficient to obtain the predicted results. Although the results of experiment 2 argue against this possibility, additional research is needed to completely address this issue. Second, it may be that a ceiling effect was experienced due to the narrow-band frequency of the auditory stimuli used in this study. Each sound element consisted of a short-duration pulse of a 250-Hz computer-generated tone. This stimulus would have activated only a limited subset of auditory-nerve fibers, primarily those responsive to a signal frequency of 250 Hz. The intensity increments may have had a limited impact on the overall levels of neural activation, and this may have led to the overall limited perceptual changes observed. Robin *et al.* (1990a) used short-duration pulses of a white-noise stimulus. This broad-frequency-band stimulus would produce overall greater changes in the levels of neural activation with changes in signal intensity (e.g., Abbas, 1979), and might produce a clearer set of results regarding the relationship between sound-element intensity and auditory pattern organization.

A third possibility may be that the perceptual organization of these auditory sequences is not determined solely by the pattern of the neuronal responses proposed to underlie the run and gap principles, but may also be influenced by other organizing factors. For example, Povel (1981), Povel and Okkerman (1981), and Essens and Povel (1985) have identified several important factors in the perception of rhythm using temporally structured tone sequences similar to those used in the baseline conditions of this study. These factors include tempo, accent distribution (beats), starting point of the sequence, and inter-tone-interval ratios. Although in the present study the effects of starting point were controlled by randomly selecting the starting point of the sequence on each trial, the influence of the remaining factors on the perceptual pattern organization in this study is unknown and warrants further investigation.

V. CONCLUSIONS

The data from this study provide preliminary support for Robin *et al.*'s (1990a) notion that the relative pattern of neuronal response amplitude (i.e., the pattern of neuronal adaptation due to repeated stimulation and recovery from adaptation following a pause in stimulation) may underlie the run and gap principles that determine the perceived organization of cyclic auditory sequences. Variations in the intensity of specific sound elements in the sequences, which should have produced specific changes in the relative pattern of neuronal response amplitude, produced predictable changes in the perceived pattern organization reported by human listeners. However, not all of the predictions were supported by the data. The source of this discrepancy is unclear, but may be related to the narrow range of signal increments tested, the narrow-band nature of the stimuli used, or the presence of other organizing factors such as the distribution of perceived accents. Although the data clearly suggest an association between the perceptual organization of temporally structured auditory sequences and the pattern of neuronal response amplitude, additional research is needed to substantiate the link with regards to human listeners. Further verification of the hypothesis requires studies using techniques such as auditory evoked responses. Preliminary data by Hug *et al.* (1989) using auditory brainstem responses indicate that the neurosen-

sory responses of humans listening to the same ambiguous and unambiguous sequences as used in this study are similar to those of the cats studied by Robin *et al.* (1990a). A more extensive continuation of this work is needed.

ACKNOWLEDGMENTS

The research was supported by NINDS Grant No. PO-NS19632 on which D.A.R. is an investigator. The authors gratefully acknowledge the technical assistance of Bruce Clark, David Wood, and Marty Milder, the statistical assistance of George Woodworth, and the sound advice of Paul Abbas. The data for experiments 1 and 2 were collected by Mary Krapfl in partial fulfillment of her honor's research thesis in the Department of Speech Pathology and Audiology at the University of Iowa, and the data for experiment 3 were collected by Anup Kubal in partial fulfillment of the requirements of the University of Iowa Secondary Student Training Program. The authors wish to acknowledge the helpful critiques of Stephen Handel and an anonymous reviewer on a previous version of this manuscript. Portions of this research were presented at the 37th Annual Meeting of the Psychonomic Society, November, 1996, in Chicago. Correspondence should be addressed to Lynn D. Zimba, Laboratory of Speech and Language Neuroscience, Department of Speech Pathology and Audiology, University of Iowa, 13 WJSHC, Iowa City, IA 52242-1407 (e-mail: lynn-zimba@uiowa.edu).

Abbas, P. (**1979**). ''Effects of stimulus frequency on adaptation in auditory-nerve fibers,'' J. Acoust. Soc. Am. **65**, 162–165.

American Psychological Association (**1992**). ''Ethical principles of psychologists and code of conduct,'' Am. Psychol. **47**, 1597–1611.

Bregman, A. S. (**1990**). *Auditory Scene Analysis: The Perceptual Organization of Sound* (MIT, Cambridge, MA).

Deutsch, D. (**1980**). ''The processing of structured and unstructured tonal sequences,'' Percept. Psychophys. **28**, 381–389.

Deutsch, D. (**1981**). ''The octave illusion and auditory perceptual integration,'' Hearing Research and Theory **1**, 99–142.

Efron, R. (**1963**). ''Temporal perception, aphasia, and deja vu,'' Brain **86**, 403–424.

Essens, P. J. (**1986**). ''Hierarchical organization of temporal patterns,'' Percept. Psychophys. **40**, 69–73.

Essens, P. J. (**1995**). ''Structuring temporal sequences: Comparison of models and factors of complexity,'' Percept. Psychophys. **57**, 519–532.

Essens, P. J., and Povel, D.-J. (**1985**). ''Metrical and nonmetrical representations of temporal patterns,'' Percept. Psychophys. **37**, 1–7.

Garner, W. R. (**1974**). *The Processing of Information and Structure* (Erlbaum, Hillsdale, NJ).

Garner, W. R., and Gottwald, R. L. (**1968**). ''The perception and learning of temporal patterns,'' Quarterly Journal of Experimental Psychology **20**, 97–109.

Gfeller, K., Woodworth, G., Robin, D. A., Witt, S., and Knutson, J. F. (**1997**). ''Perception of rhythmic and sequential pitch patterns by normally hearing adults and adult cochlear implant users,'' Ear and Hearing **18**, 252–260.

Handel, S. (**1973**). ''Temporal segmentation of repeating auditory patterns,'' J. Exp. Psychol. **101**, 46–54.

Handel, S. (**1974**). ''Perceiving melodic and rhythmic auditory patterns,'' J. Exp. Psychol. **103**, 922–933.

Handel S. (**1993**). *Listening: An Introduction to the Perception of Auditory Events* (MIT, Cambridge, MA).

Handel, S., and Oshinsky, J. S. (**1981**). ''The meter of syncopated auditory polyrhythms,'' Percept. Psychophys. **30**, 1–9.

Hug, L. N., Robin, D. A., and Abbas, P. J. (**1989**). ''Neurophysiologic correlates of temporal pattern perception in humans,'' paper presented at the American Speech-Language-Hearing Association, St. Louis, MO.

Keppel, G. (**1991**). *Design and Analysis: A Researcher's Handbook* (Prentice Hall, Englewood Cliffs, NJ), 3rd ed.

Kirk, R. E. (**1982**). *Experimental Design* (Brooks/Cole, Monterey, CA), 2nd ed.

Longuet-Higgins, H. C., and Lee, C. S. (**1982**). ''The perception of musical rhythms,'' Perception **11**, 115–128.

Longuet-Higgins, H. C., and Lee, C. S. (**1984**). ''The rhythmic interpretation of monophonic music,'' Music Perception **1**, 424–441.

Martin, J. G. (**1972**). ''Rhythmic (hierarchical) versus serial structure in speech and other behavior,'' Psychol. Rev. **79**, 487–509.

Massaro, D. W. (Ed.) (**1975**). *Understanding Language: An Information-Processing Analysis of Speech Perception, Reading, and Psycholinguistics* (Academic, New York).

Pisoni, D. G., and Swausch, J. R. (**1975**). ''Some stages of processing in speech perception,'' in *Structure and Process in Speech Perception*, edited by A. Cohen and S. Nootboom (Springer-Verlag, Heidelberg), pp. 1–19.

Povel, D.-J. (**1981**). ''Internal representation of simple temporal patterns,'' Journal of Experimental Psychology: Human Perception and Performance **7**, 3–18.

Povel, D.-J. (**1984**). ''A theoretical framework for rhythm perception,'' Psychol. Res. **45**, 315–337.

Povel, D.-J., and Essens, P. J. (**1985**). ''Perception of temporal patterns,'' Music Perception **2**, 411–440.

Povel, D.-J., and Okkerman, H. (**1981**). ''Accents in equitone sequences,'' Percept. Psychophys. **30**, 565–572.

Preusser, D., Garner, W. R., and Gottwald, R. L. (**1970**). ''Perceptual organization of two-element temporal patterns as a function of their component one-element patterns,'' Am. J. Psychol. **83**, 151–170.

Robin, D. A., Abbas, P. J., and Hug, L. N. (**1990a**). ''Neural responses to auditory temporal patterns,'' J. Acoust. Soc. Am. **87**, 1673–1682.

Robin, D. A., Royer, F. L., and Abbas, P. J. (**1987**). ''The perception of repetitive auditory temporal patterns,'' in *Auditory Processing of Complex Sounds*, edited by W. A. Yost and C. S. Watson (Erlbaum, Hillsdale, NJ), pp. 87–103.

Robin, D. A., Tranel, D., and Damasio, H. (**1990b**). ''Auditory perception of temporal and spectral events in patients with focal left and right cerebral lesions,'' Brain and Language **39**, 539–555.

Royer, F. L., and Garner, W. R. (**1966**). ''Response uncertainty and perceptual difficulty of auditory temporal patterns,'' Percept. Psychophys. **1**, 41–47.

Royer, F. L., and Garner, W. R. (**1970**). ''Perceptual organization of nine-element auditory temporal patterns,'' Percept. Psychophys. **7**, 115–120.

Royer, F. L., and Robin, D. A. (**1986**). ''On the perceived unitization of repeated auditory patterns,'' Percept. Psychophys. **39**, 9–18.

Gap detection as a measure of electrode interaction in cochlear implants

Johan J. Hanekom[a)]
Department of Electrical and Electronic Engineering, University of Pretoria, Pretoria, 0002, South Africa

Robert V. Shannon
House Ear Institute, 2100 West Third Street, Los Angeles, California 90057

(Received 14 July 1997; revised 15 June 1998; accepted 29 June 1998)

Gap detection thresholds were measured as an indication of the amount of interaction between electrodes in a cochlear implant. The hypothesis in this study was as follows: when the two stimuli that bound the gap stimulate the same electrode, and thus the same neural population, the gap detection threshold will be short. As two stimuli are presented to two electrodes that are more widely separated, the amount of neural overlap of the two stimuli decreases, the stimuli sound more dissimilar, and the gap thresholds increase. Gap detection thresholds can thus be used to infer the amount of overlap in neural populations stimulated by two electrodes. Three users of the Nucleus cochlear implant participated in this study. Gap detection thresholds were measured as a function of the distance between the two electrode pairs and as a function of the spacing between the two electrodes of a bipolar pair (i.e., using different modes of stimulation). The results indicate that measuring gap detection thresholds may provide an estimate of the amount of electrode interaction. Gap detection thresholds were a function of the physical separation of the electrode pairs used for the two stimuli that bound the gap. Lower gap thresholds were observed when the two electrode pairs were closely spaced, and gap thresholds increased as the separation increased, resulting in a ''psychophysical tuning curve'' as a function of electrode separation. The sharpness of tuning varied across subjects, and for the three subjects in this study, the tuning was generally sharper for the subjects with better speech recognition. The data also indicate that increasing the separation between active and reference electrodes has limited effect on spatial selectivity (or tuning) as measured perceptually. © *1998 Acoustical Society of America.* [S0001-4966(98)02710-6]

PACS numbers: 43.66.Mk, 43.66.Ts, 43.66.Ba, 43.64.Me [JWH]

INTRODUCTION

The individual electrodes in a modern multi-electrode cochlear implant are intended to selectively stimulate discrete neural populations. However, the assumption that discrete neural populations can be activated is not always true. It is widely assumed that stimuli applied between closely spaced or adjacent bipolar electrode pairs lead to the localized activation of neurons, whereas widely spaced bipolar electrode pairs (including monopolar stimulation) will lead to broad electrical fields and wide areas of neural activation (van den Honert and Stypulkowski, 1987; Busby *et al.*, 1994). Even for a closely spaced electrode pair, a broad region can be activated at high current levels (van den Honert and Stypulkowski, 1987). The consequence is that when two sets of bipolar electrode pairs are stimulated, and these two sets are closely spaced, overlap can occur in the neural populations excited by the stimulation currents. This overlap of neural populations can occur regardless of whether the stimuli are nonsimultaneous or simultaneous. Simultaneous stimuli give rise to direct electrical field interactions, which pose additional problems for electrical stimulation, but even nonsimultaneous stimuli may produce activation of overlapping neural regions.

If two electrode pairs stimulate the same neural population or overlapping neural populations, the implication is that sound sensations elicited by the two stimuli might be confused or might even be indistinguishable. This may reduce the number of independent channels of information that can be conveyed to the cochlear implant user's auditory system, presumably resulting in a deterioration of speech recognition ability. If two electrode pairs stimulate the same population of neurons and are perceptually indistinguishable, they probably cannot convey two separate channels of information.

The number of information channels in an implant

Recent work by Fishman *et al.* (1997) and Lawson *et al.* (1993, 1996) indicates that increasing the number of electrodes does not necessarily lead to better speech recognition. In fact, very slight or no improvement was evident when the number of electrodes used was increased from 7 to 20. For some speech recognition tasks, no improvement in performance was found when the number of electrodes used increased from 4 to 20. In these experiments, all spectral information that is usually presented across all 20 electrodes, was applied to a limited number of electrodes, i.e., no spectral information was discarded. This result suggests that the actual number of information channels available to these patients was not a function of the number of electrodes, and that the actual number of information channels might be limited to somewhere between 4 and 7. Interestingly, in a study with normal-hearing listeners, Shannon *et al.* (1995) used

a)Electronic mail: jhanekom@postino.up.ac.za

four channel processors and found that listeners achieved near-perfect speech recognition, implying that four information channels might be adequate, at least in quiet listening conditions.

In another study, on patients with the Nucleus cochlear implant device, Hanekom and Shannon (1996) showed that for several different seven-electrode speech processors, speech recognition performance was a function of which set of seven electrodes were used. This indicates that different choices of which electrodes are used in a processor might lead to different numbers of information channels. A reduced number of electrodes, including only discriminable electrodes, were also used in the speech processors of 11 Nucleus cochlear implant users who participated in a study by Zwolan *et al.* (1997). While some subjects showed significant improvement in specific speech recognition tasks, others showed a decline in speech recognition performance. Although no strong relationship between electrode discrimination performance and speech recognition was observed, this study again indicates that the choice of electrodes in a reduced electrode processor influences speech recognition ability in some implant users. This supports the suggestion that the number of information channels is a function of the choice of electrodes in a reduced electrode processor. Lawson *et al.* (1996) measured a larger difference in performance between two different selections of 6 electrodes than between 6 and 20 electrodes. This suggests that there should be a way to maximize the number of information channels used for a specific subject by judicious choice of electrodes. Further maximization may be possible using electrical field focussing (Townsend *et al.*, 1987), or by compensating for a missing patch of nerve, or by shifting the speech analysis filters to better match the electrode location (Fu and Shannon, submitted). No maximization of this sort is presently done in implant programming strategies, partly because measurement tools are not yet available and partly because the relation between the electrode interaction and information channel capacity is not well understood.

Physical factors affecting electrode interaction

To fully account for the effects of electrode interaction we must (1) identify the factors in the patterns of speech that are most important for speech recognition (Shannon *et al.*, 1995), (2) be able to measure the electrode interaction pattern in an individual implant patient, and (3) use the information from both (1) and (2) to optimize the reception of the most important speech pattern information for an individual patient.

A number of variables can influence the interaction of electrodes in a cochlear implant user. These include the electrode placement within the cochlea and nerve survival at the cochlear level and also at the central auditory level.

Electrode placement

The proximity of the electrode to the surviving neurons, as well as the impedance and paths of current flow between the electrode and the neural population, will determine the spatial selectivity of the stimulation. The impedance and the current pathways could be influenced by new bone formation in the implanted cochlea and encapsulation tissue around the electrode (Grill and Mortimer, 1994). Broad spread of activation will occur if the electrode is physically distant from the excitable neurons (along the lateral wall of the cochlea for example, rather than next to the modiolus) or if nerve survival is poor immediately adjacent to the electrode. Although not routinely used, techniques such as spiral tomography (Wang *et al.*, 1996) are available to measure the exact placement of the electrodes inside the scala tympani. The absolute electrode location can then be used to deduce which nerve fibers will be activated. Finley *et al.* (1990) modeled nerve fiber activation in a finite element model with idealized electrode placement, but no work has been reported using real electrode placement data.

Although it is clear that placement of electrodes further from the modiolus requires higher stimulus levels to reach threshold, and consequently leads to larger current spread, the influence of electrode placement is not yet quantified regarding the interaction or independence of information channels. It is generally assumed that placement of electrodes close to the modiolus is preferable because more focused stimulation can be achieved (Rebscher *et al.*, 1994). Unfortunately, very few tools are available for perceptually assessing and quantifying electrode absolute location and spatial selectivity and their exact influence on speech recognition.

Nerve survival

A second factor that should affect electrode interaction is the nerve survival pattern in an individual patient. Several anatomical post-mortem studies (Zimmermann *et al.*, 1995; Linthicum *et al.*, 1991; Fayad *et al.*, 1991) have shown from human temporal bones that nerve survival patterns vary greatly among subjects, even for the same disease. It is not clear how the amount and pattern of neuron survival affects implant performance. However, with fewer neurons, the distance between the stimulating electrode and neurons might be larger. Certainly, the further the neurons are distant from the electrode, the larger the current required for activation and the broader the spread of activation. This, in turn, may reduce the number of independent information channels.

It is clear that it is necessary to quantify the available auditory abilities and to optimize the use of the available information channels, i.e., to optimize information transfer in current implants. Tools are needed to establish the number, the location, and the characteristics of information channels available in each individual cochlear implant user. In this article, gap detection is proposed as one such tool.

Gap detection as a measure of tonotopic spread

Gap detection has traditionally been used as a measure of temporal processing (Plomp, 1969). At moderate levels and higher, normal-hearing listeners can detect 3–5 ms gaps in a stimulus when identical stimuli are bounding the gap, irrespective of the frequency of the stimuli (Penner, 1976; Fitzgibbons, 1983; Florentine and Buus, 1984; Hall *et al.*, 1996; Shailer and Moore, 1983). We characterize this result as the ''within-channel'' temporal resolution. However,

TABLE I. Subject information for the three subjects who participated in this study. Insertion depth refers to the number of electrode bands inside the cochlea. The first 22 electrodes are active. Speech recognition scores for these subjects were obtained in a previous study (Fishman *et al.*, 1997). Recognition of words from sentences was measured with the CUNY everyday sentences. For consonant and vowel recognition tests, 16 medial consonants in a v/C/v context and 8 vowels in a h/V/d context were used.

Subject	Age	Gender	Age of onset of profound hearing loss	Time of implant use	Processor type	Insertion depth	Cause of deafness	Sentence recognition (%)	Vowel recognition (%)	Consonant recognition (%)
N3	55	Male	45	6 years	SPEAK	27	trauma	61	58	46
N4	39	Male	35	4 years	SPEAK	26	trauma	95	92	95
N7	54	Male	47	6 months	SPEAK	22	unknown; progressive hearing loss	71	98	75

when the frequencies or levels of the two stimuli that bound the gap are different, gap detection thresholds increase about an order of magnitude to 30–50 ms (Divenyi and Danner, 1977; Divenyi and Sachs, 1978; Formby and Forrest, 1991; Formby *et al.*, 1992). In this case, even the standard stimulus with no gap is perceived as having a discontinuity. The discontinuity that identifies the actual gap must be long enough to be distinctive from this no-gap, standard condition. This temporal comparison must be done centrally ''across-channels'' in that the two stimuli bounding the gap are processed through largely independent neural pathways. A simple model of peripheral frequency resolution can largely explain these results, indicating that gap detection can indicate the degree of neural population overlap between two stimuli (Heinz *et al.*, 1996).

In cochlear implant users, Chatterjee *et al.* (1998) observed that ''within-channel'' gap detection thresholds increase when the stimuli marking the gap were of unequal amplitude or unequal pulse rate. They concluded that the perceptual discontinuity caused by dissimilar markers complicated the gap detection task, and suggested that under these conditions gap detection thresholds may be a function both of limitations caused by peripheral mechanisms and a central perceptual distance detector. Their results also emphasize the importance of loudness balancing the stimuli marking the gap.

Shannon (1989) measured gap detection thresholds in cochlear implant users as a function of stimulus level, for both closely spaced (bipolar) and widely spaced (monopolar) electrode configurations, using sinusoids and pulsatile stimuli. He found that gap detection thresholds were a strong function of stimulus level, with the shortest gap thresholds in the order of 1.5–3.1 ms regardless of the separation between the active and reference electrodes. He concluded that the temporal resolution for implant subjects was as good as or better than for normal-hearing listeners. However, all measures were made with the stimuli marking the gap on a single electrode pair, i.e., no cross-channel gap detection was done.

The present study measures gap detection thresholds as an indicator of the characteristics of the available neural channels, i.e., the number of channels available, the position of these channels (which electrodes provide independent channels) and the width of the channels. We hypothesize a simple conceptual model which relates gap detection thresholds to neural excitation. When the two stimuli that bound the gap are presented on different electrode pairs, it is expected that gap thresholds will be short if the two electrode pairs stimulate the same neural population. Gap detection in this case is presumably determined by a ''within-channel'' temporal mechanism and so is determined by the time constant of the peripheral auditory system. As the electrode pairs are separated and the amount of neural overlap decreases, temporal information is carried in separate neural pathways, the stimuli sound more dissimilar and the gap thresholds are expected to increase. Gap detection in this case is presumably limited by the time constant of the centrally located auditory integration because the comparison is made ''across-channels.'' As the two electrodes defining each of the electrode pairs are separated, moving from BP stimulation mode (bipolar between adjacent electrodes) toward BP $+3$ stimulation mode (bipolar between nonadjacent electrodes with three electrodes separating the stimulation pair), the amount of neural overlap between the two electrode pairs is also expected to increase, resulting in increased gap thresholds. Using the same argument, the gap thresholds should presumably also be higher for lower levels of stimulation, as there would be less spread of excitation. According to this model, gap detection thresholds can be used to infer the amount of overlap in neural populations stimulated by two pairs of electrodes.

I. METHODS

A. Subjects

Three users of the Nucleus cochlear implant participated in this study. All were users of the Nucleus Spectra speech processor, which implements the SPEAK speech processing strategy (McDermott, 1989; McDermott *et al.*, 1992). They were highly trained in various psychoacoustic experiments, having participated in many similar experiments over a period of months. Table I contains detailed demographic information on the three subjects.

B. Electrode parameters

All three subjects used the Nucleus 22 electrode array (Clark *et al.*, 1990), implanted into the scala tympani. The electrodes are numbered from 1 at the basal end to 22 at the apical end. Adjacent electrodes were separated by 0.75 mm.

Electrode pairs are referenced by their basal-most member (the *active* electrode); the *reference* electrode is the apical-most member of an electrode pair.

The Nucleus speech processor allows different stimulation modes. Stimuli were presented either in bipolar mode between adjacent electrodes (BP); bipolar between nonadjacent electrodes for electrode separations up to 3 mm (BP+1: 1.5-mm separation; BP+2: 2.25-mm separation; BP+3: 3-mm separation); or in pseudo-monopolar mode, using the apical-most electrode as reference electrode. Pseudo-monopolar mode is not a true monopolar mode, as the reference electrode is not located remotely, but inside the scala. In this mode, which we will call AR (apical reference) mode for simplicity, the actual mode of stimulation varies with the active electrode position, so that, for example, when electrode 20 is used as active electrode, the mode is BP+1. The spread of the current field should be larger for larger spacing between the active and reference electrodes of the pair.

C. Stimulus parameters

All stimuli were charge-balanced, 200-μs/phase biphasic pulses, with anodic phase first, and were presented at a stimulation rate of 1000 pulses per second. Stimuli were presented at a comfortable level of stimulation. The stimuli were loudness balanced across electrodes before the start of the experiment, using a bracketing loudness balance procedure. First, thresholds and upper loudness levels were obtained in each stimulation mode. Then the subjects were asked to choose a comfortable level of stimulation on electrode 10. All subjects chose comfort levels somewhere between 50% and 85% of their dynamic ranges in the various stimulation modes. All other electrodes were then loudness balanced to this electrode by instructing the subject to adjust the loudness of an adjustable stimulus to be just louder than, then just softer than and finally equal to the reference stimulus. Loudness was adjusted by adjusting pulse amplitude. This was repeated as many times as was necessary to obtain consistent decisions about the relative loudnesses. Loudness balancing was repeated for all conditions (each level of stimulation in each stimulation mode).

Gaps were presented between two 200-ms stimuli. These two stimuli were presented on the same electrodes in the baseline condition and on different electrodes otherwise. Gap thresholds were measured as a function of the separation of the two electrodes. In a single run, the first electrode position was held constant, and gap thresholds were measured for different positions of the second electrode. The experiment was performed in BP, BP+1, BP+2, BP+3, and a pseudo-monopolar mode as described above.

A computer program generated the appropriate stimuli and recorded the subject responses. The stimuli were encoded in the correct format to enable presentation directly to the internal receiver of the Nucleus device (without using the subjects' processors), via a custom interface (Shannon *et al.*, 1990).

D. Psychophysical procedure

Gap thresholds were collected using an adaptive, two-interval, forced-choice procedure. The gap was initially 100 ms and two consecutive correct decisions led to a decrease in gap size, and one error increased gap size. This procedure estimates the gap size required for 70.7% correct responses (Levitt, 1971). Initially the increase or decrease was by a factor of 2, but after four reversals this factor was 1.3. Data collection was for 12 reversals and the mean of the last 8 reversals was used to estimate the gap threshold.

Gap detection thresholds were obtained in BP+1 mode for all three subjects using all the even-numbered electrodes as standard (the first stimulus). For each standard, the gap thresholds were measured as a function of probe electrode separation from the standard. Three repetitions were made for each measurement, which resulted in six measurements of gap threshold for each combination of stimulation electrodes when using both orderings of electrodes. Also, gap detection thresholds were obtained in BP, BP+2, BP+3, and AR modes for all three subjects using electrodes 6, 10, and 14 as standard. Again, gap thresholds were measured on even-numbered electrodes as a function of probe electrode separation from the standard. In this task two to six measures were taken at each probe electrode location.

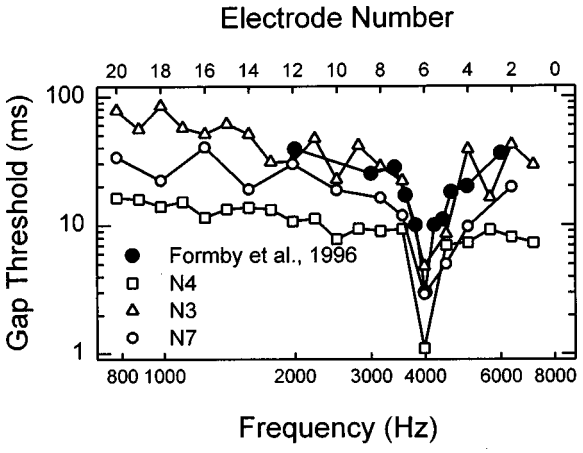

FIG. 1. Comparison of gap detection as a function of electrode separation with comparable results from Formby *et al.* (1996) on gap detection as a function of frequency separation between marker stimuli. The electrode number axis (top) has been reversed and scaled to match the approximate location and extent of the electrode according to Greenwood's (1990) formula.

II. RESULTS

A. Gap threshold as a function of electrode separation

Figure 1 compares gap threshold data from Formby *et al.* (1996) (in normal-hearing listeners) to gap threshold data from cochlear implant patients. Formby *et al.* (1996) measured gap thresholds as a function of marker frequency separation and we measured gap thresholds as function of electrode separation in cochlear implant patients. The electrode axis in Fig. 1 is scaled to match the approximate location of the linearly spaced electrodes to the cochlear frequency-position function of Greenwood (1990). There is good agreement between the two sets of data in the shape of the gap threshold curves and in the absolute values of gap thresholds for implant subjects N3 and N7. Gap thresholds

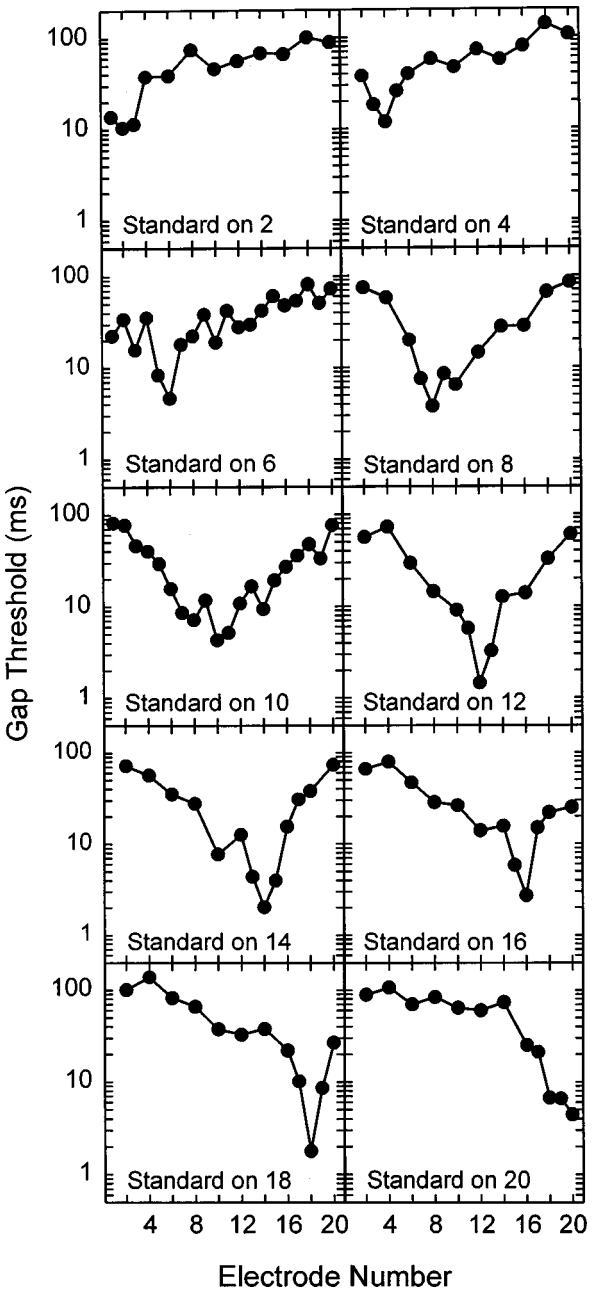

FIG. 2. Gap detection for N3 as a function of separation between electrodes. One of the marker bursts was presented to the standard electrode pair and the other to another electrode pair. Gap detection ''tuning curves'' are shown for all even numbered electrodes as standard. Gap detection thresholds were measured on all even-numbered electrodes.

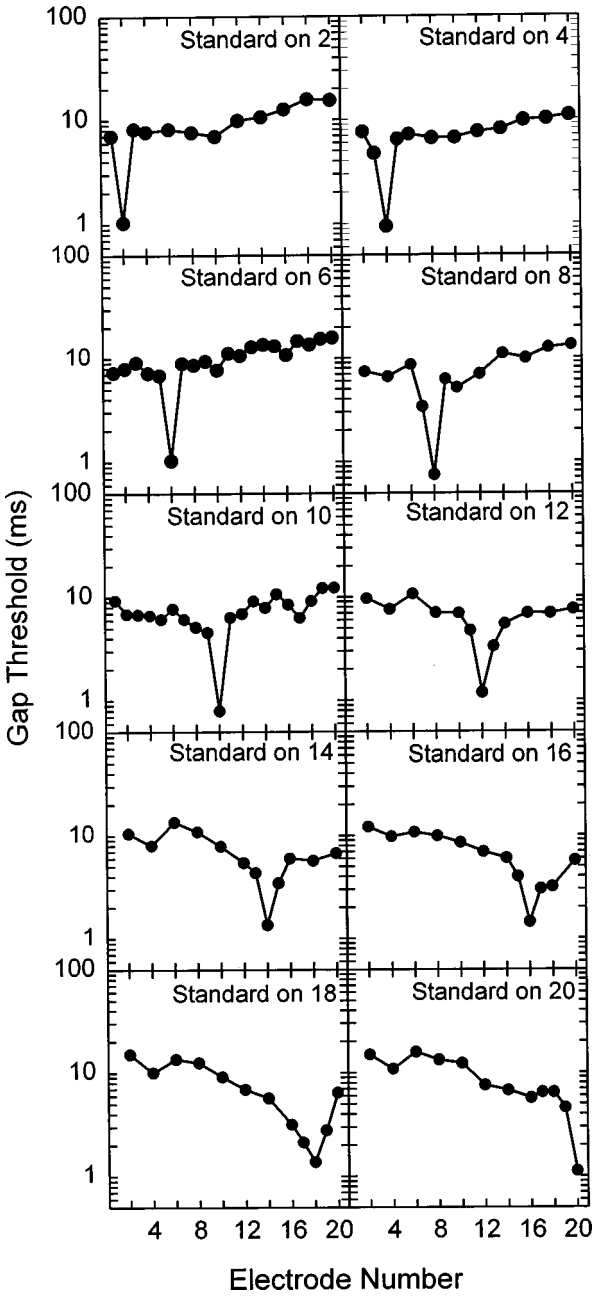

FIG. 3. Same as Fig. 2, but for subject N4.

for implant listener N4 were consistently lower than those from Formby *et al.* at every comparison point.

Gap thresholds were measured as a function of electrode separation for ten standard electrodes (all the even-numbered electrodes) for each of the three subjects (Figs. 2–4). The lowest gap thresholds were always achieved when the two stimuli that bound the gap were presented on the same electrode. The minimum values of gap threshold were near 1 ms for most electrodes for N4 and 3–4 ms for the other two subjects. This is consistent with the range of gap thresholds reported by Shannon (1989).

Gap thresholds increased considerably as electrode separation increased. In general, gap thresholds increased by almost a factor of 10 as the two electrodes were separated. The absolute values and ranges of gap thresholds varied considerably among the subjects, particularly when electrodes were widely separated. Subject N4 had gap thresholds of between 10 and 20 ms for widely separated electrodes, while subject N7 had maximum gap thresholds of 20–70 ms, and N3 had maximum gap thresholds of 100–200 ms.

For most electrodes toward the basal end of the array, the spatial selectivity of the gap threshold curves was sharpest for N4, while N7 had broader selectivity, and N3 had broad ''spatial tuning'' that covered most of the length of the electrode array. For simplicity, we will refer to the gap threshold curves as ''tuning curves.'' Many of the gap detection tuning curves have two portions: a sharply tuned ''tip'' region in the vicinity of the standard electrode, and a shallow, bowl-shaped portion for electrodes distant from the

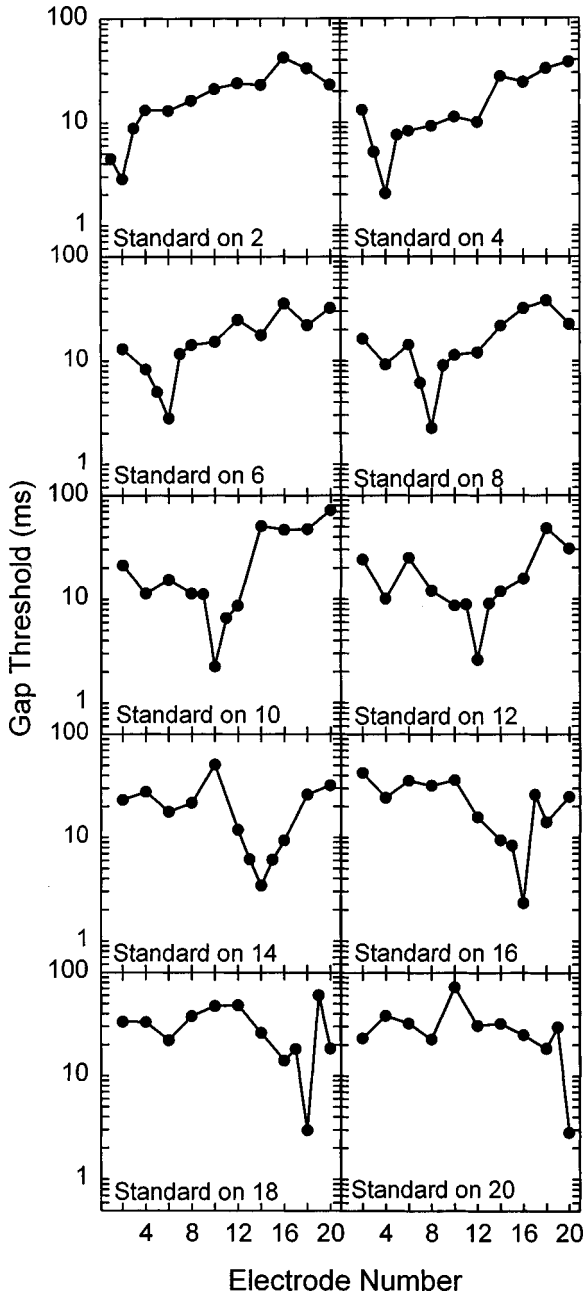

FIG. 4. Same as Fig. 2, but for subject N7.

standard. These two sections may reflect two different mechanisms relating electrode similarity to gap detection.

Figures 2–4 show a general tendency for the slopes of the bowl-shaped portion to become steeper on the apical side of the gap threshold tuning curves (i.e., towards electrode 20) and shallower on the basal side as the standard moved from base to apex. For electrodes near the base, asymmetry was towards the apex (slopes were shallower on the apical side). This is consistent with measurements of electrode interaction in the same three subjects, using forward masking (Chatterjee and Shannon, 1998). The shallower slopes toward the base (for apical electrodes) suggest larger current flow toward the basal region, but the shallower slopes toward the apex (for basal electrodes) suggest larger current flow toward the apex. Previous measures of electrode interaction using forward masking (Lim *et al.*, 1989) suggested larger

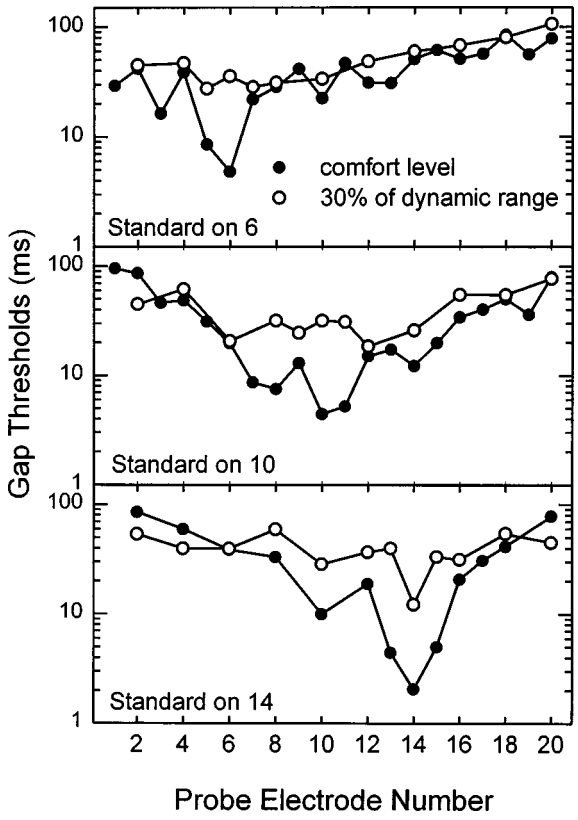

FIG. 5. Gap detection tuning curves for N3 for two stimulation levels. The comfortable stimulation level was at 81% of the dynamic range. Each panel represents a different standard electrode location.

current flow toward the basal region for stimulated electrodes at all cochlear locations, but the data presented here do not confirm this observation.

B. Gap threshold as a function of level of stimulation

Figures 5–7 show the gap thresholds for two levels of stimulation for each of the three subjects, for three standard electrodes. Stimulation was either at a relatively loud level (comfort level was at 81% of the dynamic range for N3, 84% for N4, and 69% for N7) or a softer level (around 30% of the dynamic range for all subjects). BP+1 stimulation mode was used throughout. The most striking difference between the gap threshold tuning curves at high and low levels is the absence of the sharp tip region in most cases at low levels. In the region of the tuning curve tips gap thresholds increased at the softer levels in every case. In addition to the loss of the sharp tips, for N4 there was also a 5–10 ms increase in gap thresholds across the whole pattern at the lower level. Subjects N3 and N7 did not show a clear shift in gap thresholds with level away from the tip region.

C. Gap threshold as a function of mode of stimulation

Figures 8 to 10 show the gap threshold tuning curves for different stimulation modes for standard electrodes 6, 10, and 14 for each subject. Stimulation was at comfort level. To compare the sharpness of the tips of the gap threshold tuning curves, the curves were interpolated to determine the elec-

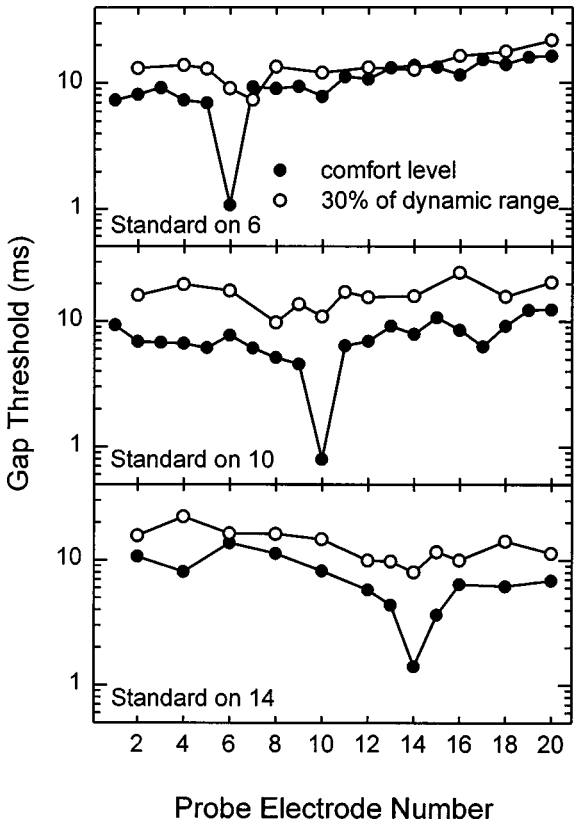

FIG. 6. Gap detection tuning curves for N4 for two stimulation levels at three standard electrode locations. The comfortable stimulation level was at 84% of the dynamic range.

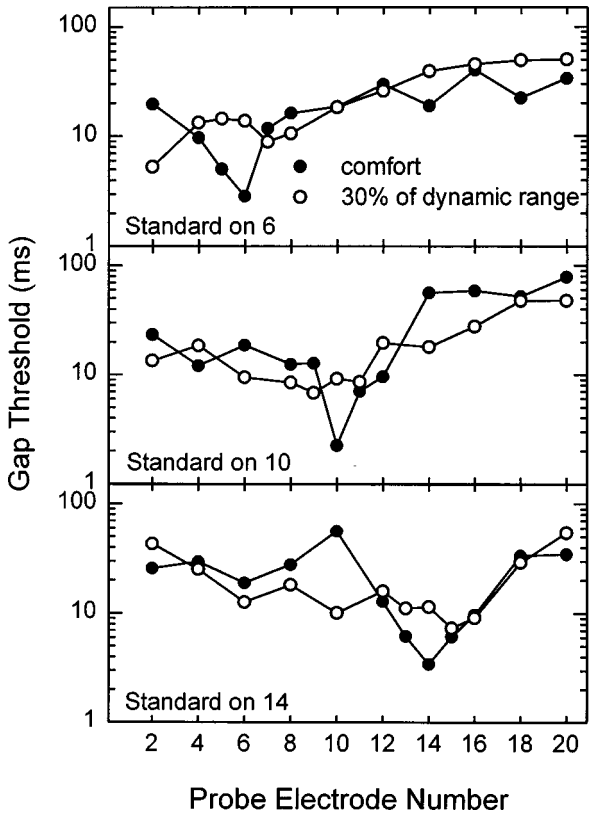

FIG. 7. Gap detection tuning curves for N7 for two stimulation levels at three standard electrode locations. The comfortable stimulation level was at 69% of the dynamic range.

trode separation that would result in a gap threshold that was twice the value at the tip. This electrode separation was then converted to a width in mm (using the electrode separation of 0.75 mm). Figure 11 presents the tuning widths at the tip from Figs. 8–10 as a function of stimulation mode with standard electrode location as the parameter.

N3 (Figs. 8 and 11) exhibited the sharpest tuning in BP+1 mode and poorer tuning in all other modes, with the exception of sharp tuning in AR mode when the standard was on electrode 6. Surprisingly, his poorest tuning occurred in BP mode, which should produce the most localized current field. Tuning curves were so flat in BP+2 mode and in AR mode when the standard was on electrode 6 that tuning curve widths could not be calculated. Gap thresholds were greater than 10 ms even at the tip of the tuning curve. There was a 10-ms difference between the AR and the BP gap threshold curves near the tip and a difference as large as 50 ms across stimulation modes away from the standard electrode.

N4 (Figs. 9 and 11) demonstrated almost the same sharp tuning in most stimulation modes, with decidedly broader tuning in AR mode. The difference between the stimulation modes was most pronounced for electrode 6, with BP having a significantly steeper slope than AR. At the tip of the tuning curve, BP+1 produced the lowest gap threshold among the stimulation modes.

For N7 (Fig. 10), tuning did not change dramatically across all conditions. Overall, BP exhibited the widest tuning—even wider than AR mode. Lowest gap threshold also did not change for N7 across all stimulation modes and standard electrode locations.

Overall, these three implant listeners showed quite different patterns of tuning as a function of stimulation mode. Based simply on electrical field spread we would have expected that tuning curve widths would have broadened as the separation between active and reference electrodes in each pair increased. We expected that AR mode would produce the poorest tuning. No subject showed this expected pattern, although N4 at least showed the poorest tuning in AR mode. N3 showed the lowest gap thresholds and the sharpest tuning in BP+1 mode, which was the stimulation mode used in his normal speech processor. There was no clear change in the pattern of tuning for different standard electrode locations—similar tuning was generally observed for a given listener whether the standard electrode was 6, 10, or 14.

III. DISCUSSION

A. Relation between spatial selectivity and gap detection thresholds

The hypothesized relationship between gap detection thresholds and neural activation is reflected in the graphs of gap detection as a function of electrode separation (Figs. 2–4). Short gap detection thresholds were found where neural interaction was assumed to be large (zero or small electrode separation) and larger gap detection thresholds were found as the separation between the two electrode pairs in-

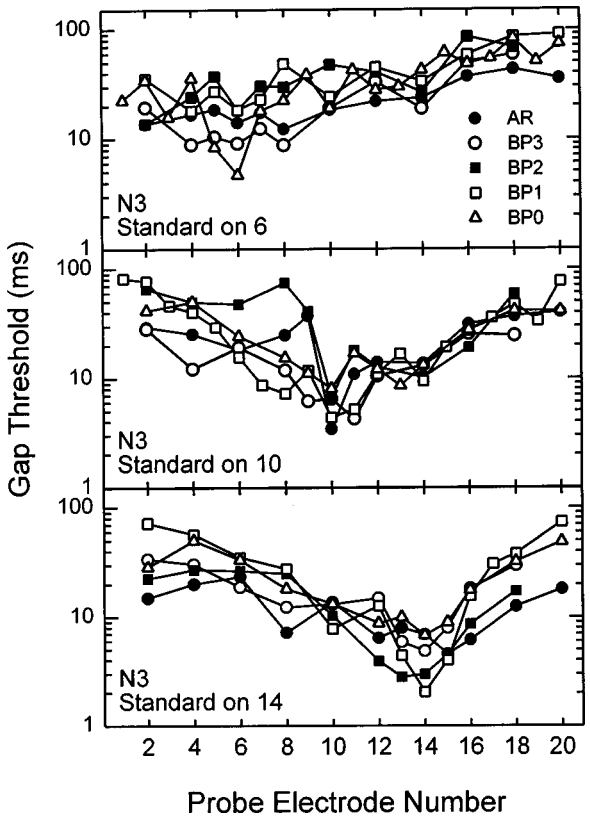

FIG. 8. The five curves in each panel are gap detection tuning curves for N3 for five different spacings between the two electrodes of a bipolar pair (i.e., five stimulation modes). The three panels represent measurements at three standard electrode locations.

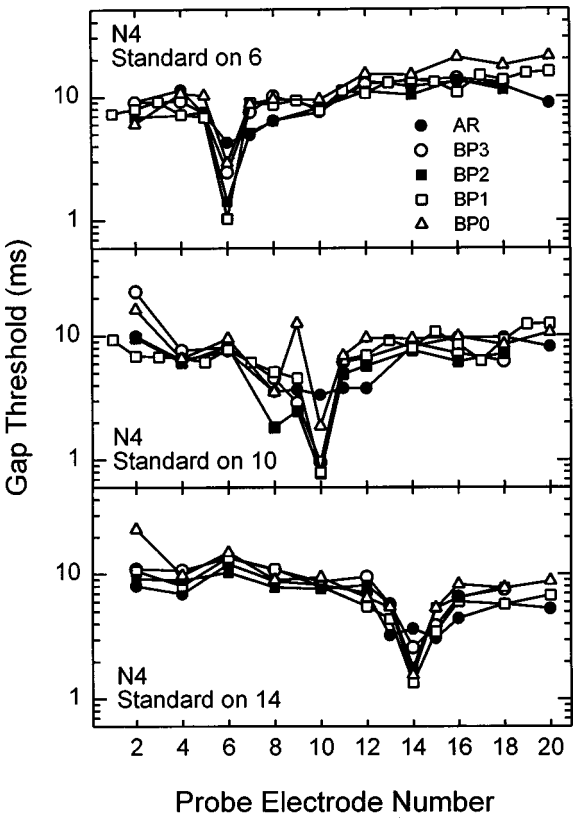

FIG. 9. Same as Fig. 8, but for subject N4. Gap detection tuning curves for five stimulation modes at three standard electrode locations.

creased. We conclude that a narrow ''tuning'' in the gap detection thresholds is an indication of good neural selectivity.

The data in Fig. 11 were used to calculate a two-factor ANOVA, to test the statistical relationship between tuning width and two factors: stimulation mode and subject. The ANOVA indicated a statistically significant difference between the tuning widths obtained for the three subjects [$F(2,30)=4.74$, $p=0.016$]. For these data, the sentence recognition scores (Table I) were higher in subjects with smaller tuning widths, although this cannot be stated as a general rule as the statistical sample was too small.

The shortest gap thresholds observed at the tip of the tuning curves were similar across subjects, 1–4 ms. This is consistent with the results of Shannon (1989) who saw similar gap thresholds across patients at the highest stimulation levels. The two studies thus indicate that there is little relation between the best gap thresholds and speech recognition performance. Both studies found similar gap thresholds across subjects and included subjects with a wide range of speech recognition performance.

However, the longest gap threshold, generally observed for widely separated electrodes, may be related to speech recognition performance. Gap thresholds in this case differed by an order of magnitude between the best and poorest implant user. It is not clear what factor might underlie such a large difference in gap thresholds. The two curve segments (sharp tip and shallow bowl) may indicate the selectivity of two mechanisms of similarity between electrodes (Fig. 12). The sharp tip may reflect a peripheral/neural process that indicates the amount of overlap in the neural populations excited by the two electrodes. The ''shoulder'' of the gap threshold tuning curves may indicate a point of transition to a condition where electrodes do not stimulate overlapping neural populations. When electrodes are moved even further apart, a further increase in gap detection thresholds would not be expected according to our conceptual model. However, the shallow bowl portion of the function may indicate a weak effect of perceptual similarity for two electrodes that do not activate overlapping neural populations. Although the gap detection must be performed centrally in this case, the shallow bowl-shaped function may indicate that there is a also a mild effect of overall perceptual similarity on gap detection. The transition that is heard between electrodes that are highly distinctive complicates the gap detection task. Electrodes that are highly distinctive require longer gaps for detection than two electrodes that are less distinctive, even if no neural populations are in common in either case.

Our original hypothesis was that the longer gap detection time was indicative of the time constant of a central mechanism comparing outputs from different peripheral neural channels. If this is the case, then the long gap thresholds exhibited by N3 may be long enough to interfere with recognition of speech transitions across channels. Long gap thresholds can presumably lead to the misinterpretation or missing of important temporal cues for the identification of consonants (e.g., voice onset time; Divenyi and Sachs, 1978), resulting in poorer speech recognition performance.

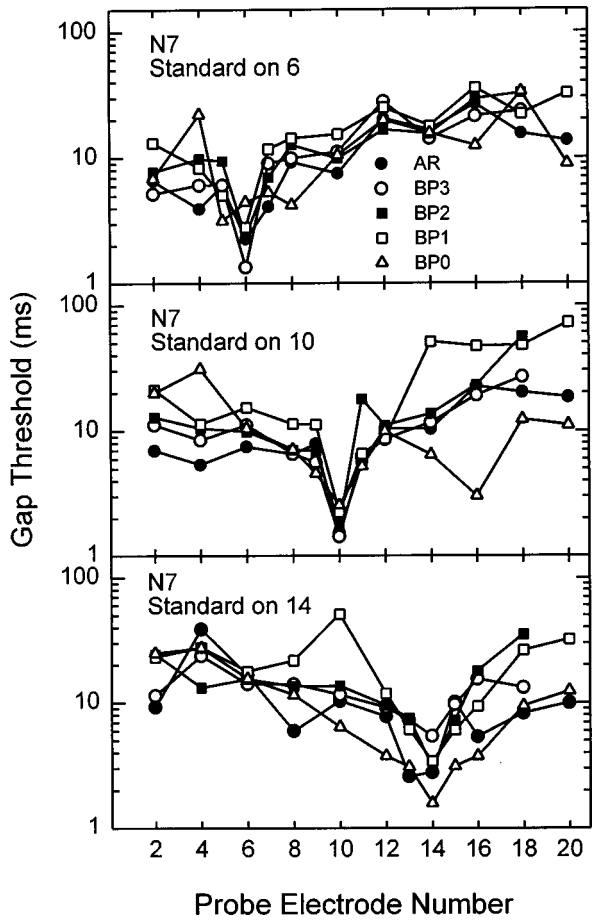

FIG. 10. Same as Fig. 8, but for subject N7. Gap detection tuning curves for five stimulation modes at three standard electrode locations.

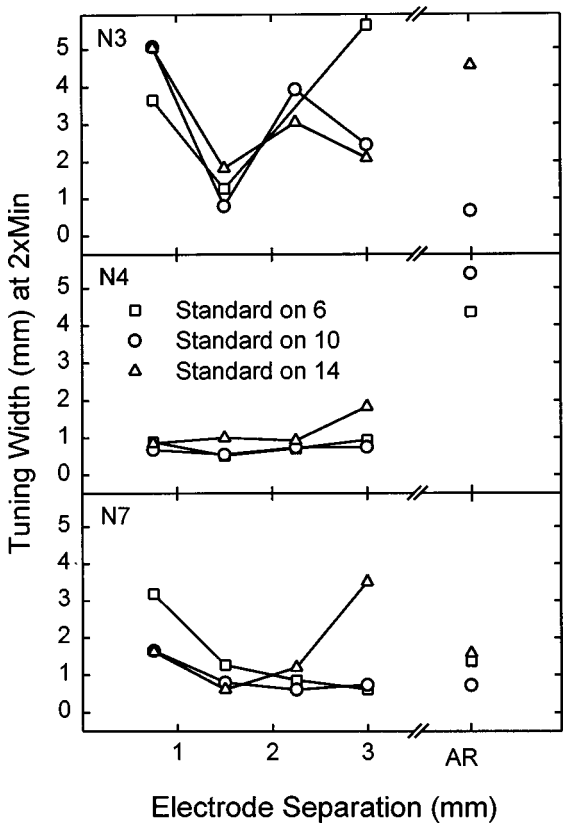

FIG. 11. Width of the gap detection tuning curves at twice the gap threshold value at the tip as a function of the separation of active and reference electrodes. The three curves in each panel represent the tuning width measures for three standard electrode locations.

In the case of N4, poorest gap detection was still 10–20 ms, which may be rapid enough to allow processing of all relevant cross-channel speech transitions. It may be that within-channel gap detection is not a limiting factor for speech recognition, but that long, central cross-channel comparison times can interfere with speech temporal distinctions. It is not clear what might cause the large difference observed in these gap thresholds between different subjects. It appears that there is a larger range of individual differences in the implant results than in similar conditions with acoustic hearing in normal listeners (Formby *et al.*, 1991).

B. Relation between stimulation level and spatial selectivity

Gap thresholds are a strong function of stimulus level in cochlear implant users (Shannon, 1989). All of Shannon's measurements were made with identical markers before and after the gap, a condition similar to the tips of the tuning curves in the present data. The data in Figs. 5–7 also show longer gap thresholds at softer stimulus levels around the tip region. However, gap thresholds did not change as much with level away from the tip region, resulting in the loss of the sharp tips of the tuning curves at lower levels. We would expect less interaction at lower stimulus levels, because the region of neurons activated should be smaller. Our conceptual model would predict narrower tips at low stimulus levels rather than no tips. However, interpretation of the present data is confounded by the strong change in gap thresholds with level. In conditions where the markers before and after the gap were on different electrodes (away from the tip region), little change in gap thresholds with level was observed in two of the three subjects. According to our conceptual

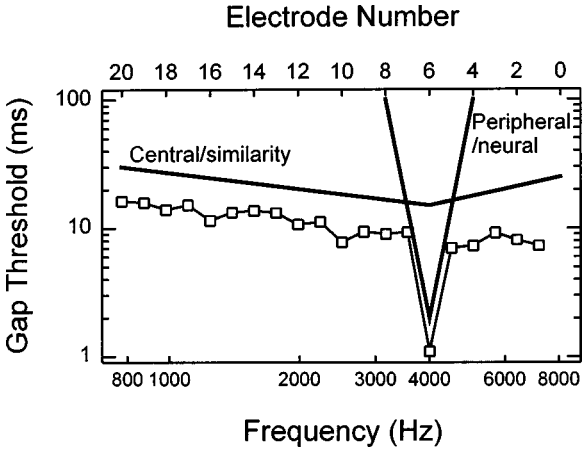

FIG. 12. Schematic representation of a conceptual model of gap detection. When the two markers defining the gap excite overlapping neural populations gap thresholds are lowest, but this mechanism is not useful if the neural populations do not overlap. When the neural populations of the two markers do not overlap the gap threshold is determined by a slower, central mechanism. This hypothesized mechanism is only broadly tuned in that markers that are more similar produce slightly lower gap thresholds than markers that are highly dissimilar.

model this suggests that central mechanisms of gap detection are less dependent on stimulus level than peripheral mechanisms of gap detection. Clearly, more data are needed to validate this suggestion.

C. Relation between stimulation mode and spatial selectivity

As the active and reference electrodes in a bipolar pair are separated the electric field becomes more diffuse and spatial selectivity decreases. In general, we did not find broader tuning in the gap detection threshold curves as the active and reference were separated. What was not expected was the inconsistency across subjects—gap thresholds varied much more across subjects than across stimulation modes. The ANOVA on the data in Fig. 11 indicated a statistically significant difference between the tuning widths obtained for the three subjects, but no statistical difference between tuning widths for different stimulation modes.

Three possible explanations are proposed. The first is that current spread is already so large that the effect of using stimulation modes with widely separated electrodes has little additional effect (see Lim *et al.*, 1985). A second explanation is that stimulation modes with larger electrode separation do not increase current spread as much as expected. The electrical field model of Finley *et al.* (1990) predicted a broadly spreading field around banded electrodes, such as those used in the Nucleus implant. Other electrode designs with more localized current distributions might produce more significant and consistent variations in gap detection thresholds in different stimulation modes. A third explanation is that the effects of changing stimulation mode were confounded by the fact that stimulation current level also changed with stimulation mode. Lower currents were used in the stimulation modes with larger spacing between the active and reference electrodes, because these modes produce lower thresholds and uncomfortable loudness levels. The original goal was to change the extent of the neural population activated by using more widely spaced electrodes in a stimulation pair. However, widely spaced electrodes in a stimulation pair result in lower stimulation currents, presumably exhibiting less current spread, and so may partially offset the increased neural extent due to the electrode separation. The net observed result was that sharpness of the gap threshold tuning curves remained effectively unchanged. So it is possible that the effect of stimulation modes with anticipated larger current spread was offset by using lower currents in these stimulation modes.

An additional unanticipated result is that in AR stimulation mode gap thresholds were not the very low values that should correspond to wide spread of stimulation. For wide spread of stimulation, all neural channels receive similar input and there are more channels to aid in gap detection, so a flat tuning curve with very low values of gap thresholds was expected for all separations of electrode pairs. In fact, although AR mode had a slightly flattened curve, the curve was not entirely flat and in most instances the lowest gap threshold values were higher than the tip region of the other stimulation modes. Because we did not use true monopolar stimulation, the current paths were directed toward the apical region (where the reference electrode was situated). When detecting the gap between, for example, stimuli on electrode pair (10,22) and electrode pair (19,22), gap detection is performed for an electrode pair with wide current spread activating a large neural population and an electrode pair activating a subset of the same neural population. This complete neural overlap would have been expected to produce low values of gap thresholds. This observation again suggests that the amount of neural overlap is not the only factor in determining the gap detection thresholds. Perceptual dissimilarity between the two stimuli may have confounded the peripheral gap detection mechanism. Our simple conceptual model about this peripheral mechanism cannot explain all the data presented here, and some of the trends might be ascribed to central mechanisms. This is the interpretation in Chatterjee *et al.* (1998), who found short gap thresholds only when the two stimuli bounding the gap were identical; gap thresholds were long if the two stimuli were perceptually different in any way (pitch or loudness). This result suggests that even if the two stimuli marking the gap activate mostly overlapping neuron populations, the differences in neuron activation may produce a sufficiently different percept that the gap detection decision is primarily central. However, the relative importance of central and peripheral processing mechanisms is unknown.

D. Channel characteristics

We have used gap detection threshold as a tool to provide more insight into the channel characteristics, i.e., the number of channels, the location of channels, the width of channels, and the factors that determine channel characteristics. The present results show that the gap detection tuning curves are wider for some choices of electrodes and stimulation modes, and also vary widely across subjects. However, it is not clear at this time how to interpret the gap detection tuning curves in terms of information channels. We propose the following two assumptions to aid in defining channel width:

(1) Each subject has a minimum gap threshold when the two stimuli are presented to the same electrode and a large gap threshold when the two electrodes are widely separated. We have initially assumed that the value of the gap threshold corresponds to the relative amount of neural interaction. Thus for each electrode for each subject, there exists a value of gap threshold relative to the minimum such that larger values of gap threshold correspond to negligible channel interaction.

(2) We then need to make an assumption as to how much neural interaction is negligible, i.e., how much interaction can be tolerated between two neural channels for them to still be distinct channels. This value is unknown, but it might correspond to the ''shoulder'' of the gap threshold ''tuning curves.'' We speculate that this shoulder indicates the point of transition from a peripherally limited task to a centrally limited task (Fig. 12). As a first approximation a fixed gap threshold value at 40% between the lowest and highest gap threshold can be used, which is in the general vicinity of the shoulder of the gap threshold tuning curves. Another candidate measure for deciding whether two elec-

trode pairs correspond to two different channels is electrode discriminability. As the electrode pairs are separated and the amount of neural overlap decreases, the stimuli become easier to discriminate. The electrode separation at a chosen level of electrode discrimination (say 75% correct) may be used to find the corresponding gap threshold (from the gap threshold tuning curves). This defines a minimum gap threshold value for electrodes to be discriminable. Gap thresholds larger than this value correspond to two electrodes constituting two different channels.

Electrode discriminability was measured in these same subjects (Hanekom and Shannon, 1996), but the 40% measure does not match very well with the electrode discriminability measure. The electrode discrimination measure may be too strict. Two electrodes might be discriminable if there is any difference in the neural populations that they stimulate, but that might not be enough difference to allow them to be independent information channels. Better choices than the 40% measure may be available, but this gives an example of how channels may be defined and this measure was used in the discussion that follows.

Using these assumptions, we can deduce the following from the results:

1. Number of channels

The number of distinct channels may be small. Estimating the number of channels from the above assumptions, we find that N3 (a relatively poor user) may have only a few information channels available, and the upper limit in the number of available channels may be around six or seven (for N4, the best user in the group). Clearly, the number of channels will generally be less than the number of electrodes. One key question raised by this observation is whether improvements in speech recognition can be achieved by selecting electrodes appropriately (Zwolan *et al.*, 1997; Henry *et al.*, 1997; Hanekom and Shannon, 1996). Specifically, can better speech recognition be achieved with a smaller number of independent electrodes or a larger number of interacting electrodes?

When speech processors are programmed with a subset of the total number of available electrodes, many combinations of electrodes are available from which to select. Because of the pattern of interactions in an individual subject, processors with the same number of electrodes can be selected that will have quite different numbers of independent channels (Hanekom and Shannon, 1996). Hanekom and Shannon (1997), using 14 different seven-electrode processors, made a very simple estimation of the number of channels using gap detection thresholds and the assumptions above and found significant correlation between vowel recognition and the estimated number of channels. Presumably, this relation was due to a clearer formant structure when a larger number of distinct channels were available.

2. Width and location of channels

The shapes of the gap threshold curves suggest that the tuning may be broad or that channels are relatively wide and typically span many electrodes. Channels become only slightly wider when using stimulation modes with widely spaced active and reference electrodes. Channels are in general wider for the poorest user (N3) and narrower for the best user (N4) in the group. Using the assumptions above, channel width may be between 2 electrodes for N4 (1.5 mm) and 14 electrodes for N3 (10.5 mm). The location of the best (most selective) channels may be deduced directly from the gap detection curves.

3. Factors determining the characteristics of channels

At least four physical factors determine channel characteristics: (1) electrode placement relative to the remaining nerve fibers; (2) electrode design, which determines the electrical field distribution (Finley *et al.*, 1990), e.g., the Nucleus has a banded electrode design while the Clarion device (Schindler and Kessler, 1993) has a radial electrode placement; (3) nerve survival (Zimmerman *et al.*, 1995); and (4) the current pathway that the stimulation current follows between the active and reference electrodes. In existing implants we can only control the current pathway and current spread to some degree by choice of the stimulation electrode pair. Results reported here for the Nucleus device indicate very little difference between the gap threshold tuning curves for different stimulation electrode pair separations and larger variations across subjects. Electrode placement and nerve survival are fixed for an individual implant patient and so cannot be modified after surgery to achieve a larger number of channels.

Although much research has focused on the physical factors influencing cochlear implant user performance, the important question is how these effect the information actually received. We propose that we need to concentrate more research on how the channel capacity depends on or is related to the physical aspects of cochlear stimulation (electrode design, electrode placement, electrical fields patterns, and nerve survival patterns).

E. Implications for cochlear implants

1. Comparison of electrode designs

Different electrode designs exhibit different current spread characteristics (Finley *et al.*, 1990). The results suggest that electrode designs cannot be compared by simply calculating which design produces the most localized current field. All the subjects in our study had the same electrode design, but large differences in selectivity were observed. Selectivity is not a linear function of either current spread or the spacing between the stimulation electrode pair.

2. Reduced electrode processors

In any nonsimultaneous delivery of biphasic pulses to a number of electrodes there is an inherent trade-off between the number of electrodes and the overall pulse rate. As the number of electrodes decreases a higher pulse rate can be maintained on each electrode. However, the trade-off between pulse rate and number of electrodes is not well understood in terms of their importance to speech recognition. Several recent studies (Fishman *et al.*, 1997; Lawson *et al.*, 1993, 1996) suggest that implant patients are not making full

use of all electrodes. It is possible that better speech performance could be achieved with a smaller number of electrodes, selected to be maximally independent channels, that are stimulated at a higher pulse rate. Techniques such as gap detection, forward masking (Shannon, 1983; Lim *et al.*, 1989; Chatterjee and Shannon, 1998), electrode discrimination (Hanekom and Shannon, 1996; Kileny *et al.*, 1997; Zwolan *et al.*, 1997; Henry *et al.*, 1997), or loudness summation (Fu *et al.*, 1996) could be used to help select electrodes for inclusion or exclusion in a processor that uses only a subset of all available electrodes.

3. Choice of electrodes for a reduced electrode processor

Gap detection thresholds may also be used to compare different choices of speech processors regarding the number of channels, using the assumptions mentioned earlier. Although the actual number of channels is unknown, this method could be used to find the speech processor that maximizes the number of calculated channels. As discussed earlier, Hanekom and Shannon (1997) found that seven electrodes in a processor can lead to a quite different number of distinct channels depending on which electrodes are chosen. Thus a simple relationship between number of electrodes and quality of speech recognition cannot be assumed.

4. Choice of electrode pair separation (stimulation mode)

It has been widely assumed that closely spaced bipolar electrodes are necessary for achieving good spatial selectivity in a cochlear implant. However, the present gap detection tuning curves show only minor differences in spatial selectivity as a function of the separation of the bipolar pair. Indeed, in a recent study electrode discrimination and speech recognition were each similar for monopolar and bipolar stimulation (Zwolan *et al.*, 1997). To the extent that stimulation mode does effect channel interaction, the optimal configuration may change from one end of the electrode array to the other. This may result in the use of multi-mode speech processors, with each information channel optimized by choosing the electrodes and stimulation modes that result in the best selectivity. Present clinical speech processor fitting software for the Nucleus device allows mixed-mode processor designs, but this feature is not generally used.

IV. CONCLUSIONS

(1) Gap detection thresholds are a function of the physical separation of the electrode pairs used for the two stimuli that bound the gap. Gap thresholds increase from a minimum when the two stimuli are presented on the same electrode pair to a maximum when the two stimuli are presented on widely separated electrode pairs. This change may be due to a changeover from a peripheral, within-channel gap detection process for closely spaced electrode pairs to a central cross-channel process for widely spaced electrode pairs.

(2) When the two marker bursts are presented to the same electrode, gap detection thresholds are similar across subjects at 1–4 ms. Gap thresholds for widely separated electrodes vary considerably among subjects and may be related to speech recognition performance, with better implant users having lower gap thresholds in this condition.

(3) The area of neural activation by each electrode (as inferred from the width of the tip region of the gap detection tuning curves as a function of electrode pair separation) varies across subjects and across electrodes. For the three subjects in the present study, the better implant users exhibit sharper tuning, i.e., a smaller area of neural activation around each stimulation pair.

(4) Using stimulation modes with larger separation between active and reference electrodes has limited effect on spatial selectivity. AR stimulation mode, although presumably having larger current spread, has better neural selectivity than BP mode for some subjects. This implies that there is no fixed optimal stimulation mode, but that the optimal stimulation mode may vary across subjects and from one end of the electrode array to the other.

ACKNOWLEDGMENTS

This research was supported in part by the NIDCD. The research was made possible by travel grants toward the first author by the University of Pretoria, South Africa and by the House Ear Institute, Los Angeles. We wish to thank the subjects for patiently and faithfully participating in the psychoacoustic experiments.

Busby, P. A., Whitford, L. A., Blamey, P. J., Richardson, L. M., and Clark, G. M. (**1994**). ''Pitch perception for different modes of stimulation using the cochlear multiple-electrode prosthesis,'' J. Acoust. Soc. Am. **95**, 2658–2669.

Chatterjee, M., and Shannon, R. V. (**1998**). ''Forward masked excitation patterns in multielectrode cochlear implants,'' J. Acoust. Soc. Am. **103**, 2565–2572.

Chatterjee, M., Fu, Q.-J., and Shannon, R. V. (**1998**). ''Within-channel gap detection using dissimilar markers in cochlear implant listeners,'' J. Acoust. Soc. Am. **103**, 2515–2519.

Clark, G. M., Tong, Y. C., and Patrick, J. F. (**1990**). *Cochlear Prostheses* (Churchill Livingstone, Edinburgh), pp. 99–124.

Divenyi, P. L., and Danner, W. F. (**1977**). ''Discrimination of time intervals marked by brief acoustic pulses of various intensities and spectra,'' Percept. Psychophys. **21**, 125–142.

Divenyi, P. L., and Sachs, R. M. (**1978**). ''Discrimination of time intervals bounded by tone bursts,'' Percept. Psychophys. **24**, 429–436.

Fayad, J., Linthicum, F. H., Jr., Otto, S. R., Galey, F. R., and House, W. F. (**1991**). ''Cochlear implants: Histopathologic findings related to performance in 16 human temporal bones,'' Ann. Otol. Rhinol. Laryngol. **100**, 807–811.

Finley, C. C., Wilson, B. S., and White, M. W. (**1990**). ''Models of neural responsiveness to electrical stimulation,'' in *Cochlear Implants. Models of the Electrically Stimulated Ear*, edited by J. M. Miller and F. A. Spelman (Springer-Verlag, New York), pp. 55–96.

Fishman, K., Shannon, R. V., and Slattery, W. H. (**1997**). ''Speech recognition as a function of the number of electrodes used in the SPEAK cochlear implant speech processor,'' J. Speech Hear. Res. **40**, 1201–1215.

Fitzgibbons, P. (**1983**). ''Temporal gap detection in noise as a function of frequency, bandwidth, and level,'' J. Acoust. Soc. Am. **74**, 67–71.

Florentine, M., and Buus, S. (**1984**). ''Temporal gap detection in sensorineural and simulated hearing impairment,'' J. Speech Hear. Res. **27**, 449–455.

Formby, C., and Forrest, T. G. (**1991**). ''Detection of silent temporal gaps in sinusoidal markers,'' J. Acoust. Soc. Am. **89**, 830–837.

Formby, C., Sherlock, L. P., and Forrest, T. G. (**1996**). ''An asymmetric roex filter model for describing detection of silent temporal gaps in sinusoidal markers,'' Aud. Neurosci. **3**, 1–20.
Formby, C., Morgan, L. N., Forrest, T. G., and Raney, J. J. (**1992**). ''The role of frequency selectivity in measures of auditory and vibrotactile temporal resolution,'' J. Acoust. Soc. Am. **91**, 293–305.
Fu, Q.-J., and Shannon, R. V. (**submitted**). ''Effects of electrode location and spacing on speech recognition with the Nucleus-22 cochlear implant,'' J. Acoust. Soc. Am.
Fu, Q.-J., Shannon, R. V., Zeng, F.-G., and Chatterjee, M. (**1996**). ''Electrode interactions measured by loudness summation in cochlear implant listeners,'' J. Acoust. Soc. Am. **100**, 2631.
Greenwood, D. D. (**1990**). ''A cochlear frequency-position function for several species—29 years later,'' J. Acoust. Soc. Am. **87**, 2592–2605.
Grill, W. M., and Mortimer, J. T. (**1994**). ''Electrical properties of implant encapsulation tissue,'' Ann. Biomed. Eng. **22**, 23–33.
Hall, J. W., Grose, J. H., and Joy, S. (**1996**). ''Gap detection for pairs of noise bands: Effects of stimulus level and frequency separation,'' J. Acoust. Soc. Am. **99**, 1091–1095.
Hanekom, J. J., and Shannon, R. V. (**1996**). ''Place pitch discrimination and speech recognition in cochlear implant users,'' South African Journal of Communication Disorders **43**, 27–40.
Hanekom, J. J., and Shannon, R. V. (**1997**). ''Gap detection thresholds as a measure of spread of excitation in cochlear electrical stimulation,'' in Abstracts of the 1997 annual midwinter meeting, Association for Research in Otolaryngology, #307.
Heinz, M. W., Goldstein, M. H., Jr., and Formby, C. (**1996**). ''Temporal gap detection thresholds in sinusoidal markers simulated with a multi-channel, multi-resolution model of the auditory periphery,'' Aud. Neurosci. **3**, 35–56.
Henry, B. A., McKay, C. M., McDermott, H. J., and Clark G. M. (**1997**). ''The relationship between speech information perceived by cochlear implantees in different spectral regions and electrode discrimination,'' in Program and Abstracts: 1997 Conference on Implantable Auditory Prostheses, Asilomar Conference Center, Pacific Grove, California, 17–21 Aug., p. 74.
Kileny, P., Zimmerman-Phillips, S., Zwolan, T., and Kemink, J. (**1992**). ''Effects of channel number and place of stimulation on performance with the cochlear corporation multichannel implant,'' American Journal of Otology **13**, 117–123.
Lawson, D., Wilson, B., and Finley, C. (**1993**). ''New processing strategies for multichannel cochlear prostheses,'' in *Natural and Artificial Control of Hearing and Balance*, edited by J. A. Allum, D. J. Allum-Mecklenburg, F. P. Harris, and R. Probst, Progress in Brain Research (Elsevier, Amsterdam), Vol. 97, pp. 313–321.
Lawson, D. T., Wilson, B. S., Zerbi, M., and Finley, C. C. (**1996**). ''Speech processors for auditory prostheses,'' Third Quarterly Progress Report, NIH Contract N01-DC-5-2103.
Levitt, H. (**1971**). ''Transformed up–down methods in psychoacoustics,'' J. Acoust. Soc. Am. **49**, 467–477.
Lim, H. H., Tong, Y. C., and Clark, G. M. (**1989**). ''Forward masking patterns produced by intracochlear stimulation of one and two electrode pairs in the human cochlea,'' J. Acoust. Soc. Am. **86**, 971–980.
Linthicum, Jr., F. H., Fayad, J., Otto, S. R., Galey, F. R., and House, W. F. (**1991**). ''Cochlear implant histopathology,'' American Journal of Otology **12**, 245–311.
McDermott, H. J. (**1989**). ''An advanced multiple channel cochlear implant,'' IEEE Trans. Biomed. Eng. **36**, 789–797.
McDermott, H. J., McKay, C. M., Vandali, A. E., and Clark, G. M. (**1992**). ''A comparison of speech perception of cochlear implantees using the Spectral Maxima Sound Processor (SMSP) and the MSP (Multipeak) processor,'' Acta Oto-Laryngol. **112**, 752–761.
Penner, M. J. (**1976**). ''The effect of marker variability on the discrimination of temporal intervals,'' Percept. Psychophys. **19**, 466–469.
Plomp, R. (**1964**). ''Rate of decay of auditory sensation,'' J. Acoust. Soc. Am. **36**, 277–282.
Rebscher, S. J., Heilmann, M., Talbot, N., Bruszewski, W., and Merzenich, M. (**1994**). ''Studies on pediatric auditory prosthesis implants,'' Sixteenth Quarterly Progress Report, NIH Contract N01-DC-2401.
Schindler, R. A., and Kessler, D. K. (**1993**). ''Clarion cochlear implant: phase I investigational results,'' Am. J. Otolaryngol. **14**, 263–272.
Shailer, M., and Moore, B. C. J. (**1983**). ''Gap detection as a function of frequency, bandwidth, and level,'' J. Acoust. Soc. Am. **74**, 467–473.
Shannon, R. V. (**1983**). ''Multichannel electrical stimulation of the auditory nerve in man: II. Channel interaction,'' Hearing Res. **12**, 1–16.
Shannon, R. V. (**1989**). ''Detection of gaps in sinusoids and pulse trains by patients with cochlear implants,'' J. Acoust. Soc. Am. **85**, 2587–2592.
Shannon, R. V., Adams, D. D., Ferrel, R. L., Palumbo, R. L., and Grandgenett, M. (**1990**). ''A computer interface for psychophysical and speech research with the Nucleus cochlear implant,'' J. Acoust. Soc. Am. **87**, 905–907.
Shannon, R. V., Zeng, F.-G., Kamath, V., Wygonski, J., and Ekelid, M. (**1995**). ''Speech recognition with primarily temporal cues,'' Science **270**, 303–304.
Townshend, B., Cotter, N., Van Compernolle, D., and White, R. L. (**1987**). ''Pitch perception by cochlear implant subjects,'' J. Acoust. Soc. Am. **82**, 106–115.
van den Honert, C., and Stypulkowski, P. H. (**1987**). ''Single fiber mapping of spatial excitation patterns in the electrically stimulated auditory nerve,'' Hearing Res. **29**, 195–206.
Wang, G., Vannier, M. W., Skinner, M. W., Kalender, W. A., Polacin, A., and Ketten, D. R. (**1996**). ''Unwrapping cochlear implants by spiral CT,'' IEEE Trans. Biomed. Eng. **43**, 891–900.
Zimmerman, C. E., Burgess, B. J., and Nadol, J. B. (**1995**). ''Patterns of degeneration in the human cochlear nerve,'' Hearing Res. **90**, 192–201.
Zwolan, T. A., Collins, L. M., and Wakefield, G. H. (**1997**). ''Electrode discrimination and speech recognition in postlingually deafened adult cochlear implant subjects,'' J. Acoust. Soc. Am. **102**, 3673–3685.
Zwolan, T. A., Kileny, P. R., Boerst, A. K., Collins, L. A., and Telian, S. A. (**1997**). ''Electrode discrimination using monopolar and bipolar stimulation with the Nucleus multichannel cochlear implant,'' in Abstracts of the 1997 annual midwinter meeting, Association for Research in Otolaryngology, #231.

Temporal processing in the aging auditory system

Anne Strouse,[a] Daniel H. Ashmead, Ralph N. Ohde, and D. Wesley Grantham
Division of Hearing and Speech Sciences, Vanderbilt University School of Medicine, Nashville, Tennessee 37232

(Received 29 December 1997; accepted for publication 10 July 1998)

Measures of monaural temporal processing and binaural sensitivity were obtained from 12 young (mean age=26.1 years) and 12 elderly (mean age=70.9 years) adults with clinically normal hearing (pure-tone thresholds ≤20 dB HL from 250 to 6000 Hz). Monaural temporal processing was measured by gap detection thresholds. Binaural sensitivity was measured by interaural time difference (ITD) thresholds. Gap and ITD thresholds were obtained at three sound levels (4, 8, or 16 dB above individual threshold). Subjects were also tested on two measures of speech perception, a masking level difference (MLD) task, and a syllable identification/discrimination task that included phonemes varying in voice onset time (VOT). Elderly listeners displayed poorer monaural temporal analysis (higher gap detection thresholds) and poorer binaural processing (higher ITD thresholds) at all sound levels. There were significant interactions between age and sound level, indicating that the age difference was larger at lower stimulus levels. Gap detection performance was found to correlate significantly with performance on the ITD task for young, but not elderly adult listeners. Elderly listeners also performed more poorly than younger listeners on both speech measures; however, there was no significant correlation between psychoacoustic and speech measures of temporal processing. Findings suggest that age-related factors other than peripheral hearing loss contribute to temporal processing deficits of elderly listeners. © *1998 Acoustical Society of America.* [S0001-4966(98)05210-2]

PACS numbers: 43.66.Mk, 43.66.Pn, 43.66.Sr, 43.71.Lz [JWH]

INTRODUCTION

One of the factors identified in psychoacoustic experiments as contributing to poor speech perception is the reduced temporal resolving power of the auditory system (Dreschler and Plomp, 1985; Ginzel *et al.*, 1982; Price and Simon, 1984; Schneider, 1997; Tyler *et al.*, 1982). Processing of temporal information may occur via monaural and/or binaural inputs. Monaural processing refers to what happens to the signal arriving at a single ear (although this normally occurs in parallel for the signals at both ears). Binaural processing refers to the analysis of the *differences* between signals arriving at the two ears. They operate at different time scales (a few milliseconds for monaural resolution versus small fractions of a millisecond for binaural resolution), and monaural temporal processing is more involved in following a speech signal whereas binaural processing contributes to separating the signal from competing sounds. Consequently, monaural and binaural aspects of temporal resolution may each contribute uniquely to speech perception.

A. Monaural temporal processing

The most common way of investigating monaural temporal processing is by means of gap detection, defined as the ability to detect a brief period of silence between two test signals. Numerous studies have reported that listeners with hearing loss have larger gap detection thresholds (Buus and Florentine, 1985; Glasberg and Moore, 1989; Irwin and McAuley, 1987; Moore and Glasberg, 1988; Moore *et al.*, 1989; Tyler *et al.*, 1982). Because most elderly listeners have some degree of hearing loss, it is important to determine whether changes in temporal processing occur independent of peripheral hearing loss.

Several studies have attempted to control for the confounding effect of age-related hearing loss on gap detection thresholds (Moore *et al.*, 1992; Schneider *et al.*, 1994; Snell, 1997). Moore *et al.* (1992) measured thresholds for the detection of temporal gaps in sinusoidal signals as a function of frequency in elderly hearing-impaired subjects and elderly subjects with ''near-normal'' hearing (audiometric thresholds ≤25 dB HL from 250 to 2000 Hz). Results were compared to previous data collected from young normally hearing subjects (Moore *et al.*, 1993), revealing that elderly subjects with near-normal hearing had higher gap detection thresholds than young subjects. Moore *et al.* (1992) attributed this result to the inclusion in the elderly group of some individuals who had large gap detection thresholds. Nevertheless, when they compared gap thresholds in elderly subjects with near-normal hearing to those with hearing impairment, they found no difference between the two groups. Schneider *et al.* (1994) reached a similar conclusion. In this study, thresholds for detecting a gap between two Gaussian modulated 2000-Hz tones were measured in young and elderly listeners with pure-tone thresholds ≤25 dB HL from 250 to 3000 Hz. Gap detection thresholds were longer and more variable for elderly listeners than for young listeners. Snell (1997) more rigorously controlled for high-frequency hearing loss in elderly subjects, measuring gap detection thresholds for noise-burst stimuli in young and elderly listeners with pure-tone thresholds ≤20 dB HL from 250 to 4000

[a]Current address: VA Medical Center, Audiology Service (126), Mountain Home, TN 37684. Electronic mail: anne.strouse@med.va.gov

Hz. Again, gap thresholds were significantly larger in elderly subjects. Thus the studies agree in that all found some elderly individuals who exhibited losses in temporal resolution that were unrelated to degree of hearing loss. Therefore it is reasonable to consider factors other than peripheral hearing loss that could account for age-related differences in monaural temporal resolution.

Whether gap detection ability is important for accurate perception of speech remains questionable. It is widely accepted that many speech events that are critical for speech perception are of short duration (Dorman *et al.*, 1979; Pickett and Decker, 1960; Repp *et al.*, 1978). For example, gap detection ability has been linked to a listener's ability to process time events related to distinctions in speech between voiced-voiceless cognates and various manners of syllable transition (DeFillippo and Snell, 1986). It has also been demonstrated that in adverse listening situations, segment duration may be an especially important cue to phonetic identity (Wardrip-Fruin, 1982). The relationship between gap detection and speech perception has been widely studied using multivariate correlation analyses. Several investigations reveal significant correlations between gap detection and speech recognition ability even when audiometric threshold is factored out (Dreschler and Plomp, 1985; Glasberg and Moore, 1989; Tyler *et al.*, 1982; Tyler and Summerfield, 1980). Reduced gap detection ability has been associated with poorer performance on speech in noise tests and discrimination of syllables varying in duration of voice onset time (VOT) (Dreshler and Plomp, 1985; Tyler *et al.*, 1982). Thus it is conceivable that perceptual problems with short duration stimuli such as those observed in temporal gap experiments may partially underlie the communication problems of the elderly. Other studies, however, find no significant correlation between these factors (Divenyi and Haupt, 1997; Festen and Plomp, 1983; Lutman and Clark, 1986; van Rooij and Plomp, 1990). Thus the relationship between gap detection and speech perception has not been firmly established.

The perception of temporal differences in speech can be measured directly by examining categorical perception of temporal aspects of speech such as duration of formant transitions, duration of frication, or differences in VOT. VOT, defined as the temporal interval between the burst or release of a stop consonant and the onset of periodic vibration of the vocal cords, is one of the major parameters distinguishing voiced and voiceless consonants (Lisker and Abramson, 1970). Several investigators have used categorical perception to study temporal factors in speech perception. Some have reported that neither age nor mild-to-moderate hearing impairment affect a listener's ability to make phonetic judgments based on temporal stimulus properties (Dorman *et al.*, 1985; Tyler *et al.*, 1982). On the other hand, Godfrey and Millay (1978) found that about half of their sample of hearing-impaired listeners were unable to identify stimuli which varied in the duration of formant transitions. Price and Simon (1984) found that older listeners (who had good hearing for their age, but higher pure-tone thresholds than younger listeners) required longer silence durations to report hearing differences in stop consonants. Age-related difficulties in identification have also been reported for stimuli in which vowel duration, voice onset time, and fricative noise duration were manipulated (Ginzel *et al.*, 1982).

B. Binaural temporal processing

Older adults with peripheral hearing loss show reduced performance on such binaural tasks as the masking-level difference (Findlay and Schuchman, 1976; Olsen *et al.*, 1976), interaural time discrimination (Herman *et al.*, 1977; Kirikae, 1969; Matzker and Springborn, 1958), and the precedence effect (Cranford *et al.*, 1990). However, little age-related change in binaural processing has been reported by other researchers (Kelly-Ballweber and Dobie, 1984; Palva and Jokinen, 1970).

Much of the psychoacoustic literature directed toward the effects of aging on binaural processing has focused on sensitivity to interaural time differences (ITD) (Herman *et al.*, 1977; Kirikae, 1969; Matzker and Springborn, 1958). These studies have varied widely in method, age groups tested, and stimuli, however, a consistent finding has been that younger adults have lower thresholds for ITDs than older adults. Little attempt was made, however, to control for the effects of hearing loss on ITD thresholds despite use of experimental stimuli containing higher-frequency spectra such as clicks and wideband noise.

Herman *et al.* (1977) recognized the possible confounding effects of high-frequency hearing loss on ITD thresholds and thus attempted to control for such an effect by testing individuals with normal pure-tone thresholds below 2000 Hz. Although all subjects in this study had normal hearing below 2000 Hz, older subjects had substantially greater hearing loss than young subjects at higher frequencies. Pure-tone loss in the elderly group increased from 4.38 dB at 2000 Hz to 44.38 dB at 4000 Hz, while loss for young subjects increased from -4.0 dB at 2000 Hz to only 1.56 dB at 4000 Hz. Thus it is not clear whether the reported age-related loss in the ability to lateralize the source of a sound on the basis of interaural time delay observed in elderly individuals was caused by aging, *per se*, or by the high-frequency peripheral hearing loss. Hearing loss in younger individuals has been shown to adversely affect binaural abilities (Durlach *et al.*, 1981; Hausler *et al.*, 1983).

To the extent that there are age-related changes in binaural processing, older people might be expected to have problems in situations where binaural hearing is useful, such as sound localization and comprehending speech in noisy settings. Although age-related changes in speech perception have not been tightly linked to binaural processing deficits, older adults tend to do worse than younger adults at various dichotic listening tasks (Kelly-Ballweber and Dobie, 1984; Martin and Cranford, 1991; Roush, 1985).

A common measure of binaural processing for speech is the masking level difference (MLD). The MLD is a phenomenon resulting in improved binaural hearing sensitivity when a phase reversal is imposed on either a primary signal or its masking noise. Several theories have been proposed to account for this phenomenon, but all are based on binaural analysis of interaural differences in time and intensity for dichotically presented stimuli (Moore, 1982). Several studies

have indicated that elderly subjects have reduced MLDs compared to younger subjects (Findlay and Schuchman, 1976; Tillman *et al.*, 1973; Warren *et al.*, 1978). In a recent investigation, Grose *et al.* (1994) compared MLDs for speech in a group of elderly listeners with normal hearing through 2000 Hz to those obtained from a group of young normal-hearing listeners. Results again showed that elderly subjects performed more poorly than the young listeners. Although these findings may be due, in part, to age differences, peripheral hearing loss in the older subjects may have accounted for their smaller MLDs compared with those of the young normal-hearing groups, since it has been established that presence of peripheral hearing loss significantly reduces the MLD (Jerger *et al.*, 1984). Nonetheless, several studies have examined the MLD, accounting for peripheral effects, and have found statistically significant differences between young and elderly subjects, suggesting further decline in binaural processing with advancing age (Olsen *et al.*, 1976; Pichora-Fuller and Schneider, 1991).

To determine whether losses in temporal resolution are attributed to age-related factors other than sensorineural hearing loss, temporal resolution must be measured in an elderly population with good hearing sensitivity. Findings of previous studies may have been confounded by age-related hearing loss since high-frequency audiometric thresholds were not included in selection criteria of older subjects with normal hearing. For the present investigation, we were in a unique position in that elderly subjects available for study had audiometric thresholds $\leqslant$20 dB HL from 250 to 6000 Hz. By more rigorously controlling for degree of peripheral hearing loss over a wider range of audiometric frequencies, any changes in temporal processing ability could be more strongly attributed to factors associated with aging. Thus for the present sample, if temporal processing is normal as long as hearing is normal, regardless of age, this would mean that reported decreases in temporal processing ability in older listeners are primarily the result of reduced hearing sensitivity. On the other hand, if temporal processing is ''abnormal'' in older subjects even when hearing is better than 20 dB HL, this would imply that there exist age-induced alterations in auditory structures and/or processes which are not detected by conventional pure-tone measures.

I. METHOD

A. Subjects

Two groups of subjects were tested, 12 normally hearing young adults, aged 20–30 years (mean=26.1, range 22–30) and 12 normally hearing elderly adults aged 65–75 years (mean=70.9, range 66–75). The groups were matched for gender (ten female and two male subjects) and hearing sensitivity. Normal hearing was defined as 20 dB HL or better pure-tone thresholds for the frequencies 250–6000 Hz bilaterally. At 8000 Hz, close matching of young and elderly subjects could not be achieved despite extensive audiometric screening of potential subjects. Regarding the interpretation of ''normal hearing,'' some researchers have used published age-relative norms, whereas others have selected subjects who meet criteria established for young adults. We used the latter approach, based on evidence that reduced temporal processing ability is associated with hearing impairment, independent of age (Florentine and Buus, 1984; Moore and Glasberg, 1988; Moore *et al.*, 1989). The present study included older subjects with pure-tone thresholds as close as possible to those of a control group of young subjects, to help ensure that any resulting age differences would not be attributable to peripheral hearing loss, although this means that the older subjects had better hearing than is normal for their age. The mean pure-tone audiometric thresholds (in dB HL *re:* ANSI, 1969) for each group are shown in Table I. Hearing thresholds for all subjects were symmetrical (interaural differences $\leqslant$10 dB at each frequency), with no conductive component. There was no significant difference in pure-tone thresholds between groups at any frequency. In an analysis of variance there were no significant main effects or interactions involving age [$F(1,22)=3.72$; $p=0.07$], ear [$F(1,22)=0.93$; $p=0.34$], or tone frequency [$F(1,22)=0.30$; $p=0.143$].

TABLE I. Mean audiometric thresholds (dB HL) and standard deviations (dB) for young and elderly listeners.

	Frequency (kHz)						
	0.25	0.5	1	2	3	4	6
	Young subjects ($N=12$)						
Mean—Right ear	7.9	7.5	7.9	8.3	10.4	11.2	13.8
	(4.9)	(4.5)	(3.9)	(4.4)	(3.9)	(4.3)	(4.3)
Mean—Left ear	7.1	5.0	5.8	8.8	9.6	12.9	13.3
	(4.9)	(5.2)	(4.2)	(2.3)	(2.6)	(2.6)	(3.9)
	Elderly subjects ($N=12$)						
Mean—Right ear	9.6	10.8	10.0	10.4	12.5	14.1	15.8
	(2.6)	(3.6)	(6.0)	(5.8)	(3.9)	(3.6)	(5.1)
Mean—Left ear	7.1	5.8	7.1	10.4	11.6	14.6	16.3
	(3.9)	(3.6)	(3.3)	(3.9)	(4.4)	(3.9)	(4.8)

B. Procedures

Four tasks were presented to each subject. Monaural temporal processing was measured using a gap detection paradigm. Binaural sensitivity was measured by interaural time difference (ITD) thresholds. Data were collected from the two groups at three different presentation levels (4, 8, and 16 dB), defined with respect to each individual's threshold for detecting the test stimulus. Low presentation levels were chosen based on evidence that the temporal resolution of the auditory system has been found to worsen somewhat at low sound levels for all types of stimuli (Gregory, 1974). Thresholds for the detection of a temporal gap in a noise stimulus increase when the level per critical band is less than 40 to 50 dB above the absolute threshold (Buus and Florentine, 1985; Fitzgibbons, 1983; Shailer and Moore, 1983). Further evidence is consistent with a worsening of temporal resolution at low sound levels. For example, the rate of recovery from forward masking decreases as the sensation level of the masker is reduced (Jesteadt *et al.*, 1982; Moore and Glasberg, 1983). The ability to detect amplitude modulation at various modulation rates worsens at low sound levels, again indicating reduced temporal resolution at low lev-

els (Bacon and Viemeister, 1985). Although no published data are available, researchers have examined age differences in sensitivity to interaural time differences as a function of sound level (Ashmead *et al.*, unpublished data). They tested young and older adults, obtaining ITD thresholds at each of three overall sound levels (8, 16, and 30 dB SL relative to individual detection thresholds). Findings revealed that the difference between age groups was greater at low stimulus levels.

Each subject was also evaluated on two measures of speech perception. One of these was the masking level difference (MLD), which examined the ability to utilize binaural cues including interaural temporal differences to recognize speech. The second test was a syllable identification task that included phonemes varying in voice onset time (VOT). All testing took place in a double-walled sound booth using TDH49P headphones, where subjects were seated in front of a computer. The computer monitor provided visual feedback during testing and subject responses were entered on the computer keyboard (with the exception of the responses for the MLD task, which were repeated aloud). The order of presentation for the four tasks was randomized across subjects. Subjects were tested in three sessions, each lasting 1–1.5 h, and were paid for their participation.

C. Gap detection

1. Stimuli

Stimuli for the gap detection task were computer-generated 1000-Hz sinusoidal signals presented in a continuous background noise with a spectral notch at the frequency of the sinusoid. Signals were generated using a Dell XPSP90 laboratory computer and Tucker-Davis Technologies (TDT) Psychoacoustic System, with 16-bit digital-to-analog (D/A) converters, a 10-kHz sampling rate (low-pass filtered at 4 kHz to prevent aliasing), and a rise–fall time of 5 ms. The overall duration of each observation interval was 200 ms. To determine the duration of the signal on either side of the gap, the gap duration was subtracted from 200 ms and the result divided by two. The duration of the signal preceding and following the gap was then rounded to the nearest ms. The gap started with the signal at a positive-going zero crossing and ended with the phase needed for a given gap duration.

The 1000-Hz signal was presented in a continuous background noise, with a sharp notch at the signal frequency, designed to mask the spectral splatter associated with the abrupt gating of the gap. The noise masker was a 65 dB SPL (22-dB spectrum level) Gaussian noise with a notch arithmetically centered at the frequency of the test signal (fc); the width of the notch was 0.4fc at the 3-dB down points. The depth of the notch was 37 dB. The noise was recorded on digital audio tape (DAT), and played back through a Panasonic SV3700 DAT deck that led to a programmable attenuator. The signal and noise were combined in a weighted signal mixer and passed through a headphone buffer to the TDH49P headphones.

2. Procedure

Gap detection thresholds were measured using an adaptive two-interval forced choice (2IFC) procedure. On each trial, two 200-ms signals were presented, separated by 1000 ms. One of the two sounds was the ''signal'' (containing the gap); the other sound was the ''standard'' (no gap). The order, either signal-standard or standard-signal, was chosen randomly with equal probability. Following stimulus presentation, the subject chose the interval that contained the signal by pressing the appropriate button on the computer keyboard. Gap duration on the first trial was 50 ms so that the stimulus gap was easily detectable. On subsequent trials, gap duration was increased by a factor of $\sqrt{2}$, then rounded to the nearest ms after each incorrect response and decreased by a factor of $\sqrt{2}$ after every two successive correct responses. This two-down, one-up algorithm estimates the 71% point on the psychometric function (Levitt, 1971). In order to ensure that subjects remained attentive to the appropriate cue, gap duration was increased to the starting level of 50 ms following four incorrect responses and remained at 50 ms until the subject responded correctly. Following a correct response, testing was resumed at the gap duration being evaluated before the jump to 50 ms occurred. Trials measured at 50 ms were not considered in gap threshold calculations. Testing continued until ten reversals occurred and gap threshold was estimated as the geometric mean of the gap durations at the last eight reversals.

Before testing began, a practice run was administered at a level of 30 dB relative to the masked threshold for a 1000-Hz continuous tone[1] to ensure that subjects were familiar with the task. Following the practice run, each subject contributed three gap threshold estimates at levels of 4, 8, and 16 dB relative to masked threshold.

Stimuli were presented monaurally to the ear with the least pure-tone threshold loss. If there was no difference between ears, the test ear was chosen randomly. The order of presentation level was randomized across subjects. The mean of the three gap threshold estimates obtained at each intensity level was taken as the gap threshold value.

D. Interaural time differences (ITD)

1. Stimuli

Stimuli for the ITD task were 400-ms-long trains of 40 rectangular clicks, each click lasting 50 μs with an interclick interval of 10 ms. Signals were generated using the same equipment as for the gap detection task, but with a 200-kHz sampling rate. Interaural time differences were implemented by delivering the signal to one ear by an integer multiple of the sampling period (5 μs).

2. Procedure

Thresholds for interaural time differences were measured using an adaptive 2IFC procedure. On each trial, two successive 400-ms click trains were presented. The first click train was presented with a 0-μs ITD, thus presented to both ears simultaneously. For the second click train in the series, the desired ITD was created by offsetting the clicks to the two channels in 5-μs intervals. Thus the auditory impression

was of a sound image that occurred first at midline and then to the side (left or right, depending on the trial). The ear receiving the delayed click train was chosen randomly with equal probability. Following stimulus presentation, the subject indicated whether the sound image was perceived to the left or to the right by pressing the appropriate button on the computer keyboard. The ITD on the first trial was 100 μs. On subsequent trials, step size was 20 μs through the first reversal and 5 μs thereafter. In order to encourage subjects to remain attentive to the appropriate cue, ITD duration was increased to a level of 400 μs following four incorrect responses and remained at 400 μs until the subject responded correctly. Following a correct response, testing was resumed at the ITD being evaluated before the increase occurred. Trials measured at 400 μs were not considered in ITD threshold calculations. Testing continued until ten reversals occurred and ITD threshold was estimated as the geometric mean of the ITD from the last eight reversals.

Initially, a practice run was administered at a level of 30 dB relative to the binaural click threshold.[2] During testing, each subject contributed three ITD threshold estimates at levels of 4, 8, and 16 dB relative to binaural click detection threshold. The order of the presentation level was randomized across subjects. The mean of the three ITD threshold estimates obtained at each intensity level was taken as the ITD threshold value.

E. Voice onset time (VOT)

1. Stimuli

VOT was examined by creating a sound continuum which varied in the duration of VOT in small steps. A continuum of consonant–vowel (CV) syllables ranging from /ba/ to /pa/ was created using the Computerized Speech Research Environment (CSRE) cascade/parallel synthesis program modeled after Klatt (1980) (AVAAZ Innovations, Inc., 1994) and a laboratory computer. Acoustically, the stimuli differed only in VOT. VOT ranged from 0 to 60 ms in 10-ms steps, creating a continuum of seven stimuli. A /ba/ syllable with a duration of 300 ms was synthesized at a sampling rate of 20 kHz. Fundamental frequency ($F0$) contour began at 103 Hz and rose to 125 Hz over the duration of the syllable. During a 40-ms transition period, the three lowest formant onset frequencies moved until they reached appropriate steady-state values (Blumstein and Stevens, 1980). For generation of the six additional members of the continuum, VOT variations were accomplished by altering the onset of voicing and the duration of aspiration in 10-ms steps following the initial burst.

2. Procedure

Listeners identified and discriminated the /ba/–/pa/ continuum. Stimuli for both tasks were presented to the subject's better ear at an individually determined most comfortable loudness level. Subjects listened to conversational speech through headphones and adjusted the level of the speech using the computer keyboard to their preferred listening level. Because young and elderly subjects had similar hearing sensitivity, presentation levels did not vary significantly between groups [$F(1,23)=0.362$; $p>0.05$]. Presentation levels ranged from 68 to 86 dB SPL.

For the identification task, subjects initially responded to the series of seven stimuli representing the ordered continuum from /ba/ to /pa/. This set was then repeated to familiarize the listener with the range of stimuli involved. Following familiarization, stimuli were presented randomly. A set of ten stimulus blocks (70 trials) was used to generate identification functions. Data were collected using a single-interval forced-choice paradigm. After presentation of each stimulus, subjects identified the initial consonant of each syllable as either /b/ or /p/.

The discrimination task involved one-step and two-step presentations of a pair of stimuli in an AX (same–different) format. The stimulus pairs contained either two identical stimuli (i.e., ''catch'' trials), or two stimuli which differed in VOT. In the one-step condition, pairs of CV stimuli that differed by 10-ms VOT were presented, resulting in six pairs of experimental trials. Pairs were each presented 20 times, in random order, with 500-ms interstimulus intervals. Intermixed with the 120 experimental trials were 120 catch trials. The 240 stimuli were arranged in 20 blocks, each containing 12 randomized stimulus pairs. In the two-step condition, pairs of experimental stimuli that differed by 20-ms VOT were presented, resulting in five pairs which were each presented 20 times. Intermixed with the 100 experimental trials were 100 catch trials. The 200 stimuli were arranged in 20 blocks, each containing ten randomized stimulus pairs. After presentation of each stimulus pair in both one- and two-step tasks, the subject indicated whether the stimuli were the ''same'' or ''different.''

F. Masking level difference (MLD)

1. Stimuli

The MLD was measured using speech as the stimulus and was determined by presenting a continuous speech noise binaurally and in-phase (N_0), then determining the speech reception threshold when the binaural speech signal was presented interaurally in-phase (S_0) and interaurally out-of-phase 180° (S_π). The threshold difference (in decibels) between the two masking conditions (S_0N_0 minus $S_\pi N_0$) defined the MLD.

Both the speech signal and masker were presented through a standard two-channel clinical audiometer (GSI-10) which has a network allowing phase reversal of either the noise or test signal. The stimuli for the speech MLD were the 36 spondaic words of the CID W-1 list. The spondaic words, and their associated calibration tone, were presented using a compact disc recording (Department of Veterans Affairs, 1991) played on a JVC XL-V161 compact disc player routed through the audiometer. The recording consisted of two randomizations of the CID W-1 word list for a total of 72 spondaic words separated by 4-s interstimulus intervals. The masker for the speech MLD was a broadband noise with equal energy per Hz from 250 to 1000 Hz with 12 dB/oct rolloff from 1000 to 6000 Hz. During the experiment, the masker was presented continuously at an overall level of 65 dB SPL. Presentation levels of both the speech signal and

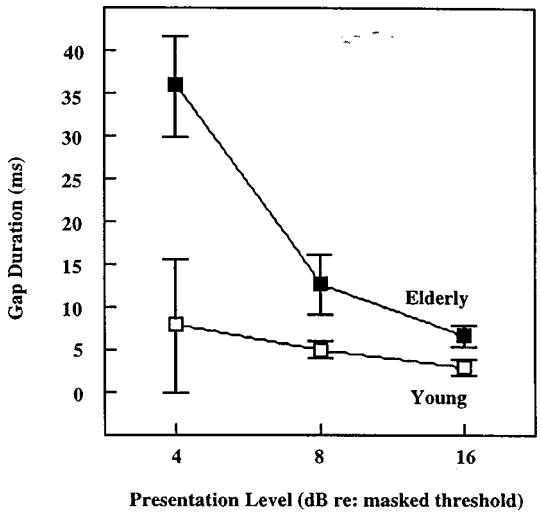

FIG. 1. Mean gap detection thresholds for young and elderly adult listeners at the 4-, 8-, and 16-dB sound levels presented relative to individual masked thresholds. Error bars indicate ± standard error.

masker were verified using sound level measurements (Larson-Davis Laboratories, model 800B).

2. Procedure

To familiarize listeners with the test materials, a written list of the CID W-1 spondaic words was provided for subjects to read before testing began. Each listener was then presented with a randomization of the stimuli at a comfortable listening level in the absence of masking noise. To obtain the MLD, threshold was determined for spondee words in the diotic (S_0N_0) and dichotic ($S_\pi N_0$) conditions in the presence of a continuous masking noise. To determine threshold, a one-up, one-down adaptive procedure was used. The first word of each test sequence was presented at 85 dB SPL, representing a level that was 20 dB greater than the level of the continuous noise masker. The subject reported aloud the perceived word. Following each correct response, the level of the speech was attenuated in 5-dB steps until an incorrect response was recorded. Thereafter, the level of the signal was decreased in 2-dB steps following a correct response and increased in 2-dB steps following an incorrect response. Testing continued until ten reversals occurred, and the mean of the final eight reversal levels was taken as an estimate of threshold. Once thresholds for both diotic and dichotic conditions were obtained, the dB difference between the two conditions was recorded as the speech MLD.

II. RESULTS AND DISCUSSION

Results of the present study indicated significant age differences on measures of gap detection, ITD thresholds, slope of the VOT identification function, discrimination of VOT cues, and MLD thresholds. Thus elderly subjects performed more poorly than their younger counterparts on these tasks, even though all subjects had normal-hearing sensitivity.

A. Gap detection

Figure 1 shows mean gap detection thresholds obtained at the 4-, 8-, and 16-dB sound levels (relative to individual masked thresholds). Data were examined using an analysis of variance (ANOVA) with sound level as the within-subjects factor and age group as the between-subjects factor. Results indicated significant effects of age group [$F(1,22) = 23.57$; $p < 0.0001$], sound level [$F(2,44) = 27.13$, $p < 0.0001$], and the interaction of age group and sound level [$F(2,44) = 14.05$, $p < 0.0001$]. As shown in Fig. 1, the difference in performance between young and elderly adults was especially large at very low sound levels. Performance was significantly different between age groups at all three sound levels (4 dB: [$F(1,22) = 14.49$, $p < 0.001$]; 8 dB: [$F(1,22) = 6.71$, $p < 0.05$]; 16 dB: [$F(1,22) = 21.45$, $p < 0.0001$]).

To further assess the relationship between gap detection performance and signal level, a linear regression line was fit for each individual subject (linear fits were used as they proved as good as linear plus quadratic fits during regression analysis), and slopes were averaged across subjects within each group. The mean slope values based on individual best-fit linear regression lines were significantly [$F(1,22) = 15.33$, $p < 0.001$] different for young adults (-0.44) as compared to those for the elderly group (-2.45).

Present findings are in agreement with earlier studies using sinusoidal stimuli which reported larger gap detection thresholds in elderly listeners with minimal hearing loss (Moore *et al.*, 1992; Schneider *et al.*, 1994). In fact, gap detection thresholds for young and elderly adult subjects measured at the highest presentation level in the present study (2.8 and 6.7 ms for young and elderly subjects, respectively) are quite similar to those reported by Schneider *et al.* (1994) (young = 3.8 ms; elderly = 6.2 ms) using suprathreshold stimuli. Collectively, findings of Moore *et al.* (1992), Schneider *et al.* (1994), and the present investigation are similar in that each identified some elderly individuals who exhibited deficits in temporal processing that were unrelated to hearing loss. Snell (1997) also observed larger thresholds for detection of gaps using noise-burst stimuli for elderly subjects with audiometric thresholds similar to those obtained for the present study.

Previous studies reported temporal processing ability as measured by the ability to detect gaps in sinusoids at relatively high sound levels. Moore *et al.* (1992) obtained gap detection thresholds at 25, 40, 55, 70, or 80 dB SPL and subjects were tested only at levels for which the signal was clearly audible. Schneider *et al.* (1994) evaluated three young control subjects at 10, 20, 40, and 60 dB SL, but elderly listeners were evaluated at a single high-intensity signal level. Thus the only information reported regarding performance of elderly subjects on gap detection tasks was measured well above audiometric threshold.

Schneider *et al.* (1994) did not find an effect of level on gap detection thresholds over most of the range of levels tested in their three young control subjects (with the exception of 10 dB SL). Therefore they concluded that it was not likely that the poorer gap detection performance of the older subjects was due to the effect of sensation level. Their use of Gaussian-enveloped tones minimized the likelihood that spectral differences contributed to the ability to detect temporal gaps. They showed that spectral differences within notched noise were much larger for gaps in continuous noise (used in the present study) than for gaps between two

Gaussian-enveloped tones. Thus it is possible that the increase in gap detection thresholds at lower presentation levels may have been influenced by spectral differences. Since all subjects in the present study had hearing within normal limits, however, we would expect the contribution of spectral cues, if any, to have a similar effect on gap threshold for all listeners regardless of age. Thus the large differences between groups at low sensation levels cannot be entirely explained by spectral cues. It is possible that the effect of level is only apparent closer to audiometric threshold, as even two of three young control subjects in the Schneider *et al.* (1994) study had elevated gap detection thresholds at the 10-dB sensation level (compared to the 20-, 40-, and 60-dB levels in the same study). Since stimulus levels in the present study were defined with respect to individual thresholds, and since the groups had comparable pure-tone thresholds, the age differences cannot be attributed to overall hearing sensitivity. Rather, results suggest that there is a general tendency for decreased performance on the gap detection task at low sound levels.

B. Voice onset time

Figure 2 shows mean identification functions for the /ba/–/pa/ syllable series. All listeners in both groups identified two clear phoneme categories. Phoneme intercept values (phonetic boundaries) along the identification functions were determined for each subject by performing a linear regression across *z*-transformed identification scores for stimuli on the continuum. The mean phonetic boundary for the young adult group was 27 ms, which is in agreement with previous findings for normal-hearing young adults (Lisker and Abramson, 1970; Tyler *et al.*, 1982). For the elderly adult group, the mean phonetic boundary was 32 ms. ANOVA on the data revealed that there was no significant difference in mean phonetic boundary between young and elderly listeners [$F(1,22)=2.41$, $p>0.05$], indicating that the two groups used a similar criterion for identifying VOT. The mean slope of the boundary was also determined for each subject using linear regression. The mean slope value was -1.41 for the young adult group and -0.93 for the elderly adult group. This identification slope for the younger group was significantly steeper than that of the elderly group [$F(1,22)=4.30$, $p<0.05$].

In Fig. 3, the open symbols show mean one-step and two-step discrimination functions for the /ba/–/pa/ continuum from each subject group. Predicted discrimination functions (shown by filled symbols) were derived from the identification responses using the procedures described in Pollack and Pisoni (1971), which are based on the assumption that subjects rely on phonetic labels in the discrimination task (Liberman *et al.*, 1967). The peak of the predicted curve depends on the position and slope of the phoneme boundary in the identification function. Predicted scores were calculated for each subject using the following formula:

$$P_{c(a,b)}=0.5[(1-P_{a1})^2+(1-P_{b2})^2]+P_{a1}P_{b2},$$

where $P_{c(a,b)}$=predicted percent correct for any pair of stimuli along a continuum. P_{a1}=probability that the first stimulus in the pair is identified as a member of a given phoneme category. P_{b2}=probability that the first stimulus in the pair is identified as a member of another phoneme category. The phonetic model is based on the assumption that sounds are coded as one phoneme or another. Thus this model indicates the classical categorical perception phenomenon. That is, sounds that are of different categories should be discriminable whereas sounds in the same category should not be discriminable. When both stimuli involved in a comparison come from one phoneme category, the predicted percent correct discrimination scores are near chance (50%). When the pair of stimuli come from two different phoneme categories, the predicted score is greater than chance, with the magnitude of the score dependent on consistency of the identification performance.

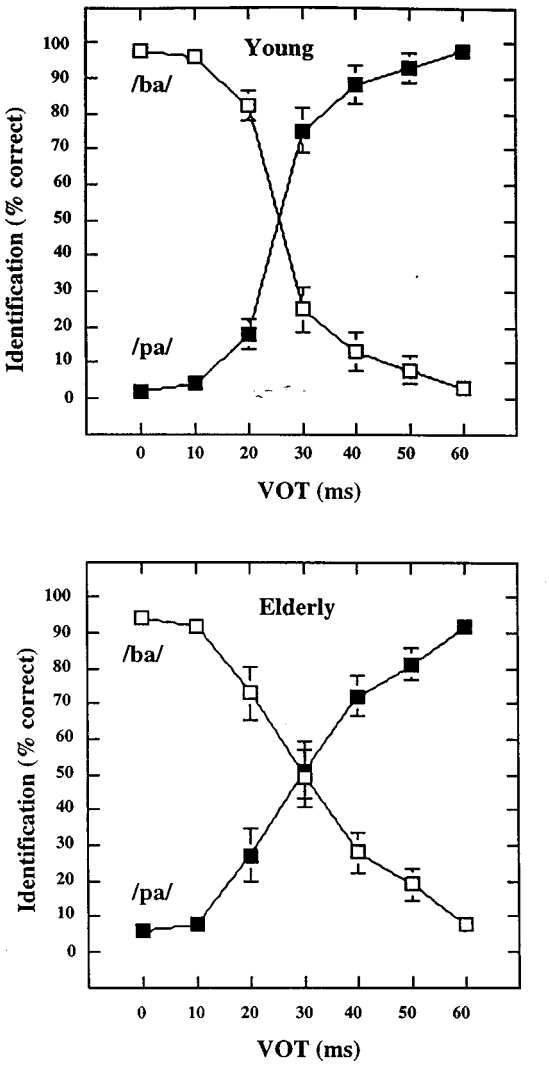

FIG. 2. Mean identification functions including standard error values for young and elderly listeners for the seven-step /bɑ/–/pɑ/ continuum.

Figure 3 (top) displays mean one-step discrimination scores for young and elderly adult listeners. Data were examined using an ANOVA with score type (obtained versus predicted) and stimulus pair as within-subjects factors and age group as the between-subjects factor. Results revealed a significant effect of age group [$F(1,22)=23.1$, $p<0.0001$], stimulus pair [$F(5,110=12.76$, $p<0.0001$], and a significant interaction between score type and stimulus pair [$F(5,110$

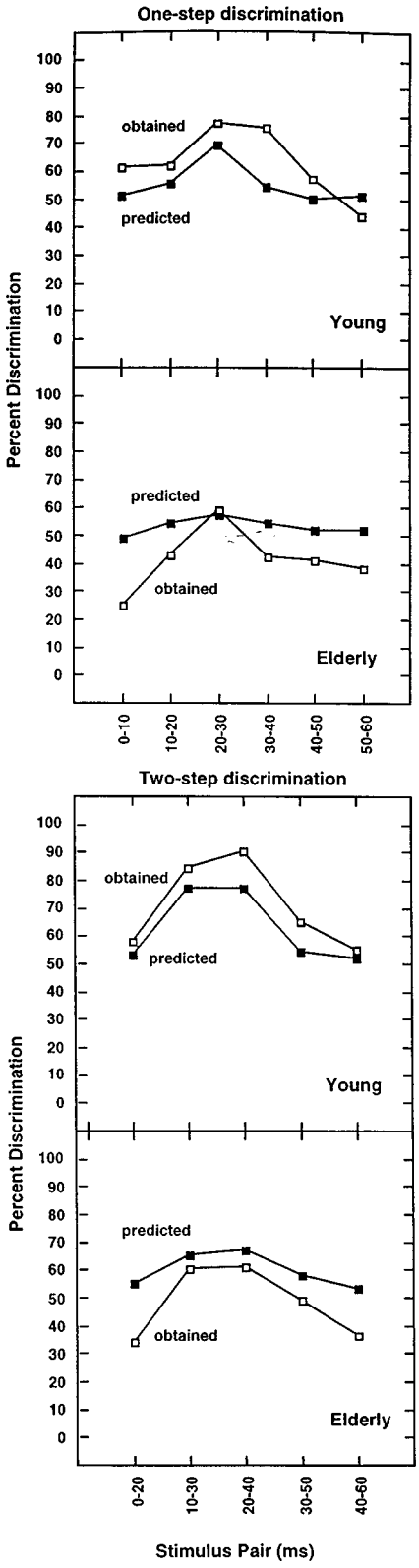

FIG. 3. Mean discrimination scores for the one- and two-step discrimination conditions for young and elderly adult listeners.

$=3.8$, $p<0.01$]. There was a significant interaction between age group and score type [$F(1,22)=17.15$, $p<0.0001$], indicating that the relationship between obtained and predicted scores differed between groups. All listeners exhibited improved discrimination performance at or near the phoneme boundary. An obvious difference is that obtained scores were higher than predicted scores for young adult subjects but not for the elderly subjects. As observed by others (Stevens *et al.*, 1969; Sharf *et al.*, 1988), actual discrimination performance for the young adult group exceeded that predicted by identification data on the one-step discrimination function. For elderly listeners, discrimination performance was poorer than predicted by identification data. To interpret the interaction effect of age group×score type, the simple main effect of age group at each of the two conditions was assessed. Comparisons revealed a significant difference between groups for both predicted and obtained scores at the $p<0.01$ level.

Figure 3 (bottom) shows two-step discrimination scores for young and elderly adult listeners. There was a significant effect of age group [$F(1,22)=16.12$, $p<0.001$], stimulus pair [$F(4,88)=24.36$; $p<0.0001$], and a significant interaction between score type and stimulus pair [$F(4,88)=2.73$, $p<0.05$]. The interaction between age group and score type was also significant [$F(1,22)=12.94$, $p<0.01$]. All listeners exhibited improved discrimination performance at or near the phoneme boundary. Actual discrimination performance for the young group exceeded that predicted by identification data for all stimulus pairs. For the elderly group, although performance increased near the phoneme boundary, overall discrimination ability was lower than predicted values for all stimulus pairs. *Post hoc* comparisons using simple effects testing revealed a significant difference between groups for both predicted and obtained scores ($p<0.01$).

Results of the present study indicate that elderly listeners have reduced sensitivity to differences in VOT as compared to younger listeners. Identification performance revealed a more gradually sloping phonetic boundary, indicating that elderly subjects were less able to clearly distinguish phoneme boundary categories. Discrimination data revealed that actual performance on both one-step and two-step discrimination tasks followed a similar pattern as predicted scores for both groups; the percent correct discrimination scores increased at areas near the phoneme boundary. Actual percentage scores of elderly listeners, however, were lower than what was predicted based on identification data, again indicating decreased ability to distinguish the temporal cue of VOT. The fact that young and old listeners performed differently as a function of predicted and observed discrimination indicates that the categorical model performed differently for these populations. It is likely that the difference in the populations relates to their ability to use auditory cues. Young adults appear to utilize temporal auditory cues within sound categories as evidenced by higher obtained than predicted scores. Older adults are limited in this auditory ability as reflected in poorer obtained than predicted scores across stimulus pairs. This may also indicate that the younger subjects might have been using acoustic as well as phonetic information in forming their discrimination judgments. In the future, one way to assess the auditory component would be to examine predicted functions using the dual-coding model that includes both an auditory and phonetic component (Fujisaki and Kawashima, 1970).

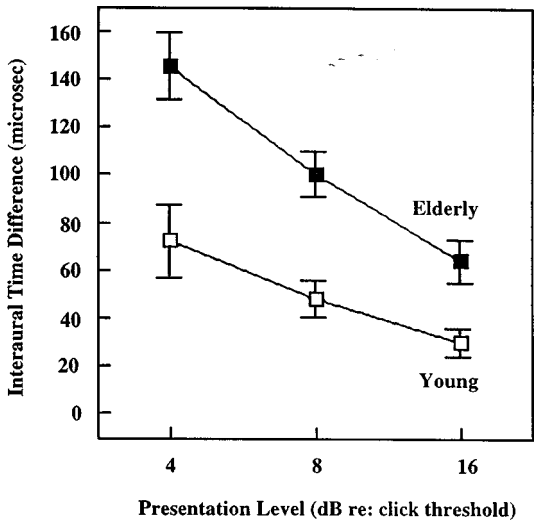

FIG. 4. Mean ITD thresholds for young and elderly adult listeners at the 4-, 8-, and 16-dB sound levels presented relative to individual detection thresholds. Error bars indicate ± standard error.

C. Interaural time differences

Figure 4 shows mean ITD thresholds for young and elderly adults at the 4-, 8-, and 16-dB sound levels. As in the gap experiment, the ITD thresholds of younger adults were lower than those of older adults at all presentation levels. Data were examined using an ANOVA with sound level as the within-subjects factor and age group as the between-subjects factor. Results indicated significant effects of age group [$F(1,22)=19.06$, $p<0.0001$], sound level [$F(2,44)=97.9$, $p<0.0001$], and the interaction of age group and sound level [$F(2,44)=9.52$, $p<0.0001$]. Performance was significantly different between groups at the 16 dB [$F(1,22)=9.18$, $p<0.0001$], 8 dB [$F(1,22)=16.98$, $p<0.0001$], and 4 dB [$F(1,22)=22.59$, $p<0.0001$] sound levels. The mean slope values based on individual best-fit linear regression lines were significantly [$F(1,22)=24.22$, $p<0.01$] different for young adults (-3.55) as compared to those for the elderly group (-6.78). Results for young adult listeners are in agreement with previous findings reporting increased thresholds for detecting interaural phase differences at low sensation levels (Zwislocki and Feldman, 1956).

Previous studies have examined the effects of aging on binaural hearing by measuring sensitivity to ITDs (Herman *et al.*, 1977; Kirikae, 1969; Matzker and Springborn, 1958), however, little attempt was made in these studies to adequately control for the effects of hearing loss on ITD thresholds despite the use of experimental stimuli containing higher-frequency spectra such as clicks and wideband noise. The present data for elderly subjects with normal-hearing sensitivity demonstrate a clear age-related loss in the ability to lateralize the source of a sound on the basis of an interaural time delay. Similar to findings of Herman *et al.* (1977), data revealed that older listeners required approximately twice the interaural time delay as young listeners for the same level of performance. The interaction of age and sound level indicated that a decrease in stimulus level had a more deleterious effect on ITD discrimination in the elderly group than in the younger group.

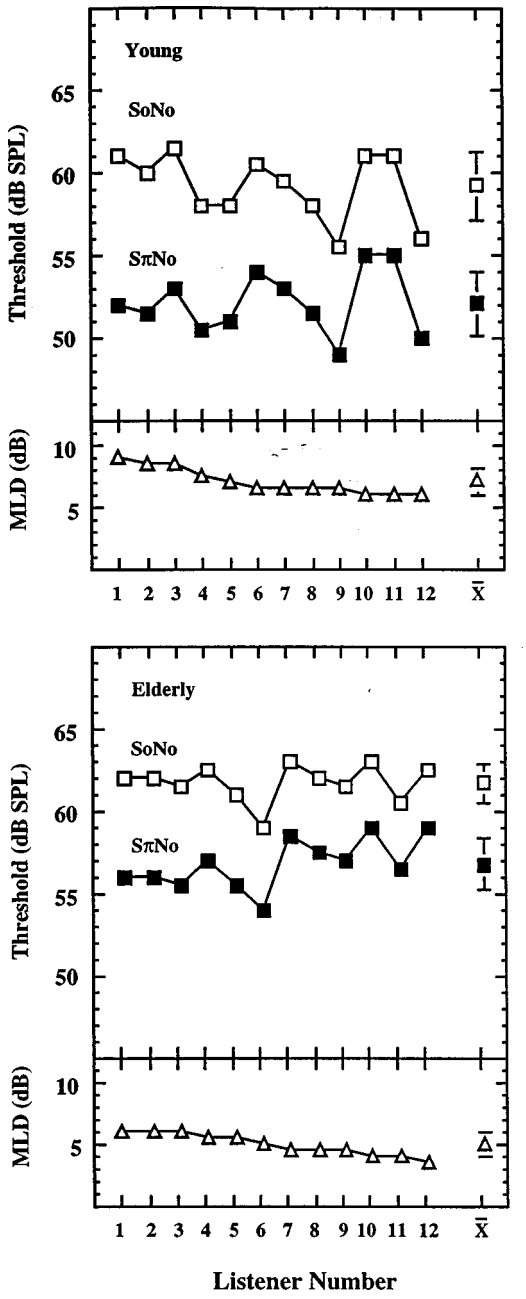

FIG. 5. Individual and group mean speech thresholds for S_0N_0 and $S_\pi N_0$ for young and elderly listeners. Individual listeners are ordered by magnitude of masking level difference, within each age group.

D. Masking level difference

The mean MLD was 7.0 dB for the young listeners, which is consistent with previous MLD studies using similar stimuli (Grose *et al.*, 1994; Wilson *et al.*, 1982). The elderly group had a mean MLD of 4.9 dB. This age difference was significant, as shown by a *t* test [$t(22)=5.31$, $p<0.0001$].

Individual thresholds for the S_0N_0 and $S_\pi N_0$ conditions are displayed in the two panels of Fig. 5 for young and elderly listeners. Pichora-Fuller and Schneider (1991, 1992) using pure-tone stimuli, and Grose *et al.* (1994) using speech stimuli, found that elderly listeners with normal hearing sen-

TABLE II. Correlation coefficients between psychoacoustic and speech measures of temporal processing for young adult subjects.

		GAP(4)	GAP(8)	GAP(16)	GAP(slope)	ITD(4)	ITD(8)	ITD(16)	ITD(slope)	VOT1	VOT2	MLD
Gap Detection	GAP(4)	--------	.856**	.077	.988**	.843**	.838**	.620*	.886**	-.148	.121	-.090
	GAP(8)		--------	.373	.799*	.721*	.805*	.705*	.655*	.021	-.076	-.215
	GAP(16)			--------	-.075	.190	.370	.469	.006	.345	.284	-.448
	GAP(slope)				--------	.816**	.781*	.551	.886**	-.202	-.164	-.029
Interaural Time Discrimination	ITD(4)					--------	.921**	.886**	.962**	-.229	-.178	-.346
	ITD(8)						--------	.873**	.853**	-.116	-.137	-.222
	ITD(16)							--------	.726*	.011	-.044	-.423
	ITD(slope)								--------	-.345	-.237	-.264
Voice Onset Time	VOT1									--------	.697*	.145
	VOT2										--------	.005
Masking Level Difference	MLD											-------

*p<0.05, **p<0.001

sitivity from 250 to 2000 Hz, exhibited an elevation in $S_\pi N_0$ thresholds but not S_0N_0 thresholds as compared to younger listeners. Present data show differences between the young and elderly groups for both S_0N_0 and $S_\pi N_0$ conditions. This was assessed using an ANOVA with signal condition (S_0N_0 vs $S_\pi N_0$) as the within-subjects factor and age group as the between-subjects factor. Results revealed significant effects of age [$F(1,22)=29.66$, $p<0.0001$] and signal condition [$F(1,22)=892.67$, $p<0.0001$], as well as a significant interaction [$F(1,22)=28.19$, $p<0.0001$]. Unlike past studies, S_0N_0 thresholds were more variable in the young group as compared to the elderly group. Nonetheless, intersubject variability of both groups was relatively small ($S_0N_0=2.0$ and 1.1 standard deviations; $S_\pi N_0=1.9$ and 1.5 standard deviations, for young and elderly groups, respectively). To interpret the interaction effect, the simple main effect of age group at each of the two conditions was assessed. In contrast to previously reported findings, analysis revealed that the two groups differed significantly for both the S_0N_0 condition at the $p<0.0001$ level and for the $S_\pi N_0$ condition at the $p<0.001$ level. Although both were statistically significant, differences in threshold between groups were greater in the $S_\pi N_0$ (4.6 dB) than in the S_0N_0 (2.5 dB) condition.

Previous research has reported age-related deficits in binaural processing reflected by reduced MLDs in elderly listeners (Grose *et al.*, 1994; Pichora-Fuller and Schneider, 1991; Tillman *et al.*, 1973; Warren *et al.*, 1978). Findings may have been due, in part, to age differences, although peripheral hearing loss in the older subjects may have accounted for their smaller MLDs since the presence of peripheral hearing loss significantly reduces the MLD (Jerger *et al.*, 1984). Present data support that binaural release from masking declines significantly as a function of advancing age, independent of peripheral hearing loss.

E. Correlations among measures

There was no significant correlation between the experimental measures and individual pure-tone thresholds or age for either subject group. Pearson *r* correlation coefficients were calculated to examine the relationships among experimental measures. The correlation analysis used the following variables: GAP(4), GAP(8), GAP(16), GAP(slope), ITD(4), ITD(8), ITD(16), ITD(slope) (representing mean gap and ITD thresholds at each presentation level and mean slope values for both tasks), MLD, VOT(slope), VOT1 and VOT2 (representing the slope of the identification function and percent identification scores at the phoneme boundary for one- and two-step discrimination tasks). For the following discussion we refer to the gap detection and ITD thresholds as ''psychoacoustic measures'' and the VOT scores and MLDs as ''speech measures.'' The correlation matrices for young and elderly adult subjects are presented in Tables II and III, respectively.

For young adult subjects, the slope measures of ITD and gap functions were strongly correlated. A significant relationship was found between GAP(4) measures across all ITD variables. The same finding was observed between GAP(8) measures and all ITD variables. No significant correlations were found for the GAP(16) condition and ITD variables. ITD(16) scores had lower correlations with the gap tasks than the ITD(4) and ITD(8) scores. Taken together, these patterns suggest that when trying to identify individual differences across tasks, it may be best to challenge the auditory system by working at low sound levels. When only suprathreshold levels are used, individual differences may be difficult to find. For elderly subjects, ITD thresholds were negatively and significantly correlated with gap detection thresholds at lower sound levels, however, this relationship was only of moderate statistical significance. There was no sig-

TABLE III. Correlation coefficients between psychoacoustic and speech measures of temporal processing for elderly adult subjects.

		GAP(4)	GAP(8)	GAP(16)	GAP(slope)	ITD(4)	ITD(8)	ITD(16)	ITD(slope)	VOT1	VOT2	MLD
Gap Detection	GAP(4)	--------	.460	.028	.984**	-.598*	-.575*	-.508	-.175	.226	.017	.060
	GAP(8)		--------	.155	.427	-.624*	-.464	-.308	-.430	-.106	-.322	.194
	GAP(16)			--------	-.153	-.244	-.115	-.155	-.130	.329	.346	-.148
	GAP(slope)				--------	-.547	-.781	-.475	-.149	.284	.079	.086
Interaural Time Discrimination	ITD(4)					--------	.926**	.643*	.524	-.253	-.004	-.019
	ITD(8)						--------	.790*	.269	-.467	-.157	.013
	ITD(16)							--------	-.316	-.602*	-.280	-.154
	ITD(slope)								--------	.356	.311	.148
Voice Onset Time	VOT1									--------	.822**	.088
	VOT2										-------	.423
Masking Level Difference	MLD											-------

*p<0.05, **p<0.001

nificant correlation between the slopes of ITD and gap functions for the elderly adult group. Overall, correlations between gap and ITD thresholds did not show a strong or consistent relationship for elderly subjects.

The relationship between speech measures was also examined. There were no significant correlations between MLD and VOT measures for either age group, indicating that performance on the MLD task was independent of performance on the VOT tasks.

Finally, there were no significant correlations observed between psychoacoustic and speech measures for young adult listeners. For elderly adult listeners, ITD thresholds obtained at 16 dB were moderately correlated with performance on the one-step discrimination task ($r=-0.602$). No other significant correlations were observed, however, suggesting an incidental relationship.

III. GENERAL DISCUSSION

A. Aging and monaural temporal processing

In the limited amount of research available on monaural temporal processing ability in elderly listeners, results have been mixed, and interpretation has been complicated by the presence of peripheral hearing loss in the elderly samples. Present data for normally hearing elderly listeners demonstrate a clear deficit in the ability of elderly subjects to process temporal information, as measured by detection of temporal gaps. Results are in agreement with recent studies by Moore *et al.* (1992), Schneider *et al.* (1994), and Snell (1997) who reported larger gap detection thresholds in elderly listeners with minimal hearing loss. Additional studies measuring gap discrimination thresholds and duration discrimination thresholds support that there is an age-related deficit in monaural temporal processing that is independent of hearing loss (Abel *et al.*, 1990; Fitzgibbons and Gordon-Salant, 1994; Trainor and Trehub, 1989).

A similar result was observed for monaural temporal processing of speech stimuli, as measured by sensitivity to changes in VOT. Elderly subjects were less able to clearly distinguish phoneme categories and were less accurate at discriminating speech stimuli which differed in VOT duration. Findings suggest that elderly listeners may be at a functional disadvantage in the perception of temporal changes in the acoustic waveform that comprise everyday conversational speech.

The question of whether deficits in temporal processing ability contribute to speech perception difficulties is an area of considerable controversy. Reduced temporal processing has been linked to some speech perception errors made by hearing-impaired listeners (Erber, 1972; Price and Simon, 1984; Tyler *et al.*, 1982), and similar errors have been demonstrated by normal-hearing listeners as a consequence of changes in temporal relations among signal components (Klatt, 1975; Schouten, 1980). In relation to gap detection, several investigations have revealed significant correlations between gap detection thresholds and speech recognition ability, even when audiometric threshold is factored out (Dreschler and Plomp, 1985; Glasberg and Moore, 1989; Tyler *et al.*, 1982). Taken together, these results suggest that poorer speech perception might be related, in part, to abnormal temporal processing. Despite this evidence, auditory temporal processing measures have not consistently proven to be strong predictors of speech perception performance in elderly listeners (Festen and Plomp, 1983; Lutman and Clark, 1986; vanRooij and Plomp, 1990). Results of the present investigation support this latter finding.

As Dorman *et al.* (1985) have suggested based on previous research, observed differences between young and elderly listeners on psychoacoustic measures, although statistically significant, may be small when compared to the magnitude of the differences in acoustic segment duration which signal phonetic contrasts in normal speech. In the case

of gap detection, there is no doubt that silent intervals in continuous speech can have linguistic importance. For example, introduction of a period of silence between the [s] and [l] in the word ''slit'' results in the perception of the word ''split'' (Bastian *et al.*, 1961; Marcus, 1978). Relative duration of the silent interval is also important. One of the cues to voicing in intervocalic stops (e.g., rapid–rabid) is the duration of closure for the stop consonant (Lisker, 1957). The question, therefore, may not be whether periods of silence are linguistically important but, rather, whether gap detection thresholds are so elevated in elderly listeners that these silent periods are poorly perceived. For example, in speech, when a silent interval signals the presence of a stop consonant in a cluster, that interval is on the order of 80 ms or longer, while the absence of a stop is signaled by intervals of less than 20 ms (Dorman *et al.*, 1985). The distinction between ''slit'' and ''split'' is evoked with a pause of at least 30–45 ms. Relative to the present data, the poorest gap detection threshold measured at the loudest presentation level among elderly listeners was approximately 15 ms, and most elderly listeners exhibited even better resolution at this sound level. Therefore linguistically relevant silent periods in speech should be easily perceived by these listeners if the signal-to-noise (S/N) ratio is adequate. However, at near-threshold levels, gap detection thresholds for elderly listeners ranged from 6 to 60 ms (as compared to the 4–15-ms range for young adult listeners), suggesting that the magnitude of the loss in some elderly listeners may be such that speech perception is adversely affected.

It may also be the case that the failure to find a significant correlation indicates that the mechanisms underlying detection of temporal gaps are somehow different from mechanisms underlying the ability to distinguish temporal characteristics of speech. Although a complete discussion is beyond the scope of this paper, there is evidence that speech stimuli are perceived and processed in a different way from nonspeech stimuli. The evidence derives from studies of categorical perception, the phenomenon that speech sounds can be discriminated only when they are identified as being linguistically different (Liberman *et al.*, 1967); from studies of cerebral asymmetry, which indicate that certain parts of the brain are specialized for dealing with speech (Broadbent and Gregory, 1964; Kimura, 1964); and from the speech–nonspeech dichotomy, which shows that when a listener is presented with speechlike sounds there is a perceptual dichotomy in that the sounds are either perceived as speech or they are not (House *et al.*, 1962; Stevens and House, 1972). Thus it appears that the perception of speech sounds may be fundamentally different from that of nonspeech stimuli, which could account for the lack of significant correlation observed between measures of monaural temporal processing in the present study. Finally, significant correlations might have been found if a similar presentation level was used for both psychoacoustic and speech perception measures or if different tasks had been used.

Despite the lack of observed correlations and potential differences in the underlying processes involved in temporal processing of speech and nonspeech stimuli, results of the present investigation still suggest an age-related decline in monaural temporal processing of elderly listeners for both speech and nonspeech stimuli, even when peripheral hearing sensitivity is considered clinically normal. Importantly, these deficits are likely to be exaggerated in listeners with hearing loss.

B. Aging and binaural processing

The present data demonstrate a clear age-related loss in the ability to lateralize the source of a sound on the basis of an interaural time delay, replicating results first reported by Matzker and Springborn in the late 1950s. Similar to findings of Herman *et al.* (1977), the present data revealed that older listeners required approximately twice the interaural time delay as young listeners for the same level of performance.

To examine how decreased sensitivity to interaural time differences might contribute to speech perception difficulties, binaural processing for speech was measured using the MLD. Because binaural processing is acutely sensitive to interaural time differences, any loss of temporal resolution in the nervous system would be expected to reduce the size of the MLD (Durlach, 1972). It was found that elderly listeners performed more poorly than young listeners, primarily for the $S_\pi N_0$ condition, contributing to a 2-dB age effect on the MLD. This supports ITD findings that the elderly have a reduced ability to process interaural time cues, even when they have normal hearing. The MLD difference, while not large numerically, is important because it represents another way in which the effects of age probably reduce hearing efficiency in complex listening situations. It has been demonstrated that a loss of 1 dB S/N ratio may result in as much as a 20% reduction in speech intelligibility (Plomp, 1986). Thus a loss of 2 dB S/N ratio could result in considerable difficulty in everyday listening. Furthermore, it should be remembered that while the experimental group in this study was composed of elderly individuals, they did not manifest clinical symptoms of hearing impairment. The deficits which they showed in binaural signal processing are likely to be exaggerated in listeners with significant hearing loss.

Since ITD and MLD thresholds both measure aspects of binaural processing of auditory stimuli, it was hypothesized that performance on the ITD task may be related to the ability to use directional cues to perceive speech in noise as measured by the MLD. Correlations between mean ITD threshold and mean MLD scores for subjects in the present study, however, did not reach statistical significance. This lack of significant correlation between the two measures is consistent with findings of Warren *et al.* (1978) using similar binaural measures. The failure to find a significant correlation is perhaps not surprising since the mechanisms involved in binaural signal analysis are complex. As previously suggested, results indicate that the binaural mechanisms underlying discrimination of interaural time differences are likely different from those of binaural processing for speech. Again, significant correlations might have been found if a similar presentation level was used for both psychoacoustic and speech perception measures or if different tasks had been used.

Although no significant correlations between measures of binaural processing were found, present findings do indi-

cate an age-related decline in binaural processing of temporal information in both speech and nonspeech stimuli. The reduced ability of elderly listeners to utilize interaural time cues has implications for tasks involving lateralization or localization. More importantly, the introduction of binaural, dichotic time cues has been shown to significantly improve the detection and perception of speech signals, especially in a background of noise. Although some of this ability arises from monaural cues such as frequency, timing, or syntax of the source, binaural cues improve the range of situations in which effective communication is possible. If the aging auditory system fails to preserve these cues, older adults may be at a functional disadvantage in the perception of speech in any situation where surrounding auditory space is noisy.

C. Relationships between psychoacoustic measures

Previous research has shown that temporal resolution worsens at low sound levels (Ashmead *et al.*, unpublished data; Buus and Florentine, 1985; Shailer and Moore, 1983; Viemeister, 1979). Present results revealed a significant interaction between age and sound level, indicating that at a given stimulus level older adults performed more poorly than younger adults, and this age difference increased as the overall stimulus level decreased. This interaction between age and signal level was found consistently across gap detection and ITD tasks. Thus the temporal resolution of elderly listeners was more adversely affected by low stimulus level, even when level was specified relative to individual thresholds. The contribution of spectral cues to the ability to detect temporal gaps as reported by Schneider *et al.* (1994), however, cannot be ruled out.

Correlations between the slopes of ITD and gap detection functions showed a highly significant positive relationship for young adult subjects, suggesting that changes in performance as a function of signal level were comparable across monaural and binaural types of processing. For elderly subjects, however, there was no significant correlation between the slope of the ITD function and that of the gap detection function. This result indicates that although there was a significant interaction of age and signal level across tasks, changes in performance as a function of signal level for elderly listeners were not consistent across measures. Thus the relationship between ITD and gap detection thresholds was quite different for young versus elderly subjects, indicating processing difficulties of the aging auditory system at low sound levels that are not attributable to a single, simple factor such as temporal resolution loss in the auditory periphery. Rather, the two types of temporal processing measured in this study may be affected differently by the aging process. It is likely that central factors play a role as well, especially with regard to ITD discrimination (vonWedel *et al.*, 1991; Yin and Chan, 1988). It also may be the case that binaural performance on the ITD task may have been affected by differences in monaural performance between ears on the gap detection task. Results for gap detection in the present study were obtained for one ear of each subject. Schneider *et al.* (1994) found that in older listeners, there were sometimes large differences in gap detection thresholds within the same subject between the two ears. Thus the fact that a significant correlation was found between gap detection and ITD performance in young but not older subjects may be because there are only small interaural differences in the gap detection thresholds of young listeners but larger differences may occur in older listeners.

IV. CONCLUSION

The results of this study support an age-related decrease in temporal processing ability. Elderly listeners had higher thresholds versus younger listeners on gap detection and ITD tasks, were less able to benefit from binaural release from masking, and were less accurate in discriminating changes in voice onset time. Importantly, these findings were observed in elderly listeners with no clinical symptoms of hearing loss. Findings support the following conclusions:

(1) Elderly persons with excellent hearing sensitivity nonetheless perform worse than younger persons on measures of temporal resolution and speech perception. It should be noted that although strict criteria were used to select subjects for the present study, future studies could apply more stringent criteria to ensure that elderly subjects have auditory peripheries that match those of young subjects.

(2) On measures of monaural and binaural processing of temporal information, elderly persons are more adversely affected than younger persons by having to listen at very low sound levels, even when those sound levels are defined with respect to individual thresholds.

(3) For younger persons, monaural performance (of one ear) and binaural performance were related when testing was performed at low sound levels (suggesting that the auditory system must be challenged in order to see individual differences), but for elderly persons there appeared to be no relation between measures of temporal resolution (perhaps suggesting unique effects of aging on specific auditory abilities).

(4) There is no evidence that individual differences in speech perception can be accounted for by temporal resolution abilities. This result is based on a limited number of subjects and a limited range of tasks.

ACKNOWLEDGMENTS

This work was supported by a Dissertation Enhancement Award through the Graduate School at Vanderbilt University. The authors express appreciation to Gene Bratt and Leslie Smith for constructive comments on an earlier version of this paper, Xuefeng Yang, for assistance in computer programming, and the Audiology staff at the VA Medical Center, Mountain Home, for comments and suggestions.

[1]To obtain masked thresholds for the gap detection task, each subject was presented with a 75 dB SPL continuous 1000-Hz pure tone. Using the computer keyboard, the subject manually attenuated the level of the tone until it was just barely audible in the noise background (descending series). A second threshold was measured using an ascending series, where the tone was initially presented at 0 dB SPL and the subject again adjusted the level of the tone until it was judged as barely audible. A third threshold was measured with the initial amount of attenuation adjusted to match the individual subject's threshold based on the first two threshold approximations, and the subject manually adjusted the level of the tone for a third time to a level just barely audible in the noise background. The mean of the three estimates was considered threshold. Masked tone thresholds ranged from 43 to 51 (mean=47.1) dB SPL for the young adult group and from 43 to

50 (mean=47.3) dB SPL for the elderly group. Masked gap detection thresholds for the 1000-Hz tone did not differ significantly between groups [$F(1,23)=0.073$, $p>0.05$].

[2]To obtain binaural click detection thresholds for the ITD task, each subject was presented with a 70 dB SPL continuous click train. A method of adjustment was used to determine individual thresholds, identical to that used in the gap detection task. Click thresholds ranged from 14 to 26 (mean=20.3) dB SPL for young adult listeners and from 18 to 28 (mean =23.3) dB SPL for the elderly group. Click thresholds did not differ significantly between groups [$F(1,23)=2.30$, $p>0.05$].

Abel, S. M., Krever, E. M., and Alberti, P. W. (**1990**). ''Auditory detection, discrimination and speech processing in aging, noise sensitive and hearing-impaired listeners,'' Scand. Audiol. **19**, 43–54.

ANSI (**1969**). ANSI S3.6-1969 (R 1973), ''Specifications for Audiometers'' (American National Standards Institute, New York).

Ashmead, D. H., Tetzeli, M., Chandler, D., and Thomas, A. (unpublished data). ''Aging and sound level effects in interaural time discrimination: Efficiency of auditory processing.''

AVAAZ Innovations, Inc. (**1994**). *Computerized Speech Research Environment* (Ontario, Canada).

Bacon, S. P., and Viemeister, N. F. (**1985**). ''Temporal modulation transfer functions in normal-hearing and hearing-impaired listeners,'' Audiology **24**, 117–134.

Bastian, J., Eimas, P. D., and Liberman, A. M. (**1961**). ''Identification and discrimination of a phonetic contrast induced by a silent interval,'' J. Acoust. Soc. Am. **33**, 842.

Blumstein, S. E., and Stevens, K. N. (**1980**). ''Perceptual invariance and onset spectra for stop consonants in different vowel environments,'' J. Acoust. Soc. Am. **67**, 647–662.

Broadbent, D. E., and Gregory, M. (**1964**). ''Accuracy of recognition for speech presented to the right and left ears,'' J. Exp. Psychol. **16**, 359–360.

Buus, S., and Florentine, M. (**1985**). ''Gap detection in normal and impaired listeners: The effect of level and frequency,'' in *Time Resolution in Auditory Systems*, edited by A. Michelson (Springer-Verlag, Berlin).

Cranford, J. L., Boose, M., and Moore, C. A. (**1990**). ''Effects of aging on the precedence effect in sound localization,'' J. Speech Hear. Res. **33**, 654–659.

DeFillippo, C. L., and Snell, K. (**1986**). ''Detection of temporal gaps in low-frequency narrow-band signals by normal-hearing and hearing-impaired listeners,'' J. Acoust. Soc. Am. **80**, 1354–1358.

Department of Veterans Affairs (**1991**). *Speech Recognition and Identification Materials (Disc 1.1.)* (Auditory Research Laboratory, VA Medical Center, Long Beach, CA).

Divenyi, P. L., and Haupt, K. M. (**1997**). ''Audiological correlates of speech understanding deficits in elderly listeners with mild-to-moderate hearing loss. III. Factor representation,'' Ear Hear. **18**, 189–201.

Dorman, M. F., Marton, K., Hannley, M. T., and Lindholm, J. M. (**1985**). ''Phonetic identification by elderly normal and hearing-impaired listeners,'' J. Acoust. Soc. Am. **77**, 664–670.

Dorman, M. F., Raphael, L. J., and Liberman, A. M. (**1979**). ''Some experiments on the sound of silence in phonetic perception,'' J. Acoust. Soc. Am. **65**, 1518–1532.

Dreschler, W. A., and Plomp, R. (**1985**). ''Relations between psychophysical data and speech perception for hearing impaired subjects. II,'' J. Acoust. Soc. Am. **78**, 1261–1270.

Durlach, N. I. (**1972**). ''Binaural signal detection: Equalization and cancellation theory,'' in *Foundations of Modern Auditory Theory*, edited by J. V. Tobias (Academic, New York).

Durlach, N. I., Thompson, C. L., and Colburn, H. S. (**1981**). ''Binaural interaction in impaired listeners: A review of past research,'' Audiology **20**, 181–211.

Erber, N. P. (**1972**). ''Speech-envelope cues as an acoustic aid to lipreading for profoundly deaf children,'' J. Acoust. Soc. Am. **51**, 1224–1227.

Festen, J. M., and Plomp, R. (**1983**). ''Relations between auditory functions in impaired hearing,'' J. Acoust. Soc. Am. **73**, 652–662.

Findlay, R. C., and Schuchman, G. I. (**1976**). ''Masking level difference for speech: Effects of ear dominance and age,'' Audiology **15**, 232–241.

Fitzgibbons, P. J. (**1983**). ''Temporal gap detection in noise as a function of frequency, bandwidth, and level,'' J. Acoust. Soc. Am. **74**, 67–72.

Fitzgibbons, P. J., and Gordon-Salant, S. (**1994**). ''Age effects on measures of auditory duration discrimination,'' J. Speech Hear. Res. **37**, 662–670.

Florentine, M., and Buus, S. (**1984**). ''Temporal gap detection in sensorineural and simulated hearing impairments,'' J. Speech Hear. Res. **27**, 449–455.

Fujisaki, S., and Kawashima, K. (**1970**). ''Some experiments on speech perception and a model for the perceptual mechanism,'' Annual Report of the Engineering Research Institute, Faculty of Engineering, University of Tokyo, Tokyo, Vol. 29, pp. 207–214.

Ginzel, A., Pedersen, C. B., Spliid, P. E., and Andersen, E. (**1982**). ''The role of temporal factors in auditory perception of consonants and vowels,'' Scand. Audiol. **11**, 93–100.

Glasberg, B. R., and Moore, B. C. J. (**1989**). ''Psychoacoustic abilities of subjects with unilateral and bilateral cochlear impairments and their relationship to the ability to understand speech,'' Scand. Audiol. **32**, 1–25.

Godfrey, J., and Millay, K. (**1978**). ''Perception and rapid spectral change in speech by listeners with mild and moderate sensorineural hearing loss,'' J. Am. Audiol. Soc. **3**, 200–208.

Gregory, R. L. (**1974**). ''Increase in neurological noise as a factor in aging,'' in *Concepts and Mechanisms of Perception*, edited by R. L. Gregory (Duckworth, London).

Grose, J. H., Poth, E. A., and Peters, R. W. (**1994**). ''Masking level differences for tones and speech in elderly listeners with relatively normal audiograms,'' J. Speech Hear. Res. **37**, 422–428.

Hausler, R., Colburn, S., and Marr, E. (**1983**). ''Sound localization in subjects with impaired hearing,'' Acta Oto-Laryngol. Suppl. **400**, 6–62.

Herman, G. E., Warren, L. R., and Wagener, J. W. (**1977**). ''Auditory lateralization: Age differences in sensitivity to dichotic time and amplitude cues,'' J. Gerontol. **32**, 187–191.

House, A. S., Stevens, K. N., Sandel, T. T., and Arnold, J. B. (**1962**). ''On the learning of speechlike vocabularies,'' J. Verb. Learn. Verb. Behav. **1**, 133–143.

Irwin, R. J., and McAuley, S. F. (**1987**). ''Relations among temporal acuity, hearing loss, and the perception of speech distorted by noise and reverberation,'' J. Acoust. Soc. Am. **81**, 1557–1565.

Jerger, J., Brown, D., and Smith, S. (**1984**). ''Effect of peripheral hearing loss in the masking level difference,'' Arch. Otolaryngol. **110**, 290–296.

Jesteadt, W., Bacon, S. P., and Lehman, J. R. (**1982**). ''Forward masking as a function of frequency, masker level, and signal delay,'' J. Acoust. Soc. Am. **71**, 950–962.

Kelly-Ballweber, D., and Dobie, R. A. (**1984**). ''Binaural interaction measured behaviorally and electrophysiologically in young and old adults,'' Audiology **23**, 181–194.

Kimura, D. (**1964**). ''Left-right differences in the perception of melodies,'' J. Exp. Psychol. **16**, 355–358.

Kirikae, I. (**1969**). ''Auditory function in advanced age with reference to histological changes in the central auditory system,'' Intern. Audiol. **8**, 221–230.

Klatt, D. H. (**1975**). ''Voice onset time, frication, and aspiration in word-initial consonant clusters,'' J. Speech Hear. Res. **18**, 686–706.

Klatt, D. H. (**1980**). ''Software for a cascade/parallel formant synthesizer,'' J. Acoust. Soc. Am. **67**, 971–995.

Levitt, H. (**1971**). ''Transformed up-down methods in psychoacoustics,'' J. Acoust. Soc. Am. **49**, 467–477.

Liberman, A. M., Cooper, F. S., Shankweiler, D. P., and Studdert-Kennedy, M. (**1967**). ''Perception of the speech code,'' Psychol. Rev. **74**, 431–461.

Lisker, L. (**1957**). ''Closure duration and the inter-vocalic voiced-voiceless distinction in English,'' Language **33**, 42–49.

Lisker, L., and Abramson, A. S. (**1970**). ''The voicing dimension: Some experiments in comparative phonetics.'' in *Proceedings of the VI International Congress of Phonetic Sciences* (Academia, Prague).

Lutman, M. E., and Clark, J. (**1986**). ''Speech identification under simulated hearing-aid frequency response characteristics in relation to sensitivity, frequency resolution, and temporal resolution,'' J. Acoust. Soc. Am. **89**, 1030–1040.

Marcus, S. M. (**1978**). ''Distinguishing 'slit' and 'split'-an invariant timing cue in speech perception,'' Percept. Psychophys. **23**, 58–60.

Martin, D. R., and Cranford, J. L. (**1991**). ''Age-related changes in binaural processing. II. Behavioral findings,'' Am. J. Otolaryngol. **12**, 365–369.

Matzker, V. J., and Springborn, E. (**1958**). ''Richtungshoren und lebensalter,'' Zeitschrift fur Laryngologie, Rhinologie, Otologie und Ihre Grenzgebiete **37**, 739–745.

Moore, B. C. J. (**1982**). *Introduction to the Psychology of Hearing* (Academic, London).

Moore, B. C. J., and Glasberg, B. R. (**1983**). ''Growth of forward masking for sinusoidal and noise maskers as a function of signal delay: Implication for suppressions in noise,'' J. Acoust. Soc. Am. **73**, 1249–1259.

Moore, B. C. J., and Glasberg, B. R. (**1988**). ''Gap detection with sinusoids and noise in normal, impaired, and electrically stimulated ears,'' J. Acoust. Soc. Am. **83**, 1093–1101.
Moore, B. C. J., Glasberg, B. R., Donaldson, E., McPherson, T., and Plack, C. J. (**1989**). ''Detection of temporal gaps in sinusoids by normally hearing and hearing-impaired subjects,'' J. Acoust. Soc. Am. **85**, 1266–1275.
Moore, B. C. J., Peters, R. W., and Glasberg, B. R. (**1992**). ''Detection of temporal gaps in sinusoids by elderly subjects with and without hearing loss,'' J. Acoust. Soc. Am. **92**, 1923–1932.
Moore, B. C. J., Peters, R. W., and Glasberg, B. R. (**1993**). ''Detection of temporal gaps in sinusoids: Effects of frequency and level,'' J. Acoust. Soc. Am. **93**, 1563–1570.
Olsen, W. O., Noffsinger, D., and Carhart, R. (**1976**). ''Masking level differences encountered in clinical populations,'' Audiology **15**, 287–301.
Palva, A., and Jokinen, K. (**1970**). ''Presbyacusis,'' Acta Oto-Laryngol. **70**, 232–241.
Pichora-Fuller, M. K., and Schneider, B. A. (**1991**). ''Masking level differences in the elderly: A comparison of antiphasic and time-delay dichotic conditions,'' J. Speech Hear. Res. **34**, 1410–1422.
Pichora-Fuller, M. K., and Schneider, B. A. (**1992**). ''The effect of interaural delay of masker on masking-level differences in young and old adults,'' J. Acoust. Soc. Am. **91**, 2129–2135.
Pickett, J. M., and Decker, L. R. (**1960**). ''Time factors in the perception of a double consonant,'' Lang. Speech **3**, 11–17.
Plomp, R. (**1986**). ''A signal-to-noise ratio model for the speech reception threshold of the hearing-impaired,'' J. Speech Hear. Res. **29**, 146–154.
Pollack, I., and Pisoni, D. B. (**1971**). ''On the comparison between identification and discrimination tests in speech perception,'' Psychonom. Sci. **24**, 299–300.
Price, P. J., and Simon, H. J. (**1984**). ''Perception of temporal differences in speech by normal-hearing adults: Effects of age and intensity,'' J. Acoust. Soc. Am. **72**, 405–410.
Repp, B., Liberman, A. M., Eccardt, T., and Pesetsky, D. (**1978**). ''Perceptual integration and differentiation of acoustic cues for stop, fricative, and affricate manner,'' J. Exp. Psychol. Hum. Percept. Perf. **4**, 621–637.
Roush, J. (**1985**). ''Aging and binaural auditory processing,'' Sem. Hear. **6**, 135–146.
Schneider, B. A. (**1997**). ''Psychoacoustics and aging: Implications for everyday listening,'' J. Speech Lang. Path. Audiol. **21**, 111–124.
Schneider, B. A., Pichora-Fuller, M. K., Kowalchuk, D., and Lamb, M. (**1994**). ''Gap detection and the precedence effect in young and old adults,'' J. Acoust. Soc. Am. **95**, 980–991.
Schouten, M. E. H. (**1980**). ''The case against the speech mode of perception,'' Acta Psychol. **44**, 71–98.
Shailer, M. J., and Moore, B. C. J. (**1983**). ''Gap detection as a function of frequency, bandwidth, and level,'' J. Acoust. Soc. Am. **74**, 467–473.
Sharf, D. J., Ohde, R. N., and Lehman, M. E. (**1988**). ''Relationship between the discrimination or /w-r/ and /t-d/ continua and the identification of distorted /r/,'' J. Speech Hear. Res. **31**, 193–206.
Snell, K. B. (**1997**). ''Age-related changes in temporal gap detection,'' J. Acoust. Soc. Am. **101**, 2214–2220.
Stevens, K. N., and House, A. S. (**1972**). ''Speech perception,'' in *Foundation of Modern Auditory Theory, Volume 2*, edited by J. V. Tobias (Academic, New York).
Stevens, K. N., Liberman, A. M., Studdert-Kennedy, M., and Ohman, S. E. G. (**1969**). ''Crosslanguage study of vowel perception,'' Lang. Speech **12**, 1–23.
Tillman, T. A., Carhart, R., and Nicholls, S. (**1973**). ''Release from multiple maskers in elderly persons,'' J. Speech Hear. Res. **16**, 152–160.
Trainor, L. J., and Trehub, S. E. (**1989**). ''Aging and auditory temporal sequencing: Ordering the elements of repeating tone patterns,'' Percept. Psychophys. **45**, 417–426.
Tyler, R. S., and Summerfield, Q. (**1980**). ''Psychoacoustical and phonetic measures of temporal processing in normal and hearing-impaired listeners,'' in *Psychophysical, Physiological, and Behavioural Studies in Hearing*, edited by G. van den Brink and F. A. Bilsen (Delft U.P., Delft).
Tyler, R. S., Summerfield, Q., Wood, E. J., and Fernandes, M. A. (**1982**). ''Psychoacoustic and phonetic temporal processing in normal and hearing-impaired listeners,'' J. Acoust. Soc. Am. **72**, 740–752.
vanRooij, J. C. G. M., and Plomp, R. (**1990**). ''Auditive and cognitive factors in speech perception by elderly listeners. II. Multivariate analyses,'' J. Acoust. Soc. Am. **88**, 2611–2624.
vonWedel, H., vonWedel, U., and Streppel, M. (**1991**). ''Monaural and binaural time resolution ability in the aged,'' Acta Oto-Laryngol. **476**, 161–166.
Viemeister, N. F. (**1979**). ''Temporal modulation transfer functions based on modulation thresholds,'' J. Acoust. Soc. Am. **66**, 1364–1380.
Wardrip-Fruin, C. (**1982**). *Final Stop Voicing: Vowel Duration the Primary Cue in Noise*, Meetings of the American Speech and Hearing Association, November.
Warren, L. R., Wagener, J. W., and Herman, G. E. (**1978**). ''Binaural analysis in the aging auditory system,'' J. Gerontol. **33**, 731–736.
Wilson, R. H., Hopkins, J. L., Mance, C. M., and Novak, R. E. (**1982**). ''Detection and recognition masking-level differences for the individual CID W-1 spondaic words,'' J. Speech Hear. Res. **25**, 235–242.
Yin, T. C. T., and Chan, J. C. K. (**1988**). ''Neural mechanisms underlying interaural time sensitivity to tones and noise,'' in *Auditory Functioning: Neurobiological Bases of Hearing*, edited by G. M. Edelman, W. E. Gall, and W. M. Cowan (Wiley, New York).
Zwislocki, J., and Feldman, R. S. (**1956**). ''Just noticeable differences in dichotic phase,'' J. Acoust. Soc. Am. **28**, 860–864.

Analyzing head-related transfer function measurements using surface spherical harmonics

Michael J. Evans
Electronic Engineering Group, University of Reading, Reading RG6 6AY, United Kingdom

James A. S. Angus and Anthony I. Tew
Department of Electronics, University of York, York YO10 5DD, United Kingdom

(Received 30 October 1996; revised 17 June 1998; accepted 22 June 1998)

A continuous, functional representation of a large set of head-related transfer function measurements (HRTFs) is developed. The HRTFs are represented as a weighted sum of surface spherical harmonics (SSHs) up to degree 17. A Gaussian quadrature method is used to pick out a set of experimentally efficient measurement directions. Anechoic impulse responses are measured for these directions between a source loudspeaker and the entrance to the ear canal of a head-and-torso simulator (HATS). Three separate SSH analyses are carried out: The first forms a SSH representation from the time responses, with the variable onset delay caused by interaural differences intact, by applying the analysis to each time sample in turn. The second SSH model is formed in exactly the same way, except using impulse responses in which the variable onset delays have been equalized. The final SSH analysis is carried out in the frequency domain by applying the technique on a frequency bin by frequency bin basis to the magnitude and unwrapped phase responses of the HRTFs. The accuracy and interpolation performance of each of the computed SSH models is investigated, and the usefulness of the SSH technique in analyzing directional hearing and, particularly, in spatializing sounds is discussed. [S0001-4966(98)01310-1]

PACS numbers: 43.66.Pn, 43.66.Qp, 43.66.Ba [RHD]

INTRODUCTION

Human sound localization makes use of the filtering which sound is subjected to between its source and the tympanic membrane. These acoustic transfer functions are known as head-related transfer functions (HRTFs) and arise due to directionally dependent filtering caused by the head, torso, and pinna shape. Notionally, a pair of HRTFs, one corresponding to the path from source to the left ear and the other the right, contains all the acoustic cues that the auditory system will use to make a localization judgement. Therefore, a sound signal filtered with HRTFs and reproduced over headphones, or a suitably setup loudspeaker system, should be perceived as emanating from the appropriate direction. (See Wightman and Kistler, 1989, among others.)

However, the application of HRTF data to sound spatialization is subject to a severe drawback if effective and flexible spatialization is required: In general, we would wish to be able to create the illusion of sound emanating from an arbitrary direction, and not merely those at which experimental measurements have been made. To simulate every conceivable direction, create sound sources which appear to move smoothly through space, or to include head tracking so that spatialization is resilient to head movements requires an extremely large (ideally infinite) set of HRTFs. Measuring a particular HRTF pair is merely a process of sampling one direction in auditory space, a space which, ideally, should be represented continuously.

This problem of restricted directional resolution can be alleviated by forming a continuous, functional representation of an HRTF data set, expressing the HRTFs mathematically, as a continuous function of direction. Two functional representations of HRTF measurements have previously been investigated: The first of these applied principal components analysis (PCA) (Kistler and Wightman, 1992) to a large set of HRTF magnitude responses (256 directions for each of 10 subjects). The analysis yielded a set of principle components present in each of the HRTFs, and weights expressing the contribution of each of these components to each particular HRTF. Thus each HRTF in the set could be expressed in the form of a weighted sum of these principal components. The authors verified the psychoacoustic effectiveness of the technique by means of perceptual tests. However, this PCA representation was not continuous. Simulation of directions at which no experimental measurements were taken was impossible because the PCA weights for these directions were not available.

A second technique of functional representation, employed in Chen *et al.* (1995), uses the Karhunen–Loeve expansion to represent complex frequency domain HRTFs as a series of orthogonal Eigentransfer functions (EFs). From the point of view of continuous spatialization, this is a very useful representation as it is genuinely continuous, allowing unmeasured directions to be simulated, and includes phase as well as magnitude data. Additionally, resonances in the EFs may highlight a number of important frequencies for a model of the human ear.

This paper develops an alternative form of continuous, orthogonal representation by expressing an HRTF data set as a weighted sum of surface spherical harmonics (SSHs)—a hierarchical set of basis functions which are orthogonal upon the surface of a sphere. The SSH weights are calculated from

a limited set of experimental measurements by means of a discrete Fourier analysis. The resulting spherical harmonic representation is continuous, yielding a modeled HRTF for any arbitrary direction. It is also hierarchical, in that the more harmonics that are included the greater the accuracy of the model. Third, the representation has a meaningful spatial structure, with particular SSH weights expressing particular patterns of directional variation in the HRTF set. Analysis is carried out in the time and frequency domains, in order to assess the usefulness of the representation to data in both these forms.

I. SPHERICAL HARMONIC ANALYSIS

A. Surface spherical harmonics as basis functions

Conventional, one-dimensional signal processing makes use of sinusoidal harmonics as the basis functions of Fourier analysis. Surface spherical harmonics (SSHs) may be similarly applied to the analysis of functions on the surface of a sphere—$f(\theta,\phi)$ where $0°\leqslant\phi<180°$ and $0°\leqslant\theta<360°$. This is possible because SSHs form a complete, orthogonal set over this surface (Kaplan, 1981). Spherical harmonics arise as the solution to the Laplace equation expressed in spherical polar coordinates. SSHs are the special case spherical harmonics in which the distance coordinate is constant. We may define the SSHs (normalized so that their integrals over the surface of the sphere are unity) as

$$u_{0n}(\theta,\phi)=\frac{(2n+1)}{4\pi}\cos m\theta P_n^m(\cos\phi),\quad m=0,$$
$$u_{mn}(\theta,\phi)=\frac{(n-m)!(2n+1)}{2\pi(n+m)!}\cos m\theta P_n^m(\cos\phi),\quad m=1,...,n,$$
$$\nu_{mn}(\theta,\phi)=\frac{(n-m)!(2n+1)}{2\pi(n+m)!}\sin m\theta P_n^m(\cos\phi),\quad m=1,...,n, \tag{1}$$

where P_n^m are the *associated Legendre functions* defined by

$$P_n^m(x)=-1^m(1-x^2)^{m/2}\frac{d^m}{dx^m}\times\left[\frac{1}{2^n n!}\frac{d^n}{dx^n}(x^2-1)^n\right],\quad n=1,2,\ldots. \tag{2}$$

The parameter n represents the degree of each particular harmonic: u_{00} is the fundamental SSH. The three first-degree harmonics are denoted by u_{01}, u_{11}, and ν_{11}. There are five second-degree harmonics, seven third-degree harmonics, and so on. The first few SSHs, listed below, will have a structure familiar to chemists as they form the electron shell patterns of ''*s*'' (fundamental), ''*p*'' (first-degree), ''*d*'' (second-degree), and ''*f*'' (third-degree) orbitals;

$$u_{00}=\sqrt{\frac{1}{4\pi}},\quad u_{01}=\sqrt{\frac{3}{4\pi}}\cos\phi,$$
$$u_{11}=-\sqrt{\frac{3}{4\pi}}\cos\theta\sin\phi,$$
$$\nu_{11}=-\sqrt{\frac{3}{4\pi}}\sin\theta\sin\phi,\ldots.$$

Because these harmonics form a complete, orthogonal set any function of (θ,ϕ) can be approximated by a weighted sum of SSH components, up to the desired degree:

$$f(\theta,\phi)\approx U_{00}u_{00}+U_{01}u_{01}+U_{11}u_{11}+V_{11}\nu_{11}+U_{02}u_{02}+U_{12}u_{12}+V_{12}\nu_{12}+U_{22}u_{22}+V_{22}\nu_{22}+\cdots.$$

The weights required to express a function $f(\theta,\phi)$ in this way can be calculated by Fourier analysis:

$$U_{mn}=\int_{\phi=0}^{\pi}\int_{\theta=0}^{2\pi}f(\theta,\phi)u_{mn}(\theta,\phi)\sin\phi\,d\phi\,d\theta,\quad 0\leqslant m\leqslant n, \tag{4}$$

$$V_{mn}=\int_{\phi=0}^{\pi}\int_{\theta=0}^{2\pi}f(\theta,\phi)\nu_{mn}(\theta,\phi)\sin\phi\,d\phi\,d\theta,\quad 1\leqslant m\leqslant n. \tag{5}$$

B. Calculating SSH weights from HRTF data

Equations (4) and (5) allow the calculation of the SSH weights given a continuous function $f(\theta,\phi)$. However, in this investigation we do not have such a function, but instead a set of HRTF impulse responses. Spherical harmonic analysis (SHA) can be applied to the responses for each individual time sample. Thus the representation will be of the form of a new set of weights for each instant of time. Equations (4) and (5) must also be adapted so that the weights U_{mn} and V_{mn} may be calculated given that only discrete values of $f(\theta,\phi)$ are available, effectively sampled at each direction in which a physical HRTF was measured. Thus it is necessary for the integration denoted in Eqs. (4) and (5) to be approximated by means of a summation over N discrete points:

$$\int_{\phi=0}^{\pi}\int_{\theta=0}^{2\pi}f(\theta,\phi)u_{mn}(\theta,\phi)\sin\phi\,d\phi\,d\theta\approx\sum_{i=1}^{N}w_i f(\theta_i,\phi_i)u_{mn}(\theta_i,\phi_i). \tag{6}$$

Equation (6) is of the form:

$$\int_s F(\theta,\phi)dS\approx\sum_{i=1}^{N}a_i F(\theta_i\phi_i). \tag{7}$$

This operation is, therefore, one of numerical integration across the region formed by the surface of a sphere. Ideally, we wish the approximation to the continuous integral to be exact.

McLaren (1963) and Stroud (1971) describe efficient methods for exact numerical integration of this form, in terms of the discrete directions and corresponding weights to use for computing up to a particular maximum SSH degree. Although such optimal sets of directions and weights minimize the number of directions that need be considered, given a particular SSH degree, in terms of *experimental* efficiency they are not, in general, suitable for HRTF analysis. Gener-

ally, the optimal directions for numerical integration on the sphere are not distributed in a pattern along which experimental measurements can conveniently be made. In Atkinson (1982) an alternative set of directions and weights for exactly this integration is developed. This set is less mathematically efficient, since it requires a greater number of individual directions to integrate exactly functions up to a given degree. However, the choice of discrete directions is more experimentally practical. The approximation is based on following relationship:

$$\int_{\phi=0}^{\pi}\int_{\theta=0}^{2\pi} F(\theta,\phi)\sin\,\phi\; d\theta\; d\phi \approx \frac{\pi}{n}\sum_{j=1}^{n}\sum_{i=1}^{2n} w_j F(\theta_i,\phi_j). \tag{8}$$

Under this approximation, measurements are made at the same set of angles of azimuth, θ_i, for each of a set of n angles of elevation, ϕ_j. The $2n$ angles of azimuth are equally spaced, thus forming a ''rectangular'' mesh of directions which permits more systematic experimental measurements. In order to gain some mathematical efficiency, and maintain the exactness of the approximate integration, *product Gaussian quadrature* is used to select the n angles of elevation. The *Gauss–Legendre* quadrature formula uses weighting and an unequal spacing of sampling points to exactly integrate functions varying between -1 and $+1$. This approach can be applied to the spherical integration region of Eq. (8) by selecting the angles of elevation ϕ_j so that that $\cos(\phi_j)$ and w_i are the Gauss–Legendre nodes and weights for degree n. [These values can be found in tables such as those of Stroud and Secrest (1966).] Using this choice of directions Eq. (8) permits the exact numerical integration of all functions $F(\theta,\phi)$ less than degree $2n$ (Stroud, 1971). In SSH analysis, since $F(\theta,\phi)$ is the product of the function under analysis and a particular SSH, it is apparent that this approximation can be used to calculate exactly the weights for SSH components up to and including degree $n-1$.

II. MEASUREMENT AND PROCESSING OF HRTFs

A. Measurement

We define the HRTF as the impulse response between a sound source and the entrance to the ear canal. A set of 648 HRTF measurements were analyzed by means of an SSH analysis. This corresponds to setting $n=18$ in Eq. (8), thus requiring measurements with a 10° azimuthal spacing at each of 18 angles of elevation; ±5.0°, ±14.5°, ±24.0°, ±34.0°, ±44.0°, ±53.5°, ±63.0°, ±73.0°, and ±82.5°, where 0° elevation refers to the horizontal plane. Such a set of HRTF measurements allows the calculation of SSH component weights of up to and including degree 17.

The impulse responses were measured by means of maximum-length sequence (MLS) analysis, using a MLSSA system (DRA Laboratories). MLSSA makes use of pseudo-random sequences to measure audio impulse responses between a source loudspeaker and a pickup microphone. The use of MLSSA in HRTF measurement is described in detail in Møller *et al.* (1995). The measurements were made in an anechoic chamber (measuring approximately 3 m×3 m×3 m) at BT Laboratories, Martlesham Heath, using a Bruel & Kjaer 4127 head-and-torso simulator (HATS) mounted on a turntable, and a Auratone loudspeaker in a movable bracket on an arched frame. It is estimated that the directional error in positioning the loudspeaker and HATS ears relative to each other was rarely more than 0.5° and never more than 1°. Schematics of the measurement setup are illustrated in Fig. 1.

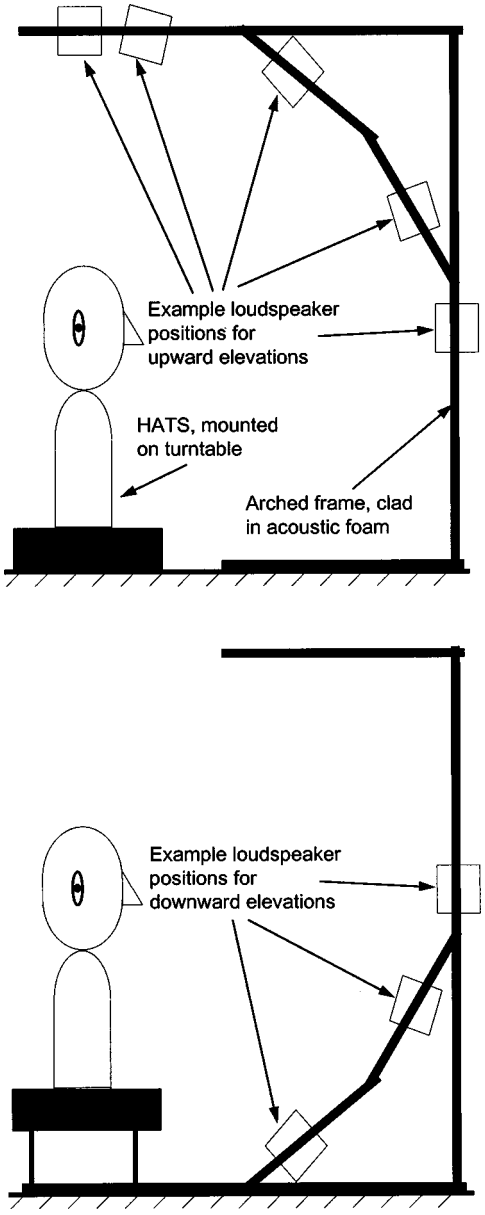

FIG. 1. Schematics of HRTF measurement apparatus in the anechoic chamber.

The HATS is a symmetrical piece of apparatus in the median plane. Therefore, measurements only had to be made using one of the in-ear microphones. MLSSA sampled the signal from the right ear microphone at 60.60 kHz, discarded the first 220 samples, which accounted for the majority of the bulk delay, and then retained a 512 sample impulse response. Each response was averaged over 16 repetitions to improve the signal-to-noise ratio.

These impulse response measurements contained the effects of the transfer functions of the loudspeaker and the

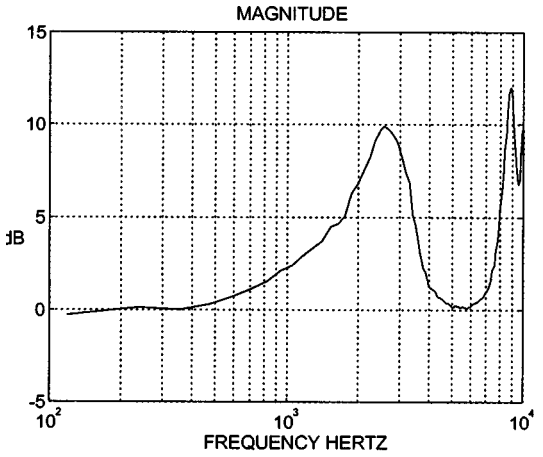

FIG. 2. Magnitude spectrum of HATS ear canal, as measured using a probe microphone.

in-ear microphone, together with a group delay which was slightly variable due to the repositioning of the speaker on the bracket. In order that these effects could be alleviated at processing time, a free-field measurement, using an identically calibrated microphone placed at the center-head position with the HATS removed, was taken each time the loudspeaker was repositioned. These responses contained the microphone and loudspeaker transfer functions, and the effects of distance between the HATS and the loudspeaker (always maintained at greater than 1 m). Also, since the HATS microphones are placed at the eardrum position and the HRTF refers to the sound as detected at the entrance to the ear canal, the impulse response of the ear canal was measured. This measurement was made by pointing the loudspeaker directly at the ear and finding the difference in response between the standard eardrum microphone, and a probe microphone placed in front of an occluded ear canal (as in Møller *et al.*, 1995). The magnitude spectrum of the ear canal response is shown in Fig. 2 and displays resonances at approximately 3 and 10 kHz.

B. Processing

The impulse response data collected in the anechoic chamber were processed using the MATLAB software package. The free-field responses and ear canal response were deconvolved out of the HATS measurements by means of a complex division in the frequency domain. (DFTs of twice the impulse response sequence length were used to avoid circular convolution effects.) This compensation yielded the impulse responses which would have been detected at the entrance to the ear canal. Some of the responses showed a small amount of reflection, probably due to the turntable surface. This reflection was windowed out. The HRTFs were downsampled to 20.20 kHz, as the effective performance of the HATS is only specified for frequencies up to 10 kHz, and truncated to a length of 96 samples. Those HRTFs measured at the lowest four angles of elevation (effectively at angles in excess of 50° beneath the horizontal plane) were extremely distorted by the structure of the apparatus. (The underside surface of the HATS, an artifact that does not exist in real listeners, occluded the direct path to the ear.) In order that the presence of these responses in the global data set did not distort the SSH analysis, these HRTFs were removed. For these four angles of elevation the HRTFs measured at the lowest reliable angle of elevation were simply reused. Thus below this angle, the HRTFs were effectively considered to be independent of elevation angle.

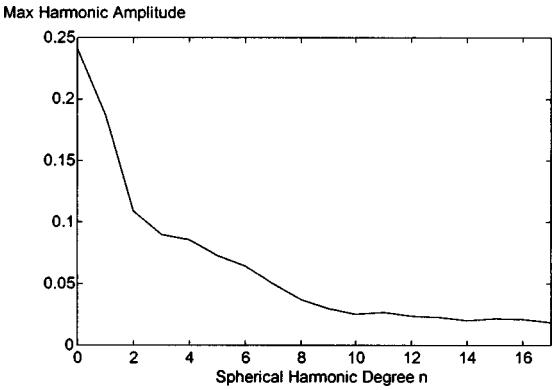

FIG. 3. Spherical harmonic spectrum of SSH representation (using maximum values over time).

III. SSH REPRESENTATION OF TIME-DOMAIN HRTFs

A. Structure of SSH representation

The HRTF data processed and measured in the previous section were sufficient to calculate SSH weights of up to and including degree 17. The SSH analysis yielded data in the form of 324 weights coefficients for each of the 96 impulse response samples. Therefore, for each sample a weighted sum of SSHs can be formed; a continuous functional representation of the HRTFs at that instant of time, as discussed in the Introduction to this paper. An alternative way of looking at this representation is to consider that the vector of weights of a particular SSH component forms a function of time; effectively a discrete-time impulse response. Thus we have broken the global set of HRTFs for all directions into a set of common components. Each HRTF is a weighted sum of these components with the weights being the value of the appropriate SSH at that direction. This view is not unlike the PCA representation of Kistler and Wightman (1992) except that the SSH representation is a continuous one.

Higher degree SSH components in the representation correspond to the finer detail on the response, in the same way that higher order sinusoidal harmonics contain the fine detail in 1-D Fourier analysis. The spherical harmonic spectrum (SHS) is defined in Pollack *et al.* (1993) as $\sqrt{\Sigma_m(U_{mn}^2+V_{mn}^2)/(2n+1)}$ for each degree n. This spectrum corresponds to the rms value of the weights of SSH components of a particular degree. Figure 3 illustrates the SHS of the time-domain HRTF model: (To take account of the time domain structure of the model, the maximum amplitude over all time samples was taken for each degree n.)

The structure of this spectrum shows a clear downward trend in the average contribution made by harmonics of increasing degree. This is a very encouraging result as it indicates a decrease in physical sensitivity for smaller changes in direction. Having said this, the harmonic amplitude at the

TABLE I. Average mean-square error percentages between measured and 17th degree SSH simulated HRTFs for each octant.

Octant	Front ($\theta \leqslant 45°; \theta \geqslant 315°$)	Shadowed side ($45° \leqslant \theta \leqslant 135°$)	Back ($135° \leqslant \theta \leqslant 225°$)	Unshadowed side ($225° \leqslant \theta \leqslant 315°$)
Above horizontal ($0° \leqslant \phi \leqslant 90°$)	1.93%	5.88%	2.60%	1.32%
Below horizontal ($90° \leqslant \phi \leqslant 180°$)	8.50% (3.67%)	10.46% (6.33%)	8.68% (2.79%)	3.01% (1.74%)

17th degree is still significant; indeed, the spectrum seems to be levelling off. This indicates the presence of even higher harmonics in the HRTF set. It seems likely that these very high-degree components arise, in part, from the ITD information in the HRTFs, which is in the form of a variable onset delay before the response begins. HRTFs in close directional proximity, even those which appear to have similarly shaped responses, will differ greatly in a sample-by-sample analysis such as this.

The existence of these delays also precludes the calculation of useful error values in the time domain. Therefore, the performance of the SSH model in accurately approximating experimentally measured HRTFs has been assessed in the frequency domain. The error metric assessed is mean-square error in the magnitude spectrum. (Phase response error values were generally found to be considerably smaller due to the dominance of group delay.) The error performance of the SSH model was investigated for two different classes of direction; those for which physical measurements were actually made and contributed toward the derivation of the model—*Recreation*—and directions for which the SSH analysis had no experimental reference—*Interpolation*.

B. HRTF recreation performance

The percentage mean-square error between the magnitude spectra of measured and simulated HRTFs for recreated response directions is shown in Table I. The figures are given as averages across each of the eight octants. (Note: The bracketed percentages are the averages obtained when the lowest four angles of elevation, for which dummy data were used in the analysis, are excluded from the error analysis.)

These values show that, in general, the recreation of HRTFs is better above the horizontal plane than below it; better at the source-facing side of the head than in the head's acoustic shadow; and generally better in the front hemisphere than in the rear. Figure 4 illustrates some example experimental HRTF measurements, with their SSH simulation overlaid.

The responses in Fig. 4 qualitatively show that the SSH model recreates the experimental responses with, generally, very high accuracy. Within the main part of the HRTFs very little difference between measured and simulated responses is visible. Much of the error that does arise seems to be as a result of the time-domain nature of the analysis, coupled with the fact that the variable onset delays were retained in the responses so that ITD would be included in the model. For example, the response for 24.5° elevation and 90° azimuth, a response corresponding to a source on the shadowed side of the head, contains a clearly visible and spurious ''pre-echo'' before the onset of the true response. This almost certainly occurs due to the presence in the SSH analysis set of those HRTFs measured on the unshadowed side of the head. These responses have a high amplitude and a short onset delay, relative to those on the shadowed side. Another source of error, generally less visible, is a ''widening'' of peaks in the simulated HRTFs due to interpolation between responses where similar peaks are separated by a few samples.

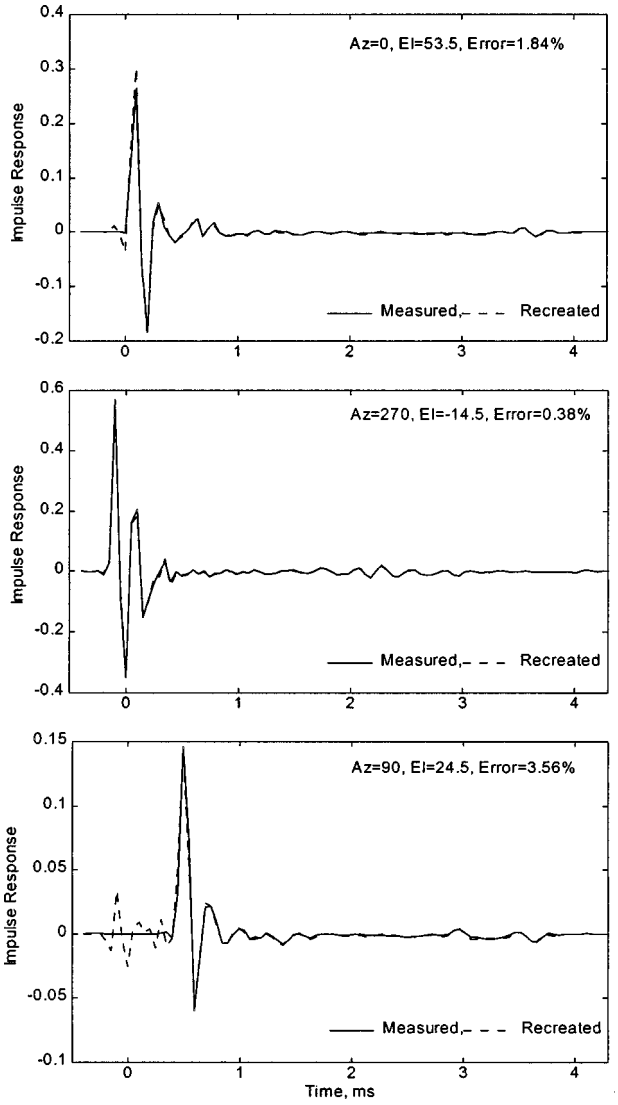

FIG. 4. Example measured and recreated HRTFs.

TABLE II. Average mean-square error percentages for different azimuths with 17th degree SSH model used for HRTF interpolation.

	$\theta=0°$	$\theta=45°$	$\theta=90°$	$\theta=135°$	$\theta=180°$	$\theta=225°$	$\theta=270°$	$\theta=315°$
Above horiz. ($0°\leqslant\phi\leqslant 90°$)	8.69%	6.93%	12.77%	7.79%	3.26%	7.82%	10.31%	8.85%
Below horiz. ($90°\leqslant\phi\leqslant 180°$)	11.06%	11.41%	15.53%	11.19%	7.33%	6.53%	19.27%	5.66%

C. HRTF simulation performance

In order to assess how accurately the SSH model can generate interpolated HRTFs an additional set of 32 experimental HRTFs was measured. These responses were processed in exactly the same way as those used in the SSH analysis. These extra measurements were spaced throughout the sphere, using angles of elevation $\pm 20°$ and $\pm 59.5°$ (the 4th degree Gauss–Legendre directions), and with an azimuthal spacing of 45°. This distribution places the measurements between the directions which were actually used in the SSH analysis. Average mean-square error percentages for the magnitude spectra of these interpolated directions are given in Table II.

The results in Table II show that the accuracy of interpolation is significantly, but not grossly, less than the accuracy of recreation. Again, in general, the upper hemisphere is simulated more accurately than the lower. However, now the rear hemisphere is simulated with significantly greater accuracy than the front, and the shadowed and unshadowed sides are approximated with a similar degree of accuracy. Figure 5 qualitatively illustrates the measured and simulated responses for some of these interpolated directions:

These responses illustrate the following significant features of the interpolated responses: They show that interpolation errors seem to occur because of the effects of averaging and, as before, of the variable onset delay. In the upper response a reduction in the height of the peaks is visible. The middle plot shows an interpolated HRTF which appears to be fractionally delayed with respect to the physically measured response, and the lower response exhibits a slight ''widening'' of the peaks in the interpolated response.

IV. ANALYSIS OF ITD EQUALIZED RESPONSES

The bulk of the approximation errors in the time-domain SSH model appear to arise as a result of the variable onset delay present in the HRTF responses being analyzed. In order to examine the actual effects of these variations on the model the time-domain SSH analysis was repeated. However, this time the onset delays, the basis of the ITD information, were equalized in order that each response should begin at the same instant. (Chen *et al.* also carried out such ITD equalization prior to their KLE analysis.) For this analysis the delays were equalized very simply by going through each of the 648 HRTFs in turn, detecting the sample at which the response first exceeded an onset threshold of 0.015, and cropping the response 4 samples before this point. This choice of thresholding was chosen as it was not affected by the very small variations in the unequalized HRTFs that occurred prior to the onset of the true response. (Note: In Sec. II the compensation of the anechoic chamber measurements using a free-field response measured at the center-head position was described. Notionally, by stripping away the ITD information from the front of the HRTFs we should be left with the responses that would have been obtained had the free-field measurements been made at the ear position.) The equalized HRTFs were then truncated to 64 samples in length.

The SSH analysis of the previous section was then repeated, exactly as it had been before, for each of the 64 time

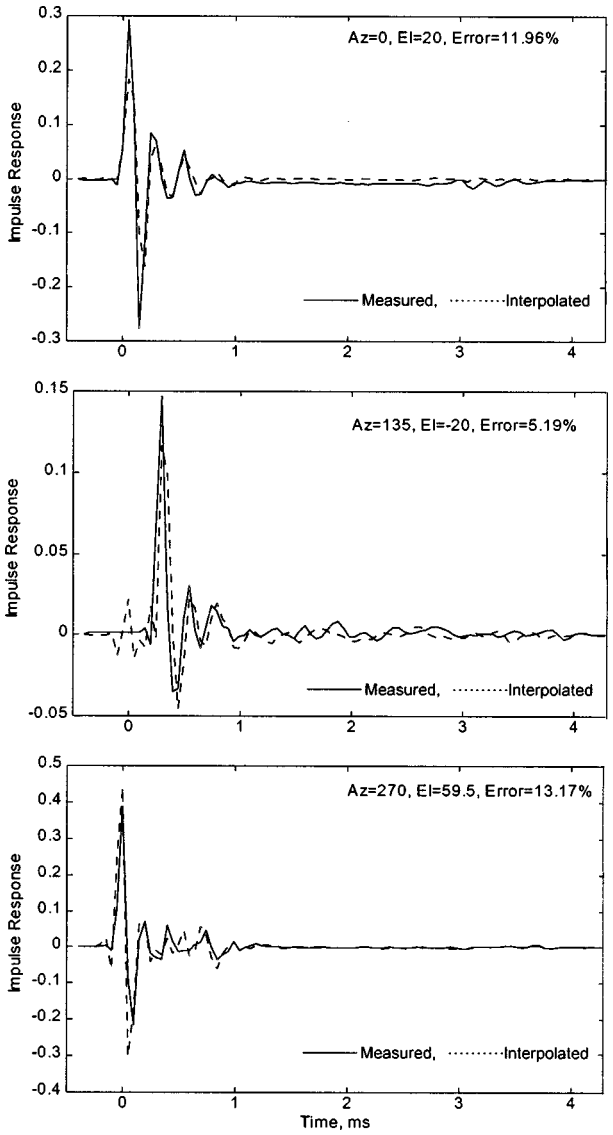

FIG. 5. Example measured and interpolated HRTFs.

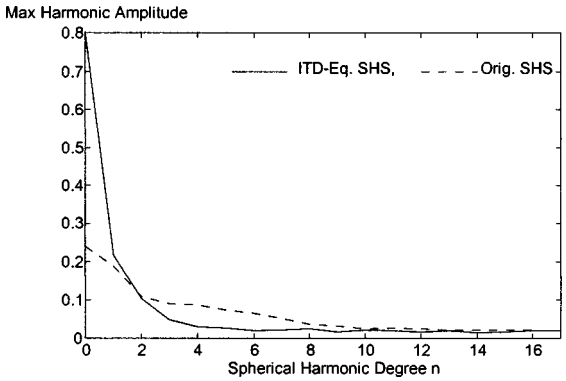

FIG. 6. Spherical harmonic spectrum (using maximum values over time) of SSH representation of ITD-equalized responses, with original SHS overlaid.

samples of the ITD-equalized HRTFs. This yielded an entirely new set of weights for SSH components up to 17th degree; and a new continuous, functional model for the HRTFs, omitting the ITD information. As before, the structure of the SSH model is illustrated by means of its spherical harmonic spectrum (SHS), shown in Fig. 6.

The SHS of the original model (shown previously in Fig. 3) is overlaid as a dotted line on the same scale. The SHS of the ITD-equalized model has a significantly higher fundamental (0th degree) amplitude and a slightly higher 1st degree amplitude. At higher degrees, however, the spectrum flattens out very rapidly, unlike the spectrum of the original model which had a much slower ''decay.'' This indicates that the new model places more of the information required to reconstitute HRTFs into lower-degree components, which should have implications for efficient reconstruction. However, as with the SHS of the unequalized responses, the response flattens out to an amplitude of approximately 0.016; meaning that higher-degree components are still present in the HRTF set.

A. ITD-equalized HRTF recreation performance

Table III presents the same information as Table I; average mean-square error percentages in the magnitude spectrum of recreated HRTFs for directions for which physical measurements were made, except that the ITD-equalized HRTFs and SSH model were used.

These figures show that the removal of the ITD information from the HRTFs has improved the accuracy of approximation of the SSH model. Performance in those octants which had previously had relatively high error percentages has been significantly improved. The same basic accuracy structure is apparent—approximations are generally better above the horizontal plane than below it, better in front than behind, and better on the unshadowed side than the shadowed; but the general effect of equalizing the delay has been to reduce the differential between these error percentages. Figure 7 qualitatively displays the approximation performance for the same directions as in Fig. 4. The most notable feature is the alleviation of the ''pre-echo'' effect. There is also some improvement in the ''peak widening'' observed previously.

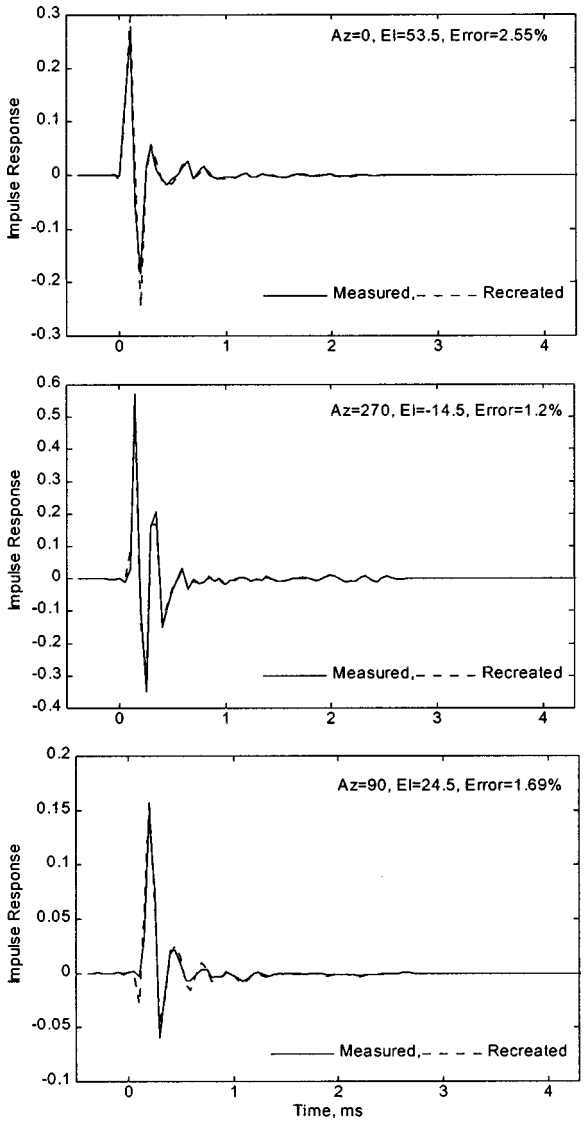

FIG. 7. Example measured and recreated HRTFs for the ITD-equalized model.

TABLE III. Average mean-square error percentages for recreated directions using ITD-equalized model.

Octant	Front ($\theta \leq 45°; \theta \geq 315°$)	Shadowed side ($45° \leq \theta \leq 135°$)	Back ($135° \leq \theta \leq 225°$)	Unshadowed side ($225° \leq \theta \leq 315°$)
Above horizontal ($0° \leq \phi \leq 90°$)	1.74%	2.97%	1.78%	1.30%
Below horizontal ($90° \leq \phi \leq 180°$)	1.49% (1.27%)	5.71% (4.60%)	2.75% (2.35%)	2.90% (2.25%)

TABLE IV. Average mean-square error percentages for interpolated directions using ITD-equalized model.

	$\theta=0°$	$\theta=45°$	$\theta=90°$	$\theta=135°$	$\theta=180°$	$\theta=225°$	$\theta=270°$	$\theta=315°$
Above horiz. ($0°\leqslant\phi\leqslant 90°$)	1.84%	3.26%	3.69%	4.19%	3.71%	4.02%	9.53%	3.92%
Below horiz. ($90°\leqslant\phi\leqslant 180°$)	7.00%	6.72%	17.55%	9.33%	8.01%	5.73%	6.61%	2.63%

B. ITD-equalized HRTF interpolation performance

The average mean-square error percentages achieved by the ITD-equalized model for interpolated directions are given in Table IV. These figures are directly comparable to those in Table II.

Here we can see again that the removal of the variable onset delay from the HRTF set has had a marked improvement on the error performance of the SSH model. The improvement apparent for some directions (such as the directly ahead above the horizontal plane) is particularly dramatic. On average the upper hemisphere is simulated with considerably greater accuracy than the lower, the shadowed and unshadowed hemispheres exhibit a similar level of performance, but, unlike the figures presented in Table II, error performance in the front hemisphere is now noticeably better than that achieved for the rear. Qualitatively, Fig. 8 shows that, in comparison to Fig. 5, the previously visible ''pre-echo'' effect has been alleviated. Also, the reduction in the height of peaks has been improved, as have the unwanted delay effects.

The results presented in this section clearly show that, as expected, equalizing the onset delay throughout the HRTF set prior to SSH analysis has improved the effectiveness of the resulting model in approximating responses for both recreated and interpolated directions. However, this improvement has been achieved at the expense of the ITD data that were previously present in the HRTFs. If the SSH model is to be used to generate HRTFs for sound spatialization then ITD will now have to be implemented separately. It is, of course, perfectly possible to keep a record of how many samples are stripped from the front of the HRTFs in the delay-equalization process and to replace them to the responses as generated by the SSH model. Unfortunately, since we will not know how much onset delay to place on simulated HRTFs for interpolated directions, the continuous nature of the SSH model will be lost. Therefore for this approach to be useful a continuous, three-dimensional model of ITD would be required (as used in Evans, 1997).

V. SSH ANALYSIS IN THE FREQUENCY DOMAIN

The spherical harmonic spectrum in Fig. 6 showed that, even with the variable onset delays equalized, the SSH analysis of the time-domain HRTFs yielded high-degree components of significant amplitude. It is possible that the occurrence of these high-degree components is inherent in the time-domain nature of the responses being analyzed, and that the presence of components of degree higher than 17 are causing much of the error in the approximation, due to their absence from the SSH model. In order to investigate if the performance of the SSH representation could be improved the technique has also been applied in the frequency domain: The set of 648 HRTFs used in analysis of Sec. III (with variable onset delays intact) underwent 96 point DFTs using MATLAB. SSH analysis was then applied to the magnitude and unwrapped phase responses of the resulting transfer functions. The analysis was applied in precisely the same way as for the time-domain analysis of the HRTFs except that, instead of applying SSH analysis separately for each instant of time, the analysis was applied, in turn, to each frequency bin. The result was two complete sets of SSH

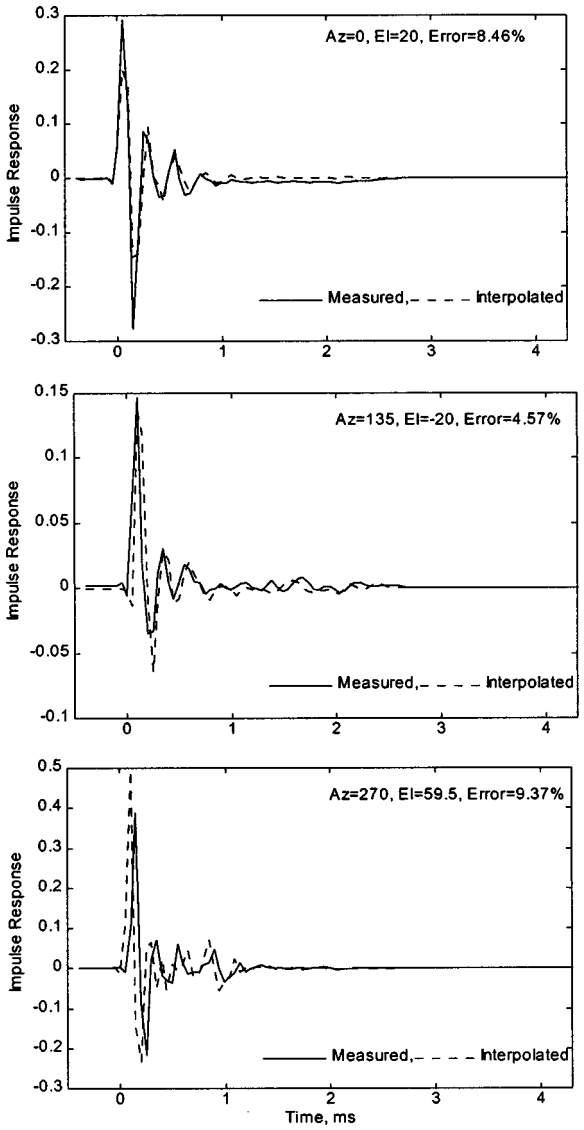

FIG. 8. Example measured and interpolated HRTFs for the ITD-equalized model.

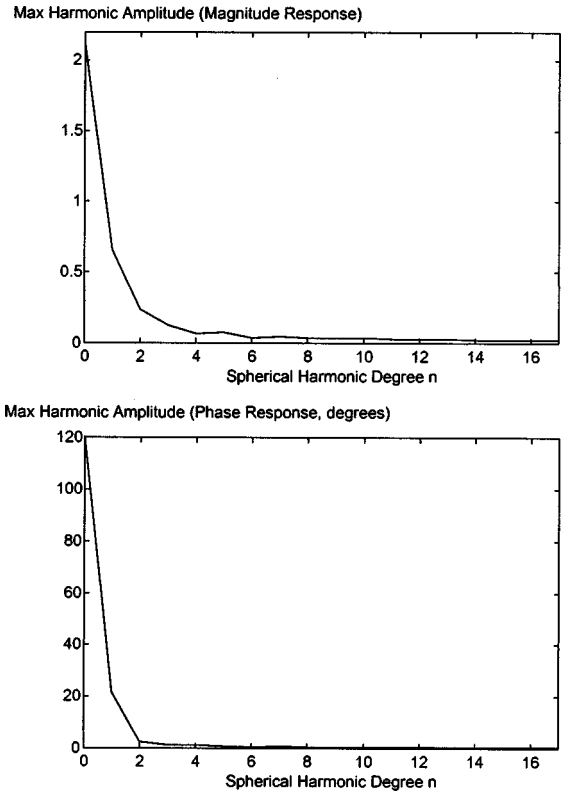

FIG. 9. Spherical harmonic spectra of SSH representation of HRTF magnitude and phase responses, using maximum values over frequency.

weights up to degree 17, allowing both the magnitude and phase responses to be expressed as a weighted sum of SSHs.

A. Spherical harmonic spectra of frequency domain model

Figure 9 shows the spherical harmonic spectra for the magnitude and phase SSH models. (Note: For each degree n the maximum value of the rms amplitude of the weights is taken across all the frequency bins.) As with the time-domain representations these spectra show a characteristic ''decay'' in the relative contribution to the HRTF set made by harmonics of increasing degree. Although the vertical axes on these spectra are not directly comparable either with each other or with those on the time-domain plots of Figs. 3 and 6, we can compare the spectra by some simple analysis. Let $S[n]$ indicate the value of a spherical harmonic spectrum at degree n. Characteristic parameters a and b are given by the following equations. Let

$$a = \frac{S[17]}{\Sigma_{n=0}^{17} S[n]}. \tag{9}$$

TABLE V. Characteristic parameters a and b for each spherical harmonic spectrum.

	Original SHS	ITD-Eq. SHS	Mag. response SHS	Phase response SHS
a	18.3×10^{-3}	13.1×10^{-3}	5.2×10^{-3}	2.2×10^{-3}
b	13	11	7	2

b is the minimum integer to satisfy,

$$\sum_{n=0}^{b} S[n] \geqslant 0.9 \sum_{n=0}^{17} S[n]. \tag{10}$$

a is effectively a measure of the contribution made to the ''energy'' of the whole spectrum by the highest-degree component present in the model. b is effectively the lowest degree at which at least 90% of this total ''energy'' is contained in that degree and lower. a and b values for the spectra in Figs. 3, 6, and 9 are tabulated in Table V.

These values show that the SSH model of frequency domain HRTF is the most efficient, both in terms of minimizing the degree containing the bulk of the variation in the responses, and also in terms of minimizing the contribution made by the highest-degree harmonics.

B. Frequency domain recreation performance

Table VI gives average mean-square error percentages between the magnitude spectra of measured HRTFs, and those recreated using the frequency domain SSH model. As in Tables I and III, for the two time-domain SSH analyses, these error figures are broken down into octants. (Note: Once again, the bracketed values ignore the lowest four angles of elevation, for which dummy data were used.)

These results show a highly significant, and global, improvement in the accuracy of the SSH approximations, in comparison to those results achieved in the time domain. It seems highly likely that this superior performance arises due to a reduced potential amplitude difference for an incremental angular change, compared to effects around the onset of impulse responses. The relative success of the model in different octants is also very similar; better above the horizontal plane than below, better on the unshadowed side of the median plane than on the shadowed side, and better in front than behind. Figure 10 shows a direct, qualitative comparison between measured HRTFs and HRTFs recreated using the frequency domain model, for the three directions previously examined in Figs. 4 and 7.

Comparing the responses of Fig. 10 to those of Fig. 4 shows that implementing the SSH analysis in the frequency

TABLE VI. Average mean-square error percentages for recreated directions using frequency domain model.

Octant	Front ($\theta\leqslant45°;\theta\geqslant315°$)	Shadowed side ($45°\leqslant\theta\leqslant135°$)	Back ($135°\leqslant\theta\leqslant225°$)	Unshadowed side ($225°\leqslant\theta\leqslant315°$)
Above horizontal ($0°\leqslant\phi\leqslant90°$)	0.47%	0.93%	0.78%	0.35%
Below horizontal ($90°\leqslant\phi\leqslant180°$)	0.69% (0.49%)	4.17% (1.67%)	1.25% (0.80%)	0.79% (0.48%)

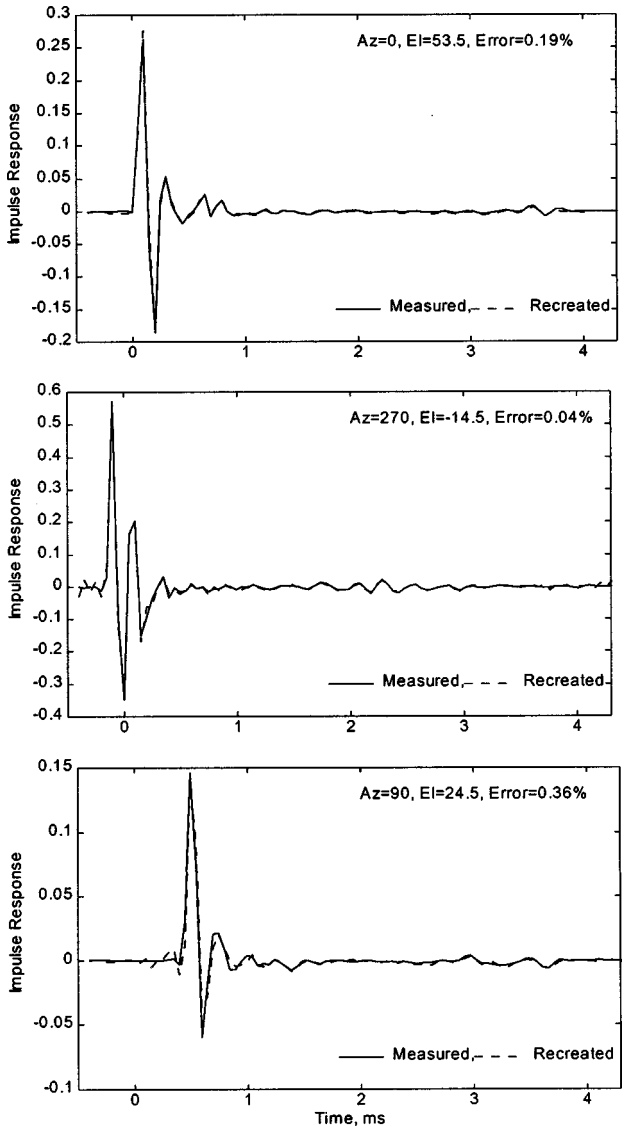

FIG. 10. Example measured and recreated HRTFs for the frequency domain model.

domain rather than the time domain has, in general, alleviated the visible discrepancies present in the previous approximations. Most significantly, the ''pre-echo'' which was previously visible in responses recreated for the contralateral side of the head is no longer present. Less obviously, these plots show that peaks in the response seem less susceptible to overshoot or undershoot. The shape of the recreated responses is generally extremely close to that of their measured counterparts. The only visible fault that the frequency domain implementation of the SSH analysis appears to have introduced is a very low-amplitude high-frequency ripple, which is just visible prior to the onset of some of the responses. Since this ripple appears to be at, or very near to, the Nyquist frequency, it is likely that it is caused by a reduction in the accuracy of the approximation for the final frequency bins. In general, though, these results are a clear improvement over those achieved in the time domain, and obtained without sacrificing the ITD data stored in the variable onset delay.

C. Frequency domain interpolation performance

Table VII gives average mean-square error percentages in the magnitude spectrum, for responses interpolated using the frequency domain model. These results are directly comparable to those in Tables II and IV. The results show a marked improvement over the performance of the original time-domain SSH model for virtually all directions, and, in general, a smaller improvement on the performance achieved by the ITD-equalized SSH model. There is a much greater difference in performance between recreated and interpolated directions than was observed in the time domain. This might mean that interpolation performance is approaching a limit imposed by physiological features and the spacing of the physical measurements. Features in the responses which occur entirely between measured directions and cannot be determined by such interpolation, even though the overall accuracy of the approximation has been improved.

Figure 11 illustrates qualitatively measured and interpolated responses for the same three directions examined in Figs. 5 and 8. If we compare the responses with those of the original, time-domain SSH model we can see that the occurrence of ''pre-echo'' has been largely eliminated, and shortfalls and overshoots on some of the peaks have been reduced. Although, the overall shape of the interpolated responses is now more accurate, there are still some peak widening effects visible, together with some very slight, spurious delays of the entire response. Often, there is also the same low-amplitude, near Nyquist frequency component visible before the onset of some of the responses that was noted for some recreated responses. Clearly, though, the results from the frequency domain application of SSH analysis are an improvement over those obtained in the time domain and indicate a successful implementation of a continuous, functional HRTF model.

TABLE VII. Average mean-square error percentages for interpolated directions using frequency-domain model.

	θ=0°	θ=45°	θ=90°	θ=135°	θ=180°	θ=225°	θ=270°	θ=315°
Above horiz. ($0°\leqslant\phi\leqslant 90°$)	2.25%	2.89%	3.60%	4.21%	2.08%	3.54%	7.14%	2.58%
Below horiz. ($90°\leqslant\phi\leqslant 180°$)	8.94%	11.00%	20.92%	11.44%	8.86%	3.65%	4.54%	2.37%

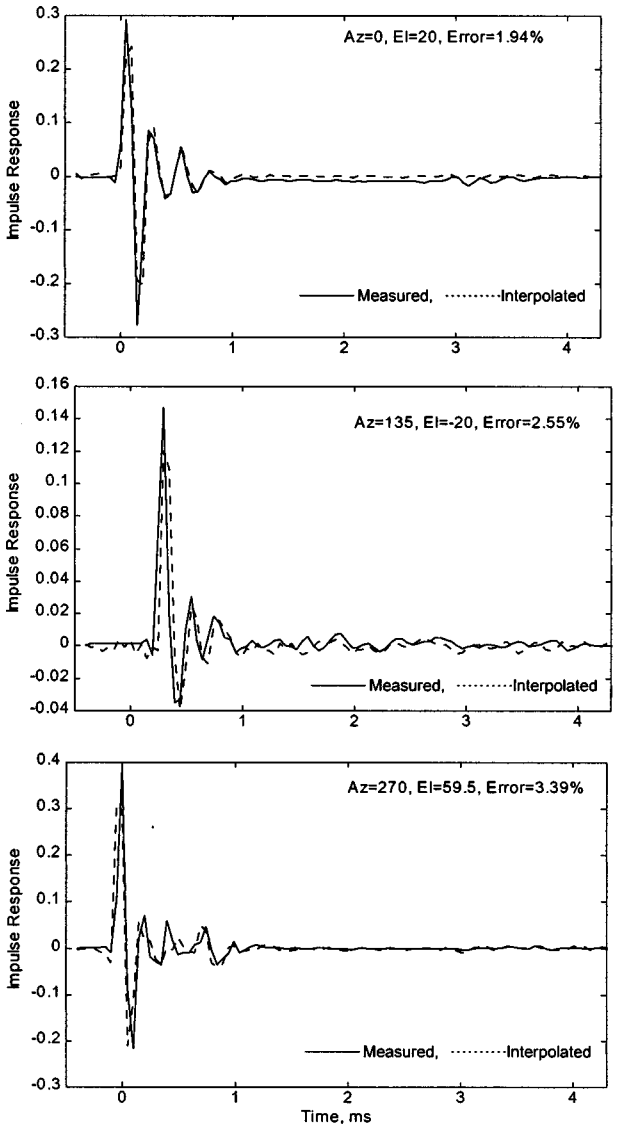

FIG. 11. Example measured and interpolated HRTFs for the frequency domain model.

D. Comparison to modeling using Eigentransfer function approach

It is in no way intended that HRTF analysis using SSHs should be perceived as a rival approach to the EF analysis of Chen *et al.* That research represented an HRTF set in a highly compact form (17 components derived from 2188 physical HRTF measurements) using basis functions derived from the measurements themselves. The SSH model in this paper uses a considerable greater number of basis functions (324, as derived from 648 measured HRTFs components). Reconstruction of HRTFs using SSHs is, therefore, less storage efficient and applications in which this is a key issue should perhaps look to the EF approach. The SSH analysis technique, however, uses a general set of spatial basis functions. As such, the weights associated with particular SSH components can be directly compared across HRTFs sets and, thus, from listener to listener or dummy head to dummy head. The EF and SSH analysis approaches, therefore, are complementary.

In terms of mathematical accuracy Table VIII gives mean-square error percentages for the EF analysis (derived from Table III in Chen *et al.*, 1995). If we compare these values to those in Table VI, calculated for the frequency domain SSH model, we see that the accuracies of the two methods are comparable overall. However, particular comparisons show that, for recreated directions, the SSH model has the more consistent performance and shows considerably less error for rearward directions. Overall, though, if the interpolation errors of Table VII are also considered, the EF model is more accurate globally than the SSH model.

VI. CONCLUSIONS

The results presented in this paper show that building a model of HRTF data from a SSH analysis has yielded a very encouraging level of performance, in terms of the mathematical accuracy of the modeled responses. In particular, the frequency domain application of the technique has alleviated some of the simplifications of the PCA analysis of Kistler and Wightman (1992) (by including a synthesis both of the phase responses, and the variable onset delay required for ITD simulation, in addition to the magnitude spectra) yet has achieved the highest level of performance in terms of the accuracy of the model. The calculated SSH model allows the direct, continuous, and accurate synthesis of a pair of HRTFs for any arbitrary direction. This capability has potential applications wherever smooth directional transitions are required in sound reproduction; for example, the simulation of moving sound sources, or the creation of soundfields which make use of head tracking to enable resilience to head movements.

The SSH component weights determined by the analysis also represent some spatial features of interest in the auditory receptivity field formed by the complete set of HRTFs. The representation complements the results of the Karhunen–Loève expansion (KLE) presented in Chen *et al.* (1995). The EF model yielded by the KLE analysis is a highly efficient one, minimizing the number of components required to

TABLE VIII. Average mean-square error percentages for the Eigentransfer function model [derived from Chen *et al.* (1995), Table III].

Octant	Front ($\theta \leqslant 45°; \theta \geqslant 315°$)	Shadowed side ($45° \leqslant \theta \leqslant 135°$)	Back ($135° \leqslant \theta \leqslant 225°$)	Unshadowed side ($225° \leqslant \theta \leqslant 315°$)
Above horizontal ($0° \leqslant \phi \leqslant 90°$)	0.52%	2.06%	0.55%	0.56%
Below horizontal ($90° \leqslant \phi \leqslant 180°$)	0.56%	3.86%	4.15%	0.59%

achieve maximum approximation accuracy by extracting and forming the orthogonal basis functions from the HRTF data itself. Such efficiency of modeling has obvious applications for any future coding or compression scheme for HRTF data. SSH analysis, meanwhile, calculates a much larger number of components, predetermined by the distribution of previous measurements. The orthogonal basis functions, instead of being extracted from the physical measurements, are a straightforward, well-known, and hierarchical set—the surface spherical harmonics. Therefore, the frequency responses and impulse responses formed by all the weights for a particular harmonic represent the presence in the HRTF set of a particular spatial pattern. For example, the three first-degree SSHs (as used in ambisonics; Gerzon, 1977) correspond to the spatial patterns of front–back, left–right, and up–down. The three frequency responses (or impulse responses) formed by taking all the weights for these harmonics therefore represent the direct contributions to the HRTFs given by the front–back, left–right, and up–down projections of the source.

The higher the degree of a SSH, the greater the level of spatial variation which it corresponds to. This allows us to look at this paper's finding that higher-degree SSH components contribute progressively less significantly to the HRTF set and, therefore, verifies the instinctive result that the highly directionally sensitive components are less mathematically significant than the effects of grosser changes in direction. The existence of higher levels of approximation error in certain directions also gives us an insight into the location of high directional sensitivity in the HRTFs. SSHs are hierarchical basis functions so the higher the maximum degree of the components used in the model the greater the mathematical accuracy of the simulated HRTFs. It is extremely important to note that errors in the signal domain do not generally map onto listeners' perceptions in a direct manner. For a full assessment of the effectiveness of SSH modeled HRTFs, psychoacoustic validation by listening tests is required. The optimum degree of SSH model, together with the accuracy of sound spatialization that can be achieved using this technique will, of course, be determined by the perceptions of individual users, together with the particular application or service the technique is employed in.

In addition to perceptual testing and validation, progress could continue to be made in this area by further work, such as a comparison of the SSH representation of different sets of HRTFs and a more detailed mathematical analysis of the error performance of the SSH model as the maximum SSH degree is varied, in the light of the perceptual tests.

ACKNOWLEDGMENTS

The authors are grateful for the helpful contributions made by the reviewers and editor of this paper. This work was funded through an EPSRC CASE studentship partly sponsored by BT. Contact: Phil Sheppard, MLB 3 7, BT Laboratories, Martlesham Heath, Ipswich, IP5 7RE, United Kingdom.

Atkinson, K. (**1982**). ''Numerical integration on the sphere,'' J. Aust. Math. Soc. B, Appl. Math. **23**, 332–347.

Chen, J., Van Veen, B. D., and Hecox, K. E. (**1995**). ''A spatial feature extraction and regularization model for the head-related transfer function,'' J. Acoust. Soc. Am. **97**, 439–452.

Evans, M. J. (**1997**). ''The perceived performance of spatial audio for teleconferencing,'' Doctoral Thesis, Department of Electronics, University of York, York, United Kingdom.

Gerzon, M. A. (**1977**). ''Design of Ambisonic Decoders for Multi Speaker Surround Sound,'' Presented at the 58th Convention of the Audio Engineering Society; New York, 4 November 1977.

Kaplan, W. (**1981**). *Advanced Mathematics for Engineers* (Addison-Wesley, Reading, MA).

Kistler, D. J., and Wightman, F. L. (**1992**). ''A model of head-related transfer functions based on principal components analysis and minimum-phase reconstruction,'' J. Acoust. Soc. Am. **91**, 1637–1647.

McLaren, A. D. (**1963**). ''Optimal numerical integration on a sphere,'' Math. Comput. **17**, 361–383.

Møller, H., Sørensen, M. F., Hammershøi, D., and Jensen, C. B. (**1995**). ''Head-related transfer functions of human subjects,'' J. Audio Eng. Soc. **43**, 300–321.

Pollack, H. N., Hurter, S. J., and Johnson, J. R. (**1993**). ''Heat flow from the Earth's Interior: Analysis of the global data set,'' Rev. Geophys. **31**, 267–280.

Stroud, A. H., and Secrest, D. (**1966**). *Gaussian Quadrature Formulas* (Prentice-Hall, Englewood Cliffs, NJ).

Stroud, A. H. (**1971**). *Approximate Calculation of Multiple Integrals* (Prentice-Hall, Englewood Cliffs, NJ).

Wightman, F. L., and Kistler, D. J. (**1989**). ''Headphone simulation of free field-listening II: Psychophysical validation,'' J. Acoust. Soc. Am. **85**, 868–878.

Binaural and monaural auditory filter bandwidths and time constants in probe tone detection experiments[a)]

Inga Holube,[b)] Martin Kinkel,[c)] and Birger Kollmeier[d)]
AG Medizinische Physik, Universität Oldenburg, D-26111 Oldenburg, Germany

(Received 2 October 1995; revised 29 July 1997; accepted 24 June 1998)

Auditory filter bandwidths and time constants were obtained with five normal-hearing subjects for different masker configurations both in the frequency and time domain for monaural and binaural listening conditions. Specifically, the masking level in the monaural condition and the interaural correlation in the binaural conditions, respectively, was changed in a sinusoidal, stepwise, and rectangular way in the frequency domain. In the corresponding experiments in the time domain, a sinusoidal and stepwise change of the masker was performed. From these results, a comparison was made across conditions to evaluate the influence of the factors ''shape of transition,'' ''monaural versus binaural,'' ''frequency domain versus time domain,'' and ''subject.'' Also, the respective data from the literature were considered using the same model assumptions and fitting strategy as used for the current data. The results indicate that the monaural auditory filter bandwidths and time constants fitted to the data are consistent across conditions both for the data included in this study and the data from the literature. No consistent relation between individual auditory filter bandwidths and time constants were found across subjects. For the binaural conditions, however, considerable differences were found in estimates of the bandwidths and time constants, respectively, across conditions. The reason for this mismatch seems to be the different detection strategies employed for the various tasks that are affected by the consistency of binaural information across frequency and time. While monaural detection performance appears to be modeled quite well with a linear filter or temporal integration window, this does not hold for the binaural conditions where both larger bandwidth and time constant estimates are found. [S0001-4966(98)00410-X]

PACS numbers: 43.66.Pn, 43.66.Ba, 43.66.Dc, 43.66.Mk [RHD]

INTRODUCTION

Temporal and spectral resolution are fundamental constraints in several auditory tasks, e.g., speech intelligibility, and therefore play an important role in normal auditory functioning. Time resolution refers to the ability of the auditory system to follow temporal variations and can be characterized by time constants. Frequency selectivity refers to the range of frequencies over which information is combined and can be characterized by the auditory filter bandwidths. Both parameters are essential for modeling the human auditory system and appear to be strongly affected in hearing-impaired listeners (Festen and Plomp, 1983; Kinkel, 1990; Moore, 1995). These psychoacoustical parameters have been examined separately in different studies, and primarily under monaural conditions. However in natural listening environments, time and frequency resolution are always combined in binaural listening conditions. In order to model the auditory system, the relations between the parameters that describe these phenomena have to be known. Therefore in this study the relationships between time and frequency resolution in various experimental conditions and in monaural and binaural hearing are examined.

Many measurement procedures have been described that can be used to determine auditory filter bandwidths or time constants in detection experiments. Auditory filter bandwidth was often determined by measuring the detection of a test tone in a noise masker which varied in the frequency domain. Monaural experiments have been performed with variations of the power density of the masking noise. Likewise, binaural experiments have been performed with variations of the interaural correlation of the masking noise. Monaural auditory filter bandwidths have been determined by Houtgast (1977) using a cosine variation of the spectral power density in the frequency domain (rippled-noise), whereas Patterson changed the power density in a stepwise (1974) or rectangular (1976) manner. Binaural auditory filter bandwidths were determined by Kohlrausch (1988) and Kollmeier and Holube (1992) using a stepwise variation of the interaural correlation, whereas Sondhi and Guttman (1966) changed the interaural correlation rectangularly.

Time constants were measured with binaural and monaural noise masker variations in the time domain. The interaural correlation of the noise masker varied cosinusoidally (Grantham and Wightman, 1979) or stepwise (Kollmeier and Gilkey, 1990) to determine binaural time constants. Monaural time constants were obtained using a cosine (Viemeister,

[a)]This paper is based on the Ph.D. theses written by the first author (Holube, 1993) and second author (Kinkel, 1990). Parts of this paper have been presented at the 1991 meeting of the German Acoustical Society (Holube *et al.*, 1991).

[b)]Current address: Siemens Audiologische Technik GmbH, Gebberststr. 125, D-91058 Erlangen, Germany.

[c)]Current address: Kind Hörgeräte, Kokenhorststr. 3-5, D-30938 Großburgwedel, Germany.

[d)]Author to whom correspondence should be addressed. Electronic mail: biko@medi.physik.uni-oldenburg.de

TABLE I. Frequency and time constants ($\nu_u + \nu_l$ and $\tau_1 + \tau_2$, respectively) for different noise masker configurations in the frequency and the time domain. The first column summarizes the results of this study, the second column reports results given in the literature, and the third column gives the results after fitting the masked thresholds given in the literature with the same procedure as in this study. The last column gives the reference.

Experiment		Current study	Literature (reported)	Literature (fit)	Reference
Frequency domain:					
	Cosine	109–166 Hz			
Binaural	Step		80–84 Hz		Kohlrausch (1988)
			56–77 Hz	56–77 Hz	Kollmeier and Holube (1992)
	Rectangle	78–103 Hz	approx. 200 Hz	92	Sondhi and Guttman (1966)
	Cosine	81–145 Hz	203–231 Hz at 1 kHz	143 Hz at 1 kHz	Houtgast (1977)
Monaural	Step		26–31 Hz	46 Hz	Patterson (1974)
			43–68 Hz	43–68 Hz	Kollmeier and Holube (1992)
	Rectangle	78–89 Hz	61–81 Hz	46 Hz	Patterson (1976)
Time domain:					
Binaural	Cosine	91–122 ms	44–140 ms	139–189 ms	Grantham and Wightman (1979)
	Step	40–69 ms	33–83 ms	33–83 ms	Kollmeier and Gilkey (1990)
Monaural	Cosine	7–33 ms	4 ms	2 ms	Viemeister (1977)
	Step	16–25 ms	12–26 ms	12–26 ms	Kollmeier and Gilkey (1990)

1977), a stepwise (Kollmeier and Gilkey, 1990), or a rectangular (Moore *et al.*, 1988) variation in the amplitude of the noise masker. The use of these different noise masker configurations has led to very different estimated values of the psychoacoustical parameters ranging in the monaural case at 500 Hz from 26 to 81 Hz for bandwidth estimates and 4–26 ms for time constants, respectively (see Table I). In addition, differing relations between monaural and binaural parameters have been found. Whereas Kohlrausch (1988) reports that monaural and binaural auditory filter bandwidths are about equal in size, Sondhi and Guttman (1966) obtained much broader bandwidths in binaural experiments.

The reasons for these differing results are unclear. One factor might be the influence of different spectra or temporal shapes of the noise maskers. Additionally, different models and thus different definitions and filter methods of auditory filter bandwidths and time constants were used. Finally, differences between measurement equipment, psychophysical measurement procedures, and subjects may have contributed to the discrepancies. An additional difficulty in comparing temporal and spectral resolution across studies is the fact that no study examined the time constants in the time domain in a way equivalent to the frequency constants (or bandwidths, respectively) in the frequency domain. Such a formally analogous treatment would definitely help to establish the relations between auditory filter bandwidths and the respective time constants.

Consequently, this study describes binaural and monaural auditory filter bandwidths and time constants obtained using different noise masker variations with the same subjects, measurement apparatus, psychophysical procedure, and model assumptions to fit the data both in the time and frequency domain. We focus on the modeling and comparison of conditions that have partially been published before (Kinkel, 1990; Holube *et al.*, 1991; Kollmeier and Holube, 1992) and draw on the fortuitous fact that many of the same listeners participated in all of these studies. To determine auditory filter bandwidth, the interaural correlation in the binaural experiments as well as the spectral power density in the monaural experiments was varied cosinusoidally, stepwise, and rectangularly in the frequency domain. The time constants were examined by a cosinusoidal and by a stepwise change of the interaural correlation or the power spectral density in the time domain. From the measured masked thresholds of the test tone the parameter for the auditory filter bandwidth and the time window were determined by applying the equalization and cancellation (EC) theory (Durlach, 1972). The results were compared with each other and with the values given in the literature.

I. METHOD

A. Subjects

All experiments were performed with two normal-hearing subjects that authored and co-authored this study [MK (male) and IH (female)]. Three additional normal-hearing male listeners participated only in a subset of the experiments (RN, CM, and SU). All listeners were between 24 and 30 years old. They were members of the research group and participated voluntarily. All had clinically normal hearing and were experienced with psychoacoustical experiments similar to those carried out here.

B. Apparatus

Stimuli were generated on a TMS 32010-based signal processing subsystem connected to a Digital Equipment PDP 11/73 computer. Three 16-bit digital-to-analog converters were used to produce the binaural noise masker and the probe tone separately at a sampling rate between 10 and 30 kHz. The level of the stimuli was controlled by separate programmable attenuators with a resolution of 0.1 dB. The noise stimuli were bandpass filtered between 0.1 and 1 kHz with two Krohn-Hite 3343 filters with a a slope of 48 dB per octave. The probe tone was also bandpass filtered between 0.1 and 1 kHz by an Ithaco 4302 filter with slopes of 24 dB per octave. The probe tone and noise waveforms were then added with an analog mixer and presented to the subject

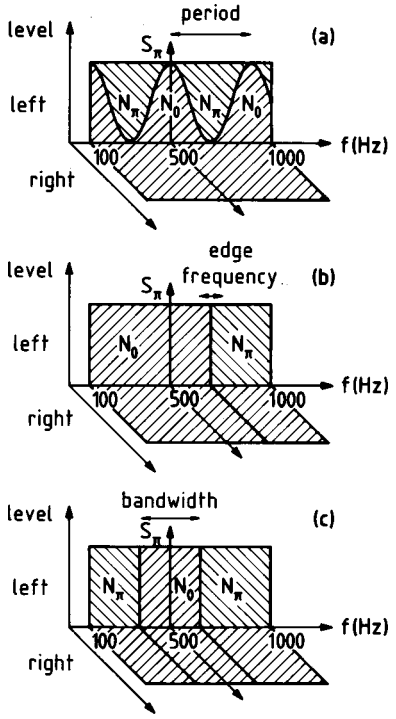

FIG. 1. Sketches of the maskers and signals employed in the experiments. In each panel, the spectral power density at the left and right ear, respectively, is plotted as a function of frequency. The interaural phase of the noise masker is changed cosinusoidally (a), stepwise (b), or rectangularly (c) from 0° (N_0) to 180° (N_π). The masked threshold of an interaurally phase-inverted probe tone (S_π) at 500 Hz is determined as a function of the period of the cosine (a), the edge frequency (b), or the bandwidth of the rectangle (c).

through DT-48 headphones in a sound-insulated anechoic chamber. Short instructions and messages for the subject were displayed on a video monitor in front of the subject. During practice runs at the beginning of each session, feedback information was provided on the monitor and by illuminating the correct-answer button of the response box.

C. Stimuli and conditions

1. Experiment 1 (frequency domain)

Figure 1 shows a sketch of the bandpass-filtered noise masker N and the probe tone S in the frequency domain for three different configurations employed to determine frequency resolution in binaural conditions (a)–(c). Data from the second condition were obtained by Kollmeier and Holube (1992). The interaural correlation was changed cosinusoidally over frequency in the first configuration, stepwise in the second configuration, and rectangularly in the third configuration. In the first and third configurations, an interaural phase shift of 0 degrees (N_0 noise) was present in the spectral region around 500 Hz whereas an interaural phase shift of 180 degrees (N_π noise) was present at frequencies above and below this region.

The noise maskers depicted in Fig. 1 were generated using 32 768 samples of a Gaussian noise for the first stereo channel [$R(f)$]. For the second stereo channel, the samples were Fourier transformed and multiplied with a cosine of variable periodicity for the first configuration [cf. Fig. 1(a)], a stepwise transition from -1 to $+1$ in the second configuration [cf. Fig. 1(b)] and a rectangular transition from -1 to 1 and back to -1 in the third configuration [cf. Fig. 1(c)]. To achieve a flat power spectrum in the second stereo channel in the first configuration, an uncorrelated second noise [$U(f)$] with the same statistics as $R(f)$ which was sinusoidally shaped in the frequency domain was added before the inverse Fourier transformation into the time domain. Therefore the amplitude spectrum $L(f)$ for the second stereo channel was

$$L(f)=R(f)\cos\left((f-f_0)\cdot\frac{2\pi}{F}\right)+U(f)\sin\left((f-f_0)\cdot\frac{2\pi}{F}\right). \tag{1}$$

$R(f)$, $U(f)$: amplitude spectra, f_0: probe tone frequency 500 Hz, F: periodicity in the frequency domain (in Hz), also denoted as ripple spacing.

The interaural correlation $\rho(f)$ thus exhibited a frequency dependence as follows:

$$\rho(f)=\cos\left((f-f_0)\cdot\frac{2\pi}{F}\right). \tag{2}$$

A modification of the configurations in Fig. 1 was also employed in which N_0 was replaced by N_π (and vise versa) by multiplying one of the stereo channels by -1. The masked thresholds of the probe tone were determined as a function of the periodicity F of the cosine-shaped variation of the interaural correlation in the first configuration, as a function of the edge frequency in the second configuration, and as a function of the bandwidth in the third configuration.

The corresponding monaural configurations exhibit a frequency-dependent variation of the spectrum level similar to that of the interaural correlation for the binaural configurations. Hence for detecting a S_π-probe tone, the N_π noise corresponds to a nonattenuated monaural noise and the N_0 noise corresponds to a monaural noise which is attenuated by 15 dB. This attenuation of 15 dB corresponds to the average masking level difference (MLD) at 500 Hz, i.e., the improvement of the masked threshold of a S_π-probe tone masked by a N_0 noise in comparison to a N_π noise. Specifically, the monaural noise masker $M(f)$ was created by mixing both stereo channels $R(f)$ and $L(f)$ of each binaural noise masker with a ratio of 0.698 that yields a maximum attenuation of 15 dB:

$$M(f)=\frac{R(f)+0.698L(f)}{1+0.698}. \tag{3}$$

The probe tone had a frequency of 500 Hz and a duration of 250 ms with 20-ms cosine-shaped ramps. It was temporally centered within the masker which had a duration of 750 ms.

2. Experiment 2 (time domain)

For the measurement of temporal resolution, configurations similar to the first two in Fig. 1 were employed, but with the frequency axes replaced by time axes. The total duration of the masking noise was set to 750 ms.

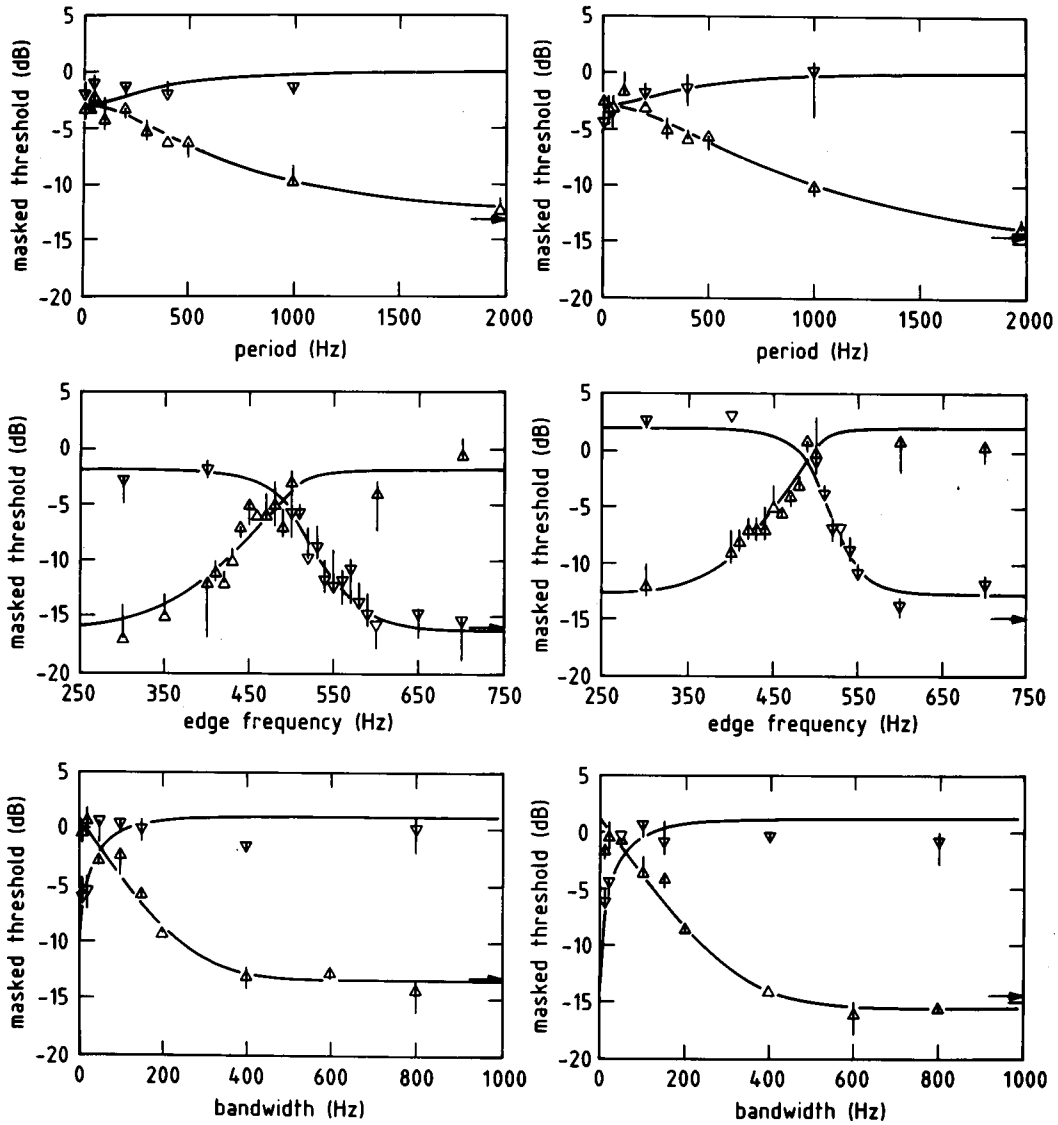

FIG. 2. Masked thresholds (median value and interquartile ranges) as functions of the periodicity (upper panels), the edge frequency (middle panels), and the bandwidth (lower panels) of the noise masker. The left panels show the results for the binaural and the right panels for the monaural conditions for subject RN. The upwards-pointing triangles (△) refer to the conditions shown in Fig. 1. The downwards-pointing triangles (▽) refer to the reversed condition where N_0 is replaced by N_π and vise versa. The same symbols are shown for the monaural conditions when the N_π noise is replaced by a nonattenuated monaural noise and N_0 noise is replaced by a monaural noise attenuated by 15 dB. In each panel, 0 dB at the ordinate denotes the individual $N_\pi S_\pi$ reference threshold and the monaural threshold for the reference masking level, respectively. The arrow at the right-hand side denotes the individual $N_0 S_\pi$ reference threshold and the monaural threshold after reducing the masking level by 15 dB, respectively. The reference thresholds were obtained without a frequency-dependent interaural phase or power density of the masker. Solid lines indicate theoretical threshold functions obtained with a double-sided exponential filter characteristic. The second condition (center left and right panel) is taken from Kollmeier and Holube (1992).

The masker was generated by selecting at random a 750-ms segment of a cyclically repeated time sequence of the masking noise and D/A converting it without shaping the envelope. The probe tone was again a 500-Hz sinusoid. It had a duration of 20 ms including 5-ms ramps. In the binaural condition it was presented with an interaural phase difference of 180 degrees (S_π). In the monaural experiment, both signal and noise masker were presented monaurally (condition $N_m S_m$).

With the cosine-shaped masker configuration, the masker always started with an interaural correlation of 1, and the period of the temporal modulation of the interaural correlation was varied. The short probe tone was always centered at a temporal position where either an N_0 or N_π noise was present. For N_0 noise, the probe tone began 240 ms after masker onset (490 ms for 1- and 2-Hz modulation frequencies) and for N_π noise, the probe tone began one-half period later (earlier for 2-Hz modulation frequency). For the largest modulation periods, however, the number of complete cycles within the masking interval was limited. Thus the duration of the masker was prolonged to 1500 ms for the 0.5-Hz modulation frequency. In addition, the interaural correlation of the masker started at -1 for the 0.5- and 1-Hz modulation frequencies if the probe tone was centered at a temporal position where N_0 was present. In addition, the masked threshold was determined with a static interaural correlation ($N_\pi S_\pi$ or $N_0 S_\pi$), where the probe tone always began after 240 ms.

With the stepwise masker configuration, the transition of

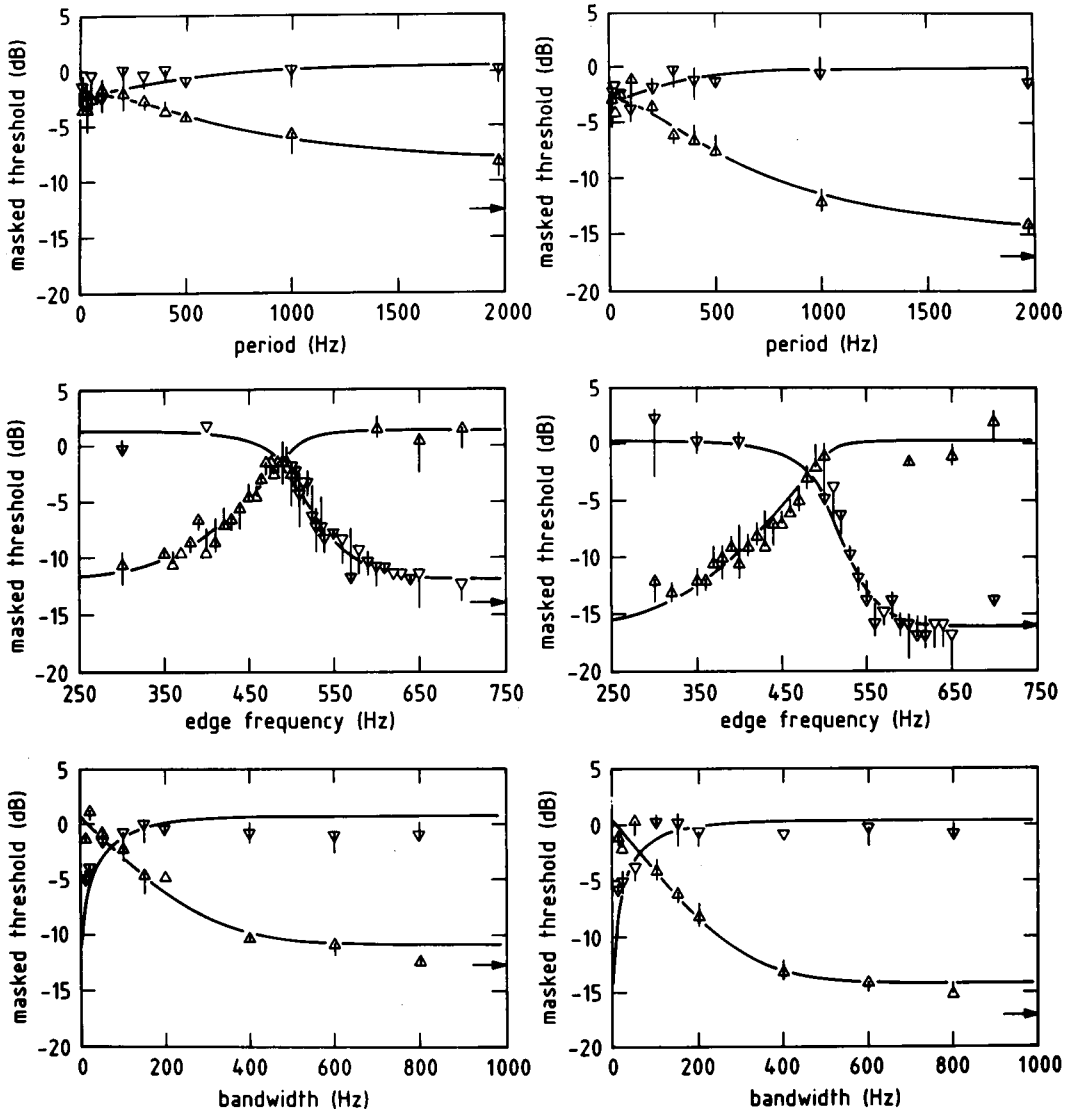

FIG. 3. Same as Fig. 2 for subject IH. Again, the second condition (center left and right panel) is taken from Kollmeier and Holube (1992).

the interaural phase of the masker occurred at 375 ms, whereas the onset time of the probe tone was varied.

The monaural noise masker $M(t)$ in the corresponding monaural configurations were derived from the stereo channels $R(t)$ and $L(t)$ in each binaural condition in the same way as for the experiment on the frequency domain described above, i.e.,

$$M(t)=\frac{R(t)+0.698L(t)}{1+0.698}. \tag{4}$$

The masker was always presented at the level 75 dB SPL. Four reference thresholds were obtained for each individual subject with the unprocessed time sequence of the noise masker. For the binaural condition, the $N_\pi S_\pi$ and $N_0 S_\pi$ thresholds were obtained by presenting the noise interaurally phase inverted or in phase, respectively. For the monaural condition, the ''nonattenuated'' $N_m S_m$ reference threshold was obtained at the standard level of 75 dB. The attenuated monaural reference threshold (-15 dB) $N_m S_m$ was obtained by attenuating the masker by 15 dB.

D. Trial structure and measurement procedure

A three-interval three-alternative forced-choice (3I-3AFC) procedure was employed. The three 750-ms observation intervals were separated by two 500-ms interstimulus intervals. In all three observation intervals, a marking light was turned on 20 ms before the time when the signal might occur. At the end of the third observation interval, unlimited time was allowed for the subject to respond. A pause of 400 ms was provided after the subject responded before the next trial began. An additional 400-ms feedback light was optionally provided to mark the interval that actually contained the probe tone. In addition, a message ''correct'' or ''miss'' was displayed on the video screen. Trial-by-trial feedback was only provided during training runs that were not included in the data presented below. The feedback can be a helpful feature for nontrained subjects to learn the task, but it can lead to unstable thresholds for trained subjects (Robinson and Watson, 1972).

An adaptive staircase algorithm was used to control the probe tone level, following the recommendations of Koll-

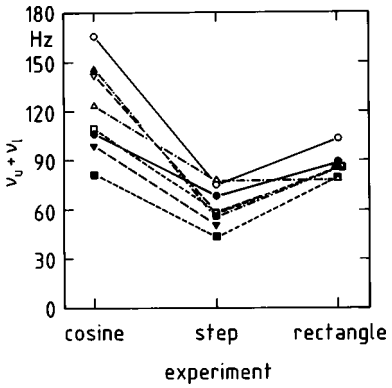

FIG. 4. Width of the auditory filters as the sum of the frequency constants ($\nu_u + \nu_l$) for the cosinusoidal, stepwise, and rectangular masker variation. Full symbols: monaural condition, open symbols: binaural condition. Subject RN: △, IH: ○, MK: □, SU: ▽. The symbols are connected by lines to get an impression of the overall performance of the subjects in different configurations.

meier *et al.* (1988). At the beginning of a run, the signal level was set well above the expected threshold and lowered by 2.0 dB after each correct response. As soon as the first incorrect response was recorded, the signal level was increased by 2.0 dB and a ''one up/two down'' rule was adopted (Levitt, 1971), which lowered the signal level after two successive correct responses at the same signal level and increased the level after one incorrect response. After the third reversal, the step size was decreased to 1.0 dB. At least 20 trials were performed using this small step size. The track was continued until an even number of reversals was completed. Following the recommendations by Kollmeier *et al.* (1988), the threshold estimate was obtained as the average of the levels presented on all trial after the third reversal. Each data point represents the median threshold estimate of six independent runs for each subject. The medians are plotted together with the respective interquartile ranges. With the monaural configuration employing a stepwise masker transition in the time domain only three runs were performed by each subject.

E. Fitting procedure

To fit the data from the various experiments performed here and from the data in the literature, a simple linear filter integrating masking energy across a certain frequency range was assumed for the frequency domain. In addition, a temporal integration window was assumed that operates in the time domain. As has been shown by Kollmeier and Gilkey (1990) and Kollmeier and Holube (1992, Appendix A), integrating across masking power for the monaural cases is equivalent to integrating across interaural correlation for the binaural case if the formulas of the EC theory are applied (Durlach, 1972). Specifically, the frequency-dependent masked threshold $L(f)$is given as

$$L(f) = L_{\text{low}} + 10\log(1 + b(f)), \tag{5}$$

where $L_{\text{low}} = L_M - 15$ dB in the monaural case (L_M denotes the masked threshold in the presence of the nonattenuated masker) and $L_{\text{low}} = L_M - 10\log(K+1)/(K-1)$ in the binaural case. Here K is determined by the individual's performance in binaural detection tasks according to the EC theory and can be directly computed from the individual N_0S_π masked threshold. $b(f)$ is the weighted average over the frequency-dependent masking energy $m(f)$ that exceeds the -15 dB reference threshold in the monaural case. This is computed as

$$b(f) = \int_{F_1}^{F_2} w(f_m - f') \cdot m(f')\,df'. \tag{6}$$

In this formula, $w(f_m - f')$denotes the frequency weighting function (i.e., filter shape), and F_1 and F_2 denote the spectral extent of the complete masker in the frequency domain. For the binaural case, the equivalent formula is given as

$$b(f) = \frac{1}{K-1} \cdot \left(1 - \int_{F_1}^{F_2} w(f_m - f') \cdot \rho(f')\,df'\right), \tag{7}$$

where $\rho(f')$ denotes the frequency-dependent interaural correlation of the masker (varying between -1 and $+1$) under the assumption that an S_π-probe tone has to be detected which exhibits the lowest masked threshold for a binaural masker with an interaural correlation of $\rho = 1$. The weighting function $w(f_m - f')$ can either be a double-sided exponential or a rounded exponential function (see Kollmeier and Holube, 1992).

For modeling threshold data in the time domain, exactly the same formulas hold if the frequency parameter f is exchanged by the time parameter t and all functions are considered as a function of time instead of frequency. The only free parameters that have to be fitted to the individual data are the frequency constants (effective bandwidths) or time constants of the weighting function w, respectively, and the magnitude of the lower ''target'' threshold L_{low}. In some cases, however, the target threshold L_{low} was fixed as the respective reference measured with an independent experiment. The fitting of the data was performed using a simplex method to minimize the squared deviation between the respective model function and the data.

II. RESULTS

Presenting figures of all the data would be beyond the scope of this paper. Therefore the following panels show the results of subjects IH, RN (frequency domain), and CM (time domain). Subject IH was chosen because she participated in all experiments and collected more data points than the other subjects. The two listeners RN and CM showed average performance in all tasks and had less training than MK and SU. The results for the remaining two subjects (MK and SU) are very similar to those shown here. Complete results were reported by Holube (1993).

A. Experiment 1 (frequency domain)

Figures 2 and 3 give the masked thresholds of the probe tone for the binaural conditions depicted in Fig. 1 (left column) and the monaural conditions (right column) for the subjects RN (Fig. 2) and IH (Fig. 3). The upper panels give the results for a cosinusoidal variation as a function of the ripple spacing (or frequency period) F. The middle panels give the results for the condition employing a stepwise tran-

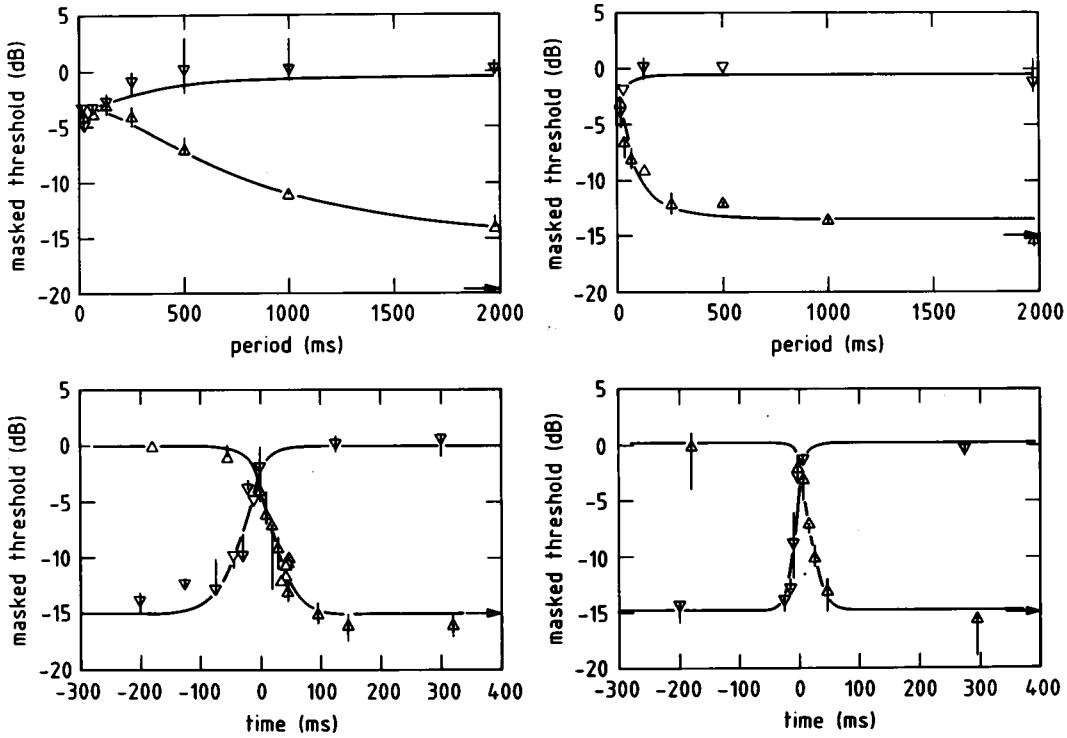

FIG. 5. Masked thresholds (median values and interquartile ranges) as functions of the temporal period (upper panels) and the time of the step (lower panels) of the noise masker variations. The left panels show the results for the binaural and the right panels for the monaural conditions for subject CM. The upwards-pointing triangles (△) refer to the conditions where N_0 noise is presented simultaneously with the probe tone (upper panels) or the N_π noise switches to N_0 (lower panels). The downwards-pointed triangles (▽) refer to the reversed condition where N_0 is replaced by N_π and vise versa. The same symbols are shown in the monaural conditions when the N_π noise is replaced by a nonattenuated monaural noise and N_0 noise is replaced by a monaural noise which is attenuated by 15 dB. In each panel, 0 dB at the ordinate denotes the individual $N_\pi S_\pi$ reference threshold and the monaural threshold for the reference masking level, respectively. The arrow at the right-hand side denotes the individual $N_0 S_\pi$ reference threshold and the monaural threshold after reducing the masking level by 15 dB, respectively. The reference thresholds were obtained without a time-dependent interaural phase or power density of the masker. Solid lines indicate theoretical threshold functions obtained with a double-sided exponential window characteristic.

sition and are taken from Kollmeier and Holube (1992). Thresholds are plotted as a function of edge frequency. The lower panels give the masked thresholds obtained in the condition with the rectangular transition [cf. Fig. 1(c)] as a function of bandwidth of the center band. The upward-pointing triangles (△) depict the listening situation with N_0 noise or a 15-dB attenuation of the monaural noise, respectively, in the spectral region around the probe tone frequency. The downward-pointing triangles (▽) denote the listening situation with N_π noise or a nonattenuated monaural noise, respectively, centered around the probe tone frequency.

In the binaural condition with cosinusoidal variation (upper left panel in Figs. 2 and 3), the masked threshold of the S_π-probe tone decreases with increasing ripple spacing for N_0 (△), because a smaller portion of the spectral region with N_π falls into the auditory filter. In the condition with the phase-inverted masker (▽) the observed increase of the masked threshold with increasing ripple spacing can be deduced from a similar argument. The two masked threshold curves intersect at -3 dB for small periodicities, which corresponds to the MLD for a S_π-probe tone in an interaurally uncorrelated noise. This is due to the fact that several ripple periods are integrated within each auditory filter resulting in an interaural correlation close to 0. A similar argument holds for the monaural condition (right upper panel in Figs. 2 and 3): An integration across at least one ripple period yields an average power density value which corresponds to 1/2 of the maximum power density value. This corresponds to a decrease in masking power of 3 dB.

In the stepwise configuration (middle panels in Figs. 2 and 3) the results show smooth threshold transitions as the edge frequency of the masker is increased beyond the probe tone frequency of 500 Hz. The slopes of these transitions are shallower in the binaural conditions (left panels) than in the monaural conditions (right panels). For edge frequencies well below or above the probe tone frequency, the obtained threshold values are expected to approach the reference thresholds.

With the rectangular configuration (lower panels in Figs. 2 and 3) the masked threshold in the binaural case (left panel) decreases for N_0 noise and increases for N_π noise in a manner similar to that for the cosinusoidal masker. For small bandwidths, however, the threshold for the probe tone in N_0 noise (△) approaches the threshold for the static configuration $N_\pi S_\pi$ and vice versa. A similar argument holds again for the monaural condition (right lower panels in Figs. 2 and 3).

Theoretical masked thresholds were fitted to the measurement results using a double-sided exponential and a rounded-exponential auditory filter centered around the probe tone. The double-sided exponential filter consists of a pair of back-to-back exponential functions. Each exponential function can be characterized by a frequency constant which describes the steepness of this function. The rounded-

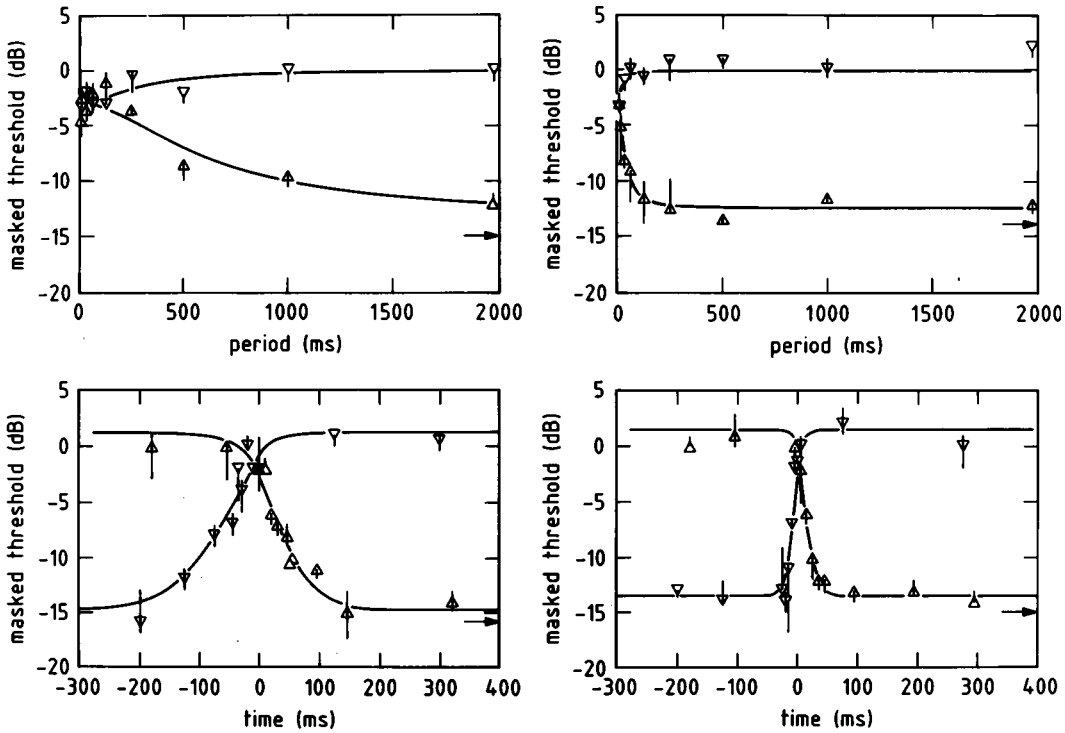

FIG. 6. Same as Fig. 5 for subject IH.

exponential filter consists also of a pair of back-to-back exponential functions with a rounded tip in the middle. For details of the underlying model assumptions and formulas see Kollmeier and Holube (1992, Appendix A). The solid lines in Figs. 2 and 3 give the masked thresholds fit using the double-sided exponential filter. The upper and lower frequency constants (ν_u and ν_l) of the double-sided exponential or rounded exponential filter, respectively, were fitted to the data. Additional parameters were the $N_\pi S_\pi$ and $N_0 S_\pi$ thresholds for the binaural case and the $N_m S_m$ and $N_{-15} S_m$ thresholds for the monaural case, respectively. However, the lower and upper frequency constants could not be determined separately in conditions where the interaural correlation is symmetric around the probe tone [Fig. 1(a) and (c)]. Hence symmetric filters were fitted to the data of these experiments.

Figure 4 gives the ''effective'' bandwidth, i.e., the sum of the frequency constants $\nu_u + \nu_l$ (as a measure for the auditory filter bandwidth) of the double-sided exponential filter for each individual subject for each of the binaural and monaural conditions. With the exception of RN, the bandwidths in the monaural conditions are always similar or smaller than those in the corresponding binaural conditions. When comparing the three conditions, the stepwise variation of the masker produces the smallest bandwidths. The rectangular variation produces the least variability across subjects and the second lowest bandwidths. The cosinusoidal masker variation produces the highest bandwidths on average and the largest variation of the bandwidths across subjects and binaural/monaural conditions. The obtained bandwidths for each individual subject are connected with straight lines for the different conditions in the binaural and monaural case. In general, these lines are fairly parallel with only a few intersections. This indicates that the rank order of the bandwidths across conditions is fairly constant. Apart from a significant absolute change of the bandwidths across conditions (discussed further below) the results with the different measurement methods are therefore consistent across subjects.

B. Experiment 2 (time domain)

Figures 5 and 6 give the masked thresholds for subjects CM and IH for the cosinusoidal transition of the masker (upper panels) and the stepwise transition of the masker (lower panels). The results for the binaural case are given on the left and those for the monaural case on the right. For the conditions with the cosinusoidal masker variation (upper panels), the masked threshold is given as a function of the temporal period of the cosine. The upward-pointing triangles ($\triangle$) denote the condition where the probe tone is presented simultaneously with N_0 noise in the binaural case and an attenuated noise in the monaural case. The downward-pointing triangles (∇) denote the condition with N_π noise presented simultaneously with the probe tone in the binaural case and a nonattenuated noise in the monaural case. In the condition with stepwise masker variation, the upward-pointing triangles ($\triangle$) denote the configuration where an N_π noise is switched to N_0 in the binaural case and the nonattenuated noise is switched to the attenuated noise in the monaural case. The downward-pointing triangles (∇) denote the transition from N_0 to N_π in the binaural case and from the attenuated noise to the nonattenuated noise in the monaural case. The general shapes of the masked thresholds as a function of the independent variable are very similar to those in the related experiments in the frequency domain (Figs. 2 and 3). However, the difference between the binaural and monaural conditions is more pronounced for the experiments in

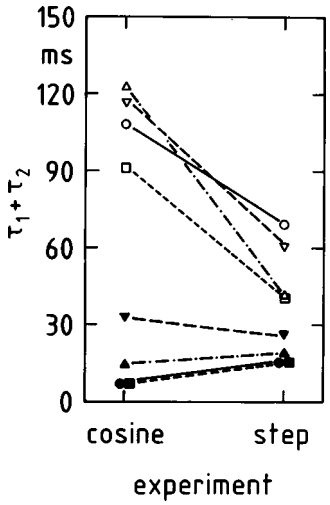

FIG. 7. Width of the time windows as the sum of the time constants ($\tau_1 + \tau_2$) for the cosinusoidal and stepwise masked variations. Full symbols: monaural condition, open symbols: binaural condition. Subject CM: △, IH: ○, MK: □, SU: ▽. The symbols are connected by lines to get an impression of the overall performance of the subjects in different configurations.

the time domain. As before, theoretical masked thresholds were fitted to the data using a procedure similar to that for the frequency domain (cf. Kollmeier and Gilkey, 1990). A double-sided exponential time window centered around the probe tone was used. The time constant τ_1 and τ_2 of this window were fitted to the data employing the stationary thresholds $N_\pi S_\pi$, $N_0 S_\pi$, $N_m S_m$, and (-15 dB) $N_m S_m$, as additional parameters. To fit the curve to the data from the condition with cosinusoidal masker variation, a symmetrical time window was assumed. Figure 7 shows the sum of the time constants $\tau_1+\tau_2$ as a measure of the time window length for the different subjects.

While only small differences occur between the cosinusoidal and the stepwise masker variation in the monaural case (Fig. 7, filled symbols), large differences occur in the binaural case (Fig. 7, open symbols). For the cosinusoidal variation, the binaural condition yields on average time constants 7.2 times larger than in the monaural case, and 2.8 times larger for the stepwise masker variation. This behavior differs significantly from the analogous results in the frequency domain and points towards different mechanisms being involved in the monaural and binaural detection experiments in the time domain. In addition, the rank order of the time constants across subjects is preserved between the two monaural experimental conditions, whereas it is not for the two binaural experiments. This leads to the assumption that different mechanisms are involved in both binaural experiments that cannot simply be described by a single time constant with a consistent variation across subjects.

Another interesting pint is the comparison of the results in the time and frequency domain across subjects. In the monaural condition, subject IH has the smallest time constants and the largest frequency constants, whereas subject SU has the largest time and the smallest frequency constants. However subject MK shows both small time and frequency constants. This indicates that no direct inverse relation between temporal and frequency resolution, as is suggested by linear filter theory, can be found in the monaural case. Similar arguments can be made for the binaural case, where again no simple relation between the findings in the time domain and the frequency domain exists across subjects.

C. Comparison with data from the literature

In the literature, several experiments have been described that measure time and frequency resolution from monaural and binaural conditions in a manner similar to that used in this study. Unfortunately, the frequency and time constants reported are based on different fitting procedures and definitions of the filter bandwidth (e.g., 3-dB-bandwidth, equivalent rectangular bandwidth) or time constants (e.g., equivalent rectangular duration, period of the cutoff modulation frequency). Therefore a comparison is made between the time and frequency constants reported in this study (first column in Table I), the time and frequency constants reported in the literature (column 2), and the constants that are obtained after fitting the data from the literature with the model assumptions used in this study (column 3).

For the experiments in the frequency domain, the experimental data provided by Kohlrausch (1988) employing a stepwise transition of the interaural correlation in the binaural case could not be fitted, because the probe tone frequency was not fixed at 500 Hz, but was varied during the experiment. The values reported by Kohlrausch are higher than the corresponding values reported here. This may be due to the fact that he employed a trapezoidal filter function instead of the double-sided exponential filter function employed here which is a triangular filter function on a dB scale. Sondhi and Guttman (1966) employed a rectangular transition in the frequency domain for the binaural case and reported a transition region of approximately 200 Hz. When their original values are fitted with the same method as for our data, an average frequency constant of 92 Hz results, which is in good agreement with the frequency constants reported here. In the monaural case, however, the frequency constants reported in the literature appear to be smaller than those reported here. However, several experimental parameters differ from this study. Houtgast (1977), for example, only employed a sinusoidal variation of the masking level across frequency with a maximum depth of 11 dB instead of the 15 dB employed here. If one assumes an approximate doubling of the frequency constants with a doubling of the center frequency from 500 Hz to 1 kHz, the value fitted to the data of Houtgast (i.e., approximately 72 Hz) appears to be very close to the values reported here for a similar condition. Patterson (1974, 1976) varied the spectral density of the masker across frequency both in a stepwise and a rectangular way. He attenuated the respective spectral component up to the maximum obtainable dynamic range instead of the 15 dB employed here. After employing the same model assumptions for the two sets of experimental data reported by Patterson, similar frequency constants of 46 Hz result both for the stepwise and the rectangular variation of the masking level. Although this value agrees well with our finding for the stepwise variation, the close match between the frequency constants found in both experiments does not correspond well with the frequency constants reported here.

For the experiments in the time domain (binaural case), Grantham and Wightman (1979) used a sinusoidal temporal variation of the masker's interaural phase. The time constants fitted to their data with the methods described here are higher than those reported by the authors originally and, in addition, are higher than those derived in our experiment. One difference between their data and those presented here is that they only included few modulation frequencies. This limits the accuracy of time constants fitted to their data. Another difference is that their maskers had a bandwidth of 400–600 Hz, whereas the maskers employed in this study were low-pass filtered at 1 kHz. For the stepwise temporal transition both in the binaural and monaural case, Kollmeier and Gilkey (1990) used the same method as in this study to fit their data. Their time constants agree very well with the time constants found in this study. Viemeister (1977) employed a sinusoidal modulation of the masker and found time constants much smaller than the ones reported here. However, they are based on detecting a probe tone in a 100% modulated noise carrier instead of an incomplete modulation (attenuation of the minima: 15 dB) employed here. If his data are fitted by the model used in this study, a very small time constant of 2 ms results instead of the period of the −3-dB point corresponding to 4 ms reported originally.

In general, the values reported in the literature appear to be more consistent across conditions and with the data found here, if they are fitted in a consistent way. This underlines the need for standard procedures to report time and frequency constants that are as independent as possible from the model assumptions underlying the fitting procedure.

III. DISCUSSION

The main findings of the current study can be summarized as follows:

(i) The different masker configuration employed here yield considerably different bandwidth estimates and time constants across conditions even though the same subjects, the same psychoacoustical procedures, and the same fitting procedures have been employed. These variations are largest for the binaural case and for the difference between the stepwise (aperiodic) and cosinusoidal (periodic) variation of the masker across frequency or time. They are much less pronounced for the monaural case and for the difference between stepwise and rectangular (aperiodic) variation in the frequency domain.

(ii) The differences between the binaural and the corresponding monaural case is largest for the cosinusoidal (periodic) variation and is least for the stepwise variation of the masker both in the frequency and the time domain.

(iii) No systematic covariation of bandwidth and time constants across subjects is found for the corresponding experiments in the time and frequency domain.

A. Masker variation in the frequency domain (experiment 1)

The differences in bandwidth estimates for the different masker configurations within the same subject may be influenced by several factors:

(a) The shape of the auditory filter function employed for fitting the data

(b) The shape of the maker variation as a function of frequency (periodic versus aperiodic variation and continuous versus abrupt transition across frequency).

(c) The inappropriate usage of a basically linear filter model to explain nonlinear properties of the auditory system.

With respect to factor (a), it should be noted that the respective filter shape has a significant influence on the magnitude of the estimated bandwidth which may differ across subjects and experimental conditions in an unsystematic way (cf. Kollmeier and Holube, 1992). However, this difference across filter shapes is not nearly sufficient to explain the discrepancies between the different masker configurations observed here. For the double-sided exponential filter employed here, the bandwidth estimate (binaural case) averaged across subjects is 75 Hz for the stepwise versus 135 Hz in the cosine experiment, whereas it averages to 33 Hz for the stepwise and 112 Hz for the cosinusoidal periodic variation if a rounded exponential filter is used. Also, the effect of ''off-frequency listening'' might yield a larger bandwidth estimate for the rounded exponential filter if properly accounted for in the stepwise masker variation across frequency (cf. Kollmeier and Holube, 1992). However, this effect only yields an increase of approximately 5% for the binaural case and 10% for the monaural case (Kollmeier and Holube, 1992). Thus the effect of different assumed filter shapes (and the possibility for off-frequency detection associated with certain filter shapes) might only be able to explain some parts of the discrepancy across conditions for the monaural case, but does not add significantly to explaining the large differences in the binaural case.

With respect to factor (b) it should be noted that in the current experiment only the combination of a cosinusoidal and periodic variation and the combination of a stepwise and aperiodic variation were employed. To check the respective influence of the factors ''periodic versus aperiodic variation'' and ''cosinusoidal versus stepwise variation,'' a set of additional measurements was performed with only one subject (IH). Both the combination of the periodical, stepwise variation and the combination of a periodical, cosinusoidal variation of the masker across frequency were employed for the monaural and the binaural case. All other experimental parameters were the same as for experiment 1 described here [see Holube (1993) for a detailed description of the experiments and the results]. Table II gives the fitted ''effective'' bandwidths (i.e., the sum of the frequency constants ν_u and ν_l both for the double-sided exponential and the rounded exponential filter shape) for all the conditions for experiment 1 and the additional experiment for subject IH. These data indicate that the bandwidths derived for both types of periodic variations of the masker across frequency coincide very well and differ significantly from both types of nonperiodical variation across frequency. Although the data from a single subject should only be interpreted with caution, these results indicate that the factor ''aperiodic versus periodic'' variation of the masker across frequency has a considerably larger

TABLE II. Binaural and monaural estimated bandwidths (i.e., sum of frequency constants $\nu_u + \nu_l$ for rounded and double-sided exponential filters in Hz) fitted to data of IH for periodic and nonperiodic rectangular and cosinusoidal masker variations.

		Double-sided	Rounded
Rectangle periodic	binaural	165	106
	monaural	102	70
Cosine periodic	binaural	166	117
	monaural	106	75
Rectangle nonperiodic	binaural	103	67
	monaural	89	58
Cosine nonperiodic	binaural	86	53
	monaural	80	52
Rectangle nonperiodic (fixed masked threshold)	binaural	113	73
	monaural	101	66
Cosine nonperiodic (fixed masked threshold)	binaural	106	68
	monaural	88	58

influence on the data than the factor ''cosinusoidal versus stepwise'' variation.

One factor which contributes to this large difference between aperiodic and periodic conditions might be the fact that in the aperiodic condition the lower reference threshold L_{low} [cf. Eq. (3)] is not quite approached for the limiting case of very large bandwidths. This individual threshold is given by arrows in the right-hand sides of Figs. 2 and 3, respectively, and denotes the individual threshold obtained for the limiting case of (-15 dB) $N_m S_m$ in the monaural case and $N_0 S_\pi$ in the binaural case. Since the fitting procedure treats the ''target'' threshold as a free parameter which is fit to the data in an optimum way, some of the resulting fitted threshold functions deviate substantially from the expected thresholds for large masker bandwidths. To eliminate this factor, a different fit to the data was obtained by using the measured reference masked thresholds as the ''target thresholds,'' i.e., by forcing the fitted curve to end at the arrows given in Figs. 2 and 3, respectively (cf. Sec. I E). The resulting ''effective'' bandwidths for these fixed masked thresholds are also reported for Subject IH in Table II. Obviously, these values are higher than for the nonperiodic cases without a fixed masked threshold. In the monaural case, virtually no difference between these values and the periodic conditions occur, whereas in the binaural case, still a large difference remains to the periodic variations of the masker across frequency. Hence a satisfactory agreement may be achieved between the different conditions for the monaural case, whereas the large difference across conditions in the binaural case seems to be mostly due to the periodic versus aperiodic variation of the masker across frequency.

With regard to factor (c) (adequacy of a linear filter approach for explaining the data), it should be noted that the assumption of a linear critical band filter has proven to be very successful for a wide variety of monaural psychoacoustical tasks in the frequency domain, especially if only a limited dynamic range is involved so that the compressive nonlinearity of the auditory system does not have to be accounted for. This concept also seems to hold for the monaural conditions considered here if appropriate corrections are employed for off-frequency detection (assuming a rounded exponential window) and for the possible mismatch between reference threshold and ''target threshold'' (see above). In the binaural case, however, such a linear filter concept obviously is not able to explain both the data for the periodic cosinusoidal variation and the aperiodic stepwise and rectangular variation of the masker across frequency, respectively. The respective ''effective'' bandwidth averages to 135 Hz for the periodical cosinusoidal variation as opposed to 66 Hz in the stepwise and 89 Hz in the rectangular aperiodic variation. Thus a factor of approximately 1.2 is found between the binaural and monaural bandwidths for the aperiodical stepwise or rectangular variation, whereas a factor of approximately 1.5 is found between binaural and monaural bandwidths for the periodical cosinusoidal variation. Note that such a factor of 1.2 coincides well with the differences in auditory filter bandwidths between monaural and binaural conditions found in broadband experiments and the factor of 1.5 coincides well with the factor of 1.7 found in ''band-narrowing'' experiments [as discussed by Kollmeier and Holube (1992)]. Also, the difference between the ''effective'' bandwidths found between the aperiodic stepwise or rectangular variation versus the periodical cosinusoidal variation can neither be explained by off-frequency detection (this would only yield an increase of 5%, see above) nor by using the reference thresholds as ''target thresholds'' when fitting the data. The latter procedure yields a significant decrease in the goodness-of-fit parameter B_{nl} [see Kollmeier and Holube (1992)] indicating that the underlying model function does not adequately describe the data. Taken together, the performance of the binaural system in the experiments both here and in the literature cannot be described by a linear filter approach (in combination with an equalization and cancellation mechanism) in a way analogous to the monaural case.

One parameter which obviously exerts a strong influence on the performance of the binaural system in the detection tasks considered here seems to be the consistency or ''straightness'' of binaural information across frequency, as has already been pointed out by Stern *et al.* (1988). In the aperiodic stepwise, rectangular, or sinusoidal variation of interaural phase across frequency, the binaural information is quite consistent over a large frequency range and varies only in a limited frequency region. This obviously produces less spectral disturbance (and hence a lower ''effective'' bandwidth estimate) than the case for periodical cosinusoidal (or even rectangular) variation of interaural phase across frequency. Such a condition provides much less consistent binaural information across frequency than the other conditions and hence produces a less clear ''internal auditory image'' of the masker. A (linear) single-frequency channel model would assume the same ''effective'' bandwidth in both cases and obviously fails to predict the observed data. Hence a more elaborate model of binaural image decomposition, one capable of using the consistency of binaural information across the peripheral auditory frequency channels, would be required to explain the data.

B. Masker variation in the time domain (experiment 2)

The general finding for the experiments in the time domain are very similar to those in the frequency domain: While for monaural conditions, only slight variations are found between the different masker configurations, considerable differences in time constants are found between the periodical sinusoidal variation and the aperiodic, stepwise variation of the masker as a function of time. Thus the approximation of the temporal behavior of the auditory system by a sliding linear time window appears to be valid for the monaural conditions employed here. This agrees well with findings from the literature (cf. Table I), although Viemeister (1977) reported smaller values (4 ms) for the cosinusoidal masker variation and Moore *et al.* (1988) obtained 6 ms for the sum of time constants for a rectangular masker variation as well as a variety of other experiments in the time domain. This somewhat smaller value is still comparable to the results of at least two of the four subjects employed in this study. For the binaural case, however, this simple linear sliding window approach cannot account for the large differences (approximately a factor of 2.1) in the cosinusoidally varying masker versus the stepwise variation of the masker. Similar to the frequency domain, a model would rather be applicable that does not only monitor the time period covered by the temporal window, but also evaluates the consistency of any ''binaural image'' across a longer period of time. Such a model could produce a different response to the stepwise change in interaural correlation from one well-defined ''binaural image'' to another as opposed to the case with periodically changing interaural correlation, where no consistent and distinct binaural image can build up over time.

The comparatively large time constants of such an integrative binaural image model would correspond well to the comparatively large time constants of about 200 ms reported by Blauert (1972) in directional hearing and by Grantham and Wightman (1979) who found binaural time constants between 100 and 400 ms. These large values might also be explained in terms of the EC theory (Durlach, 1972): In the cosinusoidal configuration, the interaural correlation changes continuously. Therefore the outputs of different binaural processing channels with various ''E'' mechanisms must be compared. Of these outputs, the one with the largest signal-to-noise ratio has to be chosen. This procedure can be a source of an additional sluggishness and may lead to larger binaural time constants than for conditions with a predetermined ''optimal'' detection strategy (e.g., a stepwise change in interaural correlation). While the latter sluggishness of the binaural system was termed ''channel sluggishness'' by Kollmeier and Gilkey (1990) who found approximately 2.8 times larger time constants in the binaural than in the monaural case for the stepwise variation, the former sluggishness can be denoted as ''strategy sluggishness.''

It is unclear if this additional ''strategy sluggishness'' is the only reason for the difference between cosinusoidal and stepwise masker variation in the binaural case and the extreme difference of a factor 7.2 between the binaural and monaural condition with a cosinusoidal variation. Since nonlinearities are especially important for describing temporal aspects of auditory processing (cf. Püschel, 1988; Dau *et al.*, 1996), a refined model of the effects considered here should definitely incorporate some of these nonlinear properties of the auditory system.

C. Relations between the individual estimated bandwidths and time constants

A major aim of the current study was to correlate the variability across subjects in one experimental condition to the variation in the other experimental conditions in order to estimate the number of independent parameters necessary to characterize the individual's performance in the time and frequency domain. Since the variability across subjects is not much higher than the measurement accuracy for the estimated bandwidths and time constants from each experiment, respectively, only rank order of the estimates for each individual subject should be considered across different experiments. For the monaural case the rank order is preserved for the experimental conditions in the frequency domain with one exception (cf. Fig. 4) and is completely preserved across conditions in the time domain (cf. Fig. 7). However, the rank order in the frequency domain is not related at all to the rank order in the time domain, i.e., the subjects with the largest bandwidth estimates (IH) and with the respective lowest bandwidth estimate (MK) both show the smallest estimated time constants for both experiments in the time domain. This indicates that the individual auditory bandwidth has approximately the same influence for all masker configurations in the frequency domain employed here and is comparatively independent of the individual time constant. This individual time constant in turn seems to influence the performance in both experiments in the time domain in a similar way. Taken together with the notion that the linear model employed here for fitting the data is quite appropriate in the monaural case, this indicates a single bandwidth estimate and a single (independent) time constant estimate might be sufficient to characterize the individual performance in various monaural detection experiments at a certain center frequency. Note that no inverse relation exists between bandwidth and time constant as would be assumed on the basis of the uncertainty principle.

For the binaural conditions, on the contrary, the rank order for the subject's estimates of bandwidth or time constant is neither maintained across experiments in the frequency domain (cf. Fig. 4, open symbols) nor in the time domain (cf. Fig. 7, open symbols). This also precludes any systematic relation between the individual's time constant and bandwidth estimate across subjects. This finding provides another piece of evidence that the detection mechanisms employed for the binaural conditions are not well characterized by the simple linear filter or temporal window employed here to fit the data. Rather, more complex, integrative functions seem to be involved to obtain the optimum performance in the binaural case. This also goes in line with the finding that both the bandwidth estimates and the time constant estimates in the binaural case are considerably higher than in the monaural case, which again would not be predicted from the uncertainty principle. Rather, these increased parameters correspond to a higher degree of ''smear-

ing'' both in the frequency and time domain in the binaural case as compared to the monaural case. The advantage of such an operation might be the increased stability of localization judgments that are based on interaural differences. Its positive effect has been demonstrated by Kollmeier *et al.* (1993) and Peissig *et al.* (1994) who achieved an improved performance of an artificial binaural noise reduction system and a binaural localization model where a fair amount of temporal and spectral integration was included.

IV. CONCLUSIONS

(1) This study shows that a linear filter or temporal window approach is an adequate first approximation to model the masked thresholds in the used probe tone detection experiments in the monaural case and to a much lesser degree in the binaural case. Since not all configurations could be modeled with the same accuracy, a nonlinear extension of these model assumptions appears desirable, especially in the binaural case where a higher degree of spectral and temporal integration can be observed.

(2) In the monaural conditions, all masker configurations lead to about the same frequency and time constants. The estimated auditory bandwidth at 500 Hz averaged over the rectangular and cosinusoidal masker variations for a rounded exponential filter in the frequency domain is 67 Hz. It is 38 Hz for the stepwise masker variation which might be increased by approximately 10% with off-frequency listening and symmetrical filtering. In the time domain, the average time constant is 17 ms for all configurations for a double-sided exponential window. These results are consistent with data given in the literature.

(3) Although the frequency and time constants found in the binaural conditions are consistent with the data from literature in those cases where previous experiments have been reported, considerable differences occur for the different masker configurations. The estimated effective bandwidth at 500 Hz is 43 Hz for the stepwise, 58 Hz for the rectangular, and 95 Hz for the periodic cosinusoidal masker variations in the frequency domain for a rounded exponential filter. A possible explanation for these differences is the reduced consistency or ''straightness'' of interaural parameters across frequency in the latter case. In the time domain, the sum of time constants is 53 ms for the stepwise and 109 ms for the cosinusoidal masker variation for a double-sided exponential window. A possible explanation is the additional ''strategy sluggishness'' that might play a role in the latter condition.

(4) The binaural frequency constants are up to a factor of 1.5 and the binaural time constants are up to a factor of 7.2 larger than the monaural constants. This higher degree of ''smearing'' or integration both in the frequency and temporal domain might be related to an increased stability of interaural parameter estimates.

(5) In the monaural case, a single bandwidth and time constant estimate might be sufficient to assess the individual performance for detection experiments. However, time and frequency constants measured for the same subjects appear to be largely independent of each other both in monaural and binaural conditions.

ACKNOWLEDGMENTS

Work supported by the Deutsche Forschungsgemeinschaft and BMBF (01 VJ 8903). Thanks to Armin Kohlrausch for helpful hints and discussion, Angela Sievers, Peter Wagner, Karin Bramstedt, and Ralph Nolte-Holube for helping to prepare the manuscript and Liane Martens and Gisela Kirschmann-Schröder for technical assistance. We also thank Brian C. J. Moore for comments on a previous version of the manuscript.

Blauert, J. (**1972**). ''On the lag of lateralization caused by interaural time and intensity differences,'' Audiology **11**, 265–270.

Dau, T., Püschel, D., and Kohlrausch, A. (**1996**). ''A quantitative model of the effective signal processing in the auditory system. I. Model structure,'' J. Acoust. Soc. Am. **99**, 3615–3622.

Durlach, N. I. (**1972**). ''Binaural signal detection: Equalisation and cancellation theory,'' in *Foundations of Modern Auditory Theory, Vol. II*, edited by J. V. Tobias (Academic, New York), pp. 369–462.

Festen, J. M., and Plomp, R. (**1983**). ''Relations between auditory functions in impaired hearing,'' J. Acoust. Soc. Am. **73**, 652–662.

Grantham, D. W., and Wightman, F. L. (**1979**). ''Detectability of a pulsed tone in the presence of a masker with time-varying interaural correlation,'' J. Acoust. Soc. Am. **65**, 1509–1517.

Holube, I. (**1993**). ''Experimente und Modellvorstellungen zur Psychoakustik und zum Sprachverstehen bei Normal- und Schwerhörigen,'' dissertation, Universität Göttingen.

Holube, I., Kinkel, M., and Kollmeier, B. (**1991**). ''Messungen zur monauralen und binauralen Zeit- und Frequenzauflösung,'' in *Fortschritte der Akustik—DAGA 91* (DPG-Kongreß GmbH, Bad Honnef), pp. 549–552.

Houtgast, T. (**1977**). ''Auditory-filter characteristics derived from direct-masking data and pulsation-threshold data with a rippled-noise masker,'' J. Acoust. Soc. Am. **62**, 409–415.

Kinkel, M. (**1990**). ''Zusammenhang verschiedener Parameter des binauralen Hörens bei Normal- und Schwerhörigen,'' dissertation, Universität Göttingen.

Kohlrausch, A. (**1988**). ''Auditory filter shape derived from binaural masking experiments,'' J. Acoust. Soc. Am. **84**, 573–583.

Kollmeier, B., and Gilkey, R. H. (**1990**). ''Binaural forward and backward masking: Evidence for sluggishness in binaural detection,'' J. Acoust. Soc. Am. **87**, 1709–1719.

Kollmeier, B., Gilkey, R. H., and Sieben, U. (**1988**). ''Adaptive staircase techniques in psychoacoustics: A comparison between theoretical results and empirical data,'' J. Acoust. Soc. Am. **83**, 1852–1862.

Kollmeier, B., and Holube, I. (**1992**). ''Auditory filter bandwidths in binaural and monaural listening conditions,'' J. Acoust. Soc. Am. **92**, 1889–1901.

Kollmeier, B., Peissig, J., and Hohmann, V. (**1993**). ''Real-time multiband dynamic compression and noise reduction for binaural hearing aids,'' J. Rehab. Res. Develop. **30**, 82–94.

Levitt, H. (**1971**). ''Transformed up-down methods in psychoacoustics,'' J. Acoust. Soc. Am. **49**, 467–477.

Moore, B. C. J. (**1995**). *Perceptual Consequences of Cochlear Damage* (Oxford U.P., London).

Moore, B. C. J., Glasberg, B. R., Plack, C. J., and Biswas, A. K. (**1988**). ''The shape of the ear's temporal window,'' J. Acoust. Soc. Am. **83**, 1102–1116.

Patterson, R. D. (**1974**). ''Auditory filter shape,'' J. Acoust. Soc. Am. **55**, 802–809.

Patterson, R. D. (**1976**). ''Auditory filter shapes derived with noise stimuli,'' J. Acoust. Soc. Am. **59**, 640–654.

Peissig, J., Albani, S., and Kollmeier, B. (**1994**). ''A real-time model fm binaural sound source localization resolving spatial ambiguities,'' J. Acoust. Soc. Am. **95**, 3004.

Püschel, D. (**1988**). ''Prinzipien der zeitlichen Analyse beim Hören,'' dissertation, Universität Göttingen.
Robinson, D. E., and Watson, C. S. (**1972**). ''Psychophysical methods in modern psychoacoustics,'' in *Foundations of Modern Auditory Theory, Vol. II*, edited by J. V. Tobias (Academic, New York), pp. 99–131.
Sondhi, M. M., and Guttman, N. (**1966**). ''Width of the spectrum effective in the binaural release of masking,'' J. Acoust. Soc. Am. **40**, 600–606.
Stern, R. M., Zeiberg, A. S., and Trahiotis, C. (**1988**). ''Lateralization fm complex binaural stimuli: A weighted-image model,'' J. Acoust. Soc. Am. **84**, 156–165.
Viemeister, N. F. (**1977**). ''Temporal factors in audition: A system analysis approach,'' in *Psychophysics and Physiology f Hearing*, edited by E. F. Evans and J. P. Wilson (Academic, London), pp. 419–428.

Vowel posture normalization

Michiko Hashi, John R. Westbury,[a] and Kiyoshi Honda
Waisman Center and Department of Communicative Disorders, University of Wisconsin—Madison, Madison, Wisconsin 53705-2280

(Received 12 January 1998; accepted for publication 19 June 1998)

A simple normalization procedure was applied to point-parametrized articulatory data to yield quantitative speaker-general descriptions of ''average'' vowel postures. Articulatory data from 20 English and 8 Japanese speakers, drawn from existing x-ray microbeam database corpora, were included in the analysis. The purpose of the normalization procedure was to minimize the effects of differences in vocal tract size and shape on average postures derived from the raw data. The procedure resulted in a general reduction of cross-speaker variance in the *y* dimension of the normalized space, within both language groups. This result can be traced to a systematic source of variance in the *y* dimension of the raw data (i.e., palatal height) ''successfully removed'' from the normalized data. The procedure did not result in a comparable, general reduction in cross-speaker variance in the *x* dimension. This negative result can be traced partly to the new observation that some speakers within the English sample habitually placed their tongues in a fronted position for all vowels, whereas other speakers habitually placed their tongues in a rearward position. Methods for evaluating articulatory normalization schemes, and possible sources of interspeaker variability in vowel postures, are discussed. © *1998 Acoustical Society of America.* [S0001-4966(98)00710-3]

PACS numbers: 43.70.Aj, 43.70.Bk [AL]

INTRODUCTION

Vowels form an important part of the sound system in every human language. Basic problems for speech science include descriptions of kinematic, acoustic, and perceptual properties of vowels, within and across gender, dialect, age, and language groups. Defining those speaker-general characteristics of vowels that are *normal* is an important task within this broad view of speech research.

Speaker-general descriptions, in principle, should be derived from data collected from many speakers. Data from multiple speakers are necessary to quantitatively estimate central tendencies among vowel postures, and limits of normalcy, without excessive bias due to speaker-specific idiosyncracies. The unfortunate fact is that many generalizations about vowel articulation are based on single-speaker data (e.g., Fant, 1960). Relatively little is known about the actual articulation of vowels by many speakers (but cf. Wood, 1979; Johnson *et al.*, 1993; and references cited therein).

One of the reasons that multi-speaker articulatory studies are scarce relates to the difficulty and cost of data acquisition. It has only been within the last 15 years or so that technological developments and refinements (e.g., MRI, ultrasound, electromagnetic-articulometry, x-ray microbeam) have made it possible and feasible to record certain kinds of articulatory data (e.g., postural and kinematic) from many speakers. Another reason for the scarcity of multi-speaker studies relates to unspoken assumptions about homogeneity of articulatory behaviors across speakers in a population. Assumptions of this type, common to single-speaker studies, appear to be ill founded in the face of growing numbers of accounts of interspeaker variability (e.g., Lubker and Gay, 1982; Delattre and Freeman, 1968; Hagiwara, 1995; Johnson *et al.*, 1993; Westbury *et al.*, 1995). These reports show the homogeneity assumption to be false for several aspects of articulatory behavior. This general fact suggests, in turn, a need for reliable, accurate estimates of the degree and nature of interspeaker variability that can be obtained only from additional studies. X-ray microbeam (XRMB) speech production databases—one that is publicly available, including 57 speakers of American English (Westbury, 1994a); and, one including 19 speakers of Japanese—have been developed partly in response to this need. These resources provide an opportunity to study vowel productions by relatively many speakers and, thus, a potential basis for valid, informed generalizations about vowel articulations across speakers.

A key methodological challenge associated with cross-speaker descriptions of articulatory postures for vowels relates to data representation. Speakers obviously differ in size and shape of the articulators (cf. Beck, 1997), and these differences may cause their articulatory behaviors to appear more different than they are. Information shown in Fig. 1, for three Japanese speakers (top panel), and three American English speakers (bottom panel), hints at the problem of anatomical differences in a concrete way. Midsagittal outlines of the palatal vault are shown for each speaker, terminated to the right (at the origin [0,0]) by the location of the lower edges of the central maxillary incisors (CMI) in the maxillary occlusal plane (MaxOP), and to the left by a line segment representing the mid-sagittal outline of a portion of the posterior pharyngeal wall. The sources of these outlines, and procedures necessary to obtain them, are described in subsequent sections of this report.

Among the three Japanese speakers, J7 has the tallest and longest oral cavity, while J2 has the shortest. Speaker J5 has a distinctive ''hump'' in the mid-palatal region. Among the three English speakers, E43 has the tallest palatal vault,

[a]Electronic mail: westbury@facstaff.wisc.edu

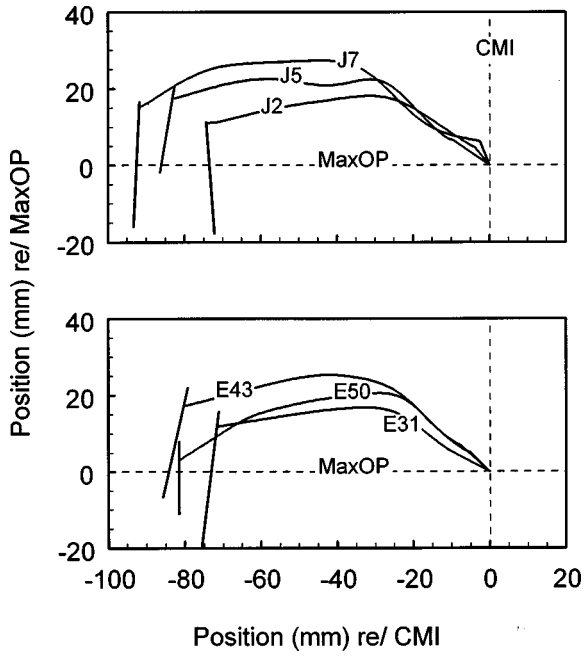

FIG. 1. Examples of anatomical differences in three Japanese speakers (top panel), and three American English speakers (bottom panel). Mid-sagittal outlines of the palatal vault are shown for each speaker, terminated to the right, at the origin (0,0), by the location of the lower edges of the central maxillary incisors (CMI) in the maxillary occlusal plane (MaxOP), and to the left by a line segment representing the mid-sagittal outline of a portion of the posterior pharyngeal wall.

and speaker E50 the longest outline, from the CMI to the posterior pharyngeal wall. Speaker E31 has the shortest of the palatal vaults, and the shortest palatal outline. Anatomical differences such as these might easily affect postures and movements associated with speech sound articulation, from one speaker to the next. In turn, these anatomical differences might also influence estimates of cross-speaker variance in statistical summaries of such materials, if the summaries are based upon raw data. Ideally, postural and kinematic data from multiple speakers should be represented in some form that minimizes differences in size and shape of the vocal tract such as those illustrated in Fig. 1. A normalization step of this type should precede an attempt to develop meaningful group descriptions, based upon data from multiple speakers.

Up to now, normalization schemes have not been emphasized in speech kinematic studies, probably due to the dominance of single-speaker analyses. However, a few approaches to the problem of normal representation have been considered. For example, Harshman *et al.* (1977) and Maeda (1991) applied mean corrections, within talkers, to postural and kinematic measures from lateral-view cineradiographic data. Harshman *et al.* (1977) manipulated their data in this way presumably to facilitate comparisons between talkers. Maeda's (1991) manipulation facilitated comparisons of kinematic data from different articulators, as well as data of different types (e.g., kinematic and acoustic). However, no approaches to articulatory normalization have been proposed that are directly and easily applicable to so-called point-parametrized data, of the type generated by XRMB or electromagnetic-articulometric techniques. These techniques involve less risk, and lower time costs for data reduction than flood-field cineradiography. Both factors make these newer techniques better suited for multiple-speaker studies, and, in turn, motivate an attempt to develop a normal representational scheme for their data.

The study summarized in this report represents such an attempt. The central goal of the study was to develop a simple normalization procedure that yields a speaker-general space within which descriptions of central tendencies and variabilities of the vowel postures are possible. The procedure was applied to XRMB data taken from two readily accessible language samples. Acoustic data were included in the present study to verify the normalcy of speakers and to allow comparisons of normalized articulatory data with traditional phonetic descriptions of vowel postures and their acoustic correlates. Normalized postural/kinematic data were examined relative to inferences drawn from accompanying acoustic data, and existing literature, regarding the relationship among vowels within each language, and between the two vowel systems.

I. METHODS

A. Speakers

Twenty native English speakers (ten males and ten females), and eight native Japanese speakers (four males and four females), all with normal speech and hearing, were selected from existing XRMB Speech Production Database samples as subjects for this study. The English speakers are designated as {E12,E14,E15,...,E59,E61},[1] and the Japanese speakers as {J1,J2,...,J7,J8}. All English speakers were essentially monolingual, and from Wisconsin, USA. Dialect homes for the English speakers, expressed in terms of the communities in Wisconsin in which they grew up, can be found in Westbury (1994a). All Japanese speakers were bilingual, but variably proficient in English. Seven of the Japanese speakers were Tokyo-dialect speakers. One male Japanese speaker was not from the Tokyo area but his formant frequencies were well within the range of the Tokyo dialect speakers. For that reason, he was also included in the study. The mean age and standard deviation were 22.8 and 4.8 years for English speakers, and 25.6 and 7.4 years for Japanese speakers.

B. Speech tasks

Isolated productions of the five vowels /i ɛ ɑ o u/ were analyzed for English speakers. Speakers' productions of these vowels were cued by (but not contained in) the CVC words {*beet, bet, hot, boat, boot*}. For the Japanese speakers, the five vowels /i e a o ɯ/ were elicited by katakana prompts. Phonetically trained listeners judged all tokens. Vowels considered distorted or off target (e.g., /u/ for E25 and E27) were excluded from analysis. One English production of /ɛ/ (by E31), one Japanese production of /ɯ/ (by J2), and articulatory data for one of the tongue pellets (T4) for J2 were not available due to pellet mistracking by the XRMB system. Thus, the number of speakers for each vowel varied from 6–8 among Japanese talkers and from 18–20 among the English talkers. From phonation onset to offset, the English

talkers' vowels averaged about 390 ms ($\sigma \cong 75$ ms), while the Japanese talkers' vowels averaged about 270 ms ($\sigma \cong 90$ ms).

C. Acoustic data

Speech data from the 20 English and eight Japanese speakers included synchronous records of the sound pressure wave, sampled at 21 739 Hz, and fleshpoint kinematic data. Formant frequencies for each available vowel spoken by each talker were identified through a LPC-based formant tracking algorithm in Cspeech (Milenkovic and Read, 1992). The number of LPC coefficients was set at 24. The formant tracking results were supplemented by spectrographic measurements made independently of the formant tracking. Dynamic range for the spectrograms was adjusted to best reveal formants. Bandwidths of 300 and 500 Hz were used for male and female speakers, respectively. Formant estimates from the tracking algorithm were accepted when the differences between the tracks and spectrographic measures were within 30 Hz for $F1$, 60 Hz for $F2$, and 80 Hz for $F3$. Estimates from the spectrograms were accepted when the formant tracks overtly deviated from the spectrogram. Fundamental frequencies were measured using the Cspeech autocorrelation-based pitch-extraction utility, supplemented by narrow-band spectrographic readings. Readings from the narrow-band spectrogram were accepted when the result of automatic pitch extraction overtly deviated from the spectrogram. The correlation coefficient, for a linear least-squares regression calculated between repeated acoustic measures made by one of the authors, for ten English speakers and seven Japanese speakers, was 0.98.

The frequencies of the first three formants were measured at the temporal midpoint of the *acoustical steady state* in each vowel production from each talker, following conventions established in well-known speech acoustic investigations (e.g., Hillenbrand *et al.*, 1995; Peterson and Barney, 1952). The acoustical steady state in the present study was defined as the entire region within each isolated vowel where changes in first ($F1$) and second ($F2$) formant frequencies were less than 40 Hz over successive 20-ms periods. For isolated English /o/, which speakers tended to produce as a diphthong, steady states were identified before the [u]-like off-glide.

Figure 2 shows the sound pressure waveform, wideband spectrogram, measurement time (=0), and selected coordinate histories and trajectories for tongue and lip fleshpoints, for /u/ spoken by one English talker (E15). The acoustical steady state in this example spans the 200-ms interval centered at the measurement time (i.e., the steady-state midpoint). A vertical cursor, indicating the measurement time, passes through a solid circle and cuts coordinate histories for upper-lip (UL) and tongue-dorsum (T3) pellets shown in the middle panel. Steady articulatory states in both UL coordinates, and in the *y* coordinate for T3, are apparent during the acoustical steady state. These steady positions are accompanied by a modest 2-mm rearward drift in the *x* position of T3. Sagittal-plane trajectories for tongue and lip fleshpoint, traced during the 560-ms interval illustrated in the spectrogram, are shown in the lower panel. Fleshpoint positions at the measurement time are indicated by filled circles. Unfilled (open) circles indicate fleshpoint positions 260 ms after the measurement time, at about phonation offset for the vowel, when the speaker has moved well away from the posture associated with the acoustical steady state. The typical example shown in this figure suggests the degree to which single-time-slice measurements of formant frequencies, and articulatory postures reflected by fleshpoint positions, are representative of the acoustical steady states of isolated vowels analyzed for this study.

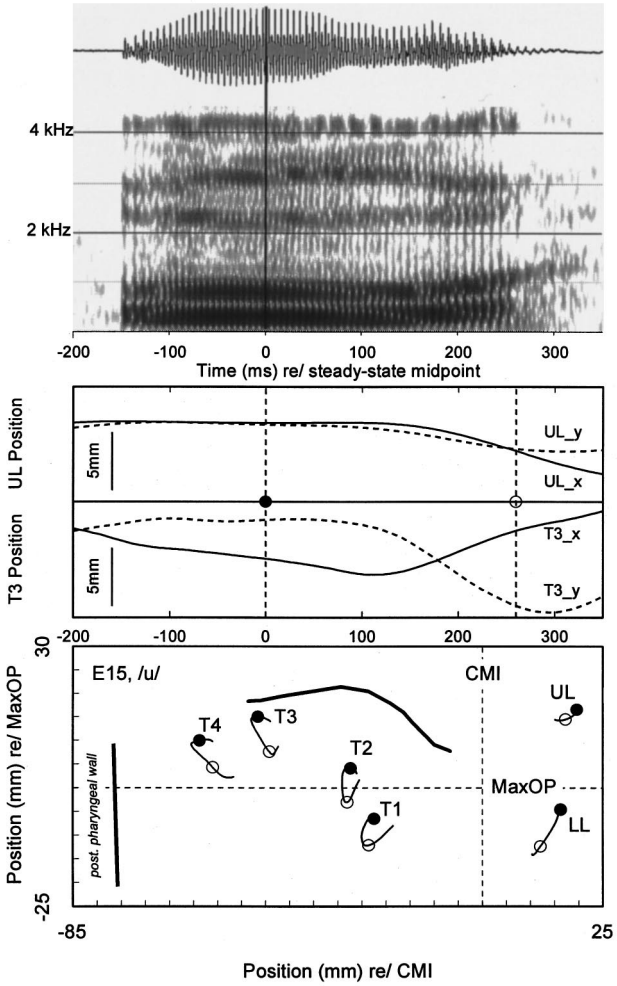

FIG. 2. A representative vowel token produced by one male English speaker (E15). The upper panel shows the sound pressure waveform, wideband spectrogram, and steady-state midpoint (=0) at which formant frequencies $F1$, $F2$, and $F3$ were measured (in this example, 320, 797, and 2261 Hz, respectively). The middle panel shows (relative) *x*- and *y*-coordinate histories for upper lip (UL) and tongue dorsum (T3) fleshpoints. The dashed vertical lines cutting the coordinate histories, and passing through filled and unfilled circular symbols, indicate respectively the measurement time for fleshpoint coordinates, and a later moment during the vowel at about phonation offset. The bottom panel shows sagittal-plane paths traced by tongue and lip fleshpoints during the time interval represented in the upper two panels. Fleshpoint positions at the measurement time (during the acoustical steady state) are indicated by filled circles, while those at phonation offset are indicated by unfilled circles.

D. Articulatory data

Speech kinematic data from the available corpora represented sagittal-plane positions of markers (gold pellets,

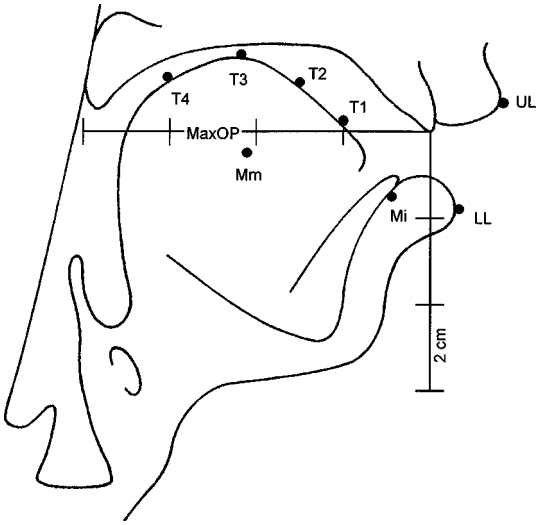

FIG. 3. A schematic illustration of the standard, midsagittal eight-pellet placement constellation, in a cranial coordinate system. The *x* axis corresponds roughly to the maxillary occlusal plane (MaxOP). The *y* axis is normal to MaxOP, and intersects it at the tips of the central maxillary incisors (CMI).

2.5–3 mm in diameter) attached to the tongue, jaw, and lips, recorded 40–160 times/s by the University of Wisconsin XRMB system. Figure 3 schematically represents pellet placements.

Four pellets (T1–T4) were arrayed along the longitudinal sulcus of the tongue. The general rule was to place T1 roughly 10 mm posterior to the apex; T4 as far back as the speaker could easily tolerate without gagging (usually about 60 mm behind the apex); and, then, T2 and T3 so that the spacing between adjacent pellets was roughly equal. Average placements, standard deviations, and ranges, measured from the apex of the extended tongue, using hand-held calipers, are indicated in Table I for each language group. Across speakers, T1 placement varied least and T4 placement varied most. The last two rows of Table I also indicate averages, standard deviations, and ranges of *x* coordinates (measured along lines parallel to the maxillary occlusal plane) of English speakers' tongue pellets measured during prespeech rest postures observed within the first 50 ms of each isolated vowel-task record. Across speakers, by pellet, variation in placement was positively but not strongly related to rest position. For example, Pearson product coefficients of correlation between placements and rest posture *x* coordinates were {0.43, 0.43, 0.47, 0.71} for {T1, T2, T3, T4}. In short, nominal pellet placements on the tongue seemed to explain no more than 50% of the variation in pellet position, across speakers, for resting prespeech postures.

One pellet was also attached in the midline at the vermillion border of each lip (UL and LL), and two others (incidental to this study) were attached to mandibular teeth (Mi, at the incisors, and Mm at a molar). Mid-sagittal plane positions of the four tongue pellets and two lip pellets, at the midpoint of the acoustic steady state during each vowel produced by each talker, were the primary focus of analysis in this study.

E. Articulatory data transformation

Raw articulatory data represented the positions of articulator pellets expressed relative to coordinate system axes defined by the speaker's own maxillary occlusal plane (MaxOP), according to conventions described elsewhere (Westbury, 1994b). A normalization method was applied to raw pellet data, to remove positional effects due to cross-speaker variation in size and shape of the oral cavity and lips. The method was based in part on a procedure described by Beckman *et al.* (1995), and another procedure described in our own recent work dealing with lip pellet positions in vowels and consonants (Westbury and Hashi, 1997). In general, the normalization procedure involved re-expressing tongue pellet positions relative to the palate, and lip pellet positions relative to one another. These transformations have the effect of defining separation between upper and lower boundaries of the upper vocal tract, and must be supplemented by procedures to scale data from different talkers to a common size.

Figure 4 shows raw pellet position data, reflecting articulatory configurations of the upper vocal tract, for the vowels /ɑ/ and /u/ spoken by one male English talker (E12). Line segments have been drawn between adjacent tongue pellet positions associated with each vowel posture, to suggest tongue shape. The rear of the mouth, toward the left of the figure, is bounded by a straight line approximating position and orientation of the posterior oropharyngeal wall. The top of the mouth is bounded above by an outline of the ''hard'' palatal dome, represented by a thick solid line. The palatal outline does not extend all the way back to the pharyngeal wall, though the normalization method required a complete contour of the palate. Thus, an approximation of the missing portion of the palatal contour, represented by a dashed line, had to be devised.

TABLE I. Summary statistics for nominal tongue pellet placements (in mm, behind the apex of the extended tongue), for 8 Japanese speakers (J: top two rows), and 20 English speakers (E: middle two rows); and, for tongue pellets' *x* coordinates for prespeech resting postures (in mm behind the CMI) for 20 English speakers only (bottom two rows).

	*T*1	*T*2	*T*3	*T*4
Placement (J): $\bar{x}$ (σ)	−8.0 (0.76)	−24.3 (1.91)	−42.8 (4.13)	−59.4 (4.83)
Range (J): max, min	(−9, −7)	(−27, −22)	(−48, −37)	(−66, −52)
Placement (E): $\bar{x}$ (σ)	−8.5 (1.05)	−25.3 (1.90)	−45.0 (2.48)	−61.2 (3.07)
Range (E): max, min	(−11, −7)	(−29, −22)	(−49, −39)	(−67, −55)
Rest_*x* (E): $\bar{x}$ (σ)	−9.7 (2.07)	−24.3 (3.51)	−42.1 (4.34)	−54.7 (4.79)
Range (E): max, min	(−1.4, −6.4)	(−29.0, −17.5)	(−50.5, −33.3)	(−62.3, −46.2)

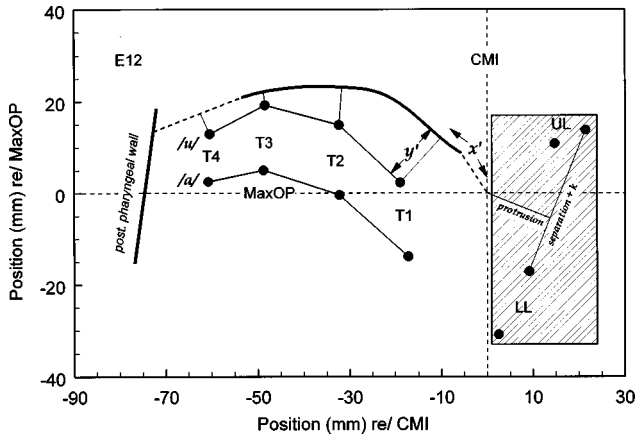

FIG. 4. Raw pellet position data for /ɑ/ and /u/ spoken by one male English talker (E12). Line segments connect adjacent tongue pellet positions associated with each vowel posture. A thick solid line at the top of the mouth represents the original midsagittal outline of the hard palatal dome. An approximation of the completed contour of the palate is represented by a dashed line. The minimum distance between T1 and a point on the palatal contour is represented by y'. The distance along the palatal curve, from the origin to the point where the distance between the palatal curve and the pellet was a minimum, is represented by x'. Key parameters for lip opening, derived from upper and lower lip pellet positions, are illustrated in the shaded rectangle for lip pellet positions associated with /u/.

For the English speakers, the hard portion of the palatal outline, from slightly behind the upper teeth to about the dorsal margin of the horizontal plate of the palatine bone (i.e., the juncture of the hard and soft palates), was based upon an averaging scan of a stone model of the upper (maxillary) dental arch (including the teeth and palatal surface), carrying a chain of a dozen or so gold pellets fixed along the midline of the palatal vault. For the Japanese speakers, the same portion of the palatal outline was based upon a trace created by tracking the motion of a pellet attached to a small wand. Positions of chain pellets for E12 are shown as small solid circles in Fig. 5. The palatal outline behind the rearmost chain pellet (or the end of the palate trace) could be extended for a short distance ($\leqslant$15 mm) through a collection of extreme positions of the T4 pellet observed in records of connected speech, clear speech, consonant inventories, and liquid swallows. A set of eight such extrema, extending the

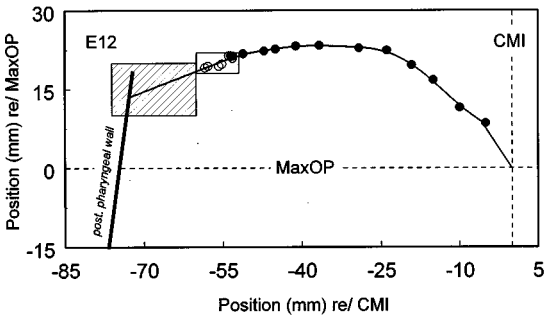

FIG. 5. An approximation of the complete mid-sagittal palatal outline. The small filled circles represent positions of chain pellets attached to a stone model of the upper teeth, along the midline of the palatal vault, for E12. Unfilled circles surrounded by the smaller of two rectangles are extreme positions of the T4 pellet during selected speech and nonspeech tasks. The larger of the rectangles, filled by cross-hatching, represent the extended portion of the palate.

outline for E12 about 6 mm beyond the end of the pellet chain, are represented by open circles surrounded by the smaller of two rectangles in the upper left of Fig. 5.

For each speaker, the piecewise continuous boundary line formed by segments connecting adjacent chain pellet centers (or position samples in the palate trace), and extreme T4 positions, was resampled at approximately 0.5-mm intervals, and smoothed using a 17-point moving weighted average. The resulting curve was then extended rearward to intersect the posterior pharyngeal wall by a line segment with a slope given by the last pair of samples in the smoothed curve. This extension, for E12, is surrounded by the larger of the rectangles in Fig. 5, filled by cross-hatching. The palatal outline was also extended forward to the origin by a line segment drawn between the frontmost sample in the smooth curve, and (0,0). The entire outline, formed by a smooth curve in the middle, joined by line segments at both ends, was again resampled into nearly equal-length segments no longer than about 0.7 mm.

The palatal outline, constructed in this way, was important for transforming tongue pellet positions.[2] The distance between each tongue pellet, and the point on the extended palatal curve nearest to the tongue pellet, was calculated.[3] This distance was considered to be the minimum midsagittal distance between the palatal curve and the tongue pellet. Distances of this type are indicated by straight lines in Fig. 4, intersecting the palatal curve and drawn through tongue pellet positions for the vowel /u/. The lengths of these lines (e.g., y' for T1 in Fig. 4), multiplied by (-1), were treated as new y coordinates for the pellets. The transformed y coordinates for tongue pellets thus indicate their respective distances below the palate, regardless of the shape and height of the speaker's palate above the maxillary occlusal plane.

Distances along the palatal curve, from the origin to the point where the distance between the palatal curve and the pellet was a minimum (e.g., x' for T1 in Fig. 4), were also found for all pellets. These distances, indicating location of the mid-sagittal minimum distance associated with each of the four tongue pellets, were divided by the total distance from CMI to the pharyngeal wall, measured along the speaker's extended palate, and then multiplied by the mean CMI-to-pharyngeal-wall distance computed across speakers for the language group. In this way, the pellets' new x coordinates were scaled for size of the oral cavity.

Key concepts of the transformation method applied to lip pellet data are represented in the right-hand portion of Fig. 4, in the area surrounded by the shaded rectangle. A line segment has been drawn to connect UL and LL positions associated with the vowel /u/. This line represents midsagittal separation between the lip surfaces, plus some distance k corresponding to the lips' combined thickness. Lip separation can be estimated by subtracting an index of lip thickness from the length of the UL–LL line. In this study, lip pellet separation at the initial closure moment for the labial consonant in /ɑbɑ/ was used as the index of lip thickness (cf. Westbury and Hashi, 1997). The resulting estimate of lip separation became the new y coordinate of the lips (Ly).

Protrusion of the lips was estimated as the length of a

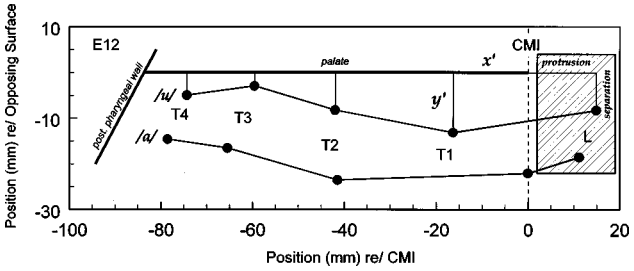

FIG. 6. Transformed articulatory data for /u/ and /ɑ/ produced by speaker E12.

line segment drawn tangent to the lower edges of the CMI, and normal to the UL–LL line. This raw measure of protrusion also incorporates a measure of lip size that should be removed before data from different speakers can be combined. Size normalization was accomplished by multiplying each speaker's raw protrusion measures by the ratio of an extreme speaker-specific protrusion to the cross-speaker mean for the same extreme protrusion. The largest raw protrusion measure from a record of VCV tokens containing all consonants of the language was chosen as the extreme value for each speaker. The new x coordinate (Lx) derived from lip pellet data represents lip protrusion normalized for lip size.

Midsagittal tongue and lip data, for /u/ and /ɑ/ vowel postures produced by speaker E12, transformed according to these methods, are replotted in Fig. 6. The new coordinates of the four tongue pellets (T_x',T_y'), plotted to the left of the CMI, correspond to their respective locations between the CMI and posterior pharyngeal wall, and their distances below the flattened palate. The new lip coordinates, plotted in the shaded area to the right of the CMI, represent estimated lip aperture (Ly), and normalized lip protrusion (Lx).

II. RESULTS

A. Acoustic measures

Scatterplots shown in the upper half of Fig. 7 illustrate the distribution of first and second formants, for vowel steady-state midpoints, across speakers in each of the two language groups. Male speakers are represented with unfilled symbols and female speakers with filled symbols. Different vowels are represented by different symbol types. Ellipses are drawn to surround the distributions of speakers' formant frequencies for each vowel, with major and minor axes two standard deviations (i.e., two-σ) in length, oriented along the principal components of the ($F1$,$F2$) scatter. The distortion of the ellipses is due to logarithmic scaling of $F2$. The expected gender difference in vowel formant frequencies is easy to see.

Scatterplots in the lower half of Fig. 7 show similar information, in similar ways, but for normalized acoustic data expressed in Bark difference scale, in an $F1-F0$ by $F3-F2$ plane. The Bark difference transformation produced greater overlap among male and female speakers for all vowels except /i/, for both language groups, and /a/ for the Japanese group. Acoustic data illustrated in Fig. 7 are in general agreement with other reports for English and Japanese vowels (e.g., Hillenbrand *et al.*, 1995; Hirahara and Kato, 1992).

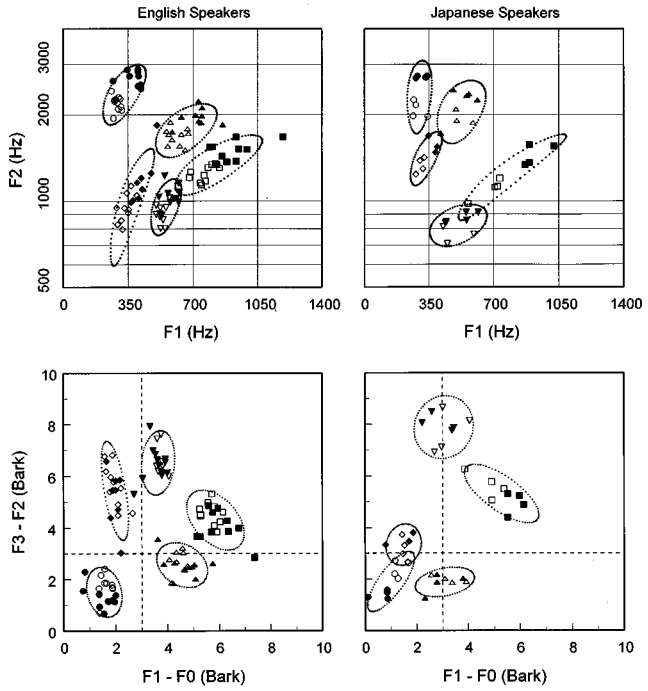

FIG. 7. Distributions of vowels, in formant-frequency ($F1$,$F2$) planes (upper two panels) and in Bark-difference ($F1_{\mathrm{Bark}}-F0_{\mathrm{Bark}}$, $F3_{\mathrm{Bark}}-F2_{\mathrm{Bark}}$) planes (lower two panels). Horizontal lines in the upper panels indicate selected frequencies along the logarithmic scale applied to $F2$; vertical lines represent selected frequencies along the linear scale applied to $F1$. Data from English speakers are to the left, and those from Japanese speakers are to the right. Male speakers are represented with unfilled symbols, and female speakers with filled symbols. Different vowels are represented by different symbol types; circles=/i/, triangles=/ɛ/ and /e/, squares=/ɑ/ and /a/, reversed triangles=/o/, and diamonds=/u/ and /ɯ/. Ellipses are drawn with major and minor axes two standard deviations (i.e., two-σ) in length, oriented along the principal components of the scatter for each vowel.

B. Pellet position measures

Scatterplots in the left columns of Figs. 8 and 9 illustrate the distributions of raw pellet locations (in cranial space), across speakers, separately for each vowel steady-state midpoint. Data from English speakers are shown in Fig. 8, and data from Japanese speakers are shown in Fig. 9. Tongue pellet locations with respect to CMI and MaxOP, are represented by appropriate numerals, while upper and lower lip pellet locations are represented by capital letters U and L, respectively. Scatterplots in the right columns of both figures illustrate the distributions of normalized pellet locations. Coordinates for lip protrusion and separation, derived from raw UL and LL data, are represented by the single capital letter L. For convenience, the ordered pair of lip (protrusion, separation) values are also referred to as normalized pellet coordinates. Two-σ ellipses, with major and minor axes oriented along principal components, are drawn around each pellet-by-vowel distribution.

The normalization procedure translates pellet position data into a normal space where average pellet locations, computed across talkers for each vowel in each language group, can be calculated. Average normalized pellet locations for each vowel are shown in Table II, for English speakers in the upper five rows and for Japanese speakers in the lower five rows. The number of speakers represented in

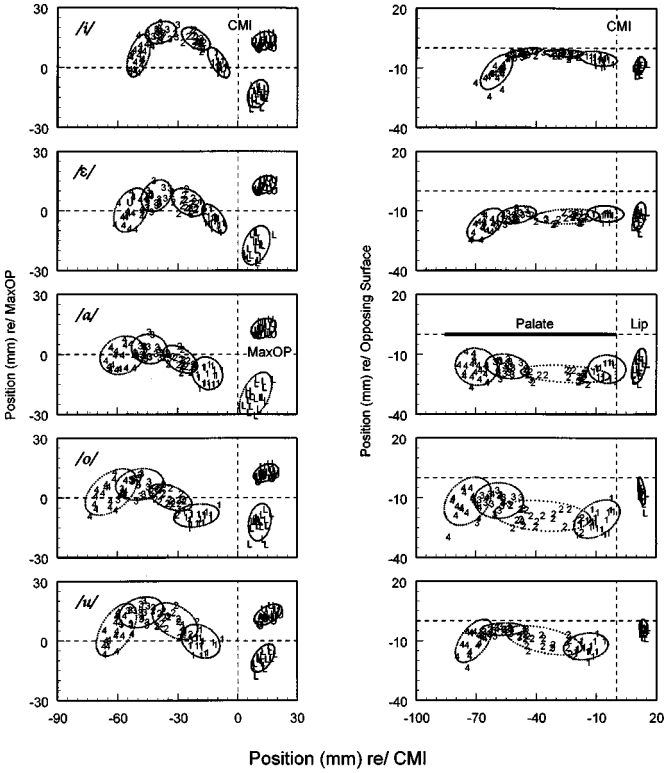

FIG. 8. Distributions of raw (left column) and normalized (right column) pellet locations for each vowel for English speakers. The numerals 1–4 represents pellets T1–T4, respectively. The letters U and L in the raw data (in the left column) represent upper and lower lip pellet locations, respectively. The letter L in the normalized data (in the right column) represents coordinates for lip protrusion and separation. Two-σ ellipses, with major and minor axes oriented along principal components, are drawn around each pellet-by-vowel distribution.

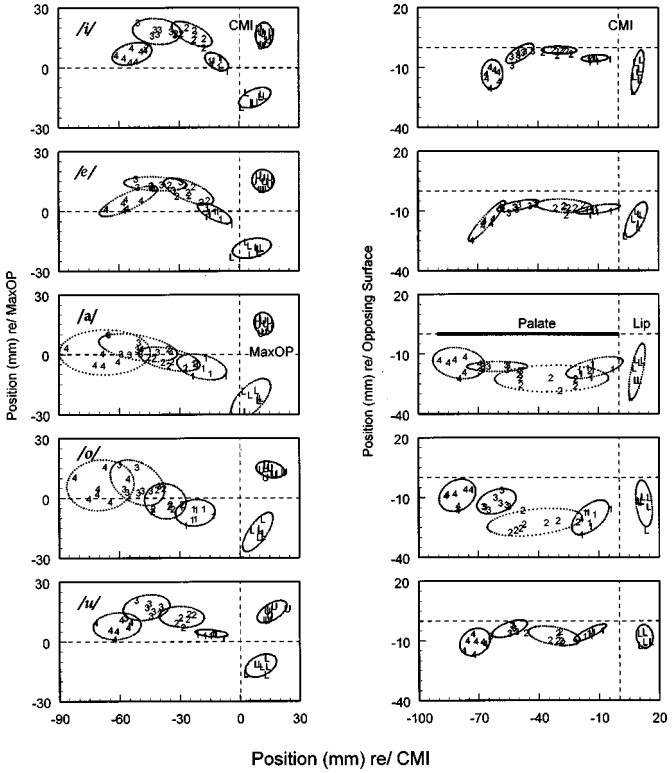

FIG. 9. Distributions of raw (left column) and normalized (right column) pellet locations for each vowel for Japanese speakers.

each English cell is 20, and in each Japanese cell 8, unless noted differently.

Average data shown in Table II are consistent with broad descriptions of vowel postures that can be found in other phonetic accounts of speech production. For example, average normalized *y* coordinates for tongue pellets, especially for T2 and T3, indicated that /i u ɯ/ were *high* vowels, that /e ɛ o/ were *mid*, and that /ɑ a/ were *low*. The tongue-to-palate distances for the high vowels were surprisingly small.[4] Normalized *y* coordinates also suggested that Japanese /ɯ/ may have involved greater constriction, forward in the mouth, than English /u/. Normalized *x* coordinates for tongue pellets indicate that /i e ɛ/ were relatively *front* vowels, and that /ɑ a o u ɯ/ were *back*. In fact, /o/ seems to have been the most *back* of the five vowels for both language groups.[5] This last observation echoes comparative illustrations of vowel postures described by Ladefoged and Maddieson (1996, pp. 284–285).

Average normalized articulatory measures also conformed to formant data in certain expected ways. Formant scatterplots for the two language groups suggested Japanese /e/ to be *higher* than English /ɛ/, Japanese /ɯ/ to be *fronted* relative to English /u/, and Japanese /o/ *back* relative to English /o/. These acoustically based inferences seemed to be reflected in average normalized pellet position data.

Normalized coordinates for the lips indicated greatest separation for /ɑ a/, least separation for /u ɯ/, and greater protrusion for /o u ɯ/ than the other vowels, in both language groups. Japanese /ɯ/ in Tokyo dialect is often described as not involving substantive lip protrusion, though as we have noted elsewhere (cf. Westbury and Hashi, 1997) the extent of lip protrusions for Japanese /o ɯ/ seems to be about the same.

No systematic relationship was found between gender or oral cavity size and normalized pellet coordinates. Males and females, and speakers with relatively large and small mouths, were scattered in similar ways about the distributions of normalized coordinates for each pellet-by-vowel combination.

Articulatory normalization tended to reduce cross-speaker variance in pellets' (new) *y* coordinates, but not their (new) *x* coordinates. Cross-speaker standard deviations of raw and normalized coordinates of tongue pellets are compared in Fig. 10. Comparisons for *x* and *y* coordinates are shown in the upper and lower panels, respectively. Data for the English speaker group are shown to the left, and those for the Japanese speaker group are shown to the right. Symbols for different vowels are the same as in Fig. 7, and numerals plotted within symbols indicate pellet identity. In each panel, the normalized-coordinate standard deviation, computed across speakers, is plotted against the raw-coordinate standard deviation, for matched pellets and vowels.

In the lower panels of Fig. 10, most datapoints fall below the $y = x$ line. This fact indicates that normalization generally reduced the variance across speakers in pellets' *y* coordinates. Modest exceptions can be identified, where cross-speaker variance was greater in normalized than raw data (e.g., for the *y* coordinates of all pellets for the vowel /ɛ/ in

TABLE II. Average normalized pellet locations for vowels, by language group. The abbreviations *pro* and *sep*, heading the last column, represent estimated lip *protrusion* (normalized) and *separation*, respectively. Numbers in square brackets indicate sample sizes for conditions when fewer than 20 English speakers, or 8 Japanese speakers, were available.

	T1 (*x*,*y*)	T2	T3	T4	L (*pro*,*sep*)
i	−9.1, −5.3	−26.3, −2.5	−46.4, −2.3	−59.9, −12.2	11.5, 8.8
ɛ [19]	−5.4, −11.5	−24.6, −12.9	−49.7, −12.2	−65.5, −17.0	11.4, 12.6
ɑ	−4.6, −17.5	−25.3, −20.0	−54.4, −16.3	−69.8, −16.4	11.3, 15.8
o	−9.7, −20.8	−36.8, −19.2	−58.6, −11.6	−74.1, −11.9	12.6, 6.8
u [18]	−15.2, −13.1	−36.0, −10.0	−56.6, −4.4	−71.2, −10.3	13.5, 3.8
i	−11.7, −5.4	−29.4, −1.4	−49.0, −3.1	−62.8, −13.5 [7]	9.5, 12.1 [7]
e	−10.2, −9.2	−27.0, −7.6	−50.1, −7.5	−65.6, −15.2 [7]	8.7, 14.4 [7]
a	−12.0, −17.1	−33.4, −22.5	−60.5, −16.5	−79.7, −14.8 [7]	9.0, 18.9 [7]
o	−14.3, −20.1	−42.0, −22.5	−61.0, −12.1	−80.6, −9.0 [7]	12.4, 13.1 [7]
ɯ [7]	−14.7, −6.0	−32.6, −7.6	−54.7, −4.1	−72.1, −10.7	12.4, 8.0 [6]

the English group). However, the median reduction in the cross-speaker standard deviation, across pellets and vowels, was on the order of 1 mm in both language groups. This decrease in variance may seem small, but should be interpreted with reference to the relatively small articulatory range for the *y* dimension in the oral cavity.

The reduction in *y*-coordinate variance associated with normalization probably results from elimination of an effect of vertical size of the oral cavity in the raw data. The top panel of Fig. 11 illustrates the association between palatal height and tongue pellets' *y* coordinates in raw data, for the vowel /o/ in English. Tongue pellet positions for 4 of 20 English speakers with the highest palates are represented by unfilled circles, while those for four speakers with the lowest palates are represented by filled triangles. In the raw data, speakers with high and low palates had higher and lower *y* coordinates, respectively, than other speakers, especially for the T2 and T3 pellets. This effect of palatal height disappears in normalized data, shown in the lower panel of Fig. 11, because pellet locations in normalized data are defined relative to the palatal surface above, rather than the occlusal plane below.

Normalization did not provide a comparable, broad reduction in cross-speaker variance in pellets' *x* coordinates. Instead, as the top two panels of Fig. 10 show, cross-speaker standard deviations in the *x* coordinates for at least one pellet, T2, were substantially larger in normalized than raw data, for some vowels in both language groups. Symbols for

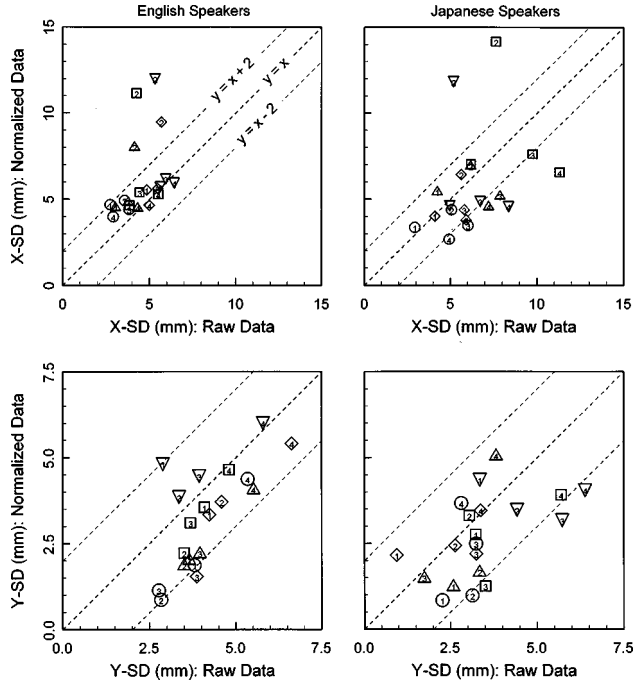

FIG. 10. Comparisons of cross-speaker standard deviations of raw and normalized coordinates of tongue pellets. Data for the English speaker group are shown in the left panels, and those for the Japanese speaker group are shown in the right panels. Comparisons for the *x* and *y* coordinates are shown in the upper and lower panels, respectively. Symbols for different vowels are the same as in Fig. 7, and numerals plotted within symbols indicate pellet identity.

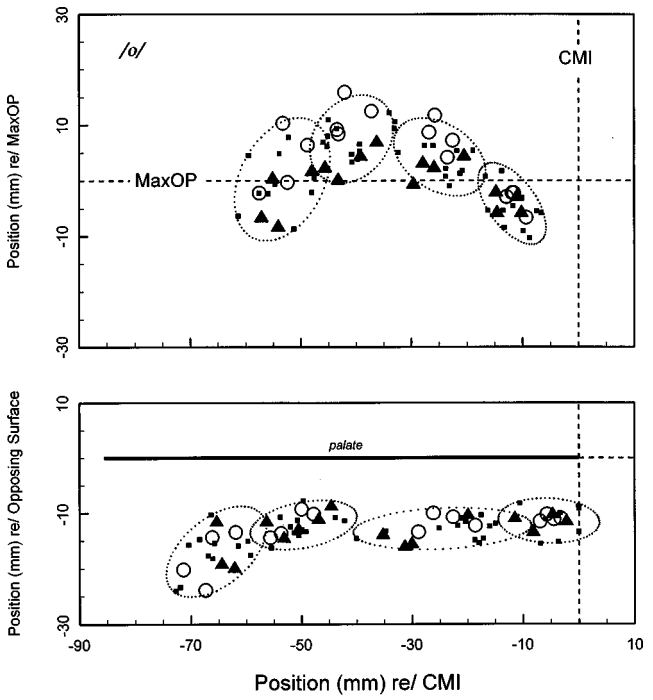

FIG. 11. The effect of palatal height on tongue pellets' *y* coordinates in raw and normalized data, for English /o/. The top panel shows the raw data, and the bottom panel the normalized data. Tongue pellet positions for 4 of 20 English speakers with the highest palates are represented by unfilled circles, while those for four speakers with the lowest palates are represented by filled triangles. The rest of the English speakers are represented by dots.

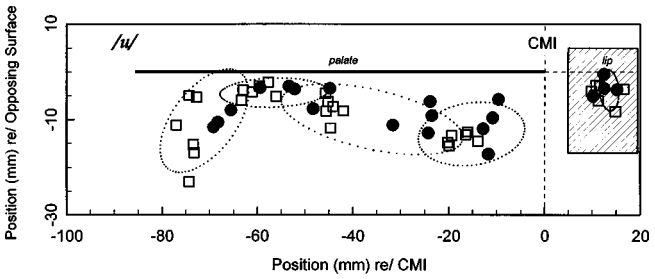

FIG. 12. Normalized pellet-position data for the vowel /u/, produced by four English speakers (filled circles) who habitually positioned their tongues more forward, and six speakers (unfilled squares) who habitually positioned their tongues more rearward.

these vowels, labeled with the numeral 2, are well above the $y=x$ line. Cross-speaker variances for other pellets' raw and normalized x coordinates were about the same in the English group. In the upper left panel of the figure, for example, most symbols cluster about the $y=x$ line. In the Japanese group, cross-speaker standard deviations tended to be smaller among pellet's normalized than raw x coordinates. Some symbols in the upper right panel of Fig. 10 also cluster about the $y=x$ line, though relatively more symbols fall below that line.

The relatively large increase in cross-speaker variance in the normalized x coordinate for the T2 pellet is probably a consequence of the normalization procedure itself. The T2 pellets usually occupied a region bounded above by the part of the palatal curve with the most rapidly changing slope (i.e., in the knee region, forward of the horizontal portion of the palate, and above and behind the alveolar ridge). Flattening the curve of the palate, as the normalization procedure requires, would tend to stretch and magnify differences among speakers in pellets' raw x coordinates in the vicinity of the palate that curves most sharply.

The fact that normalization did not reduce cross-speaker variance in tongue pellets' x coordinates in the English group may be due to a curious articulatory ''habit'' manifest among some English speakers. Detailed inspection of the data revealed a group of four (E16, E31, E34, and E43) who habitually positioned their tongues more forward along the palatal curve, for all vowels, than other speakers in the sample. Another group of six (E12, E14, E29, E35, E41, and E61) habitually positioned their tongues more rearward for all vowels. Figure 12 contrasts normalized data for the vowel /u/ produced by these ten English speakers. Speakers with forward and rearward postures are represented by filled circles and unfilled squares, respectively. The approximate constriction locations and shapes of the oral portion of vocal tract appear to be similar for the two groups. However, the underlying (muscular) mechanisms required to achieve these similar configurations would probably be quite different, assuming that each of the four tongue pellets represents approximately the same part of the tongue for each speaker in each group.

The average difference in matched pellets' x coordinates for the tongue-forward and tongue-rearward subgroups of English speakers, computed across all pellets and vowels, was on the order of 10 mm. No comparable subgrouping was

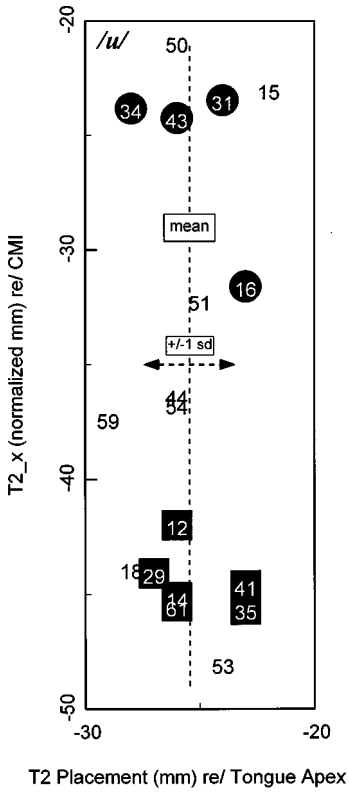

FIG. 13. Normalized x coordinates of the T2 pellet during /u/ produced by 18 English speakers, plotted against their respective nominal T2 placements behind the apex of the extended tongue. Subject numbers are used as plotting symbols. Plot positions of four speakers with habitually forward normalized tongue–pellet positions are surrounded by filled circles, while those belonging to six habitually rearward speakers are surrounded by filled squares.

found among the Japanese speakers. Graphical and linear-least-squares-regression analyses involving all English speakers indicated that postural variation (e.g., including, but not limited to forward and rearward subgroups) was unrelated to variation across speakers, for any of the following variables: (1) gender, (2) oral cavity size, (3) vowels' formant frequencies, (4) pellet placement, (5) concurrent lip pellet positions, and (6) different indices of mandible size, including bigonial diameter, gnathion-to-incisor distance, and pogonion-to-gonion distance.

The basic approach and results of these analyses are illustrated in Fig. 13, where the normalized x-coordinates for pellet T2, measured during /u/ for 18 available English speakers, have been plotted against the nominal placement of the T2 pellet behind the apex of the extended tongue (cf. Table I). Subject numbers are used as plotting symbols. The plot positions of four speakers with habitually forward normalized tongue–pellet positions are surrounded by filled circles, while those belonging to six habitually rearward speakers are surrounded by filled squares. The 18 speakers varied about the mean nominal T2 placement in a relatively normal fashion. It is clear, however, that there was no systematic relationship between this modest placement variability, and the much larger variability—in the limit, almost 30 mm—in normalized x position for this pellet-by-vowel condition. The same negative result was obtained from all comparisons involving normalized x coordinates of tongue pel-

lets, on the one hand, and acoustic and anatomic variables, on the other. In short, no reliable correlate of the forward-talker/rearward-talker distinction among the English speakers could be found.

III. DISCUSSION

In this study, a normalization scheme involving scaling and re-expression was applied to point-parametrized vowel postures recorded from 20 English and 8 Japanese speakers with differently shaped and sized vocal tracts. Normalized data were added together within groups, to compute fleshpoint-position averages and standard deviations for postures for five vowels. The results of the study can be evaluated on several different levels. For example, at a superficial but nonetheless necessary level, we can argue that the normalization scheme succeeds because the average postural results are easy to interpret. It is easy to tell which vowels, expressed in averaged, normalized form have tongue positions that are relatively front, back, high, and low in the mouth. Also, it is easy to tell which vowels have protruded lip configurations, with narrow or large (vertical) lip openings. These cross-speaker interpretations conform to descriptive generalizations about vowel articulations established by other methods (e.g., palatography, cineradiography, MRI), and to inferences derived from our own intergroup differences in vowel formant frequencies.

A more interesting and substantive benefit of the normalization scheme is that its result conveys a better sense of the geometry of the oral portion of the vocal-tract tube than does the raw fleshpoint data. For example, mid-sagittal degrees of constriction between the tongue and palate, and between the lips, at those locations defined by attached markers, are more obvious after normalization. This advantage comes simply from the fact that transformed fleshpoint locations are expressed relative to an opposing boundary of the vocal tract (i.e., the palate, or opposing lip), against which the pellet-carrying surfaces work, rather than relative to the occlusal plane about which they move.

Perhaps the most significant success of the normalization scheme lies in its general reduction of cross-speaker variance in the *y* dimension of the transformed space, within both language groups. This reasonable result can be traced to a systematic source of variance in the *y* dimension of the raw data (i.e., height of the palatal vault above the occlusal plane) that was ''removed'' from the normalized data. It is noteworthy, however, that the normalization scheme did not reduce cross-speaker variance in the *x* dimension of the data, consistently, across language groups. Within the English group, cross-talker variance in fleshpoints' *x* coordinates was about the same or even increased after normalization. A significant part of this negative result can be traced to what appears to be a real difference among some English speakers in how they use and position their tongues to create comparable vowels. Some speakers habitually placed their tongues in a forward position compared to the rest of the speakers, across all vowels, whereas another subgroup habitually placed their tongues in a rearward position. These positional differences, perhaps analogous to articulatory settings mentioned by Laver (1980) and recently investigated by Nolan and Kuhnert (1995), yield broadly similar vocal tract shapes, and thus would not be apparent in conventional flood-field x-ray images that emphasize shape of the (continuous) tongue, as a whole. The unique emphasis of fleshpoint kinematic techniques, on parts of the tongue, may be necessary to expose articulatory differences between speakers such as these, differences that are undoubtedly significant at underlying neuromuscular levels, but possibly insignificant at the level of vocal-tract area function and/or listeners' perceptions.

The front-to-back variance in English speakers' tongue positions was unrelated to oral-cavity-size measures from the speakers or any other variable. Thus, it is natural that the size-and-shape normalization scheme did not remove the effect from the speakers' group data. At present, the source of the *x*-dimension variability in tongue postures for vowels has yet to be identified. We are confident, however, that this variability is not an artifact in the data, in view of its magnitude, its generality across vowels, and the relatively large number of speakers in the sample. It is interesting, to us, that we were prompted to see the differences in speakers' tongue postures precisely because our normalization scheme failed to reduce variance in the *x* dimension of the transformed space.

It is possible that broad postural differences for vowels among some English speakers take their root in variables that are hard to see clearly (if at all) in XRMB data. It is important to remember, for example, that XRMB data provide a rough outline of tongue shape, and only that in the mid-sagittal plane, for the upper, oral portion of the vocal tract. No information is available regarding the lower half of the vocal tract. Constrictions in the pharynx and adjustments in larynx height are out of view, though these are known to have strong acoustic effects (Fant, 1975). Recent inferences from an independent analysis-by-synthesis study (Milenkovic, submitted) involving one tongue-rearward talker (E12) and one tongue-forward talker (E16), suggest in fact that significant differences in pharyngeal geometry may exist between the talkers, particularly along the *z* dimension (width) of the vocal tract. These limitations must be taken into account when interpreting results of this study.

Another word of caution regarding results of this study relates to the generally greater variance in *x* than *y* dimensions of the normalized space (cf. Figs. 8 and 9). This result cannot automatically be interpreted as an indication that formant frequencies are differentially sensitive to variations in *degree* versus *place* of vocal tract constrictions. Other investigators (e.g., Perkell and Nelson, 1985; Beckman *et al.*, 1995) have examined the significance of articulatory variability for vowel productions along locally orthogonal dimensions in the vocal tract, using single-speaker data with replicates. The outcomes of those analyses have been interpreted to suggest greater freedom in the front-to-back dimension. However, multi-speaker data, of the kind reported in this study, may not be suitable for addressing the *differential sensitivity* hypothesis. Using our data for this purpose would require us to discover, and be capable of evaluating, a normalization scheme that removes all sources of anatomical variation from the multi-talker data set. Only then would we be in a position analogous to other investigators, for whom

anatomical variation (in a single speaker) could not have been a concern.

An underlying goal of this study was to explore the need for, and benefits of, a simple normalization scheme for point-parametrized articulatory data. There is no intent to claim that the scheme described in this study is right or best. In at least an indirect way, trying to evaluate our proposed scheme forces some light on the interesting issue of how any speaker-normalization method might be evaluated. It has been customary in the speech acoustic/perception literature to evaluate speaker-normalization methods partly by the degree to which they reduce systematic (e.g., gender and age) variability within vowel categories, while maintaining differences across categories (cf. Fant, 1975; Syrdal and Gopal, 1986; Miller, 1989). An acoustic normalization scheme that reduces intracategory variance among speakers—producing greater overlap amongst speakers than before normalization—is successful precisely because the scheme appears to capture underlying commonalities among vowels produced by different speakers. The expectation that such commonalities exist is driven by listeners' perceptions that vowels from different speakers are the same, despite measurable differences in their spectra. In short, acoustic normalization schemes can be judged successful when and because their results match listeners' expectations that vowels, produced by speakers from different gender and age groups, should collapse into distributions undifferentiated by such variables.

This same simple criterion may be appropriate for evaluating an articulatory normalization scheme whenever variance in the raw data, due to anatomy, is reduced in the normalized result (e.g., as for the *y*-dimension effect described in this study). However, when variance does not decrease after normalization, we need not automatically conclude that normalization has failed. Our expectations about speech production are complicated by the fact that articulatory variance can result from any of at least three sources. These include (1) anatomical variation that is in view but poorly understood (e.g., key differences in oral-cavity geometry not captured by our few simple measures); (2) anatomical variation that is not in view (e.g., key differences in oral- and/or laryngopharyngeal geometry, especially in the dimension normal to the sagittal-plane slice represented in XRMB data); or, (3) variations in speakers' *choices* of behaviors that are not themselves driven by corresponding differences in anatomy. This third source of variation warrants special comment. It is well known that the map from acoustics to articulation is not one-to-one. The spectrum of an isolated, sustained vowel, for example, is determined by size, shape, and hence static posture of the vocal tract. However, the same spectrum can be obtained from more than one vocal tract configuration. In principle, speakers may have vocal tracts that are the same size, bounded by walls that are the same shape, but choose to use their mobile articulators differently to achieve the same spectral result. In cases of this type, we might reasonably say that speakers have adopted different *strategies* for producing the acoustic spectrum belonging to the vowel. The fact that a range of acoustic signals can be associated with one nominal vowel means that the room for such strategies/choices in vowel articulation might be substantial. This last possibility, in particular, clouds any expectations about variance reduction we might bring to the problem of evaluating a normalization method. Additional information about the range and nature of interspeaker anatomical variation, and incorporation of these kinds of information in normalization methods, are necessary to refine our expectations of such methods and, ultimately, our views of their success.

ACKNOWLEDGMENTS

Research was supported by USPHS Grant No. DC00820, and a collaborative research agreement between the University of Wisconsin—Madison and ATR Human Information Processing Research Laboratories (Kyoto, Japan). We are grateful for constructive criticisms from Jim Dembowski, Phil Hoole, Associate Editor Anders Lofquist, and one anonymous reviewer.

[1]Identification numbers for English speakers included in this analysis {12,14,15,16,18,25,27,29,31,34,35,41,43,44,50,51,53,54,59,61} are the same as in the publicly available XRMB Speech Production Database (Westbury, 1994a), while the English speech task corresponds to the *vowel* record (*tp*014) from that corpus. Seventeen speakers (ten English and seven Japanese) of the twenty-eight described in this report are the same group described in a preliminary analysis, presented at the 127th Meeting of the Acoustical Society of America, 6–10 June 1994, Cambridge, MA (cf. Hashi *et al.*, 1994).

[2]The full palatal outline estimate, extending from the teeth to the pharyngeal wall, is a necessary convention for our work, though we recognize that our estimates of such outlines, especially in the velopharyngeal region, are neither fully certain, nor realistic. They are uncertain for the obvious reason that there is no real information, aside from pellet-position extrema themselves, to guide any estimate of the shape of the palate beyond the end of the pellet chain, or trace. We can never be sure if the dorsal pellets, at their extrema, touched the palate or not. The outline estimates in the soft palate region are unrealistic for at least two reasons. Shape and position of the soft portion of the palate both change during speech. Our outline is fixed. The outline estimate may also be unrealistic because the resultant smooth curve does not look much like most lateral-view radiographs we have seen (cf. our own Fig. 3). In such images, the palatal shape in the vicinity of the posterior pharyngeal wall is complex and footlike, and certainly not well approximated by a straight or gently curved line.

[3]Estimates of nearest-palate-point coordinates for tongue pellets may be influenced by the transformation method in at least four ways. One of these relates to the fact that the transformation method forces some pellets that are forward in the mouth (e.g., T1 for /ɑ/, in Fig. 4) to have nearest-neighbor points at the CMI, even though lines passing through their original locations cannot be normal to the palatal outline at that point. A second problem relates to the fact that pellets far back in the mouth may also be closer to the pharyngeal wall than the palatal ceiling (e.g., T4 for /ɑ/). However, in such cases, the transformation identifies the nearest palatal point near the sharp and unrealistic knee formed by the intersection of the palatal and pharyngeal outlines. We do not allow points on the pharyngeal wall to be nearest neighbors to tongue pellets, because we know of no realistic way to turn the corner from an already unrealistic palatal outline, to join the rear wall of the pharynx. A third problem relates to the fact that tongue pellets bounded above by a roughly circular portion of the palatal outline may be very nearly equidistant from many points on such a surface. This fact means that small errors in measurement, or small changes in the selection of the measurement time, may produce significant shifts in the location of some pellets for some talkers. It is important to carefully examine the source of the transformed *x* coordinate of each pellet, for example by determining its distribution of nearest-neighbor distances relative to all palatal points. In the great majority of cases in the present study, there was a salient minimum value within each distribution. The location of a tongue pellet's nearest palatal neighbor will depend upon the palatal curve itself, which is affected by at least three factors: (1) extreme values available for rearward extension, (2) the spatial sampling frequency, and (3) the smoothing function applied to the curve. We recognize the influence of these kinds

of methodological problems on results from the transformation, but know of no simple or final solutions.

[4]True physical separation between the tongue surface and palate is difficult to capture in XRMB data. In principle, procedures that define the palatal outline, and determine the positions of pellets at any moment in time, will allow the outline to intersect pellet centers. At such moments, separation between a rigid (hard) palate, and any other rigid surface carrying the pellet, would correspond to the diameter of the pellet itself (ca. 2.5 mm), rather than zero. Of course, the tongue is not rigid, and may deform locally about a pellet glued and packed down into its surface. Nevertheless, we can guess that a correction of about 2 mm might be applied to normalized *y*-coordinate data shown in Table II. Thus, the narrow tongue-to-palate constrictions of about 2 mm at T2 and T3 for the vowel /i/ in either language group could well be closer to 4 mm in the real world.

[5]Fleshpoint kinematic data provide location information only about those points on ''soft'' articulators (e.g., the tongue) where pellets are attached. Partly for this reason, it is impossible to know the exact location(s) of tongue-to-palate constrictions for vowels. Thus, it is important to be cautious when making inferences about constriction location from these kinds of data.

Beck, J. M. (**1997**). ''Organic variation of the vocal apparatus,'' in *The Handbook of Phonetic Sciences*, edited by W. J. Hardcastle and J. Laver (Blackwell, Cambridge, MA).

Beckman, M. E., Jung, T., Lee, S., de Jong, K., Krishnamurthy, A. K., Ahalt, S. C., and Cohen, K. B. (**1995**). ''Variability in the production of quantal vowels revisited,'' J. Acoust. Soc. Am. **97**, 471–490.

Delattre, P., and Freeman, D. C. (**1968**). ''A dialect study of American R's by x-ray motion picture,'' Language **44**, 29–68.

Fant, G. (**1960**). *Acoustic Theory of Speech Production* (Mouton, The Hague).

Fant, G. (**1975**). ''Non-uniform vowel normalization,'' in *Speech Transmission Laboratory Quarterly Progress and Status Report* (Royal Institute of Technology, Stockholm), **2–3**, 1–19.

Hagiwara, R. (**1995**). ''Acoustic realization of American /r/ as produced by women and men,'' UCLA working papers in phonetics, 90, Department of Linguistics, UCLA.

Harshman, R., Ladefoged, P., and Goldstein, L. (**1977**). ''Factor analysis of tongue shapes,'' J. Acoust. Soc. Am. **62**, 693–707.

Hashi, M., Westbury, J. R., and Honda, K. (**1994**). ''Articulatory and acoustic variability of vowels in Japanese and English,'' J. Acoust. Soc. Am. **95**, 2820.

Hillenbrand, J., Getty, L. A., Clark, M. J., and Wheeler, K. (**1995**). ''Acoustic characteristics of American English vowels,'' J. Acoust. Soc. Am. **97**, 3099–3111.

Hirahara, T., and Kato, H. (**1992**). ''The effect of *F*0 on vowel identification,'' in *Speech Perception Production and Linguistic Structure*, edited by Y. Tohkura, E. Vatikiotis-Bateson, and Y. Sagisaka (Ohmu-sha, Tokyo).

Johnson, K., Ladefoged, P., and Lindau, M. (**1993**). ''Individual differences in vowel production,'' J. Acoust. Soc. Am. **94**, 701–714.

Ladefoged, P., and Maddieson, I. (**1996**). *The Sounds of the World's Languages* (Blackwell, Oxford, UK).

Laver, J. (**1980**). *The Phonetic Description of Voice Quality* (Cambridge U.P., Cambridge).

Lubker, J., and Gay, T. (**1982**). ''Anticipatory labial coarticulation: Experimental, biological, and linguistic variables,'' J. Acoust. Soc. Am. **71**, 437–448.

Maeda, S. (**1991**). ''On articulatory and acoustic variabilities,'' Journal of Phonetics **19**, 321–331.

Milenkovic, P. (**1998**). ''Articulatory model for determining the vocal tract area function from point-parametrized data,'' submitted to J. Acoust. Soc. Am.

Milenkovic, P. H., and Read, C. (**1992**). Cspeech Version 4 User's Manual, Madison, WI.

Miller, J. D. (**1989**). ''Auditory-perceptual interpretation of the vowel,'' J. Acoust. Soc. Am. **85**, 2114–2134.

Nolan, F., and Kuhnert, B. (**1995**). ''The articulatory correlates of descriptive categories for supralaryngeal voice qualities,'' in *Proceedings of the XIIIth International Congress of Phonetic Sciences*, edited by K. Elenius and P. Branderud (Stockholm Univ., Stockholm), Vol. 2, pp. 470–473.

Peterson, G., and Barney, H. (**1952**). ''Control methods used in a study of the vowels,'' J. Acoust. Soc. Am. **24**, 175–184.

Perkell, J. S., and Nelson, W. L. (**1985**). ''Variability in production of the vowels /i/ and /a/,'' J. Acoust. Soc. Am. **77**, 1889–1895.

Syrdal, A. K., and Gopal, H. S. (**1986**). ''A perceptual model of vowel recognition based on the auditory representation of American English vowels,'' J. Acoust. Soc. Am. **79**, 1086–1100.

Westbury, J. R. (**1994a**). *X-ray microbeam speech production database user's handbook* (version 1.0) (UW-Madison, Madison).

Westbury, J. R. (**1994b**). ''On coordinate system and the representation of articulatory movements,'' J. Acoust. Soc. Am. **95**, 2271–2273.

Westbury, J. R., and Hashi, M. (**1997**). ''Lip-pellet positions during vowels and labial consonants,'' Journal of Phonetics **25**, 405–409.

Westbury, J. R., Hashi, M., and Lindstrom, M. J. (**1995**). ''Differences among speakers in articulation of American English /r/: An x-ray microbeam study.'' in *Proceedings of the XIIIth International Congress of Phonetic Sciences*, edited by K. Elenius and P. Branderud (Stockholm Univ., Stockholm), Vol. 4, pp. 50–57.

Wood, S. (**1979**). ''A radiographic analysis of constriction locations for vowels,'' Journal of Phonetics **7**, 25–43.

Measures of auditory–visual integration in nonsense syllables and sentences

Ken W. Grant and Philip F. Seitz
Walter Reed Army Medical Center, Army Audiology and Speech Center, Washington, DC 20307-5001

(Received 21 September 1997; revised 12 May 1998; accepted 2 July 1998)

For all but the most profoundly hearing-impaired (HI) individuals, auditory–visual (AV) speech has been shown consistently to afford more accurate recognition than auditory (A) or visual (V) speech. However, the amount of AV benefit achieved (i.e., the superiority of AV performance in relation to unimodal performance) can differ widely across HI individuals. To begin to explain these individual differences, several factors need to be considered. The most obvious of these are deficient A and V speech recognition skills. However, large differences in individuals' AV recognition scores persist even when unimodal skill levels are taken into account. These remaining differences might be attributable to differing efficiency in the operation of a perceptual process that *integrates* A and V speech information. There is at present no accepted measure of the putative integration process. In this study, several possible integration measures are compared using both congruent and discrepant AV nonsense syllable and sentence recognition tasks. Correlations were tested among the integration measures, and between each integration measure and independent measures of AV benefit for nonsense syllables and sentences in noise. Integration measures derived from tests using nonsense syllables were significantly correlated with each other; on these measures, HI subjects show generally high levels of integration ability. Integration measures derived from sentence recognition tests were also significantly correlated with each other, but were not significantly correlated with the measures derived from nonsense syllable tests. Similarly, the measures of AV benefit based on nonsense syllable recognition tests were found not to be significantly correlated with the benefit measures based on tests involving sentence materials. Finally, there were significant correlations between AV integration and benefit measures derived from the same class of speech materials, but nonsignificant correlations between integration and benefit measures derived from different classes of materials. These results suggest that the perceptual processes underlying AV benefit and the integration of A and V speech information might not operate in the same way on nonsense syllable and sentence input. [S0001-4966(98)03510-3]

PACS numbers: 43.71.An [WS]

INTRODUCTION

The ability to understand speech can be greatly impaired by many factors such as noise, reverberation, and hearing loss. One method individuals use to improve speech recognition is to combine auditory (A) cues with visual (V) cues available through speechreading. Past research has indicated that the benefit due to speechreading can be substantial for most listeners, often allowing near-perfect comprehension of otherwise unintelligible speech (Sumby and Pollack, 1954; ANSI, 1969; Summerfield, 1992; Grant and Braida, 1991; Grant and Walden, 1996). For hearing-impaired (HI) patients, improvements as great as that derived from speechreading are seldom seen with the use of individualized hearing aids, counseling, or training (Walden *et al.*, 1981, 1987, 1996).

The amount of benefit derived from combining A and V speech cues (''AV benefit'') is dependent on a number of factors, including the degree of auditory impairment, speechreading ability, language skills, etc. (Grant and Walden, 1995, 1996). In the present study, we examined a variety of different measures of AV integration in individual hearing-impaired subjects to determine whether individual differences in integration abilities was a significant factor for predicting individual variability in AV consonant and sentence recognition.

Methods for studying AV integration in groups of normal-hearing (NH) subjects have employed measures using both congruent and discrepant AV speech materials (e.g., McGurk and McDonald, 1976; McGrath and Summerfield, 1985; Pandey *et al.*, 1986; Massaro, 1987; Braida, 1991; Massaro *et al.*, 1996). Congruent AV materials, like those produced in natural speech, have a single visible sound source, the articulating face, which is in synchrony with the auditory signal. Discrepant AV materials, on the other hand, are ''out of sync,'' and have been created by either temporally misaligning acoustic and visual channels or by dubbing the acoustic production of one sound onto the visible production of another sound. Because there are no well-established methods for quantifying an individual's ability to integrate A and V cues, a number of methods using both congruent and discrepant stimuli were employed in the present study based on specific hypotheses about the possible effects of such manipulations. One goal of using varied methodologies to measure integration abilities across listeners was to establish the construct validity of AV integration as an independent pro-

cess operating for both congruent and discrepant speech segments and sentences.

Recently, two models of AV speech integration have been proposed which have the potential to scale subjects with regard to their integration abilities (Massaro, 1987; Braida, 1991; Massaro *et al.*, 1996). In the Pre-Labeling Model of Integration (Braida, 1991), a maximum likelihood prediction of AV recognition is made from A and V confusion matrices. The model purports to be an optimum processor in that all information extracted from both unimodal conditions is preserved in the multimodal case, with no interference (e.g., masking) or biasing from the other modality. Thus the predicted AV recognition performance should always be equal to or better than unimodal recognition, and more importantly, predicted AV speech recognition should always be equal to or better than the AV recognition obtained from real observers. Recent tests of the Pre-Labeling (PRE) Model of Integration with normal-hearing and hearing-impaired subjects (Braida, 1991; Grant and Walden, 1995) have confirmed these expectations. The value of the PRE model as an optimum processor is that it provides a rational basis for the development of rehabilitative efforts for improving AV speech recognition. For example, simple differences between predicted and obtained AV scores can be used as an index of AV integration skill. If subjects obtained AV scores that are close to predicted scores, the presumption is that they are integrating in a nearly optimal way and any rehabilitative effort to improve AV scores beyond those already observed should be targeted at improving the unimodal (A or V) recognition scores by the use of better technology (i.e., improved hearing aids, visual aids, etc.), auditory training, visual (speechreading) training, or a combination of these approaches. If, on the other hand, predicted AV scores far exceed obtained AV scores, then the subject is not integrating the available A and V cues optimally and may profit from training methodologies that facilitate the integration A and V cues. Previous results using consonant and vowel confusion data (Braida, 1991; Grant and Walden, 1995) have shown that groups of normal-hearing and hearing-impaired observers tend to combine A and V cues in a highly efficient manner. That is, differences between predicted and observed group AV data have been relatively small. In tests with individual HI subjects, however, the PRE model has been shown to over predict AV performance by as much as 19 percentage points (Grant and Walden, 1995) suggesting potentially large improvements from rehabilitative efforts that focus on A and V cue integration.

In the Fuzzy Logical Model of Perception (FLMP), a different approach is taken for describing AV integration (Massaro, 1987; Massaro *et al.*, 1996). Whereas the FLMP can be used to predict AV scores in much the same way as the PRE model, the preferred method for applying the FLMP is to fit the model to the data from A, V, *and* AV experimental conditions. Assumptions underlying the FLMP are (1) all sources of information (A, V, and AV) are evaluated independently; (2) the information (i.e., cues) obtained from any one source is compared to prototypes in memory to determine the degree to which the cues from a given source specify the various response alternatives; (3) all sources (A, V, and AV) are integrated relative to prototypes in memory to determine the overall degree of support for each response alternative; and (4) identification responses are determined by the overall degree of support among the alternatives (Massaro *et al.*, 1996). Similar to the PRE model, the FLMP uses data from stimulus/response confusion matrices to estimate the probability that a particular stimulus presentation will result in a particular response alternative. The model is fit iteratively to A, V, and AV conditions (unlike the PRE model which only considers A and V matrices) assuming a multiplicative rule of integration such that the root-mean-squared deviation (rmsd) between predicted and observed results are minimized. The degree of fit that the model is capable of achieving can be construed as a measure of integration. That is, good integration should result in good model fits (small rmsd's) whereas poor integration should result in poorer model fits (large rmsd's). In a recent test of the FLMP's sensitivity to measure integration in a syllable test with asynchronous AV tokens, Massaro *et al.* (1996) demonstrated that integration of audible and visible speech remains intact for AV asynchronies up to approximately 250 ms but deteriorates for larger asynchronies near 500 ms. No discussion was provided regarding possible differences in integration abilities across individual subjects.

A lingering concern with the FLMP approach for measuring integration is whether it is sensitive to small variations in integration efficiency among individual subjects. The iterative procedure used in fitting the FLMP tends to produce very small rmsd's for a wide range of data (Massaro, 1987). This suggests that the vast majority of subjects integrate quite well for a variety of different stimulus manipulations (additive noise, filtering, synthetic speech, synthetic faces, etc.). However, the consistently excellent fits achieved by the FLMP may also suggest that the model is less sensitive in recognizing subtle changes in integration efficiency because so many parameters are available for manipulation during each fit. In pilot tests of the FLMP to determine its suitability for studying integration abilities of individual subjects, we fit the data for two simulated subjects who had identical A and V consonant recognition confusion matrices, but different AV confusion matrices. One AV matrix was an actual response matrix obtained by an HI subject. The other AV matrix was the predicted AV matrix from the PRE model. The PRE model overpredicted the actual AV performance by approximately 16%, suggesting that this subject failed to optimally integrate the available A and V cues. The FLMP fits for these two cases were both excellent in terms of the correlation and root mean squared deviation between predicted and observed scores ($r=0.997$ and 0.988, rmsd$=0.013$ and 0.020 for subject 1 and subject 2, respectively). Differences of this order are probably not significant (Massaro *et al.*, 1996). Thus relatively large differences in AV speech recognition performance (given identical A and V performance) may be difficult to detect using the FLMP. For the purposes of this study, therefore, only the PRE model was used to obtain a measure of integration for congruent AV materials.

A second proposed measure of AV integration uses AV consonant materials in which the A and V stimulus components are dubbed from different consonant productions, for

example, an auditory /bɑ/ dubbed onto a visual /gɑ/. When these two discrepant stimuli are presented to listeners who have been instructed to report what they heard, the response /dɑ/ or /ðɑ/ is often obtained. This result, referred to as the ''McGurk effect'' (McGurk and MacDonald, 1976), is a fairly compelling example of the influence of visual speech cues on speech perception (Massaro, 1987; Walden *et al.*, 1990; Green *et al.*, 1991). Even when instructed to ignore what they see and report only what they hear, subjects in these McGurk experiments find themselves unable to ''turn off'' the visual channel. In the current study, individual susceptibility to the McGurk effect was measured for a number of discrepant AV tokens; the assumption being that individuals who integrate A and V stimuli in a near optimal way will be more susceptible to the McGurk effect than individuals who integrate less well. Thus the McGurk effect is interpreted as a natural consequence of the integration process whereby individuals cannot help but use all the available information at their disposal to interpret speech.

A concern in using either PRE model predictions (with congruent stimuli) or the McGurk paradigm (with discrepant stimuli) to study integration is that both approaches can only be applied to data that can be represented by a set of stimulus/response confusions. This means that data obtained with connected speech materials, such as sentences, cannot be used. Because connected speech materials have greater face validity for studying an individual's speech recognition than isolated consonant or vowel productions, the use of segment data to gauge integration ability may be limited. In particular, it is possible that an individual who integrates near-optimally for isolated consonant or vowel productions, may not do as well with connected speech. One reason for this may be the additional demands placed on the integration process when forced to operate in a continuous sampling mode at the faster rates associated with running discourse. With isolated AV segments or even AV words, one can use sensory buffers (Baddeley, 1990, 1996; Campbell, 1990) or working memory (Massaro, 1972; Winkler *et al.*, 1993) to store, and then recall, A and V cues used in the integration process. In contrast, with running discourse, speech segments continuously flow into sensory buffers overwriting previously stored input, and the demands on working memory are significantly increased. Recent studies on speechreading help elaborate this point. For example, Bernstein and Auer (1996) and Demorest *et al.* (1996) have shown that for NH subjects the correlations between speechread nonsense syllables and speechread words or sentences are not as high as the correlations between speechread words and speechread sentences. Highly similar results were obtained by Grant *et al.* (1998) in a study comparing nonsense syllable recognition to sentence recognition for A, V, and AV modalities. However, in the Grant *et al.* study, the correlations between syllables and sentences were significantly higher for A and AV modalities ($r \approx 0.7$) than for the V modality ($r \approx 0.5$). This suggests that the lack of experience with V-only speech recognition by NH or HI subjects may promote differences in processing strategies between nonsense syllables and meaningful speech signals that are not as readily observed under the more familiar A and AV conditions. In any case, there are a number of physical and psycholinguistics differences between nonsense syllables and meaningful speech to warrant the investigation of AV integration for both types of speech materials.

One method for studying integration at the sentence level is to misalign temporally the A and V stimuli with respect to the other (e.g., McGrath and Summerfield, 1985; Pandey *et al.*, 1986). McGrath and Summerfield (1985) measured AV sentence recognition as a function of auditory delay for normal-hearing subjects. The auditory signal was a pulse train that was modulated by the vocal pitch of the talker. When presented alone, this signal yielded essentially 0% intelligibility. Similarly, Pandey *et al.*, (1986) measured AV sentence recognition under six conditions of AV asynchrony with two S/N ratios and two levels of context. For both studies, AV scores were substantially greater than A-alone scores and remained basically unaffected by delay over a range between ± 80 ms. However, when the data obtained from the best speechreaders were analyzed separately (McGrath and Summerfield, 1985), the effects of auditory delay were more apparent and AV scores decreased for delays as short as 20 ms. For the purposes of the current study, it was assumed that subjects who integrate A and V cues with a high degree of efficiency, would also be affected by relatively small AV asynchronies [as were the better speechreaders in the McGrath and Summerfield (1985) study]. Further, it was assumed that the overall effect of asynchrony (as measured by a decline in speech recognition relative to the synchronous case) would be greater for better integrators. The logic motivating these assumptions was that better integrators (as opposed to poor integrators) probably pay closer attention to, and are able to extract more information from, the natural associations between the movements of the lips and jaw and the resultant speech sound modulations. Correlations between area of mouth opening and speech envelope, for example, may serve as a cue signaling the occurrence of high-amplitude acoustic events in the speech waveform. This temporal correspondence between visual speech and audible speech may draw the listener's attention to a particular point in time when important speech information is presented, thereby improving speech recognition (Summerfield, 1987). With the introduction of AV asynchrony, the temporal associations between A and V cues would be disrupted and speech recognition would suffer for those subjects attuned to this information.

To summarize, the amount of benefit derived from combining A and V speech cues is influenced by the ability to integrate A and V cues. In the present study, we measured integration using a variety of AV materials (isolated speech segments and sentences) having both congruent and discrepant properties. The overall goal of the study was to relate the different measures of integration ability to each other and individually to a measure of AV sentence benefit. Specifically, this study addressed two basic questions:

(1) Are the different measures of integration ability correlated with each other? In particular, this question addresses whether AV integration processes are similar for isolated segments (e.g., consonants) and connected speech (e.g., sentences).

(2) Can AV benefit for consonants and sentences be predicted by one or more measures of integration ability? This question addresses whether integration ability per se is an important factor for understanding AV consonant and sentence recognition.

I. METHODS

A. Subjects

Forty-one adults between the age of 41 and 76 ($\bar{x}=66$) with acquired moderate-to-steeply sloping hearing losses ranging from mild to severe served as subjects. The average three-frequency pure-tone threshold (500, 1000, and 2000 Hz) was 39 dB HL (ANSI, 1989). The average two-frequency pure-tone threshold (2000 and 4000 Hz) was 59 dB HL. All subjects were native English speakers with normal or corrected-to-normal vision (visual acuity equal to or better than 20/30 as measured with a Snellen chart). All auditory testing was conducted binaurally using headphones. Each subject participated in approximately fourteen hours of testing.

B. Stimuli

Three different sets of speech stimuli were used, all spoken by the same female speaker. They included low-context sentences (IEEE/Harvard), vowel–consonant–vowel (vCv) segments, and consonant–vowel (Cv) segments. The sentences were taken from the IEEE/Harvard (1969) sentence corpus, which is comprised of 720 phonetically balanced low-context sentences each containing five key words (e.g., ''The birch canoe slid on the smooth planks''), and organized into 72 lists of 10 sentences each. The sentences were videotaped and subsequently transferred to an optical disk recorder (Panasonic TQ-3031F). The audio portion of each sentence was digitized (16 bit A/D, 20-kHz sampling rate), normalized in level to have the same overall rms, and stored on a personal computer for later playback. The personal computer was capable of independently controlling both the visual and audio playback for each sentence. Precise and independent control of AV playback allowed variable alignment of the audio and visual signals within ± 2 ms.

The vCv stimuli consisted of the consonants /p,b,t,d,k,g,m,n,s,z,f,v,θ,ð,ʃ,ʒ,tʃ,dʒ/ interposed between two /ɑ/ vowels. Ten productions of each /ɑ–consonant–ɑ/ (/ɑCɑ/) stimulus were recorded directly onto optical disk and the audio tracks of the disk were digitized and normalized in level as described above.

The Cv stimuli consisted of the consonants /b,p,m,v,g,k,d,s,f,θ,ʃ,dʒ,tʃ,ʒ/ followed by the vowel /ɑ/. Ten productions of each Cv stimulus were recorded directly onto optical disk and the audio tracks were digitized and normalized in level in the same manner as the IEEE and vCv stimuli.

IEEE sentences and vCv nonsense syllables were presented in filtered noise shaped to match the long term spectrum of the target speech materials. A 20-s sample of shaped noise was digitized and stored on computer. During each A and AV presentation trial, a segment of noise 100 ms longer in duration than the target speech stimulus, was selected randomly from the 20-s noise file. The noise started 50 ms before the speech and ended 50 ms after the speech stimulus was over. A 10-ms cosine gate was used to ramp the noise on and off.

All audio test signals (whether presented in noise or in quiet) were output through separate channels of a dual channel 16 bit DAC (TDT DD1) and routed through an 8.5-kHz antialiasing filter (TDT FLT3), separate programmable attenuators (TDT PA4), mixer (TDT ADD1), head phone driver (TDT HBUF3), and stereo headphones (Beyer Dynamic DT770). The overall presentation level of the speech or speech-plus-noise stimuli, as measured at the output of the headphones in a 2-cc coupler, was approximately 95 dB SPL. For AV presentations, video signals from the optical disk were routed through a digital timebase corrector (FOR A FA-310) before being sent to a 21 in. color monitor (Sony PVM 2030).

C. Procedures

The study comprised four separate experiments from which two measures of AV benefit and four measures of AV integration were derived. The four experiments were: (1) A, V, and AV sentence (IEEE) recognition in noise; (2) A, V, and AV consonant (vCv) recognition in noise; (3) A and AV consonant (Cv) recognition in quiet using McGurk-like stimuli; and (4) AV sentence (IEEE) recognition in noise using temporally misaligned stimuli. For all testing, subjects were seated in a sound-treated booth facing the color video monitor that was positioned approximately 3 ms away. During vCv and Cv tests, subject responses were collected via a touch-screen terminal (JUGO TID 10-0054) which displayed a fixed set of response alternatives. During sentence tests, subject responses were given via paper and pencil. The initiation of all stimulus presentations was under subject control via a confirmation button displayed on the touch screen. No feedback was provided regarding the correctness of the responses. Subjects were paid for their participation.

1. IEEE sentence recognition in noise

IEEE sentences were presented at a speech-to-noise (S/N) ratio of 0 dB to avoid ceiling effects in the AV condition. Three different lists of ten sentences each (150 key words) were presented in the A, V, and AV conditions. Visual-only lists were presented without noise. All subjects were presented with the same three lists in each receiving modality. However the order of the nine test blocks (3 lists $\times 3$ modalities) was randomized separately for each subject. Subjects wrote down their responses following each presentation and were encouraged to guess if there was any uncertainty as to what was spoken. Sentences were scored using an *exact key word* system where all aspects of the target key words (e.g., number, tense, etc.) had to be correct for credit to be given.

2. Medial consonant recognition in noise

Medial consonants (vCv) were presented at a S/N of 0 dB. Each test block consisted of 72 trials. The 18 consonants were selected randomly so that each consonant appeared 4

times per block and each presentation of a particular consonant represented a different token. On each trial, the subjects indicated their response by touching 1 of the 18 response areas on the touch screen. Response alternatives were always visible on the touch screen. Trial-by-trial responses were stored on computer for later analyses. A total of 10 blocks were presented in A, V, and AV conditions resulting in a 40 trials per consonant type per condition (or 720 trials per confusion matrix). No feedback was provided.

3. Initial consonant recognition (McGurk effect)

Four discrepant pairs of AV consonant–vowel stimuli were identified in pilot tests as good candidates for producing strong McGurk effects. These were auditory /bɑ/ paired with visual /gɑ/ (b/g), auditory /pɑ/ paired with visual /kɑ/ (p/k), auditory /mɑ/ paired with visual /dɑ/ (m/d), and auditory /vɑ/ paired with visual /dɑ/ (v/d). The expected AV response from these stimuli were /dɑ/ or /ðɑ/ for b/g, /tɑ/ for p/k, /nɑ/ for m/d, and /zɑ/ or /ðɑ/ for v/d. In the AV condition, each of these discrepant stimulus pairs were presented in quiet for identification. The subjects were instructed to watch the video screen and report what they heard. The subjects were also informed that they may notice something wrong with the stimuli and that the stimuli may appear to be ''out of sync.'' Subjects were also presented with these same stimuli in an A-alone condition (with the video monitor turned off). For both A and AV test blocks, 18 response alternatives (the same used for medial consonants) were available to the subjects on the touch screen. Each test block consisted of 60 trials. For AV test conditions, each AV McGurk pair appeared 10 times per block, drawn randomly from the 10 productions of each auditory consonant (i.e., 40 trials). An additional 20 AV trials/block were composed of a random selection of 1 of the other 10 initial consonants in the set. These additional trials were normal AV recordings (i.e., composed of congruent A and V components) and were included to encourage subjects to use the full set of response alternatives on the touch screen. The block structure was identical for A-only test conditions with the exception that there was no video. That is, the four primary auditory consonants (/b,p,m,v/) were presented 10 times in each test block of 60 trials, and the 20 remaining trials were composed of a random selection of the other 10 consonants in the set. Trial-by-trial responses were stored on computer for later analyses. A total of 5 blocks were run in both A and AV conditions yielding 50 trials per primary target token (i.e., the 4 primary auditory tokens or the 4 AV McGurk pairs).

4. Asynchronous IEEE sentence recognition in noise

Auditory–visual performance in noise as a function of auditory delay (audio lagging video) was measured using IEEE/Harvard sentences presented in noise. The S/N ratio was selected individually for each subject to produce roughly 80% AV key-word recognition for the 0-ms delay condition (synchronous condition). Thus each subject, regardless of his or her degree of hearing loss, was equated on a performance basis for key-word recognition. An adaptive procedure was used to determine the appropriate S/N for each subject. The speech level was fixed at approximately 85 dB SPL. At the beginning of the track, an IEEE sentence was presented at a poor S/N ratio (−12 dB) so that fewer than four out of five key words were recognized correctly. Subjects responded verbally after each sentence and the correctness of each key word was scored by the operator. If no key words were correctly recognized, the noise level was decreased by 2 dB and the sentence was repeated. If fewer than four key words were recognized correctly, the noise level was decreased by 1 dB and the sentence was repeated. This procedure continued until four or five key words were correctly recognized, at which point the final noise level was noted, the subject shown the correct sentence, and a new track with a different sentence began. Thus each adaptive track consisted of repeated presentations of a single sentence with continual improvements in the S/N ratio until the four or five correct key words was achieved. A total of 20 tracks per subject was obtained and the final noise levels for each track were averaged to yield the S/N required for 80% correct key-word recognition. After the appropriate S/N ratio was determined, AV sentence recognition scores at nine auditory delay values (0–320 ms in 40-ms steps) were measured using three different lists of sentences for each delay (150 words). The 27 lists of sentences (3 lists, 9 delays) were presented in a different random order for each subject, although the assignment of a given list to a delay condition was fixed. Subjects responded by writing down as much of each sentence as they could on blank answer forms.

II. RESULTS

Two measures of AV benefit (one for consonants, one for sentences) and four measures of AV integration were derived from the data sets of each individual subject. Auditory–visual benefit describes the amount of speech recognition improvement relative to a baseline condition (typically A-only) that is achieved through the addition of visual (speechreading) cues. One metric for describing AV benefit is the simple difference score between AV and A conditions (AV–A). However, this metric is biased in that high A scores necessarily lead to low benefit scores. This bias can be avoided by defining AV benefit as the difference between AV and A speech recognition scores relative to the amount of performance improvement possible given the subject's A score (Sumby and Pollack, 1954; Rabinowitz *et al.*, 1992). The relative benefit score, defined as $(AV-A)/(1-A)$ with A and AV scores expressed as probability correct, has been shown to be roughly independent of the S/N ratio (Sumby and Pollack, 1954) as well as the overall A sentence recognition score (Grant and Walden, 1995). Relative AV benefit measures are an especially useful description of benefit for hearing-impaired subjects with widely differing degrees of hearing loss. Among HI subjects, A scores for nonsense syllables and low-predictability sentences in noise (as used in the present study) tend to vary over a considerable range, whereas V scores tend to be much less variable (Grant and Walden, 1995). By expressing AV benefit relative to A performance, much of the effect of hearing loss is removed, making the relation (if any) between AV benefit and AV integration more apparent.

A. Derived measures of AV integration

1. Integration efficiency (IE)

A and V confusion matrices obtained from the vCv nonsense syllable test were used to predict AV performance with Braida's (1991) Pre-Labeling Integration Model (PRE). The ratio of obtained AV scores to predicted AV scores defined the efficiency measure. Higher ratios imply better integration. One important aspect of this measure is that perfect integration need not be associated with high overall AV performance. Overall AV intelligibility is heavily influenced by the amount and type of unimodal cues available (Grant and Walden, 1996). If a subject has very bad hearing or is a very poor speechreader, it is unlikely that they will achieve a high AV score. Nevertheless, even under these conditions, a subject may still integrate the available A and V cues in a nearly optimal manner, and if so, the integration efficiency measure should be near unity.

2. McGurk susceptibility (MS)

In pilot tests using the four AV McGurk stimuli, normal-hearing (NH) subjects responded consistently with either /dɑ/ or /ðɑ/ when presented with the stimulus b/g, /tɑ/ when presented with p/k, /nɑ/ when presented with m/d, and /zɑ/ or /ðɑ/ when presented with v/d. In contrast, when these same stimuli were presented in the A-only condition, NH subjects obtained nearly perfect recognition. With HI subjects, however, A responses are prone to numerous errors. Some of these errors are consistent with McGurk-like responses given by NH subjects, making it difficult to distinguish between a simple auditory error (i.e., no integration) and susceptibility to McGurk effects (i.e., integration). Although there is no definitive way to correct for this problem, it is possible to use the subject's A confusion matrix to infer the proportion of AV responses might have been due to errors in audition. For example, given 100 A-only presentations of the stimulus b/g, suppose that a subject responds /bɑ/ 80 times and /dɑ/ 20 times. Further suppose that the subject responds /dɑ/ 100 times in the AV condition. We can assume that of the 100 McGurk-like responses in the AV condition, 20 are likely to have arisen from auditory errors and not from the integration of auditory /bɑ/ with visual /gɑ/. Therefore, the McGurk susceptibility to this AV pair would be adjusted from 100% to 80%. Following this procedure, the responses obtained in the AV condition for the four McGurk pairs were scored for the probability of being labeled a target McGurk blend and adjusted by the error probabilities obtained in the A condition. McGurk susceptibility was defined as the average tendency across the four stimuli to be labeled as one of the target McGurk blends. Greater susceptibility implies better integration.

3. Minimum effective auditory delay (MEAD)

Percent correct sentence recognition (i.e., of the five key words per sentence) obtained from the asynchronous AV sentence test were plotted as a function of auditory delay. The mean intelligibility scores at each delay were fit with two best-fitting lines with the constraint that slope of the first line be zero (Leek *et al.*, 1991). The intersection of the best two-line fit was interpreted as the minimum delay required to produce a decrease in sentence intelligibility. A shorter minimum delay implies greater sensitivity to the concordance of A and V cues and therefore better integration.

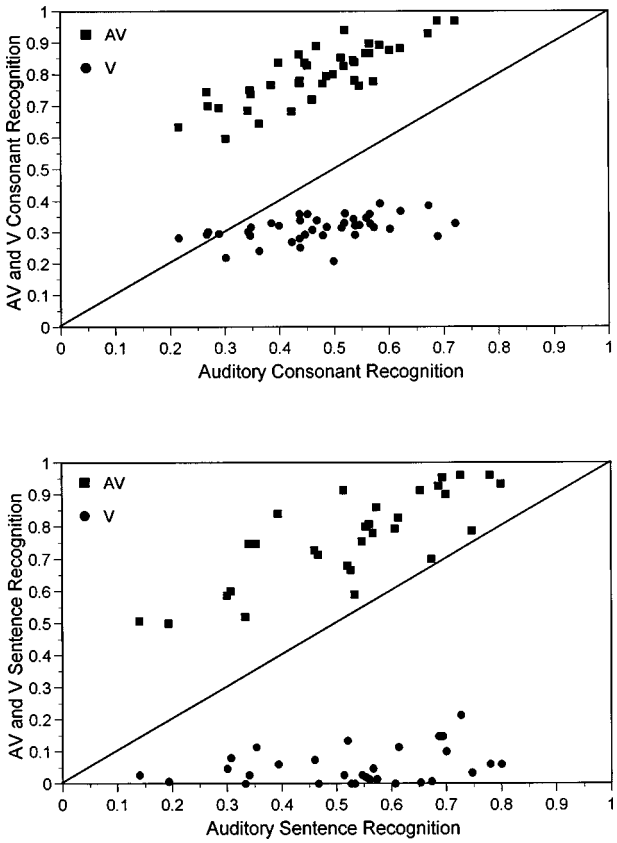

FIG. 1. Auditory–visual (AV) and visual (V) speech recognition in noise (0-dB S/N) as a function of auditory (A) speech recognition. (Top) Consonant recognition ($N=40$). (Bottom) Sentence recognition ($N=30$). Solid line shows values for A=AV and A=V.

4. Overall effect of auditory delay (OEAD)

OEAD was defined as the ratio of intelligibility scores obtained for the 320-ms delay condition (maximum delay condition) and the 0-ms delay condition (synchronous condition). This ratio represents the total amount of intelligibility decline caused by AV asynchrony. A smaller ratio (i.e., greater OEAD) implies better integration.

B. Correlations among derived measures of integration and AV benefit

Some subjects were unable to complete the full range of the tests administered in this study. Overall, the number of subjects evaluated on a given test was either 30 or 40, with 29 subjects completing all tasks. Figure 1 shows individual subject data for consonant recognition (top) and sentence recognition (bottom) in a 0-dB S/N condition. All scores are expressed as the proportion of correct responses. Forty subjects participated in the consonant recognition test and 30 subjects participated in the sentence recognition test. In both panels, V (circles) and AV (squares) intelligibility scores are shown as a function of A intelligibility. The diagonal line represents V=A and AV=A performance. For both consonants and sentences, A scores were better than V scores, with

the exception of only four subjects (10%) on the consonant test. The range of A scores for consonants (0.21–0.72) and sentences (0.14–0.8) was similar (and large) across test materials. In contrast, V scores varied over a considerably smaller range for consonants (0.21–0.39) and sentences (0.0–0.21). Auditory–visual scores were generally much higher than A or V scores for both sets of materials. However, whereas all subjects showed improved AV speech recognition for consonants, some subjects failed to show any AV improvement with sentences.

For consonant recognition (top panel), significant correlations among speech recognition scores across the three modalities were found. Specifically, AV consonant scores were significantly correlated with A ($r=0.83$, $p<0.0001$) and V ($r=0.64$, $p=0.0001$) consonant scores. In addition, A consonant scores were significantly correlated with V consonant scores ($r=0.46$, $p=0.04$). The finding of cross-modal correlations in speech recognition abilities has been noted previously (Watson *et al.*, 1996). For sentence materials, however, the situation is somewhat different. Whereas A and AV speech recognition scores were significantly correlated ($r=0.80$, $p<0.0001$), the correlation between V sentence scores and either A or AV sentence scores was not significant. One reason for failing to observe significant correlations with V-alone sentence scores may have been because of the extremely low (near-zero percent) and tightly clustered V sentence recognition.

The distribution of relative AV benefit scores ([AV−V]/[1−A]) derived from the data shown in Fig. 1 are displayed in Fig. 2. The top panel shows the results for consonants ($N=40$) whereas the bottom panel shows the results for sentences ($N=30$). Each bin width is five percentage points spanning the range from 0 to 1. The two distributions were not significantly different from a normal distribution and exhibited fairly large ranges of benefit scores across subjects. The mean relative AV benefit score for consonants and sentences was $\bar{X}=0.672$ (s.d.=0.126) and $\bar{X}=0.526$ (s.d.=0.214), respectively. Analyses comparing the two distributions for the 29 subjects who completed both tests showed that the amount of relative AV consonant benefit was significantly greater than the amount of relative AV sentence benefit (Wilcoxon Signed Ranks Test, $z=-3.51$, $p=0.0004$). Overall, 22 of 29 subjects obtained greater benefit from visual cues for consonant recognition than for sentence recognition. Furthermore, AV benefit for consonants and sentences were not significantly correlated ($r=0.06$, $p=0.74$).

The distributions of subject scores for the two derived integration measures from consonant tests are shown in Figs. 3 and 4. Figure 3 shows the data from vCv tests, whereas Fig. 4 shows the data from Cv tests. The graph displayed in the top panel of Fig. 3 shows observed versus predicted (PRE) AV scores for vCv consonants. The diagonal line represents equivalent observed and predicted scores, which according to Braida's model, reflects perfect integration (IE=1.0). Note that the predicted and observed AV scores for several subjects fall near the main diagonal, whereas observed scores for other subjects are significantly less than predicted. The mean difference between predicted and observed scores was 9.4%, with a maximum difference of

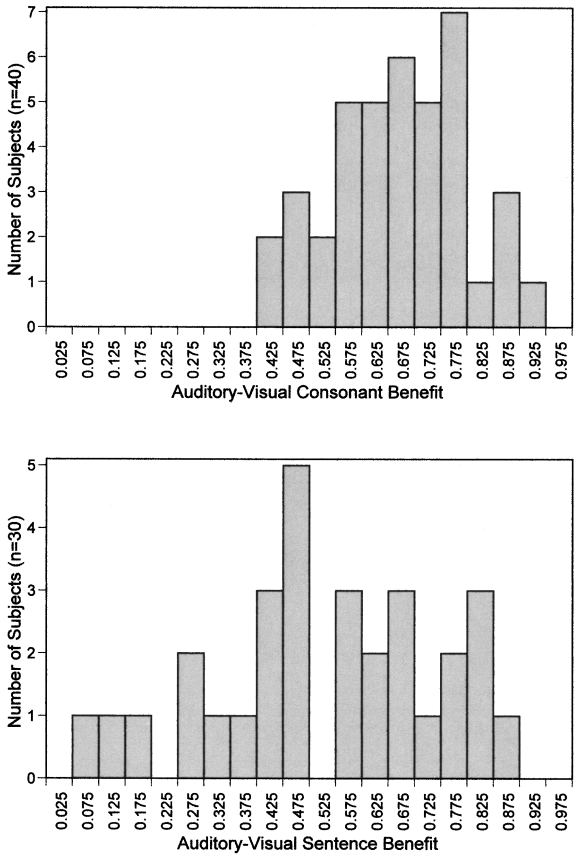

FIG. 2. Distribution of relative AV benefit scores for consonants (top) and sentences (bottom). Benefit was defined as the difference between AV and A recognition relative to the total amount of benefit possible {i.e., (AV−A)/(100−A)}.

19.9%. The bottom panel of Fig. 3 shows the results for the derived integration efficiency (IE) measure. The bin width is five percentage points. The distribution of IE ratios for 40 subjects shows that most were able to integrate A and V cues at a high level ($\bar{X}=0.89$, s.d.=0.05). However, the fairly large differences observed between predicted and observed AV consonant scores for some individuals suggests that some form of integration training would be beneficial in selected cases.

Figure 4 shows the data obtained for the McGurk stimuli. The top graph shows the average McGurk results across 30 subjects. Each bar shows the adjusted probability of responding with a target McGurk blend to the stimulus pairs listed. The last bar in the figure shows the overall average adjusted mean ($\bar{X}=0.85$, s.d.=0.14). The two stimulus pairs yielding the least McGurk-like response were b/g and v/d. This occurred because HI subjects made numerous /b/-to-/d/ and /v/-to-/ð/ errors in the A condition, making the adjusted scores substantially lower than the raw scores.

The bottom panel of Fig. 4 shows the distribution for McGurk susceptibility (MS). The distribution of individual MS scores shows that most subjects experienced typical McGurk effects. However, unlike the previous three distributions, the distribution of MS scores is left-skewed (skewness coefficient=−0.9, standard error of skewness=0.43)

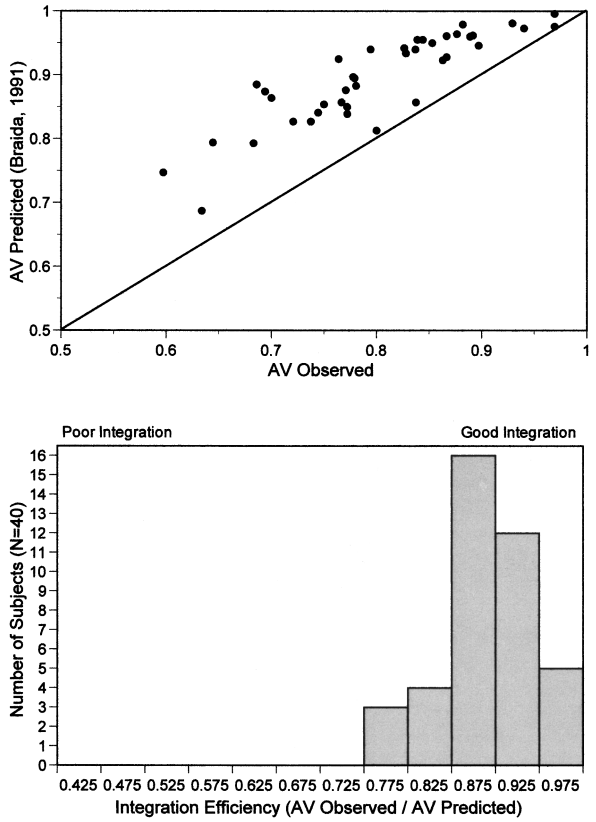

FIG. 3. Observed and derived measures obtained from experiments on consonant recognition in noise. (Top) Observed versus predicted (PRE model, Braida, 1991) AV scores. Solid line shows values for AV observed=AV predicted. (Bottom) Histogram showing distribution for integration efficiency (IE) measure.

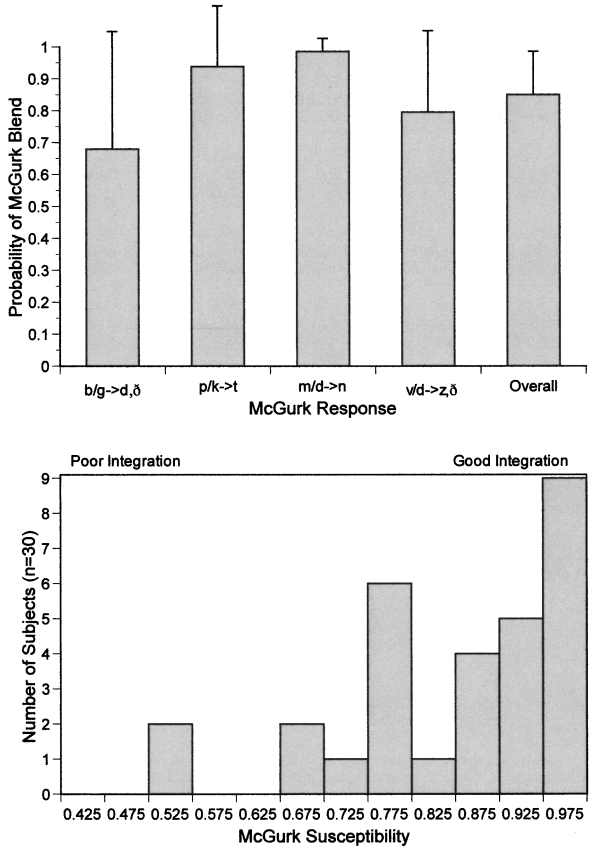

FIG. 4. Observed and derived measures obtained from experiments with McGurk consonant pairings. (Top) Group mean probability for the four McGurk blend responses and overall blend response. Error bars are ±1 standard deviation. (Bottom) Histogram showing distribution for McGurk susceptibility (MS) measure.

and significantly different from a normal distribution.

Intelligibility scores and derived integration measures obtained with asynchronous AV sentence materials are shown in Figs. 5 and 6. Figure 5 shows the average intelligibility score as a function of auditory delay. The fitted line shown is the best fit trinomial function. Consistent with previous reports of speech intelligibility with asynchronous AV sentence materials (McGrath and Summerfield, 1985; Pandey *et al.*, 1986), most subjects were relatively unaffected by delay until about 200 ms. The average intercept of the best two-line fits for individual subjects was 214.7 ms (s.d. =45.24 ms). The distribution was significantly left-skewed (skewness coefficient=−1.12, standard error of skewness =0.43).

Distributions of MEAD (top) and OEAD (bottom) measures derived from individual subject data with asynchronous sentence materials are displayed in Fig. 6. The distribution of MEAD's (top) shows that most of the subjects (27/30) were not significantly affected by AV asynchrony until the auditory signal was delayed by at least 200 ms. A few subjects, however, (6/30) showed a drop in intelligibility with substantially smaller delays. Based on suggestions by McGrath and Summerfield (1985) that better speechreaders may be more susceptible to AV asynchrony than poorer speechreaders, we examined the speechreading abilities of these six subjects for consonant and sentence recognition. None of the subjects had unusually good speechreading skills for consonant recognition compared to the average V consonant recognition ($n=40$). For V sentence recognition, two of the six subjects performed far better than the mean, whereas the performance of other four subjects was consistent with the mean speechreading performance for the group as a whole.

The bottom panel in Fig. 6 shows the distribution of

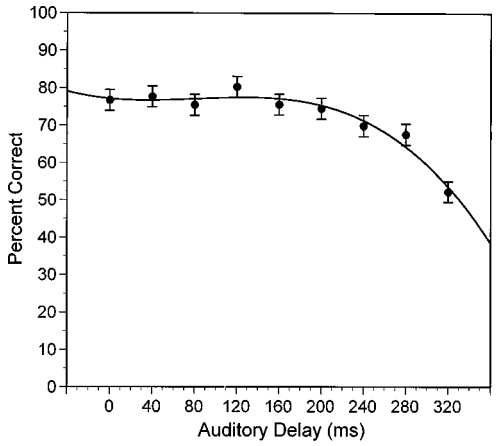

FIG. 5. Average AV percent correct key-word recognition as a function of auditory delay. Error bars are ±1 standard deviation.

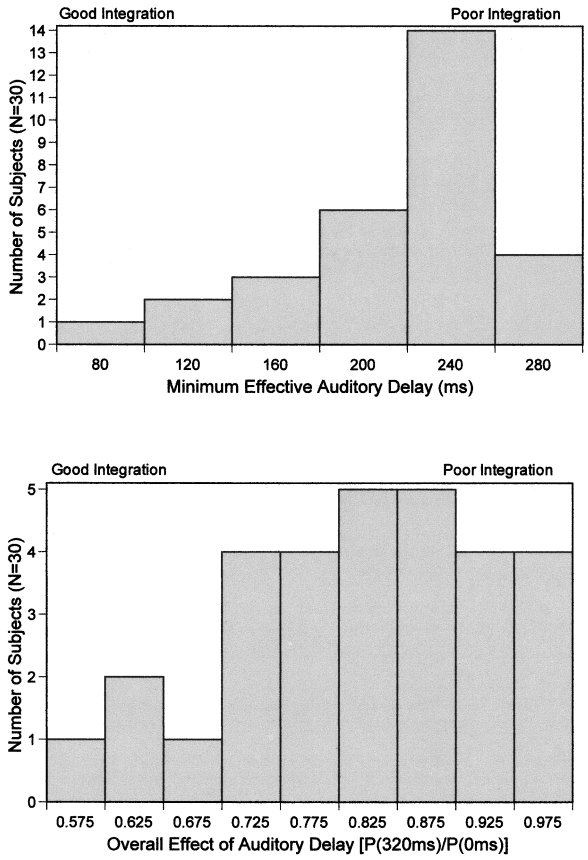

FIG. 6. Distribution of subject scores on derived measures obtained from experiments on asynchronous sentence recognition. (Top) Minimum effective auditory delay (MEAD). (Bottom) Overall effect of auditory delay (OEAD).

ratios of intelligibility scores at a 320-ms delay and 0-ms delay. The average OEAD was 0.82 (s.d.=0.11). For 8 of 29 subjects (28%), audio delays up to 320 ms had little effect on intelligibility (OEAD>0.9). However, for 12 of 29 subjects (41%), the decline in intelligibility from synchrony to a 320-ms delay was greater than 20% (OEAD<0.8). Thus although most subjects were relatively insensitive to delays up to 200 ms, once the delay was sufficiently large, AV intelligibility dropped dramatically.

A central assumption of this study was that AV speech integration is a measurable skill, independent of A and V cue extraction, that subjects use whenever A and V sources of information are available. Significant correlations among the four measures of AV integration would help validate this assumption. It was further hypothesized that individual subject performance on the different integration measures would help predict the amount of AV benefit achieved for consonant and sentence tests. Correlations among the various integration measures and the two measures of AV benefit are shown in Table I. Significance levels were determined using Bonferroni adjusted probabilities. Numbers shown in parentheses indicate the number of subjects. Among the four integration measures, only two of the six possible correlations were significant: scores for IE were significantly correlated with MS (both measures derived from tests with isolated consonant materials), and scores for MEAD were significantly correlated with OEAD (both measures derived from tests with sentence materials). Integration measures derived from recognition of isolated speech segments (IE and MS) were not significantly correlated with measures derived from recognition of words in low-context sentences (MEAD and OEAD). Analyses relating the different integration measures to AV benefit scores showed that AV consonant benefit was significantly correlated with IE and MS scores, whereas AV sentence benefit was significantly correlated with MS and OEAD scores.

To determine whether any of the four integration measures were useful for predicting AV benefit scores a stepwise multiple regression was used to identify predictor variables. Based on results from previous studies (Grant and Walden, 1995, 1996), a number of candidate predictor variables were used in the regression equation including subject variables such as age and hearing loss, speech feature recognition scores derived from subject consonant confusion matrices, and the different integration measures identified from the present experiment. Variables describing the subject's hearing loss included three-frequency (0.5, 1, and 2 kHz) and two-frequency (2 and 4 kHz) average loss for pure tones. Speech feature scores for visual place-of-articulation and auditory voicing-plus-manner were also included as possible predictor variables since these two features represent the ma-

TABLE I. Pearson correlations among derived measures of integration and AV benefit (*$p<0.05$, **$p<0.01$). Numbers in parentheses show number of subjects.

	Integration efficiency	McGurk susceptibility	Minimum effective auditory delay	Overall effect of auditory delay	AV consonant benefit	AV sentence benefit
Integration efficiency (IE)	1.0 (40)					
McGurk susceptibility (MS)	0.43* (29)	1.0 (30)				
Minimum effective auditory delay (MEAD)	0.11 (29)	−0.22 (30)	1.0 (30)			
Overall effect of auditory delay (OEAD)	0.01 (29)	−0.26 (30)	0.66** (30)	1.0 (30)		
AV consonant benefit	0.53** (40)	0.43* (29)	−0.09 (29)	−0.05 (29)	1.0 (40)	
AV sentence benefit	0.17 (29)	0.46* (30)	−0.23 (30)	−0.45* (30)	0.06 (29)	1.0 (30)

TABLE II. Predicting AV benefit.

I. AV consonant benefit ($n=29$):		
Predictor variables included		
-Age	-$A_{(Voicing+Manner)}$ Information	-Integration Efficiency
-3PTA	-$V_{(Place)}$ Information	-McGurk Susceptibility
-2PTA		
The subset model included the following predictors with $r^2=0.53$, $p<0.0001$		
Constant		
Integration efficiency		
$V_{(Place)}$ information		
II. AV sentence benefit ($n=29$):		
Predictor variables included		
-Age	-$A_{(Voicing+Manner)}$ Information	-Overall Effect of Auditory Delay
-3PTA	-$V_{(Place)}$ Information	-Minimum Effective Auditory Delay
-2PTA		-McGurk Susceptibility
The subset model included the following predictors with $r^2=0.38$, $p<0.003$		
Constant		
Overall effect of auditory delay		
$V_{(Place)}$ information		

jority of information typically extracted from A and V speech recognition conditions when noise is present (Miller and Nicely, 1955; Grant and Walden, 1996). The results of the stepwise regressions are shown in Table II. The subset model for predicting AV consonant benefit included visual place information and the IE measure obtained from Braida's PRE model. The subset model for predicting AV sentence benefit included visual place information and the OEAD integration measure. Overall, roughly 40%–50% of the variance in AV benefit could be explained by a subject's visual place recognition score and an appropriate measure of AV integration ability. Figure 7 shows scatter plots of the relation between IE and AV consonant benefit (top) and OEAD and AV sentence benefit (bottom). In both cases, the selected integration measure accounts for roughly 20%–30% of the variance observed in AV benefit.

III. DISCUSSION

The primary goals of this study were to establish appropriate measures of AV integration ability for individual subjects and to determine whether individual differences in integration ability were predictive of AV benefit. The results of the correlation and multiple regression analyses showed that we were only partially successful in meeting these goals. The various measures that were chosen to evaluate integration ability did not converge on a single construct. Instead, measures based on the perception of isolated consonants (IE and MS), and measures based on the perception of key words in sentences (MEAD and OEAD) diverged. In a similar manner, the two measures of AV benefit diverged, in that the correlation between consonant benefit and sentence benefit was not significant. In light of recent reports showing systematic relations among speech recognition scores for nonsense syllables, isolated words, and sentence materials (e.g., Bilger, 1984; Boothroyd and Nittrouer, 1988; Rabinowitz *et al.*, 1992; Watson *et al.*, 1996; Olsen *et al.*, 1997), these results are somewhat surprising. On the one hand, the existence of a common source of variance across all speech recognition tasks, independent of receiving modality (A, V, or AV) and speech material, is not hard to justify. According to Bilger (1984), speech recognition represents a single construct and therefore all scores, regardless of test conditions, must be related. Furthermore, given that these relations have been shown to hold for HI listeners with widely differing auditory capabilities (Olsen *et al.*, 1997), it has been suggested that the common skill applied by all subjects in speech recognition tests is a shared knowledge of the linguistic properties of the language and the ability to use this

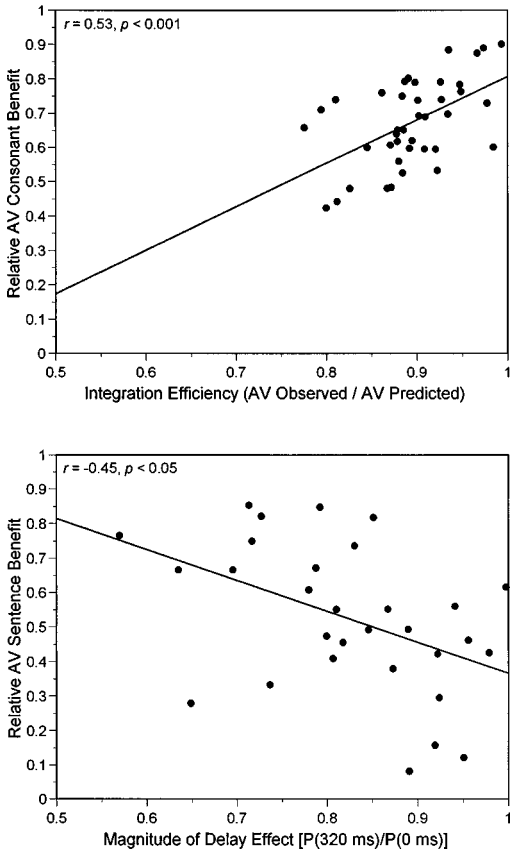

FIG. 7. (Top) Scatter plot showing relation between derived measure of integration efficiency (IE) and relative consonant benefit. (Bottom) Scatter plot showing the relation between derived measure of overall effect of auditory delay (OEAD) and relative AV sentence benefit.

knowledge to construct words from incompletely resolved segments and sentences from incompletely resolved words (Watson *et al.*, 1996).

In most of the previous studies that examined the relations between segment, word, and sentence recognition, the tests were conducted in the A modality only (but see Bernstein and Auer, 1996; Demorest *et al.*, 1996; Watson *et al.*, 1996 for exceptions). In the present study, the integration tests were conducted in A, V, and AV modalities and the materials were a mix of congruent and discrepant stimuli. It is possible that the presentation of unusual AV materials, created by delaying the audio portion of the sentence materials relative to V or by cross-dubbing V and A portions of Cv materials, fostered greater variability across subjects than one would observe with more typical speech materials. If the variability observed across subjects for the different integration tasks does not have a common origin, then the correlations among measures might be low, as was observed in the present study. In fact, when measures were confined to similar tasks, most of the correlations across materials (segments and sentences) were significant. For example, the correlations among speech recognition measures in noise (0-dB S/N) using congruent materials were all significant. That is, A segment recognition was significantly correlated with A sentence recognition ($r=0.64$, $p=0.0002$), V segment recognition was significantly correlated with V sentence recognition ($r=0.49$, $p=0.0075$), and AV segment recognition was significantly correlated with AV sentence recognition ($r=0.47$, $p=0.0102$). In addition, the two consonant recognition tasks (vCv and Cv) yielded significantly related integration indices (IE and MS). This may not be that surprising given that most subjects reported that they were unaware of the discrepant nature of AV McGurk pairs and perceived them as naturally occurring stimuli. This was true even though at the beginning of the experiment all subjects were informed that the McGurk stimuli might seem ''out of sync.'' Therefore, from the subject's point of view, the main perceptual difference between vCv and Cv tests was that the Cv McGurk pairs were administered in quiet, whereas the vCv's were administered in noise. Finally, the two measures of sentence integration (MEAD and OEAD) were significantly related. Given that they were derived from the same data set, this could have been expected.

The apparent breakdown in the relation between measures based on speech segments and those based on sentences observed in the present study (specifically, AV consonant benefit versus AV sentence benefit, and segment integration measures versus sentence integration measures) may be best explained in terms of the differences in task demands imposed by the two sets of materials. In the vCv and Cv tasks, the response set was closed and known to the subjects via the touch screen terminal. In contrast, the response set for IEEE words was open and essentially the size of subject's vocabulary in that no sentences were ever repeated and no feedback was provided. Furthermore, recognition of key words in sentences require additional processing stages involved in lexical retrieval that are not required in tests with single consonants (Bernstein and Auer, 1996; Demorest *et al.*, 1996). The combination of a larger response set and additional processing stages inherent in key-word recognition may require more processing time than the recognition of consonants to sort through the potential candidate responses. Similarly, the methodology used to test recognition of consonants and recognition of key words differed with respect to the amount of time subjects had to make their response. In tests with single consonants, no time constraints were placed upon the subject's decision process. That is, one item was presented and the subjects had as long as they needed to make their response. In contrast, for key-word recognition, approximately 3–5 words/s ($\approx$13 phonemes/s) were presented. Thus the processing of each word in the sentence may be potentially interrupted by the next incoming string of phonemes. How well each subject can handle this potential disruption depends in part on how fast they can process each word. This suggests that speed of processing in spoken language recognition may be a separate variable worthy of examination. Individual differences in processing speed for words in sentences could help explain why some subjects derived much less AV sentence benefit than AV consonant benefit. That is, subjects who require more time to process each work may fall progressively farther behind as the sentence proceeds. Such would not be the case with AV consonants because there is no interfering stimulus between initial presentation and response.

Finally, although IEEE sentences were designed to be low-context (IEEE, 1969; Rabinowitz *et al.*, 1992), it is quite possible that some subjects were able to take greater advantage of the morpho-syntactic structure of each sentence, if not the semantic context, giving them a significant contextual advantage over other subjects. In other words, the presumed common ability of native language users to take advantage of semantic and syntactic context may not be an equal skill across individuals. If individual subjects exhibit a broad range of context-usage abilities (e.g., Olsen *et al.*, 1997), then correlations between the recognition of speech segments and sentences would not be expected to correlate highly.

IV. SUMMARY AND CONCLUSION

Four measures of auditory–visual integration were derived from three separate experiments with hearing-impaired (HI) listeners. In the first experiment, auditory (A), visual (V), and auditory–visual (AV) consonant recognition in noise was evaluated. A Pre-Labeling integration model (Braida, 1991) which specifies optimum integration of A and V cues, was used to predict AV consonant recognition from A and V consonant confusion matrices. The ratio of observed to predicted (PRE) AV score was then used as an index of integration efficiency (IE) with unity representing perfect integration. In a second experiment, A and AV consonant recognition was measured using AV stimuli with discrepant auditory and visual components selected to elicit the well-known McGurk effect (McGurk and MacDonald, 1976). Susceptibility to McGurk illusions (MS) was defined as the probability of responding with a McGurk blend to discrepant AV tokens. Greater susceptibility to McGurk illusions was assumed to imply better integration ability. In a third experiment, temporally misaligned AV sentence materials were presented in noise for identification. Nine auditory

delays ranging from 0 to 320 ms in 40-ms steps were evaluated. Two derived integration measures were obtained from the sentence identification data: (1) a minimum effective auditory delay (MEAD), defined as the smallest delay resulting in a statistically significant intelligibility performance decrement relative to the synchronous case (0-ms delay); and (2) an overall effect of auditory delay (OEAD), defined as the ratio of AV scores for the longest delay condition (320 ms) and the 0-ms condition. For both sentence integration measures, it was assumed that smaller MEAD and OEAD values implied better integration. Correlations among the four measures of AV integration, as well as correlations between each integration measure and a separate measure of AV benefit for sentences in noise, were obtained.

Subjects derived substantial benefit from visual speech cues for both consonant and sentence recognition in noise, but there were substantial individual differences in the amount of AV benefit obtained. Interestingly, no relationship was observed between the amount of AV benefit obtained for consonants and the amount of AV benefit obtained for sentences, despite the fact that significant correlations were found for speech recognition scores across materials for each of the three receiving conditions tested (A, V, and AV). Among the four measures of integration ability examined as possible predictors of AV benefit, the two measures derived from tests with isolated Cv's and vCv's (IE and MS) and the two measures derived from asynchronous AV sentence materials (MEAD and OEAD) were significantly correlated with each other. However, measures derived from experiments using consonant materials were unrelated to measures derived from experiments using sentence materials. In predicting AV consonant benefit, the ability to speechread place-of-articulation and the derived measure IE accounted for roughly 50% of the variability. For predicting AV sentence benefit, the ability to speechread place-of-articulation and the derived measure OEAD accounted for roughly 40% of the variability. Other potential variables such as audiometric thresholds, age, and auditory feature recognition scores for voicing and manner-of-articulation were not useful predictors.

Since our primary focus is understanding the processes that lead to successful AV recognition and benefit in daily communication (i.e., for connected speech), it was somewhat disconcerting to find little association between integration measures derived from nonsense syllable tests and those derived from sentence tests. Models of AV speech integration (Massaro, 1987; Braida, 1991) currently require data in the form of confusion matrices, which are difficult if not impossible to obtain from sentence recognition tests (but see Bernstein *et al.*, 1994 for a possible solution to this problem). Thus one of the basic tools available for measuring individual differences in integration ability may not be applicable given our desire to study connected speech. However, it may be possible to modify nonsense syllable tests in such a way as to incorporate a number of important aspects of connected speech materials. For example, some of the major differences between consonant and sentence recognition include stimulus differences in A and V segmental cues that occur as a result of isolated nonsense syllable productions versus the more fluent productions associated with words and sentences. Intonation and stress variations important for sentence recognition may be incorporated into nonsense syllable tests by using sequences of nonsense syllables rather than isolated productions. Recognition tests involving sequenced nonsense syllables would also be more similar to sentence tests by reducing the differences in memory load that result from having to recognize short ($\approx$350 ms for isolated segments) versus long ($\approx$2.7 s for sentences) utterance durations, and by reducing differences in the number of items needed to remember before making a response (i.e., 1 ''target'' phoneme/s for isolated segments versus $\approx$13 ''target'' phonemes/s for sentences).

There are other differences separating nonsense syllables from meaningful sentences that cannot be eliminated, namely, processes involved in lexical access and retrieval and the different levels of contextual information from nonsense syllable to word, and from word to sentence. Additional studies are needed to determine whether individual subjects differ in their ability to cope with these differences in task demands. We are currently studying two factors separating isolated segment recognition and sentence recognition; the ability to use sentence context to facilitate the recognition of words, and the ability to process strings of spoken words quickly. It is hoped that individual differences in these skills will help explain further the relatively weak relations between segment and sentence integration measures observed in the present study.

ACKNOWLEDGMENTS

Portions of this research were presented at the 133rd Meeting of the Acoustical Society of America, 15–20 June 1997, State College, PA. This research was supported by Grant Nos. DC00792 and DC01643 from the National Institute of Deafness and Other Communication Disorders to Walter Reed Army Medical Center, and by the Clinical Investigation Service, Walter Reed Army Medical Center, under Work Unit #2540. All subjects participating in this research provided written informed consent prior to beginning the study. The opinions or assertions contained herein are the private views of the authors and are not to be construed as official or as reflecting the views of the Department of the Army or the Department of Defense.

ANSI (**1969**). ANSI S3.5-1969, ''American National Standard Methods for the Calculation of the Articulation Index'' (American National Standards Institute, New York).

ANSI (**1989**). ANSI S3.6-1989, ''American national standard specification for audiometers'' (American National Standards Institute, New York).

Baddeley, A. (**1990**). *Human Memory: Theory and Practice* (Allyn and Bacon, Boston).

Baddeley, A. (**1996**). ''The fractionation of working memory,'' Proc. Natl. Acad. Sci. USA **93**, 13468–13472.

Bernstein, L. E., and Auer, E. T. Jr. (**1996**). ''Word recognition in speechreading,'' in *Speechreading by Humans and Machines: NATO ASI Series F*, edited by D. G. Stork and M. E. Hennecke (Springer-Verlag, Berlin), pp. 17–26.

Bilger, R. C. (**1984**). ''Speech recognition test development,'' in *Speech Recognition by the Hearing Impaired*, edited by E. Elkins, ASHA Reports **14**, 2–7.

Boothroyd, A., and Nittrouer, S. (**1988**). ''Mathematical treatment of context effects in phoneme and word recognition,'' J. Acoust. Soc. Am. **84**, 101–114.

Braida, L. D. (**1991**). ''Crossmodal integration in the identification of consonant segments,'' Q. J. Exp. Psychol. **43**, 647–677.

Campbell, R. (**1990**). ''Lipreading, neuropsychology, and immediate memory,'' in *Neuropsychological Impairments of Short-Term Memory*, edited by G. Vallar and T. Shallice (Cambridge U.P., New York), pp. 268–286.

Demorest, M. E., Bernstein, L. E., and DeHaven, G. P. (**1996**). ''Generalizability of speechreading performance on nonsense syllables, words, and sentences: Subjects with normal hearing,'' J. Speech Hear. Res. **39**, 697–713.

Grant, K. W., and Braida, L. D. (**1991**). ''Evaluating the Articulation Index for audiovisual input,'' J. Acoust. Soc. Am. **89**, 2952–2960.

Grant, K. W., and Walden, B. E. (**1995**). ''Predicting auditory-visual speech recognition in hearing-impaired listeners,'' presented at the XIIIth International Congress of Phonetic Sciences, Stockholm, Sweden, 13–19 August 1995, Vol. 3, pp. 122–129.

Grant, K. W. and Walden, B. E. (**1996**). ''Evaluating the articulation index for auditory-visual consonant recognition,'' J. Acoust. Soc. Am. **100**, 2415–2424.

Grant, K. W., Walden, B. E., and Seitz, P. F. (**1998**), ''Auditory-visual speech recognition by hearing-impaired subjects: Consonant recognition, sentence recognition, and auditory-visual integration,'' J. Acoust. Soc. Am. **103**, 2677–2690.

Green, K. P., Kuhl, P. K., Meltzoff, A. N., and Stevens, E. B. (**1991**). ''Integrating speech information across talkers, gender, and sensory modality: Female faces and male voices in the McGurk effect,'' Percept. Psychophys. **50**, 524–536.

Institute of Electrical and Electronic Engineers (**1969**). ''IEEE recommended practice for speech quality measures'' (IEEE, New York).

Leek, M. R., Brown, M. E., and Dorman, M. F. (**1991**). ''Informational masking and auditory attention,'' Percept. Psychophys. **50**, 205–214.

Massaro, D. W. (**1987**). *Speech Perception by Ear and Eye: A Paradigm for Psychological Inquiry* (Erlbaum, Hillsdale, NJ).

Massaro, D. W. (**1972**). ''Perceptual images, processing time, and perceptual units in auditory perception,'' Psychol. Rev. **79**, 124–145.

Massaro, D. W., Cohen, M. M., and Smeele, P. T. (**1996**). ''Perception of asynchronous and conflicting visual and auditory speech,'' J. Acoust. Soc. Am. **100**, 1777–1786.

McGrath, M., and Summerfield, Q. (**1985**). ''Intermodal timing relations and audio-visual speech recognition by normal-hearing adults,'' J. Acoust. Soc. Am. **77**, 678–685.

McGurk, H., and MacDonald, J. (**1976**). ''Hearing lips and seeing voices,'' Nature (London) **264**, 746–748.

Miller, G. A., and Nicely, P. E. (**1955**). ''An analysis of perceptual confusions among some English consonants,'' J. Acoust. Soc. Am. **27**, 338–352.

Olsen, W. O., Van Tasell, D. J., and Speaks, C. E. (**1997**). ''Phoneme and word recognition for words in isolation and in sentences,'' Ear Hear. **18**, 175–188.

Pandey, P. C., Kunov, H., and Abel, S. M. (**1986**). ''Disruptive effects of auditory signal delay on speech perception with lipreading,'' J. Aud. Res. **26**, 27–41.

Rabinowitz, W. M., Eddington, D. K., Delhorne, L. A., and Cuneo, P. A. (**1992**). ''Relations among different measures of speech reception in subjects using a cochlear implant,'' J. Acoust. Soc. Am. **92**, 1869–1881.

Sumby, W. H., and Pollack, I. (**1954**). ''Visual contribution to speech intelligibility in noise,'' J. Acoust. Soc. Am. **26**, 212–215.

Summerfield, Q. (**1987**). ''Some preliminaries to a comprehensive account of audio-visual speech perception,'' in *Hearing by Eye: The Psychology of Lip-Reading*, edited by B. Dodd and R. Campbell (Erlbaum, Hillsdale, NJ), pp. 3–52.

Summerfield, Q. (**1992**). ''Lipreading and audio-visual speech perception,'' Philos. Trans. R. Soc. London, Ser. A, 71–78.

Walden, B. E., Erdman, S. A., Montgomery, A. A., Schwartz, D. M., and Prosek, R. A. (**1981**). ''Some effects of training on speech recognition by hearing-impaired adults,'' J. Speech Hear. Res. **24**, 207–216.

Walden, B. E., Grant, K. W., and Cord, M. T. (**1996**). ''Effects of amplification and speechreading on consonant recognition in persons with impaired hearing,'' paper presented a ASHA Annual Convention, Seattle, Washington, 21–24 Nov. 1996, 152(A).

Walden, B. E., Montgomery, A. A., Cord, M. T., Demorest, M. E., and Prosek, R. A. (**1987**). ''Effects of amplification and visual cues on consonant recognition,'' ASHA **29**, 77(A).

Walden, B. E., Montgomery, A. A., Prosek, R. A., and Hawkins, D. B. (**1990**). ''Visual biasing of normal and impaired auditory speech perception,'' J. Speech Hear. Res. **33**, 163–173.

Watson, C. S., Qiu, W. W., Chamberlain, M. M., and Li, X. (**1996**). ''Auditory and visual speech perception: Confirmation of a modality-independent source of individual differences in speech recognition,'' J. Acoust. Soc. Am. **100**, 1153–1162.

Winkler, I., Reinikainen, K., and Naatanen, R. (**1993**). ''Event-related brain potentials reflect traces of echoic memory in humans,'' Percept. Psychophys. **53**, 443–449.

Variable-duration notched-noise experiments in a broadband noise context

James J. Hant, Brian P. Strope, and Abeer A. Alwan
Speech Processing and Auditory Perception Laboratory, Department of Electrical Engineering, School of Engineering and Applied Sciences, UCLA, 405 Hilgard Avenue, Los Angeles, California 90095

(Received 27 April 1998; accepted for publication 30 June 1998)

A variable-duration notched-noise experiment was conducted in a noise context. Broadband noise preceded and followed a tone and notched noise of similar duration. Thresholds were measured at four durations (10, 30, 100, and 300 ms), two center frequencies (0.6, 2.0 kHz), and five relative notch widths (0.0, 0.1, 0.2, 0.4, 0.8). At 0.6 kHz, 10-ms thresholds decrease 6 dB across notch widths, while 300-ms thresholds decrease over 35 dB. These trends are similar but less pronounced at 2 kHz. In a second experiment, the short-duration notched noise was replaced with a flat noise which provided an equivalent amount of simultaneous masking and thresholds dropped by as much as 20 dB. A simple combination of simultaneous and nonsimultaneous masking is unable to predict these results. Instead, it appears that the elevated thresholds at short durations are dependent on the spectral shape of the simultaneous masker. © *1998 Acoustical Society of America.*
[S0001-4966(98)02510-7]

PACS numbers: 43.71.An, 43.66.Ba, 43.66.Dc [RVS]

INTRODUCTION

Short-duration speech signals, such as plosives, are often confused in noisy environments. To model these confusions, it is necessary to characterize our ability to resolve the spectral components of short-duration stimuli in the context of background noise. Previous notched-noise experiments using a short-duration tone and long-duration notch have shown that frequency selectivity develops nearly instantaneously (Moore *et al.*, 1987; Wright and Dai, 1994). In this paper, a variable-duration notched-noise experiment is reproduced in a noise context. Specifically, the tone and notched noise are of similar duration and surrounded in time by long-duration (300-ms) white noise. Tone thresholds are therefore determined by the combination of three potential maskers: the preceding white noise, the simultaneous notched noise, and the trailing white noise.

Previous studies suggest that a combination of maskers may result in masking which is greater than that predicted by a linear sum of each individual masker. These studies have shown masking increases of 7 dB for combinations of simultaneous maskers (Green, 1967), 15 dB for combinations of nonsimultaneous maskers (Oxenham and Moore, 1995), and 14 dB for combinations of simultaneous and nonsimultaneous maskers (Jesteadt, 1996). This ''excess masking'' can be predicted by power-law models in which the effects of the individual maskers are compressed before they are added together (for a review see Humes and Jesteadt, 1989).

In this paper, the variable-duration notched-noise data are analyzed in terms of either a linear or nonlinear combination of simultaneous and nonsimultaneous masking. To further assess this approach, a second experiment is conducted in which the notched noise is replaced by a flat noise which provides an equivalent amount of simultaneous masking.

I. EXPERIMENT 1

A. Stimuli

Figure 1 shows a schematic spectrogram of the stimuli used in the experiment. The notched-noise masker and tone signal were presented between two 300-ms white-noise segments. White noise was generated by randomly choosing 1 of 32 digitally synthesized Gaussian noise sequences. The notched noise was created by filtering the white noise with an 801-tap bandstop filter. Both the notched noise and the surrounding white noise had a spectrum level of 36 dB/Hz and were generated from different Gaussian noise sequences.

To reduce the effect of spectral splatter, all stimuli were gated on and off using raised-cosine windows with rise/fall times of 10 ms. Signal durations of 10, 30, 100, and 300 ms were defined from the half-rms level (i.e., -6 dB). Figure 2 shows a diagram of the temporal relationships between the onsets and offsets for the tone, notch, and white noise. The notched noise was centered (in time) around the tone and was 20 ms longer than the tone. This ensured that the full amplitude of the notch was in place throughout the entirety of the tone. To maintain a constant spectrum level across time in the frequency region outside the notch, the transients of the notched-noise masker were opposite to those of the white-noise masker.

The experiment was conducted at tone frequencies of 0.6 and 2 kHz. All notches were symmetric (in frequency) around the tone and characterized by $\Delta f/c_f$, where c_f is the tone frequency, and Δf is the frequency difference between the tone and either edge of the notch. The skirts of the spectral notch had slopes which ranged from -25 dB/50 Hz (at a tone duration of 10 ms) to -60 dB/50 Hz (at a tone duration of 300 ms).

Thresholds were measured for $\Delta f/c_f$ equal to (0.0, 0.1, 0.2, 0.4, 0.8) which correspond to notch widths of (0.0, 0.12, 0.24, 0.48, 0.96) kHz at a center frequency of 0.6 kHz, and

 0001-4966/98/104(4)/2451/6/$15.00

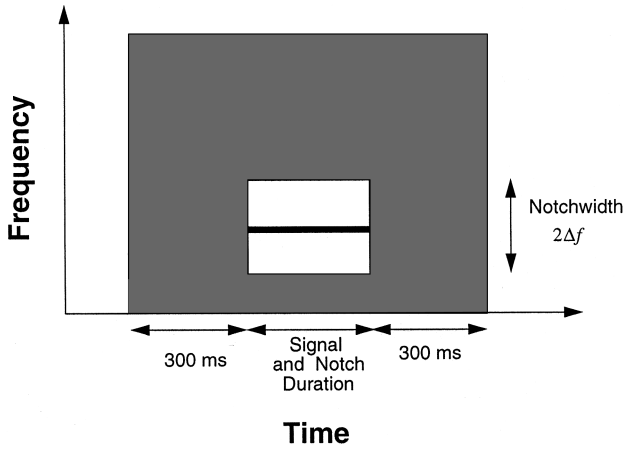

FIG. 1. Schematic spectrogram of the stimuli in experiment 1. The notched noise and tone (of a specific duration) are surrounded by two 300-ms white-noise maskers. The notch is symmetric around the tone and defined in terms of the fractional deviation from the tone's frequency ($\Delta f/c_f$).

(0.0, 0.4, 0.8, 1.6, 3.2) kHz at a center frequency of 2 kHz. To measure the amount of nonsimultaneous masking by the surrounding white noise, additional data points were collected using a wide notch width from 50 to 7950 Hz.

B. Subjects

Five audiometrically normal subjects (two male, three female) participated in the experiments. The first two authors participated as subjects and were experienced listeners in psychoacoustic experiments. The other three subjects were paid and had no previous experience as laboratory listeners.

C. Protocol

Stimuli were presented binaurally to listeners in a sound attenuating room via Telephonics TDH49P headphones. The ringing of the headphones was measured to be negligible at the frequencies and durations used in the experiment. Computer software generated the test tokens as 16 bit/16 kHz digital numbers. An Ariel ProPort 656 board performed digital-to-analog conversion. The resulting analog waveforms were amplified using the pre-amp of a Sony 59ES DAT recorder, which was connected to the headphones. The entire system was calibrated within ± 0.5 dB before each experiment using a Larson Davis 800B sound level meter.

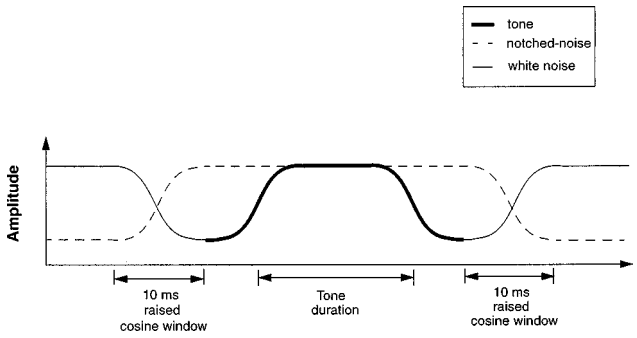

FIG. 2. Schematic of the temporal transitions for the tone, notched noise, and white noise. All stimuli are turned on and off with a raised cosine window of length 10 ms. Durations are defined from the half-rms levels.

Masked thresholds were determined using an adaptive 2I, 2AFC paradigm with no feedback (Levitt, 1971). Three correct responses determined a successful subtrial while one incorrect response determined an incorrect subtrial. Thresholds, therefore, are defined to be the 79% correct point. Step sizes were initially set to 4 dB, then reduced to 2 dB after the first reversal, and finally to 1 dB after the third reversal. From a total of nine reversals, the average of the last six determined threshold for each trial. The mean of two trials determined the final threshold. If the difference between the two trials was greater than 3 dB, a third point was taken and the median of all three trials determined the final threshold. Thresholds for the wide notch width condition were determined from one trial.

Subjects were trained for one hour before beginning the experiments. No training effects were apparent in the final data. One subject had particular difficulty detecting tones at the narrow notch widths across all durations. Despite substantial training, thresholds *increased* by nearly 5 dB between the 0.0 and 0.1 notch width conditions. Data from this subject were not included in the analyses below.

II. RESULTS AND DISCUSSION

To model the results of experiment 1, the masking contributions of the preceding white noise, the simultaneous notched noise, and the trailing white noise are considered. The results of notched-noise experiments using a short-duration tone and long-duration notch have shown that frequency selectivity develops nearly instantaneously (Moore *et al.*, 1987; Wright and Dai, 1994). The difference between these studies and experiment 1 is the noise context which adds forward and backward masking noise. Therefore, in the following analyses, the amount of simultaneous masking is determined by a traditional filtering model which uses auditory filters derived from long-duration notched-noise experiments (Glasberg and Moore, 1990). The masking contributions of the surrounding white noises are lumped together into a single nonsimultaneous-masking term. Tone thresholds are then predicted as either a linear or nonlinear combination of simultaneous and nonsimultaneous masking.

A. Predictions of a linear model

Assuming a linear combination of simultaneous and non-simultaneous masking, thresholds from experiment 1 are predicted by the following equation:

$$T_{\text{tot}} = 2K \int_b^\infty N(g)W(g)dg + T_{\text{ns}}, \tag{1}$$

where T_{tot} is the threshold prediction, g is the normalized frequency deviation from the tone center frequency, K is the threshold SNR due to simultaneous masking, b is the relative notch width ($\Delta f/c_f$), $N(g)$ is the power density of the noise, $W(g)$ is the shape of the auditory filter centered around the tone, and T_{ns} is the tone threshold due to nonsimultaneous masking.

Auditory filters are assumed to have the shape of a symmetric roex function,

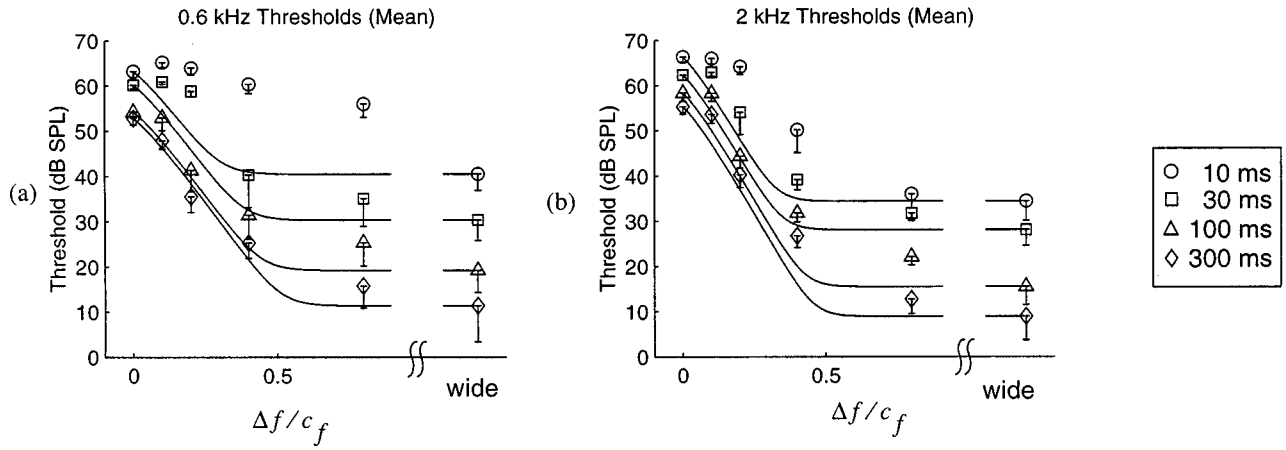

FIG. 3. Mean notched-noise thresholds. (a) Thresholds of 0.6-kHz tones as a function of the relative notch width, $(\Delta f/c_f)$, with signal duration as a parameter. Error bars, shown below the data points, represent standard deviations across subjects. Wide notch width thresholds, corresponding to a notch between 50 and 7950 Hz, are denoted by ''wide'' on the horizontal axis. (b) Thresholds of 2-kHz tones. The lines represent predictions of the linear model at each duration.

$$W(g)=(1-r)(1+pg)e^{-pg}+r, \tag{2}$$

where p specifies the slope of the filter skirts and therefore sets the filter bandwidth, and r determines the dynamic range of the filter. The filter bandwidths used were from Glasberg and Moore (1990), and r was set to -75 dB. Here, $T_{\rm ns}$ and K are determined from the wide and 0.0 notch thresholds, respectively.

Figure 3(a) plots mean thresholds of the 0.6-kHz tone as a function of the relative notch width $(\Delta f/c_f)$ with signal duration as a parameter. Standard deviations are expressed by error bars and, for clarity, are only shown below the average thresholds. The mean data at 2 kHz are shown in Fig. 3(b). Wide notch-width thresholds, corresponding to a notch from 50 to 7950 Hz, are denoted by ''wide'' on the horizontal axes of Fig. 3(a) and (b). The solid lines represent the predictions of the linear model for each duration.

At short durations (10 and 30 ms), a linear combination of simultaneous and nonsimultaneous masking underestimates measured thresholds. The discrepancy is most notable for the 10-ms thresholds at 0.6 kHz, but the trend exists throughout the data. Between the 0.0- and wide-notch conditions, the combination of masking is greater than the (linear) sum of its parts. At the longer durations (100 and 300 ms), the contribution of the nonsimultaneous masker is reduced and the linear model provides better threshold predictions.

B. Predictions of a nonlinear model

Auditory compression has been used in nonlinear models that predict combinations of forward and backward masking (Penner, 1980; Oxenham and Moore, 1994, 1995) and combinations of simultaneous and nonsimultaneous masking (Jesteadt *et al.*, 1996). Nonlinear auditory models which include adaptation (Zwislocki, 1969; Dau *et al.*, 1996) further imply time-varying compression. To predict the current data, we assume summation of simultaneous and nonsimultaneous masking after a power-law compression which, for generality, is allowed to vary as a function of the stimulus duration. The total threshold, $T_{\rm tot}$, is the sum of the thresholds due to simultaneous masking, T_s, and nonsimultaneous masking, $T_{\rm ns}$, after each term has been raised to a power, q:

$$(T_{\rm tot})^q=(T_s)^q+(T_{\rm ns})^q, \tag{3}$$

where

$$T_s=2K\int_b^\infty N(g)W(g)dg. \tag{4}$$

The parameters $T_{\rm ns}$, q, and the scaling factor K are iteratively optimized to reduce the mean squared error (in dB) of the model predictions for each duration. As with the linear predictions above, the logarithm of $T_{\rm tot}$ is used to provide threshold predictions on a dB scale.

Figure 4(a) and (b) shows the predictions of the nonlinear model at tone frequencies of 0.6 and 2 kHz, respectively. While the predictions are better than those from the linear model, the error is still considerable, especially at short durations. For both center frequencies, the optimal q values decrease with shorter durations, implying an increase in the nonlinear summation of masking.

III. EXPERIMENT 2

A simple modification of the first experiment was used to assess the utility of the current modeling approach. The simultaneous notched noise was replaced with a flat-noise masker (0–8 kHz). Figure 5 shows a schematic spectrogram of the stimuli. Assuming traditional measures of frequency selectivity, the level of the simultaneous flat noise was set to provide the same amount of simultaneous masking as the notched noise in experiment 1. With identical amounts of simultaneous and nonsimultaneous masking, we expect similar thresholds.

For a given filter shape $W(f)$ (Glasberg and Moore, 1990), and relative notch width $(\Delta f/c_f)$ equal to b, the spectrum level of the noise, $N_{\rm eq}$, which equates the amount of simultaneous masking in experiments 1 and 2, is given by the following equation:

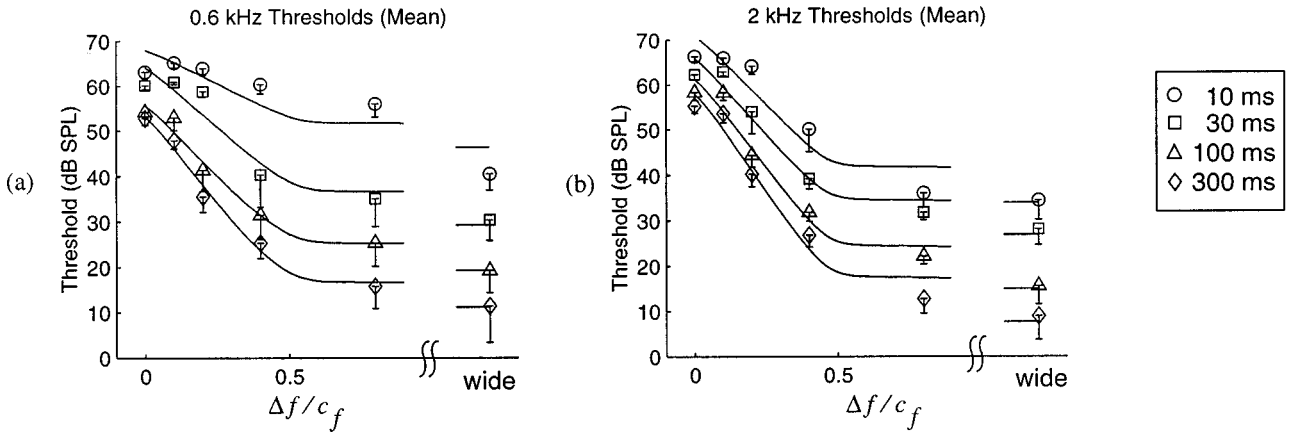

FIG. 4. Mean notched-noise thresholds. Same as Fig. 3 except the lines represent predictions of the nonlinear model.

$$N_{\mathrm{eq}}=\frac{N_0[\int_0^{(1-b)c_f}W(f\,)df+\int_{(1+b)c_f}^{8\ \mathrm{kHz}}W(f\,)df]}{\int_0^{8\ \mathrm{kHz}}W(f\,)df}, \qquad (5)$$

where N_0 is the spectrum level of the notched noise (36 dB/Hz).

The four subjects whose data were analyzed in experiment 1, participated in experiment 2. Tone thresholds were measured for equivalent noise levels, N_{eq}, corresponding to notches of 0.2, 0.4, and 0.8. The onsets and offsets of the surrounding noise, tone, and simultaneous noise masker were identical to those used in experiment 1. Tone thresholds were measured using the same procedure as in the first experiment. Measurements were made only at a 10-ms tone duration.

IV. COMPARING RESULTS

In Fig. 6, thresholds from experiment 2 (squares) are compared to the corresponding notched-noise thresholds from experiment 1 (circles) and the nonlinear threshold predictions (solid lines). For both experiments, thresholds are averaged across the four subjects with error bars representing standard deviations. The values of N_{eq} (in dB/Hz) are shown on the horizontal axes below the corresponding notch.

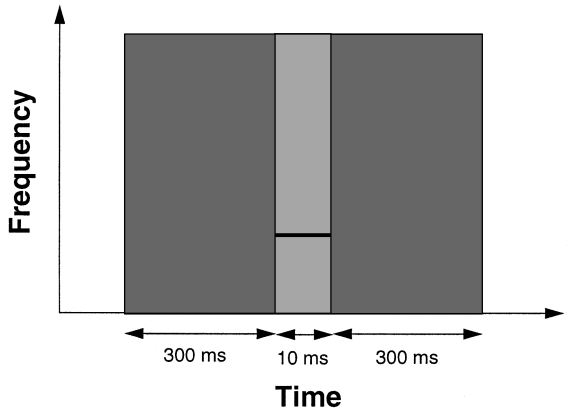

FIG. 5. Schematic spectrogram of the stimuli in experiment 2. A 10-ms tone and a flat, simultaneous masker of spectrum level, N_{eq}, are surrounded by two 300-ms white-noise maskers, each with a spectrum level of 36 dB/Hz. Tone frequencies are either 0.6 kHz or 2 kHz.

Thresholds with a flat-noise simultaneous masker are lower than those with a notched-noise masker. Despite a similar combination of simultaneous and nonsimultaneous masking, thresholds for experiment 2 are as much as 20 dB less than those for experiment 1. Therefore, no simple combination of simultaneous and nonsimultaneous masking predicts both results.

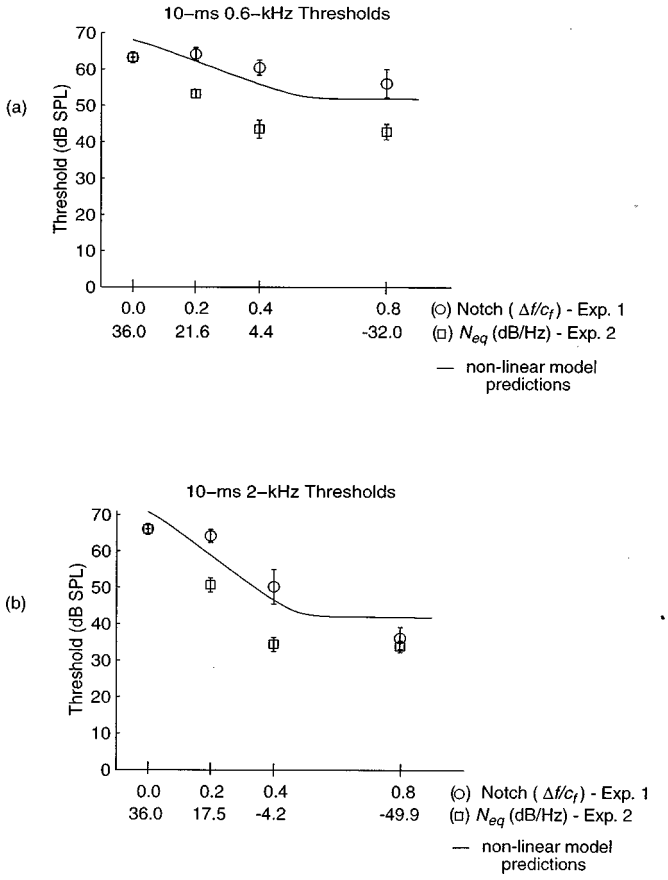

FIG. 6. Mean results of experiments 1 and 2: (a) 0.6-kHz, 10-ms tone thresholds for experiments 1 and 2 are denoted by the circles and squares, respectively. Thresholds are averaged across four subjects with error bars representing standard deviations. The values of N_{eq} (in dB/Hz) are shown on the horizontal axis below the corresponding notch. The solid line shows the threshold predictions of the nonlinear model. (b) Same as (a), at a center frequency of 2 kHz.

V. DISCUSSION

Our goal is to model the perception of short-duration speech sounds in a noise context. Toward that end, a traditional measure of frequency selectivity, the notched-noise experiment (Patterson, 1976), was reproduced in a noise context and at varying durations. The forward- and backward-masking components introduced by the surrounding noise were found to increase thresholds, especially at shorter durations, wider notch widths, and the lower center frequency. In an attempt to evaluate the suitability of ''standard'' psychoacoustic models, threshold predictions from a traditional filtering model with either a linear or nonlinear combination of simultaneous and nonsimultaneous masking were fit to these data. In a second experiment, each notched noise was replaced by a flat noise that was assumed to provide the same simultaneous masking. Thresholds were much lower with the flat noise, implying that no simple combination of masking can predict results from both experiments.

Instead, we are left to conclude that the spectral shape of the simultaneous masker influences the interaction with nonsimultaneous maskers. This result is not inconsistent with previous work that parameterized the perception of short-duration sounds in broadband noise as a reduction of usable frequency selectivity (Hant *et al.*, 1997). With such a reduction, threshold predictions for experiment 1 increase, as the tone is not as well separated from the simultaneous notch. Similarly, if ''overly sharp'' frequency selectivity estimations were used to set the noise level in experiment 2, then the amount of simultaneous masking would be lower than in experiment 1, and lower thresholds would be expected. Another pilot experiment using a narrow-band noise signal and a two-tone simultaneous masker, also surrounded in a noise context, provided a similar result.

One difficulty is defining a mechanism that reproduces these trends. An interaction between suppression and nonsimultaneous masking might appear likely. However, an interaction between the spectral shape of the simultaneous masker and a backward masker has been measured (see Fig. 12 in Hant *et al.*, 1997). Figure 7 replots these data with those from experiment 1 and shows similar trends. If suppression is considered nearly instantaneous, then there is little time for interaction with an extremely weak backward masker.

These results might still be partially attributed to an interaction of peripheral mechanisms, if 2-D differences in time-varying excitation patterns produced by an auditory model with adapting compression are considered. Similarly, at a higher level in the auditory system, thresholds might be predicted if we consider masking as the corruption of an evolving statistical estimate of the signal. Shorter durations and surrounding noise may hinder such statistical estimates.

Another strong possibility is that auditory perception is more readily characterized by the response to *changes* across time and frequency, than by the response to stationary stimuli. If so, then the extent of coherent changes across one dimension could influence the ability to detect changes in the other. For example, in experiment 1, as the duration of the notch increases, the ability to detect the spectral change

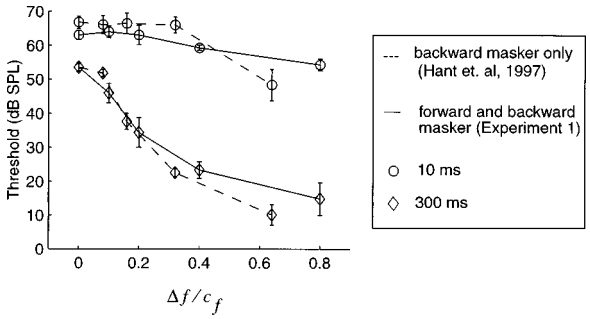

FIG. 7. Replot of the results of experiment 1 with those of a pilot notched-noise experiment from Hant *et al.* (1997). The pilot experiment was similar to experiment 1 except that the tone and notch were only followed by backward-masking noise. Thresholds from the pilot experiment, which was conducted at a center frequency of 1 kHz and relative notch widths of 0.08, 0.16, 0.32, and 0.64, are denoted by the dashed lines. 0.6-kHz thresholds from experiment 1 are denoted by the solid lines. Tone (and notch) durations are delineated by the circles (10 ms) and diamonds (300 ms). Thresholds for both experiments, are averaged across the same two subjects (JH and BS), with standard deviations represented by the error bars.

caused by the presence of the tone improves, and thresholds drop.

A similar approach may explain the discrepancy between experiments 1 and 2. In experiment 2, transients preceding and following the tone extended over a wider frequency range than in experiment 1. Well-correlated wide-bandwidth transients may have cued subjects to the low-energy valley of the masker, helping them locate ''when'' to listen for the tone and thus, lowering thresholds (Buus, 1985). However, in the 0.6-kHz 0.8-notch condition, large differences in the thresholds of experiments 1 and 2 are measured. Previous CMR data (Hall *et al.*, 1984) do not support significant decreases in threshold when the transient bandwidth increases beyond that of the 0.8 notch. Regardless, interpreting the current data in terms of ''listening to the valleys'' is difficult because the ''valleys'' in experiments 1 and 2 have different depths and unlike previous CMR studies, there's only one ''valley.'' More experiments are necessary.

Predicting the discrepancy between our results and those of Moore *et al.* (1987) and Wright and Dai (1994) also remains a significant challenge. Clearly, the addition of nonsimultaneous noise (in the spectral region of the signal) degrades our ability to perceive short-duration signals. However, the nature and time course of this degradation are still not known. Additional psychoacoustic measurements, both in a noise context and using a wider range of time-varying stimuli, will help characterize what appears to be a time-varying process and should constrain the modeling possibilities.

We can conclude, however, that a classical filtering model with either a linear or nonlinear combination of simultaneous and nonsimultaneous masking does not directly predict the current data. These models are therefore inadequate to predict the perception of short-duration speech signals in a noise context.

ACKNOWLEDGMENTS

We thank our subjects for their cooperation. We would also like to thank R. Shannon and two anonymous reviewers

for their helpful comments. This work was supported in part by NIH-NIDCD Grant No. 1 R29 DC 02033-01A1 and by the Whitaker Foundation.

Buus, S. (**1985**). ''Release from masking caused by envelope fluctuations,'' J. Acoust. Soc. Am. **78**, 1958–1965.

Glasberg, B. R., and Moore, B. C. (**1990**). ''Derivation of auditory filter shapes from notched noise data,'' Hearing Res. **47**, 103–138.

Green, D. M. (**1967**). ''Additivity of masking,'' J. Acoust. Soc. Am. **41**, 1517–1525.

Dau, T., Puschel, D., and Kohlrausch, A. (**1996**). ''A quantitative model of the ''effective'' signal processing in the auditory system. I. Model structure,'' J. Acoust. Soc. Am. **99**, 3615–3622.

Hall, J. W., Haggard, M. P., and Fernandes, M. A. (**1984**). ''Detection in noise by spectro-temporal pattern analysis,'' J. Acoust. Soc. Am. **76**, 50–56.

Hant, J., Strope, B., and Alwan, A. (**1997**). ''A psychoacoustic model for the noise masking of voiceless plosive bursts,'' J. Acoust. Soc. Am. **101**, 2789–2802.

Humes, L., and Jesteadt, W. (**1989**). ''Models of the additivity of masking,'' J. Acoust. Soc. Am. **85**, 1285–1294.

Jesteadt, W., Neff, D. L., and Kessler, C. J. (**1996**). ''Combinations of forward and backward masking revisited,'' J. Acoust. Soc. Am. **100**, 2593.

Levitt, H. (**1971**). ''Transformed up–down methods in psychoacoustics,'' J. Acoust. Soc. Am. **49**, 467–477.

Moore, B. C., Poon, P. W., Bacon, S., and Glasberg, B. (**1987**). ''The temporal course of masking and the auditory filter shape,'' J. Acoust. Soc. Am. **81**, 1873–1880.

Oxenham, A. J., and Moore, B. C. (**1994**). ''Modeling the additivity of nonsimultaneous masking,'' Hearing Res. **80**, 105–118.

Oxenham, A. J., and Moore, B. C. (**1995**). ''Additivity of masking in normally and hearing impaired subjects,'' J. Acoust. Soc. Am. **96**, 1921–1934.

Patterson, R. D. (**1976**). ''Auditory filter shapes derived by noise stimuli,'' J. Acoust. Soc. Am. **59**, 640–654.

Penner, M. J. (**1980**). ''The coding of intensity and the interaction of forward and backward masking,'' J. Acoust. Soc. Am. **67**, 608–616.

Wright, B., and Dai, H. (**1994**). ''Detection of unexpected tones with short and long durations,'' J. Acoust. Soc. Am. **95**, 931–938.

Zwislocki, J. J. (**1969**). ''Temporal summation of loudness: An analysis,'' J. Acoust. Soc. Am. **46**, 431–441.

Syllabic strength and lexical boundary decisions in the perception of hypokinetic dysarthric speech

Julie M. Liss and Stephanie Spitzer
Motor Speech Disorders Laboratory, Arizona State University, Box 871908, Tempe, Arizona 85281

John N. Caviness, Charles Adler, and Brian Edwards
Department of Neurology, Mayo Clinic-Scottsdale, 13400 Shea Boulevard, Scottsdale, Arizona 85259

(Received 13 August 1997; revised 19 May 1998; accepted 30 June 1998)

This investigation evaluated a possible source of reduced intelligibility in hypokinetic dysarthric speech, namely the mismatch between listeners' perceptual strategies and the acoustic information available in the dysarthric speech signal. A paradigm of error analysis was adopted in which listener transcriptions of phrases were coded for the presence and type of word boundary errors. Seventy listeners heard 60 phrases produced by speakers with hypokinetic dysarthria. The six-syllable phrases alternated strong and weak syllables and ranged in length from three to five words. Lexical boundary violations were defined as erroneous insertions or deletions of lexical boundaries that occurred either before strong or before weak syllables. A total of 1596 lexical boundary errors in the listeners' transcriptions was identified unanimously by three independent judges. The pattern of errors generally conformed with the predictions of the Metrical Segmentation Strategy hypothesis [Cutler and Norris, J. Exp. Psychol. **14**, 113–121 (1988)] which posits that listeners attend to strong syllables to identify word onsets. However, the strength of adherence to this pattern varied across speakers. Comparison of acoustic evidence of syllabic strength to lexical boundary error patterns revealed a source of intelligibility deficit associated with this particular type of dysarthric speech pattern. [S0001-4966(98)03410-9]

PACS numbers: 43.71.Gv [WS]

INTRODUCTION

Speech intelligibility is central to the diagnosis, treatment, and study of dysarthria. However, speech intelligibility is not a unitary construct, and it is not a simple byproduct of the quality or clarity of the speech signal. Estimates of speech intelligibility depend on how the speaker talks, on what he or she is saying, and on who is doing the listening (Connolly, 1986; Weismer and Martin, 1992; Yorkston and Beukelman, 1978, 1980a; Yorkston *et al.*, 1990).

As a result of this complexity, research on intelligibility in dysarthria has taken a variety of forms. At one end of the continuum are those investigations of the causal relationship between acoustic information in the dysarthric speech signal and the perceptual consequences of this information, particularly at the single-word level (Kent *et al.*, 1989; Tikofsky *et al.*, 1966; Yorkston and Beukelman, 1980a). Other studies have explored message and listener effects on measures of intelligibility in dysarthria, primarily in connected speech (e.g., Dongilli, 1994; Hammen *et al.*, 1991; Garcia and Cannito, 1996; Tjaden and Liss, 1995; Yorkston and Beukelman, 1980b). Taken together, these studies have delineated a wide range of variables that may affect estimates of intelligibility in dysarthria. They also have highlighted the conceptual gap between studies of single-word and connected speech perception, leading to conclusions such as those of Weismer and Martin (1992): ''The explanatory principles that are emerging from the study of single-word intelligibility are likely to be quite different than those that will be discovered in the study of sentence intelligibility'' (p. 67).

The present report is the first of a series of studies that adopts a different vantage point than those of previous investigations: the interface between the speech signal and the listener's response to that signal (see Lindblom, 1990). Our studies examine evidence of the perceptual strategies listeners use to decipher the impoverished dysarthric speech signal, and how certain aspects of the dysarthric speech signal affect these perceptual strategies. To address these issues, we selected a paradigm that would allow us to consider jointly speaker and listener variables in the identification of word boundaries in dysarthric connected speech. This task, although seemingly effortless under normal circumstances, is perhaps the single most important process in the perception of connected speech (Cutler and Norris, 1988; Gow and Gordon, 1995; Quene', 1992). Words must be extracted from the continuous acoustic stream for lexical access, and thus speech perception, to occur. No research to date has directly examined the special challenge that dysarthria poses to the task of lexical segmentation in connected speech, although it has been suggested that listeners modify their perceptual strategies when faced with impoverished acoustic signals (Forster, 1989; Marslen-Wilson, 1989; McQueen, 1991; Pisoni and Luce, 1986). If we can identify a mismatch between perceptual strategies and the available acoustic information, we will have learned something about the source or nature of intelligibility deficit. This is in contrast to other studies of intelligibility that regard listener perception as the tool or metric by which speaker performance is assessed.

The paradigm used here to study lexical segmentation of dysarthric speech derives from a model of normal speech perception, termed the Metrical Segmentation Strategy (MSS; Cutler and Butterfield, 1992; Cutler and Norris,

1988). This model has produced a growing body of evidence suggesting that listeners exploit syllabic strength, specifically the juxtaposition of strong and weak syllables, to parse the continuous acoustic stream into its component words. According to this model, strong syllables are those that contain full vowels and that may or may not receive prosodic stress, and weak syllables contain reduced vowels and do not receive prosodic stress[1] (Cutler and Butterfield, 1990, 1991; Cutler and Carter, 1987; Fear *et al.*, 1995; Smith *et al.*, 1989). Central to the MSS hypothesis is the assumption that segmentation of the speech signal is activated by the occurrence of a strong syllable (Cutler and Norris, 1988; Grosjean and Gee, 1987)

Support for the MSS hypothesis is found in the statistical probabilities of syllabic strength in the English language, as well as in perception and production studies. Cutler and Carter (1987) determined that, in English, the occurrence of strong syllables is associated with 73% of word–initial syllables or single-syllable words. They reported that words with word–initial strong syllables are most frequently open-class words such as nouns, verbs, and adjectives; weak syllables are associated most often with second syllable placement or word–initial placement (including single-syllable words) in closed-class words, such as articles and pronouns (see also Cutler, 1993). Thus when listeners recognize strong syllables as word–initial, there is a high probability that they will be successful in their lexical segmentation.

In a specific test of the MSS hypothesis, Cutler and Butterfield (1992) presented listeners with phrases containing six alternating strong and weak syllables at a very low intensity, just above threshold. The pattern of errors evident in the listeners' transcriptions was as expected if they recognized strong syllables as word onsets: Listeners were more likely to incorrectly insert lexical boundaries before strong than weak syllables, and they were more likely to delete lexical boundaries before weak than strong syllables. Moreover, they found that the words following a lexical boundary inserted before a strong syllable were most often open class, and the words following a lexical boundary inserted before a weak syllable were most often closed class. This pattern of results suggests that the listeners attended to the relatively robust acoustic cues associated with strong syllables (Smith *et al.*, 1989).

If listeners indeed rely on syllabic strength to identify word boundaries, speech with reduced syllabic strength contrasts—such as that produced by some speakers with dysarthria—should reduce the effectiveness of this perceptual strategy. Evidence for this reduction in effectiveness would be apparent in the patterns of lexical boundary errors (LBEs) the listeners produce when deciphering such speech. Specifically, we would expect to see either a more even distribution of lexical boundary insertions and deletions between strong and weak syllables than has been shown to occur with normal degraded speech, or we would see a distribution that more closely aligns with the opportunities for these errors to occur.

Hypokinetic dysarthria was chosen as a test case for the present investigation because the principal perceptual speech characteristics, by definition, serve to diminish syllabic strength contrastivity: rapid speaking rate, monotony, monoloudness, and phoneme imprecision (Darley *et al.*, 1969). The perception of reduced syllabic strength contrasts in hypokinetic dysarthria is supported indirectly by acoustic studies that have examined segmental and suprasegmental characteristics. These include demonstrations of rapid speaking rate and short segment durations (Adams, 1991; Forrest *et al.*, 1989), reduced vowel formants and trajectories (Forrest *et al.*, 1989; Weismer, 1984), consonant imprecision (Logemann and Fisher, 1981; Weismer, 1991), and the vocal characteristics of monopitch, monoloudness, and reduced stress (Ludlow and Bassich, 1984; Ramig, 1992). Thus from both perceptual and acoustic standpoints, hypokinetic speech that possesses the cardinal constellation of symptoms listed above has reduced syllabic contrastivity.

The purpose of the present study was to examine the relationship between listeners' perceptual strategies and the nature of the dysarthric speech signal to determine whether evidence of a mismatch could be identified. The variables of interest were the quantity and location of LBEs produced by the listeners as they attempted to decipher a set of phrases marked by reduced syllabic strength contrastivity. The following questions were addressed: (1) Does this hypokinetic dysarthric speech elicit LBEs; (2) Do patterns of LBEs support or refute the MSS hypothesis and the listeners' apparent reliance on syllabic strength information to segment the acoustic stream; (3) To what extent do acoustic indices of reduced syllabic strength contrastivity correspond with the number and pattern of LBEs produced by the listeners.

I. METHOD

A. Listeners

Seventy graduate and undergraduate (63 females and 7 males) students primarily from the Speech and Hearing Science Department of Arizona State University served as listeners for this experiment. Their ages ranged from 21 to 50 years, with a mean age of 27 years. All listeners self-reported normal hearing and were native speakers of Standard American English. All listeners reported having little or no experience listening to dysarthric speech.

B. Speech stimuli

The goal of speaker selection was to obtain a group of speakers with hypokinetic dysarthria whose segmental and suprasegmental characteristics were highly similar (as per the operational definition of hypokinetic dysarthria herein), and who were at least moderately impaired in intelligibility on the stimulus phrases. Therefore, only speech characteristics at the time of recording the stimulus phrases were relevant to the purposes of the present investigation. The two certified speech-language pathologists associated with this study confirmed that all speakers who participated exhibited some degree of all components of the operational definition: perceptually rapid speaking rate with monopitch and monoloudness; little use of variation in pitch or loudness to achieve differential syllabic stress; imprecise articulation that gives the impression of a blurring of phonemes and syllables; and a breathy and perhaps hoarse/harsh voice. These percep-

TABLE I. Information on speakers with hypokinetic dysarthria.

Speaker[a]	Age	Years Post-Dx	H&Y	AIDS word	AIDS sentence
HF1	48	7.0	2	92%	96%
HF2	73	5.5	3	54%	45%
HF3	74	6.5	3	20%	24%
HM1	62	8.0	···	74%	70%
HM2	80	5.5	···	76%	58%
HM3	74	17.0	3.5	96%	88%
HM4	60	27.0	3	72%	91%

[a]Note. ''HF'' and ''HM'' refer to hypokinetic dysarthric female and male speakers, respectively. Speaker's ages and the number of years that have elapsed since their diagnoses of Parkinson's disease are presented in the first two data columns. The third data column contains the Hoehn and Yahr (Hoehn and Yahr, 1967) scores that were obtained by trained neurology personnel within six months of speech sample collection. Dashes indicate no score was obtained. The last columns contain the best of two scores for the word and sentence subtests of the *Assessment for Intelligibility of Dysarthric Speech* (Yorkston and Beukelman, 1981).

tual impressions were supported by comparisons of acoustic measures taken from the hypokinetic dysarthric speech samples and those from a group of a control speakers, as will be described later.

Thirty-three people were identified by their neurologists or speech-language pathologists as potential speakers for this study. Of these, 12 people were brought in to participate in recording based on their general speech characteristics and severity levels at the time of an initial telephone conversation with the first author. Five of these speakers who provided speech samples ultimately were not used in the investigation because of additional speech characteristics either not present or not noted during the initial telephone screening. These characteristics included the presence of a distinctive regional accent, a pervasive vocal tremor and oral dyskinesia, insufficient impairment of intelligibility, and the absence of one or more components of the operational definition of hypokinetic dysarthria. The seven remaining speakers (4 men, coded HM1–4; and 3 women, coded HF1–3), all who carried a primary diagnosis of Parkinson's disease, served as speakers in this investigation. Their ages ranged from 48 to 81 years, with a mean age of 67 years (see Table I).

Speech samples from a group of neurologically normal speakers who were similar to the dysarthric speakers in age also were collected. The acoustic measures derived from these control speech samples were compared to those of the hypokinetic samples to assess the perceptual impressions of reduced syllabic strength contrastivity among the speakers with hypokinetic dysarthria. The three women (coded F1–F3) were aged 79, 52, and 56 years, and the three men (coded M1–M3) were aged 47, 54, and 73 years. The mean age of the control group was 60 years. These speakers had no history or presentation of speech, language, or hearing disorders, and they exhibited no distinctive regional accents. Speech sample collection and data analysis procedures for these participants' speech samples were identical to those described herein for the speakers with hypokinetic dysarthria. As with all speakers of this investigation, the control group was blinded to the purpose of the study.

Speech samples were collected during a single hour-long session with each speaker. The protocol included the administration of the word and sentence subtests of the Assessment of Intelligibility of Dysarthric Speech (AIDS; Yorkston and Beukelman, 1981), the elicitation of several minutes of spontaneous speech, and the production of a set of stimulus phrases.[2] The phrases were modeled after those of Cutler and Butterfield (1992) and they were designed to have low interword predictability to reduce the contribution of semantic information to intelligibility. The 60 six-syllable phrases alternated strong (S) and weak (W) syllables, such that half of the phrases contained an SWSWSW phrasal stress pattern, and the other half contained a WSWSWS phrasal stress pattern. In addition to the phrasal stress distinction, the vast majority of strong and weak syllables contained full and reduced vowels, respectively. The phrases ranged in length from three to five words, and no word contained more than two syllables. None of the words in the phrases was repeated except articles and auxiliary verbs; and all English phonemes except /ʒ/ were represented. For the purposes of the larger investigation, a portion of the phrases contained words that were deemed to have political connotation—these words have no particular import for the present study.

Digital audio recordings of the speech protocol were made in a sound-damped booth with an initial microphone-to-mouth distance of 8 in. A Panasonic SV-3700 digital audio tape recorder, a Microtech Gefell GMBH condenser microphone mounted on a stand, a Mackie 1202 mixer, and high quality digital audio tapes were used to record the speech samples. Recording levels were monitored closely. A digital Tenma 72-860 sound level meter was used to measure sound pressure level at the microphone during each speaker's sustained /a/ and connected speech, both prior to recording and at intervals during the session. When the maximum levels obtained by a speaker did not reach a minimum of 65 dB SPL at the microphone, the microphone was moved incrementally toward the mouth. No microphone-to-mouth distance was less than 5 in., none was more than 8 in. The average maximum sound pressure level for the hypokinetic dysarthric speakers across phrase productions was 73.7 dB SPL at the microphone, with a standard deviation of 5.4; the normal control speakers averaged 76.1 dB SPL with a standard deviation of 5.5. Throughout recording, the LED voltage indicator on the DAT recorder was monitored continuously to insure an identical peak voltage range for each phrase or production. For the production of the stimulus phrases, speakers were encouraged to produce them in their ''normal, conversational voice.'' All intelligibility test words and sentences and stimulus phrases were printed in large bold print on 8 $\frac{1}{2}$ by 11 in. cards and were read aloud by the speakers.

Each production of the phrases was low-pass filtered at 10 kHz, digitized at a 22-kHz sampling rate and stored in a computer file using CSpeech Laboratory Automation System (Milenkovic and Read, 1992). Each speaker typically produced four iterations of each stimulus phrase during the course of speech sample collection. The first token which contained no word omissions, substitutions, dysfluencies, or interword pauses, and which most closely represented our operational definition of hypokinetic dysarthria was selected as the experimental token. The 60 phrases per speaker were

then downloaded on to DAT audiocassettes for use in the perceptual experiment, and saved in computer files for acoustic analysis.

Seven listening tapes for the hypokinetic speakers were created. Each tape contained one production of the 60 phrases in identical order to evenly distribute any practice effects that may have accrued over the course of the listening task. Each tape contained contiguous productions from 3 speakers, the first 20 from 1 speaker, 21–40 from another speaker, and 41–60 from a third speaker. Thus each speaker's 60 phrases were distributed across 3 different tapes, such that 30 listeners (10 listeners in each tape group) would hear and transcribe the productions of each of the 7 speakers. This provided an opportunity to identify any group of listeners which may have performed significantly better or worse than any other group. Phrases were preceded by the phrase number (1–60) spoken by a neurologically normal female, and followed with a 12-s interstimulus silent interval. The subjective recording quality was judged to be high and signal intensity consistent across speakers and phrases. Identical procedures were used for the creation of listening tapes for the control speech samples. These tapes were used in the present investigation only for acoustic analysis and not LBE assessment because the normal speech was found to elicit only a negligible number of LBEs from among listeners.

To obtain acoustic evidence of the perceived decreased syllabic strength contrasts, all of the 420 digitized hypokinetic phrases (60 phrases×7 speakers) used in the listening experiment were subjected to the following acoustic measures: phrase duration, $F0$ and amplitude variation within and between phrases, and first and second formant frequencies of selected strong vowels across the phrases. Although these measures were not conducted on consecutive strong and weak syllables, they were meant to capture global reductions in prosody and vowel working space, particularly as compared to the measures from the control phrases. Reductions in phrase duration, $F0$ and amplitude variation, and vowel working space relative to the normal controls were regarded as support for the perceived characteristics of rapid speaking rate, monotony, and reduced vowel contrastivity, respectively. The same measures from the 360 phrases of the control group (60 phrases×6 speakers) were used as a source of comparison.

All acoustic measures were accomplished using the software CSpeech (Milenkovic and Read, 1992). Phrase duration was obtained during the initial editing of the phrases by placing cursors on the first and last acoustic evidence of phonemes on the spectrographic display. This included the first or last glottal pulse in the case of initial or final voiced phonemes, respectively; the beginning or end of noise energy in the case of initial or final fricatives; and the beginning or end of the of the burst release in the case of initial or final stop consonants. One hundred milliseconds of silence was then appended to the beginning and end of each phrase to reduce onset–offset effects and the entire screen was saved as a digital file for all subsequent acoustic analysis.

Fundamental frequency ($F0$) and its variation within each digitized phrase was computed automatically using the short-term autocorrelation function with center clipping. All pitch traces were inspected visually to identify and edit tracking errors which occurred in this set of phrases. The majority of tracking errors consisted of brief regions of pitch doubling that required interpolation. Approximately 10% of the phrases that required hand-editing were remeasured by a second judge to calculate interjudge reliability. One hundred percent of the interjudge differences were less than 7 Hz; 70% of these were less than 3 Hz. The rms amplitude envelope of each phrase was converted automatically to mean decibels and variation around the mean was calculated. Frequency and amplitude data were saved in computer files for the automated calculation of across-speaker values.

First and second formant frequencies were measured at the temporal midpoints of seven occurrences of the vowels /i/, /æ/, /a/, and /u/, using both broadband spectrograms and LPC displays. The vowels were taken from the strong syllables of the following words: ''teacher, release, legal, impeach, veto, appear,'' and ''eager'' for /i/; ''ballot, taxes, catch, batch, rally, attack,'' and ''fast'' for /æ/; ''congress, lobby, water, follow, solid, proper,'' and ''models'' for /a/; and ''choose, soon, nuisance, new, assume, remove,'' and ''include'' for /u/. A total of 364 vowels were measured (4 vowels×7 instances×7 hypokinetic and 6 control speakers). Means and standard deviations were used to create $F1-F2$ plots to define the vowel quadrilaterals for each speaker, and geometric area values were calculated by summing the areas of the two triangles created by bisecting each quadrilateral (see Fourakis, 1991; Turner *et al.*, 1995). Approximately 30% of the hypokinetic and 10% of the normal control vowels were remeasured and intrajudge reliability was found to be high and acceptable: 98% of the differences between the original and second measures of $F1$ were less than 20 Hz; 93% of the differences between the original and second measures of $F2$ were less than 40 Hz. Interjudge reliability was calculated on approximately 20% of all vowel measurements and also was found to be acceptable: 84% of the differences between the original and second measures of $F1$ were less than 20 Hz; 80% of the differences between the original and second measures of $F2$ were less than 40 Hz. Inter- and intrajudge differences that exceeded 40 Hz for $F1$ and 60 Hz for $F2$, which all occurred in the dysarthric samples, were reassessed and modified as appropriate.

Severity of speech intelligibility impairment was estimated by performance on the word and sentence subtests of the AIDS, as scored by two naive judges. The mean difference between the two judges' scores was 10% for both the word and sentence subtests. The highest score obtained by either of the judges for each subtest was used as an index of best case speaker intelligibility (see Table I).

Phrase duration measures support the perceptual impression of rapid rate among these speakers with hypokinetic dysarthria. Figure 1 shows the mean phrase duration and standard deviation for each of the hypokinetic dysarthric and control speakers. All but one of the speakers with hypokinetic dysarthria exhibited more rapid phrase production than any of the normal controls (HF1).

To visually compare mean intraphrase $F0$ and intensity variations across speakers and between speaker groups, coefficients of variation were calculated by dividing each stan-

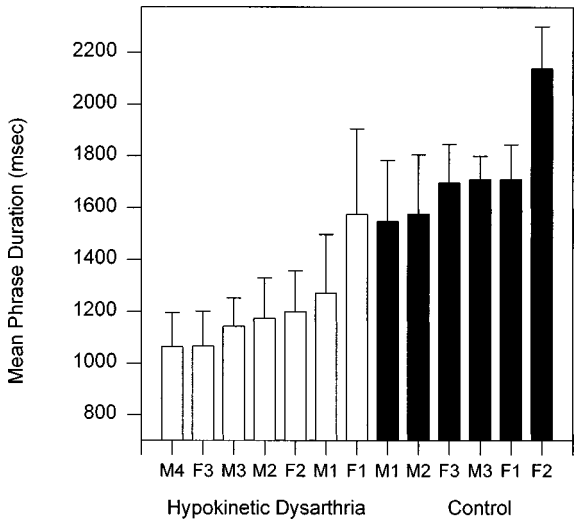

FIG. 1. Mean phrase durations are shown for all speakers. Error bars indicate one standard deviation about the mean. The open bars represent the speakers with hypokinetic dysarthria (H); the filled bars represent the means of the control speakers (C). The M and F preceding speaker numbers refer to male and female, respectively.

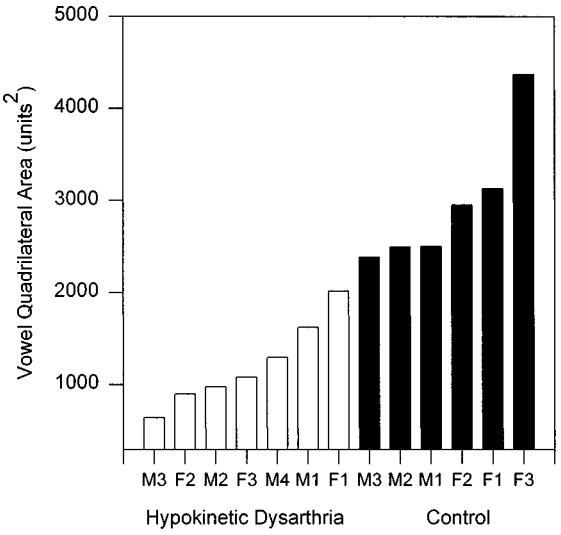

FIG. 3. Geometric areas of vowel quadrilaterals, expressed in units^2, were constructed from the mean $F1$ and $F2$ formant values. Open bars represents the speakers with hypokinetic dysarthria (H); the filled bars represent the means for the control speakers (C). The M and F preceding speaker numbers refer to male and female, respectively.

dard deviation by its mean. These values are plotted in Fig. 2 where the filled and unfilled circles represent data for the control and hypokinetic groups, respectively. Coordinates toward the upper right of the graph are associated with greater degrees of prosodic variation within phrases; those toward the lower left are associated with lesser degrees of prosodic variation. Thus control speakers M2 and F3 exhibited the greatest prosodic variation, and hypokinetic speakers HM2 and HF2 exhibited the least. The $F0$ variation appears to capture the majority of group difference, however, in that the means all speakers with hypokinetic dysarthria except $F1$ fall to the left of the control speakers. This corresponds favorably with the perception of monotony among the hypokinetic phrases.

The perceptual impression of reduced vowel strength

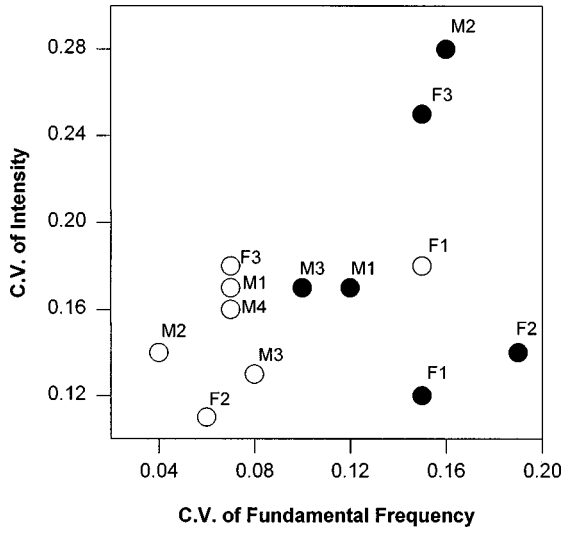

FIG. 2. Coefficients of variation for $F0$ are plotted as a function of coefficients of variation for intensity for all speakers. The open circles represent speakers with hypokinetic dysarthria; the filled circles represent the control speakers.

contrasts in the hypokinetic phrases is supported by the measures of vowel working space, namely the geometric area occupied by the vowel quadrilateral derived from vowels in strong syllables. This measure offers an estimate of the ''outer limits'' of the vowel working space for this set of phrases. By inference, smaller working spaces may be related to less capacity for strong–weak distinctions because the strong vowels are closer to ''reduced.'' Figure 3 contains the geometric area values derived from each speaker's vowel quadrilateral. All of the quadrilaterals from the hypokinetic dysarthric vowels were smaller than those of the control phrases—there was virtually no overlap between members of the two groups.

To summarize, this group of speakers with hypokinetic dysarthria produced stimulus phrases that were perceptually rapid, monotonous, and lacking in syllabic strength contrastivity. These perceptual impressions are supported by the associated acoustic measures as they compare to those of a group of control speakers.

C. Procedures

Ten listeners were randomly assigned to transcribe each of the seven tapes. Their task was to listen to each phrase and to write down exactly what they heard. They were told that all phrases consisted of real words in the English language, and they were encouraged to guess if they did not know what the speaker was saying.

The listeners were seated in individual cubicles. The audio tapes were presented via the Tandberg Educational sound system in the ASU Language Laboratory over high quality Tandberg supra-aural headphones. Equivalent sound pressure levels across headphones were verified with a headphone coupler sound level meter (Quest 215 Sound Level Meter). Listeners were instructed to adjust the volume to a comfortable listening level (in 4-dB increments up or down) during the preliminary instructions. They were directed not

TABLE II. Examples of coding lexical boundary errors from the listeners' transcriptions.

Target phrase	Listener response	Error type[a]
amend the slower page	I'm in the slower page	IS
she describes a nuisance	see this guy's a nuisance	IS
they repaired the veto	baby pass the veal	IS
ballot formal circles	battle for all circles	IW
answer dying temper	that's his dying panther	IW
wait beyond the mention	way beyond dementia	DS
watch him join the caucus	____ enjoy the carcass	DS
sticks are best for pencils	pigs are ____ eventful	DS
soon the men were asking	sooner men were asking	DW
test a law for methods	test for other methods	DW

[a]Note. IS refers to insertion of a lexical boundary before a strong syllable; IW refers to insertion before a weak syllable. DS and DW refer to deletions of lexical boundaries before strong and weak syllables, respectively.

to alter the volume once the stimulus phrases had begun. The listeners transcribed three practice phrases which were read by a neurologically normal female speaker. Listeners who made more than one word-transcription error in the practice phrases were not eligible for the study. Only one listener was excluded by this criterion.

D. Analysis

Three trained judges independently coded the listener transcripts for the presence and type of LBEs. Lexical boundary violations were defined as erroneous insertions or deletions of lexical boundaries. These insertions or deletions were coded as occurring either before strong or before weak syllables (as determined by the target phrasal stress pattern of the phrase, SWSWSW or WSWSWS). Thus four error types were possible and each phrase had the possibility of containing more than one LBE. Examples from the actual transcripts are provided in Table II.

The 60 phrases consisted of 360 syllables, 60 of which were phrase–initial syllables and were therefore not subject to LBEs. Of those 300 nonphrase–initial syllables, 102 were word–initial strong syllables; 80 were word–initial weak syllables; 48 were nonword–initial strong syllables; and 70 were nonword–initial weak syllables. The occurrence of each word–initial strong syllable in the target corresponded to the opportunity for the deletion of a lexical boundary before a strong syllable. Similarly, word–initial weak syllables corresponded to the opportunity for the deletion of a lexical boundary before a weak syllable; nonword–initial strong syllables to the opportunity for an insertion of a lexical boundary before a strong syllable; and nonword–initial weak syllables to the opportunity for an insertion of a lexical boundary before a weak syllable. Thus the opportunities for producing the different types of LBEs were not equal, but are representative of the opportunities generally available in the English language (Cutler and Carter, 1987). The proportions of opportunities across the series of phrases are shown in Table III.

The codes generated for each speaker by the three judges were merged into one composite data set that reflected instances in which there was 100% agreement among the judges. Twenty-four LBE decisions were discarded due to interjudge disagreement. The number, type (insertion or deletion), and location (before strong or before weak syllables) was then tallied for each speaker and for the group. The errors also were analyzed for the distribution of open- and closed-class words following the insertion of a lexical boundary. All words following the insertion of a lexical boundary were classified as open, closed, or nonclassifiable in the case of nonword responses.

TABLE III. Proportions of possible lexical boundary error sites based on syllable position.

	Syllable position			
	Word–Initial		Nonword–Initial	
Error type	Strong	Weak	Strong	Weak
Deletions	34.00%	26.67%	N/A[a]	N/A[a]
Insertions	N/A	N/A	16.00%	23.33%

[a]Note. N/A refers to the fact that lexical boundary deletions cannot occur in nonword–initial syllable positions, and that lexical boundary insertions cannot occur in word–initial syllable positions. Phrase–initial syllables were excluded from the count because they are not subject to LBEs.

Chi-square analyses were performed to determine the relationship between the variables of insert/delete and strong/weak, and between the variables open/closed class and insertion before strong/weak syllables. Spearman Rank Order Correlation analyses were performed to assess the strength of the speaker-rank relationships between LBE patterns and acoustic measures.

II. RESULTS

A. Lexical boundary error incidence

The first finding of this investigation is that the hypokinetic speech samples elicited many LBEs from the listeners. In all, 1596 LBEs were identified unanimously by the three independent judges. The data columns of Table IV contain values from the coded listener transcripts. The number of phrases (out of 420 total) for which listeners provided no response whatsoever ranged from 9 to 75. The percentage of words transcribed correctly ranged from 18.3% to 64.9%. The number of phrases transcribed entirely correctly for each speaker ranged from 1 to 157. The number of LBEs elicited by each speaker ranged from 151 to 317, with a mean of 228 (s.d.=71.2).

B. Lexical boundary error pattern

The second finding is that the pattern of LBEs supports the MSS hypothesis. Of the total 1596 errors identified, there were nearly three times as many insertion as deletion errors. Of these, 47% were insertions of a lexical boundary before a strong syllable, 27% were insertions before weak syllables, 10% were deletions before strong syllables, and 15% were deletions before weak syllables. Pattern strength can be expressed as two ratios, IS–IW and DW–DS. Ratio values of ''1'' indicate that insertions and deletions occur equally as often before strong and weak syllables: the greater the positive distance from ''1,'' the greater the strength of adherence to the predicted pattern. For the present data, insertion errors

TABLE IV. Listener performance on phrase transcription task by speaker. Note. The first column contains number of phrases for which listeners provided no response. The second column contains the percentages of words-correct in the 60 stimulus phrases. Column 3 contains the number of phrase transcriptions that were entirely correct. The fourth column contains the absolute number of LBEs produced for each speaker.

Speaker	No response	% Words-correct	# Phrase correct	# LBEs
HF1	11	64.9%	157	161
HF2	75	18.3%	1	317
HF3	49	26.7%	11	286
HM1	25	57.5%	132	151
HM2	9	47.7%	66	227
HM3	18	60.0%	132	161
HM4	21	43.9%	70	293

occurred 1.7 times more often before strong than before weak syllables, and deletion errors occurred 1.5 times more often before weak than before strong syllables. A chi-square analysis indicated a significant interaction between the variables of insert/delete and strong/weak [$\chi^2(1,N=4)=67.3$, $p<0.0001$].

Also, the majority of the post-boundary words created by the insertion of a lexical boundary before a strong syllable were open-class words (73.7%), and the majority of the words created by the insertion of a boundary before a weak syllable were closed-class words (74%). A chi-square analysis revealed a significant interaction between the variables of open/closed class and strong/weak syllables [$\chi^2(1,N=4)=281.8$, $p<0.0001$].

This general pattern of LBEs for the group also held for each of the seven speakers. The first four data columns of Table V contain the percentages of error types out of the total errors elicited by each of the speakers. In accordance with MSS hypothesis predictions, insertions were more common before strong than before weak syllables; and deletion errors were more common before weak than before strong syllables. The final column of this table expresses the strength of these error patterns with IS–IW ratio values:[3] Lexical boundary insertions before strong syllables outnumbered those before weak syllables by 2.70 to 1.38 times. Thus although all speakers elicited the general pattern of LBEs predicted by the MSS hypothesis, the pattern was stronger for some speakers than for others.

C. Lexical boundary error pattern and speech characteristics

The final question was the extent to which the acoustic evidence of reduced syllabic strength contrasts was associated with the listener performance patterns elicited by the seven speakers with hypokinetic dysarthria. Spearman correlation coefficients were calculated on the rank orderings of the speakers on the various measures of intelligibility; aspects of LBE patterns; and acoustic measures associated with syllabic contrastivity. This was meant to identify any intelligibility or acoustic measures that might be associated with LBE incidence or pattern strength.

The rankings of the word and sentence subtests of the *AIDS* were correlated strongly with the rankings of percent words-correct from the stimulus phrases, accounting for 79% and 56% of the variance, respectively. However, neither standard intelligibility ranking was associated strongly with that of the number of LBEs ($R=0.64$ and 0.43, for word and sentence subtests, respectively), nor with the IS–IW ratio ranking ($R=0.39$ and 0.46, respectively). Only one of the three acoustic measure rankings was associated strongly with measures of intelligibility and LBE pattern strength. The $F0$ variability ($CVF0$) and sentence subtest rankings were correlated at 0.71 ($p=0.05$). The $CVF0$ and IS–IW rankings were correlated at 0.93 ($p=0.00$).

Although the correlations of rankings provide some insight to the relationships among the variables of interest, it is the joint consideration of individual speaker patterns and LBE results that is most revealing. The speakers in this study fall roughly into three groups when the strength of the IS–IW ratio is examined. The high IS–IW ratio group consists of speakers HF1 and HM3 who also were the most intelligible, and elicited among the fewest LBEs. The low IS–IW ratio group consists of speakers HF2 and HM2 who were among the least intelligible of this group, and who produced among the greatest numbers of LBEs. The mid IS–IW ratio group consists of HF3, HM1, and HM4. Although more variable in their presentation, they obtained IS–IW ratio values in the narrow range of 1.6–1.8. Each group is addressed in turn.

The high IS–IW ratio group (HF1 and HM3) obtained high standard intelligibility scores, and elicited the highest percentages of words-correct on the stimulus phrases. Subjective impressions also support the conclusion that these two speakers had the highest levels of articulatory integrity of the group. The acoustic data for HF1 are consistent with the notion that strong–weak contrasts in her phrases were well marked. Her mean phrase durations were the longest of the hypokinetic speakers, and comparable to those of the fastest control speakers (Fig. 1). Her measures of $F0$ and amplitude variation placed her among the control speakers (Fig. 2), and her vowel quadrilateral was the largest of the

TABLE V. Distribution and type of lexical boundary errors elicited per speaker.

Speaker	% IS	% IW	% DS	% DW	IS–IW
HF1	55.28%	26.71%	8.70%	9.32%	2.03
HF2	43.85%	30.28%	9.78%	16.09%	1.44
HF3	49.65%	27.62%	10.84%	11.89%	1.78
HM1	50.33%	32.45%	5.30%	11.92%	1.56
HM2	37.44%	26.87%	11.89%	23.79%	1.38
HM3	55.90%	20.50%	11.18%	12.42%	2.70
HM4	44.71%	24.91%	11.95%	18.43%	1.78

hypokinetic speakers (Fig. 3). In contradistinction, evidence for the acoustic marking of syllabic strength contrasts for HM3 is not so apparent. His mean phrase duration was almost half that of HF1 (Fig. 1), and his vowel quadrilateral area was the smallest of the group (Fig. 3). The only positive factor was his high $CVF0$ ranking. Although substantially smaller than that of HF1, his was second highest for the group of hypokinetic speakers (Fig. 2). Thus despite equivalent LBE pattern evidence of relatively robust strong–weak syllabic distinctions, only one of the two speakers offered commensurate acoustic evidence.

The low IS–IW ratio group (HF2 and HM2) did not exhibit high levels of articulatory integrity based on their standard intelligibility scores, their percentages of words-correct on the stimulus phrases, and on subjective impressions. Acoustically, these speakers exhibited the least prosodic variation (see Fig. 2), and among the smallest vowel quadrilateral areas (see Fig. 3) of the group. Their mean phrase durations were short compared with those of the normal control, but they were in the middle of the range for the hypokinetic group (see Fig. 1). Thus the LBE pattern evidence of reduced syllabic strength contrasts was supported by the acoustic evidence for these two speakers.

Two of the mid IS–IW ratio group, HM1, and HM4, had very similar intelligibility profiles on both the standard measure and on the percent words-correct on the stimulus phrases. The third member, HF3, was the least intelligible. Acoustically, the three speakers had highly similar $CVF0$ values (Fig. 2), and they formed the midrange for vowel quadrilateral area (Fig. 3). The only acoustic measure that distinguished these speakers was phrase duration (Fig. 1): HM1 was the slowest male of the group, and HF3 and HM4 tied for the most rapid speakers. Interestingly, this corresponds with the number of LBEs elicited: HM1 elicited nearly half as many errors as HF3 and HM4.

III. DISCUSSION

The present report offers several new findings relevant to the study of speech perception and speech intelligibility. First, these hypokinetic speech samples elicited large numbers of LBEs. Also, like systematically degraded normal speech, the pattern of LBEs elicited by these hypokinetic dysarthric speakers generally is consistent with the predictions offered by the MSS hypothesis. The third and most critical finding is the evidence of diminished effectiveness of this strategy when syllabic strength contrasts were most reduced.

More than 1500 LBEs were identified in the transcribed phrases. Even speakers with high scores on the standard measures of word and sentence intelligibility elicited relatively large numbers of LBEs. Although there is no direct point of comparison, Cutler and Butterfield (1992) reported just 256 LBEs in their corpus of 864 phrase transcriptions evoked by normal speech presented at low listening levels. Their coding criteria were more stringent than those used in the present investigation, however, this cannot explain the magnitude of the discrepancy in the occurrence of LBEs. The answer may be related to the fact that degradation of normal speech results in a rather systematic and consistent manipulation of segmental and suprasegmental components. Dysarthric speech, in contrast, may vary more randomly on these dimensions, thereby providing more opportunities for lexical boundary misperceptions to occur. This question may be addressed by the evaluation of LBEs elicited by other types of dysarthria.

Having established the presence of LBEs, the next issue is that of error pattern. The primary hypothesis of this investigation was that a group of speakers who produced poor distinctions between strong and weak syllables would elicit lexical boundary error patterns that either are random, or closely aligned with the opportunity for such errors to occur. In other words, one would expect to see lexical boundary insertions distributed either equally often before strong and weak syllables, or more often before weak than before strong syllables. The opposite would be expected for lexical boundary deletions. This certainly was not the case. These data conformed precisely with the predictions of the MSS hypothesis: Lexical boundary insertions occurred most often before strong syllables and created open-class words; deletions occurred most often before weak syllables and created closed-class words. The conclusion must be, then, that listeners relied on some sufficient level of strong–weak syllabic contrastivity to make their lexical boundary decisions.

Investigations have provided evidence that, despite overall reductions in stress production, speakers with hypokinetic dysarthria are able to maintain relative stress distinctions. Ackermann and Ziegler (1991) measured sound pressure levels associated with syllable–initial stop consonants to estimate degree of articulatory closure in speakers with parkinsonian dysarthria. They reported greater degrees of articulatory closure for the initial stop consonants of stressed syllables as compared with those of unstressed syllables. Their interpretation was that, because of linguistic import, stressed syllables received articulatory attention at the expense of the unstressed syllables. Kinematic findings reported by Forrest and Weismer (1995) further support the notion of maintained stress contrasts in hypokinetic dysarthria. They documented reductions in movement amplitude and velocity for stressed syllables, and even greater reductions for unstressed syllables. It may be the case that the patterns of LBEs found in the present study conformed with the MSS hypothesis predictions because, although reduced, relative syllabic strong–weak contrastivity was maintained. However, there exists one critical difference between the present study and those of Ackermann and Ziegler, and Forrest and Weismer: All of our speakers and speech tokens (phrases) were selected because of the perceptual reductions in syllabic contrastivity, rather than the perceptual presence of correct stress, as was the case in the other two studies.

The present study indicates that the perceptual strategy of attending to syllabic strength was less effective for some speech samples than for others. This evidence is found in discrepancies in the IS–IW ratios, or the strength of pattern adherence. There exists in the literature no entirely comparable data base. However, Cutler and Butterfield (1992) report insertion and deletion values for a study of lexical boundary errors elicited by faint speech. The ratio values derived from their data indicated that insertion errors oc-

curred before strong syllables three times more often than before weak ones ($n=195$). Deletion errors before weak syllables outnumbered those before strong by nearly four times ($n=69$). In the present study these ratios were substantially lower, with an IS–IW ratio of 1.7 ($n=1180$), and a DW–DS ratio of 1.5 ($n=399$). At face value, this suggests that either the hypokinetic speech contained less strong-weak contrast information than the faint speech, or that the listeners in the present study attended less to the contrasts than did those of Cutler and Butterfield.

Support for the validity of the IS–IW ratio as an index of pattern adherence is found in the assessment of individual speaker data. From this assessment, three conclusions can be drawn. The first two are related: The rankings of IS–IW ratios were strongly associated with the rankings of *CVFO*; and the lowest IS–IW ratios were elicited by speakers with the most overall acoustic evidence of decreased syllabic contrastivity. An interpretation of the first finding is that larger variations in $F0$ within phrases correspond to larger prosodic distinctions between strong and weak syllables. When these strong and weak syllables are most perceptually distinctive, and when listeners use this distinction to motivate lexical segmentation, the IS–IW ratio is largest. Even though overall low performance on the acoustic measures was related to low IS–IW ratios, the rankings of these measures did not line up precisely with LBE pattern rankings. This may reflect the nonspecific nature of the measures of phrase duration and vowel space relative to syllabic strength. Relative durations of syllabic strength, specifically ratios of strong to weak durations, may be more valuable indicators of syllabic strength contrastivity in the temporal domain. Similarly, comparisons of strong to weak vowel formant data would provide information specific to vowel quality differences that were not presented here.

The final conclusion is that the speakers with highest measures of intelligibility elicited the highest IS–IW ratios, even when syllabic contrastivity apparently was most reduced (HM3). However, when measures of intelligibility were lower, the degree of syllabic contrastivity seemed to ''matter more'' for the IS–IW ratios. In other words, the IS–IW ratio appeared to be more vulnerable to decrement when articulatory integrity was most impaired. This supports the proposal of Cutler and Butterfield (1992) that, ''it is precisely under the conditions of phonetic uncertainty that rhythmic segmentation proves most useful'' (p. 233). In the present case, the listeners may rely on the rhythmic information when articulatory integrity is reduced, but their success is restricted by the available syllabic strength acoustic information.

The findings of this study must be viewed within the limitations of the methodology and design. First, syllabic strength was defined herein as a relative prosody-based entity with secondary vowel quality constituents. Although most of the strong and weak syllables of the stimulus phrases contain full and reduced vowels, respectively, not all do. If it were found that vowel quality has primary perceptual saliency for strong–weak distinctions, the findings of this study would have to be revisited (see Fear *et al.*, 1995). Second, as mentioned earlier, this study did not use relative intersyllabic measures to document the acoustic correlates of syllabic stress reductions. Because of the perceived reductions, it is expected that finer acoustic measures, such as strong–weak syllable duration ratios, will offer greater predictive value than the ones used here. Finally, individual listener patterns were not presented. Although all listener error patterns generally conformed to the group results, there was a range of performance across listeners. For example, some listeners appeared to be more vigilant than others in their transcription attempts, as evidenced by the number of ''no responses'' they produced. The design of the listening tapes did reduce potential listener effects by having each listener transcribe 20 phrases from three different speakers. However, the potential for different listening (and segmentation) strategies across the listeners should be considered.

IV. CONCLUSION

The examination of lexical boundary errors revealed that listeners attended to syllabic strength information to segment the connected hypokinetic dysarthric speech, just as they have been shown to do in the segmentation of normal speech. In general, adherence to the predicted pattern of errors was weakest for speakers with the greatest evidence of reduced syllabic contrastivity. This constitutes a mismatch between the perceptual strategy and the available acoustic information, and is therefore a source of intelligibility deficit for these speakers.

ACKNOWLEDGMENTS

This research was supported by research Grant No. 5 R29 DC 02672 from the National Institute on Deafness and Other Communication Disorders, National Institutes of Health. Gratitude is extended to the patients of the Mayo Clinic—Scottsdale who participated in this investigation, and to Shannon Beatty and Michele Marshall for their assistance on the project.

[1]This definition of syllabic strength is distinguished from that of prosodic phonology which holds that all strong syllables are stressed, and weak syllables are unstressed (Halle and Keyser, 1971). The relative importance of vowel quality versus prosodic stress in the perceptual designation of syllabic strength remains to be determined (Fear *et al.*, 1995; Gow and Gordon, 1995; van Ooijen *et al.*, 1997).

[2]The list of phrases is available electronically from the first author.

[3]Analogous data for the strength of deletion error patterns are not provided because of the relatively small numbers of deletion errors for several of the speakers. For example, speakers HF1, HM1, and HM3 elicited only 29, 26, and 38 deletion errors, respectively. These small numbers would render a comparison of DW–DS ratios across speakers difficult to interpret.

Ackermann, H., and Ziegler, W. (**1991**). ''Articulatory deficits in Parkinsonian dysarthria: An acoustic analysis,'' J. Neurol. Neurosurg. Psychiat. **54**, 1093–1098.

Adams, S. G. (**1991**). ''Accelerating speech in a case of hypokinetic dysarthria: Descriptions and treatment,'' in *Motor Speech Disorders: Advances in Assessment and Treatment*, edited by J. Till, K. Yorkston, and D. Beukelman (Paul H. Brookes, Baltimore), pp. 213–228.

Connolly, F. (**1986**). ''Intelligibility: A linguistic view,'' British Journal of Disorders of Communication **21**, 371–376.

Cutler, A. (**1993**). ''Phonological cues to open- and closed-class words in the processing of spoken sentences,'' Journal of Psycholinguistic Research **22**, 109–131.

Cutler, A., and Butterfield, S. (**1990**). ''Durational cues to word boundaries in clear speech,'' Speech Commun. **10**, 485–495.
Cutler, A., and Butterfield, S. (**1991**). ''Word boundary cues in clear speech: A supplementary report,'' Speech Commun. **9**, 335–353.
Cutler, A., and Butterfield, S. (**1992**). ''Rhythmic cues to speech segmentation: Evidence from juncture misperception,'' Journal of Memory and Language **31**, 218–236.
Cutler, A., and Carter, D. M. (**1987**). ''The predominance of strong syllables in the English vocabulary,'' Comput. Speech Lang. **2**, 133–142.
Cutler, A., and Norris, D. (**1988**). ''The role of strong syllables in segmentation for lexical access,'' J. Exp. Psychol. **14**, 113–121.
Darley, F., Aronson, A., and Brown, J. (**1969**). ''Differential diagnostic patterns of dysarthria,'' J. Speech Hear. Res. **12**, 246–269.
Dongilli, P. (**1994**). ''Semantic context and speech intelligibility,'' in *Motor Speech Disorders: Advances in Assessment and Treatment*, edited by J. Till, K. Yorkston, and D. Beukelman (Paul H. Brookes, Baltimore), pp. 175–192.
Fear, B. D., Cutler, A., and Butterfield, S. (**1995**). ''The strong/weak syllable distinction in English,'' J. Acoust. Soc. Am. **97**, 1893–1904.
Forrest, K., and Weismer, G. (**1995**). ''Dynamic aspects of lower lip movement in Parkinsonian and neurologically normal geriatric speakers' production of stress,'' J. Speech Hear. Res. **38**, 260–272.
Forrest, K., Weismer, G., and Turner, G. (**1989**). ''Kinematic, acoustic, and perceptual analyses of connected speech produced by Parkinsonian and normal geriatric adults,'' J. Acoust. Soc. Am. **85**, 2608–2622.
Forster, K. I. (**1989**). ''Basic issues in lexical processing,'' in *Lexical Representation and Process*, edited by W. Marslen-Wilson (MIT, Cambridge), pp. 75–107.
Fourakis, M. (**1991**). ''Tempo, stress and vowel reduction in American English,'' J. Acoust. Soc. Am. **90**, 1816–1827.
Garcia, J., and Cannito, M. P. (**1996**). ''Influence of verbal and nonverbal contexts on the sentence intelligibility of a speaker with dysarthria,'' J. Speech Hear. Res. **39**, 750–760.
Gow, D. W., and Gordon, P. C. (**1995**). ''Lexical and prelexical influences on word segmentation: Evidence from priming,'' J. Exp. Psychol. **21**, 344–359.
Grosjean, F., and Gee, J. (**1987**). ''Prosodic structure and spoken word recognition,'' Cognition **25**, 135–155.
Halle, M., and Keyser, S. J. (**1971**). *English Stress: Its Form, Its Growth, and Its Role in Verse* (Harper and Row, New York).
Hammen, V. L., Yorkston, K. M., and Dowden, P. (**1991**). ''Index of contextual intelligibility: Impact of semantic context in dysarthria,'' in *Dysarthria and Apraxia of Speech: Perspectives on Management*, edited by C. Moore, K. Yorkston, and D. Beukelman (Paul H. Brookes, Baltimore), pp. 43–53.
Hoehn, M. M., and Yahr, M. D. (**1967**). ''Parkinsonism: Onset, progression, and mortality,'' Neurology **17**, 427–442.
Kent, R., Weismer, G., Kent, J., and Rosenbek, J. (**1989**). ''Toward phonetic intelligibility testing in dysarthria,'' J. Speech Hear. Dis. **54**, 482–499.
Lindblom, B. (**1990**). ''Explaining phonetic variation: A sketch of the *H* and *H* theory,'' in *Speech Production and Speech Modeling*, edited by W. J. Hardcastle and A. Marchal (Kluwer Academic, Dordrecht, The Netherlands), pp. 403–439.
Logemann, J. A., and Fisher, H. B. (**1981**). ''Vocal tract control in Parkinson disease: Phonetic feature analysis of misarticulations,'' J. Speech Hear. Dis. **46**, 348–352.
Ludlow, C. L., and Bassich, C. J. (**1984**). ''Relationships between perceptual ratings and acoustic measures of hypokinetic speech,'' in *The Dysarthrias*, edited by M. R. McNeil, J. C. Rosenbek, and A. Aronson (College Hill, San Diego), pp. 163–195.
Marslen-Wilson, W. (**1989**). ''Access and integration: Projecting sound onto meaning,'' in *Lexical Representation and Process*, edited by W. Marslen-Wilson (MIT, Cambridge), pp. 3–24.
McQueen, J. (**1991**). ''The influence of the lexicon on phonetic categorization: Stimulus quality in word-final ambiguity,'' J. Exp. Psychol. **17**, 433–443.
Milenkovic, P. H., and Read, C. (**1992**). CSpeech (Version 4) [Computer software], Madison, WI.
Pisoni, D. B., and Luce, P. A. (**1986**). ''Speech perception: Research, theory, and the principal issues,'' in *Pattern Recognition by Humans and Machines: Speech Perception*, edited by E. C. Schwab and H. C. Nusbaum (Academic, Orlando), Vol. 1, pp. 1–50.
Quene', H. (**1992**). ''Durational cues for word segmentation in Dutch,'' Journal of Phonetics **20**, 331–350.
Ramig, L. O. (**1992**). ''The role of phonation in speech intelligibility: A review and preliminary data from patients with Parkinson disease,'' in *Intelligibility in Speech Disorders*, edited by R. D. Kent (John Benjamin, Amsterdam), pp. 120–155.
Smith, M. R., Cutler, A., Butterfield, S., and Nimmo-Smith, I. (**1989**). ''The perception of rhythm and word boundaries in noise-masked speech,'' J. Speech Hear. Res. **32**, 912–920.
Tikofsky, R. S., Glattke, T. J., and Tikofsky, R. P. (**1966**). ''Listener confusions in response to dysarthric speech,'' Folia Phoniatr. **18**, 280–292.
Tjaden, K., and Liss, J. M. (**1995**). ''The influence of familiarity of judgments of treated speech,'' American Journal of Speech-Language Pathology **4**, 39–48.
Turner, G. S., Tjaden, K., and Weismer, G. (**1995**). ''The influence of speaking rate on vowel space and speech intelligibility for individuals with amyotrophic lateral sclerosis,'' J. Speech Hear. Res. **38**, 1001–1013.
Van Ooijen, B., Bertoncini, J., Sansavini, A., and Mehler, J. (**1997**). ''Do weak syllables count in newborns?'' J. Acoust. Soc. Am. **102**, 3735–3741.
Weismer, G. (**1984**). ''Articulatory characteristics of Parkinsonian dysarthria: Segmental and phrase-level timing, spirantization, and glottal-supraglottal coordination,'' in *The Dysarthrias*, edited by M. R. McNeil, J. C. Rosenbek, and A. Aronson (College Hill, San Diego), pp. 101–130.
Weismer, G. (**1991**). ''Assessment of articulatory timing,'' in *Assessment of Speech and Voice Production: Research and Clinical Applications*, NIDCD Monograph, Vol. 1, pp. 84–95.
Weismer, G., and Martin, R. (**1992**). ''Acoustic and perceptual approaches to the study of intelligibility,'' in *Intelligibility in Speech Disorders*, edited by R. D. Kent (John Benjamin, Amsterdam), pp. 67–118.
Yorkston, K. M., and Beukelman, D. R. (**1978**). ''A comparison of techniques for measuring intelligibility of dysarthric speech,'' Journal of Communication Disorders **11**, 499–512.
Yorkston, K., and Beukelman, D. (**1980a**). ''A clinician-judged technique for quantifying dysarthric speech based on single-word intelligibility,'' Journal of Communication Disorders **13**, 15–31.
Yorkston, K. M., and Beukelman, D. R. (**1980b**). ''The influence of passage familiarity of intelligibility estimates of dysarthric speech,'' Journal of Communication Disorders **13**, 33–41.
Yorkston, K. M., and Beukelman, D. R. (**1981**). *Assessment of the Intelligibility of Dysarthric Speech* (Manual) (CC Publications, Oregon).
Yorkston, K. M., Hammen, V., Beukelman, D. R., and Traynor, A. (**1990**). ''The effect of rate control on the intelligibility and naturalness of dysarthric speech,'' J. Speech Hear. Disord. **55**, 550–560.

Speech recognition with altered spectral distribution of envelope cues

Robert V. Shannon,[a] Fan-Gang Zeng, and John Wygonski
House Ear Institute, 2100 West Third Street, Los Angeles, California 90057

(Received 12 September 1997; revised 1 May 1998; accepted 30 June 1998)

Recognition of consonants, vowels, and sentences was measured in conditions of reduced spectral resolution and distorted spectral distribution of temporal envelope cues. Speech materials were processed through four bandpass filters (analysis bands), half-wave rectified, and low-pass filtered to extract the temporal envelope from each band. The envelope from each speech band modulated a band-limited noise (carrier bands). Analysis and carrier bands were manipulated independently to alter the spectral distribution of envelope cues. Experiment I demonstrated that the location of the cutoff frequencies defining the bands was not a critical parameter for speech recognition, as long as the analysis and carrier bands were matched in frequency extent. Experiment II demonstrated a dramatic decrease in performance when the analysis and carrier bands did not match in frequency extent, which resulted in a warping of the spectral distribution of envelope cues. Experiment III demonstrated a large decrease in performance when the carrier bands were shifted in frequency, mimicking the basal position of electrodes in a cochlear implant. And experiment IV showed a relatively minor effect of the overlap in the noise carrier bands, simulating the overlap in neural populations responding to adjacent electrodes in a cochlear implant. Overall, these results show that, for four bands, the frequency alignment of the analysis bands and carrier bands is critical for good performance, while the exact frequency divisions and overlap in carrier bands are not as critical.
 [S0001-4966(98)02210-3]

PACS numbers: 43.71.Ky, 43.71.Es, 43.66.Ts [WS]

INTRODUCTION

Speech pattern recognition has been evaluated under a wide variety of conditions that alter and reduce spectral and temporal information. Speech has proven to be a robust signal that is resistant to many forms of distortion and information reduction. For example, speech can be recognized even when the spectral information is reduced to three sinusoids that track the formant transitions over time (Remez *et al.*, 1981). Even removing all spectral cues in speech results in a surprisingly high level of speech phoneme discrimination and recognition (Schroeder, 1968; van Tasell *et al.*, 1987, 1992; Rosen, 1992; Drullman, 1995; Turner *et al.*, 1995; Shannon *et al.*, 1995), and provides significant assistance for lip reading (Erber, 1972; Grant *et al.*, 1985, 1991).

Cochlear implants present an interesting case for understanding speech pattern recognition. In cochlear implants a relatively small number of electrodes activate tonotopic patches of neurons with a portion of the speech signal. However, the physiological response to electrical stimulation is quite different from the normal acoustic response. Among other differences, all neurons activated by an electrode are driven in a highly deterministic fashion (van den Honert and Stypulkowski, 1984, 1987; Hartmann *et al.*, 1984). Even with these abnormal properties in the physiological response, patients with as few as four electrodes have demonstrated high levels of speech recognition—higher levels than most researchers have predicted might be possible with such severe quantization of spectral information. This observation indicated how little was understood about recognition of speech under conditions of minimal or distorted spectral information.

In the design of prosthetic devices we face a dilemma which has both theoretical and practical implications: how do we maximize the speech information transmitted, given the limitations of the prosthetic device interface to the nervous system? Hill *et al.* (1968) partitioned the problem into two parts: analysis issues and presentation issues. The analysis problem is concerned with how to parcel speech information in a way that preserves the maximum amount of information, given the limitation of a small number of channels. The presentation problem is then to define the optimal mapping of the channels of speech information into perceptual/neural channels via the prosthesis.

A. The analysis problem

The analysis problem depends primarily on the distribution of critical speech pattern information in frequency and time. What temporal and spectral patterns of information are most critical for speech recognition? If we are limited in either the temporal or spectral domains, what are the most important speech cues remaining within those limitations? For example, if we could determine that a listener had only two potential receiving channels for speech information, what is the best way to divide speech information into two channels to preserve the maximum number of distinctions across different talkers and listening conditions? One indication comes from the original research on the articulation index (AI) which attempted to define an importance function for each spectral segment of speech (Fletcher and Steinberg,

[a]Electronic mail: Shannon@hei.org

1929; French and Steinberg, 1947). Fletcher and colleagues used high-pass and low-pass filtered speech to find that 1500 Hz was the frequency around which low-frequency and high-frequency contributions were equal for speech recognition. Articulation theory further defined the importance of each spectral region's contributions to the recognition of speech.

Using a different approach, Shannon *et al.* (1995) systematically reduced spectral information in speech to one, two, three, or four bands of modulated noise. The surprising result was that speech was highly recognizable with only three or four bands of noise, each modulated by the envelope from that same spectral band in speech. However, even with this result it is not clear that the four frequency bands chosen by Shannon *et al.* were the optimum for speech information content. One of the purposes of the present study is to study the importance of spectral parameters for speech pattern recognition.

The amount of temporal information required for speech recognition has recently been evaluated in conditions of reduced spectral information (Van Tasell *et al.*, 1987; Turner *et al.*, 1995; Shannon *et al.*, 1995; Dorman *et al.*, 1997a). In these studies envelope information was low-pass filtered at successively lower frequencies and used to modulate bands of noise or a sinusoid as a carrier. No change was observed in vowel, consonant, or sentence recognition as long as the low-pass envelope filter cutoff was 50 Hz or higher. Removing envelope fluctuations above 50 Hz had no effect on recognition, while removing envelope fluctuations between 20 and 50 Hz resulted in reduced phoneme discriminability and reduced speech recognition. Thus speech recognition is possible with only four bands of noise, even when each band is modulated with low-frequency envelope information below 50 Hz.

B. The presentation problem

In sensory prosthetic devices the goal is to convey information through an impaired sensory modality or through an alternate sensory modality. Thus we must understand the limitations and capabilities of the impaired or substitute sense to fully utilize its information carrying capacity. In the case of cochlear implants, acoustic information is being presented to the auditory system, but electrical stimulation activates the auditory system in a manner that produces highly unnatural patterns of neural activity. Some of the differences between acoustic and electrical stimulation are critical limitations for conveying speech information, while other differences may be of only secondary or no importance. To achieve the best match between the speech features extracted from the acoustic signal and the information transmitted to the electrically stimulated nerve, we must understand which patterns of neural activity are critical for speech recognition and which are secondary.

Psychophysical experiments with cochlear implants have demonstrated that temporal processing in implant patients is relatively normal (Shannon, 1983, 1986, 1989, 1990, 1992). Intensity processing is abnormal in implant listeners, but is still capable of restoring normal loudness growth with the proper loudness mapping function in the speech processor. However, implant listeners only have 20–40 discriminable intensity levels (Zeng and Shannon, 1992, 1994; Nelson *et al.*, 1997), which may be adequate for speech. In contrast, spectral resolution in an implant depends on many factors, including the number of electrodes, the proximity of the electrode to the remaining neurons, and the degree of neuronal survival in the individual patient. Because several of these factors are difficult to evaluate in implanted patients, we have developed an acoustic model of implant speech processing that allows us to parametrically measure the effect of tonotopic distortions in the speech pattern in normal-hearing listeners.

C. Rationale of present study

To simulate the limited spectral cues available to cochlear implant listeners Shannon *et al.* (1995) developed an acoustic simulation of a cochlear implant that systematically reduced spectral information. In this simulation speech was divided into several contiguous frequency bands. The envelope of each band was extracted by full-wave rectification and low-pass filtering at 160 Hz. This envelope was then used to modulate a band of noise. In the original experiments Shannon *et al.* (1995) changed the number of bands and the cutoff frequency of the envelope filter. High levels of speech recognition were possible with only four modulated bands of noise, modulated at relatively low rates. These results were obtained in normal-hearing listeners in whom the global pattern of speech information, while spectrally reduced, was at least presented to the appropriate tonotopic region of the cochlea via the modulated noise bands.

Recent studies (Dorman and Loizou, 1998; Dorman *et al.*, 1997a; Fishman *et al.*, 1997) validated the noise-band simulation of cochlear implants by comparing the simulation results to performance of cochlear implant patients with the same number of channels. The performance of normal-hearing listeners with the noise-band simulation sets an upper bound on the performance of implant listeners with the same number of channels. The results from the best performing implant listeners were similar to those from the normal-hearing listeners for the same number of channels. Poor performing implant listeners may be using fewer effective spectral channels, or there may be other processing deficits underlying their poor performance.

But how would speech recognition be affected by tonotopic alterations in the minimal pattern of information? When the central auditory system is already working with a minimal spectral representation of speech (as in implants), how would recognition be affected by changes in the spectral distribution of information along the nerve array? In cochlear implant listeners the neural population stimulated by a given electrode may be larger or smaller than for the adjacent electrode. If uniformly spaced electrodes stimulate nonuniformly spaced segments of nerve, this would result in a warping or stretching of the spectral distribution of envelope cues. In the present experiments we systematically alter the spectral location and extent of four bands of speech envelope information. Since four was the minimum number of bands that provided a high level of speech recognition, any detrimental manipulation of the pattern of envelope information should result in a reduction in speech performance. These manipu-

lations may not only provide insights into the difficulties faced by cochlear implant patients, but may also demonstrate the sensitivity of normal speech pattern recognition to alterations in the spectral distribution of information.

I. METHOD

A. Subjects

Subjects were eight native speakers of American English, normal-hearing adults, ranging in age from 22 to 50 years old. Their hearing was tested in a standard audiometric fashion to ensure that their thresholds were better than 20 dB HL. Two of the authors (RVS and JW) were two of the eight subjects.

B. Equipment and signal processing

All signals were digitized at a 10- or 20-kHz sample rate and passed through a pre-emphasis filter (−6 dB/octave below 100 Hz). Signals were then split into frequency bands (third to fourth order Elliptical IIR filters). For the standard condition (STD) the output from each filter was 15 dB down from the level in the passband at the frequency where adjacent filters overlapped. For conditions with increasing overlap between adjacent filters the same nominal cutoff frequencies were used as in the STD condition, but the slopes of the filters were reduced to the specified value. Thus conditions with shallower slopes had more energy at the crossover point between adjacent filters. The envelope was extracted by full-wave rectification and low-pass filtering (−6 dB/octave Elliptical IIR filter with cutoff frequency of 160 Hz, selected to be well above the 50-Hz value where previous research had shown no deterioration in temporal cues). The envelope derived from each band was then used to modulate a white noise. The modulated noise was frequency limited by filtering with a bandpass filter (third to fourth order Elliptical IIR filters). This last bandpass filtering reduced the modulation depth to some degree because it removed the modulation sidebands. The resulting modulated noise bands were then combined, low-pass filtered at 4 kHz (8 kHz for experiment III) (Kronhite 3343: 24 dB/oct), amplified (Crown D75) and presented to the listener through headphones (TDH-49). Overall levels were calibrated for each combination of parameters to produce an average A-weighted output level of 75 dB for continuous speech.

C. Test materials

Consonant and vowel stimuli were taken from the sound track of the Iowa audiovisual speech perception laser videodisc (Tyler *et al.*, 1989). A single male talker was used for both vowels and consonants. Three exemplars of each token were selected randomly. Consonant confusion matrices were compiled from 10 presentations of each of the 16 medial consonants /b d g p t k l m n f s ʃ v z j θ/ presented in an /a/-consonant-/a/ context. Vowel confusion matrices were compiled from nine presentations of each of the eight vowels in an /h/-vowel-/d/ context (heed: /hi̱d/, hawed: /hɔd/, head: /hɛd/, who'd: /hu̱d/, hid: /hɪd/, hood: /hʊd/, hud: /hʌd/, had: /hæd/, heard: /hɜ˞d/, hoed: /ho̱d/, hod: /hʊd/, hayed: /he̱d/). Recognition of words in sentences was measured using the sound track from the City University of New York laser videodisc everyday sentences (Boothroyd *et al.*, 1985). Data were collected for 24 sentences, representing 100 key words, from each subject. The sentences were of easy-to-moderate difficulty, presented with no context, and no sentences were repeated to an individual listener. No feedback was provided other than the overall score for each condition.

D. Data analysis

In each experiment the experimental conditions were tested for significant differences from a comparison condition using a standard paired *t*-test. In addition, the results of experiments II were tested against a single-channel condition to evaluate the loss of spectral information. Results of all tests of significance are presented in Tables I–IV.

II. EXPERIMENT I: LOCATION OF BAND DIVISIONS

The first experiment investigated the importance of the spacing of the cutoff frequencies that define the four bands. Three conditions were tested: linear spacing of the four bands (LIN), tonotopic spacing (LOG), and one intermediate spacing (STD). In the linear (LIN) condition the crossover frequencies (−15 dB down) of the four filters were nominally 1000, 2000, and 3000 Hz. The filter crossover frequencies in the standard (STD) condition were 800, 1500, and 2500 Hz which were selected to be the same as the filters used by Shannon *et al.* (1995). In the tonotopic (LOG) condition the frequency spectrum from 80 to 4000 Hz was divided into four equal distances on the basilar membrane, corresponding to crossover frequencies of 332, 845, and 1886 Hz (assuming a 35-mm cochlear length and using the formula of Greenwood, 1990). Fourth-order IIR elliptical filters were then designed to implement these crossover frequencies. In this experiment the same filters were used for the analysis and for filtering the noise carrier bands. The STD data are taken from the results of Shannon *et al.* (1995), collected earlier with the same eight subjects with the same test materials. The LIN and LOG conditions were run in randomized order for each listener.

Experiment I: Results and discussion

Figure 1 presents the results of experiment I for sentences, vowels, and consonants, and Table I presents the tests of significance between the experimental conditions and the STD condition. In the STD condition sound-only performance was 90%–95% correct on all three tests. Performance on sentences and vowels was significantly lower in the LIN–LIN condition and performance on all measures was significantly lower in the LOG–LOG condition. Although these scores are lower than the STD condition, they still represent high levels of speech recognition. Consonant recognition was slightly (but significantly) better in the LIN–LIN condition than in LOG–LOG, while vowel recognition was slightly better in the LOG–LOG condition.

These results indicate that the exact crossover frequencies in a four band representation are relatively minor factors in speech recognition. We speculate that the STD condition

TABLE I. Paired *t*-tests of significance for the data from experiment I.

	LIN–LIN vs STD–STD	LOG–LOG vs STD–STD	LIN–LIN vs LOG–LOG
Sentences	7.26[a]	4.76[a]	−0.21
Vowels	8.77[a]	3.33[b]	−3.41[b]
Consonants	0.85	4.11[a]	2.41[b]

[a]Significant at <0.01 level (df=7).
[b]Significant at <0.05 level (df=7).

had slightly higher scores because there was a band transition at 1500 Hz, a frequency known to divide high from low second formants and a frequency division point commonly used in automatic speech recognition systems to separate voiced from unvoiced stimuli. This is probably due to the fact that the central pattern recognition system has adapted to the variety of talkers and listening conditions. Information provided by second formant varies across talkers, room acoustics, and competing noise conditions. A specific, fixed set of frequency divisions might be best for a given talker, but a specific set of filter divisions may not be optimal across a range of different talkers or listening conditions. For example, the best dividing point may be different for male and female talkers due to differences in their formant frequencies. In a normal ear with many effective processing channels this is probably not a problem, but in processors with a reduced number of channels 1500 Hz probably represents a compromise frequency which provides the best dividing point for distinguishing coarse speech features (Zue, 1985).

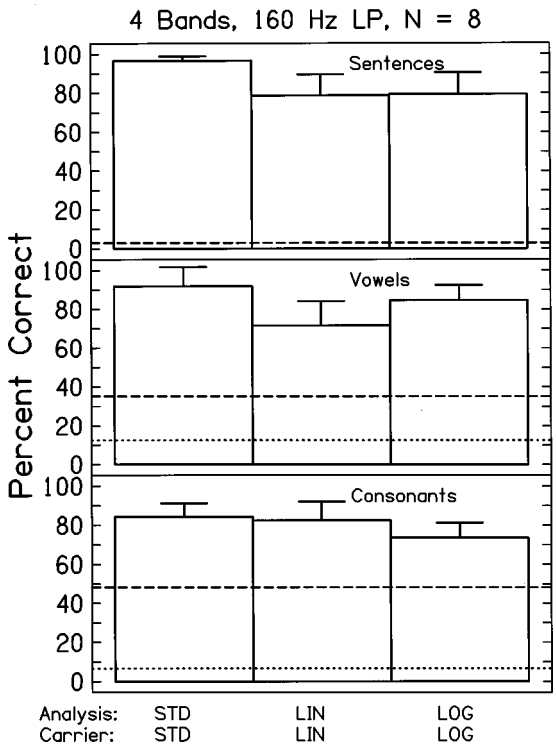

FIG. 1. Results of experiment I: Location of band divisions. Percent correct recognition of sentences (top), vowels (middle), and medial consonants (lower) for three frequency divisions. All conditions used matched analysis bands and noise carrier bands, 4-band processors and a 160-Hz, low-pass envelope filter. In all figures error bars indicate one standard deviation. Dotted line indicates chance level of performance and dashed line indicates the level of performance with no spectral cues (single-channel results from Shannon *et al.*, 1995).

III. EXPERIMENT II: WARPING THE SPECTRAL DISTRIBUTION OF ENVELOPE CUES

In cochlear implants the extent of auditory nerve excited by each electrode depends on many factors, including the electrode bipole orientation, the proximity of the electrode to surviving neurons, and the location and uniformity of surviving neurons. For example, some pathologies may produce poor spiral ganglion survival in the basal portion of the cochlear and better survival in the apical region. Other pathologies may produce relatively uniform nerve survival along the entire cochlea. Most cochlear implant speech processors divide the acoustic spectrum into equal tonotopically spaced bands and the information from each of these bands is routed to an electrode in the scala tympani. However, if the electrodes activate nonuniform regions of nerve due to a combination of the above factors, this strategy creates a mismatched condition in which the speech envelope information extracted from uniformly wide tonotopic bands are being presented to sectors of nerve of varying widths. In the example above, the basal electrode may stimulate a broad sector of nerve in a region with sparse neuronal survival, while the apical electrode may stimulate a narrow sector of nerve in a region with good survival. Since these two electrodes are presenting envelope information from comparable bands, the result is a distortion of the spatial (tonotopic) distribution of envelope information: The envelope information from high-frequency regions will activate a disproportionately wider section of the cochlea than the envelope from low-frequency regions.

To simulate such a mismatch a different frequency extent was used for the analysis and carrier bands. In this experiment the speech envelope information was extracted from linearly spaced bands and used to modulate tonotopically spaced noise bands (LIN-LOG), and vice versa (LOG-LIN). In these conditions the same envelope information was extracted as in experiment I, but the tonotopic extent of the cochlea that received that information was different from the analysis band. Thus the tonotopic representation of speech envelope cues was ''warped.''

Figure 2 presents a comparison of spectrograms for the STD–STD, LIN-LOG, and LOG-LIN conditions for the utterance ''shoo cat.'' Note how the spectral distribution of energy over time is altered for the conditions in which the analysis and carrier filters are mismatched. For a speech sound that contains a sweep in spectral energy crossing from one band to another, the transition in the processed version occurs at the right time, but in the wrong tonotopic location.

Experiment II: Results and discussion

Figure 3 presents the results for the tonotopic warping conditions on sentence, vowel, and consonant materials. Note that a dramatic and significant reduction in performance was evident in all conditions, compared to the STD–STD, LIN–LIN, or LOG–LOG conditions (Table II). The consonant scores for the mismatched conditions were only 50%–55% correct, which were not significantly different (Table II) from the consonant scores with the same subjects

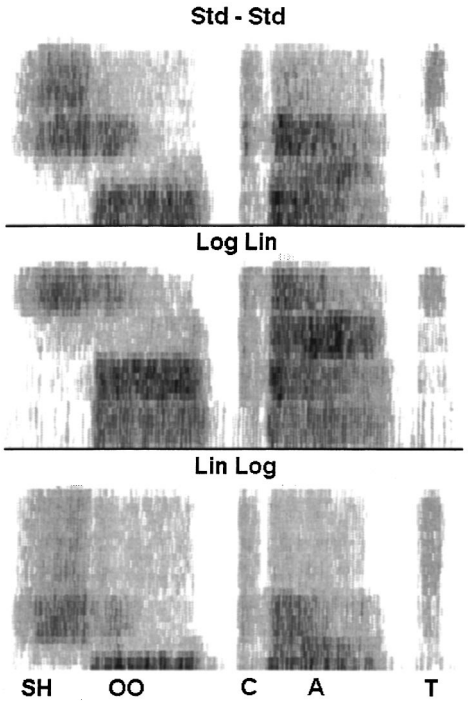

FIG. 2. Example spectrograms of the utterance ''SHOO CAT'' from conditions of experiment II: Tonotopic warping of envelope cues. Upper panel shows spectrogram from STD–STD condition: a four band processor with no tonotopic warping. In the middle panel envelope cues were extracted from logarithmically spaced filters and used to modulate noise bands that were spaced linearly (LOG-LIN) and in the lower panel the reverse (LIN-LOG).

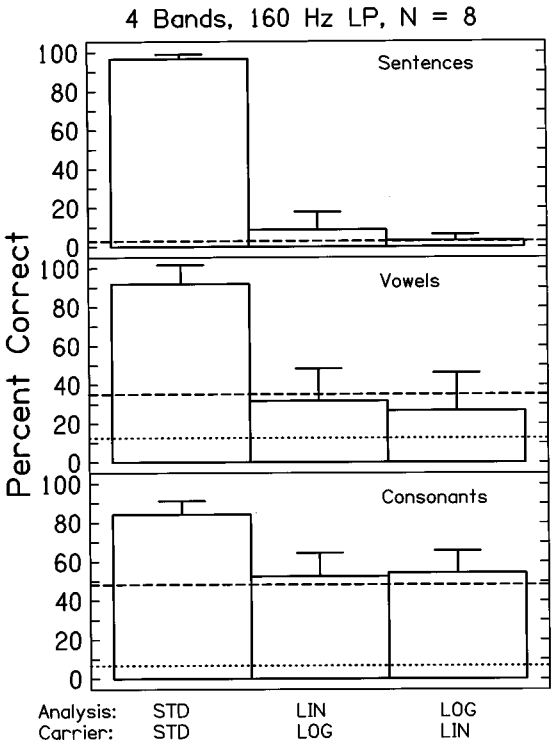

FIG. 3. Results of experiment II: Tonotopic warping of envelope cues. Dashed and dotted lines are the same as in Fig. 1.

and the same materials for a single band processor with no spectral cues (level indicated in each panel of Figs. 1, 3, 4, and 5 by a horizontal dashed line). Consonant scores in the single band condition are higher than those observed by Van Tassel *et al.* (1987) because a single male talker was used and the subjects had considerable practice with this stimulus set, which probably resulted in some incidental learning (Van Tassel *et al.*, 1992). Vowel recognition was reduced to 25% correct. Like the consonant score, this level of performance was no better (and possibly a bit worse) than the score with no spectral cues (Table II). Sentence recognition scores in the mismatched conditions were less than 10% correct.

These results indicate that the mismatching of the spectral extent of envelope cues eliminates the ability of the listener to utilize the minimal spectral cues provided by these stimuli. If the envelope cues are in their proper tonotopic locations and extents, they can be integrated for speech recognition, even with only four bands. But when the tonotopic distribution of envelope information is warped, performance falls to the level achieved in the single band case, which provides no spectral cues at all. In this case the same spectral envelope information is present as in the four band LIN–LIN or LOG–LOG conditions and the information is still distributed tonotopically. However, the central pattern recognition system apparently cannot utilize the tonotopic distribution of envelope information when the pattern is distorted. From this result we infer that the relative tonotopic distribution of envelope information is a critical dimension for recognition of speech when access to the full range of speech cues is restricted.

We speculate that people may be able to learn to recognize speech even with these distortions, because the information is still present. Prior studies of the learning time for altered or distorted speech (Blesser, 1972) indicate that several days or even weeks may be necessary for learning to understand running speech, similar to the relearning time for altered vision (Kohler, 1964).

IV. EXPERIMENT III: FREQUENCY SHIFTING ENVELOPE CUES

Cochlear implant electrodes are inserted through the round window into the scala tympani for a length of 20–25 mm. The multiple stimulating electrodes in a fully inserted device are located at tonotopic locations corresponding to frequencies of 800 Hz and above. If the electrode carrier is not fully inserted, the tonotopic location of the most apical electrode corresponds to an even higher frequency. However, all present commercial implant speech processors divide the audio spectrum into multiple, contiguous frequency bands. A processed version of the information in each of these bands (usually the envelope) is presented to a single electrode pair.

TABLE II. Paired *t*-tests of significance for the data from experiment II.

	LIN-LOG vs STD–STD	LOG-LIN vs STD–STD	LIN-LOG vs Single channel	LOG-LIN vs Single channel
Sentences	32.19[a]	83.71[a]	2.24	0.50
Vowels	15.50[a]	10.49[a]	−1.70	−3.17[a]
Consonants	9.58[a]	9.80[a]	0.66	1.22

[a]Significant at <0.01 level (df$=7$).

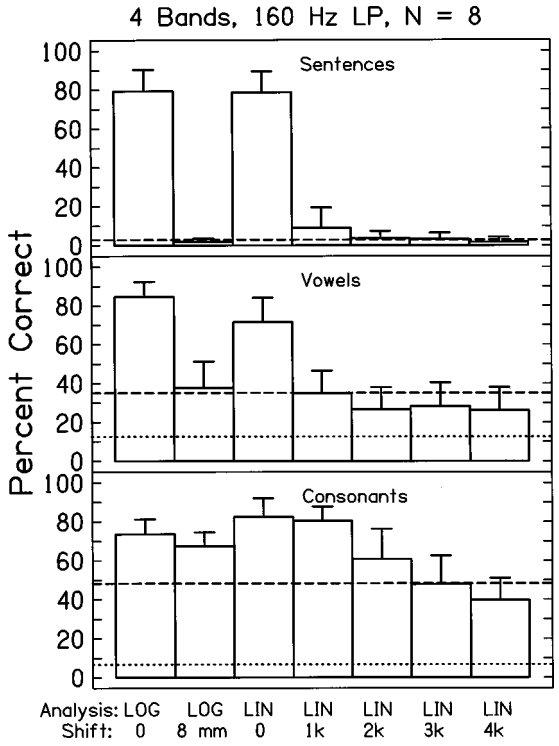

FIG. 4. Results of experiment III: Frequency shift. Dashed and dotted lines are the same as in Fig. 1.

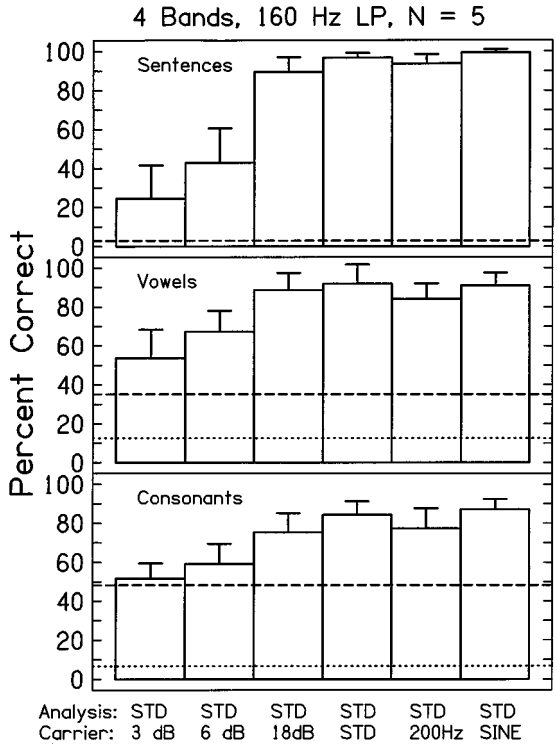

FIG. 5. Results of experiment IV: Band overlap. Dashed and dotted lines are the same as in Fig. 1.

The output of the lowest-frequency analysis band is presented to the most apical electrode pair. The output from the next lowest band is presented to the second most apical pair, and so on, until all bands are assigned to all usable electrode pairs. If we assume that each electrode is stimulating neurons near its cochlear location, this stimulation scheme will result in a basal shift of the speech pattern. If the neuron survival is uniform and the electrode proximity to those surviving neurons is uniform, the speech pattern will simply be shifted from its normal location. However, if either neuron survival or electrode location are nonuniform the speech pattern on the auditory nerve will be both shifted *and* warped.

To simulate these conditions we shifted the noise carrier bands relative to the analysis bands. In one condition the analysis bands were arranged tonotopically (LOG) and the noise carrier bands were shifted 8 mm basally in cochlear location using the Greenwood (1990) formula, which was a shift of nearly two octaves. This resulted in a condition similar to a cochlear implant that was not fully inserted. In this case the noise carrier bands were at the following frequency locations: band 1: 500–1156 Hz; band 2: 1156–2640 Hz; band 3: 2640–5052 Hz; and band 4: 5052–10 200 Hz. In another set of conditions linearly spaced analysis bands (LIN) were used and the output noise carrier bands were shifted up in frequency by 1, 2, 3, or 4 kHz from the analysis bands. This manipulation resulted in a basal shift of the speech pattern and a compression of the pattern in terms of tonotopic distance.

Experiment III: Results and discussion

Figure 4 presents the results from the frequency shift conditions for sentences, vowels and consonants. The results from experiment I (LIN–LIN and LOG–LOG) are reproduced here for comparison. For the LOG-8 mm shift condition the consonant score was not significantly reduced, but the vowel score was dramatically reduced and the sentence recognition score was reduced to essentially zero (statistical significance results are presented in Table III). Although all of the temporal cues in the four bands were preserved and the four bands maintained their relative tonotopic spacing and extent, speech recognition was completely disrupted.

In the LIN shift conditions there was a graded effect as a function of the amount of frequency shift. For a 1-kHz shift (LIN-1 k) the consonant score was similar to the unshifted condition, while the vowel score was significantly reduced. The sentence score was strongly reduced to only 10% correct from the unshifted score of 80% correct. As the frequency shift increased the consonant score decreased, while the vowel and sentence scores remained at low levels for all frequency shifts, probably indicating a floor effect.

We anticipated that the detrimental effect would be less in the LOG shift condition than for the LIN shift condition because the relative tonotopic pattern was preserved, and simply shifted in mm along the cochlea. If the central mechanisms for speech pattern recognition stored templates of *relative* speech envelope patterns in terms of mm along cochlea or along the nerve array (Miller, 1989), we would expect that the LOG shift condition would result in relatively little decrease in performance. This was clearly not the case, suggesting that the central representation is stored in terms of *absolute*, not relative cochlear place. The LIN shift conditions may have resulted in a smaller decrease in performance because the shift in terms of mm in the cochlea was smaller

TABLE III. Paired *t*-tests of significance for the conditions of experiment III.

	LIN 1 k vs LIN–LIN	LIN 2 k vs LIN–LIN	LIN 3 k vs LIN–LIN	LIN 4 k vs LIN–LIN	LOG 8 mm vs LOG–LOG
Sentences	22.24[a]	28.64[a]	27.58[a]	31.44[a]	21.27[a]
Vowels	9.77[a]	9.26[a]	11.15[a]	8.64[a]	11.43[a]
Consonants	0.74	4.33[a]	6.56[a]	9.43[a]	2.28

[a]Significant at <0.01 level ($df=7$).
[b]Significant at <0.05 level ($df=7$).

in the high-frequency regions than for the LOG shift condition.

Recent clinical surveys (Bredberg and Lindstrom, 1996; Hartrampf *et al.*, 1996; Kumakawa *et al.*, 1997) have shown poorer performance in cochlear implant patients with short electrode insertion depths, even after a substantial period of experience. Dorman *et al.* (1997b) simulated the effect of electrode insertion depth in normal-hearing listeners with the noise-band technique. They found that the performance level of normal-hearing listeners was similar to that of cochlear implant listeners when the noise carrier bands were shifted in mm to simulate typical electrode insertion depths. This result implies that the implanted listeners did not improve their performance with practice, but were performing similarly to normal-hearing listeners with the same signal processing and tonotopic shift and no practice.

Rosen *et al.* (1997) recently measured performance as a function of training in normal-hearing listeners with a four noise-band processor and a 6-mm tonotopic shift. Initial performance was reduced to chance by the 6-mm shift, a result similar to the 8-mm shift in the present experiment III. After only 3 h of training, they found substantial improvement, but performance at that point was still only half of the level achieved with the STD–STD condition. The Rosen *et al.* result indicates that some relearning is possible for tonotopically shifted speech patterns, but the clinical studies suggest that complete accommodation may not be possible even after prolonged experience.

V. EXPERIMENT IV: SPECTRAL SMEARING

In a cochlear implant it is widely assumed that good speech recognition requires selective stimulation of distinct neural populations by each electrode. It is also assumed that neural overlap is inversely correlated with electrode discrimination, i.e., that electrodes that stimulate different neural populations are easily discriminable while electrodes that stimulate overlapping neural populations are poorly discriminated. In acoustic listening, the analogous assumption is that broadened auditory filters observed in some hearing impaired listeners are the primary cause of reduced speech intelligibility in those listeners (Boothroyd *et al.*, 1996; ter Keurs *et al.*, 1992, 1993; Moore *et al.*, 1992).

Electrode interaction in cochlear implants or broadened auditory filters in impaired hearing was simulated by broadening the filter slopes on the noise carrier bands. The analysis bands were fixed at the same frequencies and filter slopes as in the STD condition. However, the slopes of the noise carrier bands were systematically varied to produce conditions of varying degrees of overlap. At one extreme the carriers were simply sinusoids near the center frequency of each band. In another condition (STD-200 Hz) the noise carrier bands were 200-Hz-wide bands of noise for each channel. In these two conditions there was no overlap in the output of the carrier bands and, in fact, the output stimulus had spectral regions in which no stimulus was present. To simulate increasing overlap between output channels the carrier noise bands were fixed at the nominal crossover frequencies of the STD configuration and the slopes of the filters broadened from -24 to -18 to -6 to -3 dB/octave. Since the filters were generally separated by an octave or less this last condition resulted in overlap such that the output level at the center of a band was only 3 dB above the level from the adjacent carrier bands.

Experiment IV: Results and discussion

Figure 5 presents the results of the carrier overlap condition for sentences, vowels and consonants, and Table IV presents the statistical comparisons. In general, the degree of overlap in the output carrier bands had relatively little effect on speech recognition. Broadening the carrier bands from sinusoids to bands of noise with -18 dB/octave slopes produced a significant effect on consonant and sentence recognition, but the absolute performance level was still quite high. For the -3 and -6 dB/octave slope conditions all results were significantly lower than the STD condition.

Consider the limiting conditions for such manipulations. We know that as the filter slopes are broadened to 0 dB/octave the output is reduced to a single-band processor and the performance would be reduced dramatically, to less than 5% correct on sentences. Yet at -3 dB/octave, which results in extensive overlap, listeners still were able to correctly identify words in sentence material at 25%. This is an encouraging result for cochlear implant speech processor design. It indicates that speech recognition is possible even with considerable overlap between electrodes. Apparently almost total overlap is necessary to reduce performance to the single-band level.

At the other end of the scale, 200-Hz-wide carrier bands and sinusoidal carriers, which result in a sparse spectral representation, still allow nearly perfect recognition of sentence material with only four modulated sinusoids, replicating a recent result by Dorman *et al.* (1997a). Earlier studies with sinusoidal vocoders required 8–10 bands to achieve similar levels of performance (Hill *et al.*, 1968), in some cases because they were using low-pass filters for envelope extraction of only 15–20 Hz. With this severe filtering, some of the more rapid temporal cues and voicing periodicity was lost, and more spectral channels had to be added to make up for

TABLE IV. Paired *t*-tests of differences from the STD–STD condition for the conditions of experiment IV.

	STD 3 dB	STD 6 dB	STD 18 dB	STD 200 Hz	STD Sine
Sentences	9.98[a]	9.20[a]	3.27[b]	2.09	−5.41[a]
Vowels	16.33[a]	9.77[a]	0.96	2.43[b]	0.29
Consonants	10.81[a]	10.35[a]	3.14[b]	2.29	−1.90

[a]Significant at <0.01 level ($df=7$).
[b]Significant at <0.05 level ($df=7$).

the loss of temporal information. In a normal cochlea, a sinusoid or narrow band of noise is represented in the neural response across a considerable tonotopic extent due to the normal cochlear processing (Rose *et al.*, 1971). So the ''sparse'' spectral representation of the sinusoidal and 200-Hz noise-band stimuli actually resulted in an internal representation on the auditory nerve that was more contiguous than the spectrum.

VI. GENERAL DISCUSSION

The present series of experiments builds on earlier work with signal correlated noise (Schroeder, 1968; Rosen, 1992; van Tassel *et al.*, 1987, 1992; Turner *et al.*, 1995; Shannon *et al.*, 1995). Those experiments removed all spectral information in speech and preserved only the broadband temporal envelope. Recognition of consonants was surprisingly high even in the complete absence of any spectral information. Turner *et al.* (1995) and Shannon *et al.* (1995) extended this technique to two bands. In their experiments speech was filtered into a high-pass band and a low-pass band, divided at 1500 Hz. The envelope from the high-pass band of speech was used to modulate a high-pass band of noise and similarly for the low-pass band. Recognition of vowels and consonants improved dramatically with two modulated noise bands compared to one. This result demonstrated that temporal envelope information, quantized into two spectral bands, was sufficient for overall high recognition performance on consonants and was sufficient for recognition of almost 100% of the voicing and manner information. In addition, Shannon *et al.* (1995) expanded the technique to three and four bands, which resulted in high levels of sound-only speech recognition. Information transmission analysis (Miller and Nicely, 1955) showed that the improvement from two to four bands was primarily due to increased information on place of articulation, as might be expected.

The present series of experiments investigated speech recognition by starting with the minimal spectral representation that resulted in good speech recognition (4 bands: STD–STD). This limited set of cues was then perturbed/distorted to see which dimensions were most critical for speech recognition. We might expect considerable robustness to small distortions in amplitude or spectral cues because these types of distortions occur commonly in everyday listening conditions. However, in listeners with limited capacity for processing acoustic signals, like the severely hearing impaired or cochlear implant listeners, the remaining cues they have available may be more delicate and more sensitive to distortion. The present experiments extend the results of previous experiments to demonstrate the robustness of speech pattern recognition to some distortions in the tonotopic pattern but not to others.

The data of experiments II and III on spectral warping and shifting demonstrate some conditions which have a more detrimental effect on vowels than on consonants. Drullman *et al.* (1994) found that conditions of temporal smearing had a larger detrimental effect on consonants than on vowels. As speech cues are reduced to a minimum it appears that reductions in temporal and spectral cues have differential effects on consonants and vowels. Shannon *et al.* (1995) demonstrated that consonantal voicing and manner cues are correctly perceived even when spectral cues are reduced to only two bands of modulated noise, indicating that those consonant contrasts require only minimal spectral information. However, vowel recognition and consonantal place of articulation required more spectral detail for high levels of recognition, indicating that vowel recognition depends more on spectral cues than on temporal cues. In the present experiments temporal cues were preserved across all conditions and spectral cues were distorted by shifting or warping. In several conditions consonant recognition was only slightly degraded while vowel recognition was reduced to single-channel levels. This result is consistent with those previous studies in that vowel recognition is more sensitive to spectral distortions than is consonant recognition. In conditions where consonant performance was relatively good and vowel performance was poor (Fig. 4, LOG-8 mm condition), sentence recognition was completely disrupted. This suggests either that both vowel and consonant phonemic recognition must achieve a certain minimal level before the linguistic retrieval can be successfully accomplished or that vowels are more important than consonants for sentence recognition.

The present experiments measured speech recognition performance without any practice in conditions of shifted and warped spectral distribution of envelope cues. Certainly, experience with the altered spectral distributions will improve performance, as demonstrated by Blesser (1972) and recently by Rosen *et al.* (1997). However, our intention was to take a ''snapshot'' of the effect of spectral alterations compared to existing normal acoustic pattern recognition. Whether or not these altered patterns can be fully learned and whether performance will ultimately return to the unaltered level is a separate and important question. From the present results it is not possible to predict which pattern of alteration from the present experiments might be learnable.

VII. SUMMARY AND CONCLUSIONS

Speech recognition is a complex and robust process that can be accomplished under conditions of severe distortion in

the original signal. Under ideal listening conditions the central pattern recognition and linguistic access mechanisms have a rich and redundant set of peripheral cues. As listening conditions deteriorate, or under conditions of peripheral pathology, the central pattern recognition must work with a reduced set of cues from the periphery. The present series of experiments tries to quantify the effect of corrupted and limited peripheral information on speech recognition.

Previous work (Shannon *et al.*, 1995) demonstrated that four bands of modulated noise were sufficient for high levels of speech recognition. The present experiments expand this previous result to define which parameters of such a reduced representation are most critical for speech recognition. Experiment I demonstrated that the exact cutoff frequencies which define the four bands were not critical for speech recognition. Experiment II demonstrated that warping the spectral distribution of envelope cues renders speech completely unintelligible. Experiment III demonstrated that a tonotopic shift of the envelope pattern resulted in poor intelligibility, even when the relative cochlear distribution of envelope cues was preserved. This result indicates that the central pattern recognition mechanisms are not robust to even linear translations of the pattern along the neural array, at least without training. Experiment IV demonstrated that the selectivity of the envelope carrier bands was not critical for speech recognition; performance deteriorated only when the bands were broadly overlapping, smearing the tonotopic specificity of envelope cues.

ACKNOWLEDGMENTS

We appreciate the help of Franco Portillo and Vivek Kamath in running subjects, and Alena Wilson and Steve Otto for their perseverance. This work was supported by Grant No. DC01526 from NIH/NIDCD.

Blesser, B. (**1972**). ''Speech perception under conditions of spectral transformation: I. Phonetic characteristics,'' J. Speech Hear. Res. **15**, 5–41.

Boothroyd, A., Hnath-Chisolm, T., and Hanin, L. (**1985**). ''A sentence test of speech perception: Reliability, set-equivalence, and short-term learning,'' City University of New York, Report No. RCI10.

Boothroyd, A., Mulhearn, B., Gong, J., and Ostroff, J. (**1996**). ''Effects of spectral smearing on phoneme and word recognition,'' J. Acoust. Soc. Am. **100**, 1807–1818.

Bredberg, G., and Lindstrom, B. (**1995**). ''Insertion length of electrode array and its relation to speech communication performance and nonauditory side effects in multichannel-implanted patients,'' Ann. Phys. (Leipzig) **104**, 256–258.

Dorman, M. F., and Loizou, P. C. (**1998**). ''Identification of consonants and vowels by cochlear-implant patients using a 6-channel continuous interleaved sample processor and by normal-hearing subjects using simulations processors with two to nine channels,'' Ear and Hearing **19** (2), 162–166.

Dorman, M. F., Loizou, P. C., and Rainey, D. (**1997a**). ''Speech intelligibility as a function of the number of channels of stimulation for signal processors using sine-wave and noise-band outputs,'' J. Acoust. Soc. Am. **102**, 2403–2411.

Dorman, M. F., Loizou, P. C., and Rainey, D. (**1997b**). ''Simulating the effect of cochlear-implant electrode insertion depth on speech understanding,'' J. Acoust. Soc. Am. **102**, 2993–2996.

Drullman, R., Festen, J. M., and Plomp, R. (**1994**). ''Effect of temporal envelope smearing on speech perception,'' J. Acoust. Soc. Am. **95**, 1053–1064.

Drullman, R. (**1995**). ''Temporal envelope and fine structure cues for speech intelligibility,'' J. Acoust. Soc. Am. **97**, 585–592.

Erber, N. (**1972**). ''Speech envelope cues as an acoustic aid to lipreading for profoundly deaf children,'' J. Acoust. Soc. Am. **51**, 1224–1227.

Fishman, K., Shannon, R. V., and Slattery, W. H. (**1997**). ''Speech recognition as a function of the number of electrodes used in the SPEAK cochlear implant speech processor,'' J. Speech Hear. Res. **40**, 1201–1215.

Fletcher, H., and Steinberg, J. C. (**1929**). ''Articulation testing methods,'' Bell Syst. Tech. J. **8**, 806–854.

French, N. R., and Steinberg, J. C. (**1947**). ''Factors governing the intelligibility of speech sounds,'' J. Acoust. Soc. Am. **19**, 90–119.

Grant, K. W., Ardell, L., Kuhl, P., and Sparks, D. (**1985**). ''The contribution of fundamental frequency, amplitude envelope, and voicing duration cues to speech reading in normal subjects,'' J. Acoust. Soc. Am. **77**, 671–677.

Grant, K. W., Braida, L. D., and Renn, R. J. (**1991**). ''Single band amplitude envelope cues as an aid to speechreading,'' Q. J. Exp. Psychol. **43A**, 621–645.

Greenwood, D. D. (**1990**). ''A cochlear frequency-position function for several species—29 years later,'' J. Acoust. Soc. Am. **87**, 2592–2605.

Hartmann, R., Topp, G., and Klinke, R. (**1984**). ''Discharge patterns of cat primary auditory fibers with electrical stimulation of the cochlea,'' Hearing Res. **13**, 47–62.

Hartrampf, R., Dahm, M. C., Battmer, R. D., Gnadeberg, D., Straus-Schier, A., Rost, U., and Lenarz, T. (**1995**). ''Insertion depth of the Nucleus electrode array and relative performance,'' Ann. Phys. (Leipzig) **104**, 277–280.

Hill, F. J., McRae, L. P., and McClellan, R. P. (**1968**). ''Speech recognition as a function of channel capacity in a discrete set of channels,'' J. Acoust. Soc. Am. **44**, 13–18.

Kohler, I. (**1964**). *The Formation and Transformation of the Perceptual World*, translated by H. Fiss (International Universities Press, Vienna).

Kumakawa, K., Tadeka, H., and Ujita, N. (**1997**). ''Determining the optimum insertion length of electrodes in the Cochlear 22-channel implant: Results of a clinical study,'' Adv. Otolaryngol. **52**, 129–134.

Miller, G. A., and Nicely, P. E. (**1955**). ''An analysis of perceptual confusions among some English consonants,'' J. Acoust. Soc. Am. **27**, 338–352.

Miller, J. D. (**1989**). ''Auditory-perceptual interpretation of the vowel,'' J. Acoust. Soc. Am. **85**, 2114–2134.

Moore, B. C. J., Glasberg, B. R., and Simpson, A. (**1992**). ''Evaluation of a method of simulating reduced frequency selectivity,'' J. Acoust. Soc. Am. **91**, 3402–3423.

Nelson, D. A., Schmitz, J. L., Donaldson, G. S., Viemeister, N. F., and Javel, E. (**1997**). ''Intensity discrimination as a function of stimulus level with electric stimulation,'' J. Acoust. Soc. Am. **100**, 2393–2414.

Remez, R. E., Rubin, P. E., Pisoni, D. B., and Carrell, T. D. (**1981**). ''Speech perception without traditional speech cues,'' Science **212**, 947–950.

Rose, J. E., Hind, J. E., Anderson, D. J., and Brugge, J. F. (**1971**). ''Some effects of stimulus intensity on response of auditory nerve fibers in the squirrel monkey,'' J. Neurophysiol. **34**, 685–699.

Rosen, S. (**1992**). ''Temporal information in speech: Acoustic, auditory and linguistic aspects,'' Philos. Trans. R. Soc. London, Ser. B **336**, 367–373.

Rosen, S., Faulkner, A., and Wilkinson, L. (**1997**). ''Perceptual adaptation by normal listeners to upward shifts of spectral information in speech and its relevance for users of cochlear implants,'' in *Speech, Hearing, and Language: Work in Progress* (Phonetics and Linguistics, University College, London), Vol. 10.

Schroeder, M. R. (**1968**). ''Reference signal for signal quality studies,'' J. Acoust. Soc. Am. **44**, 1735–1736.

Shannon, R. V. (**1983**). ''Multichannel electrical stimulation of the auditory nerve in man: Basic psychophysics,'' Hearing Res. **11**, 157–189.

Shannon, R. V. (**1986**). ''Temporal processing in cochlear implants,'' in *Sensorineural Hearing Loss: Mechanisms, Diagnosis, and Treatment*, edited by M. J. Collins, T. Glattke, and L. Harker (University of Iowa Press, Iowa City), pp. 323–334.

Shannon, R. V. (**1989**). ''Detection of gaps in sinusoids and pulse trains by patients with cochlear implants,'' J. Acoust. Soc. Am. **85**, 2587–2592.

Shannon, R. V. (**1990**). ''Forward masking in patients with cochlear implants,'' J. Acoust. Soc. Am. **88**, 741–744.

Shannon, R. V. (**1992**). ''Temporal modulation transfer functions in patients with cochlear implants,'' J. Acoust. Soc. Am. **91**, 1974–1982.

Shannon, R. V., Zeng, F.-G., Wygonski, J., Kamath, V., and Ekelid, M. (**1995**). ''Speech recognition with primarily temporal cues,'' Science **270**, 303–304.

ter Keurs, M., Festen, J. M., and Plomp, R. (**1992**). ''Effect of spectral

envelope smearing on speech reception,'' J. Acoust. Soc. Am. **91**, 2872–2880.
ter Keurs, M., Festen, J. M., and Plomp, R. (**1993**). ''Effect of spectral envelope smearing on speech reception,'' J. Acoust. Soc. Am. **93**, 1547–1552.
Turner, C. W., Souza, P. E., and Forget, L. N. (**1995**). ''Use of temporal envelope cues in speech recognition by normal and hearing-impaired listeners,'' J. Acoust. Soc. Am. **97**, 2568–2576.
Tyler, R. S., Preece, J. P. and Lowder, M. W. (**1987**). The Iowa audiovisual speech perception laser videodisc, Laser Videodisc and Laboratory Report, Dept. of Otolaryngology, University of Iowa, Iowa City, IA.
Van den Honert, C., and Stypulkowski, P. H. (**1984**). ''Physiological properties of the electrically stimulated auditory nerve. II. Single fiber recordings,'' Hearing Res. **14**, 225–243.
Van den Honert, C., and Stypulkowski, P. H. (**1987**). ''Single fiber mapping of spatial excitation patterns in the electrically stimulated auditory nerve,'' Hearing Res. **29**, 195–206.
Van Tasell, D. J., Soli, S. D., Kirby, V. M., and Widin, G. P. (**1987**). ''Speech waveform envelope cues for consonant recognition,'' J. Acoust. Soc. Am. **82**, 1152–1161.
Van Tasell, D. J., Greenfield, D. G., Logemann, J. J., and Nelson, D. A. (**1992**). ''Temporal cues for consonant recognition: Training, talker generalization, and use in evaluation of cochlear implants,'' J. Acoust. Soc. Am. **92**, 1247–1257.
Zeng, F. G., and Shannon, R. V. (**1992**). ''Loudness balance between electric and acoustic stimulation,'' Hearing Res. **60**, 231–235.
Zeng, F.-G., and Shannon, R. V. (**1994**). ''Loudness coding mechanisms inferred from electric stimulation of the human auditory system,'' Science **264**, 564–566.
Zue, V. W. (**1985**). ''The use of speech knowledge in automatic speech recognition,'' Proc. IEEE **73**, 1602–1615.

Temporal and spatio-temporal vibrotactile displays for voice fundamental frequency: An initial evaluation of a new vibrotactile speech perception aid with normal-hearing and hearing-impaired individuals

Edward T. Auer, Jr. and Lynne E. Bernstein
Spoken Language Processes Laboratory, House Ear Institute, 2100 West Third Street, Los Angeles, California 90057

David C. Coulter
Coulter Associates, Fairfax, Virginia

(Received 6 March 1997; revised 27 April 1998; accepted 30 June 1998)

Four experiments were performed to evaluate a new wearable vibrotactile speech perception aid that extracts fundamental frequency ($F0$) and displays the extracted $F0$ as a single-channel temporal or an eight-channel spatio-temporal stimulus. Specifically, we investigated the perception of intonation (i.e., question versus statement) and emphatic stress (i.e., stress on the first, second, or third word) under Visual-Alone (VA), Visual-Tactile (VT), and Tactile-Alone (TA) conditions and compared performance using the temporal and spatio-temporal vibrotactile display. Subjects were adults with normal hearing in experiments I–III and adults with severe to profound hearing impairments in experiment IV. Both versions of the vibrotactile speech perception aid successfully conveyed intonation. Vibrotactile stress information was successfully conveyed, but vibrotactile stress information did not enhance performance in VT conditions beyond performance in VA conditions. In experiment III, which involved only intonation identification, a reliable advantage for the spatio-temporal display was obtained. Differences between subject groups were obtained for intonation identification, with more accurate VT performance by those with normal hearing. Possible effects of long-term hearing status are discussed. [S0001-4966(98)03010-0]

PACS numbers: 43.71.Ma [WS]

INTRODUCTION

The substitution of the sense of touch for the sense of hearing has been explored intermittently across almost the entire twentieth century (Reed *et al.*, 1993), with the primary goal to develop portable devices to enhance speech communication by hearing-impaired individuals. Fundamental issues continue to be: (1) what speech information to encode for presentation to the skin (e.g., spectral patterns or extracted acoustic-phonetic cues); and (2) how to present the information (e.g., as mechanical or electrical stimulation; as rate displays, or spatial displays). To date, several different tactile speech perception aids have been developed and tested, encoding a variety of sources of speech information in a variety of presentation schemes designed to enhance speechreading (for reviews see Kishon-Rabin *et al.*, 1996; Reed *et al.*, 1993; Summers, 1992). Reported enhancements to speechreading have generally been in the range of 4–20 percentage points for words correct in open-set sentence identification tasks.

One type of speech perception aid, which has motivated a fair amount of research, delivers extracted voice fundamental frequency ($F0$) (Bernstein *et al.*, 1989, 1998; Boothroyd and Hnath, 1986; Eberhardt *et al.*, 1990; Grant, 1987; Hanin *et al.*, 1988; Hnath-Chisolm and Kishon-Rabin, 1988; Kishon-Rabin *et al.*, 1996; Plant and Risberg, 1983; Rothenberg and Molitor, 1979; Summers, 1992; Waldstein and Boothroyd, 1995a, b). Voice $F0$ has been studied for several reasons:(1) $F0$ characteristics contribute to speech perception at several different linguistic levels; (2) voice $F0$ is generated at the glottis, which is invisible to the speechreader; and (3) the presentation of simple *acoustic* stimuli composed of pulses generated as a function of $F0$ greatly enhances speechreading. Normal-hearing adults have been shown to improve 40–50 percentage points over speechreading alone when they speechread with an acoustic $F0$ supplement (Boothroyd *et al.*, 1988; Breeuwer and Plomp, 1984, 1985, 1986; Grant, 1987; Rosen *et al.*, 1981).

A brief inventory of the linguistic levels at which $F0$ has been shown to be a factor readily illustrates the first point above. The onset time of vocal fold vibration relative to supralaryngeal articulator release (i.e., voice onset time) is a primary contributor to perception of prevocalic consonantal voicing distinctions (Lisker and Abramson, 1967). $F0$ direction and height at the onset of prevocalic consonants also vary systematically with the consonantal voicing distinctions (Haggard *et al.*, 1970; House and Fairbanks, 1953). $F0$ is an acoustical correlate of lexical stress (e.g., *CONvert* versus *conVERT*) and sentential stress (Lehiste, 1970; Bolinger, 1958; Fry, 1955, 1958) also referred to as accent (Sluijter and van Heuven, 1996). Lexical stress patterns may be involved in the perception of word boundaries (Cutler and Butterfield, 1992). $F0$ also systematically signals syntactic structure (Bolinger, 1978; Lehiste, 1970; Pike, 1945) (e.g.,

the contrast between a sentence spoken as a statement or a question) and can signal phrase boundaries (Streeter, 1978).

The present study reports on an initial evaluation of a new design for a wearable vibrotactile speech perception aid that employs a digital processor for the automatic extraction of $F0$. The new aid was evaluated using closed-set identification of emphatic sentential stress (on the first, second, or third word of the stimulus) and intonation (question versus statement). The main questions were: (1) whether one of the two different vibrotactile displays of $F0$ (one a single-channel temporal display and one an eight-channel spatio-temporal display) was more successful for conveying $F0$; and (2) whether auditory speech perception experience was a factor in the successful perception of $F0$ information.

I. DISPLAYS

A main issue in designing an $F0$ vibrotactile speech perception aid is how to tailor the linguistically relevant characteristics of the $F0$ signal to vibrotactile perceptual characteristics. $F0$ varies over the range of approximately 70–500 Hz across children, women, and men, with individuals' voices exhibiting ranges of 1–1.5 octaves (Hess, 1983). Based on their research on $F0$, Hnath-Chisolm and Boothroyd (1992) suggested that 1/8-octave or better resolution is needed to effectively encode $F0$ tactually, but semitone (1/12-octave) resolution has also been suggested in the literature (Hermes and van Gestel, 1991).

Vibrotactile psychophysical experiments by Rothenberg *et al.* (1977) showed that the vibrotactile frequency difference limen results in at least ten discriminable steps between approximately 10 and 90 Hz with some additional steps, if the range is extended to 300 Hz. Beyond 300 Hz, frequency discrimination falls off rapidly. Therefore, a direct one-to-one transformation from acoustic pitch periods to vibrotactile rate is unlikely to be optimal. For example, the entire range of a child's voice (approximately 157–444 Hz; Hess, 1983) would be above the range at which frequency is best resolved by the skin. The $F0$ range of adult males was even found to be too large and poorly resolved with a direct acoustic-to-vibrotactile transformation (Bernstein *et al.*, 1989).

A. Single-channel temporal displays

Rothenberg and Molitor (1979) proposed to solve the problem of transforming acoustic $F0$ to vibrotactile $F0$ by using frequency range compression and frequency shifting. Detected voice $F0$ was encoded as vibrotactile pulses delivered by a single vibrator. The most favorable results were obtained when frequency was shifted so as to center around 50 Hz, with the scale factor at 1:1 or 1:0.75 (for a male talker whose untransformed 80-Hz range was centered at 125 Hz). Their experimental task was forced-choice identification of the stressed word and intonation type of a sentence, *Ron will win*, presented as a series of vibrotactile pulses. The sentence was spoken with emphasis on one of the three words and with the intonation pattern of either a question (rising) or a statement (falling). The results confirmed the prediction that perception is most accurate when vibrotactile stimuli make use of the frequencies below approximately 100 Hz. Analysis of Fig. 5 in the Rothenberg and Molitor (1979) study suggests that stress judgments were 51% correct ($n=8$ normal-hearing individuals, chance at 33%), and intonation judgments were approximately 90% correct ($n=8$, chance at 50%).

Using a similar paradigm to Rothenberg and Molitor (1979), Bernstein *et al.* (1989) tested several alternate $F0$-to-vibrotactile transformations. However, Bernstein *et al.* employed a much larger and more varied stimulus sentence set leading to higher uncertainty. In addition, because use of an $F0$ speech perception aid would necessarily involve speechreading under practical (not laboratory) conditions, they compared stress and intonation identification under tactile-alone (TA), visual-tactile (VT), and visual-alone (VA) conditions. When $F0$ was shifted into the range below approximately 100 Hz, stress and intonation patterns were perceived most accurately. Differences in display effectiveness were only observed under TA conditions. Under the TA condition, the most effective transformation produced somewhat more accurate identification of stress (approximately 60% correct for the best subject and a group mean of 52%, $n=5$ normal-hearing individuals) and somewhat less accurate identification of intonation (approximately 80% correct for the best subject and a group mean of 70%, $n=5$) than obtained by Rothenberg and Molitor (1979).

B. Multichannel spatio-temporal displays

An alternate method for solving the problem of matching the acoustic $F0$ characteristics to the skin's perceptual capabilities is to engage spatial perception, following the suggestion of Kirman (1973) who argued that temporal pattern perception is not a forte of the skin. Spatial resolution for touch is extremely good. Phillips and Johnson (1985) reported spatial resolution of the finger pad to be 0.7 mm for a moving stimulus. Blind readers of Braille can achieve rates of 80–200 words per minute (Foulke, 1991), indicating potential for high information transfer rates. Spatial $F0$ displays might deliver greater information than temporal displays and also result in more effective processing under cross-modal conditions. However, vibrotactile perception is also susceptible to distortions due to interactions between time and space (Geldard, 1985; Geldard and Sherrick, 1972). These distortions could enhance or degrade the perception of speech information (Kirman, 1973).

Boothroyd and colleagues implemented a spatio-temporal vibrotactile $F0$ display scheme (Boothroyd and Hnath, 1986; Boothroyd *et al.*, 1988; Hnath-Chisolm and Medwetsky, 1988; Hanin *et al.*, 1988; Waldstein and Boothroyd, 1995a) (for an aid employing a purely spatial electrotactile display scheme, see Grant *et al.*, 1986). $F0$ was extracted using an analog circuit and was encoded via vibration rate and vibrator location in a single-dimensional vibrator array (Yeung *et al.*, 1988). Under this scheme, frequency resolution is theoretically limited only by vibrotactile spatial resolution and the number of vibrotactile stimulators (Hnath-Chisolm and Kishon-Rabin, 1988). The spatial component of the Boothroyd display used a change of 0.16 octaves in input frequency to cause a change in selection of the vibrator for

activation.[1] The temporal component of the display was the output of a pulse on the spatially appropriate stimulator for every other detected pitch pulse.

Hnath-Chisolm and Kishon-Rabin (1988) compared this spatio-temporal display with a single-channel temporal-only display of $F0$, which also employed the every-other-pulse scheme. Their experimental tasks included identification of stress and intonation in separate conditions, and results were interpreted as showing some advantage for the spatio-temporal display (VT = 80% correct and TA = 78% correct, $n = 6$ normal-hearing individuals).[2] However, Hnath-Chisolm and Kishon-Rabin's temporal display of intonation (VT = 70% correct and TA = 64% correct, $n = 6$) failed to replicate TA intonation identification accuracy obtained by Rothenberg and Molitor (1979), and Bernstein *et al.* (1989) with several different temporal displays, calling into question the conclusion that there is a general advantage for a spatio-temporal display.

II. CURRENT STUDY

The present study used the same task employed in Bernstein *et al.* (1989) to investigate whether an eight-channel spatio-temporal or single-channel temporal display was more effective at conveying intonation and sentential stress information. The temporal display consisted of the presentation of every other detected pitch period, and the spatio-temporal display consisted of presentation of the same pulses but distributed across an eight-channel single-dimensional array. Experiment I investigated whether vibrotactile $F0$ enhanced stress and intonation identification beyond VA identification, and whether there were differential effects of display. Experiment II assessed the perception of stress and intonation information and display in the TA condition. Experiment III further investigated display effects for intonation identification under VT and TA conditions using a within-subjects design to compare displays. In addition to group comparisons, individual performance differences were examined as a function of display.

The goal of sensory substitution is to develop vibrotactile speech perception aids for hearing-impaired individuals. However, the relationship between the specialized experience of hearing-impaired individuals and vibrotactile speech perception has received little attention in the literature (e.g., Bernstein *et al.*, in press; Rothenberg and Molitor, 1979). Therefore, experiment IV examined effects of auditory experience on vibrotactile $F0$ perception by hearing-impaired adults.

III. EXPERIMENT I. VISUAL-ALONE VERSUS VISUAL-TACTILE JUDGMENTS OF STRESS AND INTONATION

In experiment I, under VA and VT conditions, subjects identified both the position of an emphatically stressed word in a sentence and the sentence intonation pattern.

A. Subjects

The 12 subjects (all female), were age 20–29 years old, with normal hearing, 20/30 or better normal or corrected vision, and English as their native language. Six were randomly assigned to the single-channel temporal display and six to the eight-channel spatio-temporal display. Subjects were paid for their time in the experiment.

B. Stimuli

1. Sentence stimuli

Four sentences were used to generate stimuli for this and subsequent experiments.

(1) We owe you a yoyo.
(2) We will weigh you.
(3) Pat cooked Pete's breakfast.
(4) Chuck caught two cats.

Phonetic content was controlled to examine the influence of continuously voiced versus interrupted vibrotactile stimulus patterns: the first two sentences (referred to as ''continuous'') have voiced continuants (resulting in almost uninterrupted voicing), and the second two (referred to as ''discontinuous'') have voiceless stop and fricative consonants (except for /b/ in ''breakfast'') (resulting in brief periods of silence). It was predicted that vibrotactile stress identification would be easier for sentences with voiceless consonants, because the silences would facilitate identifying syllable location and duration (Bernstein *et al.*, 1989). At the same time, inasmuch as those gaps interrupt intonation contours, they might reduce vibrotactile intonation identification accuracy (Bernstein *et al.*, 1989). Twenty-four stimulus sentences were generated from orthogonal combination of intonation pattern (statement or question) and position of the word receiving emphatic stress (first, second, or third). For example, the base sentence ''We owe you a yoyo.'' generated the following six sentences in which the capitalized word received emphatic stress:

WE owe you a yoyo.
WE owe you a yoyo?
we OWE you a yoyo.
we OWE you a yoyo?
we owe YOU a yoyo.
we owe YOU a yoyo?

Two tokens of each sentence in its six different instantiations were spoken by a male and a female talker (96 tokens total).

Stimuli were recorded on videotape and then stored on video laserdisc (Bernstein and Eberhardt, 1986). The 96 stimuli had been previously evaluated for production accuracy via auditory testing (98% correct stress and intonation identification) (Bernstein *et al.*, 1989). A linear-phase electroglottograph (EGG) (Synchrovoice) signal, which was passed through a high-pass filter (Glottal Enterprise) was recorded on one audio channel of the video recording. The dominant frequency in the EGG signal is the voice $F0$ (Fourcin, 1981). The EGG signals were used as input to the vibrotactile aid following gating to eliminate spurious vibrotactile output due to shifts in the noise floor as the videodisc player moved from pause to play. Video stimuli were presented on a color monitor.

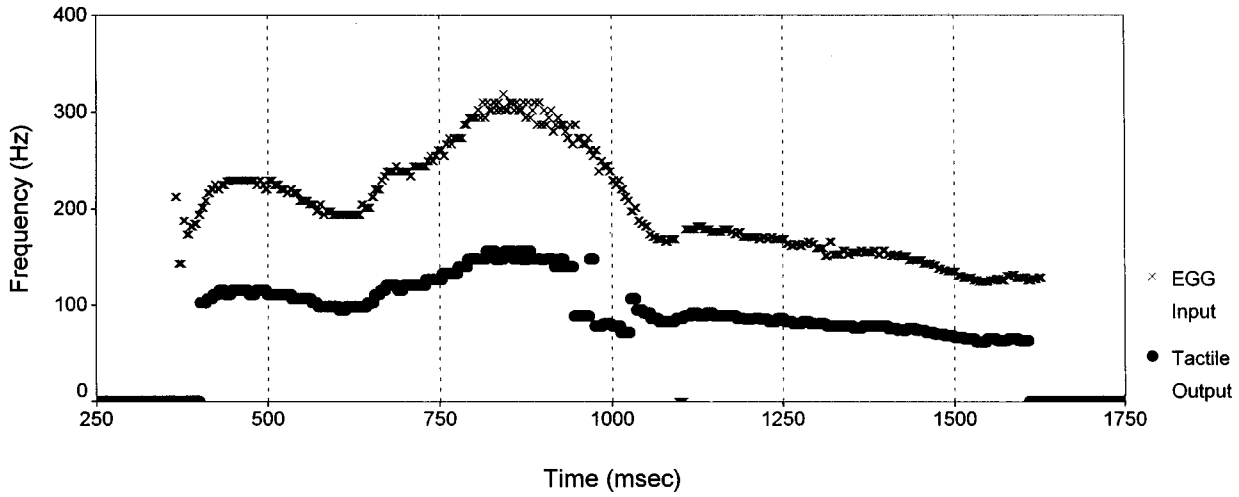

FIG. 1. Frequency in Hz is displayed as a function of time for the input EGG signal (indicated by the ×'s) and the output tactile signal (indicated by the filled circles). The statement ''We WILL weigh you.'' was spoken by the female talker. Tactile-alone stress (chance=33%) judgment accuracy for this token was 30% correct with the temporal display and 45% correct with the spatio-temporal display. Tactile-alone intonation (chance=50%) judgment accuracy was 85% correct with the temporal display and 100% correct with the spatio-temporal display.

2. Vibrotactile stimulus generation

Both vibrotactile displays in these experiments employed the same real-time $F0$ extraction algorithm. The algorithm was based on a time domain model of the decay of the acoustic speech waveform following glottal excitation. The algorithm was implemented on a Texas Instruments TMS320 digital signal processing chip. Using a set of conditions prespecified in software, the algorithm compared the decline in amplitude over a sequence of digital samples with the decay rate of the model. Criteria known to the model were adaptively updated. Initial conditions were based on likely first formant values, which determine the largest upward excursion in the speech waveform. When the amplitude of the sampled waveform exceeded criteria for decay, or the duration of the putative pitch period was within the limits of the model, a pitch period was reported by the processor. Over time, in the absence of input, the model returned to its initial values.

The performance of the current $F0$ extraction algorithm has not yet been subjected to direct comparison with other possible real-time extraction $F0$ extraction algorithms (for a comparison of three alternate algorithms, see Bosman and Smoorenburg, 1997). However, we have examined several randomly selected examples of the pitch tracking by the current algorithm (see Figs. 1–4). Frequency in Hz is displayed as a function of time for the handpicked pitch of the input EGG signal and the output vibrotactile signal. Figures 1 and 3 show better frequency tracking for continuously voiced sentences, as would be expected given the difficulty of extracting pitch from speech with many stop consonants. The figures also show that errors were made in tracking $F0$.

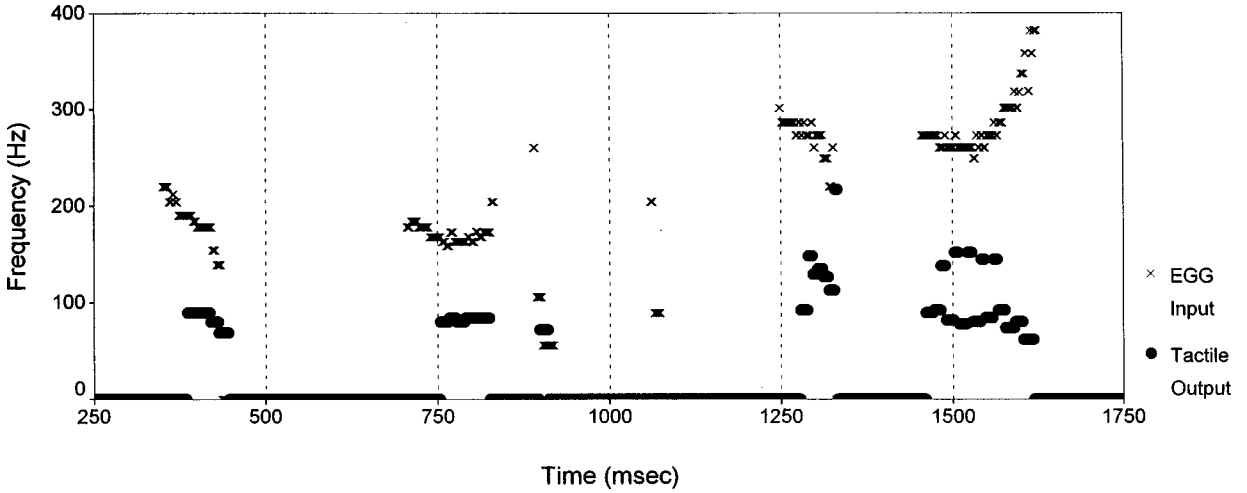

FIG. 2. Frequency in Hz is displayed as a function of time for the input EGG signal (indicated by the ×'s) and the output tactile signal (indicated by the filled circles). The question ''Chuck CAUGHT two cats?'' was spoken by the female talker. Tactile-alone stress (chance=33%) judgment accuracy for this token was 85% correct with the temporal display and 60% correct with the spatio-temporal display. Tactile-alone intonation (chance=50%) judgment accuracy was 100% correct with the temporal display and 90% correct with the spatio-temporal display.

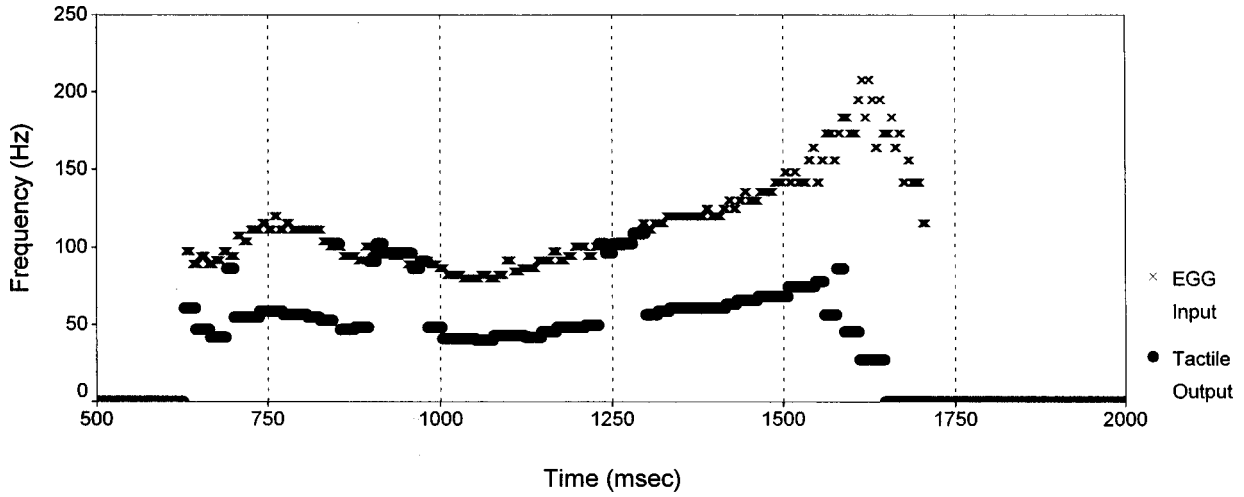

FIG. 3. Frequency in Hz is displayed as a function of time for the input EGG signal (indicated by the ×'s) and the output tactile signal (indicated by the filled circles). The question ''We will WEIGH you?'' was spoken by the male talker. Tactile-alone stress (chance=33%) judgment accuracy for this token was 40% correct with the temporal display and 70% correct with the spatio-temporal display. Tactile-alone intonation (chance=50%) judgment accuracy was 100% correct with the temporal display and 100% correct with the spatio-temporal display.

However, examination of the human performance data taken from experiment II (see captions of Figs. 1–4) suggests that with tactile information alone, stress and intonation judgments can be accurate even when tracking errors occurred. For example, despite substantial errors in the tracking of the sentence final frequency contour for the token displayed in Fig. 2, intonation judgments were highly accurate.

The processor in the vibrotactile aid was programmed to send a signal to a custom electronic circuit that initiated a square pulse for every second detected pitch pulse. This scheme was required by the spatio-temporal display in order to determine the appropriate output channel. Discarding the initial pulse introduced a variable delay in the output. Analysis of 8 of the 96 tokens suggested that onset delays ranged between 0 and 50 ms with an average onset delay (~30 ms). However, this delay was within the 40-ms limit that McGrath and Summerfield (1985) suggested as sufficient to *not* dramatically affect audio-visual speech understanding.

The scheme used to assign output channels for the eight-channel aid is shown in Fig. 5. Output channel number is plotted as a function of input rate. The lines with the open squares represent the channel selection scheme for the male talker. Channel selection was programmed on the basis of prior analysis of the frequency ranges of the two talkers (Bernstein *et al.*, 1989) and was designed to center the eight channels over the range of frequencies containing the center 90% of detected pitch periods for each talker. Frequency ranges were allocated to channels equally except for the highest and lowest channels, which were expanded to accommodate extreme pitch excursions. Spatial resolution was approximately 0.083 octaves per vibrotactile stimulator location for the male talker and 0.125 octaves for the female talker. Vibrotactile stimulation was delivered via small solenoids with contact points of 2 mm in diameter arrayed with 4-mm separation between them. The single-channel display presented every pulse on a single solenoid. Amplitude of the

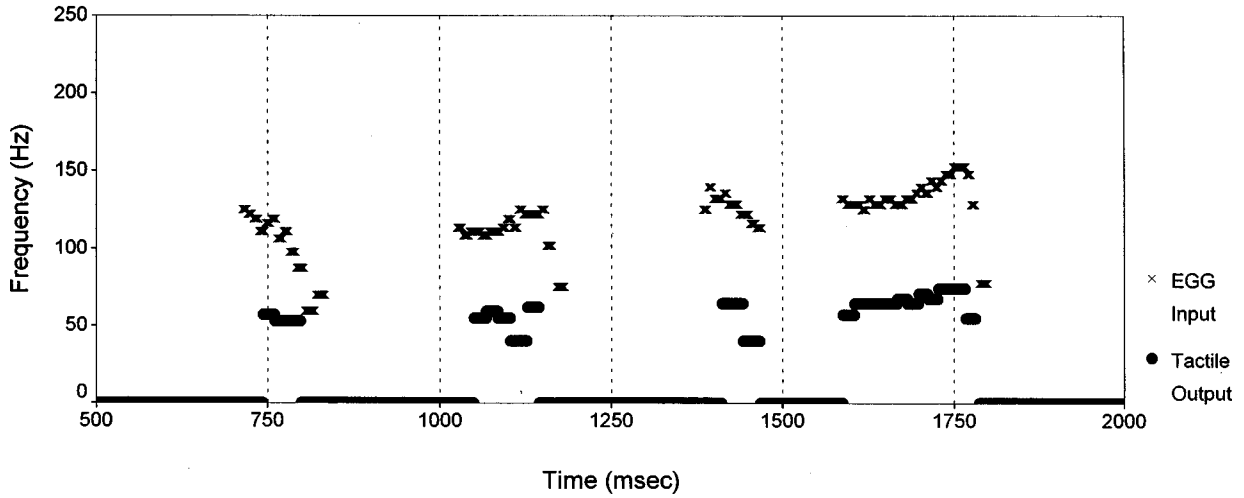

FIG. 4. Frequency in Hz is displayed as a function of time for the input EGG signal (indicated by the ×'s) and the output tactile signal (indicated by the filled circles). The question ''Chuck CAUGHT two cats?'' was spoken by the male talker. Tactile-alone stress (chance=33%) judgment accuracy for this token was 55% correct with the temporal display and 30% correct with the spatio-temporal display. Tactile-alone intonation (chance=50%) judgment accuracy was 75% correct with the temporal display and 90% correct with the spatio-temporal display.

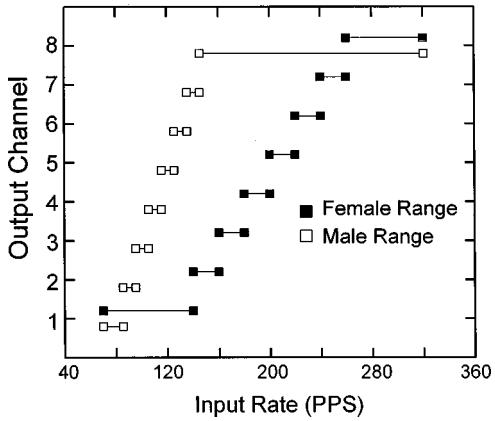

FIG. 5. Channel selection for spatio-temporal display of voice *F*0. The lines delimited by the open squares indicate the input ranges for the male display. The lines delimited by the filled squares indicate the ranges for the female display.

output signal was not modulated by the amplitude input signal. All stimuli were presented to the hypothenar of the left hand.[3]

C. Design and procedure

Stimulus presentation and response collection were computer controlled. The subject's task was to make a six-alternative forced-choice identification of the emphatically stressed word (first, second, or third word) and the intonation pattern (question or statement) of each stimulus sentence. Responses were collected using a six-button response box with ''question'' responses on the right side of the box and ''statement'' responses on the left. Buttons on each side were numbered to correspond to the position in the sentence of the stressed word.

LEDs on the response box signaled the beginning of a trial. The first frame of a video stimulus was then presented and paused briefly, with the talker in a relaxed position. The video stimulus was then played in real-time. The final frame of the stimulus was then paused with the talker again in a relaxed position. Following each response, feedback was provided by lighting an LED over the button associated with the correct response.

Subjects were tested in both VA and VT conditions, with the order of conditions counterbalanced. Sentences for a single talker were presented in blocks of 48 (2 tokens×4 base sentences×2 types of intonation×3 positions of stress). Subjects received 20 blocks in the visual condition and 30 blocks in the VT condition. The talker was alternated every five blocks, and the order of talker presentation was counterbalanced across subjects. During VT trials, subjects wore earplugs and received shaped noise through headphones to mask possible sounds caused by the stimulator. The stimulus blocks lasted approximately 60 mins, and subjects were tested in seven sessions. The subjects received at most 3 h of vibrotactile experience.

Subjects were informed of both the structure and content of the stimulus sentences and practice was administered prior to data collection. Practice preceding the VA condition consisted of audiovisual trials with 48 sentences (two talkers ×four base sentences×two intonation×three stress) and visual trials with 48 sentences, each sentence followed by the subject's response and feedback. Practice prior to the VT condition consisted of audiovisual presentation of the 48 sentences, the same sentences presented with video and EGG signals auditorily, and then presented with VT stimulation. Feedback was given following each trial.

TABLE I. Experiment I: Individual subject data in percent correct for *stress* judgments under visual-alone and visual-tactile conditions (Chance =33%). Display=1 indicates the subject used the temporal display; Display=8 indicates that the subject used the spatio-temporal display. Cont.=Continuous Sentences; Discont.=discontinuous sentences.

Subject (Display)	Visual-alone			Visual-tactile		
	Cont.	Discont.	Combined	Cont.	Discont.	Combined
1(1)	89	78	83	85	79	82
2(1)	82	74	78	74	81	78
3(1)	93	84	88	92	84	88
4(1)	85	75	80	83	85	84
5(1)	90	80	85	93	93	93
6(1)	97	93	95	88	87	88
7(8)	82	73	78	75	81	78
8(8)	77	71	74	78	69	73
9(8)	84	80	82	84	80	82
10(8)	93	84	89	86	80	83
11(8)	86	79	83	78	80	79
12(8)	82	83	82	91	88	90
Mean	87	79	83	84	82	83

D. Analyses

Separate $2\times2\times2\times2\times2$ (condition×talker×sentence type×order×display) repeated measures analyses of variance were performed on the mean percentage correct responses separately for stress and intonation.[4] Condition, talker, and sentence type were within-subjects variables, and order and display were between-subjects variables. The condition factor corresponded to whether the trials were performed VA or VT. The sentence-type factor compared the two sentences with voiced consonants to the two sentences with unvoiced consonants. Order corresponded to whether the subjects were tested in the VA condition first or second. Display corresponded to the temporal or spatio-temporal vibrotactile stimuli. Only the last five blocks of data for each talker, for each condition, were analyzed. Those blocks were considered representative of the subjects' most experienced performance within a given condition.

E. Results and discussion

VA stress and intonation identifications were reliably above chance (chance=33.3% for stress and 50% for intonation) according to the binomial test, but not at ceiling. (See Tables I and II for individual subject data.)

Stress identification did not differ as a function of condition [$F(1,8)=0.00$, $p>0.96$] (see Table I). The overall mean percent correct stress was 79% for the female talker and 87% for the male talker (chance=33%) [$F(1,8)=24.94$, $p<0.01$]. This result was consistent with previous results suggesting that the female talker was more difficult to speechread than the male (Demorest and Bernstein, 1987;

TABLE II. Experiment I: Individual subject data in percent correct for *intonation* judgments under visual-alone and visual-tactile conditions (Chance=50%). Display=1 indicates the subject used the temporal display; Display=8 indicates that the subject used the spatio-temporal display. Cont.=Continuous Sentences; Discont.=discontinuous sentences.

Subject (Display)	Visual-alone			Visual-tactile		
	Cont.	Discont.	Combined	Cont.	Discont.	Combined
1(1)	63	53	58	87	74	80
2(1)	63	55	59	70	62	66
3(1)	67	65	66	86	89	88
4(1)	76	66	71	93	88	91
5(1)	58	63	66	91	81	86
6(1)	79	68	74	81	75	78
7(8)	65	53	59	92	88	90
8(8)	61	60	61	85	70	78
9(8)	68	62	65	92	86	89
10(8)	68	65	67	84	78	81
11(8)	63	68	65	83	86	85
12(8)	62	54	58	73	66	70
Mean	67	61	64	85	79	82

Eberhardt *et al.*, 1990). Stress was more accurately identified in continuous sentences (85%) than in discontinuous sentences (81%) [$F(1,8)=20.96$, $p<0.01$]. This result was counter to the prediction that stress would be more perceptible when sentences had unvoiced consonants to mark syllable boundaries. However, because the visual stimulus appeared to provide most of the information about stress, it seemed that the mostly labial place of articulation for consonants in the continuous sentences provided the syllable boundary information. This result provides support for the hypothesis that visible changes in the rhythm of alternating mouth opening during vowels and closure or approximation during consonants provides cues to the location of emphatically stressed words in sentences (Bernstein *et al.*, 1989). Both talker and sentence-type interacted with condition. Examination of the means for both of these interactions suggested that the sentence-type (see Table I) and talker differences (VA: male=88% correct, female=78% correct; VT: male=86% correct, female=80% correct) were reduced in magnitude in the visual-tactile condition relative to the visual-alone condition. These interactions are not readily interpretable in terms of the influence of the vibrotactile speech perception aid.

Identification accuracy for *intonation* differed across conditions (82% VT and 64% VA) [$F(1,8)=58.39$, $p<0.01$] (see Table II). However, the spatio-temporal and temporal display were not different [$F(1,8)=0.20$, $p=0.66$], and display did not interact with condition (VA: temporal=66%, spatio-temporal=62%; VT: temporal=82%, spatio-temporal=82% correct). A significant main effect of sentence-type and a sentence-type by talker interaction were also obtained. These effects did not interact with condition and therefore were not interpretable in relation to the tactile information. This pattern of results provides evidence of a benefit from the tactile information for making intonation judgments. However, as in the VT condition of study I reported in Bernstein *et al.* (1989), no evidence was observed for any display differences.

IV. EXPERIMENT II. TACTILE-ALONE JUDGMENTS OF STRESS AND INTONATION

Experiment II was conducted to assess how accurately stress and intonation could be perceived by vibrotaction alone and to determine whether a difference between displays would emerge in the absence of visual stimulation.

A. Stimuli and subjects

The vibrotactile stimuli and the stimulus delivery system were the same as in experiment I. Seven subjects from experiment I were tested in experiment II. An eighth subject, a native-English speaking female, was recruited. This subject performed the experiment I protocol before proceeding to experiment II. Subjects ranged from 20 to 27 years of age. The eight subjects were divided into two groups according to their previously assigned display and performed experiment II with that display.

B. Design and procedure

A block of 48 VT trials was presented to refamiliarize the subjects with the stimuli. They then judged stress and intonation for 25 blocks of TA trials for each talker. Five blocks per talker were presented in each session. The talker was alternated every five blocks, and the order of talker presentation was counterbalanced across subjects. After day 1, subjects were informed of a monetary bonus that could be earned based on day 5 accuracy for stress identification. To earn the bonus, the subjects were required to maintain intonation accuracy while improving stress accuracy.

C. Analyses

Each subject's last five blocks of stress and intonation identification for each talker were analyzed. Separate $2\times2\times2$ (talker×display×sentence-type) repeated measures analyses of variance were performed on the mean percentages of correct responses for intonation and stress. Talker and sentence-type were within-subjects factors, and display was a between-subjects factor.

D. Results and discussion

Stress information was available from the vibrotactile stimuli at levels reliably above chance according to the binomial test (56% for the temporal display and 48% for the spatio-temporal display) (chance=33.3%) (see Table III). TA stress identification accuracy did not differ significantly as a function of displays [$F(1,6)=3.11$, $p=0.13$]. Stress was more accurately identified in discontinuous sentences (59%) than in continuous sentences (45%) [$F(1,6)=82.14$, $p<0.01$], as predicted. In addition, sentence-type interacted with talker [$F(1,6)=26.24$, $p<0.01$], such that performance was better with the female talker only for the continuously voiced sentences (Continuous Male=40% correct, Continuous Female=50% correct, and Discontinuous Male=58% correct, Discontinuous Female=61% correct). Analysis of the results showed that the bonus did not influence performance levels.

TABLE III. Experiment II: Individual subject data in percent correct for *stress* judgments under the tactile-alone condition (Chance=33%). Display=1 indicates the subject used the temporal display; Display=8 indicates that the subject used the spatio-temporal display. * indicates subject did not participate in experiment I.

Subject (Display)	Experiment I subject number	Tactile-alone		
		Continuous	Discontinuous	Combined
1(1)	3	54	69	61
2(1)	*	47	60	53
3(1)	5	40	58	49
4(1)	6	50	71	61
	Mean	48	64	56
5(8)	7	40	54	47
6(8)	8	38	42	40
7(8)	11	48	65	56
8(8)	12	43	56	50
	Mean	42	54	48

Accuracy was comparable to that for stress identification obtained earlier by Rothenberg and Molitor (1979), and by Bernstein *et al.* (1989), who used the same stimuli and a different set of vibrotactile displays based on hand-picked pitch periods. Scores were also roughly comparable to those obtained by Hnath-Chisolm and Kishon-Rabin (1988) (56% correct temporal and 51% correct spatio-temporal).

Although no statistically significant differences between displays were observed for stress judgments, the temporal display tended to convey stress more accurately. This trend was also present in the TA performance reported by Hnath-Chisolm and Kishon-Rabin (1988). However, given the evidence, obtained in experiment I, that emphatic stress tends to be highly visible, this trend was not explored further in subsequent experiments.

Intonation information was available from the vibrotactile stimuli at levels reliably above chance according to the binomial test (73% for the temporal display and 83% for the spatio-temporal display) (chance=50%) (see Table IV). The difference between performance with the temporal and spatio-temporal displays in the current study was not statistically significant [$F(1,6)=2.58$, $p=0.16$]. However, the absence of statistical significance may be a result of the subject sample size.

TABLE IV. Experiment II: Individual subject data in percent correct for *intonation* judgments under the tactile-alone condition (Chance=50%). Display=1 indicates the subject used the temporal display; Display=8 indicates the subject used the spatio-temporal display.* indicates subject did not participate in experiment I.

Subject (Display)	Experiment I subject number	Tactile-alone		
		Continuous	Discontinuous	Combined
1(1)	3	85	92	89
2(1)	*	61	68	65
3(1)	5	68	59	63
4(1)	6	69	79	74
	Mean	71	74	73
5(8)	7	93	84	88
6(8)	8	92	76	84
7(8)	11	85	85	85
8(8)	12	76	74	75
	Mean	86	80	83

Intonation identification accuracy with the temporal display was worse than that reported by Rothenberg and Molitor (1979) (90% correct) and the same as Bernstein *et al.* (1989) (70% correct). However, average performance was better than reported by Hnath-Chisolm and Kishon-Rabin (1988) (64%) for their temporal display. Intonation identification accuracy with the spatio-temporal display (83% correct) was greater than spatio-temporal performance reported by Hnath-Chisolm and Kishon-Rabin (1988) (78% correct).

Examination of the subject data suggested that the accuracy of intonation judgments by several individuals matched or exceeded the best subject's performance (81% correct) in Bernstein *et al.*'s experiment II in which pitch was hand-picked. Thus even with errors introduced by real-time $F0$ extraction, levels of accuracy were achieved with both displays that were comparable to results obtained when the tactile signal was generated off-line for the same sentence tokens (Bernstein *et al.*, 1989).

Individual differences were observed in the ability to use the tactile information (see Table IV). For example, examination of the intonation judgment performance shows that subject 1 performed exceptionally well with the temporal-display, and subject 8 performed somewhat less accurately with the spatio-temporal display. Unfortunately, the between subjects design employed limits our ability to interpret the relationship of the individual differences and display type. Experiment III examined the relationship of individual differences in performance accuracy and display type.

V. EXPERIMENT III. TEMPORAL VERSUS SPATIO-TEMPORAL DISPLAYS FOR INTONATION JUDGMENT

Given the theoretically motivated prediction of an advantage with the spatio-temporal display and the possibility of individual differences in display effectiveness, an additional experiment was conducted to attempt more sensitively to observe differential effects of display. Experiment II provided an indication, although not statistically significant, that the two displays were differentially effective for both stress and intonation judgments. However, the results of experiment I provided evidence that *only* intonation judgments were influenced by the addition of vibrotactile information. Experiment III examined the advantage for the spatio-temporal display for intonation judgments.

Arguably, the complexity of the task and the stimulus set in experiments I and II could result in performance errors that reduced sensitivity. Therefore in experiment III, one talker was presented, the subjects judged intonation only, and testing was under the two conditions employing vibrotactile stimuli, VT and TA. To enhance the power of the design, subjects received both displays in counterbalanced order and repeated measures analysis was performed.

A. Subjects and stimuli

The 21 subjects were age 18–45 years old, with normal hearing, 20/30 or better normal or corrected vision, and English as their native language. Complete data were obtained for 16 of the 21,[5] who were divided into groups of eight and received both displays in counterbalanced order. Subjects received approximately 3 h of experience with each display and had not participated in experiments I or II.

In experiments I and II, two talkers were used to increase the generalizability of the findings (Demorest *et al.*, 1996). However, the use of multiple talkers is known to increase task difficulty (Mullennix *et al.*, 1989). In the current experiment, we chose to use a single-talker to reduce task difficulty. The sentence stimuli were the 48 tokens spoken by the female talker.

B. Design, procedure, and analyses

Stimuli were presented under TA and VT conditions. Subjects made two-alternative forced-choice intonation identifications by pressing one of two buttons (one labeled ''question,'' and one ''statement''). Practice trials were presented on the first day of testing with each of the two displays. For each display, 15 blocks of trials were presented, 5 on each of 3 days. Only the data from the last five blocks of trials for each display were analyzed. For each subject, order of the 48 sentences was independently randomized within each block and condition, and the 2 conditions (VT and TA) were randomly ordered across the 5 blocks presented on a given day with the constraint that no more than 3 blocks were presented in a given condition.

A repeated measures analysis of variance was performed on percent correct intonation identification. The within-subjects factors were display (temporal versus spatio-temporal), condition (TA versus VT), sentence-type (continuous versus discontinuous), and block. The between-subjects factor was display order (temporal first versus spatio-temporal first).

C. Results and discussion

Across VT and TA conditions, intonation identification was more accurate with the spatio-temporal (91% correct) than with the temporal display (75% correct) [$F(1,14)=18.53$, $p<0.01$] (see Table V). Also, VT identification differed significantly from TA identification [$F(1,14)=9.29$, $p<0.01$]. However, a statistically significant display×condition interaction was also obtained [$F(1,14)=10.25$, $p<0.01$]: Spatio-temporal display resulted in the same performance levels across conditions (91% correct VT and TA), whereas performance varied across conditions with the *temporal* display (78% correct VT versus 72% correct TA). These results demonstrated an advantage for the spatio-temporal display under the TA and VT conditions. The advantage observed under VT conditions is important in that it suggests a difference may exist under practical (not just laboratory) conditions.

The increased accuracy with the spatio-temporal display observed in this experiment has two possible sources. First, the two displays differed in the extent to which they had been optimized for this female talker. The spatio-temporal display was optimized specifically for the presentation of the female talker (see Fig. 5). The temporal display was designed to deliver both male and female talkers and was known to be less than optimal for this female talker. Specifically, the female talker's mean $F0$ was 200 Hz, with her mean for the every-other-pulse scheme being 100 Hz. The best frequency resolution for the skin is below 100 Hz, thus the temporal display of the female talker's $F0$ is not optimally suited to the temporal resolution capabilities of the skin. Second, the advantage could be due to the use of the spatial dimension.

Although the current data alone do not allow us to decide between these two possible interpretations, examination of previous performance with tactile transformation of these stimuli can provide some insight. In their Fig. 2, Bernstein *et al.* (1989) present data on temporal displays optimized for the presentation of the same stimuli spoken by the female talker as were used in the current experiment. Average TA performance levels with the best of these temporal displays was comparable (74% correct) to the current TA performance with a temporal display (72% correct). Thus the increase in performance with the spatio-temporal display was likely due to the use of the spatial dimension and not the optimization of the display for a specific talker.

Examination of the individual subject data (see Table V) suggests that performance level varied more for the temporal display than for the spatio-temporal display. Within-subject performance levels (in percent correct) were not significantly correlated across displays for either condition (TA: $r=0.377$ and VT: $r=0.398$). The pattern of results suggests an advantage for spatio-temporal display in the stability of performance across individuals. That is, most individuals could successfully use the spatio-temporal display, whereas only some of those individuals could successfully use the temporal display.

TABLE V. Experiment III: Individual subject data in percent correct for *intonation* judgments under the visual-tactile and tactile-alone condition (Chance=50%).

	Temporal		Spatio-temporal	
Subject	Tactile-alone	Visual-tactile	Tactile-alone	Visual-tactile
1	66	65	95	94
2	55	68	89	90
3	85	91	98	95
4	93	88	83	81
5	88	90	85	92
6	65	70	93	98
7	45	53	89	78
8	87	94	93	98
9	68	75	92	94
10	83	86	95	95
11	69	78	95	95
12	45	57	72	63
13	44	65	90	97
14	84	87	95	98
15	95	97	97	96
16	83	90	88	86
Mean	72	78	90	91

TABLE VI. Display-type, age of onset in years, three-frequency (0.5 kHz, 1 kHz, 2 kHz) pure-tone averages (dB HL) and speechreading ability of sentences in percent words correct for subjects in experiment IV. NMH=no measurable hearing.

Subject (onset)	Display	Age of onset of hearing loss	Left ear	Right ear	Speechreading of sentences
1(Post)	Temporal	4	NMH	NMH	67
2(Post)	Temporal	4	NMH	NMH	37
3(Post)	Spatio-Temporal	3	110	105	61
4(Post)	Spatio-Temporal	15	103	95	28
5(Pre)	Temporal	Birth	83	92	67
6(Pre)	Temporal	Birth	87	100	72
7(Pre)	Spatio-Temporal	Birth	115	110	62
8(Pre)	Spatio-Temporal	Birth	100	105	71

VI. EXPERIMENT IV. VISUAL-ALONE VERSUS VISUAL-TACTILE JUDGMENTS OF STRESS AND INTONATION BY HEARING-IMPAIRED INDIVIDUALS

The goal of sensory substitution is to develop vibrotactile speech perception aids for hearing-impaired individuals. Having observed several hearing-impaired subjects who were less successful identifying vibrotactile stress and intonation than hearing subjects, Rothenberg and Molitor (1979) suggested that vibrotactile pitch perception could be based on experience with auditory pitch. Alternatively, the ability to judge stress and intonation could be based on experience with spoken language. That is, individuals with reduced experience perceiving spoken language, might have more difficulty with identification of stress and intonation regardless of the form of stimulation. Experiment IV, which was a modified version of experiment I, employed pre- and postlingually hearing-impaired adult subjects. In addition to testing stress and intonation judgments, a test was also given to estimate the speechreading ability of our subjects with early ages-of-onset of hearing impairment.

A. Subjects

The subjects were eight hearing-impaired adults, age 19–30 years, four with pre- and four with post-lingual hearing impairments. They were all from the Gallaudet University community. Table VI shows the three-frequency pure-tone averages (dB HL) for each of the subjects, their age at onset of hearing impairment, the display they received and their accuracy for speechreading words in sentences. All subjects reported English as their native language. They were paid for their participation.

B. Stimuli, design, and procedure

The stimuli and task in experiment IV were the same as in experiment I. The sequence of conditions was held constant across subjects. VT stimuli were used to help explain and give initial practice. It was hypothesized that the vibrotactile stimuli would aid in conveying the concept of stress and intonation, in the event that the subjects were unfamiliar with these linguistic characteristics.

Subjects were given written instructions explaining the task followed by a spoken explanation with manual sign accompaniment. The experimenter presented the subjects with examples of the different types of intonation patterns and stress patterns using live voice (and no manual signs), which was processed and transformed into vibrotactile stimulation in real-time. It was verified that the subjects had a basic understanding of the task. Subjects were then presented with practice consisting of 48 VT trials and 48 VA trials. Each trial was followed by feedback. Then subjects identified stress and intonation in 4 blocks of 48 sentences in the VA condition followed by 30 blocks of VT trials, followed by 20 blocks of VA trials. Half of the blocks were produced by the female talker and half by the male talker, with order of talker counterbalanced across subjects. The total number of trials in each condition was equivalent to that in experiment I. At the end of testing, each subject was presented with a set of 100 prerecorded sentences spoken by a different male talker to assess speechreading ability. Sentences were presented one at a time under computer control and after each sentence subjects typed what they thought the talker said.

C. Analyses

Separate $2\times2\times2\times2\times2$ (condition×talker×sentence-type×pre-post×display) repeated measures analyses of variance were performed on the mean percentages of correct responses for intonation and stress, as in experiment I, except that pre–post corresponded to whether the subjects had pre- or post-lingual hearing impairments. Again, only the last five blocks of data within the VA and VT conditions were analyzed.

D. Results and discussion

VA *stress* identification was reliably above chance for both talkers (80% correct for the female talker and 84% correct for the male talker) according to the binomial test (chance=33.3%) (see Table VII). VA *intonation* identification was reliably above chance for the male talker (66% correct) but not for the female talker (56% correct), according to the binomial test (chance=50%) (see Table VIII). The accuracy of speechreading sentences (see Table VI) is consistent with our previous studies assessing speechreading ability (Bernstein *et al.*, 1998; Auer, 1997). Specifically, individuals with early onset hearing impairments (subjects 1, 3, 5, 6, 7, 8) frequently far outperform individuals with late-onset hearing impairments (e.g., subject 4) or normal hearing.

TABLE VII. Experiment IV: Individual subject data in percent correct for *stress* judgments under visual-alone and visual-tactile conditions (Chance=33%). Display=1 indicates the subject used the temporal display; Display=8 indicates that the subject used the spatio-temporal display. Post indicates the subject had a post-lingual hearing impairment. Pre indicates the subject had a pre-lingual hearing impairment.

Subject (Display) (Onset)	Visual-alone			Visual-tactile		
	Cont.	Discont.	Combined	Cont.	Discont.	Combined
1(1)(Post)	87	82	85	75	73	74
2(1)(Post)	88	75	82	77	75	76
3(8)(Post)	95	88	92	98	88	93
4(8)(Post)	71	62	66	63	60	62
5(1)(Pre)	91	87	89	89	82	85
6(1)(Pre)	70	63	66	74	65	69
7(8)(Pre)	93	84	89	91	83	87
8(8)(Pre)	89	83	86	85	75	80
Mean	86	78	82	81	75	78

The results of experiment IV were essentially consistent with those of experiment I. The analysis of variance for *stress* identification revealed statistically significant effects of talker [$F(1,4)=15.18$, $p<0.02$] and sentence type [$F(1,4)=109.44$, $p<0.01$]. As in experiment I, stress identification was easier with the male talker and easier for continuous sentences (see Table VII). Furthermore, as in experiment I, no significant effects or interactions related to the variables of interest were revealed.

Intonation identification accuracy was enhanced by the addition of the vibrotactile $F0$ information (61% correct VA and 71% correct VT) [$F(1,4)=9.68$, $p<0.04$]. Consistent with the results of experiment I, intonation identification was easier for continuous sentences [$F(1,4)=46.07$, $p<0.01$]. However, this effect did not interact with condition and was not interpretable in relation to the tactile information. No statistically significant effects of display or pre- versus post-lingual hearing impairment were observed. Thus benefit for intonation judgment accuracy obtained with the addition of the tactile information does not appear related to the age-of-onset of the hearing impairment or the type of vibrotactile display used.

The similarity of the results for individuals with pre- and post-lingual onset of hearing impairment does not support the suggestion that vibrotactile pitch perception may be based on auditory pitch perception experience (Rothenberg *et al.*, 1977). However, experiential differences between these two populations were relevant to VA intonation judgment accuracy. The post-lingual group was better able to make intonation judgments from visual speech information [$t(6)=4.197$, $p<0.01$; Pre-lingual=56% correct, Post-lingual=66% correct]. Interestingly, this difference in VA intonation judgment accuracy was not related to speechreading ability or the magnitude of enhancement observed with the addition of tactile information.

VII. GENERAL DISCUSSION

This study was conducted within the context of a project to develop a new, wearable vibrotactile speech perception aid. The main questions with practical implications were: (1) whether one of the two different vibrotactile displays of $F0$ was more successful for conveying $F0$; and (2) whether auditory speech perception experience was a factor in the successful perception of $F0$ information.

The current studies demonstrated an advantage in intonation judgment accuracy for a spatio-temporal display over a temporal display. The advantage was observed under both VT and TA presentation conditions, but was reduced in magnitude in the VT condition. Furthermore, the advantage was

TABLE VIII. Experiment IV: Individual subject data in percent correct for *intonation* judgments under visual-alone and visual-tactile conditions (Chance=50%). Display=1 indicates the subject used the temporal display; Display=8 indicates the subject used the spatio-temporal display. Post indicates the subject had a post-lingual hearing impairment. Pre indicates the subject had a pre-lingual hearing impairment.

Subject (Display) (Onset)	Visual-alone			Visual-tactile		
	Cont.	Discont.	Combined	Cont.	Discont.	Combined
1(1)(Post)	72	63	67	70	69	70
2(1)(Post)	64	59	62	80	77	79
3(8)(Post)	73	66	69	90	77	84
4(8)(Post)	70	61	65	81	71	76
5(1)(Pre)	66	53	59	75	68	72
6(1)(Pre)	52	50	51	57	53	55
7(8)(Pre)	60	57	58	83	76	79
8(8)(Pre)	63	49	56	57	56	56
Mean	65	57	61	74	68	71

observed in the context of a temporal display that also provided a significant enhancement over the visually available information. Thus the current results appear to provide stronger evidence in favor of a spatio-temporal display than was reported in Hnath-Chisolm and Kishon-Rabin (1988). Interestingly, evidence was observed that performance was more stable with the spatio-temporal display across individual subjects. Thus if the goal of the speech perception aid is to accurately convey sentential intonation contours, then the current study supports the use of a spatio-temporal display. However, this conclusion may not hold for other linguistic levels at which $F0$ has been shown to be a factor.

A coarse level comparison of previous perceptual and linguistic experience was possible by comparing the performance of the normal-hearing subjects in experiment I and hearing-impaired subjects in experiment IV. The pattern of results for *stress* identification did not appear to differ as a function of hearing group nor the pre–post lingual onset distinction. It is interesting to note that because hearing-impaired individuals rely on visual information for speech communication, more accurate stress identification might have been predicted on their part.

VA *intonation* identification accuracy was comparable across subject groups (64% correct for normal-hearing and 61% correct for hearing-impaired subjects). VT *intonation* identification accuracy was higher for the hearing subjects (82% for normal-hearing subjects and 71% for hearing-impaired subjects).[6] This pattern of results is consistent with the suggestion that vibrotactile pitch perception may be based on auditory pitch perception experience (Rothenberg *et al.*, 1997). However, this conclusion was not supported by the comparison of pre- versus post-lingually hearing-impaired individuals (see discussion of experiment IV). Thus although it is clear that hearing-impaired subjects received less benefit than the normal-hearing subjects, determination of the nature of the experiential factors responsible for this difference between hearing groups awaits further study (e.g., Bernstein *et al.*, 1998).

VIII. CONCLUSION

The results of the present study clearly support the use of a spatio-temporal display, if the goal is to accurately convey sentential intonation contours. Furthermore, enhancements in performance over VA performance are related to previous perceptual/linguistic experience, with normal-hearing individuals obtaining the largest enhancements. However, the issues raised in Sec. VII point to the need for additional studies investigating both of these conclusions. Direct comparison of alternate display schemes, holding signal processing constant, is relatively rare (cf., Eberhardt *et al.*, 1990; Hnath-Chisolm and Kishon-Rabin, 1988; Rothenberg and Molitor, 1979). When such studies have been conducted, they have provided insights into vibrotactile speech perception and have shown that the vibrotactile system can be sensitive to how the vibrotactile stimulus is constructed. These demonstrations encourage us to believe that systematic research and engineering methods can lead to speech perception aids that optimally engage the vibrotactile system.

ACKNOWLEDGMENTS

E. T. Auer, Jr. and L. E. Bernstein collected the majority of the data for these studies while employed at Gallaudet University. The authors thank Drs. Marilyn E. Demorest and Robin S. Waldstein, Paula E. Tucker, and two anonymous reviewers for their comments. They thank Dr. Marilyn E. Demorest for her advice on the design and analysis of experiment III. They also acknowledge the very capable assistance of Paula E. Tucker, Jennifer Johnson, and Deborah Yakel. This study was supported by a grant from NIH (DC00695). Correspondence concerning this article should be addressed to Edward T. Auer, Jr., Spoken Language Processes Laboratory, House Ear Institute, Fifth Floor, 2100 West Third Street, Los Angeles, CA 90057. Electronic mail for Edward T. Auer, Jr. may be sent via Internet to eauer@hei.org.

[1]In Hnath-Chisolm and Kishon-Rabin (1988) two different figures are given for the frequency change that corresponds to a change in vibration location, 0.14 and 0.16 octaves.

[2]In Hnath-Chisolm and Kishon-Rabin (1988) percent correct was reported after correction for guessing. The values reported here are not corrected for guessing in order to facilitate comparison of results between studies.

[3]Spatial resolution on the hypothenar is less than that on the fingerpad (Cholewiak and Collins, 1991).

[4]Using the methods described in Kirk (1968) (pp. 63–67), it was determined for experiments I and II that a data transformation was not required.

[5]Of the five who did not provide complete data, two performed a portion of the training without any masking noise, one was provided with an erroneous display, and two had scheduling difficulties.

[6]The order of the VA and VT conditions was counterbalanced for normal-hearing subjects whereas hearing-impaired subjects always received the VA condition second. Therefore, a simple practice effect could explain the difference between the two groups. However, comparison of the hearing-impaired subjects' performance with only those normal-hearing subjects who received the VA condition second resulted in the same difference between the populations.

Auer, Jr., E. T. (**1997**). ''The scope of individual differences in cognitive models of spoken language understanding,'' J. Acoust. Soc. Am. **102**, 3115A.

Bernstein, L. E., Demorest, M. E., and Tucker, P. E. (**1998**). ''Speech perception without hearing,'' Manuscript submitted for publication.

Bernstein, L. E., and Eberhardt, S. P. (**1986**). Johns Hopkins lipreading corpus I–II: Disc 1 [videodisc] (The Johns Hopkins University, Baltimore, MD).

Bernstein, L. E., Eberhardt, S. P., and Demorest, M. E. (**1989**). ''Single-channel vibrotactile supplements to visual perception of intonation and stress,'' J. Acoust. Soc. Am. **85**, 397–405.

Bernstein, L. E., Tucker, P. E., and Auer, Jr., E. T. (**1998**). ''Potential perceptual bases for successful use of a vibrotactile speech perception aid,'' Scand. J. Psych. **39**, 181–186.

Bolinger, D. L. (**1958**). ''A theory of pitch accent in English,'' Word **14**, 109–149.

Bolinger, D. L. (**1978**). ''Intonation across languages,'' in *Universals of Human Language: Volume 2. Phonology*, edited by J. P. Greenberg, C. A. Ferguson, and E. A. Moravcsik (Stanford U.P., Stanford, CA).

Boothroyd, A., and Hnath, T. (**1986**). ''Tactile supplements to speechreading,'' J. Rehab. Res. Develop. **23**, 139–146.

Boothroyd, A., Hnath-Chisolm, T., Hanin, L., and Kishon-Rabin, L. (**1988**).

''Voice fundamental frequency as an auditory supplement to the speechreading of sentences,'' Ear Hear. **9**, 306–312.
Bosman, A. J., and Smoorenburg, G. F. (**1997**). ''Evaluation of three pitch tracking algorithms at several signal-to-noise ratios,'' Acustica Acta Acust. **83**, 567–571.
Breeuwer, M., and Plomp, R. (**1984**). ''Speechreading supplemented with frequency-selective sound-pressure information,'' J. Acoust. Soc. Am. **76**, 686–691.
Breeuwer, M., and Plomp, R. (**1985**). ''Speechreading supplemented with formant-frequency information from voiced speech,'' J. Acoust. Soc. Am. **77**, 314–317.
Breeuwer, M., and Plomp, R. (**1986**). ''Speechreading supplemented with auditorily presented speech parameters,'' J. Acoust. Soc. Am. **79**, 481–499.
Cholewiak, R. W., and Collins, A. A. (**1991**). ''Sensory and physiological bases of touch,'' in *The Psychology of Touch*, edited by M. A. Heller and W. Schiff (Erlbaum, Hillsdale, NJ).
Cutler, A., and Butterfield, S. (**1992**). ''Rhythmic cues to speech segmentation: Evidence from juncture misperception,'' J. Mem. Lang. **31**, 218–236.
Demorest, M. E., and Bernstein, L. E. (**1987**). ''Reliability of individual differences in lipreading,'' J. Acoust. Soc. Am. **82**, S24.
Demorest, M. E., Bernstein, L. E., and De Haven, G. P. (**1996**). ''Generalizability of speechreading performance on nonsense syllables, words, and sentences: Subjects with normal hearing,'' J. Speech Hear. Res. **39**, 697–713.
Eberhardt, S. P., Bernstein, L. E., Demorest, M. E., and Goldstein, M. H. (**1990**). ''Lipreading sentences with single-channel vibrotactile transformations of voice fundamental frequency,'' J. Acoust. Soc. Am. **88**, 1274–1285.
Foulke, E. (**1991**). ''Braille,'' in *The Psychology of Touch*, edited by M. A. Heller and W. Schiff (Erlbaum, Hillsdale, NJ).
Fourcin, A. J. (**1981**). ''Laryngographic assessment of phonatory function,'' Am. Speech Hear. Assoc. Rep. **11**, 116–127.
Fry, D. B. (**1955**). ''Duration and intensity as acoustic correlates of linguistic stress,'' J. Acoust. Soc. Am. **35**, 765–769.
Fry, D. B. (**1958**). ''Experiments on the perception of stress,'' Lang. Speech **1**, 126–152.
Geldard, F. (**1985**). ''The mutability of time and space on the skin,'' J. Acoust. Soc. Am. **77**, 233–237.
Geldard, F., and Sherrick, C. (**1972**). ''The cutaneous rabbit: A perceptual illusion,'' Science **178**, 178–179.
Grant, K. W. (**1987**). ''Encoding voice pitch for hearing-impaired listeners,'' J. Acoust. Soc. Am. **82**, 423–432.
Grant, K. W., Ardell, L. H., Kuhl, P. K., and Sparks, D. W. (**1986**). ''The transmission of prosodic information via an electrotactile speechreading aid,'' Ear Hear. **7**, 328–335.
Haggard, M., Ambler, S., and Callow, M. (**1970**). ''Pitch as a voicing cue,'' J. Acoust. Soc. Am. **47**, 613–617.
Hanin, L., Boothroyd, A., and Hnath-Chisolm, T. (**1988**). ''Tactile presentation of voice fundamental frequency as an aid to speechreading of sentences,'' Ear Hear. **9**, 329–334.
Hermes, D. J., and van Gestel, J. C. (**1991**). ''The frequency scale of speech intonation,'' J. Acoust. Soc. Am. **90**, 97–102.
Hess, W. (**1983**). *Pitch Determination of Speech Signals* (Springer-Verlag, New York).
Hnath-Chisolm, T., and Boothroyd, A. (**1992**). ''Speechreading enhancement by voice fundamental frequency: The effects of contour distortions,'' J. Speech Hear. Res. **35**, 1160–1168.
Hnath-Chisolm, T., and Kishon-Rabin, L. (**1988**). ''Tactile presentation of voice fundamental frequency as an aid to the perception of speech pattern contrasts,'' Ear Hear. **9**, 329–334.
Hnath-Chisolm, T., and Medwetsky, L. (**1988**). ''Perception of frequency contours via temporal and spatial tactile transforms,'' Ear Hear. **9**, 322–328.
House, A. S., and Fairbanks, G. (**1953**). ''The influence of consonant environment upon the secondary acoustical characteristics of vowels,'' J. Acoust. Soc. Am. **25**, 105–113.
Kirk, R. E. (**1968**). *Experimental Design Procedures for the Behavioral Sciences* (Wadsworth, Belmont, CA).
Kirman, J. H. (**1973**). ''Tactile communication of speech: A review and analysis,'' Psychol. Bull. **80**, 54–74.
Kishon-Rabin, L., Boothroyd, A., and Hanin, L. (**1996**). ''Speechreading enhancement: A comparison of spatial-tactile display of voice fundamental frequency ($F0$) with auditory $F0$,'' J. Acoust. Soc. Am. **100**, 593–602.
Lehiste, I. (**1970**). *Suprasegmentals* (MIT Press, Cambridge, MA).
Lisker, L., and Abramson, A. S. (**1967**). ''The voicing dimension: Some experiments in comparative phonetics,'' in *Proceedings of the Sixth International Congress of Phonetic Sciences*, Prague (Academia, Prague), pp. 563–567.
McGrath, M., and Summerfield, Q. (**1985**). ''Intermodal timing relations and audiovisual speech recognition by normal-hearing adults,'' J. Acoust. Soc. Am. **77**, 678–685.
Mullennix, J. W., Pisoni, D. B., and Martin, C. S. (**1989**). ''Some effects of talker variability on spoken word recognition,'' J. Acoust. Soc. Am. **85**, 365–378.
Phillips, J. R., and Johnson, K. O. (**1985**). ''Neural mechanisms of scanned and stationary touch,'' J. Acoust. Soc. Am. **77**, 220–224.
Pike, K. (**1945**). *The Intonation of American English* (University of Michigan Press, Ann Arbor, MI).
Plant, G., and Risberg, A. (**1983**). ''The transmission of fundamental frequency variations via a single channel vibrotactile aid,'' Stockholm, Sweden, Speech Transmission Laboratory, Quarterly Report, **2–3**, 61–84.
Reed, C. M., Delhorne, L. A., and Durlach, N. I. (**1993**). ''Historical overview in tactile aid research,'' in *Proceedings of the Second International Conference on Tactile Aids, Hearing Aids, and Cochlear Implants*, edited by A. Risberg, S. Felicetti, and K.-E. Spens (Akademitryck AB, Edsbruk, Sweden).
Rosen, S. M., Fourcin, A. J., and Moore, B. C. J. (**1981**). ''Voice pitch as an aid to lipreading,'' Nature (London) **291**, 150–152.
Rothenberg, M., and Molitor, R. D. (**1979**). ''Encoding voice fundamental frequency as vibrotactile frequency,'' J. Acoust. Soc. Am. **66**, 1029–1038.
Rothenberg, M., Verrillo, R. T., Zahorian, S. A., Brachman, M. L., and Bolanowski, S. J. (**1977**). ''Vibrotactile frequency for encoding a speech parameter,'' J. Acoust. Soc. Am. **62**, 1003–1012.
Sluijter, A. M. C., and van Heuven, V. J. (**1996**). ''Spectral balance as an acoustic correlate of linguistic stress,'' J. Acoust. Soc. Am. **100**, 2471–2485.
Streeter, L. A. (**1978**). ''Acoustic determinants of phrase boundary perception,'' J. Acoust. Soc. Am. **64**, 1582–1592.
Summers, I. R. (**1992**). ''Signal processing strategies for single channel aids,'' in *Tactile Aids for the Hearing Impaired*, edited by I. R. Summers (Whurr, London).
Waldstein, R. S., and Boothroyd, A. (**1995a**). ''Comparison of two multichannel tactile devices as supplements to speechreading in a postlingually deafened adult,'' Ear Hear. **16**, 198–208.
Waldstein, R. S., and Boothroyd, A. (**1995b**). ''Speechreading supplemented by single-channel and multichannel displays of voice fundamental frequency,'' J. Speech Hear. Res. **38**, 690–705.
Yeung, E., Boothroyd, A., and Redmond, C. (**1988**). ''A wearable multichannel tactile display of voice fundamental frequency,'' Ear Hear. **9**, 342–350.

Interrelation between proton transfer reactions and solvent structure studied by the ultrasonic absorption method

N. Kuramoto and S. Nishikawa
Department of Chemistry and Applied Chemistry, Faculty of Science and Engineering, Saga University, Saga 840, Japan

(Received 22 September 1997; revised 10 March 1998; accepted 19 June 1998)

Ultrasonic absorption coefficients in aqueous solutions of methanol at 1.00, 2.00, 3.00, 4.00, and 6.00 mol dm^{-3} and in those of ethanol at 1.00, 2.00, 3.00, 4.00, 5.00, and 6.00 mol dm^{-3} have been measured in the frequency range from 0.8–220 MHz at 25.0 °C. No excess absorption has been observed in any of these solutions except in the 5.00 and 6.00 mol dm^{-3} ethanol solutions, for which a Debye-type single relaxational equation has been fitted. In order to see the effects of methanol and ethanol on the dynamic characteristics of aqueous amine solutions, the ultrasonic absorption measurements have been carried out in aqueous solutions of propylamine containing 1.00, 2.00, 3.00, 4.00, and 6.00 mol dm^{-3} methanol and 1.00, 2.00, 3.00, and 4.00 mol dm^{-3} ethanol. The excess absorption has been observed, and the frequency dependence of the ultrasonic absorption coefficients has been well described by the Debye-type single relaxational equation. The cause of the relaxation is due to a perturbation of equilibrium associated with a proton transfer reaction. The rate constants have been determined from hydroxide ion concentration dependence of the relaxation frequency, and the standard volume change of the reaction has been calculated from the reactant concentration dependence of maximum absorption per wavelength. It has been found that the addition of methanol causes the decrease in the diffusion controlled rate constant and the trend of the decrease is more remarkable in the concentration range from 3.00–6.00 mol dm^{-3}. On the other hand, the rate constant in the solution with ethanol has decreased linearly with an increase in the ethanol concentration. The reverse rate constant and the volume change of the reaction have not been affected by the addition of the two alcohols. Using a theoretical equation for the diffusion controlled reaction, a diffusion coefficient of the hydroxide ion has been determined at various concentrations of the additives. These results are discussed in relation to the effects of methanol and ethanol on water structure. © *1998 Acoustical Society of America.* [S0001-4966(98)06509-6]

PACS numbers: 43.80.Cs, 43.80.Ev [FD]

INTRODUCTION

Ultrasonic absorption and velocity data have been widely utilized to investigate solution characteristics and they provide useful information of the static and dynamic properties.[1–3] Using ultrasonic absorption method, we have shown that urea and 2-propanol affect the kinetic and thermodynamic parameters of a proton transfer reaction in aqueous solutions of propylamine.[4–7] Urea and 2-propanol are considered to be a water structure breaker and a water structure promoter, respectively.[8–10] It is interesting to see how additives influence the proton transfer reaction because the reaction proceeds through the network of water hydrogen bond and additives change the reaction field. Based on the results of our ultrasonic absorption study for aqueous solutions of various alcohols,[11] it has been explored that ethoxyl group does not change the solvent water structure so much and the methoxyl group acts as water structure breaker. Comparing the results of the various additive effects on the proton transfer reaction offers the key to elucidate an interrelation between the solvent structure and the reaction. Then, in this study we have chosen methanol and ethanol as additives. This type of fundamental dynamic information is particularly desirable for understanding of more complex biological and solvent interaction reactions.

Another aim of this study is to report the ultrasonic absorption data in aqueous solutions of methanol and ethanol. Previously, Dale *et al.*[12] have performed the measurement of the ultrasonic absorption coefficients in the system of methanol–water at 25 °C from 10–50 MHz. The ultrasonic relaxation process in the same system has been found by Endo[13] and Emery and Gasse.[14] For ethanol–water mixtures, Bruun *et al.*[15] have measured the ultrasonic absorption coefficients at 25 °C in the range from 12–350 MHz, and have observed at least two relaxation processes. Takagi and Negishi[16] and Emery and Gasse[14] have also performed the measurement for the same system at different temperatures and have observed similar ultrasonic relaxations. However, the above results are not usable for our experimental study because their frequency range, concentration, and thermodynamic conditions are not suitable for our purpose. Therefore, the absorption measurement has to be carried out precisely in aqueous solutions of methanol and ethanol when they are used as solvents for the study of the dynamic properties of amine.

I. EXPERIMENTS

Methanol, ethanol, and propylamine of reagent grade were purchased from Wako Pure Chemicals Co., Ltd. Methanol and ethanol were distilled once at normal pressure just before their use. Propylamine of purity greater than 98% was

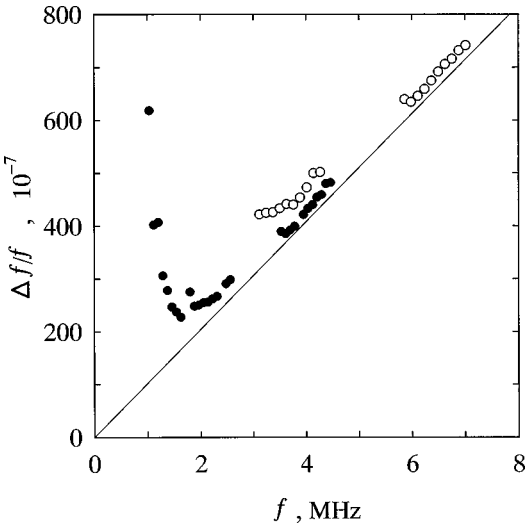

FIG. 1. Plots of $\Delta f/f$ versus frequency for an aqueous solution of 0.594 mol dm^{-3} NaCl. The solid line represents the calculated values using $\alpha/f^2 = 21\times10^{-15}$ s^2 m^{-1} and $c = 1531$ m s^{-1}. ○: by 5-MHz crystals, ●: by 3-MHz crystals. The solution used has the same acoustic impedance as that of 4.00 mol dm^{-3} ethanol aqueous solution.

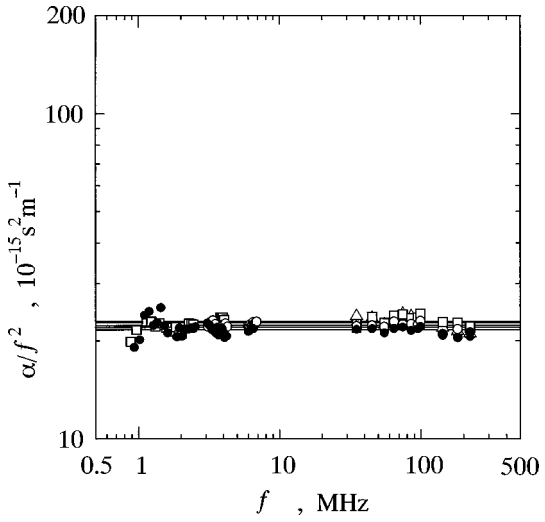

FIG. 2. The ultrasonic absorption spectra for aqueous solutions of methanol. ●: 1.00 mol dm^{-3}, ■: 2.00 mol dm^{-3}, ○: 3.00 mol dm^{-3}, △: 4.00 mol dm^{-3}, □: 6.00 mol dm^{-3}.

used without further purification. Sample solutions were prepared by water purified through a MilliQ SP-TOC system, from Japan Millipore Ltd., and were prepared from the concentrated stock solutions.

The ultrasonic absorption coefficient, α, was measured by a pulse method in the frequency range from 15–220 MHz using 5- and 20-MHz fundamental X-cut quartz crystals.[17] A resonance method was utilized to obtain the absorption coefficient in the lower frequency range. A resonator cell with 3-MHz fundamental X-cut quartz crystals, with a 4-cm diameter, was newly constructed and was applied to the measurement of the absorption coefficient in the range below 4.5 MHz. In the frequency range from 3–7 MHz, 5-MHz fundamental crystals, with a 2-cm diameter, was used. The absorption coefficient and the half-band width, Δf, are related by $\Delta f/f = (\alpha/f^2)(fc/\pi) + Q^{-1}$, where f is the frequency, c is the sound velocity, and Q^{-1} is the mechanical loss of the resonator. Figure 1 shows representative experimental values of $\Delta f/f$ as a function of the frequency. A solid line in this figure represents the calculated values. As may be seen in this figure, it is possible to obtain the almost absolute values of the absorption coefficient in the frequency range from 2–7 MHz by the two resonators, because of very small mechanical losses. However, the resonance curves are not always symmetrical in real solutions, depending on the magnitude of the ultrasonic absorption coefficient and the frequency. The data were used only when the curve symmetry was established within 10%. In other frequency ranges where the mechanical losses exit, we subtracted the losses from the measured $\Delta f/f$ values for the determination of the absorption coefficient. Using the newly constructed cell, the measurable frequency range was extended down to 0.8 MHz. The accuracy of the resonators was always checked using solvents before measuring the desired sample solutions. More details concerning the determination of the absorption coefficient is described precisely elsewhere.[5] The sound velocity was measured by the resonance method at around 3 MHz and with an interferometer at 2.50 MHz. The values of sound velocity determined by the two methods agreed well with each other to an accuracy of less than ± 1 m s^{-1}. Measurements of pH and density were carried out using a pH meter with a glass electrode (HM-60S Toa Denpa) and a vibrating density meter (DMA 60/602 Anton Paar), respectively. A Ubbelohde-type viscometer was used to determine viscosity coefficient. All of the measurements were always performed with a dry N_2 gas atmosphere in order to avoid as much as possible any contamination of carbon dioxide during the measurements. The measurement temperature was 25.0 °C. The temperature of the water bath for the cells of the pulse and interferometric apparatuses was controlled within ± 0.004 °C using a sensor equipped with Y-cut quartz crystal (around 10 MHz), the frequency of which is very sensitive to temperature. The change in the oscillating frequency was around 400 Hz per degree. The thermostated water, maintained within less than ± 0.01 °C, was circulated around the resonance cells using Lauda RM-20B.

II. RESULTS

First, the results of the ultrasonic absorption in aqueous solutions of methanol are represented. Figure 2 shows the absorption spectra for aqueous solutions of methanol in which the values of α/f^2 are independent of the frequency in the range from 0.8–220 MHz in the concentration range up to 6.00 mol dm^{-3}. It is also seen that the values of α/f^2 are almost independent of the methanol concentration. This is because the concentrations in our study are still very low, lower than those used by Dale *et al.*[12] and Brai *et al.*[18] In more concentrated solutions, the peak sound absorption phenomenon may be observed.

Next, the absorption results in aqueous solutions of ethanol are shown in Fig. 3 from 1.00–6.00 mol dm^{-3}. In the concentration range below 4.00 mol dm^{-3}, the values of α/f^2 are independent of the frequency. In 5.00 and 6.00 mol dm^{-3} ethanol solutions, the values of α/f^2 are depen-

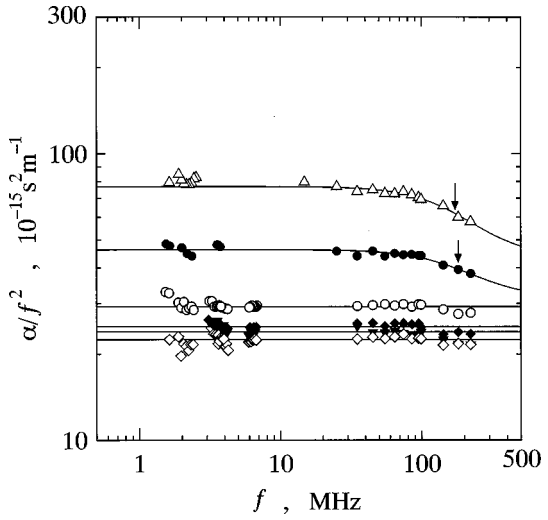

FIG. 3. The ultrasonic absorption spectra for aqueous solutions of ethanol. ◇: 1.00 mol dm^{-3}, ▼: 2.00 mol dm^{-3}, ◆: 3.00 mol dm^{-3}, ○: 4.00 mol dm^{-3}, ●: 5.00 mol dm^{-3}, △: 6.00 mol dm^{-3}. The arrows show the positions of the relaxation frequency.

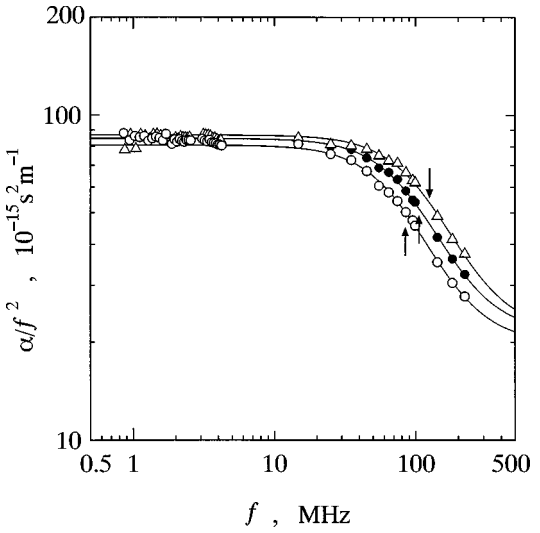

FIG. 4. The representative ultrasonic absorption spectra for aqueous solutions of propylamine containing 1.00 mol dm^{-3} methanol. ○: 0.170 mol dm^{-3}, ●: 0.306 mol dm^{-3}, △: 0.583 mol dm^{-3}.

dent on the frequency. The frequency dependence of α/f^2 has been analyzed by the Debye-type single relaxational equation,

$$\alpha/f^2 = A/[1+(f/f_r)^2] + B, \tag{1}$$

where f_r is the relaxation frequency, A is the amplitude of the ultrasonic relaxation, and B is the background absorption associated with the viscosity and thermal conductivity of the medium as well as that due to any processes with relaxation frequencies much higher than f_r for the process in question. The ultrasonic parameters, A, B, and f_r, were determined by a nonlinear least mean squares method. The solid curves in Fig. 3 are those calculated using thus determined values. The position of the relaxation frequency was estimated to be at around 200 MHz with an error of about 15%. The large error of the relaxation frequency arises from the locations of the relaxation frequency at the upper limit of the frequencies accessible to us and the small amplitude of the ultrasonic relaxation. The large background absorption suggests the existence of other relaxation processes in the higher frequency range. However, the profiles of the absorption spectra are quite similar to those reported in the range less than 220 MHz.[14–16] We consider that the observed relaxational absorption is due to a perturbation of equilibrium associated with solute and solvent interaction.[11]

These ethanol solutions (5.00 and 6.00 mol dm^{-3}) are not used as the solvent for studying dynamic characters of amine, because an additional relaxation by amine causes the complex ultrasonic absorption spectra.

In aqueous solutions of propylamine containing methanol or ethanol, the frequency-dependent α/f^2 values were observed and they were tested by the Debye-type single relaxational equation (1). Figures 4 and 5 show the representative ultrasonic absorption spectra in the presence of 1.00 mol dm^{-3} methanol and those of 3.00 mol dm^{-3} ethanol, respectively. The solid curves in the figures represent the calculated values using Eq. (1). The excellent agreement between the calculated and experimental values shows that a single relaxational process is observed over the wide frequency range even if methanol, or ethanol, coexists in the solution. The ultrasonic parameters thus obtained are tabulated in Tables I and II. Figure 6 shows the dependence of the relaxation frequency on the concentration of the amine, C_0, in which the results in other solvents[4,6,7] are also shown for comparison. The trends of the concentration dependence of the relaxation frequency are quite similar in these solutions, although the magnitudes are dependent on the solvents. Furthermore, it is seen in Tables I and II that the amplitude of the relaxation, A, tends to reach a plateau with increasing the concentration, the dependence of which is another characteristic of the ultrasonic absorption observed in relatively dilute solutions of amines.[19–21] These similar concentration dependences of the ultrasonic parameters have led us to predict that the cause of the relaxation is the same and that it is associated with a proton transfer reaction of amine.

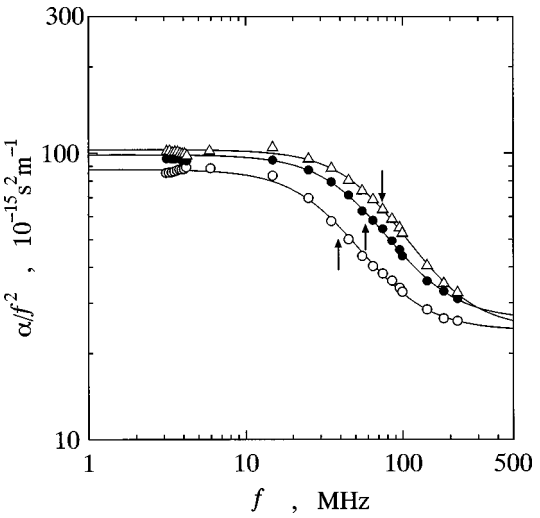

FIG. 5. The representative ultrasonic absorption spectra for aqueous solutions of propylamine containing 3.00 mol dm^{-3} ethanol. ○: 0.0894 mol dm^{-3}, ●: 0.278 mol dm^{-3}, △: 0.452 mol dm^{-3}.

TABLE I. Ultrasonic and thermodynamic parameters for aqueous solutions of propylamine in the presence of methanol at 25.0 °C.

C_0 (mol dm^{-3})	pH	f_r (MHz)	A (10^{-15} s^2 m^{-1})	B (10^{-15} s^2 m^{-1})
		1.00 mol dm^{-3} methanol		
0.0875	11.785	61±1	59.5±0.8	20.9±0.2
0.170	11.944	84.4±0.8	61.0±0.3	19.9±0.2
0.306	12.085	101±1	63.4±0.4	21.4±0.3
0.487	12.207	111±3	64.6±0.6	23.2±0.6
0.583	12.260	123±2	65.3±0.4	21.6±0.5
		2.00 mol dm^{-3} methanol		
0.119	11.842	65±1	66±1	19.8±0.2
0.166	11.907	74.0±0.7	67.2±0.4	19.7±0.1
0.303	12.070	92.5±0.7	69.9±0.3	20.3±0.1
0.499	12.205	106±2	73.7±0.6	19.9±0.5
0.596	12.259	118.3±0.8	73.3±0.2	18.5±0.2
		3.00 mol dm^{-3} methanol		
0.109	11.805	55.9±0.7	66.6±0.7	20.2±0.1
0.155	11.886	62.1±0.6	70.5±0.5	21.2±0.1
0.172	11.922	65.2±0.6	71.6±0.5	20.2±0.1
0.258	11.986	78±1	73.6±0.7	19.5±0.2
0.310	12.053	86.7±0.6	74.7±0.3	18.6±0.1
0.344	12.102	91.7±0.9	73.6±0.4	18.2±0.2
0.581	12.224	103±1	77.6±0.5	19.7±0.4
0.584	12.231	101.6±0.6	75.3±0.2	20.8±0.1
		4.00 mol dm^{-3} methanol		
0.116	11.802	50.2±0.6	73.0±0.9	21.5±0.1
0.284	12.032	73±1	77.0±2	20.7±0.2
0.352	12.083	76±1	78.5±0.7	22.0±0.2
0.436	12.139	85.1±0.9	79.5±0.5	20.4±0.2
0.569	12.218	92±1	80.8±0.5	20.8±0.3
		6.00 mol dm^{-3} methanol		
0.107	11.762	39.2±0.6	80±1	22.2±0.2
0.291	12.002	57.1±0.5	86.1±0.7	23.0±0.1
0.430	12.119	67.0±0.8	85.3±0.8	24.3±0.2
0.582	12.198	69±1	89±1	27.1±0.3

The mechanism of the reaction has been originally proposed by Eigen and it is expressed by Eq. (2):[22]

$$\mathrm{R{-}NH_3^+ + OH^- \underset{k_{21}}{\overset{k_{12}}{\rightleftharpoons}} R{-}NH_3^+ \cdots OH^- \underset{k_{32}}{\overset{k_{23}}{\rightleftharpoons}} R{-}NH_2 + H_2O}, \quad (2)$$

where the k_{ij} are the rate constants of individual steps. Following the conventional procedure of the relaxation time analysis, the relationship between the relaxation time, τ, and the reactant concentration is given by Eq. (3) including the coupling effect of the perturbation of the two equilibria on the relaxation time:

$$\tau^{-1} = 2\pi f_r = 2\gamma^2[\mathrm{OH^-}]k_{12} + k_{21}/(1 + k_{23}/k_{32}), \quad (3)$$

where γ is the activity coefficient calculated by Davies' equation. Plots of f_r vs $\gamma^2[\mathrm{OH^-}]$ in the solvents with methanol and ethanol are shown in Figs. 7 and 8, respectively, and it is seen to yield straight lines. However, the ratio $(k_{21}/k_{12})/(1 + k_{23}/k_{32})$, which is calculated from the values of the slope and the intercept, should have been the dissociation constant, K_b, defined as $K_b = \gamma^2[\mathrm{OH^-}]^2/([\mathrm{R{-}NH_3^+ \cdots OH^-}] + [\mathrm{R{-}NH_2}])$,[23,24] for which the value in water is reported.[25] Also, this is obtainable from the pH dependence in aqueous solutions using the relation,

$$K_b = \gamma^2[\mathrm{OH^-}]^2/(C_0 - [\mathrm{OH^-}]). \quad (4)$$

The literature values and the determined ones in Table III are, on the contrary, far from those obtained using Eq. (3). Even if the $1 \ll k_{23}/k_{32}$ condition is satisfied, the ratio $(k_{21}/k_{12})/(k_{23}/k_{32})$ must be close to the dissociation constant. Therefore, we have simply considered that the perturbation of the first step is the cause of the observed relaxation. Using this hypothesis, reasonable dissociation constants are obtained from a relation between the experimental relaxation time and the concentration.[23] More detail of the above assumption is described elsewhere.[23] Then, the values from the slope and the intercept lead to the rate constants, k_{12} and k_{21}, because $\tau^{-1} = 2\gamma^2[\mathrm{OH^-}]k_{12} + k_{21}$. They have been determined using a least mean squares method and are listed in Table III. The forward rate constants are reasonable for a diffusion controlled reaction. Figure 9 shows the dependence of k_{12} on the concentration of the additives, where the results in the solvents with urea[4,6] and with 2-propanol[5,7] are cited in order to make comparisons.

Another important parameter obtained from the ultrasonic absorption and velocity measurements is the maximum absorption per wavelength, $\mu_{\max}$,

$$\mu_{\max} = Af_r c/2 = \pi\rho c^2 \Gamma (\Delta V)^2/2RT, \quad (5)$$

where ρ is the density, R is the gas constant, T is the absolute temperature, ΔV is the standard volume change of the reaction, and Γ is the concentration term given by

$$\Gamma = (1/[\mathrm{OH^-}] + 1/[\mathrm{R{-}NH_3^+}] + 1/[\mathrm{R{-}NH_3^+ \cdots OH^-}])^{-1}. \quad (6)$$

The contribution of the activity coefficient to the Γ term is negligibly small[26] and the enthalpy term in Eq. (5) is approximately negligible because of the aqueous solutions. Further, the coupling effect of the second step on the first step in Eq. (2) is ignored because of the same reason for the interpretation of the relaxation time. As a result, the concentration dependence of $\mu_{\max}$ provides the value of the standard volume change of the reaction because the intermediate concentration is calculated from K_b and $K_{21} = k_{21}/k_{12}$.[23] The results are shown in Fig. 10 as a function of the concentration of propylamine, in which those in other solvents[4,6,7] are also shown. In these calculations, the values of sound velocity and density were approximated to be equal to those for the individual solvents because the changes in the sound velocity and density did not affect the magnitude of $\mu_{\max}$. As is seen in Fig. 10, the volume change is almost independent of the concentration of methanol or ethanol, and it is nearly equal to that in the absence of the additive. On the other hand, it decreases with the increase in the concentration of urea.[6]

III. DISCUSSION

The rates for the ion pair formation are reasonable as the diffusion controlled reaction, although they are dependent on the solvents. There may be two factors that affect the rate constants, k_{12}. One is the hindrance effect for the diffusing process of reactant molecules. This effect makes the value of

TABLE II. Ultrasonic and thermodynamic parameters for aqueous solutions of propylamine in the presence of ethanol at 25.0 °C.

C_0 (mol dm^{-3})	pH	f_r (MHz)	A (10^{-15} s^2 m^{-1})	B (10^{-15} s^2 m^{-1})
1.00 mol dm^{-3} ethanol				
0.105	11.868	59.9±0.9	62.0±0.8	20.9±0.2
0.181	11.983	77±1	64.1±0.6	20.4±0.2
0.363	12.160	100±2	67.9±0.6	19.3±0.5
0.479	12.239	105±3	68.5±0.8	20.2±0.7
0.542	12.269	108±3	66.2±0.8	22.2±0.8
2.00 mol dm^{-3} ethanol				
0.100	11.862	49.8±0.9	64±1	21.6±0.1
0.184	12.028	61±1	69±1	21.4±0.2
0.368	12.209	81.6±0.9	70.2±0.5	21.5±0.2
0.444	12.248	86±1	71.8±0.5	21.5±0.2
0.568	12.310	94±1	71.5±0.4	22.3±0.2
3.00 mol dm^{-3} ethanol				
0.0894	11.839	38.8±0.7	64±1	24.0±0.1
0.186	12.039	50.5±0.7	70.6±0.9	24.2±0.1
0.278	12.120	57.4±0.8	72.5±0.9	26.2±0.2
0.372	12.224	67±1	76.4±0.9	24.8±0.2
0.452	12.264	74±1	78.5±0.8	24.3±0.2
0.591	12.342	78±1	80.1±0.8	29.0±0.3
4.00 mol dm^{-3} ethanol				
0.117	11.901	36±1	70±3	29.2±0.2
0.192	12.063	43±1	76±2	31.4±0.2
0.385	12.243	59±2	86±2	35.3±0.4
0.495	12.311	64±1	88±1	39.9±0.3
0.583	12.368	69±1	95±1	43.1±0.3

k_{12} decrease and k_{12} may be dependent on the additive concentrations. The other is the effect arising from solvent water structural change due to the additives because the hydroxide ion moves through the water hydrogen bond network (the Grotthuss mechanism).[27]

As is shown in Fig. 9, it is found that k_{12} decreases with the methanol concentration and that the decreasing trend is more noticeable from 3.00 to 6.00 mol dm^{-3}. On the other hand, the rate constant in the solution with ethanol decreases linearly with increase in the ethanol concentration. These trends are considerably different from that in the solvent with 2-propanol, as is seen in Fig. 9. This behavior has been interpreted as an appearance of the water structure making effect of 2-propanol.[7]

The observed dependence of k_{12} on the methanol concentration may be explained well by the two factors by methanol. When the methanol concentration is relatively low (below 3.00 mol dm^{-3}), only the hindrance effect appears. Further addition of methanol breaks the water structure and the rate of the diffusion process of the hydroxide ion may decrease. Then, the decrease in the rate due to the disordering of the hydrogen-bonded network synchronizes with the diminution in the rate by the hindrance effect, leading to the further decrease in k_{12}. The structure-breaking effect of

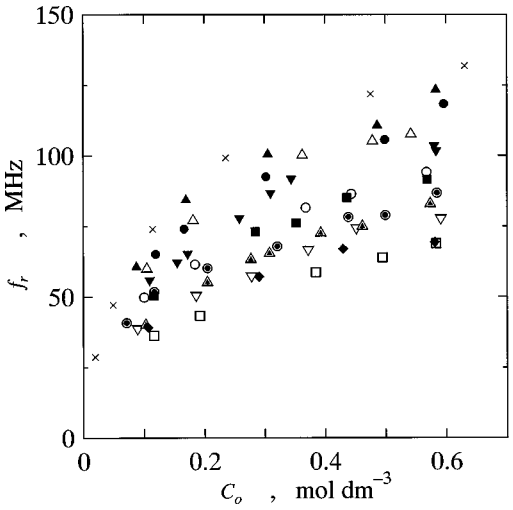

FIG. 6. The concentration dependence of the relaxation frequency, f_r, for aqueous solutions of propylamine in the absence and presence of additive. ×: no additive (Ref. 4), ▲: 1.00 mol dm^{-3} methanol, ●: 2.00 mol dm^{-3} methanol, ▼: 3.00 mol dm^{-3} methanol, ■: 4.00 mol dm^{-3} methanol, ◆: 6.00 mol dm^{-3} methanol, △: 1.00 mol dm^{-3} ethanol, ○: 2.00 mol dm^{-3} ethanol, ▽: 3.00 mol dm^{-3} ethanol, □: 4.00 mol dm^{-3} ethanol, ⊙: 2.60 mol dm^{-3} 2-propanol,[7] △: 4.00 mol dm^{-3} urea (Ref. 6).

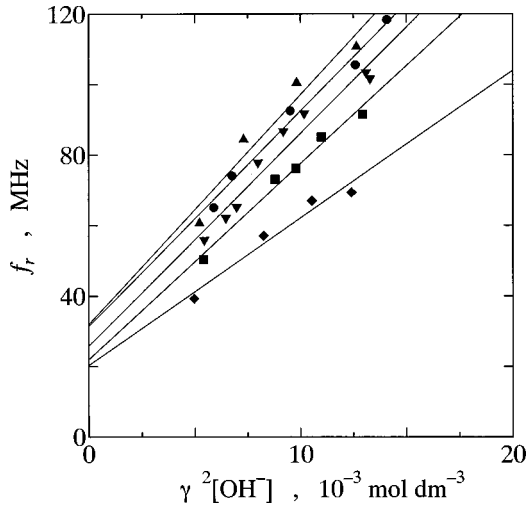

FIG. 7. Plots of f_r vs γ^2[OH$^-$] for aqueous solutions of propylamine in the presence of methanol. ▲: 1.00 mol dm^{-3} methanol, ●: 2.00 mol dm^{-3} methanol, ▼: 3.00 mol dm^{-3} methanol, ■: 4.00 mol dm^{-3} methanol, ◆: 6.00 mol dm^{-3} methanol.

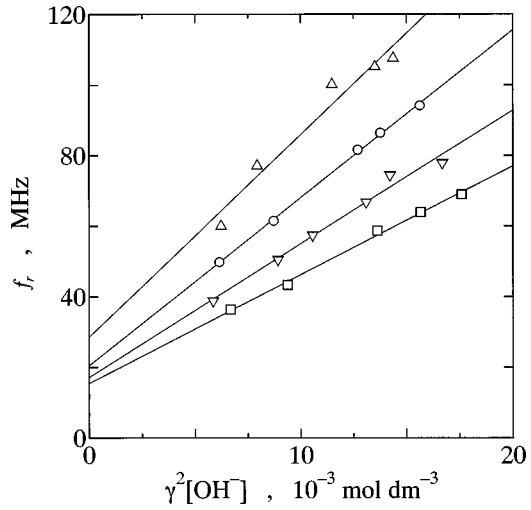

FIG. 8. Plots of f_r vs γ^2[OH$^-$] for aqueous solutions of propylamine in the presence of ethanol. △: 1.00 mol dm^{-3} ethanol, ○: 2.00 mol dm^{-3} ethanol, ▽: 3.00 mol dm^{-3} ethanol, □: 4.00 mol dm^{-3} ethanol.

TABLE III. Rate and thermodynamic parameters of the proton transfer reaction of propylamine in the absence and presence of the additives at 25.0 °C.

Additive	k_{12} (10^{10} mol^{-1} dm^{-3} s^{-1})	k_{21} (10^{8} s^{-1})	K_b (10^{-4} mol dm^{-3})	D_{OH^-} (10^{-9} m^2 s^{-1})	Reference
No additive	2.1±0.2	1.3±0.4	5.6±1.5	5.1	4
Methanol					
1.00 mol dm^{-3}	2.0±0.2	2.0±0.3	4.2±0.2	4.9	this work
2.00 mol dm^{-3}	1.92±0.08	2.0±0.2	3.9±0.3	4.6	this work
3.00 mol dm^{-3}	1.9±0.1	1.6±0.2	3.6±0.2	4.4	this work
4.00 mol dm^{-3}	1.75±0.09	1.3±0.2	3.5±0.2	4.1	this work
6.00 mol dm^{-3}	1.3±0.1	1.3±0.2	3.2±0.2	3.0	this work
Ethanol					
1.00 mol dm^{-3}	1.8±0.1	1.8±0.3	4.9±0.2	4.3	this work
2.00 mol dm^{-3}	1.49±0.02	1.29±0.04	5.6±0.3	3.5	this work
3.00 mol dm^{-3}	1.19±0.05	1.1±0.1	5.8±0.4	2.7	this work
4.00 mol dm^{-3}	0.97±0.02	0.97±0.06	6.4±0.6	2.1	this work

methanol is considered to begin at around 3 mol dm^{-3}.

On the other hand, the monotonic decrease in k_{12} observed in the solvent with ethanol up to 4.00 mol dm^{-3} suggests that the water structure is not so changed by the addition of ethanol and the effect of ethanol on k_{12} may arise mainly from the hindrance. It is also seen in Fig. 9 that the extrapolations to the zero additive concentration in the solvents with the three alcohols go through the data point obtained in the solvent without additive. In our previous papers,[6,7] the line in the solvent with urea was drawn through the value in the solvent water. However, the fairly good linear relationships of the plots in the solvents with the three alcohols have led us to reconsider the data in the solvent with urea. A better linearity in the plots of k_{12} versus the urea concentration has been found when the data, except that in liquid water, are accepted, and a new straight line has been redrawn in Fig. 9. This suggests that the water-structure-breaking effect of urea begins in the concentration below 1.50 mol dm^{-3} and that both of the hindrance and the structure-breaking effects are acting in the solvent with urea.

Furthermore, it should be noted that the slope for the alcohol concentration dependence of k_{12} progresses in the order of 2-propanol>ethanol>methanol in the concentration range, where the decreasing effect in k_{12} is mainly due to the hindrance. This order is consistent with the size of three alcohols. Thus, we have considered that the linear decrease in k_{12} with increase in the additive concentrations reflects the hindrance effect and that the magnitude of the slope may indicate the extent of the hindrance to the movement of the reactants. Although the physicochemical properties of water in aqueous alcohol mixtures have been studied widely with IR, dielectric relaxation, thermodynamic, NMR, and many other methods,[28] the assessment for the change in water structure induced by the additions of alcohols seems to be undecided. However, the present assignment concerning the effect of alcohols on water structure is qualitatively consistent with that derived from our ultrasonic absorption measurements in aqueous solutions of various alcohols.[11]

In order to see the effects of methanol and ethanol on

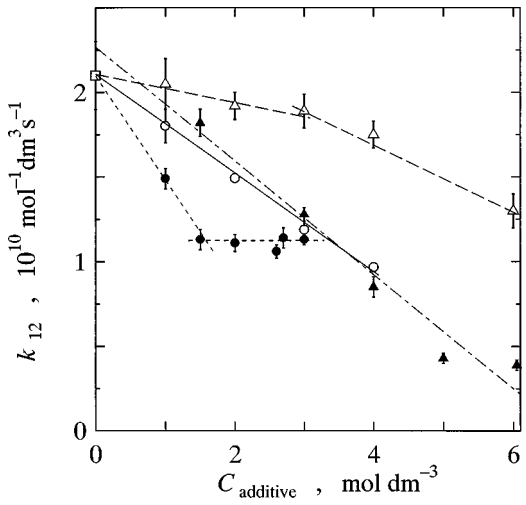

FIG. 9. The dependence of the forward rate constant of the reaction on the concentration of the additives. △: methanol, ○: ethanol, □: no additive (Ref. 4), ▲: urea (Refs. 4 and 6), ●: 2-propanol (Refs. 5 and 7).

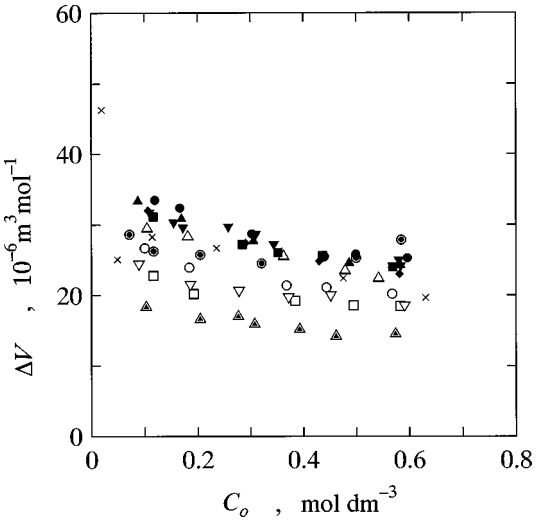

FIG. 10. The concentration dependence of the standard volume change of the reaction, ΔV, for aqueous solutions of propylamine in the absence and presence of additive. ×: no additive (Ref. 4), ▲: 1.00 mol dm^{-3} methanol, ●: 2.00 mol dm^{-3} methanol, ▼: 3.00 mol dm^{-3} methanol, ■: 4.00 mol dm^{-3} methanol, ◆: 6.00 mol dm^{-3} methanol, △: 1.00 mol dm^{-3} ethanol, ○: 2.00 mol dm^{-3} ethanol, ▽: 3.00 mol dm^{-3} ethanol, □: 4.00 mol dm^{-3} ethanol, ⊙: 2.60 mol dm^{-3} 2-propanol (Ref. 7), △: 4.00 mol dm^{-3} urea (Ref. 6).

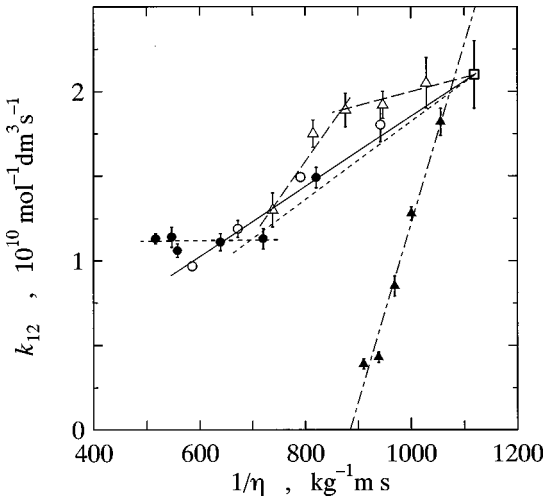

FIG. 11. Plots of the forward rate constant, k_{12}, vs the reciprocal of the viscosity coefficient of the solvent. □: no additive (Ref. 4), △: methanol, ○: ethanol, ▲: urea (Refs. 4 and 6), ●: 2-propanol (Refs. 5 and 7).

solvent water structure, we have examined the dependence of k_{12} on solution viscosity. Figure 11 shows the plots of k_{12} versus the reciprocal of the viscosity coefficient, $1/\eta$, in which those for the solvents with urea and 2-propanol are also shown.[4–7] The value of k_{12} in the solvent with ethanol increases linearly with $1/\eta$. This is simply due to the increase of the collision frequency of the reactants because the frequency is reciprocally proportional to the viscosity coefficient of the solvent following the Smoluchowski equation.[27] On the other hand, the plot in the solvent with methanol is broken in two separate lines and the rate constant decreases markedly when the solution viscosity is relatively high. This tendency is opposite to that in the solvent with 2-propanol in which the rate constant tends to be independent even when the viscosity coefficient increases. These results confirm our speculation that methanol acts as water structure breaker in the relatively high concentration range and 2-propanol acts as a water structure maker. The profile in the solvents with the alcohol is, however, different from that in the solvent with urea. The viscosity dependence of the rate constant in that with urea may not be easily interpreted only by the hindrance effect and the water-structure-breaking effect.

The migration of the hydroxide ion plays an important role in our discussion because the reaction is diffusion controlled. Busing and Horning[29] have investigated the hydration state of the hydroxide ion in strong electrolyte solutions using Raman spectroscopy for interpretation of the interaction among the hydroxide ion and water molecules. More direct information on the mobility of the hydroxide ion may be obtained from a determination of a diffusion coefficient. Debye[22] has derived an expression for the diffusion-controlled rate of the reaction of ions in solution as

$$k_{12}=\frac{\sigma N Z_{\mathrm{OH}^-} Z_{\mathrm{R-NH_3^+}} e_0^2 (D_{\mathrm{OH}^-}+D_{\mathrm{R-NH_3^+}})}{\varepsilon\varepsilon_0 kT[\exp(Z_{\mathrm{OH}^-} Z_{\mathrm{R-NH_3^+}} e_0^2/4\pi\varepsilon\varepsilon_0 r_d kT)-1]}, \quad (7)$$

where N is Avogadro's number, σ is a steric factor, e_0 is the electronic charge, Z_{OH^-} and $Z^+_{\mathrm{R-NH3}}$ are the algebraic charges of the reacting ions, ε_0 is the dielectric constant in vacuum, ε is the dielectric constant of the solvent, D_{OH^-} and $D_{\mathrm{R-NH_3^+}}$ are the diffusion coefficients of the reacting ions, k is the Boltzmann constant, and r_d is an effective radius for the reaction. The values of the dielectric constant in aqueous solutions of methanol and ethanol are available from the literature reported by Ärkerlöf.[30] The diffusion coefficient for the hydroxide ion, D_{OH^-}, is expected to be much greater than that of alkylammonium ion, $D_{\mathrm{R-NH_3^+}}$. Using the appropriate values for the effective radius and the steric factor of the reaction ($r_d=5\times10^{-10}$ m and $\sigma=0.58$),[6] which are assumed to be independent of the solvent composition, the values of D_{OH^-} have been calculated at various concentrations of methanol and ethanol, and they are listed in Table III. It is seen that the decrease in k_{12} values with the additives reflects on the diffusion coefficients. That is, the diffusion process of the reactants is considered to be altered through the hindrance of the additive and the structural change in solvent water.

Next, the effects of methanol and ethanol on the reverse rate constant, k_{21}, is considered. This constant is for the dissociating process of the intermediate in Eq. (2). The change in water structure around the reactants has not been considered to affect the value of k_{21} because this process is just a separation process into anion and cation. When the errors for the values are taken into account, the obtained values of k_{21} may be approximately the same as that in water as is seen in Table III.

Finally, the effects of methanol and ethanol on the standard volume change of the reaction are discussed. It has been indicated that the standard volume change of the reaction may be used as a probe monitoring the extent of the hydrogen-bonded network in the solvent.[4–7] The volume change tends to increase slightly, when water structure is promoted.[5,7] On the other hand, the disordering of the hydrogen-bonded network by the addition of urea has caused a remarkable decrease in the volume change.[4,6] However, as is seen in Fig. 10, the addition of methanol or ethanol does not cause a change in the standard volume change of the reaction. Taking into account the fact that the increase in the volume change due to addition of 2-propanol is slight, it is considered that the water-structure-breaking effect of methanol is not so remarkable when compared with that of urea.

In conclusion, it has been shown in this study that only one relaxational absorption is observed in the aqueous solution of propylamine in the presence of 1.00, 2.00, 3.00, 4.00, and 6.00 mol dm^{-3} methanol or in 1.00, 2.00, 3.00, and 4.00 mol dm^{-3} ethanol. The observed relaxation has been attributed to the perturbation of the equilibrium associated with the proton transfer reaction. It has been found that the addition of methanol causes a decrease in the forward rate constant and the decreasing trend in the methanol concentration range from 3.00–6.00 mol dm^{-3} is more striking than that in the dilute concentration range. On the other hand, the forward rate constant in the solvent with ethanol decreases linearly with increase in the ethanol concentration. The reverse rate constant and the volume change of the reaction are not greatly affected by the addition of methanol or ethanol. On

the basis of these results, we conclude that ethanol does not have a significant effect on the solvent water structure in the concentration range up to 4 mol dm^{-3} and methanol acts as a water structure breaker in the concentration range above 3 mol dm^{-3}.

ACKNOWLEDGMENTS

We wish to express our thanks for the Research Fellowship of the Japan Society for the Promotion of Science for Young Scientists to NK. This work was partly supported by a Grant-in-Aid for Science Research No. 09440202 from The Ministry of Education, Science and Culture of Japan.

[1] R. Behrends, M. K. Cowman, F. Eggers, E. M. Eyring, U. Kaatze, J. Majewski, S. Petrucci, K. Richmann, and M. Riech, J. Am. Chem. Soc. **119**, 2182–2186 (1997).
[2] K. U. Holmes and R. E. Challis, J. Acoust. Soc. Am. **100**, 1865–1877 (1996).
[3] F. W. Kremkau, J. Acoust. Soc. Am. **83**, 2410–2415 (1988).
[4] Y. Yoshida and S. Nishikawa, Bull. Chem. Soc. Jpn. **60**, 2779–2783 (1987).
[5] N. Kuramoto, M. Ueda, and S. Nishikawa, Bull. Chem. Soc. Jpn. **67**, 1560–1564 (1994).
[6] N. Kuramoto and S. Nishikawa, J. Phys. Chem. **99**, 14 372–14 376 (1995).
[7] N. Kuramoto and S. Nishikawa, J. Phys. Chem. **100**, 10 629–10 633 (1996).
[8] R. A. Rupley, J. Phys. Chem. **68**, 2002–2003 (1964).
[9] T. T. Herskovits and T. M. Kelly, J. Phys. Chem. **77**, 381–388 (1973).
[10] S. Nishikawa, T. Yasunaga, and M. Mashima, Bull. Chem. Soc. Jpn. **49**, 1413–1414 (1976).
[11] S. Nishikawa and M. Ueda, J. Phys. Chem. **97**, 3539–3543 (1993).
[12] W. D. T. Dale, P. A. Flavelle, and P. Kruus, Can. J. Chem. **54**, 355–366 (1976).
[13] H. Endo, K. Saijou, and G. Atkinson, J. Acoust. Soc. Jpn. **13**, 85–90 (1992).
[14] J. Emery and S. Gasse, Acustica **42**, 205–211 (1979).
[15] S. G. Bruun, P. G. Sorensen, and A. Hvidt, Acta Chem. Scand. A **28**, 1047–1054 (1974).
[16] K. Takagi and K. Negishi, Jpn. J. Appl. Phys. **14**, 953–959 (1975).
[17] S. Nishikawa and K. Kotegawa, J. Phys. Chem. **89**, 2896–2900 (1985).
[18] M. Brai and U. Kaatze, J. Phys. Chem. **96**, 8946–8955 (1992).
[19] M. M. Emara, G. Atkinson, and E. Baumgartner, J. Phys. Chem. **76**, 334–338 (1972).
[20] G. Atkinson, M. M. Emara, H. Endo, and B. L. Atkinson, J. Phys. Chem. **84**, 259–263 (1980).
[21] S. Nishikawa and R. Gouhara, Bull. Chem. Soc. Jpn. **69**, 1855–1861 (1996).
[22] M. Eigen and L. de Maeyer, in *Technique of Organic Chemistry, Vol. VIII, Part 2*, edited by A. Weissberger (Wiley, New York, 1961).
[23] Y. Yoshida and S. Nishikawa, Bull. Chem. Soc. Jpn. **59**, 1941–1945 (1986).
[24] S. Nishikawa and M. Satoh, J. Acoust. Soc. Am. **102**, 3779–3784 (1998).
[25] J. J. Christensen, R. M. Izatt, D. P. Wrathall, and L. D. Hansen, J. Chem. Soc. A , 1212–1223 (1969).
[26] S. Nishikawa, N. Arakane, and N. Kuramoto, J. Phys. Chem. **99**, 369–374 (1995).
[27] E. S. Amis and J. F. Hinton, *Solvent Effects on Chemical Phenomena* (Academic, New York, 1973).
[28] *Water, A Comprehensive Treatise, Vol. 2*, edited by F. Franks (Plenum, New York, 1973).
[29] W. R. Busing and D. F. Horning, J. Phys. Chem. **65**, 284–292 (1961).
[30] G. Ärkerlöf, J. Am. Chem. Soc. **54**, 4125–4139 (1932).

Frequency relationships for ultrasonic activation of free microbubbles, encapsulated microbubbles, and gas-filled micropores

Douglas L. Miller
Department of Radiology, University of Michigan Medical Center, Ann Arbor, Michigan 48109-0553

(Received 2 March 1998; revised 13 May 1998; accepted 29 June 1998)

The ultrasonic activation of free microbubbles, encapsulated microbubbles, and gas-filled micropores was explored using available linear theory. Encapsulated microbubbles, used in contrast agents for diagnostic ultrasound, have relatively high resonance frequencies and damping. At 2 MHz the resonance radii are 1.75 μm for free microbubbles, 4.0 μm for encapsulated microbubbles, and 1.84 μm for gas-filled micropores. Higher-pressure amplitudes are needed to elicit equivalent subharmonic, fundamental, or second-harmonic responses from the encapsulated microbubbles, and this behavior increases for higher frequencies. If an encapsulated microbubble becomes destabilized during exposure, the resulting liberated microbubble would be about twice the linear resonance size, which would be likely to produce subharmonic signals. Scattered signals used for medical imaging purposes may be indicative of bioeffects potential: The second harmonic signal is proportional to local shear stress for a microbubble on a boundary, and a strong subharmonic signal may imply destabilization and nucleation of free-microbubble cavitation activity. The potential for bioeffects from contrast agent gas bodies decreases rapidly with increasing frequency. This information should be valuable for understanding of the etiology of bioeffects related to contrast agents and for developing exposure indices and risk management strategies for their use in diagnostic ultrasound.
 [S0001-4966(98)03210-X]

PACS numbers: 43.80.Gx, 43.35.Ei, 43.35.Wa [FD]

INTRODUCTION

Contrast agents for diagnostic ultrasound consist of suspensions of microscopic gas bodies whose purpose is to enhance echogenicity of blood-filled regions for display in a diagnostic image. For example, two agents now in clinical use are Albunex® and Optison (Mallinckrodt Medical, St. Louis, MO), which consist of gas microbubbles stabilized by a thin shell of denatured albumin. The encapsulated microbubbles in Albunex contain air, while those in Optison contain perfluoropropane for greater persistence. Ultrasound contrast agents function by introducing resonance-sized gas bodies into the blood, and acoustic scattering from the gas bodies generates echos for imaging. The pulsation of the gas bodies has nonlinear characteristics which can be exploited for special forms of imaging, such as second-harmonic Doppler imaging.[1] Ultrasound exposure can also modify the encapsulated microbubbles, resulting in loss of stability of the gas bodies.[2] Destabilization of contrast agent gas bodies can result in loss of the microbubbles by dissolution under some conditions but may also result in nucleation of free-microbubble cavitation phenomena with continued exposure.[3] Theory has been developed for the interaction of ultrasound with the encapsulated gas microbubbles.[4,5] Essentially, the shell adds elasticity and damping parameters to the theory for the pulsation of free-spherical microbubbles. This theory has been utilized to describe the scattering properties of suspensions of the agents, leading to empirical values for the shell parameters.[6,7]

Gas body activation in biological media has a potential for bioeffects, and encapsulated microbubbles from contrast agents have been the subject of recent bioeffects research. Even small amounts of agent added to whole blood can significantly reduce the threshold for cavitation and hemolysis.[8] For relatively high-pressure amplitudes, the gas bodies serve as cavitation nuclei with subsequent effects resulting from free-microbubble cavitation phenomena. For lower-pressure amplitudes, the gas bodies may remain stable, with effects produced by the pulsating encapsulated microbubbles, but this aspect of the etiology of contrast-agent-related effects is presently uncertain. *In vitro* studies designed to detect ultrasonically induced bioeffects at high hematocrits with added contrast agents have demonstrated hemolysis at moderate pressure amplitudes.[9,10] The hemolysis generated by ultrasonically activated contrast agents can even be detected *in vivo*.[11] Hemolysis amounting to several percent resulted from pulsed 1.15-MHz ultrasound above a threshold of about 3 MPa applied to mice injected with Albunex®. The addition of contrast agents to the vascular system also enhances the vascular damage from lithotripter shockwaves or ultrasound, and this phenomenon persists for several hours.[12–14] Newer contrast agents such as Optison, which is based on a perfluorocarbon gas to improve persistence of the gas bodies, can produce larger effects than observed with air-based agents such as Albunex®, particularly for pulsed-mode exposures.[15]

At low cell concentrations, cell lysis can be detected at relatively low amplitudes of exposure.[16] Cultured cells in monolayer were exposed to 3.3-MHz ultrasound in the presence of Albunex® ultrasound contrast agent with simultaneous observation of ATP loss from the cells and of scattered signals. The signal scattered at the first subharmonic (half the incident frequency) and, to a lesser extent, the

second-harmonic signal were correlated with the observed cell membrane damage. Observation of transmission through the exposure chambers suggested that effects occurred above the levels needed for destabilization of the gas bodies. The strong scattering and nonlinear signals produced by ultrasonic activation of encapsulated microbubbles may indicate destabilization of the gas bodies and these emissions therefore may be predictive of the potential for cavitational bioeffects.

Presently, the biophysical ultrasonics of contrast agent bioeffects is not well understood. Even approximate models could help to elucidate the relationship between the activation, nonlinear emissions, and the bioeffects potential associated with contrast agents, and lead to the development of new exposure indices or risk mitigation strategies for medical applications. Gas body activation can take various forms, in addition to ultrasound contrast agents.[17] For example, in many plant tissues intercellular channels are filled with gas for respiration, and the channel walls stabilize the gas against dissolution. Theory for the resonance activation of the channels can be combined with theory for the acoustic microstreaming shear stress within the cells to yield prediction for cell death in the leaves of the aquatic plant Elodea, which are in rough agreement with observed bioeffects.[18] This reasonably complete description exemplifies the level of understanding possible for nonthermal bioeffects of ultrasound, which will be essential for a full appreciation and exploitation of bioeffects in medical ultrasonics. Gas-filled channels also occur in insect larvae, which are responsible for nonthermal killing of the larvae by ultrasound,[17] and the activation of these channels also may be a resonance interaction.[19] Gas can be stabilized in cylindrical micropores in thin sheets of plastic, otherwise used as precision filters, and configured for resonance excitation in the low-megahertz range.[18] The ultrasonic activation of the gas-filled micropores leads to nonthermal bioeffects on cell suspensions, probably through the physical mechanisms of radiation force, which attracts cells to the micropores, and acoustic microstreaming shear stress, which tears cell membranes.[20] Cell lysis has been demonstrated to occur from activation of gas-filled micropores even in whole blood.[21] The microscopic activity at the ultrasonically activated gas-filled micropores may mimic the activity near contrast agent gas bodies under some conditions. The purpose of this study was to examine the theory for ultrasonic activation of the free and encapsulated microbubbles in contrast agents for describing and understanding the occurrence of biological effects through application of the type of descriptive model developed for gas-filled channels in Elodea leaves.[18] In addition, gas-filled micropores were considered for comparison.

I. THEORY

For this study, relatively simple linearized models of gas body activation have been employed. These models are clearly inadequate in many relevant situations, possibly including exposures sufficient to cause destabilization of gas bodies. However, these readily accessible analytical treatments provide useful insights, particularly for the low-level near-threshold conditions of interest in bioeffects research. Most of the theoretical problems discussed here have been previously studied, and the solutions are available in the literature. The equations representing the various models were entered in the software program Microsoft Excel (Microsoft Corp.) and numerical results calculated using the iterative capability of the program.

The ultrasonically induced pulsation of free-gas microbubbles has been addressed by numerous authors.[22] The purely linear theory has been extended slightly to include the second-harmonic oscillation, which provided the basis for second-harmonic bubble detection.[23] In this theory, the microbubble radius as a function of time is expressed as a fractional displacement about the equilibrium radius R_0, and solutions are obtained for small values (i.e., less than unity) of amplitude, including the second harmonic term. The ambient pressure is $p_0 = 0.1$ MPa, with ultrasonic pressure amplitude p_1. The solution for the fundamental (or, first harmonic) amplitude A_1 in a liquid of density $\rho = 10^3$ kg m^{-3} and surface tension $\sigma = 0.072$ N m^{-2}, is given in dimensionless form by

$$A_1 = p_1 \chi_1 / \rho \omega_\sigma^2 R_0^2, \tag{1}$$

and for the second-harmonic amplitude A_2 is given by

$$A_2 = \tfrac{1}{2} A_1^2 Y \chi_2, \tag{2}$$

in which

$$\chi_1 = [(1-\Omega^2)^2 + \Omega^2 \delta^2]^{-1/2}, \tag{3}$$

$$\chi_2 = [(1-4\Omega^2)^2 + 4\Omega^2 \delta^2]^{-1/2}, \tag{4}$$

and

$$Y = \left[\left(\frac{5}{2} \Omega^2 + \frac{3\gamma(p_0 + 2\sigma/R_0)(3\gamma+1) - 4\sigma/R_0}{2\rho\omega_0^2 R_0^2} \right)^2 + \Omega^2 \delta^2 \right]^{1/2}. \tag{5}$$

In these equations, $\Omega = \omega/\omega_0$, in which the angular resonance frequency (i.e., $2\pi f_0$) of the oscillation is given approximately by

$$\omega_0^2 = \frac{1}{\rho R_0^2} \left[3\gamma \left(p_0 + \frac{k\sigma}{R_0} \right) - \frac{2\sigma}{R_0} \right]. \tag{6}$$

The symbol δ represents the sum of damping coefficients for viscous, radiation, and thermal damping mechanisms. At relatively high frequencies or viscosities, the largest damping coefficient is viscous damping, given approximately at resonance by

$$\delta_\nu = \frac{4\eta}{\rho \omega_0 R_0^2}, \tag{7}$$

in which η represents the shear viscosity of the medium. The assumed value of 0.014 N s m^{-2} for plasma at 37 °C represents a compromise between lower values for pure water and higher values for whole blood. The detailed damping coefficients were calculated according to the equations of Church.[5] The polytropic exponent γ is related to the thermal damping process, and was also calculated from this theory.

During exposure of encapsulated microbubbles, the highly nonlinear subharmonic signal (i.e., at one-half the driving frequency) can be detected at relatively low exposure levels.[16,24] The threshold for generation of subharmonic oscillations is minimal for microbubbles which are twice the size of linear resonance, and this minimum threshold is[25]

$$p_{1/2}=6\,\delta p_0. \tag{8}$$

Because this expression is independent of many of the parameters involved in microbubble oscillation, it provides a good diagnostic signal for gas bubble behavior. The simplicity of this formula has lead to the suggested use of bubbles for measuring the damping coefficient of bubbles,[26] or the viscosity of liquids.[27]

A theory for the oscillation of encapsulated microbubbles can be obtained by modifying the free-microbubble theory to include the elasticity and damping contributed by the shell.[9,10] Essentially, the shell increases the resonance frequency for a given size of microbubble by adding stiffness to the microbubble oscillation. This can be represented in a manner similar to the surface tension with the shell parameter S_p,[4] which has been found to be about 4.2 N m^{-1}.[7] The resonance frequency of the encapsulated microbubbles is given approximately by

$$\omega_e^2=\frac{1}{\rho R_0^2}\left[3\gamma p_0-\frac{2\sigma}{R_0}+\frac{2S_p}{R_0}\right], \tag{9}$$

in which the internal gas pressure has been set to the external ambient value (i.e., not to $p_0+2\sigma/R$, which implies microbubble instability by diffusion of gas out of the microbubble). The shell also contributes to the damping, through a friction parameter S_f, which has been estimated to be 5.4×10^{-6} N s m.[7] In a somewhat more complete formulation of the problem, Church used the modulus of rigidity $G_s\cong6\Delta S_p$ and shell viscosity $\eta_s\cong S_f/48\pi\Delta$, in which $\Delta=15$ nm is the shell thickness.[5] Analytical solutions from this latter formulation were used for calculations in this study,[5] using the more recent values of the parameters.[7] The shell viscosity η_s is much higher than the viscosity of water, at about 2.4 N s m^{-2}, but the damping is moderated by the thinness of the shell. The damping coefficient may be written approximately

$$\delta_s=\frac{16\,\eta_s\Delta}{\rho\omega_e R_0^3}. \tag{10}$$

The oscillation of gas-filled micropores has also been examined theoretically.[28] The gas in the cylindrical micropores forms an approximately flat air–water interface, which oscillates transversely (i.e., like a drumhead) when activated by ultrasound. Only micropores which are full of air, and twice as long as their diameter are considered here, for simplicity. The linear resonance frequency is then

$$\omega_p^2=\frac{15\pi}{8\rho R_p^2}\left[\frac{p_0R_p}{4g}+\frac{2\sigma}{R_p}\right], \tag{11}$$

in which the length of the micropore $g=2R_p$ for this study. The second-harmonic oscillation has also been worked out for gas-filled micropores.[29] However, this component of the oscillation is small, because the oscillation is primarily transverse rather than pulsatile. The subharmonic component of the micropore oscillation was not considered here. The micropore damping coefficients are similar to those for the free microbubble, except that a coefficient related to damping in the viscous boundary layers inside and outside the micropore are added. The boundary layer inside the micropore was neglected in this study, because the micropores were assumed to be full of gas.

A theoretical framework for estimating the amount of biological perturbation expected from a given microbubble exposure should be developed for use in medical applications. Although the interaction of an ultrasound field with a gas body is at least partly understood, as outlined above, the processes leading to observed bioeffects are not. Even for moderate pressure amplitudes, a number of different mechanisms may plausibly have a role in bioeffects, but detailed physical theory is not available for most.[30] Second-order, time-averaged mechanisms, including radiation forces and acoustic microstreaming have received considerable theoretical attention. The microstreaming shear stress model has proven useful in describing several bioeffects situations involving gas body activation in terms of the damage of cell membranes by shear stress in acoustic microstreaming fluid flow near the oscillating gas body.[31,32] Approximate theory is available for the shear stress generated in near-boundary acoustic streaming and can be used to estimate the pressure amplitudes required to exceed the critical shear stress for biological membranes. If a pulsating microbubble rests on a rigid boundary, then the fluid oscillating across the surface will have a boundary layer of thickness

$$\beta^2=\frac{2\,\eta}{\rho\,\omega}. \tag{12}$$

Microstreaming flow is generated with a velocity gradient near the boundary which results in a shear stress approximately given by

$$s=\omega\,\eta R_0A_1^2/\beta. \tag{13}$$

When this shear stress exceeds a critical value for membrane failure, then cells may be lysed as they are caught up in the flow. This theory should be considered to be only an approximate framework for the actual processes occurring near ultrasonically activated microbubbles in the megahertz frequency range. For example, the boundary layer thickness is typically smaller than the cell size in the MHz frequency range, so that the cells cannot be subjected to uniform stress, as is the case for low frequencies.[17,20] Nevertheless, the theory may be a useful relative indicator of bioeffects potential under various situations.

Ultrasonically activated gas bodies act as transducers of the ultrasound wave into localized activity. It seems plausible that a general indicator of the biological effectiveness of microbubbles or gas bodies might be the amplification of the ultrasonic kinetic energy near the oscillator. The ratio of the kinetic energy density E_s of the spherical wave at the microbubble surface to the kinetic energy density E_p of the incident wave is given by[33]

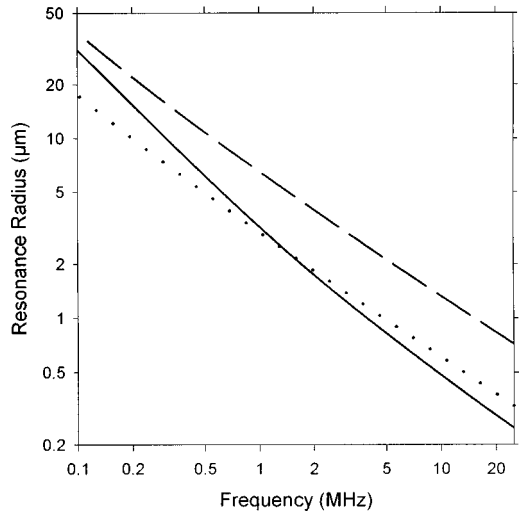

FIG. 1. The resonance radii for free microbubbles (solid), encapsulated microbubbles (dashed), and gas-filled micropores (dotted) for frequencies in the medically relevant range.

$$\frac{E_s}{E_p} = \frac{c^2}{\omega_0^2 R_0^2 \delta^2} \tag{14}$$

at resonance. Another consideration for bioeffects potential is the excess absorption expected from the ultrasonic interaction with microbubbles. The energy dissipation represented by the damping coefficients ultimately appears as heat. The excess absorption coefficient α_e is proportional to the product of the number density N of identical resonant microbubbles in the medium, and the absorption cross section[33]

$$\alpha_e = N \frac{2\pi R_0 c}{\omega_0 \delta}. \tag{15}$$

II. RESULTS

The linear activation of gas bodies is maximum for the size of resonance at the exposure frequency. The resonance size is plotted in Fig. 1 for free-gas microbubbles, encapsulated gas microbubbles, and gas-filled micropores. It should be noted that, although Fig. 1 covers a 100-kHz to 20-MHz span, most encapsulated microbubbles in contrast agents are less than about 5 μm in radius,[12] and the largest gas-filled micropores which have been useful in bioeffects research are about 6.6 μm in radius.[34] The resonance sizes are roughly inversely proportional to frequency. The shell stiffness makes the resonant encapsulated microbubble larger than the free-microbubble or gas-filled micropore, which are of similar magnitude under the assumed conditions. The ratio of the encapsulated-microbubble resonance radius to the free-microbubble resonance radius increases with frequency as shown in Fig. 2. Above about 1 MHz, the resonant encapsulated microbubbles are more than twice as large as the resonant free microbubble for a given frequency.

The ultrasonic activation of the microbubbles and gas bodies changes with frequency due mostly to the increasing viscous damping at higher frequencies. The pressure amplitude required to produce a fixed oscillation of $A_1 = 0.1$ at

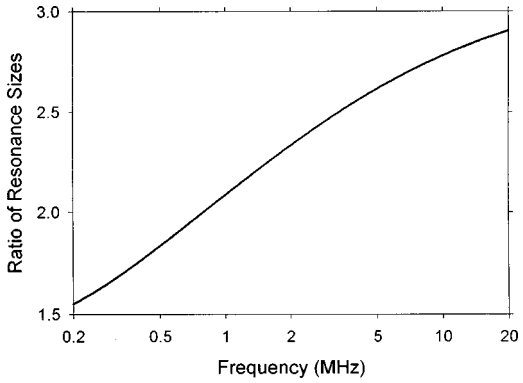

FIG. 2. The ratio of the encapsulated microbubble resonance size to the free-microbubble resonance size.

resonance is shown in Fig. 3. The pressure amplitude needed for this level of activation of the encapsulated microbubbles is generally about an order of magnitude larger than for the free microbubbles. In the important 2–20 MHz frequency range, the needed pressure-amplitude increases as $f^{1.6}$ for the encapsulated microbubbles and as $f^{0.9}$ for the free microbubbles (determined by linear regression, with $r^2 > 0.99$). In the limit that the pulsation of the free microbubble is controlled by viscous damping only, the amplitude A_1 becomes inversely proportional to frequency and reduces to

$$A_1 \cong \frac{p_1}{4\mu\omega_0} \tag{16}$$

at resonance. In the low amplitude range, the second-harmonic component of the oscillation A_2 increases as the square of the pressure amplitude as specified in Eq. (2). The oscillation generates spherical ultrasound waves which can be detected at a distance. The scattered signal levels can be readily calculated from the fundamental and second-harmonic amplitudes.[5,23] Due to the relatively low amplitude

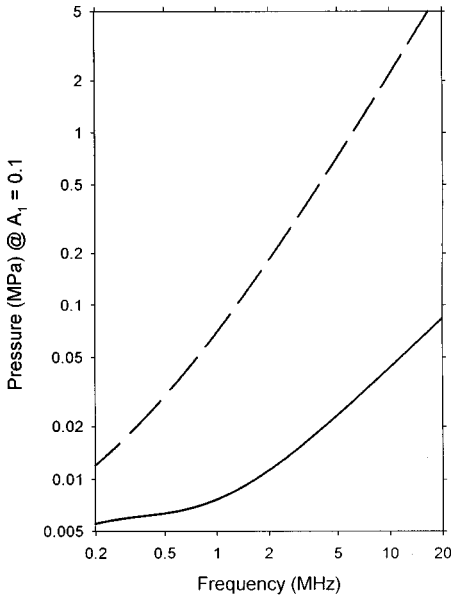

FIG. 3. The incident pressure amplitude needed to drive the resonant free (solid) and encapsulated (dashed) microbubbles with an oscillation amplitude equal to one-tenth of the radius.

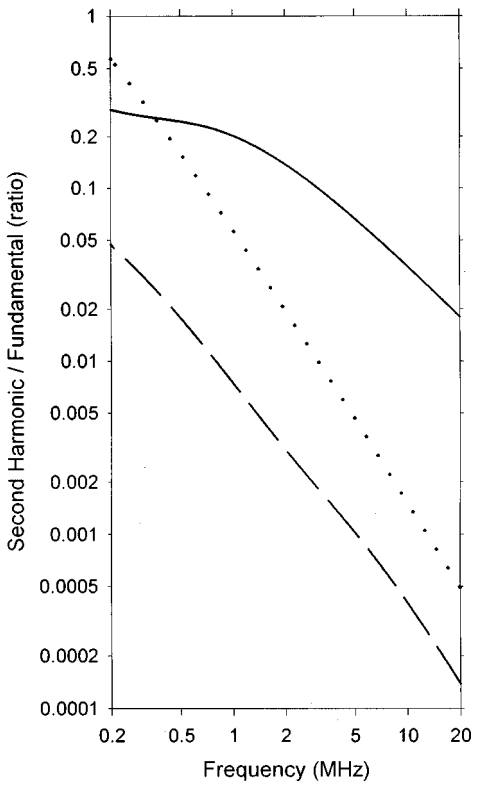

FIG. 4. The ratio of the scattered second harmonic to the fundamental component for resonant free microbubbles (solid), encapsulated microbubbles (dashed), and gas-filled micropores (dotted) for an incident pressure amplitude of 0.01 MPa.

of the encapsulated microbubbles (see Fig. 3), the ratio of scattered second-harmonic signal to scattered fundamental is typically much larger for the free than for the encapsulated microbubbles. This is illustrated for the three oscillators in Fig. 4, in which the ratio is shown for a constant $p_1 = 0.1$ MPa at resonance.

The free and encapsulated microbubbles can also engage in highly nonlinear oscillation at half the fundamental frequency (i.e., the subharmonic). The theoretical thresholds for subharmonic pulsation are displayed in Fig. 5 for free and

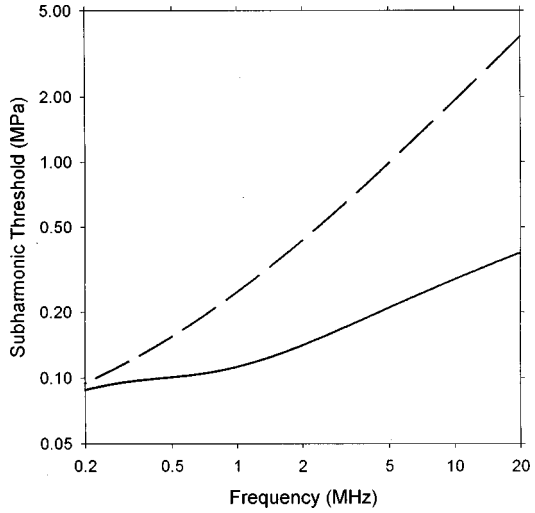

FIG. 5. Threshold for generation of a subharmonic signal at one half the fundamental for free (solid) and encapsulated (dashed) microbubbles.

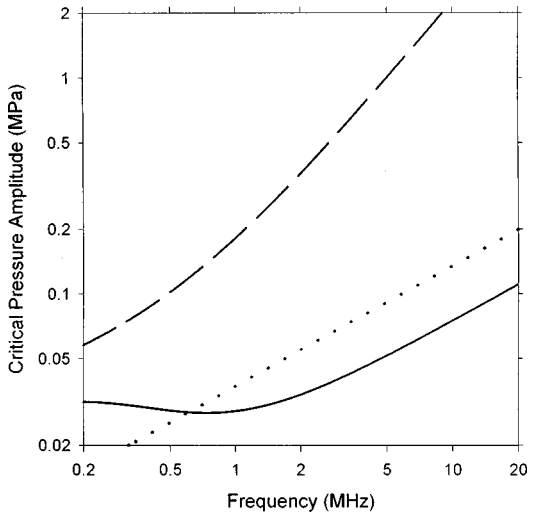

FIG. 6. The incident pressure amplitude required to produce a critical shear stress (see text) at a surface for resonant free microbubbles (solid), encapsulated microbubbles (dashed), and gas-filled micropores (dotted).

encapsulated microbubbles. From Eq. (8), the total damping coefficients can be obtained easily from these thresholds in MPa simply by dividing by 0.6. Since the encapsulated microbubbles have extra damping associated with their shells, these gas bodies have substantially higher thresholds than free microbubbles.

The shear stress generated at a surface near a small source is given by Eq. (13). This shear stress depends on the square of A_1, and thus on the square of p_1. In the shear stress model of bioeffects, a critical shear stress S_c exists, which can result in membrane damage and cell lysis. The appropriate value of S_c for the conditions considered here is uncertain, but this can be estimated by comparison to observed bioeffects. The gas-filled micropore system probably best corresponds to the shear stress model, since the gas bodies reside in a solid surface. Data on bioeffects are available for whole blood for 2-μm radius micropores exposed to 1.7-MHz ultrasound; for 16-min exposures, significant hemolysis was observed at intensities as low as 45–90 mW cm^{-1}, or about 0.05 MPa. Assuming this pressure amplitude corresponds to the shear stress threshold, S_c can be calculated from Eq. (13) to be about 5950 N m^{-2}. There are other uncertainties, such as how this value might change with the ultrasonic frequency and the duration of shear, but these likely have a small influence on results, because cells larger than the boundary layers appear to remain fixed at the micropores.[20] Assuming that S_c is approximately constant for the frequency range considered, the pressure amplitudes needed to attain this critical value can be calculated, as shown in Fig. 6 for resonance conditions. This model may also be applicable to free and encapsulated microbubbles under some conditions, and calculations are also shown in Fig. 6 for these (neglecting the additional damping near a surface). For the higher frequencies considered, the critical pressure amplitude increases strongly with frequency for all three oscillators, roughly as $f^{1/2}$ for the micropores and free microbubbles and as f for the encapsulated microbubbles. The gas-filled micropores require about ten times higher pressure amplitude at 2 MHz than do free microbubbles to reach S_c.

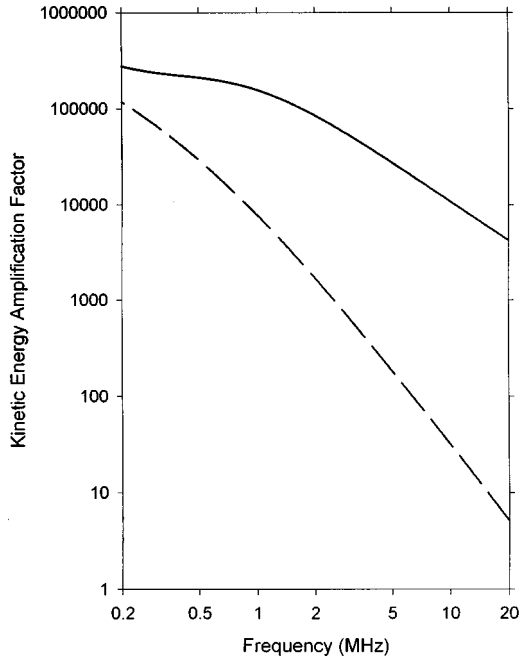

FIG. 7. The kinetic energy density amplification factor for free microbubbles (solid), and encapsulated microbubbles (dashed) plotted against resonance frequency.

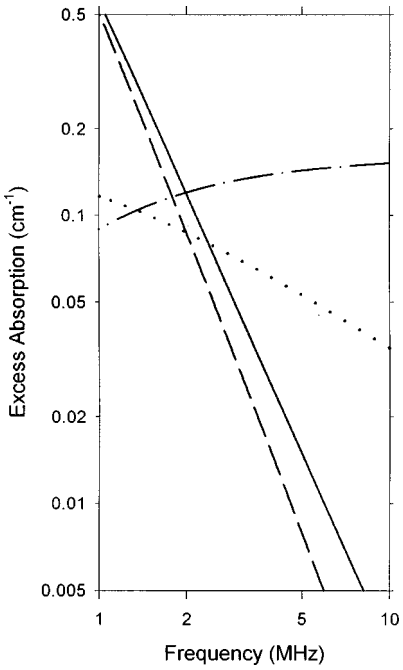

FIG. 8. The excess absorption coefficient for free microbubbles (solid), and encapsulated microbubbles (dashed) at a concentration of 2-mm^{-3} resonant microbubbles over a diagnostically relevant frequency range. For constant volume fraction of gas, relative to 2-mm^{-3} resonant microbubbles at 2 MHz, the coefficient for free microbubbles (dash–dot), encapsulated microbubbles (dotted) are less strongly dependent on frequency.

The shear stress model described above may not be generally applicable to the free and encapsulated microbubbles. More general indicators of the potential for biological effects might be the kinetic energy amplification factor [Eq. (14)] and the excess absorption [Eq. (15)] due to the interaction. The kinetic energy density amplification factor for free and encapsulated microbubbles is shown in Fig. 7 as a function of the resonance frequency. In the 2–20 MHz range, this ratio is proportional to $f^{-1.3}$ for free microbubbles and to $f^{-2.6}$ for encapsulated microbubbles. The absorption and heating resulting from activation of microbubbles depends on the number present. A concentration of about 50 mm^{-3} might be expected to occur throughout the body for a normal 0.15-ml/kg dose of Albunex® with about 3×10^8 ml^{-1} encapsulated microbubbles, and it is not implausible that a few percent could persist in a tissue of interest and have a resonance response at the diagnostic frequency. The expected excess absorption coefficient is shown in Fig. 8 for a constant $N=2$ mm^{-3}, for which the coefficients decrease rapidly with increasing resonance frequency, and for a constant volume fraction (but increasing number of microbubbles) of gas based on 2-mm^{-3} resonant microbubbles at 2 MHz (about the frequency of maximum transmission loss for Albunex®[17]). For comparison, the absorption coefficient for liver is proportional to frequency and is about 0.1 cm^{-1} at 2 MHz.

III. DISCUSSION

The difference in resonance size between the encapsulated and the free microbubbles shown in Fig. 1 has interesting implications. A sphere of radius 2.5 μm is approximately the largest size capable of passing readily through most human capillaries. For the free microbubble, this size of free microbubble resonates at about 1.3 MHz, but this size of encapsulated microbubble resonates at about 3.9 MHz. Thus the encapsulated microbubbles appear to be well suited for use a frequencies used in diagnostic ultrasound, because the resonant encapsulated microbubbles are small enough to circulate throughout the body. For example, the mean diameter of Albunex encapsulated microbubbles of 3–5 μm would be resonant in the range 8.3–3.9 MHz.

Under reduced atmospheric pressures, or high-pressure-amplitude ultrasound exposure, the encapsulated microbubbles appear to be destabilized, such that they disappear from a suspension upon cessation of the perturbation. For example, changes in transmission through Albunex suspensions are noted at 0.1–0.2 MPa, which apparently indicates destabilization of the encapsulated microbubbles in this pressure-amplitude range.[10] A plausible explanation of this phenomenon is that the shells break as a consequence of the ultrasonic activation, thus freeing the microbubble. The free microbubble then becomes subjected to compression due to surface tension and can shrink by diffusion. Microscopical observation of Albunex suspensions confirms this explanation for pulsed ultrasound.[35]

Resonance-sized gas bodies might be expected to be the most susceptable to destabilization, since they would have the strongest interaction. A resonant encapsulated microbubble, when destabilized, might liberate a free microbubble, which would then be larger than resonance size for a free microbubble. As shown in Fig. 2, the liberated free microbubble might be twice (or more) the resonance size above about 2 MHz, which coincides with the size giving the lowest subharmonic threshold. Experimentally, subharmonic signals have been obtained with Albunex at about 0.28 MPa,

or higher, for 3.3-MHz exposure. From Fig. 5, the threshold for free microbubbles, 0.17 MPa, is somewhat less than the experimental value, while that for encapsulated microbubbles, 0.67 MPa, is much higher. This lends support to the idea that the encapsulated microbubbles break, and liberate free microbubbles which generate the observed subharmonic signals.[16,24]

The differences in behavior between free and encapsulated microbubbles, which arise in comparing different contrast agents or in considering the consequences of the destabilization of gas body shells, are important for imaging of fundamental, second-harmonic, or subharmonic signals. From Fig. 3, the fundamental amplitude is different by an order of magnitude for the diagnostic frequency range. In regard to use of contrast agents in diagnostic procedures, this destabilization and amplitude enhancement might be evidenced by the phenomenon of stimulated emission, observed during Doppler examinations with contrast agents.[36] The second harmonic is important for contrast agents because this signal can be used to form an image which emphasizes the location of the agents (i.e., second-harmonic imaging[6]). A large difference exists in the nonlinear resonance response of the encapsulated and free microbubbles as shown in Fig. 4 for $p=0.01$ MPa. Above about 2 MHz, the second harmonic scattered from a resonant encapsulated microbubble is less than 1% of the second harmonic scattered from a resonant free microbubble. The sensitivity of the second-harmonic scattering to oscillation parameters of gas bodies has been utilized to determine the mode of oscillation of the gas-filled micropores,[37] and to evaluate the stability of the gas in the micropores as the excitation level was increased.[38]

Gas body activation occurs for any level of excitation, but the resulting local perturbation presumably must exceed a critical biological threshold in order to induce biological effects on nearby cells. As noted above, one useful model for cell lysis is the near-boundary shear stress model, in which cells caught up in microstreaming fluid flow near a pulsating microbubble on a boundary are damaged by the shear stress. Above a critical shear stress, the cell membrane fails, leading to cell lysis. The pressure amplitude needed to generate the critical shear stress, which was estimated from observations of lysis near ultrasonically activated gas-filled micropores, is plotted in Fig. 6. The critical pressure amplitudes needed with encapsulated microbubbles are modest, and generally within the capability of diagnostic ultrasound systems. However, the critical levels are roughly two orders of magnitude lower for resonant free microbubbles under some conditions. Thus encapsulated microbubbles in contrast agents may have a relative safety advantage compared to free microbubbles, particularly for conditions with improved stability (e.g., with lower insonation levels or use of ''unbreakable'' shells).

A noteworthy feature of the shear stress model is that the shear stress increases as the square of the incident pressure amplitude, which is the same dependence found for the second-harmonic component of oscillation, for a given oscillator. Thus the second-harmonic scattering from activated contrast agents might reflect, to some extent, the level of microstreaming shear stress near the gas bodies. This implies that a second-harmonic image might indicate bioeffects potential. However, the second-harmonic signal arises from other processes (e.g., finite amplitude propagation) and has not been strongly correlated with bioeffects.[16] The formation of images using the subharmonic signals may be a better strategy for this purpose, since this signal more clearly represents microbubble activity[39] and has been correlated with bioeffects.[16]

The use of contrast agents in diagnostic ultrasound procedures complicates the specification of indices for gauging the potential for nonthermal interaction and bioeffects. A ''mechanical index'' (MI) of the form $pf^{-1/2}$ and a ''thermal index'' (TI) indicative of temperature increases have been developed to indicate this potential.[40] This form of the MI was based on calculations of the pressure-amplitude thresholds for inertial cavitation with nuclei of optimum size. Since gas bodies do not have a threshold for activation, the threshold concept for an exposure index has reduced applicability for contrast agents. The consideration of different indices or risk management strategies for use with these agents may be desirable as they come into general use. One possibility might be the pressure amplitude needed to produce a constant level of activation of the resonant microbubbles as shown in Fig. 3. From this calculation, the form of an index in the diagnostic frequency range (2–20 MHz) would be $pf^{-1.6}$ for constant A_1 of the encapsulated microbubbles, or $pf^{-0.9}$ for free microbubbles. Alternative parameters considered in regard to bioeffect potential were the local kinetic energy, and the excess absorption. The ultrasonic activation of microbubbles greatly amplifies the local kinetic energy density as shown in Fig. 7. The kinetic energy density in the spherical wave may be important as a bioeffects indicator because it is related to the radiation force on nearby particles (e.g., cells). The excess absorption, shown in Fig. 8 for specific number densities of resonant microbubbles, may be important in predicting heating. This may influence models used for calculations of the TI. For example, the excess absorption coefficients at 2 MHz in Fig. 8 of 0.12 cm^{-1} for free microbubbles and 0.088 cm^{-1} for encapsulated microbubbles are comparable to the 0.1-cm^{-1} absorption expected in liver. Clearly, a full understanding of the etiology of contrast-agent-related bioeffects will require a detailed evaluation of many factors in order to develop exposure indices and risk management strategies for ultrasound contrast agents.

ACKNOWLEDGMENTS

This research was supported by the U.S. National Institutes of Health via Grant No. CA42947.

[1] P. H. Chang, K. K. Shung, S. Wu, and H. B. Levene, ''Second harmonic imaging and harmonic Doppler measurements with Albunex®,'' IEEE Trans. Ultrason. Ferroelectr. Freq. Control **42**, 1020–1027 (1995).
[2] B. F. Vandenberg and H. E. Melton, ''Acoustic lability of albumin microspheres,'' Journal of the American Society of Echocardiography **7**, 582–589 (1994).
[3] D. L. Miller and R. M. Thomas, ''Ultrasound contrast agents nucleate inertial cavitation *in vitro*,'' Ultrasound Med. Biol. **21**, 1059–1065 (1995).
[4] N. de Jong, R. Cornet, and C. T. Lancee, ''Higher harmonics of vibrating gas-filled microspheres. Part one: simulations,'' Ultrasonics **32**, 447–453 (1994).
[5] C. C. Church, ''The effects of an elastic solid surface layer on the radial pulsations of gas microbubbles,'' J. Acoust. Soc. Am. **97**, 1510–1521 (1995).

[6] N. de Jong, L. Hoff, T. Scotland, and N. Bom, ''Absorption and scatter of encapsulated gas filled microspheres: Theoretical considerations and some measurements,'' Ultrasonics **30**, 95–103 (1992).
[7] J. N. Marsh, C. S. Hall, M. S. Hughes, J. Mobley, J. G. Miller, and G. H. Brandenburger, ''Broadband through-transmission signal loss measurements of Albunex suspensions at concentrations approaching *in vivo* doses,'' J. Acoust. Soc. Am. **101**, 1155–1161 (1997).
[8] D. L. Miller and R. M. Thomas, ''Contrast-agent gas bodies enhance hemolysis induced by lithotripter shock waves and high-intensity focused ultrasound in whole blood,'' Ultrasound Med. Biol. **22**, 1089–1095 (1996).
[9] A. A. Brayman, P. L. Strickler, H. Luan, S. L. Barned, C. H. Raeman, C. Cox, and M. W. Miller, ''Hemolysis of 40% hematocrit Albunex®-supplemented human erythrocytes by pulsed ultrasound: Frequency, acoustic pressure and pulse length dependence,'' Ultrasound Med. Biol. **23**, 1237–1250 (1997).
[10] D. L. Miller, R. A. Gies, and W. B. Chrisler, ''Ultrasonically induced hemolysis at high cell and gas body concentrations in a thin-disc exposure chamber,'' Ultrasound Med. Biol. **23**, 625–633 (1997).
[11] D. Dalecki, C. H. Raeman, S. Z. Child, C. Cox, C. W. Francis, R. S. Meltzer, and E. L. Carstensen, ''Hemolysis *in vivo* from exposure to pulsed ultrasound,'' Ultrasound Med. Biol. **23**, 307–313 (1997).
[12] D. Dalecki, C. H. Raeman, S. Z. Child, D. P. Penny, R. Mayer, and E. L. Carstensen, ''The influence of contrast agents on hemorrhage produced by lithotripter fields,'' Ultrasound Med. Biol. **23**, 1435–1439 (1997).
[13] D. Dalecki, C. H. Raeman, S. Z. Child, D. P. Penny, and E. L. Carstensen, ''Remnants of Albunex nucleate acoustic cavitation,'' Ultrasound Med. Biol. **23**, 1405–1412 (1997).
[14] D. L. Miller and R. A. Gies, ''Gas-body based contrast agent enhances vascular bioeffects of 1.09 MHz ultrasound on mouse intestine,'' Ultrasound Med. Biol. (in press).
[15] D. L. Miller and R. A. Gies, ''Enhancement of ultrasonically-induced hemolysis by perfluorocarbon-based compared to air-based echo-contrast agents,'' Ultrasound Med. Biol. **24**, 285–292 (1998).
[16] D. L. Miller and S. Bao, ''The relationship of scattered subharmonic, 3.3 MHz fundamental and second harmonic signals to damage of monolayer cells by ultrasonically activated Albunex,'' J. Acoust. Soc. Am. **103**, 1183–1189 (1998).
[17] D. L. Miller, ''A review of the ultrasonic bioeffects of microsonation, gas-body activation, and related cavitation-like phenomena,'' Ultrasound Med. Biol. **13**, 443–470 (1987).
[18] D. L. Miller and R. M. Thomas, ''Ultrasonic gas body activation in Elodea leaves and the mechanical index,'' Ultrasound Med. Biol. **19**, 343–351 (1993).
[19] S. Z. Child, C. H. Raeman, E. Walters, and E. L. Carstensen, ''The sensitivity of Drosophila larvae to continuous-wave ultrasound,'' Ultrasound Med. Biol. **18**, 725–728 (1992).
[20] D. L. Miller, ''Particle gathering and microstreaming near ultrasonically activated gas-filled micropores,'' J. Acoust. Soc. Am. **84**, 1378–1387 (1988).
[21] D. L. Miller, ''The influence of hematocrit on hemolysis by ultrasonically activated gas-filled micropores,'' Ultrasound Med. Biol. **14**, 293–297 (1988).
[22] T. G. Leighton, *The Acoustic Microbubble* (Academic, New York, 1994).
[23] D. L. Miller, ''Ultrasonic detection of resonant cavitation microbubbles in a flow tube by their second harmonic emissions,'' Ultrasonics **19**, 217–224 (1981).
[24] O. Lotsberg, J. M. Hovem, and B. Aksum, ''Experimental observation of subharmonic oscillations in Infoson microbubbles,'' J. Acoust. Soc. Am. **99**, 1366–1369 (1996).
[25] A. Eller and H. G. Flynn, ''Generation of subharmonics of order one-half by microbubbles in a sound field,'' J. Acoust. Soc. Am. **46**, 722–727 (1969).
[26] A. Prosperetti, ''Application of the subharmonic threshold to the measurement of the damping of oscillating microbubbles,'' J. Acoust. Soc. Am. **61**, 11–16 (1977).
[27] M. H. Safar, ''The exploitation of the subharmonic pressure waves from pulsating gas microbubbles in an acoustic field in liquids,'' J. Phys. D **3**, 635–36 (1970).
[28] D. L. Miller and W. L. Nyborg, ''Theoretical investigation of the response of gas-filled micropores and cavitation nuclei to ultrasound,'' J. Acoust. Soc. Am. **73**, 1537–1544 (1983).
[29] E. A. Neppiras, W. L. Nyborg, and D. L. Miller, ''The nonlinear response of gas-filled micropores to ultrasound at MHz frequencies,'' in *Ultrasonic International 83 Conference Proceedings* (Butterworth, London, 1983), pp. 248–253.
[30] M. W. Miller, D. L. Miller, and A. A. Brayman, ''A review of *in vitro* bioeffects of inertial ultrasonic cavitation from a mechanistic perspective,'' Ultrasound Med. Biol. **22**, 1131–1154 (1996).
[31] J. A. Rooney, ''Shear as a mechanism for sonically induced biological effects,'' J. Acoust. Soc. Am. **52**, 1718–1724 (1972).
[32] W. L. Nyborg, *Physical Mechanisms for Biological Effects of Ultrasound* (Bureau of Radiological Health, Rockville, MD, 1977).
[33] W. T. Coakley and W. L. Nyborg, ''Cavitation: Dynamics of gas microbubbles: Applications,'' in *Ultrasound: Its Applications in Medicine and Biology*, edited by F. J. Fry (Elsevier Scientific, New York, 1978), Chap. 2, pp. 77–160.
[34] D. L. Miller, ''Experimental investigation of the response of gas-filled micropores to ultrasound,'' J. Acoust. Soc. Am. **71**, 471–476 (1982).
[35] J. Wu and J. Tong, ''Experimental study of stability of a contrast agent in an ultrasound field,'' Ultrasound Med. Biol. **24**, 257–265 (1998).
[36] V. Uhlendorf and C. Hoffmann, ''Nonlinear acoustical response of coated microbubbles in diagnostic ultrasound,'' in *Proceedings 1994 Ultrasonics Symposium* (Institute of Electrical and Electronics Engineers, New York, 1994), pp. 1559–1562.
[37] D. L. Miller and E. A. Neppiras, ''The oscillation mode of gas-filled micropores,'' J. Acoust. Soc. Am. **77**, 946–953 (1985).
[38] E. A. Neppiras, W. L. Nyborg, and D. L. Miller, ''Non-linear behavior and stability of trapped micron-sized cylindrical gas microbubbles in an ultrasonic field,'' Ultrasonics **21**, 109–115 (1983).
[39] P. M. Shankar, P. D. Krishna, and V. L. Newhouse, ''Advantages of subharmonic over second harmonic backscatter for contrast-to-tissue echo enhancement,'' Ultrasound Med. Biol. **24**, 395–399 (1998).
[40] AIUM, *Standard for Real-Time Display of Thermal and Mechanical Acoustic Output Indices on Diagnostic Ultrasound Equipment* (American Institute of Ultrasound in Medicine, Rockville, MD, 1992).

Playback of acoustic thermometry of ocean climate (ATOC) -like signal to bony fishes to evaluate phonotaxis

A. Peter Klimley and Sallie C. Beavers
Bodega Marine Laboratory, University of California, Davis, P.O. Box 247, Bodega Bay, California 94923

(Received 9 March 1998; accepted for publication 14 July 1998)

The aim of this study was to evaluate whether acoustic thermometry of ocean climate (ATOC) signals have a positive or negative phonotactic effect on the behavior of fish present near the sound source at Pioneer Seamount off Central California. We played back an ATOC-like signal to three species of rockfish kept within a 15×2-m field enclosure in Bodega Bay, California. Each subject was observed during a 25-min ''silent'' control period followed immediately by a test period comprised of a 5-min ''ramp-up,'' in which the sound level increased gradually to a peak level, and a 20-min period at constant peak level. The amount of time that each subject spent in 15 zones, each 1 m wide, at increasing distances from the sound transducer, was observed. It was suspended in midwater at the center of zone 1, the deepest portion of the enclosure. We observed little movement by fish in response to the playback of the ATOC signal. The subjects remained in zones 1 and 2, despite sound pressure levels present of 145.1–153.0 dB *re*: 1 μPa. Little difference existed in the behavior of fish during sound playback period and the ''silent'' control period. The median time interval that fishes occupied zone 1 was 100% of the experiment duration for both test and control periods (i.e., 6 of 11 subjects in the former remained exclusively within that zone versus 7 of 11 subjects in the latter). © *1998 Acoustical Society of America.* [S0001-4966(98)04310-0]

PACS numbers: 43.80.Jz, 43.80.Lb, 43.30.Qd [PBO]

INTRODUCTION

The time taken by a sound to propagate between two points in the ocean is an indicator of the temperature of the water along the sound path. This is because rate of travel is related to water temperature, i.e., the warmer the water, the faster the speed. A high amplitude, low frequency sound broadcast from an underwater acoustic transducer positioned along one coastal margin of an ocean can be detected by a hydrophone on the other margin. The changing rate of travel (or transit interval) over time is a potential indicator of long-term warming or cooling of the oceans (Munk *et al.*, 1994). Acoustic thermometry of ocean climate (ATOC) refers to the use of acoustics to measure ocean temperature on a global scale. The introduction of the ATOC signal into the ocean, however, changes the composition of the ambient noise and may affect the behavior of marine animals [for impact on distribution and behavior of marine mammals, see Bowles *et al.* (1994)].

On 28 October 1995, an acoustic source (Alliant Techsystems, HX-554) was placed at a depth of 941 m off Central California on the peak of Pioneer Seamount (27° 20.555′ N, 123° 26.7117′ W) (Howe, 1996). This projector will periodically broadcast a phase-modulated signal with a 37.5-Hz bandwidth centered at 75 Hz. The sound will start 5 min before each hour with a sound pressure level of 165 dB (*re*: 1 μPa) and will increase by 6-dB steps each min for an interval of 5 min until reaching a peak of 195 dB. This peak level will be maintained for 20 min. Hydrophones at sites throughout the Pacific Ocean will time the arrival of the intermittent shifts in the phase of the dominant frequency in a pseudorandum m-code sequence (common signals long used in tomography) by the process of ''match filtering'' (Munk *et al.*, 1994). Au *et al.* (1997) describe how these ATOC signals are synthesized and how they would propagate in the deep waters near the proposed Kauai source in the Hawaiian Islands.

What effect will these ATOC signals have on the distribution and behavior of fishes? This question needs to be answered because many of these species constitute important food resources for countries surrounding the ocean basins in which the signals will be propagated. The acoustic sense of fishes is their best means of acquiring information from a distance. It is used to locate prey and avoid predators (Nelson and Gruber, 1963; Banner, 1972) as well as to communicate among each other (Myrberg, 1981). To accomplish this, fishes must distinguish relevant signals from the cacophony of sounds generated by various sources. These sounds may be weather related, caused by rain or wind, or man-made, produced by ship propellers, explosions, SCUBA, or the above-mentioned ATOC source. If high in amplitude and composed of frequencies overlapping the hearing range of the species, such noise may interfere with the reception of sounds of biological relevance, a process termed ''masking'' [for review of adverse effects, see Myrberg (1990, 1997)]. If these sounds change in magnitude suddenly, they can also startle an individual and cause it to swim away from the vicinity of the source (Klimley and Myrberg, 1979). The aim of this pilot study was to evaluate whether ATOC signals have a positive or negative phonotactic effect on the behavior of a species of fish present near the California ATOC signal-source at Pioneer Seamount.

I. METHODS

The input signal of the ATOC sound source was played back to fish in an experimental enclosure in Bodega Bay using a tape recorder (Marantz, PMD430), amplifier (Pio-

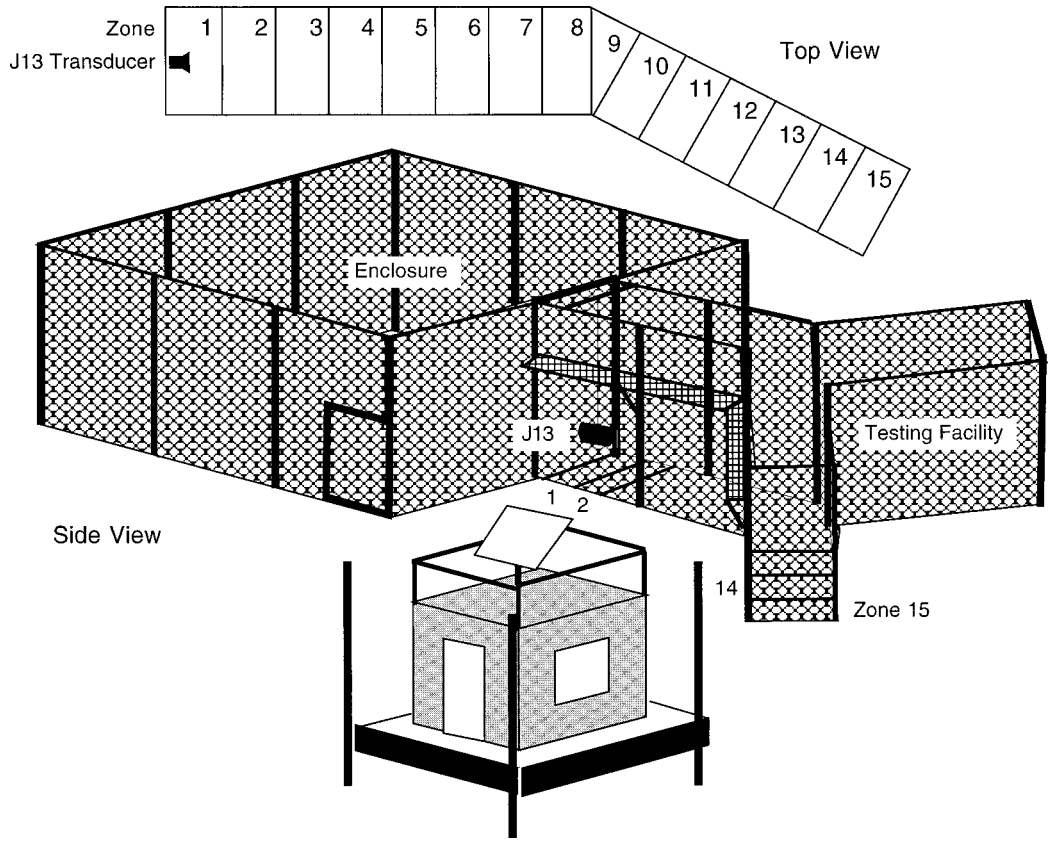

FIG. 1. Facility in which ATOC-like signals were played back to rockfish.

neer, GM-X502), and underwater transducer (U.S. Navy, J13). The signal was monitored during the tests with a hydrophone-preamplifier (sensitivity: −163 dB *re*: 1 V/μPa) and a tape recorder (Sony, DAT). The hydrophone was suspended at the same depth of the underwater speaker. Sound pressure levels throughout the enclosure were measured with a storage oscilloscope (Tektronix, 560) by comparing the peak-to-peak voltage of the waveform of the ATOC signal recorded at locations to that of a 75 Hz pure tone produced by a signal generator (Wavetek, 130). The input voltage of the pure tone equaled the output voltage of the hydrophone-preamplifier with a known sound pressure. Peak-to-peak measurements of the ATOC signal on the oscilloscope display were converted to root-mean-square pressure levels relative to 1 μPa. We determined the waveform, spectrogram, and spectrum of the sound at a distance of 0.5 m from the sound projector using Canary Bioaccoustics Workshop software (Charif *et al.*, 1995).

The experimental enclosure consisted of a 15-m-long channel with a 2-m width surrounded by fiberglass fencing and supported by wooden pilings (Fig. 1). There was a slight slope to the bottom so that the depth of water varied <0.25 m over the length of the channel. White PVC tubes were laid across this channel on the bottom at 1-m distances from the speaker, and the resulting zones were numbered 1–15. The sound projector was suspended in midwater at the center of zone 1, the deepest portion of the enclosure. The depth of water at this point varied 1.5–2.0 m during testing due to tidal variation. We observed the behavior of each fish from a platform extending the length of the channel on either side.

Individuals of three species of rockfish (size range: 33–44 cm total length) were captured by hook and line and maintained in the laboratory for a period of three weeks before the experiments were conducted upon them. These rockfish are mid-water dwellers (130–365 m) and comprise moderate to large proportions of the commercial and recreational fishery catch off northern California (Leet *et al.*, 1992). All of the rockfish fed in the laboratory prior to testing in the field enclosure. Eleven fish were tested individually in the field (9 *Sebastes flavidus*, 1 *S. ariculatus*, and 1 *S. mystinus*). A tag on its dorsal fin identified each fish. Fish were transported (<30 min per trip) within a large plastic ice cooler to the field enclosure and allowed >35 min to acclimate to the enclosure.

Each subject was observed during a 25-min control period followed immediately by a test period comprised of a 5-min ''ramp-up,'' in which the sound level increased gradually to a peak level, and a 20-min period at constant peak level. The frequency composition, phase shifting, and resulting amplitude modulation of the recorded signal were identical to those of the ATOC signal propagated at Pioneer Seamount. A second 25-min period of silence and 25-min of sound playback immediately followed the first control and test period. We noted the time on a hand-held tape recorder whenever a fish entered a new zone. From this, we calculated the frequency and duration of time each subject spent in each zone throughout the experiment.

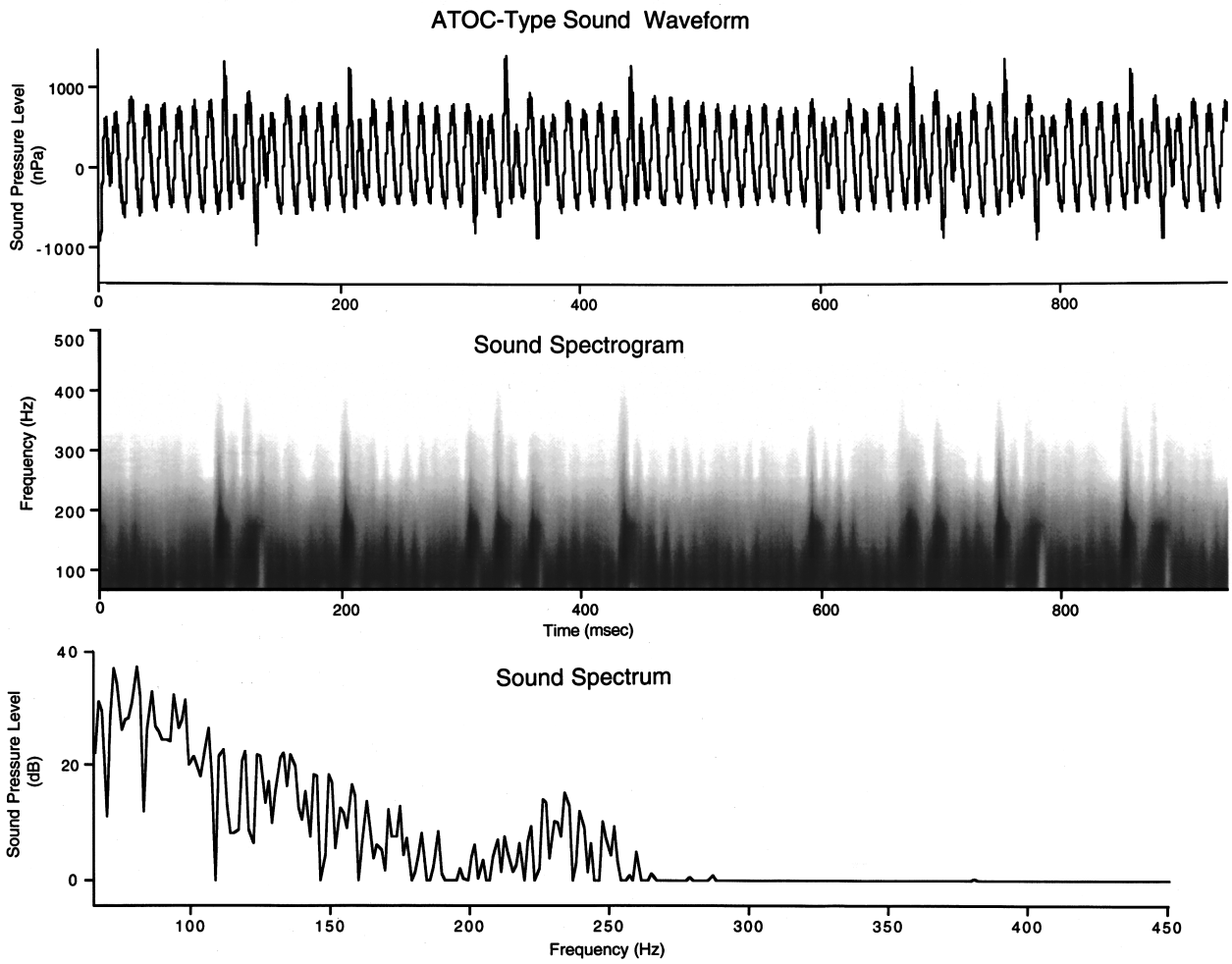

FIG. 2. ATOC-like signal of 1-s duration used in study. Shown are the waveform (above), spectrogram (middle), and spectrum of the sound (bottom).

II. RESULTS

The acoustic properties of the ATOC-type sound are evident in the waveform, spectrogram, and spectrum of the sound (Fig. 2). The period between successive peaks in the waveform is 13 ms, equivalent to a frequency of 75 Hz, and this is also evident in the spectrogram by the period between the evenly spaced dark bands. The higher peaks in the waveform and broader bands on the spectrogram at intervals of 25-150 ms are due to the phase shifts in the m-code sequence of the ATOC signal. The J13 does not accurately reproduce the sharp discontinuities between the phase-shifted waveforms (Fristrup, personal communication). For this reason, we refer to the signal as ''ATOC-like.'' The relative sound pressure levels of the various frequencies comprising the sound are shown in the spectrum. In addition to the fundamental of 75 Hz, weak harmonics are centered near 150 and 225 Hz.

The sound pressure level 1 m from the speaker was 145.1 dB. The levels measured at 2, 4, and 8 m were 133.5, 122.0, and 112.6 dB, respectively (Fig. 3). The rate of sound attenuation varied from 11.6 to 9.4 dB per doubling of the distance to the source. This exceeded the 6 dB that is expected in an unbounded acoustic medium and is probably due to destructive interference caused by the summation of the direct signal with boundary reflections from the mud substrate in the shallow channel where the facility is located. The sound pressure level 12 m from the speaker and near the end of the enclosure in zone 14 was 109.5 dB, exceeding the 105.4 peak level of ambient noise recorded in the enclosure.

We observed little movement by fish kept in the enclo-

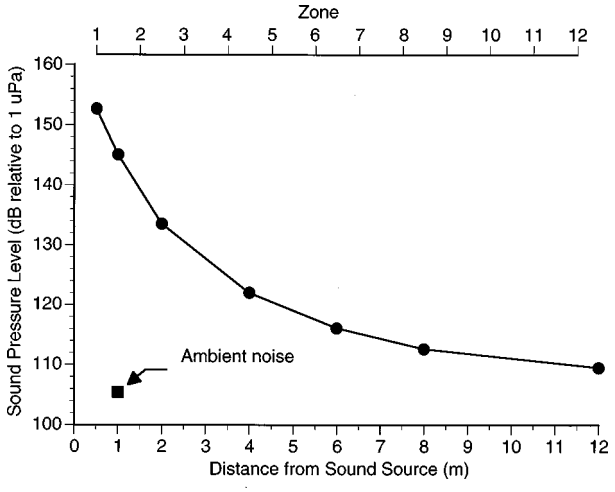

FIG. 3. Peak sound pressure levels of the ATOC-like signal (solid circles) at increasing distances from the speaker in the center of the test enclosure. Ambient noise was measured at a distance of 1 m from the speaker (solid square).

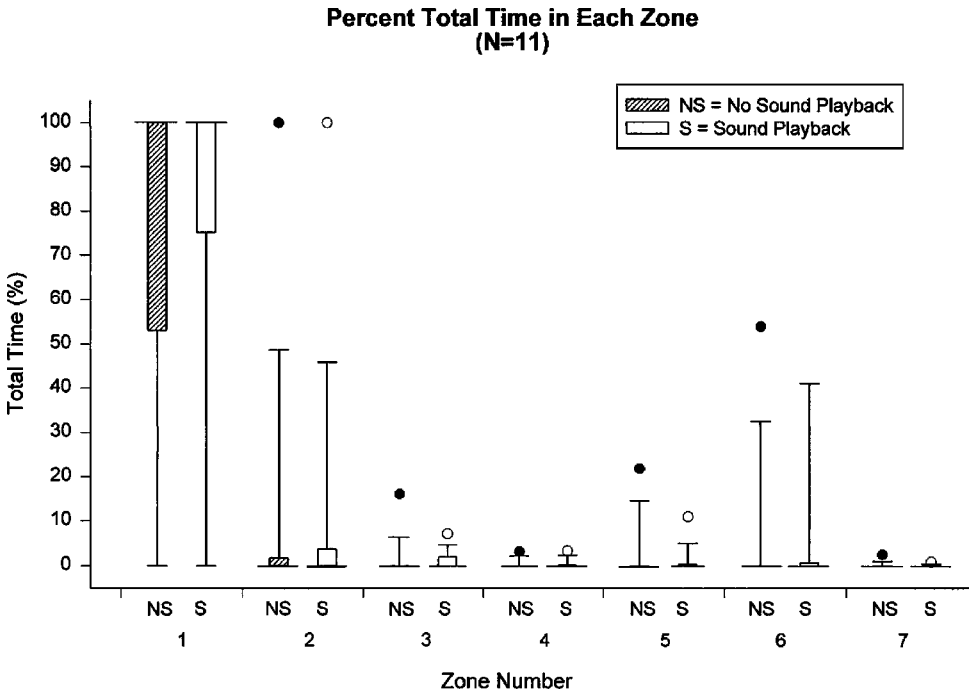

FIG. 4. Amount of time that 11 rockfish spent in seven zones, each 1 m farther from the speaker, expressed as a percentage of the 25 min duration of each experiment. Box diagrams are shown for ''silent'' control (NS) and test periods when the ATOC-like signal was played in the enclosure (S). Median percent time indicated by long horizontal lines across bars, 75th percentile by crosshatched box, and 90th percentile by short horizontal lines.

sure in response to the playback of the ATOC-like signal (Fig. 4). The subjects usually remained in zones 1 and 2, despite the high sound pressure levels present. Little difference existed in the behavior of fish during the sound playback period and the ''silent'' control period. The median time interval that fishes occupied zone 1 was 100% of the experiment duration for both test and control periods (i.e., 6 of 11 subjects in the former remained exclusively within that zone versus 7 of 11 subjects in the latter). Of the five subjects that did not stay exclusively in zone 1 during the playback period, four spent the majority of their time in zones 1 and 2, and one (No. 5) remained in zone 6 throughout the entire period. Of the four fishes that did not stay in zone 1 during the entire ''silent'' control, three spent the majority of their time in zones 1 and 2, and subject No. 5 spent its time in zones 4-7. Almost all the fish in zone 1 stayed along the edge of the enclosure, 0.5 m to the side of the J-13, where the sound pressure was 153.0 dB.

The results of the second experiment were similar to those of the first. Again the subjects remained in zones 1 and 2 despite high sound pressure levels present during the test period, and little difference existed in time spent in the same zones during the sound playback and ''silent'' control periods. The median time interval that fishes occupied zone 1 was again 100% for both test and control periods (i.e., 7 of 10 fish remained within that zone during the test versus 6 of 10 fish in control). Of the three subjects that did not stay exclusively in zone 1 during the playback period, one divided its time evenly between zones 2 and 3, another remained exclusively in zone 2, and the third stayed the entire period in zone 6. This spatial distribution varied little from that of the rest of the control fish. The five fishes not staying in zone 1 during the entire control period remained relatively close to the speaker. One fish spent 98.6% of its time in zone 1, another 100% of its time in zone 2, two spent most of their time between zones 1 and 4, and the fifth stayed in zone 6 as during the test period.

III. DISCUSSION

The presence of the ATOC signal had no apparent effect on the distribution of rockfish within the experimental enclosure. The subjects remained near the underwater transducer both during sound propagation and in its absence. The fish did not move away from the speaker in response to sound (i.e., negative phototaxis) or move toward the speaker (i.e., positive phototaxis). When in the two nearest zones, individuals usually did not swim toward the transducer either during the sound or controls periods. More likely some aspect(s) of the physical environment attracted rockfish to that part of the enclosure such as the slightly greater depth and absence of light. Avoidance of light would be consistent with their predilection to move about the enclosure along the perimeter, usually the shadiest part of the maze. These two environmental properties certainly characterize the midwater habitat of the rockfish species used in the study. In this context, it is significant that the sounds did not frighten the fishes away from a location resembling a natural refuge.

The failure of fish to show withdrawal responses to the ATOC-like signal may be explained by two acoustic properties of the signal. First, the sound pressure level to the onset of the ATOC-like signal was only 123 dB and the level slowly rose 30 dB to a peak of 153.0 dB. The level rose in 6-dB steps every min for 5 min until the final level was achieved and it was then sustained for 20 min. A similar onset rate of 6 dB/s rarely caused lemon sharks (*Negaprion*

brevirostris) to reverse their direction in a circular channel and accelerate away a sound source (Klimley and Myrberg, 1979). Consistent withdrawal responses by lemon sharks were exhibited only when the broadband of noise maintained at a level just masking broadband noise (105 dB) was increased at a rate of 96 dB/s to 123 dB. The slow onset to the ATOC signal minimizes the likelihood that it will elicit withdrawal responses from most fishes in the marine environment.

We may have elicited alarm responses by the rockfish if the sound pressure levels used our experiments had been higher. The general threshold of rockfish to impulsive sounds made by an air gun used in geophysical surveys was 180 dB (Pearson *et al.*, 1992). At this level, blue rockfish (*S. mystinus*) milled in increasingly tighter circles and schools of black rockfish (*S. melanops*) moved to the bottom. Vermilion (*S. miniatus*) and olive rockfish (*S. serranoides*), which form stationary schools on the bottom, either moved up into the water column or descended to the bottom where they remained still. Aversive responses were detected during this study in some fishes at levels as low as 161 dB.

A signal of 195 dB at a distance of 1 m from the sound projector could affect the behavior of fish in the immediate vicinity. However, the level would rapidly attenuate with distance from the speaker to a level below threshold, i.e., decreasing by 6 dB each doubling of the distance from the speaker. At this theoretical attenuation rate, the sound pressure level would decrease to 153 dB, the level at which alarm responses were not observed in the experimental enclosure, at a distance of 128 m from the sound source.

Additional experiments assessing the effect of the ATOC signal on fishes should utilize sound pressure levels closer to the 195-dB level of the actual signal. Ideally, the same sound transducer should be used to propagate the ATOC signal as at Pioneer Seamount. Tests should also be conducted on members of several species because the propensity to perform a phonotactic response may be dependent upon species-specific behavior and habitat. Two additional species worthy of testing are the Pacific hake (*Merluccius productus*) and the blue shark (*Prionace glauca*). These species are more sensitive to low-frequency sounds than rockfish (Hawkins, 1973; Banner, 1972). Furthermore, they often swim in a straight-line path and make ''yo-yo'' diving excursions within the sound fixing and ranging channel (SOFAR) [Carey and Scharold, 1990; Arnold *et al.*, 1994]. The high amplitude ATOC signal might disrupt their normal swimming patterns. The ATOC signal might further mask the low frequency, pulsed sounds used by blue sharks to localize their prey. The responsiveness of both species to high-amplitude sound could be studied either under controlled conditions in a laboratory facility or in the open ocean. In the latter case, swimming directions and depths could be recorded from individuals both when the ATOC signal is and is not being propagated at the Pioneer Seamount. Finally, although fishes may not respond overtly to the ATOC signal, repeated exposures at high amplitudes could cause damage to the hair cells of the inner ear and lateral line [see Hastings *et al.* (1996) for literature on hair cell damage to fishes].

ACKNOWLEDGMENTS

Andrew Bass helped us get the opportunity to do this study. Chris Clark graciously loaned us sound equipment and a recording of the ATOC signal. Hisham Qayum helped us observe the movements of rockfish during many experiments. Art Myrberg, Jr. read the manuscript and provided useful advice. The study was made possible by subcontract from Scripps Institution of Oceanography to us from their ATOC contract with the U.S. Department of Defense.

Arnold, G. P., Greer-Walker, M., Emerson, L. S., and Holford, B. H. (**1994**). ''Movements of cod (*Gadus morhua* L.) in relation to the tidal streams in southern North Sea,'' ICES J. Mar. Sci. **51**, 207–232.

Au, W. W. L., Nachtigall, P. E., and Pawloski, J. L. (**1997**). ''Acoustic effects of the ATOC signal (75 Hz, 195 dB) on dolphins and whales,'' J. Acoust. Soc. Am. **101**, 2973–2977.

Banner, A. (**1972**). ''Use of sound predation by young lemon sharks, *Negaprion brevirostris* (Poey),'' Bull. Mar. Sci. **22**, 251–283.

Bowles, A. E., Smultea, M., Würsig, B., DeMaster, D. P., and Palka, D. (**1994**). ''Relative abundance and behavior of marine mammals exposed to transmissions from the Heard Island Feasibility Test,'' J. Acoust. Soc. Am. **96**, 2469–2484.

Carey, F. G., and Scharold, J. V. (**1990**). ''Movements of blue sharks (*Prionace glauca*) in depth and course,'' Mar. Biol. **106**, 329–342.

Charif, R. A., Mitchell, S., and Clark, C. W. (**1995**). *Canary 1.2 User's Manual* (Cornell Laboratory of Ornithology, Ithaca).

Fristrup, K. (personal communication).

Hastings, M. C., Popper, A. N., Finneran, J. J., and Landford, P. J. (**1996**). ''Effects of low-frequency underwater sound on hair cells of the inner ear and lateral line of the teleost fish *Astronotus ocellatus*,'' J. Acoust. Soc. Am. **99**, 1759–1766.

Hawkins, A. D. (**1973**). ''The sensitivity of fish to sounds,'' Oceangr. Mar. Biol. Ann. Rev. **11**, 291–340.

Howe, B. (**1996**). ''Acoustic thermometry of ocean climate (ATOC): Pioneer Seamount source installation,'' Technical Memorandum APL-UW TM3-96, 67 pp.

Klimley, A. P., and Myrberg, Jr., A. A. (**1979**). ''Acoustic stimuli underlying withdrawal from a sound source by adult lemon sharks, *Negaprion brevirostris* (Poey),'' Bull. Mar. Sci. **29**, 447–458.

Leet, W. S., Dewees, C. M., and Haugen, C. W. (**1992**). *California's Living Resources and their Utilization*, Sea Grant Extension Publication USSCEP-92-12, 257 pp.

Munk, W. H., Spindel, R. C., Baggeroer, A., and Birdsall, T. G. (**1994**). ''The Heard Island feasibility test,'' J. Acoust. Soc. Am. **96**, 2330–2342.

Myrberg, Jr., A. A. (**1981**). ''Sound communication and interception in fishes,'' in *Hearing and Sound Communication in Fishes*, edited by W. H. Tavolga, A. N. Popper, and R. R. Fay (Springer-Verlag, New York), pp. 395–425.

Myrberg, Jr., A. A. (**1990**). ''The effects of man-made noise on the behavior of marine animals,'' Environ. Int. **16**, 575–586.

Myrberg, Jr., A. A. (**1997**). ''Underwater sound: its relevance to behavioral functions among fishes and marine mammals,'' Mar. Fresh. Behav. Physiol. **29**, 3–21.

Nelson, D. R., and Gruber, S. H. (**1963**). ''Sharks: attraction by low frequency sounds,'' Science **142**, 975–977.

Pearson, W. H., Skalski, J. R., and Malme, C. I. (**1992**). ''Effects of sounds from a geophysical survey device on behavior of captive rockfish (*Sebastes* spp.),'' Can. J. Fish. Aquat. Sci. **49**, 1343–1356.

Echolocation range of captive and free-ranging baiji (*Lipotes vexillifer*), finless porpoise (*Neophocaena phocaenoides*), and bottlenose dolphin (*Tursiops truncatus*)

T. Akamatsu
National Research Institute of Fisheries Engineering, Ebidai, Hasaki, Kashima, Ibaraki 314-0421, Japan

D. Wang
Institute of Hydrobiology, The Chinese Academy of Sciences, Wuhan 430072, People's Republic of China

K. Nakamura
Faculty of Fisheries, Hokkaido University, 3-1-1, Minatocho, Hakodate, Hokkaido 041-0821, Japan

K. Wang
Institute of Hydrobiology, The Chinese Academy of Sciences, Wuhan 430072, People's Republic of China

(Received 20 February 1998; revised 30 April 1998; accepted 19 June 1998)

The interclick intervals of captive dolphins are known to be longer than the two-way transit time between the dolphin and a target. In the present study, the interclick intervals of free-ranging baiji, finless porpoises, and bottlenose dolphins in the wild and in captivity were compared. The click intervals in open waters ranged up to 100–200 ms, whereas the click intervals in captivity were in the order of 4–28 ms. Echolocation of free-ranging dolphins appears to adapt to various distance in navigation or ranging, sometimes up to 140 m. Additionally, the difference of waveform characteristics of clicks between species was recognized in the frequency of maximum energy and the click duration. © *1998 Acoustical Society of America.* [S0001-4966(98)06609-0]

PACS numbers: 43.80.Ka, 43.80.Jz, 43.66.Gf [FD]

INTRODUCTION

Acoustic characteristics of dolphin sonar signals provide various underwater behavioral information. The waveform characteristics of clicks are different in the harbor porpoise (*Phocoena phocoena*), the Dall's porpoise (*Phocoenoides dalli*), and the bottlenose dolphin (*Tursiops truncatus*) (Kamminga *et al.*, 1996). The source level of clicks is affected by the target range (Au, 1980; Au *et al.*, 1985; Thomas and Turl, 1990).

Click intervals of free-ranging dolphins and porpoises are possibly used as an indicator of their echolocation range in the wild. Click intervals of trained dolphins have been demonstrated to be longer than the two-way transit time between the dolphin and a target. This has been demonstrated in bottlenose dolphins (Au *et al.*, 1974; Penner, 1988) and in a false killer whale, *Pseudorca crassidens* (Thomas and Turl, 1990). Penner (1988) reported that the click intervals of bottlenose dolphins were much longer in a target-absent task than a target-present task. Thomas and Turl (1990) suggested that the false killer whale may have searched for a target at several locations along the range, since miss or false alarm trials had more variable interclick intervals in the target discrimination tasks. Dolphins seemed to change their echolocation range depending on the sensory demands.

The echolocation range of free-ranging dolphins and porpoises are not well known, mainly due to the difficulty of recording high-frequency underwater sounds in open waters. Continuous observations of clicks from the baiji (*Lipotes vexillifer*), the finless porpoises (*Neophocaena phocaenoides*), and the bottlenose dolphins in open waters and in tanks were conducted, using a high-frequency adapted digital data recorder and a hydrophone.

I. MATERIALS AND METHODS

A. Dolphins

Clicks of a single baiji in a Semi-Natural Reserve and another single specimen kept in a circular tank were observed. The Semi-Natural Reserve is a horse-hoof-shaped oxbow of the Yangtze River, 1–2 km wide and 21 km long, situated in Shishou, Hubei, China. The Reserve was established as a conservation area for the highly endangered baiji. Observations were conducted in January 1996, one month after the capture of the wild female baiji from the Yangtze River. The baiji lived alone without being fed by humans in the Reserve. It was 2.29 m in body length, 150 kg in weight, and was estimated to be 10–15 years old when captured. A 6-m small boat was operated for the recordings. A hydrophone was suspended at 3 m in depth. The baiji was frequently observed in the downstream area of the Reserve, so we waited for the dolphin to appear in this area. During the recording, an engine of the observation boat was stopped and the boat drifted without an anchor. The absolute distance and swimming direction of the baiji could not be observed.

Vocalizations of a male baiji named ''QiQi,'' kept in a circular tank (13 m diameter) of the Institute of Hydrobiology, the Chinese Academy of Sciences (IHCAS), for 16 years in January 1996, were also recorded. QiQi was 2.15 m in body length, 125 kg in weight, and estimated to be 17–18 years old at that time.

Fourteen finless porpoises (nine male, four female, and

one calf) lived in the Semi-Natural Reserve in January 1996. The calf was born in the Reserve. Five or more finless porpoises were usually observed together. Vocalizations of these individuals were recorded in the manner similar to those of the baiji. Two male finless porpoises (1.90 and 1.59 m in body length, respectively) in a rectangular tank ($8\times5\times2\ m^3$) of Izu-Mito Sea Paradise, Shizuoka, Japan, were used for observations of captive finless porpoises.

Clicks of wild bottlenose dolphins around Mikura Island in the Izu Archipelago, Japan, and three captive bottlenose dolphins (one male of 2.97-m body length and two females of 2.75- and 2.72-m body length each) in a circular tank (12 m diameter) in the Shinagawa Aquarium, Tokyo, were recorded. Mikura Island is known to be a dolphin sighting area in Japan. More than one hundred dolphins were identified by underwater video camera observations of field marks (T. Hishii and R. Soeda, 1997). A 6.7-m fishing boat was used for recordings. A hydrophone was suspend at 3 m in depth. To avoid disturbing the dolphins, the boat drifted during the recordings without an anchor. The absolute distance and swimming direction of the dolphins could not be observed. Sometimes, the engine of the boat was not stopped to avoid being close to the sea shore due to currents and waves around the Island.

B. Recording and analysis equipment

A hydrophone (B&K 8103, sensitivity -211 dB *re*: 1 V/μPa$+2/-9$ dB, up to 180 kHz, or OKI ST8004, sensitivity -220 dB *re*: 1 V/μPa, $+3/-2$ dB, up to 200 kHz), a 1-kHz high-pass filter to eliminate the various low-frequency noise, and a digital data recorder (SONY PCHB 244, sampling rate of 384 kHz) were used for recordings. The frequency response of the data recorder was flat from DC to 147 kHz within 3 dB. Most of the frequencies of maximum energy in dolphin clicks are limited to the range below 150 kHz, as reviewed by Au (1993) and Richardson *et al.* (1995). The hearing ranges of the baiji, the harbor porpoise (*Phocoena phocoena*) which is the same family of the finless porpoise, and the bottlenose dolphin also stop at 150 kHz (Wang *et al.*, 1992; Andersen, 1970; Johnson, 1967). Consequently, the total frequency response of the sound recording system was sufficient to receive and to store the clicks of the recorded animals.

The echolocation sounds are composed of high-frequency clicks. The duration of a typical click is between 40 and 600 μs (Au, 1993) and the click intervals are highly variable, ranging from a few hundred μs (Amundin, 1991) to 150 ms (Hatakeyama *et al.*, 1994). The data acquisition system must have the capacity to process such high repetition rate click series for real-time data analysis. The analog-to-digital conversion, data comparison, and memory access had to be completed before the next detection of a click within the minimum click interval, such as less than 500 μs.

A signal processing circuit (Click Detector; 14 cm in length, 10 cm in width, and 4.5 cm in height, operated up to 4 h using alkaline primary cells) converted each click to a 500-μs rectangular signal with a voltage level corresponding to the peak level of the click (Fig. 1). A comparator in the Click Detector generated a trigger signal whenever the voltage level was larger than the threshold level in order to eliminate false activation of the Click Detector by background noises or reverberations of the pulse signals. The noise level lower than this threshold level did not activate the Click Detector. In the case of the analysis of bottlenose dolphins' vocalizations, a 20-kHz high-pass filter (NF FV-606T) was used to eliminate false-triggering by whistles.

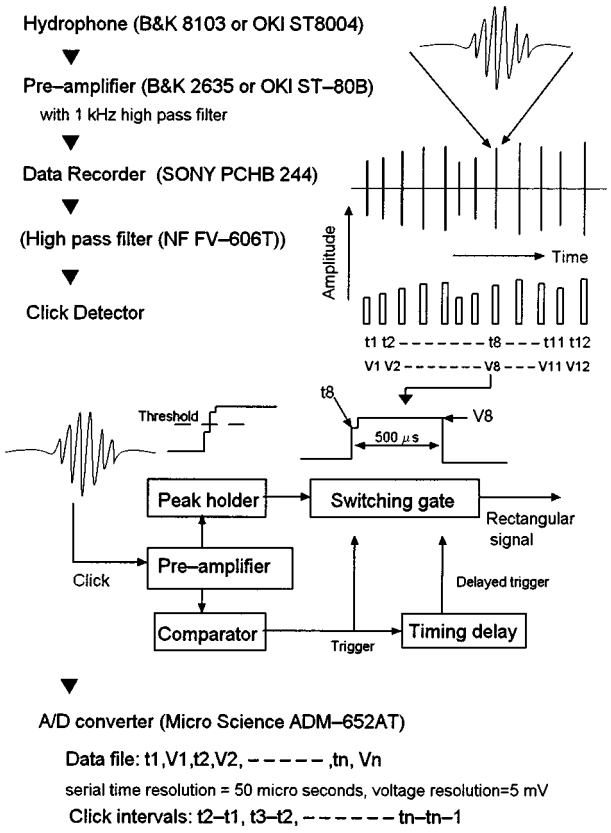

FIG. 1. Data acquisition systems and signal processing. The high-frequency recording system archived whole bandwidth sonar signals (clicks) of the dolphins. Peak sound pressure levels and the event time were recorded.

A 486 MPU (66 MHz) based personal computer with an analog-to-digital converter (Micro Science ADM-652AT) and a data acquisition program on Windows 95© were developed for real time analysis. Signal processing of the recording and the data acquisition system are illustrated in Fig. 1. The analog-to-digital converter was operated at a 20-kHz sampling rate by a data acquisition program. Serial time data and output voltage level of the rectangular signal were obtained every 50 μs. The maximum voltage level and the initial sampled time in the rectangular signal were saved in the RAM of the personal computer. This algorithm avoided a lower voltage level at an onset of the click. The detection threshold of the system was set to be 127 dB *re*: 1 μPa (rms) which was changed $+6$ dB to $+17$ dB depending on the recording conditions. The data processing was fast enough to capture all of the event time and the sound pressure level of dolphins' clicks.

The digital oscilloscope LeCroy model 9304AM was used to digitize the waveform of each click. The frequency of maximum energy and the duration of a click, half pulse width of maximum amplitude, were analyzed by using the digitized waveform.

II. RESULTS

A. Acoustic characteristics of clicks

High-frequency and short-duration click series were frequently observed in all species. The waveform characteristics were different between species as shown in Fig. 2, interspecies differences of frequency of maximum energy and duration of a click are recognizable. The finless porpoises produced narrower band and longer duration clicks than the other two species. The click duration of baiji and bottlenose dolphins was similar, but the frequency of maximum energy of the baiji was lower than that of the bottlenose dolphin. In the Semi-Natural Reserve, the baiji and the finless porpoises sometimes were observed at the same time around the observation area. However, it was easy to distinguish the species by their waveform characteristics, and sighting observations supported their identifications. The swimming direction of free-ranging dolphins could not be observed, so the data contained off-axis signals. On-axis data obtained from the captive baiji whose swimming direction were recorded by a video camera depicted in the lower part of Fig. 2 has similar frequency range as the off-axis data of the free-ranging baiji.

B. Reverberation and simultaneous vocalization

An example of click intervals and received sound pressure levels (rms), 9 dB smaller than the peak-to-peak pressure value, at the hydrophone obtained from the captive baiji are illustrated in Fig. 3. The end of a click train was defined as 1-s or more interval.

Train 3 had a 715-ms duration with 33 clicks. The mean click interval was 21.7 ms and the standard deviation was 0.81 ms. The regression coefficient between the click intervals and time elapsed was 0.00 013.

Pulse sounds reflected from the water surface, bottom, or tank wall showed alternating changes of click intervals and sound pressure levels. The reverberated pulses were mostly recorded within 1 or 2 ms after the direct path signals in a tank. Changes of sound pressure level of the reverberated signals were closely associated with the direct path signals in the time domain. Thus, 2 ms or fewer intervals were neglected for the analysis.

Simultaneous vocalization by two or more individuals also exhibit two independent changes of the sound pressure levels and the click intervals, which were clearly distinctive from the regular click. The irregular (two times or more and half or less) changes of successive click intervals were not counted as data.

C. Click intervals

Click intervals in the baiji, finless porpoise, and bottlenose dolphin are presented in Fig. 4. In the large environments such as the open ocean and the Semi-Natural Reserve, a wide variety of click intervals was observed, up to 286 ms (90% of 14 294 intervals) from a baiji, 276 ms (90% of 2506 intervals) from finless porpoises, and 200 ms (90% of 37 025 intervals) from bottlenose dolphins, respectively. On the other hand, the baiji in the 13-m circular tank frequently produced 26–28-ms click intervals, and 90% of 329 940 intervals were less than 90 ms. Finless porpoises in the rectangular tank ($8\times5\times2$ m^3) frequently produced 8–10-ms click intervals, and 90% of 36 647 intervals were less than 18 ms. The bottlenose dolphins in the 12-m circular tank frequently produced 4–6-ms click intervals.

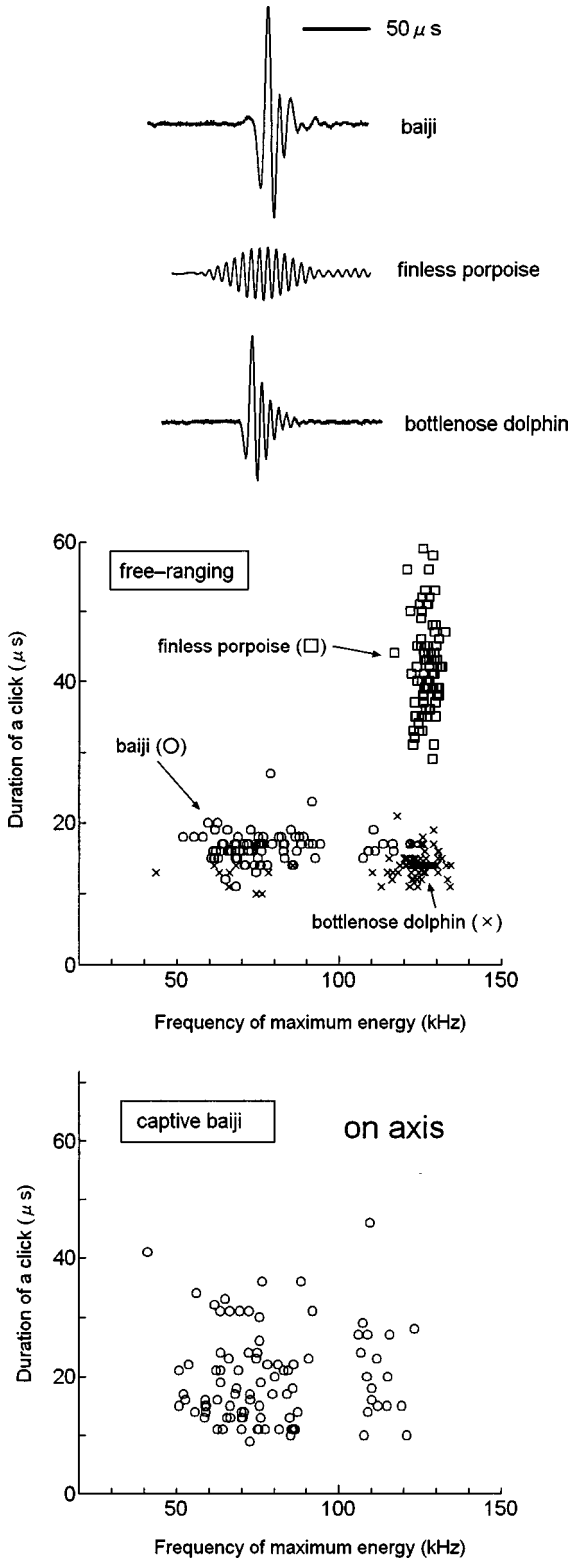

FIG. 2. Waveform characteristics of clicks and their differences between species. Waveform, frequency of maximum energy, and duration (half width of maximum amplitude) of clicks from baiji, finless porpoises, and bottlenose dolphins were depicted. Acoustic characteristic differences between these species are clearly recognizable. On-axis data obtained from the captive baiji is depicted in the lower part of this figure.

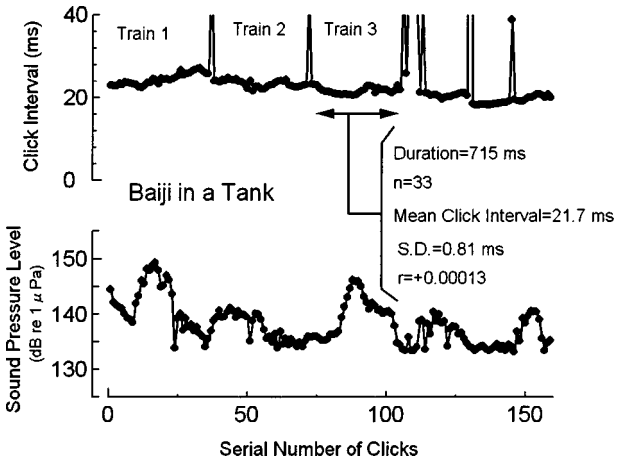

FIG. 3. Click intervals and rms sound pressure levels (dB *re:* 1μPa) of captive baiji. Duration, number of clicks, mean click interval, and its standard deviation of click train 3 are shown. A regression coefficient between the click intervals and time elapsed in train 3 was also calculated.

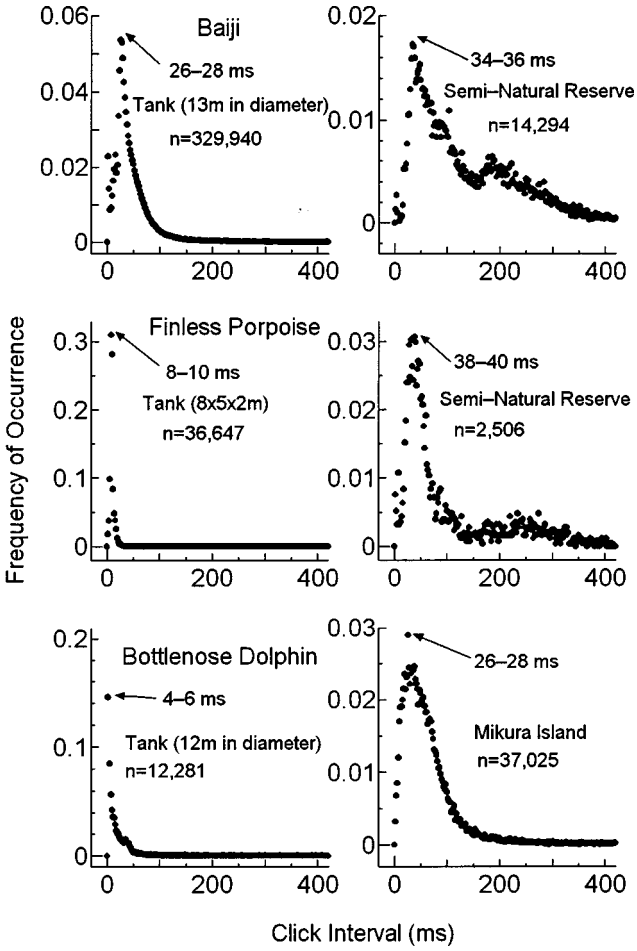

FIG. 4. Frequency of occurrence in click intervals of baiji, finless porpoise, and bottlenose dolphin. Clicks observed in open waters had a wide variety of intervals up to 400 ms. Click intervals in a tank were much smaller than in open waters. Differences of the click interval distributions between the different environments were much larger than those between species.

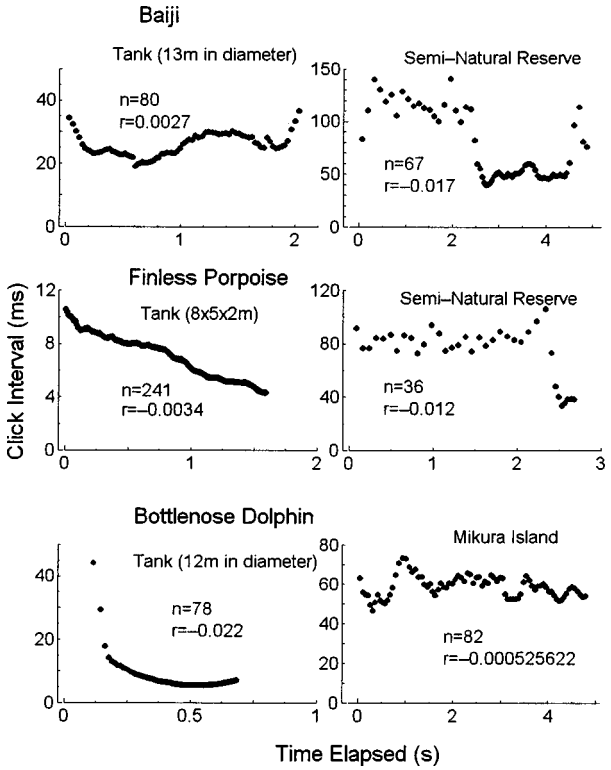

FIG. 5. Change of click intervals in a click train. The monotonous decrement of click intervals was observed in a tank. In open waters, the click intervals fluctuated in a train.

Besides a wide variety of click intervals in open waters, the difference of successive click intervals from animals in open waters were mostly less than 20 ms. In captive animals, successive click interval differences were much smaller than those in open waters.

Decreasing click intervals possibly correlated with target range were clearly observed in captive finless porpoises and bottlenose dolphins (Fig. 5). On the other hand, the change of click intervals observed in open waters did not show monotonous increment or decrement. The click intervals were fluctuated in a train and the successive click interval differences in the open waters were larger than that observed in a tank.

III. DISCUSSION

A. Differences of the waveform characteristics of clicks between species

The frequency of maximum energy and the duration of a click reflect the differences of species. Kamminga *et al.* (1996) also reported the differences of the frequency of maximum energy and the duration of a click between the *Phocoenidae* family and bottlenose dolphin. The lower frequency part in Fig. 2 might have caused by the off-axis signal due to the undetermined swimming direction of free-ranging dolphins. However, on-axis clicks of captive baiji also have a lower frequency part. This suggests that the baiji produced the clicks of double-peak spectrum.

Acoustical monitoring seems to be an effective method to detect and discriminate baiji from other species. Endangered baiji are planned to be kept in the Semi-Natural Re-

serve or in a tank without any disturbance by water traffic and fishing activities. The Yangtze River has a wide basin and quite muddy water, so the acoustic survey seems to be an effective method to detect and discriminate baiji from finless porpoise that are observed more frequently in the Yangtze River.

B. Target range of dolphin echolocation

The free-ranging dolphins and porpoises changed their echolocation range in relation to the size of their environment. The two-way transit times of 286, 276, and 200 ms, as found in the baiji, finless porpoise, and bottlenose dolphin, respectively, correspond to two-way sound transmission distances of 207, 200, and 154 m calculated by the sound velocity of fresh or sea water (Medwin, 1975). It is only natural to increase the echolocation range in the large environment. Actually, the click interval does not precisely correspond to the two-way transit time between a dolphin and a target, since there is a lag time after receiving an echo before the next click is produced (see the review of Au, 1993, p. 116). The estimated target range of a bottlenose dolphin at the 200-ms interval is about 140 m, which is the same order as the 113-m maximum detection range for a 7.62-cm metal sphere by a bottlenose dolphin reported by Au *et al.* (1974).

On the other hand, the two-way transit time of underwater sound between the center of the tank and the hydrophone of the present study was about 9.0 ms for the baiji, 5.3 ms for the finless porpoise, and 7.9 ms for the bottlenose dolphin, respectively. The click intervals observed in these captive animals were mostly around 24–26 ms, 6–8 ms, and 4–6 ms. The dolphins in captivity adapted their echolocation to short-range detection or navigation.

Previously reported click intervals seemed to be correlated to environmental size. Amundin (1991) reported 1–3-ms click intervals of harbor porpoise in a 41-cubic-meter ($7\times5\times1.2\ m^3$) tank. The click intervals of a harbor porpoise in another tank ($8.6\times6.3\times1.3\ m^3$) were less than 2 ms close to an object (Kastelein *et al.*, 1995). Verboom and Kastelein (1995) also reported 0.5–5-ms click intervals of harbor porpoise in this tank. The click intervals of a Dall's porpoise in captivity were mostly 9.5 ms in a pool ($7\times5\times3\ m^3$) and ranged from 20–48 ms in a larger pool ($12\times8\times3\ m^3$) (Hatakegama and Shimizu, 1985).

A few broadband acoustical observations in the wild have been conducted. A stable interclick interval around 27 ms was observed in wild bottlenose dolphins (Goodson and Mayo, 1995). Herzing (1996) showed a wide variety of the click intervals that ranged from 0.5–125 ms in wild Atlantic spotted dolphin (*Stenella frontalis*) in the Bahamas. The Atlantic spotted dolphins produced 2–2.5-ms click intervals during echolocation with the rostrum in the sand. Hatakeyama *et al.* (1994) conducted broadband recording of Dall's porpoise in the North Pacific Ocean and the click intervals ranged from 8–150 ms. Goold and Jones (1995) reported decreasing click intervals from 2 to 0.5 s at the beginnings of a sperm whale (*Physeter macrocephalus*) dive. The intervals were comparable to the water depth in which sperm whales were feeding.

C. Change of click intervals in a train

Changes of sonar signal intervals correlated with distance from an approaching target were observed in foraging bat's echolocation of insect (Tian and Schnitzler, 1996). Dawson (1991) also reported the decreasing change of click intervals of the wild Hector's dolphin (*Cephalorhynchus hectori*). In the present study, decreasing click intervals of dolphins, similar to the terminal phase of a target interception by bats, were only observed in short click intervals. However, few terminal phases was observed in open waters, possibly due to the large fluctuation of click intervals.

If the click intervals reflect the target distance precisely as Lucke and Goodson (1997) suggested, the -0.0034 regression coefficient observed in the finless porpoise in the tank corresponds to a 2.6-m/s approaching speed to the target which is the usually observed swim speed of free-ranging dolphins.

ACKNOWLEDGMENTS

We wish to thank Institute of Hydrobiology, The Chinese Academy of Sciences, Miyake branch of Tokyo Metropolis, Mikura-jima village office, and Mikura and Miyake fishery cooperative society. K. Fujita, M. Hohana, M. Furusawa, K. Shirakihara, M. Shirakihara, S. Demura, M. Nagata, M. Inoue, H. Shimura, and H. Kobayashi worked with us and greatly supported our experiments. Izu-Mito Sea Paradise and Shinagawa Aquarium provided finless porpoises and bottlenose dolphins for our experiments. Y. Narita and T. Matsu-ura developed analysis software and signal processing circuit. Y. Hatakeyama, A. D. Goodson, M. Amundin, K. Dudzinski, and three reviewers provided constructive criticism on this manuscript. This research was supported by the Science and Technology Agency of Japan, Tokyo Metropolis and Grant-in-aid for Scientific Research (*B*) from the Ministry of Education, Science and Culture, B09450172.

Amundin, M. (**1991**). ''Click Repetition Rate Patterns in Communicative Sounds from the Harbour Porpoise, *Phocoena phocoena*,'' in *Sound Production in Odontocetes with Emphasis on the Harbour porpoise, Phocoena phocoena* (Swede Publishing AB, Stockholm), pp. 91–111.

Andersen, S. (**1970**). ''Auditory sensitivity of the harbour porpoise *Phocoena phocoena*,'' in *Investigations on Cetacea*, edited by G. Pilleri (Hirnanatomisches Institut, Bern), Vol. 2, pp. 255–259.

Au, W. W. L. (**1980**). ''Echolocation Signals of the Atlantic Bottlenose Dolphin (*Tursiops truncatus*) in Open Waters,'' in *Animal Sonar Systems*, edited by R. G. Busnel and J. F. Fish (Plenum, New York), pp. 251–282.

Au, W. W. L. (**1993**). *The Sonar of Dolphins* (Springer-Verlag, New York).

Au, W. W. L., Carder, D. A., Penner, R. H., and Scronce, B. L. (**1985**). ''Demonstration of adaptation in beluga whale echolocation signals,'' J. Acoust. Soc. Am. **77**, 726–730.

Au, W. W. L., Floyd, R. W., Penner, R. H. , and Murchison, A. E. (**1974**). ''Measurement of echolocation signals of the Atlantic bottlenose dolphin, *Tursiops truncatus* Montagu, in open waters,'' J. Acoust. Soc. Am. **56**, 1280–1290.

Dawson, S. M. (**1991**). ''Clicks and communication: the behavioural and social contexts of Hector's dolphin vocalizations,'' Ethology **88**, 265–276.

Goodson, A. D., and Mayo, R. H. (**1995**). ''Interactions between Free-ranging Dolphins (*Tursiops truncatus*) and Passive Acoustic Gill-net Deterrent,'' in *Sensory Systems of Aquatic Mammals*, edited by R. A. Kastelein, J. A. Thomas, and P. E. Nachtigall (De Spil, Woerden, The Netherlands), pp. 365–379.

Goold, J. C., and Jones, S. E. (**1995**). ''Time and frequency domain characteristics of sperm whale clicks,'' J. Acoust. Soc. Am. **98**, 1279–1291.

Hatakeyama, Y., and Shimizu, H. (**1985**). ''Feeding Trial and Acoustic Studies on Dall's Porpoise Captured Alive,'' Document Submitted to the Meeting of the Scientific Subcommittee of the Ad Hoc Committee on Marine Mammals, INPFC, Tokyo, Japan, INPFC Document 2860.

Hatakeyama, Y., Ishii, K., Akamatsu T., Soeda, H., Shimamura, T., and Kojima, T. (**1994**). ''A Review of Studies on Attempts to Reduce the Entanglement of the Dall's Porpoise, *Phocoenoides dalli*, in the Japanese Salmon Gillnet Fishery,'' Rept. Int. Whal. Commn. (Special Issue 15), 549–563.

Herzing, D. L. (**1996**). ''Vocalizations and associated underwater behavior of free-ranging Atlantic spotted dolphins, *Stenella frontalis* and bottlenose dolphins, *Tursiops truncatus*,'' Aquatic Mammals **22**, 61–79.

Hishii, T., and Soedo, R. (**1997**). Personal communication.

Johnson, C. S. (**1967**). ''Sound Detection Thresholds in Marine Mammals,'' in *Marine BioAcoustics*, edited by W. N. Tavolga (Pergamon, New York), Vol. 2, pp. 247–260.

Kamminga, C., Stuart, A. C., and Silber, G. K. (**1996**). ''Investigations on cetacean sonar X I: Intrinsic comparison of the wave shapes of some members of the *Phocoenidae* family,'' Aquatic Mammals **22**, 45–55.

Kastelein, R. A., Nieuwstraten, S. H., and Verboom, W. C. (**1995**). ''Echolocation Signals of Harbour Porpoises (*Phocoena phocoena*) in Light and Complete Darkness,'' in *Harbour Porpoises: Laboratory Studies to Reduce Bycatch*, edited by P. E. Nachtigall, J. Lien, W. W. L. Au, and A. J. Read (De Spil, Woerden, The Netherlands), pp. 55–67.

Lucke, K., and Goodson, A. D. (**1997**). ''Characterising wild dolphins echolocation behaviour: Off line analysis,'' Proceedings of the Institute of Acoustics **19**, Pt. 9, 179–183.

Medwin, H. (**1975**). ''Speed of sound in water: A simple equation for realistic parameters,'' J. Acoust. Soc. Am. **58**, 1318–1319.

Penner, R. H. (**1988**)., ''Attention and Detection in Dolphin Echolocation,'' in *Animal Sonar: Processes and Performance*, edited by P. E. Nachtigall and P. W. B. Moore (Plenum, New York), pp. 707–713.

Richardson, W. J., Greene, Jr., C. R., Malme, C. I., and Thomson, D. H. (**1995**). *Marine Mammals and Noise* (Academic, New York).

Thomas, J. A., and Turl, C. W. (**1990**). ''Echolocation Characteristics and Range Detection Threshold of a False Killer Whale (*Pseudorca crassidens*),'' in *Sensory Abilities of Cetaceans: Laboratory and Field Evidence*, edited by J. A. Thomas and R. A. Kastelein (Plenum, New York), pp. 321–334.

Tian, B., and Schnitzler, H. (**1996**). ''Echolocation signals of the greater horseshoe bat (*Rhinolophus ferrumequinum*) in transfer flight and during landing,'' J. Acoust. Soc. Am. **101**, 2347–2364.

Verboom, W. C., and Kastelein, R. A. (**1995**). ''Acoustic Signals by Harbour Porpoises (*Phocoena phocoena*),'' in *Harbour Porpoises: Laboratory Studies to Reduce Bycatch*, edited by P. E. Nachtigall, J. Lien, W. W. L. Au, and A. J. Read (De Spil, Woerden, The Netherlands), pp. 1–39.

Wang, D., Wang, K., Xiao, Y., and Sheng, G. (**1992**). ''Auditory Sensitivity of a Chinese River Dolphin, *Lipotes vexillifer*,'' in *Marine Mammal Sensory Systems*, edited by J. A. Thomas, R. A. Kastelein, and A. Y. Supin (Plenum, New York), pp. 213–221.

Comparison of electrohydraulic lithotripters with rigid and pressure-release ellipsoidal reflectors. I. Acoustic fields

Michael R. Bailey
Applied Physics Laboratory, College of Ocean and Fishery Science, University of Washington, 1013 NE 40th Street, Seattle, Washington 98105, Applied Research Laboratories, The University of Texas at Austin, P.O. Box 8029, Austin, Texas 78713-8029, and Department of Mechanical Engineering, The University of Texas at Austin, Austin, Texas 78712-1063

David T. Blackstock
Applied Research Laboratories, The University of Texas at Austin, P.O. Box 8029, Austin, Texas 78713-8029, and Department of Mechanical Engineering, The University of Texas at Austin, Austin, Texas 78712-1063

Robin O. Cleveland[a] and Lawrence A. Crum
Applied Physics Laboratory, College of Ocean and Fishery Science, University of Washington, 1013 NE 40th Street, Seattle, Washington 98105

(Received 10 April 1998; revised 21 May 1998; accepted 7 July 1998)

The most common lithotripter, a Dornier HM-3, utilizes an underwater spark to generate an acoustic pulse and a rigid ellipsoidal reflector to focus the pulse on the kidney stone to be comminuted. The pulse measured in water with a PVDF membrane hydrophone at the external focus of the ellipsoid was a 1-μs positive-pressure spike followed by a 3-μs negative-pressure trough. When we replaced the rigid reflector in our experimental lithotripter with a pressure-release reflector, the pulse was a 1.6-μs trough followed by a 0.6-μs positive spike. The waveforms are nearly time inverses (i.e., their spikes and troughs are reversed). The frequency spectra, the maximum peak positive pressures P_+ (42 MPa, rigid and 43 MPa, pressure-release), and the maximum peak negative pressures P_- (-12 MPa and -14 MPa) are comparable. The maximum P_- occurred 20 mm closer to the reflector than did the maximum P_+, for both reflectors. However, the spatial maxima of the peak pressures (P_+ and P_-) produced by the pressure-release reflector were located 20 mm nearer to the reflector than those produced by the rigid reflector. Qualitative explanation of the waveforms and the location of pressure maxima as well as comparison to previous theoretical and experimental results is given. The alternate waveform produced by the pressure-release reflector may be a tool in determining the role of cavitation in lithotripsy because cavitation is highly sensitive to waveform. [S0001-4966(98)03110-5]

PACS numbers: 43.80.Sh, 43.25.Jh, 43.25.Yw [FD]

INTRODUCTION

For over 15 years the focused pressure pulse produced by an underwater spark at the focus of a rigid reflector has been used clinically to break kidney stones. This process, called extracorporeal shock wave lithotripsy (ESWL), also induces trauma to the kidney being treated.[1] Although exactly what causes stone comminution and tissue damage is not known, two mechanisms—direct stress (compression and tension) and cavitation—are thought to play the major roles. If we are to improve the safety of ESWL treatment while accelerating the rate of stone breakage, the precise role of each of these mechanisms must be understood. However, separating these mechanisms from one another has been difficult. Both mechanisms are sensitive to the peak positive P_+ and negative P_- pressure amplitudes produced by the lithotripter. However, the intensity of cavitation bubble collapse has been shown to be highly sensitive to the waveform.[2] Therefore, a way to alter the waveform and thus the collapse intensity without altering the peak pressure amplitudes may offer a way to assess the role of cavitation in stone comminution and tissue injury.

Previous efforts have been made to modify the waveform and the accompanying cavitation produced by a lithotripter. Chapelon *et al.*[3] built a piezoelectric device in which the waveform could be manipulated. Others tried switching the leads on a piezoelectric lithotripter or reflecting the shock wave from a pressure-release plane surface[4] to change the waveform. Müller[5] demonstrated differences in the waveform and the cavitation field produced by rigid and pressure-release ellipsoidal reflectors, but his arrangement was different from that used in lithotripsy. Müller placed his experimental spark source at the exterior focus $F2$ of the ellipsoid and measured waveforms at the interior focus $F1$. In the conventional lithotripter and in our experiment, the spark is at $F1$.

We modified the waveform but maintained the peak pressures by replacing the conventional rigid reflector of a Dornier HM-3-style lithotripter with a pressure-release reflector. The experimentally determined sound fields are reported here. The two types of reflectors produce two differ-

[a]Current address: Department of Aerospace and Mechanical Engineering, Boston University, 110 Cummington St., Boston, MA 02215.

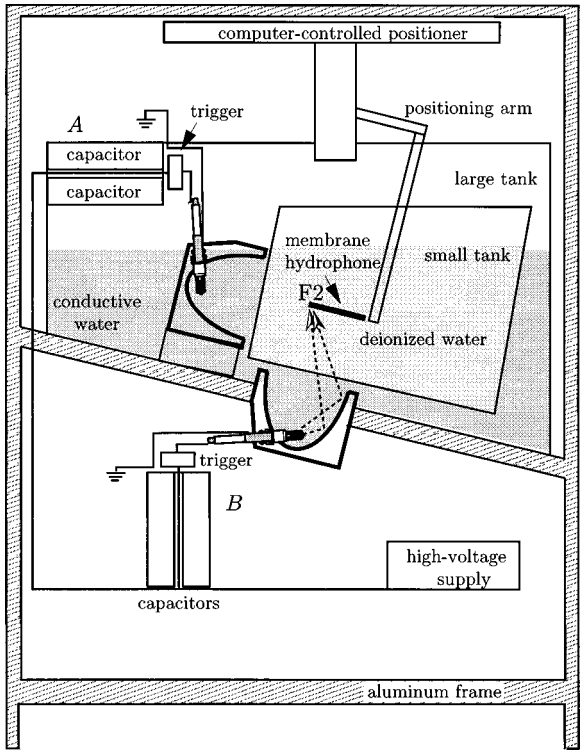

FIG. 1. Schematic of the experimental lithotripter and the added second reflector and spark generator. It was necessary to use the membrane hydrophone in deionized water. The small tank housed the deionized water. The walls of the small tank contained large, acoustically transparent windows made of a low-density polyethylene membrane.

ent waveforms with the same peak positive- and negative-pressure amplitudes, the effects of which (cavitation, stone comminution, tissue damage, etc.) can be compared. The experimentally determined cavitation fields and numerical calculations of bubble dynamics are reported in a companion paper,[6] hereafter referred to as paper II. Together the papers define the similarity in peak pressure, but the difference in cavitation, which may be exploited to assess the role of cavitation in stone comminution and tissue damage, as discussed further in paper II.

I. METHODS AND MATERIALS

The measurements were made in a research lithotripter that is similar in design and operation to the Dornier HM-3 clinical lithotripter (Dornier Medical Systems, GmbH). Peak positive-pressure P_+ produced at 18 kV (our range is 12–24 kV) was approximately 40 MPa for both an HM-3 (Methodist Hospital, Indianapolis, Indiana) and our lithotripter, and the waveforms (measured by the PVDF membrane hydrophone described below) were comparable. The lithotripter is one of three identical research lithotripters. More detail on the design was given by Howard and Sturtevant[7] and on the operational comparison to the HM-3 by Cleveland *et al.*[8] Figure 1 shows the experimental apparatus—the water bath, spark sources, reflectors, positioner, and hydrophone. A spark generated with refurbished Dornier electrodes (Servicetrends, Kennesaw, Georgia) produces a spherically diverging pressure wave. A portion of the wave travels without reflection directly to the receiver; this is the direct wave. Another portion impinges upon the ellipsoidal surface and reflects. All reflected rays focus at the exterior focus $F2$, as illustrated by the dashed ray paths in Fig. 1. Because the direct wave, which arrives at $F2$ 30 μs before the focused wave, has less than 1/30th the amplitude, the direct wave is neglected in this and most studies.

A. Water bath

The experiments were conducted in a 58×95 cm acrylic tank. The bottom of the tank has a slant of 14° similar to that of the Dornier HM-3. The maximum height of the tank is 59 cm; the minimum is 36 cm. The conductivity of the water was controlled at 600 μS/cm and tested with a Model EP water-conductivity meter (Myron L Company, Carlesbad, California). The water level for the experiments was 20 cm from the tank top.

A water-degasing system is part of the research lithotripter. A 70-gallon stainless steel tank stores the water. A pump is used to fill the tank or recirculate the water for filtering through a 5-μm pore filter (Cole-Parmer Instrument Co., Chicago, Illinois) or for degasing under vacuum through a nozzle. The vacuum draws gas from the water, and the large surface-area-to-volume ratio of the fine spray particles accelerates the process. The method makes use of both Degassing Procedures B4.2 and B11.3 in IEEE Std 790-1989. Gas content is checked with a model 51B oxygen meter (Yellow Springs Instrument Co., Inc., Yellow Springs, Ohio) and is maintained below a reading of 4 parts per million of oxygen.

A smaller acrylic tank, also with a bottom sloped at 14°, was built to hold the hydrophone and to isolate it chemically from the water in the main tank. Located within the main tank, the small tank (25×38 cm, 24-cm minimum height, 34-cm maximum height) was filled with deionized water, conductivity 1–5 μS/cm. The low conductivity allowed the hydrophone to work properly.[9] Filling the large tank with deionized water was not practical. However, sparks are more repeatable and efficient in conductive water.[10] The small tank was degased with a multiple pinhole degasing system.[11] A 100-μm membrane of low-density polyethylene was stretched across 22×22 cm windows cut in the acrylic.

The polyethylene separated the two water baths but permitted sound to enter the small tank with no measurable attenuation or distortion. Distortion was tested by comparing (1) waveforms measured in the small tank with and without a second thin membrane present and (2) waveforms measured in the large tank of deionized water with and without a membrane present. Differences in rise times and peak pressures were statistically insignificant (student's t test for $N=10$) in all four cases. Although the membrane is thicker than the width associated with the measured 30-ns risetime and will therefore attenuate high frequencies in the pulse, the membrane appears to be sufficiently far (110 mm) from the hydrophone that the shock has sufficient travel distance to ''heal.'' When the spatial extent of a shock is increased by $\Delta x = 100$ μm (the thickness of the polyethylene membrane), the risetime of the shock is also increased by an amount $\Delta t = \Delta x / c_0$, approximately 67 μs in water. The velocity of a step shock, in excess of the small signal sound speed c_0, is

given by $u_s = 0.5\beta p/(\rho_0 c_0)$;[12,13] for a 10-MPa shock in water ($\beta = 3.5$, $\rho_0 = 1000$ kg/m^3, $c_0 = 1500$ m/s) the shock velocity is approximately $u_s = 12$ m/s. If the shock can be treated locally as a plane wave it will take the shock $\Delta x/u_s = 8.3$ μs to heal the thickening. This corresponds to a propagation distance of approximately 12.5 mm. A 30-MPa shock would require 4.2 mm of propagation to heal the same thickening.

B. Spark sources

The two spark-reflector systems in the tank produced beams offset by 90° with respect to each other but having a common external focus $F2$ (see Fig. 1). For spark-generating system *A*, a pair of 50-nF, low-inductance capacitors (100 nF total) made by Maxwell Technologies, San Diego, California, were charged to 18 kV and triggered by an open-air, spark-gap switch.[14] Spark system *B* employed a pair of 40-nF, low-inductance capacitors (80 nF total), 18 kV, and a nitrogen-enclosed, spark-gap switch (EG&G, Princeton, New Jersey). System *A* had higher inductive and resistive losses, and therefore the acoustic outputs from both sparks were equal. The data discussed in this paper were obtained with the pressure-release reflector positioned on the left and the rigid reflector on the bottom. However, both types of reflectors were tested in both positions with no observable change in results. Only one spark was triggered at a time. Electrodes were ''burned in'' with 150 sparks before use and replaced after 2000 sparks. Coleman *et al.*[15] showed pulse amplitude increased 0.01%/3 sparks in this electrode age range and saw no change in wave shape. We did not observe any change in waveform as a function of electrode wear and did not collect sufficient data to verify an increase in pulse amplitude.

C. Reflectors

Brass and polyurethane foam reflectors were tested; results with one brass reflector and one polyurethane foam reflector are reported. Brass is nearly acoustically rigid in water (normal pressure amplitude reflection coefficient R is 0.94).[16] Polyurethane foam (General Plastics, Tacoma, Washington) is nearly pressure release ($R = -0.88$).[17] Although neither reflector acoustically is perfectly rigid ($R = 1$) or pressure release ($R = -1$), we use these descriptors to emphasize that differences in the reflector outputs are more attributable to acoustic impedance than to other material properties. The two reflectors (Fig. 2) have the same ellipsoidal dimensions as the brass reflector in a Dornier HM-3 clinical lithotripter (major half axis $a = 13.8$ cm and minor half axis $b = 7.75$ cm). The pressure-release reflector is semiellipsoidal. The rigid reflector (and the Dornier reflector) are 12.5 cm deep which is 1.3 cm less than semiellipsoidal. The slight difference in dimension produced no measurable difference when compared to a brass semiellipsoidal reflector. Aberrations in the surface due to machining were estimated to be less than 25 μm, or 1/300th the length of the acoustic pulse and 1/20th the size of the active spot of our hydrophone.

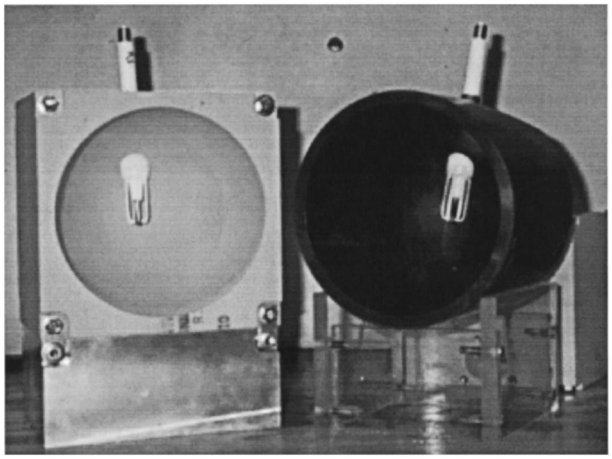

FIG. 2. Photograph of the pressure-release reflector (left) and the rigid reflector (right) that were used in the experiments.

D. Positioning system

Velmex (Bloomfield, New York) microstepping motors and slides located above the tank positioned the hydrophone within the tank and interfaced with the computer. The motor resolution was 200 steps per millimeter. The three axes were controlled with a handheld controller or via an RS-232 connection from the computer. The axis of the reflector perpendicular to the aperture of the reflector was designated the axis of the reflector or the z axis. The axial distance from the aperture to the external geometric focus $F2$ is 11.4 cm for the pressure-release reflector and 12.7 cm for the rigid reflector. $F2$ was designated $z = 0$ with negative z toward the reflector.

E. Hydrophone system

A Reference Shock Wave Hydrophone (Sonic Technologies, Hatboro, Pennsylvania)[9] was used to map the acoustic fields. Figure 1 shows a side view of the hydrophone aligned to measure the focal waveform produced by the rigid reflector on the bottom. The hydrophone consisted of a 5×5 cm membrane window of unshielded polyvinylidene difluoride (PVDF) in a $0.75 \times 7.5 \times 9.2$ cm plastic cassette, which could be detached from the submersible preamplifier and replaced. The geometric diameter of the sensitive element on the hydrophone was less than 0.5 mm, and the electrodes and element were not electrically shielded from the water. According to manufacturer's specifications,[9] the frequency response was flat (± 2 dB) up to 50 MHz. Because spark jitter (inherent lack of repeatability in the precise location, shape, and strength of the spark) caused variation in the waveforms measured at each location, ten waveforms ($N = 10$) were recorded. The peak pressures were averaged and are presented (Fig. 6) plus and minus the sample standard deviation, and the waveform that possessed most nearly the average pressures is also presented (Fig. 7).

Two possible short comings—membrane waves and cavitation nucleation—of an unshielded PVDF membrane hydrophone should be kept in mind. Both affect representation of the negative tail in the waveform produced by a rigid reflector. Membrane waves and reflections result when the

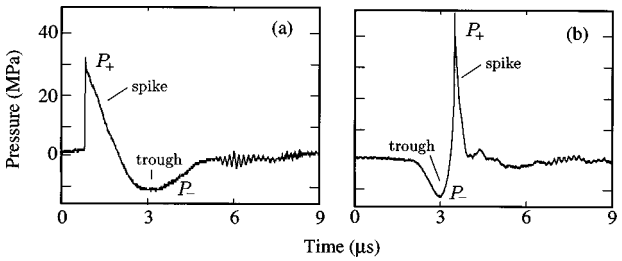

FIG. 3. Focal waveforms produced by (a) a rigid reflector and (b) a pressure-release reflector. Charging potential was 18 kV. P_+ and P_- are the maximum positive and negative pressures of the waveform. Pulse durations, P_+, and P_- are comparable, but the wave shapes differ. The spike-then-trough waveform of the rigid reflector and the trough-then-spike waveform of the pressure-release reflector are reproducible although amplitudes, durations, and the noise following each pulse varies among individual measurements because the amplitude, shape, and location of individual sparks varies.

edge of the membrane scatters sound,[18] and these artifacts of the measurement system add to the signal sensed by the active spot of the membrane. The membrane wave signals are delayed because they must travel from the edge of the membrane but may arrive in time to contaminate the tail portion of the focused-pulse signal. Contamination is worse for small hydrophones and strong pulses. For example, if we try to measure the acoustic pulse 30 mm off the reflector axis, the lithotripter focuses on the hard plastic case, not on the PVDF window, of our hydrophone, and reflections are unavoidably strong. We therefore limited the region of study to within 20 mm of the axis; with this restriction no strong distortion by membrane waves or reflections was discerned.

Cavitation nucleation can occur at the bare metal electrodes and at the PVDF membrane of unshielded hydrophones. Staudenraus and Eisenmenger[19] suggest that when a PVDF membrane is used to measure a lithotripter pulse, cavitation on the membrane surface shortens the apparent duration of the negative tail. Using a fiber optic hydrophone of their own design, they measured a longer negative tail. They presented only waveforms measured at the focus of their lithotripter. Although in paper II[6] we used Staudenraus and Eisenmenger's results to propose a correction to focal waveforms measured with an unshielded PVDF hydrophone, unmodified waveforms are presented here because no ''correction'' is known for off-axis waveforms or for any pressure-release reflector waveforms.

The hydrophone signals were recorded on a Tektronix 744A DSO digital oscilloscope and passed to a computer via GPIB. Interfacing was done with LabVIEW (National Instruments, Austin, Texas) software and boards. Sampling rates were 100–250 MHz.

II. ACOUSTIC FIELD RESULTS

A. Focal waveforms

Figure 3 shows focal waveforms produced by the rigid reflector and the pressure-release reflector. The wave shapes differ. The rigid-reflector waveform has a positive spike followed by a drawn out negative-pressure trough. When the pressure-release reflector is used, the trough precedes the spike. Our experimentally determined waveforms agree well

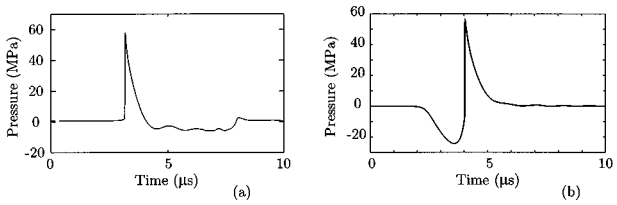

FIG. 4. Focal acoustic waveforms calculated numerically by Averkiou and Cleveland (Ref. 20) for (a) a rigid reflector and (b) a pressure-release reflector with the dimensions of a Dornier HM-3 reflector. With the rigid reflector, the trough comes after the spike; with the pressure-release reflector, the trough comes before the spike.

with the focal waveforms (Fig. 4) predicted by Averkiou and Cleveland[20] whose theoretical model is the Khokhlov–Zabolotskaya–Kuznetsov (KZK) equation.[21] The KZK equation accounts for nonlinear distortion, thermoviscous absorption, and diffraction in the parabolic approximation. The numerical code solves the KZK equation in the time domain using finite differencing. The code describes the propagation of shock waves from the aperture of the reflector. The source condition at the aperture is obtained using geometrical acoustics to model propagation within the reflector. Agreement between Fig. 3(b) and Fig. 4(b) is particularly good, whereas the measured trough in Fig. 3(a) is shorter than predicted in Fig. 4(b). As with each results subsection, further discussion is left to Sec. III.

Although the pulses in Fig. 3 differ in shape, they have similar peak positive pressures ($P_+ > 30$ MPa), and they have similar peak negative pressures ($P_- < -10$ MPa). The pulse durations for both are a few microseconds. The rigid reflector produced a spike 1 ± 0.1 μs long and a trough 3 ± 0.4 μs long. The pressure-release reflector produced the shorter but comparable values 0.6 ± 0.1 μs and 1.6 ± 0.1 μs. Again, the numbers are averages and standard deviations of ten measured waveforms. The waveforms are reproducible, and the standard deviations on the durations and amplitudes (Fig. 7) give a quantitative indication of the reproducibility.

The frequency content of the rigid- and pressure-release reflector waveforms is also similar as seen in Fig. 5. The peak in the rigid-reflector spectrum is lower and narrower than the peak in the pressure-release reflector spectrum. Although centered at slightly different frequencies, the structure of the spectra is similar. The decays at higher frequencies closely track each other.

B. Field map of pressure waveforms

Figure 6 shows waveforms measured along the axis of the reflector. Both types of reflectors produced high positive and negative acoustic pressures in a region 80 mm long. Peak pressure amplitudes and pulse durations are comparable, but pulse shapes differ between the left and right panels.

In the left column, the positive-pressure spike always precedes the negative-pressure trough. The spike sharpens with increasing z. The pulse has the highest amplitude (42 ± 5 MPa for 10 pulses) and the shortest duration at $z = 20$ mm. An arrow indicates the edge wave (the wave scattered from the edge of the aperture)[22,23] trailing the main

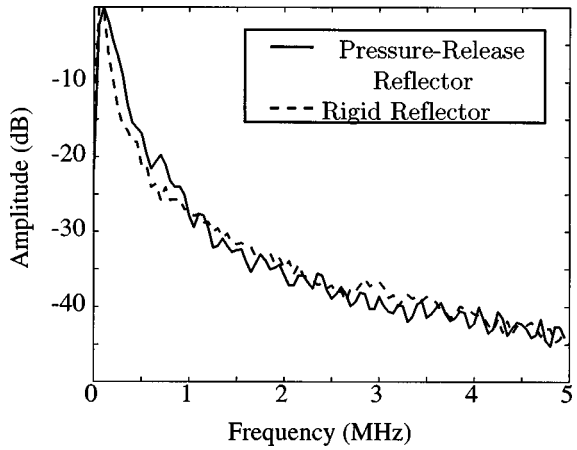

FIG. 5. Fourier transform of the focal waveforms shown in Fig. 3. The 6 μs (1500 points) centered at the waveform spike were padded front and back with 274 zeros, and the fast Fourier transform was computed. The transform of pressure-release reflector waveform is shown as a solid line; the transform of the rigid-reflector waveform is dashed. The frequency content of the waveforms is very similar.

spike at $z=-40$ mm and then leading the the main spike at $z=+40$ mm. The focused pulse arrives first at $z=-40$ mm because the paths are shorter for the focused rays than for the edge rays. The opposite is true at $z=+40$ mm. At $F2$ the rays are the same length. A delay of 6 μs was calculated between the shortest ray path (the axial one) and the edge ray path, and 5 μs were measured. Agreement is good, the difference likely occurred because the axial ray path is blocked by the bubble generated by the underwater spark.

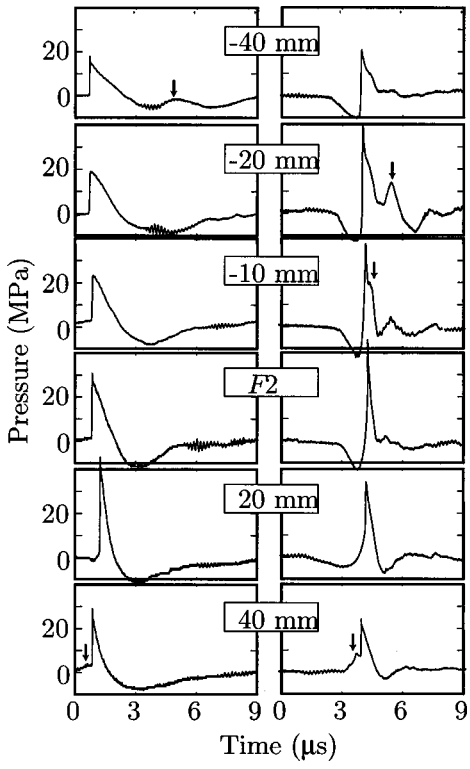

FIG. 6. Comparison of pressure waveforms produced along the axis of a rigid reflector (left) and a pressure-release reflector (right). The positive direction is away from the reflector, and zero is at the geometric focus $F2$, 114 mm from the aperture of the semiellipsoidal reflector. Arrows indicate the edge wave.

The shape of the waveform produced by the pressure-release reflector changes more dramatically. The positive-pressure spike appears after the negative-pressure trough at $z=-40$ mm and before the trough at $z=+40$ mm. As z increases from -40 and $+40$ mm, the spike moves toward the front of the waveform. The pulse has the highest amplitude (43 ± 6 MPa for 10 pulses) and the shortest duration at $F2$ ($z=0$). The maximum trough-to-peak swing (57 MPa) produced by the pressure-release reflector is comparable to, and in fact larger than, the 42-MPa trough-to-peak swing produced by the rigid reflector. Arrows indicate the edge wave. The waveforms not only indicate the earlier relative arrival of the edge wave as z increases, but the waveform at $z=-20$ mm in particular shows the inverted shape of the edge wave. The edge wave created by an aperture takes the inverted form of the wave passing through the aperture. In this case the leading negative-pressure trough of the focused wave is inverted to a leading positive-pressure spike in the edge wave, and the trailing positive-pressure spike is a trailing negative-pressure trough. Negative-pressure spikes quickly lengthen to troughs as nonlinear effects cause high amplitude, negative-pressure regions of the pulse to propagate more slowly than low amplitude regions.[24]

C. Field map of pressure amplitudes

Figure 7 shows spatial maps of the peak pressure amplitudes P_+ and P_-. For both reflectors the focal region is long along the axis and narrow across the axis at $F2$. As Coleman and Saunders[25] found, the -6-dB region (i.e., the region where the pressure amplitude is greater than half the maximum) of the rigid reflector is a cigar-shaped region 12 cm long by 1.5–2 cm. For the pressure-release reflector, the -6-dB region of P_+ is at least 10 cm long, but the -6-dB region of P_- is shorter, 8 cm. The focal region of the pressure release-reflector is also narrower, $\sim$1 cm. The maximum values are on the axis of the reflector in the transverse map.

Axially, the location of the maximum peak pressures $\hat{P}_+$ and $\hat{P}_-$ varies between the two reflectors. The pressure-release reflector produced its $\hat{P}_-=-14\pm1$ MPa at $z=-20$ mm and its $\hat{P}_+$ at $F2$. The rigid reflector yielded its $\hat{P}_-=-12\pm1$ MPa at $F2$ and its $\hat{P}_+$ at $z=+20$ mm. P_- peaks before P_+. The maxima of the pressure-release reflector field occur 20 mm nearer the reflector than do those of the rigid reflector field. Percent standard deviation is highest at the pressure maxima. In addition, percent standard deviation in P_+ is higher than that in P_-. P_- is perhaps limited by the tensile strength of the water[26,27] which P_+ is not; the limiting may account for the lower standard deviation in P_-.

The behavior of the peak pressure along the axis is in qualitative agreement with the numerical calculations of Averkiou and Cleveland.[20] For the pressure-release reflector the model predicted $\hat{P}_-$ at -5 mm and $\hat{P}_+$ at $F2$, and for the rigid reflector the model predicted $\hat{P}_-$ at -20 mm and $\hat{P}_+$ at $+5$ mm. In both calculation and measurement, P_- maximized ahead of P_+, and $\hat{P}_+$ produced by the pressure-

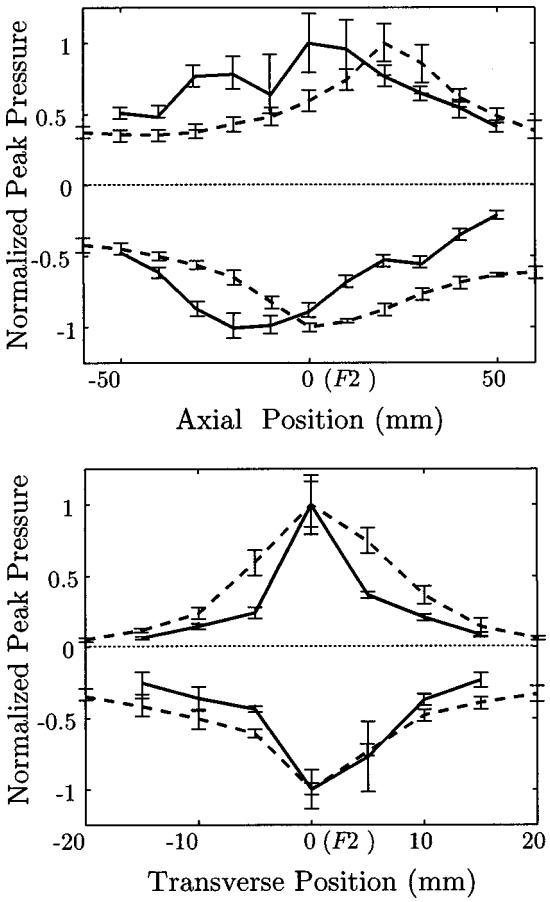

FIG. 7. Maps of peak pressure amplitudes. The top is the map along the axis of the reflector, and the bottom is the map across the axis at $F2$. A value greater than zero is the peak value of a spike P_+, normalized to the highest spike measured in the map $\hat{P}_+$. A value less than zero is the lowest pressure obtained by a trough P_-, normalized to the lowest trough $\hat{P}_-$. A solid line connects data produced by the pressure-release reflector; a dashed line connects data produced by the rigid reflector. The high standard deviation ($N=10$), particularly at $F2$ where it is 20%, is a result of spark jitter (the pulse–pulse variation in the exact location and strength of the spark at $F1$). Jitter at $F1$ moves and degrades the focus around $F2$ (Ref. 10).

release reflector occurred nearer to the reflector than did $\hat{P}_+$ produced by the rigid reflector. A possible explanation for the discrepancy in the exact location of the peaks is that the source condition used in the calculations for the pressure-release reflector was simply a triangular, negative-pressure pulse. Although the model accounts for nonlinear distortion from the aperture of the reflector outward, the source condition neglected nonlinear distortion of the pulse before it reached the aperture. The effect of nonlinear distortion on the waveform within the reflector is addressed in Sec. III.

III. DISCUSSION

Although the waveform of a plane wave reflected from a pressure-release surface is amplitude-inverted relative to that for a wave reflected from a rigid surface, the waveforms produced at $F2$ by rigid and pressure-release reflectors are not inverses in amplitude but are more nearly inverses in time. The rigid reflector produced a spike followed by a

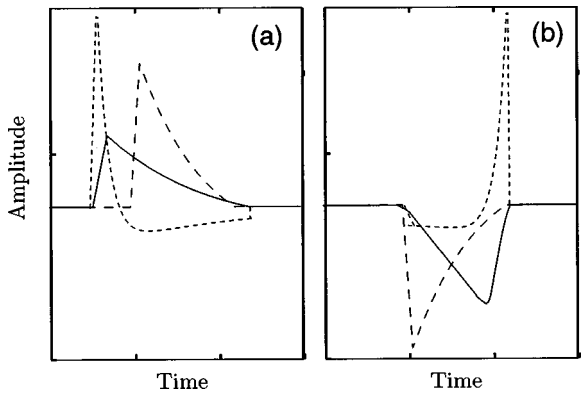

FIG. 8. Simplified models of the reflected pulses at the surface (dashed) and in the aperture (solid) of (a) a rigid reflector and (b) a pressure-release reflector. Focusing and finite-amplitude effects distort the waves as they propagate. At the focus, the waveforms are most similar to the time derivative (dotted) of the solid pressure pulse and are no longer amplitude inverses of each other. The artificially abrupt beginning and termination of each idealized pulse are exaggerated in the derivative of the pulse.

trough, and the pressure-release reflector produced a trough followed by a spike. The amplitudes of both spikes and both troughs were comparable.

Hamilton[22] obtained an analytical solution for small signals focused by a rigid ellipsoidal reflector. He found that the focal waveform is proportional to the time derivative of the waveform at the surface of the reflector. Because nonlinear effects play a significant role in our experiments, Hamilton's model cannot be used for quantitative predictions of results found here. However, the pressure waveform in the farfield of a uniformly driven, circular piston (plane or focused) also has the shape of a time derivative, in this case, of the pressure waveform at the piston face.[28–30]

Next, we use the piston model and elementary nonlinear acoustical theory to qualitatively discuss the shape of our measured waveforms. It is, however, recognized that (1) the uniform piston is too simple a model of the aperture of an ellipsoidal reflector, since the aperture is shaded,[22] and (2) a more rigorous accounting of nonlinear effects[31] would include the phase difference between nonlinearly generated higher harmonics and the fundamental. The qualitative description is only reasonable speculation. Future calculations and pressure measurements in the aperture are needed to determine whether the nonlinear and shading effects are strong enough to validate our explanation.

Description of the rigid-reflector waveform as a derivative is straightforward because the shape of the reflected wave changes very little. Let the positive, dashed idealized waveform in Fig. 8(a) represent the spark-generated pulse shortly after reflection from the rigid, ellipsoidal surface. The reflected pulse has the same shape as the initial spark-generated pulse. When the reflected pulse reaches the aperture, let the aperture be modeled as a piston, which radiates the positive pulse. The change in duration and amplitude from the dashed waveform to the solid waveform results from finite-amplitude distortion and attenuation. The derivative [dotted line in Fig. 8(a)] of the solid, positive pulse (really either positive pulse) is a short, strong positive spike followed by a long, weak negative tail. A positive spike and

a negative tail are exactly what we have measured.

The same approach works with the wave reflected by the pressure-release surface; however, consideration of nonlinear distortion is necessary to explain why the positive spike of the focal waveform is so strong. Initially, on reflection from the pressure-release surface, the pulse resembles the dashed, negative pulse shown in Fig. 8(b); however, as the pulse propagates to the aperture, nonlinear effects cause the peak of the negative-pressure pulse to move to the back of the waveform.[24] Therefore, on our aperture/piston face, the negative pulse [solid line in Fig. 8(b)] has a slow fall to the lowest pressure and then an abrupt rise. The time derivative [dotted line in Fig. 8(b)] of such a pressure waveform is a long, weak trough and a short, strong spike, similar to what we measured.

The foregoing discussion may also explain the measured difference in lengths of the focal pulses produced by the rigid and pressure-release reflectors. The negative pulse in Fig. 8(b) does not lengthen until its minimum has fallen to the tail of the waveform and formed a shock (a discontinuous increase in pressure).[24] In contrast, the shocked, positive pulse lengthens continually throughout its propagation. The derivative of a short pulse is also a short pulse which would explain the shorter duration measured at the focus of the pressure-release reflector (Fig. 3).

Few experimental measurements with pressure-release reflectors exist to which we can compare our measurements. Wurster *et al.*[32] measured extremely high negative pressures (-59 MPa) with a fiber-optic hydrophone and a parabolic pressure-release reflector. Müller[5] made measurements with an ellipsoidal pressure-release reflector, but his arrangement was sufficiently different that little comparison can be made to our results. With a spark at $F2$, a needle hydrophone at $F1$, and shallow brass and polyurethane ellipsoidal reflectors, Müller obtained nearly unipolar pulses less than 1 μs in duration. The rigid reflector produced a positive-pressure pulse (50 MPa); the pressure-release reflector produced a negative-pressure pulse (-9 MPa). Müller's scattering angle of the edge wave, propagation distance of the finite-amplitude focused wave, and angle of incidence of the focused and edge waves at the hydrophone were different from ours. The differences conceivably contribute to the differences in the waveforms measured. It should be noted that Müller's measurements with a rigid reflector and a spark at $F1$ are in good agreement with our rigid-reflector waveforms and those of Coleman *et al.*[15]

We have reported that the peak negative pressure P_- maximizes nearer to the reflector than peak positive pressure P_+ does and that the -6-dB focal region of the pressure-release reflector is smaller than that of the rigid reflector. Both observations appear to be consistent with self-refraction, which is the bending of rays caused by the contribution of the sound field itself to the propagation speed.[33] For example, a localized negative-pressure region on the acoustic wavefront causes the rays to converge, i.e., focuses the wavefront. Focusing occurs because the sound speed is lower in the negative-pressure region. In similar fashion, a localized positive region on the wavefront pushes rays away, and the front diverges or defocuses.

In lithotripsy the focused waves are inherently strongest on the axis. Therefore, rays bend either toward the axis or away from the axis, and the focus either tightens or broadens. The strong negative-pressure trough at the front of the waveform produced by the pressure-release reflector creates, by self-refraction, a focus in front of $F2$. Because the positive spike must overcome defocusing by self-refraction, its focus is delayed beyond $F2$.

For our purposes, the principal result is that at the focus, the rigid-reflector waveform has a positive-pressure spike followed by a negative-pressure trough, whereas the pressure-release reflector waveform reverses that sequence. The wave shapes are different, yet the amplitudes and durations are comparable. The maximum positive pressure $\hat{P}_+$ for the rigid reflector is 42 MPa, and the largest negative pressure $\hat{P}_-$ is -12 MPa. The corresponding values for the pressure-release reflector are $\hat{P}_+ = 43$ MPa and $\hat{P}_- = -14$ MPa.

ACKNOWLEDGMENTS

The authors express thanks to Lewis A. Thompson and Dr. Robert L. Rogers at Applied Research Laboratories (ARL), University of Texas at Austin, for help with the spark generating system and to Don Artieschoufsky, Mechanical Engineering Department, University of Texas at Austin, for cooperation and assistance in machining the reflectors. Work done at ARL was supported by the Office of Naval Research and the ARL IR&D program, while that at APL was supported by National Institutes for Health through Grant No. DK 43881.

[1] A. P. Evan and J. A. McAteer, ''*Q*-effects of shock-wave lithotripsy,'' in *Kidney Stones: Medical and Surgical Management*, edited by F. L. Coe, M. J. Favus, C. Y. C. Pak, H. J. Parks, and G. M. Preminger (Lippincott-Raven, Philadelphia, 1996), pp. 549–570.

[2] C. C. Church and L. A. Crum, ''A theoretical study of cavitation generated by four commercially available extracorporeal shock wave lithotripters,'' in *Proceedings of the 12th International Symposium on Nonlinear Acoustics*, edited by M. F. Hamilton and D. T. Blackstock (Elsevier Applied Science, London, 1990), pp. 433–438.

[3] P. A. Lewin, D. Cathignol, J.-L. Mestas, A. Birer, and J.-Y. Chapelon, ''A novel method to control P^+/P^- ratio of the shock wave pulses used in the extracorporeal piezoelectric lithotripsy (EPL),'' Ultrasound Med. Biol. **16**, 473–488 (1990).

[4] M. R. Bailey, D. Dalecki, S. Z. Child, C. H. Raeman, D. P. Penney, D. T. Blackstock, and E. L. Carstensen, ''Bioeffects of positive and negative acoustic pressures *in vivo*,'' J. Acoust. Soc. Am. **100**, 3941–3946 (1996).

[5] M. Müller, ''Experimental investigations on focusing of weak spherical shock waves in water by shallow ellipsoidal reflectors,'' Acustica **64**, 85–93 (1987).

[6] M. R. Bailey, D. T. Blackstock, R. O. Cleveland, and L. A. Crum, ''Comparison of electrohydraulic lithotripters with rigid and pressure-release ellipsoidal reflectors. II. Cavitation fields,'' J. Acoust. Soc. Am. (in preparation).

[7] D. Howard and B. Sturtevant, ''*In vitro* study of the mechanical effects of shockwave lithotripsy,'' Ultrasound Med. Biol. **23**, 1107–1122 (1997).

[8] R. O. Cleveland, J. A. McAteer, O. A. Sapozhnikov, M. R. Bailey, B. Sturtevant, A. P. Evan, and L. A. Crum, ''Design and characterization of a research electrohydraulic lithotripter patterned after the Dornier HM3,'' J. Acoust. Soc. Am. (in preparation).

[9] Specifications Manual for Reference Shock Wave Hydrophone, Sonic Technologies, Hatboro, PA (1994).

[10] D. Cathignol, J. L. Mestas, F. Gomez, and P. Lenz, ''Influence of water conductivity on the efficiency and the reproducibility of electrohydraulic shock wave generation,'' Ultrasound Med. Biol. **17**, 819–828 (1991).

[11] A. R. Kaiser, C. A. Cain, E. Y. Hwang, J. B. Fowlkes, and R. J. Jeffers, ''A cost effective degassing system for use in ultrasonic measurements: The multiple pinhole degassing (MPD) system,'' J. Acoust. Soc. Am. **99**, 3857–3860 (1996).
[12] D. T. Blackstock, ''Nonlinear acoustics (theoretical),'' in *American Institute of Physics Handbook*, edited by D. E. Gray (McGraw-Hill, New York, 1972), 3rd ed., pp. 3-183 to 3-205.
[13] M. F. Hamilton, ''Fundamentals and applications of nonlinear acoustics,'' in *Nonlinear Wave Propagation in Mechanics*, edited by T. W. Wright, AMD-Vol. 77, Book H00346 (American Society of Mechanical Engineers, New York, 1986), pp. 1–28.
[14] M. R. Bailey, ''Isolation of a negative-pressure pulse and studies of irregular edge diffraction,'' M. S. thesis, The University of Texas at Austin, Austin, Texas, 1994, pp. 50–56.
[15] A. J. Coleman, J. E. Saunders, R. C. Preston, and D. R. Bacon, ''Pressure waveforms generated by a Dornier extra-corporeal shock-wave lithotripter,'' Ultrasound Med. Biol. **13**, 651–657 (1987).
[16] L. E. Kinsler, A. R. Frey, A. B. Coppens, and J. V. Sanders, *Fundamentals of Acoustics* (Wiley, New York, 1982), 3rd ed., p. 461.
[17] Specifications Sheet for Last-a-Foam, General Plastics Corp., Tacoma, WA (1996).
[18] D. S. Campbell, H. G. Flynn, D. T. Blackstock, C. Linke, and E. L. Carstensen, ''The acoustic fields of the Wolf electrohydraulic lithotripter,'' J. Lithotripsy and Stone Disease **3**, 147–156 (1991).
[19] J. Staudenraus and W. Eisenmenger, ''Fibre-optic probe hydrophone for ultrasonic and shock-wave measurements in water,'' Ultrasonics **31**, 267–273 (1993).
[20] M. A. Averkiou and R. O. Cleveland, ''Modeling of the Dornier HM3 using the KZK equation,'' J. Acoust. Soc. Am. (submitted).
[21] E. A. Zabolotskaya and R. V. Khokhlov, ''Quasi-plane waves in the nonlinear acoustics of confined beams,'' Sov. Phys. Acoust. **15**, 35–40 (1969).
[22] M. F. Hamilton, ''Transient axial solution for the reflection of a spherical wave from a concave ellipsoidal mirror,'' J. Acoust. Soc. Am. **93**, 1256–1266 (1993).
[23] W. M. Wright and D. T. Blackstock, ''Focusing of *N* waves in air by an ellipsoidal reflector,'' J. Acoust. Soc. Am. **102**, 741–746 (1997).
[24] *Nonlinear Acoustics: Theory and Application*, edited by M. F. Hamilton and D. T. Blackstock (Academic, San Diego, 1997), Chap. 4, pp. 65–71.
[25] A. J. Coleman and J. E. Saunders, ''A survey of the acoustic output of commercial extracorporeal shock wave lithotripters,'' Ultrasound Med. Biol. **15**, 213–227 (1989).
[26] L. A. Crum, ''The tensile strength of water,'' Nature (London) **278**, 148 (1979).
[27] T. Christopher, ''Modeling the Dornier HM3 lithotripter,'' J. Acoust. Soc. Am. **96**, 3088–3095 (1994).
[28] P. M. Morse, *Vibration and Sound* (Acoustical Society of America, Woodbury, NY, 1981), pp. 326–336, 344–346.
[29] A. D. Pierce, *Acoustics: An Introduction to Its Physical Principles and Applications* (McGraw-Hill, New York, 1981), pp. 225–231.
[30] H. T. O'Neil, ''Theory of focusing radiators,'' J. Acoust. Soc. Am. **21**, 516–526 (1949).
[31] T. S. Hart and M. F. Hamilton, ''Nonlinear effects in focused sound beams,'' J. Acoust. Soc. Am. **84**, 1488–1496 (1988).
[32] C. Wurster, M. Köhler, R. Pecha, W. Eisenmenger, D. Suhr, U. Irmer, F. Brümmer, and D. Hülser, ''Negative pressure measurements of water using the glass fiber hydrophone,'' Ultrasonics World Congress 1995 Proceedings, 635–638.
[33] *Nonlinear Acoustics: Theory and Application*, edited by M. F. Hamilton and D. T. Blackstock (Academic, San Diego, 1997), Chap. 10, p. 295, Chap. 12, p. 373.

LETTERS TO THE EDITOR

This Letters section is for publishing (a) brief acoustical research or applied acoustical reports, (b) comments on articles or letters previously published in this Journal, and (c) a reply by the article author to criticism by the Letter author in (b). Extensive reports should be submitted as articles, not in a letter series. Letters are peer-reviewed on the same basis as articles, but usually require less review time before acceptance. Letters cannot exceed four printed pages (approximately 3000–4000 words) including figures, tables, references, and a required abstract of about 100 words.

Surface waves above honeycombs

Julian Tizianel, Jean F. Allard, and Bruno Brouard
Institut d'Acoustique et de Mécanique de l'Université du Maine, UMR 6613 CNRS, Avenue O. Messiaen, 72085 Le Mans Cedex 9, France

(Received 14 February 1997; revised 19 June 1998; accepted 1 July 1998)

The phase velocity of surface waves above honeycomb structures has been evaluated with the near-field holography method developed by Tamura [J. Acoust. Soc. Am. **88**, 2259 (1990)]. A simple empirical expression is suggested to predict this velocity, by analogy with the case of comblike structures and layers with square cross-sectional shaped holes. © *1998 Acoustical Society of America.* [S0001-4966(98)02410-2]

PACS numbers: 43.28.−g, 43.20.Fn [LCS]

INTRODUCTION

Experimental evidence of acoustic surface waves above a comblike structure have been obtained by Ivanov-Shits and Rozhin,[1] in 1959. A simple modeling for these waves can be obtained as follows. A plane wave impinging on a comblike structure with an angle of incidence θ is represented in Fig. 1. The plane of incidence is *xOz*. The spatial period is *S*, the distance between the plates is *a*, and the thickness of the structure is *d*. The time dependence $\exp(-j\omega t)$ and the orientation of the axes are the same as in the book by Brekhovskikh and Godin.[2] Let k and Z be the wave number in free air and the characteristic impedance, respectively. The *z* and *x* components of the wave number vector of the reflected wave are

$$k_z = k \cos \theta, \tag{1}$$

$$k_x = k \sin \theta. \tag{2}$$

The comblike structure can be considered as an anisotropic porous material having a porosity $\Phi = a/S$, and air inside the structure can be replaced by an equivalent fluid where the wave number is k_1, and the characteristic impedance Z_1. A surface wave over the structure is related to a pole of the reflection coefficient. The surface impedance of the structure at $z=0$, if only the piston mode which propagates parallel to the *z* axis inside the structure is taken into account, is given by

$$Z_s = -j \frac{Z_1}{\Phi} \cot k_1 d. \tag{3}$$

The reflection coefficient R is given by

$$R = \frac{Z_s + Z/\cos \theta}{Z_s - Z/\cos \theta}, \tag{4}$$

and has a pole at $\theta = \theta_p$ given by

$$\cos \theta_p = j \frac{Z\Phi \tan k_1 d}{Z_1}. \tag{5}$$

The *x* wave number vector component is given by

$$k \sin \theta_p = k \sqrt{\left(1 + \frac{Z^2\Phi^2}{Z_1^2} \tan^2 k_1 d\right)}. \tag{6}$$

If the distance *a* is much larger than the viscous skin depth, the equivalent fluid is not noticeably different from free air, and $k = k_1$, $Z = Z_1$. Then Eqs. (5)–(6) can be rewritten

$$\cos \theta_p = j\Phi \tan kd, \tag{7}$$

$$\sin \theta_p = (1 + \Phi^2 \tan^2 kd)^{1/2}. \tag{8}$$

The reflected wave propagates in the *x* direction with a velocity c_e given by

$$c_e = c/(1 + \Phi^2 \tan^2 kd)^{1/2} = c/\sin \theta_p, \tag{9}$$

where c is the velocity in free air. Velocity in the *x* direction is smaller than the velocity in free air and $\sin \theta_p$ is larger than one. This simple model has been presented by Tolstoy[3] for $\Phi = 1$. If $\tan kd > 0$, this wave is evanescent in the *z* direction with a damping coefficient $\Phi k \tan kd$ and is a true surface wave.[3] The two parameters that characterize the structure are Φ and *d*, and with this model the rectangular grooves can be replaced by square or circular cross-sectional shaped holes, or by honeycombs, with the same Φ and *d*. Several experiments have been performed to measure c_e and the damping coefficient over comblike structures.[1,4–6] Equations (7) and (9) overestimate the damping and underestimate c_e. More elaborate models have been worked out for comblike structures,[6] and layers with square holes[7] having a spatial periodicity *S* along two perpendicular axes. These

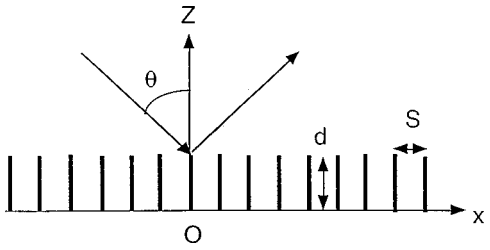

FIG. 1. Incident and reflected acoustic plane wave over a comblike structure.

models take into account the higher diffraction modes above the structures and the higher modes inside the grooves or the holes. They are inspired by previous studies concerning diffraction of electromagnetic waves.[8–11] (The transposition to acoustics of previous works concerning electromagnetic surface waves and diffraction of light can be used for other shapes of grooves[12] and porous layers.[13]) With a simple correction on d, Eqs. (7)–(9) provide predictions similar to the ones obtained with these models. More precisely, d must be replaced by $d-(a/\pi)\log 2$, a being the thickness of the grooves (respectively, the side of the square holes), and Eqs. (7) and (9) must be replaced by

$$\cos\ \theta_p = j\phi\ \tan\ k(d-(a/\pi)\log 2), \tag{10}$$

$$\sin\ \theta_p = (1+\phi^2\ \tan^2\ k(d-(a/\pi)\log 2))^{1/2}. \tag{11}$$

For rectangular grooves with infinitely thin blades ($\Phi=1$), the correction can be obtained directly by an analytical calculation.[6,8,9] When Φ is noticeably smaller than 1, comparisons between predictions obtained with a modal model[6,10] and by Eq. (11) have been performed in Ref. 6. It can be verified that the agreement is also good for the case of square holes in Ref. 7, Φ being now equal to $(a/S)^2$. In the models presented in Refs. 6 and 7, and in Eq. (11), the effects of the viscous forces and the thermal exchanges between air inside the grooves or the holes and the structure are neglected and losses are not taken into account. These effects are negligible for the evaluation of c_e when a is much larger

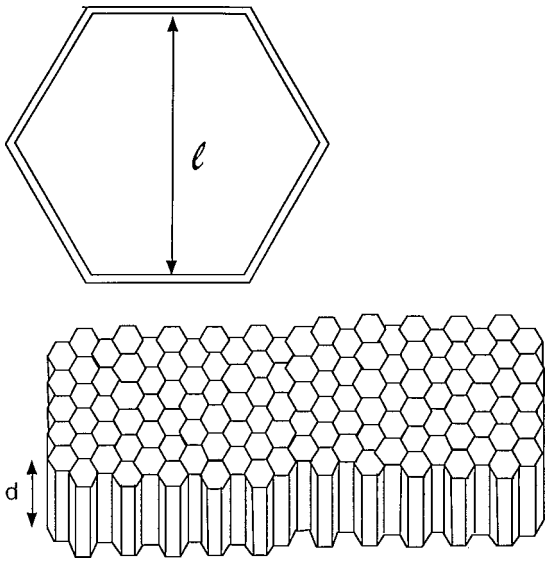

FIG. 2. Honeycomb structure.

TABLE I. Two honeycomb structures.

	Distance l (cm)	Porosity Φ	Thickness d (cm)
First structure	5.3 cm	0.88	3.3
Second structure	0.26 cm	0.9	5

than the viscous skin depth. In the present work, new experiments performed with the near-field holography method[14] over honeycomb structures are presented. The honeycomb structure has a double periodicity along two axes with an angle between these axes equal to $\pi/4$. The diffraction field for doubly periodic structures has been described by McPhedran *et al.*[11] The modal models used for comblike structures or square holes cannot be transposed easily, due to the complexity of the modes for the honeycomb geometry. Predictions obtained with a simple phenomenological correction on d as in Eqs. (10)–(11) will be compared with measurements.

I. CHARACTERIZATION OF THE SURFACE WAVES OVER HONEYCOMB STRUCTURES BY THE NEAR-FIELD ACOUSTICAL HOLOGRAPHY METHOD

The near-field acoustical holography method[14] (NAH) was used in a previous study to localize in the complex sin θ plane a pole of the reflection coefficient of a porous layer.[15] The method can be used to measure the reflection coefficient on the Re(sin θ) axis at normal and oblique incidence ($0 \leqslant \sin\theta \leqslant 1$) and for evanescent waves ($\sin\theta > 1$). The source is a loudspeaker and can be considered as a dipole. When a pole in the complex sin θ plane, located at $\sin\theta_p$, is sufficiently close to the real axis, the reflection coefficient can reach large values on the real axis in the neighborhood of $\sin\theta_p$. Let θ_M be the angle of incidence related to the maximum of $|R|$ on the Re(sin θ) axis in the neighborhood of $\sin\theta_p$, $\sin\theta_p$, and $\sin\theta_M$ can be very close to each other if $\mathrm{Im}(\sin\theta_p) \ll 1$. Due to the damping inside porous layers, the pole is close to the real axis only for layers having a small thickness. In comblike and honeycomb structures, the damping is much smaller than in porous layers, and the NAH method is well suited to the measurement of the real part of

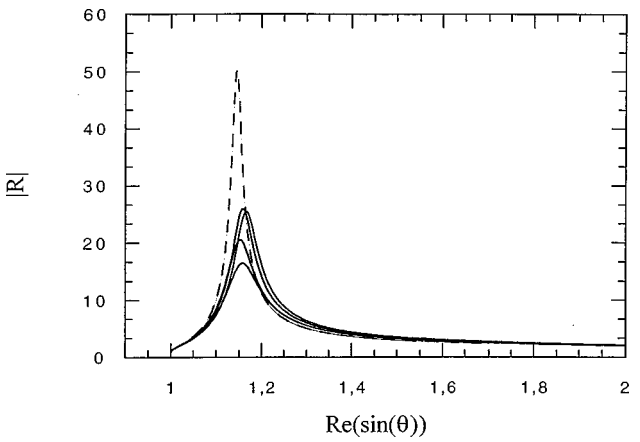

FIG. 3. Modulus of the reflection coefficient of the second structure (see Table I). Prediction with the modified thickness ----------. Measurement ———.

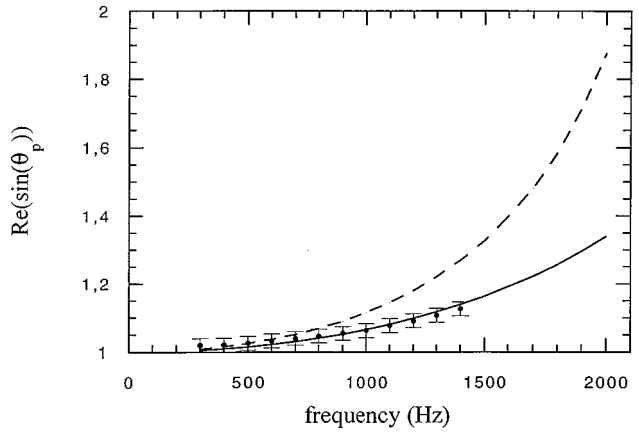

FIG. 4. Re(sin θ_p) for the first structure (see Table I) as a function of frequency. Prediction without correction of the thickness --------. Prediction with corrected thickness ———. Measurement ⏚.

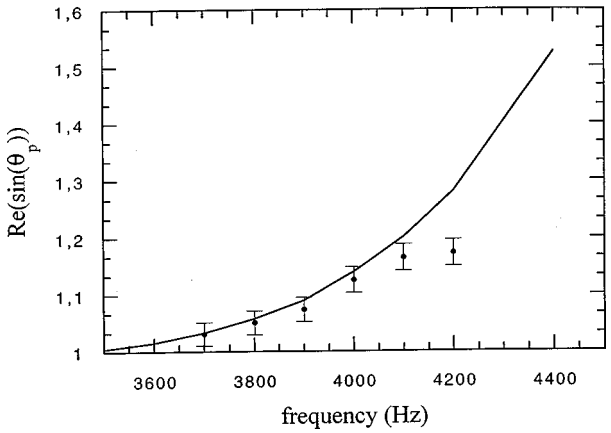

FIG. 6. Re(sin θ_p) for the second structure (see Table I) and the second mode. Prediction (corrected thickness) ———. Measurement ⏚.

sin θ_p for the evanescent waves which will be taken equal to sin θ_M in what follows. Moreover, due to the small damping inside the structures, the imaginary part of k sin θ_p can be neglected and the damping coefficient of the surface wave can be evaluated from the measured sin θ_M with a good approximation by

$$\mathrm{Im}(k\ \cos\ \theta_p)=(k^2\ \sin^2\ \theta_M-k^2)^{1/2}. \tag{12}$$

II. MEASUREMENT WITH THE NAH METHOD FOR TWO HONEYCOMB STRUCTURES AND VALIDATION OF A SIMPLE PHENOMENOLOGICAL MODEL

Two honeycomb structures are studied. Distance l between two parallel sides of the honeycomb aperture (see Fig. 2), porosity Φ and thickness d for both structures are indicated in Table I. Preliminary experiments have been performed to verify the isotropy in the xy plane of the acoustic properties of the structures. In Fig. 3, an example of localization of a pole by the NAH method is given. The modulus of the reflection coefficient $|R|$ is represented as a function of sin θ at 600 Hz for the second structure. If losses are neglected, $|R|$ presents a singularity on the Re(sin θ) axis. Losses are taken into account very approximately by using Eqs. (3)–(4) to predict $|R|$, Z_1 and k_1 being the characteristic impedance and the wave number for the equivalent damped fluid in a circular cross-sectional-shaped cylinder[16] of diameter l. By analogy with the case of square grooves and square holes, d is replaced by $d-(l/\pi)\log 2$. This correction will be used for both structures. The peak is sharp, and the calculated and measured maxima are different. Several measurements are represented in Fig. 3 to show the dispersion. The measurement of the maximum amplitude is not reliable, but the location of the maximum on the Re(sin θ) axis is measured with a weak dispersion. Moreover, it may be noticed that the maximum calculated with Z_1 and k_1 on the Re(sin θ) axis is very close to the singularity obtained by replacing Z_1 and k_1 by Z and k, which is located at sin θ_p, given by Eq. (11) where a is replaced by l.

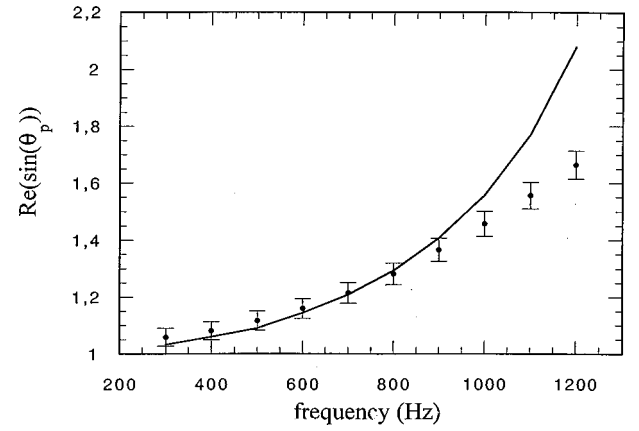

FIG. 5. Re(sin θ_p) for the second structure (see Table I) and the first mode. Prediction (corrected thickness) ———. Measurement ⏚.

In Figs. 4, 5, and 6, the measured values of Re(sin θ_p) are represented as functions of frequency for structure 1 and structure 2, and compared with sin θ_p obtained from Eq. (11), a being replaced by l. In Fig. 4 the measured Re(sin θ_p) for the first structure is compared with predictions obtained without corrections, and when d is replaced by $d-(l\ln 2)/\pi$. It appears that without correction the agreement between measurement and prediction is very bad. In Figs. 5 and 6, Re(sin θ_p) is represented for the first mode ($0<kd<\pi/2$) and the second mode ($\pi<kd<3\pi/2$), respectively. The second mode had never been set in evidence hitherto. The agreement between measurement and prediction obtained with the thickness d replaced by $d-(l/\pi)\log 2$ is good for both structures when Re(sin θ_p) is smaller than 1.2. The effect of the correction $(l/\pi)\log 2$ is very important for the first structure, and almost negligible for the second one, l being much larger in the first case.

III. CONCLUSION

From previous works concerning electromagnetic waves, it appears that surface waves above comblike structures can be characterized with a simple classical model but the thickness of the structure must be modified to take into account diffraction and higher modes inside the grooves, the correction being proportional to the spacing between the plates of the structures. For the case of honeycomb structures, precise measurements obtained with the near-field

acoustical holography method indicate that with a similar correction to the thickness, good agreement between prediction and measurement can be obtained.

[1] K. M. Ivanov-Shits and F. V. Rozhin, ''Investigation of surface waves in air,'' Sov. Phys. Acoust. **5**, 510–512 (1959).
[2] L. M. Brekhovskikh and O. A. Godin, *Acoustics of Layered Media II, Point Source and Bounded Beams*, Springer Series on Wave Phenomena (Springer-Verlag, New York, 1992).
[3] I. Tolstoy, *Wave Propagation* (McGraw-Hill, New York, 1973).
[4] R. J. Donato, ''Model experiments on surface waves,'' J. Acoust. Soc. Am. **63**, 700–703 (1978).
[5] G. A. Daigle, M. R. Stinson, and D. I. Havelock, ''Experiment on surface wave over a model impedance plane using acoustical pulses,'' J. Acoust. Soc. Am. **99**, 1993–2005 (1996).
[6] L. Kelders, J. F. Allard, and W. Lauriks, ''Ultrasonic surface waves above rectangular-groove gratings,'' J. Acoust. Soc. Am. **103**, 2730–2733 (1998).
[7] J. F. Allard, L. Kelders, and W. Lauriks, ''Ultrasonic surface waves above a doubly periodic grating,'' J. Acoust. Soc. Am. (submitted).
[8] R. A. Hurd, ''The propagation of an electromagnetic wave along an infinite corrugated surface,'' Can. J. Phys. **32**, 727–734 (1954).
[9] L. A. Vajnshtejn, ''Electromagnetic surface waves on a comblike structure,'' Zh. Tekh. Fiz. **26**, 385–397 (1996).
[10] A. Hessel, J. Schmoys, and D. Y. Tseng, ''Bragg-angle blazing of diffraction gratings,'' J. Opt. Soc. Am. **65**, 380–384 (1975).
[11] C. McPhedran, G. H. Derrick, and L. C. Bolten, ''Theory of crossed gratings,'' in *Electromagnetic Theory of Gratings*, edited by R. Petit (Springer-Verlag, New York, 1980).
[12] W. Lauriks, L. Kelders, and J. F. Allard, ''Surface waves above gratings having a triangular profile,'' Ultrasonics (accepted for publication).
[13] W. Lauriks, L. Kelders, and J. F. Allard, ''Poles and zeros of the reflection coefficient of a porous layer having a motionless frame in contact with air,'' Wave Motion **28**, 59–67 (1998).
[14] B. Brouard, D. Lafarge, J. F. Allard, and M. Tamura, ''Measurement and prediction of the reflection coefficient of porous layers at oblique incidence and for inhomogeneous waves,'' J. Acoust. Soc. Am. **99**, 100–107 (1996).
[15] J. Tizianel, J. F. Allard, W. Lauriks, and L. Kelders, ''Experimental localization of a pole of the reflection coefficient of a porous layers,'' J. Sound Vib. **204**, 600–604 (1997).
[16] J. F. Allard, *Propagation of Sound in Porous Media: Modelling Sound Absorbing Materials* (Chapman & Hall, London, 1993).

Electromagnetic exposure safety of the Carstens Articulograph AG100

Mark Hasegawa-Johnson[a)]
Department of Electrical Engineering, UCLA, Los Angeles, California 90095

(Received 13 February 1998; accepted for publication 10 July 1998)

Extremely strong magnetic fields at the frequencies used in an electromagnetic articulometer (EMA) system may pose a risk to the health of a subject. To avoid such risks, the field strengths produced by any EMA system should be measured, and compared to published permissible exposure standards. This Letter reports measurements of the 2–50 kHz magnetic field strength of the Carstens Articulograph AG100. The measured field strength (35 μT at a distance of 7.5 cm) is permissible under local standards in Austria, Germany, the UK, and the USA (except Massachusetts), but may be impermissible under the 1995 European Community Prestandard, and in Canada. © *1998 Acoustical Society of America.* [S0001-4966(98)04110-1]

PACS numbers: 43.70.Jt [AL]

I. MOTIVATION

Electromagnetic midsagittal articulography (EMA) is a technique for obtaining real-time data about the motion of points on the surface of the tongue and other articulators using relatively low-cost, lightweight, and noninvasive equipment (Schönle *et al.*, 1987; Perkell *et al.*, 1992). The EMA relies on alternating magnetic fields to measure the distance between fixed transmitter coils and movable receiver coils fixed to the surfaces of the articulators. The Carstens Articulograph AG100 is, at the time of this writing, the only commercially available EMA system capable of correcting for small misalignments of the receiver coils using a redundant third transmitter (Hoole and Nguyen, 1996).

Alternating magnetic fields generate electric current in any conducting medium, including human bones and blood. Fields of moderate strength at the frequencies used in the Articulograph (10–20 kHz) have not been conclusively linked to any health risk, but caution dictates that unnecessary exposure should be minimized. In particular, the American National Standards Institute (ANSI) has endorsed a standard which limits exposure to magnetic fields at frequencies above 3 kHz (IEEE, 1992). The purpose of this article is to very briefly review the relevant safety considerations, and to describe measurements which show that the Articulograph AG100 meets the ANSI-approved maximum permissible exposure standard.

II. HEALTH RISKS ASSOCIATED WITH ALTERNATING MAGNETIC FIELDS

The current induced in biological tissue by an alternating magnetic field can usually only be computed using numerical simulations, but in certain extremely simple cases, the current distribution can be expressed analytically. For example, if the medium is assumed to be infinite and homogeneous, the current density in a circular path of radius r perpendicular to a sinusoidally varying magnetic field of frequency f is

$$J=\sigma\pi rBf, \tag{1}$$

where J is the current density (in A/m^2), σ is the conductivity of the medium [in Ωm^{-1}], and B is the magnetic flux density (in Tesla).

At 10–100 kHz, blood has been reported to have a conductivity of 0.55–0.68 $(\Omega\text{m})^{-1}$, while bone and brain tissue have conductivities of approximately 0.0133–0.0144 and 0.12–0.17 $(\Omega\text{m})^{-1}$, respectively (Foster, 1995). Thus, in an infinite conductor with the properties of brain tissue, a field of 100 μT (microtesla) at 20 kHz will induce a current density, in a circle of radius 10 cm, of approximately 10 μA/cm^2. In a real human body, nonlinear tissue properties and boundary effects are likely to raise or lower this number by an order of magnitude or more. Standards for maximum permissible exposure are therefore typically based on computational and physical studies using realistic heterogeneous models of the human body.

Current induced by alternating magnetic fields has two readily quantifiable health effects: induced current can heat tissue, causing thermal damage, and it can stimulate electrically excitable cells, interfering with cellular communication. At frequencies below approximately 100 kHz, the current necessary to significantly heat biological tissue is greater than the current necessary to stimulate electrically excitable cells. At extremely low frequencies (ELF: 0–300 Hz), excitable cells can be stimulated by current densities of 10–100 μA/cm^2 (IRPA, 1990). At very low frequencies (VLF: 3–30 kHz), the threshold for stimulation of excitable cells is a function of frequency. In the VLF range, the lowest reported thresholds for cell stimulation are greater than $(35f)\,\mu$A/cm^2, where f is expressed in kilohertz (IEEE, 1992).

At amplitudes which are too low to stimulate excitable cells, ELF electric and magnetic fields have been conclusively linked to a small number of health effects, and other health effects have been suggested but not proven. According to the review by Stuchly (1995), exposure of healthy male volunteers to 20 μT magnetic fields at 60 Hz has been linked to a statistically significant slowing of the heart rate, and to changes in a small fraction of the tested behavioral indicators. There is evidence that nocturnal exposure to 60 Hz magnetic fields affects melatonin production. Case stud-

a)Electronic mail: mhj@icsl.ucla.edu

TABLE I. Magnetic field exposure standards at 20 kHz, expressed in microtesla.

Institution	Occupational	General public
ACGIH (1996 TLVs and BEIs)	200	
ANSI/IEEE (C95.1-1991)	205	205
Austria		440
Canada (H46-2/90-160E, 1993)	6.16	2.75
European Prestandard (ENV 50166-1, 1995)	52.8	21.1
FRG (VDT 0848 Teil 2, 1986)	314	314
Massachusetts (105 CMR 122.000, 1997)	1.99	
United Kingdom NRPB (1993)		80
USAF (AFOSH 48-9, 1997)	205	205

ies have suggested that exposure to ELF electromagnetic fields may promote the growth of cancer, but laboratory tests involving rodents have been almost entirely negative.

The only source of VLF magnetic fields which most people encounter in their daily lives is the horizontal deflection circuitry of a video display terminal (VDT) or television set, which produces both VLF (15–80 kHz) and ELF (30–100 Hz) fields. Haes and Fitzgerald (1995) measured the magnetic field strength at a distance of 50 cm in front of 141 VDTs by 38 manufacturers, and found VLF flux densities between approximately 0.002 and 0.1 μT.

Kavet and Tell (1991) describe 14 epidemiological studies and four laboratory studies with rodents seeking to establish a link between VLF magnetic fields and either spontaneous abortion or birth defects. The larger laboratory studies found no link between VLF fields and reproductive outcome, although one of the smaller studies reported a link (which Kavet and Tell question). Of the 14 epidemiological studies, two found a link between VDT use and first trimester spontaneous abortion. A recent epidemiological study not cited by Kavet and Tell (Lindbohm *et al.*, 1992) correlated pregnancy outcome with ELF and VLF field strengths and exposure time, and found that frequent exposure to strong ELF fields increases risk, but that exposure to VLF fields does not.

III. EXPOSURE STANDARDS

Table I lists a selection of magnetic field exposure standards which apply between 10 and 20 kHz, and which do not apply exclusively to VDT emissions. Standards originally quoted in units of amps/meter were converted to microtesla using a conversion factor of $\mu_0 = 4\pi \times 10^{-7}$ T/(A/m). The ANSI/IEEE, ACGIH, Canadian, Massachusetts, and USAF standards were reviewed in the preparation of this article. Other standards in Table I are as cited in Polk and Postow (1996) or Kavet and Tell (1991).

Many exposure standards are based on the industrial standard practice set by either the 1982 or 1991 ANSI/IEEE standards. The ANSI/IEEE standard is designed to keep the induced current in biological tissue at least a factor of 10 below the lowest reported stimulation thresholds for electronically excitable cells. The 1982 standard (ANSI C95.1-1982) sets a threshold limit value (TLV) of approximately 2 μT in the VLF frequency range, based on relatively simple models of induced current. Research since 1982 using more realistic heterogeneous human models indicates that there is no danger of cell stimulation at levels below approximately 2000 μT, so, after taking into account a margin of safety, the IEEE published the new standard, C95.1-1991, cited in Table I. C95.1-1991 recommends that the average exposure, averaged over any 6-min period and over a cross section of the human body, should not exceed 205 μT. Less stringent standards apply to partial-body exposures, but the less stringent standards specifically do not apply to the eyes.

In designing the standard, the committee considered peer-reviewed articles investigating the relationships between electromagnetic fields and 14 different categories of health effect, without regard for the mechanism causing each effect. The mechanisms of tissue heating and cell stimulation were chosen as the basis for standard exposure thresholds because they are quantifiable, and because ''no reliable scientific data exist indicating that nonthermal (other than [electric] shock) or modulation-specific sequelae of exposure may be meaningfully related to human health.''

Most standards applicable in the United States have been modified since 1991 based on the research cited in C95.1-1991. The ACGIH standard TLV was raised from 2 to 200 μT in 1995, and the US Air Force standard was raised in 1997. The existing Commonwealth of Massachusetts law is justified based on citations of the old ANSI and ACGIH standards, so the law will probably be changed to reflect the new standards after a reasonable period of review.

IV. ARTICULOGRAPH FIELD STRENGTH

Alternating magnetic fields generated by the Articulograph AG100 in the VLF range were measured at several distances from each of the transmitter coils. The generated fields were 140–160 μT on the surface of each transmitter coil, and 33–38 μT at a typical subject distance of 7.5 cm. This level is permissible under most published exposure standards.

Magnetic field strength was measured using a Narda model 8532 Precision ELF/VLF Gaussmeter.[1] This meter uses an induction coil to measure rms magnetic field strength along a single axis, with an accuracy better than $\pm 5\%$ (typically 1%) over the specified frequency range. The frequency range switch was set to the VLF range (2–50 kHz), in order to filter out contributions from ELF fields. All measurements reported in this article have been converted from milligauss to microtesla using the conversion 10 mG=1 μT.

The transmitter coils in the Articulograph were turned on more than 2 h before testing, in order to let them reach a steady operating temperature, as recommended in the manual (Carstens, 1993). All three transmitters were set to operate at maximum power (E value=255).

The strength of the field perpendicular to the midsagittal plane was measured at 1-cm increments along a line connecting each coil to the center of the Articulograph, as shown in Fig. 1. The results are shown in Table II. The minimum distance in Table II, 3.5 cm, is the sum of the 2.5-cm radius of the transmitter coil and the 1-cm radius of the probe coil.

Fields generated by the blue transmitter coil were also measured in two directions parallel to the midsagittal plane. These fields were much weaker than the fields perpendicular to the midsagittal plane, and also much more variable: over

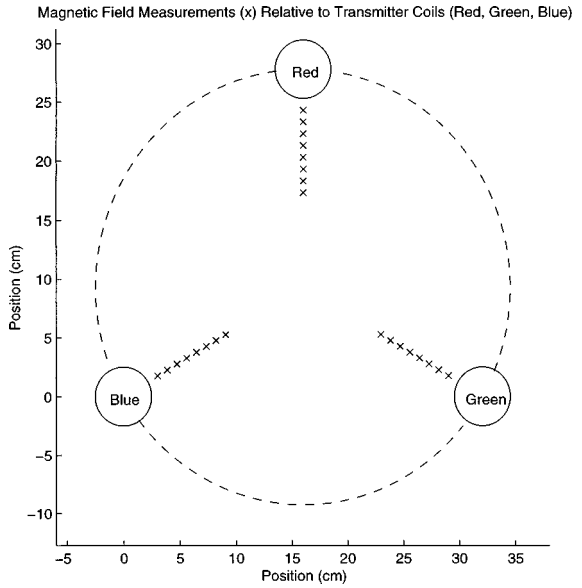

FIG. 1. Schematic of the Articulograph in the midsagittal plane; transmitter coils are shown as solid circles of radius 2.5 cm. Magnetic field strength was measured at the points marked ''×.'' These points are 1-cm increments along a line connecting each transmitter coil to the center of the Articulograph.

the course of several seconds, the strength of a parallel magnetic field sometimes varied by as much as a factor of 2. Representative values at several distances are given in Table III. In this table, ''vertical fields'' were measured parallel to, and ''horizontal fields'' perpendicular to, a straight line in the midsagittal plane passing through the blue and green transmitters.

The rms field strength B perpendicular to the midsagittal plane at each measurement position was approximated using a function $\hat{B}(d_r, d_g, d_b)$ of the distances d_r, d_g, and d_b to the red, green, and blue transmitter coils, respectively:

$$\hat{B}(d_r, d_g, d_b) = \sqrt{\left(\frac{\alpha_r}{d_r^{\beta}}\right)^2 + \left(\frac{\alpha_g}{d_g^{\beta}}\right)^2 + \left(\frac{\alpha_b}{d_b^{\beta}}\right)^2}. \quad (2)$$

The model parameters β, α_b, α_g, and α_r were optimized using a gradient search in order to minimize the mean-squared log error, $(\log(\hat{B}) - \log(B))^2$. The minimum-error exponent was $\beta = 2.1$. The scaling constants were $\alpha_b = 2240\ \mu\text{T cm}^2$, $\alpha_g = 2180\ \mu\text{T cm}^2$, and $\alpha_r = 2150\ \mu\text{T cm}^2$.

TABLE II. Magnetic field strengths perpendicular to the midsagittal plane. Distances shown are the distances between transmitter axis and probe axis; a distance of 3.5 cm is obtained by resting the probe on the surface of the transmitter. The three transmitter axes form an equilateral triangle with sides of length 32 cm (Carstens, 1993).

Distance (cm)	Blue coil (μT)	Green coil (μT)	Red coil (μT)
3.5	150.0	132.8	131.1
4.5	100.0	93.4	100.0
5.5	66.5	65.3	70.0
6.5	48.0	48.0	45.0
7.5	38.2	33.6	35.3
8.5	26.5	25.3	22.0
9.5	20.0	18.4	18.4
10.5	15.7	16.3	13.7

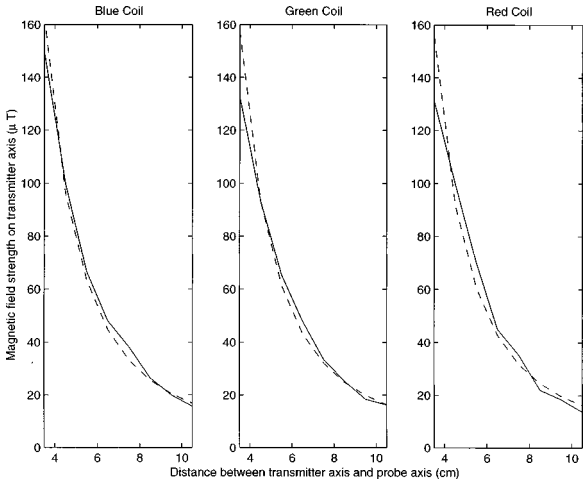

FIG. 2. Measured field strengths (solid line) and modeled field strengths (dotted) as a function of distance from each of the transmitter coils.

Figure 2 shows the measured field strengths and best-fit model field strengths as a function of the distance to the nearest transmitter coil. The discrepancy between measured and modeled field strengths at $d = 3.5$ cm may be caused by capacitive loading between the transmitter and probe coils, whose surfaces touched at this distance. If the $d = 3.5$-cm measurements are excluded from analysis, the model parameters become $\beta = 2.2$, $\alpha_b = 2810\ \mu\text{T cm}^2$, $\alpha_g = 2800\ \mu\text{T cm}^2$, and $\alpha_r = 2630\ \mu\text{T cm}^2$.

As noted in Eq. (1), transmitted field strength is proportional to signal frequency. The exact frequencies of transmission of the three coils were not measured in this study. According to one of the reviewers of this paper, however, the Articulograph circuits are designed so that the red coil, which is closest to the subject in normal use, always operates at the lowest frequency and therefore at the lowest magnetic field strength.

V. DISCUSSION

Measurements of the magnetic field strength generated by a Carstens Articulograph AG100 show that the field strength is approximately 100 μT measured near the surface of the coils ($d = 4.5$ cm), and decreases as $1/d^{2.2}$ at greater distances from each coil. This field is below the 205-μT maximum permissible exposure defined in ANSI/IEEE standard C95.1-1991. In normal use, the surface of a subject's head is typically at least 5 cm from the surface of any of the transmitter coils, or 7.5 cm from the axis of any transmitter. At this distance, the subject is exposed to a field of less than or equal to approximately 35 μT over the entire volume of the head; in particular, the eyes of the subject are exposed to

TABLE III. Magnetic field strengths generated by the blue transmitter coil along axes within the midsagittal plane.

Distance (cm)	Vertical fields (μT)	Horizontal fields (μT)
3.5	10	15
4.5	3.4	4.5
6.5	1.9	1.8
10.5	0.4	0.4

a field of approximately 35 μT. Under this assumption, it is possible to integrate the square of Eq. (2) to show that the rms average exposure of the head in the midsagittal plane is approximately 30 μT.

Epidemiological and laboratory studies suggest that the VLF magnetic fields produced by a video display terminal do not increase the risk of spontaneous abortion. It should be noted, however, that there are important differences between exposure to the VLF fields of a VDT and exposure to the fields generated by the Articulograph, which make comparison difficult.

First, the fields to which a subject is exposed in an Articulograph are several orders of magnitude higher than the VLF fields of a VDT. This is in part because the Articulograph transmitters produce stronger fields than any VDT, and in part because subjects are closer to the Articulograph transmitters than they would be to a VDT. If the head of a subject is approximately 7.5 cm from the axis of the nearest transmitter coil, the subject is exposed to fields of up to approximately 35 μT. For comparison, subjects would receive similar exposure by sitting 50 cm from a coil with the strength of 350 worst-case VDTs (VDTs taken from the top of the range measured by Haes and Fitzgerald), or 2600 typical VDTs (VDTs taken from the logarithmic midpoint of the Haes and Fitzgerald range).

Second, exposure to the fields of an Articulograph is acute (usually lasting less than a few hours), while exposure to a VDT is chronic (often continuing 8 h a day for many years). Although neither acute nor chronic exposure to VLF fields has been linked to any health risk, the study of Lindbohm *et al.* (1992) suggests that exposure to ELF fields carries a risk which increases with the duration of exposure.

The Canadian Ministry of National Health and Welfare and the Massachusetts Department of Labor and Industries do not permit exposure to fields as strong as those produced by the Articulograph, but the magnetic field strength limits under both Canadian and Massachusetts law do not apply to devices which can be shown to cause a specific absorption rate (SAR) of less than 0.4 W/kg (0.2 W/kg for the general public, under the Canadian regulation). ANSI C95.1-1991 implies, but does not explicitly state, that the SAR caused by a 200 μT source at frequencies below 100 kHz can be shown to be less than 0.4 W/kg using modern heterogeneous models of the human body. Researchers in Canada and Massachusetts interested in purchasing an Articulograph may therefore wish to investigate the possibility of justifying the Articulograph based on calculated SAR.

Finally, the European Commission Prestandard (ENV 50166-1) seems to allow use of the Articulograph at full power only if exposure is judged to be ''occupational:'' under most standards, this term refers to exposure accepted willingly by a worker trained to understand and minimize the potential health risks. If researchers in Europe do not wish to categorize their experimental subjects as trained workers, they can probably satisfy the requirements of ENV 50166-1 by operating the Articulograph at half power.

If researchers in any country or province find that local standards do not permit use of the Articulograph, they may wish to consider purchasing the other commercially available EMA system, the Botronic Movetrack. According to Hoole and Nguyen (1996), both the Botronic Movetrack and the MIT EMMA system (not commercially available) expose subjects to fields of less than 1 μT, which is permissible under all of the exposure standards listed in Table I. Hoole and Nguyen note that the accuracy of the Movetrack is limited by its two-transmitter construction, which makes it considerably more susceptible than the Articulograph to tracking errors caused by misalignment of the receivers.

[1]An initial measurement with a broadband meter calibrated for 60-Hz fields (the Magnetic Sciences International MSI-25) resulted in measurements which were an order of magnitude too large. Examination of the meter specifications revealed that the sensitivity of the MSI-25 increases with frequency in an unspecified way, and is therefore unsuitable for VLF field measurements.

American College of Governmental Industrial Hygienists (**1996**). *1996 Threshold Limit Values for Chemical Substances and Physical Agents and Biological Exposure Indices* (Cincinnati, OH).

Canadian Ministry of National Health and Welfare (**1993**). *Safety Code 6: Limits of Exposure to Radiofrequency Fields at Frequencies from 10 kHz–300 GHz*, Catalog No. H46-2/90-160E (Canada Communication Group, Ottawa).

Carstens Medizinelektronik GmbH (**1993**). *Articulograph AG100 User's Handbook* (Göttingen).

Commonwealth of Massachusetts Department of Labor and Industries (**1997**). ''Nonionizing radiation limits for: The general public from nonoccupational exposure to electromagnetic fields, employees from occupational exposure to electro-magnetic fields, & exposure from microwave ovens,'' Code of Massachusetts Regulations 105 CMR 122.000 (Boston, MA).

Foster, K. R. (**1995**). ''Dielectric properties of tissues,'' in *The Biomedical Engineering Handbook*, edited by J. D. Bronzino (CRC, Boca Raton, FL).

Haes, D. L., and Fitzgerald, M. (**1995**). ''Video display terminal very low frequency measurements: The need for protocols in assessing VDT user 'dose,' '' Health Phys. **68**(4), 572–578.

Hoole, P., and Nguyen, N. (**1996**). ''Electromagnetic articulography in coarticulation research,'' in *Instrumental Studies of Coarticulation*, edited by W. J. Hardcastle and N. Hewlett (Cambridge U.P., Cambridge).

(IEEE) (**1992**). ANSI Standard C95.1-1991, ''IEEE standard for safety levels with respect to human exposure to radio frequency electromagnetic fields, 3 kHz to 300 GHz'' (IEEE, New York).

International Radiation Protection Association (**1990**). ''Interim guidelines on limits of exposure to 50/60 Hz electric and magnetic fields,'' Health Phys. **58**(1), 113–122.

Kavet, R, and Tell, R. A. (**1991**). ''VDTs: Field levels, epidemiology, and laboratory studies,'' Health Phys. **61**(1), 47–57.

Lindbohm, M-L., Hietanen, M., Kyyrönen, P., Sallmén, M., von Nandelstadh, M., Taskinen, H., Pekkarinen, M., Ylikoski, M., and Hemminki, K. (**1992**). ''Magnetic fields of video display terminals and spontaneous abortion,'' American Journal of Epidemiology, **136**(9), 1041–1051.

Perkell, J. S., Cohen, M., Svirsky, M., Matthies, M., Garabieta, I., and Jackson, M. (**1992**). ''Electromagnetic midsagittal articulometer (EMMA) systems for transducing speech articulatory movements,'' J. Acoust. Soc. Am. **92**, 3078–3096.

Polk, C., and Postow, E. (Eds.) (**1996**). *Handbook of Biological Effects of Electromagnetic Fields* (CRC, Boca Raton).

Schönle, P. W., Gräbe, K., Wenig, P., Höhne, J., Schrader, J., and Conrad, B. (**1987**). ''Electromagnetic articulography: use of alternating magnetic fields for tracking movements of multiple points inside and outside the vocal tract,'' Brain and Language **31**, 26–35.

Stuchly, M. A. (**1995**). ''Low-frequency magnetic fields: Dosimetry, cellular, and animal effects,'' in *The Biomedical Engineering Handbook*, edited by J. D. Bronzino (CRC, Boca Raton, FL).

United States Air Force (**1997**). ''Radio frequency radiation (RFR) safety program,'' AFOSH Standard 48-9 (Washington, DC).

Erratum: "Consonant–vowel intensity ratios for maximizing consonant recognition by hearing-impaired listeners" [J. Acoust. Soc. Am. 103, 1098–1114 (1998)]

Elizabeth Kennedy
Department of Communication Sciences, Temple University, Philadelphia, Pennsylvania 19122

Harry Levitt, Arlene C. Neuman, and Mark Weiss
Center for Research in Speech & Hearing Sciences, City University of New York, 33 West 42nd Street, New York, New York 10036

(Received 17 June 1998; accepted for publication 18 June 1998)

[S0001-4966(98)00110-6]

PACS numbers: 43.66.Sp, 43.66.Ts, 43.71.Kg, 43.10.Vn [JWH]

There is an error in Table V of this paper. The text describing the table reads ''Analyses of variance for CRmax: Consonant recognition...,'' whereas it should read ''Analyses of variance for CRmax-Consonant recognition... .''

 0001-4966/98/104(4)/2533/1/$15.00